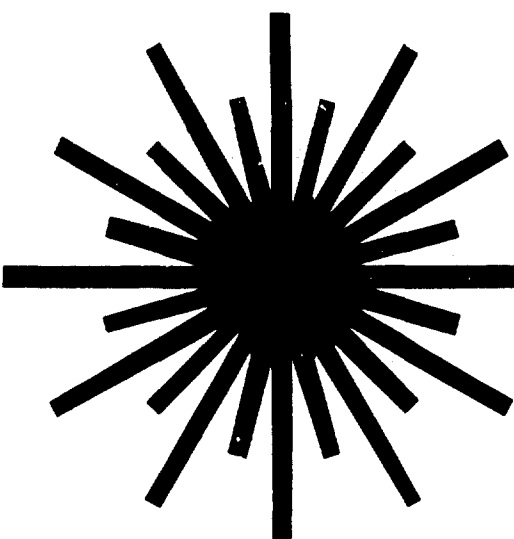


ADA 282545

PROCEEDINGS
OF THE
INTERNATIONAL CONFERENCE
ON

LASERS '87



LAKE TAHOE, NEVADA

DECEMBER 7-11, 1987

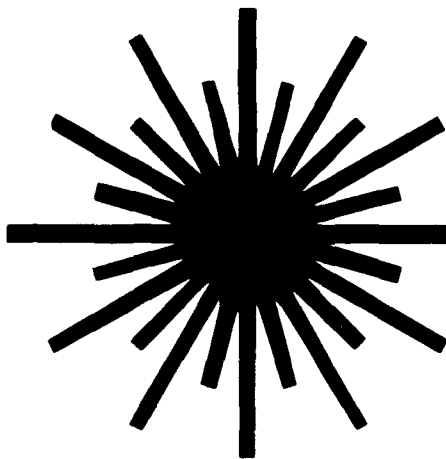
F.J. Duarte
Editor

CONFERENCE SPONSORED BY
THE SOCIETY FOR OPTICAL & QUANTUM ELECTRONICS

STS PRESS • McLEAN, VA • 1988

**Best
Available
Copy**

PROCEEDINGS
OF THE
INTERNATIONAL CONFERENCE
ON



LASERS '87

Accession For	
NTIS CRA&I	<input checked="" type="checkbox"/>
DTIC TAB	<input type="checkbox"/>
Unannounced	<input type="checkbox"/>
Justification	
By	
Distribution /	
Availability Codes	
Dist	Avail and/or Special
A-1	

DTIC QUALITY INSPECTED 3

CONTENTS

FOREWORD	XV
CONFERENCE COMMITTEE	XVII
KEYNOTE AND PLENARY SESSION	
KEYNOTE ADDRESS	
On The Detection Of Gravitational Radiation By Means Of A Simple Ring Laser Systems <i>M. O. Scully and L. Z. Wang (Invited)</i>	1
PLENARY ADDRESSES	
Coherent Dynamics Of Lasers: A Source Of Instabilities And Noise <i>L. W. Hillman (Invited)</i>	4
Dynamical Instabilities And Chaos In Lasers <i>R. G. Harrison, J. S. Uppal, W. Forysiak and J. V. Moloney (Invited)</i>	11
Optical Computing For SDI <i>H. J. Caulfield (Invited)</i>	18
LASER PHYSICS AND THEORY	
Enhanced Squeezing Under Degenerate Parametric Wave Interaction <i>E. P. Gordov, A. I. Zhiliba and N. P. Konopleva (Invited)</i>	20
On The Chemistry Of Superconductivity <i>R. More and E. Teller (Invited)</i>	26
VUV AND X-RAY LASERS	
Development And Analysis Of Pulsed-Power, Photopumped X-Ray Laser Sources At The Naval Research Laboratory <i>J. P. Apruzese, P. G. Burkhalter, G. Cooperstein, J. Davis, D. Mosher, P. F. Ottinger, J. E. Rogerson, S. J. Stephanakis, V. E. Scherrer, J. W. Thornhill, F. C. Young, G. Mehlman and B. L. Welch (Invited)</i>	37
X-Ray Lasing In An Imploding Krypton Z-Pinch Plasma <i>J. Davis, R. Clark, J. Apruzese and P. Kepple (Invited)</i>	44
Population Inversion And Possible Lasing At 150.6, 154.6, And 187.3Å In Pulsed Power Driven Z-Pinches <i>M. Krishnan, T. Nash and P. D. LePell (Invited)</i>	51
XUV Amplification In Cylindrically Expanding Laser Plasmas <i>O. Willi, V. Barrow, D. Bassett, S. Coe, J. Edwards, M. Grande, M. Key, G. Kiehn, C. Lewis, D. O'Neill, G. Pert, S. Ramsden, C. Regan, S. Rose, R. Smith and J. Wark (Invited)</i>	59
Photopumped Short Wavelength Lasers In Xenon And Krypton <i>H. C. Kapteyn and R. W. Falcone (Invited)</i>	66
EXCIMER LASERS	
Excimer Lasers In Eureka: A Proposal For A 3 KW Laser Source <i>T. Letardi, F. Burlamacchi, M. Fantini, U. Perito and R. Salimbeni (Invited)</i>	73
High Power Excimer Laser <i>H.-J. Cirkel (Invited)</i>	86

Gain Absorption And Saturation Intensity Measurements Of A Discharge Pumped, X-Ray Preionized XeCl Laser	95
<i>T. Letardi, P. Di Lazzaro, G. Giordano, E. Sabia, V. Boffa, S. Bollanti, T. Hermsen and C. E. Zheng</i>	
Use Of Magnetic Materials In Excimer Laser Circuits	103
<i>M. Vannini, R. C. Sze and F. Hommeau</i>	
Temperature Dependence Of Spectra And Efficiency For An Electron-Beam Pumped XeF Laser	111
<i>D. G. Harris, T. T. Yang, D. H. Burde, G. A. Merry, L. A. Pugh, J. H. Tillotson, C. E. Turner, Jr. and D. A. Copeland</i>	
Spectral Sweep In An Electron Beam Pumped XeF Laser	126
<i>D. G. Harris, D. H. Burde, R. J. Malins and J. H. Tillotson (Invited)</i>	
Optimization Of Electron-Beam Pumped Excimer Laser	133
<i>T. F. Lowum and J. L. Swecker</i>	
Xenon Excited State Density Measurements In XeCl	139
<i>F. Kannari, W. D. Kimura, J. F. Seamans and D. R. Guyer</i>	
A XeCl Excimer Laser With Automatic Preionization	146
<i>J. P. Singh</i>	
High Power And Efficient X-Ray Preionization XeCl Laser With A Pulse Transmission Line	150
<i>T. Hasama, K. Miyazaki, K. Yamada and T. Sato</i>	
Influence Of UV-Radiation And Shock Waves On Population Inversion Mechanisms In Inert Gas Mixture Lasers And Active Medium Formation In Sper-Lasers	155
<i>V. V. Apollonov, S. I. Derzhavin, A. M. Prokhorov and A. A. Sirotkin</i>	
Core-Excited Alkali Atoms And Ionic Excimers As VUV/XUV Laser Sources	160
<i>L. Frey, S. Kubodera, P. S. Millar, T. Petersen, G. Warwar, P. J. Wisoff and R. Sauerbrey (Invited)</i>	
Recent Progress On The Los Alamos Aurora ICF Laser System	164
<i>L. A. Rosocha and L. S. Blair (Invited)</i>	
Repetitively-Pulsed Excimer Lasers	176
<i>V. Y. Baranov, V. M. Borisov, Y. Y. Stepanov, V. P. Novikov, Y. B. Kiryukhin, O. B. Khristoforov and A. Y. Vinokhodov</i>	
Experimental And Theoretical Investigation Of E-Beam Pumped Xe-Cl Lasers	182
<i>B. A. Adamovich, V. Y. Baranov, A. A. Deryugin, I. V. Kochetov, A. P. Napartovich, D. D. Malyuta, Y. B. Smakovskii, A. P. Strel'tsov and I. V. Kurchatov</i>	
CHEMICAL LASERS	
High Power Hydrogen Fluoride Chemical Lasers; Power Scaling And Beam Quality	190
<i>J. Miller (Invited)</i>	
Space Based Chemical Lasers For Ballistic Missile Defense (BMD)	205
<i>N. Griff and D. C. Kline (Invited)</i>	
Short-Wavelength Laser Development	218
<i>J. M. Herbelin (Invited)</i>	
High Efficient Chemically Pumped Oxygen Iodine Laser	223
<i>S. Yoshida, H. Fujii, S. Amano, M. Endoh, T. Sawano and T. Fujioka</i>	
Pulse Operation Of A Chemical Oxygen Iodine Laser	230
<i>N. G. Basov, P. G. Kryukov, V. S. Paziuk, N. P. Vagin and N. N. Yuryshev (Invited)</i>	
NUCLEAR PUMPED LASERS	
The Nuclear Pumping Of Lasers - Revisted	234
<i>R. T. Schneider and J. D. Cox (Invited)</i>	

Refractive Index Gradients In Nuclear-Reactor-Pumped Lasers: Gasdynamic Effects	241
<i>J. R. Torczynski and R. J. Gross (Invited)</i>	
Radiation Effects On Nuclear Pumped Laser Optics	249
<i>G. H. Miley, R. Chapman, J. Nadler and W. Williams (Invited)</i>	
BLUE-GREEN AND METAL-VAPOR LASERS	
Narrow-Linewidth XeCl Lead Vapor Raman Converter Laser System	257
<i>H. Rieger (Invited)</i>	
Diode Pumped Promethium Laser For Submarine Laser Communications	262
<i>R. W. Solarz, R. Beach, M. Shinn and W. F. Krupke (Invited)</i>	
Discharge Excitation Of The XeF C To A Transition	268
<i>R. C. Sze, D. P. Greene, I. J. Bigio, T. M. Shay, A. W. McGown, J. F. Figueira, P. Smith, M. Vannini, R. Sauerbrey and F. K. Tittel (Invited)</i>	
Phase Preservation In High Gain Raman Applications	272
<i>B. W. Nicholson, J. A. Russel, D. W. Trainor, T. Roberts and C. Higgs</i>	
Copper And Gold Vapor Lasers: Recent Advances And Applications	276
<i>C. E. Webb (PLENARY ADDRESS), (Invited)</i>	
Recent Developments And Applications Of White-Light Lasers	285
<i>K. Fujii (PLENARY ADDRESS), (Invited)</i>	
DYE LASERS	
Engineering Of A Multi-Beam 300-Watt Flashlamp-Pumped Dye-Laser System	291
<i>P. N. Everett and B. G. Zollars (Invited)</i>	
Performance Of A Prototype Module Of A 300-Watt Flashlamp-Pumped Dye Laser	297
<i>B. G. Zollars and P. N. Everett</i>	
Dye Laser/Laser Dye Research At The U.S. Army Missile Command	304
<i>J. J. Ehrlich and S. P. Patterson</i>	
Spectral Instabilities In Flashlamp Dye Lasers	308
<i>F. J. Duarte and J. J. Ehrlich</i>	
Long Pulse Dye Laser	316
<i>S. E. Neister</i>	
A Flashlamp Pumped Zig-Zag Slab Dye Laser	320
<i>J. J. Dearth, V. V. Vaughn, R. B. McGowan, J. Ehrlich and R. W. Conrad</i>	
A Solid-State Flashlamp-Pumped Dye Laser Employing Polymer Hosts	330
<i>D. P. Pacheco, H. R. Aldag, I. Itzkan and P. S. Rostler</i>	
Solid Hosts For Dye Laser Rods - Part 1 Criteria For Choosing A Host Material	338
<i>G. F. Erickson</i>	
Solid Hosts For Dye Laser Rods - Part 2 Some Experimental Results	342
<i>G. F. Erickson</i>	
Saturation Characteristics Of UV Dyes For ps XeCl Laser Pulses	349
<i>M. Watanabe, A. Endoh and S. Watanabe (Invited)</i>	
A Long Pulse Duration, Good Beam Quality, Supersonically "Scanned-Beam" Dye Laser	356
<i>G. S. Janes, H. R. Aldag, D. P. Pacheco and R. E. Schlier</i>	
Beam Divergence Theories For Prismatic Pulsed Dye Lasers	364
<i>F. J. Duarte</i>	
Intense Picosecond Light Generation By Amplified Spontaneous Emission	370
<i>P. Sperber, W. Spangler, B. Meier and A. Penzkofer</i>	
Dye Vapors-New Nonlinear Optical Material For Vis, UV and VUV Generation?	378
<i>K. S. Aleksandrov, A. S. Aleksandrovsky, S. V. Karpov, V. F. Lukinykh, S. A. Myslivets, A. K. Popov, and V. V. Slabko</i>	

Statistical Properties Of Pulsed Dye Laser Radiation <i>E. Berik and V. Davidenko</i>	381
Fluctuation Properties Of Liquid Ring Laser With An Injected Signal <i>V. S. Smirnov and A. Z. Fazliev (Invited)</i>	387
SOLID STATE LASERS	
Recent Results In VUV Laser Spectroscopy <i>C. R. Vidal (PLENARY ADDRESS), (Invited)</i>	394
Upconversion Coefficient Measurement In TM^{3+} , HO^{3+} : YAG At Room Temperature <i>G. Kintz, T. D. Abella and L. Esterowitz</i>	398
Materials Selection And Optimization Of Diode-Pumped Lasers <i>J. T. Lin</i>	404
Injection-Seeded Nd:YLF Q-Switched Laser <i>G. Ball, W. Seka and S. Letzring</i>	412
Design Of Annular Type Of Solid State Laser For A Few Kilowatts <i>Y. Takada, H. Saito and T. Fujioka</i>	413
Resonators With Intracavity Optics For Solid-State Lasers <i>S. De Silvestri, P. Laporta and V. Magni</i>	416
Room Temperature Vibronic Laser Action In Cr^{3+} : Mg_2SiO_4 <i>V. Petricevic, S. K. Gayen, R. R. Alfano, K. Yamagishi and K. Moriya</i>	423
Low Jitter Passive Mode-Locking Of A Nd:YAG Laser Utilizing Active Q-Switching <i>S. J. York</i>	426
Output Pulse Shape Control On A High-Power Solid-State Laser Using Electronic Feedback <i>R. P. Johnson, N. K. Moncur and L. D. Siebert</i>	432
Spatial Dependence Of Electromagnetic Field In Loaded Q-Switched Laser Resonators <i>D. Hanzel, M. Copic and M. Lukac</i>	437
SEMICONDUCTOR AND DIODE LASERS	
Monolithic Two-Dimensional Diode Laser Arrays <i>J. Z. Wilcox, J. J. Yang, M. Jansen, L. Lee, M. Sergeant and S. Ou (Invited)</i>	441
Responsivity And Noise Properties Of A Highly Stabilized MOM Point Contact Diode For High Power Mid IR Detection And Mixing <i>C. Yu and C.S. Tan</i>	449
CO_2 LASERS	
Compact TEA CO_2 Lasers <i>G. D. Spiers, A. Sylvan, A. Vass and R. G. Harrison (Invited)</i>	456
TE CO_2 Laser Development At The Defence Research Establishment, Valcartier <i>P. Pace, P. Mathieu and S. Wong (Invited)</i>	463
Ultrastable Carbon Dioxide (CO_2) Lasers <i>C. Freed (Invited)</i>	468
Experimental And Theoretical Analysis Of CO Under Blackbody Optical Excitation <i>J. M. Sirota and W. H. Christiansen</i>	478
Surface Discharge Preionized CO_2 Laser Development <i>M. J. Yoder, R. B. Schaefer, J. O'Brien and J. Connolly</i>	485
Tunable SFUR TEA CO_2 Laser <i>R. Barbini, F. Colao, A. Palucci, A. Petri and S. Ribezzo</i>	493

Small Signal Gain Of CO ₂ -Lasers Pumped By A Volume Self-Sustained Discharge V. V. Apollonov, G. G. Baitsur, K. N. Firsov, I. G. Kononov A. M. Prokhorov and V. A. Yamschikov	498
Quantitative Applications Of The Thermal Lens R. T. Bailey, F. R. Cruickshank and D. Pugh (Invited)	502
CO ₂ -Lasers For Industrial Materials Processing G. Herziger and P. Loosew (Invited)	510
Operation Of A Downstream-Mixing CO ₂ Gasdynamic Laser Utilizing High-Temperature Decomposed Gas Of Liquid N ₂ O S. Takemori, M. Hachijin, K. Sugimoto, T. Hashimoto, S. Nakano and T. Miyoshi	518
Regenerative CO ₂ Amplifier Of A Nanosecond Pulse Train V. V. Apollonov, A. M. Prokhorov, V. R. Sorochenko and Y. A. Shakir	525
The Development Of A High Power Optically Pumped D ₂ O Far Infrared Laser For Collective Thomson Scattering Experiments In The TCA Tokamak M. R. Siegrist, R. Behn, M. A. Dupertuis, P. A. Krug, I. Kjølberg and S. A. Salito	531
FIR LASERS	
A Stable, High Power Optically Pumped Far Infrared Laser System J. Farhoomand and H. M. Pickett (Invited)	539
The Use Of FIR-Lasers In Solid State Research P. Janssen, F. Herlach, L. Van Bockstal, M. van der Burgt and J. Witters	544
Optically Pumped Submillimeter Lasers And Their Application To Plasma Diagnostics B. W. James, I. S. Falconer, M. D. Bowden, P. A. Krug, L. B. Whitbourn, P. A. Stimson and J. C. Macfarlane	550
Infrared And Far-Infrared Laser Development For Plasma Diagnostics At Oak Ridge National Laboratory W. H. Casson, C. A. Bennett, L. K. Fletcher, H. T. Hunter, D. P. Hutchinson, J. Lee, C. H. Ma, R. K. Richards and K. L. Vander Sluis	555
ULTRAFAST PHENOMENA	
Frontier Of Ultrafast Laser Technology And Applications R. R. Alfano (PLENARY ADDRESS), (Invited)	559
Femtosecond Dynamics Of Charged Solitons In Trans-Polyacetylene L. Rothberg, T. M. Jedju, S. Etemad and G. L. Baker (Invited)	565
Ultrafast Transient Dynamics Of Phonons And Electrons In Semiconductors W. E. Bron (Invited)	570
Subpicosecond Time-Resolved Raman Studies Of Electron-Phonon And Phonon-Phonon Interactions In GaAs-Al _x Ga _{1-x} As Multiple Quantum Well Structures K. T. Tsen and H. Morkoc (Invited)	575
Dispersionless-Like Propagation Of Induced Spectral Broadened Pulses In ZnSe (Non-Phase-Matched Second Harmonic Cross-Phase-Modulation) P. P. Ho and R. R. Alfano (Invited)	580
NONLINEAR PHENOMENA	
Nonlinear Beam Propagation In Semiconductors E. W. Van Stryland, Y. Y. Wu, D. J. Hagan, M. J. Soileau and K. Mansour (Invited)	584
A Design Of Optical Switching Elements Through Laser Subharmonic Phase Shifts K. P. Chung	599
Applications Of High-Efficiency Nonlinear Crystals For Tunable Lasers (0.19-4 Microns) J. T. Lin	604

Coupling Of Laser Modes By A Single Sideband Intracavity Modulator - A Non-Linear Coupled-Mode Analysis <i>O. P. McDuff and B. Badreddine</i>	612
A Non-Linear Coupled-Mode Analysis Of Gain-Modulated Lasers <i>O. P. McDuff and D. Thati</i>	620
A Study Of Transients And Stability In Mode-Locked Lasers By Means Of A Non-Linear Coupled-Mode Analysis <i>O. P. McDuff and A. Z. Arnous</i>	628
WAVE MIXING AND DYNAMIC GRATINGS	
Beam Amplification And Optical Phase Conjugation Via Multiwave Mixings In A Nonlinear Medium: New Theoretical Perspective And Experimental Results <i>I. C. Khoo (Invited)</i>	636
Waveguide Gratings And Optical Damage In LiNbO_3 : Ti^{3+} :Fe <i>P. Hertel, E. Kratzig and H. Pape (Invited)</i>	643
Enhanced Four-Wave Mixing In Three Level System <i>R. Shuker and I. Golub (Invited)</i>	648
PHASE CONJUGATION	
Phase-Conjugation Using Nd:YAG-Lasers <i>H.-J. Eichler, J. Chen and K. Richter</i>	653
Stimulated Scattering Of Radiation With Incomplete Speckle Modulation <i>M. A. Beedle and R. J. Lysiak</i>	657
Retroreflective Psuedo-Phase Conjugator <i>V. V. Vaughn, R. Conrad and J. Erlich</i>	665
Study Of Nonlinear Optical SBS Phenomena In Mid IR Fibers <i>C. Yu and C. K. Fong</i>	674
Stimulated Brillouin Scattering Experiments With Flashlamp-Pumped Dye Lasers <i>S. D. Russell, J. J. Ehrlich, S. P. Patterson, R. W. Conrad D. E. Klimek and S. F. Fulghum</i>	680
LASER RADARS AND REMOTE SENSING	
Autodyne Laser Transceiver <i>D. U. Fluckiger and R. J. Keyes (Invited)</i>	685
A Four-Wavelength Infrared Differential Absorption Lidar (DIAL) System <i>P. L. Holland, J. E. van der Laan, K. Phelps and S. Gotoff</i>	694
Future Applications Of Solid-State Lasers For Space Remote Sensing <i>J. W. Cox and C. L. Moore (Invited)</i>	696
Design Of A Mobile Differential Absorption CO_2 Direct-Detection Lidar System <i>J. Jones, J. van der Laan, P. Holland, L. Fletcher J. Comeford, K. Phelps and S. Gotoff</i>	703
Dial-Lidar System For Remote And Selective Detection Of Natural Gas Leaks Using A Frequency-Mixed CO_2 Laser <i>J. E. van der Laan, R. Warren and J. Jones</i>	707
Low-Pressure Gain Cell Laser Detector Operation With A CO_2 Transversely Excited Atmospheric (TEA) Laser <i>J. E. van der Laan, R. Warren and J. Jones</i>	714
High-Sensitivity Remote Laser Spectroscopy Using Behavior Of Nonlinear Optical Systems In The Vicinity Of Critical Points <i>A. P. Godlevskii, E. P. Gordov, A. Z. Fazliev, A. I. Zhiliba, V. E. Zuev and P. P. Sharin</i>	721

Multi-Wavelengths Laser Transmittance For The Lidar Monitoring Of The Atmospheric Parameters	729
<i>A. L. Butakov, V. I. Voronov, G. S. Evtushenko, V. V. Zuev, V. E. Zuev, A. E. Kirilov, A. N. Mal'tsev, S. Y. Mirza, Y. P. Polunin, V. B. Sukhanov and V. O. Troitskii</i>	

ADAPTIVE OPTICS AND PROPAGATION

Airborne Laser Communications Scintillation Measurements: Final Results	733
<i>R. J. Feldmann and S. K. Rogers</i>	
Segmented Mirror Laser Resonators	740
<i>S. De Silvestri, P. Laporta, V. Magni and O. Svelto</i>	
Unstable Resonators With Gaussian And Supergaussian Reflectivity Mirrors	744
<i>S. De Silvestri, P. Laporta, V. Magni, and O. Svelto</i>	
Raman Gain Suppression Calculations	750
<i>A. Flusberg and R. Holmes</i>	
Propagation Of A High Energy UV Laser Pulse Through Absorbing Aerosols	758
<i>S-H Lin and M. P. Thomas</i>	

IMAGING

Image Analysis For Laser-Written Hardcopy	764
<i>R. Shaw (Invited)</i>	
Ignition And High Speed Photography Of Energetic Materials With A Copper Vapor Laser	770
<i>L. R. Dosser, J. W. Reed, T. C. Girmann and M. A. Stark</i>	
Design Of A Two-Lens Gaussian Beam Waist Transformer	774
<i>J. E. Adams, Jr.</i>	
Engineering Applications Of Pulsed Laser Velocimetry	783
<i>I. Grant and G. H. Smith</i>	
Application Of Laser Light Scattering To Intracellular Streaming	791
<i>D. Pileri</i>	
The Internal Fractal Structure Of Aggregates Of Silver Particles And Its Consequences On SERS Intensities	802
<i>O. Siiman and H. Feilchenfeld (Invited)</i>	
Interaction Of Monochromatic Waves And Bodies Of Nonhomogeneous Morphology	810
<i>S. K. Salib</i>	
Digital Disk Sub-Systems For Real-Time Image Processing	826
<i>R. Mulgaonkar</i>	
Near Specular Light Scatter Measurements	832
<i>J. C. Stover</i>	

FIBER OPTICS

Bidirectional Optical Transmission System Experiment With WDM Devices	837
<i>R. C. Menendez, K. P. Chung and T. R. Hsing</i>	
Coherent Backscatter: Its Provenance And Control In Fiber Optic Applications	839
<i>G. A. Hill</i>	
Electro-Optic Device Requirements For Short High Speed Optical Links	846
<i>A. J. Cooper</i>	

The Performance Of Low Cost 1300 nm Semiconductor Lasers <i>L. Bickers, P. K. Fitch and P. Hutt</i>	851
Self-Propelled Self-Focusing Damage In Optical Fibres <i>R. Kashyap</i>	859
LASER SPECTROSCOPY	
Solvation And Twisted Intramolecular Charge Transfer In Aminophenyl Sulphones <i>J. D. Simon, S. G. Su and M. Baner</i>	867
Scientific Aspects Of The Ukaea Laser Isotope Separation Programme <i>B. J. H. Wort (Invited)</i>	875
The Supersonic Molecular Beam Predissociation Spectrum Of $^{16}\text{O}^{12}\text{C}-\text{H}^{19}\text{F}$ <i>K. McMillan and J. H. Bevan</i>	882
Broadband Modulators For Spectroscopy <i>B. Lax, P. M. Martin and R. S. Eng</i>	889
A 1,2, Fluorine Migration In The Multiphoton Isomerization Of Tetrafluorocyclopropene <i>P. C. Tardy, R. B. Friedrich and D. J. Burton</i>	898
Laser-Induced Ionization Spectrometry: Alternate Atom Reservoirs <i>E. B. Green and M. D. Seltzer (Invited)</i>	902
Determination Of Cadmium, Lead, And Zinc In Aerosols By Laser-Induced Breakdown Spectrometry <i>J. Sneddon</i>	908
Sample Introduction Using Laser Ablation For Atomic Absorption And Plasma Emission Simulation <i>J. Sneddon</i>	913
"AB Initio" Theory Of Stimulated Rotational Raman Scattering And Numerical Simulation <i>C. G. Parazzoli and C. Drutman</i>	917
Multiplex CARS For Combustion Diagnostics <i>J. P. Singh and F. Y. Yueh</i>	925
Interaction Induced Light Scattering (IILS) From The ν_2 Mode Of CO_2 In $\text{CO}_2\text{-N}_2$ Supercritical Mixtures <i>A. Hecura and F. G. Baglin</i>	931
State Mixing In Collisions Involving Highly Excited Barium Atoms <i>M. Allegrini, E. Arimondo, E. Menchi, C. E. Burkhardt, M. Ciocca, W. P. Garver, S. Gozzini, J. J. Leventhal and J. D. Kelley (Invited)</i>	936
Multiphoton Bound-Free Transitions: Role Of The Field Properties <i>S. Basile, F. Trombetta and G. Ferrante</i>	939
Energy Pooling Collisions In Na-K And Na-Rb Vapor Mixtures <i>S. A. Abdullah, M. Allegrini, C. Gabbanini, S. Gozzini and L. Moi</i>	947
On Resonantly Enhanced Two-Photon Transitions In Potassium <i>P. Bicchi, F. W. Dalby and K. R. Mah</i>	955
Preliminary Results On Energy-Pooling Ionization <i>P. Bicchi, M. Meucci and L. Moi</i>	959
Light Mechanical Actions On Vapors <i>L. Moi and J. H. Xu</i>	966
LASER DYES	
Dyes For Dye Lasers: A Manufacturer's Viewpoint <i>S. E. Neister (Invited)</i>	971

New Efficient UV Laser Dyes Through Molecular Engineering <i>H. Gusten and M. Rinke (Invited)</i>	985
Synthesis Of New Coumarin Laser Dyes Based On 1,1,7,7-Tetramethyl-8-Hydroxyjulolidine <i>C. H. Chen and J. L. Fox (Invited)</i>	995
Dye Chromophores: To Lase Or Not To Lase <i>J. H. Bentley</i>	999
Two-Photon Laser Photochemistry Of A Coumarin Laser Dye <i>R. J. von Trebra, R. P. Mahoney and T. H. Koch</i>	1003
Effects Of Detergents, Viscosity Modifiers, And Temperature Differential On The Output Of Certain Laser Dyes <i>R. F. Kubin, A. N. Fletcher, M. C. Pietrak and D. E. Bliss</i>	1005
LASERS IN MEDICINE	
The Free Electron Laser Medical Program <i>B. L. Arnoff (Invited)</i>	1010
Effects Of The Nd:YAG Laser On Normal Human Fibroblast Cultures Sensitized With Q-Switch II Dye: Study Of A New Fluorochrome <i>D. J. Castro, R. E. Saxton, H. R. Fetterman, D. J. Castro and P. H. Ward</i>	1014
The CO ₂ Laser As A Tool For Corneal Surgery <i>J. M. MacDonald, O. A. Simpson, B. E. McCarey and G. O. Waring, III (Invited)</i>	1020
Laser Optic Fiber System Removal Of Primary Invasive Skin Cancers <i>H. Ward</i>	1026
Incision Healing After Milliwatt CO ₂ Laser Welding: A Comparison Of Results Achieved With Instruments Of Varying Design <i>C. H. Greene, D. A. DeBias, W. L. Young, M. J. Henderson K. I. Lehmann and S. A. Cosmi (Invited)</i>	1033
Laboratory Models For Utilizing Laser Techniques In Education And Research <i>D. A. DeBias, C. H. Greene, R. A. Kirschner and L. H. Finkelstein (Invited)</i>	1038
Arterial-Venous Side To Side Anastomosis Using A Computerized 1.32um Nd:YAG Laser <i>R. Nelson, D. Dew, T. Hsu, S. Martin and M. Cohen</i>	1042
Argon Laser Vascular Welding: Thermal And Thrombogenic Aspects <i>G. E. Kopchok, R. A. White, R. Fujitani, G. H. White, J. Vlasak, L. Daykhovsky and W. S. Grundfest</i>	1045
Lasers In Dentistry <i>D. E. Antonson and M. D. Benedetto (Invited)</i>	1048
Objective Laser Determination Of Caries <i>M. D. Benedetto and D. E. Antonson (Invited)</i>	1051
Oral Biopsy By Pulsed CO ₂ Laser <i>C. Liebow and R. E. Braun</i>	1053
OPTICAL DEVICES AND MEASURING TECHNIQUE	
Ultrashort AR Ion Laser Pulse Shapes By Double Mode-Locking In The CPM Regime <i>E. Bourkoff (Invited)</i>	1057
Variable Cavity Mode Locked Nd:glass Laser <i>N. H. Schiller, X. C. Liang, C. X. M. Zhao, L. M. Wang and R. R. Alfano (Invited)</i>	1062

Design Of A Differential Mode Heterodyne Interferometer <i>S. Huber</i>	1065
A New Optical Method For Measuring Small Angle Rotations <i>P. Shi and E. Stijns</i>	1069
Laser-Excited Optical Filters: Comparison Of Red- And Blue-Shifting Filter Concepts <i>T. M. Shay</i>	1073
Fundamental Noise Processes In A Laser Excited Optical Filter <i>E. C. Apel, T. R. Gosnell, T. M. Shay and R. Samadani</i>	1077
Mode-Locked And Synchronously Pumped CW Lasers And Time-Correlated Single Photon Counting: A Time Resolution Study <i>A. van Hoek and A. J. W. G. Visser</i>	1083

LASER INDUSTRIAL APPLICATIONS

Materials Surface Processing With Excimer Lasers <i>D. J. Elliott and B. P. Piwczyk</i>	1090
Excimer Laser Ablation Of Metallic Thin Films: Application To Adhesion Measurements <i>P. H. Wojciechowski, F. J. Duarte and A. L. Hrycin</i>	1097
Laser Cutting Machine For Textile Industry <i>F. D. Carvalho, M. R. Teixeira, F. C. Rodrigues, C. Pais J. Alonso and D. Appelt</i>	1105
High Thickness Laser Cutting <i>G. Manassero</i>	1109
Utilizing Lasers In Television <i>L. Libin</i>	1117
Carbon Isotopes Production By The Combined Method Of IR Multiphoton Dissociation Of Difluorochloromethane Molecules And Low-Temperature Rectification Of Carbon Monoxide <i>V. J. Baranov, A. B. Bakhtadze, V. M. Vetsko, A. G. Kudziev and G. A. Tevzadze</i>	1124
Thermochemical Effect Of The Continuous Wave And High-Repetition Rate Lasers On Metal <i>V. Y. Baranov, N. A. Zheleznov, F. K. Kosyrev, D. D. Malyuta V. S. Mezhevov, A. V. Rodin and A. Y. Sebrant</i>	1130

LASERS IN STRATEGIC DEFENSE

Overview Of The SDI Program In Short Wavelength Chemical Lasers <i>C. R. Jones (Invited)</i>	1139
Advances In Laser Technology For Strategic Defense <i>J. H. Hammond, N. Griff, R. L. Gullickson, B. J. Pierce and E. W. Pogue (PLENARY ADDRESS), (Invited)</i>	1146

SDI PANEL DISCUSSION

Maturity Of Laser Technology For Strategic Defense <i>Moderator: R. Sproull, Participants: R. Biggs, L. Goldman, J. Hammond, J. Miller, A. Kantrowitz, C. Patel, E. Teller and W. Seka</i>	1153
Author Index	1173

FOREWORD

The tenth International Conference on Lasers and Applications, Lasers '87, was held at Lake Tahoe, Nevada, December 7-11, 1987. According to the opinion of most participants, the program was solid, timely, and above all interesting. In addition, Lake Tahoe provided all the right ingredients conducive to a pleasant atmosphere where discussions on laser science and technology were stimulated in surroundings perfect for skiing and amicable social interaction. To those interested in statistics, the program of Lasers '87 contained some 360 papers and registered attendance was well over 500. This was despite adverse weather conditions.

International participation was strong with the following countries being represented: Australia, Belgium, Canada, China, England, France, Germany, Israel, Italy, Japan, Portugal, The Netherlands, Scotland, Switzerland, USSR, and Yugoslavia. There were official delegations from Portugal and the USSR. The Russian delegation included scientists from the Kurchatov Institute of Atomic Energy, Lebedev Physics Institute, and the General Institute of Physics.

Traditionally, this series of conferences has emphasized laser physics and technology. As determined by the scientific nature of the program, there is no doubt that Lasers '87 provided further evidence of this emphasis. Indeed, a large proportion of the papers in the program could be integrated in the area of laser development. This is evident by the numerous and excellent sessions on topics ranging from VUV and x-ray lasers to far infrared lasers. However, if we consider the vigorous representation of sub-fields such as ultra-fast phenomena, nonlinear phenomena, spectroscopy, laser radar, laser medicine, adaptive optics, and other applications, we should conclude that the conference provides a unique forum for the review of recent advances in quantum electronics and related fields.

A characteristic of Lasers '87 was a series of superb plenary papers. The keynote address was provided by Dr. Marlan O. Scully, Distinguished Professor of Physics and Director of the Center for Advanced Studies at the University of New Mexico and head of the Theory Division at the Max-Planck Institut fur Quantenoptik. The paper by Professor Scully was entitled "Laser Probes of the Micro and Macro Cosmos." This paper and other plenary papers are included in these proceedings.

Papers submitted to the conference were reviewed in two stages. First, the papers were promptly screened by the Program Chairman and then they were sent to the respective session chairman for final approval. In cases of doubt, relevant members of the Program Committee were consulted.

In regard to the proceedings of this series of conferences, it is fair to indicate that many of the papers published in earlier editions enjoy excellent quotation status. This is particularly evident in the field of laser development. This year, an effort has been made to ensure publication of the Proceedings of the International Conference on Lasers '87 in the early part of 1988. An additional modification is the organization of papers by subject matter rather than by individual session. At the end of the proceedings, the transcription of the discussion on strategic defense is included.

The theme of the panel discussion was "Maturity of Laser Technology for Strategic Defense." This was a very well-attended event in which every panel member was given approximately 10 minutes to outline his opinion. This was followed by an intense and sometimes rather entertaining question time. The Program Chairman is grateful to the panel moderator Professor R. Sproull and to all the panelists, in particular Dr. E. Teller and Dr. C. K. N. Patel.

The "Lasers '87 Award" consisting of a gold-plated plaque and a cash prize, sponsored by EG&G Princeton Applied Research, was shared by the following papers:

"Phase Preservation in High Gain Raman Amplification"
B. W. Nicholson, J. A. Russell, D. W. Trainor, T. Roberts
(Avco Research Laboratory),
and C. Higgs (MIT Lincoln Laboratory)

"Photodynamic Therapy Using the Nd:YAG Laser and Q-Switch II Dye as a Chemosensitizing Agent for Human Fibroblast Cultures..."

D. J. Castro, R. E. Saxton, H. R. Fetterman, and P. H. Ward,
(UCLA Medical Center)

Papers were nominated by the Program Committee and the selection process was done by a subcommittee composed of Drs. M. Birnbaum, H. J. Caulfield, F. J. Duarte, L. Goldman, and R. C. Sze. Papers by members of the Program Committee were excluded from consideration.

The success of Lasers '87 is due to several factors. First, the active and enthusiastic participation of members of the Program Committee. In particular, I would like to thank Drs. R. R. Alfano, J. J. Ehrlich, R. Gullickson, S. Scott, D. J. Spencer, C. Turner, R. A. Walters, and R. W. Waynant. In addition, we were fortunate to have the support of several organizations including Eastman Kodak Company, EG&G Princeton Applied Research, U.S. Army Research Office, and U.S. Air Force Office of Scientific Research.

At Eastman Kodak Company, I would like to thank J. C. Kinard and Drs. J. Merrigan, J. P. Terwilliger and B. B. Snavely. Also, I am grateful to the Eastman Kodak Company Document Preparation Center for their diligent processing of many manuscripts.

Finally, on behalf of the Program Committee of Lasers '87, I would like to thank Kathleen Corcoran from the Society for Optical and Quantum Electronics for an excellent performance in handling the logistics of the conference.

F. J. Duarte
Program Chairman

Conference Committee

CONFERENCE CHAIRMAN

V.J. Corcoran, Potomac Synergetics, Inc.

PROGRAM CHAIRMAN

Frank J. Duarte, Eastman Kodak Company

ADVISORY COMMITTEE

A. Kantrowitz, Dartmouth College

J. Caulfield, University of Alabama

J. Gallagher, Georgia Institute of Technology

CHAIRMAN OF INTERNATIONAL ARRANGEMENTS

William B. LaCina, Hughes Aircraft Company

Program Committee

R.R. Alfano — City College of New York
M.A. Akerman — Oak Ridge National Lab
H.E. Bates — Towson University
M. Benedetto — Center for Ophthalmic Research
P. Benetti — University of Pavia
M. Bernardini — ENEA
A. Bhowmik — Rockwell International
M. Birnbaum — Aerospace Corporation
H.J. Caulfield — University of Alabama, Huntsville
P.K. Cheo — United Technologies
R.W. Conrad — U.S. Army, MICOM
B. Couillaud — Coherent
D.K. Dew — Orlando Regional Medical Center
F.J. Duarte — Eastman Kodak Company
J.G. Eden — University of Illinois
J.J. Ehrlich — U.S. Army, MICOM
L. Figueroa — University of Florida
A. Flusberg — AVCO Everett
T. Fujioka — Ind. Research Institute, Japan
L. Goldman — University of Cincinnati
R. Gullickson — SDIO
R. Gupta — University of Arkansas
J. Hunter — Griffis Air Force Base
L.W. Hillman — Cornell University
P.P. Ho — City College of New York
R.R. Jacobs — Spectra Physics
R. Kirschner — Institute of Applied Laser Surgery
D. Klick — MIT Lincoln Laboratories
D. Korff — Northeast Research
W.B. LaCina — Hughes Aircraft Company
J.T. Lin — University of Central Florida
R. Lysiak — Texas Christian University
D. Mansfield — Princeton University
R.W. McMillan — Georgia Tech
K. McMillan — University of Texas A&M
R.M. Measures — University of Toronto
W.J. Miceli — O N R
L. Moi — CNDR
T.G. Pavlopoulos — Naval Ocean Systems
E. Pogue — Strategic Defense Initiative Organization
R.J. Pressley — X M R Inc.
L. Rimai — Ford Motor Company
S. Salib — Eastman Kodak Company
S. Scott — British Aerospace

Program Committee (continued)

T. Shay — Los Alamos National Laboratory
O. Simpson — Environmental Laser Systems
A.L.S. Smith — Advanced Kinetics Incorporated
J. Sneddon — California State University
D.J. Spencer — Aerospace Corporation
R.C. Sze — Los Alamos National Laboratory
C. Turner — Rockwell International
D. van der Ziel — AT&T Bell Labs
J. Walling — Light Age Incorporated
J. Wallace — Far Field Incorporated
R.A. Walters — University of Central Florida
C.P. Wang — Optodyne Incorporated
R.W. Waynant — F & D A
J.J. Yang — TRW
T.T. Yang — Rockwell International

International Conference Committee

China

F.F. Deng — Shenzhen University
L. Zaiguang — Huazhong University

Germany

W. Demetroder — Kaiserlautern
H.J. Eichler — Technische Univ. Berlin

Italy

M. Bernardini — ENEA

Japan

T. Fujioka — Ind. Research Institute

Switzerland

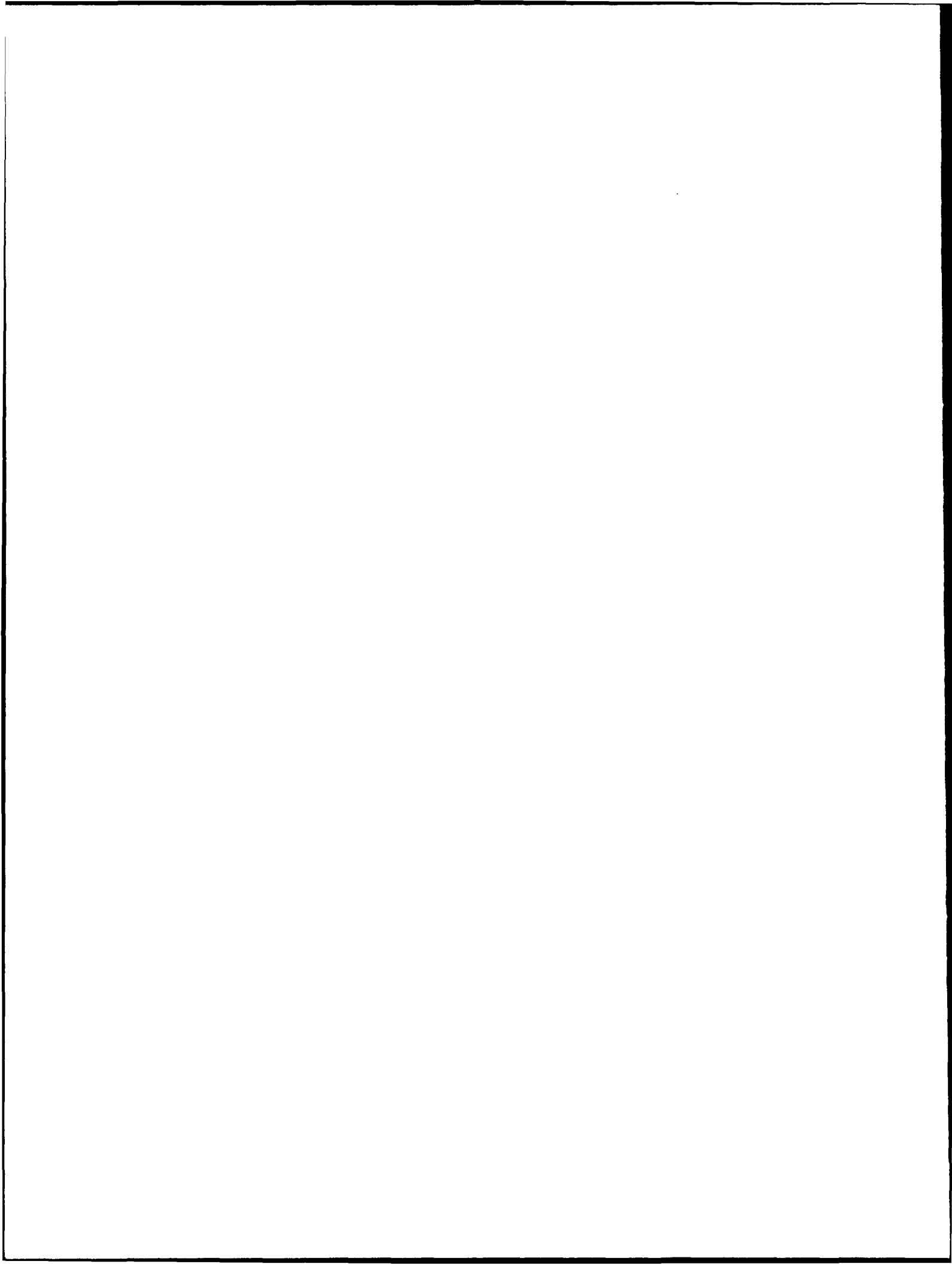
F.K. Kneubuhl — Swiss ETH

United Kingdom

S. Scott — British Aerospace

USSR

N.G. Basov — Lebedev Physics Institute



ON THE DETECTION OF GRAVITATIONAL RADIATION BY MEANS OF A SIMPLE RING LASER SYSTEMS

Marlan O. Scully and L. Z. Wang
Max-Planck Institut für Quantenoptik
D-8046 Garching bei München
and

Center for Advanced Studies and
Department of Physics and Astronomy
University of New Mexico
Albuquerque, New Mexico 87131

Abstract

It is shown that a conventional laser gyro system can, in principle, serve as a detector of gravitational radiation. Such laser devices could be quite sensitive.

We show, contrary to prevailing wisdom,¹ that a conventional² Sagnac ring laser gyro may be used as a gravitational wave detector. This is of interest for several reasons.

First, as we show in the following paragraphs, the class of devices discussed could provide sensitive detectors of gravitational radiation [see MTW].³ Furthermore, optical interferometric⁴ detectors of gravitational radiation are very sensitive to fluctuations of the mirrors⁵ and future such detectors will even be hampered by quantum⁶ uncertainties of mirror position. As is well known, ring laser gyro devices are not so susceptible to this type of random noise. To see this, we need only recall that a laser gyroscope functions⁷ by propagating two oppositely directed beams of light around the same optical path. These two beams reflect from the same mirrors differing only in their directions of propagation. Thus the two optical trains experience "identical" phase shifts due to random motion of the mirrors. The Sagnac frequency shift between the two light beams is measured by beating the counterclockwise and the clockwise running waves on a photodetector where the heterodyne cross term

$$E_{cw}^* E_{ccw} = |E_{cw}| |E_{ccw}| e^{i\Delta\nu t + i(\phi_{cw} - \phi_{ccw})} \quad (1)$$

measures the Sagnac beatnote $\Delta\nu$ which is proportional to the rotation rate. Since $\phi_{cw} = \phi_{ccw}$, the phases associated with the stochastic motion of the mirrors cancel. Thus we see that the uncertainties (classical or quantum) of the mirror positions can cancel.

Furthermore, ultrasensitive⁸ laser gyro's have recently been proposed^{9,10} for testing various aspects of metric gravity, e.g. the Lense-Thirring magnetic gravity effect and as a means of putting tight new constraints on the PPN parameter α of preferred frame cosmologies.

Clearly high risk-high payoff experiments of this type become more attractive if similar apparati could be used for a variety of measurements, i.e. a single class of devices capable of investigating gravitational radiation, magnetic gravity and cosmology, etc., would be of substantial interest. With these motivations in mind, we next briefly consider those aspects of the Sagnac physics relevant to the detection of gravitational radiation.

The Sagnac phase difference $\Delta\phi$ between the two counterpropagating laser beams in a ring gyro is given by

$$\Delta\phi = \frac{2}{\lambda c} \oint \oint (\vec{\nabla} \times \vec{g}) \cdot d\vec{\sigma} \quad (2)$$

λ is the laser wavelength divided by 2π , and the vector \vec{g} is formed from the time-space components of the metric, i.e., g_{0i} .

Let us proceed to calculate the metric, and therefore the \vec{g} vector for the case of a gravitational wave traveling in the x_0 direction while the gyro is rotating about the z_0 axis as depicted in Fig. 1. In such a situation we may write the metric for the gravitational wave as

$$h_{\mu\nu} = \begin{bmatrix} 0 & & 0 \\ & 0 & \\ 0 & & 1 \\ & & & -1 \end{bmatrix} h \sin(\omega t - kx_0) \quad (3)$$

h denotes the gravity wave amplitude. Transforming into a frame rotating at a rate Ω , the metric for the gravity wave driven gyro yields \vec{g} , which is found to be

$$\begin{aligned} \vec{g} = & \left\{ \frac{\Omega}{c} y + \frac{\Omega}{c} h \sin(\omega t - \vec{k}\vec{r}) \right. \\ & \times \left[\frac{x}{2} \sin 2\Omega t - y \sin^2 \Omega t \right] \Big\} \hat{x} \\ & + \left\{ -\frac{\Omega}{c} x + \frac{\Omega}{c} h \sin(\omega t - \vec{k}\vec{r}) \right. \\ & \times \left[-\frac{y}{2} \sin 2\Omega t + x \cos^2 \Omega t \right] \Big\} \hat{y} \end{aligned} \quad (4)$$

where the wave vector in the rotating frame is

$$\vec{k} = (k_x, k_y) = (k \cos \Omega t, -k \sin \Omega t)$$

x and y are coordinates measured in that frame.

Upon inserting Eq. (4) into Eq. (1) and carrying out the integration we find the phase difference between the counter propagating waves to be given by¹¹

$$\begin{aligned}
\Delta\phi = & -\frac{16ab\Omega}{\chi_c} \\
& + \frac{4\Omega h}{\chi_c} \left\{ \sin 2\Omega t \left[\frac{\sin k_y b}{k_y^2} - \frac{b}{k_y} \cos k_y b \right] \sin k_x a \right. \\
& + \sin 2\Omega t \left[\frac{\sin k_x a}{k_x^2} - \frac{a}{k_x} \cos k_x a \right] \sin k_y b \\
& + \frac{2a}{k_y} \cos^2 \Omega t \cos k_x a \sin k_y b \\
& \left. + \frac{2b}{k_x} \sin^2 \Omega t \sin k_x a \cos k_y b \right\} \sin \omega t \quad (5)
\end{aligned}$$

We note that when the wavelength of the gravitational radiation is large compared to typical gyro dimensions, i.e. ka and kb are small compared to unity, Eq. (5) reduces to

$$\Delta\phi = -\underbrace{\frac{16ab\Omega}{\chi_c}}_{\text{agnac}} + \underbrace{\frac{8ab\Omega h}{\chi_c}}_{\text{g-wave}} \sin \omega t \quad (6)$$

Thus we see, from Eqs. (5) and (6), that a ring laser gyro could, in principle, be used as a gravity wave detector. However, ring laser gyros have not been previously considered as gravity antennas since it was thought that the sum of the influence of a gravity wave on the various legs of the ring would cancel.

Rather than physically rotating the ring laser it is experimentally much more efficacious to use a nonreciprocal element (or some other optical technique) to break the symmetry between the cw(+) and ccw(-) running waves. This will be discussed in a future paper.

ACKNOWLEDGMENTS

It is a pleasure to thank D. Anderson, R. Chiao, D. Finley, J. Gea-Banacloche, G. Leuchs, L. Pedrotti, R. Price, W. Schleich, H. Walther, and the Max-Planck gravity wave group for stimulating and helpful discussions. It is also a pleasure to thank the Office of Naval Research for their support of the UNM portion of this work. Preliminary version of this work was presented at the 1985 Winter Colloquium on Quantum Electronics, Snowbird, Utah.

REFERENCES

1. Physics of Quantum Electronics Laser Gyro Conference, Snowbird, Utah (1984) and; 1981 Nato Advanced Study Institute of Quantum Optics and Experimental General Relativity, Bad Windsheim, Germany, 1981.
2. We note, however, that R. Chiao has made the interesting suggestion that more complicated laser gyro configurations, such as that associated with the light paths following a figure eight or the stitches on a baseball would be possible detectors of gravitational radiation, see R. Chiao in proceedings of Laser Gyro, Snowbird Conference, 1984; to be published. Another

interesting scheme has been suggested by V. Braginsky and M. Mensky (see MTW) involving a circular wave guide in which a unidirectional electromagnetic wave has different parts of the wave train blue-shifted or red-shifted due to gravitational radiation. This scheme is clearly very different from the conventional bidirectional ring laser configuration envisioned here. Further discussion on the connection with these and other experiments will be presented elsewhere.

3. For a review see: K. Thorne, Rev. Mod. Phys. **52**, 285 (1980). See also the classic book by J. Weber, *General Relativity and Gravitational Waves*, Interscience Publishers, 1961, or *Gravitation*, by C. Misner, K. Thorne and J. Wheeler (Freeman, San Francisco, 1973), hereafter referred to as MTW.
4. For an early discussion of laser interferometer detection of gravitational radiation, see R. Weiss, Massachusetts Institute of Technology Report No. 105, 1972. p. 54 (unpublished). For general background we have found the article by K. Thorne, Rev. Mod. Phys. **52**, 285 (1980) to be helpful. A more up to date review of work at the California Institute of Technology and at the University of Glasgow is described in the article of Drever, et al., and that of the Max-Planck Gravity Wave Group in the paper by H. Billing, et al., may be found in *Quantum Optics, Experimental Gravitation and Measurement Theory*, Vol. 94, NATO ASI series, edited by P. Meystre and M. Scully (Plenum, New York, 1983). For a review of recent optical g-wave detection work see the articles by C. Borde and co-workers, in Ann. Phys. (Paris **10**, 201 (1985)).
5. Actually, the cancellation of phase error is a somewhat subtle problem and will be treated in more detail elsewhere. In fact one may choose a circular (e.g. fiber optics) path in which phase shift can be cancelled. For the purposes of the present paper, we want to take a simple system in which a gyro can be seen as a possible gravity wave detector in principle.
6. For a very comprehensive and readable review of this subject including the work of V. Braginsky and co-workers in the Soviet Union, as well as their own, see the paper by C. Caves, K. Thorne, R. Drever, V. Sandberg, and M. Zimmerman, Rev. Mod. Phys. **52**, 341 (1980).
7. The article by F. Arnonowicz in *Laser Applications*, Vol. 1, Academic Press, 1971 is especially to be recommended. A more recent review of the physics of ring laser gyros by the University of New Mexico/Max-Planck group will be forthcoming shortly in the Reviews of Modern Physics.
8. See especially the paper by S. Ezekiel, et al., in "Laser Inertial Rotation Sensors," SPIE, Vol. 157, 69 (1978).
9. V. Braginsky, C. Caves, and K. Thorne, Phys. Rev. D15:247 (1977).
10. M. Scully, M. Zubairy and M. Haugan, Phys. Rev. A24, 2009 (1981).

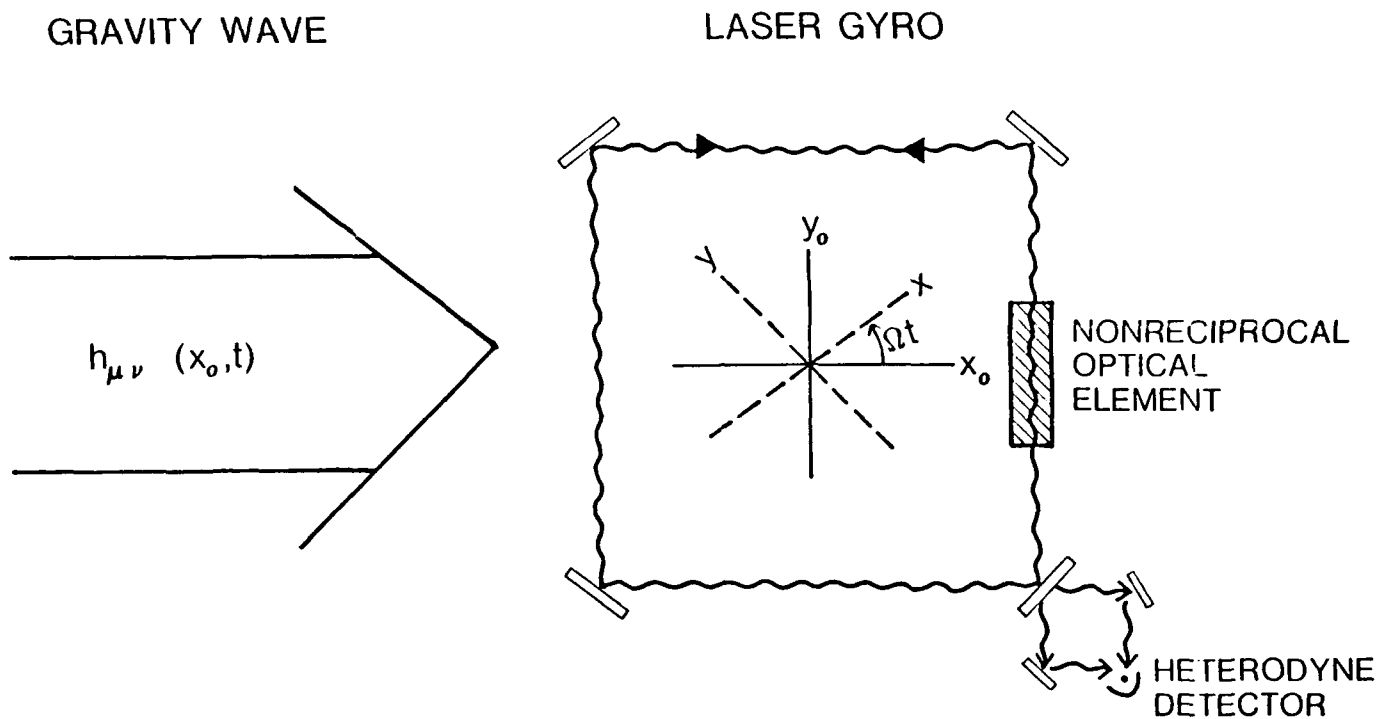


Figure 1: Gravitational wave propagating in \hat{x}_0 direction driving laser gyro of side $2a$ along x axis and $2b$ along y axis, rotating in counterclockwise sense with rate Ω . The counterpropagating waves impinge on heterodyne detector which measures frequency difference between counterpropagating waves and thus the rotation rate.

COHERENT DYNAMICS OF LASERS: A SOURCE OF INSTABILITIES AND NOISE

Lloyd W. Hillman
School of Electrical Engineering
Cornell University
Ithaca, New York 14853

Abstract

Most laser applications require precisely controlled light. We often find that the amplitude, frequency, and polarization of a laser randomly fluctuate. This limits the laser's utility. Laser noise is frequently the result of outside disturbances and random perturbations. This paper reveals another source; erratic behavior can arise from the dynamics intrinsic to all laser. Laser theory predicts such behavior only if we retain coherence in the dynamics. We review the basic principles of how light and matter interact and develop both the coherent and non-coherent theories. In a laser, two types of changes occur to the gain material due to its interaction with the optical field. The static gain saturates and the dynamic damping rates of the gain medium change. This paper compares and contrasts the coherent and non-coherent theories and discusses the onset of instabilities in a simple homogeneously broadened laser.

Introduction

How does a laser work? We all know the answer. Or do we? On my bookshelf alone, I count seventeen textbooks with **Laser** as the primary title. These books discuss many laser systems--gas lasers, solid-state lasers, dye lasers, diode lasers, and free-electron lasers. All lasers amplify light by exploiting stimulated emission. Clearly, the diversity of laser systems shows that we understand the principles of laser physics. A rational conclusion is that laser theory is a mature topic; no new fundamental progress is possible. Engineers and scientists need only to develop the technology that will optimize the gain and performance of a given laser system. This pragmatic viewpoint is partially true. We do understand the quantum mechanical interactions that are necessary for optical gain. Unfortunately, we often neglect an important component, namely coherence, when we model the dynamics of a laser. The absence of coherence in the dynamical model leads to false conclusions about the laser's linewidth, noise spectrum, and stability. Experimentally, we may therefore strive to achieve the impossible.

Maiman's demonstration of the ruby laser¹ in 1960 verified the theoretical predictions of Schawlow and Townes.² Still

today, laser technology continues to grow and mature. We find lasers at work in factories welding cars, in hospitals curing cancer, and in homes playing music. With this long and fruitful history, a pragmatic person will ask several questions: Why should laser theory be a hot topic? Is new fundamental progress being made? Who cares? These questions deserve answers; in course, the answers raise new questions.

Noise and Instabilities

Maiman's first laser opened a Pandora's box. Although the pumping pulse varied smoothly, the output of his ruby laser consisted of a random train of spikes. Dynamically, the ruby laser was "noisier than it should be." Subsequent experimental observation of other laser systems gives evidence that this "noisier than expected" conclusion is the general rule. This is all too familiar to anyone who has built a laser. What is the origin of this noise and erratic behavior? A complete answer to this question depends on the specifics of a given laser system. Nevertheless, we can separate the sources of erratic behavior into three classes: stochastic, technical, and intrinsic.

Stochastic sources of noise are non-controllable, random processes. An example is spontaneous emission, which occurs in all lasers. In addition, this class includes such processes as collisions between molecules in gas lasers. Technical noise sources are either controllable or avoidable. Cost, environment, and design determine their contribution. Technical noise sources include mechanical vibrations, impurities, pump noise, and thermal drift. In addition, spatial hole burning and spectral hole burning are technical noise sources. We can eliminate these two contributions by using a unidirectional ring cavity and by choosing a homogeneously broadened gain media.

The final source of erratic behavior is the intrinsic dynamics that govern the laser. Mathematically, we model a laser's dynamics with coupled nonlinear differential equations. How can this deterministic physics be a source of noise? This question is the key to why laser theory is now a hot topic. A 1966 paper on quantum fluctuations by Haken³ furnished the first clue. Haken found that power fluctuations grow, or are unstable, when

the light intensity is above a critical value. A few years later, Risken and Nummedal⁴ published a semiclassical model that shows this same instability. Most notable is that these papers treat the full coherent dynamics or Maxwell-Bloch equations. Previous theories dealt with only the non-coherent population rate equations, which fail to predict this instability. Unfortunately, the majority of the technical laser community overlooked this work.

Risen and Nummedal attributed their instability to the onset of self-mode-locking of lasers.⁴ In 1975, Haken⁵ expanded the dynamical significance of the instability. He demonstrated that the Maxwell-Bloch equations for a single-mode laser are equivalent to equations studied by Lorenz.⁶ Lorenz's equations model hydrodynamic flow. They are of physical interest because they predict turbulent or chaotic flow. By analogy, we pose the question: Can the unexplained noisy behavior of a laser be chaotic dynamics? This is where new fundamental progress in laser theory is being made. History of this development is in review articles by Abraham et al.^{7,8} and Casperson.⁹ Special issues of journals,^{10,11} conferences,^{12,13} and books^{14,15,16} discuss the recent progress in the field.

Light-Matter Interactions

In the preceding section, we made the comment that coherence is the key ingredient for describing erratic laser dynamics. It is the purpose of this paper to compare and contrast coherent and non-coherent laser theories. We will explain the physical origin of coherent laser instabilities. We limit the discussion to an ideal laser, one that has no technical noise sources. We therefore present only the role of intrinsic dynamics, which are present in all lasers.

Light Propagation

Before undertaking the prescribed task, let us recall a few elementary principles about light-matter interactions. The first principle arises from everyday observations--matter affects the propagation of light. One of the greatest achievements in physics is the work of J. C. Maxwell. We all know that Maxwell's equations describe how electromagnetic waves propagate. For non-magnetic dielectric materials, Maxwell's equations reduce to a single equation for the electric field,

$$\nabla^2 \underline{E}(\underline{r}, t) - \frac{1}{c^2} \ddot{\underline{E}}(\underline{r}, t) = \frac{4\pi}{c^2} \ddot{\underline{P}}(\underline{r}, t), \quad (1)$$

where $\underline{P}(\underline{r}, t)$ is the polarization density of the material. The atomic properties of the material determine the relationship between $\underline{P}(\underline{r}, t)$ and $\underline{E}(\underline{r}, t)$.

For a planewave traveling in the z-direction, we can express the electric field as,

$$\underline{E}(\underline{r}, t) = 2\text{Re}\{\underline{E}(z, t) e^{i[kz - \omega t - \phi(z, t)]}\}, \quad (2)$$

Upon propagation, the amplitude, $\underline{E}(z, t)$, and the phase, $\phi(z, t)$, of the field can change. Variation in the amplitude equates to either loss or gain; the phase change is dispersion. In a non-coherent model only amplitude changes, or the absorption and emission of photons, enter the dynamics. Coherent theory dynamically includes both amplitude and phase.

Atomic Dynamics of Matter

Our next objective is to understand how light acts upon the matter. We rely upon a simple model based on atomic physics. Our material consists of an ensemble of non-interacting atoms. Furthermore, we assume homogeneous broadening and that all atoms are alike. With this model, the task is to find the induced polarization, which appears in Eq.(1).

Classical Theory of Resonance. Around 1900 before the invention of quantum mechanics, Lorentz published an atomic model describing resonant interactions of light and matter.¹⁷ Atoms consist of a positively charged nucleus surrounded by negatively charged electrons. A net separation of the electrons from the nucleus results in the generation of a microscopic dipole. Lorentz assumed elastic binding between the electrons and nucleus. By combining Newtonian mechanics with electromagnetic forces, Lorentz found that the atomic dipoles behave like driven harmonic oscillators. Hence, the polarization induced by the electric field obeys the equation

$$\ddot{\underline{P}}(\underline{r}, t) + \frac{2}{T_2} \dot{\underline{P}}(\underline{r}, t) + \omega^2 \underline{P}(\underline{r}, t) = g \underline{E}(\underline{r}, t). \quad (3)$$

Equations (1) and (3) form the basis for the classical theory of resonant absorption and dispersion of light. This linear theory describes properly the coherent or wave aspects of light-matter interactions. With slight modifications in the electron's binding potential, this theory becomes a basis for nonlinear optics. The failure of this theory is that it does not describe the quantum or particle aspects of the interaction.

Quantum Theory of Resonance: Non-Coherent Theory.

In quantum theory, we again deal with the concept of resonant interactions; however, the physical picture is different. We divide the interaction into two parts. First, we treat the atomic system of charged particles with coulomb interactions, but ignore any possible radiation. Secondly, we consider the dynamics that result when the radiation

part of the field interacts with the atom. For the present purpose, we need only consider a single electron orbiting a fixed nucleus. Quantum mechanics tells us that the electron will only exist in special stationary states. Each state has a specific energy. The radiation field causes the electron to undergo quantum transitions. The state-of-the-electron changes through the absorption and emission of photons. Three processes describe the dynamics: stimulated emission, stimulated absorption, and spontaneous emission. These processes are resonant, in that the energy of the photon equals the energy change of the electron's state.

A laser works by exploiting stimulated emission. We limit our discussion to the case where the laser field is only resonant with a single transition. This is the two-level approximation. We denote the upper state, $|2\rangle$, and the lower state, $|1\rangle$. To achieve optical gain, the rate of stimulated emission must be greater than the rate of stimulated absorption. This means that the population density of atoms in the upper state, N_2 , must be greater than that in the lower state, N_1 . It is the inversion, the difference between the two populations, that determines the gain.

$$\text{Inversion: } W = N_2 - N_1 \quad (4)$$

To create a population inversion, one must employ a pumping scheme that involves other levels. Figure (1) depicts a pumping method that uses four levels. The pumping is important in determining the overall efficiency and dynamics of a laser. Nevertheless, we will drop the pumping dynamics in our model and deal with an ideal two-level system. This fundamental model contains the basic and necessary

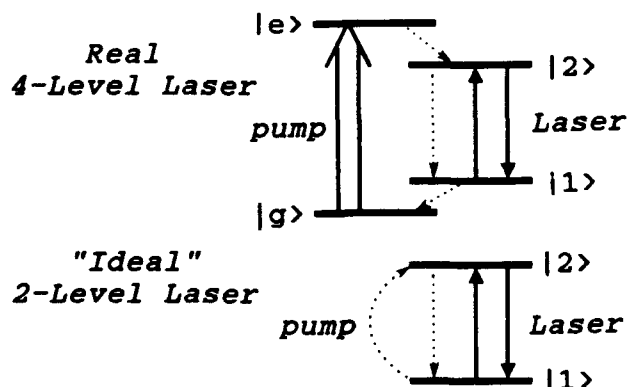


Fig. 1. Two-level laser approximation. Only the $|2\rangle$ to $|1\rangle$ transition interacts resonantly with the laser's field. Real lasers systems, such as the 4-level laser, use other levels to pump the gain medium into level $|2\rangle$ thereby creating an population inversion. We model this with an effective pumping process that transfers population from level $|1\rangle$ to $|2\rangle$.

physics. Lasers instabilities can emerge from the intrinsic interaction between a two-level resonance and a resonant optical field. By necessity, this interaction occurs in all lasers.

Quantum Theory of Resonance: Coherent Theory. Up to this point, coherence is absent in our quantum picture. Where is the induced polarization that drives Eq.(1)? This question requires us to rethink the absorption and emission process. Although it is the basis for much of our intuition, the photon picture conceals the important coherent or wave aspects of the interaction.

Recall that quantum mechanics yields the stationary states for the electron. Associated with each state is a wavefunction: a solution to the time-independent Schrodinger equation. We interpret the squared modulus of the wavefunction as the probability density of the electron's position. Loosely speaking, the electron distributes itself around the nucleus. Figure (2) illustrates two possible wavefunctions. The atomic charge distribution has no dipole moment when the electron is in one of its stationary states.

When a radiation field interacts with the atom, the electron's wavefunction changes according to the time-dependent Schrodinger equation. The electron is no longer exactly in one quantum level or another. Rather, it's wavefunction is a quantum-state mixture or superposition. An example of a mixed-state wavefunction appears in Fig.(2). In this superposition

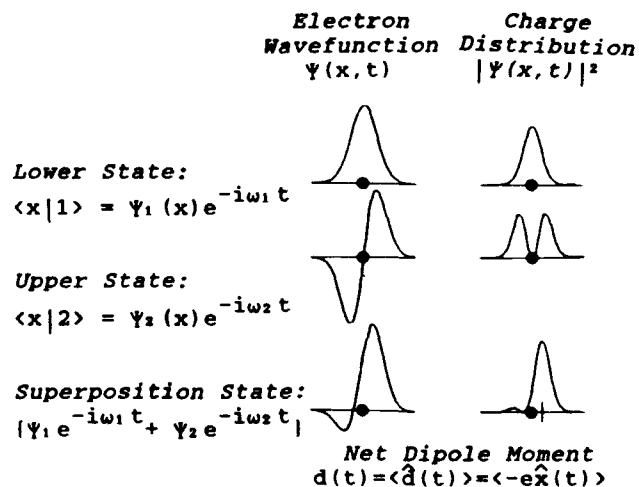


Fig. 2. Quantum picture of the coherent dipole. We illustrate two wavefunctions for an electron in state $|1\rangle$ and $|2\rangle$. In both cases the charge distribution is symmetric about the nucleus. The quantum mixing of the two state by the radiation field results in charge distribution with a net dipole moment. The dipole's resonance is at the transition frequency.

state, the distribution of the electronic charge is asymmetric about the atom's nucleus. This charge separation corresponds to a classical microscopic dipole. For a two-level system, the dynamical evolution of the polarization and inversion follow the equations,

$$\ddot{\underline{P}}(\underline{r}, t) + \frac{2}{T_2} \dot{\underline{P}}(\underline{r}, t) + \omega^2 \underline{P}(\underline{r}, t) = -g W(\underline{r}, t) \underline{E}(\underline{r}, t) \quad (5)$$

and

$$\dot{W}(\underline{r}, t) = -\frac{2}{\hbar \omega_a} \underline{P}(\underline{r}, t) \cdot \underline{E}(\underline{r}, t) - \frac{1}{T_1} [W(\underline{r}, t) - W_0] \quad (6)$$

We note that Eq. (5) is identical to Lorentz's equation (3), except that the coupling to the field depends on the inversion. In fact, the quantum picture shows that the atoms coherently radiate like a collection of classical dipole oscillators. In Eq. (6), we model the pumping by specifying a value for W_0 ; this determines the unsaturated gain. Equations (1), (5), and (6) form the basis of coherent laser theory. They are the most elementary description of resonant light-matter interactions.

A simple connection exist between the coherent and non-coherent quantum theories. In many systems, the damping time of the polarization, T_2 , is much less than the lifetime of the inversion, T_1 . The polarization then adiabatically follows the inversion and field. We approximate the polarization by replacing the dynamical equation (5) with the constitutive relationship for its complex amplitude,

$$\underline{P}(\underline{r}, t) = \tilde{\chi}(\omega) W(\underline{r}, t) \underline{E}(\underline{r}, t) \quad (7)$$

In Eq. (7), $\tilde{\chi}(\omega)$ is the complex electric susceptibility due to the resonance. The atomic dynamics and optical gain then depends only on the inversion, namely,

$$\dot{W}(\underline{r}, t) = -\frac{1}{T_1} W(\underline{r}, t) I(\underline{r}, t) - \frac{1}{T_1} [W(\underline{r}, t) - W_0] \quad (8)$$

where $I(\underline{r}, t)$ is the intensity of the optical field. Equations (1), (7), and (8) are the basis for non-coherent laser theory.

Lasers Dynamics

By laser dynamics, we mean the time evolution of the optical field and the gain material. This also includes the reaction of the laser system to noise sources. The dynamics establish the amplitude stability and spectral purity of the output field. These parameters affect the sensitivity, reliability, and performance of devices that use laser light. We obtain the dynamics by self-consistently solving the equations that describe the matter-light interaction. In general, this is a

formidable task best left to computer simulation. Every laser system will present a different set of technical problems. We therefore limit our discussion to the bare-bone model of an ideal homogeneously broadened ring laser.

Feedback Oscillators

Dynamically, how do the coherent and non-coherent laser theories differ? We examine this question by noting that the laser is an optical feedback oscillator. Its operation principle is like any electronic feedback oscillator--amplification plus positive feedback equals oscillation. To illustrate this, we consider a ring cavity as shown in Fig. (3). The gain medium amplifies the light; the cavity mirrors supply the feedback. The length of the cavity and the material dispersion determine the positive feedback frequencies. We call this set of frequencies the laser's modes.

The basic operation of a laser is simple. A pumping process excites the gain medium and creates a population inversion. This sets a value for W_0 in Eqs. (6) and (8) and establishes the gain. The gain medium amplifies optical fields with frequencies near the transition resonance. The inverse of the polarization decay time, $(1/T_2)$, sets the bandwidth of optical gain. Coherent optical oscillation grow when the gain at a modal frequency is greater than the total round-trip loss. This is the well-known threshold condition for a laser. The lasing threshold is the same for both the coherent and non-coherent theories.

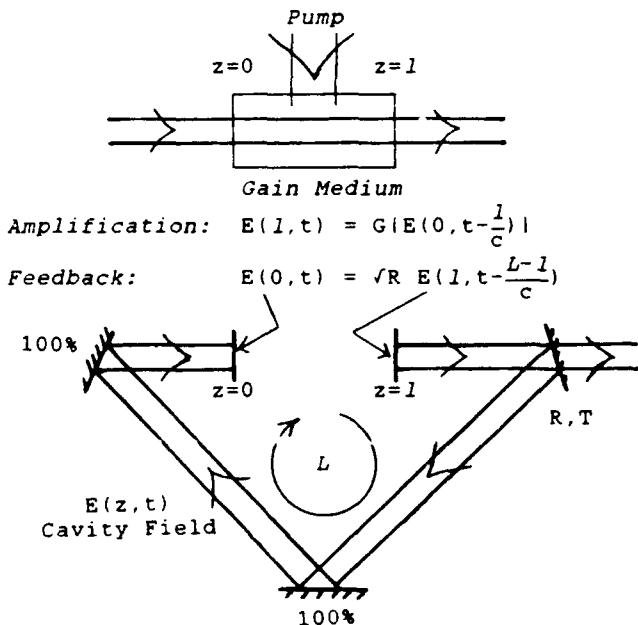


Fig. 3. The parts of a simple ring laser. The gain medium amplifies the field; the cavity furnishes feedback. The laser is therefore an optical feedback oscillator.

In all feedback oscillators, nonlinearities of the amplifier eventually limit the growth and amplitude of the oscillations. The amplification process in a laser is self-limiting because the light actively modifies the response of the gain material. We group these nonlinear changes into two categories: static and dynamic.

Static Change: Saturation

As the intensity of the optical field increases, the gain of the material decreases. We refer to this static change as saturation. The gain saturation results from quantum transitions between the upper and lower levels due to stimulated emission. This lowers the population inversion and hence the static gain. When the saturated gain is equal to the round-trip loss, no further growth in optical field is possible. Gain saturation therefore stabilizes the amplitude of the light in the cavity. Again, we find that the stationary predictions of the coherent and non-coherent theories agree. In this stationary state, an ideal homogeneously broadened laser oscillates at a single optical frequency. An increase in the pump or excitation rate leads to a proportional growth in the light intensity. Does the single-frequency oscillation remain dynamically stable at higher pumping rates? According to many textbooks, an ideal homogeneously broadened laser will only oscillate at a single frequency.¹⁸ This conclusion is wrong! It is this prediction about the dynamical stability where the coherent and non-coherent theories disagree.

Dynamic Change: Atomic Damping

What determines the stability of a single-frequency laser oscillator? The theory of feedback oscillators provides the answer. The time dynamics of an oscillator consists of two parts, the stationary oscillation (i.e. steady state) and the decay of transients. A feedback oscillator is stable if the gain at all frequency except one is less than the round-trip loss. Only one frequency or mode oscillates, the others decay. This same conclusion is true for a single-frequency laser. To answer the question of stability, we therefore must determine the gain at other optical frequencies. This problem is the same as finding the gain of probe field in a pump-probe experiment.¹⁹ The field of the laser is the pump, other fields that satisfy the cavity-boundary conditions are the probes. We refer the reader to other papers for the specific details on this calculation.^{20, 21} In this paper, we examine only the dynamical difference between the coherent and non-coherent theories.

Electrical engineers describe the behavior of an amplifier by its frequency response or transfer function. For a

fixed-frequency input, the amplifier will either amplify or attenuate the signal's amplitude. We can quantify the frequency dependence of the transfer function with its complex poles. The poles characterize the decay rate of transients, or how the amplifier relaxes to its stationary response. It is the poles of the amplifier and the feedback network that determine the stability of a feedback oscillator. In a laser, the atomic relaxation rates fix the poles of the optical amplifier and therefore determine the laser's stability.

Non-Coherent Theory. Even though the coherent and non-coherent theories predict the same stationary oscillation, their decay to this state is dynamically very different. In figure (4), we give block diagrams that represent a laser feedback oscillator. In addition to gain saturation, the strong monochromatic field in the laser dynamically alters the decay rates of the gain medium. This actively alters the response of medium to other optical fields. In the non-coherent theory, there is only one decay constant,

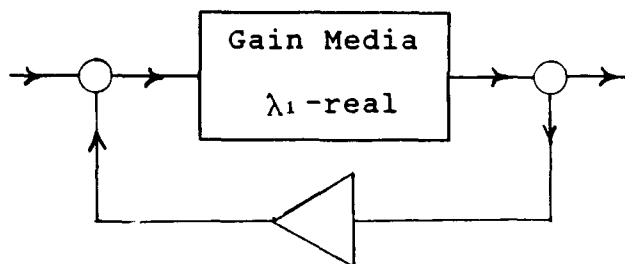
$$\lambda = \frac{1}{T_1} [1 + I_0] \quad (9)$$

We obtain this decay rate from Eq.(7). For a fixed field intensity, the population inversion exponentially decays to its stationary value. The damping rate increases as the intensity, I_0 , increases. The non-coherent amplifier has a simple real-value pole. Because of this, the non-coherent theory predicts that the laser is always stable. When we solve the matter and field equations self-consistently, the non-coherent theory does predict relaxation oscillations. These transient oscillations always decay leaving the single-frequency oscillation. To persist, relaxation oscillations require a noise source; this noise is absent in our ideal model.

Coherent Theory. In the coherent theory, a second order, Eq.(5), and a first order, Eq.(6), differential equations describe the gain medium. We can transform these equation to three coupled first order equations. The new set of equations are the Optical Bloch Equations.²² Since three degrees-of-freedom describe the gain, there are three characteristic decay rates. The coherent optical amplifier therefore has three poles. As before, these decay rates are intensity dependent. We obtain the three poles by finding the roots of a cubic polynomial whose coefficients depend on the field intensity.

The question of the laser's stability is now the same as a feedback oscillator with a three pole amplifier, as pictured in Fig.(4). One of the decay rates is always real; however, the other two poles can be complex. We identify these two poles with a resonance in the amplifier. The decay

Population Rate Equation



Bloch Equations

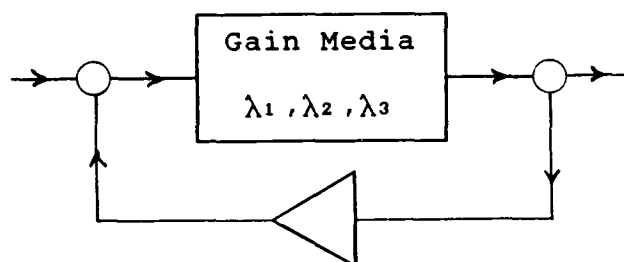


Fig. 4. Block diagrams for the feedback oscillators. The amplifier for the non-coherent theory has simple real pole. The coherent theory's amplifier has three poles. This amplifier has a field induced resonance at the Rabi frequency. Resonant amplification occurs when a probe field's detuning is equal to the Rabi frequency.

dynamics associated with this resonance is like the transient decay in a harmonic oscillator. At large intensities, the resonance becomes proportional to the amplitude of the laser's electric field. We call the frequency of this field-induced resonance, the Rabi frequency. Physically, the Rabi frequency is a measure of the interaction or coupling energy between the gain medium's resonance and the optical field.

In the stability analysis of a single-frequency laser, we treat the non-lasing modes as probe fields. The gain medium's induced resonance profoundly alter the optical gain of these probe fields. Resonant excitation occurs when the detuning of a probe field from the lasing frequency is equal to the Rabi frequency. The optical gain at this frequency can be greater than gain at the laser frequency. The amplitude of this probe field will therefore grow; the single-frequency oscillation is unstable!

Conclusions

The instability found in the coherent theory is intrinsic to a laser's dynamics. Only the coherent nonlinear interactions between an atomic resonance and the optical field are necessary. When does this instability occur? We find a definite

answer for exact resonance, which means the laser's frequency and atomic resonance are equal. The instability can occur when the laser's pumping rate is nine times above lasing threshold rate. Mode pulling and detuning lowers this value.⁴⁴ In addition, technical noise lowers the instability threshold. Computer simulation shows that the instability is hard or bistable. Once unstable, the laser does not return to its single-frequency state upon decrease of the pumping rate. Noise therefore can drive the laser into the unstable regime.

What are the laser's dynamically characteristics when the single-frequency operation is unstable? How does noise effect the stability and dynamics? These are current research questions. Computer simulations find regular pulsed solution, bichromatic solutions, and chaotic solutions. The whole nature of the solutions change as we vary the atomic relaxation times, the cavity round-trip time, and the cavity losses. The choice of initial conditions in these numerical studies is important since multi-stable solutions are possible. It is clear that lasers can operate in many states, only a few well understood. In addition, many lasers systems do not fit the simple two-level model. This includes gain media where stimulated emission occurs between bands of levels. Example include the vibrational-rotational bands of molecular dye lasers⁴⁴ and the conduction and valence band of diode lasers.⁴⁵ As we strive to tame the erratic behavior of our lasers, we need to keep in mind the important role coherence plays in their dynamics.

Acknowledgments

The physics and thoughts in this paper I obtained through lively conversations with many people. In particular, I express my thanks to C. R. Stroud, Jr., K. Koch, S. Chakmakjian, and M. Sargent III. I acknowledge support by the Eastman Kodak Company and by the National Science Foundation through the Presidential Young Investigators program.

References

1. T. H. Maiman, "Stimulated optical radiation in ruby maser," *Nature* **187**, 493-494 (1960).
2. A. L. Schawlow and C. H. Townes, "Infrared and Optical Masers," *Phys. Rev.* **112**, 1940-1949 (1958).
3. H. Haken, "Theory of intensity and phase fluctuation of a homogeneously broadened laser," *Z. Phys.* **190**, 327-356 (1966).
4. H. Risken and K. Nummedal, "Self-pulsing in lasers," *J. Appl. Phys.* **39**, 4662-4672 (1968).
5. H. Haken, "Analogy between higher instabilities in fluids and lasers," *Phys. Lett* **53A**, 77-78 (1975).

6. E. N. Lorenz, "Deterministic nonperiodic flow," *J. Atmos. Sci.* **20**, 130-141 (1963).
7. N. B. Abraham, et al., "Experimental evidence for self-pulsing and chaos in cw-excited laser," in *Proceedings of the Third New Zealand Symposium on Laser Physics*, J. D. Harvey and D. F. Walls, Eds., Springer Verlag Notes in Physics **128** (Springer-Verlag, Berlin, 1983), pp. 107-131.
8. N. B. Abraham, "A new focus on lasers instabilities and chaos," *Laser Focus* **19**, 73-81 (May 1983).
9. L. W. Casperson, "Spontaneous pulsations in lasers," in *Proceedings of the Third New Zealand Symposium on Laser Physics*, J. D. Harvey and D. F. Walls, Eds., Springer Verlag Notes in Physics **128** (Springer-Verlag, Berlin, 1983), pp. 88-106.
10. Special Issue on Instabilities in Active Optical Media, *J. Opt. Soc. Am. B* **2** (Jan. 1985).
11. Special Issue on Nonlinear Dynamics of Lasers, *J. Opt. Soc. Am. B* **5** (1988) (in press).
12. *Optical Instabilities*, Proceeding of the International Meeting in Instabilities and Dynamics of Lasers and Nonlinear Optical Systems, University of Rochester (June 18-21, 1985), R. W. Boyd, M. G. Raymer, and L. M. Narducci, Eds., (Cambridge University Press, 1986)
13. International Workshop on Instabilities, Dynamics, and Chaos in Nonlinear Optical Systems, Il Ciccio, Lucca, Italy (July 8-10, 1987).
14. *Lasers and Synergetics: A Colloquium on Coherence and Self-Organization in Nature*, R. Graham and A. Wunderlin, Eds., Springer Proceedings in Physics **19** (Springer-Verlag, Berlin, 1987).
15. *Instabilities and Chaos in Quantum Optics*, F. T. Arecchi and R. G. Harrison, Eds., Springer Series in Synergetics **34** (Springer-Verlag, Berlin, 1987).
16. L. M. Narducci and N. B. Abraham, *Lectures on Laser Physics and Laser Instabilities* (Taylor and Frances, New York, 1987).
17. H. A. Lorentz, *The Theory of Electrons*, (Dover Publication, New York, 1952).
18. For example see: A. E. Siegman, *Lasers*, (University Science Books, Mill Valley, California, 1986) pp.462-3; A. Yariv, *Quantum Electronics 2nd ed.*, (John Wiley & Sons, Inc. New York 1975) p.257.
19. B. R. Mollow, "Stimulated emission and absorption near resonance for driven systems," *Phys. Rev. A* **5**, 2217-2222 (1972).
20. L. W. Hillman, R. W. Boyd, and C. R. Stroud, Jr., "Natural modes for the analysis of optical bistability and laser instability," *Opt. Lett.* **7**, 426-428, (1982).
21. S. T. Hendow and M. Sargent III, "The role of population pulsations in single-mode laser instabilities," *Opt. Commun.* **40**, 385-390 (1982), and "Effects of detuning on single-mode laser instabilities," *Opt. Commun.* **43**, 59-63 (1982).
22. L. Allen and J. H. Eberly, *Optical Resonance and Two-Level Atoms*, (John Wiley & Sons, Inc. New York 1975).
23. L. W. Hillman and K. Koch, "Multimode instabilities in homogeneously broadened lasers," in *Optical Instabilities*, R. W. Boyd, M. G. Raymer, and L. M. Narducci, Eds., (Cambridge University Press, 1986) pp.256-258.
24. F. Hong and H. Haken, "A band-model for dye lasers and the low threshold of the second instability," *Opt. Commun.* **64**, 454-456 (1987).
25. L. W. Hillman, "Coherent optical interaction in semiconductor lasers," presented at the Optical Society of America 1987 Annual Meeting, Rochester, New York, paper WO10, abstract in *J. Opt. Soc. Am. A* **4**, P74 (1987).

DYNAMICAL INSTABILITIES AND CHAOS IN LASERS

R.G. Harrison, J.S. Uppal, W. Forysiak and J.V. Moloney

Department of Physics
Heriot-Watt University
Edinburgh EH14 4AS
U.K.

Abstract

Lasers provide nearly ideal systems for quantitative investigations of deterministic nonlinear dynamics. Aspects of these developments in regard to instabilities and chaos in single mode lasers are discussed for both 2 and 3-level systems

Introduction

Since its advent more than a quarter of a century ago, the laser has evolved as a unique device for both fundamental investigation and applications in optical science and technology. In providing a coherent and intrinsically stable emission, lasers are fundamentally different from conventional light sources for which the excited atoms (or molecules) emit spontaneously resulting in a signal comprising a statistical average of random or uncorrelated emissions. However the conventional concept of laser emission as an ordered and time invariant process provides a description of but one aspect of operation. Motivated by profound mathematical discoveries in recent years which have revolutionised our understanding of nonlinear science, it has since been found that lasers, along with many other nonlinear systems in a wide range of sciences, exhibit a rich variety of dynamical behaviour which are common features of their operation. As well as exhibiting regular and repeatable behaviour, these systems also exhibit unstable, even chaotic, solutions. Furthermore the transition from stable to chaotic behaviour, on varying a control parameter of the system, e.g. in a laser, cavity tuning, excitation, etc., follows specific, well defined routes of temporal or dynamical behaviour which are universal in the sense that they are independent of the physical properties of the system they describe. It is these signatures which have been a major impetus to experimentalists in the subsequent search for physical systems that exhibit these phenomena.

The recent exciting discovery that lasers exhibit such deterministic instabilities is particularly significant since they provide nearly ideal systems for quantitative investigations due to their simplicity both in construction and in the mathematics that describe them. Following a brief overview of nonlinear dynamics, aspects of these developments in regard to instabilities and chaos in single mode lasers are discussed for both 2 and 3-level systems.

General Aspects of Nonlinear Dynamics

Unlike linear systems, nonlinear systems must be treated in their full complexity, and there is no general analytical approach for solving them.

The temporal evolution in the behaviour of such systems can be characterised when presented as a trajectory of a point in the phase space of its dynamical variables. If an initial condition of a dissipative nonlinear dynamical system such as a laser is allowed to evolve for a long time, the system, after all the transients have died out, will eventually approach a restricted region of the phase space called an attractor. A dynamical system can have more than one attractor in which case different initial conditions lead to different types of long-time behaviour.

The simplest attractor in phase space is a fixed point; the nonlinear system is attracted towards this point and stays there. For other control conditions the system may end up making a periodic motion. The limit or attractor of this motion is a periodic cycle called a limit cycle. However, when the operating conditions exceed a certain critical value, the periodic motion of the system breaks down into a more complex chaotic pattern which never repeats itself. This motion represents a third kind of attractor in phase space called a chaotic or strange attractor.

These various types of attractor are shown in Fig. 1 for the familiar mechanical example of a damped, periodically forced nonlinear oscillator, the Duffing oscillator with displacement x given by

$$\ddot{x} + k\dot{x} + x^3 = B\cos\omega t$$

Its behaviour can be described by the motion of a point in a three dimensional phase space whose coordinates are position, velocity and time of the oscillators motion. A fixed point solution is obtained when the forcing term is set to zero, the system then relaxing to a unique stable equilibrium point (Fig. 1(a)). Stable periodic motions are sustained by the presence of the driving term over a range of values of k and β , the limit cycle behaviour being also determined by the initial, or start conditions (Fig. 1(b)). For other parameter values, the range of which is quite extensive, the behaviour breaks down into chaos. In a true 3 dimensional representation, rather than the 2 dimensional plot of Fig. 1(c), the trajectory, in contrast to those for a fixed point and limit cycle, never intersects itself, consistent with aperiodic behaviour. Evidently 3 variables, or degrees of freedom are the minimum to ensure non intersection of the trajectory in phase space.

A trajectory on a chaotic attractor exhibits most of the properties intuitively associated with random functions, although no randomness is ever explicitly added. The equations of motion are purely deterministic: the random behaviour emerges spontaneously from the nonlinear system. Over short times, the trajectory of each point can be followed, but over longer periods small differences in position are greatly amplified making the predictions of long-term behaviour impossible. Such arbitrarily close initial conditions can lead to trajectories which after a sufficiently long time diverge widely: in marked contrast to that of the fixed point and limit cycle attractors which settle down to the same solutions.

Erratic and aperiodic temporal behaviour of any of the systems' variables implies a corresponding continuous spectrum for its Fourier transform which is, therefore, also a further signature of chaotic motion. However, other factors including noise can lead to continuous spectra and distinguishing chaos from noise is one of the major problems of the field. Hence, although time series, power spectra and routes to chaos collectively provide strong evidence of deterministic behaviour further signatures are desirable for its full characterisation and in discriminating it from stochastic behaviour. Here analysis of trajectories of a point in the phase space of its dynamical variables is required. However, for a system with, say, N degrees of freedom it seemed that it would be necessary to measure N independent variables: an awesome if not impossible task for complex system. Consequently mathematicians have long tried to develop practical techniques for extracting specific finite dimensional information from the limited output provided by experiment: typically the time record of a specific physical observable; that is, one variable of the system, e.g. the laser intensity. Here embedding theorems have been recently used to reconstruct phase portraits from which Lyapunov exponents may be determined that measure the average rate of exponential separation or contraction of nearby points on the attractor. These measure intrinsically dynamical properties, unlike power spectra, and provide quantitative measures by which chaotic motion may be distinguished from stochastic behaviour. The reader is referred to references (1-4) for more comprehensive treatments on the general principles of nonlinear dynamics

Chaos in Lasers

Two-Level Laser

Chaotic behaviour in lasers may exist in even the simplest of systems: one in which population inversion is established between two discrete energy levels of the medium and where the lasing transition between these two levels is homogeneously broadened and lasing is on a single mode⁵ at gain centre. Prediction of such behaviour was initially identified by Haken⁵ through the mathematical equivalence of the equations describing laser action, the Maxwell-Bloch equations, and those derived earlier by Lorenz⁶ to describe chaotic motion in fluids. These are

<u>Maxwell-Bloch</u>	<u>Lorenz</u>
$\dot{E} = -\kappa E + \kappa P$	$\dot{x} = -\sigma x + \sigma y$
$\dot{P} = \gamma_{\perp} E D - \gamma_{\perp} P$	$\dot{y} = -x z + r x - y$
$\dot{D} = \gamma_{\parallel} (\lambda + 1) - \gamma_{\parallel} D - \gamma_{\parallel} \lambda E P$	$\dot{z} = x y - b z$

where for the Maxwell-Bloch equations κ is the cavity decay rate, γ_{\perp} is the decay rate of atomic polarisation, γ_{\parallel} is the decay rate of population inversion, λ is the pumping parameter, E is the field inside the cavity, D is the population inversion and P is the atomic polarisation. Consider the trajectory of the Lorenz attractor where in the equivalent laser system the dynamic variables x , y and z are the field amplitude (E), polarisation of the medium (P), and the population inversion (D).

Fig. 2(a,b,c) shows a sequence of trajectories on increasing the control parameter r in the Lorenz equations. For r near zero all trajectories approach stable equilibrium at the origin, the topological structure of the basin of attraction being hyperbolic about zero. For the laser equations this corresponds to operation below lasing threshold for which the magnitude of the control parameter (laser gain) is insufficient to produce lasing. As r is increased the basin lifts at its zero point to create an unstable fixed point here but now with two additional fixed points located in the newly formed troughs either side of the zero point which is now a saddle point. This is illustrated in Fig. 2(b) where the system eventually settles to one or other of the two new and symmetric fixed points depending on the initial conditions. This corresponds to d.c. or constant lasing as defined by the parameter values of one or other of these points. Note the trajectories in traces a) and b) do not spiral in as for the case of the fixed point solution of the Duffing oscillator shown in Fig. 1(a). Pictorially think of a conventional saddle shape comprising a hyperbolic and inverted hyperbolic form in mutually perpendicular planes and connected tangentially at the origin. With the curve of the inverted hyperbola turned up at its extremity and filling in the volume with similar profiles which allow the two hyperbolic curves to merge into a topological volume one sees that a ball placed at the origin is contained to move most readily down either side of the inverted hyperbola into one or other of the troughs formed by this volume. Chaotic behaviour occurs at larger values of the parameter r when all three fixed points become saddles. Since none of the equilibrium points are now attracting, the behaviour of the system cannot be a steady motion. Though perhaps difficult to visualise topologically it is then possible to find a region in this surface enclosing all three points and large enough so that no trajectory leaves the region. Thus all initial conditions outside the region evolve into the region and remain inside for all subsequent time. A corresponding chaotic trajectory is shown in Fig. 2(c). A point outwardly spirals from the proximity of one of the new saddle points until the motion brings it under the influence of the symmetrically placed saddle, the trajectory then being towards the centre of this region from where outward spiralling again occurs. The spiralling out and switching over continues forever though the trajectory never intersects.

For the laser, such behaviour not only requires a cavity with high transmission but also a gain of at least nine times that required to produce lasing making the experimental realisation of such operation rather impracticable for most lasers of this simple type. A notable exception are optically-pumped far-infrared molecular lasers which are discussed below.

Consequently attention has been given to alternative, though more complex systems, generally with external control (see below) for which such restrictions are in part relaxed. Investigations here have yielded a wealth of identifiable dynamic instability phenomena some in reasonable agreement with theoretical predictions. Recent reviews of these developments are given in references (7-12).

Three-level laser

Realisation of instability phenomena in the system prescribed by Haken nevertheless remains especially appealing in view of its fundamental simplicity and recently optically pumped far infrared lasers have been identified as perhaps the most promising candidates in this regard.

Evidence for Lorenz-type chaos in an NH_3 laser emitting at $81\ \mu\text{m}$ optically pumped by an N_2O laser has been recently reported¹³. Fig. 3, taken from this work, shows motion typical of a Lorenz system, the spiralling around two centres with random jumps from one centre to the next. The abrupt transition from stable to chaotic emission observed with increasing pump strength provides further support for this interpretation.

Nevertheless optically pumped systems comprise three levels involving pump and laser transitions with a common level (Fig. 4, inset). The consequent coherent interactions between these fields can considerably modify the shape of the gain distribution (see below) from the Lorentzian profile of a two-level system. Indeed the equivalence of 3- to 2-level schemes is only possible for weak pumping and in molecular systems where the polarisation (de-phasing) decay rate for the pump transition is considerably greater than that for the lasing transition: effectively resulting in incoherent pumping^{14,15}.

On increasing the pump signal the gain peak changes from a single peak at resonance, characteristic of 2 level systems to a double peak, the separation of which increases with pump signal. The corresponding dispersion curves show typical anomalous dispersion for small pumping which becomes significantly modified for increased pumping. This effect (Rabi splitting) arises from coherent interaction between the pump and lasing transitions.

In general both the pump field and the initial lasing field are responsible for the profile distortion^{15,16}, yielding laser emission and dispersion profiles typical of those

shown in Fig. 4 which also shows the mode line (dashed) which defines single mode operation on line centre. The intersections of the mode line with the dispersion curve determine those frequencies, which through the modified dispersion, have the same wavelength. Evidently periodic and chaotic emission implies that the signal comprises more than one frequency. For low pumping (profiles 1) mode line intersection is at line centre alone giving stable emission. For pumping above values corresponding to curve 3, two additional mode line intersections with the dispersion curves occur, the corresponding laser emission profiles showing emission at these new frequencies but not for that at line centre. The laser signal then exhibits oscillations at the beat frequency (Rabi oscillations) constituting limit cycle behaviour. Over this range the oscillation frequency increases with pump signal as the peaks separate until curve 4 when the mode line dispersion intersection frequencies lie just outside the lower frequency limits of the emission frequency profiles when lasing terminates. Returning to conditions where the pump level is just insufficient to give further intersections than that at line centre (a pump level around that for curve 3), it is in this region that chaotic emission prevails.

The mechanism behind the generation of chaotic emission here is somewhat similar to the Duffing oscillator though here the oscillatory driving or forcing term is provided internally by the Rabi oscillation. Noting that like all oscillators the laser has a natural relaxation oscillation frequency (which normally relaxes to a d.c. signal or to zero in the case of the Duffing oscillator (Fig. 1(a)) then when another oscillation is impressed on the system (here Rabi oscillations) with frequency close to resonance with the natural frequency (in Fig. 4 by decreasing the pump from 4 to around 3) the emission becomes chaotic. Examples of the time series and corresponding phase portraits in 2 dimensions are shown in Fig. 5. The chaotic attractors in the second and third plots are bounded top and bottom by corresponding limit cycle which dominates one or other of the chaotic motions. The top limit cycle is that of sustained relaxation oscillations and occurs on increasing the pump signal to a boundary or bifurcation value where the hitherto steady signal bursts into periodic emission. A further fractional increase in pump signal gives rise to the associated aperiodic signal (second row) and for a further increase the aperiodic or chaotic attractor identifies more with the Rabi type limit cycle behaviour which dominates for subsequently higher pumping (lower trace). As a laser system with its own internal and yet controllable drive (the laser pump), it is a particularly attractive nonlinear system for analysis and relatively easy experimentation, providing along with these illustrations a wealth of other dynamical behaviour, for comparison with the predictions and speculations of mathematical nonlinear dynamics.

Conclusions

Nonlinear optics, in particular lasers, is proving valuable to the field of nonlinear dynamics and deterministic chaos providing simple optical systems which exhibit the most interesting classes of chaotic behaviour. On the other hand, lasers and related nonlinear optical devices have a large and growing technical application, and the understanding, control and possible exploitation of sources of instability in these systems has considerable practical importance.

Of the wide range of lasers, optically pumped molecular systems represent perhaps the canonical laser dynamical system, retaining simplicity in the underlying physics while being amenable to a dynamical system's analysis at a level of, say, the Lorenz equations.

Acknowledgements

We wish to thank the Science and Engineering Research Council for support of this work.

One of us (JSU) is on leave from the Laser Division, Bhabha Atomic Research Centre, Bombay, India.

References

- 1) Thompson, J.M.F. and Stewart, H.B., Nonlinear Dynamics and Chaos (John Wiley and Sons Publications, 1987).
- 2) Schuster, H.G., Deterministic Chaos, Physik-Verlag (1984).
- 3) Haken, H., Synergetics - An Introduction (Springer, Berlin, 1983).
- 4) Haken, H., Advanced Synergetics (Springer, Berlin, 1983).
- 5) Haken, H., Phys. Lett., 53A, 77 (1975).
- 6) Lorenz, E.N., J. Atmos. Sci., 20, 130 (1963).
- 7) Instabilities and Chaos in Quantum Optics (Arecchi, F.T. and Harrison, R.G., eds.), Synergetic Series (Springer-Verlag, 34, 1-253, 1987).
- 8) Harrison, R.G. and Biswas, D.J., Progress in Quant. Elec., 10, 147 (1985).
- 9) Akerhalt, J.R., Milonni, P.W. and Shib, M.I., Phys. Rep., 128, 205 (1985).
- 10) Instabilities in Active Optical Media, Special Issue of J. Opt. Soc. Am. (Abraham, N.B., Lugiatto, L. and Narducci, L.M., eds.) 2, 1-272 (1985).

- 11) Optical Instabilities (Boyd, R.W., Raymer, M.G. and Narducci, L.M., eds.), Cambridge University Press (1986).
- 12) Lasers and Synergetics (Graham, R. and Wunderlin, A., eds.), Springer Proceedings in Physics, Vol. 19 (Springer, Berlin, 1987).
- 13) Weiss, C.O. and Brock, J., Phys. Rev. Lett., 57, 2804 (1986).
- 14) Dupertuis, M.A., Salomaa, R.R.E. and Siegrist, M.R., Opt. Commun., 57, 410 (1986).
- 15) Uppal, J.S., Harrison, R.G. and Moloney, J.V., Phys. Rev. A, 36, 4823 (1987).
- 16) Mehendale, S.C. and Harrison, R.G., Phys. Rev., 34, 1613 (1986).
- 17) Moloney, J.V., Uppal, J.S. and Harrison, R.G., Phys. Rev. Lett., 59, 2868 (1987).
- 18) Harrison, R.G., Moloney, J.V., Uppal, J.S. and Forysiak, W., in Instabilities and Chaos in Quantum Optics, NATO ASI Series (Arecchi, F.L., Abraham, N.B. and Lugiato, L.M., eds.) (in press).
- 19) Lanford, O.E., in Lecture Notes in Physics (Bernard, P. and Raitu, T., eds.), (Springer, Berlin, 1977).

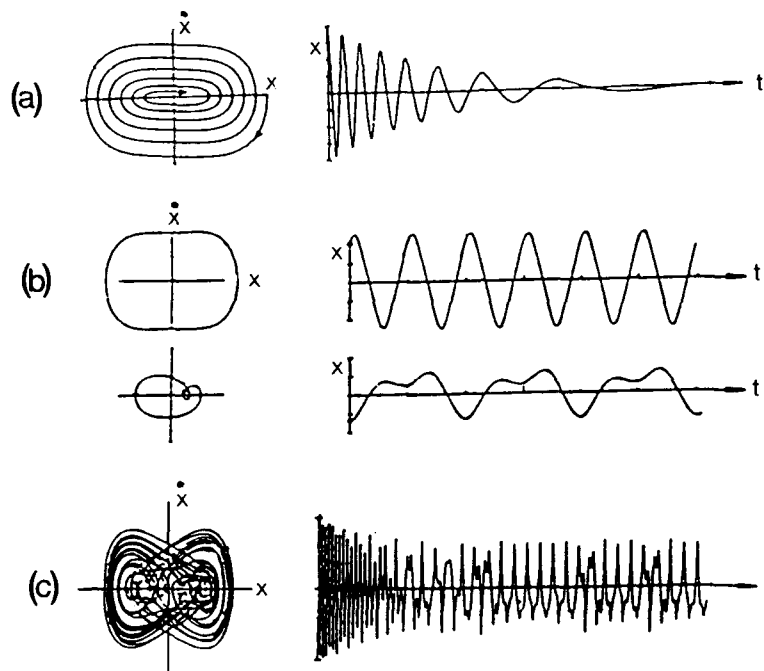


Fig. 1. Behaviour of a Duffing oscillator; a) unforced behaviour showing damped transient oscillation to a fixed point; b) coexisting periodic or limit cycle attractors with different start conditions, c) transients setting to steady state chaos (from ref. 1).

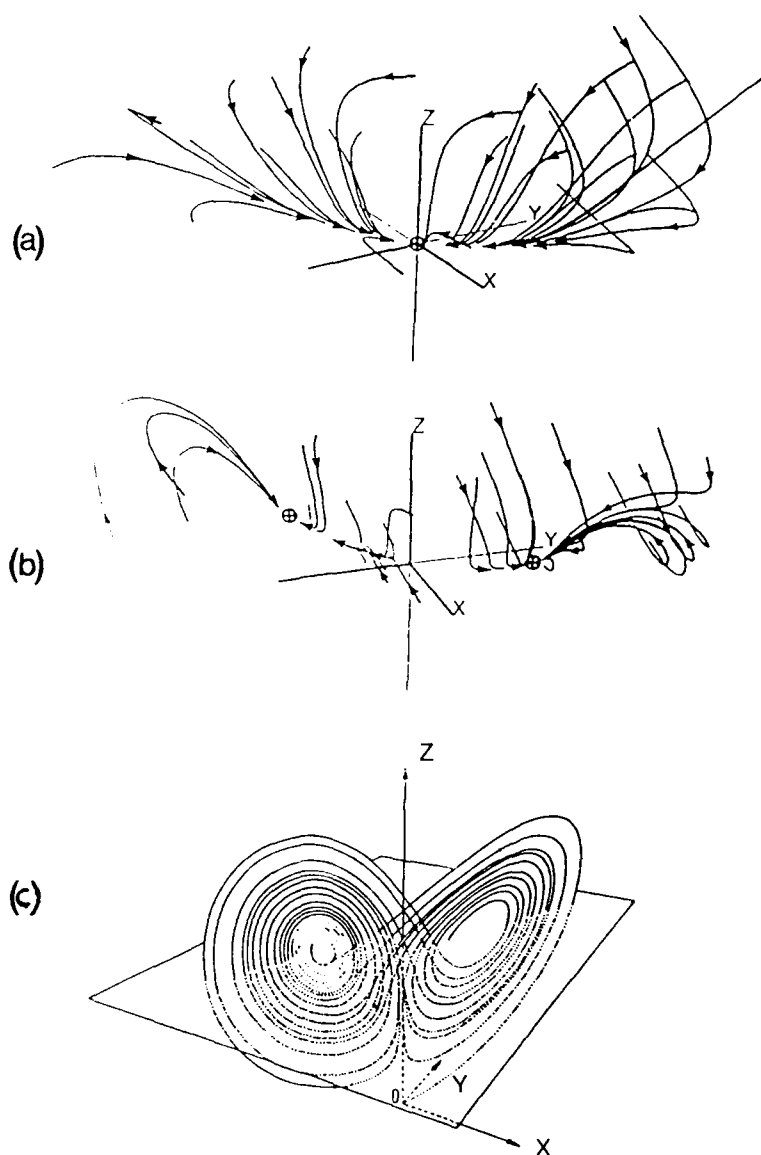


Fig. 2. Trajectories in the three dimensional phase space of the Lorenz attractor. a) Parameter r is less than 1, and all trajectories approach stable equilibrium at the origin. b) Trajectories attracted to two new stable equilibria for r just greater than 1. c) Chaotic trajectory for $r = 28$. a) and b) from ref. 1 and c) from 19.

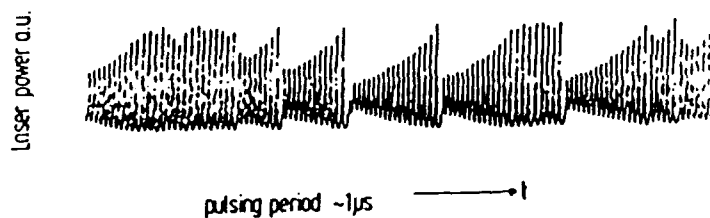


Fig. 3. Lorenz type chaos in NH_3 laser emitting at $81 \mu\text{m}$ optically pumped by a N_2O laser (from ref. 13).

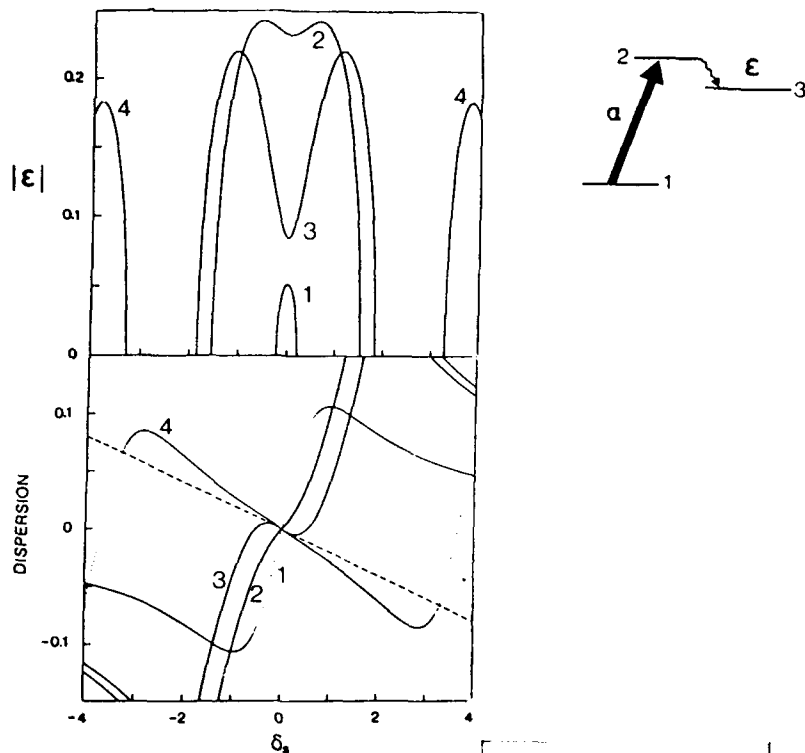
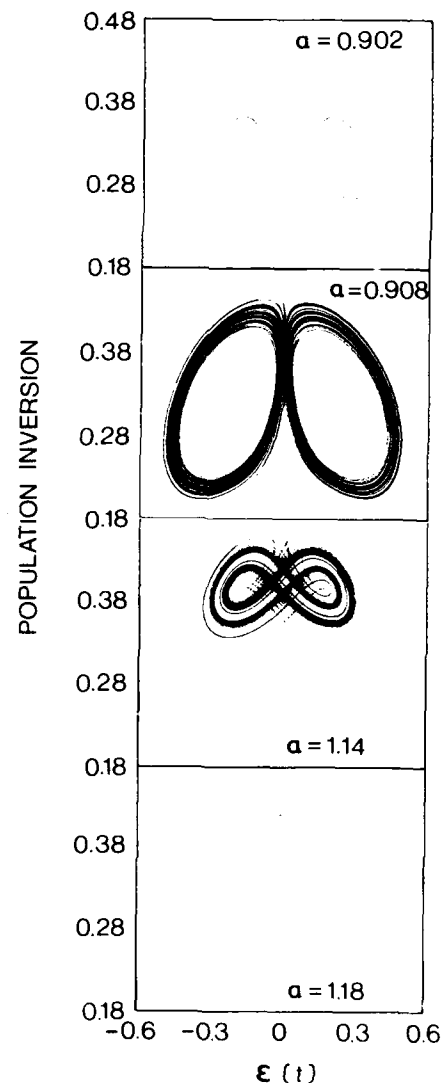
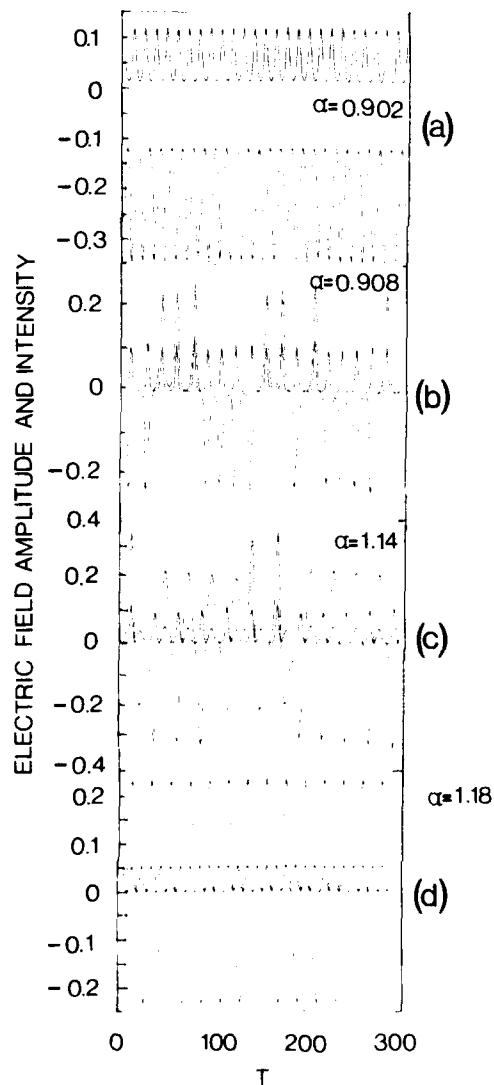


Fig. 4. Laser amplitude $|\epsilon|$ profiles (top) and cavity dispersion profiles along with mode line (dashed) (bottom) against laser signal detuning δ_s (from gain line centre) for a three level optically pumped laser on increasing the level of pumping (curves 1 to 4 respectively). Inset shows 3 level system where α is the pump signal and ϵ the laser emission (from ref. 17).

Fig. 5. Time series and corresponding phase portraits of population difference between levels 2 and 3 (see inset of Fig. 4) against laser field amplitude for increasing pump α . The dashed lines in the time series are for laser field amplitude and the full line for laser field intensity. a) Sustained relaxation oscillations, b) chaotic solution associated with a), c) chaotic solution associated with Rabi oscillations which are shown in d) (from ref. 18).



OPTICAL COMPUTING FOR SDI

H. J. Caulfield, Director
Center for Applied Optics
The University of Alabama in Huntsville
Huntsville, AL 35899

Abstract

SDI has recognized that computing complexity and speed must be increased substantially in order to achieve its goals. Its critics claim those increases are impossible. Under its Innovative Science and Technology program, SDI has sponsored a number of efforts in optical computing to address this problem. This paper reviews three of the results of that effort. This selection is a personal one and in no way implies judgement of the other efforts as less important. Rather the choices were made on two bases: my familiarity with them and the span of approaches from analog to hybrid to digital.

The SDI Problem

As SDI is still a program being defined, it is as foolhardy to condemn to failure as it is to pronounce it a success. A common thread through all proposed SDI methods is that computers (many of them--earth, weapon, and satellite based) must receive a tremendous data flux and decide rapidly

- (1) where the objects of interest are,
- (2) which ones are reentry vehicles and which are decoys, and
- (3) how to intercept and destroy the reentry vehicles.

The scenario and signals are only partially predictable a priori.

The Companion Industrial Problem

In manufacturing, the product is produced at a great rate. It is important to sense incipient and actual defects but to ignore other irregularities. These defects and irregularities are many and only partially predictable a priori.

	Number of Items	Response Time	A Priori Knowledge	Importance of Either False Positives or False Negatives
SDI	Huge	Very Short	Partial	Many lives
Industry	Huge	Very Short	Partial	Many \$

1. Problem Comparison

"Nation"	Primary Purpose
USSR	SDI (Their version)
Japan	Industry
Europe	Industry
USA	Both

2. Major "National" Optical Computer Errors

An Analog Optics Example

What the Japanese call the Sixth Generation Computer, we call Artificial Neural Networks, or (my preference) Neural Networks. Neural networks are based on our simple models of the brain--the only intelligent computer known. It is the only approach known to solving truly massive problems which do not yield to solution by traditional tree search, algorithmic methods. Furthermore, neural networks offer a response to the most often used "proof" that SDI (whatever it winds up being) will not work. That "proof" is based on

the supposed necessity of writing absurd numbers of lines of perfect computer code. In neural networks, we write no code at all. Rather, we instruct the neural network. Your neural network was sent to school for instruction not programmed by a schoolmaster. Furthermore, your neural network offers two other advantages:

- (1) It is largely immune to localized failures. In your brain 100,000 neurons per day die without serious effect on either your memory or your intelligence.
- (2) It can react intelligently to new situations for which it was not trained.

Obtaining all of these advantages for SDI is clearly desirable. Obviously we need both great complexity (number of "neurons" and number of interconnections) and great speed. Combining huge complex with great speed requires massive parallelism.

Under SDI sponsorship, we have shown that an analog optical neural network cannot only exceed current electronics but also vastly exceed conceivable electronics by allowing full parallel interconnect between 10^6 inputs and 10^6 outputs--a total of 10^{12} interconnects¹. Thus the situation is as follows:

Neural Network	Number of Interconnects	Interconnects Per Second
Electronic Chip	$\sim 10^4$	$\sim 10^8$
Optical	$\sim 10^{12}$	$\sim 10^{17}$
Human Brain	$\sim 10^{15} - 10^{16}$	$\sim 10^{17}$

The advance due to optics is clear, overwhelming, and sustainable against all future electronics.

A Hybrid Example

Analog optics is always fast but never very accurate. In linear algebra processors the following approximate equation holds:

$$\epsilon(R) \approx \chi(M) \epsilon(C),$$

where

$\epsilon(R)$ = a measure of the error in the result,

$\chi(M)$ = a measure called the "condition number" of the coefficient matrix, and

$\epsilon(C)$ = a measure of the inherent error of the computer error. In good analog optics, $\epsilon(C) \approx 0.10$. To achieve 10% accurate results we need $\chi(M) \sim 1$. Unfortunately in "real life" SDI problems $\chi(M)$ will range from a few hundred to infinity ("singular" matrices). This means analog linear algebra solvers for SDI are guaranteed to give meaningless results [$\epsilon(R) \gg 1$].

On the other hand, digital floating point processors are accurate enough but much slower.

Under SDI sponsorship, we have shown that we can combine the speed of analog optics with the accuracy of digital electronics by a hybrid process. The computationally intense parts are done with fast, low-accuracy optics. The accuracy-producing, computationally-easy parts are done with a digital electronics. Even with 20% accurate optics, we can solve problems of any condition number²

A Digital Example

The first and only widely successful nonbiological computers have been digital. Over the last 40 years, our skills in programming digital computers have grown immensely. Current multiprocessor and supercomputer efforts may gain another factor of 1000 over the state of the art at the price of very large size and very high pricetags.

Peter Guilfoyle of Opticomp has seen a practical method of using the massive parallel optical interconnect capability of optics (1) to do digital computing. As-yet-unpublished work by Opticomp for SDI has resulted in a working, high-speed, general-purpose optical digital computer. Several years more development will be required to exceed current supercomputers at much less cost, but no new inventions are required.

Acknowledgement and Note

The SDI/ISI optical computing program is directed by W. Miceli of ONR - Boston. The overall SDI/ISI program is directed by Dr. James Ionson. They are the individuals who should be contacted for information on the total program content and goals. By any measure, however, the program has been a great success.

My work on this paper was sponsored by SDI through ONR under Contract No. N00014-86-K-0591 administered by Mr. Miceli.

References

- ¹H. J. Caulfield "Parallel N^4 weighted optical interconnections," Appl. Opt. Vol. 26, No. 19, 4039 (1987)
- ²H. J. Caulfield, M. A. G. Abushagur, P. M. Gibson, and M. Habli "Superconvergence of hybrid optoelectronic processors," Appl. Opt. Vol. 26, No. 23 (1987)

ENHANCED SQUEEZING UNDER DEGENERATE PARAMETRIC WAVE INTERACTION

E. P. Gordov, A. I. Zhiliba, N. P. Konopleva
The Institute of Atmospheric Optics, Siberian Branch
USSR Academy of Sciences, Tomsk, 634055, USSR

Abstract

The study on the evolution of quantum fluctuations under the parametric wave interactions is reported. The theoretical development does not employ conventional approximations based on a given pump wave behavior and short-time expansion. Variations of the pump wave are shown to affect the photon bunching and antibunching. They also lead to squeezing of the fundamental mode in the process of its amplification or extinction. Moreover, the variations of the pump wave in the course of the interaction are found to limit the decrease or increase of the field quadrature component fluctuations.

Introduction

It is a well-established fact now that optical parametric processes are good candidates for manifestation of the quantum nature of light. There are a number of theoretical papers which have predicted that a significant degree of squeezing and antibunching (superclassical bunching) can be reached using these processes. Common features of these papers (see, i.e., Refs. 1-5) are the treatment of the relevant dynamical equations written in the Heisenberg picture within the framework of the following assumptions, namely, the pump wave is assumed to be fixed or the short-time approximation is to be held.

Here the basic set of equations for the field amplitudes describing degenerate parametric processes is analyzed without usage of the above approximations. The statistical characteristics of the processes under consideration are calculated numerically and a comparison with those determined for the given pump wave case is performed.

Evolution of Quantum Fluctuations

The set of equations for the field amplitude operators derived in the Heisenberg picture on the basis of the effective nonlinear Hamiltonian approach has the form

$$\begin{aligned}\dot{a}_1 &= -i\omega_1 a_1 - 2iga_1^\dagger a_2 \\ \dot{a}_2 &= -2i\omega_1 a_2 - iga_1^2\end{aligned}\tag{1}$$

Here 1 and 2 are referred to the generated and pump wave, respectively, g is the coupling constant (the effectivity of nonlinear conversion).

At the initial moment of time, the waves do not interact and the density matrix of the system ρ can be written as a product $\rho = \rho_1 \rho_2$. Averaging of the first equation from the set over the density matrix ρ_2 and the second equation over yields:

$$\begin{aligned}\dot{a}_1 &= -i\omega_1 a_1 - 2iga_1^\dagger \langle a_2 \rangle, \quad \langle a_2 \rangle = \text{Tr } \rho_2 a_2 \\ \dot{\langle a_2 \rangle} &= -2i\omega_1 \langle a_2 \rangle - ig \langle a_1^2 \rangle\end{aligned}\quad (2)$$

The self-consistent set (2) describes time evolution of the generated wave amplitude operator in the process of its interaction with the pump wave. In virtue of Eq. (2), the latter can be treated as a classical electromagnetic field wave. The use of the Bogolubov canonical transformation results in the following formal solution

$$a_1(t) = e^{-i\omega_1 t} [a_1 \text{ch} 2g \int_0^t a(\tau) d\tau - ie^{i\phi} 2a_1^\dagger \text{sh} 2g \int_0^t a(\tau) d\tau] \quad (3)$$

Here $a(\tau) = |\langle a_2(\tau) \rangle|$. In the given pump wave, approximation $a = \text{const}$ and (3) reduces to the known solution from Ref. 1. Below the formal solution (3) is used for analyzing the degenerate parametric scattering (DPS) and degenerate parametric amplification (DPA).

The Degenerate Parametric Scattering

In this case, the pump wave interacts with the vacuum fluctuations in nonlinear crystal, i.e. $\rho_1 = |0X0\rangle$. It follows from Eqs. (2-3) that the amplitude of the pump wave obeys the closed integro-differential equation

$$\dot{a} = -g \text{sh} 4g \int_0^t a(\tau) d\tau / 2 \quad (4)$$

The use of iteration with the given amplitude as the zero approximation results in (4)

$$a^{(1)}(t) = a - (\text{ch} 4agt - 1)/8a \quad (5)$$

This solution does not contain secular terms and describes the extinction of the pump wave in the process at degenerate parametric scattering. Expansion of Eq. (5) in gt leads to well-known Mandel results⁵ obtained within the framework of the short-time approximation.

The time behavior of the mean photon number of the generated mode on the frequency ω_1 can be calculated from Eq. (3) and is of the form

$$\begin{aligned}\langle n_1(t) \rangle &= \text{sh}^2 2z \\ z &= 2gat - g \left(\frac{\text{sh} 4agt}{4ag} - t \right) / 4a\end{aligned}\quad (6)$$

It follows from (6) that t grows up to the time

$$t_0 = \text{arch}(8a^2 + 1)/4ag \quad (7)$$

At moment of time t_0 , all photons from the pump waves were converted into a new mode. The conventional given pumping approximation corresponds to $z = 2gat$ in Eq. (6). It is fairly

clear that in this case the energy conservation law is violated. Figure 1 shows the time dependence of $\langle n_1 \rangle$ calculated on the basis of pumping case.

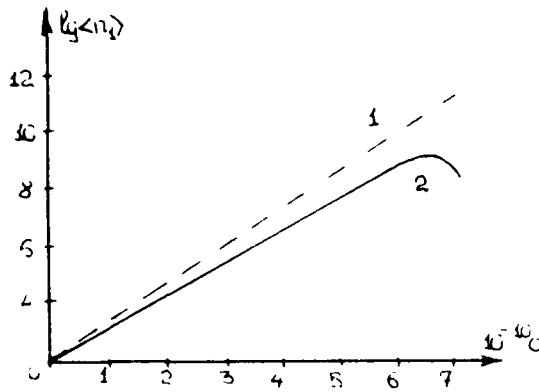


Fig.1

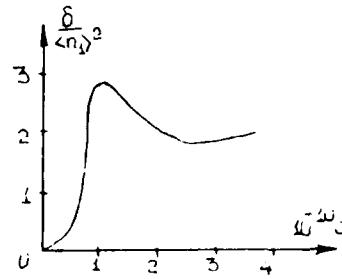


Fig.2

The variance of the photon number $\delta_1 = \langle \Delta n_1^2 \rangle - \langle n_1 \rangle$ can be written as

$$\delta_1 = \text{sh}^4 z + \text{sh}^2 z \text{ch}^2 z \quad (8)$$

The computed results are given in Fig. 2. Here z is defined by Eq. (6). It is known that $\delta = 1$ corresponds to the thermal source. It can be seen from Fig. 2 that the generated wave exhibits the superclassical bunching. The variances of the quadrature field components whose magnitudes indicate the possibility of squeezing of generated waves are of the form

$$\langle \Delta x_1^2 \rangle = \text{ch}^2 z + \text{sh}^2 z + 2 \sin \phi_H \text{ch} z \text{sh} z \quad (9)$$

$$\langle \Delta x_2^2 \rangle = \text{ch}^2 z + \text{sh}^2 z - 2 \sin \phi_H \text{ch} z \text{sh} z \quad (10)$$

where ϕ_H is the pump wave phase. The maximum squeezing is reached for

$$\langle \Delta x_1^2 \rangle = \exp(\pm 2z); \quad \langle \Delta x_2^2 \rangle = \exp(\mp 2z) \quad (11)$$

The plus and minus signs are referred to $\phi_H = \pi/2$ and $\phi_H = -\pi/2$, respectively. It can be readily seen that for $z = 2g\alpha t$ (the given pumping approximation) the wave is generated in the ideally squeezed state (see Refs. 1,2). The influence of the pump wave variation results in the increasing of the effect. The squeezing takes place up to the time t_0 , then this property of the field a_1 disappears. It should be noted that the increase of the nonlinear conversion effectivity g leads to the increase of t_0 . The same occurs with growing of the pump wave intensity. These results are illustrated in Figs. 3 and 4. The curves show that for the region $t \sim t_0$ there exists a significant discrepancy between the given pump wave approximation results and those obtained here. The consideration of the pump wave extinction makes the generation of the ideally squeezed states impossible.

Degenerate Parametric Amplification

In this case, there are two incident wave frequencies $2\omega_1 = \omega_2$, and the initial state at wave ω is given as $\rho_1 = |\beta\rangle\langle\beta|$, where $|\beta\rangle$ is a coherent state. Due to the process of nonlinear interaction, two possibilities appear for the wave with the frequency ω_1 . If $\Psi = 2\phi_1 - \phi_2 = \pi/2$, the wave begins to amplify while for $\Psi = -\pi/2$, it attenuates.

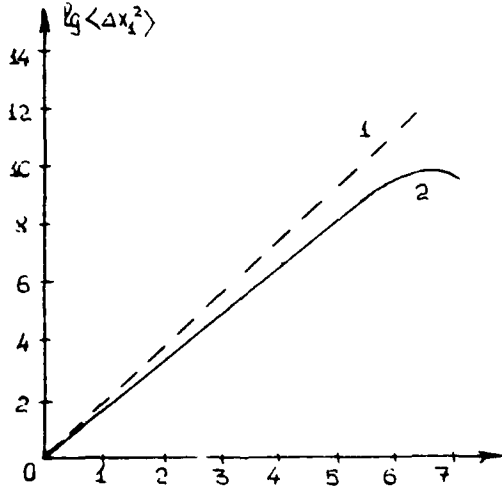


Fig. 3

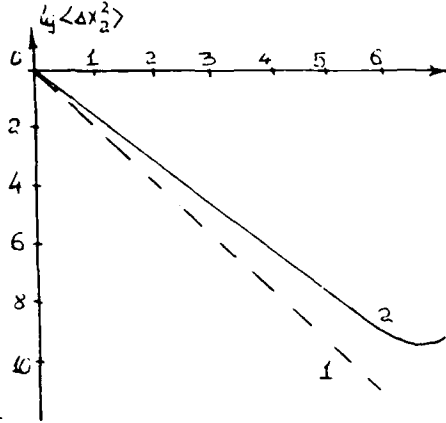


Fig. 4

Equation for a now has the form

$$a = g \left\{ |\beta|^2 \exp \left(4g \int_0^t a(\tau) d\tau \right) - \frac{1}{2} \operatorname{sh} 4g \int_0^t a(\tau) d\tau \right\} \quad (12)$$

The first iteration of Eq. (12) yields

$$a^{(1)}(t) = a - |\beta|^2 [\exp(-4agt) - 1]/4a - [\operatorname{ch}(4agt) - 1]/8a \quad (13)$$

It can be readily seen that expansion of Eq. (13) in gt degrees and averaging it over ρ_1 lead to the results coinciding with those obtained within the framework of the short-time approximation.⁵

When the wave 1 is attenuated ($\Psi = -\pi/2$), the variance δ_1 is of the form

$$\delta_1(t) = (2|\beta|^2 + 1) \operatorname{sh}^4 z + (6|\beta|^2 + 1) \operatorname{sh}^2 z - 2|\beta|^2 \operatorname{ch}^3 z - 6|\beta|^2 \operatorname{ch} z \operatorname{sh}^3 z \quad (14)$$

$$z = 2g \left\{ at + \frac{|\beta|^2}{4a} \left[t - \frac{1 - \exp(-4agt)}{4ag} \right] - \frac{1}{8a} \left[\frac{\operatorname{sh} 4agt}{4ag} - t \right] \right\} \quad (15)$$

Its behavior is shown in Fig. 6 in comparison with the results obtained for a fixed a . When photon antibunching exists, however, its degree and duration are more moderate than those for fixed. When the wave is amplified ($\Psi = \pi/2$)

$$\delta_1 = (2|\beta|^2 + 1) \operatorname{sh}^4 z + (6|\beta|^2 + 1) \operatorname{ch}^3 z \operatorname{sh}^2 z + 2|\beta|^2 \operatorname{ch}^2 z \operatorname{sh} z + 6|\beta|^2 \operatorname{ch} z \operatorname{sh}^3 z \quad (16)$$

and there appears the photon superbunching.

The variances of the quadrature components of a_1 are of the form

$$\langle \Delta x_{1,2}^2 \rangle = \operatorname{ch}^2 z + \operatorname{sh}^2 z \pm 2 \sin \Psi \operatorname{ch} z \operatorname{sh} z \quad (17)$$

If ($\Psi = \pi/2$), then

$$\langle \Delta x_{1,2}^2 \rangle = \exp(\pm 2z) \quad (18)$$

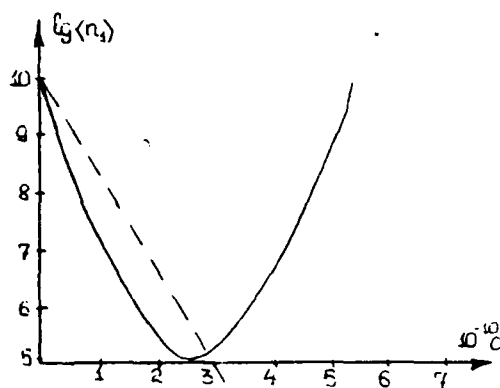


Fig.5

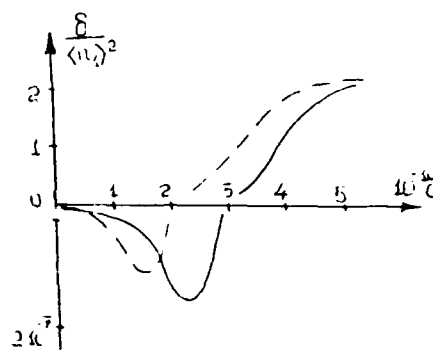


Fig.6

Figures 7 and 8 show that in process of the degenerate parametric amplification the possible squeezing is more moderate than squeezing calculated in the given pumping wave approximation.

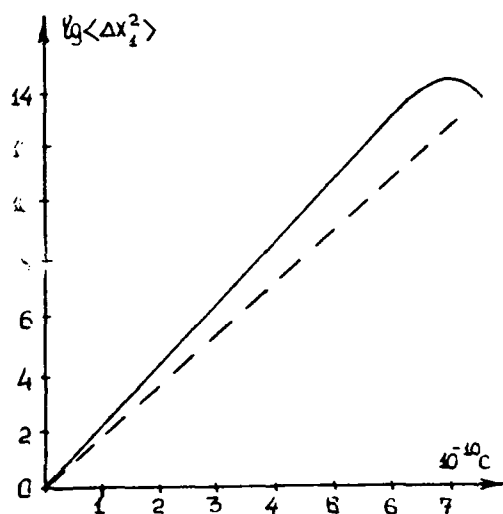


Fig.7

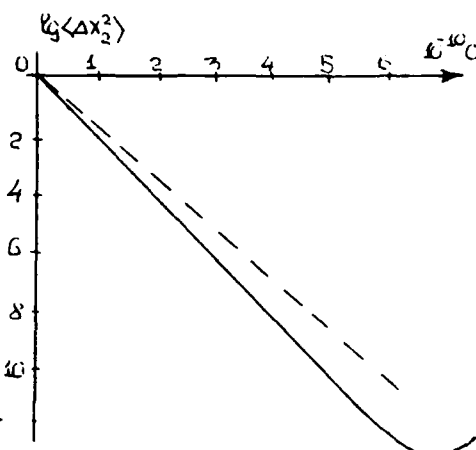


Fig.8

Conclusion

The quantum consideration of degenerate optical parametric processes in the approximation of self-consistent pumping field does not vary qualitatively the results obtained in the approximation of the given pumping field. However, there are quantitative discrepancies. The most important fact is that in the process of degenerate parametric attenuation of fundamental wave squeezing became greater than the resulting one, obtained in the approximation of the given pumping field. This is accompanied by the intensity decrease of the fundamental wave.

References

1. S. Stoler, Phys. Rev. Lett. 33, 1397 (1974)
2. H. P. Yuen, Phys. Rev. 13, 2226 (1976)
3. H. Paul, Rev. Mod. Phys. 54, 1061 (1982)
4. D. F. Walls, Nature. 306, 141 (1983)
5. L. Mandel, Opt. Commun. 46, 437 (1982)

ON THE CHEMISTRY OF SUPERCONDUCTIVITY*

R. More and E. Teller
Lawrence Livermore National Laboratory
Livermore, California 94550

Abstract

High-temperature superconductivity is observed in ceramics with complex crystal structures. In each case, perovskite-like layers (CuO_2) are found next to cation-monoxide layers (LaO or CuO). We suggest that Bloch wave functions in these two layers are hybridized. The interaction of the bottom of an energy band in the monoxide layer with the top of the perovskite band gives rise to states with a low group velocity within these layers. Superconductivity is explained by the strong interaction of these electrons with loosely bound oxygen ions which leads to pairing and ordering of the electrons. Experimental verification of this model may be obtained by observing the variation of the current due to the dependence of the group velocity on the location of oxygen ions.

Introduction

The familiar properties of superconductors appear in La_2CuO_4 and $\text{YBa}_2\text{Cu}_3\text{O}_7$ at higher temperatures and stronger field strengths than usual. The oxygen ions in these crystals, related to the perovskites, are able to interact strongly with any charged particles. The substances have a complex, layered structure.

We assume that the high temperature superconducting state is similar to that described by Bardeen, Cooper, and Schrieffer,¹ with a limited set of free electrons participating. We start by discussing the role of the perovskite layers (consisting of CuO_2) and argue that an interaction of the states of electrons in these layers with states in neighboring layers is decisive in producing the observed effects.

In carrying out this program, we assume in some cases purely ionic configurations, as for the ions Ba^{2+} and Y^{3+} . For the copper ions, we consider energy bands filled with a number of electrons not corresponding to an integral charge per copper ion; the same holds for lanthanum. In the case of oxygens in the perovskite layer, we assume somewhat less than two electrons per ion corresponding to some holes in the O^{2-} shell. All this is based on plausible speculations about the band structure. We feel that in these complex ceramics, the uncertainties of a priori calculations leave some room for alternative scenarios.

Theory and Discussion

It is not unusual, in describing conduction bands, to use hybrid wave functions on single atoms. In the case of our special ceramics, we propose to form hybrids from electron states near the bottom of an empty band [on a Cu^{3+} or La^{3+} ion] in the monoxide

*Based on a discussion in August 1987 at Erice, Italy; completed in December, 1987.

plane, and hole-like states from the top of an almost-filled band which results from states of the O^{2-} ions in the perovskite plane.

The hybridized wave function ψ can be written

$$\psi = a_m \psi_m + a_p \psi_p \quad (1)$$

where ψ_m is composed of states in the monoxide plane and ψ_p from states in the perovskite plane.² For all three wave functions we write the two-dimensional Bloch functions,

$$\psi = e^{i(k_x x + k_y y)} f_k(x, y, z) \quad (2)$$

where the 2-dimensional wave-number \vec{k} is near $k = 0$ in every case for the states of interest. We shall show that the hybridization of wave functions in the neighboring layers will reduce the group velocity of the carriers and enhance the interactions that give rise to superconductivity.

The Cu ions in the perovskite plane shall be represented in a first approximation as Cu^{2+} . For the sake of clarity and completeness we discuss these electrons even though we believe they do not contribute to superconductivity.

In the crystal field, the 3d and 4s electrons of copper are hybridized, and there are nine electrons shared between these states. More specifically, the six orbitals representing the (3d, 4s) hybrid can be symbolized by $(x^2, y^2, z^2, xy, xz, yz)$. If one considers the perovskite plane to be the x-y plane, the four orbitals (z^2, xy, yz and zx) do not strongly overlap electrons on the oxygen ions, and should generate bands which lie at lower energies and are filled by eight electrons. The ninth electron is then in the lowest part of the band formed from the (x^2, y^2) orbitals.³ These carriers can explain the observed linear specific heat and observed metallic conductivity.

In the yttrium compound, we assume the barium oxide and yttrium planes to be purely ionic, and thus to have closed bands that require no further discussion. If there is no deviation from stoichiometry we can describe the monoxide layer in the lanthanum compound as containing La^{3+} and in the yttrium compound as containing Cu^{3+} . In the Y compound the monoxide plane is represented in Fig. 1. The Cu ions have only two oxygen neighbors along the x-axis within the xy plane. However, they have two further close oxygen neighbors along the z-axis. Using similar arguments as for the perovskite plane we fill four orbitals (y^2, xy, yz , and zx) with eight electrons and obtain Cu^{3+} ions which one may consider as a closed shell.

In this first approximation we should consider all oxygens to be in the O^{2-} state. Thus we have conducting perovskite layers with no other layers participating in the conduction process.

However, there are also energy bands⁴ formed from the 2p states on the oxygen ions in the perovskite layer. These bands are filled or nearly filled and have their maxima at $k = 0$. Of these the $2p_z$ subband is of special interest. We assume that the states of

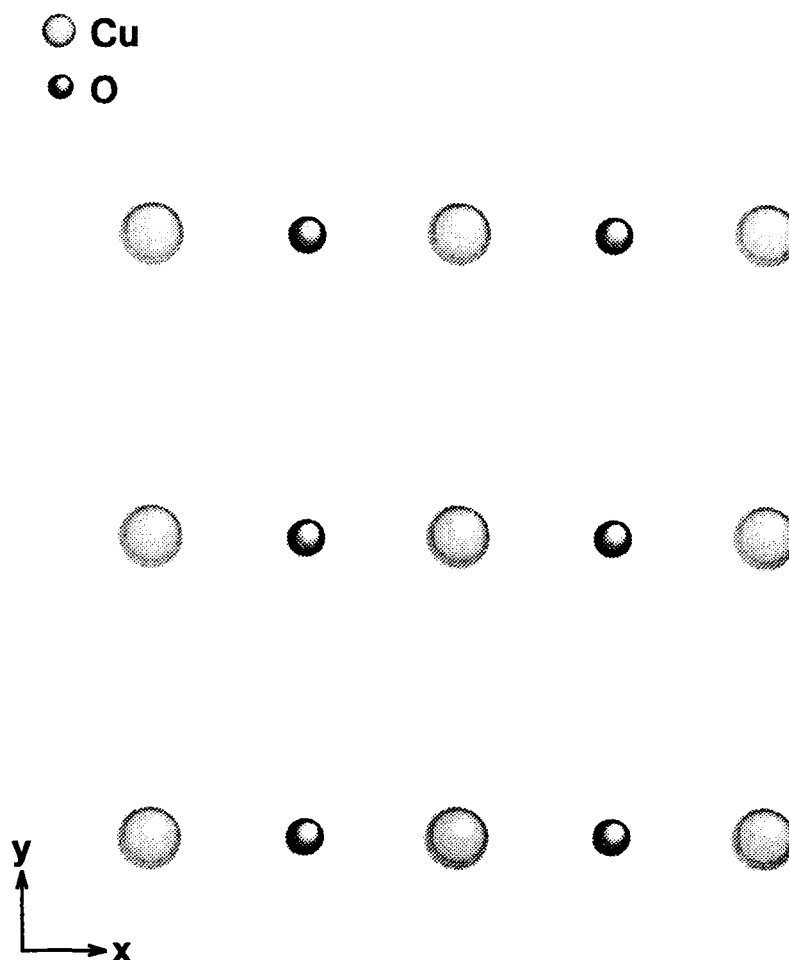


Fig. 1

this band have slightly higher energy than the $2p_x$, $2p_y$ subbands, for electrostatic reasons. Indeed, the filling of all states (x^2 , y^2 , z^2 , xy , yz , zx) would result in a spherical electrostatic potential near Cu. Absence of some x^2 and y^2 electrons raises the energy of the oxygen $2p_z$ state (relative to $2p_x$ and $2p_y$) both on account of electrostatic terms and on account of exchange terms. (However, it should be pointed out that consideration of the kinetic energy may change this argument.)

The superconductivity will be ascribed to holes from the oxygen $2p_z$ band, appropriately hybridized with electrons in the monoxide plane(s). In order to better understand this, we show the nodes of the $k = 0$ oxygen $2p_z$ wave functions as dotted lines in Fig. 2.

In Fig. 2, the plus and minus signs refer to the values of ψ_p above the node in the xy plane. This wave function does not change upon displacement of the lattice by an integral number of periods in the x - or y -directions. It therefore does correspond to zero wave-vector in the plane; the indicated changes of sign are a consequence of the fact that this state is at the top of the $2p_z$ band.

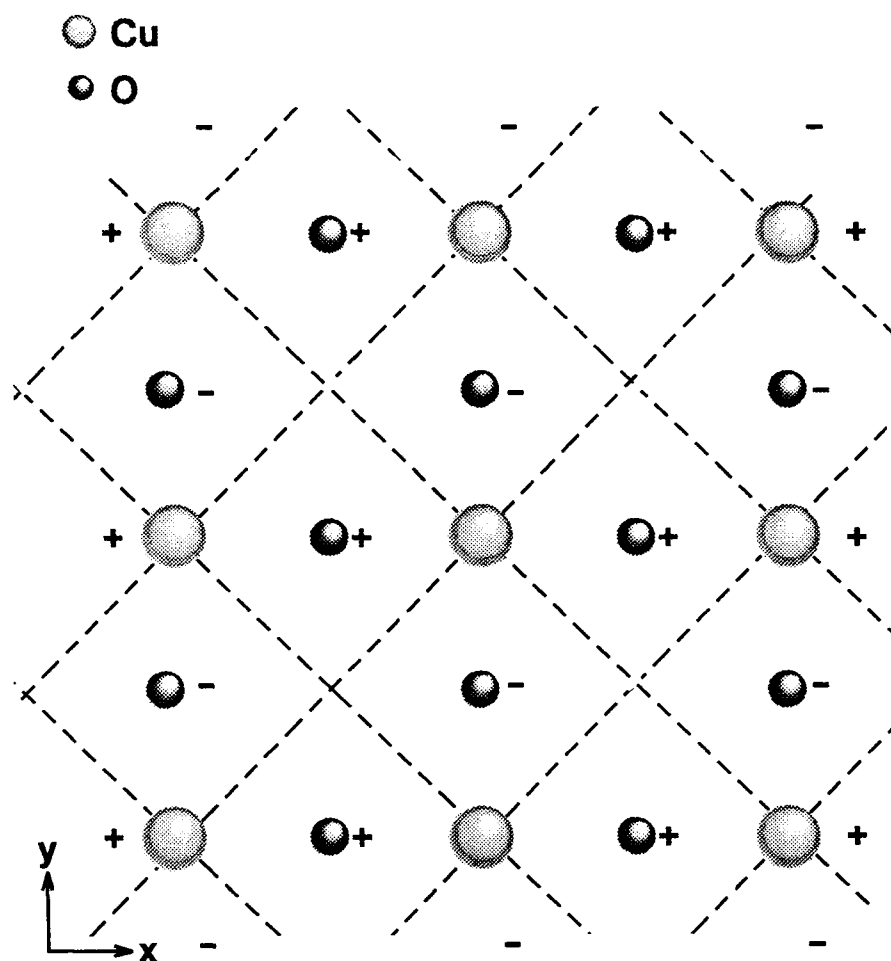


Fig. 2

In La_2CuO_4 , the La^{3+} ions are located above and below those crossing points of the nodes (Fig. 2) that are not occupied by Cu ions. Wave functions of this type are just becoming available on the La ions in the 4f state with three nodes in the xy, yz, and zx planes. We assume that splitting by the crystal field and resonance with ψ_p lowers one state so that it no longer lies above the 6s state of lanthanum as in the case of the free ion. Another possible assignment would be a resonance with a 5d orbital on the La ion. In that case only two nodes (yz and xz) are present. When Ba is substituted for La hybridization with 4f or 5d orbitals would still be possible. On the substitution by Sr the 4d orbital should be preferred. The role that Ba and Sr play in determining T_c will be influenced by the wave function selected.

We, therefore, propose that ψ_p in (1) is a wave function near $k = 0$, composed of $2p_z$ oxygen wave functions with alternating signs (Fig. 2), while ψ_m is composed of 4f wave functions on the La with xy, yz, and zx nodes in the layers on either side of the perovskite plane.

In the yttrium compound (and the similar superconductors where rare earths are substi-

tuted for yttrium) we assume that ψ_p in Eq. (1) is a wave function similar to that discussed above but extending over two perovskite layers. The wave function ψ_m extends over a single copper monoxide plane lying between the two perovskite layers. Because a BaO layer is found between the monoxide and perovskite layers, the interacting layers are now second neighbors, and their interaction should be greatly weakened.

However, the perovskite layers are puckered, the oxygens being attracted toward the Y^{3+} more strongly than toward the Ba^{2+} ions. Thus the orbits to be considered for ψ_p are not pure $2p_z$ states but rather an appropriate linear combination of $2p_z$ and $2s$ orbitals. One linear combination extends toward Y^{3+} , has lower energy, and is already occupied; the other points toward the CuO plane and has its band maximum at $k = 0$ near the Fermi level. This second band will be used for ψ_p . With this choice, the interaction between Cu layers is increased.

In the monoxide layers of the yttrium compound, we have assumed in first approximation that the copper is present as Cu^{3+} , and that the states (y^2 , xy , yz , and zx) of the $3d-4s$ hybrid are filled, leaving the states (z^2 , x^2) unoccupied. The wave function ψ_m in Eq. (1) will now be composed of x^2 -type states from the bottom of the band formed near the Cu^{3+} ions in the monoxide layer. Indeed these x^2 -type wave functions overlap more strongly along the x -axis than the states of z^2 -type, and thus the band formed from x^2 -functions will have the lower band minimum at $k = 0$.

We observe by comparison of Figs. 1 and 2 that the $2p_z$ band maximum wave function and the $3d-4s$ x^2 band minimum wave function have the same symmetry so that hybridization is permitted. The ratio of amplitudes of the coefficients in the lower hybrid state (near $k = 0$) is:

$$\frac{a_p}{a_m} = \frac{E_i}{\Delta} ; \quad \Delta = [(E_{\max} - E_{\min})^2 + E_i^2]^{1/2} \quad (3)$$

where E_i is the interaction energy of ψ_p and ψ_m , and Δ is the energy-difference between the levels, determined by the maximum energy in the perovskite layer E_{\max} and the minimum energy E_{\min} in the monoxide layer. In the yttrium compound, E_i should be small due to the distance of perovskite and monoxide layers and one should expect $a_m \gg a_p$. Thus the hybridized electrons are concentrated on the monoxide layer.

We now consider the group velocity in the xy plane,

$$v_g = \frac{dE}{dk} \quad (4)$$

for electrons with hybrid wave functions of the form given in Eq. (1). A large group velocity leads to large energy-denominators in the process of electron scattering by lattice vibrations. This then implies that the states coupled in the formation of Cooper pairs must be very near the Fermi surface. In our model for the ceramic superconductors, and particularly for $YBa_2Cu_3O_7$, the low group velocities will loosen this restriction on electron pairing and thereby enhance superconductivity.

To calculate the group velocity from (4), we write

$$E = a_p^2 E_p + a_m^2 E_m + 2a_p a_m E_i \quad (5)$$

where E_p and E_m , which are the energies in the two layers, and E_i , which is responsible for the interaction, can be expanded near $k = 0$ in powers of k . We have assumed a_p , a_m to be real.

$$\begin{aligned} E_p &= E_{\max} - \frac{\hbar^2 k_x^2}{2m_x^{(p)}} - \frac{\hbar^2 k_y^2}{2m_y^{(p)}} \\ E_m &= E_{\min} + \frac{\hbar^2 k_x^2}{2m_x^{(m)}} + \frac{\hbar^2 k_y^2}{2m_y^{(m)}} \\ E_i &= E_0 + \alpha k_x^2 + \beta k_y^2 \end{aligned} \quad (6)$$

Since in the perovskite layer we are near a maximum of the kinetic energy, the terms in k_x^2 and k_y^2 appear with a negative sign. The structure is almost tetragonal, and, therefore, the effective masses in the perovskite layer are nearly equal: $m_x^{(p)} \cong m_y^{(p)}$. They correspond to a band width of a few volts. For the lanthanum monoxide layer one can write in a similar way $m_x^{(m)} \cong m_y^{(m)}$. The electron orbits in neighboring lanthanum ions will probably overlap to a lesser extent than in the perovskite layer. We therefore assume $m^{(m)} > m^{(p)}$. The interaction energy, E_i , is smaller and its k -dependence may be neglected, $\alpha \cong \beta \cong 0$.

To obtain the group velocity, we calculate dE/dk from Eq. (5). This gives terms containing factors $\delta E/\delta E_p$, $\delta E/\delta E_m$, $\delta E/\delta a_p$, and $\delta E/\delta a_m$. However, the contributions from the latter two cancel since a_p and a_m are adjusted to give stationary values to E . This gives, for the x - and y -components of the group velocity v_g ,

$$\begin{aligned} v_{gx} &= \hbar^2 k_x \left(\frac{a_m^2}{m_x^{(m)}} - \frac{a_p^2}{m_x^{(p)}} \right) \\ v_{gy} &= \hbar^2 k_y \left(\frac{a_m^2}{m_y^{(m)}} - \frac{a_p^2}{m_y^{(p)}} \right) \end{aligned} \quad (7)$$

According to (3) the amplitude in the perovskite layers is smaller, $a_p < a_m$. But we assumed $m^{(p)} < m^{(m)}$. The group velocities may be interpreted as a superposition of a smaller electron-like velocity $\hbar^2 k/m^{(m)}$ in the monoxide layer with a higher probability a_m^2 and a faster hole-like velocity in the perovskite layer $\hbar^2 k/m^{(p)}$ with a lower probability a_p^2 .

In the lanthanum compound, the formation of Cooper pairs may be understood as in the BCS theory. The higher transition temperature T_c may be ascribed to low electron velocities, partly explained by the participation of few electrons, and partly by the cancellation of terms seen in (7).

The explanation of superconductivity will require phase-ordering of the electron pairs

in three dimensions. The electron hopping (or kinetic energy) operator plays a key role in establishing this long-range order. The wave functions of Eq. (1) will have to be used to construct full three-dimensional Bloch functions.

In the case of $\text{YBa}_2\text{Cu}_3\text{O}_7$, the high transition temperature (near 95°K) requires a more detailed explanation and greater modification of the BCS theory. In the monoxide plane the y^2 -states of the (3d, 4s) hybrid are filled, but the bottom of the x^2 -energy band is available. Crowding by the oxygen ions along the x-axis will cause the effective mass $m_x^{(m)}$ in (6) to have a low value, while $m_y^{(m)}$ will be large due to the small overlap of the x^2 -type wave function in neighboring cells along the y-axis.

As a result, the group velocities (7) will behave quite differently in the x- and y-directions. We have seen that a_p should be small. In the expression (7) for v_{gx} , the term containing a_p^2 may be neglected, and the electron velocity will be governed by $m_x^{(m)}$, which is of the order of the actual mass of an electron. The velocities will be those of electrons in common metals at appropriate k_x values.

On the other hand, for the y-component, the two terms $a_m^2/m_y^{(m)}$ and $a_p^2/m_y^{(p)}$ in (7) will be comparable. Thus, v_{gy} may well become very small. The energy may become practically independent of k_y , even for high k_y -values. Contraction of ψ_m on a single line of Cu-O-Cu-O-Cu ions along the x-axis may become possible. Such a contraction permits a strong interaction with the oxygen ions surrounding that line and a lowering of the energy will result.

Appropriate occupation of states including those of high k_y values could lead to one-dimensional behavior of the electrons in the monoxide plane and to low x-components of the velocity if the energy band is filled to a low level. Indeed, if a fixed fraction ϵ of the band is occupied, then the maximum k-value in the Fermi sea is proportional to $\epsilon^{1/3}$, $\epsilon^{1/2}$, and ϵ in three, two, and one dimensions. The velocities at the Fermi level behave similarly and become small in the one-dimensional case.

In applying the Bardeen, Cooper, Schrieffer theory of superconductivity,⁵ we have now a strong-interaction situation because the electron-lattice coupling becomes stronger than the kinetic energy of the electrons. In this case, the energy to break a pair of electrons will be greater than kT_C ; there will be many paired electrons above the critical temperature in the "normal" state; and the transition itself may be understood as the establishment of ordering and phase relations between existing pairs. For a low density of these bipolarons, the transition temperature will be inversely proportional to their effective mass. These ideas are similar to the bipolaron theory.⁶ The following discussion will be given in terms of that theory.

Let us consider the localization and pairing of electrons along a Cu-O-Cu-O-Cu chain in a more quantitative manner. Placing an electron near a Cu^{3+} ion, there will be four O^{2-} neighbors at distances of 2 Å. Assuming a double charge on the oxygen and a restoring force constant of 10^6 g sec^{-2} (corresponding to an Einstein oscillator of $\omega \cong 2 \times 10^{14} \text{ sec}^{-1}$), one obtains a polarization energy of about 1 eV.

Due to the small effective mass, $m_x^{(m)}$, the energy needed for localizing the electron is greater than 1 eV, and the electron therefore should be spread over several lattice

cells. Spreading the electron over n cells in the x -direction, the negative polarization energy will vary as n^{-1} , while the kinetic energy of localization changes as n^{-2} .

For the bottom of the energy band, the minimum might occur for an n between 3 and 7, giving a binding energy of about 0.1 eV. If not much more than 0.01 electrons per lattice cell are available to fill the bottom of the energy band, then the polarons formed in this way will not overlap. The binding energy of the polaron may have an isotope effect, but if polaron formation has progressed far enough above the critical temperature, this need not affect superconductivity.

The total energy can be represented as

$$E_{\text{bipolaron}} = 2E_{\text{kin}} - 4E_{\text{pol}} + E_{\text{repulsion}} \quad (8)$$

The positive kinetic energy term, E_{kin} , is that of two electrons. Polarization, E_{pol} , by two electrons gives a twofold displacement of the oxygens and a fourfold negative polarization energy term which may stabilize the bipolarons. Finally, $E_{\text{repulsion}}$ between the two electrons is apt to prevent bipolaron formation in most substances.

The bipolarons need to be ordered to make the crystal superconducting. In our model, the ordering is accomplished by the coupling of the bipolarons which extend along the Cu-O-Cu-O-Cu chains in the monoxide plane with the two neighboring perovskite layers. The amplitude in the latter is small, but the effective masses, $m_y^{(p)}$, as well as $m_x^{(p)}$, are small, and therefore the wave functions are not fully localized in the x - or y -direction. Thus several chains in the monoxide layer interact with the same wave function in the perovskite layer. In that way, they interact with each other, and phase relations can be established. The interaction, E_i , can be assumed to be low enough to make the amplitude a_p in Eq. (1) small, but high enough to lead to an ordering at a transition point T_c near 100°K. One might assume $E_i \approx 0.01$ eV. The ordering need not depend on the isotope, and T_c need not show an isotope effect.

The construction of the wave function Eq. (1) from contributions in the monoxide and perovskite layers should help to avoid Peierls instability. Actually, in the monoxide plane, the bipolaron is localized in the y -direction according to our model. Yet, through the coupling in the perovskite plane, it remains mobile and can carry a current.

It is probable that for a phase transition and for establishment of long-range order, three-dimensional ordering is required. In our model, we have only correlated the wave functions in three neighboring planes. Such wave functions in the triplets of planes will have to be superposed using phase factors e^{ikz} . The resulting superconductor will, of course, be anisotropic, particularly in its magnetic properties.

If a rare earth atom is substituted for yttrium the transition temperature does not change. Yet, ordering in the z -direction should depend on the coupling of the wave functions through the yttrium layer or rare earth layer that has replaced it. In the former case a 4d orbital on yttrium may be involved; in the latter case, a 5d orbital or, more probably, a 4f orbital. The coupling should be altered by the substitution in either case.

It is possible that phase-ordering of bipolarons will occur near T_c in the x - y plane.

Once this ordering has proceeded far enough the coupling across the yttrium (or rare earth) plane will become strong independent of the value of the local coupling constant because an increased 2D correlation can easily compensate for a reduced z-coupling.

A remarkable observation of the elastic properties of the yttrium compound seems to support the one-dimensional model of bipolarons. Below the transition point, the torsion frequency increases by approximately 1%. If bipolarons extend in the x-direction, and if interaction between these bipolarons is established by the phase transition in the z-direction, then an increase in the torsion frequency should indeed be expected.

Measurements performed at Bell Labs⁷ on nuclear quadrupole resonance give explicit information on the location of the superconducting electrons. The relaxation time of nuclear spins depends on the ability of adjacent electrons to accept very small amounts of energy. For Cu^{2+} in the perovskite plane, this relaxation time varies inversely with temperature and shows only a small irregularity at T_c . The behavior is similar to that found in common metals. But for the Cu^{3+} excitations, the relaxation time is practically temperature-independent above T_c , while below T_c , the relaxation time increases rapidly with decreasing temperature. One may consider this as evidence that bipolarons, which are ordered and frozen when superconductivity sets in, are found with highest probability in the monoxide planes.

Recent observations (Walstedt et al., unpublished; Kohara et al., unpublished) raise doubts about the assignment of observed resonances to the Cu ions in the monoxide and perovskite layers. Our theory agrees with the original assignment. The observed relaxation times have been interpreted, so far, on the basis of the interaction of Gadolinium f-electrons with the magnetic dipoles of the Cu nuclei. For a proper evaluation of the relaxation times (longitudinal or transverse) the interaction through the hybrid wave functions for electrons and bipolarons must also be considered. This could establish a strong indirect coupling between the Gadolinium f-electrons and the Cu^{3+} ions in the monoxide layer.

In the search for superconductivity at even higher temperatures, high conductivities of somewhat irregular nature were found when some of the oxygens in the yttrium compound were replaced by fluorine.⁸ Zero resistance was reported at temperatures as high as 160°K, and small magnetic anomalies showed up even above 300°K. The ion F^- is more stable than O^{2-} . If the substitution occurs in the perovskite plane, fewer electrons may become available in that layer of negative ions and fewer holes may participate in forming complex Bloch functions. Other changes may be more important. Whenever a fluorine displaces an oxygen, one more electron is injected into the system. Additional electrons may also be placed in the x^2- and y^2- orbitals in the perovskite plane. The result may be a higher or lower density of bipolarons; this will influence the ordering of bipolarons and might account for the observed phenomena above the critical temperature as well as for the increase in the critical temperature.

The coupling between layers proposed in our model may depend on the location of the O ions. Such dependence might actually be observed. The symmetric vibration of two oxygen ions on the z-axis located below and above a Cu^{3+} ion in the monoxide plane may be excited by irradiating the yttrium compound with two laser beams of different frequency, where the difference of the energy of the light quanta equals the quantum of the vibration. Since this vibration is apt to change the polarizability of the crystal near the Cu ion, an effective excitation of the vibration should be obtained.

One should expect that in the course of such a vibration, the values of a_p and a_m will change. The group velocity, v_{gy} , in (7) may change in a sensitive way in the course of such a vibration. Therefore, if a crystal carrying a strong superconducting current is irradiated, the current is modulated by the vibration, and the frequency difference of the two laser beams should be emitted in the infrared. The emission should be polarized parallel to the current and should be proportional to the square of the current.

In principle, the experiment can be carried out in a multicrystalline conglomerate, but the small currents and correspondingly small emissions may make the observation difficult. A further difficulty is that other nonsymmetric vibrations may be excited. Some are active in the infrared and will emit even in the absence of a current.

The dependence of the current on the oxygen locations is hard to predict; at the same time, if the right polarization and the right dependence on the current is observed, this would give strong support to the model we are proposing.

Our model leads to a relatively simple coupling between oxygen-displacements and the positions of bipolarons. For instance, one may find below the transition temperature T_c that bipolarons are located in every second Cu-O-Cu-O chain while the oxygens in the intervening Cu-O-Cu-O chains are polarized. This specific model relies on the bending vibrations of oxygens with particularly low frequency and low restoring force. At the same time bipolarons which are closest to each other in the x-y plane should be 180° out of phase. This would reinforce their action in the oxygens located between them. Thus the bipolarons would form a superlattice with a period four times the lattice distance. (We are, of course, considering relative displacements of nearby oxygens rather than absolute displacements.) The superlattice may become visible in the diffraction pattern giving maxima at $1/4$ of the lattice distance in the reciprocal lattice of oxygen ions.

The intensity of the subsidiary maxima should, however, be extremely small. The relative oxygen displacements are of the order of the zero-point vibrations and the observed intensities should be proportional to the square of the displacement. This results in intensities less than 10^{-3} of the regular interference spots.

If interference peaks indicating a superlattice are found this would show in an explicit manner that high-temperature superconductivity is connected with a particularly simple arrangement of the electrons.

Our model depends sensitively on specific properties of the lanthanum and yttrium compounds. High temperature superconductivity seems, indeed, to be a rarity. It may occur only under quite specific quantitative conditions. Those proposed in this paper may not be unique. Other peculiar circumstances could well lead to pairing and ordering of electrons at high temperatures and, thereby, to superconductivity.

Acknowledgments

The authors are very grateful to a number of scientists who have provided useful information, comments and questions about the ideas presented here, especially Drs. J. Smith and A. McMahan. The authors are also very grateful to Professor N. Zichichi for the hospitality of the E. Majorana Center in Erice.

References

1. J. Bardeen, L. N. Cooper, and J. R. Schrieffer, Phys. Rev. 108, 1175 (1957).
2. In the case of the lanthanum compound ψ_m represents two LaO planes surrounding one CuO_2 plane; for the yttrium compound ψ_m corresponds to one CuO plane surrounded (at a distance) by two CuO_2 perovskite planes. At the present stage of discussion we assume that the wave functions extend over a few layers in the z-direction.
3. Instead of starting from orbitals at the location of various ions, one may first construct the bonding and antibonding states belonging to neighboring ions. The difference is one of vocabulary rather than substance.
4. For calculations of the energy bands, J. Yu, S. Massidda, A. J. Freeman, and D. D. Koeling, Phys. Lett. A122, 203 (1987).
5. See, for instance, A. A. Abrikosov, L. P. Gorkov, and I. E. Dzyaloshinski, Methods of Quantum Field Theory in Statistical Physics (translated by R. Silverman) (Prentice-Hall, Inc., Englewood Cliffs, NJ, 1963).
6. B. K. Chakraverty, J. de Physique Lettres 40, L-99 (1979); B. K. Chakraverty and J. Ranninger, Phil. Mag. B52, 669 (1985).
7. W. W. Warren, R. E. Walsted, et al., Phys. Rev. Lett. 59, 1860 (1987); R. E. Walsted, W. W. Warren, et al., Phys. Rev. B36, 5727 (1987).
8. S. V. Ovshinsky, T. R. Young, et al., Phys. Rev. Lett. 58, 2579 (1987).

DEVELOPMENT AND ANALYSIS OF PULSED-POWER, PHOTOPUMPED X-RAY LASER SOURCES AT THE
NAVAL RESEARCH LABORATORY

J.P. Apruzese, P.G. Burkhalter, G. Cooperstein, J. Davis, D. Mosher, P.F. Ottinger,
J.E. Rogerson, S.J. Stephanakis, V.E. Scherrer, J.W. Thornhill, and F.C. Young

Naval Research Laboratory
Washington, D.C. 20375-5000

G. Mehlman

Sachs-Freeman Associates, Inc.
Landover, Maryland 20785

B. L. Welch

University of Maryland
College Park, Maryland 20742

Abstract

Resonant photopumping is an attractive and potentially very efficient technique for achieving x-ray lasing in plasmas. At the Naval Research Laboratory we are pursuing the realization of one of the most promising photopumped schemes wherein heliumlike sodium pumps heliumlike neon. The theoretical side of this research has revealed the conditions required for the sodium and neon plasmas to maximize the possibility of photopumped fluorescence and lasing. On the experimental side, a powerful (25 GW) z-pinch source of sodium line pumping radiation has been developed and characterized. A separate neon plasma, driven by part of the return current from the sodium-bearing plasma, has been deployed side-by-side with respect to the sodium line source at a distance of 5 cm. The presence of photopumping has been indicated in fluorescing spectra. The remaining steps toward achievement of an x-ray laser are reducing the spatial separation of the pumped and pumping plasmas, increasing the pump line power of the pumping, sodium-bearing plasma, and improving the uniformity and stability of the neon plasma.

1. Introduction

For more than a decade, line coincident (resonant) photopumping^{1,2} has been considered a promising approach for realizing x-ray lasers in a plasma medium. All x-ray lasers to date, however, have achieved population inversions either by electron collisional excitation or recombination. Moreover, the shortest lasing wavelength yet obtained³ using resonant photopumping is 2163 Å, well outside the x-ray region. Perhaps the most attractive photopumping scheme which could push the lasing wavelength an order-of-magnitude shorter is the use of the Na X $1s^2-1s2p$ 1P_1 line at 11.0027 Å to pump the Ne IX $1s^2-1s4p$ 1P_1 line at 11.0003 Å. At the Naval Research Laboratory (NRL), we have pursued this promising¹ approach in a coordinated experimental and theoretical program, and have made considerable progress toward the goal of an efficient, photopumped x-ray laser. In Section 2, the fundamental theory of lasing in this scheme, the constraints imposed by atomic physics on the plasma properties, and the diagnosis of the pumping (sodium-bearing) and fluorescing or lasing (neon) plasmas are discussed. Section 3 deals with the experiments which have been carried out using NRL's Gamble II generator to produce both the pumping and pumped plasmas in order to demonstrate fluorescence. Finally, in Section 4 our principal conclusions and the outlook for obtaining lasing using this method are summarized.

2. Theory of the Sodium-Neon Lasing System

The essence of this approach to x-ray lasing is depicted in Figure 1. The very strong $1s^2-1s2p$ 1P_1 line of heliumlike Na X lies at a wavelength which differs by 2 parts in 10^5 from that of the $1s^2-1s4p$ 1P_1 line in heliumlike Ne IX. The existence of this line coincidence and its significance for x-ray lasing were first pointed out by Vinogradov, et al¹ in 1975. This wavelength difference corresponds to only one Doppler width at typical sodium plasma temperatures (200 - 500 eV) required to optimize radiation from the heliumlike stage. Thus there is no question as to the adequacy of the wavelength match. The Ne IX wavelength of 11.0003 Å was calculated as described in Refs. 9 and 10. The Na X wavelength of 11.0027 Å was calculated by Ermolaev and Jones.¹¹ According to Martin and Zalubas,¹² the accuracy of such calculations for a two-electron system in this atomic number range is at least 1 part in 10^5 (i.e., much smaller than a thermal line Doppler width). Therefore, sodium line radiation of sufficient power streaming into a properly prepared neon plasma

would be expected to overpopulate the Ne IX $n=4$ singlet levels, leading to lasing in the 4-3 and 4-2 transitions, and possibly also the 3-2 lines. The lasing wavelengths would be 230 Å, 58 Å, and 82 Å, for the 4-3, 4-2, and 3-2 transitions, respectively.

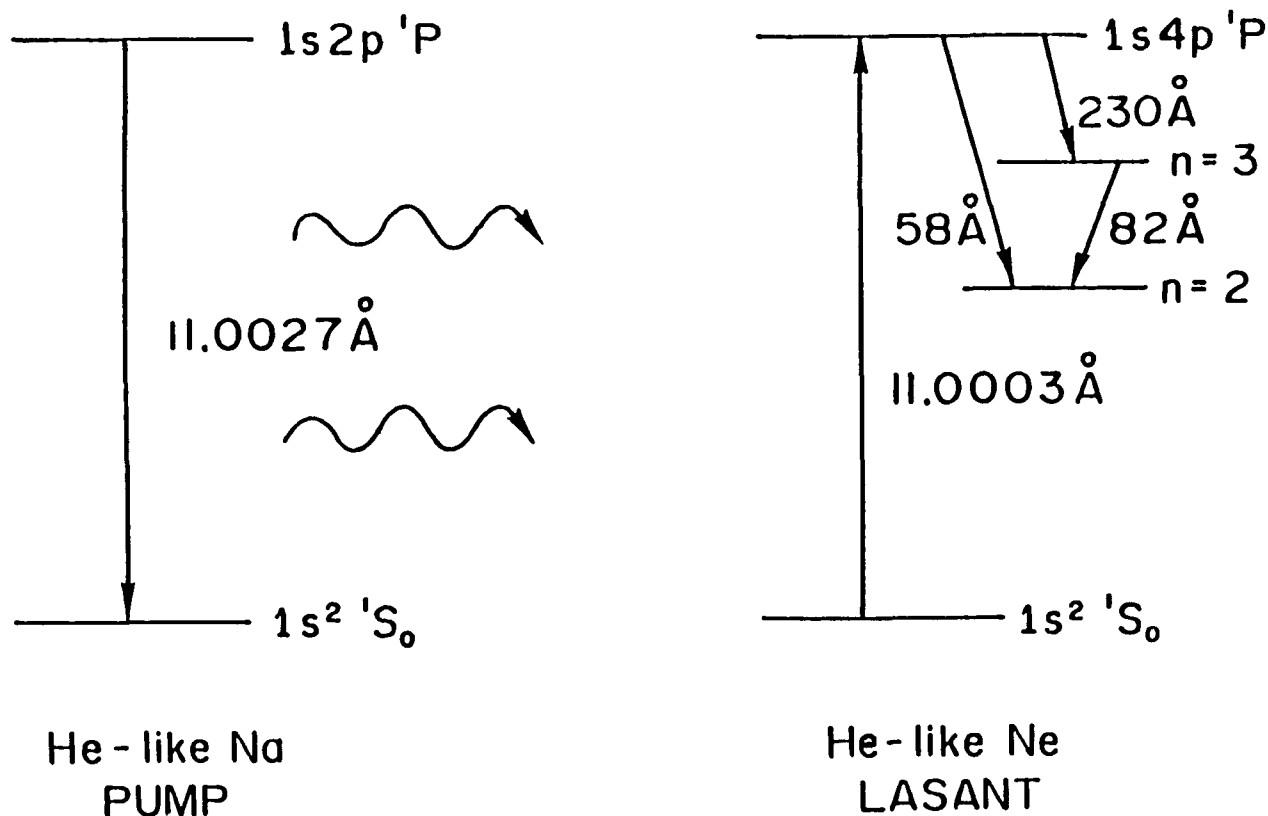


Figure 1. Simplified energy level diagram for sodium-neon resonant photopumping.

In the approach to fluorescence and ultimately lasing, we have followed a step-by-step approach. First, develop and characterize an adequate sodium-bearing plasma pump source. Then, develop and characterize a neon lasant plasma of proper conditions. Finally, deploy the neon plasma close enough to the sodium plasma to facilitate resonant pumping - resulting in fluorescence or possibly lasing. We now consider the desired characteristics of such a system from a theoretical viewpoint. Section 3 describes the experiments and the results obtained to date.

2.1 Desired properties of sodium pump source.

Detailed analysis of what is required for the heliumlike sodium line pump source has been presented in Refs. 4 and 6. In brief, the gain achievable in the neon lasant plasma is nearly linear in the pump line strength. Therefore, the greater the power radiated in the 11.0027 Å $1s^2-1s2p\ ^1P_1$ line of Na X, the better, with one caveat. If the sodium plasma becomes so optically thick due to size, density, or combination of both that the continuum power becomes competitive with that of the resonance line, over the same frequency interval, all of the Ne IX levels will be optically pumped, extinguishing the gain. In practice this condition has not occurred in any laboratory sodium-bearing plasma, but it must be kept in mind as higher power plasma configurations are designed.

To obtain adequate pump power from a sodium-bearing plasma the density should be high and the temperature should be in the upper end of the proper range for a substantial fraction of the ions to be in the heliumlike stage. These factors promote substantial collisional population of the upper radiating level without overionization into the hydrogenic stage. In practice, an appropriate temperature range is 200-500 eV. Generally, the highest density possible is desirable with the proviso, explained above, that the continuum radiation remain well below that of the lines. Densities at least an order of magnitude higher than those currently achieved (Table I) would be even more effective in generating pump power.

A sodium-fluoride capillary discharge plasma source has been developed and used on the Gamble-II generator at NRL to produce a 4-cm long sodium fluoride z-pinch implosion. This source is discussed in Section 3. Spatially resolved sodium K shell x-ray spectra have been measured and used in conjunction with a detailed atomic model of sodium to determine the properties of this plasma, which contain as many fluorine ions as sodium ions. Properties of this plasma, based on the analysis of Ref. 13, are summarized in Table I below.

Table I. Properties of Sodium Fluoride Z Pinch Plasmas

Shot	Diam.(cm)	Pulsewidth(ns)	Pump Line Yield(J)	$N_e(\text{cm}^{-3})$	$T_e(\text{eV})$
A	0.22	20	610	3.6×10^{20}	240
B	0.28	14	380	8.2×10^{19}	490
C	0.32	17	350	6.7×10^{19}	470

The quantities in this Table have been spatially averaged along the z-pinch axis. Ref. 13 should be consulted for the detailed spatially-resolved analysis. The pulsewidth given in Table I is the full-width-at-half-maximum of sodium K shell radiation. Note that Shot A was most effective in producing pump line radiation, converting 6% of the 10 kJ of electrical energy coupled into the plasma into 610 J in the pump line. If a pure sodium source were used, this efficiency is likely to increase to at least 10%, as half the energy coupled to the sodium fluoride plasma is wasted in stripping and exciting fluorine ions. Inspection of Table I reveals that for these z pinch plasmas, moderate temperature and high density is most effective for x-ray production, as opposed to high temperature which in this case is associated with considerably lower density. This behavior was also found by Gersten and co-workers¹⁴ for aluminum wire z pinch plasmas.

2.2 Desired properties of the neon lasant plasma.

We now consider the neon plasma properties required for fluorescence and/or gain. The lower lasing levels of this system are the $n = 2$ and $n = 3$ singlet levels of heliumlike neon. It is clearly desirable to minimize the population of these levels. Therefore, the neon plasma should remain at the lowest possible temperature that supports a substantial heliumlike ground state population. Such a temperature range has been found to be 50-100 eV by detailed numerical calculations.⁴ At these relatively low temperatures the collisional excitation rates of the lower lasing levels are nearly negligible and the population dynamics will be controlled completely by the radiative pumping of the $1s4p\ ^1P_1$ level and the resulting cascade. The optimum densities for the neon lasant plasma are controlled by the usual tradeoffs. At high density, collisional mixing of the lasing levels spoils the gain, whereas, if the lasing plasma density becomes too low, there are simply not enough lasing ions to support a significant gain. For Ne IX, the high-density cut off occurs near $N_e = 2 \times 10^{20} \text{ cm}^{-3}$ for the 4-3 transitions at 230 Å but substantial gain may be possible, depending on the pump strength, at considerably lower electron densities ranging down to $4 \times 10^{18} \text{ cm}^{-3}$.

With respect to the neon plasma size, the limiting factor is the optical depth of the 1-2 and 1-3 resonance lines which through photon trapping, can enhance the populations of the $n = 2$ and $n = 3$ singlet levels, thus quenching the gain. Numerical calculations have shown that optical depths up to about ten in the $1s^2-1s2p\ ^1P_1$ line of heliumlike neon can be tolerated.⁶ This applies to a stationary plasma. Differential mass motions would relax this limit as some of the photons would be Doppler-shifted out of the highly absorbing line core. At an ion density of 10^{18} cm^{-3} with 50% heliumlike neon, the optical depth limit corresponds to a diameter of 0.7 mm, for the pessimistic case of a stationary plasma.

2.3 Theoretical fluorescent spectra and achievable gain.

If the pump line strength is expressed in terms of equivalent blackbody brightness

temperature T_p , the gain in the 4f-3d singlet transition (230 Å) is given approximately by

$$k(\text{cm}^{-1}) = 10^4 \exp(-1127/T_p(\text{eV}))$$

at the favorable electron density of 10^{19} cm^{-3} . We have assumed one-sided irradiation of the neon in the above expression. Our best Gamble-II sodium implosions with a yield of 600 J in the pump line cannot be directly translated to monochromatic intensity because high resolution line profile measurements have not been made. However, for the somewhat conservative assumption that the sodium line is ten times wider than the neon pumped line (due to greater Doppler and opacity broadening) a gain of 0.1 cm^{-1} is determined for a separation of 5 cm. This gain is inversely proportional to the distance between the plasmas and directly proportional to the pump line yield. As a first step toward establishing the presence of photopumping, calculations have been performed of the neon K-shell spectra expected to be emitted from both pumped and non-pumped neon plasmas. The non-pumped neon spectra are characteristically thermal, and the intensities of the heliumlike resonance lines decrease monotonically with higher series lines. For neon plasmas pumped with the Gamble-II source at a distance of 5 cm, the calculations predict that the $1s^2 - 1s4p$ P_1 line, of Ne IX should be anomalously bright for all temperatures from 50 to 150 eV. At the higher end of this temperature range the $1s^2 - 1s2p$ P_1 line is brighter than the pumped 1-4 line, but the pumped line is stronger than the adjacent 1-3 line. If the neon plasma temperature is less than 100 eV, the 1-4 line intensity exceeds even that of the 1-2 line. As will become evident in Section 3, types of fluorescent spectra corresponding to both the high and low ends of this temperature range have been produced on Gamble-II, providing direct evidence of x-ray photopumping.

3. Fluorescence Experiments

The experimental setup used for the fluorescence experiments is shown in Figure 2. The Gamble II generator is located to the left of the figure and is charged negative with respect to ground. An externally driven capillary discharge source injects sodium fluoride plasma across the 4-cm diode gap. A confining nozzle (1 to 2-cm dia) restricts radial expansion of the plasma from the capillary source. Up to 1.2-MA of current from Gamble II is driven through this low impedance load to implode the plasma. The capillary discharge source and properties of sodium fluoride plasmas imploded on Gamble II have been described elsewhere.^{15,16} Such implosions have produced total sodium K-shell x-ray powers in excess of 50 GW and sodium He- α pump line powers of up to 25 GW. Current from the Gamble II generator flows from the wire mesh cathode through the sodium fluoride plasma and back to ground through an array of current return rods equally spaced azimuthally around the axis. For this experiment, one of these rods is replaced with a neon plasma column as shown in Figure 2. Only a fraction of the total current flows through the neon. It is estimated that about 200 kA of current is required to heat the neon to 50-100 eV temperature. The neon column is produced by puffing gas through a fast opening valve and a 6-mm diameter copper tube aimed as shown. The neon mass is adjusted by varying the plenum pressure upstream of the valve. No effort has been made to optimize the gas flow (e.g., by using a supersonic nozzle instead of an open tube), and as a result the neon implosions are far from ideal.¹⁷ Currents through the sodium fluoride and neon plasmas are measured with the Rogowski current monitors shown in Figure 2.

X-ray radiation from both plasmas was measured in the radial direction. The sodium fluoride plasma was viewed through gaps between the current return rods. Diagnostics included time-resolved x-ray diodes (sodium K-shell and neon L-shell), time-integrated pinhole cameras (sodium K-shell and neon L-shell) and a KAP curved crystal spectrograph. The spectrograph was aligned to the neon plasma in order to record neon K-shell emission. The sodium K-shell emission, which reached the crystal from a different angle, was reflected in second order and collected at a different location on the film, well separated from the neon spectrum. The primary purpose of the spectrographic measurements was to detect fluorescence through anomalously strong He- γ (11 Å) line emission from the neon plasma.

Current and x-ray diode traces for a shot where the sodium fluoride and neon plasmas were imploded are shown in Figure 3. A peak current of 1 MA flows through the sodium fluoride plasma while only 150 kA flows through the neon plasma. The sodium implosion occurs 110 ns after the start of the current with the emission of an intense burst of K-shell x-rays. The neon implosion, as evidenced by the peak in the L-shell radiation, precedes the sodium fluoride implosion by 25 ns.

The neon K-shell x-ray spectrum for this shot is compared in Figure 4 with the spectrum from a shot where no sodium plasma was present. For the top spectrum in Figure 4, the sodium plasma was replaced with a 1-cm dia metallic rod. The presence of both NeIX and NeX line emissions in these time-integrated spectra indicates that the neon was significantly hotter than the desired 50-100 eV temperature at some time during the implosion. The spectrum without the sodium was produced with 240 kA through the neon. This spectrum is more intense and represents a significantly hotter and/or denser plasma than the spectrum

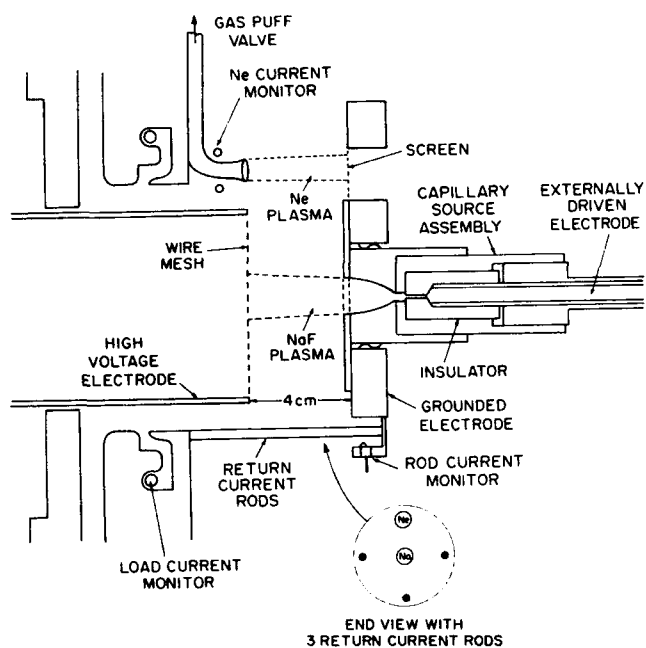


Figure 2. Experimental arrangement on Gamble II for sodium/neon fluorescence experiments.

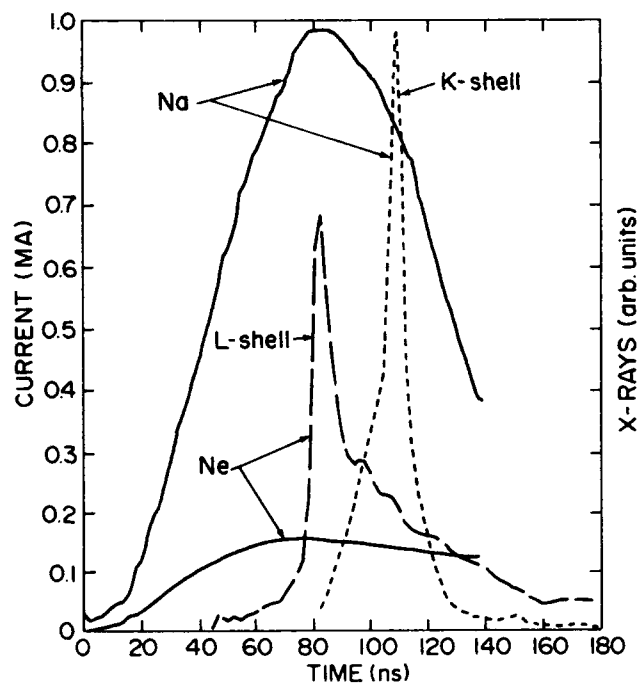


Figure 3. Current and x-ray traces for sodium fluoride and neon implosions. The K-shell trace is for sodium x-rays, and the L-shell trace is for neon x-rays.

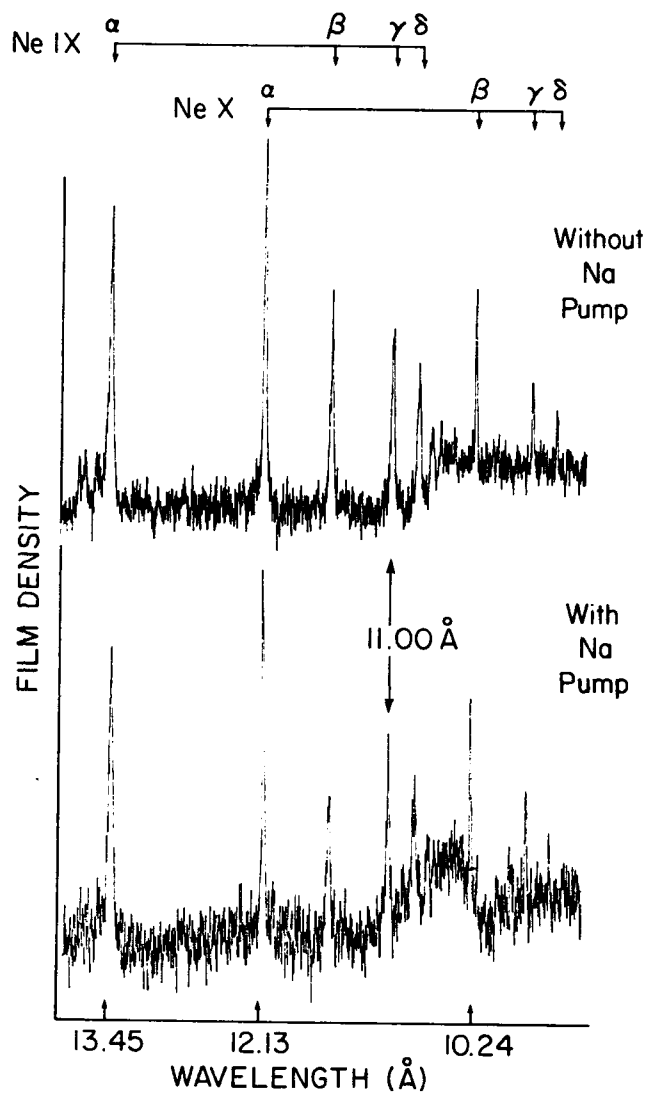


Figure 4. X-ray spectra recorded on shots with the sodium pump (bottom) and without the sodium pump (top). Spectral lines from NeIX and NeX are identified. The bottom spectrum is for the shot presented in Figure 3.

with the sodium pump. The top spectrum is representative of a thermal neon plasma,^{13,18} while the reversal in the ratio of the NeIX He- γ and He- β line strengths in the bottom spectrum is striking in comparison. We have no reasonable explanation for the He- γ /He- β line ratio exceeding unity in this spectrum except by resonantly photopumped fluorescence. There is no spectral evidence of sodium or fluorine line radiation from possible migration of sodium fluoride plasma into the neon implosion. Two points should be emphasized. First, these spectra are densitometer traces, not x-ray intensities, so relative amplitudes of lines will change upon further analysis without however changing the basic conclusion that fluorescence is observed. Second, the spectrum is time-integrated, thus the strong NeX L- α and NeIX He- α lines were probably emitted during the neon implosion (85 ns in Figure 3) rather than at 110 ns when pumping occurred. Since the spectra indicate that the neon is significantly hotter than the desired 50-100 eV at implosion, this delay in the sodium fluoride implosion may allow the neon plasma to cool before the pump radiation is emitted. We can speculate that a time-resolved spectral measurement would show a stronger fluorescing He- γ line relative to the other NeIX lines in the spectrum at the time of pumping.

On another shot, the crystal spectrograph was configured to measure K-shell x-ray emission in first order from both the sodium fluoride and the neon implosions. The relative timing of the implosions was similar to that shown in Fig. 3 so that the condition of the neon plasma could well be appropriate for fluorescence at the time of the sodium fluoride implosion. The spectral film recording for this shot is presented in Fig. 5. The spectrum is dominated by intense NaX and NaXI line radiation. Several of these sodium K-lines are saturated. Because the sodium and neon plasmas are separated in space, their K-shell spectra

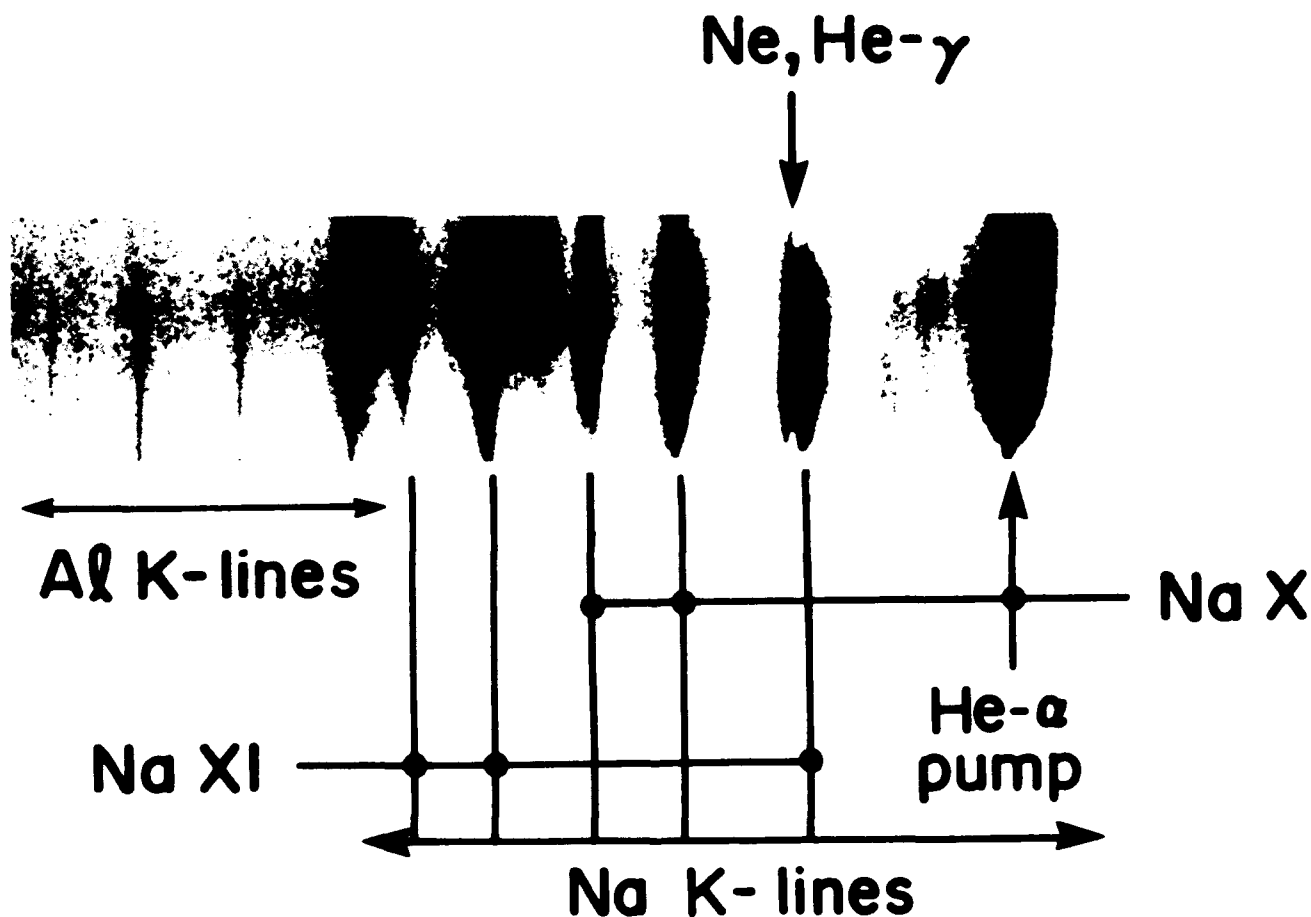


Figure 5. Film recording of the K-shell x-ray spectrum for a shot where both sodium fluoride and neon are imploded. The neon He- γ line is just to the left of the Na XI Ly- α line. The aluminum lines arise from the use of an aluminum nozzle.

are not coincident, even for the same wavelength. We can calculate, knowing the separation of the two sources, exactly where each neon line should appear relative to the sodium lines. The narrow line just to the left of the NaXI L- α line appears at exactly the location where the neon He- γ fluorescence line is expected. No emission was detected corresponding to the NeIX He- α and He- β lines. The presence of the He- γ line and the absence of the He- α and He- β lines are consistent with resonance photopumping of a relatively cold (~ 50 eV) and tenuous ($N_e < 10^{18}$ cm $^{-3}$) neon plasma. At higher electron densities, collisional coupling in the cascade process would lead to detectable He- α and He- β emission.

4. Conclusions and Outlook

In summary, we have taken theoretical predictions of resonant photopumping of neon by the sodium He- α line and have devised an experimental system to test these predictions. The theory indicates that a reversal of the normal ratio of the He- γ and He- β lines due to coincident photopumping should be detectable on Gamble II. The experimental geometry permits us to drive different currents through each of the plasmas on the same Gamble-II shot and thereby to achieve conditions appropriate for fluorescence. The preliminary spectroscopic results provide evidence for fluorescence on some shots.

For the nominal separation of 5 cm between the sodium and neon plasmas, a gain of about 0.1 cm $^{-1}$ in the 4f - 3d singlet lasing transition is theoretically obtainable with the optimum experimental pump power. This gain is proportional to the pump power and inversely proportional to the separation. Several improvements are planned to confirm the fluorescence observations and possibly to provide conditions necessary for lasing on Gamble II. We plan to improve the sodium pump by replacing the sodium fluoride capillary discharge with a pure annular sodium plasma source⁹ which is under development. Such a source will not only nearly double the pump line radiation by eliminating the fluorine, but because of its thin annular shape and uniform density, will produce better behaved, axially simultaneous implosions which should further increase the pump line power. Improvements in the neon plasma include replacing the open tube with a supersonic mini-nozzle and driving the neon plasma independently of the Gamble II generator with an external capacitor bank. With better collimated sodium and neon plasma sources, the distance between the two plasmas may be decreased by at least a factor-of-two.

5. Acknowledgments

We thank the Gamble II technician crew, J. W. Snider, F. Hollis, J. Negri, G. Langley, and T. Robinson for supporting the experiment. Work Supported by SDIO/IST.

6. References

1. A.V. Vinogradov, I.I. Sobelman, and E.A. Yukov, Sov. J. Quantum Electron 5, 59 (1975).
2. B.A. Norton and N. J. Peacock, J. Phys. B. 8, 980 (1975).
3. P.L. Hagelstein, "Physics of short wavelength laser design," unpublished Ph.D. thesis, University of California Report No. UCRL-53100 (1981).
4. J.P. Apruzese, J. Davis, and K.G. Whitney, J. Appl. Phys. 53, 4020 (1982).
5. J. Trebes and M. Krishnan, Phys. Rev. Lett. 50, 679 (1983).
6. J. P. Apruzese and J. Davis, Phys. Rev. A 31, 2976 (1985).
7. R.C. Elton, T.N. Lee, and W.A. Molander, Phys. Rev. A 33, 2817 (1986).
8. N. Qi and M. Krishnan, Phys. Rev. Lett. 59, 2051 (1987).
9. C.L. Pekeris, Phys. Rev. 112, 1649 (1958).
10. Y. Accad, C.L. Pekeris, and B. Schiff, Phys. Rev. A 4, 516 (1971).
11. A.M. Ermolaev and M. Jones, J. Phys. B 7, 199 (1974).
12. W.C. Martin and R. Zalubas, J. Phys. Chem. Ref. Data 10, 153 (1981).
13. J.P. Apruzese, G. Mehlman, J. Davis, J.E. Rogerson, V.E. Scherrer, S.J. Stephanakis, P.F. Ottinger, and F.C. Young, Phys. Rev. A 35, 4896 (1987).
14. M. Gersten, W. Clark, J.E. Rauch, G.M. Wilkinson, J. Katzenstein, R.D. Richardson, J. Davis, D. Duston, J.P. Apruzese, and R. Clark, Phys. Rev. A 33, 477 (1986).
15. F.C. Young, R.J. Comisso, G. Cooperstein, D.D. Hinshelwood, R.A. Meger, D. Mosher, V.E. Scherrer, S.J. Stephanakis, B.V. Weber, and B.L. Welch, in Record 1986 IEEE International Conference on Plasma Science, Cat. No. 86CH2317-6, p. 87.
16. F.C. Young, S.J. Stephanakis, V.E. Scherrer, B.L. Welch, G. Mehlman, P.G. Burkhalter, and J.P. Apruzese, Appl. Phys. Lett. 50, 1053 (1987).
17. D. Mosher, B.V. Weber and S.J. Stephanakis, Bull. Am. Phys. Soc. 32, 1339 (1987).
18. G. Mehlman, P.G. Burkhalter, S.J. Stephanakis, F.C. Young, and D.J. Nagel, J. Appl. Phys. 60, 3427 (1986).
19. M. Gazaix, H.J. Doucet, B. Etlicher, J.P. Furtlehner, H. Lamain, and C. Rouille, J. Appl. Phys. 56, 3209 (1984).

X-Ray Lasing In An Imploding Krypton Z-Pinch Plasma

J. Davis, R. Clark, J. Apruzese, and P. Kepple

Naval Research Laboratory
Plasma Radiation Branch
Washington, D.C. 20375-5000

ABSTRACT

A scheme employing neonlike krypton ions is under intensive theoretical and experimental investigation to determine the feasibility of developing a pulsed-power driven laboratory x-ray laser. The scheme depends on discharging 100's of kilojoules of electrical energy through co-axial cylindrical krypton gas puffs generating a dense, hot, uniform, homogeneous, and highly ionized krypton plasma. The outer plasma is accelerated radially inwards and achieves speeds approaching $4-5 \times 10^7$ cm/sec. When it impinges and stagnates on the inner plasma, an inwardly propagating shock wave is produced, and the inner plasma reverberates and bounces outward. Near the interface between the two interacting plasmas, and along the axis, conditions appear to be conducive to the establishment of a population inversion with the subsequent emission of coherent soft x-rays with measurable gain. The theoretical analysis and numerical simulations are based on a fully coupled self-consistent one-dimensional non-LTE radiation hydrodynamics model including the effects of opacity and radiation transport. The multi-level ionization dynamics is evaluated in the collisional radiative equilibrium (CRE) approximation for the manifold of both ground and excited states distributed throughout the various stages of ionization. In addition, particular emphasis is placed on the atomic structure of the neonlike ionization stage which in our model consists of 48 excited levels in j-j coupling. The evolution of the level populations as functions of the various atomic processes provides information on the conditions necessary to establish population inversions and the emission of coherent radiation in the lasing transitions. At the densities of interest the spectral line profiles are represented by Voigt functions.

INTRODUCTION

Since the successful laboratory demonstration of soft x-ray lasing using a laser produced plasma^{1,2}, either as the gain medium or as a broadband x-ray source to photopump specially designed targets generating conditions conducive to lasing, a number of alternative drivers have been proposed. Chief among the alternative technologies is the pulsed-power capacitively discharged z-pinch plasma. In the past, pulsed power driven z-pinch plasmas were developed as intense high brightness x-ray radiation sources for application in materials testing, spectroscopy studies of high-z ions, and x-ray lithography.

Unfortunately, the history of these plasmas has not made them prime candidates for x-ray laser gain mediums because of their unstable behavior. A major reason for this predicament is that pulsed power driven material loads have not enjoyed the benefit of long years of detailed studies in target design; a hallmark of the laser fusion program. Recently, however, advances in the technology of load materials and configurations combined with an improved theoretical understanding of the load dynamics has led to a revival of the z-pinch plasma as a potential source of x-ray lasers.

Experiments at both the Naval Research Laboratory (NRL) and Physics International Company (PI) have indicated the possibilities for this new emerging technology. At NRL the sodium/neon system, which is the prototype of the line coincidence photopumping schemes, is under intensive investigation. Preliminary results appear to indicate that resonance fluorescence³ has been achieved in the pumped transitions. The scheme involves imploding and heating a sodium plasma on the GAMBLE II generator to temperatures commensurate with producing the sodium He-like resonance pump line to photopump the He-like $1s^2-1s4p$ ¹P transition in a relatively cool neon plasma in a side by side configuration. These experiments are very encouraging and methods and techniques will continue to be investigated in order to increase the power in the pumping line sufficiently to achieve measurable gain in the lasing transitions. Another series of pulsed power z-pinch experiments at PI involves stagnating an outer gas puff plasma onto a cylindrically symmetric coaxial core plasma located on the axis. Two different configurations have been investigated; the first involves concentric krypton gas puffs⁴ and the second involves a neon puff gas plasma stagnating onto an aluminum coated parylene post on the axis.⁵ The krypton design explores the possibility of creating an inversion and gain in the lasing transitions of neonlike krypton. The experimental results are somewhat uncertain because of the existence of line admixtures at the lasing wavelengths. On the other hand, the theory supports the existence of gain for a given set of implosion conditions discussed in the text. Preliminary experimental results from the second configuration strongly suggests gain in the lasing transitions in lithiumlike aluminum as the aluminum plasma expands, cools, and recombines after collision with the inward moving neon gas puff plasma. All these new experimental results indicate that with proper design, z-pinch plasmas have a

promising future as a potential source for laboratory x-ray lasers.

In support of the experimental program there has been significant advances both in the theoretical and computational description of the dynamics characterizing a variety of load configurations and geometries. With applications ranging from fusion plasmas to x-ray source development, the theoretical models vary in their degree of complexity ranging from the simple Bennett pinch equilibrium models to the sophisticated multidimensional MHD models. The major emphasis in the past, and to some extent today, has focused on the hydrodynamic behavior of the implosion/explosion phenomenology. For low- z plasmas, or more specifically hydrogen plasmas, radiation cooling is described by bremsstrahlung, and the MHD models do reasonably well in describing the plasmas evolution. However, for partially ionized higher- z plasmas radiation loss from recombination and line radiation far exceeds any bremsstrahlung and must be incorporated into the models because it represents a major energy loss and will affect the dynamics in ways that are obvious and in ways that are quite subtle. Although this problem is well recognized by now, it is still inadequately dealt with; recourse is oftentimes made to models involving blackbody radiators or LTE average atom models. Radiative loss terms represented by blackbody emitters grossly overestimate the radiation cooling rate and provide an erroneous description of the dynamics. Similarly, the average atom model resorts to Local Thermodynamic Equilibrium (LTE) arguments constraining the plasma to be in LTE and averages over the details of atomic structure vitiating any meaningful comparison between theory and experiment. Due to the efforts of the NRL group, major improvements have been made in the modeling of radiating z -pinch plasmas. The capability now exists to model self-consistently the full non-LTE radiation MHD behavior of z -pinch plasmas, including opacity effects on the heating and cooling rates as well as the influence of radiation on the instability growth rates. In an x-ray laser environment the interplay and feedback between the atomic processes, radiation, and hydrodynamics is an extremely important and delicate interaction that ultimately determines whether lasing becomes a reality.

To model the experiments at PI and in the spirit of our earlier work⁶ we investigate the behavior of a krypton gas puff plasma impinging and stagnating onto another krypton gas puff plasma located on the axis. It has been found experimentally that upon collapse the inner plasma has a strong stabilizing influence on the outer plasma and appears to retard the development of plasma instabilities, creating a fairly uniform plasma in the interaction region where lasing may thus be expected to occur. The strategy is to choose initial conditions such that in the interaction region between plasmas, the temperature and density support the existence of sufficient quantities of neonlike krypton for times long enough for the various atomic

processes to create a population inversion in the upper 3p and 3d levels, which will subsequently radiatively decay to the 3s and 3p levels, respectively, in the lasing lines. The model used to describe the implosion dynamics is a 1-D radiation hydrodynamics model including a self-consistent treatment of: (a) hydrodynamics and thermal conduction, (b) atomic dynamics, and (c) radiation emission and transport.

The basic hydrodynamic variables of mass, momentum, and total energy are transported in one dimension using a numerical scheme with a sliding-zope version of flux corrected transport. A special gridding algorithm is used that moves zones in a Lagrangian fashion and adjusts the mesh in order to resolve gradients in the flow. A single temperature assumption is made in the core plasma, where the equilibration time is of the order of picoseconds, and is adequate in the stagnation region, where the equilibration time can be of the order of nanoseconds; the time scale for significant changes in temperature is about an order of magnitude longer. The local rate of change of energy resulting from radiation transport, ϵ_{rad} , will be discussed below.

Most gas-puff implosion experiments employ an azimuthal magnetic field driver, whereas the calculations we will describe do not consider the effects of magnetic fields, but instead assign an initial radial velocity to the puff-gas plasma. This allows us to study the physics of imploding plasmas in an idealized framework, without the complications of an external driver and coupled circuit. We have codes that include the magnetic field and intend to consider more general configurations in future work. In a driven implosion with an optimized load, we expect a nearly uniform velocity to be ultimately achieved, but density and temperature gradients will be produced in the puff, particularly near the outer edge, where Joule heating produces a layer of hot plasma.

The atomic level populations in the plasma are determined by a set of rate equations. For sufficiently dense plasmas, the effective population and depopulation rates are generally fast compared with the hydrodynamic response. Under these circumstances, an equilibrium assumption can be justified, which involves dropping the explicit time dependence. The plasma is then said to be in collisional-radiative equilibrium (CRE), whereby the plasma ionization state responds instantaneously to changes in hydrodynamic quantities.

The atomic model for krypton consists of about 100 levels and 300 emission lines. This includes all the ground states and selected excited states distributed throughout the M-, L-, and K-shells. In addition, a detailed neonlike model in j - j coupling containing an additional 48 excited levels is incorporated into the overall atomic model in order to provide a better picture of the dynamics of the neonlike levels and the lasing transitions. The rate coefficients that are used to calculate level

populations are obtained using various atomic calculational methods. The processes included in this simulation and the methods used in generating the corresponding rate coefficients are summarized elsewhere. An abbreviated Grotian diagram illustrating the lasing lines along with their wavelengths and spontaneous decay rates is shown in Figure 1.

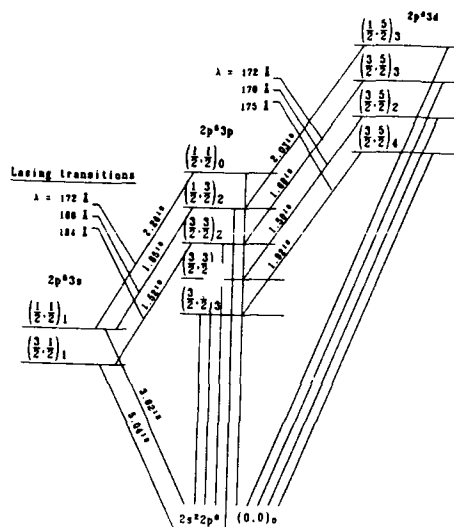


Figure 1. Energy Level Diagram for neonlike Krypton.

Inner-shell opacities are included in the model, since these processes are very important in the cool, dense plasma regions. Inner-shell photoionization cross sections for the neutral element are calculated as described in Duston et al. and the positions of the ionization-dependent absorption edges in the low density limit are taken from the Hartree-Fock calculations of Clementi and Roetti.

Radiation emission from and absorption by a plasma are dependent on the local atomic level population densities. Except for optically thin plasmas, the level populations depend on the radiation field, since optical pumping via photoionization and photoexcitation can produce significant population redistribution. Thus, the ionization and radiation transport processes are strongly coupled and must be solved self-consistently. In this model, an iterative procedure is used, where level populations are calculated using the radiation field from the previous iteration, then using these populations to calculate a new radiation field and recalculating populations until convergence is reached.

A probabilistic radiation transport scheme is employed, which forms local angle and frequency averaged escape probabilities for each emission line and for each bound-free process. Free-free radiation is treated with a multifrequency transport formalism. The escape probabilities calculated for the

transport of bound-bound radiation take into account Doppler and Voigt line profiles. The method can treat comprehensive atomic models and provides good overall energetics, but cannot calculate accurately certain spectral details and lines with very high optical depths. Multifrequency transport of lines and continuum is adequate for the above but requires lengthy computer simulations.

Results

The numerical simulations were performed for an outer hollow cylindrical annular krypton puff gas with a gaussian mass density distribution of $140 \mu\text{g}/\text{cm}^3$ with its centroid located 15mm from the origin and an inner coaxial cylindrical krypton puff gas with a gaussian mass distribution of $20 \mu\text{g}/\text{cm}^3$ with its centroid located 1mm from the origin. The configuration is schematically illustrated in Figure 2. The initial temperature and particle density of the puff gas and core plasma are 2.5 eV and $2 \times 10^{19} \text{ cm}^{-3}$ and 0.5 eV and $2 \times 10^{21} \text{ cm}^{-3}$, respectively. A tenuous background plasma was placed between the puff and core plasmas with a mass density of $5 \times 10^{-7} \text{ gm}/\text{cm}^3$. The results of the simulation are insensitive to this value, which was chosen for numerical convenience. Finally, the outer gas puff plasma is given an initial kinetic energy corresponding to a radial implosion velocity of $4.5 \times 10^7 \text{ cm}/\text{sec}$.

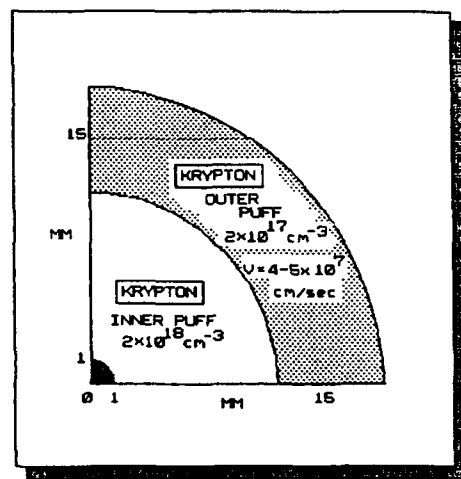


Figure 2. Initial conditions for Gas Puffs.

The outer plasma continues to move radially inward until its leading edge makes contact with the boundary of the core plasma where it stagnates onto and begins to cause compression of the core. During this phase of the implosion, the kinetic energy of run-in is redistributed into thermal, ionization, radiation and kinetic energy associated with the generation and propagation of weak shocks and rarefaction waves as well as the outward motion of material after the "bounce." This oscillatory motion continues until it is damped by viscous forces. As energy is converted during the stagnation process

photons are emitted over a broadband spectrum extending from the visible to the soft x-ray regime preheating the core plasma which itself begins to radiate. The interface region between the interacting plasmas and, especially, the compressed core plasma is where we expect conditions conducive to lasing to occur.

The phenomenology of the assembly phase of the implosion dynamics is best characterized by the behavior of the hydrodynamic variables, particularly the temperature, density, and pressure and the cooling rate by radiation. Specifically focusing on the times corresponding to the first assembly phase we present, in the next three figures, the temporal variation of these variables as a function of displacement, extending from the origin out to 0.08 cm. The ordinate is normalized in order to illustrate the behavior of all the variables on a single figure. The scale factor for each variable is given by: density $\times 1 \text{ gm/cm}^3$, temperature $\times 1 \text{ ev}$, pressure $\times 10^{12} \text{ erg/cm}^2$, velocity $\times 10^{11} \text{ cm/sec}$, and $\dot{E}_{\text{rad}} \times 10^{27} \text{ erg/sec cm}^3$. For example, from Figure 3, the graph value of the velocity at 0.08 cm is 4.5×10^{-11} multiplied by the scale factor (10^{11}) yields $4.5 \times 10^0 \text{ cm/sec}$, the initial velocity.

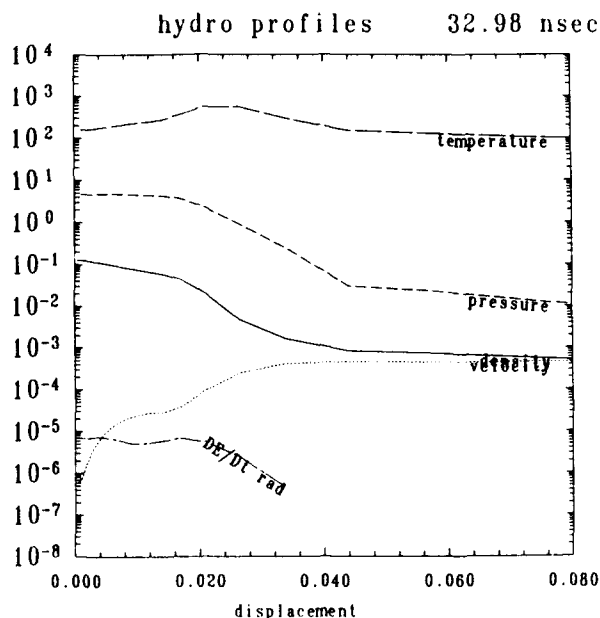


Figure 3. Hydrodynamic Profiles as a function of Displacement at 32.98 nsec.

Based on the sequence of events, the following conclusions can be drawn from the hydrodynamic profiles. Figure 3 presents a snapshot view of the spatial variation of the profiles at about 33 nsec into the simulation. As the inward propagating shock reaches the central axis at about 28 nsec, there is strong heating near the axis. The temperature reaches about 750 ev, but radiation cooling and hydrodynamic effects quickly reduce the temperature on axis. Ion number density monotonically increases at the

origin until about 34 nsec and the temperature decreases. The plasma remains quite warm, however, a short distance from the origin, where the density begins to fall off sharply. By 33 nsec. the temperature at the origin has dropped to about 150 ev; however, at about 0.025 cm the temperature peaks in excess of 700 ev. From the velocity gradients at this time, it is evident that the plasma is compressing in the vicinity of the hot shell. Notice that the velocity is negative (directed toward the origin) everywhere at 33 nsec. Contour plots of density and temperature over space and time will be discussed below. By referring to the contour plot of temperature, it will be seen how the shell of warm Krypton evolves. Also note that because the gradients in temperature and density are in opposite directions the radiation cooling rate is subject to relatively large variations over relatively small gradient scale lengths. Just after 33 nsec, plasma near the origin begins to expand in a complicated fashion: parts of the plasma move outwards while other parts are moving inwards. This behavior produces compressions and rarefactions in the core plasma leading to heating and cooling in localized regions. At 34.22 nsec, it is seen on Figure 4 that plasma a short distance (0.008 cm) from the origin is expanding radially, while plasma is moving radially inwards elsewhere. The contour plot of temperature will clearly exhibit the localized regions of rapid heating and cooling from 33 to 36 nsec.

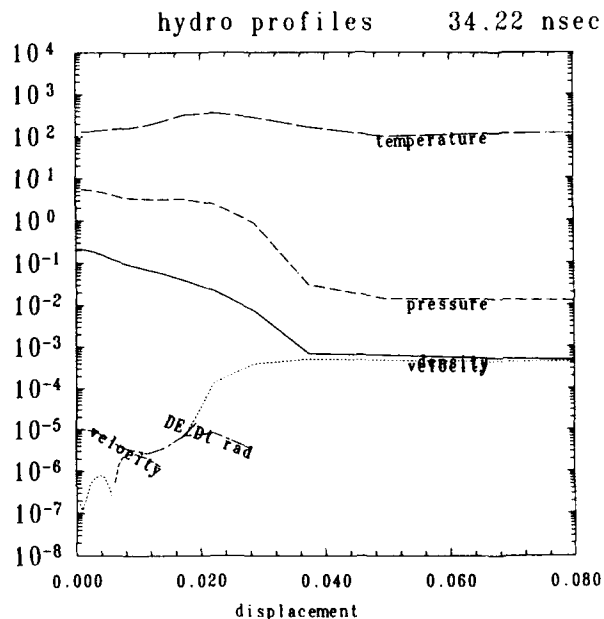


Figure 4. Hydrodynamic Profiles as a function of Displacement at 34.22 nsec.

Relief of the very large pressure gradient which built up at 34.22 nsec results in a virtual stagnation at about 0.035 cm, shown on Figure 5 at 35 nsec. Plasma is now moving radially outward within the region and colliding with imploding plasma. As a

result, a fairly broad shell of hot plasma (1kev) has been produced. Since the ion density is fairly small over much of this region, the radiative cooling rate is correspondingly reduced, and the high temperatures can be maintained.

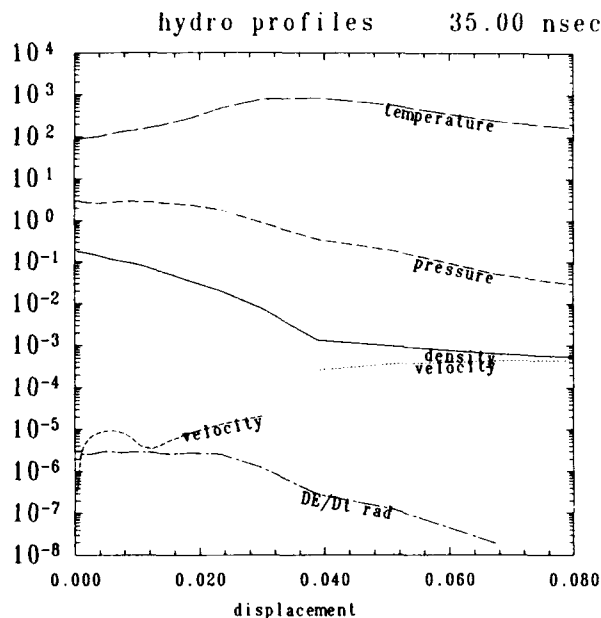


Figure 5. Hydrodynamic Profiles as a function of Displacement at 35 nsec.

A novel way of presenting the results of the numerical simulations is to illustrate by contour plots the behavior of the hydrodynamic variables. The contour plots complement our earlier figures as well as provide a better picture of the course of events. In the following figures time runs along the vertical axis from 27 to 36 nsec and displacement (or radius) runs along the horizontal axis from the origin out to 0.08 cm. The values of the different colors are coded on the Right Hand Side (RHS) of the figures. There are several ways to understand and interpret the results. One of the easiest is to choose a time and then observe how the parameters vary from larger to smaller displacements and simply repeat the process for increasing times. Also, much of what has already been said is repeated here in order to provide commentary with the results. The radial temperature history is shown on Figure 6 over distances mainly confined to the compressed core plasma and the interaction region.

The brighter regions are primarily the result of compressional wave heating or weak shocks. The expanding darker regions later in time extending from the axis outward reflect the effects of radiative cooling while the brighter regions from 34 nsec on indicate heating due to weak shocks moving outwards. The temperature peaks around 1 kev in this region. The ion density is shown on Figure 7 where it is seen that as time increases the density along the axis

increases where the plasma is compressing. These high pressures near the origin slow down the incoming plasma creating velocity gradients at about 33 nsec. Thus, kinetic energy is constantly being thermalized in this region, commencing just after the on-axis assembly. Radiation cooling in this region falls off sharply with radius following the corresponding density falloff. Just after 33 nsec, the plasma near the origin exhibits both inward and outward flowing plasma. This produces compressions and rarefactions leading to heating and cooling in localized regions. At just after 34 nsec, the plasma at about 0.008 cm from the origin is expanding radially while elsewhere the plasma is moving radially inwards. From the contour plot of temperature shown on Figure 6, it can be seen that alternating rapid cooling and heating is produced from 33 to about 36 nsec in localized regions. At about 35 nsec a pronounced stagnation is produced, as warm plasma recoiling radially outwards collides with imploding plasma. This results in the formation of a fairly broad shell of hot plasma (about 1 kev).

The fraction of neonlike krypton ions in the ground state is shown on Figure 8. Since the fractional abundance of neonlike ions is strongly temperature dependent and only weakly density dependent, it is not too surprising to observe that the number of neonlike ions tracks the temperature. The greater abundances occur for temperatures in excess of about 400 ev which is about the temperature commensurate for the appearance of neonlike krypton.

Shown on Figure 8 are a number of localized regions where the fractional abundance of neonlike ions exceed 50 % and a few regions where it is upwards of about 70%, i.e., in those regions of the plasma anywhere from 50 to 70 percent of all the ions are in the neonlike ground state. A very propitious situation, indeed, for our proposed x-ray laser scheme!

Conditions conducive to a population inversion leading to gain in the lasing transitions were achieved for six of the lines considered: the 172, 186 and 184 A 3p to 3s transitions, and the 172, 170 and 175 A 3d to 3p transitions. Reference to Figure 1 shows the details of the respective transitions. Gain contours for the 172 A and the 184 A 3p-3s lines are shown on Figures 9 and 10, respectively. Gains of one or more occur in highly localized regions eventually achieving values in excess of 10/cm for the 172 A line; and 3/cm for the 184 A line. The atomic processes contributing to the gain are predominantly due to recombination and electron impact excitation. The gain for the 172 A line extends over the largest radial region extending from the origin out to about 0.048 cm from 28 to 29 nsec. A more localized region occurs from 34 to 36 nsec. Gain for the 184 A line, which is due predominantly to electron collisional excitation, is confined to a smaller region peaking around 35 nsec. Note, that on the scale on the RHS of the gain profiles some of the values represented are negative numbers

and correspond to the absorption of radiation.

An identical simulation was performed for an initial velocity of 4.0×10^7 cm/sec. The reduced implosion velocity resulted in a lower temperature and a correspondingly smaller fraction of neonlike krypton near the axis. The resulting gain in the 172 Å 3p-3s line is shown in Figure 11; gains in excess of 5/cm are achieved over temporal and spatial scales comparable to those in Figure 9. Gains in the other transitions considered were somewhat smaller than those obtained at an implosion velocity of 4.5×10^7 cm/sec.

The major point to be made is that it is possible to achieve a population inversion and gain in all of the expected lasing lines from our imploding plasma simulations. The final confirmation of whether this approach is feasible is currently unfolding with the analysis of the experimental observations.

ACKNOWLEDGEMENTS

We would like to thank Jonathan Workman for his assistance in making a number of production runs.

This work was supported by the Innovative Science and Technology Office of the Strategic Defense Initiative Organization.

REFERENCES

1. A recent source of advances in x-ray laser research can be found in the Proceeding of an "International Colloquium on X-Ray Lasers," Jour. De Physique, C6 (1986).
2. G. Y. Yin, S. E. Harris, et al., Optics Lett. 12,331 (1987).
3. J. Apruzese, R. Comisso, et al., "Pulsed Power Driven Photopumped X-Ray Laser Research at the Naval Research Laboratory." This conference.
4. M. Krishnan, R. Nash, P. Le Pell, and R. Rodenburg, "Krypton on Krypton Z-Pinch X-Ray Laser Experiment," Physics International Rept. PIT-87-02 (1987).
5. M. Krishnan, R. Nash, and P. Le Pell, "Evidence For Population Inversion And Possible Lasing In Pulsed Power Driven Z-Pinches," Physics International Rept. PITS-3411-01 (1987).
6. J. Davis, R. Clark, and F. Cochran, Phys. Fluids 29, 1971 (1986).
7. D. Duston, R. Clark, J. Davis, and J. Apruzese, Phys. Rev. A. 27, 1441 (1983).
8. E. Clementi and C. Roetti, At. Data Nucl. Data Tables, 14, 177 (1974).

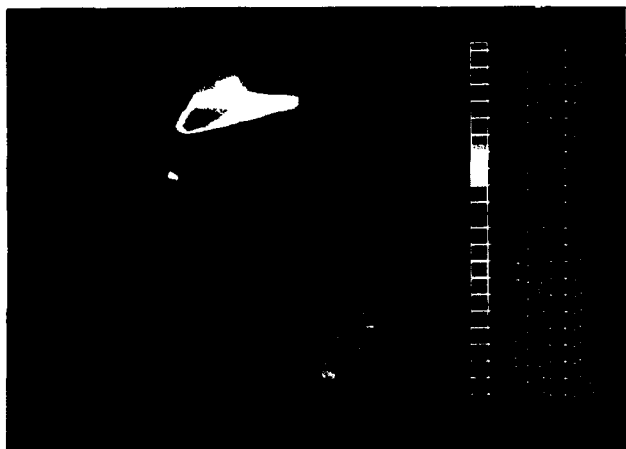


Fig. 6 Temperature contours as a function of displacement and time.



Fig. 9 Gain/cm contours of the 172 Å line as a function of displacement and time.

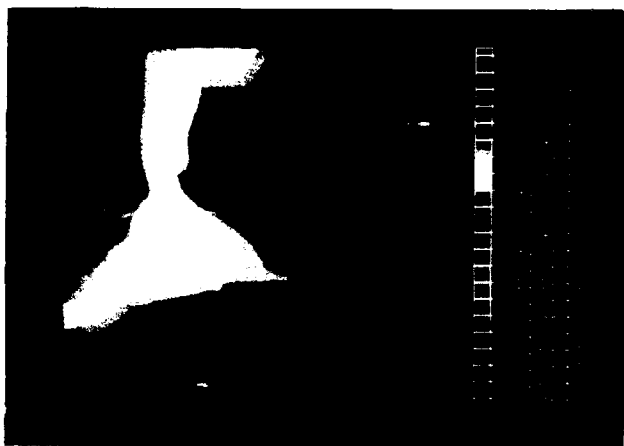


Fig. 7 Ion density contours as a function of displacement and time.



Fig. 10 Gain/cm contours of the 184 Å line as a function of displacement and time.

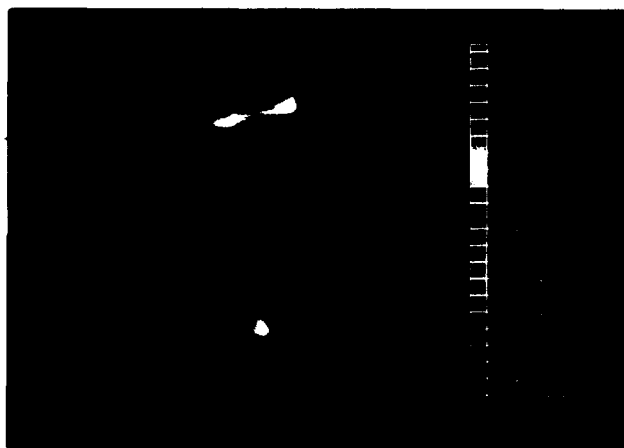


Fig. 8 Neonlike ion fraction contours as a function of displacement and time.



Fig. 11 Gain/cm contours of the 172 Å line as a function of displacement and time. $V_0 = 4 \times 10^7$ cm/sec.

POPULATION INVERSION AND POSSIBLE LASING AT
150.6, 154.6 AND 187.3Å IN PULSED POWER DRIVEN Z-PINCHES*

M. Krishnan, T. Nash, P. D. LePell

Physics International Company
P.O. Box 1538, 2700 Merced Street, San Leandro, California 94577

Abstract:

The DNA/PITHON pulsed power generator was used to produce hot, dense, aluminum plasmas in a Z-pinch configuration. The pinch produced 3-cm- and 5-cm-long Al plasmas with densities $\sim 10^{20} \text{ cm}^{-3}$ and temperatures $\sim 500 \text{ eV}$, with a 25 ns duration. After the implosion, the Al plasma expanded and cooled for the next 50 ns, producing Li-like Al XI ions by recombination from He-like Al XII ions. A time-gated, grazing incidence spectrograph captured three consecutive 25 ns duration spectra from the plasma. These spectra provide evidence for population inversion and possible lasing at 150.6 (4d-3p) and 154.6Å (4f-3d) in Al XI, and also at 187.3Å (4-3) in Ne X. A rough estimate of the gain-length product for these lines is 3-4. From measured K-line yields in neon, using branching ratios and detector response, it was estimated that the total energy output of these laser lines $\approx 60 \text{ mJ/pulse}$. Further confirmation of lasing requires length scaling and simultaneous on-axis/off-axis measurements.

1. Introduction

Research is underway at NRL, Sandia Labs and Physics International to demonstrate pulsed power driven X-ray lasers. Such lasers are inherently more efficient than laser-driven X-ray lasers because focused electrical energy is the most efficient means for pumping an active, X-ray laser medium. Several laboratories have demonstrated X-ray lasers driven by longer wavelength lasers.¹⁻⁵ Pulsed power driven Z-pinches can be used directly as the laser gain media, or alternatively, the copious X-ray emissions from these pinches can be used to photo-pump adjacent media. The research effort at PI has studied neon-like krypton lasers in krypton-on-krypton gas puff Z-pinches, resonant photo-excitation of neon ions by sodium ions from a Z-pinch, and recombination pumped lasers in expanding Z-pinches of neon and aluminum. This paper reports time-resolved measurements of XUV emissions from recombining Ne and Al plasmas. Evidence is presented for anomalous brightness of the 4d-3p and 4f-3d lines of Al XI at 150.6 and 154.6Å, and of the Ne X 4-3 line at 187.3Å. The spatial and temporal variations of these line intensities, when compared with several $n = 3-2$ and $n = 4-2$ lines of Al XI and Ne X, suggest inversions and gains. Gain-length products of 3-4 are estimated. The energy/pulse in these laser lines is estimated to be $\approx 60 \text{ mJ}$.

2. Experimental Results

Figure 1 is a schematic drawing of the experimental configuration that was used to produce the Ne and Al plasmas. Neon gas puff Z-pinches are driven by the DNA/PITHON generator.⁶ Multi-megampere currents cause the puff to implode on to a 1.6-mm-diameter capillary load on axis. The capillary is of low mass parylene with an aluminum coating on the outside. The neon implosion heats the Al to form a linear plasma, which is estimated to have a density (during the 25 ns implosion) of $\approx 10^{20} \text{ cm}^{-3}$ and a temperature of $\approx 500 \text{ eV}$. X-ray spectra reveal that the Ne and Al plasmas are in K-shell ionization states during the 25 ns implosion. After the implosion, the plasma at the capillary surface expands and cools, producing Li-like Al from He-like ions and H-like neon from fully stripped ions.

The recombination that produces Al XI and Ne X ions proceeds in two ways: radiative recombination favors the ground and lower levels of the recombined ions; three-body recombination favors the higher lying (Rydberg) levels. For densities $\sim 10^{20} \text{ cm}^{-3}$ and temperature $\sim 30 \text{ eV}$, it is estimated that strong population inversions can be produced in the $n = 4$ levels of Al XI and Ne X.

Figure 2 shows the arrangement of the diagnostics. X-ray spectra were obtained transverse to the Z-pinch axis. A time-resolved, X-ray pinhole camera also viewed the pinch in a transverse direction. The grazing incidence spectrograph (MCPIGS) viewed the pinch along its axis. A set of three cross-slits imaged the pinch on to the three framing strips of the MCPIGS. In this manner, the time-gated spectra were also radially resolved. The radial

*Research supported by SDIO/IST and directed by NRI

resolution was ≈ 1 mm. The field of view covered by each strip was ± 4 mm about the axis of the pinch.

Figure 3 shows 5 ns X-ray pinhole images of the neon-on-aluminum pinches. To the right of the images is a trace of the time-varying voltage from a filtered X-ray diode. This X-ray diode detects X-rays with energies > 1 keV, i.e., it is sensitive only to the K-shell emissions of Ne and Al. As such, this diode measures the hot portion of the Z-pinch. The temporal locations of the twelve 5-ns frames relative to the X-ray diode trace are shown below this trace. The pinhole images are identified by frame number as shown. It is observed that the pinch grows from the cathode end and is fully developed along the 3-cm length of the capillary in frames 5, 6, and 7, which are coincident with the peak X-ray emission. Also shown on the X-ray diode trace are three 25-ns time-frames, labeled A, B, and C. These are the frames which were used to capture the XUV spectra with the MCPIGS, as described later. Note that frame A includes frames 3 through 9 of the pinhole images. Frames B and C correspond to the post-pinch, expansion phase, during which the K-shell X-ray emissions are observed to be greatly decreased. During frames B and C, the aluminum and neon plasmas expand and cool, allowing the Al XII and Ne XI ions to recombine to Al XI and Ne X. The pinhole camera did not record plasma images during this recombination phase. The homogeneity of the plasma must be measured by other means. Under the right conditions of density and temperature in the recombining plasmas, recombination lasers are produced.

We turn now to the MCPIGS spectra. Figure 4 shows the three spectra from a 5-cm-long, neon-on-aluminum pinch for time frames A, B, and C, as defined in Figure 3. In frame A very few XUV lines appear, as the pinch is hot, most of the ions are in the K-shells of Al and Ne, and the radiation is predominantly above 1 keV. A few Li-like Ne lines are observed, extending to large radii (≈ 4 mm) from the pinch axis. In frame B, as the K-shell X-ray emissions decrease rapidly (see Figure 3), the XUV emissions from the L-shells of the Al and Ne increase dramatically. It is observed that the Ne-like emissions extend to large radii from the pinch, while the Al lines are confined to the first millimeter or so in radius. Of particular significance is the fact that the Al XI, 4f-3d and 4d-3p lines (at 150.6 and 154.6Å) appear visibly brighter than the Al XI, 4d-2p line. This is very significant, because the grating, detector and film response favor the 4d-2p wavelength. The anomalous brightness of the 4-3 lines suggests a population inversion in Al XI. In the third frame, C, it appears that the 4d-2p line becomes brighter than the 4-3 lines. This is as expected in a non-inverted medium, and rules out systematic effects as the cause of the strong anomaly observed in frame B.

Digitized spectra from a 3-cm-long, Ne-on-Al Z-pinch are shown in Figure 5. These spectra correspond to time frames A and B (as shown), with the continuum background subtracted, and with the instrument dispersion as well as overall response unfolded. It is pointed out that although they are not apparent in Figure 4, the 4-2 and 4-3 lines of Al XI do appear on the raw film in Frame A, and thus in Figure 5. The 4-3 lines are shown at 150.6 and 154.6Å on the figure. A double arrow points to the 4d-2p line at 39.2Å. It is obvious from Figure 5 that the 4-3 lines are brighter than the 4-2 line in frame B, but much weaker than the 4-2 line in frame A. This reversal in line intensities strongly suggests an $n = 4-3$ inversion, and possible lasing at 150.6 and 154.6Å. The results shown in Figure 5 were obtained with a 3-cm-long pinch. To examine whether a longer pinch would produce more dramatic increases in the Al XI 4-3 lines, a 5-cm-long pinch was tried.

Figure 6 shows a single time-frame (corresponding roughly to frame B of Figure 5), of the XUV spectrum from this longer pinch. Again, the 4f-3d and 4d-3p lines are the brightest lines in the entire spectrum. Both lines are more intense than the 4d-2p line, significantly more so than for the 3-cm-long pinch. The high intensity of the 4f-3d and 4d-3p lines strongly suggests lasing. Figure 6 also shows evidence for possible lasing in Ne X on the 4-3 line at 187.2Å. The Ne X, 4-2, Balmer- ρ line is at 48.55Å, which is not resolved from the Al XI, 3p-2s resonance line at 48.3Å. Although it is not obvious on the digitized spectrum (because these spectra were averaged over radii up to 2 mm), the raw film from the MCPIGS does resolve these lines, and the Ne X, 4-2 line is about half as bright as the Al XI, 3p-2s line. With this estimate, the Ne X, 4-3 line on Figure 6 is then a factor of two to three times brighter than the 4-2 line. Under non-lasing conditions, the 4-3 line should be three times weaker than the 4-2 line. Again, this anomalous brightness of the 4-3 line is presented as evidence for lasing at 187.2Å in Ne X. The presence of many Ne VIII lines in this frame suggests that the Ne X lasing might have occurred during an early portion of the 25-ns frame duration. Finer time-resolution might reveal more striking evidence for lasing. In any case, the factor of nine higher intensity of the Ne X, 4-3 line implies a laser with a gain-length product of ≈ 3 .

As a further check, a Z-pinch of pure neon was produced by imploding a neon-on-neon double puff, with no capillary on axis. In this configuration, an annular, supersonic Ne puff is imploded on to an inner coaxial Ne puff. A single 25-ns frame of the time-resolved spectrum from this pinch is shown in Figure 7. Here it is clearly seen that the Ne X, 4-2, Balmer- ρ line is brighter than the 4-3 line. This is as expected in a non-inverted medium

and confirms the lasing observed in Figure 6. That is, errors in unfolding the instrument response, etc., are not responsible for the anomalous spectra shown in Figure 6. In comparing the relative intensities of the Ne X, 4-2 and 4-3 lines, it is important to assess the effects of optical trapping on these lines. A worst-case estimate of the 4-2 opacity was made by assuming that recombination fed the $n = 2$ level as rapidly as the $n = 3$ and 4 levels. This gave the $n = 2$ level population during the 25-ns interval. For this population, the line-averaged optical depth of the 4-2 line was estimated to be 0.01 cm^{-1} . For a plasma length of 3 cm, this gives an opacity of 0.03, which allows the neglect of optical trapping effects.

A crucial test of whether the Al XI and Ne X lines are indeed lasing would be to simultaneously measure the XUV spectra on-axis and off-axis with two MCPIG spectrographs. These measurements are planned for the near future. Another acid test of lasing in such ASE media is to perform a methodical length scaling. If the lasing lines exhibit exponential growth, while non-lasing, optically thin lines show linear growth, lasing will be confirmed. For example, the 4p-3s line of Al XI at 141.5 Å is one such non-lasing line. Comparison of 4d-3p and 4f-3d lines with this line would allow confirmation of lasing. Since these lines are separated by only a 15 Å wavelength interval, the de-convolution of the spectrograph and micro-channel detector response is more reliable. At this stage, we offer the spectra of Figures 5, 6, and 7 as tentative evidence for lasing at 150.6, 154.6, and 187.3 Å.

Another argument for lasing at 150.6 and 154.6 Å in Al XI proceeds as follows: the absolute yields on the Ne X, 2-1 and 3-1 lines (in the X-ray spectrum) were measured using thermoluminescent detectors (TLD) and calibrated X-ray crystal spectrometers, as 2000 and 400 joules, respectively. These values are shown in Table 1. The table also shows yields for several other lines, which are derived from these measured line yields. For example, by a simple branching ratio from the 3-1 line, the Ne X, 3-2 line at 65.5 Å (in the XUV MCPIGS

Table 1. Measured and estimated line yields; NeX and AlXI.

Line	Wavelength (Angstroms)	Yield (Joules)	Method by Which Yield was Determined
NeX, 2 to 1	12.13	2,000	Thermoluminescent detectors (TLDs) and crystal spectroscopy
NeX, 3 to 1	10.24	400	X-ray crystal spectroscopy and oscillator strengths
NeX, 3 to 2	65.5	16	Branching ratio from $n = 3$
AlXI - 4f to 3d	154.5	50 (into 4π ster.) OR 0.05 (lasing into 10^{-3} ster.)	Estimated MCPIG response and intensity relative to the H-like neon 3 to 2 line. (Lasing is assumed into 0.001 steradian)
AlXI - 4d to 3p	150.5		
AlXI - 3d to 2p	52.4	12	
AlXI - 3p to 2s	48.3	11	
AlXI - 4d to 2p	39.2	9	Intensity with respect to NeX, 3 to 2 line

spectrum, Figures 5, 6, and 7) emits 16 joules. With this 65.5 Å line as a reference, the Al XI lines listed in the table were all assigned estimated yields, by comparison with the reference line in the XUV spectra. This comparison shows that the 4d-3p and 4f-3d lines should have emitted 50 joules into 4π steradians, to account for their relative strengths on the film. But a non-inverted medium would allow these lines to emit no more than ~ 1 joule each, if the 4d-2p line emits 9 joules. There is clearly an anomaly. This anomaly may be removed if the 4-3 lines were emitted into a smaller solid angle in the direction of the MCPIGS spectrograph. The spatial localization of the 4-3 lines on the film gives an estimate of the solid angle for axial emission of $\sim 10^{-3}$ steradian. With this small solid angle, ~ 50 mJ of emission on the 4f-3d line would account for the observed spectra. We conclude that the anomalous brightness of the 4-3 lines in Figures 5 and 6 is consistent with 50 mJ lasers emitting into a narrow solid angle in the direction of the axial, MCPIGS spectrograph. At a distance of 2.0 meters from the pinch (the location of the MCPIGS imaging cross-slits), the "footprint" of these lasers is estimated to be ~ 7 cm in diameter. Since the cross-slits were only 9 mm apart, alignment of the instrument with the laser beams is clearly not a problem. Optical trapping of the 4d-2p line could also be responsible for the anomaly described above. The effects of opacity require a detailed atomic model.

A rough estimate of the gain in these lasers is made as follows: from a simple branching ratio one expects the 4d-2p line to emit about three times as many photons as the 4d-3p line. Taking into account instrument response, we record the 4d-3p line as emitting nine times as many photons as the 4d-2p line on axis. The 4d-3p line, therefore, is anomalously bright by a factor of 27. A factor of 27 anomaly corresponds to a gain-length product of 4.8. For a 3-cm-long plasma the gain is then 1.6 cm^{-1} . It should be noted that optical trapping of the 4d-2p line (which could be important in the Al XI plasma) would reduce this gain. Such gain coefficients are consistent with recombination lasing, based on a density of $\sim 10^{20} \text{ cm}^{-3}$ and a temperature of $\sim 30 \text{ eV}$. To reiterate, this gain estimate has neglected the effects of opacity on the 3d-2p line, collisional excitation of the 3d level from the 2p level, non-uniform plasma conditions, etc. A more refined estimate requires detailed atomic modeling. Such models are under development.

3. Discussion

Time-gated, XUV spectra from rapidly recombining plasmas of Al and Ne have shown that the 4f-3d and 4d-3p lines of Al XI are much brighter than the 4d-2p line. Also, the 4-3 line of Ne X was shown to be brighter than the Ne X, 4-2 line. These anomalous line ratios, combined with the spatial and temporal localization of the 4-3 lines, suggest inversion and lasing on these lines at wavelengths of 150.6, 154.6, and 187.3 Å. Rough estimates of the gain ($\sim 1.6 \text{ cm}^{-1}$) and energy/pulse ($\sim 60 \text{ mJ}$) of these lasers is consistent with a three-body recombination pumping mechanism. Further confirmation of lasing requires simultaneous on-axis/off-axis measurements, which are in preparation. Length scaling is also planned. The data presented in this paper are offered as early evidence for the first pulsed power driven X-ray lasers. Even in their unoptimized state, these lasers have already produced power levels ($\sim 2 \text{ MW}$) comparable to those demonstrated at Livermore^{1,2} using glass laser drivers. The energy/pulse estimated for these lasers is a factor of 100 higher than that produced in glass-laser driven X-ray lasers. The efficiency of this pulsed power driven approach is higher. Saturation of these recombination lasers could produce $\sim 1 \text{ J}$ laser bursts.

4. Acknowledgments

The authors express deep appreciation to the DNA/PITHON machine crew for their expert assistance with these measurements. L. Burr helped with digital data analysis. Fruitful discussions with J. Davis, J. P. Apruzese, F. Young, B. L. Whitten, O. Willi, and J. Trebes are gratefully acknowledged.

5. References

1. D. L. Mathews et al., Phys. Rev. Lett. 54, 110 (1985).
2. M. D. Rosen, Paper 4-A-1, 6th APS Conference on Atomic Processes in Plasmas, Sept. 28-Oct. 2, 1987, Santa Fe, NM.
3. A. Jamelot et al., Paper 4-B-5, 6th APS Conference on Atomic Processes in Plasmas, Sept. 28-Oct. 2, 1987, Santa Fe, NM.
4. O. Willi, Paper 4D-1, 6th APS Conference on Atomic Processes in Plasmas, Sept. 28-Oct. 2, 1978, Santa Fe, NM.
5. S. S. Suckewer, Proceedings of the Lasers 87 Conference, Lake Tahoe, NV, Dec. 7-11, 1987.
6. P. Sincerny et al., J. Appl. Phys., 54, (12) Dec. 1983.

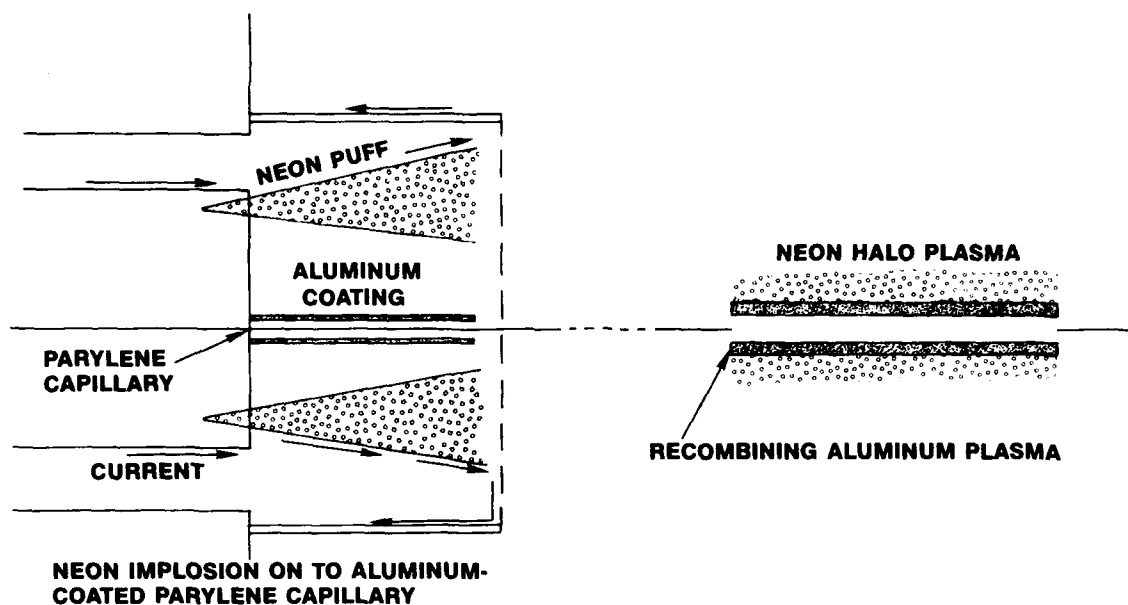


Figure 1. Schematic drawings of experimental configuration which produced aluminum and neon plasmas.

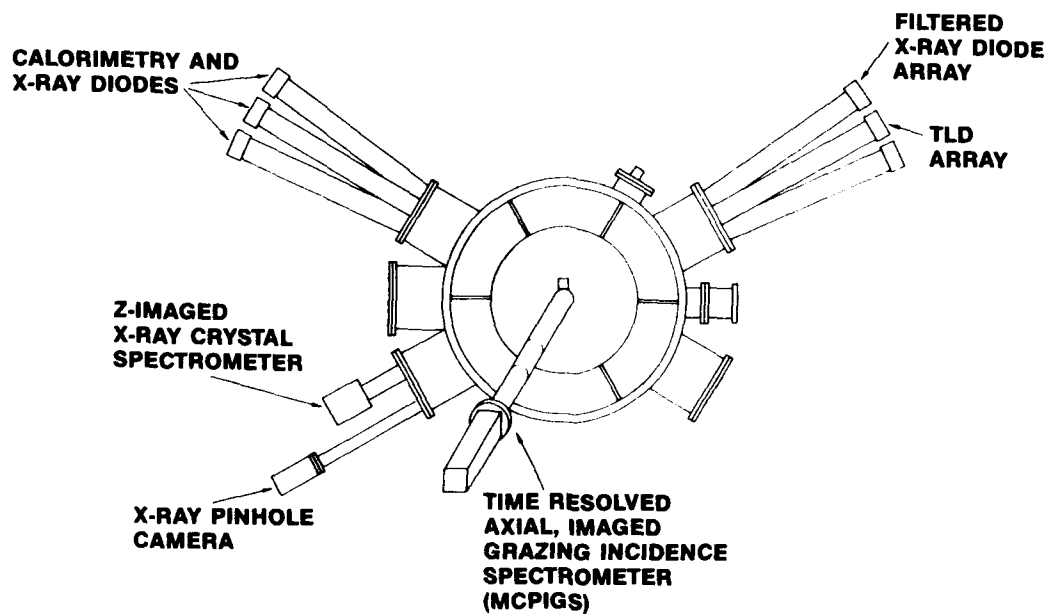
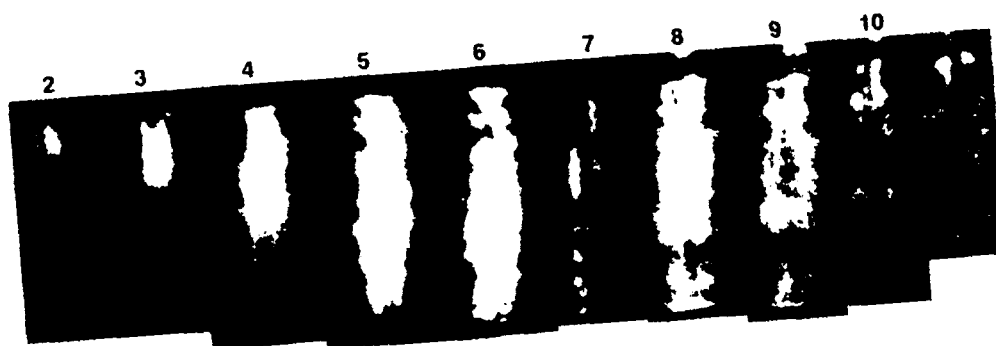


Figure 2. Schematic drawing of experimental apparatus used to diagnose Z-pinch plasmas produced on PITHON.



• 5 ns time frames

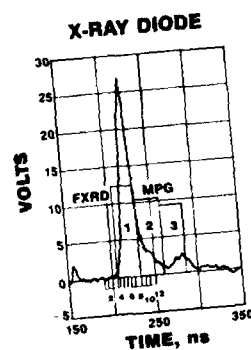
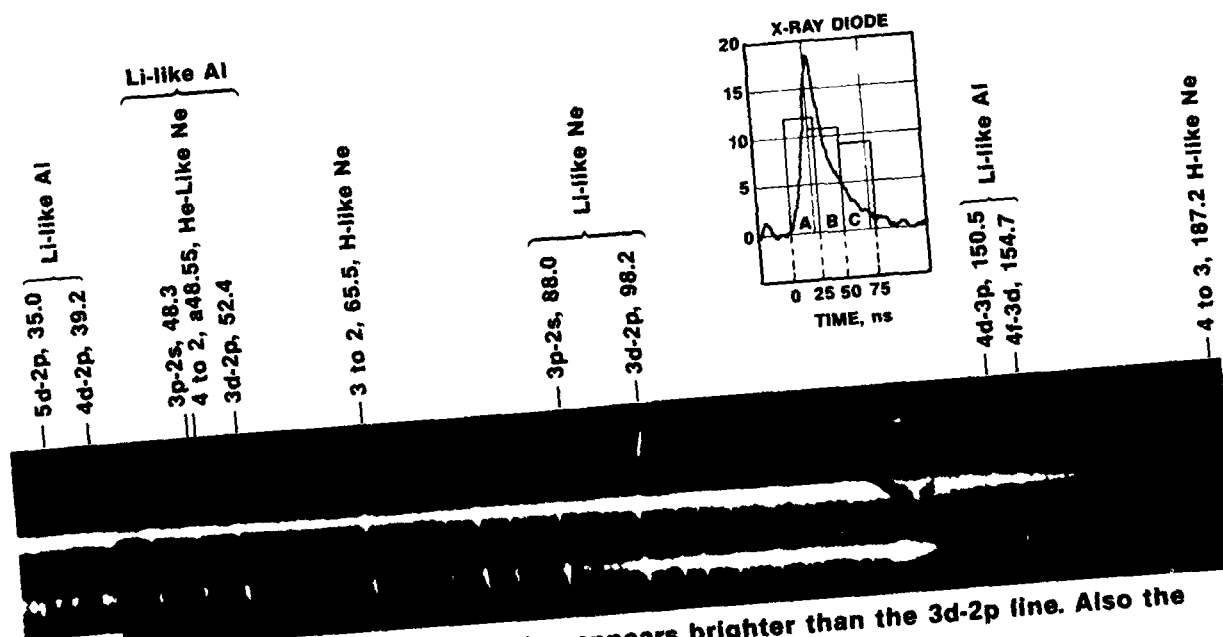


Figure 3. Time resolved pinhole camera images from Shot 4436: neon gas puff imploding onto an aluminum coated capillary.



Notice that the Li-like Al 4f-3d line appears brighter than the 3d-2p line. Also the H-like neon 4 to 3 line appears brighter than the 4 to 2.

Figure 4. Time-resolved XUV spectra from shot 4452: neon gas puff imploding onto a 5 cm long, aluminum coated capillary. Each time frame represents a 25 ns exposure.

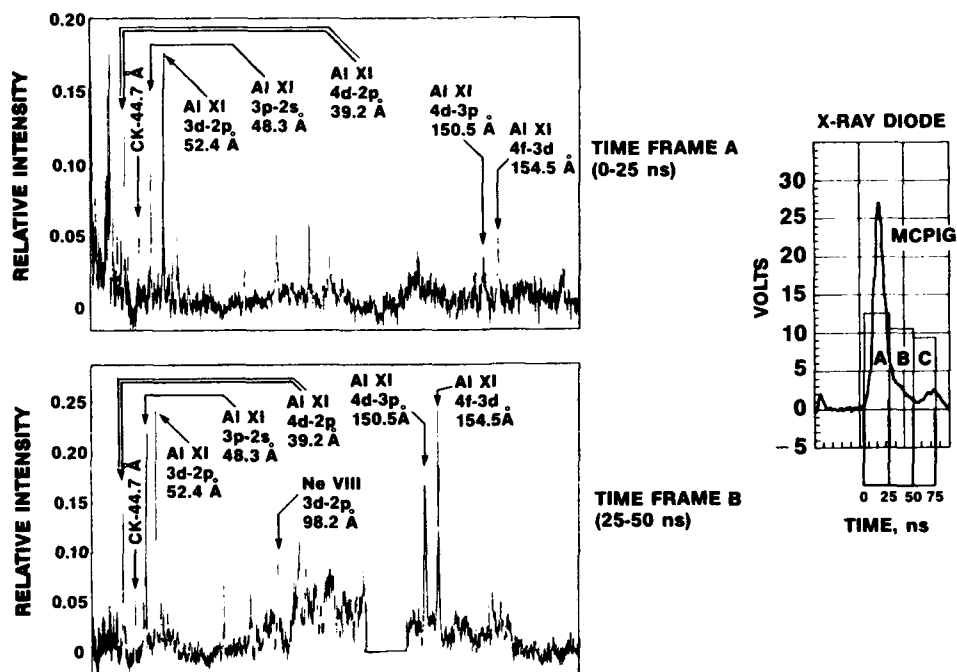


Figure 5. Digitized XUV spectra from a 3 cm long neon-on-aluminum Z-pinch. The two spectrums each represent 25 ns of emission.

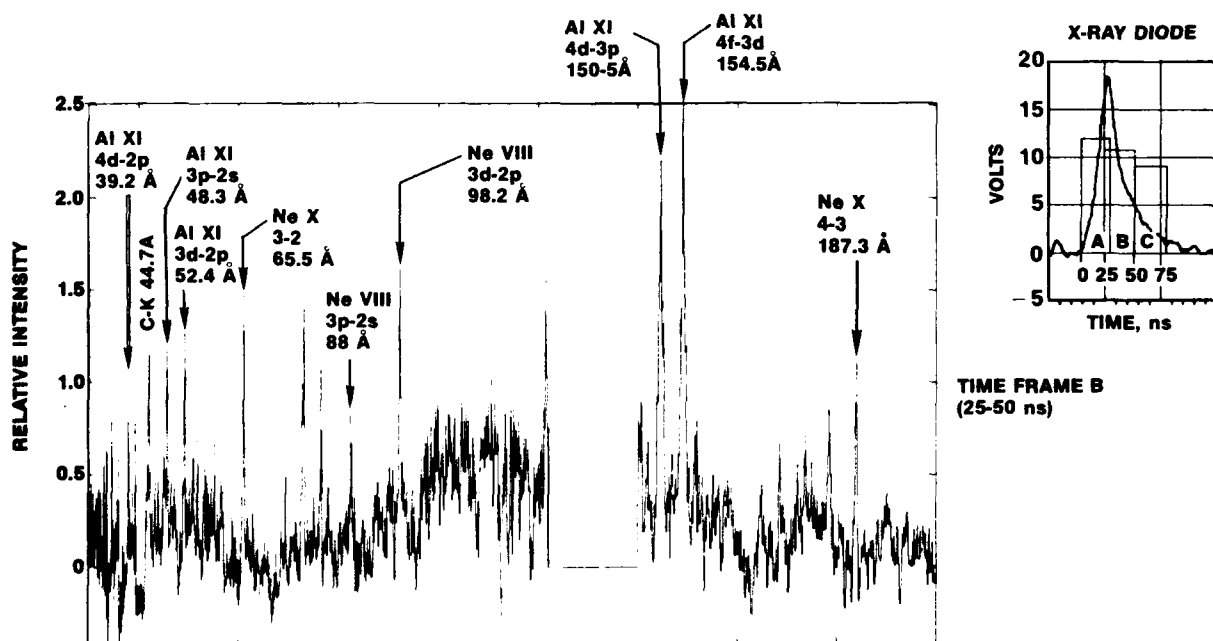


Figure 6. Digitized XUV spectrum from a 5 cm long, neon-on-aluminum Z-pinch. The emissions were recorded for 25 ns following peak X-ray output.

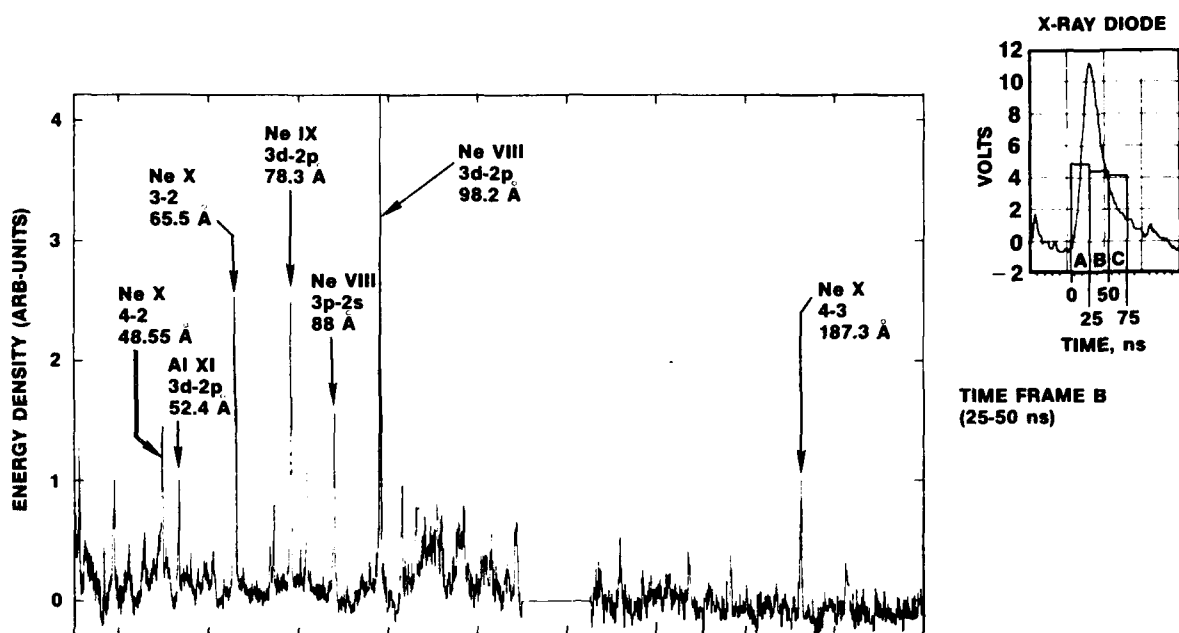


Figure 7. Digitized XUV spectrum from a neon-on-neon (double puff) Z-pinch. The emissions were recorded for 25 ns.

XUV AMPLIFICATION IN CYLINDRICALLY EXPANDING LASER PLASMAS

O Willi*, V Barrow*, D Bassett*, S Coe*, J Edwards*, M Grande**, M Key**, G Kiehn*,
C Lewis*, D O'Neill*, G Pert**, S Ramsden**, C Regan**, S Rose**, R Smith*, J Wark*

* The Blackett Laboratory, Imperial College of Science and Technology,
London SW7 2BZ, UK

** Rutherford Appleton Laboratory, Chilton, Oxon OX11 0QX, UK

+ Queen's University Belfast, Belfast BT7 1NN, UK

++ York University, York YO1 5DD, UK

+++ University of Hull, Hull HU6 7RX, UK

Abstract

This invited paper describes recent experimental results demonstrating amplification of spontaneous emission in the XUV spectral region. The gain medium is a rapidly expanding recombining cylindrical plasma produced by laser irradiation of thin fibre targets. Moderately large laser gain between $1-5 \text{ cm}^{-1}$ has been observed in transitions of hydrogenic (C VI and F IX) and Li-like (Al XI and Cl XV) ions. This work has been carried out at the Central Laser Facility of the Rutherford Appleton Laboratory by various groups using the high power VULCAN laser.

Introduction

In recent years, considerable progress has been made in the field of XUV laser research. Amplification has now clearly been demonstrated in several discrete transitions in the VUV/XUV spectral wavelength region between 50 to 250 Å. In all the successful experiments, laser produced plasmas were used as the gain media where pumping was achieved either via collisions (Ne-like and Ni-like schemes^{1,2}) or via recombination (H-like^{3,4} or Li-like systems⁵). This paper reviews the current status of the x-ray laser program carried out at the Central Laser Facility of the Rutherford Appleton Laboratory by various university groups and in-house RAL staff. The work concentrates on the recombination pumped scheme and its isoelectronic scaling to shorter wavelengths. Both, hydrogenic (C VI and F IX) and Li-like systems (Al XI and Cl XV) have been investigated in plasmas produced by laser irradiation of thin fiber targets. The Li-like results will be discussed by P Jaegle elsewhere in these proceedings. Preliminary spectrographic x-ray observations taken from aluminium targets irradiated by a picosecond high power KrF laser pulse are described. In addition, initial experimental results studying the hydrodynamics of ribbon targets are given. Finally, a joint recombination-photopumping x-ray laser scheme for amplification in the 'water window' is discussed.

Background

Highly ionized plasmas produced by optical lasers have long been identified as potential media for laser amplification in the XUV spectral region. Population inversion can be obtained either by collisional excitation, photo-pumping, or by recombination. In the latter case, the inversion arises as the highly ionized plasma cools and recombines preferentially into the upper states which cascade to the ground states. If the upper laser level is sufficiently populated by collisional recombination and the lower laser level is rapidly depleted by radiative decay, large gains can be developed on the 3-2, 4-3 and 5-4 transitions in H-, Li-, and Na-like ions, respectively.

Rapid cooling of the plasma is essential for the recombination scheme. This can be achieved either by adiabatic expansion of a cylindrical plasma or by doping the plasma with medium to high Z ions to increase the radiative losses. Adiabatic cooling has been extensively investigated using the carbon fiber scheme. A thin carbon fiber 7 μm in diameter uncoated or coated with various elements is heated with a short 70 ps laser pulse. Due to the small diameter of the fiber target, rapid expansion occurs resulting in an efficient cooling. Secondly, the small mass reduced optical trapping of the lower laser level. Computer simulations have well established the optimum energy content of the plasma as a function of its mass and the duration of the heating pulse⁶. Two regimes exist; a thin layer of the fiber target is ablated or the fiber is burnt completely. The first regime is energetically advantageous. All the experimental results described in this paper were obtained when a thin layer of the target was ablated.

The recombination scheme can easily be scaled to shorter wavelengths by moving along the isoelectronic sequence to higher Z ions. The wavelength λ is proportional to Z^{-2} . The pump energy can be estimated by comparing the collisional radiative model and the laser ablation model. The electron temperature scales as $T_e \propto Z^2$ (from the CR model) and $T_e \propto Z^{2/9} I^{4/9}$ (from ablation model). It follows that the required pump laser intensity

scales as $n_e \propto Z^7$, consequently, to produce shorter wavelength x-ray lasers the heating laser pulse must be of shorter duration and wavelength.

Facility and Diagnostics

The VULCAN high power Nd:glass laser is being used for XUV/x-ray laser experiments. The laser provides 150 J in 70 ps pulses on target in six second harmonic beams. Each beam is focused onto a cylindrical target by using a lens and off-axis mirror arrangement⁷. The line foci are 7 mm long and 25 μ m wide. The six laser beams are arranged as three pairs of opposing beams. All the pairs are either superimposed or each pair can be spatially translated along the length of the target to obtain a longer line focus length. The targets are aligned to an accuracy of a few microns in space and less than 1 mrad in direction by using a split field imaging system.

The principle diagnostics are a pair of time resolving flat field XUV spectrographs⁸. One of the instruments is aligned along the plasma axis, while the other views the full length of the plasma at an angle of 35 degrees to the axis. The temporal and spectral resolution of both instruments is 100 ps and 0.5 A, respectively. These instruments, including filters, have been absolutely calibrated using synchrotron radiation⁹. Additional diagnostics included x-ray pinhole cameras to measure the plasma length and uniformity, and a plasma calorimeter array to record the laser energy absorbed in the plasma.

Experimental Results

a) Hydrogenic Carbon (C VI)

Carbon fiber targets 7 μ m in diameter were irradiated with one pair of opposed laser beams for lengths up to 5.5 mm and with two axially displaced pairs for lengths between 5.5 mm and 9.5 mm. The beams were masked to vary the irradiated target length and care was taken to ensure that irradiation was as uniform as possible. The carbon fibers were supported at one end only to provide unrestricted access to the XUV spectrograph viewing the system axially. The incident laser energy was 25 J cm⁻¹ in 70 ps. With a measured absorption fraction of about 10% of the incident laser energy, the absorbed energy was 2.6 ± 0.6 J cm⁻¹. The heated plasma lengths were varied from 1.5 to 9.5 mm. The time resolved spectrograph was absolutely calibrated with synchrotron radiation and after allowing for the measured contributions to the H β and H γ lines of high-order grating reflections of resonance lines, the absolute intensities of the Balmer lines were determined as a function of time for each plasma length. Figure 1 shows the line intensities of H α and H β versus length 975 ps after the peak of the laser pulse. A clear exponential growth of line intensity with length is observed on the H α transition at 182 A. The data was fitted by the function $\exp(gl-1)$, resulting in a best fit of $g = 4.1 \pm 0.6$ cm⁻¹. This corresponds to an amplification of about 50 in the longest plasma case. Computer modelling of the data predicts a gain coefficient which is larger at earlier times and does not persist for as long as observed experimentally.

b) Hydrogenic Fluorine (F IX)

The isoelectronic scaling of the hydrogenic recombination scheme to shorter wavelengths was investigated by using fluorine as the lasing ion when carbon fibers 7 μ m in diameter were coated with 0.5 μ m of LiF. All six green laser beams were superimposed to give the required energy per unit length and irradiation uniformity. The incident laser energy was varied over a large range from 50 to 150 J cm⁻¹, allowing the dependence of the gain as a function of the input laser energy to be studied. The laser pulse duration was 70 ps. Axial and transverse spectrographs were used to time resolve the emission in the range of 40-100 A. A comprehensive set of data was taken for targets lengths from 1 to 5.5 mm. Analysis of the pinhole camera brightnesses, relative intensities of H-like and He-like transitions and laser beam energies resulted in the classification of three distinct regimes. These three groups correspond to absorbed energies of 6 ± 2 J cm⁻¹, 10 ± 2 J cm⁻¹, and 14 ± 2 J cm⁻¹. Although the absorbed laser energies were not measured directly, these values were derived from the known absorption fraction, measured in similar fiber target experiments to be 10% of the incident laser energy. Figure 2 shows the ratio of axial to transverse H α intensity at as a function of target length 250 ps after the laser pulse.

As clearly can be seen in figure 2, three distinct regimes are observed. In the very low E/L case no amplification is observed. In fact, the measurements can be fitted by an attenuation coefficient of -0.5 ± 0.5 cm⁻¹. A large gain coefficient of 5.5 ± 1 cm⁻¹ is observed for the medium energy range. Whereas, the gain coefficient is reduced to 3 ± 1 cm⁻¹ for very large absorbed energies, indicating that the plasma is overheated. These three distinct regimes are also observed when the intensities of H α obtained from the axial spectrograph are plotted as a function of target length. A similar behaviour of the peak gain as a function of the coupled laser energy is observed in simulations. A

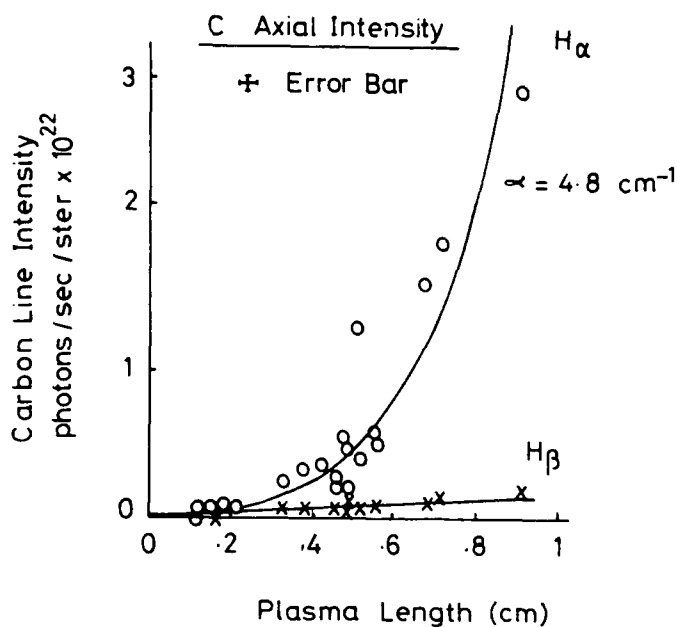


Figure 1. Absolute intensity of H_{α} and H_{β} transitions measured from streaked spectra 975 ps after the peak of the laser pulse.

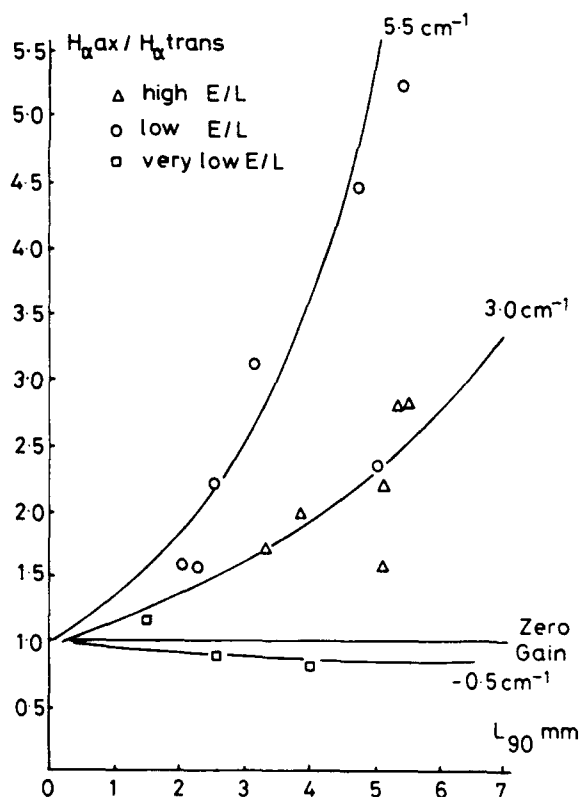


Figure 2. Gain coefficients for the F IX H_{α} transition at 81 Å deduced from axial to transverse line intensity ratios at the time of peak gain for various absorbed energies.

one-dimensional Lagrangian hydrocode is used for modelling of the experimental data. The code also predicts the three gain regimes as observed experimentally. See figure 3. Below an absorbed energy of 4 J cm^{-1} no significant gain is calculated. Whereas, a gain coefficient of about 4 cm^{-1} is obtained for absorbed energies from $10\text{--}15 \text{ J cm}^{-1}$. The gain begins to fall off for energies larger than 15 J cm^{-1} .

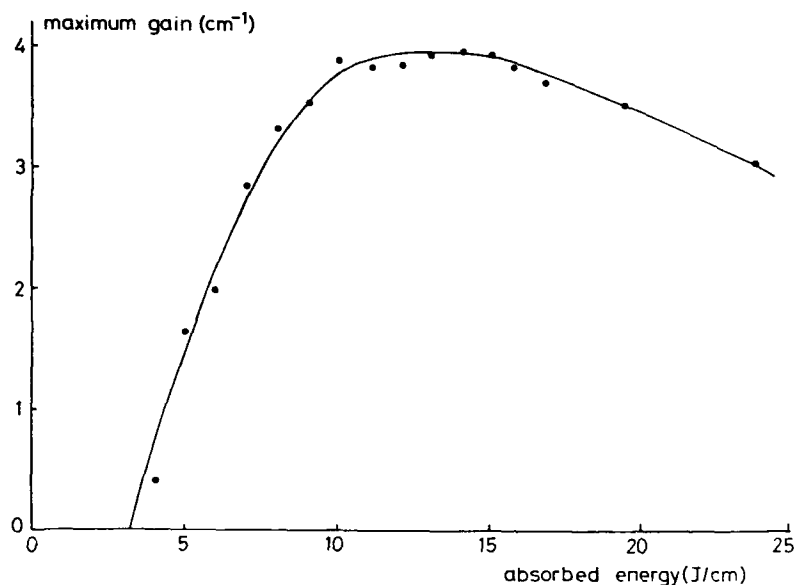


Figure 3. Calculated maximum gain for the F IX H_{α} transition as a function of absorbed laser energy assuming 1 mm and 10 mm length fibers.

The measured peak gain as a function of time was also compared with the simulations for an absorbed energy of 10 J cm^{-1} . See figure 4. The code predicts a similar peak gain and is in much better agreement with the experiment than in the previous carbon work. This is due to the inclusion of Stark broadening and p-level splitting in the code. The measured peak gain occurs, however, slightly later in time and has a broader temporal profile than the code results. It is unclear whether the disagreement on the time behaviour is due to incomplete modelling of the expansion, or to small scale laser plasma instabilities affecting the uniformity of expansion at early times.

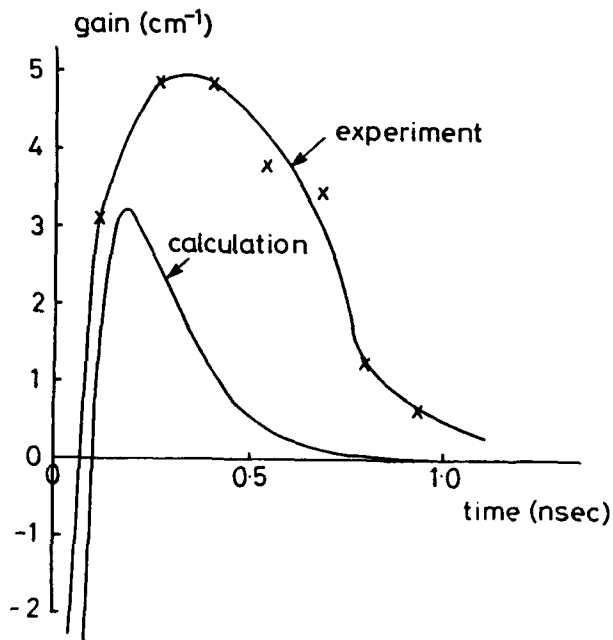


Figure 4. Temporal behaviour of measured and calculated gain for the F IX H_{α} line, calculated using H_{α} intensity from 2.1 mm and 5.5 mm lengths.

c) Hydrogenic Aluminium (Al XIII)

Initial experiments have been carried out to study the ionization balance of an aluminium plasma produced with a picosecond high power KrF laser. The use of picosecond short wavelength laser pulses is essential for recombination pumped aluminium x-ray lasers with the lasing transition in the water window. This is due to the strong scaling of the initial electron density with atomic number ($n_e \propto Z^7$).

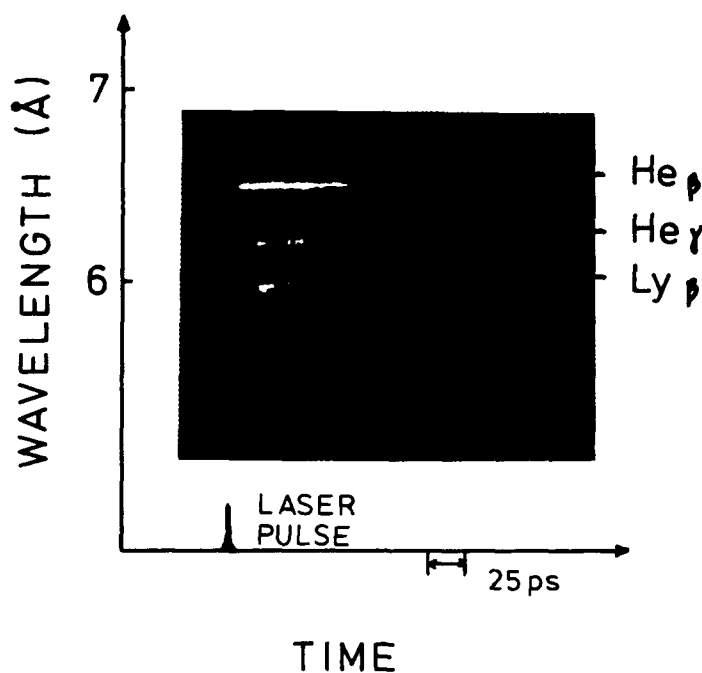


Figure 5. Time resolved x-ray spectrum recorded from an Al plasma, indicating a plasma density of 2×10^{22} and temperature of 400 eV.

Aluminium targets have been irradiated with 3 ps, ≈ 1 J KrF laser pulses. The laser beam was focused onto the target with an f/2.5 aspheric lens. Irradiances of up to 10^{17} W cm $^{-2}$ were achieved on the target surface. The primary diagnostics were time integrating and time resolving x-ray spectrographs. These instruments allowed the electron temperature and density to be determined via line ratios and Stark broadening measurements. The diameter of the focal spot was measured with an x-ray pinhole camera. Figure 5 shows a streak record taken of an aluminium plasma produced with an irradiance of 3×10^{16} W cm $^{-2}$ on the solid target. H-like and He-like transitions are clearly observed. Preliminary analysis of the x-ray spectrum with RATION indicates a density of about 2×10^{22} cm $^{-3}$ with a temperature of about 400 eV. The short picosecond pulse was, however, preceded by a relatively large prepulse 10 ns in duration. Consequently, a large plasma corona was produced before the main short pulse interacted with the target. The x-ray emission then primarily occurs from densities near the critical density. When the prepulse was kept small the x-ray spectrum was distinctly different. The Al He γ transition is now very broad and intense, while the Al He β and Ly β lines are almost nonexistent. This spectral behaviour is consistent with x-ray emission from very dense plasmas. These x-ray spectra are the first single shot x-ray measurements taken on targets which were irradiated with picosecond laser pulses.

Hydrodynamics of Stripe and Ribbon Targets

Amplification with moderate gain has clearly been demonstrated on various discrete transitions in the XUV spectral wavelength region between 81 Å and 182 Å. Population inversion by recombination was obtained by rapidly cooling a cylindrical plasma produced by laser irradiation of small mass thin fiber targets. This approach has, however, several shortcomings. Not only are fiber targets difficult to handle, but also the coupling of the incident laser energy is inefficient. Further, fiber targets are not very well suited for multipass cavity operation. Consequently, initial experiments have been carried out to investigate stripe and ribbon targets for recombination pumped x-ray lasers. In particular, the hydrodynamic behaviour of thin foil formvar targets overcoated with a narrow stripe of aluminium (50 μ m wide and 300 μ m in thickness) and free standing Al ribbon targets (350 μ m in thickness) was examined. Preliminary results show that the formvar targets did not behave as expected. Laser energy spilling and lateral energy transport over onto the plastic substrate seem to create two large regions of cold overdense plasma on either side of the expanding stripe. This restricts the cylindrical flow causing a slower rate of expansion and cooling than predicted by modelling. In addition to this, fluid instabilities have been observed at the hot aluminium-cold plastic plasma interface. On the other hand,



TIME = 0.69ns



TIME = 1.59ns

Figure 6. Schlieren images of free standing aluminium stripe targets.

the expansion of the ribbon targets followed theoretical predictions more closely. Figure 6 shows two optical Schlieren images of a laser irradiated aluminium ribbon target.

Joint Recombination-Photopumping Scheme

A novel x-ray laser scheme is proposed which is based on the adiabatically cooled recombination laser, but augmented with a line coincidence photopump. The photopumping relies on the accidental coincidence between a transition in Be-like Mn which acts as the pump, and either a hydrogenic fluorine or a Li-like calcium transition to obtain gain at 81 Å or 39 Å, respectively. In the first case Mn $1s^2 2s 2p^3 P_2 - 1s^2 2s 3d^3 D_3$ pumps the F IX $1s - 3p$ transition, whereas in the latter case the Mn line is used to pump the Ca $1s^2 2s^2 S_{1/2, 3/2} - 1s^2 5p^2 P_{1/2}$ transition.

The experimental arrangement for the Li-like Ca laser is shown in figure 7. Three laser beams delivering about 75 J in 70 ps are focused on a CaF_2 coated carbon fiber. The photopumping flashlamp separated from the fiber target by about 50 μm consists of a 1 μm thick plastic foil supporting a thin layer of Mn. Three laser beams are focused onto the Mn target and are delayed 100-200 ps in time relative to the beams which heat the fiber target. Numerical simulations show a gain of about 2 cm^{-1} is obtained when a photopump of modal photon density of 0.01 is present. No gain is seen in the simulations if the photopump is turned off.

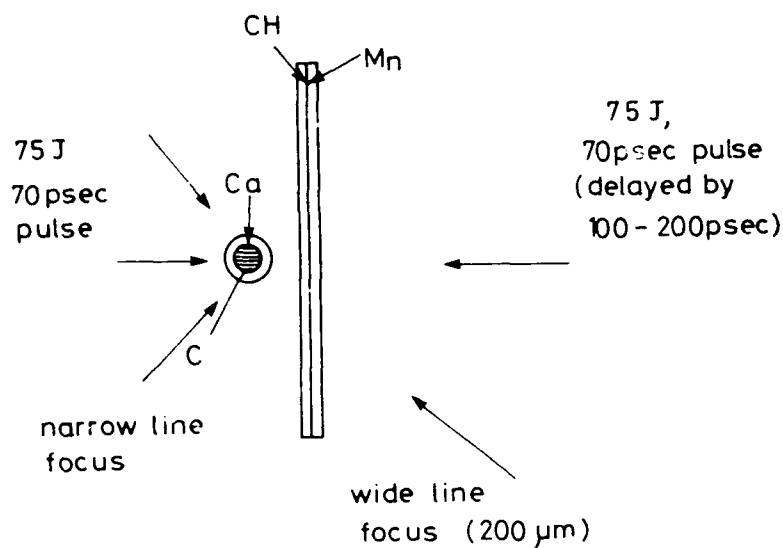


Figure 7. Schematic of the experimental arrangement for a possible joint recombination/photopumping scheme.

Conclusions

Recombination pumping in the XUV spectral wavelength region has been demonstrated in H-like and Li-like ions using low mass thin fiber targets. Isoelectronic scaling towards shorter wavelengths has been carried out for both ions. By changing the incident laser energy the gain of hydrogenic fluorine has been optimized. Theoretical modelling of hydrogenic C VI gives higher gains than measured early in the expansion and lower gains in the later stages. Better agreement is obtained for H-like fluorine. The hydrodynamic expansion of ribbon targets has been studied, indicating great promise as potential targets for future x-ray laser schemes. A joint photopump/recombination scheme is proposed which may result in amplification in the water window.

Acknowledgements

We would like to acknowledge the technical support given by the Central Laser Facility staff. This work was supported by various SERC grants.

References

- 1) D L Matthews et al, Phys Rev Lett, 54, 10 (1985).
- 2) B MacGowan et al, Phys Rev Lett, 59, 2157 (1987).
- 3) C Chenaïs-Popovics et al, Phys Rev Lett, 59, 2161 (1987).
- 4) C Willis et al, SPIE, 698, 2 (1986).
- 5) G Jamelot et al, J Phys B, 18, 4647 (1985).
- 6) G Pert, Plasma Phys, 27, 1427 (1985).
- 7) I Ross et al, Appl Opt, 26, 1584 (1987).
- 8) G Kiehn et al, Appl Opt, 26, 425 (1987).
- 9) G Kiehn, PhD Thesis, Univ of Oxford (1987).
- 10) S Rose, private communication.

PHOTOPUMPED SHORT WAVELENGTH LASERS IN XENON AND KRYPTON

H.C. Kapteyn and R.W. Falcone

Department of Physics
University of California at Berkeley
Berkeley CA 94720

Abstract

We report studies of short wavelength lasers in Xe III at 108.9 nm and in Kr III at 90.7 nm. The inversion mechanism in these systems is inner shell photoionization followed by selective Auger decay. Data presented include the demonstration of gain and the measurement of the upper and lower level natural lifetimes of the laser transitions. Computer models used to simulate the output of the gain demonstration experiments are discussed. These simple models can explain the observed output, without need to consider any effects other than amplified spontaneous emission on the dynamics of the system.

The first demonstration of a short wavelength laser pumped by Auger decay following photoionization was recently reported by the authors.¹ In this experiment, soft x-rays emitted from a laser produced plasma ionize inner-shell 4d electrons in neutral xenon gas. The resulting highly excited Xe* atoms rapidly undergo Auger decay to various excited states of Xe⁺⁺. The relative Auger decay rates and level degeneracies are such that a population inversion is created between the Xe⁺⁺ 5s⁰5p⁶ ¹S₀ and 5s¹5p⁵ ¹P₁ states, and laser gain is observed at the transition wavelength of 108.9 nm. The analogous transition in krypton, Kr⁺⁺ 4s⁰4p⁶ ¹S₀ to 4s¹4p⁵ ¹P₁, is similarly inverted at a wavelength of 90.7 nm.²

The experimental apparatus used to demonstrate gain is shown in Fig.1.¹ A Nd-doped glass laser pulse (40-70 J, 0.1-1 nsec) is focused onto a tantalum target to form a thin, 9 cm long plasma soft x-ray source. Radiation from the plasma ionizes xenon or krypton gas in a 3mmx3mmx9cm channel opposite the plasma and 1-2 cm away from it. The channel is covered with a 150 nm thick parylene filter which confines the active region since it is transparent to the pump soft x-rays but opaque to the short wavelength laser radiation. The excited length of the gain region is varied by shadowing portions of the channel from the pumping radiation; emission from gas in the channel is expected to increase non-linearly with pumped length if there is laser gain. The photodetector is a specially designed soft x-ray streak camera using a microchannel plate photocathode.³ The camera views the gas in the channel through a vacuum spectrometer. The system has a spectral resolution of 1.5 nm, a time resolution of 200 psec, and is sensitive to single photons. The spectrometer is separated from the target chamber by a LiF window in the case of Xenon, and by a capillary array window and differential pumping arrangement in the case of Krypton.

Gain is observed at both the Xe⁺⁺ 108.9 nm transition, as seen in Fig.2, and at the Kr⁺⁺ 90.7 nm transition, as seen in Fig. 3.² The data were fitted using a spectrally integrated brightness function,¹ which yields the line center gain coefficient. The xenon data were taken using 55 J of laser pump energy in a 1 nsec pulse, with a target-channel distance of 2 cm. The curve yields a gain coefficient of 0.8 cm⁻¹. 80% enriched ¹³⁶Xe was used for these measurements to limit the effects of hyperfine splitting on the gain of the transition. For Krypton, no separated isotope was used, the pump pulse width was narrowed to 0.5 nsec, and the target-channel distance was narrowed to 1 cm. The indicated curve (a) is a fit to data taken with 50 J of pump energy, yielding a gain coefficient of 0.5 cm⁻¹ and (b) is a fit to data taken with 38 J of pump energy, yielding a gain coefficient of 0.7 cm⁻¹.

In the case of the xenon, the output pulse width is generally about 600 psec, narrowing to 450 psec at the highest intensities, and widening to somewhat over 1 nsec at the lowest intensities. A double pulse structure is often observed at intermediate intensities, for which our best explanation is superfluorescent ringing. In the case of Krypton, the pulse width is always less than 300 psec, near the resolution limit of our detector.

Measurements were made using a single end mirror with the xenon laser to enhance output in a double pass geometry. The reflector used was a lithium fluoride window, which has a calculated surface reflectivity of about 10% at 108.9 nm.⁴ In this experiment, the pump laser is focused to a line 9 cm long inside a 1 cm deep by 3 mm wide slot. Emission is observed from a region close to the plasma target. About 4 J of laser energy is necessary to show substantial gain on the 108.9 nm transition in this geometry. Gain is measured by alternately blocking and unblocking the mirror and varying the pumped length. As shown in Fig. 4, the mirror enhances the output. Curve (a) is a fit to data with the reflector and curve (b) fits data without the reflector. The relatively small enhancement of output intensity in the multipass geometry, relative to the measured gain along the channel, may be explained by output saturation and the fact that gain is present in the system for a time comparable to or shorter than the optical round trip time in the channel.

In addition to studying these xenon and krypton transitions, we searched for other lines in the wavelength range of 50 to 100 nm in xenon, krypton, and argon. No other lasing transitions were found in either the channel configuration or in the slot configuration using a 30 J, 100 psec pump pulse.

The lifetimes of the upper and lower laser levels in xenon and krypton were measured using the technique of time correlated photon counting⁵ (TCPC) in conjunction with a high repetition rate laser produced plasma x-ray source.^{2,6} In TCPC, single photons are detected from the excited gas following repetitive impulsive excitation. The time interval between the excitation pulse and detection of a fluorescence photon is measured and after many detected photons, a histogram of photon arrival times is constructed showing decay of the excited state. The apparatus is shown in Fig. 5. A q-switched, mode-locked Nd:YAG laser is focused onto a rotating metal target rod. The output of the laser consists of bursts of about 20 pulses at a 10 nsec interpulse interval, with each pulse 100 psec long. The burst repetition rate is up to 500 Hz. Each pulse has an energy of up to 70 μ J and is focused by a 10 cm lens to a power density of about 10^{11} W/cm² on the target. Soft x-rays from the resulting plasma excite gas surrounding the target, and fluorescence is detected by a microchannel plate photodetector at the exit slit of a vacuum monochromator. The target cell is separated from the spectrometer by a differential pumping system. Since some of the fluorescence lines have energies above the neutral gas ionization threshold, the capillary array window is placed within 1 cm of the excited gas region to minimize absorption. Care was taken to direct gas flow through the target chamber in such a way that debris from the plasma does not clog the capillary window. The detection electronics consists of two constant fraction discriminators, one triggered by a photodiode looking at the laser output, and the other triggered by the photodetector after amplification. Discriminator outputs are connected to the start and stop inputs of a time-to-amplitude converter, whose output is fed to a computer. The data is then displayed and fit to an exponential decay function.

The time resolution of the system was estimated by observing the emission of a short-lived transition in Kr^{II} at 55 nm. Figure 6(a) shows this measurement. The resulting pulse has a FWHM of <300 psec and a risetime of 125 psec. Figure 6(b) shows a measurement of the Kr^{II} 90.7 nm laser transition at 1 torr pressure, along with the resulting fit to the lifetime. The observed lifetimes of the states vary with pressure due to neutral gas collisional quenching; data is thus taken at several pressures and extrapolated to zero pressure to get the natural lifetime. The upper state lifetimes in both xenon and krypton, and the lower state lifetime of krypton, were determined in this manner. In the case of the xenon lower level, the system was modified by the insertion of an electro-optic pulse selector, so that only one pulse in each burst is passed. This was done since the upper level lifetime feeds into the lower level on a time scale similar to the 10 nsec pulse separation, which would have made measurement of the lower level lifetime difficult to fit to using the original setup. For both lower levels, the lifetime was fit to data at times after the upper level had substantially decayed. The measured data including the lifetimes and the quenching coefficients is shown in Table 1.

Computer simulations were developed to model the laser systems. These simulations involve two types of calculations. The first is a simple, time independent calculation assuming instantaneous pumping of the xenon gas by the plasma x-rays. This yields cumulative electron and ion densities, as well as the net gain coefficient. The second simulation is time dependent and takes into account amplified spontaneous emission. This is done to predict the temporal behavior of the output and to relate predicted local gain coefficients to the experimentally measured gain of the system as determined by the gain curve fit.

In these simulations, we assume that the plasma spectrum resembles a blackbody emitter with a 30 eV temperature and that the conversion efficiency of input laser energy to soft x-ray emission is 7%.⁷ By calculating absorption of this radiation in the parylene filter⁸ and in the gas (using cross sections⁹ for the 4d, 5s and 5p electrons), the densities of inner-shell and outer-shell ionized atoms and the total electron density can be determined. Secondary electron production due to electron avalanche ionization is also taken into account. Excitation densities include integration over the line focus geometry of the system, assuming the plasma radiates uniformly in all directions. The population inversion density is calculated using relative Auger decay fractions^{2,10} of 0.044 and 0.051 for decay of the 4d hole state into the upper and lower laser levels, and the gain cross section is calculated using standard formulas assuming Doppler broadening. Calculations for the xenon gain experiment using this time independent model predict an exponential gain coefficient of 1.5 cm^{-1} along the 9 cm channel. The excited state density along the slot is calculated to be constant to within 20% of the average value over 80% of the slot length, and the maximum electron density is predicted to be $1 \times 10^{15} \text{ cm}^{-3}$.

Since the observed output pulse from the xenon is shorter than the pump pulse, the gain computed above is expected to be only a rough estimate of the actual measured gain. Thus we developed the time dependent model to more accurately predict the gain observed, and also to enable us to understand the pulse width behavior of the system under varying conditions. In this model, three major approximations are made to simplify the implementation. First, the excited state density of the system is assumed to be uniform over the entire slot. Second, the photon transit time through the slot is assumed to be small compared to the characteristic time of both the pump pulse and the output pulse. And third, superfluorescence effects¹¹ are ignored and the output is assumed to be determined solely by amplified spontaneous emission.

The time dependent model approximates the effects of amplified spontaneous emission on the dynamics of the system by generating a function which, as a function of gain of the channel, approximates the number of photons exiting the excited region for each spontaneous emission photon emitted in the region. This function is generated in two steps. The first step is to do a Monte Carlo simulation to generate a distribution function of how far a photon emitted in a random direction from a random place in the channel will travel before exiting the region. Then, for any given gain in the channel, this distribution function is integrated to determine the average number of photons exiting the excited region. Also generated in this process is a function which indicates how many of these photons will exit in an f30 cone along the axis, approximating the output beam observed in the experiment.

This spontaneous emission enhancement function can then be used in a simple rate equation model determining the dynamics of the system and the intensity of the output beam. In the simulation the upper and lower levels are filled by Auger decay, and the upper level decays to the lower level through amplified spontaneous emission. The Monte Carlo and rate equation codes can then be run for several different excited lengths, and the simulation data fit to the same function the experimental data is fit to. Given a pump pulse length of 1 nsec and a total pump flux identical to that determined in the time independent model, the time dependent model predicts a fitted gain parameter of 0.95 cm^{-1} . This is in reasonable agreement with the measured 0.8 cm^{-1} gain. The model predicts also that this measured gain is close to saturation in the system.

According to the results of the simulation, the output pulse length should shorten with increasing output intensity until saturation, when the output pulse has a width of 430 psec. At higher output intensities the pulse width again increases. Figure 7 shows the experimental pulse width data as a function of intensity; fits to the time dependent model data are shown as solid lines. Curve (a) is the model result assuming the predicted pump flux which, as discussed above, yields a reasonable fit to the intensity versus length data. However, the pulse length in this simulation is longer and increases more rapidly with decreasing length than the experimental data. By assuming only a 30% higher pump flux and thus higher gain, we obtain better agreement with the data as shown by curve (b). Thus the behavior of the amplitude and pulse length of the output can be reasonably accurately simulated using this model with only one empirical parameter. Although the model involves many simplifying assumptions (for example, it ignores possible electron quenching of the laser level) we conclude that amplified spontaneous emission is the dominant process determining the behavior of the xenon laser system.

The model does not, however, predict the observed double pulse output. Possible explanations include non-uniformities in the pumped gain region such as spatially dependent depletion rates, transit time effects, electron quenching of the lower level or coherent effects. Superfluorescent behavior might be expected in our high gain, narrow linewidth gain medium since the coherence time (which is on order of the upper state lifetime) is longer than the optical transit time through the gain region. Double output pulses have been predicted and observed in superfluorescent systems.¹¹

Efficient extraction of energy from these laser systems is of interest not only in developing practical applications, but also as a prototype for other photopumped short wavelength lasers. Sher, Macklin, Young, and Harris¹² have demonstrated saturation and extraction of 20 μJ of energy from a travelling wave amplifier using the Xe III 108.9 nm transition. Resonators are another possibility for extracting a coherent beam. Since the transition is short lived and self terminating, any resonator would have to be either very short, or synchronously pumped. In the case of short resonators, computer simulations may be helpful to determine the tradeoff between high single pass gain and the reduced number of passes resulting from an amplified spontaneous emission reduced gain lifetime. In the case of a synchronously pumped resonator, the resonator transit time could be made longer than the lower level decay lifetime, and repetitive excitation pulses could produce gain synchronously with a propagating pulse. This concept may be more practical with the krypton than with the xenon transition, since it has a shorter lower level lifetime.

In conclusion, we demonstrated gain in two new short wavelength laser systems pumped by inner-shell photoionization and Auger decay. We measured lifetimes and quenching of the important states, and demonstrated the use of a reflector for multipass amplification. Time dependent simulations were used to model the temporal behavior of these systems and to demonstrate that the primary effect determining the output pulse length of the laser under our pumping conditions is amplified emission. Further studies could include development of short cavity length or synchronously pumped resonators for these lasers, and the extension of the Auger pumping scheme to shorter wavelengths.

The authors thank Margaret Murnane, Richard Lee, Mau Chen, Jim Scofield, Geoffrey Kolbe and Gary Power for their assistance. This work was supported by the National Science Foundation, the Institutional Research and Development Program at Lawrence Livermore National Laboratory, the Center for X-Ray Optics at Lawrence Berkeley Laboratory, AT&T Bell Laboratories, Schlumberger Doll Research, AMOCO, and Newport Corporation.

References

1. H.C. Kapteyn, R.W. Lee and R.W. Falcone, Phys. Rev. Lett. 57, 2939 (1986).
2. H.C. Kapteyn and R.W. Falcone, Phys. Rev. A, (to be published).
3. H.C. Kapteyn, W.W. Craig, G.D. Power, J. Schachter and R.W. Falcone, Proceedings of the SPIE # 832 (to be published).
4. D.M. Roessler and W.C. Walker, J. Opt. Soc. Amer. 57, 835 (1967).
5. D.V. O'Connor and D. Phillips, Time-correlated Single Photon Counting (Academic Press, London, 1984).
6. H.C. Kapteyn, M.M. Murnane and R.W. Falcone, Optics Letters 12, 663 (1987).

7. R.G. Caro, J.C. Wang, R.W. Falcone, J.F. Young and S.E. Harris, *Appl. Phys. Lett.* **42**, 9 (1983); R.G. Caro, J.C. Wang, J.F. Young and S.E. Harris, *Phys. Rev. A* **30**, 1407 (1984).
8. R. Stern and F. Paresce, *J. Opt. Soc. Amer.* **65**, 1515 (1975).
9. J. Berkowitz, *Photoabsorption, Photoionization and Photoelectron Spectroscopy* (New York, Academic Press, 1979).
10. L.O. Werme, T. Bergmark and K. Sigbahn, *Physica Scripta* **6**, 141 (1972); S. Southworth, U. Becker, C. Truesdale, P. Kobrin, D. Lindle, S. Owaki and D. Shirley, *Phys. Rev. A* **28**, 261 (1983); H. Aksela, S. Aksela and H. Pulkkinen, *Phys. Rev. A* **30**, 865 (1984).
11. M.F.H. Schuurmans, Q.H.F. Vreken and D. Polder, *Ad. At. Mol. Phys.* **17**, 167 (1981).

Tables

	Transition	Wavelength (nm)	Lifetime (nsec)	Quenching Coef. (torr-sec) ⁻¹
Xe	Upper 5s ¹ 5p ⁵ ¹ P ₁ - 5s ⁰ 5p ⁶ ¹ S ₀	108.9	4.75 ± 0.15	2.8 ± 0.2 × 10 ⁷
Xe	Lower 5s ² 5p ⁴ ³ P ₀ - 5s ¹ 5p ⁵ ¹ P ₁	90.2	20.5 ± 2.0	2.3 ± 0.5 × 10 ⁷
Kr	Upper 4s ¹ 4p ⁵ ¹ P ₁ - 4s ⁰ 4p ⁶ ¹ S ₀	90.7	2.0 ± 0.1	3.4 ± 0.6 × 10 ⁷
Kr	Lower 4s ² 4p ⁴ ¹ D ₂ - 4s ¹ 4p ⁵ ¹ P ₁	78.6	4.5 ± 0.3	1.8 ± 1.1 × 10 ⁷

Table 1: Lifetime data for the xenon and krypton upper and lower laser levels. The wavelength, decay time and collisional quenching coefficient are indicated.

Figures

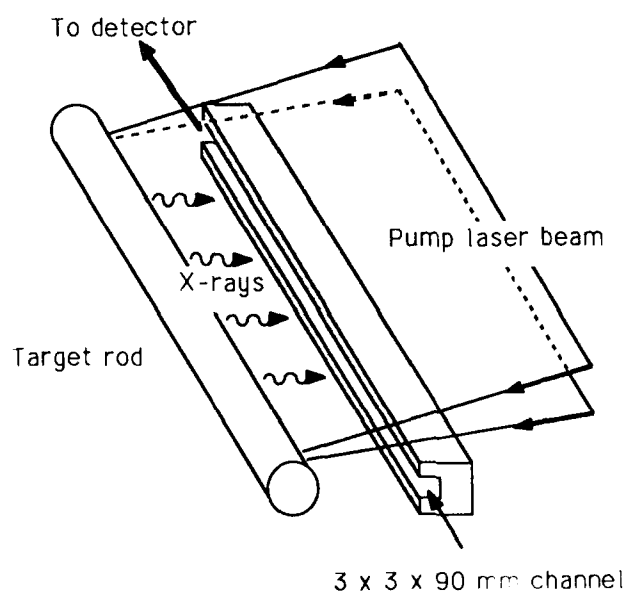


Figure 1 Gain measurement apparatus showing the pump laser focused to a line on the target rod and the emission of soft x-rays from the resulting plasma. The channel confines the observed region of the photoionized gas.

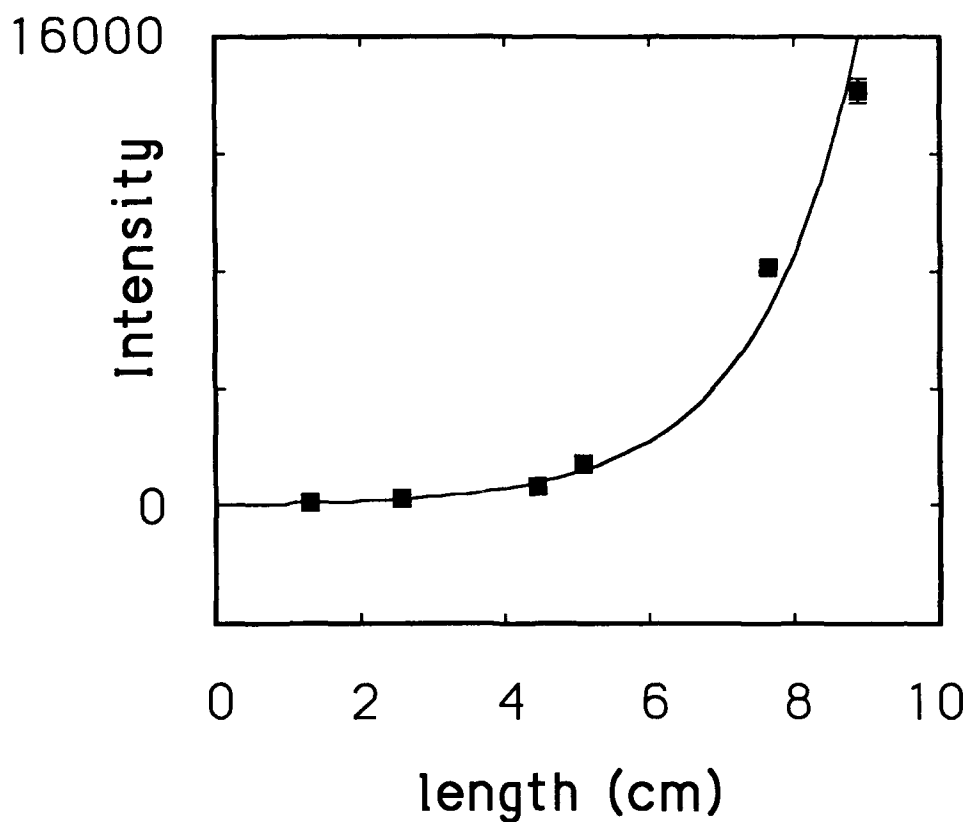


Figure 2 Intensity as a function of pumped length for xenon emission at 108.9 nm. The solid line indicates the fit to the data for a gain coefficient of 0.8 cm^{-1} .

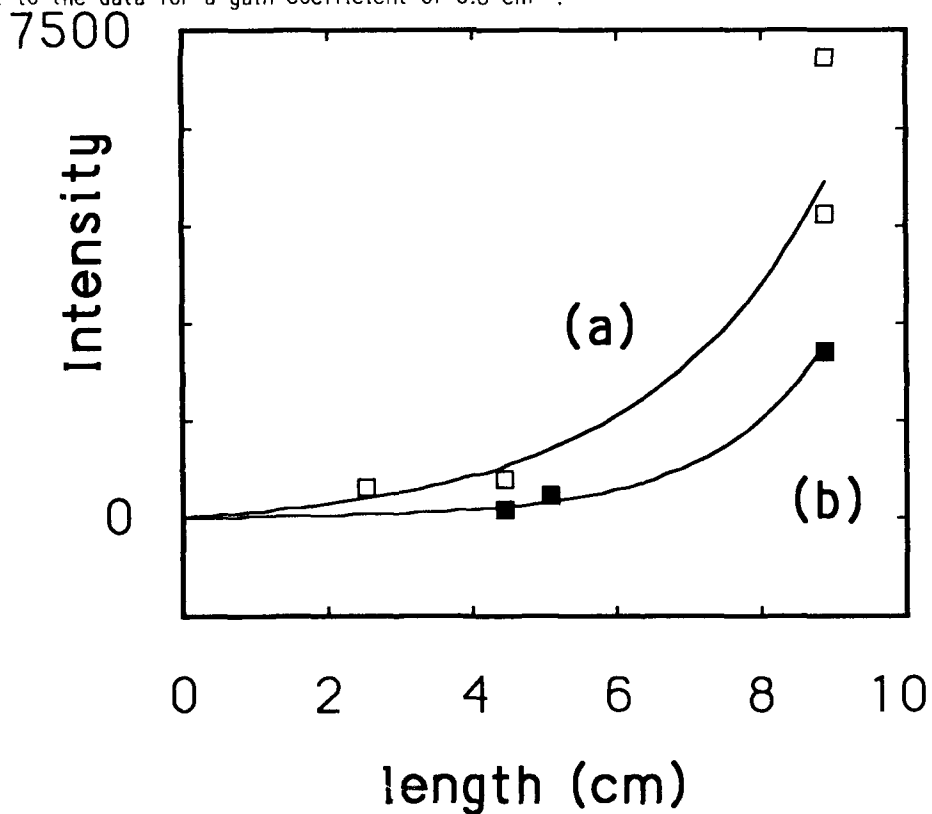


Figure 3 Intensity as a function of length for krypton emission at 90.7 nm. Curve (a) indicates a fit to data taken with a pump energy of 50 J yielding a gain coefficient of 0.5 cm^{-1} . Curve (b) indicates a fit to data taken at a pump energy of 38 J yielding a gain of 0.7 cm^{-1} .

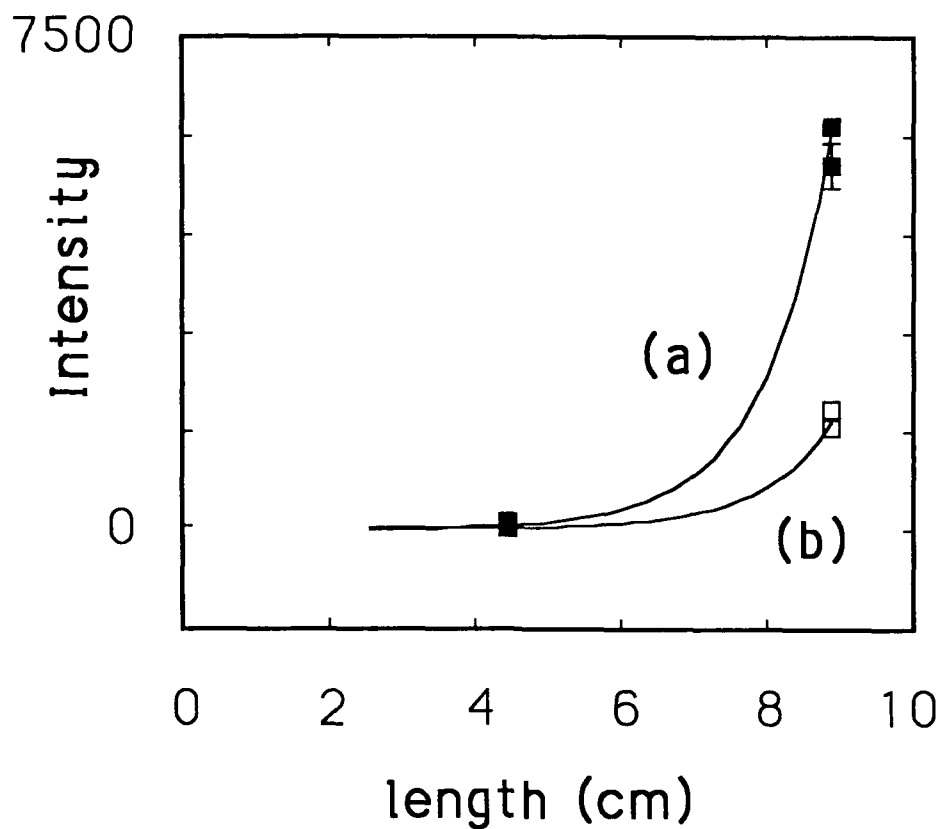


Figure 4 Intensity as a function of length for xenon 108.9 nm emission. Curve (a) indicates a fit to data taken with a lithium fluoride reflector yielding a gain coefficient of 1.12 cm^{-1} . Curve (b) indicates a fit to data taken without the reflector and yields a gain of 1.09 cm^{-1} .

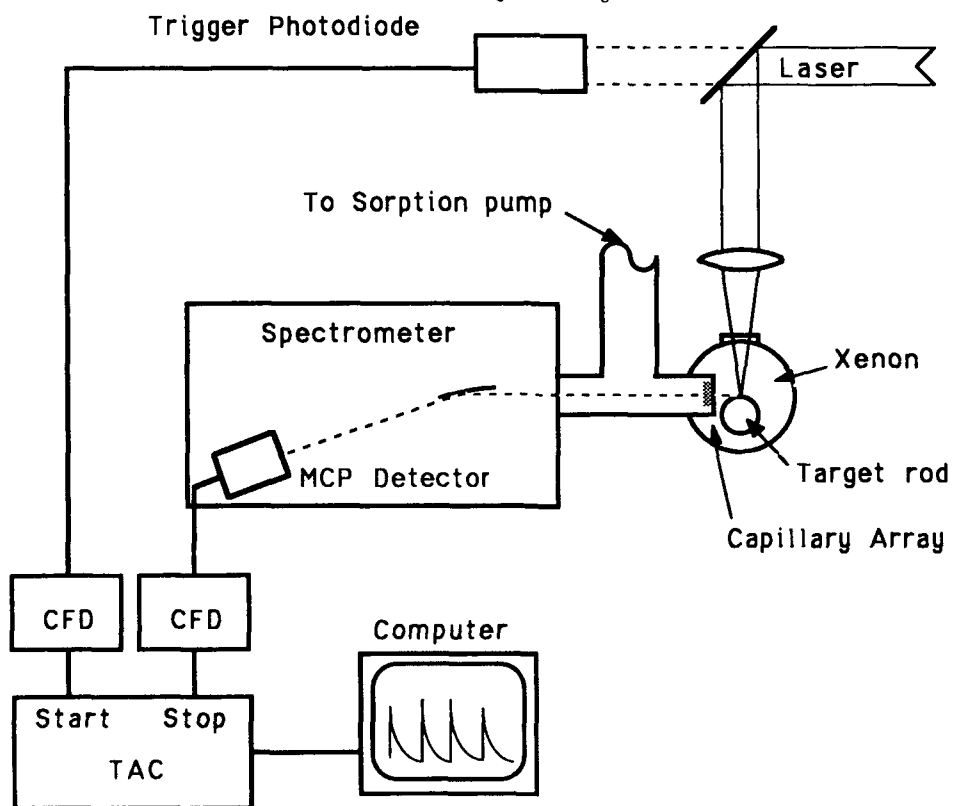


Figure 5 Time correlated photon counting apparatus.

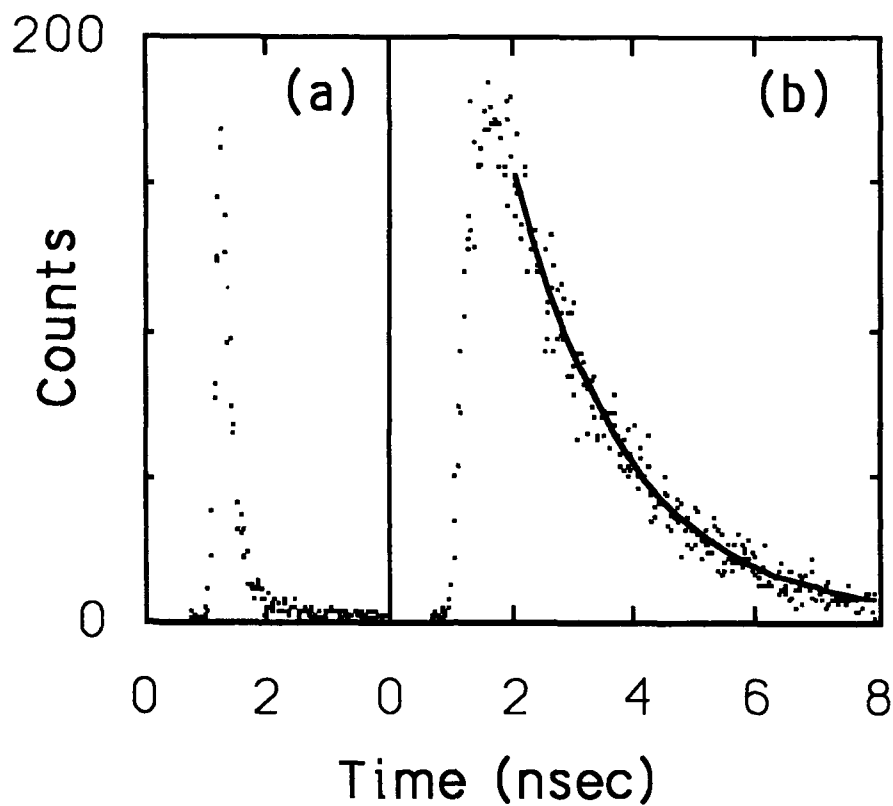


Figure 6 Time correlated photon counting data. (a) shows the time response of the system and (b) shows the decay of the krypton 90.7 nm transition at 1 torr pressure, with a fitted decay time of 1.84 nsec.

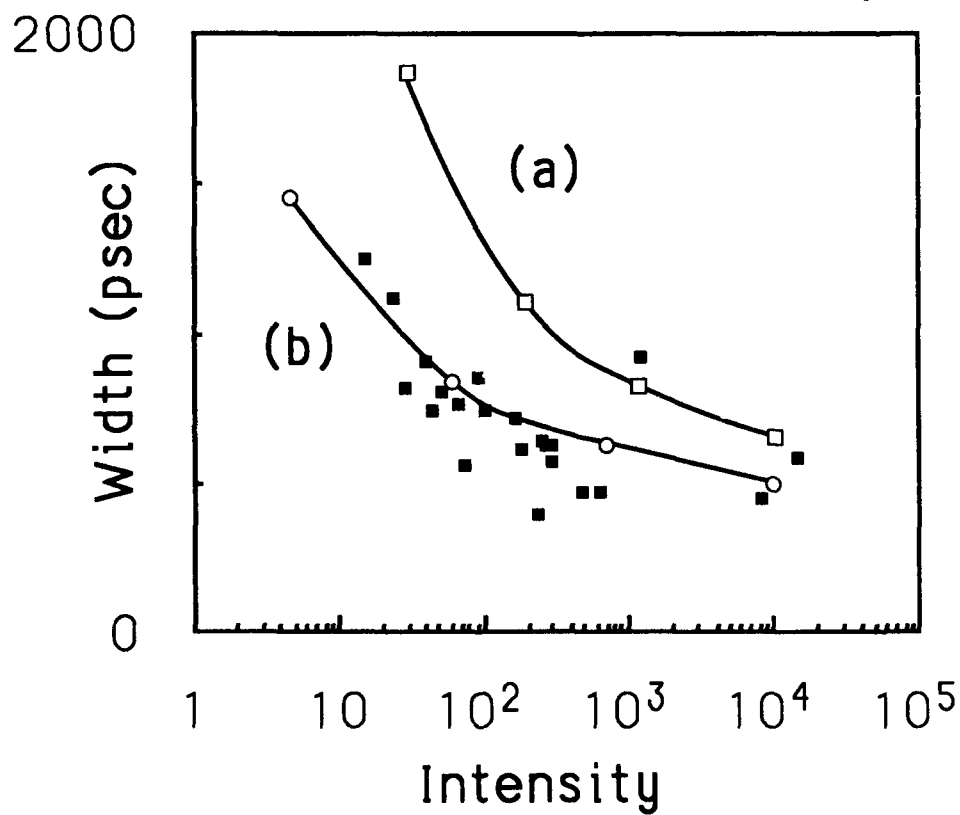


Figure 7 Pulse length as a function of output intensity for the xenon transition at 108.9 nm. The solid lines are the model predictions. Curve (b) assumes a 30% higher gain than curve (a).

EXCIMER LASERS IN EUREKA
A PROPOSAL FOR A 3 KW LASER SOURCE

T. LETARDI
ENEA, TIB-FIS DEPARTMENT - CRE FRASCATI, P.O.Box 65, 00044 FRASCATI (ROME) ITALY
P. BURLAMACCHI
UNIVERSITY OF CAGLIARI - 09100 CAGLIARI - ITALY
M. FANTINI
IRVIN SYSTEMS - Via dell'Industria S.N.C. - 04011 APRILIA (IATINA) ITALY
U. PERITO
OFFICINE GALILEO - Via Einstein, 35 - 50013 CAMPI B. (FIRENZE) ITALY
R. SALIMBENI
ISTITUTO DI ELETTRONICA QUANTISTICA (C.N.R.) - Via Panciatichi, 56/30
50127 FIRENZE - ITALY

ABSTRACT

In the EUREKA EUROLASER Project it was required the study of excimer laser sources with a final power up to 10 kw. At the same time the possibility of developing systems with final power in a lower range has been investigated by some countries. The Italian group has studied the general characteristics of a system delivering a beam with 3 kW power.

The main features of the system will be: operation with a self-sustained discharge pumping system after x-ray preionization, and optimization for XeCl, but with the possibility of operation also with F compounds.

During the development of the project, special attention will be dedicated to cavity studies for the control of the beam quality, to kinetic codes for the control of the discharge phenomena, and to specific studies for the control of pulse duration, both for short and long pulses. Exploratory work on application studies is also foreseen all along the development phase of the project.

Some information on distribution of the work, time schedule, costs and international cooperations will be finally illustrated.

INTRODUCTION

With the declaration of Hannover signed on November the 6th 1985, eighteen European countries agreed to start a scientific and technological cooperation which goes under the name of EUREKA.

Subsequently, following the conferences held in London in June the 30th and September 16th 1986 the Eureka project was given a framework within which procedures for preparation, evaluation, financing and management have been set.

The countries which joined the Eureka program are listed in Table 1. The main objectives set up by the Eureka program are:

- 1) Increase the productivity and the competitiveness of industries and national economies on international market.
- 2) Increase welfare and occupation.
- 3) Control and exploration of vital technologies for European future development.

The organization structure is the following:

- a committee formed by the ministers of scientific research and technology in charge of approving the presented projects;
- a committee of government's high representative formed by people of outstanding political and scientific weight capable of steering each national activity;
- a committee of government delegates in charge of each project capable to drag and enunciate the interests of scientific community and companies toward an industrial competitive project.

The main conditions set up for approval are the followings:

- * belong to one of the Eureka specified areas of interest.
- * Cooperation among some of the Eureka participating nations.
- * Outstanding benefits of the cooperation.
- * Development and exploration of new technologies.
- * Assurance of a technological progress.
- * Qualification of participants.
- * Fair autofinancing of participants.
- * Civil objectives only.

EUROLASER (EU6) OBJECTIVES AND ACHIEVEMENTS

At the date of september 15th 1987 the Italian participation to the Eureka approved projects is related to an overall number of 47 projects. The laser field is covered by six projects three of which have been a natural spin off of the Eurolaser (EU6) project.

The EU6 project was approved and took into consideration the definition phase for:

- A) Present interests: Carbon dioxide laser; Solid state laser; Excimer laser.
- B) Future interest: Carbon monoxide laser; Free electron laser.
- C) Other lasers for industry

The originating partners for the Eurolaser (EU6) program were originally:
Federal Republic of Germany, France, Italy, United Kingdom

To this original set of countries other countries added later on to the definition phase. They are: Austria, Belgium, Denmark, France, F.R.G., Greece, Italy, Netherland, U.K., Spain.

The Eurolaser program has so far generated five independent laser programs as a natural spin off. Two CO2 laser projects; two excimer projects and one solid state project. (see Table 2 for general informations).

EUROLASER: EUROPEAN EXCIMER GROUP ORGANIZATION

An overall number of about 80 companies and scientific organizations have participated to the Eurolaser excimer definition phase. The project was subdivided in work packages and these workpackages grouped in five main areas. Each area was coordinated by one of the national coordinators as follows:

- 1) application and market analysis. (U. Schmidt - KWU - F.R.G.)
- 2) Excimer laser concept and system aspects. (E.J. Spalding - UKAEA - UK)
- 3) Excimer laser components. (T. Letardi - ENEA - Italy)
- 4) Excimer laser discharge (M. Gaillard - Laboratoires de Marcoussis - France)
- 5) Excimer laser optics (U. Brinkmann - Lambda Physik - F.R.G.)

The outcome of this work will not be described here. We will limit ourselves in this article to describe the italian contribution to the definition phase of the Eurolaser (EU6) excimer group which constituted the basis for the spin off of the EU213 Excimer laser project (Hipulse) indicated in Table 2.

EUROLASER: ITALIAN EXCIMER GROUP ORGANIZATION

The participation of the Italian Excimer group to the Eurolaser excimer definition phase brought up a proposal for a lower power excimer laser (3 kW) than originally proposed by the international Eurolaser excimer group (10 kW).

The italian working group was organized in a way similar to the international working group (Table 3) and each group of workpackages was headed by a coordinator. The coordinators were in charge of coordinating the work performed by each company and scientific institution involved in the respective workpackages of interest. In the reference list are indicated the contribution which made possible the completion of the italian definition phase and which are the basis of this communication [1 through 20].

THE ITALIAN 3 KW PROPOSAL

1. General features

The cooperation among the italian participants brought up the proposal of a rare gas halide (RGH) laser system which might deliver a laser radiation with a power of 3 kW. This kind of high power UV laser output system could be very useful for industrial application. In particular, if the system is combined with other laser technologies, the high power laser beam can have different characteristics, such as:

- 1. the low far-field divergence (up to diffraction limit);
- 2. the wavelength tuning or wavelength shift;
- 3. the controlled laser output pulse duration (up to picosecond);
- 4. the spatially uniform intensity output.

A laser beam with these features is very attractive for material processing, photochemistry and so on. ^{5,12}

The mean power of a pulsed laser source can be increased varying the repetition rate, which in turn effects the gas flow speed in the discharge region, or varying the energy per pulse.

In order to increase the energy per pulse the active volume must be increased, because it has been experimentally verified that the efficiency decreases as the energy density in the active volume increases, so that the energy per pulse must be increased with the discharge volume at constant energy density. Currently, few J/l can be extracted from an efficiently operated RGH source.

The maximum length of the active volume is limited by absorption processes and by con-

siderations about the problems concerning the amplification of spontaneous emission, to about 1 m. A further increase in the active volume can be done only increasing the cross section of the laser beam.

2. Discharge region features

Usually the discharge transverse dimensions (H, W) cannot be too much different, so that we can realistically assume $H \sim W$.

However, there are several factors which limit the discharge dimensions. We can summarize them as follows.

1. Rise time of the discharge current in the laser cell. Indeed the discharge circuit inductance, which the rise time of the discharge current is proportional to, is increased with the discharge cross section. On the other hand, the useful pumping time, for present systems, is always lower than about 1 μ sec, which imposes a limitation on the inductance.
2. Skin depth effects, which limit the maximum height of the discharge to the penetration of the current in the active volume. If we take the discharge conductivity of $0.02/\Omega \cdot \text{cm}$ for the usual XeCl discharge, a simple estimation shows that the skin depth is ~ 20 cm.

It is well known that discharge in F_2 mixtures are less stable than in HCl mixtures, and these limits, therefore, are more and more severe with increasing the active volume. So, the active volume may be different for F_2 mixture or HCl mixture. In conclusion, in order to reach the final goal of a 3 kW laser system, we took into consideration two kinds of technologies, first: the high repetition rate laser, and second the high energy per-pulse laser.

Typically they might be (see Table 5)

no. I system:

1 J/pulse; repetition rate 3 kHz; active volume 1 Liter;

no. II:

10 J/pulse; repetition rate 300 Hz; active volume 10 Liter.

3. Optical cavity features

Usual configurations of optical cavities, such as stable configurations or plano-plano mirrors, easily achieve divergence of the laser beam in the region of few milliradians, which means more than an order of magnitude higher than the diffraction limit. However, the possibility of decreasing the divergence is very attractive because in this way the power density can be increased, with higher accuracy of material machining. Recently many schemes of unstable cavities have been used with excimer lasers, both in the positive branch and in the negative branch configuration. It is now clear that low divergence diffraction limited beams can ideally be obtained without serious reduction of extraction efficiency. However, further studies still need to be done. For some schemes there are problems of stability and criticiness (especially in the positive branch), in other cases (negative branch, SFUR) there are problems of limited volume of the mode. So, for large aperture systems further investigations should be done in order to choose the best optical configuration. ⁷

4. Power supply features

Operation of the laser requires the utilization of an adequate power supply-system. It consists of a Main Power Supply section (MPS), a Prepulse Power Supply (PPS), and a X-Preionization Power Supply section (XPS).

MPS typical specifications might be the following: average power of 50 kW, voltage level on the storage line from 30 to 60 kV with a risetime of ≤ 10 μ s. To fulfill these requirements a resonant transformer command charging system will be employed, with the benefit of a low voltage power section, solid state (thyristor) command charge switch, with relatively high energy transfer efficiency. ¹⁶

The PPS section provides a voltage level ranging from 80 to 100 kV with an average power of 5 kW to the prepulse storage capacitor. Switching-mode systems could be employed for optimum control and stabilization. Similarly this solution will be chosen for the XPS section, providing voltage levels between 150 and 200 kV and average power of 10 kW. ¹⁴

5. Switch features

One of the most important technological issues in high power pulsed gas lasers is the problem of switching energy in a very short time from the source to the load. In this respect excimer lasers requirements to the excitation process are extremely severe in terms of peak current and voltage risetime. Usual high power switches employed so far during the development of this class of lasers have been quite often at the limits of the operative parameter ranges. In the last few years the general trend has been a wide investigation on the potential advantages offered by magnetic materials (MM) in comparison with traditional components such as Spark-gaps (single arc or in a rail geometry) or Thyratrons. Indeed in suitable geometries a fast flux saturation produces a sudden reduction of the imaginary part of the impedance opposed otherwise to the current flow, with good risetimes and reasonable losses. Several companies have deve-

loped MM for low losses high frequency operation. These materials can be divided in two main classes: ferrites and steel alloys, allowing different choices in terms of various parameters, such as saturation flux, unsaturated permeability, losses, design geometries, hysteresis, loop shapes or others.

For all these types of different switching requirements MM will be employed both as switches (MDS) or magnetic compressors (PDS, XGS) besides high power ceramic thyristors. During the preliminary device development various MM will be tested to evaluate their effectiveness in terms of switching time, losses and component lifetime.

On the other hand preliminary evaluations on the cost incidence of magnetic compressors indicate the necessity to develop studies on the use of different pumping schemes.

6. Energy Storage Systems Features

If we fix the efficiency of the laser system to a level of 2%, the storage capacitors must:

- 1) Store an energy from 50 J to 500 J;
- 2) Transfer a power of 150 kW.

Solid state (mylar) or water capacitors may be used: stored energy density in mylar can be a little higher than in water, but the water capacitors are essentially self-repairing in case of internal discharge, and can easily dissipate the heat. On the other hand, water capacitors, for the reason of the limited insulating properties, can be charged only for times not longer than few microsecond. So, the two system are both attractive for an industrial system, and the final decision must be taken after the collection of further elements. Any way, a suitable development must be undertaken for solid state system in order to reduce the losses which limit the power handling capabilities of most commercial capacitors, when used in fast discharge circuits.

7. Preionization System Features

Of the different preionization system, U.V., corona, e-beam, X-ray, only the X-ray seems to be suitable for the preionization of large active volumes, especially, for large volume or high pressure discharge systems.

Theoretical studies set a lower limit of $\approx 10^5$ e/cm for the preionization density to obtain uniform discharges and experimentally, it has been verified that, at least for XeCl, 10^7 e/cm is a sufficient preionization density for this purpose.

From the experience gained up to now in X-ray preionized discharges, the voltage of the X-ray tube must be in the region of 100 kV. Usually a stored energy of 10 J for X-ray diode is sufficient for a uniform discharge in a 10-l volume.

If we keep in mind that the discharge energy safely desposited in such active volume can be of the order of 1 kJ, one sees that the power in the preionization system can be of the order of percent of the power of the main discharge.

For efficient preionization, cathodes that can deliver current peak-pulses of ≈ 1 kA, for 100 nsec, are necessary. Even if such cathodes are today existing (plasma cathodes, cold emission cathodes, etc.) their ability to work in the kHz range for more than 10 pulses must still be proved.

8. Automation of control features

Gas Mixture Processing

The laser will operate with several mixtures, depending on the required wavelength of the output radiation. The conventional approach up to the present time is to create a static fill of the appropriate gas composition and partial pressures and then recirculate the gas trough the electrodes by means of a fan and eventually a wind tunnel.

The following sequence of operations will be required: a) Evacuation of the laser head; b) Fill up with the appropriate gases with controlled pressures; c) Recirculation of the gas mixture in an appropriate gas purifier.

Starting program

After the gas fill is performed an automatic warm up of all the components will start. The high voltage power supplies are set in a stand-by position until the gas flow system and all the cooling systems are in operation.

Beam Characteristics

The output beam can be controlled for different possible applications.

The wavelength can be selected by a tuning system consisting in a selective cavity or by changing the gas mixture. As the mirror reflectivities and spectral response are different in the various cases an automatic switch is required. More complicated automations can be optional if the optical cavity geometry has to be varied (stable versus unstable resonators and so on). The optimization for different gas compositions or different output characteristics may require the substitution of the electrodes.

Power Delivering Control

The laser output which reaches the working station must be controlled in several ways.

- a) Energy per pulse, for the appropriate dose at each pulse. b) Average power, c)

repetition rate, d) Sequences of pulses. This control will be determined by an appropriate program, depending on the particular application which have to be performed at the working station.

System Master Control

Automatic check of the following parameters at various points in the system will have to be performed:

a) temperature, b) pressure, c) gas flow, d) cooling liquids flow, e) electrical parameters.

Each check point must be indicated by appropriate displays with indication of failure. An intelligent decision has to be taken in case of failure to predict the kind of "intervention" (complete switch off of the system, stand by, alarm and so on).

9. Recirculation features

The evaluations have been essentially carried out by SNIA BPD ²⁰ and we report here some results.

The recirculation system of the EUREKA 3 kW excimer laser differs from those of previous, lower-power lasers mainly because the high gas velocity required in the discharge region makes the power absorbed by the recirculation fan comparable to or greater than the power absorbed by other subsystems of the laser. Therefore it becomes necessary to adopt aerodynamical optimization techniques which were unnecessary in the past.

Another consequence of the high gas velocity is that compressibility effects become significant, and may lead to noticeable changes in temperature and pressure of the gas through the system.

One problem that may arise because of the high power of the recirculation system is vibration. Vibrations in a closed-loop recirculation system are caused both by the rotating mass of the fan and by whistling in the ducts, and in a system of the size considered here are such that they must be explicitly taken into account in the mechanical design of the wall ducts.

The evaluation of the possible laser parameters involved in the recirculation system to try to assess general performance criteria and make some trade off, starts from a well known relation. ²¹

$$P(L) \approx \frac{T}{\ln(1/R)} I_s W H d_0 \quad (1)$$

where:

I_s = $h\nu/2\sigma\epsilon_f$ = saturation energy
 d_0 = $\sigma(N_2 - N_1)_0$ = small signal gain
 T = $1 - R$ = mirror transmittivity

A simple manipulation of (1) shows that:

$$P(L) \approx R E_d \nu A = \text{laser power output where:} \quad (2)$$

A = $L \cdot H$ = gas flow cross section

ν = gas flow velocity

L = active volume length

H = active volume height

W = active volume depth

E_d = stored energy per pulse

R_c = proportionality constant (function of resonant cavity characteristics)

In case of high frequency operation equation (1) is modified as follows: ²²

$$P_{MAX}(L) = R_c E_d \nu A / K(E_{PUMP}) = R_c E_d V / K(E_{PUMP}) \quad (3)$$

where:

$K(E_{PUMP})$ = $(1/f)/t_f$ = clearing factor ²²

$P_{MAX}(L)$ = total power output at the P.R.F. in which laser starts arcing ²²

t_f = gas flow transit time

V = $\nu \cdot L \cdot H \cdot W$ = volume flow rate

E_{PUMP} = pump energy

f = pulse repetition frequency

A useful parameter in a recirculation gas systems is the energy ratio E_R defined as the ratio of kinetic energy flow rate in the highest-velocity (smallest area) part of the hydraulic loop to the absorbed power.

The energy ratio of a given system becomes approximately independent of operating conditions once a fully turbulent regime is achieved so that a useful comparison among the proposed operating specifications in terms of power requirements may be obtained

The energy ratio is:

$$P(F)/P(R) = E_R \quad (4)$$

where:

$$P(F) = \frac{1}{2} (V \cdot d \cdot \rho^2) = \text{kinetic energy flow in the fluid stream} \quad (5)$$

$P(R)$ = power absorbed by fan
 d = gas laser density

The value of E_R is generally around 0.6 for small excimer lasers mean while reaches values of 3 to 7 for well optimized wind tunnels. By use of equation (3) introducing the values of V and of ρ into (5) it is possible to express $P(F)$ in function of laser specifications and finally with (4) derive fan power

$$P(R) = (1/R_c^3) (1/E_R) [K^3 (E_{PUMP}) P_{MAX}^3 (L) d / 2 E_p E_d^2 L] \quad (6)$$

E_p = total stored energy per pulse.

Using specifications given in Table 4 it is possible to derive Table 5 and Table 6.

Table 5 shows the energy flow rates for the two kind of systems taken into consideration in Table 4 both for a low energy ratio and a high energy ratio. It is possible to see that even in a well optimized wind tunnel, fan power consumption can be a consistent fraction of power input to the laser head depending on design and buffer gases. Table 6 shows some evaluation about pressure drops and dimension of commercially available fans capable of satisfying the design requirements.

The design gas velocity in the discharge region of the EUREKA excimer laser is a non-negligible fraction of the speed of sound. When the Mach number is not small, noticeable changes in gas temperature and pressure take place because of compressibility effects. In particular, when the gas is accelerated from zero speed to a given velocity its temperature decreases, in a manner that can be calculated from the Bernoulli equation and the equation of state when the flow is isentropic, as it may reasonably be assumed in a well-designed contraction.

Table 7 shows the increments in temperature and pressure which are foreseen to be maintained in the stagnation region (low speed part of the recirculating system) and particular at the entrance of the convergent leading to the discharge region if 50°C and 2 atmospheres are to be maintained in the discharge region itself.

10. Cooling features

As can be observed, compressibility effects are relevant for the type I configuration, in which a temperature difference of 65°C for argon and 33°C for neon exists between the discharge region and stagnation conditions. This temperature difference may be advantageous in that a smaller heat exchanger is necessary.

The EUREKA excimer laser recirculation system must include a suitable cooling device in order to dispose of the heat generated both by electric discharge and by friction in the ducts.

In order to estimate the approximate specifications of the heat exchanger, the relevant parameters are the thermal power to be transferred, the flow rate and temperature of the two fluids, and the maximum allowable pressure loss due to friction. It will be assumed that the coolant fluid is running water.

Typical values of the heat exchanger parameters for the different conditions foreseen for the EUREKA excimer laser are collected in Table 8, for an inlet water temperature of 20°C and exit gas temperature of 50°C at a pressure of 2 or 5 atm. In the same table an estimated indicative value of face area is given

11. Overall recirculation system features

In table 9 are indicated the main components which make up the recirculation system for type I laser. If a high energy ratio is to be achieved, each of these components must be carefully designed and tested.

The possible locations of the cooling unit are indicated in Table 9 before or after the fan or at the end of the second bend before the convergent. The overall size of the loop may be of the order of 2 by 0.8 metres, indicatively.

A similar system for the type II discharge section configuration is also easy to be made. The main differences would be in the use of sharp bends with guiding vanes, preferable because of the thicker cross-section and use of a 3:1 rather than 4:1 diffuser to shorten the loop (the somewhat worse energy ratio that this will entail, is probably tolerable given the lower power involved).

The overall size of the type II loop may be estimated in 3.5x1.5x1 metres.

Of course, the dimensions indicated in these two examples are only indicative, and are intended to serve as a guide in finalizing system specifications.

The discharge region is the highest velocity part of the loop and particular care must be taken to design it in such a way to achieve good aerodynamic efficiency (energy ratio).

Gasdynamic and electrical properties must be taken into account. For instance particular care must be taken in designing a high velocity region without protrusions, sharp corners and sudden cross-section variations. A peculiar and important aerodynamic problem is that created by the release of energy from the discharge itself. The performance of the downstream diffuser might be strongly effected by such a behaviour and even the energy ratio might be adversely influenced.

The perturbation induced in the gas conditions by the electric discharge has been observed in the past to effect unfavourably the stability of subsequent discharges. Numerical simulations could be set up to study the evolution of this perturbation and the recovery of uniformity. Experimental techniques to properly assess discharge behaviour by means of optical diagnostic of the active medium with holographic interferometry will be implemented by groups having already proven experience. ^{1,24}

12. Gas purification and material compatibility features

Gas purification and material compatibility are essentially engineering problems but not less important ones. Gas purity is generally achieved by means of cryogenic cooling so to freeze compounds formed in the discharge region. The most harmful component for the discharge region are nitrogen oxides from residual air and halides from reaction of activated halogen atoms with the container walls. Elimination of the impurities and replenishment of the consumed halogen donor (F_2 or HCl) can increase by several times the duration of a gas refill.

Replenishment of the halogen donor is an easy operation requiring only periodic additions of F_2 or HCl and does not require further discussion. A closed loop refrigerating unit will be the best solution for cryogenic cooling.

From the specifications of the EUREKA excimer laser it can be obtained that one passage through the trap every 10 shots requires a gas flow rate of the order of 3 l/s for both the type I and type II discharge region configuration. Refrigeration of this quantity of gas from $+50^\circ$ to $-50^\circ C$ requires a refrigerating power of between 400 and 1000 kcal/h depending on the composition and pressure of the laser mixture.

Material compatibility is of course another important engineering problem.

Most common metals of construction are self-passivating and compatible for use in a pure fluorine environment. All metals burn in pure fluorine if heated to the ignition temperature, but of course self-ignition is inhibited in a mixture of inert gases with a low fluorine content because of the effect of thermal conduction.

Different is the situation in the presence of hydrofluoric acid, which forms complex compounds leaving the surface of the metal exposed to further corrosion.

An important source of hydrofluoric acid is water impurity, which reacts spontaneously with fluorine to form hydrofluoric acid. Moisture itself can also react with the passivating fluoride film, forming complex compounds and leaving the metal surface exposed to further corrosion. Therefore one imperative precaution to be taken in fluorine-handling systems is to eliminate carefully any trace of moisture.

Depending on the composition of the gas used different materials are available the most resistant of which are copper, brass and stainless steel.

Among less common materials, tantalum displays a very good resistance to hydrochloric acid but is rapidly corroded by hydrofluoric acid, while a nickel alloy known by the commercial name of hastelloy shows very good resistance to both compounds.

RESULTS OF THE MARKET STUDY

A market study has been commissioned to a specialized company to back up the technical work of this proposal. ²⁴

Presently excimer lasers are mainly used for research. Also the excimer lasers installed for industrial material processing purposes are nearly exclusively used in application laboratories for process development and application studies. The same is true for medical excimer lasers which are presently only used for experimental work.

In the future industrial, medical and measurement applications are to be expected. Especially in industrial material processing high power excimer lasers (with an average power in excess of 500 W) are expected to find applications as well as low power excimer lasers.

Table 10 shows how this market study has been subdivided in application sectors to properly assess the market potentials. We do not report here the complete results of this market study which is a proprietary study but we show in Table 11 the overall result of the potential accumulated market for Europe up to year 2000, for low power (less than 500 W) and high power (more than 500 W) excimer lasers.

The results of this study are indicative of to day know how and don't take any notice of improvements in the technologies and break through which are likely to happen in the future years.

The analysis of present market potential shows that mainly low power excimer lasers are expected to be needed. In addition to the general guidelines of low price/power ratio, high reliability and up time, development of the application technology and systems suited for industrial use (which is extremely important), the need to follow specific requirements are:

- 1) Good shot to shot repeatability is necessary for microelectronic applications (better than 2%).
- 2) A uniform beam profile is important for microelectronic applications.
- 3) Reduced linewidth (achieved e. g. by injection locking) is important to overcome the imaging difficulties (it is very difficult to develop an achromatic lens of the required

- red size).
- 4) An up-time of 95% or more as well as an easy to maintain construction is required for an integration of excimer lasers into production lines.
 - 5) Lasers with long pulse length are needed for fibre optical beam delivery (i.e. for medical applications), as well as for some material processing and scientific applications.
 - 6) In order to avoid plasma formation when strong focusing is necessary a high repetition is to be preferred to a high peak power (e.g. for many materials processing applications)

CONCLUSIONES

A study has been carried out within the frame of the EUREKA organization to assess the necessity and feasibility of a high power excimer laser of up to 3 kW output. The conclusion has been that such a machine is feasible but that is worthwhile concentrating on lower power excimer laser (up to 1 kW) with peculiar beam and versatile characteristics. This is the basis for the already started EUREKA EU 213 HIPULSE PROJECT.

ACKNOWLEDGMENTS

Thanks are given to all the scientists (see references from 1 to 20) and organizations who factively participated to this overall proposal with meetings, discussions, reports and proposals which have been the basis for this feasibility study.

REFERENCES

1. A. DE ANGELIS, F. GAROSI, ENEA-TIB, FRASCATI, ITALY, Private Communication
2. V. AQUILANTI, BRUNETTI, VECCHIOCATIVI, UNIVERSITY OF PERUGIA, ITALY, Private Communication
3. M. BERTOLOTI, C. SIBILIA, 1st UNIVERSITY OF ROME, ITALY, Private Communication
4. E. BORSELLA, R. LARCIPRETE, ENEA-TIB, FRASCATI, ITALY, Private Communication
5. M. CANTELLO, CRUCIANI, RTM, VICO CANAVESE, ITALY, Private Communication
6. M. CAPITELLI, R. CELIBERTO, UNIVERSITY OF BARI, ITALY, Private Communication
7. G. DATTOLI, T. HERMSEN, A. TORRE, ENEA-TIB, FRASCATI, ITALY, Private Communication
8. P. DI LAZZARO, ENEA-TIB, FRASCATI, ITALY, Private Communication
9. A. DI PACE, E. SABIA, ENEA-TIB, FRASCATI, ITALY, Private Communication
10. G. EMILIANI, ENEA-TIB, CASACCIA-ROME, ITALY, Private Communication
11. R. FANTONI, R. LARCIPRETE, ENEA-TIB, FRASCATI, ITALY, Private Communication
12. A. GIARDINI-GUIDONI, A. MELE, S. LORETI, R. TEGHIL, E. PENCO, UNIVERSITY OF ROME "LA SAPIENZA", ROME, ITALY, Private Communication
13. T. HERMSEN, ENEA-TIB, FRASCATI, ITALY, Private Communication
14. T. LETARDI, C.E. ZHENG, ENEA-TIB, FRASCATI, ITALY, Private Communication
15. A. LUCHES, V. NASSINI, M.R. PERRONE, UNIVERSITY OF LECCE, ITALY, Private Communication
16. F. MUZZI, EL. EN., FLORENCE, ITALY, Private Communication
17. U. PERITO, OFFICINE GALILEO, FLORENCE, ITALY, Private Communication
18. R. SALIMBENI, IEQ-CNR, FLORENCE, ITALY, Private Communication
19. F. SCUDIERI, 2nd UNIVERSITY OF ROME, ITALY, Private Communication
20. Gas Recirculation and Cooling Subsystem of EUREKA 3 kW Excimer Laser, SNIA-BPD REPORT, SNIA-BPD, COLLEFERRO, ITALY, Unpublished
21. A.J. DE MARIA, Principles of Laser Plasmas, 1986, G. BEKEFI, Ed (JOHN WILEY & SONS) pp. 341-350
22. G.S. DZAKOWIC, S.A. WUTZKE, J. Appl. Phys. 44, (11), 5061, (1973)
23. S. MARTELLUCCI, Nuovo Cimento, Serie I, 5, 642, (1967)
24. A. MAYER, N. SCHRODER, Prognos report, 1987

TABLES

- TABLE 1 - Eureka participating countries
 TABLE 2 - Eureka Eurolaser spawned project
 TABLE 3 - Eurolaser Italian excimer working group
 TABLE 4 - 3 kW Excimer laser characteristics
 TABLE 5 - Recirculation system energy flow rate
 TABLE 6 - Recirculation system fan requirements
 TABLE 7 - Recirculation system compressibility effects
 TABLE 8 - Heat exchanger specifications
 TABLE 9 - Recirculation system layout
 TABLE 10 - Excimer application sectors
 TABLE 11 - Excimer European market

<u>EUREKA OVERALL PARTECIPANTS</u>	
AUSTRIA BELGIUM CEE DENMARK FRANCE FINLAND FRG GREECE IRELAND ITALY	LUXEMBOURG NORWAY THE NETHERLAND PORTUGAL UNITED KINGDOM SPAIN SWEDEN SWISS TURKEY
TABLE 1	

<u>EUREKA EUROLASER SPINNED OFF PROJECTS</u>	
CARBON DIOXIDE	
EU 180.- 10 Kw CARBON DIOXIDE LASER AND RELATED SYSTEMS	
PARTICIPANTS	: BELGIUM, AUSTRIA, ITALY, SPAIN
INVESTMENT	: 41.6 M.E.C.U.
DEVELOPMENT TIME	: 5 YEARS
EU 114.- INDUSTRIAL APPLICATION EVALUATION FOR HIGH POWER LASERS	
PARTICIPANTS	: AUSTRIA, DENMARK, FRANCE, F.R.G., ITALY, SPAIN, U.K., GREECE
INTERESTED	: BELGIUM
INVESTMENT	: 37.7 M.E.C.U.
DEVELOPMENT TIME	: 5 YEARS
EXCIMER	
EU 205.- HIGH POWER EXCIMER LASERS	
PARTICIPANTS	: FRANCE, F.R.G., NETHERLAND
INVESTMENT	: 14.6 M.E.C.U. FOR 30 MONTHS
DEVELOPMENT TIME	: 9 YEARS
EU 213.- HIPULSE (HIGH POWER ULTRAVIOLET LASER SOURCE)	
PARTICIPANTS	: ITALY, NETHERLAND
INTERESTED	: U.K.
INVESTMENT	: 10 M.E.C.U. PLUS OTHER 6 FROM U.K.
DEVELOPMENT TIME	: 4 YEARS
SOLID STATE	
EU 226. HIGH POWER SOLID STATE LASER	
PARTICIPANTS	: FRANCE, F.R.G.
INTERESTED	: ITALY, U.K., THE NETHERLAND, SPAIN
INVESTMENT	: 19 M.E.C.U.
DEVELOPMENT TIME	: 5 YEARS
TABLE 2	

EUROLASER ITALIAN EXCIMER WORKING GROUP

- | | |
|--|--|
| <p>1. OFFICINE GALILEO (PERITO)</p> <ul style="list-style-type: none"> - APPLICATION STUDIES (SOITAAE, IEQ, GALILEO, RTM, ROME I AND II) - MARKET ANALYSIS (ENEA, CISE) <p>2. OFFICINE GALILEO (BURLAMACCHI)</p> <ul style="list-style-type: none"> - GENERAL SYSTEM DESIGN (IEQ, OFF. GALILEO, ENEA) - SYSTEM CONTROL AND AUTOM. (SOITAAE) - SAFETY SYSTEM - ENGINEERING (CONTEK, OFF. GALILEO) <p>3. IRVIN SYSTEM (FANTINI)</p> <ul style="list-style-type: none"> - MATERIAL COMPATIBILITY (SNIA BPD) - ENERGY STORAGE SYSTEM - PREIONIZATION SYSTEM (IRIN, ENEA) - POWER SUPPLIERS (ELEN, IRVIN) - SWITCHES (IEQ, IRVIN) - RECIRCULATION SYSTEM (ENEA, SNIA-BPD, IEQ) - COOLING (SNIA-BPD) - GAS PURITY (SNIA BPD) | <p>4. IEQ (SALIMBENI)</p> <ul style="list-style-type: none"> - PREIONIZATION SYSTEM II (IEQ, ENEA, IRVIN) - KINETIC CODES AND SIMULATION (ENEA) - DISCHARGE REG. DESIGN (IEQ, ENEA, OFF. GALILEO) - NEW SCHEMES (OFF. GALILEO, UNIV. OF LECCE, UNIV. OF BARI) <p>5. ENEA (LETARDI)</p> <ul style="list-style-type: none"> - BEAM MONITORING AND CONTROL - DIELECTRIC COATINGS (SELENIA, OFF. GALILEO) - BEAM QUALITY AND OPT. CAV. DESIGN - QUANTY SYSTEM, UNIV. OF PAVIA, GALILEO, ENEA) - WAVELENGTH SHIFT (IEQ) - ULTRASHORT PULSES (UNIV. OF ROME I, ENEA) - OPTICAL COMPONENTS AND NON LINEAR OPT. (GALILEO) |
|--|--|

TABLE 3

LASER SPECIFICATION

LASER POWER P(L): 3 KW
 DISCHARGE POWER = 150 KW
 Ed = 1-2 J/LITRE
 TYPE I DISCHARGE REGION 3x3x80 cm
 GAS SPEED 250 m/s
 PULSE REP. RATE 2 kHz 1 J/P
 TYPE II DISCHARGE REGION 10x10x100 cm
 GAS SPEED 100 m/s
 PULSE REP. RATE 300 Hz 10 J/P
 GAS: Ne, Ar PRESSURE 2-5 bar

TABLE 4

KINETIC ENERGY FLOW RATE

TYPE	GAS	PRESS. bar	P(F) KW	P(R)(ER=1.6) KW	P(R)(ER=2.5) KW
I	Ne	2	300	500	50
I	Ne	5	760	1300	130
I	Ar	2	610	1010	101
I	Ar	5	1500	2500	270
II	Ne	2	30	130	12
II	Ne	5	200	230	32
II	Ar	2	160	260	27
II	Ar	5	400	670	67

TABLE 5

FAN REQUIREMENTS FOR THE EXCIMER LASER RECIRCULATION SYSTEM

(ENERGY RATIO E = 5)

DISCHARGE REGION	FLOW RATE	FAN HEAD	APPROXIMATE DIAMETER	ABSORBED POWER
TYPE I	6 m/s	40 cm of water	25 cm	60-200 Kw
TYPE II	10 m/s	10 cm of water	55 cm	10-30 Kw

TABLE 1

COMPRESSIBILITY EFFECTS

DISCHARGE REGION	GAS	MACH NUMBER	STAGNATION	
			PT (°C)	DP (bar)
I	Ne	. 55	13	. 5
I	Ar	. 73	65	1.2
II	Ne	. 22	5	. 08
II	Ar	. 21	10	. 17

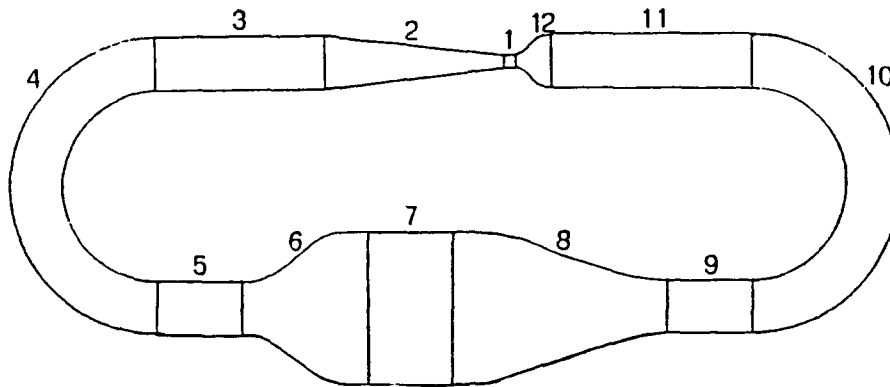
TABLE 2

HEAT EXCHANGER SPECIFICATIONS

DISCHARGE REGION	GAS	OPERATING PRESSURE	FLOW RATE	TRANSFERRED HEAT	ESTIMATED FACE AREA
TYPE I	Ne	2 bar	6 m/s	110 Kw	. 13 m ²
TYPE I	Ne	5 bar	6 m/s	200 Kw	. 15 m ²
TYPE I	Ar	2 bar	6 m/s	270 Kw	. 20 m ²
TYPE I	Ar	5 bar	6 m/s	450 Kw	. 21 m ²
TYPE II	Ne	2 bar	10 m/s	165 Kw	. 58 m ²
TYPE II	Ne	5 bar	10 m/s	190 Kw	. 42 m ²
TYPE II	Ar	2 bar	10 m/s	190 Kw	. 60 m ²
TYPE II	Ar	5 bar	10 m/s	190 Kw	. 46 m ²

TABLE 3

TYPE I RECIRCULATION SYSTEM



GENERAL LAYOUT OF THE RECIRCULATION SYSTEM IN THE TYPE I CONFIGURATION.

1: DISCHARGE SECTION. 2: 4:1 DIFFUSER. 3: STRAIGHT DUCT. 4: 180° SMOOTH BEND.
 5: POSSIBLE HEAT EXCHANGER LOCATION. 6: 35 CM-DIAMETER FAN. 8: FAN DIFFUSER AND
 ROUND-TO RECTANGULAR ADAPTER. 9: POSSIBLE HEAT EXCHANGER LOCATION. 10: SECOND BEND.
 11: POSSIBLE HEAT EXCHANGER LOCATION OR TURBULENCE-CONTROL HONEYCOMB. 12: CONVERGENT.

TABLE 9

APPLICATION SECTORS AND APPLICATIONS OF EXCIMER LASERS

APPLICATION SECTOR	APPLICATIONS
MICROELECTRONICS	LITHOGRAPHY, DIRECT WRITING, ANNEALING, LASER ETCHING, DOPING, DEPOSITION, LINK BREAKING, X-RAY GENERATION
PHOTO CHEMISTRY	ISOTOPE SEPARATION, CHEMICAL SYNTHESIS, CATALYSIS, POLYMERIZATION, MATERIAL PURIFICATION, SINTERABLE POWDER PRODUCTION, PHOTODESTRUCTION OF POLLUTANTS
MATERIAL PROCESSING	CUTTING, DRILLING, WELDING, SURFACE ALTERATION, ABLATION AND MICROSTRUCTURING, METALLIZING AND DRILLING OF PRINTED CIRCUIT BOARDS, STRUCTURING OF CERAMICS, POLYMERS, AND COMPOUNDS, MARKING
MEASUREMENT AND RESEARCH	DYE LASER PUMPING, SPECTROSCOPY, LIDAR TECHNIQUES

TABLE 10

MARKET FOR EXCIMER LASERS IN EUROPE

(ACCUMULATED MARKET IN UNITS)

APPLICATION SECTOR	LOW POWER LASERS (LESS THAN 500 W)	HIGH POWER LASERS (MORE THAN 500 W)
MICROELECTRONICS		
PESSIMISTIC	100	0
MOST LIKELY	1000	0
OPTIMISTIC	4000	250
PHOTO CHEMISTRY		
PESSIMISTIC		0
MOST LIKELY		120
OPTIMISTIC		700
CUTTING, DRILLING, WELDING, MARKING, SURFACE ALTERATION		
PESSIMISTIC	45	15
MOST LIKELY	130	130
OPTIMISTIC	630	540
MEASUREMENT AND RESEARCH		
PESSIMISTIC	1500	10
MOST LIKELY	2500	20
OPTIMISTIC	3500	50
TOTAL		
PESSIMISTIC	1645	25
MOST LIKELY	3630	270
OPTIMISTIC	8130	1540
TABLE 11		

High Power Excimer-Laser

H.-J. Cirkel

Siemens AG, Hammerbacherstraße 12 + 14, D-8520 Erlangen
Fed. Rep. Germany

Abstract

For excitation of high power excimer lasers a pulse forming network (PFN) has been developed which is made up of a large number of paralleled waterline capacitors arranged normal to the optical axis of the laser. An elongated x-ray gun employing a hollow cathode preionizes the laser of 45 cm gain length. Up to 4 J optical energy have been measured at 308 nm. Between 1 J and 2.5 J the laser emits at other known rare gas-halides wavelengths for a lower stored energy in the PFN. With an injection locked amplifier low divergence operation has been achieved. The results of a 20 channel pseudo spark switch are presented and show a current rise of $2.6 \cdot 10^{12}$ A/s for 100 kA peak current.

Introduction

For advanced industrial applications in the fields of material processing, photochemistry and especially laser isotope separation, high power excimer lasers are of special interest. Consequently the Kraftwerk Union group of the Siemens Corporation started a development program.

System description

Figure 1 shows the components of a high power excimer laser. At about 5 cm distance the laser head houses the elongated electrodes, the grounded one of which is transparent to the x-rays for preionization. The pulse forming network made up of low inductance waterline capacitors stores the electrical energy, which is transferred to the laser after closing the switch S. The charging unit connected with the public grid provides the electrical energy for the laser. For high rep rate operation a flow loop composed of blower, cooler and gas processor produces a homogeneous gas flow through the laser head transverse to the optical axis.

The aerodynamically designed bars of the laser head (fig.2) bear a shielding to prevent against sliding sparks and the current returns from the grounded electrode to the pulse forming network (PFN), consisting of many paralleled waterline capacitors. These stripline capacitors are stacked along the optical axis and use deionized water as a dielectric because of its high dielectric strength of more than 100 kV/cm, high dielectric constant of about 80 and its good cooling properties. A variety of low inductance switches such as spark gaps, rail gaps, thyratrons or pseudo sparks can be used with this type of PFN.

The PFN composed of paralleled waterline capacitors of negligible electrical length, is formed by stainless steel plates immersed in deionized water and arranged vertically to the optical axis of the laser ¹. Different circuits of the PFN can easily be realized by connecting the plates with the different electrodes E_1 , E_2 of the laser head K and the switch S. By choosing only current compensated geometries for the plates, all the inductance of the excitation circuit has to be located in the laser head with its current returns.

The LC-inversion circuit (fig. 3a) allows doubling of the charging voltage across the laser electrodes. The smallest unit representing this circuit is shown in fig 3b. Many of this unit are paralleled in the PFN. The charge transfer circuit (fig. 4a) is also in widespread use for excitation of excimer lasers. By changing the plate area and/or the thickness of the dielectric, the capacitance ratio C_L/C_K can be varied (fig. 4b), so that the measurable peak voltage across the laser electrodes is between one and two times the charging voltage of the PFN. The ICT-circuit represents a combination of the above mentioned circuits (fig. 5). The achievable voltage across the laser electrodes depends on the capacitance ratios and is between one and two times the charging voltage of the PFN.

Because of the properties of the water dielectric pulse charging via a solid state capacitor C_Z and a switch S_L is required (fig. 6). The electronic control of the laser triggers the charging unit and the switch S_L . After the energy transfer from the capacitor C_Z to the waterline capacitors the switch S is activated. In case of two thyratrons EGG HY 3202 or EEV CX 1625 being paralleled for the switch, both tubes have to be synchronized actively within ± 1 ns. During the voltage rise across the laser electrodes the control unit fires the x-ray pulse of about 50 ns halfwidth for preionization of the laser gas.

X-ray preionizer

The required 100 kV voltage pulse for the x-ray gun is generated by a pulse transformer ², of which the primary windings are the load of a pulse generator (fig. 7). Substituting the x-ray gun by a 50 Ohm or 100 Ohm resistive load, the characteristics of the pulse transformer are recorded (fig. 8). This type of transformer, which can reliably be run at repetition rates up to several hundred Hertz, is characterized by a very low stray inductance and a coupling of more than 99.9 %. Because of the problems associated with field emission cathodes we have developed an x-ray preionization unit employing a hollow cathode.

The hollow cathode turns out to be superior to the cold or field emission cathode (fig. 9). Progressing in time the x-ray gun with field emission cathode shows a degradation of its emission caused by a melting and a concomitant sputtering from the thin cathode. Employing the hollow cathode no decline in x-ray intensity is observed even after several million shots and at repetition rates up to several hundred Hertz. A very stable and homogeneous x-ray distribution along the optical axis of the laser is measured for this type of preionizer.

Results

The laser itself has been operated at low repetition rates with a gain length of 45 cm and an electrode gap of 53 mm. Neon at 5 bar is used for buffer gas with 0.5 % to 1 % Xe and about 0.1 % to 0.2 % HCl and an addition of 0.02 % H₂. The inductance of the excitation loop is measured at about 10 nH. According to the burn pattern of the laser pulse the discharge width depending on the stored energy in the PFN varies between 40 mm and 53 mm. The optical pulse P_{opt} (fig. 10a) of nearly 60 ns halfwidth extends about 10 ns beyond the exciting current pulse. After closing the switch the voltage U_L across the laser electrodes rises for about 200 ns until gas breakdown occurs and the laser current I_L starts to pump the laser (fig. 10 b). In the computer plot (fig. 10 c) the measured voltage is corrected for the inductive voltage drop in the excitation circuit of the discharge. Immediately after gas breakdown a constant voltage of about 100 ns duration is established feeding the high pressure glow discharge at characteristic E/P values. The resistance of the gas discharge collapses to 0.15 Ohm (fig. 10 d) driven by an excitation circuit of 0.28 Ohm characteristic impedance. Between 70 % and 80 % of the total energy dissipated in the discharge is injected into the laser gas during the first current peak.

In the leading edge of the voltage pulse U_L (fig. 10b) the laser has to be preionized by the x-ray pulse of sufficient intensity. About 110 ns prior to the breakdown time (fig. 11), which remains nearly constant during the experiments at about 180 ns after start of the voltage rise across the laser electrodes, the laser has to be preionized for optimum performance during a time window of about 50 ns duration. Under these conditions the laser pulse of about 2.7 J shows an energy stability of 1.5 %, whereas at too late a timing the strong fluctuating pulse energy drops dramatically associated with a very poor discharge quality. Premature preionization leads also to an unstable discharge of low energy output. The performance of the laser also greatly depends upon the properties of the PFN.

By the above described system output energies at low rep rate operation between 2.5 J and 4 J are achieved at efficiencies ranging from 2.5 % to 3 %. At E/P values of 540 V/cm bar - slightly dependent on the gas mix - the high pressure glow discharge phase of the XeCl-laser is established at current densities of 410 A/cm². The optical energy density varies between 2.2 J/l and 3.1 J/l.

In addition to the XeCl mode this laser has been successfully operated at other excimer wavelengths. For KrF the x-ray preionizer of 50 ns to 80 ns pulse width has to be timed within 80 ns (fig. 12). At a charging voltage of 29 kV and about 110 J stored energy 3.1 J have been measured for the XeCl-laser employing a plane-plane resonator of 5 % output mirror reflectivity (fig. 13). The somewhat less efficient KrF-laser peaks for 30 % output mirror reflectivity at 2.5 J. Remarkable 1.5 J for the XeF-laser are achieved and in the ArF- and KrCl-mode the laser still emits 0.95 Joule. For buffer gas all different lasers use Neon. The maximum pulse length of about 50 ns has been achieved by the KrF-laser (2.9 bar Ne, 0.1 % F₂, 2.6 % Kr) compared to about 40 ns of the XeCl- (4.75 bar Ne) and XeF-laser (4.0 bar Ne, 0.1 % F₂, 0.25 % Xe). For the KrCl- (4.0 bar Ne, 0.05 % HCl, 3% Kr) and ArF-laser (4.0 bar Ne, 0.05 % F₂, 4 % Ar) the pulse length drops to about 30 ns.

Injection locked amplifier

Employing a plane-plane resonator the divergence of the laser is measured at several mrad. To improve the beam quality a combination of an oscillator and amplifier ³ is used (fig. 14). With an unstable resonator of magnification 8 the oscillator starts emitting at some mrad, narrows after several roundtrips to some 100 μ rad, until in the trailing edge a divergence of less than 100 μ rad - about two to three times the diffraction limit -

is finally reached. By a proper timing of the oscillator and the amplifier discharge only laser light of high optical quality can be amplified, so that the output pulse of the system has from the beginning a superior optical quality. By this selection technique the extraction efficiency of the amplifier is raised and the pulse envelope smoother [11,12].

High repetition rate operation of the laser

The high rep-rate operation of excimer-laser is of special interest for many applications. At an energy per pulse of about 2 J the laser system is designed for about 240 W average power at 100 Hz repetition rate. In first preliminary experiments 140 W average power at 308 nm are achieved. To analyse the behavior of the system at higher rep rates a Mach-Zehnder interferometer has been installed (fig. 16). By a framing camera the evolution of the discharge and the inhomogeneities of the gas caused by the energy dump of the excitation pulse are recorded at high time resolution. Before gas breakdown (fig. 17) a regular undisturbed pattern with a fringe distance corresponding to $\Delta\rho/\rho = 1.5 \cdot 10^{-3}$ is observed. At the rise of the laser current the fringes are regularly bent indicating a homogeneous electron density between 2 and $3 \cdot 10^{15}$ per cm³. In this field nearly covering the whole picture, the excimer molecules are created by the high pressure flow discharge. Inside this region 50 ns to 100 ns after breakdown a small and constricted area of high electron density gradually emerges. This time correlates with the beginning of the reverse current in the laser discharge. Progressing in time the interferometer reveals a very rapid energy transfer to the laser gas from the electrons contained in this narrow ribbon. A very turbulent zone with distinct boundaries arises, expands at the speed of sound and covers the entire cross section after more than 20 μ s. Outside the primary small region a regular shaped compression wave and the concomitant wave of lower pressure - the rarefaction wave - develops within 10 μ s. This wave of 1.3 higher density than the surrounding gas is built up by thermalization of the energy contained in the high pressure flow discharge and causes an adiabatic pressure rise of 85 mbar and a temperature rise of 2 K. In a static gas all kind of waves originating from the short discharge are damped within roughly 1 μ s. After this period the next discharge can be fired without any loss in optical pulse energy.

From these experiments a necessary condition for high rep-rate operation has been deduced. For optimum efficiency the density fluctuations within the laser gas must be kept well below 0.1 % before the next discharge can be ignited. This condition poses stringent requirements on the PFN, the laser head and the flow loop design.

Multi channel pseudo spark switch

Besides high rep-rate operation a high energy per pulse is also required for high average power excimer lasers. The 4 J laser mentioned before has a halfwidth of about 50 ns and is excited by a peak current of about 100 kA (fig. 18a). Two thyratrons working at 15 kV are used for the switch in the PFN, wired as LC-inversion circuit. The peak current in forward direction for one thyatron is measured at about 24.5 kA (fig. 18b); the peak reverse current amounts to 8.5 kA. Besides these values a severe ringing stresses also the thyratrons used in the 4 J laser. Within the rated specifications the thyratrons are operated for a 2 J laser.

A new switching element based upon the pseudo spark ⁴ provides a solution to higher peak and reverse currents. The pseudo spark is a low pressure gas discharge working on the left branch of the Paschen curve. By an insulator both electrodes are kept in a distance much smaller, so that an avalanche discharge bridging both electrodes on the shortest path cannot develop (fig. 19). Whereas electrons traveling in the axis of the facing holes in the electrodes can ionize the gas and thereby short the gap.

Based upon this concept a new switching element ⁵ has been developed (fig. 20). After triggering the device electrons from the hollow cathode discharge are injected into the axial field between the cathode and anode of the switch and accelerated in the high field. In the backspace of the anode high energy electrons are collected on the surface of a metallic cup. The pseudo spark switch is characterized by a very compact design and a commutation phase of less than 1 ns; both prerequisites for a low inductance switch. By the hollow cathode structure lifetime limiting erosion processes on the electrodes are avoided. Also large reverse currents do not cause any harm to the switch. In a rotational symmetric geometry a direct replacement of the thyatron by the pseudo spark is possible.

For use in high power excimer lasers a pseudo spark switch composed of several pseudo sparks in parallel ⁶ is of special interest (fig. 21). This device resembles a rail gap switch but avoids its technical drawbacks.

A 20 channel pseudo spark switch has been tested at a hold off voltage of 35 kV and the peak current was measured at about 100 kA giving a di/dt of $2.5 \cdot 10^{12}$ A/s (table). The on resistance of the device is smaller than 10 mOhm and the inductance smaller than 5 nH. Limited by the power supplies the switch has been operated in a test bench at 40 Hz without any degradation and damage. In other experiments the multichannel pseudo spark successfully replaced the thyatrons in a laser system emitting the same pulse energies for a XeCl-laser from 3.1 J to 3.5 J.

hold off voltage:	35 kV
peak current:	100 kA *
$\frac{di}{dt}$:	$2.5 \cdot 10^{12} \frac{A}{s}$ *
current rise:	20 ns *
reverse current:	< 50 A < 100 A possible
on resistance:	< 10 mOhm
inductance:	< 5 nH
jitter:	± 1.5 ns
* limited by PFN	

Table: Parameters of a 20 channel pseudo spark switch

Conclusions

From our results we are confident, that reliable excimer lasers of much higher average power will become feasible and would be an useful tool in industrial applications.

Acknowledgements

Part of the work has been performed under contract No. BMFT 13 N 5357/3 (Bundesministerium für Forschung und Technologie).

References

- / 1 / H.-J. Cirkel, W. Bette, D. Friede, R. Müller
in Proceedings, Pulse Power for Lasers
T. R. Burkes, Ed. (SPIE v. 735, 1987) pp 50-54
- / 2 / H.-J. Cirkel, W. Bette, German patent DE 2932 781 C2
- / 3 / H.-J. Cirkel
in Proceedings of the 7th International Congress Laser '85
W. Waidelich, Ed. (Springer 1986) pp 706-709
- / 4 / J. Christiansen, C. Schultheiss
Z. Phys. A 290, 35 (1979)
- / 5 / K. Frank, E. Boggasch, J. Christiansen, A. Goertler, W. Hartmann, C. Kozlik
in Proceedings, Pulse Power for Lasers, T. R. Burkes, Ed.
(SPIE v. 735, 1987) pp 74-81
- / 6 / Mechttersheimer, Kohler
J. Phys. E: Sci Instr. 20, 27 (1987)

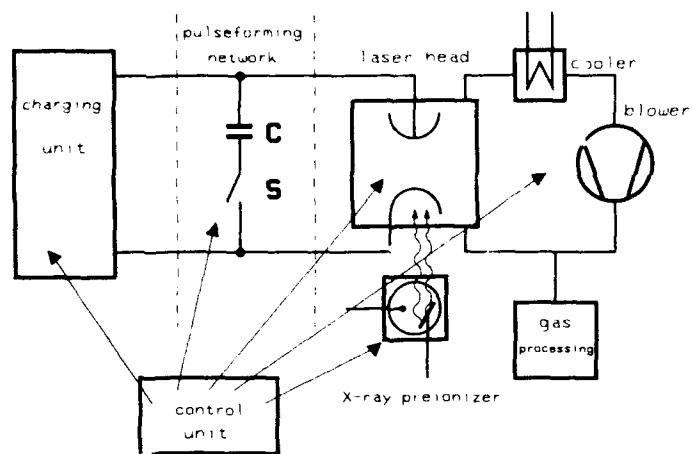


Fig. 1: Components of an excimer-laser

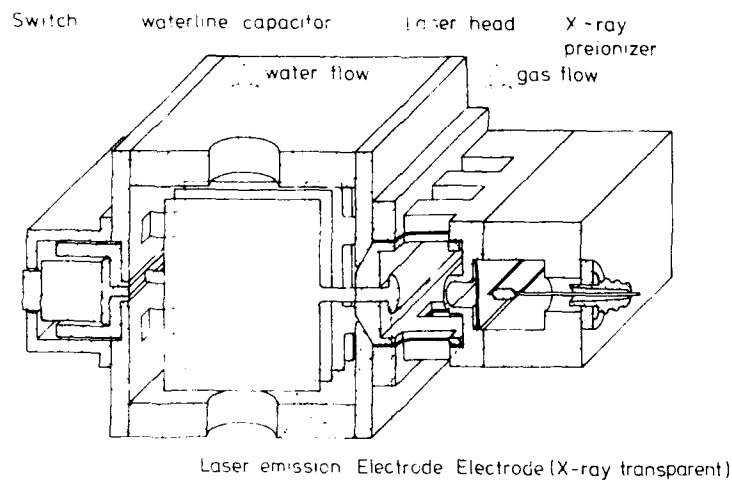


Fig. 2: Schematic drawing of the laser

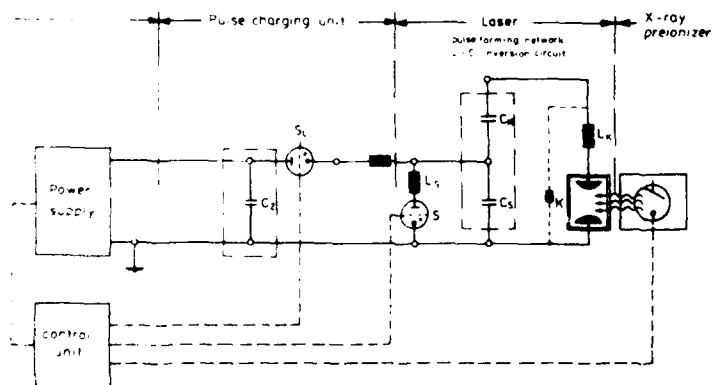


Fig. 6: Circuit diagram of an excimer laser with waterline capacitor

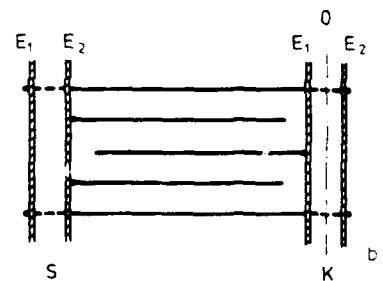
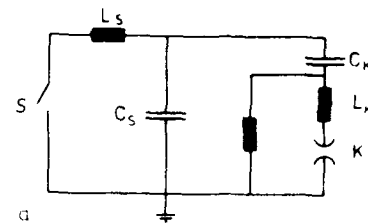


Fig. 3: LC-inversion circuit
a) circuit diagram
b) geometrical arrangement

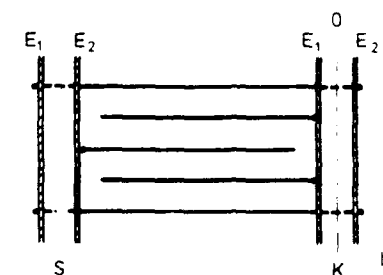
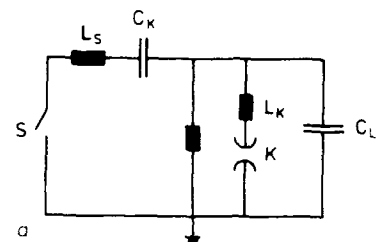


Fig. 4: Charge transfer circuit
a) circuit diagram
b) geometrical arrangement

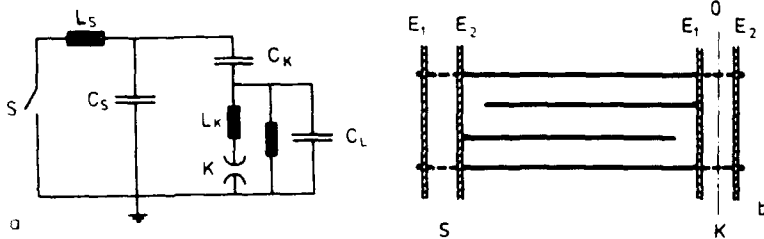


Fig. 5: ICT-circuit
a) circuit diagram
b) geometrical arrangement

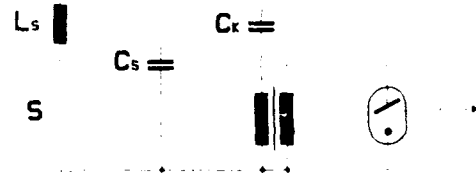
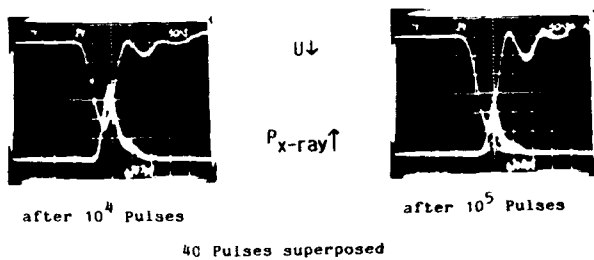


Fig. 7: Pulse generator for x-ray gun

X-Ray Gun with Field Emission Cathode



X-Ray Gun with Hollow Cathode

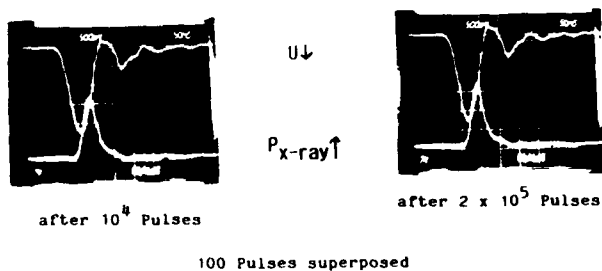


Fig. 9: Features of an x-ray preionizer with field emission cathode and hollow cathode (50 ns/div)

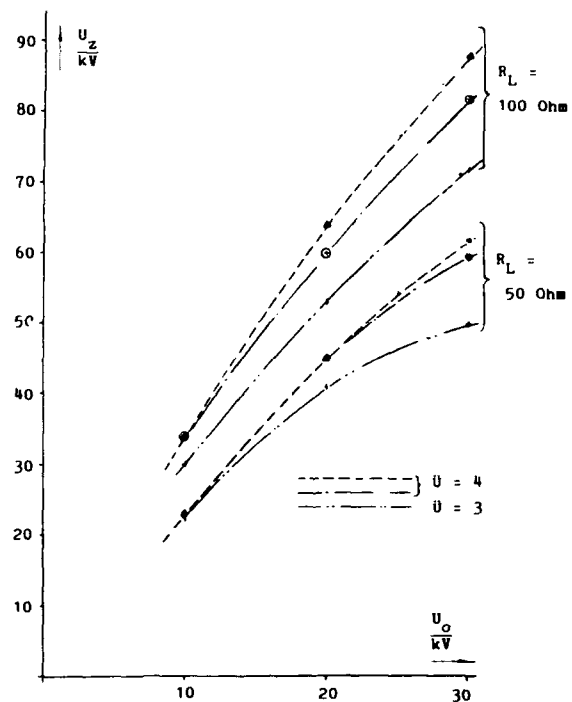


Fig. 8: Characteristics of the pulse transformer with different transformation ratios \bar{u} .

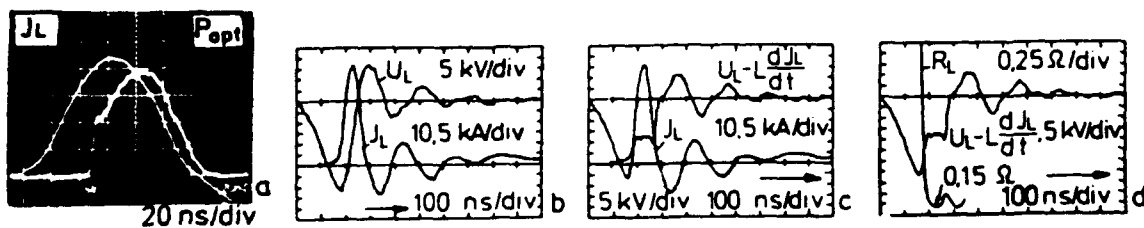


Fig. 10: Pulse traces of an XeCl-laser

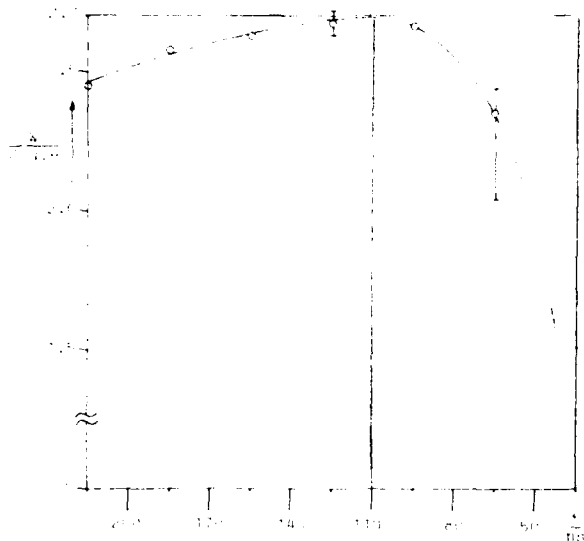


Fig. 11: Timing of the x-ray pulse before gas breakdown (XeCl)

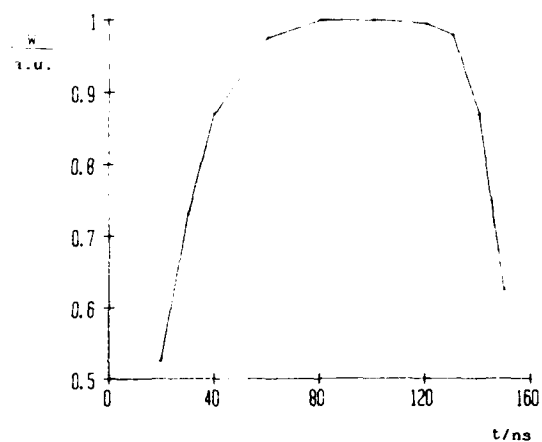


Fig. 12: Timing of the x-ray-pulse before gas breakdown (KrF)

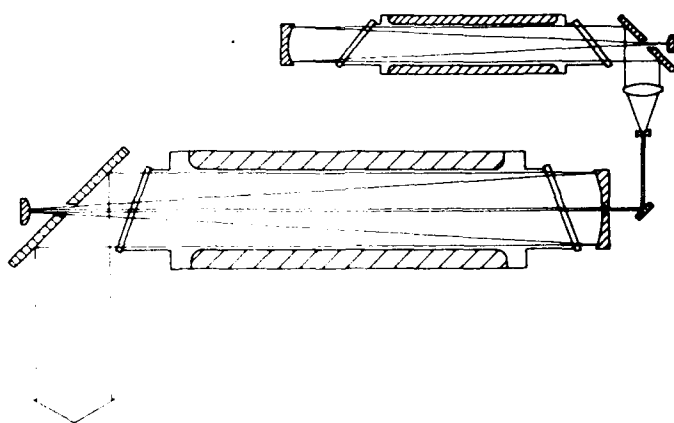


Fig. 14: Amplifier stage with injection laser

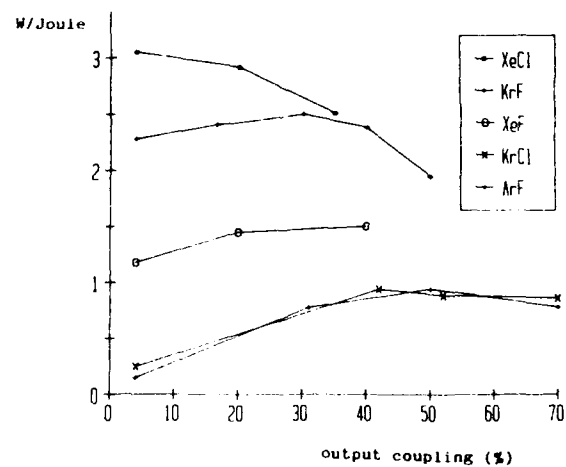


Fig. 13: Output energy vs output mirror reflectivity

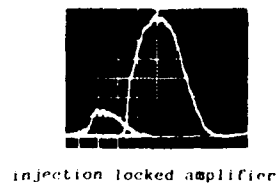


Fig. 15: Amplifier with injection laser (20 ns/div)

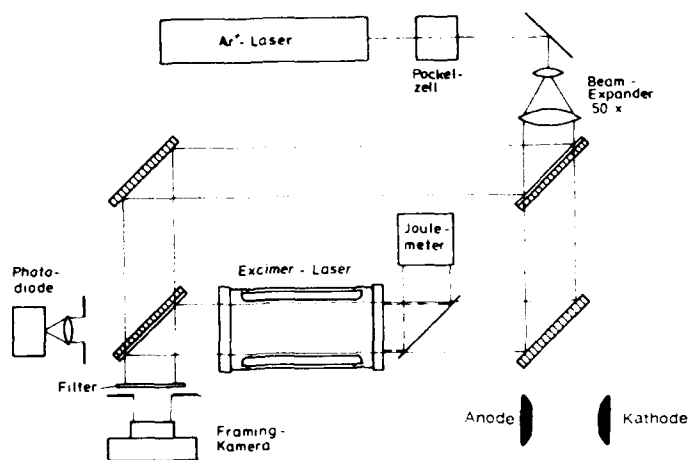


Fig. 16: Mach-Zehnder interferometer

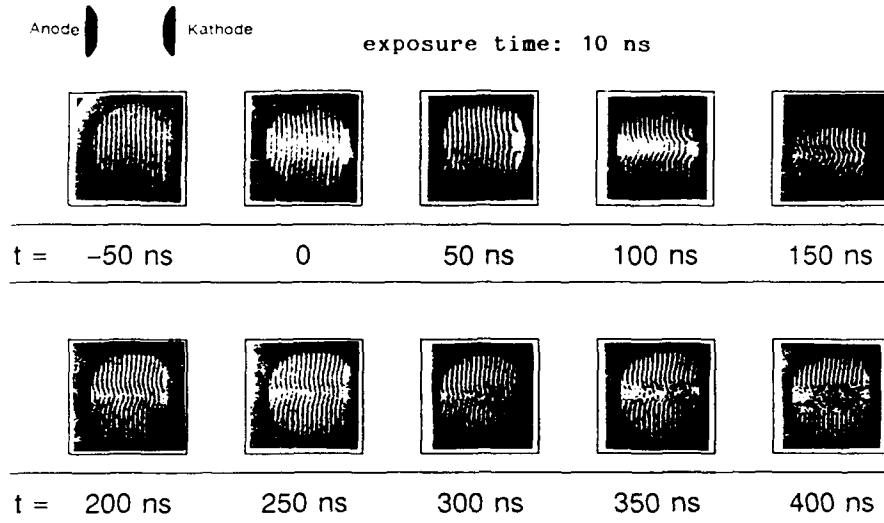
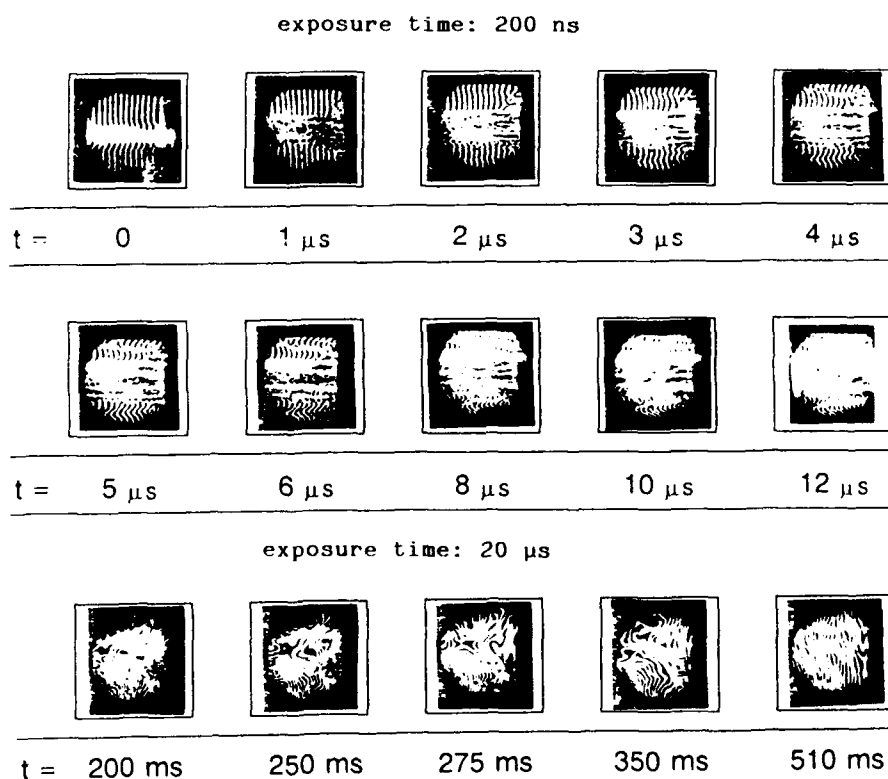


Fig.17: Temporal evolution of gas inhomogeneities (static gas fill) after gas breakdown ($t = 0$)



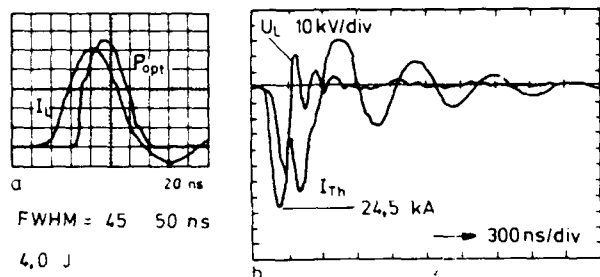


Fig. 18: 4 J XeCl-laser pulse

- a) laser current I_L and optical pulse P_{opt}
- b) thyatron current I_{Th} and laser voltage U_L

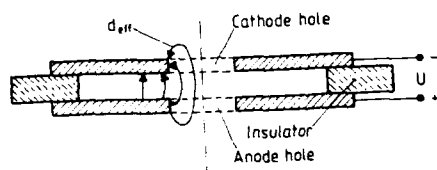


Fig. 19: Scheme of a pseudo spark discharge

after K.Frank et al SPIE Vol. 735 (74 - 81)

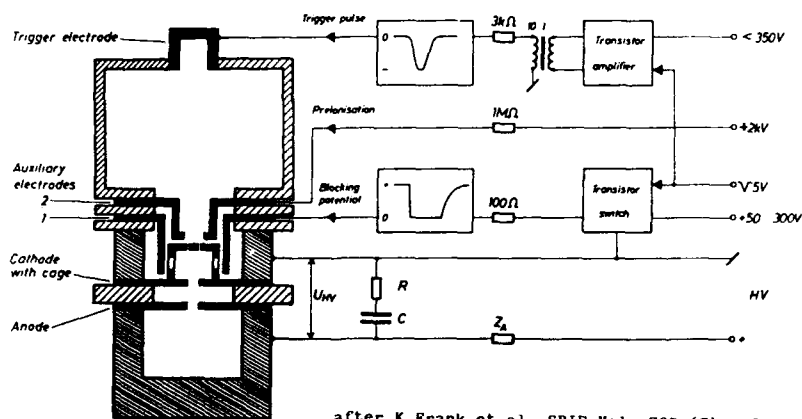


Fig. 20: Pseudo spark switch design

after K.Frank et al SPIE Vol. 735 (74 - 81)

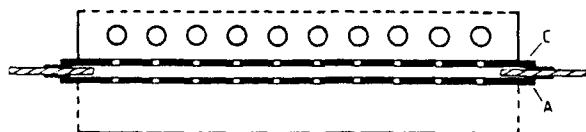


Fig. 21: Multi channel pseudo spark switch (longitudinal section)

after Mechttersheimer, Kohler J. Phys. E 20 (1987) 270

GAIN, ABSORPTION AND SATURATION INTENSITY MEASUREMENTS OF A DISCHARGE PUMPED, X-RAY
PREIONIZED Xe-Ce LASER

T. Letardi, P. Di Lazzaro, G. Giordano, E. Sabia, V. Boffa*, S. Bollanti*,
T. Hermesen*, C.E. Zheng**

ENEA, Dip. TIB, U.S., Fisica Applicata, C.R.E. Frascati,
C.P. 65 - 00044 Frascati, Rome (Italy)

Abstract

The small signal gain and absorption coefficients of a high uniformity, X-ray preionized Xe-Ce laser have been measured. Their time evolution and wavelength dependence have been simultaneously detected with high resolution.

Two distinct estimates of the saturation intensity were obtained by means of a Rigrod-type analysis of the intracavity intensity and by using saturated gain measurements.

I. Introduction

We present the results of a detailed experimental study of the gain characteristics of a high uniformity, X-ray preionized, self sustained discharge Xe-Ce laser, entirely realized at the ENEA center of Frascati.

The laser system, described in Ref. 1,2,3 consists of a laser cell with an active volume of about 1 liter (dimensions $3,5 \times 3,5 \times 80$ cm³), filled with a gas mixture of HCl/Xe/Ne (1:6,7:2019) at a total pressure of 4 atm. The active medium is uniformly preionized by X-rays using a 3 kA, 50 ns pulsed plasma cathode and a resonantly charged tungsten target anode.

In order to gain a deeper insight into the physical characteristics of this device, the time and spectral dependence of the small signal gain and absorption coefficients together with the saturation intensity have been investigated. Due to the intrinsic nonsaturable absorption, the extraction efficiency of excimer lasers depends on the parameters $g_0 \cdot \ell$ and $r = g_0/a$, where g_0 is the small signal gain coefficient, a is the non-saturable absorption coefficient and ℓ is the active medium length. It is therefore necessary to know the temporal evolution of these parameters in order to predict and to optimize the performance of any Rare Gas Halide laser.

The time and spectrally resolved gain and absorption measurements were performed using the frequency doubled output of a long pulse, flash-pumped dye laser to probe the active medium in the wavelength range around the main laser transition lines. Thus the high resolution ($\Delta\lambda = 0,5$ Å) spectral profile of the gain and the time evolution (resolution $\Delta T = 5$ ns) of both the gain on the four B-X transitions and the absorption coefficients have been obtained.

Finally, two different measurements were performed to obtain an estimate of the saturation intensity. Both make use of a Rigrod analysis of the intracavity intensity at different reflectivities of the output coupler, but with the difference that in the first measurement the saturation intensity was calculated directly from the measured output intensity by solving the resulting transcendental equation, while in the second measurement the saturation intensity was obtained from the mean intracavity intensity and the measured gain of a probe beam.

Most of the measurements of g_0 and a were performed at an energy deposition rate of 200 kW/cm³, but some were done at 250 kW/cm³ and 350 kW/cm³. These pumping rate density values were obtained from a numerical simulation of the discharge circuit and checked by means of a more direct method which uses the pressure jump in the laser cell during discharge⁴. All measurements of the saturation intensity refer to an energy deposition rate of 350 kW/cm³.

The paper is organized as follows: in sect II we describe the experimental setup and give the results relative to the absorption and gain coefficient measurements, while sect III is devoted to the measurements of the saturation intensity. Final conclusions are drawn in sect IV.

* ENEA Guest

** On leave from Shanghai Institute of Optics and Fine Mechanics and ENEA Guest

II. Measurement of the Absorption Coefficient and the Small Signal Gain Coefficient

Experimental Setup

The intensity I_2 of a probe laser beam at the exit of an amplifying medium can be expressed in terms of the input intensity I_1 by

$$I_2 = I_1 \exp[(g_0 - a) \ell] \quad (1)$$

where g_0 is a function of both the wavelength and time, while a is supposed to be only time dependent in the operating wavelength region; ℓ is the active medium length. The expression (1) holds only for steady state amplification and if the condition for the probe beam intensity

$$I(z) \ll I_s, \quad 0 \leq z \leq \ell \quad (2)$$

is satisfied. The saturation intensity I_s is a characteristic parameter of the active medium and in our case was of the order of 1 MW/cm^2 . Before every set of measurements, the fulfillment of condition (2) was checked through the linearity of I_2 versus I_1 .

The experimental setup is drawn in Fig. 1. The Phase-R DL 1100 flash-pumped dye laser used in the experiment has a pulse duration which can range from 100 to 250 ns, by changing the net gain of the active medium.

The small signal gain coefficient has been measured in the wavelength interval $3075 \text{ \AA} - 3085 \text{ \AA}$, while the absorption coefficient has been measured only for $\lambda > 3085 \text{ \AA}$. As a matter of fact, for wavelengths shorter than the emission peak ($\lambda < 3080 \text{ \AA}$), there is a long fluorescence tail⁵, primarily due to transitions originating from $v' > 1$ vibrational levels in the B electronic state, which do not permit absorption measurement.

The maximum output energy ranged from 0.5 to 2.0 mJ, depending on the operating wavelength. After the spatial filter P1 (see Fig. 1), a collimated laser beam with a 4 mm spot diameter was available for the measurements. The probe laser beam power and wavelength were monitored by means of an ITT FW114A photodiode and an optical spectrum analyzer (OSA) respectively. The OSA was used in conjunction with a 0,75 m spectrometer with a 3600 rows/mm grating, (overall spectral resolution: $\Delta\lambda = 0.12 \text{ \AA}$) and an optical fiber allowed the beam handling (see Fig. 1). Neutral density filters were inserted at the entrance of the Xe-Cl medium in order to limit the probe beam intensity and thus ensuring the gain linearity. An optical filtering system behind the Xe-Cl target, composed of a lens and a pinhole, increased the signal to noise ratio, where the background noise derived essentially from the Xe-Cl fluorescence. Finally the amplified beam was monitored by means of a second ITT photodiode after attenuation to ensure that the detector working point was far away from saturation.

The Absorption Coefficient a

The measured time dependence of the absorption coefficient for two different wavelengths $\lambda = 3125 \text{ \AA}$ and 3140 \AA is reported in Figs 2 and 3 respectively.

The first was chosen because of the expected negligible gain at this wavelength⁶. Corkum and Taylor⁷ assume that the absorption coefficients at these values and at 308 nm are the same due to the broad band absorption spectra of the species (e.g. Xe_2^+ , Cl^- , Xe_2Cl , Ne^{**}) which are thought to be important in the Ne based XeCl laser mixture during discharge⁸. In the following we will use the measurement results on wavelength $\lambda = 312,5 \text{ nm}$. There is about 10% difference between the absorption curves on $312,5 \text{ nm}$ and $314,0 \text{ nm}$, as can

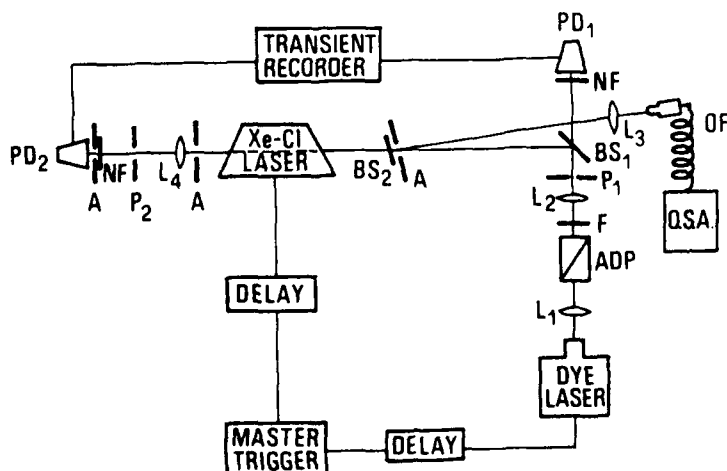


Fig.1 Experimental layout for small signal gain and absorption coefficients measurement, where

L_1 focal length = 20 cm

L_2 focal length = 15 cm

L_3 focal length = 10 cm

L_4 focal length = 15 cm

P_1 = pinhole $\phi = 4 \text{ mm}$

P_2 = pinhole $\phi = 0.5 \text{ mm}$

PD = photodiode

OF = optical fiber

BS = beam splitter

F = UG11 Schott filter

NF = neutral density filters

A = aperture

be seen from the figures, which seems to confirm the broad band absorption around the laser transition lines.

A time interval of about 500 ns was covered varying the delay between the discharge breakdown and the probe pulse. No larger times were considered because it has been observed that the measurements would be seriously disturbed because of the formation of inhomogeneities in the refractive index of the mixture after about 500 ns, corresponding to the base width duration of the current pulse ⁷.

As a result of these measurements, we calculated a peak value of the absorption coefficient $\alpha = 0,27 \pm 0,01\%$ cm at wavelength $\lambda = 312,5$ nm and with a power deposition rate of 200 kW/cm^3 .

As evident from the Figs (2,3) the absorption reaches a maximum value after the peak power deposition, in a similar way as in previously published absorption measurements using e-beam excitation ⁹ and UV preionization ⁷, both at a much higher power deposition level ($\sim 3 \text{ GW/cm}^3$). In particular, the two-component behavior of the absorption may be due, according to Ref. 7, to Xe^+ , in the high E/P region and to Xe_2^+ in the afterglow. This conjecture is supported by the different formation onset times of the two mentioned species ¹⁰.

The Small Signal Gain Coefficient g_0

Figures 4 and 5 show the measurement results of the time behavior after the discharge of the net gain coefficient $g_0 - \alpha$ for two different wavelengths corresponding to the two main laser transition lines, at a pumping rate deposition of 200 kW/cm^3 . A maximum value of $g_0 = 4.7\%/cm$ was obtained for $\lambda = 3079.6 \text{ \AA}$ (corresponding to the main laser transition line) and for a delay time of about 230 ns. Using the measured peak value of the absorption coefficient, we calculate a gain to loss ratio $g_0/\alpha = 18 \pm 1$ at the peak of the gain.

The gain and absorption coefficients measurement was repeated at an higher pumping rate density of 250 kW/cm^3 , in order to check the pumping dependence of the coefficient $\gamma = g_0/\alpha$. Figure 6 and 7 show the time histories of the small signal gain at the main transition line and of the absorption coefficient at $\lambda = 3125 \text{ \AA}$ respectively. Both time behaviors resemble those of the corresponding ones at lower deposition rate (Figs 2 and 4) and the resulting factor $\gamma = g_0/\alpha = 20 \pm 2$ is the same (within the error bars) with respect to the above reported γ value at 200 kW/cm^3 . This seems to be in agreement with the experimental results reported in Ref. 9.

Figure 8 shows the net small signal gain coefficient as a function of the wavelength for a fixed time delay of 230 ns. The corresponding measured XeCl emission spectral profile reported in Fig. 9 is a type of multimaximum having peaks at 307.6 nm, 307.9 nm, 308.2 nm and 308.4 nm, confirming that the XeCl laser takes place in the form of the bound-bound transition, as expected theoretically ¹¹. To our knowledge it is the first time that the gain profile of all four B-X transition lines have been clearly resolved for the Ne based XeCl laser mixture (for He/Xe/Cl see Ref. 12). It should be mentioned that no attempt has been made to correct this gain curve for the finite bandwidth of the probe beam, which would probably result in more pronounced difference between the minima and maxima.

Finally, in Fig. 10 we show the peak small signal gain coefficient for different energy deposition rates in the laser cell.

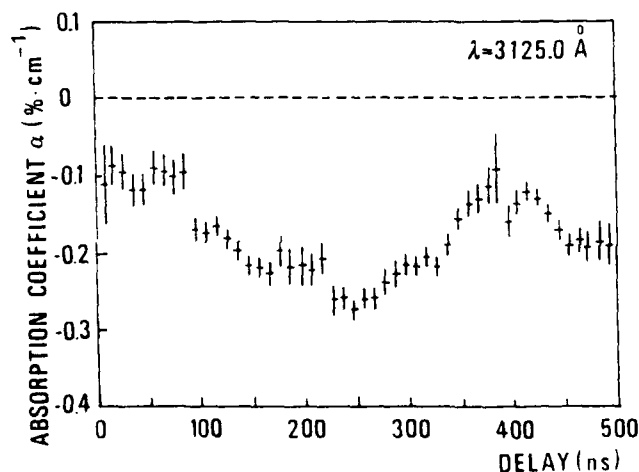


Fig. 2 Absorption coefficient α vs time for $\lambda = 3125 \text{ \AA}$

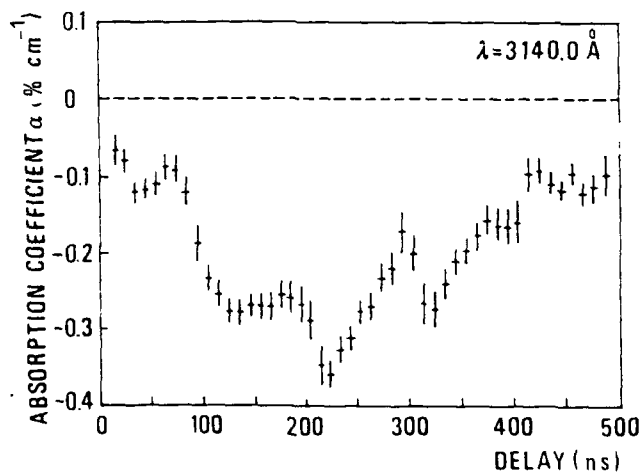


Fig. 3 Absorption coefficient α vs time for $\lambda = 3140 \text{ \AA}$

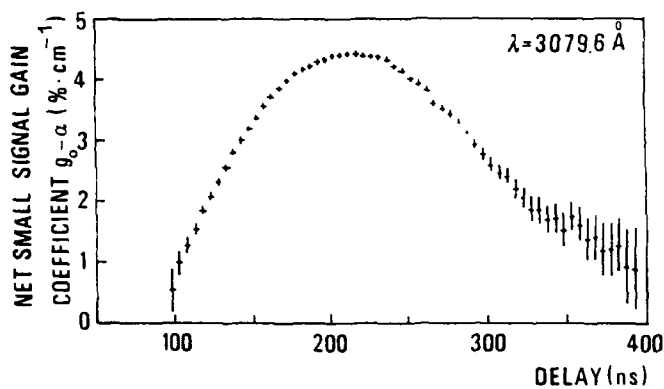


Fig. 4 Net small signal gain coefficient $g_0-\alpha$ vs time for $\lambda = 3079.6 \text{ \AA}$

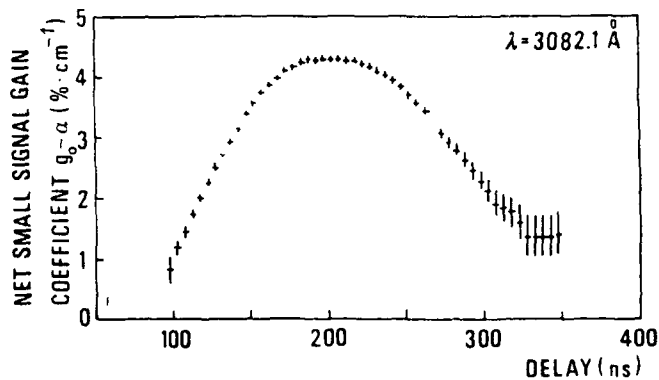


Fig. 5 Net small signal gain coefficient $g_0-\alpha$ vs time for $\lambda = 3082.1 \text{ \AA}$

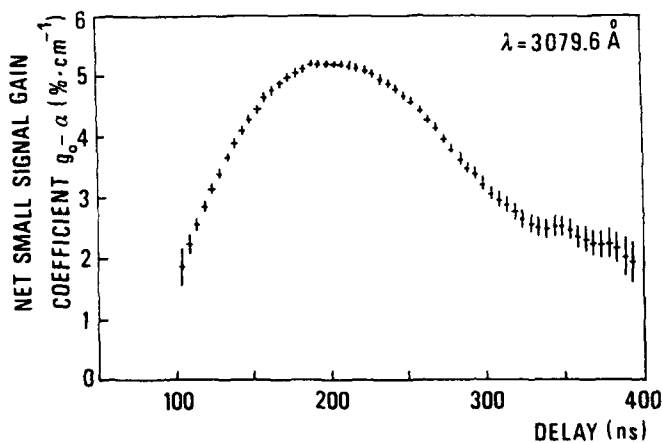


Fig. 6 Net small signal gain coefficient $g_0-\alpha$ vs time, for $\lambda = 3079.6$ and a pumping density of 250 kW/cm^3

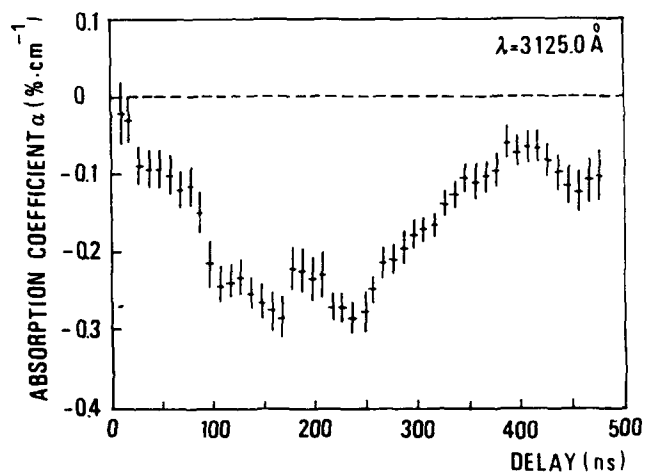


Fig. 7 Absorption coefficient α vs time at $\lambda = 3125 \text{ \AA}$ for a pumping rate density of 250 kW/cm^3

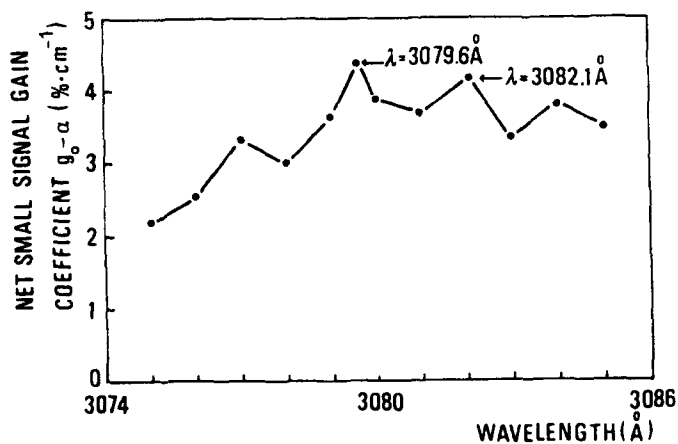


Fig. 8 Net small signal gain coefficient $g_0-\alpha$ vs wavelength λ , for delay time of 230 ns and a pumping rate density of 200 kW/cm^3

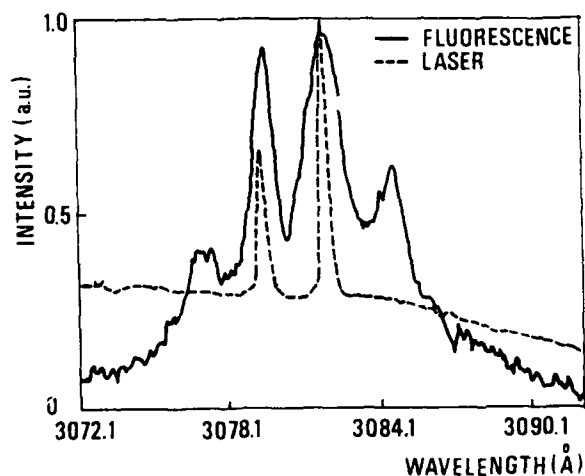


Fig. 9 Emission spectral profile of XeCf active medium

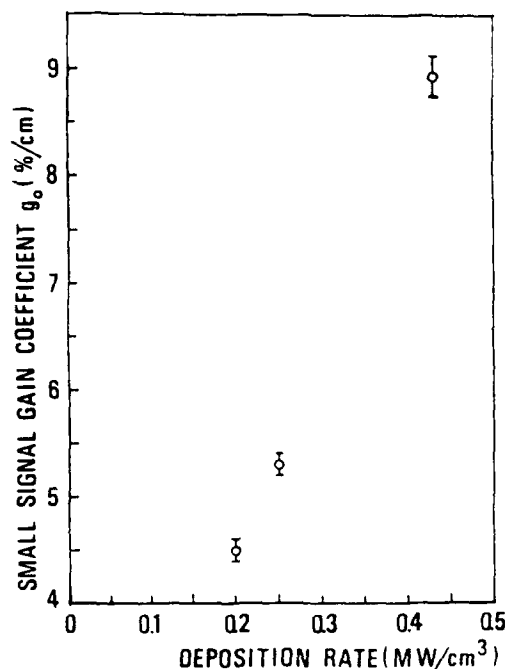


Fig. 10 Small signal gain coefficient g_0 vs energy deposition rate in the XeC₂ active medium

III. Measurements of the Saturation Intensity

To obtain an estimate of the saturation intensity of the mixture, two different experimental measurements were performed. The first makes use of a Rigrod type analysis of the laser output intensity of a plano-plano cavity, as a function of the mirror reflectivities and the saturation intensity¹³. Strictly speaking this method is only valid under stationary conditions, but one can show that for our experimental conditions the steady state approximation is well satisfied. Using a geometrical approximation one may write for the right and left travelling intensities $I_+(z)$ and $I_-(z)$

$$\frac{1}{I_+} \frac{dI_+}{dz} = \frac{g_0}{1 + \frac{I_+}{I_s} + \frac{I_-}{I_s}} - a = -\frac{1}{I_-} \frac{dI_-}{dz} \quad (3)$$

with the boundary conditions

$$\begin{aligned} I_+(L) &= I_-(L) R_2 T_f^2 \\ I_-(0) &= I_+(0) R_1 T_f^2 \end{aligned} \quad (4)$$

R_1 and R_2 are the reflectivities of the back and the output mirror respectively, and T_f the transmittance of the quartz-windows in the gas chamber. Equation (3) may be integrated to obtain a transcendental equation in the variable $\delta = I_- I_+ / I_s^2$. Solving this equation for δ as a function of the parameters R_1 , R_2 , T_f , g_0 and a , one may calculate the saturation intensity from the measured intensity I_e at the exit of mirror M_2 . To determine the peak output intensity, both the laser pulse shape and the total pulse energy were measured.

The values of the parameters used were

$$\begin{aligned} R_1 &= 98\% & g_0 &= 8.9 \pm 0.2\%/cm \\ T_f &= 99\% & a &= 1.4 \pm 0.3\%/cm \end{aligned}$$

while for R_2 three values were taken, namely, $R_2=10\%$, 23% , and 84% . The higher value of the peak small signal gain coefficient with respect to the earlier measured g_0 is due to the higher pumping rate deposition in this case (350 kW/cm^3). This implies a correspondingly higher absorption coefficient assuming a constant ratio g_0/a ⁹. The value of the effective absorption coefficient was obtained by taking the sum of the intrinsic absorption coefficient ($0.5 \pm 0.1\%/cm$) and the estimated loss due to diffraction ($0.9 \pm 0.2\%/cm$).

From these measurements three values for the saturation intensity were calculated (see Table I) with a mean value of

$$\langle I_c \rangle = 0.5 \begin{cases} +0.3 \\ -0.2 \end{cases} \text{ MW cm}^{-2} \quad (5)$$

The error bars were calculated by finding the maximum and minimum values of I_s , varying the parameters α , g_0 , and I_e within their error bars.

The second method uses the intracavity intensity dependence of the gain of a probe beam. Indeed, for the propagation of the probe beam with a sufficiently low intensity I (i.e. $I \ll I_c$) we may write:

$$\frac{dI}{dz} = \left(\frac{g_0}{1 + I(z)/I_c} - \alpha \right) I \quad (6)$$

The intracavity intensity $I_c(z)$ depends on the longitudinal coordinate z . However, it can be shown that the error made in Eq. (6) by taking its mean value over the cavity length is small, and hence the equation may be integrated to give for the amplified probe beam the following expression:

$$I_{out} = I_{in} \exp \left[\left(\frac{g_0}{1 + \langle I_c \rangle} - \alpha \right) \ell \right] = I_{in} \exp(g \ell) \quad (7)$$

where g is the net gain coefficient of the probe beam. Using a modified Rigrod analysis¹⁴ one may express the mean intracavity intensity $\langle I_c \rangle$ in terms of the intensity I_e at the output coupling mirror M_2 :

$$\langle I_c \rangle = - \frac{(1 - \sqrt{R_1 \cdot R_2 \cdot T_f^4})(\sqrt{R_1} + \sqrt{R_2})}{(1 - R_2)T_f \sqrt{R_1} \ln \sqrt{R_1 \cdot R_2 \cdot T_f^4}} \cdot I_e \quad (8)$$

In this way, by measuring the amplified probe beam intensity I_{out} and the laser intensity I_e at the exit of mirror M_2 , one may calculate the saturation intensity.

Of course, this method depends heavily on the technical possibility of separating the amplified probe beam from the much larger overall background laser intensity. This has been achieved elegantly by means of the Brewster angle quartz windows W_1 and W_2 .

The experimental set up is schematically drawn in Fig. 11. The probe beam was taken from a Lambda Physik EMG50 XeCl laser with 17 ns (FWHM) pulse duration, which was attenuated (filter A), recollimated (lenses L_1 and L_2) and spatially filtered (pinhole PH) before entering the

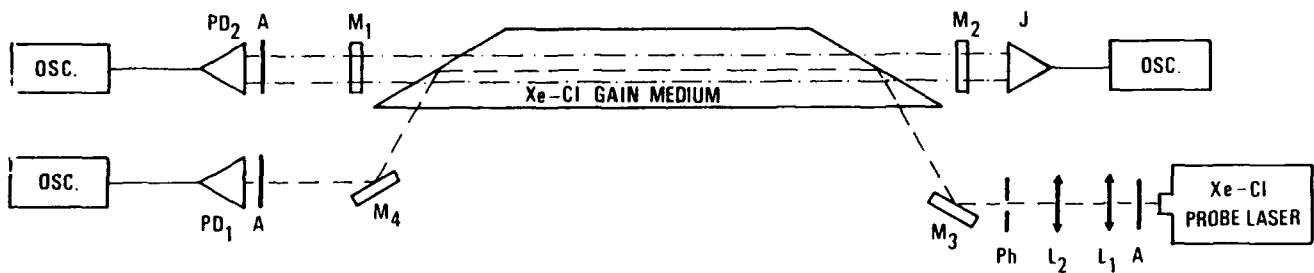


Fig. 11 Experimental setup for the second measurement of the saturation intensity (see text)

M_1 = cavity back mirror, reflectivity 99%
 M_2 = cavity front mirror
 M_3 = mirror
 M_4 = mirror
 A = neutral density filters
 L_1 = lens ($f=50$ cm)

L_2 = lens ($f=25$ cm)
 PH = spatial filter
 J = joule meter Gentec ED-1000
 PD_1 = reference photodiode ITT, FW-114A
 PD_2 = signal photodiode ITT, FW-114A

TABLE I: Results of first saturation intensity measurement

$R_2(\%)$	$I_e \text{ (Mw/cm}^2\text{)}$	$I_s \text{ (Mw/cm}^2\text{)}$	$\langle I_s \rangle \text{ (Mw/cm}^2\text{)}$
10	1.0 ± 0.2	$0.4 \begin{cases} +0.2 \\ -0.1 \end{cases}$	
23	1.0 ± 0.2	$0.5 \begin{cases} +0.2 \\ -0.2 \end{cases}$	$0.5 \begin{cases} +0.3 \\ -0.2 \end{cases}$
84	0.26 ± 0.06	$0.6 \begin{cases} +0.4 \\ -0.2 \end{cases}$	

TABLE II: Results of second saturation intensity measurement

$R_2(\%)$	$I_e \text{ (Mw/cm}^2\text{)}$	$g(\%/cm)$	$I_s \text{ (Mw/cm}^2\text{)}$	$\langle I_s \rangle \text{ (Mw/cm}^2\text{)}$
10	1.0 ± 0.2	4.9 ± 0.3	$1.4 \begin{cases} +0.7 \\ -0.5 \end{cases}$	
23	1.0 ± 0.2	3.7 ± 0.4	$1.2 \begin{cases} +0.7 \\ -0.4 \end{cases}$	$1.2 \begin{cases} +0.6 \\ -0.4 \end{cases}$
84	0.26 ± 0.06	2.23 ± 0.05	$1.3 \begin{cases} +0.5 \\ -0.4 \end{cases}$	

laser cell. The other experimental conditions (mirrors reflectivity, pumping rate, etc.) were left unchanged with respect to the first measurement.

Due to the different polarizations induced by W_1 and W_2 the probe beam and the intracavity e.m. field are split at window W_2 , after which the gain is measured by photodiode PD_1 .

The results of the measurements are shown in Table II and we calculated a mean value of the saturation intensity of

$$\langle I_s \rangle = 1.2 \begin{cases} +0.6 \\ -0.4 \end{cases} \text{ MW cm}^2 \quad (9)$$

Again, the error bars were calculated by finding the maximum variation in I_s , changing the parameters within their range.

IV. Conclusions

The absorption coefficient a and the small signal gain coefficient g_0 have been measured, both as a function of the time elapsed after discharge breakdown, and g_0 as a function of the wavelength. It should be noted that the time dependence of the absorption is rather similar to that of the small signal gain coefficient g_0 (width, onset time, peak time) leading to an approximately constant ratio g_0/a with time.

Two different measurements of the saturation intensity were performed leading to the values 0.5 Mw/cm^2 and 1.2 Mw/cm^2 respectively. However, taking into account the rather large error bars (see 5 and 9) these results are not really in contradiction but rather reflect the considerable difficulty in measuring this quantity. These considerations are, on the other hand, largely stated by the wide range of saturation intensity measured values, also for apparently similar experimental conditions ^{7,9,15,16}.

References

1. A. De Angelis, E. Fiorentino, G. Giordano, T. Letardi, E. Sabia and M. Vannini, in Proc. of the Int. Conf. on Lasers 84, K.M. Corcoran, D.M. Sullivan, W.C. Stwalley, Eds (STS Press, Mclean VA 1985) pp. 606-611.
2. T. Letardi, S. Bollanti, A. De Angelis, P. Di Lazzaro, I. Giabbai, G. Giordano, and E. Sabia, "Characterization of High Uniformity, X-ray Preionized XeCl Laser", to be published in Nuovo Cimento D.
3. V. Boffa, S. Bollanti, P. Di Lazzaro, G. Giordano, T. Hermesen, T. Letardi and E. Sabia, in Proc. 1986 European Conference on Optics, Optical Systems and Applications, S. Sottini, S. Trigari, Eds (Proc. SPIE 701, 1987). pp. 158-165.
4. E. Fiorentino, T. Letardi, A. Marino, E. Sabia, and M. Vannini, Laser and Particle Beams 3, 319 (1985).

5. J.B. Loudenlager, T.S. Pacala, I.S. Mcdermid, CLEO 81, post deadline paper.
6. J. Tellinghuisen, J.M. Hoffman, G.C. Tisone, A.K. Hays, J. Chem. Phys. **64**, 2484 (1976).
7. P.B. Corkum, R.S. Taylor, IEEE J. Quantum Electron. **QE-18**, 1962 (1982);
R.S. Taylor, P.B. Corkum, S. Watanabe, K.E. Leopold and A.J. Alcock, IEEE J. Quantum Electron **QE-19**, 416 (1983).
8. A. Mandl, Phys. Rev. **A14**, 345 (1976);
W.R. Wadt, P.J. Hay, J. Chem. Phys. **68**, 3850 (1978);
W.R. Wadt, J. Chem. Phys. **73**, 3915 (1980);
C. Duzy, H.A. Hyman, Phys. Rev. **A22**, 1878 (1980);
A. Gevaudan, B.L. Fontaine, B.M. Forestier, M.L. Sentisin, Gas Flow and Chemical Lasers, S. Rosenwaks Ed (Springer Verlag, Berlin 1987) pp. 118-124.
9. G.C. Tisone and J.M. Hoffman, IEEE J. Quantum Electron. **QE-18**, 1008 (1982).
10. L.A. Levin, S.E. Moody, E.L. Klosterman, R.E. Center, J.J. Ewing, IEEE J. Quantum Electron. **QE-17**, 2282 (1981).
11. P.J. Hay, T.H. Dunning, J. Chem. Phys. **69**, 2209 (1978).
12. A. Takahashi, M. Sumi and M. Maeda, Opt. Commun. **55**, 193 (1985).
13. W.W. Rigrod, J. Appl. Phys. **36**, 2487 (1965).
14. W.C. Marlow, J. Appl. Phys. **41**, 4019 (1970);
W.W. Rigrod, IEEE J. Quantum Electron. **QE-14**, 377 (1978).
15. R.S. Taylor, A.J. Alcock, K.E. Leopold, Opt. Commun. **31**, 197 (1979).
16. J.H. Glowing, G. Arjaualingam, P.P. Sorokin, J.E. Rothenberg, Opt. Lett. **11**, 79 (1986).

USE OF MAGNETIC MATERIALS IN EXCIMER LASER CIRCUITS

MATTEO VANNINI

Istituto di Elettronica Quantistica del C.N.R.
Via Panciatichi 56/30, 50125 Firenze, Italy

ROBERT C. SZE

Los Alamos National Laboratory
Los Alamos, New Mexico, 87545, Mail Stop E543, U.S.A.

FRANÇOIS HOMMEAU

Institute de Mécanique des Fluides
Université d'Aix-Marseille II, 1, Rue Honnorat, 13003 Marseille, France

Abstract

The use of saturating magnetic materials in laser excitation discharge systems is presented. Particular attention is given to the most important parameters of magnetic materials and to the analysis of some circuits such as single and multi-stage pulse compressor and pre-pulse isolation systems.

Introduction

The use of saturating magnetic materials in pulse forming circuits for the laser excitation of large volume avalanche discharges is becoming an important area of investigation (1-5)(7-13)(17). Such techniques find applications especially in the excitation of excimer laser systems where pulse power requirements are especially severe (17-18) present, the two main techniques are in the areas of pulse compression and circuit isolation (5). The idea of pulse compression is to use a saturating inductance as a switch that will allow a slow charge of the pulse circuit through a thyatron and subsequently provide a fast deposition of energy through a low inductance circuit to the discharge. Such a technique, therefore, permits a comfortable dI/dt for the thyatron, insuring long life operation, and at the same time deliver a short voltage risetime and fast energy deposition pulse desirable for the excitation of excimer laser systems. The use of a saturating inductor as an isolator is an even more powerful technique (5). The idea here is to overcome the necessity of charging the final stage capacitors used for energy deposition to the gas breakdown voltage while the steady state operating voltage of the discharge is some factor of four lower (8). The latter results in a discharge power supply very far from a good current generator and, therefore, yields very poor theoretical power transfer efficiencies. The use of a saturating inductor as an isolator permits the use of a separate low energy, high dV/dt pre-pulse and the subsequent deposition from a low voltage main storage pulse power circuit.

While substantial successes are reported in the application of saturating magnetic materials for these uses, very little discussion has been devoted toward elucidating the details involved that lead to the successful implementation of these results. In this communication, we wish to discuss, for example, the limits associated with the available materials for the above mentioned uses, the losses associated with a saturating magnetic inductance and the optimization associated with multistage pulse compressor.

Material considerations

Two general classes of materials are available: those of various steel alloys including splat cooled amorphous metals such as Metglass (14) and Vitrovac (15) and those of ferrites. The choice of the appropriate material depends on the speed of the circuit under consideration and the degree of compression or isolation required. The most important parameter to keep in mind is the relative permeability at the operating frequency (16). We make the important assumption of working solely with soft magnetic materials or, in other words, to employ magnetic materials with a very narrow (low coercive force) hysteresis loop. As a rough criteria we have $H < 10$ A/cm. (18). In this condition (see Fig. 1) we can define at a given frequency the "relative permeability" as

$$\mu_r^u = \mu_r^s / \mu_0 = (1/\mu_0) \Delta B_1 / \Delta H_1, \quad (u = \text{unsaturated})$$

$$\mu_r^s = \mu_r^s / \mu_0 = (1/\mu_0) \Delta B_2 / \Delta H_2, \quad (s = \text{saturated})$$

where μ_0 = free space permeability = $4 \cdot 10^{-7}$

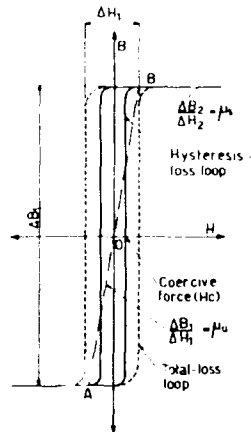


Fig. 1. Power losses during the switching time for a magnetic material device. Main losses arise only when the voltage starts to drop down and the current starts to increase. T_s = switching time, generally $\ll T_{sat}$.

It is clear that under this approximation overmentioned and illustrated in Fig. 1, a linearity between B and H is a good approximation and we can employ easier formulas in our circuits analysis. It is well known that μ_r is about equal or few times that of air. We will call in the following discussion "relative permeability" simply "permeability".

Another point to keep in mind is that although steel alloys have enormous permeabilities at low frequencies only the best materials have comparable values to those of high frequency ferrites in the region of 10MHz, and are unusable at frequencies in the 100MHz. region. Depending on the annealing process the permeability for amorphous metals can be as high as 600,000 for cases of square hysteresis loops and can also be made to have constant permeability values in the region of 5 to 30 thousand up to frequencies near the 100 KHz. range. Low frequency ferrites generally have constant permeabilities with values of 1 to 5 thousand up to 1 to 5 MHz. High frequency toroids can have constant value permeabilities of a few hundred at frequencies up to 10 to 20 MHz, and even higher frequency toroids with constant permeabilities of the order of 40 to 50 at frequencies up to one to two hundred MHz. The difference between the unsaturated permeability and the saturated permeability defines the change in inductance when the materials goes into saturation and, therefore, defines the degree of isolation. The saturating flux, B_s , between the amorphous metals and the ferrites are not very different with the amorphous metals having values about a factor of three higher. These are from .5 to 2 Teslas for amorphous metals and .2 to .5 for ferrites materials. Thus, given a desired final saturated inductance, the time to reach saturation is controlled by the unsaturated permeability which controls the leakage current through the inductor and by the nature of the B-H curve. The required amount of material necessary to hold off a given voltage is given by:

$$(1/N_t) \int_0^{T_{sat}} V(t) dt = A_m \int_{B(t=0)}^{B_s(T_{sat})} dB \quad w \quad BA_m \quad (1)$$

where $V(t)$ is the voltage across the inductor; T_{sat} is the time to saturation of the material;

ΔB is the total change in flux density and is $(2B_s)$ twice the saturation flux density if one initially reverse saturates the material.

N_t is the number of turns.

Thus, to reach a desired hold off voltage before saturation of the magnetic material, both the saturation flux density and the cross-sectional area are important parameters. Arguments using Eqn. (1) are valid when the transition time between unsaturated and saturated inductance is small compared to the overall resonance charging time (T_{sat}). When this is not the case, as is sometimes true in fast compression stages and in pulse isolation

systems, the details of the saturation process becomes important. We will discuss in the details of the transition region for different types of materials in a future paper.

The consideration of losses in saturating magnetic materials is a difficult task and can be very different for the two types of materials under discussion. Hysteresis losses, the integral of BdH , which tend to be a constant per round trip of the hysteresis loop, represent a small fraction of the energy transferred through the inductor if the current through the inductor is many times that necessary to drive the magnetic material to saturation. This is usually the case for the circuits under consideration.

The other important loss is that due to the resistivity of the material. If we look at the voltage and current characteristics as a function of time as in Fig. 2, we find that most of the power loss takes place when the inductance saturates. In steel alloys where the resistivity ($\rho \approx 100 \mu\Omega\text{cm}$) is very low the material must be formed by laminations with alternating insulating layers to allow voltage build up across the inductor structure. Due to this very low resistivity huge eddy currents counter the driving current and necessitate H values at the boundary of the lamination many times that of the saturating H -field (H_s) before a saturating wave launched in the medium travels across the magnetic material and saturates the whole thickness of the lamination. Eddy current losses in amorphous metals can be a substantial fraction of the storage energy if care is not used in the design of saturating inductors. In ferrite materials the resistivity is rather large and can vary from 50 to as high as $10^6 \Omega\text{cm}$ and saturation of the material medium can be determined purely by the rising local H -field. Losses can be calculated by integration in space and time using the local induced electric field in the medium and the resistivity. However, the calculation of the local electric field is complicated by the change in the local permittivity as sections of the medium saturates. There is indication that the permittivity decreases at saturation. In addition, there are frequency dependencies of the resistivity and permittivity caused by differences in the resistivities of varying grain sizes in the material at low frequencies and by a phase lag loss that becomes important at higher frequencies.

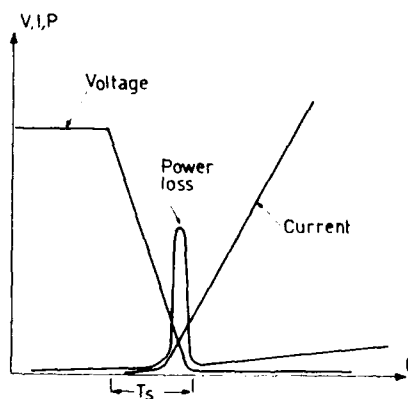


Fig. 2. Solid line: narrow hysteresis loop that allows to make the described approximation, the linearity between B and H fields.

Single stage pulse compression

We wish in this section to make the simplest circuit arguments for a one stage pulse compression circuit. We shall then present the first order arguments for the design of the inductor dimensions and the necessary magnetic material characteristics. Figure 3 gives the schematic for a single stage pulse compression circuit.

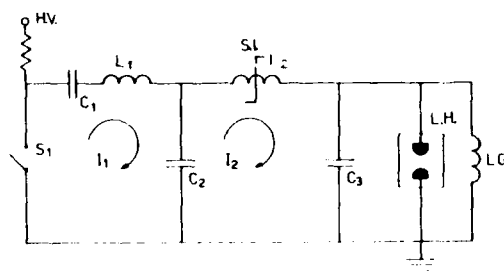


Fig. 3. Single stage pulse circuit diagram. L_G is only the ground reference for the C_1 charge. $L.H.$ is the load, in particular the laser head.

For one hundred percent energy transfer efficiency $C_1=C_2=C_3=C$. The right part of the circuit is isolated from the left by the unsaturated inductance of L_2^u . For an efficient charge of C_2 , $L_1 \ll L_2^u$.

In order to make \dot{I}_2 much larger than \dot{I}_1 , $L_2^s \ll L_1$. For satisfying these two inequalities we put:

$$L_1/L_2^s = L_2^u/L_1 \approx 10 \quad (2)$$

$$\text{Where: } L_2^u = \mu_0 \mu_r^u \frac{N_t^2}{l_m} \frac{A_m}{l_m} \quad (3)$$

$$L_2^s = \mu_0 \mu_r^s \frac{N_t^2}{l_m} \frac{A_m}{l_m} \quad (3')$$

With: N_t = number of turns ; A_m = magnetic cross-sectional area; l_m = magnetic field path length

So, μ_r^u must be at least equal to 100⁽¹⁾. We remark that the expressions given for (3) and (3') are valid when soft magnetic materials are employed (narrow B-H loop). Under the assumption that two parts of the circuit are isolated by the unsaturated inductance, calling $C_{12} = [C_1 C_2 / (C_1 + C_2)] = C/2$, we can write the equation when the switch S_1 closes at $t=0$ for $I_1(t)$ with C_1 initially charged to V_{\max} by observation,

$$I(t) = V_{\max} [C_{12}/L_1]^{1/2} \sin(\omega_1 t) \quad (4)$$

where $\omega_1 = (1/L_1 C_{12})^{1/2}$. The voltage across the capacitor C_2 , $V_2(t)$, is then given as:

$$V_2(t) = V_{\max} (C_{12}/C_2) (1 - \cos(\omega_1 t)) \quad (5)$$

Assuming that the current required to saturate L_2 is small compared to the peak current through L_2 after saturation, the voltage across the capacitor C_3 , $V_3(t)$ is approximately at ground potential and the current through L_2 before saturation is simply written as

$$I_2(t) = (1/L_2^u) \int_0^t V_2(t') dt' = V_{\max} (C_{12}/C_2) L_2^u [t - (1/\omega_1) \sin(\omega_1 t)] \quad (6)$$

We define the "Pulse compression ratio" ⁽¹⁾ as:

$$\delta = T_1/T_2 \quad (7)$$

where $T_1 = \pi/\omega_1$; $T_2 = (C_{23} L_2^s)^{1/2}$, $C_{23} = C_2 C_3 / (C_2 + C_3) = C_{12} = C/2$

It is clear now that T_2 is the duration of the secondary current pulse of amplitude I_2 after saturation of L_2 . Furthermore we immediately recognize $T_1 = T_{\text{sat}}$ by definition and from Eqn(5) $V_2(T_1) = V_{\max} (C_{12}/C_2)$ or the maximum voltage across the capacitor C_2 . If losses are neglected and sinusoidal waveforms are assumed, the law of conservation of charge gives:

$$I_1 T_1 = I_2 T_2$$

and from (7) :

$$\dot{I}_2/\dot{I}_1 = (I_2/I_1)(T_1/T_2) = \delta^2 \quad (8)$$

Thus, for example, a pulse compression ratio of 5 reduces dI/dt in the thyatron by 25.

Integrating Eqn. (1), (Faraday's law), we obtain the fundamental ⁽¹⁻⁴⁾⁽¹³⁾⁽¹⁷⁻²⁰⁾⁽²⁵⁾:

$$N_t A_m = V_{\max} T_{\text{sat}} / 2 \Delta B \quad (9)$$

with $\Delta B = 2B_s$, biased magnetic core near the reverse saturation
 $\Delta B = B_s$, unbiased magnetic core.

Thus, depending on the resonant charging time in the primary subcircuit, we are able by means of Eqn.(9) to calculate the cross-sectional area of magnetic material (A_m) that we need in a given circuit. In Eqn. (9) the compression factor defined by Eqn.(7) does not appear; by means of Eqns. (3), (3') and (9), and recalling Eqns.(7) and (2) with the explicit expressions for T_1 and T_2 , we have the required magnetic material volume for a given single stage pulse compressor, as:

$$V_m = (\pi^2/4) \mu_0 (1/\Delta B^2) (C V_{\max}^2/2) \delta^2 \quad (10)$$

with: $V_m = A l_m$, the magnetic material volume; $C_1 = C_2 = C_3 = C$, the capacitors.

An application of pulse compression is to allow a very slow charge of the pulse circuit through a solid state switch instead of a thyatron and, subsequently to obtain a fast deposition of energy to the discharge. General dI/dt requirement for an excimer laser is 100KA/100ns. Unfortunately the maximum dI/dt for a high power solid state switch such as a thyristor, is about 1KA/1 μ s, thus $\delta \approx 1000$ and consequently by (10), the required volume and the associated losses become huge.

Multi-stages pulse compression

We have looked at the minimization of magnetic material needed as a function of the number of stages and we have found that there exists a number where the magnetic material needed is a minimum.

Figure 4 gives the schematic for a multistages pulse compression circuit:

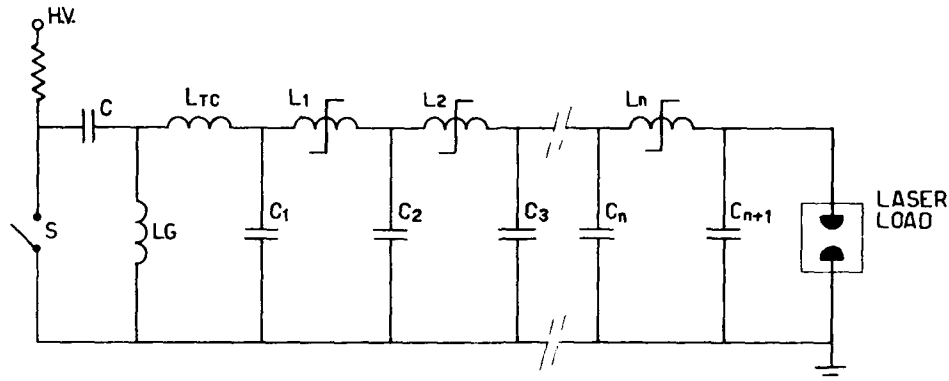


Fig. 4 Multi-stages pulse circuit diagram. L_{TC} corresponds to L_1 in Fig. 1, and may be high due to the slow current rise-time in the first stage.

We consider the circuit lossless⁽¹⁸⁾⁽¹⁹⁾, purely inductive and capacitive. For one hundred percent energy transfer efficiency we put:

$$C_1 = C_2 = C_3 = \dots C_{n+1} = C \quad (11)$$

For such a multi-stage efficient resonant energy transfer system, the condition of Eqn. (2) generalizes to

$$\frac{L_{TC}/L_1}{L_1/L_2} = \frac{L_1/L_2}{L_2/L_3} = \dots = \frac{L_{n-1}/L_n}{L_n/L_{n+1}} = \frac{L_{TC}}{L_1} \quad (12)$$

We realize a compression factor δ with n-stages of different compression factor d_i

$$d_1 < \delta$$

Moreover, the saturation flux B_s has the same value up to the final highest frequency (but it is not necessarily the same material); thus we write

$$\delta = \pi_{i=1, \dots, n}^{d_i} \quad (13)$$

$$V_m^t = \sum_{i=1, \dots, n} k_i d_i^2 = k \sum_{i=1, \dots, n} d_i^2$$

where:

V_m^t = the total magnetic material volume

$k_i = k = \mu_0 (\pi^2/4) (1/\Delta B^2) (C/2) V_{\max}^2$, the same value under our condition for each stage.

We demonstrated that V_m^t is minimum when d_i is the same for each stage.

Thus (13) become:

$$\delta = d^n$$

$$V_m^t = n k d^2 = n k (\delta^2)^{1/n} \quad (14)$$

Looking at the minimization of V_m^t as a function of the number of stages assuming, as currently done, $n \in \mathbb{R}^+$, we found that there exists a minimum for n given by the equation:

$$n = 21n(\delta) \quad (15)$$

Keeping in mind that n is the number of stages, as a result of (15), we take the first integer that approximates (15). Generally the smaller number is picked to avoid building one more stage. As a numerical example we take a compression factor, $\delta = 31$, ($\delta^2 \approx 1000$), and with one stage only:

$$V_m \approx 1000$$

From (15) we have $n=6$, thus the total volume needed is from the second of (14):

$$V_m^t \approx 19$$

Thus it is clear that substantial material savings results in going to multi-stage pulse compressors. The losses associated with increasing number of stages is counter-balanced by the larger and larger losses of a single stage device as k increases. In discussing some theoretical aspects of a multi-stages pulse compressor, it may be convenient to give a first hint for a practical evaluation of the device expense; calling C the "cost" for a required n -stages magnetic compressor, we have:

$$C = nH(\delta^2)^{1/n} + nK \quad (16)$$

Where: H = magnetic material cost per stage.
 K = capacitors cost per stage.

Minimizing (16) as done in (15), the minimum cost is given by the following equation for the optimized number of stages:

$$n = 21n(\delta) / [1 + \sigma / (\delta^2)^{1/n}] \quad (17)$$

Where: $\sigma = K/H$.

It is easy to recognize (15) for $K=0$.

Pre-pulse isolation circuit

Similarly, as done for obtaining equations (4), (5), and (6), we can write the equations for the pre-pulse isolation circuit given in Fig. 5.

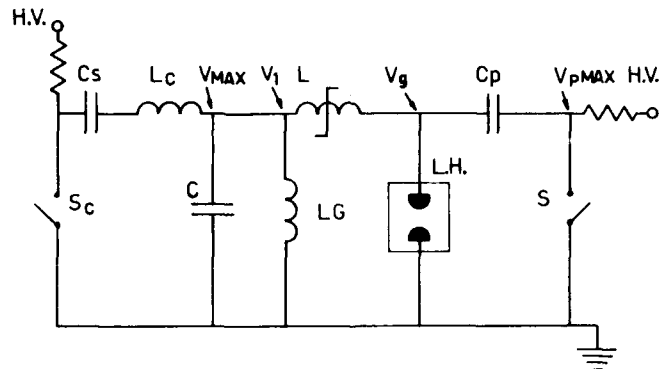


Fig. 5, General pre-pulse circuit diagram. On the left hand part to respect L: main storage energy subcircuit, generally set at low voltage. On the right hand part to respect L: pre-pulse subcircuit or "spiker".

The conditions here are that C is slowly charged to potential V_{max} so that both V_l and V_g are at this potential. The storage capacitor of the pre-pulse circuit C_p ($C_p \ll C$) is charged to V_{pmax} and is some factor of 4 higher than V_{max} . With the circuit voltages set at these values, the pre-pulse switch is closed. L acts as a high impedance barrier until the laser gap breaks down. In this process L is driven in the reverse direction and if driven to reverse saturation some of the energy in the pre-pulse will be dumped into the main capacitor C . It is seen that there will be a substantial delay after the laser gap

breakdown because the inductance L has been driven in the negative direction. The time delay is the time necessary to drive the inductance L to saturation in the forward direction. Assuming that L^u successfully isolates the left part of the circuit, then we can write the voltage across the laser (V_g) as:

$$V_g(t) = V_{\max} + [(V_{p\max} - V_{\max})(C_p / (C_p + C_g))] [1 - \cos(\omega_p t)] \quad (18)$$

with: C = laser head capacitors $1/2$
 $\omega_g = 1 / [(L(C_p C_g / (C_p + C_g)))]^{1/2}$
 L_p = laser head and pre-pulse inductance

The current flowing through the inductor L is governed by the large unsaturated inductance (L^u). We treat V_g as a time varying voltage source in calculating the current through the inductor L on the left hand part of the circuit. The capacitor C is a very large capacitor compared to the capacitor in the pre-pulse circuit (C_p) and thus effectively acts as a short. The current flow in the left hand part of the circuit then is written as:

$$I_p(t) = -(1/L^u) \int_0^t [V_g(t') - V_{\max}] dt' =$$

$$= -[(V_{p\max} - V_{\max}) / L^u] [C_p / (C_p + C_g)] [t - \sin(\omega_p t) / \omega_p] \quad (19)$$

We want to make sure that the magnetic core of L does not go into reverse saturation until $V_g = V_{g\max}$. Otherwise, some of the energy in the pre-pulse will be dumped into the capacitor C and may adversely affect the breakdown of the laser gas. From Eqn. (18) we see that $V_{g\max}$ is reached in time,

$$T = \pi / \omega_p \quad (20)$$

The voltage $V_{g\max}$ is given by,

$$V_{g\max} = V_{\max} + 2[(V_{p\max} - V_{\max})] [C_p / (C_p + C_g)] \quad (21)$$

The current at T in the left hand part of the circuit is then,

$$I_p(t) = -\pi [(V_{p\max} - V_{\max}) / L^u \omega_p] [C_p / (C_p + C_g)] \quad (22)$$

The saturating inductance should be designed such that the inductance does not go into reverse saturation when the current reaches $I(T)$. Further, the pre-pulse should be set so that gas breakdown in the laser medium is near $V_{g\max}$. After breakdown of the discharge the laser gap becomes a low impedance source and power begins to flow from the main storage capacitor, C , at time $t=T$. The current I is given as:

$$I(t) = (V_{\max} / L^u \omega) \sin[\omega(t-T)] \quad (23)$$

with $\omega = 1 / (L^u C)^{1/2}$.

Conclusions and Considerations

In both the pulse compression circuit and the pulse isolation circuit discussed above, the initial function of the saturating inductor is to hold off a certain voltage. In pulse compression L_2 must not saturate until V_2 reaches maximum voltage, $V_{\max}(C_{12}/C_2)$, and, similarly, in the pulse isolation circuit L must remain unsaturated until V_g reaches $V_{g\max}$ as given in Eqn. (21). Equation (1) is a convenient form of the Faraday's law that should easily allow us to calculate the desired area A_m for a given material with saturation flux characteristics of B . In pulse compression where the pulse compression ratio is large, that is, when the charging time is long compared to the saturation time, the integration over t to T^{sat} is easily determined since T^{sat} is simply the time for V_2 to reach maximum voltage. However, when very fast voltage risetimes are desired as in the last stage of a pulse compressor chain (multi-stage pulse compressor), the pulse compression ratio must be very small because, for example, at 20MHz, ferrites with unsaturated μ_r of only a couple of hundreds are available. Thus, the best that can be achieved are compression ratios of the order of 3. Under these conditions the exact time for T^{sat} becomes ambiguous. In the case of pulse compression we need to make sure that the inductor completely saturates before V_2 reaches maximum voltage, so that the stored energy in C_2 can be transferred more rapidly to the load or the next pulse compression stage. If this is not done the partially saturated core will transfer energy initially at slower rate until the current through the core

reaches levels to completely saturate the core. The trade-off is between saturating the core slightly before C_2 reaches maximum voltage resulting in decreased energy transfer or saturating the core after C_2 reaches maximum voltage resulting in increased energy transfer time. Although this choice is relatively unimportant when the compression ratio is large, it is very important when the ratio is only of the order of 3. Our preference for low compression ratio situations is to sacrifice the amount of energy transferred rather than the increased time delay.

For pulse isolation circuits we want the core as small as possible but at the same time successfully isolate the pre-pulse from the main energy storage circuit. Further, we do not want any of the core to reach reverse saturation during the rise of the pre-pulse voltage across the discharge gap as this may result in possible dumping of the energy in the pre-pulse into the main storage capacitors. Since the voltage risetime of the pre-pulse is generally made as fast as possible, it is necessary to use fast ferrites which have unsaturated permeabilities of only a few hundred.

In conclusion we described the important parameters of magnetic materials for a proper choice in pulse compression and in pulse isolation systems. We gave the explicit expression for the magnetic material volume needed in a single stage pulse compressor and we obtained a relation for the minimum magnetic material volume needed in a multi-stages pulse compressor. We have given, also, the explicit expression for the current in pulse isolation systems.

However, we have not discussed in detail the approximation to Faraday's law when the time to saturation is comparable to the saturation time T_{sat} ; we have not given the explicit calculation of the change in permittivity for saturated and unsaturated material that is important in calculation of resistivity loss in ferrite materials. Furthermore we have not discussed changes in resistivity as a function of frequency.

Acknowledgments

This work was carried and supported at the "Universite d'Aix-Marseille II", "Institute de Mecanique des Fluides", "Equipe Nouveaux Laser", 1, Rue Honnorat, 13003 Marseille, France.

One of the author (M. V.), wishes to thank Dr. R. Salimbeni, Dr. P. Mazzinghi, Dr. M. Matera and Dr. L. Fini, of his Institute, for some fruitful discussions during the first period of the study. We appreciated the hospitality at the "Equipe Nouveaux Laser", in particular Professor B. Fontaine and Professor B. Forestier, for having given fundamental papers and materials.

References

1. I. Smilanski, S. R. Byron, and T. R. Burkes, Appl. Phys. Lett. 40, 547, (1982)
2. R.C. Sze, SPIE, Vol. 701 1986 European Conference on Optics, Optical Systems and Applications (ECOSA '86), p.105 (Florence 1986)
3. T. Shimada, K. Noda, M. Obara, and K. Midorikawa, Jap. J. Appl. Phys. 24, L855, (1985).
4. T. Shimada, M. Obara, A. Noguchi, Rev. Sci. Instrum. 56, 2018, (1985)
5. C. H. Fisher, M. J. Kushner, T. E. DeHart, J. P. McDaniel, R. A. Petr, and J. J. Ewing, Appl. Phys. Lett. 48, 1574, (1986)
6. W. H. Long, Jr., M. J. Plummer, and E. A. Stappaerts, Appl. Phys. Lett. 43, 735, (1983)
7. R. S. Taylor, and K. E. Leopold, Appl. Phys. Lett. 46, 335, (1985)
8. R. S. Taylor, and K. E. Leopold, Appl. Phys. Lett. 47, 81, (1985)
9. T. J. Pacala, I. S. MacDermid, and J. B. Laudenslager, Appl. Phys. Lett. 44, 658, (1982)
10. S. Watanabe, M. Watanabe, and A. Endoh, Rev. Sci. Instrum. 57, 2970, (1986)
11. R. R. Butcher, and T. S. Fahlen, presented at the CLEO 84, Conference on Lasers and Electro-Optics, Anaheim, CA (1984), paper THP1
12. D. F. Crosjean, Air Force Wright Aeronautical Laboratories, AFWAL-TR-84-2074, (1985)
13. D. Basting, K. Hohla, E. Albers, H. v. Bergmann, Laser & Optoelektronik 2, 128, (1984)
14. Data sheets of ALLIED CORPORATION Metglass Products Department, (1981)
15. Data sheets of VACUUMSCMELZE GMBH "Vitrovac" Amorphous Metals, (1983)
16. The VACUUMSCMELZE Handbook: "Soft Magnetic Materials", R. Boll ed. (Siemens Aktiengesellschaft, Heyden & Son Ltd, London, 1978), pp. 13-123
17. H. J. Baker, and Seddon, J. Phys. E: Sci. Instrum. 19, 149, (1986)
18. W. S. Melville, Proc. IEE 98, 185, (1951)
19. W. C. Nunnally, Los Alamos National Laboratory Report No. LA-8862-MS, (1981)
20. D. L. Bix, E. J. Lauer, L. L. Reginato, J. Schmidt, and M. Smith, Lawrence Livermore National Laboratories, UCID-18831, (1980)
21. C. G. Koops, Phys. Rev. 83, 121, (1951)
22. J. E. L. Bishop, and P. Williams, J. Phys. D: Appl. Phys. 10, 225, (1977)
23. S. H. Charap, J. Appl. Phys. 50, 7701, (1979)
24. C. H. Smith, IEEE Trans. Nucl. Sci. NS-30, 2918, (1983)
25. D. L. Bix, E. J. Lauer, L. L. Reginato, D. Rogers, Jr., M. W. Smith, and T. Zimmerman, Proceedings 3rd IEEE International Pulsed Power Conference, Albuquerque, NM, (1981), pp. 262-267

Temperature Dependence of Spectra and Efficiency for an Electron-Beam Pumped XeF Laser

D.G. Harris, T.T. Yang, D.H. Burde, G.A. Merry,
L.A. Pugh, J.H. Tillotson, C.E. Turner, Jr., and D.A. Copeland

Rockwell International-Rocketdyne Division
Canoga Park, California 91304

Abstract

An analysis is made of the lasing efficiency and spin-split spectra of the XeF(B-X) system as observed in an e-beam pumped laser. The intricate rotational and vibrational structure in the 351-nm and 353-nm lasing emission is investigated in an attempt to gain insight into the processes responsible for the spectral features of this laser.

Introduction

Since the first demonstration of improved performance of e-beam pumped XeF laser operation at elevated temperature¹ there has been considerable interest in trying to understand mechanisms responsible for this performance improvement. At room temperature, laser power is emitted predominantly in the 353 nm band on XeF(B,v'=0) \rightarrow XeF(X,v''=3) transitions. As the temperature is increased, the 351-nm band increases in intensity. This band includes both (B,v'=1) \rightarrow (X,v''=4) and (B,v'=0) \rightarrow (X,v''=2) transitions.

Several suggestions¹ have been advanced to explain the improved performance at high temperature. Hsia et al.¹ attributed the improved energy extraction to a combination of increased vibrational relaxation within the B state and increased dissociative rate of the weakly bound X state. Subsequent experiments by Champagne et al.² indicated that a decrease in narrowband absorption with increasing temperature in the 351-nm band region might also contribute to improved energy extraction.

The objective of our experimental program was to obtain lasing spectra and efficiency from 300 K to 450 K under consistent and reproducible conditions. To this end, the electron beam parameters were held constant and the laser medium density was kept at 3 Amagats to ensure the same pump rate at all temperatures.

Experimental Apparatus

The experimental apparatus used for the measurements is the Rocketdyne electron-beam excimer laser (REBEL) system. The electron gun is driven by a three-stage Marx bank which yields current densities at the anode foil of 10-12 A/cm². Typical operating parameters of the electron-beam driver are a 270-390-kV voltage with a 0.25-1.0- μ s pulse length. The laser chamber consists of a Monel box 114 cm long with a 10- x 10-cm² clear aperture along the lasing axis. This chamber is separated from the high-vacuum electron-gun chamber by a titanium alloy foil mounted on a hibachi frame. An interior shroud of nickel-plated copper limits the volume pumped by the electron beam to 100 x 10 x 10 cm³, and an 800-Gauss magnetic field is employed to improve the pumping uniformity of the gas. The laser chamber has been operated at pressures up to 5 atm at 450 K. The experimental results reported in the present paper were obtained using a Ne buffer gas at a density of 3 Amagats, a pulse length of 1 μ sec and gas mix of Ne/Xe/NF₃ = 99.425/0.5/0.075. For the gas volume corresponding to the aperture over which laser energy is extracted, the average pump rate is approximately 90 kW/cm³ as estimated by the standard technique of measuring the gas cell pressure rise in conjunction with 3-D Monte Carlo electron-beam energy deposition calculations.

A flat/flat resonator with 100/50% reflectivities was employed in all the present studies. For this resonator the threshold gain is approximately 0.35%/cm, which ensures, at the above operating conditions, that the data were obtained well above threshold with the medium well saturated. Lasing was restricted to a uniformly pumped volume within the REBEL cavity by using 4-cm diameter mirrors. High-resolution, approximately 0.05 Å, spectra were recorded on film using a 1-m monochromator with a 1200-line/mm grating in fourth order. Both bands were simultaneously recorded. Additionally, spectral data were simultaneously recorded with an optical multichannel analyzer (OMA 2 system, EG&G Princeton Applied Research). The detector head was mounted

on a 0.3-m monochromator operated in second order with a 2400-line/mm grating. To monitor the consistency of the lasing operation, voltage and current waveforms were recorded on each shot, and the temporal profiles of the 353- and 351-nm lines were monitored using appropriately filtered vacuum photodiodes. The laser output energy was measured with a volume absorbing calorimeter. A schematic of the apparatus is shown in Figure 1.

Results

High resolution film spectra were taken at several temperatures between 300°K and 450°K, these are presented in Figures 2 through 5. It may be noted that at 300°K the lasing emission occurs predominately in the 353-nm band. Only a weak lasing spike appears in the 351-nm band at 300°K. As the temperature increases to 350°K a second spike appears. Increasing the temperature even further to 450°K shows the spikes growing and some structure appearing between the spikes. The relative energy in the 351-nm and 353-nm band could be inferred from OMA data and corroborated by the waveforms recorded with the appropriately filtered photodiodes. This data is presented in Figure 6, as lasing efficiency versus temperature. These results are in agreement with those of Hsia et al.¹, in that the 351-nm emission increases dramatically with temperature. The lasing efficiency of the XeF laser improves markedly because the energy in the 351-nm band increases while that in the 353-nm band remains virtually unchanged.

Some general qualitative observations may be noted. The structure and efficiency of the 353-nm band at 450°K are very similar to those at room temperature. In contrast the 351-nm spectrum is different in character from that of the 353-nm spectrum. At elevated temperature the 351-nm spectrum is dominated by two strong spikes with some structure between them. The 351-nm band also changes markedly with temperature growing from a single spike at 300°K to two intense spikes with structure at $T \geq 400^\circ\text{K}$.

Discussion

Potential energy curves of the molecular states important to the XeF laser are shown in Figure 7. The 353-nm band emission comes primarily from the $\text{XeF}(B, v'=0) \rightarrow \text{XeF}(B, v''=3)$ transition whereas the 351-nm band is composed of radiation from the $\text{XeF}(B, v'=1) \rightarrow \text{XeF}(X, v''=4)$ and $\text{XeF}(B, v'=0) \rightarrow \text{XeF}(X, v''=2)$ transitions. Each vibrational transition has four rotational branches: $P_e, R_e, P_f,$ and R_f , where e and f represent spin "up" and "down", respectively, for the $\Sigma \rightarrow \Sigma$ transitions.

A. 353-nm Emission

The 353-nm band is considered first. A typical high resolution lasing spectrum is shown in Figure 8. The experimental spectra consistently showed modulations and peaks whose positions were reproducible, independent of gas mixture, temperature and resonator configuration. The modulations were also observed in previous experiments with an unstable resonator³. Tellinghuisen et al.⁴ have attributed these modulations to the effects of cooperative lasing on the overlapped rotational lines of the 0-3 band and the very high-J lines of the 0-2 band. An alternative mechanism for the modulations is absorption due to rotational transitions in light diatomic molecules. It was recently suggested that excited-state absorption of N_2 is significant in the 353-nm lasing band when a substantial amount of N_2 is added to the gas mixture.⁵ Another possible mechanism for these modulations will be considered below.

The small-signal spectrum of the 0-3 band computed using the REXKAL code^{6,7} is shown in Figure 9. The spectroscopic constants used in this calculation are those reported by Tellinghuisen et al.^{8,9} The four branches, $R_e, R_f, P_e,$ and P_f and the corresponding bandheads for ^{131}XeF are shown in Figure 10. There are very small wavelength shifts and a slight broadening of the transitions due to the multitude of naturally occurring isotopes of xenon. The calculated small-signal gain in Figure 9 includes these pressure broadening and isotopic blending effects,^{6,7} which are insufficient to completely smooth the structure of the gain spectrum.

The 1-ns time integrated high-resolution spectrum displayed in Figure 8 shows several clusters of rotational lines and suggests rotationally inhomogeneous laser extraction. This type of broad, complex spectral structure has also been observed in short-pulse (~50ns) experiments¹⁰ at moderate to high spectral resolution. Furthermore, low spectral resolution (~1Å) gated-OMA experiments¹¹ have shown that the broad emission in our experiments occurs even during 100-ns time windows. From these observations we conclude that the inhomogeneous lasing seen in Figure 8 is representative of the spectra for much shorter time intervals, less than tens of nanoseconds, and an indication of restricted XeF rotational relaxation. This conclusion

is further corroborated by the recently reported spectral sweep observed in XeF.¹²

In addition, a comparison of the structure in the experimental laser spectrum of Figure 8 with the structure of the theoretical small-signal gain spectrum of Figure 9 shows that the moderate undulations in the small-signal gain spectrum appear to be accentuated in the laser spectrum. This accentuation, if not caused by absorption or cooperative lasing on high-J (0-2) lines, could be interpreted as due to wavelengths with slightly higher gain accessing neighboring rotational states to some extent but not enough to lead to truly rotationally homogeneous narrowband emission. The energy stored in XeF resides in a multitude of rotational states which must be collisionally coupled on time scales that are short compared to the stimulated emission rate for narrowband emission. Thus the appearance of several clusters (or even a broad smooth distribution) of rotational lines lasing relatively independently suggests that the rotational relaxation rates may be too slow in the B and/or X states to allow narrowband lasing. This hypothesis is supported not only by the recently reported spectral sweep observed in XeF^{11,12} but also the well-known difficulty in achieving efficient injection-locking when the small-signal gain \gg threshold gain.¹³⁻¹⁶

Another observed feature of the spectrum may be plausibly explained by examining the relative positions of the rotational bandheads in the 353 nm band. Although lasing is observed at 3531.6 Å, which is the R_p bandhead, it is consistently much weaker than that observed at 3531.8 Å, which is the R_c bandhead. Both bandheads originate from the lower rotational levels of the XeF(B, $v''=0$) manifold. While the computed small-signal gain indicates that the gain is only slightly larger at the R_c bandhead, lasing on the R_p bandhead is significantly suppressed. As shown in Figure 10 the low-J R_p bandhead at 3531.6 Å is located at the far left of the rotational structure and does not overlap spectrally with the other branches, while the R_c bandhead near 3531.8 Å overlaps with the P_c , P_f , and R_c branches of the 0-3 band. Thus lasing at 3531.8 Å (R_c bandhead) optically accesses XeF molecules in both the e and f spin states, whereas lasing at 3531.6 Å (R_p bandhead) does not optically access both spin states. Since the e and f spin states are optically coupled at the R_c wavelength but not at the R_p wavelength, saturation at the R_c bandhead at 3531.8 Å is expected to be more efficient than at the R_p bandhead at 3531.6 Å and may in turn suppress R_p lasing. Collisional spin relaxation between the e and f branches could also cause depletion of the f levels when the R_c bandhead begins to lase. This tends to reduce the gain of the R_p bandhead. However, the rates for collisional spin relaxation are expected to be much slower than spin conserved rotational relaxation and, as will be noted below, the laser spectrum at 351 nm tends to imply slow collisional spin relaxation.

B. 351-nm Emission

The 351-nm emission includes rotational transitions of both the (B, $v'=1$) \rightarrow (X, $v''=4$) and (B, $v'=0$) \rightarrow (X, $v''=2$) bands of XeF. A typical high-resolution spectrum of the 351-nm lasing emission obtained with the REBEL laser at elevated temperature is shown in Figure 11. A REXKAL small-signal gain spectrum is shown in Figure 12, while in Figure 13 are shown the corresponding 1-4 and 0-2 rotational branches and bandheads which can be correlated with the peaks of Figures 11 and 12. A very striking feature of the REBEL laser spectrum is the lack of significant lasing at 3510.5 and 3510.9 Å, where the predicted small-signal gain is large.

The lack of significant lasing in our data at 3510.5 and 3510.9 Å compared to what might be expected on the basis of the small-signal gain calculation may be understood by reference to Figure 13. The lower levels at these wavelengths are centered at a rotational quantum number of 15 for the R_p branch and 5 for the R_c branch. Since these rotational states are relatively far from the dissociation limit, during long-pulse lasing a population will build up in these states and lasing action at these two wavelengths will be affected by lower-level bottlenecking. Then lasing might shift to other spectral regions able to sustain gain during saturated extraction (e.g., high J bandheads, see below).

Some insight into other possible mechanisms for the suppression of lasing at these wavelengths can be seen by referring to the energy level diagrams of Figures 14 and 15. Strong lasing in the 0-3 band at 3531.8 - 3533.0 Å can decrease the gain on the low-J R_c and R_p bandheads of the 1-4 band by two related mechanisms. First, the 0-3 lasing emission originates from the rotational states of the $v'=0$ level for J values up to 30, as shown in Figures 8 and 10. Due to the finite rate of rotational relaxation, lasing tends to depopulate the molecules with J above, but near J ~ 30, more than those above, but far from J ~ 30. Rotational states in the vicinity of J ~ 45 of the $v'=0$ level, which are depleted by stimulated emission, are expected to be rapidly

replenished by the efficient vibrational-rotational (V-R) energy transfer from $J = 1$ -15 of the $v'=1$ level.^{17,18} This transfer will be especially rapid for the low rotational states of the $v'=1$ level due to the high density of states and their near resonance with the $v'=0$ rotational states. Consequently the low-lying rotational states of the $v'=1$ level are indirectly depleted by V-R transfer associated with 0-3 lasing, which in turn reduces the gain at the low- J R_e and R_f bandheads of the 1-4 band. This cascading process is illustrated in Figure 14. Second, a reverse effect would occur in the $XeF(X)$ state. The 0-3 lasing fills the rotational states up through $J \sim 30$ of the $v''=3$ level. The V-R relaxation in the XeF system is expected to be somewhat slower than in the HF system due to its larger reduced mass. However, because of the small energy defects of these rotational states and the low-lying rotational states of the $v''=4$ level, near-resonant V-R energy transfer between them would be efficient, as indicated schematically in Figure 15. This V-R relaxation will tend to overpopulate the low-lying rotational states of the $v''=4$ level and decrease the gain on the corresponding 1-4 transitions. Thus 0-3 lasing can decrease the gain on the low J transitions of the 1-4 band by a combination of two effects: depletion of the upper lasing level low-lying rotational populations and a corresponding buildup of the lower lasing level low-lying rotational population. The combination of these two processes is believed to be largely responsible for the absence of lasing at 3510.5 and 3510.9 Å when the 0-3 band lases for the conditions of the present experiments.

In contrast, Figure 11 demonstrates intense, relatively narrow-band, lasing at 3511.2 Å and 3512.6 Å. Reference to Figure 13 shows clearly that these peaks strongly correlate with the high- J (i.e., $J \sim 50$) R_e and R_f rotational bandheads, respectively, of the 1-4 band. Although these high- J rotational transitions are relatively unaffected by the V-R energy transfer process associated with the 0-3 lasing discussed above, vibrational-translational (V-T) energy transfer will never-the-less tend to populate the $v''=4$ level. Lasing (1-4) transitions with $J \geq 52$ are unbound and should have ground states lifetimes of order of a vibrational period, $< 10^{-13}$ s. The 1-4 lasing transitions between $40 < J < 50$ terminate on rotational resonances which are bound only by a small rotational barrier ($< 100 \text{ cm}^{-1}$) in the effective ground-state potential, or, alternatively viewed, terminate on bound levels within about $\pm kT/2$ of the dissociation limit. Tellinghuisen et al.,^{4,8} have noted that the rotational resonances lying above the dissociation limit can predissociate. More importantly, molecules near the dissociation limit can dissociate quite rapidly via collisions at high density. Collision-induced dissociation rates for molecules whose energies are in the range $(D_e \pm kT/2)$ were calculated by Yang et al.,¹⁹ to be of the order of 10^{10} to $10^{11} \text{ cm}^3/\text{s}$. At laser medium densities of $3\text{--}4 \text{ Amagat}$, these rates correspond to ground-state lifetimes of 0.01-0.1 ns. Regardless of the predissociation rates for $v''=4$, $40 < J < 50$, levels (very sensitive to the details of the effective potential and J), the collisional dissociation rates appear to be sufficiently fast to ameliorate bottlenecks.

Since the high- J rotational states of the $v''=4$ level can dissociate efficiently, the effective ground-state lifetime for these high- J levels is much shorter than the low- J $v''=4$ levels or most levels of $v''=2$ or 3, and lasing at 3511.2 Å might be expected to be more efficient than at other wavelengths. Similarly, the lasing at 3512.6 Å, which correlates strongly with the 1-4 high- J R_e bandhead, presumably should be enhanced by reduced bottlenecks in the lower levels. However, from Figure 13, it is clear that the 1-4 R-branch high- J bandheads are optically coupled with the gain (or loss) associated with other low- to intermediate- J 1-4 branches. And furthermore, lasing at the 1-4 high- J R_e bandhead (3512.6 Å) also couples to the net gain (or loss) associated with several 0-2 transitions at J -values between 10 and 25. On the other hand, lasing at the 1-4 high- J R_f bandhead (3511.2 Å) does not access any 0-2 transitions. The low- J spectral components at the high- J (1-4) bandheads may affect the extraction efficiency to varying degrees at the e and f lines at different temperatures.

The coupling to 0-2 transitions at 3512.6 Å is probably the reason for the absence of emission there at 300 K (see Figure 2). The reason for rather low energy at the 3511.2 Å bandhead is discussed below. In these experiments at approximately 90 kW/cm^2 , the 300°K lasing at 3511.2 Å occurred at a low level throughout the 1 μsec pulse in contrast to the behavior observation at higher pump rate.²¹ The temporal dependence of the 351-nm emission and the 353/351 energy ratio appear to be very sensitive to pump rate and small signal to threshold gain ratio. The narrowness of the spin-split 351-nm peaks is attributed to fast rotational relaxation in the B state²² in conjunction with rapid X state dissociation for at least the high- J component. The persistence of lasing at both e and f high- J bandheads manifests a spin inhomogeneity due to slow collisional spin relaxation.²²

C. Discussion of Improved Efficiency at Higher Temperature

As was seen in Figure 6, the improved efficiency of the XeF laser at elevated temperature results from an increase in energy in the 351-nm band. In particular, the growth of the two narrow spikes at 351.12-nm(λ_1) and 351.26-nm(λ_2) account for most of the increase with some weak emission occurring between the spikes. As was noted above, the emission at 351.12-nm is due to pure $v'=1 \rightarrow v''=4$ transitions, primarily many overlapping lines of the high-J bandhead of the R_6 branch. The 351.26-nm emission is due to a combination of the high-J R_6 bandhead of the 1-4 transition, other low-J (1-4) components, and overlapping lines ($10 < J < 25$) of the 0-2 transition.

1. $\lambda_1 = 351.12$ -nm

The overlapping high-J 1-4 transitions, which terminate on rotational resonances in the X state and account for about 60% of the calculated small-signal gain, are expected to dominate the energy extraction at λ_1 . Though lasing at λ_1 couples weakly to some low-J (1-4) transitions there is no coupling to the more highly bound 0-2 transitions. Therefore, it seems unlikely that the dramatic increase in elevated-temperature energy extraction at λ_1 can be completely attributed to decreased bottlenecks in the X state. Rather, it appears that shifts in the B state vibrational and rotational populations, and faster V-R, V-T, and R-T rates play an important role.

As temperature increases, the vibrational population of XeF(B, $v'=1$) tends to increase due to enhanced vibrational Boltzmann factors for the B state population and, perhaps, an increased B/C population ratio. Because the rotational levels of the XeF(B) state are closely spaced, there is also a significant shift to higher J as the temperature increases and the rotational population increases for high-J. These effects tend to increase the upper level populations available for lasing at λ_1 . The small signal gain at λ_1 is, therefore, expected to increase somewhat as the temperature is increased simply due to population shifts in the B state.

This effect may at least partially explain the increase of small signal net gain with temperature seen in earlier experiments by Champagne using an argon-ion laser probe at 351.11-nm.² In those studies, a strong absorption at room temperature in pure Ne plasmas was seen. However, addition of NF₃ or Xe to the Ne dramatically decreased this absorption. A further reduction in absorption in Ne/Xe and Ne/NF₃ binary mixtures at 351.11-nm was observed as the temperature was increased to 150 C.² As noted above, substantial increases in small signal net gain in mixtures of Ne/Xe/NF₃ was noted.² However, the magnitude of the increased gain appeared greater than could be explained due to decreased background absorption alone. The combined effect on background absorption at 351-nm of the addition of both Xe and NF₃ to Ne has not been determined experimentally. Since the addition of either species alone to Ne was seen to drastically decrease background absorption even at room temperature, one might expect that the addition of both species together would reduce absorption more than either alone.

Extensive modeling by Finn et al.,²³ and Yang et al.,^{6,7} has revealed that the only species that decreases significantly when Xe or NF₃ is added to Ne is Ne₂. Champagne attributes the narrowband absorption to excited atom absorption,² Ne. In either case,²³ the most probable candidate absorber is expected to be related to neon. Finn et al.²³ and Yang et al.⁶ both predict that the broadband absorption in laser mixtures at 351.11-nm is relatively low (gain/loss ~ 10) at room temperature. Further modest reduction at elevated temperature would not greatly increase net gain or lasing efficiency.

In an attempt to clarify the situation, e-beam pumping of Ar/Xe/NF₃ mixtures was carried out to see if 351-nm band lasing could be observed at room temperature. Since no neon was present and there are no known argon or argon-related narrowband absorbers at 351-nm, there should have been no strong selective absorber to inhibit 351-nm lasing. No significant lasing at 351-nm was observed. In fact, the energy ratio E(351-nm)/E(353-nm) appeared even smaller in argon than neon.

Therefore, we conclude that the increase in small signal net gain at λ_1 observed with increasing temperature is due primarily to a real increase in gain due to population shifts rather than to a significant decrease in background absorption. The increased small-signal gain at λ_1 , with a corresponding increase in $v'=1$ production rate due to faster V-T, R-T, and V-R relaxation in the B state, supports more efficient extraction by increasing the effective gain to loss ratio and saturation intensity.

2. $\lambda_2 = 351.26 \text{ nm}$

The narrowband lasing emission at 351.26 nm is even more complex. Both high-J transitions of the (1-4) R_e bandhead, (1-4) P_e (18 < J < 27) lines and overlapping 0 - 2 (10 < J < 25) lines are contributing.

The high-J 1-4 transitions are to lower weakly bound states (as at λ_1) and should not be significantly affected by bottlenecking at any temperature. However, the gain would be enhanced at high temperature by a population shift in the upper states analogous to that described at λ_1 . The 0-2 transitions at λ_2 do go to more strongly bound lower states, therefore, a global increase in the $\text{XeF}(X)$ dissociation rate with temperature would decrease bottlenecking and improve lasing for this component of λ_2 .

Thus at λ_2 several mechanisms appear to improve energy extraction as the temperature is raised. B- and C- state population shifts and enhanced V-T/V-R/R-T relaxation improve the 1-4 lasing component. Additionally, a global ground state dissociation rate increase improves bound low-J (1-4) and (0-2) lasing contributions.

In view of the substantial differences in low-J gain (or loss) contributions at λ_1 and λ_2 , it is not obvious that the energy partitioning between λ_1 and λ_2 should be about equal as appears to be qualitatively inferred by the film spectra of Figures 3-5. Only minor differences in the film spectra peak heights were observed with factor of two changes in relative Xe and/or NF_3 concentration. Due to the difficulty in interpreting film spectra, we are reluctant to draw conclusions about the relative importance of ground state dissociation versus upper state effects with respect to enhanced 351-nm emission at elevated temperature.

Summary

A correlation between the experimental lasing spectra, the theoretical small-signal gain, and the rotational branch structure of XeF has been described. The absence of lasing at the low-J spin-split bandheads of the $\text{XeF}(B, v'=1)$ to $\text{XeF}(X, v''=4)$ rovibronic transitions can be explained by near-resonant V-R energy transfer associated with lasing at 353-nm on the $\text{XeF}(B, v'=0)$ to $\text{XeF}(X, v''=3)$ transitions. Strong narrowband lasing on the high-J spin-split bandheads of $\text{XeF}(B, v'=1)$ to $\text{XeF}(X, v''=4)$ at 3511.2 and 3512.6 Å is attributed to rapid collisional dissociation of the high-J lower laser levels near the dissociation limit and rapid rotational relaxation in the $\text{XeF}(B)$ state. Comparable lasing intensities at the two high-J (1-4) R_e and R_e spin bandheads (3511.2 and 3512.6 Å) manifest a clear spin inhomogeneity and appears to indicate relatively slow collisional spin mixing rates for the $\text{XeF}(B)$ state. The collisional spin mixing rate may affect the ability to obtain efficient single narrow-line lasing in the 351-nm band. The essential absence of lasing at the low-J R_e bandhead of the $\text{XeF}(B, v'=0)$ to $\text{XeF}(X, v''=3)$ transition is likely due to optical coupling at similar and low-J of the two spin states for the (0-3) transition, a mechanism which seems much less effective in the high-J (1-4) case due to a large J difference between R_e and R_e at 3511.2 Å.

The improved efficiency of the XeF laser at elevated temperature results from increased energy in the 351-nm band. This behavior was not found to be very sensitive to mix variations of a factor of two in Xe and NF_3 concentration. The enhancement results from upper state population shifts and faster relaxation rates as well as faster ground state relaxation for low-J components of gain (or loss) at the observed wavelengths of strong emission.

References

1. J. C. Hsia, J. A. Mangano, J. H. Jacob, and M. Rokni, "Improvement in XeF Laser Efficiency at Elevated Temperatures", *Appl. Phys. Lett.* **34**, 208 (1979).
2. L. F. Champagne, "Temperature-dependent Absorption Processes in the XeF Laser", *Appl. Phys. Lett.* **35**, 516 (1979); "Transient Optical Absorption in the Ultraviolet", in *Applied Atomic Collision Physics*, Vol. 3, *Gas Lasers*, E. W. McDaniel and W. L. Nighan, Eds. (Academic Press, New York, 1982), p. 349.
3. J. H. Tillotson, D. Burde, D. Harris, and R. Malins, Rocketdyne Excimer Laser Final Report, 20 December 1982 (unpublished).
4. J. Tellinghuisen, P. C. Tellinghuisen, G. C. Tisone, J. M. Hoffman, and A. K. Hays, "Spectroscopic Studies of Diatomic Noble Gas Halides III, Analysis of XeF 3500 Å Band System". *J. Chem. Phys.* **68**, 5177 (1978).

References (continued)

5. A. Mandl and H. A. Hyman, "N₂ Excited State Absorption in XeF Lasers", Appl. Phys. Lett. 49, 841 (1986).
6. T. T. Yang, J. A. Blauer, C. E. Turner, Jr., and D. A. Copeland, "Multiline Model for E-beam Pumped XeF(B-X) Laser", in Lasers in Fluid Mechanics and Plasmadynamics, Proceedings, AIAA Sixteenth Fluid and Plasmadynamics Conference, 12-14 July 1983, Boston; also AIAA J. 23, 741 (1985).
7. J. A. Blauer, T. T. Yang, C. E. Turner, Jr., and D. A. Copeland, "Excimer Kinetics and multiline Model for the Electron-Beam Pumped XeF(B-X) Laser", Appl. Opt. 23, 4532 (1984).
8. P. C. Tellinghuisen, J. Tellinghuisen, J. A. Coxon, J. E. Velazco, and A. K. Hays, "Spectroscopic Studies of Diatomic Noble Gas Halides IV, Vibrational and Rotational Constants for the X, B, and D States of XeF", J. Chem. Phys. 68, 5187 (1978).
9. P. C. Tellinghuisen and J. Tellinghuisen, "B-X Transition in ¹³⁶Xe¹⁹F", Appl. Phys. Lett. 43, 893 (1983).
10. J. Tellinghuisen, G. C. Tisone, J. M. Hoffman, and A. K. Hays, "Analysis of Spontaneous and Laser Emission from XeF", J. Chem. Phys. 64, 4796 (1976).
11. D. G. Harris, D. H. Burde, R. J. Malins, and J. H. Tillotson, "Spectral Evolution in an Electron Beam Pumped XeF Laser", Appl. Phys. Lett. 51, 1224 (1987).
12. D. M. Guthals, J. F. Osmundsen, D. J. Sox, and T. T. Yang, "Transient Spectral Properties of an Electric Discharge XeF Laser" Lasers '87, Lake Tahoe, NV (1987).
13. J. B. West, H. Komine, and E. A. Stappaerts, "Efficient Injection-locking of an E-beam-Excited XeF Laser", J. Appl. Phys. 52, 5388 (1981).
14. J. Goldhar, J. Dickie, L. P. Bradley, and L. D. Pleasance, "Injection-Locking of a Xenon Fluoride Laser", Appl. Phys. Lett. 31, 677 (1977).
15. H. Komine, S. J. Brosnan, W. H. Long, Jr., J. Holliday, and E. Stappaerts, "Scaling Studies of Efficient Raman Convertors", NRTC-83-09R, Final Report, Northrop Research and Technology Center, 1 July 1983, p. 15.
16. I. J. Bigio and M. Slatkin, "Injection-Locking Unstable Resonator Excimer Lasers", IEEE J. Quantum Electron, QE-19, 1426 (1983).
17. T. T. Yang and J. A. Blauer, "Analysis of Rotational Non-equilibrium Behavior in Hydrogen Fluoride/Deuterium Fluoride Systems", J. Appl. Phys. 53, 2831 (1982).
18. H. Haugen, W. H. Pence, and S. R. Leone, "Infrared Double Resonance Spectroscopy of V-T, R Relaxation of HF(V=1): Direct Measurement of the High-J Populations", J. Chem. Phys. 80, 1839 (1984).
19. T. T. Yang, J. A. Blauer, C. E. Turner, Jr., and G. A. Merry, "XeF Ground State Kinetics Analysis", Appl. Opt. 26, 2533 (1987).
20. G. Herzberg, Molecular Spectra and Molecular Structure I. Spectra of Diatomic Molecules (Van Nostrand, New York, 1950), p. 409
21. A. Mandl and H. A. Hyman, "XeF Laser Performance for F₂ and NF₃ Fuels", IEEE J. Quantum Electron. QE-22, 349 (1986).
22. T. T. Yang, D. H. Burde, G. A. Merry, D. G. Harris, L. A. Pugh, J. H. Tillotson, C. E. Turner, Jr., and D. A. Copeland, "Spectra of Electron-Beam Pumped XeF Lasers", Appl. Opt. 27, 49 (1988).
23. T. G. Finn, L. J. Palumbo, and L. F. Champagne, "A Kinetics Scheme for the XeF Laser", Appl. Phys. Lett. 33, 148 (1978).
24. D. H. Burde, T. T. Yang, D. G. Harris, L. A. Pugh, J. H. Tillotson, C. E. Turner, Jr., and G. A. Merry, "Mechanisms for Improved XeF Laser Performance at Elevated Temperatures", Appl. Opt. 26, 2539 (1987).

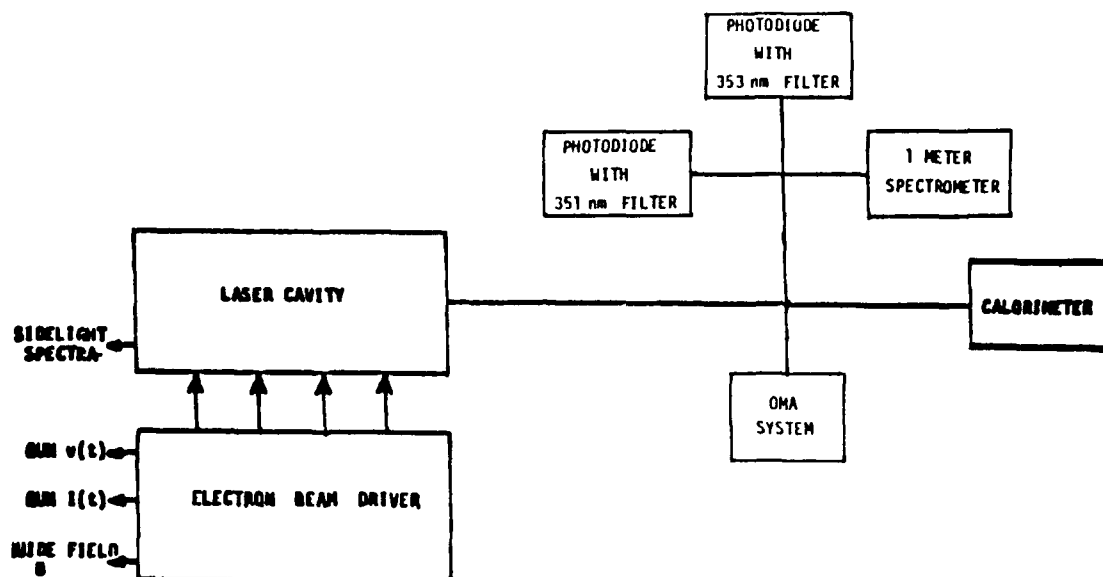


Figure 1. Schematic of Experimental Apparatus.

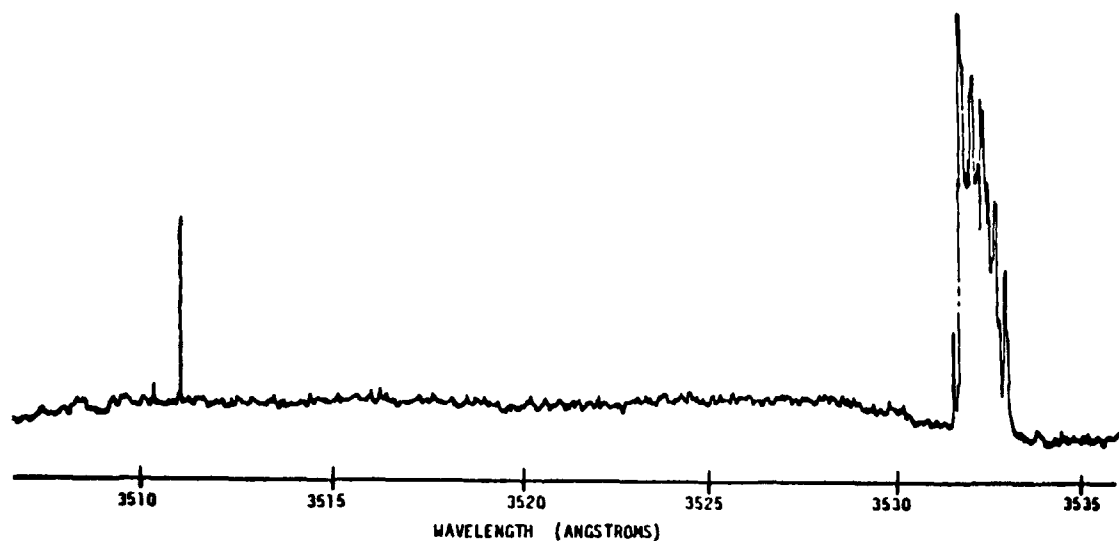


Figure 2. Multiline Laser Spectrum at 300°K.

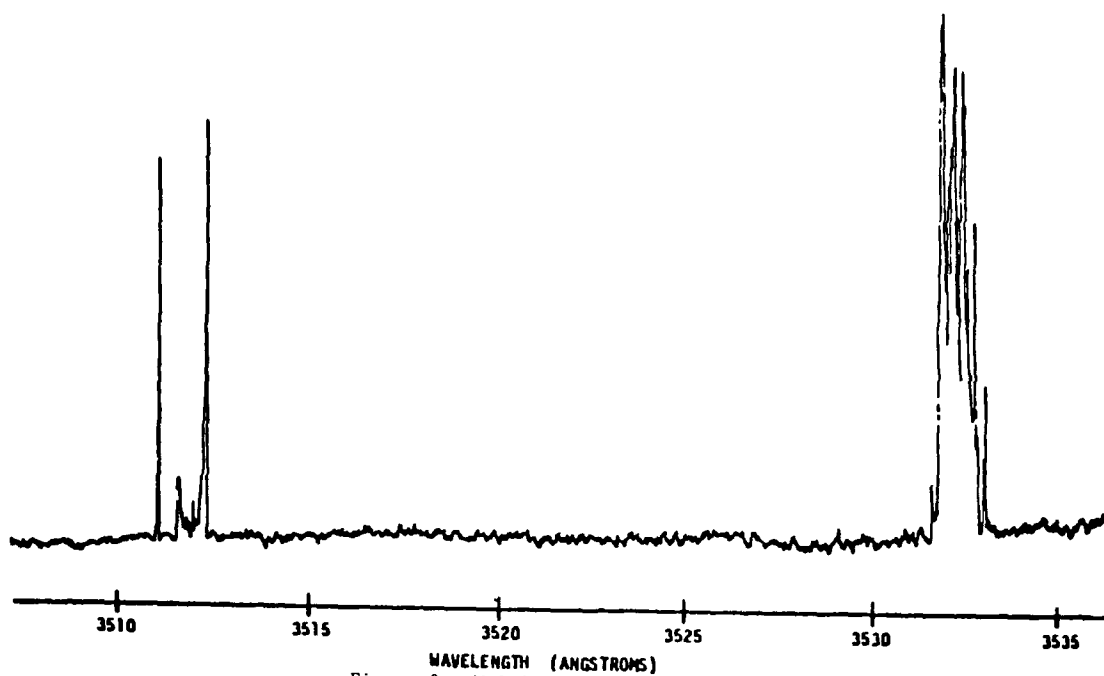


Figure 3. Multiline Laser Spectrum at 350°K

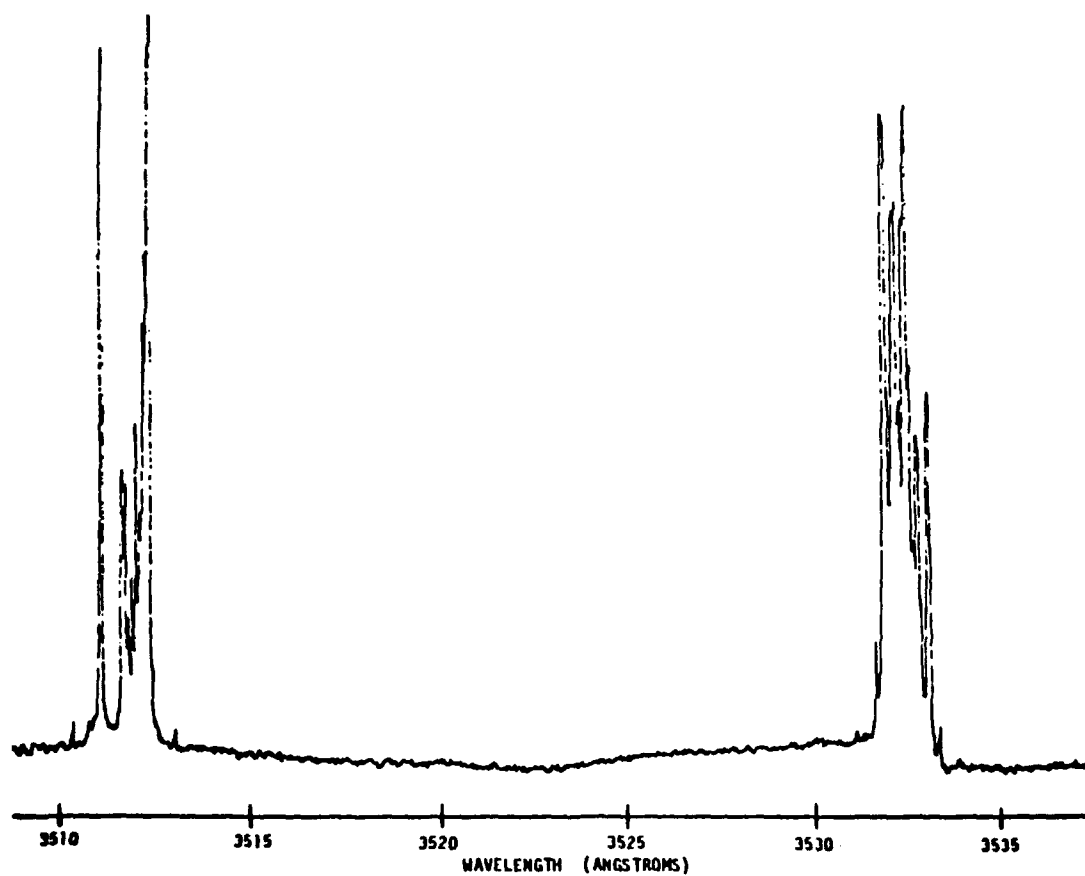


Figure 4. Multiline Laser Spectrum at 400°K.

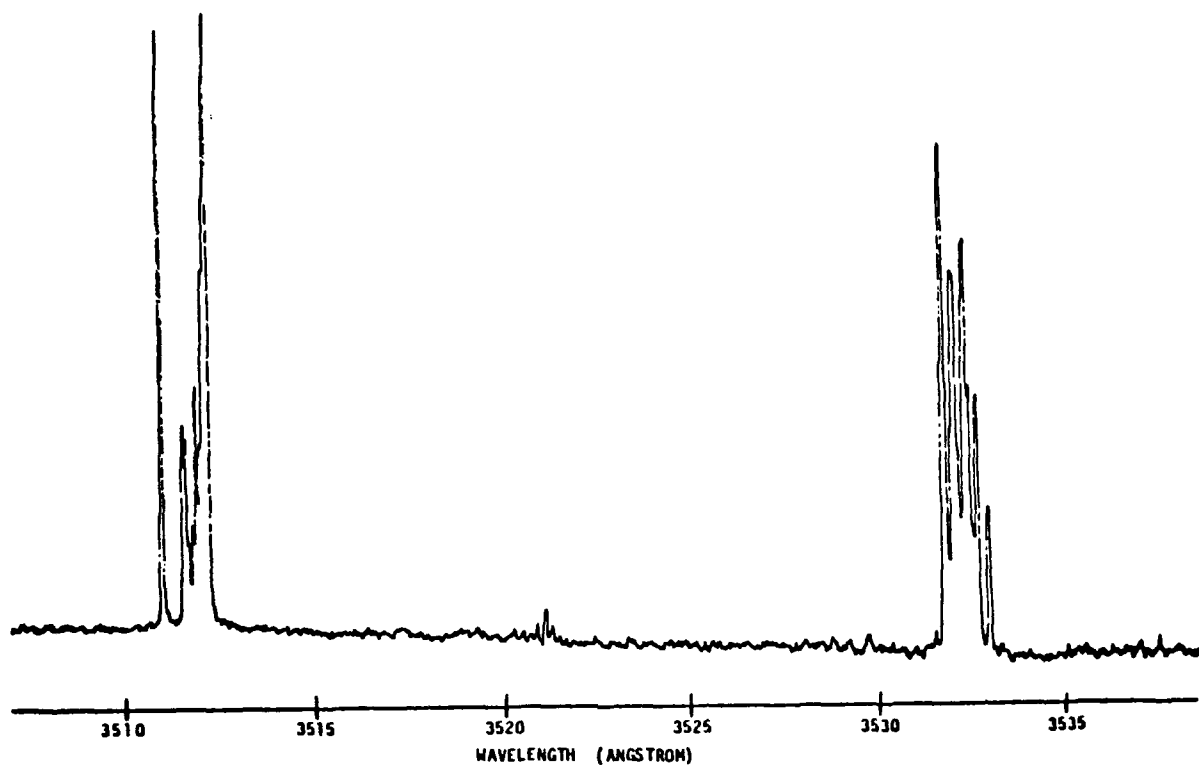


Figure 5. Multiline Laser Spectrum at 450°K.

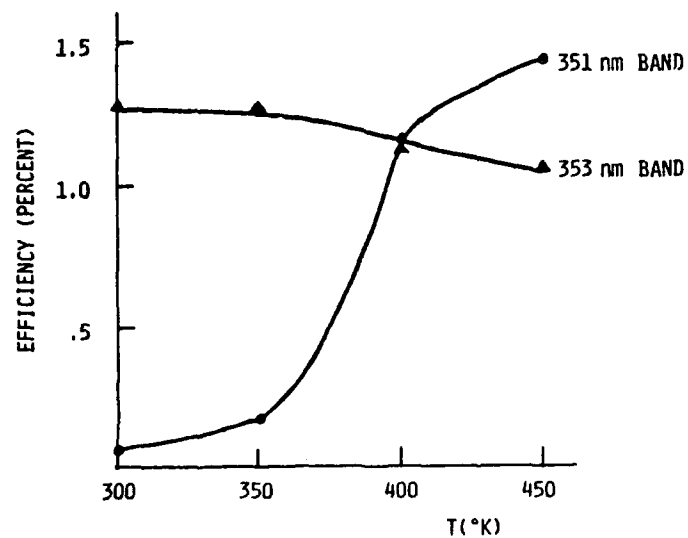


Figure 6. XeF Laser Efficiency Versus Temperature.

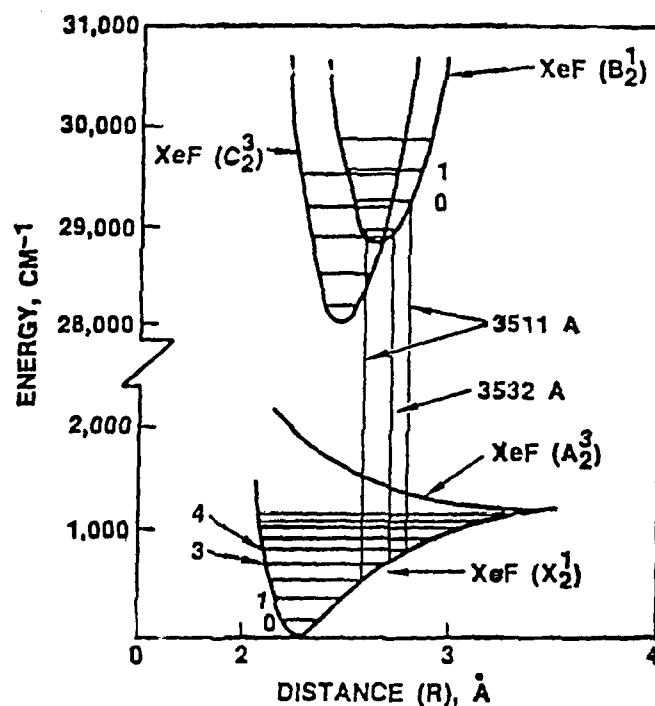


Figure 7. XeF Potential Energy Curves

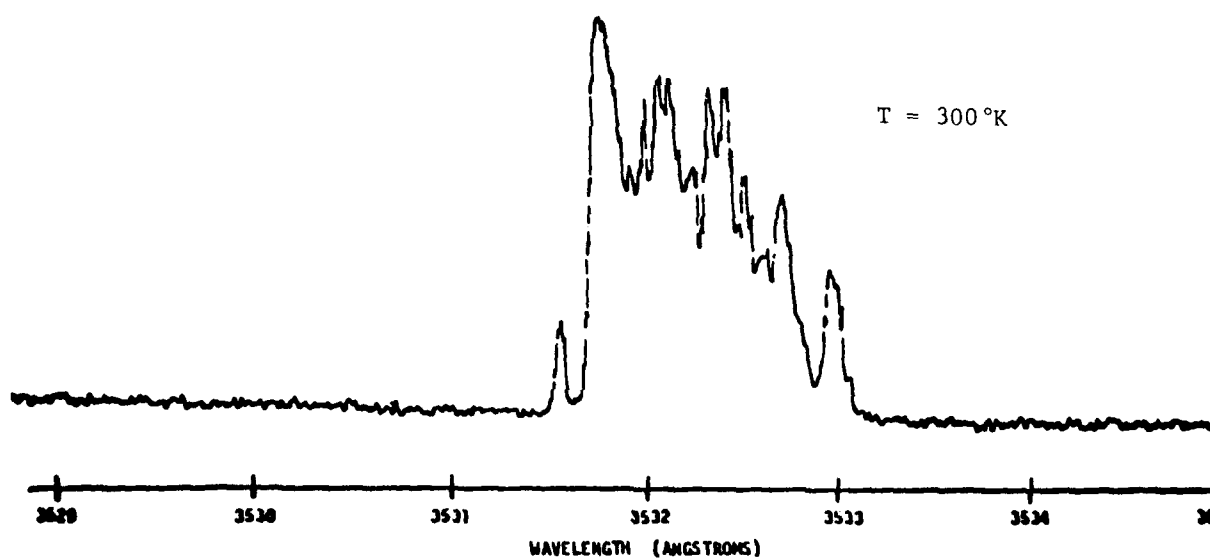


Figure 8. High Resolution XeF Laser Spectrum at 353 nm.

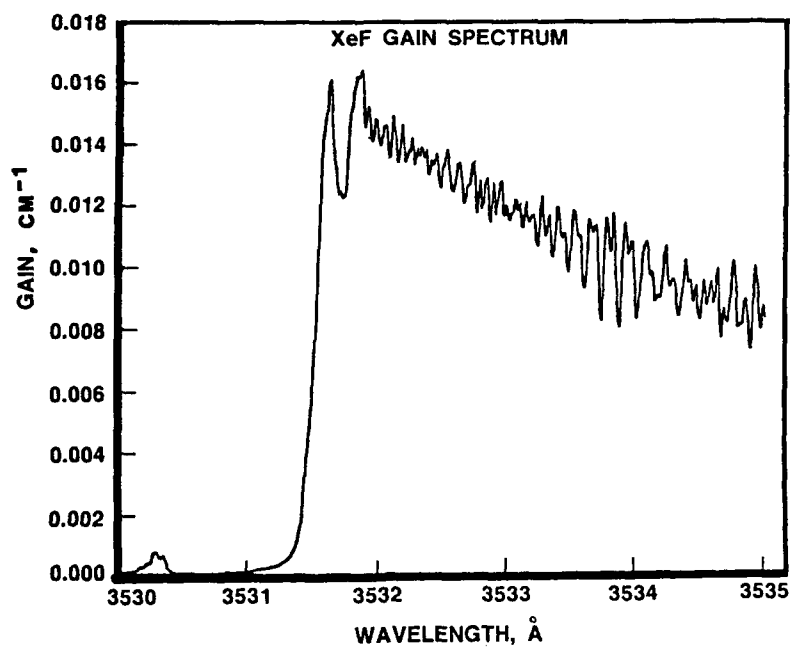


Figure 9. Calculated Small-signal Gain for 353-nm Band.

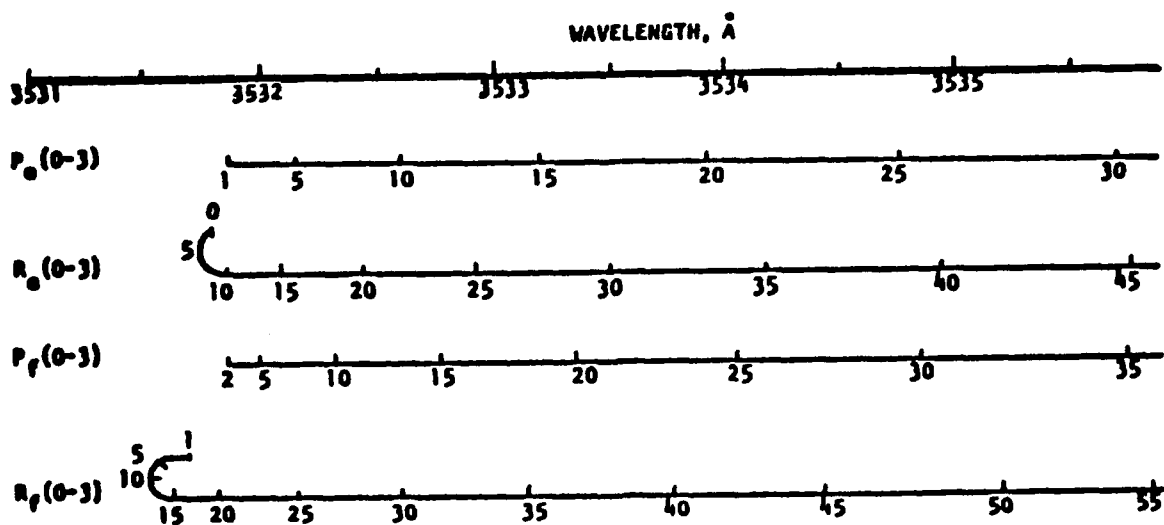


Figure 10. Rotational Branch Structure for 353-nm Band.

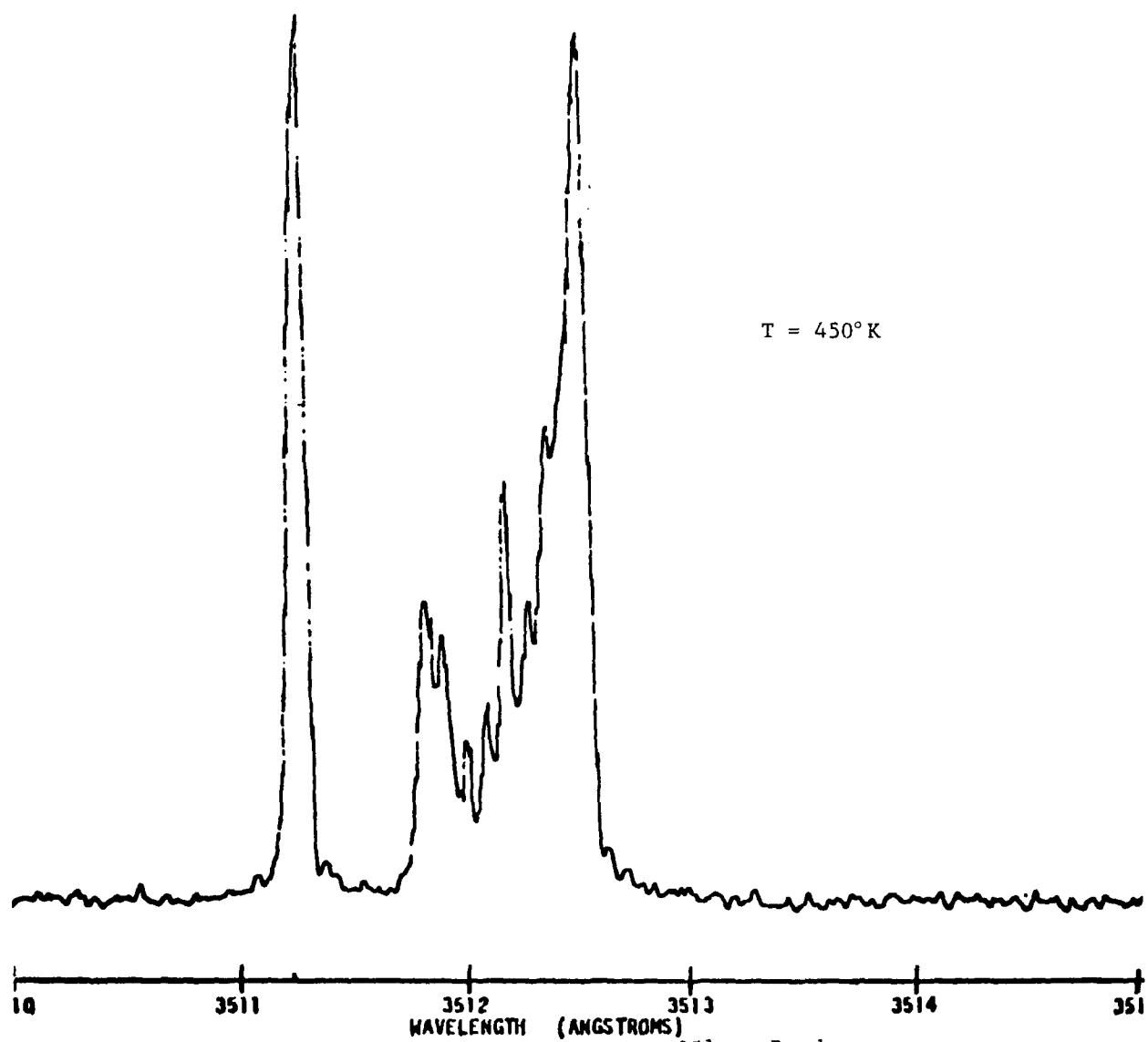


Figure 11. XeF Laser Spectrum at 351-nm Band.

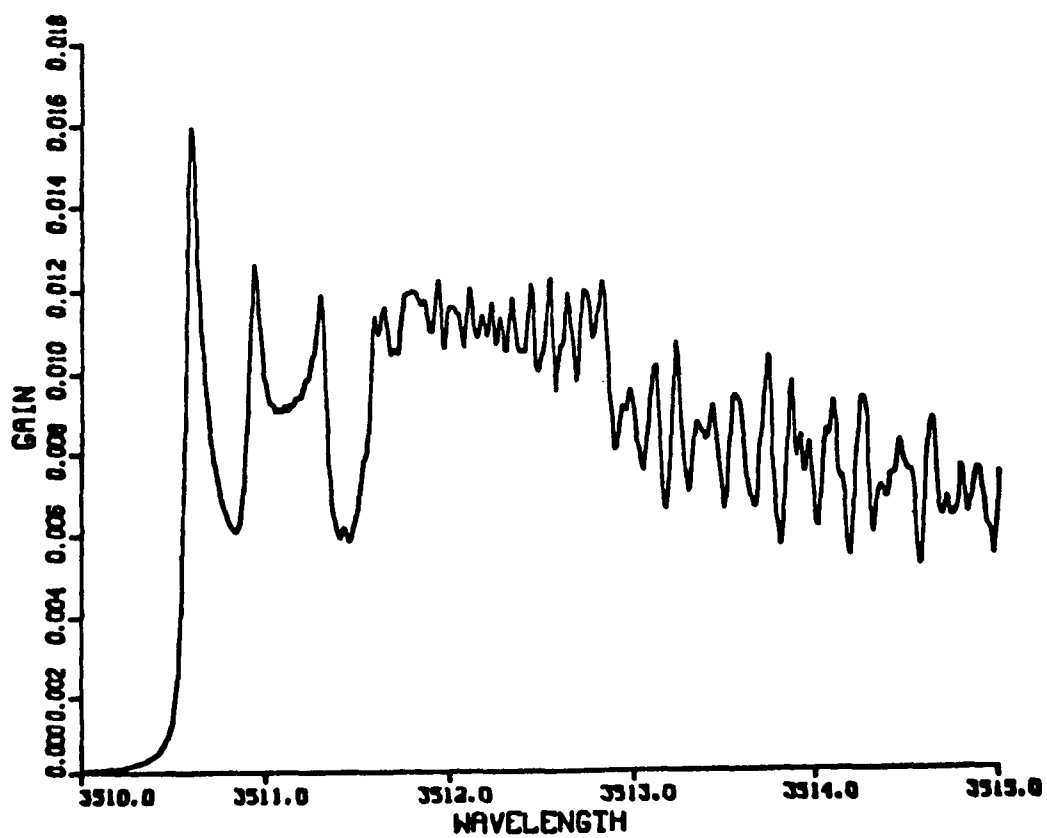


Figure 12. Calculated Small-signal Gain of XeF Laser Near 351-nm.

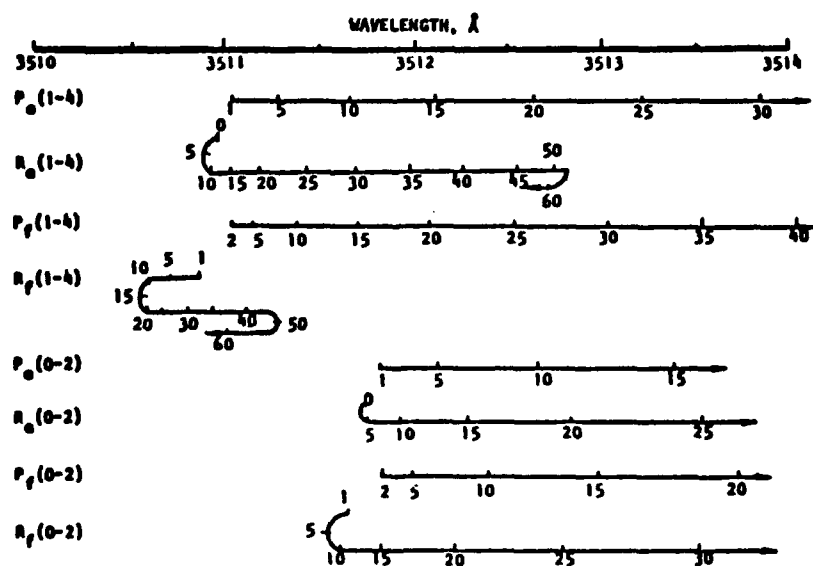


Figure 13. 351-nm Band Structure.

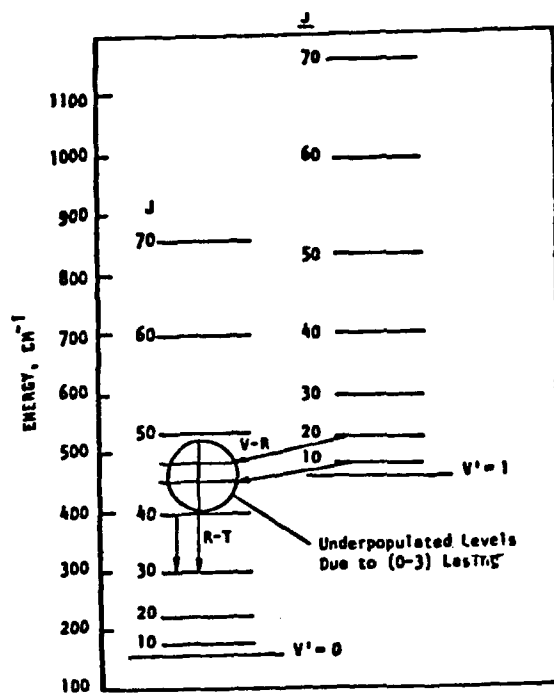


Figure 14. Rovibrational Energy Diagram of $\text{XeF}(\text{B}, v')$ for $v'=0$ and $v'=1$.

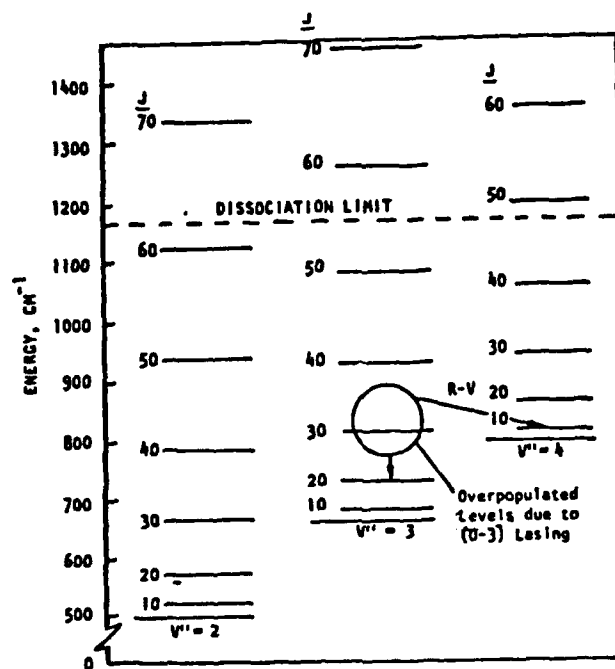


Figure 15. Rovibrational Energy Diagram of $\text{XeF}(\text{X}, v'')$ for $v''=2, 3$, and 4 .

Spectral Sweep in an Electron Beam Pumped XeF Laser

D. G. Harris, D. H. Burde, R. J. Malins,*
and J. H. Tillotson**

Rockwell International-Rocketdyne Division
Canoga Park, California 91304

Abstract

A spectral sweep in the 353 nm band of an electron beam pumped XeF laser has been investigated. The time-integrated lasing spectra broadens as the pulse length, electron beam pump rate, and intracavity flux are increased. Several possible explanations are discussed.

The XeF laser is an efficient source of near-ultraviolet (UV) radiation (Ref. 1,2). However, many proposed applications require a spectral linewidth that is considerably narrower than that obtained from a free-running laser. Injection-locking has been demonstrated to be a practical technique for controlling the linewidth of high power lasers (Ref. 3). The efficiency with which this technique can extract energy in a narrow bandwidth depends on the vibrational and rotational relaxation rates relative to the stimulated emission rate. Unfortunately, there is little information available about the rotational relaxation rates of the low lying vibrational levels of the XeF(B) electronic state that are of importance to laser action. We have attempted to gain some insight into the degree of inhomogeneous broadening of an electron beam pumped XeF laser by investigating the spectral evolution of the 353 nm band of the lasing radiation.

These experiments were performed using an electron beam pumped XeF laser at the Rocketdyne Experimental Laser Laboratory. This device is a versatile research tool having a variable pulse length (0.25 to 1.0 microsecond) and adjustable electron gun voltage (270 to 390 kV). The electron gun is driven by a three-stage Marx bank and yields currents at the anode foil of approximately 10 amp/cm². The laser chamber consists of a monel box 114 cm long with a 10 x 10 cm² clear aperture along the lasing axis. This chamber is separated from the high vacuum electron gun chamber by a Ti alloy foil mounted on a hibachi frame. An interior shroud of Ni-plated copper limits the volume pumped by the electron beam to 100 x 10 x 10 cm. An 800-Gauss magnetic guide field is employed to improve pumping uniformity of the gas. The laser was operated at room temperature with a mixture of NF₃/Xe/Ne in the ratio of 2/6/2600 at a total pressure of 3.4 atm.

A schematic of the experimental apparatus is shown in Figure 1. The principal diagnostic instrument for these experiments was the optical multichannel analyzer (OMA 2 System, EG&G Princeton Applied Research). With this instrument, we were able to obtain data on the 353 nm band of XeF as either a 50ns time slice of the lasing spectrum or a time integrated spectrum of the full lasing pulse. The detector head was mounted on a 0.3 meter monochromator operated in second order with a 2400 1/mm grating. High resolution, time-integrated spectra were simultaneously obtained on Polaroid type 55 positive/negative film using a 1-meter monochromator with a 1200 1/mm grating used in fourth order. These spectra also showed weak lasing on the 351nm band of XeF. To monitor the consistency of the lasing operation, voltage and current waveforms of the electron gun were obtained on each shot. In addition, the temporal profiles of the 353 and 351nm bands were monitored using appropriately filtered vacuum photodiodes. The voltage, current, and photodiode waveforms were displayed on high speed oscilloscopes. The lasing energy was measured with a volume absorbing calorimeter. The energy deposited by the electron beam was determined by the pressure rise technique using a 10,000 Torr MKS Baratron. For typical operating conditions, the average power deposited into the laser mixture by the electron beam was approximately 90kW/cm².

During the initial experiments, the integrated lasing spectrum of the 353nm band was measured for several pulse lengths. These experiments were performed with a confocal unstable resonator of magnification 2.7. Data from the OMA are shown in Figure 2 for pulse lengths of 250, 500, and 750 ns. There is a distinct trend in these data: as the pulse length increases, the red portion of the 353nm band is progressively more accentuated. Emission in this band is due to transitions between the $v = 0$ to $v = 3$

*Present address: BDM Corporation, Huntsville, Alabama

**Present address: Northrop Electronic Systems, Hawthorne, California

rotational manifolds of the XeF(B-X) transition. This shift represents a shift to higher rotational levels as the pulse evolves. This trend was confirmed by the high resolution film spectra. Further experiments were carried out using the OMA to obtain time slices of the lasing spectrum. The OMA gate was set to obtain a 50ns wide snapshot during a lasing pulse. By varying the delay between the initiation of the laser and the gating of the detector window, a series of snapshots of the lasing spectra were taken, which spanned the entire lasing pulse. The pulse-to-pulse reproducibility of the laser were verified by the data from the other diagnostics. Characteristic results are shown in Figure 3 for the $M = 2.7$ unstable resonator. These data show a definite shift of the spectrum to the red portion of the band as the pulse progresses. The time slicing and pulse length variation experiments were repeated with two additional resonator configurations that provided higher intracavity flux: a 50 percent feedback stable resonator and a 70 percent feedback stable resonator. These data show spectral sweeps similar to that observed with the unstable resonator.

To compare the data from several resonator configurations, the spectral sweep was quantified by dividing the 353nm band into five equal wavelength regions. The number of detector counts in each wavelength region was determined and then divided by the total number of counts in the entire band. Since the OMA curve represents time-integrated intensity, i.e., energy emitted during the time that gated detector is on, the resulting numbers measure the fraction of energy emitted in each wavelength segment during the period of the detector gate. This procedure was carried out for each time slice and for each of the resonator configurations. The results are presented in Table 1 and a graph of some of the data are shown in Figure 4. It is apparent from Table 1 and Figure 4 that the magnitude of the spectral sweep as well as the speed with which it occurs increases with the resonator feedback (i.e., as intracavity flux increases).

That a pulsed laser may exhibit a time-dependent lasing spectrum is not a new concept. The behavior observed in XeF is reminiscent of, but may not be necessarily related to, that seen in other types of pulsed lasers. For instance, smooth and continuous shifts of the lasing wavelength are well known effects in pulsed dye lasers (Ref. 4,5). In addition, the evolution seen here for XeF is similar to the line hopping phenomena observed in pulsed chemical lasers (Ref. 6,7).

Bottlenecking of the lower level and depletion of the upper level are two possible mechanisms that could contribute to the observed spectral sweep. (A 50°K temperature rise is the maximum that can occur in the gas during the laser pulse from the electron beam. Boltzman population shifts due to this temperature rise are insufficient to account for the observed spectral shift). In the case of a bottlenecking mechanism, the stimulated emission rate exceeds the rate of ground state removal. As particular rotational states of the lower laser level become filled, the lasing action shifts to adjacent states in the upper rotational manifold. Recent numerical and thermodynamical calculations modeling pulsed chemical lasers have shown that bottlenecking can cause spectral sweeps even if rotational equilibrium is maintained in both upper and lower laser levels (Ref. 8,9). Upper state depletion can result when the stimulated emission rate exceeds the rate at which an upper lasing rovibrational state is filled by relaxation from adjacent states. Consequently, the upper lasing level is emptied and lasing shifts to adjacent transitions in the rotational manifolds.

Neither of these possible mechanisms is consistent with our observations. Increased pulse length allows a longer time for the spectral sweep to occur by both mechanisms and would consequently result in a broader spectrum. The increased cavity flux caused by the higher resonator feedback increases the stimulated emission rate and hence can terminate lasing on a particular transition by more rapidly emptying an upper state (depletion) or more rapidly filling the lower state (bottlenecking).

As a further examination, spectra were taken by varying the pumping rate (electron gun current) while maintaining a constant 500ns pulse length. An attempt was also made to measure the spectral and temporal dependence of the sidelight fluorescence. This fluorescence is a monitor of the upper state population. It was found that the sweep increased with increasing pumping rate, resulting in a wider time-integrated bandwidth. Unfortunately, the result of the sidelight fluorescence were not conclusive, so that it was not possible to correlate the rate of wavelength sweep with an upper state population redistribution.

It is unclear if either of the above mentioned mechanisms can account for the observed spectral sweep because of the complicated nature of the XeF spectrum. The XeF rotational lines are closely spaced and collisionally broadened to the point of overlapping. One therefore does not observe single rotational lines turning on and off as in a pulsed chemical laser but rather a group of lines that sweep in intensity, with the location of the group moving across the manifold. It is this aspect of the spectrum that makes it difficult to differentiate between the possible mechanisms. In the absence of detailed

rotational relaxation information, an accurate kinetics model of this effect is not feasible. We note however, a recent phenomenological model was developed by Juramy et al., (Ref. 4) to analyze the spectral sweep observed in pulsed dye lasers. It was demonstrated that if the spectral dependence of the emission and absorption cross sections were taken into account, then a spectral sweep follows naturally from a rate equation description of a homogeneously broadened laser. Moreover, their model predicts an increased rate of spectral shift with increased cavity flux.

In summary, we have observed a spectral sweep in the 353nm band of an electron beam pumped XeF laser. This sweep manifests itself as progressive broadening of the time-integrated spectrum as the pulse length, electron beam pump rate, and intracavity flux increase. The spectral evolution could result from bottleneching in the lower level or depletion of the upper laser level.

Acknowledgement

The authors wish to thank Drs. D. A. Copeland and C. E. Turner, Jr. for several enlightening discussions and E. L. Rinehart for his skillful technical assistance. This work was supported by Rockwell International/Rocketdyne Division Internal Research and Development Program.

References

1. E. R. Ault, R. S. Bradford, Jr., and M. L. Bhauwmik, Applied Physics Letters, 27, 413 (1975).
2. T. A. Mangano, J. H. Jacob, and T. B. Dodge, Applied Physics Letters, 29, 426 (1976).
3. I. J. Bigio and M. Slatkin, IEEE J. Quantum Electron, QE-19, 1426 (1983).
4. P. Juramy, P. Flamant, and Y. H. Meyer, IEEE J. Quantum Electron, QE-13, 855 (1977).
5. Y. Meyer, and P. Flamant, Optics Communications, 19, 20 (1976).
6. M. J. Berry, J. Chemical Physics, 59, 6229 (1975).
7. M. J. Berry, "Chemical Laser Studies of Energy Partitioning into Chemical Reaction Products", Molecular Energy Transfer, Eds. R. D. Levie and J. Jortner, (Wiley & Son New York, 1976), 114.
8. A. Ben-Shaul, S. Feliles, and O. Kafri, Chemical Physics, 36, 291 (1979).
9. A. Ben-Shaul and O. Kafri, Chemical Physics, 36, 307 (1979).

Table 1. Analysis of Spectral Red Shift

RESONATOR	TIME SLICE,	% PEAK AREA IN REGION*				
		I	II	III	IV	V
UNSTABLE (M=2.7)	0 TO 50	15.7	50.3	27.0	7.9	0.8
	100 TO 150	8.9	36.8	34.6	15.9	3.7
	200 TO 250	5.7	29.2	34.7	22.1	8.3
	300 TO 350	5.1	27.0	34.1	23.2	10.6
	400 TO 450	6.2	27.8	33.7	21.7	10.6
STABLE** (50% R)	0 TO 50	17.1	39.7	28.9	11.6	2.6
	100 TO 150	9.7	30.6	34.1	19.6	6.0
	200 TO 250	4.9	22.1	32.7	26.9	13.4
	300 TO 350	4.2	21.0	32.9	26.9	15.0
	400 TO 450	-	-	-	-	-
STABLE*** (70% R)	0 TO 50	14.6	40.4	29.2	12.5	3.3
	100 TO 150	5.5	26.1	33.0	24.6	10.9
	200 TO 250	3.5	20.7	32.1	27.8	15.9
	300 TO 350	2.4	20.4	32.4	27.7	17.1
	400 TO 450	2.6	20.0	33.2	27.0	17.2

*The (0 to 3) band was divided into 5 equal width wavelength regions;
Region I is the Blue most region and Region V is the Red most region.
Each Region is about 0.05 nm wide.

**For this resonator the output coupler is a 50% R Mirror.

***For this resonator the output coupler was a 70% R Mirror.

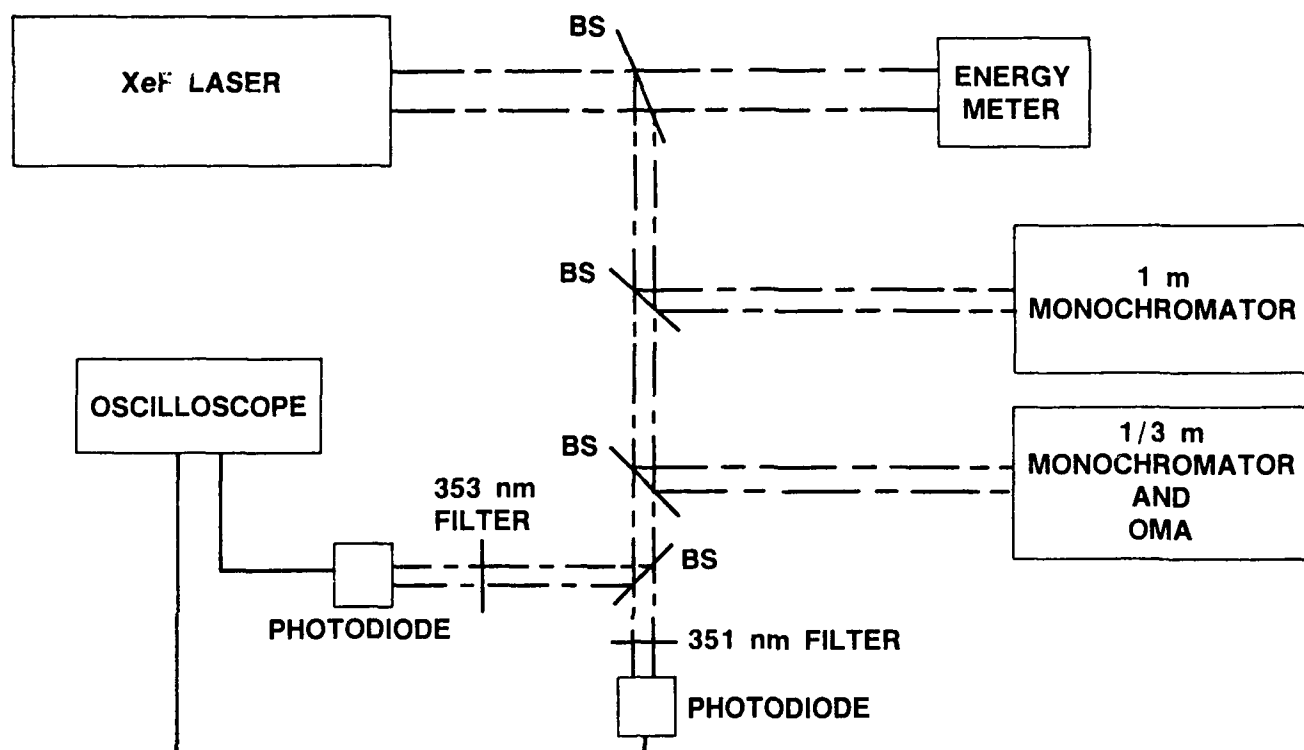


Figure 1. Schematic of the apparatus used for the spectral evolution experiments.

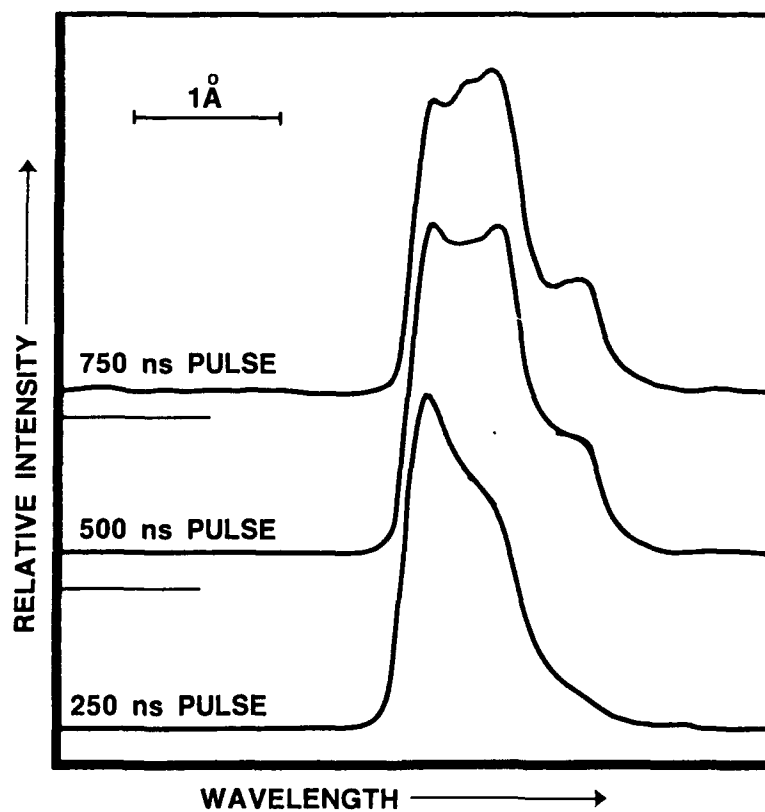


Figure 2. Lasing spectra of the 353nm band of XeF for three pulse lengths. An $M = 2.7$ unstable resonator was utilized.

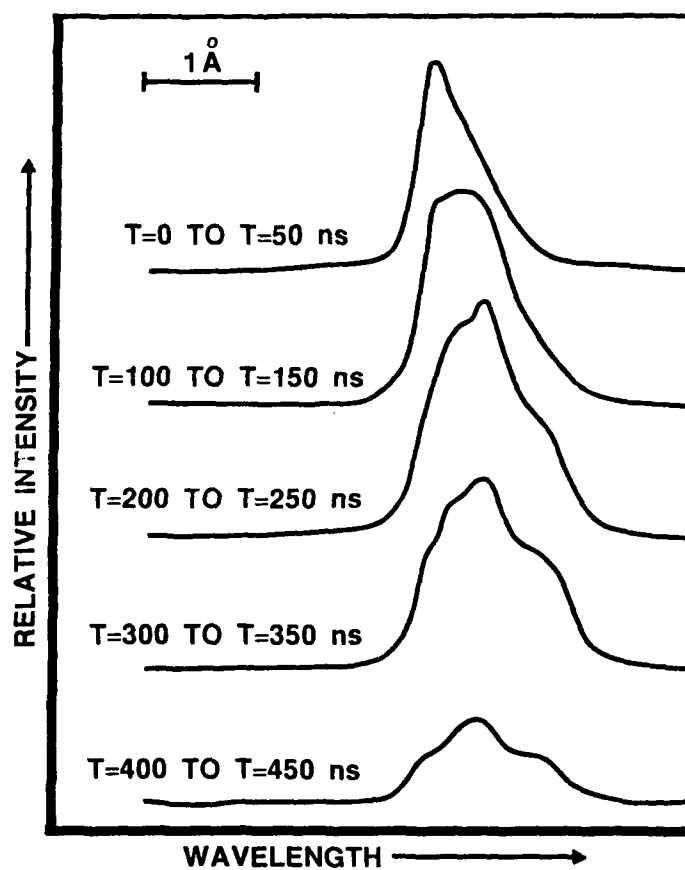


Figure 3. Lasing spectra of 353 nm band of XeF at several interval during the lasing pulse. Time, $t = 0$, is the beginning of the e-beam. An $M = 2.7$ unstable resonator was utilized.

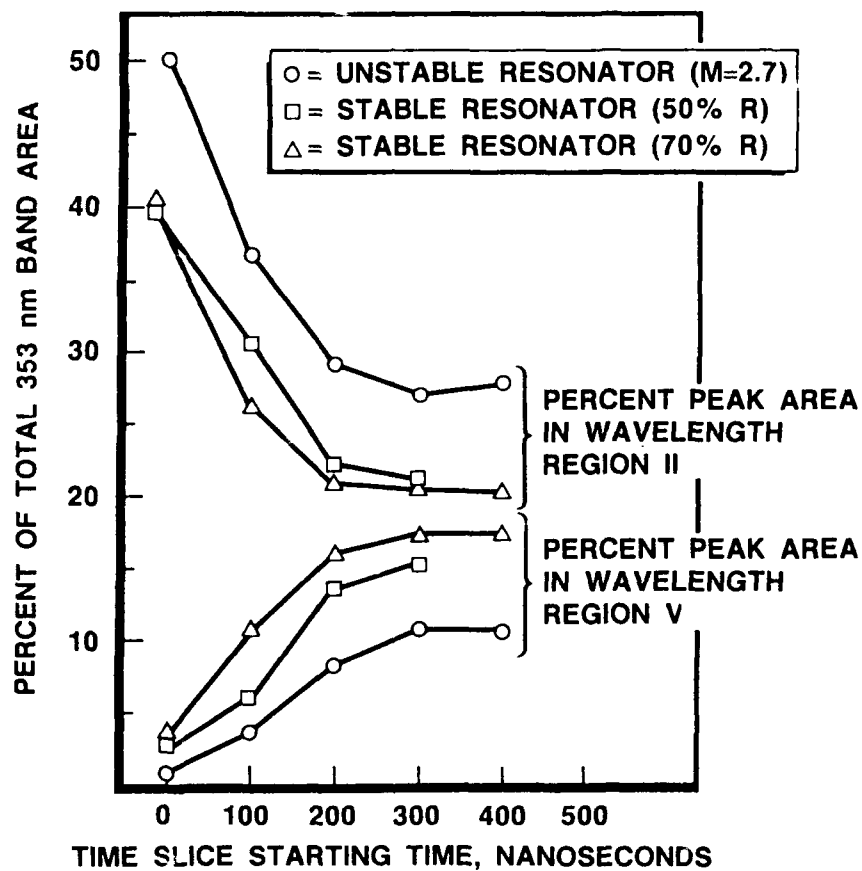


Figure 4. Results of analysis of the shift in wavelength location of peak area for 0 to 3 transition in XeF. Region II is the second most blue region. Region V is the red most region.

OPTIMIZATION OF ELECTRON-BEAM PUMPED EXCIMER LASER

T.F. Lowum and J.I. Swecker
Air Force Weapons Laboratory, AFWL/ARBM
Kirtland Air Force Base, New Mexico 87117-6008

Abstract

We significantly increased the output energy of an electron-beam pumped Xenon Fluoride laser by optimizing certain electron gun and gas mix parameters. The optimized e-gun parameters include anode-cathode spacing, magnetic field strength, and cathode voltage. The optimized laser gas parameters include NF_3 concentration, Xe concentration, and total pressure.

We found that the shortest anode-cathode spacing (9 cm), the strongest magnetic guide field (1600 Gauss), and the highest cathode voltage (375 kV) gave the highest laser output. The optimum gas concentrations were .05% NF_3 , .3% Xe, with Ne added to bring the total gas pressure to 60 psia. The energy degraded by 2% per shot with this gas mix.

Introduction

Electron beams are widely used to pump excimer lasers because of their scalability to large volumes and long pulses. However, this type of laser is often unpredictable and unreliable. Much controversy also exists over the optimum concentrations of NF_3 , Xe, and Ne in a Xenon Fluoride laser. In this work, we describe experiments to characterize the electron gun and to optimize the concentrations of NF_3 , Xe, and Ne in the laser gas mixture. Our aim was to find an optimum configuration for the laser in terms of energy output and reliability.

Electron Gun Optimization

A ten-stage Marx tank, actually a pulse-forming network (PFN) or Guillemin Type C network, provides energy to produce the electron beam. An individual stage of the Marx circuit can be charged up to 100 kilovolts to provide a maximum voltage of 1 megavolt upon erection of the ten stages.

The PFN feeds a cold cathode covered with a 10 x 75 cm piece of carbon felt. The spacing between the cathode and the anode (the hibachi foil support) is nominally 10 cm, but this spacing can be reduced by inserting a spacer behind the cathode. The A-K spacing establishes the impedance of the diode, and therefore determines the fraction of the PFN voltage delivered to the cathode. For example, when the A-K spacing is 8.9 cm, a PFN charging voltage of 75 kV per stage delivers a total of 312 kV to the cathode. This voltage produces a cathode current of approximately 9,150 amps. An external magnetic field guides the electrons into the laser chamber and reduces scattering by the foil and the high pressure laser gases (see Fig. 1).

The cylindrically shaped laser chamber is 125 cm long with a diameter of 15 cm. Since the emitting area of the cathode is only 10 x 75 cm, the e-beam pumps less than half of the total volume of gas. The energy deposited into the gas was determined by measuring the pressure rise in the chamber due to heating of the gas by the e-beam. Neon gas was used for energy deposition measurements since it is the major component of the excimer laser gas mixture. Since neon fluoresces, the rise in pressure accounts for only part of the total deposited energy. To estimate the loss to fluorescence, we measured the pressure rise with nitrogen gas which is essentially non-fluorescing. Allowing for the slight differences in the electron stopping power of the gases¹, we found the amount of energy deposited in both gases (neglecting fluorescence) to be approximately equal. Therefore, the energy lost to neon fluorescence is small and was neglected in our determination of the total deposited energy².

To study the effect of the anode-cathode (A-K) spacing on laser output, the energy deposited into the laser chamber was determined at different separations. Decreasing the A-K gap lowers the diode impedance, thus increasing the current emitted by the cathode³. This current increase is somewhat offset by a decrease in the cathode voltage caused by the lower diode impedance (due to the impedance mismatch between the PFN and the cathode). However, if the A-K gap becomes too short, the cathode voltage arcs directly to the anode and the diode shorts; the cathode will not produce an electron beam. Our measurements confirm that decreasing the A-K gap results in more energy being deposited in the laser

chamber. Table I lists the results of these measurements. Although the change in average cathode voltage and current was small, the energy deposited into the gas increased by 30%. Laser output also increased 30% with the smaller separation.

TABLE I. Effects of Anode-Cathode spacing on electron beam parameters.

A-K Spacing (cm)	I_K avg (kA)	V_K avg (kV)	V_K peak (kV)	E_{dep} (Joules)
10.2	9.01	318	377	956
8.9	9.15	312	353	1242

The strength of the magnetic guide field was varied to determine its effect on energy deposited into the chamber. As figure 1 shows, two magnets surround the laser chamber in a Helmholtz configuration. These magnets serve the dual purpose of guiding the electrons into the laser chamber and of increasing an electron's effective path length through the gas. Each magnet has a maximum field strength of 800 Gauss (limited by the power supply), so the total B field available is about 1600 Gauss. To vary the field strength, one or both of the magnets were turned off or a resistor was inserted in series with the magnet to decrease the current. Figure 2 shows the deposited energy versus field strength. The curve suggests that higher magnetic field strength would yield significantly more energy deposited into the laser chamber, but we are unable to explore this with the current configuration.

Figure 3 depicts energy deposited into the laser chamber versus cathode voltage. The theoretical curve was determined from the Child-Langmuir prediction for current density³, measurements of cathode voltage and pulse width, and the transmission of the hibachi and foil. We accounted for the increase in current density due to closure of the diode using a 4-5 cm per microsecond closure velocity⁴. Since the A-K separation is on the order of one of the cathode dimensions and the current density is non-uniform, the Child-Langmuir relationship is not strictly applicable. However, general trends are predictable. Note that as cathode voltage increases, the data fall below the theoretical curve by an increasing amount. This disparity arises because as cathode voltage increases, the kinetic energy per electron increases and more electrons impact the back wall of the laser chamber⁶ instead of depositing all of their energy into the gas. Increasing the effective stopping power of the gas (by increasing the depth of the laser chamber or raising the pressure of the gas) would reduce this loss.

Gas Mix Optimization

After completing the characterization of the electron gun, we next optimized the concentrations of NF_3 and Xe in our gas mixture. We knew that an optimum concentration of NF_3 and Xe had to exist, since both of the gases produce absorbing compounds when excited. To find the optimum gas mix, we measured the output energy of the laser as the concentrations of NF_3 and Xe were varied. An off-axis, unstable, confocal resonator was used to extract the energy from the gain medium. We aligned the resonator so that the optical axis was near the foil (and thus near the electron gun). A Scientec 8" volume absorbing calorimeter measured the energy in the 10x10 cm output laser beam. Figure 4 shows a diagram of the experimental set-up.

We first varied the Xe concentration, keeping the NF_3 concentration constant at .085%. Figure 5 shows the average output energy for the first ten shots at different concentrations of Xe. The laser produced the most energy with only .2% Xe, a significantly lower value than other investigators have reported.

Keeping the Xe concentration constant at .3%, we next varied the NF_3 concentration from .03% to .1%. As figure 6 shows, the laser produced the most energy with the NF_3 concentration at .05%, which is also lower than "normal". Further tests confirmed that the optimum concentration was indeed .05% NF_3 / .3% Xe, but .2% Xe lowered the output only slightly. We did all of these tests with the E-gun pumping level at 1200 Joules and the total gas pressure at 60 psia. Additional tests indicated that this was also the optimal gas mix for a wide range of pumping energies. We also measured the shot-to-shot degradation of this gas mix. The energy output of the laser degraded approximately 2% per shot, which is typical of NF_3 gas mixes.

Our optimum gas concentrations were significantly lower than others reported elsewhere^{2,8,9}, but our total gas pressure was higher. In 1977, Champagne¹¹ claimed that an optimum number density of NF_3 and Xe existed for XeF lasers. If this is so, then the optimum concentration will change with total pressure. To allow comparison of our results with others at lower pressures, we calculated the optimum number density (or partial pressure) of both species. The corresponding optimum number densities at various operating pressures are listed in Table 2. Our results agree favorably with those of Champagne (NRL) and Feiock (Maxwell Labs) as shown in Table 2 also.

TABLE 2. Optimum Concentrations of NF_3 and Xe at Various Total Pressures.

	5 atm	4 atm	3 atm
% NF_3	.041	.051	.068
% Xe	.16-.24	.2-.31	.27-.41
Maxwell (1984) ¹⁰		.067% NF_3 , .2% Xe	
NRL (1977) ¹¹		.06% NF_3 , .18% Xe	

Since the laser gas has greater electron stopping power at higher pressure, the electron gun deposits energy into the gas more efficiently. At lower gas pressure, however, the electron gun deposits energy more uniformly across the chamber. Figure 7 illustrates both of these points. The data taken at 50 psia show that a significant number of electrons reach the far side of the chamber. Thus, many of the electrons strike the far wall of the chamber rather than depositing their energy into the gas. The data taken with a gas pressure of 60 psia show that the gain has decreased to almost zero at the far wall of the chamber; the gas stops almost all of the electrons. As the two gain curves in Figure 7 show, the gain is more uniform across the chamber at the lower gas pressure, but higher total energy can be extracted at higher chamber pressure.

The pressure of the laser gas controls this trade-off between pumping efficiency and pumping uniformity. An application requiring maximum laser output energy calls for the highest possible gas pressure, while an application requiring maximum intensity uniformity across the beam would call for a lower gas pressure.

Conclusion

Table 3 lists the parameters of the laser when configured for maximum output energy. The laser output energy of 16.4 Joules represents an order of magnitude increase over the output energy before we started the characterization and optimization work. The deposited energy increased by 30% when we decreased the A-K spacing by 1.2 cm. The addition of a 1600 Gauss guide field increased the deposited energy by a factor of four. A higher total gas pressure gives more efficient pumping because it stops more electrons, but a lower total gas pressure gives more uniform pumping across the chamber. Optimization of the gas mixture was the most significant factor in increasing the laser output energy. Our optimum mix has lower concentrations of NF_3 and Xe, but does agree with two other investigations.

Additionally, we learned several things about the electron beam deposition. A small decrease (1.2 cm) in the A-K spacing resulted in a 30% increase in deposited energy. The addition of a 1600 Gauss magnetic field increased the deposited energy by a factor of four. Finally, we found that deposition could be tailored by varying the total pressure of the lasing medium. This implies that uniform and efficient pumping cannot be achieved with a single electron gun unless the back wall of the laser chamber can be made to reflect the electrons which strike it.

Table 3. Optimum Laser Configuration.

Cathode Voltage	310 kV	Gas Mix	.05% NF3 / .3% Xe
Cathode Current	9.2 kA	Chamber Pressure	60 psia
A-K Spacing	8.9 cm	Pulse Length	1.1 microsec
Magnetic Field	1600 Gauss	Output Energy	16.4 Joules
Deposited Energy	1450 Joules		
Extracted Volume	7.5 Liters		
Chamber Volume	18 Liters		
E-Beam X-Section	10x75 cm		

References

1. L. Pages, E. Bertel, H. Joffre, and L. Sklavenitis, in Atomic Data 4 (Academic Press, Inc, New York, 1972), pp. 1-127.
2. A. E. Mandl and H. A. Hyman, IEEE J. Quantum Electron. QE-22, 350 (1986).
3. R. K. Parker and R. E. Anderson, in Record of the 11th Symposium on Electron, Ion and Laser Beam Technology, edited by R. F. M. Thornley (San Francisco Press, Inc, California, 1971), p. 456.
4. R. M. Gilgenbach, L. D. Horton, R. F. Lucey, Jr., S. Bidwell, M. Cuneo, J. Miller, and I. Smutek, in Proceedings of the 5th IEEE Pulse Power Conference, (Arlington, VA, 1985), p. 126.
5. D. T. Thomas, Engineering Electromagnetics (Pergamon Press, New York, 1972), p. 152.
6. A. Mandl and E. Salesky, J. Appl. Phys. 60, 1565 (1986).
7. J. C. Hsia, J. A. Mangano, J. H. Jacob, and M. Rokni, "Interim Report - One Meter KrF Laser", Semi-Annual Tech. Rep., Feb 1977-Aug 1977.
8. J. C. Hsia, J. A. Mangano, J. H. Jacob, and M. Rokni, Appl. Phys. Lett. 34, 208 (1979).
9. W. D. Kimura, D. R. Guyer, J. F. Seamans, and D. H. Ford, Appl. Phys Lett. 51, 1063 (1987).
10. F. D. Feiock, J. R. Oldenettel, and G. R. Miscikowski, J. Appl. Phys. 56, 676 (1984).
11. L. F. Champagne and N. W. Harris, Appl. Phys. Letters, 31, 513 (1977).

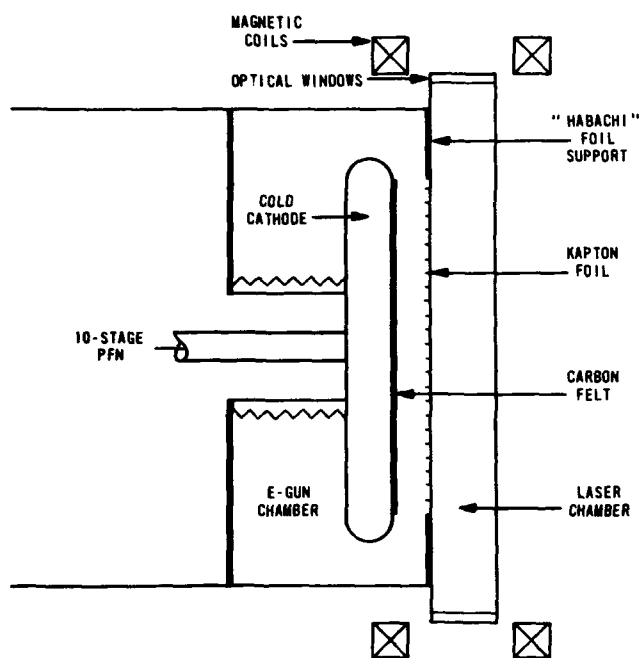


Fig. 1 - Schematic of Excimer Laser

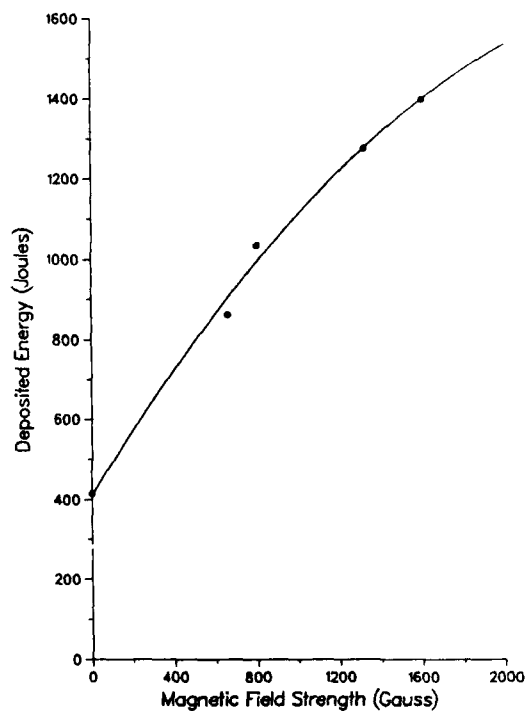


Fig. 2 - Effect of magnetic field strength on energy deposited into the lasing medium. Curve is a second order fit to the data.

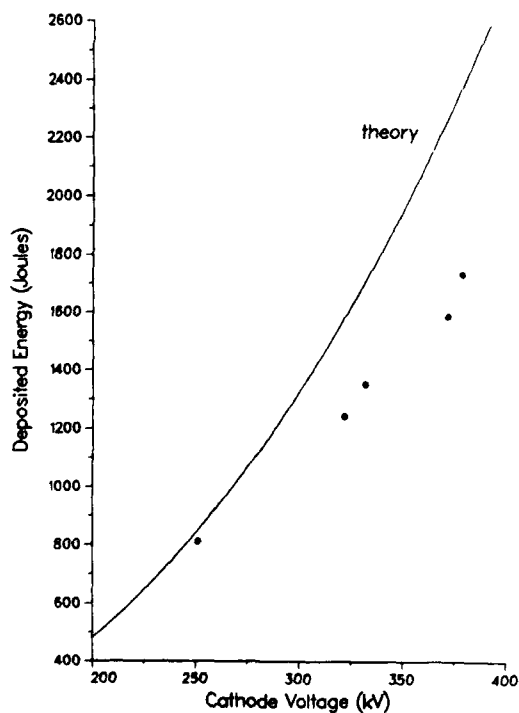


Fig. 3 - Effect of cathode voltage on energy deposited into the lasing medium. Curve represents theoretical energy deposition based on Child-Langmuir relationship.

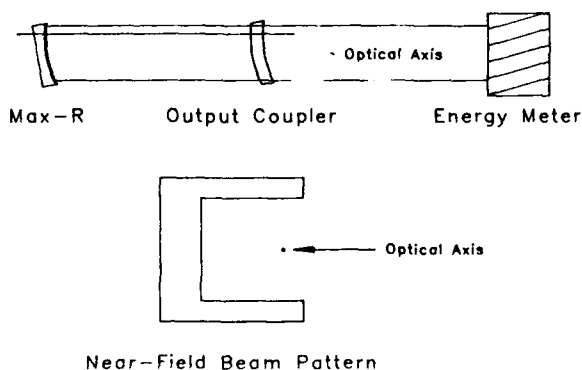


Fig. 4 - Experimental setup for gas mix optimization

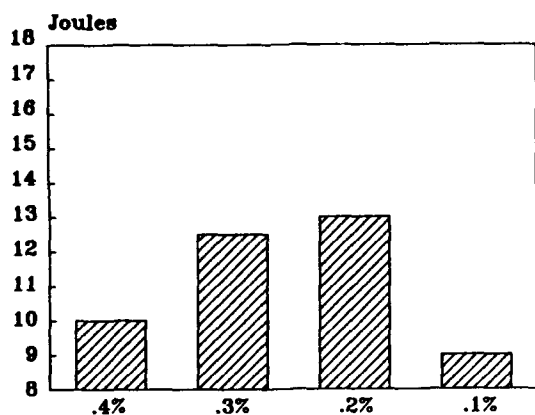


Fig. 5 - Effect of Xe concentration on laser output. NF_3 concentration held constant at .085%, total gas pressure was 60 psia.

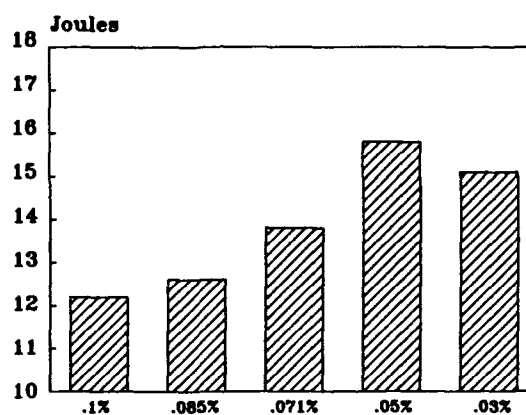


Fig. 6 - Effect of NF_3 concentration on laser output. Xe concentration held constant at .3%, total gas pressure was 60 psia.

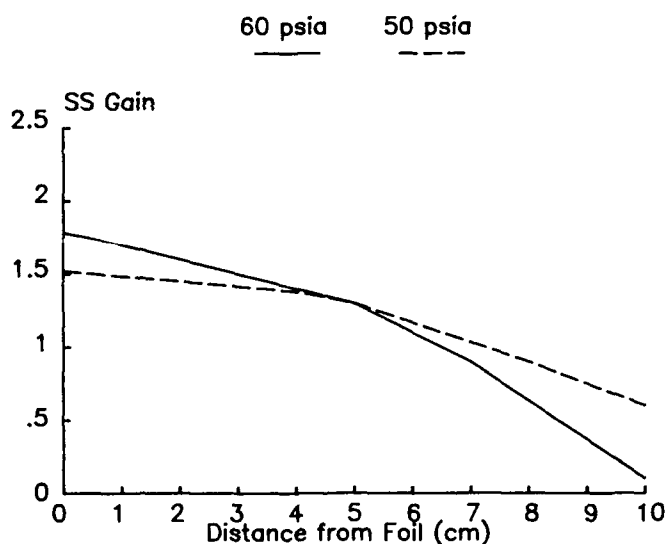


Fig. 7 - E-gun energy deposition across the laser chamber, determined from small-signal gain measurements. Net gain for a small signal input is plotted in units of percent per centimeter for a 75 cm gain length.

XENON EXCITED STATE DENSITY MEASUREMENTS IN XeCl

F. Kannari, W. D. Kimura, J. F. Seamans, and D. R. Guyer

Spectra Technology, Inc.
2755 Northup Way
Bellevue, WA 98004-1495

Abstract

To increase the kinetics data base and refine the understanding of XeCl lasers, time-dependent measurements of lower level xenon excited state densities in electron-beam pumped XeCl laser mixtures have been performed. Measurements are obtained using hook interferometry under nonlasing conditions at an average excitation rate of $\approx 250 \text{ kW/cm}^3$ and e-beam pulse widths of 0.4 and 1 μs . The population differences, ΔN^* , between four different electronic transitions [three in the $\text{Xe}^*(6s)-\text{Xe}^{**}(6p)$ manifold, and one in the $\text{Xe}^{**}(6s')-\text{Xe}^{***}(6p')$ manifold] are examined as a function of halogen concentration. A dramatic change in the excited xenon density, caused by a change in the energy flow mechanism in the XeCl kinetics due to HCl burn-up, is observed. As long as a relatively high HCl density exists in the mixture, ion-ion recombination reactions (e.g., $\text{Xe}^+ + \text{Cl}^-$) intercept dissociative dimer-ion recombination reactions (e.g., Xe_2^+) and suppress the excited xenon densities. When a certain amount of HCl is consumed, the energy flow channel switches to dimer-ion recombinations, resulting in an abrupt increase of the xenon excited state density.

Introduction

Historically, the understanding of XeCl laser kinetics has tended to lag the other major excimer lasers.¹ The major differences between the XeCl formation mechanism and those of others using fluorine as the halogen donor are as follows: 1) Reaction of the first excitation state of xenon ($5p^56s$) with vibrational ground state HCl is nearly thermoneutral with respect to XeCl^* formation. 2) The dissociative attachment reaction rate of ground state HCl with electrons is much less than that for F_2 . Several experimental and theoretical studies have shown that high XeCl^* formation yield can be achieved through higher excited states of xenon^{2,3} and/or vibrationally excited HCl^4 through the neutral reaction channels. Only vibrationally excited $\text{HCl}^{5,6}$ has a high dissociative attachment reaction rate that results in efficient XeCl^* formation through the ion channel. Numerical kinetic models have been also developed for e-beam pumped XeCl lasers⁷⁻⁹ which are in reasonable agreement with the results of laser experiments. However, measurements and analysis of only the laser output characteristics are not enough to clearly characterize kinetic processes occurring in the gas mixtures excited by the e-beams. In fact, some inconsistent experimental results have been observed.^{9,10}

To refine our understanding of XeCl lasers and increase the kinetics data base, the fundamental kinetics parameters of time-dependent electron density and burn-up of HCl have been measured at Spectra Technology, Inc. This paper presents experimental measurements of the lower level xenon excited state densities in e-beam pumped XeCl mixtures.

As mentioned before, the density of lower level excited xenon is not a key parameter with regard to XeCl^* formation, because reactions with vibrational ground state HCl do not produce XeCl^* . However, it is a key parameter to understand the energy flow from the buffer gas system to the xenon system and the balance of the other reactions. Figure 1 is a block diagram showing key kinetics pathways in Ne/Xe/HCl mixtures. In Ne/Xe mixtures (without HCl), neon ions and excited neons, produced by the primary electrons of the e-beam and by high energy secondary electrons, produce xenon ions through three-body charge transfer reactions and Penning ionizations. Xenon excited states are then produced through dissociative recombination reactions with xenon-based dimer ions (Ne_2^+ , NeXe^+). The fraction of xenon excited states formed directly by electron collisions is negligible due to the low density of xenon compared to neon gas in these laser mixtures.

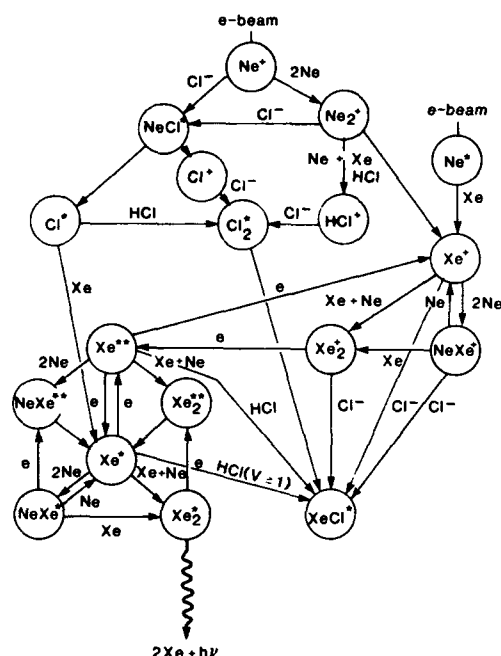


Fig. 1. Block diagram showing key kinetics paths in the Ne/Xe/HCl rare gas halide system.

When a trace of HCl is present in the mixture, dissociative attachment reactions with vibrationally excited HCl control the secondary electron density, and fast ion-ion recombination reactions (e.g., Xe^+Cl^-) interrupt the usual recombination reactions of the dimer ions. Therefore, if the measured xenon excited state densities in mixtures containing HCl are lower than those in Ne/Xe mixtures by a factor higher than that expected from just the quenching rate of excited xenon by HCl, then this is indirect evidence of high Cl^- density. However, the dominant source of Cl^- is dissociative attachment from vibrationally excited HCl and there are experimental results indicating that the density of vibrationally excited HCl is low.¹⁰

Experimental Technique

Xenon excited state densities are measured using classical hook interferometry combined with pulsed dye laser technology. The experimental apparatus and the principle of this technique are described in detail elsewhere;^{11,12} a schematic of the experimental set-up is shown in Fig. 2. The total optical path of the excited laser medium is 70 cm, and the e-beam excitation rate is $\approx 250 \text{ kW/cm}^3$.

Figure 3 is a partial energy level diagram showing the transitions examined during the experiment: 1) 823.2 nm ($6s[3/2]_2^0 - 6p[3/2]_2^0$); 2) 828.0 nm ($6s[3/2]_1^0 - 6p[1/2]_0^0$); 3) 834.7 nm ($6s'[1/2]_1^0 - 6p'[3/2]_2^0$); and 4) 840.9 nm ($6s[3/2]_2^0 - 6p[3/2]_1^0$). Measured oscillator strengths for these lines are 0.23, 0.12, 0.37, and 0.012, respectively.¹³

Because hook interferometry gives the density difference between two states, to obtain the absolute density of the lower state requires the upper state population to be either negligibly small or estimable through other means. If the collisional mixing by either neutral species or electrons is fast, the initial formation distribution will be quickly reduced to a steady-state distribution. Comparing collisional deactivation rate constants and radiative lifetimes measured by Inoue, et al.¹⁴ with rates for stepwise excitations by electrons, it is reasonable to expect that the later processes will effectively compete with the former processes. If the distribution in the xenon excited state manifold is characterized by a secondary electron temperature of 1.5 eV, which is a typical average electron temperature predicted by our model for our experimental conditions, the upper state density of the probed transitions would be 23%, 12%, and 36% of the lower state density for the 823.2, 828.0, and 840.9 nm transitions, respectively. This represents an upper limit for the higher state populations since other heating sources do not exist. In fact, even if the electron mixing processes are dominant, the fast ionization processes of the higher xenon excited states tend to decrease the population of the upper states.

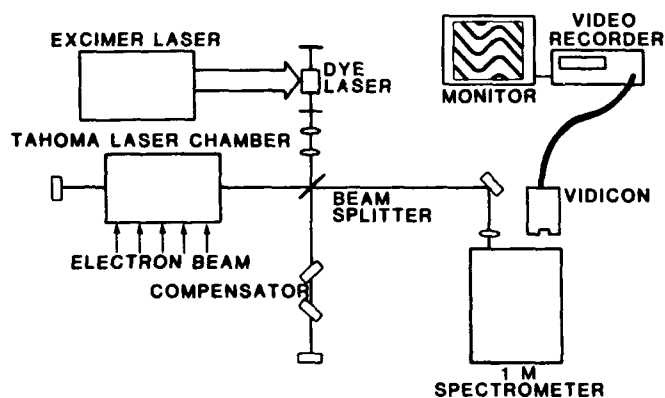


Fig. 2. Schematic of xenon excited state density measurement system.

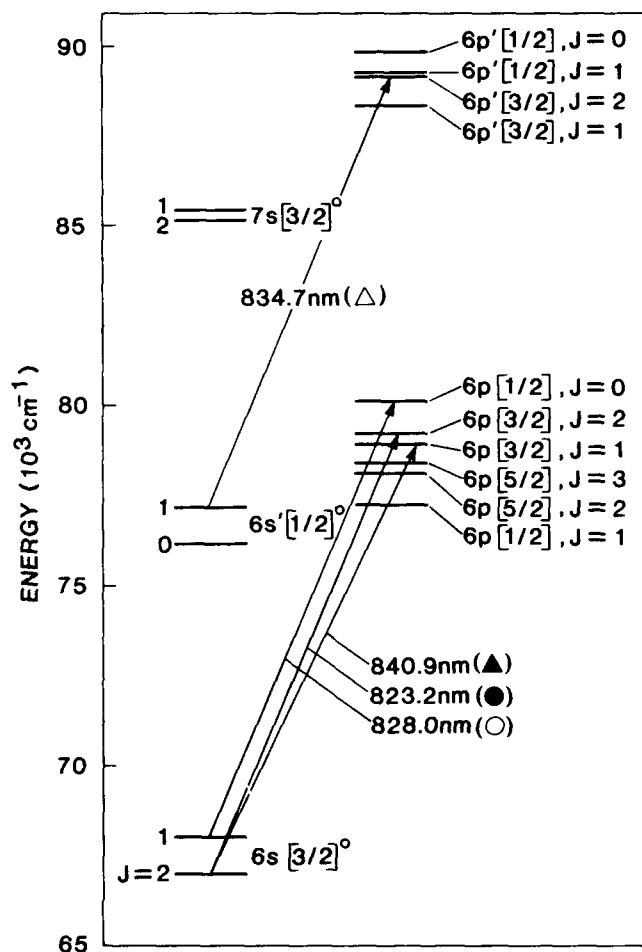


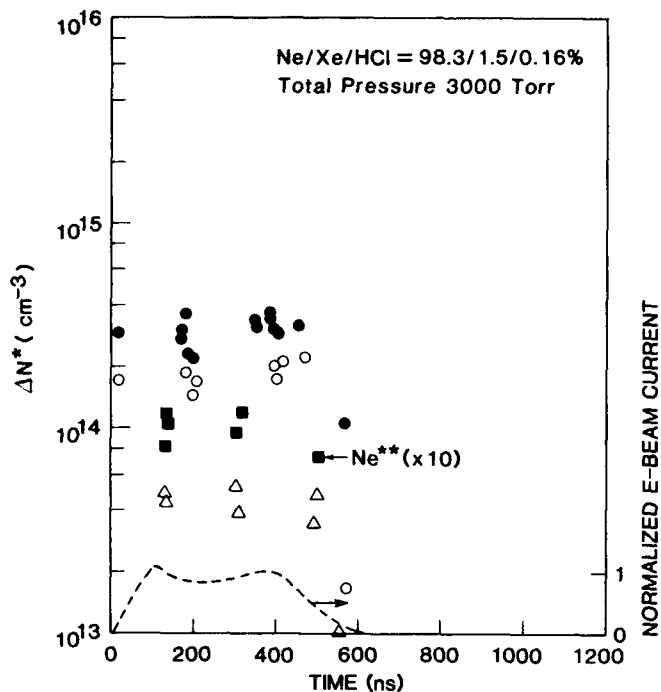
Fig. 3. Energy level diagram for Xe from 65000 to 90000 cm^{-1} . The 5d, 7p, and 6d states are not shown. The four transitions measured during the experiment are indicated.

The analysis is further complicated by the fact that at least part of the xenon manifold must be in nonequilibrium as evidenced by the existence of infrared xenon lasers. Lasing occurs between the 5d and 6p xenon excited states when mixtures of Ar/Xe or Ne/Xe at >1 atm are excited by e-beam or e-beam sustained discharges.^{15,16}

Therefore, in order to avoid biasing the data with an assumption of the upper state densities, all the data presented in this paper represent the population difference, ΔN^* , between the upper and lower state of the transition examined.

Results And Discussion

Figures 4 and 5 show typical experimental results obtained at the 828.0, 823.2, and 840.9 nm transitions, for XeCl laser mixtures with an initial HCl concentration of 0.16% and 0.08%, respectively. The XeCl laser mixture is 1.5% Xe in Ne diluent at a total gas pressure of 3000 Torr. A normalized e-beam current pulse shape [400 ns (FWHM)] is shown at the bottom of the figures. As can be seen in Fig. 4, the density differences of ΔN^* (823.2 nm) and ΔN^* (828.0 nm) are relatively constant during the e-beam pumping, and decay rapidly at the termination of the e-beam pulse. For 0.08% HCl (see Fig. 5), the ΔN^* density increases abruptly at ≈ 350 ns into the e-beam pulse. During the electron density



87-15663

Fig. 4. Time-dependent ΔN^* densities of a XeCl mixture (1.5% Xe, balance Ne to 3000 torr) for an initial HCl concentration of 0.16%. Solid and open circles, and open triangles correspond to ΔN^* (823.2 nm), ΔN^* (828.0 nm), and ΔN^* (834.7 nm), respectively. Solid squares correspond to ΔN^* densities for the neon excited state ($3p[5/2]_3 - 3d[7/2]_4$) transition at 837.8 nm.

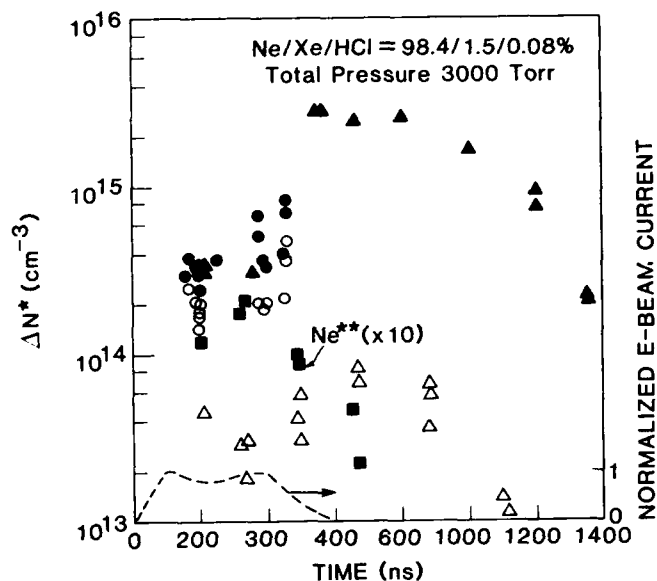


Fig. 5. Time-dependent ΔN^* densities of a XeCl mixture for an initial HCl concentration of 0.08%. Other parameters are the same as in Fig. 4. Plot parameters are the same as in Fig. 4, except solid triangles correspond to ΔN^* (840.9 nm).

measurements, the electron density also increases abruptly at a certain point during the e-beam pumping. These points tend to occur at earlier times as the initial HCl concentration is lowered. The consumption of HCl during the pump pulse increases the secondary electrons and reduces the Cl^- ions resulting in an increase in electron-dimer ion recombinations.

Also shown in Fig. 4 are results of measuring the ΔN^* density of the neon ($3p[5/2]_3 - 3d[7/2]_4$) excited state transition at 837.8 nm. Since neon excited states are mainly produced by high energy electron excitations, the neon excited state density does not increase abruptly like the xenon densities, but rather follows the e-beam pumping.

Figures 6 and 7 show time-dependent ΔN^* densities obtained under extended (1 μs) e-beam excitation for an initial HCl concentration of 0.32% and 0.16%, respectively. Sidelight fluorescence of $\text{XeCl}^*(\text{B-X})$ is shown at the bottom of each figure with the normalized e-beam current pulse. For 0.32% HCl, the ΔN^* density does not stay constant, but gradually increases towards the end of the e-beam pulse. This gradual increase may be caused by an increase in the gas temperature during the e-beam pumping which leads to a decrease in the ion-ion recombination rates.¹⁷ For 0.16% HCl, the ΔN^* density increases abruptly at ≈ 600 ns into the e-beam pulse. The sidelight fluorescence for the 0.16% HCl mixture begins to decrease at approximately the same time as the increase of the ΔN^* density.

It is also observed that, if the HCl is consumed during the e-beam pulse, the lifetime of the excited xenon is extremely long after termination of the e-beam pulse. A long lifetime is also observed in halogen-free rare gas mixtures. Note in Fig. 1 that energy transfer processes from excited Cl atoms are another possible path to form xenon excited

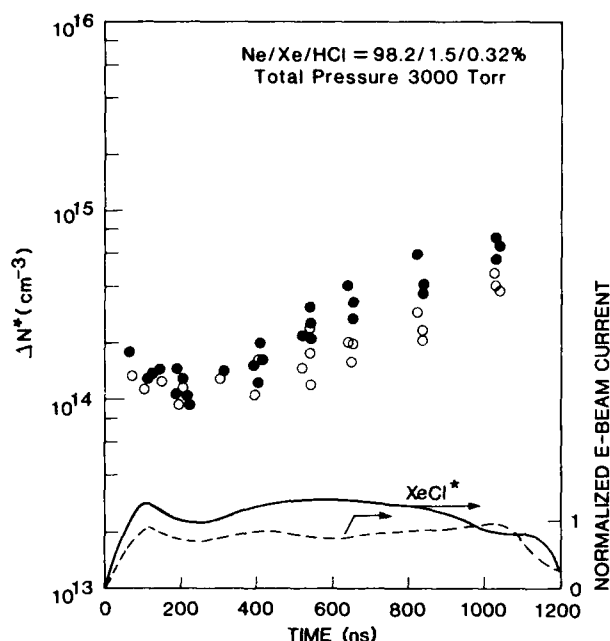


Fig. 6. Time-dependent ΔN^* densities of a XeCl mixture for an initial HCl concentration of 0.32%. Other gas parameters and plot parameters are the same as in Fig. 4.

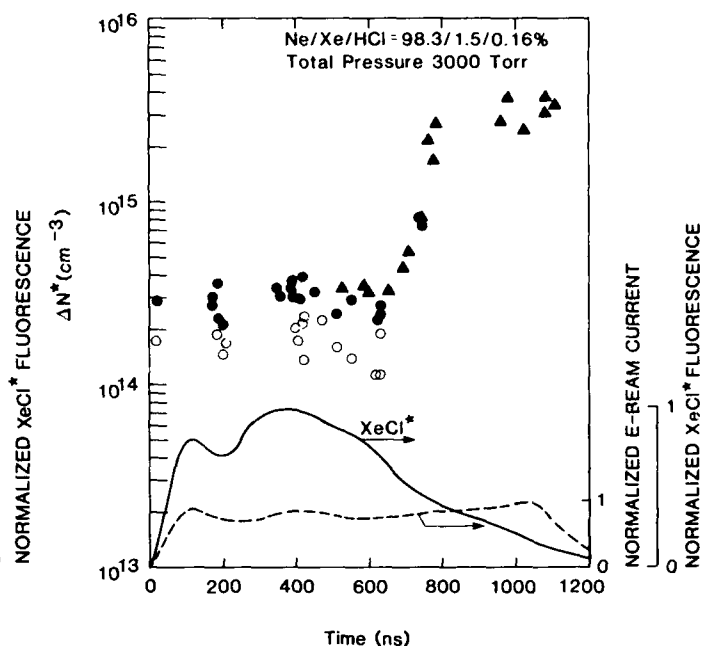


Fig. 7. Time-dependent ΔN^* densities of a XeCl mixture for an initial HCl concentration of 0.16%. Other gas parameters and plot parameters are the same as in Fig. 4.

states. To eliminate the effects of the halogen, Ne/Xe and Ar/Xe mixtures were examined, and the results are shown in Fig. 8. The xenon excited state densities increase quickly, and a peak ΔN^* of $\approx 5 \times 10^{15} \text{ cm}^{-3}$ is observed at the end of e-beam pulse. For the Ne/Xe mixture, the lifetime of $\text{Xe}^*(6s)$ is surprisingly long, and its decay behavior is not purely exponential.

In neon based mixtures, the populations of heteronuclear molecules, such as NeXe^+ or NeXe^* , are very low due to their low binding energies ($< 0.05 \text{ eV}$). In addition, xenon dimer formation through three-body collision with neon buffer is also slow. Therefore, the quenching rate of excited xenon is significantly low in neon based mixtures. Furthermore, because the dimer ion formation rate is also low for the same reasons, the population of xenon ions is quite high, and is balanced with the high density of secondary electrons which exist even after the e-beam termination. Therefore, the slow feeding processes of dimer-ion recombinations continue even after the e-beam termination, and help keep the xenon excited state density high. Moreover, because of the high density of xenon excited states, Penning ionization ($\text{Xe}^* + \text{Xe}^*$) also becomes important.

As a result of these effects, energy circulates within the xenon ion and excited xenon system, and is gradually quenched by very slow excited xenon dimer formation and radiative decay processes, thereby leading to long Xe^* lifetimes. This interpretation is supported by the results for the Ar/Xe mixture shown in Fig. 8. In Ar/Xe mixtures, the quenching rate of Xe^* , producing ArXe^* dimer, is faster than in the Ne/Xe mixtures because the binding energy of the Ar-Xe dimer is higher. Higher ArXe^+ and Xe_2^+ densities in Ar/Xe mixtures also tend to accelerate the decay of the electron density via recombination processes that result in faster energy decay of the entire system after termination of the e-beam pulse.

Conclusions

The time-dependent excited state density measurements of xenon in e-beam pumped Ne/Xe/HCl laser mixtures as a function of halogen concentration have yielded important new insights into the neutral and ionic kinetics occurring in these plasmas.

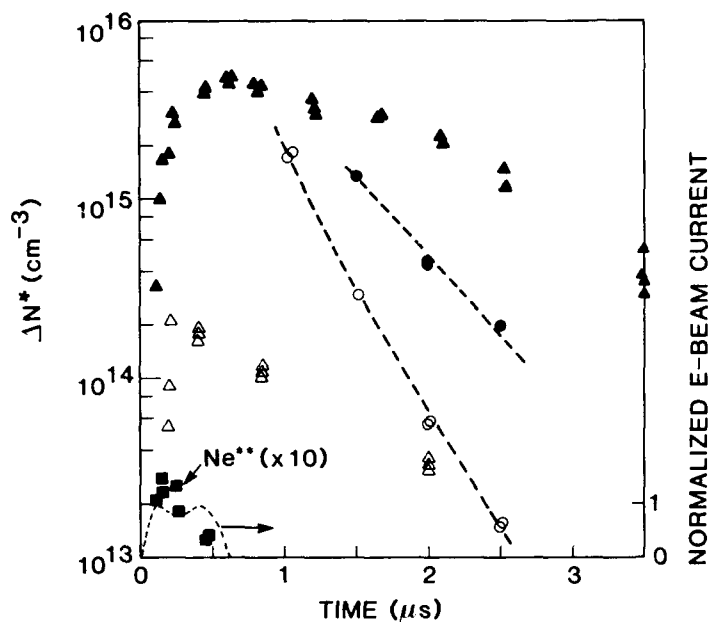


Fig. 8. Time-dependent ΔN^* densities of a Ne/Xe mixture (1.5% Xe, balance Ne to 3000 torr). Plot parameters are the same as in Figs. 4 and 5. Dotted lines with solid and open circles are $\Delta N^*(823.2 \text{ nm})$ and $\Delta N^*(828.0 \text{ nm})$, respectively, measured for an Ar/Xe mixture (1.5%, balance Ar to 1500 torr).

As long as the HCl density is high, secondary electrons and xenon ions are controlled by dissociative attachment reactions with the halogen and ion-ion recombination reactions, respectively. In addition, the amount of electron-dimer ion recombination is relatively small, which results in low xenon excited state densities. When a certain amount of halogen is consumed, the energy flow channel rapidly switches to the dimer recombination channel and the excited state density of xenon abruptly increases. This increase of the xenon excited state population is coincident with a similar increase of the secondary electrons. A population increase of the higher level xenon excited states is also observed as the halogen is burned up; this presumably results in an increase of photoionization at the laser wavelength. This may contribute to the termination of the XeCl laser output under high energy loading conditions.

Acknowledgments

The authors wish to acknowledge Dr. J.J. Ewing and Dr. S.E. Moody for their insightful discussions. This work was supported by the Office of Naval Research, Contract No. N00014-85-C-0843.

References

1. D.L. Huestis, 39th Annual Gaseous Electronics Conference, Madison, WI, Oct. 7-10, 1986, paper N-4 (unpublished).
2. D.C. Lorents, in Proceedings of the International Conference on Lasers '84, (STS Press, McLean, 1985), p. 575.
3. J.K. Ku and D.W. Setser, Appl. Phys. Lett., 48, 689 (1986).
4. R.S.F. Chang, J. Chem. Phys., 76, 2943 (1982).
5. M. Allan and S.F. Wong, J. Chem. Phys., 74, 1687 (1981).
6. W. Domcke and C. Mundel, J. Phys. B: At. Mol. Phys., 18, 4491 (1985).
7. L.A. Levin, S.E. Moody, E.L. Klosterman, R.E. Center, and J.J. Ewing, IEEE J. Quantum Electron., QE-17, 2282 (1981).
8. F. Kannari, A. Suda, M. Obara, and T. Fujioka, IEEE J. Quantum Electron., QE-19, 1587 (1983).
9. T.C. Genoni and T.H. Johnson, in Proceedings of the International Conference on Lasers '85, C.P. Wang, Ed., (STS Press, McLean, 1986), p. 582.

10. R.E. Center, J.H. Jacob, M. Rokni, and Z. Rozenberg, Appl. Phys. Lett., 41, 116 (1982).
11. F. Kannari, W.D. Kimura, J.F. Seamans, and D.R. Guyer, Appl. Phys. Lett., 51, 1986 (1987).
12. F. Kannari, W.D. Kimura, J.F. Seamans, and D.R. Guyer, "Xenon Excited State Densities in Electron-Beam Pumped XeCl and XeF", submitted to J. Appl. Phys., Dec. 1987.
13. V.R. Lazovskaya, and G.K. Tumakaev, Sov. Phys. Tech. Phys., 24, 328 (1979).
14. G. Inoue, J.K. Ku, and D.W. Setser, J. Chem. Phys., 81, 5760 (1984).
15. S.A. Lawton, J.B. Richards, L.A. Newman, L. Specht, and T.A. DeTemple, J. Appl. Phys., 50, 3888 (1979).
16. N.G. Basov, A.Y. Chugunov, V.A. Danilychev, I.V. Kholin, and M.N. Ustinovsky, IEEE J. Quantum Electron., QE-19, 126 (1983).
17. J.M. Hoffman, and J.B. Moreno, Sandia National Laboratory, Albuquerque, NM, 1980, Report No. SAND 80-1486, (unpublished).

A XeCl EXCIMER LASER WITH AUTOMATIC PREIONIZATION

J.P. SINGH
MHD Energy Center
Mississippi State University
Mississippi State, MS 39762

ABSTRACT

A high power, automatic preionization, discharge excited excimer (XeCl) laser is presented. Aluminum electrodes 81 cm long and separated by 22 mm are mounted on Al-plates which are enclosed in a pyrex tube of length 100 cm and diameter 15 cm. The electrical energy of 9J is dumped into a 107 cm³ discharge volume. 48 mJ of energy per pulse and a pulse-width of 15 nsec at 15 Hz are obtained.

INTRODUCTION

The excimer laser is one of the most powerful sources of coherent light energy in the ultraviolet region. The most common excimer laser is XeCl (308 nm) which is used in spectroscopy, photochemistry, remote sensing and to pump dye lasers. Two main techniques, discharge¹ and electron beam pumping² are used in pumping these lasers. An automatic preionized discharge pumped excimer laser is simple in construction.

During the past decade an enormous amount of work has been done on different excimer lasers.³⁻⁷ Various data have been collected to improve the understanding of the kinetics involved in laser excitation. Different techniques have been attempted for preionization to produce uniform laser discharge. Work is still continued to improve the efficiency, to improve the energy of the laser⁸⁻¹⁰ and to scale up¹¹ the laser for high energy.

This paper will present a simple, high power automatic preionized discharge pumped excimer laser. The output energy dependence with various laser parameters will be reported. The various attempts to improve the pulse repetition rate and the lifetime of the gas mixture will also be reported.

DESIGN AND FABRICATION

The design of this laser is quite similar to the one reported by Kearsley et al.¹ The cross-sectional view of the plasma tube is shown in Figure 1. The discharge electrode system is designed with two Al-plates of 100 cm x 14 cm. They are separated by 47 mm with epoxy rods of diameter 25 mm. One of the electrodes is an Al-rod of 6 mm diameter and 81 cm long which is attached to one of the Al-plates. Another electrode is fabricated from an 81 cm x 25 mm x 20 mm rectangular Al-rod and an Al-plate of thickness 5 mm. These are screwed to the middle of the second 14 cm wide Al-plate. The top of the 5 mm thick plate is a smooth and slightly curved Rogowski profile at the edges. The ends of the other electrode are also curved to avoid the arcing during the laser discharge. Two rows of 12 doorknob capacitors (Steatite and Porcelain Products Ltd. type C725) are placed symmetrically on each side of the electrode. These dumping capacitors have total capacitance of 31.2 nF. The separation between the plate electrode and dumping capacitors is critical to designing the laser. The capacitors should be close enough to the electrode to get the proper preionization but far enough away to prevent the discharge from passing through the surface of the capacitor. The complete electrode system is inside a pyrex cylinder of diameter 15 cm and length 100 cm. Two stainless steel plates with O rings are clamped to the ends of the cylinder. These plates are used to connect the laser electrodes to the capacitor and thyatron. The laser cavity is formed with an Al coated mirror of 2" diameter on one end of the plasma tube and a quartz window on the other end.

The electrical circuit diagram of the laser is shown in Figure 2. A 30 kV, 200 mA power supply is connected to a storage capacitor of 100 nF, 60 kV. The other end of the capacitor is connected to one of the laser electrodes. The other electrode is grounded with the thyatron and power supply. A homemade inductor or 5 k long resistor is connected across the electrodes of the plasma tube. The anode of the thyatron is connected to capacitor C₁ and the cathode is connected to the anode of the laser. Thyatron and storage capacitor are placed close to the plasma tube and are connected with copper strip or aluminum foil to minimize inductance in the discharging circuit. The hydrogen thyatron is triggered by a modified version of the trigger pulsed circuit of Ref. 12. The ignition coil is replaced with an EG & G pulse transformer.

OPERATION AND PERFORMANCE

The storage capacitor is charged from the H.V. power supply through the resistor R. Initially, the electrodes of the plasma tube are at the ground potential. As soon as the thyatron fires, a potential difference develops across the electrodes. This potential difference transfers to the upper end of capacitors C₂ and the top electrode which produces the breakdown of the gas medium. The capacitors C₂ are charged through the breakdown. The breakdown also produces ultraviolet photons which produce preionization of the gas media between the electrodes. The energy from the capacitors C₂ is transferred to the preionized gas mixture and produces uniform discharge. The time lag between preionization and main discharge depends upon the laser design but is typically 100 ns.

The variation of laser energy with discharging voltage and different gas mixtures has been studied to

optimize the output power. Figure 3 shows the variation of relative laser energy with charging voltage at 35 torr Xe, 4 torr HCl and 2 atm He pressure. It increases linearly with voltages from 16 kV to 24 kV and shows saturation after that. The energy of the laser is measured with a Gentec energy meter (ED-200). Figure 4 shows the laser output energy at various total pressures and also HCl partial pressures. It increases as He pressure increases from 1 atm to 2 atm. From 2 atm to 2.5 atm it remains nearly constant and starts decreasing above 2.5 atm. The power output has also been studied with varying HCl pressure in the gas mixture. It increases up to 4 torr of HCl then remains the same up to 5 torr and start decreasing above 5 torr. The uniformity of the laser discharge deteriorates at higher HCl pressure and the electrical energy dissipates in arcing rather than exciting the laser media.

The lifetime of the gas mixture is tested by monitoring the laser energy at different times. The plasma tube is passivated a few times with a HCl and He mixture without running the discharge. The laser gas mixture Xe: HCl: He; 35 torr: 5 torr: 2 atm is used to run the laser discharge. Initially, the mixtures have not lost long time. It has stabilized after few fillings and the power output with time is given in Figure 5. The stabilized system runs up to 2×10^5 shots in one filling. The laser power remains more than 90 percent of the peak power. The optimum operating conditions are 35 torr Xe, 4-5 torr HCl and 2 atmospheres of He at 24 kV charging voltage. The pulse width is found to be 15 nsec and laser energy per pulse is 48 mJ. The laser normally operates at 15 Hz but it can go up to 20 Hz.

The 6 mm diameter electrode is modified to produce uniform laser discharge at high pulse repetition rates.¹³ Four H carbon pencil rods of 15 mm length are fitted into the holes drilled 3 mm apart into the electrode. This improves the laser performance at high repetition rates but the power output is reduced. This laser can operate easily up to a PRF of 100 Hz. The gas mixture also deteriorates in shorter time than the previous system. The ballasted resistance technique to stabilize the laser discharge, which is suitable for the CO₂ laser, is found to not be useful for excimer laser. The gas mixture from the plasma tube is passed through a cooling system to a diaphragm pump which circulates the gas mixture. It improves the laser performance at high pulse repetition rates but the life of the gas mixture is reduced. The preionization system is also modified to get optimum laser energy. The bottom electrode is raised by 10 mm. Screws of 12.5 mm length are screwed from the top of the Al-plate to coincide with the upper ends of the capacitors. This arrangement provides the preionization discharge in the middle of main discharge and has improved the laser performance. This laser is being used at present to pump two grazing incidence dye lasers which are used in a sequential two photon absorption spectrometer.

ACKNOWLEDGEMENT

The author wishes to thank Prof. G.W. King, McMaster University, for providing the facility for the present work. This work was supported by the National Sciences and Engineering Research Council of Canada. The author has been employed by DOE, Contract No. DE-AC02-80ET-15601 during the writing of the paper.

REFERENCES

1. A.J. Kearsley, A.J. Andrews, and C.E. Webb, *Opt. Commun.* 31, 181 (1979).
2. Y. Kawamura, K. Suzuki, K. Toyoda, and S. Namba, *Opt. Commun.* 43, 134 (1982).
3. A.J. Andrews, A.J. Kearsley, C.E. Webb, and S.C. Haydon, *Opt. Commun.* 20, 262 (1977).
4. E. Armandillo, F. Bonanni, and G. Grasso, *Opt. Commun.* 42, 63 (1982).
5. R. Burnham, *Opt. Commun.* 24, 161 (1978).
6. R.C. Sze and E. Seegmiller, *IEEE J. Quant. Elect.* Q-17, 81 (1981).
7. R.S. Taylor, A.J. Alcock, and K.E. Leopold, *Opt. Commun.* 31, 197 (1979).
8. R.S. Taylor, *Appl. Phys. B* 41, 1 (1986).
9. M.H. Matsa and T. Goto, *Rev. Sci. Instrum.* 57, 534 (1986).
10. B. Lacour and C. Vannier, *J. Appl. Phys.* 62, 754 (1987).
11. W.H. Long, *Int. Con. Lasers '87*.
12. J.P. Singh and S.N. Thakur, *Research and Industry* 23, 227 (1978).
13. D.C. Hogan, A.J. Kearsley, and C.E. Webb, *J. Phys. D* 13, L225 (1980).

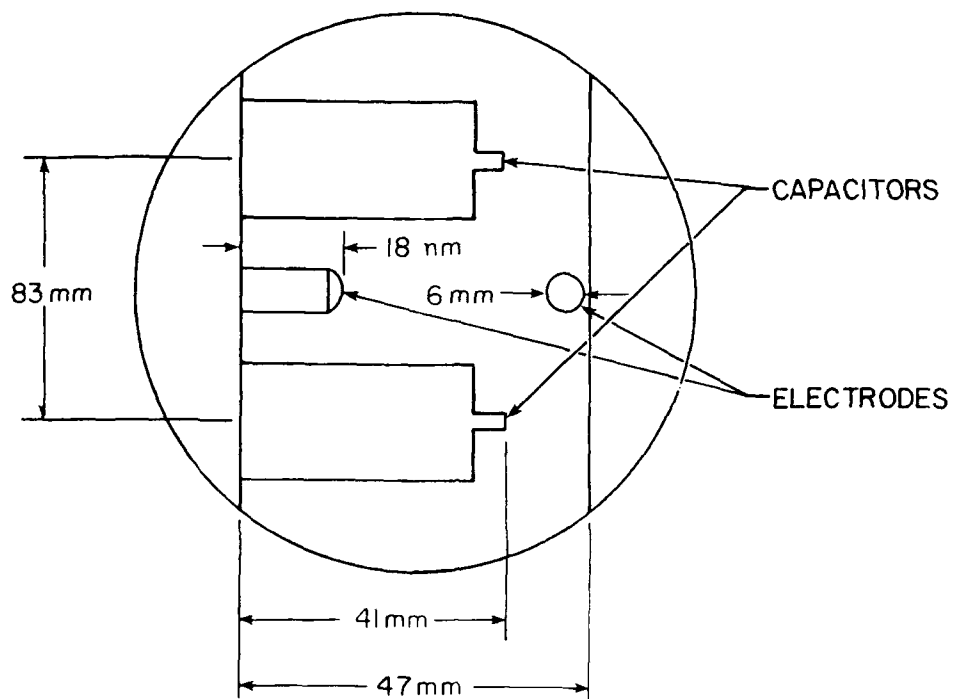


Figure 1. Cross-sectional view of the laser plasma tube.

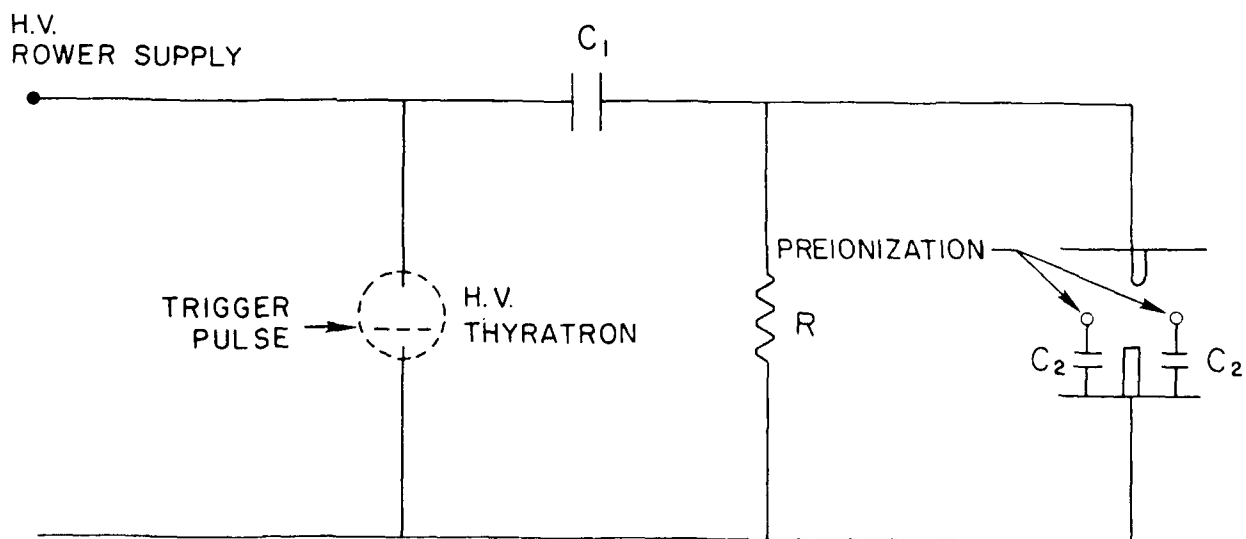


Figure 2. Schematic circuit diagram of the discharge pumped excimer laser.

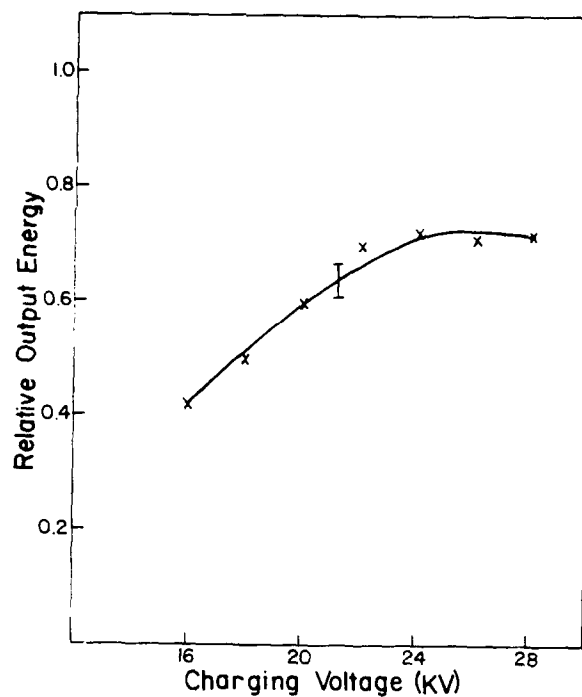


Figure 3.
Variation of the laser output energy with storage capacitor voltage at Xe:HCl: He; 35 torr: 4 torr: 2 atm.

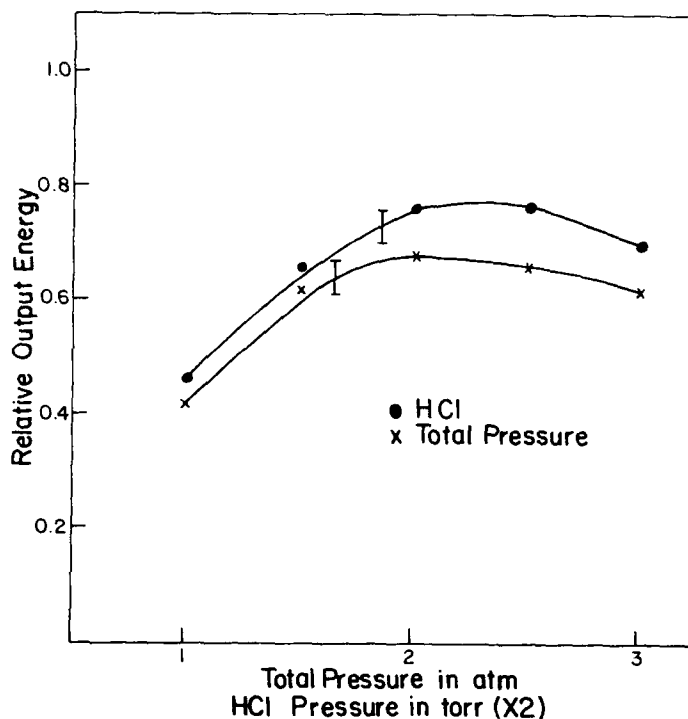


Figure 4.
Variation of relative output energy with HCl pressure and total pressure at charging voltage of 24 kV and Xe pressure of 35 torr. The total pressure was 2 atm in former and HCl pressure was 4 torr in latter.

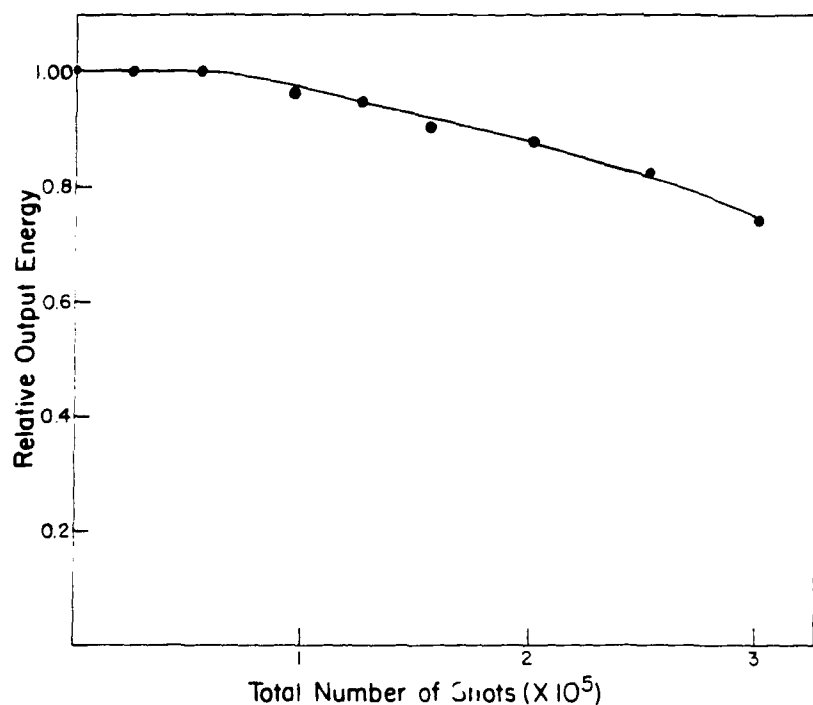


Figure 5.
Lifetime of the excimer laser without gas mixture circulations. (charging voltage 24 kV, Xe:HCl:He; 35 torr: 4 torr: 2 atm)

HIGH POWER AND EFFICIENT X-RAY PREIONIZATION XeCl LASER WITH A PULSE TRANSMISSION LINE

Toshifumi Hasama, Kenzo Miyazaki, Kawakatsu Yamada and Takuzo Sato

Laser Section, Radio- and Opto-Electronics division, Electrotechnical Laboratory,
Tsukuba, Ibaraki 305, Japan

Abstract

A high power and efficient X-ray preionized discharge pumped-excimer laser has been developed. The electrical circuit of the laser system is composed of a pulse forming line (PFL), a rail-gap switch and a pulse transmission line (PTL) to transform the PFL impedance. In order to investigate the effects of the impedance transformation of the PTL, two types of the PTL with the output impedances of 0.26Ω and 0.48Ω have been employed. The system with a lower output impedance has produced the large laser energies by 13-15 % in the range of the PFL-charging voltage from 228 to 400 kV at $\text{HCl/Xe/Ne}=4/20/4476$ Torr. The maximum energy obtained is 50 J in an 85-ns pulse (FWHM), corresponding to the peak power of 0.59 GW. The highest efficiency of 3.1 % has been achieved with an energy of 17.6 J.

Introduction

Rare-gas halide excimer lasers with high-gain and broad gain-width are available for efficient amplification of picosecond (ps) or femtosecond (fs) ultraviolet (UV) laser pulses. Recently ps or fs laser pulses with very high peak power have been¹⁻³ produced by amplification systems having XeCl, KrF or ArF laser as the amplifiers.

Since the excimer lasers have very short energy storage times, a device with a wide aperture is necessary to obtain the output energy above 1 J in an amplified ps or fs pulse. So far, an electron-beam pumping method has been mainly employed for a wide aperture device with an active volume above 10 l except for the discharge laser constructed by Champagne et. al.⁴. They have obtained a laser energy of 60 J in a 180-ns pulse with a XeCl laser.⁵ However, the detail has not been reported.

In the previous paper⁶ on an UV preionized discharge laser with a small active volume, it has been demonstrated that the output energy comparable to XeCl or KrF laser was produced by ArF laser in the high voltage operation. This result shows that the use of the discharge lasers as amplifiers enables the efficient amplification of the ps or fs pulses in the wide UV region of spectrum.

We have constructed an X-ray preionized discharge laser with a wide aperture of $10 \times 10 \text{ cm}^2$ as a main amplifier of an excimer laser amplification system to obtain 1-J class ps-pulses. The laser was designed to be operated at the high voltage of up to 400 kV. This lead a high pulse-forming-line (PFL) impedance compared with the discharge impedance. In order to reduce the output impedance of the excitation circuit, a pulse transmission line (PTL) to transform the PFL impedance has been inserted between the PFL and the laser chamber. In this paper, we report the experimental results obtained at the XeCl laser operations.

Laser design

The laser system constructed is schematically shown in Fig.1. The double PFL with deionized water as a dielectric has the capacitance of 52 nF and the line impedance of 0.87Ω . The PFL is positively charged by a Marx generator with the maximum output voltage of 500 kV and the capacitance of 50 nF. The double transit time of the PFL is 90 ns.

The PTL interconnects the PFL with the laser chamber. The transit time of the PTL is 45 ns. In order to study the effects of the impedance transformation of the PTL, two types of the PTL have been employed. One of them transforms the PFL impedance of $z_{\text{PFL}} = 0.87 \Omega$ to the output impedance of $z_{\text{out}} = 0.48 \Omega$ at the laser interface. The other transforms $z_{\text{PFL}} = 0.87 \Omega$ to $z_{\text{out}} = 0.26 \Omega$.

A rail-gap switch (RGS)^{out} with 120-cm long electrodes separated by 1 cm was set between the PFL and the PTL. The filling gas was sulfur hexafluoride and the maximum pressure of 6 atm was filled at the PFL charging voltage of $V_{\text{PFL}} = 400 \text{ kV}$. The RGS was operated with a self-breakdown mode.

The laser chamber of aluminum is designed for the maximum filling pressure of 6 atm. The laser electrodes are composed of a plain electrode with the thickness of 1 mm and a high-voltage electrode with the length of 120 cm and the width of 17 cm. The high-voltage electrode is contoured according to the expression proposed by Ernst⁷. Both

electrodes are made of nickel-plated aluminum. The maximum active volume observed was about 10 l with 10-cm electrode separation and 110-cm gain length.

X-rays for preionization are generated by colliding a cold-cathode electron-beam to a tantalum foil with the thickness of 13 μm . The X-rays generated at the tantalum foil are attenuated by two 1-mm thick aluminum plates of an X-ray window and the plain laser electrode. The X-ray generator was operated under the conditions of the maximum acceleration voltage and electron-beam current of 180 kV and 6.8 kA. The pulse width (FWHM) of the acceleration voltage was 1.0 μs .

The X-ray dose measured inside the laser chamber was 120 mR in the area of 20x100 cm^2 . The X-ray pulse observed by a photomultiplier had the pulse duration of 1.3 μs and the intensity peak at about 0.3 μs after the X-ray generation. The operation conditions were fixed in the following experiments.

Output characteristics

The discharge uniformity and stability which have strong influence on the efficient operation depend on preionization conditions. Figure 2 shows the laser output as a function of the delay time t_d from the beginning of the preionization to the discharge breakdown. The measurements were made at $V_{\text{PFL}}=154$ kV for a gas mixture of $\text{HCl}/\text{Xe}/\text{Ne}=2/20/2478$ Torr. The laser output is normalized at the laser energy of 10.3 J.

The nearly constant laser output is obtained in the wide time range of the delay time from $t_d=0.2$ to $t_d=1.8$ μs . This seems to indicate that the sufficient preionization has been achieved. Because the X-ray pulse has the intensity peak at about 0.3 μs after the X-ray generation and the pulse duration is only 1.3 μs .

Three laser pulse shapes observed at the delay times of a, b and c are also shown in the figure. The second pulse in the laser pulse shape observed at the time b has a low pulse height compared with that at the time a, though the first pulses have the same pulse height. In the laser pulse shape observed at the time c, the second pulse disappears and the pulse width of the first pulse becomes narrower than those at the times a and b. These variations of the laser pulse shapes suggest that the discharge instability which affects the laser output occurs earlier as the preionization becomes less sufficient.

The output energy of excimer lasers mainly depends on the energy deposited in the discharge plasmas as long as the stable discharge are sustained. The increase in the deposition energy caused by the increase in the total pressure and the reduction of the output impedance contributes to the improvement of the electrical efficiency.

Figure 3 shows the laser energy as a function of the total pressure for $z_{\text{out}}=0.26 \Omega$ and $z_{\text{out}}=0.48 \Omega$. The measurements were made at $V_{\text{PFL}}=154$ kV and a gas mixture of $\text{HCl}/\text{Xe}=4/20$ Torr. The increase rates of the laser energy are 70-80 % for the increase of the total pressure by 2.25 times. These imply that the electrical efficiencies has been improved by 1.7-1.8 times. On the other hand, the reduction of the output impedance leads to the increase of the laser energy above 13 % except for the total pressure of 4500 Torr. The increase rate of the laser energy for $z_{\text{out}}=0.26 \Omega$ appears to be saturated at the total pressure above 4000 Torr.

In Fig.4 are shown the voltage waveforms observed on the laser electrode at the total pressure of 4500 Torr. The waveforms after the breakdown do not represent the voltage between the laser electrodes. Because these waveforms include the inductive voltages caused by the inductance around the laser head. The breakdown at $z_{\text{out}}=0.48 \Omega$ occurs at about 60 ns after the voltage is applied on the laser electrode.

The breakdown at $z_{\text{out}}=0.26 \Omega$ occurs at about 120 ns. The long time till the breakdown indicates that the breakdown voltage is too low. The breakdown voltage is 102 kV and corresponds to the E/N value of 6.4×10^{-17} $\text{V}\cdot\text{cm}^2$. It is possible that this low voltage has brought about any discharge instability. This may explain the saturation of the increase rate of the laser energy for $z_{\text{out}}=0.26 \Omega$ at the total pressure above 4000 Torr.

The laser energy deposited in a discharge plasma during lasing duration is proportional to the charging voltage of an excitation circuit rather than the energy stored in it. Because excimer lasers have a discharge characteristic that the self-sustaining voltage does not change very much with the increase in the charging voltage. Therefore it is predicted that the laser energy increases to be proportional to the PFL voltage.

The measurements of laser energy have been made in the range of the PFL voltage from 148 to 400 kV at a gas mixture of $\text{HCl}/\text{Xe}/\text{Ne}=4/20/4476$ Torr for $z_{\text{out}}=0.26 \Omega$ and $z_{\text{out}}=0.48 \Omega$. The results of the measurements are shown in Fig.6 together with a plot of the electrical efficiency based on the energy stored in the PFL. The laser energy increase linearly for both the output impedances as the PFL voltage increases. However, the laser energies for $z_{\text{out}}=0.26 \Omega$ are large by 13-15 % compared with those for $z_{\text{out}}=0.48 \Omega$ except for $V_{\text{PFL}}=148$ kV. The maximum laser energy obtained is 50 J in an 85-ns (FWHM) pulse, corresponding to the peak power of 0.59 GW. On the other hand, the highest electrical efficiency of 3.1 % is achieved with the laser energy of 17.6 J.

Summary

The X-ray preionized discharge pumped-excimer laser with a large active volume has been constructed and the output characteristics of the XeCl laser has been studied. The glow discharge with the active volume of about 10 l has been successfully achieved by the sufficient X-ray preionization. The variations of the laser pulse shapes observed at the different delay times have suggested that the discharge instability which affects the laser output occurs earlier as the preionization becomes less sufficient.

The effects of the impedance transformation of the PTL have been studied using two types of the PTL. The laser system with $z_{out}=0.26 \Omega$ has produced large laser energies by 13-15 % compared with the system with $z_{out}=0.48 \Omega$ except for the operations under the conditions of the PFL voltage below 154 kV at the total pressure of 4500 Torr. The reduction of the increase rate of the laser energy under the above operation conditions has been considered to be due to the low breakdown voltages at $z_{out}=0.26 \Omega$.

The laser system with the lower output impedance has produced the maximum laser energy and peak power of 50 J and 0.59 GW, and an laser energy of 17.6 J with the highest electrical efficiency of 3.1 %.

References

1. J. H. Glowina, J. Misewich, and P. P. Sorokin, J. Opt. Soc. Am. B4 1061 (1987).
2. S. Szatmari, F. P. Schafer, E. M. Horsche, and W. Muckenheim, Opt. Commun. 63, 305 (1987).
3. H. Egger, T. S. Luk, K. Boyer, D. F. Muller, H. Pummer, T. Srinivasan, and C. K. Rhodes, Appl. Phys. Lett. 41, 1032 (1982).
4. L. F. Champagne, A. J. Dudas, and B. L. Wexler, presented at the Conference on Lasers and Electro-Optics, Anaheim, California (1984) (unpublished).
5. K. Miyazaki, T. Hasama, K. Yamada, T. Fukatsu, T. Eura, and T. Sato, J. Appl. Phys. 60, 2721 (1986).
6. T. Hasama, K. Miyazaki, K. Yamada, K. Ohuchi, and T. Sato, J. Appl. Phys. 61, 4691 (1987).
7. G. J. Ernst, Opt. Commun. 49, 275 (1984).

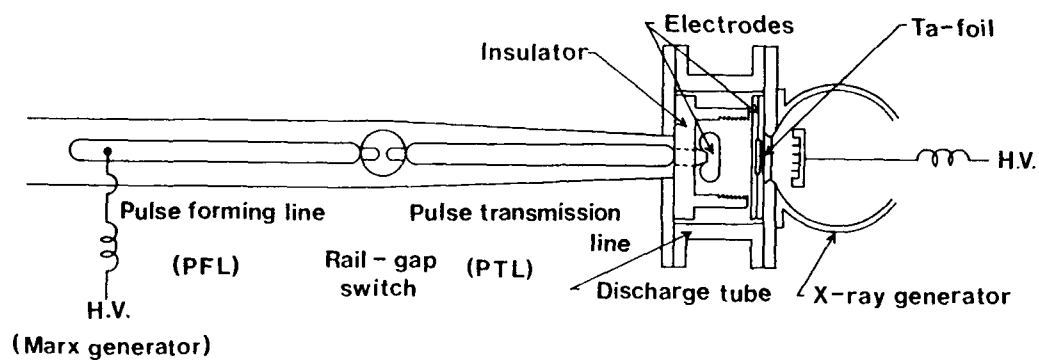


Fig.1 Schematic diagram of the X-ray preionized discharge-pumped excimer laser.

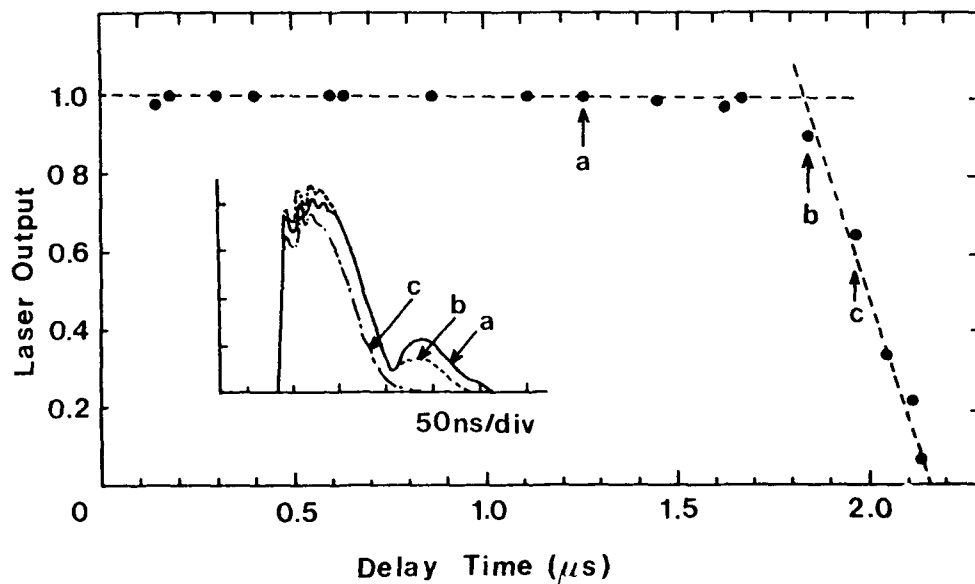


Fig.2 Laser output as a function of delay time from the beginning of preionization to discharge breakdown. Laser pulse shapes observed at the delay times of a, b and c are also shown in the figure.

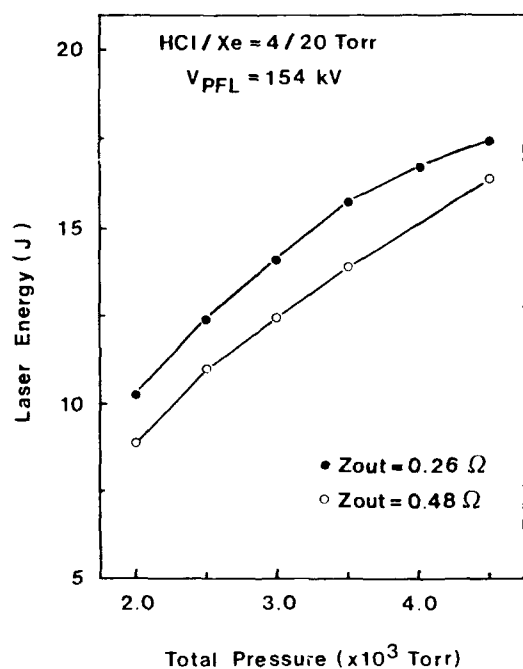


Fig. 3 Laser energy as a function of total pressure.

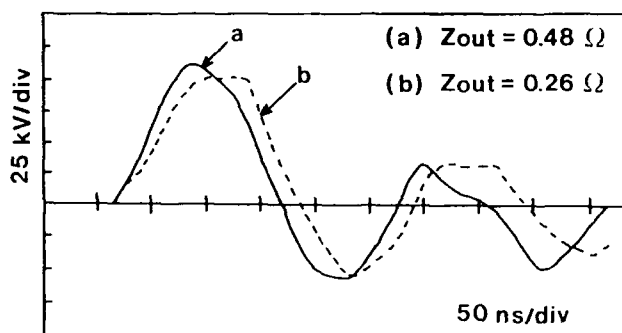


Fig. 4 Temporal behaviors of the voltages on the laser electrode. The laser was operated at the PFL voltage of 154 kV and the total pressure of 4500 Torr.

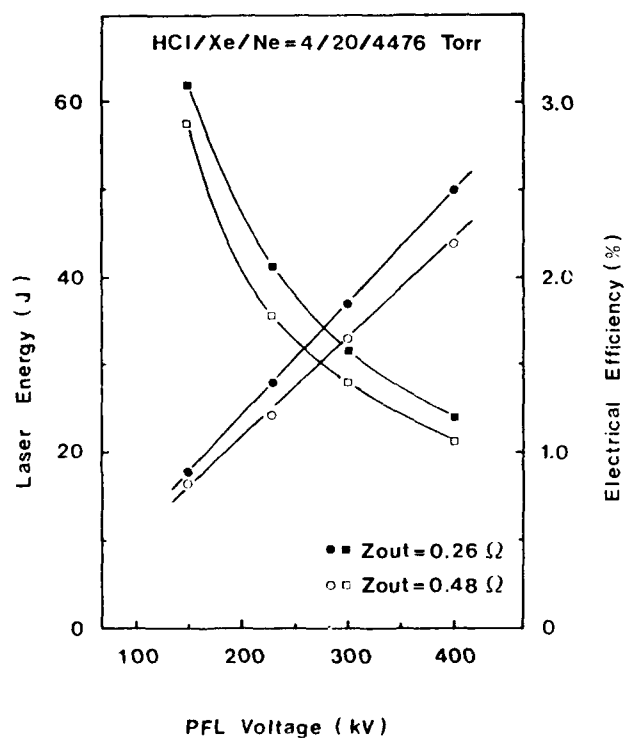


Fig. 5 Laser energy as a function of the PFL voltage.

INFLUENCE OF UV-RADIATION AND SHOCK WAVES ON POPULATION INVERSION MECHANISMS
IN INERT GAS MIXTURE LASERS AND ACTIVE MEDIUM FORMATION IN SPER-LASERS

V.V.Apollonov, S.I.Derzhavin, A.M.Prokhorov, A.A.Sirotkin

General Physics Institute, Academy of Sciences of the USSR, 38 Vavilov Street,
Moscow 117942, USSR

Part.I. Investigation of population inversion mechanisms in inert-gas mixture
lasers pumped by optical break-down

ABSTRACT

The parameters are studied of active media (AM) of He:Xe ($\lambda = 2.03; 2.65 \mu\text{m}$) and He:Ar ($\lambda = 1.79 \mu\text{m}$) lasers pumped by CO_2 -laser induced optical break-down (OB) in the mixture of these gases. The lasing is shown to occur as a result of action of UV radiation from a hot OB plasma kernel on the gas mixture under conditions of plasma shock wave (SW) compression capable of activating AM development.

It was shown earlier (W.T.Siljvast et al., V.A.Danilychev et al.) that population inversion occurs in a recombining plasma of optical break-down at the plasma scattering into ambient buffer gas. However, detailed investigations verifying this mechanism have not been conducted.

The present paper is concerned with the investigation of physical processes responsible for the active medium in lasers on inert-gas mixtures with helium pumped with OB. Lasing has been attained on He:Xe mixtures ($\lambda = 2.03 \mu\text{m}$) and He:Ar mixtures ($\lambda = 1.93 \mu\text{m}$). The CO_2 -laser radiation with a pulse duration $\tau = 300 \text{ ns}$ was focused by a cylinder lens into a 0.8 mm-wide and 9 cm-long band on an Al target placed into the chamber filled with an active mixture He-Xe = He:Ar = 1000:1. Lasing was observed in about 1 μs after OB.

The investigations of OB torch dispersion by means of a high-speed photorecorder have shown that under the conditions of pumping, when lasing is observed, the torch does not reach the region of the cavity caustic of He:Xe and He:Ar lasers, and vice versa, if OB is large the torch reaches the caustic, i.e. lasing is absent. These facts contradict to the assertion that lasing occurs in the OB recombination plasma. To solve this contradiction we have made double-exposure interferometric investigations of the optical break-down plasma.

Comparison of lasing parameters with the results of interferometric investigations of the laser AM has shown the coincidence of the lasing start with the time of shock wave arrival to the region of the cavity caustics. In this case OB plasma does not reach the lasing region and, thus, can not directly influence the population inversion formation. At the same time low gas temperature behind the SW front ($T_e \sim 0.2 \text{ eV}$, match number M 5) has shown that it can not serve either a source of AM pumping, or be the cause of high electron concentration ($n_e \sim 10^{16} \text{ cm}^{-3}$).

In our experiments the presence of excited atoms in front of CW front was confirmed by the glow of HeI, XeI, XeII lines without delay in respect to the occurring of OB. They could appear in particular as a result of resonant UV radiation diffusion from a hot kernel of the optical break-down plasma.

It is well known that the lasers operating on gas mixtures with helium, AM produced as a result of Penning reaction of the working atom with excited helium, for example, $\text{He}^+ + \text{Xe} \rightarrow \text{Xe}^+ + \text{He} + e$. In this case the rate of the Penning reaction, $R = k_p \cdot n_{\text{He}^+} \cdot n_{\text{Xe}}$ depends on the concentration of the particles n_{He^+} and n_{Xe} involved in the reaction. With a SW approach, the growth of the interacting particle concentration, a degree of compression $\eta = \xi/\xi_0 < 4$, and the gas heating $T_g \sim 0.2 \text{ eV}$ may lead to a sharp increase of the Penning reaction rate resulting in Xe(Ar) ionization. Due to a high He concentration in the operating mixture, the electrons cool down in collision with He to the gas temperature. An overcooled plasma forms in the caustic region ($T_e \sim T_g \sim 0.2 \text{ eV}$, $n_e \sim 10^{16} \text{ cm}^{-3}$), in which a recombination scheme of Xe(Ar) pumping may be attained.

Thus, we have shown that generation in lasers operating on inert gas mixtures occurs as a result of action of UV radiation from a hot OB plasma kernel on gas mixture under the conditions of plasma SW compression, as SW is capable of activating AM development. Such high-power sources of UV radiation as electrical discharge and, especially, optical break-down, can generate a great number of excited atoms in the gas mixture bulk, capable of transferring the energy efficiently to the active atoms.

Part II. MECHANISMS OF ACTIVE MEDIUM FORMATION IN SPER-LASERS

V.V. Apollonov, S.I. Derznavin, A.M. Prokhorov, A.A. Sirotkin

General Physics Institute of the USSR Academy of Sciences, Vavilov str. 39,
117942 Moscow, USSR

Abstract

Investigation of active medium parameters of lasers with segmented plasma sources of metal vapors is presented. It is shown that in the process of active medium formation of SPER-laser the following physical phenomena occur: preionization of the buffer gas; current dispersion through the volume of an expanding plasma; mixture of metal vapors and buffer gas by plasma expansion; plasmochemical reactions that occur in the expanding plasma.

Papers /1-4/ present the data on the segmented plasma excitation and recombination laser (SPER-laser) and the generation of transitions of atoms and ions into the IR, visible and UV wavelengths ranges. The authors of /1-4/ suggest the following scheme of the SPER-laser active medium formation. When a high-voltage current pulse is applied to the ends of the series of strips, high-density metal-vapor plasma is formed in each gap. This plasma (consisting of an evaporised strip material) expands hemispherically, cools down due to the expansion and collision with the low-pressure buffer gas and recombines. The population inversion on the atoms and ions transitions is formed as a result of recombination of the higher stages of ion ionization.

However, there has not been research confirming the suggested scheme of the active medium formation in the given type of lasers. This is the aim of this paper.

We used an experimental arrangement described in Fig.1. Active elements of lasers consisted of a series (numbering 30 to 60) of metal (Cd, Zn, In) electrodes ($12 \times 2 \times 1$ mm³) positioned on a glass plate so as to leave a 1-2 mm gap between them. They were pumped by rectangular current pulses $I_n = 20 \div 500$ A ($V = 10 \div 20$ kV) of a $0.5 \div 6$ μ sec. The axis of the laser resonator was parallel to a series of metal electrodes with a distance between them $r = 0 \div 20$ mm. The spectrum lines were selected by monochromator MDR-4, spectrograph DFS-452 and registered by photodiode and photomultiplier. The dynamics of the plasma expansion was studied with the help of the electronic -optical photoregister FER-7.

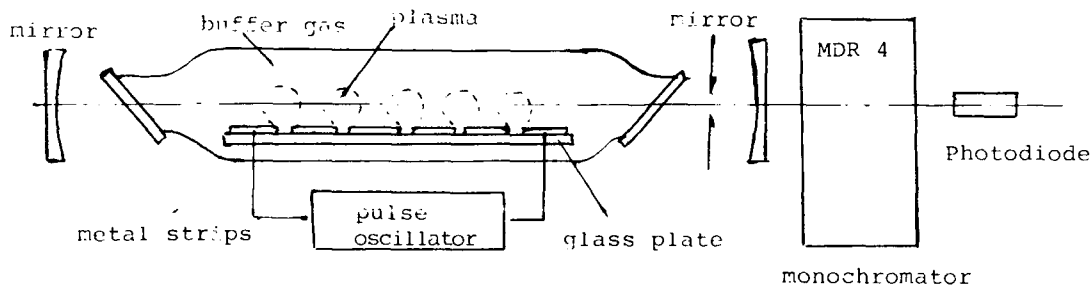


Fig.1. Schematic diagram of the experiment

In this paper the spatial-temporal distribution of the spectrum lines radiation intensity of the metal vapor and buffer gas atoms and ions, plasma expansion dynamics, and SPER-laser radiation parameters have been experimentally investigated.

The physical phenomena that occur during the SPER-laser active medium formation and are beyond the above scheme have been obtained from the analysis of the experimental data:

1. It is seen from a high-speed photo of the plasma glow (Fig.2.) that a sharp splash of glow occurs on the forefront of the pumping current pulse. It is associated with the buffer gas ionization by UV radiation /5/. Then the plasma obtained in the gaps between the electrodes expands. The experiments with the intracavity laser spectrograph showed that immediately behind the forefront I the excited buffer gas atoms are registered for r in the range of 0-16 mm. So the plasma expands in the preliminary preionized buffer gas.

2. The influence of an additional current pulse caused the plasma luminescence over all its volume not featuring a typical glow shape when expanding. If the additional current pulse coincided in time with the generation collapse for any r without time delay. It is possible when the current flows through all the gained plasma volume simultaneously, or a hard ionizer is involved. The character of the spectral lines radiation by the sharp current collapse was similar for all r , that also indicates the current dispersion over the plasma volume. Consequently, the pumping is accomplished when current pulse influences all the ex-

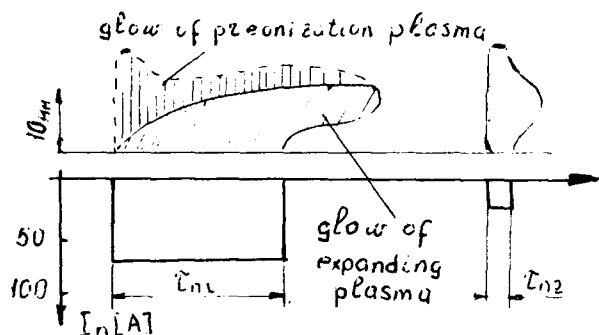


Fig.2. Schematic diagram of the high speed photo plasma glow.

the levels 9P, 8D, 6F 6G for Cd II (6P, 5D, 4F for Zn II), which can be populated as a result of the reaction recharge on He⁺ ions. The temporal character of luminescence changed for the above lines. In case of neon, on the current breakdown there was not a durable after glow characteristic of the He buffer gas, only a short recombinational splash was observed.

These experiments directly show that the process of metal ions production is connected with the recharge reaction of metal atoms with the buffer gas ions. Other plasmochemical reactions are also likely to occur.

5. It was found that the optimum duration of the laser pumping pulse τ_n was nearly equal to 3 sec. Plasma expansion velocity v_{pe} was about 4×10^5 cm/sec at $I_n = 100$ A and the buffer gas pressure $P \sim 3$ torr. During the τ_n time the plasma expands to the dimensions of 10-15 mm and after the current breakdown the plasma cooling begins. Under these conditions the estimation of the cooling velocity shows that the cooling by bumping collisions is at least an order more effective than the expansional one.

From the experimental results given above it is possible to describe the following scheme of the active medium formation of the SPER-laser.

When a high voltage pulse influences the extreme electrodes of the active element, plasma is produced in every gap between the metal stripes. It consists of atoms and ions of metal vapor and buffer gas. Plasma expands into a preionized buffer gas. Metal ions occur as a result of plasmochemical reactions with buffer gas. At the end of the current pulse the plasma is cooled in collisions with the buffer gas. Inversion may occur both as a result of triple recombination and plasmochemical reactions.

When studying the SPER-laser spatial and temporal characteristics on atom transitions we observed the oscillation region displacement in the process of plasma cooling (Fig.3 a); an increase in the time delay of the laser radiation pulse compared to the pumping current at a growing energy (Fig.4); generation breakdown by an additional current pulse (Fig.3b), - etc.

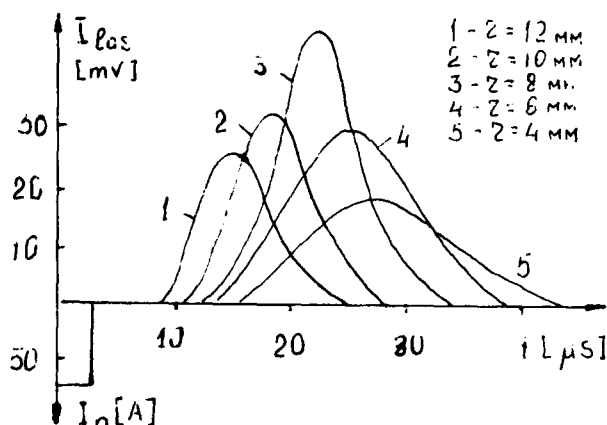


Fig.3a. Oscilloscope trace output from SPER-laser and current pulse.

expanding plasma volume.

3. In our experiments the spatial-temporal distribution of the spectrum lines intensity for He I, He II, Cd I, Cd II was similar to that of the radiation in He-Cd(He-Zn) mixtures pumped by a high-voltage discharge [6]. Their difference lied in the fact that the beginning of luminescence of metal vapor atoms and ions at different distances from electrodes was determined by the speed of the plasma expansion. It is necessary to note that simultaneous luminescence of the metal vapor and buffer gas spectrum lines was observed, i.e. in the process of plasma formation and expansion an effective mixing of metal vapor and buffer gas occurs.

4. Replacement of He by Ne in the buffer gas reduced the spectral lines intensity from

the levels 9P, 8D, 6F 6G for Cd II (6P, 5D, 4F for Zn II), which can be populated as a result of the reaction recharge on He⁺ ions. The temporal character of luminescence changed for the above lines. In case of neon, on the current breakdown there was not a durable after glow characteristic of the He buffer gas, only a short recombinational splash was observed.

These experiments directly show that the process of metal ions production is connected with the recharge reaction of metal atoms with the buffer gas ions. Other plasmochemical reactions are also likely to occur.

5. It was found that the optimum duration of the laser pumping pulse τ_n was nearly equal to 3 sec. Plasma expansion velocity v_{pe} was about 4×10^5 cm/sec at $I_n = 100$ A and the buffer gas pressure $P \sim 3$ torr. During the τ_n time the plasma expands to the dimensions of 10-15 mm and after the current breakdown the plasma cooling begins. Under these conditions the estimation of the cooling velocity shows that the cooling by bumping collisions is at least an order more effective than the expansional one.

From the experimental results given above it is possible to describe the following scheme of the active medium formation of the SPER-laser.

When a high voltage pulse influences the extreme electrodes of the active element, plasma is produced in every gap between the metal stripes. It consists of atoms and ions of metal vapor and buffer gas. Plasma expands into a preionized buffer gas. Metal ions occur as a result of plasmochemical reactions with buffer gas. At the end of the current pulse the plasma is cooled in collisions with the buffer gas. Inversion may occur both as a result of triple recombination and plasmochemical reactions.

When studying the SPER-laser spatial and temporal characteristics on atom transitions we observed the oscillation region displacement in the process of plasma cooling (Fig.3 a); an increase in the time delay of the laser radiation pulse compared to the pumping current at a growing energy (Fig.4); generation breakdown by an additional current pulse (Fig.3b), - etc.

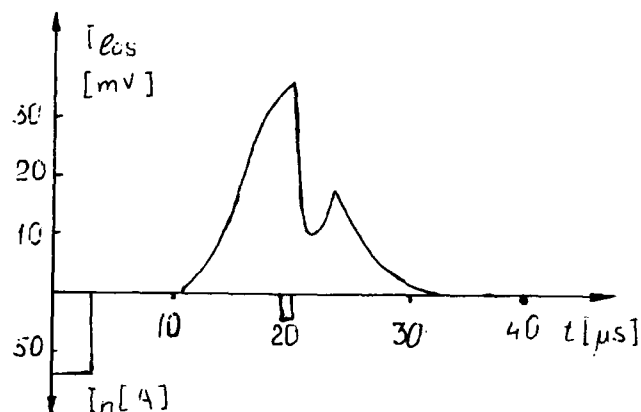


Fig.3b. Oscilloscope trace output from SPER-laser and an additional current pulse.

The experimental data enable us to state that the population inversion in SPEER-lasers on atom transitions is formed as a result of recombination of single ions, which, in turn, may

occur

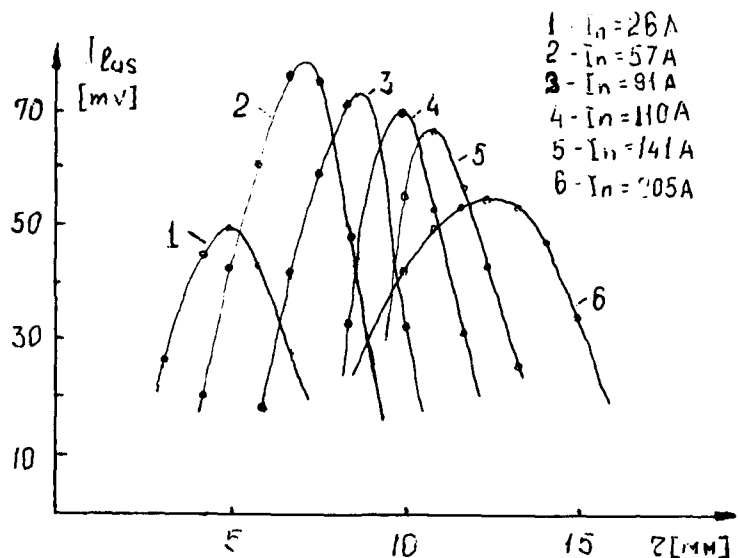


Fig.4. Phase distribution of the oscillation region.

process of metal ion formation through the recharge reaction $\text{He}^+ + \text{Cd} \rightarrow \text{He} + \text{Cd}^{++}$ ($\text{He}^+ + \text{Zn} \rightarrow \text{He} + \text{Zn}^{++}$) is almost by an order more effective than that due to electronical shock or recombination.

In /7/ it was also mentioned that the population of levels was also possible through the Penning reaction $\text{He}(2^3\text{S}_1) + \text{Cd}(5^3\text{P}_2) \rightarrow \text{He} + \text{Cd}^{++} + e$.

In /3-4/ the generation in visible and UV wavelengths ranges is described. Let us consider the question of probability of population of the upper laser levels, In III and Bi III, with the help of plasmochemical reactions.

In Fig.5 partial energy level diagrams for In and Bi are shown. It is clear that their structures are very much alike. The ground states of In^{++} and Bi^{++} are positioned near the resonance with He^+ , that is why the recharge reaction is possible simultaneously with the Penning ionization.

It is noted in /8/ that for these reactions proceeding with the total energy of electronic shells preserved, feature large cross sections ($5 \sim 10 \sim 15 \text{ cm}^2$).

More over, it follows from the diagrams (Fig.5) that for the given elements the energy gaps between the In^{++} , Bi^{++} ground states and upper laser levels, $4f^2F_5/2$ in II and $6f^2F_5/2$ in Bi III, are 20.08 eV and 20.114 eV, respectively, which are near the resonance

with metastable $\text{He}(2^3\text{S}_0)$ and $\text{He}(2^3\text{S}_1)$ states. Consequently, the transition excitation should proceed effectively according to the following scheme $\text{He}(2^3\text{S}_0) + \text{In}^{++} \rightarrow \text{He} + \text{In}^{++*}$ ($\text{He}(2^3\text{S}_0) + \text{Bi}^{++} \rightarrow \text{He} + \text{Bi}^{++*}$).

This two-step process of recharging with Penning ionization with He^+ ion and transition of excitation from He metastable may lead to selective population of the upper laser layers in InIII and BiIII.

All mentioned above makes it clear why no generation has been attained on BiIII($5f^2F_0 - 6p^2P$) transitions at $\lambda = 2074 \text{ \AA}$. This is explained through a great difference between the energy gaps of the BiIII(17.04eV) layer and He metastable and, consequently, through low-efficient excitation transmission.

Thus, the present paper shows that in the process of active medium formation of the SPER-laser the following physical phenomena are observed: 1) preionization of the buffer gas; 2) current dispersion through the volume of an expanding plasma; 3) Mixture of metal vapors and buffer gas due to plasma expansion; 4) Plasmochemical reactions that occur in the expanding plasma; 5) Mostly collisional me-

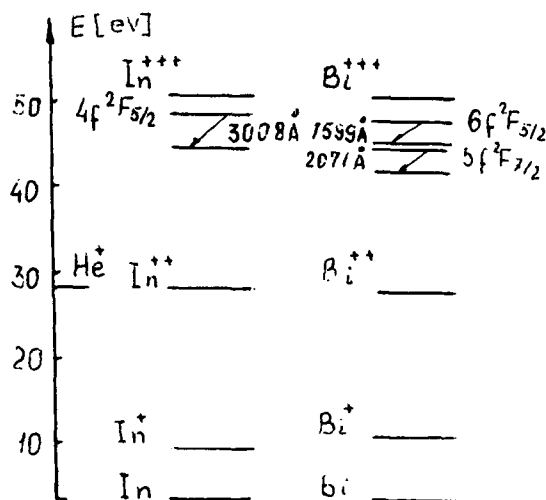


Fig.5. Partial energy level diagrams in In and Bi.

chenism of plasma cooling. It has been noted that population inversion on atom transitions is formed as a result of recombination of single ions, on ion transitions - as a result of recharging and other plasmochemical reactions.

References

1. W. T. Silfvast, L. H. Szeto, and O. R. Wood, II, Appl. Phys. Lett., v.36, pp.615-617 (1980).
2. W. T. Silfvast, L. H. Szeto, and O. R. Wood, II, Appl. Phys. Lett., v.39, pp.212-214 (1982).
3. W. T. Silfvast and O. R. Wood, II, Opt. Lett., v.7, pp.34-36 (1982).
4. J. J. Macklin, O. R. Wood, and W. T. Silfvast, IEEE J. Quantum Electronics, v.QE-18, pp.1832-1835 (1982).
5. V. V. Apollonov, S. I. Derzhevin, A. M. Prokhorov, A. A. Sirotkin, SPIE, High Intensity Laser Processes, v.664, pp.291-295 (1986).
6. V. L. Litusch, V. S. Mikhelevsky, M. F. Sem, Optika i Spektroskopiya, v.34, No2, pp.214-220 (1973).
7. A. A. Babin, I. I. Murev'ev, L. D. Shatova, A. M. Yancherina, Izvestiya Vuzov MV i SSO SSSR, Fizika, No7 (1986).
8. L.I. Gudzenko, S.I.Yakovlenko, Plasmennye Lasery, Moscow, Atomizdat (1978).

CORE-EXCITED ALKALI ATOMS AND IONIC EXCIMERS AS VUV/XUV LASER SOURCES

L. Frey,* S. Kubodera, P.S. Millar, T. Petersen, G. Warwar, P.J. Wisoff, and R. Sauerbrey

Department of Electrical and Computer Engineering, Rice University,
P.O. Box 1892, Houston, Texas 77251

Abstract

The feasibility of producing vacuum ultraviolet lasers using ionic alkali halide excimer transitions is discussed. Fluorescence at 185 nm due to the $Cs^{2+}F^{-} (^2\Sigma_{1/2}, B) \rightarrow Cs^{+}F (^2\Sigma_{1/2}, X)$ transition has been observed using a laser produced plasma to excite CsF vapor in a heatpipe. In addition, the proposed pumping of core-excited alkali transitions by collisional energy exchange with electron-beam excited rare gases is discussed.

Introduction

The interest in atomic and molecular processes leading to emission in the extreme ultraviolet (XUV) and the vacuum ultraviolet (VUV) has grown considerably because of their potential to lead to lasers in this spectral region. The extensive experimental effort in this area attests to the difficulty of obtaining an inversion between states separated in energy by 10 to 100 eV. To obtain such short wavelength transitions, most approaches to date have been to consider core-excited atomic or excited ionic transitions. In the vacuum ultraviolet region, however, another approach has recently been proposed, using excited molecular species such as the ionic alkali halide excimers.¹ The ionic alkali halide excimers ($A^{2+}X^{-}$) are isoelectronic in structure to the well-known rare gas halide excimers ($Rg^{+}X^{-}$) and, therefore, are predicted to emit in the vacuum ultraviolet on the $A^{2+}X^{-} \rightarrow A^{+}X$ transitions.

This paper reports the first observation of fluorescence from the $Cs^{2+}F^{-}$ state at 185 nm using a laser-produced plasma as the excitation source. The dependence of the ionic excimer emission on CsF vapor pressure and temporally resolved emission from $Cs^{2+}F^{-}$ are reported. In addition to these molecular transitions, this paper will discuss a method of pumping core-excited alkali atomic transitions using electron beam excitation.

Ionic Alkali Halide Excimers

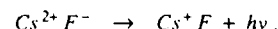
Several groups have recently shown that inner-shell transitions of atoms and atomic ions in the 10 eV to 60 eV range can be efficiently excited by the soft x-rays emitted from a laser-produced plasma.^{2,3} The $A^{2+}X^{-}$ states of the ionic alkali halides are similar to an inner-shell ionization state of an atom in that the $A^{2+}X^{-}$ states constitute the next higher ionization limit of the neutral alkali halide molecule ($A^{+}X^{-}$) above the first ionization limit corresponding to the $A^{+}X$ state. This can be seen from Fig. 1, which shows a calculated potential diagram for the $Cs^{2+}F^{-} \rightarrow Cs^{+}F$ transition. The similarity of $Cs^{2+}F^{-}$ to an atomic inner-shell ionized state suggests that laser-produced plasmas may also be suitable for excitation of these ionic excimer states.

The experimental apparatus used to produce $Cs^{2+}F^{-}$ is shown in Fig. 2. The output of an oscillator/amplifier injection-controlled KrF laser was focused onto a tantalum target inside a heatpipe cell that contained CsF vapor. The KrF laser provided a 750 mJ pulse with a 25 ns pulse width at 248 nm in a 1.5×3 cm² rectangular mode. For most of the experiments, the laser was operated at a 5-7 Hz pulse repetition frequency. The laser beam was focused by a quartz lens with a focal length of 43 cm at 248 nm. The spot size in the focus was determined to be approximately square with sides of 100 μ m in length, which corresponds to a power density of approximately 10^{11} W cm⁻² in the focus.

The heatpipe cell used to produce the CsF vapor was built according to the design described in References [2,4]. It consisted of four arms, arranged as shown in Fig. 2, each about 40 cm long. A fifth arm was tilted at a 45° angle with respect to the plane defined by the four arms shown and allowed for visual inspection of the target. A tantalum target was mounted on a hollow stainless steel tube containing an electric heater. This target rod was rotated by an electric motor to provide a new target surface on successive shots. The cell was heated by ceramic heaters wrapped in thermal insulation material and was capable of operation above 1000°C. In the present experiments, the heatpipe was typically operated between 700°C and 800°C. At those temperatures, a CsF vapor pressure of several Torr could be achieved. Stable heatpipe operation was found for CsF pressures between 1 Torr and 10 Torr, and the CsF pressure was controlled by the He buffer gas pressure.

In the apparatus shown in Fig. 2, a 10 cm focal length CaF_2 lens was used to collect the radiation from the laser plasma zone and to focus it onto the entrance slit of a 0.2 m VUV monochromator with adjustable slits. The slit widths used in these experiments ranged from 100 μ m to 250 μ m, corresponding to a spectral resolution of between 0.3 to 1 nm. The tantalum target was placed about 0.5 cm from the optical axis of the spectrometer. Fluorescence was collected from the entire interaction zone. A photo-multiplier tube equipped with a sodium salicylate scintillator was used as a detector. The rise time of this detector was about 5 ns. Single-shot temporally-resolved observation of the fluorescence was possible using a high-speed storage oscilloscope. Time-integrated spectra were obtained by a boxcar integrator triggered by a pulse from the excimer laser.

The emission spectrum obtained from laser-produced plasma excited CsF vapor at 4 Torr is shown in Fig. 3. A distinct peak at 185 nm is observed. The emission extends from about 190 nm to at least 170 nm. The 185 nm fluorescence is the only emission detected between 200 nm and 150 nm. In addition this fluorescence exhibits a temporal width of about 30 ns, as shown in Fig. 4. This is only slightly longer than the excimer laser pulse, suggesting a short radiative lifetime in qualitative agreement with the predictions of Ref. [1]. The general shape and peak position of the fluorescence emission is in good agreement with the result reported in Ref. [5], where ion beam excitation was used. The peak wavelength compares well with the prediction of Ref. [1], and it may be concluded that the emission is due to the ionic excimer transition:



Since the ionic alkali halide excimers are isoelectronic to the neutral rare gas halide excimers, the same molecular electronic states are expected. Based on the short lifetime of the $Cs^{2+}F^{-}$ state and its spectral width, the molecular band at 185 nm may be assigned to the $Cs^{2+}F^{-} (^2\Sigma_{1/2}, B) \rightarrow Cs^{+}F (^2\Sigma_{1/2}, X)$ transition. Contrary to the results shown in Ref. [5], no indication of emission at shorter wavelength was found, which may be due to the different excitation process.

The rapid rise time of the $Cs^{2+}F^{-} (B)$ fluorescence suggests a direct production mechanism of the ionic excimer state by soft x-rays emitted from the laser-produced plasma. As shown in Fig. 1, ground state CsF molecules are photoionized to the second ionization potential 17 eV above the ground state. Due to the small equilibrium inter-nuclear distance of the B-state as compared to the neutral CsF ground state, ionization should occur predominantly into higher vibrational levels of the B-state. Vibrational relaxation is slow at

*Permanent address: Physikalisches Institut der Universität Würzburg, Am Hubland, D-8700 Würzburg, F.R. Germany.

CsF ground state densities of several 10^{16} cm^{-3} and, therefore, a broad unstructured emission spectrum from a vibrationally and rotationally hot molecule is expected. This is in qualitative agreement with the experiment (Fig. 2). However, generation of electrons through photoionization of CsF by soft x-rays and subsequent electron impact ionization of CsF to the second ionization limit cannot be excluded.

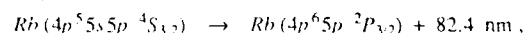
Since the cross section for stimulated emission for the 185.4 nm transition is expected to be about 10^{-16} cm^2 ,¹ upper state densities of the order of 10^{15} cm^{-3} are necessary for gains of 0.1 cm^{-1} . Such densities have been achieved in core-excited ionic systems using laser produced plasmas,⁶ but the excitation lengths are usually small $\sim 1 \text{ cm}$. Electron beam excitation of the ionic alkali halide excimers may provide larger gain lengths, but laser-produced plasma excitation provides a very suitable source for the spectroscopic examination of this interesting class of molecules. This excitation technique may also prove useful in the study of other excimer-like transitions in molecular ions described in Refs. 1 and 7.

Core-Excited Alkali Atoms

Recently, Harris, et al.,⁸ have proposed using quasimetastable alkali quartet levels for the construction of XUV lasers. These states are core-excited levels which are somewhat metastable against autoionization due to angular momentum and spin selection rules. These states, in the case of heavy alkali atoms, have high radiative rates and could be used as the upper laser level. Another possibility would be to accumulate atoms in these quasimetastable levels and then use an ultrafast tunable dye laser to transfer the stored population to a nearby upper laser level. Both of these techniques rely on first exciting large densities of quasimetastable atoms.

Harris, et al., have used microwave, hollow cathode, and laser-produced plasma excitation to generate these quasimetastable states. Another method, however, would be to use an electron beam. Using an approach suggested by Papanyan, et al.,¹⁰ an electron beam will first excite metastable rare gas atoms which will subsequently produce metastable alkali quartet atoms by collisional excitation. This technique capitalizes on the metastability of the alkali quartet storage levels by utilizing the extended lifetime of these states to achieve a large energy deposition into the active medium. In addition this method of excitation should easily produce active lengths of 10 cm or more which are appropriate for producing single-pass superfluorescent lasers. It is more difficult to achieve such active lengths using other methods of excitation such as laser-produced plasmas.

Of particular interest is the transition



which has a cross section for stimulated emission of approximately $5 \times 10^{-15} \text{ cm}^2$. This transition is shown in Fig. 5. This quartet level is a prime candidate for electron beam excitation as a result of its energy being nearly resonant with excited levels of neon. The $Rb(4p^5 5s 5p^4 S_{3/2})$ level at 16.641 eV lies between the $Ne(2p^5 3s^3 P_0)$ level at 16.71 eV and the $Ne(2p^5 3s^3 P_2)$ level at 16.62 eV.

To affect the collisional transfer of energy from the excited neon levels to the Rb quartet, Ne and Rb vapor must be mixed in an appropriate cell for electron beam excitation. The experimental apparatus is shown in Fig. 6. It consists of a heated cell with a 50 μm inconel foil for coupling in the electron beam. The cell can be operated up to temperatures of 850°K. The heated cell is thermally insulated from the cathode housing by a small air gap. The cathode housing is sealed by a 50 μm titanium foil. Both the foils on the cell and the cathode housing are supported by a Hibachi structure. The cell is coupled to a VUV detection system, consisting of a 0.2 meter vacuum spectrometer and appropriate detectors. For operation in the spectral region below 105 nm, where no window materials are available, the spectrometer and reaction cell can both be pressured with Ne up to 1.2 atm. At this buffer gas pressure, the reaction cell has

been reliably operated at up to 10 Torr of Rb vapor pressure. The rubidium vapor pressure was measured by calculating the equivalent width of a ground-state-to-resonance-level absorption profile using a white light source exterior to the heated cell.

If effective collisional energy transfer to the quasimetastables can be achieved using this technique, the established electron beam technology that has been used for many years in excimer research should prove a valuable new approach to producing XUV lasers.

Acknowledgment

This research was supported by the National Science Foundation (Contract Number ECS 85-01433), the Robert A. Welch Foundation (Contract Number C-1095), and the Air Force Office of Scientific Research (Contract Number AFOSR-87-0247). L. Frey would like to acknowledge support by the Deutsche Forschungsgemeinschaft.

References

- [1] R. Sauerbrey and H. Langhoff, *IEEE J. Quantum Electron.* **QE-21**, 179 (1985).
- [2] R.G. Caro, J.C. Wang, J.F. Young, and S.E. Harris, *Phys. Rev.* **A30**, 1407 (1984).
- [3] W.T. Silfvast and O.R. Wood, II, *J. Opt. Soc. Am.* **B4**, 609 (1987).
- [4] P.J.K. Wisoff and R.G. Caro, *Appl. Phys. B* **35**, 65 (1984).
- [5] F. Steigerwald, F. Emmert, H. Langhoff, W. Hammer, and T. Griegel, *Opt. Comm.* **56**, 240 (1985).
- [6] R.G. Caro, P.J.K. Wisoff, G.Y. Yin, D.H. Walker, M.H. Sher, C.P.J. Barty, J.F. Young, and S.E. Harris, "Soft X-Ray Pumping of Inner-Shell Excited Levels for Extreme Ultraviolet Lasers," *AIP Optical Science and Engineering Series 7 - Short Wavelength Coherent Radiation: Generation and Applications*, AIP Proceedings No. 147, pp. 145-156, 1986.
- [7] N.G. Basov, M.G. Voitik, V.S. Zuev, and V.P. Kutakhov, *Soviet J. of Quant. Electr.* **15**, 1455 (1985).
- [8] S.E. Harris, D.J. Walker, R.G. Caro, A.J. Mendelsohn, and R.D. Cowan, "Quasi-metastable quartet levels in alkali-like atoms and ions," *Opt. Lett.* **9**, 168 (1984).
- [9] S.E. Harris and J.F. Young, *J. Opt. Soc. Am. B* **4**, 547 (1987).
- [10] V.O. Papanyan, A.E. Martirosyan, and F.K. Tittel, *IEEE J. Quantum Electron.* **QE-19**, 1835 (1983).

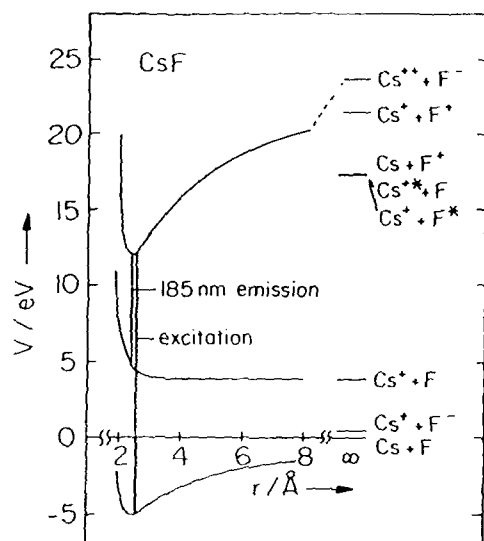


Figure 1. Schematic energy diagram for the excitation and emission process in Cs^{2+}F^- . Soft x-rays from the plasma photoionize Cs^+F^- ground state molecules to the second ionization limit. Fluorescence at 185 nm is observed on the ionic excimer transition $\text{Cs}^{2+}\text{F}^-(B) \rightarrow \text{Cs}^+\text{F}(X) + h\nu$.

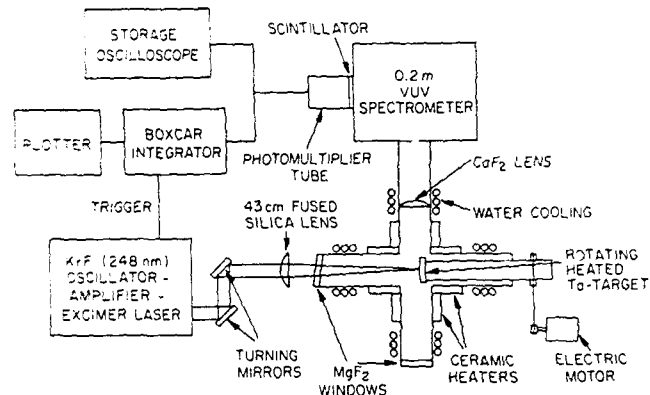


Figure 2. Experimental setup. A focused KrF excimer laser generates a plasma on a rotating tantalum target inside a heatpipe cell. The soft x-rays emitted from the plasma excite the CsF vapor, and the fluorescence in the VUV is recorded.

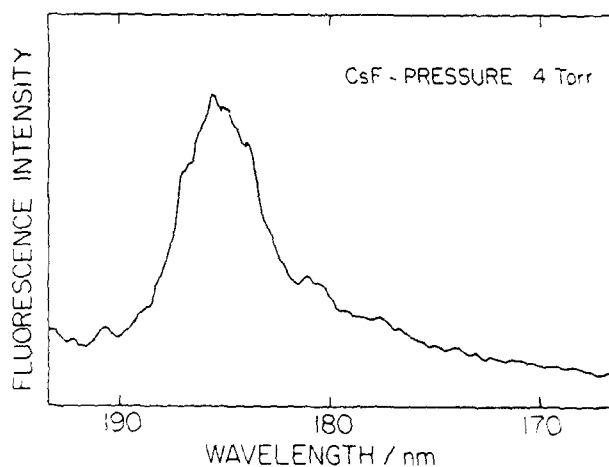


Figure 3. Emission spectrum from laser-produced-plasma-excited CsF vapor around 185 nm.

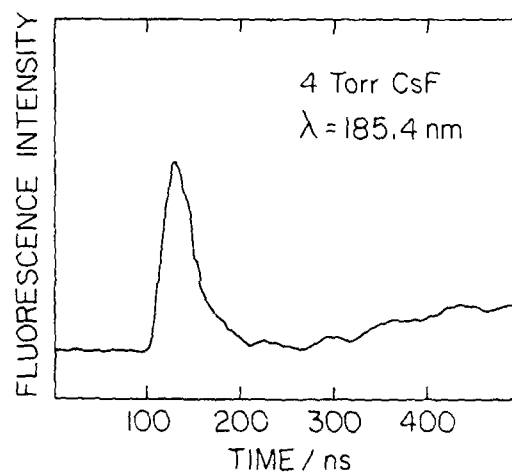


Figure 4. Temporally-resolved $\text{Cs}^{2+}\text{F}^-(B)$ fluorescence signal at 185.4 nm. The temporal width is about 35 ns (FWHM) which is slightly larger than the laser pulse width. The increasing fluorescence after about 300 ns is due to recombination of the expanding tantalum plasma.

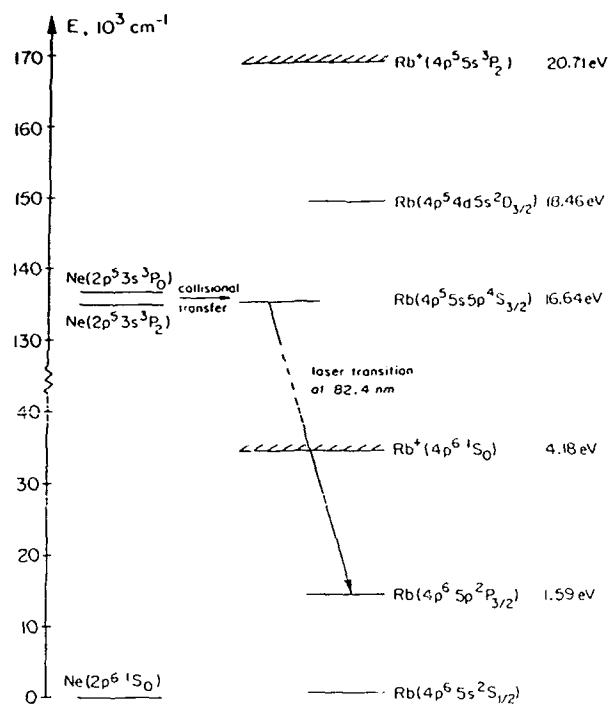


Figure 5. Schematic of *Ne* and *Rb* levels appropriate for excitation of the *Rb* ($4p^5 5s 5p^4 S_{3/2}$) level.

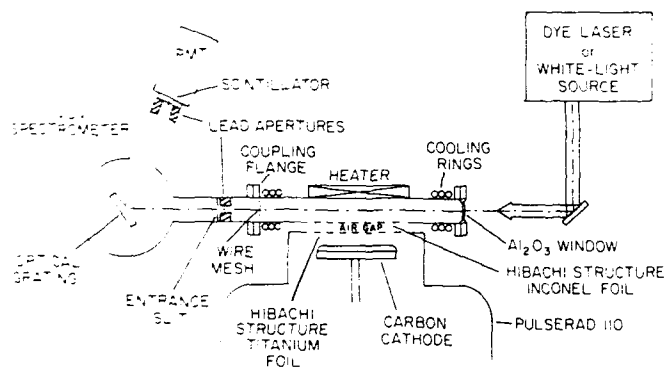


Figure 6. Electron beam apparatus for excitation of *Ne-Rb* mixtures.

RECENT PROGRESS ON THE LOS ALAMOS AURORA ICF LASER SYSTEM

by

L.A. Rosocha and L.S. Blair

Los Alamos National Laboratory of the University of California
P.O. Box 1663, MS-E548, Los Alamos, NM 87545

Abstract

Aurora is the Los Alamos short-pulse, high-power, krypton-fluoride laser system. It serves as an end-to-end technology demonstration prototype for large-scale ultraviolet laser systems for short wavelength inertial confinement fusion (ICF) investigations. The system is designed to employ optical angular multiplexing and serial amplification by electron-beam-driven KrF laser amplifiers to deliver stacked, 248-nm, 5-ns duration multi-kilojoule laser pulses to ICF-relevant targets. This paper presents a summary of the Aurora system and a discussion of the progress achieved in the construction and integration of the laser system. We concentrate on the main features of the following major system components: front-end lasers, amplifier train, multiplexer, optical relay train, demultiplexer, and the associated optical alignment system. During the past year, two major construction and integration tasks have been accomplished. The first task is the demonstration of 96-beam multiplexing and amplified energy extraction, as evidenced by the integrated operation of the front end, the multiplexer (12-fold and 8-fold encoders), the optical relay train, and three electron-beam-driven amplifiers. The second task is the assembly and installation of the demultiplexer optical hardware, which consists of over 300 optical components ranging in size from several centimeters square to over a meter square.

1. Introduction

KrF lasers are promising candidates for inertial confinement fusion drivers (ICF) because they have the following specific advantages:

- Short wavelength (which couples more efficiently to fusion targets than either infrared or visible lasers);
- Decreased superthermal electron production;
- Increased plasma penetration, which leads to high ablation pressures;
- Broad bandwidth (which tends to decrease deleterious nonlinear plasma processes);
- High intrinsic laser efficiency;
- Economical construction cost;
- High energy scalability;
- Potential for repetitive operation.

However, because of a relatively low saturation flux, large nonsaturable absorption losses, and the non-storage nature (short excited state lifetime) of the laser medium, the KrF laser must be scaled to large aperture sizes and operated in a long pulse (>100 ns) mode to produce efficient high energy (kJ- and MJ-class) outputs. Because efficient coupling of the laser energy to a fusion target requires a laser pulse duration with an energetic component of ~ 5 to 10 ns, a means of matching the target pulse duration requirement to the laser amplifier pulse duration must be provided.

At Los Alamos, we have employed the technique of optical multiplexing to accomplish this match because it utilizes existing designs and conventional optical methods. Figure 1 shows the concept. The application of multiplexing to a kilojoule-class KrF/ICF laser driver will be investigated at LANL with the Aurora system.

The Aurora KrF/ICF technology demonstration prototype system employs optical angular multiplexing and serial amplification by electron beam-pumped KrF laser amplifiers to deliver 5- to 8-kJ, 248-nm laser pulses of 5-ns duration to ICF targets. Aurora is being built in two

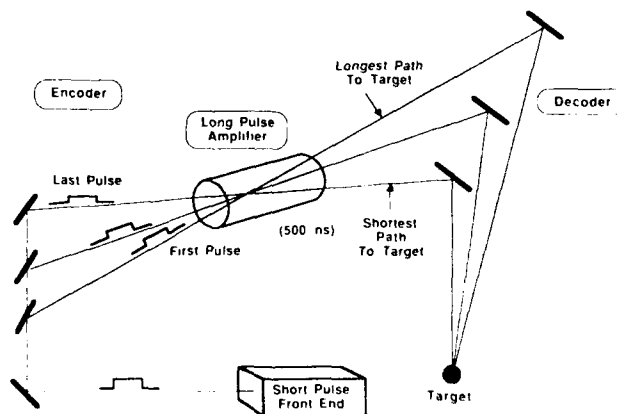


Fig. 1: A schematic diagram that illustrates the concept of optical angular multiplexing. From the front end pulse, an encoder produces a head-to-tail train of pulses that are slightly separated in path angle. This pulse train is then amplified and the individual pulses are sent along appropriate flight paths such that all the pulses arrive at the target simultaneously.

phases: the first phase (which has been essentially completed) includes the multiplexing and serial amplification features, while the second phase includes the additional end-to-end demonstrations of demultiplexing and delivery of laser pulses to fusion targets. The system has been described in great detail in several earlier publications.¹⁻³ The main power amplifier in the system, the Large Aperture Module (LAM) has a laser aperture of 1 m x 1 m and is the largest and most energetic existing ultraviolet laser of its type so far reported, having produced in excess of 10 kJ of 248-nm laser light when operated as a nonoptimized unstable resonator.^{4,5}

The Aurora prototype will demonstrate critical technologies involved in developing KrF drivers for fusion and will serve as a test-bed for some particular technological aspects of larger laser fusion systems. In particular, Aurora will examine:

- uniform electron beam pumping of large laser volumes;
- optical angular multiplexing and demultiplexing systems that are scalable to large system designs;
- staging of large KrF amplifiers;
- uv pulse propagation over long paths;
- alignment of multibeam systems;
- novel approaches to optical hardware that can lead to cost reductions for even larger systems.

Figure 2 shows a conceptual layout of the Aurora system as it is presently configured. This figure illustrates all of the main optical and laser elements from the front end through the the final power amplifier output, and on to the target system. The first phase part of the system employs the components from the front end to the LAM

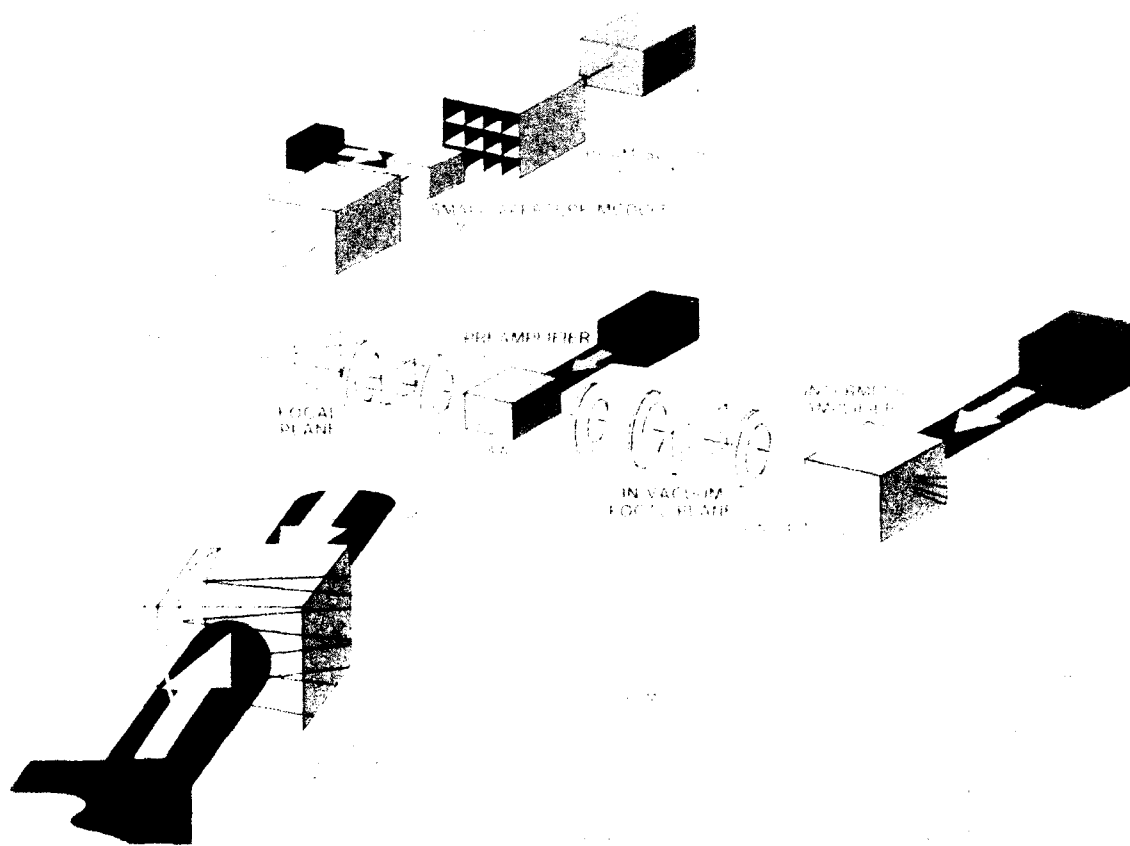


Fig. 2: A conceptual layout of the Aurora laser system. All of the main optical and laser elements from the front end, through the final amplifier output and on to the target are shown. Stage gains, number of beams, and beam energy are indicated at various points along the beam path. Typical delivered energy at the target is expected to be ~ 5 kJ in 48 beams.

output. In this phase, the basic approach is to replicate the front end output using aperture slicers, beamsplitters, and mirrors to produce a 480-ns long pulse train consisting of 96 beams each of 5-ns duration. These encoded (multiplexed) pulses, which are spatially separated, are then individually adjusted at the entrance pupil of an optical relay system. The beam train is then relayed through two single-pass laser amplifiers (the Preamplifier and Intermediate Amplifier), a double-pass laser amplifier (the Large Aperture Module), and delivered to the optical multiplexer (decoder). Beam train alignment to the multiplexer is accomplished with two automated alignment systems. One system points each of the 96 beams through the Preamplifier entrance pupil and the second keeps the Large Aperture Module primary mirror aligned in real time. In principal, a final optimized design output of 15 to 20 kJ can be expected from the LAM.

To deliver short-pulse KrF laser energy to fusion targets, the system will require decoder (demultiplexer) optics to compress the multiplexed beam train and a target facility to house and perform diagnostics on fusion targets. The second phase of Aurora will be concerned with an end-to-end demonstration of multiplexing, amplification, demultiplexing, and delivery of energy to target. Due to fiscal and programmatic constraints, only 48 beams from the set of 96 multiplexed and amplified beams will be demultiplexed and sent to target in the next one to two

years. Figure 3 shows an artist's conception of the second-phase Aurora system as it will appear with a 48-beam demultiplexer and target building in place. As configured, this system is designed to stack 48 of the 96 beams into a single multi-kilojoule 5-ns pulse at the fusion target.

In this paper, we will present brief surveys of the front end, the amplifiers, the multiplexer and relay optics, the alignment system, and the demultiplexer optics. The target irradiation apparatus, which is adequately treated elsewhere,⁶ will not be described here, other than to say that considerable progress has been made in the installation of the target chamber and associated apparatus. Progress achieved in the construction, testing, and integration of the laser system over the past year will also be discussed.

2. Front-End System

The front-end system provides the initial pulse that is replicated and then amplified for delivery to the target. The Aurora front-end system is progressing in stages that correspond to the two phases of the project. An interim front end now provides 5-ns pulses adequate for startup and initial integration of the amplifier chain. A front end to be installed later (but developed during the past year) will provide high-contrast ratio, pulse shaping, and bandwidth flexibility.

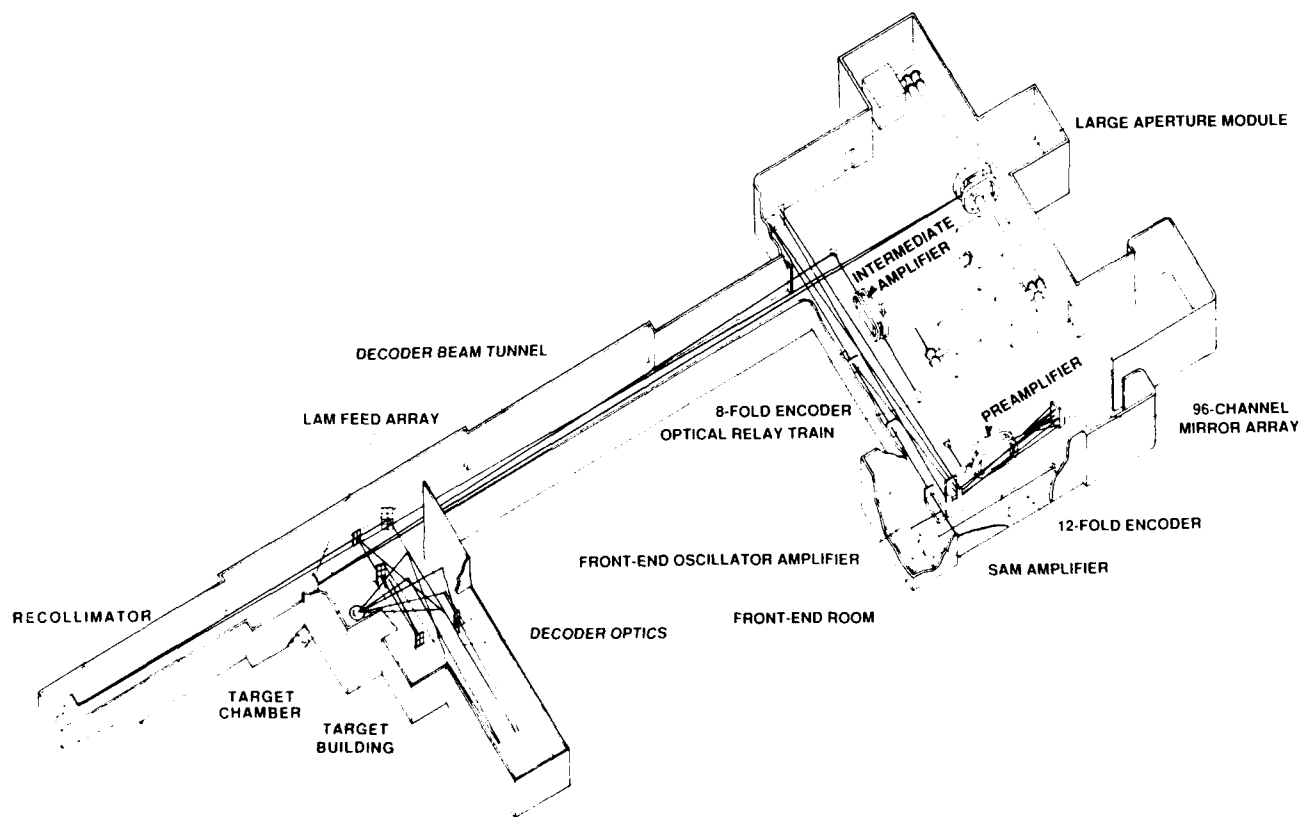


Fig. 3: An artist's conception of the Aurora system with the 48-beam decoder and target building in place. Most of the system is now built and is in the process of system integration.

2a. Baseline Front End for Multiplexing Demonstrations

The first-phase front-end system uses Pockels cells to switch out a 5-ns pulse from a longer 25-ns pulse produced by a commercial electric discharge-pumped, injection-locked KrF oscillator-amplifier system. The 5-ns pulse is then split into two identical 5-ns pulses that are then amplified by a commercial TEA KrF postamplifier and sent to the 12-fold encoder (multiplexer). The combined energy of the two pulses is approximately 250 mJ. The performance of the system (total energy, contrast ratio, and beam divergence) is determined by the characteristics of the Pockels cell, the oscillator-amplifier, and the post amplifier.

After emerging from the second switch and polarizer set, the single 5-ns pulse is split into two identical pulses by the beamsplitter and then passed through two parallel electric discharge post amplifiers. Upon emerging from the post amplifiers, the two 5-ns pulses typically contain a total energy of approximately 350 mJ; this is more than sufficient energy for the multiplexing demonstration. The shape of the 5-ns pulses emerging from the post amplifiers is determined by the effective excited state lifetime of the KrF gain medium (which is due to a short spontaneous lifetime of about 6 ns and the effect of collisional quenching). The KrF gain medium is in fact an energy storage medium with an effective lifetime of 2 - 2.5 ns, which results in an amplified pulse with a strong spike on the leading edge.

2b. Advanced Front End for Target Shooting

The above front-end configuration meets the requirements for the proof-of-principle demonstration of the technique of angular multiplexing, but will not be adequate for the delivery of energy to fusion targets since the contrast ratio is only of order 100:1. To provide a high quality target-shooter front end, Stimulated Brillouin Scattering (SBS) phase-conjugate mirrors have been used to improve the baseline front end lasers.

The modified front end⁷ (which contains many components common to the baseline front end) is shown in Figure 4. It takes advantage of commercially available units, which are then appropriately modified. A Lambda Physik Model EMG-150 KrF laser (which contains two discharge heads that are used as an oscillator-amplifier arrangement) comprise the main components of the new front end. The oscillator cavity, which consists of a 10-m concave high-reflectivity mirror and a 60% reflectance flat output coupler separated by 1.25 m with a 1-mm intracavity aperture, was operated with a moderate amount of dispersion provided by a single prism. This resulted in a bandwidth of $\sim 10 \text{ cm}^{-1}$. The 10-mJ, 20-ns pulse from the oscillator is optically delayed by 20 ns to compensate for the built-in delay between the two discharge laser heads. A polarizer placed in the output beam provides linear polarization. A beam-expanding telescope then expands the beam to overfill the 1.5-cm x 3.0-cm cross section of the preamplifier. An aperture at

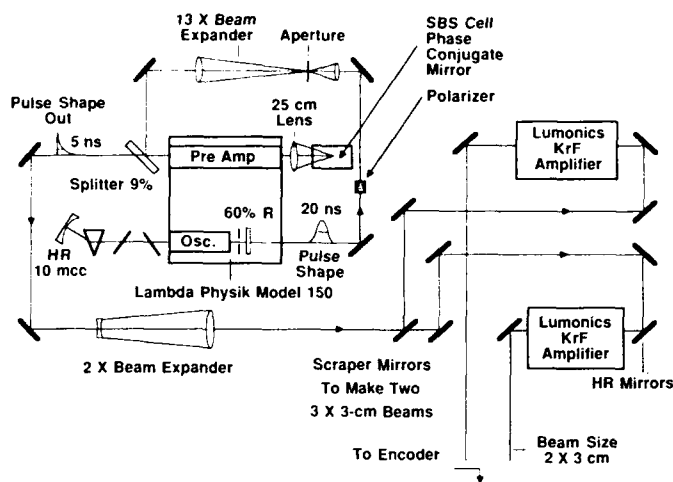


Fig. 4: Schematic diagram of the Aurora front end using phase conjugation by Stimulated Brillouin Scattering (SBS).

the focus of this telescope stops the backward amplified spontaneous emission (ASE) from damaging the telescope input lens if the oscillator fails to operate. The beam is injected into the preamplifier by a 9% S-plane reflection from an uncoated wedged beamsplitter.

After one pass of amplification, the beam is focused by a 25-cm focal length lens into the SBS cell containing 20 atm of SF_6 . The phase-conjugate reflection produced when the medium reaches threshold is returned through the preamplifier, amplified a second time, and taken through the beamsplitter. The SBS pulse width can be varied by attenuating the oscillator beam. This controls the amount of time required to reach threshold in the SBS medium. The oscillator attenuation has been adjusted to provide the required pulse width of 5 ns. This pulsewidth is very reproducible ($<0.2 \text{ ns}$ pulse-to-pulse variation).

The 1.5-cm x 3.0-cm output beam from the preamplifier is expanded with a 2x telescope to form a 3-cm x 6-cm beam. This beam is split with a scraper mirror into two identical square beams of size 3 cm x 3 cm. Each of these beams is single-pass amplified through a separate Lumonics amplifier and delivered to the encoder.

The performance of the advanced front end shows improvement in several areas when compared with the baseline front end that used Pockels cells and polarizers to create the 5-ns pulse. The prepulse has been reduced as evidenced by an instrumentation-limited measurement, which showed a prepulse energy of $<10^{-4}$ of that in the main pulse. Final beam quality from the amplifier is now 1.5 times diffraction limited ($1.5 \times \text{DL}$) as compared to $5.0 \times \text{DL}$ previously. The output energy has been doubled and the maximum pulse repetition rate has been increased from one pulse per minute to 0.5 Hz.

3. Amplifiers

The Kr/Ar/F₂ gain medium in the Aurora amplifiers is pumped by cold cathode electron guns, the details of which have been described elsewhere.^{1,8} In summary, the electron guns make use of planar cold cathode diodes with graphite felt emitters ranging in emission area from 1,200 cm² to 20,000 cm². The diodes are typically driven by Marx generator-charged pulse forming lines (PFLs) of low impedance ($\sim 2.7\Omega$ for most amplifiers). The typical electrical pulse length is 650 ns, the diode voltage 500-650 kV, and the current density 25 A/cm² at the cathode. Electron current is transported into the laser gas with $\sim 50\%$ efficiency through Ti foils and a hibachi support structure. Externally applied magnetic guide fields of 1.5 to 3 kGauss are used to provide uniform current delivery.

The main amplification chain for Aurora consists of four electron beam-driven KrF laser amplifiers ranging in aperture size from 10 cm x 12 cm to 100 cm x 100 cm. These devices are specified the Small Aperture Module (SAM), the Preamplifier (PA), the Intermediate Amplifier (IA), and the Large Aperture Module (LAM). The characteristics of these four amplifiers are summarized in Table I.

Table I

Summary of Amplifier Specifications

Device	SAM	PA	IA	LAM
Pump pulse length (ns)	100	650	650	650
E-Gun voltage (kV)	300	675	675	675
E-Gun current in gas (A/cm ²)	12	10	10	12
E-Gun area (m ²)	0.12	1.20	1.20	2.00
Input / output light energy (J)	0.25/5	1/50	50/2k	2k/20k
Stage gain	20	50	40	10
Laser aperture (cm x cm)	10x12	20x20	40x40	100x100

Figures 5-7 show some of the amplifier hardware. At present all amplifiers have been operated successfully as lasers, although the pumping of the IA needs improvement in magnitude and uniformity. The LAM is representative of all of the amplifiers in the Aurora chain, except that the PA and IA use single-sided electron beam pumping and the SAM does not use a PFL. The theoretical performance of these amplifiers has been discussed in detail elsewhere.^{1,9}

The actual performance of these laser devices has been determined by experiments conducted to measure the gain and by integrated 96-beam energy extraction measurements. Figures 8a and 8b display the measured values of small-signal gain¹⁰ for the PA and IA, while Table II gives the measured amplifier performance. The

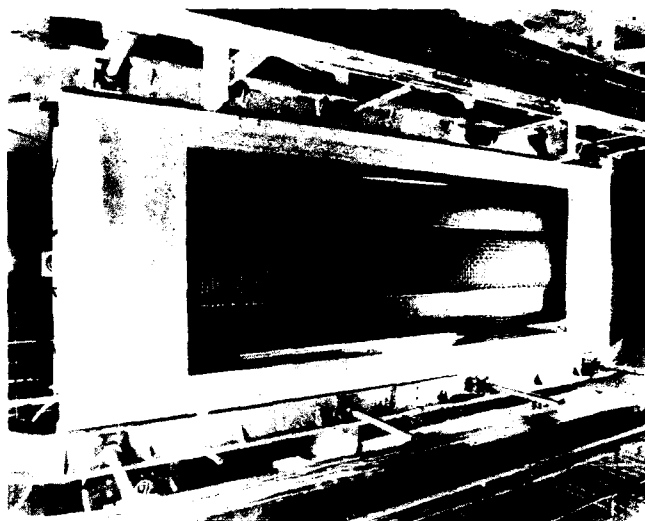


Fig. 5: Photograph showing the interior of the Preamplifier (PA) cold cathode diode.

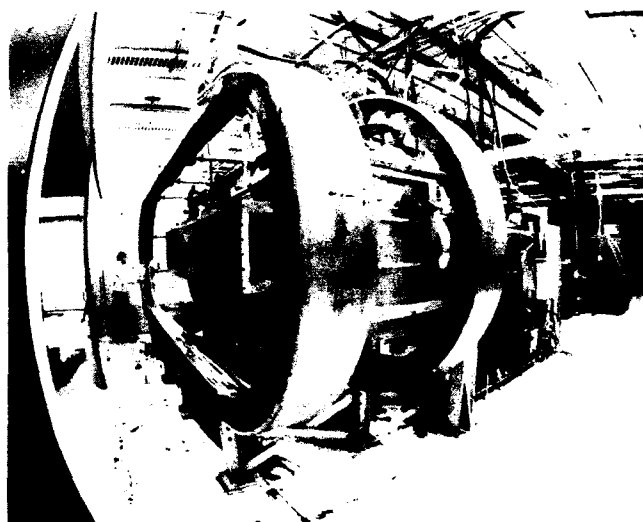


Fig. 6: A photograph showing the assembled Intermediate Amplifier (IA). The laser chamber, diode vacuum box, and the guide magnets are visible in the foreground; the Marx generator and water PFLs are slightly visible in the background.

12-element beam train shown in Figure 9a is incident at the SAM, amplified, and replicated into a 96-element beam train¹¹ shown in Figure 9b. Amplification of this 96-element train is discussed in Section 5 of this paper.

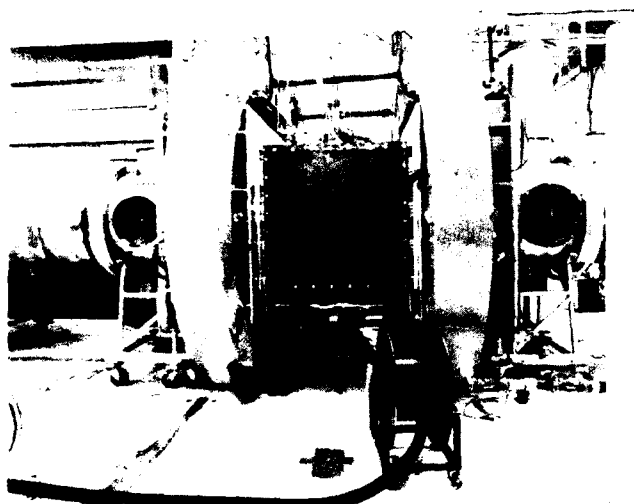
4. Optical System

4a. Multiplexer and Alignment Systems

The Aurora optical system is representative of typical angularly multiplexed systems. It is designed to match the long amplifier electrical excitation pulse time, which is determined by electrical and laser kinetics considerations, to the much shorter pulse times required for efficient



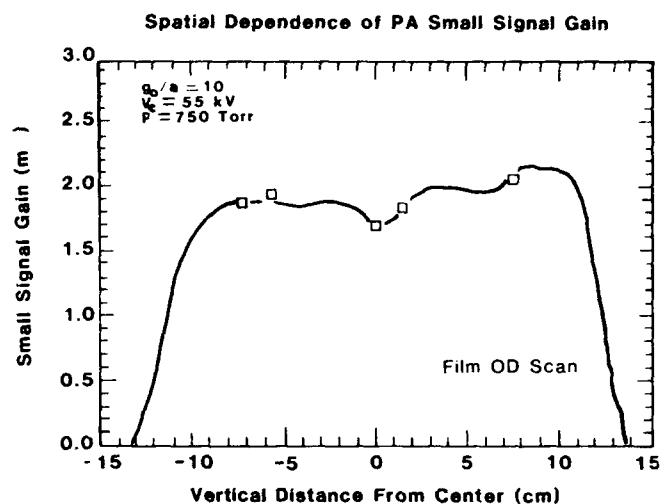
(a)



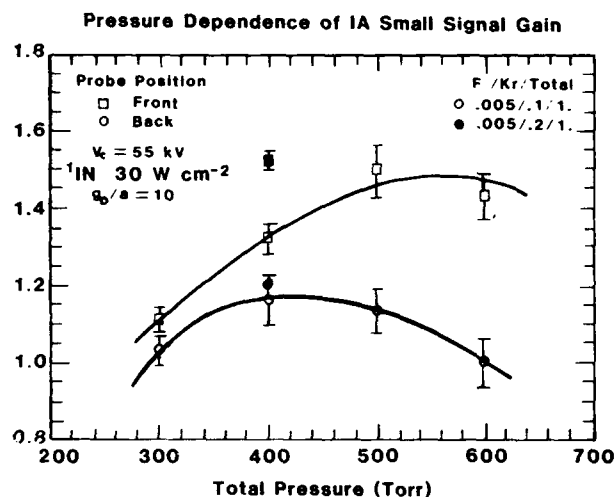
(b)

Fig. 7: Photographs showing (a) the assembly of a set of improved LANL-designed PFLs for the Large Aperture Module (LAM) and (b) the diode box, laser chamber, and guide magnets.

coupling of the laser pulse energy to inertial fusion targets. This system uses angle and time multiplexing to perform this match. Distance is used to provide the necessary time delays needed to time-encode and decode a 96-beam pulse train of 5-ns pulses. The major parts of the system are: (1) an optical encoder that replicates the 5-ns front-end output pulse to produce a 480-ns long pulse train consisting of 96 separate beams placed head-to-tail in time; (2) an angle encoder that spatially separates the beams so that they can be decoded at some later time and also helps to direct the beams through the amplifiers; and (3) a centered optical system that relays the beams through the amplifiers so that the beams expand and fill the active gain volumes; (4) an optical decoder to appropriately delay the earlier pulses in the pulse train



(a)



(b)

Fig. 8: Results of measurements of Aurora mid-chain amplifier gain at low pump rate. (a) Spatial dependence of PA small-signal gain at 80 kW/cm³. (b) Pressure dependence of IA small-signal gain at 40 kW/cm³.

relative to the later pulses so that they all arrive at the target at the same time; (5) a set of final aiming mirrors and focusing lenses that direct the beams onto the target; and (6) three optical alignment systems that control the alignment of the encoder, the final amplifier feed mirror array, and the final aiming mirrors. Figure 2 has shown a conceptual layout of the optics in Aurora. Figure 10 shows the key parts of the assembled multiplexer hardware. Figure 11 shows the automated multiplexer alignment system that can simultaneously align all 96 beams to an accuracy of 3 to 5 μ rad in approximately 3 minutes; two other separate alignment systems will be required for the fully integrated Aurora system.

Table II
Measured Performance of Electron-Beam-Pumped Amplifiers

Device	PA	IA	LAM	LAM
Marx charge (kV)	55	55	45	60
F ₂ (torr)	3.75	2.00	3.00	3.00
Kr (torr)	75	40	60	60
Total gas pressure (torr)	750	400	600	600
Deposited energy (kJ)	10	18	133	173
Volume (liters)	176	597	2000	2000
Specific energy (J/l)	56	29	67	87
Pump rate (kW/cm ³)	80	42	95	144
g ₀ (m ⁻¹), premix	2.06	1.33	2.05	Osc.
g ₀ (m ⁻¹), <i>in situ</i>	1.86	1.16	1.90	Osc.
Extracted energy (kJ)	SSG	SSG	SSG	10.7

Notes:

1. Osc.: oscillator experiments.
2. SSG: small-signal gain experiments.
3. premix: premixed laser gas.
4. *in situ*: laser gas mixed in chamber.

The optical system (multiplexer, demultiplexer, and associated alignment systems) have been described in detail in other publications.^{1-3,12} In this paper, we will deal with recent progress achieved in the assembly of the demultiplexer.¹³ Recently, several years of design, procurement and assembly have culminated in the accomplishment of a major Aurora milestone, namely the installation of all of the demultiplexer hardware, which consists of over 300 optical components ranging in size from several centimeters square to over a meter square. All optics are installed and all optical mount drive motors and motor controllers are installed and operational.

4b. Optical Demultiplexer System

Because the ICF target requires a short pulse of ~5-ns duration, the 480-ns amplifier pulse must be compressed for second-phase Aurora. The synthetic long pulse which feeds the LAM consists of a train of 96 separate 5-ns pulses. The 96 pulses that have been encoded in the multiplexer are then decoded in the demultiplexer to compress the long pulse train into a single high-power pulse. This is accomplished by sending the beams along different flight paths to the target. Initially, for budgetary and programmatic reasons, only 48 of the 96 beams will be decoded and delivered to the target.

Figure 12 is a diagram that illustrates the demultiplexer (decoder) layout. All 96 beams leave the last lens of the relay train (centered optical system), which is near a pupil, at different angles separated by 1.8 mrad. They are directed toward the LAM feed array (Fig. 13a), which is the first position after the centered optical system where the beams can again be individually pointed. The beam

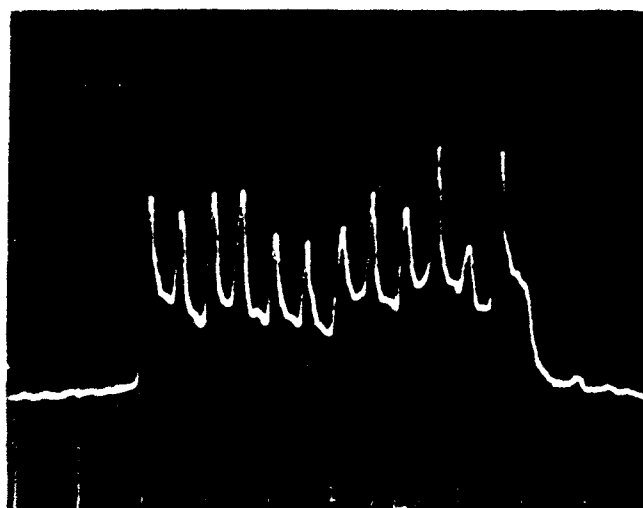
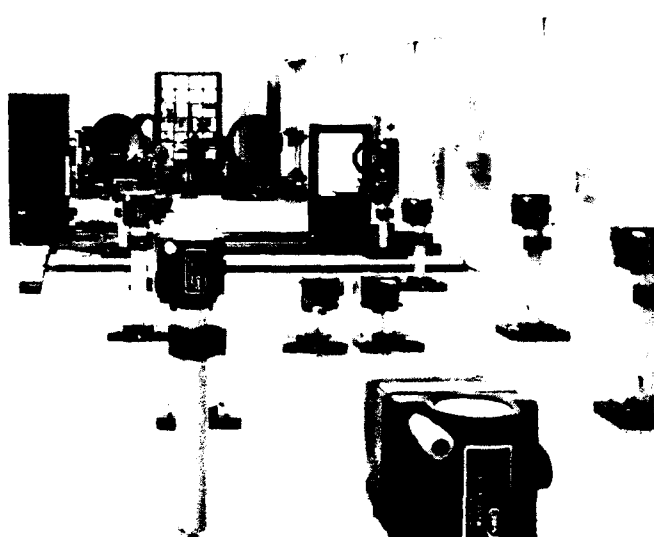
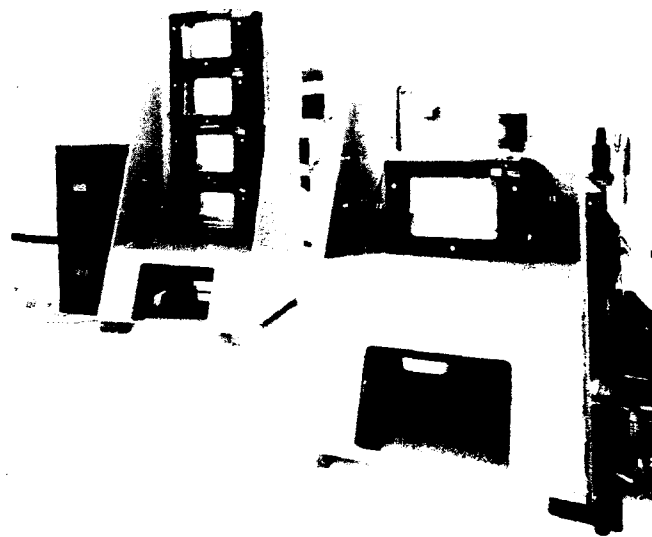


Fig. 9: (a) Twelve-element beam train incident at the SAM. (b) Ninety-six-element beam train incident at the PA.

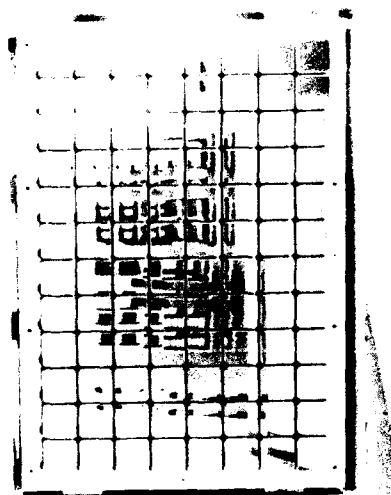
position and spacing on the feed array are determined by the recollimator array spacing and position. Each convex mirror in the feed array is 10-cm square. However, the beams on the array are only 5-cm square. The radius of curvature of the convex mirrors is 5.99 m. Each feed array mirror points at the LAM and expands the 5-cm beam to 1 m to fill the amplifier with light. The concave 107-m radius of curvature LAM mirror causes the beams to converge along the path toward the recollimator array (Fig. 13b) where the beams are again separated. The recollimator mirror spacing is 18 cm center-to-center. At the recollimator array, the beams are 14-cm square. The 17-cm square convex recollimator mirrors have a 35.12-m radius of curvature. They recollimate the beams and direct them toward the 61-cm square fold mirrors shown in Figure 14. A view of the LAM feed array, recollimator array and fold mirrors is shown in Figure 15. The fold mirrors point the beams toward the fine decoder, Figure 16, which takes out the beam-to-beam time delays and direct the beams to the final aiming array shown in



(a)



(b)



(c)

Fig. 10: Ninety-six-beam Aurora multiplexing is accomplished with three systems: (a) 12-fold encoder (aperture division), (b) 8-fold encoder (intensity division), (c) 96-element, computer-controlled angle-multiplexing mirror array.

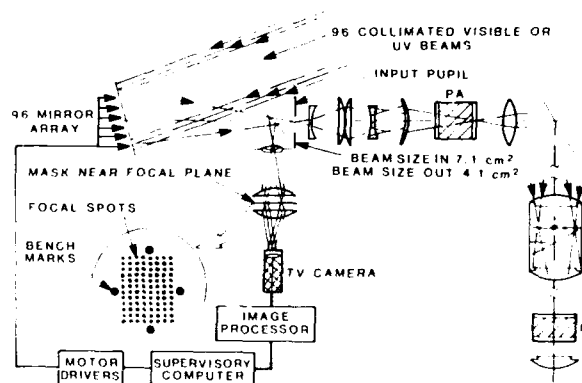


Fig. 11: The input pupil array alignment station feedback loop. A dichroic beamsplitter before the input pupil reflects collinear visible beams to a 96-spot focal plane on a mask with benchmarks. The spots are image-processed and positioned relative to the benchmarks by driving the input pupil array mirrors. From Reference 12.

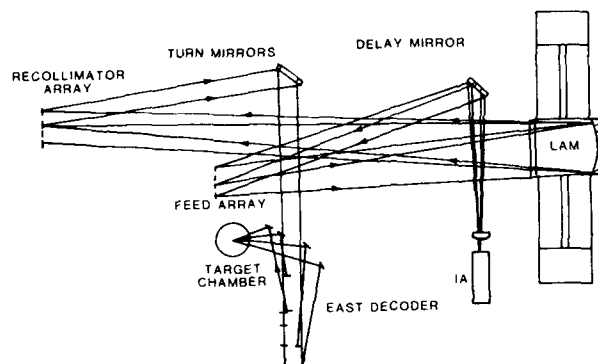


Fig. 12: Present 48-beam demultiplexer layout with one-sided target illumination (not to scale and only a few beams shown). A 240-ns delay is required; a 120-ns delay is hidden in turn and grade change from a separation tunnel in the fine decoder wing.

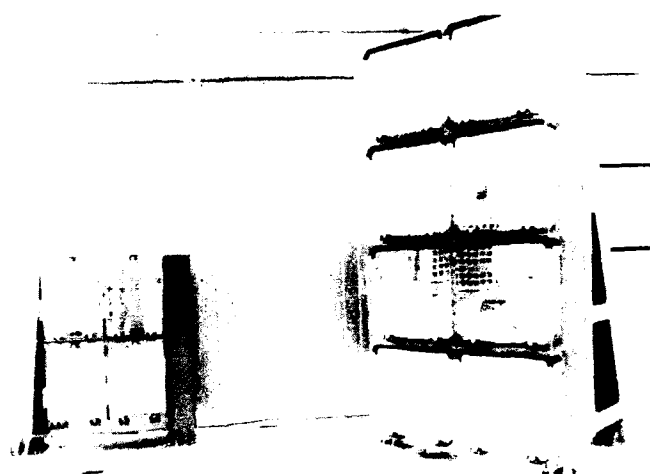
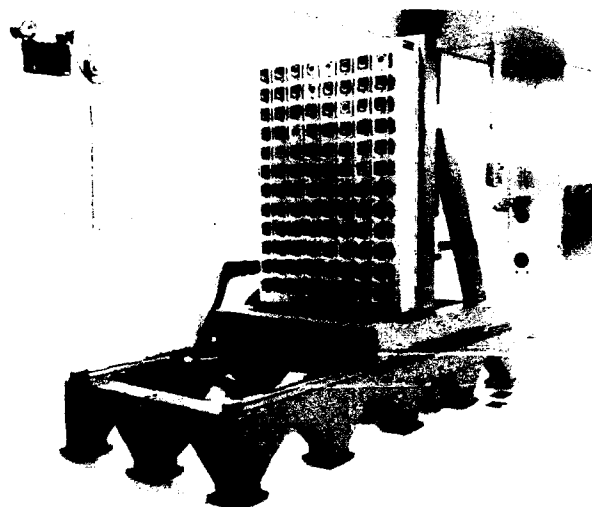
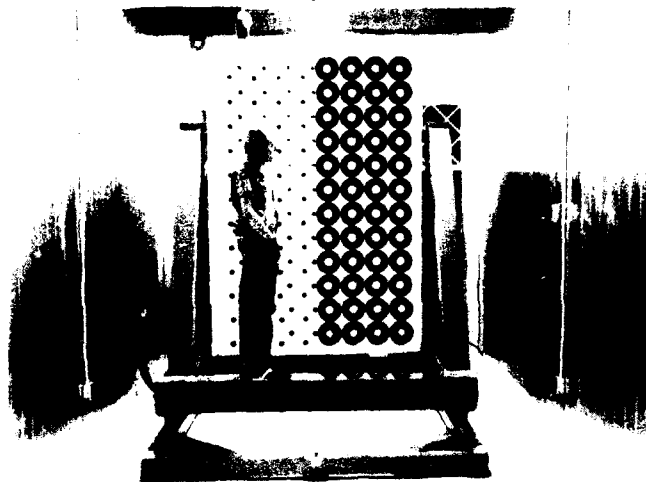


Fig. 14: Fold mirror arrays showing the stands and light-weight mirrors.



(a)



(b)

Fig. 13: (a) Ninety-six-element LAM feed array. (b) Forty-eight-element recollimator array. These arrays are assembled and integrated into the upstream optical system.



Fig. 15: A view down the beam tunnel showing the LAM feed array (left), fold mirrors (right), and recollimator array (far background).

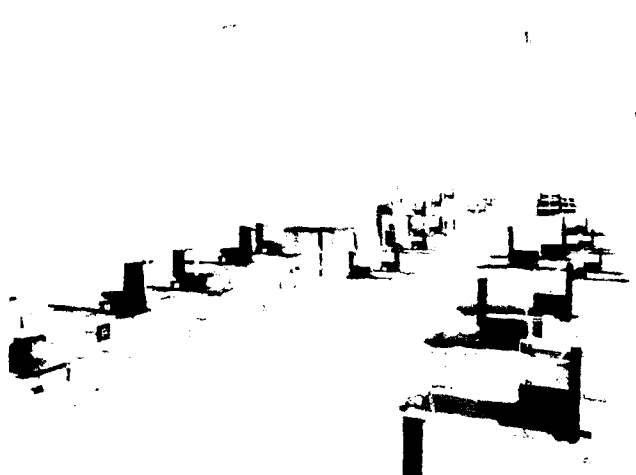


Fig. 16: The fine decoder stands and mirrors; these remove the 5-ns time delays between adjacent beams.

Figure 17. The aiming mirrors point the beams through the target lenses, shown in Figure 18, which focus all the beams onto the target plane (at a best-focus spot size of $200\text{ }\mu\text{m}$).

The fabrication of these components has been progressing for the past few years. The Aurora hardware represents a reasonable assessment of the present off-the-shelf industry capability, quality, and cost for large KrF laser system optical components. Almost all parts were specified to have a surface figure of at least $\lambda/10$ or better at 633 nm . This specification did not appear to drive the cost. For all but the largest parts, we were able to check the parts at LANL to ensure accuracy and quality.

The part-to-part tolerance for the convex LAM feed mirrors, convex recollimator array mirrors, and the target lenses were the most difficult to obtain and verify. The lightweight pyrex mirrors that are shown in Figure 14 proved to be the most cost-effective approach for the larger mirrors in the system. These mirrors now represent a proven technology that can be applied to future systems.

Ongoing work on the optical system is concentrating on the target alignment apparatus and the integration of the optical system to the amplifiers.

5. Recent Progress in System Integration

The most significant system integration milestone achieved during the past year was the extraction of amplified 96-beam energy from the Intermediate Amplifier.



Fig. 17: The final aiming mirror stand and the 48 mirrors that point the beams at the target focusing lenses.

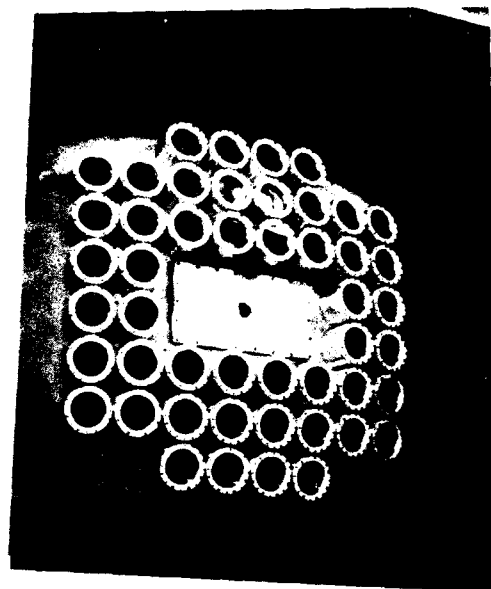


Fig. 18: A view of the lens plate and the 48 target focusing lenses.

For this demonstration, the front end, SAM amplifier, the 12-fold and 8-fold encoders, the Preamplifier, the optical relay train, and the Intermediate Amplifier were operated as an integrated chain. The experimental setup is shown in Figure 19. A 96-element beam train containing 256 J was extracted from the IA output. Although this is not the design value of $\sim 1\text{ kJ}$, it represents a significant step in the integration of the entire Aurora laser system.

At present, we have made some improvements in the SAM gain and are making some improvements in the PA and IA that should allow the extraction of near-design energy from the amplifier chain. We are now preparing another system integration experiment that will demonstrate the integration of virtually all of the Aurora system. In the upcoming experiment, the 96-element beam train from the IA will be delivered to the demultiplexer, where 48 beams will be decoded and delivered to the target plane. A modest amount of delivered energy ($\sim 100\text{ J}$) is planned for this demonstration. After that achievement, the LAM will be added to the system.

6. Remaining Issues

Aurora was built as an experiment to examine many of the technology issues related to high power KrF/ICF lasers. So far, we have demonstrated 96-beam multiplexing and energy extraction, amplifier staging, and precise optical alignment. Several other secondary issues are also in need of examination to optimize the performance of Aurora and to resolve potential problems. These are:

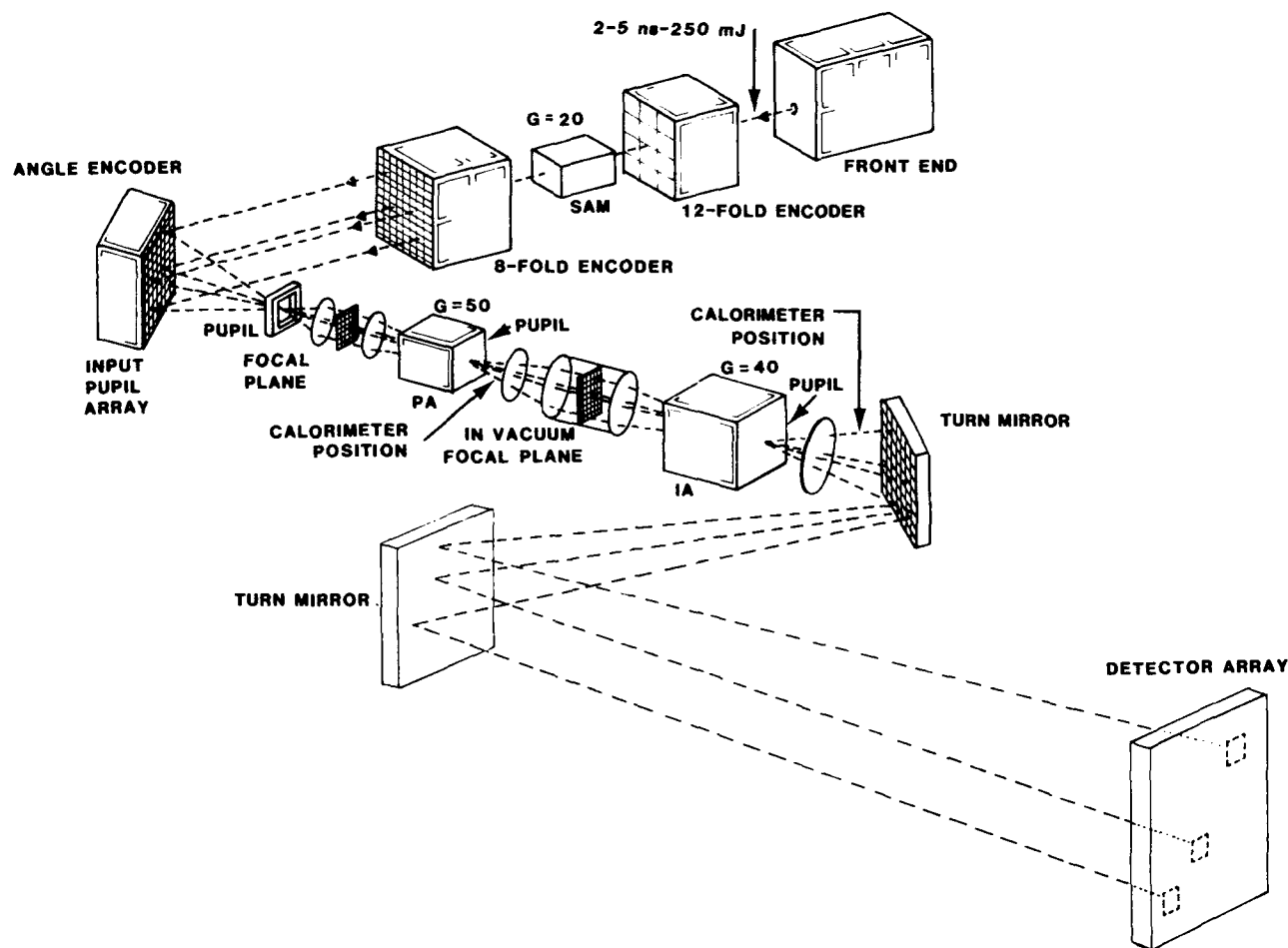


Fig. 19: Ninety-six-beam energy extraction experiments are proceeding through the Aurora amplifier chain. Amplifier chain performance to date: 256 J of 248-nm laser radiation has been extracted from the Intermediate Amplifier, driven by the front end, multiplexer, Small Aperture Module, and Preamplifier.

- Multiplexer/demultiplexer crosstalk and scattering from optical coatings that may contribute to crosstalk;
- Laser- and fluorine-induced damage to optical coatings;
- E-beam pumping uniformity limitations;
- Laser gas chemistry and contaminants;
- Long-path beam propagation;
- Pulse shaping.

These issues are now under examination and will continue to be studied during the next year.

Acknowledgments

The authors would like to express their appreciation to the entire Aurora project team for the many contributions toward progress reported in this paper. In particular, we thank Scott Thomas and Jack Hanlon for writing large parts of the front end and optics sections, respectively. We also thank Ruth Holt for work on the illustrations and photographs and Rebecca Johnson for document preparation.

References

1. L.A. Rosocha, J.A. Hanlon, J. McLeod, M. Kang, B.L. Kortegaard, M.D. Burrows, and P.S. Bowling, "Aurora Multikilojoule KrF Laser System Prototype for Inertial Confinement Fusion", *Fusion Technology*, **11**, 497(1987).
2. J.A. Hanlon and J. McLeod, "The Aurora Laser Optical System," *Fusion Technology*, **11**, 635 (1987).
3. J. McLeod, "Output Optics for Aurora: Beam Separation, Pulse Stacking, and Target Focusing," *Fusion Technology*, **11**, 654 (1987).
4. G.W. York Jr., S.J. Czuchlewski, L.A. Rosocha, and E.T. Salesky, "Performance of the Large Aperture Module of the Aurora Krypton Fluoride Laser System," *Digest of Technical Papers CLEO '85*, p. 188 (1985).
5. S.J. Czuchlewski, G.W. York, L.A. Rosocha, and B.J. Krohn, "A Large-Aperture 10-kJ KrF Laser," unpublished manuscript (1986).

6. R. Kristal, L.S. Blair, M.D. Burrows, D.C. Cartwright, P.D. Goldstone, D.P. Greene, J.A. Hanlon, A. Hauer, M. Kang, B.L. Kortegaard, J. McLeod, W.C. Mead, E.A. Rose, and L.A. Rosocha, "Aurora Status and Plans," Proceedings of the 8th International Workshop on Laser Interaction and Related Plasma Phenomena, Monterey, CA, October, 1987, to be published.
7. S.J. Thomas, K.W. Hosack, L.J. Lopez, I.J. Bigio, and N.A. Kurnit, "Improved Performance of the Aurora Front End with the Use of a Phase-Conjugate Mirror," submitted to CLEO '88 (1987).
8. L.A. Rosocha and K.B. Riepe, "Electron-Beam Sources for Pumping Large Aperture KrF Lasers," Fusion Technology, 11, 576 (1987).
9. A.M. Hunter II and R.O. Hunter Jr., "Bidirectional Amplification with Nonsaturable Absorption and Spontaneous Emission," IEEE J. Quantum Electron., QE-17, 1879 (1981).
10. D.P. Greene, Los Alamos National Laboratory, unpublished results (1987).
11. E.A. Rose, "Generation of Ninety-Six Angularly Multiplexed KrF Beams at Aurora," Proceedings CLEO '87, p. 110 (1987).
12. B.L. Kortegaard, "Pac-Man, A Precision Alignment Control System for Multiple Laser Beams, Self-Adaptive through the Use of Noise," Fusion Technology, 11, 671 (1979).
13. J.A. Hanlon, "Optical System," in L.A. Rosocha, J.A. Hanlon, and S.J. Thomas, "Chemical and Laser Sciences Annual Report, 1987, Aurora Project: Construction and Integration of a Multikilojoule KrF Laser System Prototype for Inertial Confinement Fusion," unpublished LANL report (1987).

REPETITIVELY-PULSED EXCIMER LASERS

V. Yu. Baranov, V. M. Borisov, Yu. Yu. Stepanov, V. P. Novikov,
Yu. B. Kiryukhin, O. B. Khristoforov, A. Yu. Vinokhodov
I. V. Kurchatov Institute of Atomic Energy, Moscow, USSR

Abstract

High repetition rate excimer lasers developed at the Kurchatov Institute of Atomic Energy are discussed.

Introduction

The creation of the first rare-gas halide lasers in 1975 gave birth to new high-efficiency sources of coherent ultraviolet radiation. The intensive development and investigation of these lasers result from the possibility of their wide use in photochemistry, isotope separation, microelectronics, laser purification of substances, laser thermonuclear fusion programs, atmosphere and ocean diagnostics, etc. Such applications are connected mainly with the use of the lasers capable of operating in repetitively-pulsed mode.

The program on repetitively-pulsed excimer lasers has been in progress at I. V. Kurchatov Institute of Atomic Energy since 1980. The simplest, reliable in operation, electric-discharge lasers allowing a high average output power to be attained at a high repetition rate were investigated first of all.

Experiment and Results

The various systems of space-discharge initiation with UV preionization were studied. The results of the investigations showed that the excimer laser energy depends to a large extent on the magnitude of their preionization homogeneity. Primarily this applies to rare-gas fluoride (XeF^* , KrF^*) lasers, the preionization level of which is reduced due to the intensive attachment of electrons to the donors of fluorine - F_2 , NF_3 . The use of the quadrilateral spark preionization in the lasers with metallic electrodes, as well as the use of the dielectric surface discharge as plasma electrodes, and the UV preionization sources placed as close as possible to the main space discharge zone, made it possible to develop the excimer electric-discharge lasers with an energy of 1-2J, an efficiency of 1-2% and a specific energy production of up to 6 J/l (on KrF_2 molecule). It was shown, with the gas mixtures of KrF and XeF lasers taken as an example, that under typical conditions of power input ($W \geq 2 \text{ MW/cm}^3$; $E/N \sim 10^{-16} \text{ V}\cdot\text{cm}^2$) the formation of numerous current filaments with a cross-sectional dimension of $\sim 0.1 \text{ mm}$ in the space-discharge plasma is the most probable reason limiting the duration of excimer molecule radiation ($\leq 100 \text{ ns}$). In the systems with plasma electrodes the increase in the power input as well as in the space discharge duration and aperture was reached due to both the high homogeneity of UV preionization and the principal absence of cathode and anode spots where the discharge current could be localized promoting its own spatial contraction. However, though the high homogeneity of space-discharge plasma is stable and conserved at repetition rates as

high as 10 kHz even without gas blowdown the lifetime of such systems is $< 10^6$ pulses. This results from either the breakdown of the dielectric or the sputtering of electrode materials on it.

In this connection the scheme with metallic electrodes, spark preionization and a thyatron as a commutator was taken to develop the reliable repetitively-pulsed lasers with a large lifetime. The laser electrode systems contained two discharge gaps with a common grounded electrode, the pumping made from two discharge circuits synchronized with an accuracy of 5 ns. This makes it possible to realize the "master oscillator-amplifier" scheme with a single laser.

The investigations have shown that the discharge resistance to the spatial perturbations of the parameter E/N becomes very important in the repetitively-pulsed mode of the laser operation. The accumulation of the acoustic perturbations from the preceding discharge pulses leads to the nonuniformity of power input and limits the growth of the average output power in increasing the repetition rate. It has been found that the discharge in Ne-based gas mixture is more homogeneous than that in He-based mixture at the same, as shown by the measurements, levels of acoustic interference ($(\delta N)/N \sim 1\%$). In contrast to helium-containing mixtures, with Ne as a buffer gas, the reduction of the output power per pulse is small relative to the power produced in a single pulse even at a repetition rate of ~ 500 Hz. The frequency at which the linear growth of average output power terminates equals to 300 Hz and 500 Hz for He- and Ne-based mixtures respectively, the suppression frequency being respectively 1000 Hz and 1200 Hz. The nonuniformity of the local power input $(\delta \epsilon)/\epsilon$ due to the gas density perturbation $\delta N/N$ is characterized by the parameter $\hat{\epsilon} = \partial(\ln \epsilon)/\partial(\ln N)$, $(\Delta \epsilon)/\epsilon = \hat{\epsilon} \cdot (\Delta N)/N$. It has been shown by numerical modelling that the less nonuniformity of the local power input $(\delta \epsilon)/\epsilon$ in the gas mixtures with Ne is connected with the decrease of the parameter $\hat{\epsilon}(\hat{\epsilon}_{Ne}/\hat{\epsilon}_{He} \sim 0.6-0.7$ at $\hat{E}_{He} \sim 40$) due to the weaker dependence of the Xe atom excitation frequency on E/N . The average power as high as 420 W was attained using the gas mixture $HCl:Xe:Ne = 1:10:1200$ (at 4 atm) at a gas flow velocity of ~ 30 m/s and a repetition rate $f = 500$ Hz.

The experiments were carried out to show the effect of the local temperature gradients arising on the electrode surfaces due to the nonuniformity energy input into the discharge on the discharge contraction at high repetition rates. The temperature gradients on the cathode surface were modelled experimentally acting on the cathode by the focused XeCl-laser beam with an energy ϵ_g . For different ϵ_g the minimum delay time τ_d was determined between the action on the electrode and the initiation of space discharge contracting due to the formation of metal vapor on the cathode. Figure 1 gives the dependences of τ_d on ϵ_g for various cathode materials. The open signs above the curves given in Fig. 1 denote the areas of τ_d values at which the discharge was of space nature, the full signs below the curves referring to the contracted discharge. When the energy ϵ_g increases above a certain value ϵ_g^C at which the conditions of developed evaporation on the electrode are realized the minimum delay time required to initiate the space discharge increases drastically up to $10^{-3} - 10^{-2}$ s (Fig. 1). The measurements showed that the metal splash ($10^{-7} - 10^{-5}$ g) from the area of high-current discharge channel localization is of the same order of magnitude as that under conditions of developed evaporation realized in the experiment. Thus, the cathode metal splash ($10^{-7} - 10^{-5}$ g) in the area of high-current channel localization is the sufficient cause of the discharge contraction in the subsequent pulses and the limiting factor of the repetition rate ($10^3 - 10^2$ Hz). It is seen from Fig. 1 that refractory metals are the most suitable cathode materials from the point of view of preventing the discharge contraction in repetitively-pulsed mode. To check this fact the experiments with two similar discharge sections of a repetitively-pulsed excimer laser were performed. The cathode in one of these sections was made of stainless steel and

coated with tantalum foil. The differences in generation on the gas mixture $\text{HCl}:\text{Xe}:\text{He} = 1:10:1000$ at $P = 2$ atm manifested themselves at repetition rates $f > 400$ Hz. In this case the energy production in the section with tantalum electrode was considerably, by 30%, higher and the discharge was characterized by essentially less number of high-current channels.

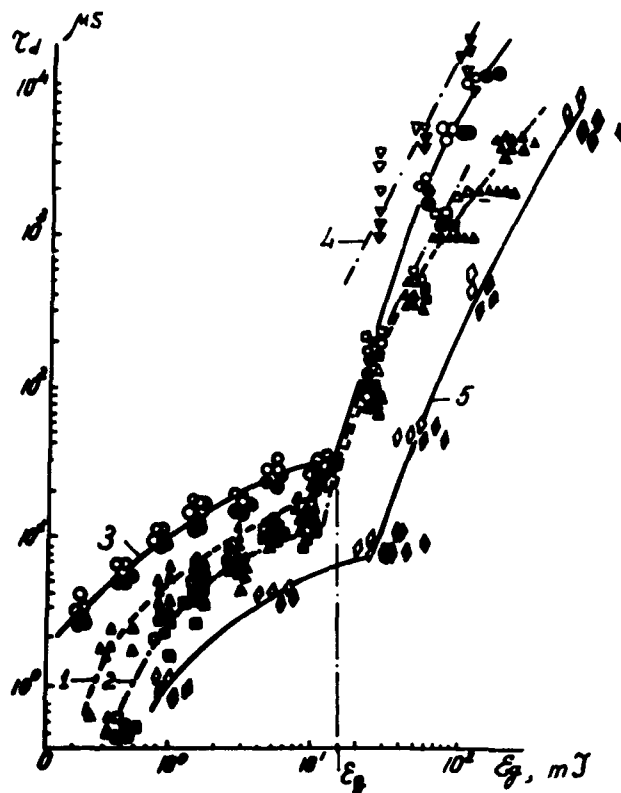


Fig. 1 The maximum delay time of discharge pulse relative to the moment of electrode exposure with the laser pulse causing the discharge contraction in He as a function of the laser pulse energy. Cathode material: 1 - Cu; 2 - Zn; 3 - Fe; 4 - W.

Thus, it was shown that at high repetition rates (> 500 Hz) the space discharge is contracted for two interrelated reasons: (1) due to the local nonuniformities of energy input resulting from the gas density fluctuations caused in turn by acoustic oscillations and (2) due to the presence of the locally-heated areas of the electrode and the metal vapors in their vicinity appearing in the areas of increased energy input from the preceding discharge pulses, which promotes the further enhancement of contraction. The inhomogeneities of refractive index connected with the acoustic field in the resonator are responsible for the observed dependence of radiation divergence on repetition rate at $f > 200$ Hz. As seen from Fig. 2, curve 2, such an influence manifests itself for the laser Ne-based gas mixtures in the direction of the smaller divergence $\theta = 2.5 \cdot 10^{-5}$ rad in the laser beam cross-section $4 \times 1 \text{ cm}^2$ in size. The theoretical analysis of divergence in terms of geometrical optics correlating with the experiment shows that the value of divergence caused by the acoustic waves in the direction transverse to the laser axis is determined in the following way:

$$\theta = \Delta n_0 \cdot \frac{\Delta N}{N} \cdot \frac{4nL}{\lambda} \cdot \text{th} \frac{\pi a}{\lambda} \quad (1)$$

This expression is true for $\Delta x \ll a, \lambda$, where $\Delta x = 2L \sqrt{\Delta n_0 \cdot \Delta N/N}$. Here λ and $\Delta N/N$ are the wavelength and amplitude of the acoustic wave, respectively; L is the length of the inhomogeneity zone; a is the laser beam width; $\Delta n_0 = n - 1$ is the difference of the refractive index of an unperturbed medium from that of vacuum. The theoretical estimates show that the frequency dependence of divergence for the He-containing mixtures is observable at $f \geq 1000$ Hz.

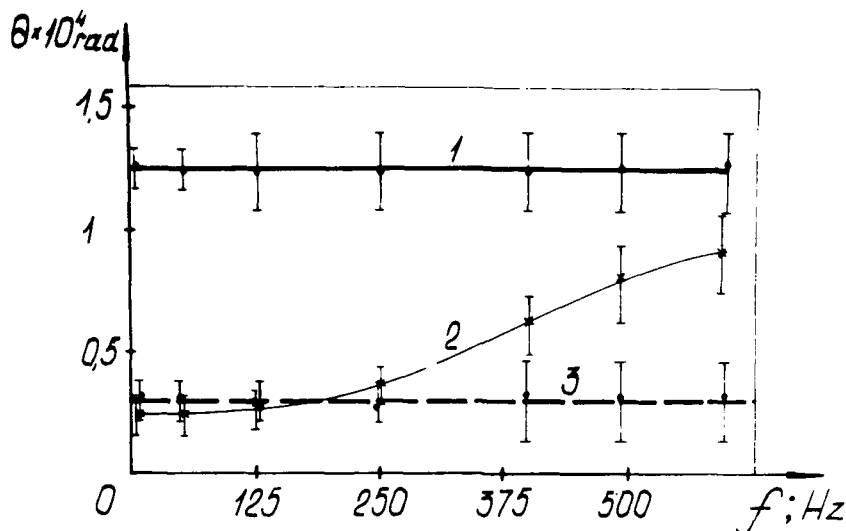


Fig. 2 The experimental dependence of divergence of the XeCl-laser radiation in the directions of minimum and maximum beam dimensions on the repetition rate for the gas mixtures with Ne (1,2) and He (1,3) as a buffer gas.

In the case of a confocal unstable resonator with a magnification $M = 12$ the divergence of radiation was $2.5 \cdot 10^{-5}$ and $1.2 \cdot 10^{-4}$ rad along two mutually perpendicular directions in the laser beam cross-section 4×1 cm² in size. These values are only 2-3 times worse than the diffraction limit. In this case radiation energy amounted to 70-75% of that in the case of the parallel-plate resonator (0.75 J and 0.2 J on Ne and He mixtures respectively).

In the SRS (stimulated Raman scattering)-transformation of the XeCl-laser wide-band radiation in compressed hydrogen ($P = 10$ atm) high energy efficiencies of transformation were attained: 45, 40 and 28% in the first, second and third Stokes components, respectively, with the total quantum efficiency exceeding 80%. It is seen from the dependences presented in Fig. 3 that in repetitively-pulsed mode the efficiency of the SRS-transformation to the second and third components decreases by 50% with the repetition rate growing up to 500 Hz. The obtained dependences are accounted for by decreasing the gain of the higher Stokes components due to heating of the medium in the repetitively-pulsed release of energy.

The lasers developed were used in the works on laser isotope separation, chloroorganic chemistry, study of radiation exposure of material surfaces, and atmospheric sounding.

Figure 4 presents the scheme of a universal mobile lidar on the basis of the developed self-sustained compact XeCl laser. Parameters: a generation energy of 1 J, an average power of 60 W, repetition rate of up to 100 Hz, a divergence along two mutually perpendic-

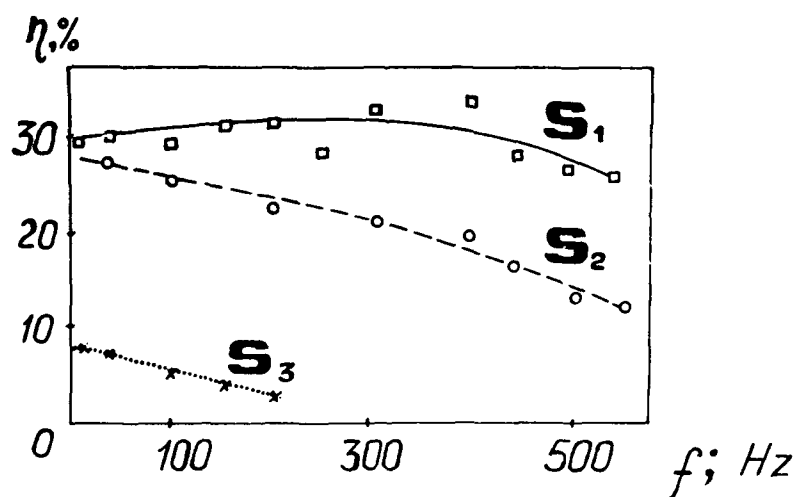


Fig. 3 The energy efficiencies of SRS-transformation of the XeCl-laser radiation in H_2 as a function of repetition rate.

ular directions of $1.2 \cdot 10^{-4}$ - $1.5 \cdot 10^{-5}$ rad, and an efficiency of 1-1.3% (depending on repetition rate). The lidar has two automated recording channels. The first channel receives and records the signal of spontaneous Raman scattering (SRS) and the signal of fluorescence with the aid of a gated spectrum analyzer - a SRS lidar. The second channel is designed for receiving and measuring the Rayleigh + Mie scattering signal on the frequency of excimer laser radiation - a route lidar.

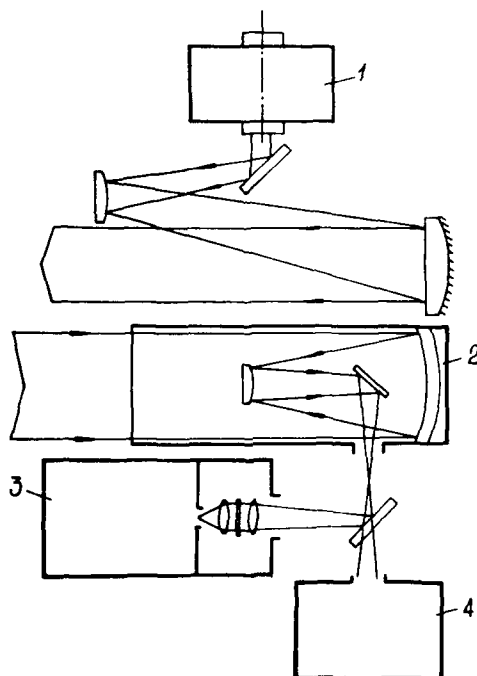


Fig. 4 The scheme of the universal lidar complex on the basis of the repetitively-pulsed excimer laser: 1 - XeCl laser; 2 - telescope; 3 - multichannel spectrum analyzer; 4 - route lidar equipment.

The lidar complex was used in the Chernobyl accident recovery works to monitor the aerosol and gas conditions, to estimate the residual capacity of the heat source under debris. The measurement showed that the aerosol fluctuations and gas composition above the accident unit do not differ from the values specific for the given area.

In the course of works on developing the wide-aperture electric discharge lasers a generation energy of 20 J was obtained in a single-pulse mode on XeCl^* and it was shown a possibility of reaching an energy of ~ 100 J using UV preionization. Figure 5 presents the scheme of the wide-aperture ($7 \times 7 \text{ cm}^2$) discharge module of the repetitively-pulsed XeCl lasers with a generation energy of 10 J/pulse. In our opinion it is not reasonable to increase the generation energy above 100 J in the repetitively-pulsed lasers with self-sustained space-discharge pumping.

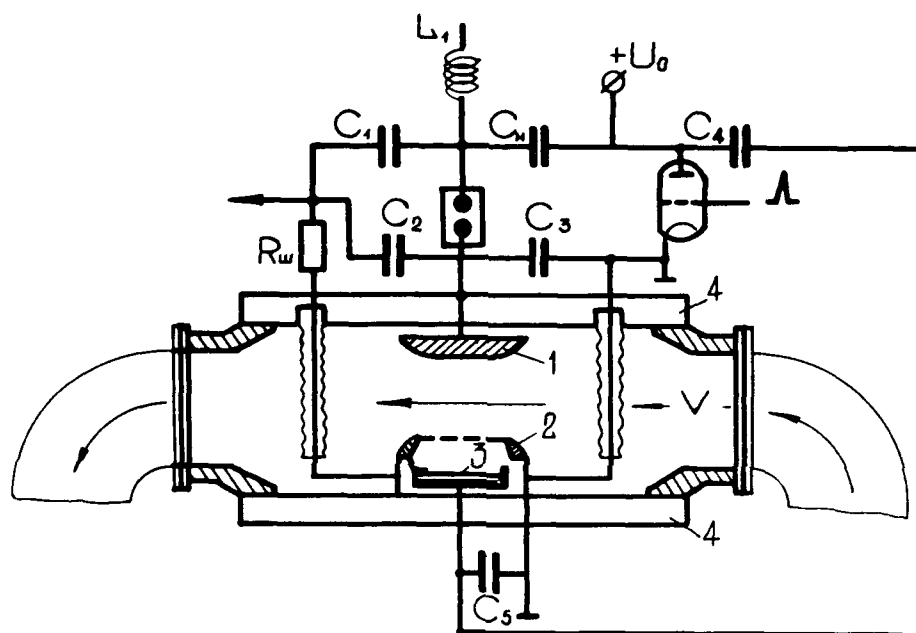


Fig. 5 The scheme of the wide-aperture ($7 \times 7 \text{ cm}^2$) repetitively-pulsed XeCl laser with an output energy of 10 J.

For further increase of energy per pulse and average power, work is in progress to develop repetitively-pulsed lasers with electron-beam pumping.

EXPERIMENTAL AND THEORETICAL INVESTIGATION OF E-BEAM PUMPED Xe-Cl LASERS

B. A. Adamovich, V. Yu. Baranov, A. A. Deryugin, I. V. Kochetov, A. P. Napartovich,
D. D. Malyuta, Yu. B. Smakovskii, and A. P. Strel'tsov
I. V. Kurchatov Institute of Atomic Energy, Moscow, USSR

Abstract

Parametric investigations of energy and spectral characteristics of the XeCl molecule under e-beam excitation are presented.

Introduction

The creation in 1975 of the first lasers on rare gas halogenides¹ has resulted in an emergence of new high-efficiency sources of powerful ultraviolet radiation. Wide promises for utilization of these lasers (medicine, semiconductor materials annealing, optical communication and location, inertial thermonuclear fusion), associated with the spectral range, high efficiency, the possibility of scaling, have given rise to a heavy growth of investigations of excimer lasers energy performances at various ways of excitation. The present-day stage of their development is characterized by widening a range of their applications, on the one hand, and depending the investigations of excimer molecular structure and physical processes in an active medium, determining their characteristics, - on the other hand. At present, the electron beam pumping of active medium provides the highest output energy of laser radiation at a 10% efficiency with respect to an expended energy. This makes it possible to consider excimer laser systems as a possible driver for LTS.

Among the family of rare gas halogenide lasers the most investigated are KrF-base molecular systems.

XeCl lasers along with XeF are the most longwave high-efficient sources of powerful ultraviolet radiation and due to less stringent requirements for radiation strength and optical elements quality, are more promising in experiments asking for high quality radiation brightness. Besides, the possibility of effective transformation of their radiation into a visible region by combination scattering opens a promise for their applications in optical communication and location.

The present paper concerns parametric investigations of energy and spectral characteristics of the XeCl molecule spontaneous and induced emissions at an excitation of an active medium by an electron beam.

The investigation results of the XeCl molecule spontaneous luminescence are presented in the second part, making it possible to determine boundaries of a number of relaxation constants and to establish their connection with a laser transition saturation intensity. Here are also the results of direct measurements of a weak signal amplification factor; and the nature of some absorbing components of visible and ultraviolet regions is discussed.

The third part considers spectral characteristics of spontaneous and laser radiations. The comparison of observed radiation spectra with calculated ones was performed. Physical factors stipulating the generation spectrum width in a dispersionless resonator were deter-

mined.

In the fourth part, the results of parametric investigations of generation specific characteristics are presented and the comparison with calculations according to the complete kinetic model was performed.

Brief Description of Experimental Installation

To excite an active medium use was made of an electron beam with the following parameters: the electron energy $E \sim 350$ keV; the pulse duration $t = 30$ nsec; the beam current density $j = 100-200$ A/cm²; the outlet window cross-section 4.5×26 cm². In investigating luminescence, within the range of pressures of ≥ 1 atm. to prevent against ASE, the excited volume was decreased to the dimension $1 \times 1 \times 1$ cm³. Time characteristics of excimer molecules spontaneous radiation at pressures of 0.1-5 atm were recorded by coaxial photoelements with time resolution of 0.5 nsec. To record luminescence at low pressures (< 0.1 atm) use was made of a preliminary calibrated monochromator - PEM system.

In experiments on measurements of active medium characteristics in the amplification mode to generate sounding pulses use was made of the amplifier's active medium part. An optical delay was selected so that the sounding pulse should get into the amplifier at the moment of attaining the amplification factor maximum.

Relaxation Processes in XeCl Laser Active Medium

An efficiency of energy extraction in excimer lasers is mainly determined by an efficiency of excited molecules formation, an intensity of saturation of laser transition, I_S ; weak signal amplification factor, g_S ; medium absorption coefficient, α . In pumping an active medium by a fast electron beam, the main channel of excimer formation is an ion-ion recombination. In this case, excited molecules are formed in various electron ($B_{1/2}$, $C_{3/2}$, $D_{1/2}$), oscillatory and vibrational states.

The ruin of excimer molecules is due to the spontaneous radiation and quenching in collisions with electrons and gas mixture components. Generation in excimer lasers occurs on the $B_{1/2}-X_{1/2}$ transition. In this case, the particles of lower oscillatory states only (as a rule, levels with $V = 0$) take place in the stimulated emission process. Therefore, the generation efficiency is determined by relation of constants of V-T relaxation, B-C exchange, collisional quenching, and by spontaneous radiation and induced emission times.

Information on relaxation process constants can be obtained from an analysis of spontaneous luminescence time behavior after the pumping switching-off. By selecting appropriately the mixture composition and pressure one can create the conditions when the luminescence intensity drop is determined in the main by a given process.

A series of experiments measuring the XeCl molecule luminescence time drop on transitions B-X, C-A enables us to determine boundaries of some constants (to draw conclusions on relaxation processes):

1. For optimum laser mixtures (1-5 torr HCl (CCl_4)/50-200 torr Xe/1-3 atm Ar) the effective quenching constant does not exceed 2×10^{-12} cm³sec⁻¹.

2. The effective relaxation constant ($K_{V-T} + K_{OC}$) in collisions CCl_4 amounts to $(5 \pm 1) 10^{-10} \text{ cm}^3 \text{ sec}^{-1}$.
3. The quenching constant in collisions with Xe is $< 5 \times 10^{-12} \text{ cm}^3 \text{ sec}^{-1}$.
4. The XeCl formation rate constant in terms of the halogen-carrier concentration is $\sim 1 \times 10^{-9} \text{ cm}^3 \text{ sec}^{-1}$.
5. The radiation lifetime of lower oscillatory levels for C-state is $\sim 100 \text{ nsec}$.
6. The XeCl laser saturation intensity at pressures of 2-3 atm is mainly determined by the B-C exchange rate.

To determine the value g_0 , the weak signal amplification factor measurements were conducted. The obtained values of g_0 and y_s are presented in Fig. 1. The assessment of weak signal amplification factor/absorption coefficient ratio has shown that under experimental conditions $g_0/a \sim 10-20$. Besides, the I_s dependence on pressure at an extrapolation at the point $P = 0$ gives the laser level radiation lifetime value (B-state, $V = 0$) $\tau = 11 \pm 3 \text{ nsec}$, coinciding with Refs. 2 and 3. In determining τ from the ratio $y_s = h\nu/\sigma\tau$ use was made of the value $\sigma = 4 \times 10^{-16}$ (Ref. 4).

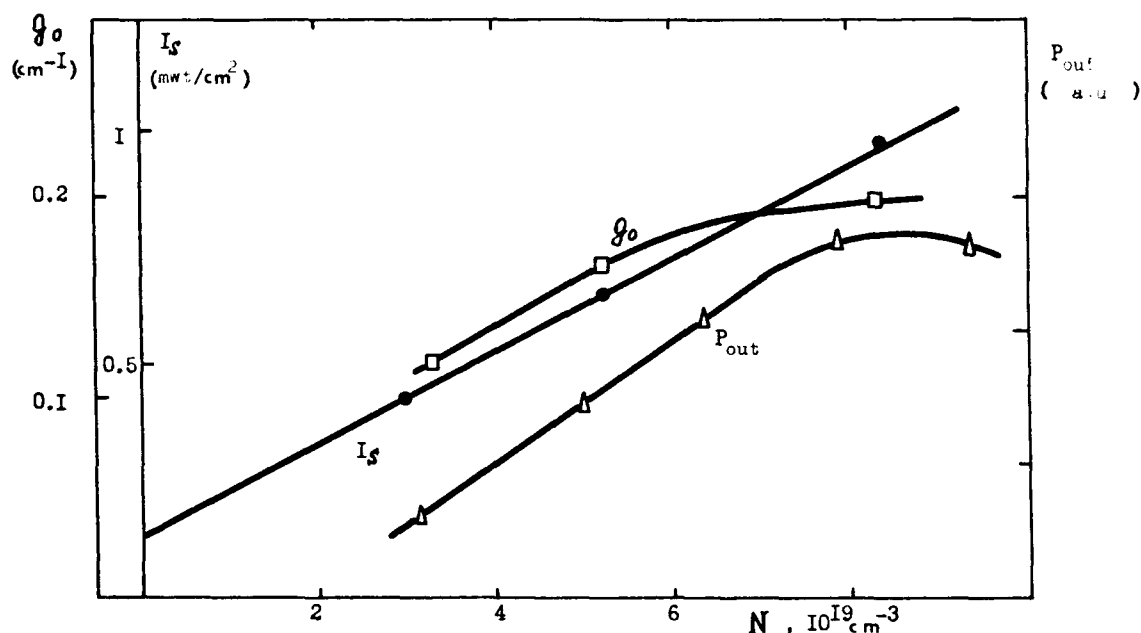


Fig. 1 Saturation intensity- I_s , small-signal gain- g_0 , and laser energy- P , as a function of pressure for $\text{Ar/Xe/CCl}_4 = 1500/15/1$ mixture.

The factor limiting the laser or amplifier output intensity is the nonsaturated absorption coefficient. The main contribution to absorption in XeCl lasers is believed to be made by rare gas positive ions and chlorine negative ions. In addition to a wide-band absorption of ions in the absorption spectrum observable are narrow-band absorption lines stipulated by transitions between rare gas excited atom states. In investigating absorption spectra in the visible and near ultraviolet region (500-350 nm), we have found that at mixture pressures of 1 atm the atomic absorption is transformed into the molecular absorption of rare gas excited dimers. An evolution of lines $\text{Xe}^* 6S[1\ 1/2]_2 - 7P[1\ 1/2]_2$ on krypton pressure is presented in Fig. 2 as an example. The given figure illustrates the increase with pressure of KrXe^* heteronuclear dimer molecular absorption portion. It was found that the red breadth of rare gas atomic absorption lines and the appearance of wide ($\Delta\lambda \sim 20\ \text{\AA}$) diffusion absorption bands shifted in the short-wave region are explained by transitions between various states of rare gas homo- or heteronuclear dimers. Note, that the photoionization of excited dimers by radiation with $\lambda < 340\ \text{nm}$ can make an essential contribution to so-called "background" ($\Delta\lambda \sim 100\ \text{\AA}$) absorption observed during the pumping pulse.⁵⁻⁷

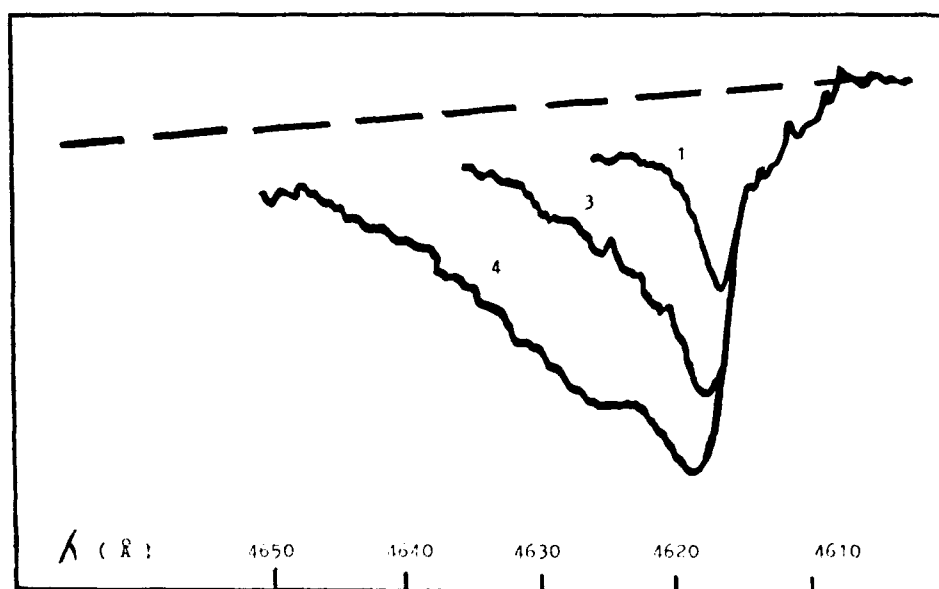


Fig. 2 Emission spectrum of Kr/Xe/NF_3 mixture near absorption transition $6S[1\ 1/2]_2 - 7P[1\ 1/2]_2$ of Xe^* . Kr pressures (atm) are indicated by numerical symbols. The pressures of the Xe and NF_3 are 60 torr and 6 torr.

Spectra of Spontaneous and Induced Emission of XeCl Molecule

The XeCl excimer molecule is characterized by the weakly-combined X-state ($D_e = 280\ \text{cm}^{-1}$), strongly distinguished rotational constants for upper and lower states as well as by the low value of X-state oscillatory quantum ($\omega_e \approx 26\ \text{cm}^{-1}$).⁸ This results in a complicated shape of radiation spectrum as consequence of which the refractive index dispersion in the amplification factor maximum can be different from zero as in the case of the XeF molecule.⁹ Then, under inhomogeneous pumping (along the cross-section) a deterioration of the laser ray divergence is possible.

Experimental investigations of spontaneous radiation spectra were carried out within the wave-length range of $300 \leq \lambda \leq 311\ \text{nm}$ under pressures of 15 torr - 4 atm and calculations of amplification and dispersion factors were performed making it possible to eluci-

date characteristic features of the B-X transition and to assess the XeCl laser divergence stipulated by the resonance dispersion.¹⁰

It was found that with the decrease in mixture pressure the effective temperature rises, characterizing the oscillatory and vibrational distribution of particles in the excited B-state. Luminescence spectra at low pressures (≤ 0.1 atm) bear out that the formation of XeCl^* molecules at the E-beam pumping takes place in high-excited states. The calculated model describing correctly the observed spectra was worked out. The calculation of active medium dispersion, carried out within the framework of the model shows the possibility of divergence deterioration due to an anomalous dispersion. For instance, on the transition $V = 0 \rightarrow V = 2$ at the active medium length of 1 m and the condition of maximum inhomogeneity of excitation along the cross-section ($g_0 = 0$ on its edge) the light beam intensity on the axis in the remote range can decrease approximately by 20%.

Based on experimental data and amplification spectral contour calculations the assessments of excited radiation cross-section value, σ , were performed on the frequency corresponding to the amplification factor maximum. The range of σ values amounted to $(4-5) \times 10^{-16} \text{ cm}^2$, which agrees with calculation results.

To predict the XeCl laser generation spectral width analytical expressions were obtained, establishing the connection of active medium characteristics (weak signal amplification factor, rotational relaxation time, lower level dissociation time, amplification contour spectral width) with resonator parameters.¹¹ It was shown that at high intra-resonator intensities ($\geq 10^7 \text{ W/cm}^2$) the generation spectrum width is determined by the amplification contour deformation near the maximum due to a weak saturation of rotational exchange rate. Besides, a heating of medium during the pumping pulse can lead to displacement in the amplification factor maximum because of the change in molecules distribution function over rotational sublevels. This also results in the increase of spectrum "width" at a time-integrated recording.

Specific Energy Characteristics of E-beam Pumped XeCl Laser

In experiments on specific generation energy measurements the laser aperture was limited by diaphragms of $d = 8 \text{ mm}$. The resonator optical axis, formed by a plane Al mirror and a quartz plate, was at 1.5 cm from the accelerator output foil. The fast electron beam current density was measured at the same distance from the foil. Apart from the generation energy, under analogous conditions for a current density, pressure and mixture composition, the measurements of XeCl molecule spontaneous luminescence intensity were carried out on the B - X transition. In this case the excited volume was reduced to dimensions of $1 \times 1 \times 1 \text{ cm}^3$.

A series of experiments on generation energy measurements from a buffer gas pressure at various HCl contents is shown in Fig. 3. Besides, luminescence dependences on the B - X transition are given in the same figure. The common feature at the content of $\text{HCl} \geq 3$ torr is the luminescence intensity saturation beginning from pressures of Ar 2.2 atm on retention of the linear growth of generation. The similar behavior of the luminescence and the weak signal amplification factor was observed also in mixtures with halogen-carrier CCl_4 (see Fig. 1). The amplification factor saturation with the growth of Ar pressure can be related to the increase in XeCl^* quenching in three-body collisions:

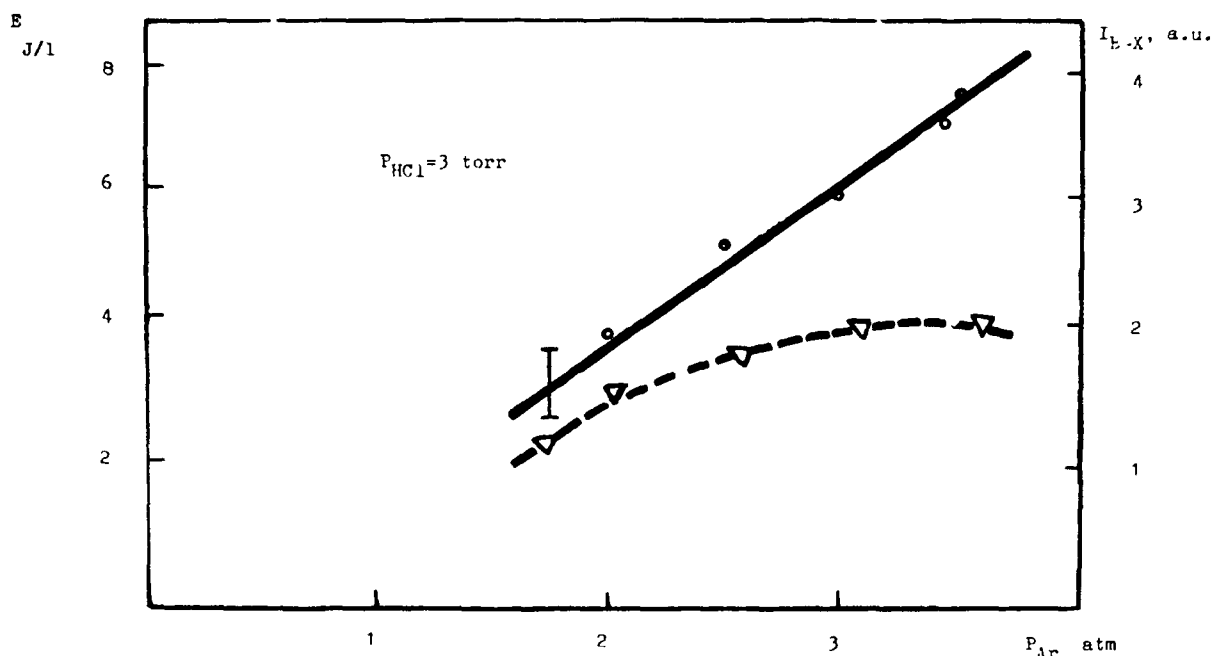
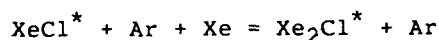


Fig. 3 The A: pressure depends on specific energy output - ●, and fluorescence intensity on B-X transition -Δ. The Xe pressure is kept at 60 torr.



Besides, the Ar pressure increase on retention of the constant concentration leads to the growth of secondary electrons concentration and, correspondingly, to the growth of quenching portion by electrons. The retention of generation energy linear growth at the weak signal amplification factor saturation is accounted for by the fact that the lifetime of excited molecules due to an induced emission remains less than due to quenching collisions.

As is seen from Fig. 3 the specific energy output amounted to 8.7 J/l at $P = 3.5$ atm. In determining efficiency with respect to the input energy to estimate the specific power of contribution use is usually made of an empirical formula of the shape:⁴

$$P = Kj \sum_i B_i [M_i]$$

where B_i is the specific power of the i -th mixture component depending on fast electrons energy M_i is the i -th component concentration; j is the beam current density; K is the numerical coefficient (usually 2-3) of fast electrons in the foil and gas, taking into account scattering. The assessment of power input according to the empirical formula with the use of beam current density measurements permits a certain arbitrary rule because of uncertainty in the correction factor K . Therefore, calibration measurements are necessary on concrete installations. We have measured the specific power input in terms of pressure drop in the excited volume. To provide homogeneity of the power input the laser chamber was poured with paraffin except the channel of $1 \times 1 \times 25 \text{ cm}^3$ close-fitting to the accelerator input foil. The measurements have indicated that in our conditions the correction factor $K = 2.9$. Thus, the XeCl laser generation efficiency at $P = 3.5$ atm and $j = 140 \text{ A/cm}^2$ amounted to 7%.

To compare with experimental results and to make more precise the XeCl laser model, calculations of the kinetic model taking into account ≥ 50 elementary processes were conducted. The main differences of the given model from that used in the paper⁴ are the following:

1. The collisional exchange between B and C states in combination with V - T relaxation was included at the upper laser level.

2. The cascade excitation of HCl molecule oscillatory states ($V = 1, 2$) was included additionally



3. The substitution reaction was included in the model:



4. The process being reverse to the XeCl molecule collisional decay in the ground state, i.e., the recombination process of Xe and Cl atoms, was included

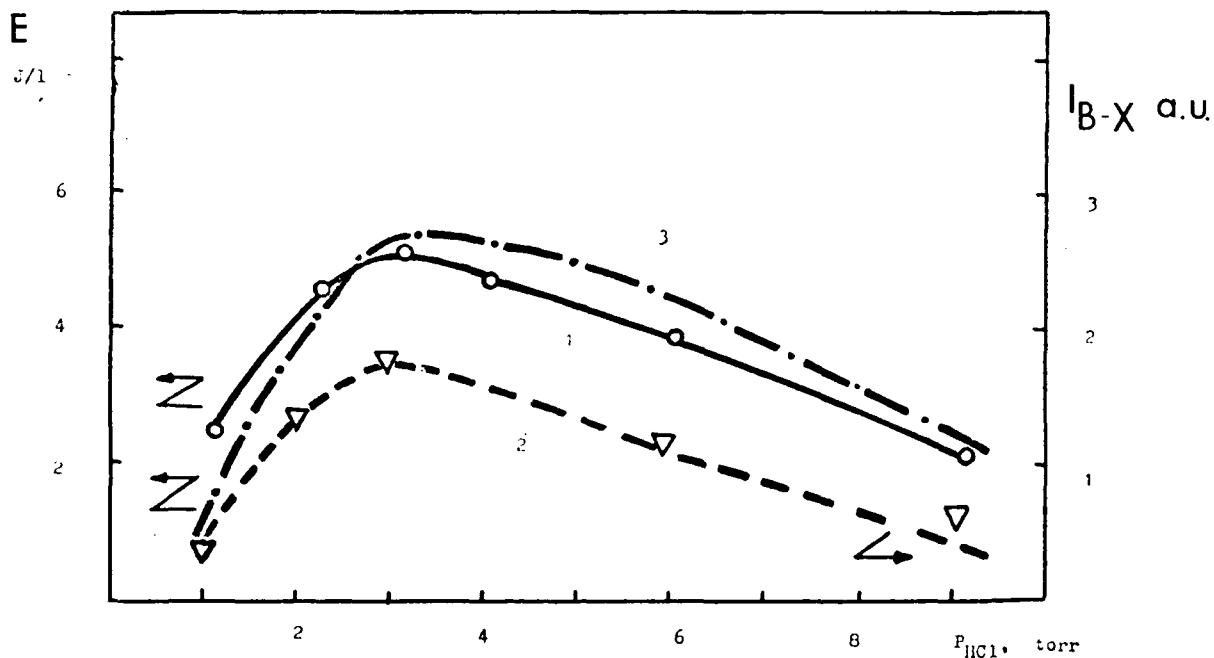


Fig. 4 Comparison of the specific output energy (1), and fluorescence intensity (2) with calculated result (3) as a function of the HCl pressure. The Ar and Xe pressures are 2 atm and 60 torr.

Figure 4 shows experimental values for generation and luminescence energies depending on HCl content at $P = 2$ atm. Here, the calculated dependence $E_{\text{gen}} = f(\text{HCl})$ is given. The amplification factor calculated dependence has a similar form. The absolute value at an HCl optimum concentration at $P = 2$ atm came up to 0.17 cm^{-1} , which agrees with the measured value (see Fig. 1). On the whole, the comparison of experimental results with calculations has found a good agreement and has demonstrated acceptability of the kinetic model to predict energy characteristics of e-beam pumped XeCl laser.

References

1. I. J. Ewing and C. A. Brau, Appl. Phys. Lett. 27, 350 (1975).
2. P. J. Hay and Th. H. Dunning, J. Chem. Phys. 69, 2209 (1978).
3. G. Jnoue, J. R. Ky, and D. W. Setser, J. Chem. Phys. 80, 6006 (1984).
4. F. Kannari, A. Suda, N. Obara, and T. Fujioka, IEEE J. Quant. Electr. QE-19, 1587 (1983).
5. E. Zamir, D. L. Huestis, H. H. Nakano, R. H. Hill, and D. C. Lorents, IEEE J. Quant. Electr., QE-15, 281 (1979).
6. F. Collier, J. B. Leblond, F. Hoffbeck, and P. Cottin, J. Chem. Phys. 74, 4372 (1981).
7. A. W. McCown, M. N. Ediger, and J. G. Eden, Phys. Rev. A. 29, 2611 (1984).
8. A. Sur, A. K. Hui, and J. Tellinghuisen, J. Mol. Spectr., 74, 465 (1979).
9. W. W. Chow and M. O. Scully, Optics Lett. 7, 316 (1982).
10. V. A. Adamovich, V. Yu. Baranov, A. A. Deryugin, I. V. Kochetov, D. D. Malyuta, A. P. Napartovich, Yu. B. Smakovskii, and A. P. Strel'tsov., Kvantovaya Electronica (Sov.) 14, 80 (1987).
11. V. A. Adamovich, V. Yu. Baranov, V. V. Likhanskii, D. D. Malyuta, A. P. Strel'tsov, and A. P. Napartovich, Kvantovaya Electronica (Sov.), 13, 2216 (1986).

HIGH POWER HYDROGEN FLUORIDE CHEMICAL LASERS;
POWER SCALING AND BEAM QUALITY

Dr. Joseph Miller
Manager, Research and Technology Operations
TRW Space & Defense Sector
Space & Technology Group
One Space Park
Redondo Beach, CA 90278

Abstract

A substantial understanding of the hydrogen fluoride laser has resulted from 17 years of research and technology development. Particularly significant experiments have been conducted under the SDI in the past year and a half, and others are imminent, addressing the limitations on power scaling with the retention of high quality beam characteristics. It is clear from this body of work that the physics of these lasers allow configurations of high power. Furthermore, recent developments establish the applications of stimulated Brillouin scattering phase conjugation techniques to HF lasers. This allows systems of even higher powers and larger projecting optics, along with reductions in requirements on laser optical quality, mirror figures, alignments and stabilization systems. Attendant reductions in engineering risks and costs result. This paper briefly reviews the basic physical processes of HF lasers, the approaches to and limitations on power scaling, and the recent results and potential applications of phase conjugation techniques to these lasers.

I. Introduction

High power hydrogen fluoride (HF) chemical lasers have been the subject of research in the United States of America for 17 years. This period has seen a methodical march to higher powers together with an increased understanding of the limitations on power scaling and beam quality.¹ The availability of high power devices has also allowed development of the technology of associated target acquisition and beam projection systems, and understanding of the effects of the high power beams on targets of interest. In recent years the more substantial work on these lasers and associated technologies has been sponsored by the Strategic Defense Initiative Office in context with the requirements for space-based boost-phase ballistic missile defense (BMD).

Recently, significant technical achievements have occurred that establish the basis for very high power, high brightness HF laser systems. Near-term, high-performance lasers in the range of megawatts, and projecting optics on the order of meters in diameter appear perfectly reasonable. At the same time, advanced technology work has established the physical feasibility of larger powers still, and high quality beams projected from optics even larger. These advanced technologies may allow the systems to be built to tolerances at mechanical rather than optical dimensional scales. Obviously this has important implications in behalf of desirable physical, engineering and cost characteristics of far term, directed energy BMD.

These remarkable conclusions are drawn from work that has been accomplished on a number of programs involving large laser devices, large projecting optics and technology development for laser beam stabilization, aberration control, pointing and tracking for space-based systems. Techniques have been demonstrated for coherently combining laser cavities to achieve very high powers, and coherently combining optical trains and elements to achieve very large projecting optics. Other programs have demonstrated the ability to build laser devices and associated optical systems to loose tolerances and then use adaptive optics techniques to sense and correct for the imperfections, and thus deliver nearly diffraction-limited beams. The techniques for synthesizing laser cavities and optics, and correcting optical imperfections, have involved technologies for wavefront sensors, deformable mirrors, and high frequency closed-loop stabilization systems. More recently, nonlinear optics phenomena have been explored; they do the same things but eliminate much of the hardware required for these functions--leading to significant engineering simplifications and cost reductions. This paper will highlight the results of some of these investigations and show how they relate to and support the projection to near-term and far-term capabilities.

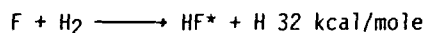
In recent public information releases and reports, the American Physical Society has commented on chemical lasers as candidates for BMD weapons that need from one to several orders of magnitude advance in power scale from currently announced kW levels.^{2,3} The statements would lead one to believe that the required advancements will be difficult. The report was published in the summer of 1987. It is derived from reviews held in mid-1986, on work essentially conducted up through 1985. This is a fast moving field. Inconsistencies exist between APS press releases, APS council statements, and the report itself; these are, in part, a reflection of the rapid advances that were occurring as the review and report writing were underway. More significantly, work accomplished since the reviews clearly establishes a different basis from which to consider the ease or difficulty of application to BMD.

This paper presents first the basic principles of operation of continuous-wave hydrogen fluoride (HF) lasers, and the resulting approaches to power scaling. The technology inherently allows the production, extraction into a laser beam and waste removal of enormous amounts of energy; these don't really limit power scaling. The limitations for useful systems come with the requirement to maintain high optical quality at high power, i.e., beam quality effects eventually limit the scale of individual devices. Two forms of devices

are described. The linear device is so-called because the chemicals that provide the source energy are injected as flowing medium from a linear plane array. Increases in the height, length and flow injection characteristics provide for the scaling within this concept. The successful history, achievement of high power and limitations within this concept are discussed. Next we describe the cylindrical laser; here the cavity injection is accomplished from a cylindrical assembly that provides a radially outward flow, thus an annulus of gain medium. This concept allows yet higher power scales, has other attributes favorable for space applications, and is the subject of a major program currently underway. Finally we discuss the techniques by which either of the basic approaches can be used as building blocks for coherent combination into very high power devices. In this regard, we report particularly on recent results using stimulated Brillouin scattering (SBS) phase conjugation in HF lasers. These results establish the physical basis for very high power, very high brightness systems, simultaneous with relaxations in requirements by factors of hundreds and thousands on component and subassembly optical quality, mirror figure, alignments and stabilizations.

II. Basic Principles of Operation of HF Lasers

Elementary descriptions of continuous-wave hydrogen fluoride lasers have been presented in several places.⁴⁻⁷ We present here a brief summary to provide context for subsequent discussions of scaling limitations. High power continuous-wave HF lasers use the chemistry



This reaction has the property that the energy release is found in the first through third excited vibrational states, not in the ground state--an inherent, nascent population inversion from which to accomplish stimulated emission. To establish this reaction in a laser optical cavity, two stages of combustion are used as shown in Figure 1. The first dissociates a fluorine compound to make F; the second injects and mixes H₂ in the laser optical cavity.

This second combustion stage occurs in the midst of a mixing, supersonic flow field. Figure 2 shows typical flow conditions for an efficient laser. As the mixing, reacting flow field progresses, new excited state molecules are born; the low pressure, cold temperature and continued flow expansion mitigates the depopulation, heating and pressure rise that ensue. The result is a modest temperature and pressure rise through the cavity as the excited states are depopulated by collisional deactivation, in competition with stimulated emission. First growth and then decay of excited vibrational-rotational states occur along the flow direction. Interestingly enough the bulk of the cavity may not contain a total vibrational state population inversion but still allow stimulated emission from a "partial" inversion. Figure 3 shows this situation, where population inversion exists only for P-branch transitions, in which the rotational state quantum number increases as the vibrational state quantum number drops ($\Delta v = -1$, $\Delta j = +1$). The lower the rotational temperature, the higher the gain for these partial inversions. It is these partial inversion P-branch transitions that are most commonly found in the multiline output of CW/HF chemical lasers (Figure 4). The use of the hydrogen isotope deuterium produces, by the same processes but a different vibrational-rotational state structure, a different laser spectral output in the range 3.6-4.1 μ .

Much of the attention of researchers has been directed toward producing a mixing, reacting supersonic flow environment to provide scalable high-power density, high-efficiency, optically clean lasers. Unfortunately, from an engineering point of view, these represent a conflicting set of requirements. Figure 5 is a view of the flow in a supersonic HF chemical laser. In this laser, slit nozzles alternately inject F and H₂ bearing flows. At the cavity entrance, the dark streams are the unreacted core flows. The triangular bright regions, which increase in transverse dimension along the flow direction, are the zones in which mixing, reaction, and excited HF production take place. Eventually, due to their increasing transverse dimension, these zones coalesce. (The radiation observed in the figure originates from excited HF molecule overtone emissions occurring along with the fundamental, but at visible wavelengths.)

To understand this complex situation, we have to look very closely at the processes occurring near the nozzle exits. Figure 6 is a representation of what occurs here for three different conditions. Here we see a combination of fluid mechanics, chemistry and optical physics phenomena. The nozzles have boundary layer viscous flows and supersonic core flows. Base regions of the nozzle can provide for continued expansion and cooling of the flow, but they set up recirculation zones that may entrain depopulated species downstream and transport them upstream to the detriment of the optical gain. The nozzle boundary layer viscous flows persist in the cavity and become wakes. As the supersonic flows enter the cavity, mix with adjacent flows, and encounter the chemical energy release, supersonic shocks occur which are another source of local optical path differences potentially detrimental to beam quality. To design a high-power laser, one has to understand this flow field, the growth and decay of each vibrational-rotational state population, and the optical disturbance features.

High efficiency requires good utilization of available reactants and a high rate of production of the excited states species (rapid mixing and chemical reaction), a high rate of stimulated emission (high optical-field strength), a low rate of deactivation (low temperature, low pressure), and rapid removal of depopulated species (high flow-field velocity). These tend to create conflicting requirements. Rapid mixing and chemical reaction argue for a fine mixing scale; however, small nozzles fill with boundary layer which gives higher temperature, higher pressure, and lower Mach number. If one tries to promote rapid mixing with boundary layer trip flows or transverse injections, the resulting shocks create temperature and pressure increases, and optical path disturbances.

The trend through the 1970's was to finer and finer nozzle scales, mixing promotion, and the heavy use of diluent gas heat capacity. Wilson⁷ reports slit nozzle structures with nozzle throats on the order of 0.1 mm, nozzle exits varying from 1.0 to 2.0 mm, and boundary layer trip injection holes along the exit edges of the nozzle blades. In addition, intricate blade internal passages and feed hole configurations exist if one attempts to provide blade regenerative cooling through the use of the source reactants. However, these fine-scale mixing laser configurations provide high density flows and allow large-scale HF and DF lasers with good pressure recovery (lower exhaust pumping requirements). Nozzles of this character are used in the Mid-Infrared Advanced Chemical Laser (MIRACL), currently located at the National High Energy Laser Systems Test Facility at the White Sands Missile Range. In this laser, the design objectives of high power, high power density, and high pressure recovery have compromised efficiency and, somewhat, optical quality. The gain path length is several meters. The optics form a simple confocal unstable resonator, as shown in Figure 1. The optical axis and the collimated output are aligned perpendicular to the flow direction and parallel to the face of the nozzle array. In MIRACL, the small local flow wakes, created by the regenerative cooling structures integral to the small blades, are designed not to be aligned along the output pass. If they were, their effects would reinforce and affect the output beam quality. By tilting the nozzle banks slightly, so as to misalign these disturbances, and thus average out rather than reinforce their effect, a significant increase in beam quality is realized. The MIRACL laser, which has been a successful scaling experience, has provided dramatic and important data in behalf of the Strategic Defense Initiative (SDI).

As HF/DF laser technology has advanced, particularly on behalf of space-based applications, it has become apparent that the fine-scale mixing nozzle is inappropriate. Fine-scale nozzles are filled with boundary layer to the extent that low-pressure, high-Mach number conditions are difficult to achieve. Since space lasers have their own natural exhaust pump and need no pressure recovery, they can operate at the high-efficiency, low-pressure, low-temperature conditions provided by large-scale nozzles. Thus the technology has turned in the direction of large primary fluorine nozzles combined with injection of the H₂ or D₂ through hypersonic wedge structures located across the primary nozzle exit plane (but misaligned with respect to the optical axis and/or output pass direction). This method provides a well-established supersonic flow in the primary nozzle, with relatively little boundary layer growth along the hypersonic wedges. Care has to be taken to assure that the shocks created by the hypersonic wedges do not block the primary nozzle or create undesirable optical path differences (OPDs) in the optical cavity. Large-scale nozzle, hypersonic wedge injection technology is being incorporated in the SDI Project ALPHA.

The design problem for a high power, efficient, high quality, HF laser is technologically complex. It is, of course, a matter of record that it has yielded to a combination of scientific understanding and engineering verification processes which now result in efficient, high power, high beam quality HF laser designs. The engineering process consists of constructing at modest scale a module of the combustor/gain generator configuration. For example, the ALPHA verification module represents such a scale and is shown in Figure 7. Such a module verifies structural, thermal, and flow-field engineering predictions. Furthermore, precise optical measurements are made on the gain medium using absorption spectroscopy, optical interferometry. Power extraction is also measured. These data are used to verify the gain model predictions in the physical optics resonator design computer codes for the growth and decay of each of the excited state populations along the flow axis in both the small signal and saturated regimes. The measurements also provide verification of input to the laser medium OPD models in these design tools. Thus, a rather explicit verification by measurement is achieved early on, assuring that the large-scale laser design tools and processes used for later design efforts are sound. The ALPHA verification module has been used in just this way, resulting in over 10,000 seconds of experimentation, to lay the foundation for the ALPHA laser. The results of the ALPHA verification module establish that path lengths in excess of 20 meters through this high efficiency gain medium are acceptable. Although flow structures such as those described in Figure 6 exist, an optically clean medium is provided through the very low pressure, the low index of refraction composition (largely helium), and careful attention to design detail. The effects experienced even with 20 meters of gain path length in a very high power laser are small in magnitude and correctable with adaptive optics.

III. Linear Chemical Lasers

The linear chemical laser is shown schematically in Figure 8. The first of the large linear chemical lasers was the Baseline Demonstration Laser (BDL) shown in Figure 9. In this case a cavity injector 10 cm in height by 150 cm in length provides excited state HF for about 3 cm in the flow direction. This gain volume is accessed by a simple confocal unstable resonator. A total flow of 0.45 kg/sec yields 100 kW of power in a laser beam that is nearly diffraction-limited.

Scaling of linear chemical lasers has proceeded by means of the Navy-ARPA Chemical Laser (NACL) and the Mid-IR Advanced Chemical Laser (MIRACL), which are shown in Figures 10 and 11. In each of these subsequent lasers the flow density and cavity injection area were to provide both a larger gain volume and a higher density of excited-state HF. The NACL doubled the gain density and the gain length. The MIRACL increased (over BDL) the gain height by a factor of 2.5, the gain length by 3.3, and the flux density of HF excited states by 3. The net result is a very high power level. The history of these advances spanned the years from 1973 to 1980. The associated program consisted of relatively straightforward technology development, engineering, and major demonstrations. The mean deviation between planned and achieved schedules for power demonstration was 1.7 months. All three of these lasers have been used in extensive test programs exploring the beam characteristics, beam control technologies in behalf of pointing and tracking, beam propagation, and beam effects. The

BDL and NACL have operated for tens of thousands of seconds. The MIRACL has been engaged in a substantial test program at the White Sands Missile Range. Most recently, on MIRACL, the high power beam output phase distribution has been sensed, and a deformable mirror has been used to actively correct phase front deviations. A clear demonstration was made of the ability of this adaptive optics technique to compensate for mirror jitter and for wave front variations whose spatial dimensional scale exceeds that of the deformable mirror actuator spacing.

The power scaling limitations of the linear bank laser have been addressed by the experiments on these and other lasers. The power scaling is limited by effects on beam quality beyond the capacity for practical adaptive optics correction. The principal effects can be categorized as shown in Figure 12, and include:

- Flow-field disturbances. These are described in Section II, and their effect depends on the total cavity length.
- Mirror distortions. High reflectivity coatings determine how much power is absorbed into the mirrors. The cooling design of the mirrors, typically multipass fine-scale heat exchangers, then determines the resultant thermal distortion of the mirrors that is manifest as a wavefront aberration of the laser beam. The thermal ripple on the mirror from the periodic nature of the buried cooling passages tends to be the distortion effect most difficult to compensate with adaptive optics because of its small spatial scale. High mirror incident power flux densities are acceptable in practical designs.³
- Fresnel diffraction. A resonator cavity that is too long relative to its transverse dimensions suffers excessive losses from diffraction of the mode outside of its geometrical optics envelope, followed by impingement of the mode onto the surrounding hardware.
- Anomalous dispersion. Multiple longitudinal mode lasers can suffer from uncorrectable anomalous dispersion induced wavefront tilt associated with the presence of gain gradients if the cavity is too long.
- Transverse spatial coherence. The resonator mode must maintain coherence over the entire mode cross section for good beam quality performance. At some point, the transverse dimensions of the mode exceed the transverse spatial coherence length.

In addition, there is clearly a limit to the flux density of HF radiation that can be achieved efficiently and within a range of optically acceptable flow conditions. Theoretical limits for premixed flow conditions range from power fluxes of 100 W/cm² of cavity flow area at efficiencies of 600 kJ/kg of total flow to 600 W/cm² at 300 kJ/kg efficiency. Since higher efficiencies are achieved at lower power fluxes, a trade-off ensues. In practice, a fair fraction of the theoretical limit may be achieved.

The above discussion allows us to scope the potential power scale of the linear chemical laser. Even higher power lasers appear reasonable. At values for the cavity height and length, a factor of two greater than MIRACL, physical effects have not yet reached magnitudes where they are of concern.

IV. Cylindrical Laser

The cylindrical laser concept is shown schematically in Figure 13. Here the cavity injector is a cylinder of revolution which injects the flow radially outward to form an annular gain region of excited-state HF. In effect the height limitation of the linear configuration has been relaxed by forming it into a circumference. Mode control and communications are provided by optical resonators of special design, one version of which is shown in Figure 14. Curvature in the radial direction on the annular mirrors allows the mode intensity level to be controlled on the compact leg mirrors.

It is easy to see how this configuration allows increased power scale. The same laser gain length that gives us high power as a linear laser, for instance a 50-cm bank height, if wrapped into a 2-meter diameter cylinder, provides 12 times the cavity injector nozzle area. This gives us many times the device power, without increasing at all the nozzle power flux, cavity injector length, or the mode width and this is done without increasing any of the effects delineated in Figure 12. Unchanged are the medium OPD, the mirror thermal loading and distortion effects, and any of the other cavity gain length related phenomena. Thus, the cylindrical laser takes us to a ten times higher power laser as far as limitations of physics are concerned.

Cylindrical chemical laser technology is under development in Project ALPHA, which has been designed, fabricated, assembled, and is nearing test. Subscale testing of the cavity injector configuration and of the optical resonator has essentially already confirmed the physics basis of the concept, and achievement of the fabrication goals has established the engineering feasibility of the full-scale gain generator and optical resonator hardware (shown in Figures 15 and 16).

V. Nonlinear Optics and the HF Laser

To build even higher power lasers, or to construct large scale systems from modules of smaller scale, the concepts of coherently combining laser cavities and optical elements may be introduced. When done properly, no beam quality effects are suffered beyond those of individual laser or optical elements. Economies are realized in nonrecurring engineering, fabrication, and assembly costs. Shorter fabrication and assembly times can be realized, and performance margins can be increased.

A number of programs are underway in which various techniques for combining laser cavities and optical elements are being successfully developed. A good example is the LAMP (Large Aperture Mirror Program), where a 4-meter diameter mirror system has been designed and fabricated, and is in final assembly at ITEK. This mirror, shown in Figure 17, has been constructed of conveniently sized segments, and has all the necessary provisions to sense wavefront aberration and correct it by aligning the mirror elements to within a small fraction of the HF laser wavelength (2.7 microns).

Quite recently, a new technology has emerged that will clearly enable the construction of systems of much higher power and higher brightness while reducing the engineering complexity and cost. This is the application of stimulated Brillouin scattering (SBS) phase conjugation techniques to the HF chemical laser.

Results from work on this technology have been presented in a number of forums within the past year and a half, following the first achievement of SBS using an HF laser by research workers at the Naval Research Laboratories.⁸ Subsequent work has resulted in the production of diffraction limited beams from aberrated HF lasers by means of phase conjugation as well as from multiple HF lasers coherently combined by phase conjugation in a common volume.⁹ Also, multiline lasers have been phase conjugated,¹⁰ and essentially continuous-wave operation (pulsed operation with a pulse length much greater than the phonon dephasing time) has been demonstrated.¹¹ Coherent optical combination of beams, optical elements and jitter compensation have been demonstrated.¹² Very high power systems engineering design issues have been addressed and resolved.

The application of SBS phase conjugation to a high power laser is shown schematically in Figure 18. A low power laser beam of high quality, represented by a flat phase in the figure, interrogates a high power laser amplifier system. It picks up phase aberrations as it encounters optical elements and power (as well as further phase aberrations) as it traverses the laser amplifier gain stages. The resultant beam is then focused on an SBS cell to intensities where the SBS process occurs, typically 1-10 G W/cm². The retroreflected beam has the conjugated phase property, i.e., it has the same phase distribution as the incident beam, but it is now travelling in the opposite direction. Therefore, what was previously a phase retardation is now a phase advancement of the same magnitude, and vice-versa. Thus, as the beam retraces its path and encounters the same optical aberrations, its phase distribution is restored to a replica of the phase distribution of the input interrogating beam. It is further increased in power by the effect of the laser amplifier stages. This system provides a high power laser beam whose phase is a replica of an input low power laser beam. Further, the low power laser, and the reflecting SBS cell can be quite inefficient without much degradation of the total power of the system, since most of the system power is derived in the final pass. All aberrations that are essentially static within the round trip transient time of the beam in the system are compensated. Typically this provides for a MHz bandwidth adaptive optics capability and includes not only spatially distributed aberrations, but also all forms of jitter (tilts). The limit on the magnitude of the aberrations that can be corrected is that which will allow a sufficient focus within the SBS cell. This is required to achieve the necessary intensities for stimulated Brillouin scattering to occur with high reflectivity.

The net result is that it is no longer necessary to have to design the high power optical system to tolerances of a tenth of a wavelength, with components thus generally tolerated to a hundredth of a wavelength. The requirements on the high power optical system are literally relaxed by a factor of a thousand. One can thus build a low power, high quality laser to interrogate a high power, low quality system and produce a high power, high quality beam. As a result of the use of SBS, this may be done with relative ease.

Furthermore, the concept allows the combination of laser amplifiers and optical systems as shown schematically in Figure 19. Here is a single interrogating laser explores a parallel array of laser amplifier stages and projecting optical elements, is phase conjugated, and results in a coherently combined set of amplifier stages in the output pass. After all, the scheme of Figure 18 applies whether it is used for compensating for aberrations in a portion of single mirror, or a segment; or similarly, for aberrations in a portion of a large laser cavity, or an individual cavity in an array.

Figures 20, 21, and 22 show results from high-fidelity HF laser phase conjugation, coherent combination of HF laser cavities, aberration correction of segmented optics performance, correction of jitter, and demonstration that high-fidelity continuous-wave operation SBS can be achieved. The latter is accomplished without suffering a transition to forward Brillouin scattering by maintaining conditions in a steady flow rather than a continuous-wave regime. This latter consideration adds the requirement for a flowing SBS cell with a medium of acceptable optical quality. Interferograms from such a cell are shown in Figure 23. The net result of this recent work has been to establish a design regime under which high-fidelity, continuous-wave, high-power, HF laser operation can be achieved. This regime is indicated in Figure 24. Detailed discussions concerning SBS experimental results, analytical techniques, and designs are being reported on a regular basis.

The introduction of the SBS process clearly allows the consideration of systems of hundreds of megawatts of power and of tens of meters of projecting optics dimensions. Individual laser amplifiers of the cylindrical configuration are combined using SBS to achieve this total power. Similarly, conveniently sized mirror segments are combined into what are essentially large phased arrays. Simultaneously, tolerances are relaxed on optical components and assemblies to dimensions measured in millimeters and sometimes even in centimeters. Wavefront sensing systems, along with high precision actuation and stabilization systems, are in many cases, eliminated altogether.

VI. Conclusions

Chemical lasers have good attributes for consideration in space applications requiring high power systems, viz,

- Direct conversion high efficiency of stored chemical energy to a laser beam
- Scalability to very high laser powers by a direct increase in the reactant flow rates and/or exit area of the unit reactor configuration
- Low index of refraction cavity composition and low density flow conditions that provide for nearly diffraction-limited beam performance in very high power configurations
- High performance reliability (simple, non-stressed hardware)
- Lightweight, compact hardware without the substantial weights that tend to accompany electrical power generation, high voltage conditioning or photoconversion processes
- Compatibility of the space vacuum with low laser cavity pressure conditions, providing easy exhaust gas pumping and high efficiency collisional deactivation conditions in the laser cavity.

In addition, a technology base has been established within the recent past that provides the physical basis for scaling very large individual HF chemical lasers and the size of the associated projecting optical systems. Phase conjugation technology has been demonstrated that allows much larger systems with major relaxations in requirements that have made such very large systems appear difficult and expensive in the past. Much of the work that leads to these conclusions is quite recent.

References

1. J. Miller, presented at the Ninth International Conference on Lasers '86, Orlando (1986), paper WM.1.
2. The American Physical Society PRESS RELEASE, for release Noon, Thursday, April 23, 1987; and the APS Council Statement on the Strategic Defense Initiative dated April 24, 1987.
3. D. Pines (Editor), Reviews of Modern Physics, 59, 3, Part II (American Physical Society, New York, 1987), pp. S1-S202.
4. K. L. Kompa, Chemical Lasers, 37 (Springer-Verlag, New York, 1973).
5. R. W. F. Gross and J. F. Bott, Handbook of Chemical Lasers (John Wiley & Sons, Inc., New York, 1976).
6. W. R. Warren, Jr., Astronautics & Aeronautics, 13, 4, 36, (1975).
7. L. E. Wilson, J. De Physique, Colloque 09, Supplement au n 11, Tome 41, C9-1-C9-3 (1980).
8. M. T. Duignan, B. J. Feldman, and W. T. Whitney, Optics Letters, 12, 111, (1987).
9. M. Farey, et. al, presented at the Opto-Electronics and Laser Applications in Science and Engineering (O-E/LASE '88), SPIE, Los Angeles (1988), paper number 874-17.
10. R. Moyer, M. Valley, M. Cimolino, and M. Sones, presented at the Conference on Lasers and Electro-Optics (CLEO '86), San Francisco (1986), paper THD4.
11. A. A. Jacobs, K. A. Bowler, presented at the Opto-Electronics and Laser Applications in Science and Engineering (O-E/LASE '88), SPIE, Los Angeles (1988), paper number 874-10.
12. M. Valley, G. Lombardi, and R. Aprahamian, J. Opt. Soc. Am. B, 3, 10 (1986).

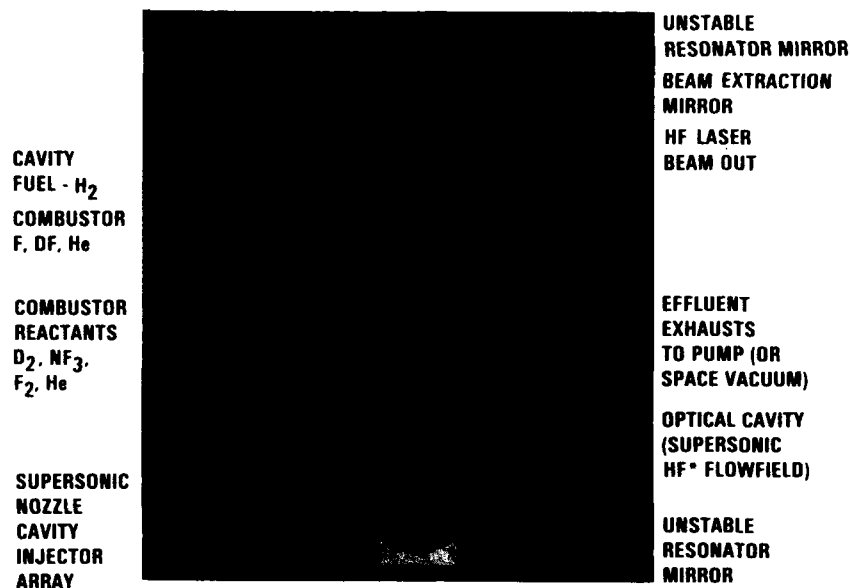


Figure 1. CW HF Chemical Laser

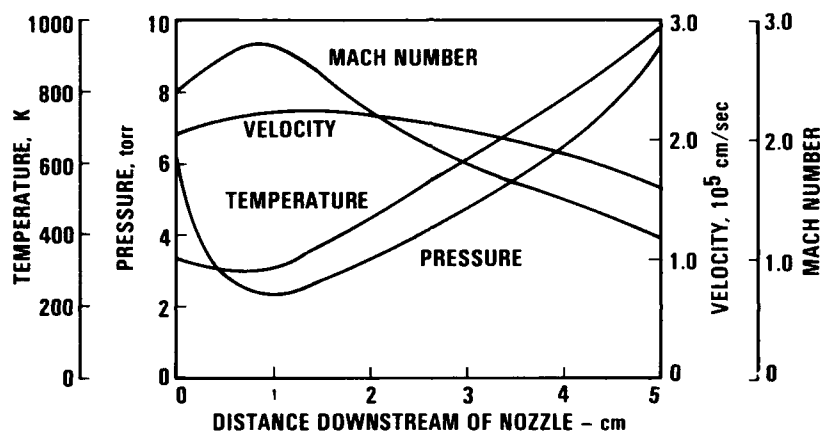


Figure 2. Typical Cavity Flow Conditions (Cavity molar flow composition 0.1 HF, 0.1 DF, 0.3 He, 0.5 H_2)

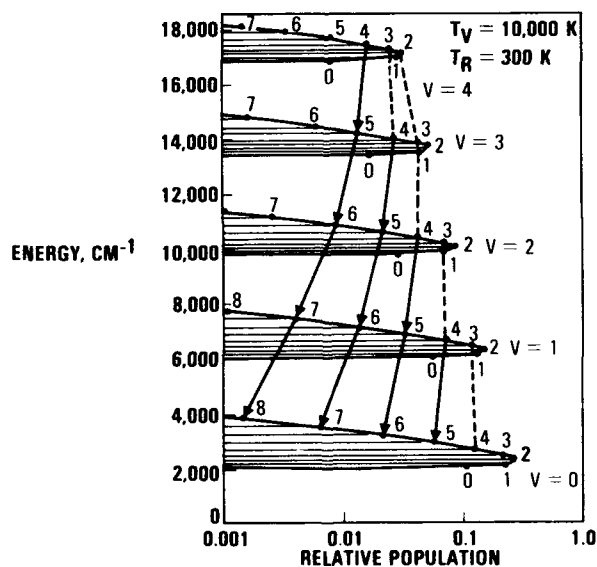


Figure 3. Energy-Level Diagram for Excited HF Molecules

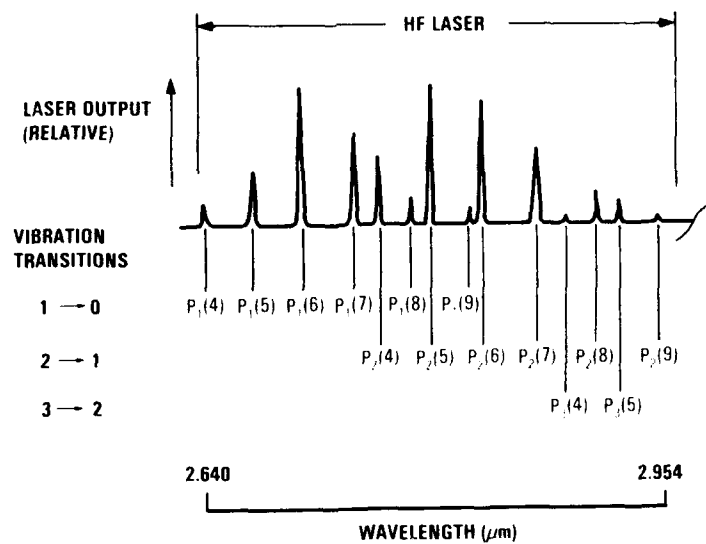


Figure 4. Typical CW HF Laser Beam Spectral Content

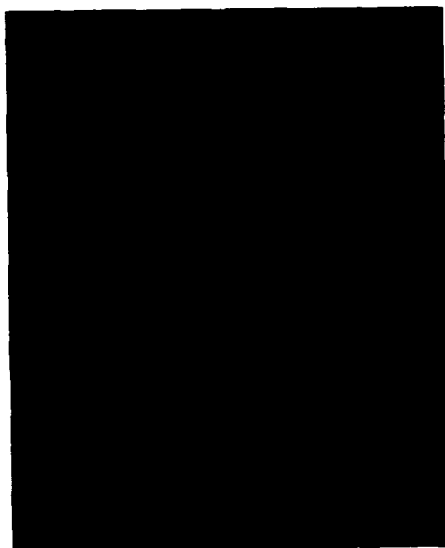


Figure 5. Supersonic, Mixing, Reactive Chemical Laser Flow Field

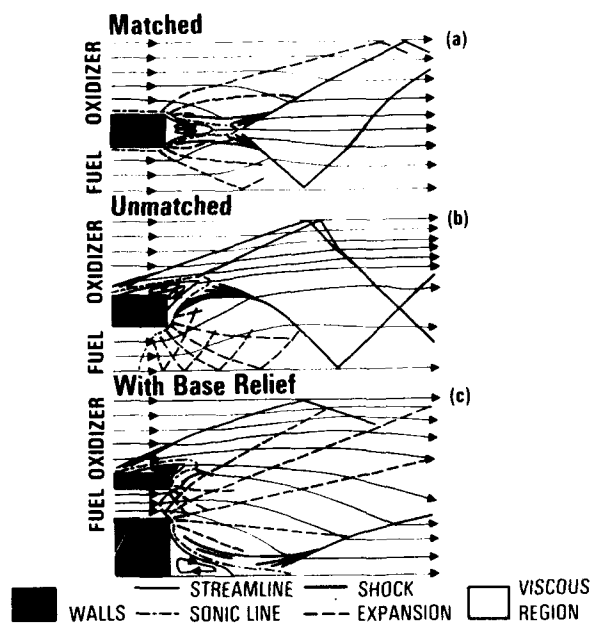


Figure 6. Supersonic Nozzle Exit Flows



Figure 7. ALPHA VM Module

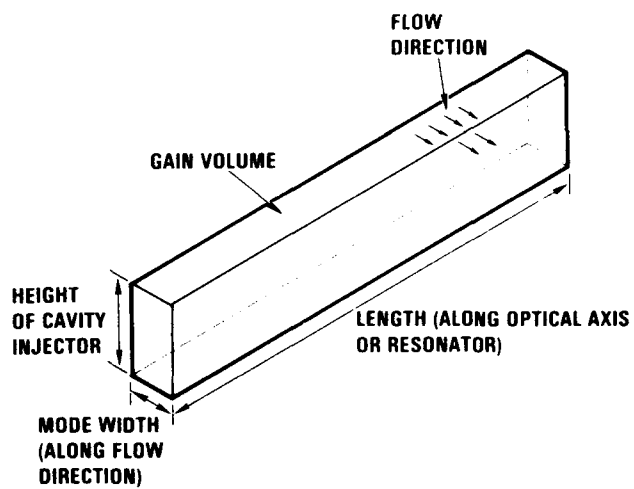


Figure 8. Linear Chemical Laser Configuration



Figure 9. Baseline Demonstration Laser

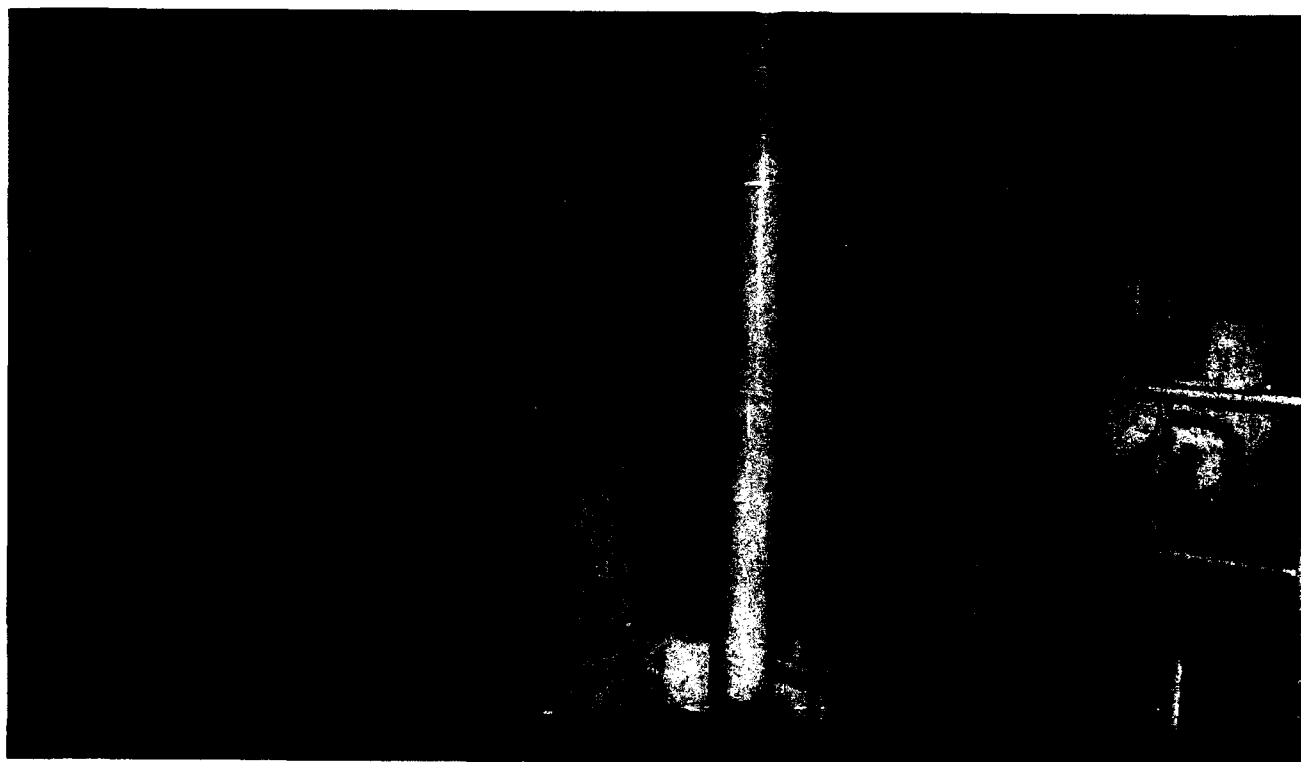


Figure 10. Navy ARPA Chemical Laser

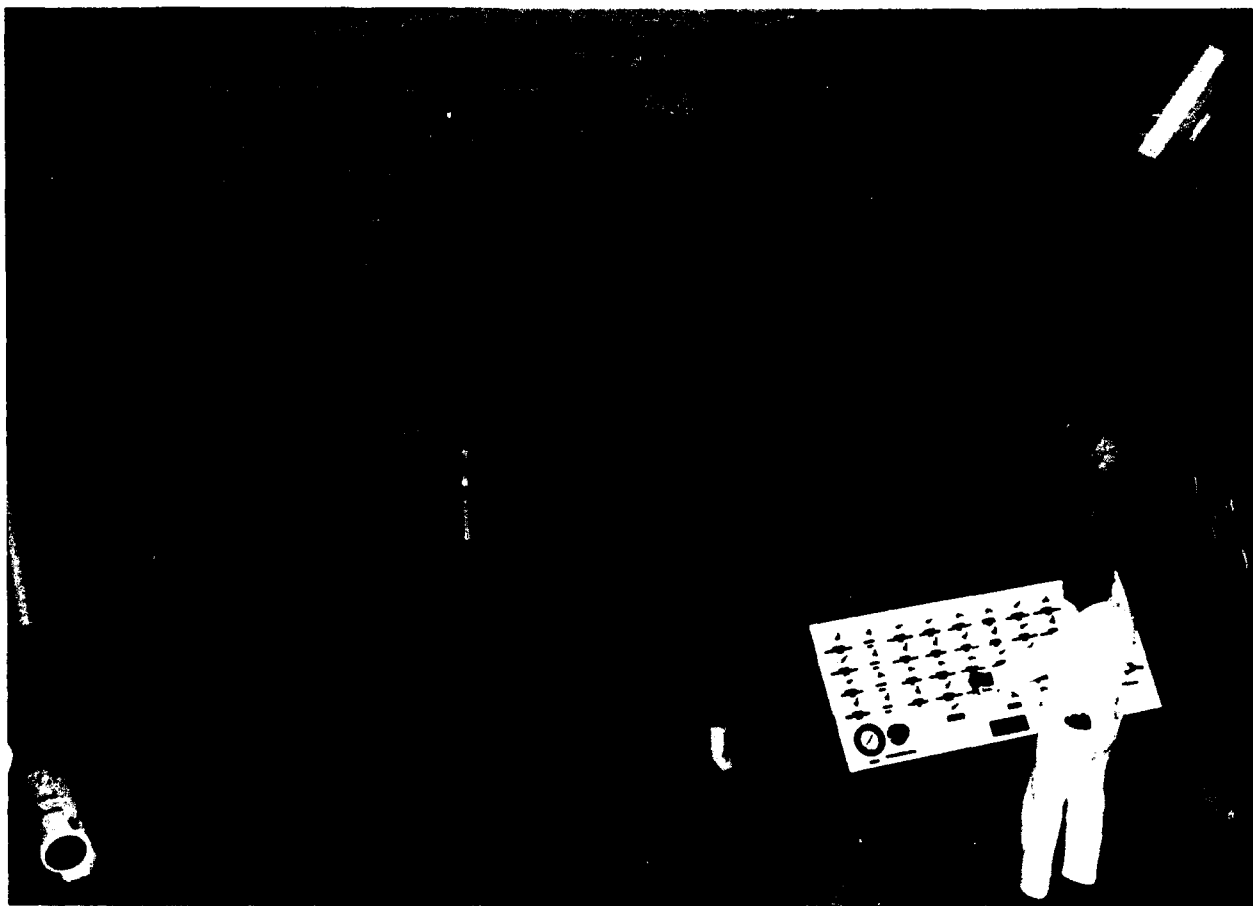


Figure 11. Mid-IR Advanced Chemical Laser (MIRACL)

Design Parameter	Beam Quality Effects					
	Flowing Medium Optical Path Difference (OPD)	Mirror Distortions	Diffraction Losses	Amplified Spontaneous Emission	Anomalous Dispersion	Resonator Mode Control
Cavity Injector Height						•
Cavity Injector Length	•	•	•	•	•	
Cavity Mode Width			•	•		
Flux Density of HF*	•	•		•	•	

Figure 12. Scaling Considerations for Linear Chemical Lasers

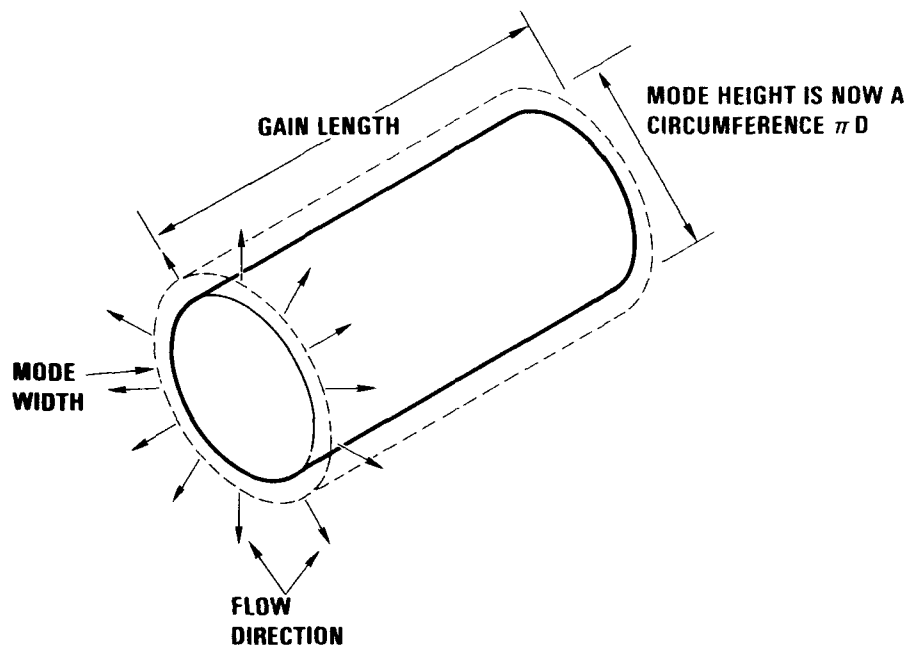


Figure 13. Cylindrical Chemical Laser

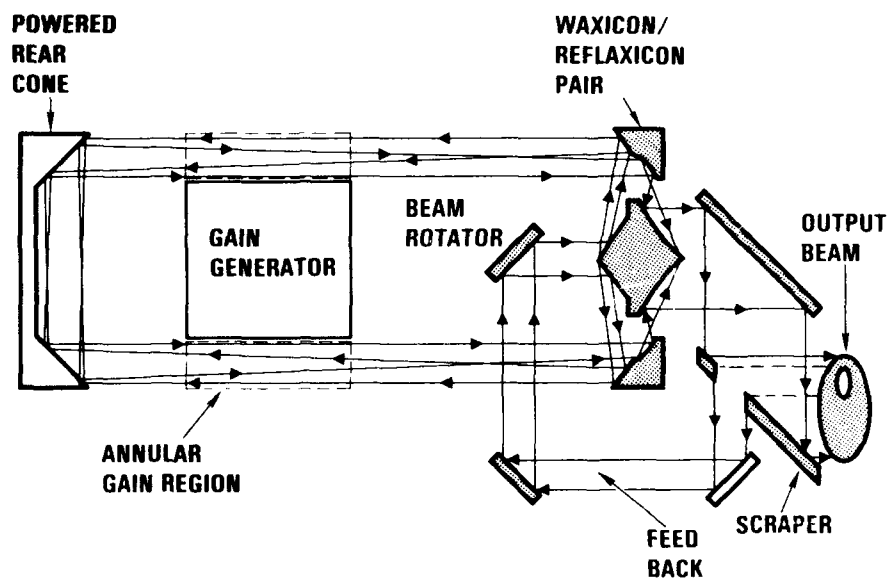


Figure 14. Cylindrical Laser Resonator



Figure 15. ALPHA Cylindrical Gain Generator Assembly

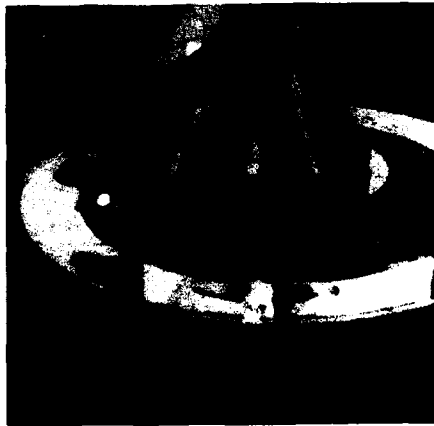
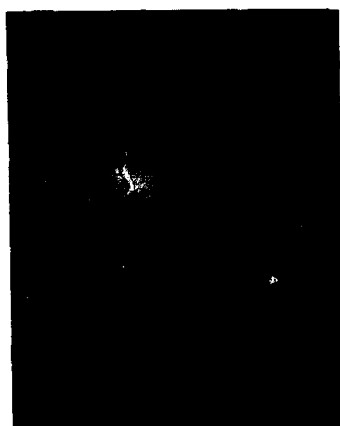
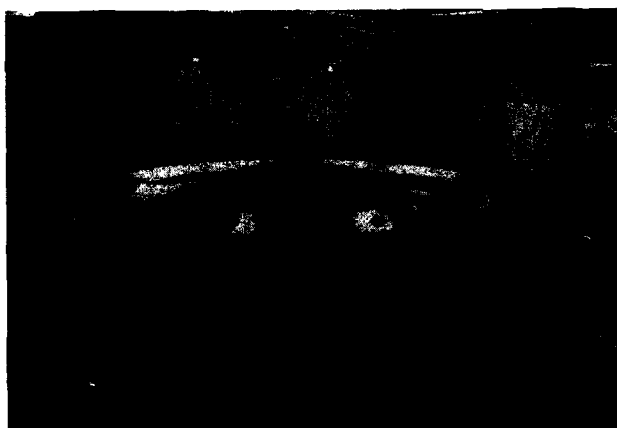
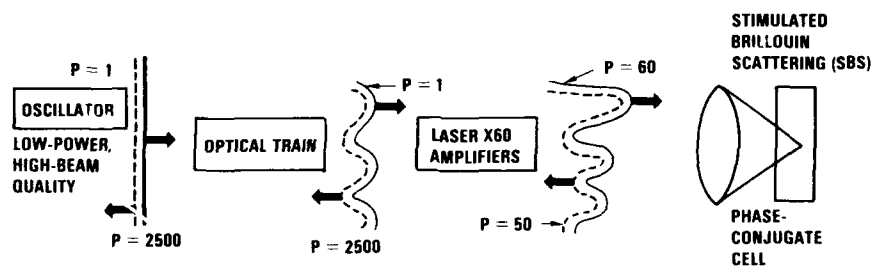


Figure 16. ALPHA Annular Optics



Figure 17. 4m Lamp Mirror



- Low-power, high-quality beam interrogates the system and picks up phase aberration (and power)
- Phase-conjugate beam returns and deconvolves phase aberration, with further power amplification
- High-power beam exits with phase replicate (and jitter replicate) of low-power oscillator input

Figure 18. SBS Phase Conjugation Applied to a High-Power Laser System

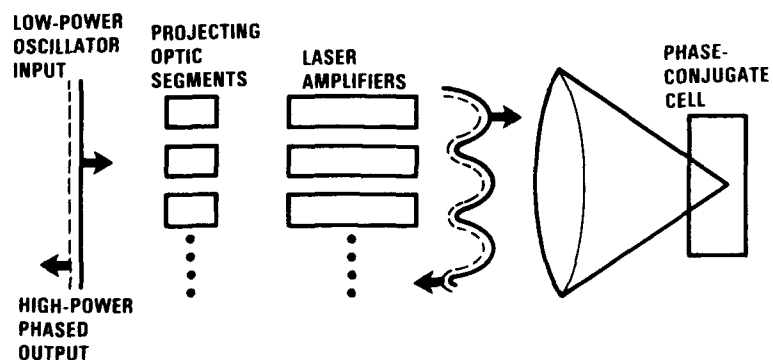
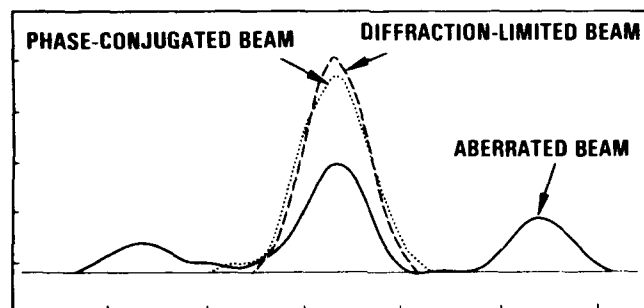


Figure 19. Phase Conjugation Laser Cavity Combining and Optics Phasing

Far-Field Intensity Profiles



Aberrator $BQ = 1.64$ corrected to $BQ = 1.03$

Figure 20. High-Fidelity HF Laser Phase Conjugation Correction of Aberrations

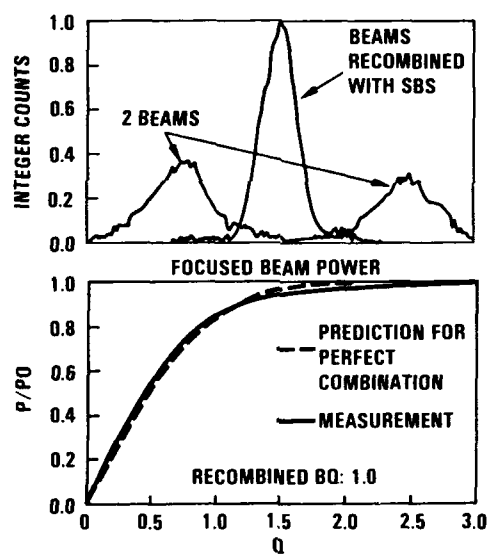
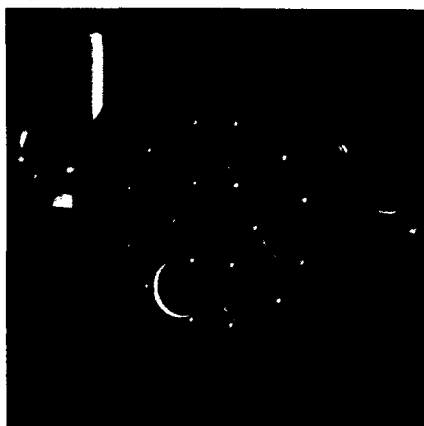


Figure 21. Aberration Correction Plus Coherent Combination of HF Laser Cavities to Diffraction Limited Beam Performance

Segmented Primary Mirror



Far-Field Patterns

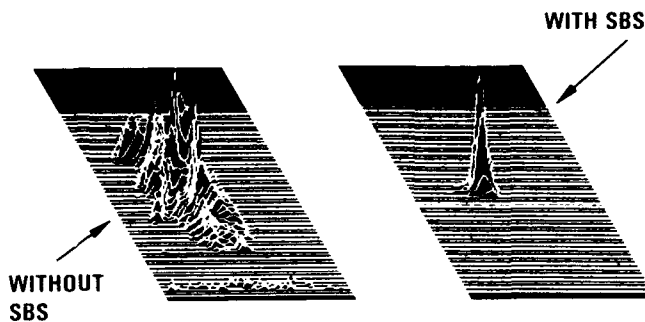
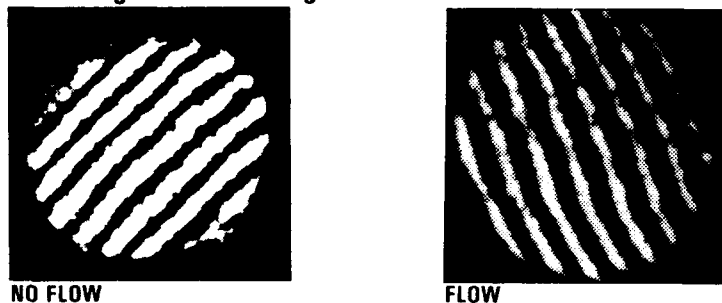


Figure 22. Use of Phase Conjugation to Obtain Diffraction Limited Performance from an Array

Interferograms of Flowing SBS Cell



Good optical quality demonstrated

Figure 23. Flowing SBS Cells Allow Operation Without the Development of Competing Forward SBS Processes

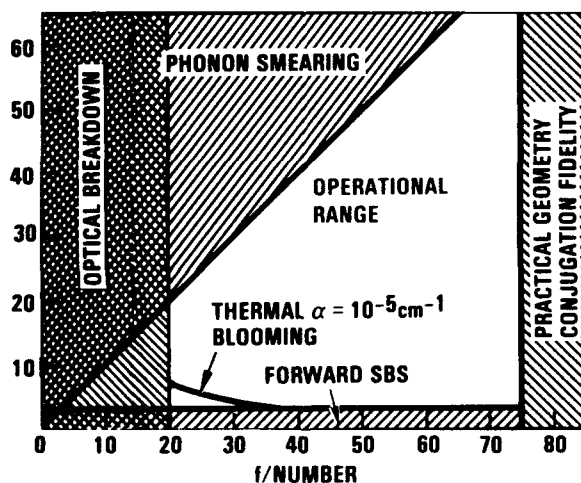


Figure 24. An Acceptable Design Space Exists for SBS Application to Very High Power Laser Systems

SPACE BASED CHEMICAL LASERS FOR BALLISTIC MISSILE DEFENSE (BMD)

N. Griff, SBL Program Manager, Strategic Defense Initiative Office (SDIO/T/DE), Washington, D.C.

D. C. Kline, Director, Special Projects, W.J. Schafer Assoc, Arlington, VA

ABSTRACT

The paper begins with a brief review of the history of ballistic missile defense, including President Reagan's dissatisfaction with the condition of an offensive dominated deterrence, which eventually led to the formation of the Strategic Defense Initiative (SDI). Also discussed is the view that the requirements for an early directed energy weapons (DEW) system are far different from those beyond the year 2000. Generalized top level performance requirements for a Space Based Chemical Laser (SBCL) are then discussed, after which the concept of phasing SBCL modules together on-orbit to obtain very high brightness systems is introduced. A discussion of the application of SBCLs to the area of interactive discrimination is then presented. Turning to SBCL technology readiness, chemical laser devices, beam control, large optics, acquisition/tracking/pointing, rapid retargeting, and coherent beam combination are briefly discussed. To complete the picture, a discussion of the survivability of SBCLs in the context of the entire SDI system is presented, including possible adversary's responses, design features to increase survivability, and a separate discussion of the threat of an adversary's ground based laser ASAT to an SBCL and SDI defense system.

I. BACKGROUND

Soon after the conclusion of World War II scientists and the military in the United States and the Soviet Union began to focus on the weapon potential that an intercontinental ballistic missile force could provide. By the 1950's, both the US and the Soviet Union had developed a small force of missiles armed with nuclear warheads that could threaten each other's heartland, thus ushering in the age of nuclear destruction by remote control. It soon became apparent that a defense against this near-instantaneous devastation was highly desirable, and both sides began working on ground based ballistic missile defense (BMD) systems. Both sides later signed the Anti-Ballistic Missile (ABM) Treaty in 1972 that limited each side to one ABM site with a total of 100 interceptors. The US began the construction of their one allowed site in Grand Forks, North Dakota, but soon lost interest because of the limited defense of the US population such a system could offer. The situation in the early 1980's was that the US had no defense against ballistic missiles, while the Soviet Union opted to complete their one authorized defensive site, located around Moscow.

After being elected to the presidency, Ronald Reagan became interested in the possibility that, unlike the defenses technologically possible in the 1960's and early 1970's, new technologies being developed in the US might actually be able to achieve population defense against a nuclear ballistic missile attack. On March 23 1983 he announced his intention to establish a major research program to investigate the feasibility of developing and deploying a ballistic missile defense, and established the Strategic Defense Initiative Organization (SDIO) in early 1984. The short history of the SDIO is familiar to all.

One of the new technologies that made the President feel that a very capable BMD was possible was directed energy weapons (DEWs). Throughout the 1970's, all three of the military Services had aggressive programs in various DEW technologies aimed at tactical applications, mostly in the arena of air defense. At the same time, the Defense Advanced Research Projects Agency (DARPA) was investigating the application of various DEW technologies to strategic problems, namely BMD, anti-satellite (ASAT) and strategic air defense. Technologies being investigated throughout the DoD spanned the entire spectrum of "conventional" DEW candidates.¹

In the context of ballistic missile defense, one point of possible confusion that has permeated many of the discussions about the role of directed energy weapons, and space based lasers in particular, is a delineation of near term versus longer term requirements for such systems. As one might expect, these requirements tend to be not only worlds, but universes apart, depending on the points of view of the debaters.

In fact, the phenomenon that is occurring is one that is totally predictable; in the early days of BMD and SDI very little was known about the physical nature of the adversary's threat with which SDI systems might have to contend. This deficiency is of little consequence in the world of kinetic energy weapons (KEWs), since if one can hit an ICBM or RV with almost any form of KEW, there is little doubt that destruction of both objects will occur and the defense will be successful (in that engagement). In the case of DEWs things are startlingly different. Depending upon the assumptions made as to the "hardness" (laser radiation resistance) of an adversary's boosters, which remain the primary targets for DEWs when used as a

¹ D.C. Kline, "A Case for Space Based Chemical Lasers in the Strategic Defense Initiative", Preprint Number AIAA-87-1389, June 1987.

weapon, systems capable of negating such targets range from something that could be available early to systems that might take decades to develop. The truth is that as more information has been gained about the hardness of boosters in both the near-term, and countermeasures to make them harder in the longer-term, it is evident, with some fair degree of certainty, that the problem is not nearly as tough as originally postulated. This is very important, since it not only reduces the requirements for an early system, but allows a much more orderly transition from the near to the longer term DEW systems.

II. SPACE BASED CHEMICAL LASERS

UTILITY:

The extent to which a Directed Energy Weapon can penetrate the atmosphere has a significant effect on its utility in the boost phase battle. In the case of the HF chemical laser this lower altitude limit can be considered to be the cloud tops, where a significant amount of water vapor begins to appear in the atmosphere. This is at an altitude of approximately 10 Km. Clearly, this constraint is not uniform, and under some geographical and meteorological conditions high power HF beams can penetrate to an altitude of several kilometers. It should be pointed out, however, that even at 10 Km this constraint is not at all serious, since missile detection at altitudes below the cloud tops is highly unlikely. This ability to penetrate the atmosphere deeply without significant loss of laser energy allows SBCLs to be primary candidates for the ABM boost phase battle.

Because of its desired low pressure operating regime for high efficiency operation and exhaust management issues, space is a natural environment for chemical lasers. Since the conversion of chemical energy to laser energy is relatively efficient, the Space Based Chemical Laser (SBCL) is a particularly attractive option when one considers a space based defensive system involving directed energy weapons (DEW). In general, the top-level requirements for a Space Based Chemical Laser are as follows:

- o Many megawatts of operating power
- o Good beam quality
- o High reactant utilization efficiency
- o Lightweight components
- o "Agile" beam (ability to rapidly retarget)
- o High quality projecting optic (primary mirror)
- o High performance beam control and correction subsystem
- o Accurate acquisition, tracking and pointing (ATP) subsystem²

Chemical laser devices with good beam quality exist today that are very near the power levels expected to be required for boost phase intercept up until the year 2000 and beyond. Specifically, the MIRACL chemical laser, which was first tested in 1980 is within a factor of 5 or 6 of the power levels, and within a factor of 2 of the beam quality, required for an early SBL system.

In addition, confidence is being steadily gained in new technologies, such as phasing individual modules together on-orbit, that can allow an early space based chemical laser constellation to grow in capability (brightness) as the threat responds so that no hardware obsolescence occurs. From the brightness equation,

$$B = \frac{P D^2}{\pi \lambda^2 [1 + (BQ^2 - 1) + \sigma_j^2 + \sigma_{wfe}^2]}$$

where

- B = Brightness (Watts/Steradian)
- P = Device Power (Megawatts)
- D = Projecting Optic Diameter (Meters)
- λ = Wavelength (Microns)
- BQ = Beam Quality (Dimensionless)
- σ_j = System Jitter (1 σ)
- σ_{wfe} = Wave Front Error (1 σ)

one can see that the projecting optic diameter is a major driver in achieving very high brightness systems of interest for ballistic missile defense. The concept of phasing HF SBCLs offers the ability to build and deploy "modules" in packages that can be made compatible with existing and planned launch vehicle capabilities and assembling them together on orbit, thus allowing (theoretically, at least) unlimited growth potential.³

Our confidence is based upon the results of small scale experiments conducted at government and contractor facilities at low powers, but which we believe can be scaled to high power lasers of interest. We have, for many years, devoted substantial resources to building and updating very complex computer codes that we have shown the ability to accurately predict the outcome when scaling from small laboratory experiments to high powers.

^{2,3} op cit

Another important utility area for SBCLs is interactive discrimination (IAD). From the time of the Fletcher study to present, there has been a spirited debate both within and outside of the SDI community concerning the issue of discriminating warheads from penetration aids and a variety of decoys that might be deployed as a countermeasure to an SDI system. Many concepts have been investigated that have varying degrees of effectiveness and utility in this role. Over the past several years the utility of using a multi-purpose space based chemical laser as both a boost phase weapon and an interactive discriminator has been investigated and appears to have great potential.

The interactive discrimination task with SBCLs and DEWs in general involves three technology areas - - observables/sensors, target handling/rapid retargeting, and interaction phenomenology. The SDIO Sensors Office is developing the space surveillance and tracking system (SSTS), which will allow the observation of the interactively discriminating event - either burnthrough or large velocity vector changes in decoys relative to RVs. Rapid retargeting has been discussed previously.

In the area of target interaction phenomenology, the DoD high energy laser program has a long history of laser interaction with materials programs conducted under the titles of damage and vulnerability (D&V), lethality and target hardness (L&TH), etc. Because most of these programs predate the SDI, they have not dealt specifically with laser interactions with balloons and decoys made from a variety of materials in exact ICBM geometries. However, much of the large volume of experimental work done for tactical and various strategic targets and materials go a long way towards giving us confidence in our modelling and simulations in evaluating SBLs and other DEWs in the IAD role.

One very attractive feature of the space based chemical lasers concept is that platforms which participate in the boost phase of the battle spend most of their on-board reactants in the task of negating boosters. However, the "absentees" (platforms that are on the other side of the earth at the time of launch) can perform the task of discriminating RVs from penetration aids for eventual kill by kinetic energy weapons as their orbits bring them into the vast midcourse battle space. Thus, for the price of a constellation that can participate with the space based kinetic kill vehicles in the boost phase of the battle, we can also achieve a very high discrimination percentage of the leakers into midcourse.

TECHNOLOGY READINESS:

The initiation of the major technology programs that are required to successfully demonstrate the readiness of space based chemical lasers for accomplishing the BMD mission were undertaken in the late 1970's. These basic ground based programs, which were initially sponsored under the auspices of DARPA, are now SDIO programs in their final stages and all have or will soon succeed in their technical goals. These programs include the Alpha chemical laser device, Large Optics Demonstration Experiment (LODE) beam control demonstration, and LODE Advanced Mirror Program (LAMP) large space based mirror, as well as an impressive array of technology programs aimed at developing all aspects of the technologies needed to meet all of the requirements stated previously for an SBL system.

The Alpha device, based upon subscale tests at the 20 - 30 Kw level, is projected to have excellent beam quality (Figures 1 - 3). Alpha I was designed to be easily scalable to power levels more than a factor of 2 - 3 beyond the power levels required for an early system, with little or no degradation in beam quality. It should also be pointed out that the power level of the Alpha I device was set not by the maximum scaling thought possible in 1980 when the program began, but by monetary constraints imposed by the facility cost to simulate the vacuum of space.

Beam clean-up, or phase correction is required to maintain good beam quality within a laser system designed for use in the BMD role. This requirement is more stringent for strategic defense than for a tactical laser system because of the great distances involved in the engagements. For a space based laser, for instance, the average engagement range for a constellation of approximately 50 platforms at 1000 Km altitude is between 1000 - 2000 Km. In a typical tactical scenario, the ranges tend to be 10 - 20 Km. In order to avoid unacceptable losses of energy, the beams must be near the diffraction limit. For space based HF chemical lasers, this beam cleanup can be done in a very straight forward manner. This has been demonstrated conclusively in the LODE program, in which a severely aberrated beam was input to a combination of small and large mirrors and the phase front "cleaned-up" to less than 1800 angstroms total error. In this experiment, small high-bandwidth mirrors remove high temporal/low spatial frequency aberrations and work in conjunction with a large primary mirror with holographic optical elements and outgoing wavefront sensor to correct high spatial/low temporal frequency aberrations (Figure 4).

A critical component in the operation of a space based chemical laser system is the projecting optic or "primary" mirror. The LAMP mirror, which is in its final testing phase, was designed specifically for use as the primary mirror for a near term HF SBL demonstrator (Figure 5). LAMP is a 4 meter, high quality, segmented mirror which has actuators that "deform" the mirror almost microscopically to correct for aberrations in the high power beam.

The acquisition, tracking, and pointing (ATP) requirements for SBLs (and GBLs) are well understood. The final space component, be it an SBL platform or a GBL fighting mirror, must have a variety of sensors and active illuminators (low power lasers) in order to effectively deal with not only the ICBM boosters but the post-boost vehicles, and perhaps most important, midcourse objects including RVs, balloons, replica decoys,

chaff, etc. To this end, all laser conceptual designs for operational systems include at least two and as many as four different sensors and from one to three illuminators to maintain a robust capability across all target types and variants. Typically, an SBL platform will have an unaided (passive) wide field of view LWIR sensor to accomplish the acquisition and coarse track function. Once coarse track is established, a moderate field of view aided or unaided MWIR sensor takes over during the intermediate track phase of the engagement. Finally, fine track is established using either an aided narrow field of view SWIR or visible sensor. This hierarchy allows each SBL battle station to handle a large number of targets very efficiently. In addition to the sensors and illuminators described above, in the far-term such responses as rotating boosters have been postulated causing the need for yet another illuminator/sensor combination -- a carbon dioxide laser radar (LADAR). The LADAR is useful in determining the direction of rotation of the booster, and has an excellent capability to perform damage assessment in the boost and post-boost phases, and to aid in the discrimination process in the midcourse phase of the battle.

The ability to retarget rapidly from one target to the next is a stringent requirement for any DEW system. As in the case of ATP, retargeting is accomplished according to a hierarchy based upon the angular distance between targets. Almost all SBL concepts have gone to a three element telescope design in order to allow very rapid retargeting within the field of view of the telescope. This three element design allows approximately +/- 10 milliradians retargeting through optical steering, which utilizes a small (approx 30 cm) mirror with a high bandwidth to move the beam within the field of view. At the next level within the retargeting hierarchy, the beam expander is used to retarget within a range of +/- 5 degrees. This is accomplished via a gimbal between the main body of the spacecraft and the beam expander. At the final level, the spacecraft itself is slewed to accommodate very large retargeting angles. Typical parameters for the spacecraft slew are an acceleration of 3 deg/sec² and a velocity of 6 deg/sec. To further reduce the retarget time, the spacecraft and beam expander can be kept in a continual (during engagements) predictive slew pattern, such as the "sheepdog" in which the engagements are accomplished around the perimeter of an assigned group of targets.

Combining beams coherently, which is a major growth option for space based HF chemical lasers has not as yet been demonstrated at high power. However, great confidence has been gained in the ability to accurately model the outcome of scaling to high power levels based upon subscale experiments using conventional Master Oscillator/Power Amplifier (MOPA) technology and advanced non-linear optical techniques (Figures 5 & 6). Such small scale experiments have been successfully conducted at both government and contractor facilities. Thus, there is great confidence that this exciting new technology could be available for future generations of space based HF chemical lasers when the higher power levels (and higher brightness) would be required to defeat the responsive threat.

In the course of these major technology programs, much has been learned about what it will actually take to manufacture and deploy a space based chemical laser. In fact, these programs, along with a multitude of supporting technology ("tech base") programs, have substantially increased optimism as to the difficulty and time required to produce a space based chemical laser system capable of accomplishing vital near-term functions for the SDI. One example is the fabrication of large mirrors for a space based chemical laser system. As recently as 5 years ago projections as to how long it would take to build enough mirrors for even a modest SBL constellation were very pessimistic. Today, with the experience gained in the LAMP program, projections are far more optimistic, and are to the point that by merely applying "brute force", that is replicating existing optical fabrication processes, a production rate of at least several complete optical systems per month can be attained with an investment in facilities of less than 1% of the total system cost.

SURVIVABILITY:

Functional survivability of a space (or a ground) based BMD system is critical. This is not to say, however, that any given single component can or must be able to be absolutely defensible against all possible threats. By the very nature of military warfare, the appearance of particular weapon and/or sensor systems have historically elicited a response, or counter-measure, from the opposing side. A strategic defense system will be no exception. Some of the pertinent questions in this chain of measure, countermeasure, counter-countermeasure, etc are;

- A. What is the effectiveness of a particular countermeasure against the entire BMD system? Does degrading effectiveness against one element of the defense actually enhance the effectiveness of others?
- B. What is the cost of implementing the countermeasure? What is the relative cost-effectiveness to the offense of various countermeasures? Would it actually be more cost effective to proliferate offense rather than pursue countermeasures?
- C. What is the likelihood that the offensive countermeasures can be easily and cost effectively circumvented by the defense (counter-countermeasures)?
- D. How much faith does the offense have that they actually understand the details of how the defense works, to the extent that they can accurately assess the effectiveness of postulated countermeasures?
- E. Are various countermeasures in consonance with offensive dogma, strategy, and political thinking?

In addition to these questions, perhaps the most critical of all is "When can the offense have particular countermeasures in place?" This question is especially relevant to the issue of survivability of a defensive system during an early deployment. One fact should be kept in mind when considering the vulnerability of an ABM system which contains one or more boost phase components; the system is designed to intercept the most likely adversary response to the presence of an ABM system in the near-term - direct ascent ASATs. In addition, the initial deployment of the space components could be into orbits that are relatively inaccessible to direct ascent ASATs and totally inaccessible to an adversary's GBL ASAT system. Later they can be changed to more optimum operational orbits.

Specifically, for a Space Based Laser system, several factors must be emphasized. During quiescent states, the space platform is "buttoned up", that is, there are doors and covers in place to protect not only the optics, but the entire inside of the spacecraft. These protect the SBL from small particles of dust, meteorites, and an entire array of active Soviet countermeasures that might be applied against the SBL platform. During operations these covers are retracted and stowed. This is the period of time that the spacecraft is the most vulnerable. To reduce vulnerability, the beam expander (which includes the large primary mirror) is encased in a lightweight cylindrical metal baffle that limits vulnerability to the direction the laser beam expander is pointing. This means that the acceptance angle into the beam expander across the expanse of space is extremely small. It would thus be very difficult for an attacker to direct, e.g., an unguided object "down the barrel" of an SBL.

Hardening to x-rays and other nuclear detonation products is a greater problem. In the case of x-rays, the cylindrical baffle described above is also very effective, since it takes only minimal material to stop the penetration of x-rays in the energy spectrum associated with a nuclear weapon. To successfully defend against unshielded x-rays, optical coatings must be designed with radiation hardness ("rad hardness") in mind. Hardening is a major technology area being investigated for all SDIO space (and ground) optics. Programs exist to investigate hardening of materials against x-rays and lasers operating across a major portion of the energy spectrum, as well as against electrons and other particles. Low "Z" materials such as beryllium appear to have excellent properties for such environments and are being investigated in depth under SDIO sponsorship.

The degree to which a relatively low to modest power level adversary DEW might be a threat to an SDI BMD system depends on many eventualities. First, the effectiveness of such a countermeasure is critically dependent upon whether the adversary's DEW is on the ground or in space. A modest brightness (10^{18} w/sr) SBL can, in principle, threaten almost all satellites in low earth orbit over a relatively short (24 hours) period of time as its orbit passes within lethal range of an SDI satellite. Here, special long distance keepout ranges could be established and used in conjunction with shielding and an effective shootback policy that would limit the extent of damage caused by an adversary's SBL. However, the SBL ASAT can probably be negated easily in a shorter time by the Space Based Interceptors (SBIs) that are also part of the SDI BMD constellation. In addition, the policy of space denial for such adversary systems could be the most effective (and cost-effective) course of action, albeit one with significant political ramifications.

An adversary's GBL ASAT presents a different problem. It has virtually an unlimited magazine and can, over a longer period of time, address all satellites that overfly its location. Furthermore, a neutralization attack on an adversary's GBL could be difficult and/or provocative. However, many obstacles must be overcome before a GBL system becomes a threat to the SDI constellation. First, a GBL ASAT system without space assets is limited to attacking assets that overfly its position. Second, since SDI assets will be hardened against low level laser radiation, the GBL ASAT must be capable of substantial correction of the extreme degradation of high energy beam through divergence caused by turbulence and nonlinear effects in the atmosphere in order to threaten the SDI system at all. This will require high bandwidth real-time measurements of phase errors introduced by atmospheric turbulence and correction of the outgoing beam phase front. Practical limitations will preclude good correction beyond about 45 degrees of zenith under the best of circumstances. Further, active counters to the pointing and tracking and turbulence measurement process by the asset under attack are possible. In the longer term, when a more robust adversary's GBL ASAT might be available, is it relatively straight forward to shield space assets with lightweight ablators that can cause orders of magnitude increases in the required energy deposited by the GBL ASAT, thus making negation of the SDI space assets extremely costly or impractical.

To enhance the survivability of all space assets, the SDIO is devoting major resources to various technologies that will make it more difficult for the offense to neutralize BMD components. These include; lightweight physical barrier shielding materials, radiation hardened materials and optical coatings, hardened electronics and sensor systems, lightweight ablative shielding materials, applied stealth technologies, etc. In addition to these technology solutions to the survivability problem, various strategies and tactics are being developed to minimize the impact of some of the counter-measures. Examples include; the establishment of keepout zones around weapons and sensors, maneuvering spacecraft, rules of engagement, etc.

In summary, survivability is recognized as an integral part of the SDI BMD system. It is being pursued vigorously along with performance, cost, and operational issues as the SDI architectures mature from the conceptual design phase to the prototype phase and finally to the deployment phase.

III. CLOSING COMMENTS

In closing, it is clear that the technologies required for a near term space based chemical laser system

are among the most mature of all of the DEW candidates. In studies that have been conducted by the SDIO and others, Space Based Chemical Lasers, based upon only modest technology projections that involve engineering rather than physics issues, appear to be one of (if not the most) attractive DEW concepts for the SDIO's BMD mission. The requirements for a militarily useful system utilizing these technologies in the SDI roles of boost phase killer and midcourse discriminator appear to be within reach of a system that could be fielded in the mid-to-late 1990's. In addition, technologies have been demonstrated at small scale that could allow the direct scaling of these near term systems to systems of very robust capabilities for the longer term with no hardware obsolescence.

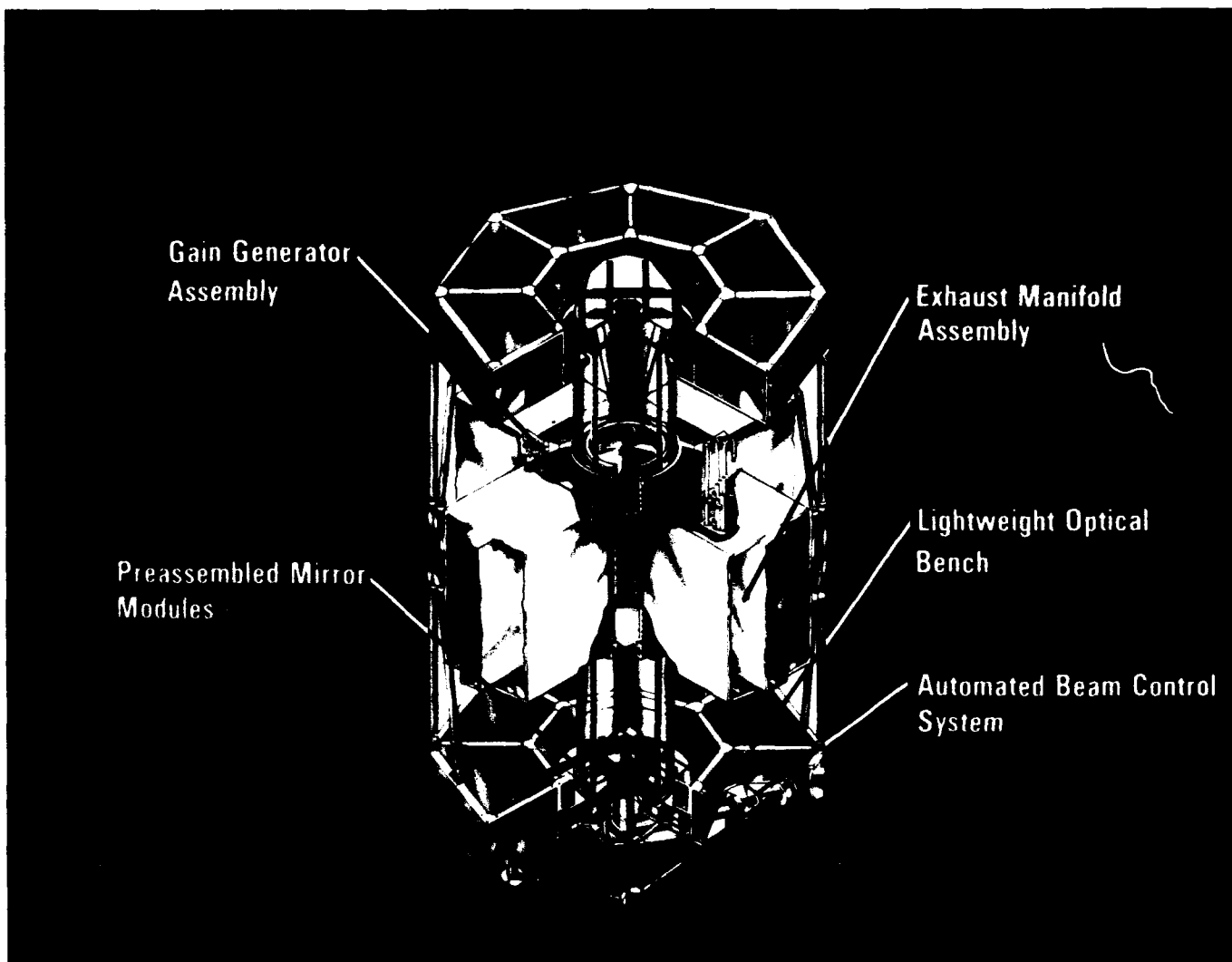


Figure 1 - Alpha HF Chemical Laser

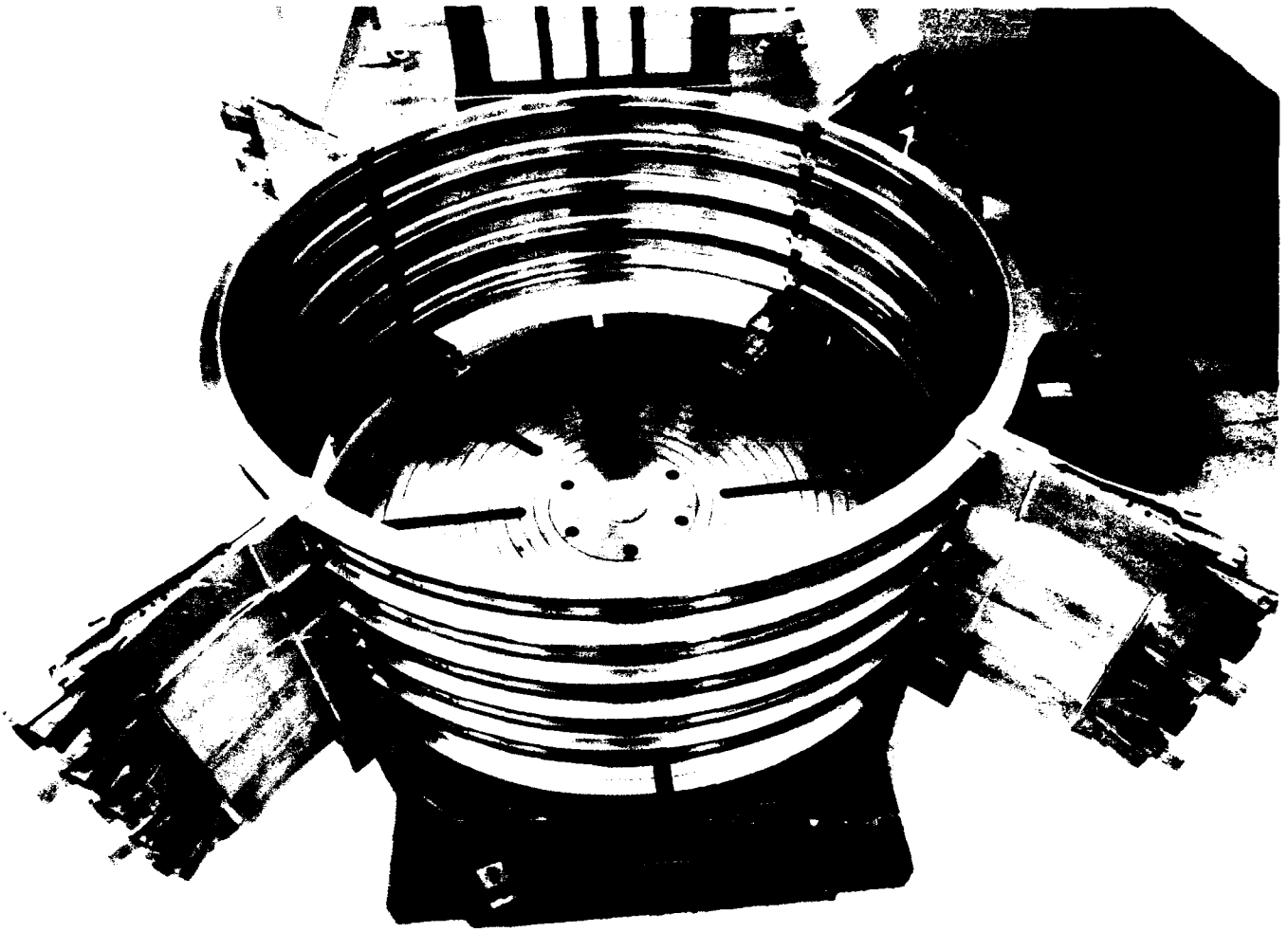


Figure 2 - Alpha Cylindrical Gain Generator

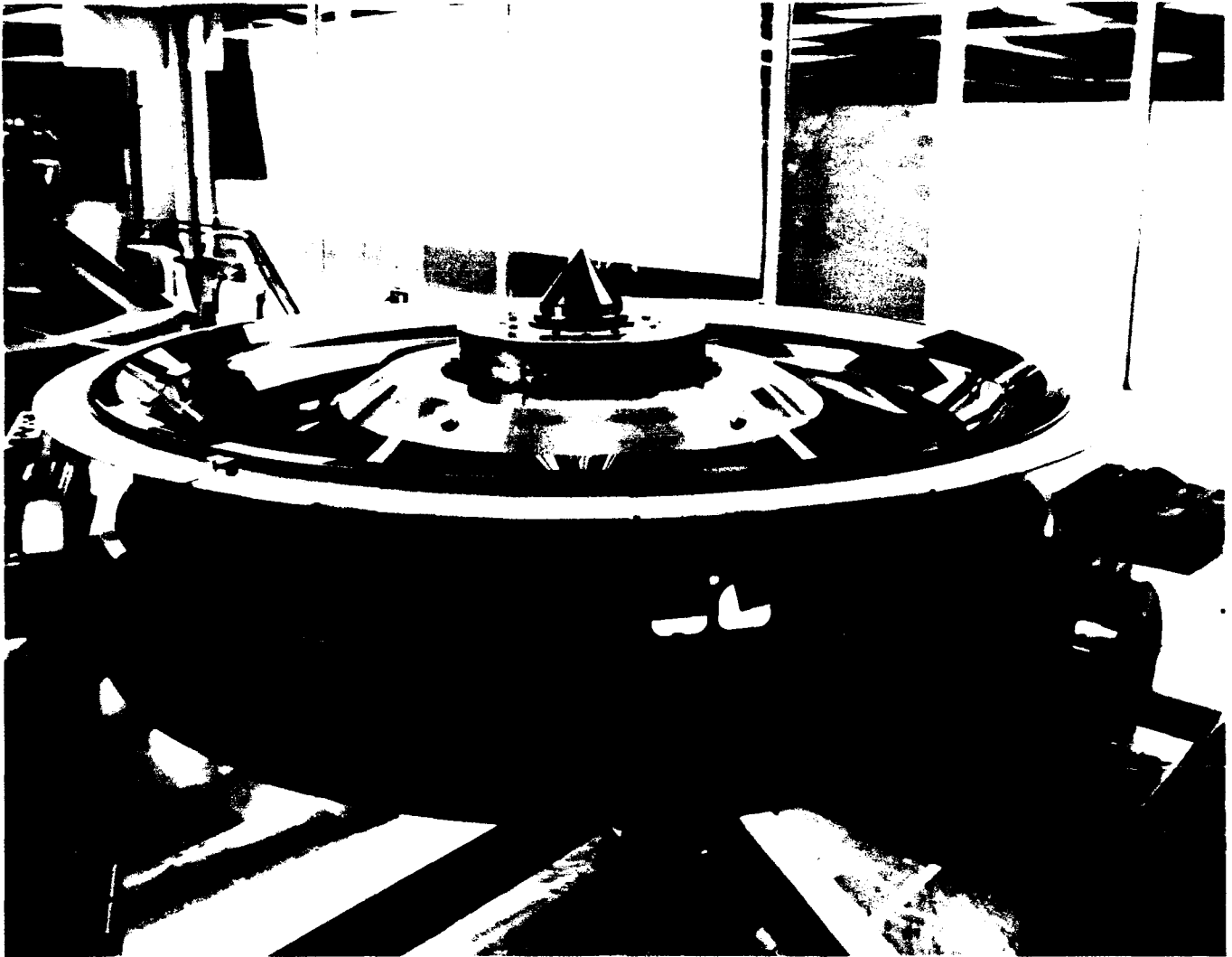


Figure 3 - Alpha Resonator Annular Optics

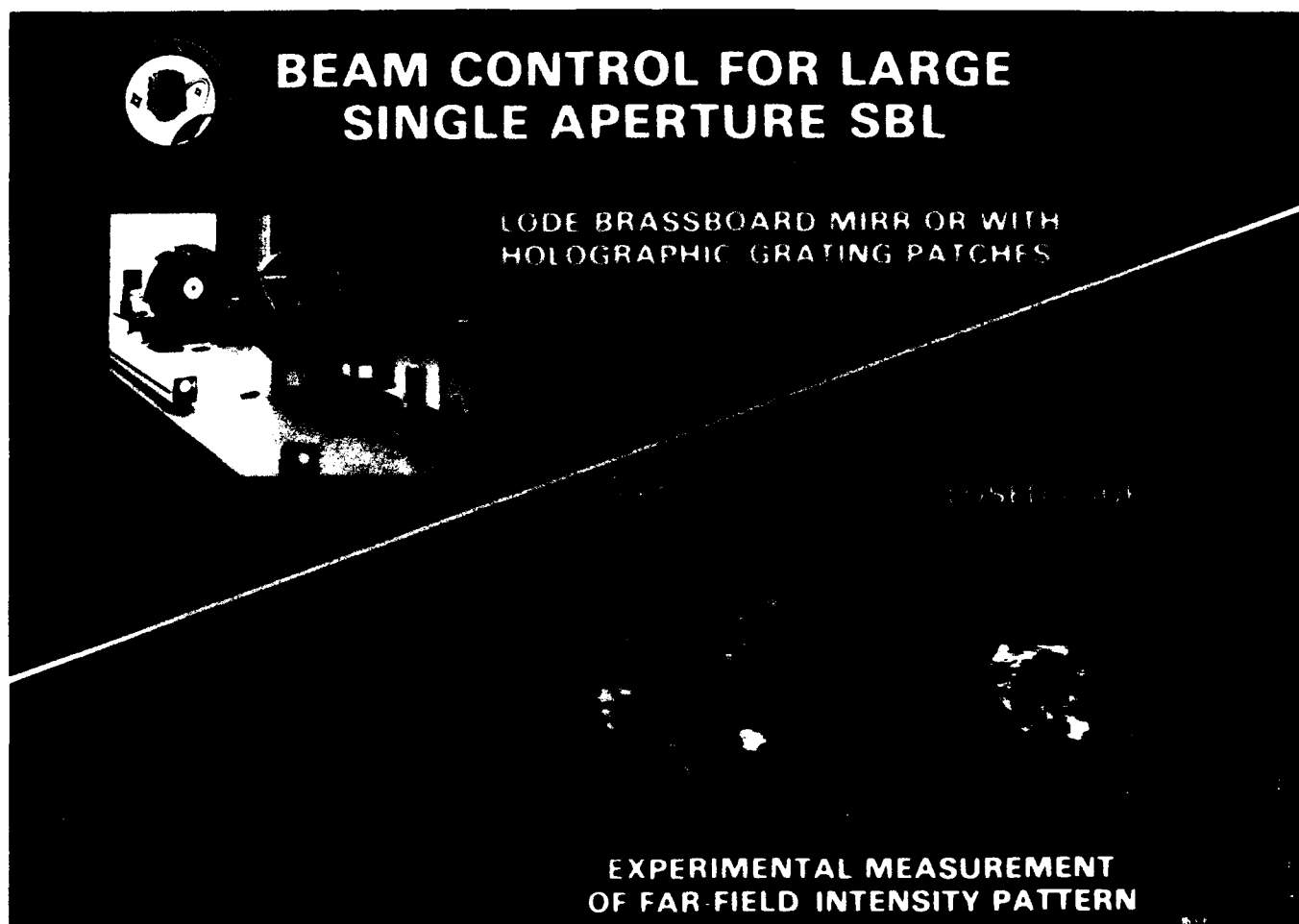


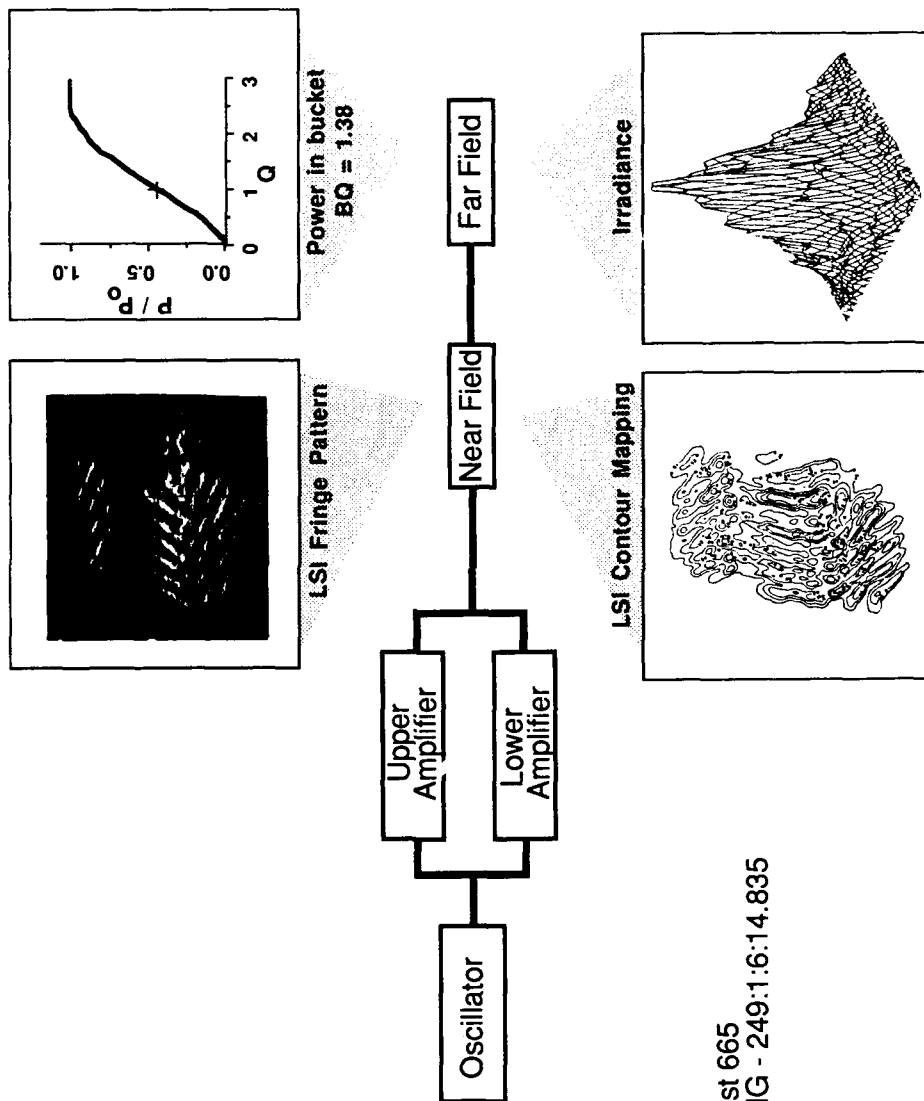
Figure 4 - Large Optics Demonstration Experiment (LODE)



Figure 5 - LODE Advanced Mirror Program (LAMP) Mirror

Multiline CW Coupled Devices

Coherent Beam Coupling Demonstrated Using the MOPA Configuration



Test 665
IRIG - 249:16:14.835

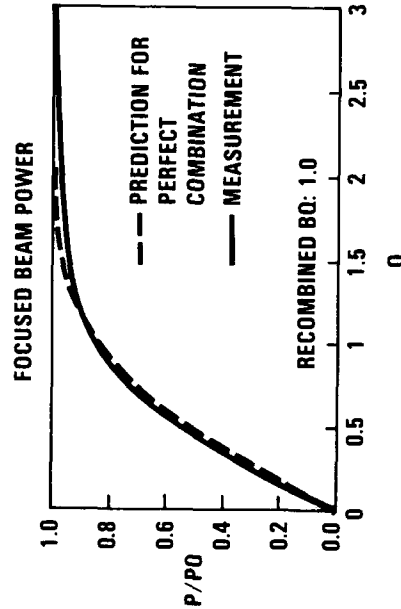
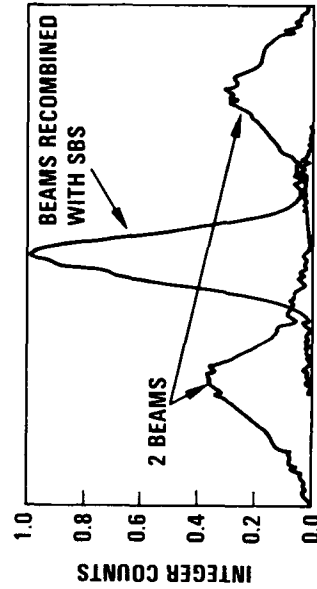
Figure 6 - HF Chemical Laser Master Oscillator/Power Amplifier (MOPA) Experimental

Phase Conjugate Beam Combination: Now Demonstrated For HF Chemical Lasers



Combination of multiple beams is a key requirement in scaling chemical lasers to SDI weapon system sizes

Beam combination using SBS phase conjugation has now been achieved for an HF chemical laser. No adaptive optics or control hardware was required



In new test results at the APACHE Test Facility, a laser beam was broken into two separate beams, which were recombined with diffracton-limited beam quality

Fractional wavelength alignment control was **not** needed: Test was performed with beams separated by several far-field diameters

Figure 7 - High Power Phase Conjugation of HF Chemical Lasers

AS-1

SHORT-WAVELENGTH LASER DEVELOPMENT

J. M. Herbelin

Aerophysics Laboratory, The Aerospace Corporation, P.O. Box 92957, Los Angeles, CA 90009

A subsonic laminar flamesheet facility has been developed for studying the reactive flow between electronically excited nitrogen fluoride, $\text{NF}(a)$, and ground-state bismuth. Initial measurements are reported and are shown to agree qualitatively with a simplified flamesheet model.

Introduction

Since its discovery, the reactive flow formed by mixing ground-state atomic bismuth with electronically excited bismuth has been the subject of numerous investigations into its potential as the power source for a continuous-wave (cw) visible chemical laser system.¹⁻⁵ The major accomplishments of those studies can be summarized as follows: Theoretical and experimental confirmation of fast and efficient excitation of bismuth fluoride, $\text{BiF}(A)$; experimental confirmation that $\text{BiF}(A)$ has a radiative lifetime of an appropriate magnitude for continuous operation; measurement of slow, electronic quenching of the excited state, $\text{BiF}(A)$; measurement of fast vibrational relaxation rates for that excited state; evidence of bismuth-atom recycling in low-density flows; demonstrated scalability of excited-state $\text{BiF}(A)$ through electrical initiation of a premixed combustive mixture using TMB (trimethylbismuthine) as the bismuth source; and demonstrated scalability of excited-state $\text{Bi}(D)$, the precursor to $\text{BiF}(A)$, in a supersonic flow.

Each of the above accomplishments represents a solid step toward the eventual demonstration of a chemical blue-green laser; however, three important questions must be answered before feasibility and efficiency of a continuous-wave laser system based on the BiF molecule can be determined:

1. Does the $\text{BiF}(A)$ excited-state density scale in a cw mixing flame in a predictable manner?
2. Is the recycling process of bismuth atoms via the reaction of $\text{BiF}(X)$ with hydrogen atoms? and if so, Is it effective in the high-density conditions required for laser action?
3. Finally, Is the relaxation of the lower levels, the vibrational states of the ground state, $\text{BiF}(X)$, as rapid as was observed for the excited state?

In this paper, we report our initial efforts toward answering these critical questions.

Experimental Approach

To answer 1., the scalability question, it is necessary to study the interplay of the chemistry and fluid dynamics in a simple flamesheet. Consequently, we selected an experimental approach that relies on (1) independent control of the starting reagents, and (2) the ability to completely characterize important $\text{NF}(a^1\Delta)$, $\text{Bi}(D)$, and $\text{BiF}(A)$ density profiles within the flame. For these purposes, we designed and built a specialized subsonic flow facility. A close-up of the reactor section is presented in Fig. 1.

In the reactor, the reagents are controlled as follows. Into a stream of fluorine atoms, F , and difluoroamine radicals, NF_2 , which are flowing from right to left in the upper section, molecular hydrogen, H_2 , is introduced so that the desired $\text{NF}(a^1\Delta)$ is prepared according to the following reactions:



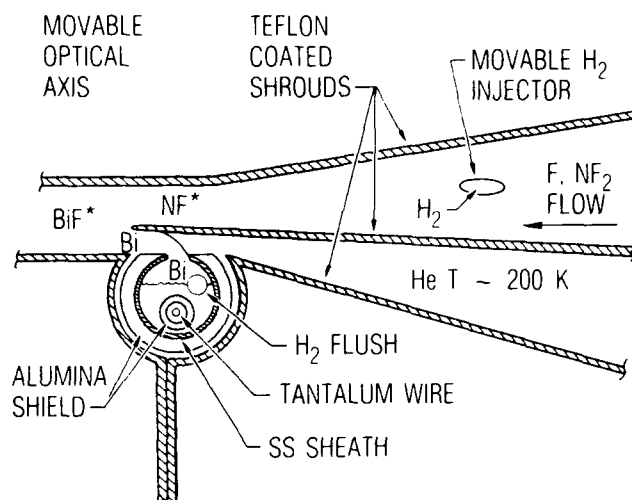
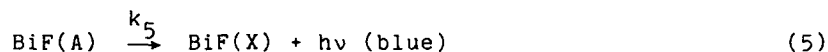
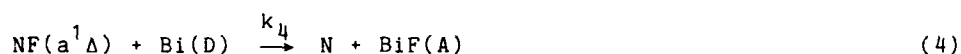


Fig. 1. Side view of reaction section of the fast-flow facility. Electronically excited $\text{NF}(a^1\Delta)$ (upper) is mixed with bismuth atoms (lower) in a carefully controlled laminar flamesheet to produce $\text{BiF}(A)$.

In the lower section, a stream of helium is passed over a specially designed bismuth boiler to produce a uniform stream of bismuth atoms. The two flows are then carefully joined to form a flat, laminar flamesheet in which the following reactions are believed to proceed to produce a brilliant blue flame:



The experimental setup to operate and characterize this reactor is depicted schematically in Fig. 2. The reactor is located in the center and is operated by a flow console, which includes a flow-system computer to monitor 16 channels of data: the flow rates, four temperatures, pressure, heater power, and spectrometer signals. The data are recorded and stored automatically for posttest analysis.

To obtain the emission spectra, such as the $\text{BiF}(A-X)$ spectrum shown in Fig. 3, we constructed and carefully calibrated a computer-controlled spectrometer, which is located to the right in Fig. 2. The spectrometer is preprogrammed to record the desired spectra in a minimum of run time, because the bismuth heater has a limited operating time at full-scale flow rates.

In addition to the blue $\text{BiF}(A)$ emission spectrum, emissions from the excited states of $\text{NF}(a^1\Delta)$, $\text{Bi}(D)$, $\text{HF}(3)$, and $\text{N}_2(B)$ are recorded. Figure 3 displays a close-up of a portion of the BiF experimental (dotted) and simulated (solid) spectra used to determine the rotational and vibrational temperatures of the molecule. The relative widths of the bands are quite sensitive to the rotational temperature, which here is $600 \pm 50^\circ\text{C}$. The relative heights of the band peaks fit a Boltzmann distribution at a slightly elevated temperature of $825 \pm 50^\circ\text{C}$. As expected, the vibrational distribution is quite sensitive to total pressure, and at pressures below 4 Torr it no longer obeys a Boltzmann distribution. The spectrum of Fig. 3 was measured at a total pressure of 6 Torr.

For this first series of experiments, the optical train of the spectrometer was designed to scan its axis along the flow to record the integrated intensity as a function of the flow distance. To obtain the detailed density profiles of the species across the flamesheet, we employed an optical multichannel analyzer (OMA) mounted on a 0.24-m Jarrell-Ash (J-A) spectrometer at a 90° rotation to the conventional position. Because of the excellent response of the OMA in the blue, the spectrometer can be operated with an aperture of less than 1 mm and thereby achieve a spatial resolution of $\sim 100 \mu\text{m}$ for the $\text{BiF}(A)$ profile.

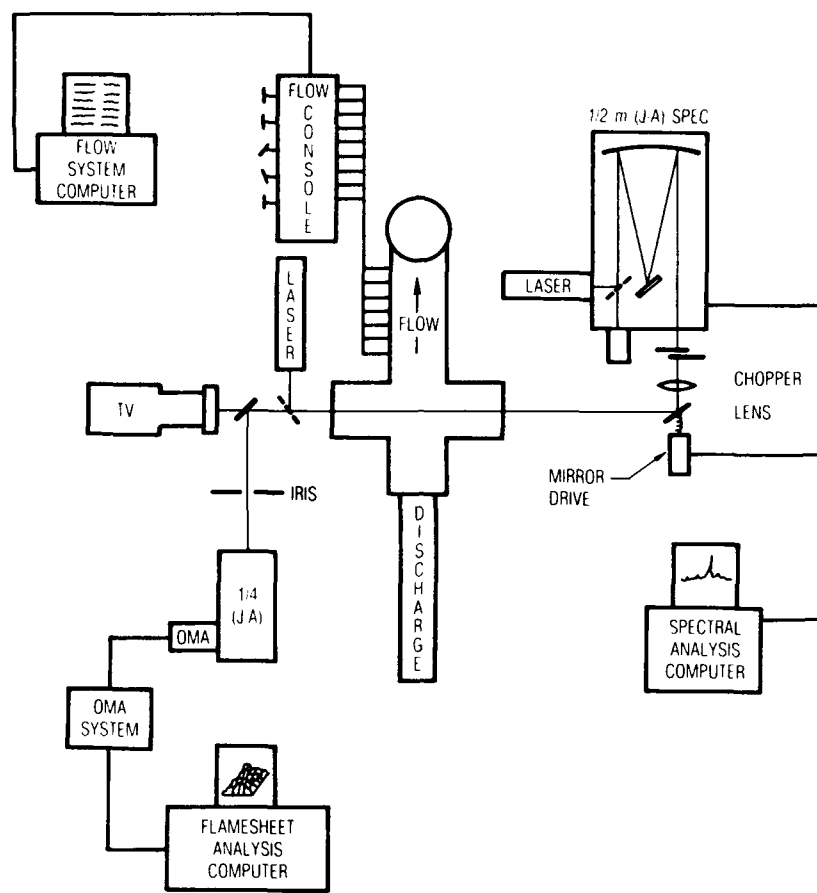


Fig. 2. Schematic of computerized flow-facility diagnostics, consisting of flow console/computer system (upper left); an automated spectrum-analyzing system (right); and OMA/TV flamesheet profile acquisition system (lower left).

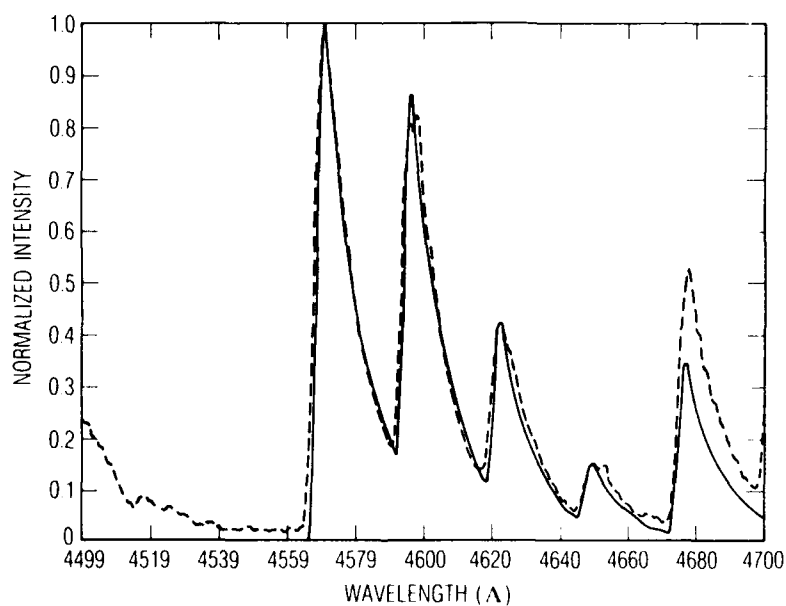


Fig. 3. Comparison of high-resolution experimental (dotted) and simulated (solid) spectra of the BiF(A-X) (0-2) band system from which the vibrational and rotational temperatures were deduced to be $825 \pm 50^\circ\text{C}$ and $600 \pm 50^\circ\text{C}$, respectively.

Results and Discussion

Figures 4a and 4b present the transverse flamesheet profiles for Bi(D), BiF(A), and NF(a¹Δ) for hydrogen-atom-lean and hydrogen-atom-rich conditions, respectively. The profiles have been normalized for ease of comparison. The BiF(A) and NF(a¹Δ) profiles were obtained directly from the OMA, whereas the Bi(D) profile was deduced from those two profiles, using the simple expression

$$[\text{Bi(D)}] = A[\text{BiF(A)}]/k_4[\text{NF(a}^1\Delta)] \quad (6)$$

in which the Einstein coefficient, A, and rate coefficient, k_4 , are known constants. (This simple expression follows directly from the solution of the mass-transport-reaction equations by applying the usual steady-state approximation.)

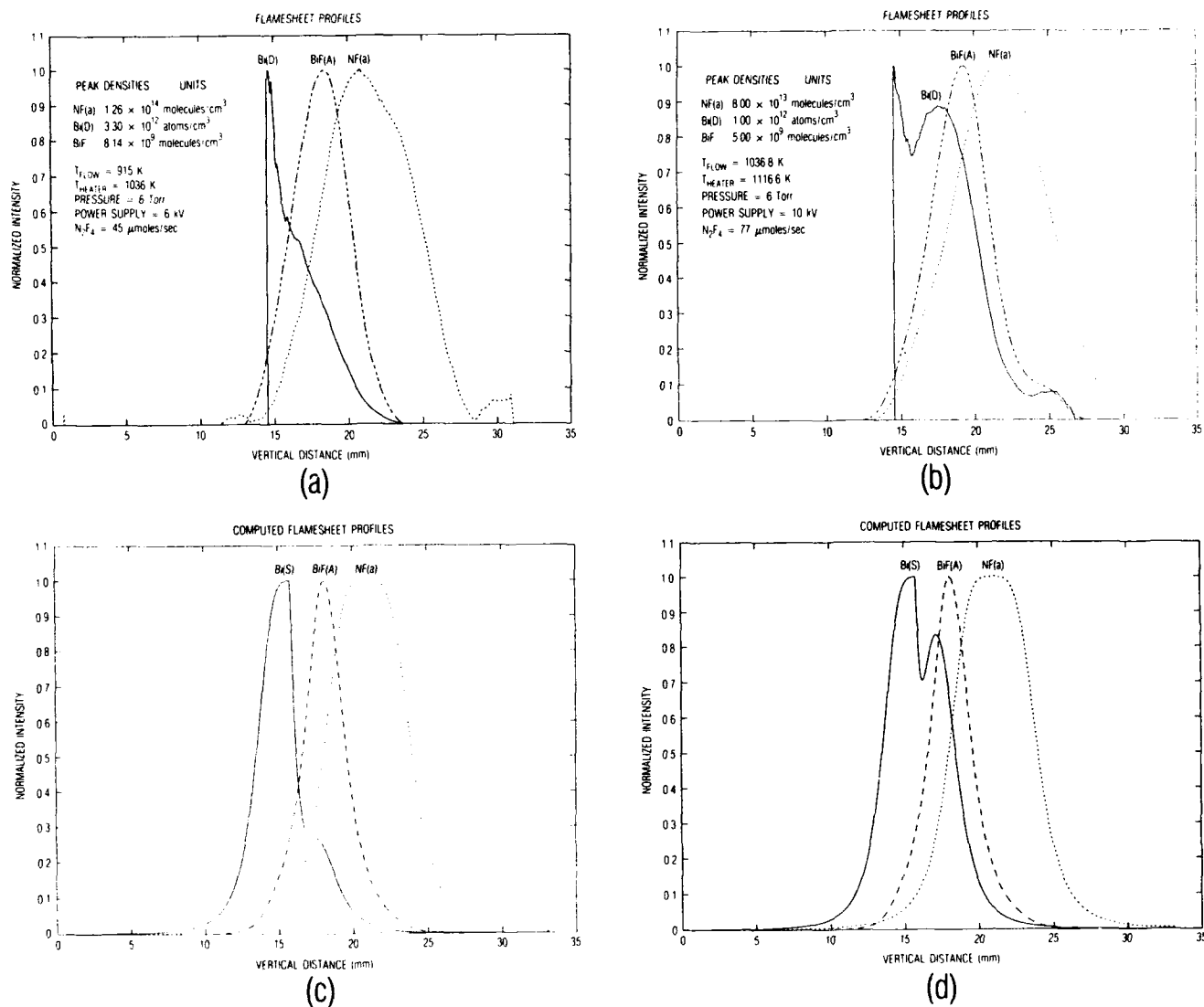


Fig. 4. High-resolution transverse flamesheet density profiles for the Bi(D), BiF(A), and NF(a¹Δ) excited states: (a) experimental, hydrogen-atom-lean conditions; (b) experimental, hydrogen-atom-rich conditions; (c) theoretical, hydrogen-atom lean; and (d) theoretical, hydrogen-atom rich. The extra width of the Bi(D) profile suggests bismuth-atom regeneration via reactions of hydrogen atoms with BiF(X).

Figures 4c and 4d present the results of a simplified flamesheet analysis we developed for the purpose of guiding the experiments. For comparison, Figs. 4a and 4c are the experimental and computed flame profiles for conditions that have been purposely adjusted to produce a deficiency in hydrogen atoms. Under those conditions, the Bi(D) profile is observed to be quite narrow, owing to the consumption of the bismuth atoms as they diffuse

into the NF(a) stream. However, when the conditions are changed to ensure the presence of hydrogen atoms, Figs. 4b and 4d, the Bi(D) profile is observed to increase in width and to actually display a hump. The computed curve suggests that this hump can be attributed to the regeneration of bismuth atoms via the reaction



But we must reemphasize that the Bi(D) distributions of Figs. 4a and 4b are deduced, not measured. A direct measurement of the Bi(D) state remains to be done.

Because of weight and mixing considerations, bismuth-atom regeneration within the flamesheet is absolutely essential to the efficient operation of a cw laser system. The results give evidence of that regeneration.

Although the data are only preliminary, the results thus far obtained are encouraging. Obviously, a great deal of work lies ahead to refine both the experimental measurements and the modeling results before the remaining questions can be answered completely. Nevertheless, the prospects of a cw chemical visible laser based on the NF(a)-BiF reaction system continue to be promising.

References

1. J. M. Herbelin, "Efficient Production of Electronically Excited BiF(AO⁺) via Collisions with NF(a). II," in Proceedings, International Conference on Lasers '86, Orlando, FL (1986).
2. J. M. Herbelin, Chem. Phys. Lett. 133, 331 (1987).
3. J. M. Herbelin, "Blue-Green Chemical Laser Development," in Proceedings, AIAA/SDIO High Power Laser Device Conference, Boulder, CO (1987).
4. J. M. Herbelin, presented at the AIAA 19th Fluid Dynamics, Plasma Dynamics and Laser Conference, Honolulu, HI (1987), paper 1391.
5. J. M. Herbelin, "Efficient Production of Electronically Excited BiF(AO⁺) via Collisions with NF(a). II," Report No. ATR-85(8315)-2 (The Aerospace Corporation, El Segundo, CA, 22 June 1987).

HIGHLY EFFICIENT CHEMICALLY PUMPED OXYGEN IODINE LASER

S. Yoshida, H. Fujii*, S. Amano, M. Endoh, T. Sawano, T. Fujioka

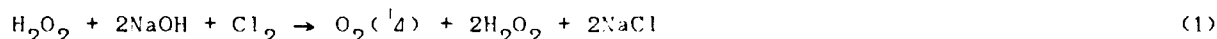
Laser Laboratory, Industrial Research Institute
1201 Takada, Kashiwa, Chiba 277, Japan

Abstract

A chemically pumped oxygen iodine laser has been developed with industrial application of the laser in mind. The system has been operated employing 35 wt% hydrogen peroxide rather than commonly used 90 wt% solution. Laser power as high as 270 W has been extracted. The maximum overall efficiency of 40%, which is almost twice as large as the previously reported best data, has been achieved. Typical experimental data are analyzed in details. It has been shown that the performance of singlet oxygen generator is a key issue of the entire system. Using the present system, we have also performed a preliminary experiment of material processing. A steel plate of 1-mm thick has successfully been drilled.

Introduction

The chemically pumped oxygen iodine laser (COIL) is a powerful and efficient radiation source in the near infrared region. Among the currently available chemical lasers, the COIL is the only laser that utilizes an electronic transition of lasing medium. The lasing action of this laser may be represented by the following reaction.



The first reaction is an energy extraction process in which the chemical energy originally contained in hydrogen peroxide is stored in the excited state oxygen (singlet oxygen). The hydrogen peroxide solution should be alkalized so as to achieve realistic reaction rate. The second reaction is an energy transfer process to generate the excited state iodine atom which is the upper laser level. Since this is a reversible reaction, the ratio of the concentration of excited state oxygen to that of ground state oxygen must be sufficiently high in order to obtain high degree of population inversion in iodine atoms. The excited state iodine then loses according to reaction (3) and generates optical output at 1.315 microns in wavelength.

The operating wavelength of COIL, 1.315 microns, lies in the minimum loss range of silica fibers as shown in Figure 1. Therefore it is feasible to transmit high cw output of a COIL system through optical fibers with high transmission efficiency. The optical power delivery through fibers offers many advanced technologies such as three dimensional processing or remote processing of various materials.

Besides the advantage of fiber transmission, the COIL wavelength is also attractive from the view point of laser-material interaction. Figure 2 shows the reflectivities of various metals as a function of wavelength. As is seen in this figure, the reflectivity at 1.315 microns is much less than at the wavelength of CO_2 laser, the most commonly used industrial laser. Combining this effect with the better focusability associated with the shorter wavelength, a COIL system may be expected more power effective than a CO_2 laser system of the same power level. In terms of medical applications, there are also some new exciting applications of the 1.3 micron-radiation such as tissue fusion.

In spite of these fascinating properties, nobody has tried to apply this laser to industrial applications probably because of some technical difficulties. This situation motivated us to develop a stable COIL device with its industrial applications in mind. Thus we have dared to start a fairly long term project in which we attempt to develop a kW-class COIL system of reasonable operation duration.

As far as industrial applications are concerned, the efficiency of the total system becomes one of the most significant parameters because it is related to the dimension and operation cost of the system. In the case of a COIL, experimentally achieved efficiencies

*Present address, Opto-Engineering Laboratory, Technical Institute, Kawasaki Heavy Industries, Ltd. Kobe, Japan

are still far below the theoretically predicted limit for the time being. Therefore we focus our primary effort on this subject, as the initial stage of the project, and have developed a highly efficient COIL system of a reasonable output range. The key to achieve high overall efficiency of a COIL system is to develop an efficient SOG (singlet oxygen generator), one which is efficient in that the ratio of the concentration of excited oxygen to that of ground state oxygen is high. In fact, in our case, the performance of the SOG almost governs the efficiency of the entire system as will be discussed later in this paper. The reason for this is obvious if one recalls that the energy transfer reaction (2) is a reversible process so that the ratio of excited oxygen to ground state oxygen is important.

It should be noted that the operation cost is strongly dependent on the concentration of hydrogen peroxide used for the excited oxygen generation. A solution of 35 wt%, for example, is more cost effective than the commonly used 90 wt% solution by the factor of 5. Thus we employed 35 wt% solution in our system. The only problem associated with employing such a dilute solution is that it generates more water vapor which quenches the excited state iodine and oxygen. We have solved this problem by designing the SOG and WVT (water vapor trap) properly.

Experimental

The schematic view of the present system is depicted in Figure 3. Excited oxygen is generated in a sparger type SOG in which Cl_2 gas is introduced into the alkaline hydrogen peroxide solution through 8-mm-i.d. teflon tubes. The WVT consists of five 36-mm-i.d., 1200-mm long straight glass tubes arranged in parallel. The glass tubes are immersed in ethanol which is cooled to dry ice temperature. The laser duct, made of polyvinylchloride, is 35-cm wide and 2 cm high. The iodine injector is a 1/4-inch-diam. copper tube placed horizontally in the laser duct. Holes of 0.5-mm-diam. are drilled on the downstream-side of the injector so that iodine vapor may spout out into the active region. The iodine container is heated up to 70 deg. by an electric heater. Nitrogen gas was used to carry iodine vapor in the container to the iodine injector. A rare gas is usually used for this purpose because the quenching rate of excited iodine is low, but we employed nitrogen for an economical reason. We compared nitrogen with argon but did not see any difference with respect to the quenching problem. The optical cavity of a 5-m curvature total reflector and a flat partial reflector. The cavity length is 60 cm. The center of the optical pass is about 1.5 cm down stream of the iodine injection point. The effective pumping speed in the laser duct is about 80 l/s which is equivalent to flow speed of 10 m/s in the active region.

9000 cc 35 wt% hydrogen peroxide and 1000 cc NaOH solution was initially introduced to the SOG. Before starting Cl_2 bubbling, the solution was cooled down to 253 K by bubbling nitrogen which encouraged water evaporation and thereby decreased the solution temperature by removing the latent heat. During operation the solution temperature rose because of the reaction heat and reached equilibrium at around 263 K. Our preliminary experiment has shown that such a temperature rise does not affect system performance. When the alkalinity in the SOG fell down, the same amount of NaOH solution was added so that the pH value of the solution might be kept over 10. Excessive NaOH addition at one time caused reduction of NaOH crystals. This was not observed when 90 wt% hydrogen peroxide was used. The solution temperature rose above 273 K when alkali was added, but the initial temperature was easily restored by nitrogen bubbling. The temperature recovery time in the case of 35 wt% hydrogen peroxide was about half of that of 90 wt% hydrogen peroxide owing to higher pressure of saturated water vapor.

Results and discussion

The COIL system has been operated many time with various operational conditions. Controlled parameters include the pumping speed, iodine carrier gas flow rate, gas flow velocity in the active region, total reflectivity of the cavity, distance between the iodine injector and the optical axis of the cavity, etc. The discussion here focuses on one specific run with a set of parameters listed in Table 1. This parameter set is not optimized in terms of the flow velocity and the reflectivity of partial reflector. We need more experiments to optimize these parameters.

To discuss the present experimental results we introduce several efficiencies defined by following expressions:

$$\eta_r = W_{\text{O}_2} / W_{\text{Cl}_2} \quad (4)$$

$$\eta_{\text{exc}} = W_{\text{O}_2^*} / W_{\text{O}_2} \quad (5)$$

$$\eta_{\text{ext}} = P_L / (E_{O_2} W_{O_2} (\eta_{\text{exc}} - \eta_{\text{exc}}^0)) \quad (6)$$

$$\eta_{\text{chem}} = P_L / (E_{O_2} W_{O_2}) \quad (7)$$

$$\eta_{\text{ov}} = P_L / (E_{O_2} W_{Cl_2}) \quad (8)$$

where W_{O_2} , W_{Cl_2} , $W_{O_2}^*$ are flow rates of total oxygen, singlet oxygen, and input chlorine, respectively, expressed in mol/s. E_{O_2} is energy stored in 1 mol singlet oxygen, and P_L is laser power. We call η reaction efficiency, η_{exc} excitation efficiency, η_{ext} extraction efficiency, η_{chem} chemical efficiency and η_{ov} overall efficiency. The reaction efficiency represents how efficiently oxygen is generated. The excitation efficiency is the ratio of excited oxygen concentration to ground state oxygen. The extraction efficiency represents the efficiency of optical power extraction from the excited iodine. η_{exc}^0 which appears in the denominator of this expression denotes the minimum excitation efficiency required to obtain population inversion. The extraction efficiency is related to the efficiency of singlet oxygen/iodine mixing in the active region. The chemical efficiency is the ratio of laser power to the energy consumption rate of hydrogen peroxide whereas the overall efficiency is the ratio of laser power to the maximum energy consumption rate of hydrogen peroxide expected from the input Cl_2 flow. The overall efficiency becomes equal to the chemical efficiency if the reaction efficiency is unity. The overall efficiency can be expressed by other efficiencies as

$$\eta_{\text{ov}} = \eta_r \eta_{\text{chem}} = \eta_r (\eta_{\text{exc}} - \eta_{\text{exc}}^0) \quad (9)$$

As we already pointed out the performance of SOG is a key issue of a COIL system. The most significant parameter of a SOG is the excitation efficiency defined by eq. (5). We evaluated this efficiency as the ratio of singlet oxygen pressure to total oxygen pressure in the cavity. Singlet oxygen pressure was measured by a Ge detector which monitored the 1.27-micron emission. Since direct measurement of total oxygen pressure is difficult, we measured input Cl_2 flow rate and total volume flow rate in the cavity, instead, and calculated theoretical oxygen pressure using the Boyle-Charles law with the assumption that the reaction efficiency [See eq. (4)] was 100%.

Excitation efficiency obtained in the present work is plotted as a function of Cl_2 flow rate in Figure 4. The data are fairly good as compared with previous data shown in Table 2. The dotted line in Figure 4 is a theoretical calculation which takes only homogeneous quenching of singlet oxygen into account as deactivation processes. It shows fairly good agreement with the experiment indicating that only homogeneous quenching is important as loss mechanism of singlet oxygen. The discrepancy between the experiment and theory at higher Cl_2 flow can be ascribed to poor reaction efficiency. In fact our preliminary experiments imply that reaction efficiency of the present SOG becomes slightly less than unity for Cl_2 flow rate over 400 mmol/min.

Laser power and overall efficiency are also plotted as a function of Cl_2 flow rate in Figure 5. It is seen that as Cl_2 flow rate increases the laser power saturates and thereby the overall efficiency decreases. We ascribe this tendency to the dependence of excitation efficiency on Cl_2 flow rate [see Figure 4]. To clarify this, the overall efficiency data are plotted as a function of excitation efficiency in Figure 6. It is seen that the overall efficiency increases in proportion to the excitation efficiency. This implies that the performance of the SOG governs that of the entire system. It should be noted that the slope of Figure 6 is the product of reaction efficiency and excitation efficiency [see eq. (9)]. Assuming that the reaction efficiency is unity and that the minimum excitation efficiency required for the population inversion is 25%, as Churassy et al. point out, the extraction efficiency of the present experiment is evaluated about 55%.

Although the maximum laser power and overall efficiency under the present condition are 120 W and 24.8%, we have achieved higher power and efficiency as high as 270 W and 40%, respectively, in other runs. Details of these results will be discussed elsewhere in near future. Besides system analyses, we also made some preliminary experiments on material processing using the present system. So far we could successfully drill a 1-mm thick steel plate with laser power of 60 W. Results of these experiments may also be presented in future.

Conclusion

Having industrial applications in mind, we have operated a COIL system with very high overall efficiency. It has been revealed that a COIL can be efficiently operated with dilute hydrogen peroxide implying that relatively high concentration of water vapor can be tolerated in the active region. This is quite favorable from industrial point of view because the concentration of hydrogen peroxide is a dominating factor of the operation cost. 35 wt% solution, for example, is five times more cost effective than commonly used 90 wt% solution. It has been shown that the performance of SOG almost dominates that of the

entire system. In fact, the overall efficiency of the present system was almost proportional to the excitation efficiency. Comparison of experiments with theory suggests that the only loss mechanism of singlet oxygen to be taken into account is homogeneous deactivation. This makes system designing much easier. Being encouraged by the present result, we plan to construct a system of higher power.

References

- ¹D. J. Benerd, W. E. McDermott, N. R. Pchelkin, and R. R. Bousek, Appl. Phys. Lett. 34, 40 (1979)
- ²R. J. Richardson and C. E. Wiswall, Appl. Phys. Lett. 35, 138 (1979)
- ³C. E. Wiswall, S. L. Bragg, K. V. Reddy, H. V. Lilenfeld, and J. D. Kelley, J. Appl. Phys. 58, 115 (1985)
- ⁴D. J. Miller, C. W. Clenderning, W. D. English, J. G. Berg, and J. E. Trost, in CLEO 82 Conference on Lasers and Electro-optics, Phoenix, AZ (Optical Society of America, Washington, DC, 1982), p. 170
- ⁵K. Watanabe, S. Kashiwabara, K. Sawai, S. Toshima, and R. Fujimoto, J. Appl. Phys. 54, 1228 (1983)
- ⁶J. Bonnet, D. David, E. George, B. Leporecq, D. Pigache, and C. Verdier, Appl. Phys. Lett. 45, 1009 (1984)
- ⁷H. Yoshimoto, H. Yamakoshi, S. Shibukawa, and T. Uchiyama, J. Appl. Phys. 59, 42 (1986)
- ⁸K. Watanabe, S. Kashiwabara, and R. Fujimoto, J. Appl. Phys. 59, 42 (1986)
- ⁹N. P. Vagin, A. F. Konoshenko, P. G. Kryukov, D. Kh. Nurligareev, V. S. Pazyuk, V. N. Tomashov, and N. N. Yurishchev, Sov. J. Quantum Electron. 14, 1138 (1984)
- ¹⁰S. Yoshida, H. Fujii, T. Sawano, H. Endo, and T. Fujioka, Appl. Phys. Lett. 51, 1492 (1987)
- ¹¹S. Churassy, R. Bacis, A. J. Bouvier, C. P. Mery, J. Appl. Phys. 62, 31 (1987)

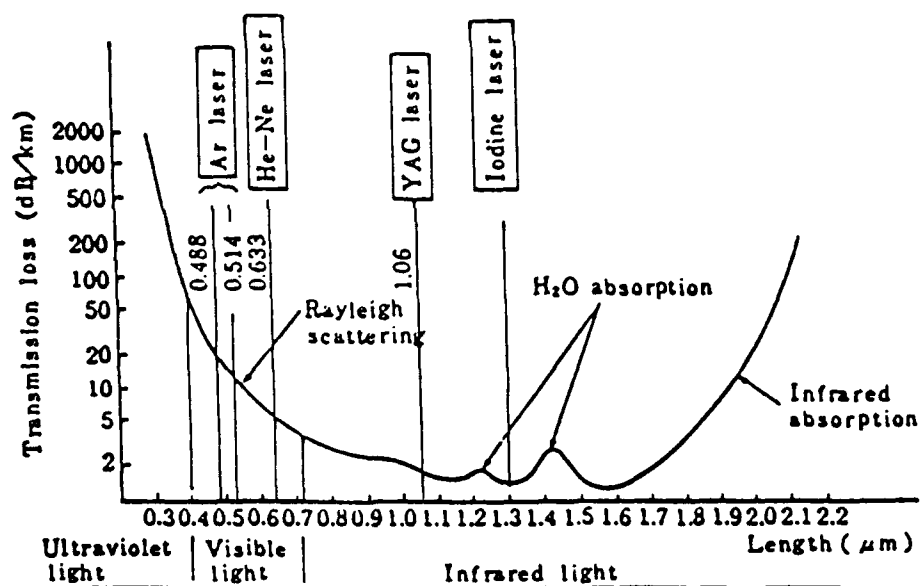


Figure 1. Transmission characteristics of silica fiber

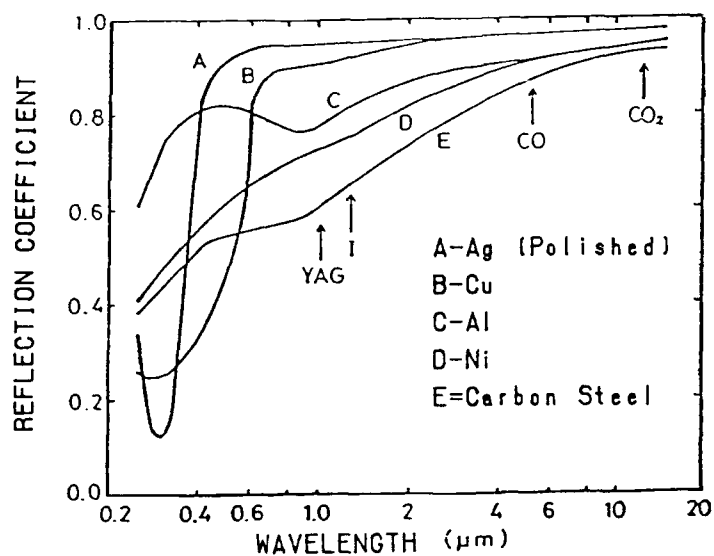


Figure 2. Reflectivity of various metallic materials as a function of wavelength

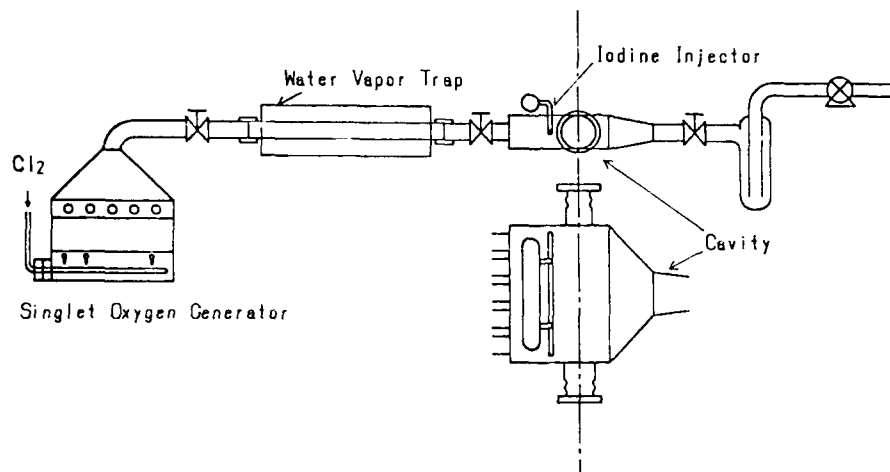


Figure 3. Schematic view of present OIL system

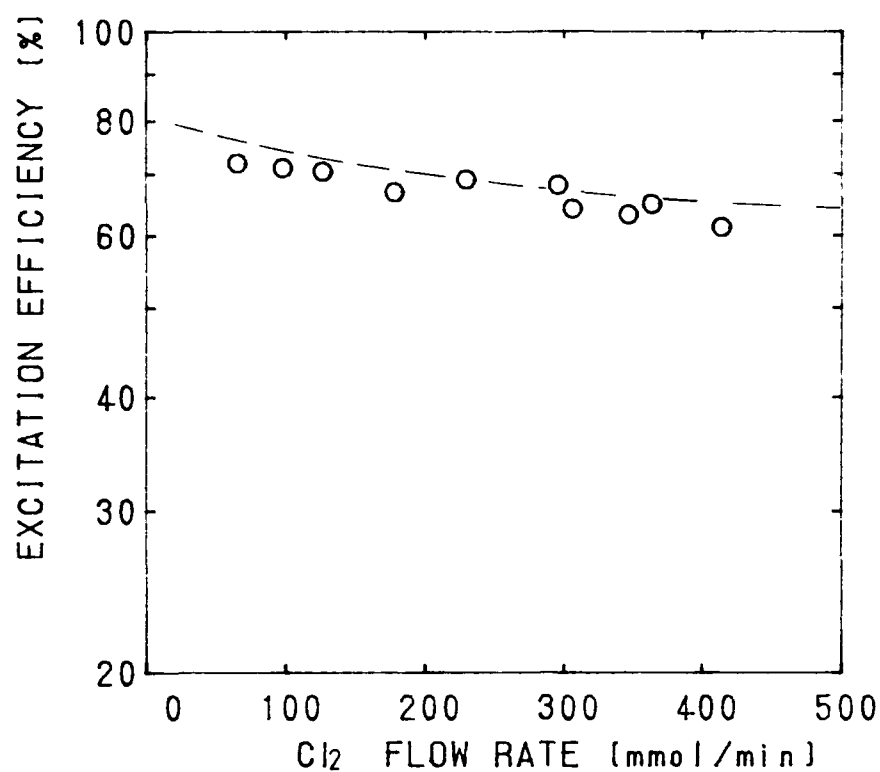


Figure 4. Excitation efficiency as a function of Cl₂ flow rate

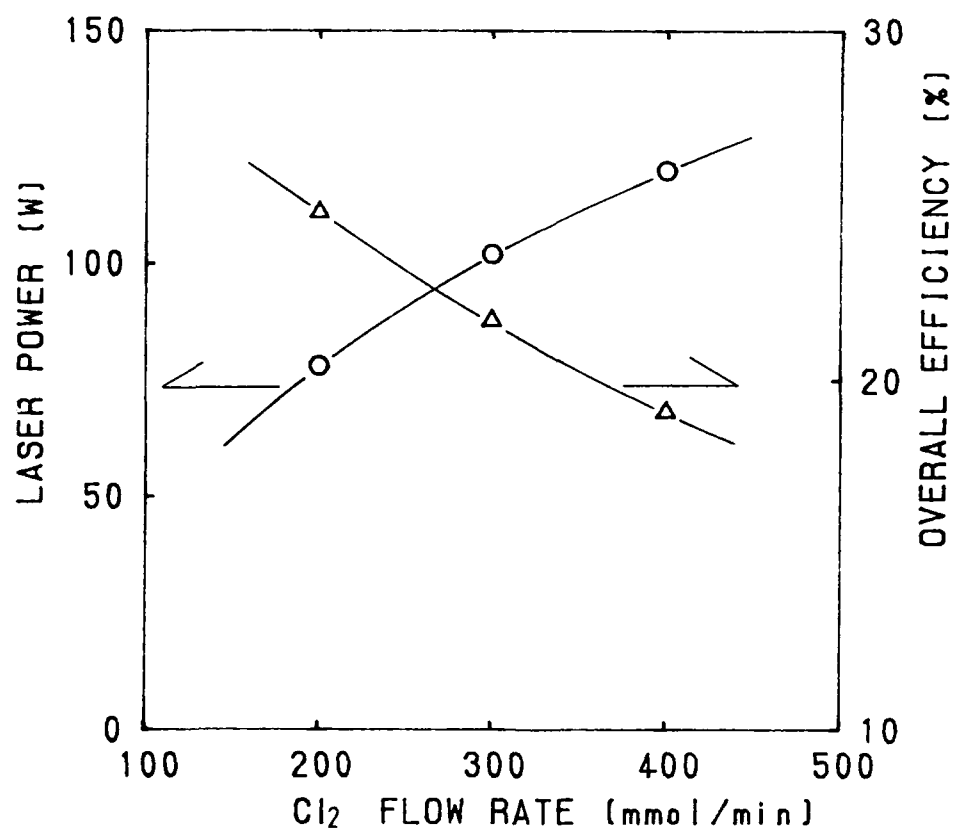


Figure 5. Laser power and overall efficiency as a function of Cl₂ flow rate

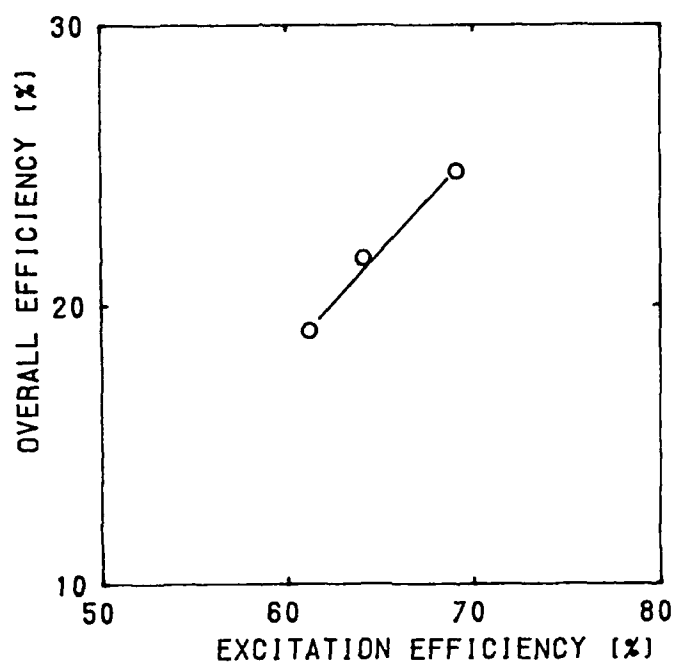


Figure 6. Excitation efficiency vs overall efficiency

Cl ₂ flow rate [mmol/min]	Volume flow [l/s]	Cavity pressure [Torr]	Total reflectance [%]	Injector distance [mm]	Iodine cell temp. [°C]
200	109	0.95	0.15	21	60
300	123	1.25	0.15	21	60
400	141	1.80	0.15	21	60

Table 1. Operational conditions of present experiment

Ref.	Cl ₂ flow rate [mmol/s]	Cavity pressure [Torr]	Flow velocity [m/s]	Excitation efficiency [%]	Laser power [W]	Overall efficiency [%]
1	30	1.0	60	40	100	3.7
2	15	...	50	30±10	10	0.7
3	19	0.9	...	40	180	10
4	80	0.82	37	50	1080	14.9
5	2.6	2.5	8	<44	11.6	4.9
6	30	0.3	40	35	80	2.9
7	6.9	1.8	15	>50	105	16.8
8	2.1	...	6	43	25	13
9	1.2	...	20	40	5	4.4
10	1.2	1.7	4.7	>60	35	20.7
This Work	5	1.25	14.0	>75	192	40.1

Table 2. Typical COIL performances

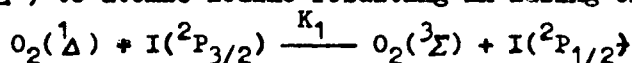
PULSE OPERATION OF A CHEMICAL OXYGEN IODINE LASER

Basov N.G., Kryukov P.G., Paziuk V.S., Vagin N.P., Yuryshev N.N.

P.N. Lebedev Physical Inst., USSR Acad. Sci., Moscow

Different methods of realizing a pulse repetition chemical oxygen-iodine laser (COIL) are discussed. Energy characteristics and efficiency of such a laser are significantly improved when iodine atoms are fastly generated in the volume filled with singlet oxygen. The pulse photolysis of the iodine containing species can be used for this purpose. The scheme for obtaining high power nanosecond pulses is proposed. It consists of a multipass ring amplifier and a second harmonic converter for extraction of output pulse.

CW Chemical Oxygen Iodine Laser based on the fast energy transfer from an electronically excited molecule $O_2(^1\Delta)$ to atomic iodine resulting in lasing on the $I(5^2P_{1/2}) \rightarrow$

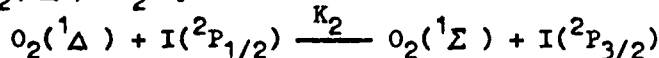


$I(5^2P_{3/2})$ transition is under investigation in the number of laboratories now. The attainable up to now energy characteristics of such a laser are rather high: output power - 2 kW (TRW, USA), specific power 211 J/gr Cl_2 (Keio Univ, Japan). The COIL may be placed among other types of powerful chemical lasers: HF, DF- CO_2 .

However, the COIL has a number of advantages. The basic advantage is a shorter wavelength of lasing, 1.315 μ m. This enables one to use glass and quartz optics and to transport the laser radiation along the quartz fibers with small losses. Moreover, since the laser operates at atomic transition under low pressure here arise some peculiarities coming from a narrow generation spectrum. These advantages make COIL attractive for industry applications.

The future of such a laser might be quite promising if one could realize pulse-repetition with high energy characteristic. Thus, the problem is to heighten the instant power of COIL with high values of average power and specific energy being the same. In this work we consider different ways of solving this problem. Note that all estimates were made for the case of laser operation at $T=300$ K.

One of the means of realization of a pulse-periodic operation regime for gas-flow COIL lasers is a preliminary mixing of singlet oxygen with molecular iodine and the continuous pumping of this mixture through the cell. When the cell is filled, the Q-switching takes place (in case of an oscillator) or an initial pulse is applied (amplifier). Besides the pumping processes in $O_2(^1\Delta) + I_2$ system there occurs the relaxation of $O_2(^1\Delta)$ electron excitation:



$K_2 = 1 \cdot 10^{-13} \text{ cm}^3/\text{s}$.

This process limits typical dimensions of the active medium along the flow by value $L = \sqrt{V\tau_{rel}}$, where V is the flow velocity, and $\tau_{rel} = 1/K_2 [I(^2P_{1/2})] \sim 1/K_2 [I]$ is characteristic time of the process. The energy E stored in such an active medium is:

$$E = O_2(^1\Delta) \cdot S \cdot V \frac{1}{K_2 [I]} h\nu,$$

where S is the flow cross-section, and $h\nu$ is the energy of the laser radiation quantum. The time of the stored energy release is determined by the time of excitation transfer i.e. $1/K_1 [I]$. This value determines either Q-switched pulse duration, or the necessary duration of the amplified pulse at amplification. Thus, the pulsed power achievable in this case is:

$$P_{pulse} = h\nu [O_2(^1\Delta)] \cdot S \cdot V \cdot K_1/K_2.$$

Taking that $h\nu [O_2(^1\Delta)] S V$ is the CW limit power we obtain that maximum power gain is equal to K_1/K_2 or $7.7 \cdot 10^2$. In fact, this gain would be less, because in order to achieve sufficient homogeneity of the medium L must be taken less than $\sqrt{V\tau_{rel}}$.

In this method the maximum pulse power and the pulse repetition frequency are directly related to CW power, and the pulse power can hardly be increased at the given average power. This follows from the fact that concentration of the atomic iodine determines both pulse energy E , and pulse duration τ_{lasing} , and does not affect as a whole the value of pulsed power. As a favourable condition, note that either E , or τ_{lasing} should be independent of the iodine concentration. Then the pulsed power might be increased with changing of the iodine concentration. This can be realised with respect to E , not τ_{lasing} . Thus, we are ready to accept the second variant of realization of the COIL pulse operation regime.

According to this method, the laser volume must be filled with singlet oxygen in ab-

sence of iodine. Immediately after filling the atomic iodine should attain the necessary concentration uniformly distributed over the laser volume. This can be achieved by adding iodine-containing substances to singlet oxygen. They do not react with it and do not cause its desactivation. The mixture subjected either to the photolysis or e-beam expansion yields the atomic iodine.

The relaxation of excitation in this case is determined by:

$$O_2(^1\Delta) + O_2(^1\Delta) \xrightarrow{K_3} O_2(^1\Sigma) + O_2(^3\Sigma),$$

$$K_3 = 2 \cdot 10^{-17} \text{ cm}^3/\text{s}.$$

The time of $O_2(^1\Delta)$ decreasing by e times is:

$$\tau_{\text{rel}}^{(2)} = 1,7/K_3 [O_2(^1\Delta)]_{\text{initial}}.$$

The time of the active volume filling, in the first method, is determined by the atomic iodine concentration, and is equal to $\tau_{\text{rel}} = 1/K_2[I]$. Since COIL is characterized by the ratio $[I]/[O_2(^1\Delta)] \sim 10^{-2}$, the time of filling, in the second method, is higher by a factor of $1,7K_2[I]/K_3[O_2(^1\Delta)] \sim 85$. Thus, in case of the photolysis-produced atomic iodine the volume of the active medium (hence, the stored energy) can be increased by nearly 85 times, as compared to the first method. Note, that the optimal relation I/O_2 for a pulse-repetition operation might be higher than that for the continuous operation, and the gain of the hybrid variant, might be higher as well. Since the pulse duration in this case is $I/I K_1$ too, the maximum power is 85 times higher as well. The atomic iodine concentration can be changed when the active volume is fixed. As a result, one can change the pulse duration at fixed energy, i.e. the pulse power might be changed within a wide interval at fixed average power.

The proposed method makes it possible to increase pressure of the active medium. One can, thus, fulfill the necessary condition of mixed lasers (time of mixing is less than time of relaxation) for higher pressures. This can open possibilities for other methods of singlet oxygen production in COIL, as for example, the method of ozone photolysis, which needs heightened pressures.

Unlike the first method, the second one requires additional sources of energy to decompose iodine-containing substances. Let's evaluate the relation of energy yielded from the active medium to the energy spent for the preparation of atomic iodine. The specific energy E_1 yielded from the active medium is $[O_2(^1\Delta)] \cdot h\nu \cdot \eta$, where η is the coefficient of singlet oxygen energy usage. In the photodissociation of iodides the production of atomic iodine per unit volume is estimated as $[I] \cdot h\nu_{\text{ph.d.}}/\eta_{\text{ph.d.}}$, where $h\nu_{\text{ph.d.}}$ is the UV quantum of a photodissociation source of $\eta_{\text{ph.d.}}$ efficiency. Let's take typical values used in CW COIL and photodissociation flash-lamp iodine lasers, i.e. $[I]/[O_2(^1\Delta)] = 10^{-2}$, $\eta = 0,4$; $\eta_{\text{ph.d.}} = 0,1$. Then we get $\eta_{\text{ph.d.}} = 80\%$. The efficiency can be increased by using photodissociation sources of higher efficiency. Quite attractive are so called excimer KrF ($\lambda=249\text{nm}$) and XeI ($\lambda=253\text{nm}$) flash-lamps, whose radiation wavelengths are in the dissociation band of iodine-containing substances, and their efficiency can attain 30%.

Another interesting property of pulse COIL is their ability to operate without low-temperature trap, which is meant to purify singlet oxygen from water vapours. Without the trap the laser is simpler and more convenient in operation; the length of singlet oxygen transport is shorter and the losses during homogeneous and heterogeneous relaxation of singlet oxygen are smaller.

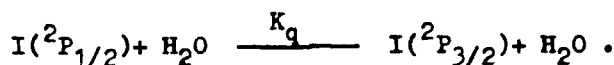
Besides, in order to provide steady-state operation of the laser it is necessary to discharge the heat released in the reaction with 113 kJ/mole Cl_2 thermal effect. The heat is discharged either from the trap or the active mixture at low-temperature operation of a singlet oxygen generator (SOG). The necessity of using a cooler in order to compensate thermal effect of the reaction limits the laser efficiency.

Without the cooler the steady-state thermal operation is sustained by water evaporation from SOG. The water vapours contained in the gas flowing from SOG are 2.7 times higher than the content of O_2 . As a result, the operation of COIL in a conventional scheme, i.e. mixing of $O_2(^1\Delta)$ with I_2 , proves to be quite impossible. This is explained by a sharp retardation of the iodine dissociation in the presence of water.

The condition when the generation energy is independent of water content in the active mixture has the form:

$$\frac{K_1}{K_q} \frac{[O_2(^1\Delta)]}{[H_2O]} \gg 1,$$

where K_q is $I(^2P_{1/2})$ quenching rate constant during



By substituting respective values in the above inequality one can see that it is well fulfilled at the abovementioned water content.

The above considerations have been experimentally checked. In the experiments we used the setups (Fig.1) of various scale: active medium volume from 300 ml up to 3 l, pumping

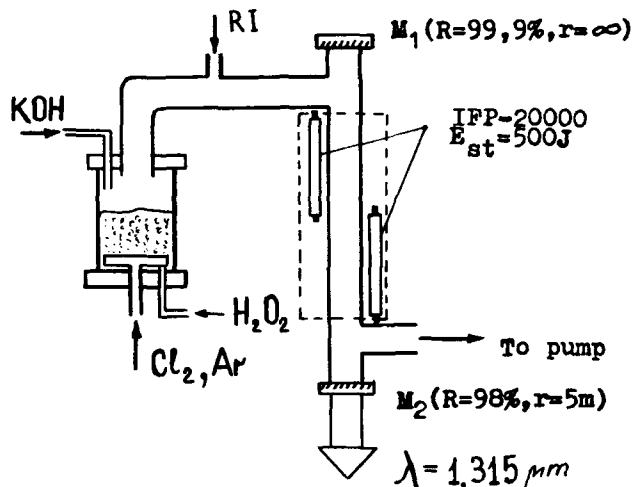


Fig.1 Schematic layout of the experimental setup.

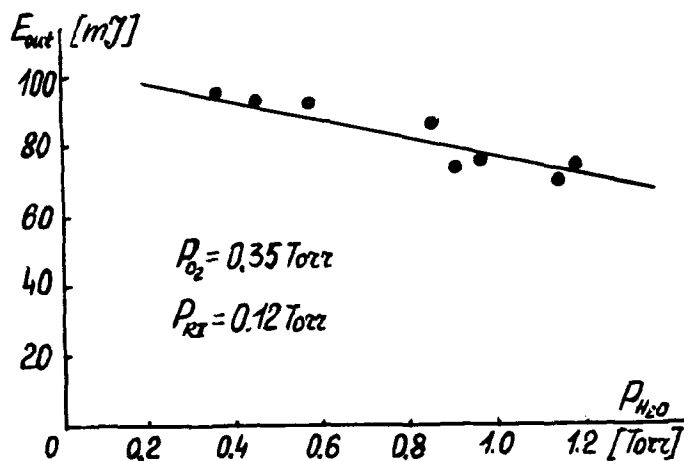


Fig.2. Output pulse energy versus the partial water pressure.

of O_2 molecule excitation energy into the laser radiation, the total efficiency of the laser system with allowance for energy expenses on the reagent reproduction, can be as high as 6% even with the up-to-date technological base. Besides, quite possible is the construction of a hybrid system including and advanced photodissociation laser (note that COIL generation occurs at the same iodine atomic transition as the iodine photodissociation lasers). To use COIL in the laser fusion it is necessary not only to implement pulse-repetition regime, but to obtain a nanosecond pulse with energy up to hundred kiloJoule.

Consider the feasibility.

Since the pulse duration is shorter than the typical duration of $O_2(^1\Delta) \rightarrow I$ transmission, it is obvious that during a round-trip the amplified pulse may extract from the active medium the energy fraction which nearly equals $[I]/[O_2]$ ratio. To extract the energy one should use multipulse scheme. This may be realized with the help of a ring scheme

Different iodides (CF_3I , CH_3I , C_2F_5I , C_3F_7I) and their efficiency as the iodine atoms donors have been studied as well as the dependences of the laser output energy and pulse shape on mixture composition, the oxygen pressure.

The best results were obtained with CH_3I . Under the same degree of iodide decomposition the output energy is decreased when CH_3I is substituted for CF_3I and C_3F_7I . The energy decrease depends on oxygen pressure.

As was earlier predicted, the presence of water vapour in the active medium of a pulsed COIL with volumic production of atomic iodine weakly affects the laser output energy (Fig.2): the laser operates successfully when the vapour concentration is three times higher than the oxygen concentration. There is evidently no need in a trap.

Like in CW operation regime the rise of the pumping rate caused the growth in the output energy that is related to the growth of singlet oxygen concentration in a flux.

Maximal specific energy released was 1.1 J/l at the pressure: oxygen, 1.3 mm Hg, CH_3I , 0.4 mmHg and Ar - 2 mmHg. Measurement of the iodide dissociation degree gives 700% of intrinsic efficiency. Chemical efficiency 16% is not less than the same best value for CW lasers.

One can see that pulse-repetition COIL possesses a number of attractive features: the absence of traps, simple control of the laser parameters. This could widen the possibilities of its application.

The idea of using COIL as a driver, i.e. as a high-power laser which heats up the target appears to be quite attractive in view of the laser fusion research. Such opportunities follow from a high efficiency of COIL operation in the closed cycle. The estimates made by Fiso and Heys [1] show that at 30% efficiency of conversion

(Fig.3). Here the perimeter exceeds the value $C\tau_1$, where C is the light velocity, τ_1 , the typical time $\tau_1 \sim 1/K_1 [O_2(\Delta)]$. The required number of round equals $[O_2]/[I]$. Such a scheme must include polarizational elements and optical shutters which can remove the pulse from the ring and prevent the system self-excitation.

To remove the pulse from the ring one can use the conversion of noncollinear beams into the 2-nd harmonic (Fig.4). In this case the beams of both rings intersect in a nonlinear crystal at an angle precisely equal to noncollinear synchronism angle. Exact peri-

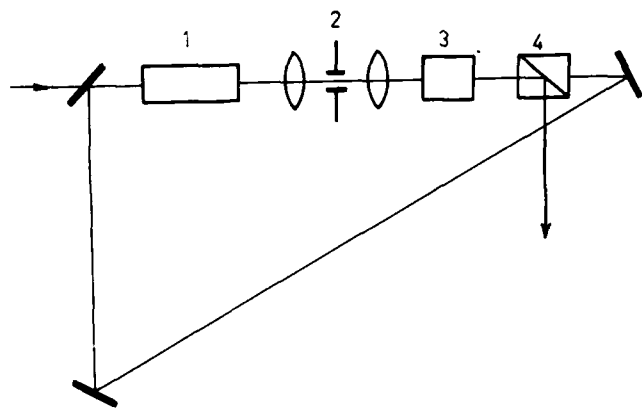


Fig.3. Ring scheme of the chemical oxygen-Iodine amplifier.

1. Amplifier cell.
2. Burned shutter (space filter).
3. Modulator.
4. Cavity dumper.

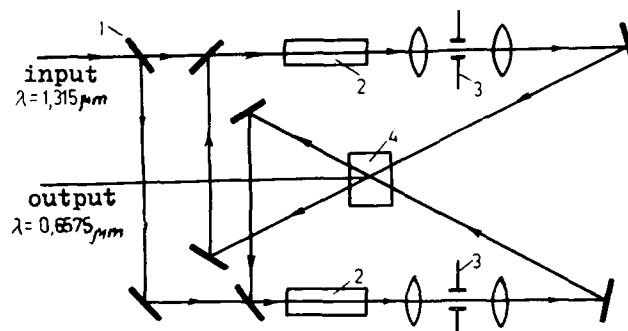


Fig.4. Chemical oxygen-Iodine amplifier - second harmonic generator.

1. Beam splitter.
2. Amplifier cells.
3. Burned filters.
4. Nonlinear crystal.

meters are chosen so that the pulses propagating in the first and second rings coincided in a nonlinear crystal only after a given number of round-trips. Here the second harmonic conversion would take place, and practically all the energy would be emitted towards bisector of an intersection angle.

Since in low-pressure (< 100 mm Hg) COIL the relation $\tau_p < 1/\Delta\omega$ ($\Delta\omega$ is the linewidth of atomic iodine) is valid for a nanosecond pulse, there is a possibility of a coherent amplification. Each round-trip will produce a two-fold energy, and this makes possible to reduce the necessary number of round trips.

To realize the proposed ideas one should first of all have the active medium with the required energy store. Fisco and Hays suggested to use the active medium of the dimensions 1.7×3 m containing 10 mmHg O_2 ($O_2(\Delta)$ - 80%) and 0.3 mmHg I_2 . However, the relaxation time in such an active medium is 0.6 ms. It is obvious that even sound velocity (300 m/s) of the flow might produce the active medium of ~ 18 cm, and this is far smaller than the required one.

However, in the second method described above for the given pressure the admissible time value is 500 times higher, and preparation of the active medium of needed dimensions becomes quite a realizable task.

The formation of large volumes of active medium may be possible under weak relaxation of the energy store. This imposes certain requirements on the selection of the iodide. As noted above, the iodide should not cause the singlet oxygen relaxation and should not produce atomic iodine in the reaction with it. In case of a chemical SOG, however, the chlorine may be present in the working mixture. This imposes an additional requirement upon RI: it should be inert to Cl_2 . Alkyl iodides (CH_3I , C_2H_5I) have been found to react with chlorine and produce atomic iodine. The rate constant of the brutto-reaction $Cl_2 + O_2(\Delta) + RI \rightarrow I + \text{products}$ was evaluated $4 \cdot 10^{-32} \text{ cm}^3 \text{ s}^{-1}$. The estimation of the relaxation time of energy store in the mixture $O_2(\Delta) + RI + Cl_2$ shows that chlorine concentration must not exceed 10^{15} cm^{-3} . At this case, the rate of energy store losses is comparable with that defined by process $O_2(\Delta) + O_2(\Delta) \rightarrow O_2(\Sigma) + O_2(\Sigma)$. Due to the noted phenomenon the creation of pulse COIL requires the selection of the type and operation regime of a SOG which ensures maximal utilization of Cl_2 .

Reference

1. G.N.Hays, G.A.Fisk, IEEE Journ of Quant.Electron., QE-17, 1823 (1981).

THE NUCLEAR PUMPING OF LASERS - REVISITED

By Richard T. Schneider, University of Florida
and John D. Cox, General Imaging Corp.,
Gainesville, Florida

Historical Overview

Nuclear pumping of lasers began shortly after the first development of the laser in 1960. Nuclear pumping has been accomplished with both nuclear reactors and nuclear explosives. In the case of nuclear explosives, stimulated emission with X rays has been reported, but much of this work remains classified. This paper, however, deals exclusively with reactor pumped lasers (rpl).

Experimentation in this field of research necessarily requires access to a reactor. Therefore, only a few institutions have proliferated research and publications in this area. These include the University of Florida, the University of Illinois (at Champaign), NASA Langley Research Center, Sandia National Laboratories and Los Alamos Scientific Laboratories. The Soviet Union has also had a vigorous study of nuclear pumping producing significant results of their own. The focus of much of the previous work was to understand the properties of nuclear excited plasmas and the measurement of small signal gain and lasing. Only a few lasers were actually pumped with fission fragments (see Table 1), all others used a simulation of the fission process where the reactor was only used as a source of neutrons and the nuclear reactions simulating the fission process took place in the laser cavity. Two simulation reactions were used almost exclusively; $B^{10}(n,\alpha)Li^7$ and $He^3(n,p)T^3$.

The boron and fission reactions were accomplished with coatings and foils while the Helium-3 reactions were in the gas phase. The reactors used were either bare core (Burst) reactors such as the Godiva at Los Alamos and the Burst reactor at Aberdeen Proving Grounds or the TRIGA type reactors found at the University of Illinois and Sandia. The Burst reactors are capable of producing a 60 microsecond pulse of fast neutrons with a peak flux of 10^{20} neutrons/cm² sec. However, the above mentioned reactions require thermal neutrons. Thermalization schemes used in conjunction with these reactor pulses produce a 200 microsecond pulse of thermal neutrons with a peak flux of 10^{17} .

Using typical cross sections and densities of boron, uranium and helium, one can estimate the power deposition (using a thermal flux of 10^{17}) into a laser gas to be on the order of 5 kw per cubic centimeter. As a point of reference, E-beam driven systems are capable of power densities on the order of 1 Megawatt per cubic centimeter. The scaling law of laser physics dictates that the lasing wavelength is inversely proportional to the threshold pumping power to the fourth power (i.e., the threshold pumping power for an ultraviolet laser is 10,000 times greater than for an infrared laser with a wavelength 10 times greater). Therefore, the laser wavelength range for reactor pumped lasers is limited to the near infrared with only a few exceptions. The low power density coupled with the typically low laser efficiencies have produced laser output powers on the order of milliwatts.

Motivations

To nuclear pump a laser requires a substantial amount of justification as with anything involving the use of a reactor. The promise of nuclear pumping is the ability of a nuclear reactor to provide "limitless" energy and extremely high energy densities with a relatively small mass (one gram of uranium stores as much energy as a ton of coal). This promise can only be kept if the device is placed in a remote location such as in outer space where shielding and other safety-related apparatus are minimal. In order to fully exploit the energy reserves of a nuclear reactor and its capability to produce extremely high energy densities, one has to optimize coupling between the reactor and the laser. It should be borne in mind that 80 percent of the fission energy is invested in the kinetic energy of the fission fragments. Therefore, it is this energy which has to be converted to laser light, not the energy of the neutrons, alpha, beta or gamma radiation. In the case of gas lasers, the fission fragment has to be able to interact with the gas atoms, and not as in conventional reactors with a matrix of solid fuel. Consequently, conventional reactor configurations are not suitable for nuclear pumping of lasers and new configurations have to be found which allow the fission fragments to interact with gaseous laser media to form a nuclear excited plasma. Nuclear excited plasmas have many unique characteristics, some of which need to be exploited, others which need to be mitigated. The fission event, in principle, is an ideal "driver" for producing excited and ionized species in a gas. Solid and liquid media suffer severe radiation damage from direct fission fragment excitation. The fission event produces almost every form of energy known, including two to three neutrons to continue the chain reaction. The energy released per reaction is about 200

NUCLEAR PUMPED LASER EXPERIMENTS
Fission Fragment Excitation

Research group & site	Wavelength (μm)	Pressure (torr)	Neutron Flux ($\text{n/cm}^2\text{sec}$)	Length of Laser Pulse (μsec)	Peak Power Deposited (W/L)	Peak Power Total (W)
Los Alamos & U. of Fla. (Helmick, Schneider)						
$^4\text{He-Xe}$	2.508	200-350	2.4×10^{16}	135	3.3×10^5	.1
Sandia Labs (McArthur)						
CO	5.1-5.6	100	3.7×10^{16}	50	1.3×10^6	2.6
$^3\text{He(n,p)}^3\text{H}$ Excitation						
NASA-LANGLEY (Hohl)						
He-Ne	1.117	400	7.65×10^{15}	400	--	--
He-Ar	1.270	466	1.8×10^{16}	220	1.0×10^5	.06
He-Cl	1.586	600	1.5×10^{16}	500	--	.04
He-Ar	1.791	200-3000	1.5×10^{16}	550	--	.05
He-Xe	2.027	200-3000	1.5×10^{16}	600	--	.085
He-Kr	2.520	200	1.5×10^{16}	200	--	.03
Los Alamos (Helmick)						
He-Xe	2.024 3.508	580	3.5×10^{16}	150	--	1.0
U. of Florida (Schneider)						
$^3\text{He-Ne}$.6328	300	$\sim 10^{12}$	C.W.	--	
$^{10}\text{B(n, } ^7\text{Li)}$ Excitation						
Univ. of Illinois (Miley, Deyoung)						
He-N ₂	.9393 .8629	150	2.5×10^{15}	6,000	3.0×10^4	1.5mw
Ne-CO ₂	1.45		2×10^{14}			
He-CO ₂	1.45	600	2×10^{14}	20,000		
He-N ₂	.9393	150	3.5×10^{15}	9,000		1.5mW
Univ. of Ill. & Sandia (Miley & McArthur, Akerman)						
He-Hg	.6150	600	1.5×10^{16}	400	3.0×10^5	1mw

Table 1

million electron volts. As pointed out above, the majority of this energy is carried away by two fission fragments (lighter elements), each with an average kinetic energy of 80 MeV and a charge of +20. In a gas where the average ionization energy is between a few electron volts and a few tens of electron volts, a fission fragment can create 100,000 ion pairs. To stop these fission fragments within a short distance (a few centimeters), relatively high gas pressures (for lasers) must be used, typically several hundred Torr. Nuclear excited plasmas can be characterized as collision dominated with very low (equilibrium) electron temperatures (usually room temperature), but high initial electron energies prior to thermalization.

A series of paradoxes are encountered when studying this phenomenon. Fission fragments have extremely high energy density per particle, yet nuclear excited plasmas have modest

power densities compared to E-beam and discharge excited plasmas. While the power densities achievable with nuclear pumping are low, very large volumes can be excited (up to several liters have been excited). Explosive-driven plasmas have incredible power densities and rise times where reactor-driven plasmas have relatively lower power densities and rise times.

The challenge to be met is to find laser media compatible with the reactor environment which are scalable to high power and/or a way must be found to efficiently couple a large percentage of the reactor power to the laser media.

Typical high-power lasers today are molecular systems (e.g., HF, iodine and CO_2) operating in the infrared which is convenient since these lasers require relatively low pumping power. However, remote operation creates a brightness problem. Brightness is the power density achievable by a light source in the far field. For the extremely large distances encountered in space applications, the brightness of a light source is diffraction limited, meaning that the maximum power density (in the far field) is limited by the inverse of the wavelength squared. That is, a one micron laser can create the same brightness as a ten micron laser with 100 times the output power. The operating wavelength of the laser also affects the size of the optics needed as well. Therefore, another criteria for the ideal nuclear pumped laser is that the operating wavelength must be short (less than or equal to one micron). The list of possible laser candidates now becomes small. Perhaps the best remaining candidates for such a laser are the excimers. The threshold power density for excimers is quite high, however, typically in the 100 kw to 1 Mw per cubic centimeter range.

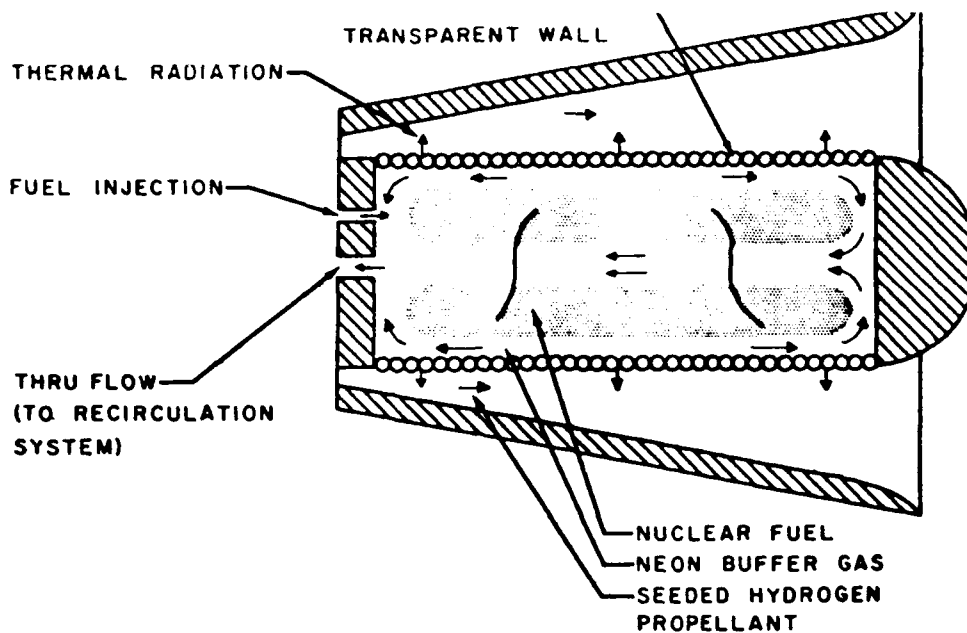
The reactor-laser interface is perhaps the most critical issue to be resolved. A way must be found to deposit a substantial fraction of the reactor power into the laser cavity at a power density sufficient to achieve laser action. At the same time, the incompatibility of the reactor core and laser cavity must be mitigated. The ideal system would be a self-critical reactor/laser where the majority of the reactor fuel is in the gaseous state. Conventional reactor designs use a solid fuel where the high-quantum (MeV) nuclear energy is degraded to thermal energy. Even if the critical mass of the reactor were in the form of foils or coatings, at least half the energy would be absorbed in the foil or substrate. The range of fission fragments in uranium is about ten microns. A coating thin enough to allow most of the fission fragments to escape would be too thin to provide any mechanical rigidity, an undesirable situation in the reactor core; therefore, supporting substrates of considerable mass would be needed. The escaping fission fragments also create sputtering effects in foils, another disadvantage.

Gas core and plasma core reactor concepts have shown promise. The gas core reactor uses one of the only stable gaseous forms of uranium, uranium hexafluoride (UF_6). In the gaseous state, nuclear fuel can transfer all of its energy to the surrounding gas. If that gas were a gaseous laser media, a homogenous reactor/laser could be constructed. A great deal of research has been done on the effects of adding UF_6 to a lasing gas and the excitation of a laser media with fissioning UF_6 . The results of this research were less than promising. Due to the many transitions the complicated UF_6 molecule has, it turns out that most of the candidate laser gases are quenched by addition of small amounts of UF_6 . There are two studies, however, which show signs of success. One is the addition of UF_6 to an operating CO_2 laser.¹⁰ Lasing was maintained with the addition of up to 2% UF_6 . Another study reports lasing of an Ar-(3%)Xe laser was maintained after the addition of 0.5% UF_6 .¹¹ In this case, 62% of the excitation was derived from the solid coating (UF_4) on the wall of the vessel, while 38% came from UF_6 directly.

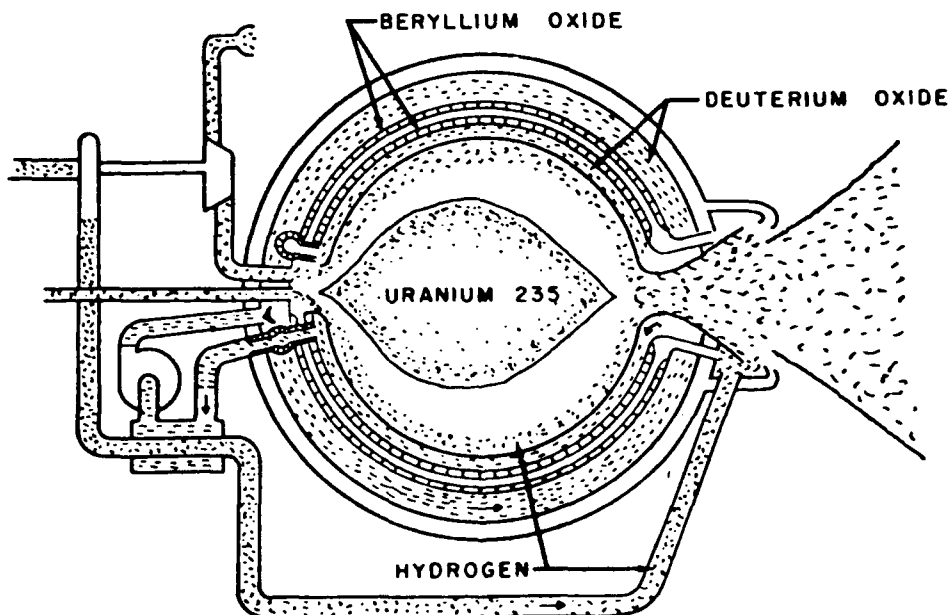
This limited success in using UF_6 would have to be improved to the point that sufficient UF_6 gas can be added to achieve criticality. Studies that have been made on the various gas core reactor concepts show that UF_6 pressures required for criticality in gas core reactors exceed five atmospheres.¹² The question still to be answered concerns the amount of quenching which would take place at these higher gas pressures.

Plasma core reactor concepts^{13,14,15,16} using atomic uranium have an operating temperature of about 40,000 degrees C, way too high for a laser. Another name given to the plasma core reactor was the nuclear light bulb. These gas core and plasma core reactors were designed for the astro-nuclear program as fourth stage boosters for deep space missions. See Figures 1A and B. It would seem that direct fission fragment pumping of a laser is a blind alley due to the incompatibility of the laser media and reactor core environment.

One method which shows promise in eliminating the reactor/laser incompatibility problem yet can achieve fairly high coupling efficiency is the transfer laser concept. Here the energy from the reactor core is absorbed by a working fluid and transferred to the laser cavity outside the core. A nuclear pumped CO_2 transfer laser was successfully demonstrated by Schneider, et al.¹⁷ Flowing nitrogen gas was excited by fission foils and exhausted through a nozzle to the laser cavity one meter away and mixed with CO_2 and helium. During transient, all of the excited states collisionally relaxed to a metastable state which is resonant with the CO_2 upper laser level. The overall laser efficiency can be quite high, the theoretical limit being 28%. A transfer laser of enormous power could be constructed using the NERVA reactor, a solid fueled, gas-cooled astro-nuclear booster. Such a laser would be capable of 100 Megawatts CW at 10.6 microns. This concept suffers from two disadvantages; the wave length is too large (low brightness, large optics) and the use of



a) CONCEPT OF NUCLEAR LIGHT BULB ENGINE



b) COAXIAL-FLOW GAS-CORE NUCLEAR ROCKET

Figure 1A and B

nitrogen as a reactor coolant would require hundreds of tons of fluid for even 30 minutes of operation. This is not any better than what a chemical laser can do.

The transfer laser concept will not scale up unless the "working fluid" is light (electromagnetic radiation). This concept, radiant transfer, was first proposed by Cox, et al¹⁸. In his proposed concept the colloidal core reactor was utilized. This reactor employs a gas vortex (in this case He) which suspends small solid particles of uranium

carbide. The temperature of the particles increases due to the fission process taking place in the uranium and is allowed to raise to a value of 3000 degrees K.

A vortex is established by tangentially blowing He-jets into the reactor cavity. In order to keep the vortex going, a like amount of helium (now containing a certain fraction of solid particles) is removed, also tangentially, and is returned consequently to the injection nozzle. Only a small fraction of the gas is circulated through this by-pass loop.

The total loading of the reactor cavity in the form of uranium carbide particles (size 0.5-5 micrometers in dia.) is 4.5 kg. The expected power density is 20 kW/cm³. Moderation is mainly achieved in the reflector-moderator (Be). For control purposes, it is necessary to generate 20% of the power in the reflector region. The reflector contains control drums which serve this purpose.

Due to the centrifugal forces, there is a density gradient from the center of the cylindrical cavity towards the outside. In order to prevent the hot particles from contacting the outer wall, a series of small jets are utilized, which tangentially inject helium to deflect the particles from the wall. Due to this, the center of the cylindrical cavity is also virtually particle free.

Here a coaxial transparent sapphire tube is inserted. The center part of the tube contains a laser liquid while the annulus contains a cooling liquid. The laser liquid is described in the next section.

The solid particles will emit light corresponding to a 3000 degree K gray body. The emissivity of the uranium carbide at this temperature is still uncertain, but it can be estimated to be around 0.75.

The light emitted by particles in the outer layer is absorbed by the particles closer to the center, which are, therefore, heated and reradiate the energy at their respective temperature.

It is, therefore, advantageous to allow the outer particles to be heated by nuclear energy to a higher temperature than the inner particles. Therefore, a radial reactor power gradient is beneficial. This gradient is established due to the gradient in the density of the fuel particles.

The coolant in the coaxial tubing can be D₂O and can be used as a partial moderator-reflector. The advantage here would be that neutron irradiation of the liquid is reduced. Also useless IR and UV components of the blackbody light are removed, reducing heating of the laser liquid. The proposed concept described above suffers from some near-term problems. These are that the colloidal core reactor is not developed to a degree that it will be available in the near future. Secondly, while plenty of laser liquids (especially laser dyes) which can be pumped optically are available, most suffer severe radiation damage. Only the aprotic Lewis acids have a chance to stand up to the severe radiation environment. However, this has not been demonstrated yet. The liquid is an inorganic solution of phosphorous-oxy-chloride (POCl₃), zirconium tetrachloride (ZrCl₄) and neodymium (Nd³⁺). The solubility of Nd³⁺ in POCl₃ is not sufficient to obtain a good concentration (3 x 10²⁰/cm³) suitable for efficient laser operation. Therefore, zirconium tetrachloride is added to the solution and acts as a Lewis acid to increase the Nd³⁺ concentration to optimum levels.

The absorption bands of the Nd³⁺ ions in the POCl₃:Nd³⁺:ZrCl₄ solution are centered around 550, 600, 750 and 820 nm. Blackbody radiation of about 3000 degrees K would serve adequately to pump this liquid. See Figure 2. Figure 3 shows a schematic of the proposed system.

The boiling point of uranium is around 4000 degrees K and most of the carbides and oxides are somewhat higher. The melting point of tungsten is 3380 K. Therefore, it is not inconceivable that a solid fuel rod with a tungsten cladding containing liquid U, UO₂ or UC₂ could be operated with a surface temperature around 3000 degrees K in a gravity-free environment. In this case, an appreciable part of the reactor energy would appear at the wavelength of the pumping band of laser liquid. Of course, all of the reactor power would eventually be radiated away as IR radiation. The unused part could be utilized for other direct energy conversion schemes.

Declaring IR as the working fluid allows the removal of the laser from the reactor environment without severe penalties, thus making it possible to pump other liquid laser media as well.

Due to the inherent limited laser efficiencies, all laser liquids need to be cooled. Low temperature waste heat rejection, which is a problem in space, is therefore limited to the part of the reactor power absorbed by the laser liquid rather than the total reactor power.

Conclusions

In the previous two decades of research a great deal has been learned about the interactions of nuclear reaction products with laser media. The most critical issue has not yet been adequately addressed, namely the development of a reactor suitable for pumping lasers. Significant problems have been encountered where attempts have been made to add UF₆ to lasing gases. A successful combination of UF₆ and a lasing gas could produce a self-critical reactor/laser, perhaps the ultimate embodiment of the rpl.

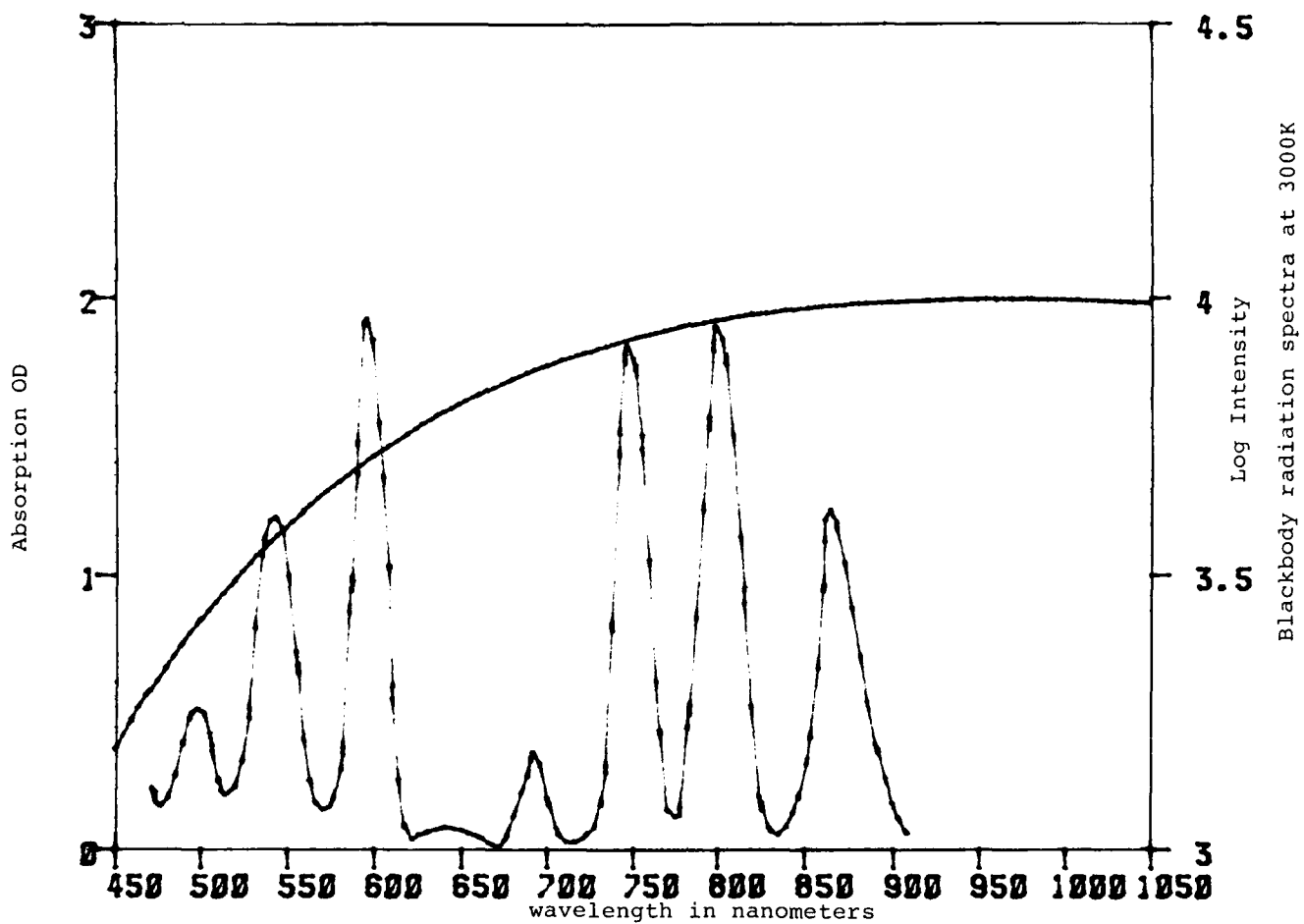


Figure 2: Absorption Spectra of Nd^{3+}

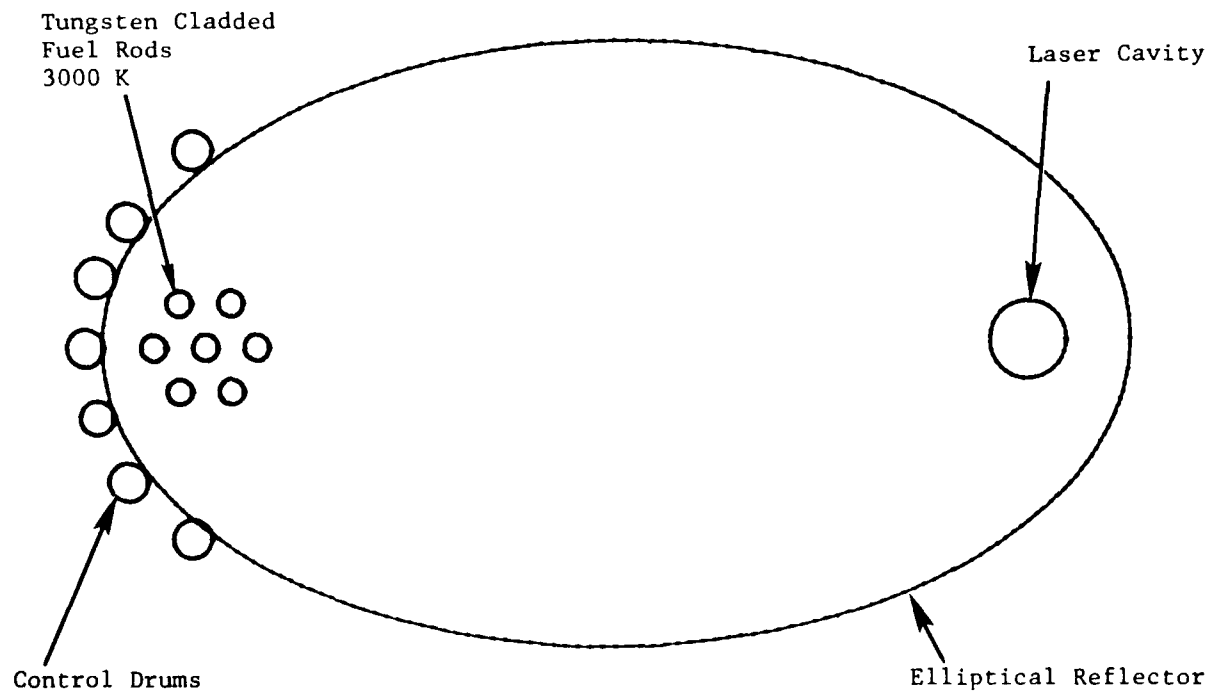


Figure 3: Reactor Concept

The only feasible alternative which maintains the promises of nuclear pumping is a radiant transfer system. Solid-fueled "lightbulb" reactors are limited by their melting points, thereby limiting the color temperature to 3000 degrees K, a marginally acceptable temperature. Gas and plasma core reactors have much higher operating temperatures and therefore are more suited for this purpose. However, development of such reactors will require hundreds of millions of dollars. Subsequent development and testing could take a generation to complete. Nevertheless, it is this approach which seems to have the most promise for success.

References

1. Wilson, J. W. and DeYoung, R. J., "UF₆-He Fission Pumped Nuclear Laser, Power Deposition", J. Appl. Phys., **49** (5), pt. 1, 989-993, March 1978.
2. Davie, R. N., Albrecht, G., Carroll, E. E. and Schneider, R. T., "Optical Radiation of Fission Fragment Excited UF₆ and Ar-N₂ Mixtures", ANS Annual Meeting, Toronto, 13-18 June 1976.
3. Skottegard, C., "Electric Field and UF₆ Impurity Effects on the Scintillation Lifetimes of Fission Fragment Excited Nitrogen, Helium, Argon, and CO₂ Gas Mixtures", Masters Project, Department of Nuclear Engineering Sciences, University of Florida, 1978.
4. Roman, W. C., "Argon/UF Plasma Experiments: UF₆ Regeneration and Product Analysis", NASA CR-3258, United Technologies Research Center, March 1980.
5. Dmitrievskii, V. A., Voinov, E. M. and Tetel'baum, S. D., "Use of Uranium Hexafluoride in Nuclear Power Plants", At. Energ., **29**, (4), 251, Oct. 1970, (in Russian).
6. Davie, R. N., Davis, J. R. and Schneider, R. T., "Optical Radiation of Fission Fragment Excited UF₆ and Ar-N₂-UF₆ Mixtures", Trans. Am. Nucl. Soc., **23**, 517.
7. Rodgers, R. J., "Initial Conceptual Design Study of Self-Critical Nuclear Pumped Laser System", NASA CR-3128, United Technologies Research Center, April 1979.
8. Krasciella, N. L., "Spectral Properties of Gaseous Uranium Hexafluoride at High Temperatures", NASA CR-3244, United Technologies Research Center, Feb. 1980.
9. Miley, G. H., "Applications of Direct Nuclear-Pumped Lasers and Gaseous Core Reactors", Trans. ANS, **26**, 526-527, 1977.
10. Rhoads, H., "Direct Nuclear Excitation of a CO₂ Laser", PhD Dissertation, University of Florida, 1972.
11. DeYoung, E. J. and Wilson, J. W., "Population Inversion Mechanisms Producing Nuclear Lasing in He-Ar, Xe, Kr, Cl, and UF₆. First Int. Symp. on Fission Induced Plasmas and Nuclear Pumped Lasers, Orsay, France, 23-25 May, 1978.
12. Bell, G. I., "Calculation of the Critical Mass of UF₆ as a Geaseous Core, with Reflectors of D₂O, Be and C", LA-1874, Los Alamos Scientific Laboratory, 1955.
13. Helmick, H. H., Jarvis, G. A., Kendall, J. S. and Latham, T. S., "Preliminary Study of Plasma Nuclear Reactor Feasibility", Los Alamos Scientific Laboratory Report LA-5679, 1974.
14. Lee, J. H., McFarland, D. R., Hohl, F. and Him. K. H., "Production of Fissioning Uranium Plasma to Approximate Gas-Core Reactor Conditions", Nucl. Technol., **22**, 306, 1974.
15. Rodgers, R. J., Latham, T. S. and Krascella, N. L., "Investigation of Applications for High-Power, Self-Critical Fissioning Uranium Plasma Reactors", United Technologies Research Center Report R76-912204, prepared under Contract NAS1-13291, Nod. 2, May 1976.
16. Roman, W. C., "High Temperature UF₆ RF Plasma Experiments Applicable to Uranium Plasma Core Reactors", NASA CR-159159, United Technologies Research Center, Oct. 1979.
17. Rowe, M. J., Liang, R. H. and Schneider, R. T., "Nuclear Pumped CO₂-Laser", 1981 IEEE International Conference on Plasma Science, c. 1981, pp 149-150.
18. Cox, J. D., Schneider, R. T. and Yang, Y. S., "Nuclear Pumped Lasers Utilizing Radiant Transfer, Laser Interaction and Related Plasma Phenomena, Vol. 6, Plenum Pub. Corp. 1984.

J. R. Torczynski and R. J. Gross
 Fluid and Thermal Sciences Department
 Sandia National Laboratories
 Albuquerque, New Mexico 87185

Abstract

In nuclear-reactor-pumped lasers, the fission-fragment energy deposition is spatially nonuniform, with less energy deposited near the laser axis than is deposited near the side walls from which the fission fragments originate. This nonuniformity causes gas to move toward the laser axis and establishes mass density and refractive index gradients perpendicular to the laser axis. In order to understand this phenomenon and describe it quantitatively, a numerical model of the gasdynamics of nuclear-reactor-pumped lasers has been developed. The numerical model simulates the two-dimensional motion of a perfect gas experiencing fission-fragment energy deposition in a rectangular or cylindrical enclosure. In addition to calculating mass density, temperature, pressure, velocity, and power density fields, ray-tracing calculations are performed to determine the beam steering caused by the varying mass density. The simulation of a representative one-dimensional rectangular case is found to be in excellent agreement with the existing analytical theory. In this case, the ray-tracing calculations indicate length limitations which result from internal focusing. Examination of cylindrical cases reveals that under certain circumstances gas motion reduces the on-axis power density to zero, a phenomenon termed axis-shielding. This phenomenon never occurs in rectangular cases. Simulations of experiments show good agreement between calculated and experimental Hartmann probe refractive index data.

1. Motivation

It is possible to pump a laser with the energetic products of fission reactions (fission fragments) induced by a pulse of moderated neutrons from a research nuclear reactor.^{1,2} Such "nuclear-reactor-pumped" lasers can take advantage of the large energy densities associated with nuclear power.³ However, since the fission fragments typically enter the gas from coatings of fissionable material located on the side walls of the chamber, the power density in the lasing gas is highest near the walls and lowest at the centerplane (rectangular geometry) or the axis (cylindrical geometry). This nonuniformity produces small pressure gradients which cause gas to flow away from the walls and toward the laser axis. Thus, fission-fragment energy deposition sets up mass density gradients perpendicular to the laser axis. Since the index of refraction is related almost linearly to the mass density,⁴ these gradients cause beam steering and under certain circumstances may be strong enough to produce an effective focal length of the gaseous medium which is comparable to the chamber length. Quantitative understanding of the temporally and spatially varying refractive index gradients in nuclear-reactor-pumped lasers is thus essential to the analysis of resonator stability, mode selection, adaptive optics compensation, and other optics-related issues.

Since the refractive index in a gas is related to the mass density, it is necessary to simulate the motion of the gas within a nuclear-reactor-pumped laser in order to determine the refractive index field. An additional benefit of such a simulation is the determination of the power density field throughout the chamber. This is an important quantity since the amount of laser power that can be extracted from the medium depends on the power density within the mode volume. Moreover, the spatial variation of the power density field is related to the mass density field in a complex manner. As the gas moves and the mass density field changes, the power density field is also modified since the power density at a point depends on both the mass density at the point and the average mass density between the point and the fission-fragment source, so a "static gas" calculation of the power density field can be significantly in error, especially when the deposited energy is larger than the thermal energy originally present in the gas. Thus, the consideration of gasdynamic effects is essential for correct prediction of the power density field.

2. The Model Problem

Consider a gas obeying the perfect gas law and having constant specific heat. The gas is initially motionless and thermodynamically uniform, and its viscosity and thermal conductivity are assumed to produce negligible effects over times and distances of interest. The gas is enclosed in a symmetric rectangular box or cylinder (see Fig. 1). The half-width or radius is denoted by L , the coordinate along this direction by x , the height by H ($H \gg L$ for most geometries of interest), and the coordinate along this direction (the laser axis) by z . The problem is assumed to be two-dimensional -- variations in thermodynamic properties, energy deposition, and gas motion are not allowed in the y -direction for a rectangular box or in the θ -direction for a cylinder.

Some portions of the side walls of this enclosure are covered with thin coatings of fissionable material called foils. When the enclosure is irradiated with a flux of thermal neutrons from a nuclear reactor, the foils emit fission fragments into the gas, as shown in Fig. 1. The fission fragments follow straight-line trajectories after creation, the origins of the trajectories are distributed uniformly throughout the foil volume, and the trajectories are isotropically distributed in solid angle.⁵⁻⁷ To find the fission-fragment power density $Q(x, z, t)$ at a point within the gas, an integral which sums up the contributions dQ at the point (x, z) at time t from each dV of foil material is performed over the foil volume.⁵⁻⁷

The power that an individual fission fragment can deposit at a given point in the chamber is not a constant. Rather, it is proportional to the mass density at the point and also depends on the line integral of the mass density along the fission-fragment trajectory through the gas, $\int \rho ds$, where ds is the incremental path length. This results from the fact that fission-fragment energy deposition in a gas is

characterized by a length scale, called the *range*, which is inversely proportional to the mass density: $l = l_0 \rho_0 / \rho$, where l_0 and ρ_0 are the range and the mass density, respectively, for the gas in its initial state (the product $l_0 \rho_0$ is a constant for a gas of given composition). Gas near a wall with a foil absorbs more energy than gas further away (the length scale of comparison is the range). The pressure gradients which result from this nonuniform energy deposition act to accelerate gas away from the foil. Near the foil, the mass density and hence the power density which drives the motion are reduced by the gas motion as time passes. Thus, the gas motion and the energy deposition are strongly coupled through the mass-density dependence of the range.⁸

The following steps are necessary to evaluate the power density at a point. For each grid point at each time step, perform the volume integral over the foil. For each dV in the volume integral, perform the integral $\int \rho ds$ from dV to the grid point along the trajectory (note that this involves interpolating the mass density field since most fission-fragment trajectories do not intersect grid points). In actuality, such a calculation is too computationally intense to be practical. However, for the high-symmetry geometries discussed above, if the neutron flux (which induces the fissions) and the mass density vary slowly in the z -direction with respect to l_0 (usually a very good assumption), then the full integral calculation can be replaced locally by a one-dimensional calculation.

The equations to be solved are given below.

$$\frac{\partial \rho}{\partial t} + \nabla \cdot \rho \mathbf{u} = 0 \quad (1)$$

$$\frac{\partial}{\partial t} \rho \mathbf{u} + \nabla \cdot \rho \mathbf{u} \mathbf{u} + \nabla p = 0 \quad (2)$$

$$\frac{\partial}{\partial t} \rho \left(e + \frac{1}{2} \mathbf{u}^2 \right) + \nabla \cdot \rho \mathbf{u} \left(e + p/\rho + \frac{1}{2} \mathbf{u}^2 \right) = Q \quad (3)$$

$$p = (\gamma - 1) \rho e \quad (4)$$

$$Q(x, z, t) = Q_0 h(t) g(z) f(x; \rho(\tilde{x}, z, t)) \quad (5)$$

The quantities \mathbf{u} , ρ , p , e , and γ represent the velocity, mass density, pressure, energy per unit mass, and specific heat ratio, respectively. Here, Q_0 is the amplitude of the power density (essentially the amplitude of the neutron flux multiplied by a constant scale factor) and has units of power per unit volume. The dimensionless functions $h(t)$ and $g(z)$ describe the temporal and spatial (along the laser axis) variation of the neutron flux. It is through the function $g(z)$ that two-dimensionality is introduced into the problem — the problem is one-dimensional when $g(z) = 1$. The dimensionless function f describes the variation of the power density in the x -direction and as such depends on the values of the mass density at all points (\tilde{x}, z) , where \tilde{x} represents any x -value between 0 and L . It is largest at the wall ($x = L$), and has a minimum at the centerplane ($x = 0$), about which it is symmetric. The shape of f depends on the parameter L/l_0 in the following way. When L/l_0 is small, the amplitude of f is small and f is relatively uniform ($df/dx \ll f/L$ everywhere). This is because the fission fragments easily traverse the chamber. As L/l_0 is increased, the fission fragments cannot travel far into the gas, so the minimum of f becomes relatively deep ($df/dx \gg f/L$ near the wall). The precise details of the function f have been published elsewhere.⁵⁻⁸ The boundary condition corresponding to no flow of conserved quantities across the boundary is $\mathbf{u} \cdot \hat{\mathbf{n}} = 0$, where $\hat{\mathbf{n}}$ is the unit vector normal to the boundary.

Equations (1) through (3) are convective equations in a conservative, Eulerian (nondissipative) form. The numerical technique used to solve such a system should be conservative, stable, accurate, and monotonic. In the last decade, a number of numerical techniques have been devised that possess all four of these characteristics for multidimensional flows. Examples are Flux-Corrected Transport (FCT),⁹⁻¹² the Piecewise Parabolic Method, and the Total Variational Diminishing technique. Strong evidence now exists demonstrating the superiority of these techniques over traditional methods such as MacCormack, Lax-Wendroff, and upwind differencing.⁹ Equations (2) through (4) are solved in the simulations presented below using FCT.

3. A Representative Simulation

Consider pure argon initially having a pressure of 50 kPa and a temperature of 300 K. Under these conditions the fission fragments will have a range slightly under 5 cm in the gas.⁵⁻⁷ The gas is contained in a rectangular box with a centerplane-to-wall distance of $L = 1$ cm and a distance along the laser axis of $H = 300$ cm. The x -dimension was chosen so that the ratio L/l_0 would be about 0.2. When this ratio is between 0.2 and 0.3, it is found that the power deposited at the centerplane is maximized, as shown in Fig. 2 (it is, however, *always* a minimum with respect to the power density at other locations in the chamber). The z -dimension was chosen to be extremely long for two reasons. The first is to allow the gas flow in the vicinity of $z = 150$ cm to remain one-dimensional (unperturbed by end effects) during the entire pulse. The calculated gas flow in this region may then be compared to the one-dimensional analytical theory.⁸ The second reason is to illustrate the length limitation placed on H by the mass density variation in the x -direction.

The fission fragments come from 13.5 μm -thick U_3O_8 foils extending from $z = 50$ cm to $z = 250$ cm on the side walls. The foil thickness was chosen arbitrarily to correspond to the maximum distance⁷ a fission fragment can travel within U_3O_8 . Since the foils do not extend the entire length of the enclosure, there will be very little energy deposition in the top and bottom 50 cm. Thus, the function $g(z)$ will be almost zero from 0 cm to 50 cm and from 250 cm to 300 cm and be almost unity from 50 cm to 250 cm in this case. The function $h(t)$, which describes the time dependence of the pulse, is chosen for simplicity to be unity for times between 0 ms and 1 ms (inclusive) and zero at all other times. The function $f(x)$ at $t = 0$ ms is shown in Fig. 3. A value of 0.4 kW/ml was selected for the quantity Q_0 . With these parameters, the pulse will deposit 0.5 J/ml on average in the gas.

Figures 4 and 5 show the mass density and the power density in the gas at $z = 150$ cm for several different times. Note as expected that the gas is moving toward the centerplane. If an infinite amount of energy were deposited in the gas, the mass density field would reach a limiting profile (shown in Fig. 4 as a dashed curve). The power density field corresponding to this mass density field is uniform (shown in Fig. 5 as a dashed curve): at this point further modifications of the mass density are no longer possible since these modifications are driven by the spatial nonuniformity of the power density field. In the above case, the limiting profiles have not been closely approached by the end of the pulse even though the amount of energy deposited is about ten times the thermal energy originally present in the gas.

Further addition of energy would drive the mass density and power density fields closer to their asymptotic limits, but the approaches will be slow, as indicated by the figures. Figures 6 and 7 show the calculated mass density and power density fields in the gas at $z = 150$ cm and $t = 1$ ms compared to the analytical theory.⁸ The agreement between theory and computation is excellent. Figures 8 and 9 show the results of ray-tracing calculations at 0.5 ms (halfway through the pulse) and 1 ms. At 0.5 ms the medium has an effective focal length of about 170 cm, and at 1 ms this length has decreased to roughly 80 cm. Thus, given the gas and pumping conditions of this case, it would be difficult to build a device exceeding a meter or so in length.

4. Rectangular vs. Cylindrical Geometries

It is instructive to investigate the differences between rectangular and cylindrical geometries, especially since no analytical theory exists for the cylindrical case. Consider argon, initially at 200 kPa and 300 K. The gas is contained either in the rectangular box described above or in a cylinder with a radius of $L = 1$ cm and a height of $H = 300$ cm. The fission-fragment range will now be slightly over 1 cm, so the fission fragments can just barely traverse the distance from the wall to the centerplane or the axis. The function f at $t = 0$ ms is shown for both geometries in Fig. 10. Note that initially the cylindrical f function is everywhere greater than the rectangular f function (a point in the cylinder interior is near to more foil than is a point in the interior of the rectangular box). All other properties of the energy deposition are the same as in the previous section.

Figure 11 shows the power density for both cases at 1 ms (the end of the pulse). Whereas the power density in the rectangular case has become more spatially uniform everywhere, this is not the situation in the cylindrical case. Although the power density field has flattened out near the wall, a region near the cylinder axis is now receiving absolutely no power. This axis-shielding results from the fact that the quantity $\int_0^L \rho dx / \rho_0 l_0$ increases with increasing time for the cylindrical case by virtue of mass conservation (it is a constant for the rectangular case,⁸ also by virtue of mass conservation). When this quantity exceeds unity, the axis is shielded from receiving further power. The on-axis power density as a function of time is shown in Fig. 12 for both cases. Although cases like these are not likely to be encountered due to their initially low on-axis power densities, ray-tracing calculations are shown for each case at 1 ms in Figs. 13 and 14. The large amount of focusing occurring in these cases is symptomatic of the relatively deep minimum of the f function. The parameter space in which axis-shielding occurs has not yet been delineated. Nevertheless, current numerical work suggests that it is necessary (but not sufficient) for L/l_0 to exceed 0.5 for this phenomenon to occur.

5. Simulation of Experiments

The simulation of one-dimensional cases provides insight into the interaction of the gasdynamics and the fission-fragment energy deposition, but the motivation for the development of this numerical model is the simulation of proposed and performed experiments. In most experiments, there will be important multidimensional effects. Such effects arise mainly from two sources. The first involves the finite extent of the foils. Even if the foils lined the side walls of the enclosure from top to bottom, points within roughly l_0 of the ends would receive less power than points further from the ends. The reason for this is that these end points "see" a smaller foil area. The consequences of this effect tend to be minor if the foil dimensions are much larger than l_0 (typically the case). The second source of multidimensionality involves the fact that in some reactor environments the neutron flux varies substantially throughout the device. Typically, most of this variation occurs along the z -direction: the neutron flux tends to be smallest near $z = 0$ and $z = H$ and largest near $z = H/2$, so again the ends receive less power than the middle (as an example, see Fig. 15). The effect of such variations is to set up pressure waves which oscillate back and forth in the z -direction. It is important to be able to calculate these pressure waves accurately since the energy deposition is usually inferred from pressure measurements and it is the energy deposition which determines the scale of the mass density variations produced in the chamber. Moreover, the flow induced by these pressure variations enhances energy transfer from the hot gas to the cold walls, further affecting the mass density field and hence the refractive index gradients.

An experiment was carried out at the following conditions.¹³ The gas was argon, initially at 103.4 kPa and 300 K. The enclosure was rectangular, with a centerplane-to-wall distance of $L = 0.75$ cm and a distance along the laser axis of $H = 10.5$ cm. In this case the ratio L/l_0 was about 0.3, within the optimal range of values. The functions $g(z)$ and $h(t)$ for this experiment are shown in Figs. 15 and 16. The amplitude of the pumping pulse was chosen to agree with experimentally measured pressure rises for similar cases (a sensitive indicator of average energy deposition). In this experiment, laser beams from a probe based on a derivative of the Hartmann technique¹³ were directed through the laser chamber, entering it parallel to the laser axis at several different x -locations. The angular deflection of each probe beam that resulted from the mass density variation was measured as a function of time.¹³ Figure 17 shows a ray-tracing (Hartmann probe) calculation after the bulk of the energy has been deposited in the gas, and Figure 18 shows a comparison of the experimentally measured angular deflections and the calculated values. The agreement is good for all probe beams and is particularly good for probe beams entering the chamber near the centerplane.

6. Conclusions

A numerical model of two-dimensional gas flow in nuclear-reactor-pumped lasers has been developed. The model can simulate rectangular and cylindrical geometries. Model simulations and available analytical results are in excellent agreement. The optical ray-tracing capabilities are useful in delineating length limits on laser chambers resulting from focusing produced by mass density variations. Axis-shielding, a new physical effect occurring in certain cylindrical cases, has been discovered numerically, and an approximate constraint for the onset of this phenomenon has been determined. Finally, simulations of experiments are able to reproduce experimentally measured refractive index data.

Acknowledgments

This work was performed at Sandia National Laboratories, supported by the U. S. Department of Energy under contract number DE AC04 76DP00789.

References

1. McArthur, D. A., and Tollefsrud, P. B. "Observation of Laser Action in CO Gas Excited Only by Fission Fragments." *Appl. Phys. Lett.* **26**, 187-190 (1975).
2. McArthur, D. A., Hays, G. N., Alford, W. J., Neal, D. R., Bodette, D. E., and Rice, J. K. "Recent Results on Reactor-Pumped Laser Studies at Sandia National Laboratories," *Laser Interactions and Related Plasma Phenomena* **8**, eds. H. Hora and G. Miley. Plenum, New York (1988).
3. Miley, G. H. *Direct Conversion of Nuclear Radiation Energy*, Chaps. 3-4, American Nuclear Society, LaGrange, IL (1970).
4. Born, M., and Wolf, E. *Principles of Optics*, Chap. 2, Pergamon, New York (1980).
5. Miley, G. H., and Thiess, P. E. "A Unified Approach to Two-Region Ionization-Excitation Density Calculations," *Nucl. Appl.* **6**, 434-451 (1969).
6. Guyot, J. C., Miley, G. H., and Verdeyen, J. T. "Application of a Two-Region Heavy Charged Particle Model to Noble-Gas Plasmas Induced by Nuclear Radiation," *Nucl. Sci. Eng.* **48**, 373-386 (1972).
7. Chung, A. K., and Prelas, M. A. "The Transport of Heavy Charged Particles in a Cylindrical Nuclear-Pumped Plasma," *Nucl. Sci. Eng.* **86**, 267-274 (1984).
8. Torczynski, J. R. "On the Motion of a Gas Experiencing Range-Dependent Volumetric Heating," *J. Fluid Mech.*, submitted (1988).
9. Book, D. L. *Finite-Difference Techniques for Vectorized Fluid Dynamics Calculations*, Chap. 3, Springer-Verlag, New York (1981).
10. Book, D. L., and Fry, M. A. *Airblast Simulations Using Flux-Corrected Transport Codes*, Rpt. 5334, Naval Research Laboratory (1984).
11. Baer, M. R., and Gross, R. J. *A Two-Dimensional Flux-Corrected Transport Solver for Convectively Dominated Flows*, Sandia Report SAND85-0613, Sandia National Laboratories (1986).
12. Oran, E. S., and Boris, J. P. *Numerical Simulation of Reactive Flow*, Chap. 8, Elsevier, New York (1987).
13. Neal, D. R., Sweatt, W. C., Alford, W. J., McArthur, D. A., and Hays, G. N. "Application of High-Speed Photography to Time-Resolved Wavefront Measurement," *SPIE Proc.* **832**, *High Speed Photography, Videography, and Photonics V*, 52-56 (1987).

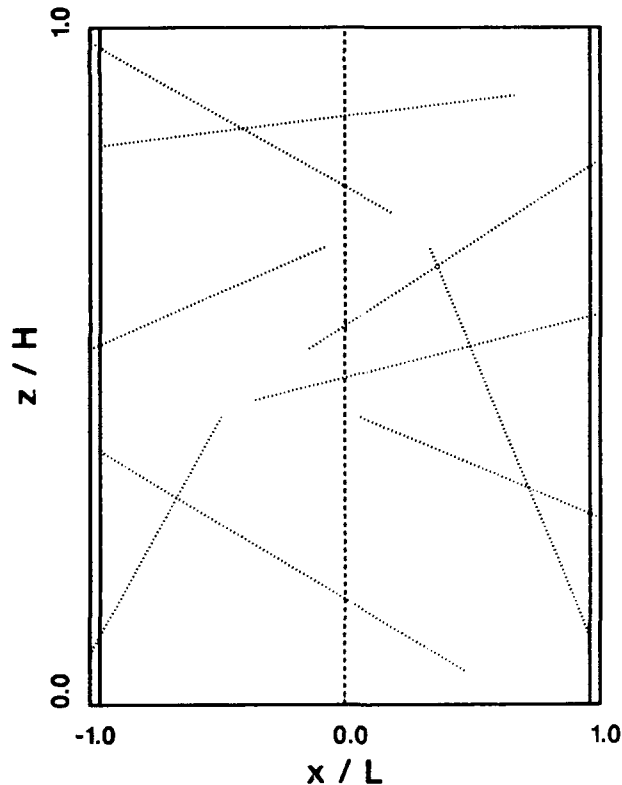


Figure 1. The lasing gas is contained in a rectangular or cylindrical enclosure (cross section shown). Fission fragments originate in thin foils of fissionable material on the side walls of the chamber and deposit energy in the adjacent gas-filled region.

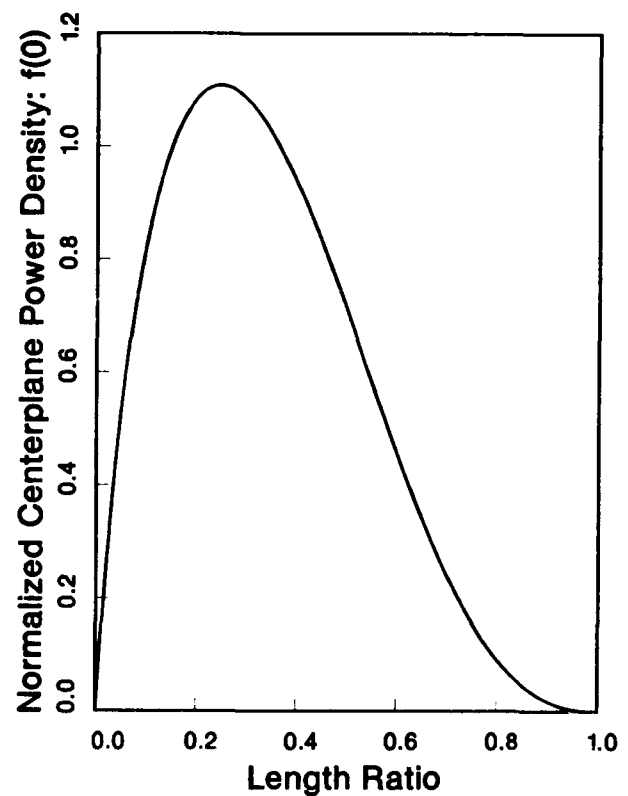


Figure 2. The maximum power that can be obtained at the centerplane for a specified geometry (proportional to $f(0)$) occurs when the length ratio L/L_0 is between 0.2 and 0.3.

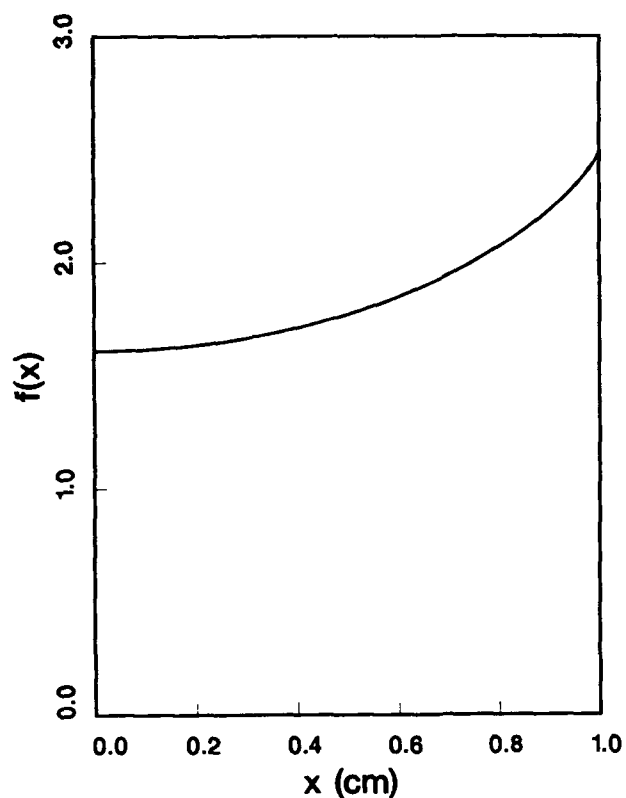


Figure 3. The function $f(x)$ at $t = 0$ ms ($\rho \equiv \rho_0$) describes the centerplane-to-wall variation of the energy deposition.

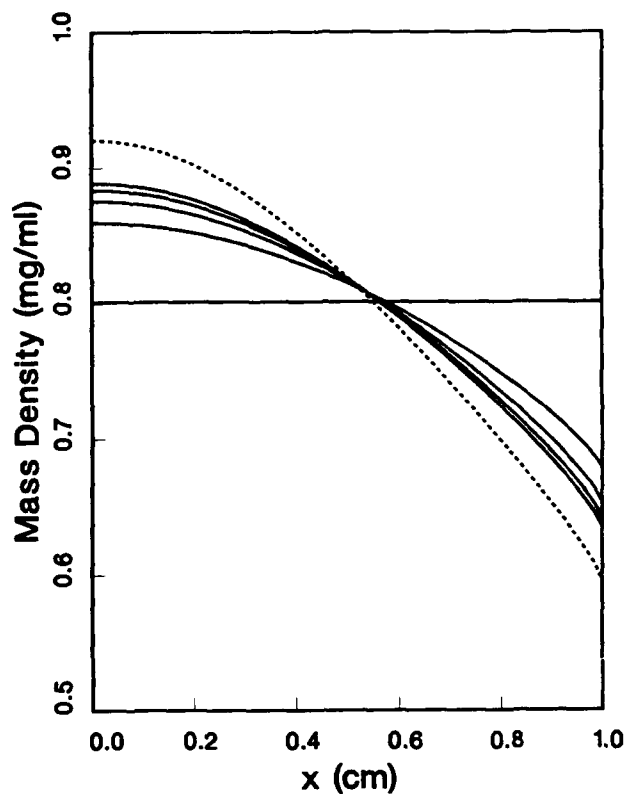


Figure 4. The mass density field, initially uniform, evolves smoothly toward the limiting profile (dashed curve) with increasing energy deposition. The curves shown are at 0.00 ms (uniform mass density), 0.25 ms, 0.50 ms, 0.75 ms, and 1.00 ms.

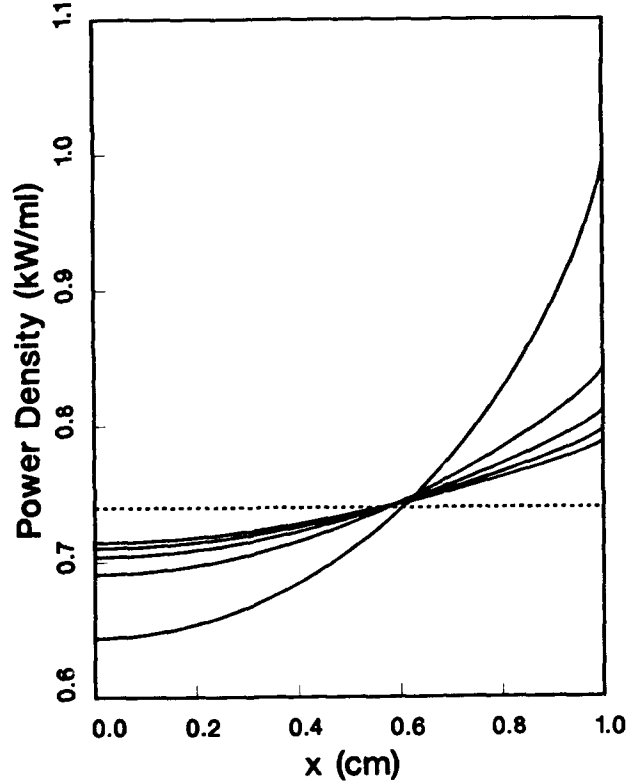


Figure 5. The power density field, initially possessing a deep minimum, evolves smoothly toward the uniform limiting profile (dashed curve) with increasing energy deposition. The curves shown are at 0.00 ms (deepest minimum), 0.25 ms, 0.50 ms, 0.75 ms, and 1.00 ms.

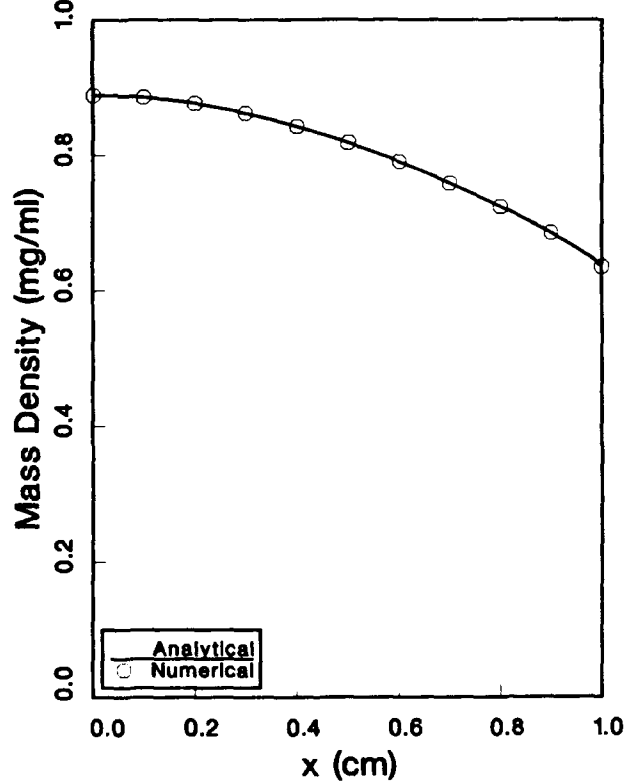


Figure 6. Analytical and numerical values of the mass density at $t = 1.0$ ms and $z = 150$ cm are in excellent agreement.

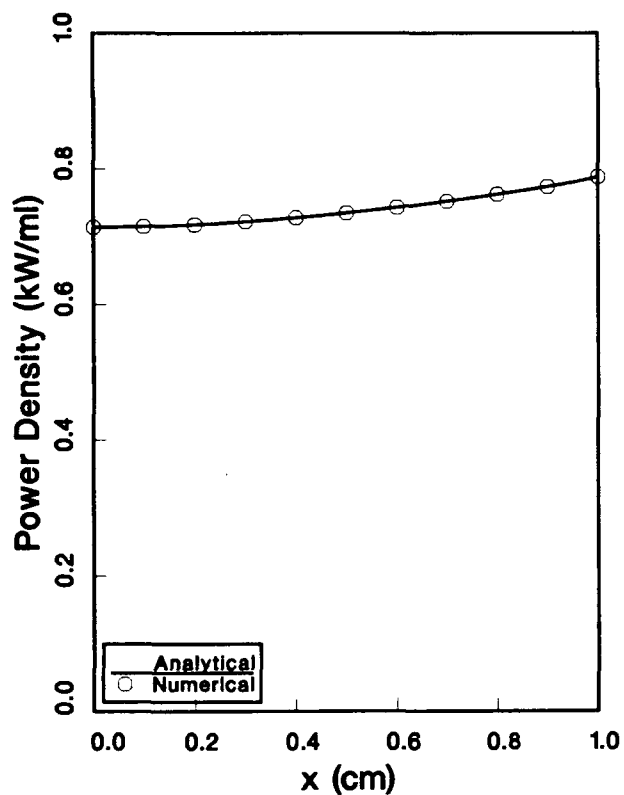


Figure 7. Analytical and numerical values of the power density at $t = 1.0$ ms and $z = 150$ cm are in excellent agreement.

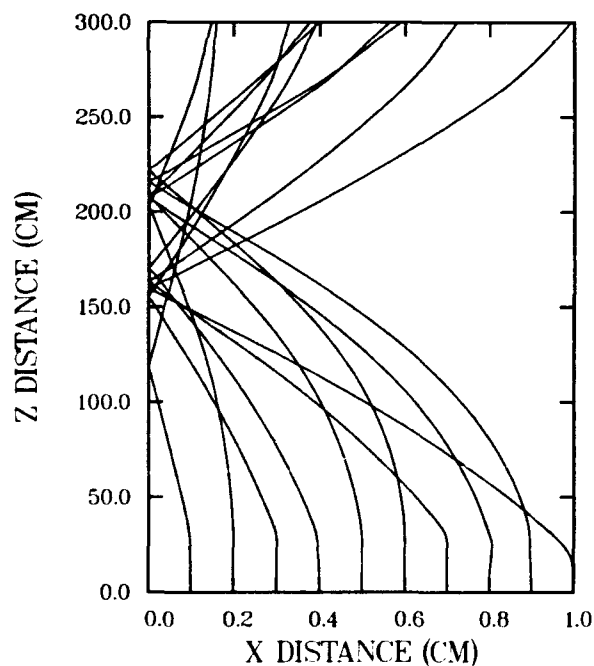


Figure 9. Light rays entering the gas parallel to the z -axis (Hartmann probe) are deflected by the mass density gradients. At 1.0 ms the effective focal length is about 80 cm although there are significant higher order aberrations.

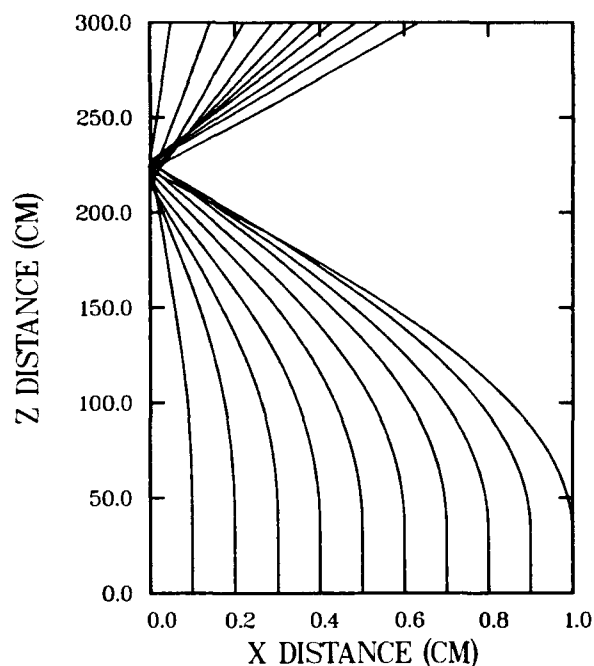


Figure 8. Light rays entering the gas parallel to the z -axis (Hartmann probe) are deflected by the mass density gradients. At 0.5 ms the effective focal length is about 170 cm.

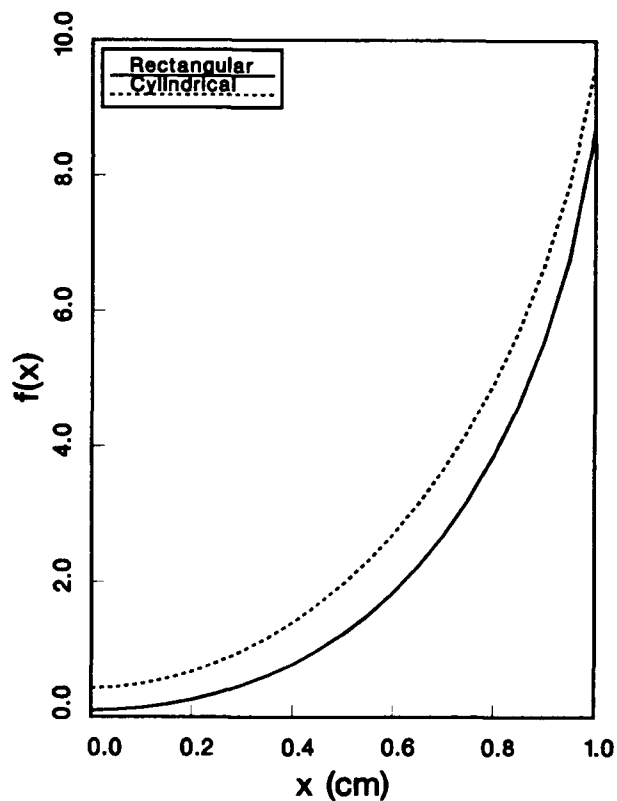


Figure 10. The function $f(x)$ at $t = 0$ ms ($\rho = \rho_0$) is shown for both the rectangular (solid curve) and cylindrical (dashed curve) cases.

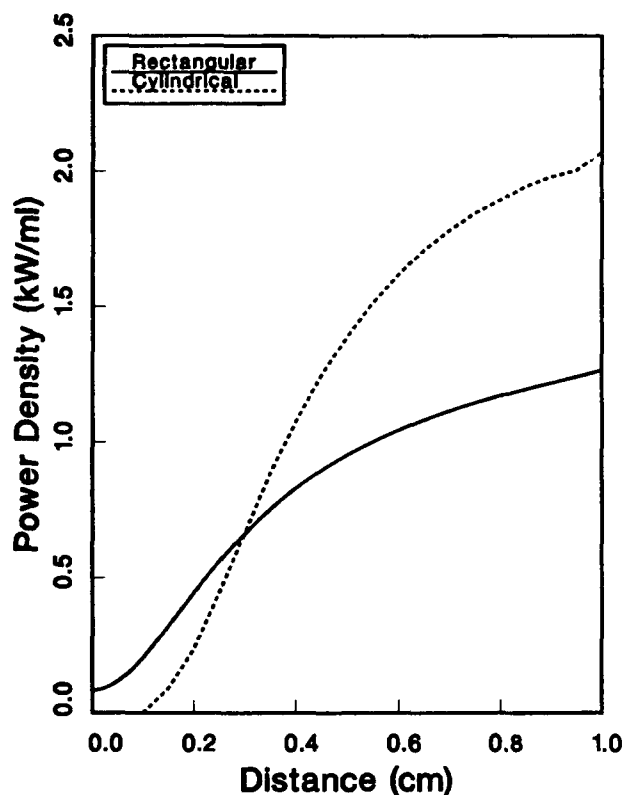


Figure 11. The power density at 1 ms is shown for both the rectangular (solid curve) and cylindrical (dashed curve) cases. Note that in the cylindrical case there is a region around the axis that receives no power (axis-shielding).

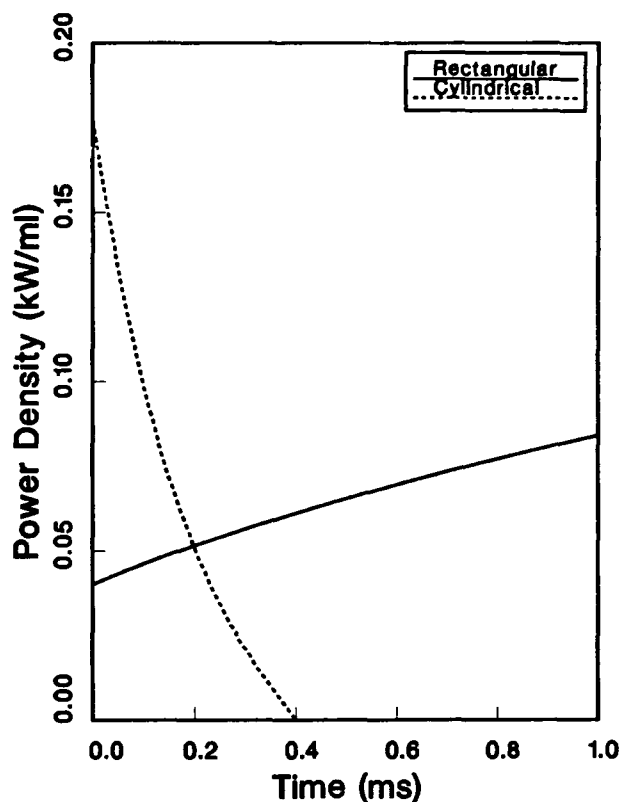


Figure 12. The power density at $x = 0$ is shown as a function of time for both the rectangular (solid curve) and the cylindrical (dashed curve) cases. The on-axis power density is initially higher for the cylindrical case but falls below that of the rectangular case around 0.2 ms and vanishes at 0.4 ms.

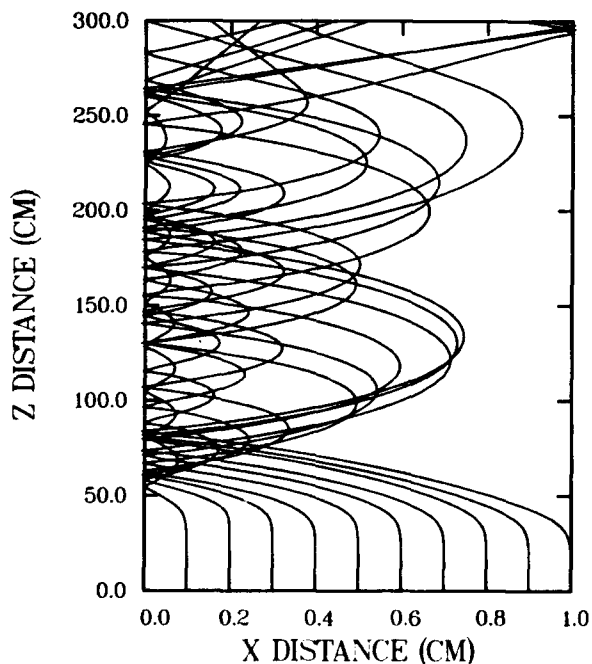


Figure 13. Ray tracing for the rectangular case at 1.0 ms.

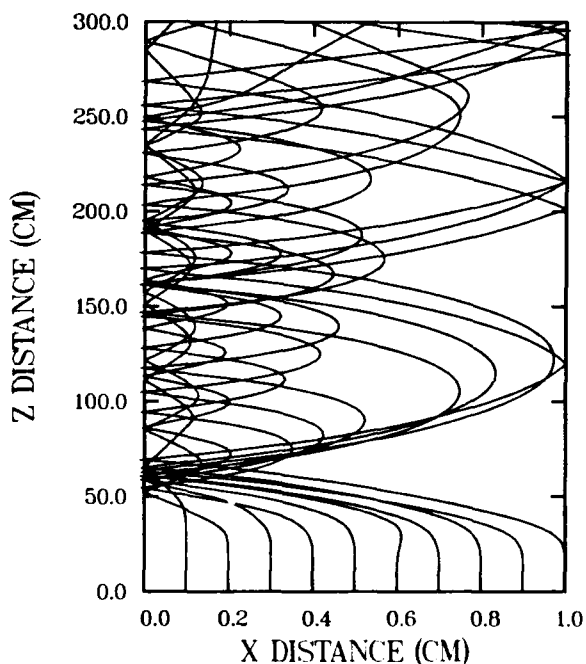


Figure 14. Ray tracing for the cylindrical case at 1.0 ms.

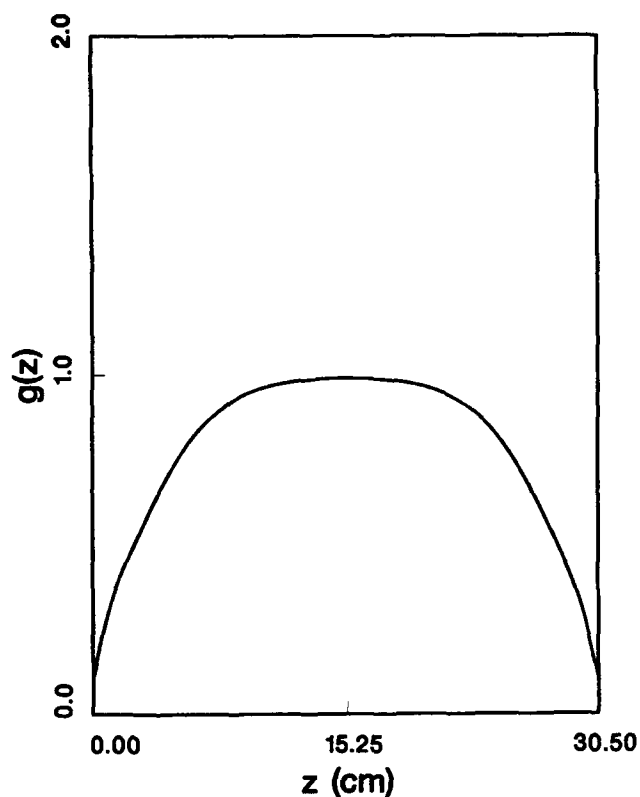


Figure 15. The function $g(z)$ describes the spatial variation of the energy deposition along the laser axis.

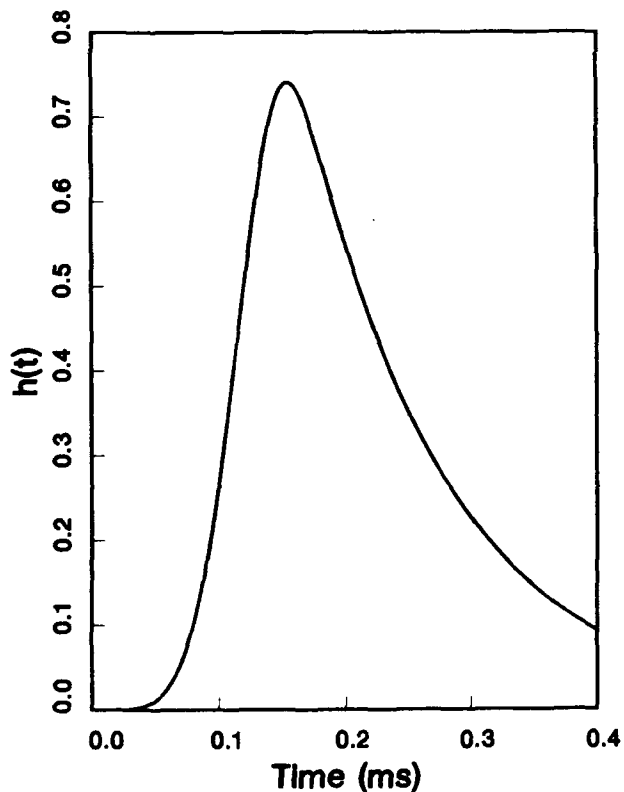


Figure 16. The function $h(t)$ describes the temporal variation of the energy deposition.

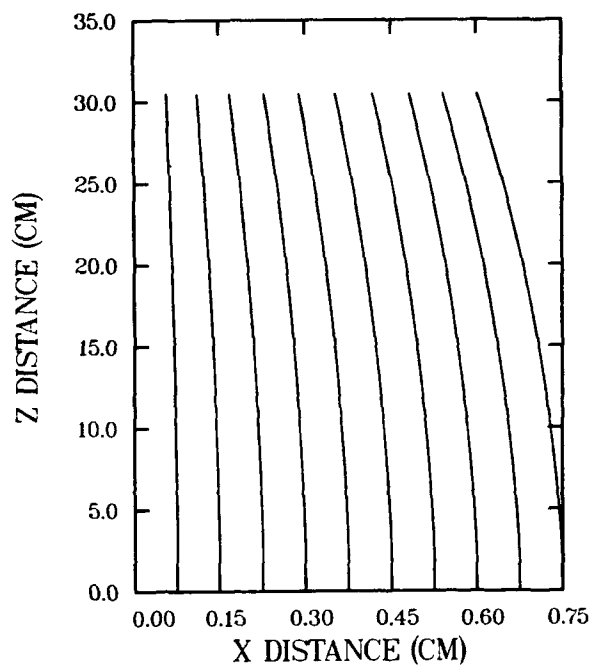


Figure 17. A sample ray-tracing (Hartmann probe) calculation performed at 1 ms (most of the energy has already been deposited). The rays end at 30.5 cm, which is the chamber length.

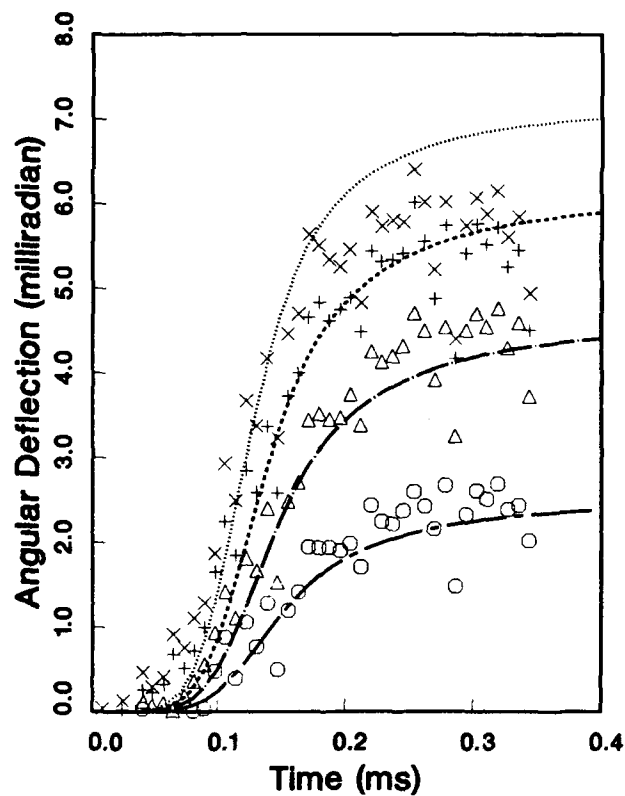


Figure 18. The experimentally measured¹³ angular deflections of probe laser beams passing through the chamber (Hartmann probe) are in good agreement with the calculated values. The circles, triangles, crosses, and diagonal crosses are experimental data corresponding to probe beams entering the chamber at x -locations of 0.15 cm, 0.30 cm, 0.45 cm, and 0.60 cm, respectively. The chain-dashed, chain-dotted, dashed, and dotted curves are the numerical results for the same locations, respectively.

RADIATION EFFECTS ON NUCLEAR PUMPED LASER OPTICS

G. H. Miley, R. Chapman, J. Nadler, and W. Williams

The University of Illinois, Department of Nuclear Engineering
103 S. Goodwin Ave., Urbana, IL 61801

Abstract

Radiation effects on the optical components of a Nuclear Pumped Laser (NPL) system can significantly impact the development of an NPL. For example, gain measurements of an NPL medium can be deleteriously affected by transient radiation-induced absorption in the window and/or substrate materials of the system. Estimates indicate that this effect can reduce the relative gain in a typical NPL system from 1.4 to below 1.0. The transient radiation-induced absorption in Corning 7740 (Pyrex) and Corning 7940 (fused silica) resulting from neutron and γ -ray irradiation has been investigated. Absorption coefficients have been measured at 632.8 nm for Pyrex and at 325 nm for fused silica during and after pulsed reactor (TRIGA) irradiation. The absorption coefficient increases rapidly to a maximum value during pulse irradiation, then decreases over a time period of > 1000 s to a permanent value after the pulse. In general, the maximum absorption coefficient increases with increasing accumulated dose and decreases with increasing temperature.

Introduction

Optical components of Nuclear-Pumped Laser (NPL) systems may be exposed to intense neutron and γ radiation environments. The radiation-induced absorption (α) in the window and substrate materials resulting from pulsed irradiation can have a great impact on the optical performance of those materials. Typically, α reaches a maximum value (α_{\max}) during pulsed irradiation and then decreases to an asymptotic permanent value afterwards. This phenomena can lead to a significant error in gain measurements in the development of pulsed NPL laser systems unless corrections are made for the transient radiation-induced absorption. In addition, laser operation itself can be severely effected.

A schematic of the mechanisms involved in radiation-induced absorption mechanisms is given in Figure 1. Excellent review papers^{1,3} on these mechanisms have been published elsewhere and therefore only a brief description of the processes involved will be discussed here.

Radiation-induced absorption is ultimately due to the formation of color centers. γ -rays interact with the material to produce Compton electrons and the neutrons interact to produce secondary electrons. At the same time, the neutrons and Compton electrons cause atom displacements to create defects in the material through momentum transfer. The Compton and secondary electrons interact with the material to generate electron-hole pairs. The electron-hole pairs can also recombine non-radiatively to create defects. The electrons or holes then become trapped at the radiation-created defects of inherent defects to form color centers.

The results of selected previous efforts on the radiation-induced absorption in optical materials are summarized in Table 1. The results of this investigation are included in the table for comparison with previous results, however only general comparisons can be made since there exists no data to enable direct comparison; can be made since there exists no data to enable direct comparisons. The borate glass has a composition of 50% B_2O_3 , 30% Na_2O , and 20% Al_2O_3 and is useful in comparing Pyrex with fused silica since Pyrex has a composition of 81% SiO_2 , 13% B_2O_3 , 4% Na_2O , and 2% Al_2O_3 ; and fused silica has a composition of 100% SiO_2 . Most of the earlier efforts concentrated on the permanent absorption^{1,2,3} resulting from low dose rate steady-state irradiations. Prior studies of the transient radiation-induced absorption in optical materials resulting from pulsed irradiation have been made at 215nm⁴ and at 257nm⁵. The present study focuses on the transient radiation-induced absorption at 325 nm in fused silica (Corning 7940) and at 632.8 nm in Pyrex (Corning 7740) as a result of pulsed reactor (TRIGA) irradiation. The radiation characteristics of a TRIGA reactor pulse are given in Table 2.

The following example illustrates the effect of transient radiation-induced absorption on gain measurements in an NPL media. Gain measurements of the XeF^* 351 nm wavelength transition in a nuclear-pumped $^3He/Xe/NF_3$ media have been made at the SPR III reactor at Sandia National Laboratory, Albuquerque, NM.¹¹ The peak relative gain (I/I_0) was reported to be 1.4 corresponding to an optimum peak gain of 0.007 cm^{-1} for a laser cell length (L) of 48 cm.

$$I/I_0 = \exp(\gamma L)$$

Table 1. Previous Work on Radiation-Induced Absorption[†]

α_{max} Dose	α_p Dose	λ (nm)	Material	Dose (MRad)	Radiation Source	Ref
1.16	.22*	633	Pyrex	0.5	Triga	pres.
---	.14			6.0		study
.014	.0002*	325	Fused	0.5	Triga	pres.
---	.0002		Silica**	7.5		study
.15	.07*	215	Fused	0.5	Triga	4
---	.04		Silica	150	Electrons	
2.17	.75	257	Fused	.05	SPR III	5
1.35	.57		Silica	.03		
---	.036	215	Cryst.	60	⁶⁰ Co	6
---	.025	257	Quartz			
---	.022	325				
---	.018	633				
---	.25	215	Borate	12	⁶⁰ Co	7
---	.31	257	Glass			
---	.40	325				
---	.13	633				
---	.04	215	Fused	40	⁶⁰ Co	8
---	.01	257	Silica			
---	.005	325				
---	.031	215	Fused	260	⁶⁰ Co	9
---	.009	257	Silica			
---	.001	325				
---	.044	215	Fused	10	⁶⁰ Co	10
---	.029	257	Silica			
---	.003	325				

α_{max} - maximum absorption measured during reactor pulse.

α_p - permanent absorption.

* - absorption measured 1000 s after the reactor pulse.

** - all fused silica in table is type-III (< 1200 ppm OH).

† - room temperature irradiations and absorption measurements.

The transient radiation-induced absorption in fused silica (Corning 7940) was also measured at the SPR III reactor at Sandia National Laboratory, Albuquerque, NM.⁵ The minimum transmission (T/T_0) at 257 nm was reported to be 76% corresponding to a maximum absorption of 0.11 cm⁻¹. Typical fused silica end windows used in these gain measurement experiments were 0.5 in. thick (l).

$$T/T_0 = \exp - (\alpha l)$$

Thus, the transient radiation-induced absorption in the end windows would reduce the measured relative gain ($(I/I_0)_{\text{meas}}$) in this example from 1.4 to below 1.0.

$$(I/I_0)_{\text{meas}} = \exp (\gamma L) \exp - (\alpha l)$$

Experimental

A schematic of the experimental set-up used for the measurement of the transient radiation-induced absorption in fused silica is given in Figure 2. A sample of fused silica was placed in a multi-pass optical cavity which was then positioned adjacent to the reactor core in the through-port of the TRIGA reactor. The multi-pass cavity utilizes a Lissajous-type resonator which increases the sensitivity of the absorption measurements 40 times due to an increase in path length through the sample. A diagram of the multi-pass cavity is given in Figure 3. The mirrors are uv-enhanced aluminum and the lens is fused silica. These materials were chosen to minimize the effects of the pulsed irradiation on the performance of the cavity.

Laser light from a He-Cd laser with a wavelength of 325 nm was directed through the sample and multi-pass cavity. The output of the multi-pass cavity was then measured by photodiode detectors and stored on a digital oscilloscope. A narrow band-pass filter ($\Delta\gamma = 2.5$ nm) was used to reduce the background signal due to the fluorescence of the sample. A

Table 2. TRIGA Reactor Pulse Characteristics

Reactivity (\$)	3.00
Peak	
γ Dose Rate (MRad/s)	35
Thermal Neutron Flux (n/cm ² s)	4.3x10 ¹⁵
Fast Neutron Flux (n/cm ² s)	4.0x10 ¹⁵
Total	
γ Dose (MRad)	0.50
Thermal Neutron Fluence (n/cm ²)	6.2x10 ¹³
Fast Neutron Fluence (n/cm ²)	5.7x10 ¹³
Pulse Width FWHM (ms)	13

laser reference signal was obtained by splitting the laser beam before it entered the multi-pass cavity to correct for any changes in laser output.

The effects of the pulsed irradiation on the multi-pass cavity optics itself were determined and found to account for 3% of the total maximum absorption measured during the reactor pulse and 75% of the total absorption measured at a time of 1000 s after the reactor pulse. The absorption attributed to the cavity optics was subtracted from the total measured absorption to yield the absorption coefficients reported for fused silica.

A parametric study of the transient radiation-induced absorption in Pyrex was conducted prior to the absorption measurements in fused silica in order to identify the dominant processes involved. The experimental set-up used for Pyrex was very similar to that used for fused silica. However, the multi-pass optical cavity was not required for these measurements due to the much larger absorption coefficients characteristic of Pyrex. A He-Ne laser was used to provide the 632.8 nm laser light and a dielectric mirror with a maximum reflectivity at 632.8 nm was used to reduce the background fluorescence signal. The effects of temperature on the transient absorption in Pyrex was investigated by maintaining the Pyrex at an elevated temperature during and after the reactor pulse. This was achieved by wrapping the Pyrex with resistive heating tape and monitoring the temperature with thermocouples.

Results

The radiation-induced absorption (α) in fused silica at 325 nm as a function of time for a room temperature pulse is given in Figure 4. α reaches a maximum value (α_{\max}) of 0.0070 cm^{-1} during the pulse then decreases to an asymptotical permanent value after the pulse. α_0 and α_{1000} are the absorption coefficients at 40 and 1000 s after the pulse respectively, and are labeled on the curve in Figure 4. For the fused silica, α decreases to 0.0001 cm^{-1} at a time of 1000 s after the pulse. This corresponds to a recovery of 99%.

The transient radiation-induced absorption in fused silica at 325 nm is compared to previous work⁴ at 215 nm in Figure 5. The previous work was done on the same material (Corning 7940) and at the same reactor (University of Illinois' TRIGA). At 215 nm, α is found to reach a maximum of 0.077 cm^{-1} with a recovery of 53% to 0.036 cm^{-1} . Since these experiments were done at different times with different quality Corning 7940 and with different experimental apparatus, there remains some uncertainty about the validity of this comparison. However, such a strong wavelength dependence for α_{\max} is expected since a similar wavelength dependence has been observed for the permanent absorption resulting from low dose rate steady-state irradiations. The ratio of α_{\max} at 215 nm to α_{\max} at 325 nm is 11, whereas the same ratio for the permanent absorption is 13. The latter ratio was obtained from averaging the three sets of values presented in Table 1 for the ^{60}Co irradiations. In addition, the recovery of α proceeds slower and to a lesser extent at 215 nm than at 325 nm. These results suggest that different color centers are responsible for absorption at 325 nm vs. 215 nm.

The radiation-induced absorption as a function of time for a series of reactor pulses is given in Figure 6. The pulses are 17 minutes apart with a dose of 0.5 MRad each. Values of α_{\max} , α_0 , and α_{1000} for each pulse in the series of pulses shown in Figure 6 are given in Figure 7 as functions of dose. In general, α increases with increasing accumulated dose. If the color centers are formed at the inherent defects, α would saturate with increasing dose. If the color centers are formed at the radiation-created defects, α would be linear with increasing dose. The experimental data shows a combination of these trends. At low accumulated doses, the color centers responsible for α_{\max} (the short-term color centers) are formed at both the inherent and radiation-created defects. At high accumulated doses, the short-term color centers are formed at only the radiation-created defects. These results are presented in terms of α_{\max}/D , α_0/D , and α_{1000}/D in Figure 8. α_{1000}/D increases with increasing dose indicating that the material recovers to a lesser extent as the accumulated dose increases. This suggests that the fused silica network bonds, broken in the creation of defects, reform to a lesser extent as the accumulated dose increases (i.e., the annealing of the long-term color centers decreases as the accumulated dose increases).

Some features of this data can be clarified by considering relative changes in α for each pulse. α' is defined as the relative absorption coefficient. It measures the absorption as a result of one pulse in a series of pulses and is normalized with the transmission through the sample just prior to the particular pulse of interest. α' as a function of time is given in Figure 9 for a sample of fused silica that had previously received 1.0 MRad and 6.5 MRad. At the lower accumulated dose, α' recovers to a greater degree (99%) than at the higher accumulated dose (73%). This again indicates that the annealing of the long-term color centers decreases as the accumulated dose increases.

The value of α in Pyrex at 633 nm as a function of time at room temperature is given in Figure 10. We see that α reaches a maximum value of 0.58 cm^{-1} during the reactor pulse and decreases to an asymptotic permanent value after the pulse. At a time of 1.5 s after the pulse, α has decreased to 0.28 cm^{-1} . The radiation-induced absorption as a function of

time in fused silica at 325 nm and in Pyrex at 633 nm are compared in Figure 11 in terms of a normalized α . It is observed that α for Pyrex decreases to 0.11 cm^{-1} at a time of 1000 s after the pulse corresponding to a recovery of 81%. Fused silica recovers slower but to a greater extent than Pyrex. The recovery for fused silica initially has a time constant of 0.51 s which continuously increases to a value of 870 s at a time of 1000 s after the pulse, while Pyrex starts out with a time constant of 0.092 and subsequently increases to 3000 s.

The value of α'_{max} for Pyrex at 633 nm as a function of temperature is given in Figure 12. At temperatures above 150°C , α'_{max} decreases exponentially with increasing temperature. A curve fit of the data yields the equation.

$$\alpha'_{\text{max}} = 0.3 \exp(-T(^{\circ}\text{C})/248.5)$$

The value of α' for Pyrex as a function of time after a reactor pulse ($t = 0$, $\alpha' = \alpha'_{\text{max}}$) at various temperatures is given in Figure 13. These curves illustrate the effect of temperature on the recovery of α' . Pyrex recovers to a greater degree and faster at higher temperatures. Indeed, α' recovers completely for temperatures above 400°C . Figure 14 shows that α recovers 100% within 60 s at a temperature 400°C .

Transmission spectra for fused silica prior to and several days after receiving an irradiation dose of 7.5 MRads are given in Figures 15 and 16. The radiation-induced absorption in fused silica is found to be strongest for wavelengths from 200 to 350 nm, much weaker for wavelengths from 350 to 700 nm, and negligible for wavelengths over 700 nm. The observed transmission spectrum for irradiated optical materials is a summation of several individual gaussian-shaped absorption bands resulting from different types of color centers. Some color centers responsible for radiation-induced absorption in fused silica have been identified.¹ Perhaps the best known color center is the E'_γ center which absorbs at 215 nm. E'_γ center is also the strongest absorbing color center which can be seen in Figure 15. Other color centers that have been identified are the E'_β and the B_2 centers which absorb at 225 nm and 245 nm, respectively. In addition, there is a color center, which is ESR inactive and thus cannot be identified, that absorbs at 260 nm.

Transmission spectra for Pyrex prior to and several days after receiving an irradiation dose of 6.0 MRads are given in Figure 17. Color centers responsible for the radiation-induced absorption in Pyrex have not yet been identified. The observed transmission spectrum for irradiated Pyrex shows that it absorbs strongly throughout the visible wavelength region, decreasing with increasing wavelength. Comparing the transmission spectra for Pyrex and fused silica suggests that there are more types of color centers formed in Pyrex than in fused silica during irradiation. This result would be expected due to the more complex composition of Pyrex.

Conclusions

The transient radiation-induced absorption in fused silica (type-III) at 325 nm and in Pyrex at 633 nm has been investigated. α for fused silica is found to reach a maximum value of 0.0070 cm^{-1} during a 0.5 MRad reactor pulse and then decreases to 0.0001 cm^{-1} at a time of 1000 s after the pulse. This corresponds to a recovery of 99%. α for Pyrex is found to reach a maximum value of 0.58 cm^{-1} during a 0.5 MRad reactor pulse and then decreases to 0.11 cm^{-1} at a time of 1000 s after the pulse. This corresponds to a recovery of 81%.

A previous study of radiation-induced absorption in fused silica at 215 nm found that α reached a maximum value of 0.077 cm^{-1} during a 0.5 MRad reactor pulse with a subsequent recovery of 53% to 0.036 cm^{-1} . The fact that α exhibits such different behavior at the two wavelengths is characteristic of absorption by different color centers. The recovery of α in fused silica is found to decrease with increasing dose. A fresh sample recovers 99% after pulsed irradiation and only 73% at an accumulated dose of 6.5 MRad. This suggests that the fused silica network bonds, broken in the creation defects, reform to a lesser extent as the accumulated dose increases.

Temperature has been found to have an immense effect on the radiation-induced absorption. The maximum radiation-induced absorption for Pyrex during pulsed irradiation decreases dramatically with increasing temperature. The value of α'_{max} is found to decrease over an order of magnitude from 0.58 cm^{-1} to 0.048 cm^{-1} as the irradiation temperature is increased from room temperature to 450°C . Also, α for Pyrex recovers to a greater extent and much faster as the temperature increases. Indeed, Pyrex is found to recover 100% within 30 s after pulsed irradiation at 450°C .

Acknowledgements

This work was supported by Sandia National Laboratory under contract 01-0371 and by EG&G Idaho, Inc. under contract C87-101376-2.

References

1. D. L. Griscom, "Nature of Defects and Defect Generation in Optical Glasses," SPIE Radiation Effects in Optical Materials 541, 38 (1985).
2. P. Levy, "Overview of Nuclear Radiation Damage Processes: Phenomenological Features of Radiation Damage in Crystals and Glasses," SPIE Radiation Effects in Optical Materials 541, 2 (1985).
3. G. H. Miley, R. Chapman, J. Nadler, and W. Williams, "Radiation-Induced Absorption in Pyrex," Southwest Optics '87 Conference; 1987 February 11-13; Albuquerque, NM (1987).
4. G. E. Palma and R. M. Gagosz, "Optical Absorption in Fused Silica During Irradiation Annealing of the C-Band," J. Phys. Chem. Solids 33, 177 (1972).
5. P. J. Brannon, R. W. Morris, and J. B. Gerrardo, "Nuclear Radiation Induced Absorption in Optical Materials," SPIE Southwest Conference on Optics 540, 451 (1985).
6. E. W. J. Mitchell and E. G. S. Paige, "The Optical Effects of Radiation Induced Atomic Damage in Quartz," Phil. Mag. 1, 1085 (1956).
7. A. M. Bishay, J. Am Ceram. Soc. 44, 289 (1961).
8. C. M. Nelson and F. H. Crawford, "Optical Absorption in Irradiation Quartz and Fused Silica," J. Phys. Chem. Solids 13, 296 (1959).
9. P. W. Levy, "Reactor and Gamma-Ray Induced Coloring of Corning Fused Silica," J. Phys. Chem. Solids 13, 287 (1959).
10. E. J. Friebele and D. L. Griscom, Treatise on Materials Science and Technology 17, 257 (1979).
11. G. N. Hays, D. A. McArthur, D. A. Neal, and J. K. Rice, "Recent Results from Nuclear Pumped Laser Studies: Gain Measurements in XeF," 7th International Workshop of the Interaction of Laser Plasmas and Related Phenomena, Monterey (1985).

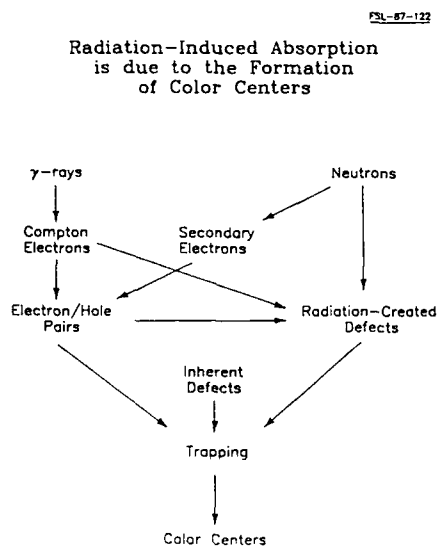


Figure 1. Schematic of radiation-induced absorption mechanisms.

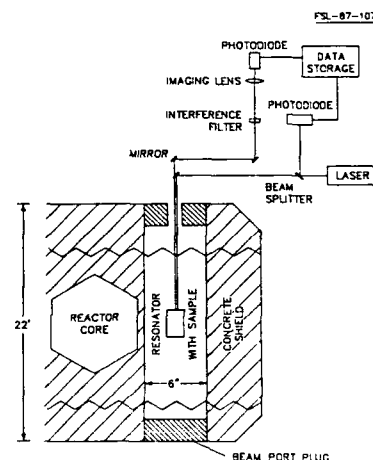


Figure 2. Schematic of experimental set-up.

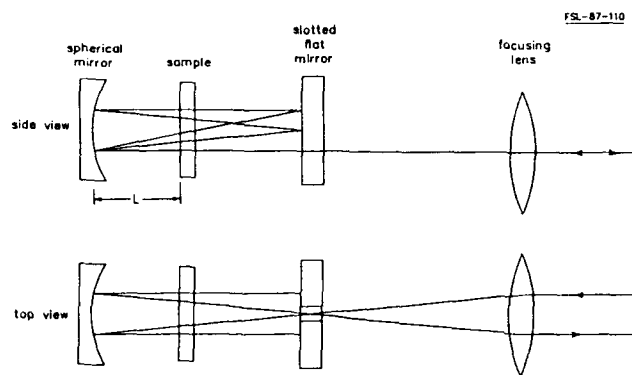


Figure 3. Diagram of multi-pass (Lissajou-type) resonator.

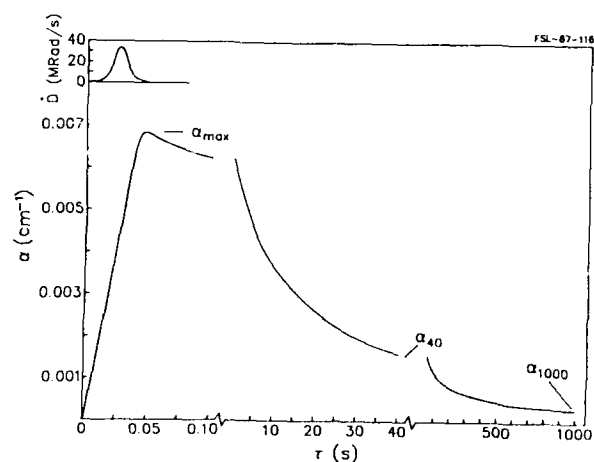


Figure 4. Radiation-induced absorption as a function of time.

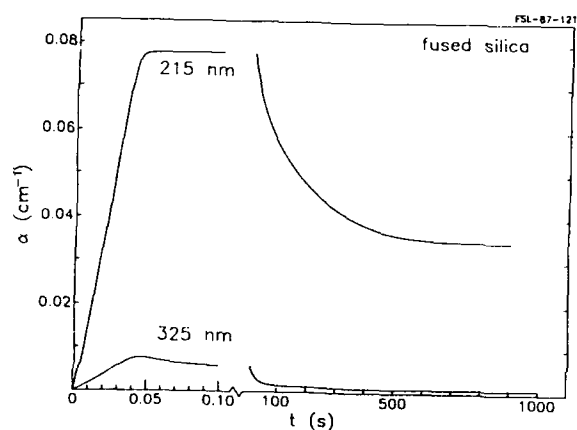


Figure 5. Comparison of radiation-induced absorption at 215 nm vs. 325 nm.

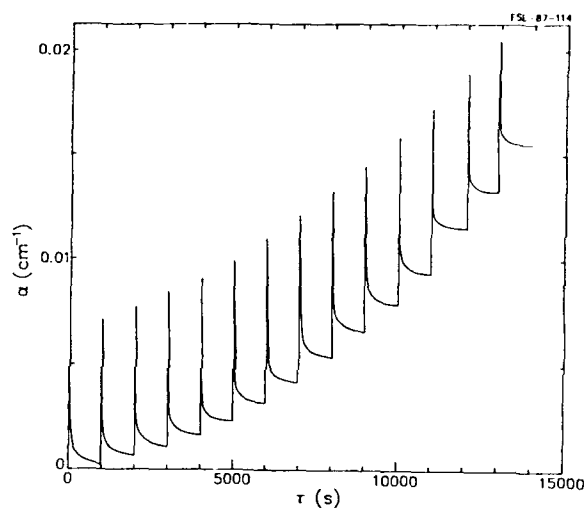


Figure 6. Comparison of radiation-induced absorption as a function of time for a series of pulses.

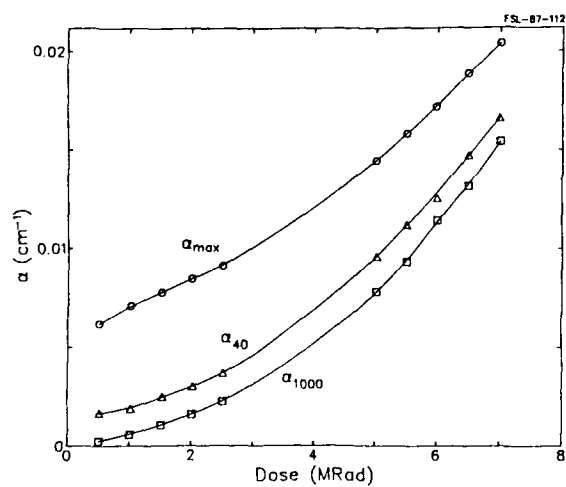


Figure 7. α_{max} , α_{40} , and α_{1000} for each pulse in a series of pulses.

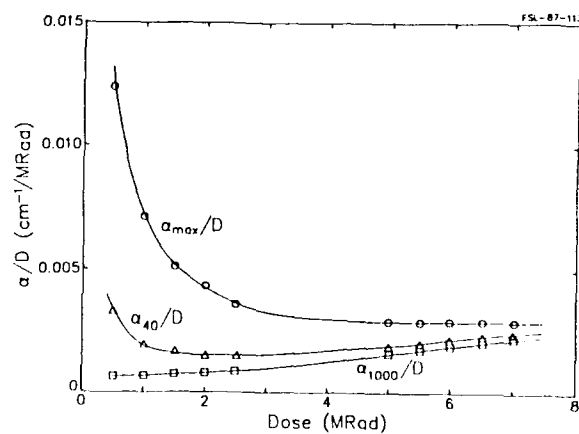


Figure 8. α_{max}/D , α_{40}/D , and α_{1000}/D for each pulse in a series of pulses.

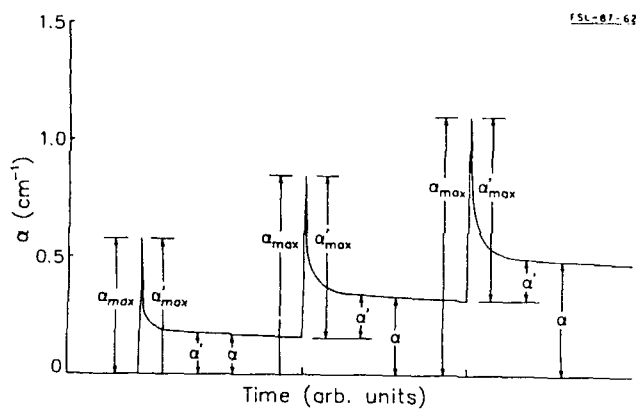


Figure 9. Definition of α and α' .

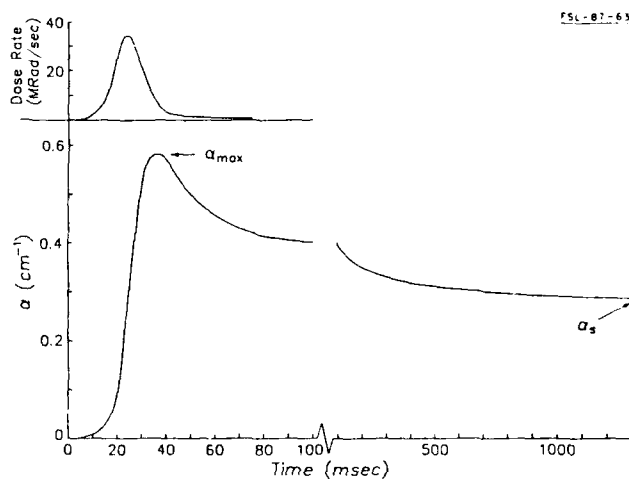


Figure 10. Absorption as a function of time for Pyrex at 633 nm.

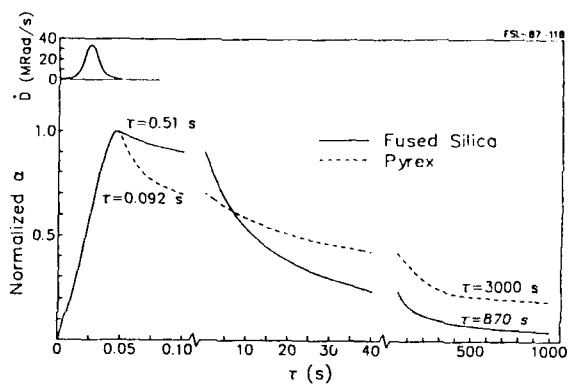


Figure 11. Normalized absorption of Pyrex at 633 nm and fused silica at 325 nm.

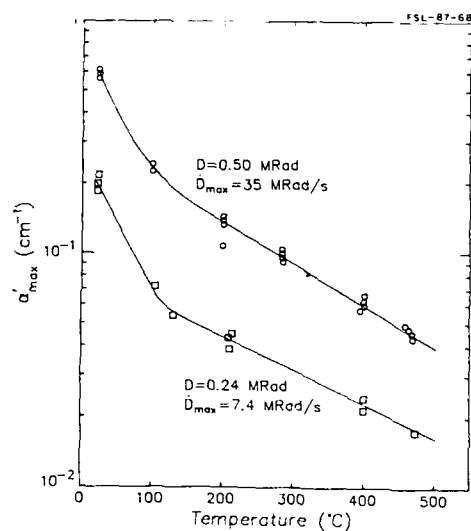


Figure 12. α'_{\max} as a function of temperature for two different size pulses.

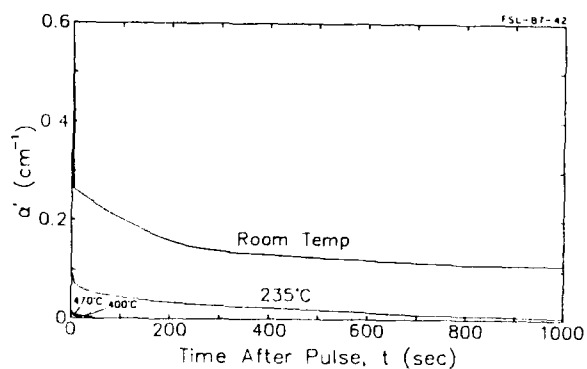


Figure 13. Absorption as a function of time for Pyrex at various temperatures.

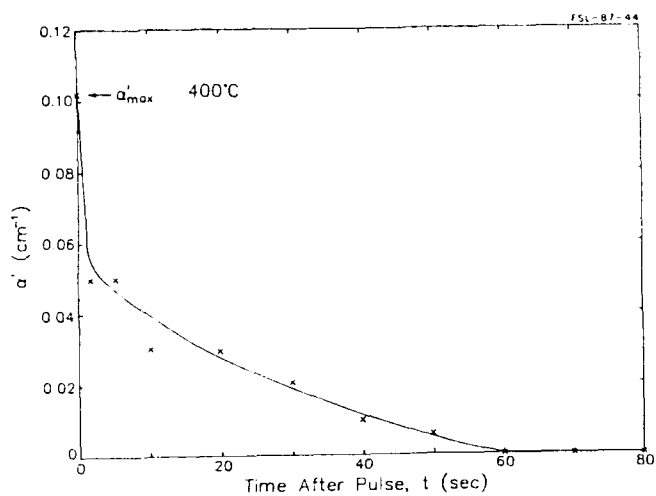


Figure 14. Absorption as a function of time for Pyrex at 400 °C.

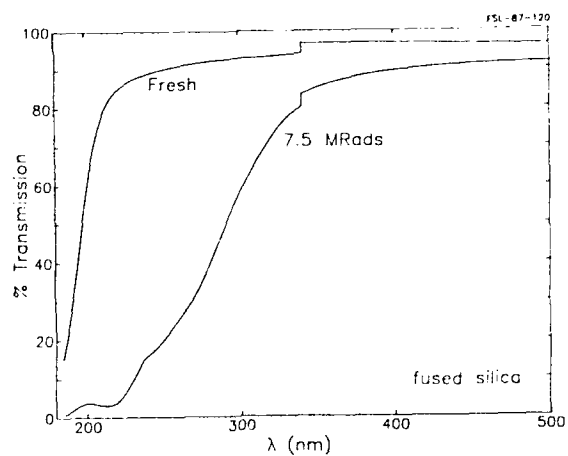


Figure 15. Transmission spectra for fresh and irradiated fused silica.

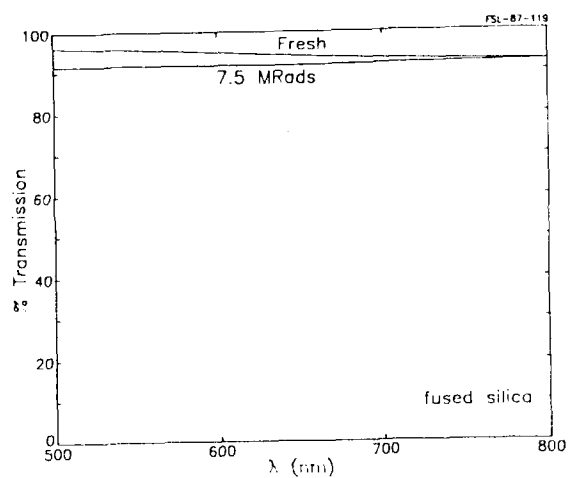


Figure 16. Continuation of Figure 15.

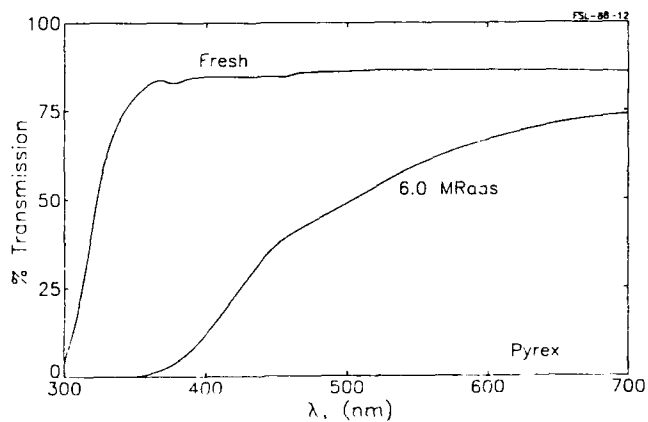


Figure 17. Transmission spectra for fresh and irradiated Pyrex.

NARROW-LINEWIDTH XeCl LEAD VAPOR RAMAN CONVERTER LASER SYSTEM

Harry Rieger
General Dynamics
Laser Systems Laboratory
5452 Oberlin Drive
San Diego, CA 92121

Abstract

Narrow linewidth and high efficiency conversion of stimulated Raman scattering (SRS) in lead vapor heat pipe was observed using a narrow linewidth and injection locked XeCl excimer laser system as the pump source.

The XeCl laser was continuously tuned over its entire B-X gain curve, from the (0-0) transition to the (0-3) transition, giving it a range of 0.8 nm (307.65 nm to 308.45 nm). The laser linewidth was narrowed down to 2 mÅ (0.02 cm^{-1}). The output energy was 310 mJ/pulse, with repetition rate up to 50 pps and good beam quality.

A lead vapor heat pipe operating at 1225°C was used as a single-pass stimulated Raman converter, shifting the radiation from 308 nm to 459 nm. Photon conversion efficiency as high as 75% with slope efficiency of 80% was achieved. A wavelength control system was incorporated to lock the wavelength within 2 mÅ.

Introduction

Stimulated Raman conversion in lead vapor heat pipe was shown to be an efficient process for shifting the UV radiation of XeCl lasers at 308 nm to 459 nm^{1,2}. Photon conversion efficiency of 66% was obtained for a free running of XeCl laser with pump energy level of 300 mJ/pulse³.

The stimulated Raman process is even more efficient for the injection-locked and narrow linewidth operation of a XeCl laser. Photon conversion efficiency of 70% in the forward direction and 5% in the backward direction was obtained.

The pump laser is an injection locked XeCl laser, capable of providing narrow linewidth down to 2 mÅ and tunable over a range of 8 Å. The combination of master and slave oscillator followed by a single-pass amplifier provided pump energy up to 310 mJ/pulse and pulse repetition rate of 50 pps.

The Stokes linewidth corresponds to the pump linewidth with some effect of gain narrowing. There was no evidence of Doppler broadening or spectral splitting by the different lead isotopes of ordinary lead.

The laser system was made to overlap and lock onto the atomic resonance absorption line of Cs vapor at 4593 Å.

The experiments reported in this paper were performed using a lead vapor heat pipe as a single-pass Raman oscillator.

Experimental Set-Up

The schematic diagram of the experimental setup is shown in figure 1. The first XeCl excimer laser is a Lumonics TE-861T-4 with high power injection-locked master/slave electrode assembly that was modified for wavelength tunability and narrow linewidth operation^{4,5}. The master oscillator contains a 100-cm^{-1} F.S.R. etalon for selecting a single transition in the XeCl B-X gain curve, an 8-cm^{-1} F.S.R. etalon for line narrowing down to 0.01 Å, an optional etalon of 0.8-cm^{-1} F.S.R. for obtaining 2-mÅ linewidth, a 3-mm aperture for mode reduction, and a flat resonator with 70% output coupler. The master oscillator beam is then injected into an unstable resonator slave oscillator that has a magnification of 4.5. Since both the master and slave oscillator are triggered by the same thyrotron, the delay time between them is fixed and determined by the ratio of the peaking capacitor banks that are connected in series. For proper locking of the slave oscillator, the unstable resonator cavity must be flooded by the injected beam prior to the excitation. The output beam energy of the master/slave oscillator is 65 mJ/pulse, pulse duration FWHM of 20 ns, and the beam divergence is 0.15 mrad. The collimated beam is then passed through a second Lumonics TE-861T-4 laser with high energy and uniform beam electrode assembly used as a single pass amplifier. Since the XeCl amplifier operates below the threshold for stimulated emission amplification, the properties of the incoming beam and the outgoing beam are identical with the exception of the beam energy and pulse duration (40 ns FWHM). The 310 mJ/pulse was obtained for an input beam of 65 mJ/pulse. The XeCl

laser system can operate up to 50 pps, which is the upper limit of the amplifier. The master/slave laser can operate up to 100 pps. The pump beam is steered and focused by a 5-m radius concave reflector at the center of the lead vapor heat pipe. The lead vapor region is 90 cm long and 1" in diameter. Xe was used as the buffer gas at total pressure of 60 to 70 torr at 1225°C.

Experimental Results

The XeCl laser system was used mainly as a 10-mÅ linewidth pump source. Blocking the beam from the master oscillator allowed a direct comparison with a free running XeCl laser operation.

Figure 2 displays the optical pulses of the pump UV, the Stokes, and the transmitted UV through the lead vapor heat pipe. Set (a) is for the case of free-running operation and set (b) is for narrow linewidth operation. The spikes on the traces for the case of narrow linewidth operation are due to mode beating.

The narrow linewidth of the pump beam causes a significant gain enhancement in the Raman cell. The threshold level of conversion, which is indicated by the peak value of the transmitted UV is the case of free-running operation, was practically eliminated under narrow linewidth operation. The moderate rise of the transmitted UV toward the end of the pulse is believed to be due to depletion of lead atoms in the ground state near the focal point.

As seen in figure 3, the improved performance of narrow linewidth operation is very substantial. Energy conversion efficiency of 45% in the forward direction and 5% in the backward direction was obtained. That energy conversion efficiency translates to 75% photon conversion efficiency. This performance is about 50% better than that for the case of free-running operation. The optimum temperature for the specific experimental apparatus was 1225°C. At lower temperatures, the Raman gain is smaller as a result of a lower number density of lead atoms; while at higher temperatures, the absorption loss by lead dimer is higher, resulting in a smaller overall gain.

The energy conversion efficiency of the Stokes beam to the depleted UV beam (UVin-UV transmitted) exhibits the effect of lead dimer adsorption. At lower temperatures, below 1150°C, the lead dimer adsorption is negligible; therefore, the photon conversion efficiency is 100%. As the temperature increases, the lead dimer number density rises faster than the lead monomer number density. As a result, a large number of UV photons and Stokes photons are lost to the lead dimer, and the efficiency of (Blue/depleted UV) goes down. In the case of narrow linewidth operation, the conversion efficiency of Stokes/depleted UV photons should be 100% at temperatures below 1150°C. However, since only the forward Stokes photons were measured, the efficiency indicated in figure 3 is a few percentage points lower. The rates of decreased conversion efficiency of Stokes depleted UV with temperature for narrow linewidth and free-running operations are slightly different. For a free-running operation, a smaller number of UV photons are being converted to blue photons compared to a narrow linewidth operation; therefore, a larger number of UV photons are being adsorbed by the Pb₂, which causes a slightly steeper reduction in efficiency with temperature.

Figure 4 shows the large improvement in performance under narrow linewidth operation. The slope efficiency for both types of operation are identical (54%), but the threshold for conversion that exists in the free-running operation causes a substantial reduction in performance, in particular for low-level pumping.

The Raman converter contains ordinary lead which is composed mainly of three isotopes (Pb²⁰⁶, 23.6%, Pb²⁰⁷, 22.5%, and Pb²⁰⁸, 52.3%). The energy level difference between the metastable state (³P₂) and the ground state (³P₀), which constitutes the Raman frequency shift, is very similar for Pb²⁰⁶ and Pb²⁰⁸ (0.001 cm⁻¹ apart). Pb²⁰⁷ has a splitted metastable state. The energy level difference for Pb²⁰⁷ does not coincide with that of Pb^{206,208}. The observed Stokes spectrum did not show any additional structure due to Pb²⁰⁷. Since Pb²⁰⁷ composes less than 23% of the lead, each of its metastable state number densities represents only 10%. This may not be sufficient to compete with the combined number densities of Pb²⁰⁶ and Pb²⁰⁸, resulting in Stokes buildup only to the metastable states of Pb^{206,208}.

The doppler broadening of the Stokes beam (459 nm) was calculated to be <4 mÅ (0.01 cm⁻¹), taking into account that both pump and Stokes beams propagate in the same direction. The linewidth diagnostics showed that the Stokes linewidth can be narrowed down to 4 mÅ, but since no further reduction of the pump linewidth was attempted, the Doppler broadening of the Pb vapor was not measured experimentally.

The Stokes beam quality is degraded when compared to the pump beam quality. There are several mechanisms that cause beam degradation.

1. The high-gain, single-pass Raman oscillator builds up the Stokes beam from noise. Since the stimulated Raman process is a highly nonlinear process, the spatial and temporal intensities are not uniform.

2. The interaction length necessary for the Stokes beam to build up and the pumping geometry will determine the Stokes beam divergence. Pumping levels well above threshold will generally cause an increase of the Stokes beam divergence.

3. The index of refraction of lead in the metastable state is higher than that of lead in the ground state; therefore, optical aberration within the converting medium exists too.

4. The nature of heat-pipe operation dictates an interface between lead vapor and buffer gas mixture in the hot zone and pure buffer gas in the cold end zones. Since the interface exhibits motion and the index of refraction is different on either side, the interface causes mild optical aberration.

The XeCl laser was tuned to the (0-3) transition so the Stokes wavelength would match the absorption line of Cs at 4593 Å. The laser system was stabilized at that wavelength using a control loop that tilted the intracavity etalon.⁸

Conclusions

Stimulated Raman scattering in lead vapor for narrow linewidth XeCl lasers was superior to that of free-running XeCl laser. Seventy-five percent photon conversion efficiency was achieved at 310 mJ/pulse of pump energy and at lead vapor temperature of 1225°C. That represents an improvement of 50% over the free-running operation. The threshold level for conversion is much smaller for the case of narrow linewidth operation, so Raman conversion can be initiated at pump intensities of $<50 \text{ Mw/cm}^2$.

Although no ordinary lead was used, the blue Stokes output was not broadened by the lead isotopes or by Doppler broadening. The blue spectrum output was slightly narrower than that of the pump UV due to gain narrowing.

The tunability of the XeCl laser was over the entire B-X gain profile ($\sim 8\text{\AA}$). All the transitions (0-0), (0-1), (0-2), and (0-3) were made to lase under narrow linewidth condition. The tunability range of the Raman beam corresponds directly to that of the pump beam ($\sim 16\text{\AA}$).

Repetition rates up to 100 pps did not affect the Raman performance in any way. One hundred percent locking of the slave oscillator was achieved with excellent wavelength stability ($<1 \text{ mÅ}$ jitters).

References

1. R. Burnham and N. Djeu, "Efficient Raman Conversion of XeCl-laser Radiation in Metal Vapors," Opt. Lett. Vol. 3, pp. 215-217, 1978.
2. S. J. Brosnan, H. Komine, E. A. Stappaerts, M. J. Plumer, and J. B. West, "High Efficiency Joule-Level Raman Generation in Pb Vapor," Opt. Lett. Vol. 7, pp. 154-156, 1982.
3. H. Rieger, "Performance Evaluation of Lead Vapor Heat-Pipe as a Stimulated Raman Converter for XeCl Lasers," IEEE J. of Quantum Elect. March 1986.
4. T. J. McKee, S. D. Hastie and R. W. Weeks, "Performance of a Noval Injection-Locked Excimer Laser," J. Appl. Phys. Vol. 56, pp. 2170-2173, 1984.
5. T. J. McKee, "Spectral Narrowing Techniques for Excimer Laser Oscillators," Canadian J. Of Phys. Vol. 63, pp. 214-219, 1985.
6. T. E. Manning, C. E. Anderson, and W. W. Watson, "Isotope Shift in the Spectrum of Neutral Lead," Phys. Rev. Vol. 78, pp. 417-419, 1950.
7. K. Murakawa, "On Some Regularities in the Isotope Effect in the Spectrum of Lead" J. of Phys. Soc. of Japan, Vol. 8, pp. 382-387, 1953.
8. T. Henderson and H. Rieger, "Wavelength Stabilization System for a Pulsed or CW Laser," Optics and Laser Technology, June 1986.

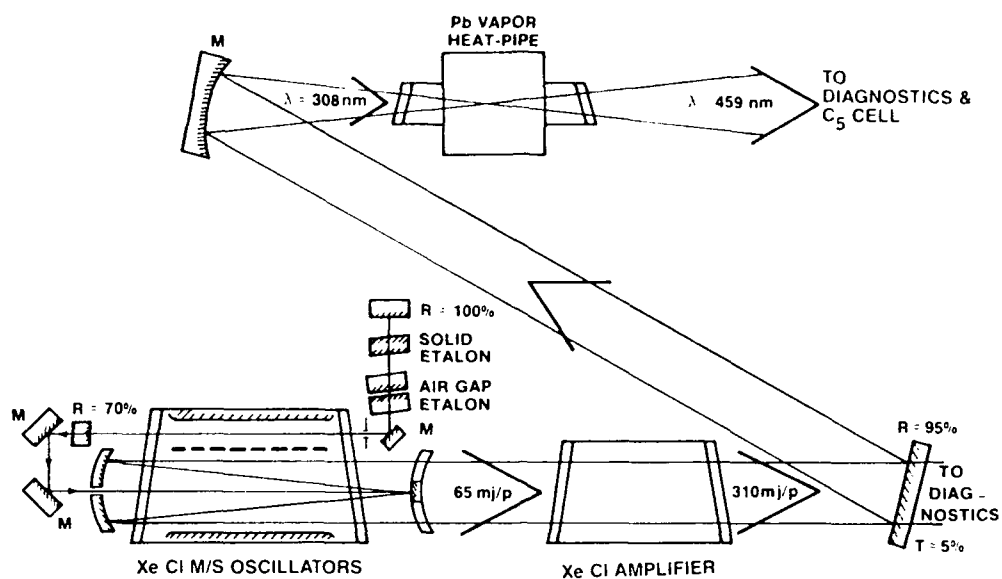


Figure 1. Schematic diagram of the XeCl laser system and the Raman converter.

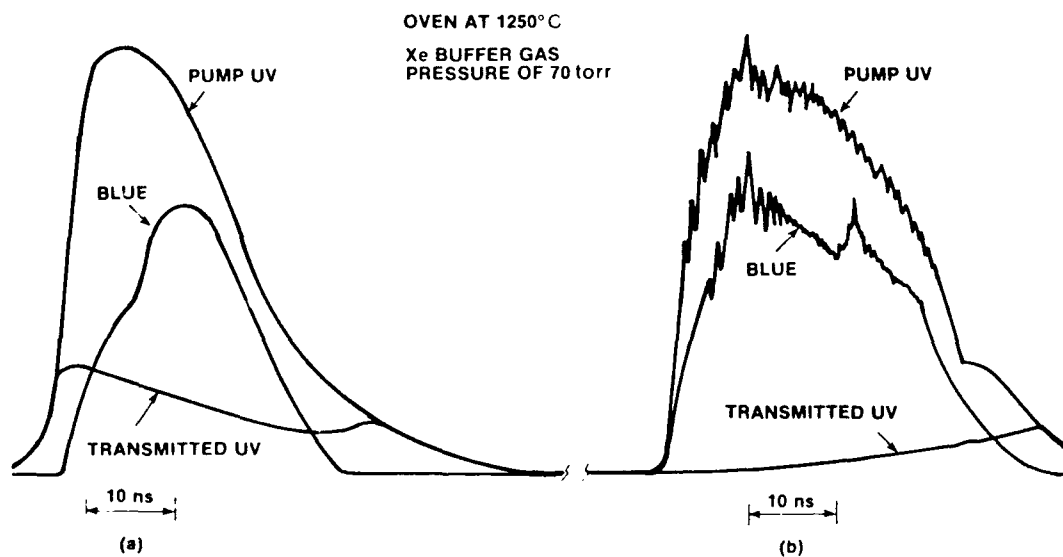


Figure 2. (a) Temporal pulses for the case of free-running XeCl laser.
(b) Temporal pulses for the case of narrow linewidth XeCl laser.

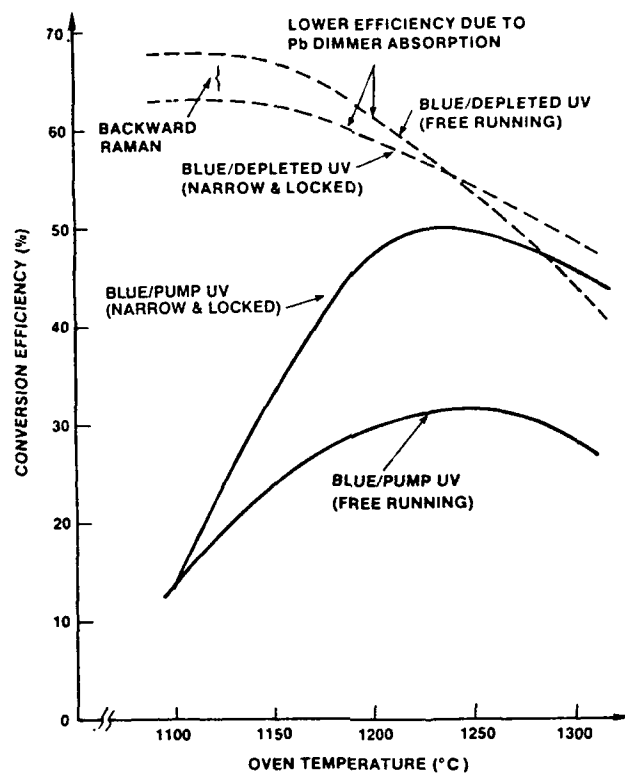


Figure 3. Conversion efficiency as a function of Pb vapor temperature.

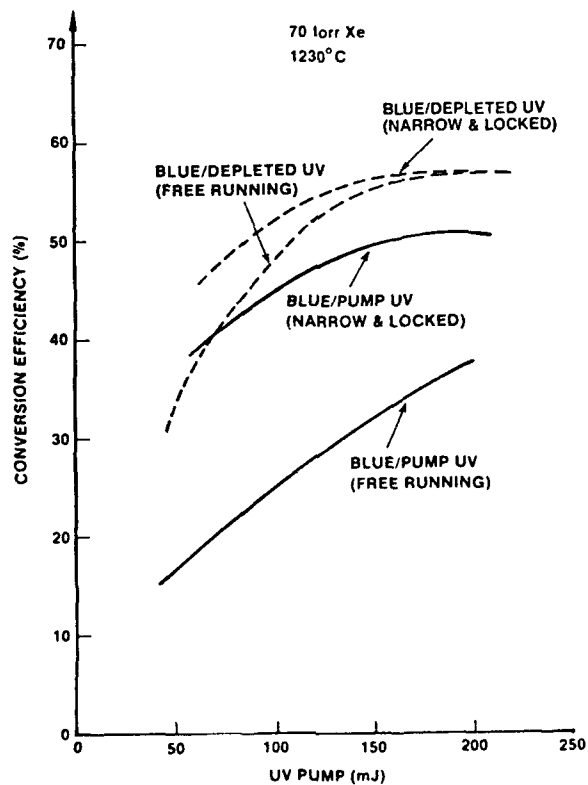


Figure 4. Energy conversion efficiency versus pump energy.

DIODE PUMPED PROMETHIUM LASER FOR SUBMARINE LASER COMMUNICATIONS

R. W. Solarz, R. Beach, M. Shinn, and W. F. Krupke
Lawrence Livermore National Laboratory
P.O. Box 808, Livermore, CA 94550

Abstract

A diode pumped promethium based solid state laser has been proposed as a candidate transmitter for a submarine communication laser system. The properties of many aspects of this laser system are reported.

Introduction

The current submarine laser communications (SLC) transmitter which is now being prototyped uses lead vapor to Raman shift the output of an XeCl laser into resonance with a cesium atomic resonance filter.^{1,2,3} Advanced SLC transmitters will have to have improved efficiency, lighter weight, superior operating lifetimes, as well as reduced system lifecycle costs when compared to the current system. With these criteria in mind a program was initiated at Lawrence Livermore National Laboratory (LLNL) to identify candidate active ions emitting at 919 nm that would allow a diode pumped all solid state laser to be constructed. Such a system could access cesium atomic resonance⁴ filters at 459 nm by simple and efficient frequency doubling. After an extensive search to identify suitable active ions having the potential for laser emission at 919 nm one promising candidate emerged in promethium.

The possibility of using Pm^{3+} as the active-ion in a four-level room temperature laser was first recognized by Krupke⁵ in 1972. Using a Judd-Ofelt^{6,7} analysis he was able to conclude that the $^5\text{F}_1 - ^5\text{I}_5$ transition of $\text{Pm}^{3+}:\text{YAG}$ at $\sim 92 \mu\text{m}$ is the analogue of the $^4\text{F}_{3/2} - ^4\text{I}_{11/2}$ transition of $\text{Nd}^{3+}:\text{YAG}$ at $1.06 \mu\text{m}$. The low-lying energy levels relevant to laser operation are shown in Figure 1 for both of these ions. Following this analysis by Krupke no experimental attempts at demonstrating lasing were reported primarily because all Pm isotopes are radioactive and one would have to have a suitably strong motivation to undertake the special procedures associated with its handling. Because of the potential for 919 nm emission and an absorption band at $\sim 770 \text{ nm}$ suitable for laser diode pumping, sufficient motivation obtained for the LLNL program to focus on Pm for the SLC application.

Before a Pm based system could be given serious consideration as a SLC transmitter it was recognized that a number of key technical issues would have to be favorably resolved. As these technical issues will form a basis for the rest of this paper, they are outlined now:

- 1) Very little spectroscopic information on Pm was available. This required initiating an experimental program to measure relevant spectroscopic parameters and identify suitable (giving 919 nm emission) host materials.
- 2) Lasing of Pm^{3+} in any host had never been demonstrated. Such a demonstration would allow a cross check to be made on the spectro-kinetic parameters derived in the spectroscopy program.
- 3) Radiation damage issues pertaining to both the host material and the diode array pumping laser needed to be addressed.
- 4) Suitable (emitting at 770 nm) long-lived diode array pump sources needed to be developed.

Pm Spectroscopy

Figure 2 shows the only Pm^{3+} emission spectrum from a solid that was available prior to the LLNL program.⁸ The salient feature of this data for the present discussion is that the emission wavelength of the $\text{Pm}^{3+} ^5\text{F}_1 - ^5\text{F}_5$ transition in YVO_4 is at 940 nm. Since this is the transition to be used for our laser, the first goal of the spectroscopy program at LLNL was to identify host materials that blue shift this emission by $\sim 21 \text{ nm}$. To guide our search for likely host materials, projections of emission wavelengths were made using a combination of the nephelauxetic effect⁹ and the known emission wavelength of the $\text{Nd}^{3+} ^4\text{F}_{3/2} - ^4\text{I}_{11/2}$ transition in various crystal and glass hosts, as shown in Figure 3. Host materials are arranged in order of increasing Nd-ligand bond ionicity going toward the origin of the ordinate axis. The regular blue shifting of the Nd emission with increasing ionicity illustrates the nephelauxetic effect. Assuming the $\text{Pm}^{3+} ^5\text{F}_1 - ^5\text{I}_5$ transition experiences such an effect similar to that of Nd and using the known emission wavelength of Pm^{3+} in YVO_4 projections of emission wavelength indicated likely materials giving 919 nm emission would be fluoride crystals and glasses. These projections were followed up by an experimental program done in collaboration with Oak Ridge National Laboratory (ORNL) in which various glass and crystal samples doped with ^{147}Pm were prepared. Figure 4 shows one example of a projected and measured $\text{Pm}^{3+} ^5\text{F}_1 - ^5\text{I}_5$ emission spectrum from a sample

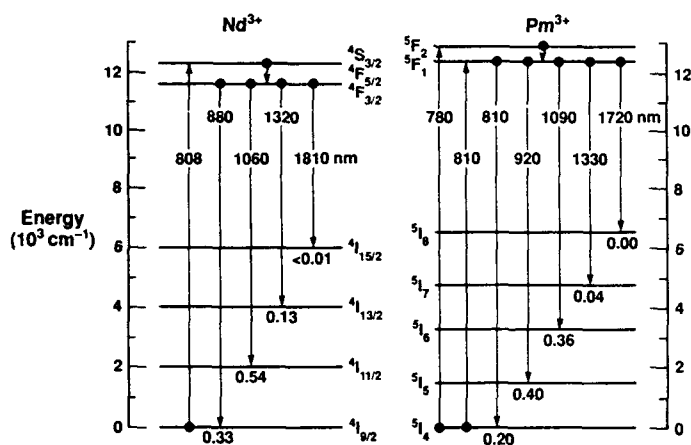


Figure 1. Level diagrams of Nd^{3+} and Pm^{3+} . The $\text{Nd}^{3+} 4\text{F}_{3/2} - 4\text{I}_{11/2}$ transition at $1.06 \mu\text{m}$ is the analogue of the $\text{Pm}^{3+} 5\text{F}_1 - 5\text{F}_5$ transition at $\sim 0.92 \mu\text{m}$.

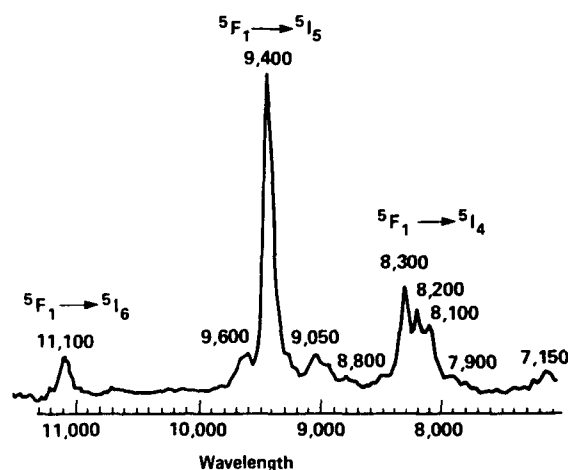


Figure 2. Pm^{3+} emission spectrum measured in YVO_4 . This was the only Pm^{3+} emission spectrum of a solid available prior to the Pm spectroscopy program at LLNL.

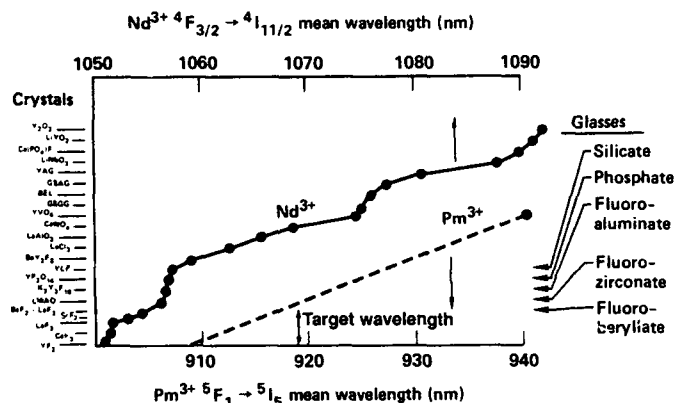


Figure 3. $\text{Nd}^{3+} 4\text{F}_{3/2} - 4\text{I}_{11/2}$ measured transition wavelengths and $\text{Pm}^{3+} 5\text{F}_1 - 5\text{I}_5$ projected transition wavelengths for various host crystals and glasses.

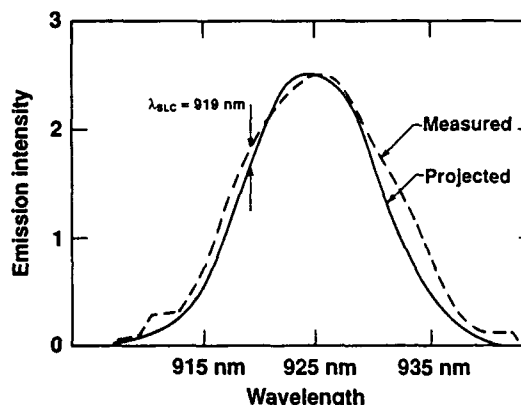


Figure 4. Measured and projected $\text{Pm}^{3+} 5\text{F}_1 - 5\text{I}_5$ emission spectrum in BeCaKAl glass.

of beryllium-calcium-potassium-aluminum (BeCaKAl) fluoride glass. This glass is being considered as a host material as it emits at 919 nm.

Having identified several potential host fluoride glasses exhibiting useful 919 nm emission, the next step in our spectroscopy program was to extract the spectro-kinetic parameters of Pm^{3+} ions in these hosts that are relevant to a laser design. To accomplish this, the Judd-Ofelt formalism was used. As this part of our program has been covered elsewhere in the literature^{10,11} only a brief summary of the important results will be given here:

- 1) The 920 nm $\text{Pm}^{3+} \ ^5\text{F}_1 - \ ^5\text{I}_5$ transition is the quantitative analogue of the 1.06 μm $\text{Nd}^{3+} \ ^4\text{F}_{3/2} - \ ^4\text{I}_{11/2}$ transition.
- 2) The $\ ^5\text{F}_1$ lifetime of Pm^{3+} in a given host is approximately equal (within $\pm 10\%$) to the $\ ^4\text{F}_{3/2}$ lifetime of Nd^{3+} in the same host.
- 3) Excited state absorption cross sections near 920 nm are very small (~ 100 times smaller than emission cross sections) in all host media.

In summary these results emphasize the similarity between our proposed Pm based system and a system based on frequency doubling the common $1.06 \mu\text{m}$ $\text{Nd}^{3+} \text{ } ^4\text{F}_{3/2} - ^4\text{I}_{11/2}$ laser transition.

Pm³⁺ Laser Demonstration

A scientific demonstration of a Pm^{3+} laser allowed us to cross check spectro-kinetic parameters derived in our Pm spectroscopy program. The host material for these experiments was a Pb-In-phosphate glass chosen primarily because of the ORNL group's extensive

experience in fabricating it. A photograph of the actual laser sample is shown in Figure 5. The dark coloration of the laser sample is due to radiation induced coloring resulting from ^{147}Pm decays. Figure 6 shows a schematic diagram of the near concentric resonator that was used to demonstrate lasing. The excitation source was a flashlamp pumped dye laser giving 2 μsec long pulses of up to 200 mJ at the excitation wavelength of 570 nm. The mirrors were appropriately coated to give a high cavity Q on either the $^5\text{F}_1 - ^5\text{I}_5$ transition at .93 μm or the $^5\text{F}_1 - ^5\text{I}_6$ transition at 1.1 μm and lasing was observed on both these transitions. While the 1.1 μm transition had a measured threshold pump energy of 44 mJ in agreement with our predictions based on spectro-kinetic parameters derived from a Judd-Ofelt analysis, the .93 μm transition threshold pump energy of 115 mJ was significantly higher than predicted. The reason for this discrepancy is likely related to Figure 7 where it is seen that absorption losses due to the radiation induced coloring of the laser sample are significantly greater at .93 μm than 1.1 μm . Fortunately, we observed that a modest increase in temperature effectively annealed out these radiation-induced losses at the laser wavelength as also shown in Figure 7. In fact, it was anticipated that heating the sample would be necessary to achieve lasing. However, we observed that several tens of excitation pulses from the pump laser effectively bleached the radiation induced coloring sufficiently enough to permit lasing without having to heat the sample. Whether the .93 μm threshold effect is due to color center losses or population of the terminal $^5\text{I}_5$ level due to sample photolytic heating is in the process of being resolved.

Pm Radioactivity

Because all Pm isotopes are radioactive it was necessary to examine possible deleterious effects of decay processes in the laser host material (color centering) and on the longevity of the semiconductor laser diode pump arrays. Table 1 lists all known Pm isotopes along with their dominant decay modes and corresponding half lives. From the table it is seen that only one isotope, ^{145}Pm , has a sufficiently long half-life to make it suitable for the SLC application. Although a process has been defined for the production of ^{145}Pm , the LLNL program has used the shorter lived but more readily available ^{147}Pm for all experiments to date.

Table 1. All known Pm isotopes, their dominant decay modes and associated half-lives.

Pm 144	Pm 145	Pm 146	Pm 147	Pm 148
363 days	17.7 years	5.5 years	2.62 years	41 days
ϵ	ϵ 70 keV and 40 keV	ϵ 735 keV	β 224 keV	β

Preliminary analysis, based on literature data on color centering in fluoride dielectric solids and 1 Mev- γ irradiation of GaAs laser diodes,¹² suggested that the radioactive decay of Pm would not significantly degrade laser performance.

Subsequent to having demonstrated lasing in the sample of Pb-In phosphate glass, host materials have been identified in which absorption at the laser wavelength due to radiation induced coloring is significantly decreased because the absorption peak of the coloring is shifted further into the UV than it is in the Pb-In-phosphate glass. One of these samples, a barium-zinc-indium-lutetium-thorium fluoride glass (BZILT) gives emission from the $\text{Pm}^{3+} ^5\text{F}_1 - ^5\text{I}_5$ transition at the desired wavelength of 919 nm and plans are currently being made to fabricate laser quality samples for further study.

To validate the projection on laser diode life insensitivity to Pm^{145} decay, commercial laser diodes purchased from Spectra-Diode Laboratories (SDL) were exposed to an x-ray spectrum approximating the spectrum that would be seen from ^{145}Pm decays. This spectrum was tailored by filtering the output of a 60 keV x-ray machine through a 100 μm thick Nd foil giving rise to radiation peaked at 38 keV, a characteristic x-ray line of Nd. This is the same x-ray line that dominates the decay spectrum of ^{145}Pm as it decays to ^{145}Nd by electron capture. During this exposure the laser diode was repeatedly cycled in drive current from 0 to a maximum of 100 ma generating a series of L-I curves, one of which is shown in Figure 8. These curves were then analyzed to extract the current threshold and the slope efficiency. To date we have exposed a laser diode to 100 MRad of this ^{145}Pm radiation. Within our experimental ability to measure the current threshold and slope efficiency ($\pm 3\%$ for both) we have not observed any degradation in these quantities. These experiments are on-going and although we have not yet exposed a laser diode to the projected mission dose of ^{145}Pm radiation, we do not expect to observe any deleterious effects. We base this projection on the so called "knock-on" model which is used to describe bulk radiation damage in metallic crystals. Experimentally it has been observed that there exists a certain threshold kinetic energy that must be transferred to a metallic nucleus to knock it out of its lattice site, for example this is about 40 keV in metallic aluminum.¹³



Figure 5. The Pm^{3+} doped Pb-In phosphate sample used in laser experiments. The actual sample is held in the center of a concentric ring which was fabricated from a Nd doped glass.

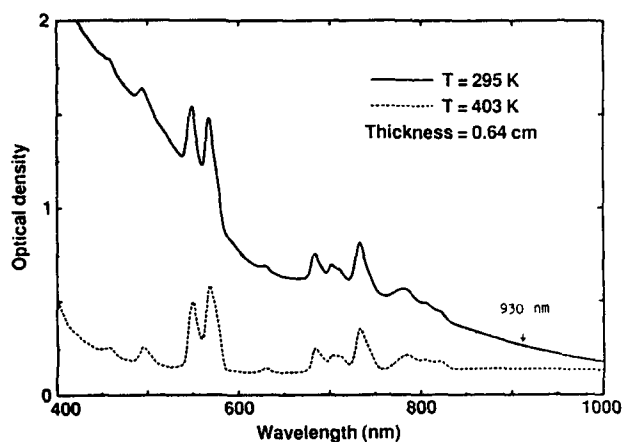


Figure 7. Absorption spectrum of the ^{147}Pm doped Pb-In phosphate glass laser sample. The room temperature spectrum shows the sharp absorption features due to Pm^{3+} superimposed on a broad feature centered in the UV which results from radiation induced coloring from ^{147}Pm decays.

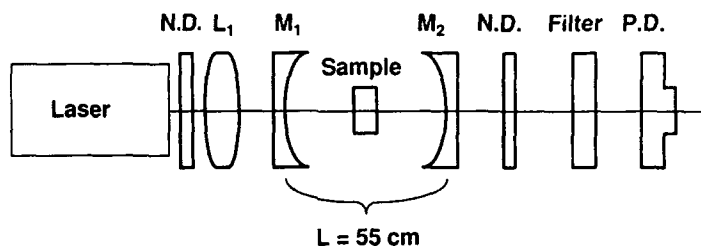


Figure 6. Schematic diagram showing the near concentric resonator that was used to demonstrate lasing on both the $^5\text{F}_1 - ^5\text{I}_5$ and $^5\text{F}_1 - ^5\text{I}_6$ transitions of Pm^{3+} .

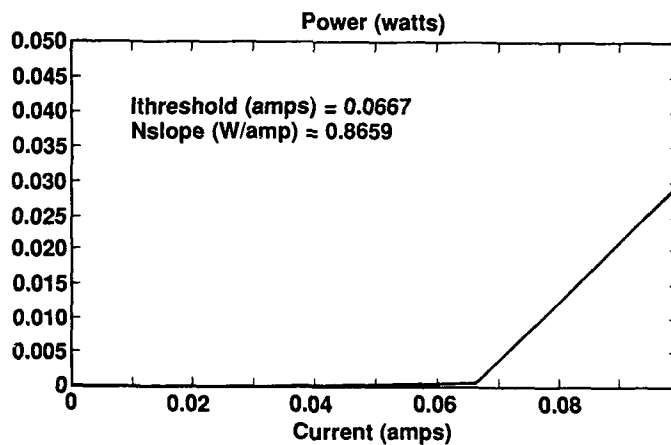


Figure 8. L-I curve taken during the exposure of an SDL laser diode to a spectrum of radiation approximately that which would be seen from ^{145}Pm decays.

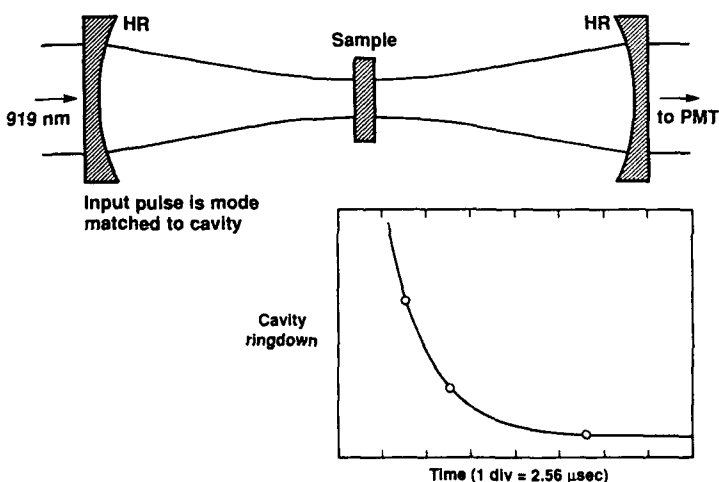


Figure 9. Schematic diagram of the cavity ring down apparatus used to measure Nd^{3+} absorption at 919 nm. Also shown is a typical output signal measured with this apparatus.

Applying the same model to AlGaAs we project that an electron would require ~370 keV of energy to knock an Al nucleus, the lowest mass nucleus in AlGaAs, out of its crystal site. Because the highest energy decay radiation produced is 72 keV occurring in a few percent of the ^{145}Pm decays which result in excited ^{145}Nd nuclei that subsequently relax by emitting a 72 keV γ -ray, we do not foresee any problems. In an effort to observe this threshold, we have repeated the above experiment in which L-I curves are continuously generated while increasing the x-ray energy. No degradation was observed in the lasing current threshold or slope efficiency until the x-ray energy reached 110 keV. This again supports our projection that the ^{145}Pm decay radiation will have no significant deleterious effect on laser diode pump array lifetime.

Finally, one important spectroscopic consideration arising from the decay of ^{145}Pm to ^{145}Nd exists. The tail of the Nd^{3+} ground state to $^4\text{F}_{3/2}$ excited state transition has the potential to absorb at the laser wavelength of 919 nm. This loss mechanism in the laser which will be most severe near the end of mission life, when the largest quantity of ^{145}Pm will have decayed to ^{145}Nd , needed to be quantified. Because the laser wavelength at 919 nm lies in the tail of the Nd transition of interest where absorption cross sections are expected to be small, a cavity ring down technique was used to measure it. Figure 9 shows a schematic diagram of the ring down apparatus used. This technique relies on injecting mode matched radiation into a very high Q optical cavity and then measuring the decay of energy within the cavity. By measuring such a ring down with and without a sample present in the cavity, it is possible to quantify very small absorption and scattering losses. To measure the Nd^{3+} absorption at 919 nm a sample of beryllium fluoride glass containing .5 mole % Nd was used. Figure 10 shows measured loss in this sample as a function of wavelength. The injected radiation in this case was generated by Raman shifting the output of a pulsed dye laser. Based on these experiments, we have been able to conclude that a typical Nd^{3+} absorption cross section at 919 nm is $\sim 2 \times 10^{-23} \text{ cm}^2$ and that losses can be held to acceptable levels.

770 nm Diode Array Development

Finally questions concerning the lifetime and efficiency of diode laser arrays emitting at 770 nm needed to be addressed. This work is being carried out by three companies under contract to LLNL: McDonnell Douglas Astronautics Company (MDAC), RCA/GE, and SDL. The technique for shifting the output wavelength of an AlGaAs laser diode down to 770 nm uses a combination of quantum wells and high Al content in the epitaxial layers. Primarily because of the high Al content required in the epi layers, there were perceived problems regarding device lifetimes and efficiencies. Questions concerning device lifetimes arose because the increased Al content in the epi layers implies increased stress between these layers and the underlying GaAs substrate. Questions concerning efficiency arose because as the Al content increases in AlGaAs the indirect bandgap becomes energetically more favorable. At 38 mole % AlAs the indirect bandgap and direct bandgap have equal transition energies. Therefore as the Al content is increased a proportionally larger number of recombination events should occur via the indirect bandgap. These nonradiative events do not contribute to the lasing process and so should negatively impact on device efficiencies.

Figure 11 shows an example of an actual 2-dimensional laser diode array constructed by RCA/GE using a rack and stack architecture.¹⁴ As an example of the progress that has been achieved to date this 2-dimensional array which measures .475 cm x .175 cm emits an equivalent peak power density of 2.1 kW/cm². The overall efficiency of the array is 35%. The emitted radiation has a spectral FWHM of 5 nm centered at 770 nm making it ideal for pumping the Pm doped fluoride glass host materials that have already been identified. Lifetesting of these devices is currently at the 10^8 shots level and on-going. Based on results to date, it is our projection (and that of our contractors) that efficient, long-lived pump arrays suitable for the SLC application can be achieved.

Conclusion

Our proposed system is the analogue of a frequency doubled, diode-pumped Nd^{3+} :glass laser system in which the $\text{Pm}^{3+} \ ^5\text{F}_1 - \ ^5\text{I}_5$ transition substitutes for the $\text{Nd}^{3+} \ ^4\text{F}_{3/2} - \ ^4\text{I}_{11/2}$ transition.

In summary, key technical issues associated with constructing such a Pm-based SLC transmitter have been addressed, quantified, and favorably resolved. It is our judgment that a Pm-based system can serve as a high performance SLC transmitter.

Acknowledgments

For their help with various phases of experiments reported here and many useful discussions, we wish to thank the following LLNL personnel: W. J. Benett, S. K. Weinzapfel, T. A. Kirchoff, P. R. Staver, M. S. Singh, H. D. Bissinger, R. T. Maney, F. P. Milanovich, R. W. Robel, and C. M. Logan. We also wish to acknowledge our collaborators at ORNL: C. B. Finch, L. A. Boatner, and C. A. Culpepper. Finally, we wish to express our appreciation and thanks to Cmdr. Ralph Chatham of DARPA for his continued encouragement and support throughout this work. Work performed under the auspices of the U. S. Department of Energy by the Lawrence Livermore National Laboratory under contract number W-7405-ENG-48 and Defense Advanced Research Projects Agency order number 5358, delivery order N00173-84-FD061.

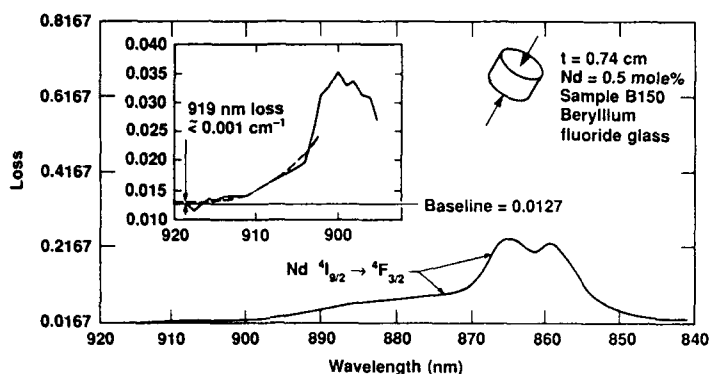


Figure 10. Nd^{3+} absorption measured at various wavelengths. The inset shows data measured using the cavity ring down apparatus of Figure 9.

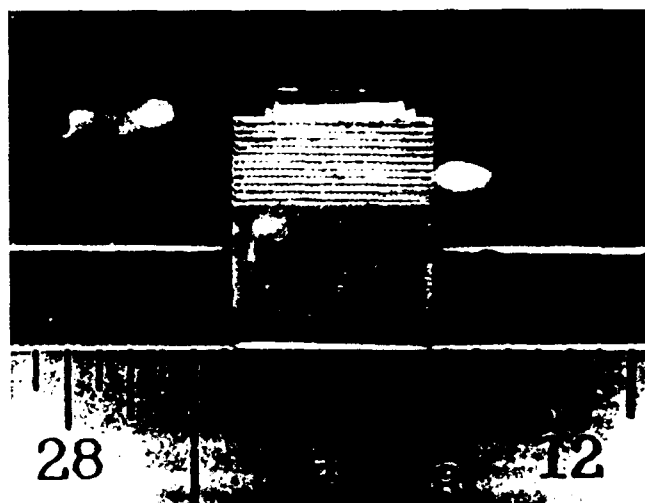


Figure 11. Two-dimensional diode laser array constructed using a rack and stack architecture by RCA/GE.

References

1. Ralph E. Chatham, "Blue-Green Lasers for Submarine Communications," Digest of Technical Papers, Conference on Lasers and Electro-Optics, San Francisco, CA, June 9-13, 1986, Paper WMI, p. 212.
2. Ralph E. Chatham, "Submarine Laser Communications," J. Defense Electronics, **10**, (1987).
3. S. E. Whitcomb, "Submarine Laser Communications (SLC) Excimer Laser Status," SPIE Proceedings, to be published, Vol. 894 (1988).
4. J. B. Marling, J. Nilsen, L. C. West, and L. L. Wood, "An Ultrahigh Q Isotropically Sensitive Optical Filter Employing Atomic Resonance Transitions," J. Appl. Phys., **50**, 610 (1979).
5. W. F. Krupke, "Assessment of a Promethium YAG Laser," IEEE J. Quan. Elec., **8**, 725 (1972).
6. B. R. Judd, "Optical Absorption Intensities of Rare-Earth Ions," Phys. Rev. **127**, 750 (1962).
7. G. S. Ofelt, "Intensities of Crystal Spectra of Rare-Earth Ions," J. Chem. Phys., **37**, 511 (1962).
8. J. Lories, P. Caro, P. Brun, and A. Babusiaux, "Self-excited luminescence of $^{147}\text{Pm}^{3+}$ in yttrium vanadate. Determination of the infrared emission spectrum and possibility of laser effect," C. R. Acad. Sci., Paris, **275**, 977 (1972).
9. P. Caro, O. Beaury, and E. Antic, "L'effect néphelauxétique pour les configurations $4f^N$ en phase solide," J. Phys. **37**, 671-676 (1976).
10. W. F. Krupke, M. D. Shinn, T. A. Kirchoff, C. B. Finch, and L. A. Boatner, "Promethium (Pm^{3+}) doped phosphate glass laser at 933 and 1098 nm," to be published in Appl. Phys. Lett.
11. M. D. Shinn, W. F. Krupke, R. W. Solarz, and T. A. Kirchoff, "Spectroscopic and Laser Properties of Pm^{3+} ," IEEE J. Quantum Electron., to be published, June 1988.
12. C. E. Barnes, "Effects of Co^{60} Gamma Irradiation on Epitaxial GaAs Laser Diodes," Phys. Rev. B **12**, 4735 (1970).
13. Private communication from C. Login to R. Beach.
14. A. Rosenberg, J. C. McShea, A. R. Bogdan, J. C. Petheram, A. Rosen, D. Bechtel, P. S. Zory, J. W. Sprague, "High Power, High Efficiency 770 nm 2D Laser Diode Array," to be published in Elec. Lett.

Discharge Excitation of the XeF C to A Transition

R.C. Sze, D.P. Greene, I.J. Bigio, T.M. Shay, A.W. McCown, J.F. Figueira
Los Alamos National Laboratory
Los Alamos, New Mexico 87545

P. Smith
St. Andrews University
St. Andrews, Scotland, U.K.

Matteo Vannini
Istituto de Elettronica Quantistica del C.N.R.
Florence, Italy

R. Sauerbrey, F.K. Tittel
Rice University
Houston, Texas

Abstract

Recent success in high efficiency and high energy laser extraction of tunable radiation in the blue-green C-A transition of XeF under intense, short-pulse electron beam excitation has renewed interest in the possibility of similar performance in avalanche discharges. We present preliminary results of discharge excited fluorescence studies in a variety of devices having different degrees of energy loading.

Introduction

The recent work by Tittel, Sauerbrey, Nighan and co-workers¹ on the XeF C-A transition laser under intense, short pulse (10ns) electron beam excitation at pump energies of 135 Joules per liter has shown efficiencies of 3 percent and energy extraction as high as 4 joules per liter. These results are obtained with very complicated five component gas mixtures that include argon as buffer with xenon, krypton, NF₃ and F₂. The most important addition is believed to be that of substantial amounts of krypton which tend to lower the absorption in the blue-green from argon species [Ar₂(³Σ_u⁺) and Ar₃⁺], to drop the population of the B-state due to enhanced B-C state mixing by krypton² and to increase absorption at the B-X transition wavelength region due to the formation of Kr₂F₂. In addition, there is increased gain on the blue side of the C-A band due to trimer emission from Kr₂F. Under e-beam excitation the B-X fluorescence steadily decreases with increasing krypton pressure. The C-A fluorescence remains relatively constant as kinetic code calculation shows that at room temperature over ninety percent of the population starts off in the C-state. Time resolved gain measurements show that during the e-beam excitation pulse there is net absorption with net gain taking place only in the afterglow of the discharge. (Recently, results at Avco Everett Research Laboratory has shown that at lower energy deposition rates substantial gain is observed throughout the e-beam pump pulse using such five component gas mixtures as described by the Rice University and United Technology work.)

Discharge Fluorescence Studies

The results of pumping with intense electron beams tend to indicate that to successfully implement similar results we need to deposit energies of the order of 10 Mwatts/cm³ in 10 nanoseconds and this needs to be done in gas mixes containing high concentrations of krypton and at static filling pressures of 6 atmospheres. Several fluorescence studies have been undertaken on the XeF C-A transition in a number of different discharge devices. This includes a long-pulse inductively stabilized laser head at relatively low power deposition (500 kw/cc), a commercial Lambda Physik EMG-50 laser at power deposition estimated in the region of 1 to 2 MW/cc, and a high power deposition device with deposition densities measured higher than 20 MW/cc.

Some initial data was obtained in a long-pulse inductively stabilized device. The power deposition is relatively low (approximately 500 KW/cc). Figure 1 summarizes the B-X and C-A fluorescence data with a gas mixture of 8 torr F₂, 8 torr Xe, 3 Atmospheres Ne and varying concentrations of Kr. Stable self sustained discharge was obtained up to 200 torrs of Kr with 100ns long electrical pulse widths. The limitation on stability in this situation is believed due to the weak corona type of pre-ionization. The rise in C-A and the drop in B-X fluorescence as a function of krypton pressure confirms the initial expectations of discharge laser pumping kinetics as indicated by the electron beam pumped laser systems.

A series of studies was undertaken in a commercial laser device (Lambda Physik EMG 50) at relatively moderate energy deposition rates which are estimated at 1-2 MW/cc. This device uses arc type pre-ionization and is capable of sustaining stable discharges with krypton partial pressures up to 500 torrs. The electrical pulse width is 25ns and He buffer is used in these studies. Figure 2 presents a typical time integrated fluorescence spectrum. Figure 3 shows the fluorescence variation as a function of krypton partial pressure in a gas mix of $F_2/Xe/Total=5/20/2500mB$ with He buffer. This device unfortunately is limited in both its pressure and power deposition rate capabilities. Note that the results of Fig.3 shows rather rapid quenching of the B-X fluorescence as expected and relatively slow decrease also in the C-A fluorescence. The relative insensitivity of the C-A fluorescence as a function of Kr partial pressure is in keeping with the explanation given in electron-beam systems that most of the excited state population resides in the C state. The gradual overall decrease in the total upper state density is an indication of increased quenching as a function of krypton pressure and is an unfortunate observation and not in keeping with the data of the inductively stabilized long pulse device using Ne buffer.

A device capable of high pressure operation but still with relatively short gain length is equipped with an inductively stabilized electrode and operated with a peaking capacitor pulse power setup that we hope will be able to operate in the 10MW/cc power deposition range. Using corona pre-ionization this device could sustain a stable discharge with 3 atmospheres. Ne buffer gas only to 50 torrs of krypton partial pressure. It was necessary to utilize an alternate form of pre-ionization. In the following fluorescence studies the discharge is pre-ionized with a krypton fluoride laser operating at 248nm as shown in Fig.4 and with the addition of trace amounts of fluoro-benzene in the gas mix. Under this technique of pre-ionization we were able to control the discharge up to 300 torrs of Kr partial pressure and at total operating pressures of over 6 atmospheres using Ne buffer. The voltage and current measurements (Fig.5) give a power deposition into a 30cmX.5cmX1cm discharge volume of 20 MW/cc. at the peak of the current pulse. Under this degree of power deposition the behavior of the C-A fluorescence with 10 torrs F_2 , 10 torrs Xe as a function of varying Ne buffer pressure and varying partial Kr pressure is given in Fig.6. In this case we observe steadily increasing C-A fluorescence as a function of increasing krypton pressure. However, the C-A fluorescence dropped precipitously beyond 4 atmospheres of Ne buffer gas. The charging voltage for all these studies were kept at 25Kv. It is not clear presently if this turn around in the C-A fluorescence can be overcome if higher charging voltages are used.

Discussion

The data presented in the above studies are a preliminary look into the possibility of obtaining high laser outputs of tunable blue-green radiation using the C-A transition of XeF with complicated multi-component gas mixtures and under the conditions of intense power deposition. As can be seen the fluorescence behavior appears to be different using neon and helium buffers. Of course, the behavior of different buffers need to be compared in the same device which up to this point have as yet to be done. The observation of increasing C-A fluorescence as a function Kr partial pressure in the neon buffer discharges at low and very high power deposition rates imply that the C and B state populations are much more evenly distributed than in the case of electron-beam excitation although the He buffer studies seem to be in accord with the e-beam excitation studies. We are presently setting up experiments to look at the gain at the argon ion laser wavelengths and to see if we can successfully obtain blue-green lasing in the high pressure device. We, however, do not look toward very strong lasing outputs because of the relatively short gain lengths of the devices under study. We need to build a laser with relatively long gain lengths using strong, uniform pre-ionization with either x-ray or arc type sources and at power deposition rates that have been reported here in order to see if strong blue-green lasers in the XeF C-A transition is a possibility.

Acknowledgements

This research is supported by the ISR internal funds of the Los Alamos National Laboratory.

References

1. F.K. Tittel, G. Marowsky, W.L. Nighan, Y. Zhu, R.A. Sauerbrey and W.L. Wilson, I.E.E.E. J. Quant. Elec., QE-22, 2168 (1986)
2. W.L. Nighan, R.A. Sauerbrey, Y. Zhu, F.K. Tittel and W.L. Wilson, I.E.E.E. J. Quant. Elec., QE-23, 253 (1987)

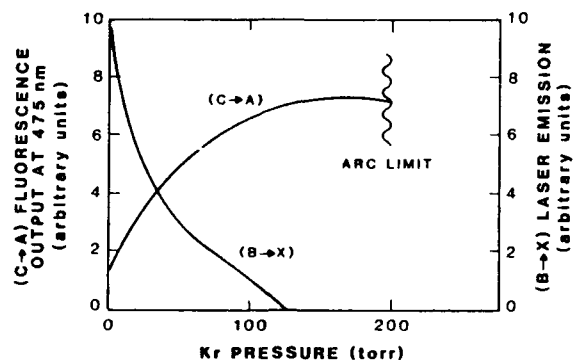


Figure 1. Fluorescence (C-A) and (B-X) versus Krypton partial pressure in a long pulse inductively stabilized long pulse laser with gas mix of 4 torrs F_2 , 8 torrs Xe and 3 atmospheres of Ne.

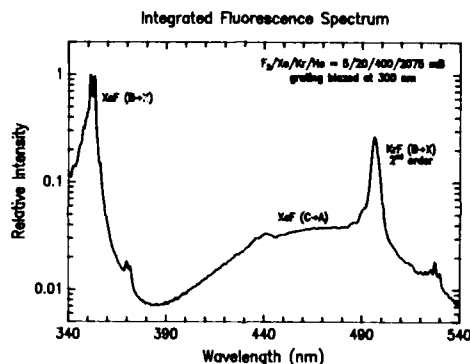


Figure 2. Integrated fluorescence spectrum from a commercial laser device (Lambda Physik EMG 50) using helium buffer with gas mixture given by $F_2/Xe/Kr/He=5/20/400/2075$ mB.

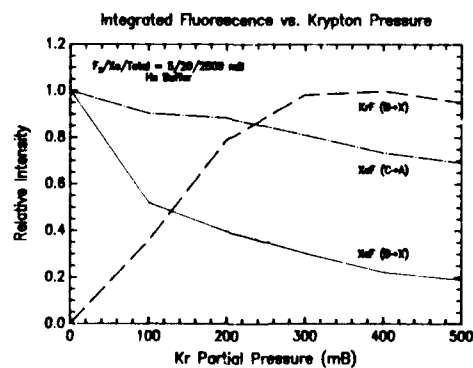


Figure 3. Fluorescence $XeF(C-A)$, $B-X$, and $KrF(B-X)$ as a function of Kr partial pressure in a gas mix of F_2/Xe Total=5/20/2500 mB.

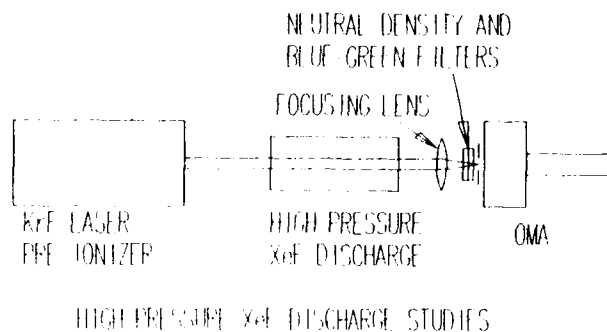


Figure 4. Schematic of high pressure XeF discharge cell with KrF laser pre-ionization.

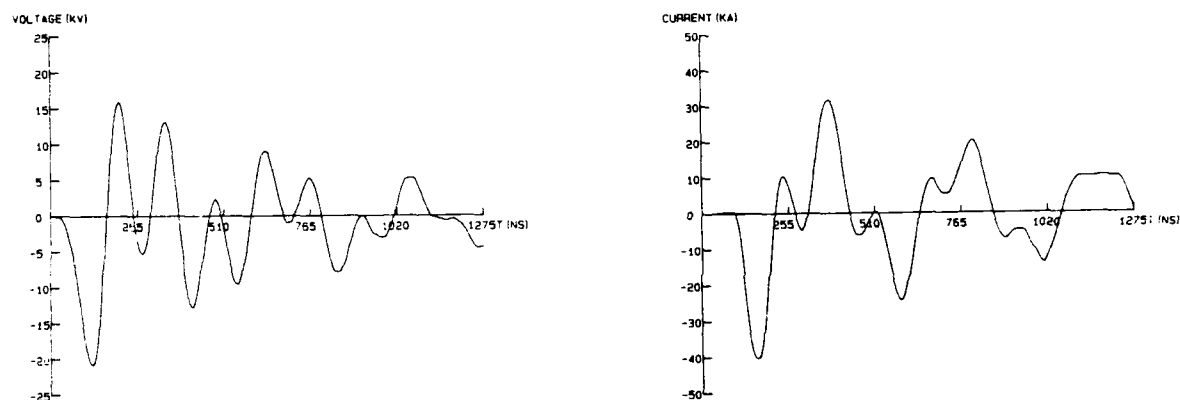


Figure 5. Voltage and Current Temporal behavior with 25 KV charging voltage and a gas mix of $F_2/Xe/Ne=10/10/2280$ torrs with no Kr.

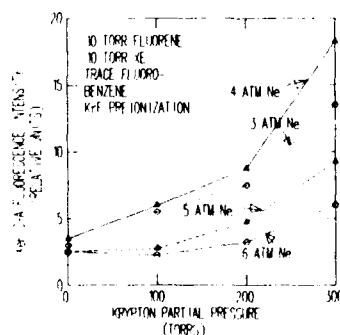


Figure 6. Fluorescence XeF(C-A) as a function of Kr partial pressure and as a function of total filling pressure using 10 torrs F_2 and 10 torrs Xe and Ne as buffer gas.

PHASE PRESERVATION IN HIGH GAIN RAMAN AMPLIFICATION

B.W. Nicholson, J.A. Russell, D.W. Trainor, and T. Roberts

AVCO Research Laboratory, TEXTRON
Everett, MA 02149
(617) 381 4754

and

C. Higgs
M.I.T. Lincoln Laboratory
P.O. Box 73, Mail Stop L-300
Lexington, MA 02173
(617) 981 3778

Abstract

The fidelity of the Raman amplification process was determined for high Fresnel number amplification in hydrogen. Phase information on the input (414 nm) Stokes beam is preserved to better than 0.1 waves rms.

Introduction

Raman amplifiers provide a means of retaining input Stokes seed beam phase upon amplification with good fidelity. Raman physics has two requirements to maintain the fidelity of the phase: that the Stokes seed and the pump are correlated, and the pump beam have a nearly uniform intensity.

The requirement of Stokes seed and pump correlation is two fold since they need to be correlated in both frequency and time. The frequency correlation is simply that the frequency of the pump photon minus the frequency of vibration of the hydrogen molecule must equal the Stokes seed photon. Achieving pump and Stokes seed frequency correlation was obtained by producing the Stokes seed from a portion of the pump beam in a focused Raman cell, separate from the main amplifier. The temporal correlation is produced when the Stokes seed beam and the pump beam arrive at the amplifier at the same time, within the correlation length of the laser. This is achieved with optical delays.

Pump beam phase has often been stated as being unimportant in Raman amplifiers, but this is subject to limits. The pump beam phase must be at least good enough such that the phase does not convert (via diffraction) to intensity over the distances traveled by the beam. This is the major reason for doing these experiments a large Fresnel number Raman amplifier. Diffraction effects are more severe in smaller beams producing unacceptable intensity non-uniformities. This is further compounded by the presence of aberrations causing distortions of the Raman process.

Experimental Approach

These experiments were conducted on the AVCO Scale-Up XeF excimer laser (Figure 1). It was operated with a confocal, off-axis, unstable resonator with a sub-aperture output window. With the full aperture window this is a multi-kilojoule device whereas in the current configuration about 500 J could be extracted from the sub-aperture. The beam quality of this sub-aperture beam is several times the diffraction limit (XDL), primarily from uncorrected spherical aberrations and astigmatism. (With the use of corrector optics, the beam can be made better than 1.2 XDL. However, these were not used in this program.) Several optical components downstream from the laser further degrade the pump beam to >100 XDL. This regime provides a stringent test of the Raman theory.

A schematic diagram of the optical train is shown in Figure 2. As the laser beam exits Scale-Up a 5 cm piece of the beam is picked off the edge and sent to the seed generator sub-assembly. This beam is further split into a small (7 mm) diameter beam for seed generation and a second beam (5 cm) with most of the energy. The smaller beam is then focused into a cell containing 10 atm of hydrogen to produce a small amount of Stokes radiation. The Stokes beam exiting the Raman cell is expanded to 5 cm and combined with the rest of the pump beam which has just imaged through a transfer tube which is under vacuum. These two beams are then sized to 1 cm and passed through a pre-amplifier hydrogen cell to increase the Stokes seed beam energy by an order of

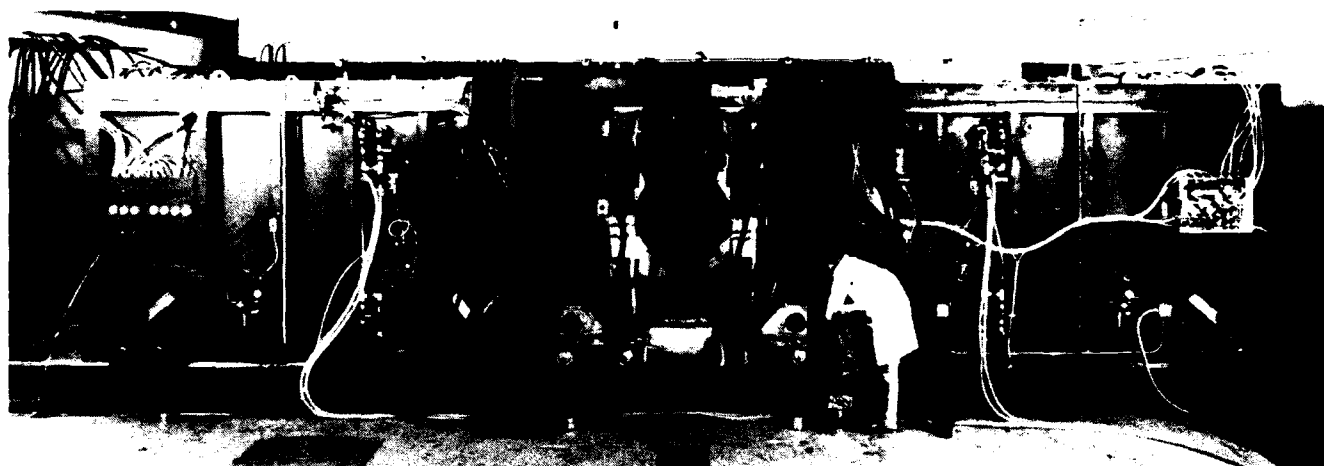


Figure 1 - View of the Scale-Up Excimer Laser used to preform high Fresnel number Raman amplification.

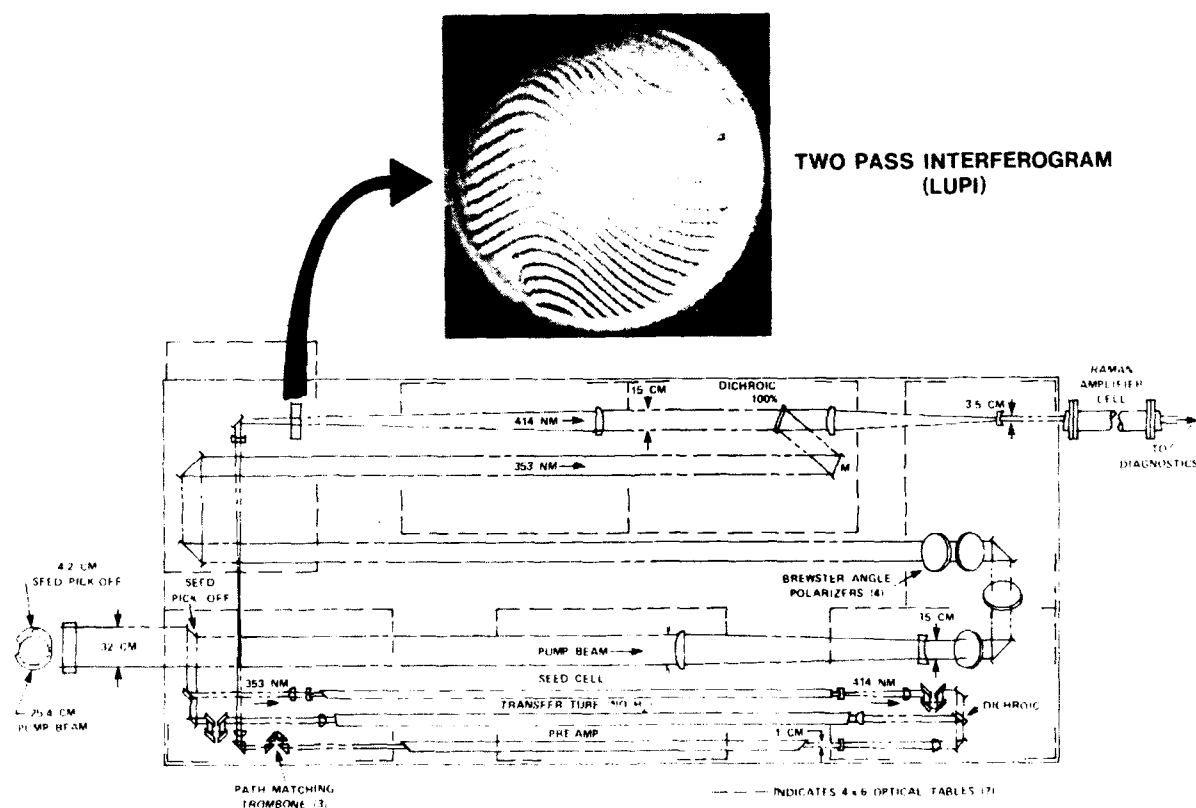


Figure 2 - Overview of the optical layout of the phase preservation experiment. The shape of the subaperture on Scale-Up is shown to the left with the pump and seed pick-off cutouts shown. The two pass interferogram (LUPI) is of the phase distorter plate also showing it position in the layout.

magnitude. The resulting beam can then be passed through a spatial filter, then a phase distorting plate, and increased in size to match the pump beam. The Stokes seed then passes through a dichroic mirror, is combined with the pump, then both are reduced in size for the Raman process and passed collimated and colinear through the Raman amplifier.

After the small beam has been picked off for the seed generator, the remaining pump radiation encounters a 25 cm diameter aperture which defines the pump beam. It was then reduced in size to 15 cm, passed through 4 Brewster angle polarizers and then on to the dichroic mirror to combine with the Stokes seed beam. The optical paths of the pump and the seed beams must be matched to 1 mm in order to meet the path matching requirements of high Raman gain. This is accomplished by very accurate laying out of the optical paths (typically less than 1 cm difference in 25 m) and the use of an auxiliary broadband dye laser, with a short coherence length (0.1 mm), injected in both legs and interfered to produce fringes.

For fidelity measurements, a surface reflection off the input window of the Raman cell supplies the input diagnostic table with a sample of the pump and Stokes seed beam. Further surface reflections are used to dump energy from these beams and direct them toward two cameras which are filtered to pass only pump or Stokes light respectively. The beams' near field images are recorded on Polaroid Type 55 film for later processing. A separate reflection is pointed toward a focusing mirror which then aims the beam into a shearing interferometer. After the beam exits the shear grating it is reimaged with a lens, passed through narrowband filters to select either the pump or Stokes signal, and captured on Polaroid Type 55 film. The output diagnostic table at the rear of the Raman cell has a similar setup for analyzing the beams after amplification. Also there are a number of photodiodes around the room to record the time history of the pump, seed, depleted pump and amplified Stokes intensity.

Results and Discussion

The first test of the system was to amplify a good Stokes beam with our poor pump beam and demonstrate that there was no degradation of the Stokes phase. For this test we took the 1.5 XDL output of the pre-amplifier cell to be our "good beam" (Figure 3). The amplified Stokes was 1.7 XDL, with a system gain of >1000. When these two wavefronts were subtracted the difference was 0.1 waves rms. We have attributed most of this error to non-common optical components that the two diagnostic tables present. This is not hard to imagine since typical errors in optical components are of order 0.02-0.05 waves rms. Since each diagnostic leg has several components, this could easily account for the observed 0.1 wave rms difference.



Figure 3 - Raman beam clean-up was demonstrated using an extremely aberrated pump beam and a good quality Stokes seed beam to produce a good quality amplified Stokes beam. The shearing interferometry data was fit to a sixth order polynomial. The resulting wavefront was Fourier transformed to provide the far-field spot simulations shown.

Next we took a phase aberrator plate (a two pass LUP1 photo is shown at the top of Figure 2) and inserted it in the Stokes seed path. This distortion amounted to 1 wave peak to valley with 2 cycles across the aperture (Figure 4). This was a wavefront error of 0.55 waves rms (>100 XDL). The amplified Stokes showed the same wavefront error. After the input and output wavefronts were subtracted the difference was 0.1 waves rms. The previous arguments about glass differences in the two diagnostics legs, of course, remain.

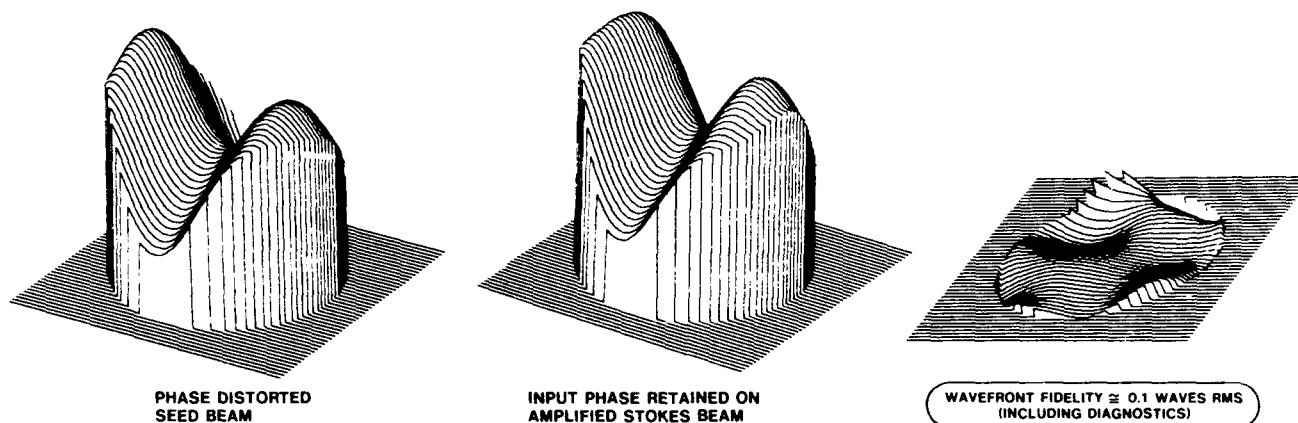


Figure 4 - Raman phase preservation was demonstrated using a phase aberrator plate to distort the Stokes seed beam and comparing the input phase with the output phase. These data are 3D representations of the phase with the full scale on the vertical axis being 2 waves. The difference between the input and output phase is the final plot with the vertical axis the same as the previous plots.

Conclusions

We have demonstrated phase preservation in a high gain (>1000) Raman amplifier. The phase preserved had 0.55 waves rms of aberration and the Raman conversion efficiencies were high (40-60%).

Acknowledgements

In conclusion, the authors would like to acknowledge the following: Sumner Freshmen and Stan Silva who ran the Scale-Up laser, Howard Stowe for laying out the optical path, and M.J. Smith, Craig Appel and Steve Fulghum for many technical discussions.

The views and conclusions contained in this document are those of the contractor and should not be interpreted as necessarily representing the official policies, either expressed or implied, of the United States Government. Funded under Massachusetts Institute of Technology Lincoln Laboratory P.O. BX-883 under U.S. Air Force Prime Contract F19628-85-C-0002.

COPPER AND GOLD VAPOR LASERS:
RECENT ADVANCES AND APPLICATIONS.
C.E. Webb

The Clarendon Laboratory, Parks Road, Oxford OX1 3PU, England.

1. Pulsed Metal Vapor Lasers.

1.1 Principles of Operation.

In 1965 Fowles and Silfvast¹ reported observation of laser action on the 723nm transition of neutral Pb, excited in a pulsed discharge containing lead vapor and a rare gas buffer. The lead vapor laser proved to be the forerunner of an entire class of lasers, of which the copper vapor laser (CVL) and gold vapor laser (GVL) are the best known examples.

Laser oscillation on the green (511nm) and yellow (578nm) transitions of atomic copper was first demonstrated by Walter et al² in 1966. The features which characterize the operation of the CVL (and all members of the class of "self-terminating" laser systems) arise from the particular arrangement of energy levels in the atomic laser species.

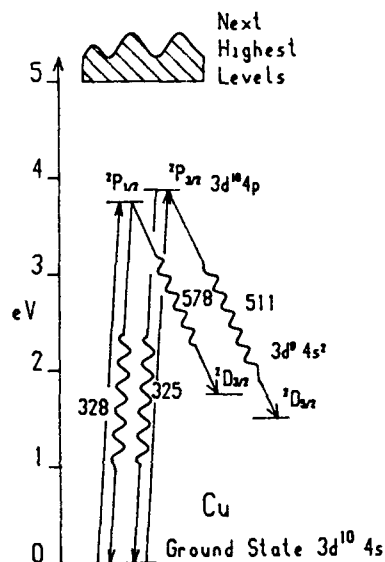


Fig.1.
Energy Levels
Atomic Copper.

As shown in Fig.1, the lowest configuration of the copper atom has one 4s electron outside a complete sub-shell of ten 3d electrons, giving rise to the $^2S_{1/2}$ ground state. Just as in the case of alkali atoms, which also have one s electron outside complete shells, there is a sequence of excited levels arising from configurations in which the outer electron is promoted into orbitals of successively higher n and l. In particular, the first such configuration $3d^{10} 4p$ gives rise to a pair of levels $^2P_{3/2}$ and $^2P_{1/2}$ which are optically connected to the $3d^{10} 4s$ $^2S_{1/2}$ ground state by the strong resonance transitions at 325 and 328 nm. However, the copper atom's energy level diagram shows a feature lacking in those of alkali atoms. In Cu, the configuration $3d^9 4s^2$ has an energy well below the ionization energy, indeed it gives rise to $^2D_{5/2}$ and $^2D_{3/2}$ levels only 1.4 and 1.64 eV above the ground state. The 2D levels are fully metastable since optical decay from them to the ground state is completely forbidden to electric dipole radiation since they have the same parity (even) as the ground state. Moreover, if the central field approximation were a completely valid description of the Cu atom, the $^2P \rightarrow ^2D$ transitions would also be forbidden since they would require two electrons to jump simultaneously. However, enough configuration interaction remains to provide moderate transition probabilities on the laser transitions;



Under conditions of practical interest for CVL operation, the density of copper in the vapor phase is sufficiently high (10^{15} atoms cm^{-3}) that radiation on the $^2P \rightarrow ^2S$ resonance lines is completely trapped. The transitions from the 2P to the 2D levels (i.e. the laser transitions) represent the only effective radiative decay route for the upper laser levels.

Because decay from the lower laser levels can occur only via collisional processes which are effective only over relatively long timescales, the CVL in common with all laser systems of this class completely fails to satisfy the necessary condition for CW operation³:

$$(A_{21})^{-1} > (g_2/g_1) \tau_i,$$

in which A_{21} is the Einstein Coefficient for spontaneous emission, g_1 and g_2 are the respective statistical weights of upper and lower levels, and τ_i is the effective decay time of the lower laser level under conditions of laser operation.

Although the cross-sections for collisional excitation of atoms by electrons do not obey rigorously the optical selection rules (especially at energies near the threshold for excitation) it is still true to say that collisional processes which involve the promotion of an inner electron tend to be of low cross-section, while those corresponding to fully allowed optical excitation of the outer electron are likely to have the highest cross-section. Hence if a fast-rising pulse of current is applied to a discharge tube containing a mixture of buffer gas (e.g. neon at 20-100 torr) and copper vapor (0.1 - 1 torr), the rate of collisional excitation of the 2P upper laser levels will exceed that of the 2D lower levels provided⁴ that the electron temperature remains above about 1.2eV. Thus, in the early part of the discharge current pulse, which might typically last for 300-500ns, a substantial population inversion can be created.

The gain on the 511 and 578 nm transitions from 2P to 2D is sufficiently strong (10^4 per single pass) that strong oscillation builds up in two or three cavity round trip times. Stimulated emission is by then dumping population into the 2D metastable lower laser levels which have no means of disposing of it on timescales of tens of nanoseconds. This precipitates a rapid switch in the behavior of the active medium - from high gain to high loss - and the laser action self-terminates well before the end of the current pulse.

A schematic representation of this change from high gain to loss based on measurements on a 40 Watt CVL by Lewis et al⁴ at the Clarendon Laboratory is shown in Fig.2.

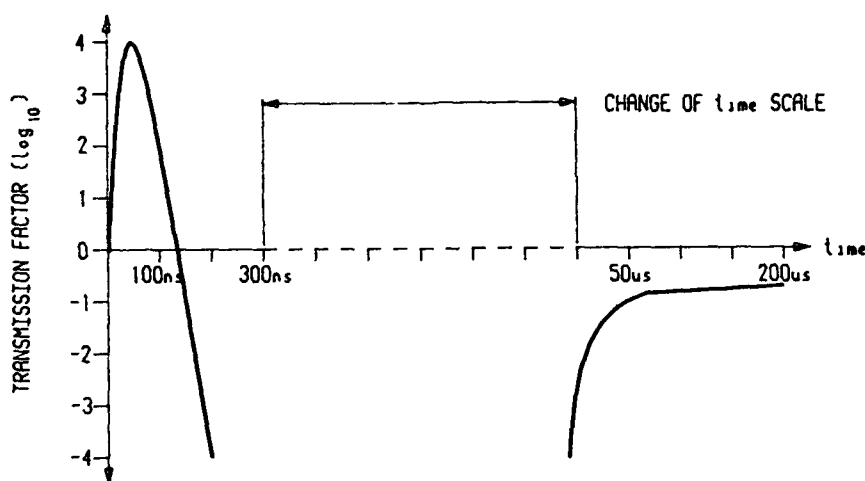


Fig. 2. Time Dependence of Gain/Loss in a 40 Watt CVL.

1.2. A Brief History of the CVL.

The earliest CVL, constructed by Walter et al² in 1966, employed an alumina discharge tube (10mm internal diameter and 80cm length) containing metallic copper pellets and helium buffer gas. To bring the density of copper vapor up to the range required for laser operation, the tube was heated to 1500°C by an external oven. A year later the same American group showed⁵ that operation in short bursts of pulses with a 1.25 kHz repetition rate within each burst, could be obtained at an efficiency of 1.2% if the power needed for the oven was not included.

In 1972, another step forward was made by researchers in the USSR with the demonstration by Isaev et al⁶ that not only was operation on an uninterrupted train of pulses possible, but that by surrounding the tube with a thick layer of thermal insulation, the heat from the discharge was itself sufficient to bring the tube up to, and maintain it at, operating temperature. By this means the Russian workers were able to demonstrate a CVL of 15 Watts mean power and an overall efficiency of 1%.

In the mid-1970s, the requirement arose for an efficient high power multi-kilohertz pulsed laser source for pumping large arrays of dye laser amplifiers in connection with the Atomic Vapor Laser Isotope Separation (AVLIS) project at Lawrence Livermore Laboratory. The CVL quickly established itself as the most promising contender for this application.

The AVLIS program⁷ provided much of the stimulus for CVL development in the USA from 1975 onwards.

The next key advance was, however, to come from a group in Israel. In 1978 Smilansky et al⁸ demonstrated efficient CVL operation in discharge tubes of considerably wider bore (40mm) and higher pressures of neon buffer gas (above 100 torr) than had previously been used. This demonstration of the volumetric scalability of the CVL showed that some process other than wall collisions was active in depopulating the metastable ²D lower laser levels in the interval between pulses. Later work at LLNL and Oxford⁴ has provided strong evidence that ²D depopulation is brought about by superelastic collisions with plasma electrons which are present in appreciable numbers throughout the inter-pulse period. Similarly, the fact that the ionization does not decay completely between laser pulses explains another surprising feature of Smilanski's results, namely the excellent uniformity with which the discharge fills the 40mm bore tube. Discharges in such wide tubes at these relatively high pressures of rare gas tend to be self-constricted and to follow irreproducible tortuous paths between the electrodes. However, the ionization remaining from one pulse to the next provides sufficiently strong pre-ionization at the start of each pulse to ensure that the discharge current builds up from an initial distribution which is uniform across the tube diameter every time.

Continued development of CVL technology over the past ten years has led to devices of high reliability and power capability. Since power can be extracted efficiently from these devices when operated as single-pass amplifiers, it is possible to couple many such units into power amplifier chains as in the AVLIS demonstration facility at LLNL. Each of the 80mm diameter amplifier units in the chain adds more than 200 Watts to the beam, resulting in a combined output of 3kW from the array⁷.

1.3 CVL Development at Oxford.

In a 1975 publication, Piper⁹ described the construction and operating characteristics of the first transversely-excited copper halide laser. Since that time the Gas Laser group at the Clarendon Laboratory has continued to make contributions to the understanding of CVL mechanisms and the development of practical CVL systems.

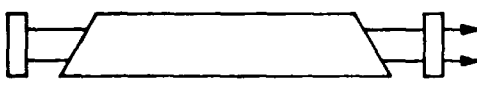
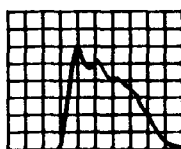
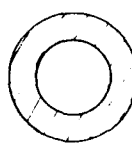
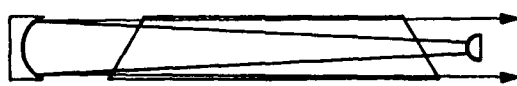
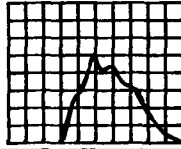
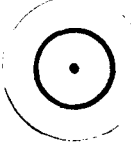
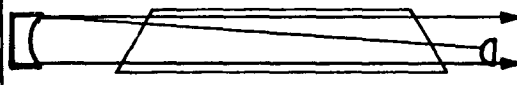
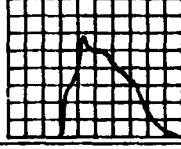

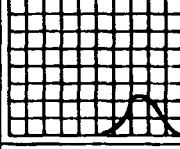
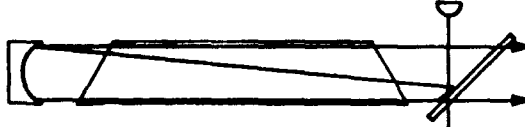
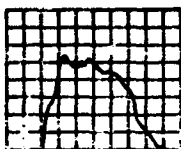

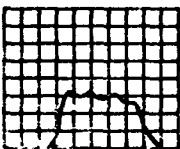
Based on those design concepts commercial production of CVLs and associated equipment was undertaken by Oxford Lasers Ltd., starting in 1980 with the introduction of the Model Cu25 laser, a CVL of 25 W mean power. Continued research and development at Oxford Lasers Ltd has enabled significant advances to be made in CVL reliability and performance. Today (1987), the company is the largest commercial enterprise specializing in the manufacture of CVL and GVL systems. To provide an indication of the performance characteristics of a state-of-the-art CVL system, the parameters of the Oxford Lasers Model Cu60 laser (the highest power CVL commercially available) are listed below:

Average Power on 511 and 578nm combined	---	60 Watts	
Green: Yellow power ratio	---	1.2 : 1	
Pulse energy -- 10mJ	Pulse width	---	15-60 ns
Pulse repetition frequency	---	5-10 kHz	
Timing jitter on command triggering	---	1ns RMS	
Beam diameter	---	42 mm	
Beam divergence (plane-plane cavity)	---	6 m rad	
Beam divergence (unstable resonator cavity)	---	0.6 m rad	
Power consumption (max)	---	8 kW	
Cooling water requirement	---	3 lit/min.	

2. Recent Advances in CVL Technology

2.1 Unstable Resonator Development.

When operated as an oscillator in the standard cavity, comprising one high reflectance plane mirror and a plane silica blank as output coupler, a Cu 40 laser (the standard 40 Watt workhorse of the Oxford Lasers range) produces a beam which in the near field is uniform in intensity over its full diameter. However, as indicated in Fig. 3a, the far field beam focus pattern is annular, and the divergence of the beam is about 6 milliradians. The annular nature of the beam pattern produced under these conditions is, as shown by Naylor¹⁰, due to the fact that the timing of gain depends on radial position within the discharge tube. At the start of each pulse, the gain rises first at positions near the tube wall, and there is a measurable delay of several nanoseconds before the gain at the tube axis reaches comparable values. Thus, the radiation which "seeds" the cavity is ASE which has an angular distribution such that when imaged by a lens it appears to have originated from a continuous ring of "point" sources near the tube wall.

POWER BASED ON A Cu40 LASER	AVERAGE POWER (V)	PULSE (10ns/div)	FOCUS 6mR	POWER WITHIN 200 μ reds (V)	PULSE WITHIN 200 μ R
<p><u>PLANE-PLANE CAVITY</u></p>  <p>EFFICIENT EXTRACTION OF POWER OVER ENTIRE LENGTH OF PULSE, HIGH PEAK POWER HIGH DIVERGENCE</p> <p>FIGURE 3a</p>	40-50			VERY LITTLE	
<p><u>UNSTABLE CAVITY</u></p>  <p>SLIGHTLY LOWER EFFICIENCY AND PEAK POWER OUTPUT LATE IN THE PULSE IS OF LOW DIVERGENCE</p> <p>FIGURE 3b</p>	30-40			10-15	
<p><u>OFF-AXIS UNSTABLE CAVITY</u></p>  <p>HIGHER POWER IN LOW DIVERGENCE MODE</p> <p>FIGURE 3c</p>	35-45			15-20	
<p><u>INJECTION CONTROLLED OSCILLATOR</u></p>  <p>FIGURE 3d</p> <p>LOW DIVERGENCE OUTPUT OVER ENTIRE LENGTH OF GAIN PERIOD</p>	45-50			30-40	

Some improvement in beam quality can be obtained by providing the laser with a confocal unstable resonator as shown in Fig. 3b. Unfortunately the light must make several round trips within the cavity before the benefit of the angular discrimination provided by the cavity becomes fully effective. Since the axial region of the 42mm diameter discharge tube of the Cu40 shows gain for only about 50ns, the number of round trips of the 2m long cavity is restricted to perhaps four or five at most. The individual round trips are visible in the far-field focus pattern as a sequence of concentric rings, with the earliest part of the gain pulse corresponding to the outermost ring and so on. Only the very last part of the gain pulse contributes to the low divergence component making up the central spot. Under these conditions the mean power of the beam within 0.2 milliradians is only 10-15 watts.

A simple modification which yields a very worthwhile improvement is to place the small convex mirror of the unstable resonator off axis as shown in Fig. 3c. Now the radiation which seeds the cavity appears to come from one pointlike source near the periphery of the tube. Since the gain rises earlier in this region than at the axis of the tube, the time available for the development of a low divergence beam is some 10ns longer. Thus the final part of the pulse contains a greater fraction of the total energy, and the beam component with a divergence less than 0.2 milliradians has a mean power in the 15-20 watt range. As indicated in Fig. 3c, the far field focus pattern in this arrangement consists of a weak halo of light which has made only one or two cavity transits. However, the bright spot of low divergence cavity-controlled light now lies on the circumference of this ring and not at its center.

2.2 Injection controlled Oscillator.

A further stage in the improvement of CVL beam quality was brought about with the development of the injection controlled device shown in Fig. 3d. In this arrangement the beam from a small CVL (whose beam divergence is limited by intra-cavity apertures) is launched into the cavity of a Cu40 laser controlled by an off-axis unstable resonator. By adjusting the relative timing so that the discharge in the small laser module fires before that in the Cu40, it is easy to ensure that the main Cu40 cavity is filled with radiation of low angular divergence before its gain pulse starts to rise. The coupling of the cavities of the two laser modules is accomplished by positioning a beam splitter to enable them to share the small convex mirror as an element common to both. With this arrangement the Cu40 can now emit low divergence light over practically the entire gain period, so that it produces a mean power in the range 30-40 watts in a beam of less than 0.2 milliradians divergence.

Extending this concept by using a Cu 60 module as a single pass amplifier following an injection locked oscillator similar to that of Fig. 3d, Naylor, Lewis and Kearsley¹¹ have recently demonstrated a device producing 100 watts mean output power, of which 80 watts is within a beam of 0.4 milliradians full angle of divergence.

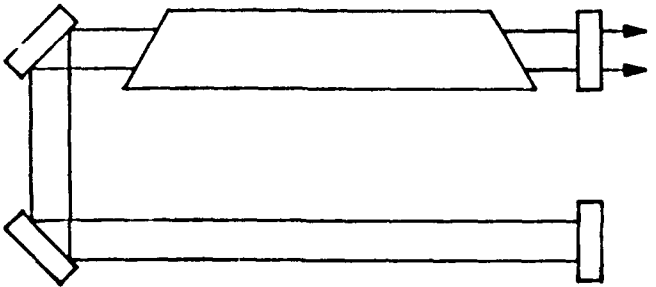
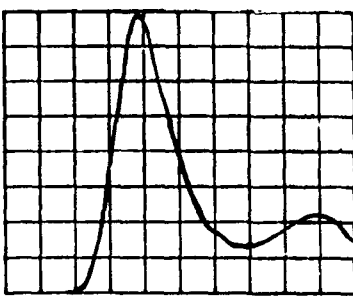

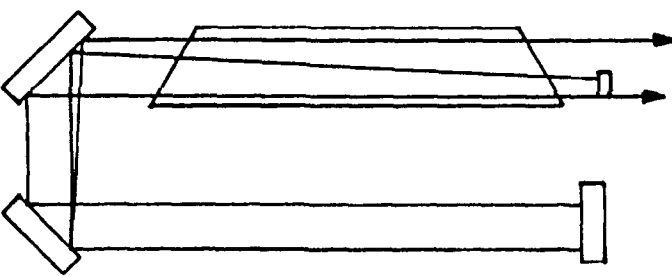
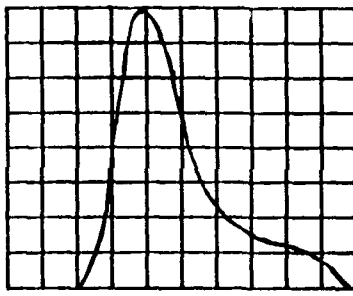

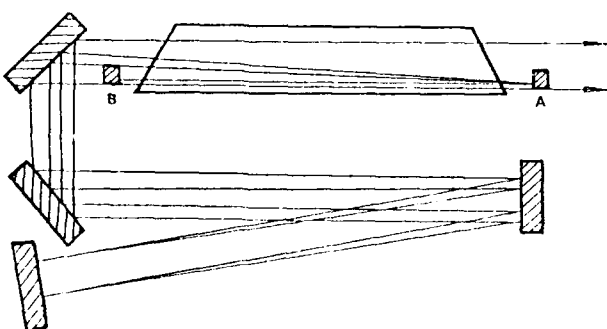
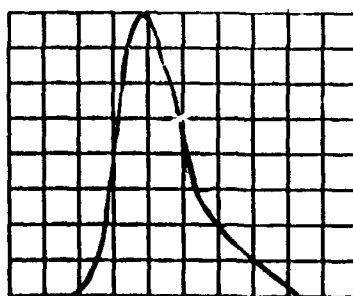

2.3 Short-pulse CVL Pump Source for femtosecond Pulse Amplification.

Synchronously-pumped mode-locked dye laser systems produce trains of picosecond pulses at a repetition rate of, typically, 80 MHz. Such pulses can be further shortened by various techniques to durations of order 100fs or less. However, each pulse in the train contains very little energy, usually not more than one nJ. In order to bring the pulse intensity up to the range where it is suitable for practical applications, it is necessary to boost the pulse energy in a dye laser amplifier.

The choice of pump source used to provide the excitation for this final amplifier has important consequences for the data rate capability. Early systems employed frequency-doubled Nd:YAG lasers for this purpose, but their limited repetition rate (typically 5-30 Hz) meant that fewer than one in a million of the femtosecond pulses in the 80MHz train could be amplified, and the data rate is limited to that of the Nd:YAG laser.

The concept of using a CVL to pump a multi-pass dye gain cell to amplify a train of fs pulses was introduced in 1984 by Knox et al¹² of AT&T Bell Laboratories. The increase of repetition rate of the pump laser from 10 Hz to 10 kHz immediately brings a thousandfold increase of data rate, and a significant increase in the mean power of the signal at the amplifier output. Moreover, since the recovery time of the dye laser gain is of order 1ns, energy can still be extracted efficiently when a given fs pulse is passed repeatedly through the gain medium up to six times during the time it is being pumped by a single CVL pulse. However, there is a problem concerning the optimum duration of the CVL pulse. If the gain cell of the dye amplifier is pumped for much longer than 12 ns then two or more neighbouring pulses in the 80 MHz train will be inside the amplifier at the same time, competing for the available gain. Obviously, this situation has undesirable consequences from the point of view of amplitude stability and reproducibility. To avoid this, it is necessary to reduce the pulse length of the CVL to 12 ns or less, without at the same time reducing its peak power.

Running the CVL at an abnormally elevated temperature can have some pulse-shortening effect, but this expedient cannot be recommended since it shortens the life of the copper charge and may damage the discharge tube.

POWERS FOR Cu40 LASER- (GREEN COMPONENT ONLY)	AVERAGE POWER (W)	PULSE (5ns/div)	FOCUS 3 mR
<p><u>SHORT PULSE OPTICS</u></p>  <p>FIGURE 4a</p>	7		
<p><u>SHORT PULSE LOW DIVERGENCE OPTICS</u></p>  <p>FIGURE 4b</p>	9.5		
<p><u>ENHANCED SHORT PULSE LOW DIVERGENCE OPTICS</u></p>  <p>FIGURE 4c</p>	11-12		

The solution to the problem, developed by Lewis and Naylor¹³, is to utilize the gain switching properties of the CVL discharge described in section 1.1 and Fig. 2. above. If, on its final transit, the pulse from a CVL is returned through the discharge with appropriate timing, its trailing edge will be strongly truncated by absorption. The pulse is thus shortened without reducing its peak power. Fig. 4a. shows a simple arrangement for implementing this scheme, which involves nothing more than removing the high reflectance mirror to a distance of 1.5 m or so from the end of the discharge tube. To make a conveniently compact layout, the cavity can be folded by plane reflectors as shown. Also as indicated in Fig. 4a. the pulse width on the 511nm transition obtained from a Cu40 laser modified in this way is 10ns FWHM, and the mean power is 7 watts on the green line only.

An improvement on this scheme due to Naylor¹⁴, combining the advantages of the off-axis unstable resonator with this pulse shortening technique, is shown in Fig. 4b. Not only has the pulse energy been increased while retaining the same pulse width, but the focussability of the beam has been improved by almost an order of magnitude.

Still further improvements on this scheme are possible, which exploit to full advantage the difference in rise time of gain at the discharge tube wall and axis. The best results to date have been obtained with such a scheme. As indicated in Fig. 4c. this has allowed a mean power of 12 watts, on the 511nm transition only, to be extracted from a Cu40 laser module, in a beam of less than 0.4 milliradians divergence.

3. The Gold Vapor Laser.

3.1 Excitation Mechanisms.

The gold vapor laser (GVL) is another member of the class of "self-terminating" laser systems to have found applications outside the laboratory. Gold lasers are similar to copper lasers in their construction and operating characteristics. This close similarity arises because gold is the only element in the entire periodic table with exactly the same arrangement of low lying atomic energy levels as copper.

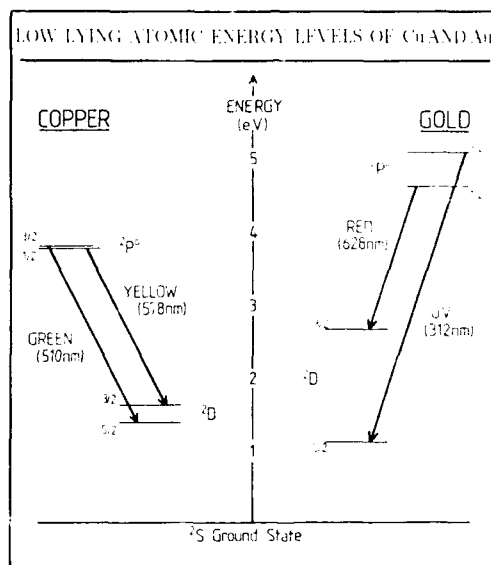


Fig.5. Upper and lower laser levels of Cu and Au.

As shown in Fig.5, which compares the energy levels of Au and Cu side by side, the configuration $5d^{10} 6s$ gives rise to the $^2S_{1/2}$ ground state in Au. However, the 2P upper laser levels of Au which arise from the configuration $5d^{10} 6p$, are almost 1eV higher in energy than the corresponding 2P levels in Cu, and show a much greater spin-orbit splitting as would be expected in a heavier element. Similarly, the 2D lower laser levels, which arise from $5d^{10} 6s^2$, are separated by four times as great a splitting as in Cu. Thus, while the $^2D_{3/2}$ level of Au (some 2.6eV above the ground state) is 1eV higher than the corresponding level of Cu, the $^2D_{5/2}$ level (at 1.0eV) is some 0.4eV lower than its counterpart in Cu.

These slight differences in the energy level schemes of Cu and Au do have some interesting consequences for laser operation in the two metal vapors. In order to provide sufficient density of gold vapor for laser operation, the tube temperature has to be increased to 1600°C because gold is somewhat less volatile than copper. At this temperature the thermal population of the $^2D_{5/2}$ is significant, and relaxation of its population between pulses is not very effective. As a consequence, oscillation on the UV 312 nm transition of Au (analogous to 511 nm in Cu) is difficult to obtain especially in discharge tubes of bore much wider than 15mm at high repetition rates.

In contrast, the emptying of the $2D_{3/2}$ level of Au between laser pulses is even more effective than its Cu counterpart, with the result that the red 628 nm transition of Au (the analogue of 578 nm in Cu) shows a constant 0.2% efficiency as the repetition rate of a 42mm diameter GVL is increased from 5 to 20kHz. Over the same range, the efficiency of a CVL of the same size decreases by a factor of three, from 1.2% at 5kHz to 0.4% at 20kHz⁴.

The fact that the efficiency of the GVL is lower than the CVL is partly due to technological considerations, since to avoid problems with laser tube construction materials the discharge must be kept at temperatures which are slightly below optimum for laser operation at 628 nm. Operation at temperatures above 1600°C for brief periods is possible with a consequent improvement in efficiency as shown by recent experimental work carried out by Lewis et al¹⁵.

For practical gold vapor lasers then, the constraints imposed by considerations of discharge tube lifetime imply that efficiencies for producing the red 628 nm output are limited to about half of that obtainable on the analogous yellow 578 nm transition of Cu. Thus, while the Cu40 is capable of producing 18 watts of output on the copper yellow line, a device of similar dimensions operated as a GVL produces 9 watts of red light. With this rating, the Oxford Lasers Model Au10 has the highest mean power of any GVL currently available commercially.

3.2 Photodynamic Therapy.

Photodynamic therapy (PDT) or Photo-radiation therapy as it is sometimes called, is an application where the red output of the gold laser is especially valuable. This form of treatment for cancer relies upon the phototoxic effect produced by certain light sensitive materials. At the moment, the best established of these is haematoporphyrin derivative (HpD), a natural chemical which is present normally in minute quantities in the blood. To treat cancer, a large dose of this chemical is injected into the patient. The bloodstream carries it to all regions of the patient's body but after three or four days its concentration in normal tissue is somewhat lower than in the cancer tissue which cannot dispose of it as effectively. At this point in the procedure the region of the patient's body where the tumor is located is flooded with light of a particular wavelength. The light does not have to be applied in a highly localized fashion since it is not the cutting or vaporizing action that is being used (as in the case of laser surgery with CO₂ or Nd:YAG lasers) but instead the light is used to promote a photochemical reaction deep within the volume of the tumor. There is a real advantage in applying the light in a broad area over the region of the tumor tissue; there may be small secondary infections in the region which are too small to detect visually and yet may still be eliminated by the technique.

The HpD works by absorbing photons of visible light which excite it to a singlet state from which it decays to a longer lived triplet state. HpD molecules in the triplet state collide with O₂ molecules in the bloodstream and pass on their excitation leaving the O₂ in the highly reactive singlet delta state. In this form the O₂ aggressively attacks everything in its vicinity, which is mainly the cells of the tumor. The major effect is to remove the blood supply to the tumor mass which then dies and is sloughed off to leave a wound which scabs over and heals in the normal way.

The light which induces the photochemical activation of HpD must have a wavelength short enough to access the singlet state of HpD, and yet long enough to escape absorption in the haemoglobin component of blood. These considerations set limits of about 610 nm to the short wavelength end and 640 nm to the long wavelength end of the spectral region that can be used. The GVL, with its output at 628 nm is ideally matched to this requirement. Gold lasers have been in use for several years now at treatment centers in the USA, Europe and Japan. For further details, the reader is referred to the medical literature on the subject¹⁶.

Since the coherence properties of the laser are not used directly in this application, it might be thought that an arc lamp might provide an equally effective light source. However, to isolate the wanted spectral band from the output of a black body source involves a massive task of filtering and cooling. Moreover, to obtain sufficient intensity in the wanted band in order to keep exposure times within reasonable bounds implies the use of an extremely powerful arc light.

Short exposure times are not the only advantage of using laser sources for PDT applications. The ability to launch laser light into narrow optical fibers with good efficiency means that the required optical radiation dose can be delivered to tumor sites anywhere within the body accessible by endoscope. Also, by implanting several fibers directly within a tumor, it is possible to irradiate a large mass of tumor from several locations simultaneously to ensure good penetration of light to all parts of the tumor. Fig.6 shows a 9 watt GVL in use at the Royal South Hampshire Hospital in Southampton, England, which is fitted with a fiber optic delivery system providing output on four separate fibers simultaneously.

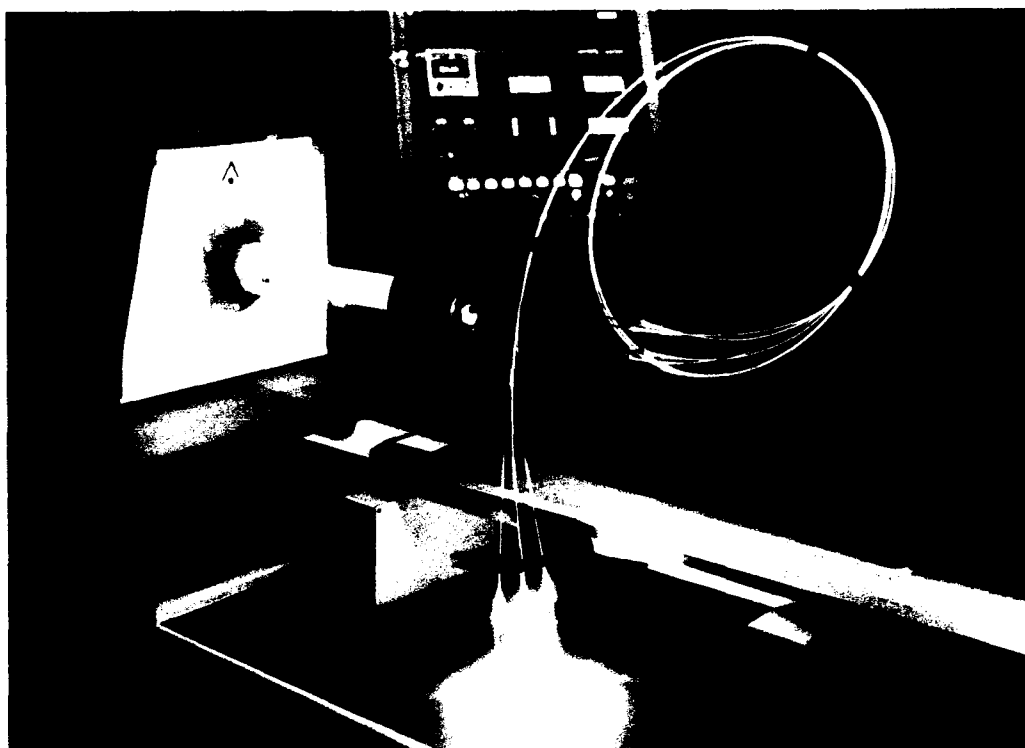


Fig.6. Oxford Lasers Model Aul0, Gold Vapor Laser fitted with 4-way Fiber Optic Delivery System (cover removed).

REFERENCES

- 1 G.R. Fowles and W.T. Silfvast, Appl. Phys. Lett. 6, 236 (1965).
- 2 W.T. Walter, N. Solimene, M. Piltch, and G. Gould, IEEE JQE, QE-2, 474 (1966).
- 3 C.E. Webb in Lasers: Physics, Systems, and Techniques, W.J. Firth and R.G. Harrison, Eds. (SS UP Publications, University of Edinburgh, 1983).
- 4 R.R. Lewis - to be published.
- 5 W.T. Walter, Bull. Am. Phys. Soc., 12, 90 (1967).
- 6 A.A. Isaev, M.A. Kazarayah, and G.C. Petrash, J.E.T.P. Lett., 33, 146 (1978).
- 7 E. Moses, presented at the International Conference on Lasers '87, Lake Tahoe (1987) paper HA3.
- 8 I. Smilansky, A. Kerman, L.A. Levin, and G. Erez, Opt. Comm., 25, 79 (1978).
- 9 J.A. Fiper, Opt. Comm. 14, 296 (1975).
- 10 G.A. Naylor, Private Communication.
- 11 G.A. Naylor, R.R. Lewis and A.J. Kearsley to be presented at SPIE Conference OE/Lasers '88 Los Angeles (1988).
- 12 W.H. Knox, M.C. Downer, R.L. Fork and C.V. Shank, Opt. Lett. 9, 552 (1984).
- 13 G.A. Naylor, and R.R. Lewis, Oxford Lasers Ltd., Application Note 6 (1986).
- 14 A.J. Kearsley, G.A. Naylor, and R.R. Lewis presented at the OSA/IEEE Conference on Lasers and Electro-Optics CLEO '87, Baltimore (1987) paper MG1.
- 15 R.R. Lewis, A.P.R. Harpin, A.J. Kearsley presented at the OSA/IEEE Conference on Lasers and Electro-Optics CLEO '87, Baltimore (1987) paper MG5.
- 16 J.A.S. Carruth and A.L. Mackenzie in Medical Lasers, Science and Clinical Practice (Adam Hilger, Bristol, England, 1986).

RECENT DEVELOPMENTS AND APPLICATIONS OF WHITE-LIGHT LASERS

Kan-ichi Fujii
Professor, Ph.D.

Department of Electrical Engineering, Faculty of Engineering, Ibaraki University
4-12-1 Nakanarusawa-Machi, Hitachi-Shi, Ibaraki, 316 Japan

Abstract

The original idea to use the negative glow for laser pumping is reviewed. Some successes in developing a He-Cd⁺ white-light laser and its application to a prototype full colour printer are described. Some ideas for giving direct modulation to the white light laser are proposed. A new candidate of a high-power white-light laser consisting of Au(I):627.8 nm (red), Cu(I): 510.6 nm (green) and Sr(II): 430.5 nm (blue) is suggested.

Introduction

1. Definition of white-light laser

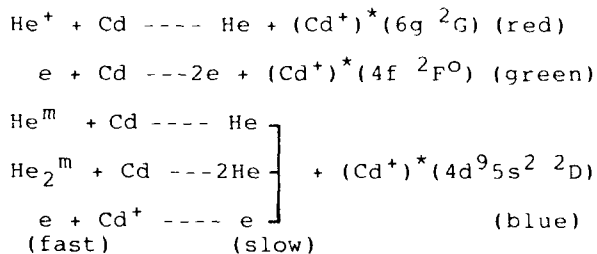
The white-light laser oscillates on the three primary colours simultaneously. In the past ten years many researches on the development of single gun system cw white-light lasers have been carried out. (1)-(10) Some of them use a rare-gas-mixtures as the laser medium (9) but others use a rare-gas-metal-vapour-mixtures. The metal-vapour are mixed with the rare-gases after being evaporated by an electric-oven or by discharge-heating itself. From the point of view of pumping source, some of them use the positive column in a low pressure glow discharge with a skilful optics (10), while the others use the negative glow mainly in a form of the hollow-cathode discharge (1)-(9).

The author and his colleagues have been successful in developing a white-light laser by using the negative glow in a hollow-cathode structure with a He-Cd mixture. The wavelengths of oscillating lines are 636.0 and 635.5 nm (red), 537.8 and 533.8 nm (green) and 441.6 nm (blue). Using a white-light laser oscillator which has similar construction as our original one⁽¹⁾ but was cultivated its performance by a manufacturing company, a prototype full colour image printer has been successfully developed⁽¹⁾ by a co-operation with a Research Institute of another production company.

In this paper, the principle of the hollow-cathode type cw white-light laser is explained, the system of full colour printer is described and the properties of its products is discussed. New aspects on the white-light laser are introduced and a new candidate of high-power white-light laser is suggested.

2. Properties of white-light laser

Figure 1 shows the partial energy diagram and laser transitions of three primary colours of Cd ion. As is clear from Fig.1, three colour laser transitions have different excitation mechanisms. Some proposals on the excitation mechanism are as follows (12)(13)



where m means the metastable state and * the usual excited state.

Figure 2 shows the CIE chromaticity diagram. Plotting the wavelengths of the three primary colours and connecting these corresponding points, one can get a triangle. The colours shown inside this triangle can be reproduced by the three

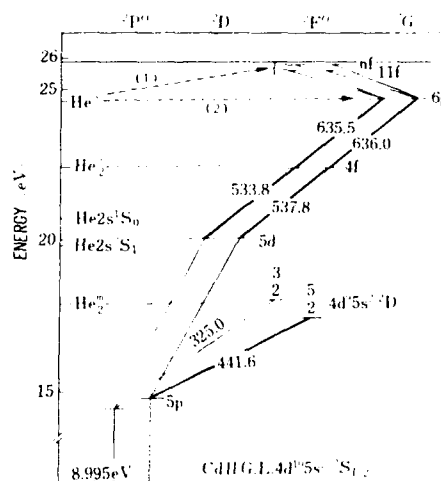


Fig.1 Energy levels of Cd ion and visible laser transitions (wavelength in nm). (1) endoergic charge transfer, (b) thermal charge transfer.

Table I Possible applications of white-light lasers

- (1) Colour display : colour holography
large scale laser TV
- (2) Medical field : diagnostics
surgery
healing of wound skin
cancer treatment
- (3) Full colour image printer
- (4) Three dimensional measurements
- (5) Multi-photon process (Isotope separation)

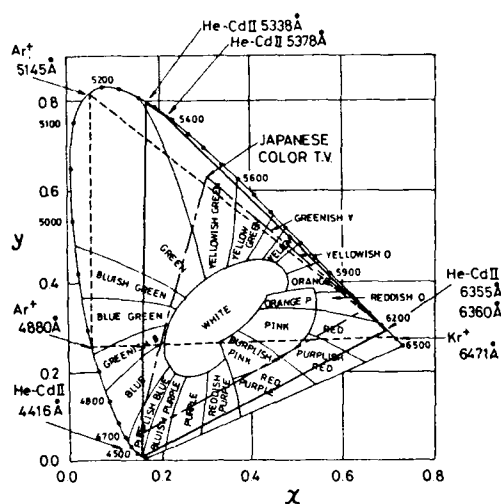


Fig.2 CIE chromaticity diagram showing reproducing characteristics of He-Cd⁺ laser (solid line) and Ar⁺-Kr⁺ laser (broken line).

colours. Therefore it is clear from produced by the He-Cd white-light laser. This is the main reason why we are keen to use this laser to the colour holography, colour printer, color TV etc..

Applications of white-light lasers

A possibility of applications of white-light lasers is summarized in Table I. Of these applications, a prototype full colour image printer was realized. Its specification⁽¹⁾ is as follows;

Resolution : 32 dots/mm (horizontal)
: 32 lines/mm (vertical)
spot size : 50 μ m
output size : 250x250 mm²
process time : 2 minutes

The system structure of the printer is shown in Fig.3. This system consists of three units, (1) data input unit, (2) data processing unit, (3) printing unit.

In the data input unit, a colour scanner for treatment of a colour image input, a magnetic tape drive for "Landsat" data input and a floppy disc drive for character data input are assembled.

The data processing unit includes three units for handling red, green, and blue colour data. The processed data are first stored in the hard disc drive (H.D.D) and are then sent to the printing unit synchronously by means of clock pulses generated in the printing unit. Each data signal drives its respective acousto-optical modulator (AOM).

In the printing unit, the white-light laser beam is splitted into three beams by dichroic mirrors. Then, each beam is individually modulated by data signals from the data processing unit. The individually modulated beams are combined again by dichroic mirrors, finally resulting

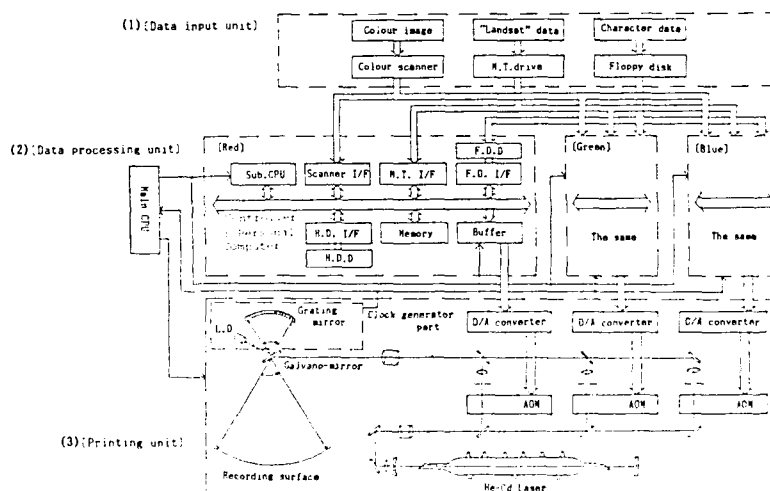


Fig.3 Schematic diagram of full colour printer He-Cd⁺ white light laser.

in a coloured beam. This coloured beam scans horizontally on the colour sensitive material that is mechanically shifted in vertical direction. Thus, a full colour picture is produced. It takes 2 minutes for a production of A4 size print.

Historical review of white-light laser

1. Comparison of pumping plasma

When the He-Ne laser was invented by Javan and his colleagues⁽¹⁴⁾ in 1960, an electrodeless rf discharge plasma was employed as the pumping source as shown in Fig.4(a). In this case the structure of the laser tube is simple, a pure positive column is obtained and problems caused by electrodes, in particular by the cathode, do not occur although some difficulties exist in getting impedance matching between power supply and laser tube.

On the other hand, Fig.4(b) shows the Asami's experiment⁽¹⁵⁾ which is interesting and important in comparison with Fig.4(a). In this case, a Ne lamp was excited by a rf power supply through the inner electrodes. When the Ne lamp was excited by a low frequency AC power, the colour of the Ne lamp was usually red. Major components of the emission spectra were from Ne gas. However, when the Ne lamp was excited by a rf power, the colour of the Ne lamp changed to blueish. Major emission spectra were from Ar gas which was mixed into the Ne in the ratio of about 0.1 %.

From these experimental results, Asami had suggested that one can control the distribution of the emission spectra by changing the frequency of the applied electric field. He interpreted this phenomenon was due to the change of electron energies in the rf discharge plasma, resulting in an influence to the dominant excitation cross-sections.

Another remarkable point is that there exists only the negative glow in the Ne lamp. Therefore, the spectra Asami observed were emitted from the negative glow only.

Further interesting and important point is the fact that a helix was already used as one of the pair of the electrodes. The helix has been revived as a long helix-cathode for a white-light laser very recently as described in the later section.

When Asami knew the invention of rf (positive column) pumped He-Ne laser, his former experiences on rf excited negative glow pushed him to attack developing a new laser by using the negative glow as a pumping source since the negative glow has different properties in electron temperature as well as in electron density from those in the positive column. Since then, our aim has been in realizing a negative glow type laser.

2. Principle of negative glow type laser

The principle of the negative glow (NG) type laser is shown in Fig.5. Shortening the electrodes-spacing by moving the anode

toward the cathode at Fig.5(a), the length of the positive column (PC) decreases, vanishing when the anode is placed in the Faraday dark space (FDS). More shorter electrode-spacing, Faraday dark space is also vanishes and only the negative glow (NG) as well as the cathode dark space (CDS) remain. Using a pair of long plane in a short distance like Fig.5(b), a long optical path of a uniform NG is obtained in perpendicular to the electric field. Using a pair of plate or a pipe cathode like Fig.5(c), these are so called hollow-cathode, a superimposed negative glow is formed and thereby an enhanced emission spectra being observed.

3. Negative glow type lasers

In 1964, a negative glow type He-Ne laser was developed by S.Kobayashi, who was one of the colleagues of Asami⁽¹⁶⁾ and his group⁽¹⁶⁾ as well as by J.Smith⁽¹⁷⁾ independently. Kobayashi used a slotted pipe-cathode, while Smith used a parallel-plate hollow-cathode, the laser characteristics,

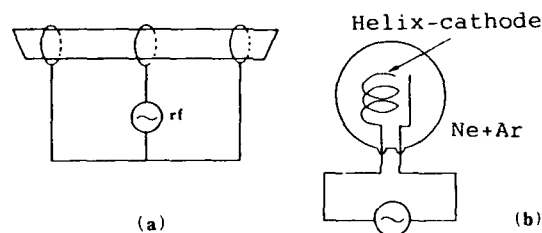


Fig.4 Comparison of laser pumping source; (a)rf-pumped He-Ne laser(use of the positive column), (b)rf-pumped Neon lamp(use of the negative glow).

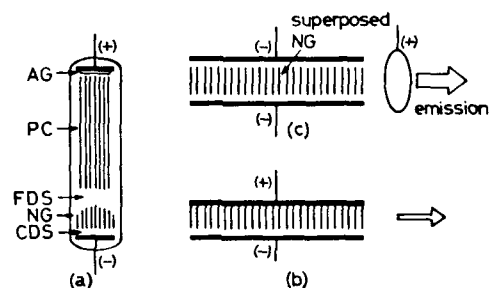


Fig.5 Discharge structure and light emission; (a)typical glow discharge, AG: anode glow, PC:positive column, FDS:Faraday dark space, NG:negative glow, CDS:cathode dark space, (b)prototype negative-glow laser, (c)principle of hollow-cathode laser.

however, being similar between both.

Thus, Asami's idea to use the negative glow for a laser became in practice. At the same time, however, some disadvantages in using the cathode region occurred. For instance, mixing of the cathode vapour by sputtering action, clean-up of the buffer gas by getter action, absorption of the buffer gas by cathode, as well.

4. Metal vapour white-light laser

As far as we use the cathode region, nobody can escape from the phenomena mentioned above. So, we turned our philosophy to use these phenomena in active. Against our expectation, however, not enough vapor for laser oscillation was obtained even using Cu, brass, Al cathode as well. So, we moved to the use of Cd which gave a laser oscillation in a positive column plasma.⁽¹⁸⁾

In 1970, many laser oscillations including visible lines were obtained by Y. Asami, S. Sugawara and their colleagues⁽¹⁹⁾ in Japan, by W.K. Schuebel⁽²⁰⁾ in the U.S.A and by F.M. Sem and his colleagues⁽²¹⁾ in the USSR almost same time but independently by using different hollow-cathode structure. In 1973, cw white-light laser oscillation was realized by K. Fujii and his colleagues⁽¹⁾⁽³⁾ in Japan and S.C. Wang and his colleagues⁽²⁾ in the U.S.A.. In Fig.6, three types of white-light laser are shown.

New aspects and developments

1. Direct modulation

As already shown in Fig.3, in the full colour laser printer, the white-light laser beam is splitted into three colour beams, then they are modulated individually in accordance with the input signals. Instead of this system, if we can get a colour beam directly from the He-Cd⁺ white light laser in time dividing method, the number of modulator and controller and the size of machine would be reduced to 1/3.

For this direct modulation, we are trying to use three means for controlling the electron energy of the discharge plasma zone, and thereby to change the excitation rate among the three colour laser lines since they have different excitation mechanism as mentioned formerly in Fig.1.

Helix-cathode: The structure of the helix-cathode type laser is shown in Fig.6(c). Using a helix-cathode, (1) cathode fall potential is controlled by changing the coil pitch, (2) it is convenient to supply the Cd vapour into the hollow-cathode region through the helix by controlled diffusion from the outer anode pipe where the evaporating Cd lining is fixed.

The helix-cathode was first used for laser oscillation by Groseva and Sabotinov⁽²²⁾ instead of hybrid-hole hollow-cathode as shown in Fig.6(b). To control the coil pitch from outside the discharge tube and to increase its frequency is the problem to be solved for direct modulation.

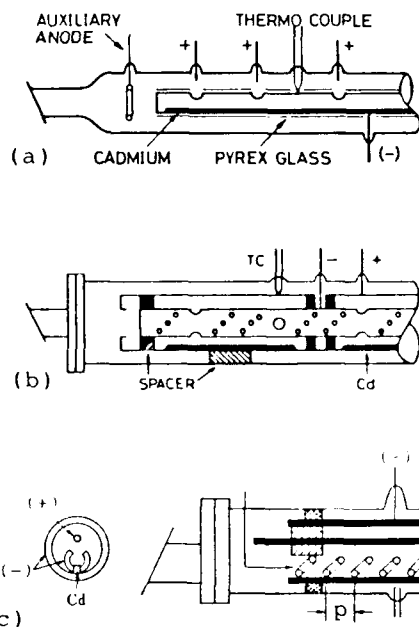


Fig.6 Tube construction of white-light lasers, (a) flute type, (b) hybrid hole type, (c) helix-cathode type (p: helix-pitch).

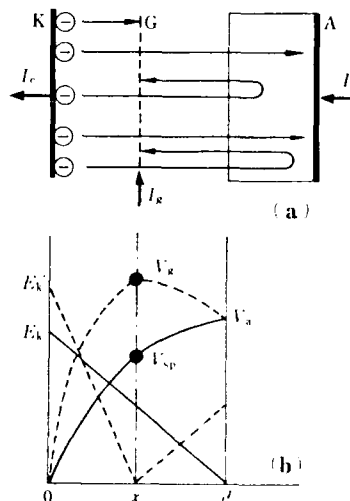
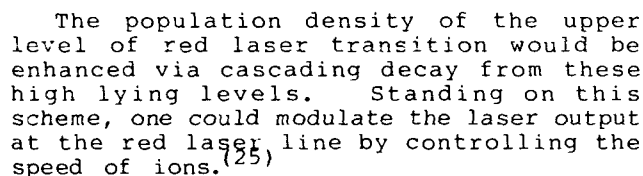
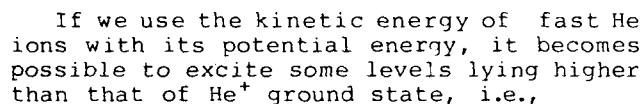


Fig.7 Model of a grid-control discharge (a) relation among currents, (b) spacial distribution of electric field (E_k) and potential (V).

Endoergic charge transfer⁽²⁴⁾: As shown in Fig.1, the red laser line is excited via thermal charge transfer like follows;



Cu(I) 510.6 nm (green), Au(I) 627.8 nm (red), and SrII 430.5 nm (blue) are a new candidate of high power white-light laser. The wavelengths of these lasers are plotted as almost same point as that of He-Cd⁺ white-light laser on the CIE chromaticity diagram shown in Fig.2.

The partial energy diagram and laser transitions of Cu(I) and Au(I) are shown in Fig.8. In these lasers, the lower laser level is in metastable state, therefore they being operating essentially in pulsative. The width of the laser output is several nano-seconds. The relaxation of the metastable state is promoted by collisions not only with the tube wall and/or other gas molecules but also with slow electrons like follows:

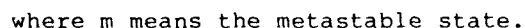
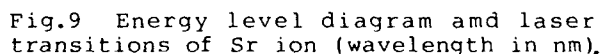
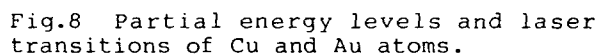


Figure 9 shows the energy level diagram



and laser transitions of Sr(II). At this laser, the upper laser level is populated by cascading decay after recombination mainly via non-radiative super-elastic collision.⁽²⁸⁾ The relaxation of the lower laser level is promoted by both radiative and non-radiative super-elastic collisions.⁽²⁸⁾

As far as we have confirmed fundamental properties of Sr^+ recombination laser as a potential high-power blue-violet laser,⁽²⁹⁾ the role of super-elastic collision is considered to be important on relaxation of the lower laser level.

For the aim getting super-elastic collisions, electrons in low energy are necessary, but high speed electrons being also necessary for getting Sr^{2+} ions by ionizing collisions. A novel idea and skillful technologies are necessary for providing both high and low energy electrons, and for an accurate measurements of plasma quantities like electron temperature, electron density, population density of relevant levels, distribution of emission spectra and so on at high repetition frequency pulse discharge.

Summary

The original idea to use the negative glow for laser pumping was reviewed. Some successes in developing a He-Cd⁺ white-light laser and its application to a full colour printer were introduced. Recent developments and new aspects on the white-light laser were discussed. The extract of this paper is summarized as follows.

Investigated

- (1) Hollow-cathode type He-Cd⁺ white-light laser was developed.
- (2) Prototype full colour printer was developed.

Expected

- (1) Some ideas for getting a direct modulation of He-Cd⁺ white-light laser were proposed.
- (2) A new candidate of high power white light laser consisting of

Au(I)	627.8 nm	(Red)
Cu(I)	510.6 nm	(Green)
Sr(II)	430.5 nm	(Blue)

 was suggested.

Acknowledgement

The author is grateful to Dr.C.E.Webb of Oxford University, U.K., Professor J.A.Piper of Macquarie University, Australia, and Dr.F.J.Duarte of Eastman Kodak Company, U.S.A. for their valuable discussions and suggestions.

References

- (1) K.Fujii: Trans.Inst.Elec.Engng.Japan 93-c, 1 (1973)(in Japanese).
- (2) S.C.Wang and A.E.Siegman: Appl.Phys., 2, 143 (1973).

- (3) K.Fujii, T.Takahashi and Y.Asami: IEEE J.Quantum Electron, QE-11, 111 (1975).
- (4) J.A.Piper and M.Brandt: J.Appl.Phys., 48, 4486 (1977).
- (5) J.Mizeraczyk, J.Konieczka, J.Wasilewski and K.Rozsa: Proc.Int.Conf. LASERS '80, New Orleans p177 (1980).
- (6) M.D.Ainsworth and A.I.McIntosh: J.Phys.D 16, L189 (1983).
- (7) W.Sasaki and T.Ohta: IEEE J.Quantum Electron. QE-18, 72 (1982).
- (8) K-H.Wong and G.C.Morgan: J.Phys.D 16, L1 (1983).
- (9) S.A.Ahmed and W.M.Keefte: J.Appl.Phys. 45 182 (1974).
- (10) H.P.Popp and E.Schmidt: IEEE J.Quantum Electron, QE-15, 840 (1979)
- (11) M.Takashima, S.Fukuda, S.Okada, H.Nishiyama and K.Fujii: Proc. 6th Int.Display Research Conf. Tokyo p446 (1986).
- (12) A.I.McIntosh, M.H.Dunn and I.K.Belal: J.Phys. D 11, 301 (1978).
- (13) M.I.Clarke and H.J.Oskam: Plasma Chem. and Plasma Proces. 1, 53 (1981)
- (14) A.Javan, W.R.Bennett, Jr., and D.R.Herriott: Phys.Lev.Lett., 6 106 (1961).
- (15) Y.Asami: Memories of the Faculty of Engng., Hokkaido Imp.Univ., 2, 1 (1929).
- (16) H.Kobayashi and Y.Oikado: Proc.Anual Meet.Inst.Elect.Communication. No.333 (1964).
- (17) J.Smith: J.Appl.Phys., 35 727 (1964).
- (18) G.R.Fowles and B.D.Hopkins: IEEE J. Quantum Electron., QE-3, 419 (1967).
- (19) Y.Sugawara, Y.Tokiwa: Japan.J.Appl. Phys., 9 588 (1970)
- (20) W.K.Scuebel: Appl.Phys.Lett., 16, 470 (1970).
- (21) E.K.Karabut, V.S.Mikhalevskii, V.F.Papakin and F.M.Sem: Soviet Phys.-Tech.Phys., 14, 1447 (1970).
- (22) M.Grozeva and N.Sabotinov: Opt.Comm. 41, 57 (1982).
- (23) K.Fujii, K.Kasai, M.Takashima and H.J.Oskam: Proc.8th Int.Conf.Gas Dis.and Their Appl., Oxford p.548 (1985).
- (24) F.Howorka and I.Kuen: Proc.XVith ICPIG Dusseldorf p560 (1983).
- (25) K.Fujii: Proc.10th Symp.Ion Source and Ion Assisted Tech., Tokyo p77 (1986).
- (26) C.E.Webb: Proc.LASERS '87, Lake Tahoe (1987).
- (27) K.Ouchi, Y.Yato and K.Fujii: Proc. Anual Meeting Appl.Phys.Japan to be published, (1988).
- (28) E.L.Latush, V.V.Zhukov, V.S.Mikhalevski and M.F.Sem: Proc.Int.Conf. LASERS '81, p1121 (1981).
- (29) K.Fujii, C.E.Little and J.A.Piper: Proc.Int.Symp.Short Wave-length Lasers and Their Appl. Osaka (1987) to be published.

ENGINEERING OF A MULTI-BEAM 300-WATT FLASHLAMP-PUMPED DYE-LASER SYSTEM

Patrick N. Everett, Staff & Byron G. Zollars, Staff

M.I.T. Lincoln Laboratory
P.O. Box 73, Lexington, Massachusetts 02173-0073

This dye-laser system will be used to conduct experiments at a field location. The engineering challenges will be discussed, as well as a 1/3-scale system which has been built to test the approach and help refine the design. Progress of the full system will be described. Operating performance of the 1/3-scale system will be described in a separate paper.

The requirements include five separate output beams, with 5 to 10 J/pulse in each beam at 10 pps. The individual pulses must be less than 2- μ s FWHM, with a spectral bandwidth less than 1 nm, at about 500-nm wavelength. Most of the energy must be within 20 times the diffraction limit. The goal is to have a significantly better beam quality. The system must perform for at least 10 minutes at full performance under mission conditions. This implies that the system must be able to run at equivalent of full power, without maintenance, for 30 minutes, allowing 20 minutes for final alignment and adjustment. A sixth beam is being added to increase reliability through redundancy.

The flashlamp-pumped dye-laser approach was selected in 1984, when the program was started, based upon equipment availability. Candela Corporation won a competitive procurement for a prototype single-beam module, and delivered the equipment in October 1985. This equipment is shown in Figure 1. It is a modified version of their commercial LFDL-20 laser. Two heads were supplied to form an oscillator-amplifier chain. Each head is 2 feet long, with a pair of linear water-cooled flashlamps. The dye flow is longitudinal in a cylindrical dye cell between the lamps. Camarin 504 dye is used, dissolved in 50/50 methanol/water mix. Modulators contain capacitors which are charged to 40 kV from the power supplies. The 500-J charge is switched into each flashlamp by triggered spark gaps. Circulator modules supply the dye and coolant flows, and include cartridges of activated carbon to clean out degraded dye and allow the solvent to be used again.

When the prototype equipment was tested at Lincoln Laboratory, it performed well enough to be considered as the basis for design of the system, but some deficiencies were noted. These included insufficient flow rate and thermal control, a tendency to arc over, and insufficient rigidity in mounting of the dye-cell windows. Candela Corporation has now delivered a second generation of equipment in which these problems have been addressed. This equipment is now in operation, and is performing satisfactorily. Some minor improvements are still being made and tested. The final hardware is now on order with expected delivery commencing before the end of 1987. Meanwhile the design of the 1/3-scale, and full-scale systems have been proceeding with the help of the following corporations.

A & R Associates	Coordination
A.L.E. Systems, Incorporated	Additional Power Supplies
Candela Corporation	Lasers & Consulting
Fels Company	Flow System Fabrication
Neurocon	(EMI Consulting)
Newport Corporation	(Vertical Optical Table)
SAIC, Incorporated	(Chemical Engineering, 1/3 Scale)
Sanders Associates, Incorporated	(EMI Testing)
Stone & Webster Engineering Corporation	(Fluid Handling Design)

A number of engineering challenges were recognized early in the program. The potential problem of flashlamp life was disposed of early, by testing at Candela that showed the lamps would last much longer than 30 minutes at 10 pps with insignificant loss in output. Beam quality has been found marginally good enough, with improvements expected. Optics have been damaged by the high lasing flux, attributed mostly to parasitics, and sometime to poor quality coatings or dust. The indications from this program and from elsewhere are that the optics should be able to withstand 10 J/cm² with the right care (2- μ m pulse). The level of oxygen absorbed in the dye solution is known to be a factor in the performance of some laser dyes. More oxygen generally decreases dye life, but often increases output for the pulse lengths by acting as a triplet quencher. In this type of system the dye is usually equilibrated with air, thus determining the oxygen content. Existing data is insufficient to estimate the effect of equilibrating at the higher elevation where the experiment will be conducted. This uncertainty will be dealt with by providing a pressurizable closed system to allow optimization of oxygen content. Other engineering challenges will be dealt with in successive paragraphs.

Output of such a dye laser drops as a result of degradation of the dye solution under the intense illumination from the flashlamps. The major problem arises from the degradation products which absorb light at the absorbing wavelength. With the currently used dye solution (solvent is acetamide/water 30% by weight), we observe a 10% drop in output when the dye solution has been exposed to about 1.5 kJ of pump energy per liter of total dye solution. At this rate an impractically large reservoir of 30,000 gallons of dye solution would be needed to run for 30 minutes with no more than 10% drop in output from dye degradation, if no real-time dye-solution regeneration were employed. For a practical system, real-time regeneration at up to the full flow rate of 360 gpm will be needed. This will be accomplished by diverting as much of the dye flow from the lasers as is necessary through a bank of activated carbon cartridges, as indicated in the flow schematic of Figure 2. The condition of the dye solution will be continually monitored by a pair of in-line optical analyzers in a diagnostic loop. One of these will have an optical path of 1 m, and will measure the optical transmission at 520 nm. This is sufficiently beyond the lasing wavelength to be just clear of the pump absorption band. However it is also sufficiently close to the lasing wavelength to catch the broad-level absorptions which will affect the lasing. It is found with this instrument that a 4% loss of transmission correlates with 10% drop in lasing output. This transmission measurement will be the input to the control

system which will regulate the speed of the pump that drives dye solution through the activated carbon. The system will strive to maintain the 520-nm transmission at a level insuring no greater than 10% loss in lasing output on this account. Since the carbon removes dye as well as degradation products, another system is needed to replenish the dye. This will be achieved by using the second optical analyzer, with a 1-mm optical path and measuring at 450-nm wavelength, to measure the dye concentration. This will control the speed of a metering pump that adds dye concentrate to the system. This control system will give automated maintenance of the dye solution under conditions of full-power output, idling at no output, or running with varying numbers of lasers. Hence it will be a very flexible system.

Temperature and flow control must be sufficiently precise whether the system is idling in standby mode, operating intermittently with a reduced number of heads, or operating with all heads at full power. Since temperature variations of even less than 0.1°C are believed to have bad effects on the beam quality (as a result of refractive-index variation within the dye cell), the system will be run with all fluids maintained close to the ambient room temperature, and to each other to minimize temperature gradients. The power dissipation into the fluids will vary between 250 kW when running at full power and maybe a few kW when idling. The schematic of Figure 3 serves for the dye and the coolant systems. In each case a feedback system controls the flow of chilled water through a heat exchanger to restore the liquid leaving the laser heads to the controlled temperature. The chilled water comes from a 10,000 gallon tank of water which will absorb the transient loads of the system and itself be cooled at a slower rate by transferring the heat to external air by a lower powered chilling system. Flow rate in each laser head will be maintained at the design value of 30 gpm for dye solution and 20 gpm for coolant, independently of how many lasers are flowing, by use of inlet and outlet manifolds maintained at a constant pressure differential. The speed of the pump will be automatically varied under the control of a feedback system to maintain the optimum pressure differential. Electromagnetic Interference (EMI) is of concern. The curve of Figure 4 was obtained by Sanders Associates when measuring the broad-band radiation from the Candela prototype system operating at reduced voltage and pulse rate. Also shown is the target curve which is desired to ensure compatibility with other equipment at the experimental field site. The situation is worst at 30 MHz, where the radiation was 100 db above target. Because of these results we are being very careful about EMI precautions in the design, and will wrap a screen room around the laser equipment.

Flammability of the dye solvent is of concern. The laser performance was initially demonstrated with a 50/50 water/methanol mix as the solvent for the coumarin 504 dye. More water helps beam quality, and reduces flammability but at the expense of output energy. There were serious concerns about flammability of even the 50/50 mix (roughly the same as 100 proof Scotch). So we have tried to find a safer solvent. We found 50/50 ethylene glycol/water would give the same beam quality, but with only 50% of the output energy. However recent tests with 30% by weight of acetamide in water, as a solvent, have yielded the same performance as the methanol/water mix but at some loss in dye life. The lower dye life can be handled by the cleaning system, so is acceptable. Because we have to provide for the possibility of a flammable solvent, the dye handling room has been designed as a Class 1, Division 2, Cutoff room, with blow-out panels.

Space is very limited at the field site where the equipment will be installed. The space problem, as well as need for short cables between Modulators and Laser Heads, and need for 144 individual fluid tubes, 24 high-voltage cables, and diagnostic cables, to enter the laser heads, has led to a vertical optical table. The Laser Heads will be mounted on the front surface, with the optics. The electrical and piping services and diagnostic cabling, will pass through from the back of the bench. Additional space will be saved by using a newer design of power supply from A.L.E. Systems Corporation. In general the design has had to be tight.

Because of the innovative features, and difficulty of doing development work on site, we embarked on a 1/3-scale system at Lincoln Laboratory. The purposes are to make sure the approach is sound, characterize the laser heads at full repetition rate, do development as necessary, and generate design information for the full system. The 1/3-scale system is now in operation and is proving very useful in the above tasks. It is also providing a test bed for developing the diagnostic and aligning techniques. It is providing valuable data to help fine-tune the design of the full system.

A photograph of the 1/3-scale system is shown in Figure 5. It uses a vertical table supplied by the Newport Corporation. The laser heads are kinematically mounted on platforms and go through a standardized alignment procedure so that minimal realignment is necessary when they are replaced. They are mounted within EMI enclosures (shown with covers removed). The services penetrate the vertical table through wave-guide tubes which cut off escape of frequencies below 2 GHz. The lasing light is likewise carried out through wave-guides to minimize EMI. The optical layout of the system will be described in more detail when discussing the full system.

The dye-handling skid for the 1/3-scale system was designed and fabricated by SAIC Incorporated, and two views of it are shown in Figure 6. It is about 6 feet tall, and contains the reservoir, variable speed pump, heat exchanger, carbon cleaning system, and control equipment. It is situated in a Class 1, Division 2, Cut-off Room so that flammable solvents can be used. The in-line optical analyzers, from Anacon Corporation are mounted on the wall above the dye skid, and are shown in Figure 7. We believe that inclusion of such instruments to give real-time monitoring and control is a new development. They are extremely useful in diagnosing problems as well as in controlling the cleanup and dye addition. The 1-m path analyzer shows virtually 100% transmission when the dye solution is optimally clean, and about 96% transmission when the degradation is such that the laser output has dropped by 10%. If this analyzer were to have a shorter path its measurements would not be sufficiently precise.

The coolant skid is shown in Figure 8. It is similar to the dye-skid except for the cleanup components. It also was designed and supplied by SAIC, Incorporated. The photograph of Figure 9 shows the services behind the vertical optical table of the 1/3-scale system. These services include the piping, manifolds, modulators, thermal equalizers, and instrumentation including a flow meter for each fluid through each laser head. The thermal equalizers are heat exchangers, one for each head, through which the dye and coolant going into a head are brought to the same temperature. This is additional to the previously mentioned active temperature control. The piping to the individual laser heads is of polypro-

pylene plastic to allow flexibility and minimize vibrations reaching the optical table. The wave-guide tubes can be seen for taking the services through the bench to the laser heads. Unions in the piping allow disconnection of the tubing so that any laser head can be withdrawn for servicing. Individual valves in all the lines make this practical.

The site where the equipment will be used is subject to some vibration. Measurements of vibration at the site, and computer modeling, indicated that a steel and concrete monolith structure, built along the lines of those used by Lawrence Livermore National Laboratory for the AVLIS program would be suitable. The photographs of Figure 10 show the bench under construction at the site, on a 3-foot thick concrete slab. Modeling indicates that all parts of the table surface will have a directional stability within $\pm 15\text{-}\mu$ radians, which is within a diffraction angle of the 1-cm beam diameter that will be used on the vertical table. The skin is of 1/4" steel plate, which acts as a former for the 18" thick filling of concrete. The first photograph shows anchors being stud-welded at 1-foot centers on the back of the skin to ensure bonding to the concrete. The second shows the plates going into position, where they are welded edge to edge, and held apart by spacer bolts on 2-foot centers. The third photograph is looking down into the top of the bench, nearly ready for the concrete pour. The network of anchors, spacing bolts, and wave-guide feed-throughs, which will be immersed in the concrete, can be seen within the bench. The fourth photograph shows the back of the bench, and some of the wave-guide tubes can be seen. This construction is sometimes referred to as Maginot Line architecture!

The proposed layout for the full-size optical table is shown in Figure 11. It closely follows the arrangement that has been developed for the 1/3-scale system. The six laser beam paths can be seen, which are independently transmitted off the table by the beam-steering mirrors at the top right-hand corner. Each beam comes from a laser made up of two laser heads within a confocal unstable resonator with a magnification of approximately 3. This "double-dip" approach overcomes some of the parasitic problems experienced with the original oscillator-amplifier approach. For alignment, a single over-sized argon-ion laser beam passes through a series of beamsplitters which divert about 5% of the beam into each of the resonators, through its annular output coupler. In each case, if alignment is correct, the "tag" beam condenses to the diffractive core as it bounces back and forth within the resonator. It then expands again on successive passes until it emerges as a collimated beam which duplicates the lasing output when the laser heads are excited. Consequently, as well as providing the alignment aid for the resonators, these "tag" beams then propagate along the output paths of the laser beams, and allow successive optical components to be correctly aligned all the way to and through the experiment. This one "tag" laser source thus provides for the alignment of all six resonators as well as their output paths. The chain of beamsplitters which directs the "tag" beams into the resonators also diverts a portion from each of the laser outputs, when they are fired, into the diagnostic system at the top middle of the vertical table. These diagnostics include pulse energy, shape and timing, spectrum and calibrated far-field distribution. The lasers are spectrally tuned using birefringent filters. These filters are placed slightly off the optimal angle so that enough lasing energy is reflected into a TV camera to monitor the internal lasing energy distribution. In addition, fiber-optic pickoffs transmit light from each of the 24 flashlamps, and are multiplexed into a centralized lamp monitoring system for diagnosis of lamp health and aging. Current transformers are also included adjacent to the lamps for monitoring the individual discharge currents. The diagnostic signals, wherever possible, will be carried away from the vertical table area, and through the screen room walls, via fiber optics passing through wave-guide feed-throughs. CAMAC equipment is being used extensively. The laser beams also will be propagated out of the screen room through wave-guides, and individually transmitted to the experiment through spatial filters for cleaning up of the beams and to give alignment references as illustrated schematically in Figure 12. The focal lengths are several feet, resulting in large enough apertures that burning is not expected to be a problem if the materials are chosen carefully.

The screen room will be wrapped around the optical table area, as illustrated in Figure 13. Its floor will cover the concrete slab which is under the vertical optical table. It will be carefully isolated from vibrations originating elsewhere. Over 200 penetrations are needed, including 48 pipes to flow about 600 gpm of fluids in and out.

The fluid handling equipment for the fixed system has been designed by Stone & Webster Engineering Corporation, and is being fabricated by the Fels Company. Photographs of the equipment, near completion are shown in Figure 14. The first photograph shows about 75% of the equipment. The other photographs show individual components. Note that the dye-cleaning equipment, although sizeable, is a relatively small part of the overall system. It is believed that, with the lessons we are learning, a future such system could be made considerably smaller. In this system we have had to design conservatively because of lack of a design base of similar systems.

The piping within the screen room is also being fabricated by the Fels Company. Because of its complexity it is being mocked up, at Fels, in a plywood model of the screen room area. A photograph of the mockup is shown in Figure 15 together with a photograph of the back of the vertical table on site, now with the concrete poured. The wooden structure in the first photograph is the model of the back of the vertical table. This area will be very full of equipment when all the pipes, thermal equalizers, modulators and instrumentation are in place.

In summary, a 1/3-scale system allowing four heads to be operated at full power, or six heads at reduced power, is now in partial operation. Its performance will be reported in a separate paper. The full system is expected to be the largest operational flashlamp-pumped dye laser system in the free world. It should be partially operational on site in March 1988, and full operational later in 1988. At least 300-W average power should be obtained, mostly within $20\lambda/D$ or better, in six independent beams each running at 10 pps with more than 5 J/pulse at about 510-nm wavelength.

We wish to acknowledge assistance from the following: E. D. Ariel, R. E. Hatch, J. M. Mahan, J. L. Swedberg.

This work is sponsored by the Defense Advanced Research Projects Agency, Directed Energy Office, through the Department of the Air Force.

"The views expressed are those of the authors and do not reflect the official policy or position of the U.S. Government."

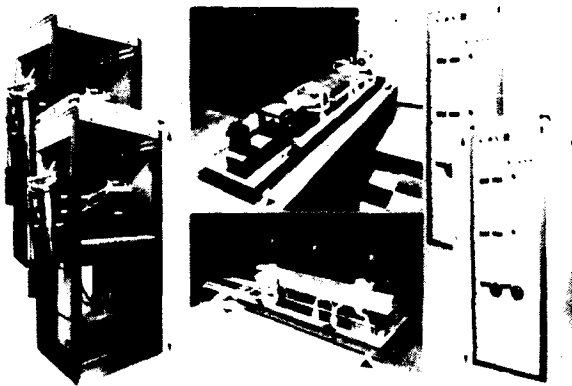


Fig. 1. Prototype laser equipment.

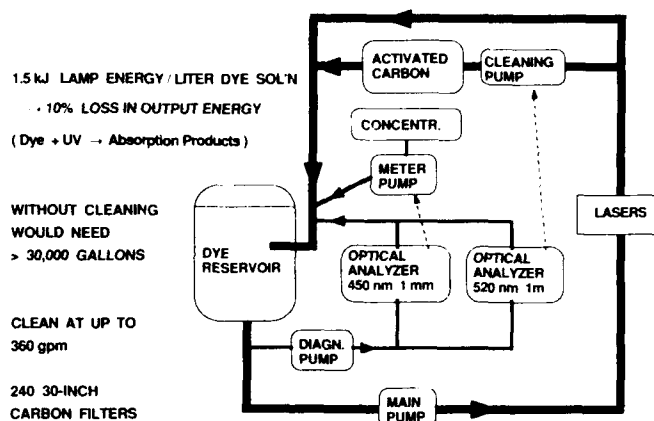


Fig. 2. Dye circulation schematic.

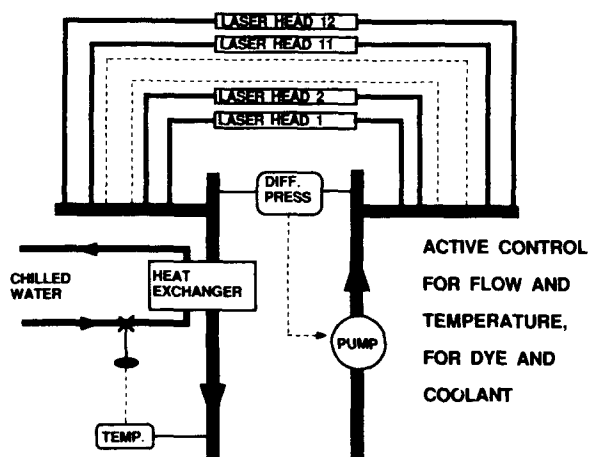


Fig. 3. Flow and temperature control.

(Prototype Tested at 5 pps, 28 kV, 2 Laser Heads)

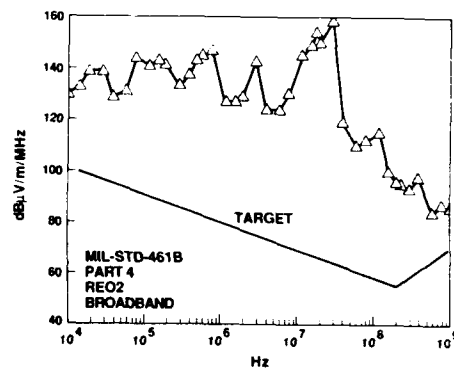


Fig. 4. Electromagnetic interference.

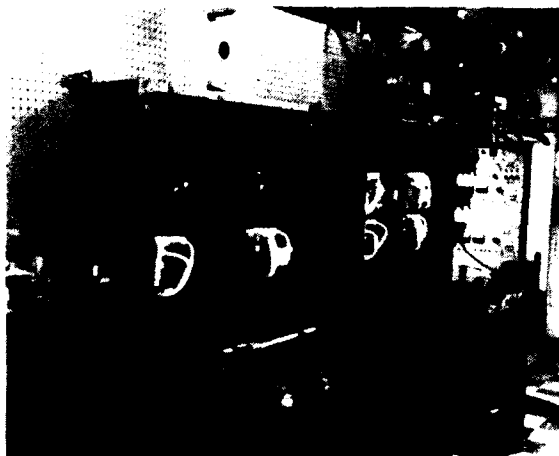


Fig. 5. 1/3-scale system.

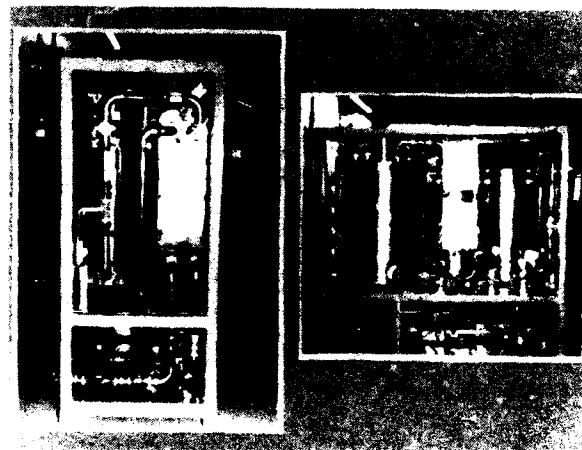


Fig. 6. 1/3-scale dye-handling skid.



Fig. 7. In-line optical analyzers.



Fig. 8. 1/3-scale cooling skid.



Fig. 9. Behind the vertical table.



Fig. 10. Progress toward the full-size table.

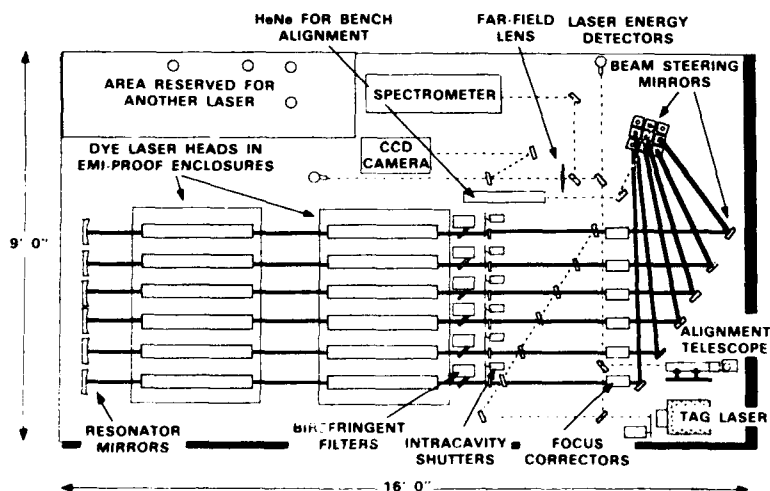


Fig. 11. Layout on final table.

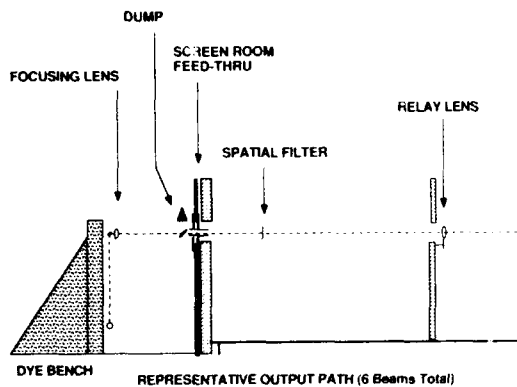


Fig. 12. Projection of beam to experiment.

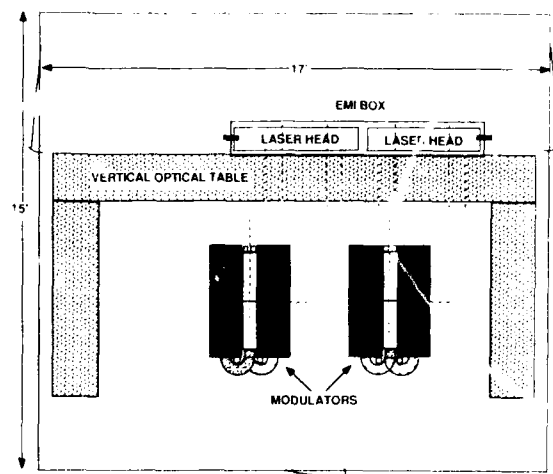


Fig. 13. Screen Room.

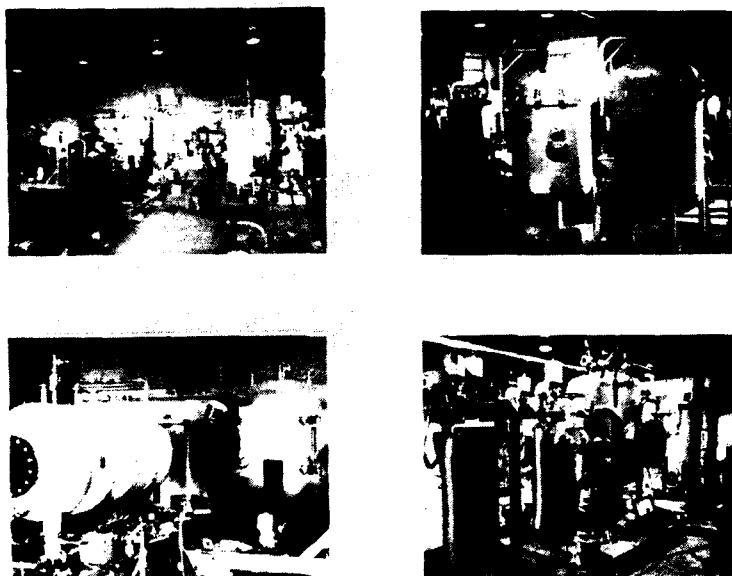


Fig. 14. Fluid handling equipment in progress.



Fig. 15. Piping mockup and vertical bench.

PERFORMANCE OF A PROTOTYPE MODULE OF A 300-WATT FLASHLAMP-PUMPED DYE LASER

Byron G. Zollars, Staff & Patrick N. Everett, Staff

M.I.T. Lincoln Laboratory
P.O. Box 73, Lexington, Massachusetts 02173-0073

ABSTRACT

Recent performance measurements on a prototype module of a multi-beam, flashlamp-pumped dye-laser system are discussed. Measurements of the total output energy of the dye laser, and its distribution in the far field are presented for operation at a 5-Hz repetition rate. The implementation of a real-time dye-regeneration system and the choice of an optimum dye solvent will be addressed.

A large, multi-beam, flashlamp-pumped dye-laser system is being constructed by Lincoln Laboratory for a field experiment. This paper presents performance measurements that were made on a prototype module of this laser system. A test bed has been assembled at the Laboratory that has the capability of supporting two of these dye-laser modules, and implements many of the unique features of the final system, such as on-line laser performance diagnostics and the capability to overcome the detrimental effects of finite dye lifetime during operation of the system.

The full-scale laser system must meet several requirements for the proposed field experiment. A total of six laser beams (one of which is a spare) must be able to operate continuously for 30 minutes at a 10-Hz repetition rate, with each laser providing from 5-10 Joules of energy per pulse, with at least 2 Joules within a $10\lambda/D$ divergence angle. The lasers are required to operate at a wavelength of approximately 500 nm, with about a 1-nm bandwidth. The requirements for wavelength and bandwidth are not stringent, and are easily met with the present equipment. Since the prototype laser module and the two-beam test bed discussed here were designed and built to satisfy the same requirements as for the full-scale laser system, the measurements presented herein are indicative of the expected performance for the dye lasers that will be used for the field experiment.

The laser system test bed has fluid control, cooling, and electrical support for two separate laser beams working at full output power. There is also a provision for operating three laser beams at a reduced power level. This system has been operational since June of this year with one laser beam installed, and has yielded valuable data on both laser performance and engineering aspects which can be directly applied toward the design of the final laser system.

Among the innovative features of the dye-laser system is the ability to run the lasers for extended periods of time without suffering the deleterious effects of dye degradation. Instruments monitor the level of photodegradation products in the dye process stream and direct a fraction of the dye into a carbon adsorber, where the degradation products are removed. Since the carbon adsorber also removes the laser dye, other instruments add the correct amount of concentrated dye solution, keeping the concentration at the desired level. Other instruments continuously control flow rates and temperatures of all the process fluids in the system.

Various diagnostic instruments also provide information on the status of the lasers. Quantities such as laser energy and beam quality, flashlamp output in the dye-pump band, and spectral lineshape are recorded on a pulse-by-pulse basis, with the aid of a Digital Equipment Corporation MicroVAX II computer. These data are then used to determine the performance of the dye lasers.

The configuration of the laser equipment is presented schematically in Figure 1. All of the optics in the laser system are mounted on a vertical optical bench. Each dye laser in the system consists of two identical laser heads, which are mounted within the same unstable optical resonator. Each laser head has a longitudinal dye flow, and is pumped by the output from two close-coupled linear xenon flashlamps. The total pump energy provided by the four flashlamps in the laser is 2,000 Joules. The dye solution consists of Coumarin 504 in a solvent of 30 wt% acetic acid amide in water. The choice of this particular dye solvent will be discussed later. Spectral control is provided by a single-plate birefringent tuning element. Currently, two laser heads are mounted in the center beam position on the optical bench.

For the present measurements, the majority of the laser output is collected by a calorimeter, which measures the total energy of each laser pulse. In addition, a small amount of the beam is collected and focused onto a CCD (charge-coupled device) camera for analysis of the focal-plane image. This image yields information about the beam divergence of the dye laser. Because the CCD camera is so sensitive, we use an uncoated fused-silica wedge to attenuate the laser beam. By tilting the wedge, beams which undergo successive reflections from the internal surfaces emerge at different angles. Each such beam has a different and easily calculated attenuation. Another advantage of this technique is that the attenuation produces no thermal wavefront aberrations.

Other beams from the attenuation wedge go to a spectrometer, a fast photodiode, and a second calorimeter which collects the energy that passes through an aperture placed in the focal plane. This calorimeter is used to provide a radiometric calibration of the CCD camera. For alignment purposes, an argon-ion tag laser beam can be injected into the laser resonator, and upon exiting, can be used to align all of the elements in the optical train. In addition, an alignment telescope is used for coarse boresight alignment of the laser heads relative to one another.

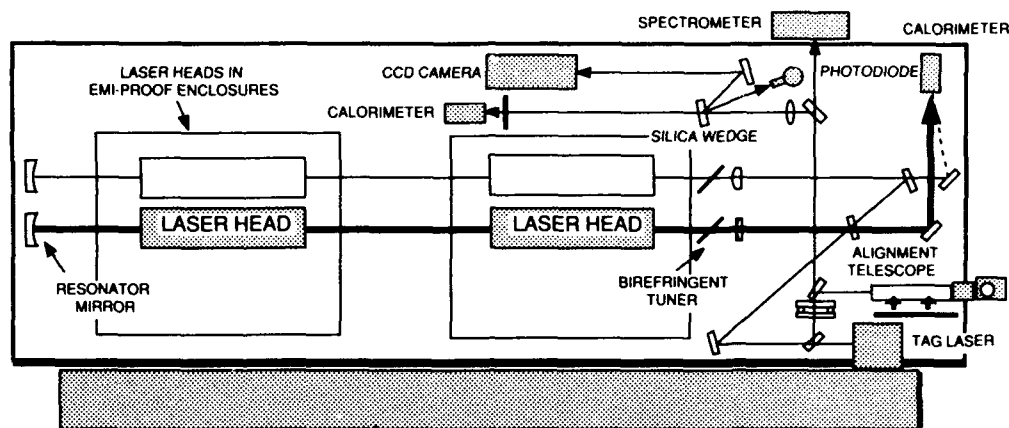


Figure 1: Dye laser equipment configuration

Figure 2 shows the total output energy of the dye laser as a function of the electrical flashlamp pump energy. The resulting curve provides data on the efficiency of the laser. The lasing threshold is observed to be about 500-J pump energy, and the efficiency at 2,000-J pump energy is about 0.35%. These data demonstrate that we can obtain about 7 J per pulse at the maximum available pumping level, which falls roughly in the middle of the 5-10 J per pulse total energy requirement for the lasers.

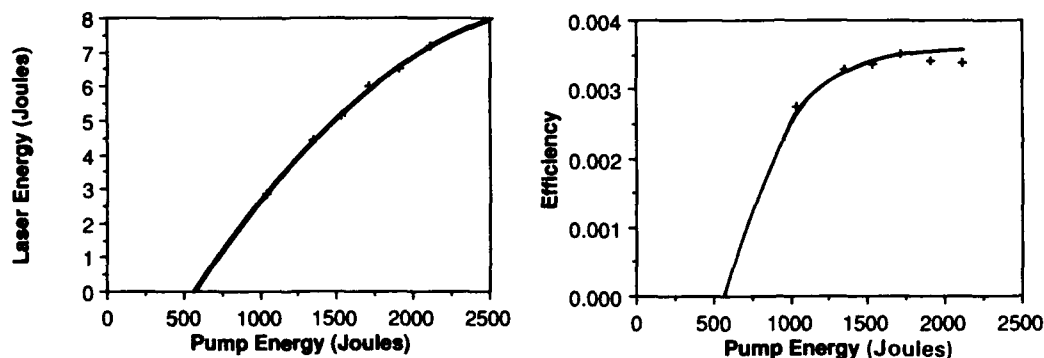


Figure 2: a) Dye laser output vs. electrical pumping energy.
b) Efficiency of dye laser as a function of pumping energy.

In order to determine the beam quality of the laser, the output is focused to the far-field with a long-focal-length lens, and the resulting focal spot is imaged with a computer-controlled CCD camera. This image is processed by the computer to yield energy-in-the-bucket curves, which are used to gauge laser beam quality. The CCD camera consists of a 64 x 64 square array of pixels. Each pixel is about 27 μm on a side, so the entire array is approximately 1.7 mm on a side. For the present measurements, the CCD array subtends about $35 \lambda/D$.

The only way to obtain unambiguous energy-in-the-bucket results from a focal plane imaging device is to radiometrically calibrate it. Figure 3 shows a schematic diagram of the apparatus used for our calibration procedure. Approximately 3% of the dye-laser output is directed through a 2.0-meter focusing lens, and then into the fused-silica wedge (attenuator) described earlier. Most of the light passes straight through the wedge and is collected by a calorimeter located past the focal plane of the lens. A 1.0-mm diameter diamond aperture is then placed in this focal plane, at a position so as to maximize the amount of laser energy transmitted through it. One of the output beams from the wedge, which has been attenuated by about 10^6 is selected and directed into the array of the CCD camera. The CCD imaging array is also located at the focal plane of the 2 meter lens.

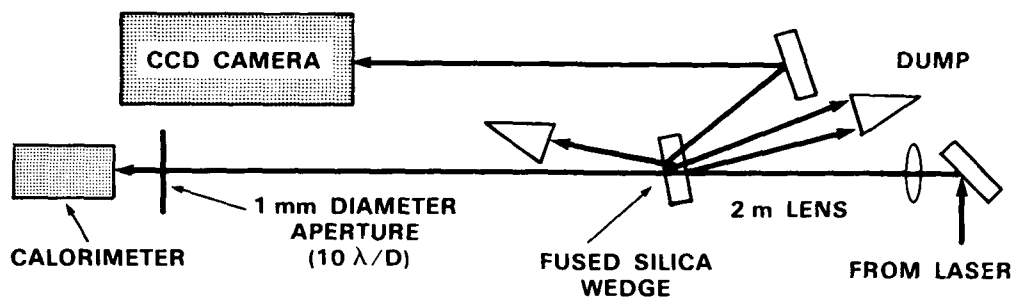


Figure 3: Apparatus used for radiometric calibration of the CCD camera.

During subsequent laser pulses, the focal plane image and the calorimeter reading are recorded. Since the dimensions of the CCD array within the camera are well known, one can, with the computer, form a circular "mask" which is 1.0-mm diameter and center this mask on the centroid of the far-field image. Now, the sum of the values of the pixels within the mask correspond directly to the energy read by the calorimeter, which also records the energy falling within a 1.0-mm aperture in the focal plane. The ratio of these numbers (and the relative attenuation in each path) gives the responsivity of the CCD camera.

Figure 4 shows a typical far-field intensity profile as recorded by the CCD camera. These data are of a single laser pulse taken from a run made at 5-Hz repetition rate. Integrating the pixel values contained in successively larger circles (centered on the image's centroid) yields the energy-in-the-bucket data for this pulse, which is shown in Figure 5.

From a qualitative inspection of the far-field image, one might be tempted to conclude that most of the energy in the laser is falling within approximately a $15 \lambda/D$ divergence angle, since the values of those pixels outside this angle have such small values. The radiometrically calibrated energy-in-the-bucket curve however, indicates that only about 4.3 J of the total energy of 7.0 J falls within a $20 \lambda/D$ angle, with the other 2.7 J of the beam energy falling within larger divergence angles, which are outside the field of view of the CCD camera. This is a graphic example of the "fried-egg effect", and points to the importance of using radiometrically calibrated far-field imaging devices for quantitative measurements of laser beam quality.

It was rather disturbing to see that only a fraction of the total beam energy resided within a $10 \lambda/D$ divergence angle, especially since dye lasers that use unstable resonators are reputed to have almost diffraction-limited output. In our case, we believe the main reason for our sub-standard beam quality is due to the flow of the dye solution through the laser head. The dye encounters several short-radius bends, restrictions, and sharp edges at the input and output ends of the laser head, and there is ample opportunity for flow cavitation and vortex shedding to occur. The resulting index variations in the media impress wavefront aberrations on the laser output. The result is relatively poor beam quality.

To test this hypothesis, we injected the diffraction-limited argon-ion tag laser beam into the laser resonator and let it sample the index variations of the laser media. This gives a simple probe of the "baseline" beam quality we can expect to obtain from the dye laser when it pulses. Figure 6 shows the results of such a measurement. The tag laser, upon emerging from the laser resonator, is passed through the same far-field imaging apparatus used for the dye-laser measurements. The beam quality parameter β (roughly the focal-spot diameter in units of λ/D) is then measured as a function of dye-flow rate through the laser head. There is obviously a strong correlation between beam divergence and the flow of the liquid media. This discovery has prompted a series of design changes to the laser head fluid distribution manifolds. Preliminary tests with these newly designed manifolds show both a more uniform and higher dye-flow rate. In spite of the poor medium quality at our operating flow rates, we can still attain approximately 3 J within a $10 \lambda/D$ divergence angle, which exceeds the basic requirements for the field experiment.

Also of interest is the fluctuation of the laser output energy during operation. During one data run at a 5-Hz repetition rate, far-field image data was taken every few seconds. The results from these measurements are shown in Figure 7. Measurements were limited to a repetition rate of 5 Hz because inadequate dye flow through the laser did not provide enough exchanges of the dye medium between pulses at higher repetition rates. The graph shows the total laser output energy, as well as the energy contained within divergence angles of 9, 14, and $18 \lambda/D$.

At the beginning of the data run, the repetition rate was slowly ramped from 1 Hz to 5 Hz and ramped back down to 1 Hz at the end of the run. As a result, the first and the last few images were taken at repetition rates lower than 5 Hz. These images seem to have a lower energy-in-the-bucket than images taken at 5 Hz, even though the total energy was roughly the same. This is really an artifact of the energy-in-the-bucket measurement. During operation, the laser media acts somewhat like a lens due to the thermal gradients induced by the flashlamp pulses. The amount of spherical power imparted to the laser output by this "thermal lens" is roughly proportional to the average heat input, and hence the pulse repetition rate. During these measurements, the CCD camera was placed at the optimum focal distance for operation of the laser at 5 Hz. When the laser is operated at any other repetition rate, the degree of "thermal lensing" will be different, and hence the far-field image seen by the CCD camera will be out of focus, leading to a lower measured energy-in-the-bucket.

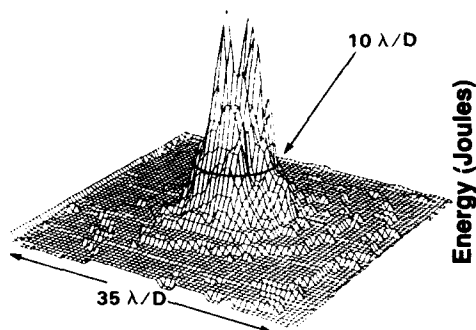


Figure 4: Far-field energy distribution of a typical dye laser pulse.

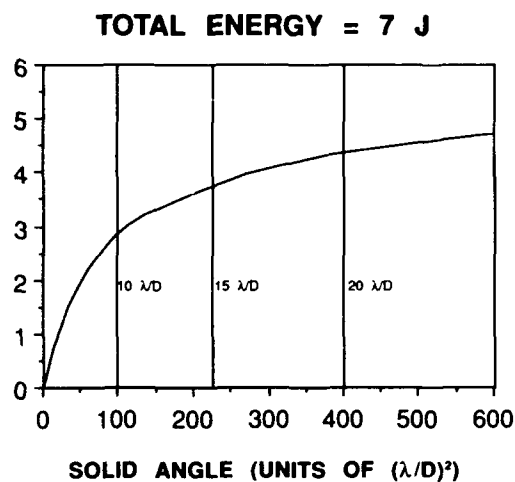


Figure 5: Energy-in-the bucket curve for the far-field distribution of figure 4.

Figure 6: Measured beam quality of the argon-ion alignment laser, as a function of dye flow rate in the laser head. The β parameter is approximately equal diameter of the focal-plane image, in units of λ/D .

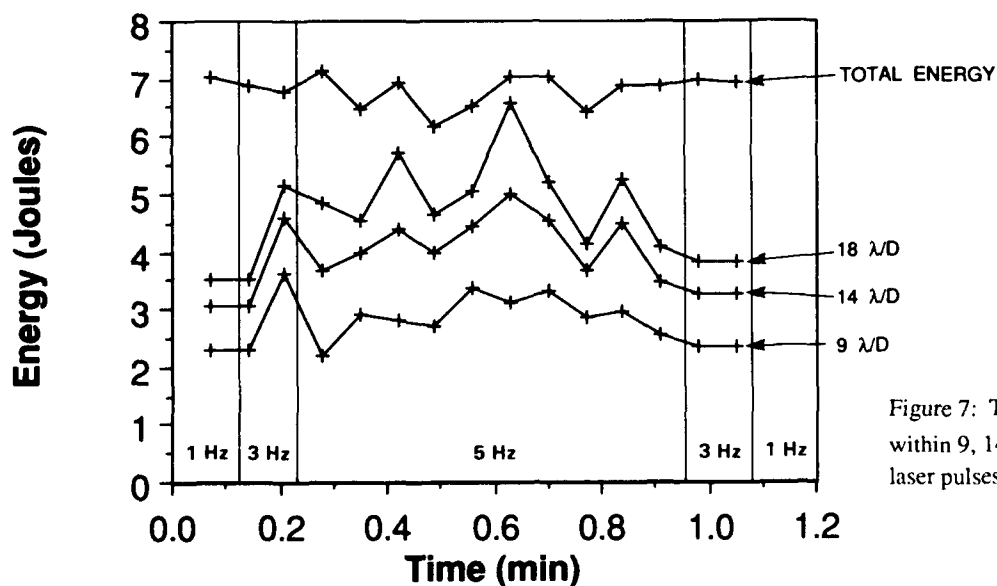
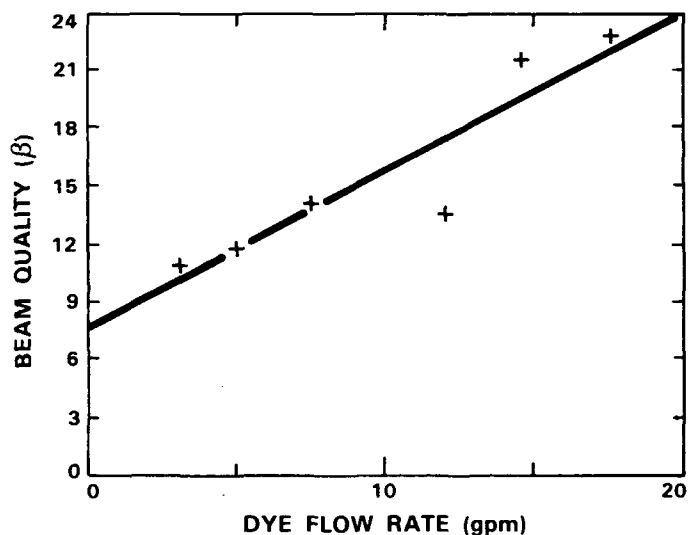


Figure 7: Total dye laser energy and energy within 9, 14, and 18 λ/D for a sequence of laser pulses taken at different repetition rates.

In an effort to measure the pointing-angle jitter of the laser, we acquired image data every few seconds during an extended run at a 5-pps repetition rate. For each of the far-field images taken during the run, the centroid of the image was found. Figure 8a and 8b show the pointing jitter about the laser axis in the X and Y directions during the run. There are no observable systematic changes in the pointing angle; the jitter appears to be random. Figure 9 shows the two-dimensional scatter of the centroid. About the X-axis, the standard deviation of the pointing jitter is $4.3 \lambda/D$, and for the Y-axis $3.1 \lambda/D$. Both of these numbers represent an uncertainty in the pointing angle of less than $1/2$ of the $10 \lambda/D$ beam diameter. This poses no problem for the field experiment. The laser head dye-flow modifications mentioned previously will most likely also improve the pointing characteristics of the lasers, since the jitter probably is a result of the tilt component of the flow-induced aberration in the media.

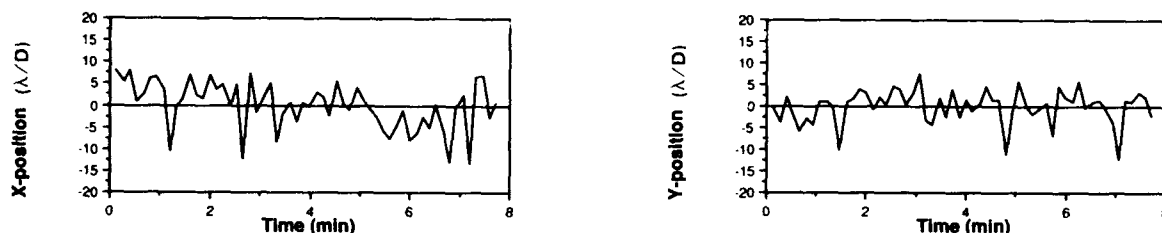


Figure 8: a) Fluctuation of the X-component of the far-field image's centroid. b) same, but for Y-component.

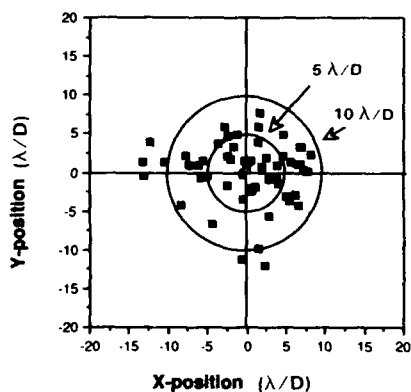


Figure 9: Two-dimensional scatter of the centroid of the far-field image. The diameters of the two circles represent motion of $5 \lambda/D$ and $10 \lambda/D$.

The finite lifetime of the laser dye against flashlamp exposure is a major concern in any large dye-laser system. The dye lifetime, for our application, is defined as the total number of kJ of pump light, per liter of dye solution, necessary to bring about a 10% reduction in the laser output. The dye molecules are allegedly destroyed in a photochemical reaction with oxygen dissolved in the dye solution. This reaction produces compounds which absorb light at the laser wavelength, leading to losses in the laser cavity, and hence lower output energy. It is also known that the solvent plays some part in the reaction, since the same dye in different solvents exhibits different lifetimes.

Figure 10 shows laser energy as a function of flashlamp exposure for Coumarin 504 dye in 30% acetic acid amide and water. The data was taken at Candela Laser Corporation (under Lincoln Laboratory contract) with a single laser head in an unstable resonator. The dye lifetime inferred from these data is 1.5 kJ/liter. It is interesting to note the impact of this dye lifetime on the operation of both the prototype and full-scale laser systems. With the 700 liter dye reservoir size of the prototype laser system, if a real-time dye-cleanup system were not available, two laser beams, each running at a 10-Hz repetition rate, would degrade to 90% of their initial energy after only 30 seconds. The full complement of 6 lasers running at 10 Hz in the full-scale laser system would need only 1 minute to reach the same fate. But the lasers are required to run for 30 minutes before losing this much output energy. Another option is to increase the size of the dye reservoir to obtain longer effective run times. If this were done for the full-scale system, the dye reservoir would be required to hold 36,000 gallons of dye solution! It seems clear that a real-time dye-cleanup system is the best option, considering the alternatives.

In an investigation of the role of dissolved oxygen on the dye lifetime, Candela removed oxygen (which is thought to be one of the photodegradation reactants) from the dye solution by bubbling nitrogen through it overnight. The resulting dye lifetime is compared to that obtained after bubbling air through the solution overnight. Figure 11 shows the results of this experiment. In both cases, the dye lifetime is about 1.5 kJ per liter, indicating that the formation of the degradation product does not seem to depend strongly on the available dissolved oxygen. It is also interesting that the energy decreases uniformly after treatment of the dye solution with nitrogen. This is probably due to the fact that oxygen is necessary in the dye solution as a triplet quencher for the dye molecule.

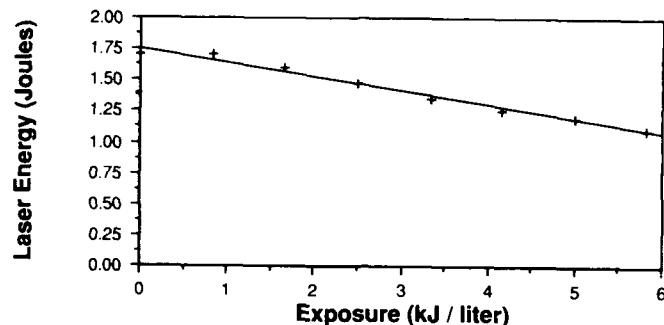


Figure 10: Laser output energy vs. flashlamp exposure. The dye solvent is 30 weight percent acetic acid amide in water.

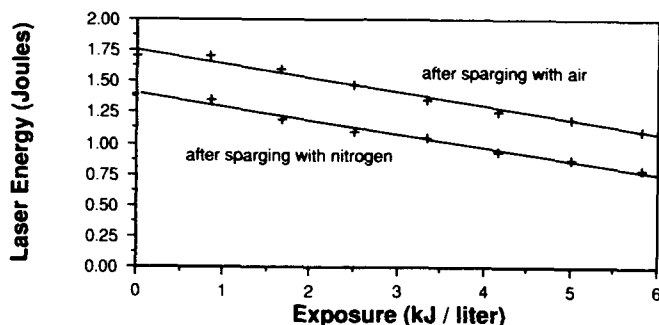


Figure 11: Laser output energy vs. flashlamp exposure, after bubbling air and nitrogen through the dye solution.

With such small values of dye lifetime, the effectiveness of the real-time dye-cleanup system becomes an important consideration. Figure 12 and 13 show the results of measurements of the degradation cleanup capability and dye-addition rate, respectively. Dye solution that had previously been degraded (by flashlamp exposure) to a level representing a 20% laser energy loss is passed through the carbon adsorber at a known flow rate, and then returned to the reservoir. The resulting exponential decrease in the concentration of the degradation component is plotted in Figure 12. The concentration of the degradation compound is directly related to the laser energy loss, and is measured with a 1.0-meter optical analyzer. Knowing the system volume and flow rate, these data yield information on the fraction of degradation product removed from the dye process stream in a single pass through the carbon adsorber. The data indicate that from 95% to 100% of the degradation component is removed by the adsorber in a single pass.

The carbon adsorber also removes dye with equal efficiency, so during operation of the laser system, dye must be added to the reservoir to replace the amount that is removed by the carbon. In the prototype laser system, for example, if all of the dye solution returning from the laser heads was passed through the carbon adsorber at maximum system flow rate, dye would be removed by the carbon at 84 $\mu\text{moles/sec}$. For the real-time dye-cleanup system to work then, we must have the capability of adding dye to the reservoir at least that fast. Figure 13 shows a measurement of dye concentration vs. time during the metered addition of a dye concentrate solution to the main dye reservoir. In this case the dye concentration was measured by a 1-mm path optical analyzer. The slope of the curve shows the capability of adding dye at rates of 90 $\mu\text{moles/sec}$, which exceeds the removal rate by the carbon adsorber. What these data demonstrate is that even under worst-case conditions, where the dye during a single laser pulse is completely converted to degradation compound, we can pass all solution returning from the laser heads through the carbon adsorber, removing virtually all of the dye degradation component. Since we can add dye at least as fast as the carbon adsorber removes it under full-flow conditions, we are assured of the ability to maintain a constant working dye concentration.

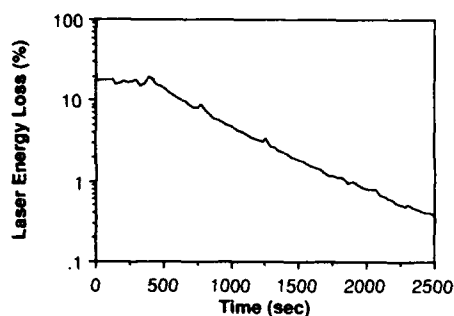


Figure 12: Concentration of dye degradation product (in terms of the laser energy loss it would produce) vs. time. The dye laser was not pulsing during this measurement.

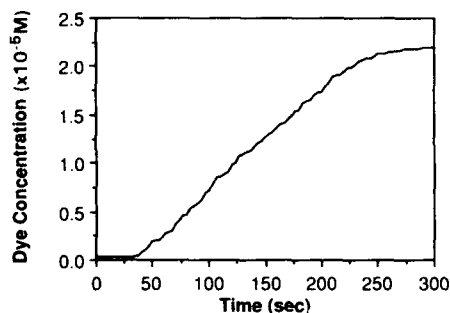


Figure 13: Dye concentration vs. time during the addition of dye concentrate solution. The working concentration is 2.2×10^{-5} moles per liter.

During development of the prototype laser system, three different dye solvents have been used, each with its own advantages and disadvantages. These are listed in the following Figure 14. The acetic acid amide solution seems to be the best choice from a performance and safety hazard point of view, because of its non-flammable and non-toxic properties. The short lifetime of C504 in this solvent is a drawback, but since the full-scale laser system is being designed with the capability to remove degradation compounds, and restore the dye to the proper concentration at the full design flow rates, the short dye lifetime will only result in additional cost due to increased usage of dye.

SOLVENT	FIRE HAZARD	TOXICITY	TOTAL ENERGY	ENERGY IN $10 \lambda/D$	DYE LIFETIME
METHANOL / WATER	MODERATE	MODERATE	6 JOULES	2.5 JOULES	7.0 KJ/LITER
ETHYLENE-GLYCOL / WATER	NONE	MODERATE	3 JOULES	1.1 JOULES	4.0 KJ/LITER
ACETAMIDE / WATER	NONE	NONE	7 JOULES	2.5 JOULES	1.5 KJ/LITER

Figure 14: Comparison of three different candidate dye solvent solutions

In summary, we have made performance measurements on a prototype flashlamp-pumped dye laser. The laser has an energy output of approximately 7 J per pulse, with more than 2.5 J in a $10 \lambda/D$ divergence angle, and a pointing angle jitter of less than $5 \lambda/D$. A dye solvent solution has been found which is non-hazardous. This solvent completely eliminates the risks of the more traditional methanol-based dye solutions, with no apparent sacrifice in output energy or beam quality. The shorter dye lifetime in the new solvent is mitigated by the use of a real-time dye regeneration system, which has the ability of removing the dye photodegradation compounds from the laser during operation.

The authors wish to extend their thanks to Robert E. Hatch, Joseph M. Mahan, James L. Swedberg, and James J. Tynan for their valued contribution to this project.

This work is sponsored by the Defense Advanced Research Projects Agency, Directed Energy Office, through the Department of the Air Force.

"The views expressed are those of the authors and do not reflect the official policy or position of the U.S. Government."

DYE LASER/LASER DYE RESEARCH AT THE
U.S. ARMY MISSILE COMMAND

John J. Ehrlich and Stanley P. Patterson
Directed Energy Directorate
Research, Development, and Engineering Center
U.S. Army Missile Command
Redstone Arsenal, AL 35893-5245

ABSTRACT

This paper reviews the research program in dye lasers and laser dyes at the U.S. Army Missile Command (MICOM). The goal of this program is the improvement of energy, efficiency, and service lifetime of flashlamp-pumped dye lasers. Topics that will be discussed include the synthesis of improved dyes, spectral line narrowing, flashlamp improvements, and non-liquid hosts.

INTRODUCTION

Research in the area of lasers has been carried on at MICOM for a number of years. In the past several types of lasers have been investigated. This paper discusses current research at MICOM in the area of dye lasers and in particular flashlamp-pumped dye lasers.

Advantages of Dye Lasers

Flashlamp-pumped dye lasers offer a number of potential advantages as compared to other types of visible laser technology. Some of these advantages are summarized here:

- ° UV To IR Spectral Coverage
- ° Moderate Tunability of Individual Dyes
- ° Wide Range of Waveforms
Pulses from Picoseconds-Microseconds
CW
- ° Optical Simplicity
- ° Potential Reliability

Applications of Dye Lasers

The unique characteristics of dye lasers give them diverse applications. Dye lasers are currently being used, or evaluated for use, in such areas as laser induced chemistry, medicine, spectroscopy, and communication. As an example of medical applications see the paper by Jim Hsia of the Candela Corporation¹. Several other applications of dye lasers are discussed elsewhere in these proceedings^{2,3}.

Problem Areas With Dye Lasers

For all of their advantages dye lasers require further development in a number of areas in order to meet present and future requirements of both the civilian and military sectors. Summarized below are a number of the problem areas with dye lasers:

- ° Efficiency
Weight
Volume
Packageability
- ° Dye Lifetime
Maintainability
- ° Beam Quality
Spatial Coherence
Temporal Coherence
Brightness
- ° Scaling to Higher Energy/Power
Flashlamps
Linear

Coaxial
System Complexity
Electrical
Fluid
Maintainability
Reliability

- ° Safety
- Flammable Fluids
- High Voltages
- Carcinogenic Dyes

We at MICOM are working to address a number of these problem areas in our dye laser technology programs which will be described next.

Applied Research in Dye Lasers

MICOM is developing dye laser technology through both basic and applied research. This section describes our applied research program and the following section describes our basic research program. The objective of our applied research program is to develop dye laser technology for the Army's needs. Our approach to developing dye laser technology is to demonstrate that scaling of current dye laser technology can be achieved and to reduce the size and weight of dye laser devices by increasing the device efficiency and lifetime.

MICOM is exploring the potential of a number of innovative areas in dye laser technology such as vapor phase dye lasers, fluorescence enhancement, multi-color dye lasers, and phase conjugation. It is expected that this technology development program will yield more efficient and reliable dye laser devices. This program is summarized as follows:

ACCOMPLISHMENTS

Transverse flow flashlamp-pumped, 7J/pulse, 1% efficiency, dye laser demonstrated. Improved flashlamp loading and lifetime demonstrated. Conceptual design of efficient color-agile system. (AVCO, 1984)

XeCL excimer laser pumped dye cell. Pump: wavelength = 308nm, energy = 4KJ, pulse length = 650 ns. Output: 600J with R6G, wavelength = 590 nm, 816J with C102, wavelength = 480nm. (Western Research, 1986)

Design of 100J/pulse, 10Hz at 10% duty cycle, flashlamp-pumped dye laser. Less than 50 XDL, efficiency at least 0.8%, lamp life at least 10**5 shots at maximum energy. (AVCO, Rocketdyne, 1987)

Design of 1KJ/pulse, 1 Hz flashlamp-pumped dye laser. Less than 50 XDL, efficiency at least 0.8%, lamp life at least 500 shots at maximum energy, sub-scale fabrication of 100 joule system, co-axial flashlamp. (Phase-R, 1987)

Demonstrated Stimulated Brillouin Scattering Phase Conjugation of a flashlamp-pumped dye laser. Oscillator-amplifier configuration, >50% reflectivity, 1500 psi CH4, 300mj, 10-100 GHz linewidth. (MICOM, 1987)

CURRENT EFFORTS

- ° Multi-wavelength dye laser
- ° Non-liquid hosts
- ° Fabricate 100 joule per pulse, 10 Hz dye laser
- ° Liquid slab dye laser
- ° Improved excitation technology

FUTURE PROGRAM

- ° Characterize 100 Joule/Pulse, 10 Hz Device
- ° Pursue Innovative Techniques
 - Excitation Technology
 - Linear Flashlamps
 - Co-Axial Flashlamps
 - Continue to Monitor Excimer Laser Technology
 - Radiation Transport
 - Coating
 - Reflector Geometry
 - Fluorescence Enhancement

Basic Research in Dye Lasers

The goal of the MICOM basic research program is the advancement of dye laser technology through the performance and advocacy of relevant basic research. This includes involving the academic community in dye laser research through the use of contracts, Short Term Analysis service contracts (STAS), colloquia, and sessions at international and national conferences. Listed here are some details of the MICOM dye laser basic research program:

ACCOMPLISHMENTS

Several new dyes offering improved efficiency and extended lifetime have been synthesized and characterized. (Various, 1986, 1987)

Stable, streamerless discharges obtained in dye vapors. (U. of I., 1986)

Narrow linewidth operation of flashlamp-pumped dye lasers.

Oscillator configuration: 250 MHz, 5 mJ, R6G.

Osc-amp configuration: 250 MHz, 600 mJ. (MICOM, 1986)

PHASE CONJUGATION

Objective: Improve the beam quality and volumetric efficiency by the development of SBS phase conjugation technology and pseudo-phase conjugators.

Issues: Laser linewidth, pulse length, frequency stability.

Approach: New cavity configurations, injection locked oscillator-amplifier, improved conjugators.

DYE SYNTHESIS AND CHARACTERIZATION

Objective: Develop more efficient, longer lived dyes spanning the near UV to near IR spectrum.

Issues: Triplet state formation, triplet-triplet absorption, dye molecule photolysis, dye molecule-solvent interaction.

Approach: Develop chromophores to move fluorescence band away from triplet-triplet absorption band, investigate alternate solvents and cover gases.

NON-LIQUID HOSTS

Objective: Develop potentially low-cost, simple sources of dye laser radiation exploiting proven solid-state technology.

Issues: Acceptable host medium, re-solvating dye media, poor optical quality.

Approach: Improve host materials, phase conjugation.

VAPOR DYE

Objective: Develop vapor dye laser radiation source of high peak power.

Issues: Discharge uniformity, dye molecule disintegration.

Approach: Develop stable, streamer free discharge in dye vapors, probe active medium.

This paper and the two dye laser and laser dye sessions at the conference are examples of our desire to involve the academic community, as well as, commercial and government concerns in dye laser research. Several papers in these proceedings are results of this effort including a paper by Jim Bentley⁴ which summarizes design tradeoffs which are required in the synthesis of new laser dyes and a paper by Stephen Russell⁵ which discusses Stimulated Brillouin Scattering Phase Conjugation. Other papers related to this work appear elsewhere in these proceedings.⁶⁻¹⁰

Conclusions

The U.S. Army Missile Command has a vigorous program in dye laser/laser dye research in both basic and applied areas. We are actively researching, supporting research, and encouraging research in dye laser technology in a number of areas including scaling of dye

laser devices, Stimulated Brillouin scattering technology, flashlamp technology, improved radiation transport, and non-liquid host technology. We are also actively pursuing laser dye technology by seeking to have new dyes synthesized which offer improved efficiency or improved lifetime.

REFERENCES

1. J. Hsia, presented at the International Conference on Lasers '87, Lake Tahoe (1987), paper MC.2.
2. J.J. Ehrlich, S.D. Russell, S. Patterson, and F.J. Duarte, presented at the International Conference on Lasers '87, Lake Tahoe (1987), paper TH.7.
3. E. Moses, presented at the International Conference on Lasers '87, Lake Tahoe (1987), paper HA.3.
4. J.H. Bentley, J.J. Ehrlich, S.P. Patterson, D.E. Klimek, and S.F. Fulghum, presented at the International Conference on Lasers '87, Lake Tahoe (1987), paper HG.7.
6. V. Vaughn, J. Ehrlich, J. Casstevens, presented at the International Conference on Lasers '87, Lake Tahoe (1987), paper HG.4.
7. F.J. Duarte, J.J. Ehrlich, presented at the International Conference on Lasers '87, Lake Tahoe (1987), paper WD.5.
8. R.B. McGowen, V.V. Vaughn, J.J. Ehrlich, R.W. Conrad, presented at the International Conference on Lasers '87, Lake Tahoe (1987), paper WD.7.
9. D.P. Pacheco, H.R. Aldag, G.S. Janes, R.E. Schlier, presented at the International Conference on Lasers '87, Lake Tahoe (1987), paper WD.8.
10. R.F. Kubin, A.N. Fletcher, M.E. Pietrak, D.E. Bliss, presented at the International Conference on Lasers '87, Lake Tahoe (1987), paper FC.9.

SPECTRAL INSTABILITIES IN FLASHLAMP DYE LASERS

F. J. Duarte
Photographic Research Laboratories - Photographic Products Group
Eastman Kodak Company, Rochester, New York 14650

J. J. Ehrlich
U.S. Army Missile Command, Research, Development, and Engineering Center
Redstone Arsenal, AL 35898-5245

Abstract

A series of measurements aimed at characterizing spectral instabilities in narrow-linewidth multiple-prism flashlamp-pumped dye lasers are presented. The discussion is centered on the spectral instabilities observed when operating under conditions favorable for double-mode ($\Delta\nu \sim 250$ MHz) oscillation.

Introduction

Recently¹ we reported, for the first time, on spectral instabilities in long pulse narrow-linewidth multiple-prism flashlamp-pumped dye laser oscillators. These instabilities were observed in the form of a lower frequency modulation superimposed on the frequency beating ($\Delta\nu \sim 250$ MHz) characteristic of double-longitudinal-mode oscillation. Here, we present and discuss a series of measurements aimed at understanding the physical origin of these instabilities.

These experiments differ from other contributions in the area in several important aspects. First, the degree of stochastic variability is reduced since we restrict oscillation to the double-mode case. Secondly, this study refers to a long-pulse coaxial flashlamp-pumped dye laser device which offers distinct difficulties in regard to active medium uniformity and thermal stability. Further, this study was motivated by the necessity of restricting the conditions originating the instabilities rather than by an interest in studying stochastic processes.

Several previous experiments²⁻⁴ provide useful background information on different aspects of performance variability in narrow-linewidth multiple-prism oscillators. Thermal effects were measured and characterized in Ref. 2. Dependence of linewidth characteristics on dye flow turbulence in high prf copper-laser pumped dye lasers is discussed in Ref. 3. Evidence of variations in the mode intensity ratio, for double-longitudinal-mode oscillation, in an homogeneous gaseous medium is presented in Ref. 4. For a discussion of stochastic processes in multimode grazing-incidence dye lasers the reader should consider Ref. 5.

Experimental

The schematics of the narrow-linewidth multiple-prism coaxial flashlamp oscillator utilized in these experiments is shown in Fig. 1. The multiple-prism expander incorporates four right-angle quartz prisms with an apex angle of 42.7° . The two small prisms have a

hypotenuse of 15 mm while the hypotenuse for the large prisms is 50 mm. The grating employed was 140 mm wide with 3000 ℓ/mm .

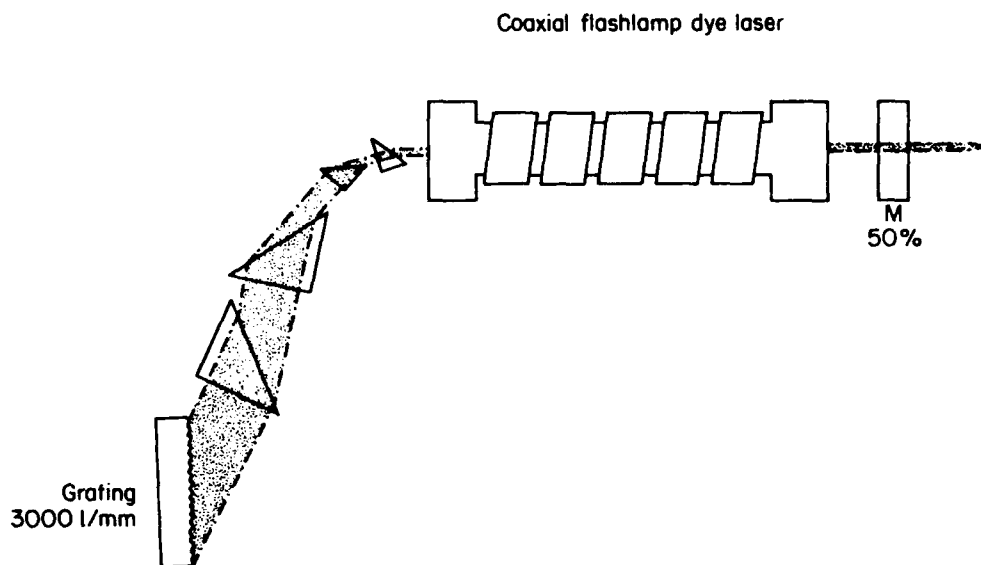


Fig. 1. Schematics of the multiple-prism Littrow coaxial flashlamp-pumped dye laser utilized in these experiments.

The laser was a small coaxial device (Phase-R model 1400) with an active length of 16 cm in a 6 mm diameter bore. When lasing with near optimum intracavity beam expansion ($250 \text{ MHz} \leq \Delta\nu \leq 375 \text{ MHz}$), the energy output was in the 5 to 10 mJ range depending on the dye concentration. Output beam diameter was $\sim 2 \text{ mm}$. Further experimental details are given in Ref. 1.

Most measurements presented are in the form of temporal pulse shapes obtained with a high-speed vacuum photodiode and a Tektronix 7834 fast storage oscilloscope.

Results

First we consider the stochastic nature of the variations as provided by a series of observations while maintaining all operational parameters fixed. These results are shown in Fig. 2. The experimental conditions here relate to a rhodamine 590 dye concentration of $2.5 \times 10^{-5} \text{ M}$, a lamp voltage of 16.5 kV, and an output energy of 6 mJ. The main feature of these results is that intensity variations were found to be $\pm 5\%$ and that the maximum amplitude of the mode beating is $\sim 22 \pm 2\%$ of the total intensity. Also, the pattern of instability as determined by the lower frequency modulation of the mode beating appears to vary somewhat from shot to shot. Variations apparent in Fig. 2 are attributed to stochastic processes.

The rather regular pattern of linewidth instability demonstrated in Fig. 2 is by no means typical. Indeed, rather exotic modes of instability can be demonstrated as shown in

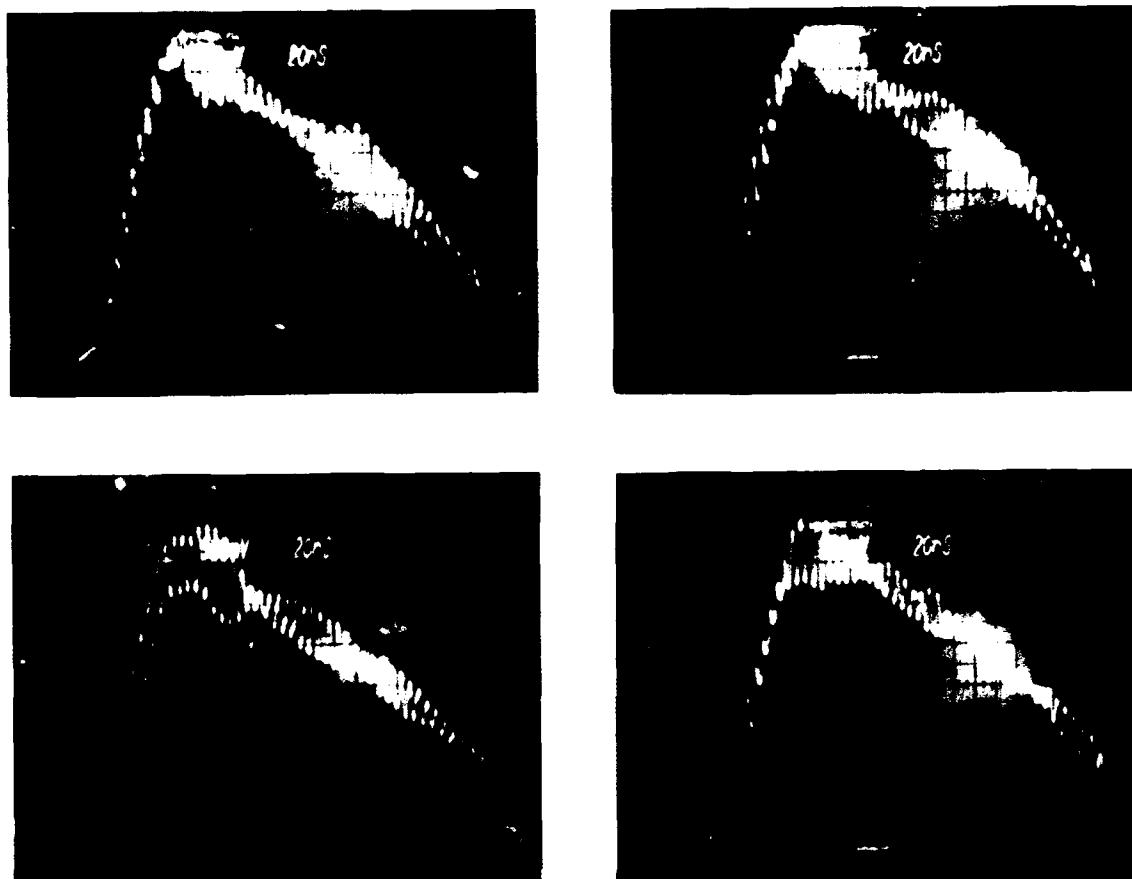
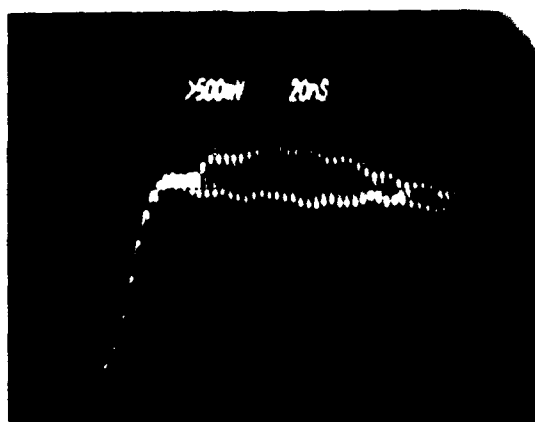


Fig. 2. Four different temporal pulses characteristic of double-longitudinal-mode oscillation. For all pulses conditions are identical. Thus, variations observed are stochastic in nature.

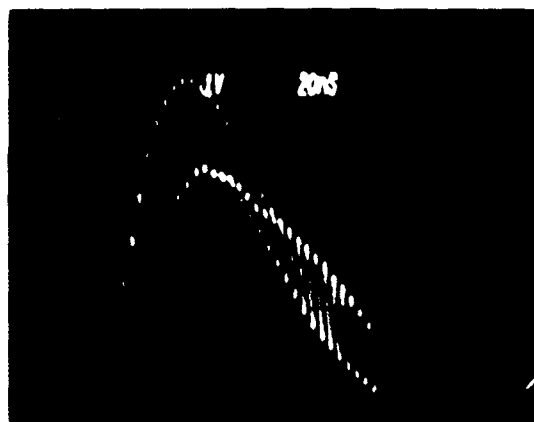
Fig. 3. The modulation of Fig. 3(a) results at an excitation voltage of 17 kV, a temperature difference (ΔT) between dye solution and cooling water of -0.8°C , and misalignment of the beam. The modulation of Fig. 3(b) was observed at a lamp voltage of 15 kV, $\Delta T -1.1^{\circ}\text{C}$, again under beam misalignment. The pattern of Fig. 3(c) is the result of the introduction of an intracavity aperture which results in a reduction of illumination at the grating. As shown in Fig. 3(d), the amplitude of the mode beating oscillation and the presence of the overimposed lower frequency modulation are reduced significantly by optimizing the beam alignment and increasing the number of grooves being illuminated at the grating. The results of Fig. 3(d) were obtained by illuminating $\sim 20\%$ more grooves than in the configuration utilized to achieve the effects shown in Fig. 3(c).

Discussion

In Ref. 1 it was shown that under optimum experimental conditions these multiple-prism oscillators can yield single-longitudinal-mode operation [see Fig. 4(a)], or when oscillating in double mode, the temporal pulse can be indicative of uniform mode beating which



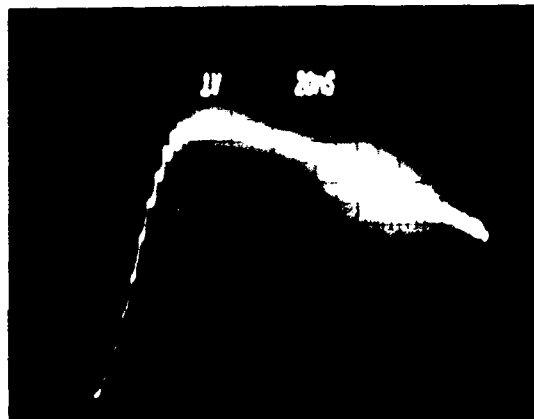
a



b



c



d

Fig. 3. (a-c) Different temporal pulses demonstrating severe changes in the mode intensity ratio (see text for explanation). (d) Amplitude of mode beating oscillation is reduced due to the oscillation of a very strong mode in conjunction with a very weak secondary mode. This is accomplished by nearly maximum beam expansion and optimum beam alignment.

in turn is representative of an unchanging mode-intensity ratio [Figs. 4(b) and (c)]. The lower frequency modulation, or instability oscillation (shown in Figs. 2 and 3), occurs due to variations in the intensity ratio of the two modes as the laser pulse evolves. Here we explore and describe possible mechanisms which may cause these variations in the mode intensity ratio.

Two possible mechanisms that can cause the instability effect are mode competition and/or frequency jitter. A description of a source of frequency jitter can be provided following consideration of the linewidth equation⁴ for multiple-prism grating oscillators

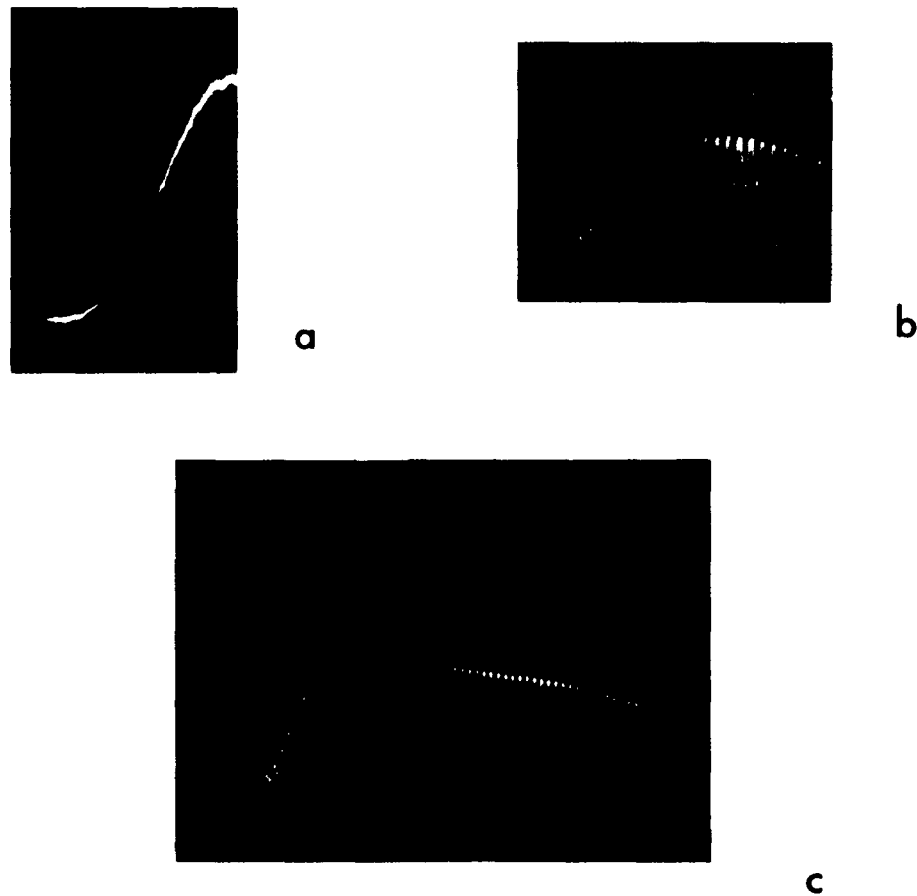


Fig. 4. (a) Smooth temporal pulse indicative of single-mode oscillation (from Ref. 1). (b) Stable double-longitudinal-mode oscillation at 10 ns/div (from Ref. 1). (c) Uniform mode-beating pattern at 20 ns/div (from Ref. 9).

$$\Delta\lambda = \Delta\theta \left[\prod_{m=1}^r k_m (\partial\theta/\partial\lambda)_G + 2 \sum_{m=1}^r (\pm 1) \left(\prod_{j=1}^m k_j \right) \tan\psi_{1,m} (dn/d\lambda) \right]^{-1} \quad (1)$$

Here, $(\partial\theta/\partial\lambda)_G$ is the grating dispersion (either in Littrow or grazing-incidence configuration), k_m the expansion factor provided by individual prisms, $\psi_{1,m}$ the refraction angle at each individual prism, and $(dn/d\lambda)$ is characteristic of the prism material. In this equation the second term corresponds to the contribution of the multiple-prism expander to the overall dispersion. This term can be made equal to zero⁶⁻⁸ by utilizing a compensating configuration such as the one shown in Fig. 1. Thus, one can describe the tuning characteristics of the oscillator using the grating equation. Under these circumstances it can be shown⁹ that a beam angular displacement of only $\sim 10^{-6}$ radians can cause a frequency shift of ~ 250 MHz. Such frequency displacement, during the laser pulse, could have a severe effect on the intensity ratio of two longitudinal modes separated by 250 MHz. A further consequence of this effect could be frequency jitter resulting from displacement

of the two modes in the frequency domain. Certainly, frequency jitter was observed interferometrically in association with temporal pulses typical of unstable behavior.⁹

From the results presented in Fig. 3 it is reasonable to assume that geometrical effects, including beam displacement and spatial constraints on the expanded beam illuminating the grating, influence the extent and magnitude of the instabilities. Indeed, it is easy to demonstrate, via Eq. 1, that a reduction in the width of the expanded beam leads to a broadening of the dispersive linewidth, which in turn allows the secondary cavity mode to increase, thus reducing the intensity ratio that results in an increase of the mode beating oscillation amplitude.^{4,10} This effect can be emphasized by comparing Figs. 3(c) and 3(d).

Using the simple notion of the dispersive linewidth being displaced in the frequency domain in an oscillatory manner (at ~20 MHz) while the two longitudinal modes remain stationary, we can closely reproduce the temporal pulse shapes of Fig. 2 using a two-mode electromagnetic wave representation.⁹ Here, omitting the high frequency terms, the intensity due to the double-mode oscillation is written as $E^2 \approx (1/2)(E_1^2 + E_2^2) + E_1 E_2 \cos(\omega_1 - \omega_2)t$, with the ratio of frequency jitter to cavity mode spacing represented by a sinusoidal function, at a frequency of 20 MHz.

At this stage it is reasonable to assume that geometrical effects can cause the instabilities demonstrated in Fig. 3. The next area of interest concerns the physical phenomena that may produce the geometrical variations. In Ref. 4 it is indicated that narrow-linewidth multiple-prism oscillators utilizing a non-flow gaseous medium do experience variations in the longitudinal-mode intensity ratio. However, these variations are from shot to shot and do not occur during the duration of a single laser pulse. The work discussed in Ref. 3 provides clear evidence that stable, single-mode oscillation is only possible when the dye flow through the cell is free from turbulence. In Ref. 2 the importance of thermal stability is highlighted. From these premises it can be assumed that stable linewidth operation requires thermal uniformity in the active medium and elimination of turbulence. Certainly, these are two conditions which are not inherent in coaxial flashlamp-pumped dye lasers. Here, it is not difficult to see that inhomogeneities in the dye medium, caused by turbulence and/or thermal spatial differences, can force slight deviations in the beam as the pulse progresses in time. To test this assumption, the laser was operated under static dye conditions which in turn neutralized the turbulence. Under these conditions the variations in the mode intensity ratio were reduced noticeably.⁹

The thermal conditions in this type of flashlamp-pumped dye laser can be described using cylindrical coordinates. If the initial and boundary conditions are independent of the angular and z coordinates (the z coordinate in this case is the optical axis) the temperature is a function of the radius and time only. Thus, under these ideal conditions the equation of conduction reduces to¹¹

$$\partial v / \partial t = \kappa [\partial^2 v / \partial r^2 + (1/r) \partial v / \partial r] \quad (2)$$

By separating variables so that $v(r,t) = R(r) T(t)$ a solution to this equation is of the form

$$v(r,t) = \sum_{n=1}^{\infty} A_n J_0(a_n r) e^{-a_n^2 \kappa t} \quad (3)$$

where J_0 is a Bessel function of the first kind. The final format of this solution depends on exact boundary conditions.¹² For the purpose of the discussion here we assume different but uniform initial dye and water temperatures. For this case, Eq. (3) clearly indicates that a definite temperature radial profile should be expected for ideal conditions of spatial homogeneity of the active medium. Hence, the refractive index of the dye solution should remain uniform for light propagating along the optical axis. All this is seriously altered by the presence of turbulence since dye solution from different temperature regions will be distributed at random.

As discussed in Ref. 1, a further source of instability is real time variations in the pumping photon flux. Investigation of this phenomena will be the subject of future experiments.

Conclusion

Measurements presented in this paper lead us to conclude that linewidth instabilities in narrow-linewidth multiple-prism pulse dye lasers have definite physical origins and are not purely stochastic in nature.

The type of coaxial flashlamp-pumped dye laser utilized in these experiment is a complex device with thermal, flow, mechanical, and excitation variables which can all contribute to the spectral instabilities. Our experience indicates that the design of a vibration-free, nonturbulent, dye flow system should contribute toward the minimization of the instabilities observed.

The present work was carried out in cooperation with R. D. Russell, S. P. Patterson and J. E. Adams. Support from Battelle Columbus Division, and U.S. Army (contract DAAL03-86-D-0001) is gratefully acknowledged.

References

1. F. J. Duarte and R. W. Conrad, Appl. Opt., 26, 2567 (1987).
2. F. J. Duarte, IEEE J. Quantum Electron. QE-19, 1345 (1983).
3. F. J. Duarte and J. A. Piper, Appl. Opt. 23, 1391 (1984).
4. F. J. Duarte, Appl. Opt. 24, 1244 (1985).
5. L. A. Westling and M. G. Raymer, J. Opt. Soc. Am. B.3, 911 (1986).
6. J.R.M. Barr, Opt. Commun. 51, 41 (1984).
7. F. J. Duarte, Opt. Commun. 53, 259 (1985).
8. R. Trebino, Appl. Opt. 24, 1130 (1985).

9. F. J. Duarte, J. J. Ehrlich, S. P. Patterson, S. D. Russell, and J. E. Adams, Appl. Opt. in press.
10. T. J. Pacala, I. S. McDermid, and B. J. Lauenslager, Appl. Phys. Lett. 45, 507 (1984).
11. H. S. Carslaw and J. C. Jaeger, Conduction of Heat in Solids, 2nd ed. (Oxford University, New York, 1973).
12. J. Unsworth and F. J. Duarte, Am. J. Phys. 47, 981 (1979).

LONG PULSE DYE LASER

S. Edward Neister

President

Phase-R Corporation

Old Bay Road, New Durham, New Hampshire 03855

Abstract:

Coaxial Flashlamps are known for pumping organic dyes with high efficiency from 0.1 μ s to 1.5 μ s pulsewidth. The requirements and results are presented which permit efficient long pulse operation into the millisecond region.

Long Pulse Dye Laser

One of the important requirements for making a long pulse flashlamp excited dye laser is UV filtering.

At Phase-R Corp., we work with our all metal to quartz sealed coaxial flashlamp. For best performance of the dye laser at high repetition rates and for long dye life, a triax configuration is used. A triax is nothing more than another tube placed inside the coax to permit an annulus for cooling water next to the flashlamp (Figure 1).

By controlling the temperature of both the dye and the water, excellent beam quality at high rate is maintained. Adding caffeine to this cooling water greatly improves dye life by filtering out the UV from the flashlamp (Figure 2,3).

Figure 4,5,6 presents some work that was done by some people at GTE. (1)* laser was terminating at a pump intensity much greater than where the dye started to lase. But in figure 5 when they filtered out the UV, the triplet quencher was more efficient and they found that the laser pulse terminated at an input intensity of a little bit less than what it was when it started. They concluded that triplet production had come to an equilibrium and certainly was not increasing. As a result, there should not be any limit to the pulsewidth. However, efficiency is reduced by at least one order of magnitude.

We decided to test this concept in a 10 microsecond laser was made. The left picture in figure 7 has only COT with no UV filtering. The rapid fall is indicative of triplet absorption.

We next added caffeine to the triax cooling water. The right picture confirms the fact that the UV was having an instantaneous affect on COT's rate of triplet state quenching.

The lower picture is a test to see if the triplet states do come to some equilibrium. We made a PFN that produced two current pulses in the flashlamp such that the intensity in the flashlamp is exactly the same on both. We got a startling result. The second laser pulse had more intensity than the first.

This says there are some things going on with triplet states that we really do not understand. In fact, what COT does with the material is quite dramatic. But we have come to the conclusion that it is very important to eliminate the UV in all these organic dyes and solvents. You have got to keep the UV away. When we say UV, we are saying below 3000A.

To further test the equilibrium theory, we made a 300us pulse. Figure 8 shows the laser pulse which followed the light pulse. It appears that Papparlardo may be correct on having no limit to the laser pulsewidth, except for the possibility of index gradient formation.

(1)* Long-Pulse Laser Emission from Rhodamine 6G: Romano Pappalardo, H. Samuelson, Alexander Lempicki; IEEE Journal of Quantum Electronics, Vol. QE-6, No. 11, Nov. 1970

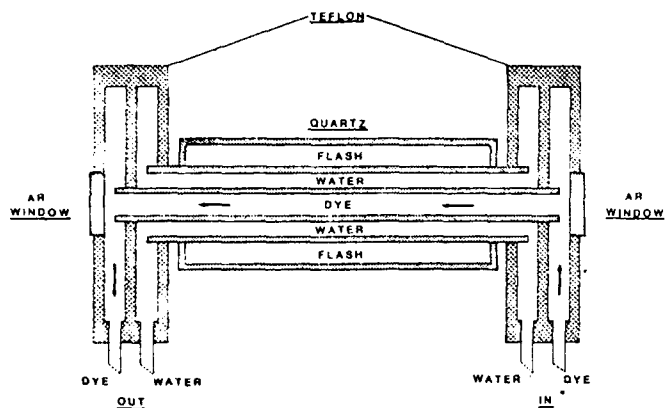


Fig. 1. Cross section of a flash tube showing fluid chambers.

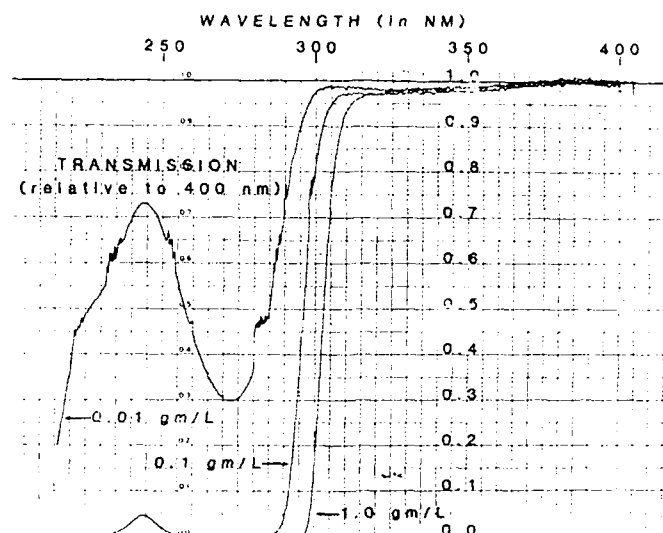


Fig. 2. The UV transmission of three concentrations of caffeine normalized at 400 nm.

LIFETIME TEST WITH CAFFEINE

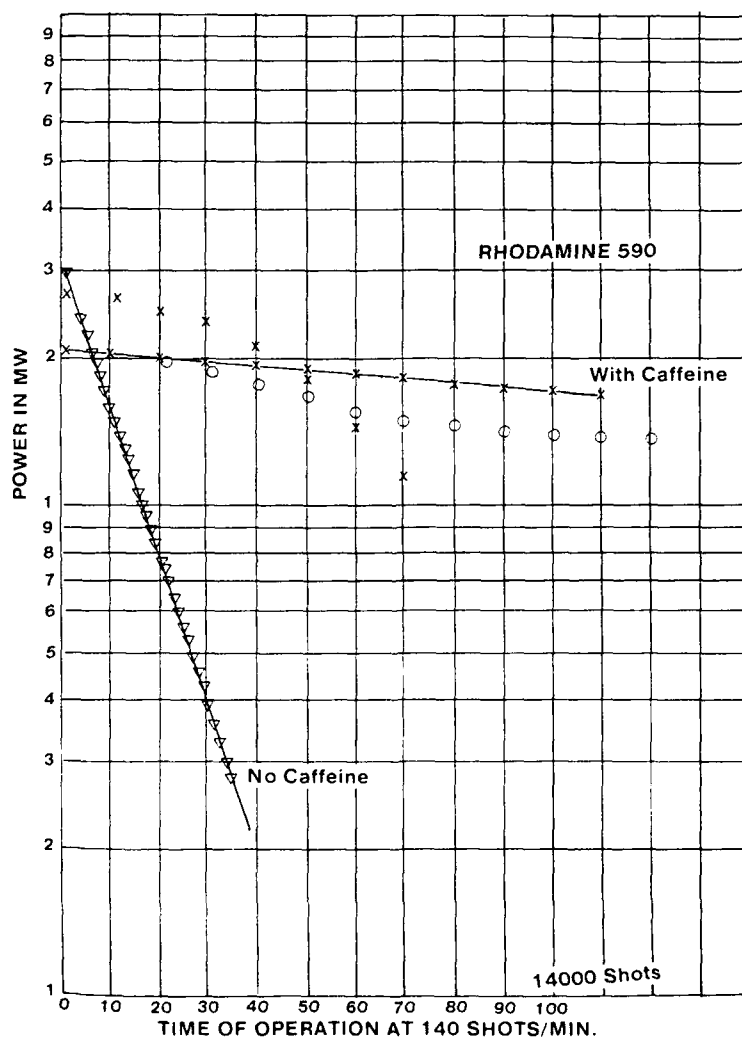


Figure 3

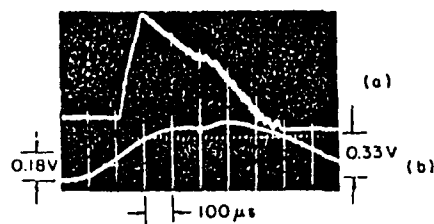


Fig. 4 Long laser emission. (a) $\approx 600 \mu s$; from a $\approx 650 \mu s$ FWHM pump. (b) Pump filtered with K_2CrO_4 solution. Input 510 joules with 524 μF . Standard laser solution. Power levels of the pump at threshold and termination are indicated.

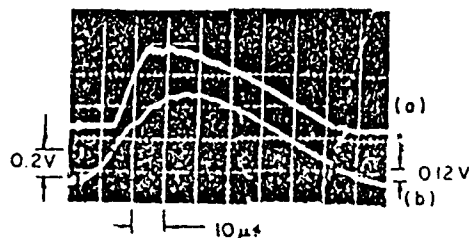


Fig. 5 Example of laser output closely following pumping-pulse outline. Solution— 5×10^{-6} M/l rhodamine 6G and 5×10^{-3} M/l COT in ethanol. Cell—3 inches long, with flat windows. Pumping—FX 42 flashlamp at 14 μF and 288 joules; Corning filter on flashlamp. (a) Laser output. (b) Pump pulse. Note the low level of the power for laser termination, which is ~ 60 percent of the threshold power.

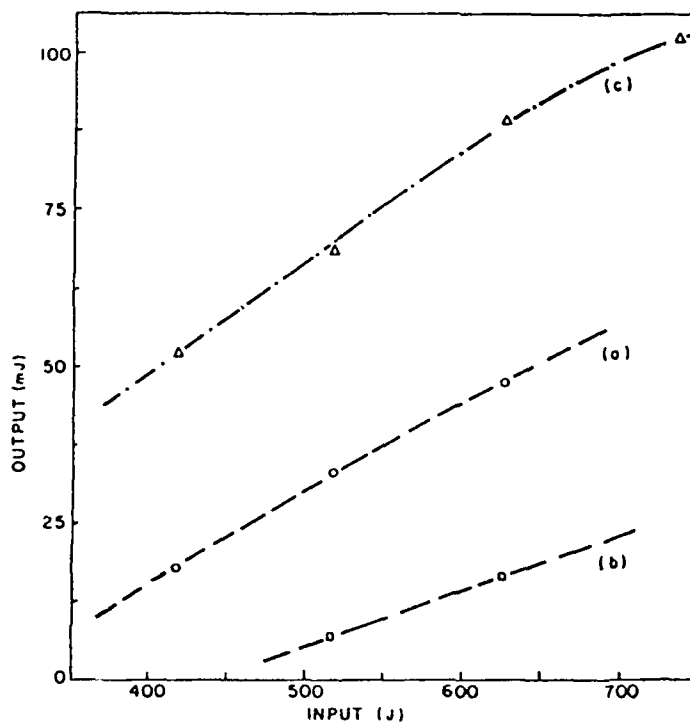


Fig. 6 Efficiency curves for an ethanolic solution of 5×10^{-6} M/l rhodamine 6G. 3-inch cell, with flat windows; output-mirror reflectivity 96.5 percent. Cavity B. (a) 5×10^{-3} M/l COT; GG 15 filters in the cavity. (b) Same, but Pyrex filters in the cavity. Note the improvement from (b) to (a). (c) 1.5×10^{-3} M/l COT; GG 15 filters in cavity.

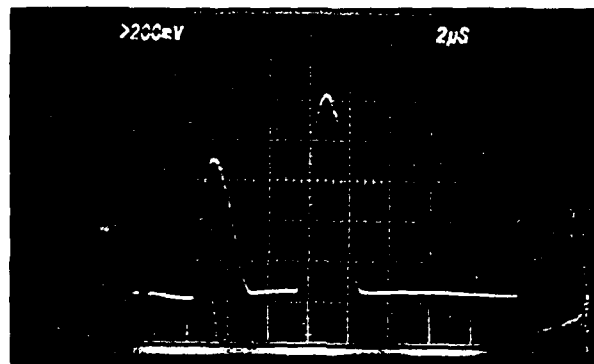
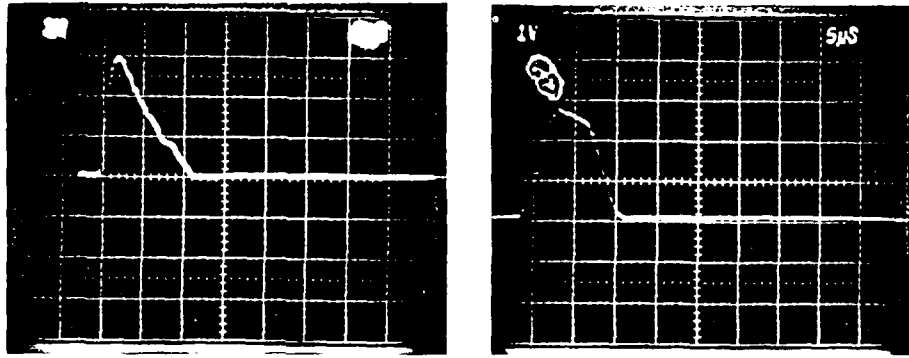


Figure 7

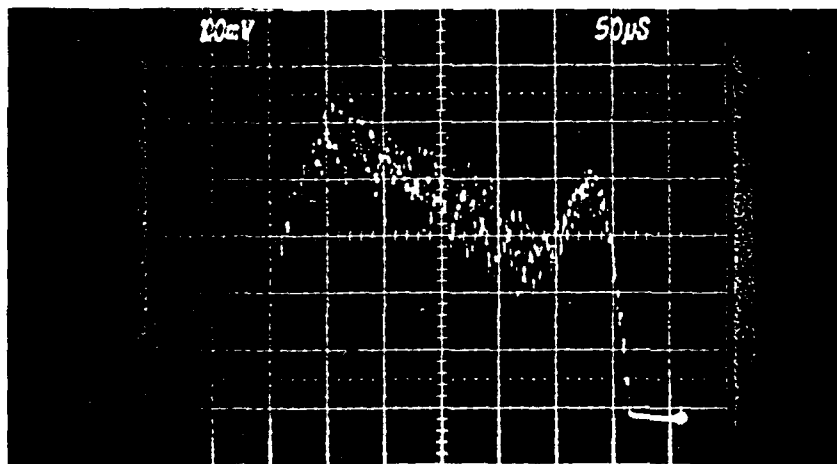


Figure 8

A FLASHLAMP PUMPED ZIG-ZAG SLAB DYE LASER

by J.J. Dearth, V.V. Vaughn, R.B. McGowan
LSI, Inc.
1900 Sparkman Drive
Huntsville, Alabama 35816

J. Ehrlich and R.W. Conrad
MICOM
Redstone Arsenal, Alabama 35898

Abstract

A zig-zag optical path through the laser cavity can potentially reduce thermal distortion. Presented is experimentation and analysis of thermally induced effects in a flashlamp pumped zig-zag dye laser system.

1. Introduction

As a laser medium is excited through a series of repetitive flashlamp pulses, zones of thermal energy concentration develop distributively from the outer edges of the dye medium decreasing in thermal amplitude inwardly toward the center. A zig-zag path which deflects throughout the dye medium from one dye cell wall to the other tends to average the thermal energy concentrations throughout the cell thus reducing their net effect on the beam quality. The work reported here extends the zig-zag principle from solid slab lasers to liquid dye lasers. A zig-zag dye laser is constructed and the laser beam quality is observed for both straight-through and zig-zag paths. Laser spots are photographed by a 35mm camera and by a high-speed framing camera. In addition, the flashlamp-pumped dye cell is placed in one leg of a Mach-Zehnder interferometer and a duplicate unpumped dye cell is placed in the other. The resultant fringe patterns, which reveal the thermal distortions of the pumped cell, are filmed at 5000 frames per second while the flashlamps are pulsed. Fringes are filmed for straight-through and zig-zag paths. The zig-zag dye cell and its associated flashlamp pumping system are described. The laser spot photographs are presented, analyzed, and discussed. The Mach-Zehnder film is described and discussed.

2. Zig-Zag Dye Cell

The sides of a zig-zag solid laser slab have no reflective coating since this might block some of the pump light. Instead, the beam is made to zig-zag by total internal reflection. An exact dye-laser analog of this system would require a monolithic dye cell. The only reported monolithic dye cells are liquid jets and solid hosts. A jet seems too experimentally complicated for the zig-zag geometry. Solid hosts have other problems[1, 2, 3]. Therefore the zig-zag dye cell for this work is designed with walls. The refractive index for a typical dye solution is near that of water which requires a wall material with a refractive index less than about 1.1 if total reflection is to occur at a practical angle with the liquid-wall interface. Instead of designing the reflection to occur at the liquid-wall interface, the zig-zag dye cell is designed with the reflections at the outer surface of the walls, which are made of vitreous quartz ($n = 1.4585$, at 0.55 micrometers). The construction of the dye cell is shown in Figure 1. The dye solution, Rhodamine 6G in methanol ($n = 1.326$), enters the lower fitting and exits the top fitting. A top view of the zig-zag beam path through the cell is shown in Figure 2. A ray trace is shown for each edge of the laser beam and for a central ray. The rays enter normal to the 50 degree slanted faces and strike each side dye-wall interface at 50 degrees off normal. The details of the wall reflections are shown in Figure 3. The rays are refracted upon entering the wall to an angle 44.14 degrees off normal. The critical angle at the outer surface is 43.29 degrees; therefore, the design meets the condition for total internal reflection at the outer surface. Some unwanted reflection occurs at the dye-wall interface since the refractive index of the wall is not a perfect match to the dye solution. These rays are shown in Figure 3 as dotted lines for the case where light enters from the left. The rays labeled a and b are calculated[4] to be about 1% of the incident light intensity for vertical polarization and much less for horizontal polarization. The ray b' is almost as strong as b. Rays a and b' are parallel to the main ray but are spaced 0.294" (7.47mm) to either side of it. Since light also travels right-to-left in the laser cavity rays similar to a and b' are produced, where the b' ray returning upon itself combines with the ray similar to a, and where the a ray returning upon itself combines with the ray similar to b'. However, rays outside the center 0.22" (5.6mm) of the laser beam have one sidebeam blocked by the exit aperture, 0.514" x 0.866" (13.1mm x 22mm).

3. Straight-Through Path

For comparison, the dye cell shown in Figure 1 is also operated with straight-through alignment. This is shown in Figure 4. Note that the beam enters and leaves the faces at 58.47 degrees off normal. This yields an effective aperture of 0.268" x 0.866" (6.80mm x 22mm).

4. Flashlamps and Reflectors

Two 6" (15.2cm) linear short-pulse Xenon flashlamps (ILC L-6209, 6mm bore, 6" arc length, 200 torr fill) provide the optical pumping for the zig-zag dye cell. Each lamp is placed in a half cylinder diffuse reflector whose diameter (0.875") fits against the side of the dye cell. The inside of the reflector is sprayed with barium sulfate and the lamp is placed as close as practical to the back wall of the reflector. The ends of the flashlamps (and leads) block the path of the beam. This obstruction can be avoided by turning the beam with prisms as shown in Figure 5 for the zig-zag path and Figure 6 for the straight-through path. Alternately, a bent flashlamp requires no prisms as shown in Figure 7 for the zig-zag path and Figure 8 for the straight-through path. A shorter reflector accommodates the bent lamp. The reflectors are not shown in Figures 5, 6, 7, and 8.

5. Laser Mirrors

Flat, dielectric mirrors are placed to form the laser cavity as shown in Figures 5, 6, 7, and 8. One mirror is rated 100% reflecting and the output mirror is 80% reflecting.

6. Power Supplies

The flashlamps are fired in parallel branches by a single triggered spark gap in the circuit shown in Figure 9, which is similar to Aldag[5], except that auxiliary spark gaps are used to allow a DC simmer. Without the auxiliary gaps, the main capacitors AC couple the flashlamps and only one lamp simmers at a time. The DC simmer supplies are shown in Figure 10. The two supplies are functionally equivalent and each provides -1100 VDC into an open circuit. The total energy into both flashlamps is given by 0.11 microfarads times the square of the high voltage. The usual 1/2 in the formula is missing because 0.11 microfarads is available for each of the two lamps. During the interferometer experiments, 15KV, or 25 joules, is used. This is near the laser threshold. When photographing the laser pulses, 20 KV, or 44 joules is used. The flashlamp pulse rise time is about 0.5 microseconds and the pulse width is about 2 microseconds, as monitored with a vacuum photodiode.

7. Mach-Zehnder Interferometer

A diagram of the Mach-Zehnder interferometer is shown in Figure 11. Data is taken for both straight-through and zig-zag paths; however, details of the paths through the prisms and the dye cells are omitted from this figure. The dye cell path details are the same as those described above using prisms except the zig-zag path has only three bounces. The input beam is a 5mw, expanded, collimated, red He-Ne laser beam which is masked to the rectangular shape of the dye cell entrance. This is split and passes through the two dye cells before being recombined with a slight tilt between the recombining beams so as to produce vertical fringes across the film plane of the 16mm Hycam camera. The beams are carefully collimated to minimize the effect of any camera vibration on the fringes. During a camera run the film rolls at 5000 frames per second and the lamps are flashed onto the test cell. Any distortion induced by the flashlamps is then displayed in the fringe pattern and recorded on the film. Note that the dye laser does not lase during this process since the laser mirrors are removed, but the flashlamps are pulsed as for normal lasing. Note also that the Hycam camera contains an LED which places 10ms timing flashes on the film. A photograph of the dye cell and the duplicate reference dye cell as used in the Mach-Zehnder interferometer is shown in Figure 12. Although the reference cell has no flashlamps to obstruct the beam, turning prisms are still used with the reference cell to match those used with the flashlamp-pumped cell. The flashlamp reflectors for the pumped cell are shown pushed back to reveal the dye cell. The diffuse coating inside one reflector is also visible, but the flashlamps are lying (on the platform) between the reflectors and the dye cell and are not readily seen in this view. Before flashing the lamps, the reflectors are repositioned against the sides of the dye cell with the lamps fitted through slots in the plexiglass holders which are bolted to the ends of the reflectors. The red He-Ne laser with its collimating attachment can be seen in the background of Figure 12.

8. Mach-Zehnder Interferometer Results

The flashlamp-induced perturbations of the interferometer fringe patterns are best observed by projecting the 16mm film at the standard 24 frames per second. This was done at the conference for a straight-through path and for a zig-zag path. (The film has also been transferred to 1" and to VHS video tape.) A detailed description of the film shown at the conference follows. The first part of the film shows the straight path case and the second part shows the zig-zag case. The film runs about 3 minutes. The film starts with a black leader showing only the 10ms LED timing flashes on the left of the screen. A splice passes and the before-pulse (actually between pulses) straight-through fringes follow. The fringes fall in a rectangle whose height is about four times its width. Six or seven, near-straight vertical fringes are visible. All the fringes are about the same width. The fringes have a general curvature of about 1 fringe width where the convex side points to the left. The fringes move left and right slowly, with a somewhat irregular periodicity, by about one fringe width giving the appearance of a body rotating back and forth. The fringes change curvature or shape perceptibly but by less than a fringe width. Then the flash from the lamp is seen (it occupies only one frame of the film) and the fringes are violently disturbed starting with the next frame. The shape of the fringes is virtually lost with the structure becoming fine grained and irregular in both horizontal and vertical directions. A typical feature is about 1/20 or less of the width of the rectangle. A rapid succession of violent pulsations (in a few ms) are followed by slower pulsations which gradually subside, with a "boiling" appearance, almost back to the prepulse appearance in about 100ms. The first rapid pulsations have a noticeable component of left-to-right or right-to-left or horizontal-squeezing motion associated with them. A splice in the film passes and some more black leader is shown--another splice--and then the before-pulse (actually between-pulses) zig-zag path fringes appear. The fringes fall in a rectangle whose height is about two and one-half times its width. The film is somewhat over-exposed. Six or seven, near-straight, vertical fringes are visible. All the fringes are about the same width except perhaps slightly wider at the top. With the exception of one short fringe in the lower left corner, the fringes have no general curvature, but there is a kink about 10% down from the top; a second, slightly larger kink is about 20% down from the top; and a third kink is about 10% up from the bottom. All three of these kinks are less than about one fringe. There are also about five or six lesser kinks of about one-third fringe. All the kinks are approximately located at equal intervals from top to bottom. The fringes have the same slowly-rotating motion as the straight-through case except the motion is about two fringes wide and has more-distinct changes in its periodicity. After the flash from the lamp is seen (it occupies one frame), the fringes react on the next frame; however, the disturbance is much less violent and it does not change the basic shape of the fringes. A rapid succession of pulses with the same, or a closely similar, timing pattern as the straight-through case but with a more pure left-to-right or right-to-left motion is seen. The motion appears to be mainly a rotation of the fringes by two or three fringe widths with little distortion of the fringe pattern. The rapid pulses are followed by slower "boiling" motions evident only as changes in the kinks of one fringe width or less. These motions subside in about the same time as the straight-through case, but their magnitude is much smaller. The overall visual impression is that the zig-zag case is much more resistant to the disturbance than the straight-through case.

9. Discussion of the Interferometer Results

Since the 16mm frames are photographed 200 microseconds apart (5000 f/s), the disturbance observed would occur after a laser pulse and some may be associated with the flow of the dye solution. However, the film indicates that the zig-zag path is showing resistance to the flashlamp-induced disturbances immediately after the pulse and later; one can reasonably infer that the zig-zag path also resists disturbances during the pulses as well. In addition, the observed effects are of direct interest to prepulse conditions in the design of repetitively pulsed dye lasers. Note that the effects recorded on the film are associated with mechanisms slower than the propagation of a shock wave. For example, since the speed of sound in methanol (at 1 atm and 25 degrees C) is 1103 m/s, the crossing time is given by $10\text{mm}/1103\text{m/s} = 9.1\text{ microseconds}$ (or 4.5 microseconds to "meet at the center").

10. Laser Spot Photographs

Photographs of the laser spots are reproduced in Figure 13 for the straight-through path and Figure 14 for the zig-zag path. The photographs are 35mm time exposures of a single pulse. The target, placed 75 ft. from the laser, is a white poster board with vertical and horizontal axes. Each axis is labeled at 2" intervals. A dot with a diameter of 1.4" is located at the center. The effective exit aperture of the dye cell is 13.1mm x 22mm for the zig-zag case and it is 6.80mm x 22mm for the straight-through case. This complicates comparison of the two spots. However, since the smallest dimension, 6.8mm, is 12,363

wavelengths, the divergence due to Fresnel diffraction is probably similar to that for a half plane at each aperture edge. Consequently, the difference in the effective aperture widths should not preclude comparison of the divergence angles for the two cases. The divergence angles are computed from the photographs by subtracting the exit dimension from the corresponding dimension of the spot, dividing by two, dividing by the target distance, and taking the arctangent. The results are listed in Table 1.

Table 1. Divergence Angles. The zig-zag case is based on the center spot (see text).

zig-zag horizontal divergence	zig-zag vertical divergence
1.00 milliradians (1.56)	1.24 milliradians (1.97)
straight-through horizontal divergence	straight-through vertical divergence
3.26 milliradians	2.57 milliradians

As shown by Table 1., the straight-through divergence is 27% larger for horizontal than vertical. The zig-zag divergence is 20% smaller for the horizontal than the vertical. This indicates that the zig-zag path reduces the horizontal divergence compared to the vertical divergence. The zig-zag divergence is also significantly smaller than the straight-through case; however, the zig-zag spot may be under-exposed and this comparison is thought to be less accurate than the first comparison of horizontal to vertical. The corresponding zig-zag divergences computed from the framing camera picture below (which is probably overexposed), are listed in parentheses in Table 1. These numbers indicate that the zig-zag case has 52% less horizontal divergence than the straight-through case. This is consistent with the first, horizontal-to-vertical ratio comparison above. The two side spots for the zig-zag case originate as described in section 2, and could therefore be eliminated by a better match between the dye-solution and the wall refractive index. Consequently, the side spots are not included in the size of the zig-zag spot.

11. Framing Camera Photographs

The framing camera photographs are shown in Figures 15, 16, and 17. Figure 15 is the zig-zag case. Figure 16 is the straight-through case with no prisms. Figure 17 is the straight-through case with the bent flashlamp and no prisms. Each framing camera picture shows two exposures where the top exposure is earlier. Each exposure is 200ns duration and the two exposures are taken 500ns apart. The target is the same as above. The extra horizontal black or very white lines which extend completely across the exposures are electron shadows of the control grid in the image converter tube and can be ignored. The straight through cases show redistribution of the beam energy during a single laser pulse. The first exposure of both straight-through cases shows a "diffraction-like" pattern but only to one side. The prism reverses the image, so the pattern is on the same side both times. Since it is only on one side, and only on the first exposure, it is thought not to be ordinary diffraction, but perhaps some type of flashlamp-induced beam wander. This pattern is not seen for the zig-zag case, indicating resistance to the flashlamp-induced disturbance during one laser pulse.

12. Practical Considerations

This design allows fine dust from the barium sulfate to collect on the dye-cell walls which causes the zig-zag output to decrease from shot to shot and to drop below threshold after 5 to 10 shots. This makes it hard to control the exposure of the photographs. Some sort of protective window or an air blast, is needed to keep the walls clean. Since total internal reflection is extremely sensitive to dust, the amount sufficient to stop lasing is invisible. Also, the glue used for this cell frequently leaks. It holds the walls in place, but has small leaks requiring frequent repair. A more appropriate glue is needed. Alignment of the zig-zag laser cavity is difficult with a red He-Ne laser due to dispersion and absorption. An orange He-Ne laser is effective for this purpose. A photograph of the alignment beam is shown in Figure 18. The beam is visible in the dye by fluorescence and at the points of total internal reflection by scattering. It is not visible in the quartz wall. Alignment of the zig-zag Mach-Zehnder interferometer required three days per experiment with only three bounces. Appreciation is expressed to Aubrey Askew for aligning and operating the system. He discovered the dust problem, too.

References

1. D.P. Pacheco, H.R. Aldag, G.S. Janes, and R.E. Schlier presented at International Conference on Lasers '87, Lake Tahoe (1987), paper WD8
2. G. Erickson, presented at International Conference on Lasers '87, Lake Tahoe (1987), paper WD9
3. G. Erickson, presented at International Conference on Lasers '87, Lake Tahoe (1987), WD10
4. F.A. Jenkins and H.E. White, Fundamentals of Optics (McGraw-Hill, New York, 1957), pp. 509-512
5. H.R. Aldag, High Power Dye Laser (Avco-Everett, 1979), prepared for the U.S. Air force (AFAL-TR-79-1059).

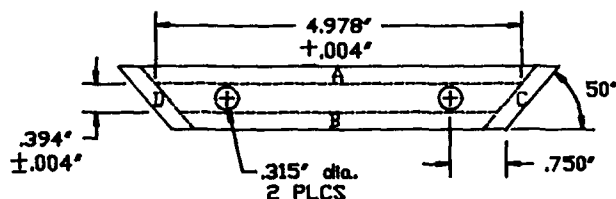
All mat'l .236" \pm .004" thick quartz
All pieces cemented with 3M epoxy ADHDP180

Pc's A-B-C-D flat $\lambda/10$ ($\lambda=.55 \mu\text{m}$)
both sides 10:5 S.D.

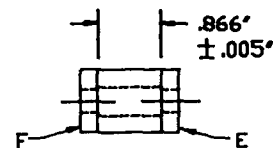
Pc's A-B to be parallel $\lambda/10$ ($\lambda=.55 \mu\text{m}$)
refractive index $n_g=1.4585$

Pc's E-F commercial grind (both sides)

Fitting for Tygon tubing to be supplied
by Zygo and cemented into each hole.
(not shown for clarity)



SIDE VIEW



END VIEW

FIGURE 1

Zig-Zag Dye Cell

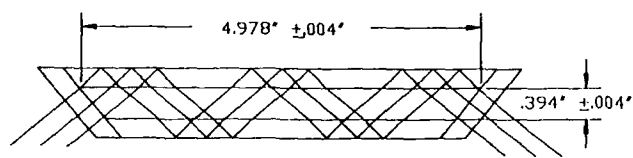


FIGURE 2

Zig-Zag Path

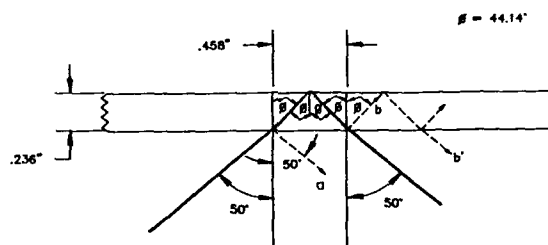


FIGURE 3

Wall Reflection Details of Zig-Zag



FIGURE 4

Straight Through Beam of Dye Cell

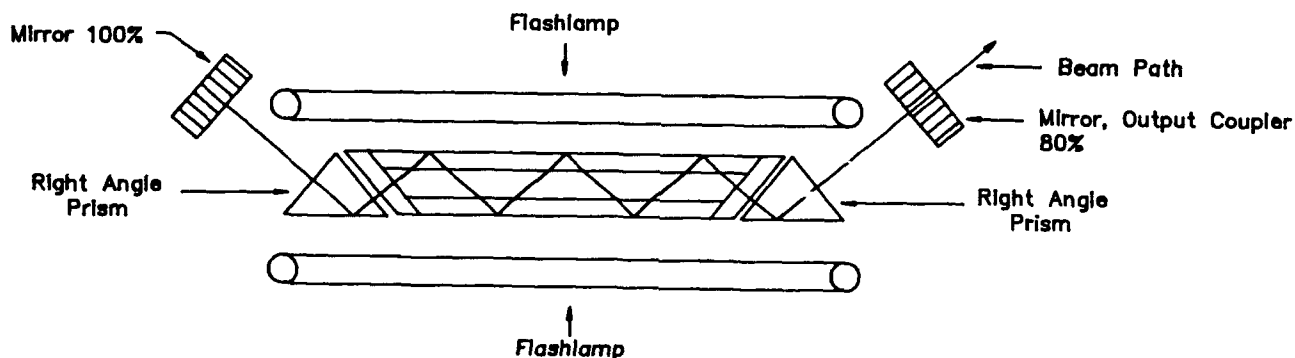


FIGURE 5

Zig-Zag Flashlamp Arrangement
with Prisms

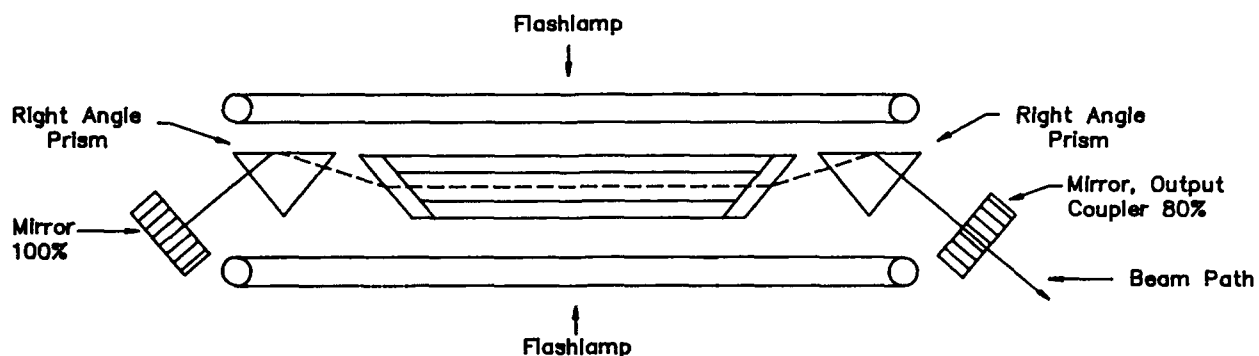


FIGURE 6

Straight Through Flashlamp Arrangement
with Prisms

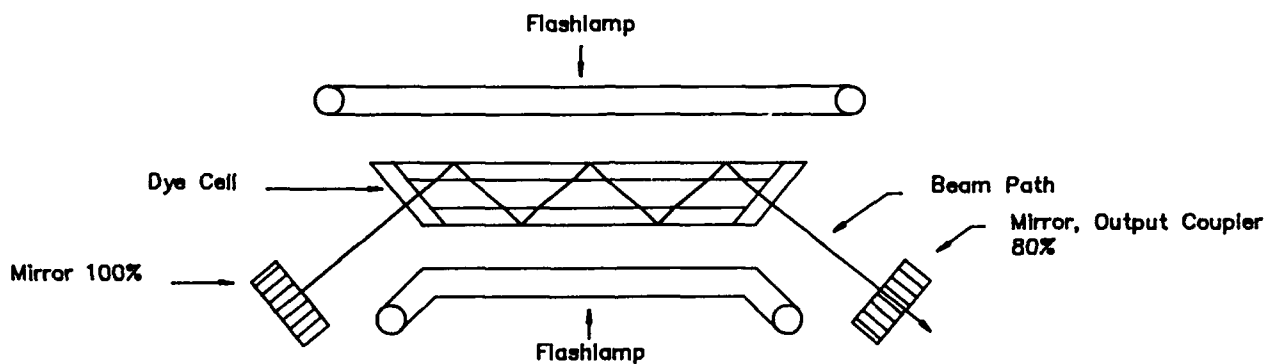


FIGURE 7

Zig-Zag Bent Flashlamp Arrangement
without Prisms

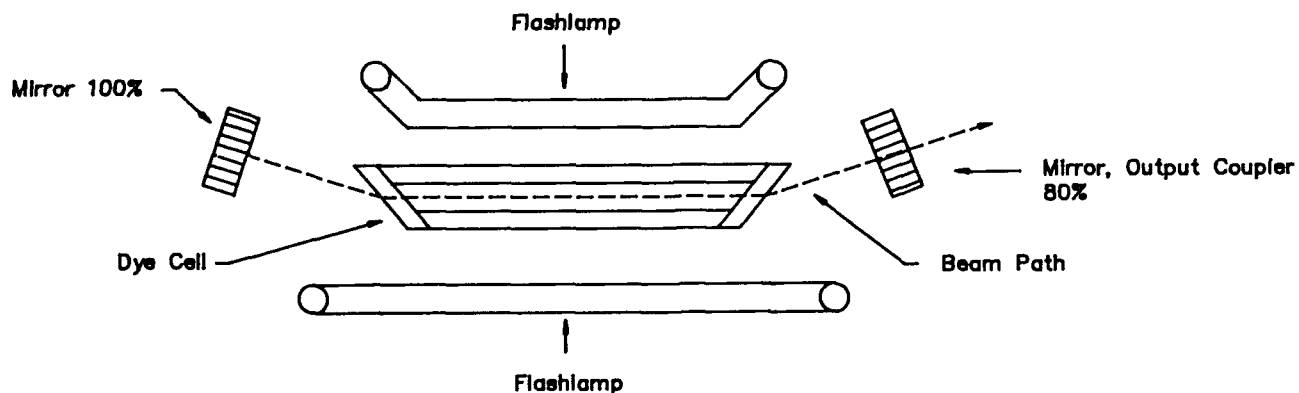


FIGURE 8

Straight Through Bent Flashlamp
Arrangement without Prisms

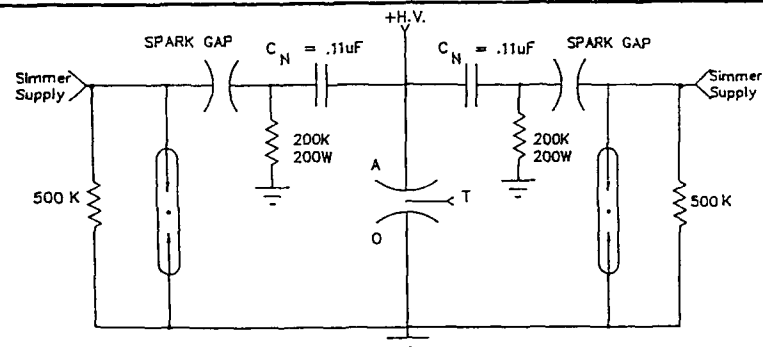


FIGURE 9

Schematic Diagram of Flashlamp Circuit

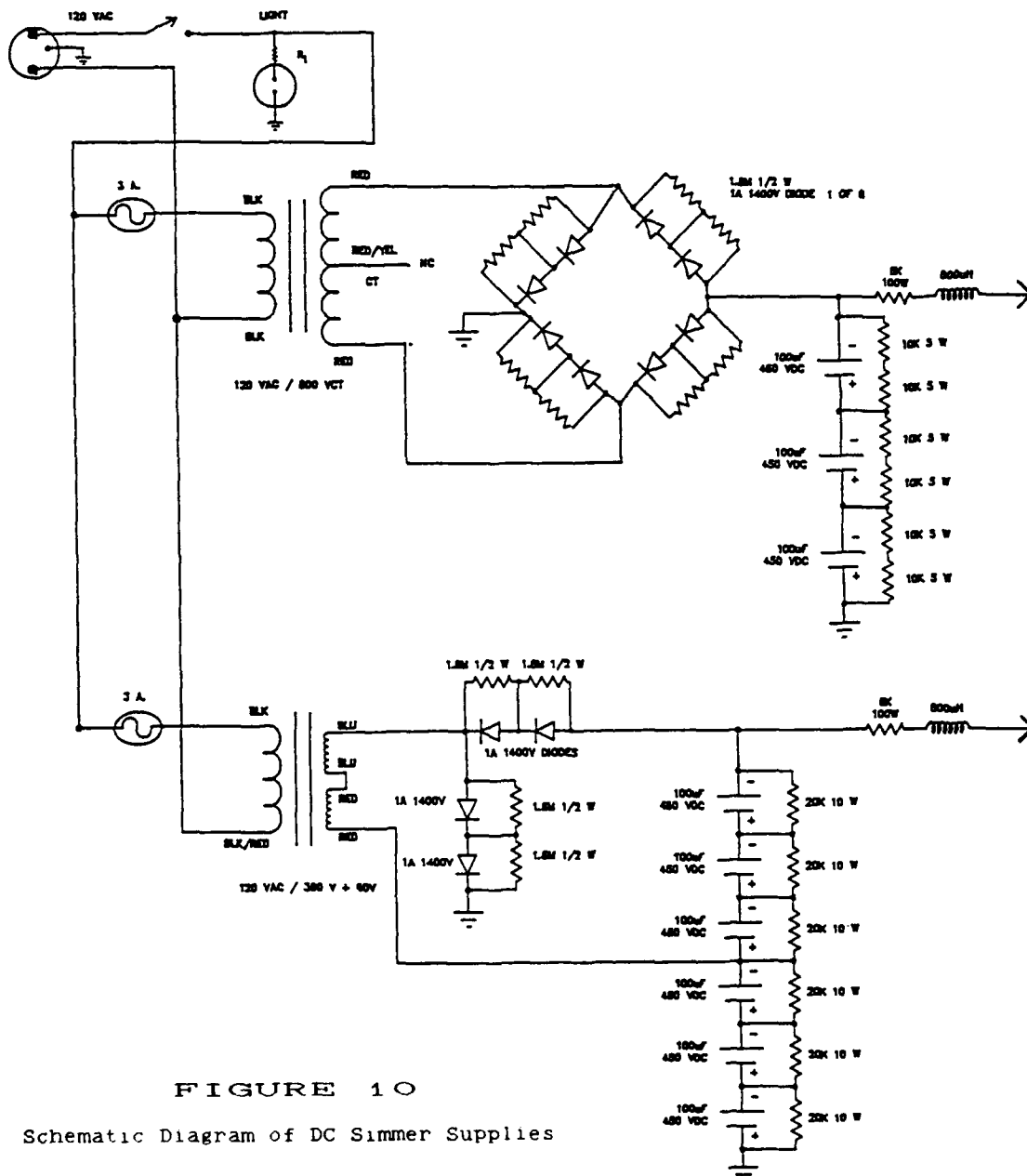


FIGURE 10

Schematic Diagram of DC Simmer Supplies

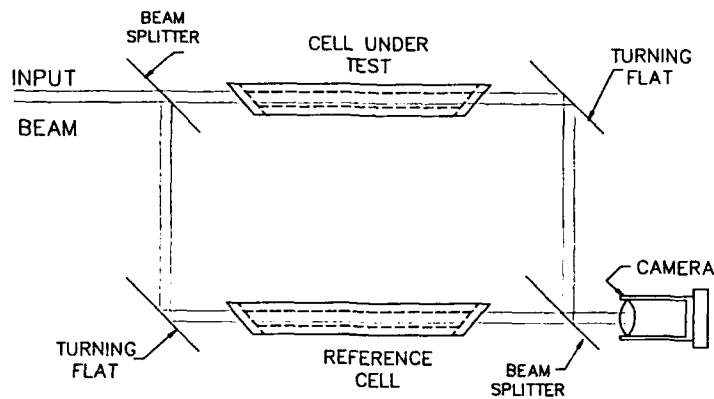


FIGURE 11

Diagram of Mach-Zehnder Interferometer

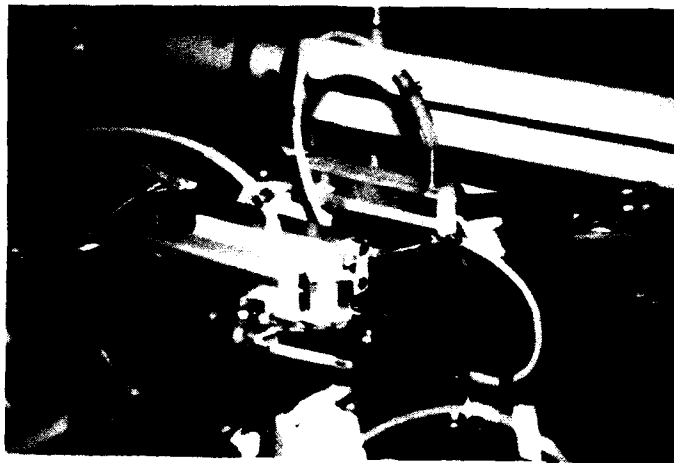


FIGURE 12

Photograph of Experimental Interferometer

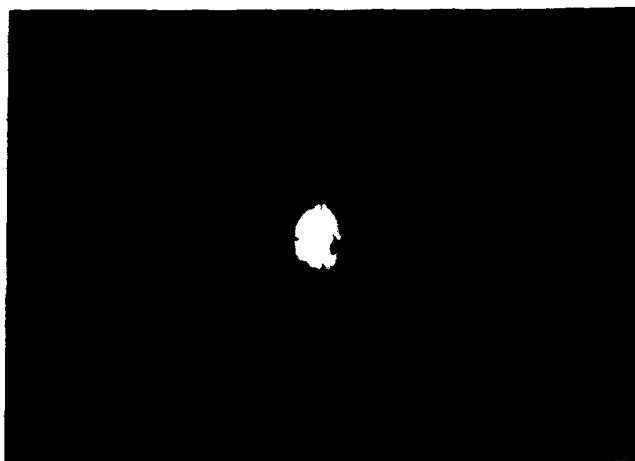


FIGURE 13

35mm Photograph of Zig-Zag Laser Spot



FIGURE 14

35mm Photograph of Straight Through Laser Spot

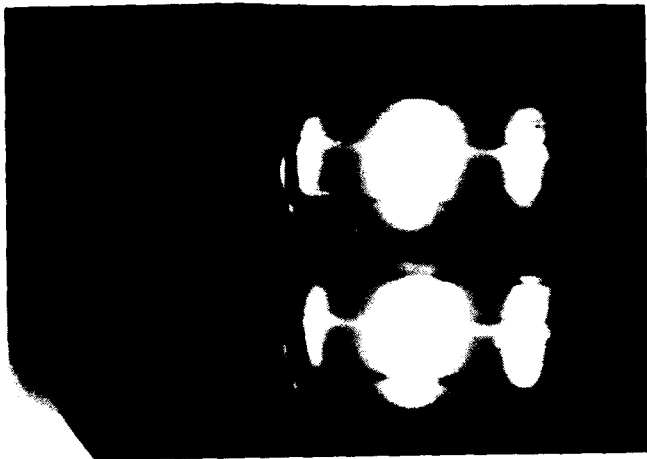


FIGURE 15

Framing Camera Photo. Zig-Zag Case

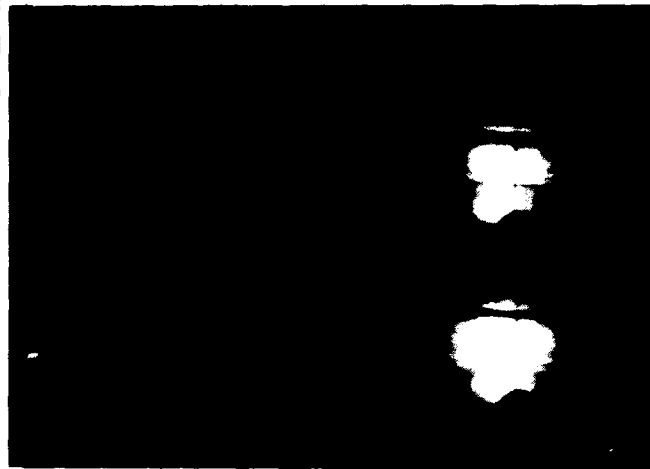


FIGURE 16

Framing Camera Photo. Straight Through Case without Prisms.

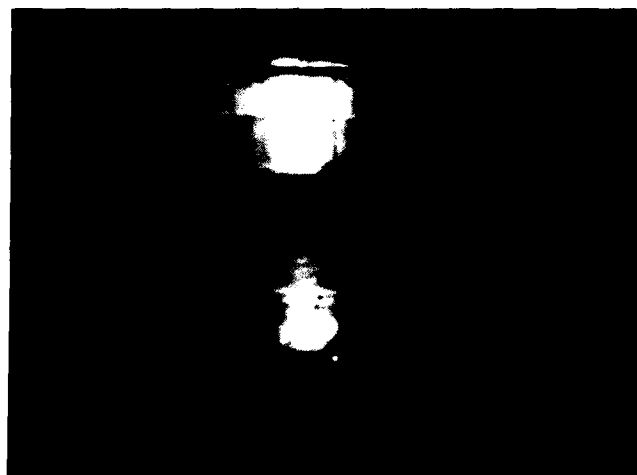


FIGURE 17

Framing Camera Photo. Straight Through Case with Prisms

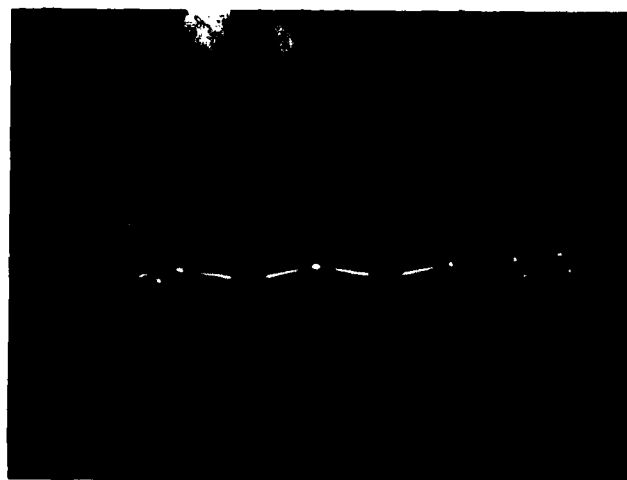


FIGURE 18

Orange HeNe Zig-Zag Alignment Beam

A SOLID-STATE FLASHLAMP-PUMPED DYE LASER EMPLOYING POLYMER HOSTS

Dennis P. Pacheco, Henry R. Aldag, Irving Itzkan
and Peter S. Rostler
Avco Research Laboratory/Textron
2385 Revere Beach Parkway
Everett, MA 02149

Abstract

This paper describes an extensive study of polymers as host materials for laser dyes in flashlamp-pumped systems. The first part of the paper discusses the differences in optical properties between polymers and conventional liquids. In the second part, data are presented on the laser performance of selected dyes in polymethyl methacrylate (PMMA) under flashlamp pumping. Finally, modeling and analysis are presented to explain the observed differences between the laser output in PMMA and in MeOH/H₂O.

Introduction

The use of polymers as host materials for laser dyes or saturable absorbers is relatively untapped. Such solid systems have the advantage of being lightweight, storable, inexpensive to fabricate and safe to handle. For dye lasers, a major benefit is that the need for a dye-flow system (and its attendant complexity) is avoided.

There have been a number of papers in the literature on the performance of dye-doped polymers under laser pumping.¹⁻⁷ In the past several years, much of it has appeared in the Russian and Japanese literature.³⁻⁷ There is relatively little information, however, on the laser characteristics of flashlamp-pumped samples.^{8,9} The purpose of this paper is to describe some recent results that we have obtained for dyes in polymers under conditions of flashlamp excitation. The paper is divided into three parts. The first section details the major differences between polymers and conventional liquids as hosts for laser dyes. The next section presents some results on laser performance for Rhodamine 590 (R590) and Coumarin 540 (C540) in polymethyl methacrylate (PMMA). Finally, we present some modeling and analysis which indicate where the problems lie in achieving laser output in polymer hosts which is comparable to that obtained in conventional liquid systems.

Factors Affecting the Laser Output in Polymer Hosts

We began by characterizing the properties of several optical polymers for laser applications. In comparing these candidates with liquids, significant differences were apparent in the areas of near-UV absorption, index-of-refraction gradients, bulk transmission losses, and differences in dye spectral properties. Each of these is discussed in turn below.

Bulk Absorption in the Near UV

Three of the most common optical polymers are PMMA, polycarbonate and polystyrene. All three show significant absorption in the near UV. The most transparent of these, PMMA, is opaque below about 290 nm, depending on the thickness. This is a problem for flashlamp pumping of laser dyes because of the high blackbody temperatures required for efficient lasing (~ 25,000 K). At these temperatures, the flashlamp output is rich in the UV, where most dyes absorb strongly. The bulk absorption of the polymer effectively excludes pumping in these bands. In the case of MeOH, for example, this UV cutoff is down around 210 nm, depending on the optical path length. Saturated polymers such as polypropylene would be expected to be more transparent in the UV than PMMA, however these materials have problems with high haze levels due to the presence of microcrystalline structures. Even "clarified" polypropylene is far too hazy for laser applications. At present, this issue of UV transparency is unresolved for the polymers. In a later section, data are presented on the effect of this bulk absorption on the unsaturated gain of the laser.

Optical Homogeneity

A second factor affecting the output of solids versus liquids is that of index-of-refraction gradients, which are much more severe in the polymers. Figure 1 indicates schematically what we have observed for both rods and sheets of PMMA. The sample behaves as a thick, negative lens in which the index gradient becomes larger as one approaches the boundaries of the piece. For purposes of modeling, we have

approximated the index variation as being parabolic. The parameter "a" in the figure is a geometric scale factor and is a measure of the homogeneity of the sample. That is, the larger the value of "a", the more homogeneous the material. In this paper, we will discuss the rod geometry only, and the variable r is the radial distance from the rod axis.

It is important to determine the impact of this static lensing behavior on the resonator design and the ultimate performance of the rod. For this reason, we devised a simple technique to measure the parameter "a" for our samples. The setup is depicted in Figure 2. Because the rod is a negative lens, the position of the focus in arrangement #1 occurs at a greater distance from the positive lens than for arrangement #2. This difference (y-x) is used to calculate the lensing effect of the rod. Using the parabolic model and geometrical optics, one can obtain formulas for l_1 and "a" in terms of readily measurable quantities. For our specimens, values of "a" typically fell in the range of 20-30 cm.

Assuming a parabolic index variation for the rod, one can determine the stability regions for a resonator in which the rod is imbedded. In Figure 3, we present the results of such an analysis for the symmetric resonator in the inset. The lenses are assumed to be close to the rod with the reflectors in turn close to the lenses. As is seen from the figure, the stable region is bounded by the functions $\coth(D/2a)$ and $\tanh(D/2a)$. As $D/2a$ becomes greater than about 2, the range of values of $n_0 f/a$ for which lasing can occur becomes quite small. In view of the dynamic lensing that occurs during pumping, there is a practical limit on the length of the rod that can be lased efficiently in such a resonator. For rods as long as 40 cm and values of "a" on the order of 20-30 cm, it is not difficult to find suitable regions in which to work. The labelled rectangles within the stable region of Figure 3 represent regions in which we have tested laser rods. The point to be emphasized here is that the homogeneity of the laser rod must be characterized first and then a resonator designed around it. Note that a resonator consisting of flat reflectors is not stable for finite values of "a".

Experimental evidence supporting the above model is given in Table 1. The first three columns refer to the resonator used, with the last giving the relative output. The resonators are arranged so that increasing applied curvature runs downward in the table. The data show that a minimum amount of applied curvature is needed before lasing can be obtained.

Table 1. Effect of Resonator Design on Lasing of R590 in PMMA

<u>RESONATOR:</u>			<u>RELATIVE OUTPUT:</u>
<u>OUTPUT COUPLER</u>	<u>MAX R</u>	<u>LENSES</u>	
R = 0.50 (FLAT)	FLAT	none	DID NOT LASE
R = 0.50 (FLAT)	20 m	none	DID NOT LASE
R = 0.50 (FLAT)	10 m	none	DID NOT LASE
R = 0.60 (3.12 m)	10 m	none	0.12
R = 0.40 (3.12 m)	10 m	none	0.28
R = 0.25 (FLAT)	FLAT	2, +250 mm	0.42
R = 0.50 (FLAT)	FLAT	2, +250 mm	1.0
R = 0.75 (FLAT)	FLAT	2, +250 mm	0.86

Bulk Transmission Losses

Another factor which differentiates polymer hosts from liquids is that of bulk transmission losses. The presence of inclusions and bubbles in the polymer gives rise to absorbing and scattering of light in excess of that observed in liquids. This is not a fundamental property of polymers, but rather represents what is presently available. Our better undoped samples show a bulk transmission loss on the order of 0.5 - 1%/cm. We have not been successful in lasing specimens with losses greater than 2 or 3%/cm. Measured losses are higher when the dye-doped rod is pumped.

Figure 4 shows that distributed losses can have a severe effect on the measured output of the rod. In the figure, the extraction efficiency η is plotted as a function of the ratio of distributed loss to unsaturated gain (α_0/g_0). This efficiency is defined as the laser output flux optimized with respect to feedback and normalized to its peak value (at zero loss). The relationship in the figure can be derived using a Rigrod analysis as described in reference 10. Note that when (α_0/g_0) = 0.5, the output is down by about an order of magnitude. Even when

$\alpha_0/g_0 = 0.1$, the output is cut in half. For convenience, several data points generated in this study have been included. The solid-phase results reveal an extraction efficiency which is down by a factor of three or four compared with that for conventional liquids. As will be shown later, the problem resides both in excessive losses and with a decrease in gain.

Differences in Dye Spectral Properties

The last major issue in comparing solids to liquids relates to differences in the spectroscopic properties of the dye because of the change of environment. The different polarity will lead to a solvent shift of absorption and emission bands (including excited-state spectra). The rigid matrix of the polymer can affect the fluorescence quantum yield by reducing the mobility of certain substituent groups. The dynamical behavior may also be affected, since the rates for intersystem crossing and triplet-state quenching can be different. A representative sampling of the spectral data we have obtained is presented in Table 2. The major item of interest is the difference in fluorescence quantum yield between liquid solvents and PMMA. In the case of the rhodamines, there is a slight decrease. For Coumarin 540A and Fluorol 555, however, there is an increase in going to PMMA. This is probably due to the decrease in mobility mentioned above. All other things being equal, these dyes should perform better in PMMA than in EtOH or MeOH.

Table 2. Spectroscopic Properties of Selected Dyes - Liquid versus Solid Host

DYE	SOLVENT	ABSORPTION λ_{\max} (nm)	EMISSION λ_{\max} (nm)	η_F	REFERENCE
R590	MeOH/H ₂ O	530	555	0.93	This work.
	PMMA	533	556	0.81	This work.
C540	MeOH/H ₂ O	470	510	0.62	This work.
	PMMA	450	- -	- -	This work.
C540A	EtOH	423	530	0.38	11
	PMMA	415	499	0.98	12
F555	MeOH	442	- -	0.68	13,14
	PMMA	430	492	0.88	13
R640	MeOH	575	- -	0.94	12,14
	PMMA	581	601	0.75	12

Experimental Results on Laser Performance in PMMA

In this investigation, two coaxial lamps were used for the lasing tests. The experimental setup is depicted in Figure 5. To minimize intracavity losses, all surfaces exposed to air were AR-coated for the appropriate wavelength range, and an index-matching fluid was used between rod and windows. Based on the dimensions of the lamps, rods of 18 cm and 42 cm lengths could be pumped. In both cases, the diameter was 0.95 cm. Because of heating of the rods during pumping, all data were taken single-shot, with adequate time between shots for equilibration. The energy input for the smaller coaxial lamp was fixed at 60 J; the larger lamp was operated at 360 J.

The usual testing procedure was to measure the "a" parameter for a given rod as described earlier and then choose lenses which allowed operation well into the stable region. A sample trace showing the power output for an 18-cm rod is presented in Figure 6. In this case the dye solution was Rhodamine 590 in PMMA (1.1×10^{-4} Moles/liter). The upper trace shows the current pulse through the lamp for purposes of reference; the time scale is 200 ns/division. For this pulse, the measured output was in excess of 50 mJ with a temporal width of 300 ns (FWHM). Figure 7 shows similar data at the same sweep speed for a 42-cm rod. The dye solution was Coumarin 540 (C540) in PMMA at a concentration of 1.4×10^{-4} Moles/liter. The energy output was 50 mJ with a pulse width of 475 ns.

An obvious issue in a solid-state dye laser is that of degradation of energy output. In the case of the 18-cm R590 rods, the observed degradation was relatively graceful. The value of the degradation rate varied somewhat from rod to rod, but fell in the range of 1.5 - 1.9%/shot. Typical data are depicted in Figure 8, in which the output was followed for more than two dozen shots. There are strategies for extending dye life, such as using modifying additives to prevent the formation of free radicals in

the vicinity of the dye molecules. Gromov et al.⁵ have reported some success in this area for their laser-pumped system.

Knowledge of the degradation rate is important in its own right, but it also allows correction of the data for shot number. For example, information on internal lasing parameters can be obtained once the effects of output degradation have been corrected for. In particular, it is of interest to extract data on the distributed loss and the unsaturated gain for the polymer rods and conventional liquids.

Rigrod¹⁰ has analyzed the case of homogeneously broadened lasers with uniform distributed loss. In his treatment, he obtains an approximate expression for the laser output power as a function of saturation flux, distributed loss, unsaturated gain and mirror reflectivity. We have used this relation to obtain information on the gain and loss parameters in both PMMA and MeOH/H₂O. The basic procedure is to measure the output of the laser as a function of mirror reflectivity and fit the results to the Rigrod relation. An example of this is given in Figure 9. The data are presented for R590 in PMMA at a concentration of 1.1×10^{-4} Moles/liter. The plot shows the energy output as a function of mirror parameter $X = -\ln(\sqrt{R})$. For purposes of reference, $X = 0.35$ corresponds to a reflectivity of 50%; higher reflectivities are to the left of this point and lower reflectivities to the right. We note that a very good fit is obtained for this sample when the unsaturated gain is about 11%/cm and the distributed loss is about 5.5%/cm.

Table 3 is a summary of some of the results that we have obtained using this approach. Note that the first two row entries correspond to R590 in MeOH/H₂O, with the next three for R590 in PMMA. For the first four entries, the concentrations are nearly the same, and so meaningful comparisons can be made. The second column of the table indicates any special conditions or changes that were made in the composition of the sample. The third column reports the bulk transmission loss measured by passing the beam from a HeNe or other light source through the sample. Fresnel losses were compensated for by measuring the transmission through different lengths of the material. This loss may be termed static or small-signal, since the sample is not being pumped. The next column shows the dynamic loss as obtained from the fitting described in connection with Figure 9. This loss can easily be higher than the static one because of the onset of time-dependent processes such as triplet-triplet absorption. The last two columns contain data on the unsaturated gain (obtained from the fitting procedure) and the extraction efficiency (as defined in Figure 4).

Table 3. Summary of Gain and Loss Parameters for Solid and Liquid Hosts

DYE SOLUTION	CONDITIONS	SMALL-SIGNAL LOSS (cm ⁻¹)	DYNAMIC LOSS (cm ⁻¹)	UNSATURATED GAIN (cm ⁻¹)	EXTRACTION EFFICIENCY(η)
R590 in MeOH/H ₂ O 7.5×10^{-5} M/l	no UV filter	- -	0.018	0.19	0.48
R590 in MeOH/H ₂ O 7.3×10^{-5} M/l	Pyrex as UV filter	- -	0.012	0.11	0.45
R590 in PMMA 7.5×10^{-5} M/l	5 percent HEMA	0.006	0.028	0.077	0.16
R590 in PMMA 6.8×10^{-5} M/l	10 percent HEMA	0.010	0.034	0.082	0.13
R590 in PMMA 1.1×10^{-4} M/l	10 percent HEMA	0.013	0.056	0.113	0.09
C540 in PMMA 1.4×10^{-4} M/l	- -	0.010	0.014	0.025	0.06

Analysis and Discussion

A number of trends can be discerned immediately. First, the extraction efficiencies of the solid samples are comparable to each other, but are a factor of three or four lower than those for the liquids. These data points are in fact the ones plotted in Figure 4. The effect of the exclusion of the near-UV bands of the dye is relatively pronounced. When pyrex was introduced to filter out the UV from the liquid

sample, the unsaturated gain dropped from about 19%/cm to about 11%/cm. In the case of the polymer host, the value was found to be about 8%/cm for a comparable concentration.

The dynamic losses in the PMMA samples are about twice as large as those for the liquids. These values are also several times larger than the small-signal measurements. Finally, there is experimental evidence that the dynamic loss scales with concentration. (See, for example, the data for R590 concentrations of 6.8×10^{-5} and 1.1×10^{-4} Moles/liter.) Together, these observations imply that there is a time-dependent loss, related to the presence of the dye, which is not as pronounced in the liquid. An obvious explanation is that the effects of triplet-triplet absorption are more severe in the solid matrix. This may in turn be due to one or more of the following: a faster intersystem crossing rate, increased triplet-triplet absorption at the lasing wavelength, or a reduced triplet quenching rate in PMMA. Since the quenching of triplets in liquids is effected by the diffusion of molecular oxygen into the immediate vicinity of the dye molecule, triplet quenching may be inhibited in the solid matrix.

For dyes in which the formation of triplets is not a major issue, the dynamic losses may remain small. This may be the case for example in C540, for which the small-signal and dynamic losses are nearly equal. This particular dye, however, has a relatively low gain in PMMA.

Summary

The principal results of this investigation may be summarized as follows:

- 1.) Index-of-refraction inhomogeneities, if symmetric enough, can be accommodated by resonator design. Our modeling of resonator stability is consistent with the experimental results to date.
- 2.) The ratio α_0/g_0 for R590 in PMMA is several times higher than that in MeOH/H₂O. This is a major factor limiting efficient performance.
- 3.) For our R590 specimens, the value of α_0 is dominated by time-dependent (dynamic) losses. A possible cause is triplet formation during the pulse.
- 4.) For a number of dyes of interest, the fluorescence quantum yield in PMMA is higher than the analogous values in liquid solution. Such dyes may perform better in PMMA than in EtOH or MeOH.
- 5.) Rods as long as 42 cm have been lased with a suitable resonator.

Acknowledgements

This work was funded in part by the Directed Energy Directorate of the U.S. Army Missile Command, Redstone Arsenal, AL, under Contract DAAH01-84-D-A031.

The authors would like to thank Drs. John Ehrlich and James Bentley of MICOM for helpful discussions throughout the performance of this work. We also acknowledge the able technical assistance of Ann Farkas, Michael Reilly, Charles Ward and Gerald Sabean.

References

- 1) H. Wang and L. Gampel, Opt. Commun. 18, 444 (1976).
- 2) R. O'Connell and T. Saito, Opt. Engineering 22, 393 (1983).
- 3) V. Danilov, A. Eremenko, S. Lan'kova, D. Savel'ev and A. Stepanov, Bull. of the Academy of Sciences of the USSR (Physics Series) 47, 86 (1983).
- 4) D.A. Gromov, K.M. Dyumaev, A.A. Manenkov, A.P. Maslyukov, G.A. Matyushin, V.S. Nechitailo, and A.M. Prokhorov, Bull. of the Academy of Sciences of the USSR (Physics Series) 48, 116 (1984).
- 5) D.A. Gromov, K.M. Dyumaev, A.A. Manenkov, A.P. Maslyukov, G.A. Matyushin, V.S. Nechitailo, and A.M. Prokhorov, J. Opt. Soc. Am. B2, 1028 (1985).
- 6) S. Muto, H. Uchida and T. Takauchi, Trans. IECE Japan E70, 315 (1987).
- 7) S. Muto, A. Ando, O. Yoda, T. Hanawa and H. Ito, Trans. IECE Japan E70, 317 (1987).
- 8) O.G. Peterson and B.B. Snavely, Appl. Phys. Lett. 12, 238 (1968).

- 9) J.M. Drake, E.M. Tam and R.I. Morse, IEEE J. Quantum Electron. QE-8, 92 (1972).
- 10) W.W. Rigrod, IEEE J. Quantum Electron. QE-14, 377 (1978).
- 11) G. A. Reynolds and K. H. Drexhage, Opt. Commun. 13, 222 (1975).
- 12) J.M. Drake, M.L. Lesiecki, J. Sansregret and W.R.L. Thomas, Appl. Opt. 21, 2945 (1982).
- 13) M.L. Lesiecki and J.M. Drake, Appl. Opt. 21, 557 (1982).
- 14) Exciton Chemical Company Catalog, Dayton, OH.

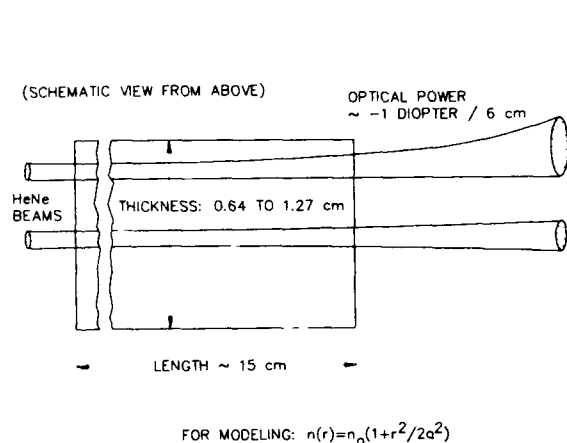


Figure 1 Optical Quality of PMMA Samples Over Long Path Lengths

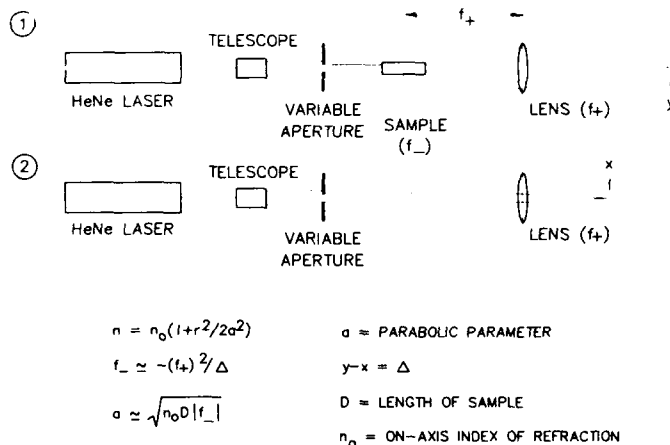


Figure 2 Experimental Setup for Measuring the Parabolic Parameter of a Laser Rod

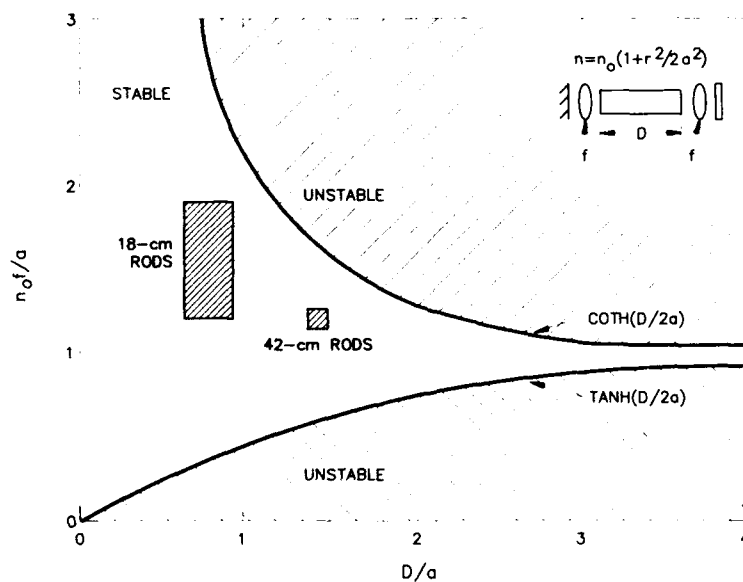


Figure 3 Map of the Stability Region as a Function of Rod and Lens Parameters

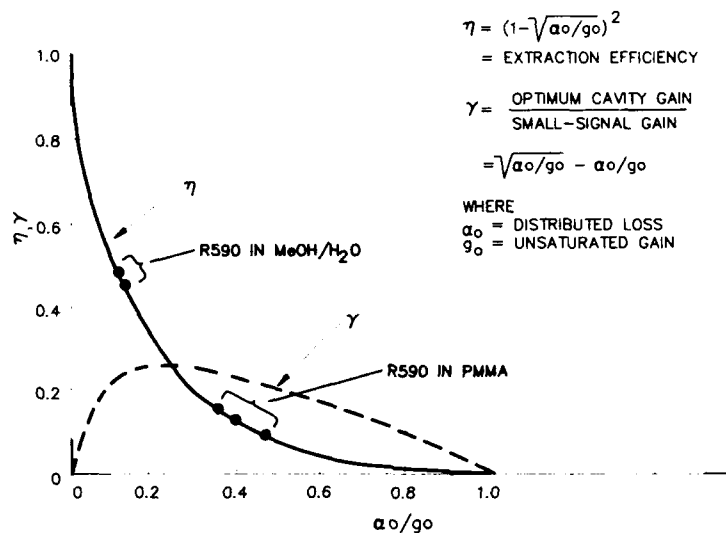


Figure 4 Dye-Laser Output as a Function of Loss/Gain Ratio

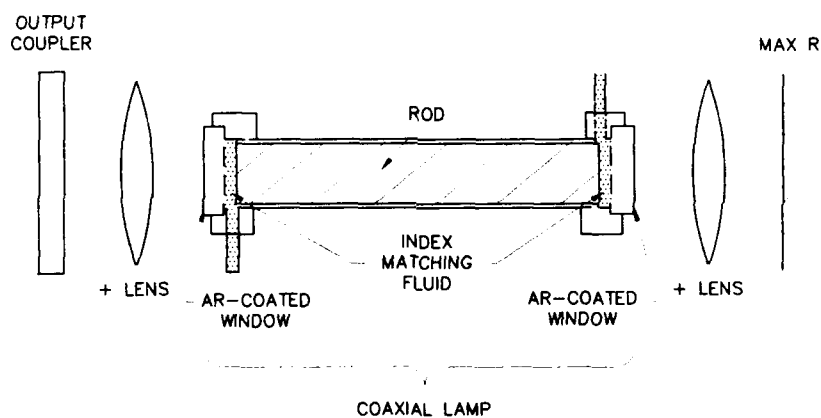


Figure 5 Resonator for Polymer-Host Laser Tests

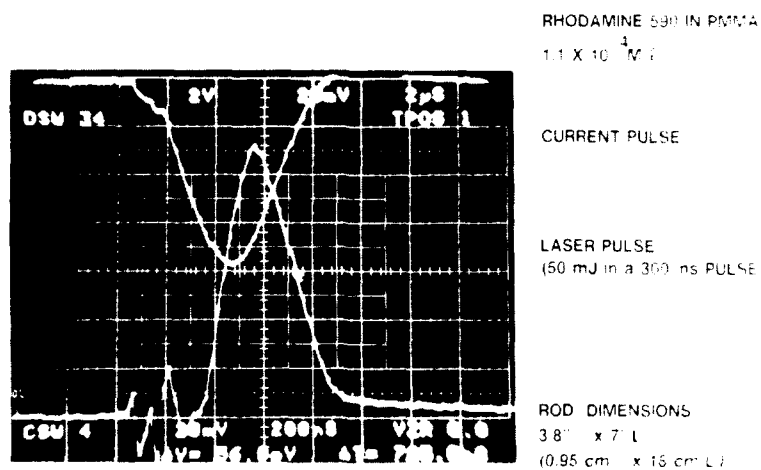


Figure 6 Laser Output of Rhodamine 590 in a Polymer Host. Sweep Speed is 200 ns/Division

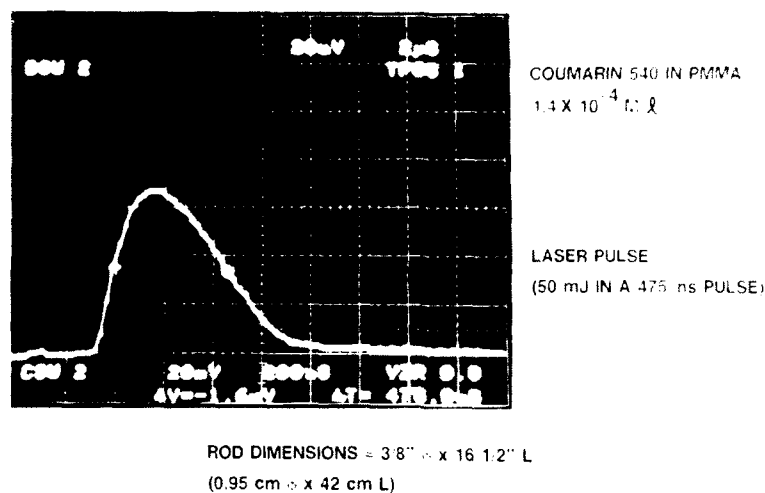


Figure 7 Laser Output of Coumarin 540 in a Polymer Host. Sweep Speed is 200 ns/Division

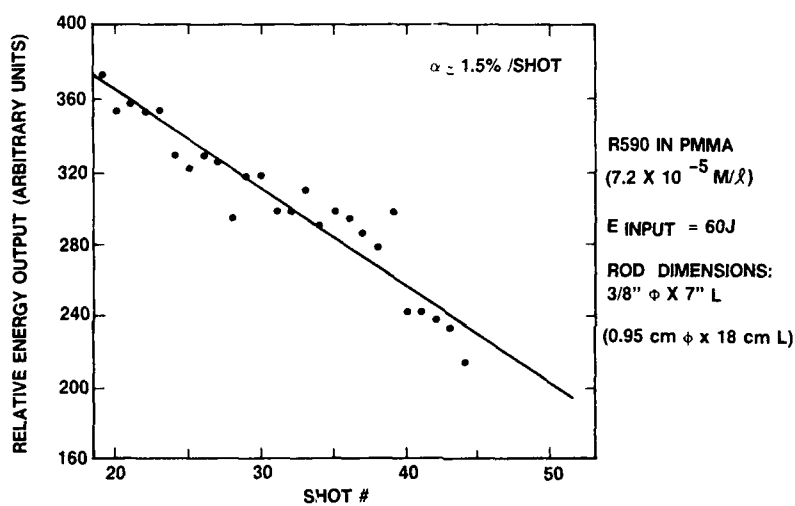


Figure 8 Degradation of Energy Output of Rhodamine 590 in PMMA

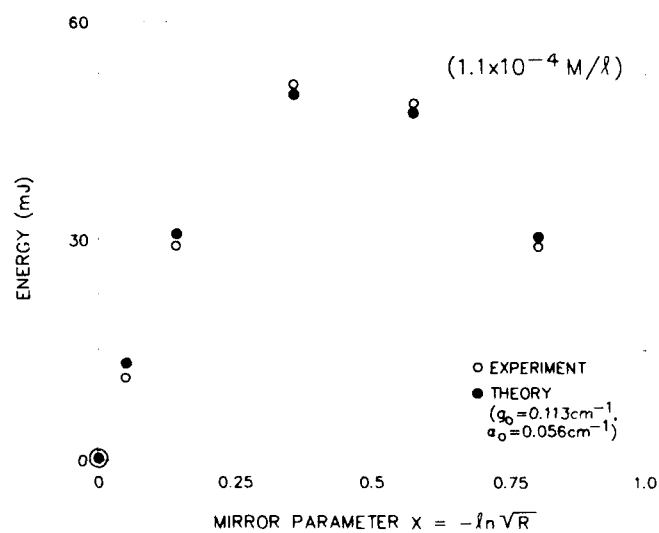


Figure 9 Theoretical Fit of Data for Rhodamine 590 in PMMA

SOLID HOSTS FOR DYE LASER RODS – PART 1 CRITERIA FOR CHOOSING A HOST MATERIAL

George F. Erickson, Staff Member
Los Alamos National Laboratory
CLS-6, MS J564
Los Alamos, NM 87545

ABSTRACT

This paper will attempt to provide selection criteria for polymers as hosts for flashlamp-pumped dye laser rods. The properties of transparent polymer materials are compared with typical inorganic crystal and glass hosts

For some time now, our group, at the Los Alamos National Laboratory has been interested in trying to produce high quality inexpensive dye-doped laser rods. The potential low cost, in volume production of dye-doped plastic rods, combined with the wide variety of lasing wavelengths available from dyes was the primary driving force for this effort. The applications have been for both single and multiple shot operation, with fast flashlamp pumping. In the single shot case, if the dye-doped rod was damaged or destroyed after lasing once, this was acceptable as we were trying to get rather large power outputs from the rods. Since we needed simple, inexpensive, storable and compact systems, flowing liquid dye solvents were ruled out. This left us with the need to find suitable dye hosts that were solids with the necessary high optical quality. Organic polymers, namely plastics, such as the acrylics have been looked at for some time for these sorts of applications by other groups world wide.

As one gets more deeply involved with the problem of plastic dye laser hosts, a number of problems become apparent sooner or later. Aside from the need for very high optical quality in the plastic rods, one encounters problems with the nature of plastics as a class, when compared to inorganic crystal and glass laser hosts. Although dye-doped plastic materials may appear attractive at first glance from a potential low cost standpoint, particularly in volume production, a comparison of the physical properties of plastics versus inorganic hosts leads to some serious consequences. If one looks at the coefficient of thermal expansion and the thermal conductivity of plastics versus inorganic glasses and crystal hosts (Table 1), one sees that the coefficient of thermal expansion for plastics is, in general, one order of magnitude greater

TABLE 1.
PROPERTIES OF PRINCIPAL OPTICAL PLASTICS

		Acrylic Polymethyl Methacrylate (Lucite) (Plexiglass)	Styrene Polystyrene (Dylene) (Sivron) (Lustrex)	NAS Methyl Methacrylate Styrene Copolymer	SAN Styrene Acrylonitrile (Lustran) (Tynil)	Polycarbonate (Lexan) (Meron)	TPX Methylpentene (TPX)	ABS	ADC Allyl Diglycol Carbonate (CR 39)	Glass BK 7
Refractive Index, n										
n _d (589.3nm)		1.491	1.590	1.533-1.567	1.567-1.571	1.586	1.467	1.538	1.504	1.517
n _c (656.3nm)		1.488	1.585	1.558	1.563	1.581	1.464		1.501	1.514
n _f (486.1nm)		1.496	1.604	1.575	1.578	1.598	1.505		1.510	1.522
Abbe Value, V _d		61.4	31.1	35	37.8	34.5	11.4		56	64.6
Rate of Change in Index with Temperature	dn/dt × 10 ⁻⁵ /°C	-8.5	12.0	14.0		-11.8 to -14.3			-14.3	-0.3
Coefficient of Linear Expansion	cm/cm × 10 ⁻⁵ /°C	6.74 @ 70°C	6.0-8.0		6.5-6.7	6.6-7.0		0.83	11.4 25 to 75°C 14.4 75 to 125°C	0.71
Deflection Temperature										
3.6°F/min 264 psi	°C	92	82		99-104	142		90		
3.6°F/min 66 psi	°C	101	110	100		146		84		
Recommended Max Cont. Service Temp	°C	92	82	93	79-88	124			100	
Thermal Conductivity	cal/sec·cm·°C × 10 ⁻⁴	4.96	2.4-3.3	4.5	2.9	4.0	4.0		5	26.6
Haze	%	2	3	3	3	3	5	12	3	
Luminous Transmittance	% Thickness 3.175mm	92	88	90	88	89	90	79-90.6*	93	99.9
Water Absorption	% Immersed 24 hr @ 23°C	0.3	0.2	0.15	0.2-0.35	0.15			0.2	
Mold Shrinkage	%	0.2-0.6	0.2-0.6	0.2	0.2-0.6	0.5-0.7	1.5-3.0			

* Luminous Transmittance 79%, thickness 6.35mm, 90.6%, thickness 0.381mm

for plastics than for the inorganic glasses and crystal hosts. The inverse is true for the thermal conductivity of plastics versus inorganic glasses. The thermal conductivity disparity of plastics, compared to many of the single crystal inorganic hosts such as sapphire and the garnets, is even more extreme because of the abnormally high thermal conductivity of these materials due to lattice phonon conduction. The change of refractive index of plastics as a function of temperature, dn/dt (Fig. 1), is closely related to the coefficient of thermal expansion. The combined effects of these two properties, as it affects plastic dye laser rods, is to aggravate the thermal stability problem by about the product of the dn/dt and the thermal conductivity ratios as compared to inorganic glasses or crystal hosts. The net result is that the optical thermal stability of plastic dye laser rods is about two orders of magnitude poorer than inorganic glass rods, approaching three orders of magnitude poorer than sapphire.

The overall effect of this very severe problem is that unless dye-doped plastic laser rods can be stored in an isothermal environment for a considerable length of time prior to firing the flashlamp, the optical properties of the plastic rod will be essentially useless if anything close to a few times diffraction limited output is needed. In the case of repetitively pulsed plastic dye laser rods, the thermal effects would be catastrophic.

A further problem related to the physical properties of plastic dye laser rods is the mechanical stability of the laser rod and cavity. Plastics are far less rigid or stiff than inorganic glass or crystal rods. Physical support under stress, vibration, G loads, etc. of plastic rods will be much more of a problem than conventional inorganic rods. Thermal gradients are apt to cause rod bending, which will throw the optical cavity out of alignment. Plastics are softer and scratch more easily than glass and most crystal hosts. About the only advantage the plastics have to offer, as far as physical properties are concerned, is resistance to mechanical and thermal shock and impact breakage. Being organic, plastics are also subject to photochemical damage. In addition, the laser dyes will undergo photochemical damage or bleaching. Photochemical damage of dye solutions is a problem in which the chemistry of the dye and the solvent system are synergistically inter-related. Polymerization without the use of initiators is desirable to obtain the best dye stability. For one shot applications, this is not too severe a problem if the rods do not bleach in long-term storage.

Probably more work has been done on acrylic, PMMA systems by numerous groups around the world than most other plastic systems for dye laser rod applications. Polymethyl methacrylate is by far the most common plastic in use for optics as it machines and polishes well, is easily moldable, has good environmental stability, and can have good uv transparency.

Acrylic's optical transmission is better than most optical plastics and can have low light scattering if clean and free of particulates (see Fig. 2). The optical damage threshold if clean is also quite good. The optical homogeneity of good quality molded acrylic optics is typically nearly two orders of magnitude poorer than good quality optical glass (see Table 1). Acrylic optics, even in well annealed, have considerable stress birefringence which is hard to remove. Adding the correct amount of a suitable plasticizer can correct the stress birefringence but can cause other problems such as loss of uv transparency, and poorer mechanical properties as well as possible interactions with the laser dye.

PMMA as such is a good solvent for the Coumarin family of dyes but is not a good solvent for Rhodamine or Kiton Red dyes which require more polar solvents. Dye triplet state formation is often aggravated in plastic host solutions. Very recently, Dr. Rob Hermes of our Laboratory, has produced some extremely fine quality acrylic copolymer rods with good solvent properties, even for dyes requiring polar solvents.

In addition to PMMA, we have looked at a number of other polymer systems as candidates for plastic dye laser rods. We looked into some clear epoxies, a rigid polyurethane-polyester copolymer sold commercially by the name, Calthane 3200, and a number of organic glasses of the glycerol borate family. We also ordered some samples of some commercial, fluorescent dye loaded, extruded, PMMA rod from Bayer AG through their U.S. subsidiary, Mobay Corporation. This commercial, fluorescent, plastic rod and sheet is available in seven colors from deep red to violet and is very inexpensive.

The epoxies had little to commend them for our application as we had trouble with dye-hardener interactions, fairly poor ultra-violet transmission, poor optical quality, and poor solvent power for dyes requiring polar solvents. The Calthane 3200 looked somewhat more promising in that the uv transparency of this material is quite good. We never were able, however, to get good optical quality from this material and the solvent power for dyes needing polar solvents was again poor. The Bayer-Mobay commercial, fluorescent, PMMA extrusions had two problems. The material had both a fluorescent and a nonfluorescent dye dissolved in the host PMMA and the optical quality of the extrusions was very poor.

The family of organic glasses based on borate esters of polyhydric alcohols was rather interesting in that these materials could be produced with a hardness ranging from a brittle glass at room temperature (glycerol borate), to a high viscosity liquid at room temperature (propylene glycol borate). The third member of this group is ethylene glycol borate which is intermediate in hardness or viscosity between the brittle glycerol borate and the syrupy propylene glycol borate.

These three borate esters can be mixed together in any proportions to temper the hardness of the resultant organic glasses. We hoped that these organic glasses would be containable as very high viscosity semisolid glasses inside fused silica cylindrical dye cells which would behave like rigid dye rods. The severe T.C.E. mismatch between the high expansion organic glasses and the fused silica would be relieved by flow in the organic glasses. An expansion space for a bubble is needed to prevent cracking of the dye cell when subjected to temperature changes. The viscosity of the organic glass is so high as to prevent convection from disturbing the optical quality of the laser medium. The glycol borate esters are again poor solvents for dyes requiring polar solvents but their uv transmission is quite good. This exercise was not successful for a number of reasons. The most severe problem is that these glycol borate esters seem to produce a swarm of tiny gas bubbles when subjected to the intense light of the xenon flashlamp and these bubbles can't be removed from the optical path without remelting the organic glass to reduce the viscosity to a low value.

One other possibility came to mind while we were working on plastic laser rods. The severe problems with thermally induced optical inhomogeneities in any high T.C.E. and low thermal conductivity, plastic dye laser rod might possibly be sidestepped by making a rigid, bonded, fiberoptic bundle, laser rod. This rod would have a dye doped, higher refractive index, plastic core material, surrounded by a clear, undoped, lower index, plastic cladding which constitutes a very thin coating between the adjacent dye doped core fibers. The solid matrix of cladding would couple the pump light into the matrix and the individual dye doped fibers would be mode coupled to one another by the evanescent wave penetrating the thin cladding between adjacent fibers. This would tend to prevent all the individual fibers in the bundle from lasing unsynchronized with one another which would make the entire fiberoptic laser bundle act as a more or less incoherent light source. If the evanescent wave coupling between adjacent fibers in the matrix works, the optical coherence should be greatly improved. The partitioning of the laser rod into many small lasing regions, each isolated from its neighbor, except for the evanescent wave coupling, would permit fairly large refractive index gradients across the cladding to exist without disturbing the lasing medium, which is the individual high index dye doped fibers. Since each fiber is bounded by the steep index gradient at the core cladding interface, the laser light would be trapped and confined to the fiber it originated in. The laser cavity mirrors would have to be in contact with the cut and polished ends of the laser fiberoptic bundle. Transverse pump light should be well coupled throughout the bundle. There would be an effective change in the cavity length across the width of the fiberoptic bundle when subjected to a temperature gradient, however, to what extent these different coupled lasers can synchronize with slightly different cavity lengths is unknown at this time.

Fabrication of such a structure although complicated might not be as difficult to accomplish at a reasonable cost as it may seem at first glance. Individual dye-doped plastic fiber with a higher refractive index than the clear cladding material could be produced in long lengths. The thin layer of clear cladding could be applied as a dip coating and cured or dried by solvent evaporation. This thinly clad fiber could then be bundled and pressure bonded, perhaps by warm isostatic pressing of warm extrusion to form the laser fiberoptic bundle. This material could then be cut to length, polished and have the flat-flat cavity mirrors cemented on the ends. The cavity mirrors may be able to be simply deposited on the polished ends of the bundle by physical vapor deposition methods and further reduce the cost of the fiberoptic laser rods. If this scheme works, it pretty much sidesteps most of the thermal problems associated with ordinary plastic dye laser rods. This system could possibly operate as a ring laser since a curved optical path could lase in a fiberoptic bundle. This device might have some interesting possibilities.

Table 1, Figures 1 and 2: "Optical Plastics: Properties and Tolerances," The Photonics Design and Applications Handbook, Book 2, 33rd Edition, pp H225-H230 (1987).

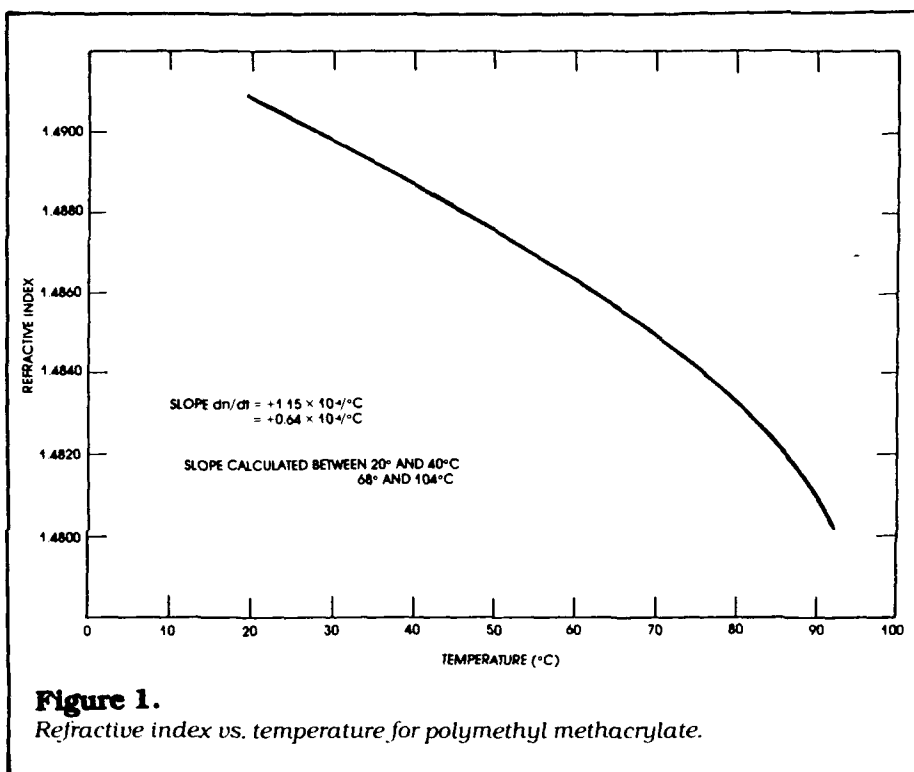


Figure 1.
 Refractive index vs. temperature for polymethyl methacrylate.

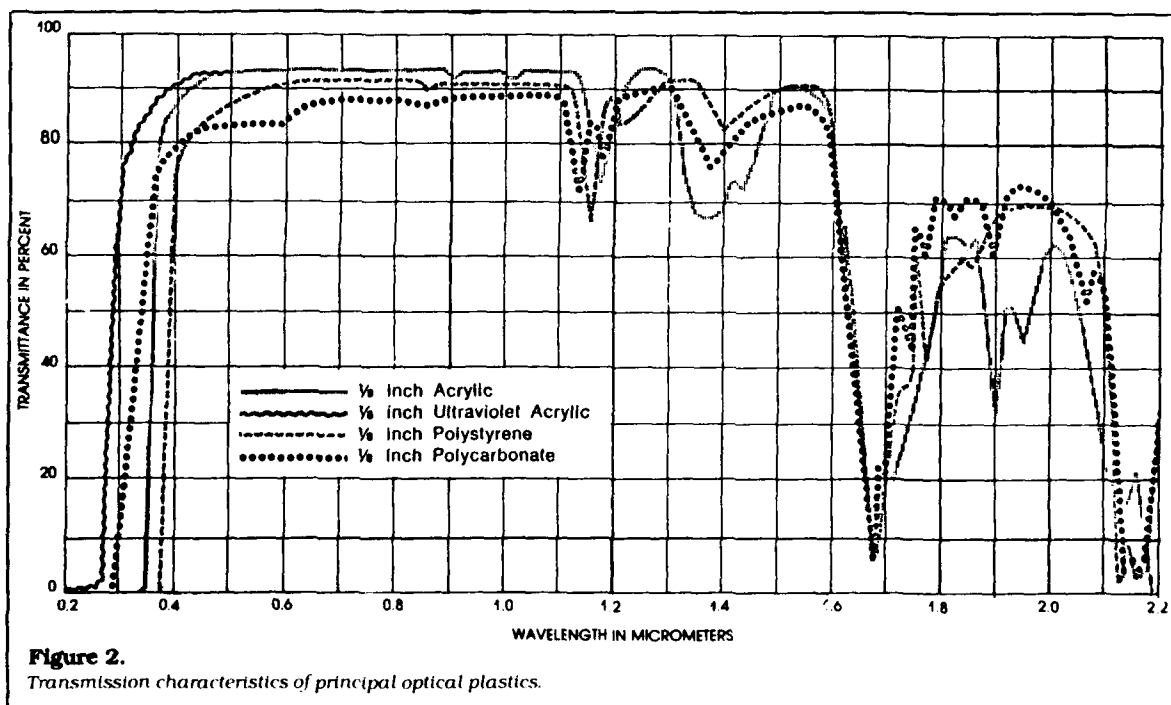


Figure 2.
 Transmission characteristics of principal optical plastics.

SOLID HOSTS FOR DYE LASER RODS – PART 2 SOME EXPERIMENTAL RESULTS

George F. Erickson, Staff Member
Los Alamos National Laboratory
CLS-6, MS J564
Los Alamos, NM 87545

ABSTRACT

This paper will describe some of the attempts and problems encountered in producing high quality polymer dye laser rods. Purification methods used on the monomer materials, curing agent problems, and gamma radiation curing are considered.

In the last paper, I tried to give an overview of the problems that exist with polymers as hosts for dye laser rods. In this paper, I will try to be more specific as to the experimental pitfalls that can occur and some of our attempts to circumvent them.

Since much of the effort by other groups working on this problem was concentrated on acrylics because of their generally desirable optical properties, we proceeded in this direction also. Our first problem was to prepare some clean, inhibitor free, MMA monomer. We used one of the recommended procedures of solvent extracting out the inhibitor, which is usually a hydroquinone type material, with an aqueous alkaline brine solution. The inhibitor-free MMA monomer, which then contains some water, was dried over anhydrous potassium carbonate and stored in a refrigerator until needed. This material after decantation contains considerable obvious suspended material which is mainly potassium carbonate. Since we wanted to work with small batches at a time, we were reluctant to set up an elaborate filtration system to filter batches as small as 50 ml of MMA monomer and dye solution only to have to clean up the entire filtration system for another batch using a different dye. We felt that for the initial trials, removing most of the suspended material by using a clinical centrifuge might suffice at least until we saw how well this method worked. Since we were only using small batches anyway, 15 ml polypropylene capped centrifuge tubes seemed like a good dual purpose container. The MMA dye solutions could be spun in the centrifuge tubes and later cured in the same tubes. Castings of this size would provide material from which one or two small laser rods could be machined. The centrifugal cleaning did seem to provide quite particulate free material with very little effort.

Our first tries at polymerizing some MMA monomer were done using small amounts of benzoyl peroxide as the initiator. This was an unqualified disaster as Fig. 1 will show. From this first trial, we found that peroxide initiators can bleach dyes, that the polymerization exotherm of MMA is hard to control, even in 15 ml quantities and that the polymerization shrinkage of MMA is very large, like 20%. We also found out that MMA while being a good solvent for the Coumarin dyes is a poor solvent for dyes like RG6 which require polar solvents. After some further trials with PMMA we looked for a polymer system which was easier to work with and had a very low shrinkage during polymerization.

Our plastics sections at the lab advised us that perhaps a rigid urethane-polyester copolymer which they liked, which is available commercially by the name of Calthane 3200, might be worth a try. Calthane 3200 has low shrinkage, a low exotherm, good clarity, can be cured overnight at room temperature and is generally quite easy to work with, except that vacuum deairing is difficult. Again Calthane 3200 is a good solvent for Coumarin dyes and does not seem to damage them in any way. However, it too is not polar enough to dissolve much RG6. After considerable experimentation with the Calthane 3200, we made a number of castings in the centrifuge tubes that were freed of any suspended material and any tiny air bubbles by using the centrifuge.

We gave some samples of this material to our optician to have him cut and polish the ends of the as-cast rods so we could look at the internal optical quality. Figure 2 shows a view through the Calthane 3200 rod using a beam expanded He-Ne laser. The optical quality is so bad that it was impossible to even get a fringe pattern using the Zygo interferometer. Looking through these rods with the unaided eye, it was even difficult to clearly see objects across the room. Although the overall clarity of the rod was quite good as indicated by the amount of light scattering using a He-Ne laser, the index of refraction striations inside the rod were so severe as to render the rod totally useless for laser applications. All further attempts to make good quality rods from Calthane 3200 were also unsuccessful for the same reason.

We also tried to use a colorless epoxy system. The suggested material, DER 332 warm cured overnight with Jeffamine T-403 hardner produces clear castings with little shrinkage. This material also dissolves Coumarin dyes quite well. We were able to get some R6G into this epoxy system by using a trace of ethanol as a dye solvent before adding the concentrated dye solution to the resin mixture. This resulted in an instant pH color change in the R6G to a nonfluorescent unusable form as the T-403 hardner is quite alkaline. Changing to an acidic hardner, hexahydrophthalic anhydride (HHPA), allows the Rhodamine to remain undamaged but the uv transmission of the epoxy is reduced. These epoxy systems even with the amine hardner have a much poorer uv transmission than either the PMMA or the Calthane 3200. Furthermore, the optical quality of these epoxy castings were not much better than the Calthane 3200 ones.

Using small amounts, up to 10% in the case of PMMA, of ethanol as a polar solvent addition, even if it doesn't inhibit the cure of the polymer system is not a long-term solution to the polar solvent problem in any of these systems. The ethanol is volatile and will slowly diffuse out to the surface of the rod causing dimensional changes as well as the loss of the solvent needed to keep the Rhodamine or Kiton Red in solution. Attempts to use less volatile polar solvents such as ethylene or propylene glycol were unsuccessful as the glycol was either immiscible in the resin system, or inhibited the cure. Ethanol merely acted like a volatile plasticizer in the PMMA system.

We returned to the PMMA system again with the hope of curing the MMA monomer in such a way as to avoid the use of initiators, the exotherm problem and also to circumvent the severe shrinkage problems. The idea was to zone cure MMA at room temperature from the bottom up using a narrow ring of gamma radiation from a radioisotope source. The polypropylene centrifuge tubes would be lowered at a controlled rate through a ring-shaped gamma ray source that is contained in a lead shield. Since the free radicals produced by the ionizing gamma radiation will initiate the polymerization of the MMA at room temperature, the MMA monomer cures from the bottom up, taking up the shrinkage in a linear fashion. As a matter of fact, the castings produced by this radiation zone curing process actually expand slightly, probably due to the swelling of the cured PMMA by the fresh MMA monomer at the zone curing interface. The radiation dose required to initiate the polymerization of the MMA is on the order of 10^4 to 10^5 rad, which does not seem to damage the dyes we have tried so far. The curing zone seems only to be about a millimeter or so thick if the source is configured correctly and has the correct gamma ray energy to just penetrate the sample. For the size of these 15 ml centrifuge tubes we are using, the radioisotope thulium 170 seems to be a good choice. Figure 3 taken from the "Chart of the Nuclides" shows that Tm 170 is easily made by neutron irradiation of natural thulium metal foil in a nuclear reactor for a few days. Tm 170 has a half-life of 129 days and emits a rather complex spectrum that consists of an 84 keV gamma ray and a couple of betas at 0.88 and 0.97 MeV. Since thulium metal is rather reactive it must be clad in thin aluminum to prevent shedding radioactive thulium oxide. The Tm 170 source will be in the form of a ring, which is about 1 in. in diameter and 0.5 in. tall. This will allow the caps of the centrifuge tubes to pass through the ring source in the lead shielded irradiation facility.

The other radioisotope choice is tantalum 182 which has a considerably more penetrating gamma spectrum as seen in Fig. 4. Ta 182 is also easily made by reactor irradiation of natural tantalum metal for only a few hours. Ta 182 has a half-life of 114.5 days and has a gamma spectrum consisting of several gammas over 1 MeV as well as tantalum and lead "K" line x-rays from the lead shield. Since tantalum metal is quite corrosion resistant, cladding of the tantalum metal tubing is unnecessary to prevent any contamination problems. The more penetrating radiation spectrum of the Ta 182 source will probably lead to a thicker gelling zone than in the case of the Tm 170 source as the more penetrating Ta 182 radiation will make it harder to control the sharpness of the radiation zone inside the lead shield.

Figure 5 shows drawings of the radiation polymerization facility. Shown are the stepper motor drive that turns a lead screw, which will lower the centrifuge tubes through the ring radiation source contained in the lead shield cask. Figure 5 also shows some details of the collet which grasps the top caps of the centrifuge tubes. The trip through the ring radiation source should take a few days to a week depending on the strength of radiation source. The steel clad lead cask will weigh about 1200 pounds. This facility is about complete. Only the pouring of the lead and the machining of the cavity in the lead shield have yet to be done plus the final assembly of the parts.

Figure 6 shows a photograph of an early experiment using a somewhat weaker Tm 170 cup shaped source used to cure some MMA containing a little ethanol as a solvent for some Rhodamine. The centrifuge tube, in this case, was not able to be lowered through the ring source. Only the bottom end of the centrifuge tube received the highest dose. This sample was removed from the source every day and examined. Each day when the sample was examined, the centrifuge tube was inverted and the thickness of the solid-liquid interface was clearly visible. These daily steps are about 1 to 2 mm thick and are clearly visible in this photograph taken by the fluorescent light coming from the Rhodamine in the PMMA. The sample was illuminated by filtered uv light in a darkened room.

The last thing that I want to cover very quickly is our attempts at making organic glasses from glycol borate esters. As I mentioned in the previous paper these materials can be made in a wide range of viscosities or hardnesses. They are simply made by boiling together the glycols and/or glycerine mixed with boric acid in the correct molar ratios. The mixture is heated in a glass beaker while being constantly stirred with a magnetic stirring bar, until a temperature of about 265°C is

reached. The Coumarin dyes can then be added as the material is cooling down but is still a low viscosity liquid. These materials have good uv transmission but are poor solvents for dyes like R6G or Kiton Red which need polar solvents. R6G and Kiton Red can be dissolved in these glycol borate organic glasses if a small amount of unreacted glycol is used as the dye solvent. A few drops of a very concentrated glycol dye solution can be added to the glycol borate as it is cooling down while still being stirred. This does work but one runs the risk of devitrification of the organic glass at a later date if very much of the unesterified glycol remains in the glass.

These organic glasses are very moisture sensitive and will devitrify and turn into a white crystalline mass if not completely sealed from contact with the air. As I mentioned in the previous paper, these organic glasses seem to generate a cloud of fine gas bubbles when subjected to intense flashlamp light which is a major drawback. This material has to be sealed inside a fused silica or glass dye cell to provide mechanical support and moisture exclusion.

So far our best looking rods by far are the PMMA copolymer material produced by Dr. Rob Hermes. This material is so new that we haven't had a good chance to get it to lase yet with flashlamp pumping (see Figure 7).

Note Added in Proof: Since this paper was presented at Lake Tahoe, we have had the opportunity to achieve laser action in one of Dr. Hermes PMMA copolymer rods using flashlamp pumping.

I wish to kindly acknowledge Dr. Shen Shey of the DARPA Directed Energy Office for funding part of this work.



Figure 1. Runaway exotherm of PMMA in an early experiment.



Figure 2. Shows poor optical quality through a Calthane 3200 rod.

CHART OF THE NUCLIDES

KNOLLS ATOMIC POWER LABORATORY

Operated by the General Electric Company under direction of

NAVAL REACTORS, U.S. DEPARTMENT OF ENERGY

THIRTEENTH EDITION — REVISED TO JULY 1983

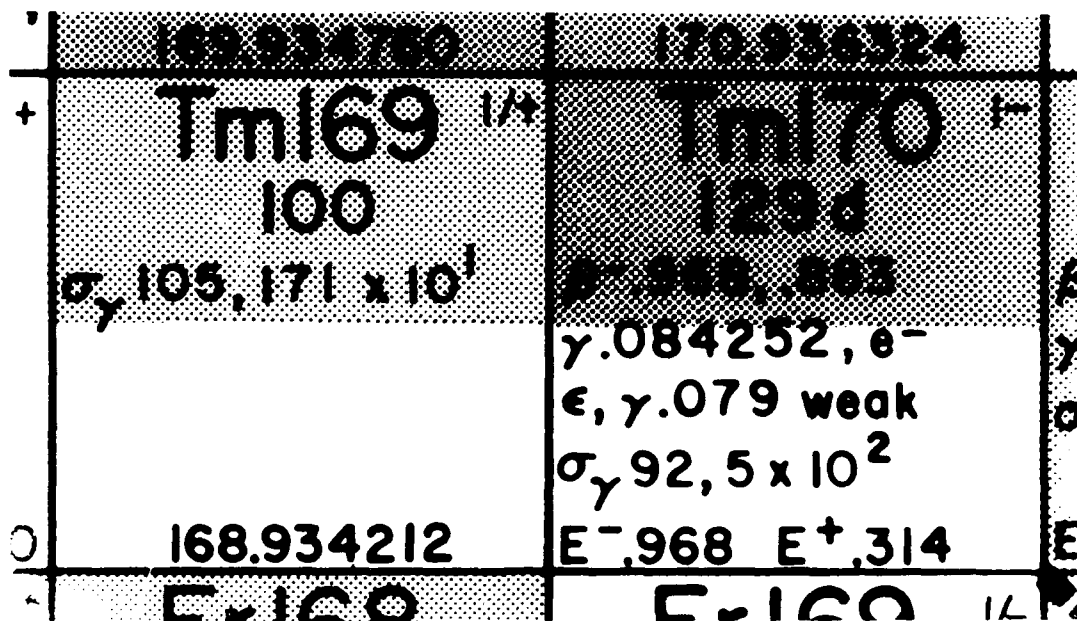


Figure 3. Excerpt from "Chart of the Nuclides" showing the nuclear properties of Tm 169 and Tm 170.

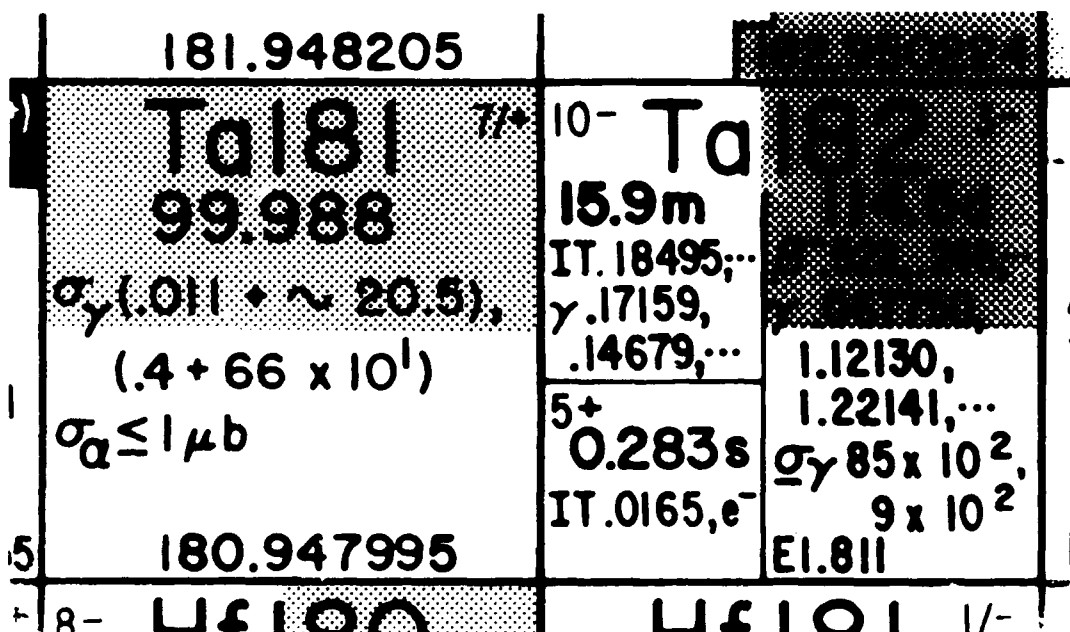
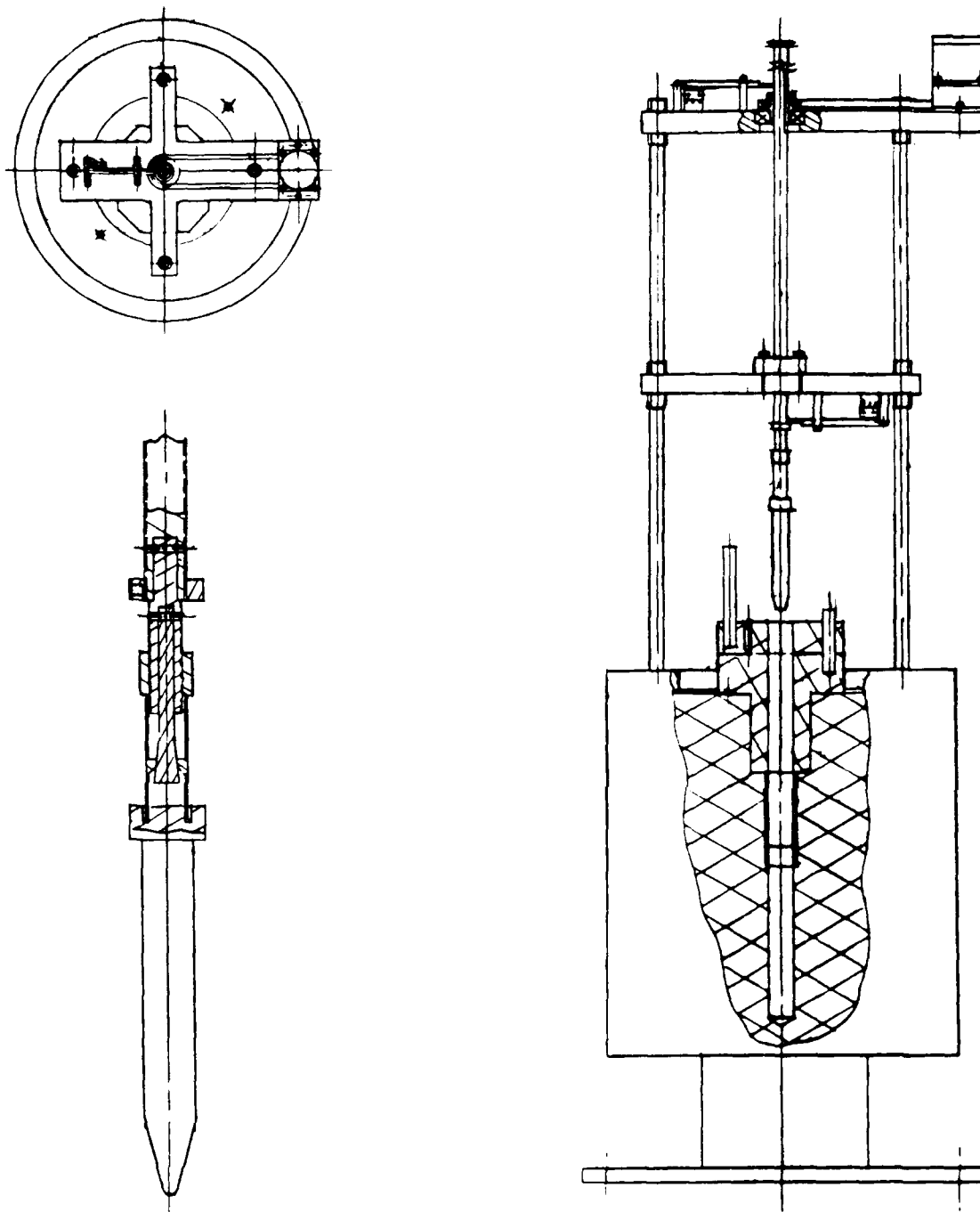


Figure 4. Excerpt from "Chart of the Nuclides" showing the nuclear properties of Ta 181 and Ta 182.



PLASTIC IRRADIATION FACILITY ASSEMBLY

Figure 5

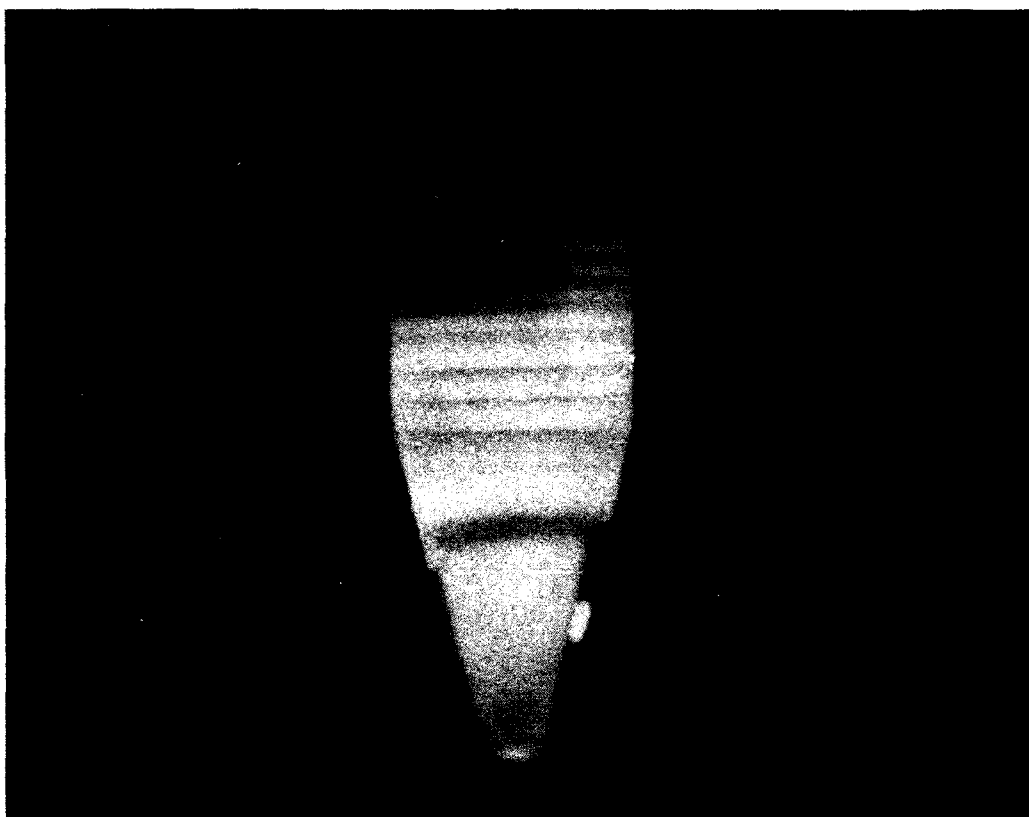


Figure 6. Gamma radiation cured PMMA fluorescing with uv light.



Figure 7. Sample of Dr. Rob Hermes new copolymer rod.

Saturation Characteristics of UV Dyes for ps XeCl Laser Pulses

M. Watanabe, A. Endoh and S. Watanabe

The Institute for Solid State Physics, The University of Tokyo
7-22-1 Roppongi, Minato-ku, Tokyo 106, JAPAN

Abstract

The peak power of 1TW was obtained in XeCl with the pulse width of 310fs and the ASE background of less than 3%. The property of ASE was analyzed for different gain. Based on this analysis, the ASE coupling between stages was completely suppressed by an appropriate spatial filter along with a relatively low gain operation. The saturation characteristics of UV dyes were investigated and analyzed for subpicosecond pulses. BBQ in cyclohexane showed the satisfactory performance for a saturable absorber in contrast and transmission.

Introduction

A multi-terawatt excimer laser is an attractive light source for studies of multiphoton ionization and x-ray laser pumping¹⁾. The development of such a system is now in rapid progress in our Institute at a picosecond and subpicosecond time regime. The schematic diagram of the laser system is shown in Fig. 1. All the amplifiers including an electron-beam pumped amplifier have been already completed. In the initial experiment an output energy of 350mJ was obtained in 20ps at KrF with two wide-aperture discharge amplifier. A synchronously pumped mode-locked dye laser was employed to reduce the pulse width to a subpicosecond region. The amplification of subpicosecond pulses has been performed in XeCl by using a partial system including two wide-aperture amplifiers. A peak power of 1TW was obtained in 310fs with an amplified spontaneous emission (ASE) background of less than 3%.

In this experiment, the obtained output energy of 300mJ was restricted by the requirement for ASE to be suppressed to a level of practical use. Spatial filters with suitable design were proved to be effective for suppressing ASE. But in some cases, especially in a double pass configuration along with a relatively high gain operation of amplifiers, the use of a spatial filter with a low divergence angle is difficult due to the limited distance between passes. Then the employment of a saturable absorber is required to decouple each pass.

In this paper we report the operation of a subpicosecond high power laser system in XeCl with an emphasis on the property of ASE and the saturation characteristics of UV dyes for subpicosecond pulses, which are desirable as saturable absorbers.

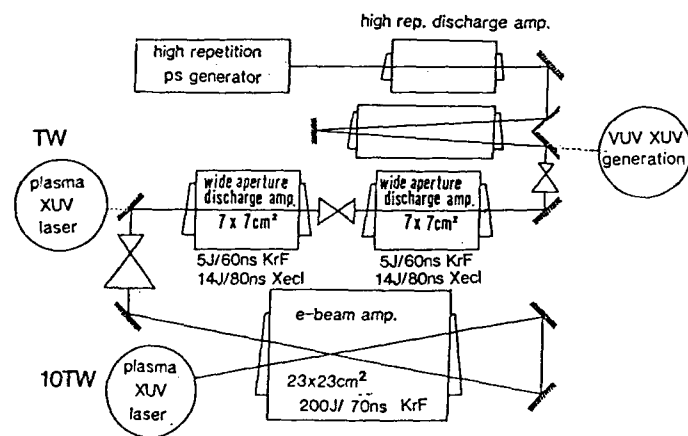


Fig.1 Multi-terawatt excimer laser system.

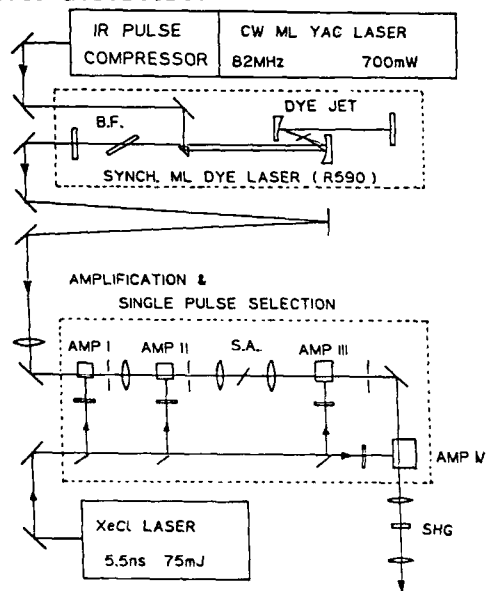


Fig.2 Schematic diagram to generate subpicosecond pulses at 308nm.

Subpicosecond pulse generation at XeCl

The schematic diagram to generate 308-nm pulses is shown in Fig. 2. The synchronously pumped dye laser generated subpicosecond pulses at 616nm. The frequency doubled output of a mode-locked cw Nd:YAG laser (Spectra Physics series 3000, PRF 82MHz) with a fiber pulse compressor (Spectra Physics 3690) was used to pump the dye laser with a pulse width of typically 3.5ps. Autocorrelation measurements showed the output pulse of the dye laser to have an actual pulse width of 320fs with some temporal wings present. The spectral width was 12.5Å. A single pulse among the pulse train was amplified in a four-stage dye amplifier chain, which was pumped by a 5.5-ns, 75-mJ XeCl laser. Kiton Red 620 and Sulforhodamine 640 were used alternatively along the stages of the amplifier chain. The growth of ASE was suppressed because the spectral gain peak of Kiton Red 620 is closely positioned to the absorption peak of Sulforhodamine 640. Malachite green saturable absorber dye jet was also used between the second and third stages. The output energy was 130μJ with an ASE background of 3%. The pulse width was 500fs at this stage. The output was frequency doubled in a 1mm-thick β-BaB₂O₄ crystal with an efficiency of 18%. Then, the output UV pulses were amplified by a two-stage high repetition rate preamplifier, which was triggered by a single thyatron and has active lengths of 30cm and 60cm, respectively. The longer laser had a double pass configuration and the pulses were spatially expanded and amplified with the cross section of 1.5cmx2cm in the final pass. The spatial filters were inserted between each pass. A typical output pulse energy was 3mJ with a negligible small content of an ASE background. The measurement of the pulse width was made at this stage by the autocorrelation method with two-photon ionization in triethylamine vapor^{8,9}. In Fig. 3 the autocorrelation trace shows a pulse width of 310fs. Figure 4 shows that the spectrum of the amplified pulse contains three of the vibronic components constituting the XeCl gain spectrum.

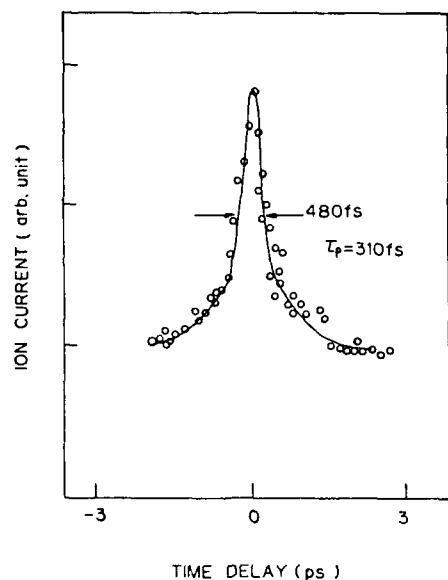


Fig.3 Autocorrelation trace of amplified UV pulses. The sech^2 pulse was assumed.

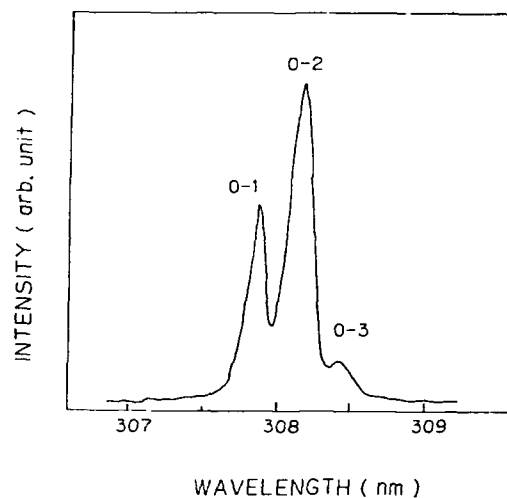


Fig.4 Spectrum of amplified UV pulses. The 0-1, 0-2 and 0-3 components of B-X transition were observed.

Measurement and analysis of ASE

In the preliminary amplification experiment, the first wide-aperture amplifier was used in a double pass configuration without a spatial filter between passes. The input pulse energy from the front end was 2.5mJ with a pulse width of 1.1ps. However, this pulse accompanied a 0.4-mJ ASE background because spatial filters were not employed in the high repetition rate preamplifier stage in this experiment. The input beam was expanded to 30cm² and fed to the first pass. The beam cross section was maintained in the second pass. An total output energy of 730mJ was obtained at a gain of 6.5%/cm but this was dominated by the considerable content of ASE. The ASE energy was 510mJ, which is 2.3 times larger than the picosecond pulse energy, while the ASE energy was 8.5mJ with the picosecond pulse energy of 51mJ before the second pass. Therefore, the serious decrease in contrast of the picosecond pulse energy to the ASE energy occurred in the second pass.

To understand the property of ASE, we measured the dependence of ASE on gain in the wide-aperture amplifier. The input pulse width was shortened to subpicosecond and its ASE background was reduced to a negligible small value by introduction of spatial filters between each pass of the high repetition rate preamplifier. The ASE energies at different gain are shown in Fig. 5 along with the saturation curves. In Fig. 6 the relation between ASE and gain is shown to be in relatively good agreement with the calculation based on the model of Ganiel et al. The used data are as follows, the radiation life time in upper state of $\tau_r=40\text{ns}$, the upper state life time of $\tau_u=2.5\text{ns}$, the stimulated emission cross section of $\sigma=2.6 \times 10^{-16}\text{cm}^2$ and the resultant saturation intensity of $I_s = h\nu / \sigma \cdot \tau_u = 0.8\text{MW/cm}^2$. The diameter and active length are 7cm and 80cm, respectively. The typical pulse width of ASE (Δt) was measured to be 40ns. The gain depletion due to ASE is proved to be negligibly small in such a relatively low gain region. Figure 7 shows the calculation in the case of small signal gain of 10%/cm. The gain depletion is within 10% over the almost entire region along the gain length. From this analysis, the ASE from the amplifier itself is shown not to be crucial at a relatively low gain. The most serious problem of ASE occurs in the case where ASE originating from the former stages is further amplified in the next stage. The serious domination of ASE in the preliminary amplification experiment is explained by this analysis. The energy growth of ASE is much faster than that of a subpicosecond pulse because the effective saturation fluence of ASE, which is defined by $I_s \times \Delta t$, is much higher than the saturation fluence of a subpicosecond pulse (E_s). The acceptable input ASE energy is severely limited by this fact. The acceptable input ASE energy is easily estimated by a simple calculation. In usual case ASE from the former stage is amplified in an unsaturation region by a factor of $\exp(g_0 L)$, where g_0 is a small signal gain coefficient and L is an active gain length. For example, if we limit the final ASE output to less than 30mJ, then the input ASE energy is limited to 370 μJ at a small signal gain of 5.5%/cm.

In the multistage amplification system like Fig. 1, the ASE background originating from the former stages should be completely suppressed before feeding a subpicosecond pulse to the final amplifier. Therefore, the use of spatial filters between each amplification stage is essential, to obtained an output pulse with good contrast. But in a double pass configuration the introduction of a good spatial filter, which is usually long, is difficult due to the limited distance between the first and second passes. Then the effective saturable absorber is required for the another approach to suppress ASE.

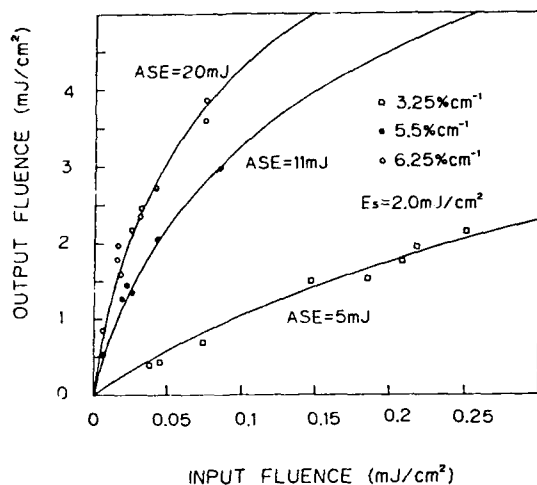


Fig.5 Saturation curves and ASE energies at different gain.

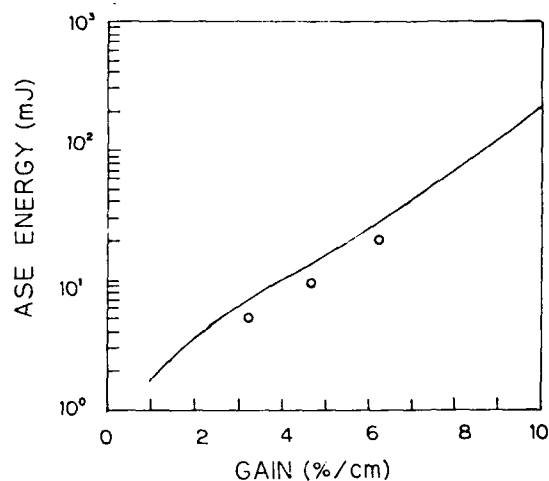


Fig.6 Calculated ASE energy dependence on gain.

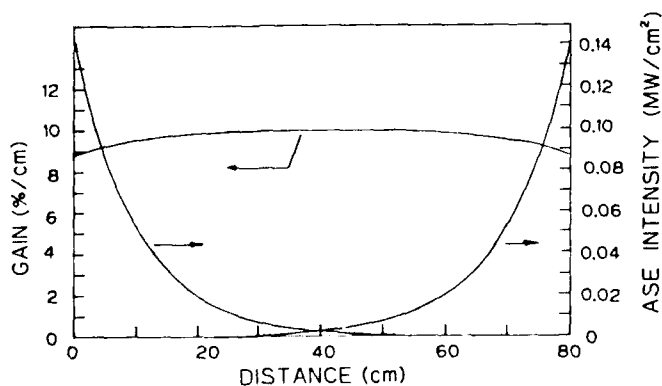


Fig.7 Calculated ASE evolution and gain depletion in the wide-aperture amplifier.

Saturation characteristics of UV dyes

We investigated the saturation characteristics of various dyes for subpicosecond pulses. A schematic of the measurement is shown in Fig. 8. The subpicosecond pulses from the front end were spatially filtered and focused by a 1-m lens on a 1-mm dye cell. The input fluence on the dye cell was varied by changing the position of the cell along the focusing beam.

First, we measured the absorption characteristics of solvents. The measurements were carried out with three well-known dye solvents (cyclohexane, dioxane and DMSO). As shown in Fig. 9, a rapid increase of absorption was observed in all solvents as the fluence exceeds tens of mJ/cm^2 . Beyond this value, evaporation occurred in all solvents. According to this data, we used cyclohexane as a solvent through this experiment. The saturation characteristics of BBQ, PBD and BPBD in cyclohexane are shown in Fig. 10. All dyes have the similar saturation fluence. BBQ in cyclohexane shows the best performance among them. A transmission contrast of 6.0 was obtained with a saturated transmission of 55%. We compared saturation characteristics of BBQ for short (subpicosecond) and long (tens of nanosecond, which is a typical pulse length of ASE) pulses. When we assume a 60-ns pulse as a long pulse and calculate the effective saturation fluence ($I_s \Delta t$) from the steady state measurement, the effective saturation fluence of a long pulse is about two orders of magnitude higher than the saturation fluence of a subpicosecond pulse (E_s). It is shown in Fig. 11. Therefore, the subpicosecond amplification system can be operated at the condition, where ASE is absorbed in an unsaturated region although a subpicosecond pulse is absorbed in a saturated region.

The saturation characteristics were analyzed by a two-level scheme with a constant absorption independent from dye levels. The pulse energy loss rate through the dye solvent is expressed as

$$\frac{dE}{dz} = -\frac{Nh\nu}{2} \cdot (1 - \exp(-\frac{E}{E_s})) - A \cdot E,$$

where E is the fluence, N is the total population density of dye, $h\nu$ is the photon energy and A is the constant absorption coefficient. The first and second term show saturation and constant loss absorption, respectively. The curve (a) in Fig. 12 is the calculation in the case of BBQ following the above equation. If we take into account a nonlinear absorption of cyclohexane, which is shown again in Fig. 12, we can almost explain the behavior of the measured absorption characteristics of BBQ in cyclohexane with E_s of $1.9 \text{ mJ}/\text{cm}^2$ and A of 2.4 cm^{-1} which is shown as the curve (b) in Fig. 12. The same fitting was carried out with PBD in cyclohexane, resulting in E_s of $2.0 \text{ mJ}/\text{cm}^2$ and A of 3.8 cm^{-1} , respectively. With a dense dye solution of $3.7 \times 10^{-4} \text{ M}$, the contrast ratio of transmission became about three times larger than that of $2 \times 10^{-4} \text{ M}$ although the decrease of saturated transmission from 55% to 38%.

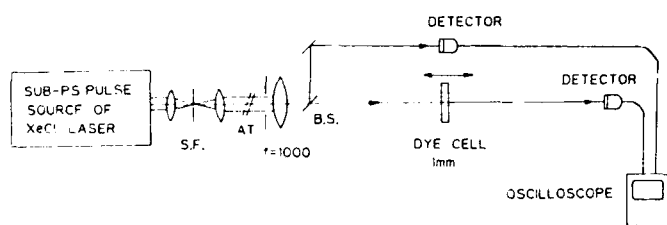


Fig.8 A schematic of the measurement.

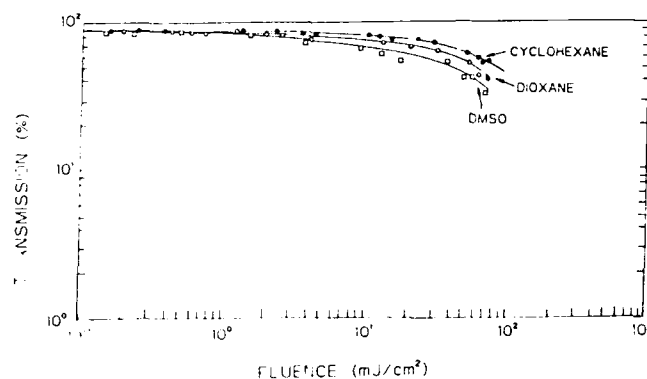


Fig.9 Transmission of solvents as a function of input fluence.

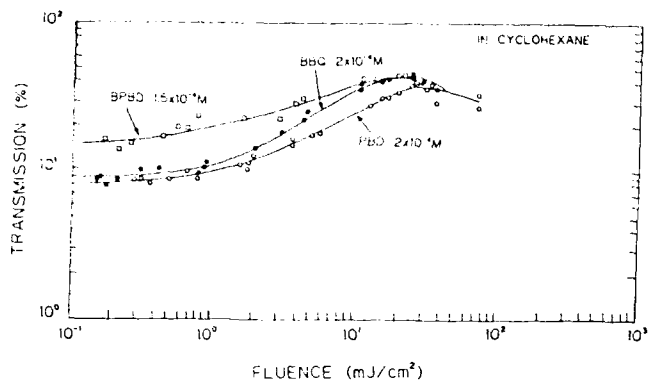


Fig.10 Transmission of BBQ, PBD and BPBD in cyclohexane.

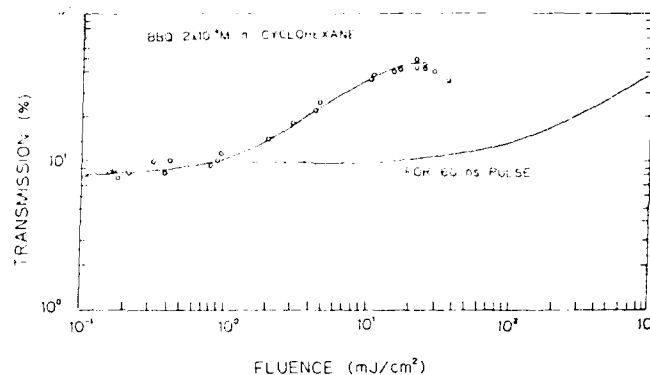


Fig.11 Transmission of BBQ for short and long pulses.

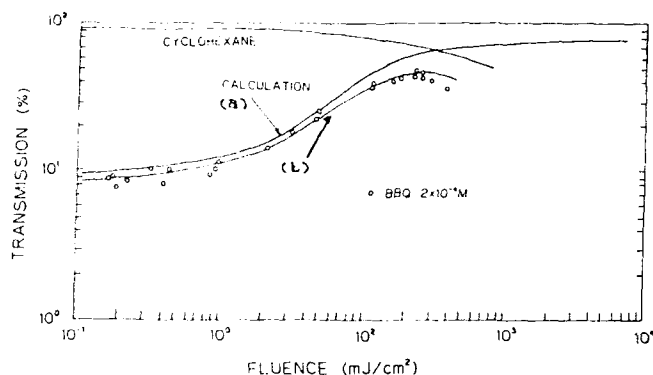


Fig.12 Calculated transmission of BBQ in cyclohexane based on a two-level scheme with a constant absorption.

Subpicosecond amplification in wide-aperture amplifiers

The block diagram of the subpicosecond amplification experiment is shown in Fig. 13. The two wide-aperture amplifiers have an identical specification of an active length of 80cm, a cross section of 7cmx7cm and capability of 14J/pulse as an oscillator.⁶⁾ Both were operated at a reduced gain level based on the measured data of ASE. The beam from the front end was spatially filtered and expanded to fill the almost entire cross section of 40cm² of the wide-aperture amplifiers. The synchronism between each stage was within 1ns jitter and the details will be described elsewhere.⁷⁾ The rail-gaps of both wide-aperture amplifiers were triggered by a single 70kV pulse generator which was also triggered by a KrF laser. The KrF laser was triggered by a thyatron and operated with an unstable resonator. The synchronism among the entire system was basically ensured by the precise timing between four thyatron-driven lasers. The relative temporal relation of the UV optical pulses including subpicosecond pulses and ASEs from amplifiers was always monitored on the oscillogram together with the trigger laser by a combination of UV fibers and a single phototube. The oscillogram at a suitable timing is shown in Fig. 14(a).

The critical issue in short pulse amplification is to suppress ASE, as mentioned above. An absorption in gain medium is not a limiting factor of energy extraction in discharge lasers. In this experiment, the spatial filter which limits the full divergence angle to 300 μ radian was employed before the final amplifier. The transmission of subpicosecond pulses through this spatial filter was 76 - 80%, while an ASE output from the first wide-aperture amplifier was almost blocked within a detecting sensitivity of a few hundred microjoules.

The amplification characteristics in the second wide-aperture amplifier are shown in Fig. 15. The laser was operated with a gas mix of 2.5Torr HCl, 15Torr Xe diluted by Ne at 4 atm. An output energy of 300mJ was obtained for an input energy of 45mJ. Then, the peak power corresponds to 1TW with the pulse width of 310fs. An ASE background was measured at 1m from the exit window of the final amplifier. When the final amplifier was operated at a relatively low gain of 4.8%/cm, the ASE background was reduced to less than 10mJ, which is 3% of the total energy. If the final amplifier is operated at the higher gain of 6.5%/cm, an output energy will increase to 400mJ, while an ASE energy will also increase to 30mJ.

To determine the origin of the ASE, we investigated the ASE coupling between the two wide-aperture amplifiers. The explicit change of the ASE background from the final amplifier was not observed between simultaneous operation, Fig 14(a), and independent operation, Fig. 14(b). Then the main contribution of ASE in this experiment was proved to originate from the final amplifier itself. But in the further critical condition, especially including a double pass configuration and a higher gain operation, the use of saturable absorber, which is discussed in the previous section, is essential to avoid the ASE coupling between passes.

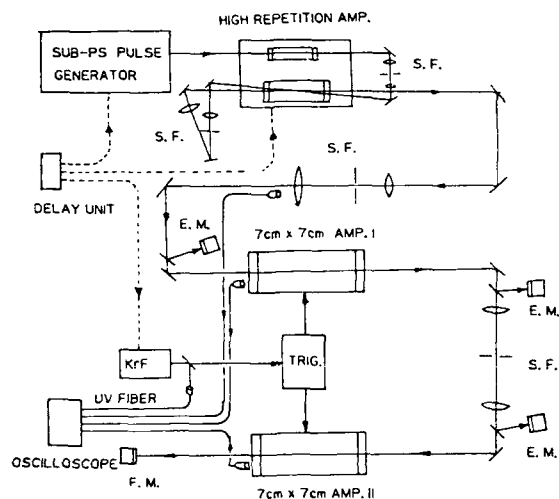


Fig.13 Experimental setup for subpicosecond amplification.

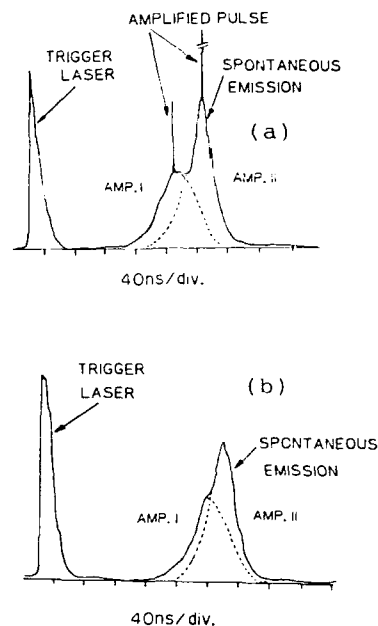


Fig.14 Temporal relation of UV pulses at simultaneous (a) and independent (b) operation.

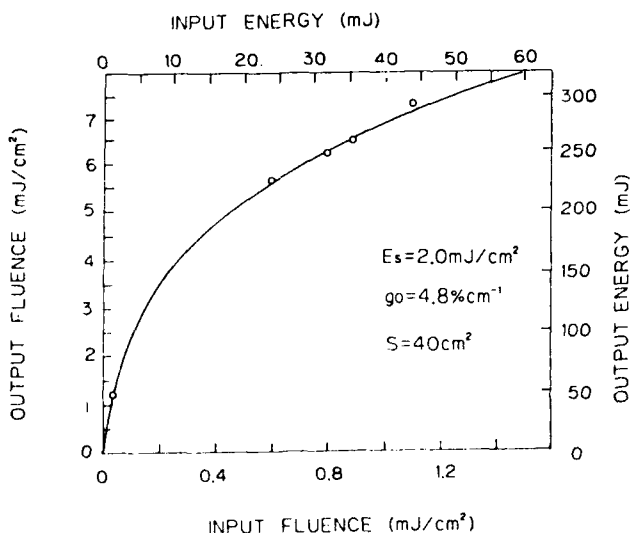


Fig.15 Amplification characteristics of the final amplifier.

Conclusion

The peak power of 1TW was obtained in XeCl with the pulse width of 310fs. The ASE background was less than 3% in energy. Based on the ASE analysis, the contribution of ASE from the former stage was completely suppressed by using an appropriate spatial filter together with relatively low gain operation of the former stage. The investigation of saturation characteristics of UV dyes were carried out for subpicosecond pulses. From the measurement BBQ in cyclohexane showed the satisfactory performance for a saturable absorber in contrast and saturated transmission.

The similar amplification experiment will be done in KrF including a 23cmx23cm electron-beam pumped amplifier, where a multiterawatt peak power is expected.

References

1. C.K.Rhodes, Sciences 229, 1345 (1985)
2. A.Endoh, M.Watanabe and S.Watanabe, Opt. Lett. 12, 906 (1987)
3. U.Ganiel, A.Hardy, G.Neumann and D.Teves, IEEE J. Quantum. Electron. QE-11, 881 (1975)
4. P.B.Corkum and R.S.Taylor, IEEE J. Quantum. Electron. QE-18, 1962 (1982)
5. R.S.Taylor and S.Mihailov, Appl. Phys. B 38, 131 (1985)
6. S.Watanabe and A.Endoh, Appl. Phys. Lett. 41, 799 (1982)
7. A.Endoh, M.Watanabe and S.Watanabe, in Digest of 6th IEEE Pulsed Power Conference (Institute of Electrical and Electronic Engineers, New York, 1987) paper 17-5
8. S.Szatmari, B.Racz and F.P.Schaffer, Opt. Commun. 62, 271 (1987)
9. J.H.Glownia, J.misewich and P.P.Sorokin, J. Opt. Soc. Am. B4, 1061, (1987)

A LONG PULSE DURATION, GOOD BEAM QUALITY, SUPERSONICALLY "SCANNED BEAM" DYE LASER

G. S. Janes*, H. R. Aldag, D. P. Pacheco, and R. E. Schlier**
Avco Research Laboratory/Textron
2385 Revere Beach Parkway
Everett, MA 02149

Abstract

This paper describes a new generic approach for obtaining an energetic, good beam quality, long pulse duration, laser pumped dye laser which avoids thermal distortion, optical window burning, and triplet problems. A small spot which is axially illuminated on the face of a wide dye cell with a pump laser, and the axis of a laser cavity are overlapped with a system of fixed mirrors, and scanned together across the face of the cell by means of a common rotating mirror. This system maintains a fixed direction and axis for the incoming pump beam, the remainder of the cavity, and the outgoing laser beam. The small area ($\sim 10^{-2} \text{ cm}^2$) of the illuminated spot results in a high cavity flux ($\sim 2 \text{ MW/cm}^2$) which permits efficient energy extraction. However, the scanning of this spot over a relatively large area ($\sim 2 \text{ cm}^2$) during the total pulse duration greatly reduces the net local fluence, and hence, thermal distortion, optical component damage, and triplet state losses. Furthermore, since the lasing spot moves faster than the speed of sound, the liquid does not have time to expand, and acoustic disturbances are left behind. Conceptually, this system is the equivalent of many continuously multiplexed, small, independent, low energy density lasers, each of which is only pumped for a short time. With this approach, efficient lasing occurs in a relatively large-area, slow moving gain medium, and fluid-dynamic heating is not a limiting factor on waste heat disposal.

Introduction

The objective of this work was to obtain the requisite information for the credible design of a repped long pulse duration ($\sim 100 \text{ usec}$), tunable pulsed dye laser system capable of operating at significant power levels ($\sim 30 \text{ kW peak}$, 300 W average) with good beam quality ($\sim 4 \times \text{DL}$). These performance criteria are deceptively difficult to satisfy. Good beam quality, tunable, CW dye lasers^{1,2} have been known for a long time, however their output is limited to a few watts.^{3,4,5} The pulsed transverse flow flashlamp pumped (Mark V) dye laser⁶ previously developed at AVCO and EXXON for laser isotope separation has met the tuning and power capability requirements. However, its beam quality seriously degrades for pulse durations in excess of a few microseconds. The most attractive option is a laser pumped laser configuration which utilizes one or more Mark V dye lasers operating in a long pulse mode to pump an optimally designed good beam quality dye cell system. Both the pump laser and the dye cell present technical problems. However, the pump laser(s) can be multiplexed, and do not need to have good beam quality. This paper is concerned with the dye cell, which has the more demanding requirements.

Technical Issues

An examination of the relevant rate constants indicates that the circulating flux or power density within the dye/solvent gain medium must of the order of 2 MW/cm^2 in order to achieve saturation and thereby avoid the losses associated with spontaneous decay within the relatively short lifetime of the excited state dye molecule ($< 10^{-8}$ seconds). This requirement for high lasing fluxes, and its companion requirement for high pump fluxes leads to three potentially serious technical problems when pulse lengths are stretched to the 100 microsecond range, and as a consequence the fluence in the gain medium and on nearby optical components approaches 100 joules/cm^2 . These problems involve; (1) Triplet state losses, (2) Damage to optical components, and (3) Thermal gradient optical distortion.

Triplet State Losses

It has long been recognized,⁷ that in the absence of an effective triplet quenching mechanism, excited dye molecules will eventually accumulate in triplet states and terminate lasing if the lasing pulse length is long relative to excited state life times. This is not a problem for very short pulse duration lasers. However it has, on occasion, caused difficulties with 1 microsecond pulse length systems, and could be a more serious problem for 100 microsecond systems. Fortunately, for many of the common dyes, triplet

*Retiree and consultant to ARL

**Retiree, currently at Candela Corp.

losses can be controlled by the presence of quenchers such as dissolved oxygen⁸ within the solvent. For this reason, triplet losses were of secondary rather than primary importance in determining our approach. (Triplet losses were not found to be a significant source of difficulty in these laboratory investigations.)

Damage To Optical Components

For conventional dye cells, the ~ 100 joule/cm² fluences associated with these long pulse durations push the damage limits of window and coating technology. For a given fluence, the optical damage mechanisms are a decreasing function of pulse duration, however this ameliorating effect has not been found to be adequate for CW dye lasers for which it was eventually necessary to resort to free jets^{9,10} in order to bypass the window burning problem. Unfortunately, this free jet approach is much less attractive for higher power lasers which require larger beam areas over which the optical quality of a free fluid surface must be maintained for beam quality considerations. (Because of the approach which we ultimately selected, optical damage will only be a significant issue for the pump laser.)

Thermal Gradient Optical Distortion

Thermal gradients in the gain medium constitute the dominant limitation on beam quality with long pulse lasers. These gradients produce local variations in the index of refraction which in turn distort the wavefront. The amplitude of the phase shift associated with this distortion is given by equation 1.

$$\Delta N = \Delta T \frac{dn}{dT} \frac{L}{\lambda} \quad \text{eq. 1)}$$

The amplitude of the phase shift measured in fringes ΔN is proportional to the product of the temperature sensitivity of the index of refraction, dn/dT , and the temperature variation, ΔT , multiplied by L/λ , the length of the optical path within the gain medium as measured in wavelengths. This phenomenon was analyzed extensively. It has two components, corresponding to slow effects occurring on the interpulse time scale, and fast intrapulse effects occurring during the laser pulse.

Interpulse Thermal Effects - The interpulse effects associated with residual heat in the system occur on a relatively slow time scale. They are primarily of concern to flash lamp pumped lasers where the optical path lengths are long, (~ 50 cm), and where differences of as much as $.01^\circ\text{C}$ can cause significant effects. Fortunately, these temperature uniformity requirements are greatly relaxed for laser pumped lasers where the dye cell need only be a few mm in length.

Intrapulse Thermal Effects The principal technical difficulty arises as a consequence of waste heat deposition which occurs within the active part of the lasing medium during the pulse. The resulting optical distortion is exceedingly difficult to correct with external optics since, with conventional dye cells, its amplitude is determined by the time integral of the pump power which increases monotonically. This effect is described by equation 2 below.

$$\Delta N = \frac{dn}{dT} \frac{(1-\epsilon)}{\epsilon \rho C_p} \frac{P \tau}{Q} \quad \text{eq. 2)}$$

It is important to note that the distortion amplitude, ΔN , measured in fringe shifts does not scale with optical path length. Instead, the terms involving temperature rise multiplied by path length are replaced by a term involving volumetric heat capacity, ρC_p , and lasing efficiency, ϵ , multiplied by the pulse duration, τ , and by the ratio of P_q , the intracavity lasing flux (MW/cm²) to the "Q" of the optical cavity. This dependence imposes a very rigid set of boundary conditions since the flux, P_q , must be large enough to achieve saturation, and the cavity "Q" is limited by absorption, and by mirror and window losses. To put this into perspective, we estimate that a "conventional," 40% efficient, 100 μsec pulse duration, laser pumped laser, with 2 MW/cm² of circulating flux, and a "Q" of 10 would exhibit 30 fringes of phase shift making the attainment of 4 X DL beam quality highly unlikely. Furthermore, the detailed spatial distribution of the resulting distortion would be difficult to control since the dominant part of the index of refraction variation is due to thermal expansion, and time dependent acoustic effects come into play once the pulse length is long enough for a sound wave to travel a distance comparable with the system dimensions.

Approach

We considered a number of approaches including the use of high "Q" cavities, the use of rigid wall dye cells in combination with very uniform waste heat deposition, the use of water-based dye solutions at close to 0°C where the coefficient of expansion is very small, the use of high speed jets as with CW dye lasers, and finally the multiplexing together of a large number of acceptable beam quality short pulse duration lasers. The high "Q" approach involves lowering the gain per pass, and was rejected because of absorption in the dye solution as well as because of optical component limitations. The rigid wall dye cell approach was rejected as being unrealistic in its spatial energy deposition uniformity requirements. The water based dye solution approach was rejected because the available dyes exhibited poor efficiency, lifetime, and solubility in these solutions. The high speed jet approach works for low power CW lasers where the spot sizes are small, so that the optical smoothness requirements of the fluid surface are reasonable, and a combination of diffusion and flow at a modest speed can serve to remove excess heat. It does not, however, scale to larger area spots where thermal diffusion would be negligible, and where the requirement for increased flow speeds leads to excessive viscous heating of the fluids. The multiplexing of discrete individual short pulse lasers can be accomplished with rotating mirrors, however it rapidly leads to unacceptable system complexity.

The "Scanned Beam" Dye Laser

Generic Concept

Although it might have been possible to achieve our objectives by some combination of the above approaches, a more promising generic option involved replacing the fluid flow method of heat removal with an approach wherein the optical axis of the laser is moved through the fluid at speeds in excess of the speed of sound in the fluid by means of a single rotating mirror. This novel scheme, which is illustrated in Figure 1, also overcomes the triplet and optical damage limitations, and is the conceptual equivalent of several hundred continuously multiplexed, small, low-energy density, independent lasers each of which is only pumped for a fraction of a microsecond.

Referring to Figure 1, we see that a small spot which is axially illuminated on the face of a wide dye cell with a pump laser, and the axis of a laser cavity are overlapped with a system of fixed mirrors, and scanned together across the face of the dye cell by means of a single common rotating mirror. This system maintains a fixed direction and axis for the incoming pump beam, for the remainder of the cavity, and for the outgoing laser beam. This is accomplished by locating the rotating mirror surface at the center of curvature of the rear mirror. The use of a small-area ($\sim 10^{-2} \text{cm}^2$) illuminated spot on the dye cell leads to high cavity fluxes ($\sim 2 \text{ MW/cm}^2$) which permit efficient energy extraction. However, the scanning of this small spot over a relatively large area ($\sim 2 \text{ cm}^2$) during the total pulse duration greatly reduces the net local fluence, and hence, both thermal distortion, and optical component damage as well as triplet state losses. At any fixed location on the dye cell, the total dwell time of the illumination is only about 1/3 of a microsecond. Since the lasing spot scans the dye cell at speeds in excess of the speed of sound, the liquid does not have time to expand ahead into the fresh dye solution and acoustic disturbances are left behind. Furthermore, since the "Scanned Beam" dye laser is a quasi-steady state device, any remaining intrapulse thermal distortion is proportional to the instantaneous power level rather than to its time integral from the beginning of the pulse. To the extent that the power is constant, any remaining thermal distortion is therefore more easily corrected with external optics. The relatively poor beam quality pump laser output is aligned with the fixed external part of the resonant cavity, which defines the lasing axis, and focused into a small spot on the dye cell with low f number optics. Figure 1 shows the beams combined with a pierced mirror, however they can also be combined with dichroic optics, and they need not be paraxial.

Experimental Configurations

Figures 2 and 3 illustrate two experimental configurations which were investigated in this laboratory. The thin 20 cm wide transverse flow dye cell shown in Figure 4 was available from previous unrelated experiments. Figure 5 shows the remainder of the apparatus. For the initial experiments, a 100 Hz rotating mirror assembly designed for laser printer applications was purchased from a commercial source. It worked as received, but was subsequently modified by the addition of coated optics. The timing of the pump laser was controlled by a delay generator triggered by a He Ne laser beam which was bounced off of the rotating mirror. As expected, our results were completely insensitive to the location of the small ($\sim 1 \text{ mm}$) lasing spot on the surface of the relatively wide ($\sim 20 \text{ cm}$) dye cell. The spot whose dimensions and location were

determined by the imaging of the pump beam aperture. Representative system parameters are given in Table 1 below which contains some limited information on the pump laser as well as on the dye cell output.

TABLE 1. REPRESENTATIVE SYSTEM PARAMETERS

PUMP LASER (508 nm)	
o	Flashlamp Pumped, Transverse Flow Dye Laser
o	Coumarin 504 in 50% ME0H/50% H ₂ O (3×10^{-5} M/l)
o	250 mJ in a 2.5 μ s Pulse (100 kW) (By End of Program, Long-Pulse Operation Extended to 50 μ s at 100-kW Power Level)
DYE CELL OUTPUT (570 nm)	
o	End Pumped (Depth Varied from 2 to 5 mm)
o	Rhodamine 590 in 50% ME0H/50% H ₂ O (9×10^{-5} M/l)
o	Temporal Output of Dye Cell Tracks Pump Beam over Times >> Dwell Time

Cavity Optics - In the Edge-Coupled Configuration (see Figure 2), the resonant laser feedback was provided by the relatively small fraction of the total radiation that passed through a small hole in the beam combining mirror, and the primary output was derived from the light that is reflected from the feedback mirror. In the Stable Resonator Configuration (see Figure 3), the feedback was provided by the coherent tuned diffraction from the grating, and the output was provided by the zero-order reflection off of the grating. In an alternative untuned stable resonator configuration, we used a partially reflecting output mirror as the feedback element. Optimum performance was obtained when the cavity lenses were located at positions corresponding to those situations in which the lasing spot on the dye cell was almost exactly focused back on itself. This is a consequence of the very small spot size at the dye cell, and the large distance to the first lens in the cavity optics system, and is in essential agreement with the results of a more detailed gaussian wave front calculation. The image of the lasing spot was greatly magnified at the feedback point, a necessary criterion for avoiding optical damage to the feedback element due to excessive fluence.

Pump Laser - Although the beam fluence was insufficient to burn the pump beam aperture, it was demagnified ($\sim 4 \times$), and intensified ($\sim 16 \times$), by the pump beam imaging optics when focused into a spot on the dye cell. For the purpose of these studies, the Mark V pump laser operated in a repped mode, and typically delivered 100 kW pulses of three to eight microseconds duration. Fifty-microsecond pulses were obtained from a Mark V laser in a separate series of experiments, but the resources were not available to combine these two elements. It is important to note, however, that even a three-microsecond pulse duration is very long in comparison to the total illumination time for a spot on the dye cell which is approximately 1/3 of a microsecond. Furthermore, it was observed that, in every case, the temporal profile of the dye cell output closely tracked the temporal profile of the pump laser indicating that steady state operation of the dye cell had been achieved.

Experimental Results

Baseline Experiments - Figure 6 displays the results of a series of measurements performed with the Edge Coupled Configuration (see Figure 2) which related the output power and conversion efficiency to the dimensions of the lasing spot as determined by the pump beam optics. These results were obtained with a 2 mm depth dye cell containing a 7×10^{-5} molar concentration of Rhodamine 590 dye dissolved in a 50-50 methanol-water solvent mix. They have been corrected for losses occurring in uncoated output optics, and clearly demonstrate efficiencies in the range of 40%. The overall results of these investigations are summarized in Table 2, which presents typical performance data for the scanned beam laser. Initial tuning investigations were undertaken, however the results, which were preliminary, are not presented here.

TABLE 2. SCANNED BEAM LASER PERFORMANCE

PUMP BEAM AT DYE CELL	
Input Power	100 kW
Beam Fluence	2.5 J/cm ²
Scan Velocity	2.5×10^5 cm/sec ($\sim 2 \times$ Sonic Velocity)
Beam Size	0.08 cm (Horizontal) x 0.16 cm (Vertical)
Beam Area	0.0128 cm ²
Beam Flux	7.8 MW/cm ²
Dwell Time	0.32 μ s

TABLE 2. SCANNED BEAM LASER PERFORMANCE (Continued)

OUTPUT BEAM	
Beam Fluence	2.0 J/cm ²
Cavity Length	660 cm
Size at Dye Cell	0.08 cm (Horizontal) x 0.16 cm (Vertical)
Size at Rotating Mirror	~ 1-1.5 cm Diameter
Efficiency	
Edge-Coupled	40-50 Percent (Broad-Band)
Stable Resonator	30 Percent (Broad-Band)
Output Power	
Edge-Coupled	40-50 kW (Broad-Band)
Stable Resonator	30 kW (Broad-Band)
Beam Quality	~ 2.5 X DL (Horizontal)
	~ 5 X DL (Vertical)

Scan Velocity Effects - The effect of scan velocity, as shown in Figure 7, was particularly interesting. Because of the long length of the optical cavity, this laser was unusually sensitive to the optical quality of the gain medium. The observed correlation between the onset of lasing, and the condition when the scan velocity exceeds the sonic velocity in alcohol water mixes (Which was characteristic of all our data.) is strong evidence for the basic validity of the generic scanned beam concept for controlling intra-pulse optical distortion of the gain medium. The observed dependences on scan velocity and spot dimensions were in rough agreement with a crude model which relates lasing efficiency to the fraction of the spot area which was unperturbed by shock waves.

Beam Quality Measurements - The beam quality was evaluated in a series of farfield measurements which determined the fraction of a focused beam, as projected by a telescope, that passed through a slit of a given width, located 6 meters away from the source. The results which are shown in Figure 8, were obtained with a dichroic mirror in place of the apertured combining mirror. The dotted vertical line corresponds to 4 X DL. The horizontal and vertical dimensions were treated separately, and the beam size was taken to be that dimension through which 90% of the full beam was transmitted. The hypothesis that the spatial quality of the beam is determined primarily by the size of the source was confirmed by far field observations in which a reduction of the spot height from 1.6 mm to 0.8 mm improved the beam quality in the vertical direction from 4.5 X DL to 2.9 X DL without producing changes in the horizontal beam quality.

Summary and Conclusions

The data obtained clearly demonstrate the concept of the "Scanned Beam" Dye Laser. This generic concept has enabled us to overcome the problems of window damage, thermal distortion, and triplet-state accumulation that have previously limited the power and beam quality of long pulse tunable laser devices. The close temporal tracking observed between pump and output pulses for times long compared to the dwell time of the lasing spot demonstrates the establishment of the quasi-steady state condition which produces long pulse capability. The dependence of performance on scan velocity (see Figure 7) dramatically demonstrates the control of acoustic disturbances in the gain medium.

Energy conversion efficiencies of up to 50% were obtained at the 50 kW peak power output level with the untuned edge-coupled configuration. This configuration appears to be superior to the stable-resonator configuration.

Good beam quality (~ 4 X DL) is achievable for the duration of the pulse. However, the farfield results indicate that further increasing the size of the spot in order to increase the power level above 50 kW will involve some compromises in beam quality.

Acknowledgments

This work was funded under Massachusetts Institute of Technology Lincoln Laboratory Purchase Order BX 586 under Air Force prime contract F19628-85-C-0002. The views and conclusions contained in this document are those of the authors, and should not be interpreted as necessarily representing the official policies, expressed or implied, of either the United States Government or M.I.T. Lincoln Laboratory.

The authors would like to thank Drs. Patrick Everett and Daniel Fouche of M.I.T. Lincoln Laboratory for their support, and for helpful discussions. We also acknowledge the able technical assistance of E. Bardho, L. Coulter, J. Gardner, and G. Sabeau.

References

1. O. G. Peterson, S. A. Tuccio, B. B. Snively: Appl. Phys. Letters 17, 245 (1970).
2. F. P. Schafer (Ed.): Dye Lasers, Topics in Applied Physics (Vol. 1), (Springer, Berlin, Heidelberg, New York, 1973 & 1977).
3. B. Wellegehausen, L. Laepple, and H. Welling: Appl. Phys. 6, 335 (1975).
4. S. Leuttyler, E. Schumacher, and L. Wost: Optics. Communications 19 197-200 (1976).
5. T. F. Johnston Jr., R. H. Brady, and W. Proffitt: Appl. Optics 21, 2307-2316 (1982).
6. H. Aldag, J. Woodroffe, R. Morton, J. Munroe: U.S. Patent 4176324.
7. F. P. Schäfer: op cit.
8. B. B. Snively, F. P. Schafer: Phys. Lett. 28 A, 728 (1969).
9. J. M. Yarborough: Appl. Phys. Lett. 24 629 (1974).
10. B. Wellegehausen, L. Laepple, H. Welling: Appl. Phys. 3 387 (1974).

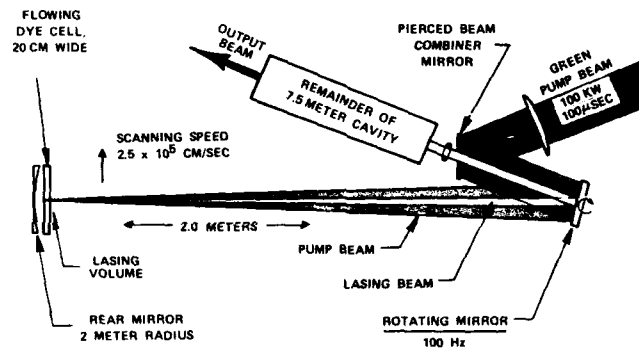


Figure 1 Scanned-Beam Laser-Pumped Laser Concept

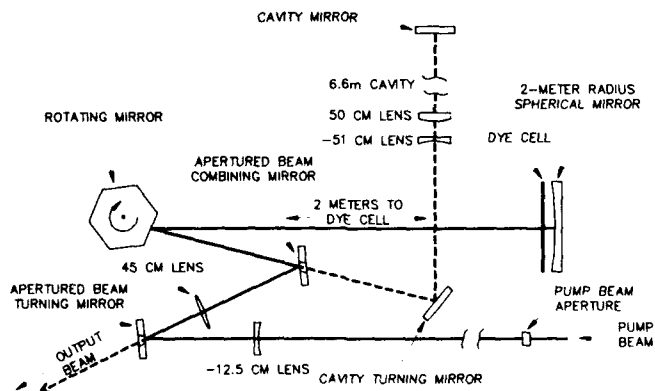


Figure 2 Scanned-Beam Dye Laser;
Edge-Coupled Configuration

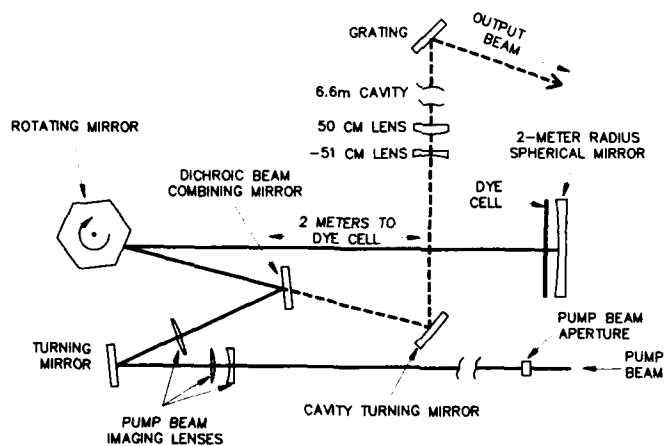


Figure 3 Scanned-Beam Dye Laser;
Stable-Resonator Configuration

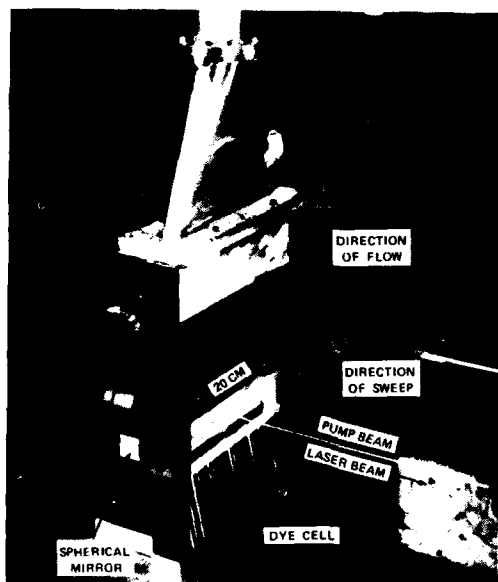


Figure 4 Flowing Dye Cell and Associated
Optics

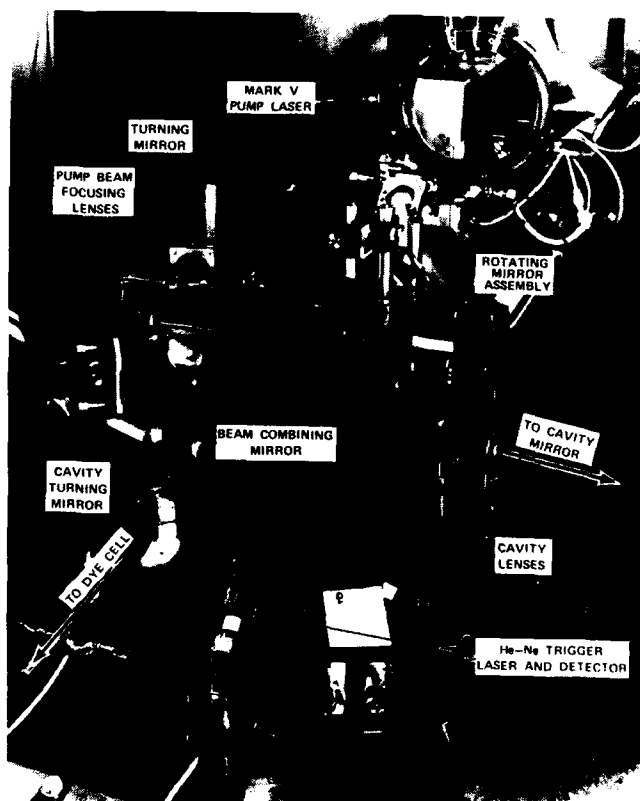


Figure 5

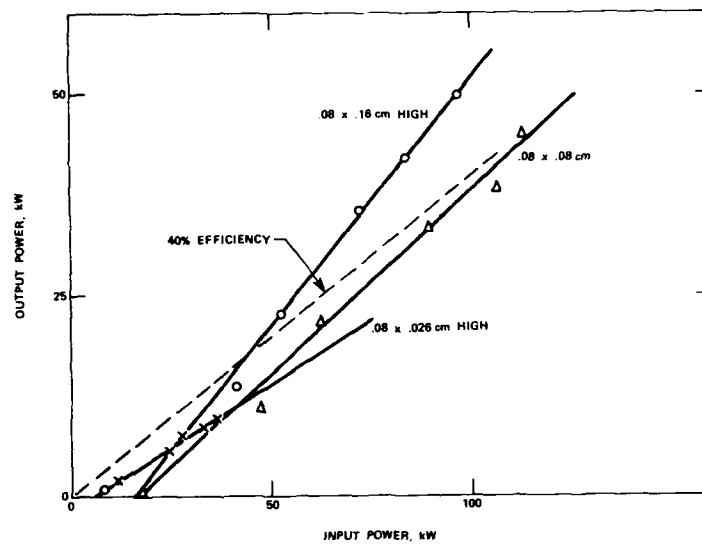


Figure 6 Laser Performance of Scanned-Beam Dye Cell in Edge-Coupled Configuration

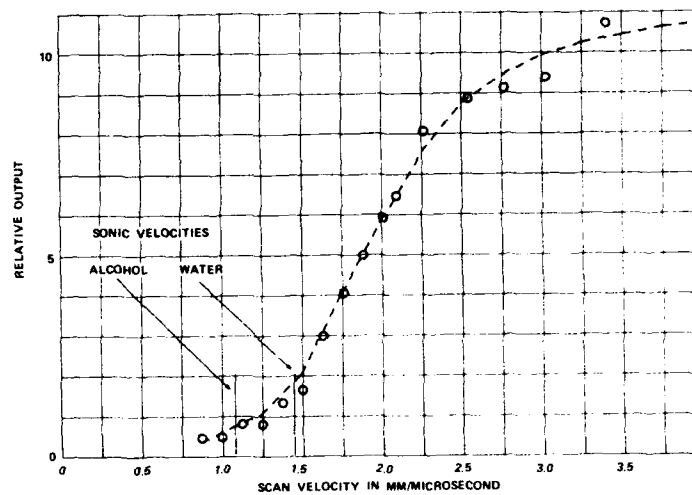


Figure 7 Dependence of Performance on Supersonic Beam Sweep Velocity Demonstrates Principles of Scanned Dye Cell

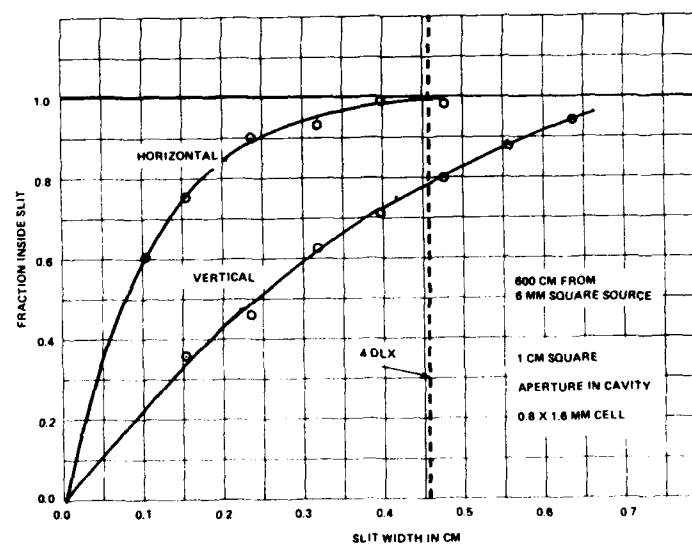


Figure 8 Far-Field Measurements for the Scanned-Beam Laser in the Stable-Resonator Configuration

BEAM DIVERGENCE THEORIES FOR PRISMATIC PULSED DYE LASERS

F. J. Duarte

Photographic Research Laboratories - Photographic Products Group
Eastman Kodak Company, Rochester, NY 14650

Abstract

Simple beam-divergence geometrical theories are compared with a complete transfer-matrix approach. A generalized transfer matrix for a typical intracavity laser multiple-prism beam expander is derived.

Introduction

Return-pass linewidth estimates in multiple-prism dye lasers use the expression $\Delta\lambda = \Delta\theta (\partial\theta/\partial\lambda)^{-1}$, where the differential term refers to the total dispersion provided by the tuning elements in the cavity, and $\Delta\theta$ is either calculated assuming Gaussian-beam propagation or obtained from measurement.¹ The usual approach to calculate $\Delta\theta$ is to employ the geometrical expressions derived by Littman and Metcalf.² In this paper we derive a generalized transfer matrix for an intracavity multiple-prism laser beam expander. This result is then applied to a double-prism dye laser oscillator using typical geometrical dimensions. The overall transfer-matrix result is then compared to the divergence estimates using the Littman and Metcalf approach. We conclude that present uncertainties in measurement do not allow a distinction between the slight differences between the two theoretical methods.

Theory

The approach of Littman and Metcalf² involves a convolution of the entrance ($\Delta\theta_1$) and the exit ($\Delta\theta_2$) slit function. For the case of a cavity length (d) much greater than the Rayleigh length,

$$\Delta\theta = [(\lambda/(\pi w))^2 + (w/d)^2]^{1/2} = (w/d) [1 + (d/L_R)^2]^{1/2} \quad (1)$$

where $L_R = (\pi w^2)/\lambda$, and w is the beam waist at the dye cell. It can be easily seen that under these conditions ($d/L_R \gg 1$) this equation can be approximated to the well known far-field expression

$$\Delta\theta \cong w/L_R = \lambda/(\pi w) \quad (2)$$

For the case of $d \ll L_R$, it is shown in Ref. 2 that

$$\Delta\theta = [(w/d)^2 + (w/d)^2]^{1/2} = [(\lambda\sqrt{2})/(\pi w)](L_R/d) \quad (3)$$

which reduces to

$$\Delta\theta = (\lambda\sqrt{2})/(\pi w) \quad (4)$$

for $L_R = d$.

The ray matrix approach for a simple mirror-end cavity incorporates the expression for the beam size at a distance from the dye cell

$$w(B) = w [A^2 + (B/L_R)^2]^{1/2} \quad (5)$$

where the transfer matrix is given by

$$\begin{bmatrix} A & B \\ C & D \end{bmatrix} = \begin{bmatrix} 1 & x \\ 0 & 1 \end{bmatrix} \quad (6)$$

If we consider a very thin dye cell with the output mirror quite close to the cell, we obtain

$$\Delta\theta_1 = w(B)/B = (w/L_R) [1 + (L_R/B)^2]^{1/2}$$

thus, using $B = x$ and $d = x$, we obtain

$$\Delta\theta = [(w/d)^2 + (w/L_R)^2 (1 + (L_R/d)^2)]^{1/2} = (w/L_R) [(L_R/d)^2 + (1 + (L_R/d)^2)]^{1/2} \quad (7)$$

for $d \gg L_R$, the far-field divergence is given by $\Delta\theta \cong \lambda/(\pi w)$, as before. For $d \ll L_R$

$$\Delta\theta \cong [(\lambda\sqrt{2})/(\pi w)] (L_R/d) \quad (8)$$

which is the Littman and Metcalf² result. For the case of $L_R = d$

$$\Delta\theta = [(\lambda\sqrt{3})/(\pi w)] \quad (9)$$

which differs slightly from the well known geometrical result.

Now, we consider a narrow-linewidth hybrid multiple-prism grazing-incidence (HMPGI) oscillator of the type shown in Fig. 1. For the prismatic beam expander the single-pass transfer matrix can be derived utilizing the analysis for tilted interfaces introduced by Turunen³ and Tache.⁴ For the case of right-angle prisms oriented for orthogonal beam exit, as used in intracavity laser beam expanders, the matrix can be written as

$$\begin{bmatrix} A & B \\ C & D \end{bmatrix} = \begin{bmatrix} k & \ell/(k n) \\ 0 & 1/k \end{bmatrix} \quad (10)$$

where k is the expansion coefficient, ℓ the path at the prism and n the refractive index. This result can be extended to a practical multiple-prism beam expander composed of r prisms separated at a uniform distance D . Assuming an equal path length at each prism, the resulting matrix becomes

$$\begin{bmatrix} A & B \\ C & D \end{bmatrix} = \begin{bmatrix} \prod_{m=1}^r k_m & (\ell/n) \left[\prod_{m=1}^r k_m \sum_{m=1}^r \left(\prod_{j=1}^m k_j \right)^{-2} \right] + \left[\prod_{m=1}^r k_m \sum_{m=1}^{r-1} \left(\prod_{j=1}^m k_j \right)^{-2} \right] D \\ 0 & \left(\prod_{m=1}^r k_m \right)^{-1} \end{bmatrix} \quad (11)$$

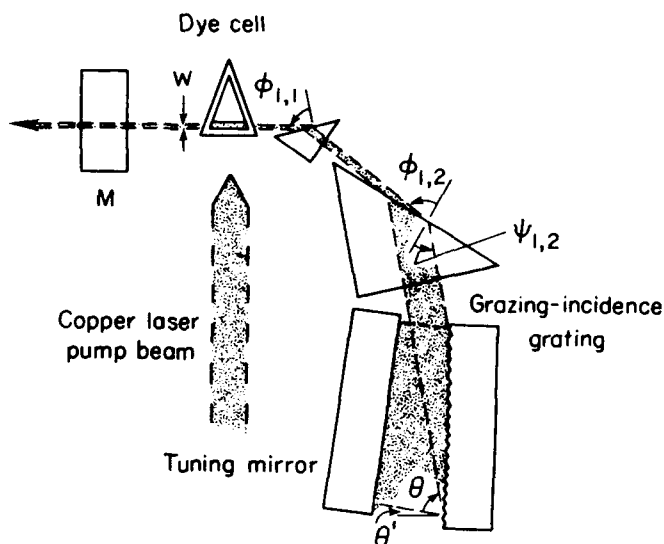


Fig. 1 Schematics of the hybrid multiple-prism grazing-incidence laser-pumped dye laser oscillator considered here. In these experiments the distance between the dye cell and the first prism was $\sim L_R$ (from Ref. 7).

Here, the overall prismatic magnification is given by⁵ $M = \prod_{m=1}^r k_m$, and $k_m = (\cos \psi_{1,m} / \cos \phi_{1,m})$, where $\phi_{1,m}$ is the angle of incidence, and $\psi_{1,m}$ the corresponding angle of refraction.

For a double-prism expander where $k_1 = k_2$ and $M = k_1 k_2$, the ray matrix at the plane of incidence is given by

$$\begin{bmatrix} A & B \\ C & D \end{bmatrix} = \begin{bmatrix} M & (\ell/n) [1 + (1/M)] + D \\ 0 & (1/M) \end{bmatrix} \quad (12)$$

Thus, the Gaussian beam at a distance x from the expander (that is located at a distance L from the dye cell) is given by

$$w(x) = w [M^2 + (B/L_R)^2]^{\frac{1}{2}} \quad (13)$$

where

$$B = [ML + D + (\ell/n) + (\ell/nM) + (x/M)] \quad (14)$$

hence

$$w(x) = w M [1 + \{[M^2 L n + D n M + M \ell + \ell + n x] / (n M^2 L_R)\}^2]^{\frac{1}{2}} \quad (15)$$

Thus, an expression for the overall cavity dispersion is given by

$$\Delta \theta = (w/L_R) [1 + (L_R/B)^2 + (L_R M/B)^2]^{\frac{1}{2}} \quad (16)$$

In the absence of prisms, $L = D = \ell = 0$ and $n = M = 1$, so that $B = x$ and Eq. (16) becomes identical to Eq. (7).

Now, for large beam expansion factors typical of laser-pumped pulsed dye lasers and a finite cell-prism length $B \cong ML$, so that

$$\Delta\theta = (w/L_R) [1 + (L_R/L)^2 + (L_R/ML)^2]^{1/2} \quad (17)$$

for the case $ML \gg L_R$, then

$$\Delta\theta = [\lambda/(\pi w)] [1 + (L_R/L)^2]^{1/2}$$

For the far-field case, $L \gg L_R$, the well-known result $\Delta\theta \cong \lambda/(\pi w)$ is obtained. For $L \ll L_R$ we get $\Delta\theta = [\lambda/(\pi w)] (L_R/L)$, and for $L_R = L$ we obtain $\Delta\theta = \lambda\sqrt{2}/(\pi w)$.

From this formulism we can work out $\Delta\theta$ for any value of M or L . For instance, in the case of flashlamp-pumped pulsed dye lasers, $10 < M < 20$, and L_R can be a few meters. So for $L \cong 1$ cm, $L_R \gg ML$ and $\Delta\theta \cong (\lambda/\pi w) (L_R/L)$.

Note that if we differentiate Eq. (15) (as suggested in Ref. 6) so that $\Delta\theta_1 = [\partial w(x)/\partial x]$, we obtain

$$\Delta\theta = (w/M L_R) [(1 + a^2 + a^4)/(1 + a^2)]^{1/2} \quad (18)$$

where $a = (M L_R/B)$, and B is given by Eq. (14).

For the case of large beam expansion we have $B \cong ML$. Thus, if $L = L_R$, we get $a = 1$ and $\Delta\theta = [\lambda/(M \pi w)] \sqrt{3/2}$. Further, in the absence of the beam expander, $M = 1$, $D = \ell = L = 0$, and $x = d$; thus, in Eq. (21) we obtain $\Delta\theta = [\lambda/(\pi w)] \sqrt{3/2}$ for $L_R = d$, $\Delta\theta = [\lambda/(\pi w)] (L_R/d)$ for $L_R \gg d$, and $\Delta\theta = \lambda/(\pi w)$ for the far-field case.

Experimental

To test the difference between the geometrical and the transfer-matrix approach, we measured the beam divergence and the linewidth from the HMPGI cavity shown in Fig. 1. In addition, identical measurements in a pure grazing-incidence oscillator were also performed. In all cases the Rayleigh length was determined measuring the beam size at the dye cell using a Galilean telescope which provided a X 20 magnification. Thus, L_R was determined to be ~ 0.11 m. For the grazing-incidence laser the cell-grating length was made equal to L_R , and for the HMPGI oscillator the cell-prism-expander length was made equal to L_R .

The excitation source was an excimer laser (XeCl , $B^2\Sigma_1^+ - X^2\Sigma_1^+$ transition at $\lambda = 308$ nm). As discussed in previous publications⁷ the pump beam was a narrow horizontal strip (10 mm wide x 0.5 mm high).

The grating utilized was a 50 mm wide holographic grating with 3000 ℓ/mm . In both cases close to 50 mm were illuminated on the grating. The two small prisms employed were made of quartz with an apex angle of 42.7° and an hypotenuse of 15 mm. The overall beam expansion factor was about 20.

The dye used in these experiments was Kodak coumarin 102-T dye ($MW = 311.32$) at a concentration of 4×10^{-3} M in ethanol. Beam divergence was determined photographically at the far field, and laser linewidths were measured interferometrically. All measurements were performed at ~ 480 nm.

The most important, and difficult to assess, experimental uncertainty in these experiments should originate in spatial variations of the pump excimer laser beam which in turn can induce changes in the dye laser beam waist. Thus, the condition of $L = L_R$ may not always be satisfied.

Results

Table I lists calculated beam divergence ($\Delta\theta_C$), measured beam divergence ($\Delta\theta_E$), calculated linewidth ($\Delta\nu_C$) and measured linewidth ($\Delta\nu_E$) for the two types of narrow-linewidth oscillators utilized in this experiment. It is immediately apparent that both measured beam divergence and linewidth are lower than the calculated values. Additional information should include the calculated linewidth using the experimental beam divergence. These values are 1.68 GHz and 1.82 GHz for the grazing-incidence and the HMPGI dye laser, respectively. For the grazing-incidence cavity $\Delta\theta_C \sim 1.7$ mrad using Eq. (4).

Table I

Cavity	$\Delta\theta_E$ (mrad)	$\Delta\theta_C$ (mrad)	$\Delta\nu_E$	$\Delta\nu_C$
Grazing-Incidence	1.1	2.11	1070 MHz	3.24 GHz
HMPGI	1.2	2.11	1070 MHz	≤ 3.24 GHz

Discussion

A comparison between the different approaches to calculate $\Delta\theta$ indicates that the Littman and Metcalf and the transfer-matrix treatments provide similar answers for the case of simple mirror-mirror or mirror-grating cavities where beam propagation is through homogeneous media. A slight difference of $\sqrt{2}$ arises between the two approaches when the case of $d \ll L_R$ is considered for cavities incorporating multiple-prism beam expansion. However, for the case yielding the lowest $\Delta\theta$ ($d \gg L_R$) the two methods provide the same prediction.

Experimentally, it is observed that for both type of cavities the beam divergence approaches its diffraction limit. This is attributed to multipass effects.⁷⁻¹⁰ The main difference between the two cavities was a larger standard of deviation in the case of beam divergence measurements corresponding to the HMPGI oscillator.

A description of the multipass effect can be found in a previous paper¹¹ where it was shown that, when dispersive elements are introduced in the cavity, a multipass analysis yields the following equation for linewidth:

$$\Delta\lambda = (\Delta\theta/R) \left[\prod_{m=1}^r k_m (\partial\theta/\partial\lambda)_G + 2 \sum_{m=1}^r (\pm 1) \left(\prod_{j=1}^m k_j \right) \tan\psi_{1,m} (dn/d\lambda) \right]^{-1} \quad (19)$$

where R represents the number of cavity return passes. In this expression $\Delta\theta$ is given by Eq. (9), (see Table I for results).

The R factor indicates that multipass effects can reduce the beam divergence when intracavity dispersive elements are utilized. A similar conclusion was reached following an intuitive description provided by Sze⁹ with the added observation that R can only reduce $\Delta\theta$ until the diffraction limit is reached.

In this discussion we have not considered possible astigmatic aberrations. Astigmatism in prismatic systems may be neutralized by making one of the prisms exit faces convex cylindrical.¹²

Conclusion

The transfer-matrix approach predicts values for $\Delta\theta$ which are only slightly different from the values predicted by the simple Littman and Metcalf description. Further, the discrepancies between predicted and measured beam divergence are far more significant than the differences between theoretical expectations. Thus, either theoretical approach can be used to estimate the likely beam divergence; however, for a more accurate estimate of laser linewidth the measured value of $\Delta\theta$ should be employed. The complete transfer-matrix formalism for the multiple-prism cavity, provided here, yields results compatible with the well known geometrical approach² when the parameters corresponding to the multiple-prism expander are given values consistent with a free-space cavity.

Finally, it should be indicated that the lowest beam divergence can be assured using a cavity length greater than L_R . The problem here is that often, for single longitudinal mode operation, the shortest cavity length is desired.

References

1. F. J. Duarte and J. A. Piper, Opt. Commun. 43, 303 (1982).
2. M. G. Littman and H. J. Metcalf, Appl. Opt. 17, 2224 (1978).
3. J. Turunen, Appl. Opt. 17, 2908 (1986).
4. J. P. Tache, Appl. Opt. 26, 427 (1987).
5. F. J. Duarte, Opt. Commun. 53, 259 (1985).
6. R. Buffa, S. Cavalieri, M. Matera, and M. Mazzoni, Opt. Commun. 58, 255 (1986).
7. F. J. Duarte and J. A. Piper, Appl. Opt. 23, 1391 (1984).
8. M. K. Iles, Appl. Opt. 20, 985 (1981).
9. R. C. Sze, in Technical Digest, Conference on Lasers and Electro-Optics (Optical Society of America, Washington, DC, 1984) paper THP6.
10. F. J. Duarte and R. W. Conrad, Appl. Opt. 26, 2567 (1987).
11. F. J. Duarte and J. A. Piper, Opt. Acta 31, 331 (1984).
12. T. Kasuya, T. Suzuki, and K. Shimoda, Appl. Phys. 17, 131 (1978).

INTENSE PICOSECOND LIGHT GENERATION BY AMPLIFIED SPONTANEOUS EMISSION

P. Sperber, W. Spangler, B. Meier, and A. Penzkofer
Naturwissenschaftliche Fakultät II - Physik,
Universität Regensburg, D-8400 Regensburg, Fed.Rep.Germany

The picosecond pulse generation in longitudinally pumped dye laser generators and amplifiers is studied. Frequency tunable pulses between 720 nm and 940 nm are generated with a picosecond ruby pump source. Energy conversion efficiencies of approximately ten percent are obtained. Besides the amplification of spontaneous emission, the seeding pulse amplification of picosecond light continua is discussed. The simultaneous occurrence of resonance Raman scattering is studied.

1. Introduction

The amplification of spontaneous emission allows the generation of frequency tunable picosecond light pulses in dye solutions if population inversion is caused by excitation with picosecond pump sources¹⁻¹¹. Longitudinal^{1,4,5,11}, transversal^{2,3,12}, and travelling-wave transversal⁶⁻¹⁰ pumping arrangements have been used. In transversally excited dye cells the duration of the amplified spontaneous emission signal is restricted by the transit time through the pumped region, and two pulses are emitted in opposite direction. The travelling-wave transverse pumping applies a grating for matching the propagation of the pump pulse to the amplified spontaneous emission signal. High gains are achieved in transverse and travelling-wave transverse pumping since excited-state absorption of the pump pulse has negligible influence on the transverse amplification of the fluorescence signal. In a longitudinally pumped dye cell the excited-state absorption at the pump-laser frequency ν_L restricts the amplification of the fluorescence light.

In this paper a versatile longitudinally pumped dye laser generator-amplifier system is described. The drawbacks of excited-state absorption at ν_L are avoided by splitting the pump pulse to pump a generator cell (amplification of spontaneous emission) and a chain of amplifier cells (signal amplification). The spectral narrowing and tuning is achieved with a grating spectrometer. The reamplification of the spectrally narrowed and tuned signals gives nearly bandwidth-limited intense picosecond light pulses.

2. Experimental

A schematic of the experimental setup is depicted in Fig.1. The pump pulses are generated in a passively mode-locked ruby laser (wavelength $\lambda_L = 694.3$ nm, duration $\Delta t_L \approx 30$ ps). The generated ASE signal in the generator cell G is collimated (lens L2) and amplified in the longitudinally pumped dye cells A1 and A2. The spectrometer SP1 is used for spectral narrowing and tuning. The reamplification of the narrowed signal occurs in the dye cell A3 which is excited with an amplified fraction of the picosecond ruby pump pulse.

3. Dyes

The investigated dyes are listed in Table 1 together with some spectroscopic data. The absorption cross-sections σ_L at the pump laser frequency ν_L are measured with a spectrophotometer. The excited-state absorption cross-sections σ_{ex} are determined by intensity dependent transmission measurements¹³. The excited-state absorptions σ_{ex}^{ASE} of the generated light are determined by simulating the light generation in the generator cell¹⁴. The fluorescence lifetimes are measured with a streak camera at low dye concentrations. The fluorescence quantum efficiencies are measured with a spectro-fluorimeter¹⁵. The stimulated emission cross-section spectra are plotted in Fig.2. They are determined from absorption cross-section spectra and fluorescence quantum distribution measurements according to¹⁶⁻¹⁹

$$\sigma_{em}(\lambda) = \frac{n_F \lambda^4 \tilde{E}(\lambda) q_F}{n_A \tau_F} \frac{\int_{em} \tilde{E}(\lambda) d\lambda}{\int_{em} \tilde{E}(\lambda) \lambda^4 d\lambda} \int_{abs} \frac{\sigma_{abs}(\lambda)}{\lambda} d\lambda \quad (1)$$

n_F and n_A are the average refractive indices of the solutions in the S_1-S_0 emission and the S_0-S_1 absorption band, respectively. $\tilde{E}(\lambda)$ is the normalized fluorescence quantum distribution ($\int_{em} \tilde{E}(\lambda) d\lambda = 1$).

4. Results

The amplification of spontaneous emission in the generator cell is studied first. Then the signal amplification, the spectral narrowing and tuning as well as the reamplification are investigated. The alternative technique of intense frequency tunable picosecond pulse

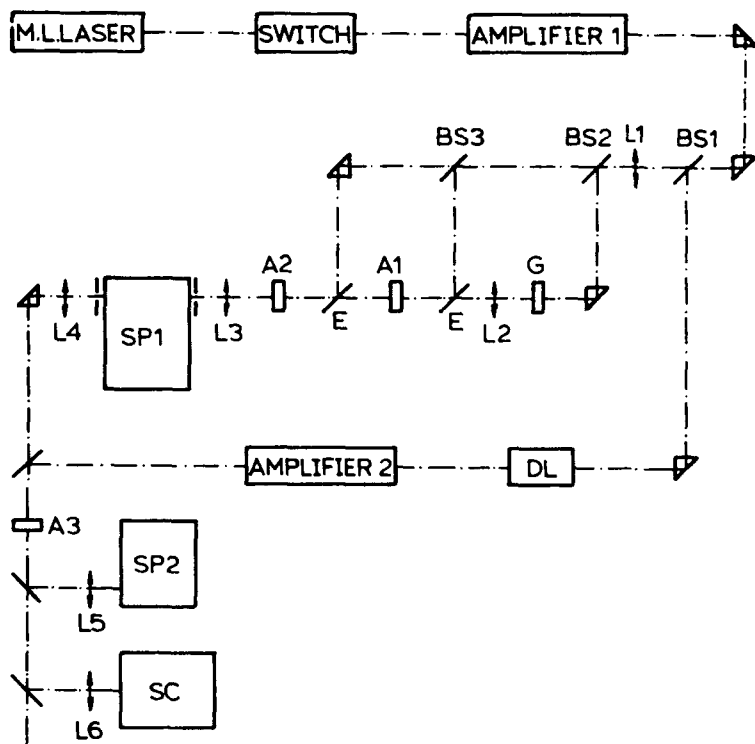


Fig.1: Experimental setup. L1-L6, lenses. G, generator dye cell. A1-A3, amplifier dye cells. SP1, SP2, grating spectrometers. DL, optical delay line. SC, streak camera. BS1-BS3, beam splitters with reflectivities $R1 = 0.1$, $R2 = 0.3$, and $R3 = 0.5$. E, edge filters reflecting the pump pulse and transmitting the generated light.

generation by seeding pulse amplification of picosecond light continua is discussed shortly. The concurrent resonance Raman scattering is mentioned.

4.1 Amplified Spontaneous Emission in the Generator Cell. In the generator cell the fluorescence signal is amplified in forward direction. The dashed curves of Fig.3 display the normalized fluorescence spectral distributions $W_F(\lambda)/W_L$ within an acceptance angle of $\Delta\theta=6^\circ$. The solid curves show the normalized spectral distribution $\eta_E(\lambda) = W_{ASE}(\lambda)/W_L$ of the amplified spontaneous emission (ASE) signals for $I_{OL} \approx 4 \times 10^4 \text{ W/cm}^2$. W_L is the pump pulse energy at the entrance of the generator cell. The amplification and spectral narrowing of the fluorescence light are clearly seen. The ASE spectra are influenced by the applied dye concentrations. Higher dye concentrations shift the emission spectra to longer wavelengths because of fluorescence reabsorption (no curves shown). The wavelength-integrated ASE energy conversion efficiency W_{ASE}/W_L versus input pump pulse peak intensity is displayed in Fig.4 (circles and solid curve) for 10^{-4} molar DDI in methanol.

The amplification in forward direction reduces the divergence of the ASE signal. The divergence $\Delta\theta$ versus I_{OL} is plotted in Fig.5 for 10^{-4} molar DDI in methanol (circles and curve 1).

The spectral bandwidth reduces with the pump pulse intensity (gain narrowing) and the emission peak shifts to shorter wavelengths (bleaching of reabsorption). This behaviour is shown in Fig.6 for 10^{-4} molar DDI in methanol. The spectral distribution of the generated spectrum is strongly structured when the observation angle is narrowed to the coherence angle $\Delta\theta_{coh} = \lambda_{ASE}/d$ (d is approximately the beam diameter of the pump pulse). The statistical nature of the spontaneous emission and the coherent amplification are responsible for the fluctuating structure^{20,21}. Integration over the full divergence angle results in a rather smooth spectrum¹⁴.

The pulse duration of the ASE signal is shortened with rising pump pulse intensity. The circles and curve 1 of Fig.7 depict the dependence of the ASE pulse duration on the input pump pulse peak intensity for 2×10^{-3} molar rhodamine 800 in methanol. The dash-dotted curve represents the pump pulse duration. When the observation angle is narrowed to the coherence angle the temporal pulse shapes are structured. The pulse shapes are rather smooth when the ASE signal is integrated over the full divergence angle.

4.2 Amplifier Chain. The following results belong to the amplified ASE signal behind the second amplifier of Fig.1. The ASE signal behind the generator cell is collimated to improve the overlap between ASE signal and pump pulse cross-section.

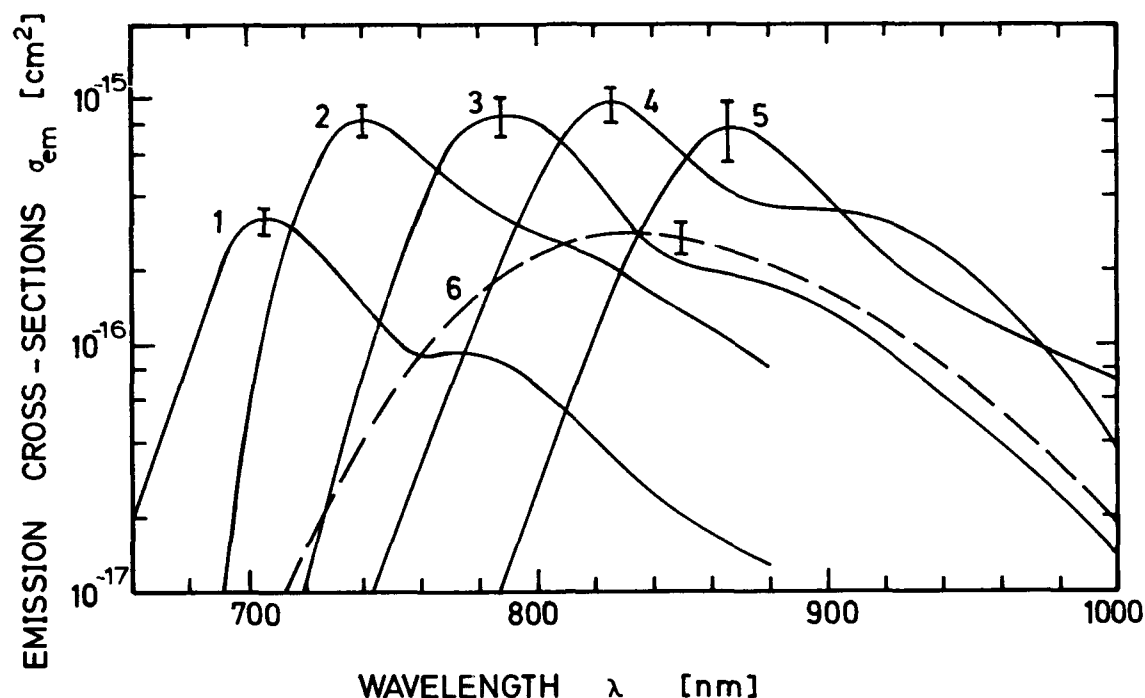


Fig.2: Stimulated emission cross-sections of investigated dyes. 1, rhodamine 800. 2, DDI. 3, HITCI. 4, HDITCI. 5, IR 140. 6, styril 9.

Table 1: Investigated dyes (all dyes supplied by Lambda Physik).

ME = methanol. EG/DMSO = 1:1 volume mixture of ethylene glycol and dimethyl sulfoxide.

DDI = 1,1'-diethyl-2,2'-dicarbocyanine iodide. HITCI = 1,1',3,3,3',3'-hexamethylindotri-carbocyanine iodide. HDITCI = 1,1',3,3,3',3'-hexamethyl-4,4',5,5'-dibenzo-2,2'-indotricarbo-cyanine iodide.

Dye	Solvent	σ_{L_2} [cm ²]	σ_{ex}^L [cm ²]	σ_{ex}^{ASE} [cm ²]	τ_F [ns]	q_F
DDI	ME	7.6×10^{-16}	5×10^{-17}	6×10^{-17}	0.017	0.004
Rhodamine 800	ME	2×10^{-16}	8×10^{-18}	1.3×10^{-17}	1.54	0.16
HITCI	ME	3.1×10^{-16}	8.5×10^{-17}	1.3×10^{-16}	0.46	0.12
HDITCI	EG/DMSO	2.2×10^{-16}	8.5×10^{-17}	1.1×10^{-16}	0.22	0.057
Styryl 9	DMSO	3.9×10^{-17}	6×10^{-17}	$\sim 1.2 \times 10^{-16}$	0.39	0.05
IR 140	EG/DMSO	1.15×10^{-16}	1.15×10^{-16}	7×10^{-17}	0.24	0.047

The dash-dotted curves of Fig.3 show the normalized spectral distributions $W_{AMP}(\lambda)/W_L$ at $I_{OL} \approx 4 \times 10^9$ W/cm². The signal amplification versus pump pulse intensity (I_{OL} is intensity in front of generator cell) is indicated in Fig.4 (dots and dashed curve).

The divergence of the amplified signal is reduced drastically as is seen by the dots and the curve 2 in Fig.5 ($\Delta\theta \approx d/l_{GA}$, d pump pulse diameter, l_{GA} distance between generator cell and amplifier cell A2).

The spectral widths are slightly narrowed in the amplifier cells (Fig.3). The wavelength peak positions are practically unchanged. The spectral shapes are slightly smoothed due to gain saturation.

The duration of the amplified signals is shortened and becomes approximately equal to

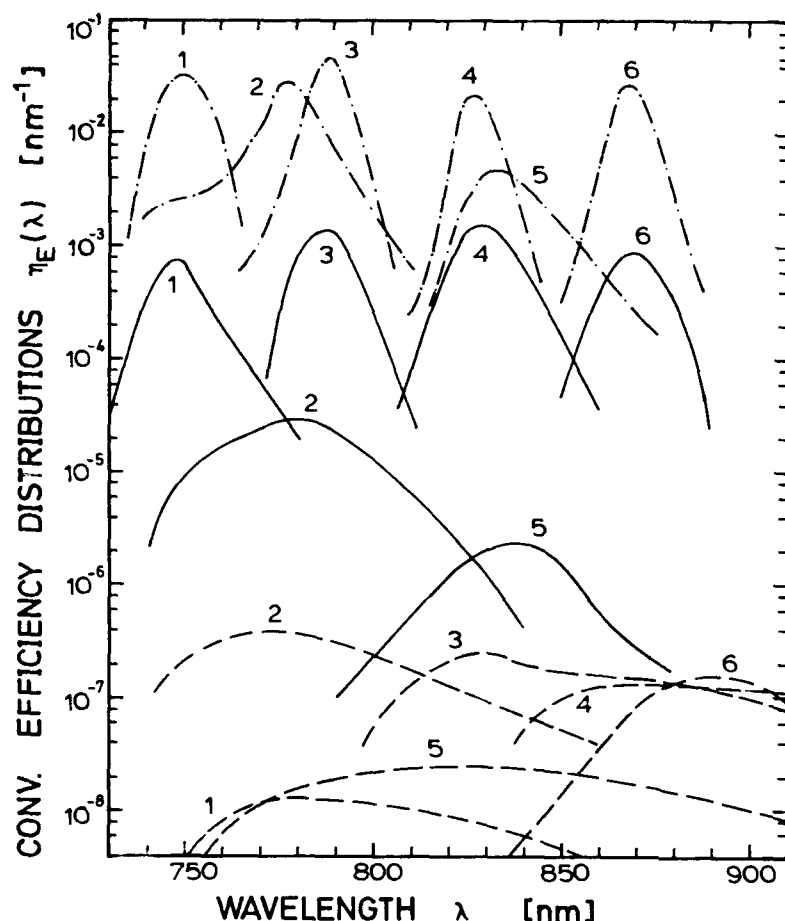


Fig.3: Conversion efficiency distributions. Dashed curves, fluorescence in forward direction within a divergence angle of $\Delta\theta=6^\circ$. Solid curves, amplified spontaneous emission signal after generator cell. Dash-dotted curves, signal behind second amplifier cell. 1, 10^{-4} molar DDI. 2, 2×10^{-3} molar rhodamine 800. 3, 7.7×10^{-5} molar HITCI. 4, 5.1×10^{-5} molar HDITCI. 5, 2.5×10^{-5} molar styryl 9. 6, 3.7×10^{-5} molar IR 140. For solvents see Table 1. Length of dye cells is $l=1$ cm.

the pump pulse duration as is seen by the triangle in Fig.7.

4.3 Tuning and Reamplification. The spectral width of the amplified ASE signal is typically 15 nm (Fig.3) and the duration is approximately 30 ps. The pulses are spectrally narrowed and tuned by passing through the spectrometer SP1. The spectral narrowing causes energy loss. The energy is restored by reamplification in the dye cell A3. The spectral narrowing, tuning, and reamplification are illustrated in Fig.8. The energy of the reamplified pulses is rather constant over a broad spectral range (higher gain at spectral wings since gain saturation occurs at the center spectral region).

4.4 Seeding Pulse Amplification. Besides the amplification of spontaneous emission the amplification of weak picosecond light continua²² in dye cells may be applied to generate intense frequency tunable picosecond light pulses^{11,14,23}. In Refs.11 and 14 the picosecond light continuum is generated in the ruby amplifier by focusing the selected single picosecond ruby pulse of the oscillator into the ruby amplifier. The main difference between amplified spontaneous emission and seeding pulse amplification (SPA) of a picosecond light continuum in a generator cell is the small divergence angle ($\Delta\theta_{SPA} \approx \Delta\theta_L$, open triangles and curve 4 in Fig.5) and the short duration ($\Delta t_{SPA} < \Delta t_L$, open caro in Fig.7). Behind the amplifier cell A2 the beam divergence (filled triangles and curve 3 of Fig.5) is slightly enlarged and the pulse duration (filled caro in Fig.7) approaches the pump pulse duration.

4.5 Resonance Raman Scattering. The ASE signal behind the generator cell is free of Raman lines in all experiments. At the position of the pump pulse peak intensity where the Raman amplification is highest, the ASE signal is still too weak to show up as an amplified Raman signal. In the seeding pulse amplification of picosecond light continua, Stokes Raman lines of the dye molecules have been observed upon the amplified continuum at high pump pulse intensities in some dye solutions^{11,14}. Behind the amplifier cells the same Raman lines were found upon the amplified ASE signals^{11,14}. The Raman transitions are resonantly enhanced by the S_0-S_1 absorption of the pump laser²⁴.

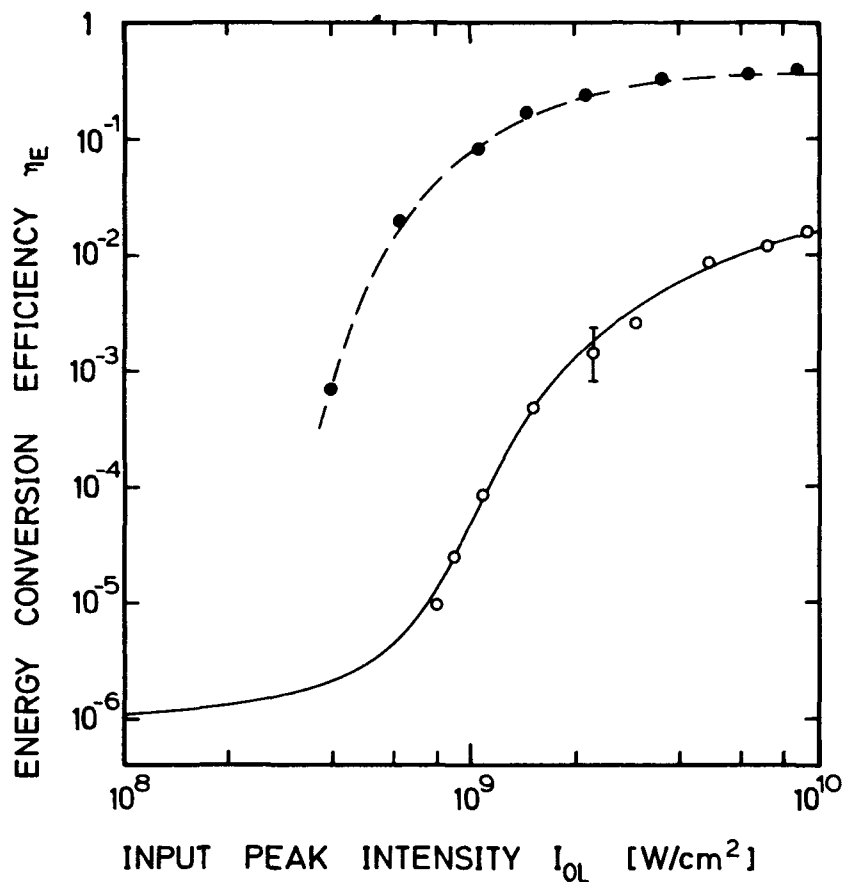


Fig. 4: Energy conversion efficiency versus pump pulse peak intensity. Dye solution is 10^{-4} molar DDI in methanol. Circles and solid curve, ASE signal behind generator cell. Dots and dashed curve, amplified signal behind second amplifier cell. Cell lengths $l=1$ cm.

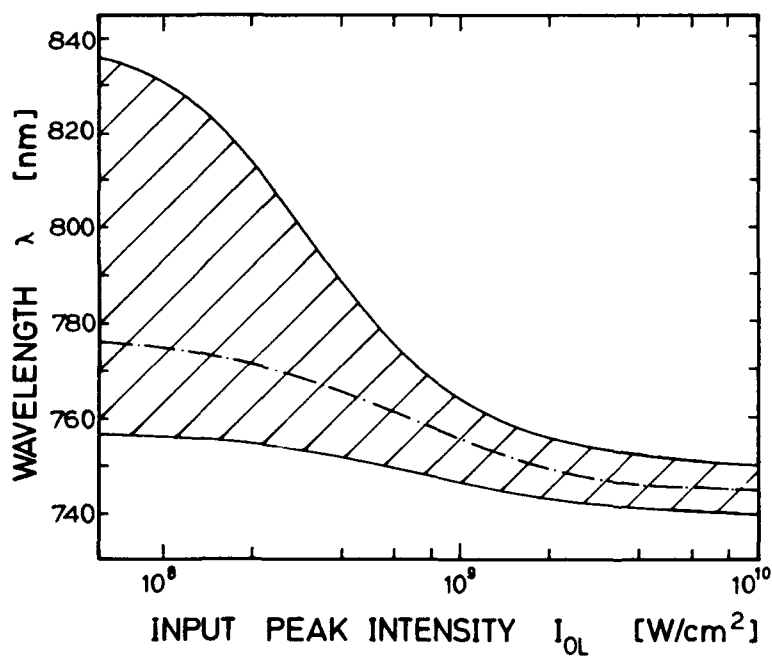


Fig. 6: Wavelength of ASE emission versus pump pulse peak intensity for 10^{-4} molar DDI in methanol. Dash-dotted curve represents peak emission wavelength. The borders of the hatched region indicate the half-heights of the signal.

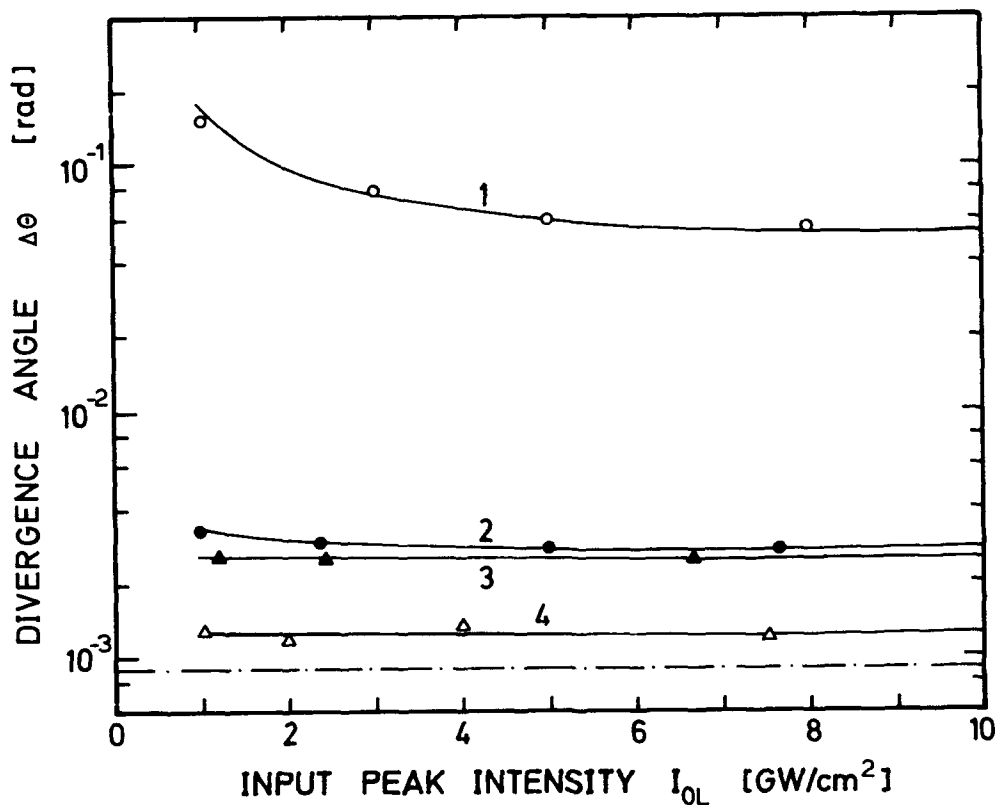


Fig. 5: Beam divergence $\Delta\theta$ (FWHM) versus pump pulse peak intensity for 10^{-4} molar DDI in methanol. The curves belong to: (1, o), ASE signal behind generator cell G; (2, ●), ASE signal behind amplifier cell A2; (3, ▲), amplified picosecond light continuum behind amplifier cell A2; (4, △), amplified picosecond light continuum behind generator cell G. The dash-dotted curve represents the beam divergence of the pump pulse.

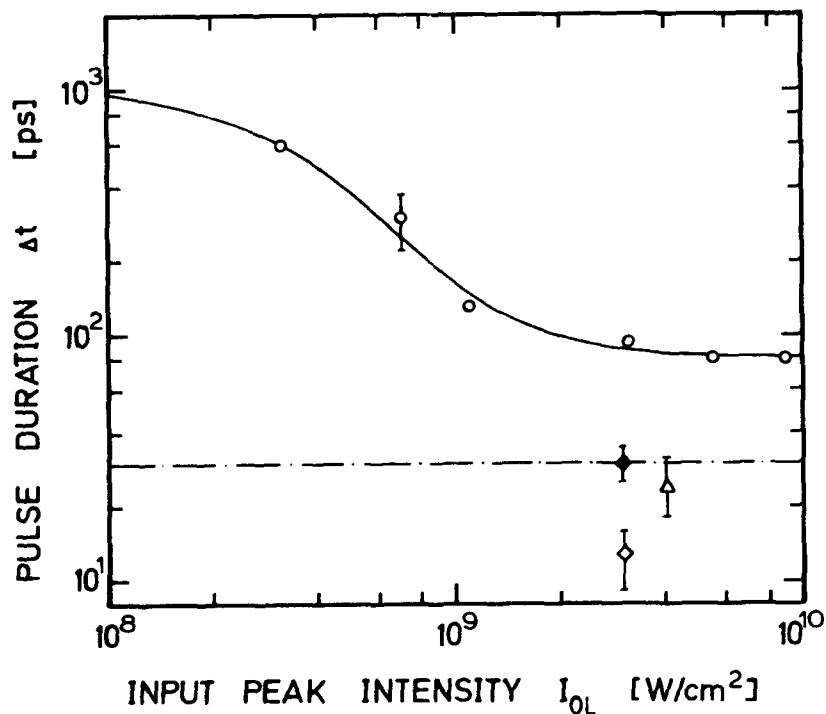


Fig. 7: Pulse durations versus pump pulse peak intensity for 2×10^{-3} molar rhodamine 800 in methanol. Solid curve and circles, ASE signal behind generator cell. Triangle, ASE signal behind amplifier cell A2. Open circle, amplified picosecond light continuum behind generator cell G. Filled circle, amplified picosecond light continuum behind amplifier cell A2. Dash-dotted line, pump pulse duration Δt_L .

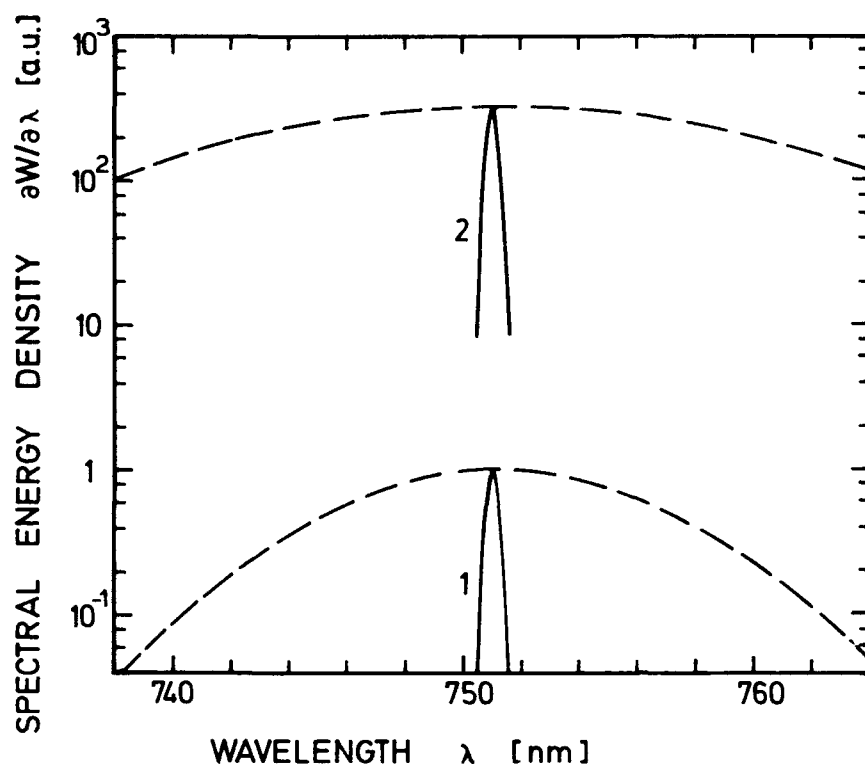


Fig.8: Reamplification of spectrally narrowed signal. Dye solution is 10^{-4} molar DDI in methanol. Solid curve 1, spectral distribution of amplified picosecond light continuum before amplifier A3. Solid curve 2, spectral distribution behind amplifier A3. The dashed curves are the envelopes of the peaks of the spectrally narrowed signals before and behind the amplifier A3.

5. Conclusions

The described dye generator-amplifier system allows the generation of intense, frequency tunable picosecond light pulses over a wide spectral range. With picosecond ruby pump pulses the frequency region between 720 nm and 940 nm was covered with 6 different dyes (in addition to Fig.3 5×10^{-4} molar rhodamine 800 extends the spectral range to 720 nm and 5×10^{-4} molar IR 140 extends the ASE signal to 940 nm). A conversion efficiency of approximately 10 % was obtained (relating to the pump pulse energy behind the ruby amplifier 1). Using other pump sources (second harmonic of mode-locked ruby laser, mode-locked Nd-lasers and their harmonics) the spectral region may be extended from the near ultraviolet to the near infrared spectral region over the full spectral range of available laser dyes or saturable absorbers²⁵⁻²⁹. In contrast to dye laser oscillators the picosecond dye laser generators may be operated as well with laser dyes of high fluorescence quantum efficiency and with saturable absorbers of low fluorescence quantum efficiency (short fluorescence lifetime τ_F , e.g. DDI in methanol)^{6,9}. The generator efficiency is expected to reduce only if $\tau_F < \Delta t_L$.

References

1. M.E. Mack, Appl. Phys. Lett. 15, 166 (1969)
2. S.L. Chin and G. Bedard, Opt. Commun. 4, 148 (1971)
3. C. Lin, T.K. Gustafson, and A. Dienes, Opt. Commun. 8, 210 (1973)
4. A.N. Rubinov, M.C. Richardson, K. Sala, and A.J. Alcock, Appl. Phys. Lett. 27, 358 (1975)
5. W. Falkenstein, A. Penzkofer, and W. Kaiser, Opt. Commun. 27, 151 (1978)
6. H.J. Polland, T. Elsaesser, A. Seilmeier, and W. Kaiser, Appl. Phys. B32, 53 (1983)
7. Zs. Bor, S. Szatmari, and A. Müller, Appl. Phys. B32, 101 (1983)
8. S. Szatmari and F.P. Schäfer, Opt. Commun. 49, 281 (1984)
9. T. Elsaesser, H.J. Polland, A. Seilmeier, and W. Kaiser, IEEE J. QE-20, 191 (1984)
10. P. Lee, C. Ning, and Z. Huang, Appl. Phys. B40, 35 (1986)
11. P. Sperber, M. Weidner, and A. Penzkofer, Appl. Phys. B32, 185 (1987)
12. A. Penzkofer, Appl. Phys. B40, 85 (1986)
13. G. Grönninger and A. Penzkofer, Opt. Quantum Electron. 16, 225 (1984)

14. P. Sperber, W. Spanale, B. Meier, and A. Penzkofer, *Opt. Quantum Electron.*, to be published
15. A. Penzkofer and W. Blau, *Opt. Quantum Electron.* 15, 325 (1983)
16. S.J. Strickler and R.A. Berg, *J. Chem. Phys.* 37, 814 (1962)
17. J.B. Birk and D.J. Dyson, *Proc. Roy. Soc. London A275*, 135 (1963)
18. O.G. Peterson, J.P. Webb, W.C. McColgin, and J.H. Eberly, *J. Appl. Phys.* 42, 1917 (1971)
19. A. Penzkofer and W. Leupacher, *J. Luminesc.* 37, 61 (1987)
20. A.A. Brütter, H.P. Weber, and R. Dändliker, *Phys. Rev.* 185, 629 (1969)
21. L. Mandel and E. Wolf, *Rev. Mod. Phys.* 37, 231 (1965)
22. A. Penzkofer and W. Kaiser, *Opt. Quantum Electron.* 9, 315 (1977)
23. A. Migus, J.L. Martin, R. Astier, A. Antonetti, and A. Orizag, in *Picosecond Phenomena III*, K.B. Eisenthal, R.M. Hochstrasser, W. Kaiser, and A. Laubereau (Springer-Verlag, Berlin, 1982) p. 6
24. M. Pfeiffer, A. Lau, and W. Werncke, *J. Raman Spectrosc.* 15, 20 (1984)
25. F.P. Schäfer, Editor, *Dye Lasers* (Springer-Verlag, Berlin 1977)
26. M. Maeda, *Laser Dyes* (Academic Press, New York, 1984)
27. U. Brackmann, *Laser-grade Dyes* (Lambda Physik, Göttingen, 1986)
28. *Kodak Laser Dyes* (Kodak Publication JJ-169, 1987)
29. H.J. Polland, T. Elsaesser, A. Seilmeier, W. Kaiser, M. Kussler, N.J. Marx, B. Sens, and K.H. Drexhage, *Appl. Phys.* B32, 53 (1983)

K. S. Aleksandrov, A. S. Aleksandrovsky, S. V. Karpov, V. F. Lukinykh,
S. A. Myslivets, A. K. Popov, V. V. Slabko
Institute of Physics, USSR Academy of Sciences, Siberian Branch,
Krasnoyarsk State University, 660036, Krasnoyarsk, USSR

Abstract

Complex organic molecules with delocalized π -electrons can display strong optical nonlinearities and phase-matching. First experiments on frequency-mixing and THG in the UV and VUV have confirmed advantages offered by this new class of nonlinear optical gaseous media.

Introduction

To obtain large nonlinear optical response in gaseous media narrow multiphoton resonances are generally used. The available choice of suitable atomic media is rather scanty. Experiments with two-atomic molecular gases, having a relatively simple spectrum, showed that due to vibrational-rotational broadening of the molecular transitions their resonant nonlinear susceptibilities are essentially lower compared to the atomic ones.¹⁻³

This paper shows that, on the contrary, very high nonlinearities can be inherent in multiatomic molecules with double-conjugated bonds despite of the wide vibrational-rotational broadening of the electronic transition.⁴⁻⁶ The presence of delocalized π -electrons leads to a substantial increase of the electric dipole moments of the transitions which compensates for the resonance broadening. The elementary qualitative theory developed describes the nonlinear optical properties of the molecules discussed. The experimental results on the frequency-tunable UV and VUV generation in the wavelength range 176.5-178.6 nm confirm the theoretical predictions. Nonlinear susceptibility has been measured for two representatives of this class: naphthalene and paraterphenyl.

Simplified Theory

A most simple treatment of the molecules with double-conjugated bonds and delocalized π -electrons is offered by a quantum mechanical model of the electron motion in an infinitely deep potential well. Within this model the wave functions ψ_n and the electric dipole moments of the transitions d_{mn} are written in terms of the molecule length L as follows⁴:

$$\psi_n = \frac{1}{\sqrt{L/2}} \sin \left(n \frac{\pi x}{L} \right),$$

$$d_{mn} = \int_0^L \psi_m \times \psi_n^* dx = \begin{cases} 0 & \text{for even } (m \pm n) \\ \frac{2eL}{\pi^2} \left[\frac{1}{(m-n)^2} - \frac{1}{(m+n)^2} \right] & \text{for odd } (m \pm n) \end{cases}$$

i.e. $d_{mn} \sim L$

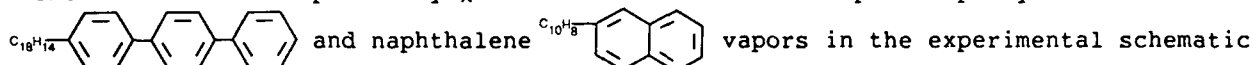
Hence the third-order nonlinear susceptibility $\chi^{(3)}$ has the form:

$$\chi^{(3)} \sim d_{mn}^4 \sim L^4$$

the estimations show that the value of $\chi^{(3)}$ for the molecules with double-conjugated bonds, even under nonresonant conditions, may be expected to be comparable with that for metal atoms under exact two-photon resonance.

Experiment

The nonlinear susceptibility $\chi^{(3)}$ has been estimated in paraterphenyl



$2\omega + 2\omega - \omega = 3\omega$ where ω is the frequency of the Nd:YAG laser radiation. In paraterphenyl vapor the frequency 2ω was tuned into the two-photon absorption band while in naphthalene vapor the resonance was absent.⁸

The nonlinear susceptibility of the paraterphenyl molecules has been measured to be $\chi^{(3)} \approx 4 \times 10^{-31}$ ESU which appears to be much larger than the resonant $\chi^{(3)}$ for the simplest molecules NO ($\chi^{(3)} \approx 10^{-32} - 10^{-33}$) and CO ($\chi^{(3)} \approx 2 \times 10^{-34}$)^{1,2} as well as the nonresonant $\chi^{(3)}$ of the dyes.⁴ This magnitude is commensurable with the quasis resonant $\chi^{(3)}$ of alkali atoms⁶ and resonant $\chi^{(3)}$ of alkali earths.³ The value of $\chi^{(3)}$ in naphthalene is about an order of magnitude lower than that in paraterphenyl. Thus the experiments have proved that double-conjugated bonds and a two-photon resonance ensure the increase of $\chi^{(3)}$.

VUV Generation

Naphthalene molecules were used to generate frequency tunable VUV radiation $2\omega + 2\omega + 2\omega = 6\omega$ where ω is the Nd:glass laser frequency tunable within the luminescence band. Figures 1 and 2 illustrate the conversion efficiency versus the cell temperature (Fig. 1) and the VUV output wavelength (Fig. 2).

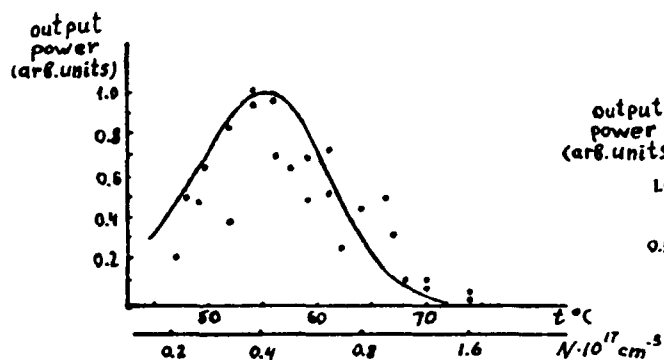


FIG. 1

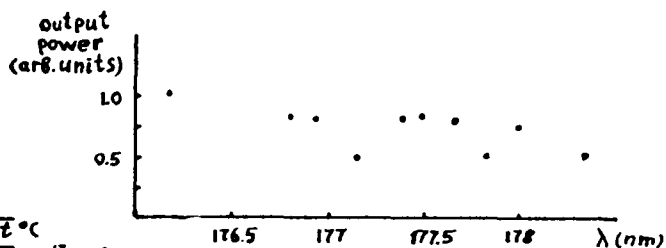


FIG. 2

As seen from the figures, the conversion efficiency is a maximum at the cell temperature

$$t = 55^{\circ}\text{C} \ (N \sim 4 \times 10^{16} \text{ cm}^{-3})$$

and is practically independent of the converted radiation frequency (Fig. 2).⁷ The tuning range of the VUV radiation depends on that of the converted radiation.

Conclusion

The estimations and preliminary experiments carried out have confirmed that the molecules with double-conjugated bonds are the promising nonlinear media for the VUV generation. This new class of nonlinear gaseous media is advantageous (low temperature, chemical inertness) over the traditional metal vapors used for this purpose.

References

1. K. K. Innes, B. P. Stoicheff, S. C. Wallace, Appl. Phys. Lett. 29, 715 (1976)
2. R. R. Vallee, J. Lukasik, Opt. Commun. 43, 287 (1982)
3. A. Timmermann, R. Wallenstein, Opt. Lett. 8, 517 (1983)
4. J. Ducuing, Optical Nonlinearities of One-Dimensional Conjugated Systems, Moscow, MIR, 1979.
5. V. F. Lukinykh, S. A. Myslivets, A. K. Popov, V. V. Slabko, Appl. Phys. B34, 143 (1985)
6. H. Eicher, IEEE J. Quant. Electr. 11, 121 (1979)
7. K. S. Aleksandrov, et. al., to be published in Doklady AN SSSR, v. 296, N 1, 1987 (USSR Acad. Sci. Rep.)
8. R. P. Drucker, W. M. McClain, J. Chem. Phys. 61, 2906 (1974)

STATISTICAL PROPERTIES OF PULSED DYE LASER RADIATION

E. Berik and V. Davidenko
Institute of Physics, 202400 Tartu, USSR

Abstract

Single-shot spectral measurements of the radiation of an excimer-pumped dye laser were performed with a high-resolution multichannel recording system in order to determine the influence of mode fluctuations and spectral instabilities of the cavity transmission band on an average laser linewidth.

Introduction

The spectral distribution of the output energy - one of the most important characteristics of any tunable pulsed laser - is usually described by one single parameter only, i.e. the linewidth (FWHM) measured by averaging over a large number of pulses.¹⁻³ However, the averaged value, obtained in this way does not take into account the spectral individualities of a single shot observable, for example, through a Fabry-Perot interferometer. Thus, a multipulse summing does not give an adequate description of laser properties and one can obtain the same linewidth for a broad-band and spectrally stable lasing as well as for a narrow-band line, shifting from pulse to pulse.

The averaged linewidth is sufficient if the laser is used in linear spectroscopy, but to apply it in nonlinear or coherent spectroscopy one must know the radiation properties more adequately. A detailed understanding of the factors determining the output linewidth is useful also for laser designing.

Theory

The spectral distribution of the energy of the pulsed laser is stochastic, each pulse having its own evolution in time, the resulting spectral form and an individual spectral position of the center of the line. In general, the recorded intensity on the wavelength λ can be written as follows:

$$I(\lambda) = \sum_{n=0}^N \int_0^{\infty} I_n(\lambda, t) dt \quad (1)$$

where the behavior of the function $I_n(\lambda, t)$ depends on a number of stochastic and deterministic processes.

Here we consider a case most typical of multimode pulsed dye lasers, when the number of modes is of the order of 5 - 25. Theoretical estimation of the linewidth have been performed already in the first publications concerning this type of lasers.^{4,5} By using a standard set of parameters (lasing wavelength λ , cavity length L , grating angle ϕ ,

transverse size of the excited zone d and beam expansion ratio M (Fig. 1)) the values have been obtained which correlate well with experimental results. The most correct expression for the laser linewidth, or, more exactly, for the Hansch-type cavity transmission band $\Delta\lambda$ has been obtained in Ref. 6. It has been shown that dependence can be written as

$$\Delta\lambda = \lambda/M \operatorname{tg} \phi [(\lambda/d)^2 + (d/2L_{\text{ef}})^2]^{\frac{1}{2}} \quad (2)$$

where $L_{\text{ef}} = L_0 + L_1/M \approx L_0$ is the distance between the active zone and the beam expander.

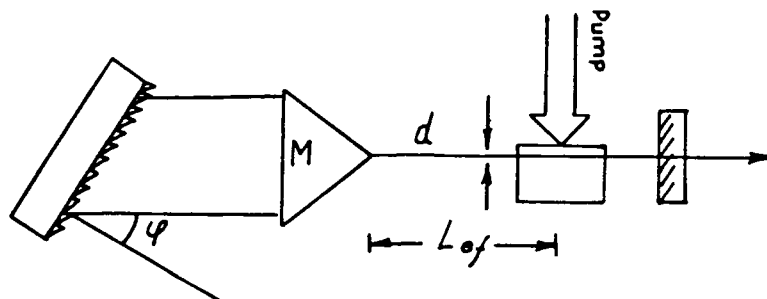


Fig. 1 Dye laser cavity parameters.

To minimize the cavity bandwidth and, accordingly, the laser linewidth one can alter all the multipliers in expression (2). However, they have different ranges of influence, therefore the increasing of the angular dispersion of the grating ($\operatorname{tg} \phi$) is the most reliable and independent way to compress the linewidth. Any possible limitation is caused by the grating properties only (finite length of substrate, surface curvature, etc.).

The enhancement of the beam expansion coefficient M also leads to a proportional reduction of the single-shot linewidth. However, the averaged linewidth will decrease to a definite level determined by spectral instabilities of the cavity transmission band, caused by the mechanical vibration of elements.

The expression under root has a minimum when $d = (2 \cdot \lambda \cdot L_{\text{ef}})^{\frac{1}{2}}$, and to optimize the laser spectrum one has to choose a proper concentration of the dye.

All the characteristics mentioned above reflect the deterministic properties of the laser cavity. The individuality of each separate shot ensues from the real condition of pulse evolution. These are mainly the mode fluctuations and spectral instabilities of the cavity transmission band. The nonreproducibility of the spectral form of each pulse is determined by stochastic processes of the mode formation due to the quantum noise. All the modes inside the cavity transmission band have the same gain because of the broad-band profile of the amplification of the active medium usually used in tunable lasers. The shot lasing time does not allow the noise-induced laser spectrum to be cut off in the smooth form of the cavity transmission profile. Therefore, the spectral form of separate shots may vary essentially, obeying statistical laws.

Spectral instabilities of the cavity transmission band, caused mainly by the vibrations of the diffraction grating, lead to nonregular shifts of the laser line. The result is the spectral broadening of the averaged profile of laser output radiation.

Both statistically described causes lead to the individualities of single pulses and

to the linewidth broadening and can not, thereby, be separated from the averaged value of the linewidth. The determination of the magnitude of the mechanical instabilities of the laser cavity is important for a proper choice of the expansion ratio M . Modern types of beam expanders (multiprism, reflecting telescopes, etc.)^{7,8} permit one to get a considerable value of M without any sufficient aberrations and losses of energy. However, the enhancement of M and thus the reduction of the single-pulse linewidth do not remove the vibrational line broadening and the ratio $\Delta\lambda_{\Sigma}/\Delta\bar{\lambda}$ can be much more than 1. Here $\Delta\lambda_{\Sigma}$ is the averaged linewidth measured in traditional manner,

$$\Delta\lambda_{\Sigma} = \int_0^{\infty} \frac{\sum N I_n(\lambda) d\lambda}{\sum I_n(\lambda_{\max})}$$

$\Delta\bar{\lambda}$ is the averaged linewidth of a single pulse

$$\Delta\bar{\lambda} = [\sum \Delta\lambda_n]/N = [\sum \int_0^{\infty} I_n(\lambda) d\lambda / I_n(\lambda_{\max})]/N$$

Wyatt, in Ref. 9, had $\Delta\lambda_{\Sigma}/\Delta\bar{\lambda} = 2.5$ when using a prism beam expander with $M = 250$. Such spectral behavior of the laser line makes impossible the application of the laser in many fields of spectroscopy. It is reasonable for commercial lasers to restrict M to the level where the difference between $\Delta\lambda_{\Sigma}$ and $\Delta\bar{\lambda}$ is less than 20 - 30%.

The task of this work was to distinguish the role of different factors in the line broadening of the pulsed dye laser and to determine the optimal value of the magnification of the intracavity beam expander M .

Experimental Details

The tunable lasers used are excimer-pumper dye lasers VL-10 and VL-18, developed in the Estonian SSR Ac.Sci.^{10,11} The lasers have modified Hansch-type oscillators with high-order ruled gratings of 600 grooves/mm and multiprism achromatic beam expanders. The lasers are of a similar design of mechanical construction and optics, except the expansion ratio M . VL-10 is provided with a four-prism 40-fold beam expander, VL-18, with a five-prism expander with $M = 100$. The lasing wavelength was chosen near the maximum of the tuning curve of Coumarin 47 dye ($\lambda = 460$ nm, $\phi = 55.8^\circ$).

The source of excitation was an excimer laser ELI-3, also produced in Estonia.¹⁰ To eliminate the negative action of thermo-optical effects on dye laser spectra the pumping energy was reduced to 3 mJ.¹² The spectral distribution of the single pulse was recorded with a 1-m home-made grating spectrophotometer provided with a diode array. The resulting spectra with a resolution of 2.2 pm were sampled and displayed by a multichannel analyzer TN-7200 (Tracor Northern). The spectral calibration of the recording system was performed with the aid of a broad-band laser radiation, passed preliminarily through a 20 mm-basis Fabry-Perrot etalon. The system permitted the recording of single-pulse and averaged spectra of the dye laser and the processing of information.

Results

The excimer and dye lasers were stabilized by one-hour operation with the repetition rate of 10 Hz. The stability of the pulse energy under these conditions was better than

5% (90% of pulses). The lasing spectrum of one of the pulses was recorded in the MCA memory. The linewidth of the pulse was calculated after subtracting the background as a ratio of the area of the spectrum to the amplitude at the maximum. The spectral forms of separate pulses were very individual, one could see asymmetrical lines or the lines with two maxima. Otherwise these were very narrow lines with high amplitudes (Fig. 2). The variety of the lineforms observed correlates well with the results of Ref. 13, where a

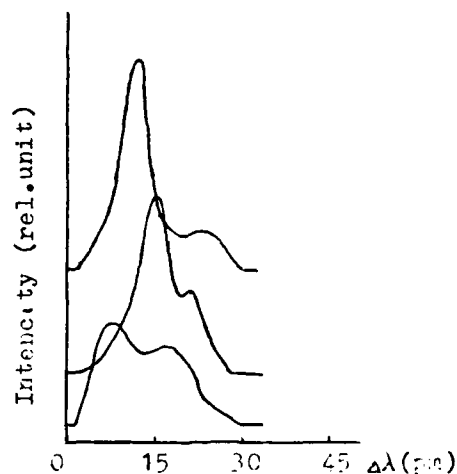


Fig. 2 Lineforms of successive laser pulses.

similar spectral method was used for the investigations of mode interaction in a pulsed dye laser with a grazing incidence grating. The 5 - 10 pulse-averaged spectra looked much smoother, and after the accumulation of 30 - 50 shots the lineform became reproducible and near-Gaussian.

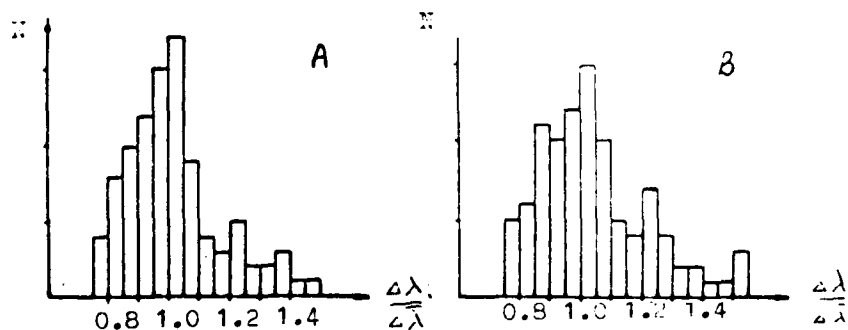


Fig. 3 Histograms of relative linewidth $\Delta\lambda_i/\Delta\bar{\lambda}$ of VL-10 (a) and VL-18 (b) dye lasers.

In Fig. 3, the results of a statistical processing of 100 independent measurement cycles are depicted. One can see that even a stabilized laser system has a two-fold variation of the linewidth as a result of the fluctuational formation of lasing. The standard of deviation of the linewidth for both lasers were calculated (see Table)

Table STATISTICAL PROPERTIES OF DYE LASER RADIATION

Laser	M	$\Delta\bar{\lambda}$ (pm)	$\Delta\lambda_{\Sigma}$ (pm)	$\delta\lambda/\Delta\bar{\lambda}$	$(\Delta\lambda_{\Sigma} - \Delta\bar{\lambda})/\Delta\bar{\lambda}$	$\Delta\lambda_c$ (pm)
VL-10	40	9.0	9.5	0.15	0.05	3.0
VL-18	100	3.7	4.7	0.17	0.25	2.9

The magnitudes of $\Delta\lambda_{\Sigma}$ for VL-10 and VL-18 dye lasers were determined by the accumulation of 100 successive pulses. This averaged value takes into account the lineshifts and is equivalent to the one obtained by the traditional methods of recording. Because of the short recording time one can neglect the line-broadening caused by slow thermal processes.

Discussion

The difference between $\Delta\lambda_{\Sigma}$ and $\Delta\lambda$ for the VL-10 dye laser is less than 5%. It shows that the contribution of the mechanical vibrations of the cavity in the line-broadening of the laser with a 40-fold expander is very small. One can say that the jumps in the spectrum of a conventional dye laser, observed visually, are the consequence of mainly the fluctuational migration of the energy inside the line profile and thus the reduction M does not lead to the proportional decrease of spectral instabilities. (The reduction proportional to $M^{1/2}$ is possible owing to the increase of the number of lasing modes.)

The standard deviation $\delta\lambda$ for VL-18 is the same as for the laser with $M = 40$. The difference in $\Delta\lambda$, obtained for VL-10 and VL-18 lasers is equal to 2.3, which indicates a small influence of the quality of the optics used. However, the difference between $\Delta\lambda_{\Sigma}$ and $\Delta\lambda$ in case of VL-18 laser with 100-fold expander exceeds 25%. This is a contribution of the spectral instabilities of the cavity transmission band $\Delta\lambda_c$. It can be defined as

$$\Delta\lambda_c = (\Delta\lambda_{\Sigma}^2 - \Delta\bar{\lambda}^2)^{1/2}$$

For the lasers VL-10 and VL-18, that have the same constructions, the calculated values of $\Delta\lambda_c$ are respectively 3.0 and 2.9 pm. The good coincidence of the magnitudes of $\Delta\lambda_c$ for different lasers confirms the correctness of the method used.

We can draw a conclusion that for an average-cost commercial pulsed dye laser it is reasonable to use beam expanders with the expansion ratio $M \approx 100$, as it does not lead to the broadening of the averaged linewidth. Though the measurements were performed by means of a dye laser with a Littrow-mounted grating, the way of the formation of the cavity transmission band does not affect on the statistics of laser spectra. Thus, the results should be valid for other types of selective laser cavities as well.

References

1. F. J. Duarte and J. A. Piper, Opt. Commun. 35, 100 (1980)
2. R. Konig, G. Minkwitz and B. Christov, Opt. Commun. 32, 301 (1979)
3. Lambda Physik, "Pulsed Dye Laser LF 2002", (1984)
4. T. W. Hansch, Appl. Opt. 11, 895 (1972)

5. F. P. Schafer, "Dye Lasers", (Springer, New York, 1973)
6. M. C. Soskin, "Tunable Lasers", Moscow, (1982)
7. R. Trebino, J. P. Roller and A. E. Siegman, IEEE J. Quant. Electron. QE18, 1208 (1982)
8. F. J. Duarte and J. A. Piper, Appl. Opt. 21, 2782 (1982)
9. R. Wyatt, Opt. Commun. 26, 429 (1978)
10. Estonian SSR Ac.Sci., "ELIS - Excimer Laser Pulsed Spectrometer", Tallinn, (1985)
11. Estonian SSR Ac.Sci., "Pulsed Dye Laser VL-18", Tallinn, (1986)
12. E. Berik, I. Berik and V. Davidenko, Trudy Institute Fiziki AN Estonskoj SSR 60, 105 (1987)
13. L. A. Wetling, M. G. Raymer and J. I. Snyder, JOSA B1, 150 (1984)

FLUCTUATION PROPERTIES OF LIQUID RING LASER WITH AN INJECTED SIGNAL

V. S. Smirnov, A. Z. Fazliev
Institute of Atmospheric Optics, SB USSR Academy of Sciences,
Tomsk, 634055, USSR

Abstract

The effect of the external-signal intensity and tuning off from resonance on the statistical properties of strong and weak fluctuations of a liquid ring laser with an external signal generating in the counter wave mode has been described.

Introduction

Dye lasers have shown good promise as light sources for laser spectroscopy. This is due to their high emitting power, adequately broad operating wavelength range, continuous laser frequency tuning capability, and other favorable properties. The majority of the experiments using dye lasers employ intracavity laser spectroscopy^{1,2} based on wide-band radiation sources. On the other hand, narrow-band dye lasers generating homogeneously broadened linewidths appear to be valuable tools for laser reception spectroscopy (LRS)³ that permits an insight into the fine structure of the stimulated Brillouin scattering. LRS provides for the amplification of the induced Rayleigh scattering components without distortion of spectral line shape within the ring laser. Krivoshechekov et al.⁴ reported LRS theoretical and experimental analysis, using a ruby laser as an emitter, and showed potentialities of this method. However, the feasibility of other light sources for that matter has not been studied.

The object of the present report is to consider statistical and spectral characteristics of a dye ring laser with an injected signal since the knowledge of these properties appears to be essential in designing LRS experiments. The results obtained show the possibility of changing the spectral properties of the laser in the counterpropagating regime. In particular, the emission linewidth can be decreased by increasing the injected intensity. The maximum narrowing is limited by the existence of the noise-induced transition between the laser modes and determined by the equality of time scale for the first-passage time (FPT) and the time required for the steady-state laser spectrum to develop.

A dye ring laser with an injected signal also permits an experimental observation of short switching times for the lasing regimes. Importantly, short FPT's can be achieved for high pumping power. It should be noted that FPT in dye lasers tends to shorten only when the pumping level is reduced.⁵⁻⁷ However, low pumping values lead to considerable color noise, which precludes from consistent analytical investigation of large statistical fluctuations.

In the discussion below the formula for FPT in a injection-locked dye ring laser is reported. Also examined is an unconventional exponential dependence that occurs when the laser detuning is taken into account.

Dynamical Behavior of Injection-Locked Dye Ring Laser

The equation of motion for the coherent amplitudes Z_q of the counterpropagating waves in a homogeneously-broadened dye ring laser with an injected signal are given by the relations⁸:

$$\frac{1}{\nu} \frac{\partial Z_q}{\partial t} = - \frac{\partial \bar{\phi}}{\partial Z_q^*}, \quad q = \pm \quad (1)$$

where ν is the cavity linewidth. The right-hand side of Eq. (1) is represented as a gradient of the complex-valued potential $\bar{\phi}$ due to the choice of the laser model, assuming that the lasing frequency coincides with the injected frequency ω .

In this case

$$\begin{aligned} \bar{\phi} &= (1 + i\delta)\phi, \quad a = \frac{a_0 - \delta^2}{1 + \delta^2}, \quad \beta = \frac{\beta_0}{(1 + \delta^2)^2}, \\ \phi &= \sum_{q=\pm} \left(-a + (\beta/2)(|Z_q|^2 + 2|Z_{-q}|^2) \right) |Z_q|^2 \frac{2\sqrt{n_0}}{1 + \delta^2} (\text{Re}Z_+ - \delta \ln Z_+). \end{aligned} \quad (2)$$

Here $\delta = (\omega - \omega_0)/\gamma_{\perp}$ is detuning from the atomic transition frequency ω_0 ; γ_{\perp} is the luminescence linewidth; a_0 , β_0 are the pumping and saturation parameters, respectively; n_0 is the injected photon number.

The dynamic behavior of the laser radiation is considered in the coordinates

$$Z_+ = x + iy, \quad Z_- = ze^{i\Phi}. \quad (3)$$

Eq. (1) rewritten in this coordinate system have the form

$$\dot{x} = -\frac{\nu}{2} \left(\frac{\partial \phi}{\partial x} - \delta \frac{\partial \phi}{\partial y} \right), \quad \dot{z} = -\frac{\nu}{2} \frac{\partial \phi}{\partial z}. \quad (4)$$

$$\dot{y} = -\frac{\nu}{2} \left(\frac{\partial \phi}{\partial y} + \delta \frac{\partial \phi}{\partial x} \right), \quad \dot{\Phi} = -\frac{\nu}{2} \frac{\delta}{z} \frac{\partial \phi}{\partial z}. \quad (5)$$

The simultaneous Eqs. (4)-(5) contain an integral of motion

$$\Phi - \delta \ln Z = \text{Const} \quad (6)$$

There are a few steady-state solutions to Eqs. (4)-(5) but only two stationary points specify steady-state laser operation in the running wave and counterpropagating wave regimes.

The metastable state with coordinates

$$x_1 = -\frac{2}{3} \sqrt{\bar{n}} \cos \left(\theta_1 + \frac{\pi}{3} \right), \quad y_1 = -\delta x_1, \quad z_1^2 = (\bar{n} - 2x_1^2)(1 + \delta^2) \quad (7)$$

corresponds to the counterpropagating wave mode. Here $\bar{n} = (a_0 - \delta^2)/\beta_0$ is the photon number in the wave (in case $n_0 = 0$); the angle θ_1 is given by the relations

$$\cos 3\theta_1 = \sqrt{\frac{n_0}{n_c}}, \quad n_c = \frac{4}{81} \frac{(a_0 - \delta^2)^2}{\beta_0}, \quad 0 \leq \theta_1 \leq \frac{\pi}{6}. \quad (8)$$

The running wave regime (the wave Z_+ follows the direction of propagation of the injected signal) is characterized by the stationary point

$$x_0 = -\frac{2\sqrt{\bar{n}}}{\sqrt{3}} \cos\left(\theta_0 - \frac{\pi}{3}\right), \quad y_0 = -\delta x_0, \quad z_0 = 0, \quad \cos 3\theta_0 = -\sqrt{\frac{n_0}{n_c}}, \quad \frac{\pi}{6} \leq \theta_0 \leq \frac{\pi}{3}. \quad (9)$$

For no injected signal ($n_0 \rightarrow 0$) the counterpropagating mode is replaced by the running regime (the wave Z_- travels in the opposite directions).

A specific feature of the bistable laser behavior model is the existence of the transition between the classical lasing modes. The steady-state transition trajectory passes through the saddle point

$$x_s = \frac{2}{3} \sqrt{\bar{n}} \cos \theta_1, \quad y_s = -\delta x_s, \quad z_s^2 = (\bar{n} - 2x_s^2)(1 + \delta^2). \quad (10)$$

The lasing condition reads $a_0 > \delta^2$. The region where the counterpropagating regime is found to occur is determined by the relation $n_0 < n_c$. Figure 1 shows the injected photon number n_0 and the square of detuning δ^2 for which the counterpropagating operation is stable (the region under the curves $a_0 = 0.1$ and 0.01). It should be pointed out that under curve A, the stationary point (7) is a node, while above curve A it is converted into focus, corresponding to the escape from the frequency-locking regime.⁹

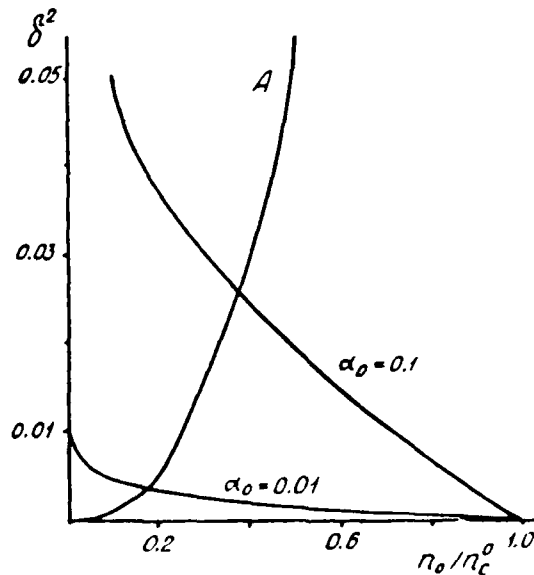


Fig. 1

The knowledge of the potential ϕ appears to simplify the analysis of the statistical properties of the injection-locked dye ring laser radiation. It is known that the mean laser intensity, field correlations, laser fluctuation spectra are entirely determined by the power series expansion coefficients for the potential in the neighborhood of the stationary points.¹⁰ The expansion of the potential up to the second-order terms ($\Delta x_\epsilon = x - x_\epsilon$, $\epsilon = 1, s$) is given by the formula

$$\phi \cong \phi_\epsilon + a_{11}^\epsilon (\Delta x_\epsilon)^2 + a_{22}^\epsilon (\Delta y_\epsilon)^2 + a_{33}^\epsilon (\Delta z_\epsilon)^2 + 2a_{13}^\epsilon \Delta x_\epsilon \Delta z_\epsilon + \dots \quad (11)$$

with the coefficients a_{ij} of the form

$$\begin{aligned} a_{11} &= ((\bar{n} - x^2)(1 + \delta^2) - 2\delta^2 x^2)\beta, \quad a_{12} = -2\delta\beta x^2, \quad a_{13} = 2(1 + \delta^2)(\bar{n} - 2x^2)\beta, \\ a_{22} &= ((n - x^2)(1 + \delta^2) + 2\delta^2 x^2)\beta, \quad a_{13} = 4\beta xz, \quad a_{23} = -4\delta\beta xz. \end{aligned} \quad (12)$$

The height of the potential barrier surmounted by the system during the transition induced by large statistical fluctuations is a critical parameter that specifies the FPT exponential part. When the counterpropagating mode switches over to the running wave regime the barrier height can be found from the expansion

$$\Delta\phi = \frac{3}{2}\beta(n_{+s}^2 - n_{+1}^2), \quad n_+ = x^2 + y^2. \quad (13)$$

Steady-State Fluctuation Spectra

The fluctuation properties of the laser radiation are discussed on the basis of the model of a laser with no detuning.¹² This simplifying assumption does not impose any stringent restrictions except for the calculation of the mean FPT where the extension to include the nonresonance is not trivial.

Running Wave Regime

In the vicinity of the steady state (9) the spectral laser fluctuation density is given by the formulae:

$$(\delta z_+^2)_{\bar{\omega}} = \frac{d}{(\bar{\omega} - \omega_0)^2 + a^2} + \frac{d}{(\bar{\omega} - \omega_0)^2 + b^2}, \quad (\delta z_-^2)_{\bar{\omega}} = \frac{2d}{(\bar{\omega} - \omega_0)^2 + c^2}, \quad (14)$$

where $a = a\nu(1 + 2\cos\theta_0)$, $b = \frac{2a\nu}{3}(2\cos 2\theta_0 - 1)$, $c = \frac{a\nu}{3}(1 + 4\cos 2\theta_0)$, d is the diffusion coefficient.

The laser linewidth due to amplitude fluctuations is found to increase with the injected intensity.

Counterpropagating Modes

In the neighborhood of the steady state (7) the laser fluctuation characteristics are of special interest because of the anticorrelation of the amplitude fluctuations. The fluctuation properties are determined by the relations:

$$(\delta Z_q^2)_{\bar{\omega}} = \frac{d}{2} \left[\frac{1 + q \frac{\beta \nu (n_{-1} - n_{+1})}{2B}}{(\bar{\omega} - \omega_0)^2 + \Delta\omega_-^2} + \frac{1 - q \frac{\beta \nu (n_{-1} - n_{+1})}{2B}}{(\bar{\omega} - \omega_0)^2 + \Delta\omega_+^2} \right], \quad (15)$$

$$(\delta Z_+ \delta Z_-)_{\bar{\omega}} = \frac{8d\beta\nu}{B} \sqrt{n_{+1}n_{-1}} \left[\frac{-1}{(\bar{\omega} - \omega_0)^2 + \Delta\omega_-^2} + \frac{1}{(\bar{\omega} - \omega_0)^2 + \Delta\omega_+^2} \right], \quad (16)$$

$$A = \frac{\beta\nu}{2}(3n_{-1} + n_{+1}), \quad B = \frac{\beta\nu}{2} \sqrt{(n_{-1} - n_{+1})^2 + 64n_{+1}n_{-1}}. \quad (17)$$

Eq. (15) shows the spectral fluctuation density to be the sum of the three Lorentzian lines. The third line results from the wave-phase fluctuations. For the wave Z_+ the line contributing to the wing of the spectrum has a width of $\Delta\omega_+ = A + B$, whereas the pedestal is formed by a narrow line with a width $\Delta\omega_- = A - B$. The phase fluctuations are responsible for the central part of the spectrum.

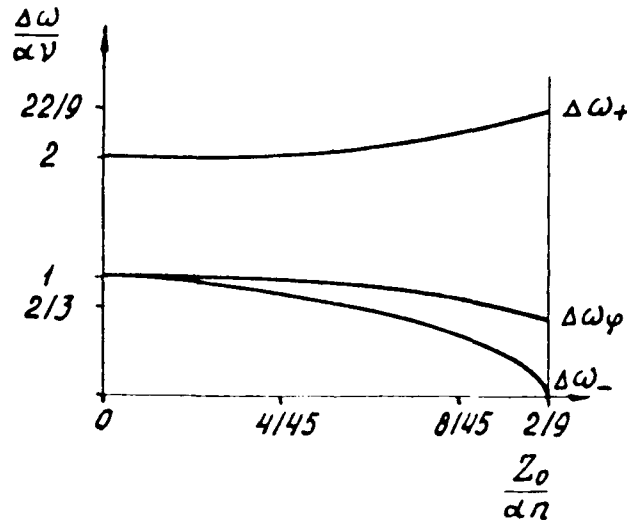


Fig. 2 The laser linewidth due to the amplitude fluctuations versus the injected signal intensity. α is the pump parameter, β is the saturation parameter, $n = \frac{\alpha}{\beta}$.

The linewidth variations characterizing the spectrum with an injected output are depicted in Fig. 2. For low intensity n_0 the contributions from the amplitude and phase fluctuations are approximately the same, whereas for n_0 falling at the neighborhood of the critical point n_c the shape of the peak is entirely determined by the line with width $\Delta\omega_-$. The maximum narrowing is limited by the time scale of large statistical fluctuations, i.e. the following equality is valid

$$\Delta\omega_- \cong \frac{1}{T}, \quad (18)$$

where T is FPT. Figure 3 plots the laser fluctuation spectrum as a function of the injected output. The curves show the feasibility of controlling the laser spectral parameters by means of a weak injected signal.

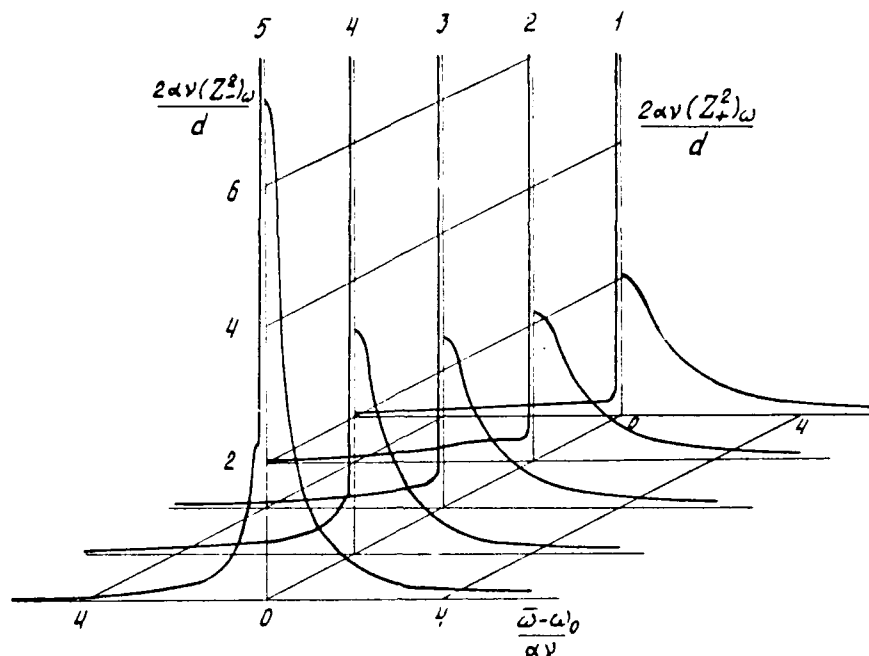


Fig. 3. Counterpropagating mode fluctuation spectra as a function of n_0 in units n_c . (1 - $n_0 = 0.01 n_c$, 2 - 0.09, 3 - 0.25, 4 - 0.49, 5 - 0.81). ν is the cavity linewidth, d is the diffusion coefficient, Z_q is the coherent amplitude ($q = \pm$).

Large Statistical Fluctuations

By large statistical fluctuations we mean fluctuations causing steady-state transitions to occur. The main quantity characterizing the fluctuations is the mean first-passage time T which is the solution to Pontryagin's equation¹³:

$$\left[d \frac{\partial^2}{\partial x^2} + \frac{\partial^2}{\partial z^2} + \frac{\partial^2}{\partial y^2} + 2\dot{x} \frac{\partial}{\partial x} + 2\dot{y} \frac{\partial}{\partial y} + 2\dot{z} \frac{\partial}{\partial z} \right] T = - \frac{2}{\nu}. \quad (19)$$

The solution of Eq. (19) based on the hypothesis of the most probable transition trajectory is derived elsewhere.¹⁴ The mean FPT formula reads

$$T = \frac{\pi r_{+1} r_{-1}}{r_{+s} r_{-s}} (1 + (f'(r_+^s))^2) \left(\frac{d^2 \phi}{dr_+^2} \Big|_{r_{+1}} \frac{d^2 \phi}{dr_+^2} \Big|_{r_{+s}} \right)^{-1/2} \exp \frac{\Delta \phi}{d}, \quad (20)$$

where

$$r_+ = \sqrt{x^2 + y^2}, \quad r_- = z, \quad f'(x_e) = \frac{a_{13}^e}{a_{11}^e - \lambda_e},$$

$$\lambda_e = \frac{1}{2} (a_{11}^e + a_{33}^e + \sqrt{(a_{11}^e - a_{33}^e)^2 + 4(a_{13}^e)^2}), \quad (21)$$

$$\frac{d^2\phi}{dr_+^2} = 2\beta (n_+ + n_- + 8f' \sqrt{n_+ n_-} + 2n_-(f')^2), \quad (22)$$

where $\Delta\phi$ is the barrier given by the Eq. (13) for $\delta = 0$.

The effect of detuning of FPT for an injection-locked dye ring laser can be calculated with an exponential accuracy. Clearly, the potential barrier height is effectively increased

$$T \cong \exp \left(\frac{\Delta\phi (1 + \delta^2)}{d} \right).$$

In conclusion, the difficulty of calculating the preexponential factor stems from the fact that the dimensionality of Eq. (19) is increased. To solve the problem would require additional hypothesis.

References

1. A. A. Kachanov, T. V. Plakhotnik, Opt. Comm. 47, 257 (1983).
2. H. Atmanspacher, H. Scheingraber, C. R. Vidal, Phys. Rev. 32A, 254 (1985).
3. G. V. Krivoshchekov, M. F. Stupak, Kvantov. Elektronika 2, 782 (1975).
4. G. V. Krivoshchekov, V. K. Makukha, V. H. Semibalamut, V. S. Smirnov, Kvantovaja Elektronika 3, 1782 (1976).
5. R. Roy, R. Short, J. Durnin, L. Mandel, Phys. Rev. Lett. 45, 1486 (1980).
6. P. Lett, L. Mandel, JOSA B2, 1615 (1985).
7. S. Zhu, A. W. Yu, R. Roy, Phys. Rev. 34A, 2044 (1986).
8. R. F. Boikova, E. E. Fradkin, Optika Spektroskopiya 22, 834 (1967).
9. G. V. Krivoshchekov, V. K. Makukha, V. S. Smirnov, M. F. Stupak, Avtometrija 6, 64 (1974).
10. L. D. Landau, E. M. Lifshitz, Statistical Physics, Moscow, 1976.
11. V. S. Smirnov, A. Z. Fazliev, Izvestija VUZ'ov, Fizika 30, 120 (1987).
12. V. S. Smirnov, A. Z. Fazliev, Optika i Spectroscopia, (1987).
13. L. S. Pontryagin, A. A. Andronov, A. A. Witt, Exp. Teor. Fiz. 3, 165 (1933).
14. V. S. Smirnov, A. Z. Fazliev, Opt. Comm. (to be published).

RECENT RESULTS IN VUV LASER SPECTROSCOPY

C. R. Vidal
Max-Planck-Institut für extraterrestrische Physik
8046 Garching, West Germany

Abstract

A short summary describing the technical parameters of typical, state of the art vuv sources is given followed by a brief review, which is restricted to the most recent developments in vuv laser spectroscopy.

Introduction

In recent years the field of vacuum ultraviolet (vuv) laser spectroscopy has matured to a point where it has promoted the field of laser spectroscopy to new spectral areas. This field requires first of all the ability to generate tunable coherent vacuum ultraviolet sources of sufficiently small linewidth and then to apply them to the numerous techniques of laser spectroscopy where the wavelength region of the vacuum ultraviolet tends to favour different methods than in the visible part of the spectrum. It is by no means intended to provide an exhaustive coverage of the field of vuv laser spectroscopy since extensive reviews have just become available.

Coherent Vacuum UV Sources

Coherent vuv sources can basically be generated in two different ways. First of all, in systems like the H₂ and the CO lasers or the noble gas excimer lasers substantial population inversions can be achieved, and these systems are able to provide peak output powers well in excess of several megawatts. However, these laser systems have only a very limited tuning range and a large linewidth and are therefore not very suitable for high resolution laser spectroscopy. For the latter application coherent vuv sources using the methods of four wave mixing in gases have proven to be by far superior. These methods have recently been reviewed by Jamroz and Stoicheff¹, by Vidal², and by Hilbig et al.³.

Since these extensive surveys a few important, new developments have occurred which are worth mentioning. Using the technique of pulsed nozzle beams⁴ for eliminating the window problem, Kung and coworkers succeeded to build highly efficient vuv sources covering the XUV spectral region below the lithium fluoride cut off limit around 106 nm⁵. Compared to differentially pumped systems pulsed nozzle beams have the great advantage that these windowless systems require moderate pumping powers because the nonlinear medium is only "switched on" during the duration of the laser pulses supplying the fundamental waves. Similar results have also been reported by Hilber et al.⁶, who investigated pulsed nozzle beams and a differentially pumped gas cell containing krypton which had a pin hole at the detector end of the gas cell. Systems of this kind are presently able to provide a linewidth of about 0.1 cm⁻¹ and smaller and typically 10¹⁰ to 10¹³ photons per shot at a repetition rate of a few Hz. This is an ample intensity for many techniques in laser spectroscopy. In addition, accurate calibrations of the absolute wavelength can easily be performed by calibrating the fundamental waves against the secondary length standards of the iodine or tellurium molecules⁷.

In view of a recent study on the short wavelength limitations of four wave mixing in metal vapor inert gas mixtures⁸, it may appear surprising that the two-photon resonant sum frequency mixing in krypton turns out to be so efficient. As an explanation one has to keep in mind that krypton around 70 to 100 nm is almost an ideal "low loss medium" as postulated by Junginger et al.⁹ having a small one-photon as well as a small two-photon absorption cross section so that one obtains a rather favourable figure of merit². This is a direct consequence of the location of the resonance line which tends to lower the two-photon absorption cross section as well as the sum frequency mixing coefficient. The latter two quantities are responsible for the figure of merit.

Using the fundamental equations of nonlinear optics and different normalized density profiles characterizing pulsed nozzle beams, Bethune and Rettner¹⁰ succeeded to obtain a reasonable agreement with the experiments. The results are remarkable because pulsed nozzle beams operating with krypton alone are by no means homogeneous and phase matched nonlinear media and it is somewhat surprising that these inhomogeneous media with a fairly small column density are capable of achieving the reported conversion efficiencies. The influence of inhomogeneities on the phase matching was first investigated by Puell et al.^{11,12} for nonlinear media with density gradients at the ends which give rise to an asymmetry of the phase matching curve, but do not noticeably lower the maximum overall conversion efficiency.

Vacuum UV Laser Spectroscopy

The previously indicated laser systems have in recent years been extensively used in various laboratories to perform laser spectroscopy in the vacuum ultraviolet part of the spectrum as reviewed by Vidal¹³. We will mention in the following only some of the recent developments.

In trying to reach atomic or molecular energy levels above 6 eV multiphoton spectroscopy was the first laser spectroscopic method used. Later two step excitation methods have also been successfully used which in conjunction with coherent vacuum uv sources had the additional virtue of pushing the effective cutoff limit well beyond the lithium fluoride limit around 106 nm¹⁴. As first shown in the visible part of the spectrum, two step excitation experiments or as they are also called, two colour optical double resonance experiments¹⁵, have the valuable property of being a state selective method. It has been for this reason that Miyazaki et al.¹⁶ tried to perform state selective spectroscopy on highly excited states by making optogalvanic double resonance experiments in which the collisional excitation in a plasma gives simple and cheap access to highly excited states. Unfortunately, due to the large Coulomb cross sections the collisional coupling of the laser excited state with its surrounding states is so large that state selectivity could only be demonstrated at very low electron densities on the example of the N₂ molecule¹⁷ where the collisional rates were minimized.

In this context it is now worth noting that Danzmann et al.¹⁸ have recently succeeded to perform Doppler-free two-photon polarization spectroscopy in an arc plasma. The result of their experiments are shown in Fig. 1 where the Lyman α profile of hydrogen is shown for an electron density of $5 \times 10^{22} \text{ m}^{-3}$ and a temperature of 11 000 K.

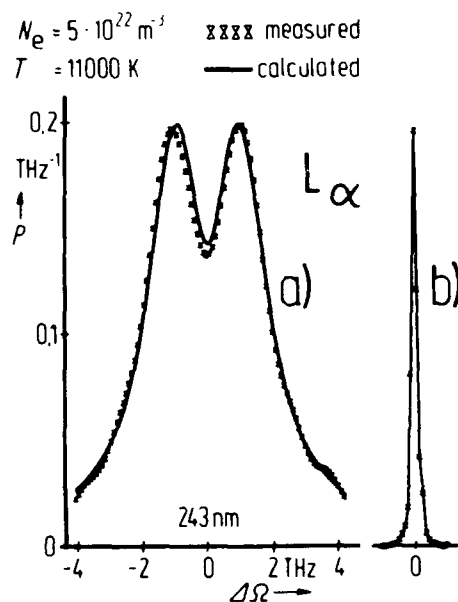


Figure 1: Lyman α line profile obtained with Doppler-free two-photon polarization spectroscopy. The measurements are taken from Danzmann et al.¹⁸.

In this case the thermal Doppler profile would have been about twice as wide as the measured Stark broadened profile of Fig. 1. For practical applications this result is extremely valuable because it allows one to determine the electron density even for situations where the Stark width is much smaller than the Doppler width and where a deconvolution would be rather inaccurate. In addition, the Lyman α line has the virtue of being theoretically the simplest one among all hydrogen lines.

In the light of the two-step excitation experiments the Doppler-free results are very interesting also from a different point of view. In the new method the measured signal is generated by the instantaneous electric field amplitudes which give rise to the two-photon absorption, whereas the two-step excitation relies on the time integrated population densities which have been accumulated in the intermediate state up to the time interrogated by the second laser and which is therefore very susceptible to a collisional population from neighbouring states and to velocity changing collisions.

With the new technique employing two-photon absorption one can anticipate state selective experiments on highly excited states which in some applications remove the necessity of performing experiments in the vacuum ultraviolet part of the spectrum. In particular, one might be able to perform state selective experiments on highly excited states in plasmas such as highly excited states in refractory metals or other sputtered materials.

In their two-step excitation experiment Klotek and Vidal¹⁴ have demonstrated for the first time a technique in the vacuum uv which they call "laser reduced fluorescence". In this method the fluorescence from the intermediate state which has been populated in the first excitation step, is modified by the laser excitation in the second step. In particular, the fluorescence from the intermediate state may be strongly reduced pumping an autoionizing or predissociating state in the second step. Recently, this technique has been used again by Spong et al.¹⁹ for conveniently analyzing core-excited levels of neutral rubidium which are otherwise difficult to reach.

In trying to push the vacuum uv laser spectroscopy further into the xuv range Kung et al.²⁰ succeeded to perform spectroscopy on the Rydberg states of H_2 by stepwise resonant two-photon ion pair production obtaining Fano-line profiles and lifetimes.

As a natural extension of the fluorescence measurements, Strobl and Vidal²¹ performed lifetime measurements of individual rotational vibrational levels of the perturbed $a'^3\Sigma^+(v=14)$ and the $e^3\Sigma^-(v=5)$ states of the CO molecule. For this application the state selectivity is absolutely essential. The results of their measurements are shown in Fig. 2. Depending on the interaction of the singlet and triplet states, the lifetimes of neighbouring levels may vary significantly giving rise to a very intricate pressure dependence which defies a simple Stern Vollmer analysis. For this reason all measurements were done under collision free conditions using a pulsed nozzle beam or a low pressure gas cell working at a pressure of about 5 mTorr and lower. As is well known, lifetime measurements are the most sensitive method of detecting weak perturbations of individual levels and are certainly more sensitive than the detection of energy level perturbations. Figure 3 shows the inverse effective lifetimes as a function of pressure. It should be noted that at elevated pressures the temporal decay of individual levels cannot be fitted by single exponential decays. This indicates a rather extensive coupling between levels of sufficiently different lifetimes. Levels with longer (shorter) lifetimes than the lifetime of the level to be investigated, act as reservoirs (sinks) which supply (remove) additional population density extending (shortening) the measured radiative decay rates. It is for this reason that a state selective measurement of individual triplet levels is absolutely crucial and this experiment serves as another striking example to demonstrate the new possibilities of vuv laser spectroscopy.

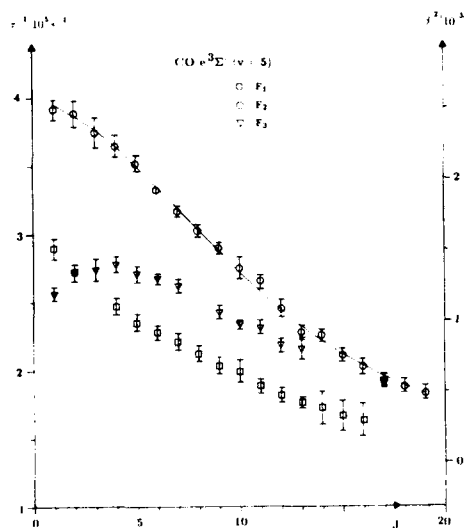


Figure 2. Measured and fitted radiative lifetimes for three different fine structure components of the $e^3\Sigma^-(v=5)$ state. The measurements are taken from Strobl and Vidal²¹.

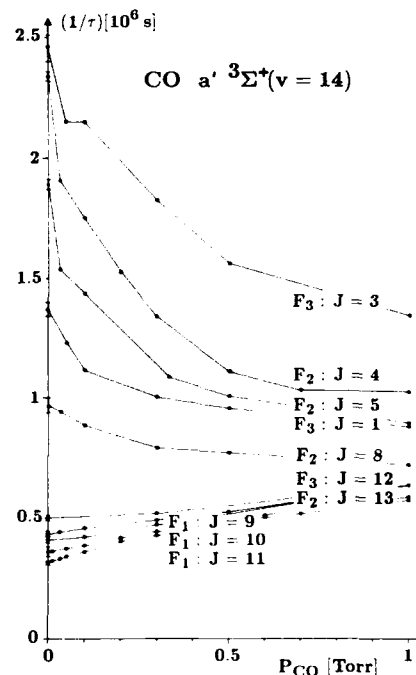


Figure 3. Anomalous pressure dependence of the inverse effective lifetime for several levels of the $a'^3\Sigma^+(v=14)$ state. The measurements are taken from Strobl and Vidal²¹.

The rather limited scope of this review served primarily the purpose of indicating future trends and new developments in vuv laser spectroscopy, and it also becomes evident that due to the different spectral range with its very different spectroscopic technology, other techniques will be favoured compared to the visible part of the spectrum.

References

1. W. Jamroz and B. P. Stoicheff, Generation of tunable coherent vacuum ultraviolet radiation, in Progress in Optics ed. by E. Wolf, (North Holland, Amsterdam, 1983), vol. 20, pp. 326-380
2. C. R. Vidal, "Four Wave Frequency Mixing in Gases" in Tunable Lasers, ed. by L. F. Mollenauer and J. C. White, Topics in Applied Physics, vol. 59, pp. 57-113, Springer, New York, 1987.
3. R. Hilbig, G. Hilber, A. Lago, B. Wolff, and R. Wallenstein, Comments on Atom. Molec. Phys. 18, 157 (1986).
4. A. H. Kung, Opt. Lett. 8, 24 (1983)
5. R. H. Page, R. J. Larkin, A. H. Kung, Y. R. Shen, and Y. T. Lee, Rev. Scient. Instr., to be published (1988)
6. G. Hilber, A. Lago and R. Wallenstein, J. Opt. Soc. Am. B4, 1753 (1987)
7. H. Scheingraber and C. R. Vidal, J. Opt. Soc. Am. B2, 343 (1985)
8. H. Scheingraber and C. R. Vidal, AIP Conf. Proc. 160, 164 (1987)
9. H. Junginger, H. Puell, H. Scheingraber and C. R. Vidal, IEEE J. Quant. Electron, QE-16, 1132 (1980); erratum: IEEE J. Quant. Electron, QE-17, 557 (1981)
10. D. S. Bethune and C. T. Rettner, IEEE J. Quant. Electron, QE-23, 1348 (1987)
11. H. Puell, K. Spanner, W. Falkenstein, W. Kaiser, and C. R. Vidal, Phys. Rev. A 14, 2240 (1976)
12. H. Scheingraber, H. Puell, and C. R. Vidal, Phys. Rev., A 18, 2585 (1978)
13. C. R. Vidal, Adv. Atom. Molec. Phys., 23, in press (1987)
14. P. Klopotek and C. R. Vidal, J. Opt. Soc. Am., B2, 869 (1985)
15. R. A. Bernheim, L. P. Gold, P. B. Kelly, C. Kittrell, and D. K. Veirs, Phys. Rev. Lett., 43, 123 (1979)
16. K. Miyazaki, H. Scheingraber, and C. R. Vidal, Phys. Rev., A28, 2229 (1983)
17. K. Miyazaki, H. Scheingraber, and C. R. Vidal, Phys. Rev. Lett., 50, 1046 (1983)
18. K. Danzmann, K. Grützmacher, and B. Wende, Phys. Rev. Lett., 56, 2151 (1986)
19. J. K. Spong, J. D. Kmetec, S. C. Wallace, J. F. Young, and S. E. Harris, Phys. Rev. Lett., 58, 2631 (1987)
20. A. H. Kung, R. H. Page, R. J. Larkin, Y. R. Shen, and Y. T. Lee, Phys. Rev. Lett., 56, 328 (1986)
21. K. H. Strobl and C. R. Vidal, J. Chem. Phys., 86, 62 (1987)

UPCONVERSION COEFFICIENT MEASUREMENT IN Tm³⁺,Ho³⁺:YAG AT ROOM TEMPERATURE

G. Kintz, I. D. Abella,* and L. Esterowitz
Naval Research Laboratory
Washington, DC 20375

Abstract

Energy transfer processes in rare earth doped crystals are very important in understanding the laser properties of these materials. Recently, laser diode pumping of solid-state laser materials has renewed interest in the study of energy transfer in rare earth doped crystalline hosts. In codoped thulium-holmium YAG, an energy transfer process, upconversion, is important in determining the threshold for continuous-wave laser emission at 2.1 μ m with laser diode pumping as well as the storage capacity of this material for Q-switched operation. The upconversion from the upper laser level in the holmium ion acts as a loss mechanism affecting the room temperature 2.1 μ m laser output. Spectroscopic measurement of the dominant upconversion process in four different concentrations of Tm,Ho:YAG are conducted. The concentration dependence of the upconversion effect indicates that the mechanism is a dipole-dipole interaction.

Introduction

Upconversion or cooperative-luminescence to higher energy states in rare-earth doped crystals can be an important process in determining the laser performance in many materials.¹⁻³ It has also been shown that upconversion can populate the upper-state laser levels not normally reached by direct laser pumping.⁴⁻⁷ In some cases, however, upconversion can act as a loss mechanism by depopulating the upper laser state, which increases the threshold, as in the room temperature operation of Tm³⁺:YAG at 2.1 μ m.^{8,9} To optimize laser design parameters such as sensitizer and activator concentrations, it is important to characterize the upconversion process by a detailed measurement. In this paper, we report experimental measurements of the upconversion coefficient, α_1 , for four samples of Tm³⁺,Ho³⁺:YAG with different concentrations. The analysis is based on the solutions of the rate equations modelling the populations of the interacting levels in the Tm-Ho system. The four concentrations of Tm,Ho:YAG are listed in Table 1.

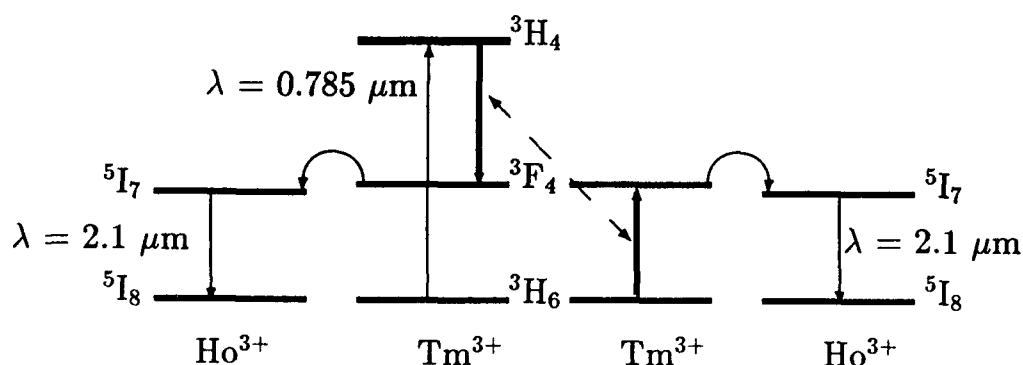


Fig. 1. The pumping diagram for the Tm, Ho:YAG system.

*Navy-Asee Summer Faculty; Permanent Address: Dept. of Physics, Univ. of Chicago, Chicago IL 60637

Energy Transfer in the Tm-Ho System

The relevant energy levels of the Tm^{3+} , Ho^{3+} :YAG system are shown in Fig. 1. Several energy transfers are important in the operation of this system with laser diode pumping. In addition to upconversion, cross-relaxation and non-resonant energy transfer affect both the laser properties of this system as well as the analysis of the data in the upconversion measurement.

The first energy transfer process important in this laser system is the cross-relaxation from the $^3\text{H}_4$ level. The $^3\text{H}_4$ absorbs the pump light from the laser diode. The cross-relaxation process produces two excited thulium ions in the $^3\text{F}_4$ level for each ion excited to the $^3\text{H}_4$ level. The quantum efficiency of the pumping process, η_p , is not the same for each sample due to the concentration dependence of the cross-relaxation process. At high concentrations, the quantum efficiency of the pumping process approaches two. Laser experiments have shown that η_p is at least 1.76 in the 5.7% Tm, 0.36% Ho:YAG sample.¹⁰ Calculations based on the lifetime measurements of the $^3\text{H}_4$ level, the known radiative branching ratios, the low concentration lifetime, and the multiphonon decay rates from the $^3\text{H}_4$ level, estimate the quantum efficiency of the pumping process to be 1.9 for the 5.7%, 0.36% Ho:YAG sample. An estimation of the quantum efficiency of the pumping process for each sample is shown in Table 1.

The second important energy transfer process in this system is the non-resonant energy transfer between excited ions in the thulium $^3\text{F}_4$ level and the holmium $^5\text{I}_7$ level. If the transfer between the thulium and holmium ions is rapid compared to the lifetime of the thulium and holmium levels, the levels can be treated as being in thermal equilibrium.¹¹ The populations of each ion can be calculated using a Boltzmann distribution over the individual Stark levels of each ion. The fractional populations, f_{Tm} and f_{Ho} , in each ion compared to the total population in the thulium-holmium manifold for each concentration are calculated and shown in Table 1.

The measured upconversion process is shown in Fig. 2. An ion in the $^5\text{I}_7$ level of holmium interacts with a thulium ion in the $^3\text{F}_4$ level. The thulium ion decays to the ground state while the holmium ion is excited to the $^5\text{I}_5$ level. The holmium $^5\text{I}_5$ level decays back to the Tm-Ho manifold by the emission of phonons, with a quantum efficiency of near unity. Because of the loss of excitation out of the Tm-Ho manifold (i.e. the upper laser level) this process is a loss mechanism and raises the threshold for a continuous-wave laser and decreases the storage capacity of the $^5\text{I}_7$ level.

A second upconversion process involves an ion in the $^5\text{I}_7$ level in holmium and a ion in the $^3\text{H}_4$ level in thulium which results in green fluorescence from the $^5\text{S}_2$ level in holmium. There is rapid decay from the $^3\text{H}_4$ pump band due to the cross-relaxation process so that we can ignore the second upconversion process in the analysis of the data. Observations of the fluorescence from the $^3\text{H}_4$ level in the 5.7% Tm, 0.36% Ho sample also indicate that this is not an important process.¹² Ignoring this upconversion effect may not be a valid approximation for the 1.5% Tm, 0.2% Ho sample due to the long lifetime of the $^3\text{H}_4$ level ($\tau = 400 \mu\text{s}$) at this low thulium concentration.

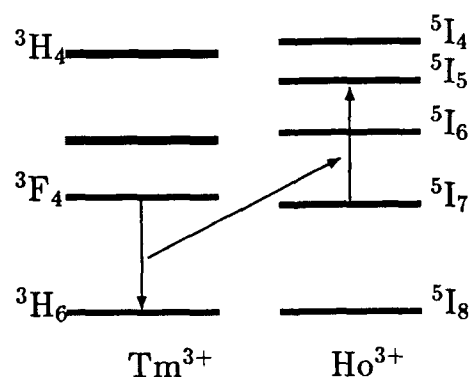


Fig. 2. The upconversion process measured in the experiment.

The rate equation describing the time dependence of the population in the thulium-holmium manifold, n_1 , can be written,¹²

$$\frac{dn_1}{dt} = \Gamma_p - \frac{n_1}{\tau} - \alpha_1(1 - \eta_r/2)f_{Tm}f_{Ho}n_1^2 \quad (1)$$

The upconversion loss term depends on the product of the populations of the holmium ions in the 5I_7 level and the thulium ions in the 3F_4 level. The quantum efficiency, η_r of the decay from the 5I_5 level to the Tm-Ho manifold is assumed to be 1. The lifetime of the Tm-Ho manifold, τ , is measured and shown in Table 1. The pump rate, Γ_p , is calculated via

$$\Gamma_p = \frac{I\alpha_p\eta_p}{h\nu_p} \quad (2)$$

where I is the intensity of the pump beam, α_p is the absorption coefficient of the pump beam, and $h\nu_p$ is the energy of the pump photons. In steady-state the equation can be readily solved,

$$n_1 = \frac{1}{\alpha_1\tau f_{Tm}f_{Ho}}((1 + 2\alpha_1\Gamma_p f_{Tm}f_{Ho}\tau^2)^{\frac{1}{2}} - 1). \quad (3)$$

The fluorescence from the Tm-Ho manifold is proportional to n_1 . In the analysis of the data, the fluorescence intensity is plotted versus $\Gamma_p\tau$.

Sample	τ (ms)	η_p	f_{Ho}	f_{Tm}	α (cm ³ s ⁻¹)
5.7% Tm, 0.36% Ho	8.5	1.9	0.57	0.43	(3.0 \pm 1.2) $\times 10^{-17}$
5.7% Tm, 0.06% Ho	12	1.9	0.18	0.82	(1.1 \pm 0.4) $\times 10^{-17}$
10% Tm, 0.1% Ho	8	2.0	0.17	0.83	(2.9 \pm 1.2) $\times 10^{-17}$
1.5% Tm, 0.2% Ho	10	1.2	0.74	0.26	(0.8 \pm 0.3) $\times 10^{-17}$

Table 1

Experimental Set-up

The experimental set-up is shown in Fig. 3. A 200 mW laser diode array is used as the pump source. The beam is collected, collimated and focused into the sample. The incident power was measured for each data point, and for each sample the absorption coefficient was measured. A 1 mm slit was used to restrict the observed region in the samples. The fluorescence signal was filtered by a Ge filter and focused onto an InAs detector. The signal was measured with an oscilloscope. The beam parameters were measured¹² and then were

calculated for a focus at the slit in the YAG sample ($n=1.8$). Using the absorption coefficient, the incident power, and the pumping geometry in the region of observation, the average pump rate was calculated. The signal was then plotted versus the average pump rate in the sample. The fluorescence signal as a function of pump rate times the lifetime of the manifold for the 10% Tm 0.1% Ho sample is shown in Fig. 4. The steady-state solution to the rate equation was used to fit the data points with a weighted least squares program. The calculated values of α_1 are shown in Table 1. The average pump rate in the crystals is not well known due to the complicated spatial distribution of the laser diode array. This is a major source of error in the experiment and accounts for the large uncertainty in α_1 .

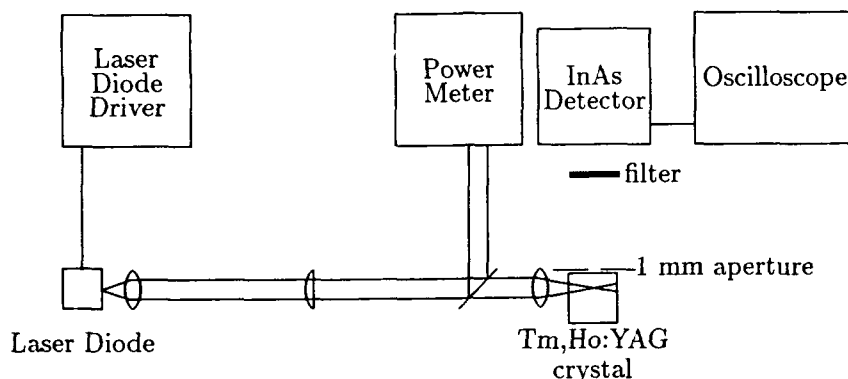


Fig. 3. The Experimental Set-up

In a separate experiment, the upconversion coefficient was measured for the 5.7% Tm, 0.36% Ho sample using the time dependent solution to the rate equation describing the population in the Tm-Ho manifold. A Q-switched Alexandrite laser with 200 ns pulse duration was sampled by an energy meter, and focused onto the $\text{Tm}^{3+}, \text{Ho}^{3+}:\text{YAG}$ sample. The fluorescence at $1.88 \mu\text{m}$ was selected by a 0.23 m infrared monochromator. As in the previous experiment, the same collection optics and slit to restrict the region of observation were used. The signal from the detector was amplified and recorded by a transient digitizer averaged over 500 shots. The laser was operating in a TEM_{00} mode, and the calculated beam waist of $91 \mu\text{m}$ compares well with the measured value using a scanning pinhole. From the measured pulse energy, the measured absorption coefficient, and calculated beam waist, the distribution of absorbed photons in the region of observation can be calculated. Six waveforms were taken at different average energies. The same rate equation was used to fit the time dependent fluorescence decay, and the calculated value of α_1 is the average of the calculated values for each waveform. The uncertainty in the calculation is possibly due to the large (30%) fluctuations in the shot to shot pulse energy. The agreement between the two methods is very good, for the time dependent method $\alpha_1 = (4 \pm 1) \times 10^{-17}$ and for the steady state method $\alpha_1 = (3 \pm 1.3) \times 10^{-17}$. The value of α_1 calculated by Fan¹² is 2.4×10^{-17} .

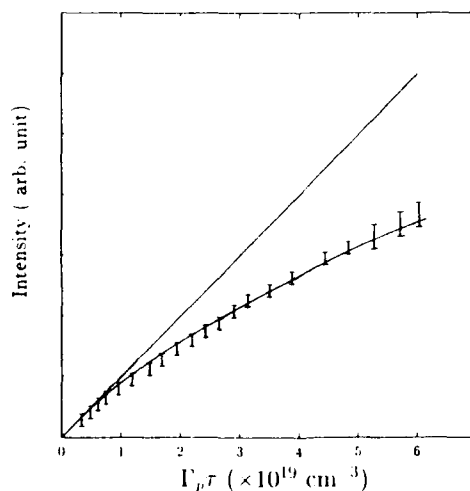


Fig. 4. Data for the 10% Tm, 0.1% Ho sample.

Concentration Dependence of Upconversion

An important part of this work is to determine the concentration dependence of this upconversion process. If the upconversion process is a dipole-dipole interaction, the upconversion coefficient should get larger as the product of the concentrations. In Fig. 5, the upconversion coefficient is plotted versus the product of the concentration of the thulium and the holmium, and the curve is approximately linear. However, a more precise measurement of the upconversion coefficient is needed to actually determine the concentration dependence. In addition, the effects of rapid migration among the thulium ions^{14,15} and higher order electrostatic interactions¹⁶ may effect the concentration dependence of the upconversion.

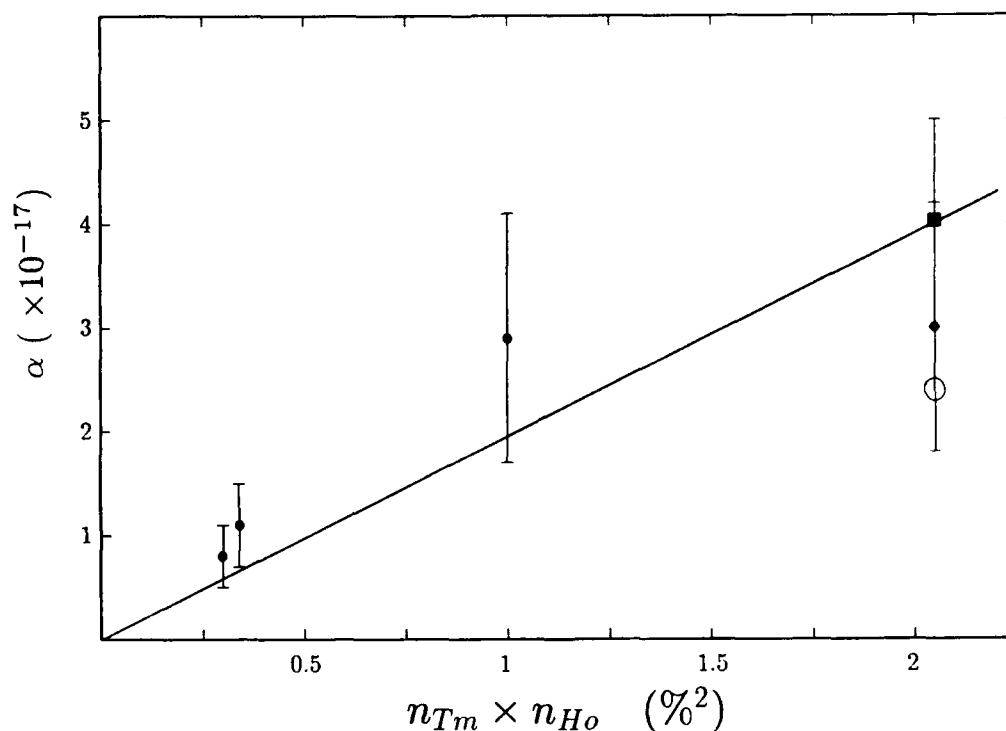


Fig. 5. Plot of the upconversion coefficient versus the product of the thulium and holmium concentrations, (in % doping squared). The data points marked by circles, ●, are measurements from the steady-state experiment, the data point marked by a square, is from the time resolved measurement, and the data point marked by an open circle is from Ref. 12. The straight line is a weighted least squares fit to the five data points discussed in the text.

Summary

In summary, the upconversion coefficients for four different concentrations of Tm^{3+}, Ho^{3+} : YAG are measured. In addition, a preliminary determination of the concentration dependence of the upconversion effect indicates that the upconversion involves a dipole-dipole interaction between the thulium and holmium ions. The effect of upconversion on the laser performance of the 2.1 μm transition must be modelled in detail to optimize the thulium and holmium concentrations to achieve the best performance of this potentially very efficient diode pumped laser system.

References

1. P.O. Feofilov, and V.V. Ovsyankin, Appl. Opt. 6, 1828 (1967).
2. L.F. Johnson, H.J. Guggenheim, T.C. Rich, and F.W. Ostermayer, J. Appl. Phys. 43, 1125 (1972)
3. B.M. Antipenko, S.P. Voronin, Sh. N. Gifeisman, R.V. Dubravyanu, Yu.E. Perlin, T.A. Privalova, and O.B. Raba, Opt. Spectrosc. (USSR) 56, 780 (1985).
4. L.F. Johnson and H.J. Guggenheim, Appl. Phys. Lett. 19, 44 (1971).
5. B.M. Antipenko, A.A. Mak, V.B. Nikolaev, O.B. Raba, K.B. Seiranyan, and T.V. Uvarova. Opt. Spectrosc. (USSR) 56, 780 (1985).
6. A.J. Silversmith, W. Lenth, and R.M. Macfarlane, Appl. Phys. Lett. 51, 1977 (1987).
7. G. Kintz, L. Esterowitz, and R. Allen, presented at the Tunable Solid-State Lasers Conference '87, Williamsburg (1987), paper WE5.
8. T.Y. Fan, G. Huber, R.L. Byer, and P. Mitzscherlich, Opt. Lett. 12, 678 (1987).
9. G. Kintz, L. Esterowitz, and R. Allen, Electron. Lett. 23, 616 (1987).
10. G. Kintz, R. Allen, and L. Esterowitz, presented in Postdeadline Papers, Conference on Lasers and Electrooptics (Optical Society of America, Washington, D.C., 1987), paper ThU4.
11. D.E. Castleberry, "Energy Transfer in Sensitized Rare Earth Lasers," Ph.D. Thesis, Massachusetts Institute of Technology, Cambridge, MA (1975).
12. T.Y. Fan, "Diode Laser Pumped Solid-State Lasers," Ph.D. Thesis, Stanford University, Stanford, CA (1987).
13. G. Kintz, R. Allen, and L. Esterowitz, Appl. Phys. Lett. 50, 1553 (1987).
14. M. Yokota and O. Tanimoto, J. Phys. Soc. of Japan. 22, 779 (1967).
15. H.C. Chow and R. Powell, Phys. Rev. B. 21, 3785 (1980).
16. V.M. Agranovich and M.D. Galanin, Electronic Excitation Energy Transfer in Condensed Matter (North Holland Publishing Company, New York, 1982) (and references therein).

MATERIALS SELECTION AND OPTIMIZATION OF DIODE-PUMPED LASERS

J. T. Lin

Center for Research in Electro-Optics & Lasers
University of Central Florida, Orlando, FL 32816

ABSTRACT

The critical issues of materials selection for diode-pumped miniature lasers are discussed quantitatively by a mathematical model. They include the emission cross section and fluorescence lifetime of the rod, the spectral-matching of the rod-absorption and diode-emission wavelength, optical coupling, spatial(transverse coordinate) mode-overlap of the pump and the signal beam, total cavity round-trip loss and the pumping power density. Optimal conditions are discussed for low threshold and high slope efficiency. Various assumptions in previously reported model are removed in this model for larger validly regime including pumping power far above threshold. The optical materials discussed in this paper include the high-efficiency nonlinear crystals of KTP, potassium niobate and MgO-doped lithium niobate. Various diode-pumping schemes including SHG and sum-frequency-mixing(SFM) for both internal and external cavity are presented for a variety of laser host crystals (such as YAG, YAP, YLF, BeL) in various dopants (such as Nd, Ho, Er, Tm, Cr). Analytic and numerical results for the threshold power, slope efficiency and output power are presented.

I. INTRODUCTION

In this paper we shall first discuss the advantages of diode-pumped lasers and their applications. The critical issues of materials selection for diode-pumped systems including laser host crystals and nonlinear crystals are presented in Section II. Various schemes for miniature lasers using frequency conversion techniques for the generation of IR and visible coherence sources are shown in Section III. In Section IV, we present a rigorous model which predicts the output power and slope efficiency in diode-pumped systems including the effects of transverse mode overlap, spot waists and the focal geometry of the pumping and signal waves and the round-trip cavity loss. Optimal conditions for various system parameters are derived within this model. Finally, tunable coherence sources using high-efficiency nonlinear crystals such as KDP and KNbO in diode-pumped systems are discussed.

ADVANTAGES OF DIODE-PUMPED LASERS

The advantages of using laser-diode as a pumping source versus flash-lamp pumping may be summarized as follows:

- (1) fundamental mode operation,
- (2) compact and long lifetime (10,000-50,000 hrs),
- (3) High gain/efficiency and low threshold,
- (4) easily temperature-tuned,
- (5) passive air cooling of the pumped rod.
- (6) efficient laser mode matching volume and very high pumping density (for focused end-pumping systems).

Furthermore, in comparison to the direct output of diode-laser, diode-pumped lasers provide the following advantages:

- (1) wider wavelength ranges may be achieved by pumping Nd, Ho and Er-doped rod for 1, 2 and 3 micron lasers (see table 1) and frequency doubling for visible sources (see Table 2),
- (2) High frequency stability and good beam quality,
- (3) High energy storage and short cavity for Q-switch, and
- (4) beam multiplexing and frequency mixing.

APPLICATIONS

The unique features of diode-lasers and diode-pumped lasers promise various applications which include but not limited to:

- (1) space-qualified (compact, long-lived) communication,
- (2) coherence sources for micromachining, microsurgery, detector and fiber characterization, atmospheric studies,
- (3) optical disk recording and image processing, printing, bar-code reader,
- (4) detector calibration, finger print detection, trace gas detection,
- (5) spectroscopy and optical damage testing, chemical reaction dynamics,
- (6) ranging, tracking, surveying,
- (7) injection seeds for high-power lasers
- (8) all-solid-state tunable laser systems using harmonic generation and optical parametric oscillation/amplification.

II. CRITICAL ISSUES OF MATERIALS SELECTION

We shall now discuss the critical

issues of materials selections for both laser host and nonlinear crystals.[1-38] In a previous paper, [38] we have discussed the selection rules for nonlinear crystals, we shall now summarize the materials selection rules for the diode-pumped laser host rods as follows:

- (1) high optical coupling using gradient-index lens (GRIN) or microscope objective lens (SELFOS),
- (2) good spectral-matching of the pumped rod (absorption spectrum) and the pumping diode (emission spectrum),
- (3) good spatial mode-matching between the pumping beam and the signal (lasing) cavity mode,
- (4) coating of the entrance surface (HT at the pump and HR at the signal wavelength) and the outcoupling mirrors (with transmission of 1% to 5% for 20 mW to 500 mW pumping diode),
- (5) low threshold and high slope efficiency.

Item (5) is characterized by transmission of the outcoupling mirror, round-trip-loss of the cavity, emission cross section and fluorescence lifetime of the rod, the spot sizes of the pump and signal beam and the mode-matching (spatial and spectral) of the system. Quantitative discussion by a mathematical model will be shown in Section IV.

Various laser host crystals have been pumped by laser diodes with emission wavelength of 780-810 nm. Results are summarized in Table 1. [1-25]

The nonlinear crystals suitable for frequency conversion of diode-pumped lasers using second harmonic generation (SHG) and sum-frequency-mixing (SFM) include KTP, KNbO₃, MgO-doped and proton-exchanged wave-guided lithium niobate. [26-37] Blue green (or visible) sources in diode and/or dye pumped systems are summarized in Table 2. The conversion techniques shown in Table 2 include internal and external cavity SHG direct doubling of laser-diodes, SFM of the pumping diode and the diode-pumped output, SFM of diode lasers and the two photon processes in diode pumped rods.

We should note that to achieve high conversion efficiency, the noncritical phase match (NPM) condition is usually required. This NPM may be achieved in temperature-tuned crystals. Examples are: (1) 188 degree C for SHG of 1064 nm using potassium niobate and 107 degree C using MgO-doped lithium niobate; (2) room temperature NPM for SFM of 809 nm and 1064 nm using KTP, SFM of 659nm and 1318 nm (i.e. tripling of Nd:YAG at 1318 nm) using potassium niobate(KN), (3) room temperature NPM of SHG of 860 nm using A-cut KN and 986 nm using B-cut KN, and SHG of 1340 nm (output from Nd:YAP) using B-cut KN.[39, 40]. Greater details for tunable diode-pumped lasers (visible to IR spectral ranges) using nonlinear crystals may be found in Ref. [39].

III. SCHEMES OF DIODE PUMPING

As shown in Fig. 1, various pumping geometries may be achieved by using one or more than one laser diodes as the pumping sources. The advantages and specific features of these schemes are summarized as follows:

- (1) Scheme (A) provides the first demonstrated pumping scheme which promises a very low threshold power and frequency stabilized fundamental mode.
- (2) With a Q-switch, scheme (B) promises output with high peak power, short pulse duration, passive air cooling, TEM₀₀-mode and good pulse to pulse stability.
- (3) The intracavity SHG provides high-efficient visible source from the diode-pumped rod, where very high circulation power inside the cavity makes the SHG conversion very efficient. However, instability caused by mode-mode(longitudinal) competition may be a problem.
- (4) Scheme (D) of intracavity SFM provide the image feature of spectral-matching between the peak absorption wavelength of the rod and the lasing wavelength, examples are 809 nm and 946 nm, where noncritical-phase-matching crystals of KTP and potassium niobate may be used respectively.[39]
- (5) The external cavity SHG, scheme (E) has several advantages versus the intracavity SHG of scheme (C): (i) the IR source from the diode-pumped laser may be optimized independently with the SHG cavity; (ii) high-power diode array may be incorporated into this scheme by using side-pumping; (iii) mode-mode competing in scheme (C) may be avoided.
- (6) Frequency doubling of the direct output from diode lasers(780-860 nm, 904 nm etc) requires a better optical coupler and high-efficiency nonlinear crystals, such as potassium niobate and proton-exchanged lithium niobate in a wave-guide geometry. Organic crystals such as DAN and PNN with nonlinear coefficients hundreds times of that of KDP may also be good candidates.[38]
- (7) Tunable diode lasers in the visible spectral regimes may be achieved via SFM of two diodes which are temperature tuned in the ranges of 780-860 nm with tuning range of 0.3 nm per degree. Noncritical phase-matching conditions using KTP and potassium niobate crystals have been defined for this scheme, see Ref.[39] in this Proceeding.
- (8) High-power IR sources at 1, 2 and 3 micron may be achieved by side-pumped slab geometry as shown in scheme (H) whose output may be in conjunction with schemes (B), (E) and (F) and (G) for visible lasers.
- (9) The double end-pumping scheme (I) promises an alternative of side-pumping for high-power diode-pumped lasers. However, volume-mode-matching of the

Table 1. DIODE-PUMPED LASER CRYSTALS

DOPANT	LASER HOST CRYSTAL	MAJOR EMISSION WAVELENGTH(um)	FLUORESCENCE LIFETIME(ms)	PUMPING (um)	REF.
Nd:	YAG	0.946,1.064,1.319	0.23	809	[1-5]
	glass	1.053	0.3	800	[6]
	YLF	1.047,1.053	0.5	791	[7-9]
	YAP(YALO)	1.08,1.34	0.18	808	[10]
	YVO ₄	1.064,1.34	0.095	809	[11-13]
	BeL	1.08,1.34		810	[14]
	Mgo:LiNbO ₃	1.085,1.387	0.085	813	[15-17]
	LiNdP ₄ O ₁₂	1.048	0.32	810	[18]
Ho:	YAG	2.1 (77° K)	5.0	785	[19]
	YLF	2.06 (77° K)	0.05	785	**
	YAP	2.92	0.9	808	**
Er:	YAG	1.65/2.94	9.1/0.1	-	**
	YLF	1.73,2.8	4.3	797	[20]
	YAP	1.66	0.13	808	**
	glass	1.54	-	904	**
Tm:	YAG	2.02	16	785	[21]
	YLF	2.31	-	781	[22]
Ho:Tm:	YAG	2.09	-	785	[23]
	YLF	2.08,2.31		791	[24]
Cr:Yb:Er	glass	1.54	-		[25]
Cr:Tm:	YAG	2.02	-	-	**
	YAP	2.27	0.77	-	**
Cr:Nd:	YAG	1.064	0.21	-	**
	YAP	1.064	0.18	-	**
Er:Ho:Tm:	YLF	2.07 (77° K)	20	-	**

* Note that except the indicated low temperature cases, all are operated at the room temperature. The pumping diode wavelengths are optimized at the absorption peaks of the rods. However, for those laser hosts with broad absorption bands the exact pumping wavelengths of the diode lasers are not critical.

** Work may be done but has not been reported at the present time.

pumped rods must be optimized for efficient output.

- (10) High-power IR source with high beam quality and frequency stability may be achieved via the injection-seed scheme (J). The seed-generator may also be in collaboration with scheme (C), (D), (E), (H) and (I) for optimal operation. Furthermore this seed may also be used in the conventional flash-damp-pumped lasers for high quality output.

In addition to the above described schemes, beam combination and frequency complexing may also be achieved in conjunction with optical fibers. Finally, tunable all-solid-state miniature lasers with output spectra of 400-700 nm, 1-5 micron are possible when the appropriate laser host crystals and nonlinear crystals are available. For example, using KTP or other high-efficient crystals as the intracavity optical parametric oscillation (OPO) crystal in the diode-pumped lasers (cw or pulsed operation) may be a potential technique for this purpose.

IV. THEORY OF DIODE PUMPING

We shall now present a rigorous model for the quantitative discussion of the critical issues described in Section II.

Previous theoretical analyses of diode-pumped lasers for the threshold pumping power and slope efficiency are based upon a simplified model which involves several assumptions: [3,18,41]

- (1) Steady-state solution for the population inversion and the photon density, in both time and space,
- (2) high-Q cavity or low round-trip loss system, where the low-gain approximation is valid,
- (3) effective or average pumping rate is used to eliminate the z-dependence of the gain function, [18,41],
- (4) z-dependence of the Gaussian waist of the pump and the signal beam is ignored, [18],
- (5) The calculated slope efficiency is valid only near the threshold, where the first-order expansion of the saturation term in the overlap function is used, [41]

Table 2. Blue green lasers from diode/dye-laser pumped systems

Laser Material	Pump Source	Conversion Technique	Nonlinear Crystal	Output (nm)	Ref.
Nd:YAG	diode	SHG(1)	KN	473	26
	diode	SFM(1)	KN	436	27
	diode	SHG(2)	MgO:LN	532	17
	diode	SHG(3)	MgO:LN	532	28
	dye	SHG(2)	KTP	459	29
	diode	SHG(2)	KTP	459	30
Nd:YLF	dye	SHG(1)	MgO:LN	523.6	8,15
Nd:YAP(YALO)	diode	SHG(2)	KTP	540	31
Nd:MgO:LN	dye	SHG(self-doubling)		598	15
Er:YLF	dye	Two-photon process		549.8	32
Nd:YLF	dye	Two-photon process		523.6	9
wave-guide	DSHG		LN	420	33
diode-laser	SFM		KN	430	34
diode-laser	DSHG		KN	414	35
diode	(direct output) from AlGaInP			600,680	36,37

* notations used in Table 2:

SHG(1):intracavity second harmonic generation (SHG)

SHG(2):external cavity SHG

SHG(3):external ring cavity SHG.

DSHG:direct SHG of diode-laser at 840 nm

SFM(1): sum-frequency-mixing of diode laser (at 809 nm) and diode-pumped Nd:YAG (at 1064 nm)

SFG(2): SFM of diodelaser (at 809 nm) and diode-pumped Nd:YAG (at 946 nm)

MgO:LN: MgO-doped lithium niobate crystal.

KN: potassium niobate crystal.

(6) a confocal geometry is assumed, where both the pump and the signal beams are focused at the center of the rod.

In the following model, we shall remove the assumptions of (3)-(6) and still obtain some tractable analytic results in addition to the numerical results.

The time-independent, steady-state signal intensity of diode-pumped system may be described by

$$dI/dz = gI/(1+sI) - \Gamma I, \quad (1)$$

where g is the unsaturated gain function proportional to the pumping rate, s is a saturation parameter and Γ is a loss constant. Assuming Gaussian transverse profiles for the pumping beam and the signal beam (normalized forms):

$$I(r,z) = P(z) f_s(r,z), \quad (2.a)$$

$$g(r,z) = G \exp(-\alpha z) f_p(r,z), \quad (2.b)$$

where α is a absorption coefficient of the pumped-rod and the normalized Gaussian functions are defined by

$$f_{p,s} = \exp(-2[r/w_{p,s}(z)]^2) / \pi w_{p,s}^2, \quad (3)$$

and the z -dependent beam spot sizes are related to the waist radii (located at the focal point) by

$$w_{p,s}(z) = w_{p,s} \sqrt{1 + D(z)(z - z_{p,s})^2}, \quad (4)$$

with a z -dependent parameter of $(n_{p,s}$ being refractive index)

$$D_{p,s}(z) = [\lambda_{p,s} / \pi n_{p,s} w_{p,s}(z)]^2, \quad (5)$$

where $D=1$ for unfocused plane wave case.

Substitution of Eqs.(2)-(5) into Eq.(1), we obtain the equation of motion for the signal power

$$dP/dz = [G \exp(-\alpha z) F(z) - \Gamma] P, \quad (6)$$

where $F(z)$ is an overlap function given by

$$F(z) = mB \int_0^\infty \frac{e^{-(m+1)x}}{1 + sPB e^x} dx, \quad (7)$$

where we have defined $m=Bp/Bs$ and

$$Bs(z) \equiv B(z) = 2/\pi w_s^2(z). \quad (8)$$

We note that Eq.(6) can be solved only numerically due to the complicated z -dependence of the overlap function $F(z)$ whose integration over the spatial transverse coordinate, $x=r$, general can not be solved analytically. For the special cases of integer values of m , the analytic expression of F is available.[10] For the perfect mode matching case, $m=1$,

$$F(z) = [1 - \ln(1 + sPB) / sPB] / sP. \quad (9)$$

We shall now calculate the F-function and in turn the output power, threshold power and the slope efficiency as follows. For systems with low single-pass gain, the steady-state output power may be obtained by equating the sound-trip gain to the sound-trip loss, i.e. $dP/dz=0$ in Eq.(6), and yield

$$(G/\delta) \int_0^{2L} F(z) \exp(-\alpha z) dz = 1, \quad (10)$$

where δ is the total round-trip loss including the cavity internal loss and the outcoupling mirror transmission (T) loss, i.e., $\delta = 2\Gamma L + T$, L being the rod length.

We shall now derive some tractable results by Taylor expansion of the saturation term in Eq.(7), up to the second-order, which is valid for $sPB < 1$. The integration of these expanded terms may be done exactly and Eq.(10) becomes a second-order polynomial of sPB which may be easily solved as follows

$$P_2 = [b - (b^2 - 4c)^{1/2}] / 2, \quad (11)$$

where P_2 and P_1 are the reduced output power (by twice of the saturation value $2s$) and the normalized input power (by the threshold value, $1/A_1$) and

$$b = A_2/A_3, \quad (12.a)$$

$$c = (A_1/A_3)(1 - 1/F_1), \quad (12.b)$$

and the coefficients of A_s may be integrated numerically

$$A_1 = mB \int_0^{2L} \left(\frac{\exp(-\alpha z)}{(m+1)E_p} \right) dz, \quad (13.a)$$

$$A_2 = mB \int_0^{2L} \left(\frac{\exp(-\alpha z)}{(m+2)E_p E_s} \right) dz, \quad (13.b)$$

$$A_3 = mB \int_0^{2L} \left(\frac{\exp(-\alpha z)}{(m+3)E_p E_s^2} \right) dz, \quad (13.c)$$

where

$$E_{p,s}(z) = [W_{p,s}(z)/W_{p,s}]^2 \quad (14)$$

other parameters are previously defined in Eqs. (4), (5) and (8), noting the z-dependence of $m(z) = B_p(z)/B_s(z)$

In Eq.(11), the normalized input (pumping) power should be restricted in the range of

$$1 \leq P_1 \leq 1/[1 - A_2^2/4 A_1 A_3], \quad (15)$$

and the threshold power may be easily found to be $1/A_1$, by equating $P_2=0$ in Eq.(11).

For a typical high-Q diode-pumped cavity with an outcoupling mirror transmission T, the explicit forms for the output power (P_{out}) and the threshold power (P_{th}) may be rewritten as: [18]

$$P_{out} = \left(\frac{\hbar \omega_s}{2L \sigma \tau} \right) T P_2, \quad (16)$$

$$P_{th} = \frac{\hbar \omega_p \delta}{2L A_1 \sigma \tau}, \quad (17)$$

where $\delta = (2\Gamma L + T)$ is the total round-trip cavity loss and σ and τ are the emission cross section and the fluorescence lifetime of the rod.

The slope efficiency, based upon Eq.(11) then may be exactly solved

$$\begin{aligned} \zeta_s &= d(P_{out})/d(P_{in}) \\ &= (T/\delta) (A_1/A_3) / [(b^2 - 4c)^{1/2} P_1]. \end{aligned} \quad (18)$$

We should note that Eq.(16) reduces to that of Ref.[18] for the near threshold case, i.e., $A_3=0$, $P_1=1/A_1$. Our results for the slope efficiency and the output power are still valid for input power above threshold, defined by Eq.(15).

The complexity of the above described calculations is mainly caused by the z-dependence of the Gaussian waists of the beams which are strongly coupled to the exponentially-decaying absorption of the rod (or the pumping power). By further assuming the averaged (over z) beam waists, the A_s coefficients in Eq.(13) may be obtained analytically and a simplified expression for the threshold power may be obtained.

$$P_{th} = \left(\frac{4\pi \hbar c}{\lambda_p} \right) \left(\frac{\delta}{2L \sigma \tau} \right) \pi \bar{w}_p^2 (\bar{m} + 1) / \zeta_a \quad (19)$$

where the averaged quantities are defined by

$$\begin{aligned} \bar{w}_p^2 &= \int_0^L w_p^2(z) dz / L \\ &= w_p^2 [1 + DL/12], \end{aligned} \quad (20.a)$$

$$D = \left[\lambda_p / \pi n_p w_p \right]^2, \quad (20.b)$$

$$\bar{m} = [\bar{W}_s / \bar{W}_p]^2, \quad (20.c)$$

and the total absorption efficiency is given by

$$\eta_a = \int_0^{2L} e^{-\alpha z} dz = [1 - \exp(-\alpha z)] / \alpha. \quad (21)$$

The major features based upon Eqs. (10) - (21) may be summarized as follows:

(1) To reduce the threshold power, we may use a smaller transmission (T) of the outcoupling mirror, typically (0.1-0.2)%, or maximize the overlap function A1 which in turn is a decreasing function of the beam waist. See Eqs. (13) and (17).

(2) Small T reducing the threshold power, however it also reduces the slope efficiency, see Eq.(18). Therefore the optimal condition for the choice of T depends upon the pumping power. By choosing a larger T (2-5%), slope efficiency may be significantly improved but high threshold power is also expected.

(3) The slope efficiency in general is not a constant. The nonlinear slope is caused by the input-power-dependence term in Eq.(18) which may be ignored only near the threshold, in which $p_1 = 1/A_1$ and the discussion in (2) is quite true.

(4) Based upon Eq.(20), there is an optimal pump waist which provides the minimal waist and hence reduces the threshold. By minimizing Eq.(20), we obtain the optimal waist of the pump

$$W_p^* = \left[\lambda p L / (\sqrt{12} \pi n_p) \right]^{1/2}, \quad (22)$$

which depends on the laser rod length (L), where the pump waist is assumed to be located at the center of the rod, i.e., $z = L/2$ in Eq.(4). We should note that this optimal condition is obtained within the frame of averaging procedure and the strong-coupling between the beam waist expansion and the $\exp(-z)$ absorption term is ignored. The true optimal condition

should be numerically solved based upon our model. Furthermore this optimal condition also depends upon the actual waist locations of the pump and the signal beams, i.e., z_p and z_s in Eq.(4). Eq.(22) used in Refs.[3, 41] is valid only for the confocal geometry, i.e., when $z_p = z_s = L/2$ and within the averaging-approximation. The case of cavity geometry of flat-curved mirrors, with $z_p = L/2$ and $z_s = 0$, we did not find the optimal pump waist which provides a maximal slope efficiency.[42]

(5) The threshold power is a decreasing function of the product of the emission cross section (σ) and the fluorescence

lifetime (τ), see Eq.(17). Therefore laser rods with longer lifetimes are preferred for achieving lower threshold. Examples based upon Eq.(17) are shown in Table 3.

Table 3. Relative threshold power (Pth) for various diode-pumped lasers.

Laser Rod	λ (nm)	τ (us)	$(\times 10^{-19} \text{ cm}^2)$	Pth
Nd:YAG	1064	230	2.4	1
Nd:YLF	1047	480	1.8	0.64
Nd:glass	1053	315	4.2	0.42
Nd:YAP	1080	170	3.7	0.88

Results based upon the numerical expressions of Eqs.(11) - (16) are shown in Fig. 2. We note that these results are valid for the situation where the Taylor expansion of Eq.(7) is relevant, i.e., when SPB is smaller than 1. This approximation, up to the second-order expansion of SPB, is much better than that of the reported first-order expansion.[18, 41]. In general the double integration defined by Eqs.(7) and (10) should be solved for results valid for all ranges of SPB.

Furthermore, to remove the low-gain-approximation used in Fig. 2, Eq.(6) should be solved numerically for both the forward and backward signal beams in the cavity. The strong z-dependence gain function may be rigorous included by considering the following travel wave rate equations for the forward (P^+) and backward (P^-) power of the signal:

$$dP^\pm/dz = \pm (G^\pm - \Gamma) P^\pm, \quad (23)$$

where the two-direction gain function $G^\pm(z)$ has a strong z-dependence due to the Gaussian overlap function $F(z)$ and the end-pumped absorption coefficient. Numerical investigation based upon above equations are in progress in our laboratory.[42].

REFERENCES

- [1] T.J. Kane, B.Zhou and R.L. Byer, Appl. Opt. 23, 2477 (1984).
- [2] B. Zhou, T. J. Kane, G.J. Dixon and R.L. Byer, Opt. Lett. 2, 62(1985).
- [3] T.Y. Fan and R.L. Byer, IEEE J. Quant. Electron. QE-23, 605(1987).
- [4] M.K. Reed, W.J. Kozlovsky, R.L. Byer, G.h. Harnagel and P.S. Gross, Opt. Lett. 13, 204(1988).
- [5] D.L. Sipes, Appl. phys. Lett. 47, 74(1985).
- [6] W.J. Kozlovsky, T.Y. Fan and R.L. Byer, Opt. Lett. 11, 788(1986).
- [7] T.M. Pollak, W.F. Wing, R.L. Grasso, E.P. Chicklis and H.P. Jessen, IEEE J. Quantum Electron. QE-18, 159(1982).

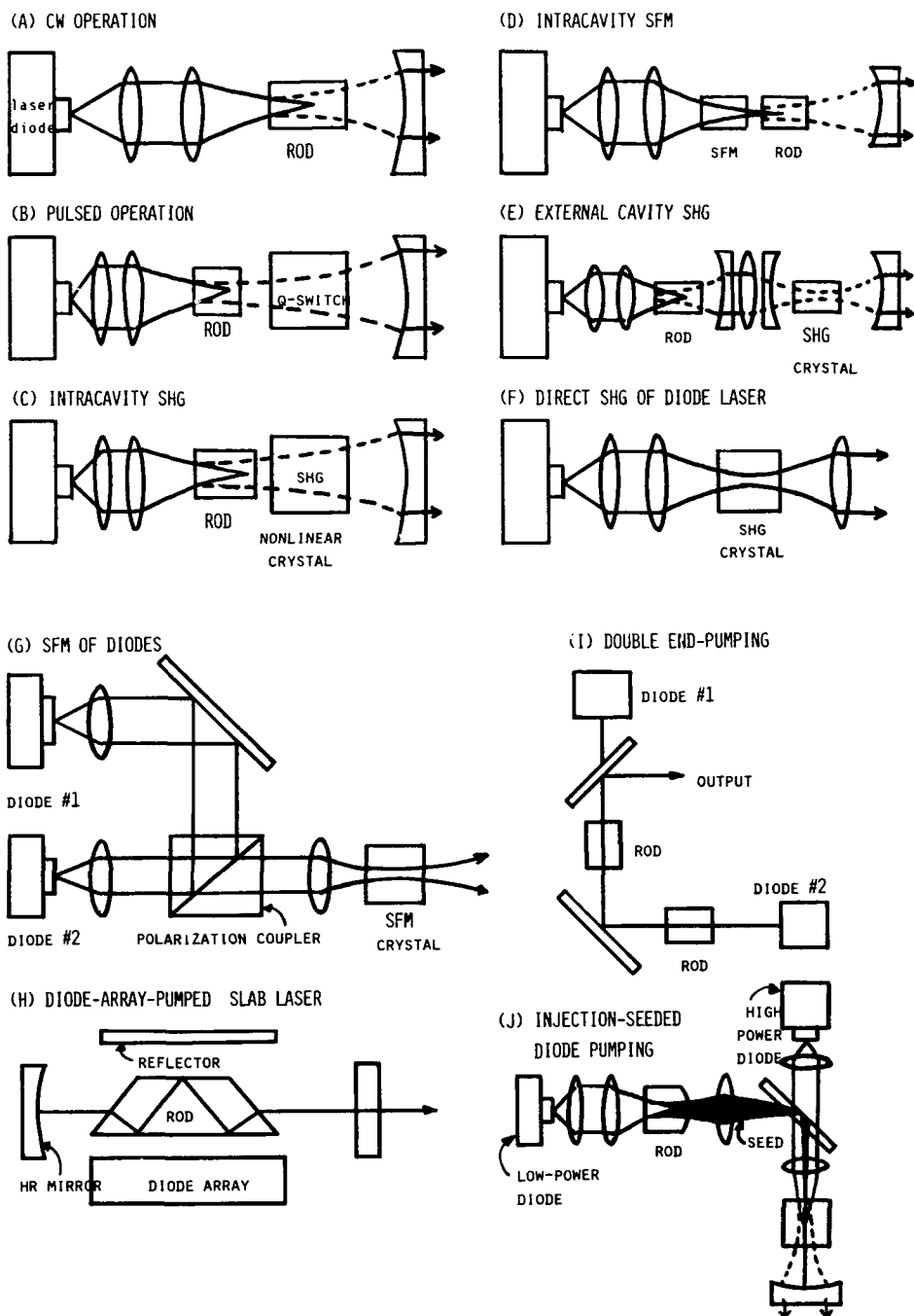


Fig. 1 Schematics of diode-pumped miniature lasers at various pumping geometries (the advantages of various schemes are discussed in the text): (A) IR source in CW operation, (B) pulsed operation, (C) intracavity SHG, (D) intracavity SFM, (E) external cavity SHG, (F) frequency doubling of direct output of diode laser by high-efficiency nonlinear crystals or wave-guided crystals, (G) SFM of two diodes, (H) diode-array-pumped slab laser, (I) double end-pumping and (J) injection-seeded diode pumping.

- [8] T.Y. Fan and G.J. Dixon and R.L. Byer, Opt. Lett. 11, 204(1986).
- [9] T.Y. Fan and R.L. Byer, J. Opt. Soc. Am. B. 3, 1519(1986).
- [10] J.T. Lin, S. Savrda and L. Chow, SPIE Proc. No.898 (1988), in press.
- [11] A.W. Tucker, M. Birnbaum and C.L. Fincher, J. Appl. Phys. 52, 3067(1981).
- [12] R.A. Fields, M. Birnbaum, C.H. Fincher, Technical Digest of CLEO'87, paper No. FL4 (1987).
- [13] R. K. Jain et al, ThB5, CLEO'88.
- [14] R. A. Fields et al, FL4, CLEO'87.
- [15] T. Y. Fan et al, J.Opt. Soc. Am. (B) 3, 140 (1986)
- [16] A. Cordova-Plaza, IEEE J. Quant. Electron. QE-23, 262 (1987)
- [17] W.J.Kozlovsky et al, Opt. Lett. 12, 1014 (1987).
- [18] K.Kubodera and K. Otsuka, J. Appl. Phys. 50,653 (1979).
- [19] R.Allen et al, Electron, lett. 22, 947 (1986).
- [20] G.J. Kintz et al, Appl. Phys. lett. 50, 1553 (1987).
- [21] G.J.Kintz et al, FB2, CLEO'88.
- [22] H. H. Zenzie et al, ThJ5, CLEO'88.
- [23] T.J. Kane and R.W. Wallace, FB3, CLEO'88.
- [24] G.J. Kintz et al, Proc. LASER'87,paper WB4.
- [25] E.Heumann et al, Appl. Phys. Lett. 52, 255 (1988).
- [26] G. J. Dixon et al, ThU 12, CLEO'88.
- [27] G. J.Dixon et al, FE5, CLEO'88.
- [28] W. R. Trutna et al, Opt. lett. 12,248 (1987).
- [29] W.P. Risk et al, Appl. Phys. lett. 52, 85(1988).
- [30] W. P. Risk et al, FE4, CLEO'88.
- [31] J. T. Lin and M. Y. Yao, to be published.
- [32] A. J. Silversmith et al, Appl. Phys. lett. Dec.(1987)
- [33] G. Johmon et al, SPIE O-E/LASE'88, Proc. vol. 898 (1988.)
- [34] H. Looser et al, ThA4, CLEO'87.
- [35] J.C. Baumert and P. Gunter, Appl. Phys. Lett. 50, 554 (1987)
- [36] O. Kumagai et al, SPIE O-E/LASE'88, Proc.vol. 898(1988).
- [37] K.Kohayashi et al, SPIE O-E/LASE'88, Proc. vol. 898 (1988).
- [38] J. T. Lin, Proc. of LASER'86 (STS press, VA), p.262-269 (1986).
- [39] J. T. Lin, Proc. of LASER'87 (STS press, VA), in press (1987).
- [40] J. T. Lin, Proc. of Topical Meeting on Laser Materials and Laser Spectroscopy, July 25-27 (1988) Shanghai, China.
- [41] M. J. F. Digonnet and C. J. Gaeta. Appl. Opt. Vol. 24, 333 (1985).
- [42] J. T. Lin, to be published in J. Opt Soc. AM. (B).

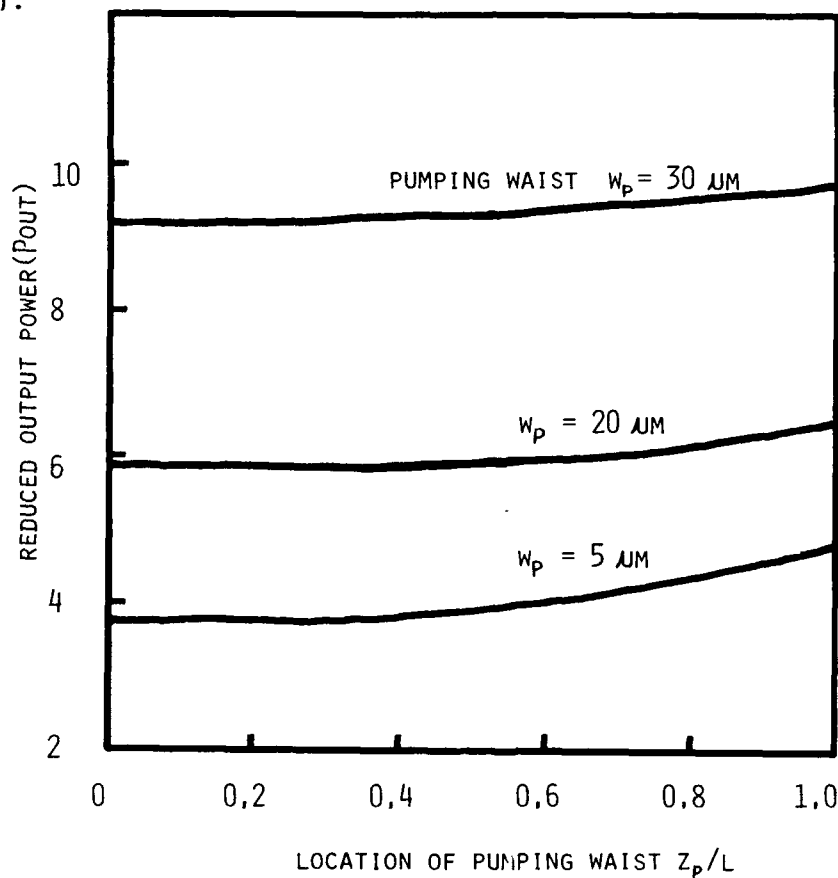


Fig. 2 Reduced output power vs. location of the focused pumping waist (Z_p/L) for fixed signal waist of 20 μm (located at the entrance plane $z=0$) and pumping power 1.2 times of threshold at various pumping waists.

Injection-Seeded Nd:YLF Q-Switched Laser

G. Ball,^a W. Seka, and S. Letzring
Laboratory for Laser Energetics
University of Rochester
Rochester, NY 14623-1299

Abstract

We report on the operational characteristics of a single-mode (axial and transverse) Q-switched Nd:YLF laser of milli-joule output energy which is injection-seeded by a diode pumped mini Nd:YLF master oscillator.

We have investigated the operational characteristics of a single axial and transverse mode Q-switched Nd:YLF laser (slave laser) which was seeded by a miniature Nd:YLF master oscillator. The latter was optically pumped by a diode laser. It was found that linear slave laser cavities are ill suited for this purpose since the gain characteristics of Nd:YLF force linear polarization within the active medium. The resulting spatial hole-burning severely degrades the single mode output but a unidirectional ring cavity alleviates this problem completely. The unidirectional operation is easily achieved by a compact (and inexpensive) intracavity Faraday rotator which also very effectively isolates the diode from the slave laser. In addition, simulations have shown that this configuration combined with a biased, slowly rising Q-switch ($t_r \approx 100$ ns) is optimal for injection locking.

Longitudinal mode-matching between the master and slave laser is achieved via a piezo-driven mirror in the slave laser. Single axial mode operation is observed over a range of ~ 30 per cent of the free-spectral range (FSR) of the slave laser. It was found that, in general, the limitation on the injection seeding range for single-mode operation comes from simultaneous injection into two neighboring modes albeit with rather different final amplitudes. However, the mode beating due to these neighboring modes are easily seen even at intensity differences of 100:1 and concomitant 20 to 50 ns differences in pulse buildup times.

The output characteristics of the slave laser can either be given in terms of the contrast of the single-mode output to the multi-mode (noise) background or the single mode pulse buildup time. The former is difficult to measure while the latter is easily accessible and compared to existing theory. Simulations based on Siegman's¹ phasor analysis yielded tuning dependent pulse buildup times which are in excellent agreement with our experimental results.

The Esherick-Owyoung² feed-back system developed for a strain-induced birefringent Nd:YAG master oscillator is easily adapted to Nd:YLF although the detailed shapes of the polarization and frequency dependent reflection from the master oscillator differ from those published by Esherick and Owyoung. This feedback system yields a signed error signal which controls the piezo-driven slave laser mirror and allows operation of the master and slave laser right on resonance.

* This work was supported by the U.S. Department of Energy Office of Inertial Fusion under agreement No. DE-FC08-85DP40200 and by the Laser Fusion Feasibility Project at the Laboratory for Laser Energetics which has the following sponsors: Empire State Electric Energy Research Corporation, General Electric Company, New York State Energy Research and Development Authority, Ontario Hydro, and the University of Rochester. Such support does not imply endorsement of the content by any of the above parties.

^a present address: United Technologies Research Center, East Hartford, CT.

References

1. A. E. Siegman, Lasers (University Science Books, Mill Valley, CA, 1986), Chapter 29.
2. P. Esherick and A. Owyoung, J. Opt. Soc. Am. B. 4, 41-47 (1987).

DESIGN OF ANNULAR TYPE OF SOLID STATE LASER FOR A FEW KILOWATTS

Youichi Takada, Hideaki Saito and Tomoo Fujioka

Laser Laboratory, Industrial Research Institute
1201 Takada, Kashiwa-shi, Chiba-ken 277, Japan

Abstract

A laser with an annular solid-state gain medium is shown to be suitable for a solid-state laser above a few kilowatts.

Design of solid-state gain medium

Recently, much attention has been paid to high average power lasers above 1 kW for their applications in material processing. Presently, YAG lasers with an average power above 1 kW are realized.^{1,2} These YAG lasers have three or four YAG rods, which are typically 150 mm long and 8 mm in diameter, in line in their cavities. For high power solid-state lasers, a zig-zag slab solid-state gain medium was proposed and has been studied in the past.³⁻⁹ Here is proposed and discussed an annular gain medium as another type of solid-state gain medium suitable for high power operation.

The pumping power per unit length is limited in a conventional rod gain medium. The maximum pumping power per unit length doesn't depend on the diameter of the rod and given by $P_{\max} = 8\pi(1-\nu)k\sigma/(\alpha\eta E)$, where α , ν , E are the thermal expansion coefficient, Poisson's ratio and Young modulus, respectively, and η , k , σ are a heat to pumping power ratio, the thermal conductivity and the rupture stress, respectively. A rod gain medium doesn't have therefore power scaling with the diameter. It also doesn't have unlimited power scaling with the length, because amplified spontaneous emission (ASE) and parasitic oscillation increase exponentially with the length and because thermal lensing and thermal birefringence increase linearly with the length. One of solutions to these problems is the zig-zag slab gain medium. This type of medium can eliminate thermal lensing and birefringence at least in ideal condition. On the other hand, the problem of enhanced ASE and parasitics, which appear naturally between two parallel side surfaces that are optically flat must be overcome for high power operation using the slab gain medium.

An annular gain medium shown in Fig.1, which we propose, is superior to a rod gain medium, or to a zig-zag slab gain medium, regarding a few properties. They are;

a) Power scaling with the cross section of the gain medium

An annular gain medium has power scaling with the outer diameter, because thermal stress depends only on the thickness of the annular medium and the gain volume can be increased by enlarging the outer diameter without increasing thermal stress.

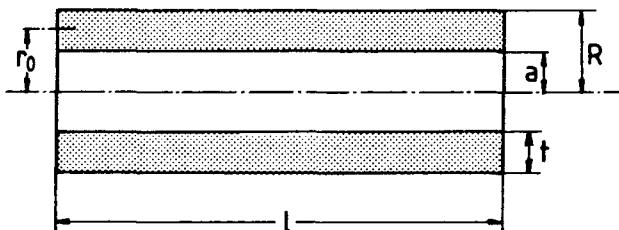


Fig. 1 Annular gain medium

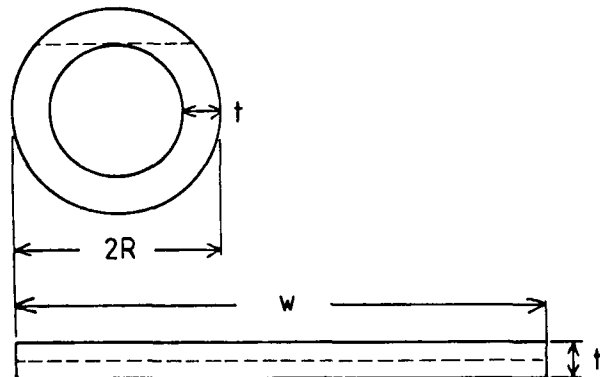


Fig. 2 Cross sections of annular and slab gain media

b) Low ASE and parasitics

An annular gain medium shows far lower ASE and parasitics than a slab gain medium because of two reasons. One reason is that an annular gain medium doesn't have wide area of two parallel side surfaces between which ASE and parasitics grows but an slab gain medium has them. The other is that an annular gain medium has in the cross section of the gain medium shorter straight optical path along which both ASE and parasitics grow than the slab gain medium, as shown in Fig. 2, where the optical path is denoted by a broken line. The path length in the annular gain medium is, roughly speaking, one-third of that in the slab gain medium, if same area and thickness are assumed for cross sections of an annular and a slab gain media.

c) Good use of material

If, again, same area and thickness are assumed for cross sections of an annular and a slab gain medium, the transverse dimension of an annular gain medium is, roughly speaking, only one-third of that of an slab gain medium. This is an advantage of an annular gain medium, especially if the medium is made of a crystalline host material.

Because of these superior properties of an annular gain medium, design of a solid-state laser above a few kilowatts become possible using an annular Nd:YAG rod. Here is assumed an annular Nd:YAG rod which is 22 mm in outer diameter, 14 mm in inner diameter, 126 mm long. Thermal stress that is generated in it by optical pumping is shown in Fig. 3, where a pumping power of 30 kW, a heat to pumping power ratio of 0.05 are assumed, the inner and outer side surfaces are assumed to be adiabatic and cooled at a constant temperature, respectively. Largest thermal stress appears on the outer side surface and is about one-half of the ruptured stress. A pumping power of 60 kW can be used without breaking the annular Nd:YAG rod if both of its side surfaces are cooled. A Nd:YAG laser has typically a output power to pumping power conversion efficiency of 3 %. Therefore, an output power of 2 kW may be expected using this annular Nd:YAG rod with a pumping power of 60 kW.

Both a rod and an annular gain media show thermal lensing and birefringence. Lensing effect may be evaluated by $(n_2)^{1/2}l$, where n_2 is the thermally changed refractive index and l is the medium length.¹¹ The thermally changed refractive index n_2 is given by $n_2 = 2(dn/dT)\delta T/(nR^2)$ for a rod gain medium of the radius R , and $n_2 = 2(dn/dT)\delta T/(nt^2)$ for an annular gain medium of the thickness t , where n is the refractive index of the medium and δT is the largest temperature difference in the medium. A conventional rod and an annular gain media have the maximum thermal stress and $(n_2)^{1/2}l$ shown in Fig. 4, where the stress is represented by a broken line and $(n_2)^{1/2}l$ is represented by a solid line. In this calculation, an annular Nd:YAG rod and assumed conditions are the same as mentioned above and a pumping power of 30 kW is assumed. A conventional rod is assumed to have the same gain volume as the annular rod and its diameter is varied to show the dependence of thermal effects on the length. Uniform pumping of 30 kW is also assumed. Both of the thermal stress and lensing effect of the rod gain medium can not be reduced at the same time, as is clear from Fig. 4. On the other hand, a quite low lensing effect is realized on the annular gain medium without increasing thermal stress. Thermal birefringence follows the similar discussion. It is then concluded that an annular gain medium shows lower thermal effects than a rod gain medium.

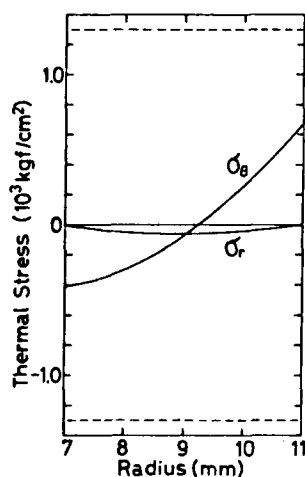


Fig. 3 Thermal stress in the Annular Nd:YAG crystal

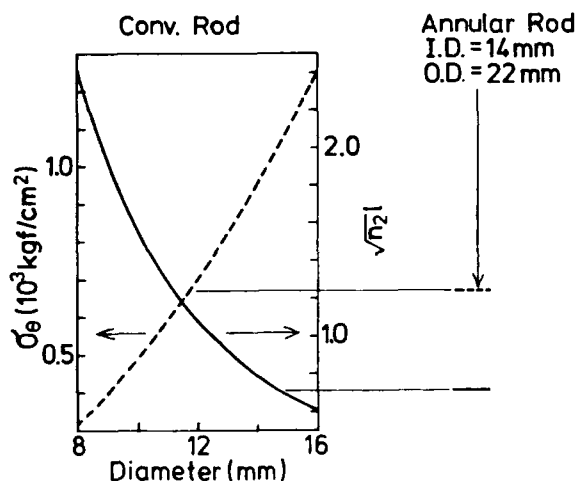


Fig. 4 Thermal stress and lensing effect in a rod and an annular Nd:YAG crystals

A laser with an annular gain medium

A laser with an annular gain medium outputs an annular beam. Its beam divergence in the far field is not sensitive to the beam outer diameter but mainly determined by its thickness, as shown in Fig. 5, where the vertical axis is the beam divergence (half width) and t is the thickness of the annular laser beam in the near field. In this calculation, a flat wave front and a uniform beam intensity is assumed on the annular laser beam in the near field. Eigen mode of an annular stable resonator has been also studied analytically.¹² The mode is approximately is an "annular Hermite Gaussian" mode, if the thickness of the annular beam is sufficiently smaller than its mean radius. Especially, the fundamental mode is the "annular Gaussian" mode. The design of such annular stable resonator is then completely the same as that of a conventional stable resonator.

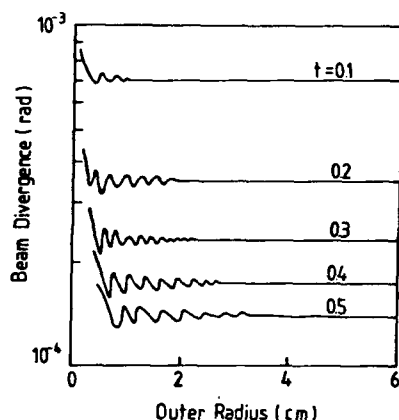


Fig. 5 Beam divergence of an annular laser beam

Summary

It has been shown that an annular gain medium is expected to have better power scaling than a rod or a zig-zag slab gain media. Output power of 2 kW has been shown to be possible using an annular Nd:YAG rod that is 22 mm in outer diameter, 14 mm in inner diameter and 126 mm long. An annular gain medium has been shown to have lower thermal lensing and birefringence than a rod gain medium. Beam characters of a laser with an annular gain medium is also discussed.

References

1. S. Watanabe, K. Okino, I. Shibano, T. Yamane and H. Miura, in Extended Abstracts, The 48th Autumn Meeting, 1987, The Jap. Soc. Appl. Phys., No. 3, p. 688, 19p-ZC-5
2. S. Nishimura, S. Yoshida, Y. Fujimori and K. Ishikawa, in Extended Abstracts, The 48th Autumn meeting, 1987, The Jap. Soc. Appl. Phys., No. 3, p. 689, 19p-ZC-6
3. J. M. Eggleston, T. J. Kane, K. Kuhn, J. Unternahrer and R. L. Byer, IEEE J. Quantum Electron. QE-20, 289 (1984)
4. T. J. Kane, J. M. Eggleston, R. L. Byer, IEEE J. Quantum Electron. QE-21, 1195 (1985)
5. S. Basu, T. J. Kane and R. L. Byer, IEEE J. Quantum Electron. QE-22, 2052 (1986)
6. S. basu and R. L. Byer, Opt. Lett. 11, 617 (1986)
7. J. M. Eggleston, G. F. Albrecht, R. A. Petr and J. Zumdick, IEEE J. Quantum Electron. QE-22, 2092 (1986)
8. G. F. Albrecht, J. M. Eggleston, J. J. Ewing, IEEE J. Quantum Electron. QE-22, 2099 (1986)
9. H. Hayakawa, K. Maeda, T. Ishikawa, T. Yokoyama and Y. Fujii, Jap. J. Appl. Phys. 26, L1623 (1987)
10. Y. Takada, H. Saito and T. Fujioka, in Proceeding of SPIE vol. 801, pp. 62-66
11. A. Yariv, Optical Electronics, 3rd Edition (Holt-Saunders, New York, 1985), pp. 31-35
12. to be published in the January issue of IEEE J. Quantum Electron. in 1988

RESONATORS WITH INTRACAVITY OPTICS FOR SOLID-STATE LASERS

S. De Silvestri, P. Laporta, and V. Magni

Centro di Elettronica Quantistica e Strumentazione Elettronica, C.N.R.,
Istituto di Fisica, Politecnico di Milano
Piazza Leonardo da Vinci 32, 20133 Milano, Italy

Abstract

A unified formulation for the analysis of linear and ring stable resonators containing a lens of variable focal length, which represents the rod of a solid-state laser, and other intracavity optical systems is presented. The stability, the mode spot sizes, the dynamical stability and the misalignment sensitivity are investigated and general properties valid for any resonator are derived. Some important practical consequences for resonator design are discussed. A new figure of merit for solid-state laser materials is introduced and critically evaluated for different crystals and glasses of practical interest.

1. Introduction

The rod thermal lensing plays a fundamental role in determining the performances of cw or high repetition rate solid-state lasers because of the considerable values of dioptric power that can be reached even at moderate pump power levels. Since the dioptric power of the rod is proportional to the lamp input power, beside the gain of the active medium, also the resonator stability, the mode spot size, the diffraction losses, the resonance frequencies and the sensitivity to misalignment depend on the pumping rate. The resonator design is further complicated by requirements of large volumes of the fundamental mode, dynamical stability, and low misalignment sensitivity. Many solutions and different design ideas for stable resonators have been proposed: compensation of thermal lens^{1,2} concave-convex resonators³, dynamically stable resonators^{4,5}, telescopic resonators^{6,7}. The sensitivity to misalignment has been also studied by several authors⁸⁻¹⁰ and has been demonstrated to become a key factor for designing stable resonators with large mode volume¹¹⁻¹³. At present, the understanding of simple stable resonators only containing a variable lens and the optimization procedure for linear dynamically stable resonators with large mode volume and low misalignment sensitivity are well established¹¹⁻¹³. However, improvements of the performances of single transverse mode solid-state lasers will probably require some additional intracavity optics (such as lenses, telescopes, adaptive optics), as the experimental results obtained with telescopic resonators have demonstrated.

The purpose of this work is to present a unified analysis, which prescind from the particular configuration and considers multielement stable resonators in their generality. Using the matrix approach for gaussian beam propagation, basic properties regarding the resonator stability, the mode spot size in the rod, and the misalignment sensitivity are derived, both for linear and ring resonators. It is also shown that the pump power stability range is a typical character of the laser material and is independent of the particular resonator configuration.

2. Preliminary remarks

To allow a very general analysis of solid-state laser resonators only two elements have to be considered: the intracavity optics and the rod. A generic optical system is described by the suitable ray transfer matrix and any possible misalignment of some element is treated using a 2x1 vector in addition to the usual 2x2 matrix appropriate for aligned systems. For a generic optical system, the position and the slope of the rays, measured with reference to the optical axis of the aligned system, at the output plane (x_o, θ_o) , are related to the corresponding quantities at the input plane (x_i, θ_i) , by an equation that, like for perfect alignment, is linear, but non longer homogeneous:

$$\begin{pmatrix} x_0 \\ \theta_0 \end{pmatrix} = \begin{pmatrix} A & B \\ C & D \end{pmatrix} \begin{pmatrix} x_i \\ \theta_i \end{pmatrix} + \begin{pmatrix} s \\ \sigma \end{pmatrix} \quad (1)$$

The elements of the misalignment vector $\begin{pmatrix} s \\ \sigma \end{pmatrix}$ give the position and the slope of the output ray when the input ray coincides with the reference axis of the system. Being Eq. (1) linear, the misalignment vector of an ensemble of optical elements is the sum of the output ray vectors obtained assuming an input ray coincident with the reference axis and taking one misaligned element at a time. In practice, s and σ result in linear combination of tilting angles and displacements of the various decentred elements.

The rod, which for a uniform pumping has a parabolic radial refractive-index profile can be treated as a thin lens provided that the distances are measured with reference to the principal planes of the rod, whose positions are independent of the pump power. The focal length is given by

$$\frac{1}{f} = \frac{k}{\pi r^2} P_{in} \quad , \quad (2)$$

where r is the rod radius P_{in} is the electrical input power to the lamp, and k is a constant related to the opto-mechanical properties of the laser rod and to the pumping efficiency.

3. Stability and mode volume

A generic resonator of a solid-state laser can be modeled, as shown in Fig. 1, by two plane mirrors that enclose a lens of variable focal length f between two generic optical systems.

As a function of the rod dioptric power, there are always two stability zones of the same width given by¹⁴

$$\Delta \frac{1}{f} = \min \left| \frac{1}{B_1 D_1} \right|, \left| \frac{1}{B_2 D_2} \right| \quad (3)$$

The spot size w_3 of the TEM_{00} mode on the lens, calculated by assuming that a Gaussian beam reproduces itself after one round trip, is given by

$$w_3^4 = - \left(\frac{2\lambda}{\pi} \right)^2 \frac{\eta^2}{(\eta^2 - u^2)(\eta^2 - v^2)} \quad , \quad (4)$$

where:

$$\eta = \frac{1}{f} - \frac{1}{2} \left(\frac{A_1}{B_1} + \frac{C_1}{D_1} + \frac{A_2}{B_2} + \frac{C_2}{D_2} \right) \quad , \quad (5)$$

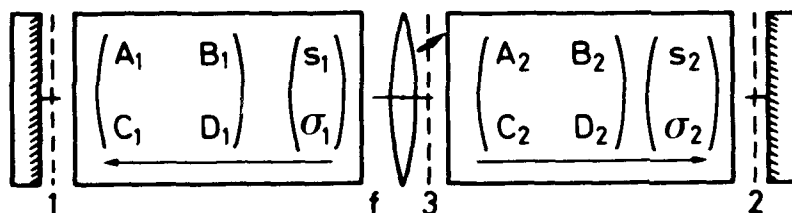


Fig. 1 - Linear resonator with an internal lens of variable focal length f and other intracavity optical systems. The arrows indicate that the matrices and the vector represent the paths from the lens to the mirrors. The dashed lines are reference planes.

$$u = \frac{1}{2B_1D_1} - \frac{1}{2B_2D_2} , \quad (6)$$

$$v = -\frac{1}{2B_1D_1} - \frac{1}{2B_2D_2} . \quad (7)$$

The diagram of Eq. (4) as a function of η , i.e., of the rod dioptric power $1/f$, is plotted in Fig. 2(a). This plot shows that the spot size goes to infinity at the stability limits and reaches a minimum in each stability zone. In correspondence to the minimum of w_3 the resonator is dynamically stable since the spot size in the rod is, at the first order, insensitive to variations of the rod focal length. Equating to zero the derivative of Eq. (4) and solving for η gives:

$$\eta = \pm (|uv|)^{\frac{1}{2}} . \quad (8)$$

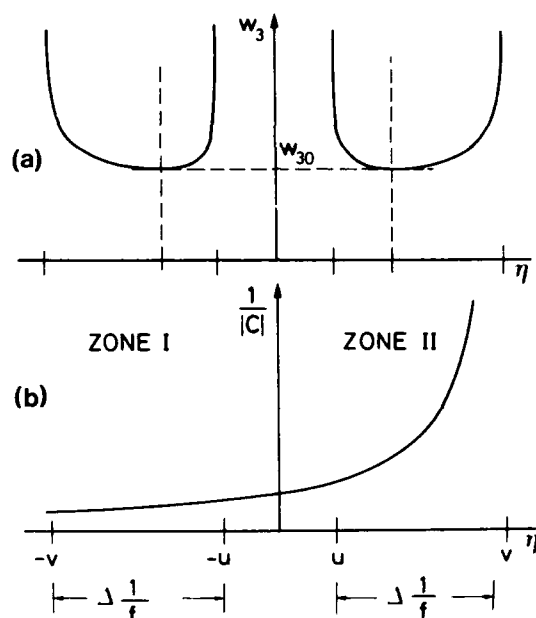


Fig. 2 - Spot sizes and misalignment sensitivity of a linear resonator with an internal variable lens for $uv > 0$ and $|u| < |v|$ as a function of η (dioptric power of the lens shifted by a constant amount). (a) Spot size on the lens. (b) Absolute value of the focal length of the optics between mirrors (including the mirrors' power) which determines the misalignment sensitivity. The dashed vertical lines correspond to the dynamical stability.

The value w_{30} of the spot size w_3 for both these values of η is

$$w_{30}^2 = \frac{2\lambda}{\pi} \frac{1}{\Delta \frac{1}{f}} , \quad (9)$$

where $\Delta(1/f)$ is given by Eq. (3). The above relationship indicates that, independently of the resonator configuration, the volume of the TEM_{00} mode in the rod at the dynamical stability is inversely proportional to the range of rod dioptric power for which the resonator is stable. The proportionality coefficient depends only on the laser wavelength.

4. Pump power stability range

A more practical expression for the stability range is obtained by expressing the rod focal length as a function of the pump power. Combining Eq. (2) with Eq. (9) yields

$$\Delta P_{in} = \frac{2\lambda}{k} \left(\frac{r}{w_{30}} \right)^2 \quad (10)$$

For single-transverse-mode operation, on the assumption that the rod represents the limiting aperture of the resonator, the ratio r/w_{30} ranges at most from 1.2 to $2^9, 11, 13$. Therefore the pump power stability range for dynamically stable TEM₀₀ lasers is a characteristic of the laser material that does not depend on the resonator configuration.

To give some interesting numerical examples, we have considered a few solid-state materials of practical relevance, namely Nd:YAG, Nd:glass (from different manufactures), Nd:Cr:GSGG, and Alexandrite, for which, assuming $r/w_{30} = 1.5$, we have calculated ΔP_{in} from the data available in the literature. The results are summarized in Table I.

Table I: Pump Power Stability Ranges ΔP_{in}

Laser Material	ΔP_{in} (W) ^(a)	Reference
Nd:YAG	313	[15]
Nd:Glass-Shott LG706	70	[2]
Nd:Glass-Kigre Q-98	134	[2]
Nd:Glass-Hoya LHG8	154	[2]
Nd:Cr:GSGG	53	[16]
Alexandrite	373(b)	[17]
	527(c)	[17]

(a) $r/w_{30} = 1.5$

(b) Pump pulse energy 400 J

(c) Pump pulse energy 200 J

Among Nd-doped materials, Nd:YAG presents the wider range, while the glass Shott LG 706, together with Nd:Cr:GSGG, show the smallest interval of pump power. This is related to the thermal focusing of glass and GSGG that is much stronger than that of YAG. In the case of glasses, the stronger thermal lensing is essentially due to the much smaller thermal conductivity (one tenth), even if a contribution comes also from the broader absorption bands. In the case of GSGG, the main factor is the enhanced thermal loading due to the presence of the broad red and, particularly blue, pump bands of Cr; however, a contribution comes also from the smaller thermal conductivity (about two thirds of that of YAG). For Alexandrite, the dioptric power has been found¹⁷ proportional to the product of the square root of pump pulse energy by the average pump power; accordingly, we have reported in Table I two different values of ΔP_{in} corresponding to different pump pulse energies. Pump power stability ranges of Alexandrite are even larger than that of YAG; this essentially depends on the thermal conductivity of Alexandrite which is about twice that reported for YAG. In general, depending on the material and on the pumping efficiency, typical pump power ranges for stable operation in single mode vary from a few tens to a few hundred watts. The stability range might be extended by increasing the ratio r/w_{30} , which implies either multimode operation or an inefficient utilization of the rod volume. This makes it evident that no optical compensation of the resonator, no matter how it is done, can effectively increase the stability range of a dynamically stable TEM₀₀ solid-state laser. The solution should be based on the use of athermal rod materials or on the reduction of the unused radiation absorbed by the rod. It should be noted, however, that since the relative stability range $\Delta P_{in}/P_{in}$ decreases as the average pump power increases, the limited stability range may become a problem mainly for cw or high-repetition-rate lasers.

5. Misalignment sensitivity

The additional power losses introduced by misalignment of some component of the resonator essentially arise from the displacement of the mode axis, and of the field pattern, on the plane of the limiting (mode-selecting) aperture, which in solid-state laser having a mode that fully utilizes the active material is generally constituted by the rod cross section. The position and the axis of the resonator modes coincides with the ray that retraces itself after one round trip around the resonator, which for a perfectly aligned resonator obviously coincides with the optical axis of the system. If we denote by $\begin{pmatrix} x_3 \\ \theta_3 \end{pmatrix}$ the position and the slope of the axis at the reference plane marked by 3 in Fig. 1, the solution of the self-consistency equation gives

$$\begin{pmatrix} x_3 \\ \theta_3 \end{pmatrix} = -\frac{1}{C} \begin{pmatrix} D_2\sigma_1 + D_1\sigma_2 \\ -C_2\sigma_1 + (C_1 - D_1/f)\sigma_2 \end{pmatrix}, \quad (11)$$

where $C = -D_1D_2(\eta - v)$ is the element 2,1 of the ray matrix from mirror 1 to mirror 2 (see Fig. 1). The detailed expression of the position of the mode axis as a function of tilting and displacement of each decentered element can obviously be calculated only when a particular resonator configuration is specified. However, it can easily be shown that the effects of the mirror misalignment are given directly by Eq. (11) by substituting the tilt angles of mirror 1 and 2 for σ_1 and σ_2 , respectively. It is obvious that, whichever element is misaligned, the dependence of the axis displacement on the rod focal length is always contained only in the denominator C . The behavior, as a function of η , of $|1/C|$, which is the absolute value of the focal length of the optics between mirrors (mirrors' power included), is also shown in Fig. 2(b). From this figure it is apparent that one of the two stability zones, denoted by zone II, is much more sensitive to misalignment than the other, denoted by zone I. In particular, the presence of the asymptote in zone II might be troublesome, especially when the stability range is small, as, for instance, in high-power cw lasers.

6. Ring resonators

The model of a generic ring resonator is shown in Fig. 3. The laser rod is represented by a thin lens of variable focal length f , the remaining optics is described by a single matrix and any misalignment is represented by a single misalignment vector. In this case, as a function of the rod dioptric power, there is only one stability zone, whose width is

$$\Delta \frac{1}{f} = \left| \frac{4}{B} \right|. \quad (12)$$

The condition for self consistency of the Gaussian beam after one round trip yields for the spot size w_3 on the lens

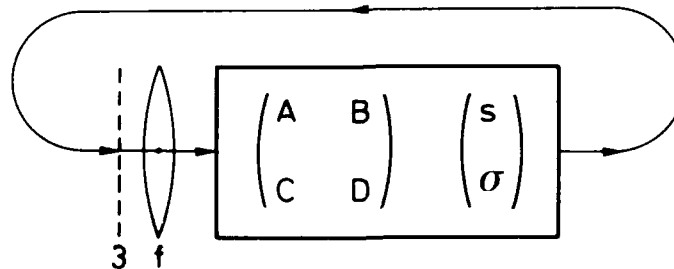


Fig. 3 - Ring resonator with an internal lens of variable focal length f and other intra-cavity optics. The matrix and the misalignment vector describe the ray path from the lens to the reference plane (dashed line).

$$w_3^* = \left(\frac{2\lambda}{\pi}\right)^2 \frac{B^2}{4 - (A+D - \frac{B}{2})^2} \quad (13)$$

As for linear resonators, the spot size on the lens goes to infinity at the stability limits. Within the stability zone, as a function of the rod dioptric power, the spot size w_3 reaches a minimum, which corresponds to the dynamical stability. Equating to zero the derivative of Eq. (13) and solving for $1/f$ gives

$$\frac{1}{f} = \frac{A+D}{B} \quad (14)$$

It can be easily shown that, unlike linear resonator, the point of dynamical stability is always at the center of the stability zone. The stationary value w_{30} of the spot size on the lens is

$$w_{30}^2 = \frac{4\lambda}{\pi} \frac{1}{\Delta \frac{1}{f}} \quad (15)$$

where $\Delta(1/f)$ is the width of the stability zone given by Eq. (12). Thus, in correspondence to the same stability range the stationary value of the spot size at the dynamical stability is $\sqrt{2}$ times larger for ring resonators than for linear ones.

Consider now a generic misalignment represented by the vector $\begin{pmatrix} s \\ \sigma \end{pmatrix}$ (see Fig. 3). The position and the slope of the mode axis in the plane of the lens, $\begin{pmatrix} x_3 \\ \theta_3 \end{pmatrix}$, where the limiting aperture is assumed to be, can be calculated with a procedure analogous to that adopted for linear resonators and can be expressed as

$$\begin{pmatrix} x_3 \\ \theta_3 \end{pmatrix} = \frac{1}{Q} \begin{pmatrix} (1-D)s & + & B\sigma \\ (C-D/f)s & + & (1-A+B/f)\sigma \end{pmatrix} \quad (16)$$

where $Q = 2 - A - D + B/f$.

The behavior of x_3 and θ_3 as a function of the rod dioptric power is similar to that of a linear resonator; in particular, in this case also, the misalignment sensitivity diverges in correspondence to a stability limit.

Another interesting property is related to the integral equation of the modes and to the diffraction losses. On the assumption that in the resonator there is only one limiting aperture of diameter $2a$ placed in the plane of the lens, the integral equation for the resonator modes can easily be written expressing the Fresnel integral in terms of the round trip matrix elements¹⁸. It can immediately be shown, through a simple variable substitution, that this equation becomes equivalent to that of a symmetric linear resonator having the apertures on the mirrors and characterized by g parameters $g_1 = g_2 = A+D-B/f$, and by a Fresnel number $N = a^2/\lambda B$. Thus, the round trip diffraction losses of the ring resonator are equal to the one-way losses of the linear resonator and can immediately be obtained, as well as the mode pattern, from the literature. In particular, a dynamically stable ring resonator results to be equivalent to a confocal resonator and therefore present the same good mode discrimination properties.

7. Conclusions

A unified formulation for the analysis of resonators containing a variable lens and an arbitrary number of optical systems has been presented. The interrelationships between mode volume, dynamical stability, and misalignment sensitivity are formulated through simple equations. Two fundamental properties independent of the resonator configuration are pointed out: (i) in dynamically stable lasers the TEM_{00} mode volume is inversely proportional to the input power stability range, (ii) if the TEM_{00} mode fills entirely the rod, the input power stability range depends only on the optomechanical properties of the rod material and can

thus be considered a novel figure of merit of the laser material. Any resonator may operate in two regions of substantially different misalignment sensitivity. A critical comparison between the thermal focusing in a few crystals and glasses has been also carried out. The results should serve as a basis for further developments and for improved design of single transverse mode solid-state lasers.

8. References

1. C.M.Stickley, IEEE J. Quantum Electron. QE-2, 511 (1966).
2. H.P.Kortz, R.Iffländer, and H.Weber, Appl. Opt. 20, 4124 (1981).
3. R.B.Chesler and D.Maydan, J. Appl. Phys. 43, 2254 (1972).
4. I.Steffen, J.P.Lörtscher, and G.Herziger, IEEE J. Quantum Electron. QE-8, 239 (1972).
5. J.P.Lörtscher, J.Steffen, and G.Herziger, Opt. Quantum Electron. 7, 505 (1975).
6. P.H.Sarkies, Opt. Commun. 31, 189 (1979).
7. D.C.Hanna, C.G.Sawyers, and M.A.Yuratich, Opt. Quantum Electron. 13, 493 (1981).
8. R.L.Sanderson and W.Streifer, Appl. Opt. 8, 2241 (1969).
9. R.Hauck, H.P.Kortz, and H.Weber, Appl. Opt. 19, 598 (1980).
10. A.Gerrard and J.M.Burch, Introduction to matrix methods in optics (Wiley, London, 1975), pp. 106-108 and 286-291.
11. V.Magni, Appl. Opt. 25, 107 (1986).
12. S.De Silvestri, P.Laporta, and V.Magni, Opt. Commun. 59, 43 (1986).
13. S.De Silvestri, P.Laporta, and V.Magni, Opt. Lett. 11, 785 (1986).
14. V.Magni, J. Opt. Soc. Am. A 4, 1962 (1987).
15. W.Koechner, Appl. Opt. 9, 2548 (1970).
16. E.Reed, IEEE J. Quantum Electron. QE-21, 1625 (1985).
17. K.P.Driedger, W.Krause, and H.Weber, Opt. Commun. 57, 403 (1986).
18. P.Baues, Opto-Electron. 1, 37 (1969).

ROOM TEMPERATURE VIBRONIC LASER ACTION IN $\text{Cr}^{3+}:\text{Mg}_2\text{SiO}_4$

V. Petričević, S. K. Gayen and R. R. Alfano
Institute for Ultrafast Spectroscopy and Lasers
Photonics Application Laboratory
Departments of Physics and Electrical Engineering
The City College of New York
New York, NY 10031

and
Kiyoshi Yamagishi and Kazuo Moriya
Electronic Materials Research Laboratory
Mitsui Mining and Smelting Co. Ltd.
1333-2 Haraichi, Ageo-Shi
Saitama 362, Japan

Abstract

Room temperature vibronic laser action in trivalent chromium ion-doped forsterite ($\text{Cr}^{3+}:\text{Mg}_2\text{SiO}_4$) is reported for the first time. The free running pulse laser emission is centered at 1235 nm of the broad ${}^4\text{T}_2 \rightarrow {}^4\text{A}_2$ fluorescence band with a bandwidth of ~ 22 nm. The spectral range for laser emission is expected to cover the 800-1350 nm range if the parasitic absorption may be minimized, making it one of the most widely tunable solid state lasers.

In this paper we present the first room temperature vibronic pulsed laser operation of Cr^{3+} -doped forsterite ($\text{Cr}^{3+}:\text{Mg}_2\text{SiO}_4$). Forsterite is a naturally occurring gem^{1,2} which can be grown by the Czochralski method.¹ The single crystal of $\text{Cr}^{3+}:\text{Mg}_2\text{SiO}_4$ used for spectroscopic and laser action measurements was grown at the Electronic Materials Research Laboratory of the Mitsui Mining and Smelting Co., Ltd., Japan. The crystal is a 9 mm x 9 mm x 4.5 mm rectangular parallelepiped with the three mutually orthogonal axes oriented along the b, c and a crystallographic axes of the crystal. The crystal contains 0.04 at.% of Cr^{3+} ions, which is equivalent to a chromium ion concentration of 6.9×10^{18} ions/cm³.

The room-temperature fluorescence and absorption spectra of $\text{Cr}^{3+}:\text{Mg}_2\text{SiO}_4$ for $\vec{E} \parallel b$ crystallographic axis are shown in Fig. 1. The fluorescence spectrum of $\text{Cr}^{3+}:\text{Mg}_2\text{SiO}_4$ was excited by the 488-nm radiation from an argon-ion laser and recorded by a germanium photodiode detector-lock-in-amplifier combination at the end of a 0.25-m monochromator equipped with a 1000-nm blazed grating. The room-temperature spectrum is a broad band covering the wavelength range 700-1400 nm. The room-temperature fluorescence lifetime is 15 μs .

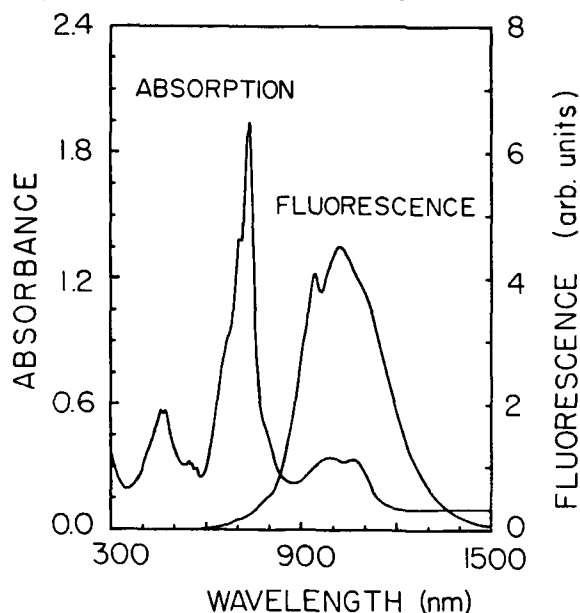


Fig. 1 Absorption and fluorescence spectra of $\text{Cr}^{3+}:\text{Mg}_2\text{SiO}_4$ at room temperature. Both the spectra were taken for $\vec{E} \parallel b$ -axis and excitation along a-axis. The thickness of the sample along a-axis is 4.5 mm.

The absorption spectrum was taken with a Perkin-Elmer Lambda-9 spectrophotometer along the 4.5-mm path length of the sample. It is characterized by two broad bands centered at 740 nm and 460 nm attributed to the ${}^4\text{A}_2 \rightarrow {}^4\text{T}_2$ and ${}^4\text{A}_2 \rightarrow {}^4\text{T}_1$ absorptive transitions, respectively, of the Cr^{3+} ion. The broad, weak absorption band between 850-1150 nm is not observed in the excitation spectrum.³ This indicates that the origin of this

absorption is not transitions in Cr^{3+} ion, but in some other impurity ions, e.g., Fe^{3+} in the host crystal.* It is evident from Fig. 1 that this background absorption overlaps a significant spectral region⁵ of $\text{Cr}^{3+}:\text{Mg}_2\text{SiO}_4$ emission, and inhibits laser action in that region.

The experimental arrangement for investigating the laser action⁶ in $\text{Cr}^{3+}:\text{Mg}_2\text{SiO}_4$ consisted of a stable resonator formed by two 30-cm-radius mirrors placed 20 cm apart. The mirrors were dielectric coated to transmit the 532-nm pump beam, and to have high reflectivity in the 1150-1250 nm spectral range. The reflectivity of the back mirror is 99.9%, while that of the output mirror is ~ 98% for normal incidence over the specified wavelength range. It is to be noted that this spectral region does not correspond to the peak of the fluorescence spectrum, but was chosen so that the background absorption is minimal. The sample was longitudinally pumped by frequency-doubled 532-nm, 10-ns full-width-at-half-maximum (FWHM) pulses from a Q-switched Nd:YAG laser (Quanta Ray DCR-1) operating at a 10-Hz repetition rate, employing an unstable resonator configuration. The pump beam was linearly polarized along the b axis and propagated along the a axis of the sample. It was focused 3 cm before the sample by a 25-cm-focal-length lens. The radius of the pump beam at the center of the sample is ~ 600 μm . The output from the laser cavity was analyzed by a 0.25-m monochromator and monitored by a germanium photodiode detector. The output of the detector was displayed on a fast oscilloscope. No dispersive element was placed in the cavity and the laser operated in a free-running pulsed mode.

Pulsed laser operation was readily obtained for pumping at or above the lasing threshold of 2.2 mJ. A single output laser pulse was obtained, implying a gain-switched operation which is a consequence of pump-pulse duration being shorter than the lasing-level lifetime. The amplitude and duration of the laser pulse varied, as expected, with the pulse-to-pulse energy fluctuation of the pump laser. The temporal duration (FWHM) of the output laser pulse varied from 200 ns at the threshold to 100 ns at 2.4 times the threshold energy. The delay between the peak of the pump pulse and the peak of the $\text{Cr}^{3+}:\text{Mg}_2\text{SiO}_4$ laser pulse also varied with pump-pulse energy, from 700 ns at the threshold to 200 ns at 2.4 times the threshold energy. This indicates that the laser cavity is highly lossy, and several hundred round trips are required to build up the laser oscillation in the cavity.

The laser threshold and slope efficiency were measured for the cavity used in this experiment and the data is displayed in Fig. 2. The laser oscillation starts to build up at an absorbed input energy of 2.2 mJ. The measured slope efficiency of 1.4% is rather low, and indicates large losses in the cavity. These losses include ~ 13% reflection loss from the uncoated sample surfaces, scattering from inhomogeneities in the crystal, and a large mismatch between the size of the pump beam and the $\text{Cr}^{3+}:\text{Mg}_2\text{SiO}_4$ cavity modes in the sample.

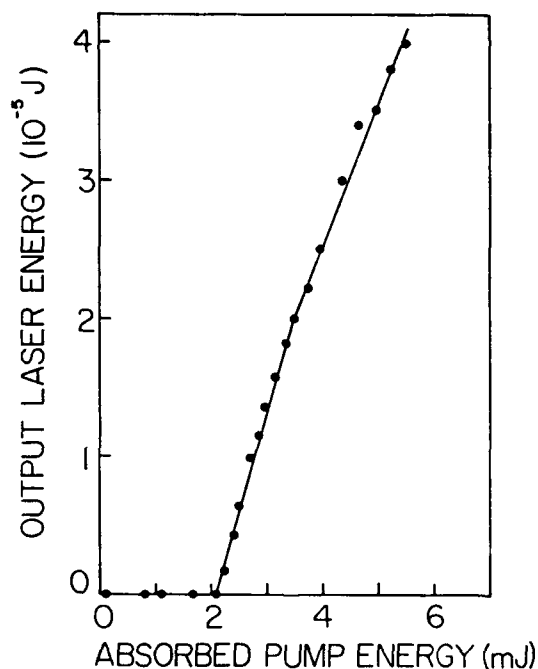


Fig. 2 The output energy of $\text{Cr}^{3+}:\text{Mg}_2\text{SiO}_4$ laser as a function of input energy.

The spectrum of $\text{Cr}^{3+}:\text{Mg}_2\text{SiO}_4$ laser is shown in Fig. 3, for an absorbed pump energy of 3.4 mJ. The spectrum peaks at 1235 nm and has a bandwidth (FWHM) of 22 nm. The spectral range is limited at the high energy end by the mirror transmission and the impurity absorption, while at the low energy end by the mirror transmission as well as by the decrease in fluorescence intensity.

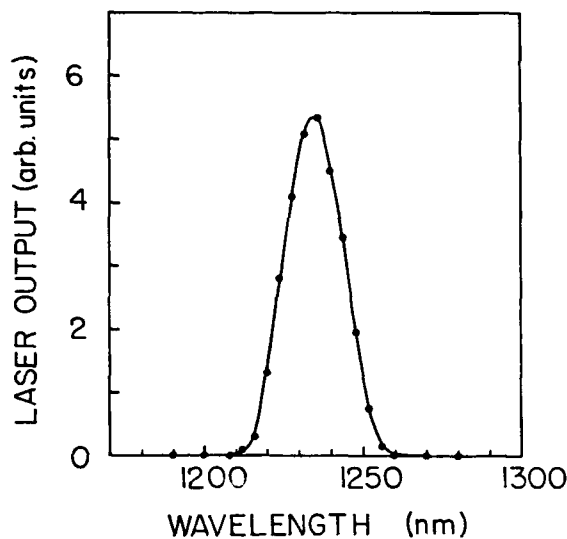


Fig. 3 The spectrum of free-running $\text{Cr}^{3+}:\text{Mg}_2\text{SiO}_4$ laser for the resonator configuration described in the text.

In summary, pulsed laser operation has been obtained in $\text{Cr}^{3+}:\text{Mg}_2\text{SiO}_4$ at room temperature. The laser emission is centered at 1235 nm and has a bandwidth of ~ 22 nm. The spectral range for laser emission is expected to extend from 850-1300 nm if the parasitic absorption may be minimized by improved crystal growth technique, making it one of the most widely tunable solid state lasers in this spectral region. The large fluorescence bandwidth of the crystal promises ultrashort pulse generation through mode locked operation.

The research is supported by National Aeronautics and Space Administration, Army Research Office, Hamamatsu Photonics KK and CCNY Organized Research.

References

1. J. R. Smyth and R. M. Hazen, *American Mineralogist* **58**, 588 (1973).
2. L. V. Bershov, J. M. Gaite, S. S. Hafner, and H. Rager, *Ph. Chem. Minerals* **9**, 95 (1983).
3. K. Yamagishi, unpublished.
4. W. A. Runciman, D. Sengupta, and J. T. Gourley, *American Mineralogist* **58**, 451 (1973).
5. V. Petrićević, S. K. Gayen, R. R. Alfano and K. Moriya, "Spectroscopic Properties of Trivalent-Chromium-Ion-Doped Forsterite: A new Potential Tunable Laser Crystal", Paper PD-8, presented at the Topical Meeting on Tunable Solid State Lasers, Williamsburg, Virginia, Oct. 26-28, 1987; and *Tunable Solid State Laser Technical Digest Series*, 1987 vol. 20, p. PD-8.
6. R. R. Alfano, V. Petrićević and S. K. Gayen, U.S. Patent pending.

LOW JITTER PASSIVE MODE-LOCKING OF A Nd:YAG LASER
UTILIZING ACTIVE Q-SWITCHING

A Summary By Stanley J. York
Laser Applications, Inc. Division of Lasermetrics, Inc.
3500 Aloma Ave., Winter Park, FL 32792 (305) 678-8995

This paper describes a method of actively Q-switching the gain of a pulsed laser cavity in order to achieve a synchronizable mode-locked pulse train derived from an intracavity dye cell. Effectively, a synchronizing trigger pulse is generated before the onset of laser action.

Introduction

A typical passively mode-locked pulsed laser can be made to emit a train of very short, high power pulses each time the flashlamp is fired (Figure 1A). But because of the inherent instabilities present in such a system, the time "window" where the mode-locked pulse train appears can be many orders of magnitude wider than the pulse train itself (Figure 2). This can make it very difficult to synchronize an extracted pulse to an external event.

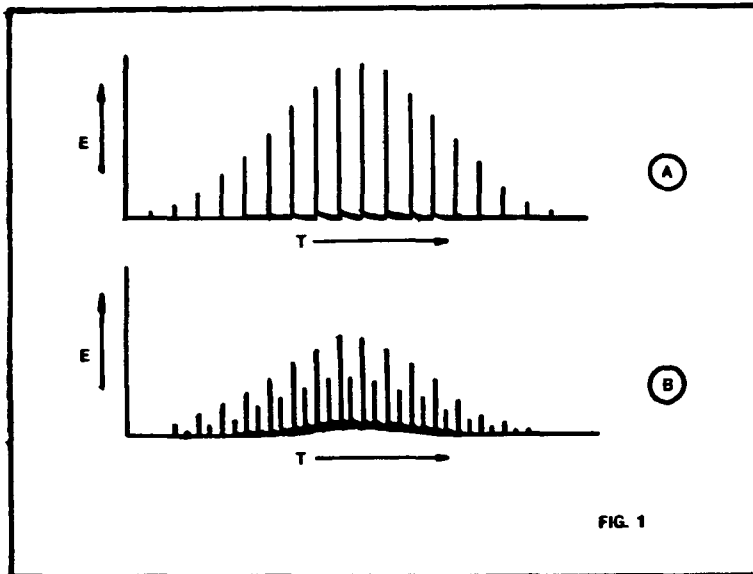


Figure 1 A and B

Shown here is a typical mode-locked pulse train obtained from a pulsed Nd:YAG laser system (A), and the results of longitudinal mode beating (B). The hump in the baseline of the lower trace is due to higher-order longitudinal mode pulses appearing more closely spaced than the two strong modes and the comparatively slow response of the photodetector at these higher frequencies.

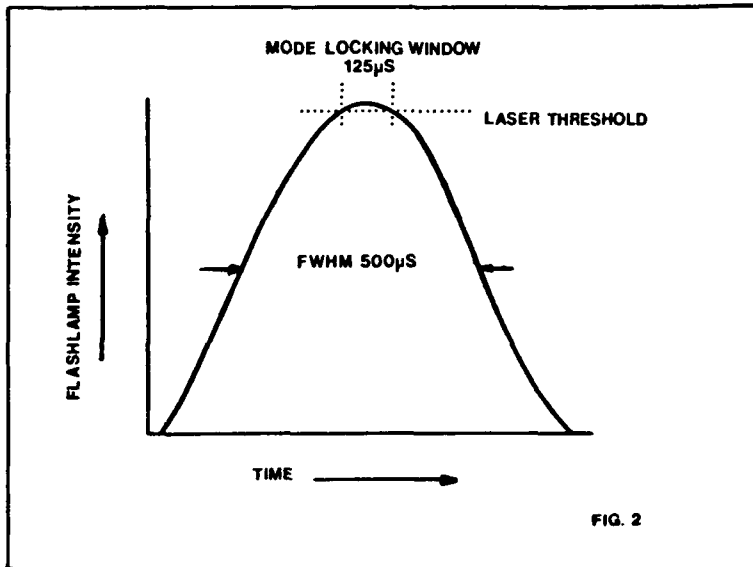


Figure 2:

This shows a typical flashlamp firing envelope, the pump level of which is chosen to produce an oscillator energy just above laser threshold. The mode-locking window in this instance is 125 µs wide, which is vastly greater than the typical mode-locked train envelope (70-100 nS. FWHM).

There are many variables in any pulsed laser system that can cause the instabilities mentioned. Among these are:

- a) Instantaneous rod temperature and its effects on the beam integrity within the cavity.
- b) Absorption of light energy in the coolant surrounding the laser rod and flashlamp.
- c) Lamp aging.
- d) The transverse and longitudinal mode structure of the laser beam.
- e) The discharge capacitor bank voltage.

Each of these problems are discussed in more detail.

The rod temperature cannot be held constant during a lamp firing pulse because of the energy being delivered to it by the flashlamp. This is a readily acceptable cause of instability due to the thermal gradient setup in the rod at the moment of lasing. The rod behaves as a long focal length positive lens, converging the beam and causing some of the reflected rays to re-enter the rod off axis, altering the energy distribution of the beam. Because of the changes in the energy distribution, the gain of the cavity can be slightly different from shot to shot. This, in turn, will affect lasing threshold, causing the mode-locked train to appear earlier or later, depending on the direction of change of gain. Mode-locking on pulsed systems is normally accomplished just above lasing threshold. Higher levels than this may cause multiple pulse trains to appear.

The absorption of light energy by the water coolant surrounding the laser rod and lamp can change, though usually on a long-term basis. Any particles suspended in the coolant could sweep past (or even adhere to) the rod and lamp. A mass of suspended particulates could absorb a large proportion of the available light energy, thereby affecting the rod pumping level.

As a lamp is used, its electrodes gradually lose the surface protection they had when new. The instantaneous temperature within the lamp body is high enough to vaporize a small portion of the electrodes with each firing, and the metal vapors are deposited onto the walls of the lamp, causing a gradual buildup that will reduce the output energy of the lamp over a period of time.

The mode structure of the beam can have an effect on the mode-locked train. If some high energy hot spots occur in an otherwise low energy pulse field, they can seriously reduce the total energy within the beam, and a pulse train of low amplitude results. This is a common occurrence in a multimode laser beam. It would follow from this, that the amplitude stability is very dependent on the uniformity of the beam spatial profile. It is also a well known fact that the damage threshold of an optical surface is much higher in the case of a TEM₀₀ beam than for a multimode beam (Reference 1). For these reasons, the mode-locked pulsed laser should always be made to operate in a TEM₀₀ mode. If more than one strong longitudinal mode is present, it too can deteriorate the mode-locked train (Reference 2). In this case, a second series of pulses can be detected in between the main pulses of the train (Figure 1B). The pulses may or may not be of equal amplitude. When this does occur, pulse frequency is apparently doubled and individual pulse extraction becomes difficult because of the now shorter time interval between pulses. One way of reducing this longitudinal mode beating is to reduce the number of parallel surfaces within the oscillator cavity. This can be done by adjusting the oscillator mirrors to produce an off-axis beam (Figure 3) the amount of skew is minor, and a 1/2-1 degree tilt should suffice. Alternatively, using a rod with wedged end faces has given the same experimental results.

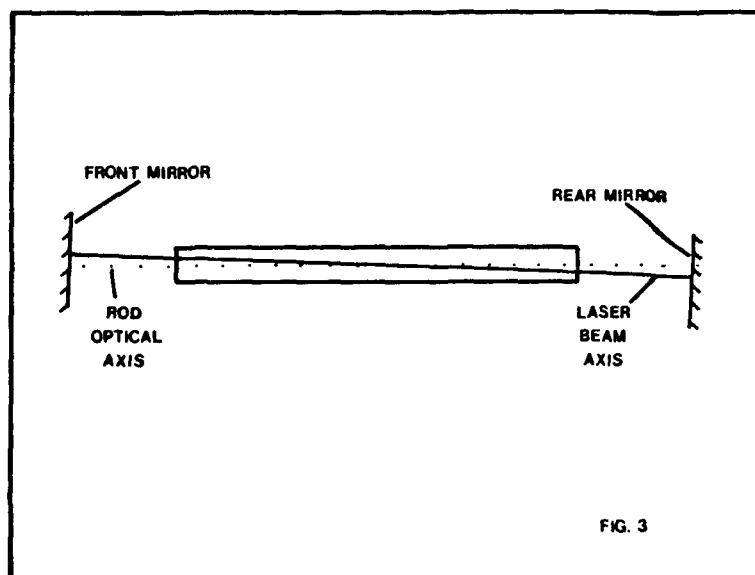


Figure 3

This illustration shows the laser beam entering the rod off axis. In this case, the displacement angle is greatly exaggerated where normally one degree should be enough to reduce the number of longitudinal modes present.

Discharge capacitor bank voltage variations have the greatest bearing on mode-locked train jitter since lamp pump energy is proportional to the square of the applied voltage. Any variations seen here will be directly reflected in the emergent beam. The mode-locked laser, as stated earlier, is operated just above laser threshold. A slight variation in bank voltage can put the rod into a lasing or non-lasing energy level, giving occasional loss of output. This is a major disadvantage of working so close to laser threshold.

Of these instabilities, the two influencing mode-locking the most are the mode structure and discharge voltage.

Theory

These experiments were performed to determine if the gain of the system could be controlled until a predetermined time had elapsed (allowing the rod to become fully populated) such that the rate of change of energy buildup within the cavity would be more uniform. This would allow the mode-locking to take place within a narrower time window.

By pumping the lamp near to the maximum capacity of the power supply used, it was felt that voltage variations would be kept to a minimum. Therefore, the energy being delivered to the lamp would be more closely controlled. (In the system used, the voltage charge on the capacitor bank is detected by a comparator circuit that gives a constant error signal across the range of charge voltage. Operating the system near to maximum will thus produce only a small error voltage on the capacitor bank. Energy is proportional to V^2 and, since dV is a smaller proportion at higher voltages, dV^2 would also be small.) This would then eliminate, as far as possible, one of the main instabilities.

The Optical Cavity

Figure 4 shows the experimental setup used. In a normal pulsed Q-switched system the Pockels cell and crossed polarizers are usually placed on the fully reflecting mirror side of the laser head in order to achieve maximum contrast ratio in the beam (Reference 3 and 4). This affords the highest energy pulse, consistent with shortest pulses time (typically 10-20 ns, depending on system configuration).

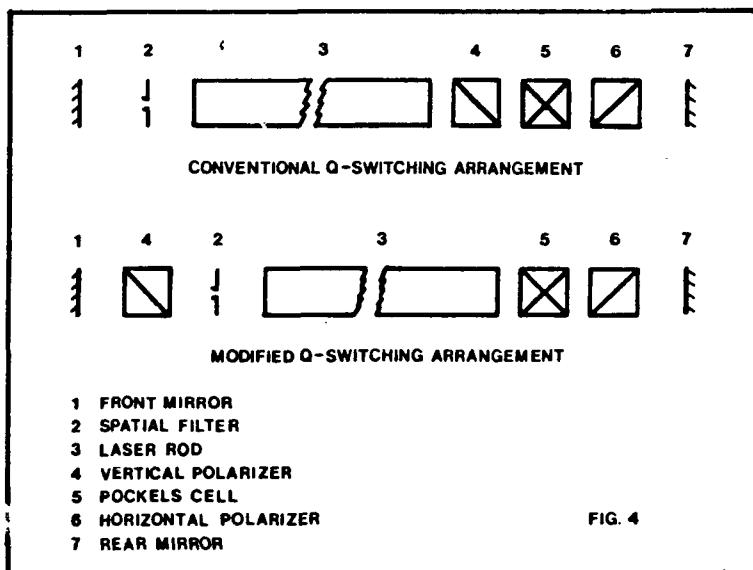


Figure 4:

Illustrated here is the comparison of optical cavities between conventional Q-switching, and Q-switching and mode-locking together. Notice how the Q-switching elements have been split (see text).

In this configuration however, the Q-switching elements have been split to allow some laser leakage. This was done to reduce the contrast ratio (and therefore the gain) of the system, when the Pockels cell switches. [(During the course of these experiments, several mirrors and a Nd:YAG rod suffered damage to the optical coatings when the conventional Q-switch layout was used. Estimated power densities exceeded 2.5×10^6 W/cm² at the time of these tests.)]

The spatial profile of the beam is controlled by the inclusion of an intracavity mode selecting filter 0.059 inches in diameter. This maintains a TEM₀₀ beam profile.

The equipment used in these experiments was all standard Laser Applications products with no modifications. The laser system was a Model 9401 high pulse rate laser utilizing a 4 x 79 mm Nd:YAG rod with 1° wedged faces. The Q-switch and driver electronics were standard Model 1059FV Pockels cell, Model GP4 high voltage pulse generator, and Model 8905B high voltage decoupling network. The polarizers were 10 mm calcite cubes AR coated for a 1.06 μ m. All optical components were mounted on a single rail extrusion 2 meters in length. The modular design of the equipment makes it very easy to change cavity configuration without seriously affecting the alignment.

The dye concentration was increased from the normal strength in order to suppress the weaker longitudinal modes, which along with the 1° wedged rod faces, appeared to work well in minimizing the secondary pulses mentioned above.

During the alignment and optimization procedure of the cavity, it was noticed that the mode locked pulse train timing would change with respect to the Pockels cell firing pulse. This can be easily explained as the result of increasing gain allowing the intracavity energy to build up to lasing levels in a shorter time and a reduced gain building up energy in a longer time (Figure 5 A and B).

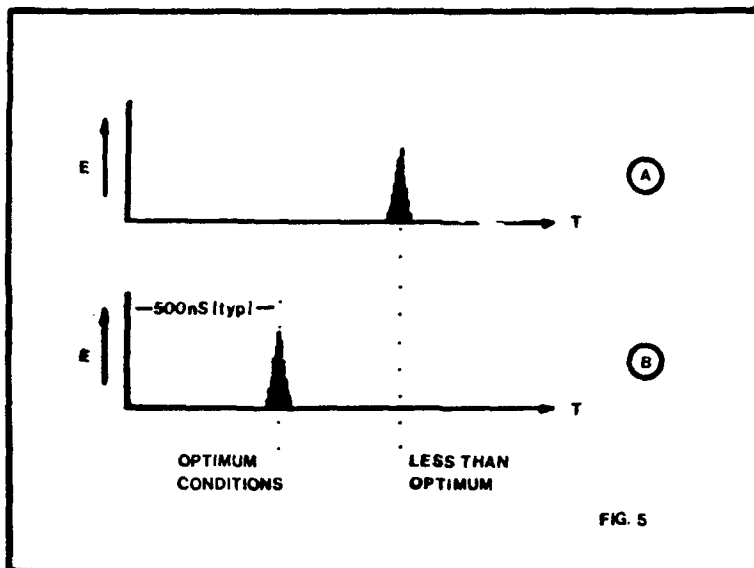


Figure 5 A and B:

This illustration shows how the mode-locked train appears on an oscilloscope triggered from the pockels cell high voltage pulse. As any of the gain changing parameters (bank voltage, mirror alignment, etc.) are adjusted, the pulse train envelope appears to "walk" toward or away from the synchronizing high voltage pulse (A). The optimum position for the pulse train is as short as possible without incurring distortion to the baseline (B).

Observations and Conclusions

The four photographs that follow show a series of multiple exposures of the mode locked train as seen on the highspeed oscilloscope. In each picture, there are approximately 30 superimposed pulse trains. This was done to see how much spread there was in the pulse train timing. It can be seen from these photographs that as the gain of the system increases, the closer the mode locked pulse train appears to the Pockels cell trigger pulse.

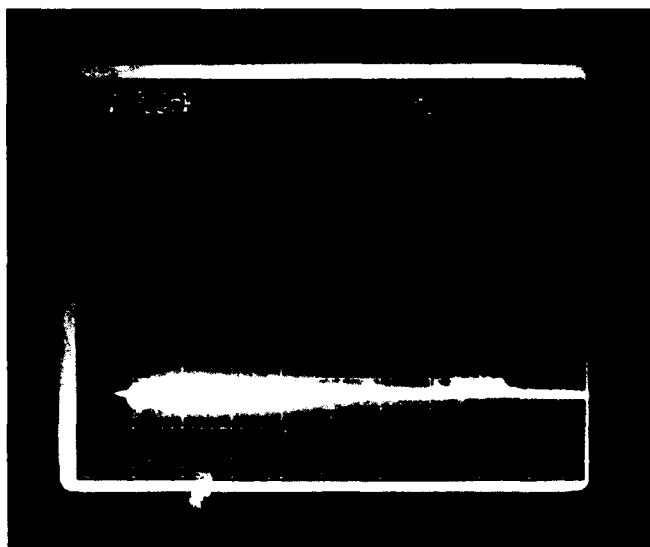


Photo 1

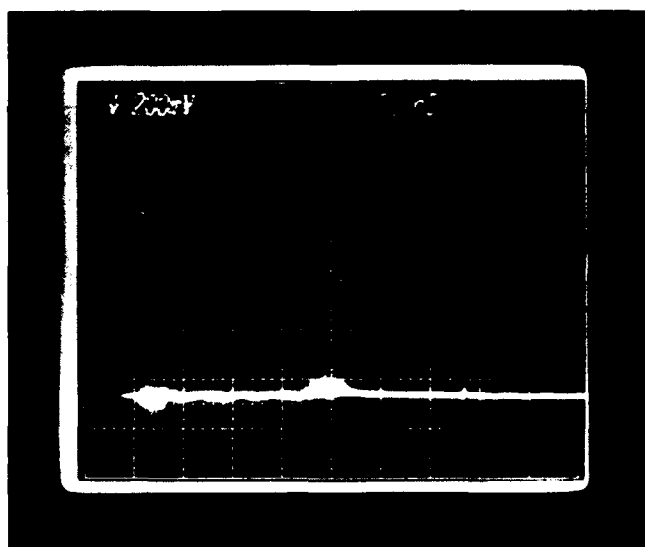


Photo 2

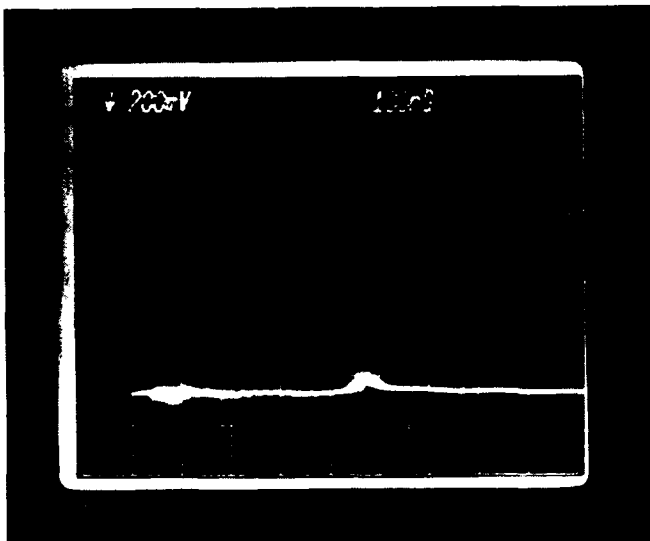


Photo 3

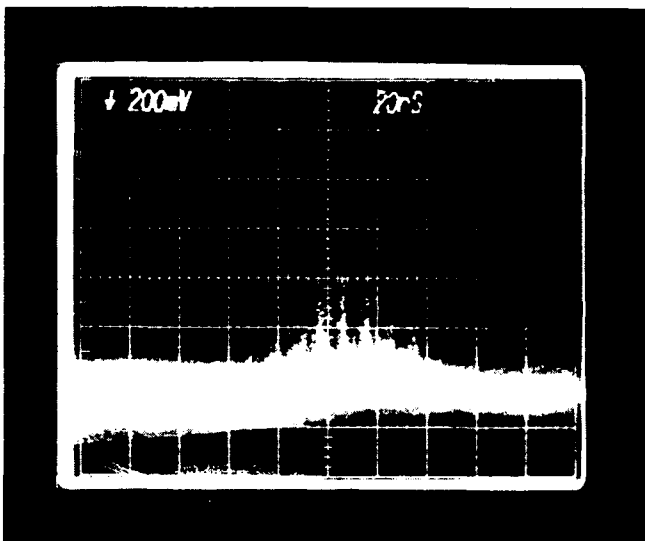


Photo 4

In Photo 1, the pulse appears approximately 3-4 μ s after the Q-switch pulse and, bearing in mind that the pulse train is only 60-70 ns wide, the timing jitter is about 10 times the width of the train. The timebase scale here is 500 ns per division.

In Photo 2, the laser gain has been increased by changing the discharge capacitor bank voltage only, all other operating parameters were left untouched. Note that the pulse train appears 800 ns after the Q-switch pulse, and that the timing jitter is down to about 200 ns. This is still not optimized, the timing jitter being 3 times the width of the mode-locked train. Timebase here is 200 ns per division.

In Photo 3, the cavity is almost optimized. The gain was increased by increasing the discharge voltage a further 5% over the last photograph. Notice now that the delay after the Q-switch pulse is only 500 ns and that the timing jitter is down to approximately one round trip time in the cavity.

Photo 4 is a 5x timebase expansion of the third shot and shows again, approximately 30 superimposed pulse trains. Where successive pulses have overlapped, there is a reinforcement of the image showing low timing errors. The broad baseline is due to multiple overwriting. Timebase speed here is 20 ns per division, and the timing jitter is ± 10 ns or one round trip time of the cavity.

Controlling the gain of the pulsed laser system in the aforementioned manner has yielded some unique and surprising data about the operation of the system. The aim of the experiment was to see if a more predictable pulse train could be produced if the gain of the system were controlled, and it would appear to be a successful venture.

REFERENCES

1. Solid State Laser Engineering. W. Koechner. 1976, p.p. 595-604
2. Passive Mode-Locking of Lasers with a Tunable Dye Cell.
G.Z. Baumann and R.L. Goldstein. Optics Letters, Vol. 7, PS23, 1982.
3. Light Modulator and Q-switch Operations Manual. Lasermetrics, Inc.
4. Pockels Cell Primer. Robert Goldstein. Laser Focus, February, 1968.

Acknowledgement

The author would like to acknowledge Laser Applications, Inc. for its support and encouragement in the execution of these experiments and subsequent writing of this paper.

OUTPUT PULSE SHAPE CONTROL ON A HIGH-POWER SOLID-STATE LASER USING ELECTRONIC FEEDBACK

R. P. Johnson
Research Scientist

N. K. Moncur
Department Head
Lasers and Optics

L.D. Siebert
Sr. Research Scientist

KMS Fusion, Inc.
P.O. Box 1567, Ann Arbor, Michigan 48106

Abstract

An electronic feedback method for the control of output pulse shape is presented that has been successfully implemented on the Nd:glass Chroma laser at KMS Fusion, Inc. With this technique, well controlled high-power pulses in the 10 to 300 μ s pulselength range, with pulse energies up to 2 kJ, have been produced. Three sampling photodiodes are used at various points in the laser system; signals from these photodiodes modulate the radio-frequency signal that drives the acousto-optic modulator in the master oscillator. With proper amplification of these photodiode signals, the system can compensate for relaxation oscillations and other instabilities in the master oscillator and for gain fluctuations in the subsequent power-amplification system.

Introduction

The Chroma laser at KMS Fusion, Inc., is a high-power master-oscillator power amplifier (MOPA) system originally designed for inertial confinement fusion experiments. The laser system was therefore designed for output pulses of nanosecond or shorter duration. Recently, however, experiments have been performed in support of strategic defense and related technology¹ that required long (0.2 to 300 μ s) pulses. Operation of the laser over these long pulselengths allows many more time-dependent pulse distortions to develop that hinder pulse-to-pulse repeatability and impede subsequent data analysis. The method described here was developed for use with laser output pulses in the 10 to 300 μ s pulselength range.

The Chroma Laser Facility

The layout of the Chroma laser is shown in Figure 1. The system consists of a Nd:YLF master oscillator and a series of Nd:glass laser amplifiers and beam-control optics. When they leave the system, the two main target-illumination beams have the characteristics shown in Table 1. A third diagnostic beam, with somewhat less total energy, is also available. The system can be operated at either the fundamental 1.053 μ m Nd:YLF wavelength or at the second harmonic (0.527 μ m).

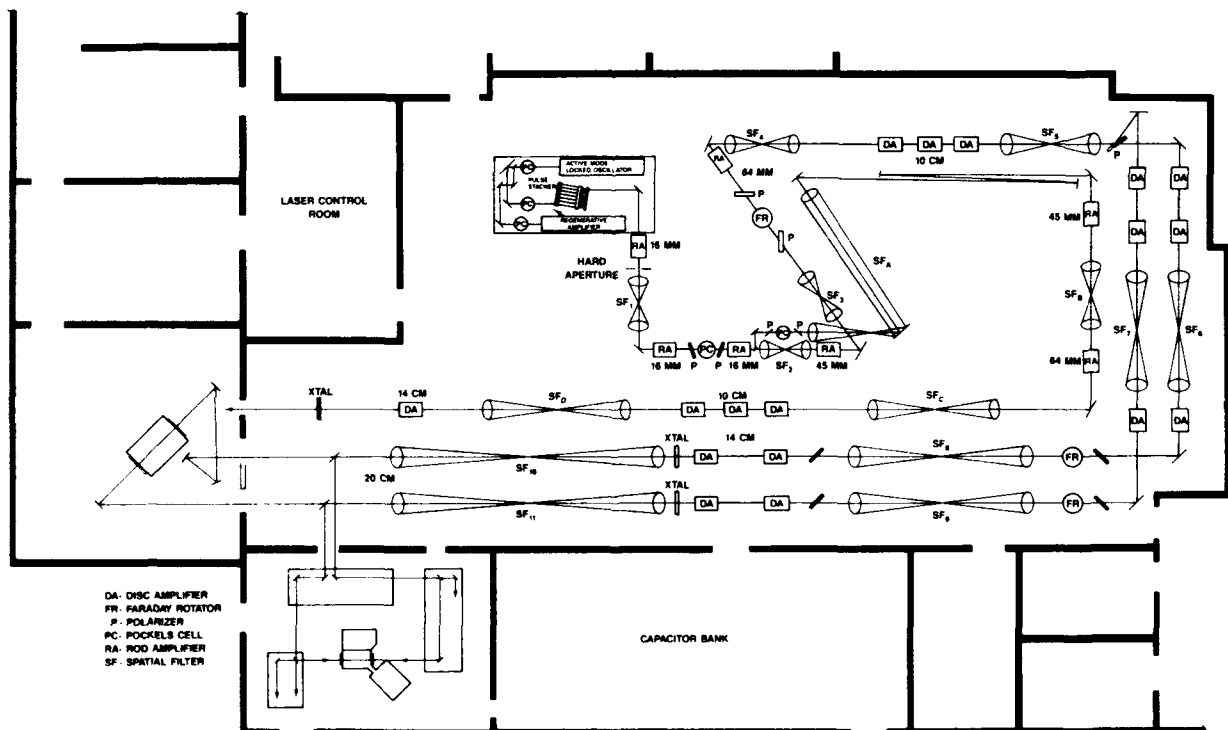


Figure 1. Schematic diagram of the Chroma laser facility. A pulse from a low-power Nd:YLF oscillator is amplified through a series of Nd:glass amplifiers.

Table 1. Capabilities of the Chroma Laser

Pulse Length	IR (1.053 μm)	Green (0.527 μm)
20—100 ps	1.8 TW	1.3 TW
0.5 ns	500 J	300 J
1.0 ns	800 J	400 J
200 ns—300 μs	2000 J	

The master oscillator design,^{2,3} shown in Figure 2, contains both an acousto-optic mode-locker and an acousto-optic Q-switch for short-pulse operation. For long-pulse operation, the mode-locker can be disabled and two etalons inserted into the laser cavity to select a single axial mode of the resonator. The oscillator is pumped with a 3.5 ms constant-current flashlamp pulse that allows the oscillator to operate at up to 10 mJ per pulse.

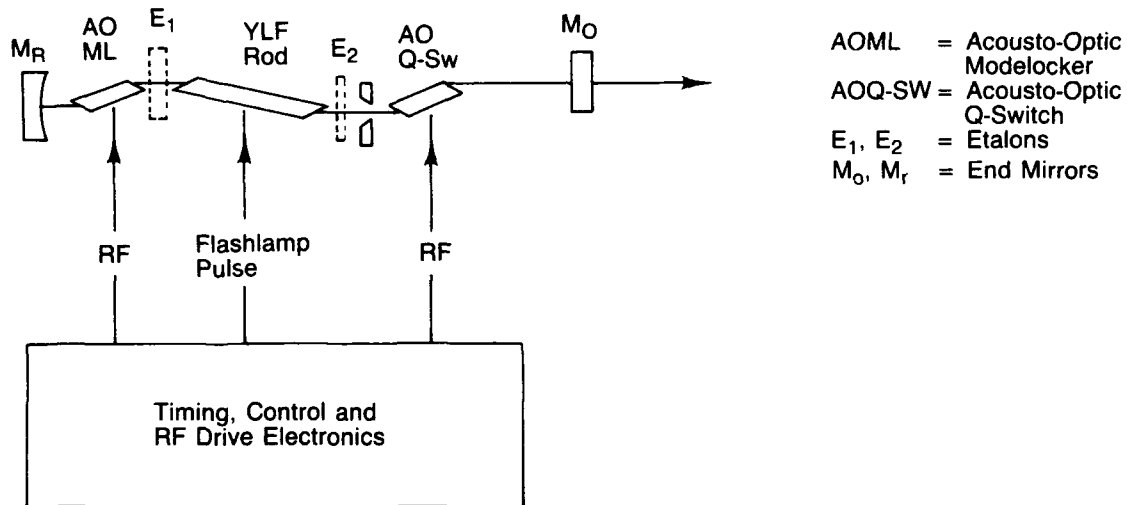


Figure 2. Chroma master oscillator design. An acousto-optic modelocker and Q-switch are available for short-pulse operation. Two etalons are available for selection of a single longitudinal mode for long-pulse work.

The uncontrolled output pulse shown in Figure 3 is typical of pulses generated during long-pulse operation of the oscillator. An appropriate-length portion of such a pulse is selected by Pockels cells and then amplified in the glass amplifier system. It can be seen from the oscillograph in Figure 3 that the uncontrolled oscillator pulse contains some features that make experiments difficult. Most notable are the relaxation oscillations, which cause spikes at the beginning of the pulse that are about an order of magnitude higher in intensity than the steady-state value. These oscillations, which occur at a frequency of about 20 kHz, dampen out significantly within a few milliseconds, but can easily be reinitiated by any disturbance within the resonator. Less obvious from the figure are mechanical and thermal fluctuations, which cause intensity variations in the frequency range of 500 Hz to 5 kHz.

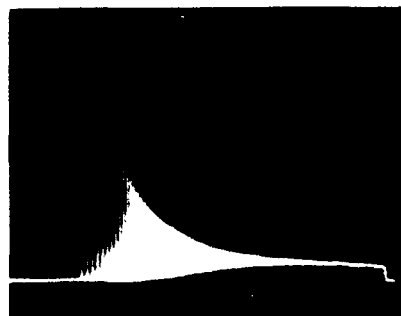


Figure 3. Oscillograph of the uncontrolled Chroma oscillator output. Relaxation oscillations cause spikes that are about an order of magnitude higher in intensity than the steady-state value.

Time-dependent gain fluctuations in the Nd:glass amplifiers also cause unwanted intensity fluctuations in the laser output. The amplifiers are pumped with flashlamp pulses that provide nearly gaussian temporal small-signal gain profiles of about $200\ \mu\text{s}$ full width at half maximum. Amplifier small-signal gain variation combines with saturation effects at high power levels to provide gain that can vary dramatically during a typical long pulse. An example of these gain variations can be seen in Figure 4. The top oscillograph trace shows the laser output pulse and the bottom trace shows the master oscillator input pulse.

The output shown in Figure 4 is typical of the laser output in the absence of feedback control. Not only does the laser output vary with time, making data reduction difficult, but pulse-to-pulse variation in total output energy can be as much as 20%. The purpose of the feedback loop is, therefore, to eliminate these intensity fluctuations and provide a well controlled, predictable laser output.

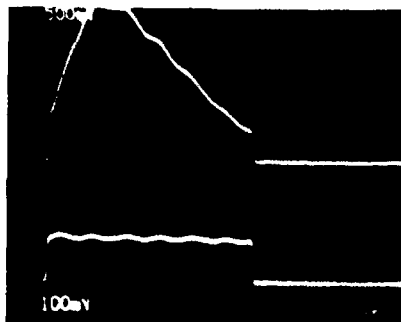


Figure 4. Bottom oscillograph trace: $250\ \mu\text{s}$ portion of the oscillator pulse selected by Pockels cells. Top oscillograph trace: Same $250\ \mu\text{s}$ pulse after amplification in the Chroma amplifiers. Effects of both flashlamp-pumped amplifier gain profile and gain saturation can be seen in the high-power pulse.

Feedback Method

The feedback employed for control of the Chroma laser uses three separate sampling photodiodes at various points in the laser system. Signals from these photodiodes modulate the radio-frequency (RF) signal that drives the acousto-optic modulator (Q-switch) in the master oscillator. A block diagram of the system is shown in Figure 5.

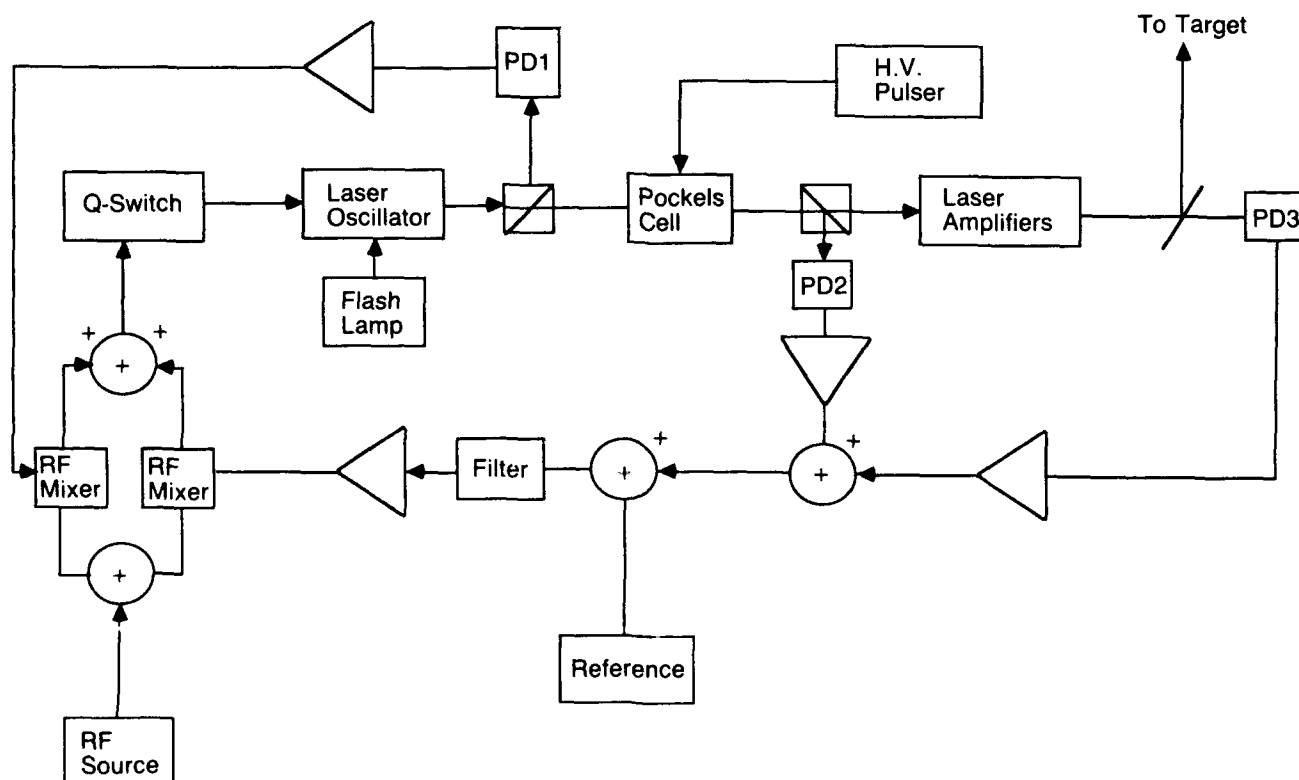


Figure 5. Block diagram of the laser feedback system. Three sampling photodiodes (PD1, PD2, PD3) are used to control laser output.

The first photodiode is located immediately outside of the oscillator cavity and monitors the light reflected from an input Pockels cell polarizer. The signal from this photodiode is amplified and fed into an RF mixer that modulates the RF signal to the Q-switch. The bandwidth of this first loop is limited only by the response time of the acousto-optic Q-switch (which is approximately $0.2 \mu\text{s}$ because of acoustic transit time in the device). This loop virtually eliminates relaxation oscillations in the oscillator, even though it has a somewhat slower response time than most previous feedback schemes that use Pockels cell modulators.^{4,5,6}

Figure 6(a) is an oscillograph of the signal from photodiode #1 after this first feedback loop is closed. Although this first loop compensates for relaxation oscillations, lower-frequency intensity variations can still be seen in the oscillator pulse. Attempts to increase the gain in the loop to compensate for lower-frequency variations force the system into high-frequency (1 MHz) feedback loop oscillations before the low-frequency variations can be controlled.

A second feedback loop is used to compensate for low-frequency intensity variations. Signals from the two photodiodes used in this loop are filtered through a low-pass filter (3 dB point at 300 Hz). One photodiode (#2 in Figure 5) samples the laser beam reflected from the output Pockels cell polarizer, while the other (#3 in Figure 5) samples the laser beam at the end of the laser amplifier system. The oscillator output, sampled by photodiode #2, is stabilized by the feedback control well before voltage is applied to the Pockels cell that switches the pulse input to the amplifiers. Figure 6(b) shows a resulting controlled oscillator pulse approximately 3.5 ms long that was recorded by photodiode #2.

When high voltage is applied to the Pockels cell, the laser beam propagates through the output polarizer, eliminating the signal to photodiode #2 and transferring the entire low-frequency control of the laser output to photodiode #3. This photodiode then drives the oscillator output to compensate for gain changes in the amplifier system. An example of the signal recorded by photodiode #2 when the full feedback system is in operation can be seen in the lower oscillograph trace in Figure 6(c). The upper trace in this figure shows the output of the oscillator during the same period. As can be seen, the response of the oscillator compensates for the gain fluctuations in the amplifier system, resulting in a square pulse at the output of the system. By varying the reference signal in the feedback loop, virtually any desired pulse shape can be produced at the output of the laser.

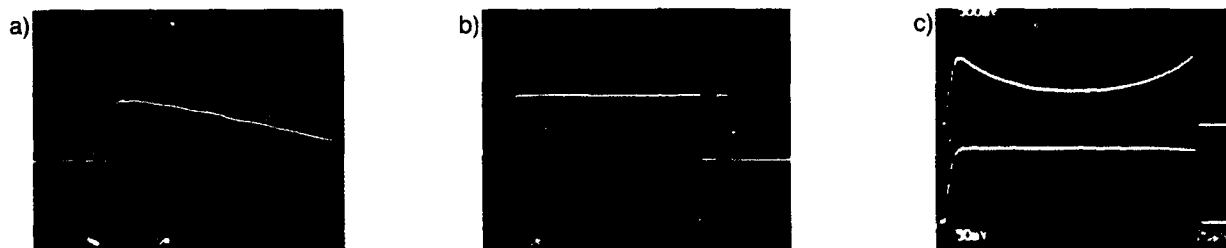


Figure 6. Operation of the Chroma oscillator with feedback control. (a) Oscillator output after closure of the first feedback loop as monitored on PD1. Relaxation oscillations are eliminated. (b) Oscillator output after closure of the second feedback loop as monitored on PD2. Low-frequency distortions are now controlled. (c) Chroma operation with entire feedback system in operation. Top trace: Portion of oscillator pulse selected for amplification. Bottom trace: High power Chroma output as monitored on PD3. The feedback system causes the oscillator output to compensate for variation in amplifier gain resulting in a flat high-power output pulse.

Results

Results of interest were obtained from both the oscillator and the system as a whole. Figure 7 shows oscillographs of various waveforms generated in the oscillator, along with the RF signals to the Q-switch that were needed to produce them. It is interesting to note that only a small amount of RF modulation is needed to produce dramatic modulation in the oscillator output at relatively high modulation frequencies (Figures 7(b) and 7(c)), while much larger RF variations are required for low-frequency modulation (Figure 7(a)). This effect is due to the dynamics of energy storage in the lasing medium.

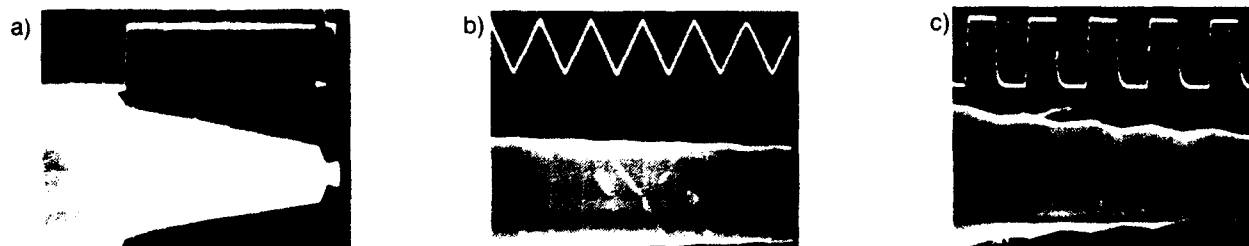


Figure 7. Oscillographs of modulated oscillator output. Top traces show oscillator output. Bottom traces show RF drive to the acousto-optic modulator. (a) 3.5 ms square pulse (b) 5.6 kHz triangle wave (modulation depth > 90%). (c) 5.0 kHz square wave (modulation depth > 95%). Modulated oscillator output with nearly any electrically producible waveform is possible using this feedback system.

Examples of high-power laser output pulses obtained using this technique can be seen in Figure 8. Similar results were obtained for both single-frequency operation and trains of mode-locked pulses. Square pulses varying from 8 to 250 μ s have been produced, as have triangular pulse shapes (which have proven useful for certain power-scaling measurements of nonlinear processes). Comparison of Figures 8 and 4 illustrates the extent of feedback control possible with this system.

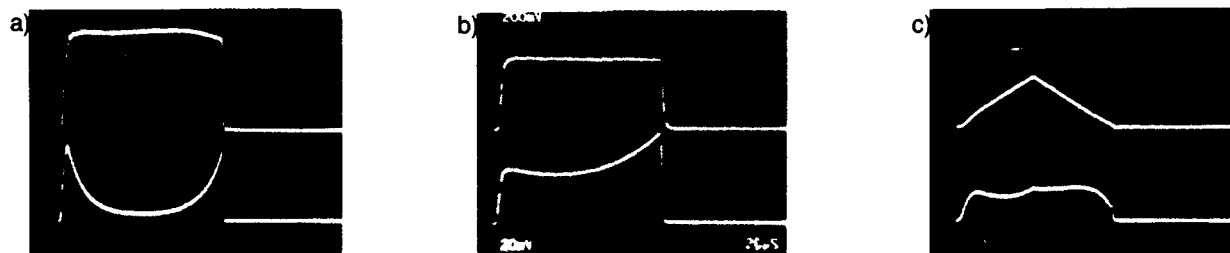


Figure 8. Examples of high power laser output pulses achieved on Chroma with this feedback technique. Top oscillograph traces: high power laser output. Bottom oscillograph traces: oscillator output used for amplification to produce the pulses shown above. Pulse parameters: (a) Single frequency; 270 J; 250 μ s. (b) 100 μ s train of 140 ps modelocked pulses, 700 J total energy. (c) Single frequency; 75 J; 250 μ s at base. The feedback system allows precise control of the laser output.

Conclusions

The performance of the Chroma laser in long-pulse operation has been significantly improved by the addition of the feedback system described here. Relaxation oscillations and other intensity variations in the master oscillator have been eliminated. Arbitrarily shaped pulses 10 μ s to 10 ms long with pulse energies up to 10 mJ can now be consistently produced by the oscillator. The system also compensates for gain fluctuations in the amplifier system, allowing for production of arbitrarily shaped high-power output pulses 10 to 300 μ s long at energy levels up to 2000 J, with shot-to-shot repeatability within a few percent.

References

1. A. Jacobs and K. Allardyce. "Steady State stimulated Brillouin scattering" paper presented at the Symposium on Lasers and Optics, O-E LASE '88.
2. M. R. Brainerd, G. W. Brink, L. D. Siebert, and J. R. Vidolich, in KMS Fusion 1979 Annual Technical Report on Inertial Fusion Research (KMS Fusion, Inc., Ann Arbor, MI, 1980), p. 4-2.
3. A. E. Siegman and D. J. Kuizenga, Opto-electronics 6, 44 (1974).
4. C. H. Thomas and E. V. Price, IEEE J. Quantum Electron. QE-2, 617 (1966).
5. E. Panarella and L. L. T. Bradley, IEEE J. Quantum Electron. QE-11, 181 (1975).
6. B. Luther-Davies, Opt. Commun. 57, 345 (1986).

SPATIAL DEPENDENCE OF ELECTROMAGNETIC FIELD IN LOADED Q-SWITCHED LASER RESONATORS

D. Hanzel, M. Copic, M. Lukac*

University E. Kardelj, J. Stefan Institute, Ljubljana, Yugoslavia

*Iskra Center for Electrooptics, Ljubljana, Yugoslavia

Abstract

Procedure for calculating the spatial and temporal distribution of electromagnetic field inside Q-switched stable and unstable laser resonators is developed. The influence of different aperture sizes and laser pumping on the laser pulse energy, beam divergence and intensity profile is in good agreement for the studied case of a Nd:YAG laser.

Introduction

Steady state laser modes in empty and active laser resonators have been extensively treated in the literature^{1,2,3,4,5,6}. These modes can then be used to describe laser output in steady state operation. The mode structure of the output beam determines the spatial coherence properties of the laser output and is therefore a basic measure of the quality of the laser beam. These properties are of equal importance in the case of Q-switched lasers as well. Due to lack of published model computations of such systems we set out to calculate in the simplest possible model the spatial behaviour of Q-switched pulsed lasers, with Nd:YAG as a particular example.

The laser pulses in such lasers build up in a few roundtrips. The influence of the initial spontaneous emission is expected to be strong. The space between the mirrors in the laser is divided in equidistant planes with active medium in between.

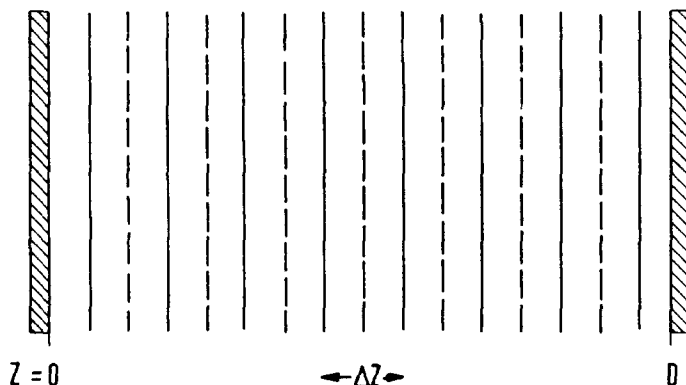


Figure 1 : Laser model. Electric field is calculated on planes denoted by solid lines. Active medium is located between these planes and is denoted by dotted lines.

The active medium is described by the population inversion only and is treated by a single rate equation. Electric field E corresponding to the spontaneous emission contribution is defined as two dimensional complex variable with random phase. This initial spontaneous emission field is free space propagated by Fourier transform algorithm^{5,6,7}. The free space propagated electric field is corrected for amplification in the active medium. Before the next free space propagation the spontaneous emission contribution is added. In the last step new population inversions in each volume element are calculated. At the mirrors the electric field is partially reflected and partially transmitted. The phase of the reflected electric field is corrected for mirror curvature. This procedure is repeated until the laser pulse is formed. This is only a brief description of the method used, details will be published elsewhere⁸.

Results

The above method has been used in the case of the two dimensional unidirectional ring laser resonator with plane mirrors and Nd:YAG as active medium. Initially the laser medium is pumped above threshold. During the pulse evolution the pumping process is neglected.

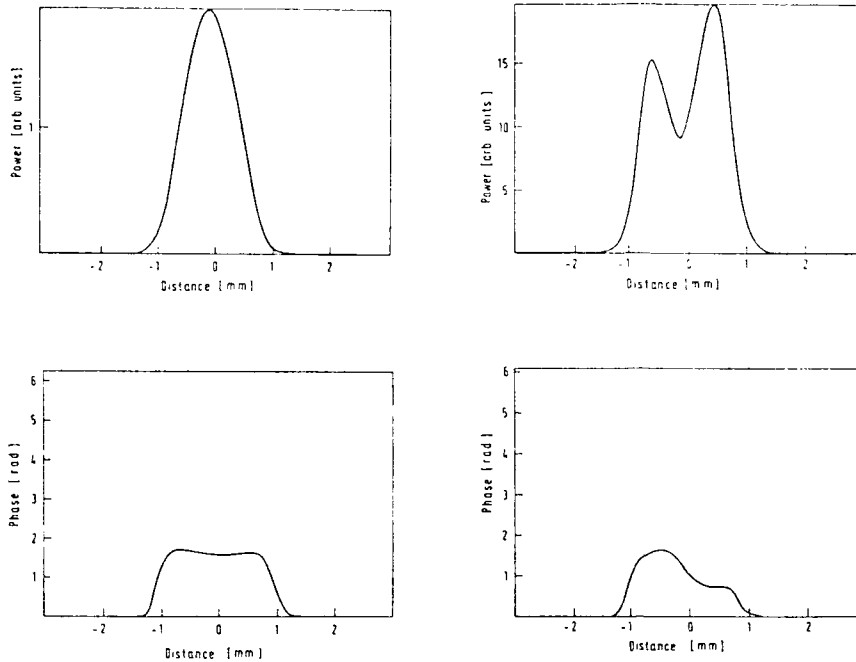


Figure 2 : Instantaneous electric field power and and phase of the electric field plot for two different population inversions :

a) $N=4.6 \cdot 10^{23} \text{ m}^{-3}$ (left side)

b) $N=6.4 \cdot 10^{23} \text{ m}^{-3}$ (right side)

Laser length is 168mm, output mirror reflectivity 15.2%, aperture diameter 2mm and active medium length 50mm.

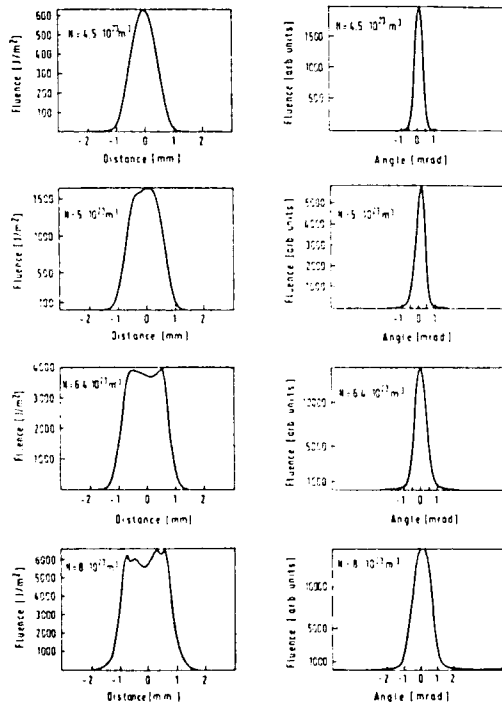


Figure 3 : Near and far field fluences for different population inversions and laser resonator with length $L=168\text{mm}$, output mirror reflectivity 15.2% , aperture diameter 2mm and active medium length 50mm.

Calculations have been made for a set of different initial population inversions above the threshold value ($N=4.5 \cdot 10^{23} \text{m}^{-3}$). Typical instantaneous power proportional to E^2 , and phase at the peak of the laser pulse for two different initial population inversions are shown in figure 2. At lower pumping ($N=4.6 \cdot 10^{23} \text{m}^{-3}$) the electric field power is bell shaped and phase is nearly constant in this region, indicating high spatial coherence degree. The electric field power at higher pumping ($N=6.4 \cdot 10^{23} \text{m}^{-3}$) shows two peaks, which are represented with two flat regions in the phase profile. The shape of power and phase profiles changes randomly in time.

Fluences have been obtained by summing up the instantaneous power profiles in near and far field respectively. Near field fluence (fig. 3) is bell shaped only for pumping at laser threshold. With increasing pumping the near field patterns show many peaks. The far field fluences are single peaked with increasing divergencies with increased pumping. Diffraction limited operation is achieved only for pumping at threshold.

The influence of aperture diameter on spatial properties of laser beams has been studied as well. The initial population inversion has been set just above threshold ($N=4.5 \cdot 10^{23} \text{m}^{-3}$). Diffraction limited operation is achieved for aperture diameter smaller than 2.3mm. With apertures smaller than 2.3mm the near field fluences are bell shaped, for bigger aperture diameters laser output contains many peaks (fig.4).

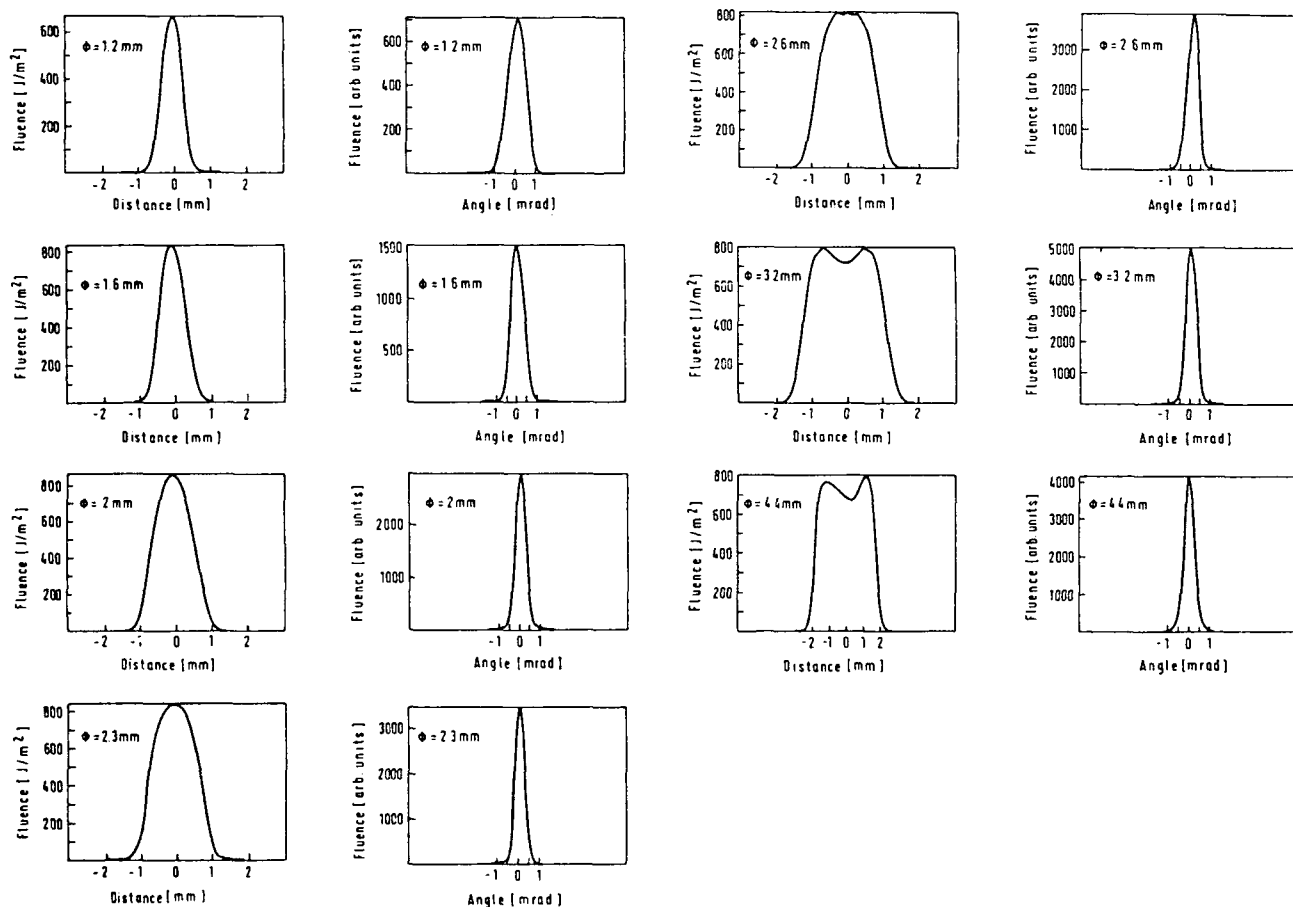


Figure 4 : Near and far field fluences for different aperture diameters and initial population inversion $N=4.5 \cdot 10^{23} \text{m}^{-3}$, resonator length $L=168 \text{ mm}$, output mirror reflectivity 15.2%, active medium length 50mm and plane mirrors.

Numerical results have been experimentally verified for the case of Nd:YAG laser with plane mirrors and electro-optic Q-switching. Near and far field energy distribution in laser beams have been measured by Spiricon 16*16 pyroelectric array. Calculated and measured divergencies are shown in figure 5. Remarkably good agreement is obtained between calculated and experimental values.

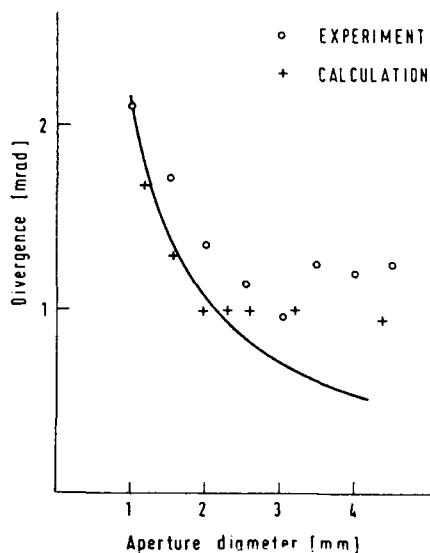


Fig. 5 : Divergence of laser beam as a function of aperture diameter. Solid line denotes diffraction limited output, calculated values are denoted by crosses, experimental values by circles.

Experimental values have been obtained as a cross section through the laser beam center in a direction perpendicular to the flash lamp-laser rod axis. Experimental energy distributions in near and far field in the flash lamp-laser rod axis show more peaks due to increased inhomogeneity of laser rod pumping in that direction. Calculated beam divergencies are smaller than experimental ones due to assumed homogeneous pumping in our model.

Conclusions

We have described a new procedure for calculating electromagnetic field distributions in pulsed Q-switched lasers. The influence of laser pumping and aperture diameters on spatial properties of laser beams has been studied. Experimental results are in good agreement with theoretical predictions. This model can be used for computer modelling of properties of laser beams from Q-switched lasers.

References :

1. H. Kogelnik, T. Li, Proc. IEEE 54, 1312(1966)
2. D.B. Rensch, A.N.Chester, Appl. Opt. 12, 997(1973)
3. D.B. Rensch, Appl. Opt. 13,2546(1974)
4. A.E. Siegman, E.A. Sziklas, Appl. Opt. 13, 2775(1974)
5. E.A. Sziklas, A.E. Siegman, Appl. Opt. 14, 1874(1975)
6. M. Lax,G.P.Agrawal,M.R.Belic, B.J. Coffey, W.H. Louisell, JOSA A2, 731(1985)
7. J.W. Goodman, Introduction to Fourier Optics, McGraw Hill, New York,1968
8. D. Hanzel, M. Copic,to be published

MONOLITHIC TWO-DIMENSIONAL DIODE LASER ARRAYS

J. Z. Wilcox, J. J. Yang, M. Jansen,
L. Lee, M. Sergeant, S. Ou

TRW, Group Research Staff, Space and Technology Group
One Space Park, Redondo Beach, CA 90278

Abstract

Surface emitting diode lasers have attracted recently much attention because of their potential as high-power monolithic two-dimensional arrays for both incoherent or coherent applications, and optical interconnects for integrated optics. Compared to the more conventional rack and stack approach to 2-D arrays, monolithic arrays offer reduced testing and production cost per unit area for large arrays. Several approaches to monolithic surface emission are available: vertical cavity, and grating and etched mirror outcouplers, and these are described in this paper. TRW results using 45 degree etched micromirrors for the fabrication of a monolithic 2-D array of 64 GaAs/GaAlAs diode lasers are reported.

I. Introduction

A monolithic two-dimensional (2-D) diode laser array can be obtained by wafer-scale integration of diode lasers which emit light perpendicular to the wafer surface. Two basic approaches are available. In the "vertical cavity" configuration,^{1, 2} the cavity is short (usually less than 10 μm) formed by mirrors at top and bottom surfaces of the wafer (Figure 1). In the "horizontal" cavity configuration, the cavity extends along the plane of the active layer, (thus offering a high gain-length product), similarly as in the more conventional edge-emitting lasers.³⁻⁷ Surface emission (SE) is obtained by light deflection: using either grating outcouplers³⁻⁷ or etched mirror deflectors¹⁰⁻¹⁶.

In addition to their use for construction of monolithic 2-D arrays, surface emitting lasers are of interest for other applications, such as optical interconnects and signal processing devices. This paper summarizes recent advances in monolithic surface-emitting arrays, and describes TRW's progress in the fabrication of 45 degree deflecting micromirrors and a large (64 element) 2-D array.

II. Approaches to Monolithic SE Lasers

Vertical Cavity

In the vertical cavity configuration (Figure 1), the optical cavity is formed by mirrors at top and bottom surfaces of the wafer¹. The electrode diameter is limited by spontaneous emission to about 20 μm , and the thickness of the gain region (in devices with top injection) by the injected carrier diffusion length to several micrometers. This results in low gain-length product, high threshold current densities, and low output powers. High reflectivity mirrors are required to lower the threshold current. CW operation was obtained recently in a lateral buried hetero structure (LBH) which provides highly efficient carrier confinement and increases the length of the gain region through transverse injection². CW threshold current 2mA has been obtained at room temperature, with far field angle 7 degrees (Figure 2).

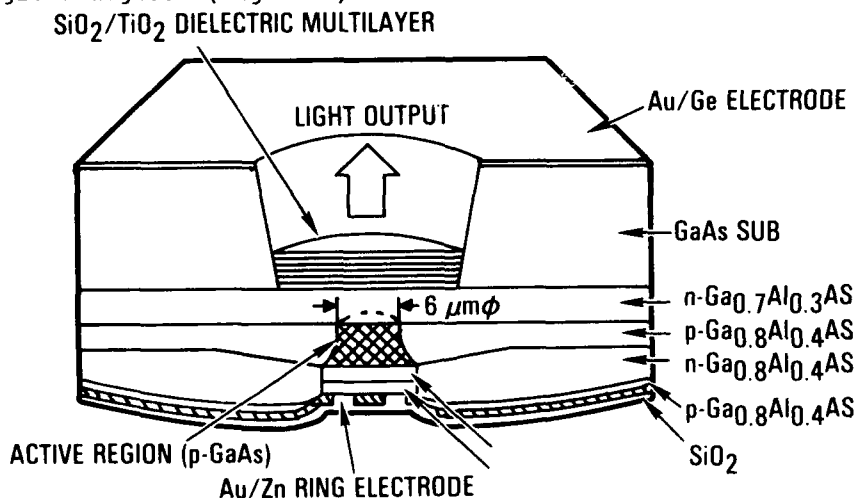
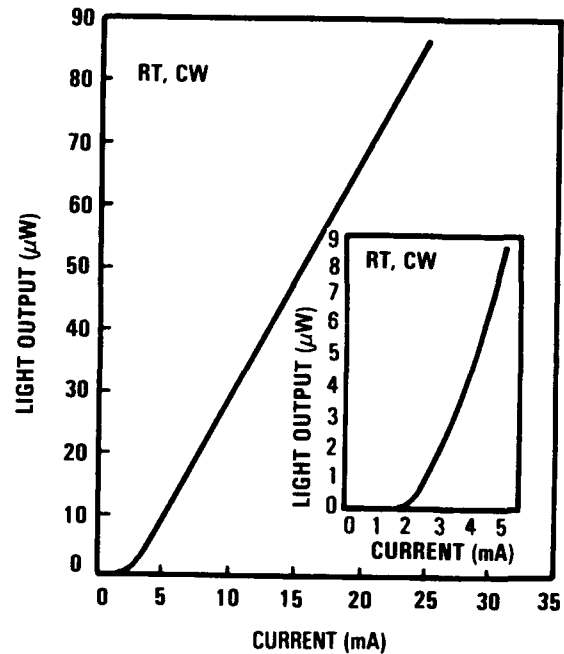
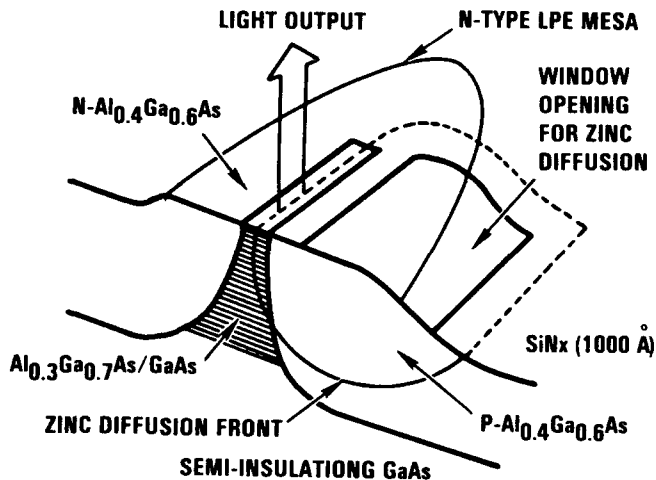


FIGURE 1. CIRCULAR BURIED HETEROSTRUCTURE SURFACE EMITTING LASERS

- Extremely low threshold current
- Single-mode operation



Ogura et al. Presented at Device Research Conf., Santa Barbara, CA, June 22, 1987
Appl. Phys. Lett. 51, 1655 (1987)

FIGURE 2. GaAs/AlGaAs VERTICAL EMITTING LASERS WITH $\lambda/4$ MULTIPLE LAYER REFLECTOR

Grating Outcouplers

In addition to the advantage of having a long cavity, grating outcouplers (Figure 3) offer wavelength stability and narrow beam divergence in direction perpendicular to the grating lines. The wavelength stability derives from frequency selective coupling of the forward and backward propagating waves. After the pioneering work in 1975,^{3,4} periodic gratings have attracted much recent attention.⁵⁻⁸ Using distributed Bragg reflector (DBR), a 0.25 degree \times 8 degree narrow far field pattern for a single emitter, and an angular divergence as low as 0.05 degrees for a linear array of fine grating outcouplers were produced.⁵ However, threshold currents tend to be high, and efficiencies low for grating outcouplers (102 mA and 3.7%, respectively, for a 4 μm ridge DBR with a 300 μm long electrode and 300 μm long second order grating).⁵ Kojima et al.^{7,8} recently obtained CW operation of DBR and distributed feedback (DFB) lasers at room temperature. To improve the outcoupling efficiency, an output window was etched underneath a metalized grating of a DFB laser to force both orthogonal emissions through the substrate; however, the threshold current was high (13 kA/cm^2) and slope efficiency low (0.05 W/A) in these early attempts.⁹

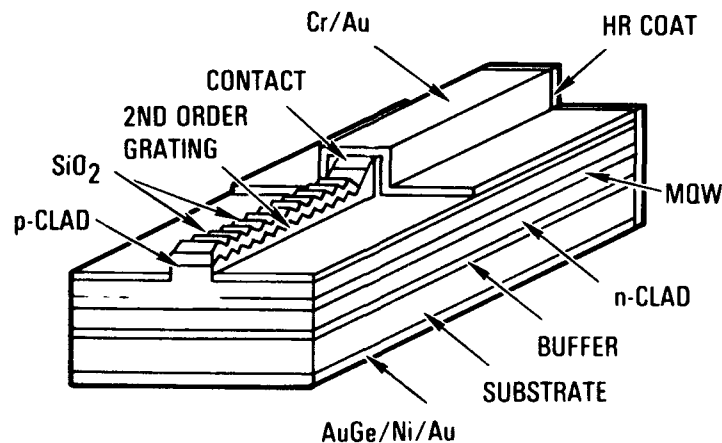


FIGURE 3. DISTRIBUTED BRAGG REFLECTOR SURFACE EMITTING LASERS

45 Degree Mirror Outcouplers

Etched mirror lasers are variations of, and offer similar benefits as Fabry-Perot cavities with cleaved facets. The cavity is formed by etched semiconductor-air interfaces, with the guided emission rotated by monolithic 45 degree micromirrors.

Figure 4 illustrates two etched mirror geometries. In Figure 4a, the micromirrors are outside the resonating cavity, and emission is through epilayers. Laser performance depends very strongly on quality of the etched mirrors. Using mass transport techniques, Liao and Walpole^{10,11} produced very smooth parabolic mirror deflectors, and fabricated 2-D arrays (112 lasers on 1 mm x 3 mm area) GaInAs P diode lasers. An average CW output of 14 mW per laser and an average optical flux of 57 W/cm² have been obtained when the array was operated one section (approximately 14% of the total area) at a time.

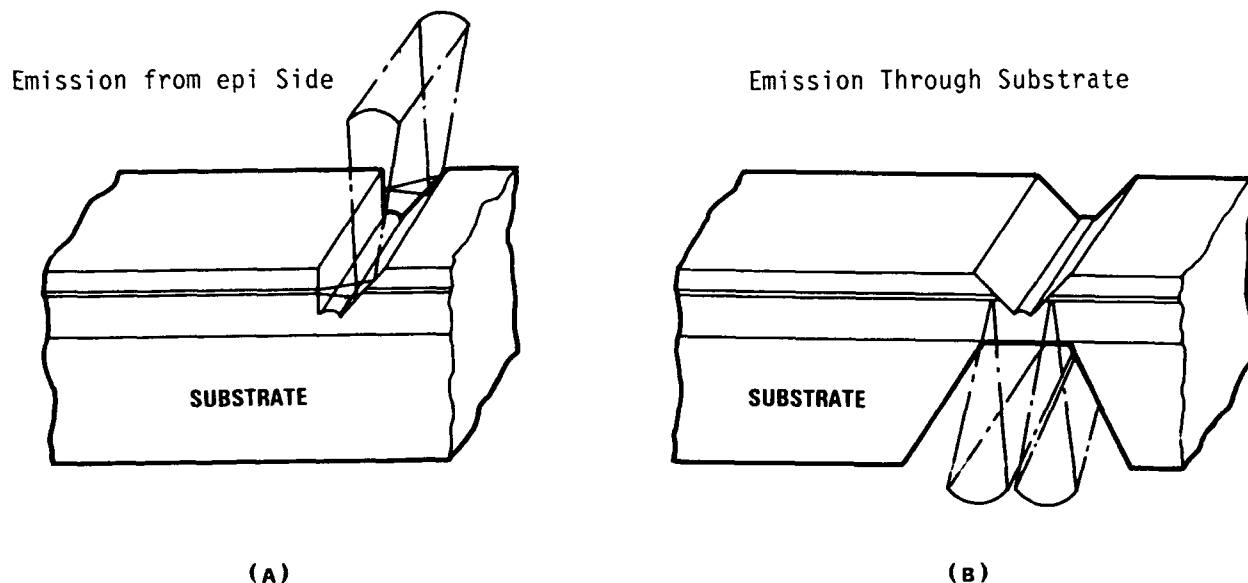


FIGURE 4. TWO DIMENSIONAL SURFACE EMITTING CONFIGURATIONS USING 45 DEGREE DEFLECTING MICROMIRROR

Mass transport techniques are not adaptable to GaAlAs, and ion beam etching or ion beam assisted etching (IBAE) must be used instead. Windhorn, Goodhue, and Donelly^{12,13} used IBAE process to fabricate a 22 element ($5\ \mu$ stripes) array. The array had 3.2 amp threshold current; the average optical flux achieved $160\ \text{W/cm}^2$ was limited by the availability of the highest (pulsed) current used, 10.5 amp, in these experiments.

In Figure 4b, the mirrors are inside the resonating cavity, and emission is through holes etched into GaAs substrate. Although there are diffraction losses between the 45 degree micromirror and the air interface, the losses are low (the estimated penalty for threshold current is less than 20%), and can be tolerated for short path length. The through-substrate emission was first proposed and demonstrated by Springthorpe¹⁴.

III. Fabrication of Deflecting Mirrors

The main issue which determines performance of surface-emitting lasers is the quality of the deflecting mirrors: surface smoothness and passivation, accuracy of 45 degrees, and in case of through-substrate emission, registration of deflecting and outcoupling mirrors. TRW has addressed all critical technologies for the development of deflecting mirrors, and fabricated both through epilayers and through substrate emitting lasers.

Emission Through Epilayers

Using ion milling technique, TRW has fabricated^{14,15} both the vertical facet and 45 degree deflecting mirrors simultaneously. A typical scanning electron micrograph (SEM) is shown in Figure 5. The smoothness of the etched mirrors is excellent. The laser performance approaches that of a side emitting laser (Figure 6). Figure 6 shows L-I curves of 10-element linear arrays (total width 50 μm) of cleaved and etched lasers. Currents at threshold differ by less than 20%. The experimental differential efficiency was lower for the etched laser because there was no AR coating on the 45 degree micromirror in these arrays. The projected (corrected by the ratio of total to partial reflectivity of uncoated 45 degree mirror) differential efficiency approaches that of the cleaved laser.

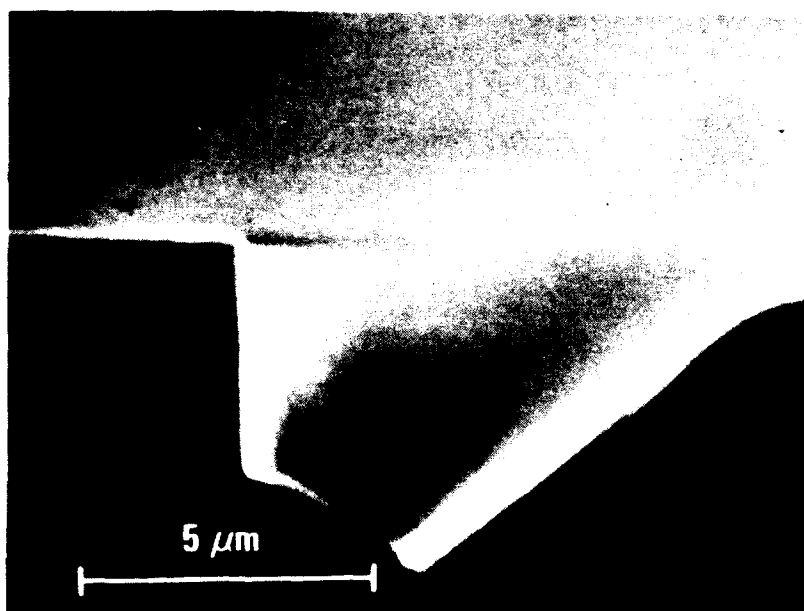
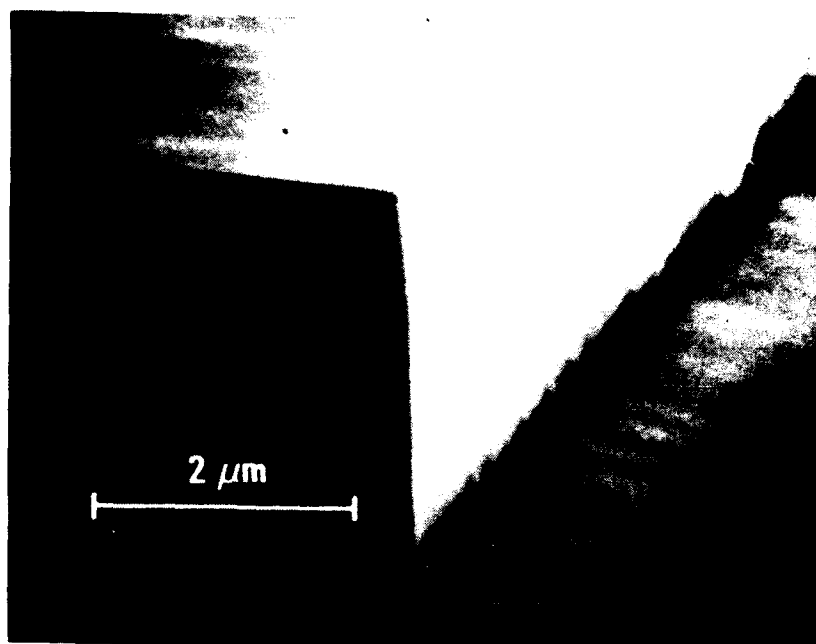


FIGURE 5. SCANNING ELECTRON MICROGRAPH OF THE ION MILLED MIRRORS

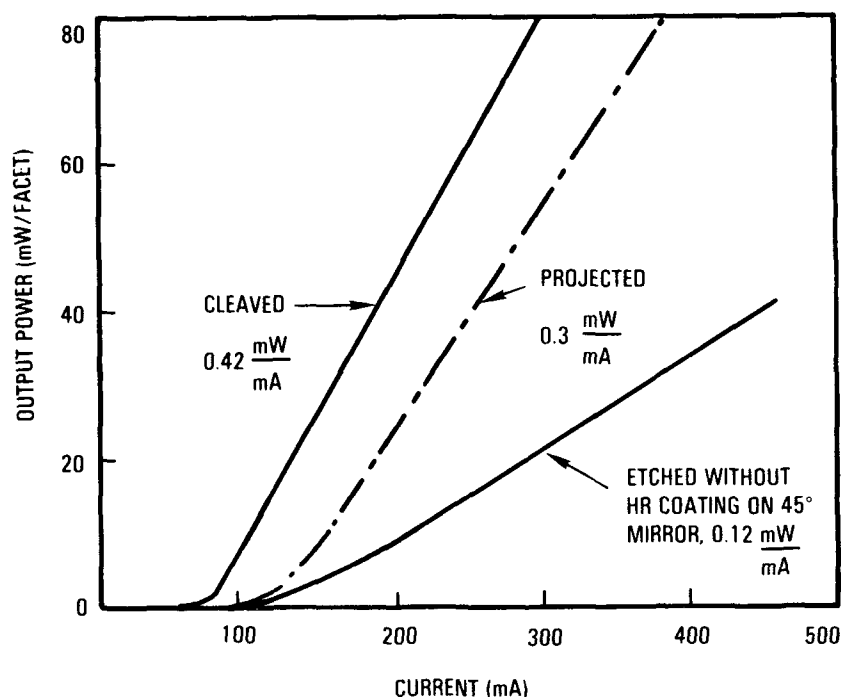


FIGURE 6. POWER-CURRENT CHARACTERISTICS OF A CLEAVED-ETCHED LASER

Figure 7 shows the top view of a typical TRW fabricated through epi emitting 2-D array. Each bright area represents emission of a 10 element array. The observed uniformity of the light intensity over the wafer surface indicates high degree of fabrication uniformity. This can be also seen from L-I characteristics of several lasers (Figure 8) which were taken at random locations on the wafer surface. For a (2 x 5) two-dimensional array of 10-element lasers (total one hundred of 3 μm -wide stripe lasers), the output power was over 1.7 W for 500 nanosecond pulses at 100 Hz. TRW has recently fabricated also a (4 x 16) 2-D array of SE emitters, with each emitter consisting of 10 μm wide stripe lasers, and 100 μm center-to-center spacing between the emitters. The cavity length was 250 μm . Figure 9 shows 128 bright shots corresponding to two-sided emission from each laser of the array.

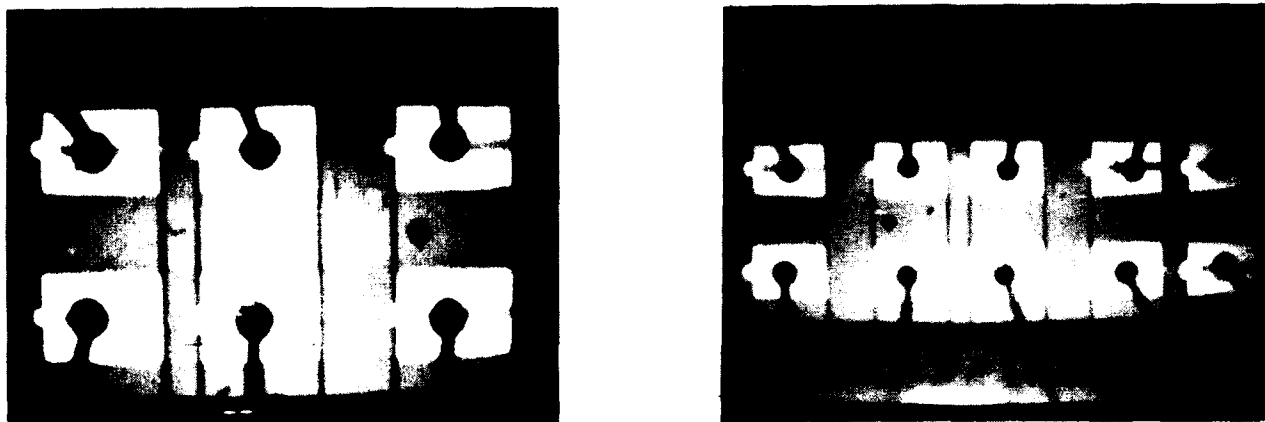


FIGURE 7. THE TOP VIEW OF A 2 x 5 SURFACE EMITTING LASER

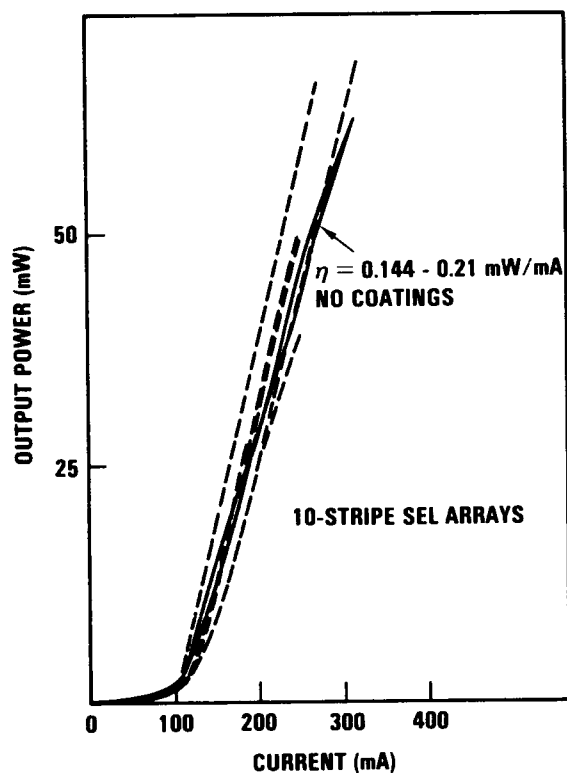


FIGURE 8. POWER-CURRENT CHARACTERISTICS
ELEMENT TWO DIMENSIONAL
SURFACE EMITTING LASER

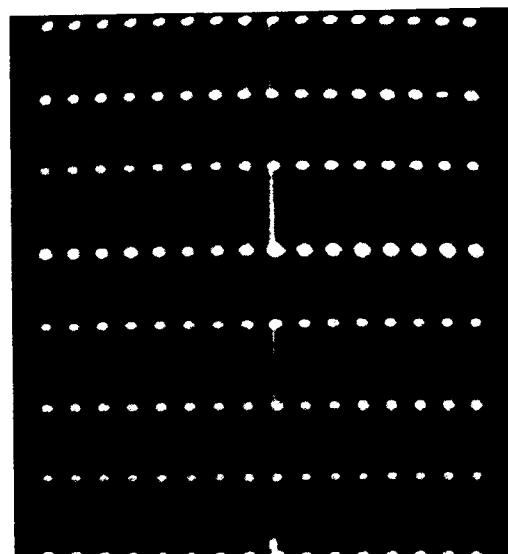


FIGURE 9. 64 ELEMENTS MONOLITHIC
TWO DIMENSIONAL SURFACE
EMITTING ARRAY

Another important issue for the fabrication of large arrays is the uniformity of the processed wafer. Typical wafer size processed in our laboratory is 0.5 in x 0.75 in. Each wafer contains hundreds of lasers. Uniformity and reproducibility studies performed at TRW showed that from a good wafer, typically more than 95% of devices lase, with threshold currents within 10% of each other.

Emission Through Substrate

For long pulses, high repetition rate, or CW operation, arrays with through-epi emission are inadequate because the waste heat must pass through GaAs substrate (which is comparatively thick, thickness > 100 μm , and a poor thermal conductor), resulting in excessive overheating. The thermal dissipation issue is similar here as for all lasers mounted epi-junction up. Lasers with emission through substrate (Figure 4b) are mounted junction side down directly on the heat sink, thus offering a solution to thermal problems associated with through-epi emission.

The 45 degree micromirrors are internal to the laser cavity. The outcoupling mirror is etched through GaAs substrate to GaAlAs stop-etch epilayer. This results in mirror-like surfaces for the outcoupling mirrors, shown in Figure 10.

One of the critical issues for substrate emitting lasers is the angular precision of the 45 degree deflecting mirror. To minimize transmission and diffractive losses (between the deflecting and outcoupling mirrors), the angular tolerance must be limited to less than 2 degrees. This puts high requirements on the fabrication process.

The first through-substrate emitting laser fabricated in our laboratory demonstrated very promising results. A typical L-I curve of a laser with one cleaved and one etched side is shown in Figure 11. The threshold current density is about 100 mA for a 10-stripe array, compared to 70 mA for a cleaved-cleaved array from the same wafer. The differential quantum efficiency is about 10%. This is rather low; however, the orientation of the deflecting mirror was only 40 degrees for this laser, which degraded the laser performance.

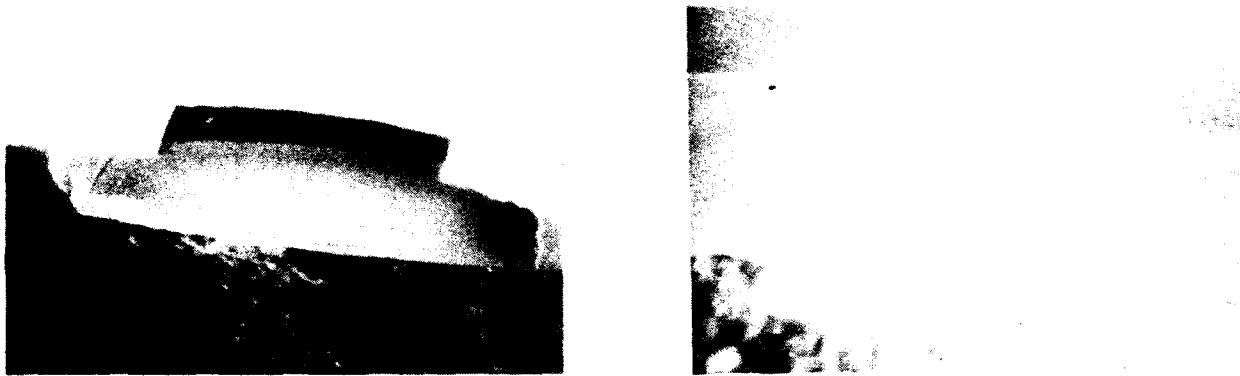


FIGURE 10. THE ETCHED FACET FOR VERTICAL EMISSION THROUGH SUBSTRATE

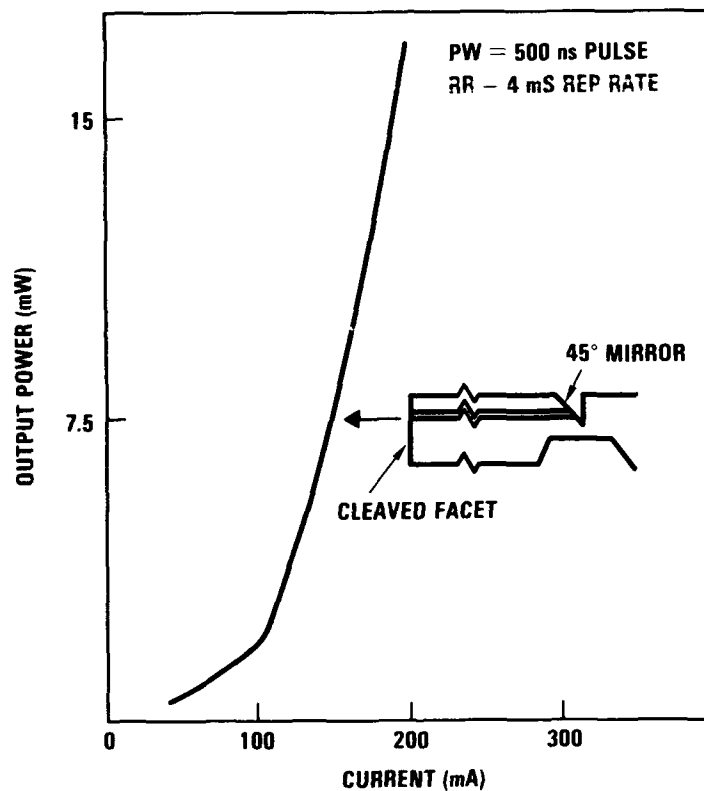


FIGURE 11. L-I CHARACTERISTICS OF VERTICAL EMISSION THROUGH SUBSTRATE

Near field patterns obtained from a (2 x 4) 2-D array (each array element consisting of a 10-stripe linear laser array shown in Figure 12b) are shown in Figures 12c and 12d. Figure 12c resolves emissions from two closely spaced array elements which are overlapped in Figure 12d.

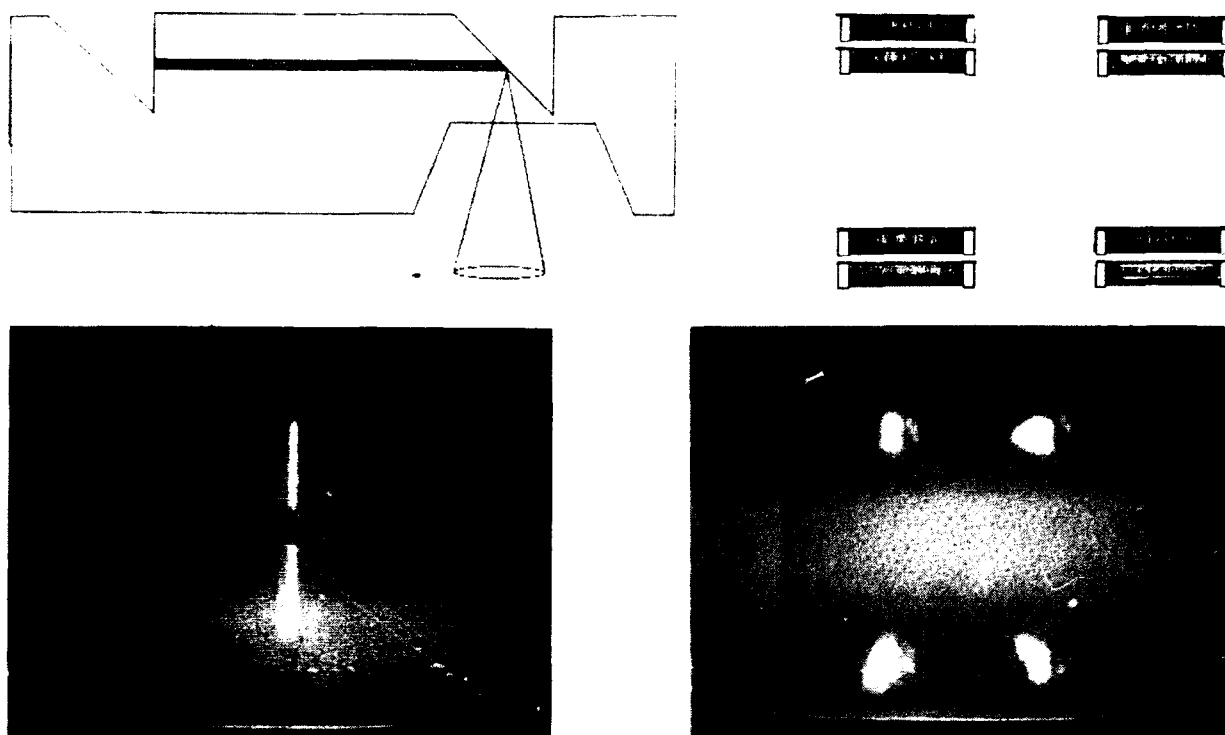


FIGURE 12. NEAR FIELD PATTERN FOR 2X4 VERTICAL EMISSION ARRAY
(THROUGH SUBSTRATE)

Another issue which must be addressed before large 2-D arrays are fabricated, is the plating of thick electrodes. TRW is developing this and other critical technologies, and is planning to fabricate a large 2-D array of through-substrate emitting lasers for pumping of solid state lasers.

REFERENCES

1. K. Iga, H. Soda, T. Terakado, and S. Shimizu, Electron. Lett., Vol. 19, pp. 457 (1983).
2. M. Ogura, W. Hsin, M. C. Wu, S. Wang, S. C. Wang, and J. J. Yang, Appl. Phys. Lett., Vol. 51, pp. 1655 (1987).
3. P. Zory and L. D. Comerford, IEEE J. Quantum Electron., Vol. QE-11, pp. 451 (1975).
4. R. D. Burnham, D. R. Scifres, and W. Streifer, IEEE J. Quantum Electron., Vol. QE-11, pp. 439 (1975).
5. G. A. Evans, J. M. Hammer, N. W. Carlson, F. R. Elia, E. A. James, and J. B. Kirk, Appl. Phys. Lett., Vol. 49, pp. 314 (1986).
6. N. W. Carlson, G. A. Evans, J. M. Hammer, M. Lurie, S. L. Palfrey, and A. Dholakia, Appl. Phys. Lett., Vol. 50, pp. 1301 (1987).
7. K. Kojima, S. Noda, K. Mitsunaga, K. Kyuma, and K. Hamanaka, Appl. Phys. Lett., Vol. 50, pp. 1705 (1987).
8. K. Mitsunaga, M. Kameya, K. Kojima, S. Noda, K. Kyuma, K. Hamanaka, and T. Nakayama, Appl. Phys. Lett., Vol. 50, pp. 1788 (1987).
9. S. H. Macomber, V. S. Mott, R. V. Noll, G. M. Gallatin, E. J. Gratrix, S. L. O'Dwyer, and S. A. Lambert, Appl. Phys. Lett., Vol. 51, pp. 472 (1987).
10. Z. L. Liau and J. N. Walpole, Appl. Phys. Lett., Vol. 46, pp. 115, (1985).
11. Z. L. Liau and J. N. Walpole, Appl. Phys. Lett., Vol. 50, pp. 528 (1987).
12. T. H. Windhorn and W. D. Goodhue, Appl. Phys. Lett., Vol. 48, pp. 1675 (1986).
13. J. P. Donnelly, W. D. Goodhue, T. H. Windhorn, R. J. Bailey, and S. A. Lambert, Appl. Phys. Lett., Vol. 51, pp. 1138 (1987).
14. J. J. Yang, M. Jansen, and M. Sergeant, Electron Lett., Vol. 22, pp. 438 (1986).
15. J. J. Yang, M. Sergeant, M. Jansen, S. S. Ou, L. Eaton, and W. W. Simmons, Appl. Phys. Lett., Vol. 49, pp. 1138 (1986).

RESPONSIVITY AND NOISE PROPERTIES OF A HIGHLY STABILIZED MOM POINT CONTACT DIODE FOR HIGH POWER MID IR DETECTION AND MIXING

C. Yu, and C. S. Tan
Department of Electrical Engineering
Greensboro, NC 27411

Abstract

Although electron tunneling devices, such as the MOM point contact diode, have proven to have fast response and be easy to fabricate, they are also plagued by fabrication related instabilities and non-reproducibilities that render them impractical and not amenable to investigations regarding their basic operating mechanisms. Mechanisms such as thermally assisted tunneling, plasmon conduction and irradiation switching impair diode responsivity and increase noise. We have arrived at a highly stabilized MOM point contact diode after extensive research that has reduced or eliminated most of the instabilities. The deliberately hooked whisker tip has removed expansion due to radiation heating, thus enabling us to study the thermally assisted tunneling mechanism. The well controlled etched whisker tip geometry enables us to clarify the role of plasmon conduction and plasmon modes in the tunneling junction. The known junction geometry aids in the understanding of switching and its prevention. Experimental results are presented on our study of these mechanisms with the stabilized diode.

Introduction

The metal-oxide-metal (MOM) point contact tunneling diode with its long, slender whisker antenna and sharp and delicate electrolytically etched tip in contact with a thin native metal oxide layer as the insulating tunneling barrier, has demonstrated its superior performance as a room temperature detector-mixer, operating from rf to the near infrared with mixing bandwidth reported in the hundreds of gigahertz. However, these highly desirable detector features, such as the long antenna with an extremely sharp tip for concentrating and enhancing the incident radiation field near the tunneling junction, are the very cause of structural instabilities that have hampered, if not, totally ruled out the practical use of such a diode. These fabrication related problems have also rendered study of diode basic operating mechanisms almost impossible. Attempts have been made by various research groups to arrive at other configurations, such as the discontinuous metal film diode¹ and the edge MOM² planar structures with some degree of success by trading electrical performance for mechanical stability.

We have long held the opinion that the MOM point contact diode is simpler to analyze and stabilize by virtue of its simple structure of a single junction. This was borne out in our successful fabrication of a stable diode. This also provides us with the opportunity to further improve the performance of the diode by the fact that we now have a handle on investigating the basic diode conduction mechanisms, since most instabilities have been removed.

Major instabilities of the diode have been identified by us to be mechanical, thermal and electrical for a typical MOM diode made up of a tungsten whisker and a nickel post with a thin layer of natural nickel oxide. By a systematic implementation of the electrolytic etching procedure, control of the oxide layer thickness and controlled hooking of the etched tip with prescribed shape, we have been able to produce and reproduce highly stabilized, hooked-tip point contact diodes with responsivity comparable to diodes with unhooked tips. Such hooked-tip diodes are highly immune to normal mechanical vibrations, electrical shocks or uncontrolled switching and ambient or incident radiation heating, thus the potential for high power operation. These diodes have thus been subjected to CO₂ laser irradiation for the purpose of establishing diode performance parameters.

CO₂ Laser and Diodes with Unhooked Tips

The typically unstabilized MOM point contact diode consists of a tungsten whisker and a nickel post with native oxide layer mounted as shown in Fig. 1. The whisker tip is moved into contact with the nickel post by a differential micrometer, and the entire diode mount is micromanipulated by an xyz θ translation stage such that the tip will be illuminated by a focused CO₂ laser beam. The detected signal is tapped from the BNC connector shown. The CO₂ laser beam is chopped and focused.

Figure 2 illustrates initial attempts at laser detection with the sharp-tip, unstabilized diode. The evidence of a detected signal is severely masked by noise, attributable to heating of the sharp tip. This is clearly verified in Fig. 3, where the laser beam is not chopped (the lower trace). A seemingly periodic signal is still recorded due most likely to periodic expansion and contraction of the sharp tip under laser irradiation. The tungsten tip expands when heated by the laser radiation deeper into the oxide layer until

contact is made with actual nickel surface. The latter then acts as a heat sink, cooling the tungsten tip in contact with it and causing it to contract. The electrical short is then broken, and the tip resumes detection. The removal of the heat sink, however, causes the tip to heat up and tip expansion ensues. This heating and cooling cycle repeats in a periodic fashion, hence the periodic signal even in the absence of chopping. This periodic signal persists even chopping resumes, and there is no correlation between their frequencies. However, as chopping rate increases, the detected laser signal frequency begins to follow the former, as is evidenced in Fig. 4. Here, thermal effect still persists as gently sloping envelopes, on which the detected signal rides as ripples. The envelopes are indications of diode resistance states under heating. As is even more vividly demonstrated in Fig. 5, where the I-V characteristic of the diode is monitored in conjunction with the detected signal. The ever changing resistance state of the diode reflects also erratic switching of the diode, as reported by others in Fig. 6. Threshold and memory switching of MOM structures has been extensively reported⁵ as the result of Joule heating by the incident field that exceeds the heat dissipation of the insulator, causing junction resistance to drop rapidly. As the ac field decreases in its cycle, the conduction channel cools down, and the high resistance state is restored. The high temperature state causes metal diffusion from the electrodes into the insulator, creating a conducting channel heavily doped with electrode metal particles. This discontinuous metal filament or channel gives rise to a nonlinear I-V characteristic, as charge carriers are forced to tunnel through high resistance insulating gaps to adjacent metal islands.

The Highly Stabilized MOM Point Contact Diode

Our major efforts in the stabilization of the point contact diode involve control of the whisker tip etching parameters, which in turn control the hooking parameters and oxide layer penetration depth of the eventual diode. By careful control of the immersion depth of the tungsten whisker into the 3N KOH solution, it is possible to control the shape of the etched tip as shown in Fig. 7. The optimum shape of the tip is deduced from its hooked shape after the tip has been mounted and brought into contact with the nickel post. It is clear that the slenderness of the initial tip controls the ultimate hook shape, as is seen in Fig. 8. For instance, Fig. 8 a indicates a blunted and damaged tip after contact; b and c show acceptable hooks, while d implies the tip is overly slender that leads to excessive hooking.

CO₂ Laser and Diode with Optimally Hooked Tip

Once an optimum slenderness is established, the whisker is mounted and brought in contact with nickel oxide layer, the penetration of which is carefully executed with the differential micrometer. Hooking of the whisker tip results from such a contacting process with an optimum shape that bears no damage to the tip and a minimum radius that places the tip at the closest proximity to the contact area.

Such a diode is then illuminated with focused chopped or pulsed CO₂ laser radiation. Detection is observed at various laser power levels and chopping speeds. Typical oscillograms are shown in Fig. 9. At higher laser power, the frequency of the detected signal follows that of the chopper with a certain degree of distortion, indicating lingering thermal effects. However, at lower laser power, the detected signal is quite well formed. This encourages us to make further refinement to the shape of the hook with expected result shown in Fig. 10. We can finally conclude that we have arrived at a simple design for a highly stabilized MOM point contact diode that can detect at reasonable laser powers.

Study of Diode Basic Parameters

The stabilized diode has been illuminated with 5 μ sec pulsed CO₂ laser radiation and also chopped cw CO₂ laser beam. The pulsed laser radiation does not introduce any heating effect, so that heating of the diode can be furnished by the cw laser. It is found that the diode sees very little thermal assisted tunneling effect, since it demonstrates highly sensitive detection characteristics to polarization or angle of incidence of the laser radiation impinging on the diode junction region. It is thus concluded that thermally assisted tunneling, if it exists, plays a minor role in the diode performance.

In view of the thermal origin of threshold and memory switching of the diode, as anticipated, the diode experiences little erratic switching unless laser heating is excessive. Further work is in progress to remove totally or utilize this type of switching by designing MOM electrode geometry and barrier thickness.

Since for frequencies ranging from the mid infrared to the visible, electron conduction on the whisker tip is nonohmic, but by surface plasmons¹ excited by the incident radiation, metal attenuation is dominant. This loss can be circumvented by forcing the major portion of the energy in the surface plasmons to be carried in the dielectric around the antenna². The tip shape factor is thus an important consideration in this respect. The polarization-sensitive data on detection is already an indication of the important role of the tip shape on plasmon conduction. We will proceed further with the correlation of the antenna pattern with the shape of the etched whisker tip.

These surface plasmons must then be guided by the whisker tip antenna and be efficiently coupled to the modes allowed in the MOM junction region in the form of a cavity bounded by metals at the two ends and filled with the thin layer of insulating oxide. The plasmon modes can no longer be excluded from the metals, leading to a very high anticipated junction attenuation. Impedance matching between the antenna and the junction cavity is thus a key factor in efficient coupling of plasmon modes to junction modes. We have observed some degree of degradation in diode responsivity due to hooking of the tip as compared to the sharp tip diode. In the case of the sharp tip, the cavity is virtually absent so that plasmon modes couple directly across the junction gap to the other electrode, resulting in very efficient coupling. On the other hand, the rounded knee of the hooked tip and the flat surface of the nickel post forms a well defined cavity, leading to high attenuation of the plasmon modes when coupled into this cavity due to very lossy metallic boundaries. A more exhaustive analysis and experimental verification is required to assess quantitatively the impact of hooking in this respect. Preliminary results have already indicated that excessive hooking renders the diode totally inoperative as a detector.

The junction plasmon modes modulate the electric field on the insulating barrier of width much shorter than a wavelength. An optical voltage due to the surface plasmon can thus be defined. This optical voltage oscillates at the frequency of the applied electromagnetic radiation and modulates the effective voltage across the barrier. The current through the barrier is hence also modulated, giving rise to a nonlinear I-V characteristic. The rectified component of this current is detectable and is proportional to the incident radiation power. Thus, study of the coupling between plasmon modes and tunneling electrons is of importance.

Conclusions

It has been discovered so far that simple hooking of the etched whisker tip without blunting has produced highly stabilized MOM point contact diodes against mechanical, thermal and electrical instabilities. As a natural next step, we have ventured into a closer look at the underlying diode operating mechanisms. Preliminary indications point to possible removal of thermally assisted tunneling and threshold switching as pluses and some degree of degradation in detection efficiency due to poor plasmon mode to junction cavity mode coupling as minuses. It is hoped a better understanding of correlation between diode structure and diode performance may lead to a hook that is not only mechanically and electrically optimum, but optically as well.

References

1. C. Yu, and A. Niczad, presented at the 10th International Conference on Infrared and MM Waves, Lake Buena Vista, Florida (1985), paper T5.8.
2. M. Heiblum, S. Wang, J. R. Whinnery, and T. K. Gustafson, IEEE J. Quantum Electron. QE-14, 159 (1978).
3. S. Manhart, J. Noncrystal. Solids 11, 293 (1973).
4. D. P. Siu, and T. K. Gustafson, Appl. Phys. Lett. 31, 71 (1977);
A. E. Craig, A. Olson, and Dror Sarid, Opt. Lett. 8, 380 (1983).

Acknowledgements: This research was performed under Navy Grant N00014-83-K-0569 and Army Research Office Grant DAAG29-83-G-0114.

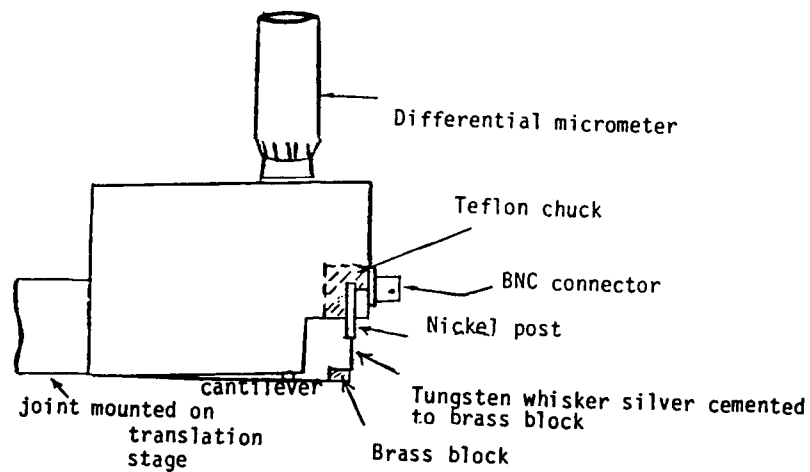


Fig. 1 . Schematic of mounting for laboratory MOM point contact diode

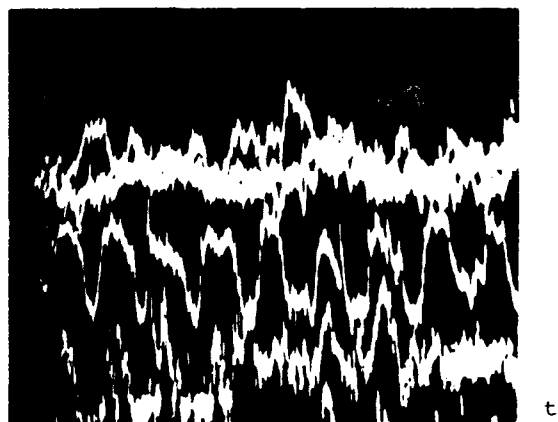


Fig. 2. Sharp tip diode response under chopped cw laser radiation.

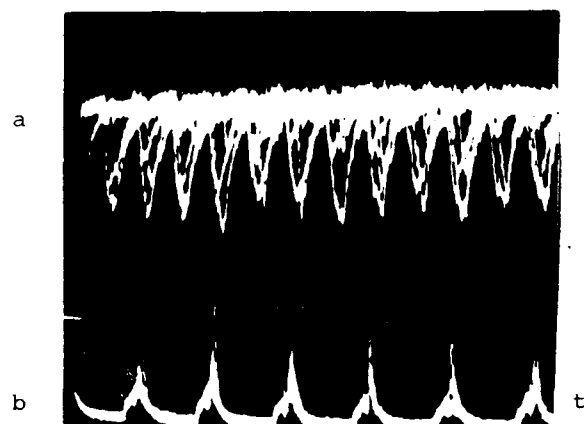


Fig. 3. Sharp tip diode response to chopped cw laser radiation (a); to unchopped cw laser (b).

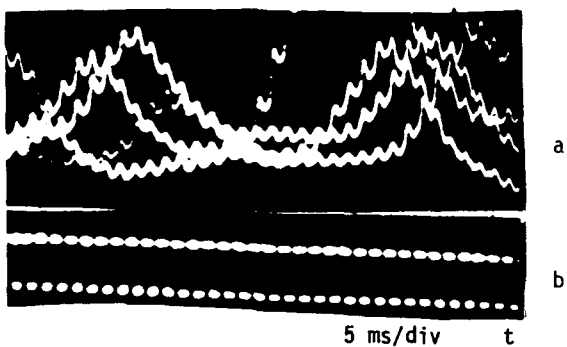
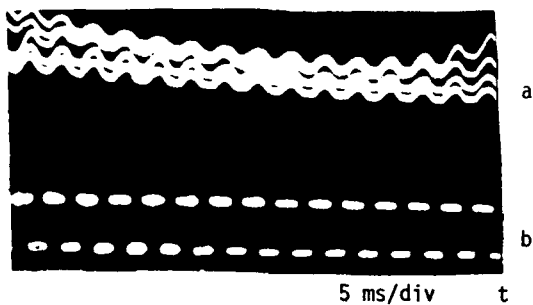


Fig. 4. MOM sharp tip diode response to chopped laser radiation (a) with varying chopper speeds (b).

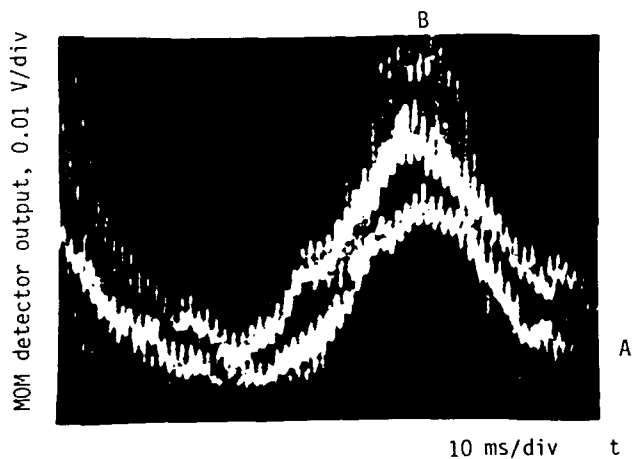
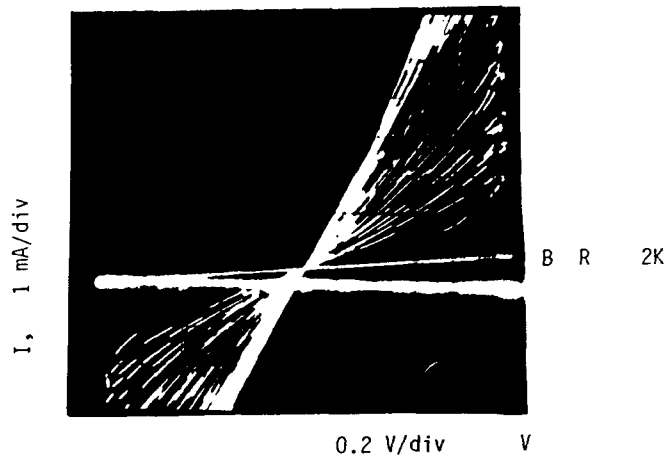


Fig. 5. Upper diagram: I-V curve of sharp tip diode, showing erratic switching;

Lower diagram: corresponding detector output signal in high and low impedance states.

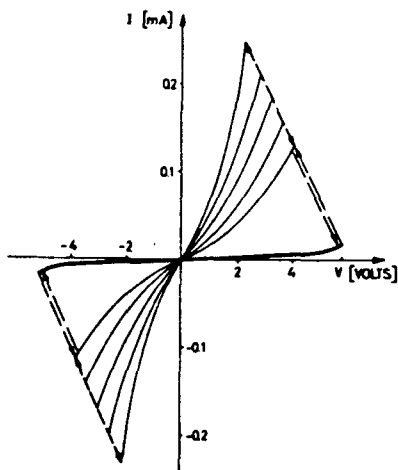


Fig. 6. Switching characteristic of the memory effect in Al-SiO-Ag with an unstable low impedance state. Element returns to high impedance state after some time. (from Ref. 4)

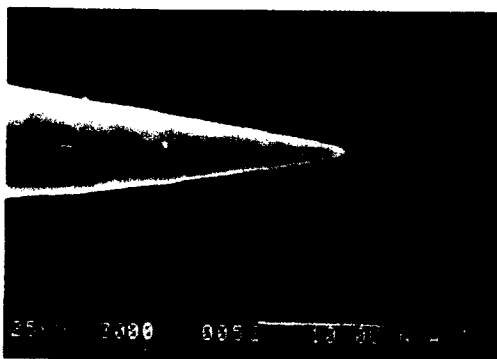


Figure 7a immersion
depth code

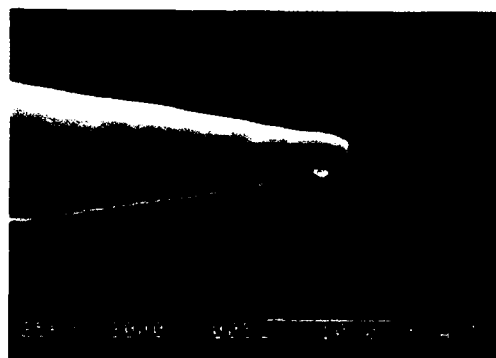


Figure 8a



Figure 7b

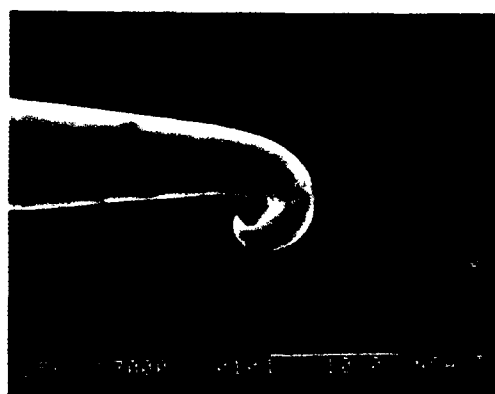


Figure 8b



Figure 7c



Figure 8c

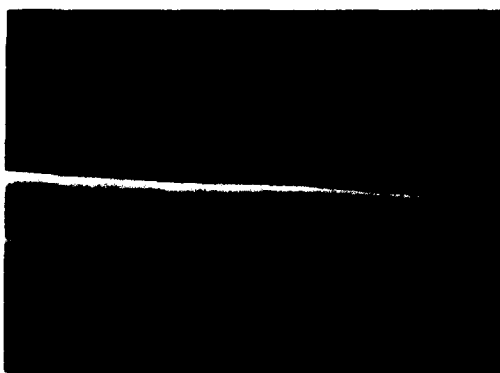


Figure 7d



Figure 8d

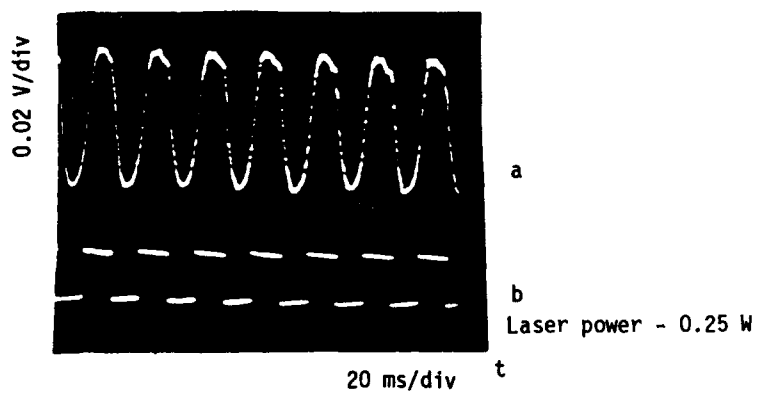
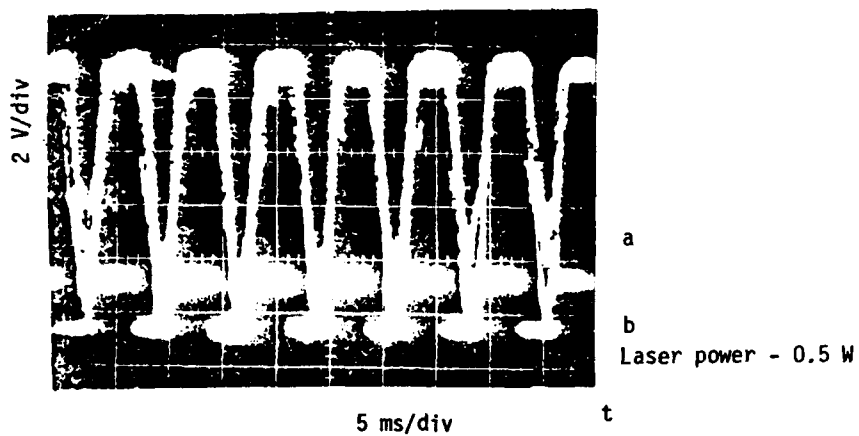
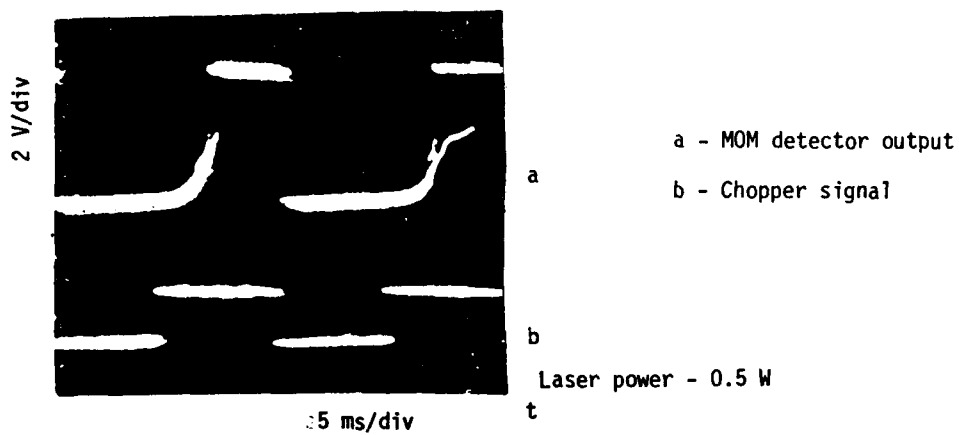


Fig. 9. Forked tip diode output at varying chopper speeds and laser power levels.

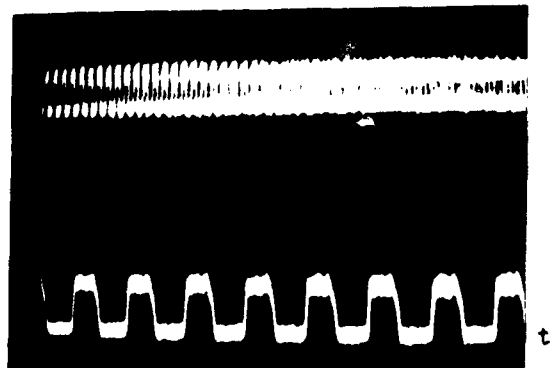


Fig. 10. Optimum hooked-tip diode output

COMPACT TEA CO₂ LASERS

Gary D. Spiers, Alan Sylvan, Alex Vass and Robert G. Harrison

Department of Physics
Heriot-Watt University
Riccarton
Edinburgh EH14 4AS, U.K.

Abstract

Following an overview of TEA CO₂ laser development a comparison of sliding spark array, corona and semiconductor preionisers was carried out using a compact, 5 cm³ discharge volume, TEA CO₂ laser. The corona technique was found to provide the best preioniser, with good pulse to pulse repeatability (~ 2%) over a wide voltage operating range from a simple and reliable device. In view of the potential longlife and robustness of all solid state drivers, such a unit was developed for this laser. This has a wallplug efficiency similar to that of the conventional thyatron and HV PSU driver.

Introduction

The first Transversely Excited Atmospheric (TEA) pressure CO₂ laser was reported by Beaulieu¹ in 1970. The major problem in obtaining a TEA discharge was the difficulty in preventing the preferential formation of arcs rather than a diffuse discharge. Beaulieu prevented this by using a series of resistively ballasted pins for the anode, thus preventing the high local currents associated with an arc discharge. In the same year Laflamme² proposed an alternative stabilisation technique using a low-voltage discharge between a third electrode and the cathode to provide a uniform electron distribution prior to the main discharge, thus enabling a uniform discharge to take place. The following year Lamberton and Pearson³ proposed a third discharge scheme utilising a trigger-wire suspended on either side of the electrodes mid-way between them; again to provide a preliminary ionising discharge. They claimed that this technique enabled higher concentrations of CO₂ to be used, resulting in a greater output power per unit discharge volume. In 1972 Javan⁴ and Levine⁵ proposed the possibility of photo-ionising the gas volume prior to discharge by either a two photon process acting on the CO₂ and N₂ molecules or a one photon process acting on an easily ionisable additive. The following year they demonstrated a photo-initiated discharge⁶ utilising Iri-n-Propylamine (InPA) as the easily ionisable additive.

In 1973 Wiegand et al.^{6,7} identified the major ions involved in the discharge kinetics and proposed that a high negative ion concentration would lead to discharge instability and eventually arcing. They also identified the formation of Oxygen as a result of CO₂ dissociation:-



In 1976 Shields et al.⁸ showed that 1-2% O₂ concentration in the lasing gas would lead to arc discharge formation.

The above summary outlines some of the early experimental and theoretical developments associated with TEA CO₂ lasers, leading to the identification of the following problems:-
(a) The need to be able to obtain a uniform diffuse discharge with high CO₂ concentrations.
(b) The need to suppress O₂ formation by CO₂ dissociation to enable sealed off operation to be achieved.

Attempts to reduce CO₂ dissociation have included the addition of CO to bias the dissociation reaction (eqn. (1)) in the reverse direction^{9,11,12,16}, the addition of H₂ to "pump up" O₂^{10,11,12,16} and the use of catalysts to recombine the dissociation products^{2,10,14,15}.

A summary of notable sealed/semi-sealed TEA CO₂ lasers is given in table 1.

Preionisation is a key factor in determining the extent of the problems outlined above and our report details work carried out on the direct comparison of various preionisers suitable for a compact sealed TEA laser.

For high pulse rates (> = 1 kHz) the lifetime of the thyatron (~ 10⁹ pulses) can become a limiting factor and in view of the potential cheapness of all solid state drivers over the conventional thyatron and HV PSU driver it was decided to investigate this technique.

Group	Year	Max. PRF	Preionisation	Life (pulses)/ Bleed Rate	Additives/ Catalysts
Stark et al. ⁹	1975	2 Hz	Trigger-wire	2×10^6	CO, H ₂
Stark et al. ¹⁰	1978	1 Hz	Sliding-spark	3×10^5	hot Pt
Pace et al. ¹¹	1978	100 Hz	3rd Electrode	2×10^6	H ₂ , CO
Menyuk et al. ¹²	1980	500 Hz	Spark	2 L/Min	InPA, H ₂
Rickwood et al. ¹³	1982	5 kHz	Semiconductor	10 L/Min	
Pace et al. ¹⁴	1982	2 Hz	Silicon Carbide	$\sim 10^6$	SnO + Pt
Stark et al. ¹⁵	1983	30 Hz	Semiconductor	2×10^7	SnO + metal
Marchetti et al. ¹⁶	1985	1 kHz	Corona	2×10^7	H ₂

Table 1. Important Compact Sealed/Semi-Sealed CO₂ TEA Lasers.

The second part of the report outlines work conducted on the development of an all solid state laser driver circuit. This utilises a semiconductor device to switch a long low voltage pulse onto a high voltage transformer. The high voltage pulse generated is then subsequently compressed in time by successive magnetic compression stages to provide a pulse of sufficiently short duration to drive the laser. The technique of using a series of saturable inductors to obtain pulse compression was first proposed by Melville¹⁷ in 1951 and the first all solid state CO₂ TEA laser driver was reported by Shimada et al.¹⁸ in 1985. This was used at a PRF of 1 Hz. In 1986 Baker et al.¹⁹ reported an all solid state driver with a PRF of ≤ 50 Hz.

Preionisation

Experimental Details

There have been many preionisation techniques applied to TEA CO₂ lasers; these have included various spark systems, corona, semiconductor, e-beam, alpha-particle and x-ray systems. Most of these are unsuitable for compact lasers and we have concentrated on sliding spark^{20,21}, corona²² and semiconductor²³ systems.

The preionisers were tested in an axial flow TEA laser, consisting of two stainless steel electrodes utilising a simple radius of curvature approximation to a Chang profile. These defined a discharge volume $9.5 \times 0.6 \times 0.8$ cm³ ($1 \times d \times w$) = 4.6 cm³. A standard 12:14:74 CO₂:N₂:He gas mix flowing at 10 L/Min was used. The resonator was formed by a gold plated mirror (R = 10 m, reflectivity 99%) and a flat ZnSe output coupler (reflectivity 85% at 10.6 μ m) to provide a 15 cm cavity.

The sliding spark preionisation consisted of 2 longitudinal spark arrays, each of four 2 mm tungsten spark gaps mounted 25 mm from the laser axis. The preionisation and main discharge circuits (fig. 1(a)) were independent, to enable the delay between the preionising and main discharges to be varied.

The corona preionisation consisted of two etched double sided pcb's each running the length of the discharge in direct contact with the electrodes. Their design was similar to that of Hasson and Brink²⁴. The back surface of the preionisers was connected to the laser anode using brass shim sheet to provide low inductance. The discharge circuit used is shown in Fig. 1(b).

The semiconductor preionisation was provided by two $1.5 \times 0.2 \times 10$ cm³ pieces of 50 Ω -cm germanium placed directly in contact with both electrodes on either side of the discharge.

Results

The optimum delay between the preionising and main discharges for the sliding spark preionisers was found to be ~ 500 ns. Figs. 2 and 3 show the energy output and relative efficiencies for the various preionisers. It was found that the maximum PRF for the sliding spark array was 18 Hz, compared to 25 Hz (power supply limited) for the other systems. A dark deposit formed on the electrodes whilst the sliding spark was in use and this led to a reduction in the output energy (fig. 4), resulting in the need to clean the electrodes at regular intervals. This deposit did not occur with the other two preioniser systems.

Discussion

In directly comparing the output energy results for the three systems care must be taken because of the change in electrical circuit between the sliding spark system and the other preionisers. The lower maximum PRF and the deposit formed on the electrodes, however, lead us to believe that this preionisation system dissociates the CO_2 more than the other systems, with the Oxygen formed reacting with the tungsten pins² to form tungsten oxide^{2b}, which is the deposit on the electrodes. This deposition has been observed previously. It was found that the highest efficiency was obtained with the sliding spark technique, whilst the semiconductor technique provided the lowest efficiency. The reliability of the spark system was not very good, due to the need to regularly clean the electrodes. The corona technique was found to be very reliable, with the current preionisers having operated for $> 10^6$ shots with no evidence of any deterioration. Based on other peoples results, it has been assumed that the semiconductor is as reliable. A comparison of simplicity of use and relative costs was made and a summary of the conclusions to this comparison is given in table 2.

Property	Sliding Spark	Corona	Germanium
Simplicity	Extra circuitry	Simple	Simple
CO_2 dissociation	High ¹	Low	Low
Efficiency	Best	Moderate	Low
Voltage range	Limited	Wide	Wide
Pulse reproducibility	5%	2%	2%
Maximum PRF ²	18 Hz	25 Hz ³	25 Hz ³
Relative costs	High	Low	Moderate
Reliability	Poor	Very good	Very good

1) Provides oxide contamination

2) For 10 L/Min gas flow

3) Limited by HV power supply

Table 2. Summary of Preionisation Techniques

As a result of these investigations, the corona preioniser was chosen as the most suitable for our purposes. It should be noted however that other authors² have shown that higher resistivity semiconductors produce better preionisation than the low resistivity type used by us.

Following on from this work, investigations were carried out into optimising the discharge circuit and the final circuit is shown in Fig. 5, where C_{store} and C_{pk} have the values 20 nF and 1.2 nF respectively. The laser was also grating tuned, to see if an SLM output could be obtained. A typical pulse is shown in Fig. 6 and the tuning range of the laser in Fig. 7. No 9 μm lines were obtained because the output coupler was coated for 10 μm only. A summary of the laser characteristics is given in Table 3. It should be noted that these figures are for the 12:14:74 $\text{CO}_2:\text{N}_2:\text{He}$ mix and for an unoptimised cavity arrangement. The laser was tested using other gas mixes and it was found that the discharge was stable for most gas mixes tried, including those with high CO_2 concentrations ($> 50\%$).

Discharge volume	4.6 cm ³
Preioniser	Corona
Cavity length	
grating tuned	18 cm
Untuned	15 cm
Single longitudinal mode demonstrated	
Peak power	200 kW
Pulse energy	38 mJ
Maximum pulse rate ¹	70 Hz
Optimum operating voltage	10 kV
Input energy densities	100-370 J/L
Wallplug efficiency	2%

1) limited by restrictions in gas flow.

Table 3. Laser Specification.

In this form the laser was used to investigate two photon absorption in InSb and a report of this work will appear elsewhere.

All Solid State Driver Techniques

Experimental Details

As mentioned above it was decided to investigate all solid state drivers because of their potential longlife and cheapness compared to conventional thyatron and HV PSU drivers. They are also more resistant to large reverse currents than the conventional circuit. Ferrite cores were chosen for the saturating inductors because they are readily available and have lower losses than the alternative amorphous metal cores. The design of the cores was based on the E-core design of Baker et al.

A simplified circuit is shown in Fig. 8, where S1, S2, S3 are the saturating inductors. The circuit uses demand charging to resonantly charge Cstore which is then discharged through the high voltage transformer into C1. S1 is designed to saturate when C1 is fully charged, enabling C1 to charge C2 through S1 in a time $T1 = \pi(S1(sat) \times C2/2)^{1/2}$. When fully charged, S2 then switches enabling C3 to charge up. When C3 is fully charged, S3 saturates enabling C3 to discharge into the load. For pulse compression to occur at each of the stages $S1(sat) > S2(sat) > S3(sat)$.

Results

Figs. 9-12 show the change in the voltage pulse as it progressively passes down the high voltage circuit at C1-C3 and the laser head respectively. A summary of the effect of the various stages is given in Table 4.

<u>Stage</u>	<u>Pulse FWHM</u>	<u>Ratio</u>	<u>Efficiency</u>
Transformer	6 μ S	-	70%
S1	2.3 μ S	2.6	96%
S2	0.8 μ S	2.9	76%
S3	0.2 μ S	4 (a)	-

(a) includes effect of peaking capacitor.

Table 4. Compression Stage Performance.

A comparison with the conventional HV PSU and thyatron technique as a function of stored energy is shown in Fig. 13. Using the solid state driver the laser has been successfully run at a PRF of 70 Hz, limited by the gas flow, and the pulser has been tested into a resistive load at PRF's up to 500 Hz with no obvious problems.

Discussion

From fig. 13 we see that the output from the magnetic system is more dependent on the stored energy than the conventional discharge technique. This is because the efficiency of the compressor stages falls away quite rapidly when they are operated away from their design specification. The magnetic pulse compressors were found to be between 75% and 96% efficient, depending on the stage, whilst the high voltage transformer was only 70% efficient. These values are not the optimum, particularly for the transformer stage, which is currently being redesigned and an efficiency of $\sim 96\%$ should be feasible²⁶ for this stage. Baker et al.²⁷ found that the slow rising edge of the voltage pulse created problems with their spark preionisation system leading to discharge uniformity problems. However, we have found that using the corona technique outlined above, no problems have so far arisen. It is noticeable that the all solid state driver has the same efficiency as the conventional HV PSU and thyatron circuit for an input energy of 1.4 J, despite the losses in the circuit elements. This suggests that either the longer pulse from the all solid state driver is coupled into the laser head more efficiently than the thyatron derived pulse or that for the small laser discharge volume used, the large thyatron discharge volume represents a significant energy loss. This is currently being investigated.

Conclusion

For the laser head under consideration, the corona preionisation technique was chosen over the sliding spark and semiconductor techniques because of its ability to provide reliable preionisation simply. An all solid state driver circuit was demonstrated to

70 Hz on the laser head with an efficiency equivalent to that of the conventional HV P50 and thyatron pulser system.

Future developments will incorporate these devices in a sealed high repetition rate laser.

References

1. A.J. Beaulieu, Appl. Phys. Lett., 16, 504 (1970).
2. A.K. Laflamme, Rev. Sci. Instrum., 41, 1578 (1970).
3. H.M. Lamberton, P.R. Pearson, Electron. Lett., 7, 141 (1970).
4. A. Javan, J.S. Levine, IEEE J. Quant. Electron., QE-8, 827 (1972).
5. J.S. Levine, A. Javan, Appl. Phys. Lett., 22, 55 (1973).
6. W.L. Nighan, W.J. Wiegand, R.A. Haas, Appl. Phys. Lett., 22, 579 (1973).
7. W.J. Wiegand, W.L. Nighan, Appl. Phys. Lett., 22, 583 (1973).
8. H. Shields, A.L.S. Smith, B. Norris, J. Phys. D: Appl. Phys., 9, 1587 (1976).
9. D.S. Stark, P.H. Cross, H. Foster, IEEE J. Quant. Electron., QE-11, 774 (1975).
10. D.S. Stark, P.H. Cross, M.R. Harris, J. Phys. E: Sci. Instrum., 11, 311 (1978).
11. P.W. Pace, M. Iacombe, IEEE J. Quant. Electron., QE-14, 263 (1978).
12. N. Menyuk, P.F. Moulton, Rev. Sci. Instrum., 51, 216 (1980).
13. K.R. Rickwood, J. McInnes, Rev. Sci. Instrum., 53, 1667 (1982).
14. P. Pace, P. Mathieu, J. Cruickshank, Rev. Sci. Instrum., 53, 1861 (1983).
15. D.S. Stark, A. Crocker, N.A. Lowde, J. Phys. E: Sci. Instrum., 16, 1069 (1982).
16. R. Marchetti, E. Penco, G. Salvetti, IEEE J. Quant. Electron., QE-21, 1766 (1985).
17. W.S. Melville, Proc. IEE (London), 98, 185 (1951).
18. T. Shimada, K. Noda, M. Obara, K. Midorikawa, Jap. J. Appl. Phys., 24, 1855 (1985).
19. H.J. Baker, P.A. Ellsmore, E.C. Sille, presented at CLEO '86, San Francisco (1986), paper WK27.
20. O.P. Judd, Appl. Phys. Lett., 22, 95 (1973).
21. M.C. Richardson, K. Leopold, A.J. Alcock, IEEE J. Quant. Electron., QE-9, 934 (1973).
22. V.N. Ischenko, V.N. Lisitsyn, V.P. Safonov, A.R. Sorokin, Sov. J. Quant. Electron., 5, 738 (1975).
23. K.R. Rickwood, J. Appl. Phys., 53, 2840 (1981).
24. V. Hasson, D.J. Brink, J. Phys. E: Sci. Instrum., 12, 976 (1979).
25. A.L.S. Smith, B. Norris, J. Phys. D: Appl. Phys., 11, 1949 (1978).
26. H.J. Baker, P.A. Ellsmore, E.C. Sille, presented at the 17th Power Modulator Symposium, Seattle (1986), paper R243.
27. H.J. Baker, P.A. Ellsmore, E.C. Sille, presented at the 8th National Quantum Electronics Conference, St. Andrews (1987), paper 21P.

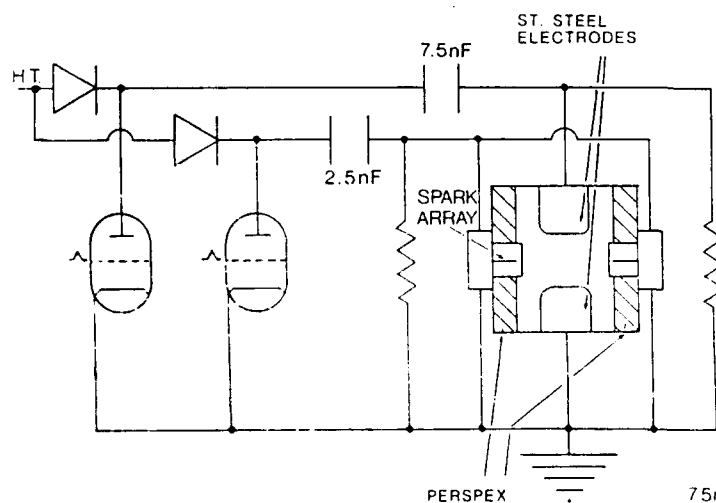
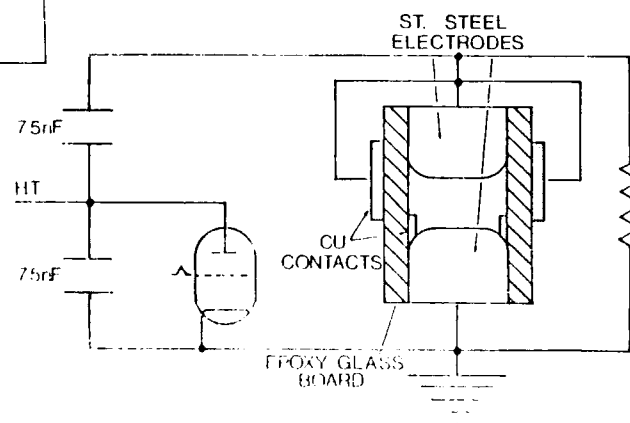


Fig. 1(a). The discharge circuit used with the sliding spark preionisers.

Fig. 1(b). The discharge circuit used with the corona and semiconductor preionisers.



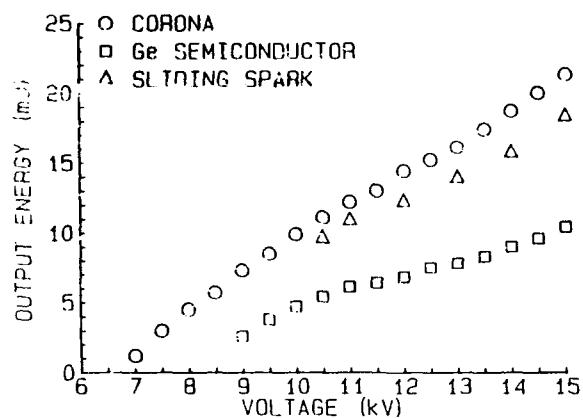


Fig. 2. The output energy dependence on charging voltage for the three preionisers.

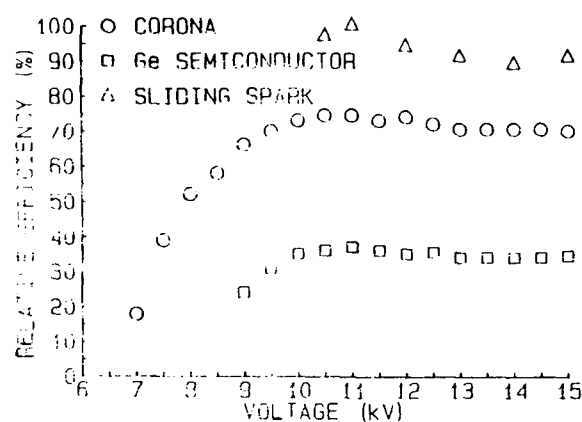


Fig. 3. The relative efficiency of the three preionisers as a function of charging voltage.

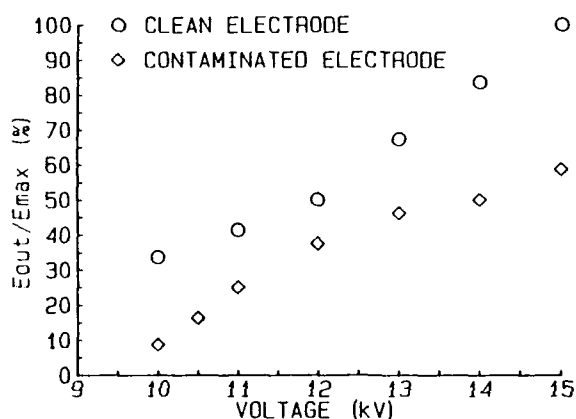


Fig. 4. The output energy dependence on contamination of the electrodes by oxide from the sliding spark preioniser.

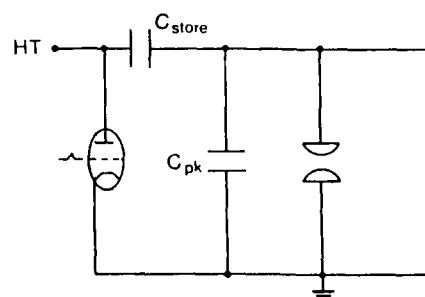


Fig. 5. The final discharge circuit, where $C_{store} = 20 \text{ nF}$ and $C_{pk} = 1.2 \text{ nF}$.

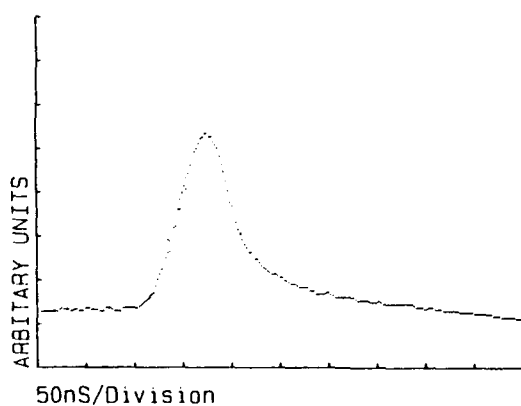


Fig. 6. A typical 50 ns output pulse from the grating tuned laser.

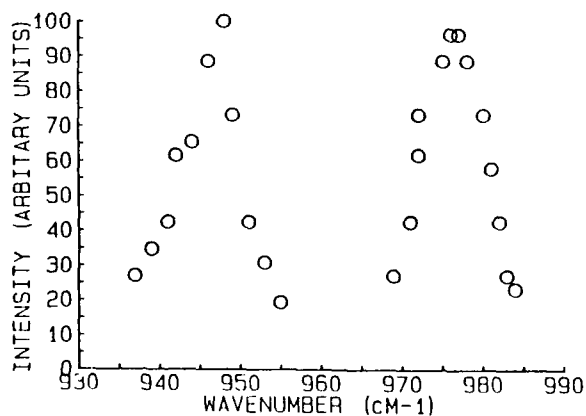


Fig. 7. The tuning range over the 10 μm P and R branches.

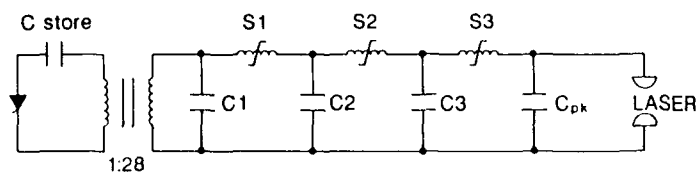
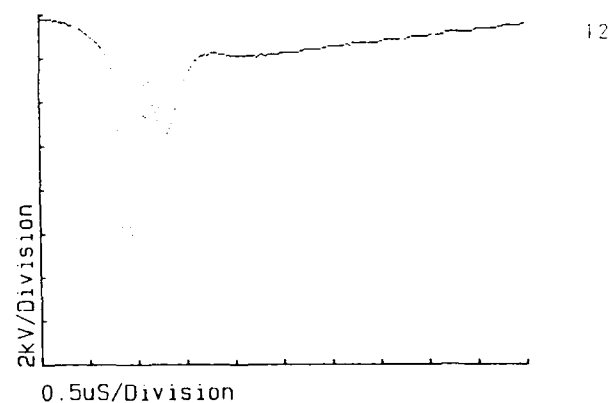
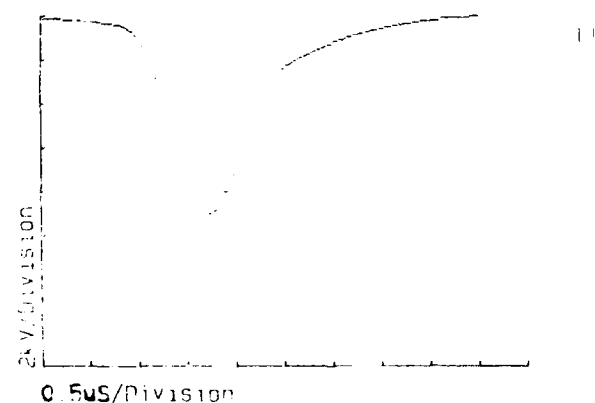
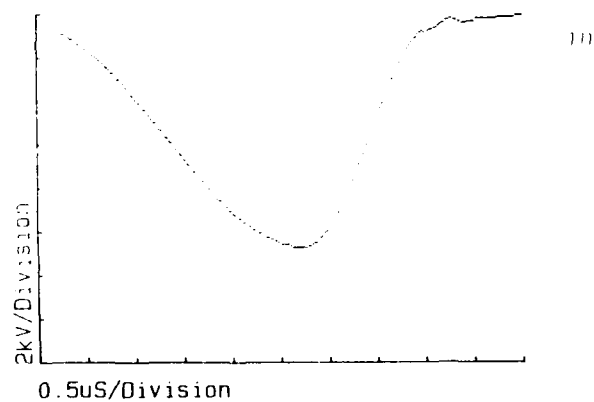
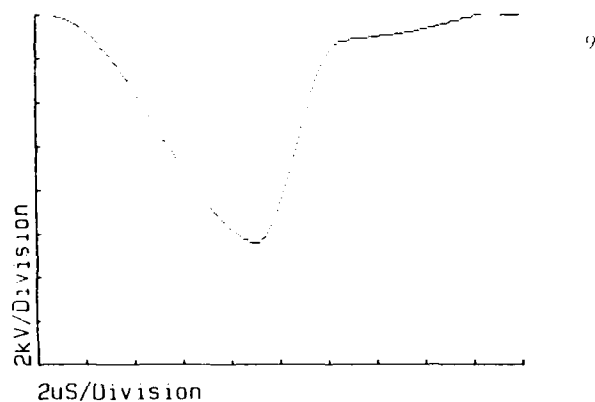


Fig. 8. The all solid state discharge circuit.



Figs. 9-12. The compression of the voltage pulse as it passes down the saturating inductor chain. The voltages were measured at C1, C2, C3 and the laser head respectively.

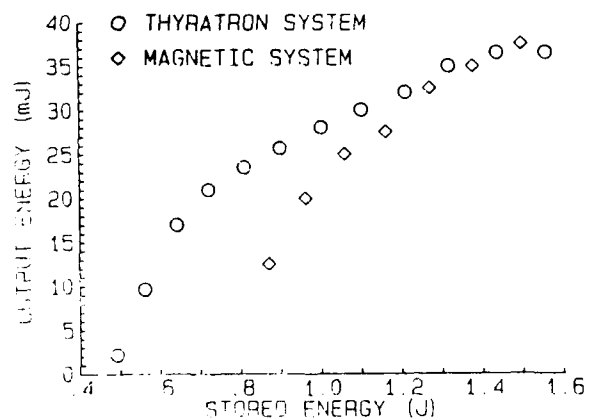


Fig. 13. The output energy dependence on the stored energy for the all solid state and conventional thyatron HV PSB driver circuits.

TE CO₂ LASER DEVELOPMENT AT THE DEFENCE RESEARCH ESTABLISHMENT, VALCARTIER

Paul Pace, Pierre Mathieu and Silvester Wong

Defence Research Establishment Valcartier
P.O. Box 8800, Courcellette, P.Q., G0A 1P0

Abstract

This paper presents a summary of results achieved in the development of TE CO₂ lasers sources. Sealing techniques (catalysts), frequency ability, graded reflectivity optics, miniaturization, and mode selection will be discussed. An indication of future research areas will also be discussed.

Introduction

This overview summarizes the work carried out at the Defence Research Establishment Valcartier during the past several years concerning the development and study of CO₂ lasers. These lasers have been developed for transmitters in coherent detection radar systems as well as miniature rangefinder systems and various other applications involving pulsed and CW CO₂ lasers. The studies have included the investigation of lifetime characteristics, frequency stabilization, sealing techniques, beam quality, pulse characteristics and waveguide laser development.

Unstable Resonators with Graded Reflectivity Mirrors

To improve the near-field beam quality and other drawbacks to standard unstable resonator CO₂ lasers, DREV has investigated the use of graded reflectivity mirrors in a Cassegrain resonator.¹ This allows the production of a fundamental transverse mode of large cross-sectional area. For the preliminary investigations, the test laser had a 50-cm long optical cavity and a 2 x 2 x 30 cm³ TE-CO₂ gain section. The unstable resonator configuration used mirrors with a Gaussian reflectivity profile and a magnification of 1.2. It was found that in a full-angle beam divergence of 1.3 mrad, the gaussian mirror system contained 70% of the total laser output while only 3% was obtained for a conventional unstable resonator and only 3% for a stable resonator was measured. By using injection-locking techniques or by using a short-laser cavity, single-mode operation has been achieved. Using heterodyne detection, "chirp" rates as low as 60 kHz/μs² have been measured. These low "chirp" rates are a result of having a large laser mode.² Also, it is expected that a pulse-to-pulse frequency instability of 500 kHz can be obtained. Therefore, this laser source can produce an output with almost all the desired characteristics for a laser radar transmitter and it may also be useful in applications involving velocity measurements.

Catalyst in CO₂ Lasers

About 10 years ago, DREV supported the industrial development of a TEA-CO₂ laser using a hot-platinum catalyst to minimize gas consumption. Although being very effective, large amounts of power were required to heat the catalyst and then cool the gas after it had been in contact with the hot platinum. More recently, we have developed a catalyst consisting of stannic oxide and noble metals.³ The use of catalysts based on SnO₂ was first reported in the United Kingdom in 1983.⁴ Tests have also been carried out by GEC Avionics where an SnO₂ catalyst on a monolith gave more than 5 x 10⁷ pulsed at a 30-Hz pulse repetition rate in a TEA-CO₂ laser. NASA Langley Research Center has also tested a Pt-SnO₂ catalyst in a commercial TEA-CO₂ laser with excellent results.

We have also developed and evaluated SnO₂ catalysts as well as bimetal and trimetal materials. Efficiencies 2-3 times greater were found for the bimetal and trimetal product over the monometal catalyst. Several experiments have been carried out in which the catalyst powder was contained in the hollow centres of sintered stainless-steel filter elements and placed in miniature TEA-CO₂ lasers. With no forced gas circulation, it was found that 5 g of catalyst were required to maintain the lasers output at 90% of its original value at a pulse repetition rate of 1 Hz over 10⁶ pulses. More recently, we have carried out the experiments in a modified Lumonics 820 TEA-CO₂ laser. The laser was capable of operating at an output level of > 1 J/pulse and at a pulse repetition rate of 50 Hz. For the initial experiments, 15 g of catalyst were placed in the stainless-steel elements and then mounted in the laser enclosure in direct contact with the high-speed transverse gas flow. No additional heating or gas circulation was provided. The results of a typical experiment are shown in Figure 1. Tests have also been carried out to more

than 2×10^6 pulses over a period of three days. It was noticed that there was almost a complete recombination of the dissociation products during the 16 hours that the laser was off overnight. It is therefore feasible to considerably reduce the gas consumption of a commercial laser using moderate amounts of catalyst. This would obviously have an impact in the operating and maintenance cost of these lasers.

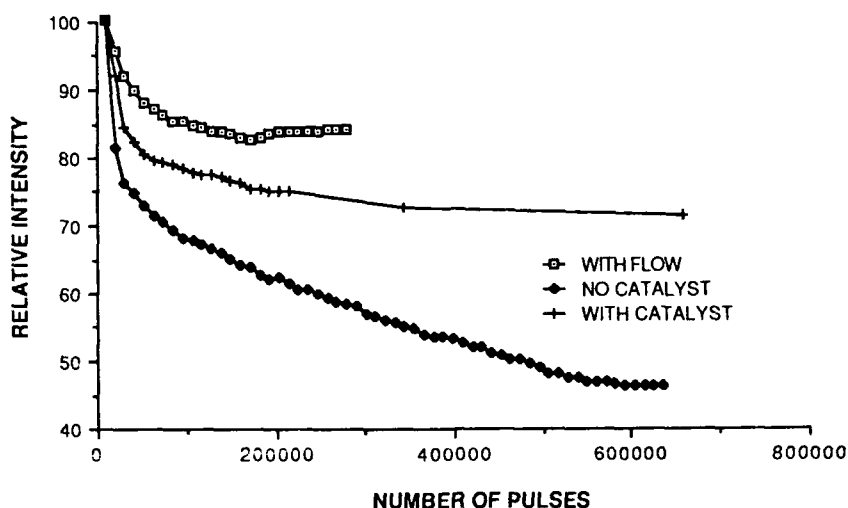


Figure 1. Relative Laser Output VS Number of Pulses "With Flow" indicated a 'make-up' flow of 14 l/min. The laser was completely sealed for test with the catalyst

Injection Locking and Mode Selection in TEA-CO₂ Lasers

In the past, DREV has devoted a considerable effort to the development of frequency stabilized sources for applications involving heterodyne detection methods. Theoretical as well as experimental studies have been performed in the areas of injection and mode selection in TEA-CO₂ lasers for stable, unstable and variable reflectivity unstable resonators. Models based on the competition between the injected signal and spontaneous emission have been developed to describe the transient evolution of the different field amplitudes and phases together with their effect on the inversion.⁵

Results have been obtained over a wide range of injection levels, detuning frequencies and resonator types.

The results indicate three zones of operation: a frequency-locking zone, a mode-selection zone and a region where the injected signal has no effect. It has been found that, because of the transient nature of the TEA laser, a competition between the noise and the injected signal takes place and a pulling of the injected signal carrier frequency toward the resonator mode frequency occurs. The competition between the noise and the injected signal will determine which one will grow more rapidly and depopulate the active medium. The noise amplitude is generally much weaker than the injection level although its effective gain is higher. The injection field is stronger, but its net gain is smaller because it suffers a phase change through each cavity transit and therefore it is no longer in phase with the original injection frequency. Depending upon the injection level and cavity detuning, either the noise or the injection signal will reach saturation first. Thus we must have high injection levels and small cavity detuning to obtain the desired result. Also, the time-varying phase experienced by the injection signal becomes a frequency modulation that pulls the frequency of the field toward that of the nearest resonator mode.

Experiments have been performed with several different TEA-CO₂ lasers. The latest version was based on a modified Lumonics 820 laser that produced an output of 1 J/pulse at a 50 Hz repetition rate. An optimized, variable-reflectivity unstable resonator was used in these experiments. A typical result for this as well as other systems is shown in Figure 2. The ordinate represents the difference between the TEA-laser-pulse frequency and the local-oscillator frequency and the abscissa shows the resonator-mode frequency. Zones of single-mode operation are shown for two different injection levels.

As can be seen from Figure 2, the cavity frequency and the heterodyne frequency are linearly related with unity slope. Therefore, the frequency of the TEA pulse follows that of the TEA resonator inside as well as outside the single-mode zone. For all injection levels investigated, the TEA pulse is influenced by the injection signal, but its frequency is that of the cavity mode and not that of the injection signal. The frequency locking range could not be studied experimentally because of the resolution of the equipment.

Another observation is the asymmetry of the mode selection range about the zero-beat frequency. We believe that this can be explained from a chirp cause by the decreasing electrons density during the tail of the excitation pulse. This effect has been explained by Willets and Harris.² This chirp occurs during the time when there is a competition between the noise and the injected signal and results in the TEA laser frequency being lower than that of the injection signal.

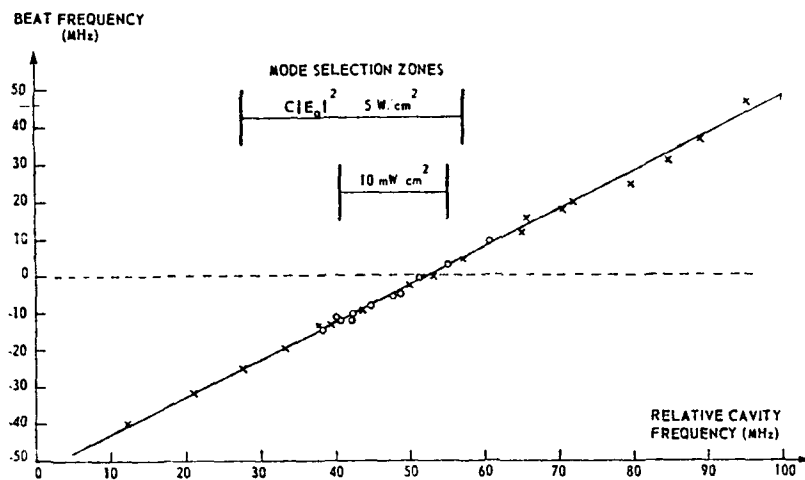


Figure 2. Experimental plot between the TEA laser pulse and a local oscillator as a function of the relative cavity detuning frequency

Miniature Sealed CO₂ Lasers

Several applications have been envisaged for small, sealed and portable CO₂ lasers. The most prevalent at the present time are target designation and rangefinding. These applications pose some unique and challenging requirements on the laser design. These volume efficient lasers must maximize optical peak power while at the same time optimizing the pulse shapes to conform with the optical detection system in use. Typically, optical pulse widths are in the range from 35-70 ns with rise times less than 25 ns. The exact shape of the pulse is also important. Pulses with a minimum tail duration are required if we wish to reduce the short range backscatter. The laser must also operate in sealed-off conditions for several million pulses.

In the design of a laser that will be used in a transportable apparatus, several factors have to be addressed. A significant effort was placed on the development of a modular system, economic construction, rugged and reliable performance, a wide temperature range of operation and resistance to harsh environmental conditions. The laser discharge was based on the standard technique or capacitive corona preionization. We used nickel electrodes defining a discharge volume of about $0.6 \times 0.6 \times 13 \text{ cm}^3$. The electrodes were profiled to give a uniform discharge. The laser resonator was formed using a total reflector and a partially transmitting output coupler separated by about 20 cm. The total reflector is a gold-on-copper design with a radius of curvature of 10 m. The output coupler was flat germanium window with a reflectivity of about 70%. The entire electrode structure and preionization were mounted inside a stainless-steel box of dimensions $5 \times 4 \times 20 \text{ cm}^3$. A catalyst was also included to promote long operational lifetimes. The stainless-steel box was designed in two sections. It was laser welded after the electrodes and catalyst were inserted. The high voltage electrical feed through was also welded to the laser enclosure. Finally, the laser mirror and output coupler were hard sealed to the enclosure using a low-temperature soldering technique.

To simplify construction and reduce the overall complexity of the laser we have used a pressure-relay initiated discharge system. The PFN consist of an energy storage capacitor (> 2 nF) and the relay. The capacitor is charged to voltages of about 20 kV by a switching supply operating in the demand recharge mode.

The laser produced output powers of about 100 mJ when operated at atmospheric pressure with a mixture $\text{He:N}_2:\text{CO}_2=50:10:40$. A low concentration of the N_2 was used to reduce the duration of the pulse tail. Beam divergence was measured to be about 5 mrad and the FWHM of the initial output spike was 37 ns. Operation to over a million pulses has been obtained and shelf life of six months has been demonstrated. The tests on storage lifetimes is continuing.

Supra-Atmospheric CO_2 -TE Lasers and Frequency Conversion by Stimulated Raman Scattering and Four-Waves Mixing

Frequency agile laser sources are needed for remote detection of atmospheric pollutants and gases, for laser photochemistry, for isotope separation and for military applications. In most of these applications, narrow-bandwidth high-energy output at the resonance vibrational frequency of selected molecules are needed. The spectral region of interest is roughly the 2 to 10 μm band. Since the different molecular lasers (CO_2 , CO, HF, DF) cover only a relatively small portion of this band, methods have to be developed to increase the spectral coverage. Nonlinear-optical methods (harmonic generation, parametric mixing, stimulated Raman scattering) can be used but much work is still needed in order to fulfill the requirements.

Because of its high efficiency and relatively broad gain-bandwidth, the CO_2 laser is one of the best pump source for frequency conversion. On the one hand, high conversion efficiency ($> 30\%$) have been achieved by stimulated rotational Raman scattering in H_2 and D_2 by using multiple pass cells.⁶ Output in the 13 to 18 and 11 to 14 μm band was thus achieved. On the other hand, resonant and near resonant pumping by a CO_2 laser of molecular gases like NH_3 , CF_4 , CH_3F , OCS , C_2D_2 and their different isotopic species has led to a large number of discrete laser lines in the 10 to 20 μm band.⁷ Particularly interesting are the recently observed effects in NH_3 and CH_3F in which four-wave mixing was demonstrated. In these experiments the absorption of one pump photon nearly resonant with an P branch absorption line led to the simultaneous emission of two rotational transition photon in the far infrared (FIR) and a P branch photon in the mid infrared (MIR).⁸⁻⁹ Since at the end of this process the molecule is in the same energy level as at the beginning, no saturation or depletion of the molecular levels is observed. This may lead to very high-efficiency conversion of the pump photons at high power levels.

If any of the frequency conversion technique, and particularly the last one, can provide an efficiency of 50% or more, then it could probably be a basis for a "beam-cleanup" system. In such a system, a poor-quality beam, but high-power pump pulse is frequency converted to a high-spatial-quality output beam. Raman "beam-cleanup" systems have been shown usefull for improving the output of excimer laser systems.¹⁰ They could also be usefull for improving the beam quality of large aperture high energy CO_2 -TEA lasers. Theoretical as well as experimental studies are needed to investigate the possibility of using the four-wave-mixing technique for beam "clean-up" systems in the infrared.

If any of the frequency conversion techniques we have discussed, the tunability of the pump source is of prime importance. For this reason the supra-atmospheric pressure, CO_2 -TE laser has proved to be the most versatile pump source.¹¹ Work at DREV on this type of source goes back to the mid 1970's.¹² More recently we have built a supra-atmospheric pressure CO_2 TE laser of a modern design which produces up to 1.2 J pulses in 50 nsec from a $1 \times 1 \times 35$ cm^3 , 12 atmosphere gain section. This laser is now being fitted with a 6X telescopic resonator and a 100 mm wide grating to produce narrow-band (0.3 cm^{-1}) = 400 mJ pulses tunable over about 60 cm^{-1} in the 9.2 to 10.8 μm band. It will be used to investigate the possibility of efficient frequency conversion and "beam-cleanup" by nearly resonant four-waves mixing in molecular gases.

Discussion

During the past several year, DREV has placed a considerable effort on the development of CO_2 laser technology. Developments such as the TEA laser, miniature laser technology, graded reflectivity mirrors, frequency control techniques, sealing and catalyst technology as well as a general understanding of CO_2 laser physics has been the result of the programme. At the present time, CO_2 laser technology is reaching a mature stage of its development. As a result we are now starting to place our efforts into other wavebands of interest. Nevertheless, work is continuing in the development of high-power and high pulse repetition-rate waveguide CO_2 lasers. Pulse rates approaching 30 kHz are possible with average output energies approaching 1 kW.

It is hoped that this innovative technology will help to provide solutions to many scientific, industrial and military needs.

Acknowledgements

The authors would like to thank Dr. Jacques Beaulieu for his valuable contributions and many helpful discussions.

References

1. P. Lavigne, A. Parent, D. Pascale and N. McCarthy, "A Compact Wide-Aperture Single-Mode TE-CO₂ Laser with a Low Chirp Rate", IEEE J.Q.E., QE-22, pp. 2200-2203, (1986)
2. D.V. Willets and M.R. Harris, "Scaling Laws for the Intrapulse Frequency Stability of an Injection Mode Selected TEA-CO₂ Laser", IEEE J.Q.E., QE-19, pp. 810-814, (1983)
3. P. Mathieu, "Method for Producing a Catalyst for Oxidizing Carbon Monoxide", U.S. Patent, 4,490,482, (1984)
4. D.S. Stark, A. Crocker and G.J. Skward, "A Sealed 100-Hz CO₂ TEA Laser Using High CO₂ Concentrations and Ambient-Temperature Catalysts", J. Phys. E. Sci. Instrum., Vol. 16, (1983)
5. J.-L. Lachambre, P. Lavigne, G. Otis and M. Noël, "Injection Locking and Mode Selection in TEA-CO₂ Laser Oscillators", DREV Report 4061/76, (1976), UNCLASSIFIED
6. H. Tashiro, K. Midorikawa, T. Higashii, K. Toyoda and S. Namba, "High Power Emission in the 11-14 μ m by Stimulated Rotational Raman Scattering in Deuterium", Opt. Commun. Vol. 60, pp. 45-48, (1986) and reference there in.
7. A.S. Grasiuk, V.S. Letokhov and V.V. Lobko, "Molecular Infrared Laser Using Resonant Laser Pumping", Prog. Quant. Electr., Vol. 6, pp. 245-294, (1980)
8. F. Julien, J.-M. Lourtioz, T.A. De Temple and S.J. Petuchonski, "Evidence of Four-Wave Parametric Interaction in Optically Pumped NH₃", Opt. Commun., Vol. 54, N°4, pp. 246-250, (1985)
9. M. Bernardini, M. Giorgi, A. Polucci, S. Ribezzo and S. Marchetti, "Resonant Four-Wave Mixing in NH₃ and CH₃F", Opt. Commun., Vol. 57, N°6, pp. 435-438, (1986)
10. R.S.F. Chang, R.H. Lehmborg, M.T. Duignan and N. Djeu, "Raman Beam Cleanup of a Severely Aberated Pump Laser" IEEE J. Quant. Electr. QE-21, pp. 477-487, (1985)
11. P. Mathieu and J.R. Izatt, "Continuously Tunable CH₃F Raman Far-Infrared Laser", Opt. Lett. Vol. 6, N°8, pp. 369-371, (1981)
12. M. Blanchard, J. Gilbert, F. Rheault, J.-L. Lachambre, R. Fortin and R. Tremblay, "Superatmospheric Double-Discharge CO₂ Laser", J. of Appl. Phys. Vol. 45, N°3, pp. 1311-1314, (1974)

ULTRASTABLE CARBON DIOXIDE (CO₂) LASERS*

Charles Freed

Massachusetts Institute of Technology
Lincoln Laboratory
P.O. Box 73
Lexington, Massachusetts 02173

Abstract

This paper reviews the spectral purity, frequency stability and long-term stabilization of CO₂ isotope lasers developed at MIT Lincoln Laboratory. Extremely high spectral purity and short-term stability of less than 1.5×10^{-13} have been achieved and will be discussed. A long-term stabilization technique, which was used to line-center lock any regular or hot-band CO₂ isotope laser transition, is described. A brief description on using CO₂ lasers as secondary frequency standards is also given.

Spectral purity and short-term stability

The theoretical linewidth of a laser above threshold was first derived by Schawlow and Townes¹ as:

$$\Delta f = \frac{\alpha \pi h f_0}{P_0} \left(\frac{f_0}{Q_c} \right)^2 \quad (1)$$

where Δf is the full width between half-power points of the laser output (FWHM); α , h , f_0 , P_0 , and Q_c denote the population inversion parameter, Planck's constant, the center frequency, power output and "cold" cavity Q of the laser, respectively.

In a well designed small CO₂ laser the "cold" cavity Q is given by:

$$Q_c = \frac{2\pi L f_0}{c T_r} \quad (2)$$

where L , c , T_r denote the cavity length, velocity of light and mirror transmission, respectively (diffraction losses are usually negligible compared to output coupling loss). In a small CO₂ laser with $L = 50$ cm, $T_r = 5\%$, Q_c is of the order of 10^7 ; thus for a typical power output of 1 to 10 Watts (which is easily obtainable with a small TEM_{00q} mode CO₂ laser) the quantum phase noise limited linewidth is less than 10^{-6} Hz.

In actual practice, however, so-called "technical" noise sources dominate^{2,3} over the quantum phase noise limited Schawlow-Townes linewidth. Examples of technical noise sources are acoustic and structure-born vibrations, power supply ripple and noise, etc. These can cause frequency instabilities by perturbing the effective cavity resonance via the sum of fractional changes in the refractive index n and the cavity length L .

$$\Delta f = f \left(\frac{\Delta n}{n} + \frac{\Delta L}{L} \right) \quad (3)$$

*This work was sponsored by the Defense Advanced Research Projects Agency of the Department of Defense, the Department of Energy, and the NASA Langley Research Center.

As an example, a change of only 10^{-3} Angstrom, about 1/1000 of the hydrogen atomic diameter, in a 50 cm long CO_2 laser cavity will cause a frequency shift of approximately 6 Hz. A 6 Hz variation in the approximately 3×10^{13} Hz frequency of CO_2 lasers corresponds to a fractional instability of 2×10^{-13} . A frequency stability at least as good as 2×10^{-13} is implied in Fig. 1, which shows the real time power spectrum of the beat signal between two free running lasers, designed and built at MIT Lincoln Laboratory. The frequency scale in Fig. 1 is 500 Hz/cm, indicating that the optical frequencies of the two lasers producing the beat note were offset by less than 3×10^3 Hz. The discrete modulation side-bands were primarily due to line frequency harmonics, fan noise and slow drift; however, each spectral line was generally within the 10 Hz resolution bandwidth of the spectrum analyzer. The measurement of the spectral width was limited to 10 Hz resolution by the 0.1 s observation time set by instrumentation and not by the laser stability itself.

Laser stabilities are most conveniently measured by heterodyning two lasers, as is shown in Fig. 1; however, the results are not altogether foolproof because the disturbances causing frequency jitter of the lasers may be at least partially correlated. In an optical radar one may compare the laser with its own output delayed by the round trip time to and from the target. Hence, effects due to disturbances with correlation times less than the round trip time of the transmitted signal will be included in the measured beat note spectrum.

Figure 2 shows a greatly simplified block diagram of a $10.6 \mu\text{m}$ laser radar at the MIT Lincoln Laboratory Firepond Facility⁵ in Westford, Massachusetts. In Fig. 2 wavy and solid lines denote optical and electrical signal paths, respectively. The 0.5 meter local and the 1.5 meter power oscillators were designed and constructed at Lincoln Laboratory^{2,6}. The higher power oscillator was phase-locked to the local oscillator with a fixed 10 MHz frequency offset between the two lasers.

The frequency stability of the CO_2 laser radar facility at Firepond was verified from observations on GEOS-III, a NASA geodetic satellite equipped with an IRTAN II solid cube corner retro-reflector. Radar returns from GEOS-III have been used to determine the radial velocity of the satellite using Doppler measurements, and to set an upper bound to the laser oscillator instability⁷. During these measurements the satellite range was 1063 km, which corresponds to a round-trip signal travel time of 7.09 milliseconds (ms). During these measurements the constant frequency, amplified CO_2 laser output signal was chopped by means of a duplexer so that a 25% duty cycle pulse train consisting of 4 ms duration pulses 16 ms apart was transmitted to the orbiting satellite.

The spectra that result from a radio frequency (R.F.) test signal of 4 ms duration processed in the same manner as the optical radar data are shown in Fig. 3. In Fig. 3, the horizontal rows simulate logarithmic displays of the power spectra of a consecutive sequence of radar return signals; this type of display is the Doppler-time-intensity (DTI) plot in radar terminology. The sinc^2 function shape of the spectra due to the 4 ms pulse duration is quite evident. The average spectral width 10 db below the peak is 383 Hz, and the standard deviation of the spectral width is 5 Hz.

Figure 4 shows the DTI plot of the actual CO_2 radar signal return from GEOS-III at a 1063 km range. Notice the striking similarity to the simulated DTI plot in Fig. 3, which was obtained from a high quality frequency synthesizer (that was also part of the radar receiver). A comparison of Figures 3 and 4 shows that the -10 db average spectral width of the radar return signal broadened from 383 to 399 Hz and the standard deviation of this spectral width increased from 5 to 18.5 Hz. These figures thus indicate that the short-term stability of the entire CO_2 radar system, including round trip propagation effects caused by fluctuations in the atmosphere, was better than 1.5×10^{-13} for the 7.09 ms roundtrip time duration.

Figure 4 also shows that the standard deviation of pulse-to-pulse centroid jitter of the spectra was 117 Hz during the test run. No effort was made to line-center stabilize either one of the lasers since the longterm stability of the free-running laser was more than adequate for typical optical radar applications. However, as mentioned previously (see Fig. 2) the power oscillator was phase-locked to the local oscillator with a fixed 10 MHz frequency offset between the two lasers. Figure 5 shows the real time power spectrum of the beatnote of the two phase-locked lasers. Note that the horizontal scale is only 2×10^{-2} Hz/division and the vertical scale is logarithmic, with 12.5 db/division. Figure 5 indicates that the spectral width of the beatnote was only 9×10^{-3} Hz at 60 db below the peak. This implies that the full spectral width between the half maximum points (FWHM bandwidth) was only about 9×10^{-6} Hz. It took 26.67 minutes of measurement time to obtain just a single scan with the frequency resolution of Fig. 5. Since tracking even by a very good servo system would still be limited by quantum phase noise, the narrow linewidth in Fig. 5 is an indirect, but clear confirmation of the high spectral purity of CO_2 lasers, as predicted by the Schawlow-Townes formula.

Laser design

Figure 6 illustrates the most basic CO₂ laser structure developed at MIT Lincoln Laboratory^{2,6} about twenty years ago. In order to achieve maximum open loop stability, a very rigid optical cavity design was chosen, which utilized stable materials. Four thermally, magnetically, and acoustically shielded low expansion superinvar rods define the mirror spacing of the optical cavity. The mirrors are internal to the vacuum envelope, and are rigidly attached to the composite granite and stainless steel mirror holders bolted to the four invar rods. In spite of the rigid structure, the laser design is entirely modular, and can be rapidly disassembled and reassembled; mirrors may be interchanged, and mirror holders can be replaced by piezoelectric and grating controlled tuners. It should be noted that the philosophy and many other aspects of the stable CO₂ laser design may be easily traced back to the original He-Ne laser design of A. Javan.

Figure 7 shows a 1.5 m piezoelectrically tunable laser which is offset-locked to a 0.5 m local oscillator reference in the coherent CO₂ radar at the Firepond facility of Lincoln Laboratory.

Figure 8 illustrates a grating controlled, stable, TEM₀₀₀ mode laser. Many variants of these basic designs exist both at Lincoln Laboratory and elsewhere. This particular unit was built for high power applications, such as optical pumping and frequency shifting. The first order reflection of the grating was coupled through a partially reflecting output mirror. For heterodyne spectroscopy, zero-order output coupling is preferable. Some of the lasers also have short internal absorption cells, which may be utilized either for frequency stabilization or for very stable high repetition rate passive Q-switching.

Long-term, line-center stabilization of CO₂ lasers

The width of the Doppler broadened gain profile of a CO₂ laser is about 53 MHz. Thus the CO₂ laser may operate anywhere up to at least tens of MHz away from the center frequency of the oscillating transition. In many applications it is therefore desirable to find a narrow reference line within the operating frequency range of the laser and lock to this reference. Attempts to use CO₂ itself as a reference via either the Lamb dip or the inverted Lamb-dip techniques⁸ yielded rather poor results due to the fact that the lower state vibration-rotational levels of the CO₂ laser transitions do not belong to the ground state, and therefore the absorption coefficient of low pressure room temperature CO₂ at 10 μ m is very low. This in turn will cause difficulty in the observation and utilization of the inverted Lamb-dip resonance directly in the full power output of the CO₂ laser. These difficulties were overcome at Lincoln Laboratory in 1970, when it was demonstrated⁹ that the standing wave saturation effect can also be detected by observing the change in the intensity of the 4.3 μ m spontaneous fluorescence emission over the entire (001) - (000) transition band as the laser frequency is tuned across the Doppler profile of the corresponding 10 μ m absorption line. The change in the entire band is due to the fact that radiation-induced change in the population of an individual rotational level is accompanied by a change in the populations of all rotational levels of the same vibrational state; this is caused by the coupling among the rotational levels, which tends to maintain a thermal population distribution. Figure 9 graphically illustrates the experimental arrangement in which low pressure, room temperature CO₂, serving as the saturable absorber, is subjected to the standing wave laser field generated in a stabilizing cell placed either internal or external to the laser cavity, with the laser oscillating in any preselected (00ⁿ1) regular or (01ⁿ1) hot band transition. In the vicinity of the absorption line center a resonant change in the 4.3 μ m fluorescence signal appears which is analogous to a Lamb-dip.

Figure 10 illustrates the Lamb-dip like appearance of the resonant change in the 4.3 μ m fluorescence signal as the laser is slowly tuned in frequency. By applying a small frequency modulation to the laser as it is tuned in the vicinity of the absorption line center, the derivative of the 4.3 μ m signal is obtained, as illustrated in Fig. 11. The 4.3 μ m derivative signal in Fig. 11 was obtained by applying a ± 100 kHz frequency modulation to the laser at a 260 Hz rate. 1.75 W of the laser's output was directed into an external stabilization cell which was filled to a pressure of 0.034 Torr with pure room temperature CO₂. It is a straightforward procedure to line-center stabilize a CO₂ laser by using the 4.3 μ m derivative signal as a frequency discriminant in conjunction with a phase sensitive detector. Any deviation from the center frequency of the lasing transition yields a positive, or negative, phase sensitive detector output voltage which is then utilized as a feedback signal in a servo-loop to obtain the long-term frequency stabilization of the laser output.⁹⁻¹⁴

Figure 12 shows the block-diagram of a two-channel heterodyne calibration system in which two low pressure, room temperature CO₂ gas cells external to the lasers were used to line-center stabilize two grating controlled stable lasers filled sequentially with 9 different CO₂ isotopic species.

Figure 13 shows a photograph of the optical portion of the two-channel heterodyne calibration system which was instrumental in obtaining the absolute frequencies, band centers, and rotational constants of the nine CO₂ isotopic species¹¹ during the last few years. In essence, optical heterodyne techniques were used to generate and accurately measure with frequency counters over nine hundred beatnotes between pairs of line-center stabilized grating controlled CO₂ isotope lasers.¹¹

The spectrum analyzer display of a typical beatnote is shown in Fig. 14. Note that the S/N ratio is greater than 50 db at the 24.4 GHz beat frequency of the two laser transitions.

Figure 15 illustrates the time domain frequency stability that has been routinely achieved with the two-channel heterodyne calibration system using the 4.3 μm fluorescence stabilization technique.¹²

The open and filled circles represent two separate measurement sequences of the Allan Variance of the frequency stability

$$\sigma_y(\tau) = \frac{1}{2M} \sum_{j=1}^M (y_{j+1} - y_j)^2 \quad (4)$$

Each measurement consisted of M=50 consecutive samples for a sample time duration (observation time) of τ seconds. Figure 15 shows that $\sigma_y < 2 \times 10^{-12}$ has been achieved for τ=10s, which means that a frequency measurement precision of about 50 Hz may be readily achieved within a few minutes.

The triangular symbols in Fig. 15 represent the frequency stability of a Hewlett-Packard (HP) model 5061 cesium atomic frequency standard as specified in the 1987 HP catalog. Clearly, the frequency stabilities of the CO₂ and the cesium stabilized systems shown in Fig. 15 are about the same.

The upper bound short-term stabilities, as measured in the laboratory (see Fig. 1) and determined from CO₂ radar returns at the MIT Lincoln Laboratory Firepond facility (see Fig. 4) are also indicated by the two crossed circle symbols in the lower left corner of Fig. 15. It is quite obvious that at least two to three orders of magnitude better short-term stabilities have been achieved in a CO₂ radar compared to Microwave Systems.

The frequency reproducibility of the two-channel, line-center stabilized CO₂ heterodyne calibration system is indicated in Fig. 16, which shows a so-called "drift-run" taken over an 8/12 hour period beginning at 1 p.m. The frequency stability measurement apparatus was fully automatic¹² and continued to take, compute and record the beat frequency data of the two line-center stabilized CO₂ isotope lasers even after about 5 p.m. when everybody left the laboratory. Approximately 100 seconds apart a data point was printed out which represented the deviation from the beat frequency which was averaged over 8 1/2 hours. A measurement time of τ=10s and M=8 samples were used for each data point, yielding a measurement accuracy much better than the approximately ±1 kHz peak frequency deviation observable in Fig. 16. Most probably this frequency drift was caused by small voltage offset errors in the phase sensitive detector driven servo amplifier outputs which controlled the piezoelectrically tunable laser mirrors. Since 500 volts was required to tune the laser one longitudinal mode spacing of 100 MHz, an output voltage error of ±2.5 mV in each channel was sufficient to cause the ±1 kHz peak frequency deviation observable in Fig. 16. By monitoring the piezoelectric drive voltage with the input to the lock-in amplifier terminated in 50 Ω (instead of connected to the InSn 4.3 μm fluorescence detector) it was determined that slow output voltage drifts of up to ±2.5 mV were indeed present in the electronics, which correspond to ±5 ppm drifts in the output. Note, that no special precautions were taken to protect either the lasers or the associated electronic circuitry from the temperature fluctuations in the laboratory which were rather significant (± several °C). Substantial improvements are possible with more up-to-date electronics and temperature controlled environment; these would indeed become necessary if the emphasis would change toward the creation of a primary frequency standard.

Perhaps the greatest advantage of the 4.3 μm fluorescence stabilization method is that it automatically provides a nearly perfect coincidence between the lasing medium's gain profile and the resonance of the saturable absorber, since they both utilize the same molecule, CO₂. Thus every P and R transition of the (00⁰1)-I and -II regular bands and the (01¹1) hot band may be line-center locked utilizing the same stabilization cell and gas fill. Furthermore, the saturation resonance is detected separately at the 4.3 μm fluorescence band and not as a fractional change in the much higher power laser radiation at 10 μm. At 4.3 μm, InSn photovoltaic detectors are available which can provide very high, background limited sensitivity.

CO₂ isotope lasers as secondary frequency standards

In CO₂ molecular lasers transitions occur between two vibrational states. Since each vibrational state has a whole set of rotational levels, a very large number of laser lines, each with a different frequency (wavelength) can be generated. Moreover, isotopic substitution of the oxygen and/or carbon atoms make 18 different isotopic combinations possible for the CO₂ molecule. Approximately 50 to 150 regular band lasing transitions may be generated for each of the CO₂ isotopic species. By using optical heterodyne techniques, the beat frequencies between laser transitions of individually line-center stabilized isotopic CO₂ laser pairs were accurately measured. As a result, the absolute frequencies, vacuum wavenumbers, band centers, and ro-vibrational constants for ¹²C¹⁶O₂, ¹³C¹⁶O₂, ¹³C¹⁸O₂, ¹²C¹⁸O₂, ¹²O¹⁷O₂, ¹⁶O¹²C¹⁸O, ¹⁶O¹³C¹⁸O, ¹⁴C¹⁶O₂, and ¹⁴C¹⁸O₂ have been simultaneously calculated from well over 900 beat frequency measurements.¹³ The accuracies of these frequency determinations are, for the majority of the transitions, within about 5 kHz relative to the primary Cs frequency standard. Consequently, in the 8.9-12.3 μm wavelength region line-center stabilized CO₂ isotope lasers can be conveniently used as secondary frequency standards. One can also utilize difference frequencies and harmonics of CO₂ lasing transitions to synthesize precisely known reference lines well beyond the 8.9-12.3 μm range. Figure 17 graphically illustrates the frequency and wavelength domain of the nine CO₂ isotopic species which were measured to date. ¹⁴C¹⁶O₂ extends the wavelength range to well beyond 12 μm, while ¹²C¹⁸O₂ transitions reach below 9 μm.

In yet another project at MIT Lincoln Laboratory the equivalent of a programmable, and highly accurate infrared synthesizer was developed¹⁴ as shown in Fig. 18.

The synthesizer output is derived from a lead-salt tunable diode laser (TDL); a small portion of the TDL output is heterodyned against a line-center stabilized grating controlled CO₂ (or CO) molecular laser. The beatnote of the two lasers is detected by a high speed HgCdTe (varactor) photodiode.¹⁵ The detected beat frequency, which is generally in the 0 to 18 GHz range is further heterodyned to some convenient intermediate frequency (I.F.) using readily available commercial R.F./microwave frequency synthesizers and wide-band double balanced mixers. The I.F. output is amplified and amplitude limited by means of low-noise, wide-band amplifiers and limiters. The limiter output is, in turn, used as input to a wide-band, delay-line type frequency discriminator (200 to 600 MHz typical bandwidth). The output of the frequency discriminator is further amplified by means of a servo amplifier/integrator, the output of which is then used to control the current which determines the output frequency of the TDL. By closing the servoloop in this fashion the TDL output is frequency offset-locked to the combination of CO₂ (or CO) laser, R.F./microwave synthesizer, and the center-frequency of the wideband I.F. discriminator which is monitored by a frequency counter. The entire infrared synthesizer system shown in Fig. 18 is controlled by a computer. If, for instance, the microwave synthesizer is frequency swept under computer control, the I.R. output frequency of the TDL would be swept too in synchronism with the microwave synthesizer, since the frequency offset-locking servoloop forces the TDL output to maintain the frequency relationship

$$f_{\text{TDL}} = f_{\text{CO}_2/\text{CO}} \pm f_{\text{synthesizer}} \pm f_{\text{I.F. counter}} \quad (5)$$

In Eq. (5) above, the frequency of the R.F./microwave synthesizer is predetermined by the operator or computer program, the I.F. frequency is very accurately measured (and averaged if so desired) even in the presence of appreciable frequency modulation (which may be necessary in order to line-center lock either or both lasers); thus the absolute accuracy of the TDL output frequency, f_{TDL} will, to a very large degree, depend on the absolute accuracy, resettability and long term stability of the reference laser(s). The most accurate results obtained to date were achieved with the use of CO₂ reference lasers.

Conclusions

CO₂ lasers have demonstrated greater spectral purity and better short term stability than any other oscillator at any frequency. These results were confirmed by laboratory measurements and also deduced from analysis of CO₂ radar returns from orbiting satellites. A long-term stabilization technique, using low pressure room temperature CO₂ gas as a reference, was also developed so that long-term CO₂ laser stabilities at least comparable to commercial grade atomic clocks can be also achieved. By using a line-center stabilized, two-channel CO₂ laser heterodyne system, the absolute frequencies of lasing transitions and the ro-vibrational constants of nine CO₂ isotopic species were determined to within about 5 kHz relative to the primary cesium frequency standard. These results allow the CO₂ system to be used as a secondary frequency standard in the infrared spectrum. Furthermore, the results described in this paper were achieved with laser designs and components which were

developed 15-20 years ago. Extensive experience gained by working with these lasers clearly indicates that at least one to two orders of magnitude improvements of both short-term and long-term stabilities should be achievable with improved designs.

Acknowledgement

The work reported here represents the cumulative efforts of many individuals at the MIT/Lincoln Laboratory Community. The author wishes to particularly thank the contributions of the following individuals (listed in alphabetical order): J. W. Bielinski, L. C. Bradley, J. W. Daley, F. R. Gurski, H. A. Haus, A. Javan, R. H. Kingston, D. G. Kocher, W. Lo, R. G. O'Donnell, K. L. SooHoo, D. L. Spears, L. J. Sullivan, and J. E. Thomas.

Originally appeared in SPIE publication Laser Research and Development in the N.E. 709-07, 1986.

References

1. Schawlow, A. L. and Townes, C. H., Phys. Rev. 112, 1940 (1958).
2. C. Freed, IEEE J. Quantum Electron. QE-4, 404 (1968).
3. C. Freed, Proceedings of the 31st Annual Symposium on Frequency Control held in Atlantic City, N.J. 1-3 June (1977).
4. R. H. Kingston, SPIE Vol. 227 - CO₂ Laser Devices and Applications, 148, (1980).
5. L. J. Sullivan, SPIE, Vol. 227 - CO₂ Laser Devices and Applications, 148, (1980).
6. C. Freed, Proceedings of the Frequency Standards and Metrology Seminar - Sponsored by the National Research Council of Canada and University Laval, Quebec, Canada, 226, (1971).
7. T. R. Gurski, J. Opt. Soc. Am. 66 1133A (1976).
8. L. S. Vasilenko, M. N. Skvortsov, V. P. Chebotaev, G. I. Shershneva, and A. V. Shisaev, Optical Spectroscopy 32, 609, (1972).
9. C. Freed and A. Javan, Applied Phys. Letters 17, 53 (1970).
10. A. Javan and C. Freed, U.S. Patent No. 3686585 issued August 22, (1972).
11. C. Freed and R. G. O'Donnell, Metrologia 13, 151 (1977).
12. K. L. SooHoo, C. Freed, J. E. Thomas and H. A. Haus, IEEE J. Quantum Electron. QE-21, 1159 (1985).
13. L. C. Bradley, K. L. SooHoo and C. Freed, IEEE J. Quantum Electron, QE-22, 234 (1986).
14. C. Freed, J. W. Bielinski, and W. Lo, Proceedings of Tunable Diode Laser Development and Spectroscopy Applications, SPIE 438, (1983).
15. D. L. Spears and C. Freed, Appl. Phys. Lett. 23, 445 (1973).

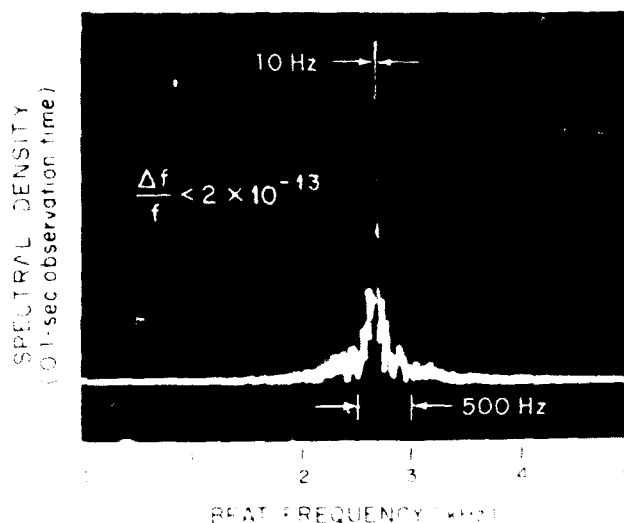


FIG. 1. REAL TIME POWER SPECTRUM OF THE BEAT SIGNAL BETWEEN TWO FREE RUNNING CO_2 LASERS.

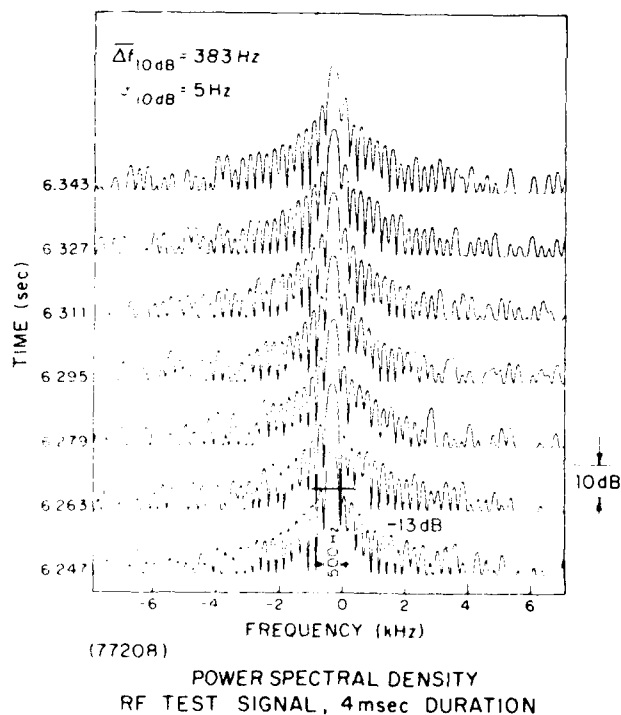


FIG. 3. DOPPLER-TIME-INTENSITY PLOT FOR A 4-msec DURATION R.F. TEST SIGNAL.

INFRARED RADAR SYSTEM BLOCK DIAGRAM

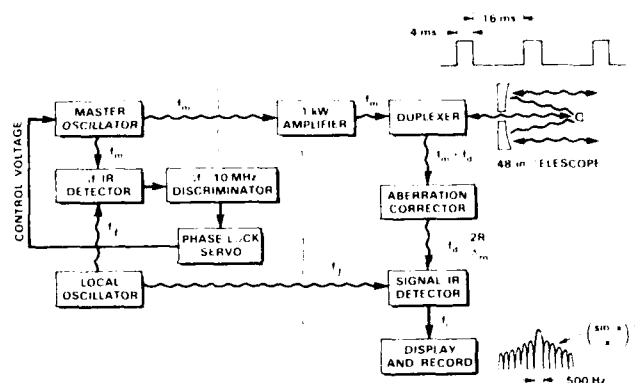


FIG. 2. INFRARED RADAR SYSTEM BLOCK DIAGRAM.

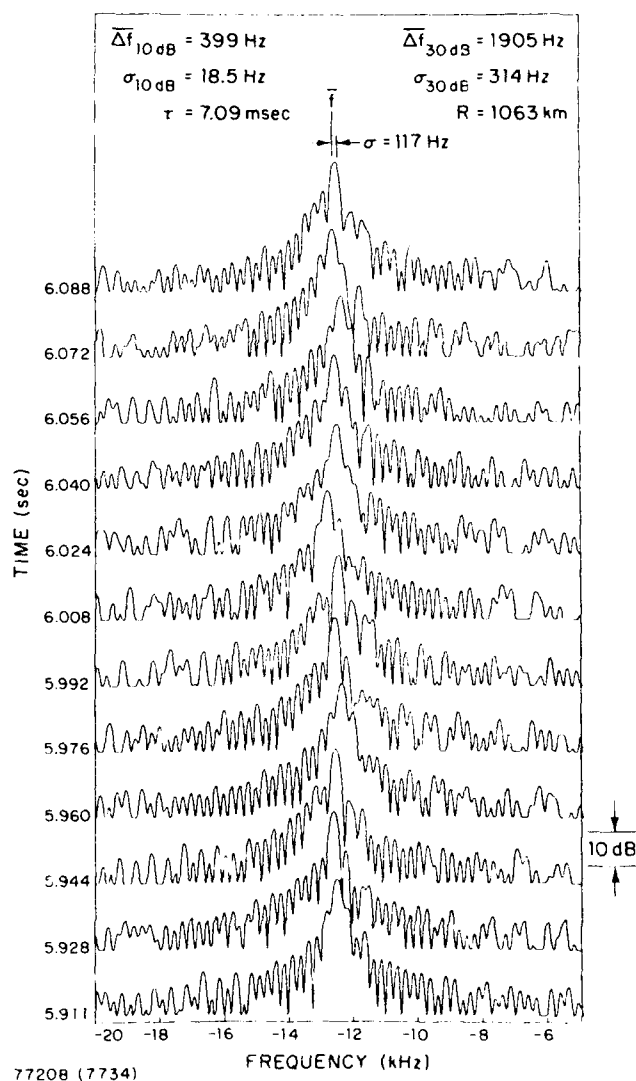


FIG. 4. DOPPLER-TIME-INTENSITY PLOT FOR THE GEOS-III RADAR RETURN SIGNAL.

SPECTRAL PURITY OF CO₂ LASERS TWO LASERS PHASE-LOCKED WITH 10 MHz FREQUENCY OFFSET

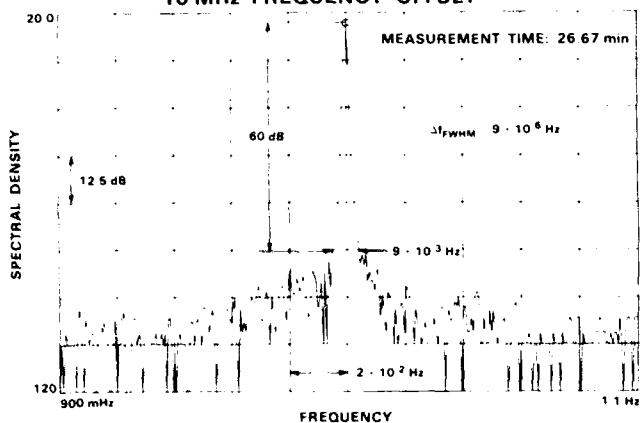


FIG. 5. SPECTRAL PURITY OF BEATNOTE BETWEEN TWO PHASE-LOCKED LASERS.

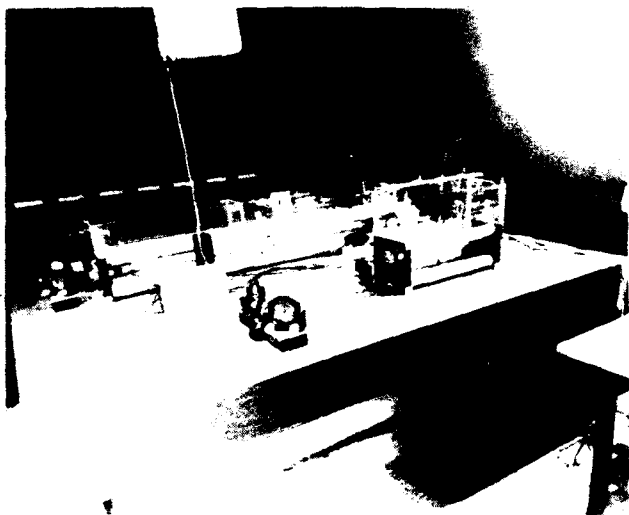


FIG. 7. OFFSET-LOCKED LASERS IN THE COHERENT CO₂ RADAR AT THE FIREPOND FACILITY.

RESONANT INTERACTION FOR $\omega = \omega_0$ [$k \cdot v = 0$]

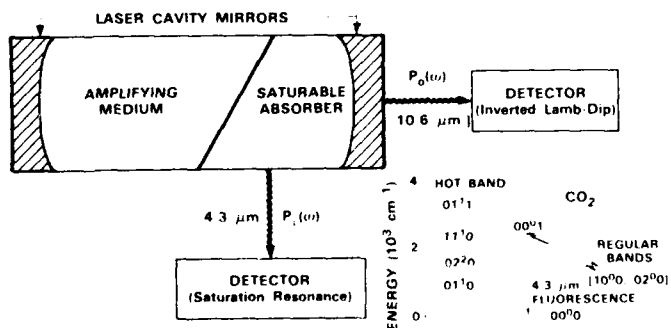


FIG. 9. GRAPHIC ILLUSTRATION OF THE SATURATION RESONANCE OBSERVED IN CO₂ FLOURESCENCE AT 4.3 μm . THE FIGURE SHOWS AN INTERNAL ABSORPTION CELL WITHIN THE LASER CAVITY. EXTERNAL CELLS MAY ALSO BE USED.

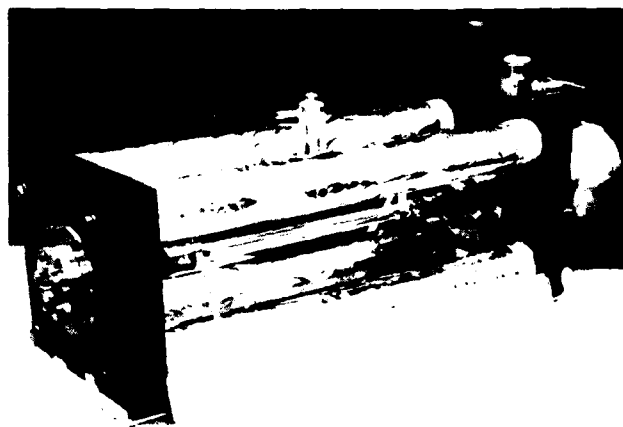


FIG. 6. BASIC STABLE LASER STRUCTURE DEVELOPED AT MIT/LINCOLN LABORATORY.



FIG. 8. BASIC GRATING-CONTROLLED STABLE TEM_{00q} MODE CO₂ LASER.

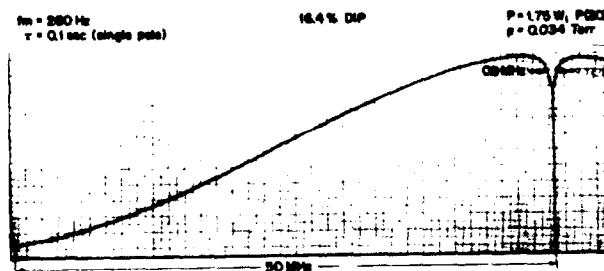


FIG. 10. LAMB-DIP LIKE APPEARANCE OF THE RESONANT CHANGE IN THE 4.3 μm FLOURESCENCE.

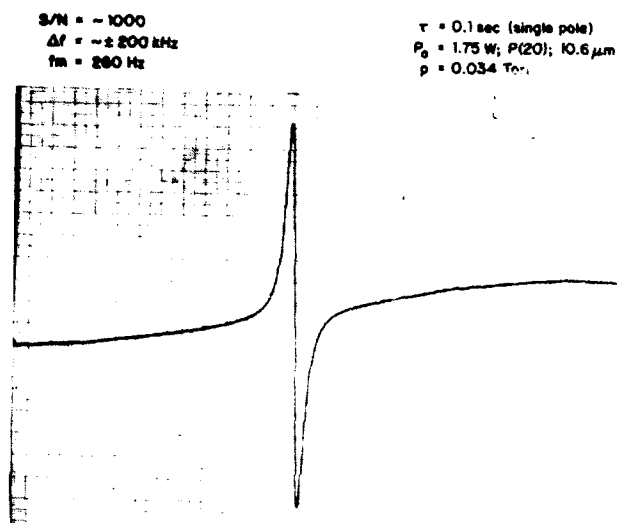


FIG. 11. DERIVATIVE SIGNAL AT $4.3 \mu\text{m}$ IN THE VICINITY OF THE STANDING WAVE SATURATION RESONANCE.

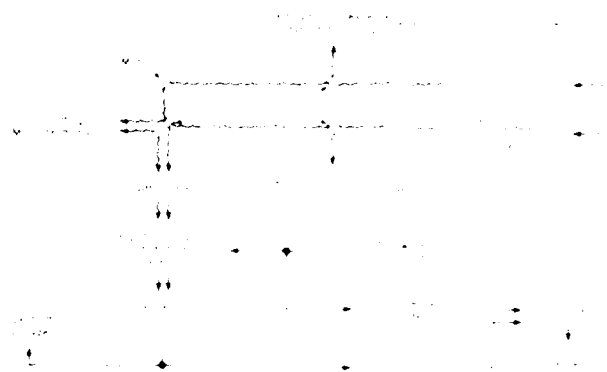


FIG. 12. BLOCK DIAGRAM OF THE TWO-CHANNEL LINE-CENTER STABILIZED CO_2 ISOTOPE CALIBRATION SYSTEM.

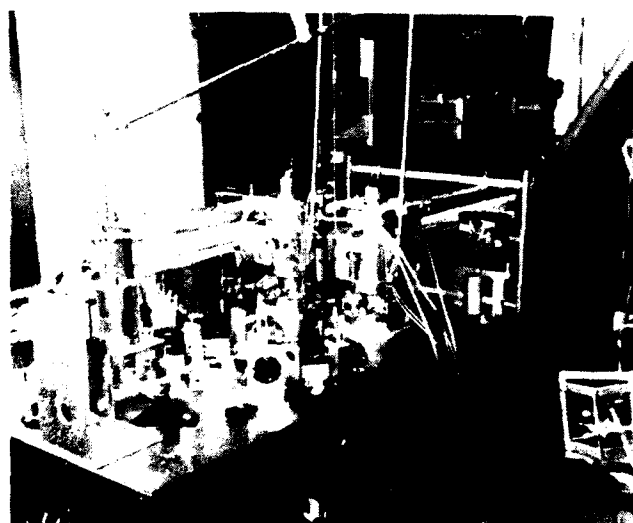
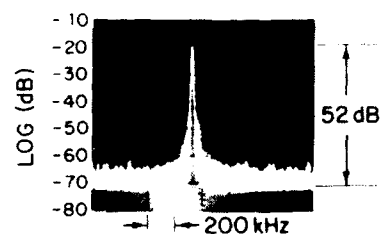


FIG. 13. PHOTOGRAPH OF THE OPTICAL PORTION OF THE TWO-CHANNEL CO_2 CALIBRATION SYSTEM.



24,410.301 MHz BEAT OF $^{16}\text{O}^{12}\text{C}^{18}\text{O}$ LASER 001-I P(12)
 AND $^{12}\text{C}^{16}\text{O}_2$ LASER 001-I P(6) TRANSITIONS

POWER LEVELS INTO PHOTODIODE :

$^{12}\text{C}^{16}\text{O}_2$ LASER: 0.42 mW

$^{16}\text{O}^{12}\text{C}^{18}\text{O}$ LASER: 0.48 mW

SECOND HARMONIC OF MICROWAVE L.O.
 10 kHz NOISE BANDWIDTH

FIG. 14. SPECTRUM ANALYZER DISPLAY OF A TYPICAL, LONG-TERM STABILIZED BEATNOTE.

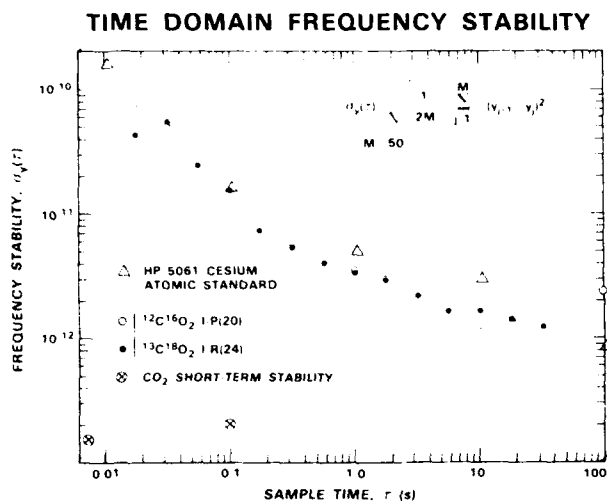


FIG. 15. TIME DOMAIN FREQUENCY STABILITY OF THE TWO-CHANNEL HETERODYNE CALIBRATION SYSTEM USING THE $4.3\mu\text{m}$ FLOURESCENCE STABILIZATION TECHNIQUE.

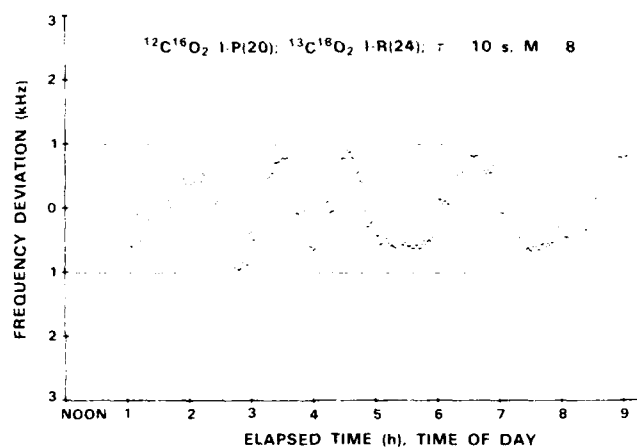


FIG. 16. SLOW DRIFTS IN BEAT FREQUENCY DUE TO SMALL DEVIATIONS FROM TRUE ZERO OF THE ELECTRONICS (CAUSED BY TEMPERATURE VARIATIONS).

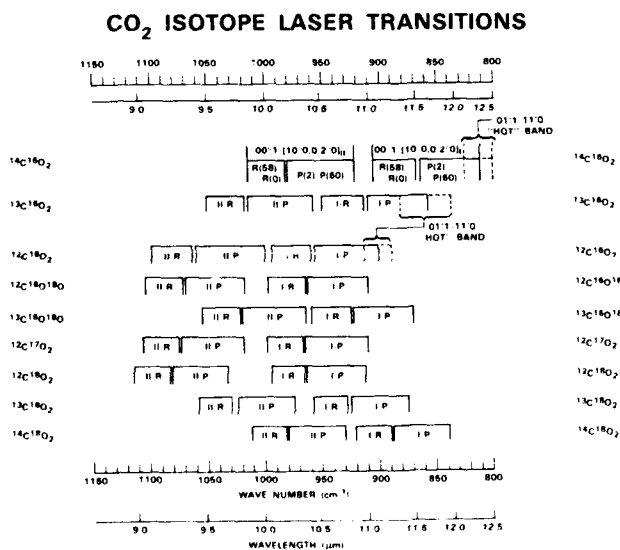


FIG. 17. FREQUENCY AND WAVELENGTH DOMAIN OF NINE CO_2 ISOTOPIC SPECIES.

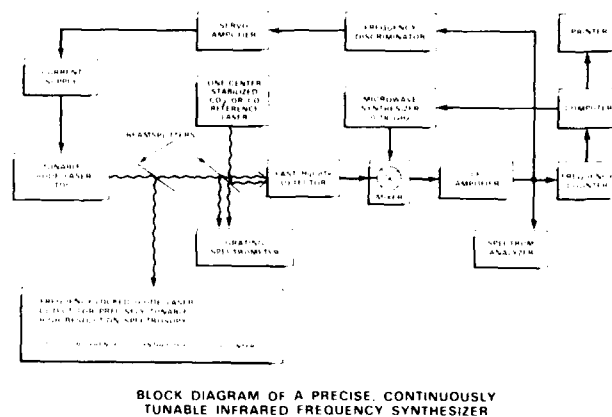


FIG. 18. BLOCK DIAGRAM OF AN ACCURATE, TUNABLE, COMPUTER CONTROLLED, kHz RESOLUTION INFRARED FREQUENCY SYNTHESIZER.

EXPERIMENTAL AND THEORETICAL ANALYSIS OF CO UNDER BLACKBODY OPTICAL EXCITATION

J.M. Sirota and W.H. Christiansen
University of Washington, FL-10
Seattle, WA 98195

Abstract

A series of experiments and modeling were performed in order to define the properties of CO-Ar mixtures as active medium for a blackbody radiation pumped laser. The vibrational temperature of the first excited state of CO(T_{v1}) was measured by the spectral line reversal method. Values of T_{v1} close to the temperature of the pumping blackbody cavity were obtained. The spatial dependence of the absorbed power per unit volume was calculated and experimentally verified. Pumping container diameters of several centimeters are possible, using high Ar content mixtures. The vibrational distribution and its time dependence were calculated by means of a numerical method that solves the rate equations of the system. Good agreement between measured and calculated values of T_{v1} was found. Radiative trapping is proposed as a method to increase the energy storage time after pumping.

Introduction

The optical pumping of lasers using a black body cavity heated by solar radiation has been proposed as an efficient method to convert solar energy into laser light¹. Several experiments have been performed to show the feasibility of the concept, and lasing in CO₂ and N₂O and their isotopes was demonstrated². While the performance of these mixtures was found quite satisfactory, the limiting factors for the absorbed power density were identified. Because the relatively fast V-T deactivation rates of these lasants the pressure of the gas could not be increased above the 10-20 torr range, limiting the number density of active molecules and also the broadening of the absorption lines.

Carbon monoxide presents much lower V-T deactivation rates, allowing higher densities and broader absorption spectrum. The absorbed power density and vibrational energy storage times can be considerably larger than for CO₂ and N₂O species. Also, because of its high quantum efficiency, a large fraction of the pumping power can be extracted as laser power. Due to the slow V-T processes, other laser schemes could be envisioned, such as transporting the excited gas and transferring the energy to other lasants, or lasing separate from the pumping region. Approximate evaluations for the efficiency of CO lasing in a blackbody pumped system have been made in Ref. 3, and values as high as 60% for high pressure operation were obtained. We report here the results of the first series of experiments and modelling aimed to define the properties of CO in a black body pumped system. Measurements of the vibrational temperature of CO and optical pumping profiles, and calculation of the vibrational population distribution and its time dependence are presented.

Vibrational Temperature Measurements

The vibrational temperature associated to the population of the first vibrational level of the CO molecule partially defines the vibrational population distribution⁴. Its measurement is necessary to evaluate the absorption and storage of energy under radiative pumping. The spectral line reversal technique⁵ was applied here with that purpose. In this technique light from a reference blackbody is passed through the sample. The reversal condition is obtained when this radiation is unmodified by the presence of the radiating gas sample. In this situation the characteristic temperature of the system under study is equal to the temperature of the reference blackbody.

The experimental set-up is shown in Fig. 1. A cylindrical electrically heated oven provides the pumping radiation. The gas mixture (CO-Ar) is flown through a sapphire tube surrounded by a cooling jacket. The components of the mixture are of research grade purity. The measurement entails observation of the gas as it exits the pumping region. The cell has calcium flouride windows and a small thermocouple monitors the gas translational temperature. The reference blackbody is a small oven in which the temperature is electronically controlled. While lenses are shown in the figure, reflective optics are used in the setup. The bandpass filter allows radiation from 4.65 μm to 4.85 μm to reach the detector. All the high intensity lines of the R band of the $v=1$ to 0 transition fall into this range at the temperatures of the experiment. The accuracy of the method is determined by the S/N ratio of the detector and associated electronics, and by the ratio between the equivalent linewidth of the gas and the bandwidth of the filter. The expression for the relative error in the measurement of T_{v1} is given in the appendix.

The values of T_{v1} measured for several pressures and mixtures are shown in Table 1, for 1500°K pumping blackbody temperature and 300°K translational gas temperature at the cell. Vibrational temperatures as high as 950°K were measured, which imply temperatures of 1300°K inside the pumping region in a steady state situation. The operating pressures are at least one order of magnitude higher than those allowed by CO₂ and N₂O in former experiments. Low concentrations of CO in the mixtures allowed deeper optical pumping. A more detailed analysis of this effect is made in the next section. Calculated values for T_{v1} are also listed in Table 1. These values were obtained using the mode described in section 4.

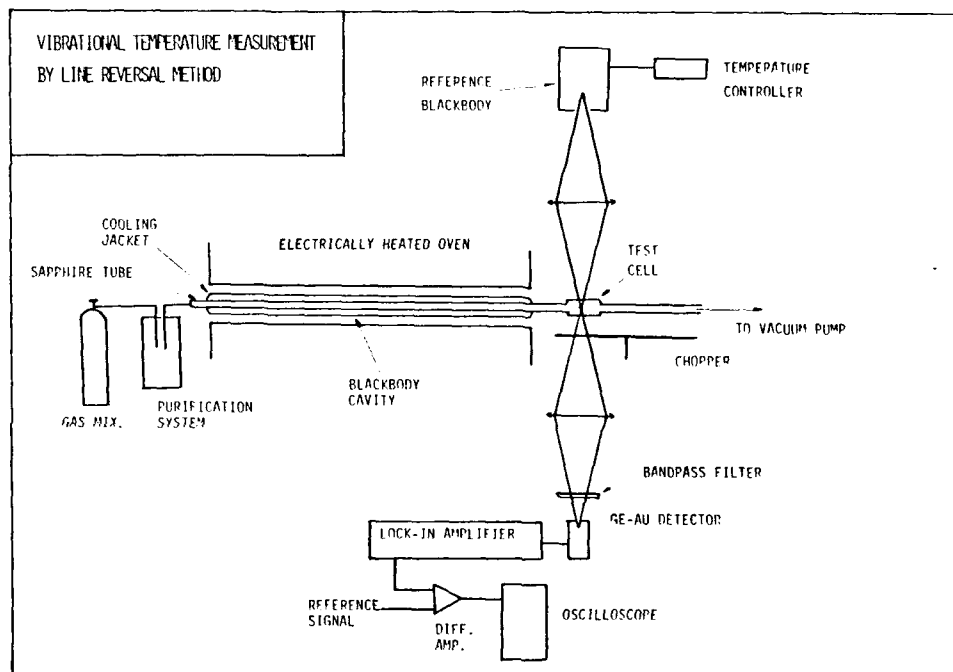


Fig. 1. Experimental set-up.

TABLE I. Vibrational temperature (T_{v1}) of CO @ the test cell.

$T_{BB \text{ pumping}} = 1500 \text{ K}$, $T_{\text{gas}} = 300 \text{ K}$, CO-Ar mixtures				
% of CO	Pressure (Torr)	Cooling jacket material	$T_{v1} \text{ meas. (K) } (\pm 5\%)$	$T_{v1} \text{ calc. (K)}$
15	200	Sapphire*	950	955
20	100	"	900	935
20	200	"	900	930
30	200	"	850	880
20	100	Quartz**	600	595
30	100	"	550	570

* Transmittance @ 4.67 μm = .77 (measured value)

** Transmittance @ 4.67 μm = .10 (measured value)

Optical Pumping Profile

The spatial distribution of excited molecules is determined, in part, by the spatial dependence of the optical excitation inside the gas mixture. Thus, as a first approximation, a one-dimensional calculation of the absorption of radiation in CO-Ar mixtures was performed. Argon presents a very low V-T deactivation probability in collisions with CO and its addition widens the spectral absorption lines of CO by collisional broadening. This yields an increase in optical depth without deleterious V-T losses. The power absorbed per unit volume was calculated using standard expressions for the integrated intensity of the bands, for Lorentzian spectral line profiles. A similar calculation, but for the total power absorbed over a certain distance, was carried in Ref. 3.

The spatial pumping profile for the one-dimensional case is shown in Fig. 2. The function G represents the power absorbed per unit volume at position x , normalized to the value of power absorbed per unit volume in the optically thin limit. The abscissa parameter (Z) is the product of the distance to the wall times the percentage of CO in the mixture. As can be seen, for mixtures containing high Ar fraction the e-folding distance is of the order of centimeters, and independent of total pressure. It must be noted that a small value of Z does not necessarily mean low density of CO molecules. The total pressure, and thus the number density of CO, can be increased without modifying the spatial pumping profile. The spatial pumping profile for CO₂ for the same conditions is plotted in the same figure for comparison.

An experimental set-up was built to verify the accuracy of this calculation (Fig. 3). A rectangular cell contained the gas mixture. Infrared pumping radiation originated by an arc lamp was focused into the cell, and the spontaneous emission radiation of the gas was measured in the perpendicular direction. The position of the measurement point was varied along the cell. The filtering and detection scheme was similar to the one shown in Fig. 1. Proportionality between spontaneous emission intensity and power absorbed was assumed for these measurements. The results obtained for mixtures with 5 and 10% CO are shown in Fig. 4. They have been normalized by dividing the signal at position X by the value for the signal at $X=0$. Good agreement between the calculated and measured spatial dependence profiles can be seen.

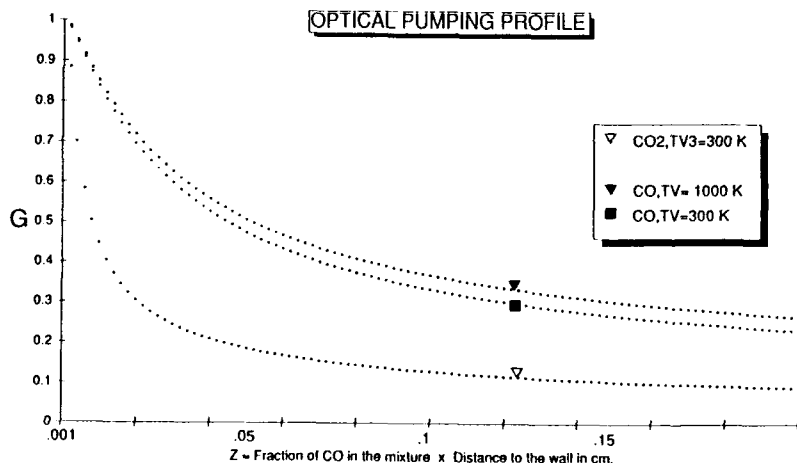


Fig. 2. Calculated radiative pumping profile for CO-Ar and CO₂-Ar mixtures.

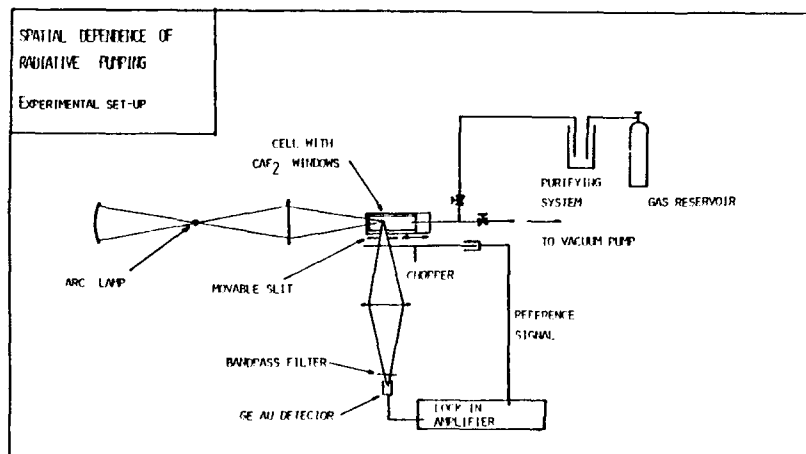


Fig. 3. Experimental set-up for optical pumping profile measurements.

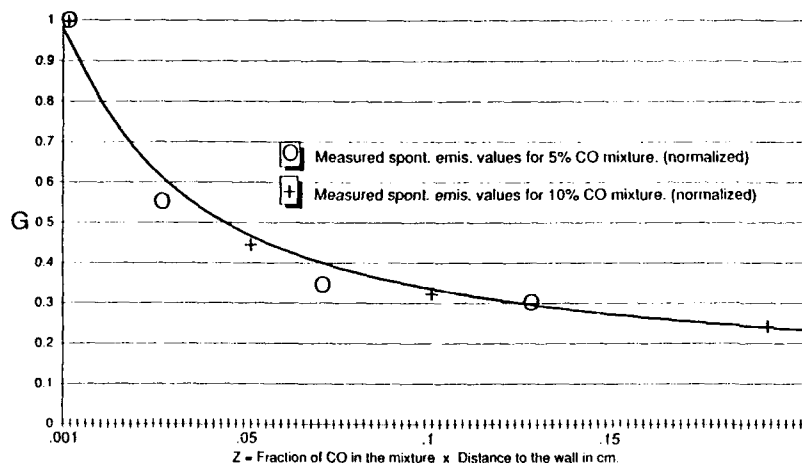


Fig. 4. Measured spontaneous emission intensities, normalized to the value at $x=0$. The curve corresponds to the calculated optical pumping profile.

Numerical Model

The rate equations for the vibrational states were formulated and solved to predict the population distribution under and after blackbody pumping. These included multilevel radiative excitation, V-V interlevel energy transfer, and V-T processes. The rate constants were calculated using experimentally proved kinetic models^{6,7}. The number of vibrational levels was adjusted according to the characteristic vibrational temperature (T_{v1}), as to include many upper vibrational levels in the Boltzmann region of the distribution. The steady state and time dependent solutions of the system were found using an initial value solver for stiff systems. Figure 5 shows an example of the steady state solution for a hypothetical case of 2100°K blackbody temperature, 200°K gas temperature, and one atmosphere total pressure. It presents the very well known distribution for anharmonic oscillators in a non-equilibrium situation. The small signal gain was calculated for the more intense rotational lines for several vibrational transitions, giving values of the order of 0.15%/cm. The model also permits one to calculate the time evolution of the distribution. Figure 6 shows the time history of T_{v1} as the gas flows through the experimental set-up shown in Fig. 1. In this particular case the gas spent 2.5 radiative lifetimes (optically thin value for $v=1$ to 0 transition) in the pumping region, and achieved a vibrational temperature of 1100°K for 1500°K blackbody pumping temperature. The values of T_{v1} for the test cell position for different cases are the ones listed as calculated values in Table 1.

As the V-T deactivation rates are very small for this molecule, and diffusion and wall deactivation can be made negligible at high pressures, the decay of stored vibrational energy downstream of the pumping region is dominated by radiative losses. Thus, radiation trapping schemes are needed to transport the excited gas efficiently. The time dependence of the total stored vibrational energy after the pumping for two radiative trapping conditions is shown in Fig. 7. The first case corresponds to the optically thin condition and the characteristic time of decay is very close to the radiative lifetime of the first vibrational level. In the second case, the expressions derived by Holstein⁸ were used to calculate the equivalent radiative lifetime for each of the lower levels for this optically thick case, adding the effect of 99% reflective walls. As it can be seen, this simple scheme allows considerable increase in the storage time.

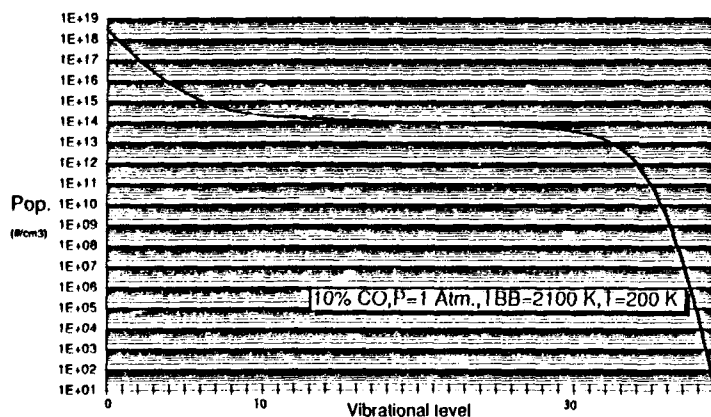


Fig. 5. Vibrational population distribution under blackbody pumping. Steady state solution.

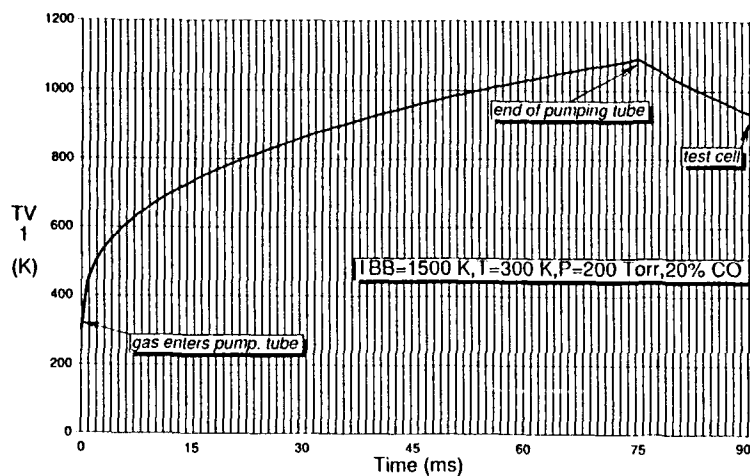


Fig. 6. Vibrational temperature history of CO in the CO-Ar mixture flowing thru the experimental system shown in Fig. 1.

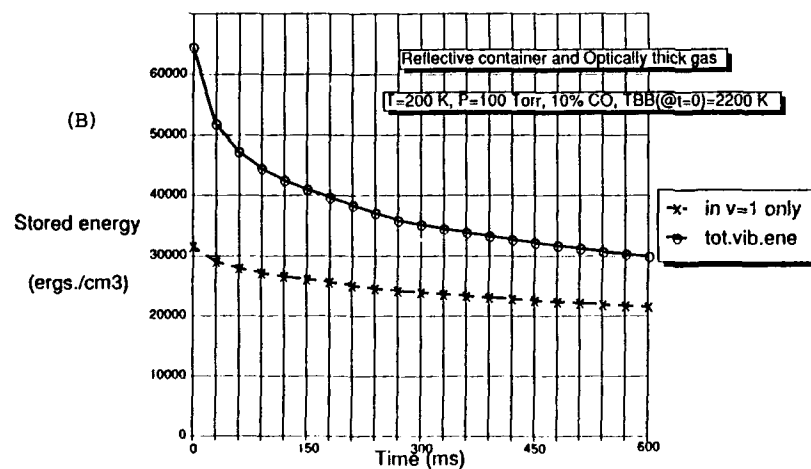
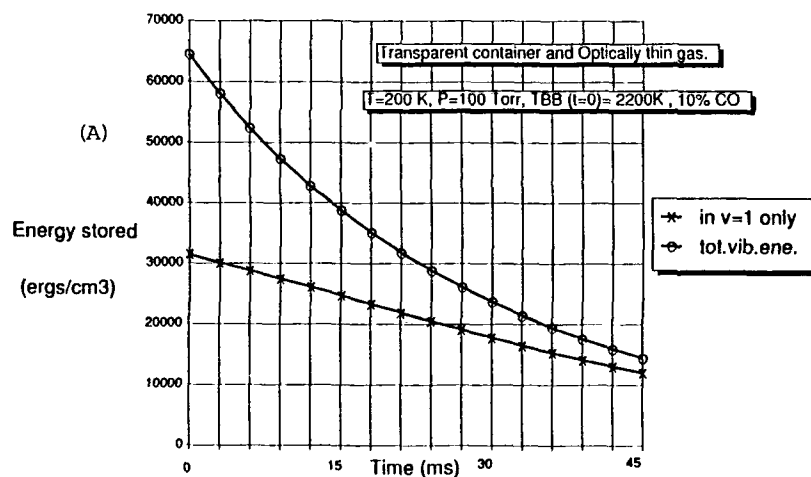


Fig. 7. Time dependence of the stored vibrational energy after the gas exits the pumping cavity. A) Optically thin case, B) Radius of transporting tube = 5 cm., and 99% wall reflectivity.

Summary

The vibrational temperature measurements have demonstrated the feasibility of exciting carbon monoxide to vibrational temperatures close to that of the pumping blackbody cavity. Some preliminary measurements have also shown that the decay of stored energy is dominated by radiative losses. The optical pumping profile calculations and measurements have shown that large pumping containers (several centimeters diameter) can be used, and that high number density of carbon monoxide is possible by maintaining high Ar content in the mixture. The implemented code for the rate equations allows prediction of the vibrational distribution and its time dependence. The calculated values for T_{v1} agree with those obtained experimentally. While the radiative lifetime of CO is inherently large (30 ms.), it is still possible to effectively increase it by radiative trapping, for energy storage or transfer purposes. The simple scheme proposed yields e-folding times of 0.5 sec., and it will be experimentally tested. V-V energy transfer by isotopes, and enlargement of storage times by addition of N₂ should further enhance the advantages of this molecule.

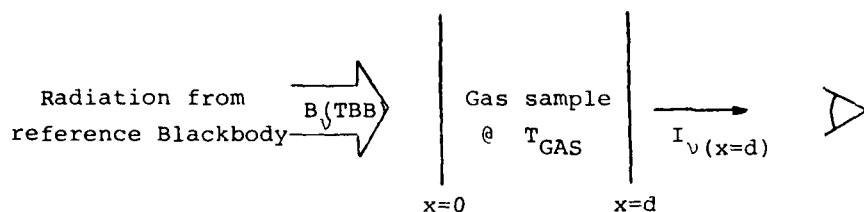
References

1. W.H. Christiansen, in Progress in Aeronautics and Astronautics, Vol. 61, Radiation Energy Conversion in Space, K. Billman, Ed., AIAA, New York (1978) pp. 347-356.
2. J.M. Sirota and W.H. Christiansen, IEEE J. Quantum Electronics QE-21, 1777 (1985).
3. C.H. Treanor, in Proceedings of the International Conference on Lasers '85, C.P. Wang, Ed. (STS Press, McLean, VA, 1986) pp. 475-482.
4. R.F. Gordiets and S. Zhdanok, in Nonequilibrium Vibrational Kinetics, M. Capitelli, Ed., (Springer-Verlag, New York, 1986) pp. 47-84.
5. S.S. Penner, Quantitative Molecular Spectroscopy and Gas Emissivities, (Addison-Wesley Co., London, 1959).
6. R.L. Deleon and J.W. Rich, Chem. Phys. 107, 283 (1986).
7. G.D. Billing, in Nonequilibrium Vibrational Kinetics, M. Capitelli, Ed., (Springer-verlag, New York, 1986) pp. 85-112.
8. T. Holstein, Physical Review 83, 1159 (1947).

Appendix

Line reversal method. Its accuracy.

Consider the following one-dimensional case:



Assuming uniform gas temperature and density, the integrated radiative transfer equation is:

$$I_v(x=d) = B_v(T_{GAS})(1 - \exp(-\alpha_v d)) + R_v(T_{BB})\exp(-\alpha_v d) \quad (1)$$

where I_v is the specific intensity; B_v is the thermal equilibrium specific intensity, α_v is the absorption coefficient of the gas at frequency ν , T_{BB} is the reference blackbody temperature and T_{GAS} is the characteristic temperature we are interested in measuring. Thus, when $T_{GAS} = T_{BB}$,

$$I_v(x=d) = R_v(T_{BB}) \quad (2)$$

which is defined as reversal condition, and T_{RR} at this point is called the reversal temperature. As $R_v(T_{RR}) \approx R_{v_0}(T_{RR}) = \text{const.}$ over all the observation bandwidth Δv , the integration of equation (1) over Δv yields:

$$I_{v_0}(d)\Delta v = R_{v_0}(T_{GAS})\delta v + R_{v_0}(T_{RR})(\Delta v - \delta v) \quad (3)$$

$$\text{where } \delta v = \int_{\Delta v} (1 - \exp(-\alpha_v d)) dv \quad (4)$$

Trying to find the blackbody temperature that verifies Eq. (2), we will be limited by the resolution of the system, and measure in fact

$$I_{v_0}(d) \cdot \Delta v = R_{v_0}(T_{RR})\Delta v(1 \pm \gamma) \quad (5)$$

where γ is the resolution of the detection system. Thus, in this situation $T_{RR} \neq T_{GAS}$. Let us define $\Delta T = T_{RR} - T_{GAS}$. As $\gamma \ll 1$ we can expand $R_v(T_{GAS})$ as function of $R_v(T_{RR})$. Replacing (3) in (5), expressing $R_v(T_{GAS})$ as function of $R_v(T_{RR})$, and after some rearrangement we obtain

$$\frac{\Delta T}{T_{RR}} = \left(\frac{KT_{RR}}{h\nu_0} \right) (1 - \exp(-h\nu_0/KT_{RR})) \left(\frac{\Delta v}{\delta v} \right) \cdot \gamma \quad (6)$$

which defines the relative error of the measurement.

SURFACE DISCHARGE PREIONIZED CO₂ LASER DEVELOPMENT *

M. John Yoder, Raymond B. Schaefer, James O'Brien, and James Connolly
W.J. Schaefer Associates, 321 Billerica Road
Chelmsford, MA 01824-4191

Abstract

A novel technique using a surface discharge preionizer and dielectric discharge plasma electrode was used to excite a pulsed CO₂ gas laser. In this approach, a plasma electrode is created by a discharge on the surface of a dielectric substrate. The plasma electrode serves both as the UV preionization source and the conductive electrode. This paper presents experimental results of a program to demonstrate high energy loading and high energy extraction from this type of electrical discharge in CO₂ gas mixtures. The results demonstrate an input energy loading in a discharge volume of 7cm x 7cm x 86cm (4 liters) of approximately 200 J/L/atm, an output laser energy extraction of 47 J/L/atm, and an electrical efficiency of 25% at 0.5 atmosphere gas pressure. Discharge times from one microsecond to 25 microseconds were obtained. The voltage and current characteristics indicate that this is a non-self-sustained electrical discharge. This surface discharge approach eliminates the need for a separate preionization source and specially contoured oversize electrodes. Much simpler, more reliable and more compact repetitively pulsed lasers for commercial and military applications can be constructed using this technique when compared to electron-beam-sustained or conventional U.V. preionized lasers.

Introduction

Large volume, near-atmospheric pressure discharges in gases are difficult to obtain. Due to the electrical nonconductivity of the gas, initial electrons must be generated for current conduction. During the discharge the free conduction electrons are lost due to electron attachment and recombination and must be replaced to "sustain" the discharge. In self-sustained discharges electrons in the high velocity "tail" of the Maxwellian drift velocity distribution generate new electrons by collisions with neutral atoms or molecules. Unfortunately this mechanism of electron production is inherently unstable. Statistical fluctuations in electron production lead to higher than average electron density in certain small volumes. These higher electron density regions subsequently generate even higher electron concentrations, which lead to high localized regions of conduction and constriction of the volumetric discharge into an arc.

An example of pulsed self-sustained discharge is the U.V. preionized discharge shown schematically in Figure 1a⁽¹⁾. The source of the initial electron distribution is a spark

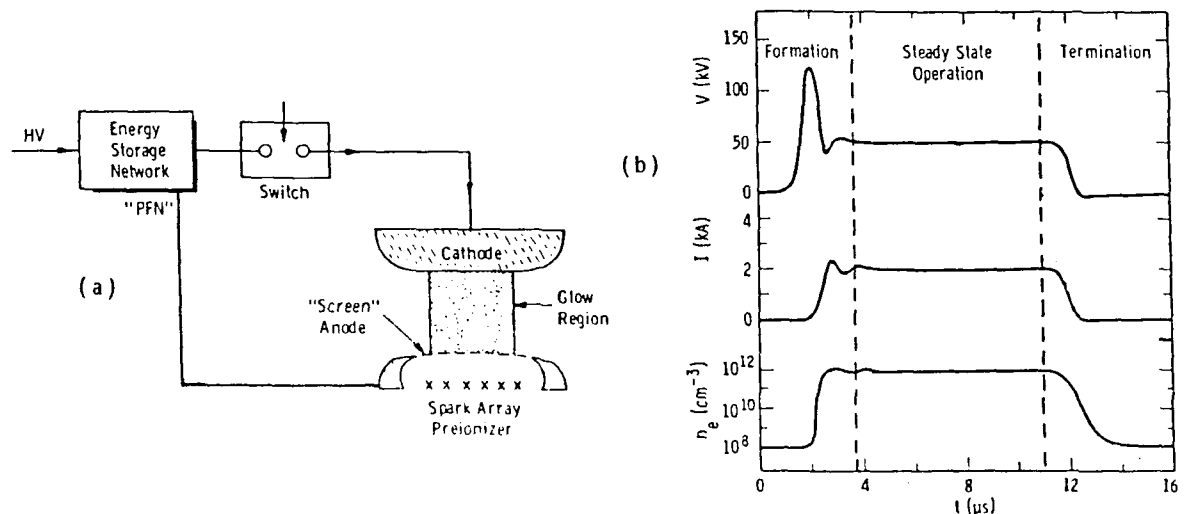


Figure 1. (a) Typical U.V. preionized laser. (b) Typical voltage and current waveforms. Approximate electron densities are also shown. (See Reference 1).

*Sponsored by Defense Advanced Research Projects Agency Contract No. DAAH01-86-C-1073 and WJSA internal research and development funds.

trodes. Large optical cross-section lasers have been demonstrated up to 15cm x 15cm, and large volume devices up to 15cm x 15cm x 80cm (18 liters) have been surface discharge pumped. Energy loadings in the range of 200 to 350 joules per liter atmosphere have been obtained with high energy extraction values of 30 to 48 joules per liter atmosphere and 15% to 25% electrical efficiency. The present research has reproduced many of these previous results and has extended the discharge times to long pulse lengths.

There are a number of issues that have not been addressed in this or previous research. The optimum operating parameter space in terms of pressure, gas mixture, discharge parameters, etc. have not been mapped. The quality of the laser in terms of gain uniformity, density uniformity or farfield beam quality has not been documented. Long lifetime electrode performance in excess of 10^4 shots has not yet been demonstrated. Candidate dielectric substrates such as Teflon, G-10, glass, quartz, ceramic, etc. have been used but not fully characterized. The basic discharge physics of this technology is not yet well understood. Finally, to these authors knowledge, no closed cycle, repetitively pulsed devices have been constructed.

Summary and Conclusions

Surface discharges have been shown to be efficient ionization sources due to their close proximity to the laser gas, high ultraviolet intensity, and the substrate induced spectral enhancement. Very high electron densities of about 10^{11} electrons per cubic centimeter were generated in the gas. Very long discharge pulse times in excess of 20 microseconds were demonstrated. These are very stable discharges for long pulse or large volume pumping at near-atmospheric pressure. High input energy density loading has been demonstrated as well as high output energy extraction and electrical efficiency. Output energy extraction with this relatively simple system is comparable with values obtained only with large electron-beam-sustained lasers or very carefully designed and aligned U.V. preionized lasers. (22)

One of the most important attributes of this surface discharge technology is the simplicity and compactness of the electrodes. Long pulse or large volume self-sustained operation using either U.V. spark, x-ray, or electron beam preionization requires very careful design of the electrode profiles to eliminate discharge instabilities. These designs result in long electrode fall-off contours that must be at least the width of the discharge region on both sides of the electrode. The alignment of the electrodes must be very precise and must be maintainable in non-laboratory systems. By contrast there are no such requirements for surface discharge plasma electrodes. No electrode profile fall-off regions are necessary and alignment requirements are not severe. Packaging this technology in a repetitively pulsed fieldable or marketable device should be much easier and compact than with conventional spark array, x-ray or electron beam preionized lasers or electron-beam-sustained lasers. Potential applications include long range laser ranging or wavelength conversion. Surface discharge lasers may also be useful for coherent CO₂ laser radar applications since long pulses are required for good velocity discrimination.

References

- (1) L.E.Kline and L.J.Denes, Applied Atomic Collision Physics, Vol.3(Academic Press, Inc. 1982), pp. 387-422
- (2) J.D. Daugherty, E.R. Pugh, and D.H. Douglas-Hamilton, Bull. Am. Phys. Soc. 16, 399 (1972); J.A. Fenstermacher, M.J. Nutter, W.T. Leland, and A.K. Boyer, Bull. Am. Phys. Soc. 16, 399 (1972).
- (3) S.I. Andreev, et.al., Zhurnal Prikladnoi Spektroskopii 5, 703 (1963).
- (4) A.A. Avdienko and M.D. Malev, Sov. Phys. Tech. Phys. 24, 581 (1979).
- (5) R.E. Beverly III, Progress in Optics, XVI, E. Wolf Ed. (North-Holland Inc., 1978). (6)W.J. Sargeant, IEEE Trans. Plasma Sci. PS-8, 216 (1980).
- (7) R.B.Schaefer, J.P.Reilly and M.J.Yoder, Final Report DNA-TR-84-222,Contract No. DNA-001-83-C-0400 (1985).
- (8) R.B. Schaefer and M.J. Yoder, Final Report WJSA-87-R-B-017, Contract No. DAAH01-86-C-1073 (1987).
- (9) E.J. McLellan, U.S. Patent No. 4, 412, 333, Ser. No. 198,028, U.S.CI. 372-87, Intl. Cl. H015-31097, Filed Oct. 17, 1980.
- (10) V.V. Apollonov, G.G. Baitsur, A.M. Prokhorov, and K.N. Firsov, Sov. J.Quantum Electron. 17, 76 (1987).
- (11) M.J. Yoder, H.H. Leger, J.H.Jacob, and D.R. Ahouse, J.Appl.Phys.49, pp. 3171-3180 (1978).
- (12) M.C. Cornell, I. M. Littlewood, H.L. Brooks, and K.J. Nygaard, J. Appl. Phys. 54, 1723 (1983).
- (13) P.M. Atanasov, V.P. Golubchenko, N.V. Karlov, I.O. Kovalev, G.P. Kuzmin, and A.M. Prokhorov, Sov. Tech. Phys. Lett. 11, 326 (1985).
- (14) N.V. Karlov, A.V. Kisletsov, I.O. Kovalev, G.P. Kuzmin, A.A. Nesterenko, and E.M. Khokhlov, Sov. J. Quantum Electron. 17, 131 (1987).
- (15) G.V. Eremenko, D. Yu.Zaroslav, N.V. Karlov, I.O. Kovalev, G.P. Kuzman, and A.M. Prokhorov, Sov. J. Quantum Electron. 13, 1996 (1983).
- (16) S.I. Andreev, I.M. Belousova, P.N. Dashuk, E. Zobov, N.V. Sidorov, L.L. Chelnokov, and M.D. Yarysheva, JETP Lett. 21, 194 (1975/A).
- (17) D.Yu.Zaroslav, N.V. Karlov, G.P. Kuzmin, and D. McKen, Sov. J. Quant. Elect. 8, 1048 (1978/B).
- (18) N.G. Basov, U.A. Danilychev, V.A. Dogikh, O.M. Kerimov, I.G. Rudoi, A.M. Soroka, and G.Yu. Tamanyan, Sov. Tech. Phys. Lett. 12, 82 (1986).
- (19) S.P. Bazhulin, N.G. Basov, S.N. Bugrimov, U.S. Zuev, A.S. Kamrukov, N.P. Kozlov, A.G. Opekan, and Yu.S. Protasov, Sov. Tech. Phys. Lett. 12, 589 (1986).
- (20) N.G. Basov and V.S. Zhev, Il NUOVO Cimento B 9, 129 (1976)
- (21) A.V. Belotserkovets, et al, Sov. Tech. Phys. Lett. 5, 80 (1979)
- (22) M.J. Pechersky, R.V. Babcock, J.F. Roach, D.R. Suhre, and R.J. Spreadbury, Proceedings of the International Conference on Lasers '84, pp. 380-389.

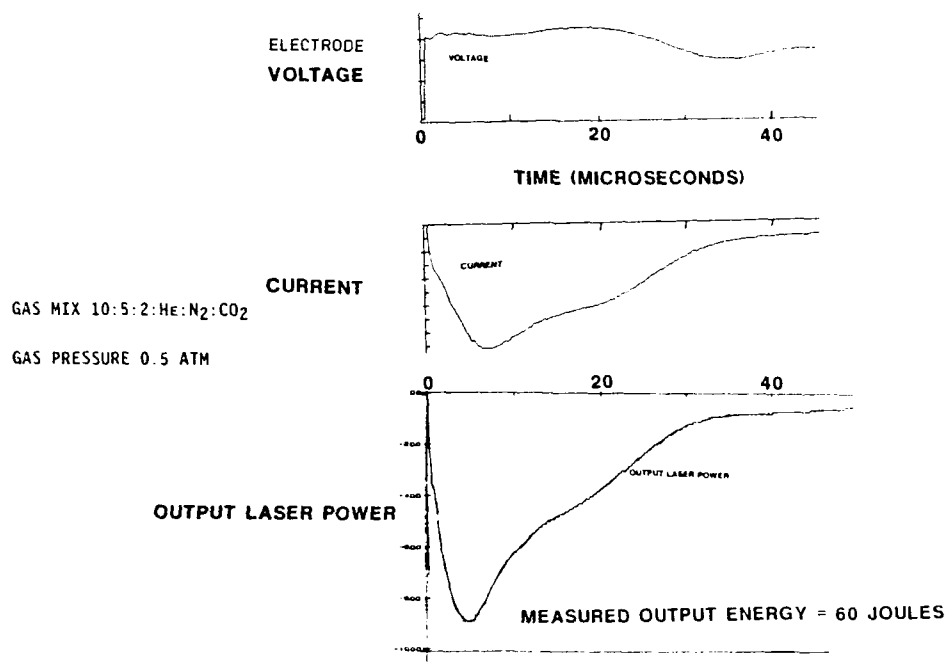


Figure 10. Input voltage, input current and output power waveforms for long pulse discharges.

follow the input current waveform profile. The measured output energy for these traces was about 60 joules, thus achieving an energy extraction of about 27 joules per liter atmosphere. (Note: the entire discharge aperture of the laser was larger than the optics so a small correction factor was applied). The small signal gain was not measured but is calculated to be about 2.5% per centimeter. The operating voltage of the discharge divided by the gas density (particles per cubic centimeter), or E/N , is measured to be approximately 2×10^{-16} which is significantly lower than the expected "glow voltage" of about 3×10^{-16} .

Contrary to expectations, U.V. preionized discharges using the plasma electrode do not behave like self sustained discharges. There are several notable differences: (1) there is no overvoltage spike; (2) the current rise is slow; (3) the operating E/N is lower than the glow voltage; (4) the electrode profiles and alignment are not critical. The lack of an overvoltage spike could be explained by the fact that surface discharges radiate much more ultraviolet radiation than spark arrays, thus directly generating electron densities in the range of 10^{11} to 10^{12} , but the other differences are not easy to explain.

Two possible explanations for this discharge imply that it is a non-self-sustained discharge. Hypothesis #1: The discharge may be photon-sustained in direct analogy to the electron-beam-sustained discharge. In this case the intense ultraviolet glow of the surface plasma generates electrons via photoionization until the electron production rate equals the loss rate due to attachment and recombination. This hypothesis is consistent with all of the above four observations. Hypothesis #2: An electron cloud is created at the cathode, and the electron lifetime is long enough that when the anode to cathode acceleration voltage is applied, a significant number of electrons reach the anode.^(9,10) Since the electron mean lifetime is approximately 4 microseconds for this mixture and gas pressure,⁽¹¹⁾ and the mean electron velocity at these applied voltages is about 5×10^6 centimeters per second,⁽¹²⁾ then the mean electron drift distance is calculated to be approximately 20 centimeters. The anticipated initial current rise time in this hypothesis is approximately 2 microseconds due to the finite velocity of the initially generated electron cloud. This hypothesis is also consistent with all four of the above observations. Further experiments and/or calculations are required to discriminate between these two hypotheses and definitively explain the discharge.

Previous and Future CO₂ Surface Discharge Laser Research

Extensive CO₂ research using this technology has been carried out in the Soviet Union since about 1975 and a large number of research papers have been published.⁽¹³⁻¹⁷⁾ Surface discharges are also applicable to pumping excimers and photodissociation lasers.⁽¹⁸⁻²¹⁾ Surface discharges have been used both as preionization sources as well as plasma elec-

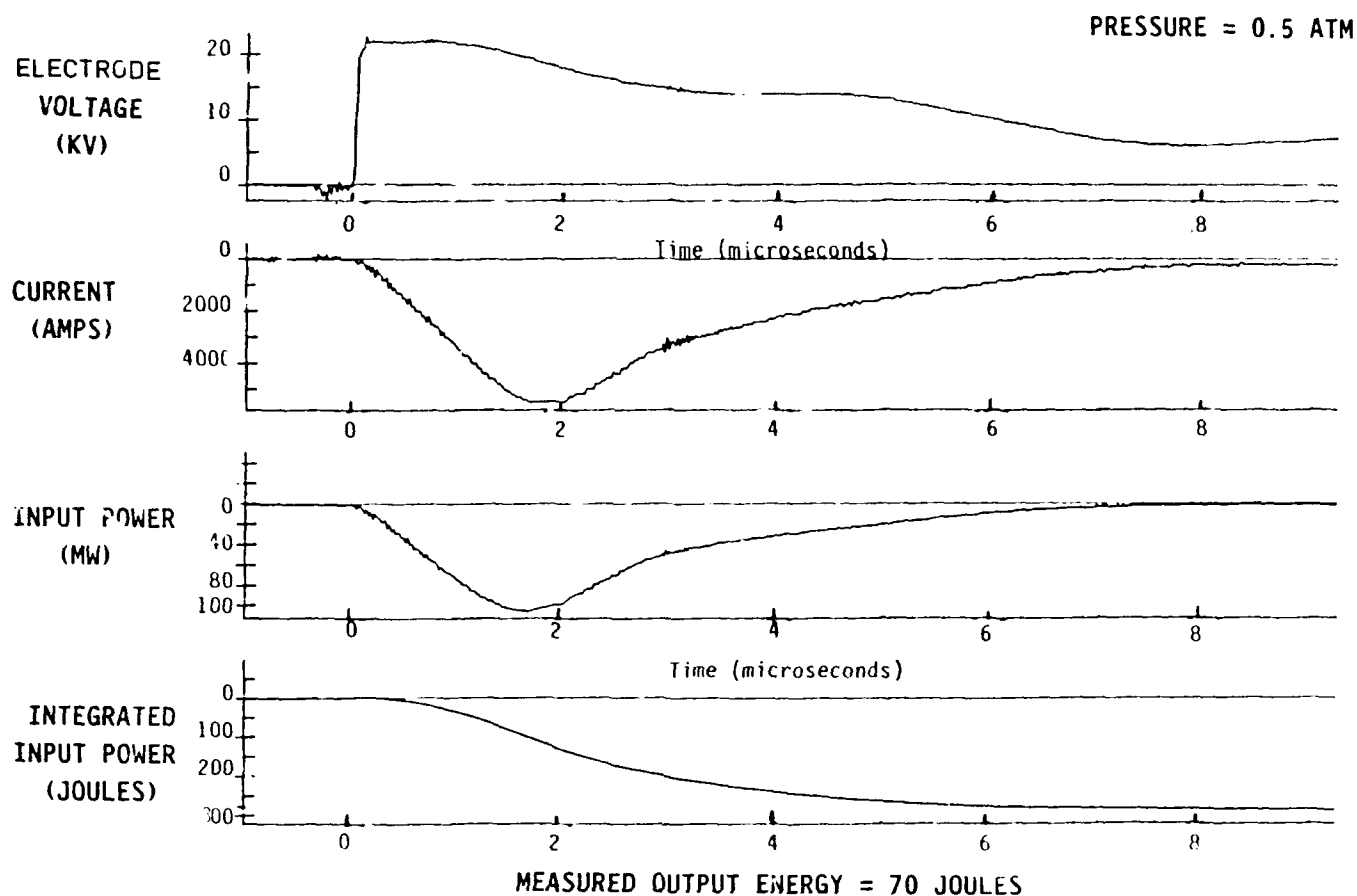


Figure 8. Voltage, current, input power, and input energy traces for a typical short pulse discharge.

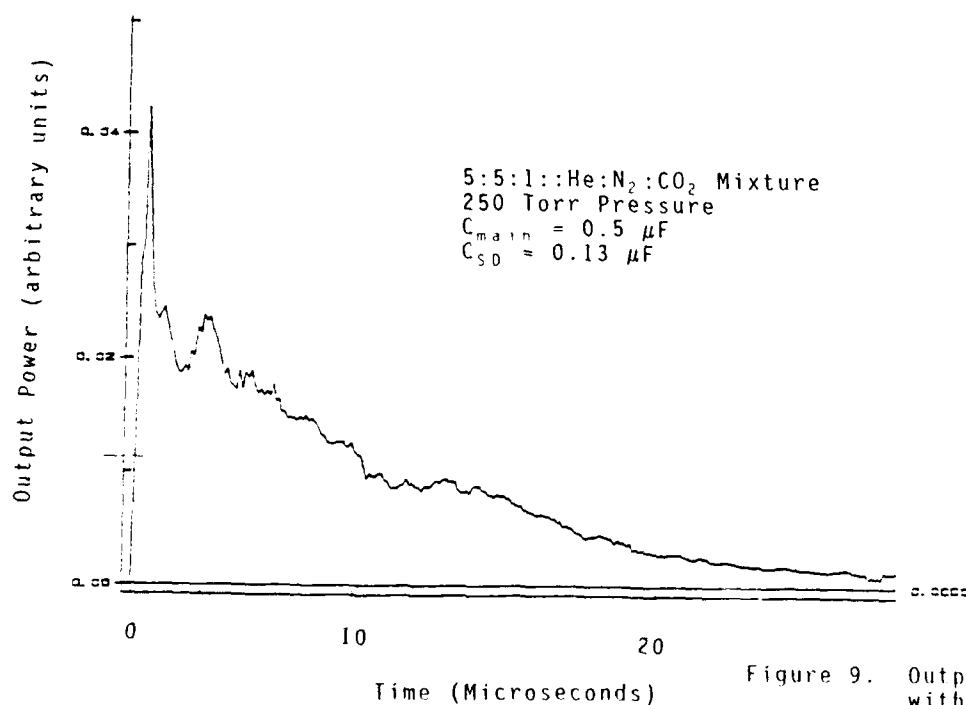


Figure 9. Output power measured with a Photon Drag Detector

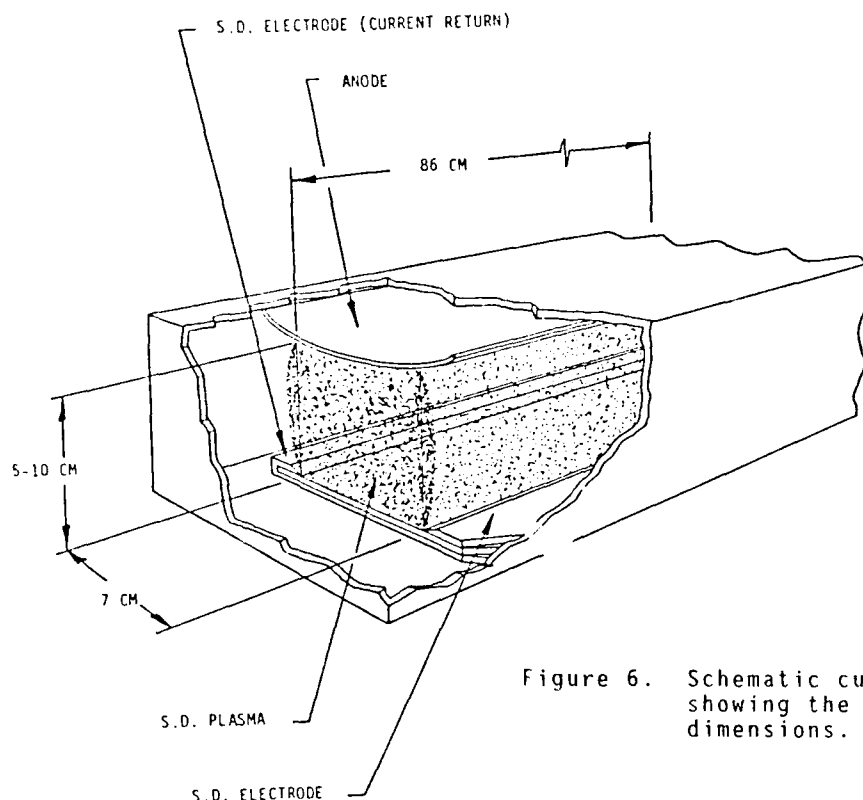


Figure 6. Schematic cut-away drawing showing the typical discharge dimensions.

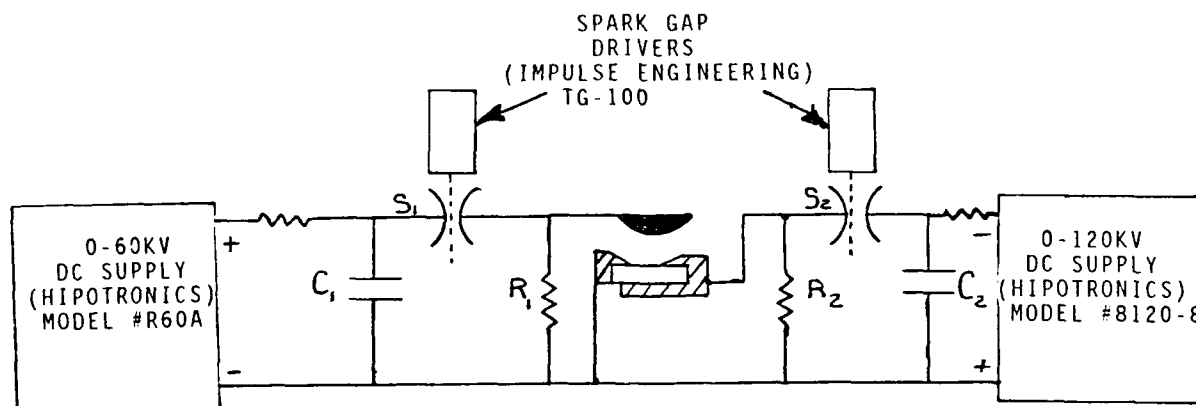


Figure 7. Electrical circuit for surface discharge laser using plasma electrodes. $C_1 = .5\mu\text{Fd}$, $C_2 = .137\mu\text{Fd}$, $R_1 = 1\text{k}\Omega$, $R_2 = 1\text{k}\Omega$, $S_1 = S_2 = \text{Modified Maxwell Air Gaps}$

calculation. No gas mixture or discharge optimization variations were carried out. The operating pressure was limited by the available capacitors, switches, and voltage supplies. Higher pressure operation should be possible.

Long pulse operation was demonstrated using a 1.5 microfarad three section pulse forming network (PFN). In this case the discharge cavity was 7cm x 8cm x 86cm (4.8 liters) and operated at 0.5 atmosphere pressure with a 10:5:2::He:N₂:CO₂ mixture plus TPA. The pressure was again limited by the available capacitors, switches, and power supplies. Voltage, current, and output power traces are shown in Figure 10. The pulse width was about 25 microseconds at the half power points and was limited by the available PFN. The voltage measured directly at the electrodes rises rapidly and then remains high. There is no voltage overshoot. The current rise and fall are gradual. These rise and fall times are not determined by circuit inductive effects but rather by the discharge characteristics and the waveform of the applied voltage. The photon drag detector trace shows the output power to

A single pulse laser employing a surface discharge electrode and a conventional contoured brass electrode was set up (similar to Figure 4b). The dielectric electrode was made by chemically etching copper-clad fiberglass circuit board to form a surface discharge of area approximately 7cm by 107cm. This extremely compact and simple to fabricate electrode and the rest of the laser are shown in Figure 5. An outer plexiglass box is used to enclose the electrodes and the laser gas. The facing brass electrode is 107cm x 19cm in area, with an elliptical contour (quasi-Rogowski). It had a flat discharge area of 86cm x 8.3cm. A diagram of the discharge electrodes and discharge volume is shown in Figure 6.

The basic configuration of the electrical circuit is shown in Figure 7. The surface discharge capacitor (0.137 microfarads) was charged typically to 35 kV and had an energy of 84 joules. Voltage traces showed surface discharge pulse lengths of approximately 0.7 microseconds. The presence of CO₂ in the gas mixture causes the surface discharge to break up into closely spaced streamers at 0.5 atmosphere pressure. The uniformity of the laser preionization, however, is still better than that obtained with discrete sparks.

The main discharge capacitor was 0.5 microfarads and was charged typically to 35 kV for a stored energy of 310 joules for the short pulse tests. Voltage and current traces were obtained from a Tektronics Model P6015 voltage probe and a Pearson Model 110 current coil. An Analogic Data Precision Model 6000 multichannel analyzer was used to collect and process the experimental results. Key features of this discharge shown in Figure 8 are the absence of an overvoltage spike and the gradual rise of the current waveform. The integrated input power (energy) was about 280 joules and the measured output energy (using a Scientech Model 364 energy meter) was 70 joules. The gas pressure was 375 Torr and the gas mixture was 5:5:1::He:N₂:CO₂ and contained a trace amount of TPA. Thus for this 5cm x 7cm x 86cm (3 liters) discharge, the input energy loading was about 190 joules per liter atmosphere and the laser efficiency was 25%. The output energy extraction was about 48 joules per liter atmosphere. Computer code calculations based on the measured input parameters exactly predict the measured output energy. The output laser waveform was monitored using an Edinburgh Instrument Model PDM-2 photon drag detector. A typical output waveform is shown in Figure 9. The shape of the output flux waveform also agrees well with the computer code

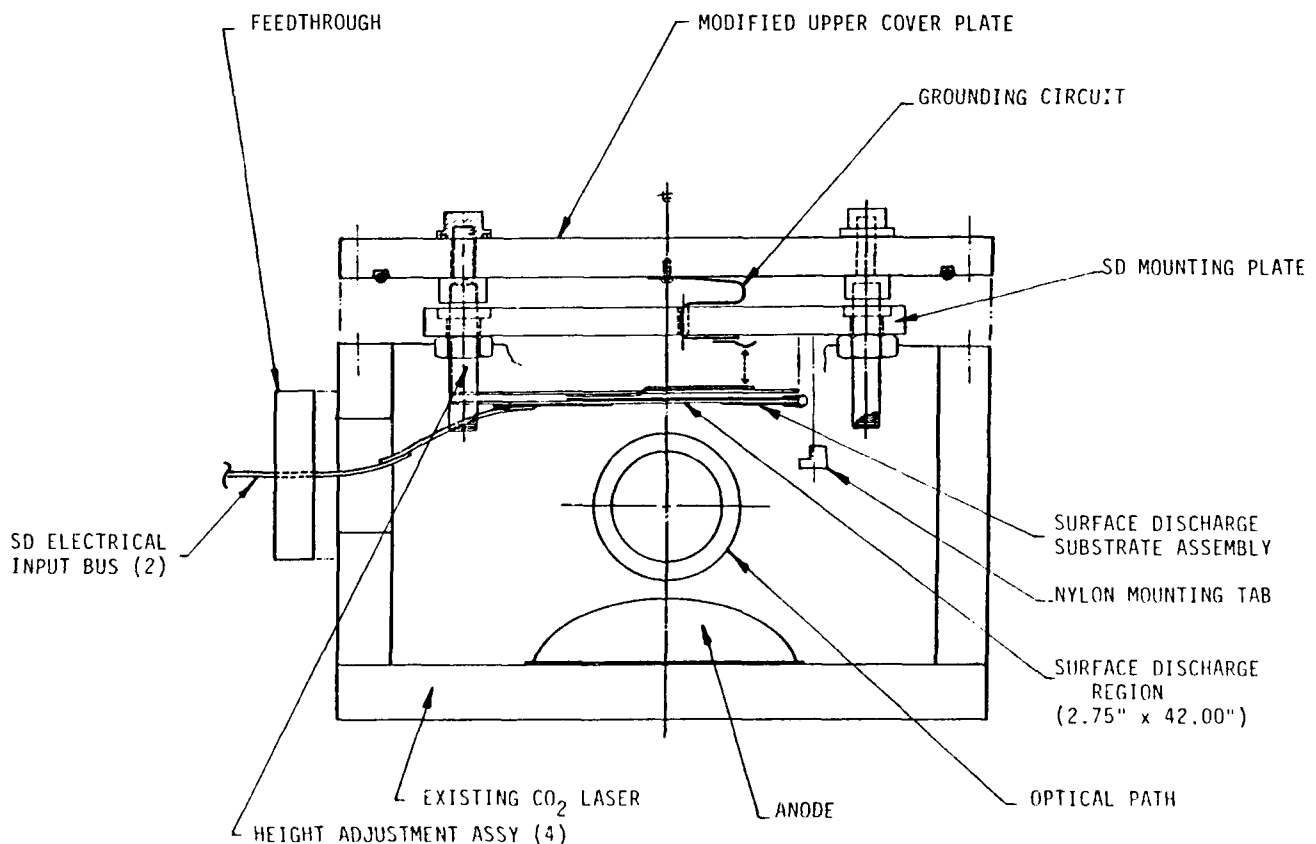


Figure 5 Single pulse laser configuration showing the surface discharge assembly.

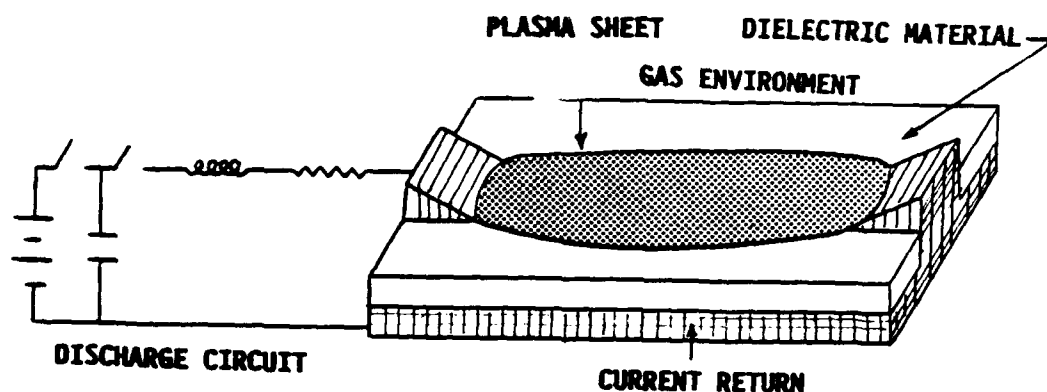


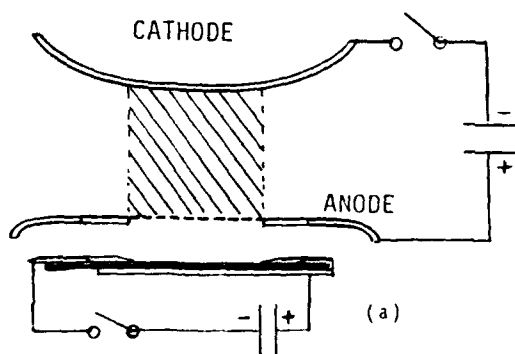
Figure 3. Schematic diagram of a surface discharge and the associated electronics circuit.

dielectric toward the anode. The surface discharge forms at relatively low voltages compared to the breakdown voltage for the anode to cathode gap spacing due to the capacitance between the electrode and the back-plate. Because of surface vaporization the conductivity of the plasma is largest near the surface so the discharge remains confined to this region. The radiation spectrum contains a strong continuum in addition to bright spectral lines characteristic of the substrate material. In particular, use of silicon containing dielectric materials matches the U.V. photoionization absorption spectrum of CO_2 and easily ionizable additive gases such as tri-n-propylamine (TPA). The radiation intensity of the surface discharge depends on several variables including the electric circuit, gas composition and pressure, substrate and electrode materials and geometric arrangement. The radiation intensity can be made very high and can be characterized by the U.V. radiation intensity in the spectral region of 150nm to 300nm as being equivalent to blackbody radiation at a temperature of 50,000K or more. The electron number density in the surface plasma approaches that of the background gas and is typically 10^{18} to 10^{19} electrons per cubic centimeter.

Experimental Design and Results

In analogy with U.V. preionized lasers the surface discharge can be used in any of several configurations shown in Figure 4. The most obvious is that of Figure 4a which simply replaces the spark array by a surface discharge. More novel configurations are shown in Figure 4b and 4c in which the surface discharge serves not only as a preionization source, but also becomes the conductive (plasma) electrode.

CONVENTIONAL APPROACH



PLASMA ELECTRODE APPROACH

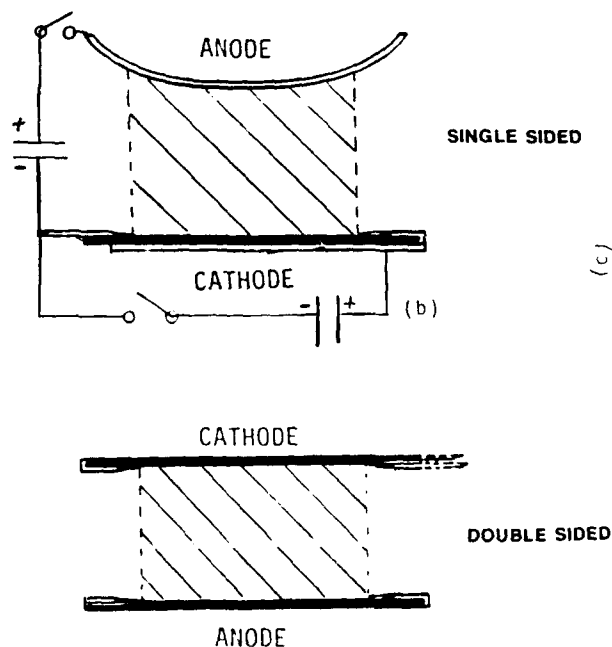


Figure 4. Alternative discharge configurations for surface discharge preionized and pumped lasers.

array located, in this case, behind the anode. This spark array generates an electron concentration of about 10^7 to 10^8 electrons per cubic centimeter by photoionization of the gas. A high voltage is subsequently applied from a capacitor bank through a high voltage switch such as a spark gap or a thyatron. The optimum high voltage pulse waveform shown in Figure 1b has a short duration "spike" which is 1.5 to 2 times higher than the equilibrium "glow voltage" steady state. During this overvoltage spike the electron density avalanches a factor of 10^3 to 10^4 to an equilibrium value of 10^{10} to 10^{12} electrons per cubic centimeter. During the steady state, electron production just balances electron losses. These devices work well but due to the inherent instability of this type of discharge, oversized, carefully contoured and well aligned electrodes are required to provide very uniform electric fields. Electrode widths are typically three times the discharge width. Arcs will still form but at longer and longer times (depending on the uniformity of the electric fields, ionization, and the gas density). In any given device the discharge is terminated before the arcs have a chance to form. The discharge characteristics of note are the initial overvoltage spike, the rapid increase in electron density during the spike, the rapid rise of current and the equilibrium "glow voltage" characteristic of each gas mixture and pressure.

Other types of preionization involving x-rays, electron beam injection, and U.V. surface discharge arrays are possible. In all of these cases the initial electron density is higher than with spark arrays so electron density avalanching requirements are not as severe.

It is also possible to sustain the electron distribution by using an external source. This type of discharge is called an externally sustained or non-self-sustained electric discharge. An example is that of the electron-beam-sustained discharge shown in Figure 2a⁽²⁾. In this case a broad area beam of electrons is obtained from a high voltage electron gun. The electrons are accelerated from the cathode through a vacuum and penetrate a thin foil into the discharge volume. These (primary) electrons generate a larger number of secondary electrons in the gas which are accelerated by a set of discharge electrodes at a much lower voltage. This second discharge collisionally excites the gas internal energy levels and heats the gas. The electron production mechanism is thus decoupled from the laser pumping mechanism and the resulting discharge is inherently very stable. Typical current waveforms are shown in Figure 2b. A constant voltage is applied to the gas from a capacitor. The square wave pulsed primary electron current from the electron beam results in a GRADUAL rise in the secondary electron current until the loss rate (which depends primarily on the instantaneous electron concentration) equals the secondary electron production rate. Electron conduction occurs at any voltage and usually is maintained lower than the glow voltage of the gas to prevent arcing. The primary disadvantage of this type of externally sustained discharge is the large, complex, high vacuum, delicate and marginally reliable broad area electron guns that are required.

Surface Discharges

Very high intensity discharges⁽³⁻⁸⁾ can be obtained on the surface of dielectric materials by the circuit shown schematically in Figure 3. Two conductive electrodes are placed on a thin dielectric surface in contact with a conductive "backplate". A voltage of several tens of kilovolts is applied through a switch from an external capacitor. Due to the capacitance between the cathode and the back-plate (at anode potential) a discharge occurs in the form of a diffuse series of streamers which propagate along the surface of the

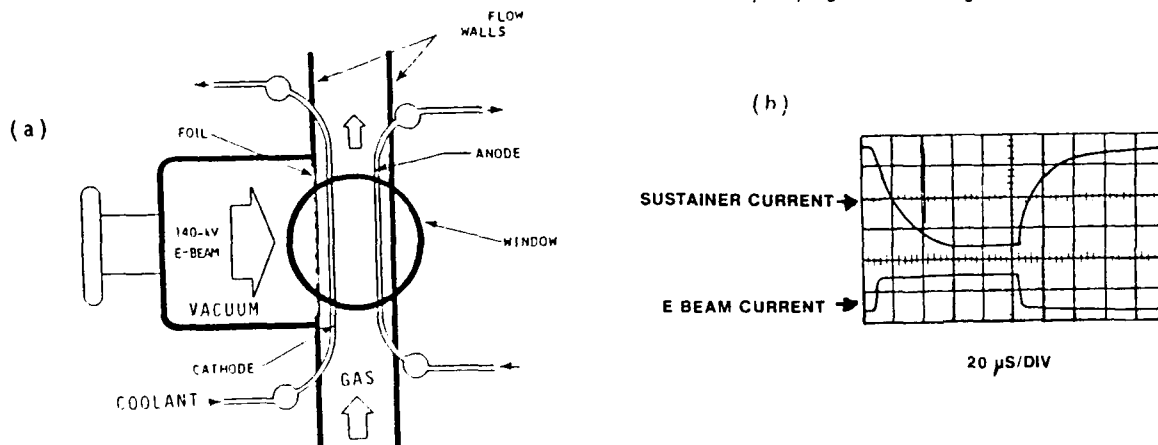


Figure 2. (a) Electron beam sustained laser. (b) Typical electron current and main discharge current traces. The applied sustainer voltage is constant.

TUNABLE SFUR TEA CO₂ LASER

R.Barbini, F.Colao*, A.Palucci*, A.Petri, S.Ribezzo

ENEA, Dip. TIB, U.S., Fisica Applicata, C.R.E. Frascati,
C.P. 65 - 00044 Frascati, Rome (Italy)

Abstract

In this communication we report the results of the first tunable TEA CO₂ laser using Self-Filtering Unstable Resonator (SFUR).

By this technique we obtained tunability over 64 lines, single transverse and longitudinal mode operation and diffraction limited divergence.

Introduction

Active remote sensing of the environment requires efficient laser sources with high pulse energies, wavelength tunability, short pulse-lengths, low divergence beams, single transverse and longitudinal mode patterns, mechanical stability.

To attain these aims, we developed a new design of a TEA CO₂ laser¹ to be used as a LIDAR transmitter in the infrared spectral region.

The laser cavity is a Self Filtering Unstable Resonator (SFUR)^{2,3} which provides transverse mode selection, good far field brightness and efficient energy extraction. This source has also been made line tunable over a broad emission spectrum, for exploiting multi-gas detection capability in the ENEA IR DIAL (Differential Absorption Lidar) system.

In this paper we present the operating principle of the laser resonator and the experimental results, together with numerical laser fields computations.

Operating Principle

The SFUR is a negative branch confocal unstable resonator with a field limiting aperture of radius "a" placed at the common focal plane of mirrors M₁ and M₂ (fig. 1a).

To understand the cavity behaviour let's consider a plane wave proceeding from the right toward M_p: it is at first diffracted in passing through the aperture, then reflected on mirror M₁ and shaped in a Airy pattern with its first zero at $r_0 = \sqrt{0.61 \cdot f_1 \cdot \lambda}$. If we choose $a = r_0$ only the Airy disk is allowed to pass beyond the aperture.

Reflection on mirror M₂ magnifies the field which is partly extracted by M_p and partly transmitted through the aperture, starting a new roundtrip cycle.

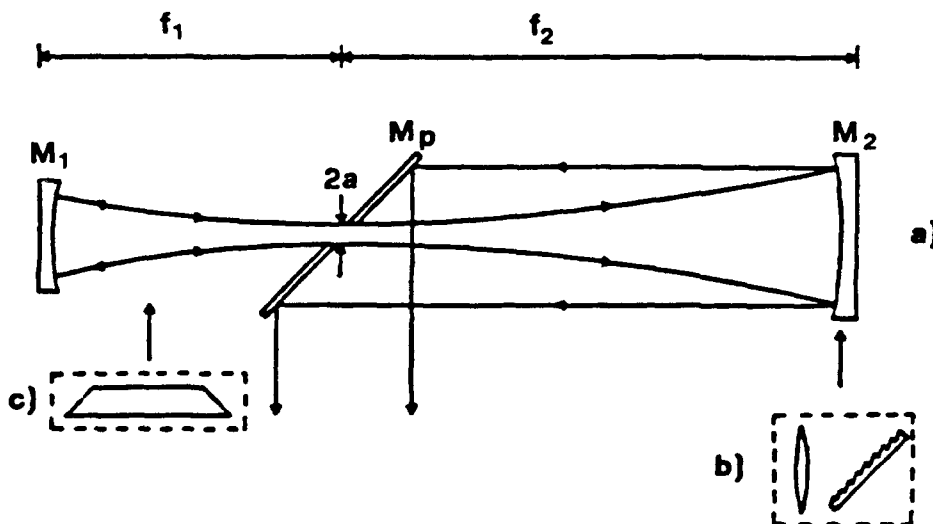


Fig.1 The tunable SFUR TEA CO₂ laser: a) basic design, b) lens-grating assembly replacing end mirror M₂, c) low pressure cw CO₂ cell inserted for longitudinal modes

* ENEA Guest

Laser Design

The optical elements forming our cavity are actually:

- 1) M_1 : a fully reflecting copper mirror with a focal length $f_1 = 62.5$ cm, PZT controlled;
- 2) M_p : a flat copper mirror, placed at the cavity confocal point, with a central aperture radius $a = 2$ mm, which selects the lowest order transverse mode for $\lambda = 10.6$ μm , and is also the output coupler;
- 3) M_2 : a ZnSe lens plus plane grating (150 grooves/mm) assembly (fig 1.b). The lens focal length ($f = 500$ cm) reproduces the confocal condition, at the location of M_p , with a total cavity length $L = 312.5$ cm. Rotation of the grating allows for line selection.

Experimental Results

Our tunable SFUR configuration provides high energy extraction efficiency over 64 lines on branches P and R both at 9 and 10 μm (fig. 2), the maximum output energy being $E = 3.8$ J for the 10P20 line. The pulse length for all the lines is around 80 ns.

The beam divergence has been evaluated by reconstructing the beam profile in the focal plane of a lens ($f = 10.7$ m) placed close to the extraction mirror: we measured the energy transmitted by a 1 mm diameter pinhole, scanning across the beam, and fitted the experimental points with an Airy curve, as shown in fig.3:

$$A(r) = C_1 \cdot \left[\frac{J_1(y)}{y} \right]^2 \quad \left[y = \frac{r - C_2}{C_3} \right] \quad (1)$$

where $J_1(y)$ is the Bessel function of the first kind of order unit and C_1, C_2, C_3 are best fitted by the computer routine to the experimental data. The $1/e^2$ Airy radius turned out to be $w_f = 5.3$ mm leading to a far field divergence half angle $\theta_\infty = w_f/f = 0.5$ mrad. We also measured the beam profile at various distances downstream of the extraction mirror M_p , finding best fit values $w_0 = 6.4$ mm a $z_0 = 6.7$ m for the waist and its distance from M_p , respectively.

Numerical Simulation

Experimental results have been checked by a numerical procedure which computes the field amplitude and phase inside and outside the cavity, by solving the Fresnel diffraction integral⁴.

In the following, we shall consider complex field amplitudes $U_i(r, \phi)$ ($i = 1, 8$) before and after each cavity element, where r and ϕ are polar coordinates in the plane normal to the

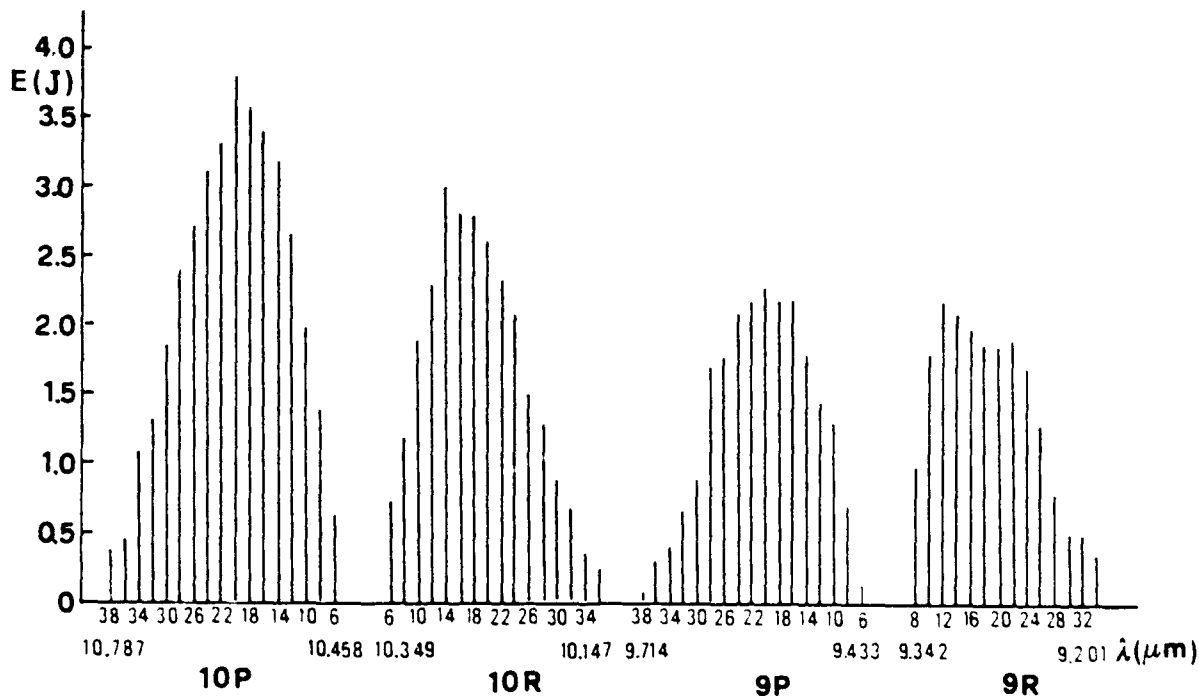


Fig. 2 Line emission spectrum of the SFUR laser.

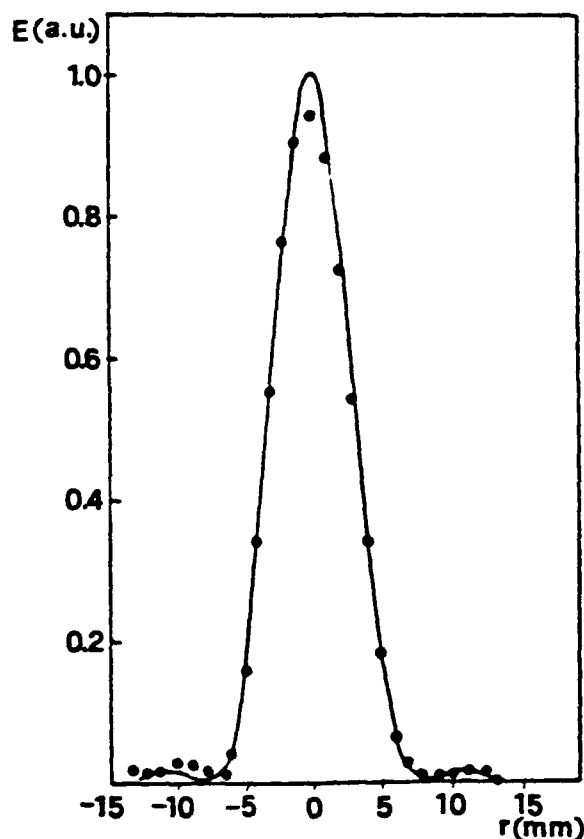


Fig. 3 Beam profile measured with 1 mm pinhole fitted by Airy curve (• = experimental data).

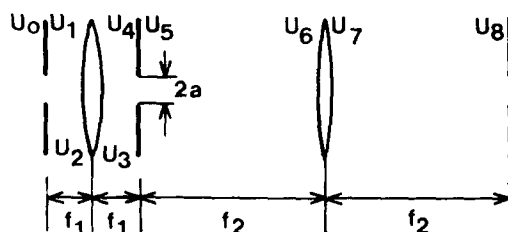


Fig. 4 Lens equivalent circuit of the SFUR Resonator.

propagation axis. Referring to fig. 4 (which is optically equivalent to fig 1.a), a complete radiation roundtrip can be disassembled in the following steps:

a) truncation of the incoming field U_0 by the aperture:

$$U_1(r, \phi) = \begin{cases} U_0(r, \phi) & \text{for } r < a \\ 0 & \text{for } r \geq a \end{cases} \quad (2)$$

b) propagation through a drift space $d = f_1$ (Fresnel integral):

$$U_2(r, \phi) = \int_0^a r' dr' J_n(krr'/d) U_1(r', \phi) e^{ik \cdot (r'^2 + r^2)/2d} \quad (3)$$

where n is the mode index;

c) phase shifting by cavity mirror M_1 with focal length f_1 :

$$U_3(r, \phi) = U_2(r, \phi) e^{-im^2 \Lambda f_1} \quad (4)$$

d) propagation through $d = f_1$, which completes the half roundtrip:

$$U_4(r, \phi) = \int_0^a r' dr' J_n(k r r' / d) U_3(r', \phi) e^{ik \cdot (r^2 + r'^2) / 2d} \quad (5)$$

An identical sequence can then be written with f_2 instead of f_1 , leading to complex amplitudes from U_5 up to U_8 .

Starting with a plane wave, iteration of equations (2), (3), ... etc. leads, after few roundtrips⁵, to the fundamental stationary solution⁶. Actually, the numerical calculation is stopped when

$$\max_{\text{over } r, \phi} \left| \frac{U_8(r, \phi) - U_0(r, \phi) \cdot \Gamma}{U_0(r, \phi)} \right| < \varepsilon$$

where ε is a preassigned precision limit and the eigenvalue Γ is computed as the mean value of $|U_8/U_0|$ over r and ϕ .

The eigenvalue integral equation arising from the above equations can be also written as

$$\Gamma U_0(r, \phi) = \int U_0(r', \phi') \cdot K(r, \phi, r', \phi') dr' d\phi' \quad (6)$$

where $K(r, \phi, r', \phi')$ is a suitable cavity kernel⁷. Use of equations (2) to (5) instead of (6) allows for field computation in arbitrary points along the resonator: moreover, we have a large flexibility in changing cavity parameters such as focal lengths, drift distances, their ratio, total cavity length, pinhole dimension.

Solutions involving higher order modes can be found by subtracting the previously calculated modes from the initial plane wave.

The output beam field distribution is obtained by propagating the complex amplitude U_8 , after extraction by mirror M_p , for an arbitrary drift " d ", by means of integral (3). Figure 5 gives a sketch of beam profiles, computed at various distances from M_p , from which we extracted some of the $1/e^2$ half widths plotted in fig. 6 together with the fitting function:

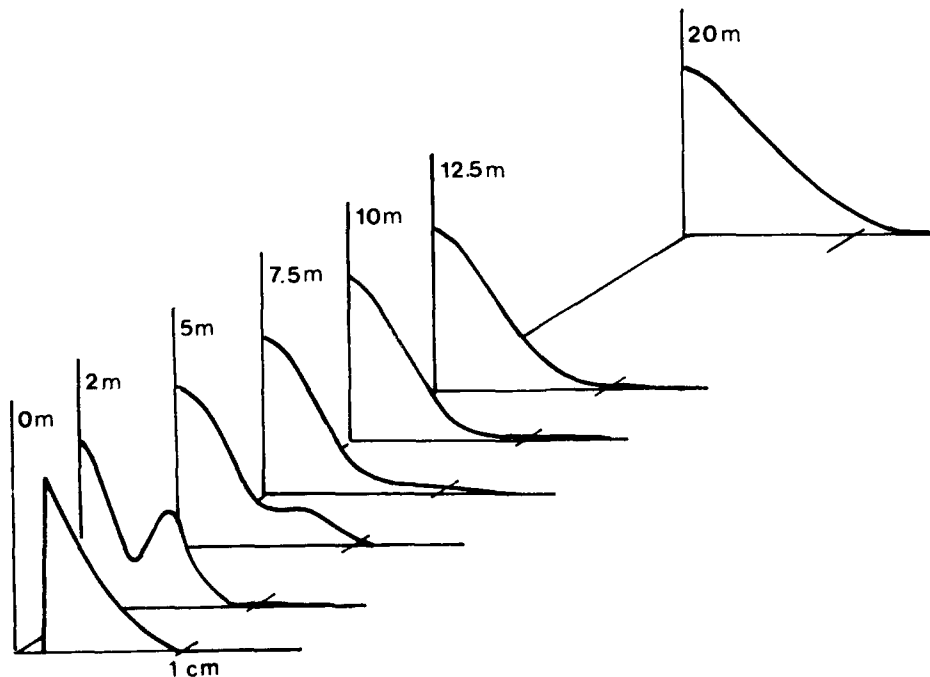


Fig. 5 Computed normalized beam intensity profiles at various distances from the extraction plane.

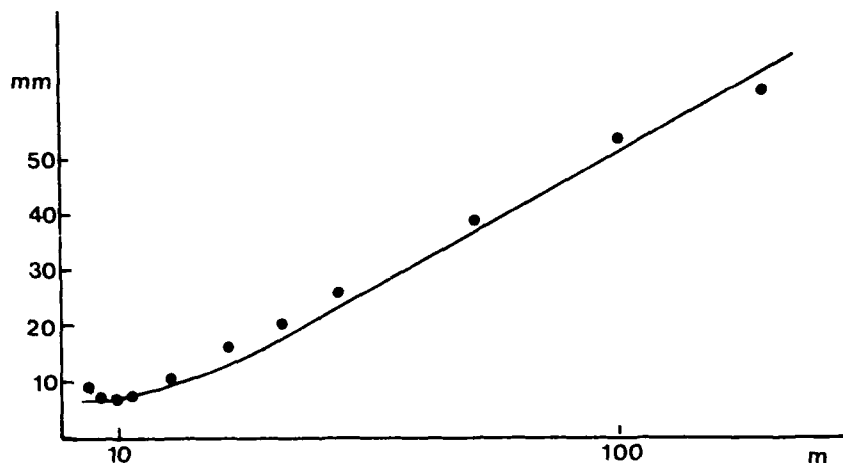


Fig. 6 $1/e^2$ half widths as derived from computed intensity profiles (•) together with fitting function (7).

$$w(z) = w_0 \left[1 + \left[\frac{\lambda \cdot (z - z_0)^2}{w_0^2 \cdot \pi} \right] \right]^{1/2} \quad (7)$$

Best fit values for the waist and its distance from M_p turned out to be $w_0 = 6.9$ mm and $z_0 \approx 8$ m, respectively, in good agreement with experimental measurements. Minor features of actual beam shapes can possibly be traceable to the active medium, whose non linear gain effect is going to be incorporated in a further version of our code.

Single Mode Operation

Single longitudinal mode emission is required for heterodyne LIDAR detection. We achieved mode locking by inserting a low pressure (10 torr) CO_2 CW section in the short arm of the resonator as shown in fig. 1c, and are at present improving the long term stability of this technique.

Conclusions

This new laser cavity design will extend the multi-gas detection capability of our IR LIDAR/DIAL apparatus, providing a diffraction limited lowest order TEM_{00} mode beam tunable over more than 60 lines. Single longitudinal mode locked pulses are also available for optical heterodyne detection of LIDAR echoes.

References

1. R.Barbini, A.Ghigo, M.Giorgi, K.N.Iyer, A.Palucci, S.Ribezzo, Opt. Comm. **60**, 239 (1986).
2. P.G.Gobbi, G.C. Reali, Opt. Comm. **52**, 195 (1984).
3. P.G.Gobbi, G.C. Reali, S. Morosi, A.S. Zarkasi, Appl. Opt. **24**, 26 (1985).
4. R.Barbini et al., "Theoretical Analysis of a CO_2 SFUR laser", ENEA internal report, to be published.
5. P.G.Gobbi, G.C.Reali, "Numerical study of a SFUR", SPIE Southwest Conference on Optics, Vol.540, (1985).
6. J.Todd, "Survey of Numerical Analysis" Mc Graw Hill, New York, 1962.
7. P.Di Lazzaro, T.Hermesen, T.Letardi, C.E.Zheng, Opt. Comm. **61**, 393 (1987).

SMALL SIGNAL GAIN OF CO₂-LASERS PUMPED BY A VOLUME SELF-SUSTAINED DISCHARGE

V.V.Apollonov, G.G.Baitsur, K.N.Firsov, I.G.Kononov, A.M.Prokhorov,
V.A.Yemshikov

General Physics Institute of the USSR Academy of Sciences, Vavilov street 38,
Moscow, 117942, USSR

Abstract

A small signal gain has been investigated of volume self-sustained discharge CO₂-lasers with the input energy density of up to 700 J/l.atm. It has been found that the volume self-sustained discharge initiation by means of a low-current electron beam or preliminary discharge gap filling with electrons in the regime of a pulled voltage front provides a more homogeneous pumping of the active medium than the UV preionized TEA discharge. The 8.2 m⁻¹ gain has been achieved in a He-free mixture.

Introduction

Small signal gain is one of the basic parameters of a CO₂-laser active medium. It shows the maximum radiation energy which may be extracted from the unit active volume. Therefore, if a suppression technique for parasitic oscillation is established, high gain media are favourable for efficient energy extraction by saturated amplification. Moreover, small signal gain is the nonlinear function of the input electrical density (W), and the upper limit of this value shows the volume discharge homogeneity for the mixture under consideration.

It is well known that the upper limit of small signal gain is about 12 m⁻¹ for the electron beam controlled discharge, whereas this value does not exceed 5 m⁻¹ for the volume self-sustained discharge (VSD) devices [1]. This drastic difference of the gain upper limits for two types of discharges is usually accounted for by a high E/P ratio (E - electric field, P - total gas pressure) required for VSD formation and support. This value is higher than that required for the optimum pumping of the CO₂ and N₂ molecules into the excited vibrational states.

Addition of properly chosen low-ionized organic substances (with ionization potential less than 7.6 eV) to the laser mixture allows to reduce significantly E/P operational value in the self-sustained discharge and simultaneously increase small signal gain and total duration of the stable VSD [2-6].

Investigations of the small signal gain upper limit for the doped self-sustained discharge are of great interest, and experimental study of this parameter is the subject of this report. It is useful to measure the maximum gain for typical large volume amplifier conditions - at the pumping pulse duration more than 1 μs. The most serious problem in this case is to provide stable discharge formation with high homogeneity of the active medium at the pumping energy density of about 700 J/l.atm.

VSD formation methods

In systems with UV-, radioisotopic and X-ray preionization one of the main reasons which make worse the medium homogeneity and limit the duration of the discharge volume stage is the formation of uncompleted channels near the cathode zone before the beginning of their avalanche multiplication because of drift in the voltage front [7]. We shall consider below the methods of formation of VSD which make possible to overcome this difficulty.

In CO₂-lasers with UV-preionization from the side of the cathode the cathode zone homogeneity becomes much better on addition of low-ionized substances into the mixture. It is associated with an increase in the concentration of photoplasma in the vicinity of the cathode and with the emergence of mechanisms distorting the electric field in the discharge gap (due to the photoplasma polarization) which prevent the electron flow off from the cathode. In our experiments we used Xe-flash lamps as a source of UV-radiation. The VSD was initiated in the volume of 1-20 l in the ordinary regime with a short front of voltage. The experimental set up is shown in Fig.1a (amplifier 1).

When the VSD is formed by means of a preliminary discharge gap filling with electrons in the regime of a specially extended voltage front the cathode zone practically loses no electrons [6]. In this case formation of inhomogeneities associated with the cathode structure becomes much less probable due to reduction of the electric field strength on the cathode by the volume charge and to the low overvoltage in the gap. Fig.1 b shows the scheme of the amplifier in which VSD is formed in the way discussed above (amplifier 2, volume 2-12 l). The auxiliary weak-current volume discharge disposed under a mesh cathode initiated by a barrier discharge was used as a source of electrons for filling the main gap.

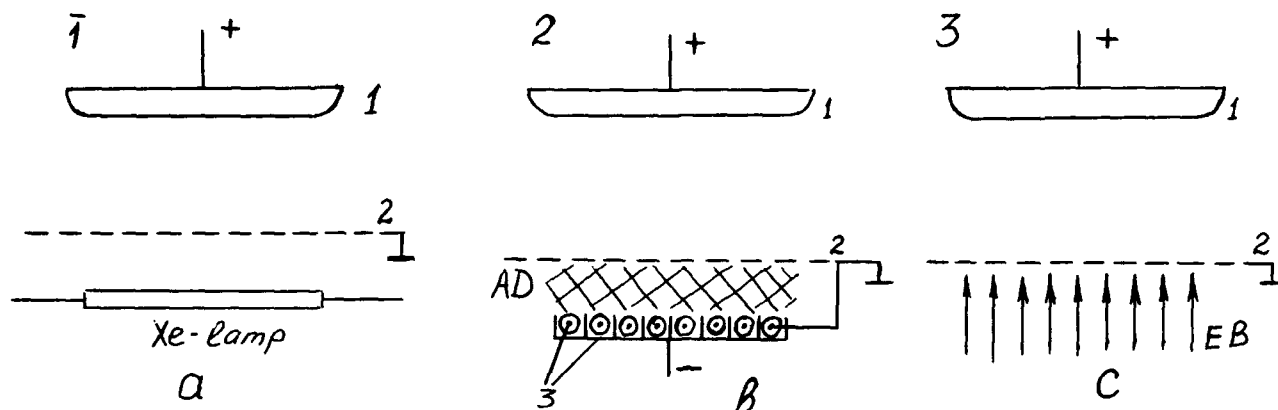


Fig. 1. Scheme of excitation of a volume self-sustained discharge:

- a - by active medium preionization with UV radiation,
- b - by preliminary discharge gap filling with electrons,
- c - by preionization with an electron beam;
- 1 - anode, 2 - cathode, 3 - electrodes for an auxiliary discharge, AD - auxiliary discharge, EB - electron beam.

The problem of inhomogeneities in the vicinity of a cathode is also solved due to a large initial concentration of electrons ($\sim 10^{12} \text{ cm}^{-3}$) achieved on initiation of VSD by a weak current beam of accelerated electrons [5]. In this case there is practically no overvoltage in the discharge gap and the energy is introduced into the VSD plasma at the quasi-stationary value of E/P, which is determined by the gas composition. This method allows to achieve the duration of a stable VSD combustion of $\sim 10 \mu\text{s}$ [5]. In our case the electron beam density in the gas chamber was $\sim 15 \text{ mA/cm}^2$, the active volume - 16 l . The scheme of the set up is shown in Fig. 1 c (amplifier 3).

Measurement results and discussion

Most of the experiments have been carried out with the 0.5-0.7 atm total pressure of He-free mixtures at the pumping duration of 1-3 μs . Triethylamine or tripropylamine (vapor pressure ~ 1 torr) were used as low-ionized additives.

Small signal gain was measured with a chopped CW CO_2 probe laser beam operating on P(20) rotational line of $10.4 \mu\text{m}$ band. The discharge was assumed to be sufficiently homogeneous if the average input pump energy for plasma without contraction exceeded

600 J/l.atm. Doped as well as undoped mixtures were used in the electron-beam preionized amplifier.

For all methods of VSD formation the maximum values of the small signal gain have been achieved with a laser gas mixture of $\text{CO}_2:\text{N}_2=1:1$. Fig. 2 shows the experimental dependence of the pumping energy on the small signal gain for this mixture doped by triethylamine (solid lines (1-3) are for amplifiers 1-3, respectively). The broken line (4) was obtained under the same conditions with a usual UV-preionized double-discharge laser with a weak level of preionization (Lamberton-Pearson type device with an active volume of 1.8 l). It is clear from curves (1-3) that for the studied pumping energy densities the small signal gain increases with increasing pumping energy and becomes saturated at $W \sim 500-600 \text{ J/l.atm}$. For Lamberton-Pearson system the gain is maximum at $W \sim 400 \text{ J/l.atm}$ and decreases with the further input energy growth. The comparison of lines (1-4) shows the advantages of the methods using VSD initiation by means of electron-beam and preliminary discharge gap filling by electrons in the regime of extended voltage front in comparison with the widely used UV-discharge preionization in the regime of a very sharp voltage front.

The maximum small signal gain value of 8.2 m^{-1} has been obtained in the electron-beam preionized device with a doped mixture. For the undoped gas the measured gain value was $\sim 7.5 \text{ m}^{-1}$ with $\text{CO}_2:\text{N}_2:\text{He} = 1:2:3$ laser gas pressure of 1 atm the small signal gain of 6 m^{-1} has been achieved at $W=350 \text{ J/l.atm}$. The gain value does not decrease for more than 20% at the increase of total pump pulse duration from 3 μs to 9 μs .

The present data show that the usual discharge formation with weak preionization cannot provide plasma homogeneity and high gain. Application of VSD formation methods discussed in our paper allow to improve discharge homogeneity to reduce the level of interelectrode gap overvoltage and optimize the regime of pump energy input for VSD plasma. As a result high gain significantly exceeding the value of 5 m^{-1} , which was supposed to be the upper limit, has been achieved for the doped as well as undoped mixtures even at large pump duration.

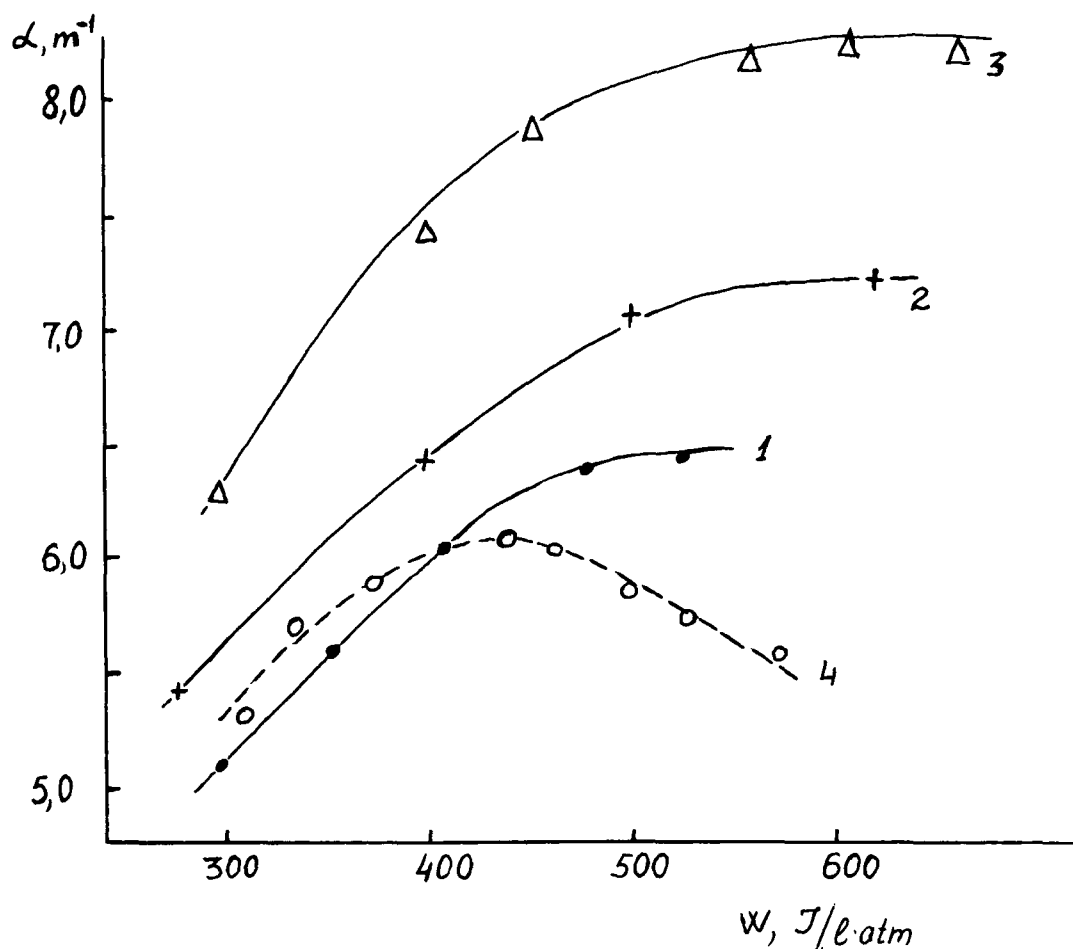


Fig.2. Amplification coefficient α vs specific energy contribution into the discharge.

Conclusion

Thus, it has been demonstrated in our paper that with a uniform enough pumping of the gas mixture the small signal gain upper limit of VSD CO₂-lasers is significantly higher than 5m⁻¹ irrespective of the discharge initiation method. The gain coefficient of 8.2m⁻¹ close to those achieved experimentally in the electron-beam controlled discharge lasers with sufficiently small active volumes [1,8] has been obtained.

References

1. Yu. V. Afonin, W. Biszewski, A. G. Ponomarenko, R. I. Soloukhin, V. N. Tischenko, Opt. Commun. 10, No1, 11 (1974).
2. V. V. Apollonov, F. V. Bunkin, S. I. Derzhavin, I. G. Kononov, K. N. Firsov, Yu. A. Shakir, V. A. Yamschikov, Sov. J. Quantum Electron. 6 (1979).
3. V. V. Apollonov, N. Ahunov, F. V. Bunkin, S. I. Derzhavin, I. G. Kononov, K. N. Firsov, Yu. A. Shakir, V. A. Yamschikov, Symposium Optica 80, Lectures, Budapest (1980), p.94.
4. V. V. Apollonov, G. G. Baitsur, K. N. Firsov, A. M. Prokhorov, Sov. J. Quantum Electron. 13 (1986).
5. V. V. Apollonov, K. N. Firsov, I. G. Kononov, A. M. Prokhorov, V. A. Yamschikov, Lett. to Sov. Journal of Techn. Phys. 12, No7 (1986).
6. V. V. Apollonov, N. Ahunov, G. G. Baitsur, K. N. Firsov, V. R. Minenkov, A. M. Prokhorov, B. V. Syomkin, B. G. Shubin, A. V. Yushin, V. A. Yamschikov, in Proceedings of the International Conference on Lasers'85, C. P. Wang, Ed. (STS Press, Mc Lean, VA, 1986), p.p.681-687.

7. J. I. Levatter, S. C. Lin, J. Appl. Phys. 51, 210 (1980).
8. C. H. H. Carmichael, R. K. Garnsworthy, L. E. S. Mathias, Appl. Phys. Lett. 24, 608 (1974).

QUANTITATIVE APPLICATIONS OF THE THERMAL LENS

R. T. Bailey, F. R. Cruickshank and D. Pugh

Department of Pure and Applied Chemistry

The University of Strathclyde

295 Cathedral Street

Glasgow G1 1XL

Scotland

Abstract

The quantitative development of the thermal lens is described. Techniques for obtaining accurate values of vibrational-translational (V-T) and, less obviously, vibration-vibration (V-V) energy transfer rate constants are detailed. It is shown that initial, transient cooling of a medium does not require an endothermic energy transfer step between upper levels, but may often depend upon a fine kinetic balance between higher level relaxation and equilibration with the translational energy bath. In the case of low molecular weight gases such as helium it is clear the V-V energy transfer can have a lower rate constant than V-T transfer! These techniques are shown to give similar results, in well-characterised systems, to other large perturbation approaches.

Examination of the time constants, for the several gas dynamic processes involved, indicates that energy transfer processes will generally be separable from the thermal diffusivity controlled return of the system to ambient conditions. Analysis of the thermal diffusivity controlled decay of the thermal lens signal is shown to permit accurate (within 5%) measurement of thermal diffusivities, non-invasively and even at elevated temperatures. Where heat capacities are available, these can be converted to thermal conductivity coefficients. Anisotropic thermal diffusivities can also be measured in a variety of phases.

Introduction

The coaxial thermal lens and its refraction and reflection variants are increasingly being recognised as a valuable, non-invasive, diagnostic for an ever-widening range of phenomena. From one or two papers per annum in the 1970's, the work in these areas has grown to >100 papers per annum. Accordingly, in the short space available, it will be possible to deal with only a small part of the field. This covers a range of gas, liquid and solid phase systems quantitatively and will be described here as an indication of the accuracy and versatility of the technique.

Experimental

Only coaxial beam geometries will be considered in this discussion. Two lasers are required. One must be pulsed and of pulse length short in comparison with any kinetic event which is to be monitored and a duty cycle low enough to allow the system to relax completely to its initial state between pulses (e.g. 20-50 half lives of the decay between pulses). This "pump" laser must also have a high quality TEM beam profile. The response time of the experiment will vary as the square of the radius of this profile at the $1/e$ point, so that this diameter must be small enough to allow observation of the desired kinetics. It is immediately obvious that, even with good optics, work in the infra-red will be slower than work at visible wavelengths because of the larger diffraction-limited spot sizes obtaining at the longer wavelengths. The "pump" laser should, ideally, be tunable to allow very specific transitions to be "pumped".

The second "probe" laser requires high pointing and intensity stability, a stable TEM beam profile and is best to be in the visible wavelength range. This facilitates alignment and allows use of cheap He/Ne lasers and fast photomultipliers.

The two lasers are mixed coaxially on a beam-splitter transparent to one and reflective to the other (e.g. a Ge plate transparent to CO_2 laser radiation and reflecting 632.8nm light). The "pump" laser beam is brought to a beam waist (by telescope or simple lens; - apertures should be avoided) in the sample cell which is of such a length that this waist is parallel to $\pm 5^\circ$ or better throughout the cell. This cell can be mounted in an oven for high temperature work. The probe laser is unfocussed and, after passing through the cell, is centred on a 25 μm pinhole masking a 632.8nm narrow bandpass filter covering the photocathode of a fast photomultiplier tube. If the sample temperature rises as a result of the energy deposited in the Gaussian "pump" laser profile, the "probe" laser will diverge. This leads to a drop in signal at the photomultiplier. This is termed the rise of the thermal lens signal. Eventually the photomultiplier signal relaxes to its initial state and this is termed the decay of the thermal lens signal. Generally, the risetime of

the lens signal is several orders of magnitude faster than its decay. Accordingly, the signal is best recorded by a real time waveform digitiser capable of operating with dual timebases (one fast for the risetime data, one slow for the decay). The trigger to this instrument is obtained from the rising edge of the "pump" laser pulse via a very fast (e.g. photon-drag) detector. The trigger pulse is delayed so that it signals the timebase change-over of the signal averager, but includes some pre-laser pulse data which is used as a baseline for the signal analysis. The 16 bit data are stored on floppy disc for analysis as set out below.

In the gas phase there are several time constants which influence the interpretation of the data. These are:

Pressure wave	$\tau_p = R_g/c$	$[c = (\gamma RT/M)^{1/2}]$
V-T	τ_{s^*}	
Diffusion	$\tau_D = R_g^2/4D$	
Thermal conduction	$\tau_k = R_g^2/4k$	

Where R_g is the "pump" laser beam 1/e Gaussian radius, c is the speed of sound in the sample, D is the gas phase diffusion coefficient and k is the thermal diffusivity of the sample.

For ideal gases, it has been shown^{1,2} that $\tau_k/\tau_D = \gamma$ which is close to unity. However, for most gas phase work, $\tau_p \ll \tau_k, \tau_D$. In the gas phase, energy transfer rates increase with pressure whereas thermal diffusivity decreases with pressure. A pressure range can be selected, therefore, where these two rate processes can be sufficiently different that they can be treated quite separately. The thermal lens signal risetime and its decay are accordingly analysed independently.

At high pressure, energy transfer rates may become so fast that τ_s approaches τ_p . The signal is then said to be acoustically limited. This occurrence is easily detected in the signal by appearance of an "overshoot" at the signal maximum.

A complete description of the thermal lens signal strength has been presented previously^{1,2}. If E is the energy remaining in internal modes of the sample molecules at time t , and the process of energy release is pseudo first order,

$$\psi(t_0) = (1/\tau_s) \exp(-t_0/\tau_s). \quad \dots\dots\dots(1)$$

The time dependence of the temperature rise in the sample region can then be expressed as

$$f(t) = (\tau/(\tau + t))^2 \int_0^t \psi(t_0)/[1 - t_0/(t + \tau)]^2. \quad \dots\dots\dots(2)$$

Here τ is the thermal decay lifetime of the thermal lens signal given by

$$C_p R_g^2 P/4RTK. \quad \dots\dots\dots(3)$$

where P is the pressure, T , the absolute temperature and, K , the thermal conductivity coefficient of the sample.

The thermal lens signal strength may now be defined in terms of S , the fractional modulation of the probe laser

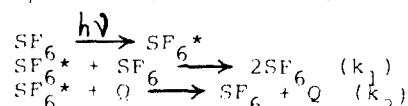
$$S = 1 - 1/(1 + \beta^2/4\{[1 - \exp(-l\lambda)][\lambda L - 1] + l\lambda\})^2. \quad \dots\dots\dots(4)$$

Here λ = sample optical extinction coefficient in reciprocal length units, l = length of the thermal lens cell, L = distance from the thermal lens cell output window to the pinhole and β is given by:

$$\beta^2 = (8/\pi) \mu \lambda R_g^2 (Q_0 RT_s/C_p T_p S) \delta_s f(t). \quad \dots\dots\dots(5)$$

Here μ = sample refractive index, p_s , T_s = the sample pressure and temperature at which this refraction index obtains, T = the actual sample temperature, R the gas constant, and $\delta_s = \mu - 1$.

Figure 1 shows the quality and sensitivity of fit obtainable with this analysis applied to the risetime of the signal. In the case of SF_6 quenched by the inert gases, the important energy transfer processes in the cell are:



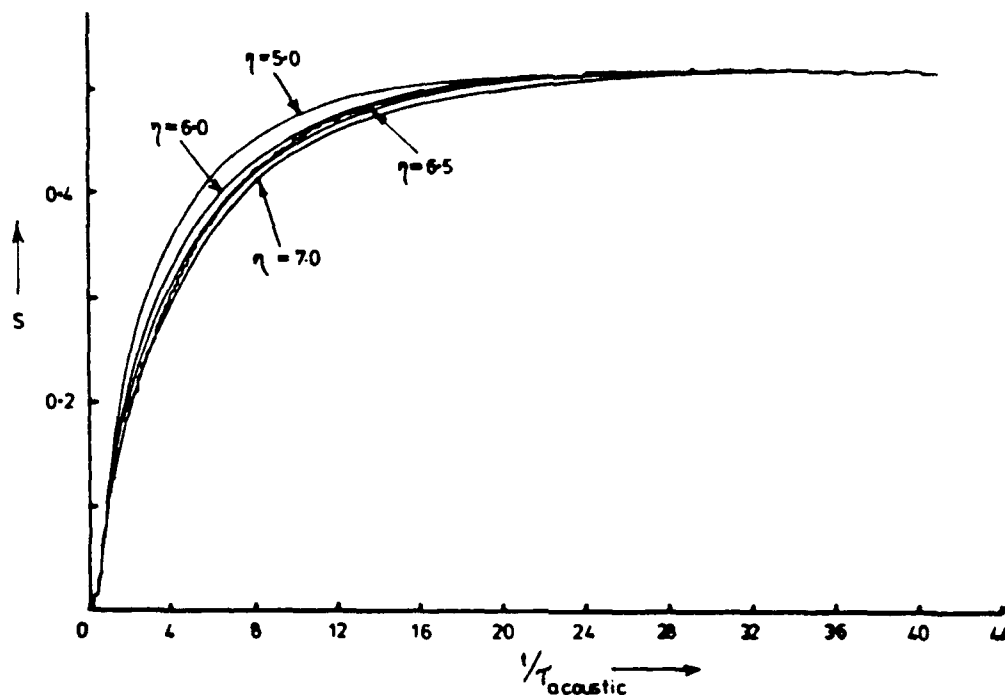


Figure 1. Fractional signal modulation, S , as a function of the dimensionless ratio t/τ_p for 1 Torr SF_6 + 252.4 Torr Xe at 330K. The best fit is where $V-T/p$ (η) = 6.5.

k_2 is obtained from the slope of the plot of the pseudo first order rate constants, for a series of studies at constant SF_6 pressure and variable inert gas pressure, against the inert gas pressure. The intercepts of such plots are $k_1 [\text{SF}_6]$, so that a plot of such intercepts, obtained from studies with different base pressures of SF_6 , against the SF_6 pressures used, yields k_1 . The results are summarised in Table 1.

Table 1. Rate constants k_2 for SF_6 + inert gas quenchers and k_1 for self quenching. * = ref 3.

Inert Gas	$P\tau$ $\mu\text{s Torr}$	$P\tau^*$ $\mu\text{s Torr}$
Xe	6250	----
Xe	4347 ^a	----
Kr	2147	3040
Ar	409	470
Ne	233	194
He	----	41
SF_6	42 ± 15	122-182

The results for SF_6 indicate that the mechanism follows the Ehrenfest condition for these gases. From Table 1, it is clear that this technique agrees satisfactorily with totally different approaches.

The energy transfer in the case of SF_6 follows a mechanism which is simple overall, but much too complex to analyse in detail due to the high density of energy levels around 1000cm^{-1} . However, in the case of CO_2 such detailed analysis is possible. Additionally, many of the rate constants are already available in the literature, so that few variables are available for fitting observed to predicted thermal lens signals. In a series of studies on pure CO_2 an endothermic dip in the signal is observed and the signal shape is very sensitive to the choice of parameters used to define the mechanism. Figure 2 shows the energy levels relating to these studies.

It has been shown^{4,5} that

$$\delta E_{\text{trans}}/\delta N = (E_x - E_z) + e^{\alpha t} [-E_x(d+h_2) - nh_3 + h_4(d+h_2)/(d+h_5)]/(d+\beta) \\ + e^{\beta t} [E_x(\beta+h_2) + nh_3 - h_4(\beta+h_2)/(\beta+h_5)]/(d-\beta) \\ + e^{-h_5 t} [E_z + h_4(h_2-h_5)/(d+h_5)/(3+h_5)]$$

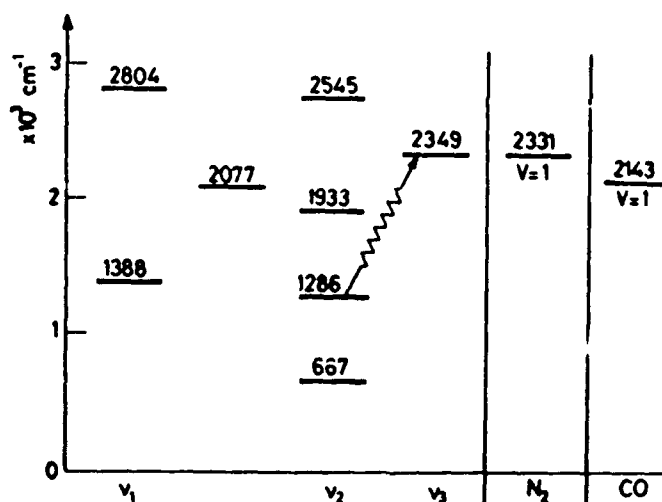


Figure 2. Energy levels for CO_2 , N_2 and CO .

Here α and β are the roots of the equation,

$$p^2 + (h_1 + h_2)p + h_2(h_1 - h_3) = 0 \text{ and}$$

$$h_1 = k_{x3} + k_{x4} + k_{x0} M_{\text{O}}^{\text{O}}$$

$$h_2 = k_{\text{ox}} M_{\text{O}}^{\text{O}}$$

$$h_3 = E_{\text{O}} + k_{x3} + E_4 k_{x4} - E k_{10} x^{\infty}$$

and

$$h_5 = k_{10} (1 - x^{\infty}).$$

Fortunately, it is possible for the modest modulations involved (<50%) to equate the thermal lens signal to E_{T} , so that the above relation can be solved numerically. k_{xn} denotes the rate constant for the relaxation of level x (001) to level n . The value of $k_{x3} + k_{x4}$ is the V-T relaxation rate constant for the 001 (x) level of CO_2 , i.e. $2832 \mu\text{s Torr}$. $k_{x4} = 512 \mu\text{s Torr}$. k_{xo} is the quenching rate constant for a diatomic buffer gas, if present, and M_{O} is its pressure. E is the lowest energy level of the CO_2 (667 cm^{-1}). The $n00$ levels are assumed to equilibrate rapidly with the $0n0$ manifold with which it is connected via Fermi resonance. The model used to derive the above equations also assumes that, following the act of absorption of the "pump" pulse, the $0n0$ stack of levels V-V equilibrates instantly within itself (and with $n00$). This is followed by equilibration with the 001 level and the translational bath. In order to achieve a good fit with the experimental signal shape, it is necessary to set $k_{x3} = 80\% (k_{x3} + k_{x4})$. It should be noted that this is the only variable used in the curve fitting apart from a normalisation factor to scale the observed maximum signal to the experimental modulation maximum. Clearly, the endothermic route from the 001 level to 040 is not favoured although it is nearer resonance with the 001 level, nor is this endothermic step significant in producing the observed thermal lens endotherm. Instead, this arises from the relaxation via translational to vibrational transfer, initially faster than V-V transfer from 001. In the case of N_2 quench gas, the endotherm is more pronounced, because the 001 population is further depleted by the fast, resonant equilibration of this level with the N_2 $V = 1$ state. Figure 3 shows the quality of fit obtainable in this case.

With CO quench gas, the 001 equilibration is endothermic by 206 cm^{-1} compared with the 18 cm^{-1} for N_2 . In this case, a fast initial exotherm is apparent in the thermal lens signal. The magnitude predicted is $206/1046.58$ of the 6% modulation, i.e. 1.2%. The observed value is 1%! The exotherm in the case of N_2 was of the order of the noise level 0.2%. Table 2 lists the data obtained from these studies^{4,5,6}.

Here, k_{qg} is the rate constant for the quenching of the excited state of the quench gas by CO_2 . In the case of CO this value carries an error of 40%. The V-T quenching value of He is very high, but is as accurate as the other values above, the typical error being <20% for k_{x3} and 10% for k_{10} .

Figure 4 shows the quality of fit to the CO data.

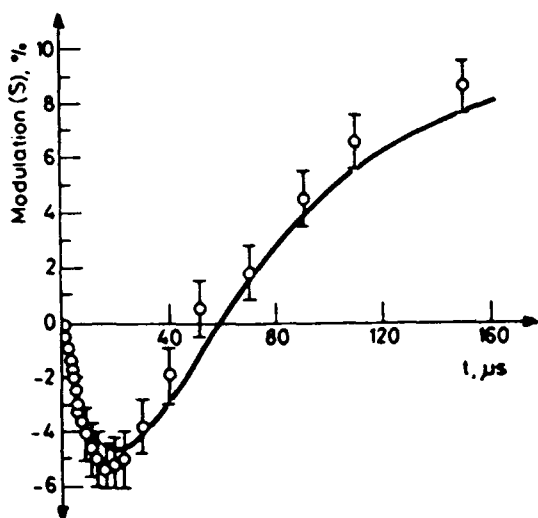


Figure 3. The best fit (full line) curve for 144 Torr CO_2 + 445 Torr N_2 .

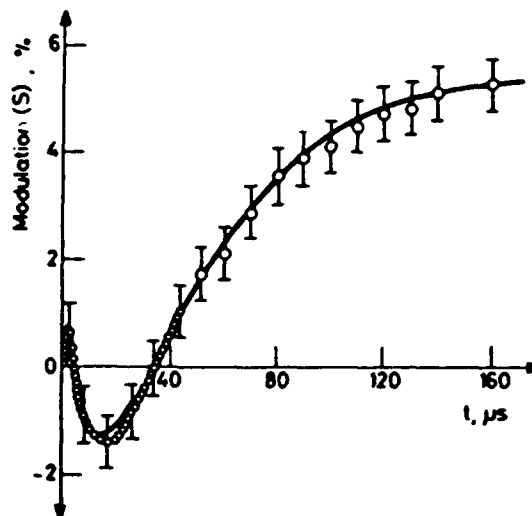


Figure 4. The best fit (full line) curve for 744 Torr CO_2 + 154 Torr CO .

Table 2.

Quench	k_{x3}	k_{10}	k_{eq}
Gas	$\text{s}^{-1} \text{Torr}^{-1}$	$\text{s}^{-1} \text{Torr}^{-1}$	$\text{s}^{-1} \text{Torr}^{-1}$
He	45	1500	----
Ar	60	27	----
N_2	60	45	>15000
CO	450	160	10000

The routine use of equation (4) to determine thermal conductivity would be tedious, but in cases where $\tau_k \gg \tau_s$ (and this is generally true above ~ 50 Torr) this equation simplifies to

$$[(1-S)^{-\frac{1}{2}} - 1]^{-\frac{1}{2}} = t/(\tau C) + 1/C$$

where C is a constant independent of time. Clearly, plots of the left side of this relation versus time will be linear and the ratio of intercept/slope gives τ . Further plots of τ against pressure yield K , the thermal conductivity coefficient, from equation (3). Figures 5 and 6 show such plots for the inert gases. In these cases, 1 Torr SF_6 was added to absorb "pump" laser radiation. With the pressures used, this introduces $<1\%$ error.

Table 3 lists the results and compares these with the best current values obtained from transient hot wire measurements¹.

Table 3

Gas	$K/$ $10^{-3} \text{Wm}^{-1} \text{K}^{-1}$	$K_{\text{hot wire}}/$ $10^{-3} \text{Wm}^{-1} \text{K}^{-1}$
Ne	48.20	48.21
Ar	18.48	17.27
Kr	10.05	9.23
Xe	6.02	5.35

High temperature operation with the heated cell allows measurements on systems where transient hot wire equipment does not perform well because of the restricted, low range of vapour pressures.

Table 4 lists the results⁷ for a variety of compounds.

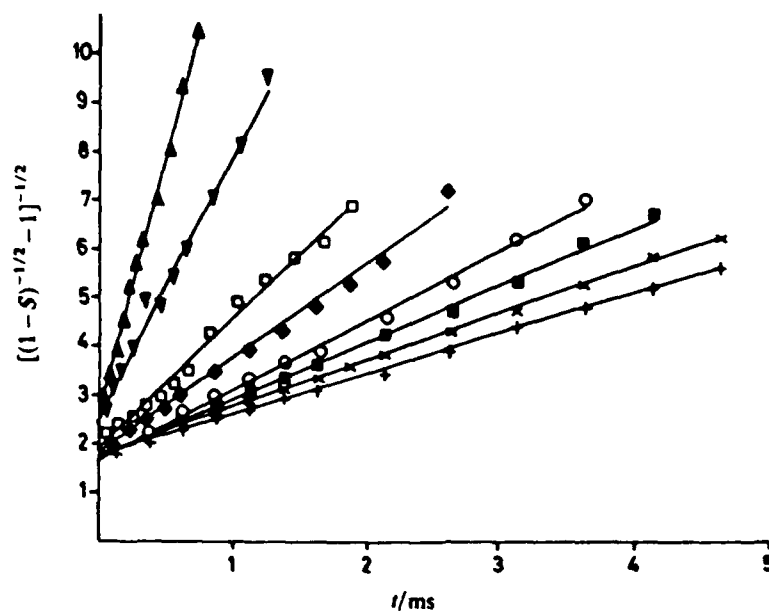


Figure 5. The $\text{SF}_6 + \text{Ar}$ system for 30, 54, 113, 160, 210, 266, 324, 385 Torr, in order of decreasing slope.

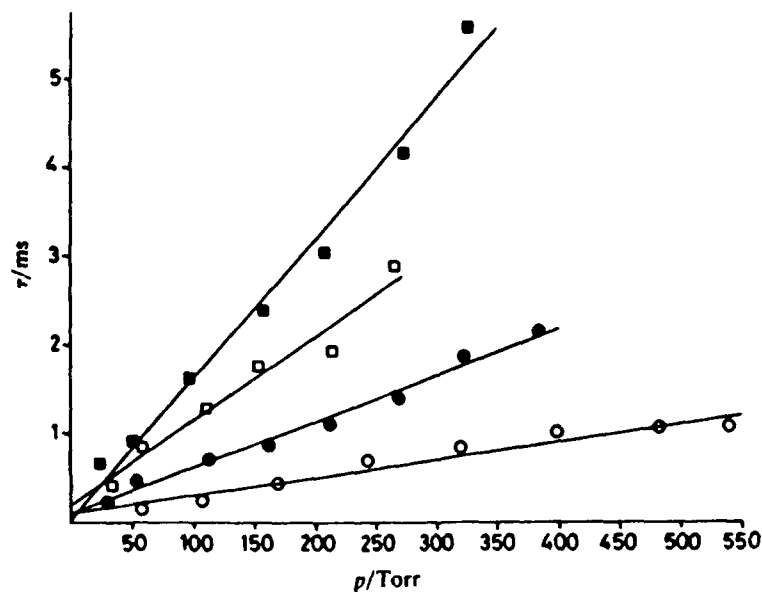


Figure 6. Plots of τ against pressure for $\text{SF}_6 + \text{Ne}, \text{Ar}, \text{Kr}, \text{Xe}$ in order of increasing slope.

Table 4

Cyclopropane		Ethyl chloride		Toluene	
Temp./K	$\text{K/Wm}^{-1}\text{K}^{-1}$	Temp./K	$\text{K/Wm}^{-1}\text{K}^{-1}$	Temp./K	$\text{K/Wm}^{-1}\text{K}^{-1}$
291	15.17	291	12.5	364	21.62
323	18.33	329.5	14.96	385.5	23.51
329.5	22.54	348	19.31	419.5	24.44
362	33.24	365	20.23		
413	41.88	390	21.15		
		414	25.44		

Nitrobenzene was also examined⁷, but, since there are no heat capacity data, the thermal diffusivity was all that could be calculated. 0.339Ns^{-1} was obtained at 429K. More complex systems can also be studied with the thermal lens technique. Methanol vapour exists as monomer, dimer and tetramer, the equilibrium constant depending on temperature and the relative concentrations of these species depending on pressure. Figure 7 shows the τ versus P plot for this system⁸.

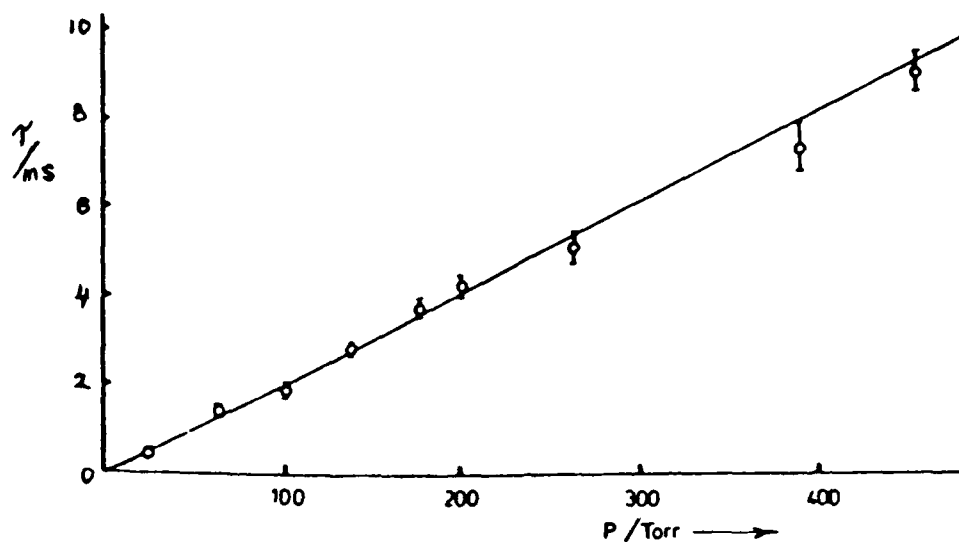


Figure 7. τ versus pressure for methanol vapour at 341K.

The thermodynamics of this system are well characterised. At high temperature, the molar heat capacity is nearly constant because the methanol is nearly pure monomer. However, at lower temperatures the "molar" heat capacity varies in a very non-linear way with pressure. Figure 8 illustrates these effects.

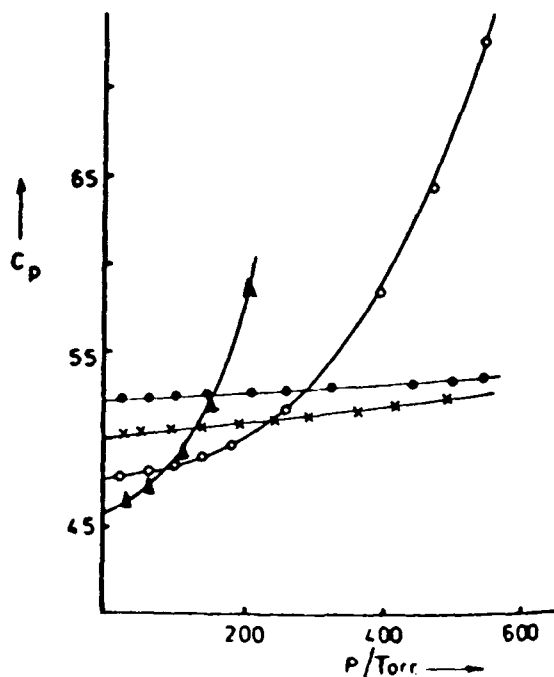


Figure 8. The variation of heat capacity of Methanol vapour with pressure. (\blacktriangle) = 321K, (\circ) = 341K, (\times) = 377K, (\bullet) = 405K

Since the γ/P plot is linear, it is clear that the thermal diffusivity is independent of pressure. Consequently, the thermal conductivity coefficient will follow the heat capacity variation with pressure.

It is possible to "pump" molecules indirectly by the stimulated Raman effect using two pulsed lasers tuned so that their frequencies differ by that of a Raman transition in the sample⁹. This allows energy transfer from Raman level to be monitored directly and the lens signal maximum is useful in recording the Raman spectrum if one of the pulsed lasers is a scanning dye laser.

The thermal lens technique has been extended to studies in the liquid and solid phases. In laser eye surgical procedures¹⁰ where high power laser pulses are projected through the cornea and lens of the eye, thermal lens effects in these will destroy the precise focus needed in e.g. the drilling of 50 μ m diameter holes in the uveal mesh through to Schlemm's canal in an effort to alleviate open angle glaucoma. The minimum time required for these lens effects to relax to ambient conditions is determined by the thermal diffusivity of the cornea. This was measured for Rabbit and baboon corneae. These are somewhat variable, but values were all within the range 1.5 - 3.0 seconds for τ_k . These compare with the values 1.79s, 1.82s and 3.04s for water, Barany's solution and chloroform respectively. All these τ_k refer to a 2mm beam diameter. The last three values reproduce within $\pm 2\%$.

In the solid phase, anisotropic, partially oriented polyethylene terephthalate sheet was examined¹¹. If the pinhole at the photomultiplier is replaced by a slit, the thermal lens experiment gives a signal containing most information on processes occurring in a direction orthogonal to the slit. Accordingly, the thermal diffusivity of the polymer sheet was measured parallel and perpendicular to the orientation direction for a variety of stretch ratios. The orientation ellipse of biaxially drawn sheet could be obtained and the clear correlation was observed between orientation and enhanced thermal conductivity. Being non-invasive and far faster and easier to use than alternative approaches, the lens technique is particularly suitable for quality control applications in this context.

Finally, one effect which emerges from the above is that the maximum temperature in an absorbing medium depends strongly on the energy transfer/thermal diffusivity kinetic balance. For example, it is customary to add an inert buffer gas to a gas phase photochemical system to increase its heat capacity and thus lower its temperature when probing the thermal component of the mechanism. However, this approach is far too simplistic. Increasing buffer gas pressure increases the release rate of energy to translational degrees of freedom and slows thermal diffusivity. On-axis temperatures will increase as a result and only the increasing heat capacity will counteract this¹². For 0.5 Torr SF₆ + Argon buffer gas the peak, on-axis temperature is reached when 20 Torr buffer gas have been added and proceeds to decrease only when this pressure is exceeded. Details of the calculations have been given elsewhere¹².

Conclusions

The brief review of quantitative applications of the thermal lens technique given above, while far from exhaustive, clearly shows why this non-invasive, versatile technique is gaining popularity as a diagnostic approach in many, diverse investigations. No attempt has been made to be comprehensive and only lack of space has prevented this and necessitated omission of much fine work of other authors for which we hope we shall be forgiven.

References

- 1 R T Bailey, F R Cruickshank, D Pugh and W Johnstone, J C S Far II, 76, 633, (1980); *ibid* 77, 1387, (1981).
- 2 R T Bailey, F R Cruickshank, R Guthrie, D Pugh and I J M Weir, Mol Phys, 48, 81, (1983); Chem Phys, 114, 411, (1987).
- 3 J I Steinfeld, I Burak, D G Sutton and A V Nowak, J Chem Phys, (1970), 52, 5421.
- 4 R T Bailey, F R Cruickshank, D Pugh and K M Middleton, J Radioanal. Nucl. Chem., 101, 383, (1986).
- 5 R T Bailey, F R Cruickshank, D Pugh and K M Middleton, J C S Far II, 81, 255, (1985).
- 6 R T Bailey, F R Cruickshank and D Pugh, Proc 5th Intl Topical Mtg. Photoacoustic and Photothermal Phenomena, Heidelberg, (1987), *in press*.
- 7 R T Bailey, F R Cruickshank, D Pugh and I J M Weir, Chem Phys, 87, 125, (1984).
- 8 R T Bailey, F R Cruickshank, D Pugh and I J M Weir, Chem Phys Lett, 134, 311, (1987).
- 9 R T Bailey, F R Cruickshank, S M G Guthrie, C H Nelson and D Pugh, J Raman Spectrosc, 18, 13, (1987).
- 10 S Venkatesh, S M G Guthrie, F R Cruickshank, R T Bailey, W Foulds and W Lee, British J Ophthal, 69, 92, (1985).
- 11 R T Bailey, F R Cruickshank, A McLeod, D Pugh and A G Faraday, Polymer Comm, 26, 23, (1985).
- 12 R T Bailey, F R Cruickshank, D Pugh, R Guthrie, W Johnstone, J Mayer and K M Middleton, J Chem Phys, 77, 3453, (1982).

CO₂-LASERS FOR INDUSTRIAL MATERIALS PROCESSING

G. Herziger, P. Loosen
Fraunhofer-Institut für Lasertechnik, Steinbachstr.15, D-5100 Aachen, W.-Germany

1. Introduction

The driving force of the laser-development program being outlined in the following is given by the interaction phenomena of laser radiation and matter such as surface and plasma absorption, heat conduction, melt dynamics and plasma formation. As a guiding example for the different types of processing (cutting, welding, surface treatment etc.), welding with CO₂-laser radiation will be used in the following.

Absorption of high-intensity laser radiation is a nonlinear function of laser intensity /2/. In order to achieve high energy coupling into metallic materials and to overcome the generally low natural surface absorption, the laser has to exceed a certain threshold intensity, which is for welding of steel within the range of $1 - 2 \cdot 10^4 \text{ W/cm}^2$ /1,2/. For laser-system development this implies, that not only the increase of laser power is an important objective, beam quality in terms of the capability of focussing the beam down to small spots, may also be significant in order to reach the threshold intensities for processing with high energy coupling.

Generally this threshold intensity is depending on:

- variations in the surface quality and materials parameters of a workpiece, which occurs frequently in industrial environment
- periodic and turbulent melt dynamics in the processing zone
- laser-power fluctuations caused by processes inside the laser source or induced by radiation reflected from the workpiece to the laser system (optical feedback /8/).

Knowledge and control of these processes may be important in order to keep the processing result within the given limits independent of the changing boundary conditions. In Fig. 1 a laser-system for flexible laser-manufacturing is proposed, which is capable to react on processing parameter fluctuations by control in a closed-loop feedback circuit. Similar systems have been demonstrated for applications like soldering /18/ and hardening /19/, where the time constants for the processes are mainly determined by heat conduction and are lying in the ms-s range. The modulation bandwidth of CO₂-laser-systems, nowadays used in industrial materials processing is in the range of several kHz, which is sufficient for regulation of these slow processes whereas regulation of fast melt dynamics and plasma processes requires modulation frequencies in the range of kHz to several hundreds of kHz, which cannot be achieved with commercial laser systems for industrial applications.

In the following some areas of fundamental research and development are discussed, which may contribute to the design of a laser-system for flexible laser manufacturing: control of intensity and optical feedback, increase of beam quality and modulation bandwidth.

2. Laser Diagnostics

In Fig. 2 the scheme of a beam analysing system is shown, capable of controlling the intensity distribution of focused as well as unfocused laser beams /4/. The system consists of a rotating hollow needle with a pin-hole in its surface directing to the laser beam. By rotating the needle through the beam cross-section and stepping the whole set-up through the beam, several tracks (typically 40) can be picked up and displayed on a personal computer. With this system, measurement of the intensity distribution, the beam radius as well as the divergence up to laser powers of several kW can easily be achieved.

The results of analysing a CO₂ laser with an output power of 1,500 W in the focal plane of a 5 inch lense is illustrated in Fig. 3 showing the intensity distribution similar to a TEM₁₀* mode. In this way several commercial CO₂ laser systems have been analyzed with regard to their normalized beam quality, which is given by:

$$K^* = \frac{\lambda}{\pi} \cdot \frac{1}{w \cdot \theta}$$

(λ - wavelength, w - beam radius, θ - far field divergence)

In contrast to the unfocused beam, where the far field divergence is not easily to obtain due to the large Rayleigh length, measurement of the divergence behind the lense and measurement of the focussed diameter can easily be achieved with the presented diagnostic system. In Fig.4 the measured normalized beam quality of different commercial laser systems is shown as a function of the rated laser power, and is compared with the theoretical figures. The normalized beam quality decreases with increasing rated laser power, by reason of beam distortions due to interaction of the beam with the amplifying medium /6/ and the

output window /7/. Lasers with a nearly Gaussian intensity distribution (TEM₀₀) have been found so far only up to a laser power of about 2 kW, a limit which is mainly given by the high power load of the partial transmitter.

In general it is not sufficient to analyse the beam parameters of a laser system in the nonprocessing case as described in Fig 4. Fig. 5 shows time-resolved measurements of the total beam power and the polarization state of a CO₂ laser system at total absorption of the laser by a beam stop: the total beam power and polarization state are nearly constant in time. In the case of partial reflection of laser radiation from the workpiece to the laser system the laser parameters may change drastically. This can only be detected by on-line diagnostics of the laser during processing, which is illustrated in Fig. 6, showing laser diagnostics during welding of aluminium. The total laser power as well as the polarization state show a chaotical temporal behavior /8/ whereas the averaged polarization remains constant. Sometimes the signal of the detector d_1 , indicating the polarization state, increases to the level of the signal of detector d_2 , what means that the polarization plane of the laser has turned by an angle of 90°. This, as well as the fluctuations in total beam power may have an influence on the processing results. The influence of the polarization state e. g. on cutting quality and efficiency is well known /9/, in laser welding with special process- and laser- parameters likewise results have been found /10/.

A simple model of optical feedback (Fig. 7) is used to discuss the basic characteristics of polarization change by optical feedback /11/. Polarization dynamics is described with a rate-equation model by assuming two orthogonal polarization modes containing the photon densities q_1 and q_2 . The flux of these photons towards the workpiece is modified and partially reflected from the interaction zone, described by the coefficients R_{ij} . The basic characteristics of feedback induced change in polarization state may be discussed with the stationary solution of this equation system (Fig. 8).

Without optical feedback the laser system operates in this example with a polarization ratio (q_2/q_1) of 0. With optical feedback a change of polarization takes place. The extend of the polarization change depends on the coefficients R_{11} and R_{21} , describing the coupling of photons of one polarization mode with the other by the workpiece. The greater this coupling (summarized by b_1), the greater is the change in polarization. Concerning the parameter b_1 this behaviour is just reverse. A great coefficient b_1 , which means large differences between the photon lifetimes in the resonator, is damping the polarization change by optical feedback. The case of random polarization occurs for equal or nearly equal resonator losses for the two polarization modes ($\tau_1 = \tau_2$). At a given coupling constant b_1 the polarization state tends towards mode 1, when the feedback coefficient R_{11} is increased. This is also true in the reverse sense for increasing R_{21} .

As a conclusion of the foregoing, a laser system is driven by optical feedback into a polarization state, which has maximum reflexion and therefore minimum absorption at the workpiece. A possible way to avoid this state is to chose the differences in the time constants τ_1 and τ_2 appropriately, e. g. by adaocted choice of material and coating of the folding mirrors.

3. Excitation Technics

The main objectives of excitation technics developement are to increase the homogeneity and stability of the discharge, which are essential prerequisites for high beam quality. Furthermore, increase of the electrical power density and operating pressure may contribute to the design of more compact laser systems, because raising the electric power density and operating pressure reduces the size of the active medium as well as the blower size (convective cooling is proportional to the product of pressure and pump capacity). An additional advantage may be seen in the fact, that the laser relaxation time decreases at higher pressure levels, allowing higher modulation frequencies.

Conventional dc-excitation, widely used in industrial CO₂-lasers, allows operation at power densities and pressures in the range of 10 W/cm² and some tens of mbars resp.. By use of a highly-turbulent swirl flow, generated by flow-shaping elements within the discharge tubes of an axial-flow laser /12/, the parameters for homogeneous and stable discharge operation could be raised to about 18 W/cm² and 90 mbar for the electrical power density and operation pressure resp. (Fig. 9).

With rf-excitation these figures could be increased considerably. In Fig. 10 the operating range of dc- and rf-excitation, known from the literature and own experiments, is indicated. Electric power densities up to about 50 W/cm² and operating pressures exceeding 200 mbar in homogeneous and stable discharges have been demonstrated. Additional advantages of rf-excitation arise by : low gas consumption and contamination when using capacitive coupling in the plasma.

The selection of an appropriate excitation frequency is governed by plasma physical, technical and economical aspects. Plasma physical processes, determining the choice of frequency are discharge stability, sheath thickness and plasma absorption length. In order to describe their frequency dependent behaviour models have been developed or modified /13/. One basic example of these investigations will be discussed later on. Additional technical and economical demands are given by:

- Cheap and reliable design of rf-generator, e.g. the use of magnetron microwave sources may have significant advantages in terms of cost reduction
- Simple, cheap and reliable design of matching network and coupling structure
- Capability of achieving high modulation bandwidth and short-term power increase.

Some of the coupling structures tested in the frequency range from some MHz up to GHz are schematically drawn in Fig. 11. A coupling structure which is today widely used in industrial high power CO₂ laser systems with axial gas flow is sketched in Fig. 11a: a simple structure which works well with the usually used generators in the 10 - 30 MHz range. At high power densities and operating pressures plasma inhomogeneities may occur due to the slightly inhomogeneous field distribution of this coupling structure. A similar coupling structure used for transverse flow lasers is shown in Fig. 11b. Inductive coupling of RF may be obtained with the structure in Fig. 11c, resembling a slow-wave structure used e. g. in travelling wave tubes in the several hundred MHz to the GHz region. Problems may occur with this structure due to radially inhomogeneous electrical field distribution, especially at very high frequencies. A structure in resonance for the radio frequency is shown in Fig. 11 d. This structure in combination with adjusted ridges has successfully been used with frequencies in the 500 MHz range /14/.

In order to describe the characteristics of coupling structures and rf-driven plasmas, a model has been developed /5/, consisting of the equations for charge-production and -relaxation, gas dynamics as well as equations describing the coupling-structure equivalent circuit shown in Fig. 12. The equivalent circuit includes the stray capacity c_s , the coupling capacity c , and the plasma, built up by the complex impedance Z_{PL} .

With the aid of this model, design and optimization of coupling structures and matching networks under consideration of frequency and power-density dependent plasma behaviour is possible as illustrated in Fig. 13 with an example of the power-dependent complex impedance of a rf-discharge (27 MHz) in an axial-flow-CO₂-laser. For a complete coupling of rf-power into the plasma in different operating regimes, design of the rf-generator and the matching network has to take into account the varying impedance shown in Fig. 13.

With Fig. 14, where the calculated electrical field in the discharge is given as a function of the electron density for two excitation frequencies (27 MHz and 500 MHz), an important basic feature of frequency-dependent plasma stability may be discussed. Increasing power density in the discharge increases the plasma conductivity and therefore reduces the electrical field. For a rf-frequency of 27 MHz this happens for this example at electron densities above $10^{19}/\text{cm}^3$. In comparison, at higher frequencies the total current is mainly determined by the capacitive part C_{PL} of the complex impedance. The electron density and therefore the plasma conductivity has to be increased to a greater extent to contribute to a reduction of the electrical field strength in the discharge. On the other hand, reduction of the electrical field strength with increasing power density is an important plasma stabilising mechanism and contributes to the adaption of the electrical field to changing gas density, which is essential e.g. in high-power systems with gas flow, where a decrease of gas density in direction of flow takes place, and where a nearly constant ratio of E/N is maintained by the processes just discussed. Control and stabilization of discharges may therefore become more complicated with increasing excitation frequency.

4. Laser Modulation

Following the discussion in section 3 (Excitation Technics), rf-excitation has several advantages with respect to high modulation bandwidth (high transmitter modulation bandwidth, operation pressure and electric power density). A typical rf- and laser-pulse of an axial-flow type CO₂-laser is given in Fig. 15 /15/. The rf power can be switched within very short times (bandwidth up to 200 kHz) whereas the laser shows the characteristic delay time at the beginning of the pulse and decay time at the end of it. For the type of modulation needed to regulate materials processing, the decay time at the end of the laser pulse is of main importance. Therefore the processes leading to a decrease of this decay time are chiefly investigated. Among gas temperature and gas mixture the operating pressure of the laser discharge determines the decay time. In Fig. 16 measurements of the laser power decay time as a function of pressure are shown /15,16/. The decay time is mainly determined by collision processes in the laser plasma, the time constant for this processes is proportional to about the inverse of the operating pressure. With pressures up

to 200 mbar, which can be achieved with rf-discharges as it was shown in section 3, laser power decay times in the range of 10 μ s can be observed. This is still above the decay time of the rf-generator, which is in the region of several μ s for the used 27 MHz type.

Fig. 17 shall illustrate a method of modulating a high-power CO₂-laser by means of modulating resonator parameters: in this example the resonator losses have been modulated by an oscillating resonator mirror with a frequency in the region of the laser-resonance frequency /17/. The picture shows the theoretical and experimental laser power, which is completely modulated with a frequency of about 100 kHz.

6. Conclusion

Laser-materials interaction phenomena indicate, that materials processing in a controlled, feed-back system may be advantageous. Additional elements of a laser source, suited for materials processing are: beam diagnostics (on-line or off-line resp.), high beam quality and modulation capability. With respect to the latter, rf-excitation has several advantages, however the optimal excitation frequency with respect to physical, technical and economical demands have not yet been finally fixed. This is the subject of current investigations.

This work was granted by the "Bundesministerium für Forschung und Technologie der Bundesrepublik Deutschland, FKZ 13N5382"

References

1. L. Cleemann (Ed.), Schweißen mit CO₂-Hochleistungslasern (VDI-Verlag, Düsseldorf, 1987), pp. 131 - 139, (in german)
2. G. Herziger in The Industrial Laser Annual Handbook, D. Belforde, M. Levitt, Ed. (Penn Well, Tulsa, 1986)
3. E. Beyer, A. Gasser, W. Gatzweiler, and W. Sokolowski, presented at the ICALEO '87, San Diego (1987), to be published
4. R. Kramer, E. Beyer, G. Herziger and P. Loosen in Proceedings, 6th International Symposium on Gas Flow and Chemical Lasers '86, S. Rosenwaks, Ed. (Springer, Berlin, Heidelberg, 1987), pp. 330 - 337
5. R. Wester, G. Herziger, and H. Schülke, in Proceedings High Power Lasers, E. W. Kreutz, Ed., SPIE Vol. 801 (SPIE, Bellingham, 1987), pp. 14 - 22
6. J. Dembowski, R. Hauck, H. P. Kortz and H. Weber, Opt. Commun. 42, 133, 1982
7. M. Berger and W. Kottler in Proceedings, 6th Int. Symp. on Gas Flow and Chemical Lasers '86, S. Rosenwaks, Ed. (Springer, Berlin, Heidelberg, 1987) pp. 82 - 89
8. P. Loosen, E. Beyer, R. Küchler, and R. Kramer in Proceedings, 7th Int. Congress Laser '85, W. Waidelich, Ed. (Springer Verlag, Berlin, 1986) pp. 353 - 358, (in german)
9. F. Olson, in DVS-Berichte (63), (Deutscher Verlag für Schweißtechnik, Düsseldorf, 1980) pp. 197 - 200
10. E. Beyer, G. Herziger, C. Höllt, K. Wissenbach and E. W. Kreutz, in DVS-Berichte 99, 2. Int. Conf. Strahltechnik '85, (Deutscher Verlag für Schweißtechnik, DVS, Düsseldorf, 1985) pp. 25 - 27
11. K. Du (PhI für Lasertechnik) and W. Seelig (TH-Darmstadt), Änderung der Polarisationsrichtung eines CO₂-Lasers durch Rückwirkung bei der Materialbearbeitung, Internal Report (Fraunhofer-Institut für Lasertechnik, Aachen, 1986) to be published
12. US-Patent 4.573.162 (1986)
13. R. Wester, Hochfrequenzgasentladungen zur Anregung von CO₂-Lasern (Thesis, RWTH Aachen, 1987), (in german)
14. K. Schmitt, H. Schülke and R. Wester in Proceedings, 7th International Congress Laser '85, W. Waidelich, Ed. (Springer Verlag, Berlin, 1986) pp. 28 - 32
15. V. Sturm, paper K9.3 presented at the "Frühjahrstagung der Deutschen Physikalischen Gesellschaft", Düsseldorf 1988
16. H. Schülke, Untersuchungen zur Strahlqualität von hochfrequenzangeregten CO₂-Hochleistungslasern, Thesis, RWTH Aachen 1987, (in german)
17. P. Loosen, Hochleistungs-CO₂-Laser mit axialer Gasströmung zum Einsatz in der Materialbearbeitung, Thesis, TH-Darmstadt 1985, (in german)
18. Electronics, July 10, 1987 (Mc. Graw Hill, Inc.)
19. A. Drenker et.al., Oberflächenveredeln mit Laserstrahlung, in press in Feinwerktechnik und Messtechnik 96, 1988, (in german)

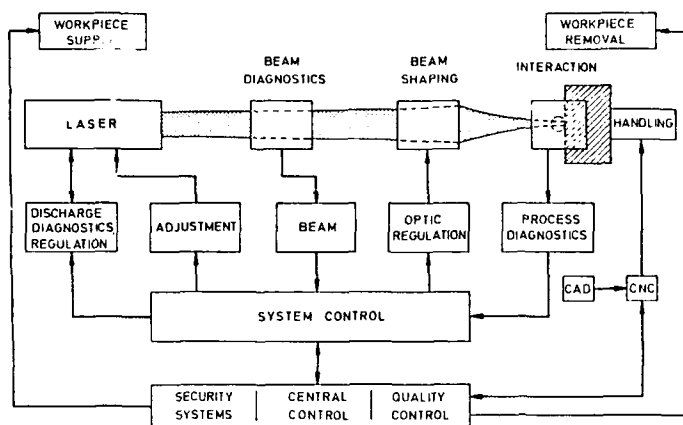


Fig 1: Scheme of a controlled laser-materials processing system

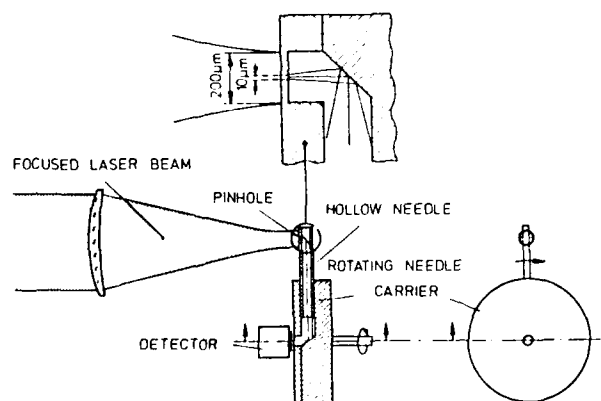


Fig. 2: Schematic set-up for diagnostics of focused and unfocused high-power laser beams.

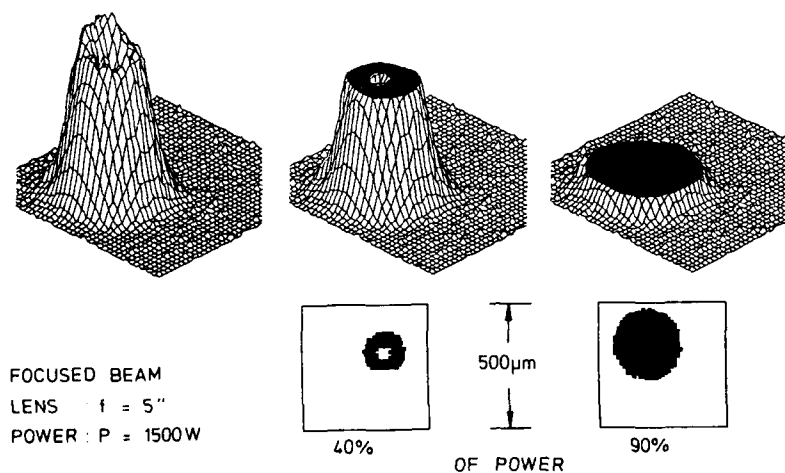


Fig. 3: Example of a measurement, taken with the set-up shown in Fig. 2.

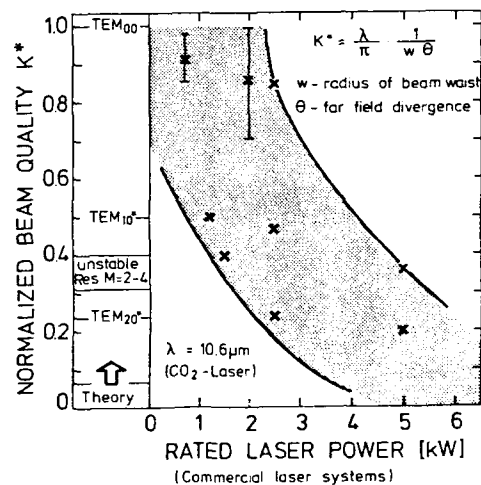
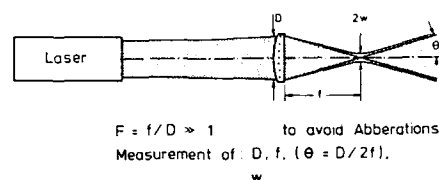


Fig. 4: Measurements of the normalized beam quality of commercial CO₂-lasers for materials processing.

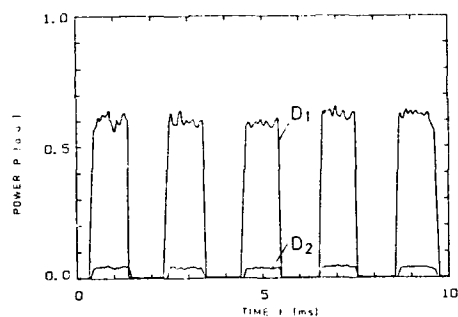
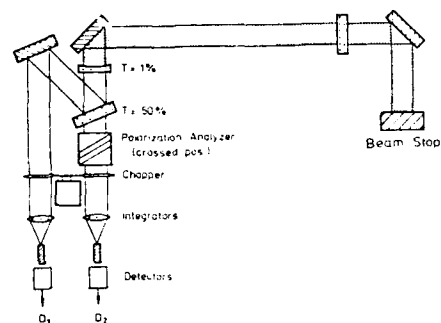


Fig. 5: Diagnostics of the total laser power of a high-power CO₂-laser, without processing.

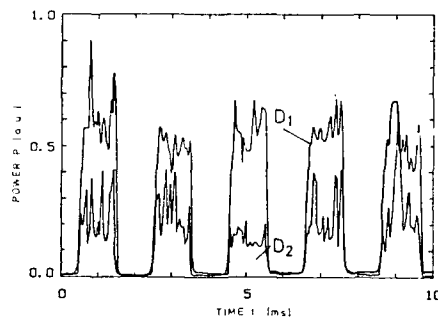
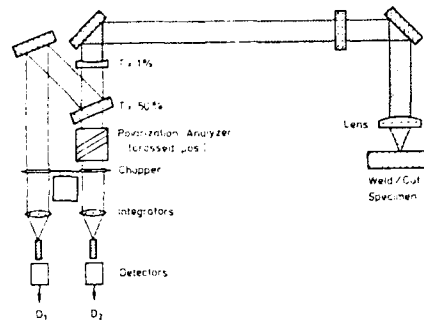
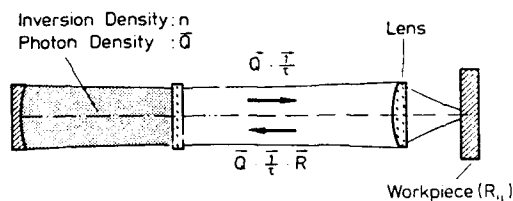


Fig. 6: On-line diagnostics of the total laser power of a high-power CO₂-laser, with processing



$$\begin{aligned} \vec{Q} &= \begin{pmatrix} q_1 \\ q_2 \end{pmatrix} && - 1,2 \text{ Polarization States} \\ \vec{Q} \vec{1} \tau &= \begin{pmatrix} q_1/\tau_1 \\ q_2/\tau_2 \end{pmatrix} && - \text{Photon Flux to Workpiece} \\ \vec{Q} \vec{1} \tau \vec{R} &= \begin{pmatrix} R_{11}q_1/\tau_2 + R_{12}q_2/\tau_2 \\ R_{21}q_1/\tau_2 + R_{22}q_2/\tau_2 \end{pmatrix} && - \text{Photon Flux from Workpiece} \\ \frac{dn}{dt} &= P - n/\tau_c - B n (q_1 + q_2) \\ \frac{dq_1}{dt} &= A F n + B q_1 n - q_1/\tau_1 + Q_1 \\ \frac{dq_2}{dt} &= A F n + B q_2 n - q_2/\tau_2 + Q_2 \end{aligned}$$

Fig. 7: Rate equation model for optical feedback- induced polarization dynamics (τ_1, τ_2 - resonator lifetimes of the photons in polarization mode 1 and 2, n - inversion density, p - pump density, τ_c - collisional lifetime, A, B - Einstein coefficients, F - filling factor)

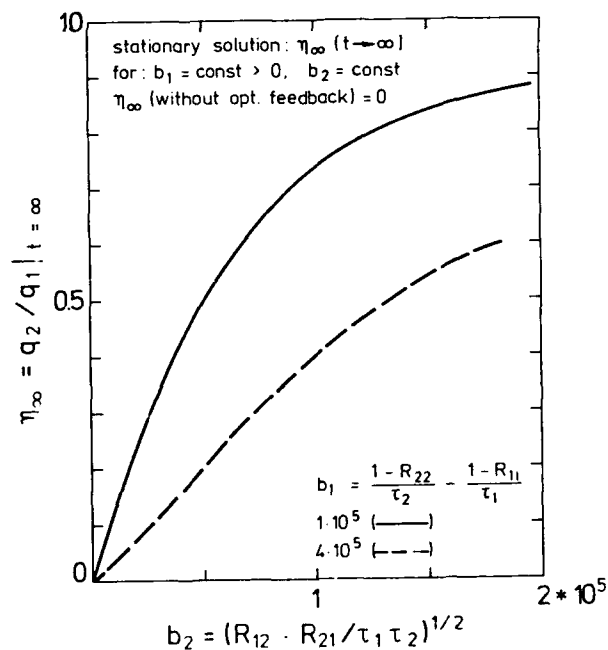


Fig. 8: Stationary solution of the equations, given in Fig. 7.



DC-DISCHARGE IN A HIGHLY-TURBULENT SWIRL FLOW

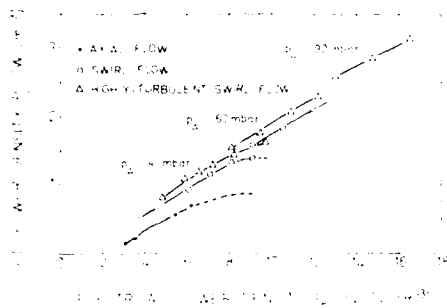


Fig. 9:
Homogenization of a dc - discharge by highly-turbulent swirl flow.

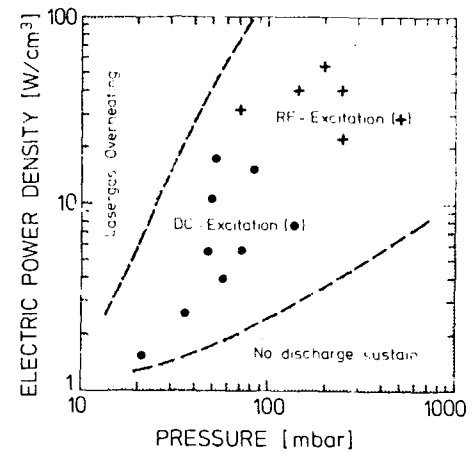


Fig. 10: Typical operating regimes for dc - and rf-excited discharges (27 MHz).

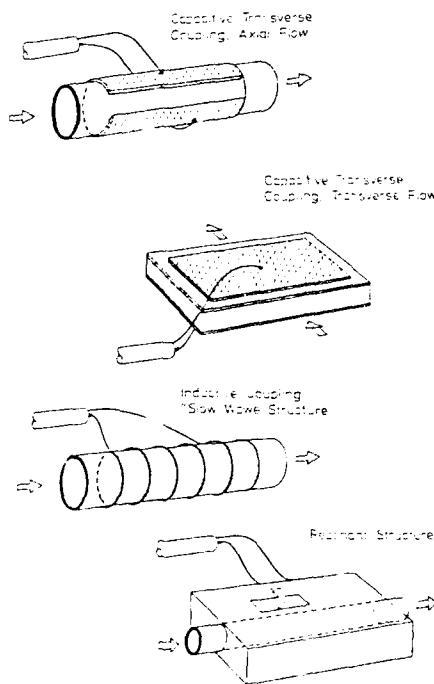


Fig. 11:
Examples of rf- coupling structures

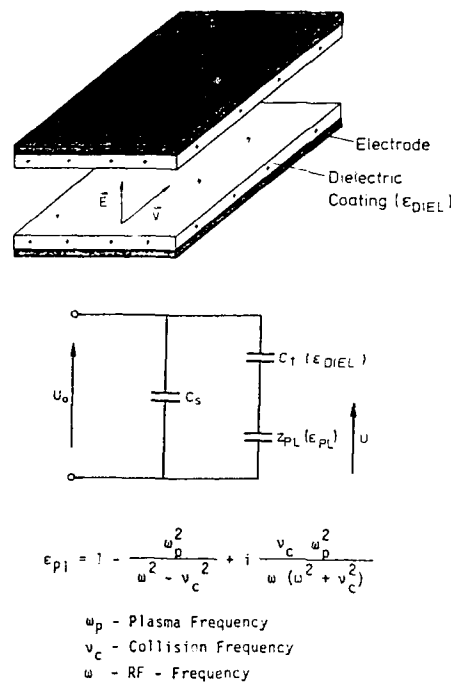


Fig. 12:
Modelling of rf-coupling (C_s -stray capacity, C_t -coupling capacity, Z_{PL} -Plasma impedance).

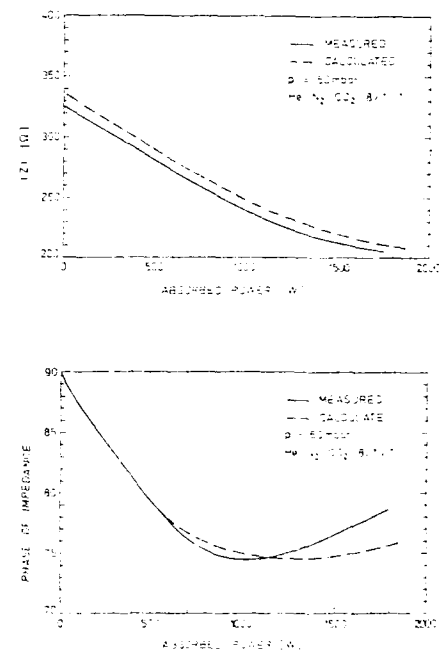


Fig. 13
Example for the power-dependent impedance of a CO₂-laser-discharge with axial flow (tube length 30 cm, inner diameter 2.4 cm).

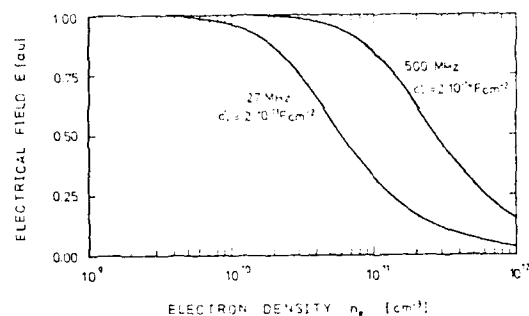
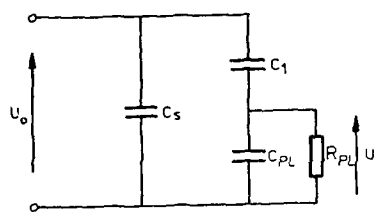


Fig. 14: Calculation of the electrical field in rf-excited plasmas as a function of electron density at two rf-frequencies.

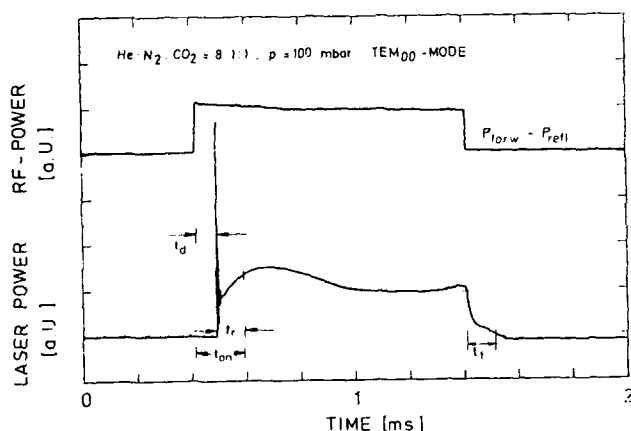


Fig. 15: Gain-switching of a high-power CO₂-laser with axial flow and rf-excitation: rf-pulse and corresponding laser pulse.

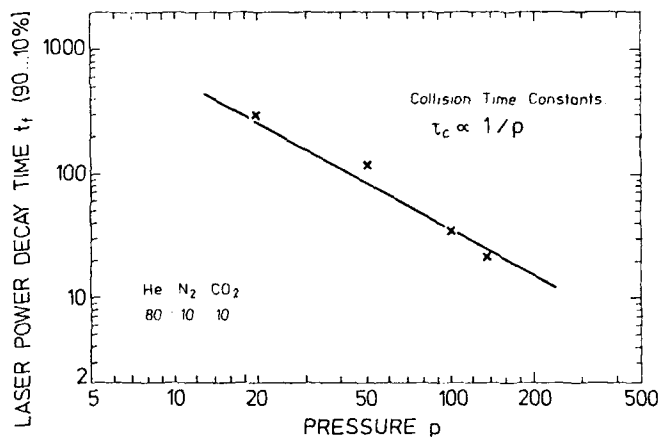


Fig. 16: Laser-power decay time as a function of discharge operating pressure.

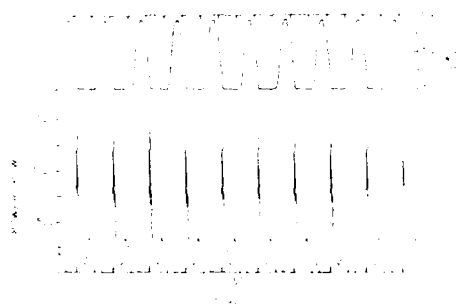
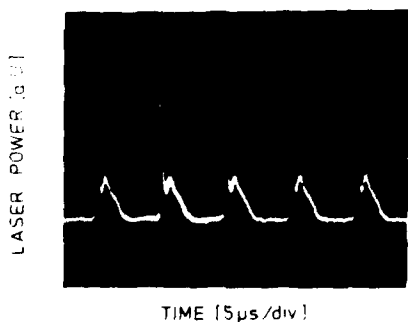


Fig. 17: Modulation of a high-power CO₂-laser: resonant-optical modulation of resonator parameters by oscillation of a resonator mirror.



OPERATION OF A DOWNSTREAM-MIXING CO₂ GASDYNAMIC LASER
UTILIZING HIGH-TEMPERATURE DECOMPOSED GAS OF LIQUID N₂O

Satoshi Takemori
Researcher

Hitachi Research Laboratory, Hitachi Ltd.
4026 Kuji-cho, Hitachi-shi
Ibaraki-ken, 319-12 Japan

Michio Hachijin Kunji Sugimoto
Senior Engineer Engineer

Hitachi Works, Hitachi Ltd.
3-1-1 Saiwai-cho, Hitachi-shi
Ibaraki-ken, 317 Japan

Takashi Hashimoto Susumu Nakano
Senior Researcher Researcher
Mechanical Engineering Research Laboratory
Hitachi Ltd.
502 Kandatsu-cho, Tsuchiura-shi
Ibaraki-ken, 300 Japan

Takashi Miyoshi
Senior Engineer
Defense Technology Development Division
Hitachi Ltd.
4-6 Kanda-Surugadai, Chiyoda-ku
Tokyo, 101 Japan

Abstract

Experimental and theoretical studies have been carried out to evaluate a potential performance characteristics of a downstream-mixing CO₂ gasdynamic laser (GDL) equipped with a screen nozzle and a passive supersonic diffuser, and utilizing high-temperature decomposed gas of liquid N₂O as the donor gas. A small-signal gain coefficient up to 0.5 %/cm and a laser output power as high as 10 kW have been measured with a typical operating condition of a total mass flow rate of 2 kg/s and a gas mixture of mole fraction of 11.3%CO₂/65.1%N₂/0.3%H₂O/23.3%O₂ in the laser cavity. In order to explain the experimental results, a mixing loss factor is introduced in an analytical model incorporating the three-temperature kinetics model combined with the gradually-mixing model utilizing a specified mixing length and a mixing rate. The studies have shown that significant laser potential performance exists for the downstream-mixing CO₂ GDL utilizing the decomposed gas of the liquid N₂O as the donor gas.

1. Introduction

A significant reduction in weight and volume of a downstream-mixing CO_2 gasdynamic laser (GDL) system is possible by replacing N_2 gas by liquid N_2O utilizing a combustion with an appropriate fuel.¹ In the nozzle expansion of the donor gas including contaminants such as CO_2 , H_2O , and O_2 generated by the combustion, vibrational energy is lost from the hot N_2 gas through collisions especially with CO_2 and H_2O gases. These collisional processes deteriorate the laser performance of the mixing GDL system. It is, therefore, required that the mixing GDL system be incorporated with a combustion technique which produces the donor gas with as small amount of contaminants as possible.

The main purpose of this research program is to investigate the feasibility of the high laser performance of the downstream-mixing GDL system utilizing high-temperature decomposed gas of liquid N_2O as the donor gas for its compactness.

2. The Laser System

A schematic diagram of the downstream-mixing GDL system is shown in Fig.1. The system consists of a supplying system of the donor gas and the laser gas, a combustor generating the donor gas by the decomposition of the liquid N_2O with a small amount of gas mixture of CO and H_2 , a downstream-mixing screen nozzle with 10-degree half-angle conical nozzle units, a multimode single-path laser cavity, and a passive supersonic diffuser. The donor gas includes non-preheated N_2 gas for dilution. The additional N_2 gas requires only small percentage of the overall mass throughput, because the N_2 gas itself is used for the pressurization in the supplying system.

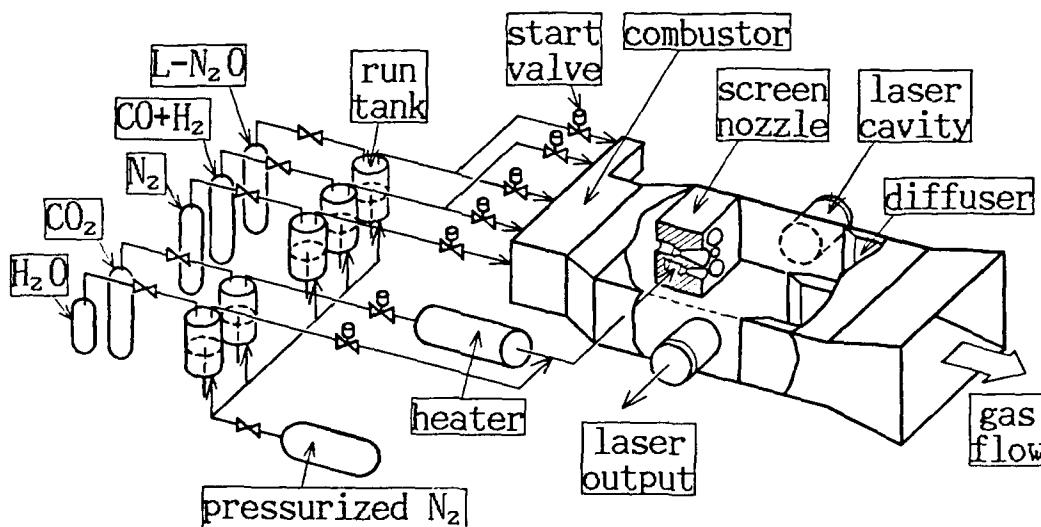


Fig.1 Schematic diagram of the downstream-mixing CO_2 gasdynamic laser

A photograph of the GDL system is shown in Fig.2. The supplying system, the laser cavity, and the cavity duct are mounted on a stand. The stand is approximately 1.5 m wide, 2.5 m long, and 1 m high. The gas flow passing through the cavity duct and a silencer is exhausted directly to the atmosphere. The laser cavity is 75 cm in length and 3.5 cm in diameter, and it contains the gas flow of 52 cm in length along the optical path.



Fig.2 Photograph of the downstream-mixing CO₂ gasdynamic laser system

3. Laser Performance

Fig.3 shows donor-gas combustion characteristics of the liquid N₂O with the gas mixture of CO and H₂ for various stoichiometric ratios ϕ . Mole fractions of N₂, CO₂, O₂ and H₂O, and combustion temperature at a combustion pressure of 100 atm are computed² by an equilibrium combustion model described by the following reaction equation,



Several experimental studies on the combustor have been performed in order to establish a stable combustion with a relatively low stoichiometric ratio. As a result, a stable decomposition of the liquid N₂O has been realized with an extremely small amount of gas mixture of CO and H₂, corresponding to a stoichiometric ratio as low as 0.06.

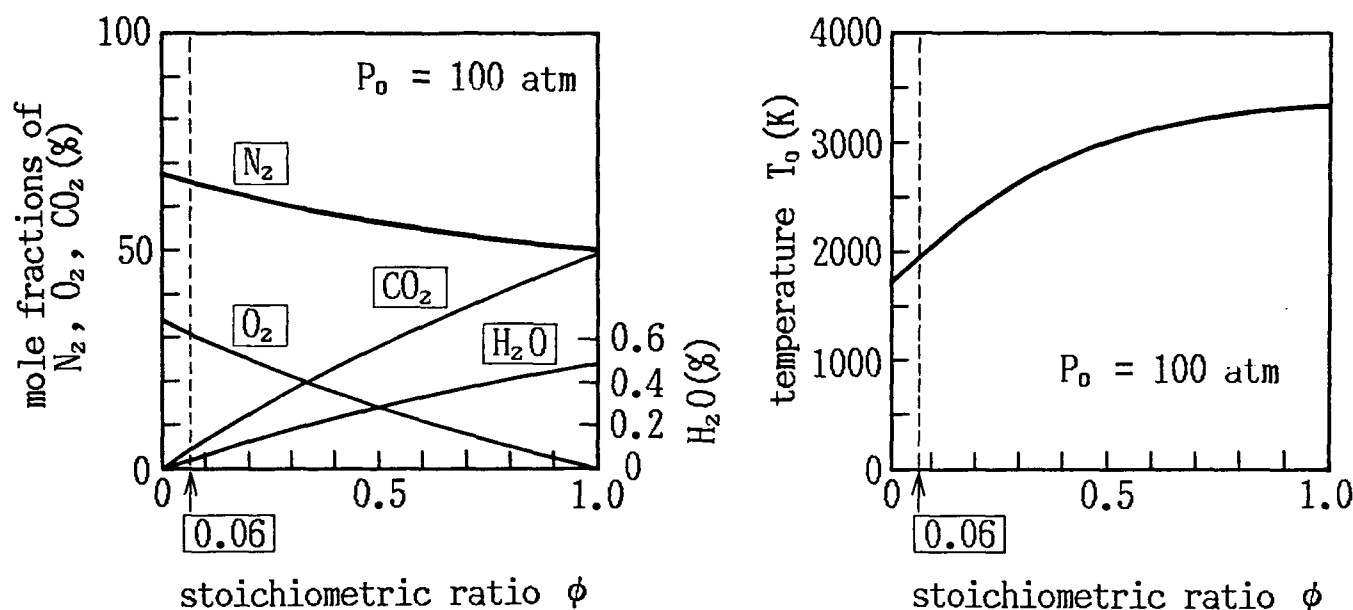


Fig.3 Combustion characteristics of liquid N_2O and mixture of $CO+H_2$

Fig.4 shows a comparison of measured gain distributions along the gas flow with calculated ones under a typical operating condition described in the upper part of the figure. A maximum gain has been measured to be 0.5 %/cm at point in the laser cavity 7 cm downstream of the nozzle exit plane.

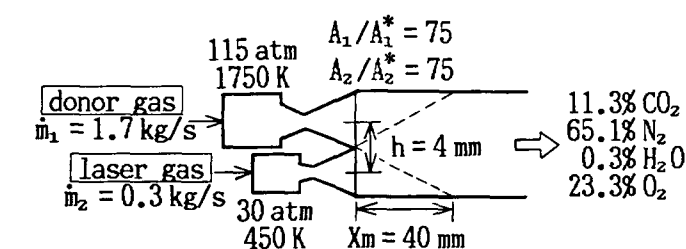
In order to explain the experimental results, small-signal gain coefficients have been computed by the three-temperature kinetics model³ combined with the gradually-mixing model⁴ utilizing a specified mixing length and a mixing rate. A mixing loss factor ζ is introduced in the analytical model to evaluate the effect of translational gas temperature increase caused by the kinetic energy loss due to the turbulence generated by the velocity difference between the two supersonic flows. The mixing loss factor in the mixed flow region is defined by the following equation,

$$u = (1 - \zeta)u_0, \quad (2)$$

where u is a flow velocity with a mixing loss, and u_0 is that without the mixing loss.

A decrease in the small-signal gain is associated with an increase in the mixing loss resulting in the static temperature increase which enhances collisional deactivation of the upper laser level population as well as depression of the small-signal gain. When the mixing loss factor ζ is specified to be 1.5 %, the calculated gain distribution is best-fitted to the measured ones.

Fig.5 shows calculated maximum-available-laser-energy⁵ distributions along the gas flow under the typical operating condition. A specific maximum-available-laser-energy of 10 kJ/kg has been calculated with the mixing loss factor ζ of 1.5 %. It is known that a specific laser power on the order of half of the maximum-available-laser-energy can be extracted from a well-designed laser cavity.⁵ Consequently, a predicted laser output power approximately amounts to 10 kW with a total mass flow rate of 2 kg/s.



predicted laser power

$$P_L = \sim 0.5 \times E_{\max} \times \dot{m}$$

$$= \sim 0.5 \times 10 \text{ kJ/kg} \times 2 \text{ kg/s}$$

$$= \sim 10 \text{ kW}$$

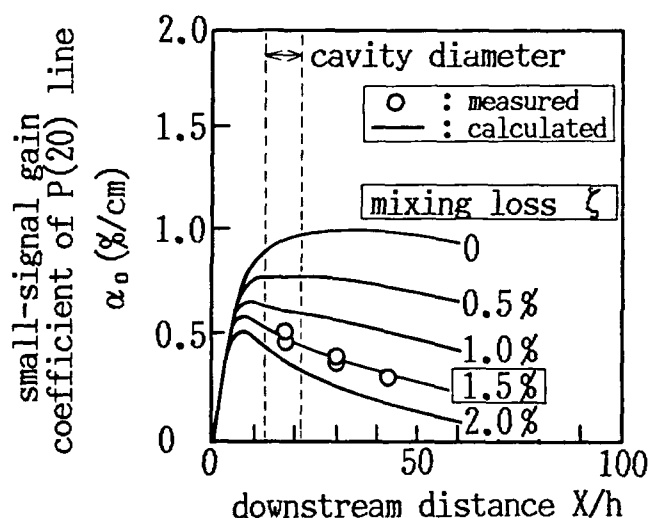


Fig.4 Comparison of measured gain distributions with calculated ones

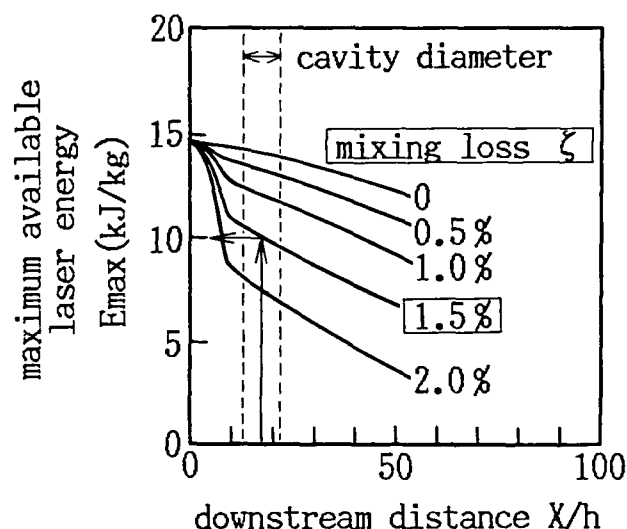


Fig.5 Calculated maximum available laser energy distributions

Fig.6 shows experimental laser output characteristics for various output mirror reflectivities under the above mentioned operating condition. A maximum laser output power of 10 kW has been obtained with a 92.5-% reflectivity output mirror. The result is in good agreement with the calculated laser output power. This indicates that the analytical model is quite capable of predicting the gain and the available energy.

A solid curve is fitted to the measured powers using the Rigrod power extraction model⁶ in order to calculate a saturation parameter. As a result, it is found to be as high as 6.0 kW/cm² with the measured small-signal gain coefficient of 0.5 %/cm.

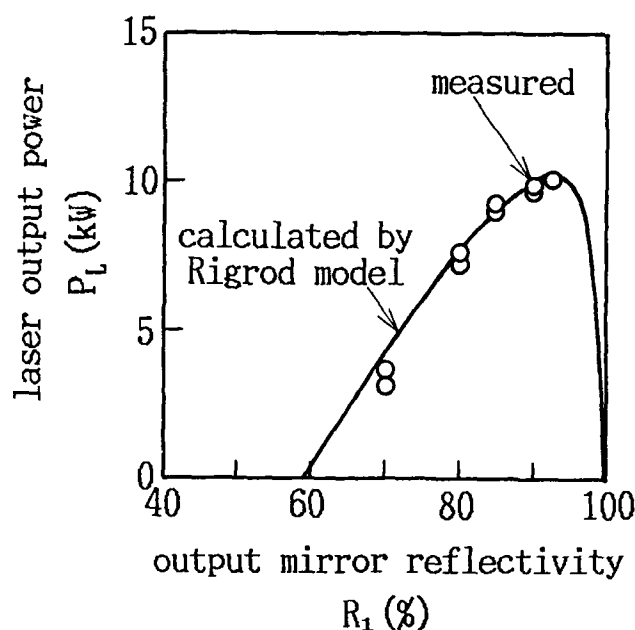


Fig.6 Laser output characteristics

Typical oscillograms are shown in Fig.7 for the laser output power and the static pressures in the combustor and in the laser cavity. The cavity is evacuated down to 40 Torr with the establishment of the stable decomposition of the liquid N_2O at a pressure around 120 atm. The laser output power of 10 kW is obtained for one second in the continuous wave mode.

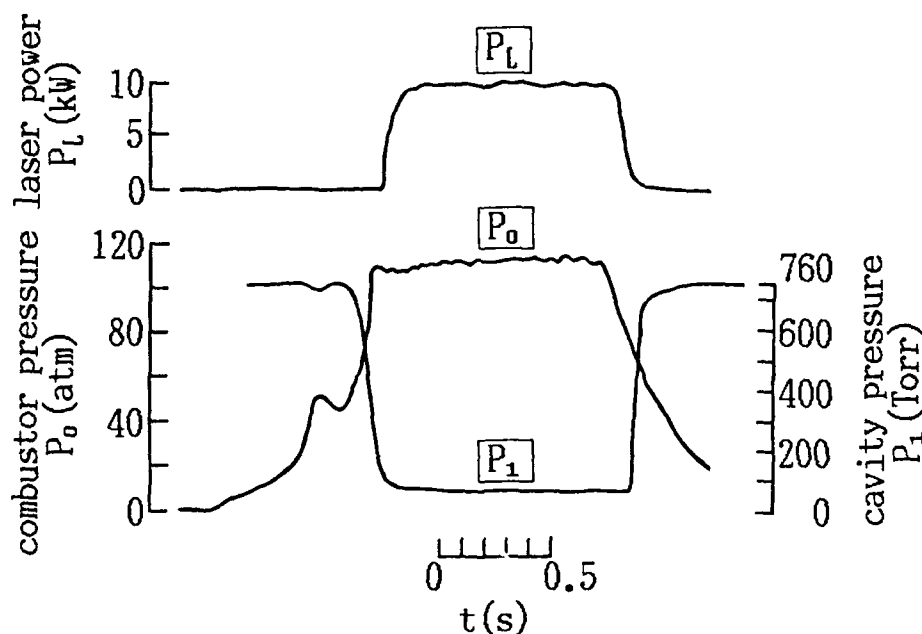


Fig.7 Typical oscillograms of laser output power and pressures in the combustor and in the cavity

4. Concluding Remarks

A further optimization of the experimental parameters such as the reduction of the mixing loss is yet to be performed to investigate an ultimate laser performance potential of the downstream-mixing GDL system utilizing the high-temperature decomposed gas of the liquid N_2O as the donor gas.

5. References

1. K. Kitagawa and K. Komatsu, Appl. Phys. Lett. 47, 558 (1985)
2. S. Gordon and B. McBride, NASA SP-273 (1971)
3. A. T. Jones, J. Phys. D: Appl. Phys. 9, 1193 (1976)
4. R. W. F. Gross and J. F. Bott, Handbook of Chemical Lasers (John Wiley & Sons, 1976)
5. J. D. Anderson, Jr., Gasdynamic Lasers: An Introduction (Academic Press, 1976)
6. W. W. Rigrod, J. Appl. Phys. 36, 2487 (1965)

REGENERATIVE CO₂ AMPLIFIER OF A NANOSECOND PULSE TRAIN

V.V. Apollonov, A.M. Prokhorov, V.R. Sorochenko, Yu.A. Shchekir

General Physics Institute, USSR Academy of Sciences, Vavilov st., 38, Moscow, USSR

Abstract

Regenerative amplification of a nanosecond pulse train in the 50 l active volume CO₂ laser has been investigated both numerically and experimentally. The area in which RA takes place was determined when varying the injected radiation parameters. The nanosecond pulse train utilization as an injected radiation instead of monopulse was shown to broaden significantly the injection time "window" and to enable variation of an individual pulse time structure in the output train.

Introduction

Nanosecond pulse regenerative amplifiers have been developed by many researchers [1,2,3]. The absence of any switches or modulators in the resonator, which limits both beam aperture and intensity, enables the construction of CO₂ regenerative amplifiers with large volumes or apertures of the active medium. A 200 J train of nanosecond pulses generated in a 30 l active volume CO₂ laser was reported in [2]. In order to carry out a number of physical experiments it is of interest to obtain a nanosecond pulse train with a higher energy and wide range of time structure variation. For example, successive interaction of the electron beam with the laser train of pulses in the same focal volume (s.c. cyclic acceleration) should permit to significantly increase the efficiency of laser acceleration of particles [4]. It is effective to use numerical calculation of the regenerative amplification (RA) process in order to estimate the borders in which RA takes place at the varied injected radiation parameters [5,6].

The present paper reports the numerical calculation results and experimental research of RA in the CO₂ laser with a 50 l volume active medium (L₁), moreover the injected radiation was a nanosecond pulse train with an interpulse time interval $\Delta T = 2L_1/c$ (where L_1 is the L₁ resonator length), obtained in a separate regenerative amplifier (L₂). The aim of the research was the determination of the RA area borders, as well as the study of the changes in the pulse train envelope and amplified spontaneous radiation (ASR) level by the variation of injected radiation parameters.

In [6] we reported the results of numerical calculations of nanosecond pulse RA in the 1.8 l active volume TEA-CO₂ laser with a stable resonator. In the present paper the same numerical calculation algorithm was used [6], but some changes caused by a significant difference between the active medium cross section size and injected beam diameter and also the type of injected radiation (pulse train).

Specifically, the following items have been taken into consideration:

1. The injected radiation gradually fills in the fundamental transverse mode of an unstable telescopic resonator.
2. The resonator is divided into 2 zones in which only one or two oppositely directed radiation fluences propagate.
3. The injected radiation is a nanosecond pulse train with the envelope close to the experimental data (Fig.1).

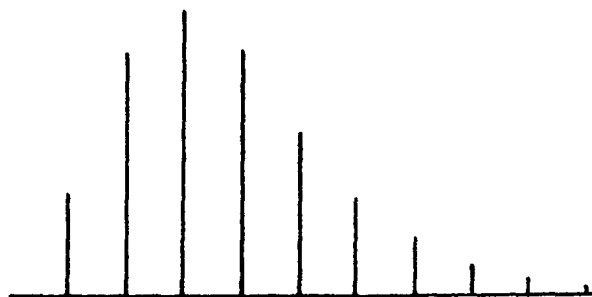


Fig.1. Nanosecond pulse train injected into L₁.

Let us introduce the following designations: T_1 is the instant of injection of the first pulse in the train into L₁ resonator in respect to the pump pulse starting, T_{thr} is the instant of the threshold gain in L₁, E_1 is the injected radiation energy. Note that the parameters of the resonator and active volume used in the calculations correspond to the experimental set up.

One of the main parameters of the RA scheme is the injection "window", that is the region of T_1 variation at a fixed E_1 , inside which ASR level does not exceed a given value. In the present paper we assume that inside the injection "window" the ratio of the pulse train maximum pulse peak power P_N (N is the number of the maximum pulse in the train) to the ASR power P_{ASR} exceeds 10. According to [3], in this case the following propagation of the radiation through the saturable absorber

(8+10 torr SF₆ + 6 atm He) allows to obtain the ratio $K = P_N/P_{ASR} > 10^4$ in the output,

this value is sufficient for the majority of physical experiments.

The calculation results for the case $T_i = T_{thr}$ are shown in Fig.2. The P_N value grows up with a decreasing injected train peak power P_i (Fig.2,a), because the maximum output train pulse is formed at a higher amplification of the active medium. P_N reaches a maximum value simultaneously with K parameter at $P_i = 10^{-3} W$ (Fig.2,b). Note that with P_i decreasing from 1 to $10^{-3} W$ (Fig.2,e) the peak power P_{ASR} also decreases, but the total ASR energy, E_{ASR} , in the L_1 pulse grows up. (See Fig.2,c) presenting the dependence of $A = E_{tr}/(E_{tr} + E_{ASR})$ on P_i , where E_{tr} is the total energy of the L_1 pulse train). This is due to a more intensive saturation of the active medium.

It follows from Fig.2,b that $K \geq 10$ if $P_i \geq 2 \cdot 10^{-5} W$, that is the minimum injected energy $E_i^* = 3 \cdot 10^{-13} J$.

The train envelope form depends significantly on the E_i value. For $E_i = 1.5 \cdot 10^{-3} J$ (experimental data) the front peak of the envelope is insignificantly higher than the main part of the envelope due to the shift of the generation start into the time interval with a smaller amplification (similarly to the generation of a smooth long pulse at one longitudinal mode performance of the injection locked laser Fig.3,a). When E_i is attenuated up to $1.5 \cdot 10^{-9} J$ the first peak power is much higher than the "tail", but the ASR level increases ($K \approx 15$) (Fig.3,b).

Thus, in order to obtain maximum output peak power the injected power must be far lower than that needed for a complete suppression of ASR ($A_1 \approx 1$). If the output peak power has a maximum, A_1 is only about 0.4 (Fig.2,c).

The numerical calculations have shown that, unlike [5,6], injection window is not symmetric relative to T_{thr} , i.e. for $E_i = 1.5 \text{ mJ}; T_{thr} = 1.5 \text{ } \mu\text{sec} < T_i < T_{thr} + 0.75 \text{ } \mu\text{sec}$. This difference is caused by the use of the pulse train as injected radiation, instead of monopulse [5,6]. If the value $T_i^M = T_i + \Delta T(M-1) < T_{thr}$ (M is the number of pulses in the train), then the train pulse with j number will be attenuated by the resonator

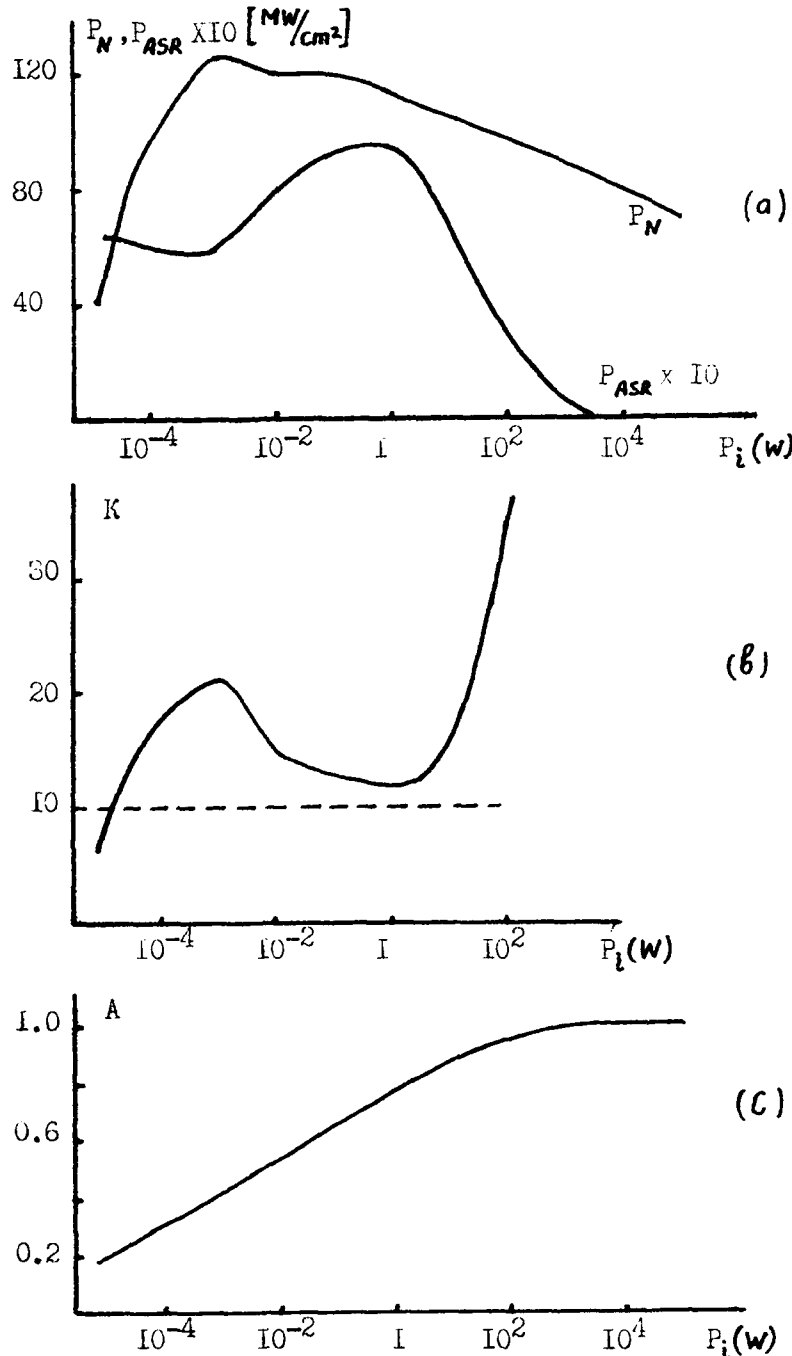


Fig.2. Dependence of P_N , P_{ASR} (a), $K = P_N/P_{ASR}$ (b) and $A = E_{tr}/(E_{tr} + E_{ASR})$ (c) on P_i - peak power of the injected train.

losses proportionally to the number of passes through the resonator in the time interval from $T_{ij} = T_i + \Delta T(j-1)$ to T_{thr} . Therefore, the last pulse in the train has the minimum losses and in numerical calculations the injection of the last train pulse with the addition of all previous pulses with different attenuation in the resonator has been considered. An equivalent power of the pulse injected at a T_i^M instant depends not only on the train maximum pulse peak power P_i , but also on the resonator parameters, T_i , and

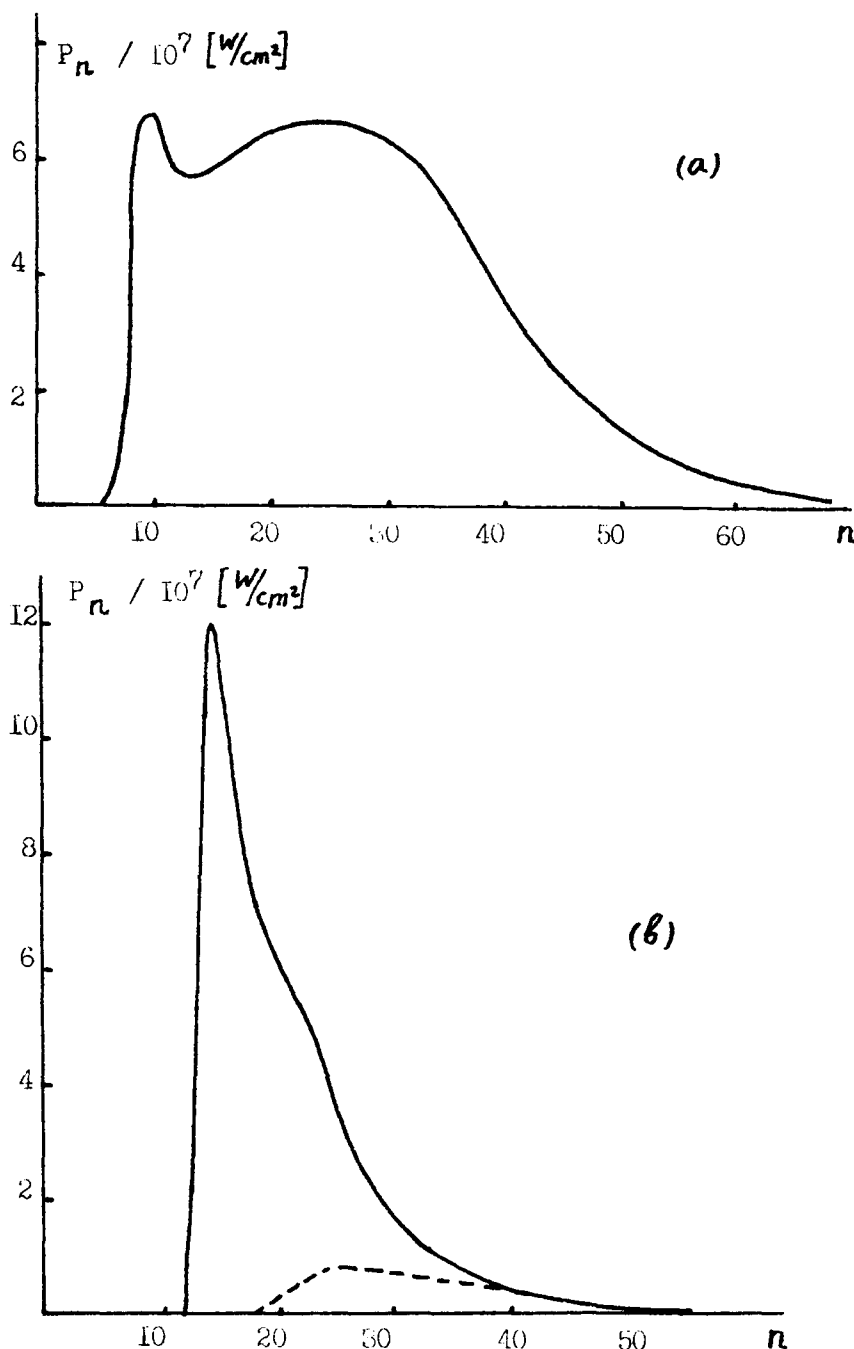


Fig. 3. Calculated envelopes of nanosecond pulse train (solid line) and amplified spontaneous radiation (ASR) (dashed line) for two values of E_1 : a) $E_1 = 1.5 \cdot 10^{-3} \text{ J}$, b) $E_1 = 1.5 \cdot 10^{-2} \text{ J}$, (n - number of a pulse in the train, P_n - power density of the train pulse with the n -th number).

the train envelope form. At the other parameters fixed the left border of the "injection window" moves further from T_{thr} with an increase in the full duration of the injected train. If $T_i > T_{thr}$ only 2-3 first pulses in the train influence the RA process due to a rapid increase of the light intensity in the resonator after the threshold.

Note that in the vicinity of the "injection window" borders the dependence of K upon T_i is similar to that shown in Fig. 2, b. When T_i approaches the border K increases from ≈ 12 up to the maximum value ≈ 20 and then rapidly drops down.

Thus, when nanosecond pulse train is used as injected radiation instead of monopulse (with the same peak power P_1) "injection window" broadens by the value close to the full duration of the injected train ($\sim 10 \text{ } \mu\text{sec}$ in the present case).

Experimental set up

The CO_2 laser (L_1) with a $20 \times 20 \times 125 \text{ cm}^3$ active medium has operated in a self-sustained discharge regime initiated by an electron beam, with a low-ionization additive (triethylamine) in a gas mixture [7]. The telescopic resonator mirrors were disposed at the edges of a 2 m^3 volume gas chamber. The resonator length $l_1 = 8.6 \text{ m}$, magnification $M = 2.1$, mirror apertures 20 and 9 cm. The injected radiation was introduced into resonator through a 4 mm diameter hole in the concave mirror center (Fig. 4). The L_1 worked on the $\text{CO}_2:\text{N}_2:\text{He} = 1:1:3$ (1 atm) gas mixtures with triethylamine (TEA) additive (1 torr), $\text{CO}_2:\text{N}_2 = 1:2$ and $\text{CO}_2:\text{N}_2 = 1:4$ (0.5 atm) with TEA (1 torr) and H_2O (2 torr) [7, 8]. Pump energy of the active volume was up to 10 kJ, electron beam energy did not exceed 200 KeV. Maximum output energy of L_1 was $\approx 1200 \text{ J}$ for $\text{CO}_2:\text{N}_2 = 1:4$ mixture.

The radiation injected into L_1 was the nanosecond pulse train generated in TEA CO_2 laser (L_2) with a 1.8 l active volume similar to [9]. The L_2 active length was 50 cm, resonator length $l_2 = l_1$ with a 1 cm accuracy. When operated on the $\text{CO}_2:\text{N}_2:\text{He} = 1:1:3$ (1 atm) mixture and 160 J/l pump L_2 output energy was $\approx 0.2 \text{ J}$ at the fundamental transverse mode. Nanosecond pulse train (Fig. 1) was formed on injecting into the L_2 resonator a 3 ns duration and about 10^{-12} J pulse cut off by electrooptical switch (S_1) from the 1 W CW CO_2 laser (L_3). The L_3 generated at a 10 P(20) line. Pulse duration in the train was close to 2 ns due to the saturation effect.

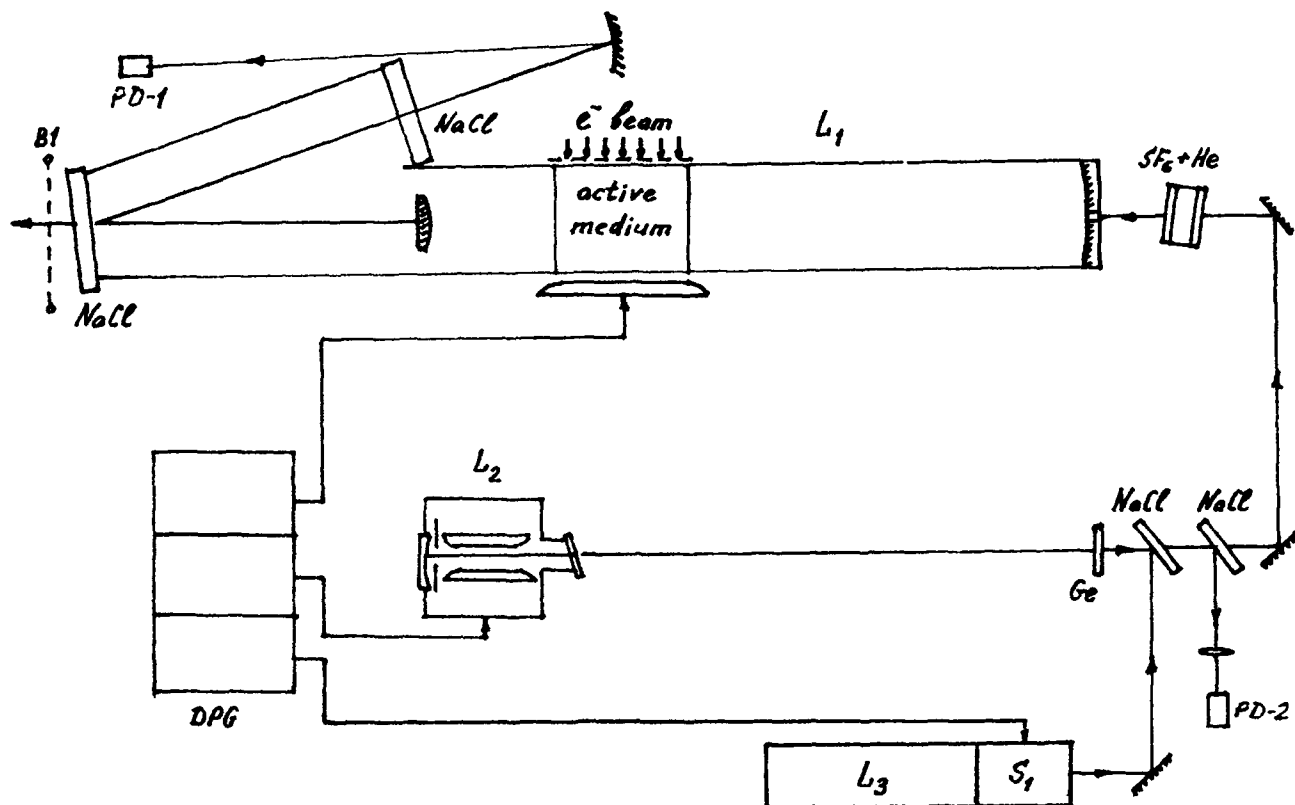


Fig.4. Experimental set up.

The contrast ratio of the train peak power to the L_2 ASR level exceeded 300:1 (measured by Tektronix 7104 oscilloscope). High peak power of the L_2 train ($\sim 10^6 + 10^7$ W) was much higher than the L_1 spontaneous emission power at the injection instant, that is why the experimental set up exhibited a very reliable performance and the "injection window" was rather wide.

Photon drag detectors PD-1 and PD-2 have been used to control the L_1 and L_2 radiation. The L_1 energy was measured by a communicating B_1 bolometer connected with a resistance bridge. B_1 was calibrated by the calorimeters matrix. The energy measurement accuracy was 15%. L_1 , L_2 and S_1 , as well as the oscilloscopes to control the set up parameters were synchronized by a many channel delayed pulse DPG generator.

When L_1 worked on the $\text{CO}_2:\text{N}_2:\text{He} = 1:1:3$ p = 1 atm mixture, RA "window" was $T_{\text{thr}} - 1.6 \mu\text{sec} < T_i < T_{\text{thr}} + 0.6 \mu\text{sec}$ for $E_i = 1.5 \cdot 10^{-3} \text{ J}$. Fig.5, a presents the L_1 radiation oscillogram for this value of E_i and $T_i = T_{\text{thr}}$.

For $T_i = T_{\text{thr}} = 0.6 + 0.7 \mu\text{sec}$ RA took place in L_1 (that is $K \geq 10$) when E_i was attenuated up to $1.5 \cdot 10^{-11} \text{ J}$. With smaller values of E_i the "injection window" width was close to the experimental jitter of $T_i = \pm 100 \text{ nsec}$, that is why it was difficult to determine an exact value of E_i . With an optimum value of $E_i = 1.5 \cdot 10^{-10} \text{ J}$ P_N had the maximum about 1.5 times higher than its value at $E_i = 1.5 \cdot 10^{-3} \text{ J}$. Fig.5, b shows the train of pulses at $E_i = 1.5 \cdot 10^{-9} \text{ J}$.

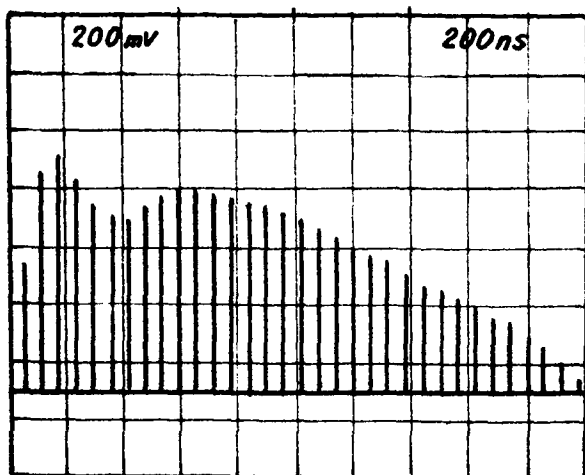
Thus, the experimental values of the "injection window" and minimum E_i^* , as well as the train envelopes for two values of E_i are close to the calculated values.

When the L_2 resonator length is varied relatively to L_1 , the output train pulses are broadened at the base due to the delay of each successive pulse in the input train to the previous one having completed its cavity round trip (Fig.6, a). At a significant difference in the resonators' lengths $\Delta t = 2L_2/c - 2L_1/c > \tau_i$ (τ_i - is an individual pulse duration) each pulse in the output train is also a train of pulses separated by a Δt interval (Fig.6, b). The train of such a type may be of interest for different experiments of radiation interaction with matter.

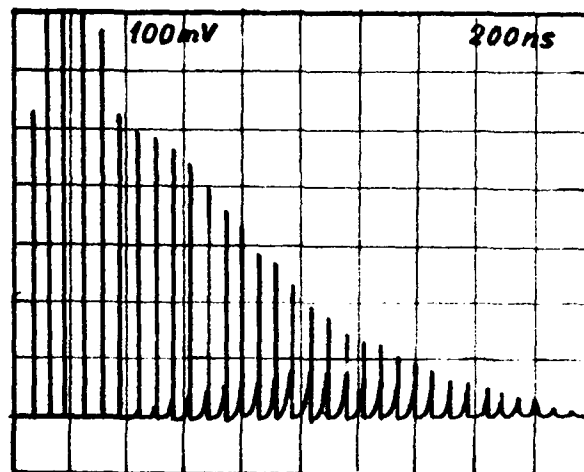
Conclusion

Thus, in the present report:

1. The borders of regenerative amplification regime in the 50 l active volume CO_2 laser

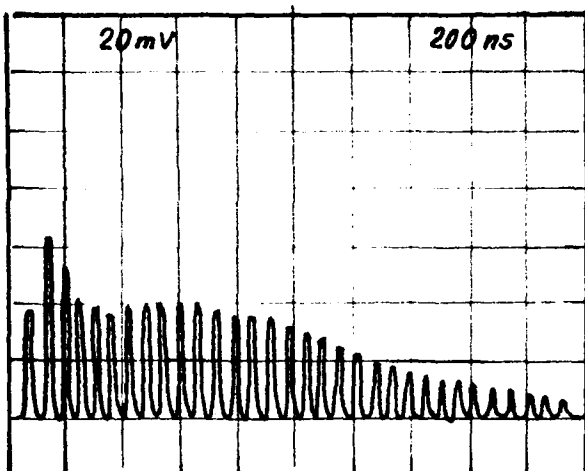


a) $E_i = 1.5 \cdot 10^{-3} \text{ J}$

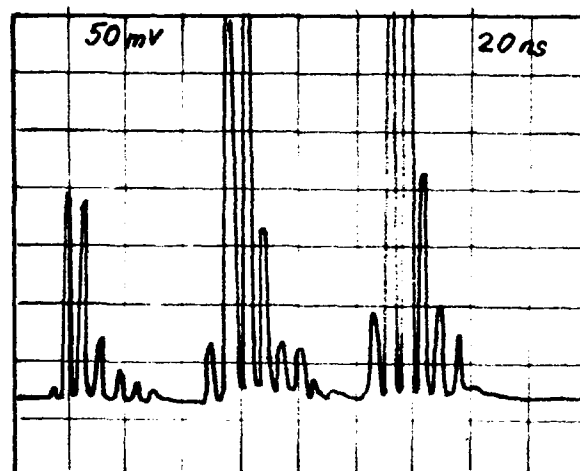


b) $E_i = 1.5 \cdot 10^{-4} \text{ J}$

Fig.5. L_1 radiation oscillograms for the case $T_i = T_{thr}$.



a) $2l_2/c - 2l_1/c < \tau_i$



b) $2l_2/c - 2l_1/c \sim \tau_i$

Fig.6. L_1 radiation oscillograms for the case $l_2 \neq l_1$.

- are determined both numerically and experimentally at varied parameters of the injected radiation (which is a train of nanosecond pulses).
2. The nanosecond pulse train utilization as injection radiation instead of monopulse was shown to broaden significantly the "injection window" and to enable the individual pulse time structure changing in the output train.
3. The possibility of controlling the peak power and envelope form in the train, as well as the amplified spontaneous emission level by varying the injected power was demonstrated both numerically and experimentally.
4. The numerical calculation results correspond satisfactorily to the experimental data.

References

1. P.A.Belanger, J.Boivin. Can. J. of Phys., 54, 720, (1976).
2. P.A.Belanger, R.Trembley, P.Lapierre. Opt. Commun., Vol.26, p.256, (1978).
3. V.V.Apollonov, P.B.Corcum, R.S.Taylor, A.J.Alcock, H.A.Baldis. Optics Letters, Vol.5, No8. p.333, (1980).
4. V.V.Apollonov, A.J.Artemiev, Yu.L.Kalachov, A.M.Prokhorov. Submitted to Applied Phys. Letters.
5. K.J.Andrews. Analysis of injection mode locking of high power CO₂ laser system (Internal report, LPI/77/3, May, 1977).
6. V.V.Apollonov, A.M.Prokhorov, V.R.Sorochenko. Modelling, Simulation & Control. A, Vol. 11, No3, (1987), p.29-38.
7. V.V.Apollonov, K.N.Firsov, I.G.Kononov, A.M.Prokhorov, V.A.Yamschikov. Lett. to Sov. Journal of Techn.Phys., 12, No7, (1986).
8. V.V.Apollonov, G.G.Baitsur, V.V.Kralin, K.N.Firsov and S.K.Semionov. Preprint of General Physics Institute, (1988).
9. V.V.Apollonov, G.G.Baitsur, V.V.Brutkov et al. Lett. to Sov. Journal of Techn.Phys., Vol. 10, No19, (1984), p.1192.

THE DEVELOPMENT OF A HIGH POWER OPTICALLY PUMPED D₂O FAR INFRARED LASER FOR COLLECTIVE THOMSON SCATTERING EXPERIMENTS IN THE TCA TOKAMAK

M.R. Siegrist, R. Behn, M.A. Dupertuis, P.A. Krug, I. Kjelberg, S.A. Salito
Centre de Recherche en Physique des Plasmas
Association Euratom - Confédération Suisse
Ecole Polytechnique Fédérale de Lausanne
21, Av. des Bains, CH - 1007 Lausanne/ Switzerland

Abstract

Results are reported of an attempt to measure the ion temperature in the TCA tokamak by collective Thomson scattering of the radiation of an optically pumped D₂O far infrared laser. Consistent results are obtained in the correct range of temperatures. While the precision obtained so far is still unsatisfactory, there are no indications of any adverse effects precluding a precise measurement with a more sensitive state-of-the-art detection system.

Time- and frequency resolved measurements of the far-infrared laser emission proved that the bandwidth and the frequency shift during the pulse (chirping) are still acceptable for a collective Thomson scattering experiment.

During this study we showed that the emission frequency depends on the intensity of the pump- and the FIR beam as well as on the D₂O pressure. We also observed an influence of the time history of the emission resulting in a doubly-peaked pulse shape of the FIR laser.

Introduction

Measuring the ion temperature of a tokamak plasma by Thomson scattering will be of particular interest to plasma physicists as soon as a precision of about 10% can be reached by this method. Our preliminary results showing scattered spectra do not achieve this goal yet. For this reason the emphasis will be on the development of the tools, mainly the optically pumped far-infrared laser where we encountered a few quite interesting problems.

The presentation is divided into two parts:

- 1) Development of a plasma diagnostic experiment to measure T_i by collective Thomson scattering.
- 2) time-resolved linewidth and lineshape measurements of a pulsed optically pumped far-infrared D₂O laser.

T_i measurement by collective Thomson scattering

In a tokamak plasma, the ion temperature is an important parameter and considerable efforts are made to develop methods that can provide measurements with good temporal and spatial resolution. Since Thomson scattering of ruby or Nd: YAG laser radiation has become the standard method to measure the electron temperature, the question arises whether the same method could be used to determine T_i ? Before discussing the problems encountered, we will first compare the different available methods and their advantages and disadvantages. Four of the main methods are listed in table I.

The most commonly used method is based on charge exchange neutrals. On JET, for example, five neutral particle analyzers are installed which look at different chords. The beams are mass and energy resolved and recorded with channel multipliers to obtain the temperatures of both ion types, the density ratio and the fast ion distribution function during additional heating. The limitation, at least in large machines, is given by the opacity of the plasma to neutrals escaping from the central plasma.

Spectroscopic techniques have also been used with success. The main drawback is that the method gives the temperature of the impurity ions in a particular ionization state and additional measurements or assumptions are required to obtain T_i . Impurities are also concentrated at the plasma edge and hence it

is difficult to obtain information about the plasma center.

Neutron analysis methods can only be used in D-D and D-T plasmas with sufficiently high neutron flux.

A reliable temperature measurement via collective scattering of laser light has not yet succeeded on a tokamak. This fact alone suggests that it is obviously not a simple technique. Potentially the method has several advantages:

- does not disturb the plasma
- good temporal and spatial resolution
- direct method (does not rely on model assumptions)
- eventually other parameters can be measured simultaneously (n_e , T_e , Z_{eff} , Bp)
- insensitive to neutrons
- insensitive to small populations of non-thermal particles

We will briefly review some important points to consider for the set-up of a Thomson scattering experiment to determine T_i .

1) The scattered radiation observed is essentially due to the electrons. The mobility of ions is so much smaller that their contribution is negligible. Hence one tries to observe the ion motion by collective scattering from the electron clouds which form around each ion in order to shield its charge. The scattering scale length is thus much larger than in the non-collective regime, which means that also the laser wavelength has to be larger. If one does not want to work at FIR wavelength, very small scattering angles will be required. This results in a loss of resolution and problems with stray light.

2) Because of the small cross-section for Thomson scattering, the scattered intensity is very small. The ratio of the power collected by the detection system to the incident laser power is typically (as for example in our case) of the order of 10^{-14} . Hence a powerful laser system in the FIR and a very sensitive detection system are required.

3) A careful study is required to make sure that the signal containing the information on the ion temperature is not masked by contributions due to other effects in the spectral region of interest. Significant undesirable contributions could be due to scattering from impurities or microturbulences, ECE radiation and parasitic stray light. Under certain conditions, the influence of the magnetic field can distort the thermal spectrum. Most of these effects influence the central part of the observed spectrum only. In the range from 600MHz to 2GHz offset from the D₂O laser frequency which we use for the evaluation of T_i we only have to consider the influence of the magnetic field, whereas the other perturbations can be neglected.

4) The laser beam should have a spectral width considerably smaller than the width of the scattered spectrum and it should also be stable in frequency. Otherwise a complicated deconvolution procedure is required, with all the associated uncertainties. The second part of the paper deals with this subject.

We have developed a system which in principle is capable of measuring the ion temperature in a single shot. In practice we haven't achieved this result yet and we are currently investigating why this is so.

Figure 1 is a schematic of our set-up. The system is installed on the TCA tokamak, a medium size tokamak used mainly for heating experiments. An optically-pumped D₂O vapor far-infrared laser produces pulses of 1-2J within 1μs. The

Collective Thomson Scattering Experiment on TCA

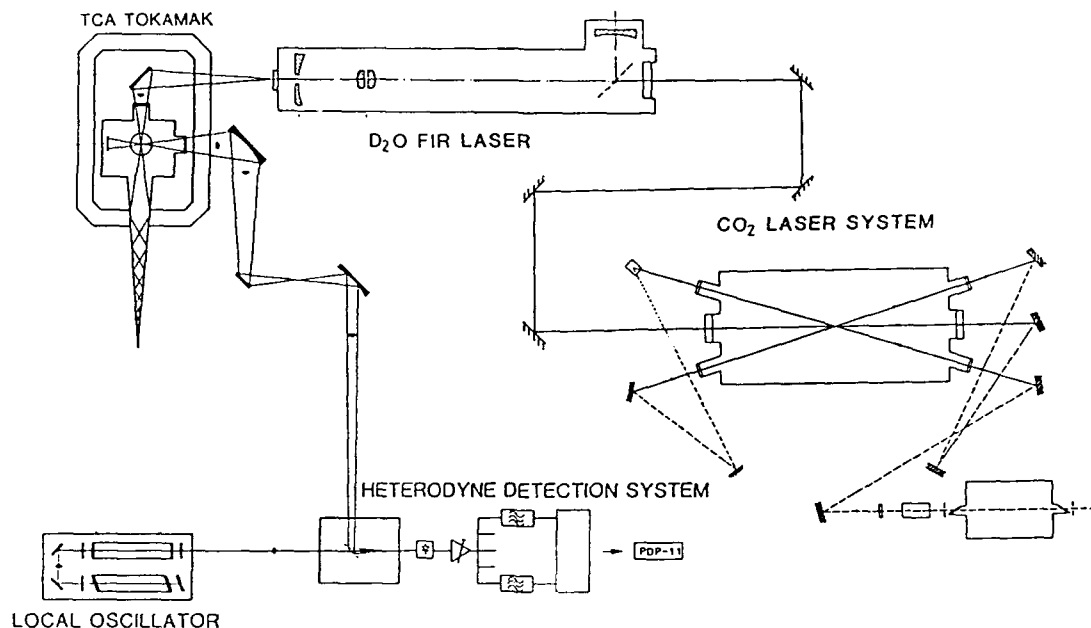


Figure 1

Configuration of the experimental system showing the CO₂ oscillator, the e-beam amplifier operated in a triple-pass configuration, the FIR laser with unstable resonator, the scattering arrangement on the TCA tokamak and the heterodyne detection system consisting of an optically pumped CD₃Cl laser as local oscillator, a diplexer and a multi-channel receiver system with a Schottky diode mixer.

beam is focused by a parabolic mirror into the center of the plasma and scattered radiation is observed at 90°. A shallow conical pyrex beam dump is used to absorb the main beam and the detection system looks at a deeply grooved Macor ceramic viewing dump. The purpose of these two devices is to suppress stray light as much as possible. We use a heterodyne detection system with an optically-pumped CD₃Cl FIR laser used as local oscillator. Its emission is combined with the scattered radiation in an optical diplexer and mixed in a Schottky diode. The resulting IF signal centered around 3.6GHz is amplified and split into a range of 20 different channels, each 80MHz wide. After amplification and integration the signals are digitized by CAMAC units and sent to the local computer for analysis.

Calculated spectra for H and D plasmas, respectively, are shown in Fig.2. In each case three curves are presented referring to different conditions (only one half of the symmetric spectrum is shown.) Curve 1 gives the spectrum for a pure plasma containing only a single ion species. Spectrum 2 is obtained when small concentrations of impurity ions are included. The species and concentrations were chosen in agreement with typical tokamak plasma conditions ($Z_{eff}=2.5$). Finally, curve 3 shows a spectrum that also takes into account the influence of the magnetic field which becomes important when $k \perp B$.

The combination of these effects leads to a considerable distortion of the central part of the spectrum out to about 600MHz. In order to avoid complications in the analysis, like multi-parameter fits, the central part should be excluded from an evaluation of T_e . A variation of the temperature of the majority ions affects essentially the wings of the spectrum.

We have developed a computer code based on a Monte-Carlo technique to simulate the signal statistics and the background noise encountered in a scattering experiment. In Fig 3 we show a spectrum for our current experimental conditions (the central part, which is not used for the analysis, has been omitted), but assuming a somewhat better sensitivity of the receiver system.

The width of the band indicates the error bars obtained from repetitive measurements at fixed plasma conditions. The ion temperature could be obtained with 10% accuracy in this case. In an actually measured spectrum the error bars should be of comparable size.

In Fig. 4 we show the results of a scattering experiment obtained from a single shot. The background, obtained from the average of nine acquisitions before and nine acquisitions after the laser pulse, has been subtracted. A fit for a plasma density of $5 \cdot 10^{13} \text{ cm}^{-3}$, an electron temperature of 800eV, a Z_{eff} of 2.5 and a toroidal magnetic field component of 1.5T at an angle of 1° with respect to the direction normal to the scattering plane, suggests an ion temperature of 390eV. The observed fluctuations of the signal are obviously much larger than predicted. However, the ion temperatures obtained by fitting the spectra of five different shots are quite consistent with a mean of 280eV and a standard deviation of 25% for a single measurement. Also shown in the figure is a fit which does not include the effect of the magnetic field. The correspondence with the measured data is obviously much worse, suggesting that magnetic field effects are indeed important for the particular geometry used in our experiment. This adds an additional uncertainty, mainly due to the averaging over a range of angles. At this stage it is difficult to discuss systematic effects; it is more useful to compare error bars in order to find out how far away we still are from a measurement. The answer is: a factor of 5 to 10. Possible ways to achieve this required factor are the following:

- 1) At present the laser power is not limited by the pump laser system, but by the damage threshold of the FIR laser entrance window. Modifications of the optical system could alleviate this problem.

- 2) Our detection system does not represent the state of the art. At present systems of similar design achieve NEPs which are up to 10 times better.

- 3) With the installation of a mirror in the place of the

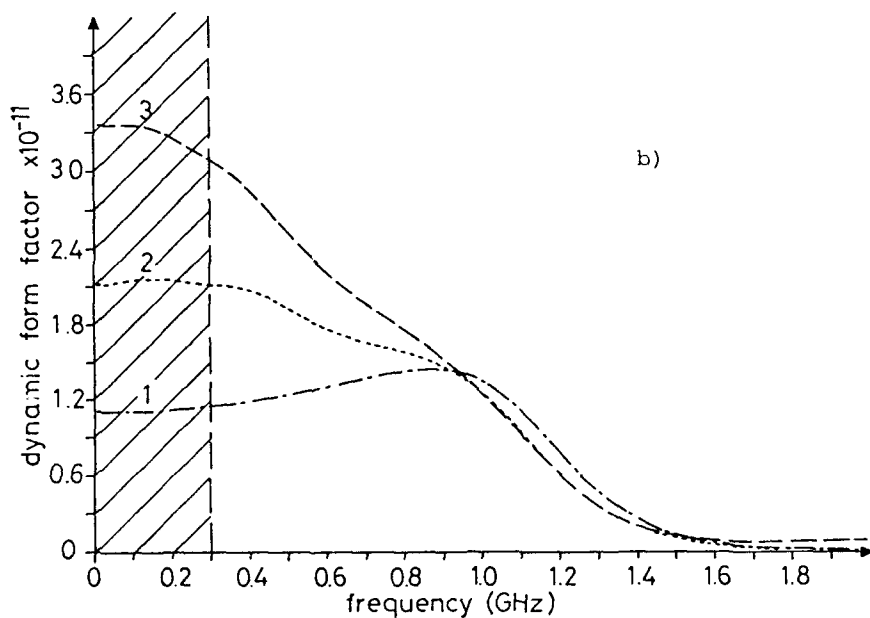
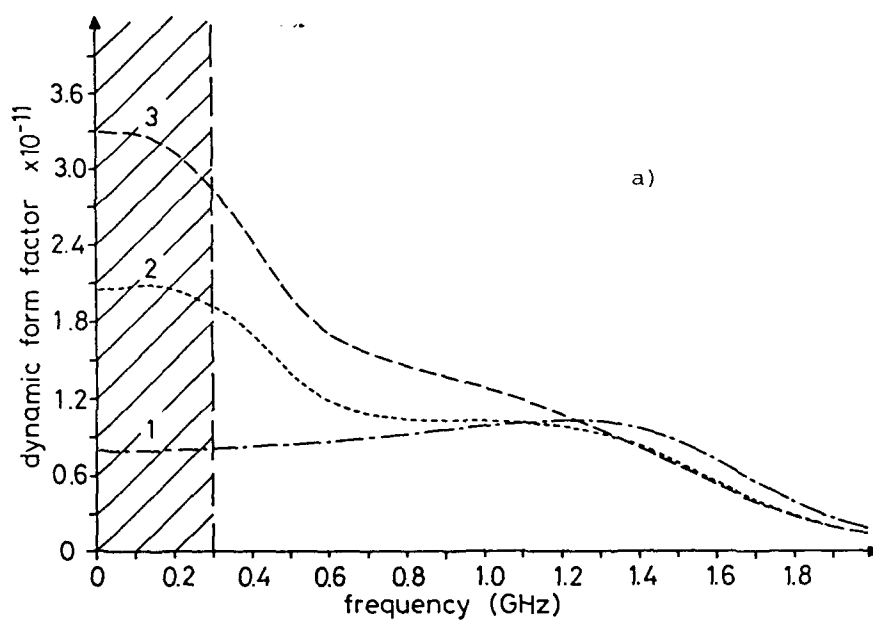


Figure 2

Calculated spectra for typical TCA plasma conditions ($T_e=800\text{eV}$, $T_i=400\text{eV}$, $n_e=5\cdot 10^{13}\text{cm}^{-3}$, $Z_{\text{eff}}=2.5$, $B_T=1.5\text{T}$, $\angle(k,B)=88^\circ$) for a hydrogen plasma (a) and a deuterium plasma (b). In curve 1 neither the effect of the impurities nor of the magnetic field are included, in curve 2 impurities are included but not the magnetic field effect and curve 3 includes both effects. In the shaded region other contributions (parasitic stray light, microturbulence) will be noticeable.

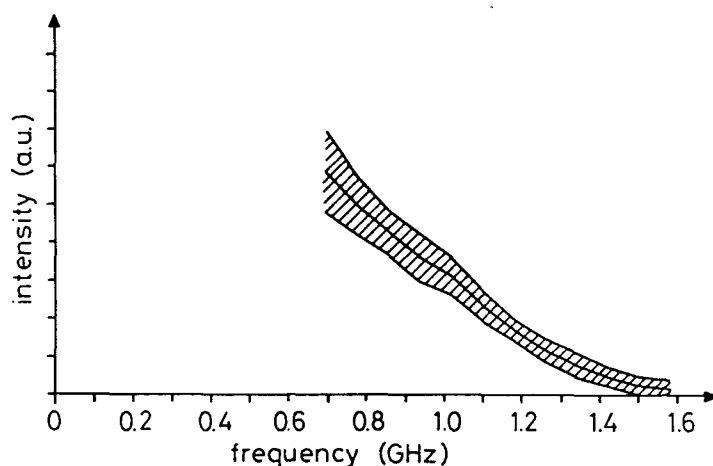


Figure 3

Simulation of a "measured" spectrum for typical TCA conditions with a band indicating the error bars corresponding to repetitive measurements at fixed plasma conditions. The ion temperature could be obtained with 10% accuracy in this case.

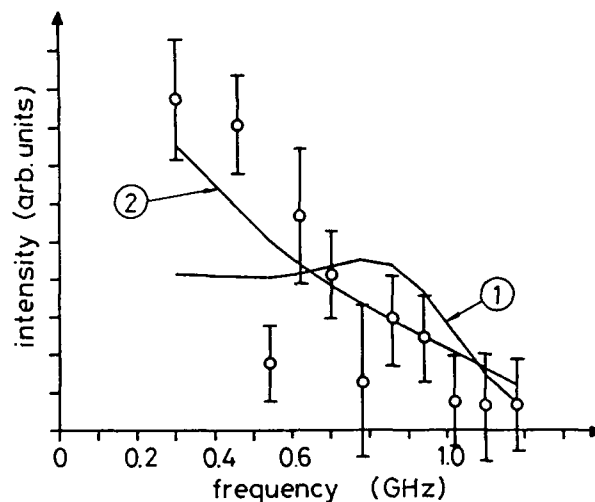


Figure 4

Experimental results obtained from a single shot. The points show the measured signal in each channel with the average background subtracted. The solid curves are fits for $T_e=800\text{eV}$, $n_e=5\cdot 10^{13}$, $Z_{\text{eff}}=2.5$. Curve 2 also includes the magnetic field effect ($B_T=1.5\text{T}$, $\angle 1.5(B,k)=89^\circ$).

viewing dump radiation with an oppositely directed wave vector could be collected and sent towards the detection system. In this way the amount of collected radiation could be doubled.

4) With several mirrors of our optical system being attached to the structure of the tokamak, which is exposed to large forces during a discharge, there may be a dynamical misalignment which is difficult to estimate. (During earlier experiments we had severe problems caused by eddy currents in our full metal mirrors which consequently had to be replaced).

Taking all these improvements into account it should be possible to get into the region where T_i can be measured in a single shot. It should be pointed out at this stage that a first demonstration of this method has been reported by a group at MIT [1]. Due to severe problems with parasitic stray light and the electron cyclotron emission background caused by the strong magnetic field on Alcator C, an evaluation of T_i could not be attempted. While we are still reluctant to call our results a T_i -measurement, we have not run into any problems which could preclude such a measurement with a more sensitive detection system.

Time-resolved linewidth and lineshape measurements

In this second part we report time-resolved linewidth and lineshape measurements. The main purpose was to investigate the spectral purity and stability of the D_2O laser emission frequency. In optically-pumped FIR lasers, especially if they are pumped off-resonance, there are several mechanisms which can lead to chirping or to a time variation of the width of the emission profile. The peaks of the gain profile vary in frequency due to the AC Stark effect induced by the pump and far infrared laser fields and also due to saturation mechanisms. If single mode emission is not imposed by external means, mode competition effects also profoundly alter the gain profile.

In our experiment the scattered radiation has a spectral width of the order of 1 GHz. If the frequency variation of the laser does not greatly exceed 10%, hence about 100MHz, we estimate that the complications of a deconvolution procedure can be avoided.

The experiment was carried out using equipment of an earlier Thomson scattering feasibility study. The basic differences were the following :

- no e-beam laser, but 6 TEA CO_2 laser units
- FIR laser pumped by 2 beams
- energies lower: CO_2 : 2 times 60J, D_2O : approx. 200mJ during 1 μs (2 to 3 modes)
- stable resonator configuration
- spherical metal target used to scatter some laser energy into the detection system
- strong attenuation of the beam to protect the detector

In many respects the equipment was not optimised for these time-and frequency- resolved measurements. In particular, the 80MHz spectral resolution, defined by the width of the channels, was insufficient to resolve individual resonator modes separated by 40 MHz. Hence mode competition effects could not be directly observed. Only shifts of the envelope of the spectral emission profile could be observed. The temporal resolution of 31ns was defined by the 32MHz sampling rate of the CAMAC units with 8 bit resolution. Since the laser was optimised for long pulse operation (approx. 1 μs) this time resolution was adequate to follow the temporal evolution during the pulse. Signal analysis was performed at the intermediate frequency by seven coaxial filters, with a bandwidth of 80MHz each. Four channels were centered around the Raman frequency and three around the line center frequency. Digital oscilloscopes were used to record the pulse shapes of the CO_2 pump laser and the D_2O FIR laser. For numerical analysis all data were transferred to a PDP-11 computer.

At each D_2O gas pressure of interest a series of typically ten laser shots was fired. The raw data show the time evolution of the FIR power for each frequency channel with a resolution of 31ns. A separate calibration of the total gain of each channel by means of a black body source allowed scaling of the signals so that spectral profiles could be obtained.

Results and discussion

For narrow band FIR emission single mode pumping is essential. It has been shown theoretically [2] that two pump modes create multiple FIR gain peaks separated from each other by the intermode spacing and not just two peaks at the corresponding Raman frequencies. This is due to nonlinear effects resulting from the induced beating of the population densities. Hence one would expect broad band emission in the FIR as soon as the pump beam is multimode. This is indeed observed. We show in Fig. 5 the recorded signals of 7 channels for two consecutive shots. On the left hand side the pump pulse was single mode, whereas on the right hand side the modulation of the pulse indicates multimode operation (beat signal not resolved).

Each channel was 80MHz wide and is labeled by the offset of its center frequency from the Raman frequency. While the three channels around the line center, namely 400, 320 and 240MHz, quite clearly show a signal on the right hand side (multimode pumping) there is, apart from an initial spike, practically no signal in the single mode pump case. The presence of the spike indicates that a mode on or near line center starts to develop, but is rapidly and efficiently suppressed by the Raman mode. Also, for multimode pumping, the emission around the Raman frequency shows a larger spectral spread.

Figure 6 shows a series of curves representing the D_2O laser emission as recorded by 4 spectral channels covering a band of 320MHz around the Raman line. Each curve corresponds to a particular instantaneous pump power and represents an average over 10 shots. The curves are arranged to form a 3D-plot. The 30 curves refer to the falling part of the CO_2 pulse and to a pressure of 3.5torr. The emission maximum occurs quite clearly at the Raman frequency for the weak pump intensities and is shifted outwards by a full channel width at maximum pump power, a clear indication of the pump induced AC Stark effect [3]. The behavior is similar during the rising part of the CO_2 pulse. However, the maximum frequency shift is smaller in this case. It seems that the short rise time (300ns) of the CO_2 pulse is insufficient for the buildup of new modes at a shifted frequency, whereas this does take place during the 1 μ s long tail of the pump pulse.

In Fig. 7 we again show data for 12 averaged shots and for a pressure of 1 torr. This time the FIR power is plotted as function of frequency and time. Again, FIR emission starts at the Raman frequency where a local maximum is rapidly reached (peak 1), earlier than the peak of the pump pulse occurring at the time of 280ns. Even with the limited resolution, the frequency shift towards a new maximum (peak 2) at an offset of -80MHz and at a time of 770ns is clearly visible. Later, at decreasing pump power, the FIR frequency of maximum emission shifts back towards the Raman frequency. A third local maximum (peak 3) is reached late in the pump pulse, at 1.4 μ s. The emission spectrum is noticeably narrower during this part where the pump power is fairly constant. Obviously rapid variations in pump power are not favorable for a stable and narrow emission profile. Flat-topped pump pulses would probably give much better results.

Figure 8 shows the major results summarized in three curves for each D_2O pressure investigated. On the left hand side the FIR power integrated over all spectral channels is shown as a function of pump power during the full pulse duration. In this representation we obtain curves that show a hysteresis-type behaviour. Certain points, equidistantly spaced in time, are marked for comparison with the middle and right hand side diagrams. These show the frequency and power of the emission maximum as function of time. The analysis of these diagrams reveals the following facts:

When we follow the time evolution of the FIR power in case (a) (going round the curves in the sense of increasing numbers of the time markers) we note a distinct pressure dependent behavior.

At low pressure the FIR power increases steeply as function of pump power before it levels off, indicating a saturation effect. During the time interval of decreasing pump power the FIR

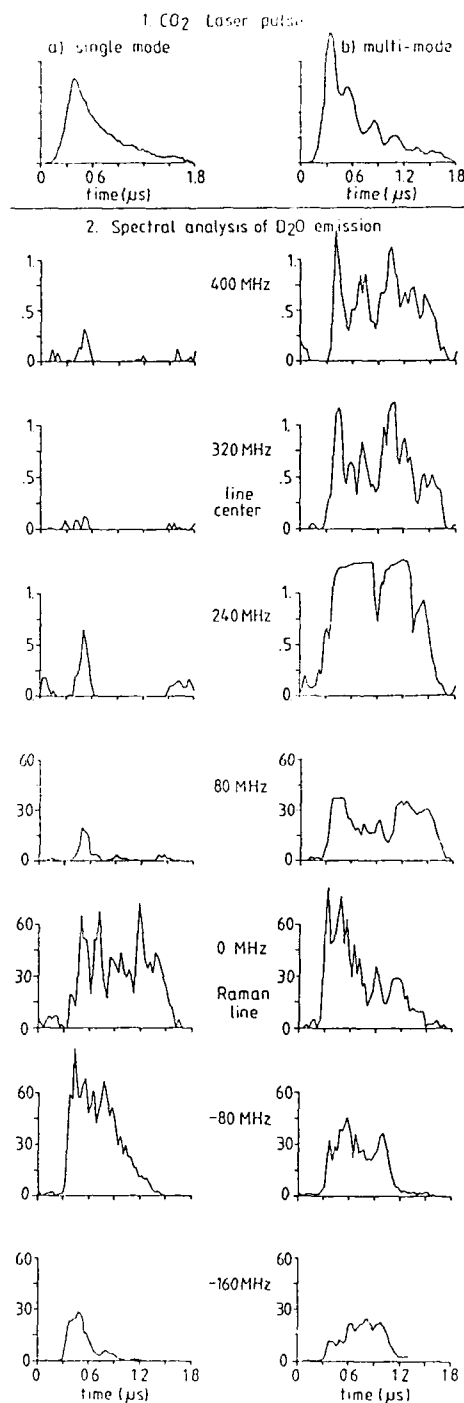


Figure 5

The signals recorded in each channel (correctly scaled) for two shots: the pump pulse was single mode on the LHS and multi-mode on the RHS. (Note that for clarity negative signals are not shown. The small spikes close to the base line at 320MHz in Fig. 5a, for example, are within the noise level, with a similar amount of negative going spikes.)

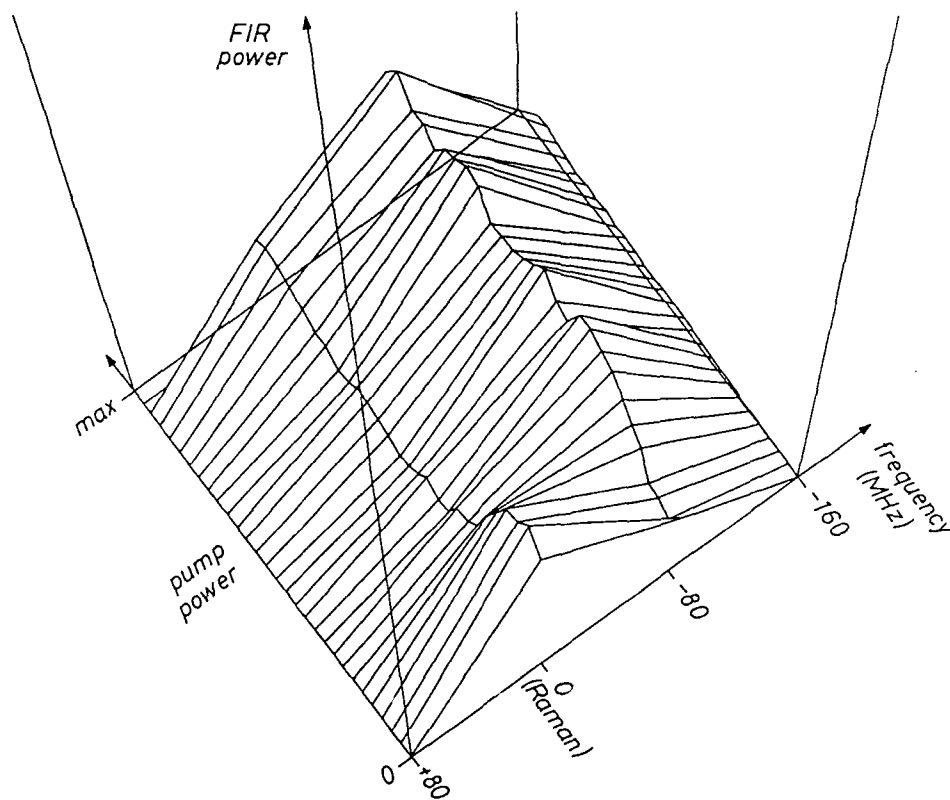


Figure 6

Averaged spectra of ten shots at a D_2O pressure of 3.5 torr, presented as function of pump power, for the falling part of the pump pulse only.

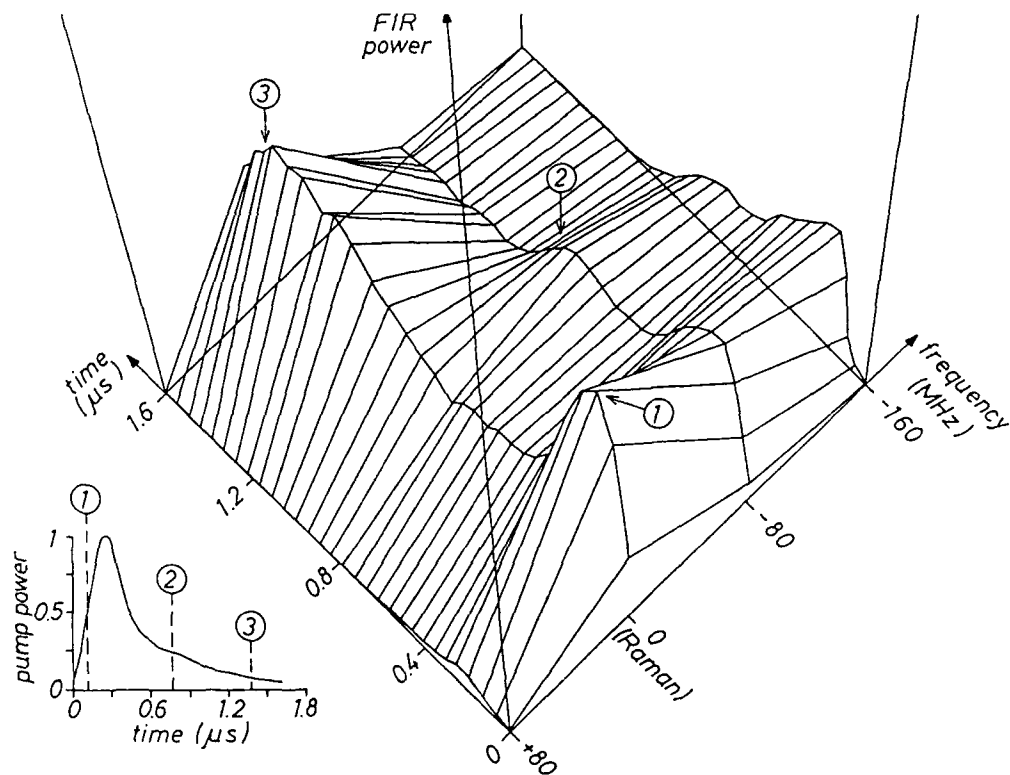


Figure 7

FIR emission as function of frequency and time. (Average of twelve shots at a pressure of 1 torr).

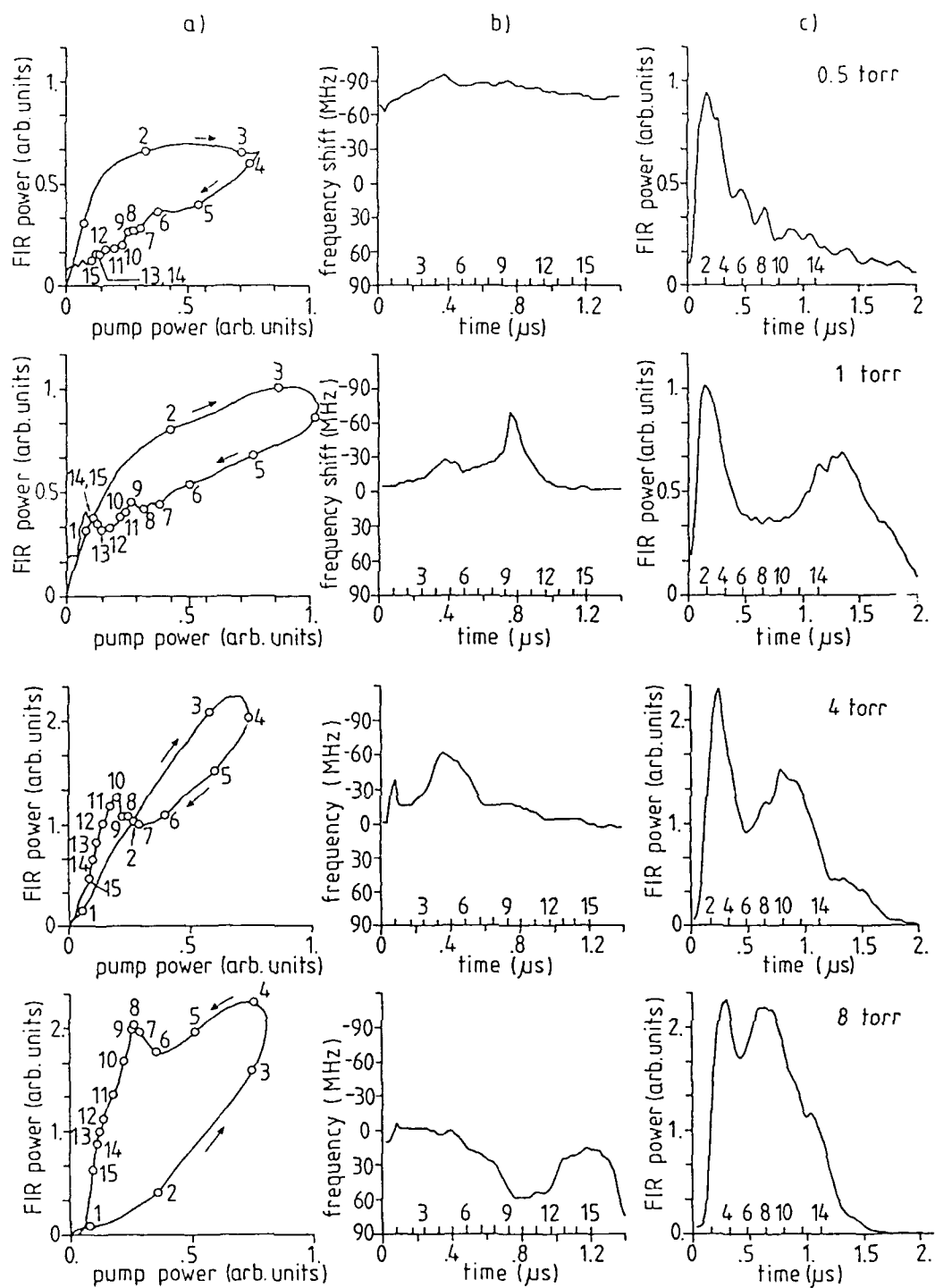


Figure 8

Spectrally integrated FIR laser emission vs pump power, and frequency and power of the FIR peak as function of time for four different D_2O pressures. The time evolution is marked with numbered points (8a) which are also indicated along the time axes (8b, c).

Table I

Charge exchange neutrals	Penetration problems for large, dense plasmas. Can be improved by active beam techniques.
Doppler broadening of spectral lines	Needs separate measurement of impurity density profiles to determine spatial location of the impurity ion.
Collective scattering of laser light	Potentially a promising technique, but in spite of the investment of much effort, still to be demonstrated in tokamaks.
Neutrons	Promising for D-D and D-T plasmas. Needs high resolution neutron spectrometers.

emission is considerably lower. The situation is reversed at high D_2O pressure (8 torr). Only at the intermediate pressure of 4 torr (which yields maximum FIR energy output per pulse) does the FIR power follow the pump power almost linearly. At low pressure the Stark effect appears to be quite important. At 0.5 torr the FIR radiation develops at a frequency which is shifted by 80 MHz from the Raman line center and stays there. The FIR grows very rapidly into a saturated region where it remains up to the peak of the CO_2 laser pulse. It then decays almost proportionally with the pump.

At 1 torr the FIR power still grows rapidly and shows signs of saturation. The emission peak is initially at the Raman frequency and moves outwards to reach a maximum shift at the time when the CO_2 laser power has returned to one quarter maximum, but the FIR laser power is still about half its maximum. After this point the frequency rapidly returns to the Raman frequency and a secondary power peak develops. Hence a doubly peaked FIR pulse is observed whereby the two peaks occur at roughly the same frequencies.

This double peaked structure is also observed at 4 torr and again the two peaks occur at similar frequencies, while the time of the intervening trough coincides with the time of maximum frequency shift. During the first 400 ns the pump and FIR powers grow and decay almost in proportion to each other.

At high pressure (8 torr) two peaks are still observed, this time with slightly different frequencies; the second one is displaced inwards, towards the line center. The FIR power remains at a high level for an extended time. Hence FIR pulses with long, reasonably flat top can be obtained under these conditions.

At 8 torr we also note that the frequency remains fairly constant, at least up to the second maximum. Later a frequency shift towards the line center position is observed. This is only the case at 8 torr, whereas for all lower pressures a shift in the opposite direction is observed.

A more detailed account of this experiment including a theoretical analysis and interpretation of the observations is shortly to appear in print [4].

Conclusions

We have reported a first attempt to measure the ion temperature in the tokamak TCA by collective Thomson scattering of far infrared radiation. The ion temperature has been obtained by fitting theoretical spectra with T_i as free parameter to the measured data. Consistent temperature values in the correct range are obtained, although the precision is still unsatisfactory and a more detailed analysis of systematic errors has to be carried out. Replacing the current detection system with one representing the state-of-the-art would allow us to measure the ion temperature with a precision around 10%.

A particular problem in connection with this experiment has been investigated in detail: the width and stability of the emission frequency of the D_2O laser.

Frequency and time-resolved investigations of an optically pumped FIR laser have been carried out using a heterodyne receiver with spectral resolution of 80 MHz. Some of the observed effects can be explained, at least qualitatively. Several others are not, at present, well understood.

Stable operation of the laser with a spectrally narrow emission profile involved the following considerations: high pressure operation (about 8 torr) is required for frequency stability. But a compromise has to be found if high output power is required in addition to a stable frequency and narrow bandwidth. In our system maximum output power is achieved around 4 torr. Rapid variations of the pump power are undesirable and could be avoided by flat-topped pump pulse shapes, which are, however, not easy to produce.

The pump induced Stark effect has clearly been demonstrated. However, the FIR power can also shift the frequency; in fact for certain combinations of the two effects a shift in the opposite direction to the Stark shift can be obtained.

A much weaker emission has occasionally been observed at the line center frequency. It is rapidly and efficiently suppressed by mode interaction effects, except in the case of a multimode pump. If observable, the line center emission also manifests a Stark shift in the direction opposite to the Stark shift of the Raman frequency.

Saturation effects are observed at low, but not at the higher pressures.

A double-humped, pressure dependent temporal pulse shape is observed. Except at 8 torr the trough between the pulses seems to occur at the time of maximum frequency shift and thus is probably linked to the buildup of new, shifted frequencies.

Repetition of these investigations with a detection system which allows resolution of individual modes (resolution 10-20 MHz) could be extremely valuable. Much of what remains at present somewhat speculative could then probably be explained.

And finally, as an answer to the original question: The frequency stability and spectral width of our D_2O laser are just good enough for the Thomson scattering measurement. Any possible improvements, however, would be quite beneficial.

References

- [1] P. Woskoboinikow, W.J. Mulligan, J. Machuzak, D.R. Cohn, R.J. Temkin, T.G. Sollner, B. Lax, "385 Micron D_2O Laser Collective Thomson Scattering Ion Temperature Diagnostic", 11th EPS Conf. Contr. Fusion Plasma Phys., Aachen, paper E21, (1983).
- [2] M. A. Dupertuis, R.R.E. Salomaa, M.R. Siegrist, "Two-mode Optical Pumping of a Laser", IEEE J. Quant. Electron. QE-20(4), 440-449 (1984).
- [3] R.L. Panock, R.J. Temkin, "Interaction of Two Laser Fields with a Three-Level Molecular System", J. of Quantum Electron. QE-13(6), 425-434 (1977).
- [4] R. Behn, M.A. Dupertuis, P.A. Krug, I. Kjelberg, A.S. Salito, M.R. Siegrist, "Time-resolved Linewidth and Lineshape Measurements of a Pulsed Optically-pumped far Infrared D_2O Laser", to be published in the March 1988 Special Issue of the Journal of Quantum Electronics.

A STABLE, HIGH POWER OPTICALLY PUMPED FAR INFRARED LASER SYSTEM

Jam Farhoomand* and Herbert M. Pickett

Jet Propulsion Laboratory
California Institute of Technology

ABSTRACT

We report the generation of 1.25 watts of CW laser power at the $119\mu\text{m}$ (2522.8 GHz) methanol line. The maximum frequency fluctuation of the free running laser is less than ± 100 KHz per hour. This laser has also been tested on numerous other lines ranging from 403.7 GHz (HCOOH) to 5260 GHz (CH₃OD) with improved power and stability.

I. INTRODUCTION

Within the last few years, CO₂ pumped far infrared (FIR) lasers have been improved to generate higher CW output power. These lasers, used mainly in plasma diagnostics experiments, have generated laser radiation close to 1 watt CW at the $119\mu\text{m}$ methanol line¹. The main objective in improving the FIR lasers has been, so far, to increase the output power with little or no attention to their absolute frequency stability. With the development of tunable laser sidebands systems and their applications in spectroscopic studies^{2,3,4}, the frequency stability of the FIR lasers has become very important. Following the work of Mansfield et al.¹ at Princeton, we have successfully developed an FIR laser which generates 1.25 watts CW laser radiation at the $119\mu\text{m}$ methanol line with CO₂ pump power of 125 watts. The maximum frequency drift of this laser has been measured to be within ± 100 KHz per hour at this laser frequency.

The details of the design and performance of this laser have been published previously⁵. In this paper we present the main features of this system.

II. DESIGN PARAMETERS

The optical layout of the system is shown in Fig. 1 and a summary of the laser parameters is given in Table 1.

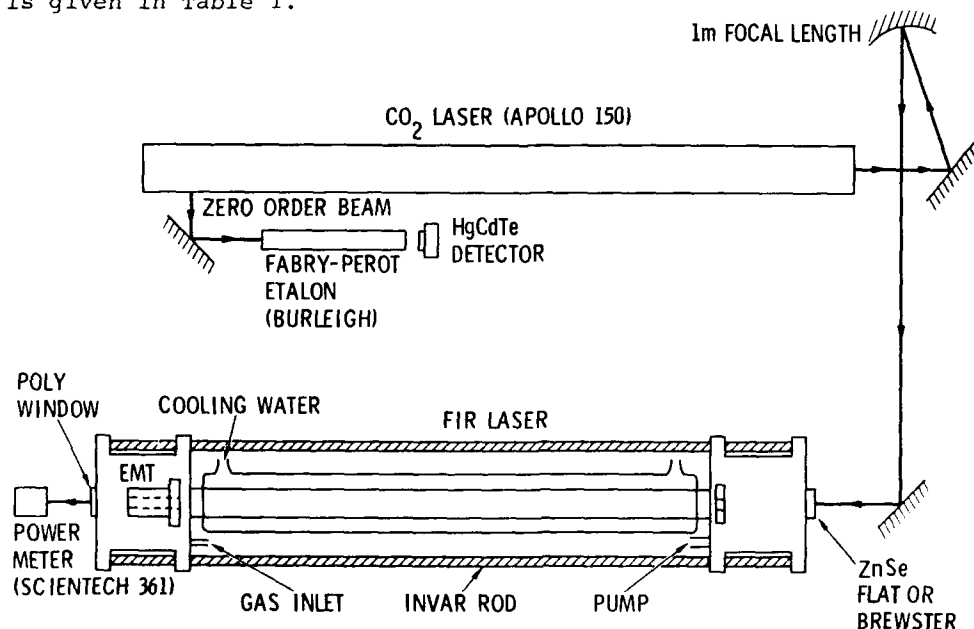


Figure 1 - The optical layout of the Far Infrared laser system.

*Presently with Sterling Software at NASA Ames Research Center, Moffett Field California

TABLE 1. FIR LASER PARAMETERS

Pumping:	Coaxial, input and output hole coupling.
Pump optics:	Folded with 1 m focal length gold coated spherical copper mirror.
Resonator:	Pyrex, 240 Cm long, 3.4 Cm ID. Coaxial water jacket.
Input coupler:	Flat gold coated copper mirror with 5 mm on axis hole. Water cooled.
Output coupler:	Flat gold coated copper mirror with 10 mm on axis hole and a Z-cut quartz window with dielectric coating. Water cooled.
Adjustments:	Gimbals (Lansing) on input and output, coarse and fine (EMT, MPB Technologies) length adjustments. All within the lasing medium, no bellows.
Windows:	ZnSe Brewster input, high density white polyethylene output.

III. POWER MEASUREMENTS

All the power measurements were done using a Scientech 361 power meter with the corresponding correction factor at $119\mu\text{m}$ wavelength as given by Foote and Hodges⁶.

We measured the FIR output power vs the CO_2 pump power with and without the addition of a buffer gas. To see the effect of the resonator wall temperature, the temperature of the cooling water was also varied. All the data were taken at constant $300\mu\text{m}$ Hg methanol pressure. Both the FIR cavity length and the CO_2 frequency were adjusted each time to optimize the FIR power. The results are plotted in Fig. 2.

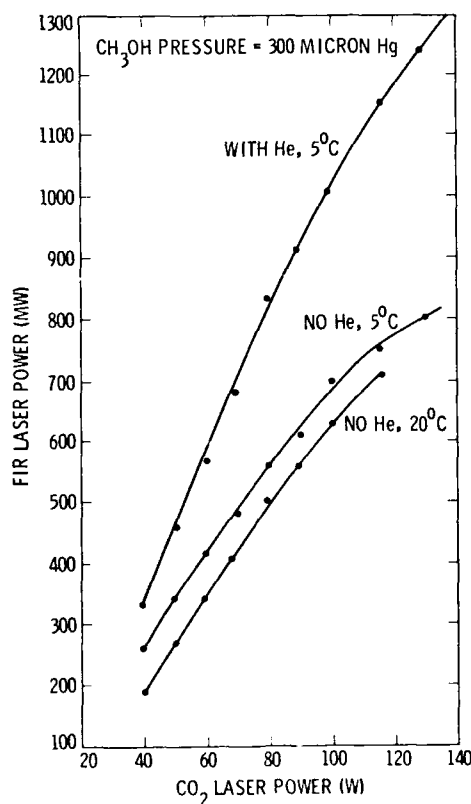


Figure 2 - FIR laser power at the $119\mu\text{m}$ methanol line vs the CO_2 pump line.

As indicated by the graphs in Fig. 2, the FIR output power was increased by more than 50% by the addition of He as the buffer gas. This increase in power is attributed to breaking of the vibrational bottle-neck^{1,7,8}. The maximum FIR power with the addition of He was measured to be 1.25 watts. The optimum power was obtained with 125 watts of CO₂ pump power, the FIR resonator wall temperature of 5°C, the methanol pressure of 300µm Hg, and the total methanol and He pressure of 550µm Hg. All the power measurements are consistent with the results obtained by Mansfield et al.

The FIR power was also measured as a function of the methanol pressure having a 115 watts of CO₂ pump power. The test was done without the addition of a buffer gas and the peak power was obtained at 300µm Hg. The results are plotted in Fig. 3.

Table 2 is a summary of the optimum power performance of this laser.

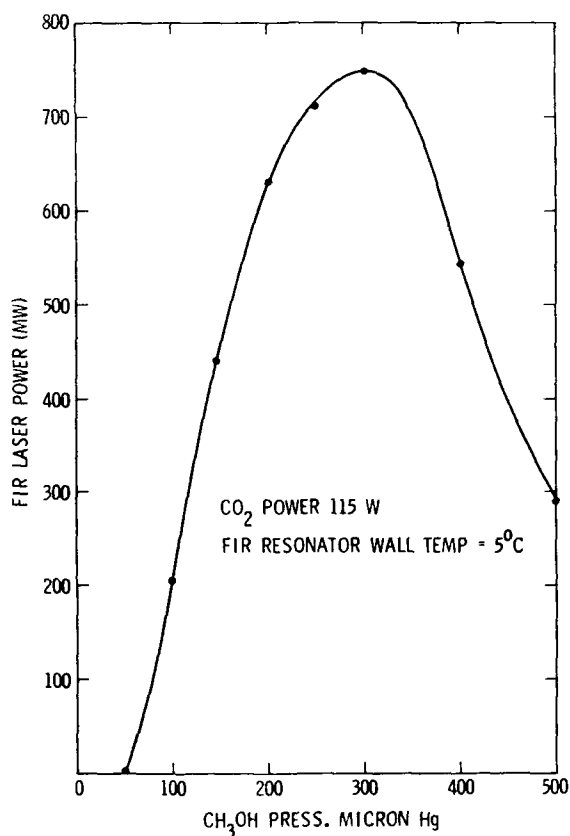


Figure 3 - FIR laser power at the 119µm methanol line vs the methanol pressure with 115 watts of CO₂ pump power and no buffer gas.

TABLE 2. POWER PERFORMANCE

FIR Power:	1.25 Watts CW with He. 0.8 Watts CW without He.
FIR Frequency:	2522.8 HGz, 119µm. Methanol line
Buffer Gas:	Helium
Methanol Pressure:	300 micron Hg.
Pressure + He pressure:	550 micron Hg.
Resonator Wall Temp:	5 degrees C.
Pump:	CO ₂ , 9 P36, 125 Watts. Locked to an external Fabry-Perot etalon (Burleigh CFT 500 IR).

IV. FREQUENCY MEASUREMENTS

We measured the frequency stability of the laser by monitoring the frequency of the absorption line of SO_2 at 2442.3 GHz. This was done by mixing an 80.5 klystron with the 2522.8 GHz laser line and generating sidebands at 2442.3 GHz and 2603.3 GHz². Using the lower sideband, we scanned the klystron through the absorption of SO_2 and measured the line frequency. The measurement was repeated every 15 minutes for several hours on different days. By measuring the SO_2 line frequency as a function of time, we determined the maximum fluctuation of the laser frequency to be less than ± 100 KHz per hour.

We have also tested this laser at other laser lines with different lasing molecules such as HCOOH , CH_2F_2 , CH_3OD , $^{13}\text{CH}_3\text{OH}$, etc. all with improved performance. The frequency fluctuation of the laser at lower frequencies is far less than ± 100 KHz per hour and it roughly scales with frequency as expected. The results are summarized in Table 3.

TABLE 3. FREQUENCY PERFORMANCE

Stability:	Free running. ± 100 KHz/hour maximum at 2522.8 GHz (119 μm CH_3OH). (Better than 2.5 parts in 10^7 .)
Lasing Range:	Tested from 403.7 GHz (HCOOH) to 5260 GHz (CH_3OD) on discrete lines.

V. SUMMARY

Far Infrared CW laser radiation of 1.25 Watts has been obtained at the 119 μm (2522.8 GHz) methanol line with a CO_2 pump power of 125 Watts. This is the highest power and the conversion efficiency reported to this date on this laser transition. The maximum frequency fluctuation of the free running laser is measured to be less than ± 100 KHz per hour. The improved performance of the FIR laser was achieved by: 1) Using reflecting optics wherever possible to minimize CO_2 mode degradation caused by damaged anti-reflection coating of transmitting optics. 2) Enclosing the input and output assemblies within the lasing medium to minimize the external effects on the cavity length as well as eliminating the mechanical instabilities associated with the use of bellows. 3) Cooling the input and output couplers to ensure frequency stability. 4) Cooling resonator wall to 5°C and adding He as the buffer gas to break the vibrational bottle-neck. The combined pressure of the CH_3OH and He was about 550 μm Hg.

This laser, which has also been tested at other frequencies ranging from 403.7 GHz to 5260 GHz with improved results, will prove to be essential in generating tunable laser sidebands for spectroscopic measurements or other experiments which require a frequency stable FIR source.

VI. ACKNOWLEDGEMENT

We would like to thank Glenn McRae and Tim Crawford for many useful discussions on the subject and for their help in making some of the measurements. We would also like to thank Dennis Mansfield and Tony Peables for their expert advice on the design. This research was performed by the Jet Propulsion Laboratory, California Institute of Technology, under contract with the National Aeronautics and Space Administration. Jam Farhoomand is presently with Sterling Software at NASA Ames Research Center in Moffett Field California.

REFERENCES

1. D.K. Mansfield, E. Horlbeck, C.L. Bennett, and R. Chouinard, Int. J. IR and MM Waves 6, 867 (1985).
2. J. Farhoomand, G.A. Blake, M.A. Frerking, and H.M. Pickett, J. Appl. Phys. 57, 1763 (1985).
3. H.R. Fetterman, P.E. Tannenwald, B.J. Clifton, W.D. Fitzgerald, and N.R. Erickson, Appl. Phys. Lett. 33, 151 (1978).
4. D.D. Bicanic, B.F.J. Zuiberg, and A. Dymanus, Appl. Phys. Lett. 32, 367 (1978).
5. J. Farhoomand and H.M. Pickett, Int. J. IR and MM Waves 8, 441 (1987).
6. F.B. Foote, D.T. Hodges, and H.B. Dyson, Int. J. IR and MM Waves 2, 773 (1981).
7. T.Y. Chang and C. Lin, J. Opt. Soc. America 66, 362 (1976).

8. N.M. Lawandy and G.A. Koepf, Opt. Lett. 5, 336 (1980).

Jam Farhoomand: NASA Ames Research Center, M/S 244-10, Moffett Field,
California 94035.

Herbert M. Pickett: Jet Propulsion Laboratory, M/S 168-314, 4800 Oak Grove Drive,
Pasadena, California 91109.

THE USE OF FIR-LASERS IN SOLID STATE RESEARCH

P. Janssen, F. Herlach, L. Van Bockstal, M. van der Burgt and J. Witters
Katholieke Universiteit Leuven
Laboratorium voor Lage Temperaturen en Hoge-Veldenfysika
Celestijnenlaan 200D, B-3030 Leuven (Belgium)

Abstract

Far infrared lasers are useful research tools in solid state physics. To underline this, we discuss a number of reasons for this usefulness and illustrate these with results obtained in our laboratory. In particular, EPR in rare earth compounds has been extended to high magnetic fields. This helps to separate nearby lines, to decompose complicated line structures, to saturate the magnetisation and to extend the region in which the energy levels can be mapped. Ferromagnetic resonance in metals is illustrated for the case of nickel. The effect of intrinsic damping is more pronounced at higher frequencies. Cyclotron resonance in semiconductors is illustrated for the case of HgCdTe, using an unconventional technique, i.e. FIR thermomodulation. The influence of high magnetic fields on the antiferromagnetic transitions of one-dimensional systems as TMMC and CMC (which are examples of one-dimensional Heisenberg systems) were studied in the FIR. Organic crystals showing one-dimensional behaviour were studied in the FIR for special effects of a gliding charge density wave on the a.c. conductivity at high frequencies and for the effect of the so-called spin phase transition.

Introduction

Several interactions in the solid state fall into the frequency range of the far infrared, broadly defined as the wavelength range between 30 μm and 3 mm. Examples are magnetic interactions between electron spins, related interactions with the crystal field, energy levels in semiconductors, and the average phonon energy at ordinary temperatures. This research has greatly benefited from the development of convenient sources of far infrared radiation, together with improved methods of detection and infrared optics. The first practical far infrared laser was the HCN laser developed by Gebbie [1]. The optically pumped FIR laser was developed shortly afterwards [2] and is now in general use. In this device, laser action is obtained between two rotational sublevels of a suitable vibration level in a molecule. Excitation of this vibrational level is obtained by tuning the pump laser precisely to the energy of this level. A grating tuned CO_2 laser is commonly used for this purpose. A recent compilation [3] lists over 3000 FIR lines that can be obtained in this way in the wavelength range 10.332 μm to 2.923 mm with continuous pumping. This large frequency range, together with reasonable power output (typically

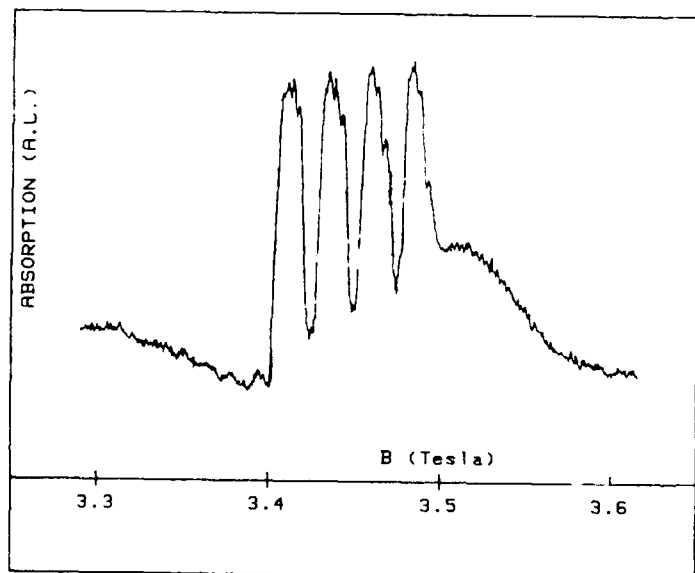


Figure 1: EPR signal in LiTbF_4 at 4.2 K, showing hyperfine structure. This was taken with the HCN laser at 0.337 mm wavelength.

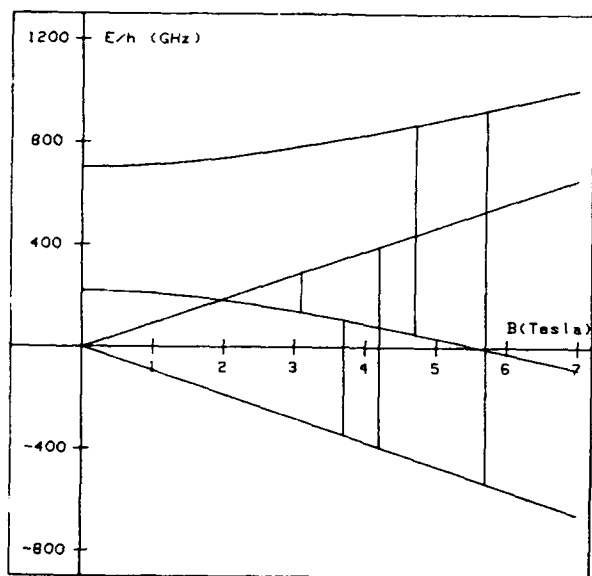


Figure 2: The lowest energy levels in LiHoF_4 versus magnetic field. The vertical lines indicate the observed transitions.

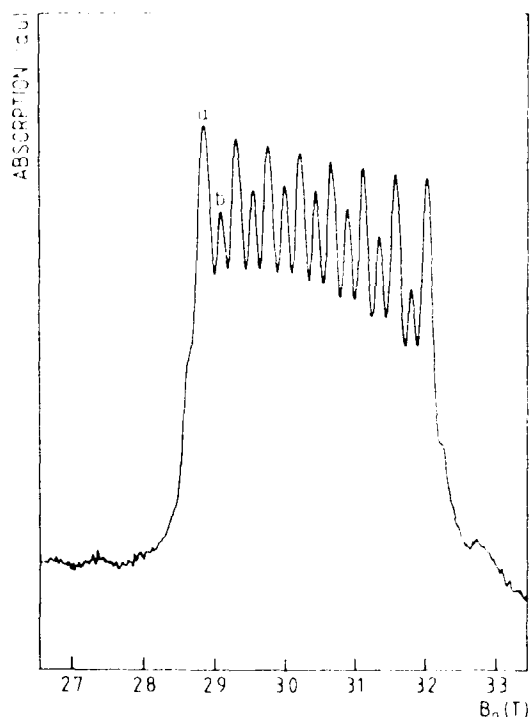


Figure 3: Resonance signal in LiHoF_4 at 4.2 K, taken with the optically pumped laser at the 0.513 mm wavelength of HCOOH . The signal corresponds to a transition of the ground doublet. Two sets of hyperfine lines can be identified, one in which the nuclear spin is changed and one in which it is unaffected.

10 mW) and stability, make the optically pumped FIR laser an excellent tool for solid state research. We want to give some general ideas on this research and illustrate it with examples from the research done at our laboratory.

EPR in High Magnetic Fields

The resonance condition for a paramagnetic resonance signal can be written in its most simple form as

$$h\nu = g\mu_B B \quad (1)$$

where ν is the resonance frequency, B the magnetic field and g the "g-factor" of the spin under study. There are several reasons for using very high magnetic fields in these experiments:

- i) The separation in field between two lines with closely spaced g-factors is increased. If a resonance signal is composed of several lines, the study of the different contributions becomes easier in a high field.
- ii) If magnetic coupling between the different spins in the solid is appreciable, the line width may be decreased by using high magnetic fields. This can be of great help in decomposing a complicated line structure e.g. for the analysis of hyperfine splitting.
- iii) In many materials there is a considerable difference between the applied magnetic field and the actual field seen by the ions. This difference is related to the magnetization in the sample; it becomes constant in sufficiently high magnetic fields where the magnetization is saturated. The correct g-factor can be obtained from the slope of the resonance field versus frequency in the high field range.
- iiii) The analysis of a complex energy level structure is easier when the behaviour of the resonances can be followed over a larger field range.

In very high magnetic fields, the resonance frequencies are usually shifted into the far infrared. Thus the optically pumped FIR laser is a most suitable source of radiation in the high field range.

This can be illustrated with experimental results obtained at our laboratory. For fields below 7 T, we use a superconducting magnet and bolometer detection of the chopped laser radiation. For higher fields up to 50 T, a pulsed magnet is used. The very high power required to generate such strong magnetic fields is obtained from the discharge of a capacitor bank (5 kV, 50-1000 kJ). Instead of continuous cooling, the coil is precooled by liquid nitrogen, and the energy is absorbed adiabatically by the heat capacity of the coil. The field is recorded by an inductive probe, calibrated with the DPPH resonance, and the infrared radiation is measured by a fast detector (InSb, GaAs and Ge:Ga). Recently, experimentation and data reduction has been greatly facilitated by digital recording and data processing.

Fig. 1 shows the EPR signal of LiTbF_4 [4]. Thanks to the relatively high magnetic field, the lines are sufficiently narrow to observe the hyperfine structure.

The energy level structure of LiHoF_4 is shown in fig. 2. The doublet and the two lowest singlets are in the range of our d.c. spectrometer. A typical experimental result is shown in fig. 3 [5].

The complicated energy level structure of LiErF_4 has been studied in both d.c. and pulsed magnetic fields [6]. The results are shown in fig. 4 together with theoretical predictions.

A number of unexpected effects have already been observed: crystal deformations in TmVO_4 [7] and non-stoichiometry in DyAlG [8]. These effects could only be seen in the far infrared part of the spectrum.

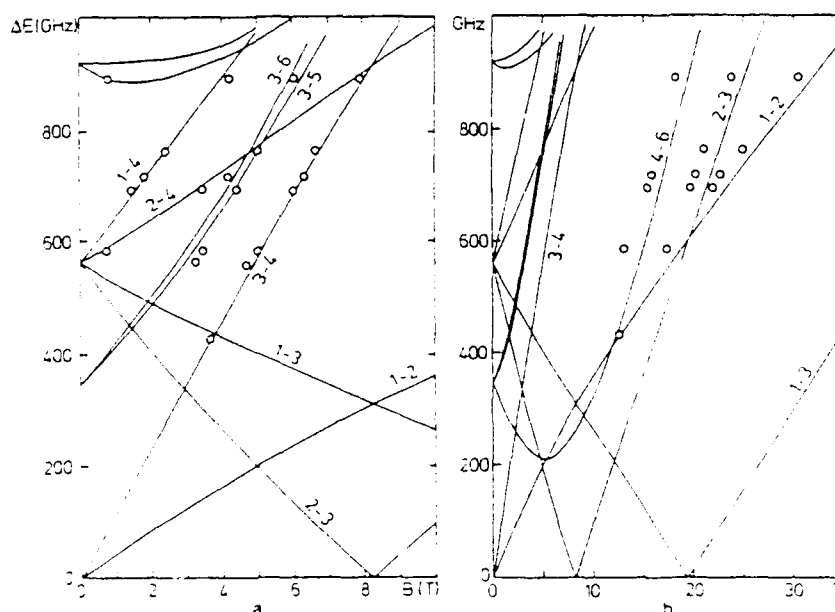


Figure 4: Measured energy levels versus magnetic field in LiErF_4 (dots). The full lines indicate the theoretical behaviour.

Ferromagnetic Resonance in Metals

In all the ferromagnetic metals of the 3d group, the intrinsic damping of the ferromagnetic resonance absorption is proportional to the frequency ω . This type of damping is described by the Landau-Lifshitz damping parameter λ :

$$dM/dt = \lambda / (\gamma M_S^2) M \times dM/dt \quad (2)$$

where M is the magnetization, γ the gyromagnetic ratio and M_S the saturation magnetization. The Landau-Lifshitz parameter does not depend on the frequency; for most of the 3d-metals it is only slightly dependent on the temperature.

In order to retrieve the intrinsic lifetime of the ferromagnetic magnon modes from the lineshape of the FMR absorption, additional contributions to the line shape must be taken into account. Due to eddy currents induced by the motion of the magnetization there is an additional damping which is proportional to $\sqrt{\omega}$. The effect of the intrinsic damping is more pronounced at high frequencies and thus at high magnetic fields because it is proportional to ω .

Our measurements at fields up to 35 T show that the temperature dependence of the Landau-Lifshitz damping is reduced at higher frequencies (Fig. 5). At microwave frequencies the Landau-Lifshitz damping at low temperatures is 8 times stronger than at room temperature. At 469 GHz and at 685 GHz, this ratio is 3.0 and 2.0, respectively.

Several theories were developed to explain this behaviour. Our results are in best agreement with the theory of Korenman [9]. He showed that the Landau-Lifshitz damping is due to the relaxation of the conduction electrons if the Fermi surface is strongly dependent on the direction of the magnetization. This damping mechanism is proportional to the dynamic conductivity which is limited - due to the anomalous skin effect - to a value proportional to the cube root of the frequency. This theory fits our results at FIR frequencies as well as those obtained at microwave frequencies. This particular damping mechanism becomes important in Ni at temperatures below 150 K and is limited at around 70 K as the propagation constant bottoms out sooner and therefore the increase in damping at lower temperatures is reduced.

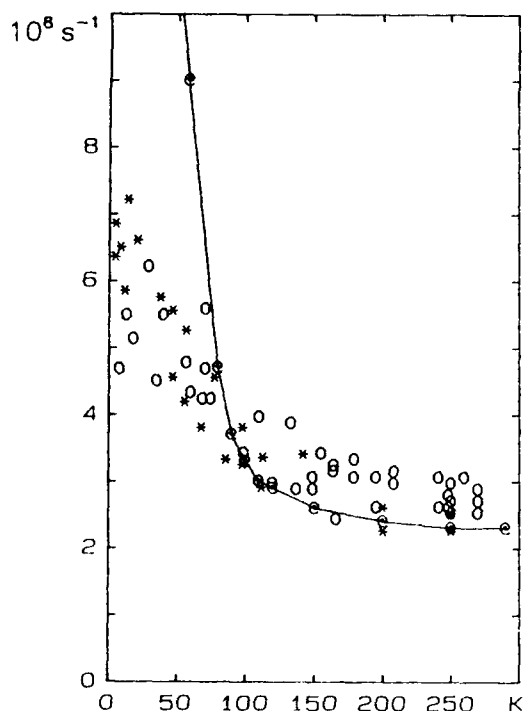


Figure 5: Landau-Lifshitz damping parameter as a function of temperature. Data with * and o are at 425 GHz and 693 GHz, respectively. The full line approximates the microwave data.

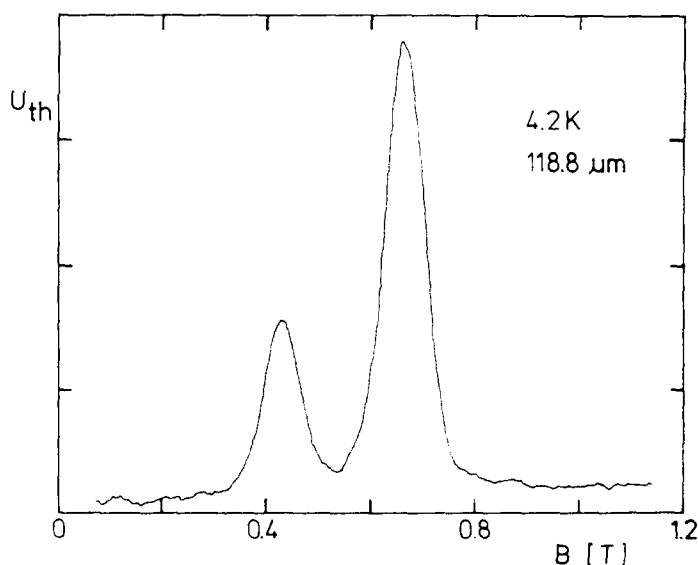


Figure 6: Thermomodulation voltage versus magnetic field of HgCdTe, measured with the optically pumped laser.

Semiconductors

In semiconductor physics, FIR radiation is used in the first place to study cyclotron resonance of conduction electrons. The resonance frequencies give information on the effective mass of different types of charge carriers and on the non-parabolicity of the energy bands. The measurement of the linewidth is a contactless method for determining the electrical resistivity. The first experiments were done in 1956 on InSb [10]. A great many experimental results have been published since then [11], and the technique was extended into the megagauss range [12].

At our laboratory, we recently measured cyclotron resonance in the narrow gap semiconductor HgCdTe in an unconventional way i.e. by means of FIR thermomodulation. As the sample is heated locally by the chopped laser beam, this results in an oscillatory thermoelectric voltage across the sample. At resonance, more radiation is absorbed and thus the heating and the thermoelectric voltage is increased, resulting in fairly strong resonance signals with a good signal-to-noise ratio. By changing the chopper frequency, it can be verified that the signal is indeed of thermal origin and not photovoltaic which would not show the thermal inertia. A typical result is shown in fig. 6. The resonances at 0.66 T can be identified as conduction electron resonance with an effective mass of $7 \times 10^{-3} m$. The resonance at 0.43 T can be interpreted as a resonance between impurity levels. However, it cannot be completely excluded that this second resonance is due to a second laser line which is simultaneously excited by the same pump line. This occasional ambiguity is one of the drawbacks of the optically pumped FIR laser.

In a FIR transmission experiment, several resonances in a ptype GaAs/GaAlAs heterojunction were observed [13]. These experiments were done in both pulsed and d.c. fields; experimental results are shown in fig. 7. Besides cyclotron resonance, both spin-flip and harmonic transitions have been identified, and there are a few resonances at the highest fields that have not yet been theoretically explained. These experiments are still in progress and will be extended to include heterostructures and semimagnetic semiconductors.

Low Dimensional Systems

TMMC (tetramethyl ammonium trichloromanganate) and CMC (cesium manganese chloride) are examples of one-dimensional Heisenberg systems. These were studied in the temperature range from 4.2 to 300 K, in order to observe the influence of very high magnetic fields on the antiferromagnetic transition [15]. Due to the strong absorption at resonance, the line shape is strongly distorted, and there is a "forbidden" region with total reflection. Another distortion of the lineshape results from the fact that the sample dimensions are larger than the wavelength. An example of an experimental recording is shown in fig. 8.

A class of materials which promises interesting results in the FIR resonances are the organic crystals. Many of these behave as quasi-one-dimensional systems. They exhibit a rather peculiar behaviour of the electrical conductivity as a function of temperature. Tentative explanations for this are given in terms of phase transitions. These include transitions from insulator to semiconductor and further to metallic behaviour. In some cases a superconducting state has been demonstrated. EPR at FIR frequencies could be a

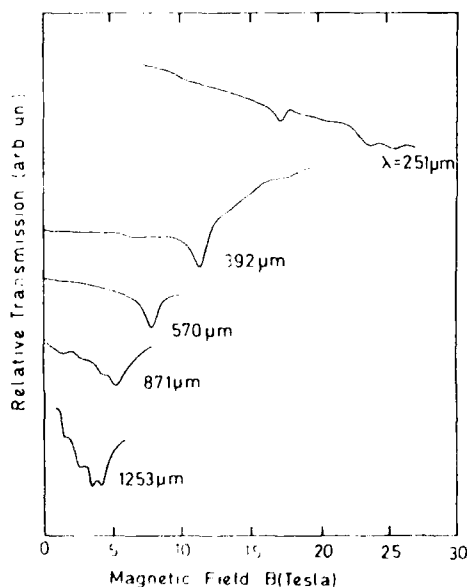


Figure 7: Magnetotransmission spectra of a GaAs/GaAlAs-heterojunction at helium temperature.

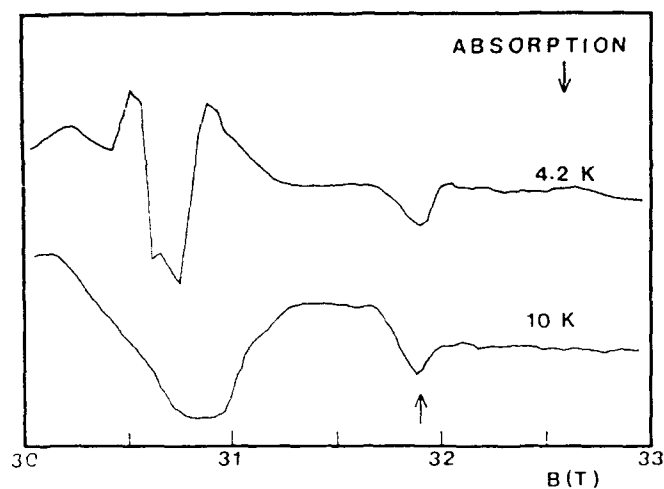


Figure 8: Absorption spectra of TMMC with the magnetic field parallel to the c-axis, using the HCN laser at 0.337 mm wavelength.

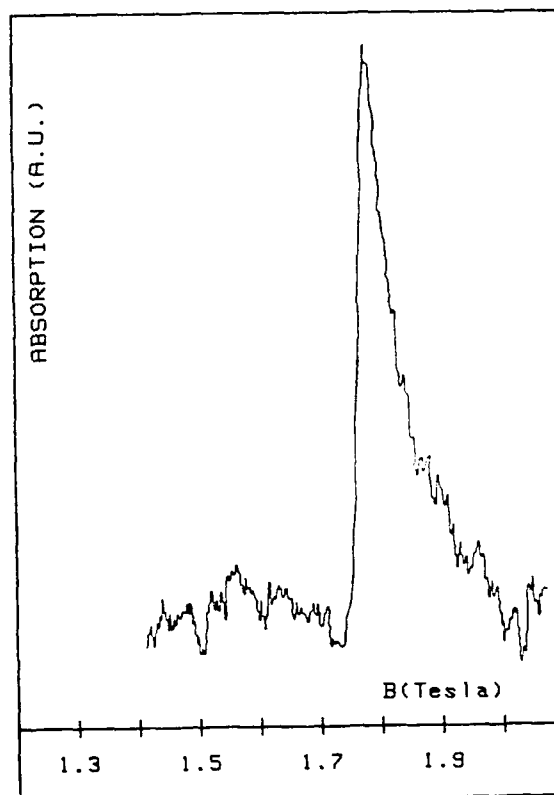


Figure 9: The most pronounced of several features seen in the transmission spectrum of $[\text{Pd}(\text{C}_6\text{H}_{12}\text{N}_2)]\text{Br}_{1.77}$ at 1.5 K, using the optically pumped FIR laser at the 1.899 mm wavelength

valuable tool to investigate the so-called spinphase transition, manifest as a change in the magnetic susceptibility. This transition can occur at different temperatures than those where the conductivity changes. Furthermore, there is a theoretical prediction that effects of a gliding charge density wave could become visible in the FIR. We are currently studying $[\text{Pd}(\text{C}_6\text{H}_{12}\text{N}_2)]\text{Br}_{1.77}$, a mixed valence palladium complex of cyclohexanediamine. A preliminary study has revealed interesting features in the transmission vs. magnetic field. The most pronounced of these is shown in fig. 9.

References

- 1 H.A. Gebbie, N.W.B. Stone and F.D. Finlay, *Nature* **202**, 685 (1964)
- 2 T.Y. Chang and T.J. Bridges, *Opt. Commun.* **1**, 423 (1970)
- 3 N.G. Douglas (private communication)
- 4 P. de Groot, F. Leempoels, J. Witters and F. Herlach, *Solid State Commun.* **37**, 681 (1981)
- 5 P. Janssen, I. De Wolf and I. Laursen, *J. Phys. Chem. Solids* **46**, 1387 (1985)
- 6 P. de Groot, P. Janssen, F. Herlach, G. De Vos and J. Witters, *Int. J. Infrared and mm-waves* **5**, No.2, 135 (1984)
- 7 I. De Wolf, P. Janssen and B. Bleaney, *Phys. Lett.* **108A**, 221 (1985)
- 8 P. Janssen, M. Mahy and W.P. Wolf (to be published in *Phys. Rev.*)
- 9 V. Korenman and R.E. Prange, *Phys. Rev.* **B6**, 2769 (1972)
- 10 R.J. Keyes, S. Zwerdling, S. Foner, H.H. Kolm and B. Lax, *Phys. Rev.* **104**, 1804 (1956)
- 11 N. Miura and F. Herlach, "Pulsed and Ultrastrong Magnetic Fields", in Strong and Ultra-strong Magnetic Fields and Their Applications, Topics in Applied Physics Vol. 57, ed. F. Herlach, (Springer Verlag Berlin Heidelberg 1985) pp. 247-350
- 12 F. Herlach, J. Davis, R. Schmidt and H. Spector, *Phys. Rev.* **B10**, 682 (1974)
- 13 M. van der Burgt, P. Janssen, L. Van Bockstal and F. Herlach, in "High Magnetic Fields in Semiconductor Physics" Vol. 71, ed. G. Landwehr (Springer Berlin Heidelberg 1987) p. 478
- 14 W. Erhardt, W. Stagnuhn, P. Byszewski, M. von Ortenberg and G. Landwehr, G. Weimann, L. Van Bockstal, P. Janssen, F. Herlach and J. Witters, *Surface Science* **170**, 581 (1986)
- 15 M. Motokawa, L. Van Bockstal and F. Herlach, *J. Phys. C* **18**, 5009 (1985)

OPTICALLY PUMPED SUBMILLIMETER LASERS AND THEIR APPLICATION TO PLASMA DIAGNOSTICS

B.W. James, I.S. Falconer, M.D. Bowden and P.A. Krug
School of Physics, University of Sydney, NSW 2006, Australia.

L.B. Whitbourn
CSIRO Division of Mineral Physics and Mineralogy, Lindfield, NSW 2070,
Australia.

P.A. Stimson and J.C. Macfarlane
CSIRO Division of Applied Physics, Lindfield, NSW 2070, Australia.

Abstract

Submillimeter wavelengths (0.1 mm - 1 mm) are particularly suitable for the interferometric measurement of electron density in magnetically confined plasmas. The most commonly used sources are optically pumped molecular lasers such as the CO₂ laser pumped formic acid and menthol vapour lasers. It is shown that a formic acid vapour laser can be operated simultaneously on three lines of a rotational cascade sequence. As there is an almost constant difference in frequency between adjacent cascade transitions for the nearly symmetric top formic acid molecule, a low frequency mixing product at about 1 MHz is produced when the three lines are incident on a non-linear detector such as a Schottky diode. Utilisation of this phenomenon to achieve a phase-modulated interferometer is proposed and the design of such an interferometer is discussed.

Introduction

The submillimeter wavelength region of the electromagnetic spectrum ($0.1 \text{ mm} < \lambda < 1 \text{ mm}$) is particularly suitable for the interferometric measurement of electron density of magnetically confined plasmas encountered in controlled fusion research. The wavelength is sufficiently short that beam bending by density gradients is negligible; on the other hand the wavelength is sufficiently long for fringe shifts of the order of 1 - 10 fringes to be generated in typical situations.

A common technique is to use an interferometer where the phase difference between the two arms is modulated¹ at a frequency of $\sim 10 \text{ kHz} - 1 \text{ MHz}$. This can be achieved by generating two beams at different frequencies, f_1 and f_2 . As shown in Fig 1, one beam (f_1) passes

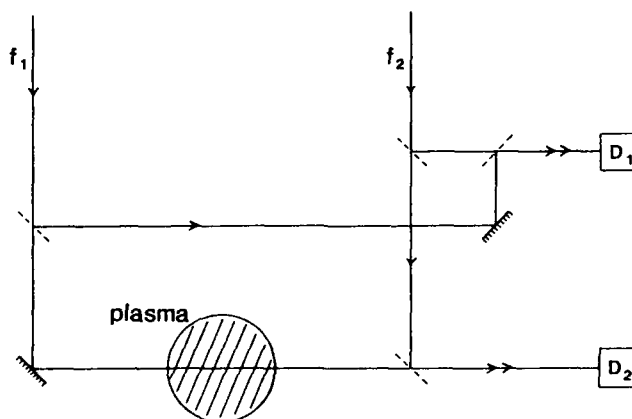


Fig. 1 A phase-modulated interferometer using two beams of different frequencies. One beam (f_1) passes through the plasma while the other (f_2) follows a reference path. The line integral of electron density along the beam path through the plasma is determined by comparing the fringes from detector D_2 with reference fringes from detector D_1 .

through the plasma while the other (f_2) traverses a reference path. The two beams are then combined and detected by a square law detector. In the absence of the plasma, there is a constant rate of change of phase of one beam with respect to the other leading to a beat signal from the detector at the difference frequency, $f_1 - f_2$. When the plasma is present any change in electron density causes a change in phase of the beam passing through the plasma which in turn causes a change in the phase of the beat signal. If some of the input radiation at each frequency is split off to produce reference fringes using a second detector (see Fig. 1), the line integral of electron density along the beam path through the plasma can be determined by comparing the phases of the two beat frequency signals.

An interferometer of this kind has been used by Veron² who produced a beam at an offset frequency by splitting off some of the laser beam and reflecting it from a rotating grating. In this way two beams with a frequency difference of up to about 1 MHz can be obtained using a single laser. A similar result has been obtained by Wolfe et al³ who used twin CH_3OH lasers pumped by a single grating tuned CO_2 laser. By careful control of the small difference in resonator length between the two lasers, two beams with a constant frequency difference of the order of 1 MHz were produced.

This paper describes a method of obtaining a phase-modulated interferometer using a single optically pumped formic acid (HCOOH) vapour laser operating simultaneously on three lines of a cascade sequence. Phase modulation at a frequency of ~ 1 MHz is achieved as a result of the mixing of the three lines in a non-linear detector.

The Laser

The CO_2 laser pumped formic acid vapour laser has four strong lines at 394 μm , 419 μm , and 513 μm . In each case, as a result of an absorption line of the HCOOH molecule closely coinciding with a CO_2 laser line, molecules are excited from a rotational sublevel of the ground vibrational state to a rotational sublevel J of an excited vibrational state thereby creating a population inversion between rotational levels J and $J-1$ as shown in Fig. 2. It is also possible that, due to rotational relaxation, population inversions may be produced for cascade transitions i.e. between rotational levels $J-1$ and $J-2$, $J-2$ and $J-3$, etc.

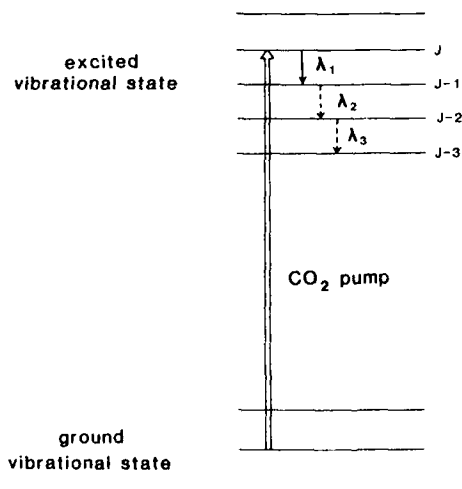


Fig. 2 Energy levels for an optically pumped submillimeter laser.

The HCOOH laser used for these studies is pumped by a 30 W beam from a grating tuned CO_2 laser focused through a small hole in one of the resonator reflectors, a polished, gold-plated copper mirror. The other reflector, the output coupler, is an aluminium strip grating deposited on a fused quartz substrate, the rear surface of which is coated with a layer of Teflon approximately one-quarter-wavelength thick to minimise the effect of multiple reflections of the submillimeter beam within the substrate. The output coupler is mounted on a translation stage which is driven axially to acquire laser resonator interferograms (submillimeter output power as a function of cavity length). A Pyrex waveguide of length 1.5 m and internal diameter 48 mm was used in these studies. A detailed account of the performance of the laser is available elsewhere⁴.

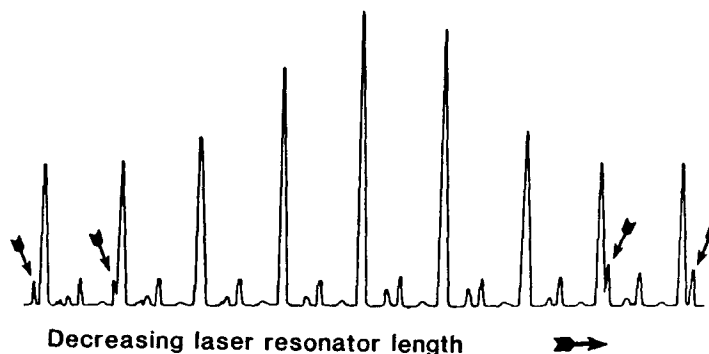


Fig. 3 Laser interferogram for a HCOOH laser pumped by the 9R(20) line of the CO₂ laser. In addition to modes of the directly pumped 433 μm line this shows the EH₁₁ mode (arrowed) of its 446 μm cascade partner.

At submillimeter wavelengths, where the separation between adjacent laser cavity modes is much greater than the linewidth of the lasing transitions, laser action is usually possible on only one transition and mode at a time. Figure 3 shows a laser resonator interferogram when the laser is pumped by the 9R(20) line of the CO₂ laser, the large peaks being due to the EH₁₁ dielectric waveguide mode of the 433 μm transition which is directly pumped by the CO₂ laser. However, it is evident that lasing also occurs on its 446 μm cascade partner (the EH₁₁ mode of the 446 μm line is arrowed in Fig. 3). The presence of another lasing wavelength is easily detected due to the different spatial periodicity of its modes in the interferogram. It is clear that when lasing occurs simultaneously on both transitions the total output power increases to a level significantly greater than the sum of the powers of each transition lasing alone. This effect, which can be used as a means of extracting more power from the laser, is discussed at length elsewhere⁶.

When the cavity is simultaneously resonant for the same waveguide mode of two different transitions the cavity length must be equal to half-integer multiples of the wavelengths for each transitions. Thus for wavelengths λ_1 and λ_2 , simultaneous resonances will occur for cavity lengths which are separated by intervals of

$$\frac{\lambda_1 \lambda_2}{2(\lambda_1 - \lambda_2)}$$

For the two lines under consideration this interval is equal to 7.3 mm.

Figure 4 shows a Fabry-Perot interferometer scan of the laser output when the cavity length is set to a value corresponding to the largest peak in Fig. 3. A third line which is at a measured wavelength of $460.5 \pm 1.0 \mu\text{m}$ is also present. This wavelength is consistent with the calculated value of 460.004 μm for the next cascade transition obtained by Dangoisse et al⁷. The simultaneous resonance of these three wavelengths in the laser resonator is a result of almost constant difference in frequency between adjacent cascade transitions for the nearly symmetric top HCOOH molecule. Similar results have been observed for the cascade sequences starting with the 394 μm and 419 μm transitions but not for the cascade sequence commencing with the 513 μm transition⁶. In each case, no evidence was found of the third transition of the cascade sequence lasing alone, suggesting that stimulated emission on the transition above was necessary for achieving a population inversion.

When all three lines of a cascade sequence are allowed to fall on a non-linear detector such as a Schottky diode many mixing products are generated. If f_1, f_2, f_3 are the frequencies of the three lines there will be a mixing product at frequency $f_1 - 2f_2 + f_3$ arising from the fourth order term in the Taylor expansion of the diode characteristic about the bias point. Because of the almost constant difference in frequency between adjacent cascade transitions for HCOOH, $f_1 - f_2 \approx f_2 - f_3$ and as a consequence the frequency of this mixing product will be very low. For all three sets of cascade sequences this frequency has been measured to be $\sim 1 \text{ MHz}$.

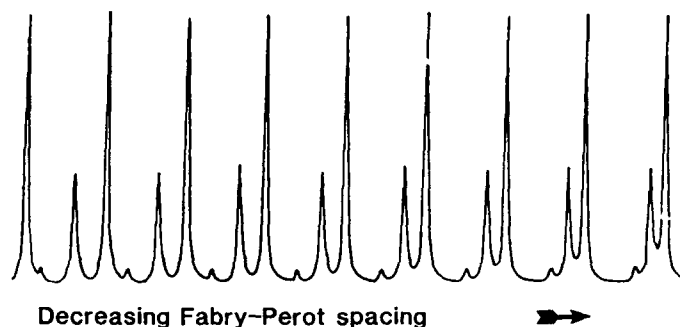


Fig. 4 Fabry-Pérot interferogram of the submillimeter laser output when the resonator length is adjusted to be resonant simultaneously for both the 433 μm and 446 μm transitions. (This is length which corresponds to highest peak in Fig. 3.)

Application to Interferometry

It is proposed that a HCOOH laser operating simultaneously on three lines of a cascade sequence be used as the basis for a phase-modulated interferometer as shown in Fig. 5. The beam from the laser, consisting of three frequencies, $f_1 > f_2 > f_3$, is split into two beams. One beam is incident upon a Fabry-Pérot etalon which allows passage of f_2 only through the plasma, rejecting f_1 and f_3 . The other beam is incident upon a Fabry-Pérot etalon which allows passage of f_1 and f_3 while rejecting f_2 . The beams are recombined for detection by a Schottky diode or some other non-linear detector (D_2). A time varying phase change $\phi(t)$ due to the plasma will appear as a phase change of $2\phi(t)$ in the beat frequency signal from the detector at frequency $f_1 - 2f_2 + f_3$. A reference beat frequency signal can be readily generated by splitting off some of the original beam to a second detector (D_1) as shown in Fig. 5. Comparison of the zero crossing times of the two beat signals allows $\phi(t)$ to be determined with a time resolution equal to the beat frequency period.

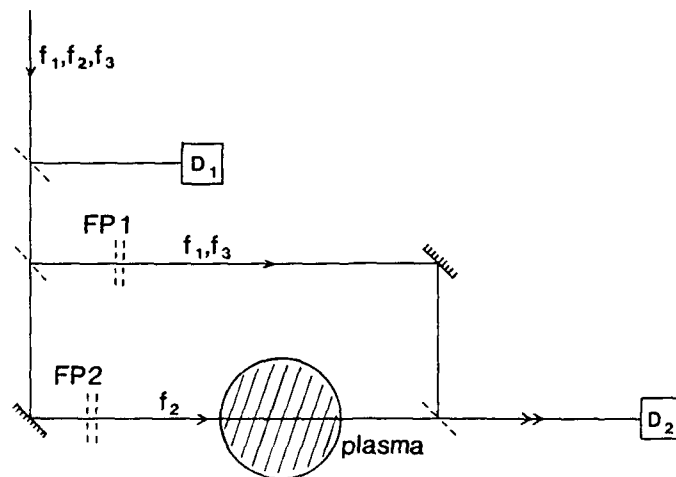


Fig.5. Schematic diagram of an interferometer using simultaneous triple cascade operation to achieve phase modulation. FP1 is a Fabry-Pérot etalon which passes f_2 and rejects f_1 and f_3 , while FP2 is a Fabry-Pérot etalon which passes f_1 and f_3 and rejects f_2 .

As the beat frequency is the result of differences among much higher frequencies, very small changes in these frequencies will result in significant change in the beat frequency. Changes in the laser output frequencies will occur due to frequency pulling effects associated with any variation in formic acid vapour pressure (which affects the Q of the pressure broadened rotational transitions) and any variation in cavity length (which affects the cavity resonance frequency). However as such frequency changes will occur on a time scale long compared to the beat period, they are not expected to be a problem.

Conclusion

It has been shown that it is possible to operate an optically pumped formic acid vapour submillimeter laser simultaneously on three lines of a rotational cascade sequence. These three lines produce a beat frequency in a non-linear detector at about 1 MHz. A phase-modulated interferometer for the measurement of plasma electron density, based on this phenomenon, has been proposed.

Acknowledgements

The authors acknowledge support from the CSIRO/University of Sydney Collaborative Research Fund and the University of Sydney Science Foundation for Physics. We are grateful to Rex Binks, Peter Dencher and Richard Phillips for excellent technical assistance.

References

1. D. Véron, Infrared and Millimeter Waves (K.J. Button, Ed.), 2, 69 (1979).
2. D. Véron, Opt. Commun. 10, 95 (1974).
3. S.M. Wolfe, K.J. Button, J. Waldman and D.R. Cohn, Appl. Opt. 15, 2645 (1976).
4. D. Véron and L.B. Whitbourn, Appl. Opt. 25, 619 (1986).
5. L.B. Whitbourn, J.C. Macfarlane, P.A. Stimson, B.W. James and I.S. Falconer, to be published in Infrared Phys. (1988).
6. P.A. Stimson, B.W. James, I.S. Falconer, L.B. Whitbourn and J.C. Macfarlane, Appl. Phys. Lett. 50, 786 (1987).
7. D. Dangoisse, E. Willemot, A. Deldalle and J. Bellet, Opt. Commun. 28, 111 (1979).
8. A.E. Siegman, Lasers (University Science Books, Mill Valley, California, 1986) P468.

INFRARED AND FAR-INFRARED LASER DEVELOPMENT FOR
PLASMA DIAGNOSTICS AT OAK RIDGE NATIONAL LABORATORY

W. H. Casson,* C. A. Bennett,** L. K. Fletcher,† H. T. Hunter, D. P. Hutchinson,
J. Lee,†† C. H. Ma, R. K. Richards, and K. L. Vander Sluis

Oak Ridge National Laboratory, § Oak Ridge, Tennessee 37831-6372

Abstract

Three IR and FIR based diagnostics will be developed and installed on the Advanced Toroidal Facility (ATF) at ORNL. An interferometer operating at 119 μm will measure plasma density along 14 vertical chords across the plasma cross-section. A small-angle Thomson scattering experiment using a 10.6- μm pulsed laser will determine the feasibility of measuring alpha particle distributions in a burning plasma. Plans are being developed for installing an FIR-based scattering experiment on ATF to measure density fluctuations.

Introduction

New fusion devices are being designed and constructed which place demanding requirements on the design and operation of laser based plasma diagnostics. Increased plasma densities, density gradients, and surface curvature are pushing the usable wavelengths toward smaller values in order to avoid serious refraction effects. Most severely affected is the FIR interferometer system because of the critical nature of the beam path. New interferometer systems are being developed at Oak Ridge National Laboratory (ORNL) for use on the next generation of plasma devices.¹ A system has been designed and is being installed on the Advanced Toroidal Facility (ATF) that is based on a high power FIR lasers system operated at 119 μm . Development work is underway on an IR system at 10.6 μm for installation on the Compact Ignition Tokamak (CIT) and other burning plasma devices.²

Many of the new generation of plasma devices will have sufficient density and temperature to be near or in the burning plasma regime. In these devices alpha particle production and heating will play a major role in the physics of fusion confinement. To assess the effects of alpha particles several alpha particle specific diagnostics are being developed. At ORNL a pulsed carbon dioxide laser source and a complex filter and receiver system is being developed and tested for use in measuring small-angle Thomson scattering from plasma electrons which will prove the feasibility of using a similar system for measuring alpha particle distributions in a burning plasma.³

To understand the important role that ion waves, density fluctuations, and ICH driven waves play in confinement and heating in a fusion device, direct measurements must be made of these properties. Future plans for the ATF device include installation of an FIR scattering experiment to fill these needs. Several options are being considered and which design will be chosen will depend on budget levels, time restraints, and needs of the experiment.⁴

Interferometer

The laser source for the interferometer system is a dual optically pumped FIR cavity system. The carbon dioxide pump lasers are illustrated in Fig. 1 and feature a modular design, no internal Brewster windows, ground potential end electrodes, and a fully isolatable center high-voltage section. Preliminary tests have shown stable operation on the 9P36 line at power levels in excess of 150 W. External optics for the pump laser beam are all reflective to eliminate distortion from the effects of high power on transmission optics. The FIR cavities are 240 cm in length and 2.3 cm internal diameter. Output powers on a daily basis exceed 1 W cw with maximum power levels reaching 1.26 W. External Stark cell stabilization provides stable output for periods in excess of two hours.

*Midwest Technical, Inc., Oak Ridge, TN 37830.

**University of North Carolina, Asheville, NC 28814.

†Tennessee Technological University, Cookeville, TN 38501.

††University of Tennessee, Knoxville, TN 37996.

§Operated by Martin Marietta Energy Systems, Inc., for the U.S. Department of Energy under Contract No. DE-AC05-84OR21400.

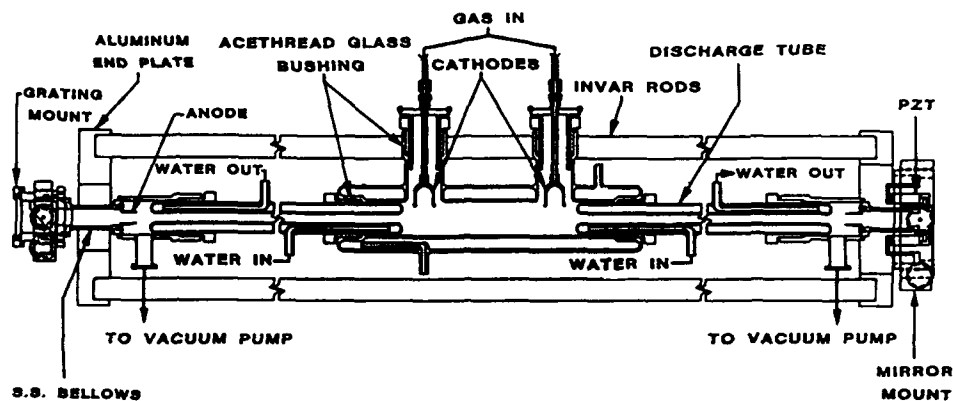


Fig. 1. Modular CO₂ laser design capable of 150 W cw output on the 9P36 line.

The laser systems are located on the ground floor two levels below the floor of the ATF device (Fig. 2). Beams are focused through a 12-in.-diam. pipe to the ATF area and the main beam is refocused onto a set of beam expansion optics (Fig. 3) located on an 18 ft high stand directly over the upper vacuum interface window. The expanded beam measures approximately 2 cm by 45 cm. After passage of the beam through the plasma and the lower window the beam is combined with the reference beam which has gone through a similar set of optics. An array of optical elements divides the beam into 14 separate channels and focuses each channel's beam onto the corresponding Schottky diode detector. A portion of the probe beam is split off prior to going through the plasma and is mixed with the reference beam to provide a reference for the phase. Data will be analyzed by the Vax computer network and the resulting temporal density profile will be available to experimental users immediately after the shot.

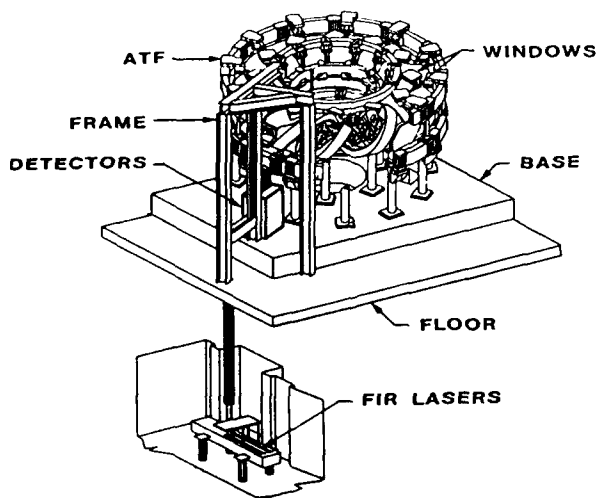


Fig. 2. Installation layout of the FIR interferometer system on ATF.

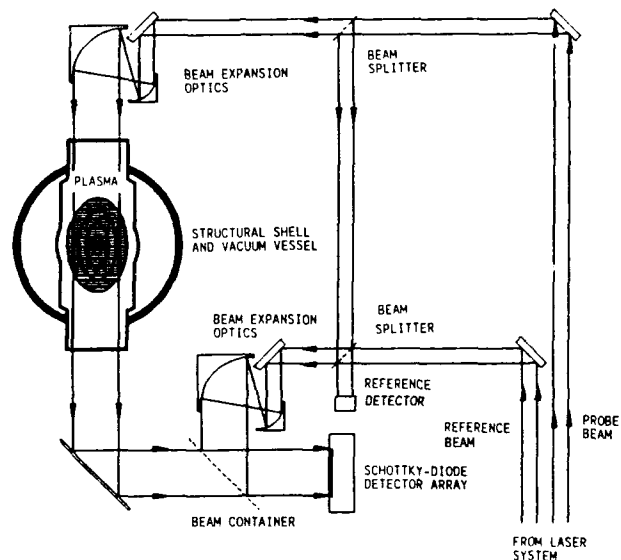


Fig. 3. Optics configuration for the FIR interferometer to be installed on ATF.

Alpha Particle Diagnostics

A diagnostic system for the measurement of fusion product alpha particles is under development at ORNL. The purpose of the diagnostic is to measure the density and velocity distribution of fusion product alpha particles; the slowing down of these particles from their initial 3.5 MeV energy is crucial in a fusion reactor to heat the fuel and maintain ignition.

The diagnostic is based upon the Thomson scattering of 10.6 μm CO₂ laser radiation (Fig. 4). A high power, long pulse, CO₂ laser as a source for this radiation has been

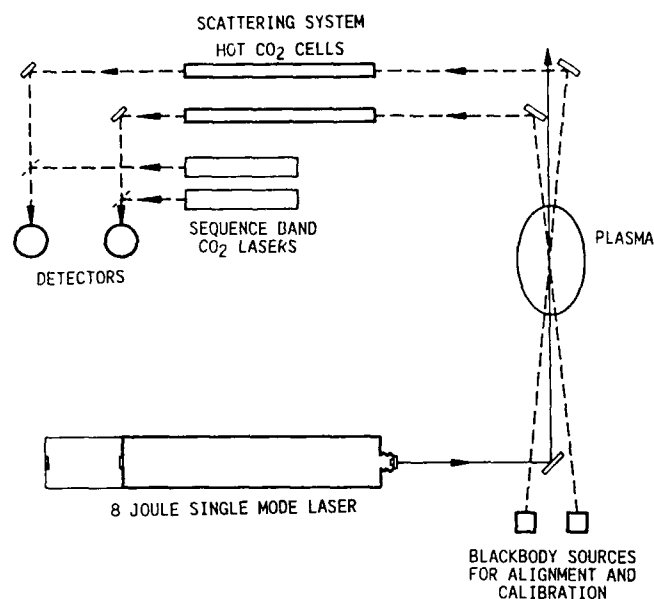


Fig. 4. Schematic of the alpha particle diagnostic system.

constructed and tested. Initial tests of a commercial TEA 103 laser modified by the addition of a low pressure cell within the cavity produced 8 Joule pulses up to 2 μsec long. This laser used unstable resonator optics which generated a small beam divergence (2×10^{-4} radians). However, a single wavelength could not be consistently produced. This problem was solved by removing the low pressure cell and injecting a low power, cw, grating tuned, waveguide CO_2 laser through a small hole in the back optic. This technique produced the same results for the pulsed laser as the low pressure cell operation except the wavelength was now consistently fixed at $10.6 \mu\text{m}$.

Detection of the scattered radiation is to be made with a series of heterodyne detectors which make use of the lengthened laser pulse to improve the signal-to-noise ratio. The local oscillator for each detector is to be a separate laser with a wavelength near the $10.6 \mu\text{m}$ CO_2 laser. The spectrum of the scattered radiation will then be measured by the selection of a series of local oscillators. To measure the alpha particle velocity distribution will require observation of approximately a 20 GHz shift from the $10.6 \mu\text{m}$ source. Tests of the detector subsystem have found that with commercially available detectors (here used as mixers), the heterodyne quantum efficiency can exceed 40%.

Thomson scattering which is characteristic of the alpha particle velocity distribution will only occur at small angles (typically 1°). This requires a special consideration in maintaining detector alignment and a reduction of stray laser radiation. To maintain alignment, an automatic tracking system is being designed which also serves the dual function of supplying a continuous calibration of the detector quantum efficiency.

To reduce the stray laser radiation, an absorption cell consisting of hot CO_2 gas is being developed. Tests of a prototype cell were able to reduce stray laser radiation by a factor of 20 with negligible ($<1\%$) reduction of signal from a black body source; the heterodyne local oscillator for this test was a sequence band CO_2 laser line shifted 11 GHz from the source CO_2 line, thus representing a central frequency of the alpha particle spectrum.

Far Infrared Scattering

The need for more information about the role played by fluctuations and plasma wave phenomenon in the confinement of a fusion grade plasma has encouraged interest in a scattering experiment which can characterize the parameters involved. So far scattering experiments have been limited and little data has been gathered from any major confinement device that was well enough diagnosed to provide adequate information for complete analysis. A far-infrared scattering device is being designed to diagnose the ATF device. Because of the magnetic field configuration and the limited access to the plasma there will be severe limitations to the design and capabilities of the system. However progress has been made in evaluating the requirements and a preliminary design is underway.

Conclusions

During a period of time when construction was underway on the ATF device, development work was done on providing three new diagnostic systems capable of yielding data on density, fluctuations, and alpha particle production. Each of these systems will exceed the available state-of-the-art design limitations and will provide a new level of diagnostic support for fusion energy research.

References

1. W. H. Casson, D. P. Hutchinson, C. H. Ma, and J. Lee, Development of an FIR Interferometer for ATF, to be published as an ORNL/TM report, Oak Ridge Natl. Lab., Martin Marietta Energy Systems, Inc.
2. C. H. Ma and D. P. Hutchinson, "Feasibility Study of an Infrared Interferometer/Polarimeter System for CIT," presented at the 29th Annual Meeting of the Division of Plasma Physics, APS, San Diego, Calif., Nov. 1987.
3. R. K. Richards, K. L. Vander Sluis, and D. P. Hutchinson, Feasibility of Alpha Particle Measurement in a Magnetically Confined Plasma by CO₂ Laser Thomson Scattering, ORNL/TM-10363, Oak Ridge Natl. Lab., Martin Marietta Energy Systems, Inc., Aug. 1987.
4. W. H. Casson, Far-Infrared Scattering on ELMO Bumpy Torus and Impurity Study Experiments, Ph.D. dissertation, University of Tennessee, 1985.

FRONTIER OF ULTRAFAST LASER TECHNOLOGY AND APPLICATIONS

R. R. Alfano
Institute for Ultrafast Spectroscopy and Lasers
Photonics Application Laboratory
Departments of Physics and Electrical Engineering
The City College of New York
New York, NY 10031

Abstract

Ultrafast laser technology encompasses both the generation and diagnostic techniques of picosecond (10^{-12} s) and femtosecond (10^{-15}) laser pulses, and their applications in direct temporal studies of extremely rapid phenomena in nature. The new frontier in optics emerged with the discovery of high-power picosecond light pulses in 1966, and developed by the ever enthusiastic search for increasingly higher temporal resolution has evolved over the last two decades to the point where pulses as short as 6 fs have been generated. This presentation highlights the state of ultrafast pulse generation and detection, reviews some key spectroscopic techniques, and describes self and coupled modulations and laser cancer diagnosis.

Introduction

Many fundamental processes in the submicroscopic world are extremely rapid ranging from femtoseconds to picoseconds. From such primary processes as transfer of excitation in the visual pigment that initiates vision, to such exotic events as electron-momentum relaxation in semiconductors, there is a plethora of these ultrafast phenomena in various disciplines of science and engineering.^{1,2} The relevant time scales of a number of these processes from many diverse fields are presented in Table 1:

Table 1. Relevant Time Scales of Typical Fast Processes

EVENT	TIME(S)
Biology	
Vision	$\sim 10^{-8} - 10^{-14}$
Photosynthesis, relaxation processes	$\sim 10^{-9} - 10^{-12}$
Electron transport steps in reaction centers	$\sim 10^{-12}$
Chemistry	
Singlet-triplet nonradiative transition	$\sim 10^{-10} - 10^{-13}$
Molecular reorientation in solvents	$\sim 10^{-12}$
Photodissociation, photoionization	$\sim 10^{-12} - 10^{-13}$
Solvent caging, H-bonding	$\sim 10^{-13} - 10^{-14}$
Transition state	$\sim 10^{-12} - 10^{-14}$
Physics	
Thermalization of hot electrons	$\geq 10^{-13}$
Vibrational dephasing in excited molecules	$\geq 10^{-13}$
Fluorescence risetime	$\sim 3 \times 10^{-14}$
Relaxation of electron-momentum distribution	$\sim 2 \times 10^{-14}$
Electron-electron and electron-hole scattering	$\sim 10^{-14}$
Electronic cloud deformation	$\sim 10^{-15}$

A major breakthrough in clocking fast events in the time domain occurred in 1966 with the discovery of mode-locked glass lasers producing light pulses several picoseconds in duration. The advent of high power picosecond pulses in turn revolutionized the field of nonlinear laser spectroscopy. Many nonlinear effects in condensed matter, unobserved in the past, were discovered which in turn helped the generation of even shorter pulses. One particularly major example which has shaped the growth of ultrafast laser technology, is the discovery in 1970 of self phase modulation (SPM) responsible for the generation of ultrafast white light or supercontinuum pulses.³⁻⁵ Self phase modulation has turned out to be a key process for femtosecond pulse generation. Methods of mode-locking developed rapidly, and by 1972 continuously mode-locked dye lasers were producing pulses on the order of a picosecond. This laser was improved further leading to the generation of pulses shorter than a picosecond in 1974. The development⁵ of the colliding-pulse mode-locking technique in 1981 pushed the limit of attainable pulse widths even shorter to less than 100 fs. Novel shaping and pulse compression techniques⁶ have led to the shortest reported optical pulse width of 8 fs and now down to 6 fs!

The field of ultrafast laser spectroscopy developed to clock extremely fast events directly in the time domain.^{1,2,7} Over the past two decades an impressive amount of new information on rapid phenomena in matter,

including molecular dynamics in liquids, relaxation and transfer of excitation in physical and biological systems, kinetics of chemical reactions has been obtained using sophisticated and novel optical techniques.^{1,2,7} While the early picosecond research could provide qualitative information and set limits for some of these processes, higher resolution and better techniques today make detailed quantitative studies possible. A history of the progress achieved in the capability of measuring faster events with increasing temporal resolution is presented in Fig. 1.

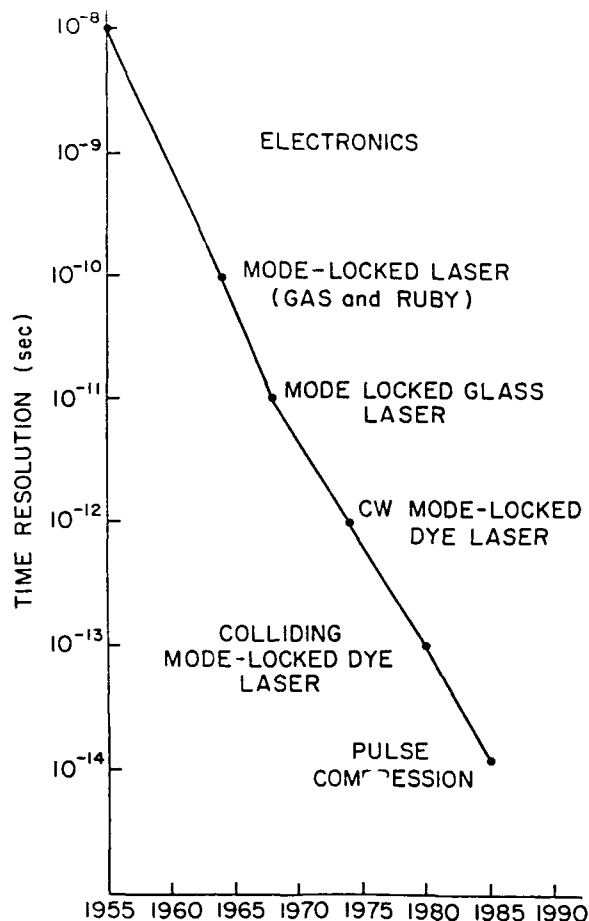


Fig. 1 Progress in measuring time.

New frontiers in Ultrafast Laser Spectroscopy will undoubtedly arise with the discovery of new phenomena. It has the potential to revolutionize the testing of high-speed electronic devices, refine our understanding of quantum and optics theories, increase data transmission capacity in optical communication using coupled modulation, open new fields in optical switching and computing, and medical diagnosis. We will focus some of the clocking methods, describe applications of nonlinear coupled phase modulations and cancer medical diagnosis.

Ultrafast Spectroscopic Techniques

In order to clock extremely rapid phenomena in nature several general ultrafast interrogation techniques have been developed and successfully used. These are streak camera, optical Kerr gate, up-conversion gate, excite-and-probe technique and transient grating method, to name a few. In this section we present a brief description of only the streak camera, optical Kerr gate, and excite and probe.

A. The Streak Camera

The technique most widely used for ultrafast luminescence measurements incorporates a streak camera.^{1,2} In this technique, shown in Fig. 2, light emitted from a sample photoexcited by an ultrafast laser pulse, is focused on to a photocathode. Photoelectrons are released by the photocathode. The flux of electrons emitted is proportional to the light intensity hitting the photocathode. These electrons are accelerated and then deflected by an applied voltage which sweeps the electrons across a phosphor screen. The electrons

released at different times from the photocathode strike the phosphor screen at different positions. This causes a track, or streak, which has a spatial intensity profile directly proportional to the incident temporal intensity profile of the luminescence. This phosphorescent streak is then analyzed electronically by a video system. In one shot, a complete fluorescence profile in time can be measured. The temporal resolution of streak cameras commercially available approach one half a picosecond with UV or IR spectral sensitivity.

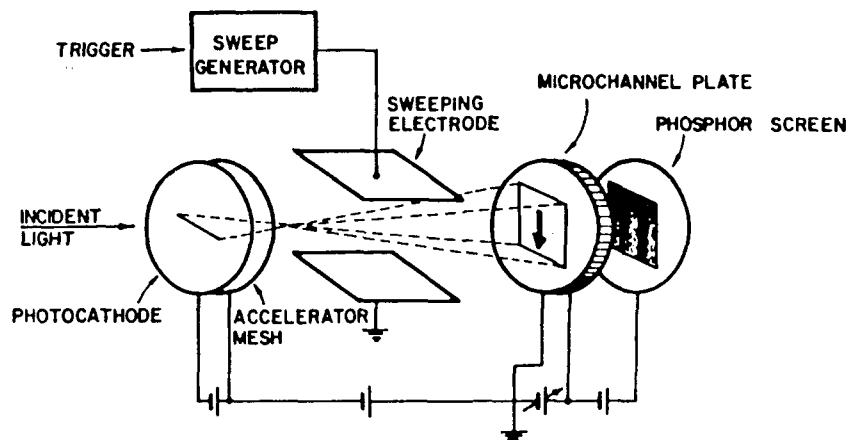


Fig. 2 Schematic diagram of streak camera

B. The Optical Kerr Gate

The earliest ultrafast luminescence studies utilized the optical Kerr gate⁷ which consists of a Kerr active liquid, such as carbon-disulfide (CS_2), situated between two crossed polarizers (see Fig. 3). Because of the crossed polarizers the gate is naturally closed. Under the action of an intense electric field associated with an ultrafast laser pulse, the molecules of the liquid experience a short-lived induced birefringence. This causes light, which happens to be passing through the Kerr shutter at the same time as the laser pulse, to become elliptically polarized. A portion of this elliptically polarized light is then able to pass through the Kerr gate. Thus, light can only pass through the gate when it temporally coincides with the intense gating laser pulse. The intense laser pulse can be used to carve out successive portions of the temporal profile of the emitted luminescence by varying the delay time of the gating pulse, using a movable prism. Typically, this takes 100 measurements to form an intensity profile in time. A wavelength spectra, at a given delay, is obtained by using a spectrometer and video system.

KERR SHUTTER

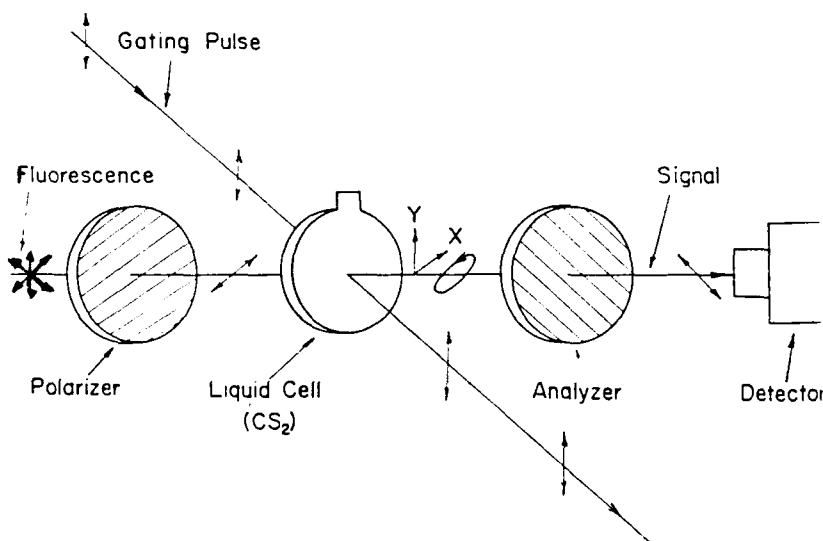


Fig. 3 Optical Kerr gate

The resolution of the optical Kerr gate depends upon the duration of the gate pulse and/or the reorientation time of the molecules of the active Kerr medium. For CS₂, one of the fastest Kerr active media available, the reorientation time is 2 picoseconds. Using polymers the resolution can be on the order of 100 fs.

C. Excite-and-Probe Technique

The excite-and-probe technique is a sensitive spectroscopic technique to study the kinetics of the excited states of matter.^{1,2,7} In excite-and-probe measurements, two incident ultrashort light pulses spatially overlap on the sample under investigation. The intense pump pulse excites the sample. The changes initiated in the sample by the pump pulse are monitored by the weaker probe pulse. The time evolution of the excited state is investigated by varying the time delay between the pump and the probe pulses. The probe pulse may be used to monitor such processes as induced absorption, bleaching, induced Raman scattering...

Excite-and-probe technique has been widely used to study the time behavior of excited states of a variety of biological, chemical and physical systems. Although the basic principle is the same, there is a wide variation of the experimental arrangement. The pump and the probe pulses may, in principle, be derived from two different lasers, but for picosecond or femtosecond applications it is extremely difficult to synchronize the timing of the two pulses to below 5 ps. So, for ultrashort time resolution both the pump and the probe pulses are generally derived from the same primary laser pulse to give femtosecond resolution. Nonlinear frequency shifting techniques like harmonic generation, sum and difference frequency generation, stimulated Raman scattering, ultrafast supercontinuum, to be described next, are used to generate the pump and the probe pulses of desired frequency. If time and wavelength resolved absorption spectra of excited states are required the probe pulse may be frequency broadened by self-phase modulation in a suitable media. The excited state is interrogated by the ultrafast supercontinuum probe pulse and a spectrograph or an optical multichannel analyzer is used for recording the absorption spectrum. A simultaneous three-dimensional recording of intensity, time and wavelength is thus obtained with a resolution of ~ 20 fs.

Applications

A. Self and Coupled Modulations

Nonlinear optics is an important field of science and engineering because it can generate, transmit and control the spectrum of laser pulses in solids, liquids, gases, and fibers. When an intense laser pulse propagates through such materials, it changes the refractive index. This in turn changes the phase, amplitude, and frequency of the incident laser pulse. A phase change can cause a frequency sweep within the pulse envelope. This process is called **self-phase modulation (SPM)** and is shown in Fig. 4.

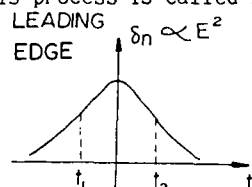
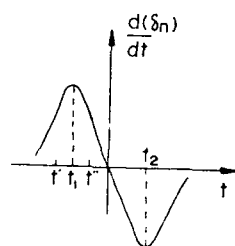
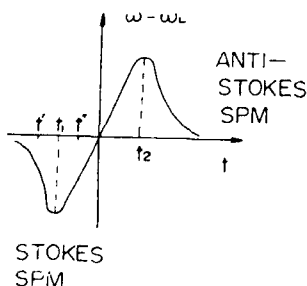


Fig.4: Self-phase modulation: index change, time derivative of index, and frequency chirp in time.



Photons at the laser frequency can also parametrically generate photons at Stokes and anti-Stokes frequencies in an angular pattern due to the required phase matching condition. The four-photon parametric generation process usually occurs together with the SPM process. These processes are mainly responsible for generation of the ps-fs white light supercontinuum (see Laser '85).

When two laser pulses of different wavelengths propagate simultaneously in a condensed medium, coupled interactions (cross modulation and gain) occur through the nonlinear susceptibility coefficients.⁸ These coupled interactions of two different wavelengths can introduce phase modulation, amplitude modulation, and spectral broadening in each pulse due to the other pulse.^{8,9} We will discuss three recent observations of spectral broadening arising from the coupled interaction of two laser pulses with different wavelengths. These processes have been termed: cross phase modulation and induced phase modulation.



When a coherent vibrational mode is excited by a laser, stimulated Raman scattering (SRS) occurs. SRS is an important process which competes with and can couple with SPM. The interference between SRS and SPM which causes the change of the emission spectrum and the phase modulation of pulse envelopes is called **cross-phase modulation (XPM)**. The Stokes pulse broadens due to a combination of XPM and Raman parametric amplification. The spectral broadening measured about the SRS wavelengths in liquids and recently in glass fibers originates from both SPM and XPM processes.⁸

Another important spectrally broadened process similar to XPM is called the **induced phase modulation (IPM)**. The experimental arrangement of this process is similar to the optical Kerr effect, namely, a weak pulse at a different frequency propagates through a disrupted medium whose index of refraction is changed by an intense laser pulse. The phase of the weak optical field can be modulated by the time variation of the index of refraction originating from the primary intense pulse. Both the weak and strong pulses are produced outside the medium and can be controlled by the researcher. (See article by Ho and Alfano in Laser '87, this conference for details.)

The spectral broadening of picosecond and femtosecond laser pulses is called the supercontinuum in condensed matter due to SPM covers a frequency band up to $10,000\text{ cm}^{-1}$ from uv to IR with picosecond to femtosecond pulse durations. Over the years, this ultrafast supercontinuum pulse source has been applied to time resolved absorption spectroscopy, nonlinear optical effects, pulse compression, squeeze states,¹⁰ and fiber diagnostics.⁹ The frequency broadened pulses can play an important role in ranging, imaging, remote sensing, communications, and other fields.¹¹ It is a key process behind the generation of 8-fs laser pulses.⁶ The newly observed induced spectral broadening due to XPM and IPM has important features for communications and signal processing by allowing pulse coding in different frequency regions and solitons generation. On the one hand, SPM, XPM, and IPM in optical fibers could be a source of noise on signals due to interference in multi-band communications and signal processing applications. It could be used to code and switch information from one frequency to another.⁸

B. Time Resolved Fluorescence Spectroscopy from Lung and Breast Cancer Tissues

Recently, there have been major breakthroughs in the use of laser spectroscopy as a unique and sensitive approach to reveal changes in the physical and chemical properties that occur in healthy and abnormal cells in tissues. Alfano and coworkers^{13,14} have established that the fluorescence spectroscopy and fluorescence recombination relaxation times from malignant and normal rat tissues were different. The differences were attributed to the transformations of local environment surrounding the fluorophors assigned to be flavins and porphyrins in the normal and cancerous rat tissues. Most recently, we have extended our laser spectroscopy research from animal to human tissues.¹⁵ Three different wavelengths were used to photo-excite the spectra from normal and tumor lung tissues. The fluorescence kinetics from lung tissues was also measured.

An Argon ion laser beam at 514.5 nm, 488 nm and 457.9 nm was focused on the front surface was collected and focused into the entrance slit of a double spectrometer. The output of the PMT was connected to a lock-in-amplifier and an X-Y recorder combination to display each spectrum. Picosecond time resolved fluorescence measurements were performed using a streak camera system and 8-ps pulse at 530 nm from a mode-locked glass laser. The tissue samples were solid chunks, not cut to any particular specificity and were a few millimeters thick. No chemicals or dyes were added.

Typical fluorescence spectra from normal (N) and tumor (T) human lung tissues are shown in Fig. 5. The principal spectral peaks excited at 457.9 nm are located at 496 nm, for normal tissues, and at 503 nm for tumor tissues, respectively. There is one subsidiary maximum located at about 605 nm in the normal lung tissue spectra. The tumor tissue spectra only showed a monotonic decrease with less structure. Similar results are obtained for 488 and 514.5 nm and for breast tissues.

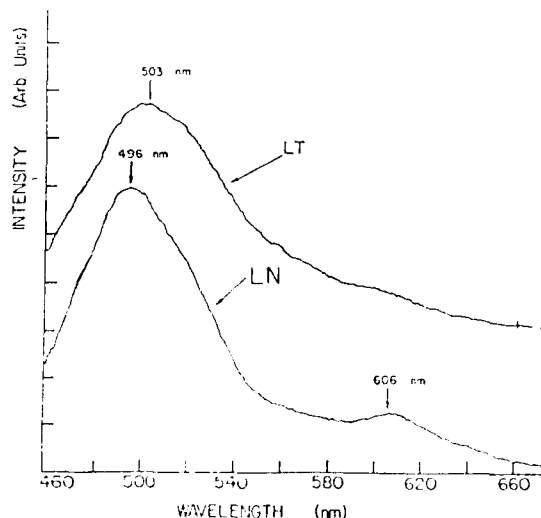


Figure 5: Steady state laser fluorescence spectra of human lung tissues: labeled (a) LN=normal (17mw) and (b) LT=tumor (10mw) excited by 457.9 nm, 1 mV sensitivity.

The fluorescence profiles in time for spectral band at wavelength center at 600 nm excited by 8 picosecond 530 nm laser pulse. The profiles were found to be nonexponential in time. To fit the curves, a double exponential $I(t)=A_{fe}e^{-(t/\tau_f)}+A_{se}e^{-(t/\tau_s)}$ was used where τ_f and τ_s are the decay times for the fast and slow components. The fluorescence decay times of the fast and slow components from the normal lung were about 220 ps and 2650 ps, respectively, while the fluorescence decay time of the fast and slow components for the tumor tissue of the lung were about 120 ps and 2600 ps, respectively.

The experimental results using 457.9 nm excitation for lung tissues indicate about 7 nm spectral red shift from normal to tumor lung tissue spectrum. A red shift of 6 nm was also observed using 488 nm and 514.5 nm excitation. A blue shift was observed in rat kidney tissue. The tumor lung tissue spectra are much smoother than normal lung tissue spectra. The lack of structure at 605 nm in tumor tissue may be associated with intensity and bandwidth increase of the second band at wavelength center at 555 nm or decrease in the native porphyrins. The observed 6 nm red shifts of the main peak and the smoothing of spectra for tumor lung tissues are attributed to the physiological and biochemical transformation of the lung cells from the normal tissues. The observed red shifts in the main maxima of the human lung tumor spectra suggest an accumulation of

negative charge ions in the malignant cells' intracellular environment. The flavin band observed for the normal breast tissue near the 515 nm peak exhibits a blue shift of about 10 nm in the tumor tissue spectra. This is opposite to the red shift observed for lung tissues. This blue shift may suggest a buildup of positive ions in the breast tumors. The time-resolved fluorescence shows that the decay time of tumor tissues is faster than that of normal tissues. This suggests an enhancement of the nonradiative processes in tumors.

Research at the IUSL is supported by AFOSR, ARO, NASA, NSF, ONR, SDIO, and Photonics Management Corporation.

References

1. Alfano, R. R. (Ed) Biological Events Probed by Laser Spectroscopy, Academic Press, New York (1982) and references therein.
2. Alfano, R. R. (Ed) Semiconductors Probed by Ultrafast Laser Spectroscopy, Academic Press, New York (1984) and references therein.
3. Alfano, R. R., and Shapiro, S. L., Emission in the Region 4000 to 7000 Å via Four Photon Coupling in Glass, *Phys. Rev. Lett.* 24, 584 (1970).
4. Alfano, R. R., and Shapiro, S. L., Observation of Self-Phase Modulation and Small Scale Filaments in Crystals and Glasses, *Phys. Rev. Lett.* 24, 592 (1970).
5. Shank, C. V., Measurement of Ultrafast Phenomena in the Femtosecond Time Domain, *Science* 219, 1027 (1982) and references therein.
6. Knox, W. H., Fork, R. L., Downer, M. C., Stolen, R. H., Shank, C. V., and Valdmanis, J. A., Optical Pulse Compression to 8 fs at a 5 kHz Repetition Rate, *Appl. Phys. Lett.* 46, 1120 (1985) and references therein.
7. Shapiro, S. L., (Ed.) Ultrashort Light Pulses, 2nd ed., Springer Verlag, New York (1984) and references therein.
8. R. Alfano, Q. Li, T. Jimbo, J. Manassah and P. Ho, "Induced spectral broadening of a weak picosecond pulse in glass produced by an intense ps pulse", *Opt. Lett.* 11, 626-8 (1986).
9. R. Stolen and C. Lin, "Self-phase modulation in silica optical fibers", *Phys. Rev.* A17, 1448-1453 (1978).
10. M. Kitagawa and Y. Yamamoto, "Numer-phase minimum uncertainty state with reduced number uncertainty in a Kerr nonlinear interferometer", *Phys. Rev.* A34, 3974-3988 (1986).
11. J. Manassah, P. Ho, A. Katz and R. Alfano, "Ultrafast supercontinuum laser source", *Photonics Spectra*, 53-59, Nov. (1984).
12. L. M. Mollenauer, "The future of fiber communications: Solitons in all optical system", *Optics News* 12, 42-46 May (1986).
13. R. R. Alfano, D. B. Tata, J. J. Cordero, P. Tomashefsky, F. W. Longo, and M. A. Alfano, Laser induced fluorescence spectroscopy from native cancerous and normal tissues, *IEEE J. Quantum Electron.* QE20, 1507-1511 (1984).
14. D. B. Tata, M. Foresti, J. Cordero, P. Tomashefsky, M. A. Alfano, R. R. Alfano, Fluorescence Polarization Spectroscopy and Time-Resolved Fluorescence Kinetics of Native Cancerous and Normal Rat Kidney Tissues, *Biophys. J.* 50, 463-469 (1986).
15. R. R. Alfano, G. C. Tang, W. Lam, D. S. J. Choy, E. Opher, Fluorescence spectra from cancerous and normal human breast and lung tissues, *IEEE J. Quantum Electron.* QE20, 1806-1811 (1987).

FEMTOSECOND DYNAMICS OF CHARGED SOLITONS IN TRANS-POLYACETYLENE

L. Rothberg and T. M. Jedju

AT&T Bell Laboratories
600 Mountain Avenue
Murray Hill, NJ 07974

S. Etemad and G. L. Baker

Bell Communications Research
331 Newman Springs Road
Red Bank, NJ 07701

ABSTRACT

Time-resolved absorption using probe wavelengths of 2.5 - 5.5 μm has been used to study photoexcitations of the quasi-one-dimensional semiconductor, trans-polyacetylene. The experiment has 0.5 ps resolution, sufficient to observe a 0.5 - 1 ps decay of photogenerated Su-Schrieffer charged soliton pairs which form after intrachain electron-hole pair excitation. The decay is nonexponential and due to geminate recombination. The tunability of our infrared probe permits us to observe spectral relaxation during soliton formation which corresponds to conformational equilibration of the solitons. Saturation of the absorption is due to volume filling of the lattice by charged solitons and provides an estimate of the third order nonlinear susceptibility of trans-polyacetylene.

I. Introduction

The photoexcitations of organic semiconductors are very different from the traditional electron and hole picture.¹ The quasi one-dimensional nature of organic polymer chains leads to a strong propensity for free electrons and holes to be dressed by the lattice and to form quasiparticles such as polarons and bipolarons. In trans-polyacetylene, the unique symmetry between degenerate ground states permits charged soliton pairs to be the energetically preferred excitations.² These take the form of mobile domain walls between the two ground states (bond alternation phases) coexisting on a single chain. The existence of photogenerated charged solitons has now been well documented^{3,4} experimentally. They are characterized by a midgap absorption around 0.5 eV. Studies of the picosecond dynamics of that absorption^{5,6} have established that both intrinsic² and defect mediated⁷ mechanisms contribute to charged soliton photogeneration. The intrinsic solitons are from intrachain electron-hole pair excitations as described by Su and Schrieffer.² Previous work suggests that these form in $<10^{-13}$ seconds^{2,8} and decay in ~ 0.5 ps.⁶ The purpose of the present paper is to investigate the formation and decay of these photogenerated lattice deformations.

In order to measure these directly, we have developed an apparatus capable of monitoring subpicosecond transient absorption in the mid-infrared where charged solitons absorb. In section II, the apparatus is described in detail. Results on both the spectroscopy and dynamics of the photoinduced midgap absorption in trans-(CH)_x are presented in section III. These are obtained with 0.5 ps time resolution and interpreted in terms of formation and decay of charged solitons.

II. Experimental

The experiments were all performed on thin films ($<1000\text{\AA}$) of Shirakawa polyacetylene⁹ on glass slides. These are grown as cis-polyacetylene and thermally isomerized to the trans form. The chain directions are thought to be primarily in the plane of the substrate but to be isotropically distributed in that plane over the laser spot size (~ 1 mm). The samples are sealed under vacuum in glass ampules and studied at room temperature. It was previously determined that there was very little temperature dependence to the behavior of the photoinduced absorption in question.⁶

The method we have chosen to generate probe frequencies in the mid-infrared is based on the technique of optical parametric generation in nonlinear crystals. Instead of building up from vacuum noise, however, we "seed" the parametric conversion with a white light continuum generated by self-phase modulation of intense light in a water cell. This permits us to use short crystals so that group velocity dispersion does not degrade our time resolution.

A schematic of the apparatus is shown in Figure 1, and a detailed description can be found elsewhere.^{10,11} A dye laser is synchronously pumped by a fiber compressed and frequency

doubled CW modelocked Nd³⁺:YAG laser. The dye laser operates around 585 nm and has pulses of <0.3 ps duration and 1nJ energy with a repetition rate of 82 MHz. A double Q-switched Nd³⁺:YAG laser is synchronized to select 10 pulses per second for amplification to the millijoule level. Spatial filtering and saturable absorbers are used to discriminate against amplified spontaneous emission and 350 fs pulse durations are routinely obtained for the amplified pulses.

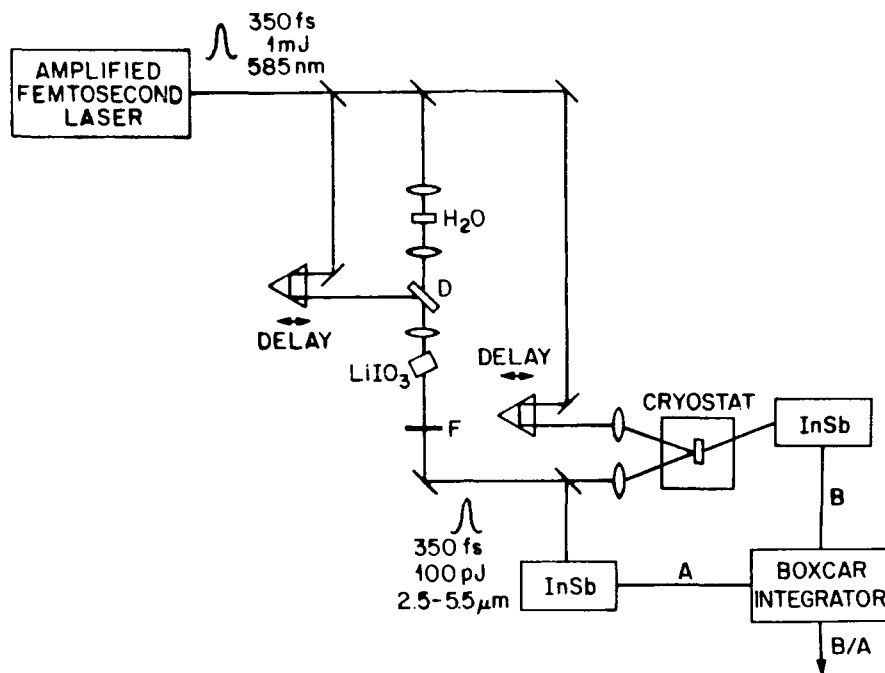


Figure 1. Schematic of seeded parametric amplifier and transient absorption apparatus.

The amplification process is essential to the wide tunability of our infrared probe since it makes continuum generation¹² possible. This broadband continuum extends from <300 nm to >1 μ m and can be difference frequency mixed with a portion of the amplified 585 nm beam in a 0.5 mm LiIO₃ crystal cut at 21° to its optic axis. Infrared pulses of picjoule energies tunable between 2.5 μ m and 5.5 μ m are obtained by parametric down conversion. The tuning is accomplished by adjusting the LiIO₃ crystal angle, thereby selecting a portion of the white light continuum which is phase matched with the monochromatic beam. The bandwidth of the infrared probe is determined by phase matching and is approximately 300 cm⁻¹ at 3 μ m.

A portion of the amplified 585 nm beam is used as a pump to generate charge soliton pairs in the sample. The infrared beam is overlapped with the pump on the sample with variable delay to measure the soliton dynamics. One InSb photodetector monitors the transmitted infrared radiation and a second monitors a portion of the incident beam so that normalization of pulse to pulse fluctuations is possible. Photoinduced absorptions of <1% are readily studied.

III. Results

Figure 2 illustrates the photoinduced change in infrared transmission for Si (a) and trans-(CH)_x (b). The transmission drop in Si is primarily due to free carrier absorption and its onset is presumed to represent the instrumental resolution of the apparatus. The free carriers are long-lived (ns) so that the derivative of the absorption turn on should be the cross-correlation between visible and infrared pulses. The probe wavelength of 2.8 μ m (.44 eV) is at the maximum of the charged soliton absorption as determined in previous work.⁴⁻⁶ Figure 2(b) shows that the absorption onset in polyacetylene is instrumentally limited and that the fall occurs in <1 ps, but in a non-exponential manner. The rise of <<0.5 ps is consistent with the predictions of numerical simulations^{2,8,13} based on the Su-Schrieffer-Heeger Hamiltonian¹⁴ which show that the domain walls form in ~100 fs. The rapid decay of these pairs suggests geminate recombination of the charged solitons by an electron hop as discussed by Kivelson and Wu.¹⁵ From our data, we estimate the survival probability of charged soliton pairs to 10 ps to be .02 \pm .03. Fewer than five percent escape and their contribution to photoconductivity on timescales >10 ps is questionable.¹⁶ The non-exponential decay has been ascribed to one dimensional diffusion limited recombination kinetics.¹⁷

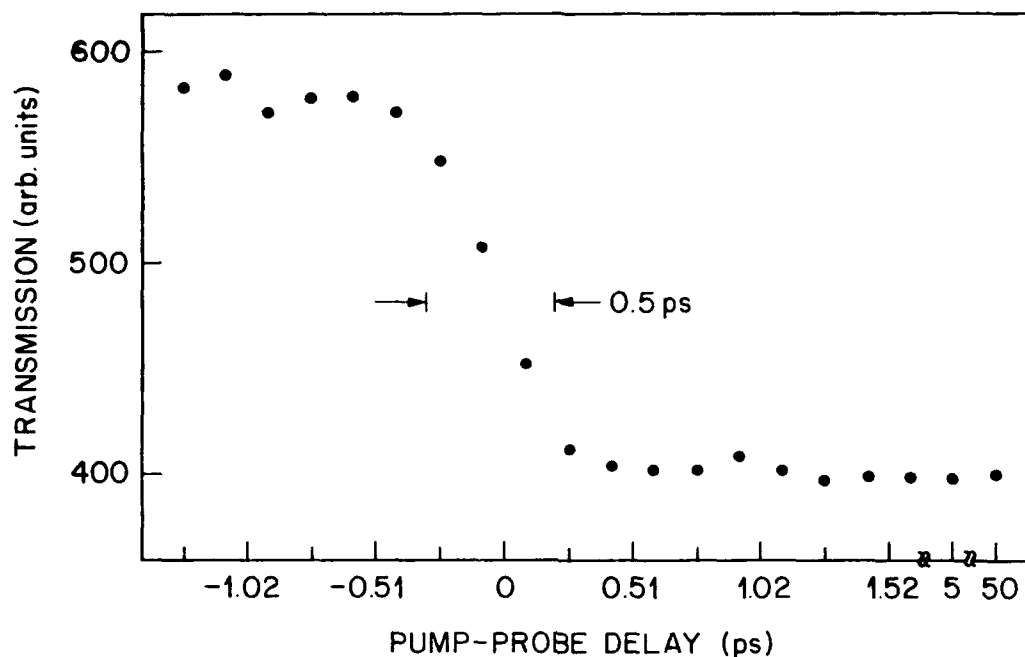


Figure 2. (a) Photoinduced transmission decrease due to free carrier generation in Si. Pump wavelength is 585 nm and probe wavelength is 2.8 μm .

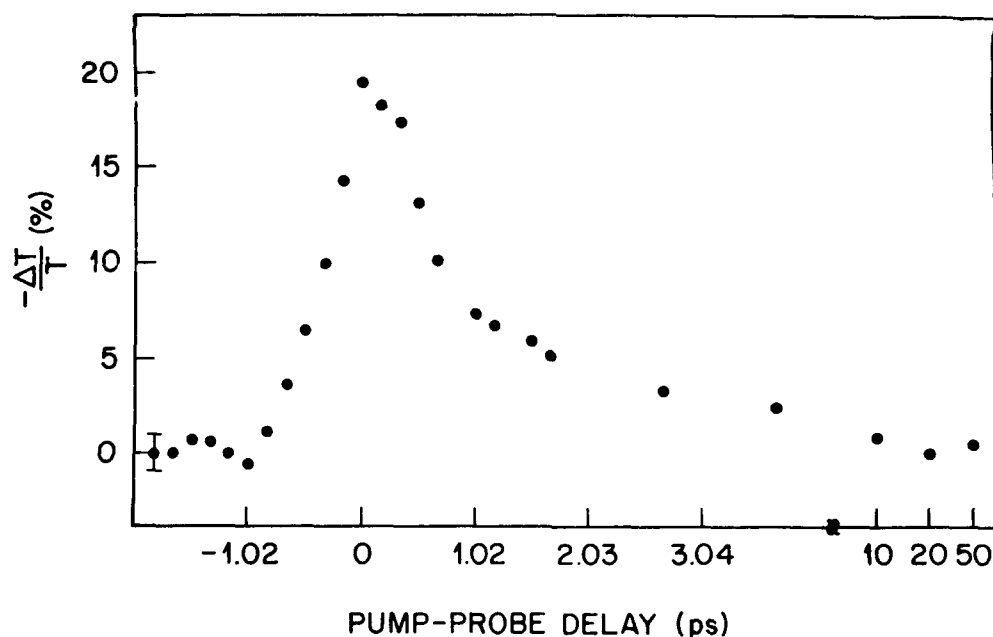


Figure 2. (b) Photoinduced transmission decrease due to charged soliton pairs in trans-polyacetylene. Pump wavelength is 585 nm and probe wavelength is 2.8 μm . Zero of time is chosen arbitrarily as maximum of photoinduced absorption.

In previous work,^{5,6} we showed that the spectrum of Su-Schrieffer charged soliton pairs at 5 ps was close to that of isolated charged solitons observed milliseconds after photoexcitation.¹⁸ This is consistent with the idea that the charged solitons are well formed within about 100 fs and do not interact very strongly.

Figure 3 illustrates that we can observe deviations from the isolated soliton spectrum with our improved time resolution. Our spectral measurements to the red of the peak are limited by the glass substrate. The data are taken by accumulating complete decay curves at each wavelength to guard against artifacts due to group velocity dispersion in the continuum and angle tuning of the crystal.¹¹ When the pulses are temporarily overlapped, the spectrum is significantly red shifted. By 500 fs delay, when the pump and probe pulses are well resolved, the spectrum has relaxed to its long time value. We believe that the red shift at short times has to do with observing the lattice prior to its conformational relaxation to a pair of well formed charged solitons. As demonstrated by the simulations of Kippelen et al.,¹³ the soliton electronic levels split off from valence and conduction bands and reach their midgap positions within 100 fs. This would produce red shifted absorptions at times <100 fs which we would not be able to time resolve. It is possible that the red absorption has to do with shape distortion of the solitons due to high initial velocity or to population of internal vibrational degrees of freedom, but we consider these to be less likely.

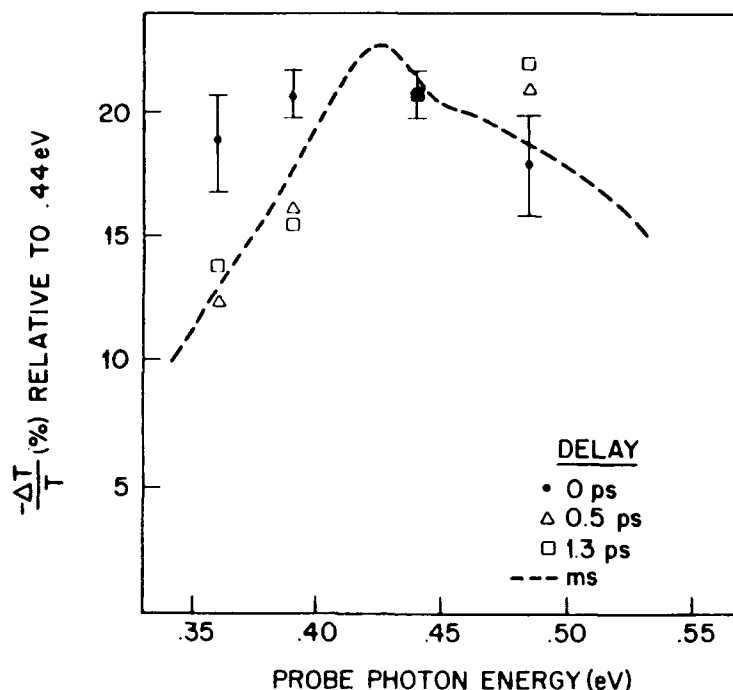


Figure 3. Spectral relaxation of the transient midgap absorption in trans-polyacetylene. Signals at each delay are normalized to the photoinduced absorption at 0.44 eV (2.8 μ m). The dashed line represents the millisecond delay photoinduced absorption as obtained from reference 16.

Shank et al.¹⁹ did photoinduced absorption experiments probing between 0.8 and 1.4 eV, and have observed a similar red shift in that band edge transient absorption at short times. They did not assign the absorption band and ascribed the spectral relaxation to cooling. We believe that these concomitant rapid decays of red shifted absorption support the picture^{6,15,16} of the 1.4 eV transient as bound neutral soliton pairs formed by rapid geminate recombination of separating charged soliton pairs. The red shifted absorption of neutral soliton pairs would be associated with charged solitons which recombine before their conformational relaxation to equilibrium has occurred. This supports our previous conclusion^{5,6} that Su-Schrieffer solitons are a precursor to the 1.4 eV transient.

In our previous work, we established that the transient midgap absorption dynamics⁶ and transient bleaching recovery dynamics⁸ were similar. This is merely a reflection of the high quantum yield for charged soliton pair generation. The onset of saturation of the absorption and bleaching also occur at the same intensity, and we have shown the saturation mechanism to be volume (phase space)²⁰ filling by charged solitons.^{6,21} From the magnitude of the bleaching we can estimate the value of $\chi^{(3)}$ to be $\sim 10^{-8}$ esu. The large susceptibility has to do with the fact that the solitons are delocalized so that each absorbed photon creates two solitons which occupy some 30 lattice sites and perturb an even longer length of chain. The low saturation intensity and rapid recovery of the absorption make this type of system an excellent candidate for optical switching applications.

IV. Conclusion

Transient absorption measurements with <0.5 ps resolution and probe wavelengths in the mid-infrared have been used to study the formation and decay of photogenerated charged soliton pairs in trans-(CH)_x. A non-exponential decay with $\sim 0.5 - 1$ ps decay time is observed along with rapid (<0.5 ps) spectral relaxation which we interpret as conformational equilibration of the solitons. The dominant decay mechanism is geminate recombination. Saturation of the photoinduced absorption and bleaching corresponds to volume filling of the sample by the delocalized solitons, resulting in large rapid $\chi^{(3)} \sim 10^{-8}$ esu. These intrachain excitations are only part of the story in polyacetylene, and work on interchain excitation of electron-hole pairs in oriented material is in progress in our laboratory and others.

References

1. J. Orenstein in Handbook of Conducting Polymers, T. A. Skotheim, Ed. (Dekker, New York, NY 1986).
2. W. P. Su and J. R. Schrieffer, Proc. Natl. Acad. Sci. USA 77, 5626 (1980).
3. J. Orenstein and G. L. Baker, Phys. Rev. Lett. 49, 1043 (1982).
4. G. B. Blanchet, C. R. Fincher, T. C. Chung and A. J. Heeger, Phys. Rev. Lett. 50, 1933 (1983).
5. L. Rothberg, T. M. Jedju, S. Etemad and G. L. Baker, Phys. Rev. Lett. 57, 3229 (1986).
6. L. Rothberg, T. M. Jedju, S. Etemad and G. L. Baker, Phys. Rev. B 36, 7529 (1987).
7. J. Orenstein, Z. Vardeny, G. L. Baker, G. Eagle and S. Etemad, Phys. Rev. B 30, 786 (1984).
8. A. R. Bishop, D. K. Campbell, P. S. Lohmdahl, B. Horovitz and S. R. Phillpot Phys. Rev. Lett. 52, 571 (1984).
9. H. Shirakawa, T. Ito and S. Ikeda, Macromol. Chem. 179, 1565 (1978).
10. T. M. Jedju and L. Rothberg, Appl. Opt. 26, 2877 (1987).
11. T. M. Jedju and L. Rothberg, Appl. Opt. 00, 0000 (1988).
12. R. R. Alfano and S. L. Shapiro, Phys. Rev. Lett. 24, 584 (1970).
13. A. R. Bishop, D. K. Campbell, P. S. Lohmdahl, B. Horovitz and S. R. Phillpot, Synth. Met. 9, 223 (1984).
14. W. P. Su, J. R. Schrieffer and A. J. Heeger, Phys. Rev. Lett. 42, 1698 (1979).
15. S. Kivelson and W-K. Wu, Phys. Rev. B 34, 5423 (1986).
16. M. Sinclair, D. Moses and A. J. Heeger, Synth. Met. 17, 343 (1987).
17. Z. Vardeny, J. Strait, D. Moses, T. C. Cheung and A. J. Heeger, Phys. Rev. Lett. 57, 3229 (1982).
18. Z. Vardeny, J. Orenstein and G. L. Baker, J. Phys. Paris Colloq. 44, C3, 325 (1983).
19. C. V. Shank, R. Yen, J. Orenstein and G. L. Baker, Phys. Rev. B 28, 6095 (1983).
20. B. I. Greene, J. Orenstein, R. R. Millard and L. R. Williams, Phys. Rev. Lett. 58, 2750 (1987).
21. L. Rothberg, T. M. Jedju, S. Etemad and G. L. Baker, IEEE J. Quant. Elect. 00, 000 (1988).

W. E. Bron
 Professor
 University of California, Irvine
 Physics Department
 Irvine, CA 92717

Abstract

We have recently expanded our previous work on the dynamics of coherent longitudinal optical phonons in compound semiconductors, to include studies of the interaction of these phonons with one- and with two-component plasma. We find an unexpected difference in the effect of the two types of plasma; namely, we find that a two-component (e-h) plasma does not change the phonon lifetime but instead hinders the formation of the coherent phonon state, while a one-component plasma does not hinder phonon generation but markedly changes the phonon lifetime.

Coherent Phonon Generation

The standard technique to determine the "lifetime" of optical phonons is to measure the spectral width of the incoherent Raman scattering cross section. Since spectral width and temporal duration are related by a Fourier transformation, information on the temporal duration of the optical phonon excitation can, in principle, be obtained in this way. More recently it has become apparent that we may circumvent the transformation by simply making measurements of the optical phonon dynamics directly in the time domain. Since, however, optical phonon "lifetimes" are of the order of picoseconds, experimental techniques capable of resolution within that very short temporal domain have had to be developed. Modern synchronously pumped mode-locked dye laser systems have proven to be the answer. Since phonon energies correspond to the far infrared (FIR) region of the electromagnetic spectrum, it would be necessary to construct a picosecond source in this spectral range. Unfortunately, to date no such source has been demonstrated. On the other hand, many pico- and even femtosecond lasers with energies in the visible spectrum have been demonstrated. It is, therefore, possible to use nonlinear difference mixing of two visible laser frequencies to form a FIR excitation source of phonons providing the phonons involved are Raman active.¹ The apparatus involves dual synchronously pumped dye lasers which produce synchronized trains of pulses with picosecond and (subpicosecond) duration at two different wavelengths. We have used such laser systems to generate near-zone-center coherent optical phonons in GaP, ZnSe and ZnTe through coherent Raman excitation (CRE), and to study the subsequent dynamics of the coherent longitudinal optical (LO) phonon state, plus the response of the electronic system to nonlinear excitation. These investigations were carried out directly in the time domain through time resolved coherent anti-Stokes Raman scattering (TRCARS).¹ Only the results on GaP will be discussed here.

Coherent Raman excitation (CRE) and coherent anti-Stokes Raman scattering (CARS) are particular forms of nonlinear mixing of laser fields. Two electromagnetic fields E_p and E_s , with photon energies $\hbar\omega_p$ and $\hbar\omega_s$ and wavevectors \vec{k}_p , \vec{k}_s , can in general give rise to a series of nonlinear interactions in a solid. One interaction leads to a virtual excitation of the electronic system at a frequency $\omega_p - \omega_s$. Of particular interest here is the case in which $\omega_p - \omega_s$ corresponds to a Raman active vibrational excitation. In the resultant CRE, the energy $\hbar(\omega_p - \omega_s)$ and wavevector $\vec{q} = \vec{k}_p - \vec{k}_s$ of the active mode are in the ideal case exactly specified, and the phase space available to the excited vibrations is severely limited. In this sense it differs markedly from stimulated and spontaneous Raman scattering for which the available phase space is much larger. Thus, the occupation probabilities of the components of the coherent state produced through CRE may be very high as compared to those of incoherent Raman excitation. Generation of intense coherent oscillations by CRE was first described for molecular systems by Garmire, et al.² Large amplitude coherent excitation of lattice vibrations was soon thereafter described by Giordmaine and Kaiser.³

The coherent excitation may be probed by a third laser field, E_p , whose energy $\hbar\omega_p$ is taken for convenience to be $\hbar\omega_s$. The nonlinear interaction of this field, with the coherent lattice vibrations results in yet another nonlinear polarization⁴ which drives an electromagnetic field with energy $\hbar\omega_c = \hbar(2\omega_p - \omega_s)$. It is further required through wavevector conservation (the phase-matching condition) that $\vec{k}_c = \vec{k}_p + \vec{k}_p - \vec{k}_s$, where \vec{k}_p and \vec{k}_c are the wavevectors associated with the probe pulse and the anti-Stokes pulse, respectively. The probe technique clearly involves coherent anti-Stokes Raman scattering, giving rise to the CARS designation for the entire nonlinear process.

The coherent phonon state mentioned above is defined by a superposition of states of different occupation probabilities, but whose component states have, at least initially, a fixed relative phase relationship among each other. The resultant excitation of the solid resembles most closely a classical harmonic oscillator.⁴

The experimentally observable parameter in the CARS experiment is the intensity of the TRCARS signal at the energy $\hbar\omega_c = \hbar(2\omega_l - \omega_s)$. This intensity is proportional to the absolute square of the nonlinear polarization induced in the vibrational and electronic systems due to the three laser fields \vec{E}_l , \vec{E}_s and \vec{E}_p . Thus an expression for this quantity can be written as,⁵

$$I_c(\Delta t) = AS \int_{-\infty}^{\infty} dt |\vec{E}_p^+(t+\Delta t) \times [N(\vec{R}_4 \cdot \vec{q}) Q^+(t) + \chi_{eff}^{(3)} \vec{E}_l^+(t) \vec{E}_s^-(t)]|^2, \quad (1)$$

In Eq. (1), the factor S goes to unity as the phase mismatch $\Delta \vec{k}$ goes to zero, Δt is the temporal difference between the probe pulse and that of \vec{E}_l and \vec{E}_s (which are set as close as possible to zero time overlap, $\delta t=0$), N is the number of primitive cells per unit volume, $\chi_{eff}^{(3)}$ is the effective third-order nonlinear electronic susceptibility, \vec{q} is the unit phonon polarization vector, \vec{R} is the Raman matrix element and Q is the displacement amplitude of the coherent phonon state.

It is clear from Eq. (1) that there are two contributions to $I_c(\Delta t)$, i.e., one due to the response of the lattice and one to the response of the electronic system. The duality can be clearly seen in the experimental results as illustrated in Fig. 1.

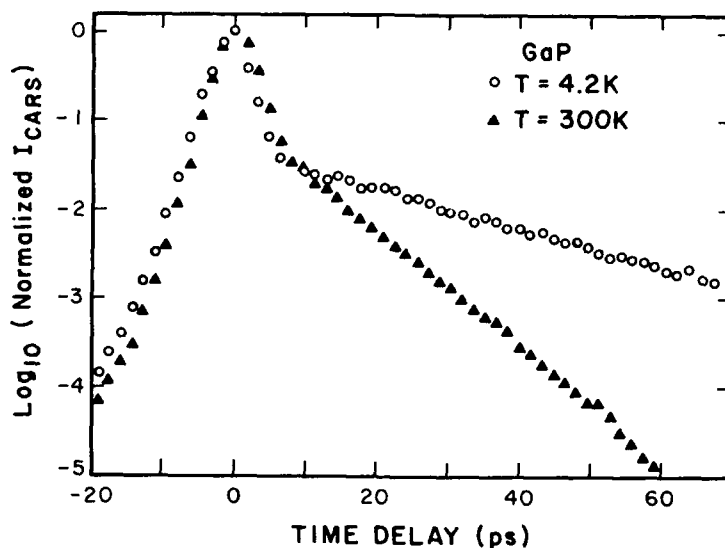


Figure 1. Logarithm to the base ten of the normalized cars signal, $I(\Delta t)$, as a function of the delay between the probe pulse, $E_p(t)$, and the coherent LO phonon generation at $\Delta t=0$.

Figure 1 illustrates typical normalized TRCARS intensities as a function of the time delay Δt between the two pump beams (E_l , E_s) relative to the probe beam (E_p) for the of GaP held at 4.2K and 300K, and with $\omega_l - \omega_s = \omega_{LO}$ so that the coherent LO phonon state is excited. The two components of $I_c(\Delta t)$ are clearly visible. The first component near $\Delta t=0$, which can be independently observed when $\omega_l - \omega_s \neq \omega_{LO}$, is a slightly asymmetric "bell-shaped" curve. This component of $I_c(\Delta t)$ is attributed to the nonlinear, electronic response of the crystal. The remaining part of $I_c(\Delta t)$ decreases exponentially with delay time for $\Delta t \gg 0$ and can be observed to do so over several orders of magnitude. Thus for these experimental conditions the time interval over which the coherent phonon state is observed to decay is long compared to the time interval over which the purely electronic signal is observed. The slope of the logarithm of the "phonon" part of $I_c(\Delta t)$ is then equal to the dephasing time, traditionally referred to as $T_2/2$.

In general, phonon dephasing in solids results from scattering at crystal boundaries, lattice imperfections, electronic carriers, or through population decay brought about by anharmonic interactions. The relative contribution to the dephasing by these scattering sources depends on the particular crystal under investigation. We have demonstrated earlier^{1,7} that for particularly pure samples the dephasing can be demonstrated to arise

almost exclusively from anharmonic decay of the LO phonon into acoustic phonons. In the particular case of GaP it can, moreover, be shown that the dephasing occurs predominantly through the decay of the zone center LO phonon into two longitudinal acoustic (LA) phonons each with half the LO phonon energy, and with equal but opposite signed wavevectors.

Under these circumstances, the rate of LO phonons at some temperature T , relative to that at $T=0K$, depends solely on the occupation probability of the LA phonon states. This ratio can, therefore, be determined directly from Bose-Einstein statistics. As can be expected, the higher the ambient temperature the shorter is the dephasing time (see Fig. 1). A comparison between experiment (symbols) and (solid line) for a range of ambient temperatures from 4.2K to 300K is summarized in Fig. 2.

The temperature dependence of $T_2/2$ has also been determined through linewidth measurements of the spontaneous Raman scattering intensity. The results are displayed in Fig. 2 as crosses for LO phonons in GaP. For completeness we also include similar data for a different crystal in GaP as reported by Bairamov, *et al.*⁸ marked BPTU in the figure.

Note should be taken of the following additional results depicted in Fig. 2. (i) the results of the linewidth studies agree among the two experimental groups, and (ii) agreement also exists between the results obtained from the linewidth and from the temporal measurements. It should be further noted that the temporal measurements show quite clearly that the coherent LO phonon state is not destroyed as a result of the dephasing process, rather $\langle Q \rangle^2$ persists through many orders of $I_c(\Delta t)$ and simply decreases its magnitude exponentially.

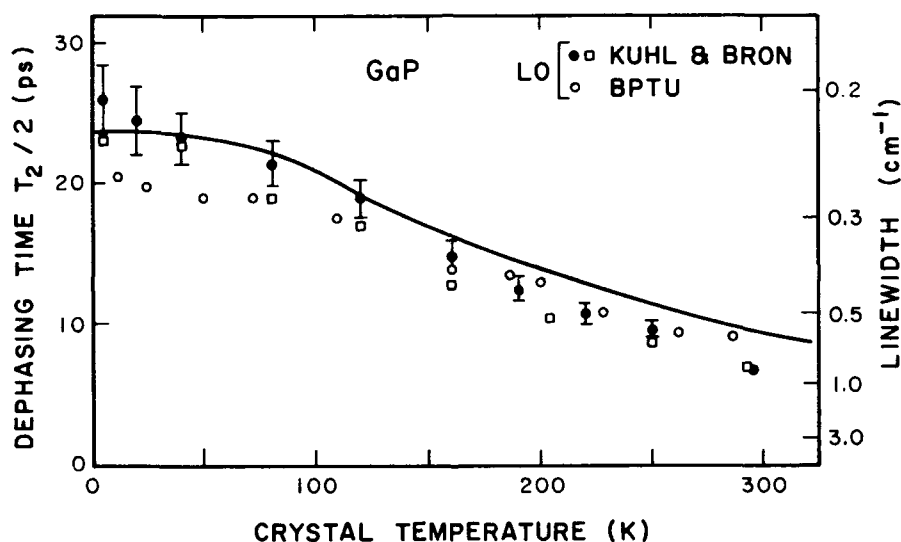


Figure 2. Temperature dependence of the phonon dephasing time as measured by time resolved CARS (solid circles), and by incoherent Raman measurements of linewidths (open squares, open circles (Ref. 8)).

Electron-Phonon Dynamics

As already noted above, coherent phonon dephasing may be caused by phonon interaction with electronic carriers. We have argued elsewhere⁷ that the LO phonons under investigation by our methods cannot interact with single particle states near the band edge. Thus the dominant carrier-phonon interaction observed in the experiments must proceed via the collective states of any plasma which is present.

We report here on a recent comparison between a phonon interaction with a one- and a two-component plasma. At the time of the writing of this paper, a part of these results are rather new and not yet fully analyzed. All the same, the preliminary analysis suggests a marked difference in the characterization of the resulting carrier-phonon interaction.

In a recent papers^{1,9} we discuss briefly the creation of a two-component (electron-hole; e-h) plasma in addition to LO phonons created through coherent Raman excitation. The experiment of Ref. 6 is different in a number of ways from the TRCARS measurements described above. In this case the two laser beams with ω_L and ω_S were generated in dye

lasers pumped by a pulsed N_2 -laser. Moreover, detection of the LO phonons and the LA phonons produced through LO phonon decay, is accomplished through vibronic sideband phonon spectroscopy.^{10,11} Coherent phonon generation proceeds through nonlinear interaction in GaP of pulse trains emitted from two dye lasers driven simultaneously by 5 ns duration pulses from a N_2 -laser. One dye laser is operated at a frequency $\omega_l = 18,275 \text{ cm}^{-1}$, which together with another laser at $\omega_s = 18,322 \text{ cm}^{-1}$, makes up the difference frequency $\omega_{LO} = \omega_l - \omega_s = 403 \text{ cm}^{-1}$ required to excite coherent LO phonons. The maximum energy per laser pulse is $\sim 60 \text{ } \mu\text{J}$ resulting in an initial LO phonon concentration $n_{LO} \approx 5 \times 10^{16} \text{ cm}^{-3}$, located within the overlap volume of the two laser beams.

The laser operating at ω_l also serves to excite the luminescence from the bound exciton in GaP (zero phonon line at $18,688 \text{ cm}^{-1}$) with which the vibronic sidebands are associated. In Fig. 3 we present the observed dependence of the anti-Stokes vibronic sideband intensity, as measured at the LO and the LA peak frequencies, as a function of the power in the s-laser when the power of the l-laser is fixed at 135 MW/cm^2 .

It can be shown⁹ that the intensity of the anti-Stokes vibronic sideband should be proportional to the product of the power of the two lasers (l and s lasers) which drive the coherent phonon generation. The results shown in Fig. 9 obviously disagree with this prediction. Moreover, it was observed that vibronic sideband bandwidth was essentially independent of the laser interaction.

We have shown in reference (9) that these observations can be accounted for by the presence of an e-h plasma generated by the photoexcitation of electrons from the valence band to the conduction band of GaP followed by decay of these hot carriers to the band minimum at the X-point. The excitation occurs most likely through two-step, two-photon absorption; i.e., $\omega_l + \omega_s$ and/or $\omega_l + \omega_s$. The plasma itself contributes to the third order electronic susceptibility, $\chi^{(3)}$, and, in effect, screens the coherent phonon generation process, but does nothing to the phonon lifetime. The solid and dotted lines of Fig. 3 represent a theoretical fit to the experimental results. (The dashed line should be ignored in the present context.)

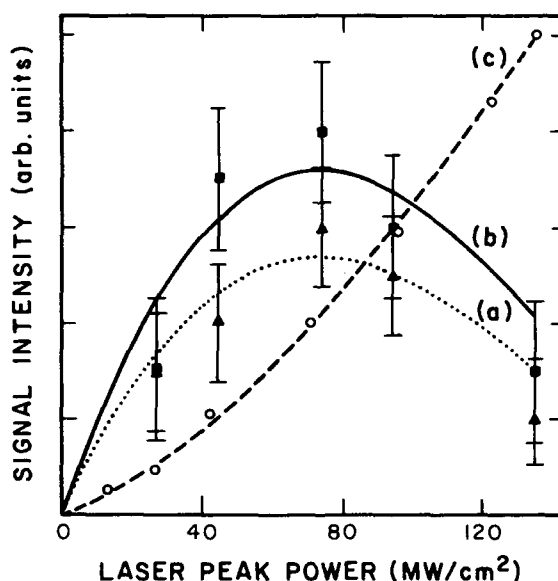


Figure 3. Dependence of the vibronic sideband peak intensity for LO (curve a) and LA (curve b) phonons as a function of the s-laser peak power. The l-laser intensity fixed at 135 MW/cm^2 .

Most recently we have also measured the dephasing time and the linewidth of coherent LO phonons in n-type GaP in the presence of a one-component plasma (at the X-point minimum) produced by thermal excitation of donor electrons into the conduction band. Forward scattering incoherent Raman spectroscopy was used in the linewidth measurement. Corresponding dephasing times were converted into linewidth measurement and also displayed in Fig. 4. The results of three different samples are shown. The data in an undoped sample (curve a) repeats the results of Fig. 2. The other two samples contain $3.2 \times 10^{17} \text{ cm}^{-3}$ (curve b) and $1.1 \times 10^{18} \text{ cm}^{-3}$ (curve c) impurity concentrations. It is observed at temperatures below $\sim 80 \text{ K}$ that the linewidth is essentially temperature independent. This region is tentatively assigned to the effects of impurity scattering. At $\sim 100 \text{ K}$ thermal

excitation of the carrier commences and reaches a maximum near 150K. Thereafter the donor states approach depletion ($\sim 250\text{K}$). The dashed lines in Fig. 4 have been arbitrarily drawn to emphasize these effects. Note that the linewidth varies strongly with the carrier concentration. But it is observed that the integrated intensity of the signal is not affected by the carrier concentration.

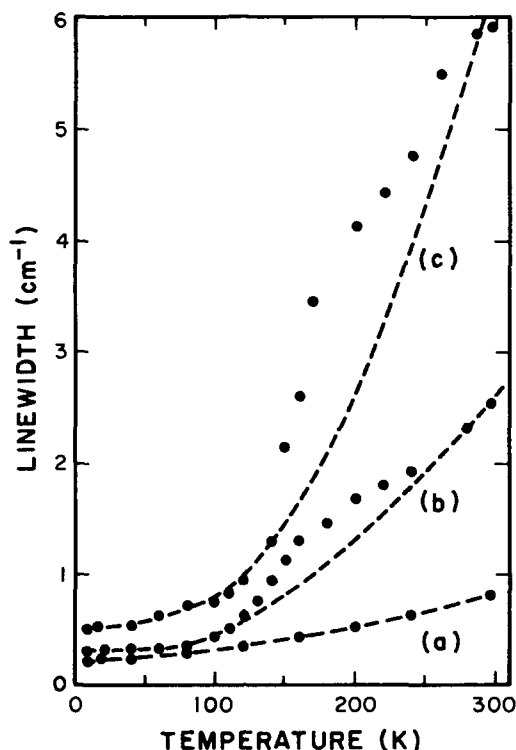


Figure 4. Dependence of the Raman linewidth on temperature for samples of varying concentration of donor states.

Thus we have observed a significant difference between the effects of one- and two-component plasma on the dynamics of coherent optical phonons in GaP. We are currently examining various factors which might contribute to this difference and hope to report on the resolution of these differences in the near future.

The author wishes to thank J. Kuhl and S. Mehta for their collaboration in the measurements on the one-component plasma. The author is also grateful for support through NSF DMR8603888.

References

1. E. Garmire, F. Pandereese and C. H. Townes, *Phys. Rev. Lett.* **11**, 160 (1963).
2. T. A. Giordmaine and W. Kaiser, *Phys. Rev.* **144**, 676 (1966).
3. See, for example, W. E. Bron, *Nonequilibrium Dynamics in the Time Domain in "Nonequilibrium Phonon Dynamics,"* Vol. 124, edited by W. E. Bron (Plenum Press, New York) 1985.
4. L. L. Schiff, "Quantum Mechanics," third edition (McGraw-Hill, New York, 1968). See also, W. A. Harrison, "Solid State Physics" (McGraw-Hill, 1970) pp. 408 ff.
5. B. K. Rhee, W. E. Bron and J. Kuhl, *Phys. Rev.* **B30**, 7358 (1984).
6. W. E. Bron, J. Kuhl and B. K. Rhee, *Phys. Rev.* **B34**, 6961 (1986).
7. W. E. Bron, *Nonequilibrium Electron-Phonon Dynamics in "Phonon Scattering in Condensed Matter V,"* ed. by A. C. Anderson and J. P. Wolfe (Springer, Berlin, Heidelberg and New York, 1986) pp. 328 ff.
8. B. Kh. Bairamov, D. A. Parshin, V. V. Toporov and Sh. B. Ubaidullav, *Pis'ma Zh. Tekh. Fig. 5*, 1116 (1979) [*Sov. Techn. Phys. Lett.* **5**, 466 (1979)].
9. B. K. Rhee and W. E. Bron, *Phys. Rev.* **B34**, 7107 (1986).
10. W. E. Bron and W. Grill, *Phys. Rev.* **B16**, 5303 (1977).
11. W. E. Bron and W. Grill, *Phys. Rev.* **B16**, 5317 (1977).

SUBPICOSECOND TIME-RESOLVED RAMAN STUDIES OF ELECTRON-PHONON AND PHONON-PHONON INTERACTIONS IN $\text{GaAs-Al}_x\text{Ga}_{1-x}\text{As}$ MULTIPLE QUANTUM WELL STRUCTURES

K.T. Tsen

Physics Department, Arizona State University, Tempe, AZ 85287

H. Morkoc

Coordinated Science Laboratory, University of Illinois, Urbana, IL 61801

Abstract:

The population relaxation time of non-equilibrium LO phonons with wavevectors perpendicular to the layers of $\text{GaAs-Al}_x\text{Ga}_{1-x}\text{As}$ multiple quantum well structures has been measured by time-resolved Raman scattering on a subpicosecond time scale. The experimental results have revealed the generation as well as decay of these excitations, and $\tau_{\text{LO}} \approx 6\text{ps}$ is deduced for their population relaxation time at $T \approx 80\text{K}$. This observed lifetime when compared with that in bulk GaAs, implies that the zone-folding effect plays little role on the determination of their lifetime. From the estimated rise time of the anti-Stokes signal, the average electron-LO phonon scattering time for electrons occupying the unbound states is determined to be $\tau_{\text{el-LO}} \approx 0.2\text{ps}$. These measured τ_{LO} and $\tau_{\text{el-LO}}$ have been found to be independent of either the width or the depth of the GaAs quantum wells.

Recently, the dynamics of photoexcited carriers in semiconductors and semiconductor multiple quantum well structures (MQWS) has attracted tremendous attention, and much valuable information about electron-phonon, electron-electron and phonon-phonon interactions has been obtained.¹⁻³ This information is both of fundamental interest and of great usefulness to modern ultrafast device applications such as optoelectronic devices. The development of picosecond/subpicosecond laser systems has made time-resolved Raman spectroscopy a powerful tool for probing the time evolution of nonequilibrium excitations in these materials, in particular, when the pump/probe configuration is employed. For example, time-resolved Raman scattering has been used to interrogate the generation and decay of non-equilibrium LO phonons in GaAs;⁴⁻⁶ the average electron-LO phonon scattering time⁵ and the population relaxation time of LO phonons⁴ in GaAs have thus been directly measured. In this paper, we have used time-resolved Raman scattering as a probe for the population relaxation time of non-equilibrium LO phonons having wavevectors perpendicular to the layers of $\text{GaAs-Al}_x\text{Ga}_{1-x}\text{As}$ MQWS. The experimental results have revealed the generation as well as decay of these excitations, and $\tau_{\text{LO}} \approx 6\text{ps}$ is deduced for their relaxation at $T \approx 80\text{K}$. From the estimated rise time of the anti-Stokes signal, the average electron-LO phonon scattering time for electrons occupying the unbound states has been determined to be $\tau_{\text{el-LO}} \approx 0.2\text{ps}$. These two time constants have been found to be independent of both the thickness of the GaAs quantum wells and the aluminum concentration of the $\text{Al}_x\text{Ga}_{1-x}\text{As}$ barriers.

The ultrafast pulses used in the experiment were generated either from a DCM double-jet dye laser (for measuring the population relaxation time of LO phonons) or from a DCM double-jet dye laser (for measuring the average electron-LO phonon scattering time), which were synchronously pumped by the second harmonic of a cw mode-locked YAG laser. The pulses had an autocorrelation full width at half maximum (FWHM) of 800fs, 4.8ps for double-jet and single-jet dye lasers, respectively. The average power was about 60mw and the repetition rate was about 76MHz. In our experiment, two successive ultrashort pulses with the same frequency and intensity but different polarizations were used to pump and probe the $\text{GaAs-Al}_x\text{Ga}_{1-x}\text{As}$ MQWS. The first pulse (pump pulse) sets up the non-equilibrium excitations (i.e., LO phonons) and the second pulse (probe pulse) detects these excitations through spontaneous anti-Stokes Raman scattering. These two beams, after being suitably polarized, were made to overlap on the surface of the samples. An appropriate analyser was placed in front of the entrance slit of the double monochromator so that the scattered signal from the pump pulse was effectively eliminated while the scattering from the probe pulse was allowed to be detected. The anti-Stokes Raman signal was collected in a backscattering geometry and by a computer-controlled Raman system. In order to take advantage of the resonance enhancement, the dye lasers were chosen to operate at $\hbar\omega \approx 1.92\text{eV}$ very close to the $E_0 + \Delta_0$ gap of GaAs.

The undoped GaAs-Al_xGa_{1-x}As MQWS investigated in this work were grown by molecular-beam epitaxy on a (001)-oriented undoped GaAs substrate. They consist of ~30 periods of 100Å-thick Al_xGa_{1-x}As (x varies from 0.1 to 0.3) and different thickness of GaAs layers (which ranges from 50Å to 300Å). The samples were mounted on the cold finger tip of a liquid nitrogen dewar. The effective temperature of the laser-irradiated area was estimated to be about 80K. The average photoexcited carrier density was about 10¹⁷cm⁻³ and the occupation number of the excited non-equilibrium LO phonons was about 0.08.

The wavevectors of the non-equilibrium LO phonons probed in the backscattering configuration are perpendicular to the layers. We believe that these LO phonons are generated as follows: The photons from the dye lasers optically excite the electron-hole pairs with an excess energy; in polar semiconductors such as GaAs, the carriers lose their excess energy primarily by emitting LO phonons.⁷ However, once the electrons are trapped inside the GaAs quantum wells, they are restricted to move within these two-dimensional layers. We can classify the thermalization of the electrons inside the wells into (1) intersubband transitions and (2) intrasubband transitions. For intersubband transitions of electrons, it is not difficult to realize that the LO phonons emitted cannot contribute to our light scattering measurements for the particular sample parameters used. For intrasubband transitions of electrons, conservation of momentum requires that the LO phonons emitted during their thermalization to the bottom of the subbands propagate almost along the layers. These LO phonons which have wavevectors almost parallel to the layers cannot be involved in the backscattering geometry employed in our experiment. Therefore, as indicated in Fig. 1 (for samples with x = 0.15) only about 0.25eV (or about seven times the LO phonon energy) can be used to generate LO phonons which are active under our current experimental measurements.

In Fig. 2, the anti-Stokes signal (monitored at 295cm⁻¹) is plotted as a function of the time delay Δt between the pump and the probe pulses for a GaAs-Al_xGa_{1-x}As MQWS with x = 0.15 and well-width = 200Å. Here, the time delay is taken to be the time interval between the peak intensity of the pump and that of the probe pulses. The scattering intensity increases very sharply from negative Δt and reaches a maximum at $\Delta t = 1.5$ ps, then decreases slowly to the background level at large Δt . This variation of the signal with time delay provides direct evidence of the generation and relaxation of the non-equilibrium LO phonons. The rise of the signal represents the growth of the LO phonon population as a result of the emission of the LO phonons by the photoexcited hot electrons, and the subsequent decrease corresponds to the relaxation of these LO phonons.

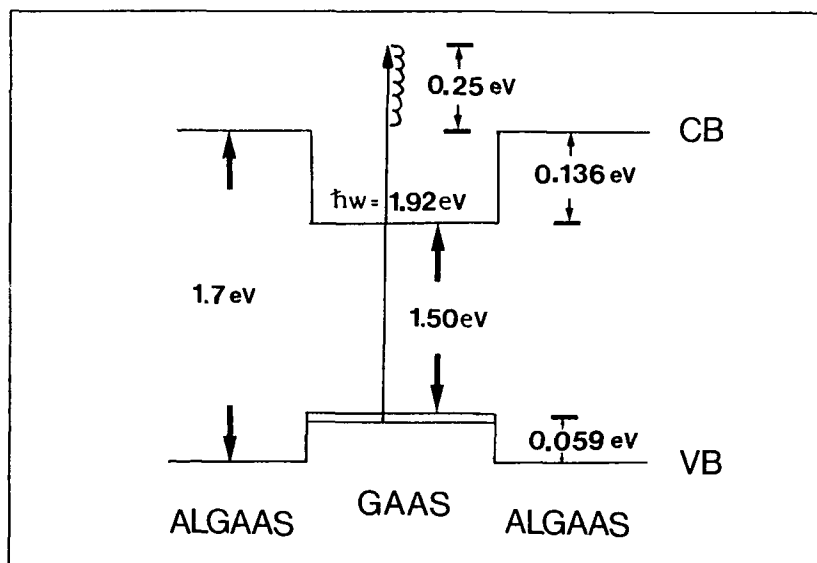


Fig. 1: Conduction-band (CB) and valence-band (VB) profiles of the GaAs-Al_xGa_{1-x}As MQWS demonstrated in this experiment. The electrons photoexcited to the continuum states will lose about 0.25eV of their excess energy before they are trapped inside the wells. Here, the band off-sets have been assumed to be 70-30% for conduction and valence bands, respectively; and effective masses have been taken to be 0.067m_e and 0.45m_e for conduction band electrons and heavy holes, respectively.

Because the pulse width of the single-jet dye laser used in this measurement is about 3ps, we do not think that the average electron-LO phonon scattering time can be estimated from the observed rise time of the anti-Stokes signal. It's determination will be postponed until a double-jet dye laser is employed.

The decrease of the anti-Stokes signal which has been stated to indicate the relaxation of the non-equilibrium LO phonons is supported by Fig. 3 in which the logarithm of the signal is plotted against the time delay Δt . The data points are very well represented by an exponential of the form $\exp(-\Delta t/\tau)$, with $\tau \approx 6$ ps. The fact that this value is very close to the population relaxation time of the LO phonons observed in bulk GaAs, suggests that the zone-folding has little effect on the population relaxation time of the LO phonons having wavevectors perpendicular to the layers of GaAs-Al_xGa_{1-x}As MQWS.

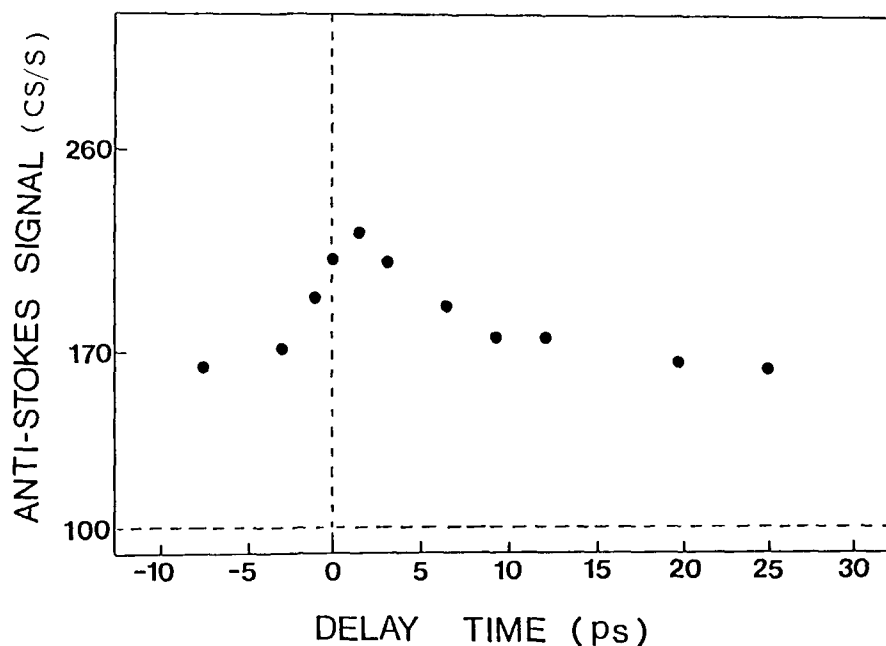


Fig. 2: Measured anti-Stokes Raman signal vs the time delay Δt for the LO phonons of the GaAs-Al_xGa_{1-x}As MQWS at T=80K. The background counts are indicated by a dashed horizontal line. Filled circles represent data points.

Fig. 4 shows the anti-Stokes Raman signal as a function of the time delay Δt between the pump and the probe pulses for the same sample as in Fig.2, but a double-jet dye laser which has pulse width of about 0.5ps is used in making the measurement. We observe that it takes about 1.5ps for the population of non-equilibrium LO phonons that have wavevectors perpendicular to the layers to reach its maximum value. Because as discussed before the number of Raman-active LO phonons emitted by the carriers is about seven, the average electron-LO phonon scattering time for electrons occupying the continuum states is deduced to be 200 ± 50 fs. The fact that this measured value of the average electron-LO phonon scattering time is about the same as that (~ 165 fs) found in bulk GaAs demonstrates that the presence of the wells has almost no influence on the relaxation of the carriers occupying the continuum states.

We have also carried out similar experiments on samples that have aluminum concentration x ranging from 0.1 to 0.3 and well-thickness from 50Å to 300Å. The experimental results have shown that both the average electron-LO phonon scattering time for electrons occupying the unbound states and the population relaxation time for LO phonons having wavevectors perpendicular to the layers of GaAs-Al_xGa_{1-x}As MQWS are rather insensitive to these parameters.

In conclusion, the population relaxation time of non-equilibrium LO phonons with wavevectors perpendicular to the layers of GaAs-Al_xGa_{1-x}As MQWS has been measured by time-resolved Raman scattering on a subpicosecond time scale. The experimental results have shown that the zone-folding effect plays little role on the determination of their lifetime. The average electron-LO phonon scattering time for electrons occupying the

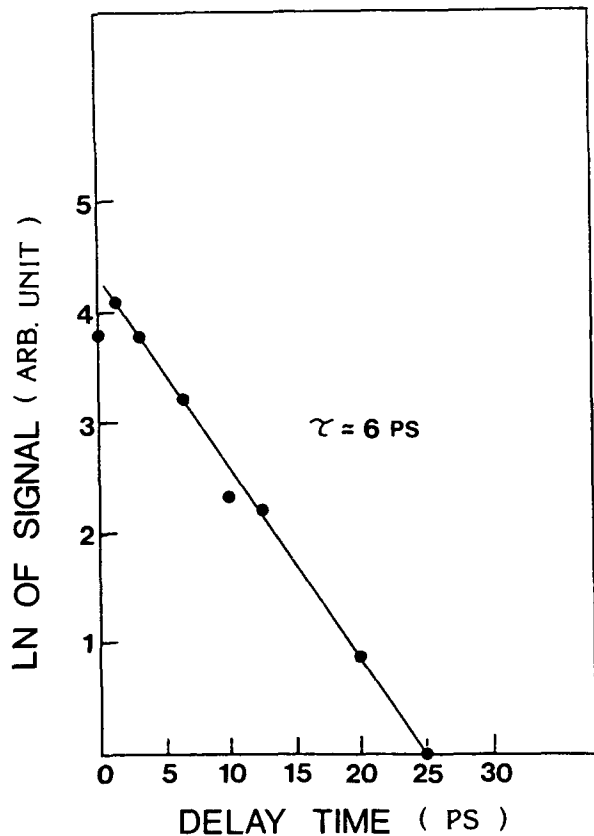


Fig. 3: The logarithm of the anti-Stokes signal is plotted as a function of the time delay Δt . The experimental data are well represented by a straight line. From the slope of this straight line, the population relaxation time of the LO phonons having wavevectors perpendicular to the layers is determined to be about 6ps.

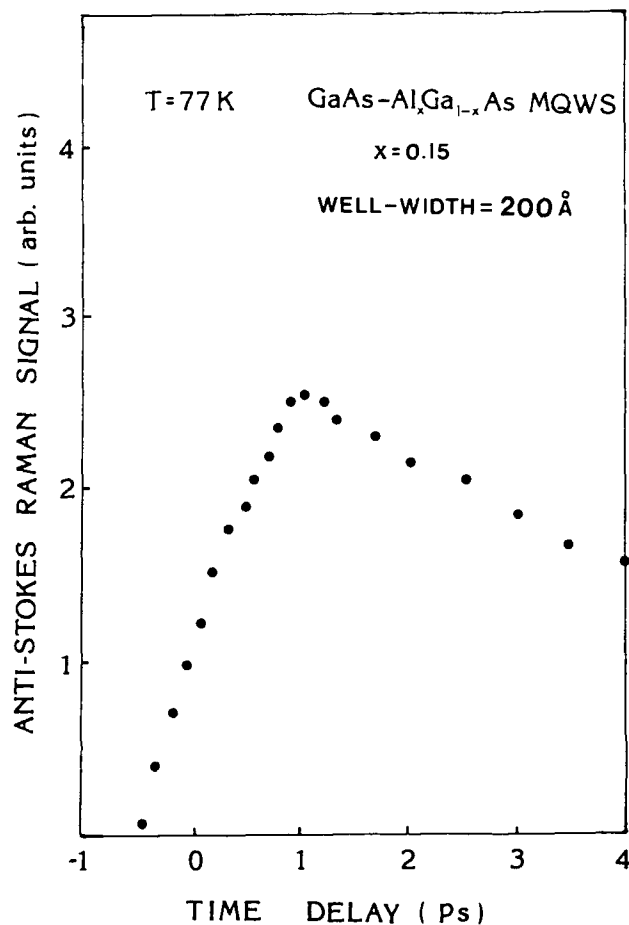


Fig. 4: Spontaneous anti-Stokes Raman signal of LO phonons having wavevectors perpendicular to the layers is plotted against the time delay Δt for a GaAs- $\text{Al}_x\text{Ga}_{1-x}\text{As}$ MQWS sample with $x=0.15$ and well-thickness=200Å. The rise of the signal is well-resolved and has been used to estimate the average electron-LO phonon scattering time for electrons occupying the unbound states in GaAs- $\text{Al}_x\text{Ga}_{1-x}\text{As}$ MQWS.

unbound states is estimated to be about 200fs. The measured values of the population relaxation time of LO phonons and the average electron-LO phonon scattering time has been found to be independent of either the width of the GaAs quantum wells or the aluminum concentration of the barriers.

References:

1. J. Shah, J. Phys. (Paris) Colloq. 42, C7-445 (1981).
2. K. Kash, J. Shah, D. Block, A. C. Gossard and W. Wiegmann, Physica 134B+C, 189 (1985), and references therein.
3. J. F. Ryan, Physica 134B+C, 403 (1985), and references therein.
4. D. von der Linde, J. Kuhl and H. Klingenburg, Phys. Rev. Lett. 44, 1505 (1980).
5. J. C. Tsang, J. A. Kash and S.S. Jha, Physica 134B+C, 184 (1985).
6. J. A. Kash, J. C. Tsang and J. M. Hvam, Phys. Rev. Lett. 54, 2151 (1985).
7. E. M. Conwell and M. O. Vassel, IEEE Trans. Electron Devices 13, 22 (1966).

DISPERSIONLESS-LIKE PROPAGATION of INDUCED SPECTRAL BROADENED PULSES in ZnSe (Non-Phase-Matched Second Harmonic Cross-Phase-Modulation)

P. P. Ho and R. R. Alfano

Institute for Ultrafast Spectroscopy and Lasers, and Photonic Application Laboratory
Department of Electrical Engineering, The City College of New York, New York, N.Y. 10031

Abstract

Ultrashort pulse propagation of non-phase-match generated second harmonic and its induced spectral broadened laser pulses have been directly measured in ZnSe. Newly generated wavelengths from 500 nm to 570 nm in ZnSe by the pump 1054nm pulse appear to be emitted at the same time as the 1054 nm pump pulse. The observed temporal property of these newly generated wavelengths can be explained by the destructive interference and parametric amplification of the non-phase-match generated cross-phase modulation waves in ZnSe. This modulation can lead a new way to optically encode ultrafast information.

I. Introduction

New laser frequency generation processes¹⁻⁶ by ultrashort pulses in condensed matter provide scientific knowledge of the wave interaction in matter as well as technological applications in lasers and optical communications. Self¹⁻³, induced^{7,8}, and Cross⁹⁻¹³-phase modulation processes are responsible for wide spectral band ultrashort laser pulses generation. Self-Phase Modulation (SPM) occurs when an intense laser pulse propagates through a medium and disturbs the refractive index where in turn changes the phase, amplitude, and frequency of the incident laser pulse. This causes a frequency sweep within the pulse envelope. Induced-phase-modulation (IPM) occurs when a weak pulse at a different frequency propagates through a disrupted medium whose index of refraction is changed by an intense laser pulse. The phase of the weak optical field can be modulated by the time variation of the index of refraction originating from the primary intense pulse. Most recently, cross-phase-modulation (XPM) was observed in optical glass fibers from the coupled interactions between stimulated Raman scattering (SRS) and SPM. The spectral width at the SRS wavelengths in liquids and glass fibers was broadened twice more than the spectral width of the incident laser. In this paper, we report a new class of XPM of a weak non-phase matched second harmonic pulse was produced from the propagation of an intense picosecond laser pulse through ZnSe crystals. The spectral broadened pulse spread from 500-nm to 570-nm was found to travel at near the same speed as the 1054-nm pump pulse in ZnSe.

In table 1, phase modulation processes responsible for the spectral broadening from various susceptibility coefficients are summarized. The bracket indicates the intensity of laser pulses at a given frequency. In the SPM process, the spectral broadening process involves only one principle wavelength. In the IPM process, strong and weak laser pulses at different wavelengths are generated outside the interaction material. Then pulses enter the sample to induce additional spectral broadening on the weak pulse. In the Raman-XPM process, a principle wavelength generates a Stokes Raman line and its width is broadened through the coupling of the laser wavelengths and internally generated Raman wavelengths. In the SHG-XPM process, the second harmonic generated inside the sample becoming spectral broadened from the primary pulse. This is similar to Raman-XPM with SHG pulse replacing Raman pulse. However, SHG-XPM has a unique dispersionless-like propagation property.

Table 1. Types of Spectral Broadening from Phase Modulation Processes

	INPUT	COUPLING	OUTPUT	PROCESS
<u>Self-Phase Modulation (SPM)</u>	$[\omega_1]$	\rightarrow χ^3	$[\omega_1 \pm \Delta\omega_1]$: SPM
<u>Induced Phase Modulation (IPM)</u>	$[\omega_1]$	\rightarrow χ^3	$[\omega_1 \pm \Delta\omega_1]$: SPM
	$[\omega_2]$ weak	\rightarrow χ^3	$[\omega_2 \pm \Delta\omega_2]$: SPM
			where $\Delta\omega_1 \gg \Delta\omega_2$	
	$[\omega_1] + [\omega_2]$	\rightarrow χ^3	$[\omega_1 \pm \Delta\omega_1]$ + $[\omega_2 \pm \Delta\omega_2]$: SPM : IPM
			where $\Delta\omega \gg \Delta\omega_2$	
<u>Cross-Phase Modulation (XPM)</u>				
<u>Raman XPM</u>	$[\omega_1]$	\rightarrow χ^3	$[\omega_1 \pm \Delta\omega_1]$: SPM
		\rightarrow χ^R	$[\omega_1 - \Omega \pm \Delta\omega_R]$: XPM
			where $\Delta\omega_R \sim 2\Delta\omega_1$	
<u>Second Harmonic XPM</u>	$[\omega_1]$	\rightarrow χ^3	$[\omega_1 \pm \Delta\omega_1]$: SPM
		\rightarrow χ^2	$[2\omega_1]$: SHG
		\rightarrow χ^2, χ^3	$[2\omega_1 \pm \Delta\omega_2]$: XPM
			where $\Delta\omega_2 \sim 1,000 \text{ cm}^{-1}$	

II. Theory of XPM

In the theoretical analysis of Raman-XPM, the spectral bandwidth of the Raman line is increased as the pulses travel in the medium. By assuming the phase matching and neglecting group velocity dispersion and higher-order Raman processes, a coupled wave equation can be written as

$$\partial a_1 / \partial \eta = i [\beta (|a_1|^2 + 2|a_2|^2) a_1 + \phi a_2], \quad (1a)$$

$$\partial a_2 / \partial \eta = i [\beta (|a_2|^2 + 2|a_1|^2) a_2 + \phi^* a_1] \quad (1b)$$

where ϕ is proportional to the phonon amplitude and $\partial \phi / \partial \xi = -\phi + i \delta a_2^* a_1$, a_1 and a_2 denote the pulse envelope function of the incident laser and the first Raman Stokes, respectively. A predicted ratio of the Stokes spectral width to the primary spectral width without dispersion is

$$X = \Delta \omega_{\text{Raman}} / \Delta \omega_{\text{Laser}} = 2 [1 + (\delta/2\beta)^2]^{0.5}, \quad (2)$$

$$\text{where } \beta = 3 n_2 \omega^3 / (\Gamma n_0 c^2), \\ \delta = \zeta^2 \omega^3 / (16 \pi \mu \Omega n_0 c^2 \Gamma^2),$$

and ω : incident laser frequency, Ω : phonon frequency, μ : effective oscillator mass density, n_0 : linear index of refraction, n_2 : nonlinear index of refraction, ζ : coupling strength between the phonon field to the electromagnetic field, and Γ : phonon decay rate. Using the values for parameters in Equ. 14, such as: $\omega = 3.54 \times 10^{15} \text{ sec}^{-1}$, $\Omega = 8.3 \times 10^{13} \text{ sec}^{-1}$, $\mu = 1$ (estimated), $\zeta = 10^6$ (estimated), $n_0 = 1.5$, $n_2 = 1.2 \times 10^{-13} \text{ esu}$, and $\Gamma = 5.7 \times 10^{12} \text{ sec}^{-1}$, we can obtain the ratio $X = 2$. The spectral broadening of the Raman line is larger than that of the laser line. The measured ratio of these spectral broadening was 2.9 ± 0.1 in agreement with XPM theory.

In the SHG-XPM, when an intense laser pulse propagates through non-centrosymmetric media where both χ^2 and χ^3 are operative, coupled spectral broadening around the non-phase matching second harmonic frequency occurs. An approximated first order partial differential equation¹² of the wave equation with slowly varying time and space envelope function is used. High order derivatives of the wave equation are neglected. If the SH signal is weak in comparison to the pump pulse, the quasi-linear partial differential wave equation can be written as¹²

$$\partial E_{10} / \partial z + 1/v_1 \partial E_{10} / \partial t = i \gamma |E_{10}|^2 E_{10} \quad (3)$$

$$\partial E_{20} / \partial z + 1/v_2 \partial E_{20} / \partial z = \frac{i \sigma E_{10}^2 \exp[-i(k_2 - 2k_1)]}{\text{SHG}} + \frac{2i\gamma |E_{10}|^2 E_{20}}{\text{XPM}} - \frac{\alpha E_{20}}{\text{Absorption}} \quad (4)$$

where E_{10} and E_{20} are the electric field envelope amplitude of the pump and the SH frequencies, respectively; v_1 and v_2 are group velocities for ω and 2ω , respectively; and k_1 and k_2 are wave vectors for ω and 2ω , respectively; α is the absorption coefficient at 2ω ; $\sigma = \mu_0 \omega_1 \chi^2 / 2$; χ : second order nonlinearity; $\gamma = 3\omega_1^2 \mu_0 \chi^3 / 8k_1$; χ^3 : third order nonlinearity.

By assuming the pump laser intensity to be constant, $\alpha \rightarrow 0$, and $\chi^3 \rightarrow 0$, the solution of E_{20} from eq.4 can be expressed as:

$$E_{20}(t-z/v_2) = i\omega\chi^2 \int_0^z E_{10}^2 \{ [t-z/v_2 - z'(1/v_1 - 1/v_2)] \} \exp[-i(k_2 - 2k_1)z'] dz' \quad (5)$$

If χ^3 and α are non-negligible, the solution of E_{20} from the coupled eqs. 3 and 4 can be written as¹²

$$E_{20} = i\sigma A_0 \exp[-\alpha z + i(2\gamma A_0^2) \int_0^z F^2(U + \eta z') dz'] \times \\ \int_0^z F^2(U + \eta z') \exp[i2\gamma A_0^2 F^2(U + \eta z') z' - i\xi z'] \exp[\alpha z' - 2i\gamma A_0^2 \int_0^{z'} F^2(U + \eta z'') dz''] dz' \quad (6)$$

where $U = (t-z/v_2)/\tau$; $\eta = (n_2 - n_1)/c\tau$; $\xi = (n_2^p - n_1^p) 2\omega/c$; n_1, n_1^p, n_2 , and n_2^p are the group and phase indices of refraction at ω and 2ω , respectively; A_0 is the initial magnitude of ω -pulse; F is the primary pulse shape envelope; τ is the pulse duration.

In both cases ($\chi^3 = 0$ and $\chi^3 = \text{nonzero real number}$), the observed temporal distribution of SHG and SHG-XPM¹² have shown a destructive interference pattern as long as the non-phase matched coefficient: $k_2 - 2k_1$ is large enough in comparison to the length of the crystal. Since E_{10}^2 is an even function and $\exp[-i(k_2 - 2k_1)z']$ is a sinusoidal function, when $k_2 - 2k_1$ is nonzero for a non-phase matched condition, the SHG emitted at the crystal exit surface at time t is an integrated solution of eqs. 5 and 6. For a given length $z = L$, if the phase factor $\exp[-i(k_2 - 2k_1)z']$ oscillates over more than one period, the integration washes out which results in E_{20} becoming zero due to the summation of many SH pulses generated at different z' with + and - phases. This is a destructive interference phenomenon. Only at the entrance and exit parts of the crystal, part of the SHG pulses will not be cancelled out from the free space boundaries. As long as the group index difference and the crystal length are large enough such that $(n_2 - n_1)L/c > \tau_1$, two separated peaks should be observed in time under the assumption of a non-depleted input and no absorption of the incident pump pulse. These two peak will be separated in time by $\Delta nL/c$. For example, in a ZnSe crystal, using $\lambda = 1054\text{-nm}$, $\tau_1 = 6/\sqrt{2} \ln 2 \text{ ps}$, and $n_2 - n_1 = 0.77$ the length of the crystal should be greater than 4-mm for a clear observation of two peaks. The newly generated SHG and XPM wavelengths appear only to be generated at the entrance and slit surfaces of the crystal. The absorption coefficient α only affect the two peak ratio.

III. Experimental of SHG-XPM

An 8-ps 2-mJ 1054-nm laser pulse was weakly focused into the ZnSe sample. The spot size at the sample was about 1.5-mm in diameter. The second harmonic produced in ZnSe samples was about 10-nJ. The incident laser energy was controlled by changing the neutral density filter. The output signal was sent through a 1/2 meter Jarrell Ash spectrograph to measure the spectral distribution of the signal light using polaroid films and optical multichannel analyzers. A reference pulse at 527 nm was produced in a KDP crystal. Using a beam splitter, 1054-nm and 527-nm pulses were separated into two different paths. The weak 527-nm reference pulse was used for calibration and traveled through a fixed distance in air to set the zero reference time for the streak camera. Only a 1054 nm pulse was used to pump the ZnSe samples. The temporal profile and the propagation time of pulses which exited from the sample and the reference pulse were measured by a 2-ps resolution streak camera system¹⁴. Polycrystalline ZnSe samples of 2, 5, 10, 22, and 50-mm thickness were purchased from Janos Inc. and a single crystal ZnSe of 16 mm thickness was grown at Philips¹¹.

A. Spectral Behavior The spectra were measured using photographic films and OMA for non-phase-matching SHG and induced spectral broadening generated in a 22-mm long ZnSe crystal by a 1054-nm laser pulse. The spectra from ZnSe and quartz samples are displayed in fig. 1. The salient features of ZnSe spectra indicate that the extent of the spectral broadening about the second harmonic line at 527-nm depends on the intensity of the incident 1054-nm laser pulse. When the incident laser pulse energy was 2mJ, there was significant spectral broadening of about $1,100 \text{ cm}^{-1}$ on the Stokes side and 770 cm^{-1} on the anti-Stokes side. There was no significant difference in the spectral broadening distribution measured in the single and polycrystalline material.

The spectral broadening generated by sending an intense 80- μJ 527-nm 8-ps laser pulse alone through these ZnSe crystals was also measured to compare with the $\sim \pm 1,000\text{-cm}^{-1}$ induced spectral broadening discussed in the last paragraph. The observed spectral broadening was only $\sim 200 \text{ cm}^{-1}$ when the pulse energy of 527-nm was over 0.2-mJ. This measurement suggests that the self-phase modulation process from the 10 nJ SHG pulse in ZnSe is insignificant to be the observed $\sim 1,000 \text{ cm}^{-1}$ of ISB. The second order nonlinearity : Pockels coefficient r_{ijk} of ZnSe is about $2 \times 10^{-12} \text{ m/V}$ and the third order nonlinearity : $n_2 \sim 10^{-11} \text{ esu}$. Replacing ZnSe with a quartz crystal, only a narrow line of 527 nm was observed in fig. 1d. This observation can be explained by the lower n_2 value of quartz which is about 50 times smaller than n_2 of ZnSe. It follows that $\Delta\nu(\text{quartz})$ is 50 times narrower than $\Delta\nu(\text{ZnSe})$.

B. Temporal Behavior The temporal profile and propagation time of a weak 527 nm calibration pulse, intense 1054 nm pump pulse, and induced spectral broadened pulses propagating through a 22-mm ZnSe polycrystalline sample is shown in fig. 2. When a weak 3-nJ 527-nm calibration pulse propagated through the 22-mm ZnSe, a time delay of about 249-ps was observed (Fig. 2a). A pulse delay of $\sim 189\text{-ps}$ at 1054-nm was observed in fig. 2b when an intense 1054-nm pulse passed through the crystal. In fig. 2c and 2d, the propagation time of 530-nm and 550-nm are displayed, respectively. The salient features of the trace in fig. 2d indicated that the XPM pulses are emitted at nearly the same time as the 1054-nm incident pulse (fig. 2b).

The temporal behavior of the pulse shape and duration of a selected 10-nm band portion centered at 530-nm produced from the 1054-nm generated spectral broadening shown in figs. 2c and 2d is quite different from that of the 1054-nm pump pulse (fig. 2b) and a weak 527-nm calibration pulse (fig. 2a). The $\sim 60 \text{ ps}$ long emission tail (from 249 ps to 189 ps) is the result of SHG of the 1054-nm pulse at different locations inside the ZnSe. The additional sharp spike located at 189 ps is coincident with the time that it takes the 1054-nm pulse to propagate through the crystal. Fig. 2d displays the temporal profile of an XPM pulse centered at 550-nm with a 10-nm bandwidth.

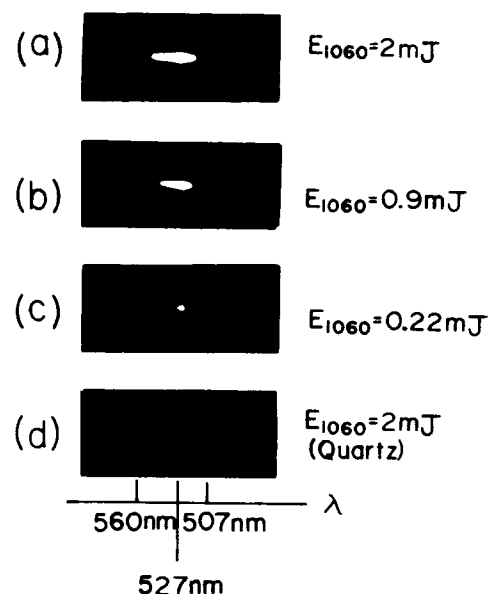


Fig. 1. SHG-XPM spectra of a 22-mm ZnSe excited by 1054-nm laser pulse of different intensity. In (d), ZnSe crystal was replaced by a 37-mm long quartz crystal.

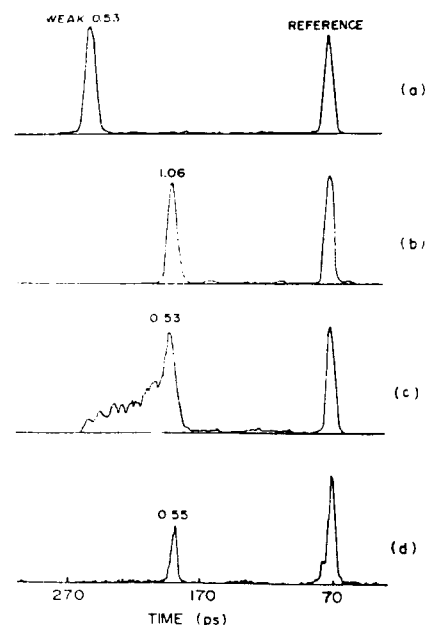


Fig. 2. Temporal profile and propagation delay time of (a) incident 527-nm (b) incident 1054-nm (c) generated 530-nm and (d) generated 550-nm XPM in a 22-mm ZnSe measured by a 2 ps resolution streak camera. The reference pulse time was obtained by removing the ZnSe.

The emission time for all the SHG, the spectral broadening about SHG, and the 1054-nm pump pulses in the crystal were near the same. The duration of the 550 nm pulse is ~ 5 ps which is about half the duration of the incident 1054-nm pulse. The spectral broadened 500-nm pulse showed a similar characteristics as that of the 550-nm pulse.

The difference in the propagation times of a weak 527 nm calibration pulse (fig. 2a) and a 1054 nm pump pulse (fig. 2b) through a ZnSe crystal can be accounted for by group velocity dispersion. The measured group refractive indices of ZnSe obtained from data displayed in figs. 2a and 2b can be fitted to be $n_{g,527} = 3.39$ and $n_{g,1054} = 2.57$, respectively. These values are in good agreement with the calculated values¹⁵ from the wavelength dependence of the group index of refraction: $n_{g,527} = 3.35$ and $n_{g,1054} = 2.58$. Therefore, dispersion can account for the difference for in propagation time for pulses at different wavelengths which pass through ZnSe. However, a sharp spike of the SHG and the ISB pulses generated in the crystal appears to have nearly the propagation time as the pump 1054 nm pulse (figs. 2c and 2d).

IV. Discussions

Experimentally, $E_{2,\omega}(t-z/v_2)$ generated in ZnSe crystals were directly measured by a streak camera. The time t is the only variable in eqs.3 and 4 after integration which is determined by the streak camera. The envelope function of the 1054-nm pump laser pulse has been measured to be a Gaussian function¹⁶ with $\tau_1 = 6/\sqrt{2\ln 2}$ ps. Sharp spikes of the generated 550-nm and 530-nm displayed in figs. 2d and 2c which appeared to be emitted together with the 1054-nm can be responsible by the imaginary part of χ^3 term in XPM. The imaginary part of χ^3 in ZnSe most likely arises from the two-photon absorption. This lead to an amplitude gain equation for the SHG-XPM signal at 550-nm as $E(XPM) \sim \exp(\chi^3 |E_0|^2)$. That may be why there is only a sharp spike appeared to be emitted at the end of the crystal or travelled at the same speed as the pump wavelength.

Several mechanisms which may account for the observed dispersionless-like propagation of the SHG and the spectral broadened pulses relative to the 1054-nm pump pulse. The first possible model is the enhanced surface phenomenon such as the SHG of the SPM process of 1054 nm. However, three observations contradicted the surface model. First, the output intensity of the ISB pulse was found to vary linearly with the sample thickness from 2-mm to 22-mm. Second, there was no difference in the output intensity or time dynamics of ISB when the ZnSe as placed in ethylene glycol or CS_2 to reduce the index mismatch between the crystal and air. Third, using different ZnSe crystals with varied surface roughness, the output spectral broadened signal intensity remained to be the same. These three observation may rule out the possibility of surface effect. The second possibility is the compensation of the group velocity dispersion in ZnSe by the negative nonlinear index of refraction. In the the negative n_2 model, the delay time of the ISB should be sensitive to the 1054 nm power density (incident energy). However, no apparent change was observed in our measurements. The third possible model is the two-photon-like excitonic polariton¹⁷. This model is also ruled out from a temperature dependent measurement of the output signal strength. The output spectral broadened pulse intensity remained the same from 4°K to 300°K.

V. Summary

Spectral broadened second harmonic XPM pulses seem to be emitted at the same time as the primary pulse and are independent to the crystal structure, surface roughness, and temperature. The observed temporal behavior of XPM pulses propagation can be a signature of all ultrafast nonlinear non-phase matched frequency generation processes. These temporal and spectral behaviors of non-phase-matched XPM may have an impact in optical communications and information coding.

Acknowledgement

This research is supported in part by NSF-OIR 84-13144, PSC/CUNY, and Hamamatus Photonics K.K..

References

1. R.R. Alfano and S.L. Shapiro, Phys. Rev. Lett., **24**, 584, 592 (1970)
2. R.H. Stolen and C. Lin, Phys. Rev. A **17**, 1448 (1978)
3. R.L. Fork, C.V. Shank, C. Hirlimann and R. Yen, Opt. Lett., **8**, 1 (1983)
4. D. Kleinman, Phys. Rev., **128** 1761 (1962)
5. Y. R. Shen, in M. Cardona, ed. "Light Scattering in Solids", Springer-Verlag, Berlin, (1975), p275.
6. R. Byer and R. Herbst, in Y. Shen ed. "Nonlinear infrared generation", Springer Verlag, Berlin (1977), p81.
7. R.R. Alfano, Q. Li, T. Jimbo, J. Manassah and P.P. Ho, Opt. Lett., **11**, 626 (1986)
8. J. Manassah, M. Mustafa, R. Alfano and P.P. Ho, Phys. Lett.A, **113**, 242 (1985)
9. R. Alfano, P. Baldeck, F. Raccach, and P.P. Ho, Appl. Opt., **6** 3491 (1987)
10. M. Islam, L. Mollenauer, R. Stolen, J. Simpson, and H. Shang, Opt. Lett., **12** 625 (1987)
11. R.R. Alfano, Q.Z. Wang, T. Jimbo, P.P. Ho, R. Bhargava and B. Fitzpatrick, Phys. Rev. A **35**, 459 (1987)
12. J. Manassah and O. Cockings, Opt. Lett., **10**, 1005 (1987)
13. J. Gersten, R. Alfano, and M. Belic, Phys. Rev. A **35**, 1222 (1980)
14. P.P. Ho, A. Katz, R.R. Alfano and N. Schiller, Opt. Comm., **54**, 57 (1985)
15. H.H. Li, J. Phys. Chem. Ref. Data, **13**, 103 (1984)
16. Q.Li, T. Jimbo, P. Ho, and R. Alfano, Appl. Opt. **25** 1869 (1986)
17. R. Alfano and P. Ho, Proc. of Laser'86 conference, STS press, McLean,VA (1987) pp84-93.

NONLINEAR BEAM PROPAGATION IN SEMICONDUCTORS

E.W. Van Stryland, Y.Y. Wu, D.J. Hagan, M.J. Soileau and Kamjou Mansour

Center for Research in Electro-Optics and Lasers
University of Central Florida
Orlando, Florida 32816

We present a detailed characterization of the output of passive semiconductor based optical limiters. These devices utilize two-photon absorption along with photogenerated carrier defocusing within the material to limit the output fluence and irradiance. In addition to protecting downstream optical components, the focusing geometry combined with these nonlinearities make the devices self-protecting. Such devices have a broad working wavelength range since both the initial two-photon absorption and the subsequent carrier refraction are slowly varying functions of wavelength. For example, ZnSe should have a useful range of from 0.5 to 0.85 μ m. In this material, we have observed the onset of limiting at input powers as low as 80 Watts using 10ns, 0.53 μ m input pulses. At the same wavelength using 30ps pulses into a monolithic ZnSe limiter, limiting begins at \approx 300 Watts or 10nJ. We also monitored the output spatial energy distribution along with the temporal response at each position using a 2 picosecond resolution streak camera. We find that the output fluence along with the output irradiance is effectively limited below detector damage thresholds over a four orders of magnitude input range. Additionally, since both two-photon absorption and the associated self-defocusing increase with decreasing band-gap energy, similar devices using narrow gap semiconductors should have considerably lower limiting thresholds.

I. Introduction

Passive optical limiting results from irradiance-dependent nonlinear optical processes in materials.^{1,2} The ideal optical limiter has the characteristics shown in Fig. 1. It has a high linear transmission for low input (eg. energy E or power P), a variable limiting input E or P, and a large dynamic range defined as the ratio of the E or P at which the device damages (irreversibly) to the limiting input. Since a primary application of the optical limiter is for sensor protection, and damage to detectors is almost always determined by fluence or irradiance, these are the quantities of interest for the output of the limiter. Getting the response of Fig.1 turns out to be possible using a wide variety of materials; however, it is very difficult to get the limiting threshold as low as is often required and at the same time have a large dynamic range. Because high transmission for low inputs is desired, we must have low linear absorption. These criteria lead to the use of two-photon absorption (2PA) and nonlinear refraction. In this paper we present the detailed operational characteristics and a theoretical description of optical limiting devices based on 2PA and the subsequent photogenerated free-carrier defocusing in semiconductors. Such devices can be made to have low limiting thresholds, large dynamic ranges, and broad spectral responses. For example, a monolithic ZnSe device limits at inputs as low as 10nJ (300W), and has a dynamic range greater than 10^4 for 0.53 μ m, 30ps (FWHM) pulses. Also, the input/output characteristics of this device should not change significantly for input wavelengths from 0.5 to 0.85 μ m. While the devices demonstrated operate in the visible, we give theoretical arguments why considerably lower limiting thresholds should be obtainable in the infrared using narrow band-gap semiconductors.

II. Background

Early observations of irradiance-dependent phenomena related to optical limiting were in liquids.^{3,4} In 1964, Leite *et. al.* used "self-action" (nonlinear refraction) as a means to measure very low absorption in liquids.⁵ In 1966, Reickhoff reported irradiance dependent self-defocusing in liquids.⁶ One year later Leite *et. al.* demonstrated an optical limiter which used thermal blooming in nitrobenzene and, along with a spatial filter, regulated the output power of a cw argon laser to 30mW.⁷

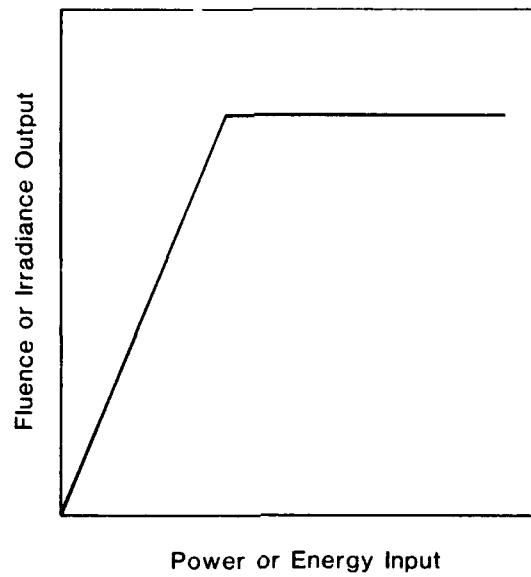
In 1980, CS₂ was tested as a limiting medium.⁸ The experiments, using a focused geometry similar to that of Leite *et al.* but with nanosecond pulses, showed that the mechanisms which limit the transmission of this device are self-focusing and absorption associated with the resulting laser-induced breakdown.^{8,9} An apparent advantage of liquid based limiters is that they self-heal, allowing high dynamic ranges limited only by damage to cell windows. The response time has been shown to be 2ps in the visible.¹⁰ Even larger nonlinearities were found at 10 μ m using CO₂ pulses which demonstrates the potential of extremely broad-band operation.¹¹ Additionally, the limiting power can be varied by adjusting the concentration of CS₂ in solvents. However, the critical power P_C is often too high for many applications (eg. P_C \approx 8 kW at 0.5 μ m) and can only be raised by mixing with solvents, not lowered.

Large refractive nonlinearities (several orders of magnitude higher than that of CS₂) have been found in liquid crystals; however, this occurs at the expense of speed (response times usually nanoseconds or longer).¹²⁻¹⁴ When picosecond pulses were used in a comparative study of limiting in seven liquid crystals, Soileau *et al.* found that two-photon absorption was responsible for the limiting behavior.¹⁵

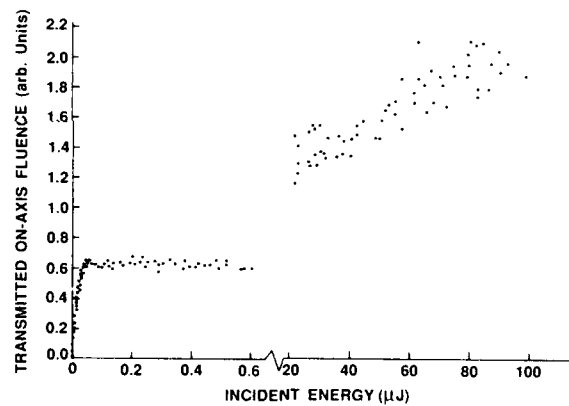
Atomic vapors have also been used to build optical limiters. Bjorkholm *et al.* built a device utilizing self-focusing in sodium vapor due to near-resonant excitation at a wavelength of 590nm.¹⁶ This device also exhibited optical bistability.

Some of the largest nonlinearities exhibited to date are in semiconductors.¹⁷ Unfortunately, from the standpoint of optical limiting, these extremely large nonlinearities are associated with near band-gap resonance and thus are in a region of relatively high linear absorption. In addition solids undergo irreversible optical damage. Even so, using other mechanisms, effective limiting has been demonstrated. In 1969, Geusic *et al.* reported limiting behavior in Si attributed to stepwise nonlinear absorption with 1.06 μ m radiation.¹⁸ Later, Boggess *et al.* showed fluence limiting in Si which was due to a combination of nonlinear absorption with a refractive contribution induced by the photoexcitation of free carriers.¹⁹ Power limiting experiments were conducted by Ralston and Chang in a series of semiconductors such as CdS, GaAs and CdSe.²⁰ This was the first report of the use of two-photon absorption (2PA) for optical limiting. Those studies utilized nanosecond pulses where absorption by the 2PA generated free carriers was significant. In addition, though not noted at that time, the refractive index change caused by the photogenerated carriers was strong and also useful in the limiting process. In particular, this defocusing limits the transmitted fluence. Another type of limiter, which uses the combination of 2PA and nonlinear refraction at 10 μ m was developed by Walker *et al.*²¹ This device relies on the etalon properties of the nonlinear sample, and the device also exhibits regions of bistability.²² While this device has the advantage of not requiring a spatial filter (ie. it is a true power limiter as opposed to a fluence limiter), the range of input energies over which limiting is obtained is small. Boggess *et al.* were the first to use the combined effects of 2PA and carrier defocusing to obtain optical fluence limiting.²³ The geometry used was to focus picosecond 1.06 μ m pulses onto the surface of a thin sample of GaAs, refocus the beam, and monitor the transmission of an aperture. Since the damage prone surfaces are subjected to the maximum fluence of the input pulses, the range over which these devices function without incurring damage is low. What we have found, is that by using *thick* samples, the large nonlinearities of the semiconductor can actually be used to prevent damage.²⁴ The trick is to simply focus the light tightly into the bulk of the material. Nonlinear absorption combined with nonlinear refraction keep the irradiance within the semiconductor below the damage threshold and the device is self protecting. One problem now is that the wave equation can no longer be separated into two propagation equations, one for the irradiance and one for the phase. This makes even numerical solutions very difficult. However, we find the analysis of thin limiters qualitatively describes the operation of thick limiters.

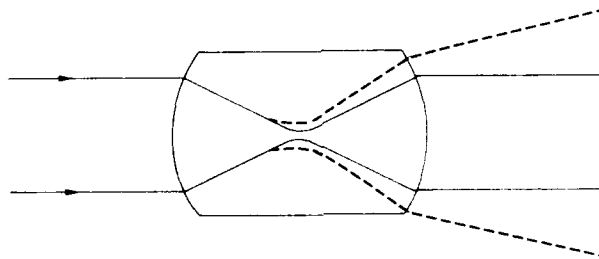
We have recently used this combination of nonlinearities to build optical limiters for the visible based on ZnSe and ZnS.²⁴ These work exceedingly well for picosecond inputs where carrier absorption is negligible while carrier defocusing is still strong.²⁵ Figure 2 shows the geometrical arrangement of a monolithic optical limiter. The device acts as a unity power inverting lens for low inputs. For high inputs the beam is depleted by 2PA and is defocused following the path shown schematically by the dashed line in Fig.2. Figure 3 shows the output fluence as detected through an aperture, as a function of the input energy of 30ps, 0.53 μ m pulses. The laser used in the picosecond experiments is a passively mode-locked Nd:Yag laser with a single pulse switched out. Residual linear absorption of



1. The fluence or irradiance output of an "ideal" optical limiter as a function of the input power or energy. P_L and E_L are the limiting power and energy inputs respectively.



2. A schematic of the monolithic optical limiter showing optical paths for low (solid line) and high (dashed line) inputs.



3. A plot of the output of a monolithic ZnSe limiter (interpreted as the on-axis fluence detected through an aperture) as a function of the input energy of 30ps FWHM, $0.53\mu m$ pulses.

$\approx 0.4\text{cm}^{-1}$ in the chemical vapor deposited ZnSe causes the linear transmission at low inputs to be $\approx 30\%$. The limiting begins at $\approx 10\text{nJ}$ input which corresponds to ≈ 300 Watts. Note the change of scale in Fig.3. If the original scale were continued, and the ordinate were three inches, the page would have to be extended for nearly 20ft. The slope shown is indeed extremely small. The device was tested up to a few hundred microjoules input, demonstrating a dynamic range of greater than 10^4 . However, the device was not tested to destruction and it should withstand pulses of a few millijoules input. In what follows we describe in greater detail the operation of this device, its limitations, and possible extension to other wavelengths using the results of a fundamental study of 2PA and self-refraction in several semiconductors

III. Mechanisms

As will be seen, the primary limiting mechanism is two-photon-induced free-carrier refraction. In earlier work we measured the 2PA coefficients β of ten different semiconductors. These experiments were performed on thin samples (1-5mm thickness) using collimated $\approx 1\text{mm}$ beam radius picosecond pulses. In this geometry self refraction is "external", the sample acts as a thin lens, and the transverse Laplacian can be neglected in the wave equation for propagation within the nonlinear material.²⁶ This allows separation of the wave equation into:

$$\frac{dI}{dz} = -\alpha I - \beta I^2 \quad (1)$$

and

$$\frac{d\Phi}{dz} = -\gamma N = \frac{2\pi}{\lambda} \Delta n, \quad (2)$$

where I is the irradiance, α the linear absorption coefficient, Φ the slowly varying phase of the field, γ the Drude contribution to the index change including band-blocking, Δn the change in refractive index, and N is the density of two-photon generated free carriers.² The equation governing the carrier generation, with $\hbar\omega$ the photon energy, is:

$$\frac{dN}{dt} = \frac{\beta I^2}{2\hbar\omega}. \quad (3)$$

In writing equations 1-3 we have made use of the fact that for picosecond pulses free-carrier absorption can be neglected, as we experimentally verified.²⁷ We also verified in 4-wave mixing experiments that recombination and diffusion of free-carriers can be ignored within the 30ps pulsewidth. Nonlinear refraction (Eq.2), observed in free-space propagation experiments, was entirely explained by carrier defocusing. This last observation allowed us to neglect bound electronic self-focusing. Carefully collecting all the transmitted energy on large area uniform response detectors in the very near field allowed us to use Eq.1 and measure the 2PA coefficients directly. Using measurements of β for ten semiconductors we verified that,

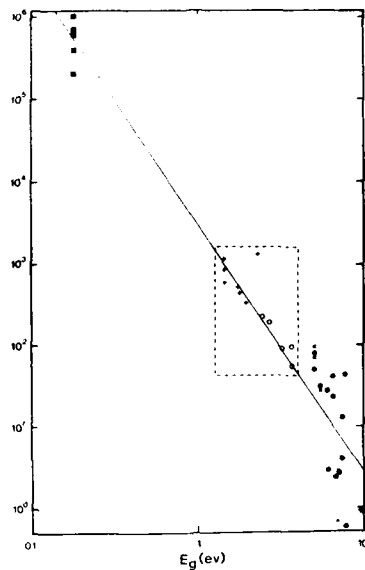
$$\beta \propto \sqrt{E_p} \frac{F_2\left(\frac{2\hbar\omega}{E_g}\right)}{n^2 E_g^3} \quad (4)$$

where n is the linear refractive index, and E_p is related to the transition matrix element and is nearly material independent.²⁷ The function F_2 , as calculated for two simple parabolic bands, is given by;

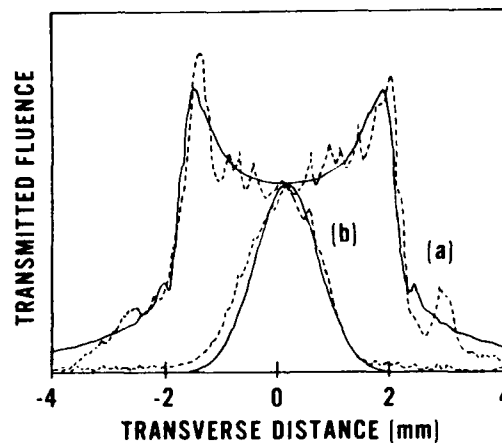
$$F_2(x) = (x-1)^{3/2} / x^5. \quad (5)$$

The constant of proportionality in Eq.4 found in these experiments is $(3.1 \pm 0.5) \cdot 10^3$ where E_g and E_p are in eV. Using these results we can predict 2PA coefficients for other materials at other wavelengths as shown in Fig.4 given only n , E_p , E_g and $\hbar\omega$. Figure 4 is a log-log plot of the data shown to emphasize the primary dependence of β on E_g . Our data is enclosed within the dashed box. The solid line has a slope of -3 and best fits the data within the box. It is extended to higher and lower values of E_g in order to predict β for other materials. Toward higher values of E_g we are no longer looking at semiconductors but insulators (e.g. ADP, KDP, SiO_2).²⁸ The fact that even here β is given, in most cases, to within better than a factor of four is quite remarkable. Toward the left, however, there is little available data except for InSb at $10\mu\text{m}$.²⁹ The line goes through the "center of mass" of these points even though this is nearly a four orders of magnitude extrapolation of β .

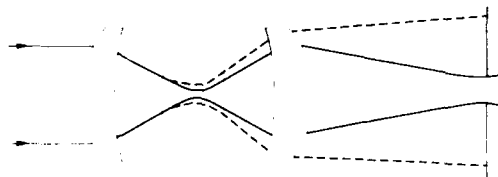
In addition to measuring 2PA, defocusing caused by the 2PA generated carriers was measured by monitoring the free-space propagation in the near field.³⁰ Figure 5, taken from Ref.30, shows the normalized near-field spatial energy distribution for low and high input irradiance picosecond $1.06\mu\text{m}$ pulses transmitted through a 2mm thick CdSe sample and propagated a distance of 0.5m. The solid line is a single parameter fit for the defocusing produced per carrier (γ in Eq.2) given the 2PA generation rate (Eq.3) as measured in Ref.27 and shown in Fig.4. This defocusing agrees with Drude theory including interband blocking (see Eq.7 in section VI).



4. A logarithmic plot of the scaled two-photon absorption coefficient β as a function of the band-gap energy E_g in eV. E_p is nearly material independent ($\approx 21\text{eV}$), F_2 is a function of the ratio $2\hbar\omega/E_g$, and n is the refractive index. The straight line is a fit to the data within the dashed box for a line of fixed slope -3. The data to the right of the box is taken from reference 28 using the third (x) and fourth (•) harmonic of $1.06\mu\text{m}$ picosecond pulses. The data to the left of the box is taken from reference 29 using $10\mu\text{m}$ nanosecond pulses which carefully accounted for free-carrier absorption.



5. Vidicon scan of 92ps FWHM $1.06\mu\text{m}$ pulses of spot radius $\omega_0=1.0\text{mm}$ transmitted through a 2mm thick sample of CdSe and viewed at a distance of 0.5m behind the sample. The dashed lines are for a) $1\text{GW}/\text{cm}^2$ and b) $30\text{MW}/\text{cm}^2$. The solid lines are theoretical fits for the defocusing per carrier. This figure reproduced from reference 30.



6. A schematic drawing of the thick limiter geometry. The solid line shows linear beam propagation for low inputs, and the dashed lines show the beam for high inputs.

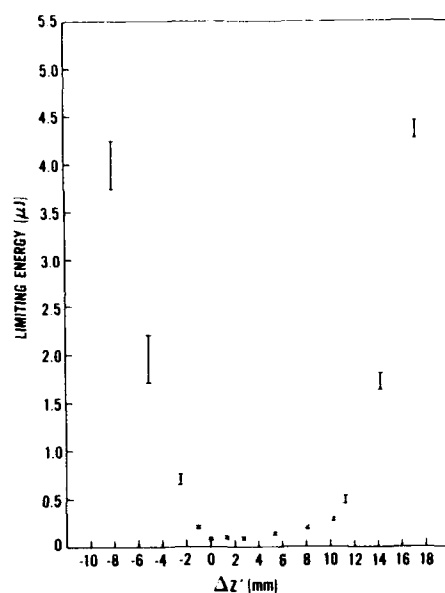
IV. Application to Limiting

Looking at Fig.5 we see the fluence limiting possibilities of a semiconductor based limiter. Not only will 2PA deplete the transmitted beam, but carrier defocusing spreads the beam in space, thus, reducing the energy density. Such limiting using thin samples has been demonstrated by detecting the energy transmitted through an aperture after free-space propagation.²³ Limiters used in this thin sample "external" self-refraction geometry have been extensively analyzed by Herman *et al.*^{31,32} The limitation of such devices is their low dynamic range. Since the light is focused onto the sample in order to get a low limiting threshold, the fluence is high on the damage prone surface, and irreversible damage occurs within one or two orders of magnitude of limiting.²³ A method to alleviate this problem is to use thick samples (thickness larger than the depth of focus), and focus into the bulk of the material reducing the irradiance on the damage prone surface. We find that this geometry, shown in Fig.6, gives something extra. Not only is the irradiance reduced on the surface, but for *high* inputs the 2PA and defocusing reduce the irradiance in the bulk preventing damage. This happens while maintaining a low limiting threshold. Unfortunately, Eq.1 and 2 are no longer valid and a quantitative description is difficult. What happens can be qualitatively described as follows.

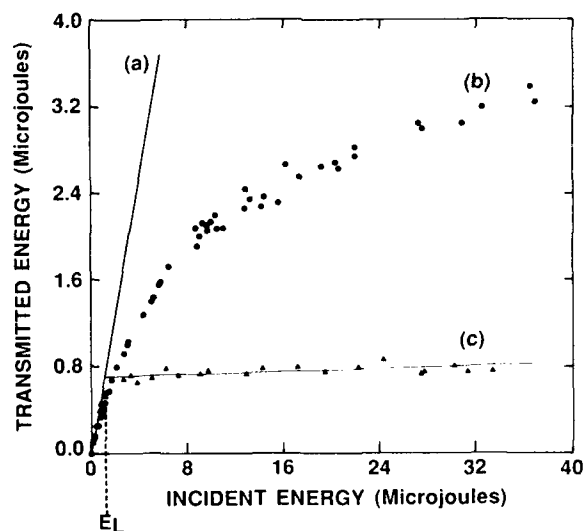
At very low inputs, the thick limiter acts linearly as does the thin limiter. For inputs near the thin limiter's threshold, the thick limiter behaves linearly except in a region near the focal position as determined by linear optics. Only in this region (within the focal volume) does the irradiance become high enough to have significant 2PA along with subsequent carrier defocusing. Thus, it is not surprising that the threshold remains constant to within a factor of two to three as the position of focus within the thick limiter is varied. This is shown experimentally in Fig.7 where the limiting threshold is plotted as a function of the position of the linear focus with respect to the front surface of a 1cm thick ZnSe slab.²⁵ At *higher* inputs the irradiance becomes large enough to have significant 2PA well in front of the linear focal position. This has two consequences. First, the beam at focus will be depleted making it more difficult to damage. Secondly, and more importantly, the negative phase change induced on the wave front by the photogenerated carriers negates the beam convergence prior to focus. The beam is defocused and damaging irradiances are never reached within the material. The dynamic range is now only limited by front surface damage. In principle this threshold can be made arbitrarily high by making the optics larger.

Figure 8 shows the output of a thick limiter device using an aperture placed ≈ 30 cm behind the second lens. The limiting is very weakly dependent on the focal length of the second lens and the distance to the aperture. Also shown is the limiting effect of 2PA by itself when all of the transmitted energy is collected. The primary limiting mechanism (fluence limiting as shown in Fig.8) is seen to be defocusing. Using limiters in this configuration with picosecond $0.5\mu\text{m}$ pulses and tight focusing, we have obtained limiting energies down to $\approx 14\text{nJ}$, corresponding to a peak power of $\approx 400\text{ W}$, with a dynamic range of $\approx 10^3$. With nanosecond pulses the limiting power is actually reduced. This is true because for a fixed irradiance longer pulses create more free-carriers, as shown by Eq.3, which more effectively defocus the beam; thus, the fluence at some distance toward the far field will be limited. Figure 9 shows the limiting energy obtained with 18ns FWHM $0.53\mu\text{m}$ pulses focused into a 1cm thick ZnSe slab as a function of the linear optics focal position. The limiting energy of less than $2\mu\text{J}$ when focused in the bulk, corresponds to a peak input power of less than 100 Watts. Again, the device was self protecting in the bulk.

We have done experiments using picosecond pulses to give approximate scaling relations to optimize limiting by changing the focusing geometry and sample thickness.²⁵ If the only limiting process were 2PA (eg. as occurs in many liquid crystals¹⁵), the limiting energy E_L would be independent of the focusing geometry. This is true since the irradiance I is proportional to $1/w_0^2$ (w_0 is the spot radius at focus) while the effective interaction length in the sample is the depth of focus which is proportional to w_0^2 . Thus, the product βIL (L is the sample length), which determines 2PA (see Eq.1), is independent of the focal length. As shown in section VII, if self-defocusing is dominant even at the limiting threshold, we expect $E_L \propto w_0$. Indeed, our experiments confirm the importance of self-refraction, however, the results for the limiting energies in ZnSe using two different focal length lenses more closely fit an even stronger dependence on spot size (nearly w_0^2).²⁵ Assuming that we focus as far into the sample as possible (ie. on the back surface), we have the limiting energy independent of L but proportional to w_0 . The damage energy E_D , however, depends on the beam area at the surface, which is proportional to L^2/w_0^2 . This gives us a dynamic range E_D/E_L that depends on L^2/w_0^3 . While the data giving this empirical scaling relation are limited, and



7. A plot of the limiting energy E_L as a function of the distance behind the front surface of a 1cm thick slab of ZnSe to the linear focal position. The pulsewidth is 30ps FWHM and the beam size at the 3.75cm focal length lens is 1mm.



8. Input/output characteristics of a ZnSe thick optical limiter showing a) the linear transmission b) the effects of two-photon absorption (ie. all energy collected) c) a plot of the transmitted energy through an aperture (ie. fluence in arbitrary units) as a function of the input 0.53 μm picosecond pulses.

extrapolating the results is suspect, it is clear that tight focusing (small w_0) and thick samples should give a larger dynamic range and lower limiting threshold.

V. Monolithic Limiter

These design criteria were taken to the extreme by making the monolithic limiter shown in Fig.2. This design takes the damage prone surface as far from focus as is possible while maintaining high irradiance within the bulk, thus, maximizing the dynamic range. The output of the frequency doubled single pulse mode-locked Nd:YAG laser was collimated to a spot size w_0 ($HW1/e^2M$) of 1mm and directed into the device. Two devices were made, one of ZnSe and one of ZnS. We have previously reported²⁵ (see Fig.3) the ZnSe device to have a limiting energy of ≈ 10 nJ, which corresponds to ≈ 300 W for 30 ps FWHM input $0.53 \mu\text{m}$ pulses, and a dynamic range of greater than 10^4 . Optical damage to the bulk of the material is prevented by the combined effects of beam depletion due to 2PA and carrier defocusing prior to the focal position determined by linear optics. This monolithic limiter is, thus, self-protected against high irradiance picosecond pulses. It was expected that the device would also be self-protected against nanosecond pulses as was true when we focused less tightly into plane parallel ZnSe samples. Unfortunately, however, both devices suffered bulk damage. When we focus extremely tightly as in the monolithic device, the focal volume becomes so small that the temperature change due to nonlinear absorption of the more energetic nanosecond pulses may give rise to a thermal nonlinearity which in ZnSe is a self-focusing nonlinearity. The thermal self-refraction for very tight focusing may overcome the free-carrier defocusing and cause beam collapse and damage. The problem can be overcome, however, by using materials with a negative thermal nonlinearity or by not focusing as tightly. Not focusing as tightly though, raises the limiting energy.²⁵

VI. Band-gap and Wavelength Dependence

The dimensions of the ZnSe and ZnS devices were slightly different so that, accounting for the different refractive indices, the calculated (by linear optics) spot sizes in the center of both devices, were the same. The behavior of the ZnS device was qualitatively similar to the ZnSe device; however, the limiting energy E_L measured under similar conditions was 130 nJ, a factor of 13 higher than for ZnSe. A reason for the large difference in limiting energies is the dependence of nonlinear refraction on band-gap energy. Using the model first calculated by Auston *et. al.*,³³ the nonlinear refractive index is given by:

$$\Delta n = - \left(\frac{8\pi P^2 e^2 N}{3n(\hbar\omega)^2 E_g} \right) \frac{1}{1 - (\hbar\omega/E_g)^2} \quad (6)$$

where n is the linear refractive index, P the Kane momentum parameter ($E_p = 2P^2 m / \hbar^2$ with m the electron mass), and $\hbar\omega$ is the photon energy. From Eq.3 the carrier density N is given by:

$$N(t) = \int_{-\infty}^t \left(\frac{\beta I^2(t')}{2\hbar\omega} \right) dt' \quad (7)$$

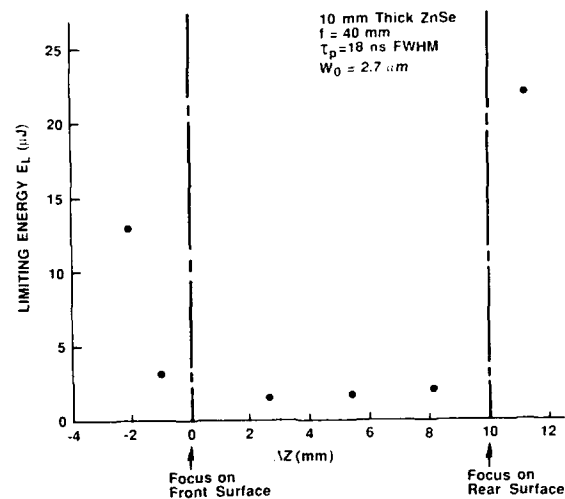
Thus, N and hence Δn is proportional to $\beta/\hbar\omega$, so that using Eq.4, we obtain the frequency and band-gap dependence of the index change as;

$$\Delta n \propto \frac{E_g}{(\hbar\omega)^8} \frac{(2\hbar\omega/E_g - 1)^{3/2}}{1 - (\hbar\omega/E_g)^2} \quad (8)$$

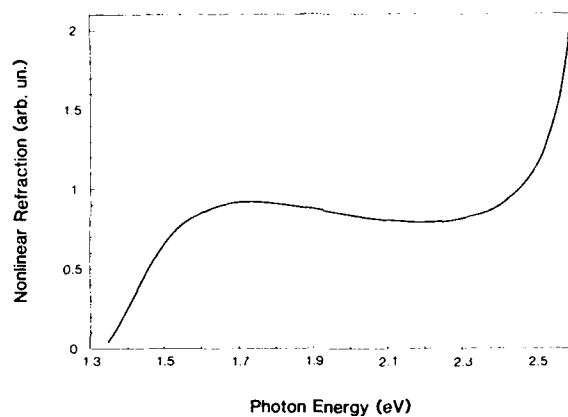
The laser frequencies are the same ($\hbar\omega = 2.34$ eV), but the energy gap for ZnSe is 2.67 eV compared to 3.66 eV for ZnS. Therefore, for identical pulsewidths and irradiances $\Delta n(\text{ZnSe}) \approx 8.3 \times \Delta n(\text{ZnS})$. This accounts for most of the factor of 13 difference in measured limiting energies. As the 2PA coefficients of the materials differ by less than a factor of three ($\beta_{\text{ZnSe}} = 5.5 \text{ cm/GW}$, $\beta_{\text{ZnS}} = 2.0 \text{ cm/GW}$), we conclude that the primary limiting mechanism is the 2PA induced free-carrier self-refraction.²⁷

If we assume that the limiting begins when the overall change in phase $\Delta\Phi$ is on the order of 2π , and occurs within the depth of focus $z_0 = \pi w_0^2 / \lambda$, we have the change in optical path length $\Delta n z_0 \propto \lambda$ (see Eq.2). For a fixed ratio $\hbar\omega/E_g$, this assumption using Eq.7 in Eq.6 along with $\beta \propto E_g^{-3}$ gives the limiting energy $E_L \propto I w_0^2 \propto (\hbar\omega)^{5/2} w_0$. The diffraction limited spot radius w_0 is proportional to λ giving the scaling relation $E_L \propto (\hbar\omega)^{3/2}$. We see immediately that we can expect much lower limiting energies at longer wavelengths using narrow gap semiconductors.

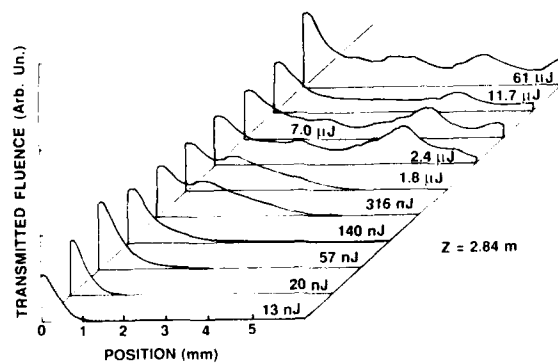
Figure 10 shows the dependence of Δn (Eq.8) on the incident photon energy for ZnSe. This highlights the flat response of the limiter over almost all of the range $E_g/2 < \hbar\omega < E_g$. The sharp rise in Δn from zero at $\hbar\omega = 1.33$ eV indicates the onset of 2PA at the two-photon resonance. The flat region between 1.55 and 2.4 eV (corresponding to $\lambda = 800$ to 500 nm) results from the slowly decreasing generation



9. A plot of the limiting energy E_L as a function of the distance behind the front surface of a 1cm thick slab of ZnSe to the linear focal position. The pulsewidth is 18ns FWHM and the beam size at the 4cm focal length lens is 2.5mm .



10. Theoretical plot of the functional dependence of Δn (Eq.8 in text) versus photon energy for ZnSe.



11. The transmitted energy at 2.8m behind the ZnSe monolithic limiter as detected by a vidicon as a function of position at various input energies.

rate combined with the slowly increasing free carrier refraction in this frequency range. As the frequency approaches the band-gap resonance, Δn rapidly increases. However, linear absorption will dominate in this region, which is undesirable for limiting. This figure clearly illustrates the broad-band nature of the two-photon induced free-carrier nonlinearity employed in these limiting devices. In what follows we show the results of a careful characterization of the output of the ZnSe monolithic limiter for picosecond input pulses in both space and time.

VII. Temporal and Spatial Response

If we place a vidicon at $\approx 2.8\text{m}$ behind the ZnSe device (toward the far field) we see the fluence limiting characteristics of Fig.11. Here the temporally integrated spatial energy distribution is shown as a function of position for input energies from 13nJ to 61 μJ . For the data shown, no filters were changed in front of the vidicon. As the input energy is increased, the energy simply gets spread out in space, limiting the fluence and thus protecting the sensitive vidicon photocathode. If we just look at the on-axis portion of this light through a 0.4mm aperture, we get the input/output characteristics shown previously in Fig.3.

Sending the pulse through the limiter onto the entrance slit of a 2ps resolution streak camera allows us to look at the spatial and temporal energy distribution simultaneously on the vidicon screen. What we see at low inputs, shown in Fig.12, is the Gaussian spatial distribution and a nearly Gaussian distribution in time. At higher input (Fig.13), as the pulse develops, the energy spreads out in space into two "wings". At still higher energies shown in Fig.14, the energy appears to be nearly uniformly spread in space for later times in the pulse. This is clearly advantageous from the standpoint of protecting optical components. In order to compare these results with the thin sample results, Fig.15 shows the spatial energy distribution at various times for a 125 μm spot radius beam traversing a 0.3cm thick ZnSe sample and propagating 11cm in free space to the streak camera. While there is certainly a quantitative difference in the output, qualitatively the results are remarkably similar. This gives us confidence in using the analysis for thin samples to predict the performance of thick limiters.

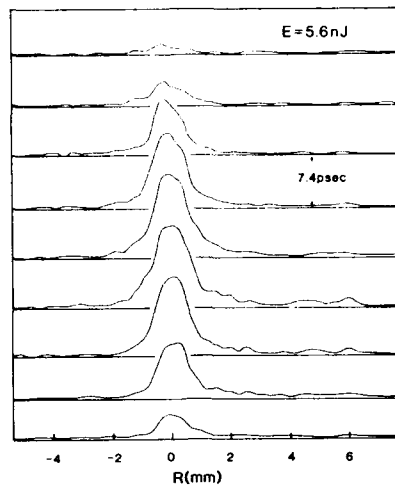
Figure 16 shows the transmitted temporal structure of the output of the ZnSe monolithic limiter for a 20 μJ input pulse at various positions in the beam. The reference beam shows the position of the center of the pulse in time (ie. when the beam is detected for low input). We see the center far advanced in time and advanced to a lesser degree as we look farther out in the beam. The original beam only extended 1mm. What is happening is that at very early times in the pulse for high input, 2PA creates free-carriers which defocus subsequent parts of the pulse. This defocusing increases with time since the carrier density increases with the time integral of the square of the irradiance over time as given in Eq.7. Therefore, later portions of the beam spread out more in space and the irradiance as well as the fluence are limited.

VIII. Conclusion

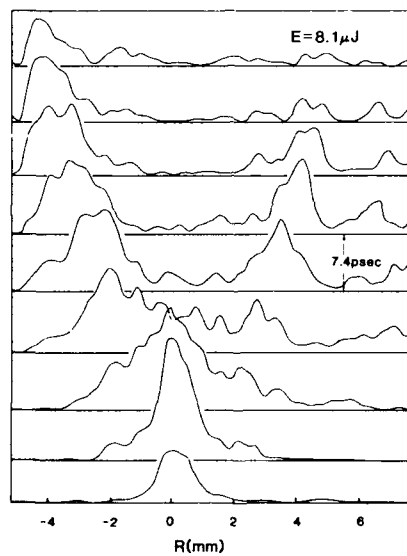
We have developed a quantitative understanding of two-photon absorption (2PA) leading to a predictive capability. That is, given n , E_g , E_p and $\hbar\omega$ we can give the 2PA coefficient. We understand the associated defocusing as being due to the 2PA generated free-carrier Drude/band-blocking effects. We have used a combination of these two nonlinearities to build optical limiting devices. By employing a "thick" limiter geometry where we focus tightly into the semiconductor material, we have greatly extended the dynamic range of these devices. Defocusing by two-photon excited carriers makes these devices self-protecting. We have obtained limiting energies as low as 10nJ which corresponds to ≈ 300 Watts for the picosecond pulses used, and the dynamic range is greater than 10^4 . In the case of nanosecond pulses, limiting powers below 100 Watts were obtained. We have determined that there are no possibly damaging hot spots in either space or time. Since 2PA is broad band, these devices are broad band (eg. ZnSe should work from 500 to 850 nm). Also, from our study of the band-gap energy dependence of two-photon absorption and the scaling of the resulting nonlinear refraction with wavelength, we expect limiters using narrow gap semiconducting material will have considerably lower limiting inputs in the infra-red.

IX. Acknowledgement

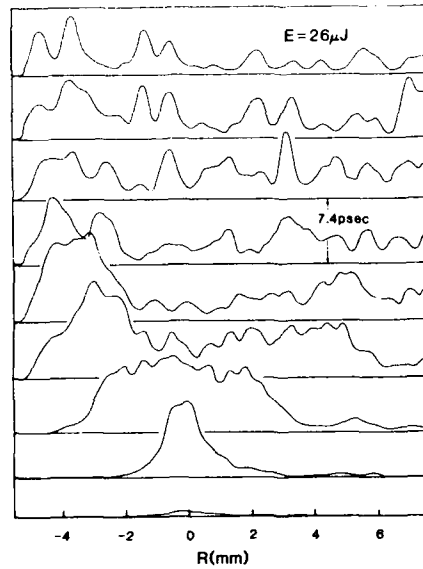
We gratefully acknowledge the support of the National Science Foundation (ECS-8617066), and we wish to express our thanks to B.S. Wherrett for useful input during the preparation of this manuscript.



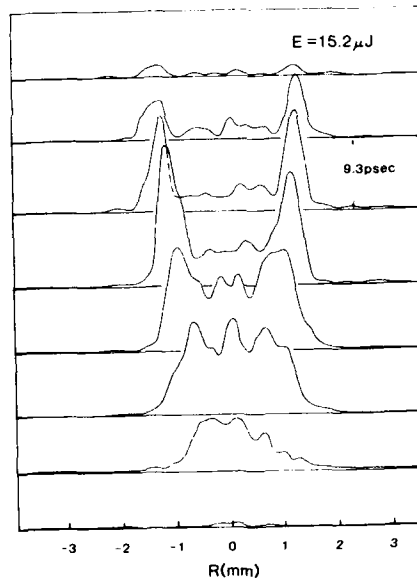
12. The spatial energy distribution at 2.8m behind the ZnSe monolithic limiter at various times, as detected by a streak camera/vidicon system for an input energy of 5.6nJ.



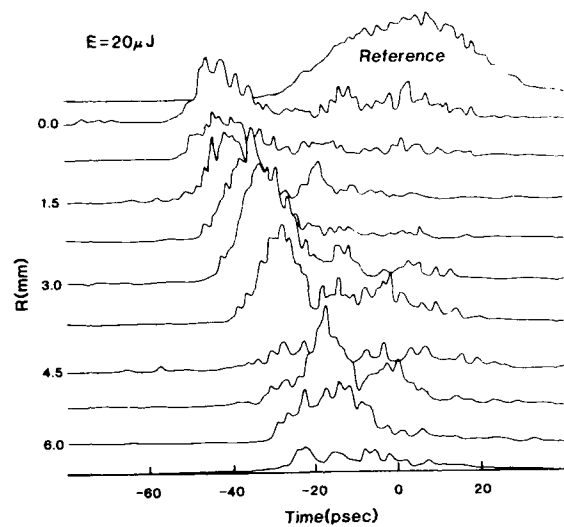
13. Same as Fig.12 for an input energy of 8.1μJ.



14. Same as Fig.12 for an input energy of $26\mu\text{J}$.



15. The spatial energy distribution at 11cm behind a thin (2mm thick) ZnSe sample at various times as detected by a streak camera/vidicon system for an input energy of $15\mu\text{J}$.



16. The temporal energy distribution at 2.8m behind the ZnSe monolithic limiter at various positions in the beam. A reference pulse indicating the zero time and the original pulsewidth is shown at the top.

REFERENCES

1. S.A. Akhmanov, R.V. Khokhlov and A.P. Sukhorukov, "Self-Focusing, Self Defocusing, and Self Modulation of Laser Beams", in Laser Handbook V. 2, 1151-1228 ed by F.T. Arecchi and E.O. Schultz-Dubois, North Holland, 1972.
2. E.W. Van Stryland, H. Vanherzelle, M.A. Woodall, M.J. Soileau, A.L. Smirl, S. Guha and T.F. Boggess, "Two photon absorption, nonlinear refraction, and optical limiting in semiconductors", Opt. Eng., 24, 613 (1985).
3. J.P. Gordon, R.C.C. Leite, R.S. Moore, S.P.S. Porto, and J.R. Whinnery, Bull. Am. Phys. Soc. Sec., 119, 501 (1964).
4. J.P. Gordon, R.C.C. Leite, R.S. Moore, S.P.S. Porto, and J.R. Whinnery, "Long-transient effects in lasers with inserted liquid samples", J. Appl. Phys. 3 (1965).
5. R.C.C. Leite, R.S. Moore and J.R. Whinnery, "Low absorption measurements by means of the thermal lens effect using an He-Ne laser", Appl. Phys. Lett., 5, 141 (1964).
6. C.E. Rieckhoff, "Self-induced divergence of CW laser beams in liquids -- a new nonlinear effect in the propagation of light", Appl. Phys. Lett., 9 (2), 87 (1967).
7. R.C.C. Leite, S.P.S. Porto and P.C. Damen, "The thermal lens effect as a power limiting device", Appl. Phys. Lett., 10 (3), 100 (1967).
8. M.J. Soileau, "Passive intensity limiter based on nonlinear optics", Annu. Meet. Opt. Soc. Amer., Chicago, IL, Oct (1980). Abstr. in J. Opt. Soc. Amer., 20, 1051 (1980).
9. M.J. Soileau, W.E. Williams and E.W. Van Stryland, "Optical power limiting with picosecond response time", IEEE J. Quantum Electron., QE-19, 731 (1983). See also W.E. Williams, M.J. Soileau and E.W. Van Stryland, "Optical switching and n_2 measurements in CS_2 ", Opt. Comm., 50, 256 (1984).
10. E.P. Ippen and C.V. Shank "Picosecond Response of a high repetition rate CS_2 Optical Kerr Gate", Appl. Phys. Lett. 26, 92 (1975).
11. M. Mohebi, P.F. Aiello, G. Reali, M.J. Soileau and E.W. Van Stryland, "Self-Focusing in CS_2 at $10.6\mu m$ ", Opt. Lett. 10, 396 (1985).
12. D.V.G.L. Narashimha Rao and S. Jayaraman, "Self-focusing of laser light in the isotropic phase of a nematic liquid crystal", Appl. Phys. Lett., 23, 539 (1973).
13. G.K.L. Wong and Y.R. Shen, "Study of pretransitional behavior of laser-field-induced molecular alignment in isotropic nematic substances", Phys. Rev. A, 10 1277 (1974).
14. I.C. Khoo, "Nonlinear light scattering by laser- and dc-field-induced molecular reorientations in nematic-liquid-crystal films", Phys. Rev. A 25, 1040 (1982).
15. M.J. Soileau, S. Guha, W.E. Williams, E.W. Van Stryland and H. Vanherzeele, "Studies of the nonlinear switching properties of liquid crystals with picosecond pulses", Mol. Cryst. Liq. Cryst., 127, 321 (1985).
16. J.E. Bjorkholm, P.W. Smith, W.J. Tomlinson and A.E. Kaplan, "Optical bistability based on self-focusing", Opt. Lett., 6, 345 (1981).
17. D.A.B. Miller, C.T. Seaton, M.E. Prise and S.D. Smith, "Bandgap-resonant nonlinear refraction in III-V semiconductors", Phys. Rev. Lett., 47, 197 (1981).
18. J.E. Geusic, S. Singh, D.W. Tipping and T.C. Rich, "Three photon stepwise optical limiting in silicon", Phys. Rev. Lett., 19, 1126 (1969).
19. T.F. Boggess, S.C. Moss, I.W. Boyd and A.L. Smirl, "Nonlinear-optical energy regulation by nonlinear refraction and absorption in silicon", Opt. Lett., 9, 291 (1984).

20. J.M. Ralston and K.R. Chang, "Optical limiting in semiconductors", Appl. Phys. Lett., 15, 164 (1969)
21. A.C. Walker, A.K. Kar, Wei Ji, U. Keller and S.D. Smith, "All-optical power limiting of CO₂ laser pulses using cascaded optical bistable elements", Apl. Phys. Lett., 48, 683 (1986).
22. A.K. Kar, J.G.H. Mathew, S.D. Smith, B. Davis and W. Prettl, "Optical bistability in InSb at room temperature with two photon excitation", Appl. Phys. Lett., 42, 334 (1983).
23. T.F. Boggess, A.L. Smirl, S.C. Moss, I.W. Boyd and E.W. Van Stryland, "Optical limiting in GaAs", IEEE J. Quantum Electron., QE-21, 488 (1985).
24. D.J. Hagan, E.W. Van Stryland, M.J. Soileau and Y.Y. Wu "Semiconductor Optical Limiters with Large Dynamic Range", OSA annual meeting, Seattle, 1986.
25. D.J. Hagan, E.W. Van Stryland, M.J. Soileau, and Y.Y. Wu "Self-protecting semiconductor optical limiters", to be published Opt. Lett., April 1988.
26. A.E. Kaplan, Radiophys. Quantum Electron. 12, 692 (1969).
27. E.W. Van Stryland, M.A. Woodall, H. Vanherzeele and M.J. Soileau, "Energy band-gap dependence of two-photon absorption", Opt. Lett., 10, 490 (1985).
28. P. Liu, W.L. Smith, H. Lotem, J.H. Bachtel and N. Bloembergen, "Absolute two-photon absorption coefficients at 355 and 266 nm", Phys. Rev. B17 4620, 1978.
29. J. Dempsey, J. Smith, G.D. Holah and A. Miller, "Nonlinear absorption and pulse-shaping in InSb", Opt. Commun. 26, 265 (1978), A.M. Johnson, C.R. Pidgeon and J. Dempsey, "Frequency dependence of two-photon absorption in InSb and HgCdTe" Phys. Rev. B22, 825 (1980); C.R. Pidgeon, B.S. Wherrett, A.M. Johnston, J. Dempsey and A. Miller, "Two Photon Absorption in Zinc-Blende Semiconductors" Phys. Rev. Lett 42, 1785 (1979).
30. "Self-Defocusing in CdSe induced by charge carriers created by two-photon absorption", S. Guha, E.W. Van Stryland, M.J. Soileau, Opt. Lett. 10, 285-287, 1985.
31. J.A. Hermann, "Beam propagation and optical power limiting with nonlinear media", J. Opt. Soc. Am., B1, 729 (1984).
32. J.A. Hermann, "Simple model for a passive optical power limiter", Opt. Acta, 32, 541 (1985).
33. D.H. Auston, S. McAfee, C.V. Shank, E.P. Ippen and O. Teschke, "Picosecond spectroscopy of semiconductors", Solid-State Electron, 21, 147 (1978).

A DESIGN OF OPTICAL SWITCHING ELEMENTS THROUGH LASER SUBHARMONIC PHASE SHIFTS

K.P. Chung
Bell Communications Research
Morristown, New Jersey

ABSTRACT

An experiment designed to explore a new approach in optical switching element is presented. The new mechanism involves digital locking of phase shifts of subharmonic waves generated by nonlinear optics. The physical phenomenon of phase locking of subharmonics is analyzed.

The design scheme has several advantages over many of the methods tried in other laboratories, in term of cascability and elimination of electrical devices in computationally critical paths. Certain problems of alignments and timing control are discussed.

1. INTRODUCTION.

Recent advances in fiber optics have resulted in high speed communication, while VLSI circuits are still mainly responsible for computation. Aside from the necessity of conversions between electric and light signals, which require additional components and degrade performance, there are basic limitations of the semiconductor circuits which cannot be overcome in the current state of the art.

As chip size and circuit density increase, the communication bandwidth of the interconnections between the chip and the outside world become severely restricted and expensive, due to the limited number of pins available and the complications associated with circuit layouts for communication purposes. In this regard, recent work on optic interconnects may be helpful to a certain extent, even though the necessary technology is still in its infancy. To what extent the emerging technology of optical interconnect will alleviate the communication bottleneck of the current generation of IC circuitry remains to be seen in the next few years.

The question whether optical switching is ever going to be feasible or is even a good idea has been debated for sometime. The history of optical switching is long and frustrating. Any attempt to substitute integrated circuits wholly or partially and thereby improve upon the technology has been beset by a different set of problems [1].

The primary requirements of optical switching elements are cascability, speed, parallelism, and compactness. The quality of signal should be maintained without degradation along successive steps. Also, the nature of input and output signals should remain the same for simplicity in integrating elements. For example, if the digital input state is coded in terms of phases, output states should not be distinguished by different amplitudes. The output should also maintain the same frequency profile. Some of the schemes in the literature indeed violate cascability in the sense described above.

2. SUBHARMONIC WAVE PHASE SHIFT

This paper presents work done to come up with a new idea on how to utilize nonlinear optics for optical switching. For this purpose, degenerate parametric oscillation is investigated as a means of subharmonic wave generation. Then a mechanism for controlling the phase shift of the generated subharmonics is predicted. Once this process is accomplished, the paper shows how to implement optical switching in this framework.

The initial phase of the work is concerned with the establishment of basic principles without much attention given to neatness and compaction. The experiment in the first stage is conducted in bulk optics. Subsequent phases of the work will focus on the realization of the same ideas in integrated optics. In recent years, lithium niobate wave guides have been successfully used for observation of harmonic wave generation, parametric oscillation, parametric fluorescence and other related second-order phenomena by W. Sohler and his colleagues [2].

Parametric oscillation in mechanics was studied as early as the 19th century. In Melde's experiment, the string attached to a tuning fork is given a periodic variation of tension by the vibrating tuning fork. If the tuning fork vibrates at frequency $2f$, the string vibrates at steady state with a second subharmonics of frequency f (Fig. 1). When the string is made to oscillate at a steady subharmonic frequency, there is an ambiguity in the phase shift of subharmonic waves, as noticed by M. Faraday and Lord Raleigh [3]. In the case of 2nd subharmonics, there are two possible phase shifts, different from each other by π radians.

In general, for the generation of n th subharmonics, there are n possible phase shifts,

$$0, \frac{2\pi}{n}, \frac{4\pi}{n}, \dots, \frac{(n-1)2\pi}{n},$$

where $m = n - 1$.

Incidentally, no such ambiguity arises in harmonic waves.

For the purpose of this paper, the rest of the discussion will be confined to the 2nd subharmonic case only, with the understanding that corresponding circumstances for other subharmonics may be valid also.

It is not hard to see the origin of this ambiguity in terms of classical damped oscillation. Suppose that a classical mechanical damped oscillator without a driving force has a spring constant modulated at frequency w_p . The equation for displacement can be written in the form

$$\frac{d^2h}{dt^2} + \kappa \frac{dh}{dt} + (w_0^2 + 2\alpha \sin w_p t) h = 0 \quad (1)$$

where κ is a damping constant and α is a modulation index.

The consequence of the parametrically driven oscillation is that under certain conditions sustained oscillation at frequency w_0 is possible. For a proof, let us assume a solution of the form

$$h = A \cos (wt + \phi).$$

After neglecting nonsynchronous terms for oscillation frequency of $w_p + w$, we have

$$(w_0^2 - w^2) e^{i(wt + \phi)} + i\kappa e^{i(wt + \phi)} - i\alpha e^{i(w_0 - w_p)t + \phi} = 0 \quad (2)$$

Thus the steady-state oscillation is possible if

$$w = w_0 \quad (3)$$

$$w_p = 2w$$

$$\alpha = w\kappa$$

$$\phi = 0 \text{ or } \pi.$$

The condition $\alpha = w\kappa$ indicates the threshold strength of the pumping to overcome the losses. If the pumping power is stronger, the generated subharmonic wave will get stronger in the linear region but eventually will stabilize to a maximum amplitude for subharmonics because of the nonlinearity. The classical equation can be more precisely studied for small modulation parameter $\alpha (< w_0^2/2)$ in terms of Mathieu's equation and Hill's techniques [4]. For strongly nonlinear cases, certain interesting analytical results can still be obtained along the lines of analogous electrical circuit problems as in the work of radio engineers many years ago [5].

The analysis presented above applies in general to an oscillator whose energy storage parameter is modulated at pumping frequency w_p . In order to extend the analysis to optical physics, it is convenient to consider the parallel RLC circuit. If the capacitance is modulated in the form

$$C = C_0 \left[1 + \frac{\Delta C}{C_0} \sin w_p t \right], \quad (4)$$

then the voltage across the circuit can be written, for $\Delta C \ll C_0$ as

$$\frac{d^2 V}{dt^2} + \kappa \frac{dV}{dt} + \frac{1}{LC_0} \left(1 + \frac{\Delta C}{C_0} \sin w_p t \right) V = 0 \quad (5)$$

This equation is similar in form to the parametric oscillation equations already discussed.

For the purpose of relating nonlinear optical properties to the mathematical forms as above, let us consider a nonlinear medium in which the polarization P is induced with a second order term in applied field E .

$$P = \epsilon_0 \chi E + dE^2 \quad (6)$$

If a parallel-plate capacitor of area A and separation S is filled with a nonlinear medium with the polarization indicated above, the capacitance is

$$C = \epsilon_0 (1 + \chi) \frac{A}{S} + \frac{AdE}{S} \quad (7)$$

When the externally applied electric field is given by

$$E = -E_0 \sin w_p t,$$

then the capacitance becomes

$$C = \frac{\epsilon_0 (1 + \chi) A}{S} - \frac{AdE_0}{S} \sin w_p t$$

This expression has the same form as equation (4). Therefore, the application of an electric field with a pumping frequency of w_p to nonlinear dielectric material is seen to be formally equivalent in a mathematical sense to the time modulation of capacitance in lumped RLC circuit.

The phase shift of the subharmonic wave being generated is normally determined by the phase of the noise at the moment when the subharmonic wave is beginning to form. However, the ambiguity in phase shift of a factor of π for 2nd subharmonics can be removed by an application of a seeding wave whose frequency is the same as that of the subharmonic. The amplitude of the seeding wave should be comfortably above the noise level but is small in comparison to the pumping wave amplitude. The timing relation between the pumping wave and the moment of subharmonic wave creation at threshold has to be satisfied. The seeding wave is required to overlap in time the particular instant when the subharmonic wave appears at threshold.

One factor of importance related to phase stability is the accuracy required of the seeding wave phase shift. It can be shown that if the seeding wave has a phase shift falling in the range $\alpha_0 \pm \frac{\pi}{2}$ then the induced subharmonic phase will stabilize to β . For the seeding wave phase shift range $\alpha_0 + \frac{\pi}{2} \pm \alpha \pm \alpha_0 + \frac{3\pi}{2}$, the corresponding subharmonic wave will settle with a phase shift of $\beta + \pi$. Thus, there is considerable latitude in the phase shift of the seeding wave. This effect will help in maintaining phase shift relations in successive steps of the cascading sequence.

3. EXPERIMENTAL SETUP

The experimental configuration for observation of the locking of the second subharmonic wave phase shift is schematized in Fig. 2. The second subharmonic wave is produced through the degenerate parametric oscillation in which the signal and idler frequencies are the same. The pumping source is the frequency-doubled beam at 532 nm of a Q-switched Nd:YAG laser source at 1064 nm.

The purpose of Q-switching is twofold. It will better meet the high power need for efficient nonlinear bulk interaction and also provide the pulsing of the pumping wave for new seeding at each pulse, as long as there is no leak between pulses. The nonlinear material is a barium borate crystal (BBO). For type I phase matching in which the incoming beam is extraordinary while both signal and idler waves are ordinary, the collinear phase matching angle between the optic axis and the incoming ray is approximately 22.9 degrees.

The source beam is divided into two parts by the beamsplitter. The seeding wave is first generated in the crystal and, after passing through the filter for elimination of fundamental frequency, is modulated by an electrooptic phase modulator to either 0 or π . This phase modulation pattern is determined by the square wave voltage pattern generator attached to the phase modulator. The pattern generator and Q-switching signals need to be synchronized. Generally the input voltage pattern provides the input information to be processed in the experiment. The delay component between BS1 and BS2 in the schematics is to synchronize seeding and pumping. Note that the same crystal and filter are used for both creation of the seeding wave and later subharmonic phase control.

As shown in the schematics, the delay component between BS3 and BS4 is to delay the reference beam so that it will arrive at the beamsplitter BS4 simultaneously with the phase-controlled subharmonic. The interferometer is a modification of the Mach-Zehnder type. After proper alignment, the beam can be made to switch to either one of the detectors, depending on the relative phase difference between the two beams, as either constructive or destructive interference takes place.

4. CONCLUSION

The approach taken in this work indicates the possibility of building optical switching components through Mach-Zehnder configuration. The early part of the experiments will focus on the verification of the phase control mechanism proposed using configurations for bulk optics. Subsequent phase of the work will be aimed at implementation of integrated optics based on waveguides of cross sectional diameter of the order of the wavelength.

Many practical experimental details need to be probed. These include alignment with submicron accuracy and control of phase jitter and amplitude noise within reasonable bounds. Also, stable phase matching for degenerate parametric oscillation needs much investigation.

The proposed mechanism provides an alternative to the currently predominant techniques in optical processing involving bistability and other mechanisms directly or indirectly related to the change of the refractive index. The need for exploration of new types of logical elements remains acute.

ACKNOWLEDGEMENTS

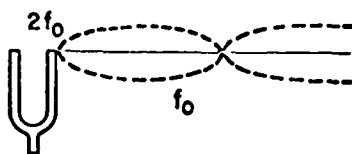
The author acknowledges with gratitude many discussions held with his colleagues within Bellcore and outside, in particular, A. Albanese, P. Smith, J. Heritage, A. Weiner, C. Brackett, G. Stegeman and W. Sohler.

REFERENCES

- [1] A. Huang, "Architectural Considerations Involved in the Design of an Optical Digital Computer", pp 780-786, *Special Issue on Optical Computing*, PROC IEEE, (1984)
- [2] W. Sohler, et al, "Integrated Optical Parametric Devices", *Jrl. of Lightwave Technology*, Vol LT-4, No. 7, (1986)
- [3] Lord Rayleigh, "On Maintained Vibrations", pp 229-235, *Phil. Mag. S5*, Vol. 15, No. 94, (1883)
- [4] E. T. Whittaker and G. N. Watson, "Modern Analysis".
- [5] E. Goto, "Parametron, a Digital Computing Element Which Utilizes Parametric Oscillations", pp 1304-1316, *PROC IRE*, Vol. 47, No. 8, (1959)

FIGURE CAPTIONS

1. Melde's experiment and steady state string oscillation with two possible phases.
2. Schematic of the experimental setup for observation of subharmonic wave phase-locking mechanism and optical switching.



MELDE'S EXPERIMENT

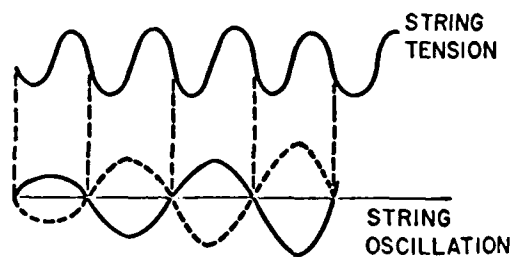


FIG. 1

SUBHARMONIC PHASE SHIFT CONTROL EXPERIMENT

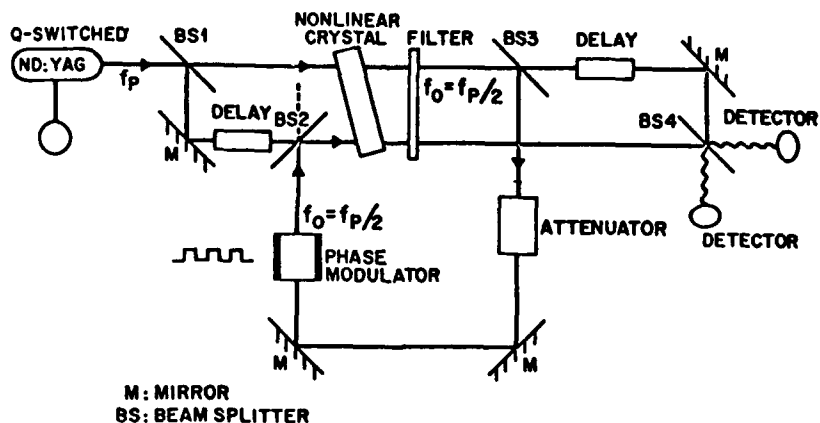


FIG. 2

APPLICATIONS OF HIGH-EFFICIENCY NONLINEAR CRYSTALS FOR TUNABLE LASERS(0.19-4 MICRONS)

J. T. Lin

Center for Research in Electro-Optics & Lasers
University of Central Florida, Orlando, FL 32816

ABSTRACT

Frequency conversion schemes including SHG, THG, SFM, DFM, OPO are presented for tunable coherence sources ranging from UV to mid-IR. The phase matching curves of BBO crystal used as SFM of dye lasers are shown. The key parameters of OPO including cavity and crystal lengths, mirror reflectivities, gain function and bandwidth are analyzed. The OPO phase matching curves of BBO and KTP for various pumping wavelengths are calculated and the effective nonlinear coefficients are compared for various configurations. Novel schemes of rapid-tuning(wavelength steering) using tunable pumping sources in OPO (such as dye-laser, Ti-sapphire laser and Alexandrite laser) are explored via the phase matching curves of BBO crystal. Noncritical phase matching conditions in diode-pumped system are calculated and the potential applications for tunable diode-pumped lasers with visible and mid-IR spectral ranges are presented.

I. INTRODUCTION

Recent technology of optical materials growth, both in laser materials and nonlinear crystals, generates many new coherence sources with tunable spectral regimes which are difficult or can not be achieved by conventional lasers and materials.[1-12] In this paper we shall review the recent progress and applications of new laser sources generated from new nonlinear crystals via various frequency conversion techniques. For frequency up-conversion, these techniques include second-harmonic generation(SHG), sum-frequency-mixing(SFM) and anti-Stokes in stimulated Raman scattering(SRS). On the other hand, for frequency down-conversion, techniques shall include optical parametric oscillation (OPO), difference-frequency-mixing(DFM) and Stokes in SRS.

The spectral regimes to be discussed in Section II shall include XUV (38-120 nm), VUV (189-200 nm), UV(200-400 nm), visible (400-700 nm) and IR (1-8 micron) generated from frequency conversion of various lasers including solid-state lasers, fiber lasers, free-electron-lasers, gas lasers, dye lasers and the newly-developed diode-lasers.

In section III, we introduce the applications of BBO crystal for tunable UV sources and another new crystal called lithium-borate(LBO). The key parameters for OPO and the phase matching curves using BBO and KTP crystal and the novel scheme of rapid-tuning are shown in Section IV. In Section V, we explore the noncritical phase matching crystals with applications to diode-pumped lasers.

II. TUNABLE LASER SOURCES

Applications

Coherence sources with spectral ranges of XUV to IR cover a variety of application areas including research, industry, medicine and military. Specific examples are: (1) laser sources in 3-5 and 8-12 micron for military IR countermeasure; (2) 1.4-2.5 micron for remote sensing in lidar and DIAL systems; (3) 1.54 micron for eyesafe radiation used in tactical training systems; (4) tunable visible sources (400-700 nm) and UV sources (200-400 nm) for materials and optical processing, biomedical studies and various military systems, (5) XUV (38-120 nm) sources for photochemical and spectroscopy studies.

Frequency Conversion Schemes

In Fig. 1, we have shown the direct output spectra of various lasers without using frequency conversions. We note that most of the gas lasers (excimer, ionic and metal vapor lasers) provide only discrete spectra of radiation whereas free-electron lasers, dye lasers, color-center lasers, diode lasers and some of the newly developed solid-state lasers generate tunable sources. New lines generated from a He-Ne laser have been recently developed. They include the visible wavelengths of 543, 594, 612 and 633 nm as well as 1152, 1523, 2396 and 3392 nm infrared wavelengths.

Frequency conversion techniques using both Raman gas media and solid-state (crystals) provide not only many new discrete laser lines but also spectral

regimes with new tuning ranges. In Fig. 2, we have shown UV and visible tuning ranges generated from SHG, SFM, OPO and SRS in the Nd:YAG laser and the YAG pumped Ti:sapphire lasers. We note that, except for some small spectral gaps, tunable sources covering the whole regimes from UV to visible (189-700 nm) may be achieved by achieved by these conversion schemes.

Fig. 3 shows the tuning ranges of 189-500 nm by using SFM of dye-lasers and the IR ranges of 1.3-6.4 micron by using DFM of dye and Nd:YAG lasers. Also shown are the very wide tuning ranges of harmonics of free-electron lasers, 0.2-10 micron. The new XUV radiations generated by SFM and frequency-mixing in inner gases dye-laser and harmonics of Nd:YAG and excimer lasers are shown in Fig 4. We note that a deep-UV source of 189 nm has been recently developed by Lambda Physik Co. by SFM of dye-laser outputs of 788 nm and 248.5 nm (from doubling of 497 nm).

For new laser sources in the IR regions, conversion techniques using DFM, OPO and SRS are shown in Fig. 5 and 6. Diode-lasers featuring the advantages of compact, long-lived, stable and cost effective are shown in Fig. 7, where new sources in the UV and visible regions (308-609 nm) generated by various schemes are represented. Greater details of OPO using BBO and KTP will be discussed in Section III and the noncritical phase-matching crystals for diode-pumped lasers will be discussed in Section IV.

III. NEW CRYSTALS FOR UV SOURCES

The recently discovered beta-barium-borate(BBO) crystal promises the unique applications for tunable UV sources by frequency conversion of the dye-lasers. As shown in Fig. 8, the phase matching angles of BBO (type I) indicate the cut-off wavelengths, defined by the 90-degree phase matching angle which results in $\text{deff} = \cos = 0$, for SHG, THG and SFM. It is seen that a deep-UV source of 189 nm(limited by the transparency range of BBO) may be achieved by SFM of two dye-lasers at 789 nm and 248.5 nm (generated from SHG of 497 nm). For comparison, the shortest wavelengths may be achieved by direct SHG and THG of dye-laser are 204 nm and 195 nm, respectively. Experimental results for the generation of 189 nm and SHG of high-average-power copper-vapor laser (with 4% output of 255 nm) have been reported.[13],[14]

BBO crystal has also been used for the generation of high-order harmonics of a Nd:YAG laser, up to the fifth-harmonics with an output wavelength of 212 nm and conversion efficiency of 12%. [5] Furthermore, this 212 nm sources has also been used as a pumping source for the third harmonic generation in argon gas with an output wavelength as short as 71 nm.[15]

Another borate-family crystal called lithium borate(LBO) promises the generation of deep-UV sources. This LBO crystal has transparency range of 0.16-2.5 μm and

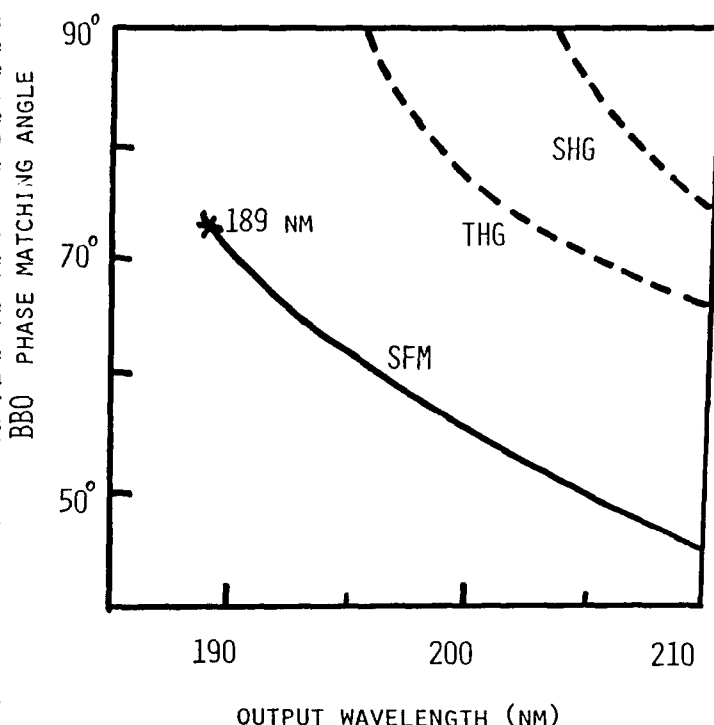


Fig. 8 Tunable deep-UV sources generated from SHG, THG and SFM in BBO(type II) where the phase matching angles are shown vs. output wavelengths. For SFM case 248 nm is suming with output from a dye laser.

rather high damage threshold, 25 GW/cm for SHG of 0.1 ns, 1064 nm YAG laser.[16]

IV. OPTICAL PARAMETRIC OSCILLATION USING BBO AND KTP CRYSTALS

Tunable coherence sources in the mid-IR spectral regime (1.8-5 micron) may be achieved via: (A) tunable color center lasers, (B) difference frequency mixing(DFM), (C) optical parametric oscillation(OPO) and amplification(OPA), and (D) stimulated Raman scattering(SRS).

We shall now discuss the key issues of optical parametric oscillation(OPO) and the tuning curves using BBO and KTP crystals.

Frequency conversion technique using OPO provides the unique tool for the generation of tunable sources. To achieve the mid-IR spectral regime of 1.8-5 microns the pump beam wavelengths for the OPO process must be in the 1-2 microns range which may be generated from several systems:

- (1) direct output (tunable) of Co:MgF₂ (1.5-2.3 μm), Ni:MgF₂ (1.62-1.8 μm) lasers.
- (2) direct output (fixed wavelength) from Nd:YAG (1.064, 1.32 μm), Nd:YAF (1.047, 1.053, 1.313), Nd:YAP(1.08, 1.34), Ho:YAG (2.06) and Er:YAG (2.94 μm).
- (3) OPO (tunable) in nonlinear crystals using the output of (1) or (2) as the pumping sources.

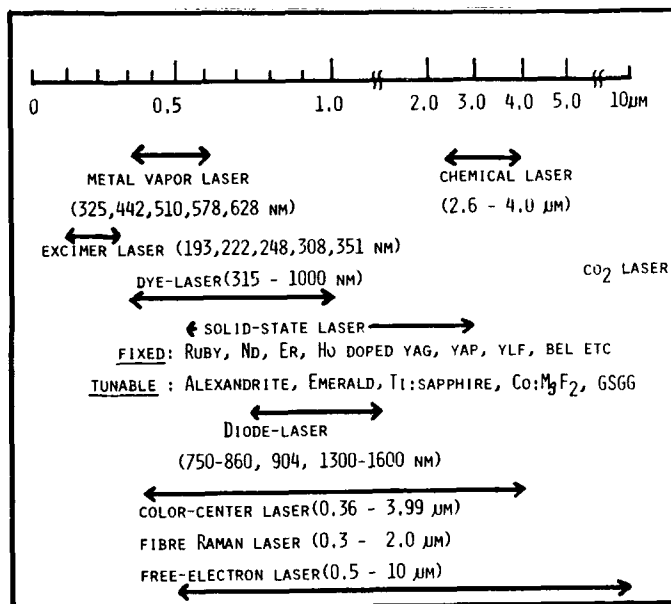


Fig. 1 Spectra of laser sources (0.2 - 10 μm) without using frequency conversion techniques.

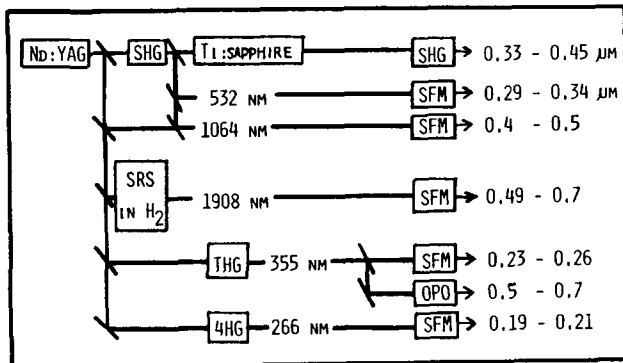


Fig. 2 Tunable new lasers in UV and visible (0.189-0.7 μm) generated from SFM and OPO in YAG-pumped sapphire.

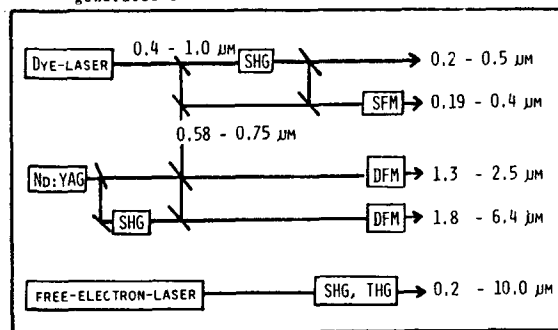


Fig. 3 New laser sources in visible and infrared using SFM and DFM in dye-laser, Nd:YAG and free-electron lasers.

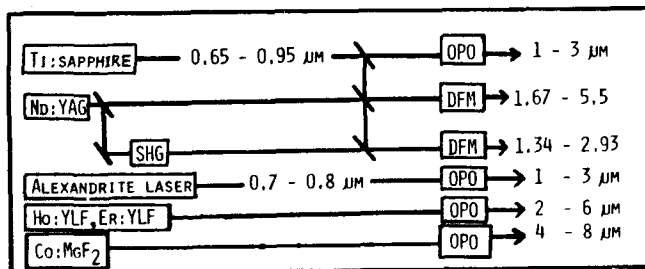


Fig. 5 DFM and OPO for new laser sources with tuning ranges of 1 - 8 μm .

Table 1—Nonlinear Crystals Transparent From 0.2-5 μm [9]

Material	Transparency Range (nm)	Phase-Matching Range (Type)	Damage Threshold (GW/cm ²)	Relative Figure Of Merit (1)
KDP	200-1500	517-1500 (I)	0.20	1.0
KDP	200-1500	732-1500 (II)	0.20	1.8
D-CDA	270-1600	1034-1600 (I)	0.50	1.7
Urea	210-1000	473-1000 (I)	1.50	6.1
Urea	210-1400	600-1400 (II)	1.50	10.6
BBO	198-3300	400-3300 (I)	5.00	26.0
BBO	198-3300	526-3300 (II)	5.00	15.0
LAP	220-1950	440-1950 (I)	10.00	40.0
LiIO ₃	300-5500	570-5500 (I)	0.50	50.0
m-NA	500-2000	1000-2000 (I)	0.20	60.0
MgO:LiNbO ₃	400-5000	800-5000 (I)	0.05	105.0
KTP	350-4500	1000-2500 (II)	1.00	215.0
POM	414-2000	830-2000 (I)	2.00	350.0
MAP	472-2000	900-2000 (I)	3.00	1600.0
KNbO ₃	410-5000	840-1065 (II)	0.35	1460/1755 (2)
COANP	480-2000	960-2000	—	4690.0
DAN	430-2000	860-2000	—	5090.0
Structure-modulated LiNbO ₃	400-5000	800-5000	0.05	2460N ² (3)

(1) The relative figures of merit are based on the value of KDP in Type I phase-matching for SHG at 1.06 μm . All are at room temperature except D-CDA, MgO:LiNbO₃ and KNbO₃, where high-temperature noncritical phase-matching is employed. The absolute value for KDP is calculated in Reference 2 as 0.025 pm/V.

(2) For KNbO₃ crystal, room-temperature 90° phase-matching at 860 nm uses d32, while phase-matching at 986 nm uses d31. Numerically, $d32 = 1.33 \times d31 = 20.4 \text{ pm/V}$.

(3) Structure-modulated LiNbO₃ is grown in quasi-phase-matching conditions, where N is the number of periodic layers of the structure-grown crystal.

Table 2—Nonlinear Crystals Transparent From 0.5-20 μm [9]

Material	Transparency Range (μm)	Absorption (cm ⁻¹ at 10.6 μm)	Damage Threshold (MW/cm ²)	Relative Figure Of Merit (1)
AgGaS ₂	0.5-13	0.090	15	1.0
CdSe	0.75-20	0.016	50	1.6
AgGaSe ₂	0.71-18	0.050	12	6.3
TAS	1.26-17	0.040	16	6.5
CdGeAs ₂	2.4-18	0.230	40	9.2
ZnGeP ₂	0.74-12	0.900	3	14.0
Te	3.8-32	0.960	45	270.0

(1) The relative figure of merit is based on the value of 14.0 pm/V for SHG at 10.6 μm in AgGaS₂.

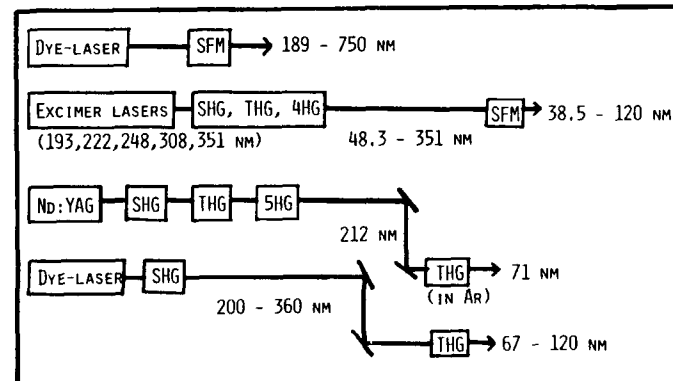


Fig. 4 XUV sources generated from SFM and THG of dye-lasers and the harmonics of Nd:YAG and excimer lasers.

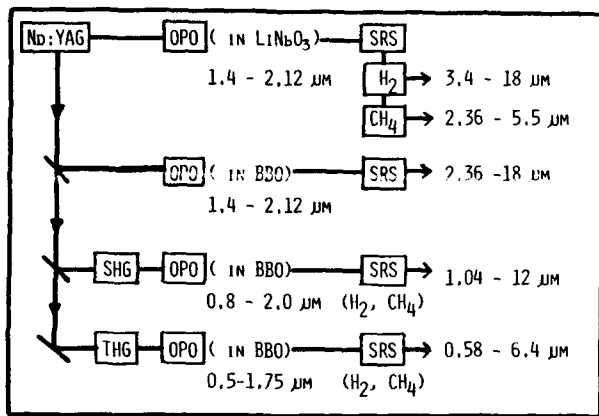


Fig. 6 Tunable new laser sources (1 - 18 μm) using OPO and Raman-shift in crystals and gas media, respectively.

Nonlinear crystals suitable for the generation of tunable mid-IR sources (2-5 microns) as shown in Tables 1 and 2. Crystals shown in Table 1 have very high damage threshold (up to 10 GW/cm²), however, they are limited by the transparency range of 0.2-5 microns. Crystals in Table 2 have much wider IR transparency ranges and higher figure of merits (1,000-30,000 times of KDP), however, they are limited by the rather low damage thresholds (up to 45 MW/cm²). Furthermore, growth technology for crystals shown in Table 2 are not as advanced as that of those shown in Table 1. Crystals (mainly in Table 1) for the generation of 2-4 microns sources via OPO/OPA processes shall include BBO, KTP, MgO-doped lithium niobate(LN), structure-modulated LN, potassium niobate and organic crystals of LAP, m-NA, POM, DAN and NPr. Furthermore, thin film and/or wave-guide crystal such as proton-exchanged lithium niobate may also be the potential candidates. In using KTP crystals, we shall note that the phase matching angles are different for flux-grown(Chinese crystal) and hydrothermally-grown (Airtron's Crystal) KTP.

We should also note that those semiconductor crystals shown in Table 2 have very high FOM, 500-5,000 times of KDP, however, they are limited by rather low damage threshold and usually can not be temperature tuned for NPM operation. Considering the transmission ranges of 0.4-5 μm for KTP and KNbO3 and their possible NPM operation, these two crystals may be as good as or even better than the semiconductor crystals for applications of OPO in mid-IR ranges.

CRITICAL ISSUES OF OPO

The critical issues of OPO may be outlined as follows:

- 1) conversion efficiency and threshold power
- 2) tunability and beam steering
- 3) cavity design
- 4) output beam quality

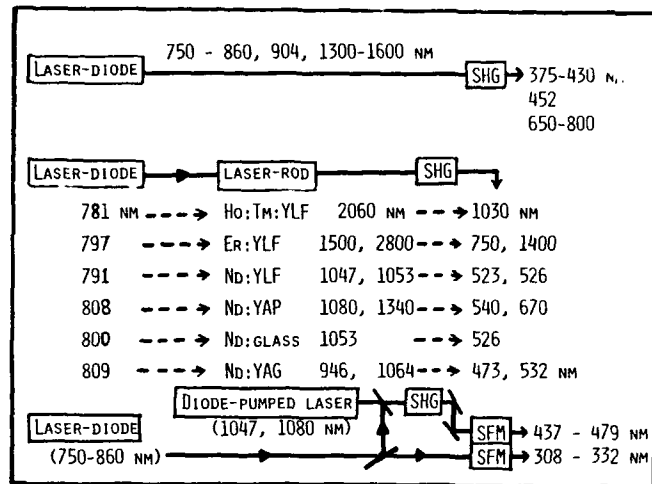


Fig. 7 Visible and UV sources(308 - 540 nm) generated from SHG and SPM of diode-lasers and diode-pumped-lasers.

Greater details are discussed as follows.

The OPO gain function is given by

$$g = [\Gamma^2 - (\Delta k/2)^2], \quad (2)$$

where the parametric gain constant is given by

$$\Gamma^2 = 8 \pi^2 \text{deff}^2 / (n_1 n_2 n_3 \lambda_1 \lambda_2 \lambda_3 c), \quad (3)$$

the effective d-coefficiency (deff) depending upon the crystal symmetry and the phase-matching angle (θ).

For BBO (type I),

$$\text{deff}(\text{esu}) = 4.26 \times 10^{-9} \cos \theta$$

For MgO:LiNbO3 (type I),

$$\text{deff}(\text{esu}) = 12 \times 10^{-9} \sin \theta$$

For POM (type I),

$$\text{deff}(\text{esu}) = 23 \times 10^{-9} \sin (2\theta)$$

For KTP (type II),

$$\begin{aligned} \text{deff}(\text{esu}) = & (d_{24}-d_{15}) \sin(2\theta) \sin(2\phi) \\ & + (d_{15} \sin^2 \phi + d_{24} \cos^2 \phi) \sin \theta \end{aligned}$$

where for KTP values of (d_{15} , d_{24}) = (6.1, 7.6) (pm/V), 1 (pm/V) = 2.4×10^{-9} (esu)

Note that $d_{36}(\text{of KDP}) = 0.43$ (pm/V) = 1.04×10^{-9} (esu).

Within the constant-pump approximation and for Gaussian spatial and temporal profiles of the pump beam, the E.T.(J) may be expressed by

$$J = (2.25 T/\text{gfL}) \times [(L/2 TC) \ln(P_n/P_c) + 2 \alpha L + \ln(2/\sqrt{R})],$$

where

$$\begin{aligned}L_2 &= L_1 + (n-1)L \\L_w &= 1.023 W_p / P, \text{ for } W_p \approx W_s \\L_3 &= L \operatorname{erf}(0.886 L / L_w) \\T &= \text{pulse duration}\end{aligned}$$

R = reflectance of the outcoupling mirror.

Where L , L_1 and L_2 are the crystal physical length, cavity length and optical cavity length, respectively (with crystal refractive index n). L_w and L_3 are the walk-off length and the effective gain length.

The beam overlap function $f = [W_p^2 W_s^2] / (W_p^2 + W_s^2 / 2)$ and the gain function, for the phase-matched case in eq. (2), is given by

$$g = 297.25 d_{\text{eff}}^2 / (n_p n_s n_i \lambda_s \lambda_i) \quad [\text{cm}^2 / \text{MW}]$$

for units of d_{eff} in (pm/V), pump intensity in (MW/cm²) and wavelength in microns.

Based upon the above discussion the important issues for the system design are addressed as follows:

- 1) E.T. may be reduced by shorter cavity (or optical) length,
- 2) Longer crystal length (L), within the limit of L walk-off length (L_w), achieves smaller E.T. which is insensitive to L , when L_w is much longer than L .
- 3) Higher coupler reflectance (60-80 %) may reduce the E.T.
- 4) Larger pump beam spot size shall reduce the walk-off effects and thus reduce the E.T. For crystals with low damage threshold longer confocal parameter, i.e., loose focusing, should be considered.
- 5) Possible direct coating on the OPO/OPA crystals will be considered for the purpose of low loss and system compactness. For high efficiency crystals OPO cavity length in the order of one cm may be achieved.

To optimize the output OPO efficiency, we propose the following issues:

- 1) Far field should be used for better beam quality and to avoid the possible "hot spot" of the pump beam.
- 2) Better beam coupling for higher SHG conversion efficiency may be achieved by using cylindrical focal lens, where the pump beam is focused preferentially in the "insensitive" direction of the crystal. In the case of type I BBO crystal, this insensitive direction is in the ordinary-ray direction.

3) High damage coating mirror should be used for the OPO cavity, where the pump beam must be focused above threshold power density in the order of 200-300 MW/cm²

4) The beam quality of the pump beam is critical for OPO efficiency. Therefore in the two-stage OPO processes, the output from the first-stage OPO (1.8-2.5 μm) which reserves the good beam quality and provides the good pumping efficiency in the second-stage OPO with output spectral ranges of 2.5-5 μm .

Tunable sources generated from OPO in BBO and KTP crystal [8,17,18,20]

Tunable solid-state lasers in the mid-IR spectral range (1.8-5 micron) may be generated from the direct output of, for example, colour-center lasers (0.65-4 micron), Co:MgF₂ laser (1.5-2.3 micron), Ho-doped laser (about 2 micron) and Er-doped laser (about 3 microns). The phase matching curves at various pumping wavelengths (0.532-1.8 microns) are calculated and the associated effective nonlinear coefficients are shown in Figs. 9-11. For BBO crystal, it is known that type I has a larger walk-off angle and is less efficient than type II. As shown in Fig. 9, we have defined the polarization directions for the pump, signal and idler waves (in order) as follows:

Type I : [e,o,o]
Type IIA: [e,e,o]
IIB: [e,o,e].

For KTP we have defined:

Type I : [e2,e1,e1]
Type IIA: [e2,e2,e1]
IIB: [e2,e1,e2],

where e1 and e2 represent the slow (large index) and fast (small index) directions of the polarized waves, noting that $n_x < n_y < n_z$ for KTP crystal.

As shown in Fig. 10, a type II KTP crystal is pumped by a Nd:YAG laser. Two configurations are defined by the polarization directions of the pump, signal and the idler beam with wavelengths of $\lambda_3, \lambda_1, \lambda_2$, respectively. The polarization of ($\lambda_1, \lambda_2, \lambda_3$) are in the axis of (x,z,x), in order, for A and (z,x,x) for B. We note that B has a wider tuning range than that of A, however the effective d-coefficient (d_{eff}) of B is smaller. Within the mid-IR tuning ranges, the values of d_{eff} of KTP vary from 5.5 to 7.5 (pm/V) which are 2.4 to 17.4 times of the d of KDP crystal. therefore the OPO gain of KTP at the degenerate point will be about 36 times of that of KDP.

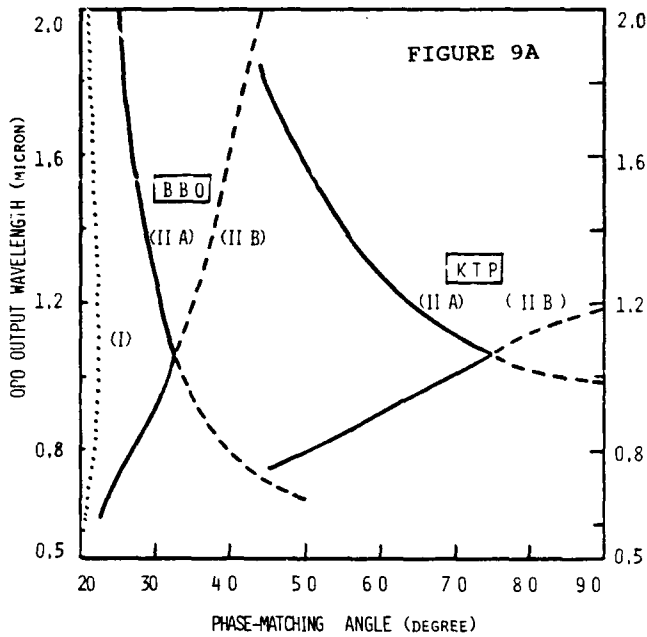


Fig. 9 Phase matching curves for BBO and KTP type I and II and the associated effective d-coefficients where double-YAG (532 nm) is used as the pumping source.

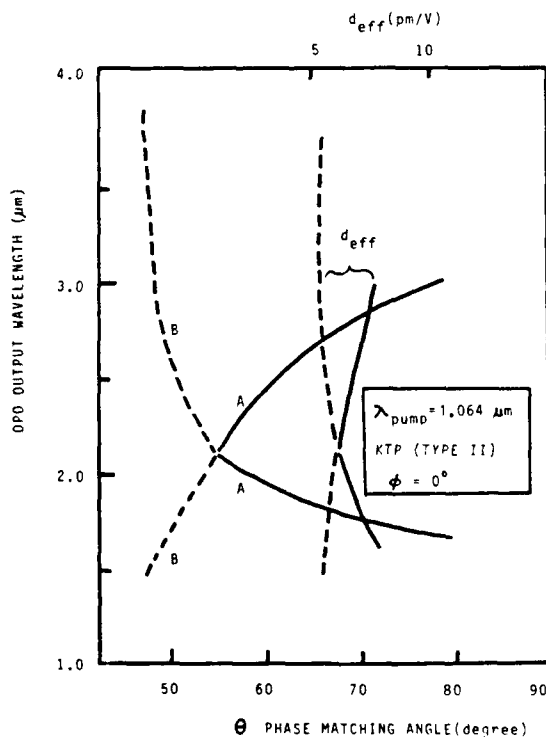
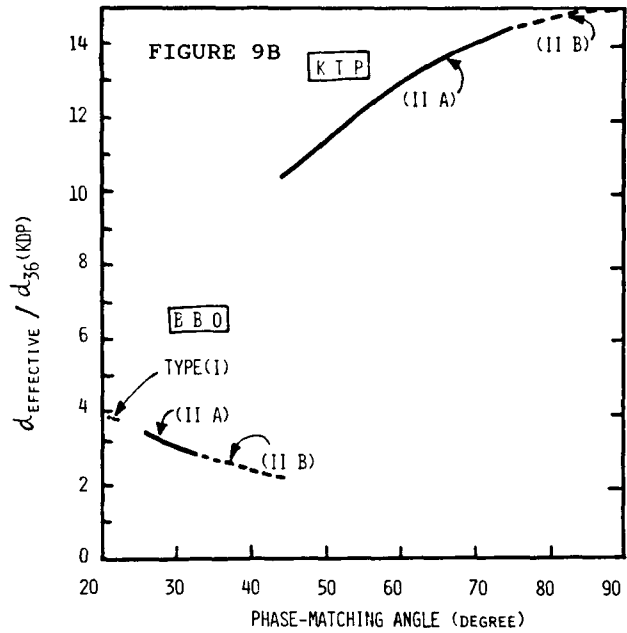


Fig. 10 Same as Fig.9 but for KTP pumped by 1064 nm (YAG).

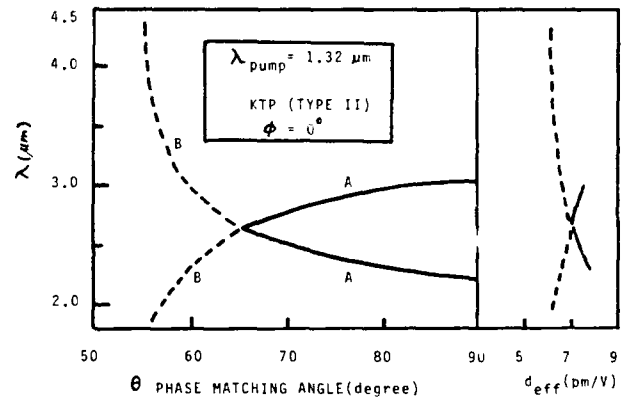


Fig. 11 Same as Fig. 10 but for 1320 nm pumping source.

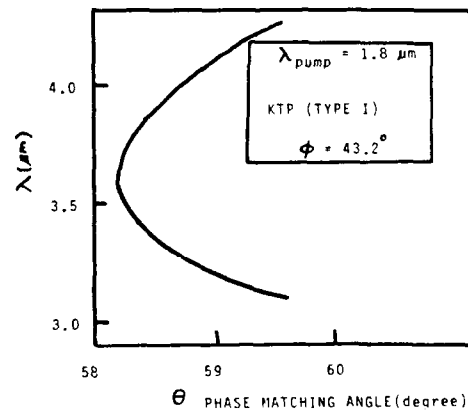


Fig. 12 Type I KTP pumped by 1.8 μm.

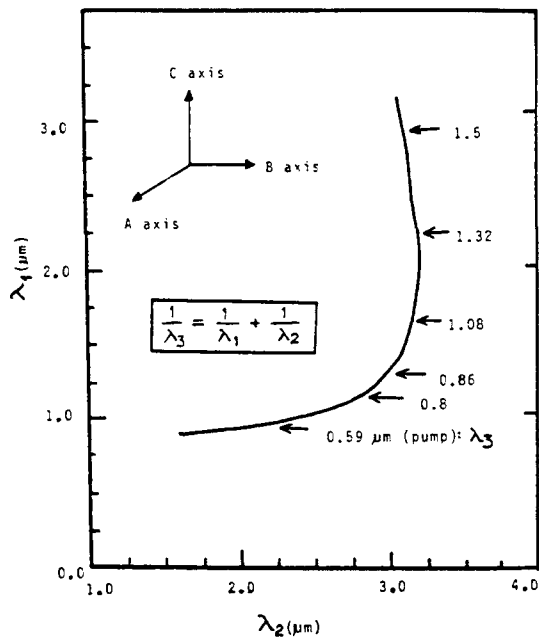


Fig. 13 Noncritical phase matching of type II KTP pumped by various wavelengths for the polarization directions [c,a,c].

As shown in Fig.11, higher deff values, 6-8(pm/V), may be achieved when a 1.32 micron laser is used as the OPO pump source. Tuning ranges near the degenerate point of 2.4 - 2.8 microns may be efficiently obtained with deff values of about 50 times that of KDP.

Fig.12 Shows the OPO curve for a type I KTP, where the type II KTP can not be efficiently phase-matched. The deff values in this case, at the degenerate point, is about 0.6 (pm/V) which is rather low compared with that of type II KTP pumped by 1.064 and 1.32 microns lasers.

The noncritical phase matching (NPM) using KTP (type II) is shown in Fig.13. Mid-IR tuning range from the signal or the idler beam may be achieved by various pumping wavelengths. The polarization directions of the pump, signal and idler beam are in the C, A and A axis, respectively. The important features of the NPM operation include: (1) Very wide angular, spectral and temperature acceptance width may be achieved in comparison with that of the critical matching case. (2) Rapid-tuning (beam steering) may be achieved via the tunable pumping sources (such as Ti:sapphire or diode-lasers), in which angle-tuning is not required. (3) Very high OPO gain may be achieved in this NPM operation.

The alternative of the generation of mid-IR tunable lasers is to use the difference frequency generation (DFG), where a laser in visible spectral regime is usually required. For example, tuning ranges of 1 - 2.9 microns may be achieved by DFG of a doubled-YAG--pumped Ti:sapphire laser (0.65-1.1 microns) and the pump itself (532 nm).



Fig.14 Phase-matching angle curves for optical parametric oscillation (OPO) in BBO (type I) crystal for various pumping wavelengths (in nm): (A) 600, (B) 625, (C) 650, (D) 700, (E) 775, (F) 825, (G) 875, (H) 925.

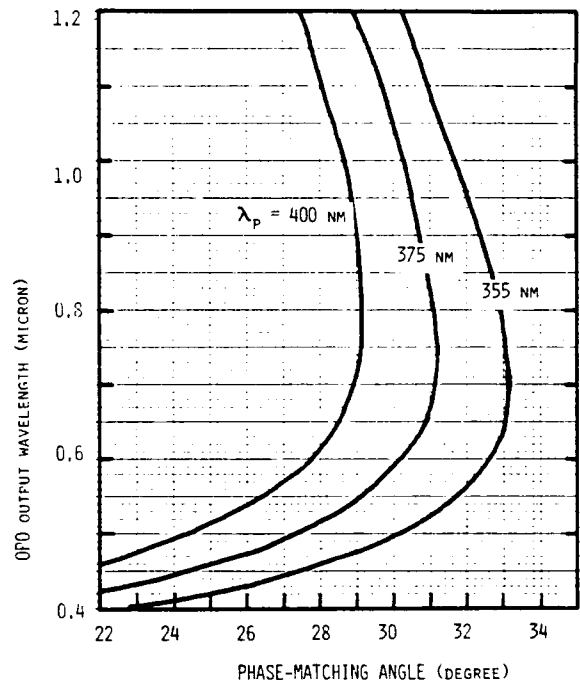


FIG.15 OPO PHASE-MATCHING ANGLES FOR TYPE I BBO CRYSTAL AT VARIOUS PUMPS λ_p .

V. NONCRITICAL PHASE MATCHING (NPM) CRYSTALS

The advantages of frequency conversion using the NPM condition include: (1) high effective d-coefficient, (2) largest acceptance widths of angle, temperature and spectrum and (3) small walk-off. Therefore crystals achieving NPM conditions by temperature-tuning or other means promise the efficient conversion of low-power lasers such as diode lasers and diode-pumped lasers. Crystals of KTP, potassium niobate (KN) and MgO-doped lithium-niobate (LN) have been identified as the best candidates for frequency conversion of diode-pumped lasers.

SHG of diode-pumped Nd:YAG using MgO-doped LN crystals operated at high temperature (107-degree C) was reported. [1] KN crystal of A-cut (for SHG of diode-lasers 830-860 nm) and of B-cut (for SHG of 1064 nm) have also been reported, [1], where temperature-tuned NPM conditions are achievable.

As shown in Fig. 16, we have calculate the NPM conditions for SFM as various polarization configurations. The conf. (A) and (B) represent the polarization directions of the three linearly polarized waves in the (bc-b) and (ac-a) axis, respectively. Special case of these curves, namely SFM of 809 nm (diode-pumping wavelength or the absorption peak of Nd:YAG) and 1064 nm (lasing wavelength) with an output of 459 nm has been reported recently. [21]

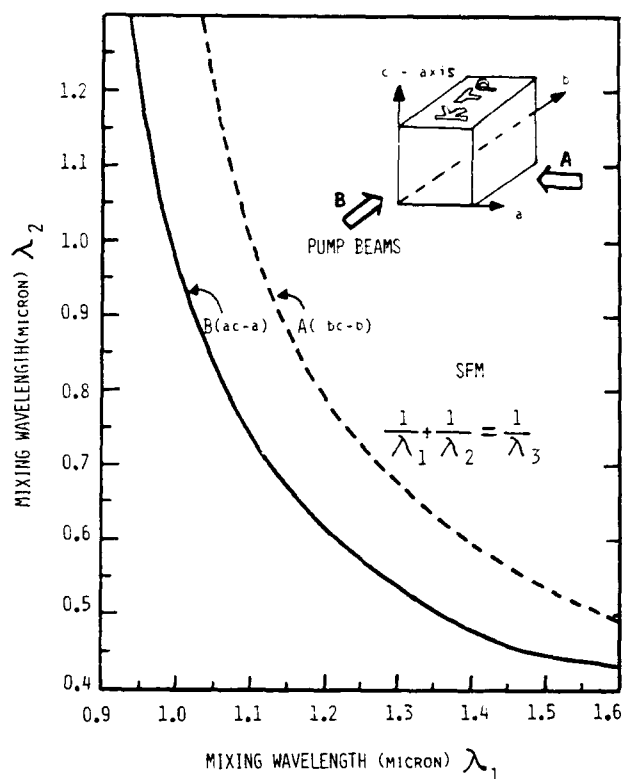


Fig. 16 Noncritical phase matching using type II KTP for two polarization configurations A: [b,c,b] and B: [a,c,a]. (see text).

REFERENCES

- [1] C. Chen, B. Wu, A. Jiang and G. You, Sci. Sin. Ser B28, 235(1985).
- [2] C. Chen, B. Wu, G. You and Y. Huang, Digest of Technical papers the XIIIth IQEC(1984), paper MCC5.
- [3] K. Kato, IEEE. J. Quantum Electron. QE-22, 103(1986).
- [4] K. Miyazaki, H. Sakai and T. Sato, Opt. Lett. 11, 797(1986).
- [5] C. Chen, Y.X. Fan, R. C. Eckardt and R. L. Byer, SPIE Proc. 681 p.12-19(1986).
- [6] D. Eimerl, SPIE Proc. 681, p.2-5(1986).
- [7] D. Eimerl, L. Davis, S. Velsko, E. K. Graham and A. Zalkin, J. Appl. Phys. 62, 1968(1987).
- [8] J. T. Lin, Proc. of LASER'86(STS Press, VA), p. 3-7(1986).
- [9] J. T. Lin and C. Chen, Laser & Optronics, P. 59, November(1987).
- [10] J. T. Lin, Digest of Technical Papers of CLEO'87, paper TuH4.
- [11] J. T. Lin, S. Savrda, J. Montgomery and R. McKinney, Program Digest OSA Annual Meeting (Rochester, NY), paper WR1(1987).
- [12] J. T. Lin, SPIE Proc. vol. 898(1988), in press.
- [13] P. Lokai et al, Technical Digest, CLEO'88, paper ThG2.
- [14] K. Kuroda et al, Technical Digest, CLEO'88, paper WV4.
- [15] A. Lago et al, Opt. Lett. 13, 221(1988).
- [16] C. Chen, Proc. Laser Materials and Laser Spectroscopy, July 24-27 (1988), Shanghai, China.
- [17] J. Q. Yao and J. T. Lin, Technical Digest, IQEC'88 (in press).
- [18] J. Q. Yao et al, Technical Digest, CLEO'88, paper TuJ5.
- [19] L. J. Bromley et al, Technical Digest, CLEO'88, paper MJ4.
- [20] J. T. Lin, Proc. Laser Materials and Laser Spectroscopy, July 24-27(1988), Shanghai, China.
- [21] W. P. Risk et al, Technical Digest, CLEO'88, paper FE4.

COUPLING OF LASER MODES BY A SINGLE SIDEBAND INTRACAVITY MODULATOR - A NON-LINEAR COUPLED-MODE ANALYSIS

Odin P. McDuff
Bader Badreddine
Department of Electrical Engineering
The University of Alabama
P. O. Box 6169
Tuscaloosa, Alabama 35487-6169

Abstract

Forced mode locking of lasers by means of intracavity phase and loss modulation has been studied extensively over the years. In addition lasers have been mode-locked by modulating the gain, such as in the case of the synchronously pumped dye laser or the current modulated diode laser. In all of these cases, from the coupled-mode point of view, the modulation couples each mode to the adjacent modes above and below it in frequency. A single sideband modulator can be constructed¹ which, in essence, shifts the frequency of the optical signal that passes through it. In the coupled mode point of view a mode could be coupled only to the adjacent mode whose optical frequency is above (or below) it by the $c/2L$ frequency. This paper reports the results of a non-linear coupled-mode analysis of a single sideband intracavity modulated laser, using techniques similar to that of McDuff and Harris.² The analysis includes the effects of laser medium saturation and mode pulling and determines the operating characteristics of the laser. The paper also presents a technique whereby a loss modulator and phase modulator can be combined appropriately to produce single-sideband-type mode coupling.

Introduction

Forced mode locking of lasers to produce short output pulses has been accomplished by either the use of intracavity phase or loss modulation and has been studied extensively both theoretically and experimentally over the years. From the coupled mode point of view, each laser axial mode is coupled to the adjacent modes which are above and below it by the $c/2L$ mode spacing frequency (assuming modulation at $\nu = 2\pi(c/2L)$). By the use of a single sideband modulator, however, which in essence shifts the frequency of the optical signal that passes through it, one would expect that mode coupling could be obtained in which an axial mode is coupled only to the adjacent mode whose optical frequency is above (or below) it by the $c/2L$ frequency. The purpose of the theoretical study reported here was to determine if laser mode-locked pulsing would be produced by the insertion of an intracavity single sideband modulator driven at the $c/2L$ frequency and to study the characteristics of the operation. Mode-locked pulsing was shown to occur. In addition, the work showed that a particular combination of intracavity phase and loss modulators also could be used to produce single sideband type mode coupling. Single sideband coupled-mode equations analogous to the regular "double sideband" equations of McDuff and Harris² were obtained and solved by numerical integration.

Combination of Phase and Loss Modulators

Although in the course of the work a rotating-wave-plate single sideband modulator of the type described by Buhrer, et al,³ was considered first, it is easier to present the theory by considering first the phase and loss modulator combination discovered later in the work.

In the papers by McDuff and Harris² on loss modulation and by Harris and McDuff⁴ on phase modulation they assumed respectively a loss modulator having loss per pass

$$\alpha(t) = \alpha_m (1 + \cos \nu_m t) \quad (1)$$

and a phase modulator having a single pass phase retardation

$$\delta(t) = \delta_m \cos \nu_m t. \quad (2)$$

The electric field in the cavity was then expanded as a sum of the normal mode eigenfunctions,

$$E(z,t) = \sum_n E_n(t) \cos(\nu_n t + \phi_n(t)) U_n(z), \quad (3)$$

where $U_n(z) = \sin(n\pi z/L)$. The $E_n(t)$ and $\phi_n(t)$ are the slowly time varying amplitude and phase of the n th mode, ν_n is its frequency, L is the cavity length, and n is the number of spatial variations of some central mode whose frequency is chosen to be closest to the center of the atomic fluorescence lines. The resulting coupled mode equations for loss modulation² are shown⁴ by McDuff and Arnous in another paper in these proceedings. The coupled mode equations for phase modulation, assuming equation (2) above, are similar to

the loss equations but have sine functions where the loss equations have cosine and cosine functions where the loss equations have sine. If both loss and phase modulators are present with $\alpha(t)$ and $\delta(t)$ as given above, the coupled mode equations include both the couplings from $\alpha(t)$ and $\delta(t)$ to both upper and lower adjacent modes. If however the phase modulator produces a phase retardation 90° out of phase with the loss modulator, i.e.,

$$\delta(t) = -\delta_M \sin v_m t, \quad (4)$$

and if the modulator drive signal amplitudes are chosen such that

$$\delta_M = \alpha_M/2, \quad (5)$$

then the couplings from the $(n-1)$ th mode to the n th mode cancel (by reversing the ac phase of either equation (1) or equation (4) the couplings from the $(n+1)$ th mode to the n th mode can be made to cancel).

The result is that one obtains "single sideband" mode coupling equations as follows:

$$(\dot{\phi}_n - n\Delta v + \frac{c}{2L} \psi_n) E_n = -\frac{c\alpha_{ss}}{L} [E_{n+1} \sin(\phi_{n+1} - \phi_n)] \quad (6)$$

$$\dot{E}_n + \frac{c}{2L} \alpha_n E_n - \frac{c}{2L} G_n E_n = -\frac{c\alpha_{ss}}{L} E_n - \frac{c\alpha_{ss}}{L} [E_{n+1} \cos(\phi_{n+1} - \phi_n)] \quad (7)$$

where

$$\alpha_{ss} = \alpha_c = \delta_c, \quad (8)$$

$$\alpha_c = \alpha_M/2, \quad \delta_c = \delta_M \quad (9)$$

and the terms Δv , α , ψ , and G are defined by McDuff and Arnous.⁵ One notes that in equations (6) and (7) that only the $(n+1)$ th mode is coupled to the n th mode, as stated above.

Direct Single Sideband Electro-Optic Modulation

The original plan was to consider a direct single sideband modulator consisting of a birefringent crystal acting as a rotating wave plate, in combination with two quarter-wave plates placed one on either side of it^{1,3} inside the laser cavity. If one assumes an optical signal input $E_x e^{jv_n t}$ to the quarterwave plate--cubic electro optic crystal combination, multiplication of the appropriate Jones matrices shows that after a round trip through the "modulator" the output is given by

$$\text{x-component: } -E_x \sin^2 \Gamma/2 e^{j(v_n + v_m)t} - E_x \cos^2 \Gamma/2 e^{jv_n t} \quad (10)$$

$$\text{y-component: } -j E_x \sin \Gamma \sin \frac{1}{2}(v_m t) e^{jv_n t} \quad (11)$$

The first term of equation (10) corresponds to an optical signal shifted by the angular frequency v_m and equal to $\sin^2 \Gamma/2$ times the input. The second term in equation (10) corresponds to an optical signal at the original angular frequency v_n and equal to $\cos^2 \Gamma/2$ times the input. The orthogonally polarized component in equation (11) represents energy lost from the input signal.

Siegman⁸ shows that a modulator with a voltage transmission given by

$$t_{AM}(t) = e^{-\Delta_m(1+\cos v_m t)} \approx 1 - \Delta_m - \Delta_m \cos v_m t \quad (12)$$

gives loss modulated mode coupled equations (which can be shown to be similar to those of McDuff and Harris² if $\Delta_m = \alpha_c$). Furthermore, Siegman shows that a phase modulator with transmission given by

$$t_{FM}(t) = e^{j\Delta_m \cos v_m t} \approx 1 + j\Delta_m \cos v_m t \quad (13)$$

gives phase modulated mode coupled equations (which can be shown to be similar to those of Harris and McDuff⁴ if $\Delta_m = \delta_c$). One can show that if

$$t_{FM}(t) = e^{-j\Delta_m \sin v_m t} \approx 1 - j\Delta_m \sin v_m t, \quad (14)$$

and if the two modulators are placed in cascade, then an overall transmission

$$t_{ss} \approx 1 - \Delta_m - \Delta_m e^{jv_m t} \quad (15)$$

is obtained, which gives single sideband coupled mode equations like equations (6) and (7).

Comparing equation (15) to equation (10), it is seen that

$$\Delta_m = \sin^2 \Gamma/2 \quad (16)$$

$$1 - \Delta_m = \cos^2 \Gamma/2 \quad (17)$$

and thus, the single sideband coupling coefficient for the rotating waveplate electrooptic modulator is given by

$$\alpha_{ss} = \sin^2 \Gamma/2. \quad (18)$$

To increase mode coupling, the electrooptically produced birefringence must be increased. At low α_{ss} , which is in fact the condition assumed in equations (12) - (17), one has approximately

$$\alpha_{ss} \cong (\Gamma/2)^2 \quad (19)$$

Solution of the Coupled Mode Equations

The coupled mode equations (6) and (7) for single sideband modulation were solved by a Runge-Kutta numerical integration procedure. The method used was the select initial mode amplitudes and phases and laser parameters and then permit the numerical integration to continue until a steady state solution had been reached (with the $\dot{E}_n = 0$ and the $\dot{\phi}_m = 0$ or all ϕ_m equal to a constant independent of n). From the mode amplitudes and phases, the pulse intensity envelope was plotted versus $v_m t$, since the laser's pulse characteristics are the basic criteria by which mode-locked performance is evaluated. Both a homogeneously broadened laser and an inhomogeneously laser were studied. A characteristic mode-locked-type output optical pulse could be obtained with both types of lasers, although the operating characteristics were different from the case of conventional "double sideband" coupling.

Results for Inhomogeneous Broadening

An argon laser was modeled as an example of an inhomogeneously broadened laser. A linewidth of 5 GHz was assumed with an axial mode spacing $c/2L = 71.6$ MHz. A fractional single pass cavity loss of 10% was assumed, meaning $\alpha_n = 0.10$. The unsaturated line center power gain was assumed to be 12.8%, meaning $G_n = 0.128$ at $n = 0$ and zero optical signal level. Figure 1 shows the resulting mode distribution at two values of cross-coupling coefficient. As the cross coupling is increased, the mode spectrum is moved farther from line center ($n = 0$ mode). The number of modes and mode amplitudes decrease as the distribution is moved toward the wings of the gain curve where there is less net gain. Figures 2, 3, and 4 show the results of these changes in the mode spectrum. As the cross-coupling α_{ss} is increased from zero, it first locks the modes together, producing a pulse whose width depends primarily on the number of free running modes. As α_{ss} is increased further, a better pulse is produced due to better mode phases. Then, continuing to increase α_{ss} , a worse pulse is produced due to the fewer and lower amplitude modes. A continuation in the increase of α_{ss} will eventually extinguish the laser. The phase of the pulse relative to the modulator drive signal changes with α_{ss} , as shown in Figure 2. At higher values of α_{ss} , the pulse phase shift approaches zero, which means that the pulse is passing through the loss modulator at its minimum loss time which is at $v_m t = \pi$ (this is like the double sideband loss modulator case²). However, the pulse then is passing through the phase modulator at the time that it has the greatest $d\delta/dt$, giving the greatest doppler frequency shift of the pulse. This is not the situation that occurs with phase-modulator-produced or FM mode locking, because there the pulse passes through the phase modulator at one of the peaks of $\delta(t)$, where $d\delta/dt = 0$. Furthermore, the shift of the mode spectrum away from line center causes the medium dispersion to change the zero effective detuning of the modulator. This causes the pulse phase shift to depend more strongly on modulator cross coupling than would be the case with double sideband mode coupling. In fact, in the simulation it is possible to remove the effect of dispersion completely by simply setting $\psi_n = 0$. This was done and the pulse phase shift remained identically zero for all values of α_{ss} .

Results for Homogeneous Broadening

A Nd:YAG laser having a 3 GHz linewidth intracavity etalon was modeled. The assumed axial mode spacing of 150 MHz then gave a ratio of mode spacing to linewidth of 0.05. Although this etalon had a smaller bandwidth than what actually might be used in practice, it was difficult to obtain steady state computer solutions with small values of the linewidth/mode-spacing ratio, and therefore this value was assumed. A fractional single pass cavity loss of 10%, or $\alpha_n = 0.1$, was assumed and a line center unsaturated single pass power gain of 16% was assumed. Figure 5 shows the mode distributions for two values of α_{ss} . The shift of the mode spectrum off to the side is noted as in the case of inhomogeneous broadening. However, here in the idealized homogeneous case, the coupling is necessary in order to establish the mode spectrum (in the idealized homogeneous case, only one mode would oscillate when $\alpha_{ss} = 0$). One also notes the relative symmetry of the mode spectrum about a center mode. For an increase in α_{ss} , the discussion for the inhomogeneous case

still applies, with the exception that here there is a larger range of α_{ss} that causes an improvement before the pulse performance deteriorates. The results are shown in Figures 6-8. Again the phase of the pulse depends strongly upon the value of α_{ss} , for the same reason as in the inhomogeneous laser. A computer run with $\psi_n = 0$ gave zero pulse shift regardless of the value of cross-coupling α_{ss} , as it did in the inhomogeneous case.

Modulator Detuning

In both types of lasers the effects of detuning the modulator were studied. The inhomogeneous laser was less affected by detuning in the negative direction while the homogeneous laser was less affected by detuning in the positive direction (the sign definition of $\Delta\nu$ used here is that of Harris & McDuff,⁴ that is, $\Delta\nu = \pi c/L - \nu$). When the mode spectrum shifts to the side of line center, the slope of the dispersion curve about the new effective center of the mode distribution changes, hence changing the actual effective zero detuning. The significance of the change is different for the two types of saturation. Large detuning also causes the pulse to deteriorate in shape, similar to the situation with double sideband mode locking.

Conclusions

Single sideband coupling between modes in a laser can produce mode-locked pulsing but with characteristics different from conventional double sideband phase or loss produced mode locking. The mode spectrum is shifted off to one side of line-center as the mode locking occurs. In the homogeneous case, the spectrum is still symmetrical and Gaussian-like, but in the inhomogeneous case, the spectrum becomes very asymmetrical. In the homogeneous case, an increase in mode cross coupling can result in improved performance; whereas, in the inhomogeneous case, a small coupling just large enough to lock the modes is preferable. This is in contrast to the double sideband mode-locked case where an increase in cross coupling can result in improved performance for both types of broadening.^{2,4} If the cross coupling is increased without limit, the laser eventually is extinguished as in the case of double sideband coupling. The single sideband mode coupling can be achieved by at least two schemes. A direct single sideband modulator using a rotating electro-optic wave plate^{1,3} can be used, or an appropriate combination of loss modulation and phase modulation can be used to obtain single sideband coupling. The studies reported apply to either type of scheme used.

References

1. C. F. Buhrer, D. Baird, and E. M. Conwell, Appl. Phys. Lett. 1, 46 (1962).
2. O. P. McDuff and S. E. Harris, IEEE J. Quant. Electr. QE-3, 101 (1967).
3. C. F. Buhrer, L. R. Bloom, and D. H. Baird, Appl. Optics 2, 839 (1963).
4. S. E. Harris and O. P. McDuff, IEEE J. Quant. Electr. QE-1, 245 (1965).
5. Odis P. McDuff and Amjad Arnous, A Study of Transients and Stability in Mode-Locked Lasers by Means of a Non-Linear Coupled-Mode Analysis, presented at the International Conference on Lasers '87, Lake Tahoe (1987), in these proceedings.
6. O. P. McDuff, Mode Coupling in Lasers, Ph.D. Dissertation, Stanford University (1966).
7. Bader Badreddine, A Theoretical Study of Single Sideband Mode Locking of Lasers, M.S. Thesis, The University of Alabama (1988).
8. A. E. Siegman, Lasers (University Science Books, California, 1986), Chapter 27.

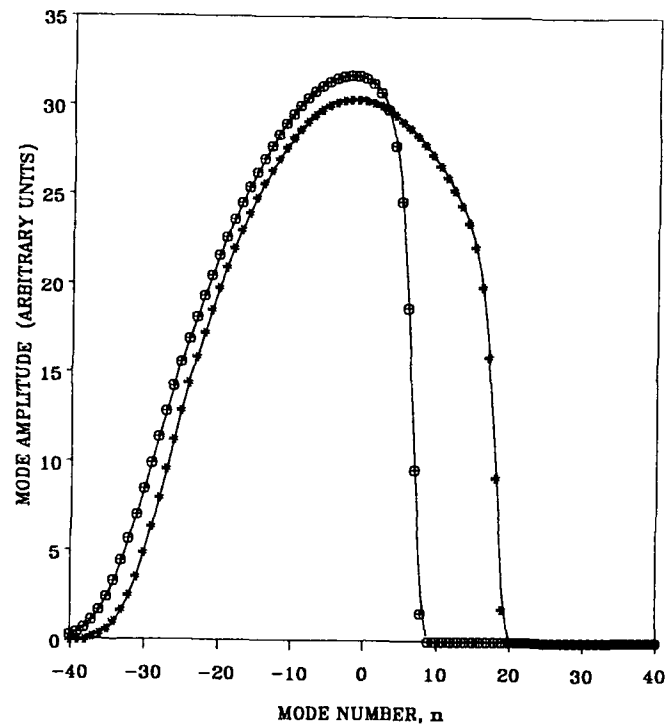


Figure 1. Mode distribution in a simulated argon laser with single sideband mode locking. Detuning $\Delta\nu = 0$ and modulator cross coupling: * $\alpha_{ss} = 0.015$; o $\alpha_{ss} = 0.027$.

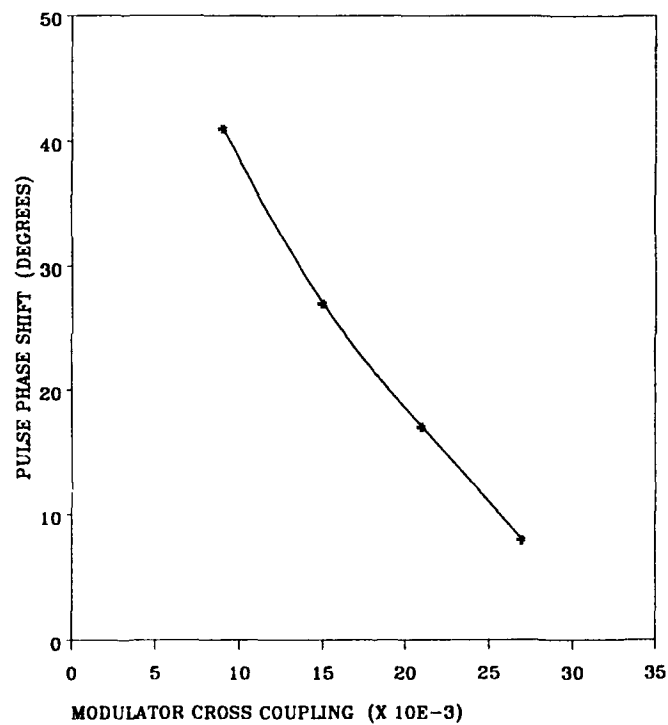


Figure 2. Phase shift of mode-locked pulse in a simulated argon laser vs. modulator cross coupling α_{ss} . Detuning $\Delta\nu = 0$.

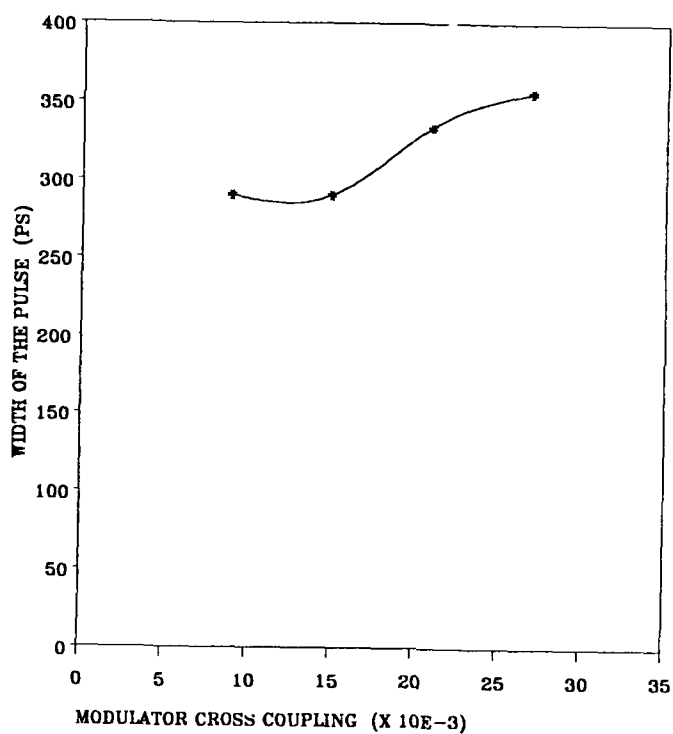


Figure 3. Width of mode-locked pulse in a simulated argon laser vs. modulator cross coupling α_{ss} . Detuning $\Delta\nu = 0$.

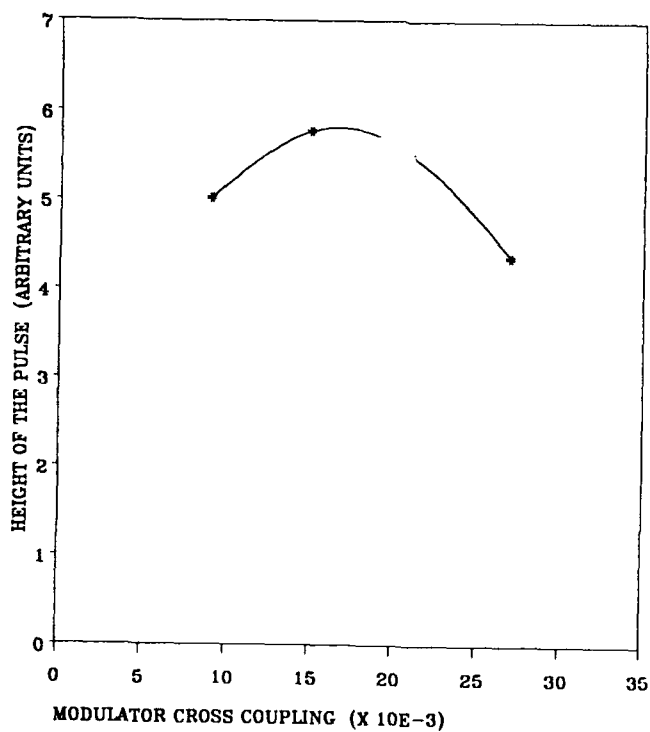


Figure 4. Peak intensity of mode-locked pulse in a simulated argon laser vs. modulator cross coupling α_{ss} . Detuning $\Delta\nu = 0$.

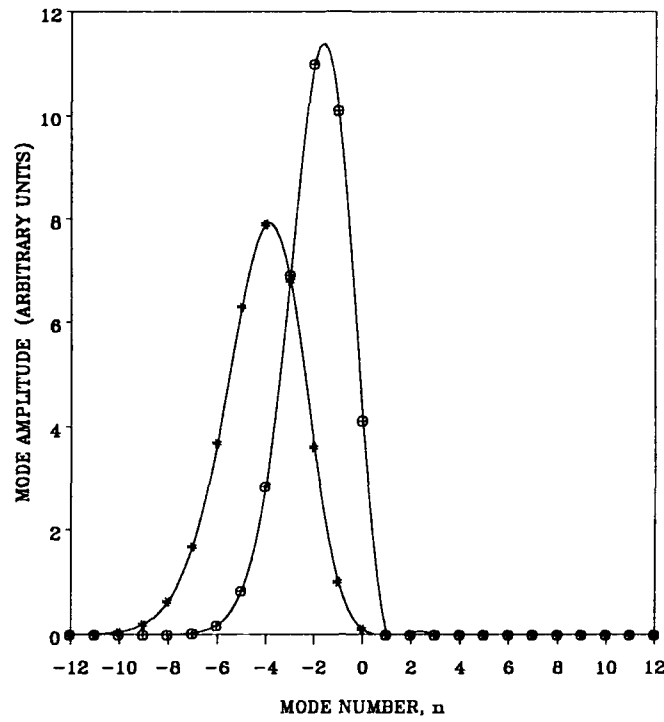


Figure 5. Mode distribution in a simulated Nd:YAG laser having a 3 GHz intracavity etalon. Detuning $\Delta\nu = 0$ and modulator cross coupling: * $\alpha_{ss} = 0.015$; o $\alpha_{ss} = 0.006$.

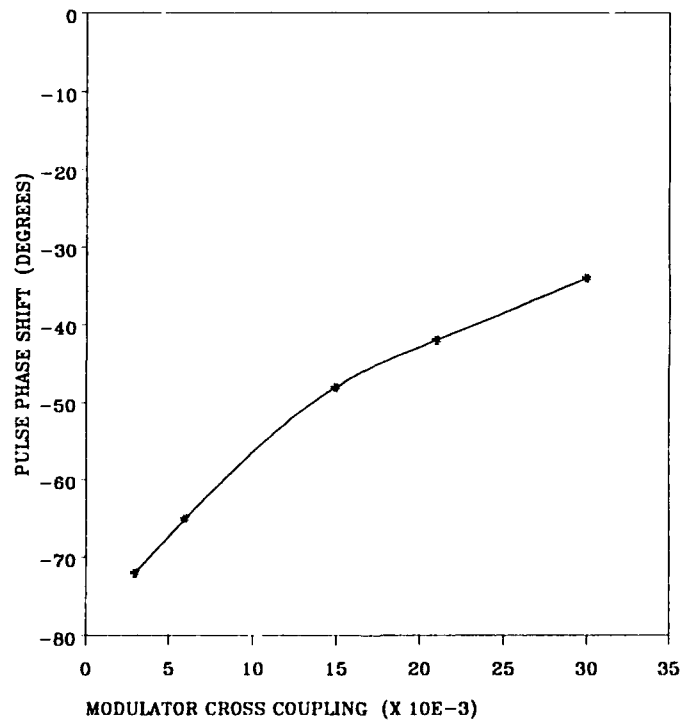


Figure 6. Phase shift of mode-locked pulse in a simulated Nd:YAG laser having a 3 GHz intracavity etalon vs. modulator cross coupling α_{ss} . Detuning $\Delta\nu = 0$.

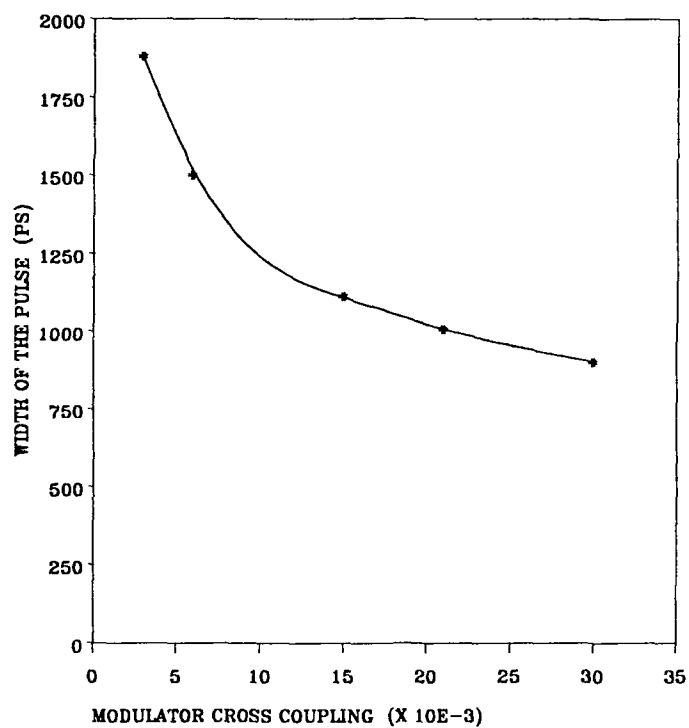


Figure 7. Width of mode-locked pulse in a simulated Nd:YAG laser having a 3 GHz intracavity etalon vs. modulator cross coupling α_{ss} . Detuning $\Delta\nu = 0$.

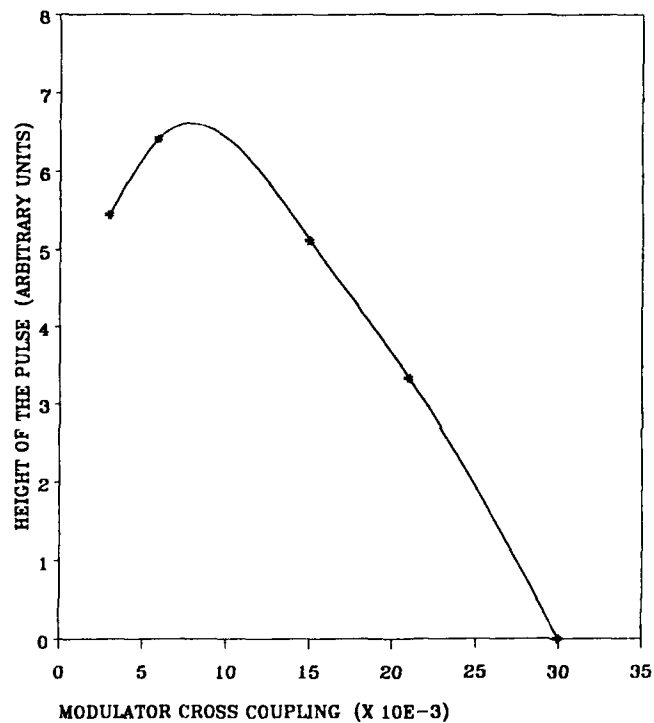


Figure 8. Peak intensity of mode-locked pulse in a simulated Nd:YAG laser having a 3 GHz intracavity etalon vs. modulator cross coupling α_{ss} . Detuning $\Delta\nu = 0$.

A NON-LINEAR COUPLED-MODE ANALYSIS OF GAIN-MODULATED LASERS

Odis P. McDuff
Dinesh Thati
Department of Electrical Engineering
The University of Alabama
P. O. Box 6169
Tuscaloosa, Alabama 35487-6169

Abstract

Forced mode locking of lasers can be accomplished by modulating the laser medium gain. In the case of synchronously pumped mode-locked dye lasers this is accomplished by pumping with the optical output of another mode-locked laser; whereas, in the case of the mode-locked diode laser, the pumping is accomplished by varying the diode current at the mode-locking repetition rate. In the dye laser the pump intensity is a repetition of short pulses rich in harmonics of the $c/2L$ frequency; however, in the diode laser the pump intensity may vary sinusoidally at the $c/2L$ frequency. This paper presents the results of a non-linear coupled-mode analysis of gain-modulated mode-locked lasers which is similar to that of McDuff and Harris¹ for loss-modulated mode-locked lasers. The analysis includes the effects of laser medium saturation and the effects of the characteristics of the pumping signal, all from the coupled mode point of view. It is shown that, due to saturation, a characteristic mode coupling occurs, irregardless of pump level, such that integrated gain and loss over the oscillating spectrum are balanced, and that the pulse width therefore depends upon the cavity loss. The effects of the pump pulse width are considered by including mode coupling terms at multiples of the $c/2L$ frequency.

Introduction

The production of mode-locked lasers by modulating the laser gain has received much attention. The synchronously pumped mode locked dye laser provides a source which can be used to produce the shortest optical pulses obtainable. The current-modulated diode laser is a possible source of an optical pulse train for use in communications.

The characteristics of the synchronously pumped mode locked dye laser have been studied by a number of researchers,²⁻¹⁴ both experimentally and theoretically.* The effectiveness of certain techniques of measurement of the dye laser output pulses e.g., the two-photon fluorescence method of obtaining the pulse width, have been questioned.¹⁵ To some extent the theoretical studies overcome the practical limitations of experimental measurements, thereby permitting a more thorough analysis of a laser system. The conclusions that have been reached in theoretical studies, however, are not entirely consistent from one study to the other.¹⁶ The authors of this paper perceived that the status of research in synchronously pumped mode-locked dye lasers could be improved by further theoretical investigations using a model which promised to give an extensive analysis of the performance under different operating conditions. The technique used was an extension of the coupled mode analysis procedure that was developed and used by McDuff and Harris^{1,17} for the study of loss-modulator and phase-modulator produced mode locking.

The Coupled Mode Model

The optical pulse from the mode-locked pump laser used in synchronous mode locking or the modulated drive current of a mode-locked diode laser can be considered as a pump which modulates simultaneously both the gain and the dispersion of the laser being mode locked. The modulation of dispersion, which in effect is the modulation of phase, is similar to the case treated by Harris and McDuff.¹⁷ The modulation of gain is similar to the modulation of loss treated by McDuff and Harris,¹ the basic difference between gain and loss being the sign of the parameter. Thus the combination of loss (or gain) modulation and phase modulation with the appropriate modifications yields the model for the pump-modulated laser. The case of sinusoidal modulation can be extended to the case where the modulation is performed by a gaussian pump pulse by treating the gaussian pulse as a combination of several sinusoidal harmonic components, the frequency of the fundamental being equal to the frequency spacing of the axial modes of the laser cavity.

* This is not meant to be an exhaustive list.

The Basic Coupled-Mode Equations

The derivation of the required nonlinear differential equations follows closely the approach developed for loss modulated and phase modulated lasers.^{1,17} The total cavity electric field is assumed to be made up of a number of axial modes as given by

$$E(z,t) = \sum_n E_n(t) \cos[\nu_n t + \phi_n(t)] U_n(z), \quad (1)$$

where $E(z,t)$ is the total cavity electric field, $E_n(t)$ and $\phi_n(t)$ are the slowly time varying amplitude and phase of the n th mode, ν_n is the radian frequency of the n th mode, and $U_n(z)$ gives the spatial variation of the n th mode. $U_n(z)$ is given by

$$U_n(z) = \sin(n_0 + n) \pi z/L \quad (2)$$

where L is the length of the cavity and n_0 is the number of spatial variations of some central mode which has been chosen to be the mode whose frequency is closest to the center of the atomic fluorescence lines. The modulating drive signal affects the driving polarization of the n th mode. Here it varies the susceptibility of the atomic medium whereas in loss and phase modulation it affects the susceptibility of the modulator. The effects of the pump modulation can be included by assuming that the optical susceptibility is a time varying quantity.

Sinusoidal Pump Modulation

First, consider sinusoidal modulation of the pump. Then we assume that the atomic susceptibility is

$$\chi(z,t) = \chi(z)(1 + \cos \nu_m t) = [\chi'(z) - j\chi''(z)](1 + \cos \nu_m t). \quad (3)$$

Thus the atomic medium gain will depend upon the time-varying quantity

$$\chi''(z,t) = \chi''(z) (1 + \cos \nu_m t) \quad (4)$$

and the medium phase shift will depend upon

$$\chi'(z,t) = \chi'(z) \cos \nu_m t, \quad (5)$$

where the constant part of the $\chi'(z,t)$ has been neglected since it only affects the mode spacing and the value of "zero-detuning" of the modulator.

In order for the time variation of χ' and χ'' to have a mode-coupling effect, the laser gain region has to extend over only a small fraction of the cavity length, preferably near one end, as required of a phase or loss modulator^{1,17} when they are used to produce mode locking.

The polarization driving the n th mode, resulting from the time variation of χ'' , is given by¹⁸

$$\begin{aligned} P_n(t) = & -\frac{c\epsilon_0}{vL\beta} K_a g_n E_n(t) \sin[\nu_n t + \phi_n(t)] \\ & -\frac{c\epsilon_0}{vL\beta} K_{c1} [g_{n+1} E_{n+1} \cos(\phi_{n+1} - \phi_n) + g_{n-1} E_{n-1} \cos(\phi_n - \phi_{n-1})] \sin(\nu_n t + \phi_n) \\ & -\frac{c\epsilon_0}{vL\beta} K_{c1} [g_{n+1} E_{n+1} \sin(\phi_{n+1} - \phi_n) - g_{n-1} E_{n-1} \sin(\phi_n - \phi_{n-1})] \cos(\nu_n t + \phi_n), \end{aligned} \quad (6)$$

whereas the polarization driving the n th mode, resulting from the time variation of χ' , is given by¹⁸

$$\begin{aligned} P_n(t) = & -\frac{c\epsilon_0}{vL\beta} K_{c1} [d_{n+1} E_{n+1} \sin(\phi_{n+1} - \phi_n) - d_{n-1} E_{n-1} \sin(\phi_n - \phi_{n-1})] \sin(\nu_n t + \phi_n), \\ & -\frac{c\epsilon_0}{vL\beta} K_{c1} [d_{n+1} E_{n+1} \cos(\phi_{n+1} - \phi_n) + d_{n-1} E_{n-1} \cos(\phi_n - \phi_{n-1})] \cos(\nu_n t + \phi_n) \end{aligned} \quad (7)$$

The total polarization driving the n th mode will be the sum of the terms in equations (6) and (7) and thus will include loss-modulator type and phase-modulator type coupling terms.

In equations (6) and (7), g_n is the unsaturated gain coefficient of the n th mode (which varies with mode number n according to the line shape function), the constants K_a and K_{c1} express the relative strengths of the dc and fundamental components of the time varying pump, d_n expresses the medium dispersive effect upon the n th mode and comes from the line shape of the atomic dispersion curve, and β is a saturation term (the saturating gain is g_n/β). Homogeneous saturation is assumed and therefore β is not a function of n and carries no subscript. The value of the saturation term β is given by

$$\beta = 1 + C \frac{\pi}{2} \Delta \nu_L \sum_n E_n^2 g_L(\nu_n), \quad (8)$$

which comes from the work of McDuff, Scott, and Taboada¹⁹ who extended the time domain saturation parameter developed by Kuizenga and Siegman²⁰ to the frequency domain. In equation (8) C is simply a saturation parameter whose value is selected in the simulation to set a convenient scale for the optical field amplitude. $g_L(\nu_n)$ is the regular Lorentzian line shape function²¹ and $\Delta\nu_L$ is the Lorentzian linewidth.²² When the polarization given by equations (6) and (7) is incorporated into the Lamb self consistency equations²² for the cavity, the mode-coupled differential equations result.

Non-Sinusoidal Pump Modulation

If the pumping time dependence is non sinusoidal, then the time dependence of $\chi(z,t)$ will include higher harmonics. This means that there will be non-zero values $K_{c2}, K_{c3}, K_{c4}, \dots$ due to these higher harmonics, where in effect the K_{c1} are the relative amplitudes of the spectral components of the pump envelope

(synchronously pumped dye laser) or current waveshape (diode laser). Rather than write out the polarization in the general case here, the complete coupled mode equations are presented for the general case¹⁸

$$\begin{aligned} (\dot{E}_n - n\Delta\nu) E_n = \frac{c}{2L\beta} \sum_{i=1}^m K_{c_i} [g_{n+i} E_{n+i} \sin(\phi_{n+i} - \phi_n) - g_{n-i} E_{n-i} \sin(\phi_n - \phi_{n-i}) \\ - d_{n+i} E_{n+i} \cos(\phi_{n+i} - \phi_n) - d_{n-i} E_{n-i} \cos(\phi_n - \phi_{n-i})] \end{aligned} \quad (9)$$

$$\begin{aligned} \dot{E}_n + \frac{1}{2} \frac{\nu}{Q_n} E_n - \frac{c}{2L} K_a \frac{g_n}{\beta} E_n = \frac{c}{2L\beta} \sum_{i=1}^m K_{c_i} [g_{n+i} E_{n+i} \cos(\phi_{n+i} - \phi_n) + g_{n-i} E_{n-i} \cos(\phi_n - \phi_{n-i}) \\ + d_{n+i} E_{n+i} \sin(\phi_{n+i} - \phi_n) - d_{n-i} E_{n-i} \sin(\phi_n - \phi_{n-i})] \end{aligned} \quad (10)$$

Equations (9) and (10) are very similar to the equations obtained when there is a combination of loss and phase modulation in the same laser cavity.²³ The difference here is that each mode is coupled not only to adjacent modes but also simultaneously coupled directly to modes located multiples of $c/2L$ away in frequency. When the number of harmonics present in the pump is m , the n th mode is coupled individually to $2m$ of the modes of the cavity, m modes lower in frequency and m modes higher in frequency.

The detuning term in equations (9), denoted by $\Delta\nu$, is defined as¹⁷

$$\Delta\nu = \pi c/L - \nu_m \quad (11)$$

and gives the mismatch between the axial mode spacing frequency and the repetition rate of the pump (frequency of the fundamental component of the time varying pump). Equation (11) may be compared with some of the time domain definitions found in the literature. For example, if δt is defined as the mismatch between the cavity transit time of the mode-locked laser pulse t_d and the period of the pump t_p as given by

$$\delta t = t_d - t_p, \quad (12)$$

then in terms of $\Delta\nu$ defined above,

$$\delta t = -\frac{2\pi}{\nu_m} \left(\frac{\Delta\nu}{\pi c/L} \right). \quad (13)$$

Thus, negative detuning in the above coupled mode terminology corresponds to the case when the mode-locked laser pulse cavity transit time is longer than the pump period.

Solution of the Coupled-Mode Equations

The coupled-mode differential equations were solved numerically using a Runge-Kutta numerical integration procedure. The technique was to assume initial values of the mode amplitudes and phases and the laser parameters and continue the integration until steady state was reached (all $\dot{E}_n = 0$ and $\dot{\phi}_n = 0$ or equal to a constant independent of n). The computer program used was a modification of that of Scott²⁴ which was developed from the early work of Harris and McDuff. Due to the presence of a large number of modes and the multiple couplings between modes, caused by the pulse nature of the pump, the solution of the equations can require a lot of computer time. The availability of a Cray X-MP/24 super computer made it possible to do this work.

Much of the initial work was done for the case of sinusoidal variation of the pump level. A computer run requires considerably less time with only the pump fundamental spectral component present, since then coupling is only to adjacent modes. The results were used to guide the pulsed-pump work and in fact predicted well many of the trends noted in the pulsed-pump case. In addition, the sinusoidal pump variation study would apply directly to the current modulated mode-locked diode laser.

Results

In doing the numerical studies, typical parameters were used rather than attempting to model any specific laser. A very important parameter in the synchronously pumped mode-locked dye laser is the mismatch between the pump cavity length and the dye laser cavity length. Here this is expressed by the detuning parameter $\Delta\nu$. Figures 1-3 show the effects of the detuning upon the laser output pulse. The ranges encompassed by the curves is that over which it was possible to obtain steady-state solutions. The phase shift is relative to the point at which the pump peak occurs. It can be noted that there is a definite asymmetry about zero detuning, with essentially only positive detunings (this corresponds to the mode-locked laser pulse transit time being shorter than that of the pump period, i.e. $t_p > t_d$) giving steady state results. A change in the pump peak intensity had little effect on the width or phase shift of the output pulse. This is because, regardless of the pump level, the coupling terms saturate down to the point where overall gain equals overall loss, giving coupling dependent on loss. As shown in Figure 4, however, the mode-locked pulse peak intensity increased linearly with the pump pulse peak intensity. A similar behavior was noticed by Shank and his co-workers during an experimental study of an intra-cavity pumped dye laser.⁴ The mode-locked laser extinguished when the pump peak intensity was reduced to 1.17 (arbitrary units). An improvement in the mode-locked pulse is expected as the pump pulse width is made shorter and Figures 5 and 6 show behavior of this nature. The importance of the cavity loss to the coupling mechanism, since the gain and hence the coupling terms saturate according to the amount of loss, was explored. Figures 7 and 8 show the effects of loss on pulse width and peak intensity for the sinusoidal modulation case. The pulse width decreases at larger cavity loss because then larger coupling terms are present (to make gain equal to loss). As the loss increases, of course, the pulse amplitude decreases as shown in Figure 8.

Conclusions

The coupled-mode approach to the analysis of gain-modulated lasers successfully describes many of the experimentally observed results.¹⁴ One result is the observation of stable and unstable regions as the detuning is varied. Catherall and New¹⁴ attributed this phenomenon to the presence of spontaneous emission noise in the case of the synchronously pumped mode-locked dye laser. The coupled-mode model does not include the effect of spontaneous emission, but yet produces the same result. The conclusion must be that the instabilities are due to the inherent non-linear coupled-mode dynamics of the dye laser. The model could be used to simulate a specific laser system. This could be either a synchronously pumped mode-locked laser or a current-modulated diode laser.

References

1. O. P. McDuff and S. E. Harris, IEEE J. Quant. Electr. QE-3, 101 (1967).
2. R. L. Kohn, C. V. Shank, E. P. Ippen, and A. Dienes, Opt. Comm. 3, 117 (1971).
3. J. M. Harris, R. W. Chrisman, and E. F. Lytle, Appl. Phys. Lett. 14, 16 (1975).
4. Z. A. Yasa and O. Teschke, Opt. Comm. 15, 169 (1975).
5. A. Scavennec, Opt. Comm. 17, 14 (1976).
6. J. N. Frigo, J. Daly, and H. Mahr, IEEE J. Quant. Electr. QE-13, 101 (1977).
7. J. Kuhl, R. Lambrich, and D. von des Linde, Appl. Phys. Lett. 31, 657 (1977).
8. D. M. Kim, J. Kuhl, R. Lambrich, and D. von des Linde, Opt. Comm. 27, 123 (1978).
9. C. P. Ausschnit, R. K. Jain, and J. P. Heritage, IEEE J. Quant. Electr. QE-15, 912 (1979).
10. S. L. Shapire, R. R. Cavanagh, and J. C. Stephenson, Opt. Lett. 6, 470 (1981).
11. J. Herrmann and U. Motschmann, Opt. Comm. 40, 379 (1982).
12. Y. A. Yasa, Appl. Phys. B. 30, 135 (1983).
13. L. M. Davis, J. P. Harvey, and J. M. Peart, Opt. Comm. 50, 49 (1984).
14. J. M. Catherall and C. H. C. New, IEEE J. Quant. Electr. QE-22, 1593 (1986).
15. E. W. van Stryland, Opt. Comm. 31, 93 (1979).
16. A. E. Siegman, Lasers (University Science Books, California, 1986), p. 1125.
17. S. E. Harris and O. P. McDuff, IEEE J. Quant. Electr. QE-1, 245 (1965).
18. D. Thati, A Theoretical Study of Synchronously Mode-Locked Dye Lasers Using the Coupled Mode Approach, M.S. Thesis, The University of Alabama (1988).
19. O. P. McDuff, D. T. Scott, and J. Taboada, in Proceedings IEEE Southeastcon '86 (IEEE Publishing Services, Piscataway, N.J., 1986), pp. 99-103.
20. D. J. Kuizenga and A. E. Siegman, IEEE J. Quant. Electr. QE-6, 694 (1970).
21. R. H. Pantell and H. E. Putoff, Fundamentals of Quantum Electronics (John Wiley and Sons, New York, 1969).
22. W. E. Lamb, Jr., Phys. Rev. 134, A1429 (1964).
23. O. P. McDuff, Mode Coupling in Lasers, Ph.D. Dissertation, Stanford University (1966).
24. D. Scott, A Computer Simulation Study of a Mode Coupled Laser, M.S. Thesis, University of Alabama (1986).

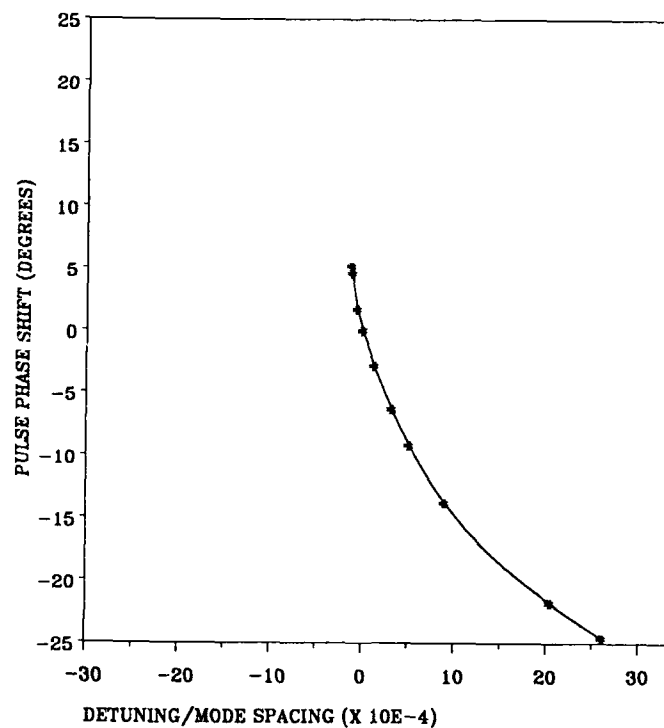


Figure 1. Phase shift of mode-locked pulse vs. detuning $\Delta\nu$. Cavity loss = 35% per pass. Peak unsaturated gain coefficient 5 times the loss. Gaussian pump pulse with FWHM = 875 psec.

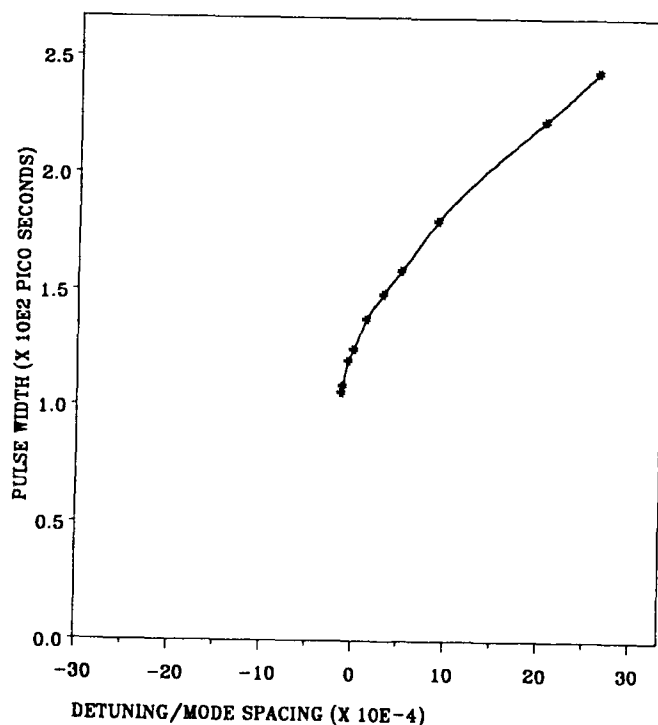


Figure 2. Width of mode-locked pulse vs. detuning $\Delta\nu$. Cavity loss = 35% per pass. Peak unsaturated gain coefficient 5 times the loss. Gaussian pump pulse with FWHM = 875 psec.

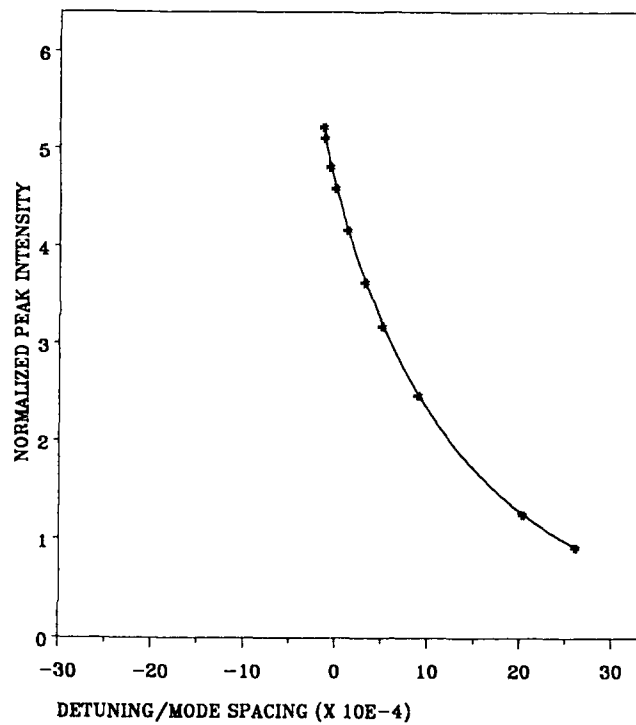


Figure 3. Peak intensity of mode-locked pulse vs. detuning $\Delta\nu$. Cavity loss = 35% per pass. Peak unsaturated gain coefficient 5 times the loss. Gaussian pump pulse with FWHM = 875 psec.

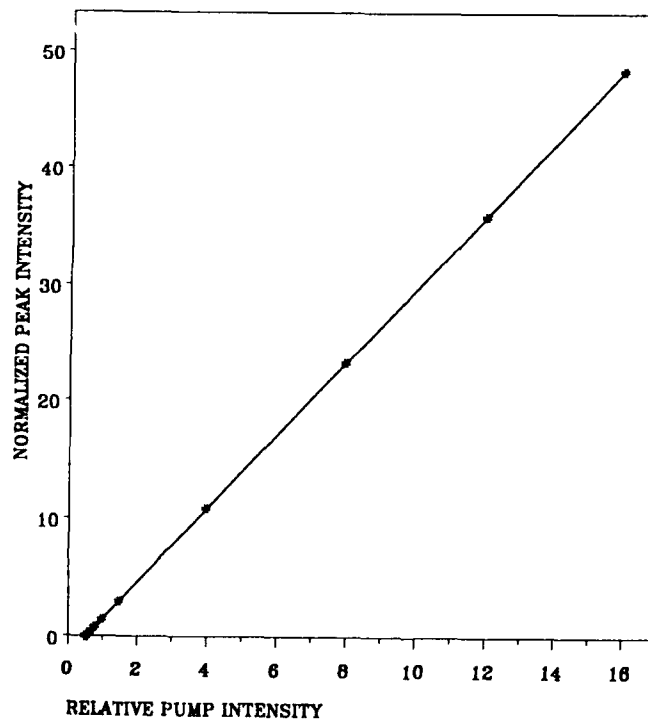


Figure 4. Peak intensity of mode-locked pulse vs. pump peak intensity. Detuning $\Delta\nu = 0$. Cavity loss = 35% per pass. Gaussian pump pulse with FWHM = 875 psec.

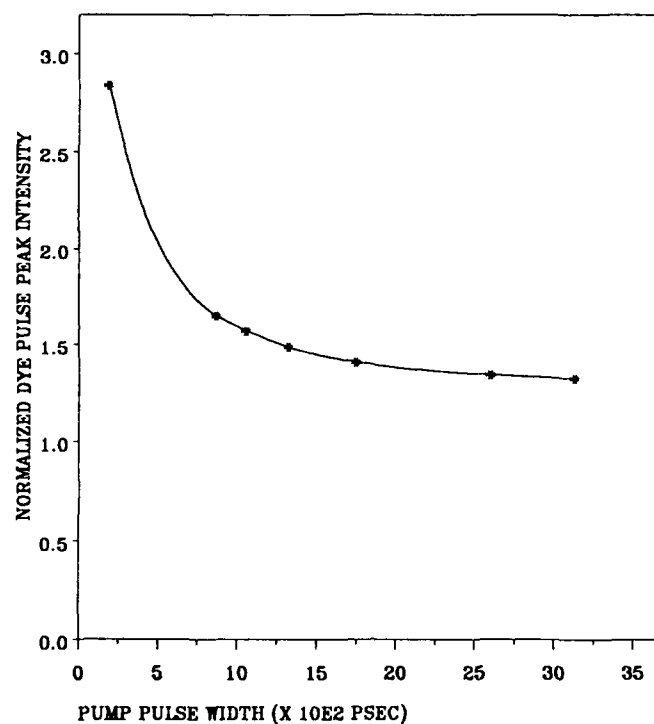


Figure 5. Peak intensity of mode-locked pulse vs. pump pulse width. Detuning $\Delta\nu = 0$. Cavity loss = 35% per pass. Peak unsaturated gain coefficient 2.5 times the loss.

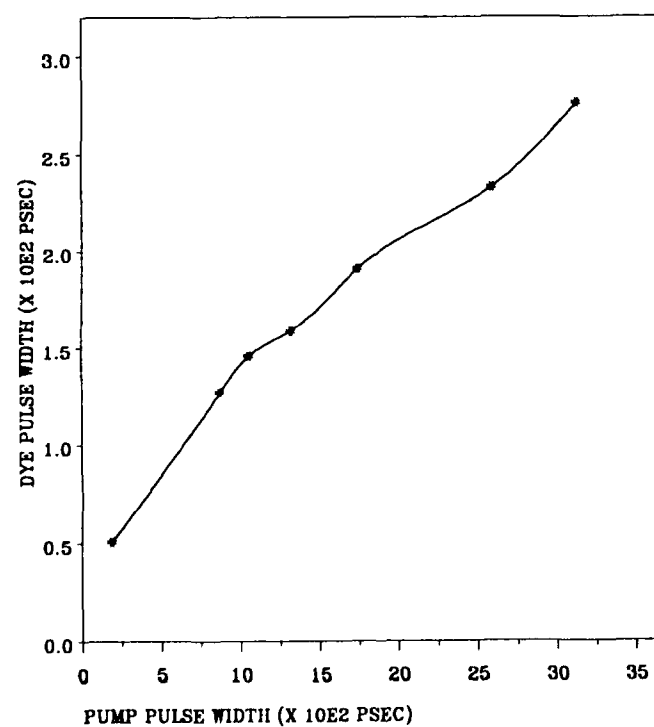


Figure 6. Width of mode-locked pulse vs. width of pump pulse. Detuning $\Delta\nu = 0$. Cavity loss = 35% per pass. Peak unsaturated gain coefficient 2.5 times the loss.

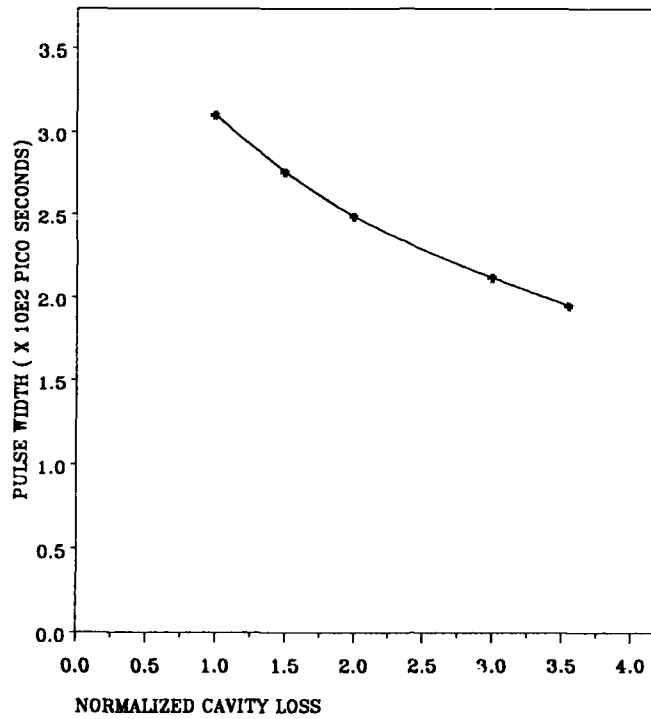


Figure 7. Width of mode-locked pulse vs. cavity loss. Peak unsaturated gain coefficient = 4.0 (on normalized cavity loss scale). Sinusoidal pump modulation.

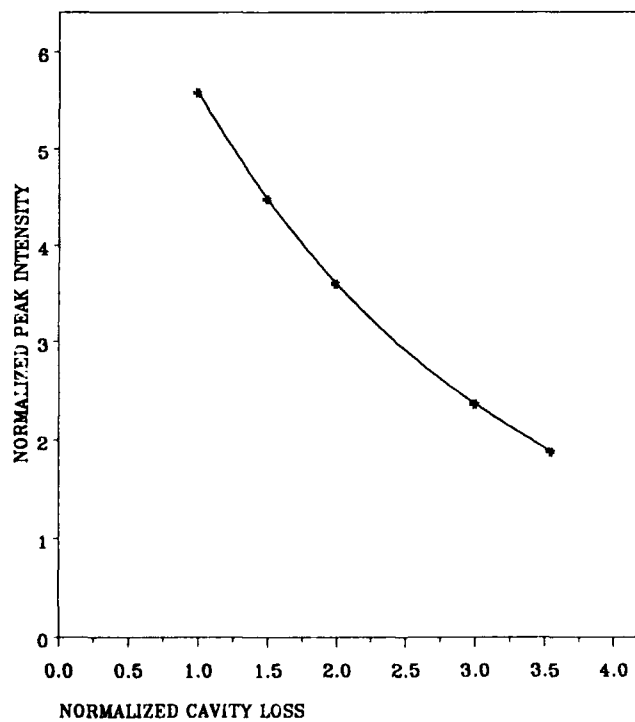


Figure 8. Peak intensity of mode-locked pulse vs. cavity loss. Peak unsaturated gain coefficient = 4.0 (on normalized cavity loss scale). Sinusoidal pump modulation.

A STUDY OF TRANSIENTS AND STABILITY IN MODE-LOCKED LASERS BY MEANS OF A NON-LINEAR COUPLED-MODE ANALYSIS

Odis P. McDuff
Amjad Z. Arnous
Department of Electrical Engineering
The University of Alabama
P. O. Box 6169
Tuscaloosa, Alabama 35487-6169

Abstract

Forced mode locking of lasers by means of intracavity phase and loss modulation has been studied extensively over the years. Analyses generally have followed the time domain approach¹ in which the optical pulse in the cavity is followed through a complete round trip, or the coupled-mode approach² in which the coupling between the multiple axial modes^{3,4} is studied. Transient effects and pulse evolution have been studied by the linearized time domain approach.^{3,4} The nonlinear coupled-mode equations of McDuff and Harris² were originally used only to determine the steady-state mode-locked behavior. However, they are written in terms of the time derivatives of the instantaneous mode amplitudes and phases and thus present a natural means of studying the transient behavior of the mode-locked laser, including the nonlinearities present. This report presents the results of such a non-linear study of the transients and stability of a mode-locked laser from the coupled mode point of view. In general the mode-locked laser is more stable at greater modulator strengths. It is less stable when the modulator is detuned. When the unsaturated excess gain is larger, the laser reaches steady state faster. Generally the laser is more sensitive to perturbations of mode phases from the steady state values than it is to perturbations of mode amplitudes. Furthermore, perturbations of mode phases have a more deleterious effect upon the mode-locked pulse shape.

Introduction

Analyses of the pulse growth and stability of solutions in an actively mode-locked laser generally have followed a linearized time domain approach in which the optical signal in the cavity² is followed through a complete round trip.^{3,4} The nonlinear coupled-mode equations of McDuff and Harris² were originally developed only to determine the steady-state mode-locked behavior. However, they are written in terms of the time derivatives of the instantaneous mode amplitudes and phases and thus present a natural means of studying the transient behavior of the mode locked laser, including the nonlinearities present.

The Coupled-Mode Equations

The work reported herein uses the coupled mode equations in the form derived by McDuff and Harris². One assumes the electromagnetic field inside the laser cavity to be expanded as a sum of the normal mode eigenfunctions,

$$E(z,t) = \sum_n E_n(t) \cos [\nu_n t + \phi_n(t)] U_n(z), \quad (1)$$

where $U_n(z) = \sin(n\pi z/L)$. The $E_n(t)$ and $\phi_n(t)$ are the slowly time varying amplitude and phase of the n th mode, ν_n is its radian frequency, L is the cavity length, and n is the number of spatial variations of some central mode whose frequency is chosen to be closest to the center of the atomic fluorescence line. The coupled-mode equations of McDuff and Harris are

$$(\dot{\phi}_n - n\Delta\nu + \frac{c}{2L} \psi_n) E_n = -\frac{c\alpha}{2L} [E_{n+1} \sin(\phi_{n+1} - \phi_n) - E_{n-1} \sin(\phi_n - \phi_{n-1})] \quad (2)$$

$$\dot{E}_n + \frac{c}{2L} \alpha_n E_n - \frac{c}{2L} G_n E_n = -\frac{c\alpha_a}{2L} E_n - \frac{c\alpha_c}{2L} [E_{n+1} \cos(\phi_{n+1} - \phi_n) + E_{n-1} \cos(\phi_n - \phi_{n-1})] \quad (3)$$

In these equations $\Delta\nu$ is the detuning of the modulator drive frequency ν_m from the axial mode spacing $\Delta\Omega$, such that $\Delta\nu = \Delta\Omega - \nu_m$. The additional round trip phase retardation seen by the n th mode as a result of the atomic medium is written as ψ_n and the fractional single pass power gain of the n th mode as G_n . Both ψ_n and G_n depend nonlinearly upon frequency and optical intensity, the actual functional dependence depending upon whether homogeneous or inhomogeneous broadening (or a mixture) occurs.^{2,5} The quantity α_n is defined in terms of the passive Q_n of the n th mode as

$$\alpha_n = \frac{vL}{c} \frac{1}{Q_n}, \quad (4)$$

and includes both dissipative and output coupling loss (mirror transmission). Since loss is small, α_n is approximately equal to the fractional single-pass power loss of the nth mode, i.e.,

$$(e^{\alpha_n} \approx 1 + \alpha_n). \quad (5)$$

In typical cases α_n is independent of n.

In equations (2) and (3) it was assumed that the expression for the attenuation of the loss modulator perturbing element, per pass through the element, could be written

$$\alpha(t) = \alpha_M (1 + \cos v_m t). \quad (6)$$

Therefore, if the loss is small α_M is approximately the average single pass fractional loss through the perturbing element. If the modulator extends over a short distance in the axial, or z direction, and has no significant spatial variation over its length in that direction, the cross-coupling loss term α_c and self coupling loss term α_a are given by the expressions

$$\alpha_c \approx \frac{\alpha_M}{2} \quad (7)$$

$$\alpha_a \approx \alpha_M \quad (8)$$

In the case of homogeneous saturation of the atomic medium as considered here, the expressions for G_n and ψ_n were taken as

$$G_n = g_o \frac{\pi}{2} \Delta v_L \frac{g_L(v_n)}{1 + C \frac{\pi}{2} \Delta v_L \sum_m E_m^2 g_L(v_m)}, \quad (9)$$

$$\psi_n = \frac{g_o \pi (v_n - v_o) g_L(v_n)}{1 + C \frac{\pi}{2} \Delta v_L \sum_m E_m^2 g_L(v_m)} \quad (10)$$

where C is a saturation constant, g_o is the unsaturated line-center power gain, and $g_L(v_n)$ is the regular Lorentzian line shape function,

$$g_L(v) = \frac{1}{\pi} \frac{\Delta v_L / 2}{(v_o - v)^2 + (\frac{\Delta v_L}{2})^2}. \quad (11)$$

Use of Coupled-Mode Equations

In previous work based on the coupled mode equations (2) and (3) the goal had been simply to look for steady state solutions which had the derivatives \dot{E}_n equal to zero and $\dot{\phi}_n$ equal either to zero or a constant independent of mode number, n. This was done by a Runge-Kutta numerical integration procedure. Here the procedure was to study the condition of the laser (mode amplitudes and phases) as the numerical integration proceeded from some set of initial conditions to a new set of conditions (maybe steady state or maybe not). Since the normal mode expansion, equation (1), is an approximation that may not be accurate at conditions when the laser oscillation is just barely building up from zero, only perturbations from an initial oscillation condition were considered.

The condition of the laser oscillation was characterized by looking at the output optical intensity pulse that would result. If the output signal of the laser is written

$$E(t) = \sum_n E_n \cos[(\omega_o + n v_m) t + \phi_n], \quad (12)$$

then the low passed portion (or envelope) of $E^2(t)$, such as would be obtained if the signal were incident on a photodetector, is given by

$$W(t) = \frac{1}{2} \sum_s \sum_n E_n E_{n+s} \cos(s v_m t + \phi_{n+s} - \phi_n). \quad (13)$$

From this output pulse envelope the pulse width and the phase shift of the pulse relative to the modulator were determined. With an assumed modulation phase as in equation (6), the pulse under ideal zero detuning conditions has its peak at $v_m t = \pi$ (lowest modulator loss).

Classic Perturbation Procedure

An alternative procedure more of the nature of a classical stability study was also used. Ho⁸ linearized the equations (2) and (3) to study the effect of noise perturbations due to spontaneous emission. Obviously if numerical techniques are used linearization is not necessary.

In this alternate procedure, it is assumed that a steady state solution to equations (2) and (3) has been reached with the corresponding values E_{no} and ϕ_{no} obtained. Then, perturbations to the E_{no} and ϕ_{no} are added. Immediately after the perturbations are added, one has

$$E_n = E_{no} + \Delta E_n \quad (14)$$

$$\phi_n = \phi_{no} + \Delta \phi_n \quad (15)$$

Substituting these relations into equations (2) and (3) and subtracting off the original steady state values, one obtains equations for ΔE_n and $\Delta \phi_n$ as follows:

$$\begin{aligned} \dot{\Delta E}_n = & -\frac{c}{2L} \alpha_n \Delta E_n + \frac{c}{2L} G_n \{E_{no} + \Delta E_n\} - \frac{c}{2L} G_{no} E_{no} - \frac{c \alpha_a}{2L} \Delta E_n \\ & - \frac{c \alpha_c}{2L} \left[(E_{no+1} + \Delta E_{n+1}) \cos(\phi_{no+1} - \phi_{no} + \Delta \phi_{n+1} - \Delta \phi_n) \right. \\ & + (E_{no-1} + \Delta E_{n-1}) \cos(\phi_{no} - \phi_{no-1} + \Delta \phi_n - \Delta \phi_{n-1}) \\ & \left. - E_{no+1} \cos(\phi_{no+1} - \phi_{no}) - E_{no-1} \cos(\phi_{no} - \phi_{no-1}) \right] \end{aligned} \quad (16)$$

$$\begin{aligned} \dot{\Delta \phi}_n = & -\frac{c}{2L} \psi_n + \frac{c}{2L} \psi_{no} \\ & - \frac{c \alpha_c}{2L(E_{no} + \Delta E_n)} \left[(E_{no+1} + \Delta E_{n+1}) \sin(\phi_{no+1} - \phi_{no} + \Delta \phi_{n+1} - \Delta \phi_n) \right. \\ & \left. - (E_{no-1} + \Delta E_{n-1}) \sin(\phi_{no} - \phi_{no-1} + \Delta \phi_n - \Delta \phi_{n-1}) \right] \\ & + \frac{c \alpha_c}{2L E_{no}} \left[E_{no+1} \sin(\phi_{no+1} - \phi_{no}) - E_{no-1} \sin(\phi_{no} - \phi_{no-1}) \right] \end{aligned} \quad (17)$$

In these equations the G_n indicates equation (9) with $E_n + \Delta E_n$ used, whereas G_{no} indicates equation (9) with E_{no} used, and similarly for ψ_n and ψ_{no} using equation (10).

In using equations (16) and (17), a steady state solution was obtained using equations (2) and (3), and then perturbations ΔE and $\Delta \phi$ were assumed and equations (16) and (17) numerically integrated using a Runge-Kutta procedure. The integration was continued until the ΔE and $\Delta \phi$ decayed back to zero. This approach is capable of handling only perturbations in mode amplitudes and phases after steady state has been reached with a given set of laser parameters. It is not capable of handling a sudden change in one of the laser parameters, such as modulation strength, whereas the first procedure directly solving equations (2) and (3) is.

Results

In doing the numerical work, constants were assumed approximately appropriate to a Nd:YAG laser with a cavity length of 1 meter. The laser parameters were assumed to be $\alpha_n = 0.1$, $g_o = 0.16$, and the linewidth 120 GHz. The saturation constant C in equations (9) and (10) was chosen to give convenient mode amplitudes and then left constant for the rest of the work, since its only effect is to set the scale. The progression of performance after a perturbation of the laser was expressed versus the number of round trips of the mode-locked pulse in the cavity. The pulse shape itself was plotted versus v_m as noted above. The figures that follow show some of the results obtained.

In Figure 1 is shown the development of the pulse when the laser is allowed to reach steady state and then the phase angles are increased by an amount $\Delta \phi = n \pi/10$. This was at zero detuning of the modulator and with $\alpha_c = 0.6$. The perturbation destroys the pulse shape but the laser recovers in ≈ 2000 cavity round trips. A similar run with $\alpha_c = 1.2$ gave a shorter recovery time of ≈ 1200 round trips. Figure 2 shows the laser recovery when the mode amplitudes are perturbed by 50%. The pulse shape is unaffected by such a perturbation and the laser recovers much quicker. Again, a larger mode coupling $\alpha_c = 1.2$ causes it to recover quicker. Figure 3 shows the transition from one steady state condition with $\alpha_c = 0.1$ to another condition with $\alpha_c = 0.088$ (i.e. the cavity loss is suddenly decreased). The pulse grows rapidly to the new peak value in ≈ 400 round trips (the final pulse also is more narrow, although it cannot be seen from the figure). Figure 4 shows that changes in modulator detuning in either direction from zero detuning require similar times for the laser to reach the new steady state. Figure 5 shows that when the modulator cross coupling is suddenly increased less time is required for the laser to reach the new steady state than when the cross coupling is suddenly decreased.

Figure 6 shows that when the laser cavity loss α is changed, similar times are needed to reach the new steady state both for an increase and a decrease in α .ⁿ Similar runs at a higher modulator cross coupling required less time to reach the new steady state. Figure 7 and 8 show a comparison of the results from the two techniques, i.e. use of equations (2) and (3) and use of equations (16) and (17).

Conclusions

Two techniques have been shown for the study of the transient behavior of a mode-locked laser. In one of them the evolution of the system from the perturbed initial conditions to the steady-state condition is followed versus time. In the other technique, a classical stability study is performed in which the decay with time of the perturbations is observed.

In general the mode-locked laser is more stable at higher cross coupling α . It is less stable when the modulator is detuned. When the excess gain is larger ($g_0 - \alpha$ is larger), the system reaches steady-state faster. Generally, the system is more sensitive to perturbations of mode phases than it is to mode amplitudes. Furthermore, perturbations of mode phases have a more deleterious effect on the mode-locked pulse shape.

The two techniques that have been shown give very useful procedures for studying theoretically the stability and transient behavior of mode-locked lasers, a problem that is extremely difficult to study experimentally.

References

1. D. J. Kuizenga and A. E. Siegman, IEEE J. Quant. Electr. QE-6, 694 (1970).
2. O. P. McDuff and S. E. Harris, IEEE J. Quant. Electr. QE-3, 101 (1967).
3. T. W. Chong and P. A. Lindsay, Int. J. Electr. 45, 573 (1978).
4. G. H. C. New and J. M. Catherall, in Proceedings International Meeting on Instabilities and Dynamics of Lasers and Nonlinear Optical Systems, June 1985, at University of Rochester, R. P. Boyd, M. G. Raymer, and L. M. Nardvici, Eds. (Cambridge University Press, 1986), pp. 197-211.
5. O. P. McDuff, D. T. Scott and J. Taboada, in Proceedings IEEE Southeastcon '86 (IEEE Publishing Services, Piscataway, N.J., 1986), pp. 99-103.
6. R. H. Pantell and H. E. Putoff, Fundamentals of Quantum Electronics (John Wiley and Sons, New York, 1969).
7. S. E. Harris and O. P. McDuff, IEEE J. Quant. Electr. QE-1, 245 (1965).
8. P. T. Ho, IEEE J. Quant. Electr. QE-21, 1806 (1985).

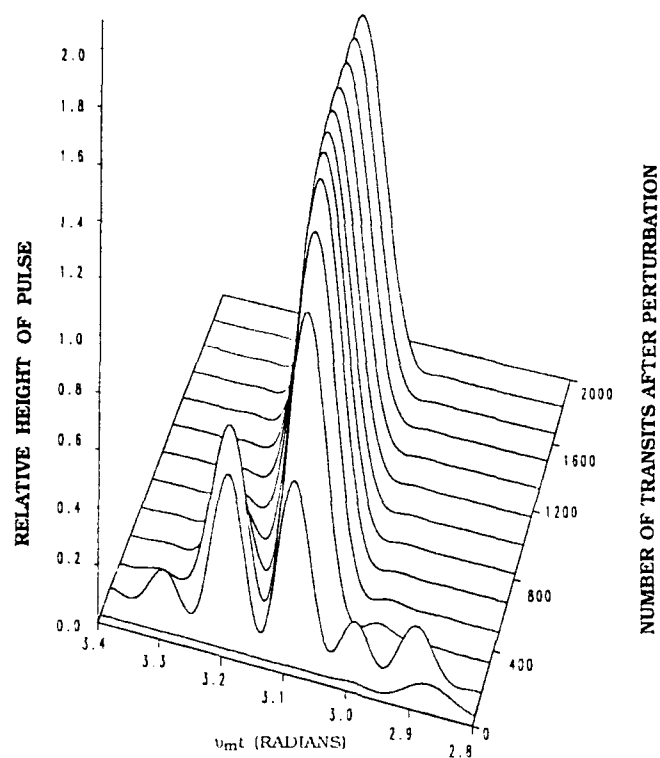


Figure 1. Development of laser pulse after each mode phase ϕ_n is increased by the amount $n \frac{\pi}{10}$. Detuning $\Delta\nu = 0$ and modulator cross coupling $\alpha_c = 0.6$.

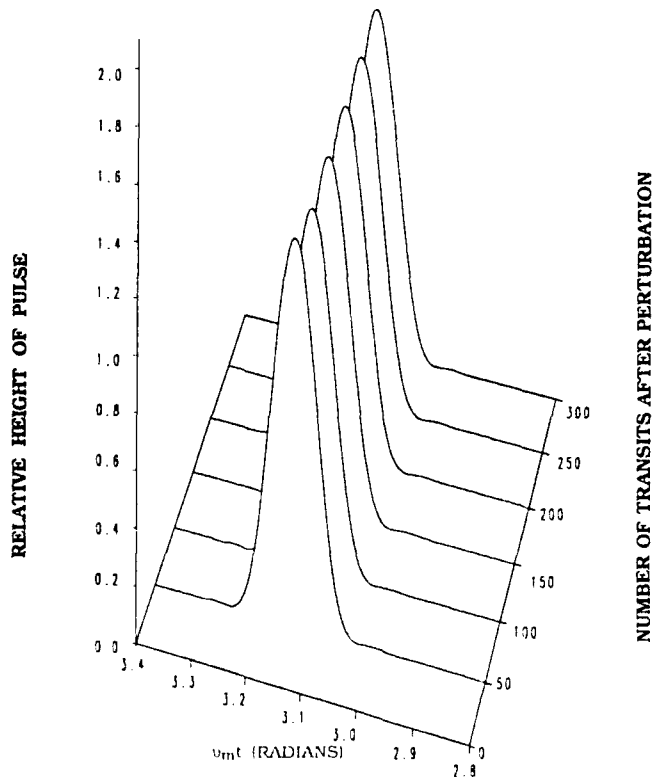


Figure 2. Development of laser pulse after each mode amplitude E_n is increased by 50%. Detuning $\Delta\nu = 0$ and modulator cross coupling $\alpha_c = 0.6$.

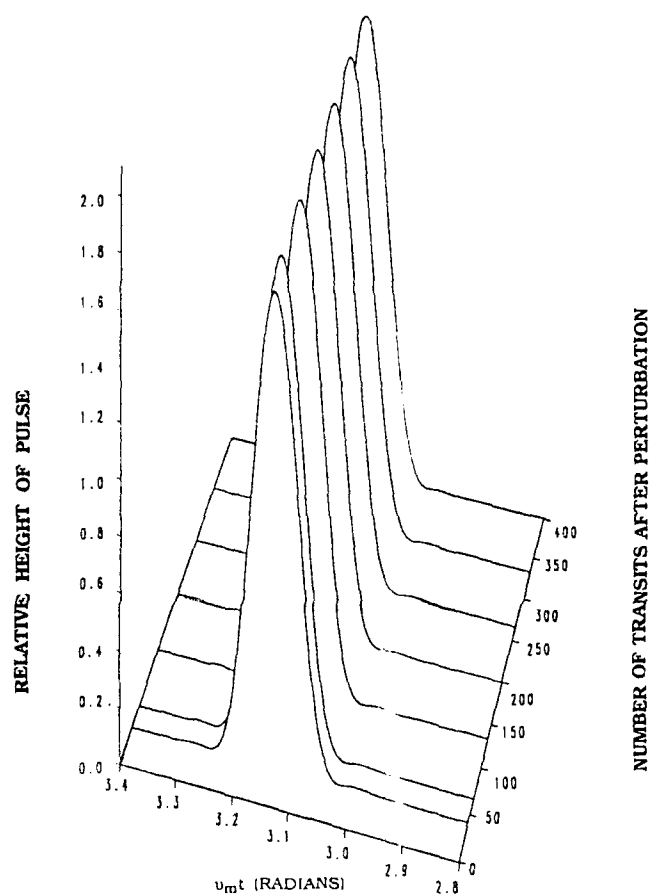


Figure 3. Development of laser pulse after the cavity loss is changed from $\alpha_n = 0.1$ to $\alpha_n = 0.088$. Detuning $\Delta\nu = 0$ and modulator cross coupling $\alpha_c = 0.6$.

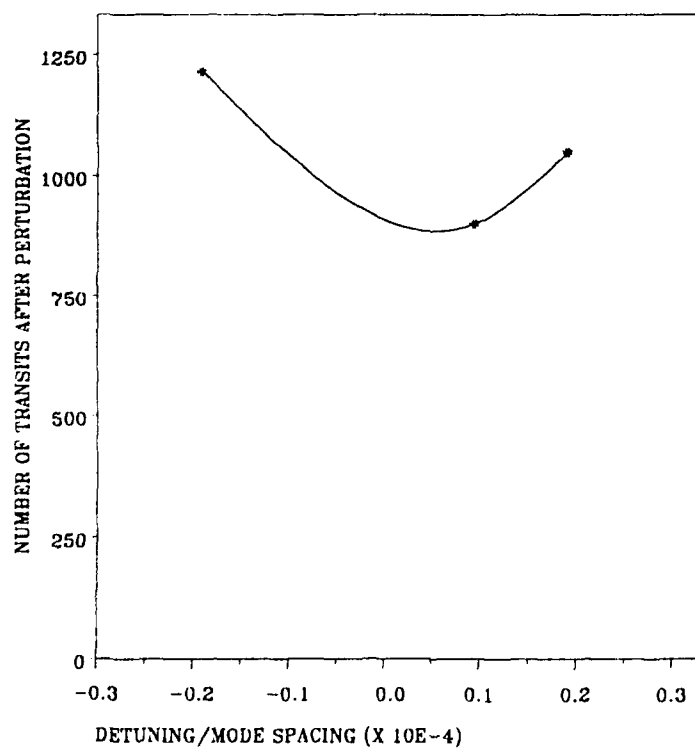


Figure 4. Number of pulse round trips in cavity to reach steady state vs. new modulator detuning. Original detuning $\Delta\nu = 0$. Modulator cross coupling $\alpha_c = 1.2$.

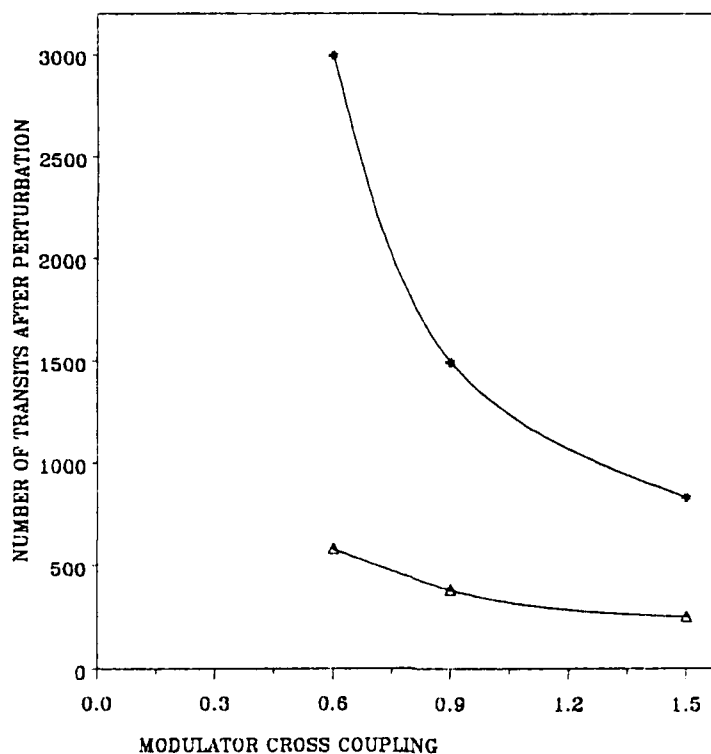


Figure 5. Number of pulse round trips in cavity to reach steady state vs. new modulator cross coupling. Original cross coupling $\alpha_c = 1.2$.

Δ Detuning/mode spacing = 0.134×10^{-4}
 * Detuning/mode spacing = 0.150×10^{-4}

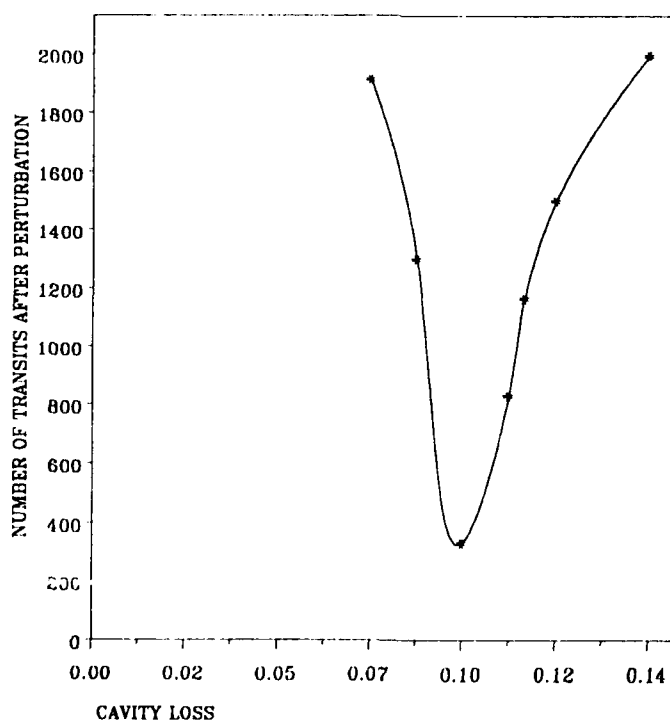


Figure 6. Number of pulse round trips in cavity to reach steady state vs. new cavity loss. Original cavity loss $\alpha_n = 0.1$. Modulator cross coupling $\alpha_c = 0.6$ and detuning $\Delta\nu = 0$.

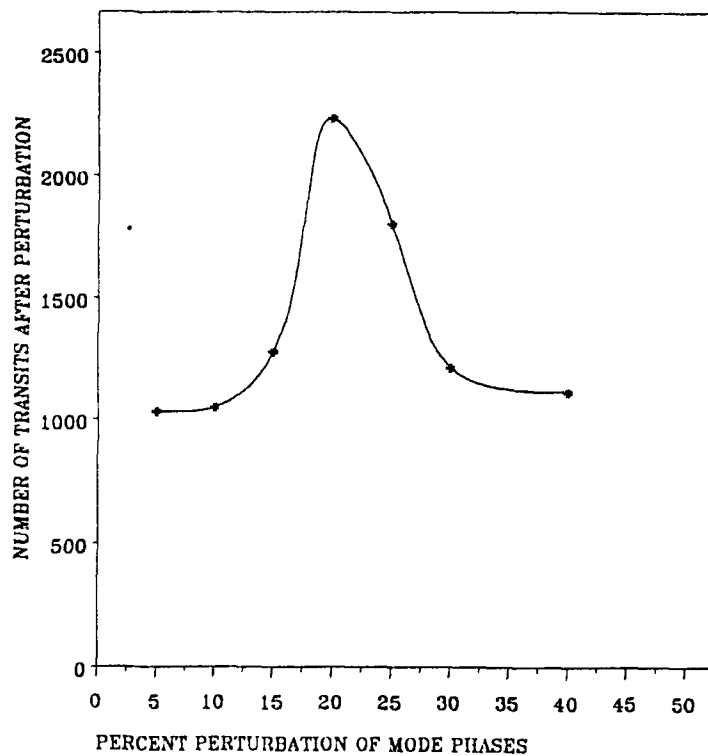


Figure 7. Number of pulse round trips in cavity to reach steady state vs. perturbation of mode phases by $\Delta\phi_n = n(\% \text{ of } \pi)$ using direct solution of coupled mode equations (2) and (3). Detuning $\Delta\nu = 0$ and modulator cross coupling $\alpha_c = 1.2$.

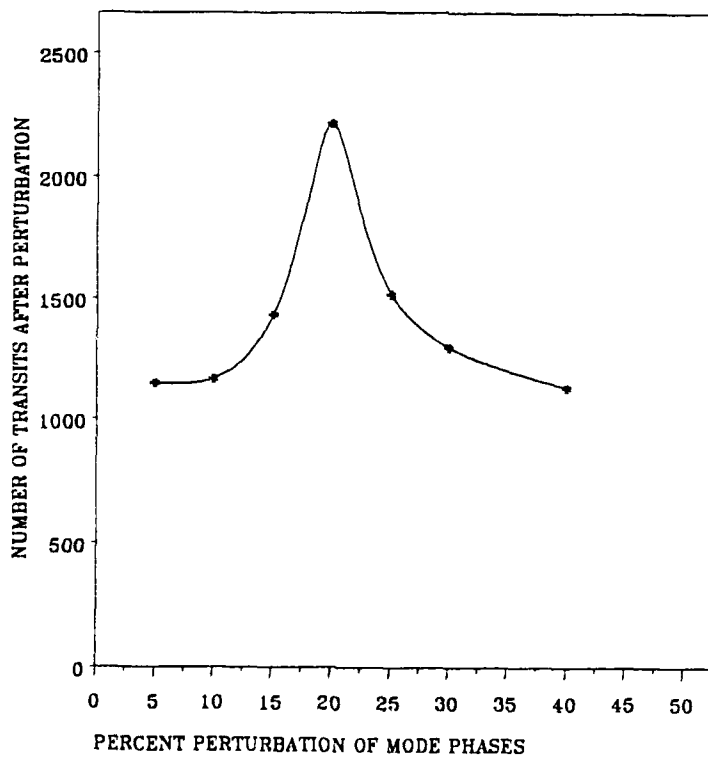


Figure 8. Number of pulse round trips in cavity to reach steady state vs. perturbation of mode phases by $\Delta\phi_n = n(\% \text{ of } \pi)$ using stability approach equations (16) and (17). Detuning $\Delta\nu = 0$ and modulator cross coupling $\alpha_c = 1.2$.

BEAM AMPLIFICATION AND OPTICAL PHASE CONJUGATION VIA MULTIWAVE MIXINGS
IN A NONLINEAR MEDIUM: NEW THEORETICAL PERSPECTIVE AND EXPERIMENTAL RESULTS

I. C. Khoo
Department of Electrical Engineering
The Pennsylvania State University
University Park, PA 16802

Abstract

Recently developed theories and observed experimental results on multiwave mixing related beam amplifications and phase conjugations are reviewed. In a highly nonlinear thin medium, the presence of the diffracted beams from the pump-probe beams induced grating modifies considerably the energy coupling between the pump and the probe beams, leading to substantial amplification of the latter. This enhanced probe beam amplification effect, in conjunction with the retroreflected pump beam (or a strong beam counter-propagating to the pump), gives rise to an increased phase conjugation reflection. Experimental results with the thermal and orientational nonlinearities of liquid crystal and electronic nonlinearity in semiconductor are in good agreement with the theoretical predictions.

Introduction

With the emergence of several highly nonlinear optical materials, the theory and practice of several nonlinear optical processes have taken an every increasing number of variations, and provided new fundamental insights and application potentials. Optical self-phase modulations, leading to self-limiting and pulse shaping and compression applications, and optical wave mixings, leading to optical phase conjugation and self-pumped phase conjugating oscillators are but a few salient examples.

In this paper, we will present some new theoretical and experimental results of optical wave mixings in a highly nonlinear thin film. Specifically, we will focus our attention on the amplification and phase-conjugated reflection of a probe beam, which occur when the probe beam is mixed with a strong pump beam in a nonlinear medium (c.f., Figure 1a and 1b). In Figure 1a, which we shall henceforth refer to as the "forward wave mixing process" (FWMP), the pump and the probe beams create the initial grating, which then scatter the pump or the probe into the various diffracted orders. New gratings among the beams are created within the medium owing to these diffracted beams, which also produce various new energy coupling and exchange mechanisms between the strong pump beam and all these other weaker beams. In Figure 1b, which we shall refer to as the "backward wave mixing process," (BWMP), an additional strong (reconstruction) beam is present, and it scatters from all the gratings created in the FWMP into an "array" of backward propagating diffracted beams, which also form new gratings with the reconstruction beam. For simplicity, we have shown only one forward and one backward diffracted beam in Figure 1b, which would have been the case if the probe beam is extremely weak compared to the pump. A situation that exists when we are dealing with self-oscillations originating from noise sources, for example.

Summary of Theories and Experiments

To fully understand these two processes, especially the exchanges of energies amongst the beams, a detailed description of the medium's nonlinear optical response is necessary. This is because many of the beams (e.g., the diffracted beam and the phase conjugated reflection) are created within the medium via the nonlinear optical responses, and the growths of these beams from their entry planes to the exit planes are governed by the spatially dependent nonlinear mechanism that couples all these electromagnetic waves together.

The nonlinear responses can take on perhaps the simplest form of a Kerr-like medium, where the couplings amongst the various beam are due to a local intensity dependent refractive index n given by

$$n = n_0 + n_2 E^2 \quad (1)$$

where n_0 is the unperturbed refractive index, n_2 is the nonlinear coefficient, and E is the amplitude of the total optical electric field (which contains several spatial frequency as well as temporal frequency components). The nonlinear coefficient n_2 can be real, or complex (i.e., $n_2 = |n_2| e^{i\phi}$), where ϕ is the phase shift between the refractive index grating and the optical intensity grating.

This Kerr-like type of coupling, and the resulting probe beam amplification and growth and decay of all the input and generated beams have been studied in detail (theoretically and experimentally) by our group.¹ In general, it is found that in a highly nonlinear thin medium, e.g., a 100 μ m thick nematic liquid crystal film, substantial probe amplification can be achieved in FWMP via the scattering of the pump beam from the pump-diffracted beam coupling. Figure 2 shows a typical dependence of the probe gain versus the pump intensity, for a constant pump-probe beam ratio. The "saturation" effect at higher pump intensities is due to the loss of the probe beam into other higher order diffracted beam directions.

A second form of nonlinearity, namely, thermal nonlinearity is slightly more complicated because of its diffusive nature, i.e., the nonlinear response of the medium depends on the boundary conditions at various planes in the medium. In general, therefore, the thermal diffusion problem is a three-dimensional one under the steady state regime (e.g., when cw lasers are used). It can be reduced to a two-dimensional problem if the beam is assumed to be very large along the dimension orthogonal to the grating wave vector. Nevertheless, complete solutions of the coupled wave equations for the FWMP and the BWMP still require very tedious self-consistent iterative numerical techniques, in order to properly account for the boundary condition (which is usually a set of initial temperatures at the input and exit planes).

A complete solution of a simplified version of this process, taking into account only one diffracted beam in the FWMP, is given in Reference 2. As we remarked earlier, this simplification is valid if the pump to probe beam ratio is large (i.e., the probe beam is very weak) and so only one diffracted beam on the pump side takes on an appreciable magnitude. In our theory, the medium is assumed to be thin, and the wave mixing angle is small (i.e., large grating constants), so that phase mismatches among the pump, probe and diffracted beams are negligible. For such a thin medium to produce an appreciable observable effect, it certainly must possess a very high thermal refractive index gradient (dn/dT). In Reference 2, the extraordinarily large thermal refractive index gradients of nematic liquid crystals near the phase transition temperature is employed. Using a cw CO₂ laser, a 100% probe gain is easily observed with a pump beam intensity on the order of a few watts/cm² (c.f., Figure 2). Figure 4 shows a typical "saturation" effect in the probe gain at high intensity, which is experimentally determined to be caused by the loss of the probe beam into higher order diffraction. By matching the thermal diffusion times with an appropriate laser pulse (a few tens of milliseconds), an even larger probe amplification can be obtained. (Up to 2000% amplification has been observed with pump pulse with a few watts in power (intensity on the order of 10 watts/cm².) (Reference 2)

Another form of optical nonlinearity, namely, electronic nonlinearity, has also been theoretically and experimentally studied in the context of the FWMP and BWMP described above³. Specifically, the intensity dependent change in refractive index caused by the creation of free carriers in silicon by nanosecond Nd:Yag laser pulses and the resultant FWMP and BWMP are studied. Although the refractive index change can also be expressed in the form $\Delta n = n_2 E^2$, the fact that several parameters responsible for n_2 (e.g., absorption coefficient) are temperature-dependent, and the temperature is, in turn, dependent on many time dependent parameters like electron-hole attenuations, recombinations, and the optical fields, contribute to complicate the problem. Several coupled equations (one describing the temperature rise, one for the free carrier concentration) and the coupled Maxwell wave equations for both the FWMP and BWMP have to be solved in a self-consistent manner. A detailed theoretical and experimental study for the FWMP has been performed. In general, the theory fits the experimental data very well. For example, it describes the dependence of the probe gain on the pump-probe beam ratio, and the probe gain dependence on the pump intensity very well (c.f., Figures 5 and 6, respectively). Recently, we have also performed some preliminary studies of BWMP in the Si sample. As plotted in Figure 5, solid circles, the phase conjugation reflectivity is shown to be dependent on the pump to probe beam ratio as one would expect from the FWMP. The main limiting factor in the probe gain is found to be due to the optical beam attenuation by the electron-hole plasma created by the laser pulse. Using the best geometry (small crossing angle ≤ 0.01 radian), one can observe up to about 20 in the probe beam amplification.

Conclusions

We have quite conclusively demonstrated that under phase-matched conditions, when diffracted beams are present, and when the pump to probe beam intensity ratio is high, a nonlinear medium can efficiently amplify a weak probe (signal) beam. This effect is therefore observable in any highly nonlinear material. This process can obviously be applied to image amplification, self-pumped ring oscillation, and wave mixing based processes (e.g., phase-locked oscillations and self-pumped oscillations). More details of the FWMP and BWMP theories for important nonlinear materials (e.g., semiconductors, liquid crystals, photorefractive materials) remain to be worked out, and they are currently being studied concurrently with experiments. These theories, and detailed experimental results, will be presented in longer articles elsewhere.

Acknowledgement

The author gratefully acknowledges the technical assistance by T. H. Liu, P. Y. Yan, R. R. Michael, G. M. Finn and R. Normandin in contributing to various theoretical and experimental aspects of this general problem. This research is supported by a grant from the National Science Foundation ECS8712078.

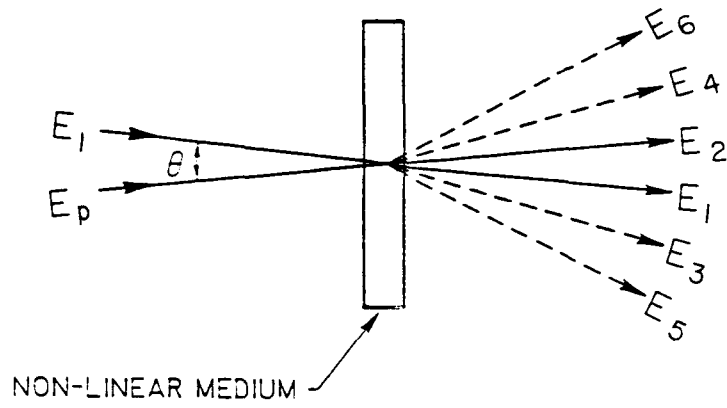
References

1. a. I. C. Khoo and T. H. Liu, IEEE J. Quantum Electron., QE23, p. 171 (1987).
b. T. H. Liu and I. C. Khoo, *ibid*, p. 2020 (1987).
2. I. C. Khoo, P. Y. Yan, G. M. Finn, T. H. Liu and R. R. Michael, J. Opt. Soc. Am. B, Feb. issue (1988).
3. I. C. Khoo and R. Normandin, Appl. Phys. Lett. Feb. issue (1988).

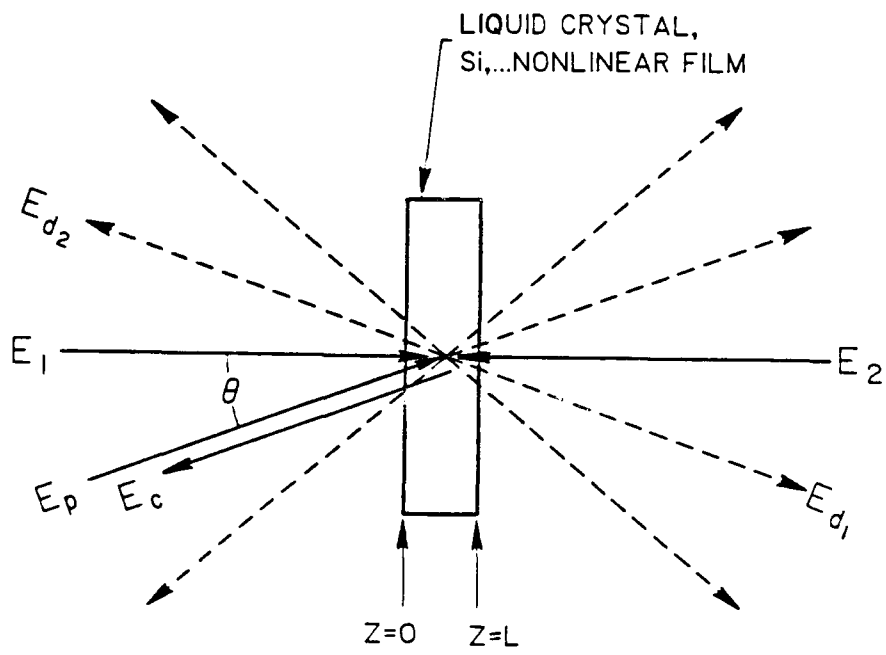
Figure Captions

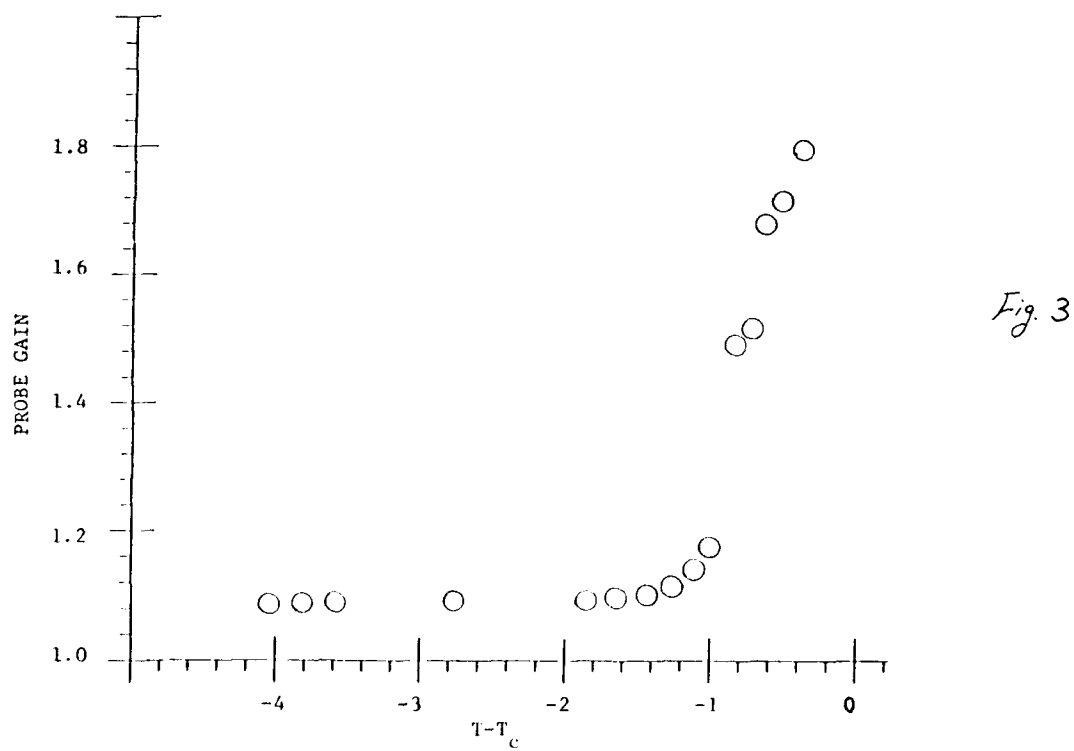
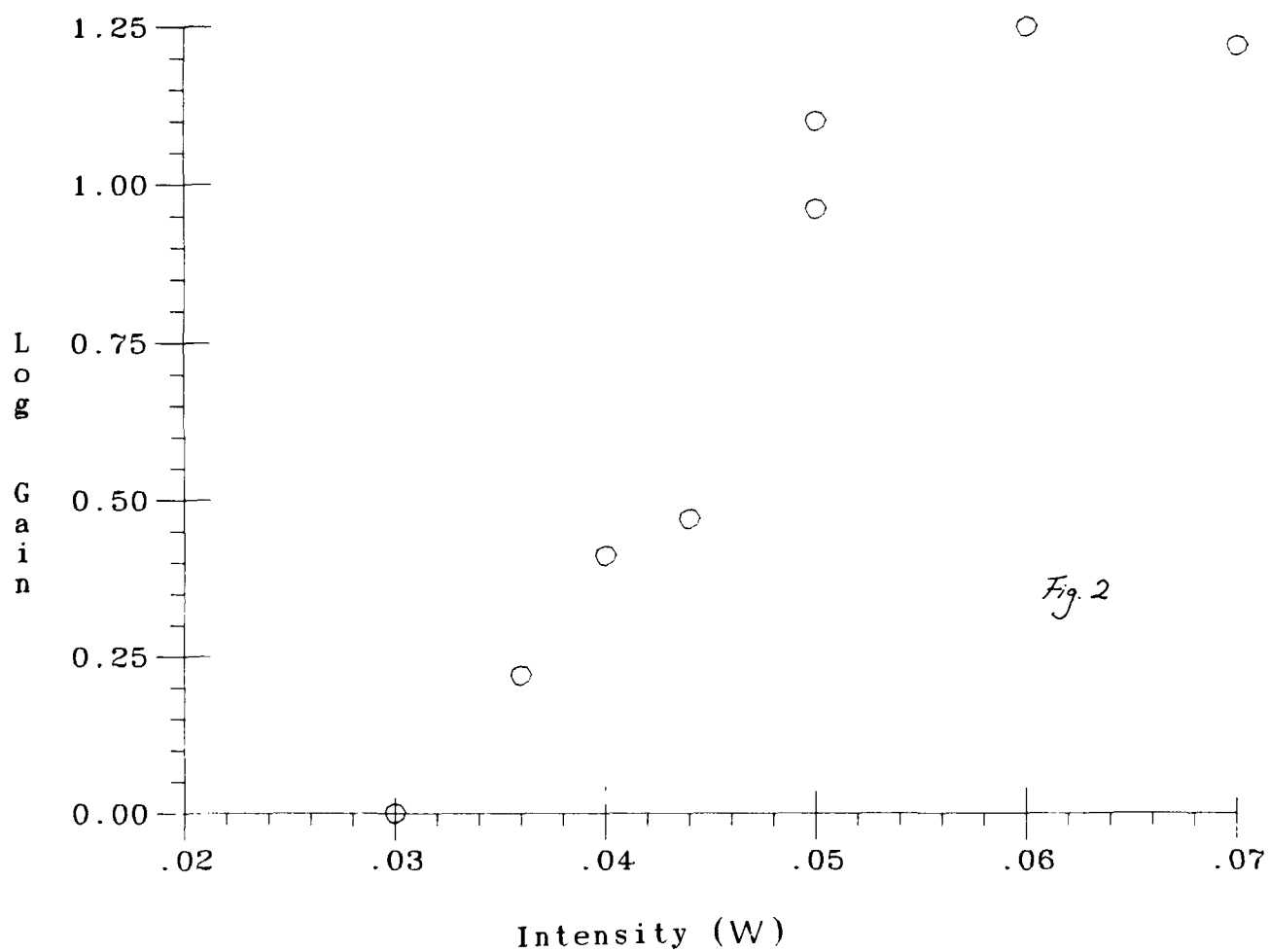
- Fig. 1a Forward wave mixing geometry, with an incident pump and a probe beam, and four diffracted beams.
- Fig. 1b Backward wave mixing geometry, showing a forward propagating pump, probe and diffracted beam, and a backward counterpropagating pump beam, phase conjugated reflection of the probe, and a diffracted beam.
- Fig. 2 Dependence of the probe gain on the pump intensity. Thickness of homeotropically nematic liquid crystal film is 170 μ m. Pump to probe beam ratio is 240:1 laser beam diameter is 2mm. Angle between the optical electric field of the linearly polarized laser and the director axis is 22°. Crossing angle between the pump and the probe is 5 mrad. For other details, see Reference 1a.
- Fig. 3 Dependence of the probe gain on the temperature. The liquid crystal used is 100 μ m thick, homeotropically aligned, and placed in a temperature cell. The pump to probe beam ratio is 175:1. The crossing angle is 2.7°. Pump power is about 3 watts. Beam diameter is 0.8 cm. The laser optical electric field is perpendicular to the director axis (i.e., the ordinary refractive index thermal gradient dn_0/dT is used.
- Fig. 4 Experimentally observed probe gain dependence on the pump intensity for the same geometry used in getting Figure 3. Above a pump power of 1.5 watt, the value of the probe gain is recorded just before the sample goes into the isotropic phase (when the probe gain drops to zero). Numerous diffracted beams can be observed at pump intensity at this level.
- Fig. 5 Circles: Dependence of the probe beam gain on the pump-probe beam ratio in our experiment with a 400 μ m thick silicon wafer. Details see Reference 3.
- Solid Circles: Dependence of the phase conjugated reflection of the probe beam on the pump-probe beam ratio. (Vertical axis is scaled to coincide with the gain at high pump-probe beam ratio of (1)). Solid line is a theoretical fit based on the theory of Reference 1b.
- Fig. 6 Dependence of the probe gain on the pump intensity showing saturation effect at high intensity. Curve a shows our theoretical fit that accounts for the electro-hole plasma attenuation effect. Curve b is a theory without accounting for the electron-hole plasma attenuation effect. For details, see Reference 3.

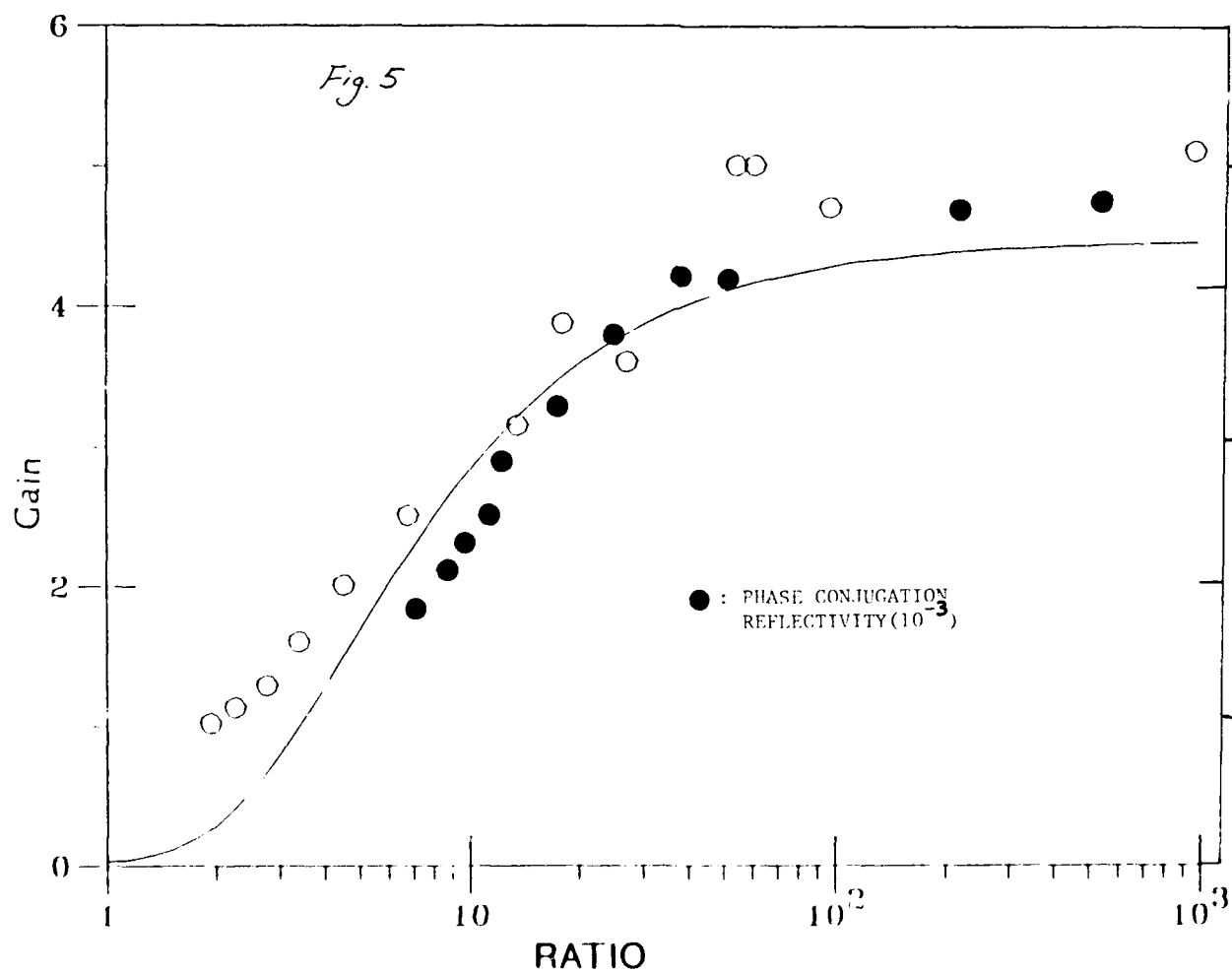
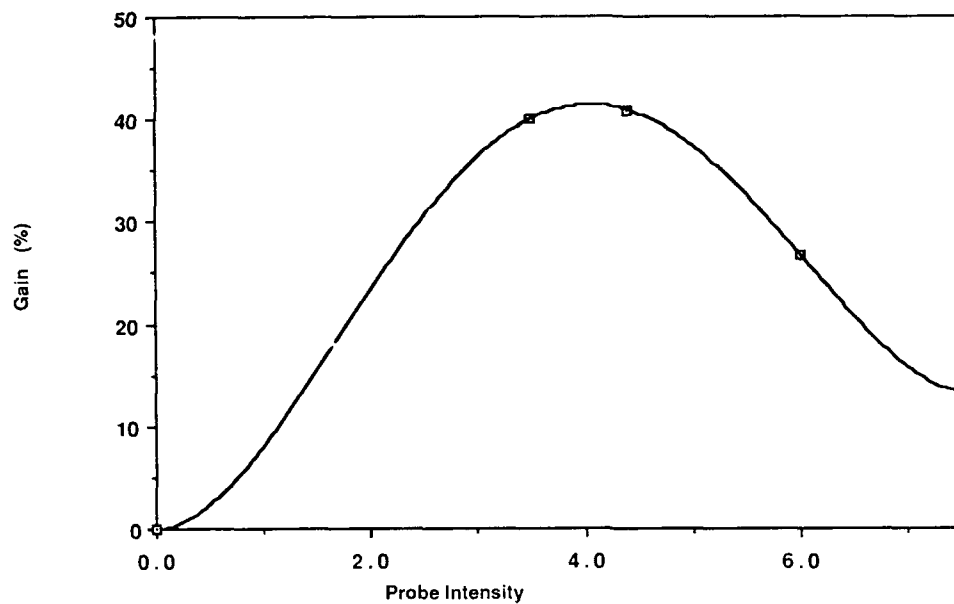
1a

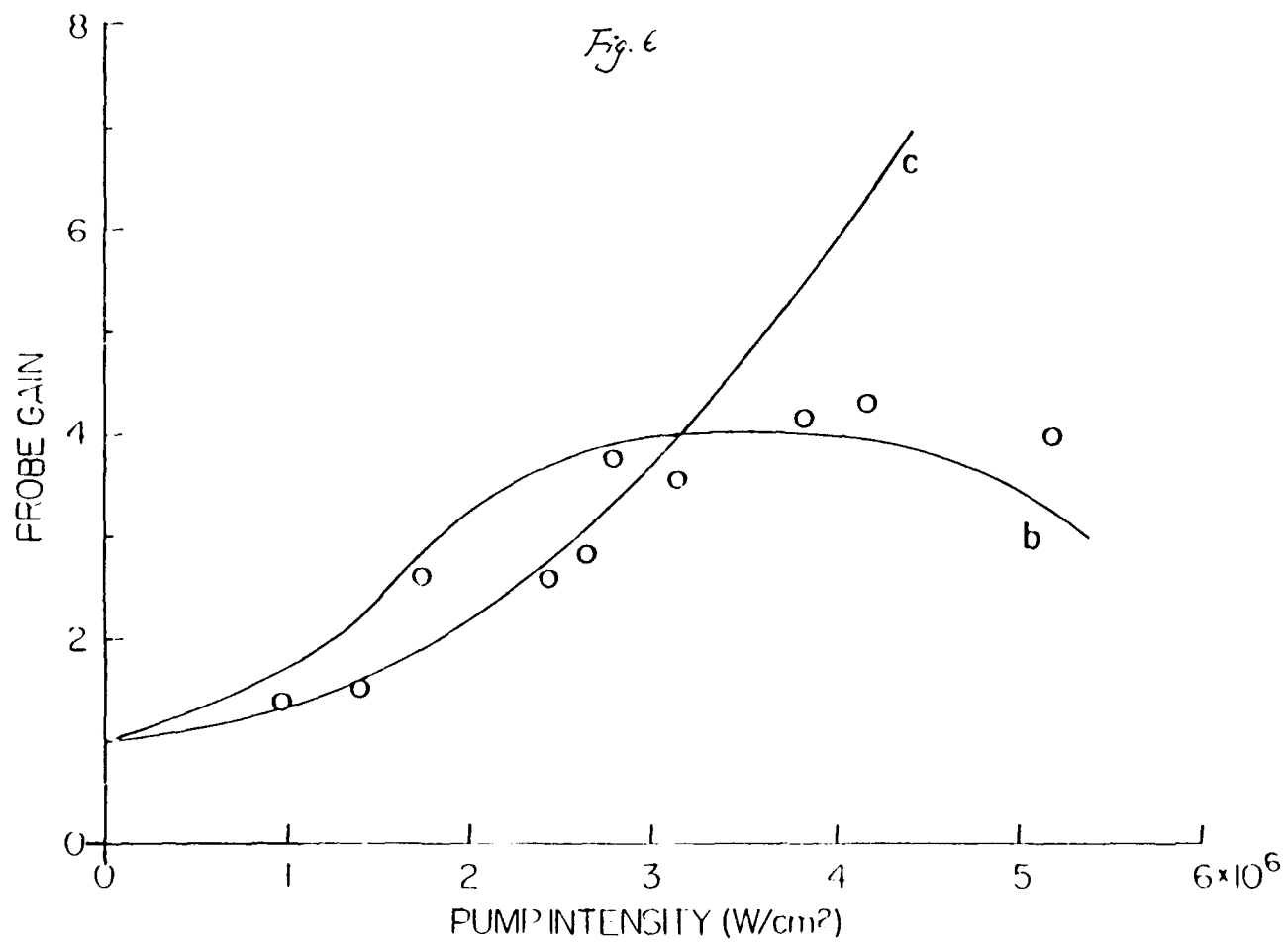


1b









WAVEGUIDE GRATINGS AND OPTICAL DAMAGE IN $\text{LiNbO}_3\text{:Ti:Fe}$

P. Hertel, E. Krätzig and H. Pape

Fachbereich Physik der Universität
Barbarastraße 7, D-4500 Osnabrück, Fed.Rep.Germany

The photorefractive effect of Fe centers in titanium-indiffused planar waveguides is studied by holographic methods. Gratings are formed by intersecting coherent guided beams and are monitored by measuring the diffraction efficiencies. Modes of different order and polarization probe the gratings at different depths for the ordinary and extraordinary light-induced refractive index change. The saturation values indicate that the total Fe concentration depends only weakly on depth. This is supported by SIMS measurements. The rates of decay upon homogeneous illumination show that the Fe^{2+} concentration increases towards the waveguide surface by a factor of about ten. Ti^{4+} ions stabilize iron in the Fe^{2+} state. A set of equations describing the photorefractive effect in $\text{LiNbO}_3\text{:Ti:Fe}$ is presented.

1 Introduction

LiNbO_3 is an artificially grown ferroelectric material with a number of outstanding properties. Infrared or visible light propagates with very little absorption, and there are various means to impose refractive index changes and thereby control the propagation of light.

The refractive indices of LiNbO_3 can be modified permanently by indiffusion, outdiffusion, implantation, and exchange of ions. In particular, linear or planar structures of increased refractive index are easy to produce. Indiffusion of titanium ions today is the preferred method to fabricate low loss dielectric optical waveguides [1].

The refractive indices of LiNbO_3 also change as a consequence of mechanical strain. This effect gives rise to interactions between acoustic waves and light, it is of interest to modern microwave technology.

An electric field likewise modifies the refractive indices of LiNbO_3 . Most devices of integrated optics, like switches, multiplexers, and modulators, are based on this effect.

An electric field may be applied externally, but it can also be an internal field. Such internal electric fields are the result of photoinduced charge transport. Upon non-uniform illumination electrons are mobilized and migrate to darker regions. The resulting space charge field generates an electric field which in turn induces refractive index changes. This photorefractive effect allows to store volume phase holograms and gives rise to wave mixing.

The photorefractive effect [2] in LiNbO_3 has been studied extensively. Even undoped crystals contain transition metal impurities, such as iron, of a few ppm, and these centers are sources and traps for mobilized electrons. Iron centers are either in the Fe^{2+} or in the Fe^{3+} state [3]. Practically all absorption, for visible light, is caused by Fe^{2+} centers [4]. Upon absorbing a photon the Fe^{2+} center decays with a certain probability into an Fe^{3+} center and an electron which is ejected into the conduction band. The electron suffers an instantaneous displacement along the crystallographic c-axis. The corresponding charge transport mechanism is known as the photovoltaic effect [5]. Before being trapped by another Fe^{3+} center the mobilized electron performs a random walk (diffusion) with a systematic drift in an electric field (photoconductivity). Note that the dark conductivity at room temperature is extremely small. An internal electric field decays, by conduction in the dark, with a time constant of up to one year.

Here we discuss the photorefractive effect in titanium diffused planar waveguides. From the waveguide point of view this effect is a nuisance, and it was therefore called 'optical damage'. Light-induced refractive index changes indeed may damage the proper functioning of waveguides as linear devices. On the other hand, holographic information storage or wave mixing in photorefractively sensitive waveguides are promising fields of investigations.

We shall report on recent studies of the $\text{LiNbO}_3\text{:Ti:Fe}$ system. It is known since long that the photorefractive effect is more pronounced in titanium indiffused waveguides as compared with bulk material [6]. We will explain why this is so: titanium ions stabilize iron impurities in the Fe^{2+} state.

In chapter 2 we describe our measurements, in chapter 3 their interpretation. We finally present the equations which describe the $\text{LiNbO}_3\text{:Ti:Fe}$ system in full generality, to our present knowledge.

2 Experiments

Our LiNbO_3 substrates have been grown from the congruent melt. The corresponding composition was checked by measuring the phase matching temperature for second harmonic generation (SHG) which depends markedly on the Li:Nb ratio. A secondary ion mass spectroscopy analysis (SIMS) indicated that Fe ions are the prevailing transition metal impurities. The Fe concentration was additionally determined by electron spin resonance spectroscopy (ESR). The crystals had been annealed in a pure oxygen atmosphere in order to transfer the predominant part of the Fe ions into the Fe^{3+} state. We found Fe concentrations which differed between 10 and 20 ppm from sample to sample.

Titanium films of typically 100 nm thickness were deposited on our y-cut substrates by vacuum electron gun evaporation. The samples were wrapped in platinum foil, placed in a ceramic pipe and heated to temperatures of 1000°C for several hours in argon atmosphere, afterwards in oxygen atmosphere to allow for reoxidation.

Fifteen planar waveguides have been made according to this procedure.

We measured the effective indices of guided transversal electric (TE) and transversal magnetic (TM) modes by the well-known prism coupling method [7]. From these data the Ti-induced refractive index profiles can be reconstructed such that the mode intensity distribution may be calculated.

The light-induced, or photorefractive index changes are determined by measuring the diffraction efficiency of holographic gratings. Two intersecting coherent beams were coupled into the waveguide by a rutile prism and out of it by a second prism (see Fig. 1). We use an argon ion laser at $\lambda = 514$ nm. The interaction length d is 7 mm, the angle 2θ between the two beams is typically 0.1 rad. The TE- and TM modes of various orders were excited by adjusting the coupling angle α and selecting the appropriate light polarization.

The diffraction efficiency is determined by monitoring the grating with one incident beam and measuring the intensities of both transmitted beams; it is defined as the ratio of the diffracted to the total transmitted intensity. We did not monitor the grating formation process since such data are difficult to interpret. There will be dynamical effects which must be taken into account. To correct for such effects a detailed knowledge of the photorefractive behaviour of $\text{LiNbO}_3\text{:Ti:Fe}$ waveguides is required - properties which are to be studied.

We therefore measured the erasure of the refractive index pattern upon homogeneous illumination. The read-out efficiency was monitored during homogeneous illumination of the entire substrate with incoherent light of $\lambda = 514$ nm. The saturation value as well as the decay rate of the holographic grating was determined for each mode and for each polarization.

3 Interpretation

We will now describe the formation and decay of holographic gratings in $\text{LiNbO}_3\text{:Ti:Fe}$ planar waveguides. The full set of equations is discussed in the next chapter, here we present a simplified formulation. This is quite sufficient for our purpose, namely to prove that the concentration of Fe^{2+} centers increases towards the waveguide surface. For a more complete discussion see [8] and [9].

We denote by y the depth below the waveguide surface. Modes propagating along the x -axis are either TE or TM; they are labelled by the number of nodes, $m = 0, 1, \dots$. We have mentioned above that propagation constants β_m were measured. By an improved inverse WKB-procedure [10] we reconstructed the Ti induced ordinary and extraordinary refractive index profiles. A simple Runge-Kutta program then allows to calculate the mode field distribution $E_m(y)$ for all modes and both polarizations. Note that the electric field is a z -component in the TE case and (predominantly) a y -component in the TM case.

Off-axis modes are described by

$$E_m^+(x, y, z) = E_m(y) e^{i\beta_m x \cos\theta} e^{i\beta_m z \sin\theta} \quad (1)$$

For sufficiently small angles θ these are indeed solutions to the mode equation, for larger angles hybrid modes must be considered. Note that both waves have identical, θ -independent propagation constants; phase matching therefore is not critical.

Superimposing two such waves with equal amplitudes gives an intensity pattern

$$I(x, y, z) \propto |E_m(y)|^2 (1 + \cos K_m z). \quad (2)$$

$K_m = 2\beta_m \sin\theta$ is the grating vector.

Assume that an refractive index grating

$$\Delta n(x, y, z) = \Delta n(y) \cos K_m z \quad (3)$$

has evolved. Since we monitor this grating with only one beam a (constant) phase shift is irrelevant for what follows.

This grating will diffract a E_m^+ mode into a E_m^- mode and vice versa with efficiency r_m . Coupling between modes of different order or different polarization is very weak because of phase mismatch. For the diffraction efficiency we calculate

$$r_m = \sin^2\left(\frac{\pi d}{\lambda} \langle \Delta n \rangle_m\right). \quad (4)$$

The intensity averaged refractive index change

$$\langle \Delta n \rangle_m = \frac{\int dy |E_m(y)|^2 \Delta n(y)}{\int dy |E_m(y)|^2} \quad (5)$$

has to be inserted into Kogelnik's [11] famous formula (4). $E_m(y)$ is from (1), $\Delta n(y)$ from (3).

Since the grating vectors are small we may safely neglect diffusion. We may likewise neglect dark conductivity. Saturation then is reached when the photovoltaic and the photocurrent balance each other. The photovoltaic current

$$J_{pv} = I c^{2+} \quad (6)$$

is proportional to the light intensity I and the concentration c^{2+} of Fe^{2+} centers. The photocurrent

$$J_{ph} = \sigma_{ph} E \quad \text{with} \quad \sigma_{ph} \propto I \frac{c^{2+}}{c^{3+}} \quad (7)$$

is proportional to the driving space charge field E , the light intensity, the number of electron sources and inversely proportional to the number of traps, i.e. the concentration of Fe^{3+} centers. It follows that the saturation electric field does neither depend on intensity nor on c^{2+} , but is directly proportional to c^{3+} . The saturation refractive index change, which is proportional to the space charge field, should likewise be independent of c^{2+} and grow linearly with c^{3+} .

Now, the saturation diffraction efficiencies η_m have been measured for all TE- and TM modes. (4) and (5) allow to calculate $\langle \delta n \rangle_m$, the intensity averaged extraordinary or ordinary photorefractive index change, respectively. Intensities refer to modes $m = 0, 1, \dots$, they probe increasingly deeper regions of the waveguide. We obtain saturation refractive index changes which only slightly depend on the mode label m . For a typical waveguide which carries four TE and four TM modes we obtain saturation values $\langle \delta n \rangle_m^{sat} = 5.9, 5.2, 5.2$, and 4.9×10^{-5} and $\langle \delta n \rangle_m^{sat} = 1.9, 1.9, 1.8$, and 1.5×10^{-5} for $m = 0 \dots 4$, respectively.

From what has been said above we conclude that the concentration of Fe^{3+} centers depends but weakly on the depth below the waveguide surface. Our waveguides have been highly oxidized in order to minimize the number of Fe^{2+} centers. Most Fe impurities are in the Fe^{3+} state. Our saturation measurements therefore indicate that the iron concentration does not vary appreciably with depth. This conclusion is supported by direct SIMS measurements of the iron concentration profile. The enhanced optical damage in Ti indiffused waveguides is not caused by an additional iron contamination.

Let us now discuss the decay of gratings upon homogeneous illumination. The space charge field will decay with the local Maxwell time constant which, in our case, is proportional to the photoconductivity. For sufficiently small erasure times we obtain

$$\langle \delta n \rangle_m(t) = \langle \delta n \rangle_m^{sat} \left(1 - \frac{t}{\epsilon \epsilon_0} \langle \sigma_{ph} \rangle_m + \dots \right). \quad (8)$$

The photoconductivity is proportional to the ratio c^{2+}/c^{3+} of electron source to trap concentration. The latter varies only weakly with depth, therefore the decay rate is directly proportional to the intensity averaged Fe^{2+} concentration.

In Fig. 2 we have plotted the averaged refractive index change - calculated from measured diffraction efficiencies - as functions of the erasure time. It is evident that the low order mode gratings decay faster. Since the low order modes propagate closer below the surface we conclude that c^{2+} is higher there. In Fig. 3 the intensity averaged Fe^{2+} concentration is plotted vs. the intensity averaged penetration depth.

The Fe^{2+}/Fe^{3+} concentration ratio close to the surface is roughly ten times higher than the bulk ratio. We conclude that, in the presence of Ti^{4+} ions, even the strongest oxidation treatment cannot bring the Fe^{2+} concentration below a certain threshold. This threshold will be higher for higher Ti^{4+} concentration.

Our data, however, do not yet allow to establish a precise functional relationship between Fe^{2+} stabilization and Ti concentration. The correct graph $(y, c^{2+}(y))$ will not, in general, pass through the points $(\langle y \rangle_m, \langle c^{2+} \rangle_m)$. Rather different functions $c^{2+}(y)$ can reproduce the data in Fig. 3, within experimental errors. Nevertheless, all fitting functions have in common that the Fe^{2+} concentration changes by a factor of about ten over a distance which is of the order of the waveguide thickness.

4 Equations for the $LiNbO_3:Ti:Fe$ System

Let us now write down the equations for dynamical holography in planar $LiNbO_3:Ti:Fe$ waveguides. They are adapted from [12] for our purpose. There is a reading and a writing part. We will use Einstein's summation convention. By E_i we denote the components of the quasistatic electric field, by e_j the light wave electric field.

The permittivity tensor has three contributions:

$$\epsilon_{ik} = \epsilon_{ik}^{bulk} + \epsilon_{ik}^{Ti} + R_{ikj} E_j. \quad (9)$$

The bulk permittivity is spatially constant, the titanium induced contribution is a function of depth only, for planar waveguides. The next term describes the electrooptic effect: R_{ikj} is related to Pockel's tensor. The quasistatic electric field E_i depends on y because gratings are written by depth-dependent light intensities. In our case it will depend on z sinusoidally. Dynamic effects, however, may also cause a variation along the propagation axis. There may be a fluctuating contribution to the bulk permittivity which can be dynamically amplified (holographic scattering).

(9) has to be inserted into the wave equation for the light wave field e_j .

The quasistatic electric field is generated by the total charge density ρ :

$$\epsilon_{ik}^{st} E_k = \rho \quad \text{with} \quad \rho + \nabla_j J_j = 0. \quad (10)$$

ϵ_{ik}^{st} are the static dielectric constants, J_j is the total electric charge current density. Let n be the density of conduction band electrons. By

$$\rho = e(3c^{3+} + 2c^{2+} - \dot{n}) = e(c^{3+} - \dot{n}) \quad (11)$$

we describe that electrons are either bound or mobilized. Charge is transported by diffusion, drift, or the photovoltaic effect, the latter being proportional to the density of Fe^{2+} centers:

$$J_i = eD_{ik}\partial_k n + \sigma_{ik}^{ph} E_k + \beta_{ikj} c^{2+} e_k e_j. \quad (12)$$

For the diffusion constants we may safely insert Einstein's relation, and the photoconductivity is proportional to the conduction band electron density:

$$D_{ik} = \frac{k_B T}{e} \mu_{ik} \quad ; \quad \sigma_{ik}^{ph} = e \mu_{ik} n. \quad (13)$$

μ_{ik} is the mobility tensor, k_B Boltzmann's constant, and T the temperature. The photovoltaic constants β_{ikj} do neither depend on the Fe^{2+} concentration nor on light intensity.

There is a balance equation for the conduction band electrons:

$$e \dot{n} - \partial_i J_i = e n^* \quad (14)$$

n^* is the production rate per unit volume of conduction band electrons. Electrons are mobilized upon light absorption by Fe^{2+} centers and trapped by Fe^{3+} centers:

$$n^* = A_{ik} c^{2+} e_i e_k - B n c^{3+} \quad ; \quad \dot{c}^{2+} = -n^* \quad ; \quad \dot{c}^{3+} = n^*. \quad (15)$$

Having written down all these equations for the photorefractive effect in $LiNbO_3:Ti:Fe$ we may restate our findings: the concentration c^{2+} in (12) and (15) depends strongly on depth. Its surface value is roughly ten times the bulk value. To establish a precise relationship between Ti concentration and c^{2+} was not yet possible, but future experiments and calculations will certainly allow to do so.

Acknowledgement

This work was performed within the program of SFB 225. We gratefully acknowledge financial support from Deutsche Forschungsgemeinschaft.

References

1. R.V. Schmidt and I.P. Kaminow, Appl. Phys. Lett. 25, 458 (1974)
2. A. Ashkin, G.D. Boyd, J.M. Dziedzic, R.G. Smith, A.A. Ballman, J.J. Levinstein, and K. Nassau, Appl. Phys. Lett. 9, 72 (1966)
3. A. Kurz, E. Krätzig, W. Keune, H. Engelmann, U. Gonser, B. Dischler, and A. Räuber, Appl. Phys. Lett. 12, 355 (1977)
4. E. Krätzig and H. Kurz, Ferroelectrics 13, 295 (1976)
5. A.M. Glass, D. von der Linde, and T.J. Negran, Appl. Phys. Lett. 25, 233 (1974)
6. A.M. Glass, J.P. Kaminow, A.A. Ballman, and D.H. Olson, Appl. Opt. 19, 276 (1980)
7. r.K. Tien and R. Ulrich, J. Opt. Soc. Am. 60, 1325 (1970)
8. J.P. Nisius, P. Hertel, E. Krätzig, and H. Pape, Integrated Optics (Springer-Verlag, 1985) p.62
9. V. Gericke, P. Hertel, E. Krätzig, J.P. Nisius, and R. Sommerfeldt, Appl. Phys. B44, 155 (1987)
10. P. Hertel and H.P. Menzler, Appl. Phys. B44, 75 (1987)
11. H. Kogelnik, Bell Syst. Techn. J. 48, 2909 (1969)
12. N.V. Kukhtarev, V.B. Markov, S.G. Odulov, M.S. Soskin, and V.L. Vinetskii, Ferroelectrics 22, 949 and 961 (1979)

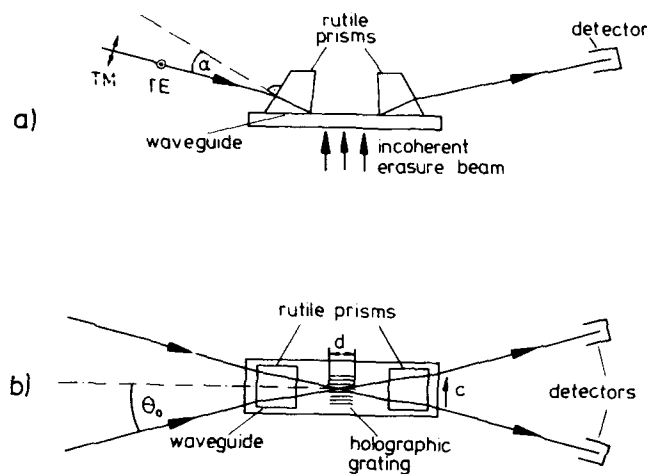


Fig. 1. Experimental setup, schematically.
a) front and b) top view.

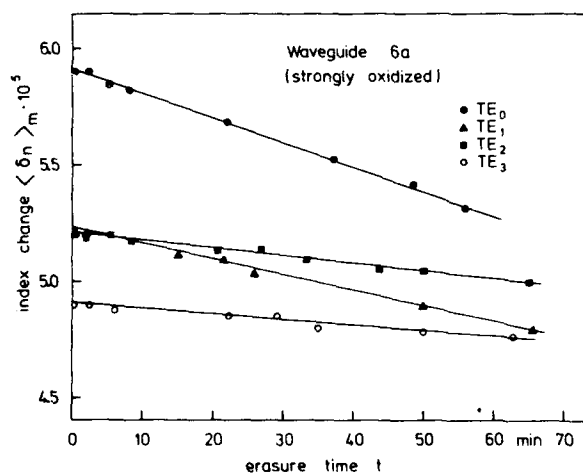


Fig. 2. Erasure of the extraordinary refractive index pattern with homogeneous light in the initial stage of illumination. The grating was written by interfering TE modes.

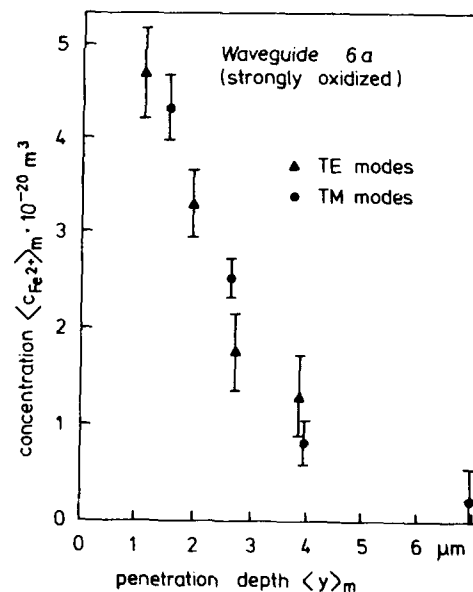


Fig. 3. Averaged Fe^{2+} concentration over grating penetration depth for various TE and TM modes. The sample has been strongly oxidized.

ENHANCED FOUR-WAVE MIXING IN THREE LEVEL SYSTEM

Reuben Shuker

Department of Physics

Ben-Gurion University of the Negev

Beer-Sheva, Israel

and

Ilya Golub

LROL, Physics Department

Laval University

Quebec, Canada.

ABSTRACT

Four-wave mixing in the vicinity of sodium double is reported. The three level system allows collinear phase-matching. The FWM is resonantly seeded and enhanced by photon splitting process of the laser photons.

We report on the enhancement of collinear nondegenerated four-wave mixing (FWM) near the sodium doublet.¹ This enhancement is related to another nonlinear effect obtained in sodium: When an intense laser beam, blue detuned from the D₂ line of sodium, propagates in sodium vapor at densities $>10^{14}\text{cm}^{-3}$ a forward coherent emission at frequency ω_B to the blue of the D₁ transition is observed - Fig.1a. This emission is attributed by us to photon splitting of the laser photon, ω_{L1} , involving the magnetic dipole $^2P_{3/2} - ^2P_{1/2}$ transition and a photon ω_B quasiresonant with $^2P_{3/2} - ^2P_{1/2}$ transition.^{2,3}

The collinear FWM occurs, when a second laser, ω_{L2} , collinear with the first one at ω_{L1} is introduced, obeying $2\omega_{L1} = \omega_{L2} + \omega_4$, Fig. 1b. This process is described by the susceptibility χ^3 and the corresponding gain is estimated by us on the order of 10^2cm^{-1} . It is resonantly seeded and enhanced by the photon splitting process. Although collinear FWM process is not possible in a two level system, the third level, $^2P_{1/2}$ of the sodium atom, relaxes the phase-matching requirements and collinear FWM becomes allowed.

First we describe briefly the photon splitting process. When a high-density ($>10^{15}\text{cm}^{-3}$) sodium vapor is illuminated by intense pulsed dye laser detuned to the blue of D₂ line, saturation, self-focusing and self-trapping occur. The forward radiation contains, apart from a conical broad band emission due to a Cherenkov-type process⁴, a stimulated emission to the blue of D₁ line - Fig.2. No counterpart to the "blue peak" at ω_{L2} , necessary for four-wave mixing process is observed. The "blue peak" emission frequency is also independent on the laser detuning Δ . Thus nonlinear processes, such as stimulated electronics Raman or four-wave mixing, which may occur in a three-level system, are excluded. Collision induced processes are also excluded since no properties of the "blue peak" depends on the buffer gas (Ar) pressure, in the range 2 - 20 torr. This stimulated emission is due to laser photon splitting into two photons, quasiresonant with $3P_{3/2} \rightarrow 3P_{1/2}$ M1 and $3P_{1/2} \rightarrow 3S_{1/2}$ E1 transition - Fig.3. Self-focusing determines the frequency of the stimulated emission to the blue of D₁ transition. Self-trapping is essential and cause gain on the order of 10^2cm^{-1} at ω_B .^{2,3} This seeds and enhances the collinear FWM. In fact the measured gain of the FWM at ω_B is on the order of 10^4 - 10^5cm^{-1} as shown below.

The energy and momentum conservation laws in the parametric FWM process for collinear propagating waves are given by

$$2\omega_{L1} = \omega_3 + \omega_4$$

(1)

$$2\omega_{L1} n(\omega_{L1}) = \omega_3 n(\omega_3) + \omega_4 n(\omega_4)$$

here ω_{L1} , ω_3, ω_4 are the frequencies of the pumping laser, the signal and the idler emissions

respectively; $n(\omega_i)$ is the index of refraction at frequency ω_i . Fig. 4 shows several FWM processes in a three-level atom.

In a two level system, for a finite laser detuning from transition $\Delta = \omega_L - \omega_0 \neq 0$, the system of (1) has a solution only for the degenerate case, i.e., for the case where $\omega_L = \omega_3 = \omega_4$. The situation is different when a third level, such as in the case of the doublet system of an alkali metal, is introduced. Here the third level relaxes the phase matching requirements. The FWM process is described by the nonlinear susceptibility $\chi^{(3)}$. The corresponding gain of g of the exponentially growing coupled waves ω_3 and ω_4 in the case of exact phase-matching ($\Delta k = 0$) and absence of losses is⁵:

$$g = 2\pi/c (\omega_3\omega_4)^{1/2} \chi^{(3)} |E_L|^2, \quad (2)$$

where E_L is the amplitude of the pumping laser field. For conditions typical for our experiments, $N = 5 \times 10^{15} \text{ cm}^{-3}$, $\Delta\omega = \omega_L - \omega_{D2} = 10 \text{ cm}^{-1}$, $\omega_4 - \omega_{D1} = 2 \text{ cm}^{-1}$, $E_L = 300 \text{ esu}$ ($I_L = 10 \text{ MW/cm}^2$), we obtain from eq. (2 and 3) $\chi^{(3)} = 10^{-8} \text{ esu}$ and $g = 5 \times 10^2 \text{ cm}^{-1}$. For comparison, a gain of $5 \times 10^4 \text{ cm}^{-1}$ was calculated for a noncollinear FWM process observed in sodium for laser intensities of $\sim 1 \text{ Gw/cm}^2$.⁶

To perform the FWM experiment we used sodium vapor with a density of 10^{15} – 10^{16} cm^{-3} produced in a 20 cm long heat pipe. A Hänsch-type pulsed dye laser with a beam splitter after the telescope and two gratings produced radiation at two independently tuned wavelengths. Each spectral component had a bandwidth of 0.6 cm^{-1} and peak power of 3–5 kW. The pulse duration was 15 nsec. By blocking one of the gratings the laser produced $\sim 10 \text{ kW}$ peak power pulses at a single wavelength. The laser radiation was focused into the heat pipe. The forward emitted radiation spectrum was measured by 1.2 cm^{-1} resolution McPhearsen 218 spectrometer. An on-axis aperture blocked the conical emission. The experiments were performed with the laser blue detuned with respect to D_2 transition, i.e. at conditions of self-focusing. The laser intensity in the focal spot is estimated to be 10 MW/cm^2 .

When the exciting laser radiation ω_{L1} is blue detuned with respect to the D_2 transition, a coherent stimulated forward emission is observed (Fig. 1a) as discussed above. When a second laser line, ω_{L2} (the signal, ω_3), collinear with the first one is introduced, a FWM obeying $2\omega_{L1} = \omega_{L2} + \omega_4$ occurs (Fig. 1b). Here an enhancement of the on-axis emission at ω_B is obtained when the frequency ω_{L2} is such that the on-axis fourth photon ω_4 is resonant with ω_B (Fig. 1b). This enhancement is achieved in spite of the reduction of the laser L_1 intensity, which occurs due to gain competition by the laser L_2 within a common dye cell. For frequencies of laser L_2 such that $\omega_4 = 2\omega_{L2}$ is different from ω_B the FWM is not observed (Fig. 1c), possibly due to a too small gain when FWM is acting alone. However, by tuning the other laser, ω_{L1} , such that the condition $\omega_4 = \omega_B$ is restored, an enhancement of emission ω_B (the frequency of which is practically constant, as mentioned above) is obtained anew (Fig. 1d). When the frequency of the laser L_2 was tuned in the region of ω_B , with the same conditions as those used to obtain the spectrum of Fig. 1a, no idler at frequency $\omega_4 = 2\omega_{L1} - \omega_{L2}$ is observed. However, this result may be due to high absorption of the laser L_2 radiation by the D_1 transition, which may render laser intensity to be too small for a nonlinear process to occur.

The collinear FWM is observed only when the idler frequency (ω_4) is within the spectral bandwidth of the emission ω_B . We conclude that the enhancement is due to the existence of a high gain at ω_B .

A more extensive description of the FWM process should be made by taking into account the saturation of the index of refraction and the shift of the levels of the three level system due to an ac Stark effect. However, for our experimental conditions (laser detuning $\Delta\omega$ from D_2 line 10 – 13 cm^{-1} and $I_L \approx 10 \text{ W/cm}^2$) the Stark shift δ of the D_2 transition levels is quite small: $\delta + (\Omega' - \Delta\omega)/2 \approx 1 \text{ cm}^{-1}$. Here Ω' is the generalized Rabi frequency. The ac Stark effect on the D_1 line is, obviously, much smaller.

In conclusion, we have observed nondegenerate collinear FWM by a three-level system in the vicinity of the sodium doublet. The third level provides the compensating dispersion and relaxes the phase matching requirements for a collinear process. The FWM is selectively enhanced by a high gain on the blue side of the D_1 transition. We hope, that the present work will stimulate research on both nondegenerate FWM by a three-level system and its relation to the emission near the D_1 transition of sodium and other alkali atoms.

References

1. I. Golub, R. Shuker and G. Erez, Appl. Phys. B **41**, 39 (1987).
2. R. Shuker, I. Golub and G. Erez, in Methods of Laser Spectroscopy, ed. Y. Prior, A. Ben-Reuven and M. Rosenbluh (Plenum: New York 1986) p.371.
3. I. Golub, R. Shuker and G. Erez, J. Phys. B: At. Mol. Phys. Letters, **20** L63 (1987).
4. I. Golub, G. Erez and R. Shuker, J. Phys. B: At. Mol. Phys. **19**, L115 (1986).
5. A. Yariv, Quantum Electronics (Wiley, New York, 1975).
6. J. Krasinski, P.J. Cauthier, M.S. Malcuit, R.W. Boyd: Opt. Commun. **54**, 241 (1985).

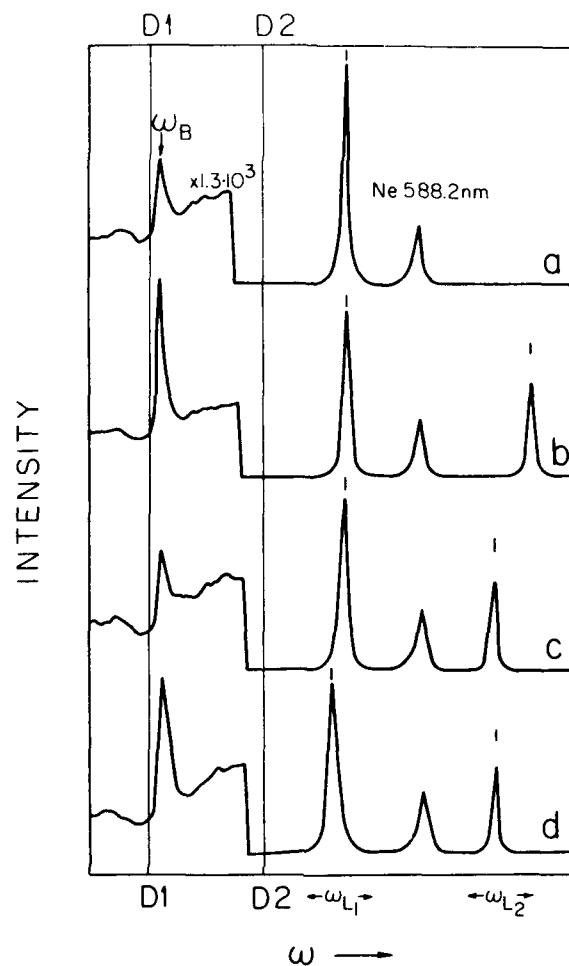


Fig.1 Spectrograph trace of the on-axis forward emission. ω_B and ω_{L1} and ω_{L2} are marked (see text). $[Na] = 2 \cdot 10^{15} \text{ cm}^{-3}$. The Ne 588.2nm line is for calibration. The jump to the left of D_2 is a scale change of the recorder.

- a) laser ω_{L1} is on and laser ω_{L2} is off.
- b) laser ω_{L2} is on. $\omega_{L2} - \omega_{L1} = \omega_{L1} - \omega_B$. Enhancement of ω_B is seen.
- c) the same as b), but ω_{L2} has been moved to the red; no enhancement of ω_B is seen.
- d) the same as c), but ω_{L1} has been shifted to reestablish $\omega_{L2} - \omega_{L1} = \omega_{L1} - \omega_B$ and enhancement of ω_B appears again.

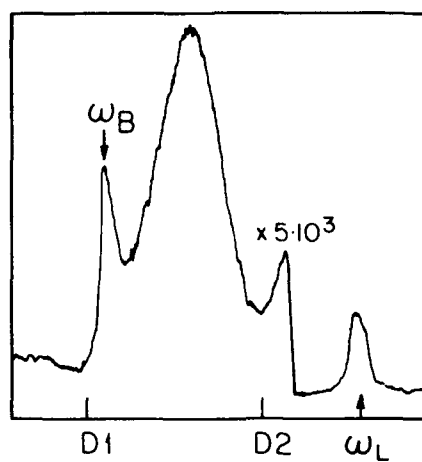


Fig. 2 Spectrum of forward emission of sodium by laser at ω_L .
 $[\text{Na}] = 1.8 \cdot 10^{15} \text{cm}^{-3}$.

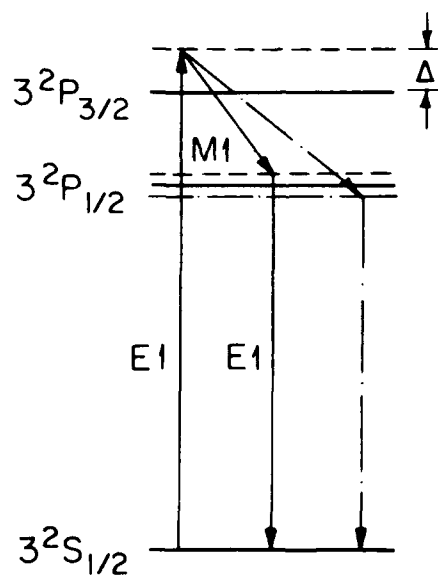


Fig. 3 Laser photon splitting by M1 and E1 transition. The broken line represents defocused emission.

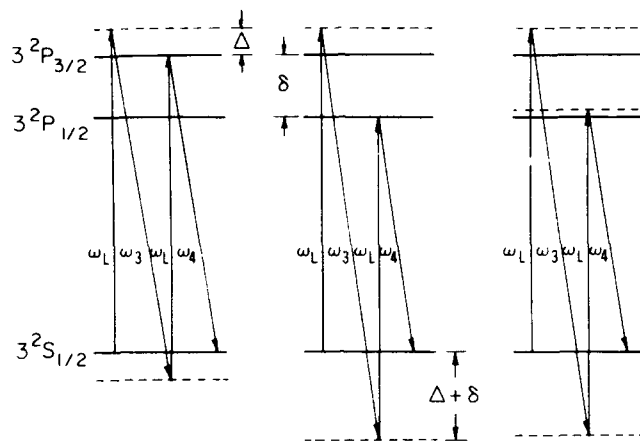


Fig. 4a-c Schemes of nondegenerate parametric four wave mixing in a sodium atom. ω_L , ω_3 and ω_4 are the laser, the signal and the idler frequencies, respectively; δ is the fine structure splitting and Δ - the laser detuning.

- FWM on two of the levels, $3^2P_{3/2}$ and $3^2P_{1/2}$
- FWM when the third level, $3^2P_{1/2}$ is also involved.
- Phase matching for a collinear FWM sets the frequency of ω_4 to the blue of D_1 transition. Note the shift between the lowest virtual levels of Fig. 1b and 1c by an amount equal to the detuning of ω_4 from the D_1 transition.

Phase-conjugation using Nd:YAG-lasers

H.-J. Eichler, Chen Jun, K. Richter
Optisches Institut, Technische Universität, D-1000 Berlin 12

Abstract

Phase conjugation has been investigated with 15 ns pulsed Nd:YAG-lasers by degenerate four-wave mixing in silicon and by stimulated Brillouin scattering (SBS) in acetone. Reflectivities of 125% by four-wave mixing and 80% by SBS have been obtained. With the phase conjugate SBS-mirror a laser has been built which compensates for phase aberrations inside the laser resonator.

Phase conjugation is a process which transforms an incident optical wave into a counter-propagating, reflected wave /1/. Mathematically in complex notation, the reversed wave amplitude is described as the complex conjugate of the incident wave. In this paper two nonlinear optical effects are described which produce conjugated waves, degenerate four-wave mixing in silicon and stimulated backscattering in various liquids.

The phase-conjugated, reversed wave is useful to compensate phase aberrations in optical systems which may be due to turbulence, vibration, heating etc. As an example for such an application we describe a pulsed Nd:YAG-laser which is Q-switched by a stimulated scattering cell replacing one resonator mirror.

1. Phase conjugation by four-wave mixing in silicon

A laser beam with 1.06 μm wavelength and a duration of 15 ns is split into three parts (Fig. 1). The signal beam E_{sig} and one of the pump beams E_{p1} produce a spatially periodic electron-hole density, which changes the refractive index, resulting in a phase grating /2/. The second pump beam E_{p2} is diffracted at the grating. The first-order diffracted beam E_{ph} is phase conjugated with respect to the signal wave. The reflectivity of this phase conjugating arrangement PCM has been obtained by measuring the pulse energy ratio of the signal and the reflected, phase conjugated beam. In Fig. 1 the measured reflectivities are shown as a function of the average pump energy density $\sqrt{E_{\text{p1}}E_{\text{p2}}}$. The silicon sample is antireflection coated and has a thickness of 400 μm . The solid curves show the theoretical results calculated from grating theory /3/. Phase conjugation can be demonstrated by placing an object with a phase aberration into the signal beam. Unlike a normal mirror, the beam reflected from a PCM, regains the initial profile after passing the phase distortion again.

2. Phase conjugation by stimulated scattering

Stimulated scattering starts from the spontaneous fluctuations of pressure (sound waves in Brillouin scattering) or temperature (Rayleigh scattering) which can be expanded into Fourier-components with all possible spatial periods and directions. The incident light is diffracted or scattered by these elementary phase gratings. The interfering incident and scattered waves couple to the material and enhance the spontaneous fluctuations if the incident wave is coherent and has sufficient power. The scattered intensity increases and may become comparable with the incident intensity. The strongest enhancement of the scattered intensity occurs for the largest interaction length and is observed in the backward direction in our experiment. The backward wave appears to be phase conjugated similarly as in four-wave mixing. However, stimulated scattering is more convenient since no additional pump waves are required. On the other side, higher PCM reflectivities are possible by four-wave mixing.

The measured reflectivity of a stimulated scattering PCM is shown in Fig. 2 for two liquids. The results were obtained by focusing Nd:YAG-laser beams into liquid cells with 10 cm length. In Table 1 the measured thresholds for stimulated backscattering in various liquids are given. The scattering mechanism has not been investigated in detail. It is

generally assumed, however, that stimulated Brillouin scattering dominates. Self-focusing seems to be important.

3. Laser with phase conjugating mirror (PCM)

High average power Nd:YAG-lasers suffer from beam distortions due to thermal lensing in the active material. It is hoped that the performance of such lasers can be improved by compensating internal phase distortions using a PCM. A pulsed Nd:YAG-laser (Fig. 3) has been set up to investigate the properties of such a laser and some preliminary results have been obtained. A Nd:YAG-rod with $2\frac{1}{4} \times 1\frac{1}{4}$ " dimensions was pumped by a flashlamp. Mirrors M_1 and M_2 are plane and have reflectivities of 40% and 100%. Initially the cavity with 60 cm length formed by these mirrors is very lossy due to the presence of the liquid cells. The laser starts in normal mode operation. The standing wave in the cell excites a reflecting grating stimulating efficient backward scattering. Since the reflectivity of this PCM device increases with the incident beam intensity, the laser is Q-switched /4/. A pulse with less than 10 ns duration and 130 mJ energy is emitted (Fig. 3). About the same energy is obtained replacing the PCM by a $R = 40\%$ mirror.

Internal distortion elimination of such a laser was proved by insertion of an etched glass plate into the cavity. Fig. 4 shows measured beam profiles of the laser with the phase-conjugating SBS-mirror and for comparison also of a laser with conventional mirrors. If we insert the scattering glass plate into the conventional resonator, the emitted laser beam profile is strongly distorted and the output energy reduced. The beam becomes divergent. In contrast, phase disturbances are eliminated in the laser with the PCM. Insertion of the etched glass plate leads to reduction of the laser energy but the nearly Gaussian beam profile is maintained.

References:

- /1/ R.A. Fisher editor, Optical Phase Conjugation, Academic Press, New York 1983.
- /2/ H.-J. Eichler, P. Günter, D.W. Pohl, Laser-Induced Dynamic Gratings, Springer Series in Optical Sciences, Vol. 50, Berlin 1986.
- /3/ H.-J. Eichler, J. Chen, K. Richter, Appl. Physics B 42, 215-219 (1987).
- /4/ D.W. Pohl, Phys. Lett. 24A, 239 (1967).

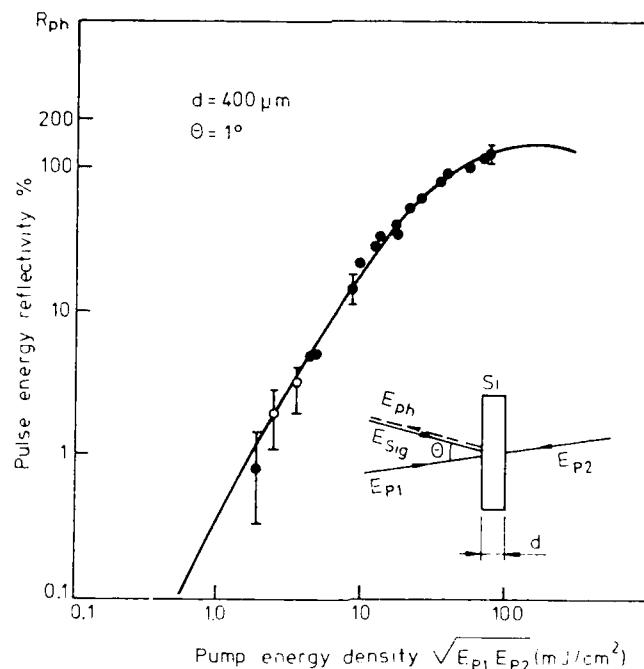


Fig. 1 DFWM reflectivity of silicon dependent on the average pump energy density.

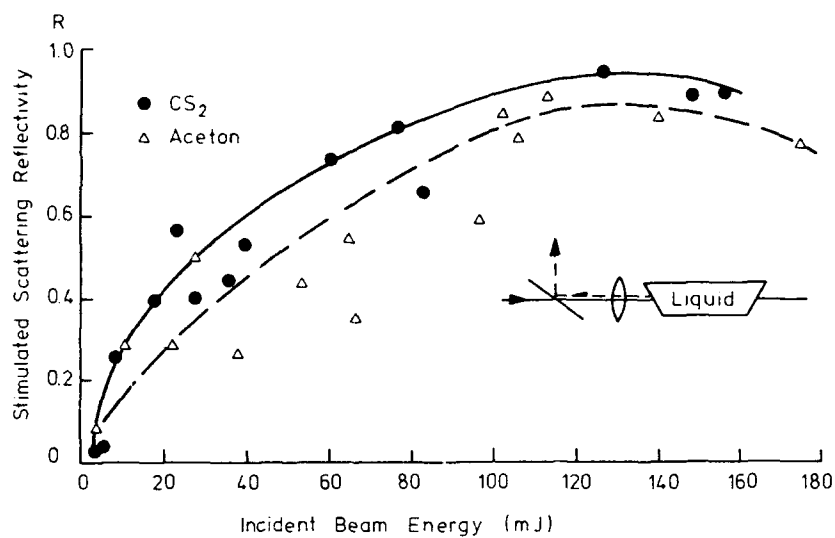


Fig. 2 Reflectivity of stimulated scattering cell as a function of the incident energy.

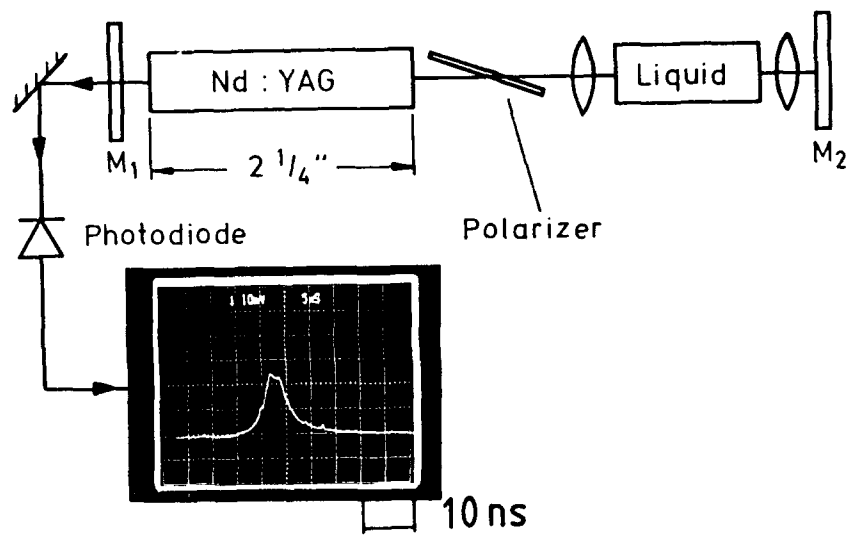


Fig. 3 Laser with PCM cell

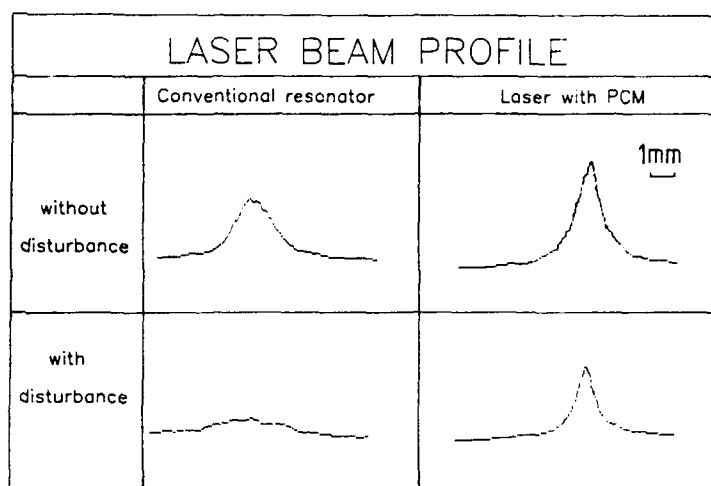


Fig. 4 Laser Beam Profiles of the conventional laser and of the laser with the phase conjugating SBS-mirror

Table 1: Threshold of stimulated backscattering in various liquids

threshold	CS ₂	acetone	heptane	methanol	water
GW/cm ²	2.3	2.6	4.3	9	13
mJ	6	7	12	24	34

STIMULATED SCATTERING OF RADIATION WITH INCOMPLETE SPECKLE MODULATION

M.A. Beedle and R.J. Lysiak
Texas Christian University, Fort Worth, Texas 76129

A theoretical calculation of the stimulated scattering of a laser beam composed of a gaussian component and a speckle part incident inside a nonlinear cell when these two parts have equal waists is presented. The intensity fraction of each component that is backscattered is dependant on the corresponding incident intensity ratio. For high incident speckle ratio the dependance is linear, however, at a ratio of .9 or lower the speckle component predominates and three different domains are identified with vastly different dependance of the output ratio to the input ratio. At low speckle ratios, the speckle portion will be preferentially amplified by a factor of 900. This behavior is in accordance with previous experimental results dating as back far as 1972. Also, a general discussion of the saturation power required by a partially speckled beams is presented and recommendations for optimum conjugation via SS are presented.

I. Introduction.

I. After B. Y. Zeldovich *et al* first discovered phase conjugation by stimulated scattering [1] his results showed conjugation had much better quality for fully speckled beams than for the scattering of the unperturbed multimode intensity. It was since then understood that the scattering of speckled fields was important to understand this behavior. Consider now the following setup in which phase conjugation by SBS (Stimulated Brillouin Scattering) is implemented. See figure 1. This setup in general, will involve a combination of non-speckled, and speckled parts. For the purpose of many applications this is convenient, while in some other cases this speckled portion is undesirable noise. Our first discussion is a continuation of the theoretical work exposed by Zeldovich in reference [2], where the SSRISM is limited to a confocal system where the waists of the speckled and non-speckled parts completely overlap. See figure 1. For this reason we prefer to only outline the procedure of this first part, and concentrate in the discussion of the results.

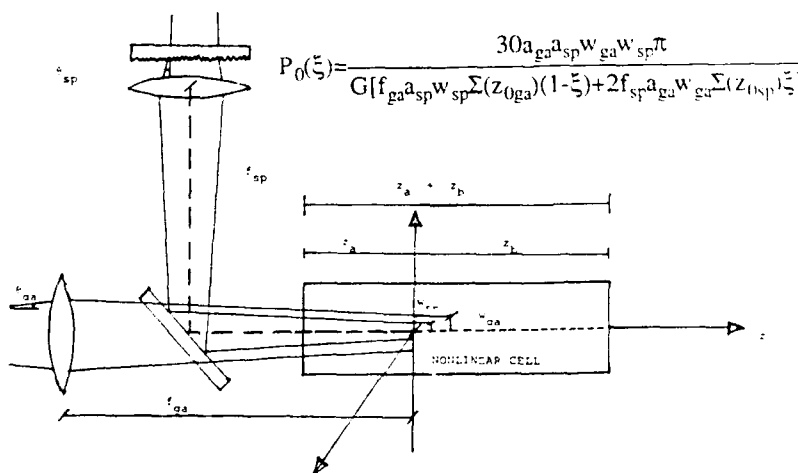


Fig. 1 Typical experimental setup for SSRISM.

II. Theory

SSRISM (Stimulated Scattering of Radiation with Incomplete Speckle Modulation), is the Stimulated Scattering of a pump beam that is partially speckled. This implies that in general the backscattered radiation will be also partially speckled. SSRISM is of particular interest because this is the way in which most Stimulated Scattering processes take place. In any application or study of OPC (Optical Phase Conjugation) there will be some noise involved, thus the beam will be in general a combination of speckled and non-speckled portions. In the SVEA (Slowly Varying Envelope Approximation) the equations describing SBS (Stimulated Brillouin Scattering) when we have normal incident plane polarized plane waves and only backscattering is considered are (pump depletion and other nonlinear terms are neglected):

$$1 \quad a) \quad \frac{\partial E_I}{\partial z} + \frac{i}{2k_I} \nabla_I^2 E_I(r, z) = 0$$

$$1 \quad b) \quad \frac{\partial E_O}{\partial z} - \frac{i}{2k_O} \nabla_I^2 E_O(r, z) = 1/2G|E_I(r, z)|^2 E_O(r, z) .$$

Where E_I and E_O are the pump and backscattered waves respectively.

Let the pump field consist of a constant plane wave and a speckle part:

$$2 \quad a) \quad E_I(r, z) = E_{Iga} + E_{Isp}(r, z) .$$

Assume that the backscattered wave is a spatial superposition of the conjugate incident beam parts:

$$2 \quad b) \quad E_O(r, z) = a_1(z)E_{Iga}^* + a_2(z)E_{Isp}^*(r, z)$$

where E_{Ipw} and E_{Isp} are the incident plane wave and speckled parts respectively. Define the ratios of incident and backscattered speckled intensity as:

$$3 \quad a) \quad \epsilon_I = \frac{I_{Isp}}{I_{I, total}} = \frac{\langle |E_{Isp}|^2 \rangle}{|E_{Iga}|^2 + \langle |E_{Isp}|^2 \rangle} ,$$

$$3 \quad b) \quad \xi_0 = \frac{I_{Osp}}{I_{O,total}} = \frac{\langle |E_{Osp}|^2 \rangle}{|E_{Oga}|^2 + \langle |E_{Osp}|^2 \rangle}.$$

Even though the backscattered wave has correlated and uncorrelated waves with respect to the pump, we consider here correlated backscattered waves with the pump of the kind of equation 2 b. In that case we obtain a system of equations for the spatial coefficients $a_1(z)$ and $a_2(z)$ after we average over the ensemble of speckle field in equations 1 a,b.

$$4 \quad a) \quad \frac{da_1}{dz} = \frac{1}{2} GI_I (a_1 + \xi a_2)$$

$$4 \quad b) \quad \frac{da_2}{dz} = \frac{1}{2} GI_I ([1-\xi]a_1 + [1+\xi]a_2)$$

When we solve for this coefficients and incorporate them back into equations 1 a,b; we may obtain the backscattered speckle intensity ratio in terms of the pump speckle ratio intensity, the gain coefficients and z .

$$5 \quad a) \quad \xi_0 = \frac{1}{1 + K}, \text{ with:}$$

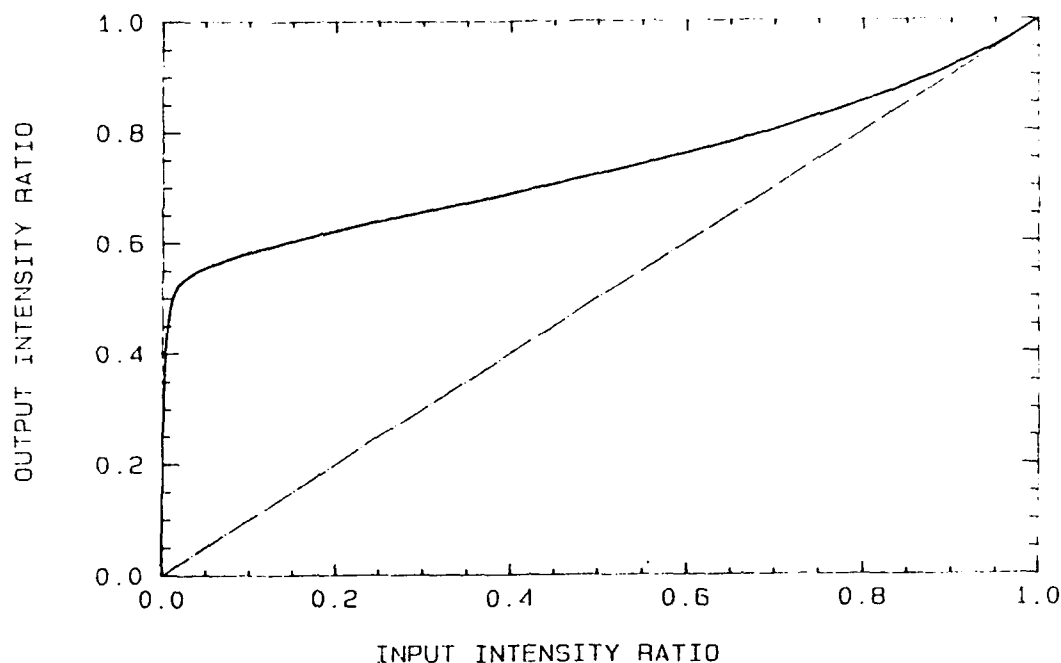
$$5 \quad b) \quad K = \frac{1-\xi}{\xi} \left[\frac{\gamma_+ - \gamma_- e^R}{\gamma_+^2 - \gamma_-^2 e^R} \right]^2,$$

$$5 \quad c) \quad R = -GI_I z \xi [\gamma_+ - 1/2] = -\frac{60}{1+\xi} \xi [\gamma_+ - 1/2],$$

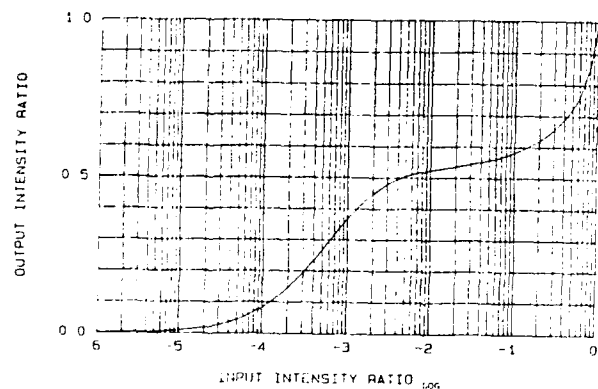
(The motivation for equating $GI_I z$ with $60/(1+\xi)$ will be apparent shortly),

$$5 \quad d) \quad \text{and,} \quad \gamma_{\pm} = 1/2 \pm [1/\xi - 3/4]^{1/2}.$$

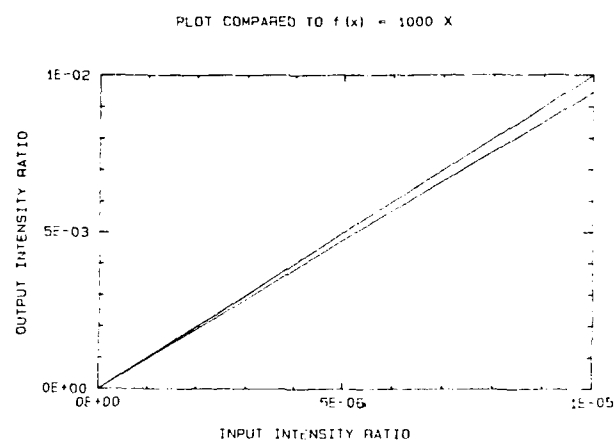
Several plots of this function of the pump speckle intensity ratio to the backscattered speckle intensity ratio are given below. Figures 2 show its behavior over the entire range $0 < \xi_I < 1$, where we identify 3 domains:



2 a)



2 b)



2 c)

Figures 2. a) Shows the behavior of the output speckle ratio with respect to the input speckle ratio over its whole domain. b) The output speckle ratio is now given in terms of the logarithm of the input speckle ratio. c) A comparison of the linear behavior of the region in which the input speckle ratio is less than 10^{-6} is given.

$10^{-5} > \xi$, where the dependance is linear;
 $10^{-5} < \xi < 10^{-2}$, a high gain region; and
 $10^{-2} < \xi < 1$, an almost linear region where the output speckle part is of the same order of magnitude of that of the pump beam.

This is an interesting result, because enables one to determine the speckled backscattered portion from the pump speckled ratio and the initial conditions. Thus it can be used as a measure of the conjugation quality. When we analyze the limit $\xi \rightarrow 0$ ($\xi < 10^{-6}$), we find that the output speckle intensity ratio ξ_0 has an approximately linear behavior with respect to the pump speckle intensity ratio ξ_I . Namely:

$$6) \quad \xi_0 \sim 900 \xi_I.$$

This implies that for low incident speckle portions, the speckle part will be amplified significantly. Recall that the Zeldovich's original experiments showed that a speckled beam had much better conjugation than his undisturbed multimode ruby laser. In the light of this discussion this can be understood by assuming that his multimode beam had a little speckled portion. That is the interacting multimodes had the same effect as a partially speckled beam with small ξ_I , therefore the backscattered speckled ratio, had to be amplified. Since the speckled portions were not measured in these experiments we cannot compare our theoretical results with them, and although we expect a similar qualitative behavior, there may be some departure from these results since the condition of overlapping waists for the speckled and non-speckled portions was not guaranteed.

We intend to do experiments at TCU to show if this behavior is as predicted by the above discussion. We know the approximation of plane waves should be valid at the focal region of a long focal lenght converging lens, and although more general treatment should include focusing, pump depletion, self focusing, as well as a more accurate accounting of the statistics, the general experimental behavior should be very similar to the above discussion, as long as the waists overlap completely.

We direct now our interest towards the power requirements of SSRISM, in the case of a confocal system like in figure 1. The calculation of the saturation power requires the definition of the focused beams. We will assume a gaussian envelope for the speckled beam, (i.e. a double gaussian).

$$7 a) \quad I_{sp}(r, z) = I_{0sp} (w_{0sp}/w_{sp}(z))^2 \exp[-2r^2/w_{sp}^2(z)]$$

$$7 b) \quad I_{ga}(r, z) = I_{0ga} (w_{0ga}/w_{ga}(z))^2 \exp[-2r^2/w_{ga}^2(z)]$$

with:

$$w_{sp} = \theta_{sp} f_{sp}, \quad w_{sp}^2(z) = w_{0sp}^2 [1 + (z/z_{0sp})^2], \quad z_{sp} = \frac{f_{sp}^2 \theta_{sp}}{a_{sp}}$$

$$w_{ga} = \theta_{ga} f_{ga}, \quad w_{ga}^2(z) = w_{0ga}^2 [1 + (z/z_{0ga})^2], \quad z_{ga} = \frac{f_{ga}^2 \theta_{ga}}{a_{ga}}$$

Where " w_i ", are the waists; " z_i ", are the waist lengths; " f_i " are the focal lengths, and " θ_i " are the divergences of the speckled and unspeckled parts.

We also know that to attain saturation at the center of the beam, or the minimum saturation power is (i.e. for higher power than that concentric circles of the beam would also attain saturation):

$$8) \quad \int_{z_a}^{z_b} GI_I(\max) dz = \int_{z_a}^{z_b} GI_I(0, z) dz \sim 30$$

We assume there is no correlation for the the speckled and unspeckled beams:

$$9) \quad \langle E_{sp} E_{ga} \rangle = 0, \text{ therefore } I_I = I_{sp}(r, z) + I_{ga}(r, z).$$

SATURATION POWER VS. SPECKLED PORTION

(for typical experimental conditions - in carbon disulfide)

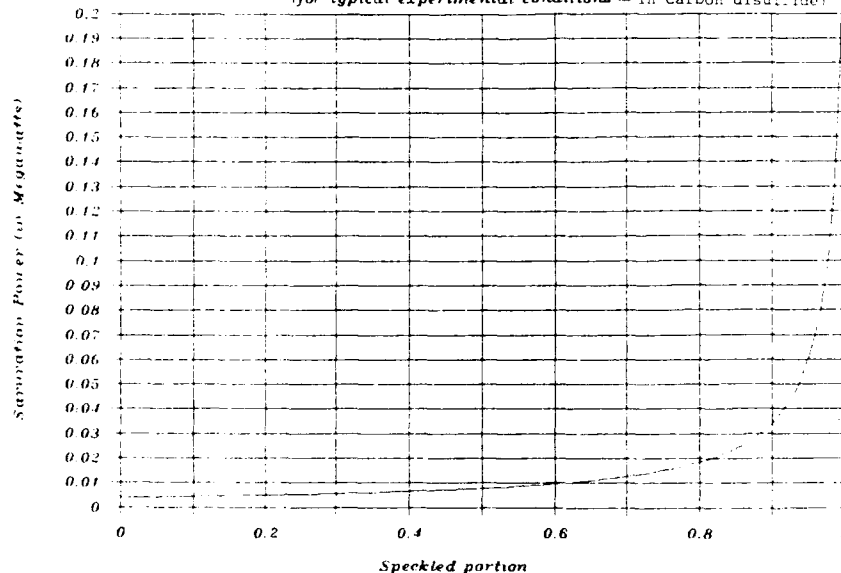


Fig. 3)

The saturation then is given as a function of the experimental conditions and the input speckled ratio after integration of equation 8:

$$10) \quad P_0(\xi) = \frac{30 a_{ga} a_{sp} w_{ga} w_{sp} \pi}{G [f_{ga} a_{sp} w_{sp} \Sigma(z_{0ga}) (1-\xi) + 2 f_{sp} a_{ga} w_{ga} \Sigma(z_{0sp}) \xi]} .$$

Where $\Sigma(z_{0i})$ is:

$$11) \quad \Sigma(z_{0i}) = \arctan(z_b/z_{0i}) - \arctan(z_a/z_{0i}) .$$

This expression above guarantees that the maximum intensity of the beam will achieve saturation, to guarantee that that a region enclosed by a certain radius (for example the radius that defines the 1/2, 1/e, or the 1/e² points from maximum intensity) achieves saturation, the above expression needs to be multiplied by the factors: 2, e, e².

To compare this result with experimental conditions let us assume typical experimental conditions. Assume equal incident beam sizes for the gaussian and speckled portions equal to 1cm., allow the gaussian mode to have a diffraction limited divergence ($\sim 2 \times 10^{-5}$ rad.) and a 2 mrad. phase plate, let the focal length of both beams equal to 1m., also assume the nonlinear medium is carbon disulfide pumped with ruby laser radiation i.e. G=.15 cm/MW in a long cell (much greater than the diffraction lengths of both components). Then the saturation power is found as a function of the incident speckled portion ξ (see figure 3):

$$12) \quad P_0(\xi) = \frac{.4 \text{ (MW)}}{100(1-\xi) + 2\xi} .$$

And for the extreme cases where $\xi = 0, 1$ this yields:

$$P_0(0) = 4 \text{ KW} \quad P_0(1) = .2 \text{ MW}$$

Although experiments under controlled conditions have not been done explicitly this results are in the order of typical experimental values see for example Mays and Lysiak [3] and, Kryzhanovskii [4], (care should be taken to compare these results with interacting cells of large dimensions). From a practical point of view, the operating points to achieve optimal conjugation, (i.e. maximum backscattered radiation with optimized quality) are implied above. If one wishes to conjugate a signal with power less than that of what a fully

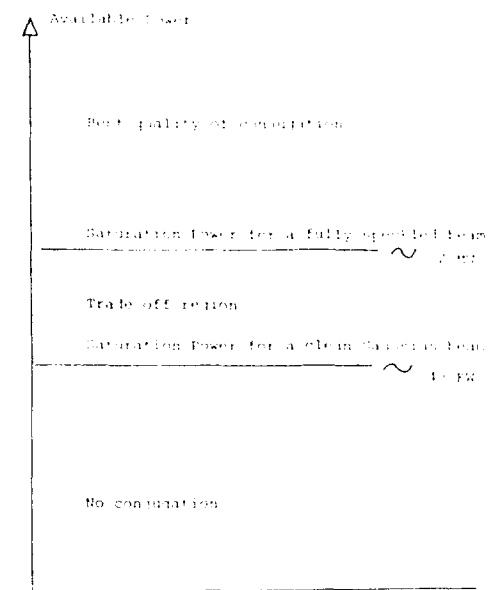


Fig 4) Power requirements for partially speckled beams.

speckled beam requires, one should be careful in choosing the amount of speckling required. In general to obtain maximum backscattered radiation one should operate in the saturation region.

For low power signals it is convenient to conjugate an unspeckled beam since they require less power to achieve saturation, however most sources of radiation within that power range operate in a multimode condition, and there are always sources of noise within the experimental setup, therefore implying that the conjugation would be of less than desired quality according to the above discussion of partially speckled beams, unless the beam is a completely "clean" Gaussian mode. To do so one would use a spatial filter (therefore decreasing even more the power). So unless one cleans the beam to a very high degree and still has enough power to guarantee saturation it is inconvenient to filter the speckle portions on a beam. In the event that the power is greater than that of the saturation power of a totally speckled beam, one should speckle the beam completely, obtaining both highest quality and maximum backscattered radiation.

- 1) B. Ya. Zel'dovich, V.I. Popovichev, V.V. Ragul'skii, and F.S. Faizullov; *Connection between the wave fronts of the reflected and exciting light in stimulated Mandel'shtam-Brillouin scattering*; P.N. Lebedev Physics Institute, USSR Academy of Sciences; ZhETF pis Red 15, no 3, 160-164 (5 February 1972).
- 2) B. Ya. Zel'dovich, N.F. Pilipetsky, V.V. Shkunov; *Principles of phase conjugation*; Springer-Verlag; New York; 1985.
- 3) R. Mays, R.J. Lysiak; *Observations of wavefront reproduction by stimulated Brillouin and Raman scattering as a function of pump power and waveguide dimensions*; Optical Communications 32 334 (1980).
- 4) Kryzhanovskii, V.I. Sov. Phys. Tech. Phys, 27(7) (1982) p 885.

RETROREFLECTIVE PSEUDO-PHASE CONJUGATOR

by Dr. Virgil V. Vaughn
President, LSI, Inc.
1900 Sparkman Drive
Huntsville, Alabama 35816

Ray Conrad and John Erlich
MICOM
Redstone Arsenal, Alabama 35898

Abstract

Improvement of the beam quality of the flashlamp pumped dye laser presents an important problem for the Army. The effort addressed here consisted of the design and development of retroreflectors for use as cavity mirrors in the subject dye laser. A retroreflector array that was tested with the data presented here showed promise that a retroreflector array could significantly improve the beam quality of the dye laser. Reflectivity better than 90% is possible providing the possibility of a high cavity gain. Fabrication techniques were developed that provided for high quality production at a reasonable cost.

1. Introduction

Improvement of the beam quality is a critical issue for the flashlamp pumped dye lasers. Conditions that result in index of refraction variations in the lasing medium induce optical phase front distortions that produce a degradation in beam quality. A methodology that helps in removing phase front distortions will result in beam quality improvement. Phase compensation is one such methodology that appears to have great promise in this application.

Phase variations are exhibited as beam intensity fluctuations as well as beam spreading and bending. Among other effects, they result from the interaction of laser dynamics effects, laser cavity path media conditions, operational mode of the laser, and wavelength. Phase variations may be compensated for by use of adaptive optics techniques, nonlinear phase conjugation or pseudo-phase conjugation[1]. Adaptive optics utilizes segmented optics or deformable mirrors which require numerous actuators and/or optical segments with a complex electronic control system. Nonlinear phase conjugation requires a somewhat less complex electronic system than that of adaptive optics yet it still requires the alignment of a number of electro-optic components. The method investigated here requires only one optical component and essentially no alignment. In this effort we examined a retroreflector used as a pseudo-phase conjugator.

The related effort included the design and development methodology of a retroreflector pseudo-phase conjugator suitable for use in a flashlamp pumped dye laser. This included examination of techniques for design and fabrication of an array of corner cube reflectors as well as right circular cones. Additional laboratory experiments were performed with Reflexite to determine its retroreflector characteristics as well as evaluate cavity performance. Evaluation of retroreflector performance to improve beam quality has been performed by several other investigators[2, 3, 4].

2. Types of Retroreflectors

Work by other investigators have included retroreflectors assembled from glass prisms as well as the commercially available material known as Reflexite[2, 3, 4, 5]. Glass prisms work well as a research device for suitable wave-lengths; however, this type of retroreflector requires a considerable amount of effort for assembly. The related effort at LSI, Inc. concentrated on types of retroreflectors which could be produced in large quantities and at a cost comparable with that of a high quality laser cavity mirror. A commercially available product produced by Reflexite Corporation is made in a variety of forms which include imprinting an array of corner cubes in plastic with or without a reflective overcoating. Samples of a electroless nickel strip of the material used in the replication process for making Reflexite, with a rhodium reflective coating, obtained from Mr. Ross Neilson of Reflexite Corporation were examined in terms of its suitability as a retroreflector in a flashlamp pumped dye laser. The several problems with this material included corner cube element size and low effective reflectivity. Reflexite performed as a diffraction limited retroreflector; however, at the wave-length of interest, the small element size resulted in divergence due to diffraction which was approximately four times

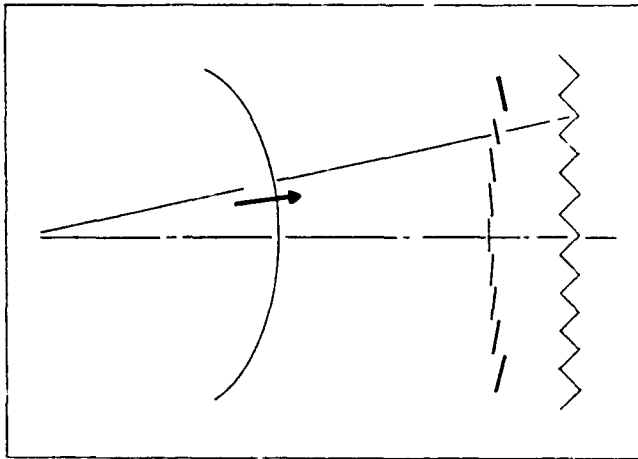


FIGURE 1

The Retroreflector Reverses the Spatial Vectors But Does Not Reverse the Time

that of the dye lasers under consideration. However, laboratory experiments showed there was considerable improvement in the dye laser beam energy distribution. The rhodium coated Reflexite retroreflector provided by Reflexite Corporation involved two reflections. Therefore $1/3$ of the incident light was lost. Although they appeared bright, the reflectivity of the sides was low giving a total effective reflectivity of the array of less than 20%. This reduced the overall efficiency of the cavity and produced a low intensity output laser beam. Consequently, an effort was initiated to design a retroreflector that was more suitable for use as a cavity mirror in the dye laser which would be more compatible with large scale production and would have a comparable cost to that of a high quality laser cavity mirror. Two types of retroreflectors were considered: an array of corner cubes and one of right circular cones.

3. Retroreflector Representations

Retroreflective arrays perform approximate wave front reversal but do not reverse the time. One can demonstrate[4, 5] that retroreflective arrays perform a function that is approximately equivalent to spatial phase conjugation. However, there is a significant difference between retroreflection and phase conjugation; Figure 1 shows a ray trace of the reflection of an incident spherical wave and illustrates one aspect of the difference. Each segment of the reflective wave in the subject Figure matches the tilt of the incident wave; however, the center of these segments propagate with the time relationship of the incident wave. The appearances are of a counter propagating wave equivalent to the conjugate wave except for a phase factor. Barrett and Jacobs present theoretical arguments which describe this behavior[4]. A separate derivation of this effect is given by Vaughn [5]. Another characteristic of retroreflection is that each of the segments expands according to diffraction for that element's geometry, size, and wave-length. Since retroreflection also occurs in nonlinear phase conjugation a similar effect should also be present in that case. With this basic understanding of the characteristics of retroreflectors, an effort to design a retroreflector for use in the flashlamp pumped dye laser was initiated.

4. Factors Considered in the Retroreflector Design

Considerations included fabrication techniques as well as the development of design specifications. A treatment of analysis methodology for the development design requirements and specifications has been given by Zel'dovich[7]. The related treatment included a similar approach with enlargement of the technique utilized as reported in this paper. The analysis included residual beam spread resulting from lateral ray shift, diffraction of elements, mismatch of the return wave on the second pass due to separation of the retroreflector from the cavity, the out of plane angle for a right circular cone, and the side misalignment angle.

Definitions of the primary variable used in this analysis are given in Figure 2. This Figure shows that the angular mismatch of the return wave is a function of the wave front tilt and the element's size. The return wave is segmented according to the array element size and results in diffraction spread. The diffraction angle results in a displacement of the return wave on the second pass and an angular mismatch of the return wave with respect to the incident wave at the cavity exit.

Treatment of the right circular cone required an additional consideration. Optical rays whose plane of incidence include a diameter of the cone are retroreflected by a conical reflector independent of the angle of incidence; however, rays which do not include a diameter in the plane of incidence are reflected with a small misalignment angle. Finally, the side misalignment angle due to manufacturing tolerances was determined so that the array would be essentially diffraction limited by the element size.

The equations which were developed to analyze the retroreflector design are summarized for convenience in Table 1. They were programmed on a microcomputer and analyses were performed to cover the range of expected wave front tilt for the flashlamp pumped dye laser. The results are presented in Figures 3 through 7 and cover the wave front slope from 1.0 to 9.0 milliradians. The analyses demonstrated that diffraction and the lateral shift of the incident rays related to the array element size dominate the results, and that the retroreflector distance L and the out of plane angle make an insignificant contribution for the optical wave-length and tilt angle ranges of interest. The data shown in Tables 2 through 6 give the residual wave front tilt as a function of the array element size and show that for a given uncorrected wave front tilt there is a preferred element size. For the wave front tilt expected in the dye laser, the best element size is predicted to be 3.0 mm.

Fabrication design techniques were planned with Optics Electronics Corporation (OEC) of Dallas, Texas utilizing their highly developed diamond turning capability and thick silicon film technology base. A methodology was developed that included cutting an array of equilateral triangular pyramids into a copper substrate, depositing a thick silicon film, etching the copper substrate leaving a free standing silicon wafer of corner cube array. A gold coating was applied as a final measure to improve the reflectivity. The issues that were to be resolved in this complex procedure included chip removal and edge sharpness of the copper substrate and similar features of the replicated silicon surfaces. The processes in either case passed tests with acceptable quality.

Several tests were performed in the laboratory with the silicon wafer and with the electroless nickel corner cube array obtained at the courtesy of Reflexite Corporation. The results of these tests are discussed in the following sections.

5. Reflexite Tests and Characteristics

Reflexite consists of a corner cube array that has been impressed into a number of plastic materials. The element size of Reflexite is .15 mm with 5 microradian side alignment error. Figure 8 shows a photomicrograph of a section of Reflexite embossed on plastic with a reflective coating. This material shows slightly crushed apices; however, the degradation due to this distortion of the individual cells is negligible in comparison to diffraction. Experiments at LSI, Inc. showed that this material performed as a diffraction limited retroreflector.

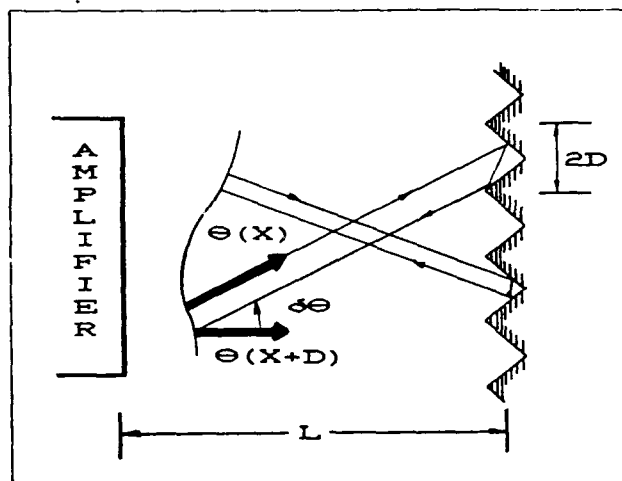


FIGURE 2

Factors Considered in the Retroreflector Design

The total beam spread was represented by $\delta\theta$:

$$\delta\theta = \delta\theta_1 + \delta\theta_2 + \delta\theta_3 + \delta\theta_4 + \delta\theta_5$$

where

$\delta\theta_1$ = the lateral shift due to the element size

$$\delta\theta_1 = \frac{d\theta}{dx}(d) \quad 2d = \text{element size}$$

$\delta\theta_2$ = diffraction spread due to each retroreflective element

$$\delta\theta_3 = \lambda/d$$

$\delta\theta_3$ = displacement relative to the first pass path

λ = optical wavelength

$$\delta\theta_3 = L \frac{\lambda}{d} \left[\frac{d\theta}{dx} \right] \quad (\text{see Figure 2.})$$

$\delta\theta_4$ = out of plane angle τ_0 of incident ray due to phase front slope

τ = out of plane angle

$$B = \tan^{-1}(\tan^2(\tau)/f2)$$

$$\cos(A) = -.5(\cos(B) - \sin(B)) + f2/4(\tan^2(\tau)\cos(2\tau))(\sin(B) + \cos(B)) - .5(\sin(2B) + \cos(2B))$$

$$\delta\theta_4 = \pi - \theta_4$$

$\delta\theta_5$ = side misalignment of retroreflector

$$\delta\theta_5 = \lambda/10d \approx 30\mu \text{ radians for } 2\text{mm element size where for a right circular cone } \delta\theta = \tan \alpha/2 \text{ where } 90^\circ : \alpha = \text{angle of cone apex.}$$

TABLE 1

Factors Considered in the Retroreflector Design

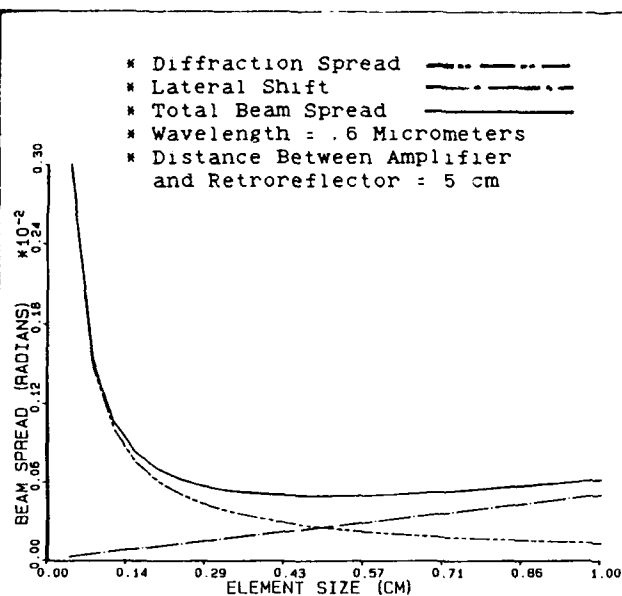


FIGURE 3

Assessment of the Effect of Element Size
 on Dye Laser Beam Quality with a Wave
 Front Tilt of .001 Radians

ELEM SIZE (CM)	LATERAL SHIFT (RAD)	DIF SPREAD (RAD)	L UNCER- TAINTY (RAD)	CONE DIVER- GENCE (RAD)	RESIDUAL BEAM SPREAD (RAD)
.04	.00002	.00300	.00001	.00000065	.00304
.08	.00004	.00150	.00001	.00000065	.00155
.12	.00006	.00100	.00000	.00000065	.00107
.16	.00008	.00075	.00000	.00000065	.00083
.20	.00010	.00060	.00000	.00000065	.00070
.24	.00012	.00050	.00000	.00000065	.00062
.28	.00014	.00043	.00000	.00000065	.00057
.32	.00016	.00038	.00000	.00000065	.00054
.36	.00018	.00033	.00000	.00000065	.00052
.40	.00020	.00030	.00000	.00000065	.00050
.44	.00022	.00027	.00000	.00000065	.00049
.48	.00024	.00025	.00000	.00000065	.00049
.52	.00026	.00023	.00000	.00000065	.00049
.56	.00028	.00021	.00000	.00000065	.00050
.60	.00030	.00020	.00000	.00000065	.00050
.64	.00032	.00019	.00000	.00000065	.00051
.68	.00034	.00018	.00000	.00000065	.00052
.72	.00036	.00017	.00000	.00000065	.00053
.76	.00038	.00016	.00000	.00000065	.00054
.80	.00040	.00015	.00000	.00000065	.00055
.84	.00042	.00014	.00000	.00000065	.00056
.88	.00044	.00014	.00000	.00000065	.00058
.92	.00046	.00013	.00000	.00000065	.00059
.96	.00048	.00012	.00000	.00000065	.00061
1.00	.00050	.00012	.00000	.00000065	.00062

TABLE 2

Assessment of the Effect of Element Size
 on Dye Laser Beam Quality with a Wave
 Front Tilt of .001 Radians

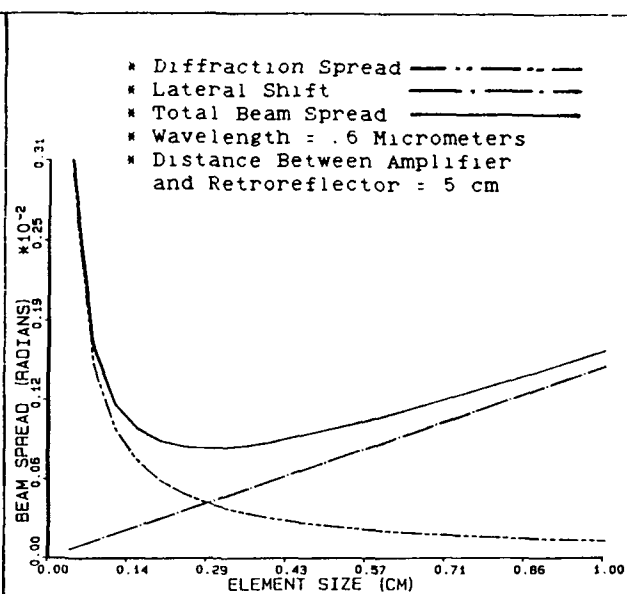


FIGURE 4

Assessment of the Effect of Element Size
 on Dye Laser Beam Quality with a Wave
 Front of Tilt .003 Radians

ELEM SIZE (CM)	LATERAL SHIFT (RAD)	DIF SPREAD (RAD)	L UNCER- TAINTY (RAD)	CONE DIVER- GENCE (RAD)	RESIDUAL BEAM SPREAD (RAD)
.04	.00006	.00300	.00005	.00000528	.00311
.08	.00012	.00150	.00002	.00000528	.00165
.12	.00018	.00100	.00001	.00000528	.00120
.16	.00024	.00075	.00001	.00000528	.00101
.20	.00030	.00060	.00001	.00000528	.00091
.24	.00036	.00050	.00001	.00000528	.00087
.28	.00042	.00043	.00001	.00000528	.00086
.32	.00048	.00038	.00001	.00000528	.00087
.36	.00054	.00033	.00000	.00000528	.00088
.40	.00060	.00030	.00000	.00000528	.00091
.44	.00066	.00027	.00000	.00000528	.00094
.48	.00072	.00025	.00000	.00000528	.00098
.52	.00078	.00023	.00000	.00000528	.00102
.56	.00084	.00021	.00000	.00000528	.00106
.60	.00090	.00020	.00000	.00000528	.00111
.64	.00096	.00019	.00000	.00000528	.00116
.68	.00102	.00018	.00000	.00000528	.00120
.72	.00108	.00017	.00000	.00000528	.00125
.76	.00114	.00016	.00000	.00000528	.00131
.80	.00120	.00015	.00000	.00000528	.00136
.84	.00126	.00014	.00000	.00000528	.00141
.88	.00132	.00014	.00000	.00000528	.00146
.92	.00138	.00013	.00000	.00000528	.00152
.96	.00144	.00012	.00000	.00000528	.00157
1.00	.00150	.00012	.00000	.00000528	.00163

TABLE 3

Assessment of the Effect of Element Size
 on Dye Laser Beam Quality with a Wave
 Front of Tilt .003 Radians

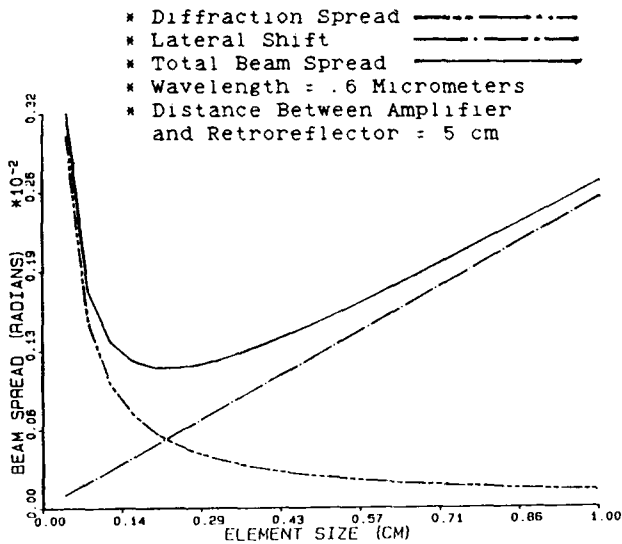


FIGURE 5

Assessment of the Effect of Element Size
 on Dye Laser Beam Quality with a Wave
 Front Tilt of .005 Radians

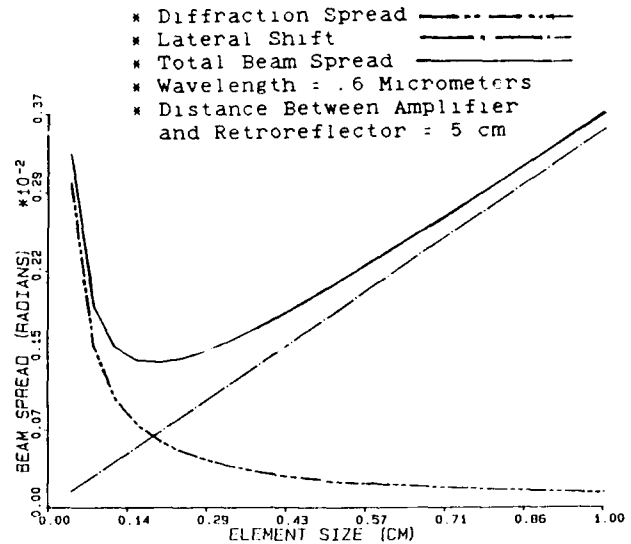


FIGURE 6

Assessment of the Effect of Element Size
 on Dye Laser Beam Quality with a Wave
 Front Tilt of .007 Radians

ELEM SIZE (CM)	LATERAL SHIFT (RAD)	DIF SPREAD (RAD)	L UNCE- TAINTY (RAD)	CONE DIVER- GENCE (RAD)	RESIDUAL BEAM SPREAD (RAD)
.04	.00010	.00300	.00007	.00001455	.00319
.08	.00020	.00150	.00004	.00001455	.00175
.12	.00030	.00100	.00002	.00001455	.00134
.16	.00040	.00075	.00002	.00001455	.00118
.20	.00050	.00060	.00001	.00001455	.00113
.24	.00060	.00050	.00001	.00001455	.00113
.28	.00070	.00043	.00001	.00001455	.00115
.32	.00080	.00038	.00001	.00001455	.00120
.36	.00090	.00033	.00001	.00001455	.00126
.40	.00100	.00030	.00001	.00001455	.00132
.44	.00110	.00027	.00001	.00001455	.00139
.48	.00120	.00025	.00001	.00001455	.00147
.52	.00130	.00023	.00001	.00001455	.00155
.56	.00140	.00021	.00001	.00001455	.00163
.60	.00150	.00020	.00000	.00001455	.00172
.64	.00160	.00019	.00000	.00001455	.00181
.68	.00170	.00018	.00000	.00001455	.00190
.72	.00180	.00017	.00000	.00001455	.00199
.76	.00190	.00016	.00000	.00001455	.00208
.80	.00200	.00015	.00000	.00001455	.00217
.84	.00210	.00014	.00000	.00001455	.00226
.88	.00220	.00014	.00000	.00001455	.00235
.92	.00230	.00013	.00000	.00001455	.00245
.96	.00240	.00012	.00000	.00001455	.00254
1.00	.00250	.00012	.00000	.00001455	.00264

TABLE 4

Assessment of the Effect of Element Size
 on Dye Laser Beam Quality with a Wave
 Front Tilt of .005 Radians

ELEM SIZE (CM)	LATERAL SHIFT (RAD)	DIF SPREAD (RAD)	L UNCE- TAINTY (RAD)	CONE DIVER- GENCE (RAD)	RESIDUAL BEAM SPREAD (RAD)
.04	.00014	.00300	.00010	.00002846	.00327
.08	.00028	.00150	.00005	.00002846	.00186
.12	.00042	.00100	.00004	.00002846	.00148
.16	.00056	.00075	.00003	.00002846	.00136
.20	.00070	.00060	.00002	.00002846	.00135
.24	.00084	.00050	.00002	.00002846	.00139
.28	.00098	.00043	.00001	.00002846	.00145
.32	.00112	.00038	.00001	.00002846	.00154
.36	.00126	.00033	.00001	.00002846	.00163
.40	.00140	.00030	.00001	.00002846	.00174
.44	.00154	.00027	.00001	.00002846	.00185
.48	.00168	.00025	.00001	.00002846	.00197
.52	.00182	.00023	.00001	.00002846	.00209
.56	.00196	.00021	.00001	.00002846	.00221
.60	.00210	.00020	.00001	.00002846	.00234
.64	.00224	.00019	.00001	.00002846	.00246
.68	.00238	.00018	.00001	.00002846	.00259
.72	.00252	.00017	.00001	.00002846	.00272
.76	.00266	.00016	.00001	.00002846	.00285
.80	.00280	.00015	.00001	.00002846	.00298
.84	.00294	.00014	.00000	.00002846	.00312
.88	.00308	.00014	.00000	.00002846	.00325
.92	.00322	.00013	.00000	.00002846	.00338
.96	.00336	.00012	.00000	.00002846	.00352
1.00	.00350	.00012	.00000	.00002846	.00365

TABLE 5

Assessment of the Effect of Element Size
 on Dye Laser Beam Quality with a Wave
 Front Tilt of .007 Radians

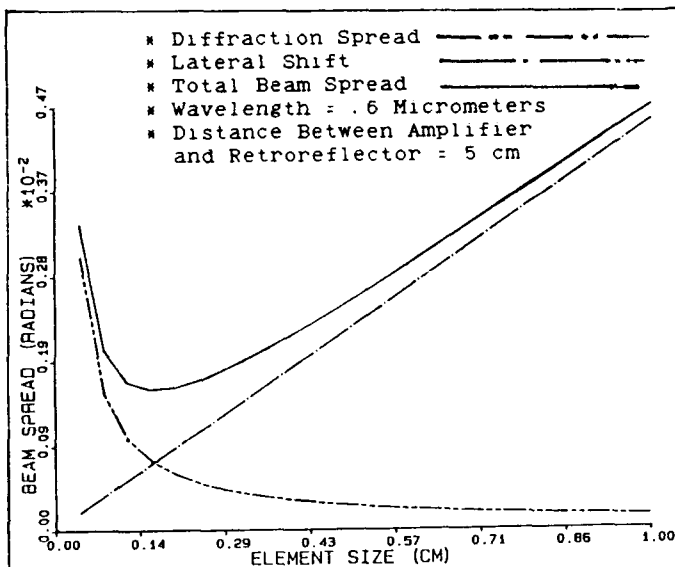


FIGURE 7

Assessment of the Effect of Element Size
on Dye Laser Beam Quality with a Wave
Front Tilt of .009 Radians

ELEM SIZE (CM)	LATERAL SHIFT (RAD)	DIF SPREAD (RAD)	L UNCER- TAINTY (RAD)	CONE DIVER- GENCE (RAD)	RESIDUAL BEAM SPREAD (RAD)
.04	.00018	.00300	.00013	.00004701	.00336
.08	.00036	.00150	.00007	.00004701	.00197
.12	.00054	.00100	.00004	.00004701	.00163
.16	.00072	.00075	.00003	.00004701	.00155
.20	.00090	.00060	.00003	.00004701	.00157
.24	.00108	.00050	.00002	.00004701	.00165
.28	.00126	.00043	.00002	.00004701	.00175
.32	.00144	.00038	.00002	.00004701	.00188
.36	.00162	.00033	.00001	.00004701	.00202
.40	.00180	.00030	.00001	.00004701	.00216
.44	.00198	.00027	.00001	.00004701	.00231
.48	.00216	.00025	.00001	.00004701	.00247
.52	.00234	.00023	.00001	.00004701	.00263
.56	.00252	.00021	.00001	.00004701	.00279
.60	.00270	.00020	.00001	.00004701	.00296
.64	.00288	.00019	.00001	.00004701	.00312
.68	.00306	.00018	.00001	.00004701	.00329
.72	.00324	.00017	.00001	.00004701	.00346
.76	.00342	.00016	.00001	.00004701	.00363
.80	.00360	.00015	.00001	.00004701	.00380
.84	.00378	.00014	.00001	.00004701	.00398
.88	.00396	.00014	.00001	.00004701	.00415
.92	.00414	.00013	.00001	.00004701	.00432
.96	.00432	.00012	.00001	.00004701	.00450
1.00	.00450	.00012	.00001	.00004701	.00467

TABLE 6

Assessment of the Effect of Element Size
on Dye Laser Beam Quality with a Wave
Front Tilt of .009 Radians

Figure 9 shows the zig-zag flashlamp pumped dye laser in which the Reflexite sample was tested as a cavity mirror and Figure 10 shows the laser output pulse. An electroless nickel sample used in the fabrication of Reflexite was used as a cavity mirror; this sample had a rhodium reflective coating when received from Reflexite Corporation. As determined by Duarte[7], it has less than 20% reflectivity. There were several reasons attributed to this. First, the array geometry allows only two reflection processes so that 1/3 of the incident light is lost; a second reason is that the low reflectivity of the rhodium coating in a two reflection process gave less than 50% effective reflectivity resulting in the combined low reflectivity which reduced the cavity efficiency and the laser output.

The rhodium coated retroreflector was placed in the laser cavity as shown in Figure 11. The laser output with the retroreflector in the cavity is shown in Figure 12; this Figure shows that the intensity is much smoother with the retroreflector than without. The elongation of the beam intensity is believed to be result of the beam walking across the flat cavity mirror since this mirror was not adjusted after the retroreflector was in place. Diffractive spreading of the beam due to the element size was sufficient to produce this effect. The spreading was limited to the vertical direction because of the two dimensional character of the retroreflective array geometry. These results demonstrate a potential for improvement of the beam quality of the flashlamp pumped dye laser using a retroreflector. However, as our analyses show the retroreflector must be fabricated with the correct array geometry and element size. The results of the design and fabrication methodology to do this is presented in the next section.

6. Fabrication and Design Results

A retroreflector design and fabrication methodology was developed with OEC. This consisted of the fabrication of a master array of triangular pyramids on a copper substrate using the highly developed diamond turning capability of OEC; replication of this array by depositing a thick silicon film that, once separated from the copper substrate, would stand alone. Separation of the silicon wafer was obtained by etching. A gold coating was applied to improve the reflectivity of the array at the dye laser wave-length.

Technology issues resolved in this part of the effort included: edge sharpness of element of the copper pyramids cut using the diamond turning process; edge sharpness of replicated elements of the silicon wafer after separation by the etching process. The ability to apply a uniform gold coating



FIGURE 8
Reflexite Micrograph 200X



FIGURE 9
Zig-Zag Flashlamp Pumped Dye Laser

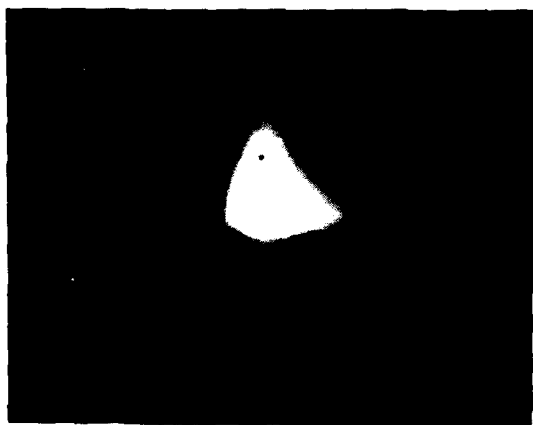


FIGURE 10
Laser Output Pulse

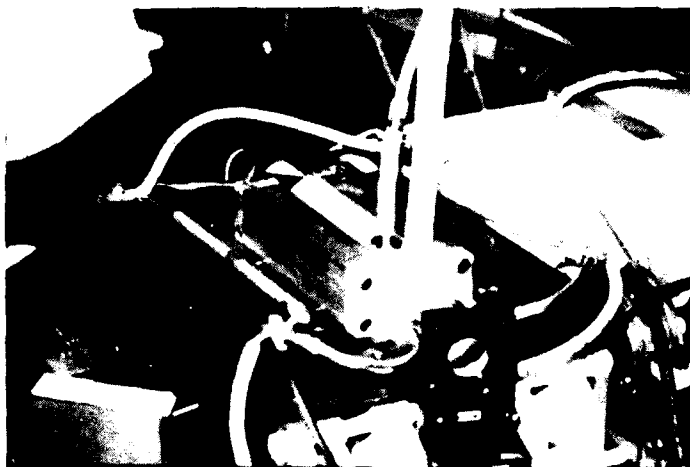


FIGURE 11
Rhodium Coated Retroreflector
in Laser Cavity

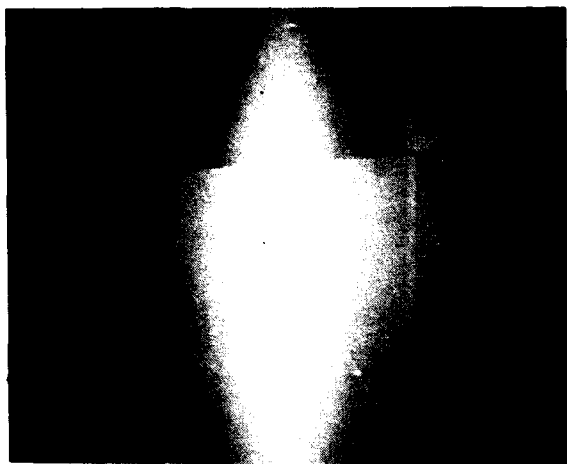


FIGURE 12

Laser Output with the
Retroreflector in the cavity



FIGURE 13

Edge View of Silicon Coated Copper Substrate



FIGURE 14

Edge View of Free Standing Silicon Corner
Cube Array After Etching the Copper Substrate

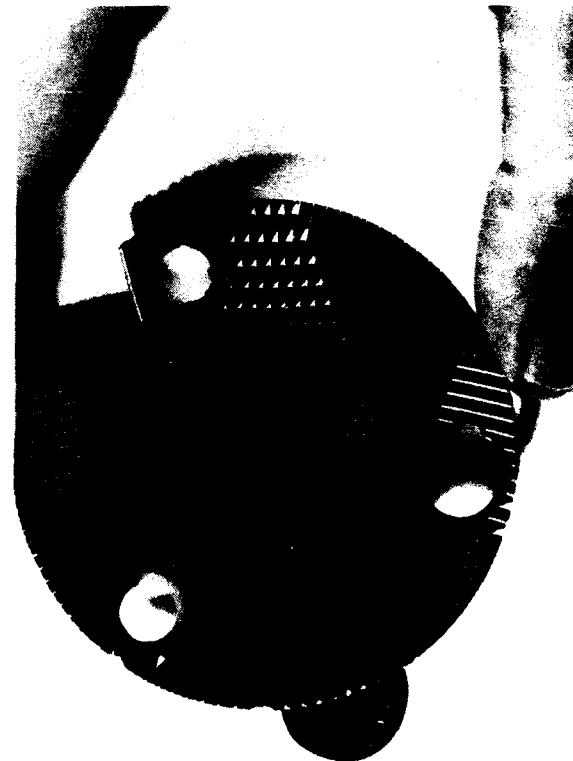


FIGURE 15

Free Standing Silicon Array
Compared with a Coin

to the resultant small corner cube elements appeared to be satisfactory. The angles between the sides of the array elements was not cut to give the proper angle. Additional fabrication design methodology was developed to give the necessary side tolerances. This methodology will be demonstrated in the next phase of the effort.

Figure 13 shows an edge view of the copper substrate before separation of the silicon wafer. A view of the sharp edges replicated on the silicon wafer after separation from the copper substrate is shown in Figure 14. The thin silicon wafer needs to be mounted to give it additional strength. The final figure shows a front view of the free standing silicon wafer before it was gold coated. The contours of the diamond cutting shows the obvious improper side angles of the individual elements.

7. Summary

Tests with Reflexite show potential for use of a retroreflector as a cavity mirror. Problems with this material are two fold: (1.) diffractive spread due to the small .15 mm element size and (2.) the inherently low reflectivity. To overcome these problems, a procedure has been developed for analyzing and fabricating retroreflectors suitable for use as a cavity mirror in the flashlamp pumped dye laser. This procedure has been partially proven and it is anticipated that the next effort will result in a high quality array that can be produced in quantity at low cost.

Other methods may be used to produce retroreflectors at relatively low cost. An array of right circular cones has been analyzed and fabrication methodologies have been examined. It may be more cost effective to make an array of right circular cones that have optical performance entirely equivalent to that of an array of corner cubes if the beam divergence or out of plane angle is small. Angles as large as several degrees may be acceptable depending on the element (i.e., cone) size. The design effort for the array of right circular cones is being continued.

References

1. C. R. Giulian, R. C. Lind, T. T. O'Mera, and G. C. Valley, Laser Focus, Feb., 55 (1983)
2. V. K. Orlov et al., Sov. J. Quantum Electron, 8 (6) 1978)
3. Z. E. Bagdasarov et al, Sov. J. Quantum Electron, 11 (11), 1465 (1981)
4. H H. Barrett, S. F. Jacobs, Optical Society America, 7, (1979)
5. V. V. Vaughn, Design of a Retroreflective Pseudo-Phase Conjugator (LSI, Inc., 1987), U. S. Army Contract DAAH01-86-P-6649
6. F. J. Duarte, A Study on Narrow-Linewidth Flashlamp-Pumped Oscillator-Amplifier Dye Lasers (1986()), U. S. Army Contract DAAG29-81-D-0100 D.O. 2346, Scientific Services
7. B. Y. Zel'dovich et al, Principles of Phase Conjugation, Springer Series in Optical Sciences, 42, (1985)
8. A. G. Fox, Tingye Li, Bell System Technical Journal 453 (1961).

STUDY OF NONLINEAR OPTICAL SBS PHENOMENA IN MID IR FIBERS

Chung Yu, and C. K. Fong
Department of Electrical Engineering
North Carolina A & T State University
Greensboro, NC 27411

Abstract

This is the first reported attempt at investigation of the sBs phenomena in mid IR fibers using externally fed or laser self generated low frequency and microwave frequency phonon waves as diagnostic probes of such processes. The observation of laser excited phonon emissions in the mid IR fiber and direct modulation of CO₂ laser pulse transmission by externally imposed low frequency radiation is the first indication of the predicted low sBs threshold in these fibers in the phonon rich mid IR spectral region. The prospect of wide applications of the sBs process in optical switching, phase conjugation and ultimately optical computing and possible deleterious effects in mid IR laser heterodyne spectroscopy, sideband modulation and transmitted power limitation is discussed.

Introduction

The Brillouin process involves scattering of light by self excited acoustic phonons in a material medium, as distinct from optical-phonon driven Raman scattering. Since the dispersion curve $\omega(k)$ is virtually flat for optical phonons near the center of the Brillouin zone, Raman scattering is isotropic and exhibits the same Stokes shift for all scattering directions. On the other hand, the linear dispersion relation $\omega = k \cdot v_s$, where v_s is the acoustic wave velocity, for acoustic phonons introduces an angular dependence to the scattered wave frequency and eliminates scattering in the forward direction. The backscattered wave undergoes a frequency shift of the order of 30 GHz for a visible pump wave ω_1 , and in the MHz and single digit GHz range for the 10.6 μm CO₂ laser pump.

It has been predicted that at low pump power densities, the losses of an optical fiber are determined by spontaneous Raman, Brillouin and Rayleigh scattering, absorption losses in the core material, scattering at the core-cladding (or other) interface and mode conversion from low loss trapped modes to high-loss cladding modes. At high pump power densities, however, stimulated scattering processes emerge within the fiber and these are pump-power dependent. Both backward Raman and Brillouin scattering will convert power in the forward traveling, information carrying wave, thus severely limiting the information capacity of fiber communication links.

The sBs threshold has been computed to be approximately two orders lower than the sRs threshold in fibers. However, this only holds if the linewidth of the laser pump is sufficiently narrow. The omnidirectional property of Raman scattering can be sustained by a much broader pump linewidth because all component lines of the pump drive the same phonons. Backward sBs require phase matching, and will thus tolerate only a pump frequency band equal to the linewidth of gain for a single Stokes wave. Efficient sBs hence requires narrowing the laser pump linewidth to about 100 MHz.

The experimentally observed low frequency emissions are confirmation of the dominance of the sBs process over stimulated Raman scattering (sRs). The existence of the sBs threshold is based on feedback theory on oscillation and thus has a finite value even for lossless fibers. Theoretical prediction has been made² for a drastic reduction in the laser pump throughput at approximately three times the initial pump threshold for the onset of backward sBs. With predicted threshold powers for visible glass fibers in the range of 35 mW³ in the sBs case, and considerably lower in mid IR fibers, the effect of sBs on laser transmission through a fiber at normal laser transmitter power levels is of great significance.

Status of sBs in Mid IR Fibers

Historically, polycrystalline KRS-5 mid IR fibers were first reported in 1977. However, these early fibers experienced progressive aging, had low power handling capability and were inherently toxic. Although substantial improvements have been made, aging and toxicity are still plaguing these fibers so that long haul, extremely low loss and nontoxic KRS-5 fibers have yet to emerge to satisfy the needs of the military, communication and medical markets.

Despite these setbacks, predicted fiber losses theoretically as low as $\sim 10^{-3} \text{ cm}^{-1}$, have prompted investigators to examine the possibility of nonlinear optical phenomena in the mid IR. Some work has been reported at 10.6 μm wavelength in KRS-5⁴, where nonlinear back scattering was observed and identified to be sBs based with a hybrid, pulsed CO₂ laser with a well tailored linewidth, pulsewidth and laser power level.

Current mid IR fibers being manufactured are of the silver halide type. Thus, Asahi is producing AgCl fibers with loss below 0.2 dB/m, and Sumitomo has provided us with such a fiber and the transmission guaranteed is 73.5% per meter at 10.6 μm wavelength. Unfortunately, no commercial or development-stage KRS-5 fibers are available. The latter type of fibers are preferred, since there is a wealth of numerical data available on KRS-5. The Sumitomo

supplied data gave a $(\text{wavelength})^{-2.4}$ dependence of fiber loss, and is certainly encouraging in view of the ultimate λ^{-4} dependence in the Rayleigh-Brillouin limit. Our intention is to study the sBs phenomena using the silver halide fibers.

The transparency band of materials in the mid IR is bounded by the shortwave electronic bandgap absorption tail, the longwave multiphonon absorption tail and Rayleigh-Brillouin scattering⁵, with Brillouin scattering dominating around the $10\text{ }\mu\text{m}$ wavelength. Preliminary calculation indicates linear or passive Brillouin scattering is a factor of 10^8 over the other absorption mechanisms. We have thus concluded that the mid IR region of the spectrum is highly phonon active. Hence, once extrinsic absorption processes, such as point defects, structural dislocations and grain boundaries and impurities are removed, the mid IR region will be most transparent, and whatever scattering that occurs will be phonon dominant.

Laser induced stimulated Brillouin or Raman scattering has been extensively investigated in the visible and near IR both in bulk materials and fibers⁵ due to the abundance of high power, narrow linewidth tunable lasers and reasonably low loss transparent materials and fibers in this spectral region. However, as mentioned above, the visible spectral region is not phonon dominant and is thus judged not to be optimum for the study of phonon related stimulated scattering. On the other hand, by going to longer wavelengths, especially the mid IR, we have chosen an optimum Brillouin active region where low linear losses are also predicted. These two factors contribute to sBs threshold being the lowest and the process should be most easily observable. This prospect is further enhanced by guided wave propagation in fibers, where the laser intensity times interaction length product is 10^7 that in bulk materials with focused laser beam in the visible. This factor will be raised by several orders when λ is increased by a factor of 20 going to the mid IR and linear loss lowered by several orders. Thus, the usual megawatt sBs threshold in bulk materials can conceivably be lowered to milliwatt threshold in mid IR fibers.

Phonons and Laser Transmission and Reflection in Mid IR Fibers

The technique employed by the authors of Ref. 4 for monitoring sBs using only the transmitted and reflected laser pulse is judged not to be a definitive means of identifying sBs. Our extensive experience in laser induced phonons in bulk material such as quartz by a ruby laser convinced us that there is a more direct way of studying sBs generation in the mid IR. A careful calculation was made using available data for the sBs induced phonon spectra of low and high frequency phonons in KRS-5. The low frequency phonon is very sensitive to index of refraction variations of the material medium, while the high frequency phonon is not⁶. If the fiber medium is dispersive, then the low frequency phonon frequency will shift with laser pump wavelength, thus facilitating phonon detection by external probes.

The first conclusive indication of CO₂ laser induced phonon emission in the 1 meter Sumitomo silver halide fiber was the observation of 2 MHz emission near the exit end of the fiber as recorded in Fig. 1 on the spectrum analyzer. The multiple lines reflect random frequency shifts of the laser pump, leading to corresponding frequency shifts in the phonon emission. This encouraging result prompted us to resort to amplification by external means.

An experimental scheme was set up, in which the fiber was placed inside a microwave waveguide that carried X band microwave radiation modulated by a 2 MHz signal. Thus, the desired 2 MHz modulation was delivered to the fiber via the X band microwave carrier. The reflected laser pulse was monitored, and the detected signals are shown in Fig. 2. The oscillograms show the direct modulation of the reflected laser pulse by the 2 MHz signal. This was apparently a rather broadband process, as seen in Fig. 3 with a 0.2 MHz modulation signal.

Installation of the fiber inside a microwave waveguide caused the transmitted laser pulse to possess a preferred longer effective interaction length with the imposed low frequency signal, and this is clearly borne out in Fig. 4. The transmitted laser pulse is seen to be more effectively modulated by the low frequency signal. A direct comparison in Fig. 5 at low and high modulation signal levels further demonstrates the more efficient interaction in the forward or transmission direction.

It is, of course, natural to proceed to high frequency (GHz) phonon effects on the fiber. The experiment is still in progress, involving fabrication of the proper waveguide and the acquisition of appropriate instrumentation.

Conclusions

There is no doubt that this first reported observation of phonon emission and direct low frequency modulation in mid IR fibers has great physical significance. It not only confirms the existence of sBs based phenomena in such phonon-active fibers, but also points to the potential of application as fiber-optic devices for optical modulation, switching, phase conjugation and the like.

References

1. C. Yu, M. Haw, and H. Hsu, Electron. Lett. 13, 240 (1977).
2. H. Hsu, and C. Yu, Electron. Lett. 9, 442 (1973);
H. Hsu, and C. Yu, Proc. IEEE (Lett) 64, 1638 (1976);

- C. Yu, and H. Hsu, J. Appl. Phys. 48, 2089 (1977).
3. R. G. Smith, Appl. Opt. 11, 2489 (1972);
K. O. Hill, B. S. Kawasaki, and D. C. Johnson, Appl. Phys. Lett. 28, 608 (1976).
 4. V. I. Kovalev, P. A. Mikheev, and F. S. Faizullov, Sov. J. Quantum Electron. 14, 1022 (1984).
 5. A. P. Belousov, E. M. Dianov, N. S. Lisitsky, T. M. Nesterova, V. G. Plotnichenko, and V. K. Sysoev, Sov. J. Quantum Electron. 9, 796 (1982);
V. G. Artjushenko, L. N. Butvina, V. V. Voitsekhovskiy, E. M. Dianov, and J. G. Kolesnikov, SPIE Vol. 618, 103 (1986).
 6. C. Yu, and C. K. Fong, presented at the Symp. on Fiber Optics and Integrated Optoelectronics, SPIE's O-E/Fiber'87, San Diego, California (1987).

Acknowledgement: This work is supported by NASA Langley Research Center Grant NAG-1-815.



a.



b.

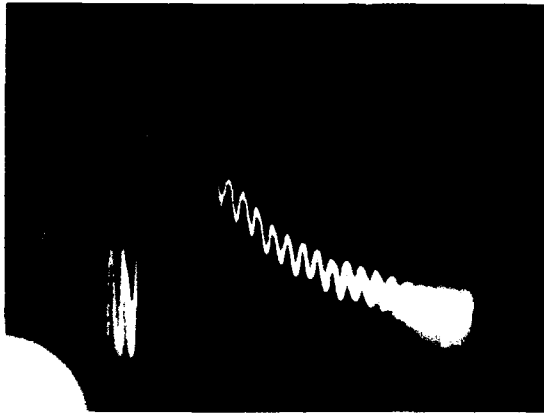


c.

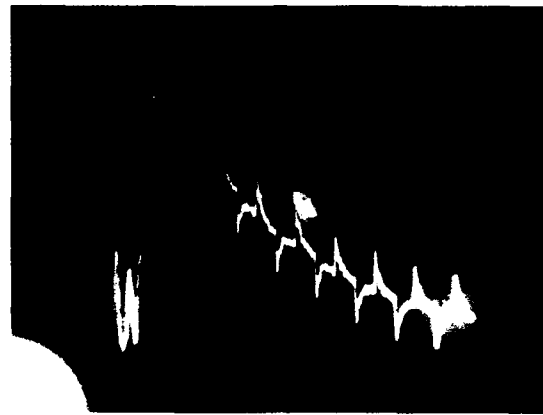
Fig. 1. Laser induced 2 MHz phonon detected by spectrum analyzer.

- 2 a - laser pulse modulated by low power 2 MHz sine wave
- b - laser pulse modulated by high power 2 MHz sine wave
- c - laser pulse modulated by high power 2 MHz sawtooth wave

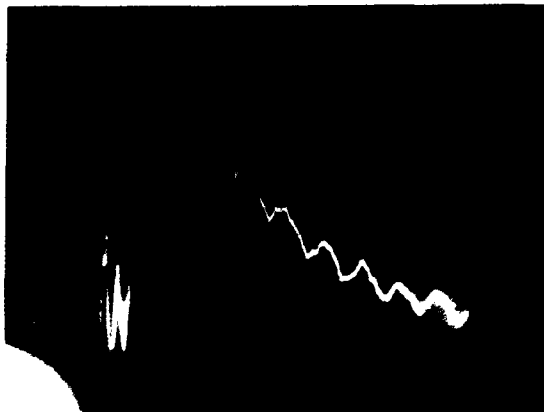
Fig. 2.



a.



b.



c.

Fig. 3.

- a - 0.2 MHz sinewave modulation on
reflected laser pulse with
microwave carrier;
- b - 0.2 MHz sawtooth wave modulation;
- c - 0.2 MHz square wave modulation



Fig. 4. a - Reflected laser pulse, b - transmitted laser pulse
Maximum 2 MHz square wave modulation

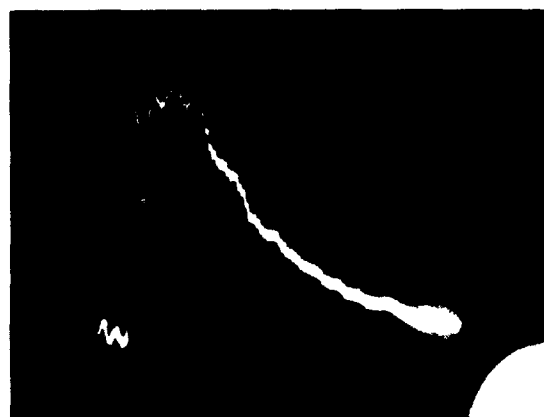


Fig. 5. a - Reflected laser pulse with low power 2 MHz saw-tooth wave modulation;
a' - reflected laser pulse with high power 2 MHz saw-tooth wave modulation;
b - Transmitted laser pulse with low power 2 MHz saw-tooth wave modulation;
b' - transmitted laser pulse with high power 2 MHz saw-tooth wave modulation

STIMULATED BRILLOUIN SCATTERING EXPERIMENTS WITH FLASHLAMP-PUMPED DYE LASERS

Stephen D. Russell, John J. Ehrlich, Stanley P. Patterson,
and Raymond W. Conrad
U.S. Army Missile Command
Redstone Arsenal, AL 35898-5245

Daniel E. Klimek and Stephen F. Fulghum*
AVCO - Everett Research Labs
Everett, MA 02149

*Stephen F. Fulghum is presently at Science Research Laboratory, Inc., Somerville, MA 02143.

ABSTRACT

In this paper, we present the first demonstration of phase conjugation via Stimulated Brillouin Scattering (SBS) with a flashlamp-pumped dye laser. This was done using an oscillator/amplifier configuration and a high pressure methane gas cell as the SBS mirror. Dye laser linewidths of 10 and 100 GHz were conjugated with SBS reflectivities of greater than 50%. Due to the reflection of SRS energy back into the laser system, a self-pumped phase conjugate resonator (PCR) was formed. This cavity could prove useful in the attainment of high energy, diffraction-limited, flashlamp-pumped dye laser systems, and is also convenient for the study of long pulse ($>1 \mu\text{sec}$) PCR's using SBS.

INTRODUCTION

Flashlamp-pumped dye lasers, on the whole, suffer from beam qualities that go from bad to worse as the output energies are scaled from a few joules to tens of joules per pulse.

This degradation can be caused in a flowing dye media by such things as turbulence, optical disturbances due to temperature gradients, and acoustic shock waves from flashlamps. Beam qualities of 50 to 100 times diffraction limited are common and spatial filtering, with significant energy loss, does not appear to be the best way to achieve a nearly diffraction-limited beam.

In recent years, many types of lasers and optical systems have benefited from the use of non-linear optical phase conjugation to compensate for optical inhomogeneities similar to those found in flashlamp-pumped dye lasers. Of the various methods for achieving phase conjugation, SBS seems to hold the most promise for use with flashlamp-pumped dye lasers.

In order to achieve SBS threshold, a combination of spectral linewidth, beam quality (divergence), and power requirements must be met. The difficulty in obtaining these often mutually exclusive requirements from a single laser cavity probably explains why SBS has not been previously demonstrated with this type of laser. One possible solution to this problem is an oscillator/single-pass amplifier configuration.

EXPERIMENTAL DETAILS

The experimental setup was as shown in Fig. 1. The oscillator was a Phase-R Model 1400 coaxial flashlamp-pumped dye laser. It was configured with a 2 meter long cavity containing 3 tuning/polarizing prisms and 2 etalons. The oscillator output was then expanded to fill a Candela LFDL-20 linear flashlamp-pumped dye laser. The laser output from this oscillator/single-pass amplifier system was then focused into a high pressure methane gas cell. One quarter-wave plate and two dielectric polarizing beamsplitters were used in combination to try to prevent the SBS return from the gas cell from re-entering the laser system. A pellicle beamsplitter was placed just before the focusing lens so that energy measurements and beam profiles could be taken of the incident and SBS returned beams. Space was left between the beamsplitter and focusing lens for the occasional insertion of an aberrator to test for the phase conjugation property of wavefront correction.

All experiments were performed using Rhodamine 6G as the laser dye with wavelength operation of the oscillator set at 590nm. The 2 etalons were removable, thus allowing linewidths of 10 GHz or 100GHz. Once the system was operational it was observed that the output of the amplifier faithfully followed the linewidth and beam quality of the oscillator.

RESULTS

SBS was successfully demonstrated in the methane cell and reflectivity data (energy out of cell vs energy into cell) was taken for various combinations of linewidth, focal length, and gas pressure. A portion of this data is presented in Figs. 2 and 3. Fig. 2 shows 10 GHz and 100 GHz operation at a constant focal length and pressure while Fig. 3 shows operation with two different focal lengths at constant linewidth and pressure.

Typical pulse waveforms taken are shown in Figs. 4-8. Figs. 4 and 5, taken when the

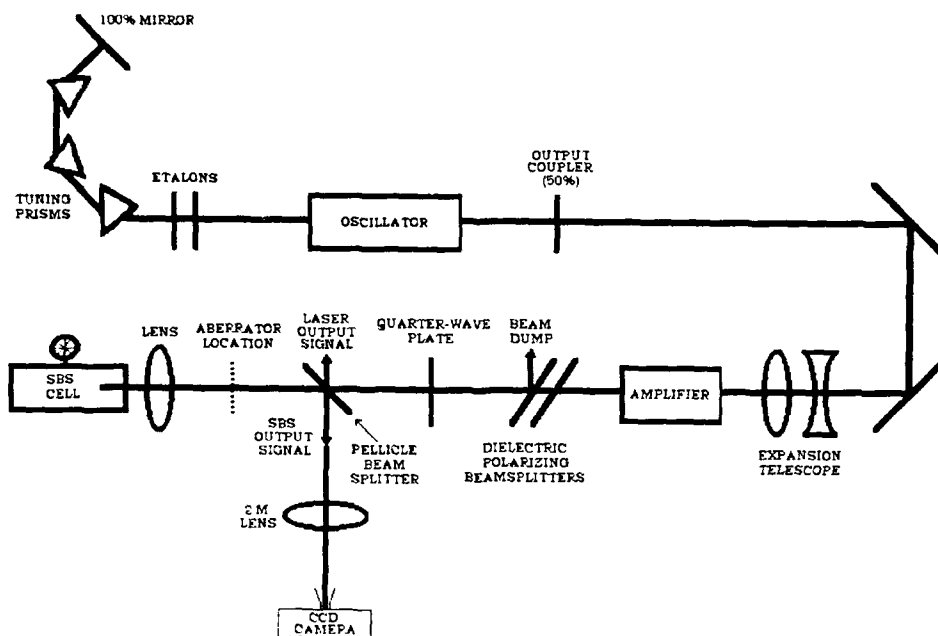


Fig.1. Oscillator/Amplifier configuration. The SBS experiment was performed by observing the SBS output signal and comparing it with the laser output signal. To investigate the phase conjugate ability of the SBS return, an acid etched glass plate could be inserted (aberrator location) and the SBS return could then be compared to the return obtained when the lens/cell combination was replaced with an ordinary mirror. The quarter waveplate/polarizers combination was intended to prevent energy from re-entering the laser system.

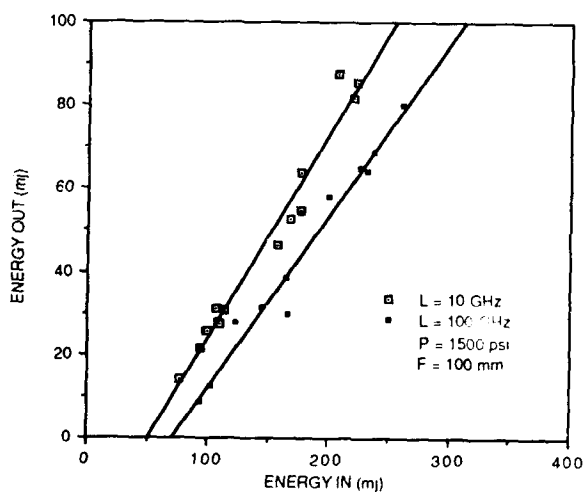


Fig. 2

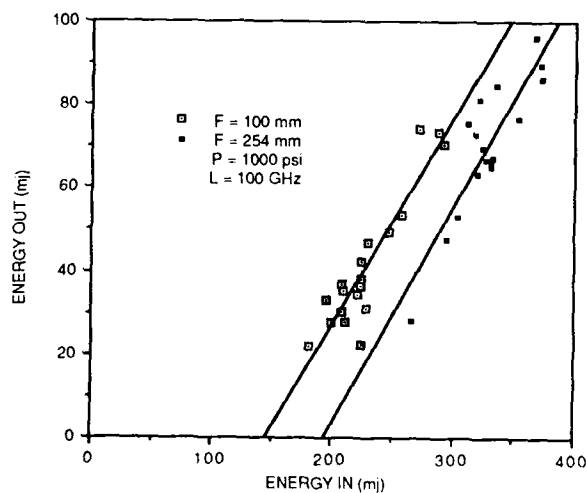


Fig. 3

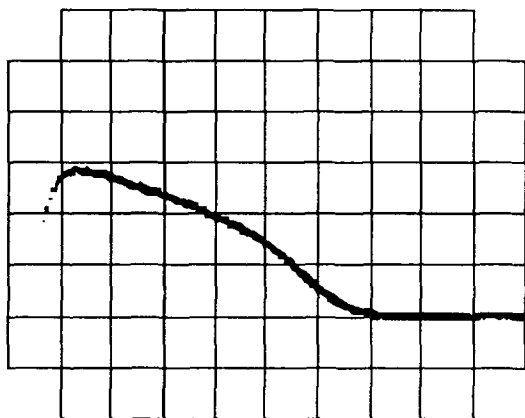


Fig.4. Oscillator pulse. 100 nSec/Division.



Fig.5. Oscillator/Single pass amplifier pulse.
100 nSec/Division.



Fig.6. Laser output waveform with SBS cell.
200 nSec/Division.



Fig.7. SBS output waveform.
200 nSec/Division.

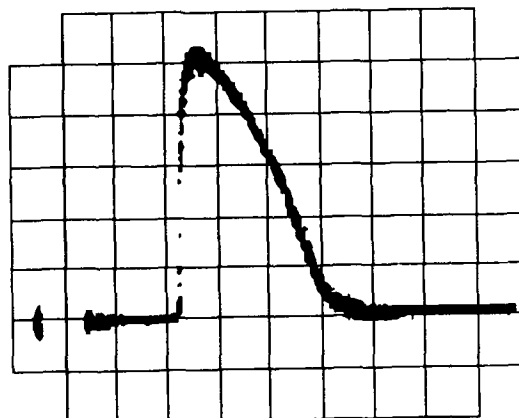


Fig.8. Laser output waveform without SBS cell.
200 nSec/Division.
This is the same as Fig.5 except for time scale.

SBS cell was absent from the setup, illustrate that the oscillator and amplifier pulse shapes were identical. Figs. 6 and 7, taken off of the beamsplitter, show input and output waveforms when the SBS cell was present and when the laser energy was well above the SBS threshold. A comparison of Fig. 6 with Fig. 8 indicates that the presence of the SBS cell caused the laser to continue to lase even after output from the oscillator had stopped. A closer inspection of this continued, apparently mode-locked lasing action (Fig. 9) revealed a period of 35 nsec which was the same as the 35 nsec round trip time for light traveling between the 100% oscillator mirror and the SBS cell. The continued lasing had two causes: first, the electrical inductance of the flashlamp circuit in the amplifier caused the amplifier flashlamp pulse to be longer than that in the oscillator; and second, laser energy from the SBS cell was getting back into the amplifier. The reason that this small amount of energy feedback into the amplifier was possibly due to a slight depolarization effect at some point. Thus, due to this feedback, a phase conjugate resonator was formed. In Fig. 10 the phase conjugate ability to compensate double-passed aberrations is displayed. The intensity profiles between the SBS mirror return and the aberrated SBS mirror return show no difference other than shot-to-shot variation, while the ordinary mirror return and aberrated ordinary mirror return are strikingly different. The spot size difference between the ordinary mirror return and the SBS mirror returns was due to the fact that the light beam incident on the mirror, SBS or ordinary, was slightly divergent. This yielded a slightly divergent return beam for the ordinary mirror and a slightly convergent return beam for the SBS mirror. Therefore, the SBS return beam reached a focus somewhat in front of the camera position.

An appreciation of phase conjugation can be found in the realization of the fact that when the SBS mirror is used, the phase plate aberrator is actually intracavity. A normal laser cavity would never lase with the presence of such an aberration plate.

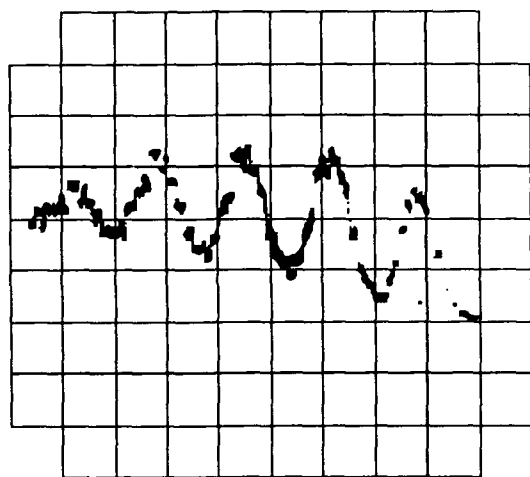


Fig. 9. Expanded view (20 nSec/Division) of the beginning of the "mode-locking" action.

CONCLUSION

Phase conjugation via SBS is possible with flashlamp-pumped dye lasers by using an oscillator/amplifier configuration. The expected bandwidth requirements for the SBS process were found to be much stricter than those observed in our laser oscillator. This was probably due to wavelength chirping in the oscillator.

A phase-conjugate resonator can be constructed around a laser gain volume by using a low energy, short pulse oscillator whose energy can be boosted above SBS threshold after a single pass through the gain volume. It may be possible to extract a significant fraction of the total available energy from a large gain volume in a nearly diffraction limited beam by such a cavity utilizing a double-pass setup.

Further experiments are required in order to understand and assess the usefulness, if any, of using this or a similar type of cavity on high energy flashlamp-pumped dye lasers, as well as other types of high energy lasers, where significant beam quality improvements can be attained via nonlinear optical phase conjugation.

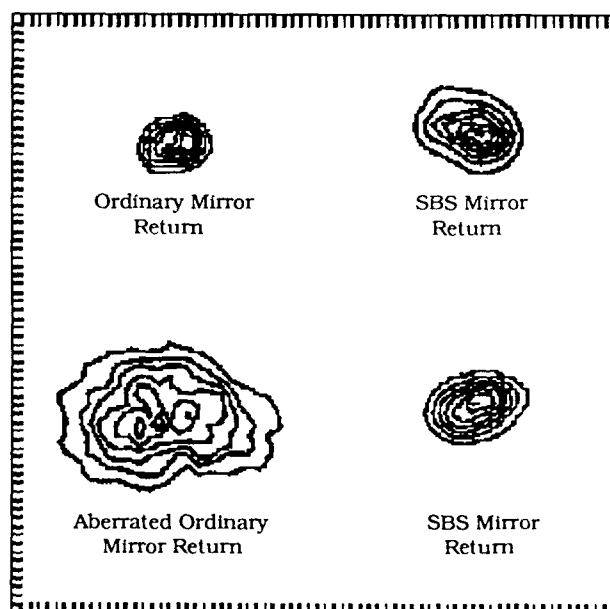


Fig. 10. Intensity contours taken with the CCD camera. The ordinary mirror return differs from the SBS mirror in that the SBS cell and lens were replaced with an ordinary laser mirror. The spot size difference is explained in the text. Both of the aberrated returns show the effect of the insertion of an aberrator placed in front of each of the mirrors.

ACKNOWLEDGEMENTS

The authors would like to thank the following: Robert A. Fisher, Frank J. Duarte, Allen M. Flusberg, and Keith A. Sage for their support and technical communications; Wayne E. Davenport and Nancy C. Guitard for major help in preparing this document and the conference presentation.

AUTODYNE LASER TRANSCEIVER*

David U. Fluckiger and Robert J. Keyes

Massachusetts Institute of Technology/Lincoln Laboratory
P.O. Box 73
Lexington, Massachusetts 02173

Abstract

The fundamental aspects of an autodyne detection laser transceiver concept are presented. A comparison between autodyne theory and measurements is made for visible wavelengths. The unique differences between heterodyne and autodyne transceiver characteristics are examined.

Introduction

Coherent detection of optical radiation is a well understood procedure in which a weak signal beam is mixed with a strong local oscillator beam on the surface of a photodetector.^{1,2} The beat-frequency portion of the resulting photocurrent contains a frequency down-translated replica of the signal field components that are copolarized and spatially coherent with the local oscillator beam. In optical heterodyne detection, the local oscillator frequency is offset from the signal frequency by an intermediate frequency (IF), and the photocurrent beat appears at this IF. No frequency offset is employed in optical homodyne detection, so that in this case the photocurrent beat is at baseband. Because of the mixing gain enjoyed by both of these coherent detection techniques, they can operate at the quantum noise limit (signal light shot noise limit) of sensitivity using photodetectors without internal current multiplication. Part of the price of this sensitivity is one of alignment tolerance; the local oscillator laser beam must closely match the polarization and the spatial mode character of the signal beam, and their frequency difference must be stable relative to the electrical bandwidth of the post-photodetection processing.

Coherent detection is becoming the technique of choice for laser-transceiver sensors because it permits the Doppler frequency shifts associated with target motion to be measured with quantum-noise-limited sensitivity. In such systems, the stringent frequency difference requirement of coherent detection can usually be met by employing a single stable laser to supply both the transmitter and local oscillator beams. Even in single laser systems, however, the spatial mode matching requirement is quite restrictive; from Siegman antenna theorem³, it follows that the received signal and local oscillator beams must be aligned to well within the diffraction limit of the receiver optics.

In this paper we will examine the use of optical autodyne detection for laser-transceiver sensors. Autodyne detection employs no local oscillator beam. It is a direct detection scheme involving self-beating between the various frequency components of the received signal beam. Autodyne detection involves the spectral analysis of the direct detection photocurrent produced by the beating of photons received from a laser illuminated target. Autodyne detection is capable of measuring the relative velocities between the components of an optically unresolved multi-element target, because they give rise to a Doppler-spread signal spectrum which is observable in direct detection. In other words, the various frequency components of the received signal light mix together on the photodetector to produce a photocurrent containing a spectrum of beat frequencies related to the relative velocity spectrum of the target complexes.

The following sections deal with the relative merits of autodyne detection as compared with heterodyne detection, and experimental results from an autodyne transceiver. Section II examines the relative merits of autodyne and heterodyne operation vis-a-vis their respective requirements for optics quality, laser frequency stability and their respective detection sensitivities. It is shown that autodyne operation greatly relaxes the stringent optics quality and frequency stability requirements of heterodyne operation. Moreover, autodyne operation can be as sensitive, if not more, as heterodyne detection at visible

*This work was sponsored by the Department of the Air Force.

"The views expressed are those of the authors and do not reflect the official policy or position of the U.S. Government."

wavelengths, because the former can make use of the internal current multiplication gain of a photomultiplier tube (PMT) to balance the mixing gain that accrues to the latter. Indeed, even at IR wavelengths, for which PMTs do not presently exist commercially*, autodyne sensitivity can approach that of heterodyne detection if due care is taken in optimizing the photodetector/preamplifier in the autodyne transceiver⁵. Section III presents experimental results obtained with a cw autodyne transceiver. Measurements of relative target motion and mixing efficiency are reported for specular and diffuse targets as functions of the diameter and optical quality of the receiver objective lens.

Autodyne Detection vs Heterodyne Detection

In the following comparison of autodyne and heterodyne detection we examine three distinct measures: detection sensitivity; required optics quality or tolerance to phase noise in the receive channel; and frequency resolution in terms of laser line stability.

Sensitivity

A measure of sensitivity for comparing heterodyne to autodyne is the Carrier-to-Noise ratio (CNR). The CNR is the ratio of the squared signal strength to the squared noise strength in the filtered photocurrent $i(t)$. To be explicit, decompose the photocurrent, $i(t)$, as follows:

$$i(t) = i(t)_{\text{light}} + i(t)_{\text{noise}} \quad (1)$$

where $i(t)_{\text{light}}$ represents the current generated by light-induced charge carrier generation within the photodetector, and $i(t)_{\text{noise}}$ represents nonlight related internal detector noise. Assume that the light current is due solely to the target return. Thus the light current includes target-light shot-noise fluctuations as well as target-return fluctuations arising from speckle; background light shot noise (if it is significant) can be lumped into the noise current. The CNR can now be defined as

$$\text{CNR} \equiv \frac{\langle T.A. [\langle i(t)_{\text{light}} \rangle_s]^2 \rangle_t}{\langle T.A. [i(t) - \langle i(t)_{\text{light}} \rangle_s]^2 \rangle_t} \quad (2)$$

where $\langle \rangle_s$ denotes ensemble averaging over the shot noise, $\langle \rangle_t$ denotes ensemble averaging over target fluctuations, $\langle \rangle$ denotes ensemble averaging over shot-noise, target, and internal-noise fluctuations, and T.A. denotes time averaging. Explicit calculations of CNR for an autodyne transceiver for specular and diffuse targets has been carried out in reference (6). From those calculations we find that

$$\text{CNR} = \frac{\text{CNR}_{\text{ref}} \text{CNR}_{\text{sig}} \epsilon_{\text{mix}}}{\text{CNR}_{\text{ref}} + \text{CNR}_{\text{sig}} + (\eta \text{NEP}/h\nu_0)^2/B} \quad (3)$$

where CNR_{ref} is the carrier-to-noise ratio associated with a sub-element of the target which is designated reference (this could be a glint feature), CNR_{sig} is the carrier-to-noise ratio associated with the remainder of the target, ϵ_{mix} is a mixing efficiency, η is the detector quantum efficiency, NEP is the detector noise equivalent power ($\text{W}/\sqrt{\text{Hz}}$), B is the IF bandwidth, and $h\nu_0$ is the photon energy. The above CNR is valid for either a diffuse (speckle) or glint (specular) target.

The CNR for a heterodyne receiver automatically achieves the quantum noise limit of performance due to the local-oscillator mixing gain. Autodyne detection can also achieve the quantum noise limit of performance which is obtained when the signal light shot noise dominates the detectors internal noise and background photon noise. In particular, when

$$\text{CNR}_{\text{ref}} \geq (\eta \text{NEP}/h\nu_0)^2/B \quad (4)$$

then autodyne detection will achieve comparable values of CNR as heterodyne (signal-light-shot noise limit). Thus to make a sensitive autodyne transceiver one should work with as low NEP detectors as possible while a heterodyne transceiver may use detectors with moderate values of NEP as long as the local oscillator shot noise can be made to dominate. The condition expressed in (4) above can often be met as is shown next.

Let us first examine visible-wavelength autodyne operation with a PMT detector. The internal current multiplication gain of the PMT is usually sufficient so that the prime contributor to NEP is background-light shot noise, namely,

$$\text{NEP} = (h\nu_0 P_B / \eta)^{1/2} \quad (5)$$

where

$$P_B = N_\lambda A_R \Delta\lambda \Omega_R \quad (6)$$

gives the received background power in terms of the background spectral radiance N_λ , the objective area A_R , the interference filter (wavelengths units) bandwidth $\Delta\lambda$, and the receiver field of view Ω_R . It follows that condition (4) for target-light shot-noise-limited autodyning is not unduly restrictive. For example, consider a 544 nm laser/PMT receiver autodyne system with $\eta = .2$, $\text{NEP} = 4 \times 10^{-14}$ W/√Hz, and $B = 1$ MHz. (This NEP corresponds to $P_B = 1$ nW collected by a 10 cm diameter objective in a 1 mrad half-cone angle field of view through a 1 nm bandwidth interference filter from a daytime sky-background spectral radiance; much lower values would apply at night. In this case we require $\text{CNR}_{\text{ref}} \geq 26.8$ dB to satisfy Eq. (5), a number that may well be realized with a glint feature. A more detailed comparison of heterodyne and autodyne sensitivities has been made by Keyes⁵, who has shown that generally for careful photodetector/preamplifier designs, direct detection systems can have sensitivities comparable to heterodyne systems.

We have considered sensitivity of autodyne detection and compared it with that of heterodyne detection. Now, we turn our attention to a comparison of the impact of optics quality on the two detection schemes. We assume that in heterodyne detection the local oscillator is injected after the objective. Degradations in the quality of the objective optic, therefore, negatively impact the heterodyne mixing efficiency.

Optics Quality

We will compare the mixing efficiency of a bistatic autodyne transceiver with that of a bistatic heterodyne transceiver in the following scenario. Suppose that both systems use identical modest-size diffraction-limited transmitter optics to illuminate a particular target and employ identical, considerably larger, receiver optics to make high spatial resolution measurements of the Doppler-spread spectrum of that target. We shall assume that the target lies in the far field of the receiver aperture, that both transceivers use identical (large-diameter) focal-plane photodetectors, and that the heterodyne transceiver introduces its local-oscillator beam after the objective optics. If both transceivers have diffraction-limited receiver optics and the heterodyne transceiver uses a local-oscillator beam (on its photodetector) that is matched to the Airy disk pattern, both transceivers will achieve high mixing efficiencies.

Now, suppose that their receiver optics are of poor quality, with an aberration-limited focal spot size N ($N \gg 1$) times the diffraction limit. In this case, the heterodyne transceiver's mixing efficiency will degrade by a factor of $\approx 1/N$, whereas the autodyne-transceiver's mixing efficiency will stay constant. The reason for this is that the phase aberration in the autodyne receiver channel is common mode, whereas in the heterodyne receiver channel the phase aberration affects the target return but not the local oscillator beam resulting in a phase-front mismatch with concomitant reduction in mixing efficiency.

Autodyne receivers can be constructed with arbitrary quality optics and are insensitive to atmospheric turbulence (as long as the received energy falls on the detector). This result has been experimentally verified as reported below. The obvious impact of being able to use large light-bucket optics for autodyne receivers is the reduction in system complexity and cost. We now turn our attention to the impact of laser frequency stability on autodyne and heterodyne detection.

Frequency Resolution/Laser Frequency Stability

Suppose the transmitter laser in a heterodyne transceiver has random frequency fluctuations with coherence time t_f and long-term linewidth σ_f , where $\delta f t_f \gg 1$. Let a portion of this laser beam be split off, acoustooptically frequency shifted, and used as

the local oscillator beam in the receiver. For long dwell time operation, the Doppler frequency resolution of this sensor will be limited by the frequency fluctuations in the IF signal. These fluctuations, for this single-laser system, are due to the decorrelation of the laser frequency that occurs over the round-trip sensor-to-target propagation delay. In particular, the frequency resolution is given by⁷

$$f_{\text{res}} = \begin{cases} 8\sigma_f(L/ct_f)^{1/2}, & \text{when } 2L/t_f \ll 1 \text{ and } 2\sigma_f L/c \gg 1 \\ 25/2\sigma_f, & \text{when } 2L/ct_f \gg 1 \end{cases}, \quad (7)$$

for a target at range L , where c is the speed of light. In the upper branch of Eq. (7), the propagation delay resolves the long-term linewidth but not the short-term linewidth. As a result, the frequency fluctuations on the target-return are highly correlated with those on the local-oscillator beam giving Doppler-measurement frequency resolution appreciably better than the long-term linewidth. When the lower branch of Eq. (7) applies, the propagation delay resolves both the long-term linewidth and short-term linewidths. Here the Doppler-measurement frequency resolution is worse than the long-term because the propagation delay is long enough that the frequency fluctuations on the target-return beam and those on the local-oscillator beam are uncorrelated.

Now consider autodyne operation, assuming the same laser frequency fluctuations. In this case, the long dwell time frequency-fluctuation-limited Doppler-measurement resolution becomes

$$f_{\text{res}} = \begin{cases} 8\sigma_f(\Delta L/ct_f)^{1/2}, & \text{when } 2\Delta L/t_f \ll 1 \text{ and } 2\sigma_f \Delta L/c \gg 1 \\ 25/2\sigma_f, & \text{when } 2L/ct_f \gg 1 \end{cases}, \quad (8)$$

where ΔL is the target depth, i.e., the range separation between the reference and signal components of the target. The interpretations of the two branches of Eq. (8) mimic those of Eq. (7), except that in the autodyne case, the appropriate propagation delay between the reference and signal frequency fluctuations is that associated with target depth rather than target range. Equations (7) and (8) imply that autodyning is far less sensitive to laser frequency fluctuations than is heterodyning. In particular, let us suppose that the two transceivers use lasers with identical frequency-fluctuation characteristics and that both operate in the regime where the short-term linewidth is unresolved. If $L=1000\Delta L$, the autodyne frequency resolution will be 30 times better than the heterodyne frequency resolution. Alternatively, with $L=1000\Delta L$, an autodyne transceiver can use a laser with 30 times worse short-term linewidth than that employed in a heterodyne transceiver, and yet both systems will have the same frequency resolution. In the regime where the path delay is sufficient to resolve the long term linewidth then the frequency resolution is given by the lower branch in Eq. (7). However, for autodyne the target depth for a large class of lasers and targets is not sufficient to resolve the long term linewidth so the upper branch in Eq. (8) still applies.

Experiment

The results presented in this section are from a series of autodyne laser-transceiver measurements made to verify the key physical aspects of the theory. The transceiver, whose block diagram appears in Figure 1, was a cw bistatic system employing a 10-mW collimated argon-ion laser transmitter operating on the 544 nm line and a direct-detection receiver consisting of a nondiffraction limited 6.8 cm diameter, 50 cm focal length, biconvex objective lens and a focal-plane photodetector. For most of the measurements, the detector was a 0.2 mm² area silicon photodiode; some measurements were made using a 1 cm diameter silicon photodiode; some measurements were made using a 1 cm diameter silicon photocell. In either case, the output of photodetector was directly applied to the 100 M Ω input impedance of a 0-30 kHz preamplifier, whose output was recorded with an analog storage oscilloscope as well as a digital oscilloscope capable of performing Fourier transformation. Throughout the measurements program, neutral-density filter attenuation of the transmitter beam was employed, as necessary, to prevent saturation of the photodetector.

The target arrangement used in the autodyne measurements is shown in Figure 2. For most of the measurements, a 50/50 beam splitter was employed to permit two target components that were well separated to appear, insofar as the autodyne transceiver was concerned, as though they were in close proximity. Low frequency choppers (9 Hz and 18 Hz) were employed, in most cases, to enable simple identification of the individual and mixing contributions to the total photocurrent. The propagation distance between the laser transceiver and the target arrangement was 100m.

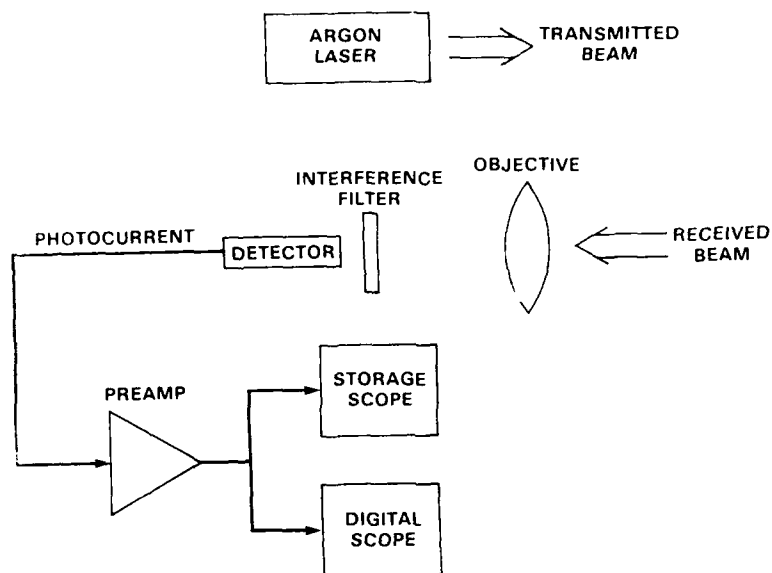


Figure 1. Block diagram of autodyne laser transceiver for experimental verification of autodyne theory.

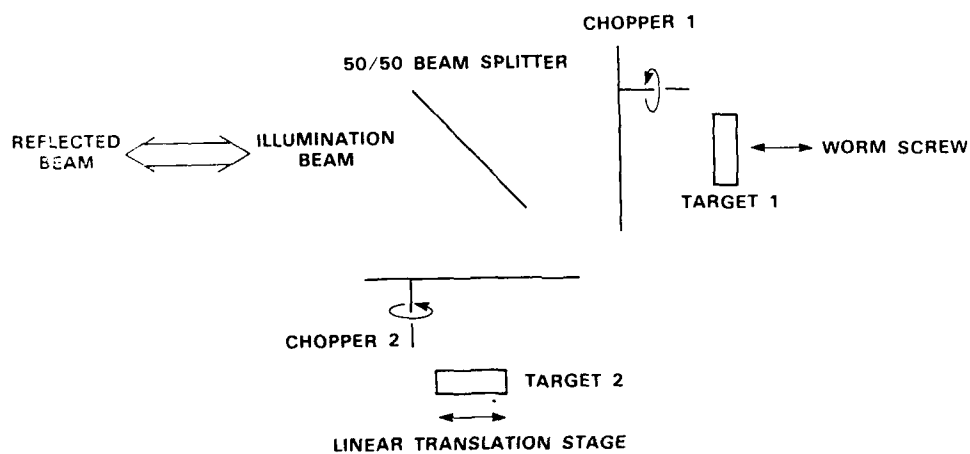


Figure 2. Schematic diagram of glint/glint autodyne target with 50/50 beam splitter.

Specular-Reference/Specular-Signal Measurements

To explore the behavior of specular-reference/specular signal autodyne, two 1 mm diameter mirrors were employed as the reference and signal components in the Figure 2 target arrangement. At a 100 m target range, this mirror size is much smaller than the 16 mm transmitter spot diameter and unresolved by the 2 mm diffraction limit of the 6.8 cm objective diameter. One mirror was mounted along the transmit/receive axis on a worm-screw-driven linear translation stage set up to provide a sawtooth relative radial motion between the two target-return components. The other mirror was mounted on a micrometer-driven linear translation stage set up to vary the transverse separation between the two target components. No effort was made to isolate the mirrors from acoustic vibrations.

The first measurement we made was to verify the expected frequency content of the specular-reference/specular signal autodyne detection photocurrent. According to the basic physics laid out in the previous section, the photocurrent obtained from the target combination should contain a beat note at the Doppler shift associated with the relative radial velocity between the two target components when both of these target elements are illuminated, and both lie within the diffraction limit of the receiver objective lines. When both mirrors were on-axis and the worm-screw drive was employed to introduce a 0.9 mm/s relative radial velocity, the photocurrent did show a clean Doppler note at the expected 3.3 kHz frequency. With no radial velocity imposed by the worm-screw drive, however, table vibrations led to an ≈ 2 kHz Doppler-spread bandwidth in the photocurrent.

Having verified the presence of the appropriate Doppler frequency beat in the photocurrent obtained with both mirrors on the transmit/receive axis, we next used the transverse micrometer drive to measure the specular-reference/specular-signal mixing efficiency achieved by our transceiver as a function of the angular offset between the two target components. This measurement was accomplished by finding the average photocurrents, I_{ref} and I_{sig} , generated by the reference and signal mirrors alone, and the average peak-to-peak photocurrent $I_{\text{p-p}}$ at the Doppler-shift frequency. These values were readable from the storage oscilloscope display because of the different chopping frequencies used in the two arms of our target arrangement. From these measurements, $\epsilon_{\text{mix}}^{\text{S}}$ is calculated via

$$\epsilon_{\text{mix}}^{\text{S}} = \frac{I_{\text{p-p}}^2}{4I_{\text{ref}}I_{\text{sig}}} \quad (9)$$

The results we obtained with the full receiver aperture and with the receiver aperture stopped down to a 1 cm diameter are shown in Figure 3. Because our 0.2 mm² area photodetector was significantly bigger than the aberration-limited blur circle of our objective lens, the mixing efficiency equals the squared magnitude of the overlap (correlation) integral between the received reference and signal fields over the entrance aperture of the objective lens. Thus, near-unity mixing efficiency should be obtained only well within the diffraction limit of this entrance aperture. This behavior is confirmed by the full-aperture data shown in Figure 3. In addition, the much broader mixing efficiency vs angular offset pattern shown in Figure 3 for the stopped-down receiver aperture is consistent with the antenna theorem view of autodyne.

There is an important aspect to these mixing efficiency curves that should be brought out at this juncture. For heterodyne-detection laser transceivers, it is generally held that diffraction-limited receiver optics should be employed. A principal reason is because the local-oscillator beam is typically injected after the objective optics. As a result, it becomes difficult to achieve good spatial-waveform matching on the photodetector between the local oscillator and received signal beams if the objective optics are not diffraction-limited. In other words, heterodyne transceivers usually need diffraction limited objective optics to approach near unity mixing efficiency. The unity, full aperture, on-axis mixing efficiency shown in Figure 3 for a nondiffraction limited objective in autodyne operation is thus a potentially valuable advantage of autodyne operation over heterodyne operation in that large diffraction-limited optics is very costly. Physically, the autodyne insensitivity to objective aberrations derives from the following considerations. First, autodyne operation with a large detector, so that all the reference-plus-signal light passing through the objective is collected, ensures that the mixing efficiency is the

degree of spatial-wavefront matching between the reference and signal fields arriving at the entrance aperture of the receiver. Second, this receiver aperture spatial-wavefront matching will be quite good whenever the two target components lie well within a single diffraction-limited field of view.

We put the insensitivity of autodyne operation to objective aberration to a severe test by placing a plastic slide coated with clear grease immediately in front of our lens. The composite optical quality of the slide and objective lens was so poor the 0.2 mm² area photodetector was smaller than the focal plane blur circle from a single-mirror reflector. Thus, we switched to a 1 cm diameter photocell for these measurements to stay in the target detector limit. We found that the mixing efficiency behavior was virtually unaffected by the presence of the severe objective aberrations in accord with the physical principles stated in the previous paragraphs.

Specular-Reference/Diffuse-Signal Measurements

Having completed the specular-reference/specular signal measurements, we replaced one of the mirrors in our target arrangement with a piece of reflective tape whose backscatter cone angle was ≈ 35 mrad. This tape introduced a spatially resolved diffuse component into our composite target. With this setup, we repeated the Doppler shift and mixing efficiency measurements with the specular-reference mirror located on the transmit/receive axis. We found that the photocurrent still contained a beat at the expected Doppler-shift frequency. We also found that the on-axis mixing efficiency, was ≈ 0.5 , in qualitative agreement with the theoretical result⁶ that specular-reference/diffuse signal autodyne efficiency is about half of that of the specular-reference/specular signal case.

Extended Rotating Cylinder Measurements

In the next series of measurements, a single multi-element target was simulated by removing the beam splitter from the Figure 2 arrangement and using a 1 cm diameter cylinder as the on-axis target. This cylinder was spun on a 1 rpm motor and canted to avoid specular reflection from the transmitter to the receiver. Within the illuminated portion of the cylinder the rotation produces a radial-velocity gradient which imparts a Doppler frequency chirp to the reflected light. The autodyne photocurrent results from self-beating between the various components of this Doppler-spread spectrum associated with reflection originating from the same diffraction-limited field of view of the receiver aperture. Thus, as the receiver aperture is masked down, with no changes in the transmitter beam or the target rotation rate, we expect that the autodyne signal bandwidth will increase because of the increased Doppler spread associated with the increased diffraction-limited field of view of the reduced receiver aperture. In Figure 4 we present plots of the photocurrent spectrum for three cases: no target rotation with full receiver aperture; 1 rpm target rotation with full receiver aperture; and 1 rpm rotation with a 1 cm diameter receiver aperture. The spectral structure seen in the absence of target rotation is principally due to 60 and 120 Hz pickup in our instruments. The key thing to observe in the Figure 4 data is the long spectral tail that exists in the 1cm aperture data that is absent from the full aperture data.

There is one additional feature of the rotating cylinder measurements that should be noted. The rotating cylinder measurements that we made were arranged so that none of the light collected by the receiver came from specular reflection. Thus the Figure 4 data verify that autodyning can be achieved in the diffuse-reference/diffuse-signal case.

Conclusion

In this initial assessment of autodyning vs heterodyning, it seems clear that autodyning and heterodyning can both measure Doppler-spread target characteristics, autodyning is far less sensitive to receiver optics quality and laser frequency stability than is heterodyning, and autodyning can be as sensitive as heterodyning. Also since autodyne reception is relatively insensitive to phase aberrations in the optics, this implies that it is also relatively insensitive to atmospheric turbulence.

Additional experimentation is underway which will address the question of quantum limited autodyne performance, i.e. how many photons per unit measurement interval are required to resolve a Doppler beat note? We are also examining the question of wide field of view optics and large detectors to explore for consequences on autodyning of aperture averaging from diffuse reflectors.

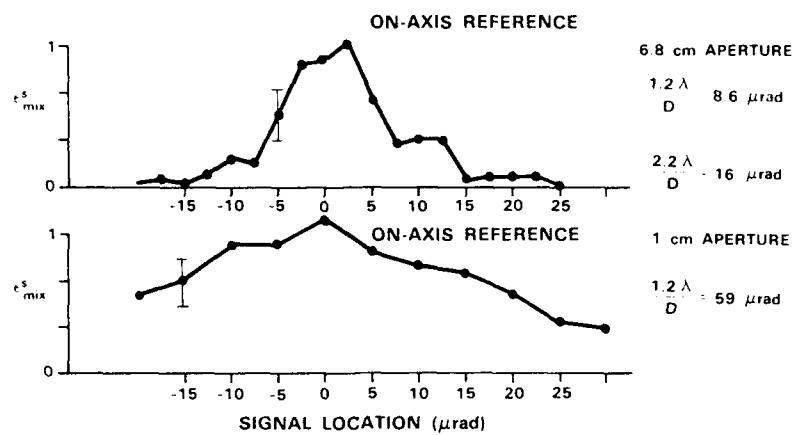


Figure 3. Experimental mixing efficiency curve for glint/glint target as a function of angular separation.

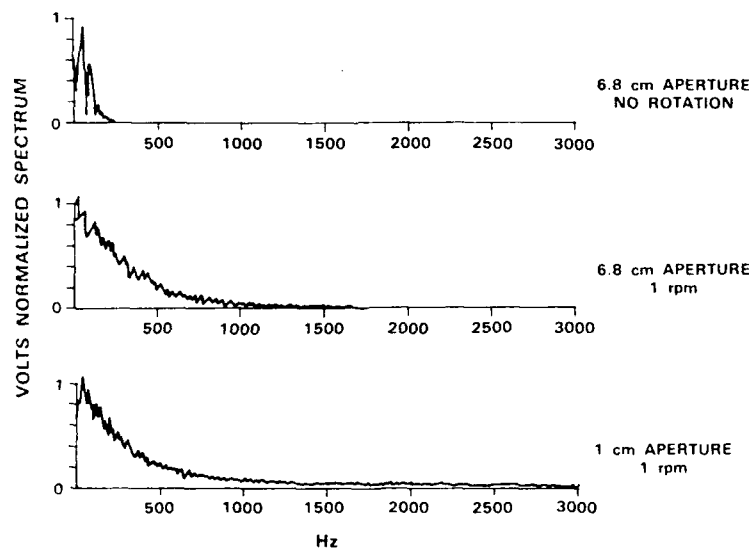


Figure 4. Autodyne signature from a resolved rotating diffuse cylindrical target.

The authors wish to express their appreciation to A.B. Gschwendtner for providing encouragement and resources for this research. We are also indebted to J.H. Shapiro of the Massachusetts Institute of Technology, Department of Electrical Engineering and Computer Science for providing insightful analysis of autodyne methodology.

References

1. S. Jacobs, Electronics 36, 29 (1963).
2. A. Yariv, Introduction to Optical Electronics (Holt, Rinehart & Winston, New York, 1971) Chap 11.
3. A.E. Siegman, Proc. IEEE 54, 1350 (1966).
4. F. Caaspasso et al., Appl. Phys. Lett. 48, 1294 (1986).
5. R.J. Keyes, Rev. Sci. Instrum. 57, 519 (1986).
6. D.U. Fluckiger, R.J. Keyes, and J.H. Shapiro, Appl. Opt. 26, 318 (1987).
7. R.J. Hull, D.G. Biron, S. Marcus, and J.H. Shapiro, "Coherent Laser Radar Remote Sensing", Final Report, MIT/Lincoln Laboratory, 30 September 1982, (DTIC AD-A139448/5), Appendix C.

A FOUR-WAVELENGTH INFRARED DIFFERENTIAL ABSORPTION LIDAR (DIAL) SYSTEM

Peter L. Holland and Jan E. van der Laan

SRI International

333 Ravenswood Avenue, Menlo Park, CA 94025

and

Kirkman Phelps and Steve Gotoff

U.S. Army Chemical Research, Development and Engineering Center

Aberdeen Proving Ground, MD 21010-5423

Abstract

A four-wavelength infrared (IR) DIAL system, developed by SRI for the U.S. Army Chemical Research, Development and Engineering Center (CRDEC), is described. The lidar detects infrared absorbing vapor clouds using the DIAL technique and performs both path-integrated (column-content) and range-resolved measurements. The van-mounted lidar contains four grating-tuned Tachisto 555-G (custom) TEA CO₂ lasers, with a nominal 1-J transmitted energy at 10P(20). The lasers are typically fired with a 100- μ s spacing to freeze the atmosphere. The IR receiver uses a 16-in. f/2.5 telescope and a liquid-nitrogen-cooled HgCdTe quadrant detector. The scanner allows pointing over a full hemisphere. The lidar data system features two DEC PDP-11/73 microcomputers and a CAMAC data acquisition system for real-time data collection, signal averaging, data analysis, color graphics display, and storage on magnetic tape. The lidar has demonstrated path-integrated measurement capability to a range of 9 km and range-resolved capability to 4.5 km. Table 1 presents the lidar technical specifications. Figure 1 shows a photograph and system layout of the lidar.

Table 1
GMBU TECHNICAL SPECIFICATIONS

Module	Specification
<u>Transmitter</u>	
Laser type	CO ₂ TEA (Tachisto 555-G Custom)
Wavelengths (μ m)	9.2 to 10.8
Energy/pulse (J on 10P20)	1.0
Pulse rate (Hz)	20 (max)
Beam divergence (mrad)	3.5 H, 4.0 V
Modes available	Multimode/single mode (TEM ₀₀)
Pulsewidth (ns)	840
Beam area (mm x mm)	18 x 20
<u>Receiver</u>	
Diameter (cm)	40 (16 in.)
Telescope type	Dall-Kirkham F2.5
Detector Type	LN ₂ -cooled photo-conducting (PC) HgCdTe (1 x 1 mm) quadrant with 4 x Ge immersion lens
Detectivity (cmHz ^{1/2} /W)	4×10^{10}
FOV (mrad)	8 x 8
Bandwidth (MHz)	2.5
Amplifier gains (dB)	12, 32, 66
Log amplifier	4 decade (oscilloscope display only)
<u>Data Acquisition</u>	
Digitization (MHz-bit)	Dual/10-12 linear, Transiac
Energy monitor detector	Room temperature photovoltaic (PV)-HgCdTe
Processor	DEC LSI 11/73
Recording (magnetic tape)	9 track, 2400 ft
Display	Character data
Visual scene	Color video
<u>Analysis Computer</u>	
Processor	DEC LSI 11/73
Hard Disk	Winchester 130 Mbyte
Display	RGB graphics

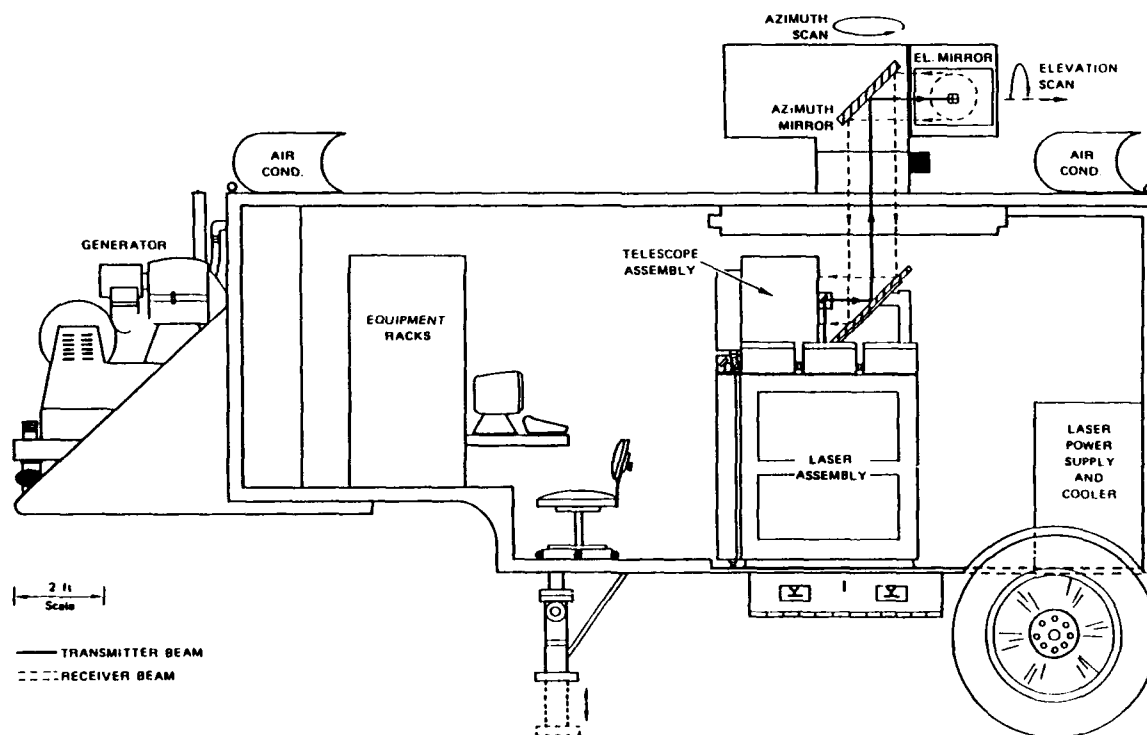
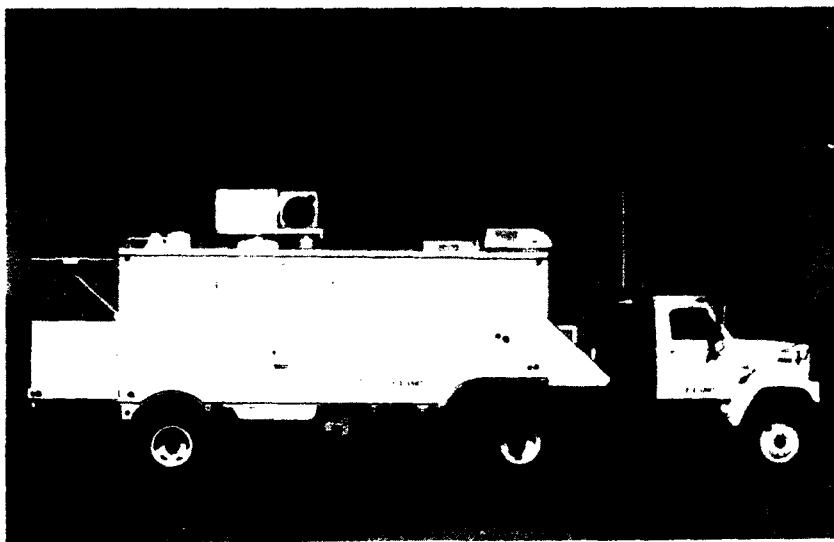


FIGURE 1 PHOTOGRAPH AND SYSTEM LAYOUT OF DIRECT-DETECTION CO₂ LASER RADAR SYSTEM

FUTURE APPLICATIONS OF SOLID-STATE LASERS FOR SPACE REMOTE SENSING

John W. Cox and Christopher L. Moore
NASA Langley Research Center
Hampton, VA 23665

Abstract

NASA's future plans include a polar-orbiting lidar platform to conduct remote sensing investigations from space. A Shuttle flight experiment is currently being developed to enhance the technology and formulate the design of this lidar system.

Introduction

NASA plans to develop a polar-orbiting remote sensing platform as part of its Space Station program. The Earth Observation System (EOS) platform will include the Laser Atmospheric Sounder and Altimetry (LASA) lidar facility.¹ LASA will provide long-term global measurements of aerosols and clouds in the Earth's atmosphere. The Lidar In-Space Technology Experiment (LITE) will demonstrate the first use of a lidar system in space, proving the technology required for future space-based lidar facilities such as LASA.² LITE is currently being developed at NASA for launch on the Space Shuttle in mid-1992.

Lidar has been utilized for remote sensing of the Earth's atmosphere since the early seventies. A lidar system fires short pulses of laser energy into the atmosphere where it is scattered by atmospheric particles and molecules. A telescope receiver collects the backscattered laser light. By measuring the strength of the return signal and its time-of-flight, a vertical distribution profile of atmospheric aerosols and other constituents can be determined.³

Early lidar systems were ground-based, and consequently could obtain aerosol profiles above only a fixed site. Currently, lidar systems are flown in aircraft, allowing measurements to be performed at remote locations and at a range of points along the flight path. This approach limits observations to a small region of the atmosphere, however. In order to map the distribution of atmospheric aerosols on a global scale, space-based lidar facilities are needed.¹

This paper will present an overview of both the LITE and LASA projects. Solid-state lasers will be utilized first in these experiments because of their proven reliability in terrestrial lidar systems. In addition, solid-state lasers can generate high-energy pulses of light at multiple wavelengths. This capability enables a single laser system to perform a variety of scientific investigations.

LITE Instrument Overview⁴

The LITE experiment is currently being developed at NASA to demonstrate the first use of a lidar system in space for remote sensing of the atmosphere. LITE is designed to be a modular experiment capable of multiple flights. It will serve as a test-bed for evolving lidar technologies such as lasers, optical detectors, and lightweight telescopes.²

The scientific objectives of LITE are to measure atmospheric aerosols and molecular densities, and to determine the height of cloud tops and the planetary boundary layer.⁵ The LITE instrument is nadir viewing, and will operate at a nominal altitude of 250 km. Data will be acquired over the course of 30 orbits.

The mechanical configuration of the LITE instrument is shown in Figure 1. The major components of LITE are a 1-Joule laser transmitter, and 1-meter diameter reflecting telescope. The laser transmitter consists of a flashlamp-pumped Neodymium-YAG oscillator with a fundamental wavelength of 1064 nm. Second and third harmonic generation is employed to obtain wavelengths of 532 nm and 355 nm. The telescope receiver collects the backscattered laser energy and converts the return signal into three channels of scientific data.

Alignment capability is provided by an actively controlled, steerable prism which maintains the laser beam parallel with the telescope axis. A 35 mm photographic camera is used to record cloud cover and the ground track of the instrument. An engineering data system acquires environmental data on the instrument during ascent and landing. The LITE

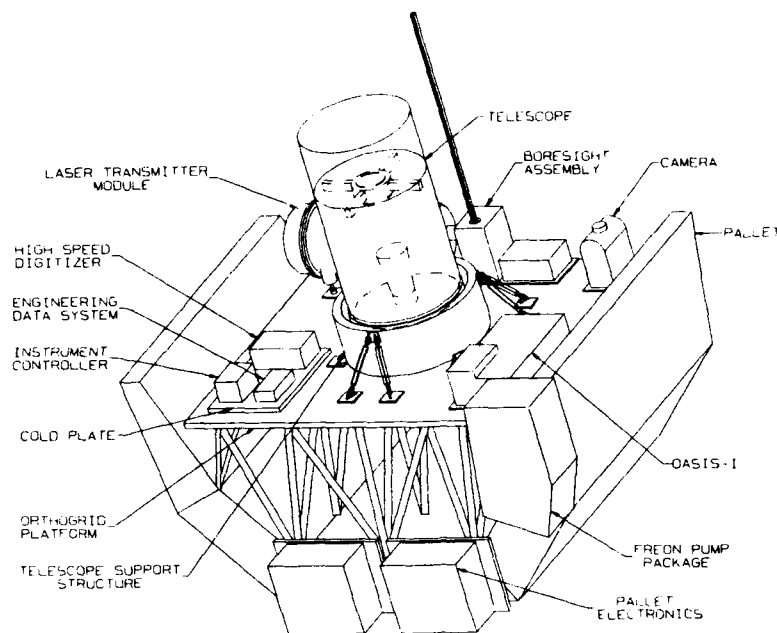


Figure 1: LITE Instrument Configuration

instrument is mounted in a Spacelab pallet which is carried in the cargo bay of the Space Shuttle Orbiter. Overall system weight, including the pallet, is approximately 2268 kg (5000 lbs).

Laser Transmitter Module

The Laser Transmitter Module (LTM) is a pressurized canister which contains the laser oscillator and its associated optics and electronics. The layout of components on the optical bench inside the canister is shown in Figure 2. Two independent laser systems are included in the LTM for redundancy. Only one laser system is operational at a given time due to Shuttle power limitations.

The Q-switched, Neodymium-YAG oscillator generates a 180-mJ pulse of laser energy. The fundamental wavelength of the oscillator is 1064 nm. The first amplifier boosts the pulse energy to 500 mJ, and the second amplifier produces an output of 1200 mJ. The oscillator and both amplifiers are excited by flashlamps.

After leaving the second amplifier, the laser beam is expanded and enters the first harmonic generator. Here a CD*A doubler crystal partially converts the fundamental wavelength to 532 nm. The remaining 1064 nm energy travels through the second harmonic generator which contains a KD*P tripler crystal. This crystal converts an additional portion of the fundamental wavelength to 355 nm. All three wavelengths are emitted simultaneously. The projected net energy per pulse is 400 mJ at 1064 nm, 400 mJ at 532 nm, and 150 mJ at 355 nm.

The pulse rate of the LTM is selectable to either one or ten pulses per second. The width of each pulse is approximately 17 nanoseconds. The laser beam divergence is 1.5 milliradians.

The laser transmitter requires about 2.2 kW of electrical power during operation. Since most of this input energy is lost as heat, the laser must be actively cooled. Ethylene glycol circulates around the laser rods, and fans are used to cool the laser canister by forced convection. Excess heat is dumped into the pallet cooling system through a heat exchanger.

The LTM optical bench is supported on three internal kinematic mounts which isolate it from deformations in the surrounding canister. The canister is in turn attached to the experiment platform by three external kinematic mounts. The projected weight of the LTM is 227 kg (500 lbs).

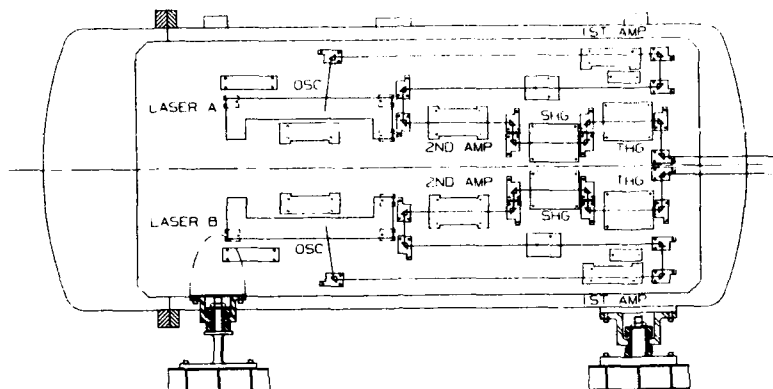


Figure 2: Laser Transmitter Module

Telescope Assembly

The telescope assembly consists of the telescope, the forward light shade, the aft optics housing, and the telescope support structure. Figure 3 illustrates the path traveled by light as it is collected by the telescope and directed into the aft optics. The telescope assembly weighs approximately 363 kg (800 lbs).

The telescope is a Cassegrainian-type reflector with a 38-inch diameter primary mirror. The primary mirror is made from cast beryllium, and has an aluminum reflective surface. The secondary mirror is made of fused quartz.

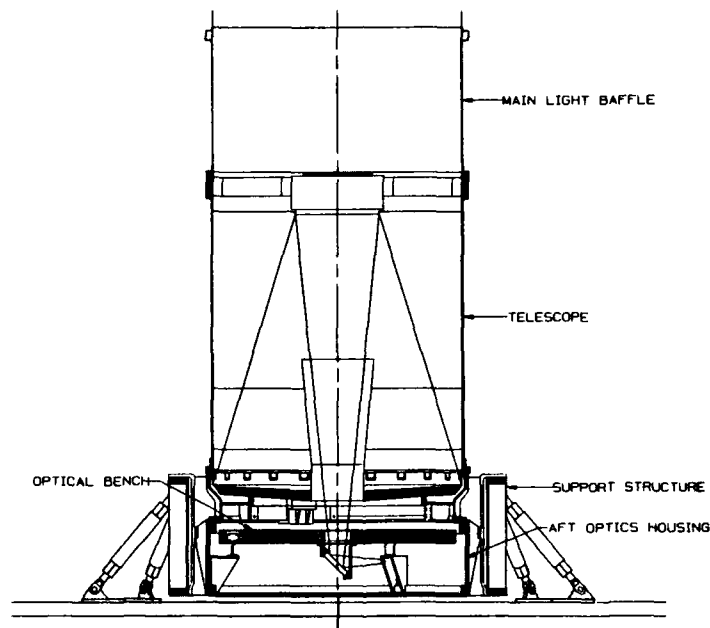


Figure 3: Telescope Assembly

Aft-Optics

The aft-optics, shown in Figure 4, contain the optical detection elements which receive and separate the return signals. The optical components are mounted on an aluminum honeycomb optical bench which is suspended below the primary mirror. The optical bench is supported on three kinematic mounts which isolate it from deformations in the surrounding housing. A series of mirrors, lenses, beam splitters, and filters separate the return signal entering the telescope into three channels of scientific data.

The 532 nm and 355 nm spectral components of the signal are detected by photomultiplier tubes. The 1064 nm channel is detected by an avalanche photodiode. A variable field stop

mechanism can be commanded to change the field of view of the instrument for either daytime or nighttime measurements. The field stop can also protect the instrument by blocking incoming light if the sun shines directly into the telescope. A microchannel-plate quadrant detector is used to sense the alignment between the receiver axis and the laser beam with a portion of the 532 nm signal.

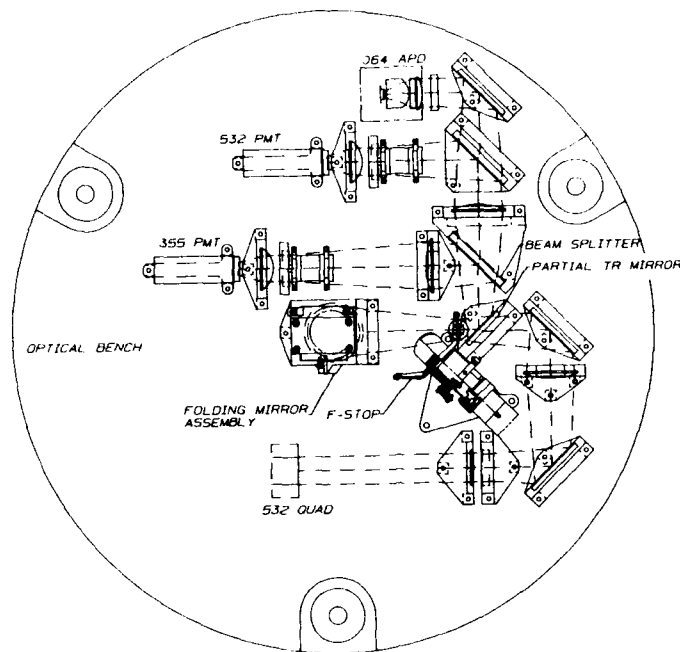


Figure 4: Aft Optics

Boresight Assembly

The boresight assembly is located near the exit of the laser transmitter module. The horizontal laser beam which emerges from the LTM canister is directed into a vertical plane by the boresight assembly. A right-angle prism reflects all three laser wavelengths by total internal reflection. This eliminates the need for multiple coatings on the reflective surface.

Alignment capability is provided by actively controlling a steerable prism to maintain the laser beam parallel with the telescope axis. A portion of the return signal entering the telescope is diverted to a quadrant detector. This detector senses the degree to which the telescope image spot is off-center. A computer generates position commands which are sent to the two-axis gimbaled prism. The gimbaled prism steers the laser beam until the telescope image spot is centered. The laser beam can be aligned to the receiver axis within 0.05 milliradians using this system.

The boresight assembly is designed to passively maintain alignment in the power off condition. It will initiate a search mode if a return signal is not detected. Total beam adjustment range is 1 degree.

System Electronics

The system electronics consist of an instrument controller unit, a high-speed digitizer unit, and an engineering data system. The instrument controller monitors and controls the operation of the laser transmitter, the boresight assembly, and the aft optics detectors. A programmable digital delay generator provides the range gate signal to activate the detectors prior to signal return.

The high-speed digitizer unit contains an analog-to-digital converter and a buffer memory which allows data from the scientific detectors to be acquired and stored at a very high rate. A high data rate tape recorder located on the aft flight deck of the Orbiter is used for data storage. The digitizer also provides the interface to the Space Shuttle Orbiter for uplink commands and downlink data transfer at a rate of 2 megabits per second.

The engineering data system records housekeeping data from approximately 300 sensors on the experiment during orbital operation. This data will be analyzed to verify functioning of the instrument. The engineering data system will acquire information on temperature, strain, pressure, and electrical power.

LASA Lidar Facility

NASA will provide the LASA lidar facility for the EOS remote-sensing polar platform. The EOS platform may be launched as early as 1995 on a Titan IV rocket. Studies are presently underway to define concepts for this platform. The concept shown in Figure 5 represents a generic complement of experiments which includes a lidar facility attached to an integral carrier.⁶ The basic carrier will furnish power, data handling, thermal control, and pointing control to the lidar facility.

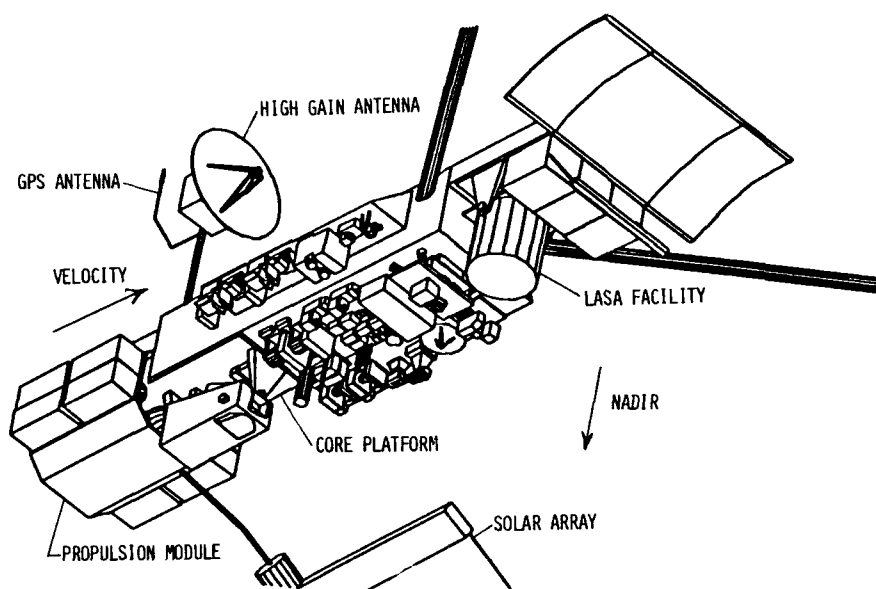


Figure 5: EOS Polar Platform

The major scientific objectives for the LASA facility are to study the distribution of atmospheric water vapor, to explore the role of aerosols and clouds in global climatic change, and to gain understanding of the processes that influence the extent of the polar ice cap.¹ Altimetry, backscattered lidar, and DIAL (Differential Absorption Lidar) techniques will be extensively employed to accomplish these broad goals. A DIAL lidar system compares the amount of energy backscattered at a particular absorption line wavelength to that backscattered at an off-line reference wavelength. This technique can be used to map the distribution of water vapor and other molecular species.³

The LASA facility will provide a telescope, optical bench, data handling system, and all interfaces to the polar platform. The lidar experiments are expected to provide the laser system, detectors, back optics and specialized electronics since these subsystems are peculiar to the experiment. In order to define the LASA facility, candidate experiments were proposed by an atmospheric and lidar science panel. Most of the proposed experiments have demonstrated aircraft flight performance, but none have any spaceflight certification. The experiments span six different laser technologies and can generally be divided into two categories--those using backscattered lidar and those using a DIAL technique.⁷ The required telescope apertures for these experiments range from 0.1 to 2.0 meters. Electrical power requirements vary from a few hundred watts to 2000 watts.

Table I lists the laser technology proposed by the science panel. Studies have been made to assess the impact on the LASA facility. The studies considered available laser technology and assumed the lasers to have outputs of 0.5 to 1.0 Joule per transmitted wavelength.⁷ Conservative engineering assessments relating to thermal issues, launch environments, and requirements to package hardware in standard "orbital replacement units" have resulted in the weights shown. These numbers are continuing to be refined as emerging laser technologies are assessed.⁸ Weights are expected to be reduced significantly with the advent of diode-pumped laser systems.

The electrical power requirements for most of the lasers are substantial. Either duty cycle operation or higher efficiency laser technology is required in order to operate within LASA facility power budgets. The inefficiency of these lasers also dictates the need for substantial systems to dissipate heat. The availability of the more efficient diode array pumping techniques not only saves electrical power, it also reduces thermal systems requirements which yield significant facility weight savings.

TABLE I
LASER SYSTEMS OPTIONS

<u>TECHNOLOGY</u>	<u>WEIGHT (LBS)</u>	<u>POWER (W)</u>
Nd:YAG 3 λ Flashlamp	1050	2025
Diode	710	435
Alexandrite Flashlamp	1210	2000
Ti:Sapphire Diode	1005	1175
Excimer 2 λ	1670	1335
CO ₂ Pulse	1675	980
CO ₂ CW	903	1300
Baseline	500	<1700

The availability of a suitable solid-state, tunable laser offers the possibility of having one laser system that meets most of the requirements of the proposed experiments. The DIAL technique could be utilized by having one transmitted wavelength on a molecular absorption line, and a second wavelength transmitted slightly off the absorption line. The second wavelength could also be used for harmonic generation to provide multiple wavelengths that would satisfy the backscattered lidar techniques. The incorporation of a short transmitted pulse capability would satisfy the altimetry portion of the experiment. A laser meeting these requirements would have the characteristics in Table II.⁷

TABLE II
SUMMARY OF SOLID-STATE LASER PARAMETERS

Tuning range	λ_{On} - H ₂ O, O ₂ absorption lines; ≤ 0.5 picometer (λ_{Off} - λ_{On}) 30-100 picometers; ≤ 2 picometer
Spectral purity	99% of energy ≤ 1 picometer
Efficiency	>3%
Energy per pulse	0.5-1.0 Joule
Repetition rate	10 Hertz
Pulse length	<100 nanoseconds
Lifetime	>10 ⁸ shots
Harmonic generation	fundamental doubled and tripled

A concept for the LASA facility is shown in Figure 6. The baseline telescope is a 1.25-meter Dall-Kirkham type instrument. The concept accommodates up to three experiment modules. Each module is assumed to be a standard Orbital Replacement Unit (ORU) which can be replaced by the Shuttle remote manipulator system or astronaut extravehicular activity. Optical ports will be used to permit steering of the received light signal to appropriate experiment modules. A fluid coolant loop will provide thermal control for the modules. Standard interfaces will be needed to permit future on-orbit change-out or addition of new modules. Evolving laser technology and experiments will be accommodated by on-orbit addition or exchange of ORU's.

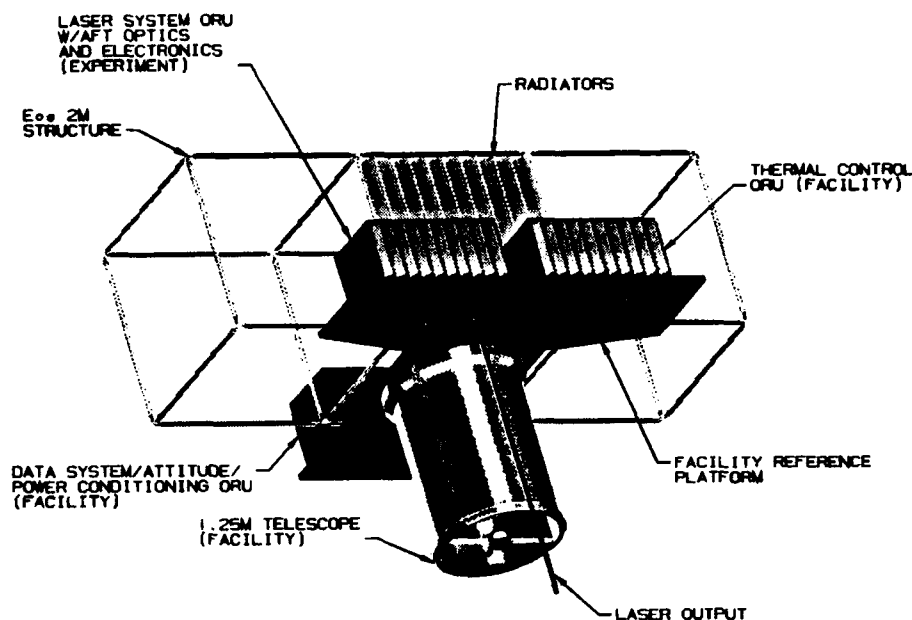


Figure 6: LASA Facility Concept

References

1. Lidar Atmospheric Sounder and Altimeter (LASA); Earth Observing System, Vol. IIId, Instrument Panel Report, NASA (1987).
2. H. E. Poole, J. W. Cox, R. H. Couch, and W. H. Fuller, Jr., "A Lidar Technology Experiment from Space Shuttle: Lidar In-Space Technology Experiment (LITE)." Laser Radar Technology and Applications, Proc. SPIE Vol. 663, pp. 196-202 (1986).
3. J. S. Levine and F. Allario. "The Global Troposphere: Biogeochemical Cycles, Chemistry, and Remote Sensing," Env. Monitoring and Assessment, pp. 263-306 (1982).
4. "LITE Preliminary Design Review Notebook," NASA Langley Research Center, Hampton, VA (1987).
5. M. P. McCormick, "The Lidar In-Space Technology Experiment (LITE)." 13th ILRC Conference, Toronto, Canada (1986).
6. "EOS Facility Instrument Briefing," presentation at Jet Propulsion Laboratory, Pasadena, CA (1987).
7. L. V. Taylor and R. R. Nelms, "Future Lidar Platforms in Space." Topical Meeting on Tunable Solid State Lasers, IEEE and Optical Society of America, Zigzag, OR (1986).
8. P. F. Moulton. "Tunable Solid-State Lasers Targeted for a Variety of Applications," Laser Focus, Vol. 23, No. 8, (1987).

DESIGN OF A MOBILE DIFFERENTIAL ABSORPTION CO₂ DIRECT-DETECTION LIDAR SYSTEM

Johnny Jones, Jan van der Laan, Peter Holland, and Leland Fletcher

SRI International

333 Ravenswood Avenue, Menlo Park, California 94025

and

Dr. Jack Comeford

U.S. Army Dugway Proving Ground
Chemical Laboratory Division/MT-C
Dugway, Utah 84022-5000

and

Kirkman Phelps and Steve Gotoff
U.S. Army Chemical Research, Development and Engineering Center
Aberdeen Proving Ground, Maryland 21010-5423

Abstract

This paper discusses the design of a direct-detection differential absorption lidar system capable of producing range-resolved vapor concentration plots of a 1000-m² grid with 20-m spatial resolution at 10-s intervals. The self-contained, modular, mobile system features four tunable 4-J, 20-Hz, TEA CO₂ lasers; automatic rapid tuning of one laser; unique plasma shutter pulse clippers to limit the pulse duration to 130 ns; a 16-in. receiver telescope with full hemispherical scanner; and a large-capacity data system based on a MicroVAX-II. The system is housed in a specially designed vehicle which features excellent environmental control and an on-board generator. The system is capable of detection, quantification, and mapping of any chemical vapor clouds having significant spectral structure in the 9 to 11- μ m region. The system has a maximum effective range of 5 km in the range-resolved mode and 20 km in the column-content mode.

System Design Goals

The design goals of the direct-detection differential absorption lidar system are:

- (1) Self-contained, mobile operation.
- (2) Column-content and range-resolved concentration measurement capability.
- (3) Detection of any chemical vapor having significant spectral structure in the 9 to 11- μ m region.
- (4) 0.02 mg/m³ sensitivity to SF₆ at 1 km.
- (5) 360° scan capability.
- (6) Near-real-time concentration map of 1000-m² grid at 10-s intervals with 20-m resolution.

System Specifications

The following is a partial list of specifications of the lidar transmitter and receiver:

Laser Transmitter

- Lasers Four tunable, pulsed, TEA CO₂ lasers (Questek model 7240)
- Pulse width Clipped with plasma shutters to 130 to 160 ns (FWHM)
- Energy 1.2 J in gain-switched spike on 10P(20)
- Repetition rate 20 Hz
- Wavelength 76 lines in the spectral region 9.2 to 10.8 μ m
- Beam divergence 4 mrad
- Tuning Automatic tuning of one laser; manual tuning of three lasers

Receiver

- Telescope 16-in. Dall-Kirkham, f2.5
- Field of view 5 mrad
- Detector HgCdTe photovoltaic, liquid-nitrogen-cooled

System Description

Vehicle and Associated Equipment

The vehicle of the lidar system is a 31-ft Front Runner manufactured by Wolverine Western (Figure 1). A floor plan of the vehicle is shown in Figure 2. A 30-kW Kohler generator mounted in the rear of the van provides electrical power for self-sufficient operation. The van engine and the generator engine use the same fuel supply. Hydraulic jacks located at each corner of the vehicle provide for leveling and stability. The vehicle includes a custom climate control system capable of temperature control to within 1°C to assure the best lidar system performance. This dual-purpose system also supplies cooling water for the lidar package. Additional features include built-in operator workstation and equipment racks, maintenance workspace, and storage. An electrical load center allows monitoring of electrical power and easy switch over from shore power to generator power.

Lidar Package

The lidar package includes four lasers with power supplies, plasma shutter pulse clippers to eliminate the nitrogen tail of the laser pulses, transmit and receive optics, built-in diagnostics, and the data acquisition and data processing subsystems. The scanner is mounted directly on top of the lidar package. The only components not included as integral parts of the lidar package are the laser cooler, the operator terminals, the display monitors, and the tape drive.

Figure 3 shows the laser access end of the lidar package. All subsystem controls, status indicators, and the data subsystem are located for easy operation and access. Access to the laser-tuning gratings is gained by opening the laser access doors. Each laser can be removed through these doors for maintenance. The laser electronic control systems are accessible through these doors without removing the lasers. Displays of laser pulse shape, energy, and wavelength are provided using digital readouts and a digital oscilloscope. The detector is readily accessible from the side of the package.

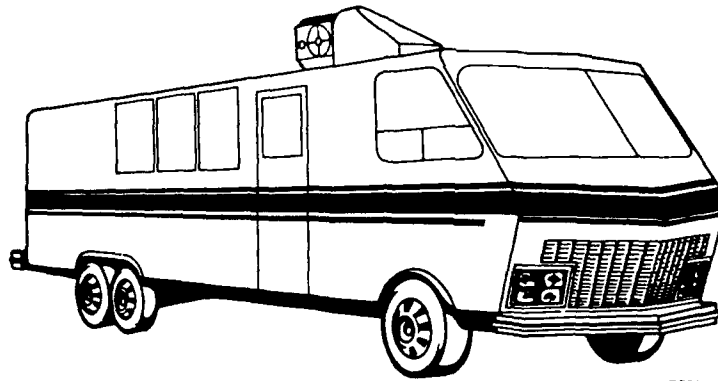
Figure 4 shows the transmit and receive optics end of the lidar package. The output beams of the four lasers are directed through four plasma shutter pulse clippers and are combined by four beam-stacking mirrors. Most of the beam energy is directed upward to the scanner, but a small fraction is directed to the beam diagnostic and monitoring system. This consists of a spectrum analyzer for measuring the laser wavelength, an X-Y error monitor for monitoring beam pointing, and the transmit power monitor. The received backscatter signal is reflected from a large turning mirror into the telescope, which focuses it onto the liquid-nitrogen-cooled detector. The transmit and receive optics are protected by airtight enclosures but easily accessible for alignment and maintenance.

Data System

Except for operator terminals, displays, and the tape drive, the data acquisition and data processing subsystems are housed within the lidar package. These are actually two separate subsystems performing separate functions. The data acquisition subsystem receives and records lidar data during each scan. At the end of each scan it sends the data to the data processing subsystem for processing and display. The two subsystems work in parallel for the greatest data throughput. While the data processing subsystem is processing data from one scan and producing an output plot, the data acquisition subsystem is recording data from the next scan.

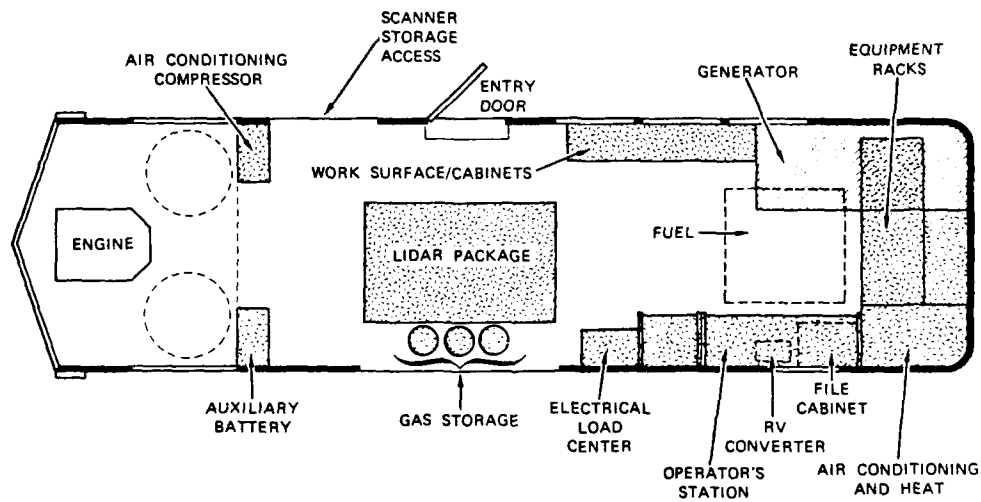
The data acquisition subsystem consists of a CAMAC crate controller, a 40-MHz coherent clock, a two-channel programmable gain amplifier, and three 40-MHz, eight-bit digitizers. One digitizer records the output energy and the waveform of the laser pulse for use in diagnostics and concentration-estimation algorithms. The other two digitizers record the lidar returns from the high-gain and low-gain channels of the programmable amplifier. Using the two eight-bit digitizers with different gains achieves an effective digitization capability of greater than 12 bits at 40 MHz. The digitizers have the capacity to store all the data from one complete scan of the test grid (125 LOS with a range of 1920 m).

The heart of the data processing subsystem is a DEC MicroVAX-II computer. While the data acquisition subsystem is recording data on a scan, the data processing subsystem is processing and displaying the data from the previous scan. (The DEC MicroVAX computer used for data processing also controls the operation of the entire lidar system.) Near-real-time data is displayed on a 19-in. color graphics monitor and a graphics printer. All data are written to a tape drive for post-test analysis and long-term storage. Detailed post-test analysis can also be performed by the MicroVAX computer.



EO041

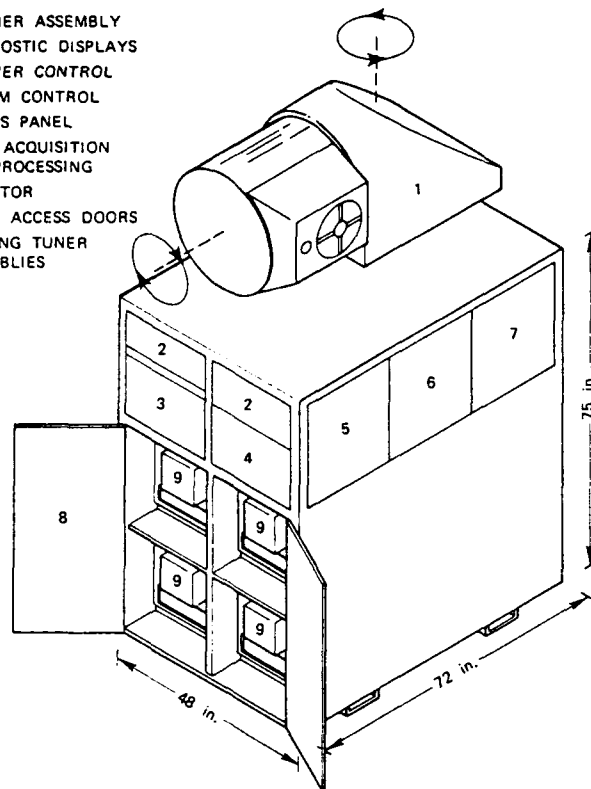
FIGURE 1 MOBILE LIDAR SYSTEM



EO041

FIGURE 2 FLOOR PLAN OF LIDAR VAN

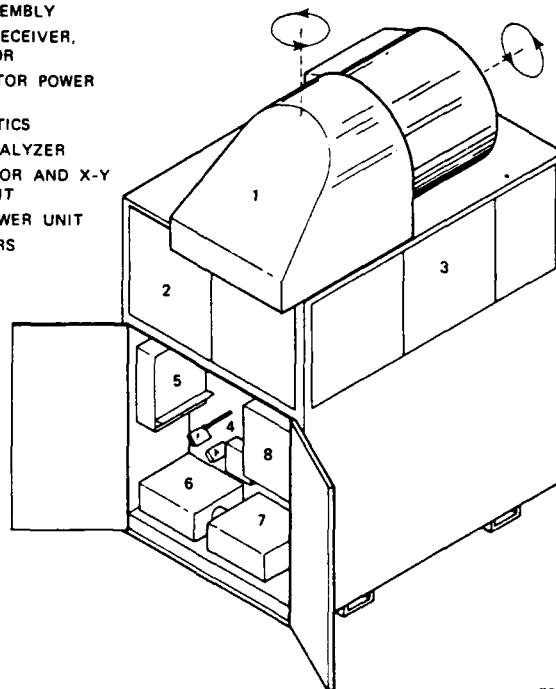
1. SCANNER ASSEMBLY
2. DIAGNOSTIC DISPLAYS
3. SCANNER CONTROL
4. SYSTEM CONTROL
5. STATUS PANEL
6. DATA ACQUISITION AND PROCESSING
7. DETECTOR
8. LASER ACCESS DOORS
9. GRATING TUNER ASSEMBLIES



EO041

FIGURE 3 LASER ACCESS END OF LIDAR PACKAGE

1. SCANNER ASSEMBLY
2. TELESCOPE, RECEIVER, AND DETECTOR
3. SCANNER MOTOR POWER SUPPLIES
4. TRANSMIT OPTICS
5. SPECTRUM ANALYZER
6. POWER MONITOR AND X-Y ERROR CIRCUIT
7. DETECTOR POWER UNIT
8. PULSE CLIPPERS



EO041

FIGURE 4 TRANSMIT AND RECEIVE END OF LIDAR PACKAGE

DIAL-LIDAR SYSTEM FOR REMOTE AND SELECTIVE DETECTION
OF NATURAL GAS LEAKS USING A FREQUENCY-MIXED CO₂ LASER
Jan E. van der Laan, William Evans, and Joseph Leonelli
SRI International

333 Ravenswood Avenue, Menlo Park, California 94025
and

L. L. Altpeter
Gas Research Institute
8600 Bryn Mawr Avenue
Chicago, Illinois 60631

Abstract

This paper describes a compact CO₂ laser DIAL system for the selective detection of natural gas. Using a novel frequency-mixing technique and nonlinear crystals, the sensor operates in the primary 3-micron band where unique hydrocarbon absorption signatures exist. By careful selection of mixing frequencies, specific hydrocarbons can be selectively detected or discriminated. In many applications, detecting a specific constituent of a gas, effectively and unambiguously identifies the gas itself.

Background

Improved detection of natural gas leaks is of interest to the gas industry. At present, gas survey trucks sample the air at the street surface. The air is then fed through a flame ionization detector (FID) to detect methane that may have leaked from a gas line below the street. This method is relatively slow, because the truck can move only a few miles per hour, and is limited in that it cannot make remote measurements of areas that are inaccessible to the truck. Furthermore, the FID reacts to any hydrocarbon in the air, resulting in a high false alarm rate.

SRI has developed a new system for the Gas Research Institute (GRI) to resolve these problems by using laser remote sensing by differential absorption. Instead of detecting methane (the main constituent of natural gas), the new system is designed to selectively detect ethane, which is present in natural gas at levels ranging between 2.8 to 8.4%,¹ but otherwise not part of the natural environment. This significantly reduces the false-alarm problem.

Unfortunately, for the strong absorption of ethane centered at 3.4 microns, there is no significant overlap of existing laser lines. This problem has been overcome by mixing CO₂ laser lines in nonlinear optical crystals to provide a significant number of new lines around 3.4 microns from which wavelengths can be selected for detection of ethane without interference of methane.

The laser remote sensor system is designed for short-range detection from a van. The sensor can look 50 m ahead of the vehicle while scanning across the street for leaks. The scan pattern and a 10-Hz pulsed laser allow speeds of up to 30 miles per hour, thereby greatly decreasing the time and expense required for surveying. A conceptual example of gas leak detection in an urban area is shown in Figure 1.

System Description

The design and development details of this system were presented at the 1985 Optical Society of America topical meeting on remote sensing of the atmosphere at Incline Village, Nevada.² Therefore, only a brief review of the design will be presented before describing the system. The block diagram shown in Figure 2 illustrates the major components of the system, which is based on the differential absorption lidar (DIAL) technique. The DIAL technique uses two closely spaced laser wavelengths for vapor detection: a strongly absorbed line and a nonabsorbed or weakly absorbed line in the IR vapor spectrum of interest. The two wavelengths are transmitted nearly simultaneously so that the laser beams pass through the same atmospheric path and are reflected by the same target while the vehicle is moving. If the laser beams pass through a gas concentration, as illustrated in Figure 2, the absorbed line signal will be received with much less intensity than the nonabsorbed signal. The amount of difference in signal can be processed to determine the concentration of gas over a given pathlength.

The basic DIAL principle is straightforward if the choice of wavelengths were unlimited; however, as indicated above, sources of laser lines in the 3-micron hydrocarbon band are very limited. The approach used in the development of the GRI sensor is an SRI-patented technique that mixes the outputs from two mini-TEA CO₂ lasers in nonlinear optical crystals to produce radiation at the selected wavelength in the 3.4-micron band. The frequency mixing is illustrated in Figure 2 by the top two lasers. The first laser output, ω_1 , is frequency doubled in a AgGaSe₂ second-harmonic generation (SHG) crystal to produce $2\omega_1$. This SHG signal is then combined with the second laser output, ω_2 , at the input to a

AgGaSe₂ summing (SUM) crystal. The output of the SUM crystal, $2\omega_1 + \omega_2$, is the desired high-absorption line for the detection of ethane. The nonabsorbed line is generated by straight frequency-tripling of the third laser output, ω_3 , using a AgGaSe₂ SHG and a AgGaSe₂ SUM crystal. The two converted frequencies, $2\omega_1 + \omega_2$ and $3\omega_3$, are then combined and transmitted as illustrated.

Figure 3 is a diagram of the nonlinear optics and beam-combining assembly used in the GRI sensor. The same nonlinear mixing and beam-combining functions described above apply to this assembly. It should be noted, however, that beam combining is accomplished using polarization techniques, so a knowledge of the polarization states is required to fully understand the beam-combining and mixing operations. The nonlinear assembly is mounted to a framework of six invar rods that also support the three mini-TEA lasers. This transmitter package, plus the receiving telescope and receiver, is housed in one of three modules, the sensor head module is shown in Figure 4. The other two modules are the support rack, which contains the processing unit, laser interface unit, and laser high-voltage power supply, and the remote control and display module. A photograph of the sensor head mounted on its scanning platform is shown in Figure 5. A dust-cover lid covers the coaxial transmit and receiver aperture, which is the larger of the two apertures shown. The smaller aperture is for a TV camera boresighted with the laser beam. Figure 6 is a photograph of the entire GRI sensor system.

Since the GRI sensor is to be used in mobile operations the operator must have a convenient real-time display. Figure 7 is an example of the GRI sensor operator display. The TV display is boresighted so that the center of the display is aligned with the zone being interrogated by the laser beam. At the bottom of the video display is a readout of the processed concentration in ppm-m units. This readout is updated at a slower rate (1 Hz) than the data being collected (10 Hz) so that the operator can read the display. A bar graph on the right side of the display presents a color-coded display of the concentration that is updated at the sample rate. If the measured concentration is below the operator-set alarm threshold, the display will be in green. When a gas concentration is detected that is above the threshold, an audio alarm is sounded and the bar graph indication above the threshold will be displayed in red. Range to target and time are also displayed so that a VCR record can be made, which will relate the visual display to digitally stored data.

Test and Evaluation

SRI is currently in the system evaluation phase of the program and performing calibration tests of the system. The diagram in Figure 8 shows two experiments designed to (1) determine the detection limits of the system and (2) demonstrate the capability of the sensor to discriminate between ethane and methane. Photographs of the actual tests being performed are shown in Figures 9 and 10. An example of the methane discrimination test data is shown in Figure 11, which is a strip-chart type presentation of the time-sequence test. With time running left to right, a calibrated gas mix consisting of 12% ethane and 88% methane was injected into the sample chamber at a specific flow rate for 1 second. The sample chamber was then pumped out with a vacuum pump until the absorbed line signal level returned to the level observed prior to the gas injection. At that time, the second calibrated gas concentration (6% ethane/94% methane) was injected into the sample chamber and then evacuated as was the first injection. This same sequence was followed by a 1% ethane/99% methane gas mix and a pure (100%) methane gas injection. The data shown in Figure 11 for the absorbed line (2997 cm^{-1}) clearly demonstrate the capability of the selected laser line to detect ethane and discriminate to methane. The reference line also demonstrates the discrimination to methane, but it also indicates that there is some absorption to ethane. This is due to a small absorption coefficient ($4\text{ atm} \cdot \text{cm}^{-1}$) on this line. This will reduce the differential absorption coefficient between the two lines to $14\text{ atm} \cdot \text{cm}^{-1}$ for DIAL measurements, but otherwise will not affect operations.

The detection sensitivity goal for ethane is 2.3 ppm-m. Assuming an ethane gas concentration of 2.8 to 8.4 percent, this will correspond to a natural gas leak detection sensitivity of approximately 25 to 80 ppm-m. This detection limit can be achieved, assuming the system noise levels are such that the measurement-limiting noise mechanism is due to speckle noise in the received signal.³ It should be mentioned that DIAL remote detection measurement units (ppm-m) are not directly comparable to FID measurements (ppm) for many reasons. However, it has been estimated from earlier SRI investigations⁴ that a DIAL system sensitivity between 15 to 30 ppm-m will be required to provide similar probability of detection statistics as the mobile FID. This observation was based on comparison tests with simulated gas leaks between a mobile FID unit and the breadboard system. The comparison does not take into consideration the increased capabilities of a mobile DIAL remote sensor or other operational modes of the system that can improve the sensitivity (i.e., integration mode). The currently observed sensitivity of the GRI sensor is about a factor of ten higher than the desired goal ($\approx 35\text{ ppm-m}$). This indicates that a noise function in the system, rather than speckle, is currently limiting the sensitivity. This problem is expected to be resolved in the near future.

Summary and Conclusions

In summary, a compact CO₂ DIAL remote sensor system that uses frequency mixing with nonlinear crystals has been developed for natural gas pipeline leak detection. The sensor has demonstrated its ability to selectively detect ethane, which is present in the environment only in natural gas. This has the potential of greatly reducing the false-alarm problems caused by other hydrocarbons using today's FID technology. In addition to the reduced false-alarm rate, the remote sensor is much faster, can interrogate areas not accessible to a mobile FID, and can be extended to many applications, including airborne measurements.

References

1. "Fuel Gas Engineering Practices," Gas Engineers' Handbook, First Edition, Industrial Press, Inc., Section 2, page 10 (1965).
2. "Optical Remote Sensing of the Atmosphere," Technical Digest, p. WC27-1, (January 15-18, 1985).
3. Leonelli, J. and J. van der Laan, "Development of Improved Detection for Natural Gas," GRI Monthly Report, SRI Project 4492, SRI International, Menlo Park, CA (15 July 1985).
4. Hawley, J., "Development of a Van-Portable Remote Sensing Laser System for Selective Detection of Natural Gas," GRI Monthly Report, SRI Project 4492, SRI International, Menlo Park, CA (May 1985).

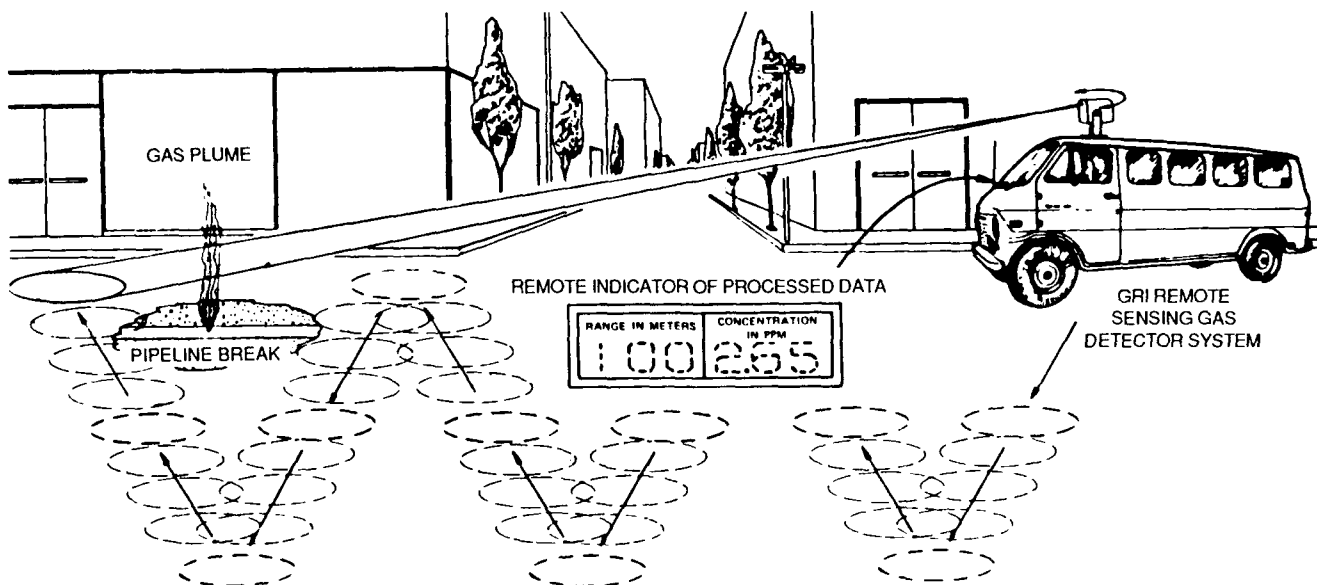


FIGURE 1 EXAMPLE OF GAS LEAK DETECTION IN AN URBAN AREA

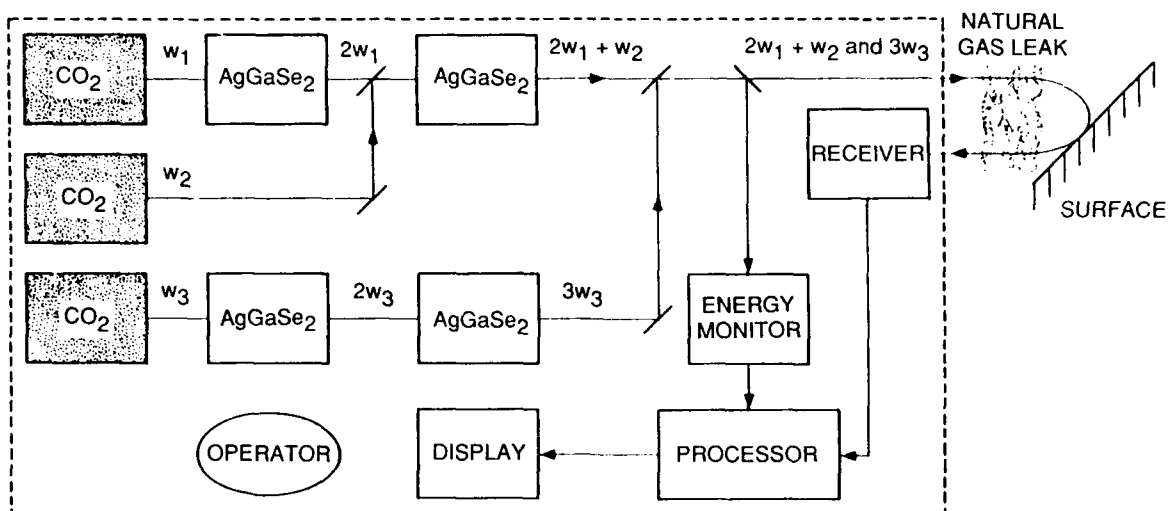


FIGURE 2 BLOCK DIAGRAM OF NATURAL GAS LEAK REMOTE DETECTION SYSTEM

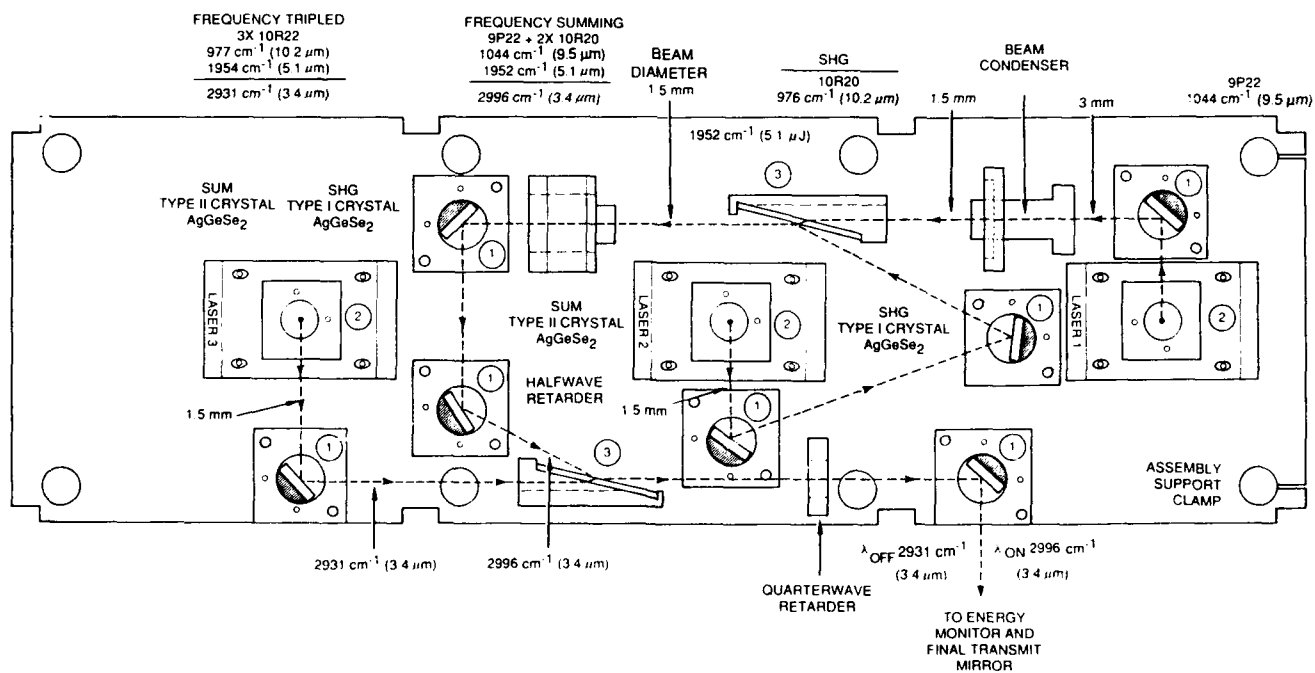


FIGURE 3 NONLINEAR OPTICS AND BEAM ASSEMBLY

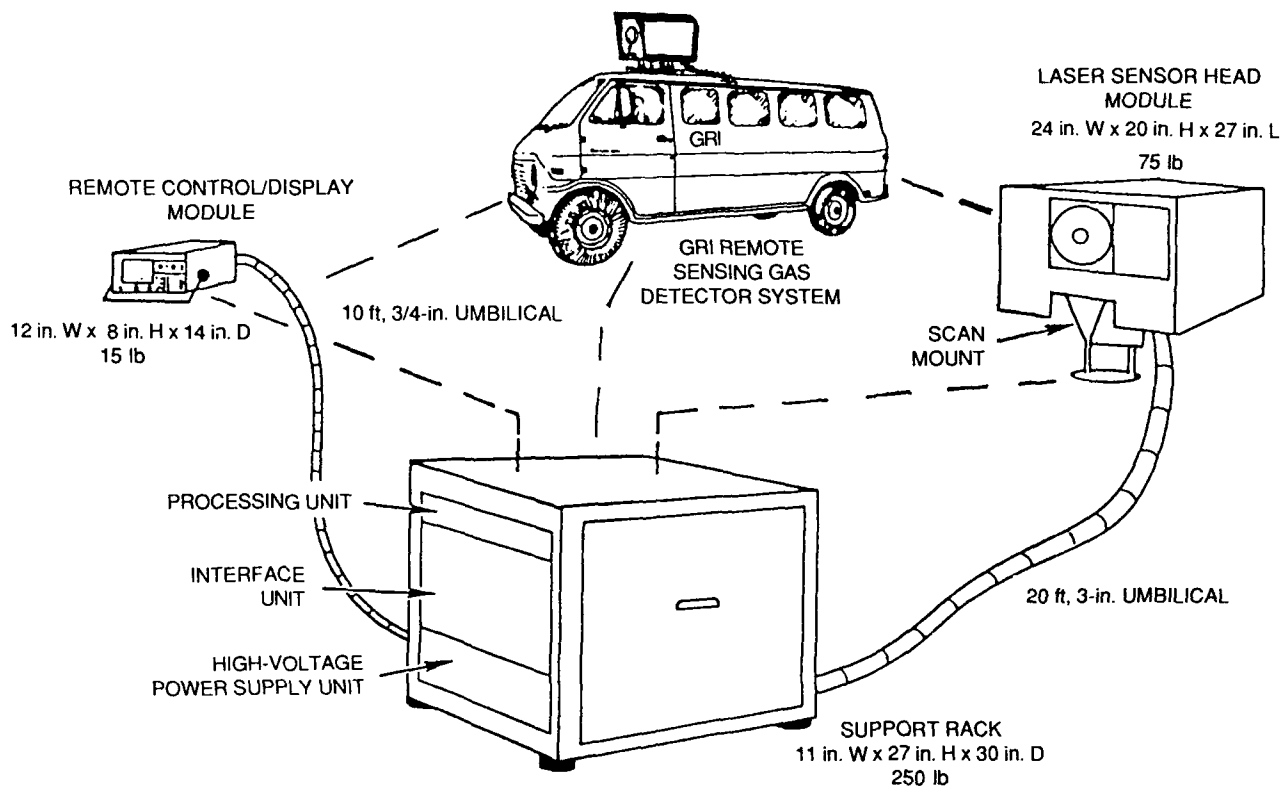


FIGURE 4 LASER REMOTE SENSOR

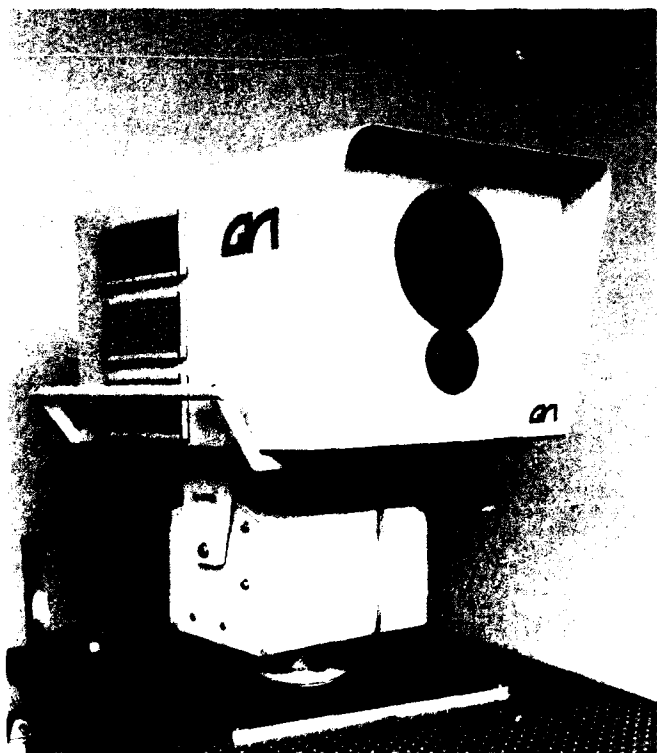


FIGURE 5 GRI SENSOR HEAD MODULE

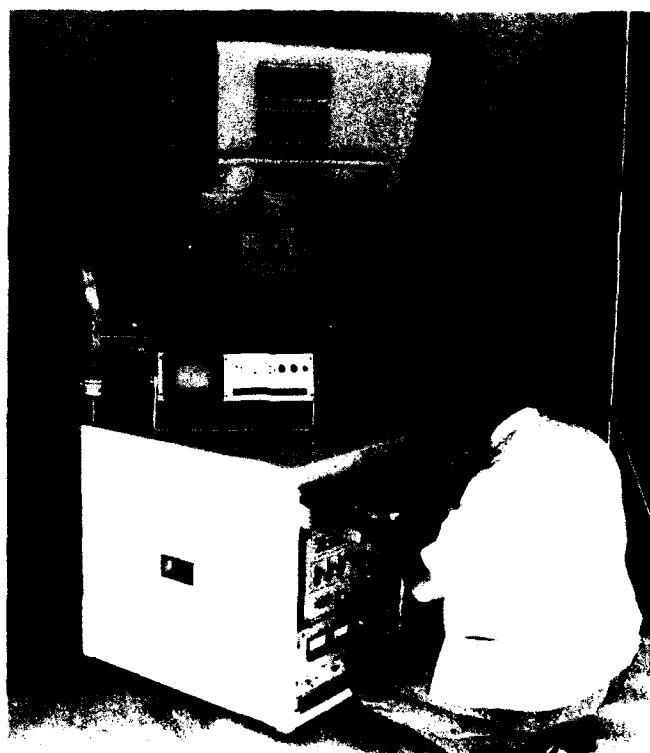


FIGURE 6 GRI SENSOR SYSTEM

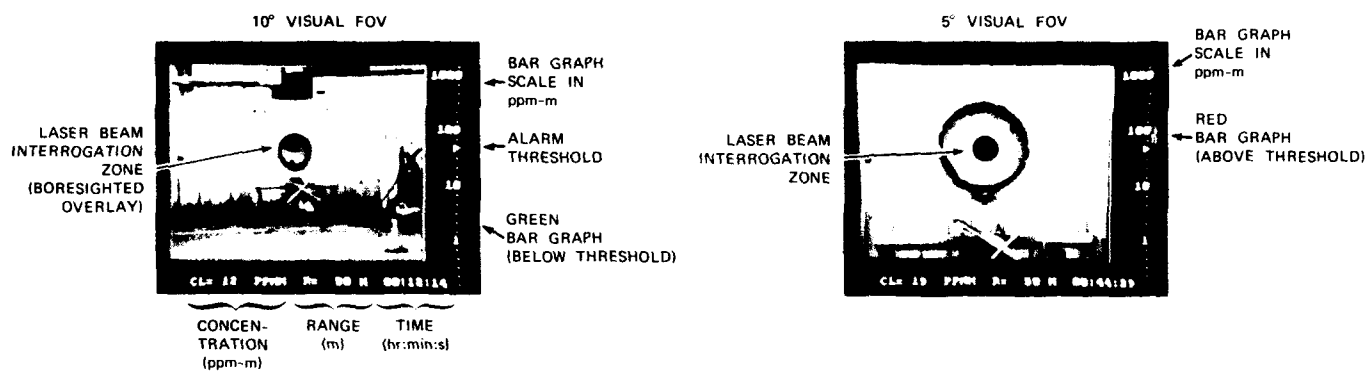


FIGURE 7 GRI SENSOR OPERATOR DISPLAY

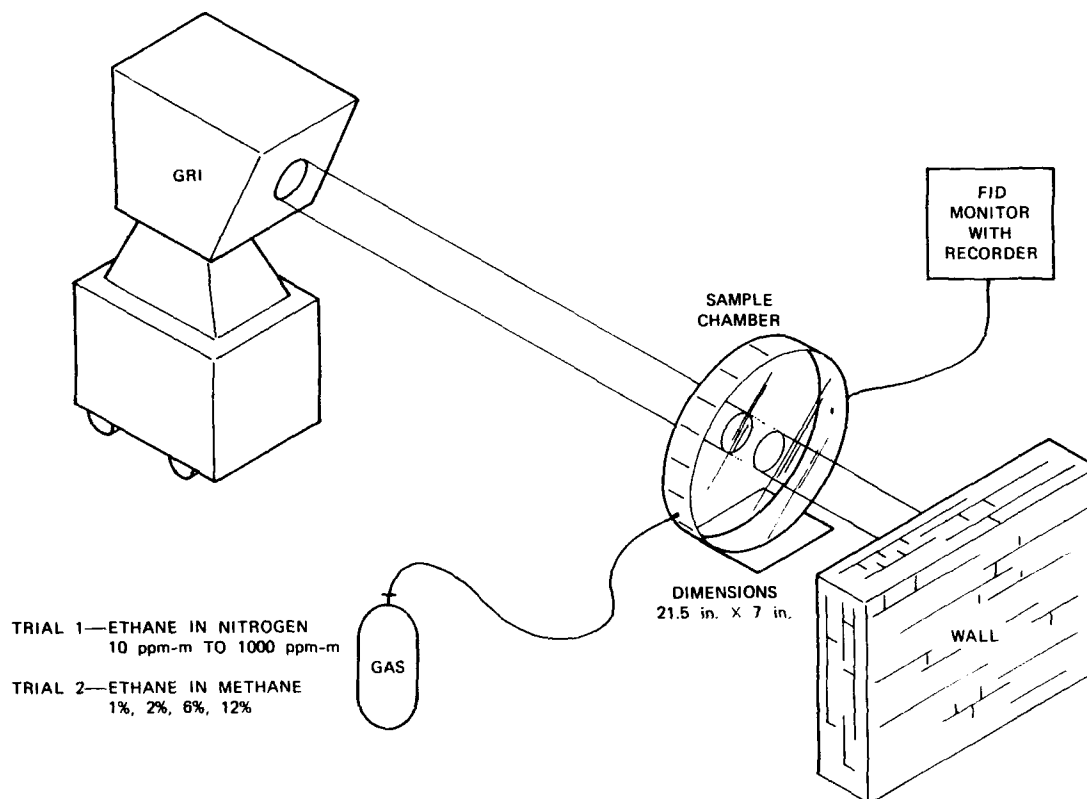


FIGURE 8 CONCENTRATION MEASUREMENT EXPERIMENT



FIGURE 9 CALIBRATION TEST RANGE (EXPERIMENT IN PROGRESS)

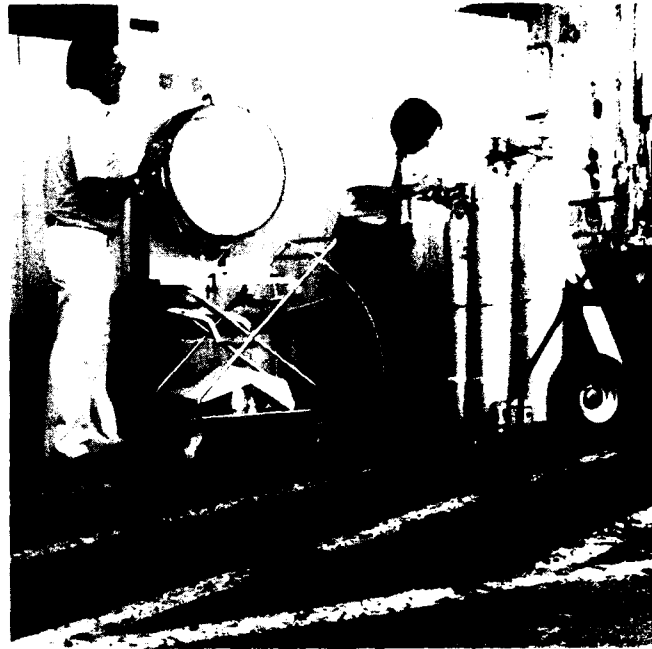


FIGURE 10 TEST RANGE SAMPLE CHAMBER (GAS FLOW CALIBRATION IN PROGRESS)

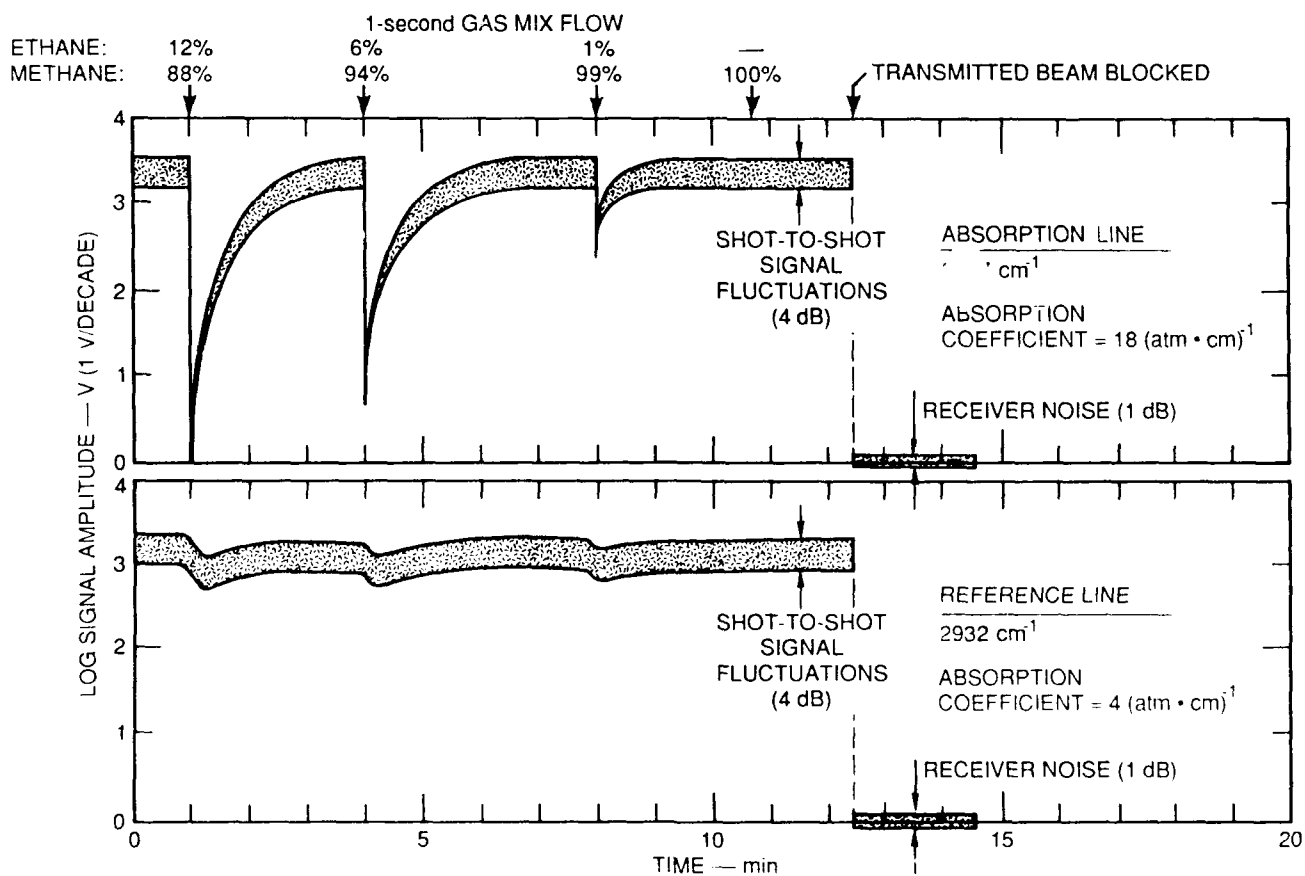


FIGURE 11 METHANE DISCRIMINATION TEST (RAW RECEIVER SIGNAL DATA)

LOW-PRESSURE GAIN CELL LASER DETECTOR OPERATION
WITH A CO₂ TRANSVERSELY EXCITED ATMOSPHERIC (TEA) LASER
Jan E. van der Laan, Russell Warren, Johnny Jones
SRI International
333 Ravenswood Avenue, Menlo Park, California 94025

Abstract

Operation of a low-pressure CO₂ gain cell is evaluated experimentally using an unmodified CO₂ mini TEA laser. Optical gains as high as 300 were observed.

Background

Recent developments using a low-pressure gain cell as an optical amplifier in laser radar (lidar) receiver applications have stimulated renewed interest in the technique. The concept of using an optical amplifier in a receiver (as illustrated in Figure 1) is not new, but early work in this area was not encouraging. A gain factor of only 2.5 observed in 1977 by Lotspeich¹ employing a 72-cm-long gain cell did not justify the added cost and complexity to lidar systems, so interest in the technique declined.

In 1985, Pulse Systems, Inc. (PSI) introduced the LDP-30, a transversely excited low-pressure gain cell amplifier, and advertised it as a laser detector preamplifier for range-finder and lidar applications. Typical gains of the order of 1000 for pulse durations of 100 microseconds were reported² for LDP-30 operating at 30 torr. A functional diagram of the LDP-30 is shown in Figure 2. The improvement in gain over previous work is attributed to the longer overall gain pathlength (280 cm) of the 7-pass 40-cm cell and the uniform transverse discharge medium. In addition, the gains observed by PSI were achieved using a low-pressure laser source in the evaluation which has a laser linewidth equal to the LDP-30 gain linewidth. The earlier work was performed using a conventional multimode longitudinal-discharge laser, which has a laser line width that is much broader than the gain cell gain linewidth. The implication of this latter fact is that the power in the laser output that is outside the gain bandwidth (in the frequency domain) of the gain cell is not amplified, although the gain measurements were made relative to the laser total spectral power output.

Recent work by Chan and Bufton³ evaluated the LDP-30 using a modified CO₂ TEA laser that utilized a low-pressure gain cell inside the laser cavity. The purpose of the intra-cavity low-pressure cell was to match the laser output linewidth to the LDP-30. The reason for limiting the TEA laser spectral linewidth is discussed in more detail later in this paper. Gains in excess of 200 were observed using this hybrid CO₂ TEA laser, including a factor of four optical insertion loss in the test setup.

The evaluation presented in this paper differs from the above studies in that a standard atmospheric-pressure-broadened CO₂ TEA laser is used to characterize the low-pressure gain cell amplifier. The purpose of this work was to determine what improvement, if any, can be achieved using a low-pressure gain cell amplifier with an unmodified CO₂ TEA laser.

Evaluation

To understand the difference between our measurements and those conducted by other researchers, it is necessary to review two characteristics of the low-pressure and atmospheric-pressure laser operation: (1) the temporal gain distribution and (2) the gain bandwidth. Figure 3 is an example of the temporal gain distribution of a low-pressure gain cell, which is similar to the gain distribution in a low-pressure laser. Note that a significant gain (> 50%) extends over several hundred microseconds in time. This is very desirable in receiver optical amplifier applications where it is now known at what time or range the signal to be amplified will be received. On the other hand, in a laser application, this long gain period results in a very long laser pulsewidth. The long pulsewidth of low-pressure lasers generally precludes its use in many lidar applications, unless some means to limit the pulse width is employed. While several techniques are available to reduce the pulse width, all add complexity to the system and reduce the output power.

The hybrid CO₂ TEA laser mentioned above is actually an example of one technique used to reduce the pulsewidth. Operating at atmospheric pressure, the TEA laser has a very short temporal gain characteristic which produces a pulsewidth of less than a few hundred nanoseconds. To help visualize this difference in pulsewidth, one can consider the width of the time marks shown in Figure 3 to be a fair representation of the TEA laser pulsewidth. Unfortunately, for the laser case, the pressure effect that reduces the temporal gain has the opposite effect on the radiation bandwidth. This is illustrated in Figure 4, which shows the gain bandwidth difference between a 20-torr CO₂ plasma and a pressure-broadened TEA laser (760 torr) plasma. Observing the gain bandwidth of the two gain mediums, it is not difficult to understand why a bandwidth-limiting modification seems necessary to achieve high gains, since only the frequencies within the gain bandwidth of the 20-torr curve will be amplified. In our investigation we operated the gain cell at a higher pressure (80 torr) to increase the gain bandwidth so that a larger amount of the TEA laser spectrum would be amplified. Figure 5 shows that the gain bandwidth is increased to about 500 MHz at 80 torr. This is still only about 15% of the bandwidth of the TEA laser, which suggests that the net gain we should expect will still be significantly lower than those reported previously, where efforts were made to match the linewidths of the laser to the gain cell.

Figure 6 is a functional diagram of the test configuration we used to characterize the gain cell operation. First, a linearity test was made to verify that the measurements were being conducted in a linear range of the amplifier. Results of this test are shown in Figure 7 which clearly indicates that, for signal levels below 30 mJ, that linear operation is achieved.

The second test was designed to measure the temporal gain distribution of the gain cell. The measurement was made by recording the relative gain as a function of laser firing time with respect to the firing time of the gain cell. The results of this test are shown in Figure 8 which also shows the gain profile of the 20-torr amplifier for comparison. Again, the pressure effect on the temporal gain is clearly observed.

The third test was the gain measurement, which was conducted by first measuring the attenuated laser beam through the gain cell with the gain cell off and then with the gain cell on. To achieve the highest gain, the laser timing was delayed with respect to the gain cell firing so that the laser signal passed through the cell at the peak of the gain cell temporal gain profile. Photographic results of one test are shown in Figure 9, which clearly demonstrates the amplifier off/on conditions. The peak amplitude in this test corresponded to an energy gain measurement of 200. This result was surprisingly higher than we had anticipated based on the comparison between gain bandwidths discussed earlier.

To resolve this apparent anomaly, we performed an analysis of the laser configuration that provides the most probable explanation for the high gains observed. The mini-TEA laser used in our test operates in the TEM₀₀ mode, but the laser does support a number of axial modes. Axial mode beating during the laser pulse will affect the distribution of spectral power over the TEA laser 3- to 4-GHz gain bandwidth. As a result of this axial mode interaction, the spectral power is redistributed over the full gain envelope into a comb of seven lines, each having a FWHM gain of approximately 50 MHz as illustrated in Figure 10. By adjusting the TEA laser cavity length, the comb of laser lines can be shifted so that the peak axial mode is centered on the gain cell bandwidth as shown. When aligned in this manner, the axial mode that lies within the gain cell gain spectrum will be amplified the maximum amount achievable. However, since our gain reference is based on total laser output (i.e., all modes), the net gain will be reduced by the percent of total energy contained in the unamplified axial modes. Nevertheless, the net gain due to the axial mode redistribution of spectral power is significantly higher than it would be if the spectral power were evenly distributed under the atmospheric gain envelope. The gain measurements were made on the 10-micron R-22 laser transition. Each laser line transition throughout the CO₂ laser spectrum will have a similar spectral line power distribution centered around the transition center frequency.

It should also be noted that the high gains observed in our evaluations cannot be fully appreciated using our current TEA laser system because of stability problems. Pulse-to-pulse frequency shifts of the axial mode relative to the gain-cell center frequency result in fluctuations in the gain, which can be observed in Figure 9 where 10 shots are overlayed. This gain fluctuation in our setup is currently the noise-limiting mechanism rather than background or spontaneous emission noise. No attempt was made to stabilize our laser.

Summary

In summary, optical amplification gains as high as 300 were observed using a standard mini-TEA laser source with a low-pressure gain cell optical amplifier. The high gains observed are attributed to the reasonably good match in gain bandwidth between the low-pressure optical amplifier and axial modes of the TEA laser. These results indicate that a standard CO₂ mini-TEA laser configuration can be used with a low-pressure optical amplifier in lidar applications if the axial modes can be stabilized.

References

1. James F. Lotspeich, "CO₂ Laser Preamplifier Capabilities for Low-Level 10.6- μ m Direct-Detection Receivers," IEEE Journal of Quantum Electronics, Vol. QE-13, No. 6., June 1977.
2. Richard Cunningham, "Gain Cell Boost Range of CO₂ Lidar," Laser and Applications, September 1983. (Reports on work by Ed McLellan of Pulse Systems, Inc.).
3. Kinpui Chan and Jack L. Bufton, "CO₂ Laser Preamplifier for Lidar Application," Laser and Optical Remote Sensing: Instrumentation and Techniques, Technical Digest Series, Volume 18, 1987.

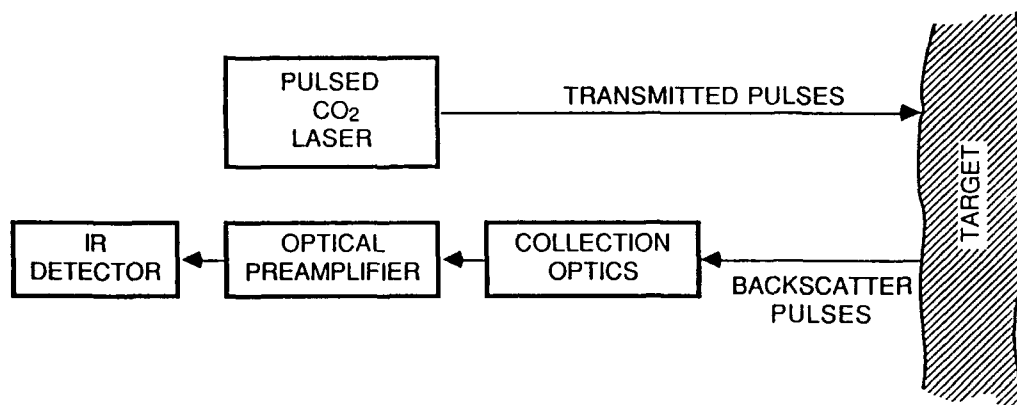


FIGURE 1 CO₂ LIDAR SYSTEM BLOCK DIAGRAM

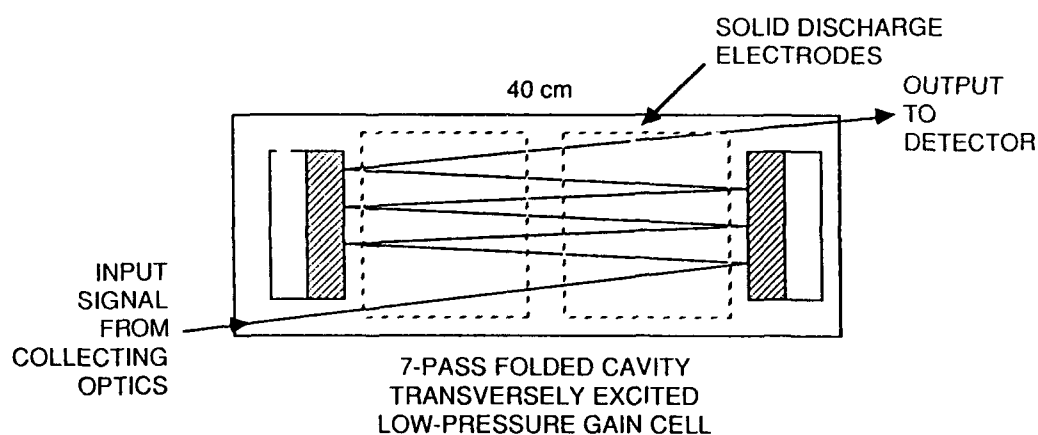


FIGURE 2 PSI/LDP-30 LASER DETECTOR PREAMPLIFIER

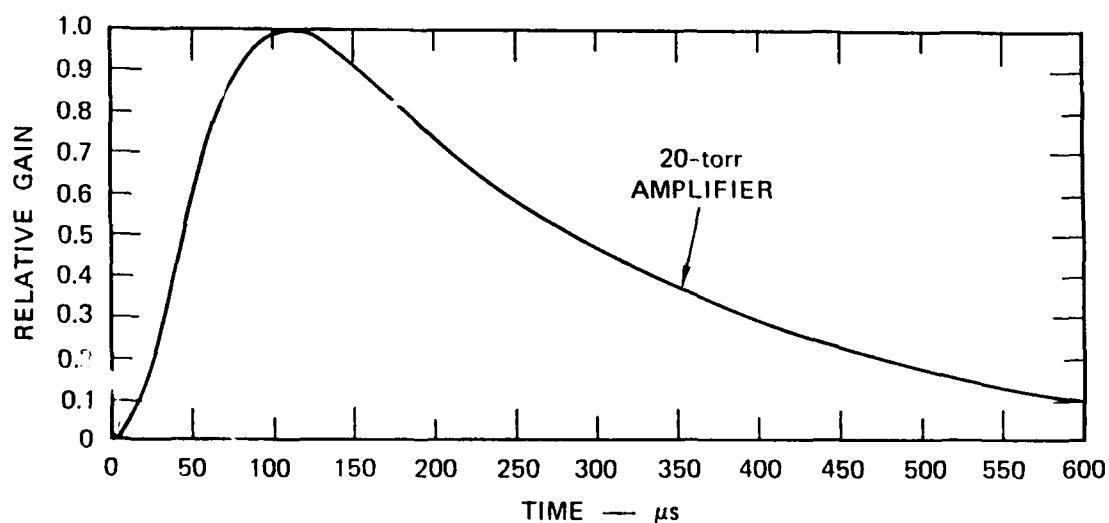


FIGURE 3 LOW-PRESSURE AMPLIFIER TEMPORAL GAIN DISTRIBUTION

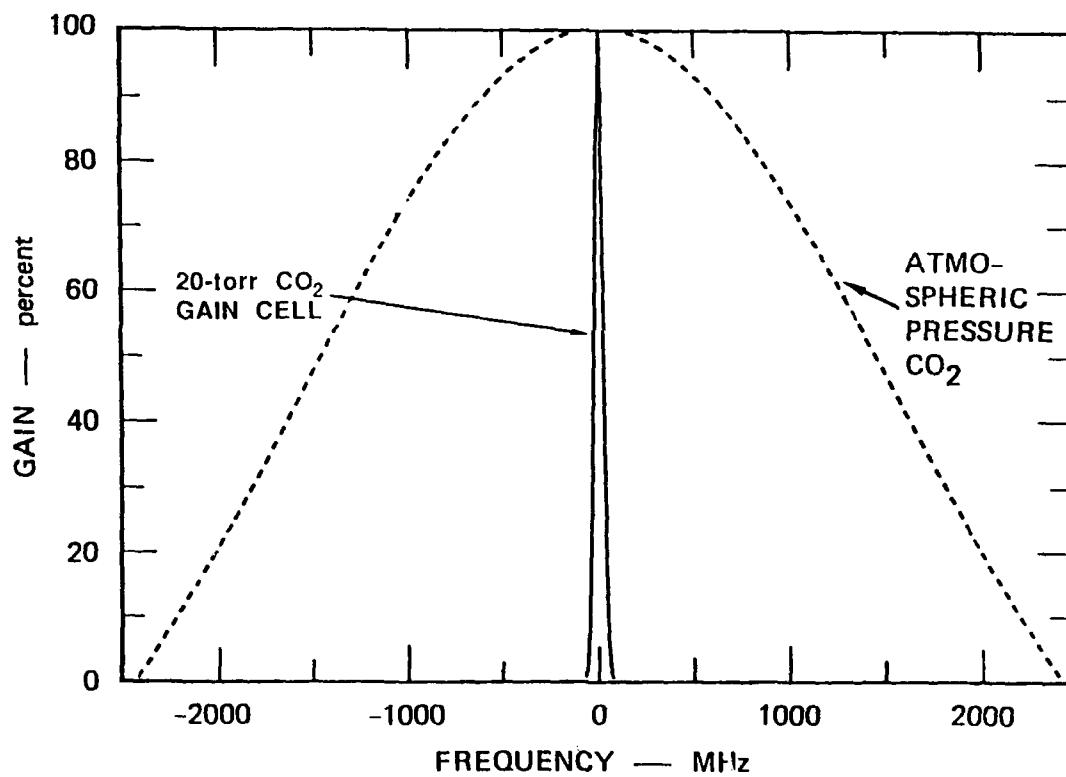


FIGURE 4 20-TORR AND ATMOSPHERIC PRESSURE CO₂ PLASMA GAIN BANDWIDTHS

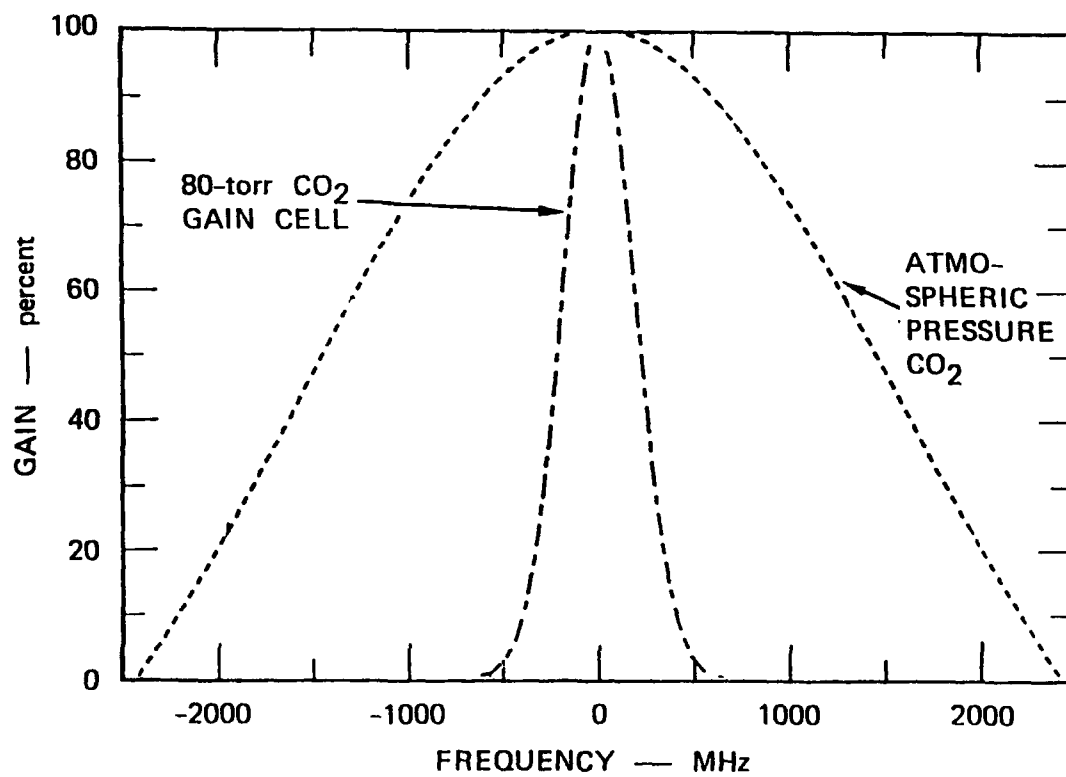
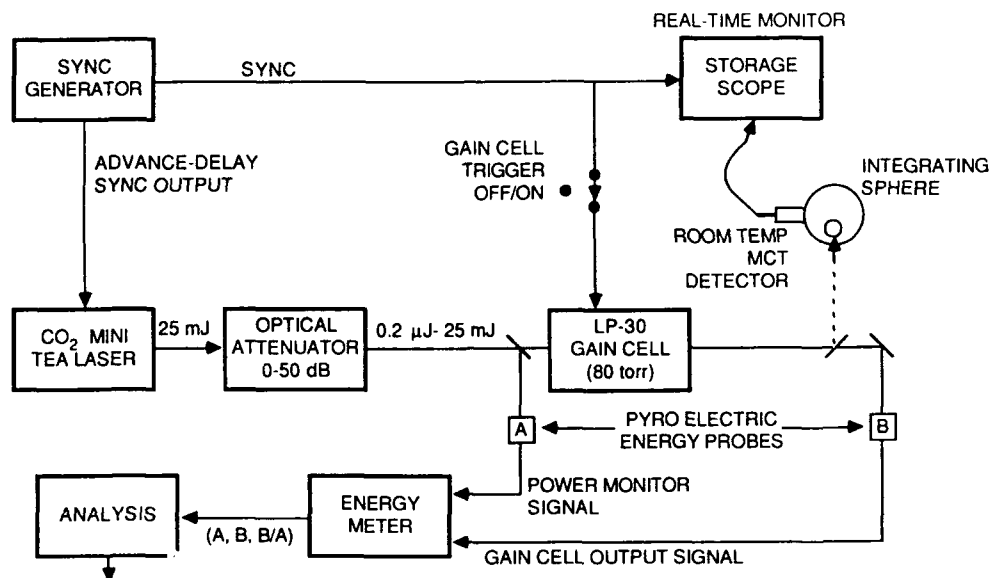


FIGURE 5 80-TORR AND ATMOSPHERIC PRESSURE CO₂ PLASMA GAIN BANDWIDTHS



1. AMPLIFIER LINEARITY -- AMPLIFIER (GAIN CELL) OUTPUT ENERGY (B) AS A FUNCTION OF INPUT ENERGY (A)
2. TEMPORAL GAIN DISTRIBUTION -- NORMALIZED ENERGY (B/A) AS A FUNCTION OF LASER TIMING RELATIVE TO GAIN CELL DISCHARGE.
3. GAIN MEASUREMENTS -- NORMALIZED ENERGY (B/A) WITH GAIN CELL TRIGGERED (ON) RELATIVE TO GAIN CELL NOT TRIGGERED (OFF).

FIGURE 6 MEASUREMENT CONFIGURATION

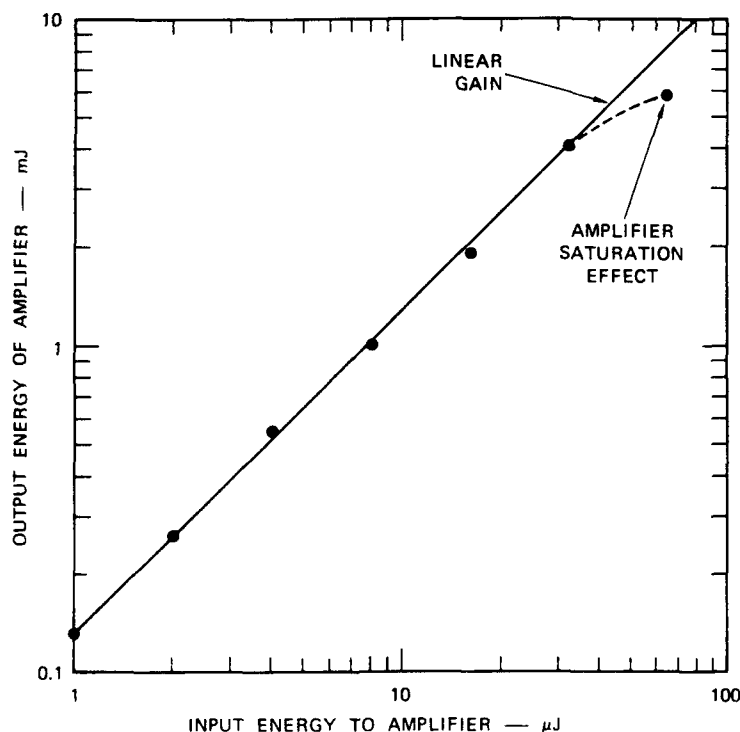


FIGURE 7 AMPLIFIER OUTPUT vs INPUT ENERGY SHOWING SATURATION EFFECT

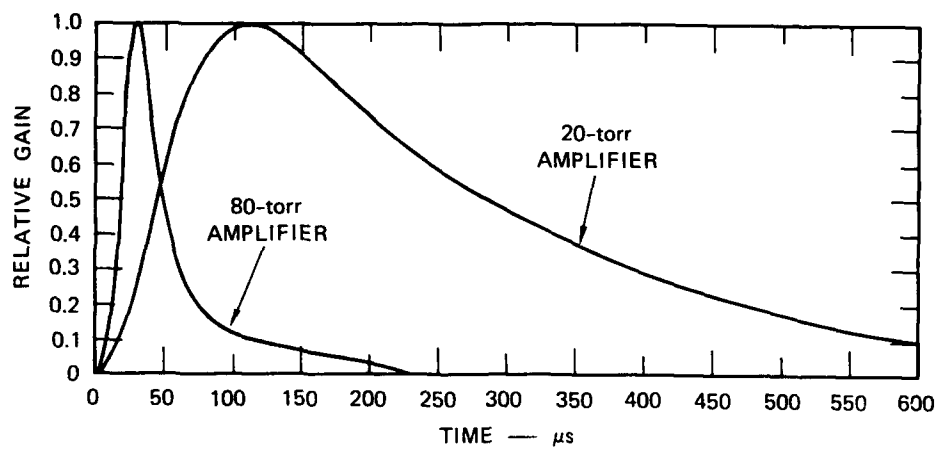
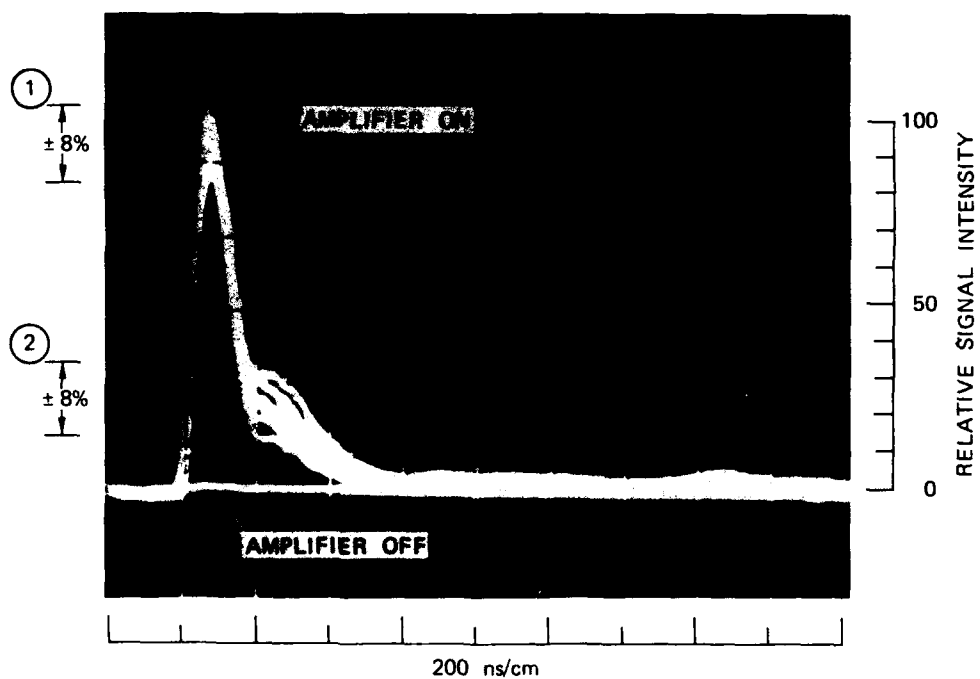


FIGURE 8 LOW-PRESSURE AMPLIFIER TEMPORAL GAIN DISTRIBUTIONS



NOTE: (1) FLUCTUATION IN PEAK INTENSITY
(2) FLUCTUATION IN NITROGEN TAIL INTENSITY

FIGURE 9 AMPLIFIER ON vs AMPLIFIER OFF SIGNAL INTENSITY—10 SHOTS OVERLAYED

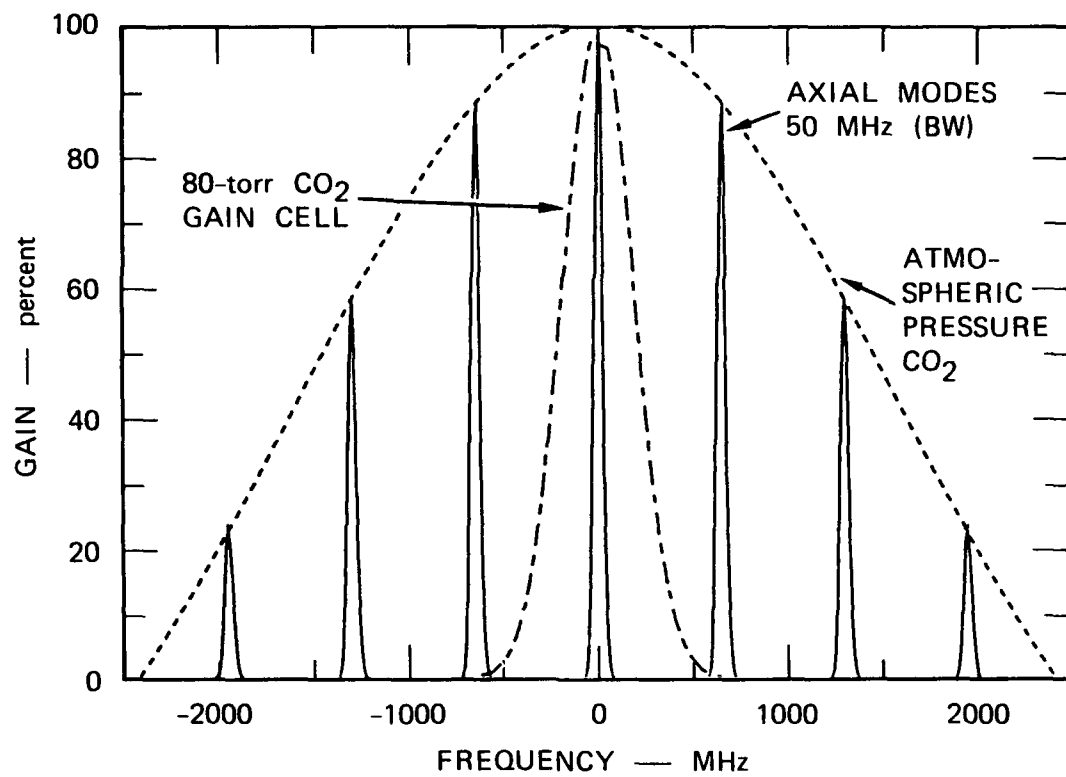


FIGURE 10 AXIAL MODES SUPERIMPOSED ON CO₂ PLASMA GAIN BANDWIDTHS

HIGH-SENSITIVITY REMOTE LASER SPECTROSCOPY USING BEHAVIOR OF NONLINEAR OPTICAL SYSTEMS IN THE VICINITY OF CRITICAL POINTS

A. P. Godlevskii, E. P. Gordov, A. Z. Fazliev, A. I. Zhiliba, V. E. Zuev, P. P. Sharin
The Institute of Atmospheric Optics, Siberian Branch
USSR Academy of Sciences, Tomsk, 634055, U.S.S.R.

Abstract

The feasibility of enhancing the sensitivity of remote laser spectroscopy using a double-frequency laser-reception lidar system or that based on a parametric oscillator is discussed.

I. Introduction

Using a well-known peculiarity inherent in the behavior of nonlinear optical systems in the vicinity of critical points, namely, the macroscopic effects caused by low external perturbations, the feasibility of increasing the sensitivity of remote laser spectroscopy has been studied.

To this end, the design features of a double-frequency laser-reception lidar system have been examined. Then the laser field behavior under the near-threshold conditions on the competing laser transition and their influence on the field dynamics during the reception of a lidar return at the fundamental frequency have been analyzed. In so doing, the minimum detectable lidar return of the system has been estimated to decrease by a factor of 10 to 100.

Based on the theoretical results, a CO₂ laser-reception gas analyzer operating at 4.3 and 10.6 μm has been developed and used for measuring the absorption coefficient along real atmospheric paths. The experimental data obtained are presented.

The paper also discusses the problem of remote atmospheric sounding by means of the conventional DIAL technique using a parametric laser oscillator as a transceiver. The theoretical analysis shows that, for the parametric oscillation in the neighborhood of the critical point, the field fluctuations are low, which provides enhanced sensitivity of remote laser spectroscopy.

II. Double-Frequency Parametric Laser-Reception Lidar

The use of the lidar return laser-reception technique for remote atmospheric gas analysis was proposed by Godlevsky et al.¹ Theoretical and experimental studies of a parametric laser-reception lidar (PLRL) designed for measuring the absorption coefficient along atmospheric paths were reported in Ref. 2. The lidar system made use of the laser radiation modulated by the oscillations of the output cavity mirror. The structure of the resulting field produced by the intracavity wave mixing of the laser output with the delayed lidar return provided information on the atmospheric absorption.

The feasibility of enhancing the sensitivity of remote gas analysis using a lidar system based on a double-frequency laser is considered. The laser emits on two competing transitions, which allows an operational regime to be chosen where the field in one of the modes is near the critical point, e.g., near threshold. The mode coupling and high sensitivity of the subthreshold mode to external perturbations dramatically increase the responsivity of the entire system. In what follows we present a preliminary theoretical analysis of the laser-reception lidar, describe the experimental set-up including a double-frequency CO₂ laser³ employed both as a transmitter ($\lambda = 4.3$ and $10.6 \mu\text{m}$; the laser transitions R₂₀ and P₂₀) and a detector, and discuss the results obtained from remote sensing of the real atmosphere.

A. Theory

The laser operation on the transitions of the A-type (see Fig. 1) has been analyzed in terms of the conventional semiclassical laser theory.⁴ The adiabatic elimination of the atomic variables and nonlinear term series expansion in the vicinity of the stationary point lead to the following set of coupled equations for the field in the laser cavity.

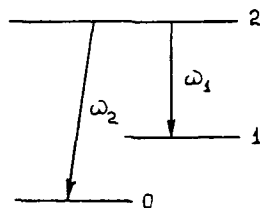


Fig. 1

$$\frac{1}{c} \frac{\partial E_{1,2}^{\pm}}{\partial t} \pm \frac{\partial E_{1,2}^{\pm}}{\partial z} + x_{1,2} E_{1,2}^{\pm} = E_{1,2}^{\pm} \{a_{1,2} (|E_1^+|^2 + |E_1^-|^2) + B_{1,2} (|E_2^+|^2 + |E_2^-|^2)\} \quad (1)$$

Here x_1 and x_2 are the decay constants for the fields within the cavity at the frequencies ω_1 and ω_2 , respectively; and $a, B_{1,2}$ are constants determined from the steady-state solution.

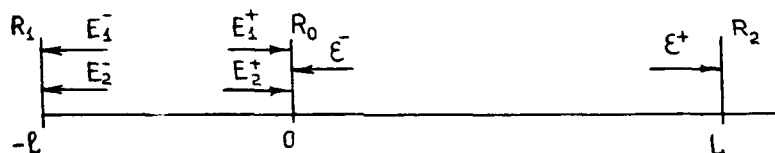


Fig. 2

A schematic diagram of lidar sounding is shown in Fig. 2, where $R_{0,1,2}$ are mirror reflectivities; T_0 is the output mirror transmission factor; l is the laser cavity length; L is the range, i.e., the distance from the natural retroreflector; ϵ^+ and ϵ^- are the probing signal and laser return fields, respectively; $a(t)$ describes the reciprocating motion of the output mirror caused by its oscillations.

The field in the atmosphere satisfies Maxwell equations (the atmospheric absorption is assumed to be linear):

$$\left(\frac{1}{c} \frac{\partial}{\partial t} \pm \frac{\partial}{\partial z} + G \right) \epsilon^{\pm}(z, t) = 0 \quad (2)$$

As seen from Fig. 2, the boundary conditions relating the cavity field with that in the atmosphere are as follows:

$$E_{1,2}^+(-l, t) = R_1 E_{1,2}^-(-l, t) \quad (3)$$

$$E_2^-(0, t) = R_0 E_2^+(0, t) \quad (4)$$

$$E_1^-(a(t), t) = R_0 E_1^+(a(t), t) + T \epsilon^-(a(t), t) \quad (5)$$

$$\epsilon^+(a(t), t) = T E_1^+(a(t), t) + R_0 \epsilon^-(a(t), t) \quad (6)$$

$$\epsilon^-(L, t) = R_2 \epsilon^+(L, t) \quad (7)$$

Equation (2) accounted for in Eq. (5) can be recast in a more manageable form at the rest point of the output mirror:

$$E_1^-(0, t) \cong (1 + 2x_1 a(t)) [R_0 E_1^+(0, t) + R_2 T^2 e^{-2G L} E_1^+(0, t - \frac{2L}{c})] \quad (5^*)$$

Equation (5*) is derived subject to the obvious condition $\dot{a}(t) \ll c$.¹ Eliminating from Eq. (2) the space variables and passing to the real variables r and ϕ for the field: $E = re^{i\phi}$, yield a set of the nonlinear differential equations with the delay term:

$$\begin{aligned} \dot{x}_1(t) + \bar{x}_1 x_1(t) - \frac{cR_1(1-2x_1 a(t))}{\ell} y_1(t) &= c x_1(t) \{a_1[x_1^2(t) + y_1^2(t)] \\ &+ B_1[x_2^2(t) + y_2^2(t)]\} \end{aligned} \quad (8)$$

$$\begin{aligned} \dot{y}_1(t) + \bar{x}_1 y_1(t) - \frac{cR_0(1 + 2x_1 a(t))}{\ell} \{x_1(t) \exp[i(\phi_1^+(0,t) - \phi_1^-(0,t))] - R_2 T^2 x_1(t - \frac{2L}{c}) \\ * \exp[i(\phi_1^+(0,t - \frac{2L}{c}) - \phi_1^-(0,t))]\} &= c y_1(t) \{a_1[x_1^2(t) + y_1^2(t)] + B_1[x_2^2(t) + y_2^2(t)]\} \end{aligned}$$

$$\dot{x}_2 + \bar{x}_2 x_2 - \frac{cR_1}{\ell} y_2 = c x_2 \{a_2(x_1^2 + y_1^2) + B_2(x_2^2 + y_2^2)\} \quad (9)$$

$$\dot{y}_2 + \bar{x}_2 y_2 - \frac{cR_0}{\ell} x_2 = c y_2 \{a_2(x_1^2 + y_1^2) + B_2(x_2^2 + y_2^2)\} \quad (9)$$

$$\left(\frac{1}{c} \frac{\partial}{\partial t} \pm \frac{\partial}{\partial x}\right) \phi_{1,2}^{\pm}(x,t) = 0 \quad (10)$$

where

$$x_{1,2}(t) = r_{1,2}^+(0,t) \quad y_{1,2}(t) = r_{1,2}^-(-\ell,t) \quad \bar{x}_{1,2} = \frac{(1 + x_{1,2} \ell)c}{\ell}$$

Because of the cubic nonlinearity and delayed arguments involved, the set of Eqs. (8)-(10) is intractable for analytic investigation. However, a preliminary analysis of Eqs. (6)-(8) made under certain simplifying assumptions indicates that the lidar sensibility can be increased by establishing the near-threshold conditions for the field E_2 . It is the behavior of the field at the frequency that reflects the lidar return changes caused by the atmospheric absorption at the frequency ω_1 . The analytical estimation shows that the threshold character of laser generation and the nonlinear coupling between the fields E_1 and E_2 within the laser cavity lead to a 10-100 fold decrease of the minimum detectable lidar return of the system as compared to PLRL technique.²

B. Experiment

The experimental program was aimed at the examination of the kinetic characteristics of a CO₂ laser where a lidar return injected into the cavity initiated simultaneous laser action on two competing transitions. The laser sensitivity (SNR) was also measured for a single- and double-frequency operation.

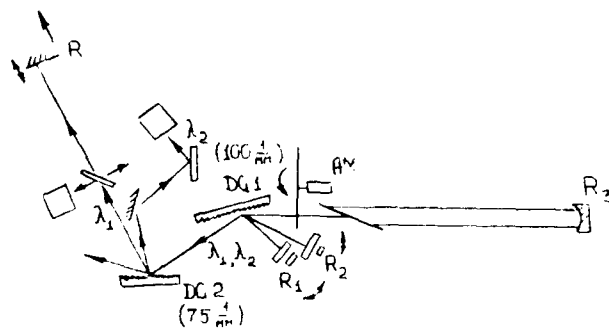


Fig. 3

An optical scheme of the experimental lidar system is shown in Fig. 3. The laser employs a standard sealed-off tube. The laser cavity configuration provides simultaneous lasing at two wavelengths in the bands $00^\circ-1-10^\circ 0$, $00^\circ-02^\circ 0$ within one vibrational branch. The wavelength tuning is made by rotating the mirrors R_1, R_2 around their axes. Fine adjustment is affected by applying a voltage pulse to the electrodes of piezoelectric transducers whereat the mirrors are mounted. CO_2 laser radiation is passed through the zero diffraction order of the grazing-incidence diffraction grating D 1, split up by another grating D 2 set for the second diffraction order, and focused onto the photodetector 2 by means of GaAs semitransmitting plates. The lidar return backscattered by a moving target is phase- and frequency-modulated due to the Doppler effect. NaCl , BaF_2 plates, rough metal surfaces, bricks, trees, etc. were used as retroreflectors.

Figure 4 shows oscillograph traces of the laser kinetics for a single-mode operation. The injected frequency modulation is due to a uniform motion of the brick target (4 and 2 cm/s). A variable component is seen to appear in the laser kinetics curve at a frequency of $\omega = 2(KV)\cos(kv)$, where k and v are the incident wave vector and the linear target velocity, respectively.

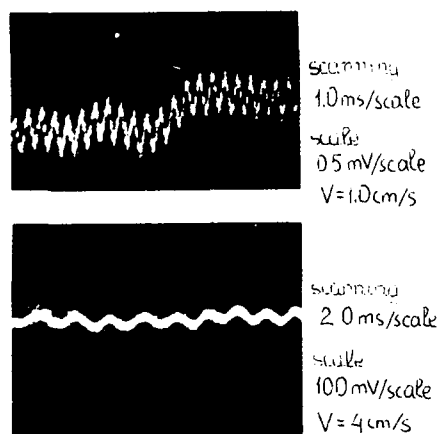


Fig. 4

For a double-wavelength operation on the transitions coupled through a common energy level, any modulation in the laser kinetics at one of the frequencies would be manifested in the kinetics of the other mode. Figure 5 illustrates laser kinetics oscillograms for the lasing on two completing transitions. The phase of the injected signal is changed. It is readily seen that the backscatter frequency is shifted relative to that of the reference beam.

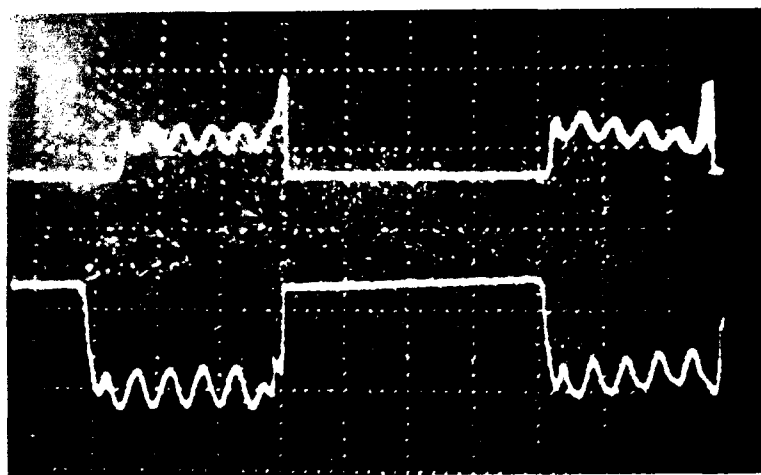


Fig. 5

Figure 6 shows a spectrogram of the double-frequency laser kinetics on the transitions $R(30)_{10}$ and $P(30)_{10}$ coupled via a common lower level. The two pronounced maxima correspond to the frequencies due to the Doppler shift of the carrier light frequencies. The signal in the low-frequency region of the trace is induced by laser noise.

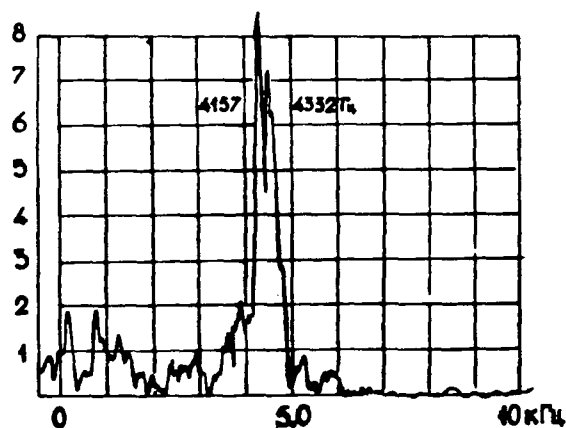


Fig. 6

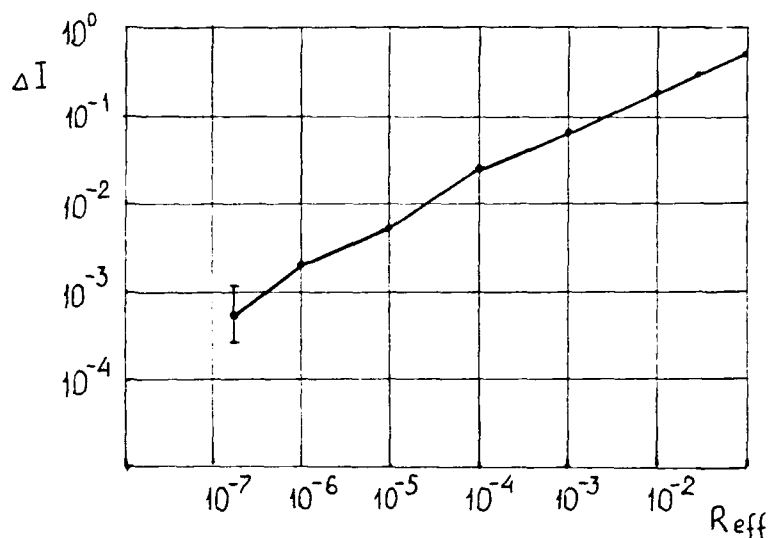


Fig. 7

The variation of the laser sensitivity with the return intensity backscattered into the laser cavity by the illuminated target was studied by means of BaF_2 and NaCl attenuating plates with a known transmission.

Figure 7 depicts the photodetector variable component at the modulation frequency (synchronous detection) as a function of the effective target reflectivity R_{eff} proportional to the lidar return intensity. This relationship is well approximated by the expression $K\sqrt{R_{\text{eff}}}$, where the proportionality factor K depending on the laser regime has the largest value near the lasing threshold. Far below threshold, K shows an appreciable decrease. In the case of interest, $K \sim 200$. For the dual-frequency operation, the laser sensitivity is strongly affected by the intensity ratio on the laser transitions. It is found experimentally that the minimum detectable lidar return of the system is observed to occur for the highest intensity ratio.

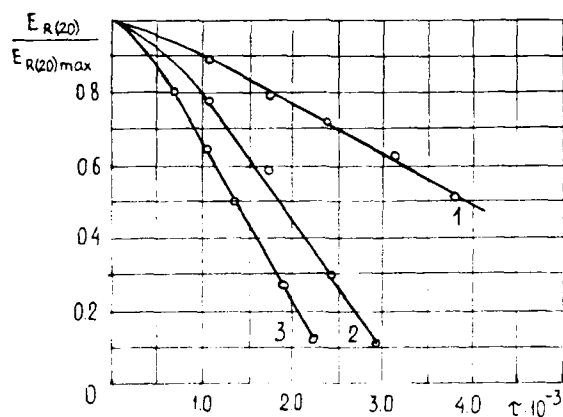


Fig. 8

Figure 8 shows the effect of the optical depth τ on the laser response normalized to its maximum value for $\tau = 0$, $R_{\text{eff}} = 0.3$. Curve 1 represents single-mode laser action on the transition $R(20)_{10}$. Curve 2 illustrates double-wavelength laser operation on the competing transitions $R(20)_{10}$ and $P(20)_{10}$ for the intensity ratio $IR(20)_{10}/IP(20)_{10} = 3$. Curve 3 depicts the same as in Curve 2 for $IR(20)_{10}/IP(20)_{10} = 8$.

III. REMOTE GAS ANALYSIS BASED ON PARAMETRIC LASER OSCILLATIONS

The parametric laser oscillation method and the relevant wavelength-tuning schemes were put forward by Akhmanov and Khokhlov,⁵ Kroll,⁶ and Kingston.⁷ The remote sounding of the atmospheric gas absorption proposed in this work is based on the use of parametric laser oscillators (PLO) and DIAL technique. It can be summarized as follows. The pumping laser output A_{30} at a frequency ω_3 enters PLO cavity (see Fig. 8). Due to the nonlinear interaction between A_{30} and the fluctuating field within the nonlinear crystal, the pumping wave is converted into the modes for which the wave synchronism relation

$$\vec{k}_3 = \vec{k}_1 + \vec{k}_2 \quad (11)$$

is valid.

Under certain conditions to be discussed later there appear light waves at ω_1 and ω_2 . In the general case, ω_1 and ω_2 can be taken to be arbitrary but they are to satisfy the relation $\omega_3 = \omega_1 + \omega_2$. It is of practical interest to consider the situation where ω_3 is tuned in the centre of the absorption band, while ω_1 or ω_2 falls at the absorption edge. After the delay time $t = 2l$ (l is the distance from the probed volume) the return signal reenters PLO, providing high immunity against incoherent background noise, i.e., PLO operates both as a light source and a narrow-band receiver. Simultaneous soundings can be carried out at the three frequencies. The photodetector eventually measures the intensities I^{ω_1} and I^{ω_2} (see Fig. 9). The minimum detectable echo for the experimental outputs I^{ω_1} and I^{ω_2} will be shown to have the lowest value for the parametric laser oscillation slightly above threshold.

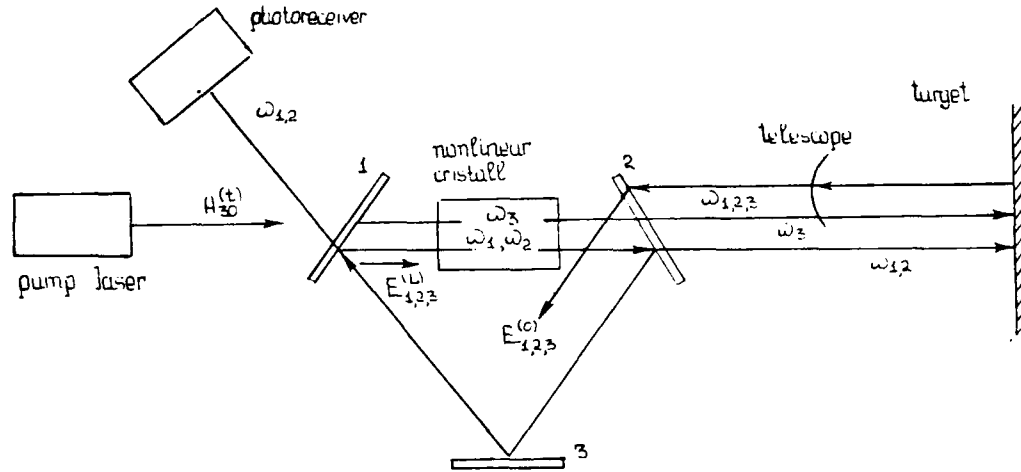


Fig. 9

The proposed method is described by the set of equations of the form

$$\begin{aligned} \dot{A}_1 &= -\gamma_1 A_1 - iG_1[A_3(z_0, t) + E_3]A_2^* + E_1 ; \\ \dot{A}_2 &= -\gamma_2 A_2 - iG_2[A_3(z_0, t) + E_3]A_1^* + E_2 ; \\ \dot{A}_3(z_0, t) &= A_{30}(t) - iG_3 A_1 A_2 z_0^2 / (2L) \end{aligned} \quad (12)$$

The external fields $E_{1,2,3}$ can be expressed in terms of the optical characteristics of the atmospheric path and the parametric laser oscillator to yield:

$$E_1 = \sqrt{1 - R_1^2} \beta_1 e^{-2x_1 l} A_1 ;$$

$$E_2 = \sqrt{1 - R_k^2} \beta_2 e^{-2x_2 l} A_2 ; \quad (13)$$

$$E_3 = \beta_3 e^{-2x_3 l} A_3(z_0, t)$$

where $A_k \sqrt{1 - R_k^2}$ is the probing field; x is the attenuation coefficient along the atmospheric path length l ; R is the target reflection coefficient.

Rearranging r.h.s. of Eq. (12) to rewrite the bifurcation and nonlinear terms in explicit form gives

$$\dot{A}_1 = (-\gamma_1 + \lambda_1) A_1 - i G_1 (1 + \lambda_3) A_{30} A_2^* - \frac{G_1 G_3 z_0^2}{2L} (1 + \lambda_3) |A_2|^2 A_1 ;$$

$$\dot{A}_2 = (-\gamma_2 + \lambda_2) A_2 - i G_2 (1 + \lambda_3) A_{30} A_1^* - \frac{G_2 G_3 z_0^2}{2L} (1 + \lambda_3) |A_1|^2 A_2 ;$$

$$\lambda_k = \beta_k \sqrt{1 - R_k^2} e^{-2x_k l} ; k = 1, 2, 3 \quad (14)$$

The formula for the threshold pumping value in the presence of the external signals E_1, E_2, E_3 reads

$$|A_{30}^{\text{thr}}|^2 = \frac{(\gamma_1 - \lambda_1)(\gamma_2 - \lambda_2)}{(1 + \lambda_3) G_1 G_2} \quad (15)$$

The return signal at a probing laser frequency reduces hard excitation threshold for parametric oscillations. The quasi-stationary solution to the equation for the measured intensities is of the form

$$\gamma_2 - \lambda_2 = \frac{G_2 G_3 (1 + \lambda_3)^2 |A_{30}|^2}{2(\gamma_1 - \lambda_1) \left(1 + \frac{1 + \lambda_3}{2(\gamma_1 - \lambda_1)} \frac{G_1 G_3^2}{2} I_2\right)} \left[1 - \frac{G_1^2 (1 + \lambda_3) I_2}{1 + \frac{1 + \lambda_3}{2(\gamma_1 - \lambda_1)} \frac{G_1 G_3^2}{2} I_2} \right] \quad (16)$$

The equation for I_1 is derived upon substitution of the indices $2 \rightarrow 1$ in Eq. (10). The minimum detectable return, say for I_2 , is estimated by finding the ratio $\Delta I_2 / I_2$ from Eq. (16). In doing so, only the cubic nonlinearity with respect to the intensity is taken into account. As a result, $\Delta I_2 / I_2$ has the form

$$\frac{\Delta I_2}{I_2} = \frac{\delta}{(\delta - 1)} \left(\frac{\lambda_1}{2\gamma_1} + \frac{\lambda_2}{\delta} + 2\lambda_3 \right) \quad (17)$$

where $\delta = I_3 / I_3^{\text{thr}}$, $I_3 > I_3^{\text{thr}}$

It follows from Eq. (17) that the parametric laser oscillation above threshold is most sensitive to the proposed sounding scheme. The resonance denominator $(\delta - 1)^{-1}$ is responsible for the abrupt enhancement of the lidar sensitivity in this regime. The detectable limit would be set by the pumping fluctuations, thermal and spontaneous emission noises induced by the nonlinear crystal.

The available PLO's suggest that a value of $(\delta - 1)$ on the order of 10^{-3} is practical without making any special provisions against the fluctuations. Moreover, the resonance denominator can be made even smaller by using a nonlinear absorption cell to optimize the pump field parameters.

IV. CONCLUSIONS

Research into the feasibility of enhancing the sensitivity of remote gas analysis has been carried out. The theoretical investigation and experimental evidence show that nonlinear optical systems offer good promise as low-power lidar return detectors. Their high-sensitivity detection capability is of critical importance because weak echo signals provide information on the laser beam attenuation by atmospheric gaseous constituents. Thus the nonlinear optical systems prove to be an excellent implementation of the general concept of a measuring instrument.

REFERENCES

1. A. P. Godlevsky, A. K. Ivanov, Yu. D. Kopytin, Kvant. Elektron. 9, 2007 (1982).
2. A. P. Godlevsky, E. P. Gordov, Ya. Ya. Ponurovsky, A. Z. Fazliev, N. P. Sharin, Kvant. Elektron. 13, 683 (1986); Appl. Opt. 26, 1607 (1987).
3. A. P. Voitovich, V. B. Dunaev, A. P. Prokopov, Zh. Prikl. Spektrosk. XII, 369 (1985).
4. W. E. Lamb, Jr., Phys. Rev. 134, A1429 (1964).
5. S. A. Akhmanov, R. V. Khokhlov, Zh. Eksp. Teor. Fiz. 43, 351 (1962).
6. N. M. Kroll, Phys. Rev. 127, 1207 (1962).
7. R. N. Kingstone, Proc. IRE 50, 472 (1962).

MULTI-WAVELENGTHS LASER TRANSMITTER FOR THE LIDAR MONITORING
OF THE ATMOSPHERIC PARAMETERS

A. L. Butakov, V. I. Voronov, G. S. Evtushenko, V. V. Zuev,
V. E. Zuev, A. E. Kirilov, A. N. Mal'tsev, S. Yu. Mirza,
Yu. P. Polunin, V. B. Sukhanov, V. O. Troitskii
The Institute of Atmospheric Optics - SB USSR Academy of Sciences,
Tomsk, 634055, USSR

Abstract

This paper describes a laser complex emitting at six wavelengths simultaneously with a mean power of about 1 W at each of them at PRF of 5 kHz and beam widths close to the diffraction limit. The complex used copper-vapor lasers for pumping the dye-lasers and also involves nonlinear crystal frequency converters.

Introduction

The investigations carried out at the Institute of Atmospheric Optics showed the perspective and possibility of making a combined lidar sensing station for monitoring the atmosphere through its entire depth in the interests of weather and climate formation studies.¹ The station "KOLIS" based on a 2 m diameter mirror is under construction now. It will allow us to measure simultaneously vertical profiles of humidity, temperature, pressure, and aerosol microphysical parameters including high-altitude lidar-ratio profiles.

In the multifrequency aerosol sounding method to be used, three or four sounding radiation lines located at 80-100 nm intervals in the atmospheric transmission windows should be available. Hence, the line width may be (10-40) Å and the wavelength reproducibility ~1 Å.

Experiments and Results

The differential absorption method requires two adjacent narrow lines with high stability to be available and imposed rigorous demands to the spectral parameters of laser radiation. The emission line width should not exceed 0.01 cm^{-1} , and the wavelength stability should be better than 5×10^{-7} . It should be noted that one line (588.0734 nm) must correspond to the H_2O molecule absorption line maximum, and the other one must be in the absorption line wing of this molecule. Moreover, to provide the required restitution accuracies of humidity and temperature profiles based on the data of lidar sounding, at least, in the troposphere, the mean laser-radiation power should be higher than 1 W at a pulse repetition rate not higher than 10 kHz. These requirements together with the demands of narrow and stable angular apertures of all the laser beams are the basis of the lidar transmitter developed. The requirements to the laser transmitter are summarized in Table 1.

Table I

Parameters of radiation	Sensing Techniques		
	Multiwavelengths	DIAL	Raman
Mean power of laser beam, W	1.0	1.0	≥ 10.0
Pulse repetition rate, kHz	3-5	3-5	3-5
Pulse duration, ns	10-30	10-30	10-30
Beam divergence, mrad	0.5	0.5	0.5
Wavelength, nm	$\lambda_1 = 510.6$ $\lambda_2 = 578.2$ $\lambda_3 = 654.0$	$\lambda_4 = 588.0734$ $\lambda_5 = 594.2572$	$\lambda_1 = 510.6$ $\lambda_2 = 578.2$ $\lambda_6 = 271.2$
Spectral width, nm	≤ 1.0	3.5×10^{-4}	-
Wavelength reproducibility, relative units	5×10^{-4}	5×10^{-7}	-

The most powerful and effective visible laser is a copper-vapor laser, which was chosen as a radiation source in the yellow-green region for aerosol sounding, for sounding by the Raman spectroscopy method and as a source for pumping dye-solution tunable lasers. To increase its energy parameters, the copper-vapor laser operating in the master generator-amplifier mode is used. The same mode is applied for increasing the energy parameters of narrow-band dye lasers.

Table II gives some energy characteristics of laboratory models of the lasers operating in both the generator and generator-amplifier modes with the use of different types of excitation.

The output radiation power was measured with a telescopic activity ($M = 14$) for the gas-discharge tubes (GDT) of 15 and 27 mm diameters. The mean radiation power with 0.2 mrad divergence for a gas-discharge tube of 15 mm diameter was 2.4 W and for GDT of 27 mm diameter it was 8.8 W. The fifth and sixth lines of Table II present the results of testing two- and three-cascade laser systems. In the two-cascade system, an optical delay of 6 m was used between the generator and the amplifier. In the three-cascade system, a collimator for 34 mm expansion of the beam and a spatial selector in the form of diaphragm were placed between the generator and the first amplifier. In this case the optical delay was 4 m. The generator in the three-cascade system operated with a telescopic cavity, and the total mean generation power given in Table II was the power in the beam with diffraction divergence.

The generation pulse of the system "generator-amplifier" has the same shape that the master generator and it was somewhat longer in duration. The maximum power of the system was obtained at 20 ns delay of the generator excitation pulse with reference to the amplifier excitation pulse. When a telescopic cavity with $M = 14$ was used, its radiation was 0.1-0.3 mrad. In our experiments, the generation duration varied from 20 ns to 50 ns.

Table II

N	Inside diameter mm	l, mm	U, kW	I, A	P _{Ne} torr	f, kHz	W, W	ΣW , W	Note
1	15	560	5.5	0.34	400	5.80	3.8	-	Two thyratrons - 1000/25
2	25	720	5.0	0.80	20	6.25	12.5	-	with water cooling, plane-parallel cavity
3	27	1000	5.5	0.63	37	7.70	15.5		
4	35	1000	5.5	0.77	70	6.67	17.0		
5	35	1000	5.4	0.95	-	5.88	11.5	22.0	Generator
	35	1000	5.2	0.57	-	5.88	14.5		Amplifier
6	15	560	4.0	0.35	300	6.25	1.5	31.5	Generator
	35	1000	6.0	1.00	200	6.25	12.0		Amplifier
	35	1000	6.0	0.70	200	6.25	14.0		Amplifier

The laser emitter generating at the wavelength λ_3 was constructed based on the oxazine-17 dye laser with transverse excitation by a two-cascade copper-vapor laser.² The generation spectrum was narrowed up to 0.07 nm using three intracavity Fabry-Perot etalons constructed by the deposition method. At a mean pumping power of 30 W the dye-laser power, without spectral selection, amounted to 9 W. The conversion efficiency of the system "copper-vapor laser - dye laser", with spectral selection, was 15%. Photostability of dye solution was tested in the 10 cm³ cell.

To transform copper-vapor laser generation to the ultraviolet range (λ_6), the KDP 2 x 2 x 4 cm crystal without forced cooling, was used (synchronism "ooe"). The efficiency of conversion (λ_1 and λ_2) to the sum frequency (λ_6) reached 5% at the mean ultraviolet radiation power 0.6 W. Variation of the basic radiation mean power in the 2 to 20 W range at constant pulse power showed that the thermal effects did not limit the conversion efficiency.

To obtain narrow-band radiation at the wavelengths λ_4 and λ_5 a three-cascade scheme of a pumping laser and a four-cascade scheme of a rhodamine C-dye laser with quasi-longitudinal pumping were used. The master generator of the dye laser was constructed using two diffraction gratings with 600 lines/mm and 1200 lines/mm, one of which operated in the grazing mode and the second one was mounted using a Littrow scheme.³ The generation spectrum width was 0.2 cm⁻¹. The master generator's radiation was transmitted through an external Fabry-Perot interferometer with sharpness ~ 30 , which decreased the generator spectrum width to the value smaller than 10⁻² cm⁻¹, and was directed to a space filter consisting of two confocal spherical mirrors with the diaphragm at their joint focus. The space filter was used to increase the signal-to-noise ratio. Then the radiation was amplified in a three-cascade amplifier. Each amplifying cell was a cell filled with dye, which was mounted at a joint focal plane of the two spherical lenses. The amplifiers pumping was quasi-longitudinal. The tests of such a system have shown that it meets the requirements for the laser transmitter parameters (spectral width and mean generation power). To obtain the required radiation reproducibility at λ_4 and λ_5 , the scheme of active stabilization, based on a wavelength meter⁴ and a microcomputer, is under develop-

ment now. The error signal between the required and real generation wavelength after the computer processing is applied to the servodrive by the angular position of the external Fabry-Perot interferometer determining spectral position of a generation line. In this scheme, the error signal is processed with time interval of ~ 1 s. The wavelength is reproduced during the time between the cycles of error-signal processing due to passive stabilization of the entire system. For this purpose, the entire laser system is mounted on a heavy plate set on supports consisting of alternating layers of vibro-absorbing materials with different amplitude-frequency characteristics.

References

1. V. V. Zuev, O. A. Romanovskii, Possibilities of Lidar Sounding of Meteorological Parameters of the Atmosphere in the Visible, *Zh. Prikl. Spektrosk.* 45, 998 (1986).
2. L. V. Masarnovskii, A. N. Soldatov, V. B. Sukhanov, Excitation of Dye Solutions and Their Mixtures by Copper-Vapor Lasers, *Kvant. Elektron.* 6, 1536 (1979).
3. S. Yu. Mirza, A. N. Soldatov, V. B. Sukhanov, Peculiarities of Efficient Transformation of Metal Vapor laser Radiation to the Dye Tuned Generation. In coll. papers: Forecast and Monitoring of Optical-Meteorological State of the Atmosphere, Tomsk: Ed. by Institute of Atmospheric Optics, SB USSR Acad. Sci., 1982, pp. 81-86.
4. A. B. Balakhnin, B. L. Bukovskii, V. I. Bobrin, et al., Operating Etalon of Wavelength Unit for Pulsed Lasers, *Izmeritel'naya Tekhnika.* 1, 17 (1987).

AIRBORNE LASER COMMUNICATIONS SCINTILLATION MEASUREMENTS: FINAL RESULTS

Robert J. Feldmann
Air Force Wright Aeronautical Laboratories (AFWAL/AAAI)
Wright-Patterson AFB OH 45433

Steven K. Rogers, PhD, Capt, USAF
Air Force Institute of Technology
Wright-Patterson Air Force Base OH 45433

Abstract

As part of the HAVE LACE (Laser Airborne Communications Experiment) program, optical scintillation data was collected and analyzed. The results of this analysis will be used to examine the effects of scintillation on air-to-air laser communications performance. The HAVE LACE terminals used direct detection of a pulsed diode laser. The random variations in received signal strength, called scintillation, are caused by the time varying index of refraction, due to atmospheric turbulence. The scintillation data that was collected is compared to a model derived from turbulence theory in an effort to validate these atmospheric turbulence models. This model can then be used to aid in the design of air-to-air laser communication terminals that provide acceptable probability of error performance.

Introduction

Successful design of an atmospheric laser communications terminal requires an understanding of atmospheric turbulence induced scintillation of the optical signal. Laser beam scintillation is small scale interference within the beam cross section due to turbulence induced fluctuations of the refractive index of the atmosphere, causing variations in the spatial power density at the receiver. The variations in the spatial power density at the receiver manifest themselves as fades and surges of the detected optical signal. By understanding the statistics and power spectrum of the fades and surges communications terminals can be designed to achieve needed levels of performance by employing optimized choices of increased link margin and error coding.

Extensive research has been done to characterize and model the effects of atmospheric turbulence on terrestrial laser communications links. However, limited work has been accomplished in collecting data for validating atmospheric scintillation models associated with airborne laser communications links.

As part of the HAVE LACE (Laser Airborne Communications Experiment) program optical scintillation data was collected and analyzed. The analysis will aid in the determination of the degree of scintillation to be expected from the air-to-air communications channel and the effects of scintillation on communications performance. The HAVE LACE terminals use direct detection of pulsed laser energy, therefore, the random variations in the received signal strength, can be used to evaluate the atmospheric turbulence induced amplitude scintillations. The collected data has been reduced and compared with a theoretical model for air-to-air communications links. The objective of the analysis is to identify deviations in the collected data from predictions based on current theory and to explain the results in terms of communications performance.

HAVE LACE Overview

The Satellite Communications Group of the Air Force Wright Aeronautical Laboratories (AFWAL) at Wright-Patterson AFB OH managed the HAVE LACE program and conducted the flight tests. In an effort to demonstrate the feasibility of air-to-air laser communications AFWAL began the HAVE LACE program in 1983 under the sponsorship of the Headquarters Air Force Systems Command, New Concept and Initiatives Office. The technology for laser communications using small semiconductor laser diodes has been available for some time. Optical acquisition and tracking systems have been developed in the past for a wide variety of applications. Early in 1984, the Air Force established a contract with GTE Government Systems of Mountain View CA, to develop two airborne laser communications terminals and furnish these terminals to the Air Force for a flight test program. These terminals were not advanced development models but feasibility models using basically "off-the-shelf" technology to quickly provide the Air Force with equipment for the HAVE LACE demonstration and test program.

In order to demonstrate the feasibility of laser communications, flight tests were

performed to analyze acquisition, tracking, communications, and scintillation, at operationally significant ranges. The HAVE LACE program was divided into three major areas: design and development of the laser terminals, modification of the testbed aircraft and installation of the terminals, and system test including both ground and flight testing. The two HAVE LACE terminals, furnished by GTE for use during the program, consisted of a laser transceiver and an acquisition/tracking system. GTE supported the aircraft modifications and terminal installation in two Air Force C-135 aircraft operated and maintained by the 4950th Test Wing. AFWAL conducted the flight test of the terminals and evaluated their performance.

The terminals consisted of a laser transmitter powered by a 100 watt peak-power diode array operating at the infrared wavelength of 904 nanometers, a quadrature receiver using four avalanche photodiodes, a gimballed optical head with 11.3 cm diameter optics, and associated controls. This equipment was installed in an equipment rack with the optical head mounted in a two-axis gimbal at the rear of the rack. The entire system was placed next to a side window in each of the aircraft.

System operation began with initialization of the acquisition process. Each operator provided inputs to their terminal designating the most probable location for the cooperating aircraft based on visual sighting, known flight paths, or other navigation inputs. These inputs defined the center point for a 10 degree by 4 degree uncertainty region. Both terminals started in the responder mode where the terminals slowly scanned its uncertainty region. When an operator wanted to initiate the link, he switched his terminal to the initiating mode and it rapidly scanned its uncertainty region until the two fields of view were mutually aligned. The initiator's fast scan covered the entire scan pattern in less time than it takes for the field of view of the slow scan of the responder to pass across a point. Mutual alignment was thus assured, to within the error allowed by the fields of view, within one scan of the responder. When the terminals were mutually aligned, an optical signal was detected by each terminal and a small scan pattern used to refine alignment. After accurate tracking was established, timing synchronization began and either communications could be evaluated or scintillation data collected.

To accurately measure the scintillation, a special mode of operation was added to the terminals. In this mode of operation one terminal sends a steady stream of 80 nsec pulses at 10 Kpps and the other terminal continuously receives these pulses and detects the peak level of each pulse. Tracking at the transmitting terminal during these measurements is accomplished using only gyro stabilization, however, measurements are limited to 30 seconds so the tracking drift is minimized. The sampling of the scintillation provides information about fades and surges with frequencies up to about 5 KHz. The scintillation spectra is not expected to contain any components greater than this. A demodulator using a peak level detector followed by a sample and hold allowed the peak levels of the short pulses to be recorded on standard recording equipment. The output of the scintillation demodulator simply tracks the fluctuations, thus requiring a recording bandwidth of only 5 KHz. Flight profiles for these tests were carefully controlled so that misalignment of the two systems did not induce fluctuations. Parallel paths were maintained at constant altitude during all scintillation tests.

The HAVE LACE test program consisted of 16 flights from which 55 hours of test data was collected. Scintillation data was collected on 6 of the test flights. Most of the scintillation data was taken at altitudes around 30,000 feet and aircraft separations of 25 nautical miles. Air speeds during the scintillation runs usually varied between 350 to 400 knots.

Scintillation

Literature on the subject of line-of-sight optical propagation through turbulence is extensive. However, the most important and influential theoretical development of the subject is that of V. I. Tatarski^{1,2} and L. A. Chernoff³. The combination of their work has been the foundation for most of the work that has followed. A collection of review articles on the subject are available⁴ and provide a concise development of turbulence theory.

Even with the extensive interest shown toward the theoretical development of this subject, predictions of the effects of atmospheric turbulence on optical propagation can be checked only by in situ measurements. The atmosphere is inhomogeneous and statistically nonstationary which precludes the use of simple models in characterizing it as a communications channel. Of interest to optical propagation research is the variation of refractive index resulting from variation of the density of the air. The air density depends on temperature and pressure. However, pressure fluctuations are

rapidly dissipated and have negligible effects when compared to that of the longer lasting temperature variations.

Sunlight incident on the earth's surface is absorbed and, in turn, as the earth re-emits this energy the surface air layer is heated. As the warmed surface layer air becomes less dense it rises, mixing turbulently with cooler air. Therefore, the air temperature varies randomly from point to point in the atmosphere (on the order of 0.1 - 1°C) and is a function of altitude and wind speed due to the turbulent mixing. These turbulent eddies cause an ever changing index of refraction of the air. The variations, which are typically on the order of 10^{-6} , result in small point-to-point differences⁴. While the refractive index variation is very small, in situations of practical interest a laser beam propagates through a large number of these inhomogeneities. This initially produces optical phase effects (leading to angle of arrival fluctuations or beam wander), intensity fluctuations (scintillation), and beam broadening. It is the intensity fluctuations of the communications signal which are of interest here.

The effect of atmospheric turbulence depends on the scale size of the turbulent eddies which range from an inner scale of a few millimeters to several hundred meters or larger for outer scale values⁵. These turbulent eddies may be envisioned as "lens" of air, each with a characteristic refractive index, which focuses or defocuses the incident light wave. The power spectral density of the turbulence may be regarded as a measure of the relative abundance of the eddies⁶. Kolmogorov⁷ initially established the form of the power spectrum of the turbulence. Subsequently, the Kolmogorov spectrum has been modified to what is known as the Von Karman spectrum which provides a more definitive spectral shape, Figure 1. The form of the Von Karman spectrum is dependent on the inner and outer scale sizes of the turbulent eddies and the refractive index structure constant, C_n^2 . Where the inner scale is given by $l_0 = 2\pi/Km$, the outer scale is given by $L_0 = 5.92/K_0$ and C_n^2 serves as a measure of the strength of the fluctuations.

The time required for light to propagate through these turbulent eddies is only a fraction of the "fluctuation time" for the random refractive index changes. Therefore, the time dependence of the refractive index changes is often suppressed and attention focused on spatial properties for the investigation of imaging properties. However, in communications the temporal properties of the turbulence are of interest and Taylor's "frozen turbulence" hypothesis is invoked. This hypothesis assumes that a given realization of the random refractive index is "frozen" and drifts across the receiver aperture with constant velocity determined by the local wind conditions. While the communications signal experiences fades and surges due to scintillation it is the signal fades which most limits the communications performance. Therefore, the frequency spectra (duration and recurrence) and the depth (probability a fade will exceed a threshold) of the fading is important to characterize.

Understanding the fading characteristics allows the design engineer to achieve a level of performance based on probability of error (P_E) by either adding signal margin and employing coding techniques or both. As more knowledge is gained about the statistical nature of the optical communications channel optimum combinations of coding and link margin can be used to achieve required communications performance levels. In particular, the long high altitude horizontal path atmospheric channel is least characterized.

Results provided by G. J. Morris⁸ involving horizontal high altitude airborne scintillation measurements over short paths and the opportunity to take part in the HAVE LACE program led to the motivation to perform the current work.

Discussion of Results

The depth of fading due to scintillation can be directly related to the probability that fades of a certain depth will occur. Tatarski's¹ and all subsequent treatments of this subject predict that the probability distribution of the logarithm of the intensity is a normal distribution. This is a reasonable assumption since the propagation of light through the many lens-like eddies can be viewed as propagation through a multiplicative noisy channel. As previously reported⁹, the HAVE LACE scintillation data was log-normally distributed.

The frequency spectra of scintillations is related to both the size of the turbulent eddies and the rate at which they move across the receiver aperture. Much data has been

analyzed for terrestrial scintillation and the frequencies have been found to range from 0.1 to 100 Hz¹⁰. Scintillation at ground level results from large turbulent eddies whose rate of motion is due to wind speeds, thus low frequencies fluctuations are expected. At altitude the turbulent eddies are much smaller and their rate of movement is, by the "frozen turbulence" assumption, the result of aircraft airspeed.

Tatarski¹ presented the first discussion of the temporal power spectral density. Equation (1) provides an expression for the reciprocal of the time required for a Fresnel-zone size disturbance to move across the line-of-sight,

$$f_o = \frac{V}{(2\pi\lambda L)^{\frac{1}{2}}} \quad (1)$$

where V is the perpendicular airspeed, L is the path length and f_o is related to the corner frequency of the spectrum, f_c ⁴, by

$$\frac{f_c}{f_o} = 1.43 \quad (2)$$

For the HAVE LACE flights (1) and (2) yield corner frequencies between 475 and 600 Hz for airspeeds of 300 to 350 knots. A representative frequency spectrum from our test flights shows f_c to be approximately 100 Hz (Figure 2). This frequency spectrum was obtained by Fast Fourier Transforming (FFT) 0.4 seconds of scintillation data and then taking the ensemble average of 74 such FFT's. The magnitude of the ensemble average is used to represent the power spectral density.

Using the flight parameters given in Figure 1 the theoretical corner frequencies as given by (1) and (2) is 502 Hz. The factor of 5 difference in the observed corner frequency led to further investigations into the theory of turbulence.

Yura^{11,12} has extended Tatarski's weak turbulence perturbation theory using a multiple scattering argument. His development accounts for the saturation phenomena associated with the log amplitude variance and reduces to the results of Tatarski in the weak turbulence regime. Yura¹² obtained the shape of the temporal power spectrum for increasing values of amplitude variance (Figure 3). The effect of strong turbulence on the frequency spectrum can be seen by the curves of Figure 3. Note from Figure 3 that while the corner frequency shifts to lower frequencies with stronger turbulence the extend of the spectral components increase.

The primary difference between the Tatarski and Yura theories is the development of a filter function which is applied to the power spectrum of the turbulence, Figure 4. The filter function is a measure of the relative efficiency of a turbulent eddy of size K^{-1} located at some arbitrary position in producing fluctuations at the receiver. It is evident from Figure 4 that Yura's approach provides a filter function which behaves on the average like Tatarski's linear theory function.

A computer model has been developed which incorporates the characteristics of the HAVE LACE terminals and Yura's scintillation theory to generate theoretical temporal frequency spectra for a comparison with the HAVE LACE data. This model provides accurate curve fits for the collected scintillation data within the bounds of the known input parameters. Atmospheric data, which is used to define the true shape of the power spectral density of the turbulence, was not available. Therefore, the initial values for l_o , L_o , and C_n^2 were chosen from reasonable estimates derived from previous work¹³ and then further refined until a good data fit was accomplished. While the model provided a good comparison with the data, Figure 1, this generally required employing C_n^2 values which were stronger than, for instance, the Hufnagel model¹³ predicted. However, values for l_o , L_o , and C_n^2 were always kept within reasonable bounds for the conditions of the flight.

Conclusion

The HAVE LACE program provided a unique opportunity to perform high altitude scintillation measurements over extended path lengths. While airborne testing is by its

dynamic nature very challenging and difficult to perform, in situ measurements are necessary if practical application of laser communications theory is to be accomplished. The results presented here offer reasonably good agreement with theory. Further analysis is in progress to more fully understand the implications of the Hufnagel C_n^2 values and those provided from the temporal frequency comparisons.

References

1. V.I. Tatarski, Wave Propagation in a Turbulent Medium, McGraw-Hill Book Company, New York, 1961.
2. V.I. Tatarski, The Effects of the Turbulent Atmosphere on Wave Propagation, National Science Foundation Report TT-68-50464, 1968.
3. I.A. Chernoff, Wave Propagation in a Random Medium, McGraw-Hill Book Company, New York, 1960.
4. J.W. Strohbehn, editor, Laser Beam Propagation in the Atmosphere, Springer-Verlag, New York, 1978.
5. R.S. Lawrence, G.R. Ochs, and S.F. Clifford, "Measurements of Atmospheric Turbulence Relevant to Optical Propagation," Journal of the Optical Society of America, Vol. 60, No. 6, pp 826-830, June 1970.
6. J.W. Goodman, Statistical Optics, John Wiley and Sons, New York, 1985.
7. A. Kolmogorov, Turbulence, Classic Papers on Statistical Theory, Wiley-Interscience, New York, 1961.
8. G.J. Morris, "Airborne laser beam scintillation measurements at high altitudes," Journal of the Optical Society of America, Vol. 63, No. 3, pp 263-270, March 1973.
9. R.J. Feldmann, L.B. Mercer, S.K. Rogers, "Airborne Laser Communications Scintillation Measurements," Proceedings of the International Conference on Lasers '86, Orlando, Fla, pp 374-378, November 1986.
10. R.S. Lawrence and J.W. Strohbehn, "A survey of clear-air propagation effects relevant to optical communications," Proc IEEE, Vol. 58, pp 1523-1545, October 1970.
11. H.T. Yura, "Physical model for strong optical-amplitude fluctuations in a turbulent medium," Journal of the Optical Society of America, Vol. 64, No. 1, pp 59-67, January 1974.
12. H.T. Yura, "Temporal-frequency spectrum of an optical wave propagating under saturation conditions," Journal of the Optical Society of America, Vol. 64, No. 3, pp 357-359, March 1974.
13. Wolfe, W.L, and Zissis, G.J. (editors), The Infrared Handbook, Washington: Office of Naval Research, Department of the Navy, 1978.

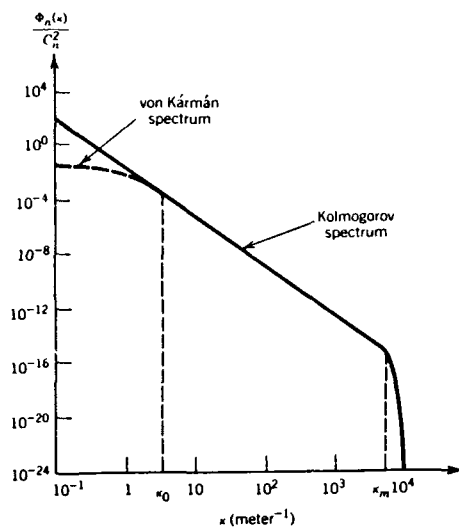


Fig 1 Representative forms of two power spectral densities of turbulence [6].

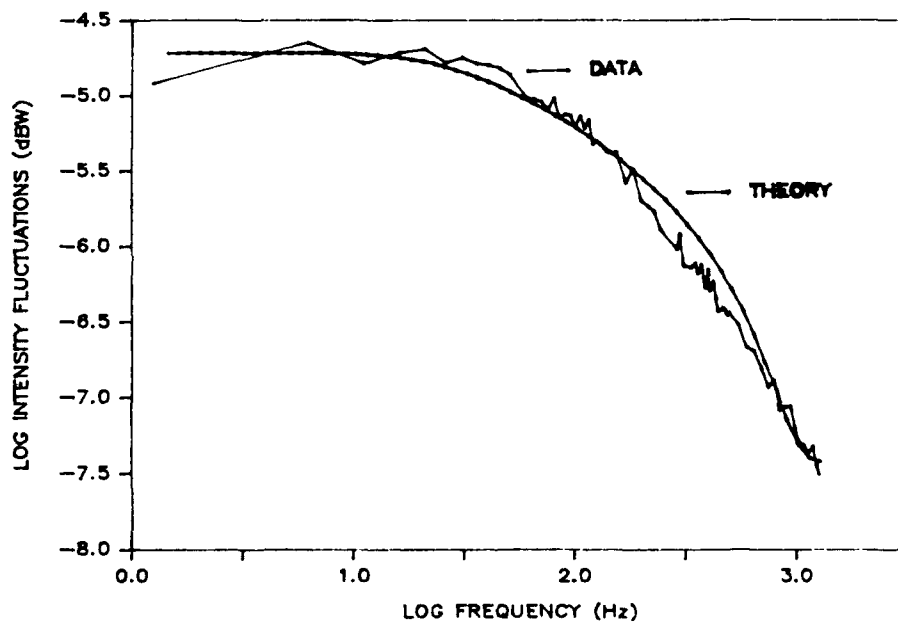


Fig 2 Measured temporal frequency spectrum for HAVE LACE flight #3, 29 Aug 85. Flight profile was 32,000 ft altitude, 350 knots air-speed, and 25 miles separation. Theoretical curve is derived from Yura.

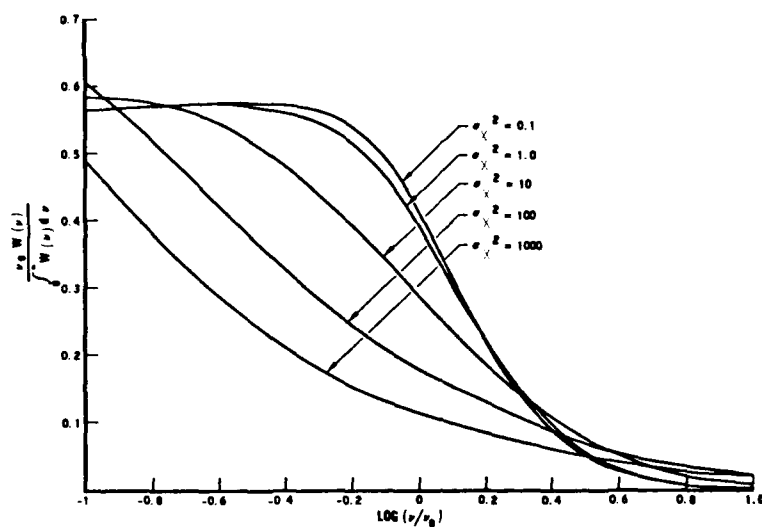


Fig 3 Theoretical temporal power spectrum for increasing values of log-amplitude variance.

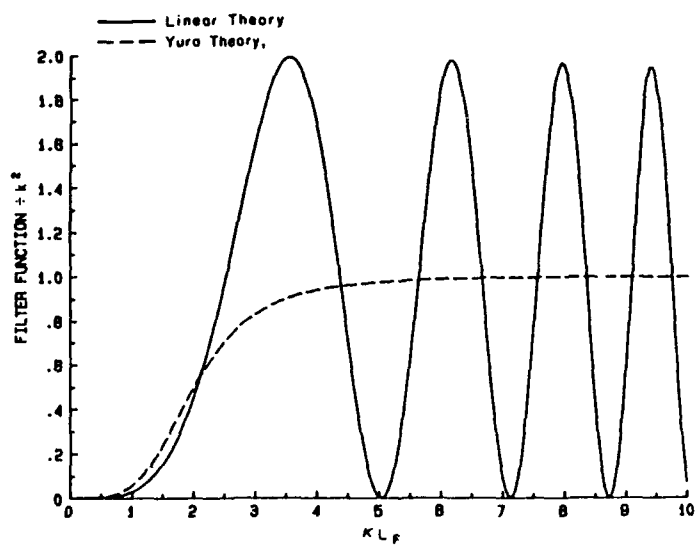


Fig 4 A comparison of two filter functions as presented by Tatarski (linear) and Yura.

SEGMENTED MIRROR LASER RESONATORS

S. De Silvestri, P. Laporta, V. Magni, and O. Svelto

Centro di Elettronica Quantistica e Strumentazione Elettronica, C.N.R.,
Istituto di Fisica, Politecnico di Milano,
Piazza Leonardo da Vinci 32, 20133 Milano, Italy

Abstract

A novel general scheme to obtain bidimensional phased-array lasers by diffraction coupling is proposed. Preliminary experiments have been performed on pulsed Nd:YAG laser to demonstrate its feasibility.

1. Introduction

Stable resonators operating in TEM_{00} mode present a noticeable drawback due to the limited portion of active medium that can be fully exploited by the laser beam. In this work we discuss a novel scheme, which should overcome this difficulty, based on the concept of in-phase locking of several TEM_{00} modes within the laser active medium by means of diffraction, which is somehow related to the recently developed phased-array semiconductor lasers¹⁻⁹. Our proposal concerns the design of a bidimensional plane mask containing suitably located holes to be inserted into the laser resonator, near one mirror, in order to simulate a segmented mirror. The mask should generate a monodimensional or two-dimensional beam array which, under appropriate conditions for the hole locations, is phase-locked by diffraction. This technique introduces a general concept in phased arrays valid for any kind of laser and in particular represents an alternative approach to the phase-locking of CO_2 wave-guide lasers^{10,11}. Preliminary experiments performed on a pulsed Nd:YAG laser have demonstrated the feasibility of our proposal.

2. Description of the Technique

The leading idea of using a mask can be understood with the help of Fig. 1, which shows a mask with two holes placed inside an otherwise conventional resonator with an active medium of suitable cross-section. The diameter of each hole is such that it can only allow oscillation on the TEM_{00} mode. For simplicity, we first assume that both mirror radii are much longer than the resonator length. Under these conditions, two distinct lobes (TEM_{00} -like modes) are expected to be emitted from the laser cavity, as shown in Fig. 1.

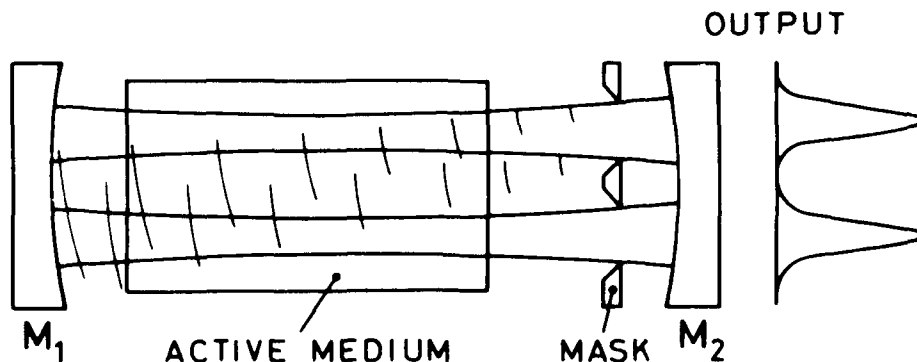


Fig. 1 - Schematic of a segmented-mirror laser resonator with a two-hole mask. Two TEM_{00} -like modes are shown along with the diffracted wavelets of one mode that couple to the field of the other mode.

Depending upon the distance between the two holes, the two beams have been observed to be: (i) unlocked, at large distance, (ii) locked in opposite phase (TEM_{01} -like mode) at suitably small distance, and (iii) locked in phase, at an intermediate distance. In fact, if the distance between the two holes of the mask is too large, the lobes do not interact and their phases are unlocked; if, however, the hole distance is sufficiently small, the diffracted waves from one hole contribute to the field of the other lobe and the two lobes are expected to lock each other. Indeed, for a suitable hole distance, the two lobes will lock 180° out-of-phase, giving a TEM_{01} mode of the cavity. The condition to be fulfilled in this case is that the phase shift $\Delta\phi$ between the diffracted wavelets of one lobe and the field of the other lobe be equal to π . To obtain in-phase locking between the two lobes, on the other hand, we must require that the phase shift $\Delta\phi$ be equal to 2π . This picture is analogous to that of supermodes in semiconductor laser arrays^{8,12}. Thus, depending upon the distance between the two holes, the configuration of Fig. 1 leads to two lobes that may be uncorrelated, 180° out-of-phase correlated, or in-phase correlated.

The extension to a more general case becomes quite straightforward: a mask containing more than two holes in a linear array, or a two-dimensional array can produce, under appropriate conditions, oscillation of many lobes all locked in phase. This would constitute a generalization of the linear phased-array lasers to two dimensions and to any active medium. The above intuitive concepts may give rise to a few critical remarks. In particular, when the radii of the two mirrors are comparable to the resonator length, the two off-axis lobes (see Fig. 1) cannot be considered as two TEM_{00} -like modes any longer. A more correct picture can be obtained considering the integral equation of a resonator in which one mirror presents zones of high reflectivity only in correspondence with the holes of the mask (segmented-mirror resonators). We can expect that, under suitable conditions, the fundamental mode will be constituted also in this case of in-phase lobes.

3. Experimental Results

The scheme previously outlined has been experimentally applied to a flash-pumped Nd:YAG laser. The pump cavity housing a 3" long \times 1/4" diameter rod, was of a reflective close-coupled type to ensure highly uniform pump energy distribution within the rod. The stable 50 cm long resonator was made of two 8 m radius of curvature concave mirrors, one of high reflectivity and the other with 60% power reflectivity. The mask, containing holes of appropriate shape and size, was placed close to the output mirror. Masks with two, three and four holes

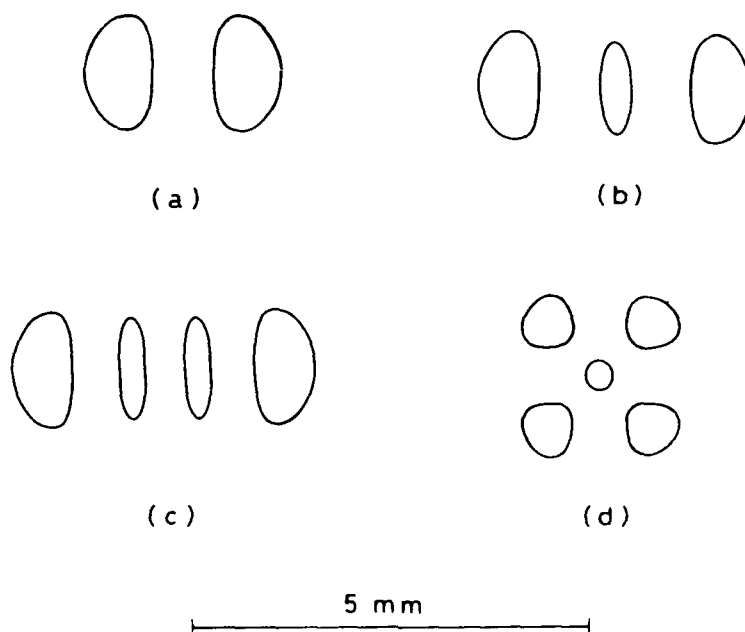


Fig. 2 - Mask hole contours giving in-phase locking: (a) two-, (b) three-, and (c) four-hole linear masks and (d) five-hole two-dimensional mask. The linear scale is indicated at the bottom.

disposed in linear arrays and five holes arranged in a two-dimensional pattern, whose shapes are shown in Fig. 2, have been used. The holes were made by chemical etching on a 100 μm thick tempered steel plate. Note that the holes are not circular and are of different size. In fact, the best hole contour would probably correspond to the iso-intensity lines of the actual mode profile of the segmented-mirror cavity. As a first approach, the hole contours have been chosen to correspond to the iso-intensity profiles of the in-phase lobes of the Hermite-Gaussian mode of a conventional spherical mirror resonator. An exact diffraction theory calculation of the mode profile is however still in progress, in order to optimize the mask patterns. As an example Figure 3(a) shows the experimental near and far-fields obtained with a two-hole resonator designed for oscillation on a fundamental mode with two lobes in phase. Figure 3(b) shows the corresponding theoretical results obtained by numerically solving the integral equation of the segmented mirror resonator.

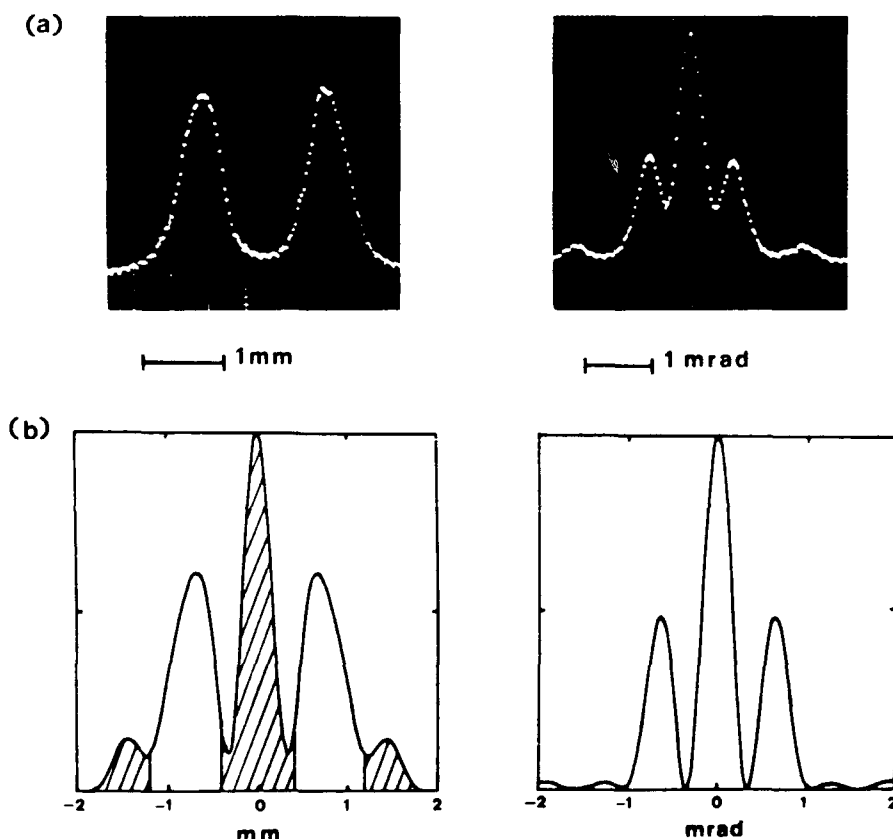


Fig. 3 - Near (left) and far-field (right) pattern of the phased output beam obtained with a two-hole segmented mirror resonator: (a) experimental; (b) theoretical. The dashed area in (b) represents the portion of the beam intercepted by the mask.

In the case of a two-hole mask with a shape similar to mask (a) in Fig. 2, but with the hole distance reduced by a factor $\sim \sqrt{2}$, the two lobes were 180° out-of-phase, corresponding to a TEM_{01} -like mode. Finally, we have noted that, if the hole separation was increased by a factor of about 1.8, the two lobes were completely uncorrelated. In this case, in fact, the far-field pattern was the same as that observed when one of the two lobes was blocked at the laser output. These results prove the validity of our scheme; the results obtained with the three- and four-hole masks shown in Fig. 2 are similar to those of the two-hole mask; in each case, using the optimum mask, good phase locking between the oscillating lobes has been observed. The results obtained with the two-dimensional five-hole mask (d) of Fig. 2 are shown in Fig. 4. To characterize the structure of the laser output beam, which is two-dimensional in this case, we have recorded the far field intensity distributions as burn

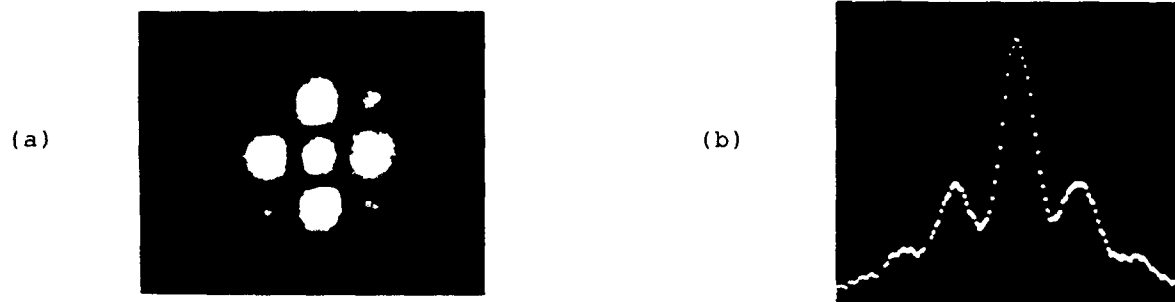


Fig. 4 - Output beam from the five-hole, two-dimensional, segmented-mirror resonator: (a) far-field burn pattern and (b) far-field profile taken along the horizontal central line of the burn pattern; the horizontal scale in (b) is 0.54 mrad/div.

patterns on a photo-sensitive paper (see Fig. 4(a)). This technique provides only for a qualitative picture of the phase locking effects, due to the non-linearity of the recording process. A quantitative analysis of the far-field patterns along selected lines has been performed by means of a linear photodetector array, and the results have shown that a reasonably good phase-locking has been obtained also in this case (see Fig. 4(b)). This represents a demonstration of phase-locking between different laser channels in two dimensions. As a general comment on the results obtained with the four masks considered in Fig. 2 we can say that, once the optimum mask was found, phase-locking was observed in a reliable way every laser shot and for a pump input energy ranging from threshold to about 2 times above threshold. The dimensions of the optimum mask are however quite critical, and changes by as much as 5% would considerably affect the phase locking condition. In all cases, the resulting output energy was also quite low, namely a few tens of mJ, compared with about 360 mJ obtained with the same laser operating at the same input energy (16 J; threshold energy 10 J) without any mask inserted in the cavity. This is due to the fact that the total area of the holes in each mask is only a fraction of the rod cross-section and to high losses introduced by the mask (see Fig. 3(b)).

As a conclusion we can say that these results demonstrate, in principle, the possibility to realize large fundamental mode by using resonators made with segmented, or more generally modulated, reflectivity mirrors. They might also shed new light on the process of diffraction coupling of diode arrays.

4. References

1. D.R.Scifres, R.D.Burnham, and W.Streifer, Appl. Phys. Lett. 41, 118 (1982).
2. D.R.Scifres, C.Lindstrom, R.D.Burnham, W.Streifer and T.L.Paoli, Electron. Lett. 19, 169 (1983).
3. J.Katz, E.Kapon, C.Lindsey, S.Margalit, U.Shreter, and A.Yariv, Appl. Phys. Lett. 43, 521 (1983).
4. D.Boetz and J.C.Connolly, Appl. Phys. Lett. 43, 1096 (1983).
5. D.F.Welch, D.Scifres, P.Cross, H.Kung, W.Streifer, R.D.Burnham, J.Yaely, and T.L.Paoli, Appl. Phys. Lett. 47, 1134 (1985).
6. D.F.Welch, P.S.Cross, D.R.Scifres, W.Streifer, and R.D.Burnham, Electron Lett. 22, 293 (1986).
7. K.K.Anderson and R.H.Rediker, Appl. Phys. Lett. 50, 1 (1987).
8. J.Katz, S.Margalit, and A.Yariv, Appl. Phys. Lett. 42, 554 (1983).
9. S.Wang, J.Z.Wilcox, M.Jansen, and J.J.Yang, Appl. Phys. Lett. 48, 1770 (1986).
10. D.G.Youmans, Appl. Phys. Lett. 44, 365 (1984).
11. L.A.Newman, R.A.Hart, J.T.Kennedy, A.J.Cantor, A.J.De Maria, and W.B.Bridges, Appl. Phys. Lett. 48, 1701 (1986).
12. E.Kapon, J.Katz, A.Yariv, Opt. Lett. 10, 125 (1984).

UNSTABLE RESONATORS WITH GAUSSIAN AND SUPERGAUSSIAN REFLECTIVITY MIRRORS

S. De Silvestri, P. Laporta, V. Magni, and O. Svelto

Centro di Elettronica Quantistica e Strumentazione Elettronica, C.N.R.,
Istituto di Fisica, Politecnico di Milano,
Piazza Leonardo da Vinci 32, 20133 Milano, Italy

Abstract

Novel output couplers with gaussian and supergaussian reflectivity profiles are proposed. An analysis of unstable resonators with supergaussian mirrors is presented. Application to a pulsed Nd:YAG laser has produced diffraction limited output beams with energy up to 200 mJ.

1. Introduction

Unstable resonators with radially variable reflectivity mirrors (VRM) offer the advantage of good mode discrimination, smooth output beam profile and large mode volume¹⁻⁴. Although these advantages have been known for many years, only a limited number of devices have been experimentally demonstrated. The proposed practical solutions include: radially varying birefringent filters⁵, apoditic filters based on frustrated total internal reflection⁶, dielectric mirror with shaped layers⁷, radially variable Fabry-Perot interferometers⁸.

Mode analysis of unstable resonators with tapered reflectivity mirrors is usually carried out assuming a gaussian shape of the reflectivity profile, which allows direct application of the matrix formalism for gaussian beam propagation⁹⁻¹⁰. A gaussian curve has long tails and, to prevent diffraction effects now coming from the rod aperture, the spot size must be rather small. For better filling of the rod other shapes of reflectivity tapering (linear, parabolic, etc.) have been proposed¹¹⁻¹³. However, the analysis of these resonators can only be carried out through machine solution of the mode integral equation, which however does not provide simple design equations for the resonator.

In this paper we show the advantage of using supergaussian reflectivity profiles and we consider the implementations of tapered reflectivity output couplers, based on thin film evaporation techniques. Applying ray analysis to the study of unstable resonators with supergaussian mirrors, simple analytic solutions are found for the lowest order mode and the corresponding loss eigenvalue. Some design considerations are also pointed out, such as: (i) spot size of supergaussian reflectivity profile for low diffraction rings; (ii) resonator magnification for low mirror misalignment sensitivity; (iii) peak reflectivity value for optimum output coupling and flat top output beam.

2. The Supergaussian Approach

The "supergaussian" intensity reflectivity profiles is defined by the following analytical form:

$$R(r) = R_0 \exp[-2(r/w_m)^n] \quad (1)$$

where R_0 is the intensity peak reflectivity, r the radial coordinate, w_m is defined as the mirror spot size, and n as the "order of supergaussianity". The choice of a such reflectivity profile provides: (i) simple analytical solution of the mode equation within the framework of geometrical optics; (ii) simple equations for the design of the resonator parameters; (iii) cavity modes bell-shaped and flatter than a gaussian curve and therefore no diffraction rings, with wide filling of the active medium; (iv) satisfactory fittings of various reflectivity profiles of existing devices.

For unstable resonators with supergaussian mirrors, geometrical optics provides for a satisfactory approximation of mode profiles and losses^{1,14}. For a supergaussian reflectivity shape of order n [see (1)], the fundamental mode solution is simply a supergaussian beam

$$u_o(r) \propto \exp[-(r/w_i)^n] \quad , \quad (2)$$

where $u_o(r)$ is the amplitude of the beam incident on the supergaussian mirror and w_i is its spot size given by

$$w_i = w_m (M^n - 1)^{1/n} \quad . \quad (3)$$

The round trip loss for the fundamental mode is

$$\gamma = 1 - \frac{R_o}{M^2} \quad . \quad (4)$$

The output beam profile $u_{out}(r)$ is obtained by multiplying the amplitude of the beam incident on the mirror by the mirror transmission:

$$u_{out}(r) = u_o(r)[1 - R(r)]^{\frac{1}{2}} \quad . \quad (5)$$

As an example, Fig. 1(a) shows the intensity profiles of the mode pattern on a supergaussian mirror ($R_o = 44\%$, $n = 2.8$) and of the transmitted beam, calculated by squaring the fields given by (2) and (5), as a function of r/w_m along with the reflectivity profile, for a given resonator magnification. The cavity mode profile is supergaussian of the same order as that of the mirror. This mode profile laying in between rectangular and gaussian shapes, should combine the advantages of both profiles. The soft smoothing avoids building up of pronounced diffraction rings typical of hard edge beam profiles. However, the large portion of the beam at almost constant intensity allows for a wide filling of the active medium and consequently for an efficient energy extraction. The output beam is no longer supergaussian and its shape depends on R_o and M : a central dip appears in the output beam for values of R_o and M such that $R_o M^n > 1$ (see Fig. 1(a)). The condition

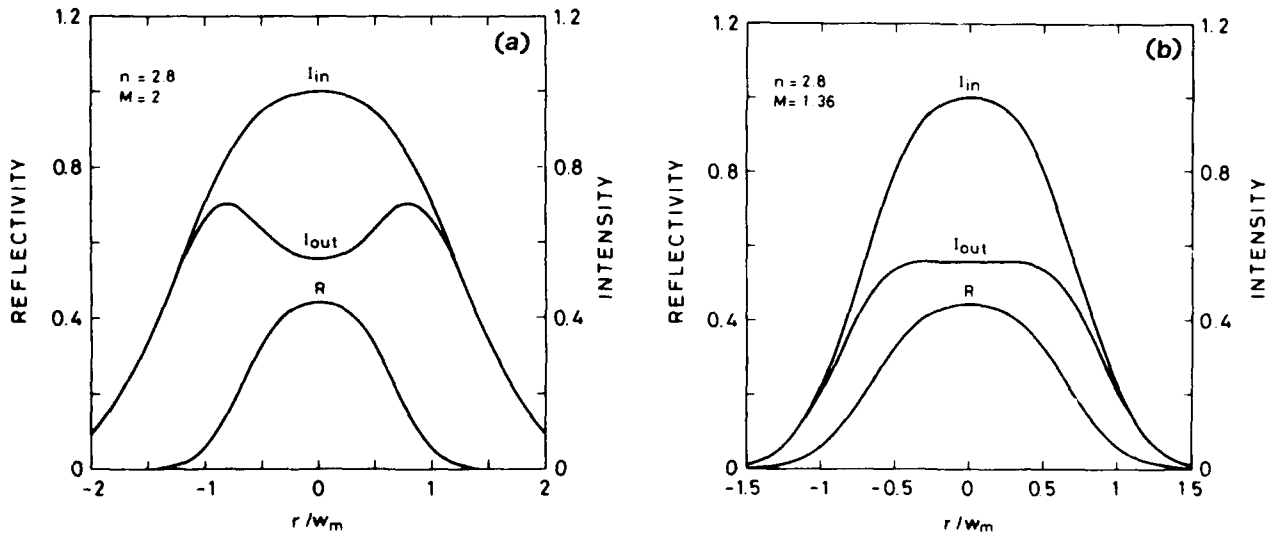


Fig. 1 - Theoretical intensity profiles of the wave incident, I_{in} , on a supergaussian reflectivity mirror (order $n = 2.8$ and $R_o = 544\%$) and of the transmitted beam, I_{out} , as a function of radial coordinate r normalized to the mirror spot size w_m , for two resonator magnifications: (a) $M = 2$; (b) $M = 1.36$. The reflectivity profile of the mirror, R , is also reported.

$$R_0 = 1/M^n$$

(6)

defines the so called maximally flat output beam. To satisfy Eq. (6) a reduction of either R_0 or M is required. Figure 1(b) shows the theoretical intensity beam profiles obtained by lowering the magnification down to $M = 1.36$; the output beam profiles appears maximally flat.

To design the resonator, the mode spot size should be optimized for a good balancing between efficient filling of the gain medium and low beam perturbations caused by diffraction at the rod aperture. For an unstable confocal resonator with Gaussian mirror the best trade-off has been demonstrated theoretically and experimentally¹⁵ to occur for a ratio of mode intensity spot size (radius at $1/e$ of the mode intensity) to rod radius between 0.4 and 0.7. This situation corresponds to an active material with an hard aperture that cuts the intensity wings at 0.002-0.13 of the central intensity peak. This criterion has also been assumed in our case as a basis to calculate the mirror spot size in a supergaussian resonator. The peak reflectivity and the magnification must be chosen with consideration of the output losses [Eq. (4)], the mode discrimination, which increases with M , the misalignment sensitivity¹⁶, and the output beam shape, which may have a central depression.

3. Practical Devices with Gaussian and Supergaussian Reflectivity Profiles

The main difficulty with tapered reflectivity output couplers is to fabricate, with standard optical techniques, practical devices which can withstand high power (if needed), and are not specific to a given laser. Up to now a few devices with radially variable reflectivity profiles have been experimentally demonstrated⁵⁻⁸.

The availability of devices whose parameters (spot size, peak reflectivity, index n) can be tuned independently, is extremely important. To this purpose, thin film vacuum evaporation techniques have been developed¹⁷, that allow to fabricate multilayer dielectric mirrors whose reflectivity profile is entirely under control. These methods are essentially based on the shadowing effect of fixed non-contact masks with a circular aperture, placed between the crucible and the substrate. One of these techniques is fully described in Ref. [18]. The mirrors consist of a glass substrate coated with an antireflection $\lambda/4$ layer of magnesium fluoride on which a second layer of cadmium telluride or zinc selenide is deposited. The thickness of the second layer is $\lambda/4$ at the center and slowly decreases to zero at the edge. Lastly, to protect the mirror, very thin film of silicon dioxide has been deposited. As an example, the reflectivity profile of two dielectric mirrors fabricated with our techniques are reported in Fig. 2. Figure 2(a) shows a gaussian ($n = 2$) reflectivity profile with a spot size $w_m = 3.9$ mm; Fig. 2(b) shows a supergaussian reflectivity profile with $n = 2.8$ and spot size $w_m = 2.2$ mm. A large variety of reflectivity profiles can be simply achieved which allow to meet the design constraints of a large number of unstable resonators.

4. Experimental Results

The supergaussian mirror reported in Fig. 2(b) was used in an unstable resonator for flash-pumped Nd:YAG laser. The pump cavity housing a $3 \times 1/4$ inch rod was a reflective close-coupled type to provide for uniform pumping of the rod. To record the near- and far-field intensity distributions of the laser output a linear array of 512 photodiodes spaced by 25 μ m was used. In the experiments the supergaussian mirror was flat and the resonator magnification was varied by changing the cavity length and the radius of curvature of the totally reflecting rear mirror. The laser rod was placed close to the rear mirror. To test the performances of unstable resonators with supergaussian mirrors two resonator magnifications $M = 1.36$ and $M = 2$ have been considered; the first was obtained with a resonator 360 mm long and a convex rear mirror of 15 m curvature radius, the second with a resonator of 375 mm and a convex 3 m mirror. The choice of an high magnification privileges the mechanical stability with respect to the output energy, while the opposite happens for the lower magnification.

Figures 3(a) and 3(b) show the shape of typical near- and far-field patterns of the output beam for $M = 1.36$. The near-field intensity distribution is quite uniform and almost flat with a diameter at half maximum $D = 5.4$ mm, in satisfactory agreement with the theoretical curve in Fig. 1(b). The spot size of the mirror, $w_m = 2.2$ mm, determines the fundamental mode

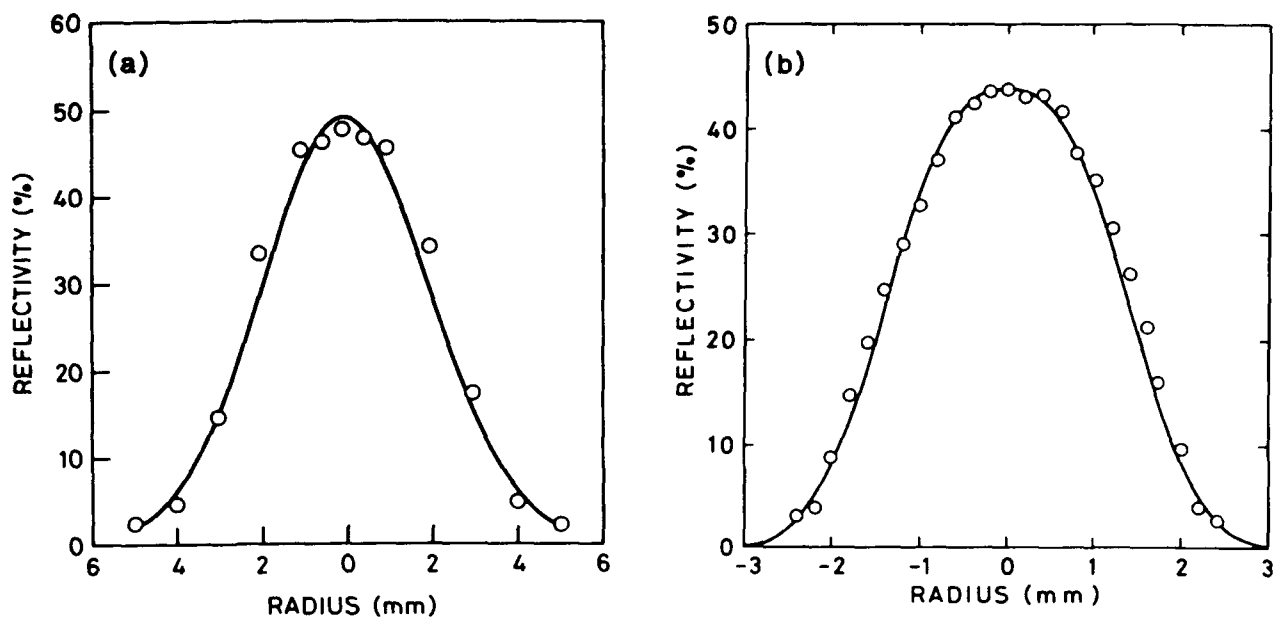


Fig. 2 - Reflectivity profiles of experimental VRM obtained by thin film deposition techniques (dots). The solid lines are fitting curves calculated assuming (a) a gaussian reflectivity profile ($n = 2$, $w_m = 3.9$ mm, $R_0 = 44\%$), (b) a supergaussian reflectivity profile ($n = 2.8$, $w_m = 2.2$ mm, $R_0 = 44\%$).

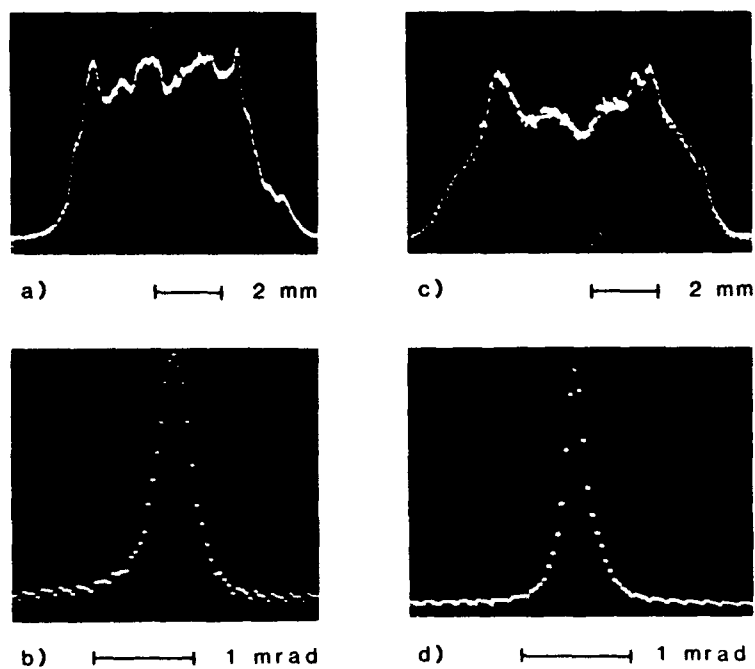


Fig. 3 - Near and far field intensity distributions of the beam coupled through the supergaussian mirror shown in Fig. 2(b) for two resonators magnifications: (a) and (c) show the near fields for $M = 1.36$ and 2 respectively; (b) and (d) the corresponding far-field.

spot size in the resonator. At the rod position the mode is cut by the rod aperture at 0.15% of the peak intensity which falls close to the lower limit established by the criterion reported in section 2. From the far-field pattern a divergence angle θ_d (at half width at half maximum) of 0.2 mrad is measured. The quantity $D\theta_d/\lambda$, equal to 1.0, almost corresponds to that of a diffraction limited beam, which for a rectangular profile turns out to be 0.6.

The shapes of typical near- and far-field intensity patterns are reported in Fig. 3(c) and 3(d) for $M = 2$. According to the theoretical plot of Fig. 1(a) the output beam shows a central dip in the near-field and the diameter of the beam at half maximum ($D = 6.8$ mm) is larger than that obtained at lower magnification. At this resonator magnification the mode is cut by the rod aperture at 5.4% of the peak intensity, which falls within the criterion considered in section 2. The divergence angle, $\theta_d = 0.12$ mrad, is slightly smaller as a consequence of a larger output beam and/or better mode. The sensitivity of the two resonators to mirror misalignment has been tested by measuring the output energy as a function of the mirror tilting angle. The value of the tilting angle that halves the output power is 0.25 mrad for $M = 1.36$ and 0.8 mrad for $M = 2$; therefore the high magnification resonator is less sensitive to mirror misalignment.

Figure 4 shows the output-versus-input energy curves for the two resonator magnifications. As expected the output energy is less for the higher magnification resonator, which however shows an output beam closer to diffraction limit and a lower sensitivity to mirror misalignment.

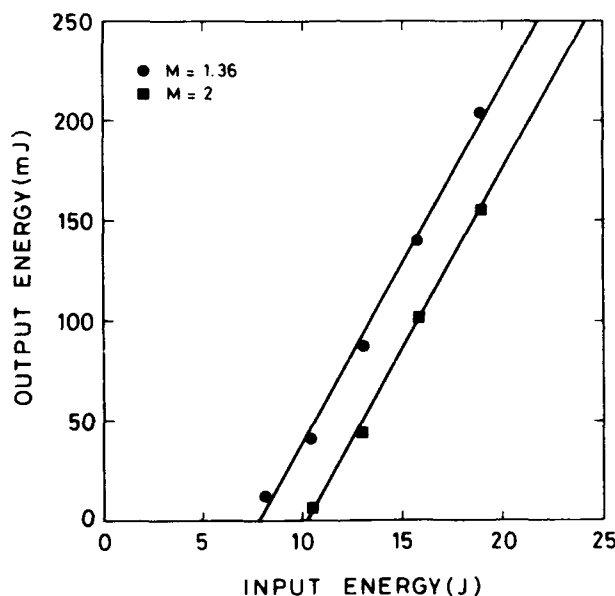


Fig. 4 - Laser output energy as a function of the electrical input energy to the lamp for the two resonators (of magnification M) considered in Fig. 3.

As a conclusion, we have introduced the supergaussian mirrors as a new class of variable reflectivity output couplers, and we have proposed a simple geometrical approach to analyze and design resonators using this kind of mirrors. A supergaussian mirror of order $n \approx 2.8$ built by special vacuum deposition technique, has been successfully tested with a pulsed Nd:YAG laser obtaining diffraction limited beams.

5. References

1. N.G.Vakhimov, Radio Eng. Electr. Phys. 10, 1439 (1965).
2. H.Zucker, Bell Syst. Tech. J. 49, 2349 (1970).
3. A.Yariv and P.Yeh, Opt. Commun. 13, 370 (1975).
4. D.M.Walsh and L.V.Knight, Appl. Opt. 25, 2947 (1986).
5. J.M.Eggleson, G.Giuliani, and R.L.Byer, J. Opt. Soc. Am. 71, 1264 (1981).

6. E.Armandillo and G.Giuliani, Opt. Lett. 10, 445 (1985).
7. P.Lavigne, N.McCarty, and J.G.Demers, Appl. Opt. 24, 2581 (1985).
8. S.De Silvestri, P.Laporta, V.Magni and O.Svelto, Opt. Lett. 12, 84 (1987);
S.De Silvestri, P.Laporta, and V.Magni, J. Opt. Soc. Am. A 4, 1413 (1987).
9. L.W.Casperson and S.D.Lunnam, Appl. Opt. 14, 1193 (1975).
10. A.E.Siegman, Lasers, Oxford University Press, 1986, pp. 913-921.
11. Y.A.Anan'ev and V.E.Sherstobitov, Sov. J. Quantum Electron. 1, 263 (1971).
12. V.E.Sherstobitov and G.N.Vinokurov, Soc. J. Quantum Electron. 2, 224 (1972).
13. G.L.McAllister, V.H.Steier, and W.B.Lacina, IEEE J. Quantum Electron. QE-10, 346 (1974).
14. A.E.Siegman and R.W.Arrathon, IEEE J. Quantum Electron. QE-3, 156 (1967).
15. A.Parent, N.McCarthy, and P.Lavigne, IEEE J. Quantum Electron. QE-23, 222 (1987).
16. W.F.Krupke and W.R.Sooy, IEEE J. Quantum Electron. QE-5, 575 (1969).
17. In collaboration with: (a) C.Zizzo, C.Arnone, C.Cali, and S.Sciortino, Dipartimento di Ingegneria Elettrica, Università di Palermo, Viale delle Scienze, 90128 Palermo, Italy; (b) B.Majocchi, TVM, Via P. Leto 6, 20100 Milano, Italy.
18. C.Zizzo, C.Arnone, C.Cali, and S.Sciortino, Opt. Lett., submitted (1987).

RAMAN GAIN SUPPRESSION CALCULATIONS

A. Flusberg and R. Holmes
AVCO Research Laboratory, Inc.
2385 Revere Beach Parkway, Everett, MA 02149
(617)381-4671

Abstract

The Raman gain for a broadband laser is reduced from the monochromatic value when the dispersion is small over a gain length for a low-Fresnel-number pump geometry for most Raman transitions.

Summary

A computer code with two transverse dimensions in a focussed geometry is used to predict the behavior of a Stokes seed generator. The presence of anti-Stokes radiation affects both the threshold and the spatial profile of the Stokes light. The computer program successfully predicts the experimental degree of gain suppression and the features of the far-field Stokes spatial profile at atmospheric pressure. The gain suppression factor for linearly polarized light in H_2 is found to depend on the Fresnel number of the focal geometry, the dispersion between the pump, Stokes and anti-Stokes, the pump power, and wavelength. This calculation also shows that the primary contribution to the Stokes is from approximately one-half the full Raman linewidth off-resonance for a tightly-focussed pump. Physically this occurs because the plane-wave gain is higher off-resonance since there is less parametric coupling of the Stokes and anti-Stokes. Additionally, the pump spatial profile causes ray-bending when off-resonance, resulting in a higher-gain configuration than that given on-resonance.

Introduction

The transmission of high-intensity light over long distances is altered by properties of the propagation medium. In particular, air results in phase and amplitude distortion of laser light. This distortion is caused by turbulence and various nonlinear processes. At lower pressure, it is thought that only a few processes have a significant effect because of the low density. Stimulated Raman scattering is expected to be the primary interaction. However, to test these expectations and measure their effect requires a difficult experiment. Hence, it is reasonable to pursue an alternative in which related, tractable experiments are performed and then to extrapolate to the upper atmosphere. Such an extrapolation should use analysis validated by the scaled-down experiments.

An analysis of Raman scattering should include diffraction, Stokes-antistokes coupling, dispersion, and laser polarization. There are numerous other aspects of Raman scattering which may be included in a detailed analysis of the Raman interaction. These effects are discussed in the next section. Those terms that are not important are dropped after brief consideration.

The third section discusses the numerical procedures used in solving the simplified equations. Economical, efficient routines are used to obtain accurate solutions with reduced computational effort. These solutions are presented in the final section, along with a discussion of the implications.

Equations of Motion

The general equations describing laser propagation in the atmosphere can be made very complicated. However, experience has shown that in clean air there are only a few major effects. Turbulence and laser-induced heating are two mechanisms which increase the angular divergence of the beam. For propagation in the upper atmosphere where the medium density is low, these effects may not be critical. Absorption is an effect which reduces the beam intensity and can result in heating of the medium. However, absorption is found to be insignificant at the higher altitudes.

Various complications to simple steady-state stimulated Raman scattering arise in particular cases. Laser pulses of very short duration result in a material oscillation

which is not in the steady-state regime. This may alter the gain behavior of the Raman interaction. Behavior off-resonance may be important for strong Stokes antistokes coupling. For high fluence and low medium density, population saturation may become important. Also, inhomogeneous Doppler broadening may dominate over collisional broadening at low densities. The nonlinear Kerr effect may also play a role in increasing the angular divergence of the beam, and in causing scintillation. Speculation regarding the importance of four-wave mixing between various Raman lines should be addressed. With these introductory remarks, one may write out the general equations of motion for a laser in the atmosphere, as follows.

Equation for propagation of laser:

$$\begin{aligned}
 \left(\frac{\partial}{\partial z} + \frac{\nabla_{\perp}^2}{2ik_m} \right) A_m = & \beta \omega_m [Q^* A_{m-1} \exp(i(k_{m-1} - k_m)z) \\
 & - Q A_{m+1} \exp(i(k_{m+1} - k_m)z)] \\
 & + ik_m (\Delta \beta_g \rho_o N_L n + \beta_g^{(0)} \rho) A_m \\
 & + ik_m \gamma_m \sum_j |A_j|^2 A_m \\
 & + ik_m \delta n_{oT} A_m - (\mu_m/2) A_m
 \end{aligned} \tag{1}$$

where

- A_m = m^{th} field; $m = 0$ corresponds to pump, $m = 1$ corresponds to Stokes
- k_m = optical wavenumber of field A_m
- ∇_{\perp}^2 = $\partial^2/\partial x^2 + \partial^2/\partial y^2$, z is direction of propagation
- β = gain constant such that ω_1 equals one-half the Stokes intensity gain
- ω_m = optical frequency of field A_m . ω_1 corresponds to Stokes
- Q = amplitude of optical phonon; the phonon is an off-diagonal density-matrix element
- $\Delta \beta_g$ = difference in Gladstone-Dale constants between ground state and Raman-excited state
- ρ_o = unperturbed gas density of ground state population
- N_L = Loschmidt number
- n = fraction of population transferred from ground state to excited state
- $\beta_g^{(0)}$ = Gladstone-Dale constant of unperturbed gas
- ρ = heating-induced perturbation of the density
- γ_m = Kerr constant for field A_m
- δn_{oT} = turbulence-induced refractive-index variations
- μ_m = intensity-absorption coefficient of field A_m

Equation for evolution of Q and n:

$$\left[\frac{\partial}{\partial t} + \Gamma_2 + i\Delta\omega + i\omega_{Dj} \right] Q = \Gamma_2 \left[\sum_j A_j A_{j+1}^* \exp(i(k_{j+1} - k_j)z) \right] (2n + n_0) + F \quad (2)$$

$$\left[\frac{\partial}{\partial t} + \Gamma_1 \right] n = \frac{\beta\omega_1}{\rho_0 N_L h \omega_1} 2\text{Re}(Q^* (\sum A_j A_{j+1}^* \exp(-i(k_{j+1} - k_j)z))) \quad (3)$$

where

- Q = amplitude of optical phonon
- n = population transferred to upper Raman level
- Γ_2 = phonon relaxation rate
- $\Delta\omega$ = detuning from material resonance
- ω_{Dj} = Doppler shift for jth atom
- n_0 = equilibrium population difference between ground state and Raman excited state
- Γ_1 = population relaxation rate
- β = gain constant
- ω_1 = Stokes optical frequency
- h = Planck's constant
- N_L = Loschmidt number
- ρ_0 = unperturbed gas density of ground state population
- k_i = optical wavenumber of field A_i
- F = noise source for phonon

Equation for heating:

$$\left(\frac{\partial}{\partial t} + v_0 \frac{\partial}{\partial x} \right) [v_s^2 \nabla_{\perp}^2 - \left(\frac{\partial}{\partial t} + v_0 \frac{\partial}{\partial x} \right)^2] \frac{\rho}{\rho_{\infty}} = - \frac{(\gamma-1)}{\rho_{\infty}} \nabla_{\perp}^2 h \quad (4)$$

$$h = \sum \mu_i |A_i|^2 + \Gamma_1 n h \omega_1 \rho_0 N_L \quad (5)$$

where

- v_0 = local wind speed in x-direction, transverse to direction of laser propagation
- v_s = speed of sound
- ρ = heating-induced density perturbation
- ρ_{∞} = unperturbed gas density
- h = heating rate
- μ_i = absorption coefficient for field A_i
- Γ_1 = population relaxation rate
- n = population transferred to upper Raman level

ω_r = optical frequency corresponding to the energy difference of the Raman shift

These equations are written for a reference frame moving with the laser pulse (the so-called "retarded" frame). Since dispersion in the upper atmosphere is weak, we have neglected differences in group velocities for the various fields A_i . We have also neglected four-wave mixing terms which couple different Raman transitions; these parametric processes are omitted in this paper.

The above equations are presently those modelled with the Avco Raman code. Each physical process is characterized with a separate subroutine of high convergence order in the dependent variables. These subroutines may be included to model the important physical effects for a given situation. Despite each subroutine's high degree of accuracy, care must be taken to obtain convergence of the overall program. The overall program for the simplified, approximate equations may be much more straightforward than that indicated above.

In order to simplify the above equations and to consider generic effects, the transient phenomena are disregarded. The resulting steady-state equations represent the propagation of most beams of interest. In addition, the Kerr effect, absorption, and turbulence are ignored for the present calculations. The resulting steady-state Raman equations are as follows:

$$\left(\frac{\partial}{\partial z} + \frac{\nabla_{\perp}^2}{2ik_m} \right) A_m = \beta_{\omega_m} [Q^* A_{m-1} \exp(i(k_{m-1} - k_m)z) - QA_{m+1} \exp(i(k_{m+1} - k_m)z)] \quad (6)$$

$$Q = \left[\sum_j A_j A_{j+1}^* \exp[-i(k_{j+1} - k_j)z] \right] / (1 + i\Delta\omega/\Gamma_2) \quad (7)$$

These are the equations modelled and the results are a consequence of the effects so described. The following section details the numerical techniques used in computerizing the solution to these equations.

Numerical Procedure

Equations (6) and (7) shown above may be viewed as a simple set of ordinary differential equations in which diffraction and nonlinear gain are the driving terms. This is the basis for a split-operator technique which computes a contribution for gain and diffraction and averages them together appropriately.

The diffraction operator contribution is performed in the usual way, by taking the fields A_m from the x-representation to the k representation using fast Fourier transforms (FFT's). Then $A_m(k)$ is multiplied by a complex phase factor $\exp(ik^2 \Delta z / 2k_m)$ and the inverse transform is performed. These transforms may be one-dimensional (1-D), circular, or two-dimensional (2-D), depending on the desired propagation geometry. The 1-D and 2-D rectilinear transforms are performed with the usual FFT algorithms. The resulting diffraction operation is denoted below as D, regardless of the propagation geometry.

The gain (i.e., Raman conversion) operator, denoted by G, is also standard. A fourth-order Runge Kutta-Simpson algorithm is used to integrate the equations (neglecting diffraction) over the interval Δz . An approximation is used to calculate $k_{m+1} - k_m$ for greater numerical accuracy of the dispersion.

Our combined algorithm for gain and diffraction is:

$$A_m(z + \Delta z) = \frac{1}{2} [DG + GD] A_m(z) \quad (8)$$

This particular scheme is an improvement on the usual split-operator algorithm mentioned in Ref. 1, since it may be shown that our scheme has an additional power of Δz in its order of convergence over the usual split-operator scheme.

In many of the cases of interest, particularly the laboratory experiments, the beams propagate through a focus. We have therefore developed a version of the Raman code which has full-focus capability. Our approach uses the Talanov lens transformation. This approach gives a result that is exact within the paraxial approximation, up to the

grid resolution. Denoting the lens transformation as T and the previous diffraction-gain split-operator as P , one obtains the following expression for the numerical technique:

$$A_m(z+\Delta z) = TP A_m(z) \quad (9)$$

This method gives reasonable results and seems to converge rapidly with decreasing Δz , even for strongly-focussed geometries.

With a description of the numerical method complete, the computational results will now be described.

Results

Of primary interest is the gain suppression of linearly-polarized light. The gain suppression factor as a result of Stokes-antistokes coupling is calculated by dividing the resonant gain increment of circularly polarized light with that of the gain-suppressed linearly-polarized light. The circularly polarized gain is multiplied by two-thirds to account for the decreased gain of linearly polarized light far from phase matching. Thus the following results show how the gain is reduced by the effect of Stokes-antistokes coupling.

Figure 1 shows the gain-suppression factor as a function of the unsuppressed gain g_0 (defined here as $2/3$ the resonant gain increment of circularly polarized light), for a focussed geometry corresponding to a 1-amagat N_2 S(8) Raman experiment (laser wavelength = 1050 nm; focal length = 15 m; beam diameter at the cell entrance = 1 cm; beam diameter at focus = 1 mm; Raman cell length = 30 m). Figure 1 gives the calculated gain-suppression factor when the beat between the pump and Stokes is exactly on resonance with the Raman transition. Far from phase-matching this would correspond to the Stokes frequency of maximum gain. However, as may be seen from the figure, because of strong Stokes-antistokes coupling in this geometry the gain at this frequency is reduced by factors of seven to ten. As the frequency offset of the Stokes is varied, the gain is seen to peak at roughly the frequency corresponding to that of Figure 2. Figure 2 shows the gain at a Stokes frequency shifted to the blue by half the Raman linewidth. The result is somewhat surprising; the gain is actually higher (less suppressed) than for the resonant calculation. The off-resonant gain is only reduced by factors of two to three. This frequency of peak gain may vary with the geometry as indicated in Ref. 1. It is also worth noting that gain suppression by a factor of approximately 2 is indicated in the N_2 experiment. This is in notably good agreement with the prediction of a gain-suppression factor of 2.3 at threshold, as shown in Figure 2, corresponding to similar conditions. The small difference may be a result of many different effects, such as the exact spatial and temporal profile of the pump. The experimental beam is not a diffraction-limited gaussian beam that is modelled in the calculation. Also the mode structure of the pump laser is such that the beam cannot be considered monochromatic as is done in the computation, since the mode spacing is much smaller than the Raman linewidth.

These results are similar to those obtained for H_2 vibrational Raman in Ref. 1, with approximately the same amount of gain reduction for comparable geometries (when the phase-mismatching length is less than a gain length). The color of the Stokes light is blue-shifted in both cases by roughly the same amount. Thus the computations appear to give estimates of the gain suppression comparable to that of the experiment and that of other authors.

It is also of interest to check the concurrence of the spatial profiles between the experiment and the computation. This is indicated in Figures 3-6. Figure 3 shows the Stokes intensity profile at the output window for various input intensities and a resonant Stokes frequency. Figure 4 shows the same relationships at a frequency shifted half a linewidth to the red. These results are of interest but are not directly comparable to the experimental profile in which the appearance is determined by the Stokes frequency of highest gain. Profiles corresponding (roughly) to the frequency of highest gain are shown in Figure 5. Far-field intensity profiles for the same frequency offset are shown in Figure 6. Several interesting features may be noted in these plots. The intensity profiles of Figure 3 show that significant energy has moved outward from the region containing the pump. This is undoubtedly because the Stokes-antistokes coupling eliminates growth in the forward direction. The highest intensity also shows a dramatically different profile compared to the other two plots. The intensity profiles of Figure 4 show that the Stokes light is more concentrated at the red-shifted frequencies compared to the profiles of Figures 3 and 5. This is a consequence of the self-focussing at the red-shifted frequencies. Nonetheless the blue-shifted frequencies for which profiles are shown in Figure 5 have the highest gain. This is in accord with

the results of Ref. 1 at the Fresnel numbers present in the experiment. Also in agreement with the result of Ref. 1 is the far-field intensity distribution which has a hole in it as shown in Figure 6. In addition, the experimental data indicates a Stokes far-field intensity which is spatially skewed with respect to the laser intensity distribution in a way which suggests a similar hole. Thus the calculated transverse profiles compare qualitatively with the experimental profiles and those of other authors.

In summary, the computational methods and approximations have resulted in predictions which agree qualitatively with the experiment and with other publications. Despite the partial agreement between theory and computation, several important features of the Stokes output are not described by the calculation. One such feature is the apparently random variation of the Raman threshold with pump laser energy for linearly polarized light. Another important and unexplained feature is the distribution of energy among the various Stokes lines. Hopefully a more complete analysis will be able to predict such behavior.

References

1. B.N. Perry, P. Rabinowitz, and D.S. Bomse, Opt. Lett. 10, 146 (1985).

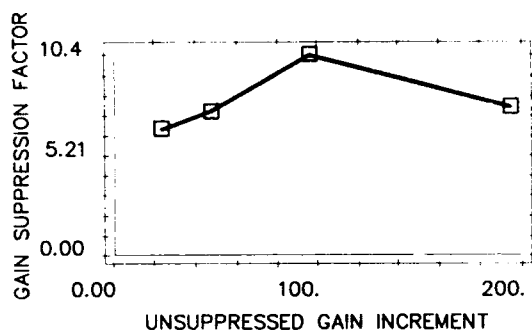


Figure 1 Computed Gain-Suppression Factor g_0/g vs Unsuppressed Gain Increment g_0 for the Laboratory Geometry at the Resonant Frequency.

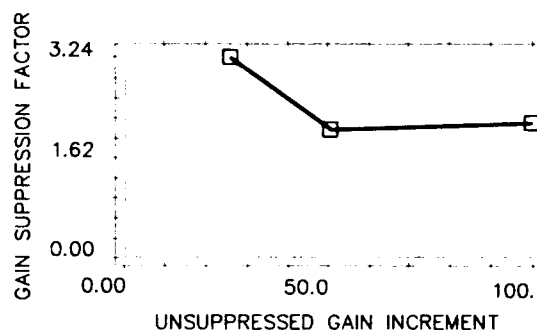


Figure 2 Computed Gain-Suppression Factor vs the Unsuppressed Gain Increment g_0 for the Laboratory Geometry. The Stokes frequency is offset so that the pump-Stokes beat is half a Raman linewidth off the Raman Resonance.

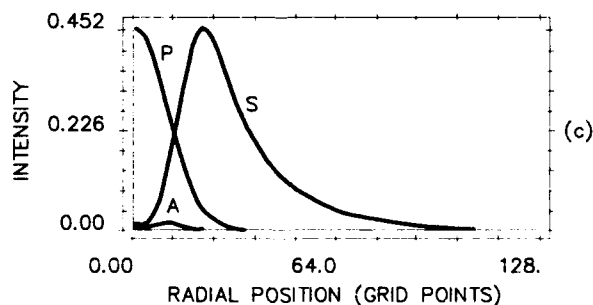
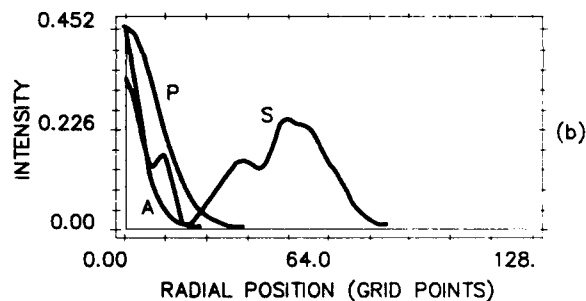
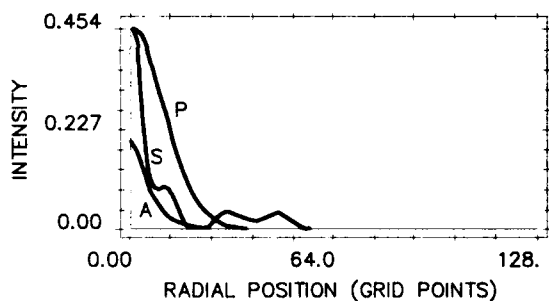


Figure 3 Computed Stokes Intensity vs Radius at Cell Exit Window for Entrance-Cell Window Intensity of: (a) 0.5 GW/cm^2 ; (b) 1 GW/cm^2 ; (c) 4 GW/cm^2 . Horizontal scale: 0-3.6 cm full scale. P - pump; S - Stokes, A - Anti-Stokes Pump and Stokes Peak Normalized to Full Scale: Antistokes Peak Normalized to that of Stokes. Only 128 of the 256 radial points used in the Calculation are Shown.

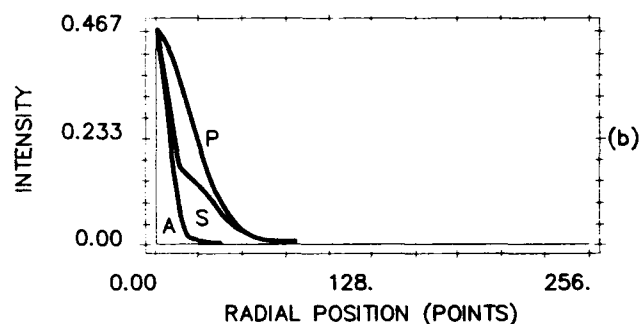
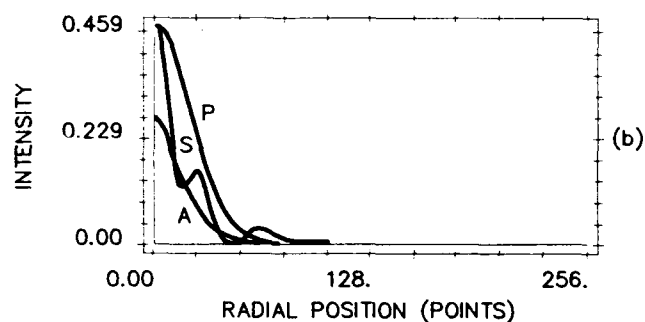
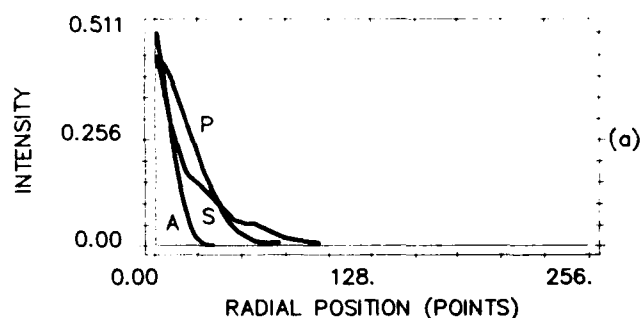
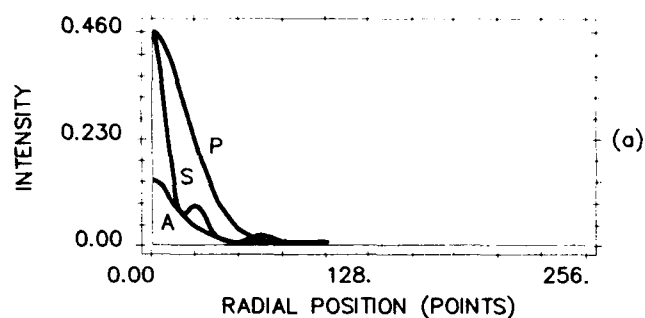


Figure 4 Computed Stokes Intensity Profile at a Frequency Shifted Half a Raman Linewidth to the Red. (a) 0.5 GW/cm²; (b) 1 GW/cm².

Figure 5 Computed Stokes Intensity Profile at a Frequency Shifted Half a Raman Linewidth to the Blue. (a) 0.5 GW/cm²; (b) 1 GW/cm². Only 256 of the 512 Radial Points Used in the Calculation are Shown.

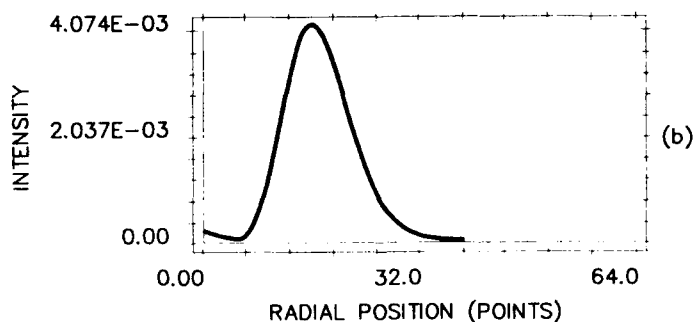
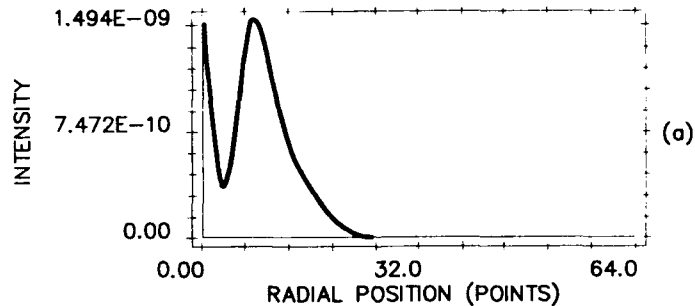


Figure 6 Computed Far-Field Stokes Intensity Profiles at a Frequency Shifted Half the Raman Linewidth to the Blue. (a) 0.5 GW/cm²; (b) 1 GW/cm². Only 64 of the 512 Radial Points Used in the Calculation are Shown.

PROPAGATION OF A HIGH ENERGY UV LASER PULSE THROUGH ABSORBING AEROSOLS

Shiow-Hwa Lin and Mary P. Thomas

Western Research Corporation
9555 Distribution Avenue
San Diego, California 92121

Abstract

The effects of propagating a high energy collimated UV laser beam through an absorbing cloud are presented. The absorption is strong enough that the aerosols undergo explosive evaporation during the laser pulse. Wavefront movements of a probing laser beam due to the high energy laser beam absorption and the cloud clearing phenomenon are discussed.

Introduction

Propagation of high energy laser beams through the atmosphere is rather complicated. The beams suffer not only from scattering and absorption by both atmospheric molecular species and atmospheric aerosols, but also more importantly from the nonlinear effects associated with changes in the atmospheric optics caused by these processes.^{1,2,3} Cloud clearing phenomenon was suggested as a means of increasing laser beam transmission by dissipating the scattering aerosols into small, and thus less efficient, scatterers through strong aerosol absorption. This phenomenon has been the subject of theoretical investigations for many years.⁴ Experimental investigation of the cloud clearing phenomenon in a laboratory simulated environment from a low power CO₂ laser beam was reported not long after the invention of the CO₂ laser.⁵ Experiments involving high flux lasers, however, have been limited to single droplet investigations so far.^{6,7}

In this paper we report the results of an experimental study on the interaction of a collimated high energy UV laser pulse with a large volume absorbing cloud in a laboratory environment. The laser beam extinction due to aerosol absorption was so strong that given the laser fluence of the experiment the aerosols were well into the explosive evaporation regime. We believe that this experiment is the first of its kind to study the interaction of a large aperture pulsed high energy laser beam with a large volume absorbing cloud which is in the explosive evaporation regime.

Experimental Setup

The experimental system which was used in performing this study is shown in Figure 1. A high energy e-beam pumped excimer laser system operated at a 308 nm output wavelength (XeCl) was used as the laser energy source. The laser pulse width was 0.9 μ s. The laser fluence delivered to the aerosol chamber was $\sim 3 \text{ J/cm}^2$ with a beam aperture of approximately 10 cm². The aerosol chamber was a 15 cm dia, one meter long cylindrical pyrex tube. Water droplets were generated by an ultrasonic humidifier and fed to the chamber through a flexible tubing. A small amount of a strong UV absorber (cinnamate salt) was dissolved in the water to achieve the necessary absorption. The absorption characteristics of the cinnamate salt solution are discussed in the next section.

The diagnostic system consisted of a large aperture Mach-Zehnder interferometer combined with a streak camera system for wavefront movement analysis, and additional standard laser power and energy diagnostics. Transmission through the cloud channel was monitored continuously by a low power collinearly propagating HeNe laser beam. This measurement provided information about the cloud densities. Input and transmitted UV laser energy were monitored to measure the total extinction of the pulsed UV laser beam. This was compared with the low power measurement which in turn gave information on the cloud droplet sizes.

Results and Discussion

Figure 2 shows the comparison of the transmission of the laser beam at two different wavelengths, namely at 633 nm (HeNe) and at 308 nm (XeCl) in the cloud. Figure 2a shows the comparison with a pure water only cloud. The total extinction in this case is due to Mie scattering by the cloud droplets since the absorption coefficient of pure water at both wavelengths is very small ($\alpha_{\text{abs}} = 6 \times 10^{-3} \text{ cm}^{-1}$ @ 308 nm and $= 3 \times 10^{-3} \text{ cm}^{-1}$ @ 633 nm).⁸ The slope of this curve, which is the ratio of the Mie

scattering efficiency of the cloud droplets at these wavelengths, is found to be 0.8. This implies that the average droplet size $\langle r_0 \rangle$ should be large compared to both wavelengths, that is, $\langle r_0 \rangle \geq 1 \mu\text{m}$. Notice that this measurement only sets the lower bound on the average aerosol size, further measurement is needed to establish the size distribution.

Figure 2b shows the same measurement, but for the UV absorbing cloud which contains the cinnamate solution. Notice that the laser fluence for this set of data was substantially less than the available fluence. This is because at a high fluence level nonlinear effects associated with explosive cloud evaporation occur during the laser pulse. The cinnamate concentration of the solution for the experiment was controlled at the 20 g/liter level. We have performed a low power absorption measurement on the cinnamate solution at very low concentration, indicating that at the 20 g/liter concentration level the absorption coefficient is 1840 cm^{-1} at 308 nm. The absorption coefficient of cinnamate solution at 633 nm was negligibly small. The slope of Figure 2b which gives the ratio of the total extinction efficiencies for the cinnamate cloud at these two wavelengths is 1.2. Since the asymptotic limit of the total extinction efficiency of aerosol particles is two, regardless of the absorption strength of the aerosol particles,⁹ the additional attenuation measured with the cinnamate cloud has to come from the background cinnamate vapor.

An important time scale concerning pulsed aerosol absorption and its subsequent explosion is the time it takes for the aerosol droplets to rise in temperature to $\sim 0.8T_c$ (where T_c is the critical temperature of the bulk liquid), and to create a pressure inside the expanding droplet greater than the surface tension of the liquid.¹⁰ At this time, the aerosol particles will undergo explosive evaporation. We can write an order of magnitude estimate for the characteristic time τ_{exp} as:

$$\alpha I \tau_{\text{exp}} = \rho C_v \Delta T + 2 \frac{\sigma}{r_0}$$

where α is the absorption coefficient, I is the incident laser flux, τ_{exp} the explosive evaporation time, ρ is the liquid density, C_v is the heat capacity, $\Delta T = T_c - T_{\text{room}}$, σ is the surface tension, and r_0 is the radius of droplet. For the case of interest in this experiment we have: $\alpha = 1840 \text{ cm}^{-1}$, $I = 3.3 \times$

10^6 W/cm^2 , $\Delta T = 220^\circ \text{ C}$, $\sigma = 7.2 \times 10^{-6} \text{ J/cm}^2$, $r_0 = 1 \mu\text{m}$ and $\tau_{\text{exp}} = 0.15 \mu\text{s}$. Calculation indicates that the aerosol absorption is strong enough that the cloud is evaporating explosively even during the laser pulse.

Figure 3 shows the wavefront movement of the probing laser beam on a short time scale, with the timing of the reference UV laser pulse shown at the left. The picture shows the time evolution of a horizontal slice of the fringe pattern from the Mach-Zehnder interferometer. Time is running vertically downward. The total time span in this figure is $5 \mu\text{s}$. It can be seen from Figure 3 that during the short (several μs) time scale, the wavefront movement is not very significant. The movement was linear with time during the laser pulse. Total fringe movement incurred at the end of the laser pulse was consistent with what one would expect if the cloud droplets in the laser beam path had evaporated completely. This wavefront movement is in contrast with the longer ($500 \mu\text{s}$) time scale behavior as shown in Figure 4 which shows a much more violent movement. After $100 \mu\text{s}$ which corresponds to the acoustic transit time across the beam aperture, the fringe pattern becomes quiet again. At longer time sweeps (1 ms) of the same measurement, the pressure wave bouncing back from the chamber wall could be clearly seen.

The cloud clearing phenomenon registered as an improvement in the low power probing beam transmission right after the high energy UV laser beam application was achieved, as is clearly shown in Figure 5. Figure 5a shows that the risetime of the visibility improvement is $\leq 100 \mu\text{s}$. There is a lot of fine structures in the signal after the cloud clearing has set in. This might be due to heated vapor forced convection in and out of the probing column. This movement might also carry the unheated droplets, which were originally outside of the probing path, into it in a turbulent fashion. Figure 5b shows that the cloud clearing which improves the laser beam transmission can last for as long as two seconds, after which the transmission returns to the prelaser application level. No experiments were performed to establish the scaling of the clearing time with other variables. Figure 6 shows the visibility improvement data from a collection of shots where the input laser fluences were between 2 and 3 J/cm^2 . The results show that at higher cloud density the cloud clearing effect can improve the beam transmission by as much as threefold, while at lower cloud density the effect is less dramatic.

Conclusion

Results from an experimental investigation of the interaction of a collimated high energy UV laser beam with a large volume absorbing cloud are presented. Measurements of the cloud extinction characteristics indicate that the average size of the aerosol droplets is probably greater than 1 μm . The absorbing droplet has enough absorption that even during the laser pulse it undergoes explosive evaporation which results in uniform, linear fringe movements during the laser pulse. Total fringe movement during this period is consistent with that expected from total evaporation of the cloud droplets. This is followed by more violent fringe movements during the acoustic wave transit time. At about this time, evidence for the cloud clearing effect appears as an improvement in the probing laser beam transmission. The cloud clearing phenomenon lasts as long as two seconds after which the transmission returns to the pre-laser application level.

Future experiments are planned to explore the scaling of the cloud clearing process and the detailed dynamics of the explosive evaporation associated with strong aerosol absorption of a high energy pulsed laser beam.

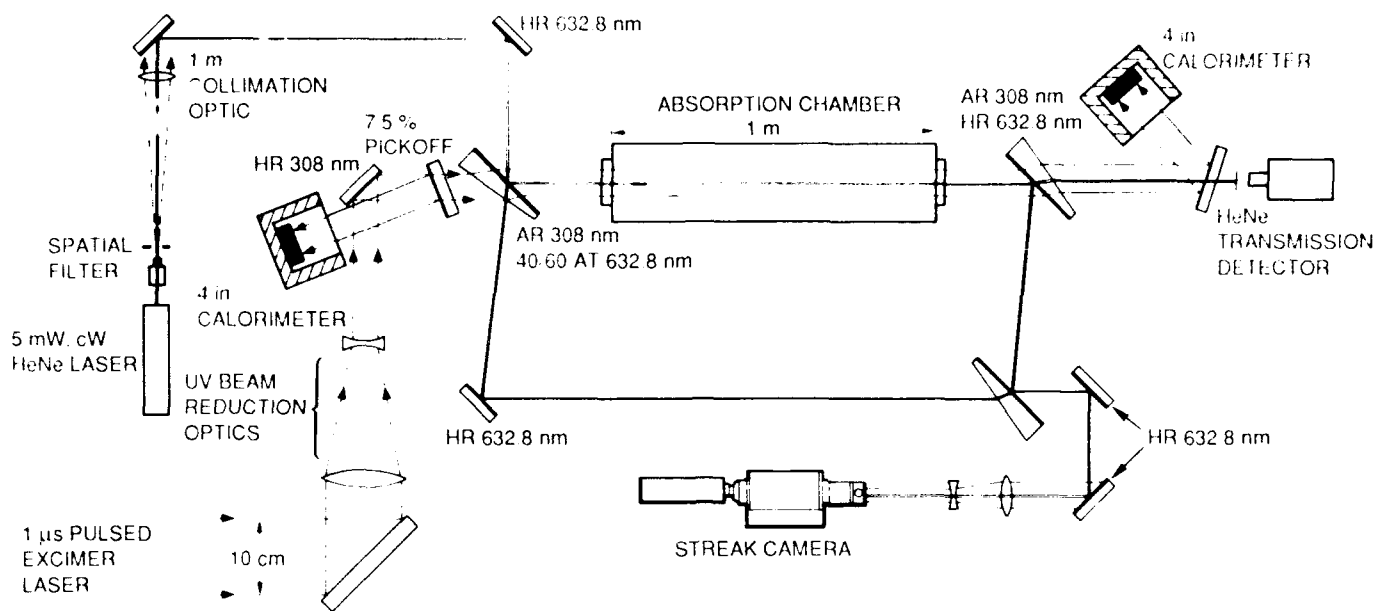
Acknowledgments

We thank Drs. E. Korevaar and L. Sverdrup for their help on the experimental

approach. We also thank M. Rivers and M. Squire for their assistance in conducting the experiments. This work was performed under the support of the Office of Naval Research, contract N00014-86-C-0302.

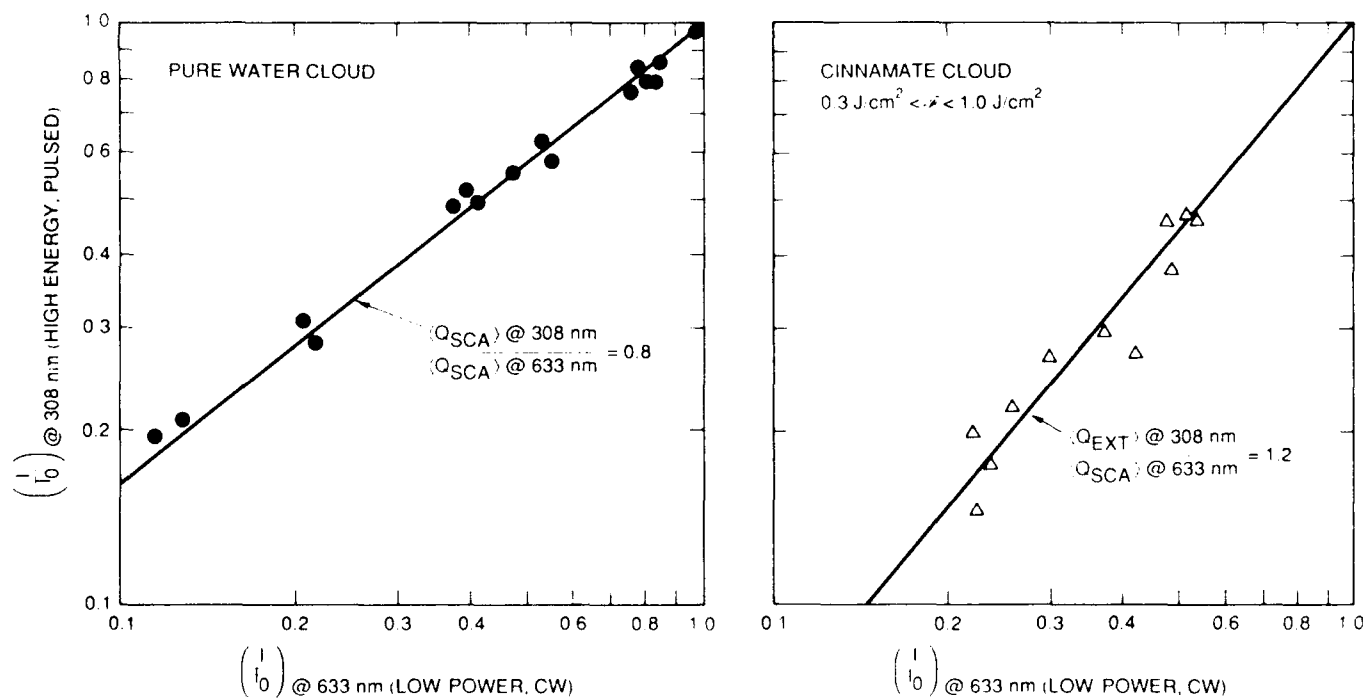
References

- (1) F.G. Gebhardt, Appl. Opt., 15, 1479(1976)
- (2) J.L. Walsh and P.B. Ulrich, Laser Beam Propagation in the Atmosphere, J.W. Strohbehn Ed.(Springer, Berlin, 1978) p.223
- (3) D.C. Smith, Proc. IEEE, 65, 1679(1977)
- (4) S.L. Glickler, Appl. Opt., 10, 644(1971)
- (5) G.J. Mullaney, W.H. Christiansen and D.A. Russell, Appl. Phys. Lett., 13, 145(1968)
- (6) P. Kafalas and A.P. Ferdinand, Jr., Appl. Opt., 12, 29(1973)
- (7) P. Kafalas and J. Herrmann, Appl. Opt., 12, 722(1973)
- (8) G.M. Hale and M.R. Querry, Appl. Opt., 12, 555(1973)
- (9) C. Bohren and D. Huffman, Absorption and Scattering of Light by Small Particles(Wiley, New York, 1983)
- (10) S.M. Chitanvis, J. Appl. Phys., 62, 4387(1987)



87-7198
Ref. 6398

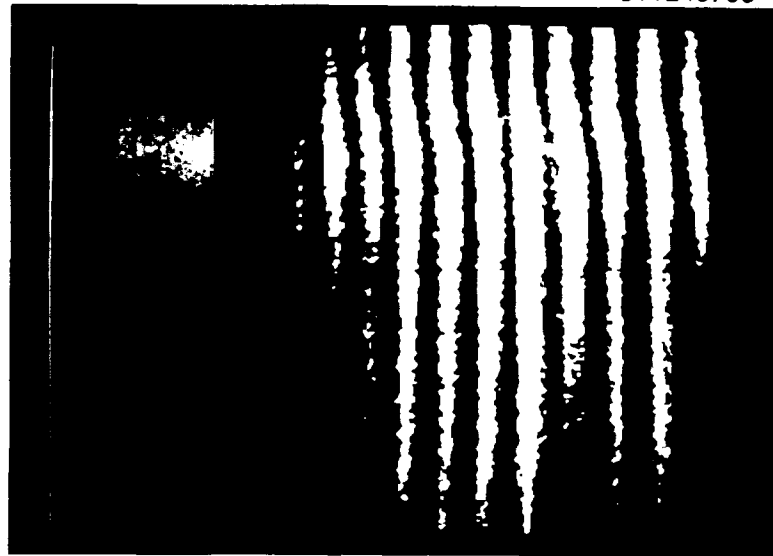
Figure 1. Schematic of the experimental system for high energy laser beam propagation experiments.



7-7342
Ref. 7202
Ref. 7203

Figure 2. Comparison of laser beam transmission at two different wavelengths for (a) a pure water cloud and (b) a cinnamate cloud.

S11248705



LASER
TIMING

SLITTED FRINGE PATTERN
5 μ s SWEEP

P-METHOXYCINNAMATE CLOUD

VISIBILITY: 52% $[(I/I_0) @ 633 \text{ nm}]$

LASER FLUENCE: 2.5 J/cm²

87-7199

LASER PULSEWIDTH: 0.9 μ s

Figure 3. The wavefront movement of the probing laser beam on a short time scale. The timing of the reference UV laser pulse is shown at the left.

S11248714



← LASER FIRED

P-METHOXYCINNAMATE CLOUD

VISIBILITY: 25% $[(I/I_0) @ 633 \text{ nm}]$

LASER FLUENCE: 2.7 J/cm²

LASER PULSEWIDTH: 0.9 μ s

SLITTED FRINGE PATTERN

87-7200 500 μ s SWEEP

Figure 4. The wavefront movement on a longer time scale (500 μ s span) is much more violent. After ~100 μ s from the high energy laser application, the wavefront becomes quiet again.

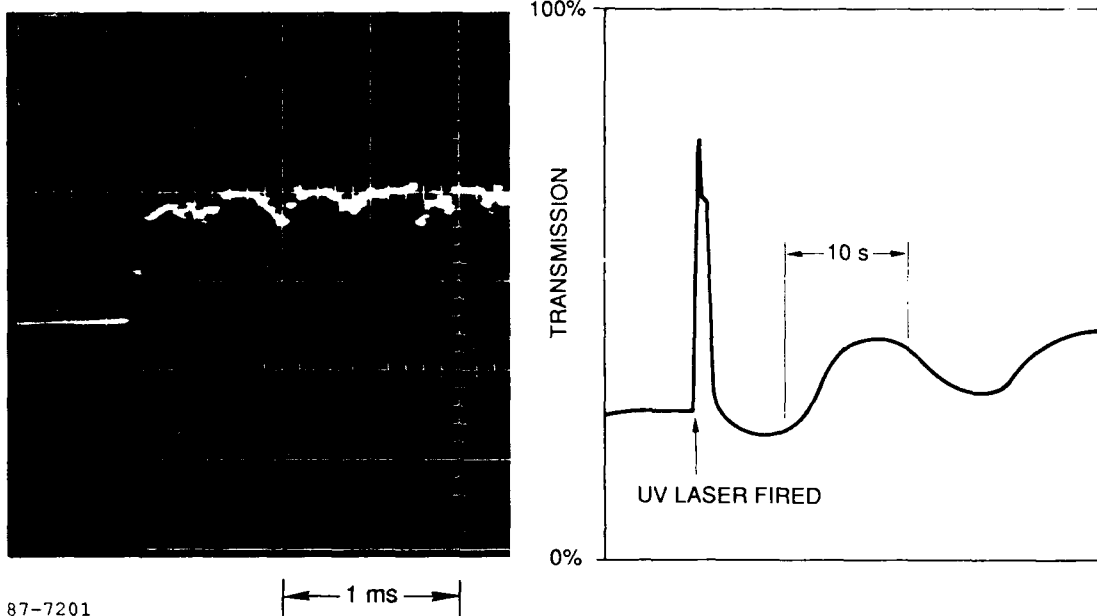


Figure 5. The cloud clearing phenomenon increases the probing laser beam transmission. (a) The rise-time of the transmission increase is $\sim 100 \mu\text{s}$. (b) The cloud clearing can last as long as 2 s.

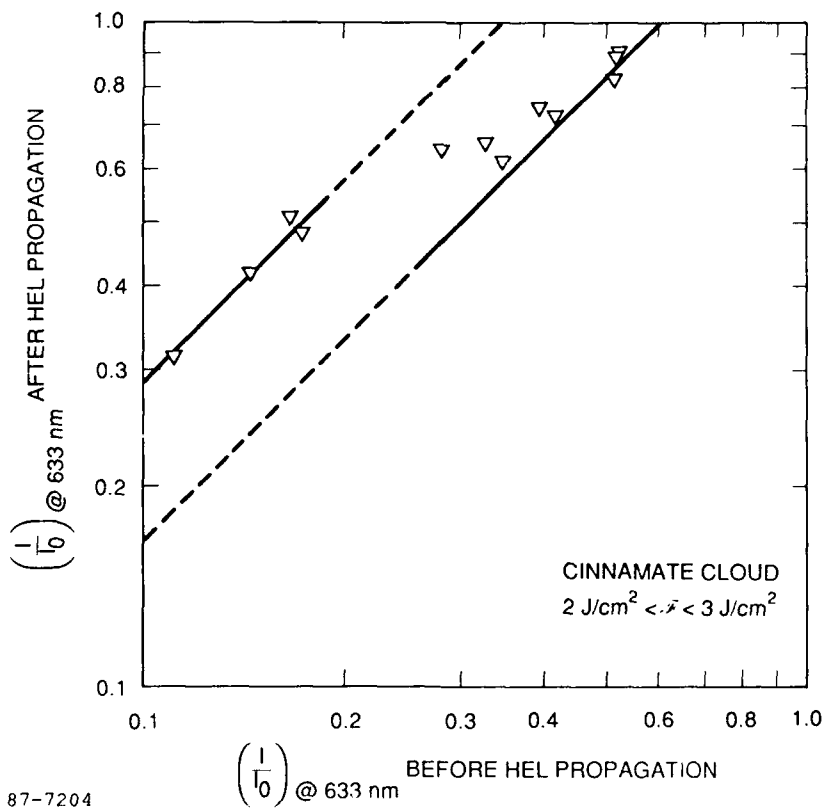


Figure 6. Comparison of the probing beam transmission before and after the high energy laser beam propagation.

IMAGE ANALYSIS FOR LASER-WRITTEN HARDCOPY

Rodney Shaw
Center for Imaging Science
Rochester Institute of Technology
One Lomb Memorial Drive
Rochester, New York 14623

Abstract

As the number of applications grow for laser-written imagery, there is an increasing interest in the manner of which the associated image quality may be expressed, and especially in the way in which new image metrics may be required. Experience shows however that existing metrics, developed in the past for more conventional types of imagery, may be readily adapted to laser-written hardcopy, with the benefits of allowing absolute comparisons. A further advantage of these metrics is that, as for conventional imaging, they readily lend themselves to systems modelling studies, aimed at identifying the mechanistic parameters, which control and limit the final image quality.

A review is given of some of the recent work in this field, and examples are given of the way in which the mechanisms of laser writers influence the associated image quality metrics.

Introduction

As laser-written hardcopy becomes a common imaging output mode, the problem is posed of expressing the quality associated with the image in a rigorous and absolute manner. Especially, as laser-writers become more sophisticated, growing importance is attached to the question of designing image quality into the system. Although there is a natural tendency to develop new, technology-specific image descriptors, experience shows that in fact it is more fruitful to look to the wider world of imaging and borrow/adapt well-established imaging systems evaluation methodologies.

It is the purpose of this paper to outline the nature and origins of existing image descriptors, and to indicate how they may be successfully applied in the present context.

Linear Systems Approach

The application of Fourier-based linear systems theory to optical and photographic images has a long history, as summarized in reference 1. However the majority of this work was carried out in the context of so-called continuous-tone imagery, as in conventional photography. The problem is thus posed of adapting this body of knowledge to cases where the image is scanned/sampled/screened, etc., or in other words takes on discrete characteristics, as in conventional halftones.

A landmark contribution was made in 1934 by Mertz & Gray², who provided a fundamental two-dimensional analysis of the role of the scanning aperture in picture transmission in the context of television systems. Almost forty years later

this work was extended by Robinson³, who also developed a rigorous mathematical approach to the analysis of a two-dimensional image screening process. More recently Huck et al.⁴ presented quantitative results on the magnitude of aliasing and blurring as a function of random radiance fields typical for natural scenes, and of spatial responses and sampling intervals typical for optical-mechanical scanners.

Information Theory Approach

The success of application of the Fourier-based linear systems approach to images of a discrete nature leads naturally to the question of overall quality criteria in these terms. An information-theory approach is then an obvious choice, and this approach has yielded conspicuous successes in many branches of applied imaging. Shannon's signal-to-noise based information theorems⁵ were subsequently adapted to two-dimensional spatial images, notably by Fellgett and Linfoot⁶ in 1955. Numerous extensions of this approach to discrete information storage⁷ and continuous recording⁸ have followed.

In 1984 Fales et al.⁹ specifically addressed the application of information theory to the performance and design of line-scan and sensor-array imaging systems. They investigated the practical design implications of the key systems components which limit and determine signal and noise for line scan arrays. For example, they considered the influence on signal transfer of the spatial lattice geometry (and hence showed the advantages of a regular hexagonal array) and the effects of sampling and quantization noise on the overall noise spectrum.

The information theory approach thus offers practical solutions to systems optimization of laser writers, and subsequent developments in this field would seem promising. However for convenience the approach adopted here is based on the closely-related concept of noise-equivalent input.

Noise-Equivalent Image Metrics

The development of noise-equivalent image metrics took place in the context of quantum limited detectors, and fundamental contributions in the imaging field were due to Rose¹⁰ and Jones¹¹, with a summary given in reference 12.

Under conditions where the input exposure in quantum-limited this approach is naturally applicable, and is based on the quantized nature of the input radiation. In other words, imaging is approached from a "particle" viewpoint, rather than the "wave" viewpoint of linear systems theory. Even when there is no input exposure criterion as such, the metric of noise-equivalent input, or noise-equivalent quanta (NEQ) still provides a universal imaging metric. We may define the efficiency of information transfer during imaging the detective quantum efficiency (DQE), where

$$DQE = \frac{\overline{\Delta Q^2}}{\Delta 0^2} \left(\frac{d0}{dQ} \right)^2$$

Q denotes exposure (input) quanta,
0 denotes output variable,

DQE thus compares input to output variances in like terms. Making use of the Poisson nature of the exposure quanta,

and in terms of the gain, g

$$\overline{\Delta Q^2} = Q,$$

$$DQE = \frac{Q}{\overline{\Delta Q^2}} g^2$$

The number of noise-equivalent quanta (NEQ) associated with the exposure Q is then derived from the relationship

$$DQE = \frac{NEQ}{Q}$$

and hence

$$NEQ = \frac{Q^2}{\overline{\Delta Q^2}} g^2$$

The link with linear systems theory can be made by the generalized expression¹³

$$NEQ(\omega) = \frac{Q^2}{\overline{\Delta Q^2}(\omega)} g^2(\omega)$$

where ω denotes the spatial frequency variable, and we are now concerned with the spatial frequency components of signal gain and image noise. Further, when these latter quantities are themselves functions of exposure level, we write

$$NEQ(Q, \omega) = \frac{Q^2 g^2(Q, \omega)}{\overline{\Delta Q^2}(Q, \omega)}$$

In terms of familiar photographic image metrics of gamma, MTF and Wiener Spectrum, we can write for the gain

$$g(Q, \omega) = \frac{\log_{10} e}{Q} \gamma(Q) MTF(\omega)$$

and for the output variance

$$\overline{\Delta Q^2}(Q, \omega) = WS(Q, \omega)$$

and finally

$$NEQ(Q, \omega) = \frac{0.189 \gamma^2(Q) MTF^2(\omega)}{WS(Q, \omega)}$$

The imaging problem can then be reduced to optimization of DQE for detection (image exposure/capture) and maintenance of captured NEQ through subsequent image systems transfer through to output, or hardcopy.

Evaluating Halftones

Both the linear-systems approach and the noise-equivalent viewpoint have been proved useful in the context of halftones. For example Kermisch and Roetling¹⁴ have calculated the Fourier spectrum of a halftone image as a function of the original continuous-tone image and the halftone process. It has also been demonstrated¹⁵ how the signal-to-noise ratio of a halftone image may be calculated in a way which leads to the determination of the number of NEQ's for a halftone system. Following this latter approach, a more detailed noise analysis of

electrophotographic halftones has shown how noise models may be developed for quantized output images^{16,17}, and especially how the Siedentopf relationship¹⁸, an image-particle model developed for continuous-tone photographic images, might be applied to electrophotographic halftones. In its simplest form this states that the low-frequency Wiener spectrum may be related to the number, N , and cross-section area, a , of the image particles in a half-tone cell by

$$WS(Q,0) = 0.189 N a^2$$

This relationship allows the number of NEQ's recorded per half-tone cell to be related to the characteristics of the imaging particles.

Evaluating Laser-Written Images

An extensive review of laser scanning for electronic printing is due to Urbach et al.,¹⁹ with special emphasis on the role of systems parameters. Bestenreiner et al.²⁰ have studied the visibility of raster lines and banding, enabling performance standards to be set for polygon mirror beam deflectors. Sullivan and Ray²¹ have considered the modification of the profile of the laser exposure beam from an image quality viewpoint. Other relevant investigations include the relationship of random and periodic noise in raster-written images²², an analysis of image noise due to position errors^{23,24}.

The specific application of noise-equivalent metrics to laser-written images was discussed by Shaw and Burns²⁵, and recently Burns^{26,27} has elaborated on this approach. Figure 1 shows a calculation of the number of NEQ's per pixel as a function of the number and size of the particles used to form the image. This calculation was based on a laser-writer as the hardcopy device for the display of detailed information from a medical radiograph²⁵.

Figure 2, due to Burns²⁷, shows a similar calculation over the complete spatial frequency and exposure working space. The NEQ values calculated here include the influence of laser and quantization noise as well as the particle size of the hardcopy process. When expressed in this way the image quality can thus be compared in absolute terms with any other type of imaging process, conventional or otherwise.

Future advances in the applications of these image metrics should allow a more detailed understanding of the factors influencing laser-written image quality, with especial benefits in systems design and optimization.

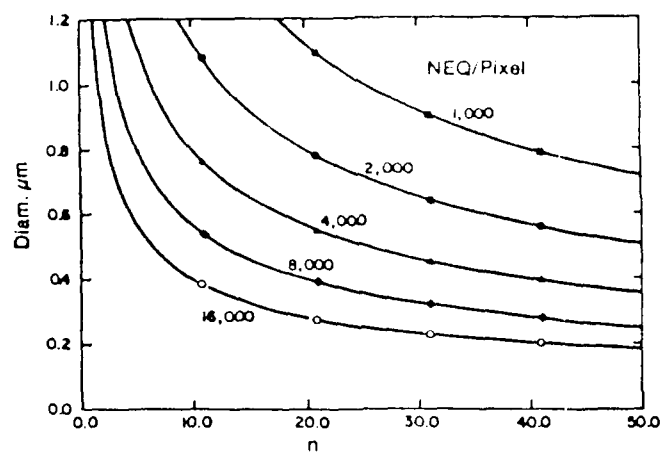


Figure 1: Calculation of NEQ's per pixel as a function of diameter and number of imaging particles.²⁵

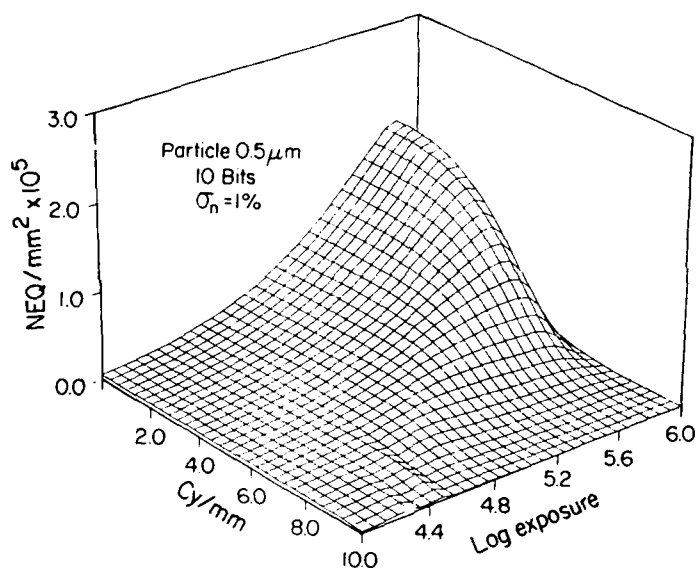


Figure 2: NEQ for a printed image, including the effects of laser and quantization noise.²⁷

References

1. J.C. Dainty and R. Shaw, *Image Science*, (Academic, London, 1974)
2. P. Mertz and F. Gray, *Bell Systems Tech. J.* 13, 464 (1934)
3. A.H. Robinson, *Appl. Opt.* 12, 1344 (1973)
4. F.D. Huck, N. Halyo and S.K. Park, *Appl. Opt.* 19, 2174 (1980)
5. C.E. Shannon, *Bell System Tech. J.* 27, 397,623 (1948)
6. P.B. Fellgett and E.H. Linfoot, *Phil. Trans. Roy. Soc. A247*, 369 (1955)
7. J.H. Altman and H. J. Zweig, *Photogr. Sci. Eng.* 7, 173 (1963)
8. R. Shaw, *Photogr. Sci. Eng.* 6, 281 (1962)
9. C.L. Fales, F.O. Huck and R.W. Samms, *Appl. Opt.* 23, 872 (1984)
10. A. Rose, *Vision, Human and Electronic* (Plenum Press, New York, 1974)
11. R.C. Jones, *Adv. Electronics and Electro Phys.* 11, 87 (1959)
12. R. Shaw, *Rep. Prog. Phys.* 41, 1103 (1978)
13. R. Shaw, *J. Photogr. Sci.* 11, 199 (1963)
14. D. Kermisch and P.G. Roetling, *J. Opt. Soc. Amer.* 65, 716 (1975)
15. R. Shaw, *J. Appl. Phot. Eng.* 1, 1 (1975)
16. R. Shaw, P. Burns and J.C. Dainty, *SPIE Procs.* 310, 137 (1981)
17. R. Shaw, P. Burns and J.C. Dainty, *SPIE Procs.* 310, 143 (1981)
18. H. Siedentopf, *Phys. Z.* 38, 454 (1937)
19. J.C. Urbach, T.S. Fish and G.K. Starkweather, *Procs. IEEE* 70, 594 (1982)
20. F. Bestenreiner, V. Greis, J. Helmberger and K. Stadler, *J. Appl. Phot. Eng.* 2, 86 (1976)
21. J. Sullivan and L. Ray, *Appl. Opt.* 26, 1765 (1987)
22. P.D. Burns, *S.P.S.E. Procs. Non-Impact Printing Technologies* 139 (1984)
23. P.D. Burns, M. Rabbani and L.A. Ray, *Appl. Opt.* 25, 2158 (1986)
24. P. Melnychuk and R. Shaw, *S.P.S.E. Procs. Non-Impact Printing Technologies* 210 (1986)
25. R. Shaw and P.D. Burns, *S.P.S.E. Procs. Non-Impact Printing Technologies* 127 (1984)
26. P.D. Burns, *SPIE Procs.* 702, 187 (1986)
27. P.D. Burns, *J. Imag. Sci.* 31, 74 (1987)

IGNITION AND HIGH SPEED PHOTOGRAPHY OF ENERGETIC MATERIALS WITH A COPPER VAPOR LASER

Larry R. Dosser, John W. Reed, Thomas C. Girmann, and Margaret A. Stark

Monsanto Research Corporation
Mound*
Miamisburg, Ohio 45342

Abstract

The reactions of energetic materials are rapid and often violent and require specialized diagnostics to study them. A method recently applied to this problem is laser illuminated high speed photography with a copper vapor laser that can record up to 10,000 laser illuminated images per second. This type of laser photography has provided images that detail the performance of a material or component in a manner never before possible. The copper vapor laser can also be used for the ignition of energetic materials. Details of such ignitions are readily observable, and the burn rate of the material can be determined directly from the film. There are indications that information useful for the modeling of energetic material reactions will become available as well. Recent results on several materials, including Ti/2B, a pyrotechnic torch, and the explosive hexanitrostilbene, are presented.

Introduction

The evaluation of the properties of energetic materials, such as burn rate and ignition, is of primary importance in understanding their reactions and how devices containing them perform their function. One method for recording such information is high speed photography at rates of up to 20,000 images per second. When a copper vapor laser is synchronized with the camera, laser illuminated images can be recorded that detail the performance of a material and/or component in a manner never before possible. The copper vapor laser used for these experiments had an average power of 30 watts and produced pulses at a rate of up to 10 kHz. The 30 nanosecond pulse width of the laser essentially freezes all motion in the burning material, thus providing stop-action pictures at a rate of up to 10,000 per second. Each laser pulse has a peak power of 170,000 watts, which provides ample illumination for the high speed photography. Laser ignition of the energetic material is also a very clean and measurable method of ignition, and the material can be ignited without other devices, such as bridgewires or electric squibs, that interfere with the photography. Several energetic materials have been studied with the copper vapor laser, and the results are presented in this paper. These include the ignition and burn rate of Ti/2B, the illumination of a functioning pyrotechnic torch, and the laser ignition of high explosives.

Experimental

The experimental configuration used to record the high speed photographs of the energetic materials is shown in Figure 1. Modifications to the optics in the area labeled "Optics" are made depending on the experiment and the information sought. During an experiment, the camera drives the laser through a delay generator that is set to a predetermined delay depending on the camera speed. This ensures that when a laser pulse is at the experimental point, the camera shutter is open and the laser illuminated image is recorded. The choice of camera lens, filters, speed, and f stop are dictated by the experiment. The camera is a rotating prism camera that provides one trigger pulse per frame. When an eight-sided prism is used in this camera, full frame images are recorded. For this work a sixteen-sided prism was used, and two images were recorded per frame. Since there is only one trigger pulse per frame, one of these images is illuminated with a laser pulse, the other is not. This provides a direct comparison between laser and non-laser illuminated images and clearly shows the usefulness of the laser for this type of photography.

Results

The configuration of the optics used for the laser ignition and burn rate studies of Ti/2B is shown in Figure 2. The part of the beam used for ignition is focused tightly on top of the pellet of Ti/2B. The pellet was 0.375 in. in diameter by 0.375 in. long. The major part of the beam was compressed into a sheet with cylindrical optics and passed across the top of the pellet to illuminate the gases and particulates produced in the ignition. The laser sheet effectively illuminated a cross section of the ignition zone and

*Mound is operated by Monsanto Research Corporation for the U. S. Department of Energy under Contract No. DE-AC04-76DP00053.

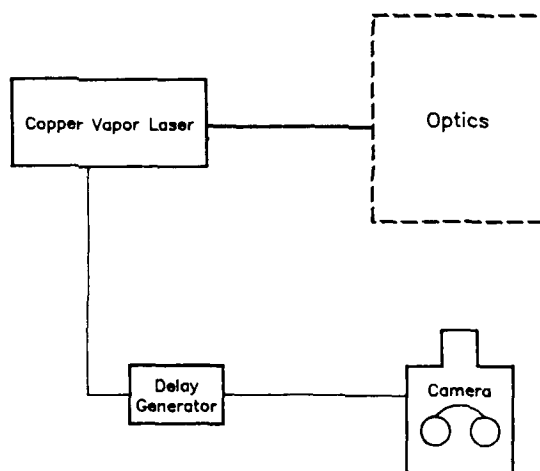


Figure 1 - Experimental configuration.

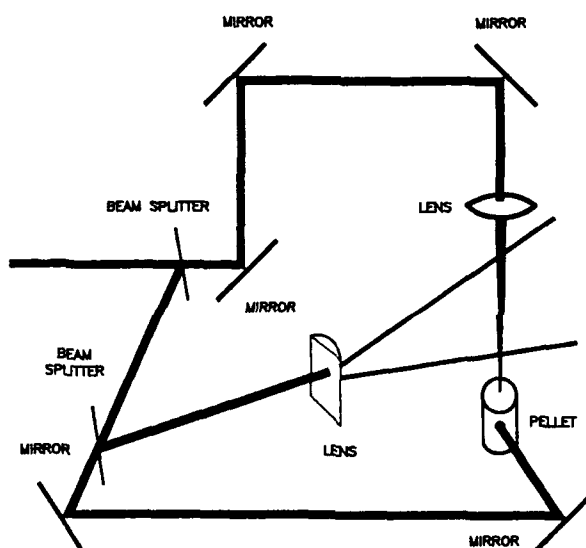


Figure 2 - Optics for laser ignition and burn rate of Ti/2B.

allowed the examination of the internal structure of this region. A small portion of the beam was used to illuminate the pellet of material. This allowed the determination of the scale of the experiment recorded on film and permitted the viewing of the material prior to ignition. The tremendous self-illumination of the Ti/2B reaction required that the photography be done through a 510-nm interference filter. The burn rate experiments were done at a laser repetition rate of 3 kHz, and a photograph of a frame from the 16-mm film is shown in Figure 3. It was found that the burn rates of different blends of materials, and the manner in which these materials ignited, could readily be observed. The ignition, as well as the turbulence created by the ignition, was clearly visible with the sheet lighting. The burn rate of Ti/2B under these conditions varied from 19 to 37 mm/s and correlated well with burn rate data taken by other methods.

A second example using the copper vapor laser to study energetic material reactions was the illumination of the flame from a pyrotechnic torch. The initial stages of ignition and burn were of primary importance to the proper functioning of this device. All of the beam was used to sheet light the region directly above the center of the torch. Part of the sheet was picked off with a right angle prism after it passed through the torch flame and was then directed to illuminate the torch body. The torch body was metal and was painted a flat white to eliminate specular reflections. The torch was filmed at a laser repetition rate of 8 kHz, and a frame of film from the initial part of the burn is shown in Figure 4. The internal structure of the flame is clearly visible with the sheet lighting. Void spaces can be seen as well as other structural features that show up from the laser illuminated smoke and particulates.

A third example of this technique was to observe the laser interaction with a high explosive up to the point of ignition. The entire beam, with an average power of 30 watts and a 6-kHz pulse repetition rate, was focused onto a small pellet of the explosive hexanitrostilbene (HNS) for these experiments. There was enough scattered laser light from the focused spot to illuminate the region above the pellet. Figures 5 and 6 show HNS just prior to ignition and just after ignition, respectively. The clouds of explosive vapor or condensable decomposition products are clearly visible above the HNS pellet in Figure 5. Examination of the film shows pulses of such clouds just prior to ignition. When the pellet ignites, it burns with a flame that is above the surface of the pellet, as shown in Figure 6.

Conclusion

The value of the copper vapor laser to illuminate and photograph the reactions of energetic materials has been demonstrated. The laser has proved to be useful as an ignition source for these materials by providing a very clean method of ignition. The structure of the torch flame should be of particular interest to those who model such reactions. For the first time it is possible to observe the internal structure of the flame. It is also possible to get some idea of the flame composition. Cold particles, for example, scatter the laser light and appear green. Hot particles appear white or yellow in contrast. The absence of scattered laser light indicates that primarily hot gases are being produced by the reaction.

Laser illuminated high speed photography of energetic materials is still in its infancy. As more progress is made in this area, it is felt that more will be learned about energetic materials and their reactions.



Figure 3 - Laser ignition of Ti/2B.

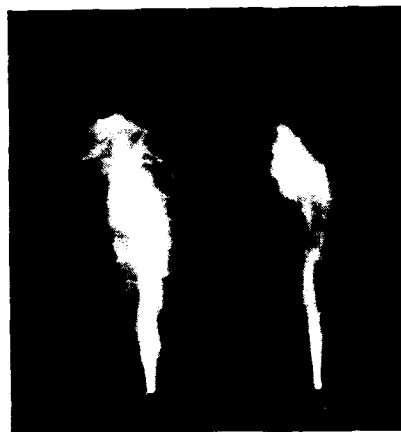


Figure 4 - Pyrotechnic torch - left image, laser sheet lighted; right image, self-illumination.



Figure 5 - HNS pellet prior to laser ignition.



Figure 6 - HNS pellet just after laser ignition (right image from self-illumination).

DESIGN OF A TWO-LENS GAUSSIAN BEAM WAIST TRANSFORMER

James E. Adams, Jr.
Photographic Research Laboratories - Photographics Products Group,
Eastman Kodak Company, Rochester, New York 14650

Abstract

The Gaussian-beam ray trace matrix equations are solved for the case of a two-lens system. Five distinct sets of input parameters are considered and the corresponding solutions derived and examined.

Introduction

The design of a laser optical system (at least for low power situations) is a simple affair as first summarized by Kogelnik and Li.¹ Recently, the author was faced with the question of how to reimage a Gaussian beam waist with as few elements as possible within given packing constraints. Tolerances, as usual, were also a concern. It was a conclusion of the author that for a large number of cases one given waist can be transformed into another waist by the use of only two catalog lens, i.e. the solution can be forced to consist of standard focal length lens.

ABCD Matrix Method

To review the premise of the ABCD matrix method is that the first order properties of most any optical system can be represented in a 2×2 matrix. With this matrix, paraxial rays may be "transferred" from the entry plane of the system to the exit plane. Figure 1 presents the nomenclature used in this paper.

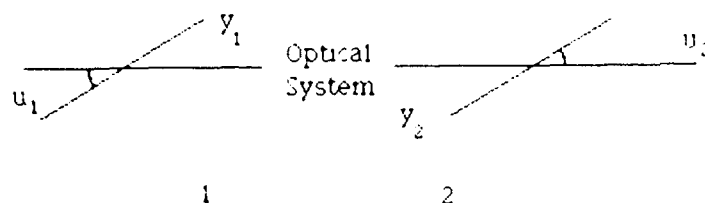


Figure 1

$$\begin{pmatrix} y_2 \\ u_2 \end{pmatrix} = \begin{bmatrix} A & B \\ C & D \end{bmatrix} \begin{pmatrix} y_1 \\ u_1 \end{pmatrix} \quad (1)$$

Gaussian Beam Definitions

We now define the complex beam parameter, both generally in (2) and at a beam waist in (3), and the Rayleigh length in (4). After this, we show how the complex beam parameter

is "transferred" from the entrance plane to the exit plane of the system in (5). The values for A, B, C and D come from the optical system's ABCD matrix.

$$\frac{1}{q} = \frac{1}{R} - j \frac{\lambda}{\pi \omega^2} \quad (2)$$

$$q_0 = j \frac{\pi \omega_0^2}{\lambda} \quad (3)$$

$$Z_R = \frac{\pi \omega_0^2}{\lambda} \quad (4)$$

$$q_2 = \frac{A q_1 + B}{C q_1 + D} \quad (5)$$

Gaussian Beam System Solution

It is a simple matter at this point to write a system of simultaneous equations that will serve as the basis of all of the subsequent mathematics in this paper. We assume there is a Gaussian beam waist at both the entrance plane (plane 1) and the exit plane (plane 2). Equations (3), (4), and (5) are combined to obtain (6). This equation is then decomposed into real and imaginary expressions in (7).

$$j Z_{R2} = \frac{j Z_{R2} A + B}{j Z_{R1} C + D} \quad (6)$$

$$\begin{cases} -C Z_{R1} Z_{R2} = B \\ D Z_{R2} = A Z_{R1} \end{cases} \quad (7)$$

ABCD Matrix for One-Lens System

As a quick review, the solution to the one-lens system is presented. There are many textbooks that arrive at this solution in a number of approaches, for example, Gaskill.² We will use the approach of ABCD matrices, expanding upon it later when discussing the two-lens system. Figure 2 shows the system layout and (8) is the corresponding ABCD matrix.

Discussion

For convenience we have expressed in (9) the lens' focal length in terms of its equivalent optical power, i.e., the reciprocal of the focal length. Also, we have defined in (10) d to be the overall length of the system from entrance plane to exit plane. There should be no confusion with this d and the D in the ABCD matrix.

Taking the expression for A, B, C, and D from the ABCD matrix and substituting them into our Gaussian beam waist system of simultaneous equations allows us to solve for the lens optical power, (11) and (12), and distance from the input waist to the lens (13). Note that there are two sets of solutions. These are discussed separately below.

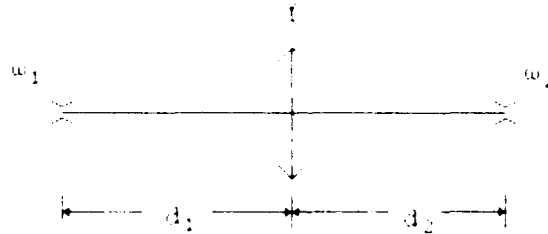


Figure 2

$$\begin{pmatrix} y_2 \\ u_2 \end{pmatrix} \begin{bmatrix} 1 - \frac{d_2}{f} & d_1 + d_2 \left(1 - \frac{d_1}{f}\right) \\ -\frac{1}{f} & 1 - \frac{d_1}{f} \end{bmatrix} \begin{pmatrix} y_1 \\ u_1 \end{pmatrix} \quad (8)$$

$$\phi = \frac{1}{f} \quad (9)$$

$$d = d_1 + d_2 \quad (10)$$

$$\phi = \frac{d}{z_{R1} z_{R2} + d_1 (d - d_1)} \quad (11)$$

$$\phi = \frac{d}{(d - d_1) z_{R1} - d_1 z_{R2}} \quad (12)$$

$$d_1 = \frac{dz_{R1} \pm \sqrt{(dz_{R1})^2 + z_{R1}(z_{R1} - z_{R2})[z_{R2}(z_{R1} - z_{R2}) - d^2]}}{z_{R1} - z_{R2}} \quad (13)$$

Real Versus Virtual Waist Solutions

Real Waist Solution

The two types of solutions are physically represented in Figure 3. The top solution takes the real input waist and creates a real output waist. The advantages of this setup are 1) smaller packaging requirements, 2) direct accessibility to the output waist, and 3) smaller clear aperture requirements on the lens.

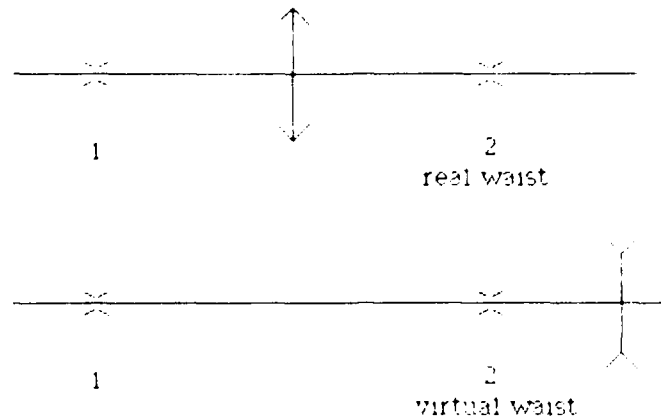


Figure 3

Virtual Waist Solution

The bottom solution takes the real input waist and creates a virtual output waist. Though it may look a bit strange, the main advantage to this setup is that it has been the author's experience that the lens power tends to be weaker than in the real waist solution. This generally carries with it the promise of looser tolerances.

ABCD Matrix for Two-Lens System

The problem with the one-lens solution is that there are no degrees of freedom left over to handle the problems of space constraint and lens focal length availability. Adding another lens (and the associated spacing) allows the designer to address these matters as well.

Discussion

The two-lens system is shown in Figure 4 and its corresponding ABCD matrix elements are given in (14). As in the one-lens case, the expressions for A, B, C and D will be substituted into our set of simultaneous equations and solved for two variables. It is understood that the remaining variables must be specified.

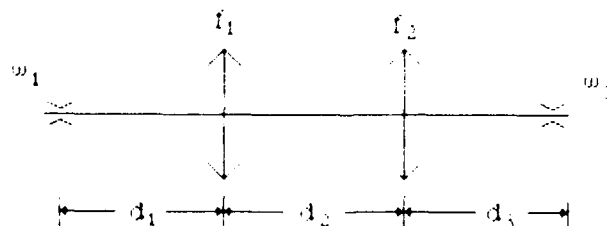


Figure 4

$$\begin{cases} A = 1 - d_2\phi_1 - d_3\phi_1 - d_3\phi_2 + d_2d_3\phi_1\phi_2 \\ B = d_1 + d_2 - d_1d_2\phi_1 + d_3 - d_1d_3\phi_1 - d_2d_3\phi_2 - d_1d_3\phi_2 + d_1d_2d_3\phi_1\phi_2 \\ C = -\phi_1 - \phi_2 + d_2\phi_1\phi_2 \\ D = 1 - d_1\phi_1 - d_2\phi_2 - d_1\phi_2 + d_1d_2\phi_1\phi_2 \end{cases} \quad (14)$$

Five Sets of Design Constraints

Five variable sets are presented below. In each case it is assumed that variables not mentioned, e.g., beam waist size, overall length, wavelength, are known.

Given d_1 and d_2 , Calculate f_1 and f_2

Discussion

By substituting the ABCD matrix values into our Gaussian beam simultaneous equations, one can first solve for the power of the first lens, (15) and (16), and subsequently eliminate it to get a quadratic expression for the power of the second lens, (17) and (18). The two solution types are illustrated in Figure 5 and generally represent whether a real intermediate waist is formed or whether a virtual intermediate waist is formed.

Figure 5 shows that we have selected conjugates so that the final waist is real. We could, of course, have also selected them so that it was virtual.

As one might expect, the powers of the lenses for the virtual intermediate waist solution are weaker and the tolerances are looser.

Special cases can add twists, however. If one solves the equations for the setup in Figure 6, one finds two solutions with real intermediate waists in the same position, just different sizes.

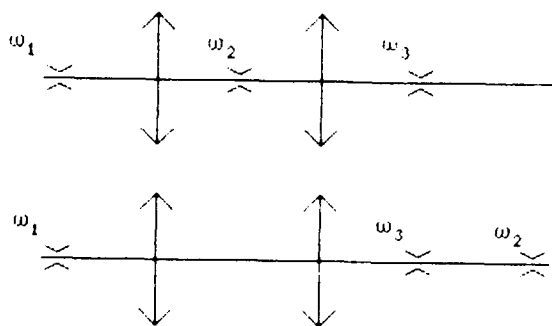


Figure 5

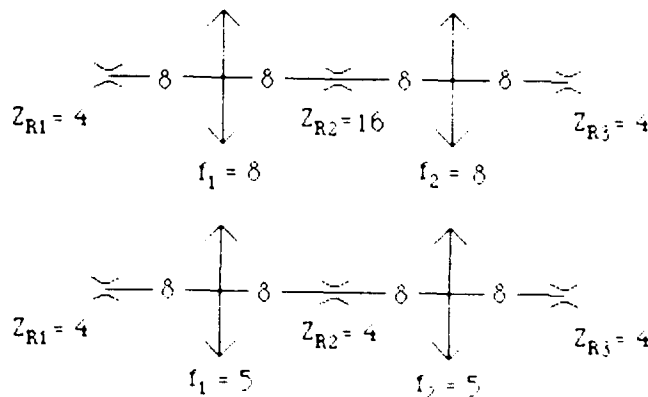


Figure 6

$$\phi_1 = \frac{d_1 + d_2 + d_3 + \phi_2(-Z_{R1}Z_{R3} - d_1d_3 - d_2d_3)}{Z_{R1}Z_{R3} + d_1(d_2 + d_3) + \phi_2d_2(-Z_{R1}Z_{R3} - d_1d_3)} \quad (15)$$

$$\phi_1 = \frac{Z_{R1} - Z_{R3} + \phi_2(Z_{R3}(d_1 + d_2) - Z_{R1}d_3)}{Z_{R1}(d_2 + d_3) - Z_{R3}d_1 + \phi_2d_2(Z_{R3}d_1 - Z_{R1}d_3)} \quad (16)$$

$$a_1\phi_2^2 + a_2\phi_2 + a_3 = 0 \quad (17)$$

$$\begin{cases} a_1 = -Z_{R1}d_2^2(Z_{R3}^2 + d_3^2) \\ a_2 = 2Z_{R1}d_2[Z_{R3}^2 + d_3(d_2 + d_3)] \\ a_3 = Z_{R3}(Z_{R1}^2 + d_1^2) - Z_{R1}[Z_{R3}^2 + (d_2 + d_3)^2] \end{cases} \quad (18)$$

Given d_1 and f_2 , Calculate d_2 and f_1

Discussion

With this set of constraints, there are four possible solutions. One begins by solving for lens separation, (21) and (22), and then calculating the power of the first lens using either (19) or (20). This solution set could be used to "test plate" the focal length of the second lens.

$$\phi_1 = \frac{d_1 + d_2 + d_3 - (d_1 + d_2)d_3\phi_2 - Z_{R1}Z_{R3}\phi_2}{Z_{R1}Z_{R3}(1 - d_2\phi_2) - d_1(d_2d_3\phi_2 - d_2 - d_3)} \quad (19)$$

$$\phi_1 = \frac{Z_{R1}(1 - d_3\phi_2) - Z_{R3}(1 - d_2\phi_2 - d_1\phi_2)}{Z_{R3}d_1(d_2\phi_2 - 1) - Z_{R1}(d_2d_3\phi_2 - d_2 - d_3)} \quad (20)$$

$$a_1d_2^4 + a_2d_2^3 + a_3d_2^2 + a_4d_2 + a_5 = 0 \quad (21)$$

$$\begin{cases} a_1 = Z_{R1}\phi_2^2 \\ a_2 = 2Z_{R1}(d_1 - d)\phi_2^2 \\ a_3 = \{Z_{R1}(d - d_1)[(d - d_1)\phi_2 + 2] + Z_{R1}Z_{R3}^2\phi_2\}\phi_2 \\ a_4 = -2Z_{R1}[(d - d_1)^2 + Z_{R3}^2]\phi_2 \\ a_5 = Z_{R1}[(d - d_1)^2 + Z_{R3}(Z_{R3} - Z_{R1})] - Z_{R3}d_1^2 \end{cases} \quad (22)$$

Given d_1 and f_1 , Calculate d_2 and f_2

Discussion

By specifying both d_1 and f_1 , all one has done is transformed the input waist into an intermediate waist and reduced the problem to a one-lens system solution. However, if one does not want to calculate the intermediate waist characteristics and solve the subsequent one-lens solution, these equations, (23) through (26), can be used to calculate d_2 directly.

$$\phi_2 = \frac{(d - d_1 - d_2)(1 - d_1\phi_1) - (d_1d_2\phi_1 - d_1 - d_2) - Z_{R1}Z_{R3}\phi_1}{Z_{R1}Z_{R3}(1 - d_2\phi_1) - (d - d_1 - d_2)(d_1d_2\phi_1 - d_1 - d_2)} \quad (23)$$

$$\phi_2 = \frac{Z_{R1}[1 - d_2\phi_1 - (d - d_1 - d_2)\phi_1] - Z_{R3}(1 - d_1\phi_1)}{Z_{R3}(d_1d_2\phi_1 - d_1 - d_2) - Z_{R1}(d - d_1 - d_2)(d_2\phi_1 - 1)} \quad (24)$$

$$a_1d_2^2 + a_2d_2 + a_3 = 0 \quad (25)$$

$$\begin{cases} a_1 = Z_{R1} - Z_{R3}[Z_{R1}^2\phi_1^2 + (1 - d_1\phi_1)^2] \\ a_2 = 2[Z_{R1}(d_1 + Z_{R1}Z_{R3}\phi_1 - d) + Z_{R3}d_1(d_1\phi_1 - 1)] \\ a_3 = Z_{R1}d(d - 2d_1) + (Z_{R1} - Z_{R3})(d_1^2 - Z_{R1}Z_{R3}) \end{cases} \quad (26)$$

Given d_2 and f_1 , Calculate d_1 and f_2

Discussion

This solution set is very similar to the case where d_1 and f_1 are given and d_2 and f_2 are calculated. This variable combination is presented for the sake of completeness.

$$\phi_2 = \frac{(d - d_1 - d_2)(1 - d_1\phi_1) - (d_1d_2\phi_1 - d_1 - d_2) - Z_{R1}Z_{R3}\phi_1}{Z_{R1}Z_{R3}(1 - d_2\phi_1) - (d - d_1 - d_2)(d_1d_2\phi_1 - d_1 - d_2)} \quad (27)$$

$$\phi_2 = \frac{Z_{R1}[1 - d_2\phi_1 - (d - d_1 - d_2)\phi_1] - Z_{R3}(1 - d_1\phi_1)}{Z_{R3}(d_1d_2\phi_1 - d_1 - d_2) - Z_{R1}(d - d_1 - d_2)(d_2\phi_1 - 1)} \quad (28)$$

$$a_1d_1^2 + a_2d_1 + a_3 = 0 \quad (29)$$

$$\begin{cases} a_1 = Z_{R1} - Z_{R3}(1 - d_2\phi_1)^2 \\ a_2 = 2[Z_{R1}(d_2 + d) - Z_{R3}d_2(1 - d_2\phi_1)] \\ a_3 = Z_{R1}[(d - d_2)^2 - Z_{R1}Z_{R3}(1 - d_2\phi_1)^2] + Z_{R3}(Z_{R1}Z_{R3} - d_2^2) \end{cases} \quad (30)$$

Given f_1 and f_2 , Calculate d_1 and d_2

Discussion

If the focal lengths of the lenses have been chosen and fixed, this solution set can be used to calculate the final positioning of the lenses. There is a possibility of four solutions but experience shows that generally only two will be real. Additionally, it is not necessarily true that one solution will involve a virtual intermediate waist and the other involve a real waist. Figure 7 shows one case where both intermediate waists are real.

This derivation begins by finding two expressions for d_1 , (31 through 34). (Note that (33) defines the optical power for the total system.) Unlike the previous situations, d_1 cannot be expressed as a simple linear equation in both cases. However, d_1 can still be eliminated from these two expressions and a quartic in d_2 produced, (35) and (36).

This is the most challenging of the systems to solve.

$$b_1 d_1^2 + b_2 d_1 + b_3 = 0 \quad (31)$$

$$\begin{cases} b_1 = \Phi \\ b_2 = -d\Phi + d_2\phi_2(2 - d_2\phi_1) \\ b_3 = -Z_{R1}Z_{R3}\Phi + d + d_2\phi_2(d_2 - d) \end{cases} \quad (32)$$

$$\Phi = \phi_1 + \phi_2 - \phi_1\phi_2d_2 \quad (33)$$

$$d_1 = \frac{Z_{R1}[(d - d_2)\Phi - (1 - d_2\phi_1)] + Z_{R3}(1 - d_2\phi_2)}{(Z_{R1} + Z_{R3})\Phi} \quad (34)$$

$$a_1 d_2^4 + a_2 d_2^3 + a_3 d_2^2 + a_4 d_2 + a_5 = 0 \quad (35)$$

$$\begin{cases} a_1 = -\phi_1^2 \phi_2^2 Z_{R1} Z_{R3} \\ a_2 = 2d\phi_1^2 \phi_2^2 Z_{R1} Z_{R3} \\ a_3 = \phi_1 \phi_2 Z_{R1} Z_{R3} [(2 - d\phi_1)(2 + d\phi_2) - 4d\phi_2 - \phi_1 \phi_2 (Z_{R1} + Z_{R3})^2] \\ a_4 = 2\phi_1 \phi_2 Z_{R1} Z_{R3} \{(Z_{R1} + Z_{R3})^2 (\phi_1 + \phi_2) + d[d(\phi_1 + \phi_2) - 2]\} \\ a_5 = (Z_{R1} - Z_{R3})^2 - Z_{R1} Z_{R3} \{(\phi_1 + \phi_2)^2 (Z_{R1} + Z_{R3})^2 - d[4(\phi_1 + \phi_2) - d(\phi_1 + \phi_2)^2]\} \end{cases} \quad (36)$$

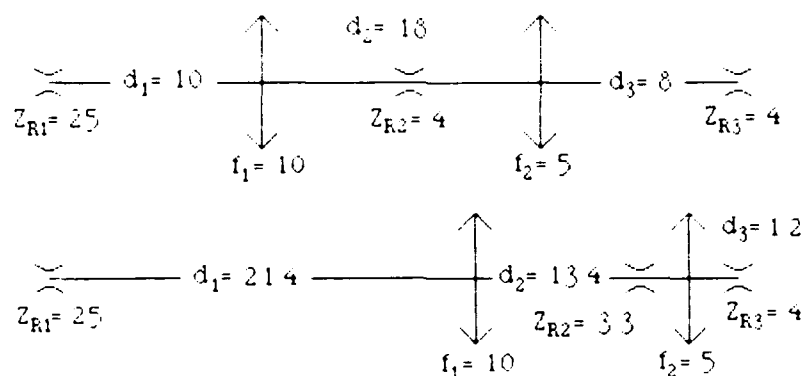


Figure 7

Afocal System Solution

Discussion

Gunter and De Young³ explored the properties of a two-lens afocal Gaussian beam transformer. These results can be recreated from our ABCD matrix setup with only a little bit

more math than their approach, (37) through (42). The important results are that 1) by imposing the additional restraint of being afocal, the system cannot be forced to consist of standard focal length lenses, (40), and 2) with an afocal setup, the position of the output waist tracks linearly with the input waist position, (42), and the size of the output waist is constant regardless of input waist position, (40).

To derive (40), (37) is generated from (7) and (14). In the limit as the system becomes afocal, it becomes necessary that (39) holds so that (38) does not become undefined.

Equation (40) follows from (39). Equation (41) also comes from (7) and (14). Immediately setting the system optical power to zero produces (42).

$$d_1 = \frac{Z_{R1}[(d - d_2)\Phi - (1 - d_2\phi_1)] + Z_{R3}(1 - d_2\phi_2)}{(Z_{R1} + Z_{R3})\Phi} \quad (37)$$

$$\lim_{\Phi \rightarrow 0} d_1 = \lim_{\Phi \rightarrow 0} \frac{Z_{R3}(1 - d_2\phi_2) - Z_{R1}(1 - d_2\phi_1)}{(Z_{R1} + Z_{R3})\Phi} + \frac{Z_{R1}(d - d_2)}{Z_{R1} + Z_{R3}} \quad (38)$$

$$Z_{R1}(1 - d_2\phi_1) - Z_{R3}(1 - d_2\phi_2) = 0 \quad (39)$$

$$Z_{R1} = Z_{R3} \frac{\phi_2^2}{\phi_1^2} \quad (40)$$

$$d_3 = \frac{Z_{R1}Z_{R3}\Phi - d_1(1 - d_2\phi_1) - d_2}{(1 - d_2\phi_2) - d_1\Phi} \quad (41)$$

$$d_3 - \frac{1}{\phi_2} = - \frac{\phi_1^2}{\phi_2^2} \left(d_1 - \frac{1}{\phi_1} \right) \quad (42)$$

References

1. H. Kogelink, T. Li, Appl. Opt. 5, 1550 (1966).
2. J. D. Gaskill, Linear Systems, Fourier Transforms, and Optics (John Wiley and Sons, New York, 1978), pp. 420-442.
3. W. D. Gunter, Jr., A. De Young, Appl. Opt. 25, 1742 (1986).

ENGINEERING APPLICATIONS OF PULSED LASER VELOCIMETRY

I Grant and G H Smith
Department of Offshore Engineering
Heriot-Watt University
Edinburgh EH14 4AS
Scotland

Abstract

This paper describes an optical technique for measuring the in-plane velocity components over an extended region of a flow SIMULTANEOUSLY. The method of application to flows of interest to the engineer is described with examples being taken from both aerodynamic and hydrodynamic experiments performed in the laboratories of Heriot-Watt University.

Introduction

All common methods used to measure fluid velocity, to date, have been 'point' measuring techniques. That is, they measure a velocity component at a particular position in the flow averaged over a small volume. They may also provide a time history of the velocity fluctuations at that point. The two most common instruments are the hot-wire and laser doppler anemometer, the latter being a non-intrusive device. The major limitation of such instruments is evident when simultaneous multi-point measurements of the flow are required. The complexity and cost of such an experiment escalates rapidly. Further difficulties are encountered if multi-component measurements at each point are required.

Pulsed Laser Velocimetry (PLV) enables the measurement of two components of velocity at many points in a flow at the same instant. Early experiments were described by Grousson and Mallik¹ and Dudderar and Simpkins². The first experiment carried out in air was described by Meynart in which he used a pulsed Ruby laser to investigate the velocity field in a low Reynolds number jet. Lourenco and Whiffen³ reported the use of a mechanically chopped Argon Laser.

Particle Image Velocimetry

The technique requires that a thin sheet of light illuminates the area of flow over which velocity measurements are required. Seeding particles are introduced into the measurement area such that the flow characteristics are unchanged. A camera is placed to collect the light scattered at 90° by the seeding particles. If the light source is pulsed rapidly and each pulse is short enough to 'freeze' the seeding particle in its flight, multiple images of each seed travelling through the light sheet will be recorded. If the time between light pulses is T , the camera optics magnification m , and the particle displacement at the image plane d_i , the magnitude of velocity at that point in the flow is given by

$$v = \frac{d_i}{mT} \quad (1)$$

with the vector displacement of the seed particle giving the vector of the velocity.

Any point in the flow where a particle occurs, and is imaged, the fluid velocity can be measured. There is, however, a 180° ambiguity in the sense of the flow vector.

PLV thus requires that the region of the flow under investigation must be illuminated by a light sheet with enough intensity such that the light scattered at 90° by seeding particles is sufficient to expose the photographic film. Seeding with the correct scattering characteristics and fluid dynamical properties must be introduced so as to cover the region of interest. Once the film has been exposed and developed it must be analysed to determine the particle displacements over the region of the negative.

In practice the light source is provided by a laser which can produce a high intensity beam that is readily steered and shaped into the required sheet. The type of laser utilised is dependent on the flow velocity and the optical properties of the flow under investigation. Continuous wave lasers can be chopped mechanically to investigate flows with low maximum velocity. The criterion relating maximum seed particle velocity to particle size and optical magnification were discussed by Lourenco and Whiffen³. Pulsed lasers with pulse durations of nano-seconds are capable of freezing flows with velocities below 500m.s⁻¹. Figure 1 shows the experimental arrangement by which a 10J Ruby laser is steered and shaped for use in the low speed wind tunnel at Heriot-Watt University.

Applications

Aerodynamics

Work in this area has been carried out at both high and low magnifications, using a variety of seeding particles.

Initially experiments were carried out in a small open-circuit wind tunnel positioned in

front of the output mirror of the laser. The tunnel working section was 70mm high by 600mm long. The width of the tunnel varied from 225mm at the inlet to 240mm at the downstream end. This compensated for the blockage caused by the increasing boundary layer.

A smooth brass cylinder of length 230mm and diameter 1mm was placed centrally in the working section. A 35mm camera was focussed on the area behind the cylinder to record the vortices being shed. Figure 2 illustrates typical vortex shedding from the cylinder. The mean air speed was 3.4ms^{-1} , giving a Reynolds number for the flow of 207. Due to the small scale of the experiment the camera magnification was high, approximately 1, providing a viewing area of 24mm by 36mm. Due to the small area under view enough seeding was provided by a DLSA aerosol generator which produced oil droplets with diameters in the range 2-5 microns at a concentration of 10cc^{-1} .

The pulsed light source was provided by a 10J Ruby laser, whose output beam had been shaped into a sheet by a simple cylindrical/concave lens pair. At this magnification and mean wind speed the pulse separation was $20\mu\text{s}$ giving a particle displacement of 68 microns at the mean wind speed. The laser pulse was chopped into two by a Pockel cell. As can be seen in Figure 2, the flow contains regions of relatively high and low seeding density. The seeding density may determine the method by which the particle displacements are measured.

Figure 3 is a vector plot of the flow behind the cylinder, in which the mean convection velocity of the vortices, taken as $0.85U_0$, has been subtracted.

The second experiment described was undertaken in the main closed-return tunnel which has a working section of $1\text{m} \times 1\text{m}$. In this case the output from the Ruby laser was transmitted to the wind tunnel using the beam guidance/shaping optics depicted in Figure 1. At no time was the beam focussed to a point as this would have resulted in ionisation of the air.

The experiment in this case was carried out at a magnification of 0.2 giving an area of view of $180\text{mm} \times 120\text{mm}$. Figure 4 shows an image of the flow over an inclined flat plate, the mean wind speed being in this case 11ms^{-1} .

The seeding density is seen to be essentially low, although of a more uniform nature than seen in the vortex shedding plate, Figure 2. When making measurements over a larger area the number of scattering centres must be greatly increased. Since the seed particles were introduced in a volumetric manner, and could not be concentrated to fill only the two dimensional sheet, the number of seeds required increased in proportion to volume rather than area. In this particular case the seeds were water droplets of mean diameter 30 microns, produced by an atomiser, which were introduced upstream of the cylinder. The number of scattering centres could have been increased by using two or more spray heads.

In this case, the laser output has been chopped into four 25ns pulses producing four images of each seed particle. Increasing the number of times each particle was imaged enhanced the ease and accuracy with which the particle could be measured.

In all the experiments involving the Ruby laser Kodak Technical Pan type 2415 was used. This film was ideal due to its high resolution, 400 lines per mm, coupled with its extended red sensitivity which gave it greater 'speed', at the Ruby output wavelength of 694nm, than other nominally faster films.

Hydraulics

Studies have been carried out in a channel fitted with a programmable flap wave generating system. Since the maximum velocities encountered under small amplitude water waves are generally below 1ms^{-1} a much longer exposure time could be utilised before the particle images began to blur. The output from a 15 watt Argon laser, chopped mechanically, was found to provide enough illumination in this case. The attenuation/scattering characteristics of water, which has an optical 'window' in the green region of the spectrum, also meant that the multi-line output from the Argon laser provided better penetration into the water, than the 694nm output of the Ruby laser. The film used in this case was Ilford HP5, nominally 400 asa, and better suited to wavelengths in the green/blue region of the spectrum. The exposure time was 1ms with the time between exposures being 0.02ms .

Figure 5 shows a typical image taken under a small amplitude water wave. Since a CW laser was used the number of particle images recorded was dependent on the time the camera shutter was open. In this case five images were recorded. The seeding was provided by aluminium particles with mean diameter 20 microns. A comparison between particle velocities derived by the PIV method with those calculated using linear wave theory was found to be excellent.

Analysis

Two methods have been found most useful in extracting the particle displacement measurements from the exposed and developed negative.

The first, most commonly used technique requires that a low powered He-Ne laser beam be passed through the negative at each successive point at which velocity information is required. If correlated particle images are present at that spot an interference pattern consisting of parallel fringes appears, embedded in a diffraction halo. The halo is produced by the individual circular particle images. If the fringes are viewed in the Fourier Transform plane the displacement d_i , of the particles at the image plane is derived from

$$d_i = \lambda f l / L \quad (2)$$

where λ is the wave length of the interrogating beam

$f l$ is the focal length of the transform lens

L is the perpendicular distance between the fringes.

The direction of particle movement is perpendicular to a line running along the fringes. Thus the magnitude of velocity at that point in the flow is, combining (1) and (2),

$$||v|| = \lambda * f l / m L T \quad (3)$$

The fringe pattern was recorded using a video camera. The resulting output was digitised and stored in a framestore, with a typical resolution of 256 x 256 pixels x 8 bits, and then transferred to a computer, Figure 6. Several techniques exist to measure the fringe spacing ranging from simple fringe compression and one-dimensional Fourier Transform to full two-dimensional analysis of the image. The particular method used depends on the processing power available, the number of points which need to be analysed and the quality of the fringe pattern recorded.

Fringes produced from the original negatives were in general of poor quality. However a marked improvement was obtained by contact printing the original negative on to higher contrast film (Pickering and Halliwell⁴). Increasing the number of times each particle was imaged also improved the fringe sharpness, in the same manner as a grating produces sharper fringes than a line pair, Figure 7.

Even with these enhancements the fringes still suffered from speckle noise. More importantly the appearance of the fringes was altered by those effects which combined to decorrelate the particle displacements and, hence, decrease the fringe visibility. These included out of plane motion, leading to a loss/gain of particles between exposures and turbulence, leading to a variation in the particle displacements in the area probed by the interrogating laser.

When the seeding density was low, only two to three particle pairs in the spot covered by the laser probe beam, accidental correlations between unrelated particle images could occur, see Figure 8, giving spurious fringes. For this reason fringe analysis was useful only when higher seeding densities could be obtained.

The second method utilised direct microscopic analysis of the negative containing the imaged flow to determine the seed displacements. This method was superior in the lower seeding density case. The dynamic velocity range of this system could be varied at analysis time by changing the power of the objective lens attached to the video camera, unlike the fringe method which fixed the dynamic range at the time of the experiment. Figure 9 shows a typical image of a small region of flow, for a low seeding density case. Direct microscopic analysis is currently under development and will be described elsewhere.

Summary

The technique of Pulsed Laser Velocimetry and its application to the investigation of large scale fluid motion has been described. The different laser requirements for aerodynamic and hydrodynamic studies led to the use of pulsed and continuous wave lasers. In particular aerodynamic studies, having mean flow velocities above 1ms, required a pulsed laser source to freeze the seed particle images whereas, for example, wave studies were possible using a continuous wave laser. The characteristics of the flow material must be considered in choosing a laser wavelength which has the best propagation characteristics through the flow.

Two analysis methods combined to allow measurements in regions of flow which have disparate seeding densities. The first, fringe analysis, was found to work when the seeding density was high but to produce ambiguous results when only a few particle pairs were found in the probe area of the laser. The second, microscopic analysis, worked very well at low and medium seeding densities.

References

1. Grousson R and Mallick S, Appl Opt 16, 2334 (1977).
2. Dudderar T D and Simpkins P G, Nature 270, 45 (1977).
3. Lourenco L M and Whiffen M C, Proc of the 2nd Intl Conf on the Application of Laser Anemometry to Fluid Mechanics, Lisbon (1986).
4. Pickering C J D and Halliwell N A, Appl Opt 23, 128 (1984).

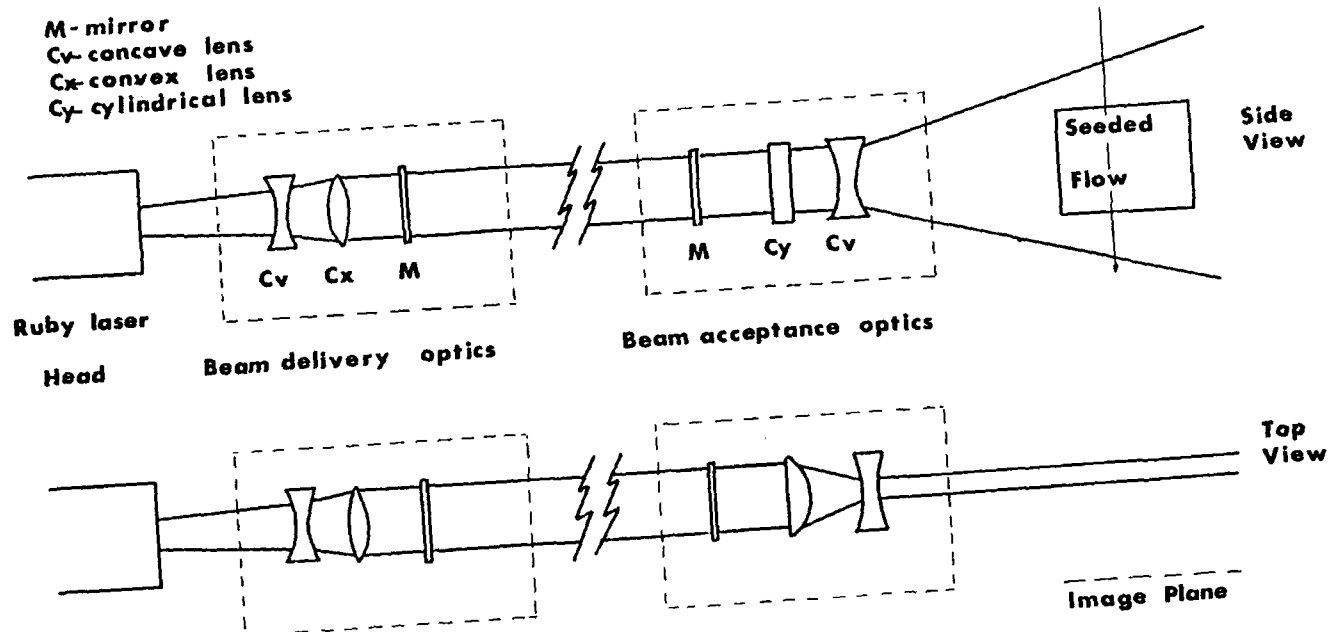


Figure 1
Beam Delivery and Production of Laser Sheet



Figure 2
Vortex Shedding From a Circular Cylinder

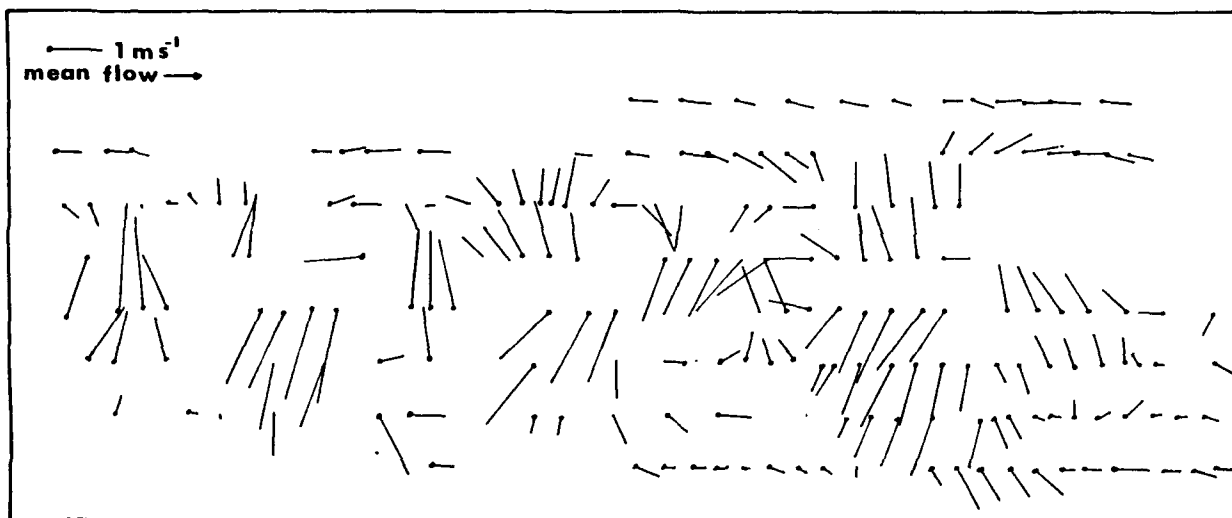


Figure 3
Velocity Vector Plot for Region Behind Cylinder

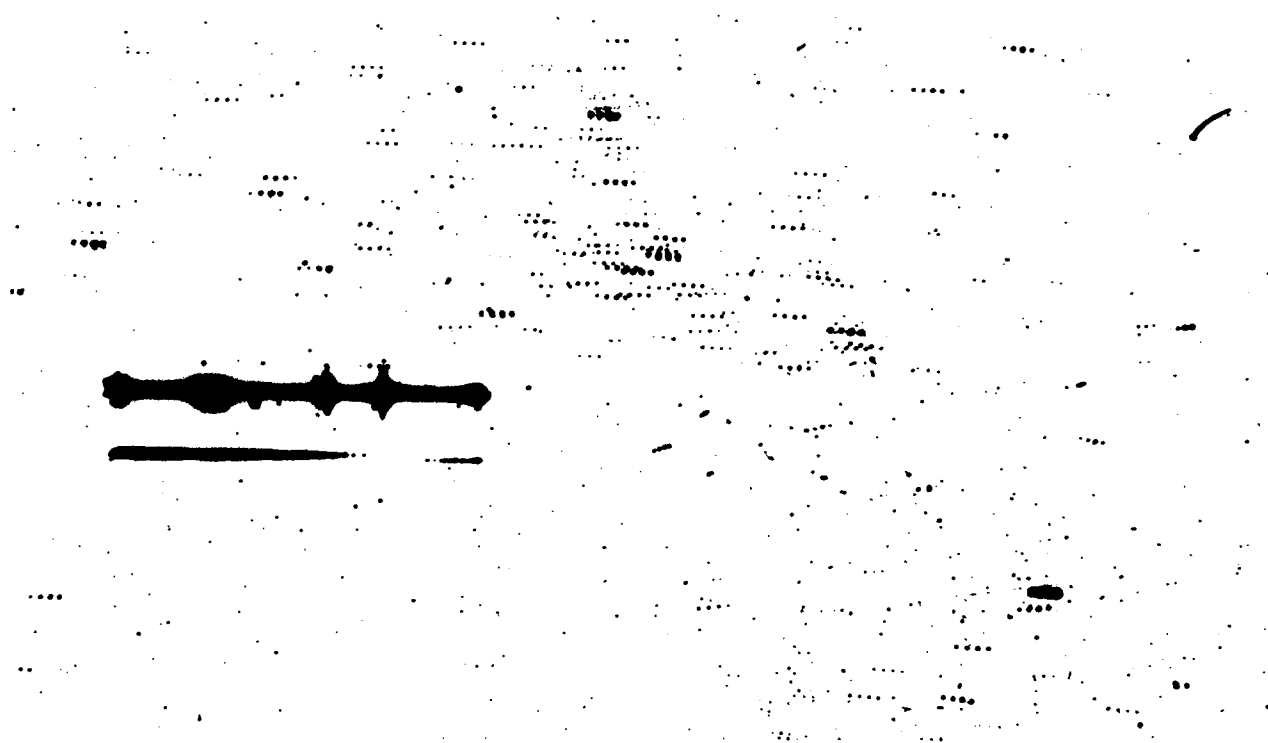


Figure 4
Flow Over an Inclined Flat Plate (Sparse Seeding)

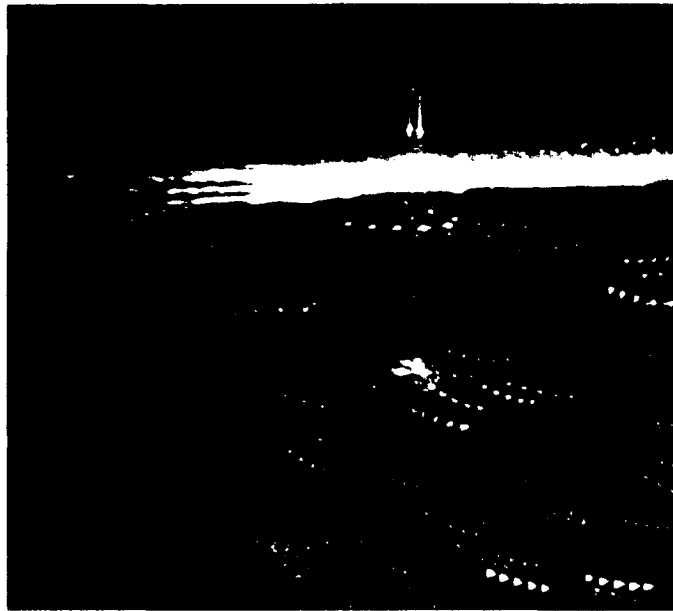


Figure 5
Particle Displacements Under a Small Amplitude Water Wave

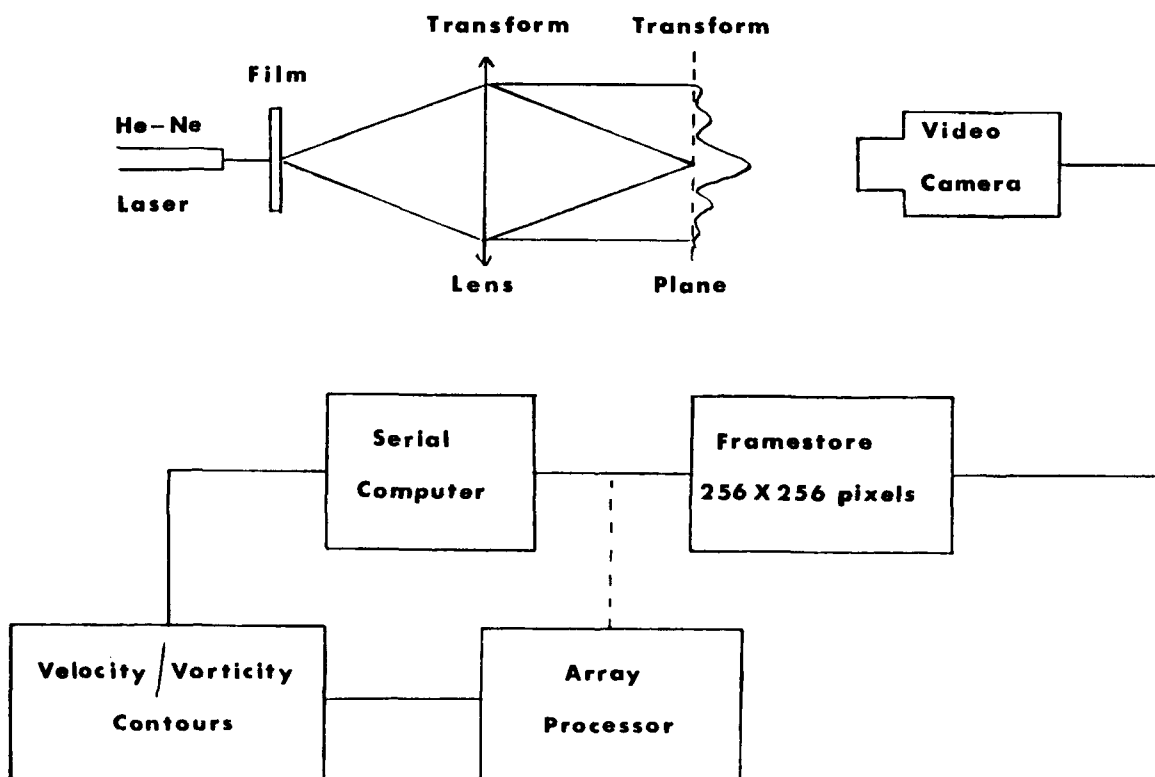


Figure 6
Fringe Processing Method

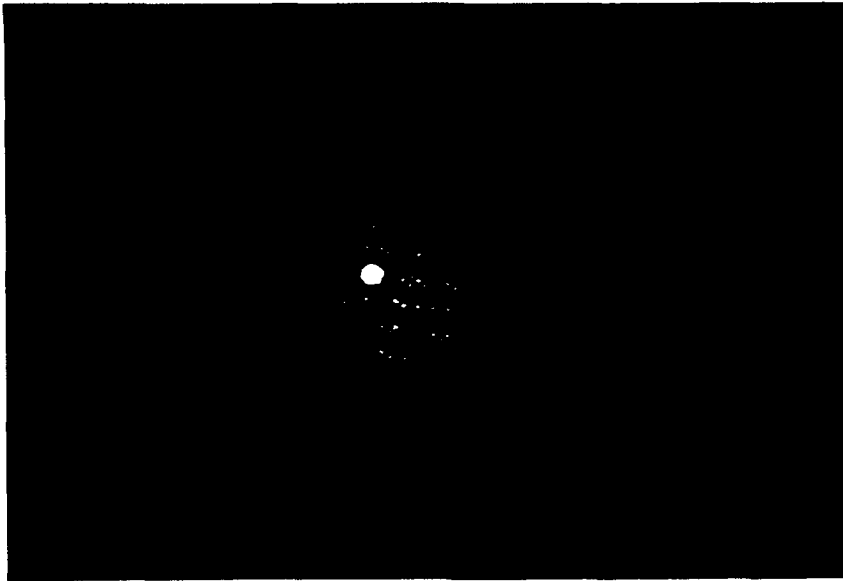


Figure 7
High Quality PLV Fringes With Little Directional Ambiguity

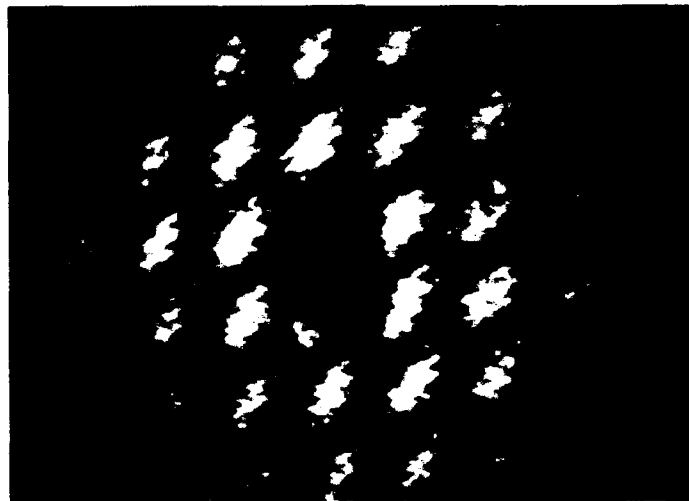


Figure 8
Total Directional Ambiguity in Fringe Pattern



Figure 9
Microscopic View of Particle Images Recorded on a Negative (Double Pulse)

APPLICATION OF LASER LIGHT SCATTERING TO INTRACELLULAR STREAMING

David Pileri
Sr. Development Engineer
Eastman Kodak Company
800 Lee Road
Rochester NY 14650

Abstract

A Laser Doppler Microscope is developed, capable of acquiring data in both the time and frequency domains. The freshwater algae *Chara globularis* is the specimen under study. Exposure of this cell to extracellular NaCl or EDTA elicits oscillatory action potentials that presumably causes the oscillation of the intracellular streaming. Data is gathered at different concentrations of each drug. Cytochalasin B effects are also monitored. The usefulness of using this approach to quantify intracellular velocity profiles in real time is apparent.

I. Introduction

The Doppler effect has many instrumentation applications in the fields of science and engineering. Since the advent of lasers, the measurement of optical Doppler shift to determine velocities has touched many technologies^{1,2}. Engineers found immediate application for this technique in measuring the fluid velocity in turbomachinery, flames, jet streams and other propulsion media.^{3,4} Vibration studies are also complimented by this technology. Chemists and physicists have applied it to study particle interactions in suspensions and emulsions.^{5,6} Health science professionals have used Doppler techniques to measure blood flow,⁶ diffusion constants,⁷ and cell motility.⁸

The advantages of using this technology for velocity measurements are numerous. The instrumentation can measure flows ranging from less than 10 $\mu\text{m}/\text{sec}$ up to Mach 8. Indeed, astronomers measure the expansion of the universe through the optical Doppler shift of stars in units of percent of the speed of light. Because this method is also non-contact, parameters can be measured accurately that would otherwise be impossible, even with the smallest (or strongest) of probes. Repetitive measurements can easily be made in real time, rendering the dynamic properties of the medium in question available for analysis. By carefully controlling the geometry of the optical setup, not only can the mean velocity be measured but the resulting velocity distribution gives insight to the "turbulence" of the flow.

Particle size measurement is also possible, although extremely difficult to model in a biological system. Biological velocimetry, specifically cytoplasmic streaming, will be the thrust of this paper. The specimen under study is the freshwater algae *Chara globularis*. To view the internal cytoplasmic streaming of this cell, a microscope was outfitted with the necessary optics and instrumentation to carry on laser Doppler velocimetry. Microcinematography studies have tracked velocities of *Chara's* streaming, but these observations are limited to visible particles whose velocity is examined over a known distance. The volume of scattered light created by the laser Doppler microscope can be accurately controlled and located for a fast, precise velocity measurement of submicroscopic particles. Besides the frequency domain, data will also be gathered in the time domain. The resultant autocorrelation curves also give insight into the velocity distribution.

Correlation is a comparison process applied to periodic electrical signals. By using correlation techniques an engineer can

- Detect a desired signal in the presence of noise or other signals
- Recognize specific patterns within analog or digital signals
- Measure time delays through various media including the human body, RF paths, electronic circuits and chemical substrates.

The correlation between two functions is a measure of their similarity. This expressed mathematically as the correlation between two functions $a(t)$ and $b(t)$.

$$C_{ab}(\tau) = \lim_{T \rightarrow \infty} \frac{1}{(2T)} \int_{-T}^{+T} a(t) b(t \pm \tau) dt \quad (1)$$

Where C_{ab} = the correlation function between two signals $a(t)$ and $b(t)$ and τ = the relative displacement between $a(t)$ and $b(t)$. The signals can be a function of essentially any variable -- wavelength, frequency, time, etc. Thus if $a(t)$ and $b(t)$ are considered to be functions of time, the correlation function C_{ab} will be related to and plotted against the relative time delay between the two signals.

For this application, the signals involved will be digitized. Here, the calculation of the correlation function is expressed as

$$C_{ab}(n \Delta t) = \sum_t a(t) b(t \pm n \Delta t) \quad n = 0, 1, 2, \dots \quad (2)$$

These signals can only be displaced by some integral number of the sampling interval, Δt . Thus, the displacement $n\Delta t$ is equivalent to τ in the previous equation.

The hardware used to gather these data employs a specific correlation scheme called autocorrelation. The autocorrelation function assumes that $a(t)$ and $b(t)$ are identical.

Intracellular particles undergoing Brownian motion and/or streaming give rise to a whole spectrum of Doppler shifted frequencies. These shifted frequencies beat either with each other or with the carrier so as to produce a fluctuating photocurrent, the frequency composition of which corresponds to the beat frequencies in their various proportions. The non-periodic bunching of signals seen in *Chara*'s intracellular flow are fitted to single exponential decaying autocorrelation functions by the digital autocorrelator.

Laser Doppler velocimeters use the Doppler shift of light scattered by moving particles to determine particle velocity and thus find the fluid flow velocity. The general equation expressing the Doppler shift (f_d) in the frequency of the scattered light as a function of the particle velocity (v) is

$$f_d = f_s - f_i = 1/\lambda \cdot v \cdot (\hat{e}_s - \hat{e}_i) \quad (3)$$

where

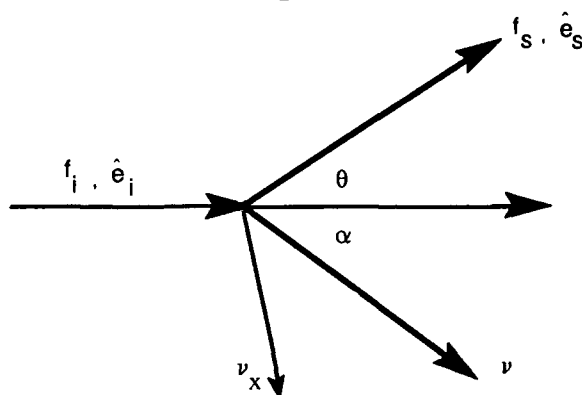
f_s = frequency of scattered light
 f_i = frequency of incident light
 \hat{e}_s and \hat{e}_i = unit vectors of scattered and incident light
and λ = frequency of incident light

The use of a monochromatic coherent light source such as a laser makes it possible to determine the values of f_i and λ ; \hat{e}_i and \hat{e}_s depend on the geometry of the system. The velocity component v_x (see below) measured by the Laser Doppler velocimeter will be in the plane formed by \hat{e}_i and \hat{e}_s and perpendicular to the line bisecting the angle formed by the two unit vectors. In this particular setup,

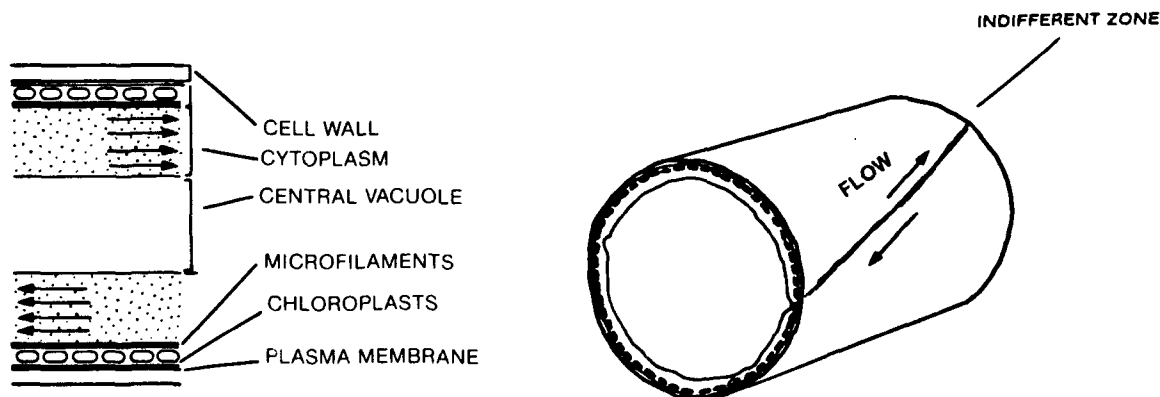
$$\alpha = 50^\circ, \theta = 40^\circ, \text{ and } \lambda = 6.328 \times 10^{-4} \text{ mm}$$

Therefore

$$\Delta \text{frequency} = \frac{K \cdot v \cdot \cos \alpha}{2\pi} \quad \text{where } K = (4\pi/\lambda) \cdot \sin(\theta/2) \quad (4)$$



The cell I have chosen to study is the fresh water algae *Chara globularis*. The largest internodal cells are approximately 20 mm long and 1 mm in diameter. The cytoplasm flows back and forth the length of these cells in two channels that are wound in a helical pattern at approximately 15° to the cell's longitudinal axis. The two opposing channels are separated by narrow regions, called indifferent zones, in which no streaming occurs. The cytoplasm is contained in a narrow cylindrical annulus surrounding the large, central vacuole. The outer cortex of the cell contains an array of chloroplasts except in the indifferent zones. The streaming cytoplasm lies between the stationary cortex and the Tonoplast membrane which lies between the vacuole and the cytoplasm. Bundles of microfilaments containing actin lie in the cytoplasm and are attached to the innermost layer of the cortex. These actin filaments have been shown to support the movement of myosin coated spheres *in vitro*.¹² See the diagram below.



II. Methods

Two experimental setups were constructed. The first was used to collect data in the time domain (Photon Correlation Spectroscopy). The second presents data in the frequency domain (Laser Doppler Velocimetry).

Photon Correlation Spectroscopy Experimental Setup

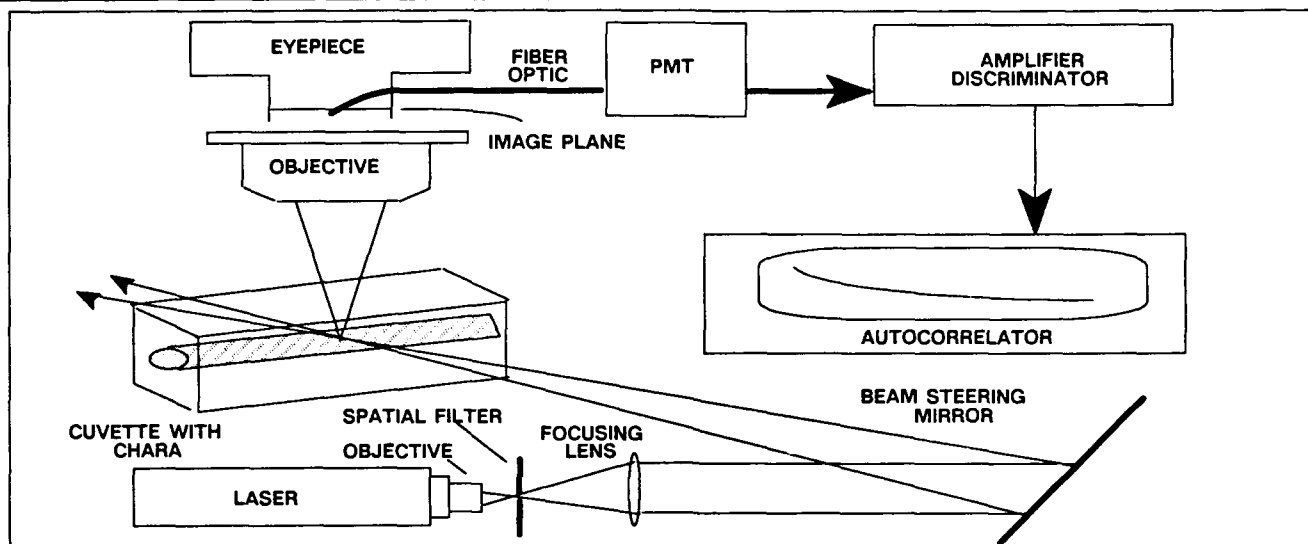


FIGURE 1. Photon Correlation Spectroscopy Experimental Setup.

Calibration of the instrument setup was confirmed by filling the cuvette with a solution of $0.525\ \mu\text{m}$ diameter, polystyrene, monodispersed latex spheres. The resulting normalized intensity autocorrelation function yielded a monotonically decaying exponential curve consistent with that expected for Brownian motion.¹³

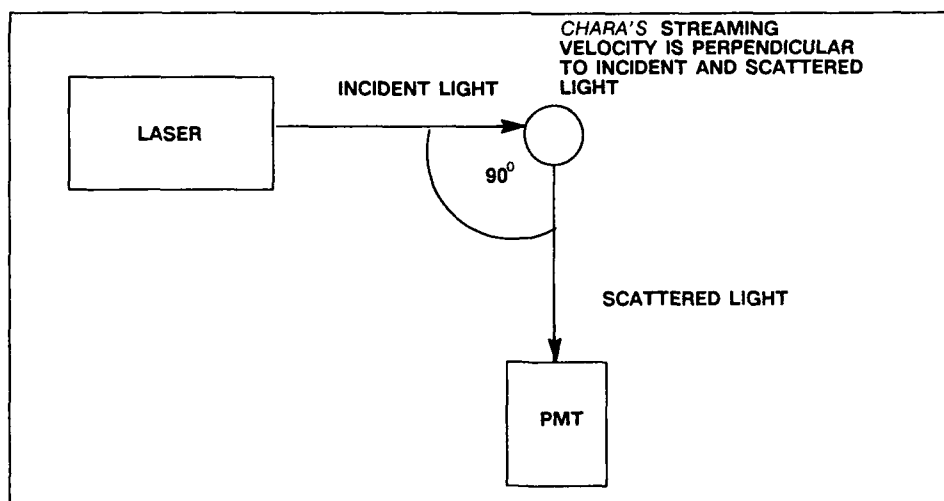


FIGURE 2 Geometry of Photon correlation apparatus.

After a *Chara* cell was cut, it was allowed to stabilize in a cuvette filled with APW for approximately 20 minutes. Then the cuvette was drained and refilled with various concentrations of NaCl or EDTA in APW. All solutions used were filtered through a $0.22\ \mu\text{m}$ filter. After a new concentration was added the cell's streaming was observed using white light illumination. When the cell began to pulse (i.e. stream and stop streaming cyclically) the time pattern was recorded. Data was gathered for both streaming and not-streaming at each concentration. Normalized intensity autocorrelation functions were output from the digital autocorrelator at 100 and 2000 μsec time delays.

Laser Doppler Velocimeter Experimental Setup

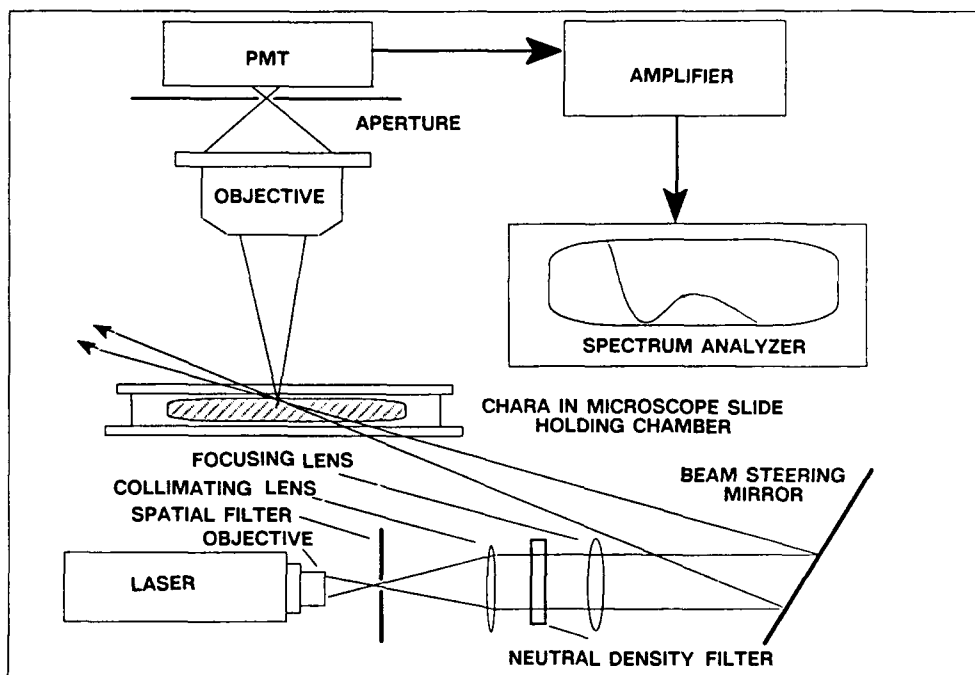


FIGURE 3. Laser doppler velocimeter apparatus.

A 25 mW HeNe neon laser, microscope objective, and spatial filter were again used as the light source. The filtered beam was then attenuated to 0.030 mW by a neutral density filter and enlarged to an 8 mm diameter by a collimating lens. A focusing lens then directed the beam into the cell through the beam steering mirror. The resulting 328 μm diameter Airy disk can easily be oriented into position within the streaming cytoplasm. A trimmed internodal cell is placed into a microscope slide holding chamber with a removable coverslip cover whose fluid contents can easily be changed. The chamber is held horizontally on the stage of a microscope such that the incoming laser beam is at 50° to the cell's axis. The cell's axis in this setup lies in the same plane that is formed by the incoming beam and the receiving optics (see Figure 4 for geometry). The light collection optics consist of a 10x microscope objective and a 1.5 mm diameter aperture in the focal plane of a photomultiplier tube. The resulting scattering volume is 150 μm . For observation of the streaming and laser alignment a prism is inserted before the PMT and all light is diverted to a viewing eyepiece. A white light illumination system is available for streaming observation. Again, a variable high voltage supply powers the PMT. The PMT's output is amplified and fed into a dynamic signal analyzer for processing. Again, all instrumentation is mounted on a vibration isolation table.

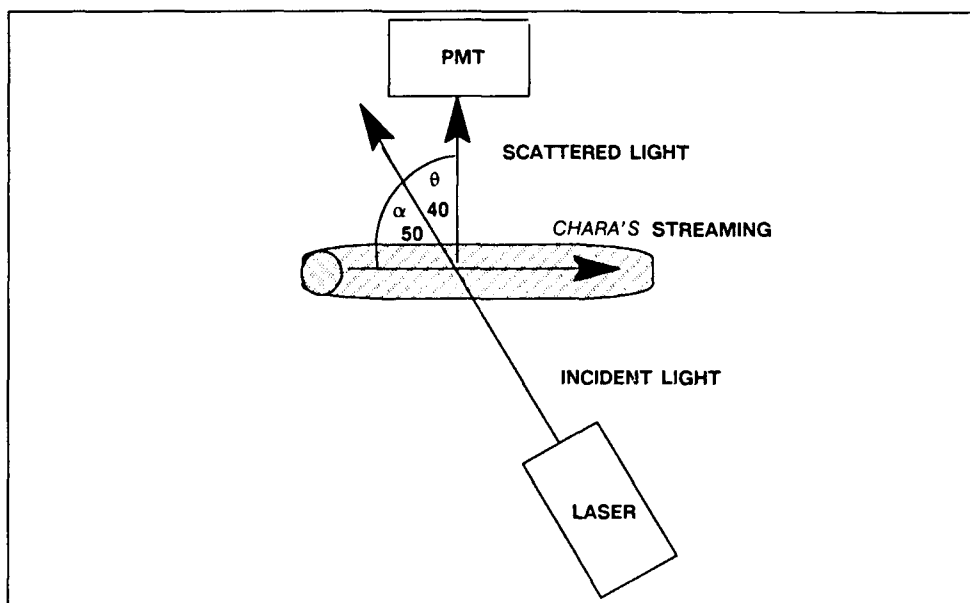


FIGURE 4. Geometry of Laser Doppler velocimeter.

Calibration of the instrument setup was accomplished by pumping a solution of polystyrene monodispersed latex microspheres through a flattened glass microtube (with a 0.3 mm wall separation) at a known rate (see Figures 5, 6, 7 and 8). The microscope objective was focused approximately in the cross-section center of the tube's flow. The resulting profile is representative of a parabolic flow¹⁴ with a peak maximum at the Doppler shifted frequency correlating with the flow velocity observed visually through the microscope. Another series of calibrations was done at 199 $\mu\text{m}/\text{sec}$ peak maximum observed flow velocity (corresponding to a Doppler shifted frequency of 138 Hz). Both the 85 $\mu\text{m}/\text{sec}$ and 199 $\mu\text{m}/\text{sec}$ observed flow velocities agreed with the calculated velocities within 1%. This error is attributed to a limited ability to accurately track and time particles in the flow during an observation.

Trimmed *Chara* cells were allowed to stabilize in APW for approximately 20 min. The chamber's fluid contents could then be perfused with a new volume of NaCl, EDTA, or Cytochalasin B in APW (pH 7.3). Real time data was gathered, averaged and mapped over time durations that included at least one stop-start cycle, depending on the frequency of pulsing. Linear scaling, rms averaging, and Hann weighting were used as measurement parameters over a 100 Hz frequency range in the spectrum analyzer. The offset mapping capability of the spectrum analyzer allows a graphic representation of the increase and/or decrease in the Doppler shifted spectrum.

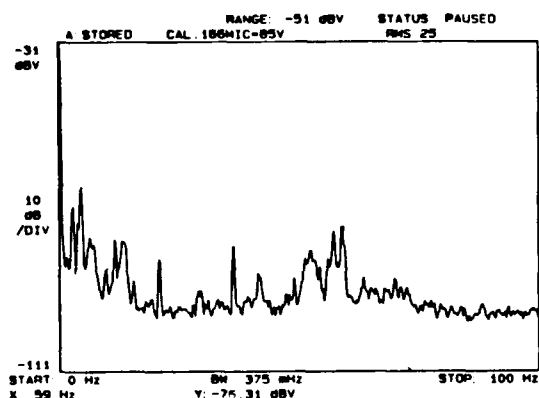


FIGURE 5. Calibration spectrum for polystyrene spheres 0.166 μm diameter: 59 Hz peak corresponds to 85 $\mu\text{m}/\text{sec}$ observed peak maximum flow velocity.

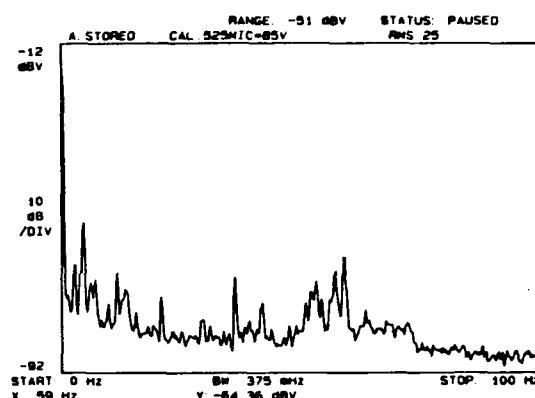


FIGURE 6. Calibration spectrum for polystyrene spheres 0.525 $\mu\text{m}/\text{sec}$: 59 Hz peak corresponds to 85 $\mu\text{m}/\text{sec}$ observed peak maximum flow velocity.

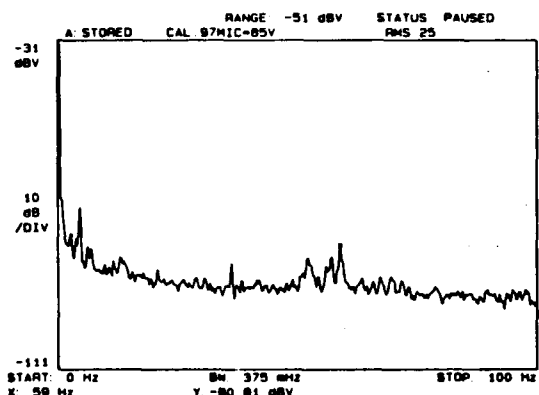


FIGURE 7. Calibration spectrum of 0.97 μm diameter polystyrene spheres. 59 Hz peak corresponds to 85 $\mu\text{m}/\text{sec}$ observed peak maximum flow velocity.

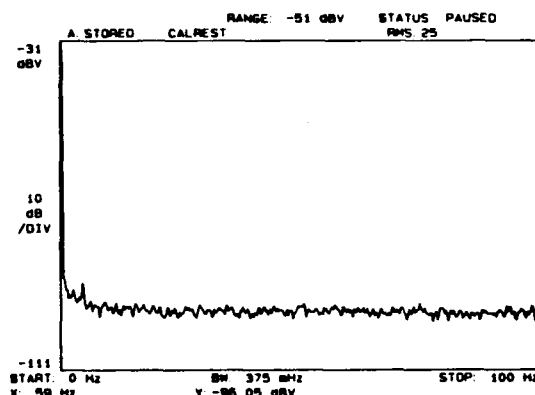


FIGURE 8. Spectrum of calibration setup with polystyrene microspheres at zero flow velocity.

III. Results

Photon Correlation Spectroscopy

Normalized intensity autocorrelation functions were recorded from the *Chara* cells using the previously mentioned experimental setup. In all, ten sets of data were gathered from ten different cells exposed to NaCl or EDTA solutions at both 100 μsec and 2000 μsec delay times (see Figure 9). Monotonically decaying autocorrelation functions resulted in all cases. The time lapse between the cessation of streaming ranged from 2 min up to 15 min depending on the chemical concentration and/or the individual properties of each cell.

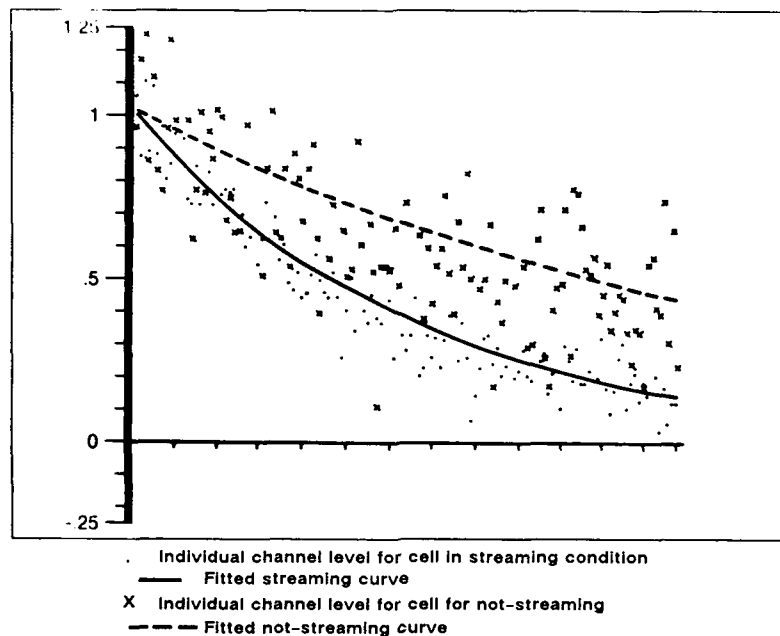


FIGURE 9. Normalized autocorrelation functions of *Chara* in 50 mM NaCl in APW using 100 μ sec delay time.

The normalized autocorrelation functions always yielded the same results. Data collected during times of streaming indicated a faster decay rate than not-streaming regardless of the delay time, drug used (or its concentration), and individual cell variability.

Laser Doppler Velocimetry

Frequency spectra were recorded from streaming *Chara* cells using the setup described in "methods." Trimmed, streaming cells were first allowed to stabilize in their holding chamber (Figure 10). The chamber could then be perfused with increasing concentrations of NaCl or EDTA. Data was recorded and/or mapped during periods of streaming and not streaming (Figures 11, 12, 13).

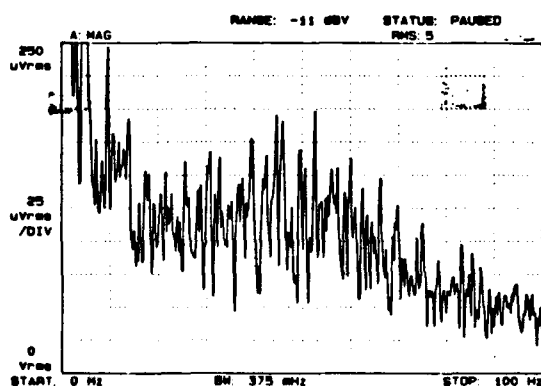


FIGURE 10. Heterodyne spectrum of *Chara* streaming in APW. Center of doppler shifted peak (52.5 Hz) corresponds to 76 μ m/sec peak maximum streaming velocity agreeing with observed velocity.

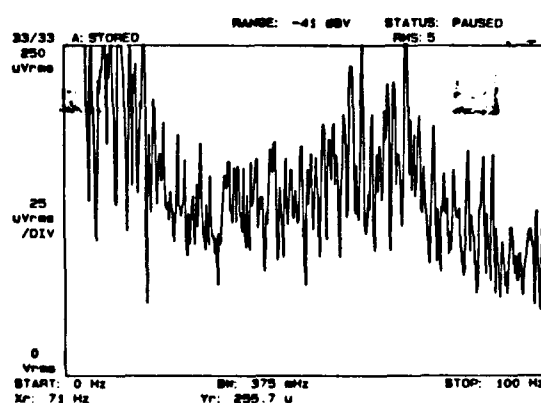


Figure 11. Spectrum of *Chara* streaming in 50 mM NaCl in APW. 71 Hz corresponds to observed 102 μ m/sec peak maximum streaming velocity.

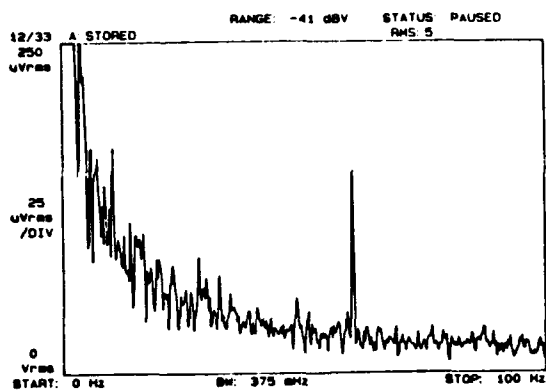


FIGURE 12. Spectrum of *Chara* with streaming cyclically stopped in 50 mM NaCl in APW. 60 Hz carrier is predominant.

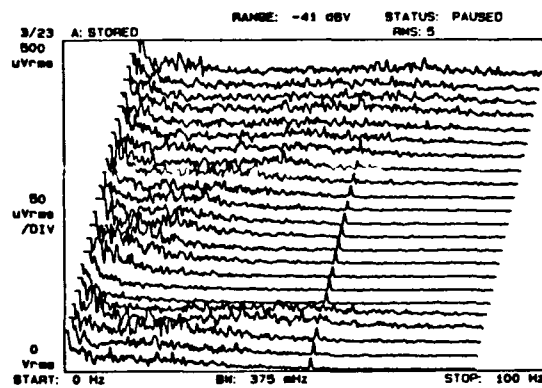


FIGURE 13. Spectral map taken at 30 second intervals of *Chara* streaming, stopping and starting again in 50 mM NaCl in APW. pH 7.3 at room temperature. 60 Hz carrier is predominant at lower velocities.

Concentrations were increased until the cell died and streaming therefore stopped (Figure 14). A 60 Hz carrier was predominant at weak signal levels or whenever the Doppler shifted spectrum moved to low frequencies.

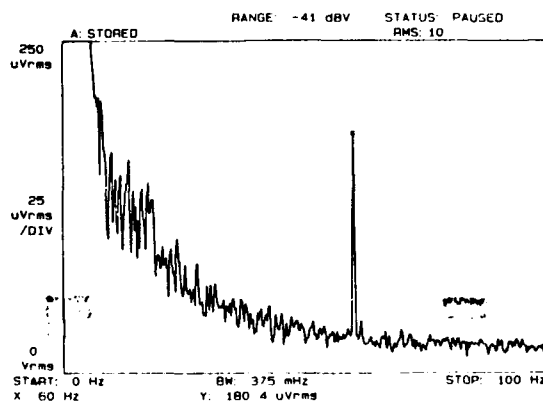


FIGURE 14. Spectrum is taken from dead cells in 75 mM NaCl in APW.

During each concentration run, the center of the Doppler shifted peak in the heterodyne spectrum that corresponds to the maximum streaming velocity was recorded. Comparison of the velocity observed through the microscope showed correlation within 1%. Minimum velocities at each concentration were also recorded. Minimum velocities were 0 if the cell was pulsing. these results are summarized in Table 1 and 2 below.

TABLE 1
NaCl in APW

Concentration	Maximum Average Velocity (#cells)	Minimum Average Velocity (#cells)
5 mM	76.5 $\mu\text{m/sec}$ (3)	0 $\mu\text{m/sec}$ (2)
7.5 mM	82.5 $\mu\text{m/sec}$ (5)	0 $\mu\text{m/sec}$ (2)
10 mM	86.1 $\mu\text{m/sec}$ (5)	0 $\mu\text{m/sec}$ (4)
25 mM	84.0 $\mu\text{m/sec}$ (5)	0 $\mu\text{m/sec}$ (5)
50 mM	87.7 $\mu\text{m/sec}$ (5)	0 $\mu\text{m/sec}$ (4)
75 mM	DEAD	DEAD

TABLE 2
EDTA in APW

Concentration	Maximum Average Velocity (#cells)	Minimum Average Velocity (#cells)
0.025 mM	88.1 $\mu\text{m/sec}$ (5)	0 $\mu\text{m/sec}$ (2)
0.050 mM	88.1 $\mu\text{m/sec}$ (5)	0 $\mu\text{m/sec}$ (4)
0.100 mM	89.8 $\mu\text{m/sec}$ (5)	0 $\mu\text{m/sec}$ (4)
0.25 mM	88.9 $\mu\text{m/sec}$ (4)	0 $\mu\text{m/sec}$ (4)
0.50 mM	68.4 $\mu\text{m/sec}$ (2)	0 $\mu\text{m/sec}$ (2)
1.0 mM	DEAD	DEAD

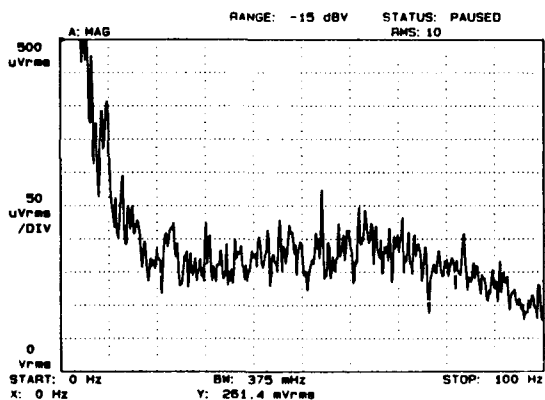


FIGURE 15. Spectrum taken from *Chara* stabilized in APW prior to addition of Cytochalasin B. 62 Hz frequency corresponds to observed peak maximum streaming velocity of 89 $\mu\text{m/sec}$.

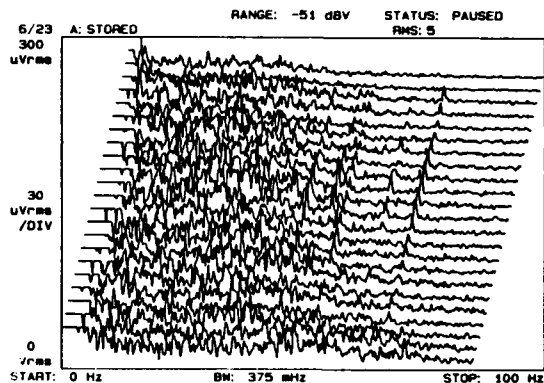


FIGURE 16. Spectral map at 4 minute intervals after the addition of Cytochalasin B. Gradual shift of doppler peak to a lower frequency correlates with slowing of streaming velocity.

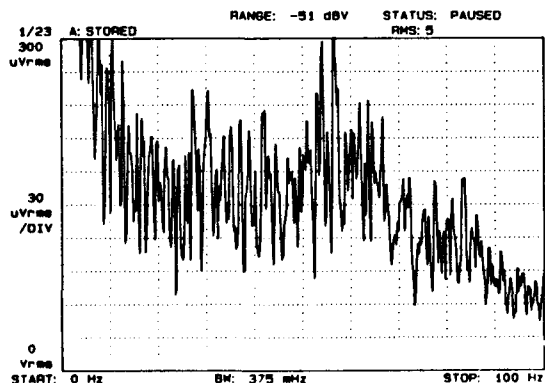


FIGURE 17. Spectrum taken 4 minutes after addition of Cytochalasin B. 56 Hz doppler shifted peak corresponds to observed peak maximum streaming velocity of 81 $\mu\text{m/sec}$.

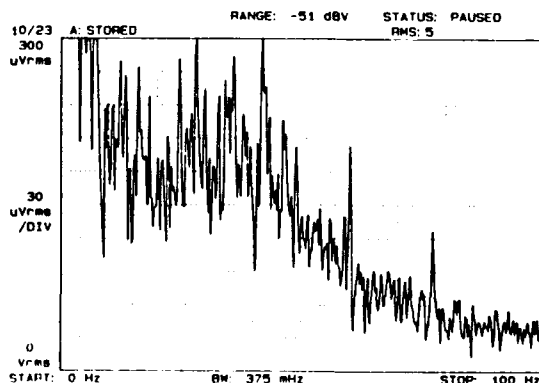


FIGURE 18. Spectrum taken 40 minutes after addition of Cytochalasin B. 42 Hz doppler shifted peak corresponds to observed peak maximum streaming velocity of 60 $\mu\text{m/sec}$.

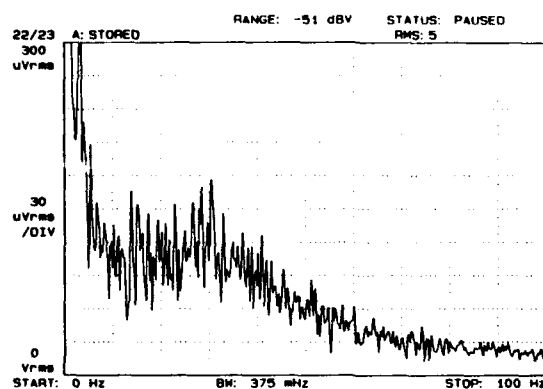


FIGURE 19. Spectrum taken 88 minutes after the addition of Cytochalasin B. 30 Hz doppler shifted peak corresponds to observed peak maximum streaming velocity of 43 $\mu\text{m}/\text{sec}$.

Cytochalasin B at a concentration of 10 $\mu\text{g}/\text{ml}$ in APW containing 1% dimethyl sulfoxide was also perfused into the chamber. During a several hour period both the observed streaming rate and the Doppler shifted spectra were seen to gradually decrease (Figures 15 and 16). Three representatives of the map shown in Figure 16 are presented separately at full scale for clarity (Figures 17, 18, and 19).

IV. Discussion

The two previously described instrumentation schemes were devised to allow fast, accurate measurements of "spectral changes" in cells under various physiological/environmental conditions. Building the instrumentation around a microscope frame allows for easy manipulation of the specimen and for comfortable viewing using standard microscope optics and illumination system. For the cell structure and streaming pattern that *Chara* exhibits, this is a distinct advantage because the direction of the streaming cytoplasm can be positioned precisely with respect to the incident light without being concerned with the angle between the streaming and the cell's longitudinal axis or the effects produced near the indifferent zones. Another advantage of this non-invasive technique is that the intensity of the incident laser light is low enough to avoid *Chara*'s photoresponse.¹³

Data gathered using light scattering instrumentation such as this help to characterize *Chara*'s cytoplasmic streaming. Photon correlation spectroscopy results consistently show a difference in decay rate between the cell's cyclic streaming and not-streaming induced by NaCl and EDTA. Since the streaming velocity was oriented perpendicular to the direction of the incident light and the scattered light, these data represent small lateral motions of the scattering particles. Shape changes in the autocorrelation functions noted during streaming are consistent with a bulk flow of cytoplasm. When streaming stops, all subcellular scatterers apparently stop together. Brownian motion is probably the sole contributor to intracellular motion when the cell is not-streaming. Other researchers,¹⁵⁻¹⁷ have worked with similar cells in the time domain, stopping the intracellular streaming using electrical stimulation. Variations in the scattering angle and the axis of the streaming have been explored with results consistent with those presented here.

Laser Doppler Velocimetry data also helps characterize *Chara*'s intracellular flow by allowing the mean velocity to be quantified. Velocity measurements obtained from fresh cells stabilized in APW agree with velocities recorded by other researchers,¹⁸⁻²² from similar cells under similar conditions using laser Doppler technique and photomicroscopy. These cited velocities on resting cells range from 40 $\mu\text{m}/\text{sec}$ to 100 $\mu\text{m}/\text{sec}$. The ability to create a spectral map collected at known intervals allows a graphic representation of a cell's response to a drug or environmental change over a specified timecourse. Mustacich and Ware,¹³⁻¹⁹ have studied the temperature dependence of streaming in *Nitella* and have found that the streaming velocity varies linearly with temperature from 5°C up to 34°C, above which the cell irreversibly stops streaming. They have also demonstrated that the low frequency portion of the spectrum is the result of amplitude modulation of the scattered light by the array of chloroplasts in the cell. Their experiments with *Nitella* and low levels (1 $\mu\text{g}/\text{ml}$) of Cytochalasin B indicate that the gradual slowing of the cytoplasmic streaming is microfilament related. These results are consistent with those presented in this paper.

The ultimate goal of any research of this type on intracellular streaming is to gain information that helps to explain the molecular mechanism for the generation of the motive force. The elicitation of spontaneous action potentials in *Nitella* was demonstrated by Kishimoto²³ using various concentrations of NaCl, LiCl, EDTA, and ATP. The cause of the spontaneous firing is theorized to be the removal of Ca^{++} from the outer surface of the *Nitella* membrane²⁴.

The role of Ca^{++} in the cytoplasmic streaming of *Chara* is not yet understood. In skeletal muscle the Ca^{++} dependence of contraction results from a conformational change of the troponin-tropomyosin complex bound to the cell's actin cables. However, in these algal cells there is no known troponin-tropomyosin complex bound to the cell's actin cables. Recent work by Vale, Szent-Gyorgyi, and Sheetz²⁵ has found that the movement of skeletal myosin coated beads on *Nitella* actin is Ca^{++} independent in concentrations between 10^{-9} and 10^{-4} M. However, if rabbit skeletal muscle troponin-tropomyosin is added, then the movement of skeletal myosin coated beads is Ca^{++} dependent. The concentration of Ca^{++} required for half

maximal activation of bead movement in the presence of troponin-tropomyosin is 10 μ M which compares favorably with the concentration required to half maximally activate ATPase by troponin-tropomyosin coated actin. They have therefore demonstrated the reconstitution of Ca^{++} dependent motility with an actin-based regulation system. Because the troponin-tropomyosin requires extensive controls with the actin filaments, these results suggest that *Nitella* actin is free to bind added proteins. Similar work by Shimmen and Yano,²⁶ using skeletal muscle tropomyosin confirms that *Chara* cells have their own Ca^{++} control system. The presence of Calmodulin has been confirmed in *Chara*,²⁷ although it assumed not to be involved in the Ca^{++} induced cessation of streaming. The Ca^{++} sensitizing component is assumed to be present within the streaming cytoplasm. Actin bundles are thought not to be the site giving Ca^{++} sensitivity to streaming. The possibility of the assembly of actin filaments being the source of cytoplasmic motility is also being investigated²⁸.

The coupling of the action potential with the oscillation of streaming is confirmed by Barry,²⁹⁻³⁰ who elicits a transient action potential through electrical stimulus. Barry varies the Ca^{++} level of his APW between 0 to 0.5 mM in order to modify the shape of the action potential. He experiences a time lag between the onset of the action potential and pressure/volume changes when the cell is only partially stimulated electrically. This time lag is of particular interest because Kishimoto's²² published action potential frequencies are an order of magnitude faster than my streaming periodicity. Barry concludes that the changes he measures in pressure and volume are the incidental consequences of a change in membrane permeability and do not necessarily imply an electro-kinetic mechanism for the action potential itself.

Other researchers,³¹⁻³² theorize that the mechanism for the action potential is generated by ion pumping instead of ion gradients. If the action potential is driven by this metabolic pump, then it is also possible that the streaming is supported by this or another metabolic process.

Both my results and other unpublished results taken in our lab indicate that both high (1.0 mM) and low (0.0001 mM) concentrations of extracellular Ca^{++} will cause *Chara* to pulse, with no pulsing seen at intermediate concentrations. The calculated³³ levels of active Ca^{++} in my APW/EDTA solutions are

- For 0.025 mM EDTA, 3.9×10^{-10} M Ca^{++}
- For 0.05 mM EDTA, 1.9×10^{-10} M Ca^{++}
- For 0.10 mM EDTA, 9.8×10^{-11} M Ca^{++}
- For 0.25 mM EDTA, 3.9×10^{-11} M Ca^{++}
- For 0.50 mM EDTA, 1.9×10^{-11} M Ca^{++}
- For 1.00 mM EDTA, 9.7×10^{-12} M Ca^{++}

At an EDTA level of 0.025mM, it takes an order of magnitude increase in total Ca^{++} concentration (from .1mM to 1.0mM) to increase the active Ca^{++} concentration by an order of magnitude (from 3.9×10^{-10} M to 3.9×10^{-9} M). This pattern of reacting only to "extreme" levels of Ca^{++} fits nicely into the scheme of a pump mechanism.

How does NaCl effect the action potential and streaming? Some researcher³⁴, suggest that there is a Sodium-Calcium exchange (sometimes referred to as Sodium-Calcium antagonism).

The instrumentation development discussed here resulted in a method to quantitatively measure intracellular flow. The actual relationship between the oscillatory action potential and intracellular streaming is still not understood. How they are coupled together—directly, indirectly, or through a time lag—would be interesting to study. The logical extension to this research is to build a chamber in which a cell could have monitored its intracellular streaming measured via light scattering and its action potential simultaneously. Varying environmental conditions and using various drugs and chemicals to couple and uncouple these two events could provide information that would help to explain the molecular and physiological mechanisms of this phenomena.

References

1. Pecora, Robert. *Dynamic Light Scattering: Applications of Photon Correlation Spectroscopy*. Plenum Press N.Y. (1985)
2. Chu, B. *Laser Light Scattering*. Academic Press, Inc. N.Y. (1974)
3. Durst, F., A. Melling, J.H. Whitelaw. *Principles and Practice of Laser-Doppler Anemometry*. Academic Press (1981)
4. Fingerson, L.M. 1982. Laser Doppler Velocimetry. *Fiberoptic Technology*. August:53
5. Chu, B., E. Gulari, E. Gulari. 1979. Photon Correlation Measurements of Colloidal Size Distributions II. Details of Histogram Approach and Comparison of Methods and Data Analysis. *Physica Scripta*. 19:476.
6. Dutiel, L., J.C. Bernengo, W. Schalla. 1985. A Double Wavelength Laser Doppler System to Investigate Skin Microcirculation. *IEEE Transactions on Biomedical Engineering*. Vol. BME-32, No. 6:439.
7. Nishio, I., J. Peetermans, T. Tanaka. 1985. Microscope Laser Light Scattering Spectroscopy of Single Biological Cells. *Cell Biophysics*. 7:91.
8. Chen, S.H., M. Holz. 1977. Medical Application of Photon Correlation Spectroscopy. *Med. Res. Eng.* 12:19.
9. Barth, H.G., S.T. Sun. 1984. Particle Size Analysis. *Anal. Chem.* 57:151R.
10. Earnshaw, J., M. Steer. 1979. Laser Doppler Microscopy. *Proceedings RMS*. 14/2:108.
11. Blank, P.S., R.B. Tishler, F.D. Carlson. 1987. Quasielastic Light Scattering Microscope Spectrometer. *Applied Optics*. Vol. 26, No. 2.
12. Sheetz, M.P., J.A. Spudich. 1983. Movement of Myosin-Coated Fluorescent Beads on Actin Cables In Vitro. 303:31.
13. Steer, M.W., J.M. Picton, J.C. Earnshaw. 1983. Diffusive Motions in Living Cytoplasm Probed by Laser Doppler Microscopy. *Journal of Microscopy*. 134:143
14. Mustacich, R.V., and B.R. Ware. 1976. A Study of Protoplasmic Streaming in Nitella by Laser Doppler Spectroscopy. *Biophysical Journal*. 16:373
15. Langley, K.H., R.W. Piddington, D. Ross, D.B. Sattelle. 1976. Photon Correlation Analysis of Cytoplasmic Streaming. *Biochimica Biophys. Acta*. 444:893
16. Sattelle, D.B., D.J. Green, K.H. Langley. 1979. Subcellular Motions in Nitella flexilis Studied by Photon Correlation Spectroscopy. *Physica Scripta*. 19:471
17. Piddington, R.W. Laser Light Scattering from Nerve and Motile Cells, in Perspective in Exptl. Biology. Vol. 1:313. Pergamon Press (1976)
18. Sattelle, D.B., P.B. Buchan. 1976. Cytoplasmic Streaming in Chara corallina Studied by Laser Light Scattering. *J. Cell Sci.* 22:633
19. Mustacich, R.V., B.R. Ware. 1974. Observation of Protoplasmic Streaming by Laser Light Scattering. *Physical Review Letters*. 33:617
20. Mustacich, R.V., B.R. Ware. 1977. Velocity Distributions of the Streaming Protoplasm in Nitella flexilis. *Biophysical Journal*. 17:229
21. Allen, N. Cytoplasmic Streaming in Plant Cells and its Relation to the Cytoskeleton, in The Application of Laser Light Scattering to the Study of Biological Motion. NATO Advanced Science Institute Series. Series A, Life Sciences : Vol. 59 :29. N.Y. Plenum (1983)
22. Shimmen, T., M. Tazawa. 1982. Cytoplasmic Streaming in the Cell Model of Nitella. *Protoplasma*. 112:101.
23. Kishimoto, Uichiro. 1966. Repetitive Action Potentials in Nitella Internodes. *Plant & Cell Physiology*. 7:547
24. Tazawa, M., T. Shimmen, T. Mimura. 1987. Membrane Control in the Characeae. *Ann. Rev. Plant Physiol.* 38:95-117.
25. Vale, R., Szent-Gyorgyi, A., Sheetz, M. 1984. Troponin-Tropomyosin Complex Confers Ca⁺⁺ Control to Myosin Bead Movement In Vitro. *Biophysical Journal*. 45:7a
26. Shimmen, T., M. Yano. 1986. Regulation of Myosin Sliding along Chara Actin Bundles by Native Skeletal Muscle Tropomyosin. *Protoplasma*. 132:129-136.
27. Tominaga, Y., S. Muto, T. Shimmen, M. Tazawa. 1985. Calmodulin and Ca²⁺ Controlled Cytoplasmic Streaming in Characean Cells. *Cell Structure and Function*. 10(4):315-325.
28. Ware, B.R., J.W. Klein. 1986. Assembly of Actin Filaments Studied by Laser Light Scattering and Fluorescence Photobleaching Recovery. *Biophys. J.* 49:147-149
29. Barry, P.H. 1970. Volume Flows and Pressure Changes During an Action Potential in Cells of Chara australis I. *J. Membrane Biol.* 3:313
30. Barry, P.H. 1970. Volume Flows and Pressure Changes During an Action Potential in Cells of Chara australis II. *J. Membrane Biol.* 3:335
31. Brashford & Pasternak. 3/11/86. Plasma Membrane Potential of Some Animal Cells Generated by Ion Pumping, Not by Ion Gradients. *Trends in Biochemical Sciences (TIBS)*. p.113.
32. Takeshige, K., T. Shimmen, M. Tazawa. 1986. Quantitative Analysis of ATP-Dependent H⁺ Efflux and Pump Current Driven by an Electrogenic Pump in Nitellopsis obtusa. *Plant Cell Physiol.* 27(2):337-348.
33. Durham, A.C.H. 1983. A Survey of Readily Available Chelators for Buffering Calcium Ion Concentration in Physiological Solutions. *Cell Calcium*. 4:33.
34. Blaustein, M.P., Liberman, M. *Electrogenic Transport: Fundamental Principles and Physiological Implications*. Raven Press (1984).

THE INTERNAL FRACTAL STRUCTURE OF AGGREGATES OF SILVER PARTICLES AND ITS CONSEQUENCES ON SERS INTENSITIES

O. Siiman and H. Feilchenfeld
Department of Chemistry
Clarkson University
Potsdam, New York 13676

Abstract

The kinetics of aggregation of colloidal silver particles as measured by surface-enhanced Raman scattering and TEM images of the aggregates were analyzed in terms of a fractal rate law and fractal structures. Transmission micrograph images of colloidal silver particles that had been induced to aggregate by oxoanions, CrO_4^{2-} , WO_4^{2-} , and PO_4^{3-} were obtained. Polymeric ions were also used to produce aggregates of varying size, in which the oxoanions function as bridging ligands between silver particle surfaces. For a series of photos with isopolytungstate on silver, the spatial dependence of the mass of silver particles in a large, low density aggregate was analyzed as a fractal object. A comparatively low fractal dimension, $D = 1.51$, was derived. Chains of silver particles on the perimeter of some aggregates were also analyzed in terms of a fractal scaling and gave $D = 1.35$. Surface-enhanced Raman (SER) spectra of chromate and phosphate on colloidal silver were used to identify two types of adsorption sites: (1) oxoanions adsorbed in a double-sided mode of coordination, bridging pairs of silver particles; (2) oxoanions adsorbed in a single-sided mode on one silver particle surface. Data on the kinetics of aggregation of colloidal silver particles as induced by NaHPO_4 showed linear, logarithmic plots of SERS band intensity against time and gave different exponents, 0.82 and 0.64, in the power law relationship, $I \sim t^\beta$, for different SERS bands. Together with similarly analyzed data for chromate and tungstate on silver a relationship between the reciprocal of β and the type of aggregate structure and mode of adsorbate coordination is proposed.

Introduction

The particular brand of Raman scattering known as surface-enhanced Raman scattering^{1,2} (SERS) is now over ten years old. There are however still problems³ in describing the mechanism of enhancement of Raman intensities in the Mie scattering formalism for small colloidal particles. The SERS enhancement (G) for an oscillating molecular dipole located on a spherical particle ($a \ll \lambda_0$) has been derived as

$$G = |(1 + 2 g_0)(1 + 2 g)|^2$$

where $g_0 = \frac{n_0^2 - 1}{n_0^2 + 2}$ and $g = \frac{n^2 - 1}{n^2 + 2}$. Thus, G becomes large if either $n_0^2 \rightarrow -2$ or $n^2 \rightarrow -2$,

i.e., if n_0 (refractive index at the incident wavelength) or n (refractive index at Raman-shifted wavelength) approach $\sqrt{2}i$. For pure silver in water this occurs at about 382 nm. The enhancements do not become infinite since even for pure silver in air the real part of the refractive index does not assume a zero value at this resonance but attains a finite minimum value.

Electrodynamic calculations,^{4,5} for silver spheres have shown that the resonances coinciding with the extinction band maxima of single spheres should also be observed in the Raman scattering intensity from molecules on the surface of small silver spheres. This however has not been realized. All of our experiments⁶⁻⁹ with colloidal metal particles have shown SERS intensity maxima that are displaced towards the red to coincide with maxima due to multiplets of single particles in clusters. The implications of these results are that (1) SERS enhancement for molecules on single isolated particles is much lower beyond our detection limit ($\sim 10^3 - 10^4$ over normal Raman scattering intensity); (2) the calculations are very sensitive to optical constants of silver that are used and comparison with experiment results depends on purity of silver in the system (The colloidal silver sols as prepared are hardly pure silver systems and no doubt the theoretical estimates must be revised downward to compare experimental against theoretical results.); (3) there may be some additional enhancement for molecules on the surface of particles in aggregates or clusters of any size (starting with a doublet) that is not present for single isolated particles and which gives the detectable SERS spectra.

Herein, we describe some of our recent results aimed at understanding more about the enhancement mechanism for SERS and SERS-active sites. The system consists of colloidal silver particles and adsorbed oxoanions, either monomeric CrO_4^{2-} , WO_4^{2-} , PO_4^{3-} ions or polymeric $\text{H}_2\text{W}_{12}\text{O}_{40}^{6-}$, isopolytungstate ions. Transmission electron micrographs of aggregated sols were used for the analysis of their internal structure and determination of their fractal dimensions. SERS spectra of aggregates, taken during their growth period,

were used to analyze the kinetics of aggregation as induced by the oxoanions. The scaling of SERS intensity with the time of aggregation was also analyzed, and together with the structural results their implications on the SERS mechanism were analyzed.

Results

Preparation and Transmission Electron Microscopy of Silver Particle Clusters

The primary Carey Lea silver sol⁶ with adsorbed citrate, diluted 1000-fold to a silver concentration of 0.002 g/L for TEM examination, consisted mainly of single silver particles and a few small aggregates (doublets and triplets). These particles have a mean diameter of 13 (± 6.3) nm. When the primary sol diluted 10-fold with distilled water was treated with an ion exchange resin (mixed bed: H^+ , OH^- form) to remove sodium and citrate ions to a conductivity of 4 $\mu\text{mho cm}^{-1}$ approaching that of distilled water, some small aggregates appeared within several hours after treatment. Aggregation increased thereafter until the sol precipitated completely after a week. TEM photos of these aggregates showed that neighboring silver particles were touching each other to form silver-silver contacts. Partial or total coalescence of particles was sometimes observed. When an oxoanion such as metatungstate $H_2W_{12}O_{40}^{6-}$ was introduced immediately after removal of sodium citrate by ion exchange, TEM examination of the aggregates that formed showed spaces between neighboring particles that had no silver-silver surface contacts and no coalescence of particles was observed.

Analysis of Aggregate Internal Structure

In a particularly favorable set of TEM photos shown in Figure 1 we have analyzed the distribution of mass in the 2-dimensional projection. In this case no overlap of silver particles occurred and thus a meaningful analysis could be performed. An enlargement of the micrograph was made and then overlaid with a square lattice of 1 mm grid graph paper. A hand-drawn image of this photo was then produced by assigning each 1 mm² square with the presence or absence of a particle. Assuming each occupied square contained the same mass of silver, the scaling of particle number (N) versus size (L) was obtained for a series of nested squares of increasing size from a common chosen origin. This analysis¹⁰ would give a power law dependence, $N \sim L^D$ for a fractal object of dimension, D. We found however that the slope of this curve in Figure 2 varied with position and gave $D = 2.02$ in the middle, $D = 1.51$ on the sides and $D = 0.99$ in the intermediate region. These results probably reflected our choice of the origin near the center of the image.

Using a second grid method due to Schlomo Alexander,¹¹ a histogram was first formed for the number of squares ($p(n_i)$) of edge length, L, containing n_i particles versus n_i . The second moment of this histogram ($\sum p(n_i)n_i^2/N$, where N = normalizing factor, total number of squares) was shown to scale as L for fractal objects and the method does not rely on a choice of origin. A logarithmic plot of second moment/ L^2 versus L gave a slope and thus fractal dimension $D = 1.51$ in good agreement with the average value, 1.55, by the first method.

Further, the inner and outer boundaries of a segment of the ribbon-like chain were analyzed by determining the number of lengths, $N(l)$, required to map the chain with a variable yardstick of length, l , as measured out on a pair of dividers. A logarithmic plot of N versus l gave fractal dimensions of 1.40 and 1.31 for the inside and outside boundaries, respectively. These values are similar to $D = 4/3$ obtained for polymer chains in dilute media and from computer simulations of the self-avoiding random walk on a 2-dimensional lattice.

Thus, fractal dimensions for aggregate structures of colloidal metal particles can span the range, 1.8 to 1.3, depending on the type of structure ($D = 1.8$ for globular clusters^{11,12}; $D = 1.5$ for less dense clusters; and $D = 1.3$ for linear chains).

Surface-Enhanced Raman Spectra of Oxoanions on Colloidal Silver

The evolution of SERS spectra of surface-adsorbed chromate and phosphate as a function of time for growing clusters of silver particles was followed. A stretching mode, $\nu_s(\text{Cr-O})$, of chromate ion in solution at 850 cm^{-1} is soon overshadowed by an intense surface counterpart at 800 cm^{-1} , shown in Figure 3. Analysis¹³ of the kinetics of aggregation established a pseudo-first order rate law. Strictly, aggregation is a second order rate process; however, under certain conditions it can assume apparent first order kinetics. In the present case the kinetics of aggregation takes on the kinetics of adsorption at relatively high total adsorbate concentrations ($\geq 10^{-3}$ M). These concentrations are much higher than the monolayer concentration of $\sim 10^{-5}$ M required to cover the entire available surface.

Further, SERS spectra in Figures 4 and 5 taken for CrO_4^{2-} and PO_4^{3-} on colloidal silver

show the presence of two sets of stretching and bending bands that might be associated with two species of adsorbed ions or the same species in different silver particle environments. For CrO_4^{2-} , these SERS bands occur at 800, 353 cm^{-1} and 937, 588 cm^{-1} ; while, for PO_4^{3-} they are found at 930, 410 cm^{-1} and 1095, 575 cm^{-1} . The second set of bands is not assignable to the dimeric species, dichromate or pyrophosphate. Thus, we have assigned them to the two different adsorption sites that are apparent in the TEM micrographs of the aggregated silver particles, i.e., single-sided or open-ended sites with no nearby adjacent particle and double-sided or bridging sites between adjacent silver particle surfaces, respectively.

Scaling of SERS Band Intensity with Time

We have also found¹³ a power law dependence of SERS intensity, I , on aggregation time, t , in intermediate time periods after an initial induction time when first order kinetics set in and before the end-point at which larger aggregates begin to sedimentate out of the suspension. Log-log plots¹³ of I versus t for $3.5 \times 10^{-3} \text{ M WO}_4^{2-}$ on silver (slow aggregation) gave a slope = $\beta = .78$ and for $5.0 \times 10^{-3} \text{ M WO}_4^{2-}$ on silver gave a slope = $\beta = .56$. Following single-sided (I_{920}) and double-sided (I_{560}) sites for PO_4^{3-} on silver gave β values of 0.82 and 0.64, respectively, from Figure 6. It appears that the reciprocal of the slope, β^{-1} , can be correlated with the structure of the aggregates that are formed.

For growth of fractal aggregates it has been suggested¹² that the radius of gyration of the aggregates, $R_g \sim t^{1/D}$. Our results suggest a scaling law for SERS intensity of the form, $I \sim R \sim t^{1/\beta}$, so that only part of the total surface area ($\sim R^2$) is SERS active. Thus, fast aggregation following $\nu(\text{WO}_4^{2-})$ assigned to a double-sided adsorption site gave $D = 1/.58 = 1.8$, the diffusion limited aggregation value assumed for globular cluster structures as previously shown for colloidal gold sols. In this limit, the particles do not have the time to discriminate between various orientations for more favorable collisions. Slow aggregation following $\nu(\text{WO}_4^{2-})$ assigned to a double-sided site gave $D = 1/.78 = 1.3$, the value assumed by linear chains. Here, singlets colloidizing with doublets or higher order multiplets of particles prefer to add in an end-on fashion instead of side-on to avoid higher coulombic repulsion from negatively-charged ions adsorbed on two or more particles. Further, slow aggregation following $\nu(\text{PO}_4^{3-})$ in a double-sided site gave $D = 1/.82 = 1.2$ like the above value for WO_4^{2-} on silver associated with linear chains but slow aggregation following $\nu(\text{PO}_4^{3-})$ of a single-sided site gave $D = 1/.64 = 1.6$. We interpret this to show that the single-sided site has no orientational preference as in the double-sided binding site which also mimics spatially the aggregate structure.

Mechanism of SERS Enhancements

SERS enhancements that we have previously determined⁶⁻⁹ for molecules adsorbed on colloidal silver and gold at various stages of aggregation fell in the $10^3 - 10^6$ range. No enhancement was observed with excitation into the single particle Mie resonances of silver and gold at 400 and 520 nm, respectively. Recently revised electrodynamic calculations¹⁴ of small single spheres of silver using new data on optical constants of silver give lower values ($10^3 - 10^4$) for the SERS enhancement than the $\sim 10^6$ figure initially computed. Since the silver sols that we have experimentally investigated by no means represent pure silver in water, these ideal theoretical estimates almost certainly need to be revised downwards for comparison with experimental results. The electrodynamic theory for two interacting silver spheres has not been completely solved. Certainly, additional dipole-dipole coupling terms not present in an array of non-interacting single spheres will become important so that to a first approximation the total SERS enhancement might be expressed as a product of enhancements from adjacent interacting spheres,

$$I_{\text{total}} = I_i \cdot I_j.$$

This would put the upper limit for SERS enhancements at $10^6 - 10^8$ which is in agreement with 10^6 or greater values that have been reported. Also, it might be expected that globular clusters ($D = 1.8$) would show higher SERS enhancements than less dense cluster ($D = 1.5$) than, in turn, linear chain clusters ($D = 1.3$). This appears to be the case from our data at identical aggregation times but there is no assurance that the comparison is for the identical number of primary silver particles in the various aggregate forms.

References

1. D.L. Jeanmaire and R.P. VanDuyne, J. Electroanal. Chem. 84, 1 (1977).
2. M.G. Albrecht and J.A. Creighton, J. Am. Chem. Soc. 99, 5215 (1977).
3. M. Kerker, O. Siiman and D.-S. Wang, J. Phys. Chem. 88, 3168 (1984).
4. D.-S. Wang, M. Kerker and H. Chew, Appl. Opt. 19, 2315 (1980).
5. M. Kerker, D.-S. Wang and H. Chew, Appl. Opt. 19, 4159 (1980).
6. O. Siiman, L.A. Bumm, R. Callaghan, C.G. Blatchford and M. Kerker, J. Phys. Chem. 87, 1014 (1983).

7. A. Lepp and O. Siiman, *J. Phys. Chem.* 89, 3494 (1985).
8. O. Siiman and W.P. Hsu, *J. Chem. Soc., Faraday Trans. 1* 82, 851 (1986).
9. H. Feilchenfeld and O. Siiman, *J. Phys. Chem.* 90, 2163 (1986).
10. S.R. Forrest and T.A. Witten, *J. Phys. A* 12, L109 (1979).
11. D.A. Weitz and M. Oliveria, *Phys. Rev. Lett.* 52, 1433 (1984).
12. D.A. Weitz and J.S. Huang, in *Kinetics of Aggregation and Gelation*, F. Family and D.P. Landau, Eds. (Elsevier-North Holland, Amsterdam, 1984), pp. 19-28.
13. H. Feilchenfeld and O. Siiman, *J. Phys. Chem.* 90, 4590 (1986).
14. M. Kerker, *J. Opt. Soc. Am. B2*, 1327 (1985).

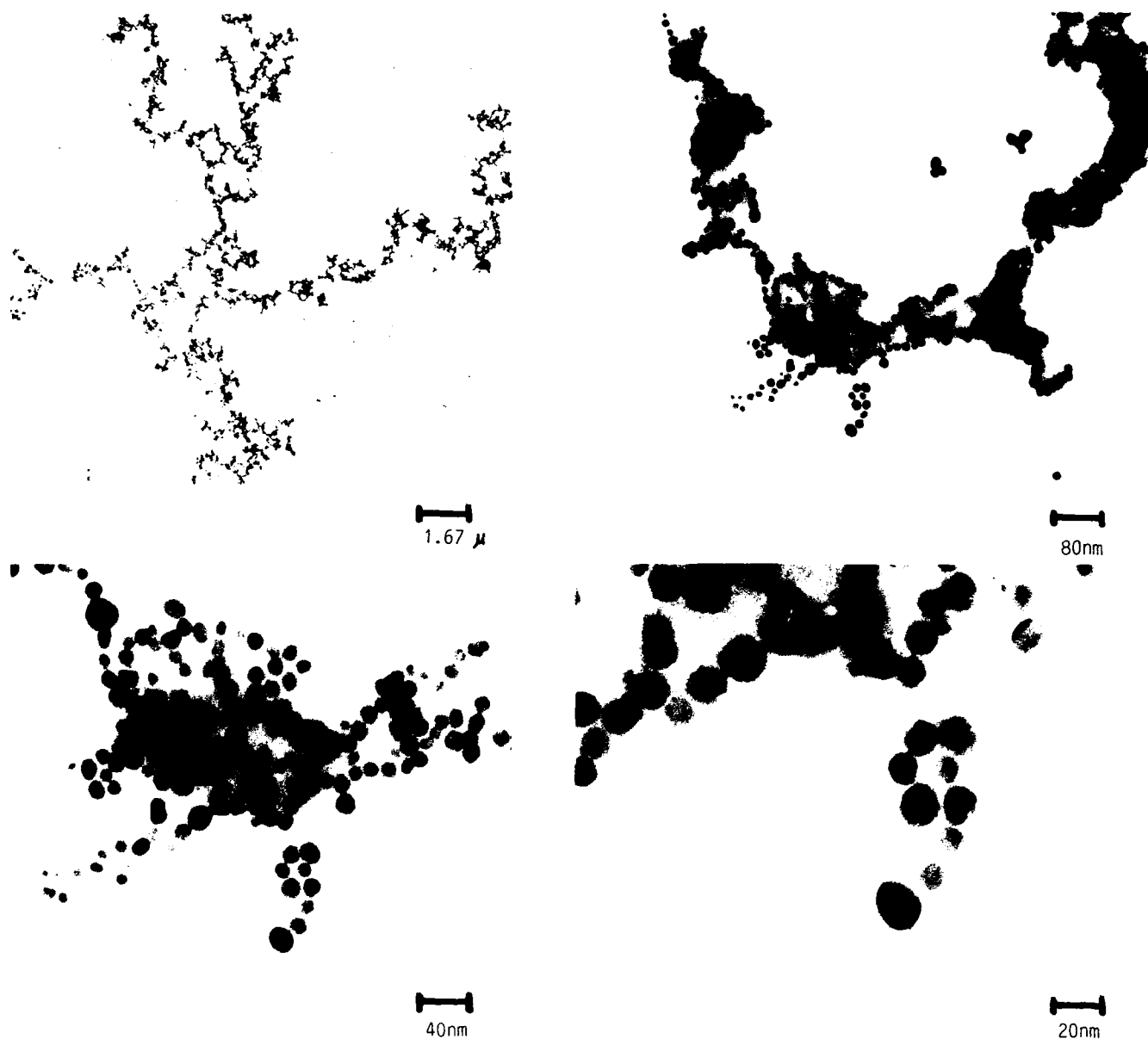


Figure 1. Transmission electron micrographs of silver particles aggregated by isopolytungstate ($6 \text{ micromho cm}^{-1}$ silver sol and $1.0 \times 10^{-3} \text{ M H}_2\text{W}_{12}\text{O}_{40}^{6-}$).

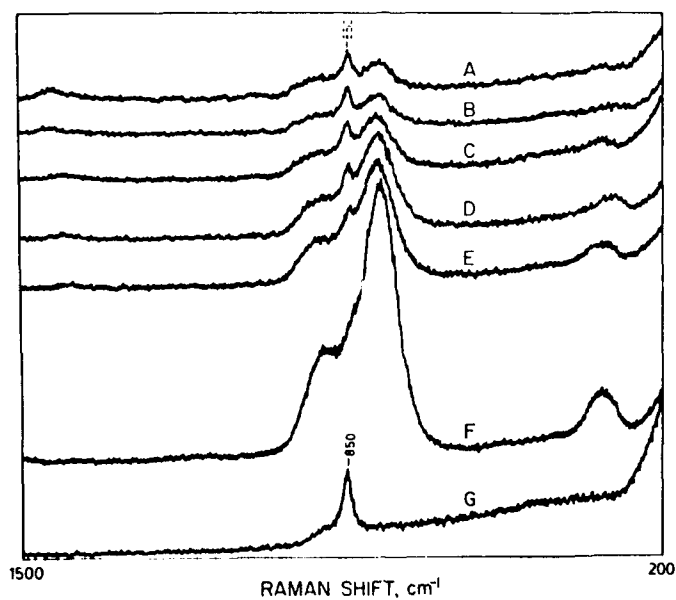


Figure 2. Time dependence of chromate (5.0×10^{-3} M) on colloidal silver (A-F) and Raman spectrum of chromate (5.0×10^{-5} M) in aqueous solution. Elapsed time (min): A, 5; B, 35; C, 65; D, 125; E, 185; F, 1235.

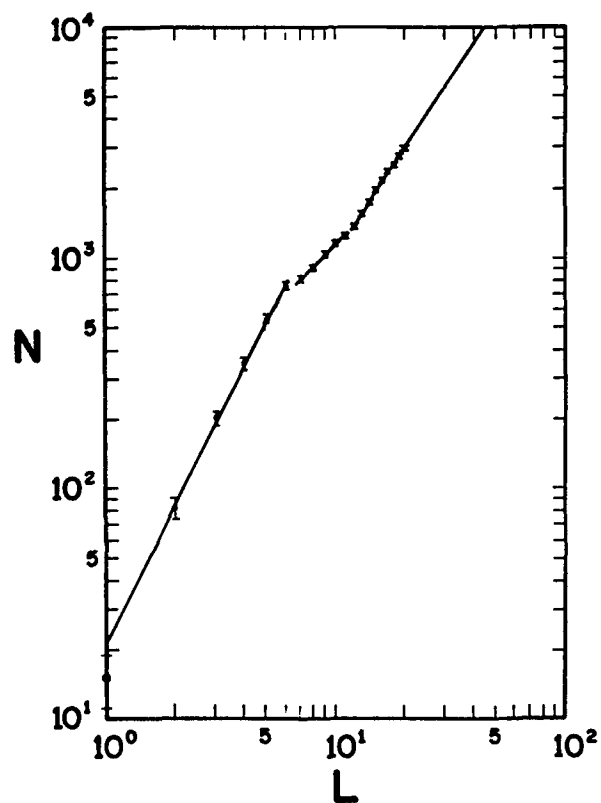


Figure 3. Internal structure analysis of micrograph in Figure 1, top, left by nested square-grid method.

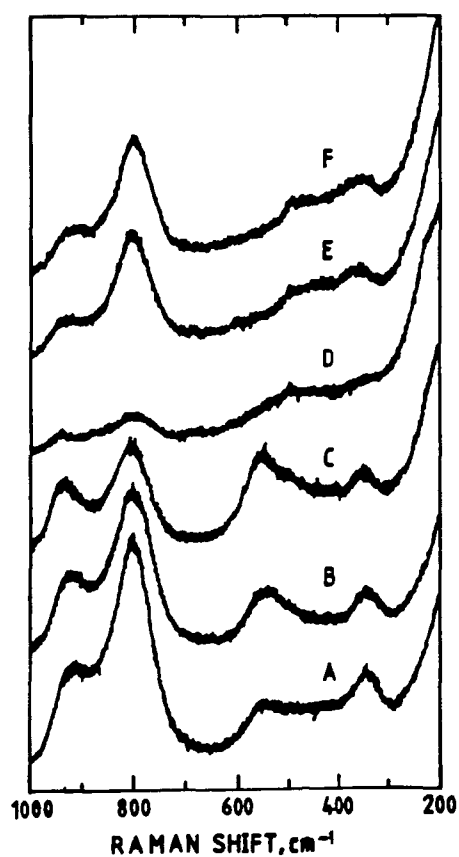


Figure 4. SERS spectra of chromate on colloidal silver. Experimental conditions: excitation wavelength, 488.0 nm Ar^+ , photon counting-time interval, 0.10 s; spectral slit-width, 7 cm^{-1} .

	Conductivity of parent sol, $\mu\text{mho cm}^{-1}$	Chromate conc M	Incident laser power, mW
A	34	1.0×10^{-4}	60
B	34	3.0×10^{-5}	60
C	34	1.0×10^{-5}	60
D	34	3.0×10^{-6}	55
E	6	3.0×10^{-6}	65
F	4	3.0×10^{-6}	65

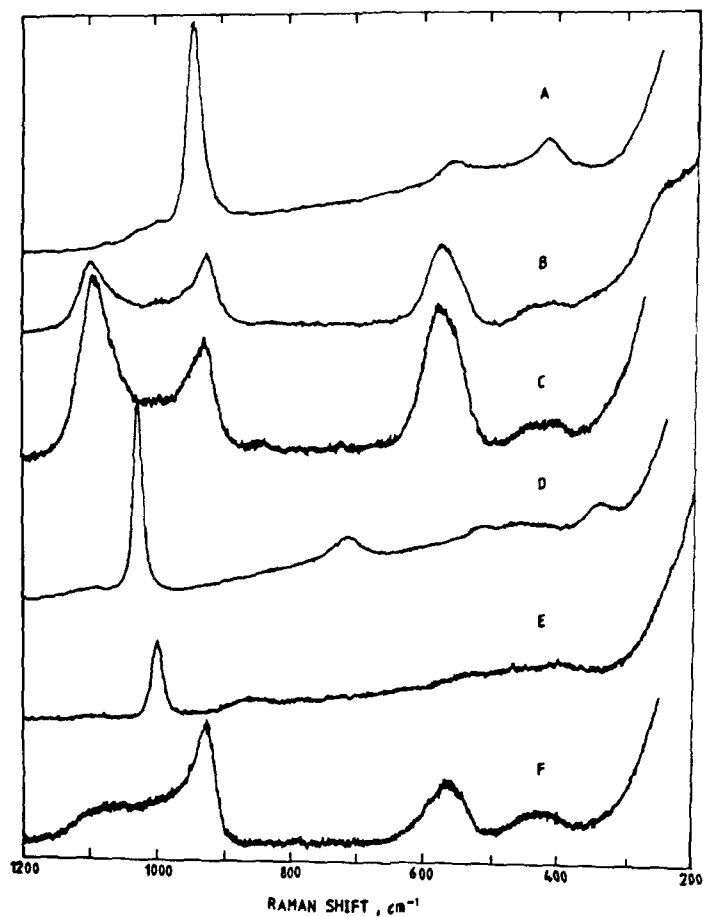


Figure 5. Raman spectra of phosphate species in solution and on colloidal silver. Experimental conditions: excitation wavelength, 488.0 nm Ar⁺; spectral slitwidth, 7 cm⁻¹.

	Species in aqueous medium	Conc, M	Incident laser power, mW	Photon counting time interval, s
A	Na ₃ PO ₄	0.50	300	.025
B	Na ₃ PO ₄ , Ag sol	5.0 x 10 ⁻³	60	.050
C	Na ₃ PO ₄ , Ag sol with PVP	5.0 x 10 ⁻³	60	.050
D	Na ₄ P ₂ O ₇	0.20	300	.025
E	Na ₂ HPO ₄	0.20	60	0.10
F	Na ₂ HPO ₄ , Ag sol	5.0 x 10 ⁻³	60	0.10

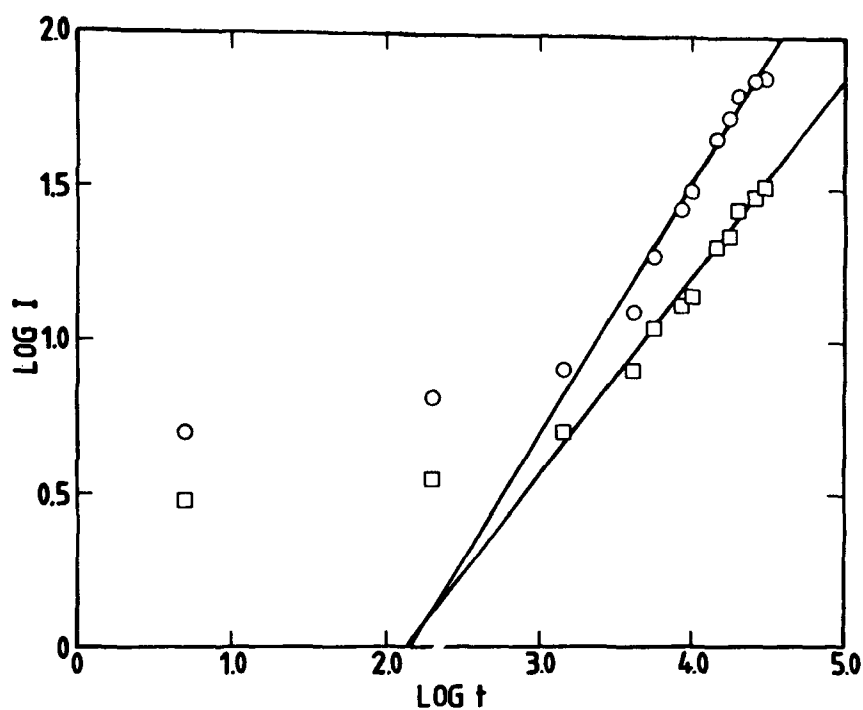


Figure 6. Power law dependence of surface Raman band intensity, I , with time, t , for aggregation of silver particles by 5.0×10^{-3} M NaHPO_4 . I_{920} (○), I_{560} (□).

INTERACTION OF MONOCHROMATIC WAVES AND BODIES OF NONHOMOGENEOUS MORPHOLOGY

S.K. Salib

Photographic Research Laboratories - Photographic Products Group
Eastman Kodak Company, Rochester, NY 14650

Abstract

A theoretical model has been developed to calculate the interaction between bodies of nonhomogeneous morphology and monochromatic radiation up to the microwave region. The theory is applied to biological studies.

Introduction

There has been a growing need to study many practical applications for systems containing nonhomogeneous bodies of multilayered structure. This has motivated us to develop a theory capable of evaluating the interaction of bodies of such configuration with nonionizing radiation. This paper deals with the development of an exact theory which would make it possible to accurately account for the absorption and the scattering of monochromatic plane polarized electromagnetic waves from arbitrary multilayered spherically symmetric bodies. The presently desired functions are more general in nature than those describing the simpler theory for the interaction of electromagnetic waves and homogeneous spherically shaped bodies embedded in dielectric and isotropic materials. For the development of such complex theory, it was necessary to follow the same basic steps used to reach the conclusions for the less complex cases.

Since these theories, for the interaction of radiation and material, are applicable to bodies whose dimensions are of the order of the wavelengths of the incident radiation, it was possible to study the electromagnetic properties of single bodies as they interact with radiations whose wavelengths range from submicrons to a few meters, depending upon the dimensions of these bodies of interest.

The derived equations have also been used to predict the fields induced inside multilayered bodies of different dimensions and electrical properties. Moreover, the distribution of the absorbed energy inside the core material has been considered. Consequently, the treatment of the nonuniform internal heating, which has in general been confined to infinitely extended flat models, has been generalized to multilayered spherical bodies.

As an application to the present theoretical investigation, the dose patterns produced in the brain of a model of a human head have been evaluated, and the results for different dimensions of the model will be presented.

Development of the Theory

Generally, the solution of any of these boundary-value problems starts with Maxwell's equations representing the incident waves in spherical polar coordinates. With these equations, the electric and the magnetic components of the incident wave can be expressed as an infinite sum of spherical partial waves. Each of such partial waves is represented by a combination of Bessel functions and Legendre polynomials. As the incident wave encounters the concentric spherical layers, scattered electric and magnetic fields are induced outside the spherical layers. These induced fields are also expressed as infinite summations of spherical partial waves with unknown coefficients. To find the values of such coefficients, we apply the boundary conditions for the electric and magnetic fields at the surfaces of the outmost layers. Moreover, electric and magnetic fields are induced inside each of the layers by the incident wave. These fields can, once more, be expressed as infinite sums of spherical partial waves with other sets of unknown coefficients which can also be determined by applying the proper boundary conditions at each of the interfaces between the layers.

For homogeneous spherical bodies, there is only one set of boundary conditions to satisfy. These boundary conditions call for the continuity of the tangential components for the E and M fields at the boundary of the homogeneous sphere. These boundary conditions are as follows:

$$E_{\theta}^i = E_{\theta}^o, \quad (1)$$

$$E_{\phi}^i = E_{\phi}^o, \quad (2)$$

$$(aM_{\theta})^i = (aM_{\theta})^o, \quad (3)$$

$$(aM_{\phi})^i = (aM_{\phi})^o, \quad (4)$$

where M_{θ} , M_{ϕ} are related to the magnetic field H_{θ} and H_{ϕ} by the relationship

$$M_{\theta} = \frac{-i\nu\mu\lambda_0}{m} H_{\theta} \quad (5)$$

and a similar relation for M_{ϕ} and H_{ϕ} . Here, ν is the frequency of the incident radiation, μ is the permeability of the medium, λ_0 is the wavelength of the incident radiation in vacuum, and m is the complex index of refraction of the particle material:

$$m = n - i\kappa \quad (6)$$

where n is the real part of the index of refraction, while κ is the imaginary part of the index of refraction. Also, a is the Mie parameter defined by the relationship

$$a = \frac{2\pi n_0 r}{\lambda_0} \quad (7)$$

where n_0 is the index of refraction of the surrounding medium, and r is the radius of the particle.

Moreover, the superscripts i and o are for the regions inside and outside the particle, respectively.

For a core-shell configuration which is sometimes called stratified body, we have to satisfy two sets of boundary conditions. The first set of boundary conditions is for the boundary at the interface between the shell and the surrounding medium, while the second set of boundary conditions which has to be satisfied is that at the interface between the core and the shell material.

The boundary conditions at the two interfaces are as follows:

$$\{E_{\theta sh}\}_{R_1=r} = \{E_{\theta c}\}_{R_1=r} \quad (8)$$

$$\{E_{\phi sh}\}_{R_1=r} = \{E_{\phi c}\}_{R_1=r} \quad (9)$$

$$m_2 \{M_{\theta sh}\}_{R_1=r} = m_1 \{M_{\theta c}\}_{R_1=r} \quad (10)$$

$$m_2 \{M_{\phi sh}\}_{R_1=r} = m_1 \{M_{\phi c}\}_{R_1=r} \quad (11)$$

and

$$\{E_{\theta} + E_{\theta}^S\}_{R_2=r} = \{E_{\theta sh}^i\}_{R_2=r} \quad (12)$$

$$\{E_{\phi} + E_{\phi}^S\}_{R_2=r} = \{E_{\phi sh}^i\}_{R_2=r} \quad (13)$$

$$\{M_{\theta} + E_{\theta}^S\}_{R_2=r} = m_2 \{M_{\theta sh}^i\}_{R_2=r} \quad (14)$$

$$\{M_{\phi} + M_{\phi}^S\}_{R_2=r} = m_2 \{M_{\phi sh}^i\}_{R_2=r} \quad (15)$$

where the subscripts c and sh correspond to the core and the shell regions, respectively, while the superscripts s and i correspond to the scattered component of the field and the component in the interior of the sphere, respectively. The component without any superscripts other than direction is that representing the incident field.

One of the most important points that we have to consider for the core-shell case is that concerning the solution in the intermediate region of the shell. The wave solution in such a region can be represented in terms of both J_n and η_n , since both functions are well behaved so that a linear combination of both functions are also a solution. To solve the more involved case of a core and two or more shells, one proceeds in the same manner as in the less involved case, of a core and a single shell.

Also, in this case, we have to remember that in the inner and outer shells, the wave solution is represented in terms of J_n and η_n , since both functions are well behaved, as I have mentioned earlier for the case of a core and one shell. By applying the boundary conditions of the three interfaces, three sets of equations can be formulated which give rise to twelve simultaneous equations to be solved. The resulting equations are written as follows:

$$m_1 g_n \psi'_n(m_2 \beta) + m_1 h_n \eta'_n(m_2 \beta) - m_2 K_n \psi'_n(m_1 \beta) = 0 \quad (16)$$

$$g_n \psi_n(m_2 \beta) + h_n \eta_n(m_2 \beta) - K_n \psi_n(m_1 \beta) = 0 \quad (17)$$

$$g_n \psi_n(m_2 \nu) + h_n \eta_n(m_2 \nu) + C_n \psi_n(m_3 \nu) - d_n \eta_n(m_3 \nu) = 0 \quad (18)$$

$$m_3 g_n \psi'_n(m_2 \nu) + m_3 h_n \eta'_n(m_2 \nu) - m_2 C_n \psi'_n(m_3 \nu) - m_2 d_n \eta'_n(m_3 \nu) = 0 \quad (19)$$

$$C_n \psi'_n(m_3 \gamma) + d_n \eta'_n(m_3 \gamma) + m_3 a_n \xi'_n(\gamma) = m_3 \psi'_n(\gamma) \quad (20)$$

$$C_n \psi_n(m_3 \gamma) + d_n \eta_n(m_3 \gamma) + a_3 \xi_n(\gamma) = \psi_n(\gamma) \quad (21)$$

$$I_n \psi'_n(m_2 \beta) + J_n \eta'_n(m_2 \beta) - L_n \psi'_n(m_1 \beta) = 0 \quad (22)$$

$$m_1 I_n \psi_n(m_2 \beta) + m_1 J_n \eta_n(m_2 \beta) - m_2 L_n \psi_n(m_1 \beta) = 0 \quad (23)$$

$$m_3 I_n \psi_n(m_2 \nu) + m_3 J_n \eta_n(m_2 \nu) - m_2 e_n \psi_n(m_3 \nu) - m_2 f_n \eta_n(m_3 \nu) = 0 \quad (24)$$

$$I_n \psi'_n(m_2 \nu) + J_n \eta'_n(m_2 \nu) - e_n \psi'_n(m_3 \nu) - f_n \eta'_n(m_3 \nu) = 0 \quad (25)$$

$$e_n \psi'_n(m_3 \gamma) + f_n \eta'_n(m_3 \gamma) + b_n \xi'_n(\gamma) = \psi'_n(\gamma) \quad (26)$$

$$e_n \psi'_n(m_3 \psi) + f_n \eta'_n(m_3 \psi) + b_n \xi'_n(\psi) = \psi'_n(\psi) \quad (27)$$

In the above equations, the following notations have been used:

$$a = 2\pi r/\lambda, \quad \beta = 2\pi R_1/\lambda, \quad \nu = 2\pi R_2/\lambda, \quad \text{and} \quad \gamma = 2\pi R_3/\lambda,$$

where R_1 , R_2 and R_3 are the radii of the core, the first shell and the outer shell, respectively. Also, r is the general distance parameter which is measured from the center of the stratified particle. Moreover, m_1 , m_2 and m_3 are the relative complex indices of the core, the first shell and the outer shell, respectively, relative to the surrounding medium.

Now by using the first six equations (16-21) and solving for a_n , the result of such solution takes the simple form:

$$a_n = \frac{[\psi\psi]_{n,\beta}'([\psi\psi]_{n,\gamma}'[\eta\eta]_{n,\nu}' - [\psi\eta]_{n,\nu}'[\eta\psi]_{n,\gamma}') - [\eta\psi]_{n,\beta}'([\psi\psi]_{n,\gamma}'[\eta\psi]_{n,\nu}' - [\psi\psi]_{n,\nu}'[\eta\psi]_{n,\gamma}')}{[\psi\psi]_{n,\beta}'([\psi\xi]_{n,\gamma}'[\eta\eta]_{n,\nu}' - [\psi\eta]_{n,\nu}'[\eta\xi]_{n,\gamma}') - [\eta\psi]_{n,\beta}'([\psi\xi]_{n,\gamma}'[\eta\psi]_{n,\nu}' - [\psi\psi]_{n,\nu}'[\eta\xi]_{n,\gamma}')} \quad (28)$$

where the following notations have been used to allow us to write a_n in such compact form:

$$[\eta\psi]_{n,\beta}' = (m_1\eta_n'(m_2\beta)\gamma_n(m_1\beta) - m_2\eta_n(m_2\beta)\psi_n'(m_1\beta)) \quad (29)$$

$$[\psi\eta]_{n,\beta}' = (m_1\psi_n'(m_2\beta)\eta_n(m_1\beta) - m_2\psi_n(m_2\beta)\eta_n'(m_1\beta)) \quad (30)$$

$$[\eta\psi]_{n,\nu}' = (m_2\eta_n'(m_3\nu)\psi_n(m_2\nu) - m_3\eta_n(m_3\nu)\psi_n'(m_2\nu)) \quad (31)$$

$$[\psi\eta]_{n,\nu}' = (m_2\psi_n'(m_3\nu)\eta_n(m_2\nu) - m_3\psi_n(m_3\nu)\eta_n'(m_2\nu)) \quad (32)$$

$$[\eta\psi]_{n,\gamma}' = (\eta_n'(m_3\gamma)\psi_n(\gamma) - m_3\eta_n(m_3\gamma)\psi_n'(\gamma)) \quad (33)$$

$$[\psi\eta]_{n,\gamma}' = (\psi_n'(m_3\gamma)\eta_n(\gamma) - m_3\psi_n(m_3\gamma)\eta_n'(\gamma)) \quad (34)$$

Similarly, by using the second six equations (22-27), the solution for b_n takes the form:

$$b_n = \frac{[\psi\psi]_{n,\beta}''([\psi\psi]_{n,\gamma}''[\eta\eta]_{n,\nu}'' - [\psi\eta]_{n,\nu}''[\eta\psi]_{n,\gamma}'') - [\eta\psi]_{n,\beta}''([\psi\psi]_{n,\gamma}''[\psi\eta]_{n,\nu}'' - [\psi\psi]_{n,\nu}''[\eta\psi]_{n,\gamma}'')}{[\psi\psi]_{n,\beta}''([\psi\xi]_{n,\gamma}''[\eta\eta]_{n,\nu}'' - [\psi\eta]_{n,\nu}''[\eta\xi]_{n,\gamma}'') - [\eta\psi]_{n,\beta}''([\psi\xi]_{n,\gamma}''[\psi\eta]_{n,\nu}'' - [\psi\psi]_{n,\nu}''[\eta\xi]_{n,\gamma}'')} \quad (35)$$

$$[\eta\psi]_{n,\beta}'' = (m_2\eta_n'(m_2\beta)\psi_n(m_1\beta) - m_1\eta_n(m_2\beta)\psi_n'(m_1\beta)) \quad (36)$$

$$[\psi\eta]_{n,\beta}'' = (m_2\psi_n'(m_2\beta)\eta_n(m_1\beta) - m_1\psi_n(m_2\beta)\eta_n'(m_1\beta)) \quad (37)$$

$$[\eta\psi]_{n,\nu}'' = (m_3\eta_n'(m_3\nu)\psi_n(m_2\nu) - m_2\eta_n(m_3\nu)\psi_n'(m_2\nu)) \quad (38)$$

$$[\psi\eta]_{n,\nu}'' = (m_3\psi_n'(m_3\nu)\eta_n(m_2\nu) - m_2\psi_n(m_3\nu)\eta_n'(m_2\nu)) \quad (39)$$

$$[\eta\psi]_{n,\gamma}'' = (m_3\eta_n'(m_3\gamma)\psi_n(\gamma) - \eta_n(m_3\gamma)\psi_n'(\gamma)) \quad (40)$$

$$[\psi\eta]_{n,\gamma}'' = (m_3\psi_n'(m_3\gamma)\psi_n(\gamma) - \psi_n(m_3\gamma)\eta_n'(\gamma)) \quad (41)$$

Only these two coefficients, a_n and b_n , out of a total of twelve unknown distribution coefficients, are necessary to describe the interaction between the incident wave and the stratified sphere as a unit.

To find the internal distribution for the induced electric field in every part of the multilayered spherical model, one should have a full knowledge of the components of the induced electric field inside each and every layer of the multilayer sphere. The components of the induced electric field in the outside shell, the intermediate shell, and also the core are written in the following equations:

$$E_{rsho} = \sum_{n=1}^{\infty} (-i)^{n+1} (2n+1) \left\{ c_n \frac{\psi_n(m_3a)}{(m_3a)^2} + d_n \frac{\eta_n(m_3a)}{(m_3a)^2} \right\} \sin\theta \pi_n \cos\phi \quad (42)$$

$$E_{\theta sho} = \sum_{n=1}^{\infty} (-i)^{n+1} \frac{(2n+1)}{n(n+1)} \left[\left\{ c_n \frac{\psi_n'(m_3a)}{(m_3a)} + d_n \frac{\eta_n'(m_3a)}{(m_3a)} \right\} \tau_n \right. \quad (43)$$

$$\left. + (-i) \left\{ e_n \frac{\psi_n(m_3a)}{(m_3a)} + f_n \frac{\eta_n(m_3a)}{(m_3a)} \right\} \pi_n \right] \cos\phi$$

$$E_{\phi sh} = \sum_{n=1}^{\infty} (-i)^{n+1} \frac{(2n+1)}{n(n+1)} \left[c_n \frac{\psi_n'(m_3 a)}{(m_3 a)} + d_n \frac{\eta_n'(m_3 a)}{(m_3 a)} \right] \pi_n \quad (44)$$

$$+ (-i) e_n \left\{ \frac{\psi_n(m_3 a)}{(m_3 a)} + f_n \frac{\eta_n(m_3 a)}{(m_3 a)} \right\} \tau_n \sin \phi$$

$$E_{r sh} = \sum_{n=1}^{\infty} (-i)^{n+1} \frac{(2n+1)}{n(n+1)} \left[g_n \frac{\psi_n(m_2 a)}{(m_2 a)^2} + h_n \frac{\eta_n(m_2 a)}{(m_2 a)^2} \right] \sin \theta \pi_n \cos \phi \quad (45)$$

$$E_{\theta sh} = \sum_{n=1}^{\infty} (-i)^{n+1} \frac{(2n+1)}{n(n+1)} \left[g_n \frac{\psi_n(m_3 a)}{(m_2 a)} + h_n \frac{\eta_n(m_3 a)}{(m_2 a)} \right] \tau_n \quad (46)$$

$$+ (-i) \left\{ I_n \frac{\psi_n(m_2 a)}{(m_2 a)} + J_n \frac{\eta_n(m_2 a)}{(m_2 a)} \right\} \pi_n \cos \phi$$

$$E_{\phi sh} = \sum_{n=1}^{\infty} (-i)^{n+1} \frac{(2n+1)}{n(n+1)} \left[g_n \frac{\psi_n'(m_3 a)}{(m_2 a)} + h_n \frac{\eta_n'(m_3 a)}{(m_2 a)} \right] \pi_n \quad (47)$$

$$+ (-i) \left\{ I_n \frac{\psi_n(m_2 a)}{(m_2 a)} + J_n \frac{\eta_n(m_2 a)}{(m_2 a)} \right\} \tau_n \sin \phi$$

$$E_{rc} = \sum_{n=1}^{\infty} (-i)^{n+1} (2n+1) \left\{ K_n \frac{\psi_n(m_1 a)}{(m_1 a)^2} \right\} \sin \theta \pi_n \cos \phi \quad (48)$$

$$E_{\theta c} = \sum_{n=1}^{\infty} (-i)^{n+1} \frac{(2n+1)}{n(n+1)} \left[K_n \frac{\psi_n'(m_1 a)}{(m_1 a)} \tau_n + (-i) L_n \frac{\psi_n(m_1 a)}{(m_1 a)} \pi_n \right] \cos \phi \quad (49)$$

$$E_{\phi c} = \sum_{n=1}^{\infty} (-i)^{n+1} \frac{(2n+1)}{n(n+1)} \left[K_n \frac{\psi_n'(m_1 a)}{(m_1 a)} \pi_n + (-i) L_n \frac{\psi_n(m_1 a)}{(m_1 a)} \tau_n \right] \cos \phi \quad (50)$$

Now, to find the explicit form of the solution for the three components of the electric field inside the core, for example, one should find the values of the partial coefficients K_n and L_n , just as we have previously done to find the values of a_n and b_n . To find the solution of K_n in terms of known parameters, we will use equations 16-21. As for the solution of L_n , we use equations 22-27. The solutions to these partial coefficients are written in an abbreviated form as follows:

$$k_n = \frac{-m_1 m_2 m_3 [\psi \xi]_{n, \gamma} [\psi \eta]_{n, (\nu \nu)} [\psi \eta]_{n, (\beta \beta)}}{[[\psi \psi]']_{n, \beta} \{m_3 \xi'_n(\gamma) (m_2 \eta_n(m_2 \nu)) [\psi \eta]_{n, (\gamma \nu)} - m_3 \eta'_n(m_2 \nu) [\psi \eta]_{n, (\gamma \nu)}\} - \xi_n(\gamma) (m_2 \eta_n(m_2 \nu)) [\psi \eta]_{n, (\gamma \nu)} + m_3 \eta'_n(m_2 \nu) [\psi \eta]_{n, (\nu \gamma)}\}} - \frac{[[\eta \psi]']_{n, \beta} \{m_3 \xi'_n(\gamma) (m_2 \psi_n(m_2 \nu)) [\psi \eta]_{n, (\gamma \nu)} - m_3 \psi'_n(m_2 \nu) [\psi \eta]_{n, (\gamma \nu)}\} - \xi_n(\gamma) (m_2 \psi_n(m_2 \nu)) [\psi \eta]_{n, (\gamma \nu)} + m_3 \psi'_n(m_2 \nu) [\psi \eta]_{n, (\nu \gamma)}\}}{ } \quad (51)$$

$$\begin{aligned}
L_n = & \frac{-m_1 m_2 m_3 [\psi \xi]_{n,\gamma} [\psi \eta]_{n,(\nu\nu)} [\psi \eta]_{n,(\beta\beta)}'}{[[\psi \psi]_{n,\beta} \{ \xi'_n(\gamma) (m_3 \eta_n(m_2\nu)) [\psi \eta]_{n,(\gamma\nu)} - m_3 \eta'_n(m_2\nu) [\psi \eta]_{n,(\gamma\nu)} \} \\
& - m_3 \xi_n(\gamma) (m_3 \eta_n(m_2\nu)) [\psi \eta]_{n,(\gamma\nu)} + m_2 \nu'_n(m_2\nu) [\psi \eta]_{n,(\nu\gamma)} \}]] \\
& - [[\eta \psi]_{n,\beta} \{ \xi'_n(\gamma) (m_3 \psi_n(m_2\nu)) [\psi \eta]_{n,(\gamma\nu)} - m_3 \psi'_n(m_2\nu) [\psi \eta]_{n,(\gamma\nu)} \} \\
& - m_3 \xi_n(\gamma) (m_3 \psi_n(m_2\nu)) [\psi \eta]_{n,(\gamma\nu)} + m_2 \psi'_n(m_2\nu) [\psi \eta]_{n,(\nu\gamma)} \}]] \quad (52)
\end{aligned}$$

The partial coefficients K_n and L_n have been written in abbreviated form besides some new ones which are defined in the following manner:

$$[\psi \xi]_{n,\gamma} = \psi_n(\gamma) \xi'_n(\gamma) = \psi'_n(\gamma) \xi_n(\gamma) \quad (53)$$

$$[\psi \eta]_{n,(\nu\nu)} = \psi_n(m_3\nu) \eta'_n(m_3\nu) - \psi'_n(m_3\nu) \eta_n(m_3\nu) \quad (54)$$

$$[\psi \eta]_{n,(\beta\beta)} = \psi_n(m_2\beta) \eta'_n(m_2\beta) - \psi'_n(m_2\beta) \eta_n(m_2\beta) \quad (55)$$

$$[\psi \eta]_{n,(\gamma\nu)} = \psi_n(m_3\gamma) \eta'_n(m_3\nu) - \psi'_n(m_3\nu) \eta_n(m_3\gamma) \quad (56)$$

$$[\psi \eta]_{n,(\gamma\nu)} = \psi_n(m_3\gamma) \eta'_n(m_3\nu) - \psi'_n(m_3\nu) \eta_n(m_3\gamma) \quad (57)$$

and similar abbreviations for similar brackets.

It should be noted that since the partial coefficients K_n and L_n are evaluated in terms of the values representing the geometry (the radii of all the layers involved) and also the properties of the different layers (the conductivity and the complex indices of refraction of each layer) in the different parts of the model, we expect a change in the distribution of the internal field in the core area as a result of a change in the morphology of the outer layers.

Numerical Evaluations

The scattering and the absorption efficiency factors for homogeneous spherical particle as a function of the particle diameter for various values of the complex index of refraction are shown in Figures 1-6. The results of our calculations show that for a relatively small value of the real part of the index, 1.2 for example, and when the extinction index k is about 0.1 or higher, the scattering efficiency factor lacks the multiple peaks behavior due to the strong damping. On the other hand, for small k values the oscillatory structure becomes apparent, and it shifts toward the larger particles. Also, as K increases, the scattering efficiency becomes very small, while the absorption efficiency rises quickly with almost no ripple structure as shown in the figures. However, increasing the real part of the index enhances the ripple structure for the scattering efficiency along with the increase in the primary and the secondary peak values and a shift in the location of such peaks toward the smaller particles.

Since the derived equations are general in their form, it is possible to evaluate the interaction between the incident wave from a laser beam and particles of sizes comparable to the wavelength of the incident beam or the interaction between microwaves and particles or bodies of dimensions in the centimeter and meter range, as long as the dielectric properties of the core and the shells materials are known in each and every region of the spectrum in which they are being investigated. For example, consider the geometry in Figure 7 to be a subcutaneous fat core while the shell is the layer representing skin. Figure 8 illustrates the total absorption as a function of the core diameter for a frequency of 433.2 MHz. It is obvious from the figures that at such low frequency, the absorption increases as the shell thickness increases. Such results should not come as a surprise to us, especially that the extinction index k for the skin layer is very high at

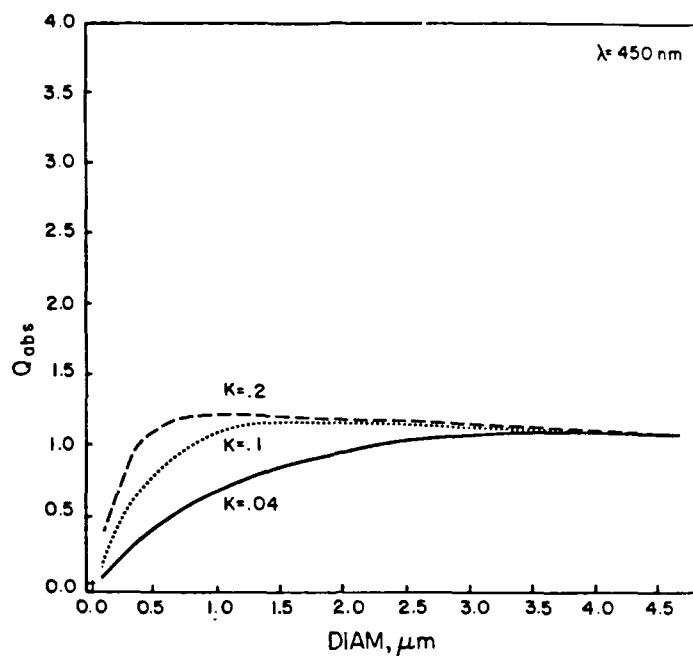


Fig. 1 The absorption efficiency factor as a function of the particle size, for $n = 1.2$, while the extinction index, k , assumes the three values shown above.

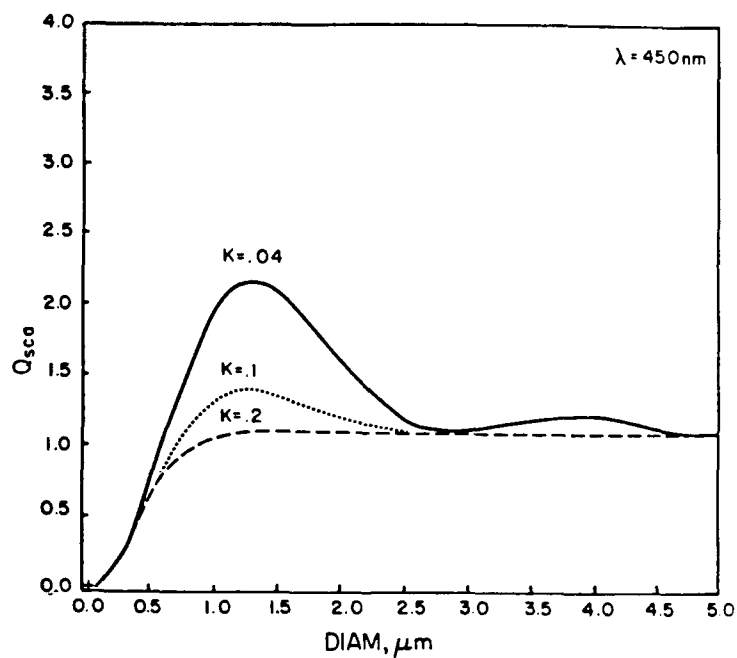


Fig. 2 The scattering efficiency factor as a function of the particle size, for $n = 1.2$, while the extinction index, k , assumes the three values shown above.

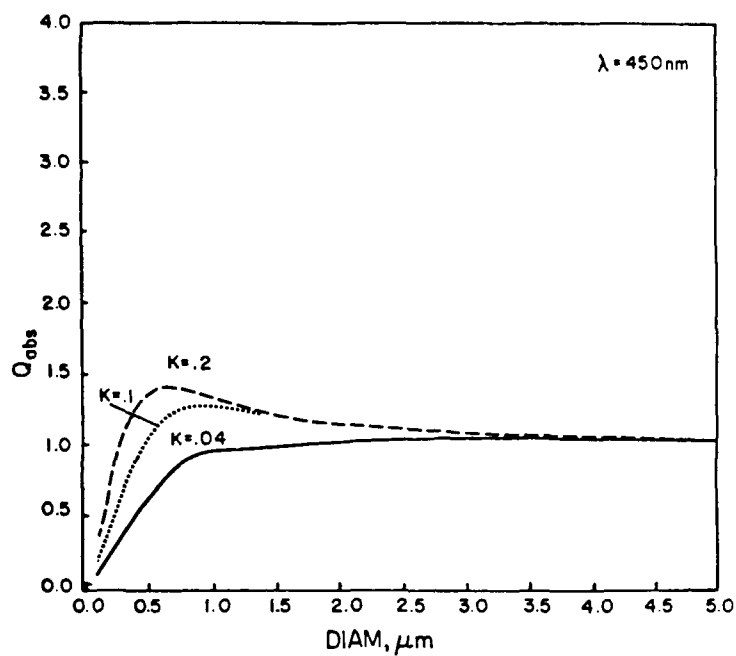


Fig. 3 The absorption efficiency factor as a function of the particle size, for $n = 1.6$, while the extinction index, k , assumes the three values shown above.

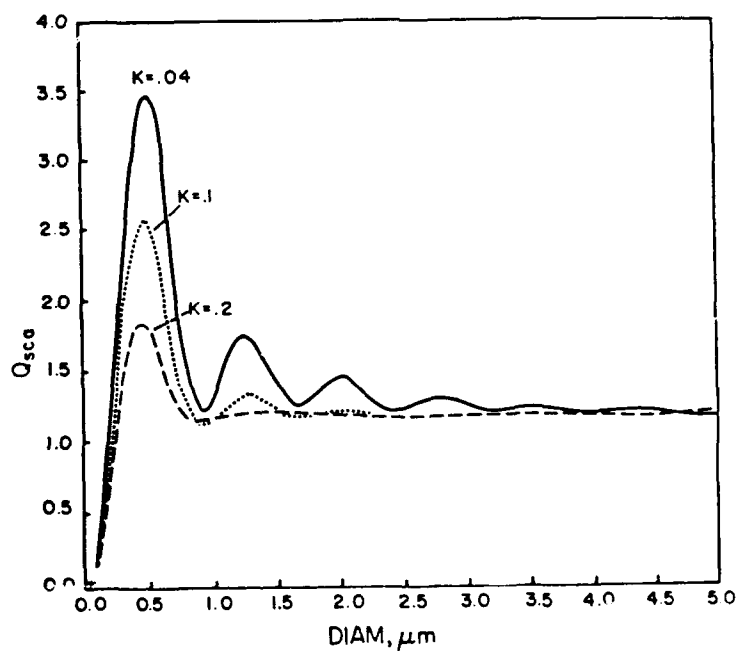


Fig. 4 The scattering efficiency factor as a function of the particle size, for $n = 1.6$, while the extinction index, k , assumes the three values shown above.

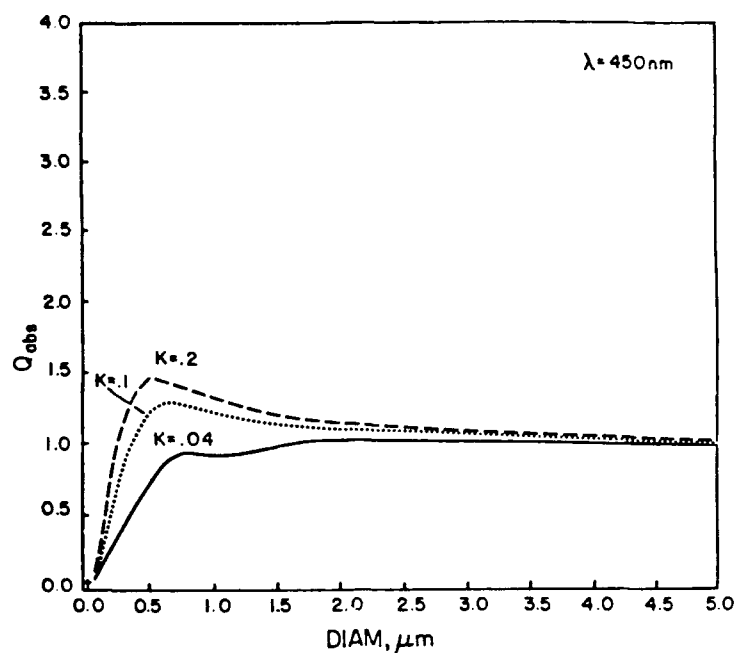


Fig. 5 The absorption efficiency factor as a function of the particle size, for $n = 1.8$, while the extinction index, k , assumes the three values shown above.

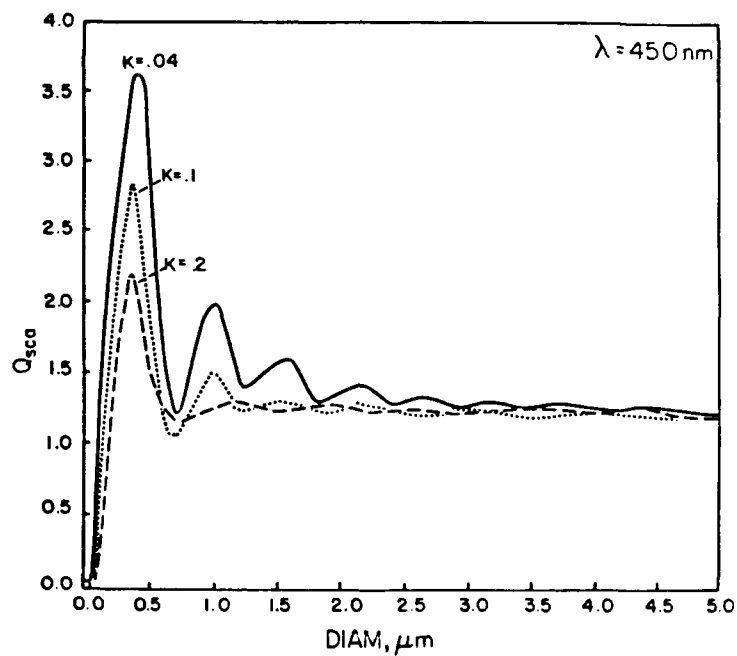


Fig. 6 The scattering efficiency factor as a function of the particle size, for $n = 1.8$, while the extinction index, k , assumes the three values shown above.

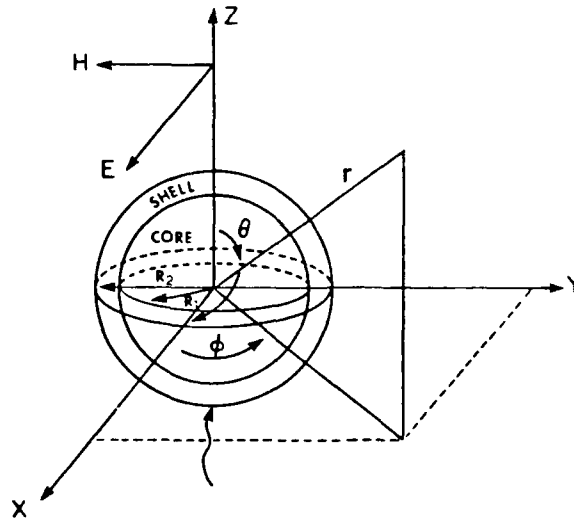


Fig. 7 Representation of a core-shell body in the form of two concentric spheres.

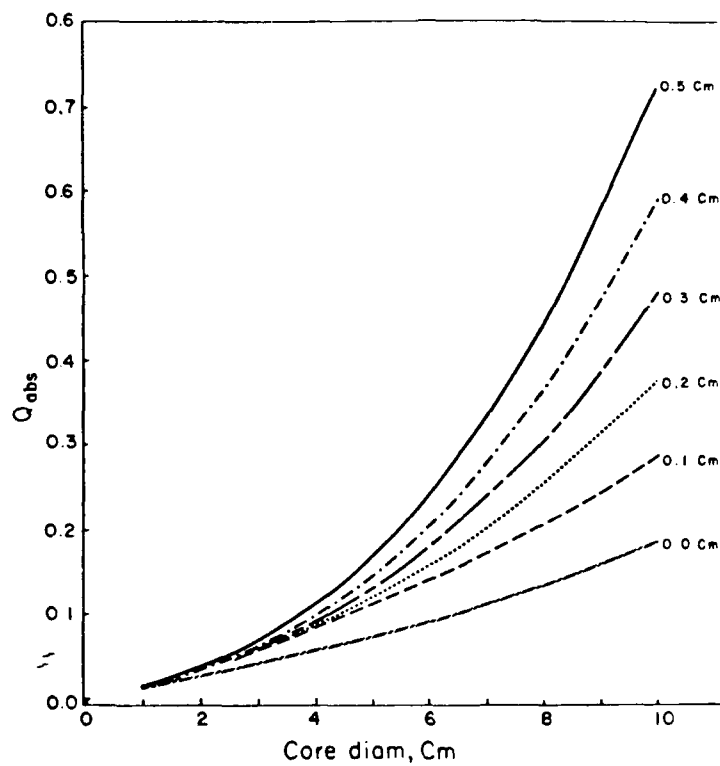


Fig. 8 The absorption efficiency factor for a fat core and a skin shell as a function of core diameter and shell thickness, at a wave frequency of 433.2 MHz.

such frequency ($k = 2.78$) in comparison to the corresponding value for the fat layer ($k = 0.328$). This value is usually a measure for the absorption characteristics of the material considered.

Also, one should realize that the diameter of the core is small relative to the wavelength of the incident radiation (at such frequency $\lambda = 69.25$ cm), and that the presence of the skin shell increases the diameter value and moves it toward the size of a more efficient absorber. Moreover, due to the small diameter-to-wavelength ratio, coupled with the high k value, the resulting scattering efficiency is expected to be relatively small. This would, in time, lead to higher absorption efficiency, especially by introducing a more efficient absorber, like the skin, on the outside. On the other hand, by examining the comparable results in Figure 9, at a frequency of 3,000 MHz ($\lambda = 10$ cm), we find ourselves confronted with a more complex situation. This is mainly because we are in a region where the diameter of the core is of the order of the wavelength of the incident radiation. In such a case, since the extinction index k for the skin is about 10 times that for the fat, the presence of the skin enhances the absorption only when the core diameter is less than 6.0 cm. It is also worth mentioning that as the skin thickness increases, the primary peak for the absorption efficiency factor moves toward a smaller core diameter as seen in the figure. This is because in the case of a small core diameter, as the skin thickness increases, the volume ratio of skin-to-fat increases much faster than for the larger core diameter. Consequently, the resulting core-shell combination becomes much richer with a more efficient absorber which leads to a significant increase in the absorption efficiency of the resulting body.

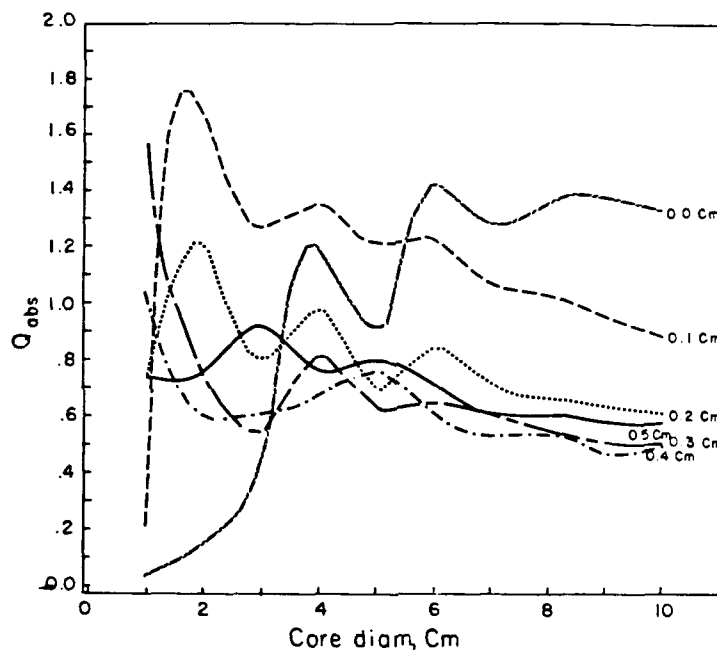


Fig. 9 The absorption efficiency factor for a fat core and a skin shell as a function of core diameter and shell thickness, at a wave frequency of 3000.0 MHz.

From the results concerning these cases, it is safe to state that the skin acts as a radiation collector for small size cores and as a shield for the larger size cores only for the high frequency radiation. For low frequency radiation, it enhances the absorption regardless of the core size. As for the intermediate frequency radiation, the presence of the skin contributes both ways, as we can deduce from the results in Figures 10 and 11.

Using the equations developed for the partial coefficients a_n and b_n for the case of a three-layered body, and by applying the relationships between the effective cross-section and these coefficients, one can find the total energy absorbed and also the energy scattered by bodies with such morphology.

By utilizing the proper values for the dielectric parameters of the tissues used in our three-layered model which represents a model head, we were able to calculate the total

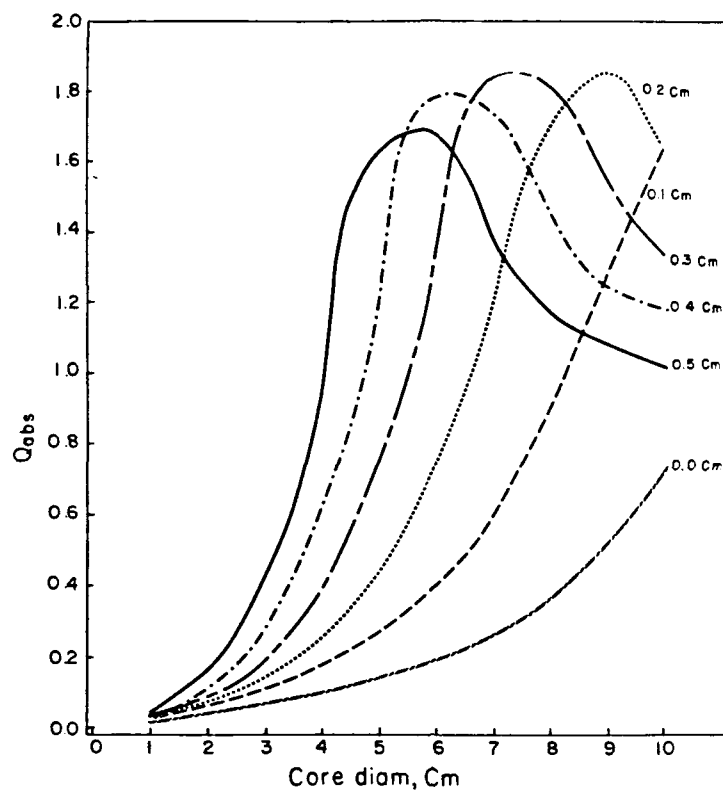


Fig. 10 The absorption efficiency factor for a fat core and a skin shell as a function of core diameter and shell thickness, at a wave frequency of 915.0 MHz.

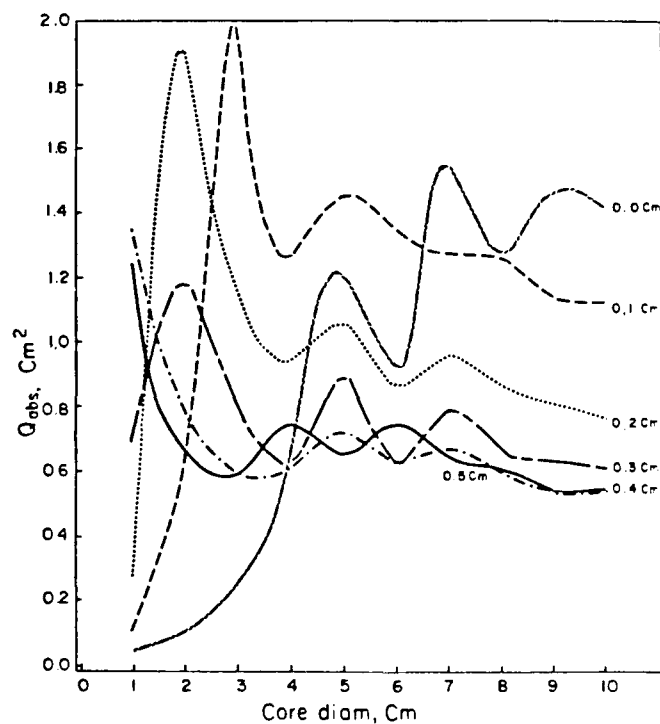


Fig. 11 The absorption efficiency factor for a fat core and a skin shell as a function of core diameter and shell thickness, at a wave frequency of 2450.0 MHz.

absorption cross-section for different brain sizes, CSF layer thickness, and also for different overall head sizes. In Figures 12, 13 and 14, we have plotted the absorption cross-section as a function of frequency for different brain and outer shells dimensions. By comparing these results, we conclude that the location as well as the absolute value of the primary absorption peak changes as the head morphology changes. This simple result demonstrates the importance of the geometry of the layers considered in the model as necessary input for predicting the total absorption of the model head.

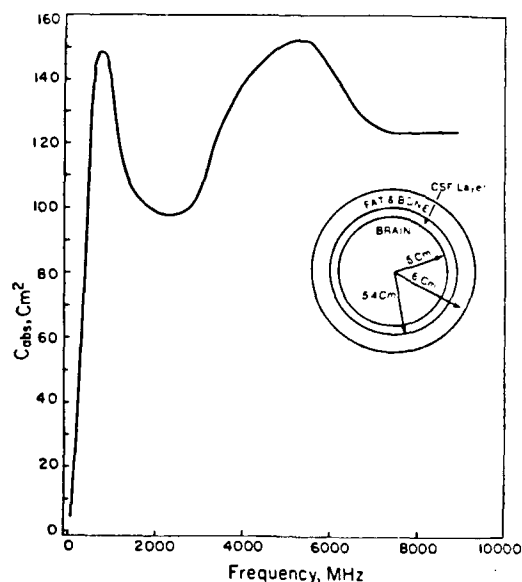


Fig. 12 The total absorption for a three-layer model head with a brain radius of 5.0 cm, a CSF layer 0.4 cm thick and a bone-and-fat layer 0.6 cm thick, as a function of frequency.

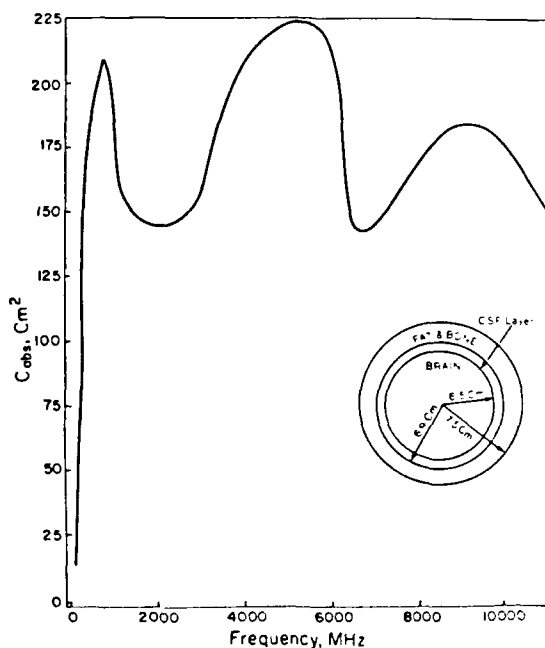


Fig. 13 The total absorption for a three-layer model head with a brain radius of 6.5 cm, a CSF layer 0.4 cm thick and a bone-and-fat layer 0.6 cm thick, as a function of frequency.

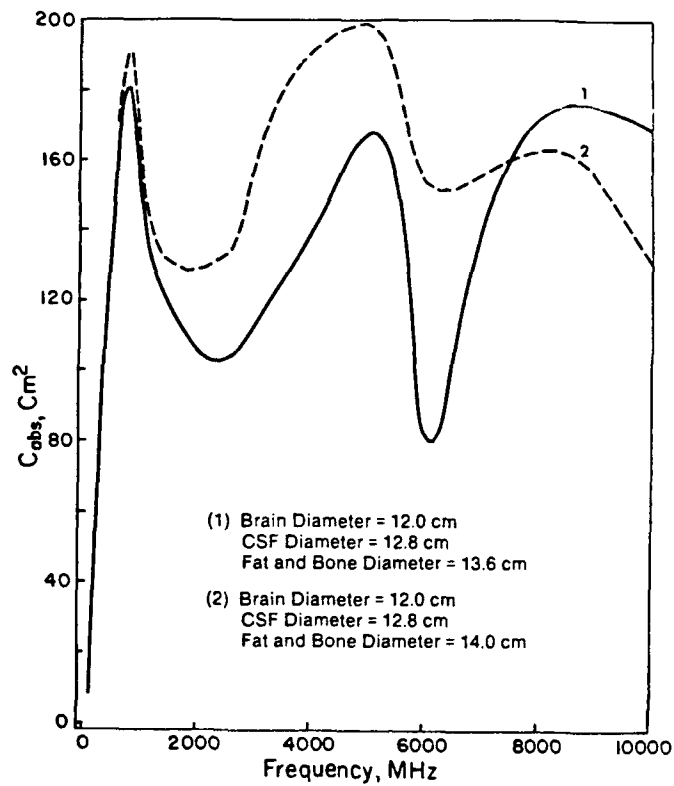


Fig. 14 The absorption cross-section in a three-layer model head as a function of frequency.

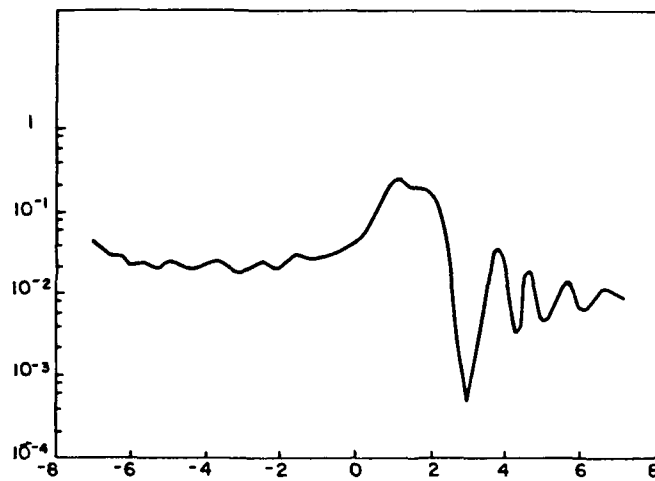


Fig. 15 The distribution of the normalized induced field inside the core (brain) of a three-layer model head, for a core diameter of 12.0 cm and an overall head diameter of 14.0 cm.

When dealing with biological specimens, it is of great importance to have a full knowledge of how the induced fields, and, consequently, the internal heating are distributed. Using the distribution coefficients describing the distribution of the induced field in the core region, we can now evaluate the uniform internal distribution of the induced electric field in the core, which is the brain for the model head. In Figures 15 and 16, we present the results of our calculations for the normalized value of the induced field inside the two geometries described in the figures for a frequency of 915.0 MHz which is known to be of practical importance as a diathermy frequency.

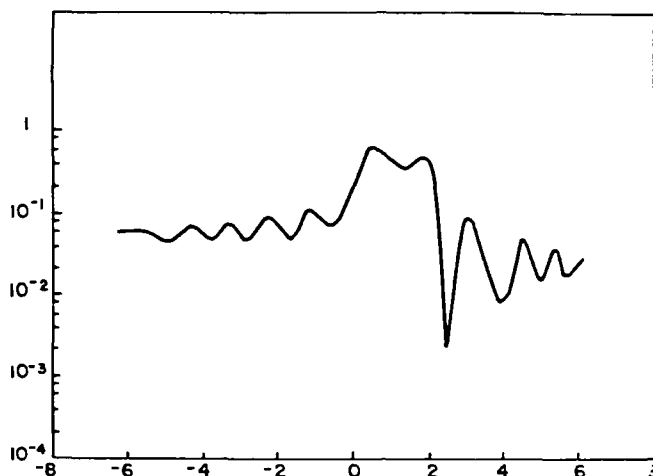


Fig. 16 The distribution of the normalized induced field inside the core (brain) of a three-layer model head, for a core diameter of 14.0 cm and an overall head diameter of 15.0 cm.

In conclusion, we can evaluate the energy absorbed by a three-layer spherical body and also the internal distribution of the induced field using a closed-form solution. Also, the outside dimensions of a three-layer model have more effect on the outcome of the absorption cross-section than does the core size. As for the model head considered in the present investigation, the maximum absorption is obviously between 570 and 4,000 MHz, a fact which has been confirmed experimentally.

Bibliography

- L. Aden and M. Kerker, J. Appl. Phys. 22, 1242 (1951)
- A. Anne, M. Saito, O.M. Salati and H.P. Schwan, Biological Effects on Microwave Radiation 1, 153 (1960)
- J.G. Burr, D.K. Cohoon, E.L. Bell and J.W. Penn, IEEE Trans. Biomedical Engng. BME 27, 452 (1980)
- R.W. Cohen, G.D. Cody, M.D. Coutts, and A. Abeles, Phys. Rev. B8, 3689 (1973)
- H.F. Cook, J. Appl. Phys. 3, 249 (1952)
- K.S. Cole and R.H. Cole, J. Chem. Phys. 9, 341 (1941)
- J.V. Dave, Appl. Opt. 8, 155 (1969)
- P. Debye, Ann. d. Physik 30, 59 (1909)
- R.H. Doremus, JCP 40, 2389 (1964)
- P.W. Dusel, M. Kerker and D.D. Cooke, J. Opt. Soc. Am. 69, 55 (1979)

Environmental Protection Agency, "Microwave Energy Absorption in Tissue," Office of Research and Monitoring Rep. WN620 T273m, 1-53 (1972)

T.S. Fahlen and H.C. Bryant, J. Opt. Soc. Am. 58, 304 (1968)

C.G. Grangvist and O. Hunteri, Phys. Rev. B18, 2897 (1978)

A. Guttler, Ann. Phys. 11, 65 (1952)

A.W. Guy and J.F. Lehmann, IEEE Trans. Bio-Med. Eng. BME-13, 76 (1966)

H.S. Ho, Ann. New York Acad. Sci. 247, 454 (1975)

H.S. Ho and A.W. Guy, Health Phys. 29, 317 (1975)

C.C. Johnson and A.W. Guy, Proc. Inst. Elec. Engrs. 60, 692 (1972)

I. Johnson and V.K. La Mer, J. Ann. Chem. Soc. 69, 1184 (1947)

M. Kerker, J. Opt. Soc. Am. 45, 1081 (1955)

M. Kerker, J. Polymer Sci. 28, 429 (1958)

M. Kerker and E. Matijevic', J. Opt. Soc. Am. 51, 506 (1961a)

M. Kerker and E. Matijevic', J. Opt. Soc. Am. 51, 87 (1965b)

M. Kerker, "The Scattering of Light and Other Electromagnetic Radiation" (Academic Press, Inc., New York, 1969)

G. Mie, Ann. d. Physik 25, 377 (1908)

M.F. Peyton, Ed., Biological Effects of Microwave Radiation, in Proc. 4th Ann. Tri.-Service Conf. (Plenum, New York, 1961)

A.S. Presman, Electromagnetic Fields and Life, F.A. Brown, Jr., Ed. (Plenum, New York-London, 1970)

H. Puschner, Heating With Microwaves (Phillips Technical Library) (Springer, New York, 1966)

Lord Rayleigh, Phil. Mag. (Sci. papers 8 and 9), 41, 104, 274 and 447 (1871)

S. Salib and M.L. Rustgi, Health Physics 42, 165 (1982)

H.P. Schwan, Microwave Power Engineering, Vol. 2, E.C. Okress, Ed. (Academic Press, New York, 1968), pp. 215

H.P. Schwan and G.M. Piersal, Am. J. Phys. Med. 33, 371 (1954)

H. Seki, Appl. Phys. Lett. 43, 1000 (1983)

A.R. Shapiro, R.F. Zulomirski, and H.T. Yurali, IEEE Trans. Microwave Theory and Techniques MTT19, 187 (1971)

J.A. Stratton, "Electromagnetic Theory," (McGraw-Hill Book Co., New York, 1941), Chapter VII

H. C. Van De Hulst, "Light Scattering by Small Particles," (Wiley, New York, 1957)

Digital Disk Sub-systems for Real-time Image Processing

Ranjit Mulgaonkar

Recognition Concepts Inc. Incline Village, Nevada.

Today's computer industry is constantly introducing faster and faster processors in the market. Although these processors can process the data at a very high speed, the overall performance of the system can be limited if the data storage devices are unable to keep up with the processor I/O requirements. In many computer applications very large amounts of data are needed to be stored, retrieved and, processed at high speeds. Digital disk sub-systems provide the high performance and high capacity that the traditional storage devices are unable to provide.

The disk sub-systems are particularly important in the image processing applications because of the video-rate or real-time acquisition, processing and, display requirements. These real-time operations must be complemented by real-time storage and retrieval of image data. For a video-rate or real-time (30 frames/sec) transfer of a 512 X 512 pixel images with 8-bits per pixel transfer rates of greater than 7,864,320 bytes/seconds have to be achieved. For the same size image with 16-bits per pixel this transfer rate requirement doubles. Many image processing applications require acquisition and storage of very large size or large number of images. A 10K X 10K LANDSAT image with 4 bands of 8-bits/pixel each takes up 100 Mbytes of disk space while a 1 minute image sequence of 512 X 512 X 8-bit images takes up 471 Mbytes.

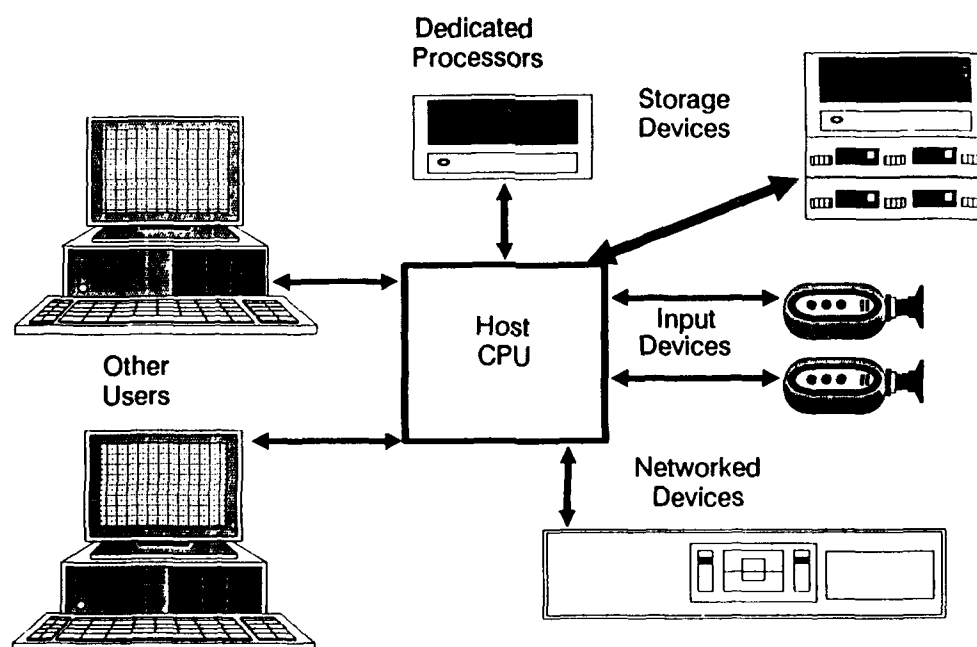


Figure 1 : Traditional imaging system

In many applications display and processing of very large images is desirable. The only way to display these very large images in real-time is to virtually roam over the data within a displayed window. Vir-

tual roam will also enable the virtual processing of such large images. These special transfer speed, processing, and storage requirements are encouraging the Image Processing industry to design disk sub-systems that are much faster in speed and larger in disk space than the traditional storage devices. The digital disk sub-systems can also be used as a virtual Random Access Memory (RAM) or a digital VCR. These disk sub-systems can be connected to the image processors by a high speed image data bus for high speed image data transfers. The entire disk sub-system is controlled by a host which communicates to the sub-system through the host bus. Other elements that may be controlled by the host that can access the disk sub-systems are a Digital Image Processor, High Resolution Display Stations, or an Array Processor. The digital disk sub-system along with an Image Processor can also be used to acquire 16 bits/pixel color images (YIQ) at real-time.

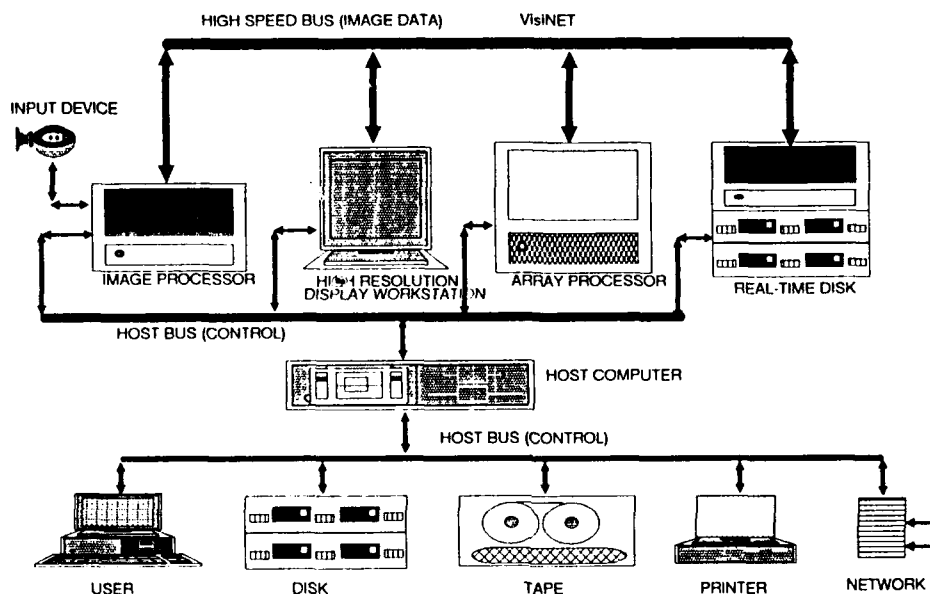


Figure 2 : Imaging network with a dedicated high speed bus

Early attempts to design high speed disk sub-systems resulted in parallel transfer disks (PTD). Many of these systems used multiple read/write heads and were very sensitive to physical damage. The time required to replace these disks was large. These disks always lacked in performance and reliability. The sustained transfer speed were significantly less than burst speed. The read/write heads had to go through a large amount of movement making the system susceptible to head crash. The second generation designs use standard winchester technology disks. These disks have a high MTBF (Mean Time Between Failure) and time required to replace a disk is minimal. There are many different possible designs of the disk sub-system. The disk sub-system design described in this paper is implemented by **Recognition Concepts Inc.** for their **TRAPIX 5500** Image Processor series. This particular disk sub-system (**VisiSTORE**) consists of a specialized master disk controller that controls multiple of standard disk controllers and hard disks of winchester technology.

The disk sub-system has five components:

1) High speed image data bus: This data path is used to move the image data to and from the disk sub-system and the user device. Examples of the user devices are image processors, high resolution display workstations, array processors etc. The data path should be fast and wide enough to handle

the real-time data transfer. **VisiSTORE** transfers image data via a dedicated bus (**VisiNET**) at a rate of up to 20 Mbytes/second. . The host processor is only used for the control and all the data transfers are done using this bus.

2) Host bus for control: This data path is used to send commands from a host computer to the disk sub-system and receive the status back. The host can also control various other processing units that access the disk sub-system through this data path.

3) Master controller: This device controls the entire disk sub-system and performs the following functions:

- (a) Interfaces between the disk sub-system and the host computer using the host bus (2).
- (b) Coordinates data transfers between the high speed image data bus (1) and remainder of the disk sub-system.
- (c) Provides local data buffers that are used as FIFO's (queues) for the data being transferred between the high speed image data bus (1) and remainder of the disk sub-system. These data buffers are useful in synchronizing the multiple disks running asynchronously. These buffers also smooth out any momentary differences between the transfer rates of the high speed data bus and the disk controllers.

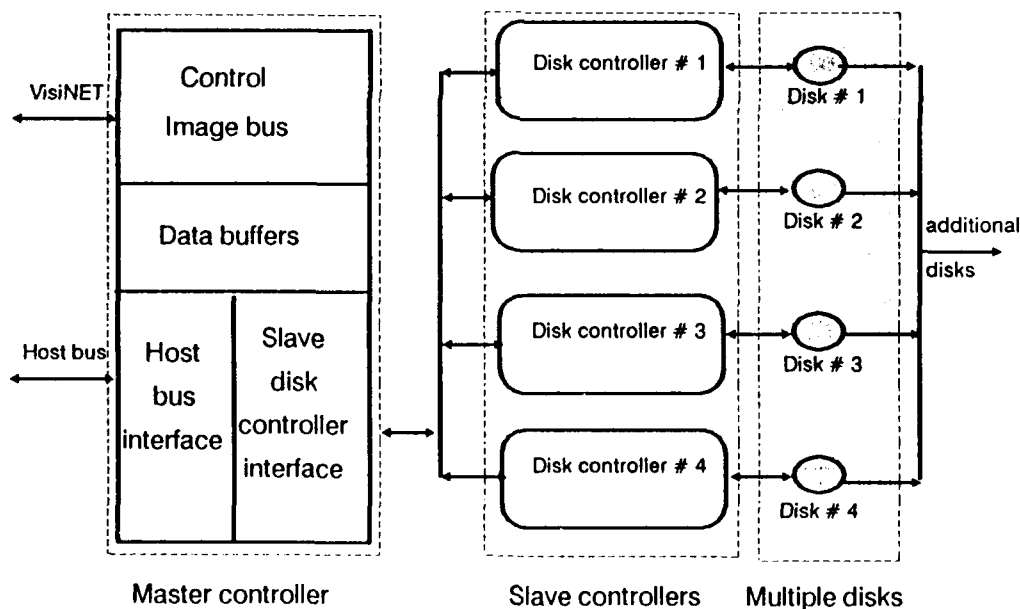


Figure 3 : Block diagram of VisiSTORE

4) Slave Disk Controllers: The master controller drives many slave disk controllers. Each of these slave disk controllers controls one or many standard winchester technology hard disks. One of the slave disk controllers keeps track of the status of all the other slave disk controllers and reports the status to the master controller. The slave disk controllers perform functions like formatting, read, write, head movement, status gathering etc.

5) Hard disks: The slave disk controllers drive these disks. The number of disks being controlled by each of the slave controllers depends upon the technique used to store the data on the disk. There are two ways to store the incoming data on the disks:

(a) Each incoming byte/pixel is stored on the next available disk. If one of the disks fails, the image stored on the disk loses the resolution, but no one image frame is lost.

(b) Each frame of an incoming image sequence is stored on the next available disk. In this case if one of the disks fails, then every N'th frame from a sequence is lost. However for the individual frames the resolution is preserved.

The method used for storing the images depends mainly upon the application. Real-time simulation would prefer the first approach in order to save the entire sequence even though it may be a lower resolution while medical imaging applications would prefer the second approach in order to maintain the resolution for each image frame. **VisiSTORE** can store up to 25 Gigabytes of image data that can be stored/retrieved at a rate of up to 18.6 Mbytes/sec (sustained) with random access to any image frame at 60 Msecs.

These disk sub-systems are mainly used as a peripheral device in a image processing system. The desirable features of a system with an image processor and a disk sub-system would be real-time image sequence acquisition, high speed processing using a pipeline image processor and a array processor, high speed storage of the acquired and/or processed image sequence on the disk sub-system, real-time retrieval and display of the image sequence from the disk sub-system, retrieval and display of images at a variable rate. The system should be able to perform basic file manipulation functions. The use of a disk sub-system along with an Digital Image Processor will enable Virtual Roam and Virtual Processing of large images stored on the disk. The disk sub-system also provides a random access to any of the frames stored on the system at a constant time (Typically 60 Msec).

The high speed data bus between the disk sub-system and various other devices has evolved into an open architecture that allows many new devices to be a part of the high speed network. **VisiNET** is one such example of high speed network made by Recognition Concepts Inc. The disk sub-system **VisiSTORE** along with the **TRAPIX 5500** image processor and the **Virtual Image Processing Software (VIP)** manufactured by the **Recognition Concepts Inc.** provides a complete image processing system with a real-time disk sub-system. Additional components like high resolution display work station **TRAPIX-PLUS** (1024 X 1024), **MARS** array processor manufactured by **Numerix Corporation**, **VisiVISION** High Resolution Display workstations (2048 X 1536) based on **Univision Technologies Inc.** **VDC-800** board or **VisiTEK** high resolution display workstations based on **TEKTRONIX** Digital Display Device can access data from the disk sub-system via the high speed network **VisiNET** in a multi-user mode. **VLDS** (Very Large Data Storage) recorder manufactured by **Honeywell** has been also interfaced to the **VisiNET** and used to backup digital data from the **VisiSTORE**.

Applications: Some of the important image processing application areas that require these types of disk sub-systems are (1) Defense Applications, (2) Medical Applications, (3) Industrial Applications, (4) Broadcasting and (5) Research and Development.

(1) Defense Applications: Success of many of the defense applications depends upon the speed of processing. For example applications like reconnaissance and simulation need real-time acquisition, processing and, replay. The images acquired may be a flying object like a plane or a missile or images acquired from an infra-red camera of moving or stationary objects. Real-time replay of stored and processed data is very desirable for flight simulation or at the test range. The disk sub-system can also be used to store images acquired at greater than 30 frames/sec. by acquiring smaller image size than 512 X 512 pixels and packing the images in 512 X 512 chunks with the help of an Image Processor. The disk sub-system can be used as security systems for airport, reactors etc. along with other security devices.

(2) Medical Applications: Many of the medical procedures need a high speed acquisition and replay of images. Images need to be acquired, processed and replayed in real-time for the digital subtraction angiography. 3-D reconstruction of organs can be done by combining large numbers of previously stored 2-D images on the disk sub-system (CAT scan, MRI, cell biology). Nuclear Medicine, Ultrasonic Imaging, Thermal Imaging and many other fields of medicine can use the disk sub-system for high speed storage. The disk sub-system can also be used to store/retrieve patient's medical records (X-rays, Ultrasonic, thermal images etc.) in digital form and can be viewed on ultra high resolution display workstations (Figure 4).

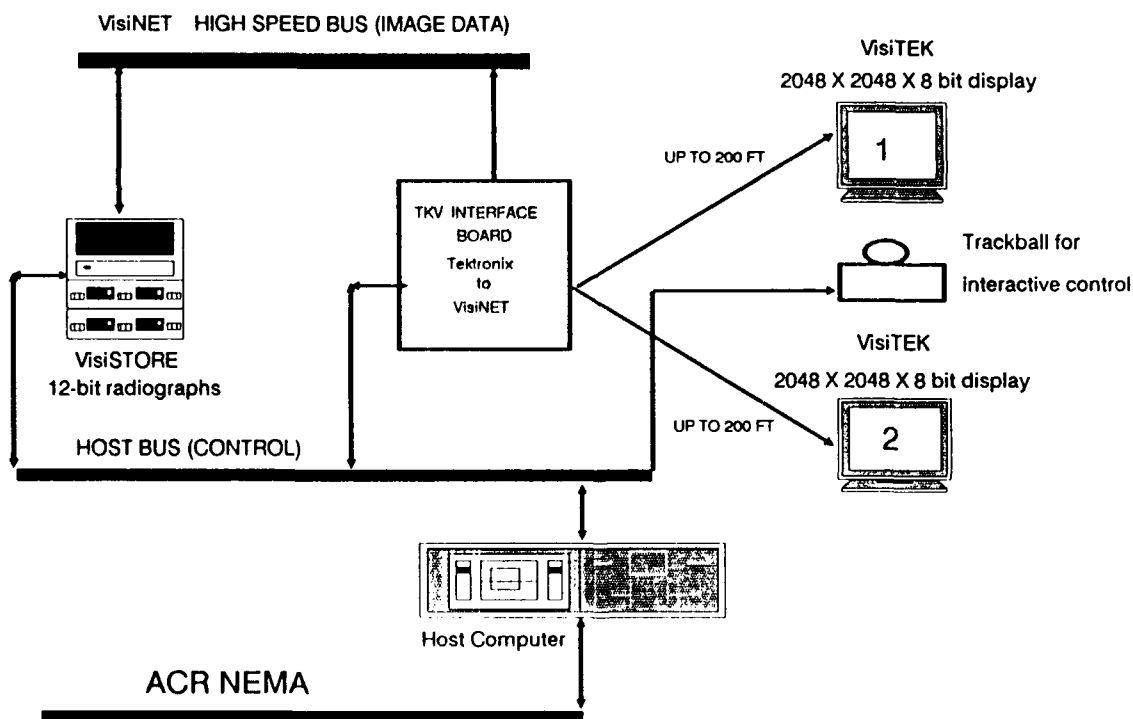


Figure 4 : Example of medical PACS system

(3) Industrial Applications: SEM and TEM applications require storage and processing of large images. These large images can be roamed around in real-time by using the disk sub-system. Remote sensing, seismic research and mapping applications can use the ability of large image acquisition, storage, processing and virtual roam. Non-destructive testing (NDT) and Machine Vision applications can also use the high speed and large storage capacity of the disk sub-system.

(4) Broadcasting: Specialized disk sub-systems can be used as a digital VCR. Images can be processed for measurements, movements etc. using the image processor at a high speed and replayed at various speeds.

(5) Research and Development: The disk sub-system can be used for all types of R&D when a fast and large data storage medium is needed. If the disk sub-system is a node of network of several processors then it can be used to continuously acquire/display images for a long time while other nodes continue processing and analysis.

Conclusion: The Real-time digital disk sub-system represents a new trend in the image processing technology. The real-time digital disk sub-system VisiSTORE and high speed network VisiNET offer open architecture that is encouraging manufactures to interface imaging peripherals to the VisiNET. As more mature disk sub-systems arrive in the market, many new applications will find the disk sub-systems useful.

Ranjit Mulgaonkar is the Product Manager for **Recognition Concepts Inc. (RCI)**. RCI is located in Incline Village Nevada and manufactures Image Processing Systems (Hardware and Software). Some of the key products of RCI are the **TRAPIX 5500 Image Processor**, **TRAPIX-PLUS** and **VisiSTATION High Resolution Display Workstations**, **VisiNET High Speed Network** and **VisiSTORE Digital Disk sub-system**.

NEAR SPECULAR LIGHT SCATTER MEASUREMENTS

John C. Stover
Toomay, Mathis & Associates, Inc.
P. O. Box 3118
Bozeman, MT 59715
(406) 586-7684

Reduction of near specular scatter from optics has become an increasingly important issue. Near specular scatter is particularly troublesome in systems where high resolution imaging is required. Modern space and aircraft optics often have to meet these type of requirements in the visible, the infrared or both. Unfortunately, a standard scatter specification is not readily available. In fact, until recently, scatter measurements closer than one or two degrees from specular were difficult or impossible to obtain. This application note presents near specular data taken on one of TMA's Complete Angle Scatter Instruments (CASI) and suggests that BRDF measurements are a viable means of specifying low scatter optics.

The CASI system utilizes variable detector apertures and a double scan technique (with and without sample) to measure near specular scatter. A complete review of this instrument is now available in the literature [1] as well as several papers describing results obtained with the system [2, 3, 4, 5, 6]. The system presents scatter data as the bidirectional scatter distribution function (BSDF). This type of format has been used for several years [1, 7], and is becoming a standard. When integrated with the users requirements it allows the generation of a measurable (and repeatable) specification. BSDF may be expressed in terms of the incident power P_i , the detected scatter power P_s , the detector aperture solid angle ω_s and the aperture angular position (from sample normal) θ_s .

$$\text{BSDF} = \frac{P_s}{P_i \omega_s \cos \theta_s}$$

BSDF is usually plotted in degrees from specular although other formats exist. The terms BRDF and BTDF designate reflective and transmissive sample respectively.

Several examples of BSDF data taken at 10.6 microns are shown in Figures 1-5 for various infrared materials. Figures 1 and 2 show the BTDF from GaAs and Ge windows plotted against $\log \theta$. In each case the sample data is compared to the focused beam profile and scatter produced from the instrument alone (without the sample in place). Instrument beam profile and scatter is referred to as instrument signature. Separation of sample scatter from the signature depends on both the sample and the instrument but usually occurs below 1° at 10.6 microns and below $.1^\circ$ in the visible. Figure 3 shows the same GaAs and Ge windows in comparison on a linear θ scale. A set of six ZnSe windows were also measured at 10.6 microns. In Figure 4, the high and low scatter samples of this set are compared. The sample variation was less than one order of magnitude over most of the range of the measurement. The lowest scatter ZnSe window is compared to the instrument signature in Figure 5 on a $\log \theta$ scale. For all the samples examined, Ge and GaAs are the better low scatter windows over the entire range of θ .

Samples which are low scatter at high angle are not necessarily low scatter near specular. Figure 6 presents data from two spherical mirrors with identical dimensions (10 cm diameter and 50 cm focal length). The cheaper of these mirrors (\$300) was purchased off the shelf from a large optical supplier. The \$1700 mirror was purchased as a special order from a vendor using a proprietary low scatter production technique. Although the expensive mirror is clearly low scatter at high angles (more than an order better) it is higher scatter in the .2 to 2 degree region near specular. This particular case was unsettling, since the requirement for this component was for a mirror with low scatter near specular. Although the instrument signature is not shown in Figure 6, it separates from both mirrors well below $.1^\circ$ from specular.

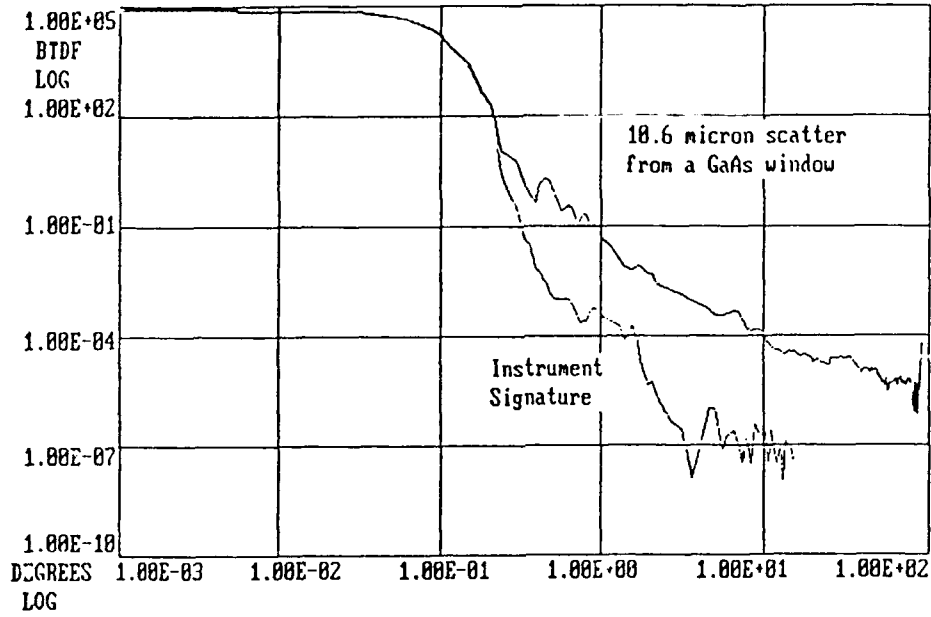
Obvious problems exist in ordering and specifying low scatter optics. It is difficult for manufacturers to respond to specifications that they cannot measure, and it has not always been clear what specifications should be used. Measurement services and systems are now available to provide near specular scatter data. The use of a BSDF limit, which measured scatter cannot exceed, can solve the specification issue. For example, the specification for the near specular mirror could have been BRDF not to exceed 10^{-1} sr $^{-1}$ over .3 to 1.0 degrees from specular at .633 microns. A ring laser gyro mirror might be specified as BRDF not to exceed 10^{-6} sr $^{-1}$ in the back scatter direction of -90 degrees from specular. The values of required BSDF, in critical regions, can be generated from the system designers requirements. Such a specification system makes a lot more sense than measuring rms roughness (by whatever means) when scattered light is the real issue.

References

1. D. R. Cheever, F. M. Cady, K. A. Klicker, J. C. Stover "Design Review of a instrument (CASI)"; SPIE Proc V 818-04; August, 1987.
2. J. C. Stover, C. H. Gillespie, F. M. Cady, D. R. Cheever, K. A. Klicker "Comparison of BRDF Data from Two Scatterometers"; SPIE Proc v 818-10; August, 1987.
3. F. M. Cady, D. R. Cheever, K. A. Klicker, J. C. Stover; "Comparison of Scatter Data from Various Beam Dumps"; SPIE Proc V818-05; August, 1987.
4. J. C. Stover, K. A. Klicker, D. R. Cheever, F. M. Cady "Reduction of Instrument Signature in Near Angle Scatter Measurements"; SPIE Pro 749-08; January, 1987.
5. K. A. Klicker, J. C. Stover, D. R. Cheever, F. M. Cady "Practical Reduction of Instrument Signature in Near Specular Light Scatter Measurements"; SPIE Pro V 818-06; August, 1987.
6. J. C. Stover "Overview of Current Scatter Measurements and the Impact on Optical Systems; SPIE Pro V776-07; May, 1987.
7. F. E. Nicodemus et al; Geometrical Considerations and Nomenclature for Reflectance, NBS Monograph 160, US Dept. of Commerce, October, 1977.

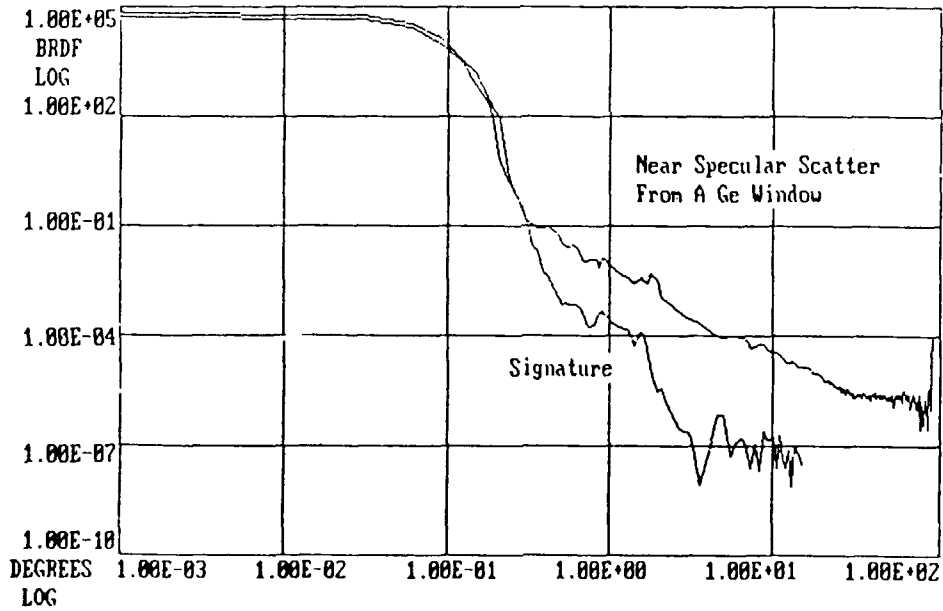
Toomay, Mathis & Associates, Inc. - Light Scatter

FIGURE 1

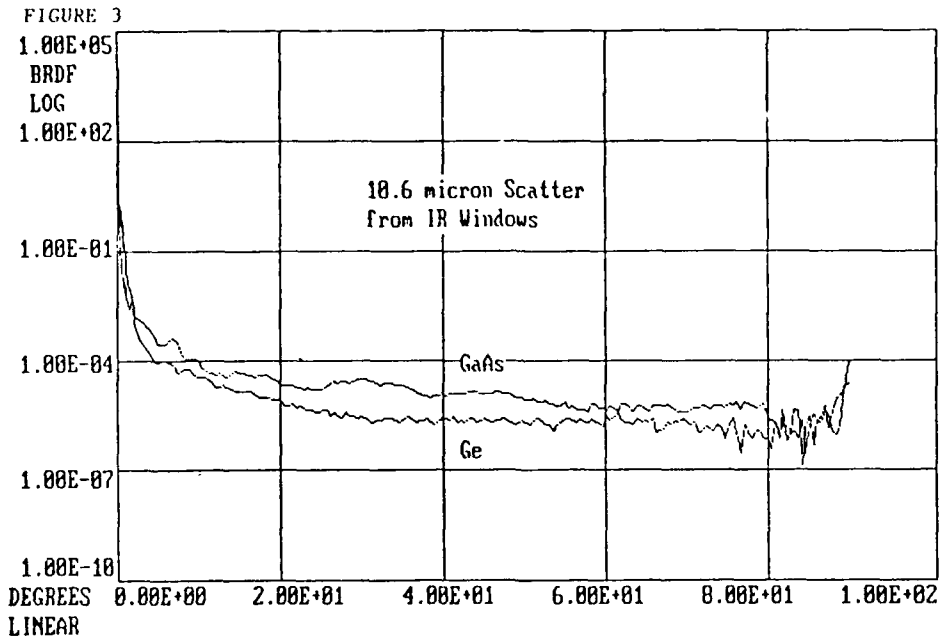


Toomay, Mathis & Associates, Inc. - Light Scatter

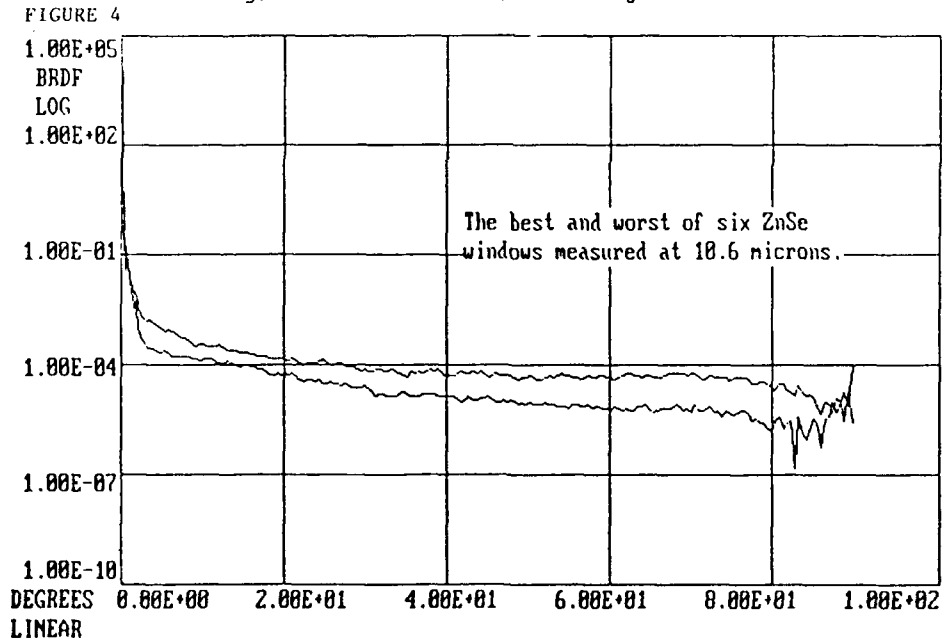
FIGURE 2



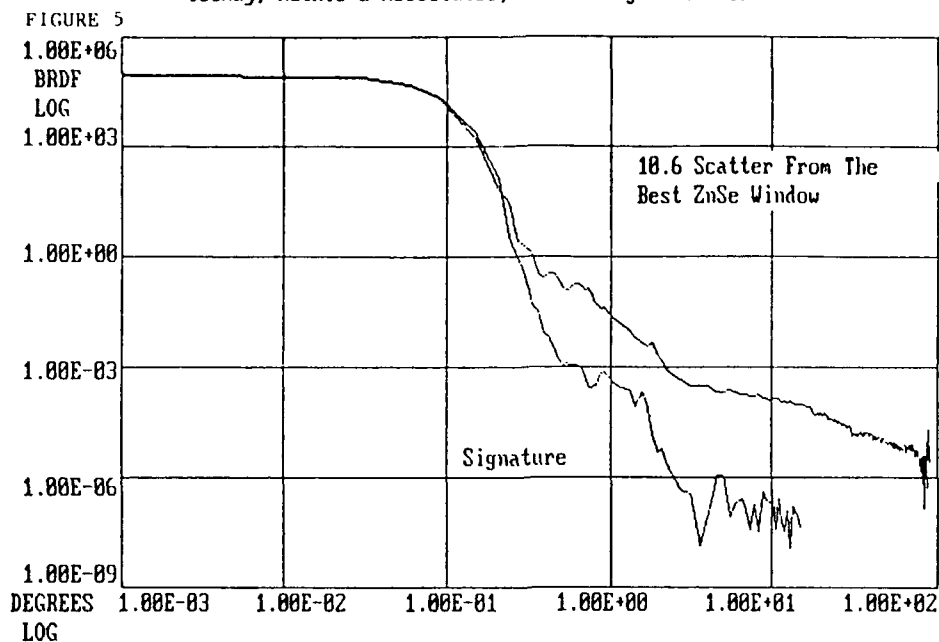
Toomay, Mathis & Associates, Inc. - Light Scatter



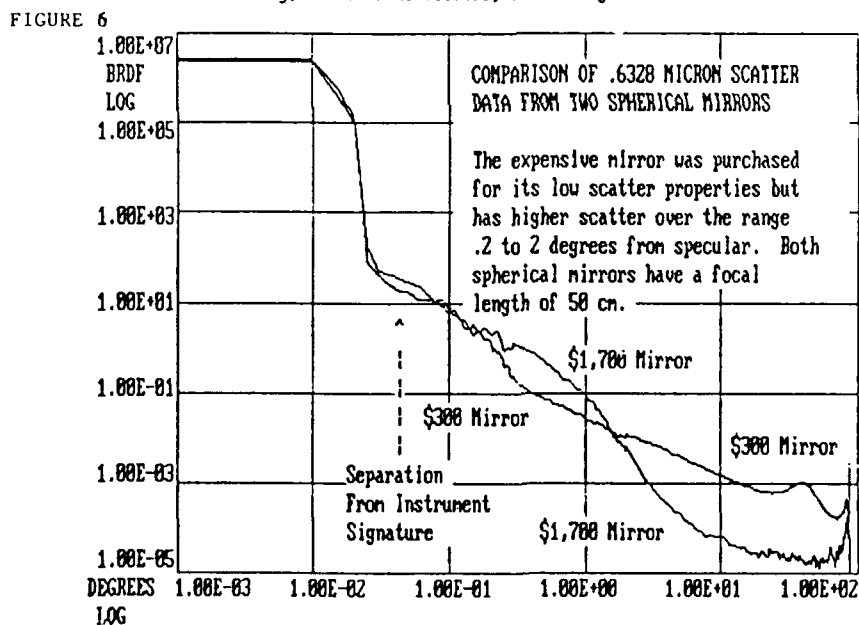
Toomay, Mathis & Associates, Inc. - Light Scatter



Toomay, Mathis & Associates, Inc. - Light Scatter



Toomay, Mathis & Associates, Inc. - Light Scatter



BIDIRECTIONAL OPTICAL TRANSMISSION SYSTEM EXPERIMENT WITH WDM DEVICES

R. C. Menendez, K. P. Chung and T.R. Hsing

Bell Communications Research
Morristown, New Jersey

ABSTRACT

Experimental results on a bidirectional optical communications system for economic configurations for local loops are presented. The transmission rate through a single-mode fiber in one direction is 140 M bits/sec and much slower in the opposite direction. Inexpensive WDM couplers are used for multiplexing and demultiplexing of light signals from LED sources.

Bit error rates for various configurations and signal levels are measured. Further, impacts of reflections and near-end cross talk on the transmission quality are reported.

There has been considerable interest recently in the application of LEDs with single-mode (SM) fiber in subscriber distribution. LEDs offer adequate performance and cost and reliability advantages over laser diodes. Similarly, there is interest in moving from two-fiber transmission to single-fiber bidirectional transmission, where the primary advantages would again be economic and operational. The economic advantage of eliminating one fiber per link must be weighed against the added cost of the couplers and possible reduced performance due to near-end crosstalk (NEXT). NEXT occurs when a portion of the optical signal from the local transmitter is reflected from some fiber discontinuity (e.g., a connector) and this undesired echo interferes with the desired signal from the remote transmitter.

Approaches utilizing one wavelength to transmit in both directions and directional couplers have been described and analyzed [1-3]. This approach introduces a minimum of 6 dB of additional loss in the link (a substantial portion of the LED/SM loss budget). NEXT problems were addressed by using fusion splices to eliminate backreflections [1] or electrical echo cancellation in the receiver [2]. An alternative which introduces less loss and mitigates NEXT is transmitting two wavelengths and relying on the isolation afforded by wavelength division multiplexer (WDM) devices. Good performance has been obtained [4] using high-isolation couplers employing dichroic filters that attenuate the echoed signal by 30 dB or more before it reaches the receiver. However, the expense of these high-quality couplers limits their applicability in loop distribution. Fused biconical taper (FBT) WDM directional couplers offer a potentially attractive compromise between these two approaches; relatively low excess loss and cost with reduced isolation. Because of the broad spectrum associated with an LED source, the isolation afforded by these devices can be only 10-15 dB.

The goal of this experiment was to determine the power penalty (receiver sensitivity impairment) introduced from fixed levels of backreflection when FBT couplers are used with LED transmitters. The experimental configuration is depicted in Figure 1. A 140 Mb/s NRZ PRBS signal from the remote transmitter is preferentially directed to an APD receiver by a 1.3/1.5 WDM-FBT coupler and passed to a BER test set for performance monitoring. The interfering source (LED2, a 1.3 μm source) was modulated by a 140 Mb/s square-wave generator. NEXT is significant here because the interfering source launches roughly 10 dB more power than the desired source. The interference signal was coupled to the trunk by the FBT coupler, and a portion of this signal was reflected back toward the coupler by a variable backreflector (VBR). The contributions of other sources of reflection were small. The optical power of the desired signal and interfering signal at the receiver are independently adjustable by the optical attenuator and VBR, respectively. The VBR monitor port taps off a fraction of the two signals propagating toward the receiver, and a high-isolation WDM coupler was used to split the two wavelengths for measurement of the two optical power levels.

Figure 2 shows the BER performance versus the received optical power level of the desired signal for five different values of the reflection coefficient of the VBR. Curve A corresponds to the case of no reflected power. Curves B-E refer to reflected power levels of -34.6, -32.6, -29.6, and -28.6 dBm, which correspond to reflection coefficients of -12.9, -10.9, -7.9, and -6.9 dB (5, 8, 16, and 20 %), respectively. For this worst-case configuration of sources, these curves indicate that the reflection penalty at a BER of 10^{-7} is about 1.0 dB for a reflection of -7.9 dB (16 %). Well-designed connectors provide a reflection of -20 dB or less, but in the worst case, the power reflection arising from an air gap at a connector can be as high as -6.7 dB (20%) [5] although a more typical maximum is -8 dB (16%). These results indicate that despite the modest isolation introduced by the broad LED spectra, this class of WDM couplers is adequate to maintain small reflection penalties (< 1 dB) for even a worst-case reflection.

REFERENCES

- [1] R. D. Hall, R. A. Betts, J. P. Moss, "Bidirectional Transmission over 11 km of Single-Mode Optical Fibre at 34 Mbit/s Using 1.3 micron LEDs and Directional Couplers", *Electronic Letters*, Vol. 21, No. 14, pp. 628-629, (1985)
- [2] P. Staubli, P. Heinzmann, "Bidirectional 2 Mbit/s Transmission over a Single Fibre Using Electrical Echo Cancellation", *Electronics Letters*, Vol. 22, No. 10, pp. 534-535, (1986)
- [3] P.P. Bohn and S. K. Das, "Return Loss Requirements for Optical Duplex Transmission", *Journal of Lightwave Technology*, Vol. LT-5, No. 2, pp. 243-255, (1987)
- [4] M. Stern, J.L. Gimlett, L. Curtis, N. K. Cheung, M. B. Romeiser, W. C. Young, and P. Shumate, "Bidirectional LED Transmission on Single-Mode Fiber in the 1300 and 1500 nm wavelength regions", *Electronics Letters*, Vol. 21, No. 20, pp. 921-922, (1985)
- [5] V. Shah, W. C. Young, and L. Curtis, "Large fluctuations in transmitted power at fiber joints with polished endfaces", Paper TUF4, OFC '86, Reno, Nevada, (1986)

List of Figures

Figure 1. The experimental configuration showing the fused biconical taper (FBT) coupler, the variable backreflector (VBR), and the power monitoring arrangement.

Figure 2. Experimental bit-error rate versus received optical power curves for a range of reflection coefficients.

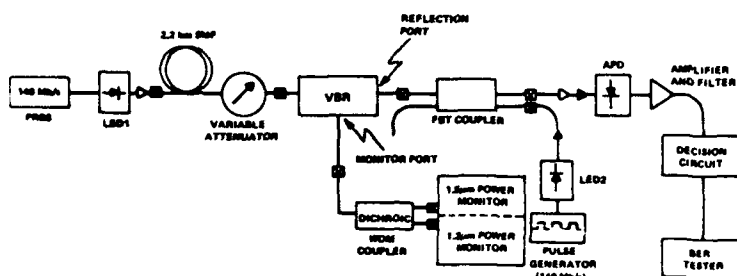


FIG. 1

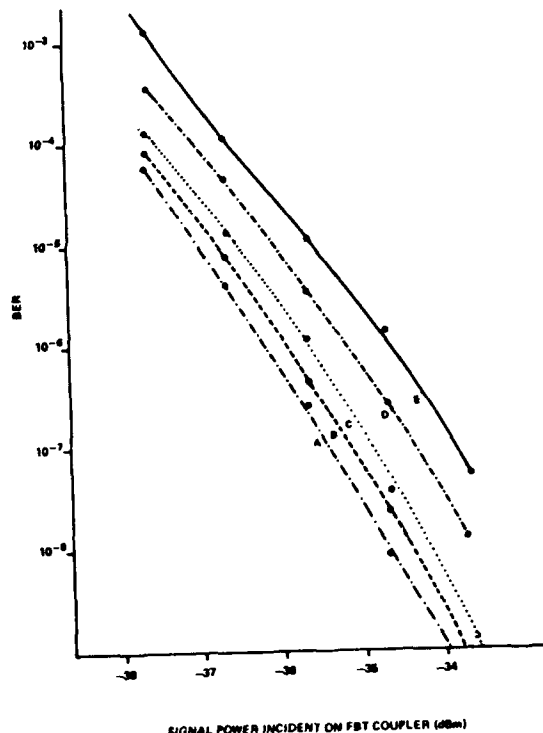


FIG. 2

COHERENT BACKSCATTER: ITS PROVENANCE AND CONTROL IN FIBER APPLICATIONS

G. A. Hill

Principal Development Physicist

Coherent Linear Ltd
9, Raynham Road
Bishop's Stortford
Hertfordshire, CM23 5PB, England.

Abstract

The classical model for the origin of non-linear optical properties is described as a basis for understanding the onset of coherent backscatter. A method utilized for increasing the coherent backscatter in novel fiber applications is discussed from a practical and theoretical point of view. Experimental data on the control of coherent non-linear backscatter in a fiber optic system is presented, along with a measurement of the Stokes frequency at 1.32 microns wavelength.

Introduction

Forward and backward scattering of light is fundamental to the process of light propagation. Both types of scattering are intimately related as evidenced by the Ewald-Oseen Extinction Theorem, which gives insight into the well known forward propagation direction of light in a medium (1). However, in certain applications the backward scattering can grow due to a coherent interaction of the light with the medium, resulting in a non-linear build up of backward scattered light (2).

The performance of the current generations of long haul optical systems is not impeded by the non-linear interaction between the optical field and the waveguide material, because of the low power density and broad spectral distribution. Future systems, however, are expected to use sources with both high power levels (20-50 mw) and narrow spectral distribution. These two features will become important in coherent optical systems where spectral widths in the megahertz range are required to obtain the high performance expected (3). Data on the non-linear backscatter (Brillouin scatter) due to lattice vibration excited by a coherent Nd:YAG laser beam at 1.3 microns wavelength is presented. An integrated LiNbO₃ optical modulator allows the coherent backscatter to be controlled (4).

Coherent backscatter can reach nearly 100% in the case of distributed fiber gratings. However, the mechanism of light induced refractive index change is not clear from the published work. A description of the origin of optical effects in fiber must be generalised in order to account for coherent backscatter and, if possible, photo-refraction.

The classical model and coherent backscatter

According to classical theory, light scattering arises from oscillations in charge and current distributions in matter induced by the incident electromagnetic wave. The precise picture for the interaction of light with a medium requires the language of quantum mechanical perturbation theory (5). However, the essential physics of optical phenomenon including non-linear effects can be qualitatively understood on the basis of the simple classical model. Here a dynamic system consisting of charge located in a potential energy binding curve is used. In the case of a crystal lattice the curvature of the energy curve is directly related to the elastic constants. Its magnitude is a function of the total energy. Similarly, since the elastic behaviour of electrons governs the dispersion of the scattered light, i.e. its amplitude and phase, the bonding of the electrons affects optical properties. The propagation behaviour of light in a medium is usually described using the phenomenological constant called the susceptibility. However the microscopic origin of susceptibility is revealed under conditions where the structure of the medium impresses its own dynamics on the optical process. This is the case with stimulated Brillouin scattering. Here the build up of backscatter starts with the random occurrence of lattice vibrations (phonons) which fall within the frequency range of the coherent source. This sets up a travelling wave interaction which results in the increased backscattering. Because the phonon is travelling at the velocity of sound the scattered wave is down shifted in frequency. This down shifted wave is known as the Stokes wave. The amount of frequency shift is proportional to the sound velocity of the appropriate propagating stress wave and therefore contains information about the elastic constant and structural origin of the scattering process.

In a waveguide the existence of core and cladding material boundary can produce frequency components which can be interpreted on the basis of the material composition. Like the elasticity, the acoustic velocity is a function of the total energy of the system. It is interesting to speculate on the possibility of producing structural transitions within a fiber core analogous to order/disorder transitions found in single crystals(7).

As the forward and backward optical waves mix via the non-linear susceptibility, the excitation of phonons at the difference frequency causes an exponential gain of light propagating in the backward direction. This latter feature follows from the wave-vector matching condition. However, the phonons have a finite lifetime due to viscous damping. It follows that, if the laser field is to build up a strong acoustic wave, the coherence time for the laser must be longer than the phonon lifetime; alternatively, the bandwidth of the laser line must be less than the spontaneous bandwidth of the phonons. At a wavelength of 1.3 microns this is 23 MHz, and implies that the laser must operate on a single longitudinal mode. On the other hand, if the phase of the laser is interrupted the acoustic wave is unable to build up. Thus modulating the phase of the laser provides a method for controlling the build up of the backscattered wave (8).

Fiber Gratings

Laser coherence time is also important in the fabrication process of fiber gratings. It is known that certain types of fiber can exhibit light induced changes in their optical properties(9). In particular, the photo-induced refractive index modulation results in an increased amount of backreflected light. A resonant filter with an extremely small bandwidth (200 MHz) is therefore 'fabricated' by the presence of the optical field. In practice the filter typically consists of a 1-m strand of Ge-doped-core fused-silica clad fiber with a NA = 0.2 and core diameter 2 micrometers. To condition the fiber to provide strong backreflection at a given wavelength (usually one of the lines from the argon ion laser) it is first exposed for about a minute to coherent contradirectional beams, until a periodic structure is formed in the core; the periodic structure results in an increase in backreflection of the fibre to a value many times that of the Fresnel reflection (4%) from the input face of the fiber.

The increased backreflection can be thought of as a special case of Brillouin scattering where the phase velocity is zero. As in the case of Brillouin scattering, the periodic dielectric perturbation is related to the wavelength of the light inducing the perturbation. By contrast to photo-elastic coupling, however, photo-induced refractive index perturbations are after a time rendered permanent. A clue to the origin of this effect might be inferred from the Hellman-Feynman Theorem (10) where it is shown that the dynamic properties of the electrons, determined by quantum mechanics, are mirrored in the electrostatics which govern the forces on the nuclei in the solid. Thus electronic processes, including laser field modified processes, in theory, 'write' on the structure of the solid. However, a 'ratchet' effect would have to be postulated in order to account for the permanent nature of the structural change. It is not yet known how such a ratchet effect might proceed but it seems likely that Quantum Size Effects (QSEs) may offer insight into photo-refractive mechanisms involving photons in the range 1-2 eV (11).

Suppression of Stimulated Brillouin Scattering using phase modulation

Experimental work was carried out using a Nd:YAG solid state laser (Quantronix 114) set up as described by Cotter (12) and operating in a single longitudinal mode at 1.32 microns. The laser output was approximately 320 mW, but, owing to losses in launching, modulator and coupler, the power available for launching into the test fibre (L = 12900m, 0.47db/km) was approximately 30 mW. The modulator (constructed by M.Grant at STL, England) was a LiNbO₃ integrated optics device with an insertion loss of 6dB, 500MHz bandwidth. For the work reported biphasic (0 and 180 deg.) modulation was used. The details of the experimental configuration are shown in Fig. 1. The laser linewidth was measured using a scanning Fabry-Perot interferometer and found to be 3MHz. On the basis of this measurement $P_{crit} = 11.75$ mW for Lorentzian spectral densities at 1.3 microns; in reasonable agreement with the measured threshold. Fig. 2 shows the spectrum of the backscattered measurement along with the effect of the phase modulation. The modulating signal consisted 140 Mbit/s data sequences, which is an important rate for the trunk network and the corresponding bit interval was less than the phonon lifetime. The control of the onset of the effect is clearly demonstrated. For the dynamic range of the experimental work there was a linear relationship between input and output indicating the suppression of the Stokes backscatter. It is noted that the Stokes' frequency off-set is approximately 12 GHz.

Within the envelope of the Stokes spectrum, the intensity of the signal is modulated. This seems to indicate that the build-up of stimulated light is occurring in bursts. Temporal structure on the laser output, due to relaxation oscillations, accounts for this. The period of the oscillations is found to be long enough for the Stokes wave to build up. Active stabilisation of the laser has been achieved with an intra-cavity acousto-optic modulator, however, the population of the resultant cavity precluded the requisite elements for simultaneously single moding it.

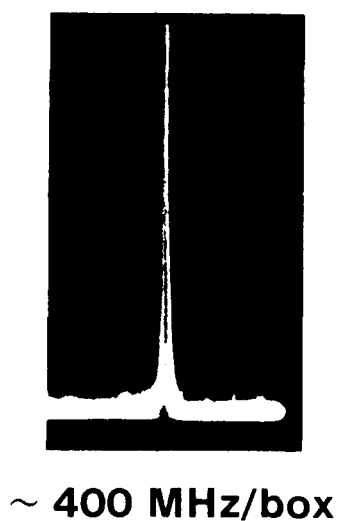
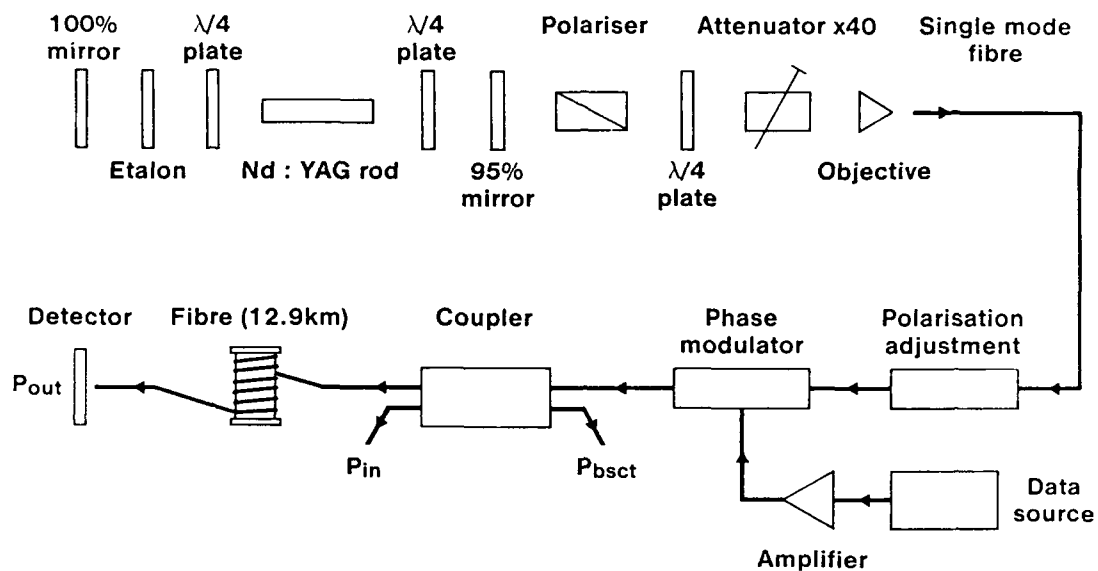
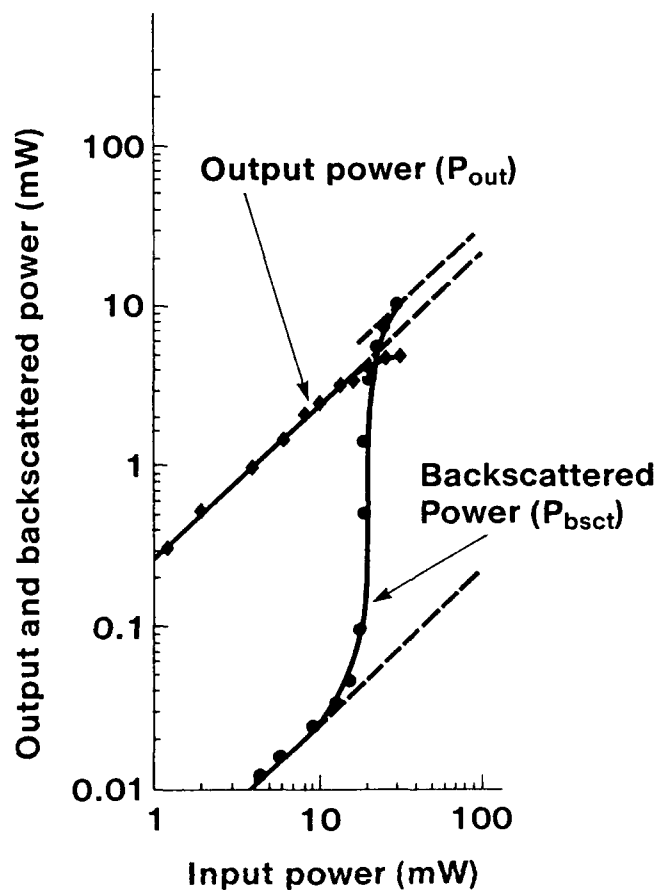
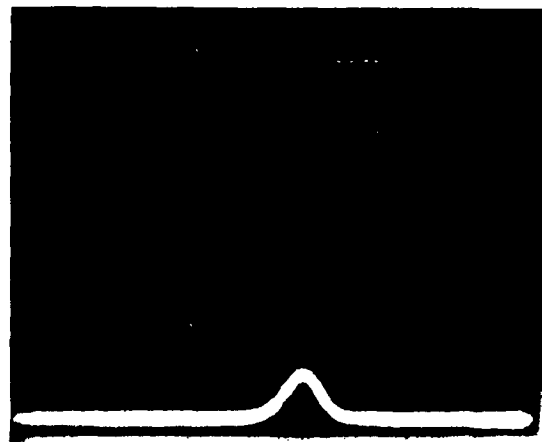
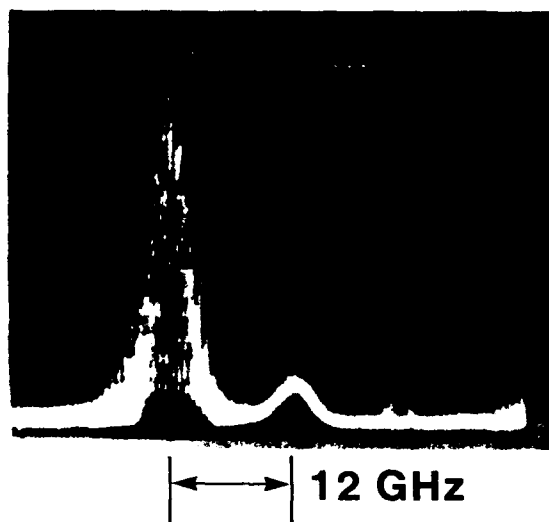


Fig. 1 Experimental set up for measuring backscatter. Laser spectrum is shown along with typical results.





$$\nu_{\text{stokes}} = \nu_{\text{laser}} - \nu_{\text{phonon}}$$

Fig. 2 Spectrum of backscatter along with spectrum with phase modulation turned on. The effect of different phase formats is shown opposite.

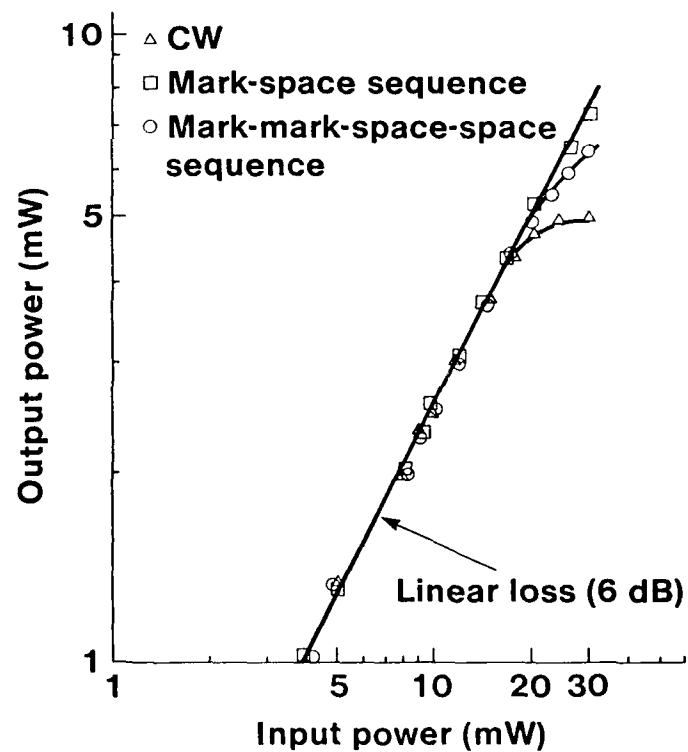




Fig. 3 The far end of a single mode fiber after heating by self-absorption initiated by contact with carbonaceous material: Propagating power was about 1W.

Fiber nonlinearity due to damage

In general, fiber based experiments allow the trade-off between laser power and interaction length. Thus the comparatively low CW threshold power required to induce coherent backscatter is partly due to the long interaction length down the fiber. This would suggest that power induced effects like self-focussing are less likely in fiber and the interaction is rather well defined. However, under CW conditions, the intensity of the light propagating in the fiber core may cause a catastrophic drop in the transmitted light due to as yet unknown form of damage mechanism. In particular cases, the far end of the fiber becomes highly absorbing and reaches incandescent temperatures. Provided an initiation effect takes place, classical inverse-bremsstrahlung may explain this phenomenon.

Conclusions

Coherent backscatter has been described in terms of its classical origin. Techniques for its control have been discussed and the opportunities that exist for studying light matter interaction have also been indicated. It is clear that laser technology is progressing along with fiber optics to the point where new ways of studying non-linearity are available. Apart from the transmission of data, fiber might provide an environment for light matter interaction studies. An understanding of coherent backscatter promises to offer improved system performance for applications such as distributed sensors for safe industrial metrology. Coherent Linear, who manufacture a versatile distance measuring interferometer, are presently developing prototypes which exploit these new opportunities.

I am very pleased to acknowledge the directors of Coherent Linear U.K., for permission to present this paper. Coherent Linear is a subsidiary of Coherent's Component Group (USA).

References

- 1) References are given in M.Born & E.Wolf.Optics(5th Edition, 1975), p.100. Also E.Hecht & A.Zajac .Optics p.44.
- 2) E.P. Ippen and R.H. Stolen, Appl. Phys. Lett., Vol. 21, No 11,539 (1972)
- 3) D. Cotter, Joun. Opt. Comm. Vol. 4, 1, 1 (1983). Also R.G.Smith , Appl Opt, 11, 2489 (1972).
- 4) A. Hadjifotiou and G. A. Hill. IEE Proceedings, Vol., 133, Pt. J, No. 4, 256 (1986)
- 6) A. D. Buckingham , Phil. Trans. R. Soc. Lon. A293,pp 239-248 (1979)
- 7) G.A. Hill, Propagation behaviour of Ultra-sonic waves near the anti-ferromagnetic critical point of CoO . Dissertation Hull University, Department Applied Physics (1969)
- 8) D. Cotter ,Elec. Lett. 18, No 5, 638 (1982)
- 9) K.O. Hill, Y. Fujil, D.C. Johnson, and B.S. Kawasaki, Appt. Phys. Lett.Vol 32,No 10, 647 (1978)
- 10) A.D. Buckingham, Department of Theoretical Chemistry, University of Cambridge, private communication. See for example, J.C. Slator, "Quantum Theory of Molecules and Solids." McGraw-Hill N.Y. (1963)
- 11) R. Dingle, Festkorperprobleme XV, 21 (1975)
- 12) D.Cotter, Opt. Commun. Vol 43, 200 (1982)

ELECTRO-OPTIC DEVICE REQUIREMENTS FOR SHORT HIGH SPEED OPTICAL LINKS

A J Cooper

British Telecom Research Laboratories
Martlesham Heath
IPSWICH
IP5 7RE
England

Summary

The realisation of short high speed optical links for Telecommunications applications imposes considerable demands on the electro-optic devices. This paper examines the system requirements based upon LED/Laser transmitters and PIN/APD receivers in particular highlighting targets for future device development.

1 Introduction

Optical fibre is continuing to penetrate all areas of the Telecommunications network and is currently being studied as an alternative to coaxial cable for installation within buildings [1,2,3]. The use of optical fibre as a transmission medium over short lengths, (< 1Km), presents a number of areas for consideration;

- a) System economics,
- b) Network architecture,
- c) Device requirements.

To allow interconnection of the in-building networks to inter-city and local loop networks the system must be capable of operating over a wide range of data rates, upto Gbit/s. This imposes a large variation in performance requirements for the transmitter and receiver devices.

This paper examines the requirements for high speed short haul optical links and considers the suitability of currently available optical devices for this application.

2 Interconnection System Requirements

In-building networks will have varying requirements specific to their function, however it is possible to produce a set of network independant requirements pertinent to the electro-optic devices.

Table 1: System Requirements

Parameter	Value	Comments
Data Rate	upto Gbit/s	The current trend in optical communications towards high speed systems indicates the need for in-building systems to be capable of interconnecting with Gbit/s systems.
Length	upto 1Km	In-building links will typically be hundreds of metres in length, however to allow for inter-building connections systems will be designed to operate over 1Km.
Device Size	small	Small devices reduce costs and ease installation.
Cost	low	A low cost is required to ensure optical interconnections are a viable alternative to coaxial cable even at low data rates.

A single solution for all architectures and interconnections is desirable since the benefits of a single system can be realised;

- * Lower cost
- * Ease of interconnection
- * Ease of maintenance/replacement
- * Ease of network reconfiguration

However, because of the wide range of data rates a single system will result in an "over-engineered" system operating at low data rates (e.g. 2Mbit/s). Therefore it may prove cost effective to consider more than one solution according to the data rate.

An optical interconnect consists of three parts; the transmitter, the receiver and the fibre, each part has a variety of options and can be investigated separately. However, it is necessary to retain an overall view of the system as it may be possible to offset one part against another. For example a highly sensitive receiver would not be used with a high launch power transmitter.

3 The Transmitter

Electro-optic device requirements for the transmitter as dictated by the general requirements of the system are presented below;

- i) The transmitter must be capable of modulation at data rates upto Gbit/s.
- ii) Launch power is not critical due to short operating distances.
- iii) The transmitter should be small with a low parts count to achieve low cost.

There are three possible options for the design of the transmitter; Datalink modules, LEDs and Lasers. The relative merits of each are discussed in the following sub-sections.

3.1 Datalink Modules

Commercially available datalink modules consist of a small, (3 x 2 x 1.5cm) dual-in-line package housing the drive electronics and optical device, (transmitter or receiver), requiring a power supply, data in/out and fibre connections. Typical datalink parameters are presented in Table 2.

Table 2: General Datalink Parameters

Module	Input	Output	Internal Retiming	Source/ Detector	Fibre	Maximum Rate Mbit/s
Transmitter	Binary electrical	Binary optical	N/A	LED	mm*	280
Receiver	Binary optical	Binary electrical	Available at < 50Mbit/s	PIN	sm*/mm	280

*mm - multimode
sm - singlemode

The main drawbacks with datalinks are; limited speed of operation, clock recovery is not widely available and multimode fibre must be used with over 90% of devices.

3.2 LEDs

Currently there are two types of LED available; Edge-emitting diodes (ELEDs) and surface-emitting diodes (SLEDs).

ELEDs can be divided into two sub-groups; the low current devices and the superluminescent diodes, (SELEDs) [4]. SELEDs are high power devices capable of coupling 160mw (-8dBm) into singlemode fibre, (power coupled into multimode fibre would typically be 10-15dB greater). They need drive currents in excess of 100mA and require some form of temperature control to stabilise the power output, which can vary by upto 1dB/10°C. As a result of such large drive currents SELEDs have a shorter lifetime than would normally be expected for LEDs, device lifetime decreases approximately as the square of the operating current density [4]. Low current ELEDs typically couple 6µw (-22dBm) into singlemode fibre, while SLEDs typically couple 1.5µw (-28dBm) into singlemode fibre. Both low current ELEDs and SLEDs can operate over the temperature range -40°C to +85°C without cooling or power output stabilisation circuitry, thus making the associated electronics both simple and inexpensive.

3.2.1 Improving LED performance

LEDs typically operate upto 280Mbit/s although system operating at speeds upto 1Gbit/s have been reported in the laboratory [5]. These devices are specially fabricated for higher speed and are heavily zinc doped to reduce minority carrier lifetime, however they are not

currently commercially available. Special drive circuits using techniques such as "current peaking" and equalisation can be used to improve LED performance to data rates of upto 565Mbit/s [6]. High speed integrated LED drives are now becoming available which are capable of providing a 1Gbit/s drive signal.

3.3 Lasers

Semiconductor lasers can currently be grouped under two headings;

- * Low cost - designed for inter-office and local loop applications,
- * Long span - designed for high launch power and high speed.

Low cost lasers are achievable by one of two methods; either a low cost package is used, such as a receptacle type with no thermoelectric cooler or the laser is designed/selected for a low power output [7]. Lasers in these packages are capable of modulation at very high bit rates, in excess of 1Gbit/s, with typical power launched into singlemode fibre of 100µW (-10dBm).

Conventional high performance 1300nm lasers are available for operation upto 1.7Gbit/s and specially packaged lasers can be obtained capable of modulation at 2.4Gbit/s. Drive circuits for these very high data rates are currently being developed.

4 The Receiver

The basic requirements of a receiver as dictated by the general system requirements are give below:-

- i) Link lengths will be less than 1Km therefore a high receiver sensitivity is not required.
- ii) A wide dynamic range is important to allow for variations in path loss and launch powers.
- iii) Devices must be capable of operation at data rates up to Gbit/s.
- iv) A low parts count is desirable to keep costs down achieve high reliability and small size.

The receiver front end can be configured in one of three ways:- (i) High impedance (ii) Low impedance (iii) Transimpedance. Comparisons of front end noise performance, equalisation circuitry and dynamic range is shown in table 3. Both APDs and PINs are available for operation upto 2.4Gbit/s.

Table 3: Comparison of Receiver Front Ends

Front End	Noise performance		Equalisation required	Typical dynamic range*
	PIN	APD		
High impedance	Very good	Very good	Yes	~20dB
Low impedance	Poor	Good	No	~20dB
Transimpedance	Good	Very good	No	>20dB

* Dynamic range figures are dependant upon characteristics of individual receivers and the type of line code used.

A comparison of PINs and APDs is presented in Table 4 below.

Table 4: Comparison of PINs and APDs

Associated Circuitry	APD	PIN
	Large reverse bias voltages (> 40V) required for avalanche breakdown. Hence the need for dc-dc converters. Temperature control.	Single power supply. Hybrid modules are available that contain front end amplifiers. No temperature control.
Noise Performance	Good with all types of front end	Good except with a low impedance front end.

Tables 3 and 4 indicate that the PIN transimpedance receiver is the optimum solution for an in building optical interconnect since it offers a wide dynamic range (-20dB) coupled with simple control and bias circuits.

5 Fibre and Wavelength

Four fibre types can be considered for this application and a review of their properties is given below.

Multimode Step Index - This fibre is modal dispersion limited and has a typical bandwidth of 6-25MHz.Km.

Multimode Graded Index - Large bandwidth typically 1GHz.Km. Operation at 850nm using LEDs is not viable at 140Mbit/s due to chromatic dispersion. Large spectral widths of LEDs, typically 150nm results in a pulse broadening of ≈ 7 ns over 500m, while at 1300nm the pulse broadening would be ≈ 0.3 ns. Coupled power levels > -10 dBm are possible due to the large core size, ($> 50\mu$ m).

Singlemode - Very large bandwidth, no dispersion at 1300nm over the required distances. Low power coupled into fibre by LEDs, (typically < -20 dBm), due to small core size, ($\approx 9\mu$ m).

Plastic Fibre - Attenuation is typically 800dB/Km making it unsuitable for this application.

6 Summary of Possible Systems

In the near future the majority of in-building interconnections will operate at data rates between 2Mbit/s and 280Mbit/s, this is based on the current British Telecom hierarchy and a 1B2B line code which is currently considered suitable for in-building systems [3,8]. Therefore it would be more cost effective to design two systems;

- Designed for operation upto 280Mbit/s using low cost devices that will meet the requirements of the majority of in-building links.
- Designed for operation in the Gbit/s range to ensure total coverage of all in-building links.

However, if requirements indicate that a significant number of interconnections operate at 2Mbit/s, it would be possible to design a third system to meet this requirement using extremely cheap devices, e.g \$5 LEDs, thereby reducing interconnection costs further.

Possible system specifications are presented in table 5.

Table 5: System Component Breakdown

	(a)	(b)
Transmitter	Low cost laser/LED†	High speed laser
Data Rate	280Mbit/s	upto Gbit/s
Launch Power	-10dBm/-20dBm	-3dBm
Fibre	singlemode	singlemode
Receiver	PIN transimpedance	PIN transimpedance
Sensitivity	-32dBm	-24dBm*
Dynamic Range	>20dB	>20dB

† Low cost lasers are now comparable in price to LEDs designed for high speed operation.

* This is an estimated sensitivity.

7 Conclusions and Future Requirements

Short high speed optical links can readily be implemented using existing electro-optic devices. However, in order to achieve cost effective in-building networks it is necessary for two, or more, systems to be designed according to the data rate requirements.

The transmitter and receiver for both systems require the use of discrete components and it is at this level that developments can be made in future devices. Advances in hybrid transmitters and receivers have resulted in modular devices such as datalinks becoming available, however fully integrated chips for transceivers are desirable. Such chips would incorporate the laser and it's associated drive circuitry and the receiver together with it's front end amplifier. The integrated circuit could be housed in a small package requiring optical and electrical inputs/outputs and the necessary power supplies, giving ease of installation and operation, reduced size and cost and improved reliability.

Acknowledgements

The author would like to thank the Director of Research and Technology at British Telecom Research Laboratories for permission to publish this paper.

References

- 1 Y. Nagata, K. Ohnishi, and Y. Tachikawa, Rev. Elec. Commun. Labs. 29, No. 11-12, (1981).
- 2 M. Sumida, and H. Tsuji, IEEE J on Selected Areas in Comms, SAC-4, No. 9, (1986).
- 3 K. Hagimoto, J. Yamada, and N. Ohta, J Lightwave Tech., LT 2, No . 5, (1984).
- 4 E. I. Gordon and D. M. Fye, Lasers and Applications, pp43-49, (1987).
- 5 W. C. King, B. H. Chin, I. Camlibel, and C. L. Zipfel, IEEE Elec. Dev. Let., ed1-6, No 7, (1985)
- 6 J. M. Senior, Optical Fiber Communications Principles and Practice (Prentice-Hall International, 1985), pp. 391-393.
- 7 L. Bickers, P. K. ffitch, and P. Huff, presented at Lasers '87, Lake Tahoe (1987).
- 8 K. Hagishima, Y. Kobayashi, and K Aida, IEEE J on Selected Areas in Comms, SAC-4, No. 9, (1986).

THE PERFORMANCE OF LOW COST 1300 nm SEMICONDUCTOR LASERS

L Bickers, P K ffitch and P Huff

British Telecom Research Labs
Martlesham Heath
IPSWICH
IP5 7RE
UK

Summary

This paper describes the characterisation of four low cost 1300 nm semiconductor laser designs developed for interoffice telecommunication applications. Measured electrical and optical parameters are compared to the required performance specification both before and after 2000 hrs of life test. Two of the designs were found to suffer from gross failure mechanisms, whilst two met the specification in all respects.

1 Introduction

Semiconductor laser technology now provides a standard range of products for a wide variety of applications, from devices used in compact disk players (≈ 800 nm wavelength), to very reliable components for undersea optical systems with 20 year lifetimes [1]. In parallel with advances in semiconductor lasers, improvements in optical fibre over the last decade have resulted in many telecom companies operating large optical fibre long-line networks. It is also recognised that optical fibre transmission can compete with alternative solutions in the interoffice and local loop environments provided that the cost of the electro-optics and fibre is economic [2]. Due to the short distances of interoffice links (< 30 km), there is an ability to relax the transmitter and receiver device specification, enabling a simplification of device design. By considering the packages and production processes of 1300 nm lasers it is possible to identify areas where a relaxed specification will produce a cost reduction. As an example, a reduction in fibre pigtail output power from -3 dBm to -10 dBm (for a given drive current) allows for ease of fibre-laser alignment.

This paper describes a specification for low cost 1300 nm lasers, followed by a description of four packages designed to meet the specification. Tests results are presented on a batch of each design, including electro-optic performance and measurements from a 2000 hr life test.

2 Specification

The low cost 1300 nm laser specification is shown in table 1 below, it can be seen that six parameters are specified, together with three other requirements.

PARAMETER	SYMBOL	RATING	UNITS
OPERATING TEMPERATURE	Tc	-5 to 65	°C
FIBRE OUTPUT POWER	Pf	> 0.1	mW
RISE TIME	tr	< 3	nS
FALL TIME	tf	< 3	nS
WAVELENGTH	λ_p	1270 to 1330	nm
RELIABILITY @ 65°C	MTTF	> 10^5	hours
MONOMODE FIBRE (9/125 μ m) PIGTAIL			
INTEGRAL REAR-FACET MONITOR PHOTODIODE			
COST TARGET \leq US \$450			

TABLE 1 SPECIFICATION

The operating temperature is specified for an equipment rack inside a building, this coupled with the low output power requirement leads to a package design which does not require thermoelectric cooling. Rise and fall times give a maximum bit rate > 160 Mbit/s to encompass both European and North American standard digital line rates, below 160 Mbit/s.

3 Package Designs

Four designs were evaluated as shown in Fig 1 (a-d).

Three included a lens to focus the laser output into the fibre core, which was terminated in an FC connector end while the other design uses a lensed fibre held by a welded strap.

The cylinder designs employ hermetically sealed sub-modules which housed the laser and photodetector. A mixture of soft solder and spot welding was used to position the submodule with respect to the cylinder, design type C also contains three grub screws to hold the rod lens and FC connector end.

Dual in line type A consists of a 6 pin package containing electro-optic components together with a rod lens, held by epoxy to the fibre mounting. Type B used an integral package design containing all the elements for alignment and fixing.

A summary description is given in table 2 below.

DESIGN	LASER TECHNOLOGY	PACKAGE TYPE
A	BURIED HETEROSTRUCTURE (BH)	DUAL IN LINE
B	DOUBLE CHANNEL - PLANAR BURIED HETEROSTRUCTURE (DC-PBH)	DUAL IN LINE
C	BURIED CRESCENT (BC)	CYLINDRICAL
D	BURIED HETEROSTRUCTURE (BH)	CYLINDRICAL

TABLE 2 PACKAGE DESIGN SUMMARY

4 Electro-optic Performance

A series of electro-optic measurements were carried out as follows:-

- . Light current characteristics
- . Voltage at threshold
- . Forward resistance
- . Rise and Fall times
- . Spectral characteristics

Fig 2 gives examples of the light current characteristics which show the differences of slope efficiency and temperature performance for each design. The overall results are summarised in table 3 below.

DESIGN	RISE/FALL TIMES nS	THRESHOLD CURRENT mA AT 25°C	FIBRE OUTPUT $I_F = I_{TH} + 20mA$ μW	EFFICIENCY mW/mA	FORWARD RESISTANCE OHMS
A	< 1	27	232	0.01	4.6
B	< 1	40	154	0.01	5.6
C	< 1	10	563	0.025	7.0
D	< 1	16	446	0.02	5.0

TABLE 3 TYPICAL ELECTRO-OPTIC RESULTS SUMMARY

Fig 3 shows the typical variation of threshold current against temperature for each design, the BC device has the lowest threshold (< 20 mA at 60°C), while the BH types lie in

the range 30-40 mA and the DC-PBH is the highest at 90 mA. Although threshold current was not specified the effect on device thermal performance has to be taken into consideration and therefore a high threshold current is undesirable.

Fig 4 gives examples of the output optical spectra under CW conditions, each of the designs was found to operate within the specified wavelength range.

5 Reliability Evaluation

The objective of this evaluation was to identify any gross failure mechanisms which would occur with the laser or package design. Samples of each type of module were operated under CW conditions with a fibre output power of 200µw, this value was maintained during the test by adjusting the laser bias current to maintain a constant photodetector monitor power.

Failure mechanisms which are thermally accelerated have a characteristic activation energy E_a such that the time to failure 't' at a test temperature TK is given by the Arrhenius equation

$$\ln(t) = A + \frac{E_a}{kT}$$

where K is Boltzmanns constant
A is a constant

Due to the relatively low maximum package operating temperatures it was only possible to carry out tests at one temperature 65°C (normally activation energies are deduced from two or more test temperatures). In addition the short life test time of 2000 hrs only allows gross failure mechanisms to be deduced. A summary of the results is shown in table 4 below.

DESIGN	SAMPLE SIZE	CONDITIONS	DURATION HOURS	GROSS FAILURES	COMMENTS
A	4	200µw:65°C	1000	0	None
B	3	200µw:65°C	2000	3	Excessive bias current increase due to laser degradations
	1	150µw:65°C†	24	1	
C	4	200µw:65°C	2000	3	Fibre coupling failure and laser degradations
D	4	200µw:65°C	2000	0	None

† unable to obtain 200µW output

TABLE 4 SUMMARY OF RELIABILITY RESULTS

It can be seen from table 4 that one device in design group B failed after only 24 hrs while the other three also suffered gross failures. Group C also had three failures, due to fibre coupling failure.

Worst case lifetime predictions are shown in fig 5, where the "end of life" is defined by a 50% increase in laser threshold current. As indicated in fig 5 designs B and C show predicted lifetimes of 10^3 and 10^4 hours respectively while A and D indicate $> 10^5$ hours, (all at 65°C package temperature).

The gross failures identified in design type B were found to be due to laser degradation in the DC-PBH laser, the package was found to be satisfactory and it is expected that a change in laser structure would provide a suitable design solution. Design type C suffered gross failures in the fibre coupling mechanism, this could be attributed to movement caused by either the grub screws, soft solder, spot welding or a combined effect.

6 Conclusions

Four designs of low cost 1300 nm semiconductor lasers have been evaluated, these preliminary investigations indicate that two of the designs (B and C) suffer from gross failures associated with either the laser chip or fibre coupling. Two package designs (A and D) were found to meet the specification in every respect. It is therefore concluded that a significant cost reduction in 1300 nm lasers can be achieved, whilst still meeting the requirements of interoffice and local loop transmission systems.

Acknowledgements

The authors would like to thank the Director of Research and Technology at British Telecom Research Laboratories for permission to publish this paper.

References

- 1 T. R. Rowbotham, B.T. Tech. J., 5, No. 1, (1987)
- 2 P. Cochrane, R. D. Hall, J. P. Moss, R. A. Betts and L. Bickers, IEEE J. SAC - 4 No. 9, (1986)

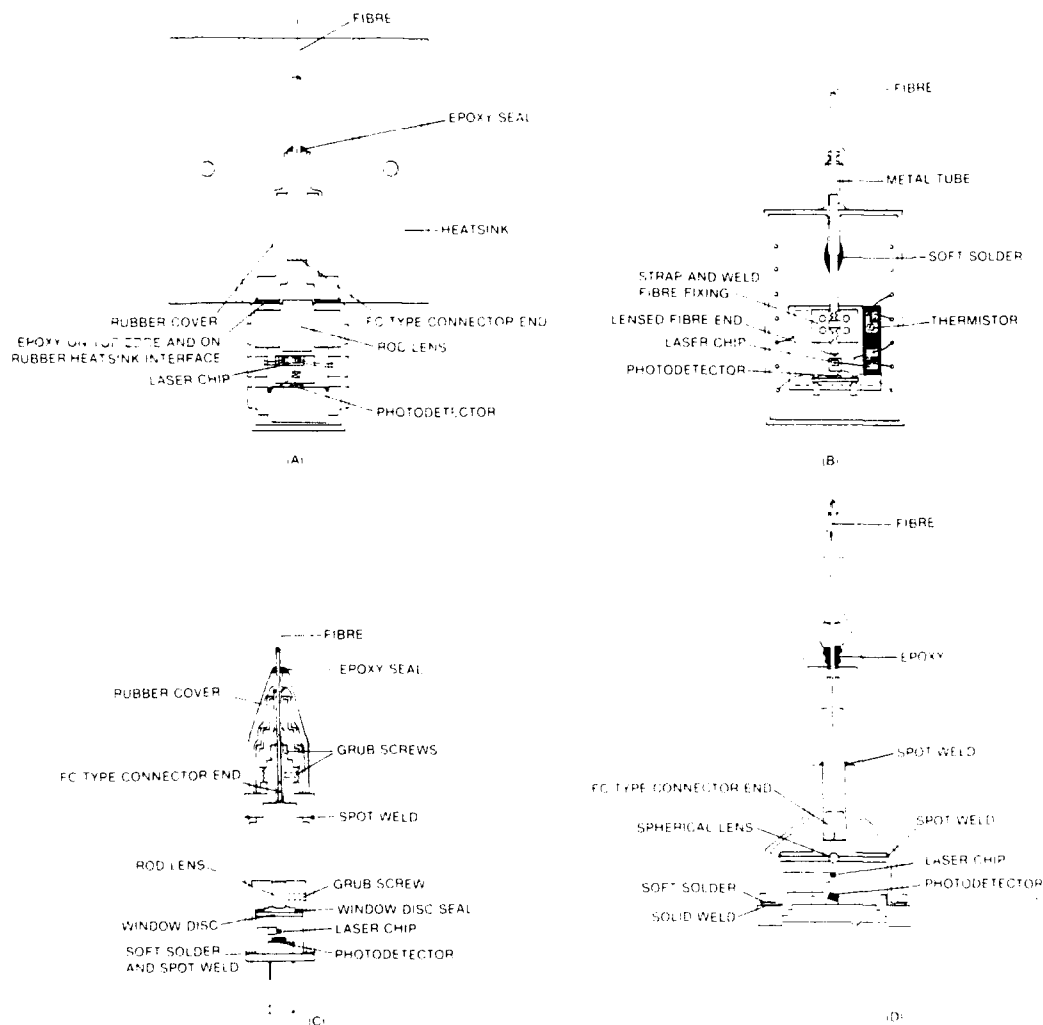
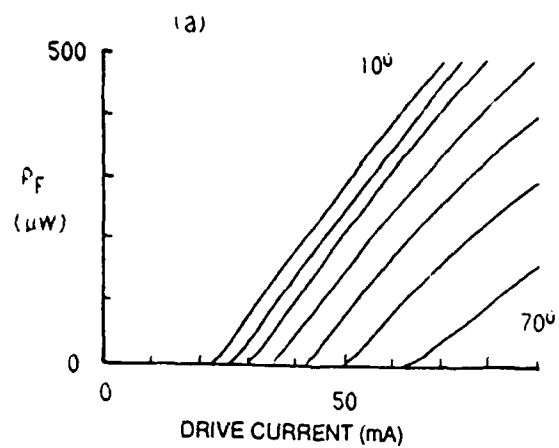
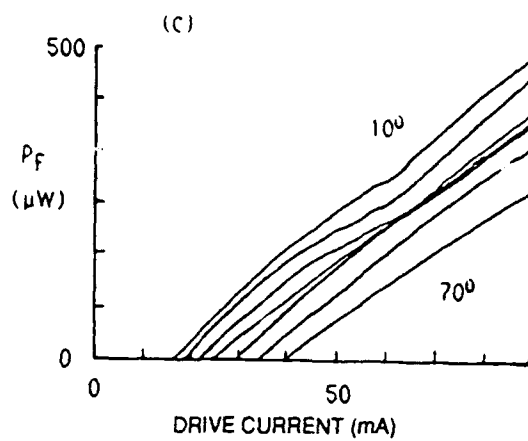


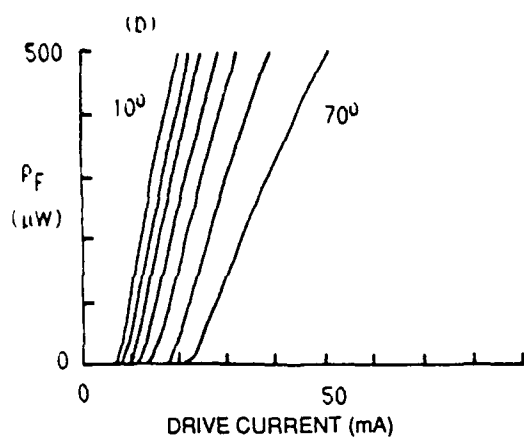
FIGURE 1 LASER DESIGNS



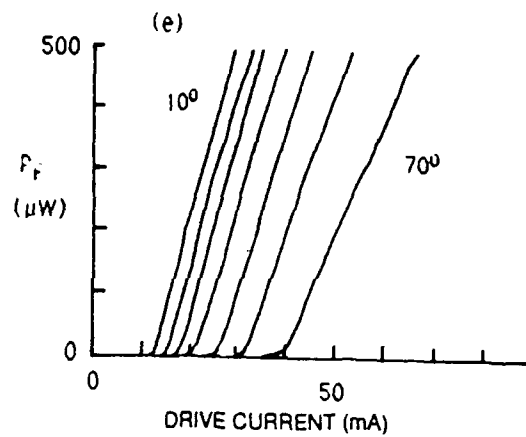
A)



B)



C)



D)

FIGURE 2 LIGHT-CURRENT CHARACTERISTICS

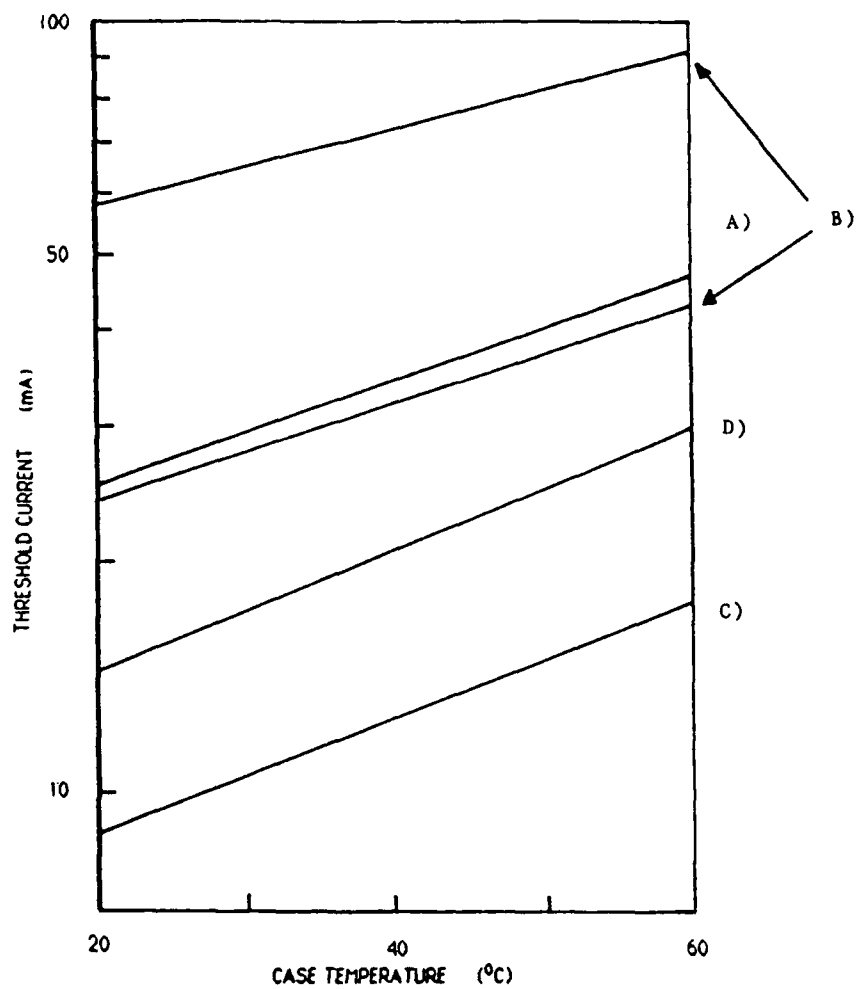


FIGURE 3 VARIATION OF THRESHOLD CURRENT WITH TEMPERATURE

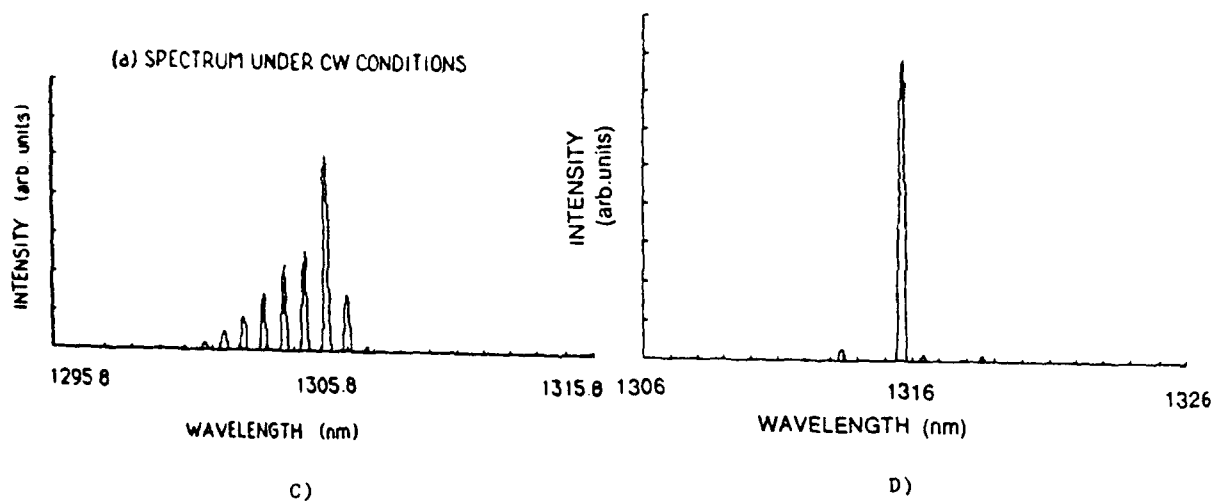
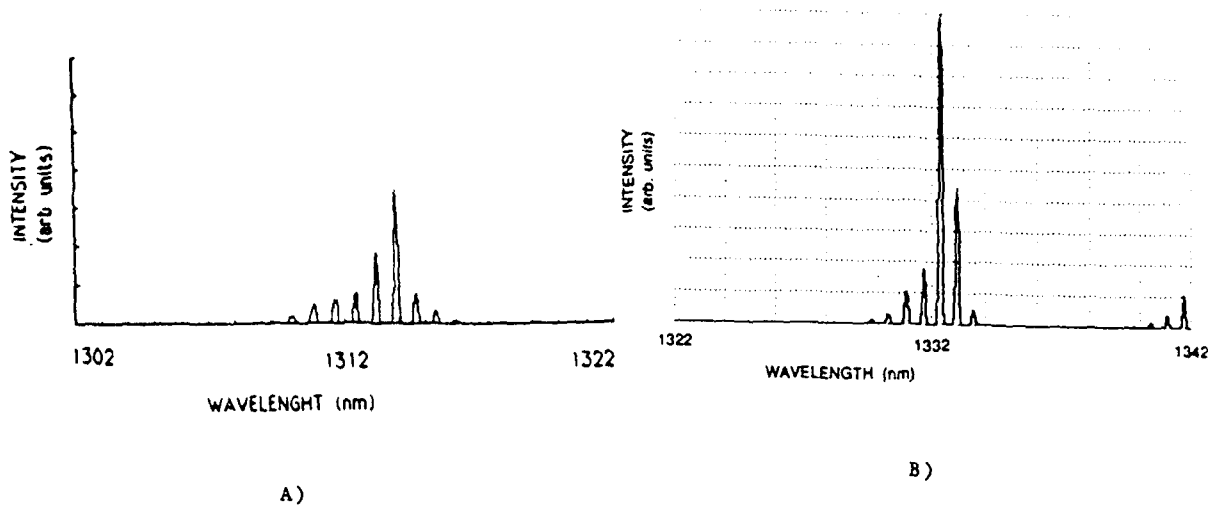
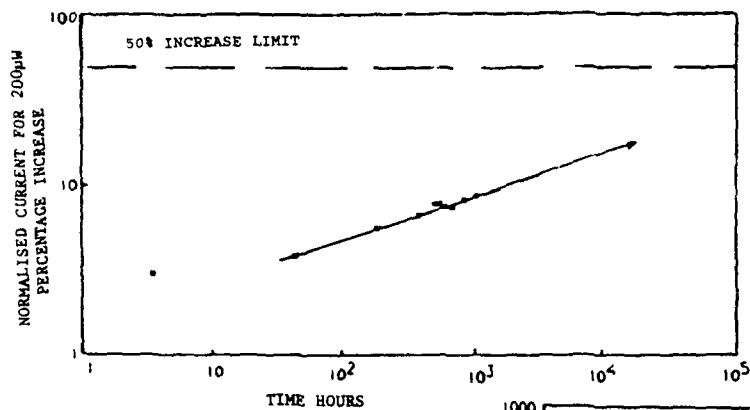
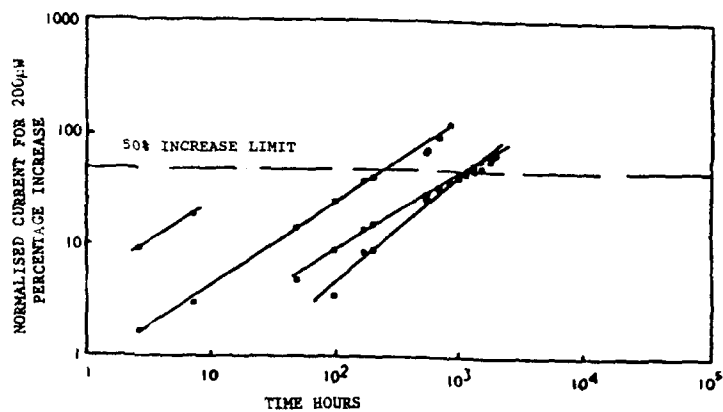


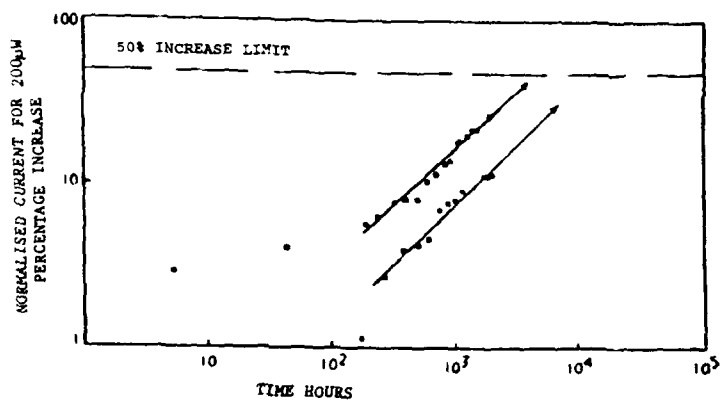
FIGURE 4 OPTICAL SPECTRA UNDER CW CONDITIONS



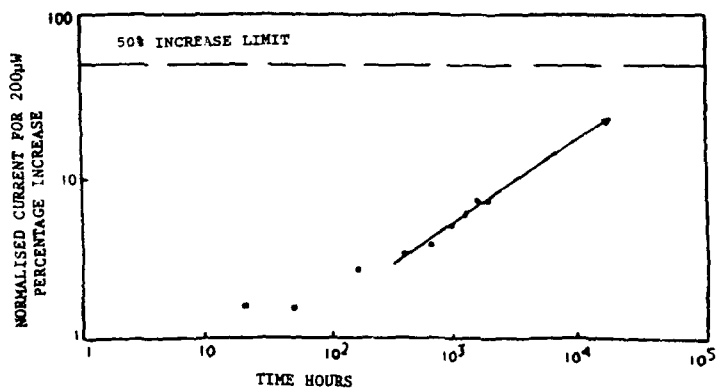
A)



B)



C)



D)

FIGURE 5 PREDICTED LIFETIMES

SELF-PROPELLED SELF-FOCUSING DAMAGE IN OPTICAL FIBRES

Raman Kashyap

British Telecom Research Laboratories, Martlesham Heath,
Suffolk IP5 7RE, United Kingdom

Abstract

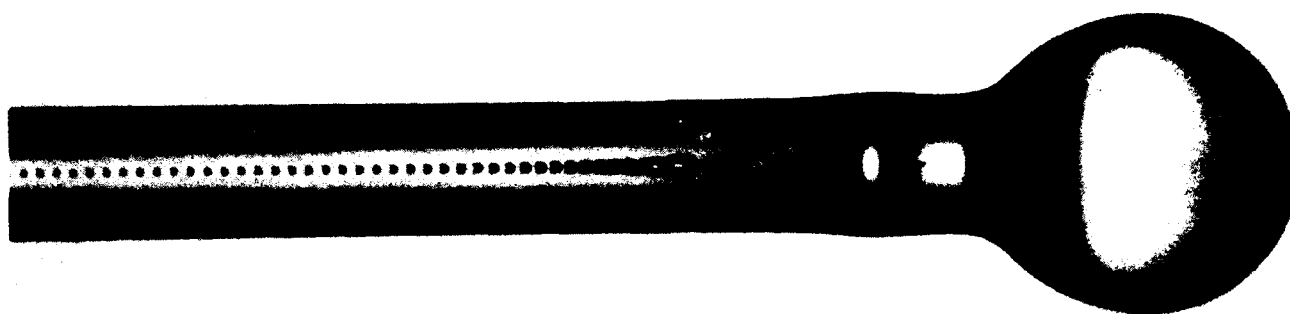
Self-focusing damage has been observed at optical power densities of 3 MW cm^{-2} (equivalent to ~ 0.5 watt) in single-mode silica optical fibres. This thermally driven phenomenon is self-propelled and has the effect of modifying the core of kilometer lengths of fibre. This paper reports on an experimental investigation into the nature and characteristics of the damage process which is accompanied by a blue-white plasma-like emission. Measurements performed on three different types of optical fibre have shown that the process is energy-density dependent. The damage results in the formation of regular cavities in the core of the waveguide, with dimensions of the order of a few wavelengths. These cavities have been shown to contain oxygen, being a chemical by-product of the damage. Further it is also demonstrated that the optical attenuation of the fibre increases rapidly above 1050°C . This is possibly due to an increase in conductivity of glass, which results in an increase in $\chi^{(3)}$ due to plasma formation. The plasma-like emission has a small temporal modulation corresponding to the formation of the cavities. Finally, it is demonstrated qualitatively with the use of a mode-locked laser that the temporal response of this thermally induced nonlinearity is in the sub-nanosecond regime. This damage process may have serious consequences for wide range of nonlinear-waveguiding devices and other fibre-based power delivery systems. Other materials for optical devices may well have damage power thresholds in the milliwatt region.

Introduction

The high damage threshold of single-mode silica fibre ($> 10\text{ GW cm}^{-2}$ [1]) has allowed the use of optical fibres for several nonlinear effects such as Raman amplification [1], soliton generation [2], ultrafast optical gates [3] and second harmonic generation [4]. The first experimental observation of self-focusing in multimode fibres using high-peak power pico-second pulses [5] has been reported, but no damage to the fibre was observed. Small-scale filament formation in dielectrics due to electronic self-trapping [6] and self-focusing damage in bulk laser materials [7] is well known. Self-focusing effects in liquids with a saturable nonlinear refractive index have also been studied using computer simulations [8]. Optical damage mechanisms involve stimulated Brillouin scattering [1] or, dielectric breakdown at high field strengths [9] using Q-switched and mode-locked lasers. Damage to optical fibres usually occurs at the launch end, where there is a finite probability of encountering contamination which then absorbs the laser energy causing the end to melt, or through intense stimulated scattering processes [1] the end fractures. Optical damage of fibres is of great concern to designers of power delivery systems in medicine and industry, and of high bit-rate non-linear devices. Power delivery systems, too, generally suffer end damage, and care needs to be taken in the safe design and operation of the fibre cables [10]. This paper presents measurements on what appears to be a new damage phenomenon in guided-wave optics which we call Self-Propelled Self-Focusing (SPSF) the observation of which was reported recently [11][12]. Optical power of about 1 watt average (10 MW cm^{-2}) in a single mode silica fibre is adequate to initiate and sustain a damage process which is accompanied by intense blue-white plasma-like emission and which propagates towards the source with devastating results for the fibre. More recently, this type of damage has been noted in fibres using Q-switched pulses of 150 ns at a repetition rate of 1 kHz and with an average power of only 0.2 watts. This process may have similarities to the degradation effects which causes catastrophic facet damage in semiconductor lasers [13], however, only melting of the laser material has been observed.

Optical Damage

Optical damage is initiated by launching about 1 watt of CW laser power into a single-mode fibre and simply heating a small section to its melting point, by using a fusion jointing machine, for example. Alternatively, the output end can be brought into contact with an absorbing surface, such as paint, metal or plastics. Some paints and metals work better than others. The contact causes local heating and initiates the damage process. Figure 1 shows the end of a fibre after the fusion-arc is struck. The spherical end of the fibre due to surface tension on melting is followed by a large drop shaped cavity. Successively smaller cavities are formed as a result of the temperature gradient, until after some distance, the damage stabilises to a more or less periodic restructuring of the core throughout the length of the fibre, and is shown in Figure 9. The photograph shows damage very similar to that seen in self-focusing in bulk materials and a possible mechanism based on nonlinear absorption [12] has been proposed whereby the melting of the glass increases the localised absorption and third-order nonlinearity, $\chi^{(3)}$. It is well known that the conductivity of glasses increases with temperature [14] which, probably results in

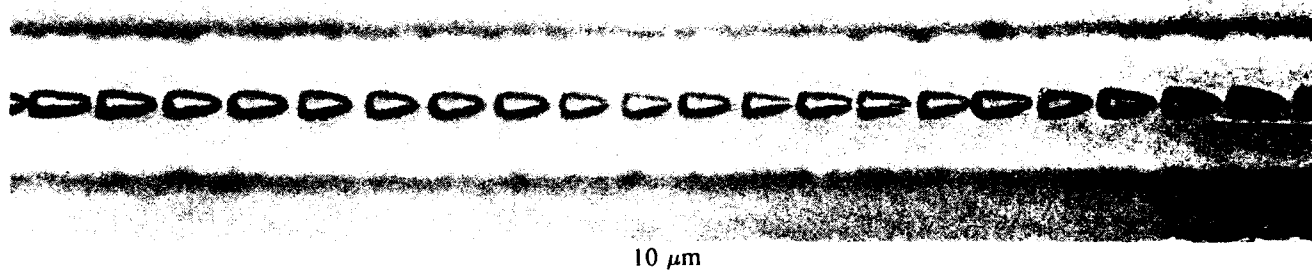


125 μm

Figure 1. Fibre end after fusion-arc is struck. The fibre melts to form the spherical end before damage process begins. The hollow cavities are the result of the damage.

plasma absorption. The detailed absorption mechanism is not understood, but measurements were performed to investigate the change in transmission characteristics of the fibre, which will be discussed later.

The shape of the damaged cavities is dependent on the state of the fibre. For example, with some of the cladding removed, as in a D-shaped fibre, the cavities are shaped more like arrow heads as shown in Figure 2. Heat diffusion must, therefore, govern the formation of the shape of the cavities.



10 μm

Figure 2. Periodic restructuring of the fibre core after damage for a fibre in which the cladding has been removed nearly exposing the core, as in a D-shaped fibre. Heat diffusion does have an effect on the shape of the cavity.

There is evidence to suggest that GeO_x and SiO_x are formed as a result of the damage process, with oxygen being liberated in the cavity. Subsequently heating a section of fibre locally causes the damage centres to coalesce forming a capillary as shown in Figure 3. The sudden expansion on heating of the cavities indicates that they are probably under some pressure.

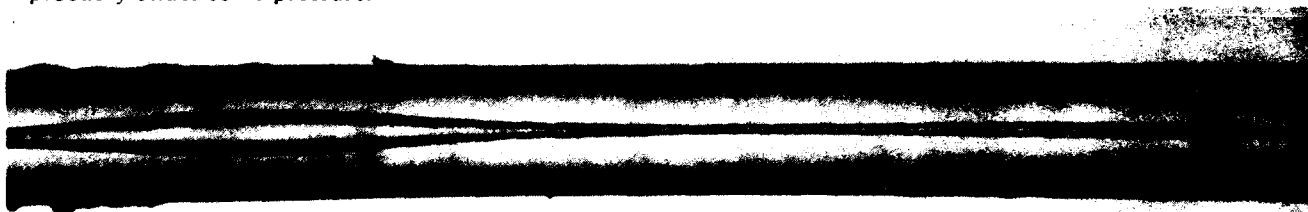


Figure 3. Expansion on heating a section of damaged fibre causes the cavities in the core to join, forming the capillary.

Micro-probe Raman studies were undertaken to detect the gases and identify the presence of sub-oxides. Initial results have shown that the cavities contain molecular oxygen at roughly 4 atmospheres pressure. The Raman spectra is shown in Figure 4 in which the characteristic vibrational band of oxygen at 1555 cm^{-1} is clearly resolved. The pressure was estimated by comparing the area under the curve with the spectra of atmospheric oxygen.

Measurements

A cw mode-locked Nd:YAG and an Argon laser were used to investigate the velocity of propagation of the

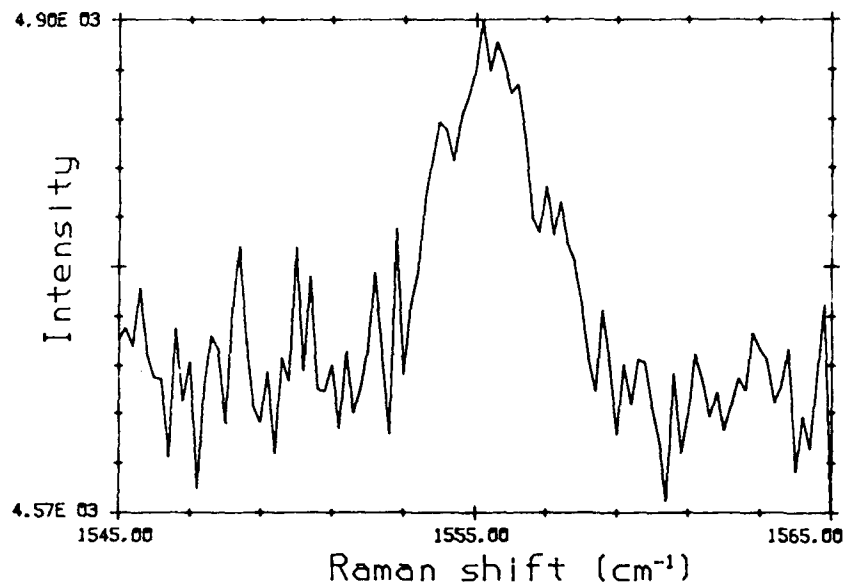


Figure 4. Raman spectra of gas in 4 μm cavity formed by the damage, showing a peak of oxygen at 1555 cm^{-1} .

damage process. The output of the laser was launched into a single-mode fibre using an optimised arrangement which enabled the continuous variation of both the numerical aperture and spot-size. An efficient launch into different types of single-mode fibre was thus possible. An optical attenuator comprising a $\lambda/2$ plate and polariser was used to select the launched power. The fibre was held in a silica V-groove in order to minimise thermal drift due to local heating of the fibre holder. The output was monitored by a power meter before each measurement. Two small area RCA silicon photodiodes with integrated fibre apertures, were placed one metre apart close to the output end of the fibre, which was stretched between them. The outputs of the photodiodes were used as triggers to start/stop an interval counter.

Three fibres A, B & C were used to compare propagation characteristics. The details of the fibres are shown in Table 1. The index profile, the core-cladding index difference, Δn , and the core radius were chosen to be different. These parameters determine the mode-field width of the optical power launched into the fibre at the laser wavelength. Several measurements were made with a Nd:YAG laser operating at 1.064 μm , both cw and mode-locked at average power levels varying between 0.7 to 2.4 watts. With an Argon laser operating at 514 nm measurements were made on fibre B for cw operation of powers ranging between 0.5 to 2.25 watts.

TABLE I : data on fibres

Fibre	Profile	Peak Δn	Core diameter	Spot size at 1.064 μm
A	step	4×10^{-3}	8.05 μm	6.04 μm
B	triangle	5.48×10^{-3}	5.40 μm	4.86 μm
C	triangle	8×10^{-3}	5.40 μm	3.94 μm

For the measurements reported in this paper, the process was initiated in two ways. An arc-fusion jointing machine was used to generate a high temperature at the output end of the fibre which was simultaneously carrying the laser power, or self-started by the heat generated on contacting the output end of the fibre with a painted or metalised surface. At 1.064 μm the initiation of the process was obvious, since an intense blue-white localised filament was seen propagating towards the launch end in the fibre. At 514 nm, the phenomenon is masked by the intense scattered visible laser radiation which, too, propagates backwards. However, the plasma-like emission is visible through the Argon line-blocking safety glasses. The start/stop trigger pulses are detected by the photodiodes as a result of the scattered radiation for both wavelengths.

Experimental Results

a. Damage Propagation:

In all over 70 measurements were performed and averaged. The data plotted in Figure 5 shows the velocity of propagation for each fibre with respect to output optical power, showing the linear relationship with different slopes. However, when the data is plotted with respect to power-density in the core, as shown in Figure 6, there

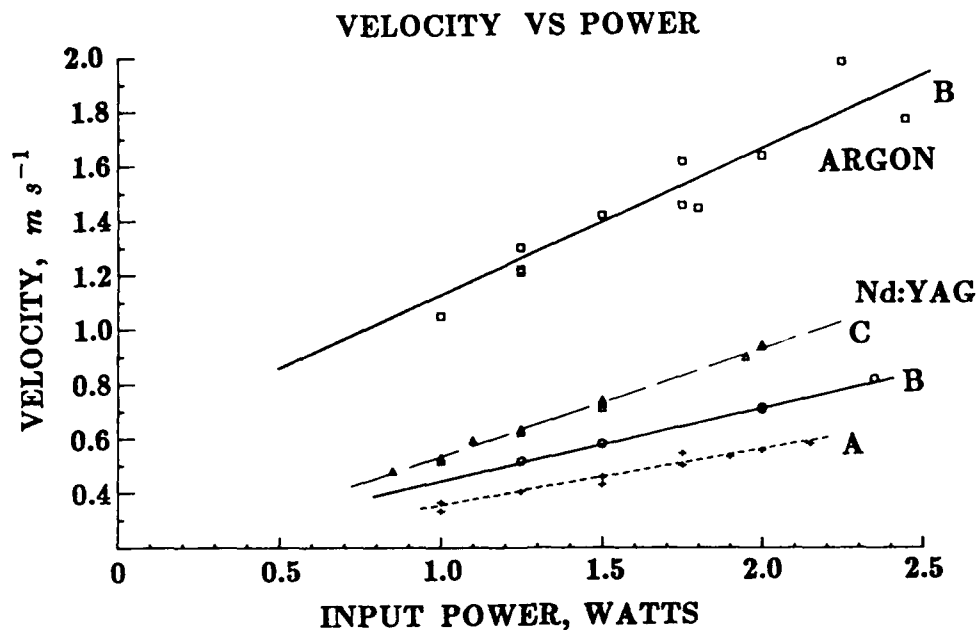


Figure 5. Velocity of damage propagation as a function of power in core for three fibres, A, B & C. There is a linear dependence on the input power, but it varies for each fibre and wavelength.

is a linear relationship with respect to the average power density in the core. The slopes in this case are virtually identical. The conclusion drawn is that the *energy density* required to cause the phenomenon is approximately constant for all the fibres. The slope is about $5 \times 10^{-12} m^3 J^{-1}$.

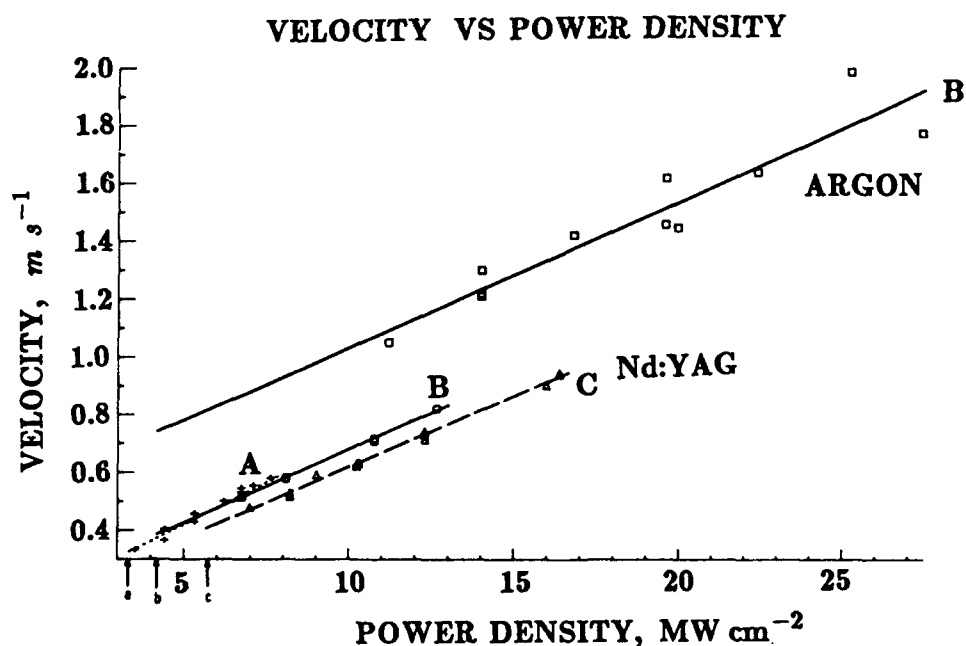


Figure 6. Velocity of damage propagation as a function of power-density in core for three fibres, A, B & C. Thresholds are indicated by a, b & c respectively. Note the near identical slopes for all measurements. It is thus concluded that the energy density required is constant for the damage process in silica fibres.

Based on the length of a damage centre of $5 \mu m$ and a nett absorption of 5% of the source power, the absorption coefficient, α , is calculated to be around $100 cm^{-1}$. The change in absorption as reflected by, α , indicates that the absorption is unlikely to be due to colour centre formation [15], since the absorption levels are far too large. It

is believed to be in part due to avalanche ionisation^[12] or increase in the conductivity of silica at elevated temperatures^[14]. Since the heat flow model is complex, a simple heat absorption calculation was performed to estimate the temperature rise, using the measured data presented here and, published data on the temperature dependence of the specific heat of silica and, allowing for the fusion energy for the formation of the sub oxides of germanium and silicon^[16]. This is around 2500 °C. However, a dynamic thermal-diffusion model using a finite element technique is being attempted to analyse the problem numerically, and will be reported elsewhere. Thresholds for sustaining the process were measured by reducing the input power until the damage propagation ceased. The thresholds are a function of the heat-diffusion time-constants which are inversely proportional to the square of the mode-field-width^[17]. Thus different thresholds for each fibre are expected. The accurate measurement of thresholds was difficult, owing to the coarse movement on the attenuator. However, the power density below which the damage was unable to propagate is indicated in Figure 6 for each fibre. The minimum level was about 3.2 MW cm⁻² corresponding to a minimum power of about 0.7 watts CW for fibre B.

The data for 514 nm is also shown in Figure 6. The presence of higher-order modes at the shorter wavelength makes normalisation difficult. The scatter in the data is the result of estimated field-widths used for calculating power-density. Again, the slope is identical to the YAG measurements, indicating similar functional behaviour. The threshold was in excellent agreement with the 1.064 µm measurement data for fibre A.

b. Nonlinear Absorption:

The mechanism involved in causing this phenomenon was thought to be related to increased absorption with temperature. Experiments were undertaken to measure the change in the throughput of a single-mode fibre, while the fibre was heated in a furnace. A one metre length of fibre was heated up to a temperature of 1100 °C, while monitoring the output power. The launched power at 1.064 µm was deliberately kept low so that increasing absorption with temperature would not cause erroneous results through optical heating. Figure 7 shows the attenuation as a function of temperature. There is a sharp increase in the loss around 1050 °C. Within 50 degrees, the attenuation increases by nearly 2000 dB km⁻¹ ($\sim 4.6 \times 10^{-3}$ cm⁻¹). At slightly elevated temperatures this seemingly exponential rise in attenuation would cause the power in the guided mode to be absorbed strongly over a very short length. It is thought that there is a corresponding increase in the third-order nonlinearity which causes self-focusing.

SINGLEMODE FIBRE ABSORPTION

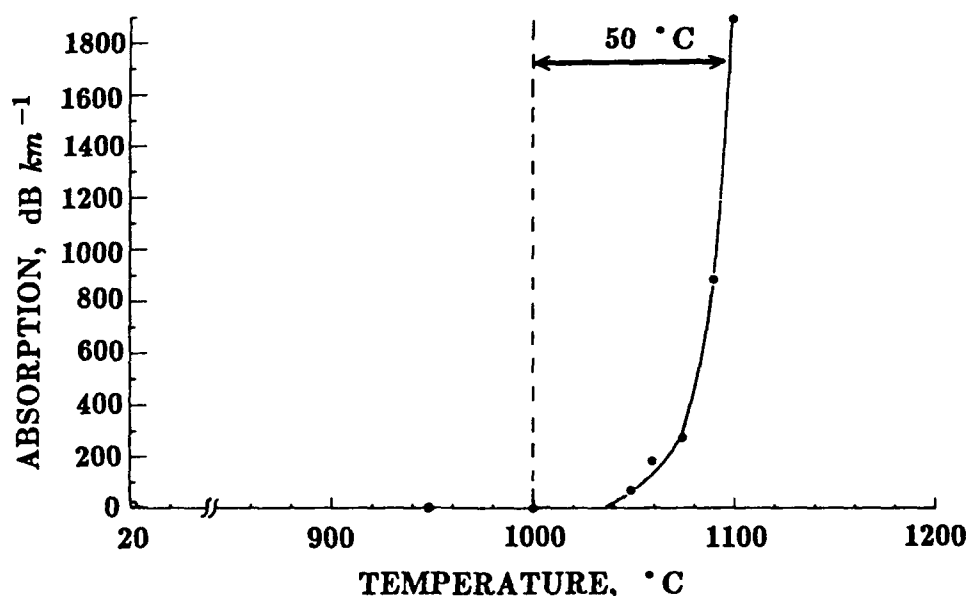


Figure 7. The absorption in single-mode fibre as a function of temperature. There is a dramatic increase above 1050 °C probably as a result of the increase in the conductivity of glass.

c. Periodic Emission:

Another experiment was performed on fibre B to detect the periodic formation of the damage centres. It was postulated that the plasma-like emission must have a modulation which would be a function of the rate of formation of the cavities. The fibre was inserted into an aluminium housing through a fine-bore capillary, so that it passed in front of a photo-multiplier tube (PMT), and out again through another similar capillary. The aluminium housing thus formed a light-tight enclosure for the PMT. With the power launched into the fibre, the damage was started just beyond the exit capillary of the housing. The output of the PMT was displayed on a 125

MHz transient digitising oscilloscope, which recorded the data as the damage swept across the face of the PMT. Filters were inserted in front of the fibre to adjust the light level incident on the PMT to ensure linearity of the output.

Several attempts were made to capture the modulation. The measurements proved to be temperamental, but the structure on the output did correlate with the damage centres. Figure 8 shows the transient digitising oscilloscope output, both unexpanded and in a smaller time window. The modulation of the light emission can be seen on a background of ambient emission, but with a small modulation-depth. This is not unsurprising; it is likely that the dynamic temperature variation remains small since the emission temperature is dominated by heat diffusion, which would tend to reduce the fluctuations.

The temporal separation between the centres as determined from measurements made on propagation velocity was approximately $33 \mu\text{s}$ (shown in the inset) for the power launched into the fibre. The measured modulation in the plasma-like emission also had a period of $33.3 \mu\text{s}$, in good agreement with the periodicity of the damage centres.

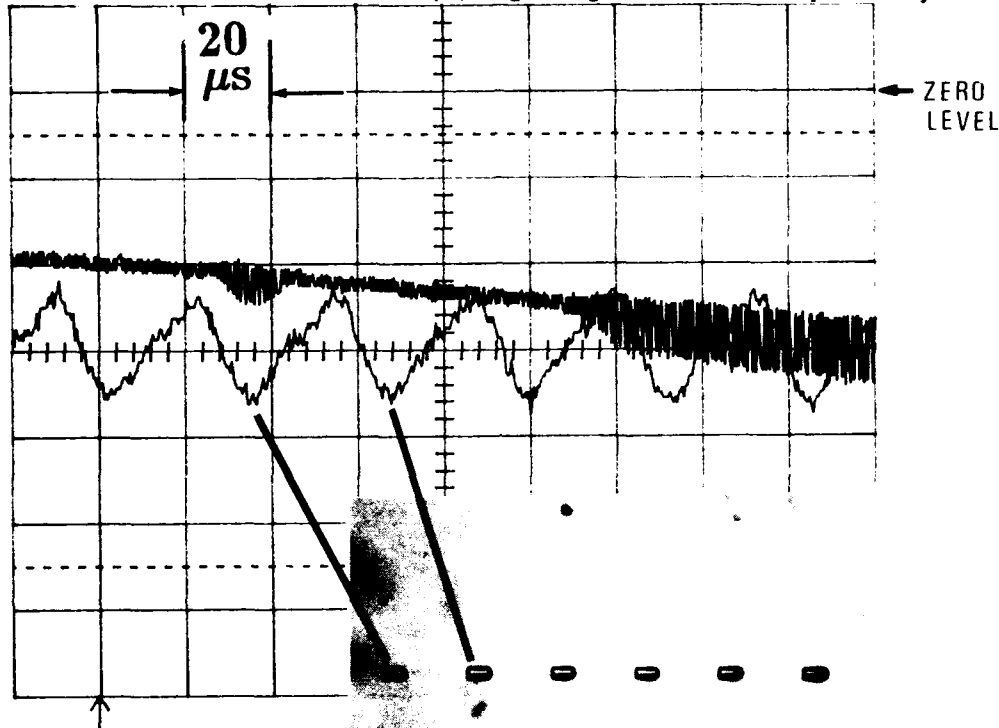


Figure 8. Data on unexpanded and expanded scale recorded on transient digitiser showing periodicity in emission of light during formation of cavities. Also shown in the inset is the region of the fibre from where the emission was captured. The cavity separation is about $33 \mu\text{s}$.

d. Temporal Effects:

Mode-locking has little effect on the velocity of damage propagation for all three fibres, but does alter the shape of the damage centres slightly. It is difficult to assess accurately the relationship between their shape, the optical pulse-widths, and the average power. But it is related to the thermal-diffusion time-constants and probably low frequency statistical fluctuations in the optical power density and local, but periodic, variations in the waveguide. It is possible to observe qualitatively the variation in the formation of the cavities with respect to the input power conditions. Figure 9a shows the type of cavities which are formed, separated by $14.8 \mu\text{m}$ when the input power is 2 watts CW for fibre A. The cavities are large drop shaped with a rounded front end. They have however, a sharp truncated tail end. The sharp boundary at the tail end is a type of feature observed in all samples examined so far. For 190 ps (FWHM) mode-locked pulses, the cavities are larger in diameter, albeit shorter in length (Figure 9b). Finally, for 100 ps mode-locked pulses, the cavities become bell like with a longer pointed front end but with a smaller average diameter (Figure 9c). These observations show that the effect is sensitive to the temporal characteristics of the input optical power, down to the narrowest pulses of 100 ps FWHM used in our experiments. It is concluded that the nonlinearity is likely to have a fast response, possibly in the picosecond region.

Discussion

These observations raise serious questions as to the operational safety and testing of optical guided-wave devices and power-delivery systems. The average power density in the fibre was about 10 MW cm^{-2} . Consequently, it



Figure 9. Temporal dependence of cavity formation. 'a' is data for cw power, 'b' for 190 ps and 'c' for 100 ps FWHM pulses. All data is for 2 watts average. The sensitivity of the cavity shape indicates that the effective nonlinearity has a sub-nanosecond response time.

puts a very low limit to the average power density in single-mode guided-wave devices, above which they will be potentially at risk of destruction. For low melting point device materials, the limit is likely to be even lower. The mechanism is also likely to be manifest in other waveguide structures such as those used in integrated-optics, and especially prone will be power delivery systems.

This phenomenon does, however, allow the investigation of laser damage processes in different materials in a 'controlled' manner. It would also allow damage investigation of specific materials by their introduction in the core of waveguides. Sandwiching thin slivers of new materials between the ends of optical fibres during the damage process may allow assessment of their suitability for optical devices.

Many fibre based applications areas using high average powers are susceptible to catastrophic damage. A type of optical-device structure using the evanescent field interaction with overlays of metals or non-linear materials, such as the fibre half-coupler block ^[16], must be used with care with high average powers to ensure its integrity.

The fast growing field of fibre-lasers ^[16] is another area where there could be a potential hazard, since the pump and cavity powers used can be high. Future fibre-lasers may well generate high powers, and thus be susceptible to such damage.

A more fundamental question arises on the origins of the absorption mechanism. The absorption is estimated to be modest. The present estimate suggests only a fraction of the optical power (5%) is being absorbed. If this were to change, for example, by the introduction of dopants or by the use of other device materials then the threshold can potentially be in the milliwatt region, causing concern for many device users.

Conclusion

In conclusion, observations on the damage to optical fibres due to self-propelled self-focusing show that long lengths can be rendered useless as a result of this process. Measurements on the velocity of damage propagation in optical fibres shows a linear dependence on power-density, with a threshold of around 3 MW cm^{-2} . Optical fibres and guided-wave components using average powers of 0.5 watt will thus be potentially at risk of failure.

Acknowledgements

The author gratefully acknowledges C A Millar, R Wyatt and K J Blow for discussions, M Dixon of Newcastle Polytechnic for providing the Raman scattering data, Peter Zory for pointing out reference [13] and the Director of Research and Technology, BTRL for permission to publish this paper.

REFERENCES

1. Stolen R H, in "Optical Fibre Communications", Miller S E & Chynoweth A G, eds., Academic Press, 1979.
2. Doran N J Blow K J, IEEJ Quant Elec 19, 1883, 1983.

3. Halas N J, Krokell D & Grischkowsky D, *Appl Phys Lett*, 50 (14), 6 April 1987.
4. Osterberg U, Margulis W, XIV Intern. Quant. Electr. Conf. IQEC 86, Tech. Digest. p102, San Francisco, 1986.
5. Baldeck P L, Raccia F & Alfano R R, *Opt. Letts.*, 12 (8), Aug 1987.
6. Alfano R R & Shapiro S L, *Phys Rev Letters*, 24 (11), 16 March 1970.
7. Giuliano C R & Marburger J H, *Phys Rev Letts*, 27 (14), 4 Oct 1971.
8. Dawes E L & Marburger J H, *Phys Rev*, 179 (3), 15 March 1969.
9. Yablonovitch E & Bloembergen N, *Phys Rev Letts*, 29 (14), 907-910, 2 October 1972.
10. Ishiwatari H, Ikeda M & Tateishi F, *Journal of Lightwave Technology*, LT-4 (8), 1273-1279, August 1986.
12. Kashyap, R & Blow, K J, Eighth National Quantum Electronics Conference, Post Deadline (Poster) Session PD7, Univ of St Andrews, UK, Sept 21-25, 1987.
12. Kashyap R & Blow K J, *Electronics Letters*, 24 (1), pp 47-48, 7th January 1988.
13. Henry C H, Petroff P M, Logan R A and Merritt F R, *J Appl Phys*, 50 (5), May 1979.
14. See for example, Sherwood E M in "High Temperature Technology", ed. Campbell I E, pp254, John Wiley & Sons, 1956.
15. Yashima H, Mitera H and Itoh Y, *Electronics Letters*, 19 (1), pp11-12, 6th January 1983.
16. CRC Handbook of Chemistry and Physics, 52nd Ed., pages D-49 and D-60, 1971-1972.
17. Carslaw H S and Jaeger J C, "Conduction of Heat in Solids", 2nd ed., Oxford University Press, 1978.
18. Kashyap R and Nayar B K, *Journal of Lightwave Technol.*, LT-1, January 1983.
19. Reekie L, Mears R J, Poole S B & Payne D B, *Journal of Lightwave Technology*, LT-4 (7), pp 956-960, July 1986.

SOLVATION AND TWISTED INTRAMOLECULAR CHARGE TRANSFER IN AMINOPHENYL SULPHONES

John D. Simon*, Shyh-Gang Su, and Matt Banet
Department of Chemistry and Institute for Nonlinear Studies
University of California at San Diego, La Jolla, CA 92093

Abstract

The dynamics of solvation in several polar solvents are studied by measuring the time resolved Stokes shift of the emission of the excited TICT state of 4,4'-dimethylaminophenyl sulphone. In addition to the experimental measurements, results from molecular dynamics simulation techniques are presented. The observed solvation dynamics cannot be accounted for by theories which model the solvent as a dielectric continuum. The experimental and simulation results clearly demonstrate the importance of molecular aspects of the solvation process.

Introduction

Interest in the molecular motions associated with chemical reactions in solution has prompted an effort to understand the dynamics of solvation. The effect of macroscopic solvent parameters (i.e. viscosity, polarity) on chemical dynamics has been extensively studied for many decades.¹ Correlations between rate constants and many such solvent variables have been reported.²⁻⁴ These studies indicate that to some extent, solvent effects on chemical reactions can be accounted for by the changes the solvent induces in the potential energy barrier and free energy of reaction.

In recent years, these issues have received considerable theoretical⁵⁻¹² and experimental¹³⁻¹⁵ attention. Advances in statistical mechanics have resulted in new treatments for equilibrium solvation which take into account molecular details of the solvent.^{16,17} However, for nonequilibrium processes, the solvent is generally described as a dielectric continuum.^{18,19} In this treatment the solvent is modeled as a structureless fluid with a frequency dependent dielectric constant, $\epsilon(\omega)$, which is usually expressed in the Debye form, equation (1).

$$\epsilon(\omega) = \epsilon_{\infty} + \frac{\epsilon_0 - \epsilon_{\infty}}{1 + i\omega\tau_D} \quad (1)$$

In the above expression, ϵ_{∞} and ϵ_0 are the high frequency and zero frequency dielectric constants, respectively; τ_D is the Debye relaxation time. Most solvents have a more complex dielectric response than given in equation (1). In the case of the normal alcohols, $\epsilon(\omega)$ is generally expressed as a sum of three regions of Debye-like behavior.^{20,21}

$$\epsilon(\omega) = \epsilon_{\infty} + \frac{\epsilon_{10} - \epsilon_{1\infty}}{1 + i\omega\tau_{D1}} + \frac{\epsilon_{20} - \epsilon_{2\infty}}{1 + i\omega\tau_{D2}} + \frac{\epsilon_{30} - \epsilon_{3\infty}}{1 + i\omega\tau_{D3}} \quad (2)$$

The three Debye relaxation times are commonly associated with the following molecular motions:²⁰ hydrogen bonding dynamics in molecular aggregates, τ_{D1} , monomer rotation, τ_{D2} and rotation of the terminal C-OH group, τ_{D3} . In addition to the Debye time, a second relaxation time, the longitudinal relaxation time, or constant charge relaxation time, τ_L , is commonly used to gauge dynamical solvent effects. The functional form for τ_L varies slightly depending on the nature of the perturbation and the value used for ϵ_{∞} (n^2 or $\epsilon_{1\infty}$).^{15,22} for the case of a point charge, τ_L is related to τ_D by $\tau_L = \frac{\epsilon_{\infty}}{\epsilon_0} \tau_D$.^{18,22-26} In polar solvents $\epsilon_0 \gg \epsilon_{\infty}$ and thus $\tau_L \ll \tau_D$. There have been several recent discussions of the importance of τ_L as a gauge of solvent dynamics. In particular, Kosower and coworkers¹⁵ have reported that the intramolecular charge transfer rates of several molecules are well correlated with τ_L^{-1} .

In this paper, nonequilibrium solvent relaxation processes are monitored by examining the time dependence of the emission spectrum of a dissolved probe molecule. In general excitation to an excited electronic state results in a change in the permanent dipole moment (magnitude and/or direction) of a molecule. The Franck-Condon principle assures that the formation of the excited state will occur on a time scale much faster than any nuclear rearrangement of the environment. As a result, the excited state species will be formed out of equilibrium with its surroundings. With increasing time, the solvent restructures, responding to the demands of the new charge distribution. This results in a lowering of the energy of the excited state, and is revealed by a red shift (or Stokes shift) in the emission spectrum.

*NSF Presidential Young Investigator

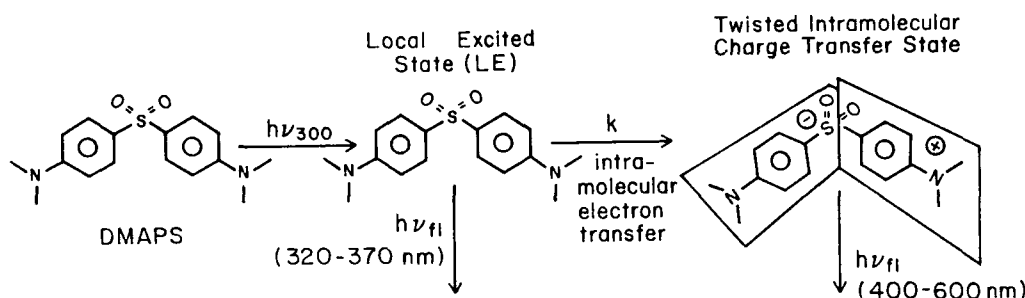
Studies on the time dependent Stokes shift have been reported for several molecules in a variety of polar solvents.²⁷⁻³⁶ In addition to states populated by direct excitation, solvation dynamics have been probed using emission from excited states populated by rapid intramolecular electron transfer^{28,37} and proton transfer³⁸ reactions.

The following correlation function is used to quantify the time dependent properties of the emission spectrum.^{36,39,40}

$$C(t) = \frac{v(t) - v(\infty)}{v(0) - v(\infty)} \quad (3)$$

In the above expression, $v(t)$, $v(0)$, $v(\infty)$ are the emission maxima at time t , zero and infinity, respectively. Thus, $C(t)$ is a function that is 1 at time $t=0$ and decays to 0 as $t \rightarrow \infty$. The time-dependent behavior of $C(t)$ provides a means of examining the relaxation of the surrounding environment on a microscopic level.

In this paper, we examine the dynamics of solvation by monitoring the time dependent Stokes shift of the emission from the twisted intramolecular charge transfer (TICT) state of dimethyl aminophenyl sulphone (DMAPS).^{27,28} The photophysics (and structure) of this class of molecules are shown in Scheme 1.



Scheme 1

Theoretical Models Connecting $C(t)$ and Solvent Relaxation

The simplest theoretical model for understanding the underlying solvent dynamics which cause the evolution of the emission spectrum would be to consider a dipole in a spherical cavity embedded in a dielectric continuum.^{39,40} If the frequency dependent dielectric constant $\epsilon(\omega)$ is expressed as in equation (1), it has been shown that $C(t)$ decays exponentially with a time constant of the longitudinal relaxation time of the solvent, τ_L . More detailed dielectric continuum treatments by Madden and Kivelson¹⁸ show that for solvents characterized by an $\epsilon(\omega)$ of the form given in equation (1) the relaxation should be biexponential, with time constants of τ_L and τ_D . Relaxation at some single intermediate time has been discussed by Nee and Zwanzig.⁴¹ All of these models attribute the relaxation of the solvent polarization to rotational motion. In solvents which are characterized by slow orientational relaxation, the dominant mechanism for solvent equilibration could involve translational motion of the solvent dipoles. This phenomenon has been termed polarization diffusion. Theoretical work by van der Zwan and Hynes predicts that this relaxation mechanism will dominate when the ratio $D\tau_D/R^2 > 1$.^{28,42,43} In this expression D and R are the self diffusion constant of the solvent and the cavity radius of the dipole, respectively. In this case, $C(t)$ is predicted to be nonexponential and relaxes to $1/e$ of its initial value on a time scale much faster than τ_L .

In addition, molecular theories^{7,9,10,44} and molecular dynamics studies^{32,45,46,57} of solvation have been reported. For medium size molecules, one expects that the majority of the relaxation takes place in the first few solvent shells. Thus, the molecular nature of the nearby solvent shells must be considered. The contribution of a range of relaxation times between τ_L and τ_D resulting from the molecular nature of the solvent was first proposed by Onsager in discussing solvation of a charge.²⁴ Near the charge, the solvent dipole would need to rotate, a time similar to τ_D . With increasing distance, the continuum model would become applicable and the time scale for relaxation of the polarization would approach τ_L . Modeling the solvent as a nonequilibrium distribution of dipoles Calef and Wolynes were able to demonstrate that the time scale for solvation around a charge depended on the distance from the charge.⁷ Nearby, a time similar to τ_D was found. With increasing distance $\tau_S \rightarrow \tau_L$. The average relaxation time (which would correspond to the experimentally observed dynamics) was nonexponential and had a $1/e$ decay time between τ_L and τ_D but closer to τ_L . Loring and Mukamel have also examined charge solvation.⁹ Expressions for calculating the solvent response are presented and results similar to the Calef and Wolynes treatment are found. Friedrich and Kivelson recently examined the effect of both a stationary and moving ion on the time dependent polarization of a dipolar solvent.⁴⁴ This work also demonstrates that the relaxation dynamics are dependent on geometric properties of the solvent molecules.

Wolynes has recently examined nonequilibrium solvent dynamics of an ion in a polar solvent.¹⁰ Solvation was found to occur on a range of time scales. However, to a good approximation, the results could be summarized by introducing a second relaxation time, τ_G , in addition to τ_L , which takes into account the cavity radius of the ion, r_c and the diameter of the solvent molecule, D_s .

$$\tau_G^{-1} = \tau_D^{-1} \frac{1 + 1/2(r_c/D_S)(\epsilon_0 + 3)}{1 + 1/2(r_c/D_S)(\epsilon_\infty + 3)} \quad (4)$$

The importance of τ_G to the observed solvation dynamics depends on the polarity of the solvent and the ratio of the volume of the ion to the solvent molecule. For $r_c/D_S \gg 1$, τ_G is similar to τ_L . However, for $r_c < D_S$, τ_G becomes comparable to τ_D . In addition, if the solvent is weakly polar, τ_G will also be close to τ_D . Even though this treatment focuses on charge solvation, the general physical conclusions should apply to the dynamics explored through $C(t)$.

Experimental

A frequency doubled CW:Nd³⁺:YAG laser is used to synchronously pump a rhodamine-6G dye laser. At 600 nm, an output power of 100 mW is obtained. Autocorrelation using a noncollinear optical arrangement indicates a pulse width of approximately 1.0 ps (FWHM).

The dye laser output is amplified using a three stage longitudinally pumped pulsed dye amplifier. The driver is a nanosecond Nd³⁺:YAG laser, providing 130 mJ at 532 nm at a repetition rate of 20 Hz. Rhodamine-640 in methanol is used as the amplifying medium. Saturable absorber jets of crystal violet in ethylene glycol are used to isolate the stages of the amplifier. The output pulse is approximately 1 ps (FWHM), 1-2 mJ/pulse, $\pm 10\%$ pulse-pulse fluctuation, at a repetition rate of 20 Hz. The pulse energy to amplified spontaneous emission (ASE) is better than 100:1.

The output of the amplifier is frequency doubled using a 0.2 cm angle tuned KDP doubler. A weak reflection of the remaining red light is focused onto an FND-100 photodiode, the output of which triggers the streak camera. Both the UV and remaining red beam are sent down optical delays of approximately 30 ft. This is made necessary by the internal delay in the streak camera. The UV is passed through a polarizer and focused onto the sample. The cell is masked so that emission over a 0.2 cm region is imaged onto the detector. The red light travels a slightly shorter delay than the UV and is used as a timing marker for signal averaging (prepulse). Fluorescence is collected 90° from excitation. The light is collimated and passed through a second polarizer which can be oriented parallel, perpendicular, or at magic angle with respect to the excitation light. The light is then focused on the input slit of a Hamamatsu C979 streak camera. Quartz input optics are used to record emission from 300 to 340 nm. The streak camera output is recorded by a Reticon detector connected to a high speed parallel computer interface. The data is transferred to an LSI-11/23+ computer system via a parallel DMA interface.

In order to control the sample temperature, a brass flow cell is used. This cell was connected to a closed cycle recirculator. The temperature of the cell could be varied over the range from -70 to +40°C. The sample temperature was monitored by a thermocouple and was stable to $\pm 0.2^\circ\text{C}$.

4,4'-Dimethylaminophenyl sulphone was synthesized by refluxing 4,4'-diaminophenyl sulphone with methyl phosphate in ethylene glycol for about 72 hours. The product was purified by repeated recrystallization from dioxane. The purified crystals were characterized using NMR spectroscopy and found to be the desired material. All solvents were dried over molecular sieves and checked for background fluorescence. Samples were purged with nitrogen and sealed with parafilm.

Static fluorescence spectra were recorded using a 1/4 meter monochromator coupled to a Reticon detector. Corrected spectra for several samples were recorded on a SPEX fluorolog. Comparison of the spectra enabled us to determine the correction factors for the monochromator-Reticon system. Data analysis was carried out on a Sun 3/110 computer system using nonlinear least squares analysis programs.

Time Dependent Stokes Shift Measurements

In Figure 1, time dependent emission spectra at several times after excitation for DMAPS in ethanol at -20°C are shown. The experimental details used to obtain these spectra are described in references 27 and 28. As can be seen in Figure 1, the emission spectrum shifts to decreasing energy with increasing time after excitation; the total shift is on the order of 40 nm. Static fluorescence data indicate that excitation to the TICT state of this molecule results in a large change in direction ($\approx 90^\circ$) and magnitude (≈ 10 D) of the permanent dipole moment.⁴⁷ From these data, $v(t)$ is extracted (insert in Figure 1). To generate $C(t)$, $v(0)$ and $v(\infty)$ need to be determined. Due to the finite time resolution $v(0)$ is extremely difficult to measure. Some recent subpicosecond studies³⁴ suggest that even on such a short time scale, a fast component of the response may be missed resulting in a misassignment of $v(0)$. On the other hand, $v(\infty)$ can be determined in an analogous manner as $v(t)$. In Figure 2, $\ln[C(t)]$ is plotted for DMAPS in ethanol at -20°C. For comparison, $-t/\tau_L$ is plotted (the continuum prediction), as well as $-t/\tau_D$. It is clear that the function $C(t)$ falls between curves corresponding to the two limiting relaxation times. In order to determine the solvation time, $C(t)$ is fit to a single exponential function. The resulting times are compared to dielectric relaxation times in Table 1.

To a good approximation, $\epsilon(\omega)$ for ethanol at -20°C is well characterized by equation 1.²¹ The τ_D reflects the dynamics of hydrogen bonding (ethanol at -20°C is $> 90\%$ hydrogen bonded).⁴⁸ However, it could be argued that monomer relaxation

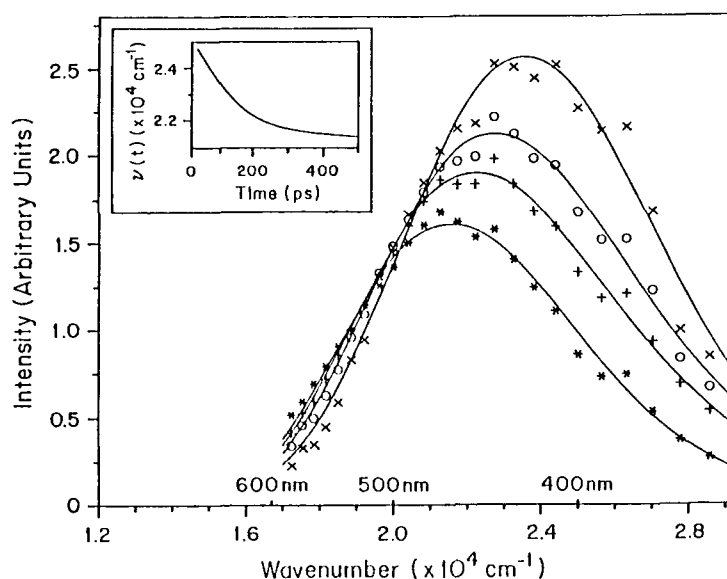


Figure 1: Time resolved emission spectra of the TICT state of DMAPS in Ethanol at -20°C are shown 100 ps (x), 150 ps (o), 200 ps (+), and 400 ps (*) after photoexcitation. The time dependence of the emission maximum is plotted in the insert.

or even the fastest dielectric dispersion region in the alcohols (C-OH rotation) should be included in the response.^{36,39} Both of these motions occur on a faster time scale than the making and breaking of hydrogen bonds. Contributions from these regions of the $\epsilon(\omega)$ response should result in an acceleration of the solvation from that calculated using just the longest time constant of the dielectric function. This would result in further disagreement between theory and experiment. For the case of two regions of Debye dispersion, Bagchi et al. have derived an expression for $C(t)$ within the continuum model.³⁹ In this case, $C(t)$ is a sum of two exponentials, weighted by a function of the dielectric constants associated with the two regions of dispersion. Studies of Coumarin 153 in propanol clearly show that the solvent dynamics are not adequately described by such a model³³. For the solvents examined here, the free monomer concentration is small. Thus the contribution to $C(t)$ is negligible.

In the above discussion, we have implied that the response is entirely accounted for by solvent motion. However, during the relaxation process, the probe molecules are also undergoing rotational diffusion, resulting in a time dependent orientation of the probe dipole. This has been treated theoretically by Bagchi et al.³⁹ For DMAPS, the rotational diffusion times are much longer than the measured solvation times.⁵⁵ In a related study by Maroncelli and Fleming on the solvation of Coumarin 153, evidence of solvation dynamics were suggested by fast components in the rotational anisotropy.³³ The time scale of this fast component was found to correlate with the solvation times derived from $C(t)$. This result suggests that there was an initial torque on the molecule, in which the new direction of the dipole moment on the solute tried to realign with the solvation structure that was present around the ground state molecule. In general, the large difference in solvation and rotational diffusion times supports the conclusion that the dominant contribution to the relaxation measured is solvent motion.

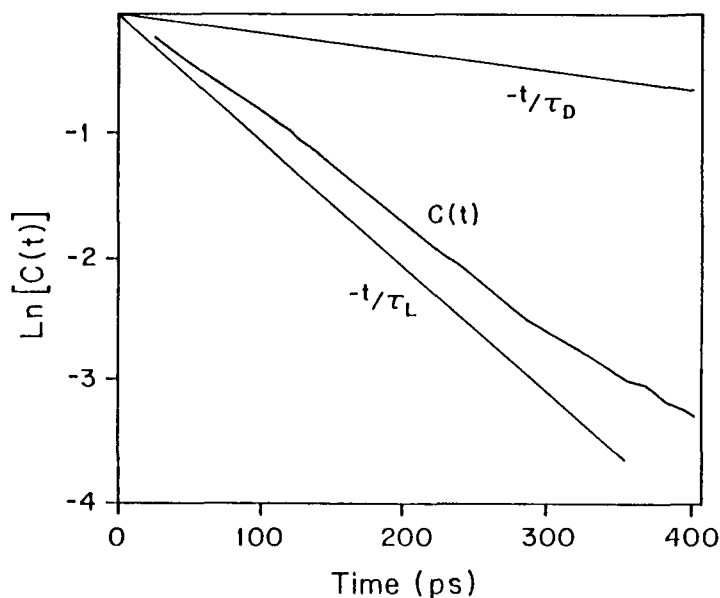


Figure 2: $C(t)$ is plotted as a function of time for Ethanol at -20°C . For comparison, decays with time constants τ_L (the continuum theory prediction) and τ_D are shown.

Temperature (K)	τ_s (psec)	τ_L (psec)	τ_D (psec)	ϵ_0	ϵ_∞
Ethanol					
273	43	60	337	26.0	4.65
263	64	72	456	29.8	4.74
253	113	96	632	31.4	4.85
243	200	132	899	33.8	4.97
233	356	185	1319	36.2	5.10
223	420	270	2001	38.7	5.24
Methanol					
213	197	81	609	56.4	7.51
223	106	56	414	52.7	7.19
233	67	41	290	49.2	6.91
Ethylene Glycol					
298	100	90	778	34.6	4

Table 1: Comparison of the solvation times of DMAPS, τ_s , longitudinal relaxation time of the solvent, τ_L , the Debye time, τ_D , and the static dielectric constant ϵ_0 , in ethanol solution.

Molecular Dynamics Simulations

Further insight into the molecular details of solvation can be revealed by computer simulation. We have used molecular dynamics (MD) to examine the time scale for the relaxation of TIP4P water to an instantaneous change in the dipole moment of a solvated Lennard-Jones (LJ) sphere.⁵⁵ The solute is modeled by a pair of equal and opposite charges embedded in an infinitely massive Lennard-Jones (LJ) sphere centered at the midpoint between the charges. The solute-solvent interaction is given by:

$$V = \sum_{\text{sites } j} \frac{q_i Q_j}{r_{ij}} + \left[-\frac{A}{R^{12}} - \frac{B}{R^6} \right] \quad (5)$$

where q_i refers to charges on the solute, Q_j to the TIP4P charges on the water molecules and r_{ij} is the corresponding site-site distance. The distance R is measured between the LJ center on the TIP4P oxygen and the LJ center on the solute. The parameters A and B are chosen to be $4.668 \cdot 10^6 \text{ kcalA}^{12} / \text{mole}$ and $2.229 \cdot 10^3 \text{ kcalA}^6 / \text{mole}$, respectively. This leads to an effective solute diameter of approximately 3.6 \AA , which is a fair model of the experimental system.^{27,33-35} The charge separation on the solute was fixed at 1 \AA . All changes in the dipole moment of the solute are carried out by changing instantaneously the charge on the sites.

Molecular dynamics (MD) simulations were performed in the NVE ensemble with the Verlet algorithm,⁴⁹ SHAKE⁵⁰ a cubic primary box and periodic boundary conditions. All interactions were truncated by a spherical cut off at 8.5 \AA , and a switching function was used between 8.1 and 8.5 \AA to change the potentials and forces smoothly to zero at the cutoff.⁵¹ No periodic images of the solute were included. The center of mass of the solute was fixed at the origin of the simulation box, and the dipolar axis was fixed along the z -axis throughout the simulations.

After equilibration the simulation was run for an additional 60 ps and configurations were recorded every 0.6 ps . These configurations provide input for the two numerical experiments. For the first experiment, the dipole moment of the solute was changed instantaneously to -4 D , thus pointing the new dipole along the negative z -axis. The system was then propagated for a further 5.4 ps without any velocity rescaling. This generated independent dynamical trajectories from each of 60 initial configuration. In the second experiment, this procedure was repeated using the same initial configurations but the dipole moment of the solute was reassigned to be 12 D along the positive z -axis with no change of direction.

In order to quantify the time dependence of solvent response to the change in the sudden solute dipole moment, the following correlation function was examined:

$$\Phi(t) = \langle \vec{M}_{\text{sol}}(t) \cdot \hat{m}_{\text{LJ}} \rangle \quad (6)$$

In the above expression, $\vec{M}_{\text{sol}}(t)$ is the total vector dipole moment of the solvent and \hat{m}_{LJ} is the unit vector along the dipole moment of the solute. Thus, $\Phi(t)$ is a measure of the time dependent projection of the total solvent dipole moment on the solute. Changes in this projection reflect rotational restructuring of the surrounding medium. In a general sense, these dynamics are a molecular measurement of the rotational motions of the solvent which contribute to the experimental correlation function $C(t)$ measured in the time resolved Stokes shift experiments. It is important to stress that the above function does not measure the entire polarization response. Translational diffusion with no rotation can contribute to the equilibration

process.^{44,52} Motions of this type are not measured by $\Phi(t)$. However, as mentioned above, dielectric continuum treatments of solvent relaxation of the type studied in this paper focus on relaxation by solvent rotational motion.

In Figure 3, $\Phi(t)$ for the 4D to 12D jump and the 4D to -4D flip are shown. $T=0$ corresponds to the time when the magnitude and/or direction of the dipole is changed. The dynamics of $\Phi(t)$ reflect the rotational restructuring process. The $1/e$ time of the relaxation for the 4D to 12D and 4D to -4D measurements is 0.5 and 0.6 ps, respectively. Due to the large fluctuations in $\Phi(t)$, it is difficult to determine whether the two cases show different total relaxation times or if the relaxation can be accurately described by an exponential function. Dielectric continuum models of solvation predict that the dynamics of relaxation should be the same for both a change in the magnitude and the direction of the solute dipole, with $\Phi(t)$ decaying exponentially with a time constant of τ_L . For TIP4P water, τ_L has a value of 0.18 ps,^{53,54} which is considerably faster than the time revealed by the relaxation data in Figure 3. However, in agreement with the experimental studies on nonequilibrium solvation, the relaxation time is between τ_L and τ_D . The result that it takes longer for the solvent to equilibrate than predicted by dielectric continuum models indicates the importance of understanding the underlying molecular motion associated with the solvation process.

In Figure 4, we have plotted $\log(\tau_s/\tau_L)$ as a function of the $\log(\epsilon_0)$. Both experimental and simulation data are plotted. The behavior shown in Figure 4 is consistent with the previous observation of Maroncelli and Fleming for Coumarin 153 in polar liquids. As can be seen, the solvation data calculated from the molecular dynamics simulation follows the trend exhibited by the experimental data. This is an encouraging sign that the molecular motions revealed by the simulation study may provide detailed insight into the molecular aspects of solvation.

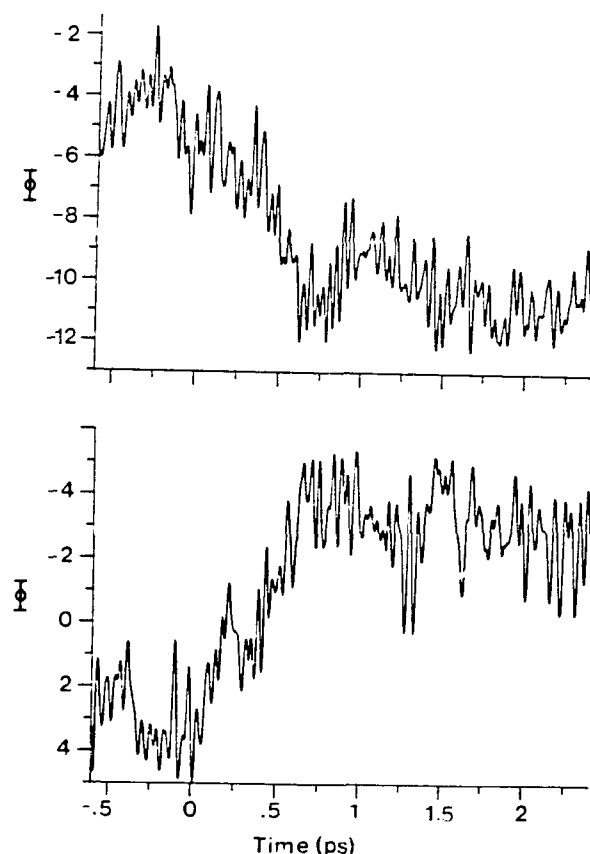


Figure 3: $\phi(t)$ is plotted for the 4D to 12D jump (top) and the 4D to -4D flip (bottom). The magnitude and/or direction of the solute dipole is changed at $T = 0$.

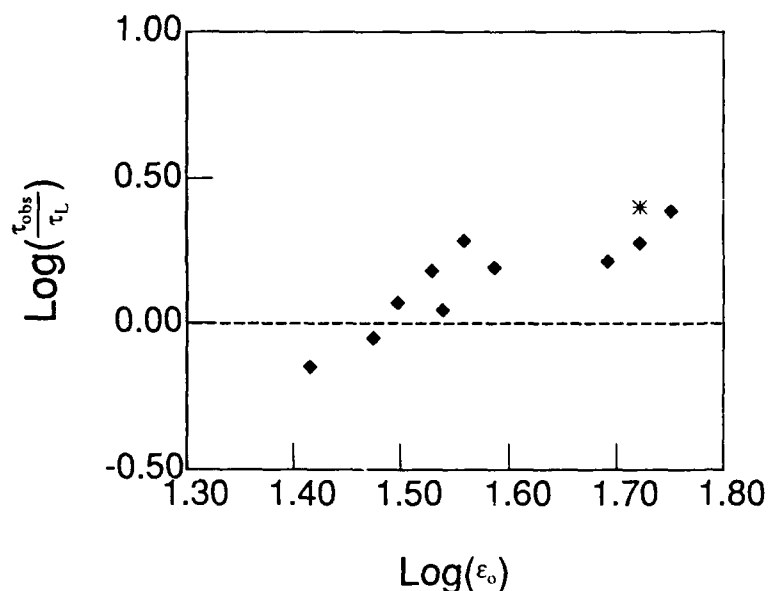


Figure 4: The function $\log \frac{\tau_{\text{obs}}}{\tau_L}$ is plotted as a function of $\log(\epsilon_o)$. The data clearly show that the solvation dynamics deviate from the continuum prediction (dashed line). The data are tabulated in Table 1. The simulation data is represented by the (*).

Conclusions

From experimental and molecular dynamics simulations of solvation, four general conclusions can be drawn.

1. The time scale for solvation generally falls between τ_L and τ_D . In all cases reported, it is closer to τ_L than τ_D .
2. The relaxation dynamics as determined by $C(t)$ are nonexponential.
3. With increasing values of the static dielectric constant, ϵ_o , the solvation time and solvent longitudinal relaxation time become more dissimilar. Not only is this true in comparing the variety of solvents examined but is also observed in a single solvent as a function of temperature where ϵ_o increases with decreasing temperature.
4. In several solvents where $D\tau_D/a^2 > 1$, the observed solvation times are longer than τ_L , in contrast to the prediction of polarization diffusion theory.

Acknowledgements

This work is supported by the National Science Foundation, the Petroleum Research Foundation administered by the American Chemical Society and the Office of Naval Research. M.B. and J.D.S. thank O. A. Karim and Professor A. D. J. Haymet for their guidance and help in carrying out the MD simulations described in this paper.

References

1. C. Reichardt, *Solvent Effects in Organic Chemistry* (Verlag Chemie, New York, 1979).
2. J. M. Hicks, M. T. Vandersall, E. V. Sitzman, and K. E. Eiseenthal, *Chem. Phys. Lett.* 135, 413 (1987).
3. J. T. Hynes, *Ann. Rev. Phys. Chem.* 36, 573 (1985).
4. J. T. Hynes, in *Theory of Chemical Reactions Volume IV*, (CRC Press, Boca Raton, 1986).
5. J.P. Bergsma, B. J. Gertner, K. R. Wilson, and J. T. Hynes, *J. Chem. Phys.* 86, 1356 (1987).
6. G. van der Zwan and J. T. Hynes, *J. Chem. Phys.* 77, 1295 (1982); *J. Chem. Phys.* 78, 4174 (1983).
7. D. F. Calef and P. G. Wolynes, *J. Phys. Chem.* 87, 3387 (1983); *J. Chem. Phys.* 78, 4145 (1983).
8. H. Sumi and R. A. Marcus, *J. Chem. Phys.* 84, 4894 (1986).
9. R. F. Loring and S. J. Mukamel, *Chem. Phys.* 87, 1272 (1987).

10. P. G. Wolynes, J. Chem. Phys. 86, 5133 (1987).
11. P. J. Rossky, Ann. Rev. Phys. Chem. 36, 321 (1985).
12. W. Nadler and R. A. Marcus, J. Chem. Phys. 86, 3906 (1987).
13. M. J. Weaver and T. Gennett, Chem. Phys. Lett. 113, 213 (1985).
14. M. McGuire, and G. McLendon, Phys. Chem. 90, 2549 (1986).
15. E. M. Kosower and D. Huppert, Ann. Rev. Phys. Chem. 37, 127 (1986).
16. D. Chandler, *The Liquid State of Matter* E. W. Montroll and J. L. Lebowitz, Eds., (North Holland, New York, 1982).
17. B. M. Pettitt and P. J. Rossky, J. Chem. Phys. 78, 7296 (1983).
18. D. Kivelson and P. A. Madden, Ann. Rev. Phys. Chem. 31, 523 (1983).
19. H. Frohlich, *Theory of Dielectrics* (Oxford Univ. Press, Oxford, 1949).
20. S.K. Garg and C. P. Smyth, J. Phys. Chem. 69, 1294 (1965).
21. M. Davies, *Dielectric Properties and Molecular Behavior* N. E. Hill, W. E. Vaughan, A. H. Price, and M. Davies, Eds. (Van Nostrand, London, 1969).
22. H. Sumi and R. A. Marcus, J. Chem. Phys. 84, 4272 (1986).
23. H. Friedman, Trans. Faraday Soc. 79, 1465 (1983).
24. L. Onsager, Can. J. Chem. 55, 1819 (1977).
25. J. Hubbard and L. Onsager, J. Chem. Phys. 67, 4850 (1977).
26. J. Hubbard, J. Chem. Phys. 68, 1649 (1978).
27. S-G. Su and J. D. Simon, J. Phys. Chem. 91, 2693 (1987).
28. Su, S-G. and J. D. Simon, J. Chem. Phys., in preparation.
30. D. W. Anthon and J. H. Clark, J. Phys. Chem. 91, 3530 (1987).
31. L. A. Hallidy and M. R. Topp, Chem. Phys. Lett. 48, 40 (1977).
32. M. Maroncelli, E. W. Castner Jr., S.P. Webb, and G. R. Fleming, *Ultrafast Phenomena V* G. R. Fleming and A. E. Siegman, Eds. (Springer-Verlag, New York, 1986).
33. M. Maroncelli and G. R. Fleming, J. Chem. Phys. 86, 6221 (1987).
34. E. W. Castner Jr., M. Maroncelli, and G. R. Fleming, J. Chem. Phys. 86, 1090 (1987).
35. V. Nagaragan, A. M. Brearley, T-J Kang, and P. F. Barbara, J. Chem. Phys. 86, 3183 (1987).
36. Y. T. Mazurenko and N. G. Bakhshiev, Opt. Spectrosc. 28, 490 (1970).
37. S-G. Su and J. D. Simon, J. Chem. Phys. submitted for publication.
38. R. S. Moog and J. D. Simon, J. Phys. Chem. submitted for publication
39. B. Bagchi, D. W. Oxtoby, and G. R. Fleming, Chem. Phys. 86, 257 (1984)
40. G. van der Zwan, and J. T. Hynes, J. Phys. Chem. 89, 4181 (1985).
41. T. Nee and R. Zwanzig, Chem. Phys. 52, 6353 (1970).
42. G. van der Zwan and J. T. Hynes, Physica A 121, 227 (1983).
43. G. van der Zwan and J. T. Hynes, Chem. Phys. Lett. 101, 367 (1983).
44. V. Friedrich and D. Kivelson, J. Chem. Phys. 86, 6425 (1987).
45. J. D. Simon, Accounts of Chem. Research accepted for publication
46. M. Maroncelli, and G. R. Fleming, in preparation.
47. W. Rettig and E. A. Chandross, J. Amer. Chem. Soc. 107, 3575 (1985).
48. Y. Sukai, Y. Sadoaka, and T. Yamamoto, Bull. Chem. Soc. Jap. 46, 3575 (1975).
49. L. Verlet, Phys. Rev. 159, 98 (1967).
50. J. P. Ryckaert, G. Ciccotti, and H. J. C. Berendsen, J. Comput. Phys. 23, 327 (1977).
51. O. A. Karim and J. A. McCammon, J. Am. Chem. Soc. 108, 1762 (1986); J. Ulstrup, Ed. (Elsevier, Amsterdam, 1986).
52. K. J. Ibuki and M. Nakahara, J. Phys. Chem. 91, 4411 (1987).
53. M. Neumann, J. Chem. Phys. 82, 5663 (1985).
54. M. Neumann, J. Chem. Phys. 85, 1567 (1986).
55. S-G. Su, and J. D. Simon, J. Phys. Chem. to be published.
56. O. A. Karim, A. D. J. Haymet, M. Banet, and J. D. Simon, J. Phys. Chem. accepted for publication.
57. M. Maroncelli, E. W. Castner Jr., B. Bagchi, G. R. Fleming, Faraday Discussion, submitted for publication.

SCIENTIFIC ASPECTS OF THE UKAEA
LASER ISOTOPE SEPARATION PROGRAMME

D J H Wort
Harwell Laboratory
United Kingdom Atomic Energy Authority
Oxfordshire
OX11 0RA
Great Britain

Abstract

Quite apart from the high power laser banks required to operate an Atomic Route Laser Enrichment plant, lasers play an important role in the supporting basic physics research. In the first place, it is necessary to determine various uranium atomic parameters, of which isotope shift is the most obvious, for each of the levels in a multistep process, and the strengths of the optical transitions between them. For the last autoionising step it is necessary first of all to find suitable levels, none being listed in the open literature, and then to measure the all important autoionising transition cross-sections. Secondly, laser diagnostics are used to characterise the stream of vapour issuing from the evaporator: parameters such as streaming velocity, kinetic and excitation temperature and degree of thermal ionisation are relevant. Thirdly, the laser may be used as a plasma diagnostic tool analysing ion motion in the extractor system, where subtle plasma physics processes operate. This paper surveys some of the measurements, the methods used and results obtained, thereby illustrating the application of lasers to what might be called the Laser Application par excellence.

Introduction

Research into the basic physics underlying the laser enrichment of uranium to levels adequate for civil nuclear reactors began at the Harwell Laboratories of the United Kingdom Atomic Energy Authority in 1974. About five years ago scientific feasibility was convincingly demonstrated, and a collaborative programme was devised to include Harwell (basic physics), Culham Laboratory (UKAEA) (primarily laser development) and British Nuclear Fuels plc (all commercial aspects including the design, construction and operation of a production plant). The primary aim of the joint programme is to ascertain the economic competitiveness of the process in the UK context: the competition being the highly successful centrifuges used at present.

Details of this programme remain restricted largely for commercial reasons. It is therefore not permissible (nor appropriate for this conference) to discuss BNF's work, and the work at Culham will eventually be described by one of their staff. Rather, this paper is confined to a largely historical review of the work at Harwell, funded by the Underlying Research Programme, with the main emphasis being placed on the role played by diagnostic lasers and the type of experiments and results obtained.

Basic Considerations

The fundamentals of the 3-colour process leading to ionisation of the uranium atom are by now too well known to bear repetition. For basic research at Harwell we have installed a small and entirely conventional MOPA Copper Vapour Laser array, (Fig 1) giving some 200 Watts output at 6KHz pulse repetition frequency (green only). This array drives a set of three dye amplifier chains, whose configuration is variable but with a design centred on 1mJ pulse energy (ie 6 Watts) tuned output per chain (Fig 2). The master colour sources at the moment are three CW ring dye lasers: this is obviously an inefficient use of CVL power but has the merit of great scientific flexibility and ease of use.

In passing, a short experimental programme has established routes for a 2-colour process, using excimer-pumped dye laser oscillators. Attractive though this process is, it is felt that technological considerations still favour the 3-colour route, although the credibility gap is gradually narrowing, primarily because of excimer laser development: dye degradation remains a problem.

We should again emphasise the purely research aspect of the Harwell work; obviously the experimental plant being installed at BNF is considerably more powerful.

Returning to the use of lasers to establish basic parameters, we recognise three main fields of activity:

1. Individual Atomic parameters
2. The behaviour of streaming vapour
3. The behaviour of ions in an extractor

These fields will be discussed individually; where possible, emphasis has been placed on the laser aspect, although in reality the primary interest lies elsewhere. We make no excuse for allowing our enthusiasm for atomic physics to show occasionally.

Atomic Parameters

The 3-colour process involves 3 transitions, and therefore the selection of 3 excited states : the last one has to be ionising.

The first excited state, at about 2eV, can be chosen from one or other of the published level lists. It must obviously have an isotope shift, and it must have the correct J-value to be coupled both to the uranium ground state and the first excited state, which at 620cm^{-1} is almost inevitably going to be present in the vapour stream to an extent making its extraction worthwhile. The strength of the coupling is also a useful parameter to know.

One of the more interesting features is the hyperfine splitting displayed by the transition in ^{235}U (the nuclear spin of $7/2$ gives rise in effect to octets). The total hyperfine width must be covered by the exciting laser, but at the same time excitation of ^{238}U must be avoided : not necessarily because it may spoil selectivity, but also to avoid a waste of photons. Ideally all selectivity is derived from the first step. Two examples of a useful and a useless transition are shown, (Fig 3) both being the result of fluorescence excitation of 235 -enriched uranium vapour using a scanning CW laser. The vapour source used was a sputter lamp, (Fig 4) which is now our standard spectroscopic source, though at various times we have used a tubular furnace, a small point source electron beam evaporator and, inevitably, an atomic beam furnace using uranium rhénide as a non-corrosive uranium source. The hyperfine structure revealed by the laser scan was analysed using an interactive computer programme, and the two controlling parameters (the Casimir A and B coefficients) deduced for several levels : this type of information is required when attempting to match 3-photon experiment to theory.

Rather as a side-issue, the effect of a magnetic field on the transitions has received some attention. In any practical uranium evaporator, a magnetic field will be present to control the electron-beam heat source. With laser fluorescence, the usual Zeeman effect is readily observed, and the less usual Paschen-Goudsmit effect on hyperfine structure gives a useful check on the validity of the structure interpretation (Fig 5).

For the second excited state, at 4eV, the choice is not so obvious. The list of levels given by Miron et al is comprehensive, at least for levels of interest, but the transition strengths from the chosen 2eV levels required to be measured. We used the branching-ratio-and-lifetime method, using both CW and pulsed lasers at various times to measure branching ratios, and either pulsed laser excitation or time delayed ionisation to measure lifetimes : the latter method (using pulsed lasers) is both experimentally easier and more accurate, and an example of the type of result obtained is shown (Fig 6).

The isotope shift of the 4eV level, which in an enrichment plant is a bonus, is relatively easily measured using CW fluorescence excitation with two lasers : absolute positions can be determined using a wavemeter calibrated against an iodine cell, or relative positions by simply relying on the calibrated frequency shift on the laser control panel! Absolute positions are of course required to determine the laser frequencies needed for a separation plant.

Just as with the 2eV level, the 4eV levels show hyperfine structure. Indeed, a double fluorescence experiment with CW lasers, one scanning and one fixed (which gives essentially doppler-free fluorescence) yields mind-bogglingly complicated results (Fig 7). One can obtain four such sets of results, all equally useless, by scanning either laser and by using parallel or opposed beams. A much more immediately appealing picture is obtained by a raster scan technique, in which both lasers are scanned, one rapidly and one slowly, and the fluorescence displayed as bright-up on an oscilloscope whose horizontal and vertical scans are matched to the two lasers (Fig 8). Even better would be a mock 3-D computer display : we were not sufficiently familiar with this technique when these experiments were performed several years ago. Again the 4eV level hyperfine parameters can be deduced and used in a

sufficiently all-embracing theory.

The third step, to a level at 6eV which ionises, was quite literally a step into the unknown. No information had been published on the position or access of levels which were either auto-ionising, or which could be induced to ionise by, say, the imposition of an electric field. We sought these levels using three pulsed lasers and an atomic beam, the first two lasers being injection locked (and single moded) by two CW lasers, each in turn actively locked to fluorescence from a uranium sputter lamp (Fig 9). All three pulsed lasers were driven by a single copper vapour laser. Pulsed lasers were required in this search partly to give a good chance of further excitation from the short lived 2 and 4eV levels (lifetimes $\sim 100\text{nsec}$) and partly because the cross-section for excitation to levels above the continuum (auto-ionising levels) was expected to be small. Continuous scanning of the third laser, with the first two locked to chosen uranium transitions, immediately yielded copious ionisation : a short length of a typical auto-ionisation spectrum is shown (Fig 10).

The auto ionising cross-section, which may well be the critical parameter determining the commercial viability of the process, was measured using a fairly conventional saturation technique (Fig 11), and has since been confirmed absolutely using vapour at known density, and known laser energies, by measuring ion current. Some levels turn out to have quite high cross-sections, in the region of 10^{-15}cm^2 . The lifetimes of these levels may be measured indirectly by measuring their spectral width : for this we used a scanning CW ring laser, pulse amplified, to ensure that the bandwidth of the laser was negligible, and the measured lifetimes ranged up to a few hundred picoseconds (and down to indefinitely small values). The accuracy of the pulse-amplified CW laser permits investigation of various exotica such as the Stark effect and coupling via parity-forbidden transitions, etc, which are not particularly relevant to this conference.

The Vapour Stream

The evaporation of uranium by electron beam heating of a melt contained in a cooled crucible has been universally adopted, not least because of the alkali-like properties of uranium. There is an evident requirement to know such parameters of this stream as velocity, temperature etc, and lasers were used extensively in this investigation. The values for these parameters depend both on the starting conditions (electron beam power, etc), and on the geometry, being different for point-source and line-source evaporators.

The vapour streaming velocity has been measured by a very simple double pass CW beam, the light being directed downwards through the upwardly streaming vapour to a mirror, which reflects it upwards again. Observation of fluorescence as the laser is scanned yields the vapour velocity as the separation between the two doppler-shifted fluorescence peaks, and also a quantity which can be identified as a kinetic temperature from the width of the peaks (Fig 12). The velocities measured, around 10^5cm sec^{-1} , are rather higher than elementary considerations would indicate due to the good transfer between internal energy of the atom (metastable states) and translational energy. Similar methods measure the line-of-sight temperature in a linear evaporator.

The excitation temperature of the vapour, a measure of the internal energy, was obtained by measuring the relative populations of various excited states, either by absorption of a CW beam or by pulsed laser fluorescence. The temperature is quite low, typically in the $1\text{--}2000^\circ\text{C}$ range (compared with the 3000°C temperature of the source), again indicating good internal-external energy transfer.

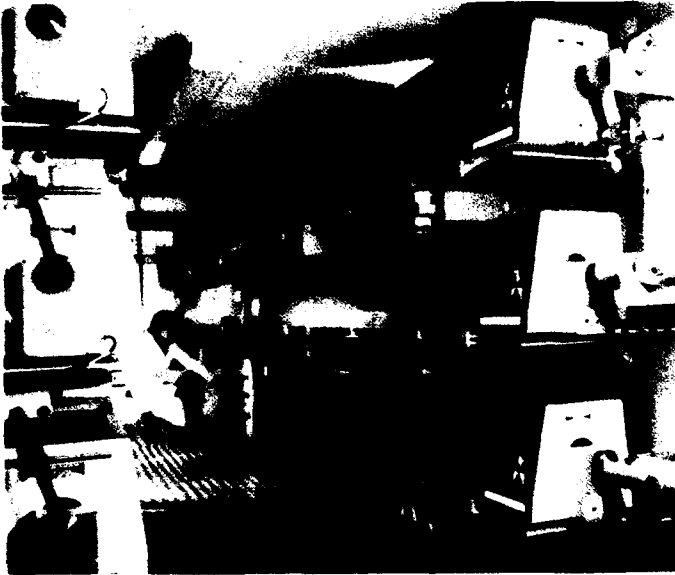
In passing, the source temperature is sufficient to give appreciable thermal ionisation, and in some sources the ion velocity, kinetic and excitation temperatures have been measured in a manner similar to the atomic parameters.

The Ion Extractor

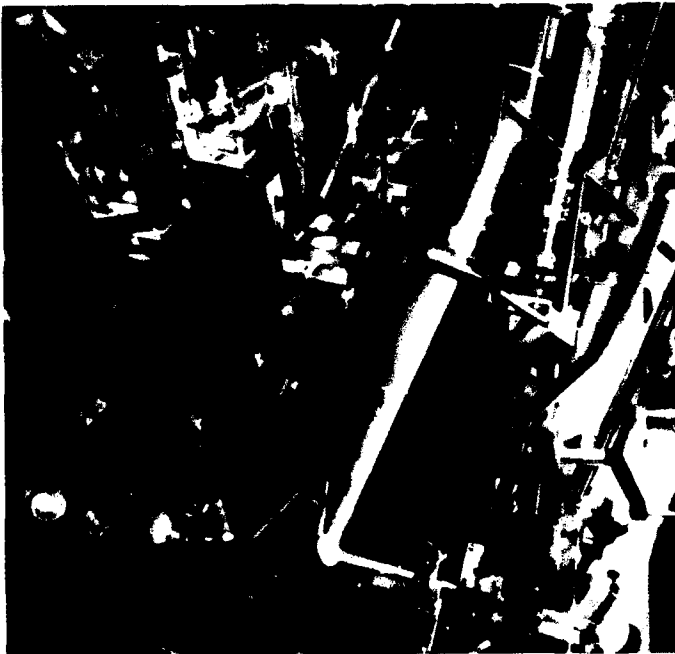
For very low densities, eg an atomic beam, elementary electrostatic collection is adequate, and we show an illustration of what we term the spectroscopic selectivity obtained in such an apparatus (Fig 13). However, at production densities ($> 10^{12}\text{ atoms cm}^{-3}$) the ion extraction becomes a plasma process, whose complexity depends on the method used. Pulsed lasers have been used to study time-resolved local ion motion by doppler-shifted fluorescence : the basic principles are not sufficiently different from the atomic stream measurements to warrant separate description. In many circumstances the laser measurements are largely an aid to the interpretation of electrical diagnostic methods.

Conclusions

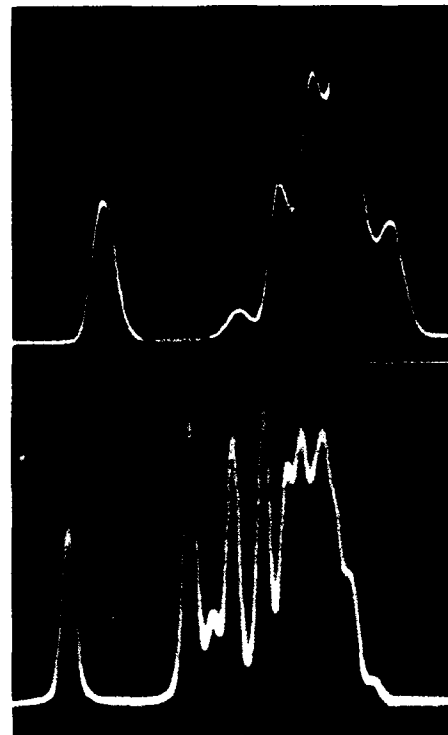
The dividing line between physics and technology in the Laser Enrichment process is shadowy. It is, therefore, difficult to say in which of these fields laser methods have made the most impact. Nevertheless, it remains true to say that without the use of lasers to establish a range of basic parameters, the development of an enrichment process would be at the very least extremely difficult. As it is, the effectiveness of the methods is shown in Figure 14, which displays the energy-resolved alpha spectra from two sample plates, briefly exposed on one collector plate in a small evaporator. One example was taken without lasers running, and shows the 238U, 235U, 234U alpha peaks in natural uranium. The other shows the effect of laser irradiation: the enrichment in 235U is about 9-fold, more than adequate for any present or future civil nuclear power programme. We conclude that the information given by laser diagnostic methods is both accurate and adequate.



1. Part of the CVL array.

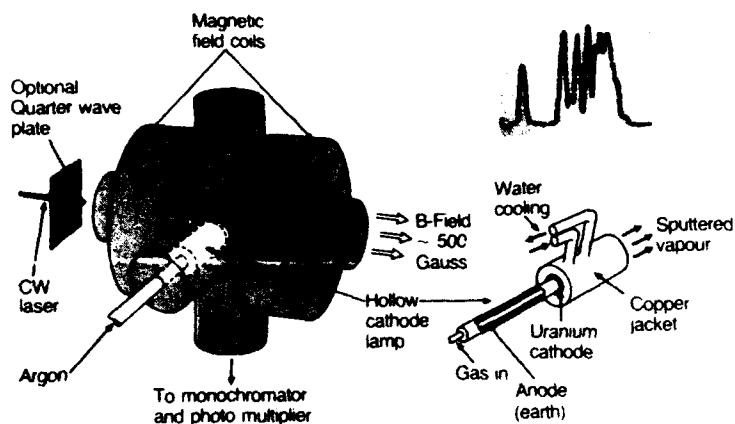


2. Dye amplifiers in operation.

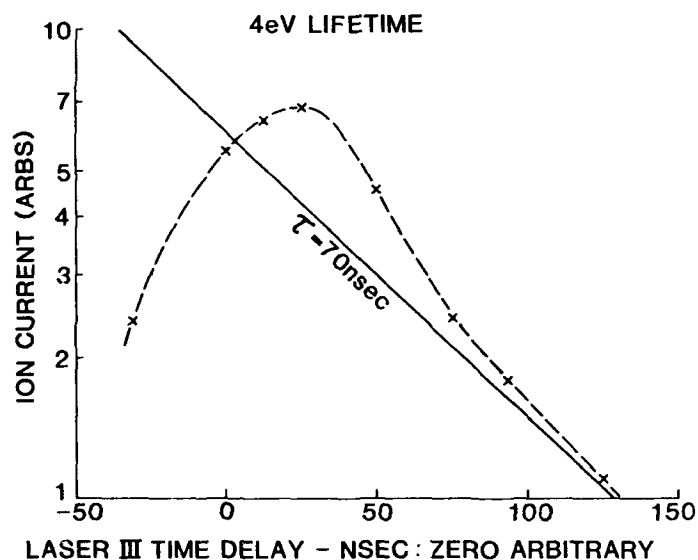


3. ²³⁵U Hyperfine structure.

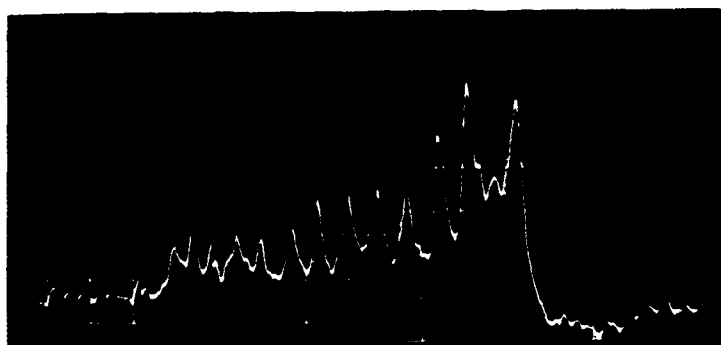
HOLLOW CATHODE LAMP



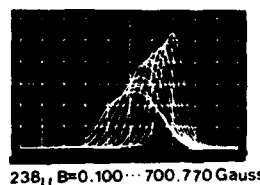
4. The Sputter Lamp.



6. Time-delayed ionisation.

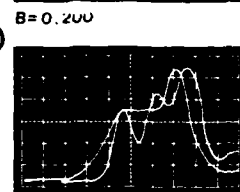
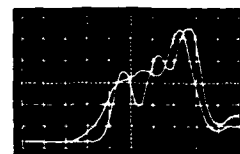
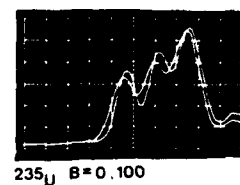


7. Two-photon hyperfine structure (4eV level).



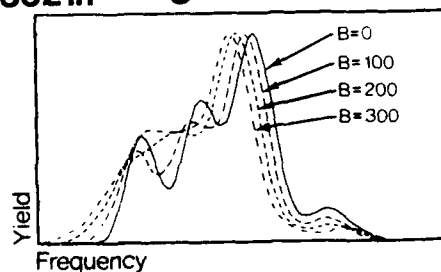
0-17362 in magnetic field ($\Delta m = -1$)

$^{238}\text{U}(I=0) ^{235}\text{U}(I=7/2)$

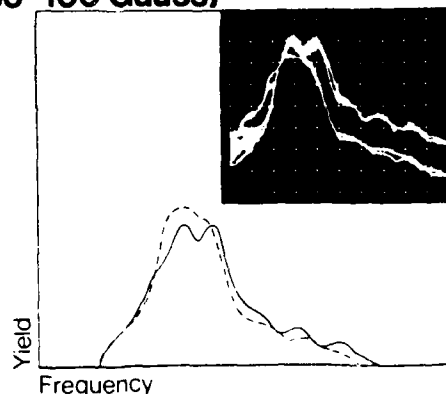


B=0.300

Theoretical Prediction for 0-17362 in ^{235}U



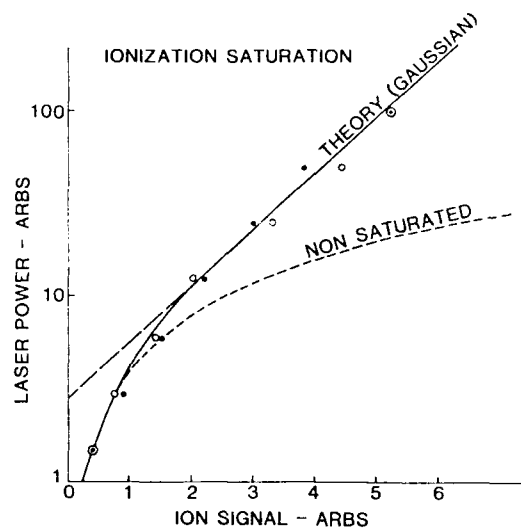
The Paschen Goudsmit Effect on the 620-17362 transition ($B \approx 80-100$ Gauss)



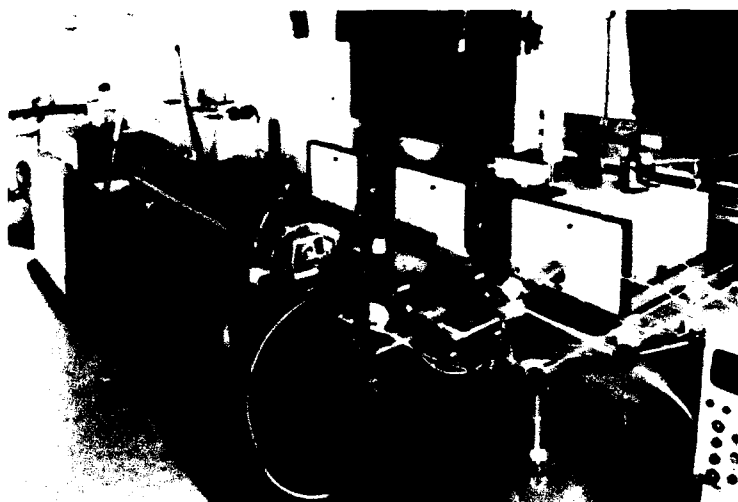
5. Zeeman effect in uranium.



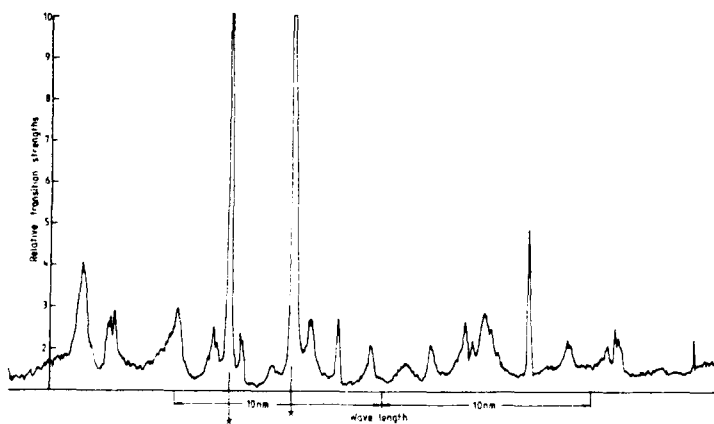
8. Two-photon raster display - 4eV hfs.



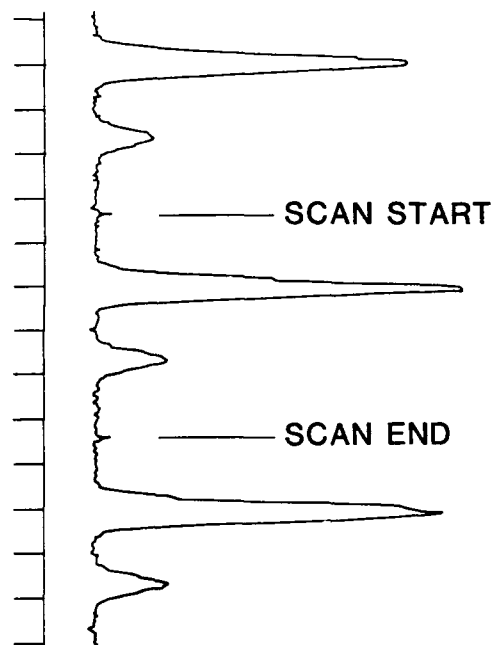
11. Ionisation saturation curve.



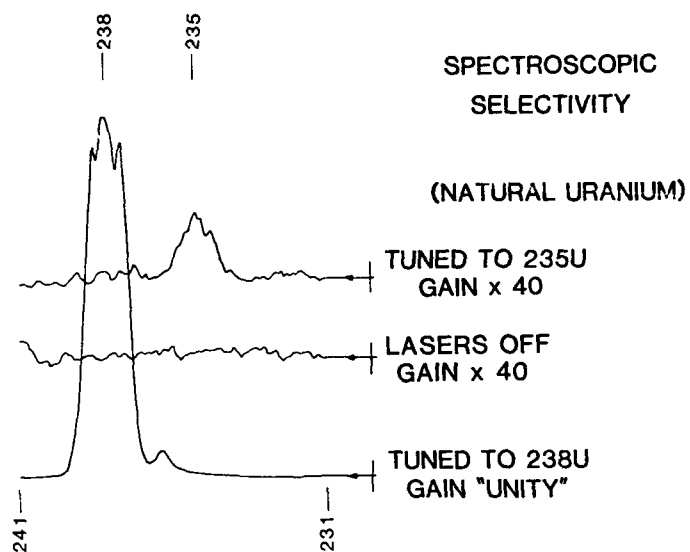
9. Injection locked dye lasers.



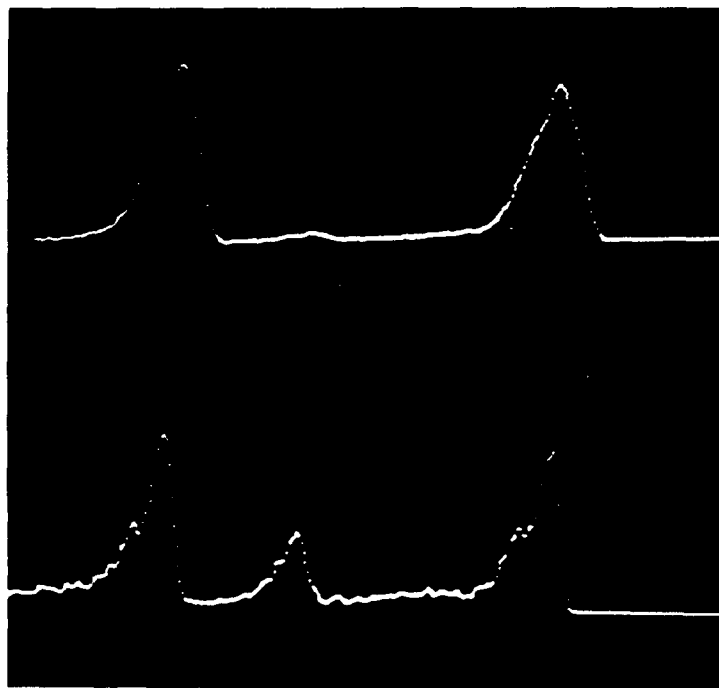
10. Typical section of autoionisation spectrum.



12. Vapour velocity measurement by fluorescence.



13. Mass-spectrometer selectivity.



14. Alpha spectrum of natural and laser-enriched uranium.

THE SUPERSONIC MOLECULAR BEAM
PREDISSOCIATION SPECTRUM OF $^{16}\text{O}^{12}\text{C}-\text{H}^{19}\text{F}$

K. McMillan and J. W. Bevan

Chemistry Department
Texas A&M University
College Station, Texas 77843

Abstract

The infrared laser predissociation spectrum of the weakly bound molecular complex OC--HF is obtained in the region of the ν_1 (H--F stretching) fundamental vibrational mode. Rovibrational analysis of the ν_1 fundamental yields values of $0.104\ 2510(20)\ \text{cm}^{-1}$ and $2.90(3) \times 10^{-7}\ \text{cm}^{-1}$, respectively, for the excited state ($1000^0 0^0$) molecular constants B' and D' . Predissociative lifetimes for unperturbed rotational levels of this excited state are determined to be $0.9 \pm 0.1\ \text{ns}$, and are found to exhibit no measurable J-dependence for $J' \leq 21$. Observation of low J transitions in the associated hot band $\nu_1 + \nu_5 - \nu_5$ allow the unambiguous J-labelling of this band and the determination of ground ($0000^0 1^1$) and excited ($1000^0 1^1$) state rotational constants.

Introduction

In the last two years, the infrared spectra of a number of weakly bound complexes between hydrogen fluoride and rare gas atoms or diatomic molecules have been observed in supersonic molecular beam experiments.¹⁻¹⁰ Two methods have been used for these studies; one, applied by Miller and coworkers, involves the bolometric detection of predissociation in an expansion from an axially symmetric nozzle source.¹⁻⁶ The other technique, which was developed by Lovejoy, Schuder, and Nesbitt, takes advantage of the larger absorption path-length and greater beam intensity possible in an expansion from a pulsed slit nozzle by detecting direct absorption of infrared laser radiation by complex molecules in the supersonic beam.⁷⁻¹⁰ Both methods allowed the rovibrational structure of the ν_1 (H--F stretching) fundamental mode to be resolved for the complexes, and, in the spectra obtained by Nesbitt and coworkers, combination and hot bands were also observed and analyzed. From these analyses of rotational structure in vibrationally excited complexes, information on the potential energy surface away from the global minimum can be acquired. The sub-Doppler nature of the spectra also permit the lifetime of the predissociating states to be accurately determined.

The infrared spectrum of the complex OC--HF in the region of the ν_1 fundamental and associated hot bands had been observed a few years ago using a sequential mode hop tuned color center laser and a low pressure, low temperature gas phase mixture of CO and HF in a White cell¹¹, but the instrumental linewidth of the laser and pressure broadening contributed largely to the 900-1500 MHz FWHM linewidth of the observed transitions. Only the ν_1 fundamental was resolved sufficiently for analysis, and the lack of pressure broadening parameters precluded more than a lower limit estimate for the excited state lifetime. In the present work we have used the supersonic molecular beam technique with bolometric detection of predissociation to reinvestigate the ν_1 fundamental in OC--HF, with the objective of obtaining more precise molecular constants and accurate excited state lifetimes. The $\nu_1 + \nu_5 - \nu_5$ hot band, which is severely overlapped with the R branch of the ν_1 fundamental in the gas phase spectrum, is resolved in the supersonic beam spectrum. Unambiguous J-labelling of this hot band allows the ground and excited state molecular constants to be determined. In addition, the linewidths of the ν_1 fundamental transitions are examined for any evidence of J-dependence in the predissociative lifetimes of the excited states. The results of this work will be compared to the recently published results of Jucks and Miller for the same complex.⁶

Experimental

The color center laser and components necessary for continuously computer-controlled scanning and monitoring the output have been described previously.¹² In this work the KCl:Li crystal of the laser is pumped with the 647.1 nm line of a Kr^+ laser. Output powers of the color center laser are of the order of 10-12 mW, and the single mode linewidth is estimated to be $\leq 3\ \text{MHz}$. Relative and absolute frequency determinations are made by simultaneously recording the transmission spectra of a 3 GHz and a temperature controlled 150 MHz marker etalon, and a reference cell containing low pressure water vapor. Water

lines in the region of the ν_1 fundamental of OC--HF require that the entirety of the infrared beam path be under vacuum.

A supersonic jet is produced by expanding a mixture of HF (0.7%) and CO (5%) in helium through the 35 μ -diam pinhole of the room temperature nozzle. The molecular beam is then formed by placing a 250 μ -diam skimmer 10 mm downstream of the pinhole. The laser output is mechanically chopped at 100 Hz and initially intersects the molecular beam 7.0 cm downstream of the pinhole. Two flat mirrors then multipass the infrared beam across the molecular beam 7.0 cm downstream of the pinhole. Two flat mirrors then multipass the infrared beam across the molecular beam a total of 27 times. The Ge:Ga bolometer, operated below the λ point of liquid helium, is positioned 52.5 cm from the pinhole. When the modulated infrared radiation is tuned to a transition to a predissociating level in a molecular complex, the resultant reduction in molecular beam momentum flux is detected by the bolometer.

Results and Discussion

Figure 1 shows the R(13) transition observed in the ν_1 fundamental spectrum. Transition frequencies are determined by reference to the water line at $3843.50529 \text{ cm}^{-1}$,¹³ and are listed for all observed ν_1 lines in Table 1. A number of these lines are split into components of varying intensity and width. In their supersonic beam study of this band⁶, Jucks and Miller reported perturbations in some of the low J transitions (J_{max} for their spectrum was 5). Here, where $J_{\text{max}} = 13$, the S/N of the low J transitions is insufficient to observe the sharp, weak sidebands those authors described, but additional perturbations can be seen for higher J transitions not observable in the colder spectrum.

The unperturbed transition frequencies were fit to the 5-parameter energy expression for a $\Sigma \leftarrow \Sigma$ transition,

$$E(\nu) = \nu_0 + B'J'(J'+1) - D'J'^2(J'+1)^2 - B''J''(J''+1) - D''J''^2(J''+1)^2, \quad (1)$$

with the ground state constants B'' and D'' constrained to the microwave values¹⁴ of $0.1022007 \text{ cm}^{-1}$ and $3.255 \times 10^{-7} \text{ cm}^{-1}$, respectively. The results of this fit are given in Table 2. Good agreement is found for the frequency separations between individual transitions in this work and that of Jucks and Miller, except for the separation between R(8) α and R(9). The tabulated data in their study indicates a separation of 0.2495 cm^{-1} , while measurements for three scans obtained on different days gave values for us of 0.2439 , 0.2449 , and 0.2444 cm^{-1} . This discrepancy produces a relative shift with respect to our data in the transition frequencies of lines R(9) through R(12), which was the highest J transition Jucks and Miller observed, and probably accounts for the difference in molecular constants obtained from these two beam experiments (Table 2).

The measured predissociative line broadening we have observed agrees well with the value of $190 \pm 10 \text{ MHz FWHM}$ given by Jucks and Miller. We have measure this linewidth for all unperturbed transitions of sufficiently high intensity ($J' \leq 21$), and have found no evidence of any increase in FWHM with increasing rotational energy.

Figure 2 shows the R(14) transition of the ν_1 fundamental, and close to it a very weak transition attributed to the P(10) line of the hot band $\nu_1 + \nu_5^1 - \nu_5^1$. This hot band, which was assigned but not analyzed in the previous gas phase study,¹¹ was not reported in the work of Jucks and Miller. Both the ground ($0000^0 1^1$) and excited state ($10000^0 1^1$) of the complex have a single quantum of energy in the doubly degenerate mode ν_5^1 . The lowest J transitions are observable in this band, allowing for an unambiguous J-labelling of the band in the absence of microwave data for the ($0000^0 1^1$) state. The S/N of the transitions is very low, and hence l-type doubling is not discernable. From a fit of this hot band data, the rotational constants are determined and are given in Table 3. The relatively high uncertainty in the values obtained reflect the low S/N, and the fit to unresolved l-doublets.

Further investigation of this region of the OC--HF spectrum will be undertaken in a subsequent analysis.¹⁵ The hot bands $\nu_1 + \nu_5^1 - \nu_1 + \nu_5^2 - \nu_5^2$, and $\nu_1 + \nu_3 - \nu_3$ are of particular interest and hence a gas phase study will be an important complement to this molecular beam work.

References

1. Z. S. Huang, K. W. Jucks, and R. E. Miller, *J. Chem. Phys.* **85**, 3338 (1986).
2. Z. S. Huang, K. W. Jucks, and R. E. Miller, *J. Chem. Phys.* **85**, 6905 (1986).
3. K. W. Jucks, Z. S. Huang, and R. E. Miller, *J. Chem. Phys.* **86**, 1098 (1987).
4. Z. S. Huang and R. E. Miller, *J. Chem. Phys.* **86**, 6059 (1987).
5. K. W. Jucks and R. E. Miller, *Chem. Phys. Lett.* **139**, 201 (1987).
6. K. W. Jucks and R. E. Miller, *J. Chem. Phys.* **86**, 6637 (1987).
7. C. M. Lovejoy, M. D. Schuder, and D. J. Nesbitt, *Chem. Phys. Lett.* **127**, 374 (1986).
8. C. M. Lovejoy, M. D. Schuder, and D. J. Nesbitt, *J. Chem. Phys.* **85**, 4890 (1986).
9. C. M. Lovejoy and D. J. Nesbitt, *J. Chem. Phys.* **86**, 3151 (1987).
10. C. M. Lovejoy, M. D. Shuder, and D. J. Nesbitt, *J. Chem. Phys.* **86**, 5337 (1987).

11. E. K. Kyro, P. Shoja-Chaghervand, K. McMillan, M. Eliades, D. Danzeiser, and J. W. Bevan, *J. Chem. Phys.* 79, 78 (1983).
12. E. K. Kyro, P. Shoja-Chaghervand, M. Eliades, D. Danzeiser, S. G. Lieb, and J. W. Bevan, *Can. J. Chem.* 63, 1870 (1985).
13. C. Camy-Peret, J. M. Flaud, G. Guelachvilli, and C. Amiot, *Mez. Phys.* 26, 825 (1973).
14. A. C. Legon, P. D. Soper, and W. H. Flygare, *J. Chem. Phys.* 74, 4944 (1981).
15. K. McMillan, D. Bender, B. A. Wofford, M. Eliades, S. G. Lieb and J. W. Bevan (submitted for publication).

Table 1. Observed transitions in the ν_1 fundamental spectrum.

The transitions marked by an asterisk were observed to be the perturbed by Jucks and Miller. The most intense component of a perturbed transition is labelled with a superscript a.

transition	observed frequency (cm^{-1})
P(14)	3841.5480
P(13)	3841.6979
P(12)	3841.8534
P(11)	3842.0114
*P(10) ^a	3842.1743
*P(9) ^a	3842.3390
P(8) ^b	3842.4995
P(8) ^a	3842.5194
P(7)	3842.6886
P(6)	3842.8682
P(5)	3842.0517
P(4)	3843.2397
P(3)	3844.4312
P(2)	3843.6269
P(1)	3843.8280
R(0)	3844.2404
R(1)	3844.4531
R(2)	3844.6691
R(3)	3844.8906
R(4)	3845.1149
R(5)	3845.3444
R(6) ^a	3845.5650
R(6) ^b	3845.5846
*R(7) ^a	3845.8138
*R(8) ^a	3846.0556
R(9)	3846.2997
R(10)	3846.5492
R(11)	3846.8022
R(12)	3847.0604
R(13)	3847.3234
R(14)	3847.5877
R(15)	3847.8581
R(16)	3848.1320
R(17) ^c	3848.3996
R(17) ^b	3848.4024
R(17) ^a	3848.4111
R(18) ^b	3848.6879
R(18) ^a	3848.6916
R(19)	3848.9772
R(20)	3849.2672
R(21)	3849.5613
R(22)	3849.8604
R(24)	3850.4690

Table 2. The molecular constants for the ν_1 (1000⁰⁰⁰) (1000⁰⁰⁰) band.

The constants marked with an asterisk for the results of ref. 6 were constrained to the corresponding values obtained in ref. 11. The constants marked with an asterisk in the present work are constrained to the microwave values of ref. 14.

	ref. 11	ref. 6	ref. 14	present work
ν_0/cm^{-1}	3844.0294(50)	3844.0278		3844.0320(2)
B''/cm^{-1}	0.102 148(14)	0.102 148*	0.102 2007	0.102 2007*
$D_j''/\text{cm}^{-1} \times 10^{-7}$	3.8(1.8)	3.8*	3.255	3.255*
B'/cm^{-1}	0.104 196(14)	0.104 208		0.104 2510(20)
$D_j'/\text{cm}^{-1} \times 10^{-7}$	3.6(1.8)	3.6*		2.90(3)

Table 3. The molecular constants obtained for the $\nu_1 + \nu_5 - \nu_5$ (1000⁰¹¹) (0000⁰¹¹) band.

ν_0/cm^{-1}	3849.4441(17)
B''/cm^{-1}	0.103 34(25)
B'/cm^{-1}	0.105 28(22)

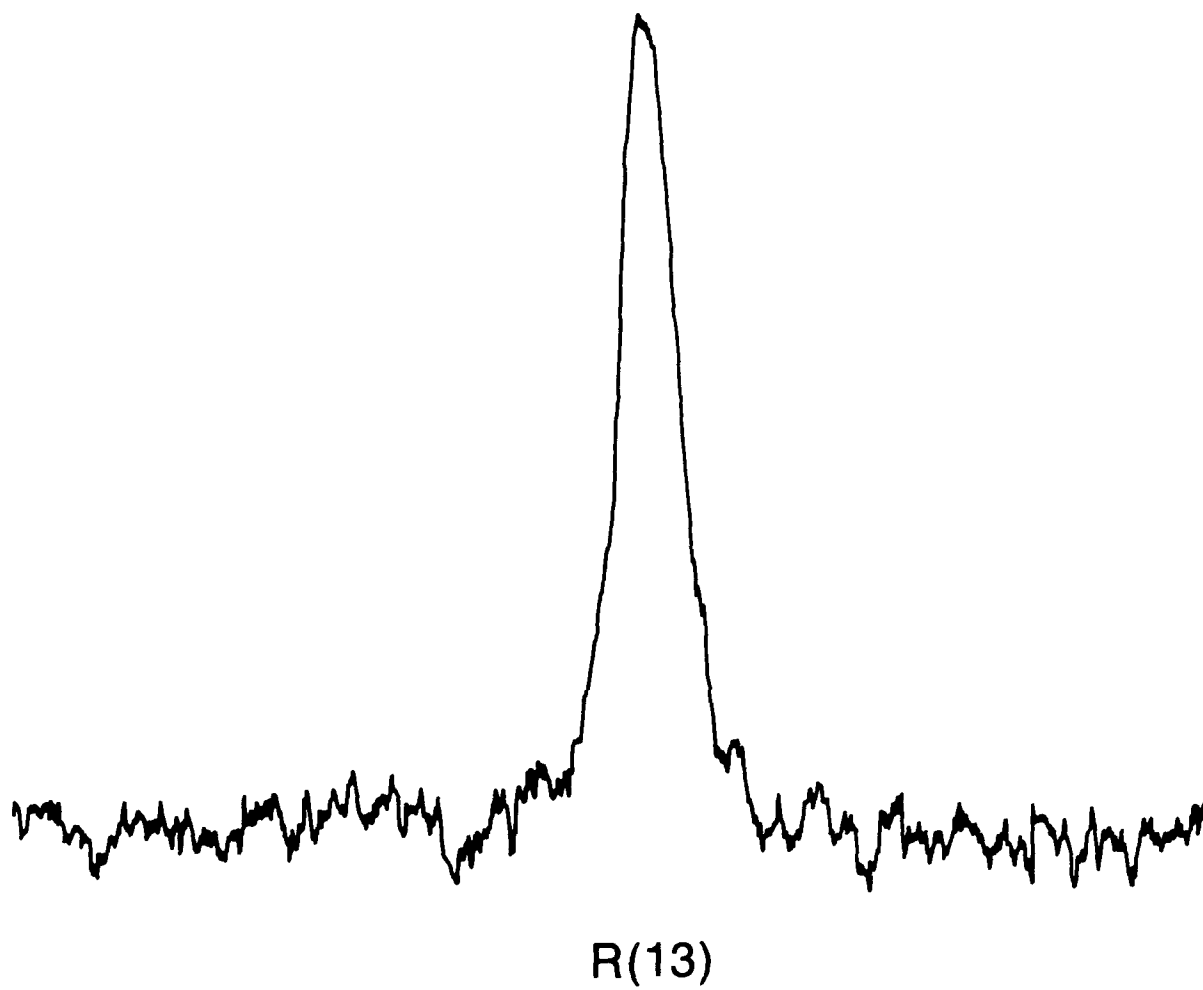


Fig. 1: The R(13) transition of the ν_1 fundamental spectrum.

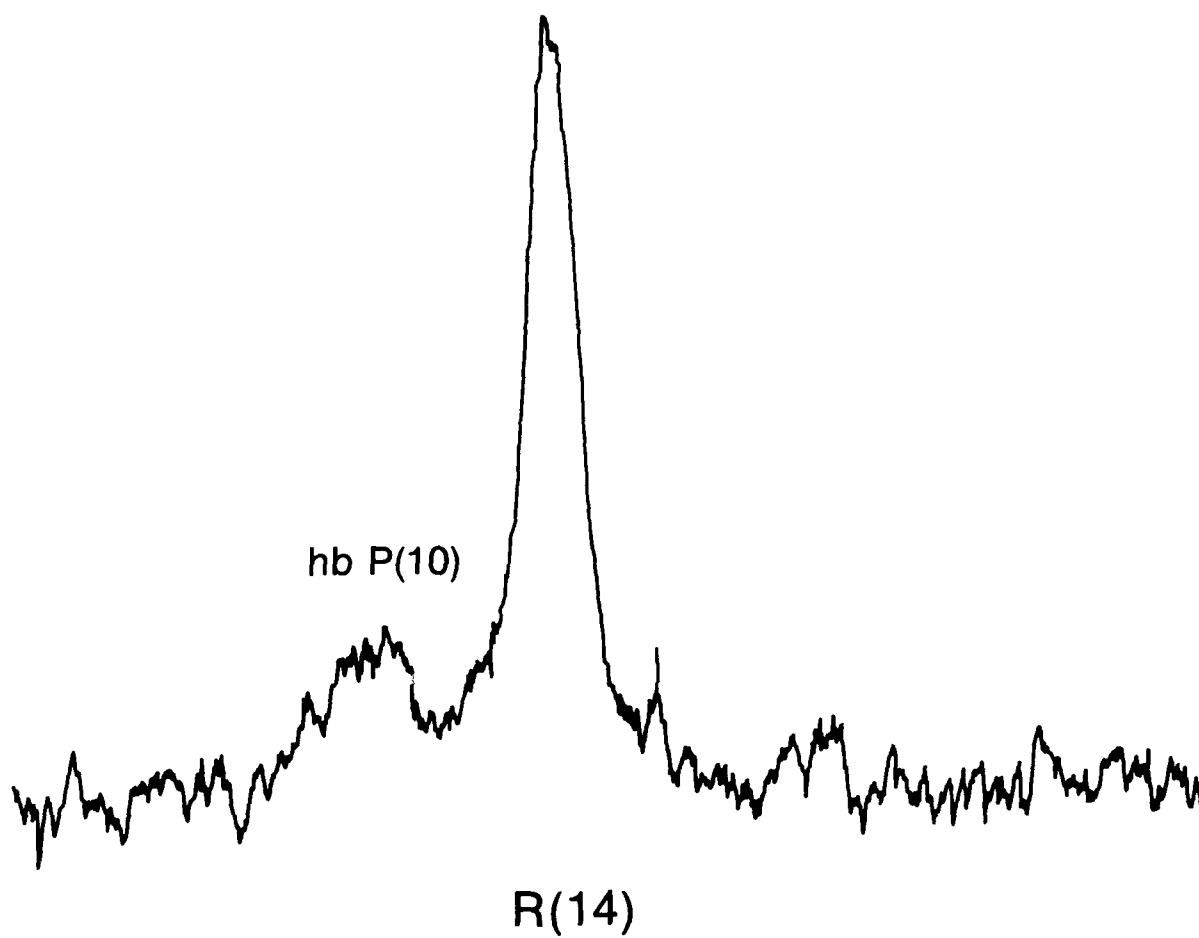


Fig. 2: The R(14) transition of the ν_1 fundamental spectrum, and the $\nu_1 + \nu_5^1 - \nu_5^1$ hot band transition P(10).

BROADBAND MODULATORS FOR SPECTROSCOPY

B. Lax
Physics Department
Massachusetts Institute of Technology
Cambridge, MA 02139

R. M. Marino and R. S. Eng
Lincoln Laboratory
Massachusetts Institute of Technology
Lexington, MA 02173-0073

Abstract

Broadbanding of single sideband (SSB) electro-optic modulators is achieved by the use of multisection dual sweep configurations. The large bandwidths suggest the application of tunable laser sources for high-resolution and nonlinear spectroscopy in solids, gases and plasmas. Resonance transitions in semiconductors; vibrational and rotational levels, including Raman and multiphoton transitions in gases can be explored. Tunable sources, optically pumped in molecular gases or mixed in second and third order nonlinear crystals can provide radiation over a wide band of frequencies in the IR and FIR regions, CW or pulsed, from about $1\mu\text{m}$ to the millimeter region. Diagnostics for cyclotron absorption and emission in fusion plasmas can be used in high field Tokamaks to measure electron temperatures. More importantly, the broadband modulator now makes it feasible to use a sensitive 4-photon coherent scattering technique (CARS) with IR and FIR lasers for measuring the temperature of alpha particles and ion species in a fusion plasma under ignition conditions.

Introduction

Single sideband (SSB) modulators have been demonstrated as useful techniques for modulating laser beams efficiently.^{1, 2} Such modulators have been primarily developed for radar and communications. The need for broadbanding these devices has motivated the development of new schemes to achieve this objective. Consequently, we have demonstrated theoretically that broadbanding is accomplished by the use of multisection modulators for identical and staggered-tuned configurations.³ In addition, a new technique of tandem dual arrangement of a SSB modulator⁴ further enhances the broadband capabilities of electro-optic modulators. The purpose of this paper is to discuss the application of the broadband modulator to the development of tunable laser sources and their use for a variety of high resolution and non-linear spectroscopic experiments in solids, gases, and plasmas.

In order to understand the method of broadbanding, it is instructive to review the principle of single sideband (SSB) modulation of a laser beam. It was first suggested by Buhrer, Baird, and Conwell¹ that SSB modulation can be achieved with an electro-optic crystal with circularly polarized light traveling along a 3-fold axis. Simultaneously a circularly polarized electric field at microwave frequencies in a traveling waveguide is applied to the crystal. Such a configuration is shown in Fig. 1a in which the laser and microwave fields are rotating in the same sense. The frequencies add, and the resultant laser beam emerges with the sum frequency, which is the SSB, circularly polarized in the opposite sense. In this case, we use a CdTe crystal oriented axially along the [111] direction, with the sides cut along $[1\bar{1}0]$ and the $[11\bar{2}]$ directions as shown in Fig. 1b. When the microwave field is fed in quadrature in time and space, the field is circularly polarized at the center of the waveguide designated by the black dot representing the size of the laser beam. This arrangement has been demonstrated by Carter and Haus² as an efficient scheme for converting the frequency of a CO_2 laser at $10.6\mu\text{m}$ to the SSB at phase match, when the crystal is sufficiently long and the microwave power is relatively high. The condition for phase matching is given by the equations:

$$\Delta\beta = \beta_1 - \beta_2 - \beta_\mu = 0 \quad (1a)$$

$$\beta_1 - \beta_2 = \frac{(\omega_1 - \omega_2)}{c} \sqrt{\epsilon} = \frac{\omega_\mu}{c} \sqrt{\epsilon} \quad (1b)$$

$$\beta_\mu = \sqrt{\left(\frac{\omega_\mu}{c}\right)^2 \epsilon_\mu - \frac{\pi^2}{a^2}} \quad (1c)$$

This work was sponsored by the Department of the Navy for SDIO.

where ω_1 , ω_2 , and ω_μ are the SSB, the laser and the microwave frequencies respectively and satisfy the relations $\omega_1 = \omega_2 + \omega_\mu$. $\epsilon = 7.2$ and $\epsilon_\mu = 10.4$ are the optical and microwave dielectric constants, which differ due to the polar character of CdTe. For $f_\mu = 16\text{GHz}$, Eq. (1) determines the value of $a = 5.2\text{mm}$, the dimension of the microwave guide.

The theory of modulating the laser beam has been solved by the use of coupled mode equations for non-linear mixing. The results are clearly presented in Yariv and Yeh³ and are expressed in their notation as follows:

$$R_s = \frac{I_1(L)}{I_2(0)} = \frac{\kappa^2}{s^2} \sin^2 sL \quad (2a)$$

$$\kappa = n^3 \bar{r} E_\mu / 1.5\lambda \quad (2b)$$

$$s = \sqrt{\kappa^2 + \delta^2}, \quad \delta = \Delta\beta / 2 \quad (2c)$$

where $I_1(L)$ is the intensity of the SSB and $I_2(0)$ that of the input laser beam, κ is the clamped electro-optic coefficient in terms of n , the refractive index, \bar{r} the effective electro-optic coefficient along the $[111]$ axis and E_μ the peak amplitude of the microwave field, where δ is the phase mismatch coefficient and L the length of the crystal. The result of Eq. (2) is plotted in Fig. 2 as the conversion efficiency, which for $L = 30.8\text{cm}$, $P_\mu = 10\text{kW}$ microwave power yields 100% conversion on phase match, i.e. $\delta = 0$. However, when the frequency is varied and $\delta \neq 0$, at 15.3GHz and 16.7GHz the SSB vanishes due to the phase mismatch between the beat optical wavelength and the microwaves. To overcome this limitation, we have devised the two schemes of multisection and dual arrangement of modulators to broadband such devices.

Broadband Modulator

To broadband the modulator, we propose to cut the crystal in sections each with its own microwave housing as indicated in Fig. 3a. The purpose of this is to correct the phase of the microwave fed into each section in order to compensate for the phase mismatch. Since the system is dispersive, the phase correction also has to vary accordingly as the frequency is tuned. In order to solve this problem, we have developed a formal theory in which we solve the couple mode equations for each section and incorporate the phase correction in the off-diagonal components of the transfer matrix which represents the solution. Then to obtain the overall output, we multiply the matrices representing the crystal sections and maximize the output by varying the phase parameters. The formal solution reduces to a compact form for the general case and is given by⁴

$$R_s^N = \sin^2 \left\{ \sum_{j=1}^N \sin^{-1} X_j \right\} \quad (3a)$$

where

$$X_j = \frac{\kappa_j}{s_j} \sin s_j L_j \quad (3b)$$

and κ_j , δ_j , L_j , and s_j are independent parameters for each section which can be staggered tuned, i.e. $\delta_j \neq \delta_i$ represent different values of length and microwave power. For identical sections, the above expression reduces to a Chebyshev form given by

$$R_s^N = \sin^2 \{ N \sin^{-1} X \} \quad (4a)$$

$$X = \frac{\kappa}{s} \sin sL \quad (4b)$$

and the phase correction between sections is given by ψ where

$$\psi = 2 \tan^{-1} \left\{ -\frac{\delta}{s} \tan sL \right\} \quad (5)$$

The results of the analysis for the multiple sections have been carried out numerically and are given in graphic form in Fig. 4. The graphs show that for a desired efficiency the bandwidth increases with the number of sections. For example, the 3dB level for a single section is 0.6GHz whereas for six sections it is 6GHz, an order of magnitude increase. In addition, we have shown analytically and numerically that the phase correction has negative dispersion with frequency. This can be achieved with a ferrite phase shifter or an appropriate negative dispersion microwave circuit. The alternative, as shown in Fig. 3b, is to use multiple TWT's connected with suitable lengths of coaxial cable, whose dispersive delay compensates for the net positive phase delay between the front end of each crystal section as calculated from theory.

To further improve the broadband characteristics of the modulators, we can place two of them in tandem as shown in Fig. 5; the first, which is in itself an efficient broadband device (can be multiple section), adds the laser and microwave frequencies, including the chirp. The second, which accepts the output of the first, subtracts the frequencies. However, the first is driven by a waveform in which the chirp is positively swept; whereas, the second is swept with the lower sideband and negatively chirped. The net result of the polarization arrangement shown in Fig. 5 is that the output of the dual tandem modulator is the recovery of the original laser base band frequency which is swept with twice the chirp bandwidth. Although there is a slight sacrifice overall in efficiency, the characteristics of the broadband curves of Fig. 4 indicate that effectively we have doubled the bandwidth of the modulator. The advantage is that it can achieve this with microwave components, whose bandwidth may also be limited. This particular dual arrangement of modulators becomes even more attractive at shorter wavelengths⁵, where solid state laser amplifiers have the bandwidth to accommodate the broadband tuning.

Tunable Sources

During the 1970's great interest was shown for the development of tunable sources. One of the applications was isotope separation which instigated a great need for tunable sources in the infrared. In particular, the TEA CO₂ laser was a favorite source for multi-photon dissociation of molecular gases.⁶ This required high power pulsed sources, which could be tuned. Usually a grating was used to obtain step tunable lines of the P and R branch transitions. The broadband microwave modulator described in this paper can now provide the fine tuning with efficient conversion to provide resonant pumping of a particular molecule for non-linearly induced multiphoton transitions. In addition, two such tunable TEA CO₂ lasers can be mixed efficiently in a third order non-linear crystal such as Ge⁷ to extend the tunable range of the CO₂ laser to the shorter and longer wavelengths in the 8 μ m and 12 μ m ranges. Thus, linear and non-linear spectroscopy can be achieved with such tunable sources in this region of the far-infrared (FIR). With the use of efficient doubling crystals such as TAS⁸, we can double these frequencies into the 4 to 6 μ m region, with fine tuning electronically by the use of the modulators, since the bandwidth of the doubling process can accommodate the modulator tuning without reorienting the birefringent crystal.

Another region of the electromagnetic spectrum that would benefit from the use of the broadband modulator is the submillimeter region. During the previous decade, Aggarwal and Lax⁹ and coworkers developed non-collinear techniques for optical mixing of two CO₂ lasers in GaAs to generate ~4000 discrete frequencies which spanned the region from 70 μ m to well into the millimeter region, about two decades. The results of their experiments⁹ are shown in Figure 6 with about 100 representative lines and some of the CO₂ laser transitions utilized to obtain them. In order to tune these transitions, the gratings of the CO₂ lasers were driven to peak at each transition, simultaneously a mirror was driven by a cam arrangement to adjust the angle between the two beams to the desired phase match angle to an accuracy less than 0.1°. The experiments achieved relatively higher efficiencies by the use of large crystals with folded geometries¹⁰ to produce ~10kW pulses at 100 μ m and a microwatt CW, still preserving the coherence of the input lasers. With further improvements and use of microprocessors this arrangement together with the electro-optic modulators, the entire frequency range can be covered automatically, overcoming the limitation of discrete tuning. Such a facility can readily replace the FEL at Santa Barbara¹¹ with superior performance and much lower funding and space requirements. This system can be readily tuned within seconds; whereas, in the FEL one has to adjust the beam energy and the wiggler separation, which takes orders of magnitude longer. The microwave TWT drivers can also drive other modulators using solid-state lasers and others lasers to cover the near and FIR regions spanning wavelengths from <1 μ m well into the millimeter region.

Spectroscopic Applications

The availability of tunable sources over a wide region of the spectrum is needed to study a variety of resonance phenomena such as cyclotron resonance, spin resonance and impurity transitions in solids, such as semiconductors. In the submillimeter region, these have been studied using Fourier transform spectrometers and fixed frequency molecular lasers with tunable magnetic fields. When the linewidths are broad, the calibration of the magnetic field or that of the Fourier spectrometer is adequate. However, if the line is relatively narrow, a broadband modulator, whose tunable microwave frequency is more precisely known, would then provide the desired high resolution. Sometimes it is more convenient to fix the magnetic field near the resonance and tune the frequency. For both linear and non-linear studies in solids this alternative is desirable.

Another application where a tunable source in the submillimeter region is useful is the study of Raman transitions⁶ in molecular gases and their application for tunable Raman lasers. For example, Raman transitions have been studied in such molecules as $^{12}\text{CH}_3\text{F}$. These have been pumped by a CO_2 TEA laser, exciting transitions between vibrational levels as indicated in Fig. 7 where the selection rules for a dipole transition $\Delta v=+1$, $\Delta J=+1, -1$, for R and P transitions respectively. The far infrared induced transition is between rotational states J and $J-1$. These transitions can be resonant if the excitation energy of the CO_2 laser is coincident with that of the molecule irradiated. In general, this is not the case since the incident photon energy is not equal to the energy separation between the lower and the upper levels. It is then assumed that a virtual transition takes place as indicated by the dotted line. Then a photon is emitted between the virtual level and the nearest lower rotational level. This is the Raman process. Thus, if one tunes the pump laser such as the CO_2 laser, one also obtains tunable radiation in the far infrared (submillimeter) region. This has been done by using grating tuning and exciting different J transitions, giving a number of selected values of δ_p or energy offset. A more systematic way of achieving the objective of tuning was to construct a high pressure multi-atmosphere TEA laser, which can be tuned continuously by a grating. An alternative which is now available is to use the broadband multisection modulator to tune a commercial atmospheric laser. The amplitude characteristics and the frequency identification of the exciting radiation are superior. Once such a source exists, the study of tunable Raman transition such as those indicated in Fig. 7 for a double Raman process can be more precisely carried out. The correlation between theory and experiment for the tuning as indicated in Fig. 8, and the relative contribution of the two competing transitions can be quantitatively examined.

Plasma Diagnostics

The use of lasers for plasma diagnostics in the submillimeter region has been demonstrated in fusion plasmas of Tokamaks. Cyclotron emission¹² and absorption¹³ have been used to measure the temperature of the electrons as a function of position. The technique has involved optically pumped lasers in which different gases were used for a few selected frequencies. The combination of a tunable CO_2 laser pumping a Raman-tuned or preferably a resonantly tuned laser in a few selected gases would provide a more versatile source for such diagnostics. The broadband tuning would make a greater number of frequencies available for a given molecular gas.

Perhaps the most significant plasma diagnostic technique that would benefit from the broadband tunable source would be the measurement of ion and alpha particle temperatures in an ignition fusion plasma. It has been demonstrated that ion temperatures in a Tokamak can be measured by Thomson scattering using high power submillimeter lasers.¹⁴ The signal-to-noise ratios in these experiments for a variety of reasons were barely marginal. However, they can be enhanced by orders of magnitude by using a coherent four wave scattering (CARS) proposed by Pradhaude, Scudder, and Lax¹⁵ in 1979. With the use of the broadband modulator pumping a Raman-tuned submillimeter laser, the technique is now feasible. For alpha particles, this would require 10-20GHz tuning to determine the spectral characteristics of the energetic ions. With two sets of lasers, which are mixed in the plasma to provide the coherent density fluctuations, this is achievable. The scheme for scattering is shown in Fig. 9, in which two intense laser beams focussed to a 1cm^3 volume within a Tokamak, would be scattered in a coherent fashion in a nearly forward direction. Alternatively, a third laser beam at right angle would be scattered by the fluctuations induced by the first two lasers. The scattered signal, which has the frequency $\omega_s = 2\omega_1 - \omega_2$ or $\omega_s = \omega_3 + (\omega_1 - \omega_2)$ is detected by a heterodyne technique. The enhancement in scattering is due to a resonance in which $\omega_1 - \omega_2$ represents the difference of the two tunable exciting lasers corresponding to the Doppler shift spread of the various ion species. Furthermore, unlike Thomson scattering, which is spontaneous and spread over a 4π steradian solid angle, the coherent scattering is confined to a small solid angle of the order 10^{-3} steradians. When these effects are incorporated into the theory, it has been shown that the relative efficiency of the CARS scattering at about $300\mu\text{m}$ would be of the order of 10^4 , four orders of magnitude larger than that of the Thomson scattering.

Conclusions

In this paper we have described two techniques of broadbanding the frequency modulation of lasers. The achievable bandwidth is about 10GHz for CO₂ lasers and even greater for shorter wavelength lasers. The techniques involve multisection modulator structures with a dual counter frequency modulation tandem arrangement. Such modulators are being developed for radar and communication applications. The spin-off for basic science in the realm of spectroscopy has been illustrated for solids, gases, and plasmas. In particular, resonance phenomena in solids and Raman spectroscopy in molecular gases were elaborated. Non-linear phenomena such as multiphoton excitation, saturation effects and non-linear tunable spectroscopic techniques were not discussed. Nevertheless, there are many such phenomena that would benefit from the use of tunable high-power laser sources. Plasma diagnostics involving cyclotron resonance and scattering in fusion plasmas are illustrative examples.

References

- (1) Buhrer, C.F., Baird, D., and Conwell, E.M., Appl. Phys. Lett. 1, 46-49 (1962).
- (2) Carter, G.M., and Haus, H.A., IEEE J. Quant. Electron, QE-15, 217-224, April (1979).
- (3) Lax, B., and Marino, R.M., and Eng, R.S., (to be published).
- (4) Lax, B., Marino, R.M., and Eng, R.S., (to be published)
- (5) Yariv, A., and Yeh, P., Optical Waves in Crystals, pp. 186-187, John Wiley and Sons, New York (1983).
- (6) Danly, B.S., Evangelitis, I.S., Jenkin, R.S., and Lax, B., pp. 195-278, Infrared and Millimeter Waves, Vol. 12, Edited by K.J. Button, Academic Press (1984).
- (7) Feichtner, J.D., and Roland, G.W., Appl. Opt. 11, , 993-997 (1972)
- (8) Aggarwal, R.L. and Lax, B., Topics in Applied Physics, Vol. 16, pp. 19-80, Edited by Y.R. Shen, Springer-Verlag, New York 1977).
- (9) Lax, B., Aggarwal, R.L. and Favrot, G., Appl. Phys., Lett. 3, 679 (1973).
- (10) Lee, N., Aggarwal, R.L., and Lax, B., Opt. Commun. 11, 339 (1974).
- (11) Elias, L.R., Ku, R.J. and Ramian, E.J., Nuclear Instruments and Methods in Physics Research A, 237, pp. 203-206 (1985).
- (12) Woskoboinikow, P.A., Praddaude, H.C., Falconer, I.F., and Mulligan, W.J., Appl. Phys. Lett. 39, 548 (1981).
- (13) Pachtman, A. and Wolfe, S., (private communication).
- (14) Woskoboinikow, P., Mulligan, W.J., Machusak, J., Cohn, D.R., Jenkin, R.J., Sollner, J.C.L., and Lax, B., Euro-physics Conference Abstract, 11th European Conference on Controlled Fusion and Plasma Physics, Vol 7D, Part II, pp. 81-84 (1983).
- (15) Praddaude, H.C., Scudder, P.W., and Lax, B., Appl. Phys. Lett. 35, 10 (1979).

"The views expressed are those of the author and do not reflect the official policy or position of the U.S. Government."

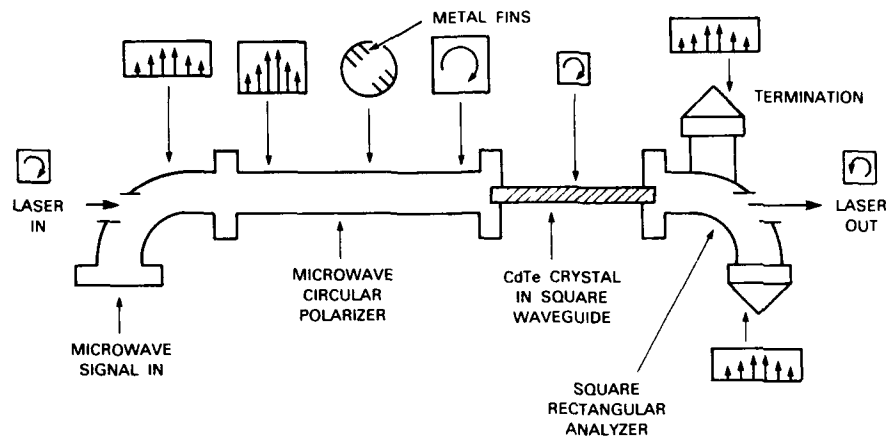


Fig. 1(a) SSB CdTe modulator showing circular polarization of laser beams (small squares) and microwave polarization (large squares) (after Ref. 2).

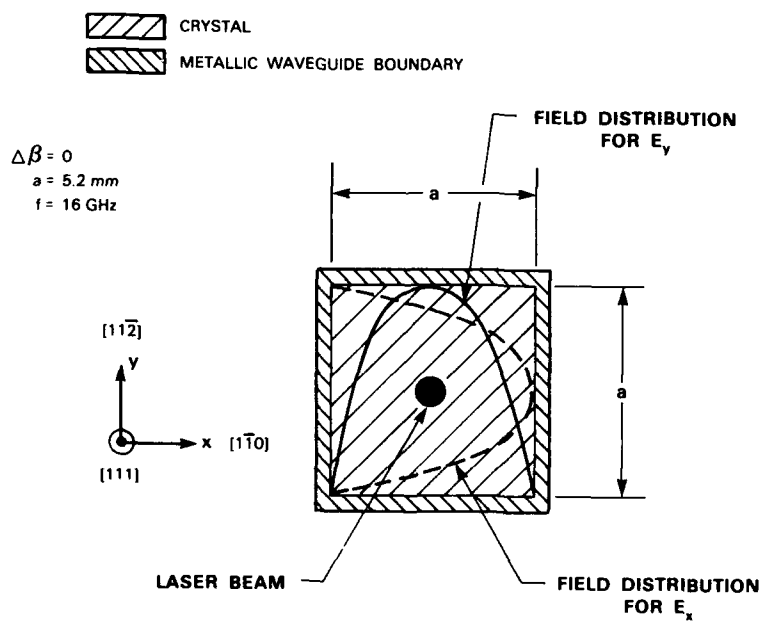


Fig. 1(b) Crystal orientation in square microwave waveguide (after Ref. 2).

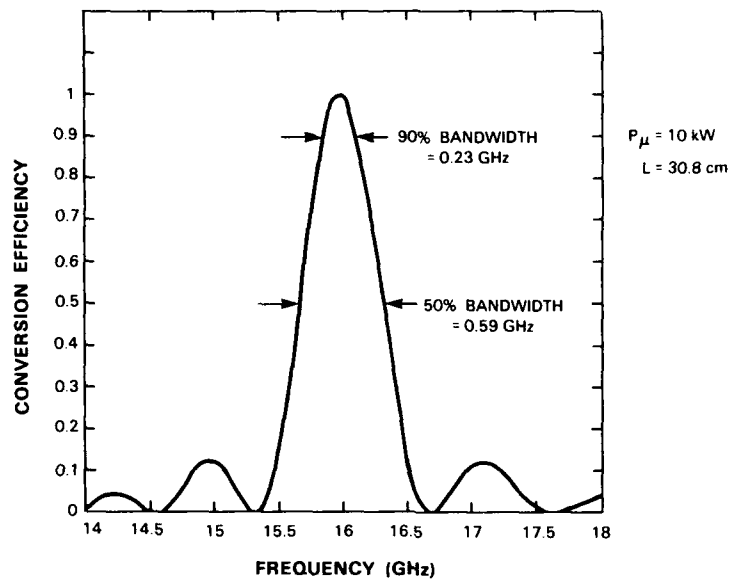


Fig. 2 Conversion efficiency of single section SSB CdTe modulator, at $10.6 \mu\text{m}$, for phase match at $f_{\mu} = 16 \text{ GHz}$, as a function of the microwave frequency (after Ref. 3).

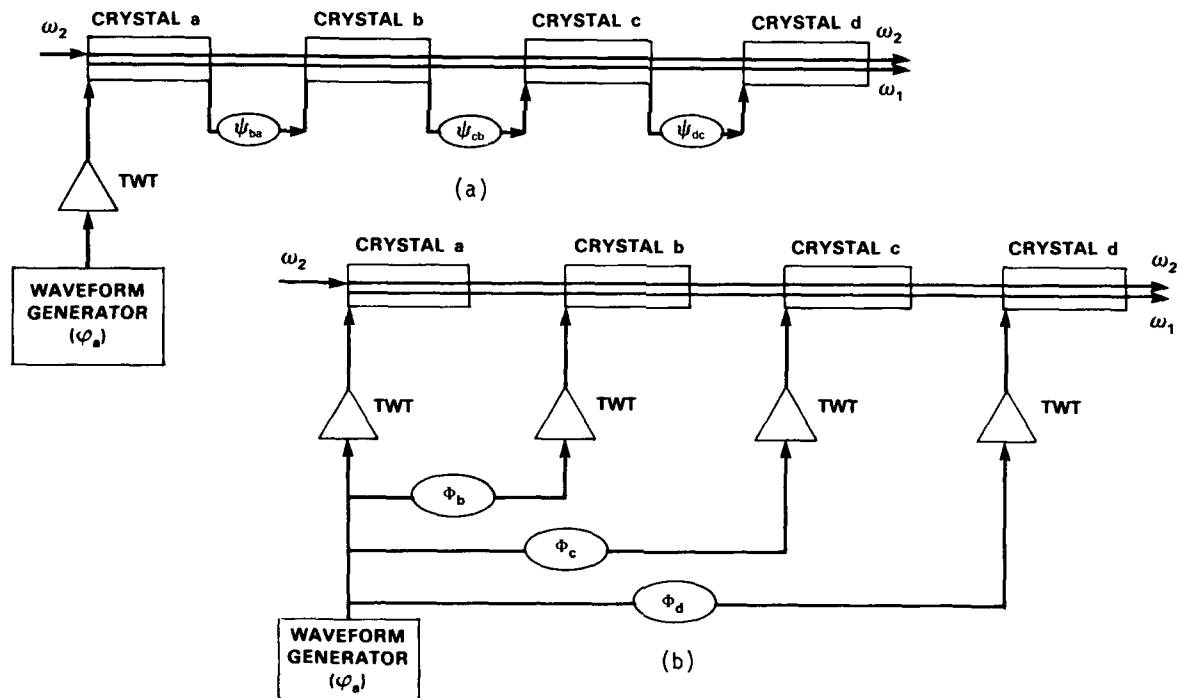


Fig. 3(a) Multisession modulator showing microwave phase corrections ψ_{ba} , ψ_{cb} , and ψ_{dc} between sections. ω_1 , ω_2 , and ω_{μ} are SSB, laser microwave frequencies, respectively. (b) Multi-TWT drive with ϕ_a , ϕ_b , and ϕ_c , which are the phase corrections of the successive sections (after Ref. 3).

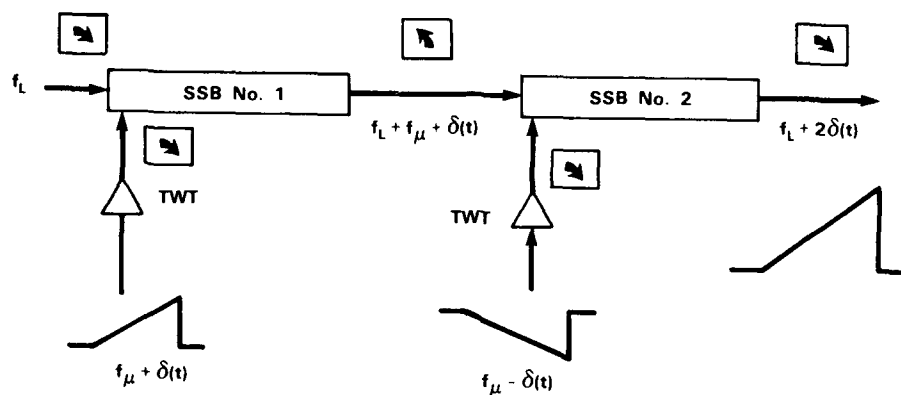


Fig. 5 Dual broadband SSB modulator with double sideband counter swept frequencies to yield the original laser frequency f_L and twice the sweep frequency (after Ref.4).

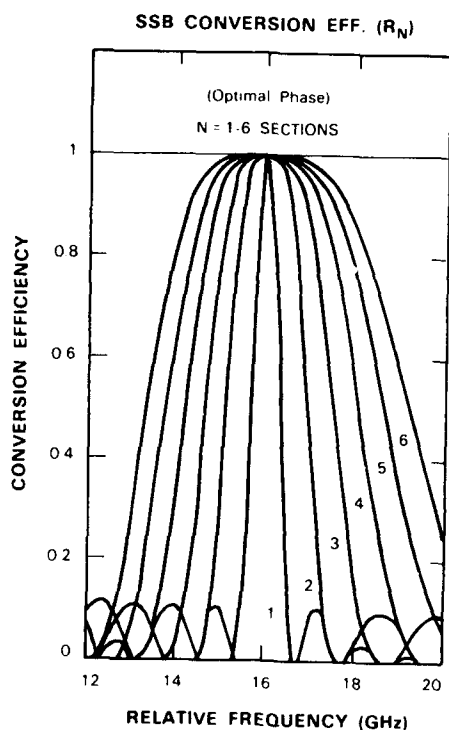


Fig. 4 Conversion efficiency of multiple section SSB modulator as a function of frequency for optimal phase adjustment (after Ref. 3).

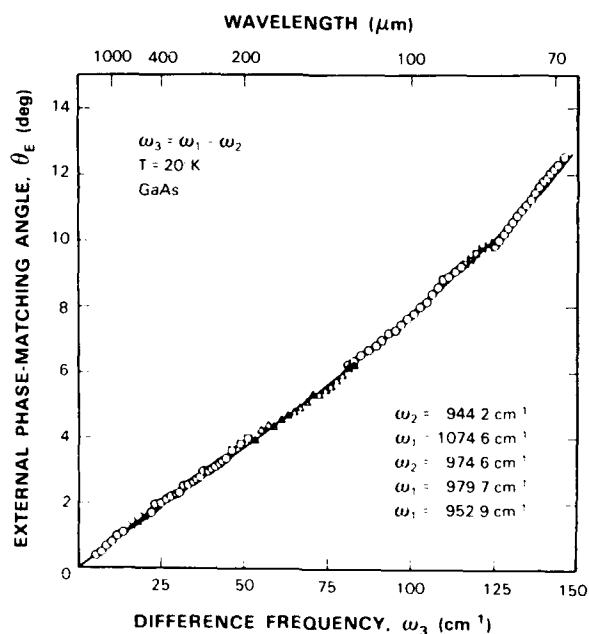


Fig. 6 Result of the non-collinear phase match optical mixing of two grating tuned CO₂ lasers in GaAs. For each discrete difference frequency from 70 μ m to beyond 1mm there is a precise phase angle (after Ref. 6).

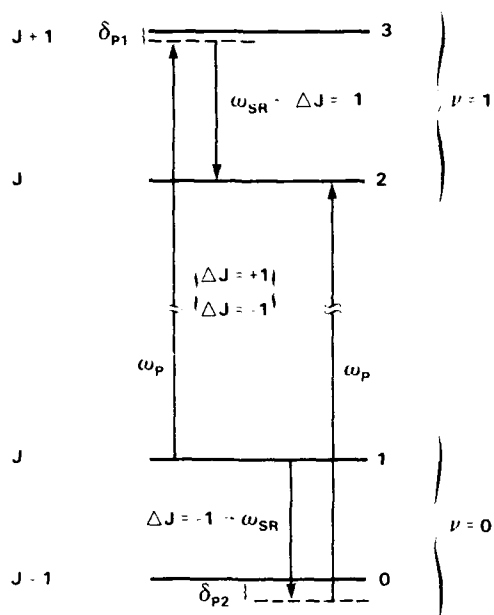


Fig. 7 Diagram of the double Raman process in a molecular gas for a tunable FIR laser, ω_p is the CO₂ pump frequency and ω_{SR} is the FIR laser emission frequency (after Ref. 6).

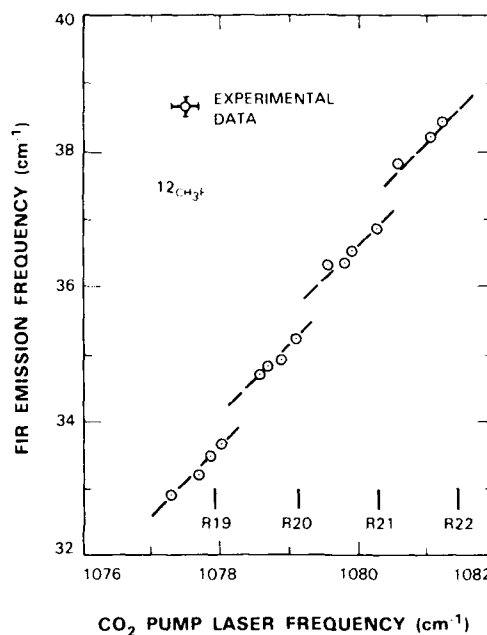


Fig. 8 Experimental results for R-branch tuning of a Raman laser. --- lines indicate results of theory (after Ref. 6).

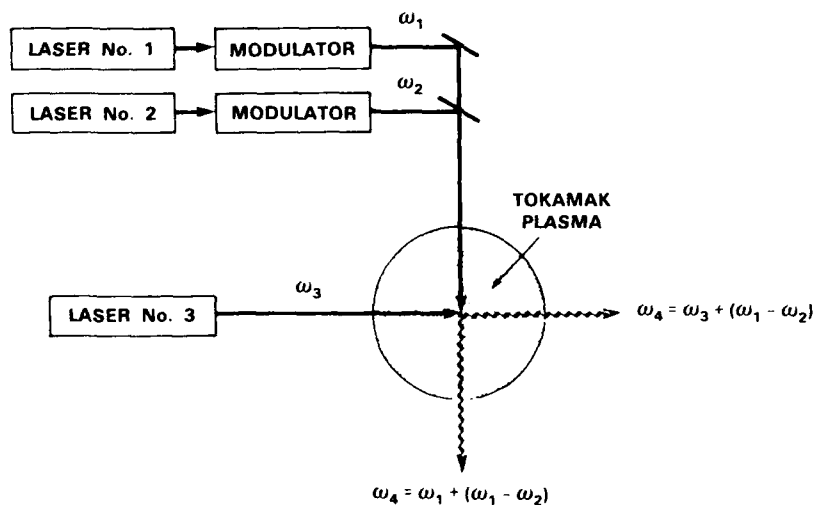


Fig. 9 Diagram of two possible arrangements of the coherent 4-wave scattering plasma diagnostic technique (CARS), ω_4 is the scattered wave and $\omega_1 - \omega_2$ = ion or alpha particle Doppler frequencies.

A 1,2 FLUORINE MIGRATION IN THE MULTIPHOTON ISOMERIZATION OF TETRAFLUOROCYCLOPROPENE

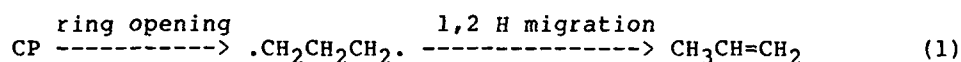
D. C. Tardy, H. B. Friedrich, D. J. Burton
Department of Chemistry, The University of Iowa
Iowa City, Iowa 52242

ABSTRACT

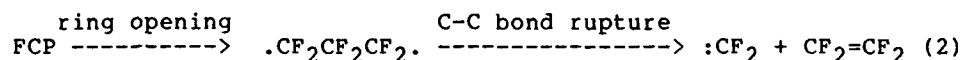
The infrared multiphoton excitation of tetrafluorocyclopropene (TFCP) leads to the unexpected formation of the tetrafluoroallene (TFA) and tetrafluoropropyne (TFP) isomers and not the elimination of CF_2 as has been reported for the decomposition of hexafluorocyclopropane. The ratio of TFP to TFA is independent of fluence and pressure; no other products are formed. The conversion per pulse increases markedly with an increase in initial TFCP pressure but decreases as the pressure of the products or a buffer gas increases. In every case, the isomerization reaction did not consume more than about 50% of the initial TFCP. The apparent intramolecular 1,2-fluorine migration required to form the products is discussed in terms of both unimolecular and bimolecular processes. The observed distribution of products and the lack of fragmentation do not support a unimolecular process after the initial excitation. However, the high conversion at low fluences and the pressure dependence are indicators that a bimolecular process may be the dominant path.

INTRODUCTION

The mechanism for the thermal or infrared multiple-photon excitation of cyclic fluoroalkanes is typically different from that for the unfluorinated analog. For example, propene is the sole product from the thermolysis of cyclopropane (CP) while the thermal decomposition of perfluorocyclopropane (FCP) leads to tetrafluoroethene; no perfluoropropene is formed. It has been shown¹ via isotopic substitution that the mechanism for CP isomerization is

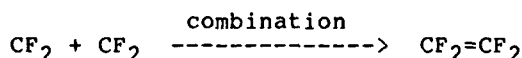
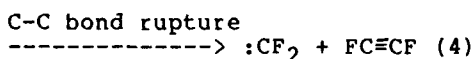
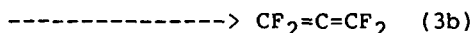
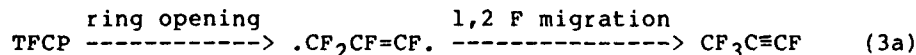


while for FCP the decomposition mechanism² is



The Arrhenius parameters³ for CP and FCP are $A=10^{15.2} \text{ sec}^{-1}$, $E_a=65.5 \text{ kcal/mole}$ and $A=10^{15} \text{ sec}^{-1}$, $E_a=43 \text{ kcal/mole}$, respectively. The ring opening of CP which is 54.8 kcal/mole endothermic has a critical energy of 64.1 kcal/mole to form the trimethylene diradical intermediate; the trimethylene can either reform the ring with a critical energy of 9.3 kcal/mole or undergo a 1,2 H migration with a critical energy of 10.7 kcal/mole. For FCP the critical energy for ring opening is 18.6 kcal/mole while the C-C bond cleavage is 23 kcal/mole; presumably this second step is lower than that for the potentially competitive 1,2 fluorine migration.

From the above analogies it was expected that tetrafluorocyclopropene (TFCP) would react by one of the following two mechanisms:



However it has been reported^{4,5} that the thermal decomposition of TFCP produces dimers and higher oligomers of TFCP. We have studied the infrared multiple-photon decomposition (IRMPD) of TFCP and find the products [tetrafluoroallene (TFA) and tetrafluoropropyne (TFP)] resulting from path 3 instead of tetrafluoroethene (from the combination of two $:\text{CF}_2$) and difluoroethyne from path 4. Thus contrary to the FCP reaction it would appear that the apparent fluorine atom migration in the TFCP system has a lower critical energy than that for the C-C bond rupture. Contrary to what is predicted for a simple unimolecular process, our IRMPD results do show a dependence for the conversion per

initial laser pulse on fluence and TFCP pressure while the product ratio is independent of these experimental parameters.

EXPERIMENTAL

TFCP was prepared by the method of Sargeant and Krespan⁵; 1,2-dichlorotetrafluorocyclopropane (DCTFCP) was prepared from the reaction of 1,2-dichlorodifluoroethene with hexafluoropropylene oxide and the DCTFCP was dechlorinated to yield TFCP. This sample had been stored for five years at room temperature without detectable (<0.1%) reaction.

A Tachisto 215G CO₂ laser tuned to the P(34) line of the 00⁰₁-10⁰₁ band (931 cm⁻¹) or the R(28) of the 00⁰₀-02⁰₀ band (1083 cm⁻¹) was used as the excitation source; these lines overlap with the symmetric C-F stretch on the CF=CF group (929 cm⁻¹) and the asymmetric C-F stretch on the CF₂ group (1093 cm⁻¹)⁶. The specific laser line was identified by an Optical Engineering model 16A CO₂ laser spectrum analyzer while the pulse energy was monitored with a Gen-Tec model ED-500 joulemeter. Most experiments were conducted with the unfocused laser beam; for other experiments a 1.5" diameter AR coated germanium lens with a 6" focal length was placed 2.5" and 3.5" from the center of the reaction cell. This amplified the fluence by factors of approximately 1.9 and 2.6, respectively.

Semiquantitative thermal reactions of TFCP were performed with a 0.15 L pyrex reactor. The tubular reactor was filled with 8 torr of TFCP and immersed into a heat bath at 250 C. After a specified time the gas was expanded into the IPMPD reactor and analyzed using the same procedure as described below for the laser excitation experiments.

Infrared spectra were obtained using an IBM Model 98 FTIR instrument at 1 cm⁻¹ resolution. The gas cells (10 cm long, 2.1 cm i.d. or 2.54 cm long, 2.54 cm i.d.) were fitted with NaCl windows. The pressure of TFCP in the cells was measured using a MKS Baratron (#22BHS) 100 torr capacitance manometer and/or infrared absorption intensities. The spectrum of the products was obtained by subtracting the spectrum of TFCP from that of the mixture of products and TFCP; band areas were obtained using Simpson's rule with a flat baseline drawn between the limits indicated below.

RESULTS

Except for weak bands due to a DCTFCP impurity the infrared spectrum of a 4 torr sample of TFCP is in agreement with that reported by Craig⁶. The spectrum of the products obtained after the spectrum of the remaining TFCP has been subtracted is almost entirely due to TFA and TFP.^{7,8}

The ratio of the area of a TFP band (integration limits 2395 to 2295 cm⁻¹) to that of a TFA band (2100 to 1975 cm⁻¹) was used to monitor the product distribution; this ratio is not equal to the actual product yield ratio. For initial TFCP pressures ranging from 0.4 to 8.5 torr, fluences from 0.8 to 2 J, and percent conversions from 1 to 50%, the ratio of areas for the 25 experiments remained constant at 0.206 +/- 0.009 independent of the laser frequency used.

The amounts of TFA and TFP formed were directly proportional to the loss of TFCP. In several cases, the total pressure was also determined as a function of percent conversion and varied from an initial pressure of 7.60 torr to 7.54 torr after 80 pulses (0.8 J/pulse) which resulted in a 26% conversion.

The conversion per pulse increased markedly with an increase in initial TFCP pressure but decreased as the pressure of the products (i.e. % reaction) increased. With unfocused radiation and an initial TFCP pressure of 0.2 torr there was no change in the spectrum after 1100 pulses, whereas with an initial pressure of 8 torr, 29% of the TFCP was converted to TFA and TFP after a single 2 J pulse. Based on the area of the burn pattern on thermal paper, the first laser pulses corresponds to about 100% conversion of the TFCP in the irradiated volume. Similar behavior was observed for all cases studied, i.e., initial pressures ranging from 0.4 to 8.5 torr. The initial extent of reaction increases markedly with pressure; a 20 fold increase in pressure (0.4 to 8.0 torr) produces a factor of 100 in the initial conversion per pulse. No quantitative studies of the reaction at higher pressures were performed, but the conversion at 8.5 torr was lower than that at 8.0 torr.

With an initial pressure of 2 torr, 128 pulses of unfocused radiation resulted in 13% conversion, but the same irradiation of a sample containing 1.5 torr of TFCP and 6.6 torr of argon produced no change in the TFCP spectrum. In every case, the apparent isomerization reaction did not consume more than about 50% of the initial TFCP using the 931 cm⁻¹ laser line; conversions up to 60% were observed when the 1083 cm⁻¹ line was used. For example, 100 pulses of unfocused irradiation for an initial TFCP pressure of 8.1 torr

resulted in 40% of the TFCP isomerized to TFA and TFP; 1000 additional pulses resulted in a total of 50% loss of TFCP, but there was also a 4% loss of TFA and a 10% loss of TFP relative to the amounts present after 100 pulses. After isomerization 42% of the TFCP in a sample with an initial pressure of 8.5 torr, the CO₂ laser frequency was changed to 1039 cm⁻¹ (P28 line of the 00⁰₁-20⁰₀ band) where TFA has a strong absorption band but TFCP does not. After 66 pulses (1.3 J each), no changes were observed in the infrared spectrum of the sample.

When the intensity of the incident beam was reduced by 50%, no dissociation of an 8.1 torr sample was observed after 32 pulses. A 30% reduction in beam intensity resulted in only 2% conversion after 32 pulses as compared to a 50% conversion with no beam attenuation (2 J/pulse). However the ratio of TFP to TFA formed by the irradiation was independent of fluence and intensity.

Our preliminary studies on the thermal decomposition of TFCP at 250 C and 8 torr have confirmed earlier reports⁴ that a high molecular weight product is formed; no TFA or TFP was observed. When a mixture of TFCP, TFA and TFP (formed by irradiating 8 torr of TFCP) was heated to 250 C both TFA and TFP uniformly disappeared while only a small amount of TFCP disappeared. Under similar conditions pure TFP did not react.

DISCUSSION

The dependence of the isomerization yield per laser pulse on the pressure of TFCP, the products, and/or a buffer gas (argon) suggests that the process is collision-assisted. The very high conversion per pulse at higher pressures and the inhibition of the reaction by argon or the products of the reaction would seem to rule out rotational relaxation or pressure broadening of the absorption line as sources of the observed pressure dependence. Intermolecular V-V or V-T/R transfer as a result of collisions of excited TFCP with cold TFCP, TFA or TFP, or a buffer gas, would be expected to cause a decrease in conversion per pulse with increasing pressure,^{9,10} but energy pooling to reach a dissociation channel as a result of the collision of two molecules at an intermediate level of excitation is a possibility.¹¹

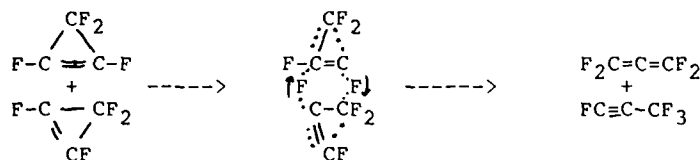
The experimentally determined exothermicity of the TFCP to TFA or TFP reaction is not known but recent quantum mechanical calculations¹² estimate TFP as being ~4 kcal/mole more stable than TFA and ~21 kcal/mole more stable than TFCP; similar calculations show propyne to be 3 kcal/mole more stable than allene while experiments give a difference of only 1 +/- 0.8 kcal/mole. Thus the TFA and TFP should be chemically activated with 21 kcal/mole in excess of the activation energy for TFA/TFP formation; this excess energy should result in greater fragmentation of the products as the pressure is decreased. The observation of constant pressure with 26% reaction indicates that the number of moles of reactants is the same as products and fragmentation is not important.

It has been demonstrated that the RRKM statistical model for unimolecular reactions adequately describes the experimental observations for IRMPD¹³. For this model the microscopic rate constant increases with increasing internal energy. The average internal energy of reacting molecules ($\langle E \rangle_r$) is determined by the energy level where the pumping rate and unimolecular reaction rate are competitive; increasing the laser intensity (fluence) will increase $\langle E \rangle_r$. For competitive intramolecular reactions the ratio of product yields for the competitive paths is a function of the difference in critical energies and the structures (vibrational frequency patterns) for the respective activated complexes. The energy dependence of this ratio has been used to determine $\langle E \rangle_r$.¹³ The observed insensitivity of the area ratio to fluence or pressure indicates that either the process is not unimolecular or that both unimolecular processes have nearly identical critical energies and structures for the activated complex.

An energy pooling collision to yield one molecule with sufficient energy for ring opening might be invoked as an excitation mechanism; this would satisfy the observed pressure dependence. However the constraints required for the simple 'one step' unimolecular step cited above would still be required.

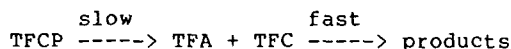
Another possible pathway which satisfies the pressure dependence would involve the collision of two TFCP molecules (either one or both supplying sufficient energy for reaction); during the collision a fluorine atom from each molecule is transferred to the other. The vibrational energy content in either TFCP molecule would be less than the threshold required to form the biradical but sufficient to promote the transfer. The TFA/TFP area ratio would be invariant with fluence and pressure; however the rate constant would show an energy dependence. This pathway would account for the difference between collisions of TFCP with argon, TFA, TFP and TFCP; the first three partners would remove the required vibrational energy from TFCP. Thus, as reaction proceeds the initial excitation is collisionally transferred to TFA and TFP instead of being directed to the reaction coordinate as is the case for collision with TFCP. At this time there is not

sufficient evidence to preclude this pathway, in fact the high conversion at low fluences and the pressure dependence are indicators that this may be the dominant path. If this is the preferred path then the product yield ratio would be 1:1. As shown below there will be a substantial decrease in entropy for the formation of the activated complex.



We are in the process of measuring absolute absorption coefficients for TFP and TFA so that the constant relating the product and area ratios can be determined.

The thermal studies at 250 C and the stability of TFC at room temperature can be used to determine limits on the activation energy if a unimolecular reaction with an A factor of 10^{15} sec^{-1} is assumed; the lower limit is 36 kcal/mole while the upper limit is 45 kcal/mole. The thermal reaction of the mixture indicates that TFA and TFP are reactive intermediates at 250 C and relatively stable at room temperature.



Thus laser excitation can be used to promote reactions with high critical energies in a low temperature environment so that consecutive reactions with smaller critical energies will be quenched. TFA and TFP appear to react stoichiometrically to produce some of the same products as the thermolysis of TFCP. Since the thermolysis of TFP does not produce TFA or the products resulting from the thermolysis of the TFCP-TFP-TFA mixture, it appears a cooperative process is involved. We plan to perform the thermolysis of neat TFA and TFA-TFP mixtures to determine this cooperative mechanism for the thermolysis.

Recently INDO calculations for 1,2 fluorine migrations in fluoro substituted ethyl radicals have been reported¹⁴. The calculated critical energy is 8.3 kcal/mole compared to 22.0 kcal/mole for a similar 1,2 H migration. Due to the formation of the pi bond in the production of TFP or TFA, we expect that the critical energy for the biradical will be reduced so that the critical energy for isomerization would be less than 26 kcal/mole.

ACKNOWLEDGMENT

This research was supported in part by a grant to D.C.T. by the Division of Chemical Sciences, Office of Basic Energy Sciences, U.S. Department of Energy Grant DE-FG02-37ER13700 and grants to D.J.B. by the National Science Foundation and the Air Force Office of Scientific Research.

REFERENCES

1. a) E.W. Schlag and B. S. Rabinovitch, J. Am. Chem. Soc. 82, 5996 (1960).
b) T.S. Chambers and G.B. Kistiakowsky, J. Am. Chem. Soc. 56, 399 (1934).
2. a) J.M. Birchall, R.N. Haszeldine and D.W. Roberts, J. Chem. Soc., Perkin Trans. 1, 1071 (1973).
b) J.M. Birchall, R. Fields, R.N. Haszeldine and N.T. Kendall, J. Chem. Soc., Perkin Trans. 1, 1773 (1973).
3. S.W. Benson and H.E. O'Neal, Kinetic Data on Gas Phase Unimolecular Reactions (U.S. Government Printing Office, 1970), NSRDS-NBS 21.
4. G. Camaggi and F. Gozzo, J. Chem. Soc. C, 178 (1978).
5. P.B. Sargeant and C.G. Krespan, J. Am. Chem. Soc. 91, 415 (1969).
6. N.C. Craig, G.F. Fleming and J.J. Pranata, J. Phys. Chem. 89, 100 (1985).
7. J.R. Durig, Y.S. Li, J.D. Witt, A.P. Zens and P.D. Ellis, Spectrochim. Acta, 33A, 529 (1977).
8. R.E. Banks, M.G. Barlow, W.D. Davies, R.N. Haszeldine and D.R. Taylor, J. Chem. Soc. C, 1104 (1969).
9. V.N. Bagratashvili, V.S. Letokhov, A.A. Makarov and E.A. Ryabov, Laser Chem. 4, 311 (1984).
10. J.S. Francisco and J.I. Steinfeld, in Advances in Multi-Photon Assisted Processes and Spectroscopy, Lin, S.H., Ed. (World Scientific, Singapore, Vol.2, 1986), pp 79-173.
11. I. Oref, J. Chem. Phys. 75, 131 (1981).
12. private communication from D. Dixon and B. Smart.
13. D.C. Tardy, L.L. Feezel and J.T. Wanna, in Proceedings, International Conference on Lasers '84, K.M. Corcoran, D.M. Sullivan and W.C. Stwalley, Eds. (STS Press, McLean, VA, 1985), pp 508-515 and references cited within this paper.
14. M. Kotaka, S. Sato and K. Shimokoshi, J. Fluorine Chem. 37, 387 (1987).

LASER-INDUCED IONIZATION SPECTROMETRY: ALTERNATE ATOM RESERVOIRS

Robert B. Green and Michael D. Seltzer
Chemistry Division, Research Department
Naval Weapons Center, China Lake, California 93555-6001

Abstract

Premixed flames have been commonly used to atomize samples for laser-induced ionization spectrometry. Detection limits have been excellent but the intrinsic sensitivity of the laser-based methods has been compromised when analyzing real samples. A total consumption flame and several energetic plasmas have been investigated as atom reservoirs for laser-enhanced ionization (LEI) and direct laser ionization (DLI) spectrometry. Ionization from a laser-excited state proceeds by collisions in LEI and absorption of photons in DLI. Laser-enhanced ionization occurs in a flame whenever a laser is tuned to an atomic transition. Whether or not photoionization (i.e., DLI) will supplement the LEI signal depends on the collisional properties of the atom reservoir and the difference between the energy required to reach the ionization potential and the energy of the photoionizing beam. The total consumption flame, active nitrogen, and argon plasmas each have advantages in terms of sample throughput, background, and interferences. The results of LEI and DLI measurements will be used to characterize and compare these atom reservoirs for laser-induced ionization spectrometry.

Introduction

Laser-induced ionization spectrometry may be viewed as a family of techniques (see Figure 1). Laser-enhanced ionization involves thermal or collisional ionization from an excited state that is populated by single-step or stepwise laser excitation.¹ In DLI, sometimes referred to as dual laser ionization,² the final step is laser photoionization. The DLI excitation schemes are similar to those used for resonance ionization spectroscopy (RIS), the distinction being the atom reservoir. Resonance ionization spectroscopy is performed in low pressure atom reservoirs, such as the source of a mass spectrometer. Laser-enhanced ionization and DLI are implemented in atmospheric-pressure plasmas, typically a flame supported by a premix burner. Laser-enhanced ionization and DLI may be viewed as complementary techniques. The former is more well developed but much of the research applies equally well to DLI. Multiphoton ionization (MPI) may also occur in flames but is not useful for trace metal determination. Multiphoton ionization can proceed by the simultaneous absorption of three or more photons of the same wavelength via bound or virtual states. A background signal may result from the MPI of added or native species in the flame, particularly at high incident laser powers. The noise carried by this additive signal can limit minimum detectable concentrations of analytes.

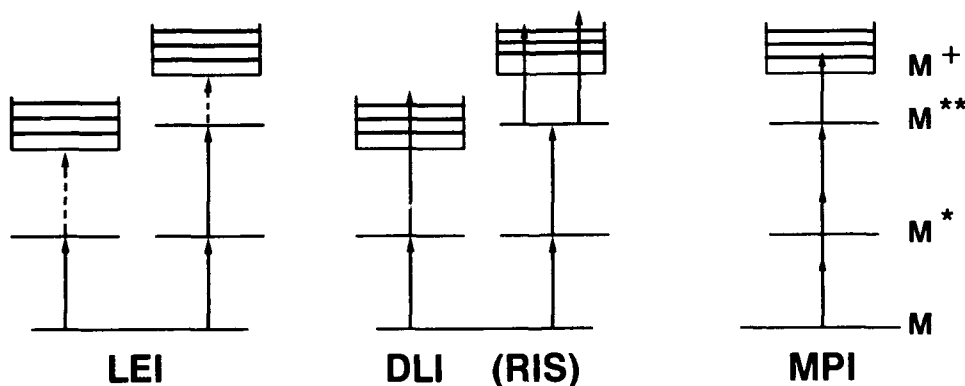


FIGURE 1. Laser-induced ionization schemes: LEI, DLI, and MPI.

Laser-enhanced ionization or DLI may be detected with biased, high voltage electrodes inserted in or near the atom reservoir. The increased current in the atom reservoir due to laser excitation is collected, preamplified, and filtered before introduction to a boxcar signal averager. A photodiode which monitors the laser output assures that the signal is sampled only during the laser pulse.

The premix burner has been the most frequently used atom reservoir. The premix burner has been the atom reservoir of choice for optically-detected spectrometry, such as atomic absorption, because it produces a stable, laminar flow flame with well-defined concentration zones. Slot burner heads provide long pathlengths which increase the signal collected. The high optical quality of the premixed flame results from mixing the fuel, oxidant, and nebulized sample solution in a chamber prior to combustion. The large sample droplets condense in the premixing chamber and return to waste via a drain. The choice of fuel and oxidant is limited to combinations that yield flames with lower burning velocities. This avoids explosive flashbacks in the premixing chamber.

The electrode configurations that have been used for laser-enhanced ionization fall into two categories: external and immersed. Either approach will produce excellent detection limits for analytes dissolved in pure, aqueous solutions. Sample matrices containing IA or IIA elements which have high ion fractions in typical analytical flames produce severe electrical interferences when external electrodes are used. This has been attributed to the formation of a space charge at the cathode.

The origin of electrical interferences may be understood by considering space charge formation at an electrode. In a flame, positive ions, electrons, and neutral species exist in the bulk phase. If the region near a negative electrode inserted in the flame is examined, several zones may be distinguished. Between the bulk phase and the electrode surface, there is a transition region where charged species separate. Near the electrode surface, cations predominate. As the concentration of cations in the flame is increased, the signal collecting field withdraws to the cathode surface. If the laser beam is outside the collecting field, none of the ions produced by laser enhancement will be sensed. When the electrodes are located outside the flame, there is no opportunity to position the laser beam within the collecting field at high ion concentrations in the flame. With immersed electrodes, the laser beam can be positioned near the cathode surface even when the ion concentration in the flame is high and the signal collection region is severely compressed. Using immersed electrodes it is possible to collect 100% of the analyte signal in the presence of sodium concentrations up to 3000 µg/mL in an air-acetylene flame.³

The periodic table in Figure 2 indicates the elements that have been determined by LEI spectrometry according to the type of flame used. (Those elements which are shown as "not determined" by LEI spectrometry have not been reported but they are amenable to flame spectrometry.) Most detection limits that have been reported were determined in the air-acetylene flame. A nitrous oxide-acetylene flame has been used for more refractory elements. It is important to recognize that although the use of an immersed electrode has mitigated electrical interferences from easily-ionized species in air-acetylene flames, the hotter nitrous oxide-acetylene flame has not yielded to this solution.⁴

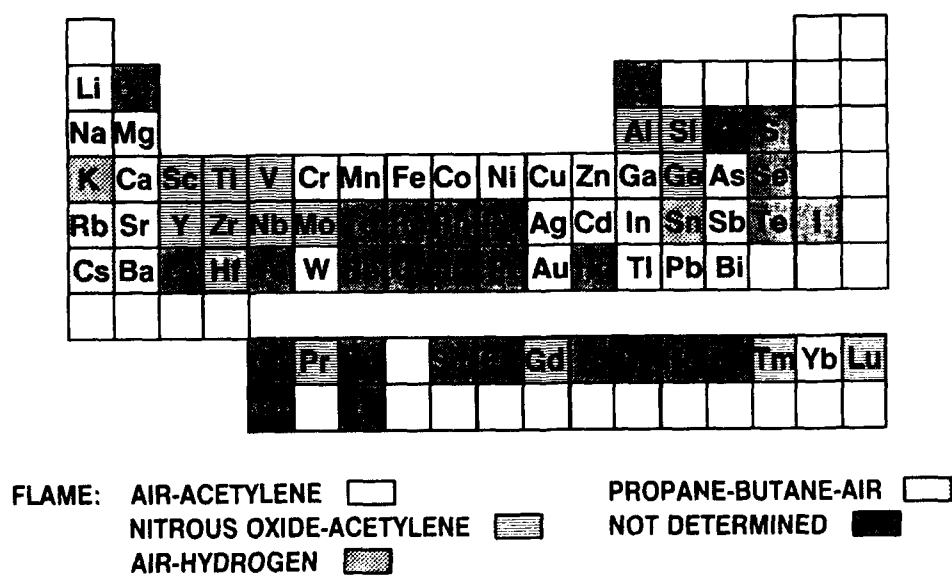


FIGURE 2. Periodic table showing types of flames used as atom reservoirs for laser-enhanced ionization spectrometry.

Results and Discussion

The limits of detection for laser-enhanced ionization in premixed flames, compiled and reported in Reference 5, establish the technique as competitive with other high sensitivity analytical methods, such as inductively-coupled plasma emission spectrometry. One component of laser-enhanced ionization spectrometry that might be improved is the atom reservoir. The search for alternate atom reservoirs was driven by the following goals: (1) increasing the analyte residence time in the laser beam, (2) increasing the quantity of analyte in the laser-excited volume, (3) reducing analyte consumption, and (4) further reduction or elimination of electrical interferences. Realistically, it should be recognized that some of these goals may be mutually exclusive.

Total Consumption Flames

One approach to increasing signal is to increase the number of atoms that can be interrogated by the laser beam. This can be accomplished by substituting a total consumption burner for the premixed burner which has been commonly used for LEI spectrometry. In the total consumption burner, the fuel, oxidant, and nebulized sample are not mixed until they exit the burner nozzle. Although 100% of the sample enters the flame, all of it is not available for laser excitation. Large droplets of sample pass through the flame without evaporation. Light scattering from these droplets is the main reason that total consumption burners are no longer used as atom reservoirs for optically-detected spectrometry. Since an electrical current is measured directly in LEI spectrometry, light scattering causes no detection problems. Even though a portion of the sample is lost to LEI, the overall increase in sample throughput over the premixed burner which rejects 95% of the aspirated sample led to a net improvement in limits of detection for the elements studied.⁶ An additional benefit of using the total consumption burner is the availability of oxygen-based flames without the threat of explosive flashback.

Laser-enhanced ionization spectrometry with a total consumption burner has some disadvantages as well. When compared with the premixed burner, the laser pathlength for the total consumption burner is reduced because the flame has a circular cross-section. Because the flame is very turbulent, the concentration gradient is diffuse and the zone of highest concentration is not well defined. The high sample throughput, the central advantage of the total consumption burner, leads to two problems: MPI background and the earlier onset of electrical interferences. The origin of the background is the MPI of flame species produced by the aspiration of water, the primary solvent for this work. The largely featureless MPI background occurs only at high incident laser powers. Since the MPI background signal was additive, it was possible to subtract it, but the random noise carried by the MPI remained. The strategy to obtain the best detection limits was to increase the laser power until MPI was observed. Then the laser power was reduced slightly below the MPI level and the detection limits were determined in the absence of MPI noise. The appearance of MPI background is also possible with a premix burner; the difference is that most of the solvent is eliminated by condensation before it reaches the flame. The earlier onset of electrical interferences due to easily-ionized species with the total consumption burner is also a symptom of the "100%" sample introduction into the flame. The actual flame concentration (or density) of ions when signal suppression occurs is probably the same for both burners. The difference is that this flame concentration occurs at much lower solution concentrations of the interferent when using a total consumption burner. It is the absolute flame concentration of interferent that determines the level of LEI signal suppression not the ratio of interferent to analyte.⁷

Sample Desolvation

Sample desolvation prior to introduction was one approach to attacking the deficiencies of the total consumption burner. Sample desolvation has long been used in atomic spectrometry but the reported sample transport efficiencies for available techniques were low. Less than complete sample transport negates the value of using a total consumption burner.

A successful approach involved using a graphite furnace to desolvate the sample prior to introduction into the total consumption burner.⁸ The liquid sample was deposited in the graphite tube, the water was driven off in a drying cycle, and the sample was atomized into a flowing stream of argon. The gas-phase sample was carried into the aspiration tube of the burner. A water vapor generator was connected in the gas line from the furnace for comparison of the introduction of dry and wet samples into the total consumption burner. Wet samples could not be introduced directly from the furnace because spattering would cause sample loss making the results equivocal.

The advantages of sample desolvation are illustrated in Figure 3. Five trials are shown. In the three trials where the manganese sample was desolvated, sharp signal peaks result. The MPI background yields a DC signal offset for the two trials with solvated samples. The increased noise carried by the signal is obvious. The reduction of peak amplitudes in the solvated trials is probably due to the cooling of the flame by water vapor introduction, thereby reducing the analyte atom fraction.

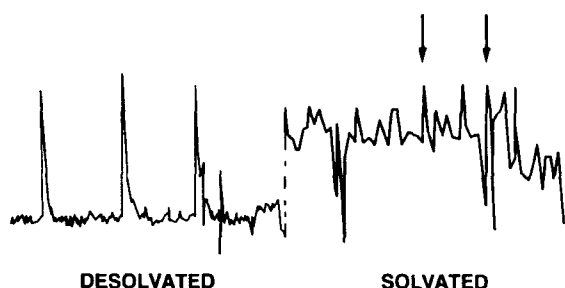


FIGURE 3. Comparison of signals for desolvated and solvated Mn samples. The arrows indicate signals for the solvated samples.

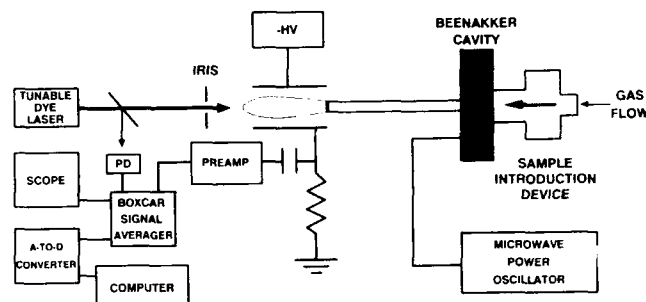


FIGURE 4. Schematic diagram of instrumentation for laser-induced ionization spectrometry in a microwave-induced plasma.

In summary, sample desolvation with the total consumption burner provides many advantages that are applicable to laser-induced ionization spectrometry.⁸ Higher laser powers can be effectively used to saturate atomic transitions. It is also possible to condense the total consumption flame by introducing it into a Vycor tube. The exciting laser beam may then be directed down the length of the flame and longer pathlength electrodes may be used. Flame condensation and pathlength extension can be applied to the total consumption flame without sample desolvation but the increased MPI noise nullifies any improvements in signal. Finally, intrinsic flame temperatures are maintained by the removal of aqueous solvents. All of these advantages lead to order-of-magnitude improvements in detection limits for laser-enhanced ionization spectrometry using total consumption burners with sample desolvation.⁸

Energetic Plasmas

Recently, microwave-induced plasmas have been investigated as atom reservoirs for laser-induced ionization. The apparatus is shown in Figure 4. The gas for plasma formation is directed through the sample introduction device. Several sample introduction devices have been used: an AC microarc, ultrasonic nebulization with solvent stripping, and a graphite furnace. The sample vapor is then carried through the microwave cavity where the plasma is generated. All of this research has involved atmospheric pressure plasmas. The plasma is conducted beyond the microwave cavity with a quartz tube. Signal collection and processing are similar to the approach used in flames.

The first plasma to be investigated was active nitrogen.⁹ Active nitrogen has interesting energetic properties and is capable of efficiently producing excited metal atoms and ions on collision with ground state species. The metal emission in sub-atmospheric pressure sources has been detected photoelectrically for analytical determinations.¹⁰ The active nitrogen in the present work was generated by adding molecular nitrogen to an argon flow in about a 1-to-10 ratio. Microwave powers in the range from 50 to 150 W were used.

Both LEI and DLI experiments were run to evaluate the collisional properties of active nitrogen. The excitation schemes for indium are shown in Figure 5. Laser-enhanced ionization occurs in a plasma whenever a laser is tuned to an atomic transition. For otherwise identical experiments, the enhancement of the DLI signal over LEI depends on the collisional environment of the plasma and how well the energy of the photon matches the energy required for photoionization. In this case, the energy overshoot was 0.34 V.

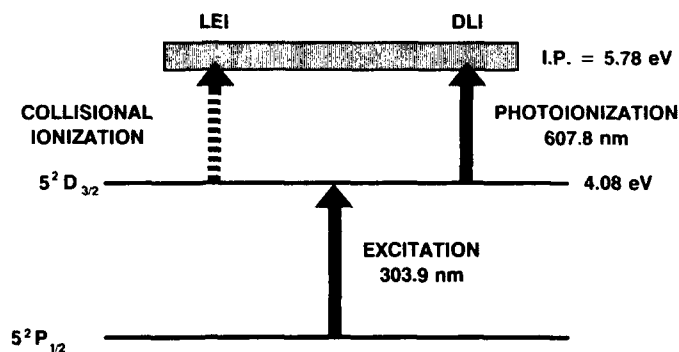


FIGURE 5. LEI vs. DLI for indium.

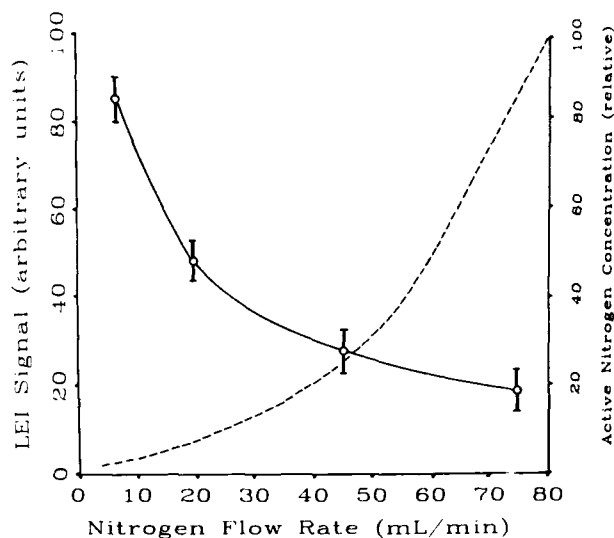


FIGURE 6. LEI and active nitrogen dependence on nitrogen flow rate.

A detection limit for DLI of indium was estimated to be 20 pg. The DLI signal was a factor of two larger than the LEI signal. Since the energy overshoot was relatively small for the photoionizing wavelength, the collisional properties of active nitrogen were judged to be good although perhaps not comparable to an air-acetylene flame.

During the optimization of the laser-induced ionization processes, some interesting signal behavior was noted. Figure 6 illustrates the results of experiments in which the LEI signal was monitored while increasing the nitrogen flow rate. As expected, the active nitrogen concentration (broken line) increased as the nitrogen flow rate was increased. The decrease in LEI signal was not expected. It was first speculated that the laser excitation prior to the signal collection region could be significantly depleting the ground state atom population. On further consideration, it seemed unlikely that a major signal suppression was caused by a relatively minor loss of atoms. Experiments in which atomic fluorescence was measured for identical concentrations of lead in both the pure argon plasma and the active nitrogen plasma (i.e., nitrogen in argon) gave essentially identical limits of detection. This suggested that quenching of the excited state analyte played a very minor role in the signal suppression observed at high nitrogen flows. Current vs. applied voltage curves (slope = $1/R$) for air-acetylene flames (sodium-seeded and unseeded) were compared with similar curves for active nitrogen and pure argon plasmas. The behavior of the sodium-seeded flame and active nitrogen plasma was very similar, suggesting that the signal suppression observed as the nitrogen flow rate was increased was due to the formation of a space charge at the electrodes. This was somewhat surprising because the currents in the active nitrogen plasma were up to two orders-of-magnitude lower than currents measured in the air-acetylene flame.

Investigations of laser-induced argon plasmas have also been initiated. Preliminary results suggested that space charge formation in argon was minimal. The laser-induced ionization background was low and featureless in the wavelength region of interest. (The active nitrogen laser-induced ionization spectrum has been characterized from 279 to 285 nm.¹¹) Because of the low background, manganese has been detected at the tens of picogram levels. No suppression of the manganese signal was observed in signal recovery experiments using sodium as an interferent over a two order-of-magnitude concentration range. Electrical breakdown occurs at a lower applied voltage in argon than active nitrogen meaning that signal collection voltages will be limited.

Conclusions

The total consumption burner has been demonstrated as a viable atom reservoir for laser-induced ionization spectrometry but further research must be undertaken before these results can be translated into practice. Energetic plasmas present some interesting possibilities. Because of its good collisional properties and long lifetime, active nitrogen plasmas may be incorporated into an interferent removal scheme.¹² Easily-ionized species could be

removed with biased electrodes prior to laser-induced ionization. Preliminary experiments with microwave-induced argon plasmas have suggested that it may be an attractive alternative to flames because of its low background and the apparent absence to electrical interferences.

Acknowledgment

In addition to the authors, many people have contributed to the body of research that is presented here. Many of them are represented in the references.

References

1. J. C. Travis, G. C. Turk, and R. B. Green, *Anal. Chem.* 54, 1006A (1982)
2. C. A. Van Dijk, F. M. Curran, K. C. Lin, and S. R. Crouch, *Anal. Chem.* 53, 1275 (1981)
3. G. C. Turk, *Anal. Chem.* 53, 1187 (1981)
4. J. D. Messman, N. E. Schmidt, J. D. Parli, and R. B. Green, *Appl. Spectrosc.* 39, 504 (1985)
5. G. C. Turk, *J. Anal. Atom. Spec.*, 2, 573 (1987)
6. M. A. Nippoldt and R. B. Green, *Anal. Chem.* 55, 554 (1983)
7. J. E. Hall and R. B. Green, *Anal. Chem.* 55, 1811 (1983)
8. J. E. Hall and R. B. Green, *Anal. Chem.* 57, 431 (1985)
9. M. D. Seltzer and R. B. Green, *Spectrosc. Letters*, 20, 601 (1987)
10. T. M. Niemczyk and H. C. Na, *Appl. Spectrosc. Rev.*, 19, 363 (1983)
11. M. D. Seltzer, E. H. Piepmeier, and R. B. Green, *Appl. Spectrosc.*, submitted
12. T. O. Trask and R. B. Green, *Spectrochim. Acta*, 38B, 503 (1983)

DETERMINATION OF CADMIUM, LEAD, AND ZINC IN AEROSOLS BY LASER-INDUCED BREAKDOWN SPECTROMETRY

Joseph Sneddon

Department of Chemistry
University of Lowell
Lowell, Massachusetts 01854

and

Marcelino Essien and Leon J. Radziemski

Applied Laser Optics Group
Department of Physics
New Mexico State University
Las Cruces, New Mexico 88003

Abstract

The repetitive breakdown spark from a Nd:YAG laser was used to generate analytically useful emission spectra of cadmium, lead, and zinc in aerosols. The system consisted of a laser operated at a pulse rate of 10Hz with an energy of 100mJ per pulse and a pulse width of approximately 15ns, and samples were generated in aerosol form using a nebulizer-heat chamber arrangement. The detection apparatus consisted of a monochromator, photomultiplier tube, and boxcar averager. The latter provided both amplification, averaging, and time resolution. The performance of the system for laser-induced, breakdown spectrometry (LIBS) will be described. The analytical performance characteristics of detection limit and linearity for cadmium, lead and zinc as well as the effect of the chemical form, perturbations and temperature of the plasma will be further presented.

Introduction

Discharge phenomena can be categorized into three distinct groups based on the frequency of the electric field that generated the discharge; low frequency region associated with low frequency constant, pulsed and oscillating fields, radio frequency region which is a broad region with an average frequency of about 1MHz, and a microwave region associated with super high frequency fields in the GHz range. The development of the laser moved the study of gas discharges into the optical region and the first observation of breakdown using optical frequencies was reported in 1963.

There are two generally accepted breakdown mechanisms for optical discharges. The first is a semi-classical description which is applicable to atmospheric pressures. In this case the electric field associated with the incident laser radiation imparts an oscillatory motion to a "seed" electron. The electron subsequently acquires energy by absorbing photons through an inversebremsstrahlung process in collisions with atoms, and becomes energetic enough to ionize an atom. Thus a second electron is produced and the process repeats itself, now with two electrons, so that a cascade ionization develops.

The second mechanism is purely quantum mechanical and dominates at low pressure. In this case the electron is ionized as a result of a multiphoton photoelectric effect, in which several photons are simultaneously absorbed by an atom. The probability of the photo-ionization of a gas by a single photon with a wavelength in the optical region is very small. This is because of the large difference between the energy of such a photon and the ionization potentials of gases. For example, the fundamental photon energy of a neodymium laser is 1.17 eV while the ionization energy of molecular nitrogen is 15.57 eV. It therefore requires a simultaneous absorption of 16 photons by a nitrogen molecule before a ground state electron can be raised into the ionization region. Thus, the probability of a multiphoton absorption is usually negligible; however, with the high irradiances created by focussing laser radiation of sufficient energy, this probability becomes large and multiphoton absorption can take place.

A medium will experience dielectric breakdown whenever it is subjected to an electric field whose strength exceeds its dielectric strength (Figure 1). In LIBS the electric field is associated with the laser radiation. The theoretical spot size generated by focussing laser radiation is given by

$$d = \frac{2f\lambda}{d_0} \quad \text{-----} \quad (1)$$

where f is the focal length of the lens, λ is the wavelength of the radiation and, d_0 is the beam diameter of the laser. However, the actual spot size is believed to be much greater than the value given by equation 1, largely because of aberrations caused by the focussing lens. To gain some measure of the spot size, it was noted that breakdown was not initiated if the laser energy fell below 60 mJ. Using this observation and the dielectric strength of air, the intensity (I) of a 60 mJ laser focussed by a 3-cm focal length lens was calculated to be $2.6 \times 10^{10} \text{ W/m}^2$.

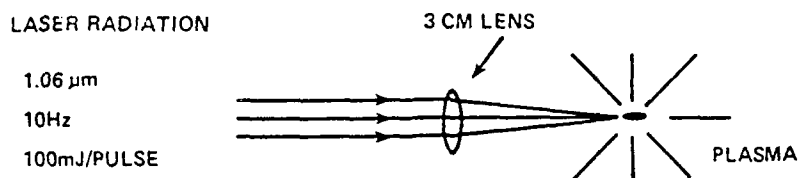


Figure 1: Dielectric breakdown using laser radiation.

This intensity corresponds to an area of $3 \times 10^{-4} \text{ m}^2$. Using this value for the area, the electric field generated by a 15 ns, 100 mJ pulse focussed by a 3-cm lens was approximated using the equation:

$$E = 2\eta\mu c^2 \quad \text{-----} \quad (2)$$

where η is the power density (I/c), μ the permittivity of free space, and c is the speed of light. The value of E was $4 \times 10^4 \text{ V/cm}$, which is greater than the dielectric strength of air ($3 \times 10^4 \text{ V/cm}$). The laser-induced plasma was found to be stable provided that the laser energy did not fall below a value of roughly 60 mJ, the approximate breakdown threshold of air at 665 torr -- Las Cruces air pressure -- using a Nd:YAG laser and a 3-cm focal length lens.

In the formation and development of the laser plasma, a gas which is normally transparent to low intensity radiation is transformed into a highly opaque plasma in a time on the order of a nanosecond. This transformation takes place in four stages. The first stage is initiation, in which ionization begins as a result of multiphoton absorption or an inverse bremsstrahlung effect.

An amplification of the number of electron-ion pairs is then produced in the second stage via a process called electron avalanche ionization. The development of this process depends on two mechanisms. The first is an increase in energy by the electron due to the applied field. The second is a loss of energy by the electron. This loss may result from collisions with atoms or ions or from the process of electron diffusion, in which the electron escapes from the region of the applied field. Therefore the rate at which the electron will gain energy is an interplay between these two mechanisms. If these energy losses can be overcome and if an appreciable level of ionization can be reached within the duration of the laser pulse, breakdown will take place when an electron density of approximately 10^{16} cm^{-3} is reached.

The third stage is called growth. This stage involves the expansion of the plasma in the direction of the laser as a result of an increased opacity of the plasma. For a laser energy in the 100 mJ range, this growth is on the order of 3mm; however, expansions of several meters have been reported using giant pulsed lasers.

The fourth and final stage is extinction, which lasts much longer than the laser pulse. It is within this stage that atomic emission takes place, along with diffusion and electron recombination.

Experimental

Apparatus

Laser. A four level pulsed neodymium (Nd) laser, with lasing occurring in the $4F_{3/2}$ to $4I_{11/2}$ transition level of the Nd ions in a yttrium aluminum garnet (YAG) matrix. The energy output was about 100 mJ per pulse, with a pulse width of 15ns, a beam width of 5mm between the e^{-2} points and a beam divergence of 2mrad. At peak performance, the laser output fluctuated by roughly 5 percent from shot to shot but had no noticeable effect on the emission from the plasma. Fluctuations of 10mJ or more did affect emission and a significant reduction of the signal occurred when the laser power fell below 60mJ.

Aerosol Generator. Wet aerosols were generated using a standard stainless steel pneumatic nebulizer capable of uptake rates of 1-8 mL/min., and a carrier gas of air at a line pressure of 60 psi. The performance of the nebulizer was stable and did not vary $\pm 3\%$ over a period of several days. An impactor device was added in order to reduce the variation in particle size and obstruct larger particles (> 10 microns). A dry or desolvated aerosol was obtained by passing the wet aerosol through a heat chamber.

Excitation. The aerosol (wet or dry) entered a six-armed cross cell which had windows placed on it. This cell contained the plasma and was useful in reducing the noise due to the hydrodynamic shock waves caused by the plasma. The power density was estimated to be about 10^{10} W/cm^2 which was sufficient for reproducible plasma formation.

Detection. The detection apparatus is shown in Figure 2 consisting of quartz focusing lens, monochromator, photomultiplier tube, boxcar averager, oscilloscope and chart recorder.

Emission from the plasma was collected by lens 2 and imaged on the entrance slit of the monochromator. The lens was positioned so that a unit magnification of the plasma was obtained at the entrance slit. The monochromator was a 0.5 m Ebert mount with scanning capabilities from 2100 to 10,000 Å. The detector was uv-visible photomultiplier tube (pmt) with a spectral response from 2000 to 7000 Å. Signals from the pmt were monitored using the boxcar's gated integrator and analog processor. The purpose of the integrator was two-fold. First this unit was used to extract small signals from the extremely noisy pmt output. In effect this suppressed random fluctuations in the pmt output and enhanced the signals from the plasma. Second the integrator provided a coincidence circuit so that time-resolved studies could be done. The integrator was triggered by an external pulse from the laser power supply, and allowed a window of variable width to be superimposed on the pmt signal at a specific delay time.

The analog processor functioned as a second-stage amplifier and was used to increase the gain on the pmt output. A modification of the apparatus involved the inability to maximize the sensitivity of the system because of noise in the system. This noise was believed to be caused by random fluctuation in the signal from the plasma. However, the amplitude of the noise increased over a period of a few weeks, until detection of even large concentrations of metals could not be performed. Closer examination

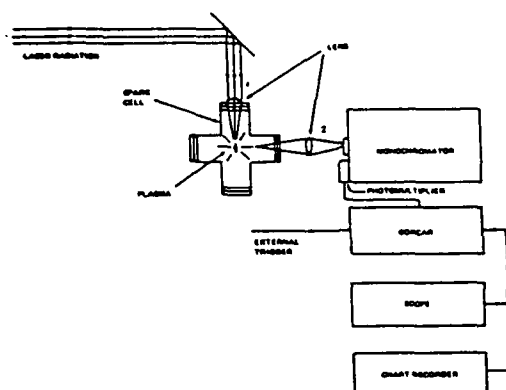


Figure 2: Detection System for LIBS

revealed that the noise was electrical and caused by a gradual deterioration of the pulse used to trigger the boxcar. The boxcar's gated integrator requires an external trigger pulse with an amplitude of 0.5 to 2 volts, and a rise time shorter than 1 μ s. If these specifications were not met an excessive jitter of the gate resulted causing the integrator to sample the input signal at different delay times, producing excessive noise (Figure 3). The coincidence circuit was improved by replacing the external trigger from the laser power supply with a fast photodiode which sensed the onset of the plasma. The amplitude of the pulse was proportional to the light incident on the diode and its rise time was less than 1 μ s. Placing the photodiode near the top of the spark cell, just above the focusing lens, generated a pulse which was sufficient to trigger the boxcar reliably.

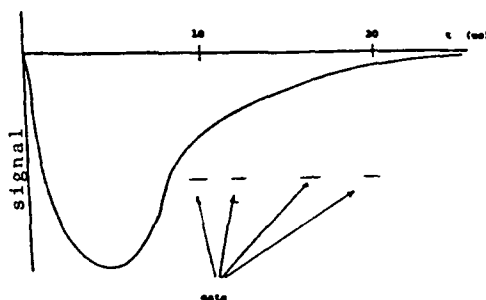


Figure 3: Excessive gate jitter caused by a faulty external trigger.

Thus the boxcar was triggered using the emission from the plasma, lessening the uncertainty in the delay time. The rate generated by this circuit exhibited negligible jitter when viewed on the oscilloscope and decreased the noise by a factor of 10. Previous results of LIBS is given in reference 1-6.

Results and Discussions

Plasma Temperature. Measurement of the plasma temperature using the two-line Boltzmann method consisted of obtaining accurate intensity ratios of the emission of the neutral 2802 Å and 4057 Å lead lines. This was done by scanning over the line four times and taking an average of the measurements. This average was then corrected for the spectral response of the system and the temperature was determined from equation 3. For example, substituting the values for the Einstein coefficients and the statistical weights for Pb I 2802 Å and Pb I 4057 Å and solving for T in equation 3, one gets

$$T = 1.44 \frac{11042}{\ln(6.07 I_2/I_1)} \quad \text{--- (3)}$$

Therefore, a ratio of $I_2/I_1 = 2$ yields an approximate temperature of 6400 K. The uncertainty in the measurement of T was determined using differential error analysis, considering T as a function of A_1 , A_2 and I_2/I_1 .

The excitation temperature was determined for delay times from 20 to 40 μ s to 5150 K at 40 μ s and are shown in Table and Figure 4.

Table 1: Temperature of the LIB plasma.

Delay (μ s)	I_2/I_1	Temperature (K)	Uncertainty
20	1.9	6500	1000
25	2.3	6000	800
30	3.0	5500	700
35	3.5	5200	600
40	3.6	5150	600

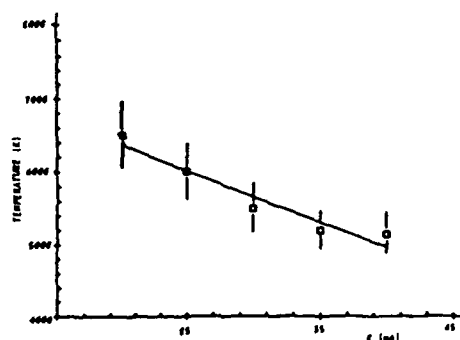


Figure 4: Temperature of the LIB plasma

Interferences. In any analytical technique, potential interferences must be determined, understood and corrected in order to obtain accuracy of the analytical measurement.

To provide some measure of the effects on the LIB plasma, the intensity of the 4057 Å lead line was recorded with no sodium present in the plasma at five different delay times, and compared to the signals obtained from this line when a concentration of sodium equivalent to approximately 780 ppm was present. The effects ranged from significant to negligible and are shown in Tables 2-4 and Figure 5.

The intensity of the background signal was lowered by approximately 30 percent at each delay time when sodium was present in the plasma. Contrastingly the signal fluctuated dramatically from 20 to 40 μs.

Table 2: Lead signal with no sodium present in plasma

<u>Delay (us)</u>	<u>Intensity (V)</u>	<u>Bkqd. (V)</u>	<u>Noise (V)</u>
20	0.35	0.58	0.0096
25	0.53	0.37	0.018
30	0.64	0.26	0.030
35	0.47	0.19	0.030
40	0.47	0.16	0.0058

Table 3: Lead emission with sodium present in plasma

<u>Delay (us)</u>	<u>Intensity (V)</u>	<u>Bkqd. (V)</u>	<u>Noise (V)</u>
20	0.63	0.36	0.003
25	0.75	0.25	0.024
30	0.65	0.17	0.037
35	0.65	0.14	0.038
40	0.55	0.11	0.012

Table 4: Emission enhancement

<u>Delay (us)</u>	<u>Percent Increase in Intensity</u>	<u>Uncertainty</u>
20	80	5.0
25	41	6.6
30	4.8	9.8
35	38	12.0
40	17	2.9

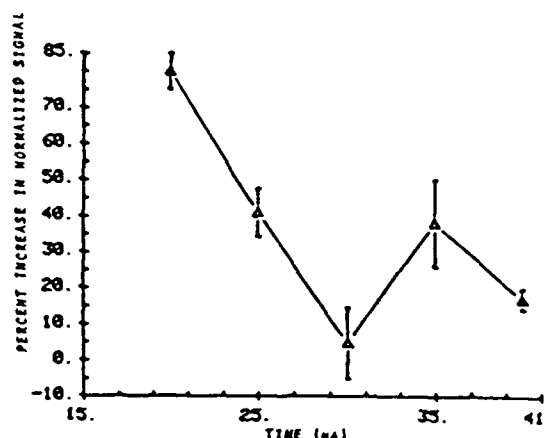


Figure 5: Emission enhancement due to sodium.

The effect of the matrix in which the analyte was dissolved was also examined briefly. In this study the emission from moderate solutions (300 ppm) of lead in acetate, chloride, and nitrate matrices were recorded, and the signal (absolute lead signal/adjacent background) was found to be constant to within 10 percent. A similar study was done for cadmium in nitrate and chloride matrices. The signal from the chloride matrix was 27 percent larger than that from the nitrate matrix.

Analytical Performance Characteristics. The results for cadmium, lead and zinc are detailed elsewhere. In general, calibration curves showed linearity a low concentration, extending over one to two orders of magnitude above the detection limit and curvature or saturation at higher concentrations. Signals from the dry aerosol were, on average about 30% percent great than those from the corresponding wet aerosol. Detection limits were in the low $\mu\text{g/g}$ (mg/m^3) level. The detection limits, threshold limit value time weighted average (TLV-TWA) of the American Conference Governmental Industrial Hygienist (ACGIH), inductively coupled plasma and direct current plasma emission detection limits for cadmium, lead and zinc are shown in Table 5.

Table 5. LIBS, TLV-TWA, ICP and DCP detection limits for cadmium, lead and zinc in aerosols.

Element	Wavelength nm	LIBS mg/m ³	TLV-TWA mg/m ³	ICP mg/m ³	DCP mg/m ³
Cadmium	288.8	0.21	0.15	0.0013	0.00015
Lead	405.7	0.019	0.05	0.00013	0.00044
Zinc	213.9	0.24	5.0	0.07	0.000033

The LIBS detection limits are lower than the TLV-TWA values for lead and zinc and comparable to lead. The ICP and DCP are 2 to 4 orders of magnitude lower than the LIBS but cannot be used to directly determine these metals in air (aerosols).

Conclusion

LIBS can be used to monitor cadmium and zinc directly aerosols at useful levels. The detection limit for lead was high than the TLV-TWA limit for lead. The absence of electrodes eliminates a source of sample contamination. The major disadvantage is the cost of the laser.

References

1. J.R. Wachter and D. A. Cremers, Appl. Spectrosc., **41**, 1042, (1987).
2. L.J. Radziemski, D.A. Cremers, and T.R. Loree, Spectrochim. Acta., **38B**, 349, (1983).
3. D.A. Cremers and L.J. Radziemski, Anal. Chem., **55**, 1252, (1983).
4. L.J. Radziemski, T.R. Loree, D.A. Cremers, and N.M. Hoffman, Anal. Chem., **55**, 1246, (1983).
5. L.J. Radziemski and T.R. Loree, Plasma Chem. and Plasma Proc., **1(3)**, 281, (1981).
6. M. Essien, L.J. Radziemski, and J. Sneddon, J. Anal. Atom. Spectrosc., Submitted, (1988).

SAMPLE INTRODUCTION USING LASER ABLATION FOR ATOMIC ABSORPTION AND PLASMA EMISSION SPECTROMETRY

Joseph Sneddon

Department of Chemistry
University of Lowell
Lowell, Massachusetts 01854

Abstract

The use of a laser for sample introduction of solid samples for metal determination in atomic spectroscopy will be discussed. The mechanism of ablation and parameters which effect the process will be further discussed. The results of the application of laser ablation for flame atomic absorption spectrometry, graphite furnace atomic absorption spectrometry, plasma emission spectrometry, and inductively coupled plasma-mass spectrometry will be presented. The design and development of a laser ablation-direct current argon plasma emission system will be presented. Results from this system including analytical performance characteristics, optimization of experimental factors and analysis of samples will be presented. Matrix effects due to real samples are a problem which will be discussed and results from various halide matrices presented. Methods to overcome these matrix effects including chemical and standard addition will be discussed. Finally, the relative merits of laser ablation used in atomic spectroscopy will be presented including disadvantages/advantages.

Introduction

The interaction of energy and matter produces three closely related analytical techniques, atomic absorption (AAS), atomic emission (AES), and atomic fluorescence spectrometry (AFS). These atomic spectroscopic techniques have become widely used and accepted for minor, trace, and ultra-trace metal determination in a wide variety of complex samples due to a number of interrelated factors including low detection limits, high sensitivity, high selectivity, low precision, a wide range (~70) of metals can be determined, ease of operation, widespread availability, modest cost per sample after initial cost of instrumentation, relative freedom from interferences and acceptable accuracy. State-of-the-art atomic spectroscopic instrumentation has become highly developed with high resolution monochromators eliminating almost all spectral overlap except in cases of near overlap, background correction devices such as continuum source, Zeeman and Smith-Hieftje eliminating molecular absorption and light scattering, leading to improved analytical accuracy, detectors with low dark current and linear response, efficient atom reservoirs, sophisticated electronics, and a high degree of automation. Despite all these developments, the major limitation appears to be the sample introduction process which is used to present the sample in a suitable form. It has been referred to as the "Achilles' heel" of atomic spectroscopy by Browner and Boorn¹ who also state that in the atomic spectroscopic measurement, the analysis can only be as good as the sample introduction. Approaches to sample introduction have been reviewed by Browner and Boorn¹ and Sneddon² who concluded that the type of system will depend on a number of variables including the physical state of the sample (solid, liquid, gas or mixture), level of analyte to be determined, amount of sample available, required accuracy and precision, and available atomic spectroscopic technique. Sample introduction techniques can be divided into two general areas, direct and hybrid, and are summarized in Fig. 1. The operation, relative merits and application of these sample introduction techniques are discussed elsewhere.²

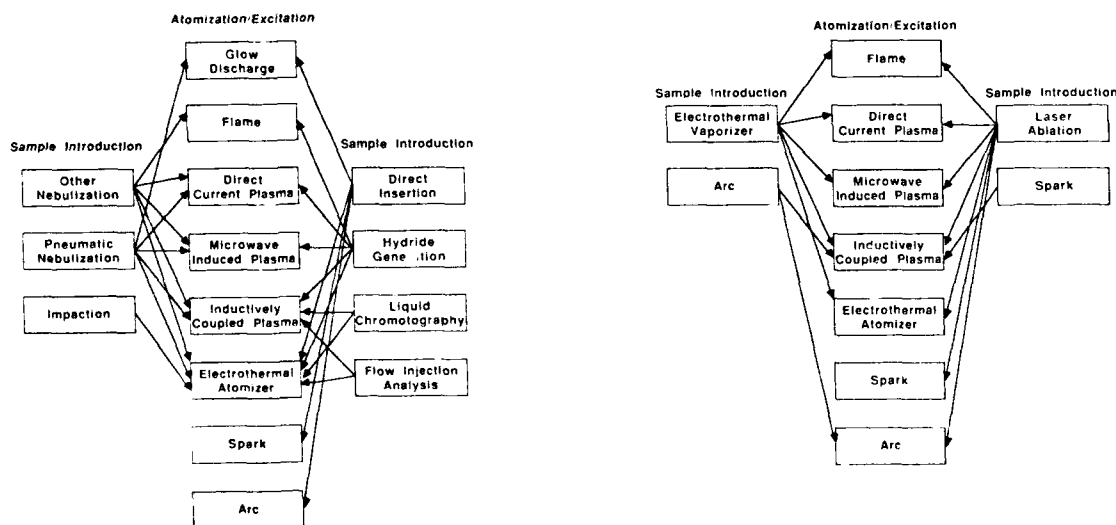


Figure 1.

Direct and Hybrid Sample Introduction Techniques.

The technique of laser ablation (vaporization) for sample introduction of small amounts of material was recognized after the invention of the ruby laser in the early 1960's, where its chief advantages are the ability to handle microgram masses of conducting and non-conducting material, ability to investigate surfaces and heterogeneities in solids, and efficient vaporization. The technique has been applied to AAS, AES, and AFS,³ and the atom reservoirs used (or potentially usable) are shown in Fig. 2. In this paper, laser ablation for sample introduction will be limited to AAS and AES with plasmas.

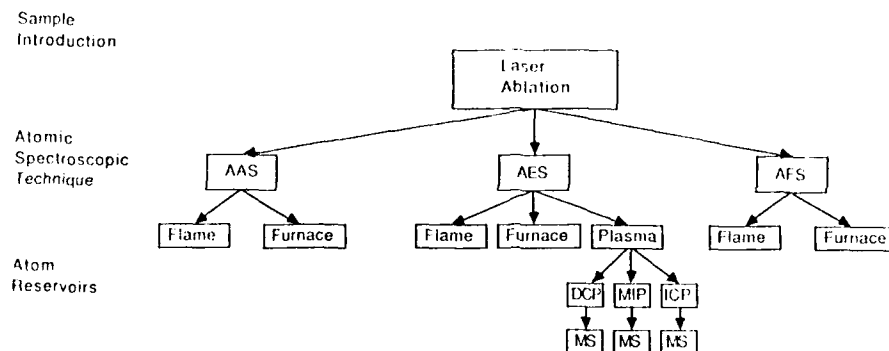


Figure 2. Atomic Spectroscopic Techniques and Atom Reservoirs Used for Sample Introduction with Laser Ablation.

Parameters Affecting the Ablation Process

When laser light is focused and absorbed by the surface of a solid sample, a variety of phenomena can occur including surface heating, ablation (vaporization), dissociation, phase changes, and excitation. A sample model has been proposed by Klocke⁴ who postulated that a portion of the light is transformed into heat energy when light flux is incident on the surface of a solid sample. The energy level of the electrons on the surrounding surface is raised and transferred to the surrounding surface by electron impact, and the electron erupts at a high velocity, leaving a crater on the surface of the solid sample. Laser parameters of wavelength, pulse rate (repetition rate) and irradiance and sample type (surface) will affect the ablation process.

(1) Laser Wavelength

Bingham and Salter⁵ compared CO₂ laser (wavelength of 10.6 μ m), ruby (wavelength 694 nm), and Nd: YAG (wavelength 1064 nm) as sources for ion production in mass spectrometry using a steel standard and concluded that the shorter the wavelength the more material ablated and subsequently the higher the sensitivity.

(2) Laser Pulse Rate and Duration

In general, the higher the pulse rate, the lower the precision and higher the sensitivity. The lower precision is attributed to reduced sample inhomogeneities and the higher sensitivity due to more material being ablated.⁶⁻¹⁰

(3) Laser Irradiance

Many solid samples can be vaporized at irradiances in the range 10^4 to 10^9 W/cm². Carr and Horlick¹¹ found a Q-switched pulse generated 25 μ g of material whereas a normal mode pulse produced 500 μ g of material. In general, the highest pulse radiance should be used to minimize the dependence on surface or sample type.

(4) Sample Type and Surface

The density of a powdered sample or hardness of a solid sample such as a steel sample will affect the emission or absorption signal when using a low power laser. Using a power of 100 mJ per pulse the effect of density of various copper⁸ and manganese^{12,13} compounds with a constant mass of copper or manganese is shown in Fig. 3. This was shown to be similar when copper is in very hard alloy steel and powder.¹²

Laser Ablation Atomic Absorption Spectrometry

Sample introduction using laser ablation has been used in atomic absorption spectrometry with a flame¹⁴⁻¹⁶ and electrothermal atomizer.¹⁷⁻²⁰ Detection limits for the flame were in the ng range for Fe, Na, Cd, Cu, and Zn and precisions around 10%.¹⁴ Using the electrothermal atomizer, Al, Cr, Cu, Fe, Mn, Mo, Ni, and V were determined in brasses, carbon steels, alloys and Al alloys with precision in the 2.1 to 10% range, and detection limits from 1.9 ppm for Fe in brass to 32 ppm for Cu in Al alloy.²⁰

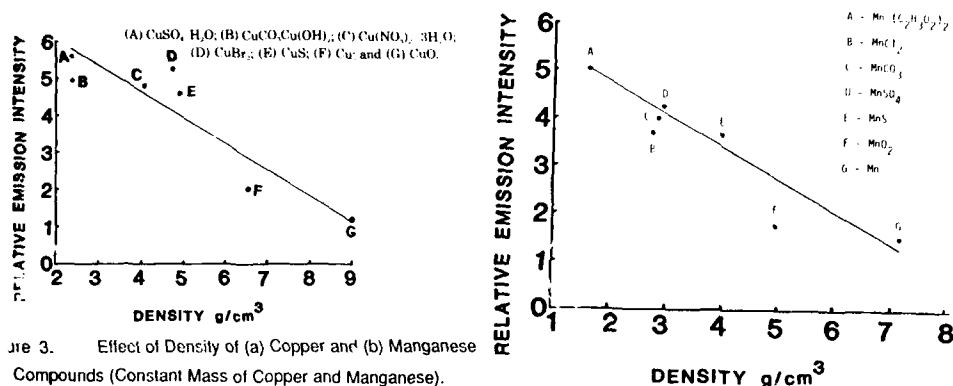


Fig. 3. Effect of Density of (a) Copper and (b) Manganese Compounds (Constant Mass of Copper and Manganese).

Laser Ablation Atomic Emission Spectrometry

Sample introduction using laser ablation has been used in atomic emission spectrometry using the inductively coupled plasma,^{11,21,22} direct current plasma,^{7-10,12} and microwave induced plasma.²³⁻²⁵ A more recent use of laser ablation has been inductively coupled plasma-mass spectrometry.²⁶⁻²⁷ In this case the ICP is used as an ion source in mass spectrometry. Detection limits for As, Sb, Te, Ag, Mn, Cd, Pb, and Bi were in the 0.04 to 0.6 $\mu\text{g/g}$ range with precision and accuracy of $\pm 5\%$.²⁷

Laser Ablation-Direct Current Argon Plasma Emission Spectrometry

Recent work from this laboratory has shown the potential of laser ablation-direct current argon plasma emission spectrometry for metal analysis in solid and powdered samples.^{7-10,12,13} Detection limits were in the $\mu\text{g/g}$ range for metals investigated, precision typically under 10%, long linear dynamic range and acceptable accuracy obtained via standard additions. However, a problem was noted that different copper¹⁰ and manganese¹² compounds with the same concentration of analyte gave different signals. Calibration curves could only be used if the matrix of unknown samples and standards were similar.

The effect of increasing concentration of various sodium halides on a constant concentration of 1000 $\mu\text{g/g}$ of copper (as $\text{Cu(NO}_3)_2$) is shown in Fig. 4.

There is no significant deviation in the emission signal when the sodium halide concentration is less than the copper concentration. However, as the concentration of sodium halide increases over the concentration of copper, a depression in the copper emission signal occurs, and at 100x concentration of sodium halide to copper, a reduction of 50-70% occurred (depending on sodium halide). A larger concentration of sodium halide would not produce a pellet due to lack of cellulose which prevented binding, but it is reasonable to assume that the greater the ratio of sodium halide to copper, the greater the magnitude of the depression. An examination of the results of Fig. 4 show that the magnitude of the depression increases $\text{NaI} > \text{NaF} > \text{NaCl} > \text{NaBr}$ and approximately correlates with the trend in density of the sodium halides but not the boiling points. It is probable that the pellet with the highest density (NaI) has the lowest emission intensity and the pellet with the lowest density (NaF) causes the highest emission intensity. In all cases, as the density of the pellet is increased, a depression will occur—the magnitude depending on the ratio of analyte to the matrix.

The effect of different sodium halides on the emission intensity of manganese metal, manganese dioxide, and manganese sulfate is shown in Table 1.

Table 1

Effect of Different Sodium Halides on Emission Intensity from Different Manganese Compounds^A

Compound	Matrix	Relative Emission Intensity
Mn	Cellulose	1.30
Mn	Cellulose + NaCl	1.18
Mn	Cellulose + NaI	1.21
MnO_2	Cellulose	4.02
MnO_2	Cellulose + NaCl	3.69
MnO_2	Cellulose + NaBr	3.73
MnO_2	Cellulose + NaI	3.73
MnSO_4	Cellulose	1.52
MnSO_4	Cellulose + NaCl	1.32
MnSO_4	Cellulose + NaI	1.33

^A Manganese concentration of 1240 $\mu\text{g g}^{-1}$ and sodium halide concentration of 1000 $\mu\text{g g}^{-1}$.

In all cases, the introduction of sodium halide concentration reduced the relative emission intensity of the particular manganese compound by 8-13%, depending on the halide and manganese compound. While different sodium halides had slightly different effects, the relative magnitudes were not considered sufficient to support the hypothesis that the density of the matrix effects the emission intensity.

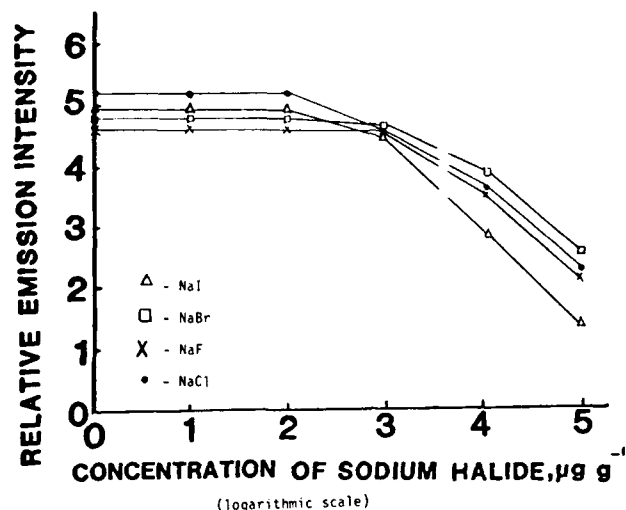


Figure 4. Effect of Increasing Mass of Sodium Halides on Copper Emission Intensity of 324.7 nm.

Conclusion

The work from this laboratory and others have shown the potential of laser ablation of solid and powdered samples for sample introduction to an atomic spectroscopic atom reservoir for quantitative metal analysis. Some potential interferences due to a matrix can occur but may be overcome using the method of standard additions. Despite the work on this area, little is known on the mechanism of laser ablation. The potential cost and reliability of the laser can be a problem. Nevertheless, it is the opinion of the author that laser ablation for sample introduction in atomic spectroscopy will continue to grow and perhaps, in the not-too-distant future, a commercial system may be available.

References

1. R.F. Browner and A.W. Boorn, *Anal. Chem.*, **56**, 786A and 875A (1984).
2. J. Sneddon, *Spectroscopy*, **1**(9), 34 (1986).
3. L. Moenke-Blankenburg, *Prog. Anal. Spectros.*, **9**, 335 (1986).
4. H. Klocke, *Spectrochim. Acta*, **24B**, 263 (1969).
5. R.A. Bingham and P.L. Salter, *Anal. Chem.*, **48**, 1735 (1976).
6. D.A. Cremers, H.C. Dilsworth, and F.L. Archuleta, *Anal. Chem.*, submitted (1987).
7. P.G. Mitchell, J.A. Ruggles, J. Sneddon, and L.J. Radziemski, *Anal. Lett.*, **18**, 1723 (1985).
8. P.G. Mitchell, J. Sneddon, and L.J. Radziemski, *Appl. Spectros.*, **40**, 274 (1986).
9. J. Sneddon and P.G. Mitchell, *American Laboratory*, **18**(11), 21 (1986).
10. P.G. Mitchell, J. Sneddon, and L.J. Radziemski, *Appl. Spectros.*, **41**, 141 (1987).
11. J.W. Carr and G. Horlick, *Spectrochim. Acta*, **37B**, 1 (1982).
12. J. Sneddon, *Proc. Int. Conf. on Lasers '86*, STS Press, Virginia, 316 (1987).
13. J. Sneddon, *Spectros. Lett.*, **6** and **7**, 527 (1987).
14. T. Kántor, L. Polos, P. Fodor, and E. Pungor, *Talanta*, **23**, 585 (1976).
15. T. Kántor, E. Pungor, J. Sztatisz, and L. Bezur, *Talanta*, **26**, 357 (1979).
16. T. Kántor, L. Bezur, E. Pungor, P. Fodor, J. Nagy-Balogh and Gy. Heincz, *Spectrochim. Acta*, **34B**, 341 (1979).
17. J.P. Matousek and B.J. Orr, *Spectrochim. Acta*, **31B**, 475 (1976).
18. K. Sumino, R. Yamamoto, F. Hatayama, S. Kitamura, and H. Itoh, *Anal. Chem.*, **52**, 1064 (1980).
19. K. Dittrich and R. Wennrich, *Spectrochim. Acta*, **35B**, 731 (1982).
20. T. Ishizuka, Y. Uwamino, and H. Sunahara, *Anal. Chem.*, **49**, 1339 (1977).
21. M. Thompson, J.E. Goulter, and F. Sieper, *Analyst*, **106**, 32 (1981).
22. H. Kawaguchi, J. Xu, T. Tanaka, and A. Mizuike, *Bunseki Kagaku*, **31**, E185 (1982).
23. F. Leis and K. Laqua, *Spectrochim. Acta*, **33B**, 727 (1978).
24. F. Leis and K. Laqua, *Spectrochim. Acta*, **34B**, 307 (1979).
25. T. Ishizuka and Y. Uwamino, *Anal. Chem.*, **52**, 125 (1980).
26. A.L. Gray, *Analyst*, **110**, 551 (1985).
27. P. Arrowsmith, *Anal. Chem.*, **59**, 1437 (1987).

"AB INITIO" THEORY OF
STIMULATED ROTATIONAL RAMAN SCATTERING
AND
NUMERICAL SIMULATION

C. G. PARAZZOLI AND C. DRUTMAN

HUGHES AIRCRAFT CO.
P. O. BOX 902
EL SEGUNDO, CA. 90250
(213) 616-6714

Abstract

An "ab initio" theory of Stimulated Rotational Raman Scattering which includes pump and population depletion, degeneracy effects, stokes and antistokes to all orders, multirotational lines, polarization effects, multiphoton processes, distributed spontaneous emission, and time dependence, is described. The theory has been derived specifically for diatomic molecule, but is readily modified to polyatomic molecules provided that the appropriate transformation coefficients are used in the Wigner-Eckart theorem. The theoretical values of the small signal gain for N_2 , obtained from the theory, agree well with the experimental values.

A numerical code based on the above mentioned theory has been written which has the complete (x,y,z,t) dependence. Preliminary results of the code indicate that the Raman small signal gain, G (cm/Tw), is a decreasing function of the pump intensity, for sufficiently large power levels (A.C. Stark effect).

The stokes-antistokes suppression effects for a plane wave has been recovered. It is shown, however, that the inclusion of diffraction severely limits the effectiveness of this suppression mechanism.

Due to the complex nature of the governing equations the code contains an artificial intelligence (A.I.) subroutine which generates a Fortran output describing the complete set of coupled differential equations for the electric fields and polarizations once the user specifies the number of rotational lines and stokes-antistokes fields that are to be included.

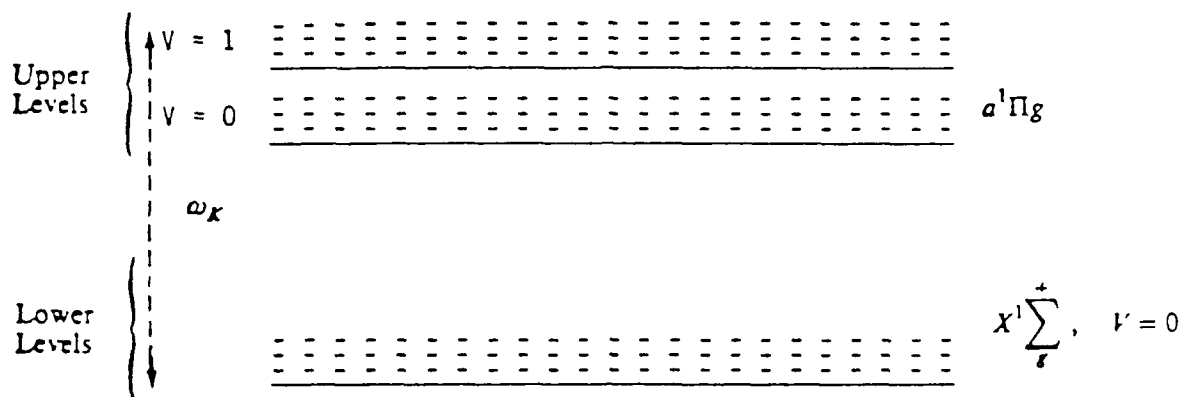
Theory

In this section we shall briefly describe the "ab initio" theory for stimulated rotational Raman scattering (SRRS). The basic elements and fundamental steps will be given without much of the intervening algebra. A future publication will give a more in depth description of the theory.

The approach followed here is similar to the one used in ⁽¹⁾. The state of the molecule is represented by the state vector $|\psi\rangle$;

$$|\psi\rangle = \sum_n C_n e^{iW_n t} |n\rangle, \quad (1)$$

where C_n is the time dependent probability amplitude of the state n and W_n is the corresponding energy. For simplicity of notation, we assume that the molecule is completely characterized by one quantum number. This assumption will be relaxed later on. The energy levels of interest for the Raman process in N_2 are shown below:



For the remainder of the paper, the convention to indicate lower (upper) energy levels with lower (upper) case subscripts will be used. Following ^(1,2) we shall expand the probability amplitudes in a series,

$$C_n = C_n^{(0)} + C_n^{(1)} + \dots, \quad (2)$$

with $C_n^{(0)} \gg C_n^{(1)} \gg \dots$, and similarly for the upper case subscript C_N .

Before proceeding with the derivation of the equation of motion of the C_n 's, the expressions for the Raman (two photon) polarizability will be given.

The standard definition of the polarizability is

$$P = \sum_{mn} d_{mn} C_m^* C_n e^{iW_{mn}t}, \quad (3)$$

where the summations extend over both the lower and upper levels. d_{mn} is the dipole moment matrix element between the m^{th} and n^{th} energy levels, and $W_{mn} = W_m - W_n$. Assuming that the molecule is infrared inactive ($d_{mn} = d_{mN} = 0$), the polarizability may be written as:

$$P = \sum_{mN} d_{mN} C_m^* C_N e^{iW_{mN}t} + c.c., \quad (4)$$

where the summation over m (N) extends only over the lower (upper) energy levels.

Substituting (2) into (4), we obtain

$$P = \sum_{mN} e^{iW_{mN}t} C_m^{(0)*} C_N^{(0)} d_{mN} + c.c.. \quad (5)$$

The equations of motion for the $C_n^{(0)}$'s are obtained from the Schrödinger equation for $|\psi\rangle$ and using of the Adiabatic Following Approximation (AFA). The Schrödinger equation is

$$(H_0 + H_1)|\psi\rangle = i\hbar \frac{\partial}{\partial t} |\psi\rangle, \quad (6)$$

where H_0 is the unperturbed Hamiltonian, and H_i is the interaction Hamiltonian. With the usual procedure we obtain the equation for the probability amplitude C_k

$$i \hbar \dot{C}_K = - \sum_{n,f} C_n e^{iW_{Kn}t} d_{Kn} \left(\mathcal{E}_f e^{i(k_f z - \omega_f t)} + c.c. \right), \quad (7)$$

where the summation over f extends to all the optical fields of frequency ω_f , wave vector \vec{k}_f , and complex amplitude \mathcal{E}_f . z is the direction of propagation. Using the AFA, we obtain the $C_k^{(0)}$ as function of the $C_k^{(0)}$ from Eq. 7, then substituting $C_k^{(0)}$ back again in Eq. 7, we obtain the following equation of motion for the $C_k^{(0)}$:

$$\begin{aligned} \frac{dC_k^{(0)}}{dt} = & \frac{i}{\hbar^2} \sum_{Nnf} d_{Nn} d_{kN} C_n^{(0)} \times \\ & \left[\mathcal{E}_f \mathcal{E}_f \frac{e^{i\{(k_f + k_f)z + \psi_1(knf)f)t\}}}{\varphi_1(Nnf)} + \right. \\ & \mathcal{E}_f \mathcal{E}_f^* \frac{e^{i\{(k_f - k_f)z + \psi_2(knf)f)t\}}}{\varphi_1(Nnf)} + \\ & \mathcal{E}_f^* \mathcal{E}_f \frac{e^{i\{(-k_f + k_f)z + \psi_3(knf)f)t\}}}{\varphi_2(Nnf)} + \\ & \left. \mathcal{E}_f^* \mathcal{E}_f^* \frac{e^{i\{(-k_f - k_f)z + \psi_4(knf)f)t\}}}{\varphi_2(Nnf)} \right], \end{aligned} \quad (8a)$$

where the ψ 's and φ 's are defined as:

$$\begin{aligned} \psi_1(knf)f &= W_{kn} - (\omega_f + \omega_f), \\ \psi_2(knf)f &= W_{kn} - (\omega_f - \omega_f), \\ \psi_3(knf)f &= W_{kn} + (\omega_f - \omega_f), \\ \psi_4(knf)f &= W_{kn} + (\omega_f + \omega_f), \\ \varphi_1(Nnf) &= W_{Nn} - \omega_f, \\ \varphi_2(Nnf) &= W_{Nn} + \omega_f. \end{aligned} \quad (8b)$$

In the expressions for P only the product

$$\rho_{mn} = C_m^{(0)} C_n^{(0)*} \quad (9a)$$

is required; this is, of course, the standard density matrix element. The equation of motion for ρ_{mn} , or alternatively, for

$$r_{mn} = \rho_{mn} e^{-iW_{mn}z/c}, \quad (9b)$$

where c is the speed of light in vacuum, will be obtained from Eq. 8a following the procedure of ⁽¹⁾. From inspection of Eq. 8a, it is clear that only the second and third terms in the [] contribute significantly to the growth of $C_k^{(0)}$, because for appropriate combinations of k , n , f , and f , ψ_2 and ψ_3 may vanish and stationary terms are obtained. Alternatively, no combinations of k , n , f , and f may null ψ_1 and ψ_4 . As usual, we assumed that there are no resonances between the pump fields and the molecular transitions. That is, the φ_1 and φ_2 will not vanish. Under these conditions, Eq. 8a may be rewritten as:

$$i\hbar \frac{dC_k^{(0)}}{dt} = \sum_n H_{kn}^e C_n^{(0)}, \quad (10a)$$

where

$$H_{kn}^e = -\frac{1}{\hbar} \sum_{Nf} d_{Nn} d_{kN} \left(\frac{\mathcal{E}_{kn+f} \mathcal{E}_f}{\varphi_1(Nkf)} e^{iW_{kn^2/c}} + \frac{\mathcal{E}_{f+nk} \mathcal{E}_f}{\varphi_2(Nkf)} e^{iW_{kn^2/c}} \right), \quad (10b)$$

where the subscript $kn+f$ stands for $W_{kn} + \omega_f$. This notation will be used for the remainder of the paper. In deriving the expression for H_{kn}^e , we used the conditions

$$\psi_2(knf^0 f) = \psi_3(knf^0 f) = 0. \quad (10c)$$

H_{kn}^e plays the role of an "effective Hamiltonian" for the equation of motion of the $C_k^{(0)}$. Effective Hamiltonians are encountered in many physical problems and are usually empirically derived; in this case, a rigorous derivation was possible. It can be shown that H^e is Hermitian. In general though, "effective Hamiltonians" may not be Hermitian because they do not represent observables.

We now explicitly describe the quantum state of the molecule by the rotational quantum number m and the magnetic quantum number μ_m . The corresponding equation of motion of the density matrix elements $r_{m\mu_m n\mu_n}$ is obtained with the help of Eqs. 10a,b;

$$\begin{aligned} \frac{dr_{m\mu_m n\mu_n}}{dt} = & \frac{i}{\hbar^2} \sum_{Nfqq'} (-1)^{q+q'} \gamma_{N\ell m\mu_m}^{qq'} r_{\ell, \mu_m - q - q', n\mu_n} \times \\ & \left(\frac{\mathcal{E}_{m\ell+f} \mathcal{E}_f}{\varphi_1(Nmf)} e_{(-q')m\ell+f} e_{(-q)f} + \frac{\mathcal{E}_{f+\ell m} \mathcal{E}_f}{\varphi_2(Nmf)} e_{(-q')f+\ell m} e_{(-q)f} \right) \\ & - (-1)^{q+q'} \gamma_{N\ell n\mu_n}^{qq'} r_{m\mu_m \ell, \mu_n - q - q'} \times \\ & \left(\frac{\mathcal{E}_{n\ell+f} \mathcal{E}_f}{\varphi_1(Nnf)} e_{(-q')n\ell+f} e_{(-q)f} + \frac{\mathcal{E}_{f+\ell n} \mathcal{E}_f}{\varphi_2(Nnf)} e_{(-q')f+\ell n} e_{(-q)f} \right) \\ & - \Gamma_{m\mu_m n\mu_n} (r_{m\mu_m n\mu_n} - r_{m\mu_m n\mu_n}^e), \end{aligned} \quad (11a)$$

where, for a diatomic molecule

$$\begin{aligned} \gamma_{N\ell m\mu_m}^{qq'} = & \frac{(N\|d\|\ell) (m\|d\|N)}{\sqrt{2m+1} \sqrt{2N+1}} \langle \ell, \mu_m - q - q', 1, q' | N, \mu_m - q \rangle \\ & \langle N, \mu_m - q, 1, q, | m, \mu_m \rangle, \end{aligned} \quad (11b)$$

where:

- $\langle | \rangle$ are the Clebsch—Gordan coefficients,
- $(\|)$ are the reduced matrix element,
- $(N\|d\|\ell) = \tilde{d}(N\|n\|i)$,
- n is a unit vector,
- \tilde{d} is related to the polarizability anisotropy (γ) of the molecule.

$\mathcal{E}_{m\ell+f}$ is the phasor of the optical fields of frequency $\omega = W_m - W_\ell + \omega_f$. $e_{(q)}$ is the q^{th} component of the electric field vector in spherical coordinates which characterizes the optical field polarization, and $\Gamma_{m\mu_m n\mu_n}$ is the relaxation rate.

The wave equation in the paraxial approximation is:

$$\nabla_1^2 \mathcal{E}_f + 2ik_f \left(\frac{\partial \mathcal{E}_f}{\partial z} + \frac{1}{c} \frac{\partial \mathcal{E}_f}{\partial t} \right) + 4\pi k_f^2 P_f^{(0)} = 0, \quad (12)$$

where

$$P_f^{(0)} = \frac{1}{\hbar} \sum_{mKn} \left\{ \left[\sum_{\mu_m q q'} (-1)^{q+q'} e_{(-q)J}^+ e_{(-q')J'+mn} \gamma_{Knm\mu_m}^{q'q} r_{n\mu_m - q - q' m \mu'_m} \right] \frac{\mathcal{E}_{f+mn}}{\varphi_1(K'nf' + mn)} \right. \\ \left. + \left[\sum_{\mu_m q q'} (-1)^{q+q'} e_{(-q)J}^+ e_{(-q')J'+nm} \gamma_{Knm\mu_m}^{q'q} r_{m\mu_m n \mu_m - q - q'} \right] \frac{\mathcal{E}_{f+nm}}{\varphi_2(Knf' + nm)} \right\} \\ + \text{Spontaneous Emission Term.} \quad (13)$$

Dispersion effects are neglected in the above expression. The system of Eqs. 11 - 13 is numerically integrated.

The Computer Model

The method of integration of Eqs. 11 - 13 will not be discussed here. It suffices to say that the time dependence and diffraction effects are treated in a mathematically consistent way. The split algorithm method and the method of characteristics are used to reduce the system of ordinary and partial differential Eqs. 11 - 13 to a system of ordinary differential equations only. These equations are then integrated by standard techniques.

In view of the complexity of Eqs. 11 - 13 for the case of numerous rotational levels and stokes-antistokes fields, an A.I. routine has been written which generates the Fortran code for these equation. The user needs only specify the rotational lines and stokes-antistokes to be considered.

The numerical code has been used to compute the small signal gain (G) for N_2 . The N_2 polarizability anisotropy is obtained from "ab initio" calculations ⁽³⁾ to be $\gamma = 7 \times 10^{-25} \text{cm}^3$. The relaxation rates for the off diagonal elements have been found in ⁽⁴⁾. From the above theory, we calculated $G = 2.25 \text{ cm/Tw}$ for the $J=8$ line for linearly polarized pump and stokes fields. This result compares with the experimental value of 2.5 cm/Tw for air at sea level. The agreement appears to be quite satisfactory in view of the fact that our calculations do not contain any adjustable parameters.

Preliminary Numerical Results

The code has been run to study the propagation from space of an HEL beam focused on a target in the atmosphere. In Fig. 1 we present the growth of the stokes energy as function of the altitude in the absence of diffractive effects. The calculations are initiated from spontaneous emission noise; pump and stokes fields only are present. The results show that as the pump energy is increased from 5 kJ to 35 kJ the altitude at which pump depletion is reached increases. A further increase in energy in the pulse from 35 to 100 kJ then brings a decrease in the pump depletion altitude. This result may be interpreted as due to the AC Stark effect which broadens the Raman gain line and decreases the peak gain ⁽⁵⁾. Fig. 2 presents the field amplitude of the pump and stokes fields as function of time at $z = 46 \text{ km}$ for the 100 kJ pulse. The diffraction effects, for the case of pump and stokes only, are shown in Figs. 3 - 4. A Gaussian beam is launched from 60 km and deplets at approximately 46 km; the beam is focused at $z = 0 \text{ km}$. The energy fluxes of the pump

and stokes are shown in Figs. 3a and 3b. The asymmetric profiles of the pump and stokes reflect the randomness of the spontaneous emission seed. In Figs. 4a and 4b a snapshot in time of the pump and stokes phases are given. The stokes phase is completely random at 60 km, but acquires the distinct parabolic shape by $z=46$ km.

In the absence of dispersion it is well known⁽⁶⁾ that when both stokes and antistokes are present in a collinear plane wave geometry a nearly complete suppression of the stokes gain takes place. The code has been run under these conditions and the results are shown in Fig. 5. As expected, the stokes Raman gain is strongly suppressed. These results are similar to the ones reported in⁽¹⁾. In the presence of diffraction, however, the suppression effect is strongly reduced as shown in Fig. 6. Observe that the growth rate of the stokes and antistokes is nearly equal to the growth rate of the stokes only in the absence of diffractive effects, as can be seen by comparing the results of Figs. 6 and 1. The energy flux of the stokes and antistokes as function of the transverse position at different altitudes is shown in Fig. 7. Observe that at higher altitudes stokes-antistokes suppression is evident at $r=0$, and at lower altitudes the effect is smeared out by diffraction effects.

Summary & Conclusion

An "ab initio" theory for SRRS has been presented which is based on the density matrix approach. This theory properly treats the field polarization effects, is time dependent, and includes an arbitrary number of stokes and antistokes fields.

Preliminary results from a numerical code based on the theory have been presented. The small signal gain for the $J=8$ of N_2 as calculated from the code is in very good agreement with the experimental value. It has also been shown that in the presence of diffraction the suppression of the stokes gain for the case of stokes and anti-stokes fields in a collinear geometry is significantly reduced relative to the case of no diffraction.

The theory presented can be readily extended to the case of polyatomic molecules by using the appropriate transformation coefficients in the Wigner-Eckart Theorem.

A more detailed presentation of the theory and results will be given in a future paper.

References

1. A. P. Hickman, J. A. Painser, W. K. Bischel, Phys. Rev. A, 33, 1788 (1986).
2. C. G. Parazzoli, to be published.
3. P. W. Langhoff, J. Chem. Phys. 57, 2604 (1972).
4. G. J. Rosasco et al, Chem. Phys. Lett. 97,435 (1983).
5. A. Flusberg, in Proceedings SPIE, R. Fisher, I. Abramowitz Ed, Vol 739, pp. 138-145, (1987).
6. N. Bloembergen, Nonlinear Optics, (W. A. Benjamin, 1965) pp. 110-119.

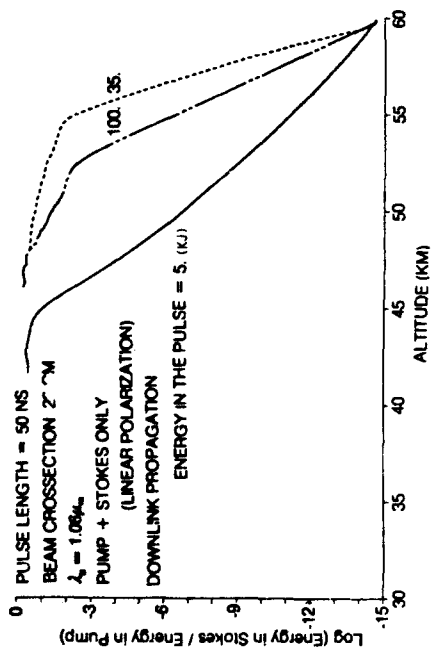


FIGURE 1. ENERGY IN THE STOKES WAVE AS FUNCTION OF THE ALTITUDE, NO DIFFRACTIVE EFFECTS

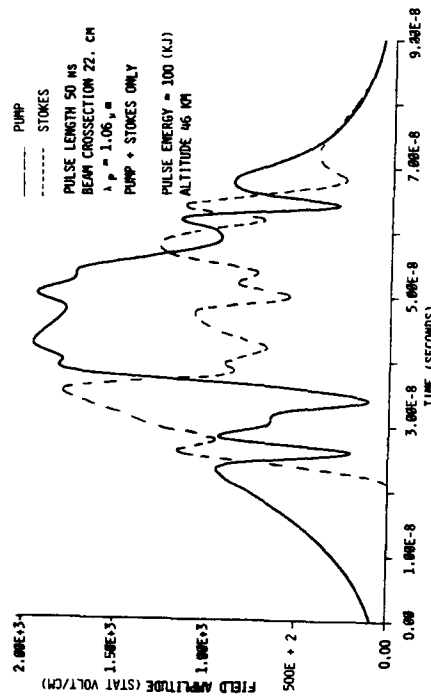


FIGURE 2. PUMP AND STOKES AMPLITUDES, SAME CONDITIONS AS FIGURE 1

PUMP AND STOKES PHASES AT $T = 40$ NS (RETARDED TIME)
PULSE LENGTH 50 NS
BEAM CROSSSECTION $\omega_0 = 24$ CM AT $Z = 46$ KM
 $\lambda_p = 1.06 \mu m$ LINEAR POLARIZATION

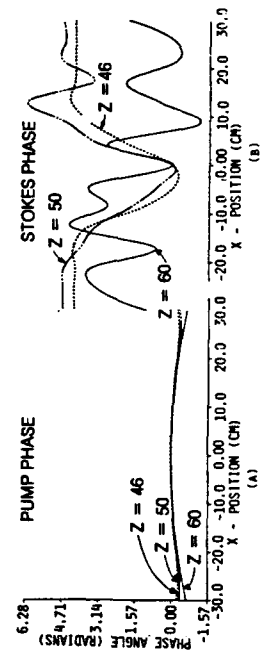


FIGURE 4. SNAPSHOT OF THE PUMP AND STOKES PHASES AT DIFFERENT ALTITUDES, DIFFRACTION EFFECTS INCLUDED

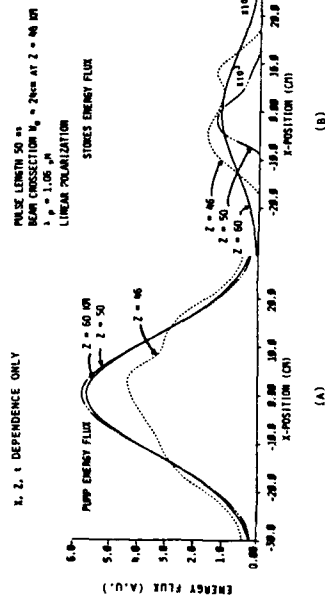


FIGURE 3. DIFFRACTION EFFECTS FOR PUMP AND STOKES ONLY, DISTRIBUTED SPONTANEOUS EMISSION IS INCLUDED IN THE CALCULATION

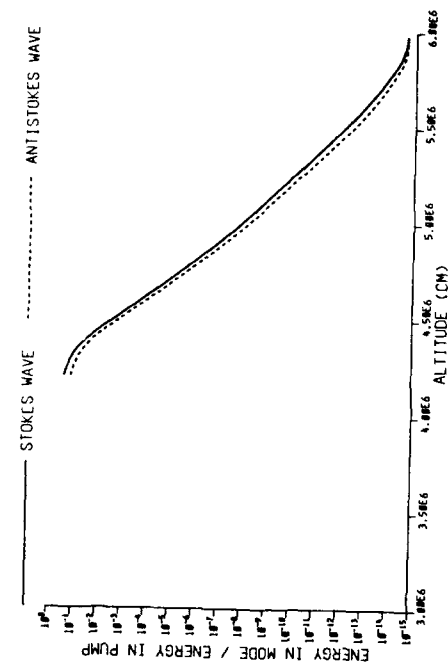


FIGURE 5. STOKES AND ANTISTOKES SUPPRESSION IN THE ABSENCE OF DIFFRACTION EFFECTS - PULSE ENERGY 5.0 KJ, PULSE LENGTH 10.0 NS, BEAM RADIUS 22.0 CM, FLAT TOP IN SPACE AND TIME, PRESSURE 1.0 OPM

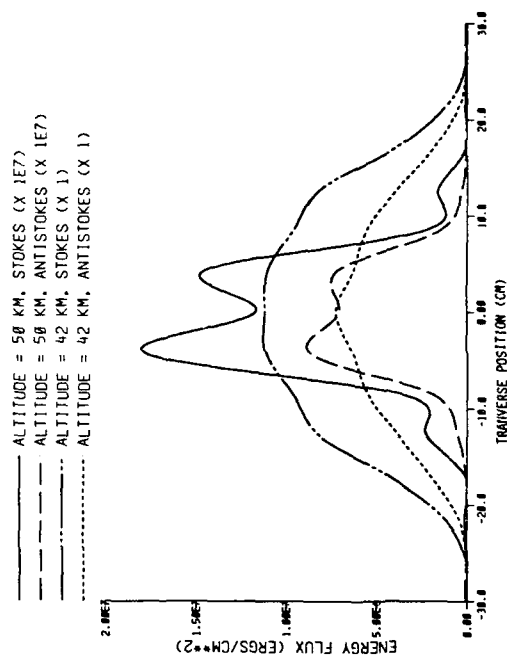


FIGURE 6. STOKES + ANTISTOKES WITH DIFFRACTION EFFECTS, PULSE ENERGY = 5.0 KJ, OTHER CONDITIONS SAME AS FIGURE 1.

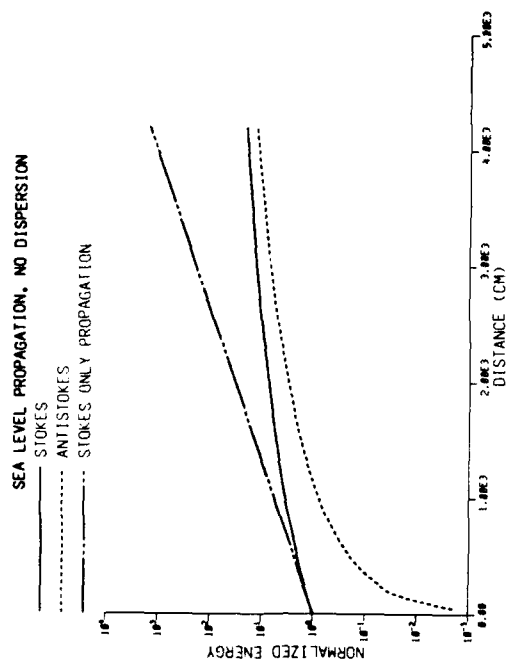


FIGURE 7. STOKES AND ANTISTOKES ENERGY FLUX AS FUNCTION OF THE TRANSVERSE POSITION AT DIFFERENT ALTITUDES, CONDITIONS SAME AS FIGURE 6.

MULTIPLEX CARS FOR COMBUSTION DIAGNOSTICS

J.P. Singh and F.Y. Yueh
MHD Energy Center
Mississippi State University
Mississippi State, MS 39762

Abstract

A multiplex coherent anti-Stokes Raman spectroscopy system (CARS) to measure the temperature and species concentration in a combustion environment is described. The nine parameter fitting program is used to compare the observed CO₂ spectra with computer simulated spectra. These measurements are performed in a methane/oxygen diffusion flame.

Introduction

Coherent anti-Stokes Raman spectroscopy (CARS) is one of the best line-of-sight techniques available for combustion diagnostics. The directional property of the CARS signal provides remote detection without much attenuation. Due to its nonlinear effect, it is produced at the focal point which gives the spatial resolution. The simultaneous recording of the broad region of spectra with multiplex CARS provides the temporal resolution.

CARS has been used to measure the temperature¹⁻⁶ and species concentration^{1,7,8} of the combustion media. The thermometry is usually done with N₂ CARS and sometimes with O₂, H₂O, and H₂ CARS. The CO₂ CARS spectra has not been explored in detail due to non-availability of its precise spectroscopic data. More refined data is coming in the literature.^{9,10} The CO₂ CARS¹¹ has been used to measure the temperature of the combustor. CO₂ CARS studies have been started to explore its full potential using the best available spectroscopic data. In this present paper it will be demonstrated that CO₂ CARS can be used to measure the concentration of CO₂. Various problems associated with modeling the spectra will be highlighted.

Theoretical Considerations

The general expression for the anti-Stokes spectral density in terms of the spectral density lineshapes of the pump and Stokes laser beams can be expressed¹²⁻¹⁴

$$I_4(\omega_4) = \int |x_{\text{CARS}}|^2 I_1(\omega_1) I_2(\omega_2) I_3(\omega_3) \delta(\omega_1 + \omega_3 - \omega_2 - \omega_4) d\omega_1 d\omega_2 d\omega_3 \quad (1)$$

where the $I_1(\omega_1)$, $I_3(\omega_3)$, and $I_2(\omega_2)$ are the pump lasers and Stokes laser spectral density functions which depend on angular frequencies and x_{CARS} is the third order susceptibility.

$$x_{\text{CARS}} = x_{\text{nr}} + 1/2 x_r(\omega_1 - \omega_2) + 1/2 x_r(\omega_3 - \omega_2)$$

If the line overlap is small, $x_r(\omega_1 - \omega_2)$ can be expressed¹¹

$$x_r(\omega_1 - \omega_2) = \frac{N}{N} \sum_j \frac{\alpha_j^2 \Delta \rho_j}{(\omega_j - \omega_1 + \omega_2) - i\gamma_j} \quad (2)$$

where N is the number density of the Raman active molecule, $\Delta \rho_j$ is the population difference between upper and lower vibrational states, α_j is the polarizability matrix element, and γ_j is the pressure-broadened linewidth (HWHM).

The CO₂ CARS measurements require the comparison between experimental data and theoretical spectra. The CO₂ CARS spectra has to be modeled carefully. CO₂ is a linear triatomic molecule. It is characterized by vibrational quantum numbers ν_1, ν_2, ν_3 of the fundamental vibrational mode and a vibrational angular momentum quantum number ℓ_2 . The accidental degeneracy, $\nu_1 = 2\nu_2$, results in the Fermi resonant effect in which the vibrational states of these two modes are mixed together. This causes a perturbation of the vibrational energy levels and rotational constants which must be considered in the theoretical calculation of CO₂ CARS spectra. The numerical simulation of the CO₂ CARS spectra has been discussed in detail.^{10,11} The depolarization of the CO₂ spontaneous Raman spectrum is relatively small.¹⁵ Therefore, the Q-branch transitions are more important than other branch transitions. The calculations in this paper include only Q-branch bands. Nineteen Q-branch bands have been observed for high temperature CO₂ CARS spectra in the spectral range 1395 - 1455 cm⁻¹.¹⁰ In order to model CO₂ CARS in this spectral range, the experimental energy level parameters given by Rothman and Young¹⁶ were employed for these bands. The influence of ℓ -type doubling on the rotational constants was taken into account for CO₂. The eigenvalue and eigenvector of the perturbed Hamiltonian matrix for each set of Fermi resonant states were solved. The perturbed eigenvector was used to calculate the perturbed polarizability matrix element following Hall's treatment.¹¹ The Raman linewidths for CO₂ were approximated by

$$\gamma_j = 0.05 (300/T)^{0.75} \quad (3)$$

It has been found that the rotational lines for the Q-branches of CO₂ are closely spaced and this results in appreciable line overlap. The pressure narrowing effect is important even at 1 atm pressure in CO₂. An analytical approach¹ to this effect has been derived by Hall based on Gordon's extended diffusion theory of rotational motion. The expression for $\chi_r(\omega_1-\omega_2)$ for all Q-branches becomes

$$\chi_r(\omega_1-\omega_2) = \left(\frac{N}{M} \sum_j \frac{\alpha^2 \Delta \rho_j}{(\omega_j - \omega_1 + \omega_2) - i \gamma_j} \right) \cdot \left(1 + i \sum_j \frac{\gamma_j \rho_j}{(\omega_j - \omega_1 + \omega_2) - i \gamma_j} \right)^{-1} \quad (4)$$

Due to the difficulty in deriving the analytical expression for CO₂ CARS intensity, the $| \chi_{\text{CARS}} |^2 = | \chi_{\text{nr}} + \chi_r(\omega_1-\omega_2) |^2$ approximation was used in Eq. (1). The anti-Stokes spectral density for the broadband Stokes laser with Gaussian laser profile then becomes approximately¹¹

$$I_4(\omega_4) \sim \exp \frac{[-(\omega_4 - 2\omega_1^0 + \omega_2^0)^2]}{(\Delta\omega_2/2\sqrt{\ln 2})^2} \cdot \int | \chi_{\text{nr}} + \chi_r(\omega_1-\omega_2) |^2 I_1(\omega_3 - (\omega_1-\omega_2)) d(\omega_1-\omega_2) \quad (5)$$

The CO₂ CARS spectra was computed using Eq. (5). Figure 1 shows the variation of the spectra as a function of concentration of CO₂ in N₂. Spectra of four concentrations (3, 5, 10, 20%) were computed at 1600 K. These spectra were convoluted with the spectrometer instrument function. It is evident that the shape of the spectra is sensitive to concentration and it may be used for CO₂ concentration measurement.

Experimental Details

The CARS system used in these measurements is shown in Figure 2 and is a modified form of the one described in Ref. 17. It has a frequency doubled Nd-YAG laser (Quanta-Ray, DCR-2A). The residual IR beam is frequency doubled again and is used to pump the oscillator of the broad band dye laser. Thirty percent of the green beam pumps the amplifier of the dye laser. The same dye cell is used as oscillator and amplifier. The amplified dye laser output is expanded 4 times and kept parallel to the optics table. The green beam is expanded 1.5 times and divided equally into two beams. Both green beams are arranged parallel to the dye laser beam. These three beams are focused into the diagnostics test region. The CARS signal generated in the focal volume is separated from the lasers using a beam block and narrow band pass filter. A glass slide is used as beam divider to send a part of the CARS signal to a 1P28 photomultiplier tube (PMT). An interference filter from Ditic Optics (15-2027) is mounted in front of the PMT. The output from the PMT is connected to a Tektronics (475A) oscilloscope. The CARS signal is focused on the entrance slit of a 0.75 m Spex spectrograph equipped with 1800 λ /mm grating. The EG & G PARC 1254E Silicon Intensified Detector (SIT) records the signal at the exit slit of the spectrograph. This signal is stored in 1215 microcomputer dedicated for recording and analyzing data from the 1254.

A typical dye solution mixture of 1.72×10^{-4} M Rh 6G and 4.4×10^{-5} M Rh610 is used to monitor CO₂ CARS spectra. It gives a dye laser peak at 579.5 nm and a FWHM of 7 nm in the present dye laser cavity. The concentrations of the dyes in the solution are changed to shift the peak of the dye laser. This provides the suitable dye profile to monitor the various regions of the CO₂ spectra and also to monitor CO₂, H₂ and O₂ CARS spectra simultaneously. The dye profile is recorded with a 0.75 m Spex monochromator interfaced with a CO₂ computer drive and a Hewlett Packard 7045A x-y recorder.

The diffusion flame burner used in the present measurement is shown in Figure 3. It has been fabricated with an aluminum block 100 mm x 65 mm x 50 mm. It has three inlets for CH₄, N₂ and O₂ gases. A stainless steel rectangular box, 100 mm x 52 mm x 16 mm open at top and bottom, is placed on the Al-block. A 100 mm x 50 mm x 1 mm stainless steel plate divides the steel box into two equal parts. One part is connected with the CH₄ inlet and the other part with O₂ inlet. There are 34 fine holes around the stainless box, 5 mm apart, in the Al-block. These holes and steel box are covered with another stainless steel box 130 mm x 65 mm x 30 mm. Nitrogen gas is passed between the stainless steel boxes through the holes to keep the flame vertical and to cool the inside box. This burner is connected with a gas handling system, as in Ref. 18, which provides the various stoichiometric CH₄/O₂ flames. It is mounted on an x-y-z translator which is attached with a stepper motor. The stepper motor power supply is controlled with a Tandy model 102 portable computer¹⁹ interfaced with Elexor Associates interface box. This provides the facility to monitor the various regions of the flame.

Results and Discussions

The flow rates of methane and oxygen are adjusted to get the flame to stoichiometry 0.85 (fuel rich). CO₂ CARS spectra were recorded on the Optical Multichannel Analyzer (OMA), as shown in Figure 4, at a distance of 2 mm from the center of the CH₄/O₂ flame towards the CH₄ side. The height of the focused laser beams are 7 mm from the burner. The dye laser peak was 575.6 nm with FWHM 7 nm. The spectrum is integrated up to 100 scans at the monochromator central position of 496 nm. It shows the various bands formed due to the Fermi resonance of symmetric stretch (ν_1) and bending stretch ($2\nu_2$). The various bands are assigned in Figure 4.¹⁰ The band at 1447 cm⁻¹ has two CO₂ bands and an H₂ pure rotational line S(5). The band progression at 1285 cm⁻¹ was recorded to compare with bands at 1388 cm⁻¹. It is clear in Figure 4 that the intense feature at 1447 cm⁻¹ is not due to CO₂. The CO₂ CARS spectrum is superimposed on the non-resonant background.

Figure 5(a) shows the fit of the model spectra with experimental spectra recorded at the previous conditions. The dye laser peak was 579.5 nm and the spectrum was averaged up to 200 scans. The nine parameter fitting program was used to compare the observed spectra with the library of computer simulated spectra. The modeling of H_2 has not yet been included in the program. The observed spectrum is in reasonably good agreement with model spectra. It gives a temperature of 868 K and a CO_2 concentration of 4.1%. CARS spectrum recorded at 1 mm from the center of the flame toward the O_2 side is shown in Figure 5(b). The spectrum is slightly poor in signal-to-noise ratio due to averaging only 50 pulses. Fitting of this spectrum with a computer simulated spectrum gives a temperature 1648.6 K and a CO_2 concentration of 11.3%. The fit of this spectrum is not as good as the previous spectrum, especially in the lower frequency wing of the bands. The shape of the band at 1448 cm^{-1} is completely different from the shape of the computed band. It might be due to the position of CO_2 bands and also due to the superposition of the H_2 S(5) line. The interference of the H_2 rotational line and the linewidth of CO_2 at higher temperatures might be possible reasons for the bad fit at higher temperatures. The spectra have also been recorded at various points across the flame at a height of 7 mm. The colder spectra were better matched with computed spectra than the hotter spectra. The observed results can be qualitatively summarized as follows. The concentration of H_2 increases as one moves away from the center towards the CH_4 side up to 4 mm and then decreases. In the same way the CO_2 concentration increases up to 3 mm. The variation in concentration across the flame may be partly due to temperature variation and to mixing of fuel and oxidizer. The spectra containing O_2 , H_2 and CO_2 has also been recorded simultaneously with the appropriate dye laser. To get the quantitative picture, the CO_2 CARS spectra will be recorded in a quartz cell placed in a furnace at different temperatures. The concentrations of CO_2 and H_2 will be changed in the gas mixture. These experiments will provide enough information to calibrate the CO_2 CARS spectra for concentration measurements. The work is also continued to get better fits of the spectra at higher temperatures using more refined spectroscopic data.²⁰

Conclusions

The CO_2 model spectra is sensitive to the CO_2 concentration and can be used for CO_2 concentration measurements in combustion media. This preliminary study of CO_2 CARS shows that the computer modeling gives a better fit for spectra at lower temperatures. Further refined spectroscopic data is needed to model the spectra at higher temperatures. The simultaneous recording of O_2 , H_2 and CO_2 CARS spectra will give concentrations of these species. This will provide information about the various combustion processes in the test media.

Acknowledgement

This work was supported by DOE Contract No. DE-AC02-80ET-15601, MHD Energy Center, Mississippi State University.

References

1. Hall, R.J., and Eckbreth, A.C. 1984. *Laser Applications*, eds. J. F. Ready and R.K. Erf, 5:213. New York: Academic Press.
2. Beiting, E.J. 1986. *Appl. Opt.* 25:1684.
3. Hall, R.J., and Boedeker, L.R. 1984. *Appl. Opt.* 23:1340.
4. Fujii, S.; Gomi, M.; and Jin, Y. 1982. *Combust. Flame* 48:233.
5. Greenhalgh, D.A.; Porter, F.M.; and England, W.A. 1983. *Combust. Flame* 49:171.
6. Bedue, R.; Gastebois, P.; Bailly, R.; Pealat, M.; and Taran, J.P. 1984. *Combust. Flame* 57:141.
7. Eckbreth, A.C., and Hall, R.J. 1981. *Combust. Sci. and Tech.* 25:175.
8. Beiting, E.J., and Yueh, F.Y. to be published.
9. Ouazzany, Y., and Boquillon, J.P. 1987. *Europhys. Lett.* 4:421.
10. Papineau, N., and Pealat, M. 1985. *Appl. Opt.* 24:3002.
11. Hall, R.J., and Stufflebeam, J.H. 1984. *Appl. Opt.* 23:4319.
12. Yueh, F.Y., and Beiting, E.J. 1986. *Comput. Phys. Commun.* 42:65.
13. Kataoka, H.; Maeda, S.; and Hirose, C. 1982. *Appl. Spectrosc.* 36:565.
14. Teets, R.E., 1984. *Opt. Lett.* 9:226.
15. Penney, C.M.; Goldman, L.M.; and Lapp, M. 1972. *Nature* 235:110.

16. Rothman, L.S., and Young, L.D.G. 1981. *J. Quant. Spectrosc. Radiat. Transfer* 25:505.
17. Beiting, E.J., and Singh, J.P. Jan. 1986. Testing and Evaluation of Heat Recovery/Seed Recovery. *Quarterly Technical Progress Report*, MHD Energy Center, Mississippi State University FE-15601-23:6-35.
18. Beiting, E.J., and Singh, J.P. 1986. *Rev. Sci. Instrum.* 57:377.
19. Yueh, F.Y.; Singh, J.P.; and Beiting, E.J. Testing and Evaluation of Heat Recovery/Seed Recovery. *Quarterly Technical Progress Report*, MHD Energy Center, Mississippi State University FE-15601-30.
20. Rosenmann, L.; Perrin, M.Y.; and Taire, J. 1988. *J. Chem. Phys.* 88.

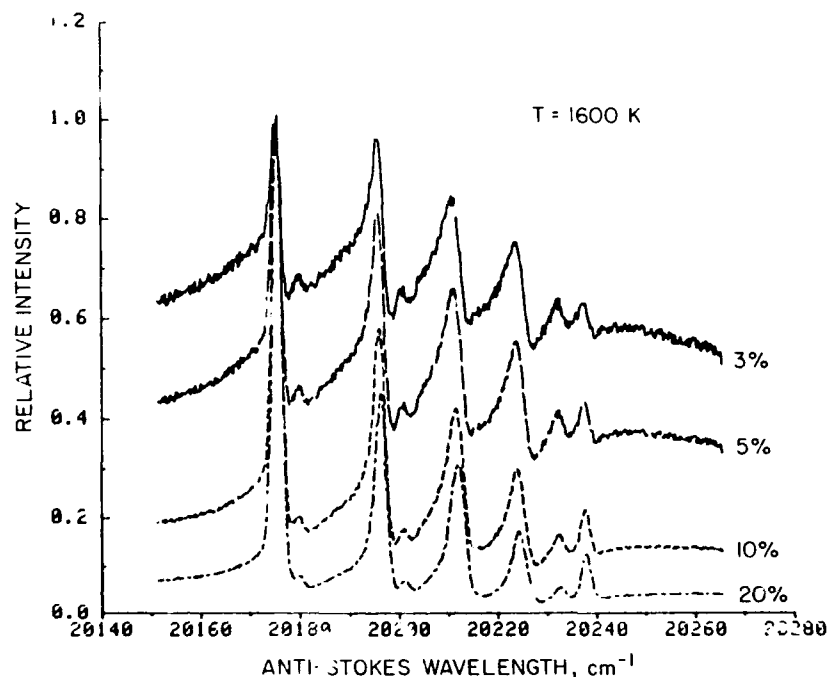


Figure 1.

CARS model spectra of CO_2 at various concentrations.

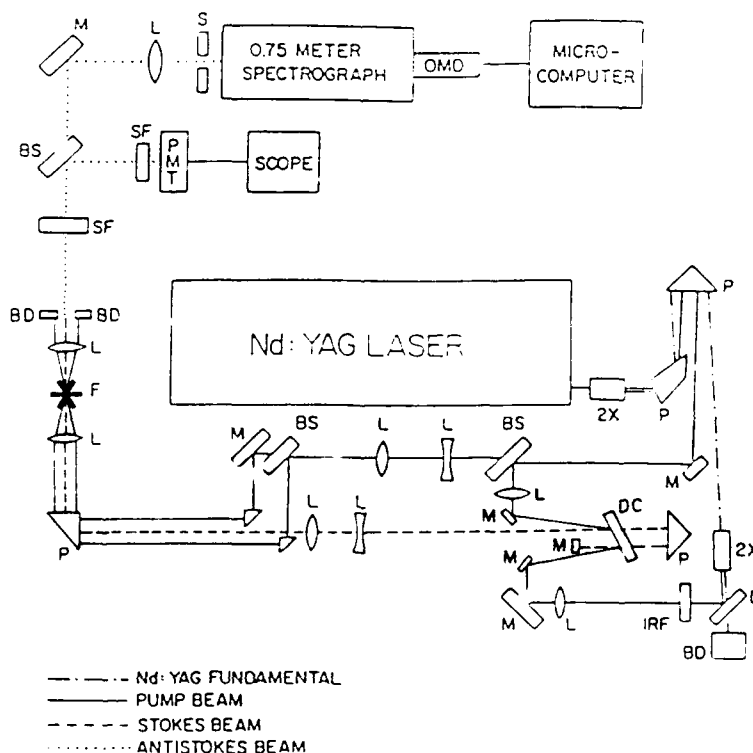


Figure 2.

Schematic diagram of the CARS instrument. Code: M, mirror; P, prism; BS, beam splitter; L, lens; BD, beam dump; DC, dye cell; 2X, DK*P doubler; IRF, infrared absorbing glass; SF, spectral filter; S, electromechanical shutter; PMT, Photomultiplier; OMD, optical multichannel detector; F, flame.

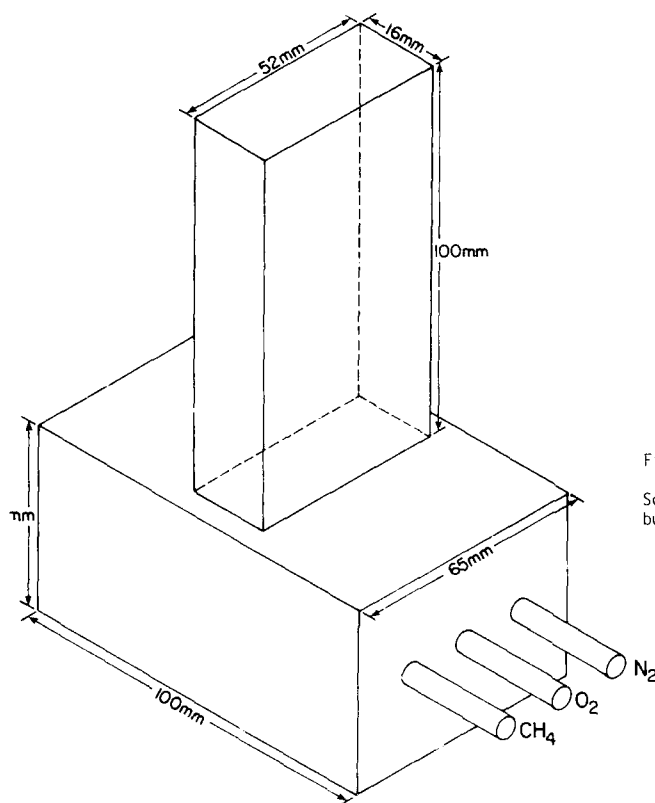
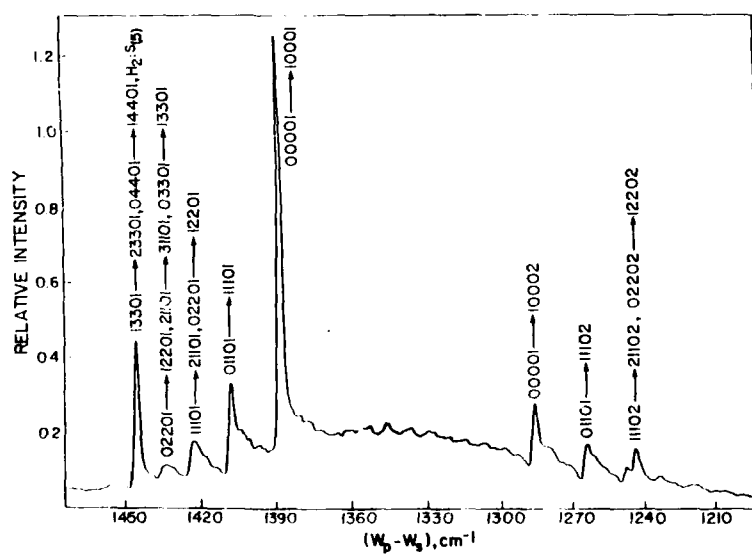


Figure 3.
Schematic diagram of the CH_4/O_2 diffusion burner.

4.
derived RARS spectrum of CO_2
in band assignment.



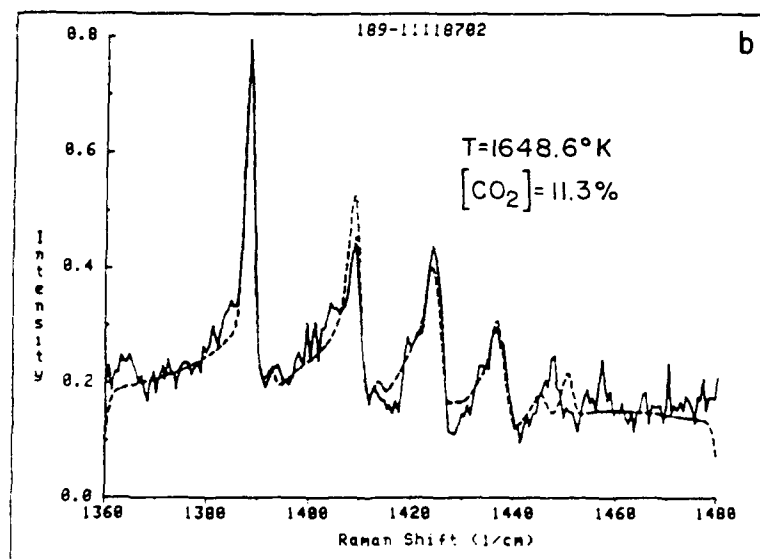
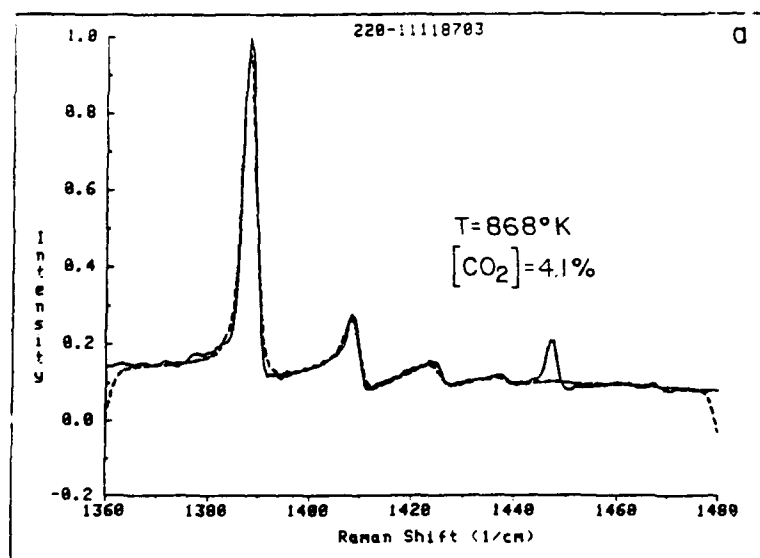


Figure 5.

Observed CO_2 CARS spectra with computer simulated spectra.

INTERACTION INDUCED LIGHT SCATTERING (IILS) FROM THE ν_2 MODE OF CO_2 IN CO_2 - N_2 SUPERCRITICAL MIXTURES

A. Hacura* and F.G. Baglin

Department of Chemistry, University of Nevada, Reno, Nevada 89557

Pure CO_2 and CO_2 - N_2 mixtures at various densities have been examined by Raman light scattering. In conjunction with molecular dynamic studies, a more complete understanding of microscopic dynamical properties of simple liquids is sought.

*Permanent address: Instytut Fizyki, Uniwersytet Slaski, ul. Uniwersytecka 4, 40-007 Katowice, Poland

INTRODUCTION

During the last ten years interaction induced Raman light scattering of simple fluids (liquid state or highly compressed gases) has been subject of several theoretical (1-5) and experimental (6-10) investigations. Interaction induced dipole forbidden Raman signals arise from electrical interactions between molecules which distort the isolated molecules point group symmetry. This distortion switches on higher order multipole electrical interaction terms. This mechanism involves translation motions of one distorted molecule relative to another and gives rise to "forbidden" signal of large width. The width is related to the duration of interaction and is clearly dominated by a very fast process. In this paper we present experimental results for CO_2 and CO_2 - N_2 mixtures at various gaseous densities which allows more accurate spectral moments and interaction induced correlation times to be obtained from the $\nu_2 \pi_u$ CO_2 signal. We have measured both isotropic and anisotropic spectra for the mode ν_2 and compared the depolarization ratios at high densities for pure CO_2 and the 1:3 CO_2 - N_2 mixture.

EXPERIMENTAL

The beam of an argon-ion laser (Spectra-Physics 2020, 1W at 514.5 nm) was focused on a single window of a three window high-pressure cell containing the gas to be studied. The 90° scattering was analyzed with a conventional Raman double monochromator (Instruments SA-1000) and detected with a nine stage photomultiplier associated with a photon counter. The temperature was monitored with a thermocouple, it could be controlled to $\pm 0.5^\circ\text{C}$. The carbon dioxide gas was Linde Precision Aquarator grade (99.9% CO_2 , 7 ppm O_2 , 10 ppm hydrocarbons) and the nitrogen, from Alphagaz Corp., has minimum purity of 99.998%. To eliminate dust, the cell was purged before experiment with supercritical CO_2 which passed through three filters of 50, 15 and 5 μm mesh. The slits were set at 4.0 cm^{-1} for the ν_2 interaction induced signal and 0.5 cm^{-1} for the ν_1 and $2\nu_2$ allowed signals of CO_2 ; both settings were considerably less than the signal width observed ($<10\%$) and deconvolution of the instrumental function from the spectra was therefore unnecessary.

RESULTS AND DISCUSSION

We have measured the Raman intensity $I(\omega)$ from the weak $\nu_2 \pi_u$ signal of pure carbon dioxide at 50°C and for the gas mixtures CO_2 - N_2 at several densities. Each experiment was repeated at least fifty times and then averaged. The normalized second spectral moments M_2 were calculated

$$M_2 = \frac{\int_{-\infty}^{\infty} (I(\omega)\omega)^2 d\omega}{\int_{-\infty}^{\infty} I(\omega) d\omega}$$

with Boltzman corrections $I_B(\omega) = 1/2 (1 + \exp(-h\omega/kT))$ which is significant for such a broad line.

Table I shows the density dependence of the second spectral moment and interaction induced correlation times $\tau = \int_0^\infty C(t) dt$, where $C(t)$ is an experimental time correlation function calculated for the $\nu_2 \text{CO}_2$ signal.

the measured total relative intensity data are displayed in Fig. 1, 2 and 3. The intensity for the

Table 1. Interaction Induced Data from CO_2 's $\nu_2 \pi_u$ signal at 50°C

Pure CO_2			CO_2 : N_2 (1:1)			CO_2 : N_2 (1:3)		
corr. time (fsec)	nor. 2nd. spectral moment	number density $1/\text{cm}^3$	corr. time (fsec)	nor. 2nd. spectral moment	number density $1/\text{cm}^3$	corr. time (fsec)	nor. 2nd. spectral moment	number density $1/\text{cm}^3$
84.7	6.46 E3	16.6 E21	65.5	7.60 E3	17.0 E21	78.9	5.86 E3	17.0 E21
66.7	28.03 E3	15.2 E21	67.4	7.25 E3	15.7 E21	71.3	3.98 E3	15.7 E21
56.5	26.06 E3	13.8 E21	65.9	7.96 E3	13.3 E21	61.5	7.02 E3	13.3 E21
66.0	3.92 E3	12.0 E21	---	---	---	---	---	---
86.7	3.99 E3	9.2 E21	70.7	6.49 E3	10.4 E21	72.0	6.44 E3	10.4 E21
84.2	0.09 E3	5.3 E21	74.3	7.16 E3	6.6 E21	59.0	5.58 E3	6.6 E21
82.1	0.01 E3	4.3 E21	83.2	4.23 E3	3.3 E21	---	---	---

Fig.1. Intensity of Raman signals from pure CO₂ "forbidden" ν_2 and from "allowed" $2\nu_2$ and ν_1 as function of density at 50°C.

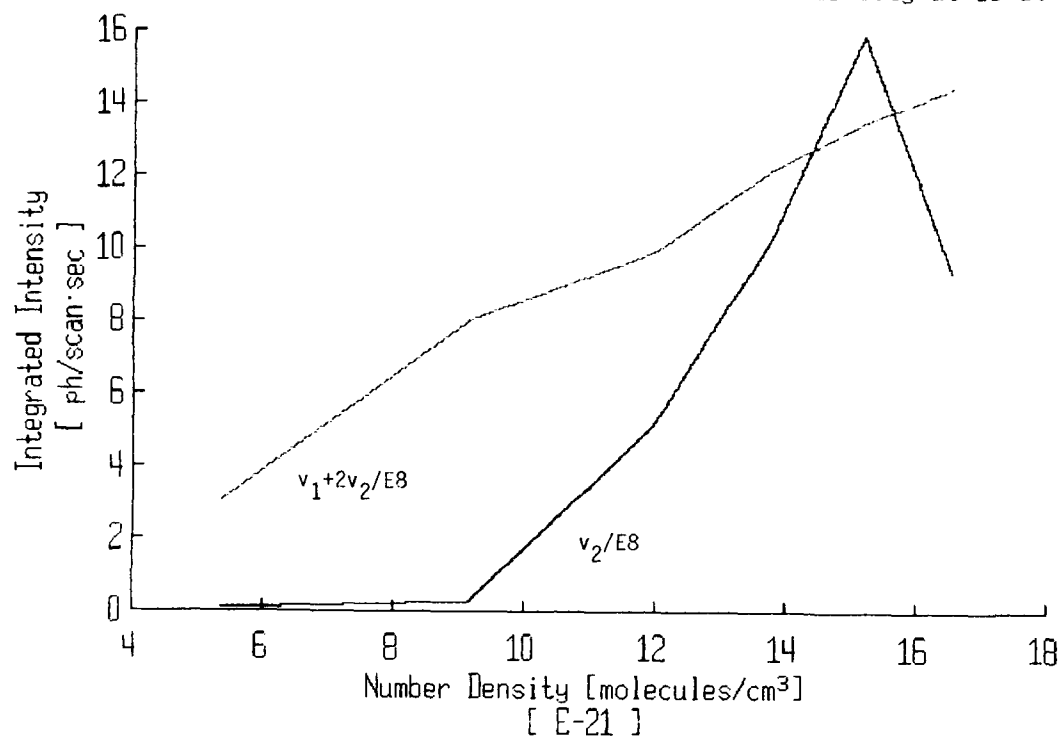


Fig.2. Same as Fig.1, but for CO₂-N₂ mole ratio 1:1 mixture also at a temperature of 50°C.

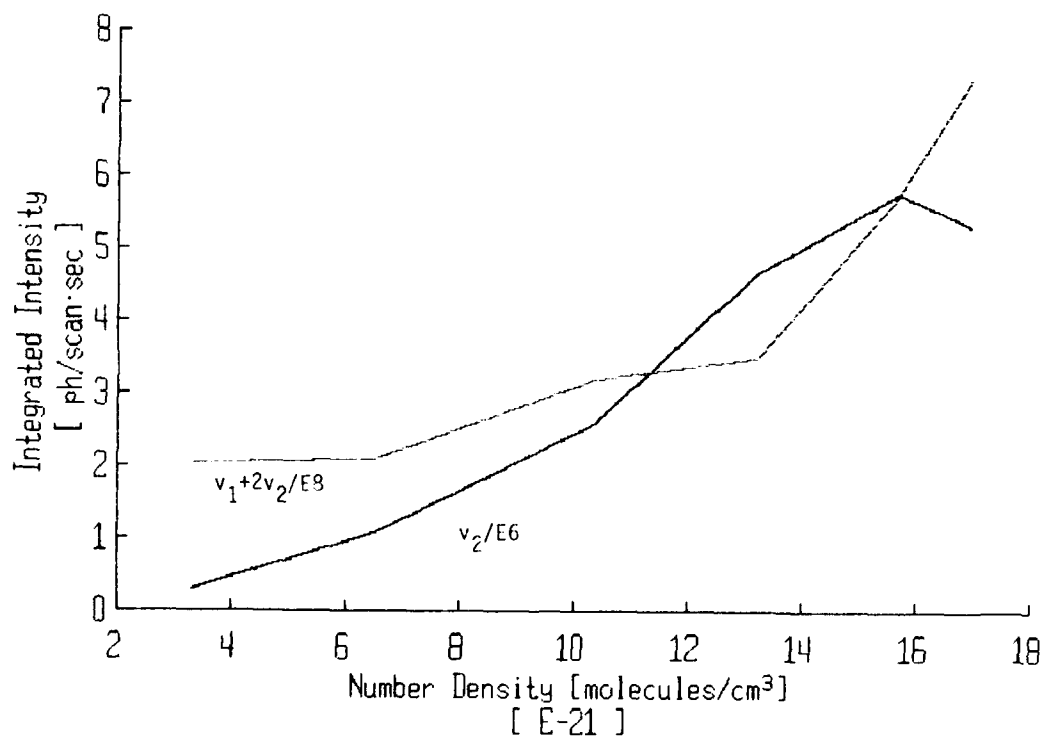


Fig.3. Same as Fig.1, but for CO₂-N₂ mole ratio 1:3 mixture also at a temperature of 50°C.

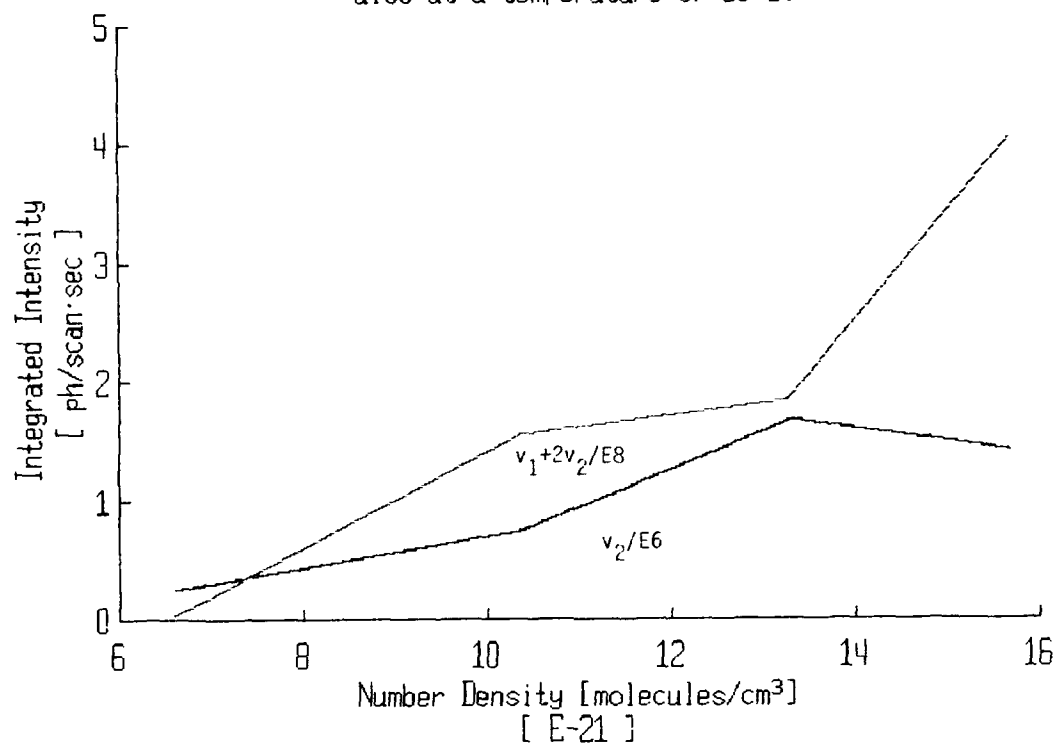


Fig.4. Depolarization ratio of CO₂ v_2 signal.

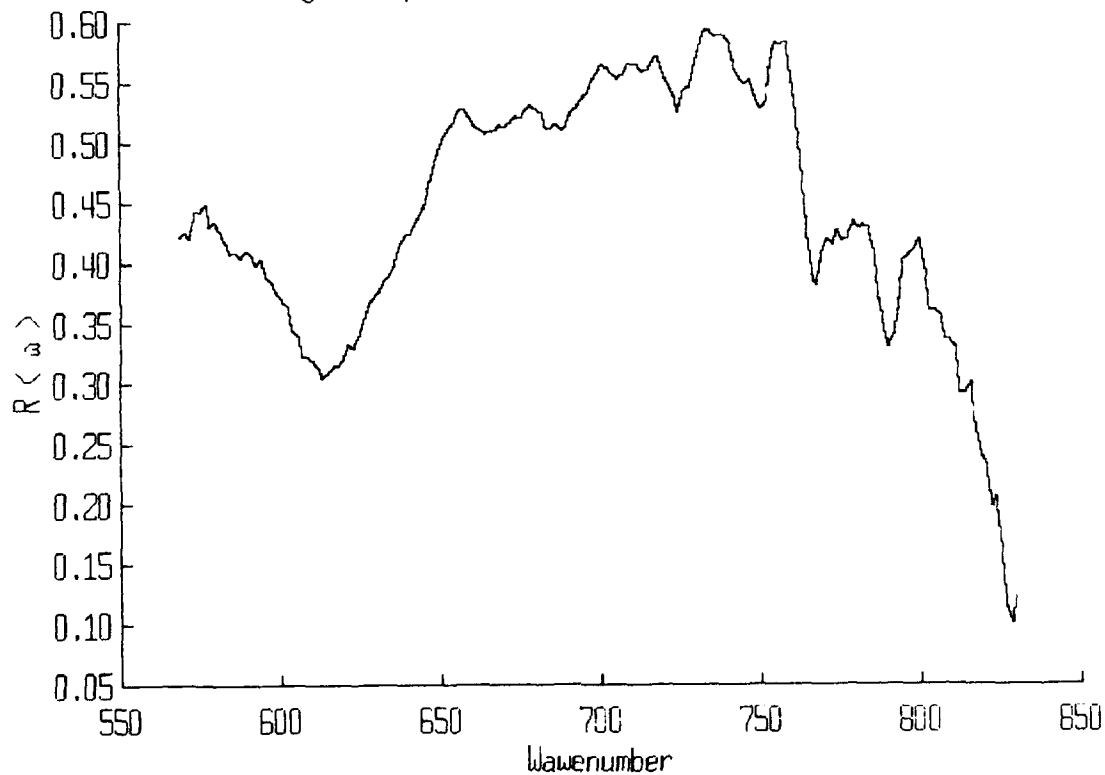
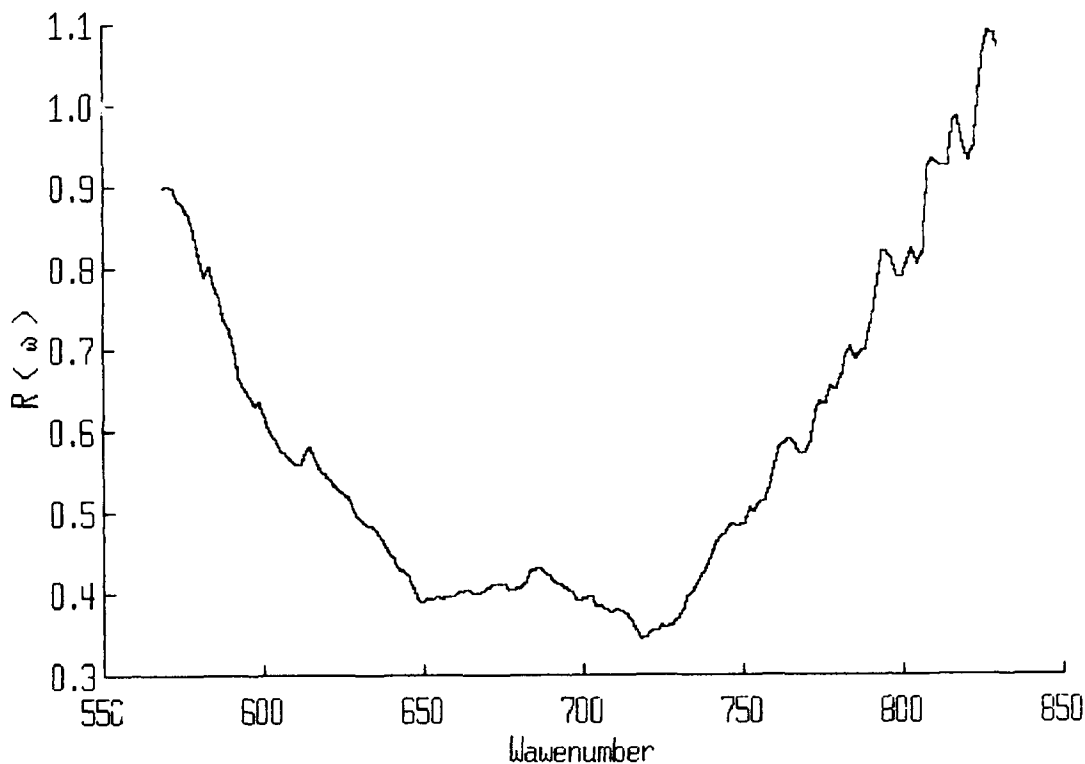


Fig.5. Depolarization ratio of ν_2 signal for $\text{CO}_2\text{-N}_2$ (1:3) mixture.



ν_1 and the $2\nu_2$ signals increases almost linearly while the intensity for the ν_2 signals increase quadratically and then gradually decreases at higher densities for pure CO_2 and mixtures. Measurements of the depolarization ratio, $R(\omega) = I_{VH}(\omega)/I_{VV}(\omega)$ for pure CO_2 and the $\text{CO}_2\text{:N}_2 = 1\text{:}3$ mixture at 50°C (for number density 15 E21/ccm was done and, as can be seen in Figures 4 and 5, shows a striking difference in behaviors as a function of energy from ω_0 (the signal center 675 cm^{-1}).

We may summarize our measurements of the ν_2 spectra of CO_2 and of $\text{CO}_2\text{:N}_2$ over a large pressure range as

follows:

- (i) a clear spectral broadening with accompanying short correlation times at a density of about 13 E21 molecules/ccm.
- (ii) a spectral narrowing at densities above 13 E21 molecules/ccm in pure CO₂ only.
- (iii) different depolarization ratio behavior in pure CO₂ and CO₂:N₂ mixtures.

The first two effects above may arise from several possible alternatives. We mention two here.

Firstly, a three-body like spectral cancellation effect (II) seen only in the pure CO₂, i.e. the intensity grows steadily as a function of number density squared until a density near 13 E21 molecules/ccm is reached. At that point three body cancellation eliminates the prominent high frequency spectral shoulder (located some 330 cm⁻¹ above ω_0). Secondly, we may not be seeing a shoulder on the ν_2 signal, but rather a dip in the spectral intensity due to exact cancellation of the component correlation functions (12) that make-up the total, observed, correlation function at very short times i.e. high frequency. At the present time either of these two possibilities is plausible depending upon one's point of view. The MD calculations on these system should help to resolve this issue.

The markedly different depolarization ratio behavior as a function of energy from ω_0 , reveals a distinct difference in the local fields about a CO₂ molecule in pure CO₂ or a nitrogen mixture. Thus, it would seem that the CO₂ tends to cluster together, much as a gas does in the vicinity of the critical point. Calculations by Amos et al. (13) have, on the basis of only two interacting CO₂ particles, shown a depolarization ratio near 0.29. In the 1:3 CO₂:N₂ mixtures we find, at ω_0 , a ratio of 0.32, which is well within experimental error. Further, studies are currently under way to understand if there is a close connection between the first two points above with this final point.

REFERENCE

1. H.A. Posch, V. Balucani and R. Vallauri, *Physica*, 123A, 516 (1984).
2. P.A. Madden and D.J. Tildesley, *Molec. Phys.*, 55, 969 (1985).
3. S. Bratos, B. Guillot and G. Birnbaum, in *Phenomena Induced by Intermolecular Interactions*, G. Birnbaum, Ed. Plenum Press, New York, N.Y., 1985) pp. 363-381.
4. G. Briganti, D. Rocca and M. Nardone, *Molec. Phys.*, 59, 1259 (1986).
5. A. DeSantis, R. Frattini and M. Sampoli, *Europhysics Letters*, 2, 17 (1986).
6. W. Holzer and R. Ouillon, *Molec. Phys.*, 36, 817 (1987).
7. M. Zoppi, F. Barocchi, D. Varshneya, M. Neuman and T.A. Litovitz, *Can. J. Phys.*, 59, 1475 (1981).
8. P.A. Madden, T.T. Cox, *Molec. Phys.*, 56, 223 (1985).
9. A. Hacura, J.H. Yoon and F.G. Baglin, *J. Raman Spec.*, 18, 377 (1987).
10. F.G. Baglin, *Spectroscopy*, 2, 26 (1987).
11. B.J. Alder, J.J. Weis and H.L. Strauss, *Phys. Rev. A*, 7, 281 (1973).
12. B. Guillot, *J. Chem. Phys.*, 87, (4), (1987) and references therein.
13. R.D. Amos, A.D. Buckingham and J.H. Williams, *Molec. Phys.*, 39, 1519 (1980).

STATE MIXING IN COLLISIONS INVOLVING HIGHLY EXCITED BARIUM ATOMS

M. Allegrini*, E. Arimondo**, E. Menchi**, C.F. Burkhardt, M. Cioocca, W. P. Garver, S. Gozzini* and J. J. Leventhal, University of Missouri-St. Louis, St. Louis, MO 63121 and J. D. Kelley, McDonnell Douglas Research Labs, St. Louis, Missouri 63166

ABSTRACT

Data acquired in experiments employing laser excitation demonstrate that the state distributions of highly excited barium atoms are drastically altered by collisions. Initially produced Rydberg ns or nd eigenstates are rapidly mixed with nearly degenerate $n'l'$ states. For initially produced states that may be viewed as admixtures of Rydberg and doubly excited independent electron eigenstates, collisions convert the distribution to one with nearly pure (but state-mixed) Rydberg character. Broadening of the absorption profiles of the highly excited states was also observed. In addition, we also report preliminary findings of experiments designed to study Penning ionization in collisions involving highly excited atoms, in this case excited Ba colliding with ground state sodium.

Introduction

Over the past decade or more, many properties of Rydberg atoms have been studied¹ both theoretically and experimentally. While much of the experimental work has been performed using "one electron" alkali-metal atoms, the two-electron alkaline-earth atoms² have also received considerable attention. Most previous studies have been directed toward elucidation of the intrinsic properties of these atoms. In contrast, the work reported here was initiated to study collisional effects on the Rydberg states of barium, a two-electron atom with high-lying energy levels readily accessible with available lasers.

It has been shown that the various states that result from a nominal $5d7d$ electronic configuration of atomic barium serve as perturbing states that alter the regularity of the Rydberg series.² For principal quantum numbers n above 20, the only significant perturber³ is the one designated $5d7d\ ^1\Omega_2$ which perturbs the $J=2$ Rydberg levels in the vicinity of $n=26$. The fact that the eigenstates have varying relative Rydberg-valence state compositions in the vicinity of the perturber has important consequences with respect to the effects of collisions on these states. In this paper we report and discuss data that illustrate some of these effects.

Just as for the alkalis⁴ we expect collisional state changing, primarily $n'l \rightarrow n'l'$. Indeed, we find this to be the case, but, not unexpectedly, only for the Rydberg component of the excited state wavefunction. As a consequence, we find that a collection of barium atoms which has been laser excited to a perturbed level with a substantial $5d7d$ fraction is rapidly converted, by collisions with other barium atoms, to a collection with a distribution over many nearly degenerate Rydberg states and essentially no $5d7d$ character.

In addition to state changing we also report our observation that the excitation profiles of the highly excited states broaden dramatically with increasing excited atom density, an effect that we deduce to be the result of quasistatic interaction between highly excited atoms during the laser excitation.⁵ While this report deals mainly with the effects of collisions with barium atoms on the initially produced highly excited barium atoms we also report preliminary results of a reactive process, Penning ionization, involving highly excited barium and ground state sodium. The dual character, Rydberg and valence state of the perturbed levels offers the opportunity to contrast the reactivities of these two, vastly different, types of states. Our early results show that Penning ionization with reactant Rydberg reactant states is orders of magnitude greater than that for perturbed levels.

The experiments were performed using a new apparatus employing a well-collimated beam of barium atoms and two grazing incidence dye lasers pumped by a single Nd:YAG laser. The collinear linearly polarized laser beams, one green and the other blue, intersected the atomic beam producing highly excited barium atoms, Ba^{**} , in two steps. The atom density N in the beam was varied over the approximate range 10^8 - 10^{13} cm^{-3} as estimated from the oven temperature and vapor pressure curves. For the Penning ionization experiments a second atomic beam oven was installed, thus providing crossed Ba and Na beams.

Two methods for detecting highly excited atoms were employed. At relatively low N , $\sim 10^8$ - 10^{10} cm^{-3} , field ionization with a preset delay time, 200 ns to 2 μ s, produced Ba^+ which were then detected with a CuPe particle multiplier. At the higher densities field ionization could not be used because of electrical breakdown of the vapor. The Rydberg states of interest in these experiments are however photoionized by room temperature blackbody radiation. The resulting Ba^+ were detectable, thus allowing this method to be used over the entire range of atom densities. Only the RRPI results will be discussed here.

*Permanent address: IFAP, Pisa, Italy.

**Permanent address: University of Pisa, Italy.

The laser beam intensities were 5 kW/cm² and 2 kW/cm² (maximum) respectively for the green and blue lasers. At these levels the green resonance transition was saturated, but the blue transition to the highly excited states was not. The intensity of the blue laser beam was reduced when necessary using neutral density filters. The bandwidth of the green laser beam was about 0.8 cm⁻¹. For most of the experiments the bandwidth of the blue laser was also 0.8 cm⁻¹. For experiments requiring careful comparison of absorption profiles, a reflection grating was used to decrease the bandwidth to 0.2 cm⁻¹.

Results and Discussion

We examine the effects of heavy body collisions on the excited state populations by comparing BRPI spectra acquired at different values on N . As N is increased the d-state signal is observed to increase with respect to the s-state signal. This result is attributed to collisional state mixing which has the effect of lengthening the excited state-lifetime. In other words, increasing N causes the initially prepared d (and s) states to be collisionally distributed over the complete l -state manifold. Increasing the l -value increases the radiative lifetime, allowing a larger fraction of initially prepared d-states to be observed. The effect enhances the d-to-s-state signal ratio because the d-state lifetimes are shorter than the s-state lifetimes. For the $J=2$ states around $n=26$ with substantial perturber (5d7d) fraction, this collisional state mixing converts such states to a distribution of states with essentially no perturber contribution.

Although these data suggest that the state-changing collisions that cause lifetime lengthening are between the highly excited barium atoms Ba^{**} and ground state, 6p1P or 5d1D barium atoms additional experiments were undertaken to investigate the possible effects of Ba^{**} - Ba^{**} collisions. First, at fixed atom density N we varied the blue laser power density from maximum to 0.1 maximum and finally to 0.02 maximum, acquiring BRPI spectra at each laser power density. The three spectra were identical.

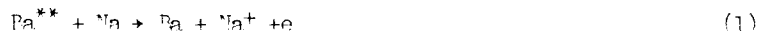
Since the excited atom density was varied by a factor of 50 in these constant N experiments, we infer that Ba^{**} - Ba^{**} collisions do not produce lifetime lengthening. We next reduced N by a factor of 50 while keeping the laser power density of the blue beam at maximum. This effectively reduces both N^{**} and N by a factor of 50. The resulting BRPI spectrum, exhibited increased s to d ratios, indicative of a tendency toward collision-free conditions. This clearly establishes Ba as the major state-changing (lifetime lengthening) collision partner.

It was also observed that as N was increased, the absorption profiles broaden. In order to assign the source of this broadening we performed additional experiments using a narrow band (0.2 cm⁻¹) blue laser. States in the vicinity of $n=40$ were prepared with $N^{**} \sim 10^{11}$ cm⁻³ and $N \sim 10^{12}$ cm⁻³. The linewidths were measured, and the blue laser power was decreased progressively to 0.1, the original level. N was kept constant. As the laser power was decreased, the linewidths decreased from about 0.6 cm⁻¹ to about 0.2 cm⁻¹.

In a second set of experiments, N^{**} was kept constant, as measured by the BRPI signal, by increasing the blue power while decreasing N . The linewidths remained constant. Thus, the broadening is independent of N , but does depend on N^{**} . These observations clearly show that the observed broadening mechanism is probably not collisional, but rather a quasistatic Rydberg-Rydberg interaction via the transition-dipole coupling matrix elements.⁵

In addition to the Ba-Ba experiments we have also begun a series of experiments designed to compare the reactivities of Rydberg states and valence states. Excited barium atoms are ideal reactants for this purpose because the highly perturbed states may be considered to have both types of character. Furthermore, as was shown in our Ba-Ba experiments, we can to some degree control the relative Rydberg-to-valence state ratio by adjusting N and N^{**} .

Our first results have been obtained for Penning ionization of Na(3s) by Ba^{**} ; that is



Because the ionization potential of ground state barium atoms is about 0.07 eV higher than that of Na(3s) Ba^{**} states, having energy higher than that of the pure Rydberg 6s16d state may cause Penning ionization. At nearly the same energy is the highly perturbed 5d7d³P₀ state so that contrast between the two types of states is possible.

The experiments are performed using the same apparatus modified so that a thermal beam of sodium atoms intersects the Ba beam and the two laser beams. Again we keep the green laser beam wavelength fixed at the Ba resonance line and scan the blue laser beam wavelength toward the blue. Na^+ and Na^+ were distinguished from each other by time of flight. Na^+ ions were first observed (scanning toward blue) when Ba (6s15d) was laser-excited. Na^+ was not observed at wavelengths other than those corresponding to production of Ba^{**} . Notable by its absence however was any Na^+ when the perturbed 5d7d³P₀ state of Ba was formed. As the wavelength was further scanned, that is toward higher Ba states, the Na^+ production at Ba^{**} wavelengths dropped off, falling to zero at about $n = 19$.

These preliminary data suggest that the Penning process is much more efficient if the excited electron is remote from the Ba^+ core. This implies that the "size" of the atom, the extent of the electron cloud, is important. More detailed data are currently being acquired and a lengthy report is contemplated.

Acknowledgements

This work supported by NSF grants PHY-8418075 and INT-8318024, DOE grant DE-FG02-84ER1327, the McDonnell Douglas Independent Research and Development Program, and the University of Missouri Weldon Spring Fund and US-NSF/Italy-CNR Bilateral Research Programs n. 19931 (M.A. and S.G.) and n.88.01280.02 (F.A. and E.M.) One of us (S.G.) wishes to acknowledge a Fulbright Fellowship. The authors wish to thank Professor T. F. Gallagher for useful discussions.

References

1. For a review see Fydberg States of Atoms and Molecules, edited by R. F. Stebbings and P. B. Dunning (Cambridge Univ. Press, Cambridge, 1983).
2. See for example, M. Aymar, Phy. Rep. 110, 163 (1984).
3. T. F. Gallagher, W. Sandner and K. A. Safinya, Phys. Rev. A 23, 2969 (1981).
4. C.E. Burkhardt, M. Ciocca, W. P. Carver, J. J. Leventhal, M. Allegrini and L. Moi, Phys. Rev A 34, 80 (1986).
5. J. M. Raimond, G. Vitrant and S. Haroche, J. Phys. B 14, L655 (1981).

MULTIPHOTON BOUND-FREE TRANSITIONS.
ROLE OF THE FIELD PROPERTIES.

S. Basile*, F. Trombetta* and G. Ferrante**

*Istituto di Fisica dell'Università,
via Archirafi 36, 90123 Palermo, Italy
**Istituto di Fisica Teorica dell'Università,
P.O. Box 50, 98166 S. Agata di Messina, Italy

Abstract. The atomic ionization process by a laser field in which an electron absorbs more photons than the minimum required to go into the continuum is considered. Within the S-matrix formalism a treatment is developed for the Multiphoton Multichannel Ionization of hydrogen atom by a strong laser field of arbitrary polarization. The effect of the laser field on the final state electrons is treated in a non perturbative way and the coulomb interaction is taken in account as well. Photoelectron energy spectra are calculated for selected values of intensity and arbitrary polarization, comparing two models of the radiation: a purely coherent field and a multimode field of vanishing bandwidth. Good qualitative agreement with known experimental results is generally obtained.

1. Introduction

The growing availability of powerful lasers and the existence of increasingly sophisticated spectroscopical techniques has permitted in recent years the study of new phenomena in the field of laser-atom interactions. One of the processes that has attracted in recent years a wide interest, both experimental and theoretical, is the Multichannel Multiphoton Ionization (M/MPI) of atoms¹. This is essentially an ionization process of an atom by a laser field in which the electrons, thanks to the high field intensities involved, can absorb from the laser more photons than the minimum required to go into the continuum; in the scattering theory language, we can say that many ionization channels, corresponding to the various numbers of photons absorbed, are simultaneously open.

In the early experiments on multiphoton ionization, only the total ions yield was generally measured, and little or no attention was paid to the electron signals. That attitude may be understood considering that at that time the experiments were performed with (relatively) low intensity lasers, when actually only one single channel was expected to be open. In a successive generation of ionization experiments with more intense lasers than before, in which attention was paid to the energy distribution of the ejected electrons, new and completely unexpected patterns were discovered, concerning photoelectron spectra. A peculiar feature of many measurements was that the photoelectron spectra could not be accounted for by any treatment based on perturbation theory in its lowest order. It was new with respect to the situation concerning instead the understanding of the single channel multiphoton ionization. Perhaps the most peculiar new information is: a) photoelectron spectra show well defined peaks, corresponding to the various numbers of photons absorbed by the electrons to arrive in the continuum; the peaks turn out to be separated by approximately the energy of one laser field photon; b) at low intensities (with the specific values depending on the atom involved), the processes with a low number of absorbed photons are the most probable; increasing the intensity, processes with higher photon multiplicity begin to appear and, for high enough intensities, become the dominant ones; c) in some experiments, a progressive disappearance of the lowest energy electrons is found by increasing the field intensity; d) in other experiments, on the contrary, only a relative decrease of the lower energy peaks with respect to the higher ones was found; e) the spectra exhibit a strong dependence on the laser polarization, with the largest effects brought about by circular polarization.

On the theoretical side, several models have been devised in the effort to explain the new features of M/MPI²⁻³, the main aim being to work out new treatments able to describe the highly nonlinear interaction process occurring between an atom and a strong radiation field. In this paper we present a theoretical approach of the multiphoton

multichannel ionization of the hydrogen atom, based on the S-matrix theory. As the properties of strong radiation fields are expected to be very important for the understanding of many measurements, in the effort to make flexible this first theoretical model as far as the radiation properties are concerned, we consider a field of arbitrary polarization, assumed: a) to be purely coherent, and b) to undergo phase and amplitude fluctuations (chaotic field). The choice of the hydrogen atom as a target is dictated not only by its paradigmatic role in the theoretical atomic physics, but also by the circumstance that recently measurements on hydrogen too have been performed⁴, and the prospects are open for more experiments in the near future.

Generally speaking, there are at least two points that deserve particular attention in any theoretical description of the M/MPI process: 1) the choice of the final state of the bound-free transition, in which the ejected electron is simultaneously interacting with the strong radiation field and the coulomb potential of the residual ion, and 2) the model assumed to describe the electromagnetic field. First, a correct description of the final electron state requires the solution of the Schrodinger equation for the motion in the presence of the laser field and of the coulomb interaction, which is not known; this solutions reduces to the Volkov states in the absence of the static field and to coulomb waves in the absence of the laser. Different approximate treatments have been proposed²⁻³, each justified by physical considerations on the problem at hand. Having in mind a far nonresonant bound-free transition occurring in a strong field, we will approximate the final electron state as a Volkov state in which the spatial plane wave part is replaced by the field-free coulomb wave⁵. This choice amounts here to describe the process as a one-step multiphoton absorption, with no account for intermediate resonances, which are expected here to be irrelevant. It may be shown that this wavefunction is just a first term of an iterative solution, and neglects at all the atomic spectrum, which will be of particular importance for low energy of the ejected electron and for resonant or near resonant laser wavelengths. Second, the experimental results are very sensitive to the properties of the laser radiation; pulse duration, number of modes involved and their statistics, spectrum bandwidth, spatial inhomogeneities and beam focussing are likely to deeply modify the measurements; to take to some extent into account the properties of the lasers actually used in the experiments we consider here as a laser model a multimode field, having a very large number of uncorrelated modes and a vanishing bandwidth (chaotic field); in this way, the fluctuations are included by simply averaging the coherent field results over the intensity distribution; this simple model appears to lead to a closer qualitative agreement with the experimental results and is probably partially representative also of other field incoherences.

2. The theoretical model

According to the usual rules, the transition rate per unit time in the S-matrix formalism is given by

$$w = \int d^3p / (2\pi\hbar)^3 \{ |S_{fi}|^2 / \lim_{T \rightarrow \infty} \int_{-T}^T dt \} \quad (2.1)$$

where, in the electric field gauge

$$S_{fi} = (i\hbar)^{-1} \int_{-\infty}^{\infty} dt \langle \psi_f | e \underline{E}(t) \cdot \underline{r} | \psi_i \rangle \quad (2.2)$$

In the above expressions, p is the final kinetic momentum, $\underline{E}(t)$ the laser electric field (taken in dipole approximation), ψ_i the initial state (the ground state) and ψ_f the final continuum state in the presence of both the radiation field and the coulomb potential.

We write the vector potential of the field as

$$\underline{A}(t) = A_0 \underline{a}(\omega t) \quad (2.3)$$

$$\underline{a}(\alpha) = (\underline{\hat{e}} \exp(-i\alpha) + \text{c.c.}) / 2 \quad (2.4)$$

$\underline{\hat{e}}$ being the complex polarization vector, given by

$$\underline{\hat{e}} = \underline{u}_x \cos(\xi/2) + i \underline{u}_y \sin(\xi/2) \quad (2.5)$$

where ξ is the so-called retardation angle and \underline{u}_j is the unitary vector in the j -direction. When ξ equals 90° , the polarization is circular, while for $\xi = 0^\circ$ and 180° the polarization is linear, respectively along the x - and y -axis. For arbitrary values of ξ , the vector $\underline{\hat{e}}$ describes an elliptically polarized radiation field.

From the expressions (2.3) and (2.4), the electric field is obtained as

$$\underline{E}(t) = E_0 \underline{e}(\omega t) \quad (2.6)$$

$$\underline{e}(\alpha) = (i \underline{\hat{e}} \exp(-i\alpha) + \text{c.c.})/2 \quad (2.7)$$

As the initial state of the transition we take the hydrogen ground state

$$\psi_i(\underline{r}, t) = (\pi a_0^3)^{-1/2} \exp(-r/a_0) \exp(i I_0 t / \hbar) \quad (2.8)$$

a_0 being the Bohr radius and I_0 the ionization energy (≈ 13.6 eV).

According to the discussion of the Sec. 1, the final state is taken in the form of a Volkov-Coulomb wave

$$\psi_f(\underline{r}, t) = \exp\left\{-i/(2m\hbar) \int_0^t (\hbar \underline{k} + e \underline{A}(\tau)/c)^2 d\tau + ie \underline{A}(t) \cdot \underline{r} / \hbar c\right\} \psi_{\underline{k}}^-(\underline{r}) \quad (2.9)$$

where $\psi_{\underline{k}}^-$ is the coulomb incoming wavefunction with asymptotic momentum $\underline{p} = \hbar \underline{k}$ and is given by

$$\psi_{\underline{k}}^-(\underline{r}) = \exp(\pi\nu/2) (1+i\nu) \exp(i \underline{k} \cdot \underline{r}) F(-i\nu, 1, -i(kr + \underline{k} \cdot \underline{r})) \quad (2.10)$$

$\Gamma(x)$ and $F(a, b, x)$ being respectively the gamma and the confluent hypergeometric functions and

$$\nu = (ka_0)^{-1} \quad (2.11)$$

We remark that in the wavefunction (2.9) attention is paid to the gauge consistence: the $\underline{A}(t) \cdot \underline{r}$ part in the exponential ensures in fact the wavefunction be physically meaningful in the electric field gauge, consistently with the S-matrix element (2.2) and with the fact that only in this gauge the hamiltonian is the energy operator. If one drops out the $\underline{A}(t) \cdot \underline{r}$ part in the exponential, the final formulas are greatly simplified; however, at expenses of loosing the physical meaning of the S-matrix as transition element between energy eigenstates; besides it has been shown to yield significant underestimates of the correct results⁶.

We can now proceed to derive the explicit expressions for the transition rate; as in most experiments one records photoelectron energy spectra along a fixed direction (usually, the field polarization for the linear case or in some direction in the polarization plane for the circular one), we give the doubly differential rate, i.e. the transition rate per solid angle and energy units; it is found as a sum over the energetically allowed multiphoton channels³ and is given by

$$d^2w/d\Omega dE = \sum_{s=0}^{\infty} (d^2w/d\Omega dE)_s \quad (2.12)$$

where

$$(d^2w/d\Omega dE)_s = C(k) (I/I_a) |M_{n_0+s}|^2 \delta(\epsilon + \epsilon_s - \epsilon_s) \quad (2.13)$$

$$C(k) = (e^2/\hbar a_0) (24/\pi^3) (2\pi\nu k a_0) (1 - \exp(-2\pi\nu))^{-1} \quad (2.14)$$

I is the laser intensity, $I_a \approx 3.51 \cdot 10^{16}$ W/cm² is the atomic unit of intensity; $\epsilon = p^2/2m$ is the electron kinetic energy, while

$$\epsilon_s = (n_0 + s)\hbar\omega - I_0 \quad (2.15)$$

with n_0 the minimum number of photons required to ionize the atom, given by

$$n_0 = [I_0/\hbar\omega] + 1 \quad (2.16)$$

[x] denoting the integer part of x; in eq. (2.15) s is the number of photons absorbed above the minimum and will be used below to label the final continuum state of an electron having absorbed n + s photons. In the expression (2.13), Δ plays the role of a shift of the ionization threshold and is given by

$$\Delta = e^2 E^2 / 4m\omega^2 = 2\pi e^2 I / mc\omega^2 \quad (2.17)$$

i.e., is the average over a field period of the oscillatory energy of an electron in a plane wave field. As may be seen from eq. (2.13), Δ fixes the energy of the ejected electron at the value $\varepsilon = \varepsilon_s - \Delta$ and is able to completely close the s-th ionization channel when the intensity is such that $\Delta = \varepsilon_s$; this result may be taken as the explanation of the sudden peak disappearance observed experimentally⁷; as we shall see in the following, this result, within the present theoretical treatment, is peculiar of the assumed coherence of the field.

The values of ε_s roughly give the position of the peaks in the photoelectron energy spectra, though if it must be remarked that the actual position will be strongly dependent on the properties of the laser radiation, mainly of the pulse duration and of the space inhomogeneities. We shall not consider such problems here, and label the final state only with reference to the number of photons absorbed by the electron to arrive into the various channels.

The basic ingredient of eq. (2.13) is the quantity M_n , that we have calculated by performing the closed form integration of the dipole matrix element of the bound-free transition and using the properties of the Bessel functions involved³; it is found as

$$M_n = - \int_{-\pi}^{\pi} B(\underline{k}, \underline{k}_G, \alpha) f_n(\alpha) d\alpha \quad (2.18)$$

$$f_n(\alpha) = \exp[i(n\alpha - \rho \cos \xi \cdot \sin 2\alpha - \underline{\lambda} \cdot \underline{a}(\alpha))] \quad (2.19)$$

$$\rho = \Delta / 2\hbar\omega, \quad \underline{\lambda} = eE_0 \underline{k} / m\omega^2, \quad \underline{k}_G = eE_0 \underline{e}(\alpha) / \hbar\omega \quad (2.20)$$

and

$$B(\underline{k}, \underline{k}_G, \alpha) = (T/S) i\nu \nu (1-i\nu) T^{-3} a_0 \underline{a}(\alpha) \cdot \{ \underline{k}_G [(T/S)(2-ika_0) + (T/S)^2(1+i\nu)(1-ika_0)/(1-i\nu) - (\nu+2i)/\nu] + \underline{k} [(T/S)(1-ika_0) - (\nu+2i)/\nu] \} \quad (2.21)$$

$$T = 1 + a_0^2(\underline{k} + \underline{k}_G)^2, \quad S = a_0^2 k_G^2 + (1-ika_0)^2 \quad (2.22)$$

For circular polarization ($\xi = 90^\circ$), the term containing ρ in the exponential (2.19) disappears as well as the term proportional to \underline{k}_G inside the parenthesis in (2.21).

Up to this point, all the results have been derived for a purely coherent field; as remarked above, any actual experiment is always performed by means of radiation fields having some source of noise. For the case of a fluctuating field of vanishing bandwidth, the average may be accomplished taking into account the fact that the correlation time of the fluctuations is very large, so that each elementary atomic act occurs at a fixed, stochastically determined value; thus, the average becomes just a weighted mean of the result found in the presence of a coherent field; the distribution of the electric field, in the case of a chaotic statistics, is gaussian, which, in terms of the threshold shift, is given by

$$P(\Delta) = \langle \Delta \rangle^{-1} \exp(-\Delta / \langle \Delta \rangle) \quad (2.23)$$

The doubly differential ionization rate to the (s+1)-th continuum state in the case of a chaotic field is then

$$\begin{aligned} \langle (d^2w/d\Omega d\varepsilon)_s \rangle &= \int_0^\infty (d^2w/d\Delta d\varepsilon)_s P(\Delta) d\Delta = \\ &= C(k) (\varepsilon_s - \varepsilon) P(\varepsilon_s - \varepsilon) |M_{n_0+s}(\underline{k}, \underline{k}_G)|^2 / \Delta_a \end{aligned} \quad (2.24)$$

where

AD-A282 545

PROCEEDINGS OF THE INTERNATIONAL CONFERENCE ON LASERS
'87 HELD AT LAKE TAHOE NEVADA ON 7-11 DECEMBER 1987(U)
SOCIETY FOR OPTICAL AND QUANTUM ELECTRONICS MCLEAN VA
1988 XD-XD

11/13

UNCLASSIFIED

NL



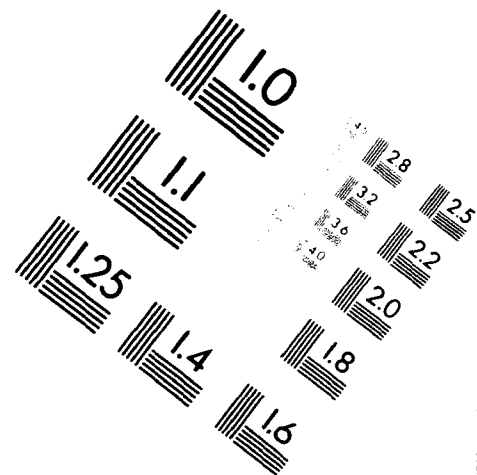
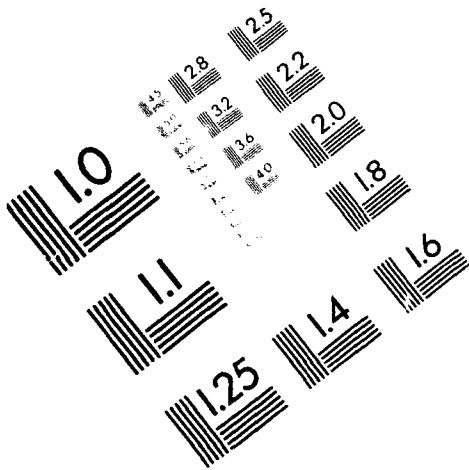


AIM

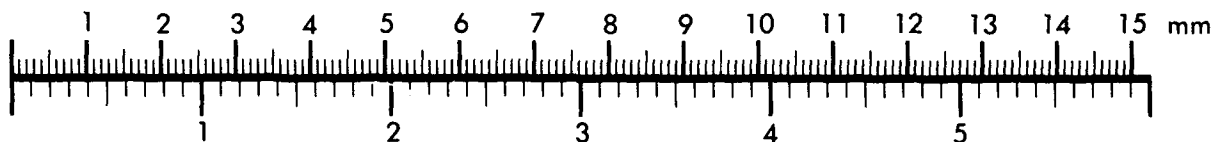
Association for Information and Image Management

1100 Wayne Avenue, Suite 1100
Silver Spring, Maryland 20910

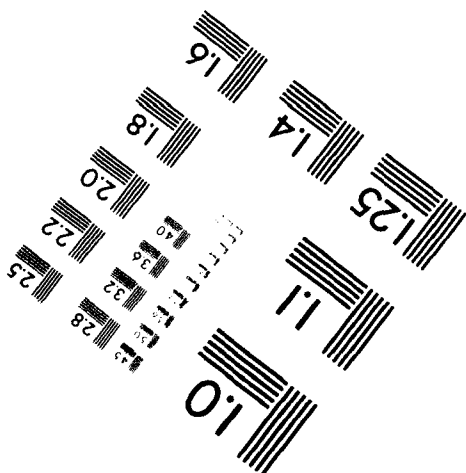
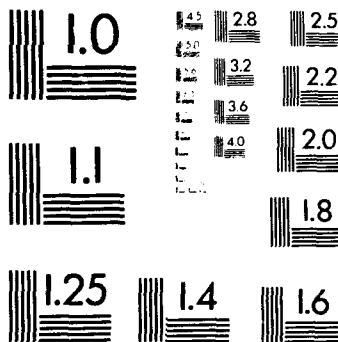
301/587-8202



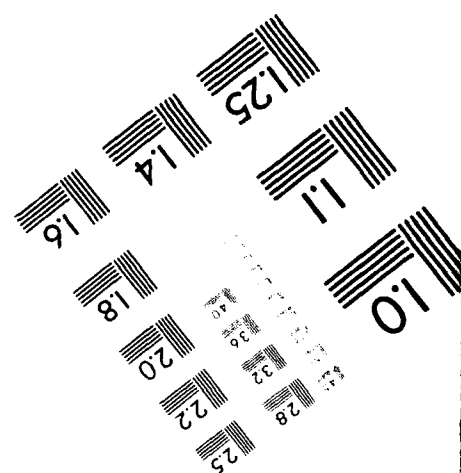
Centimeter



Inches



MANUFACTURED TO AIM STANDARDS
BY APPLIED IMAGE, INC.



$$\Delta_a = 2\pi e^2 I_a / mc\omega^2, \quad \tilde{k}_G = e\tilde{E}_0 \underline{e}(\alpha) / \hbar\omega, \quad \tilde{E}_0^2 = 4m\omega^2 (\epsilon_s - \epsilon) / e^2 \quad (2.25)$$

The mean differential transition rate is then obtained integrating eq.(2.24) over the energies allowed by (2.24), i.e.

$$\langle (dw/d\Omega)_s \rangle = \int_0^{\epsilon_s} \langle (d^2w/d\Omega d\epsilon)_s \rangle d\epsilon \quad (2.26)$$

The eq.s (2.13) and (2.26) express the rates respectively for the coherent and the chaotic field case; as reported in the next Section, they have been numerically computed for elliptically polarized light, and we will show that they correctly predict, from a qualitative point of view, several of the features exhibited by the measurements.

3. Calculations and comments

The quantities that are more commonly measured in experiments on M/MPI are:

- The angular distributions of photoelectrons of different multiphoton channels at a fixed laser intensity. They are measured detecting electrons at various values of the angle between the electron momentum and the polarization vector when this is linear, and detecting electrons at various angles in the polarization plane for arbitrary polarization⁸; obviously the angular distributions are uniform in the polarization plane in the circular case; as any the angular distribution, they are a very important test of the theoretical models.
- The total populations (integrated over ejection angles) of different channels versus the laser intensity; they are a good test of the validity of perturbation theory treatments because at low intensity the slope of the curves in a log-log scale must be proportional to the total number of photons absorbed.
- Photoelectron energy spectra along a fixed direction at different laser polarizations and intensities; they show the most peculiar feature of the process: the peak inversion with increasing intensity and the strong dependence on the polarization.

Here we restrict ourselves to reporting results referring to c) only; results for other items, obtained by us within the same theoretical model may be found elsewhere^{3,9-10}.

In Fig. 1 we show photoelectron spectra along the x axis direction at various polarizations (defined by the retardation angle ξ) and for two models of the laser radiation: purely coherent on the left and chaotic on the right side; these results reproduce qualitatively well the experimental findings on the role of the polarization, showing that the maximum peak suppression occurs in the case of circular polarization; the normalization of these curves is as follows: for the coherent case the first non vanishing rate is taken to be 1 (in this laser model suppression is absolute being linked with the energy conservation conditions); at the concerned laser intensity this term is the sixth; for the chaotic case we take as 1 the rate with s equal to zero.

In Fig. 2 we show photoelectron spectra along the x axis direction for two representative laser intensities in linear and circular polarization for the case of a chaotic field; this figure shows the role of intensity in increasing the peak suppression and shifting the maximum of spectrum towards channels with larger numbers of above threshold photons; it also shows the role of polarization at fixed laser intensity. Normalization of curves is according to figure 1.

In conclusion, we have considered the Multiphoton Multichannel Ionization of hydrogen atom by a laser field of arbitrary polarization. Within the S-matrix theory we have developed an essentially non-perturbative treatment of the process considering it as a one-step multiphoton transition without intermediate resonances. Performing calculations for selected values of intensity and polarization and improving the description of the radiation with the consideration of a multimode field of vanishing bandwidth, we have shown that our treatment is able to predict some of the most peculiar features of experimental results.

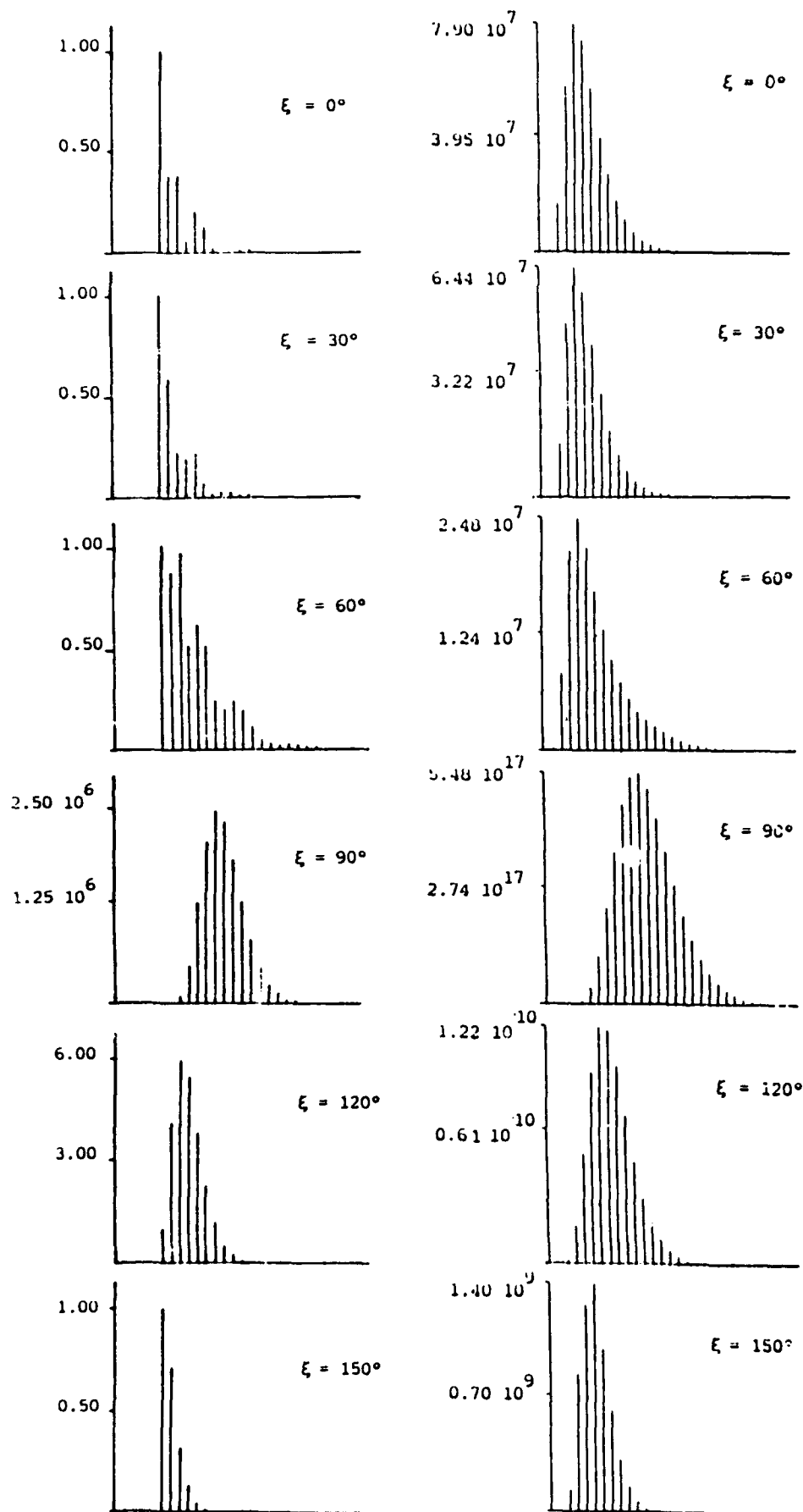


Fig.1 - Photoelectron energy spectra for the ionization of the ground state of the hydrogen atom; the number of above threshold photons runs on the horizontal axis from 0 to 30; the laser wavelength is 1064 nm; ξ is the retardation angle and identifies the ellipticity of the radiation (see eq.(2.5)). The left side refers to a coherent field of intensity $5 \times 10^{13} \text{ W/cm}^2$. The right side refers to a chaotic field of average intensity $5 \times 10^{12} \text{ W/cm}^2$. Spectra are calculated along the x axis.

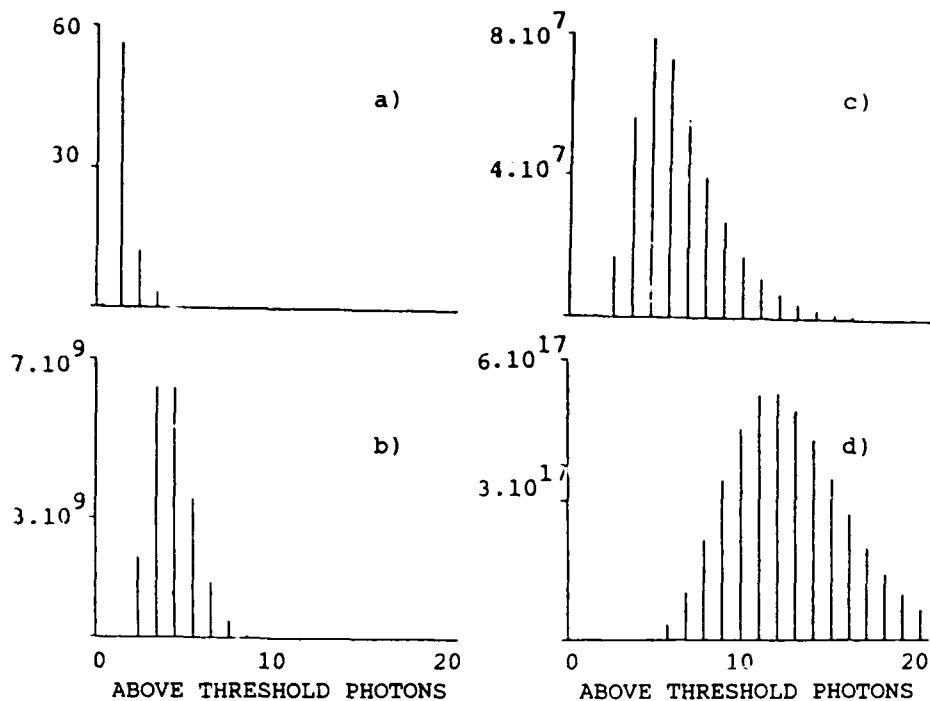


Fig. 2 - As for Fig. 1. The field is chaotic and average intensities and polarizations are: a) $7.5 \cdot 10^{11}$ W/cm², linear; b) $7.5 \cdot 10^{11}$ W/cm², circular; c) $5 \cdot 10^{12}$ W/cm², linear; d) $5 \cdot 10^{12}$ W/cm², circular.

References

1. For rather complete and up-to-date account of the many experimental and theoretical aspects of the M/MPI, see the contributions in J. Opt. Am. Soc. B 4, p. 705-856 (1987).
2. L.V. Keldysh, Sov. Phys. JETP 20, 1307 (1965); F.H.M. Faisal, J. Phys. B 6, L89 (1973); H.R. Reiss, Phys. Rev. A 22, 1786 (1980); W. Becker, R.R. Schlicher and M.O. Scully, J. Phys. B 19, L785 (1986); B. Chen, F.H.M. Faisal, S. Jetzke, H.O. Lutz and P. Scanzano, Phys. Rev. A 36, 4091 (1987).
3. C. Leone, R. Burlon, F. Trombetta, S. Basile and G. Ferrante, Il Nuovo Cimento D 9, 609 (1987).
4. H.G. Muller, H.B. van Linden van den Heuvell and M.J. van der Wiel, Phys. Rev. A 34, 236 (1986); D.E. Kelleher, M. Ligare and L.R. Brewer, Phys. Rev. A 31, 2747 (1985); D. Feldmann, B. Wolff, M. Wemhoner and K.H. Welge, Z. Phys. D 6, 293 (1987).

5. M. Jain and N. Tzoar, Phys. Rev. A 18, 533 (1978); P. Cavaliere, G. Ferrante and C. Leone, J. Phys. B 13, 4495 (1980); J. Banerji and M.H. Mittleman, J. Phys. B 14, 3717 (1981); L. Rosenberg, Phys. Rev. A 34, 4567 (1986).
6. R. Burlon, C. Leone, F. Trombetta and G. Ferrante, Il Nuovo Cimento D 9, 1033 (1987).
7. L.A. Lompré, G. Mainfray, C. Manus and J. Kupersztych, J. Phys. B 20, 1009 (1987).
8. M. Bashkansky, P.H. Bucksbaum and D.W. Schumacher, Phys. Rev. Lett. 59, 274 (1987).
9. S. Basile, F. Trombetta, G. Ferrante, R. Burlon and C. Leone, "Multiphoton Ionization of Hydrogen by a Strong Multimode Field", Phys. Rev. A 37, n.3 (1988).
10. S. Basile, F. Trombetta and G. Ferrante, "Multichannel Multiphoton Ionization and Radiation Properties. Chaotic Field Effects", Phys. Rev. A (submitted).

ENERGY POOLING COLLISIONS IN Na-K AND Na-Rb VAPOR MIXTURES

S.A. Abdullah*, M. Allegrini, C. Gabbanini, S. Gozzini and L. Moi

Istituto di Fisica Atomica e Molecolare del C.N.R.

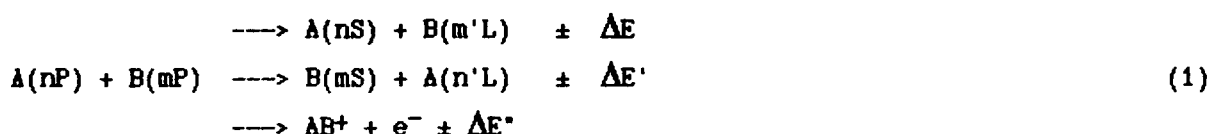
Via Del Giardino, 7 - 56100 Pisa, Italy

* Permanent address : Iraqi Atomic Energy Commission
Tuwaitha - Baghdad, P.O. 765 - Iraq

ABSTRACT We have studied the energy-pooling collisions in laser excited Na-K and Na-Rb vapor mixtures. The Na-K experiment has given quantitative results for the cross sections and also results on the influence of a foreign buffer gas. The Na-Rb experiment shows interesting molecule formation and work is in progress to determine cross section values.

Introduction

In the last few years the resonant excitation of an alkali vapor has been widely studied. Depending upon the conditions of the vapor (pressure, temperature, cell size, etc.) and upon the characteristics of the laser (pulsed or c.v., single mode or broadband, weak or strong power density) different processes occur; examples of such events are multiphoton ionization, Penning ionization, superelastic collisions and other kinds of ion and molecule formation. When the laser is operating at low power density ($\sim 1-10 \text{ W/cm}^2$) and the atomic density is relatively low ($\sim 10^{11} - 10^{13} / \text{cm}^3$), the most important processes are the energy pooling collisions and the associative ionization. In the first process two excited alkali atoms in a np state collide and the energy is transferred from one atom to the other leading the first atom to the ground state ns and the second one to a more excited state; this process is effective for levels which differ for a few kT from the sum energy $2\epsilon E(np)$. In the associative ionization process the collision of two excited atoms leads to the formation of a molecular ion. The overall reaction scheme may be written as



Since the first observation of the energy pooling effect [1], homonuclear collisions (with $A=B$) have been mainly studied. Only recently [2] the interest has been extended to heteronuclear collisions (with $A \neq B$). In this paper we will deal about energy pooling collisions in Na+K and Na+Rb mixtures. The levels of interest are shown in figure 1, in respect to the energy defect. The two alkali species are excited with two dye lasers. The interest about this kind of collisions comes from the information they give about the interatomic potentials at medium and large ranges; the experimental cross sections of such a process have been compared with theoretical calculations [3] and an agreement between them can be considered as a good test for the quantum calculations of the interatomic potentials. In the case of heteronuclear collisions the information about the interatomic potentials are even more interesting because these curves are less known. Besides that a large number of quasi resonant levels are involved into the heteronuclear collisions; a summary of that levels in the various alkali species has been given [2]. Moreover this kind of collisions allows the production of an appreciable population on levels which have forbidden transitions with the ground state. The influence of a buffer gas in the collision may be

investigated [4]; as its presence enhances three body collisions it modifies the stationary populations of the levels. With the experimental technique used in our experiment, we are able to separate the contribution of the heteronuclear collisions from that of the homonuclear ones and, in presence of a buffer gas, it is also possible to discriminate the contribution of the three body collisions involving one buffer gas atom.

In the following sections the rate equations for the heteronuclear energy pooling collisions are applied to our experiment on a mixture of Na and K atoms. Preliminary results on a running experiment in a mixture of Na and Rb are also reported.

Rate Equations

The rate equations in the stationary case describing process (1) may be written as

$$N_i \sum_{j \neq i} A_{ij} = K_i N_{np}^{(A)} N_{mp}^{(B)} \quad (2)$$

the indexes i and j are couples of quantum numbers describing the levels, A_{ij} is the spontaneous emission coefficient in the transition $i-j$, $K_i = \langle \sigma_i v \rangle$ with σ_i the cross section of the process and v the mean interatomic velocity and $N_{np}^{(A)}$, $N_{mp}^{(B)}$ are the laser excited atomic densities. As the intensity of a line coming from a transition $i-j$ can be expressed as

$$I_{ij} = \frac{V}{4\pi} \alpha_{ij} h \omega_{ij} N_i A_{ij} \quad (3)$$

where V is the fluorescence volume, α_{ij} is a factor taking into account the efficiency of the apparatus and ω_{ij} is the frequency of the transition $i-j$, it follows that

$$K_i = \frac{4\pi}{V} \frac{\alpha_{ij} \sum_{j \neq i} A_{ij}}{\alpha_{ij} A_{ij} N_{np}^{(A)} N_{mp}^{(B)}} \quad (4)$$

We want to stress out the fact that the above equations are valid if the detected signal is due only to the heteronuclear energy pooling collisions, and therefore it is of particular importance to discriminate and to eliminate any fluorescence coming from secondary processes. This can be done by adopting a special procedure described in the following section. In general it is very difficult to have the absolute values of the excited $N_{np}^{(A)}$ and $N_{mp}^{(B)}$, however we can measure the intensities of the fluorescence lines related to the atomic densities via eq.(3) where A_{ij} must be substituted by $(\tau_{np})^{-1}$, the effective lifetime of the np -level; in fact in presence of high densities of excited atoms, the radiation trapping modifies the spontaneous decay rate of the level, which must be measured from the experiment.

Experimental apparatus and procedure

The general sketch of the experimental apparatus is shown in fig.2. The vapor is contained in a cell heated at the temperature necessary to have typically an atomic density of $10^{11} - 10^{13} / \text{cm}^3$.

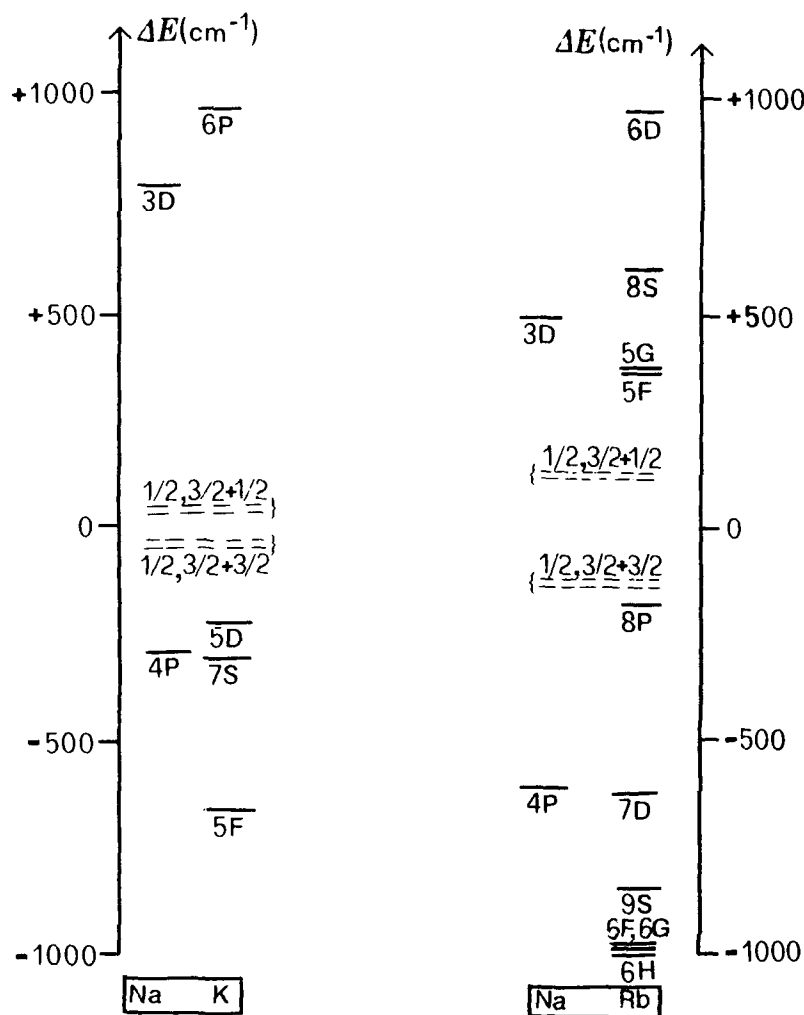


Fig. 1 Scheme of the energy levels involved in energy pooling collisions in Na-K and Na-Rb mixtures. The levels are plotted in respect to their energy defect from the center of the sum energy $A(np_i) + B(mp_j)$ with $i, j = 1/2, 3/2$.

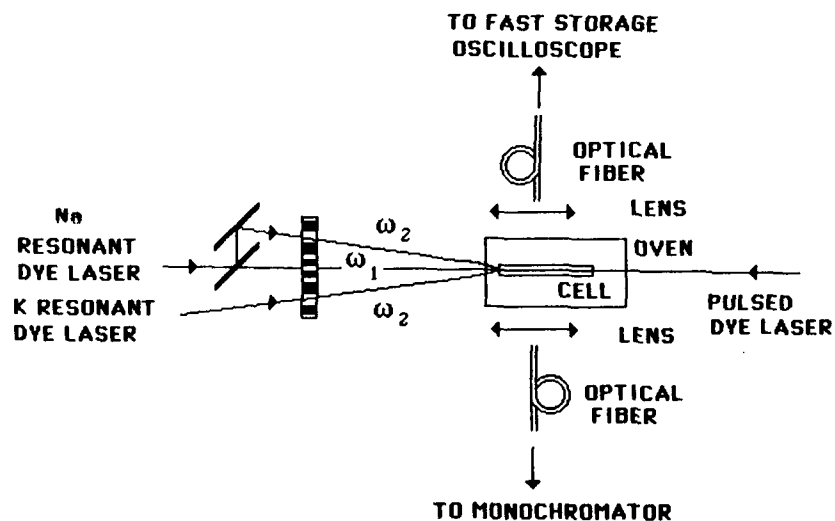


Fig. 2

Sketch of the experimental apparatus; only one of the two beams modulated at frequency Ω_2 was used at the time together with the Ω_1 modulated beam.

More care must be taken in the experiments dealing with mixtures in order to have comparable densities of the two species: assuming the Raoult law to be valid, it follows that the ratio between the vapor pressures in a mixture of two species A and B is proportional to the respective molar fractions of the two species. Following Nesmeyanov data [5] on vapor pressures of alkali atoms, the ratio $P_A/P_B \approx 1$ corresponds to an amalgam prepared with 5% K and 95% Na in the case of Na plus K experiment and 2% Rb and 98% Na in the case of Na plus Rb experiment.

To better control the fluorescence volume and to reduce the radiation trapping effect, the standard cylindrical cells have been substituted by capillary ones ($\approx 2\text{mm}$) prepared following a special procedure described elsewhere [6].

The two atomic species are excited by two c.w. dye lasers tuned to the D_2 resonance lines of the alkalis. We used a single mode Rodhamine 6G dye laser pumped by an Ar^+ laser for sodium ($\lambda = 589\text{nm}$) and a multimode Oxazine 750 Perchlorate pumped by a Kr^+ ion laser for potassium ($\lambda = 766\text{nm}$) and rubidium ($\lambda = 780\text{nm}$).

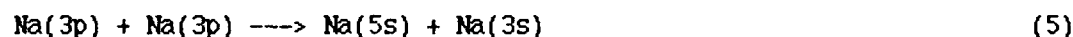
The output powers are of the order of 100mW; the beams are focussed to have laser intensities of the order of $1\text{--}10\text{ W/cm}^2$.

The beams are superimposed at the entrance of the cell; the fluorescence coming from the cell is collected at right angles and focussed on an optical fiber connected to the detection system. A 1m focal length Jobin-Yvon HR 1000 monochromator and a Hamamatsu R955 photomultiplier have been used for the visible region (300–850 nm). A 1/3 m focal length Jarrel-Ash monochromator and a PbS detector have been used to explore the infrared region (1–2.5 μm).

As we said in the previous section, we must eliminate the contribution to the fluorescence coming from different processes, and mainly from the homonuclear energy pooling collisions always present in the experiment.

At this aim, we adopted an intermodulation technique consisting in the modulation of the two beams at different frequencies Ω_1 and Ω_2 . At the same time the output of the photomultiplier is sent to a lock-in amplifier driven at the sum frequency $\Omega_1 + \Omega_2$. In this way we are able to detect signals coming only from the interaction of the species modulated at the frequency Ω_1 with the other modulated at the frequency Ω_2 . This method has shown to be very sensitive as the fluorescence signal disappears when any one of the two laser is off even if a strong fluorescence is still visible in the cell.

The measure of the rate coefficients K_i for heteronuclear collisions has been made as related to the known rate coefficient K_{55} for the homonuclear reaction



$$K_{55} = \frac{4p}{V} \frac{I_{5S-1} \sum_{i \neq j} A_{ij}}{\alpha_{5S-1} h\nu_{5S-1} A_{ij} N_{3P}^2} \quad (6)$$

where 1 is a level populated through the decay from the 5s level. In particular we found to be convenient to use the 5s–3p transition of sodium at 616nm.

For this reason, and to calibrate the apparatus, we need to measure the intensity of a transition from the 5s level of sodium with the same method. To this purpose we split the yellow beam into two components modulated at the frequencies Ω_1 and Ω_2 and we detected the signal from the desired level. Subsequently we replaced the Ω_2 yellow beam with the red one resonant with the second alkali species, and we detected the fluorescence from the levels populated by the heteronuclear collisions.

To measure the lifetime of the excited levels we sent two pulsed dye lasers resonant with the fixed transitions and we analyzed the exponential decay of the fluorescence on the screen of a fast storage oscilloscope.

K_i are related to K_{5S} of sodium by the volume independent expression

$$\frac{K_i}{K_{5S}} = \frac{\alpha_{5S-3P}}{\alpha_{ij}} \frac{A_{5S-3P}}{\sum_{l \neq 5S} A_{5S-l}} \frac{\sum_{j \neq i} A_{ij}}{A_{ij}} \frac{\omega_{5S-3P}}{\omega_{ij}} \frac{I_{ij}}{I_{5S-3P}} \frac{N_{3P}^2}{N_{np}^{(A)} N_{mp}^{(B)}} \quad (7)$$

According to the experimental procedure described previously N_{3P}^2 and $N_{np}^{(A)} N_{mp}^{(B)}$ may be better written as

$$N_{3P}^2 = [N_{3P}]_{\Omega_1} [N_{3P}]_{\Omega_2} \quad (8)$$

$$N_{np}^{(A)} N_{mp}^{(B)} = [N_{np}^{(A)}]_{\Omega_1} [N_{mp}^{(B)}]_{\Omega_2}$$

where the subscripts Ω_1 and Ω_2 indicate that the populations are modulated at these frequencies. In this way we can simplify the equation if we choose one of the atomic species, say A to be sodium modulated at the Ω_1 frequency. Eventually the equation results

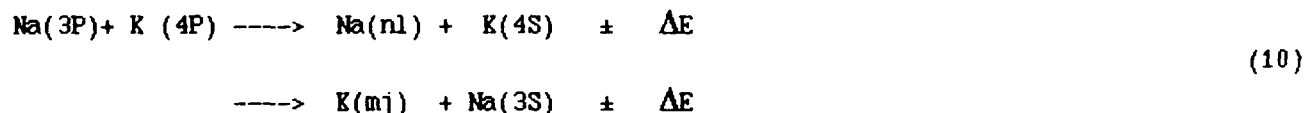
$$\frac{K_i}{K_{5S}} = \frac{\alpha_{5S-3P}}{\alpha_{ij}} \frac{\alpha_{mp-ms}}{\alpha_{3P-3S}} \frac{A_{5S-3P}}{\sum_{l \neq 5S} A_{5S,l}} \frac{\sum_{j \neq i} A_{ij}}{A_{ij}} \frac{\tau_{3P}}{\tau_{mp}} \frac{\omega_{5S-3P}}{\omega_{ij}} \frac{\omega_{mp-ms}}{\omega_{3P-3S}} \left[\frac{I_{3P-3S}}{I_{mp-ms}} \right]_{\Omega_2} \quad (9)$$

where all the quantities are known or experimentally determined.

Results

1) Na - K

We performed a first experiment on a mixture of sodium and potassium to study the exit channels of the reaction



The observed transitions are listed in table 1 along with the energy of the levels and the cross sections [7]. The measurements were performed at $T=240^\circ\text{C}$ with laser intensity of about 80mW on the red laser and 50mW on the yellow laser. The effective lifetimes of the 3p level of sodium and of the 4p level of potassium resulted to be $\tau_{3p} = 176 \pm 20\text{ns}$ and $\tau_{4p} = 287 \pm 30\text{ns}$ respectively. The obtained cross sections do not exhibit remarkable differences with those obtained for the homonuclear reactions.

An experiment was also performed in a cell containing sodium, potassium and 10 Torr of Ne as buffer gas. New features appeared in the spectra under intermodulated technique, showing some additional lines of sodium coming from more excited levels and in opposition of phase. This results from the population modification induced by the buffer gas through a three body collision of the type



where M indicates a buffer gas atom. A pure two body collision alkali atom/buffer gas atom can not change the frequency modulation and therefore does not affect the intermodulation spectrum. The effect of process (13) on the contrary is to couple atoms modulated at two different frequencies. States populated from energy transfer collisions involving these atoms are then present in the intermodulated spectrum. The signal of the fluorescence lines also indicates if the collision is responsible for a population or depopulation process, as it is clear from the spectrum reported in figure 3

Our model explains the differences observed in the spectra obtained without and with buffer gas. Moreover, by the comparison of relative fluorescence intensities in the two cases we have evaluate [4] the first lower limit for the three body rate coefficient of process (13) to be $\sim 10^{-27} \text{ cm}^6\text{s}^{-1}$.

ii) Na - Rb

The same method is applied to study an amalgam of sodium and rubidium.

As one can see from the scheme of Na and Rb (fig.1), this combination of alkali atoms gives a larger set of quasi resonant energy-pooling levels; besides that, the larger fine structure of the excited level of rubidium can carry new interesting informations about this kind of collisions following a D_1 or a D_2 excitation. In our preliminary experiment, we used one laser line at a time, exciting first the D_2 line of sodium (laser 1) and then the D_2 line of rubidium (laser 2); phase sensitive detection was used both in the infrared and in the visible part of the spectrum as in the Na-K experiment. Four different spectra for a cell temperature of 200 °C are shown in fig. 4-5; a low pass filter at 850nm was used when we recorded the infrared spectra. Fluorescence occurs from many other levels different from the first excited one; with laser 2 on, a first interesting result is that fluorescence comes not only from the more resonant homonuclear energy-pooling 5D of rubidium, as in a previous experiment with a rubidium beam [8], but also from 7S, 6D and 8S levels. In the spectra it is also clear a large molecular fluorescence coming from known states of NaRb (B-X band in the visible) and Rb_2 (A-X band in the infrared); the energy-pooling processes can be effective in populating such molecular states. Using laser 1 to excite sodium, a large population also builds in the 5P levels of rubidium; that allows us to see fluorescence from the 8p level of rubidium populated by the heteronuclear process



with $\Delta E = -50\text{cm}^{-1}$. In fig. 6 the 8P-5S fluorescence line of rubidium at 335nm is shown next to the 4P-3S line of sodium at 331nm. An experiment with the intermodulation technique as in the the Na-K amalgam is in progress to determine the cross section of the 8P level and also of other less resonant levels.

Conclusions

We report experiments on heteronuclear energy pooling in two different mixtures of alkali atoms. In the Na-K we have determined cross sections for several levels populated by this kind of collision between excited atoms and the influence of a buffer gas and consequently of three body collisions were studied. We also report preliminary results on a experiment in a Na-Rb mixture which is in progress.

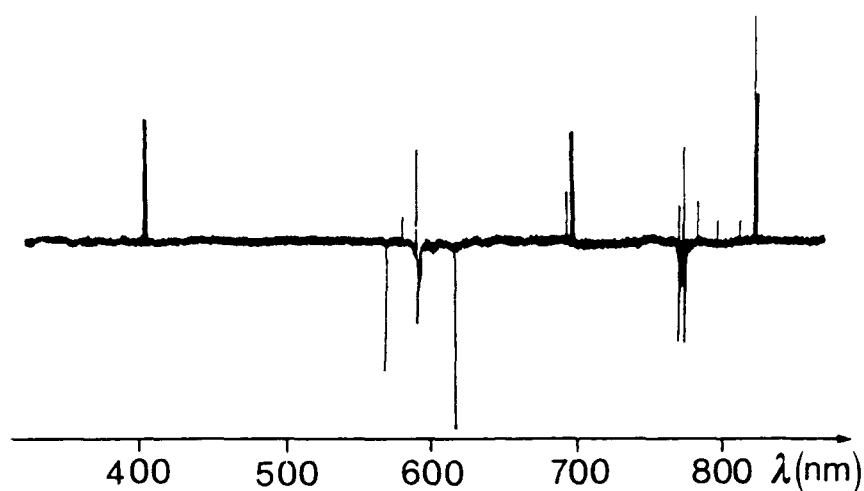


Fig. 3 Fluorescence spectrum of the Na-K mixture in presence of a buffer gas; the lines in opposition of phase come from a depopulating mechanisms.

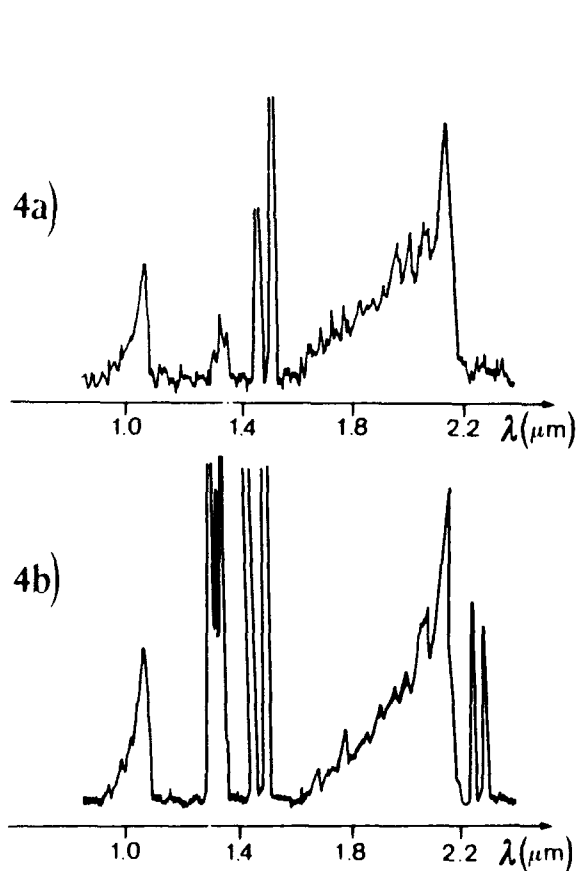


Fig. 4 Infrared spectra of the Na-Rb mixture with D_2 excitation of sodium (4a) and D_2 excitation of Rb (4b).

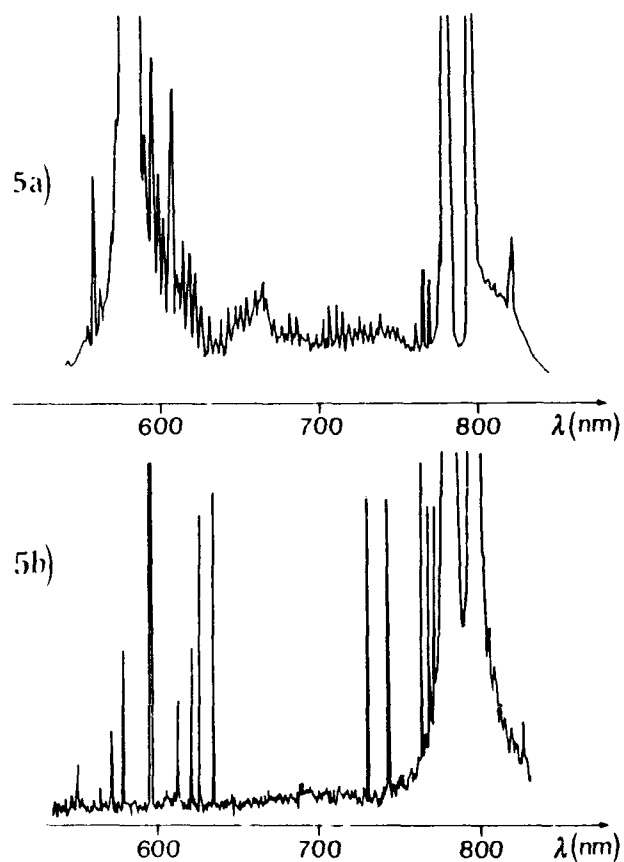


Fig. 5 Visible spectra of the Na-Rb mixture with D_2 excitation of sodium (5a) and D_2 excitation of Rb (5b).

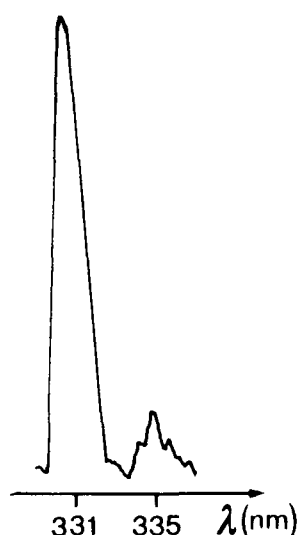


Fig. 6 Fluorescence line 8p-5s of rubidium at 335nm next to fluorescence line 4p-3s of sodium at 330nm.

TABLE 1. Heteronuclear energy pooling levels and cross sections in the Na-K mixture

Atom	Level	Energy level (cm ⁻¹)	Detected transition	λ(nm)	σx10 ¹⁵ (cm ²)
Na	3D	29172	3D-3P _{1/2,3/2}	818-820	1.4 ± 0.7
	4P	30266-30272	4P _{1/2,3/2} -3S	330	
K	6P	28999-29007	6P _{1/2,3/2} -4S	345	1.9 ± 1.0
	5D	30185	5D _{3/2,5/2} -4P _{1/2,3/2}	581-583	
	7S	30274	7S-4P _{1/2,3/2}	578-580	

References

1. M. Allegrini, G. Alzetta, A. Kopystynska, L. Moi and G. Orriols, Opt. Commun. **19**, 96 (1976)
2. A. Cremoncini, S. A. Abdullah, M. Allegrini, S. Gozzini and L. Moi, Proc. Intern. Conf. LASERS'85, C. P. Wang Ed., (STS Press, 1986), pag. 98
3. M. Allegrini, C. Gabbanini, L. Moi and R. Colle, Phys. Rev. **A32**, 2068 (1985)
4. S. A. Abdullah, M. Allegrini, S. Gozzini and L. Moi, submitted to Nuovo Cimento D
5. A. N. Nesmeyanov, Vapor Pressure of the Chemical Elements, (Elsevier, 1963)
6. M. Allegrini, P. Bicchi and L. Moi, Phys. Rev. **A28**, 1338 (1983)
7. S. A. Abdullah, M. Allegrini, S. Gozzini and L. Moi, in "Photon and Continuum States of Atoms and Molecules", N. K. Rahman, C. Guidotti and M. Allegrini Eds., Springer Proceedings in Physics vol. 16, pag. 214 (1987)
8. S. Gozzini, S. A. Abdullah, M. Allegrini, A. Cremoncini and L. Moi, Opt. Commun. **63**, 97 (1987)
9. L. Barbier and M. Cheret, J. Phys. B **16**, 3213 (1983)

ON RESONANTLY ENHANCED TWO-PHOTON TRANSITIONS IN POTASSIUM
P. Bicchi*, F.W. Dalby and K. R. Mah,
*Istituto di Fisica, Università di Siena, 53100 Siena, Italy;
Physics Dept., U.B.C., Vancouver, Canada, V6T 2A6

Abstract

We report the observation of the two-photon parity forbidden transitions 4^2S+n^2P of atomic potassium in resonantly enhanced multiphoton ionization (RMPI) spectra of a potassium vapor-argon gas mixture. The RMPI spectra were investigated over the temperature range of 150 to 240°C and the absorption to the $2P$ Rydberg levels was observed only for temperatures above 190°C where the atom densities are greater than $8 \times 10^{13} \text{ cm}^{-3}$. The characteristics of the forbidden spectra demonstrate that long range interactions between potassium atoms must be involved.

Introduction

Laser-assisted or laser-induced collision processes have been the subject of a number of investigations in atomic and molecular physics in recent years¹. In these processes, photon absorption occurs during a binary heavy-body collision. The final states of heavy-body collision products are usually inaccessible by the direct absorption laser photons or by the heavy-body collision alone. It is the simultaneous interaction of the two collision reactants and the photon or photons that allows the final product states to be accessed.

Laser-assisted collisional absorptions involving Rydberg states have permitted forbidden atomic absorption to occur in atomic sodium². Here we report the observation of two-photon parity forbidden transitions to Rydberg states of atomic potassium, K^{**} , arising from the ground $4s\ 2S$ state of potassium in a potassium vapor-argon gas mixture³. We attribute the two-photon forbidden transitions to Rydberg nP states to the absorption of two photons during a self- α -mixing collision. These transitions were observed in resonantly-enhanced multiphoton ionization (RMPI) experiments⁴⁻⁶.

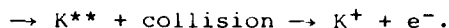
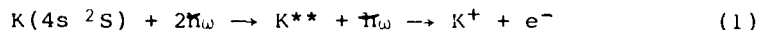
Experimental

A schematic of the simple experimental apparatus is illustrated in Fig. 1. A cylindrical Pyrex cell of 25 mm diameter and 60 mm length contains a few Torr of argon and potassium at its saturated vapor pressure. The cells are constructed with two parallel 1 mm diameter tungsten wire electrodes separated by 10 mm. Several cells, all with the same construction geometry but with argon pressures varying from 1 to 10 Torr at room temperature were used. Potassium metal containing approximately 0.05% residual sodium impurity was distilled into the side finger of the cell. This reservoir of potassium is held at slightly lower temperatures than the body of the cell to prevent condensation on the cell windows. The cell is operated inside an oven at fixed temperatures ranging from 150°C to 230°C corresponding to atomic densities of $\sim 10^{13}$ to $4 \times 10^{14} \text{ cm}^{-3}$.

A Molelectron DL300 tunable dye laser pumped by a nitrogen laser produced light with a pulse duration of 5 ns, linewidth $\sim 1.5 \text{ cm}^{-1}$, and at a repetition rate of 10 Hz. The light is focussed between the two electrodes along the axis to a minimum spot radius of $\sim 40 \text{ }\mu\text{m}$. The dye laser covered wavelengths ranging from 5000 to 7300 Å and pulse energies ranged between 40 and 250 μJ . The corresponding power densities used in the experiments varied from 160 MWcm^{-2} to 1 GWcm^{-2} at the minimum beam waist. The laser intensity is attenuated, when needed, with calibrated neutral density filters and the light is made 100% linearly polarized with an external Glan prism. When circular polarization is required, the linearly polarized light is passed through a Soleil-Babinet compensator which has been adjusted to perform as a quarter-wave plate.

Resonant absorption was detected through the collection of the free electrons and ions created by the laser-induced photoionization. The negative voltage applied to the cathode varied from 2 to 150 volts; thus the performance of the ionization detection varied from ion chamber collection to amplification through gas multiplication. After collection by the anode the current was passed through a preamplifier, monitored on an oscilloscope, processed by a PAR model 160 boxcar integrator, and displayed on a chart recorder. A typical spectrum is shown in Figure 2.

The two-photon RMPI signals are due to the process



Under all experimental conditions studied the allowed series where K^{**} is $(n+2)^2S$ or n^2D for $4 \leq n \leq 32$ are well developed. At temperatures above 190°C corresponding to K vapour densities above $(8)10^{13}\text{cm}^{-3}$ the series, forbidden by the Laporte rule, where K^{**} is n^2P for $n \leq 20$, is developed.

The ratio of the intensity of the "forbidden" 2P signals to that of the allowed 2D signals varies quadratically with potassium density. It is independent of the argon density. For K densities of $4 \times 10^{14}\text{cm}^{-3}$ the 19^2P line intensity is observed to be about 15% of the neighboring 2D lines.

The observed line widths of both the 2P and 2D signals are the same - about 4 cm^{-1} . The intrinsic widths are not measured as they are less than or of the order of twice the laser line width.

The power dependence of the "forbidden" signals is not accurately determined since the dynamic range available is small due to their relative weakness. However the "forbidden" signals appear to have the same dependence on laser power as the allowed transitions.

At sufficiently high densities the two photon transition leading to 2D , 2S and the "forbidden" 2P states are all seen if the laser light is linear polarized. With circularly polarized light, excitation to the 2S levels is not observed and excitation to both the 2D at the 2P levels is somewhat enhanced.

Conclusions

In order to fix some orders of magnitude we calculate various quantities for a potassium density of $(4)10^{14}\text{cm}^{-3}$ where the ratio of the "forbidden" 18^2P line intensity to that of the 18^2D line is 0.17. The semi-classical radius of the wavefunction for the 18^2P state is 342\AA . The average distance between potassium atoms is 840\AA . The probability of finding two potassium atoms within 342\AA or less of each other is 0.067, and within 466\AA or less is 0.17. Clearly the interaction responsible for the appearance of the 2P line must be long range.

The most obvious possible long range interaction is that due to electric fields, a Stark effect. Stark effects due the applied fields are not responsible. The forbidden lines are not seen at potassium densities below $(8)10^{13}\text{cm}^{-3}$ even for fields approaching 100 volt/cm . Moreover at higher density the lines persist for fields below 2 volts/cm .

Possible Stark mixing by microfields produced by a laser induced plasma was also investigated. We calculate that the required ion density to produce the observed forbidden lines would require more than 10% ionization in the focal volume, even when off resonance. We find this difficult to reconcile with our observations. Moreover microfields large enough to give observable signals at $n = 15$ would lead to widths and strengths for the forbidden P lines above $n = 22$ at least an order of magnitude larger than that observed; and strong Stark F state signals would be produced contrary to observation. We conclude microfield Stark effects are also not significant.

We attribute the observed effects to quasi-molecule formation. In the presence of a second atom the spherical symmetry of the atom is modified so that only a cylindrical symmetry is present. Moreover the atomic separation is much less than the wavelength of the laser light. Hence the L quantum number is not conserved. The problem is to find an interaction that is sufficiently long ranged and of sufficient strength. The Rydberg electron is only loosely bound to the K^+ core and has a de Broglie wavelength considerably greater than the radius of a ground state potassium atom. The Rydberg electron can interact strongly, scatter off such an atom with a delta function interaction, the Fermi constant potential, and change its state^{7,8}. Such an interaction can be strong and has a range equal to that of the radius of the Rydberg atom; for $n = 18$ that range is 342\AA which is marginally smaller than that required - about 466\AA . Of course this interaction is effective only for atoms whose wavefunction overlap.

For atoms whose separation is sufficiently large that their wavefunctions do not overlap the strongest interaction is

$$V = V_D + V_Q \propto \frac{\mu_1 \mu_2}{r^3} + \frac{\mu_1 Q_2 + \mu_2 Q_1}{r^4} + \dots$$

The first interaction potential V_D , the dipole-dipole interaction leads to cross sections of the order 10^9Å^2 for resonant collisions between Rydberg-Rydberg atoms with $n = 20$ (ref.9). Although the symmetry of this interaction precludes an explanation of our "forbidden" P signals, it may explain the much larger effects observed on the enhancement of the S levels which we have also observed but are not described here. The dipole-quadrupole interaction V_Q has the correct symmetry to explain our observations on the appearance of the "forbidden" P lines. We outline schematically the process where the ground quasi-molecular state $|S\rangle |S\rangle$ is excited coherently by two photon-dipole allowed transitions to virtual excited states $|S\rangle |D^*\rangle$, $|S\rangle |S^*\rangle$, and $|P^*\rangle |P^*\rangle$ and then because of the dipole quadrupole interaction V_Q to the "forbidden" state $|S\rangle |P\rangle$. ie.

$$|S\rangle |S\rangle \xrightarrow{2 \text{ photons}} |P^*\rangle |P^*\rangle + |S\rangle |D^*\rangle + |S\rangle |S^*\rangle \xrightarrow{V_Q} |S\rangle |P\rangle$$

The relative contributions of the Fermi contact and the dipole-quadrupole interactions, both long range, are now being studied.

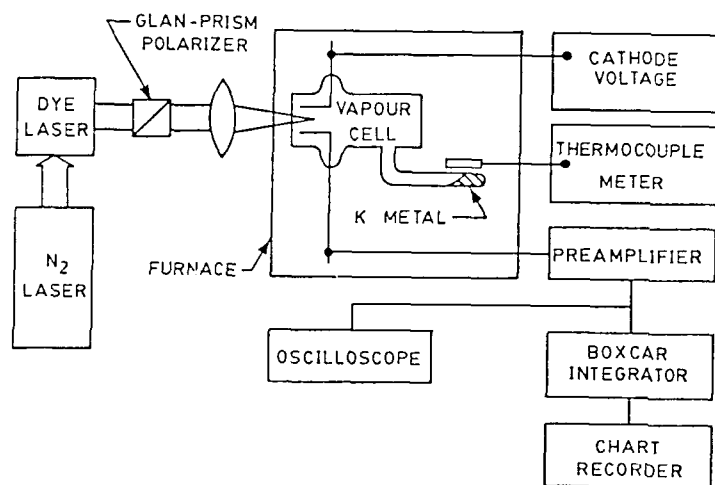


Fig. 1 Schematic diagram of the photo-ionization experiment. When circularly polarized light is required, A Soleil-Babinet compensator (not shown) is used after the Glan-prism polarizer.

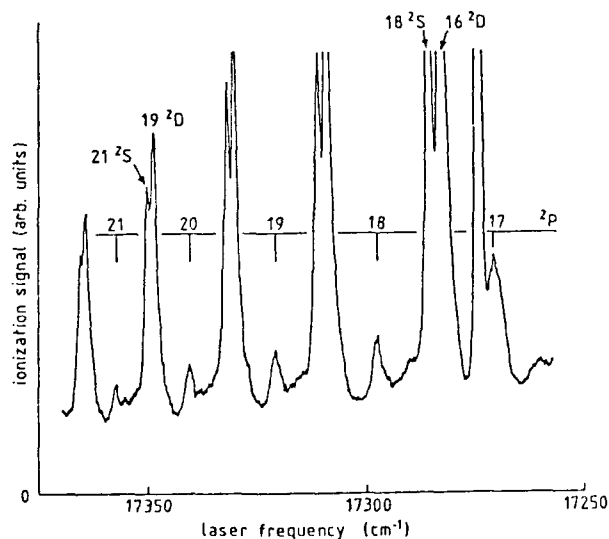


Fig. 2 Portion of a potassium resonant multiphoton ionization spectra taken at $T=232^\circ\text{C}$ and with a collection voltage of 10 volts. The laser power density was 800 MWcm^{-2} . The strong line signal near 17272 cm^{-1} is due to sodium impurity.

Acknowledgement

This work was supported by the Natural Science and Engineering Council of Canada. We thank Alak Chanda, M.H.L. Pryce, L. Sobrino and W. Unruh for helpful discussions.

References

1. See, for example, Collisions and Half Collisions with Lasers, edited by N. K. Rhaman and C. Guidette (Harwood-Academic, Chur, Switzerland, 1984); A. Kopystanska and L. Moi, Phys. Rep 92, 135 (1982)
2. C. E. Burkhardt, M. Ciocca, W. P. Garver, J. J. Leventhal, and J. D. Kelley, Phys. Rev. Lett. 57, 1562 (1986).
3. P. Bicchi, K. R. Mah, and F. W. Dalby, in Book of Abstracts of the Second European Conference on Atomic and Molecular Physics, Amsterdam, 1985 edited by A. E. de Vries and M. J. van der Wiel, p. 4.
4. G. Petty, C. Tai, and F. W. Dalby, Phys. Rev. Lett. 34, 1207 (1975).
5. P. M. Johnson, M. R. Berman, and D. Zakheim, J. Chem. Phys. 62, 2500 (1975).
6. S. E. Wheatley, P. Agostini, S. N. Dixit, and M. D. Levenson, Physica Scripta 18, 177 (1978).
7. E. Fermi, Nuovo Cimento 11, 157 (1934).
8. A. Omont, J. de Phys. 38, 1343 (1977).
9. T. F. Gallagher, D. A. Safinya, F. Gounand, J. R. Delpech, W. Sandner and R. Kachru., Phys. Rev. A25, 1905 (1982).

PRELIMINARY RESULTS ON ENERGY-POOLING IONIZATION

P. Bicchi, M. Meucci, L. Moi*

Istituto di Fisica - Università di Siena

Via Banchi di Sotto, 57 - 53100 Siena - Italy

*Istituto di Fisica Atomica e Molecolare del CNR

Via del Giardino, 7 - 56100 Pisa - Italy

Abstract

A new effect, Energy Pooling Ionization (EPI), is proposed. It gives rise to atomic ions through a collision between atoms transferred to their first excited state by resonant laser light. The atomic systems that may produce this effect are indicated and the first preliminary results obtained are reported.

Introduction

Laser assisted collisions represent a vast class of processes where an atomic transition takes place only in the simultaneous presence of a laser field and a collision. These processes have been the subject of a large number of both theoretical and experimental studies since the first work of Gudzenko and Yakovlenko⁽¹⁾.

They may be divided into two groups:

a) Collisions assisted by a laser field non resonant with any atomic transition.

b) Collisions assisted by a laser field resonant with an atomic transition.

We want to study a new effect, the Energy Pooling Ionization (EPI) which produces atomic ions via the collision of two atoms excited by resonant laser light. As it is often very difficult to make a selective triggering of only one process, it may be useful, before introducing the new effect, a brief review of these processes pointing out the relevant parameters for which they are predominant. This will help us in the determination of the experimental conditions and in the choice of the atomic species.

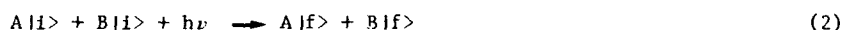
An extensive review of the most recent results can be found in references (2) and (3).

Processes belonging to group a) may be further classified into two categories. The first one is schematically represented by the reaction:



where $|i\rangle$ represents the initial state for both atoms A and B, $|f\rangle$ represents the final state of atom A and ν is the frequency of the laser photon. This reaction is referred to as "Optical Collision"⁽⁴⁾. It is characterized by the fact that one atom does not change its initial state; it only plays the role of perturbing the potential curves of atom A during the collision so that the latter can absorb the photon $h\nu$.

The second class is schematically represented by the reaction:



where $|i\rangle$ and ν have the same meaning as before and $|f\rangle$ is the final state for both atoms A and B. Reaction (2) is referred to as "Radiative Collision"⁽¹⁾ or LICET - Laser Induced Collisional Excitation Transfer⁽⁵⁾. It is characterized by the fact that both atoms change their initial state. Transition (2) can be imagined as a process in which the atom A makes a transition at a frequency corresponding to the sum of the energies supplied by the collision and the laser field. It may also be viewed as a transition induced by the laser photon in the quasi-molecule AB which is present during the interaction between the atoms.

Reactions (1) and (2) need very high photon fluxes and relatively high atomic densities. These effects, moreover, strongly depend on the laser frequency.

In processes of group b) the role of the laser is to prepare the colliding atoms in a well defined excited state. The two most important parameters are the laser power density W_L and the atomic density N . The predominance of one or the other of these parameters gives rise to several different reactions which are briefly reviewed and which may be simultaneously present in a particular experiment. The atoms most widely studied are the alkalis and a review of the results of these experiments is given in references (2), (6) and (7). The processes leading to highly excited levels are the "energy pooling collisions"



and the "associative ionization"



followed by dissociative recombination or radiative recombination

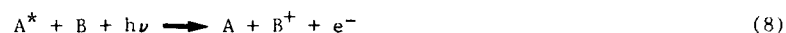


The cross section for process (3) has been measured by monitoring the fluorescence from the highly excited levels and values up to 10^{-15} cm² have been obtained⁽⁸⁻¹¹⁾ in good agreement with the theoretical calculation⁽¹⁰⁾. Several alkali atoms and alkali mixtures have been studied starting with Na in the pioneering work on the subject⁽¹²⁾. They include besides Na, K⁽¹³⁾, Cs⁽¹⁴⁾, Rb⁽¹⁵⁾, Na-K^(11,16) and Na-Rb⁽¹⁷⁾. These processes do not need very high laser power densities as well as high atomic densities. Therefore they cannot be easily

eliminated by simply choosing suitable experimental conditions.
Besides the ionization induced by multiphoton absorption(18)



other processes lead to the ionization. They are widely discussed in ref.(7). They include, besides the associative ionization (4), the "Penning Ionization"



and the ionization by collision with "hot" electrons e^*



where e^* are produced by superelastic collisions



Energy Pooling Ionization

This new process is represented by the reaction



where A^* indicates an atom in the first excited level and ΔE is the quantity

$$\Delta E = |2E(A^*) - E_i| \quad (13)$$

E_i being the ionization energy. In the collision between the two excited atoms, one of them transfers its energy to the other and goes back to the ground state while the latter sums up an energy greater than the ionization limit and is ionized (fig. 1a).

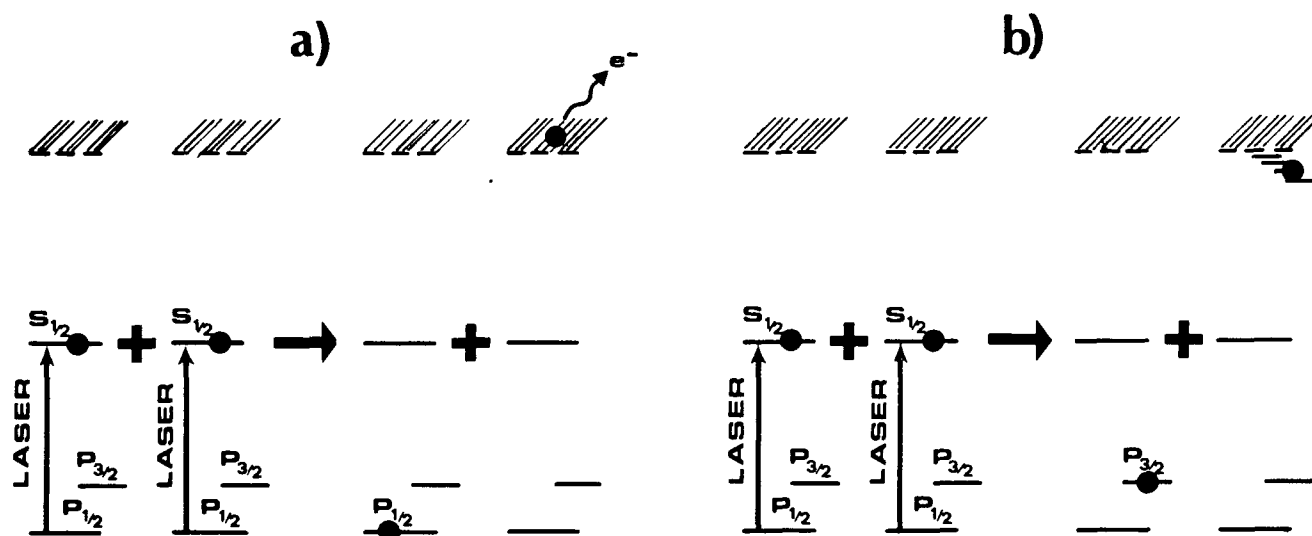


Figure 1. a) Schematic representation of the EPI process.

b) Schematic representation of the excitation of Rydberg levels [reaction (16) in the text].

It is evident that the requirement to get this effect is

$$E(A^*) \approx 1/2 E_i . \quad (14)$$

To get the process unaffected by secondary effects it is essential that the level resonant with the laser photon is the first excited one.

The interest in this process comes from the fact that it makes possible the transition of atoms from bound states to continuum through collisions. Besides it allows the study of how the cross section of this transi-

tion depends on the energy defect ΔE defined in (13). It also gives the opportunity to get informations on the quasi-molecular states of the colliding partners and to produce an atomic population in the Rydberg levels of the atomic system.

TABLE 1: Relevant parameters of Ga, In and Tl for the EPI process.

Atom	Ground level	$\tau(P_{3/2})$	Fine structure of the ground state cm ⁻¹ (eV)	First excited level	Energy of the first ex. level eV	Ionization Potential eV	ΔE_1 cm ⁻¹	ΔE_2 cm ⁻¹	n(Ryd.)
Ga	4P _{1/2}	200 s.	826.2 (0.10)	5S	3.07	6.00	1189.6	363.4	=
In	5P _{1/2}	10 s.	2212.6 (0.27)	6S	3.02	5.79	2075.7	-137.0	≈ 30
Tl	6P _{1/2}	0.23 s.	7792.7 (0.97)	7S	3.28	6.11	3688.3	-4104.4	6±10

Table 1. τ = mean lifetime of the ground state P_{3/2} sublevel; ΔE_1 = difference between twice the energy of the first excited level and the ionization potential [reaction (15)]; $\Delta E_2 = \Delta E_1$ minus the fine structure energy of the ground state [reaction (16)]; n(Ryd.) = Rydberg state reached from the atom according to reaction (16). Data from reference (19).

EPI can be detected by monitoring:

- i) the fluorescence coming from high lying levels populated by recombination processes,
 - ii) electrons and/or ions.
- In case i) the use of a collision cell is to be preferred while in case ii) an atomic beam is to be used. An atomic system suitable for EPI has to fulfill the condition (14). Those which answer this requisite are In, Tl and Ga.

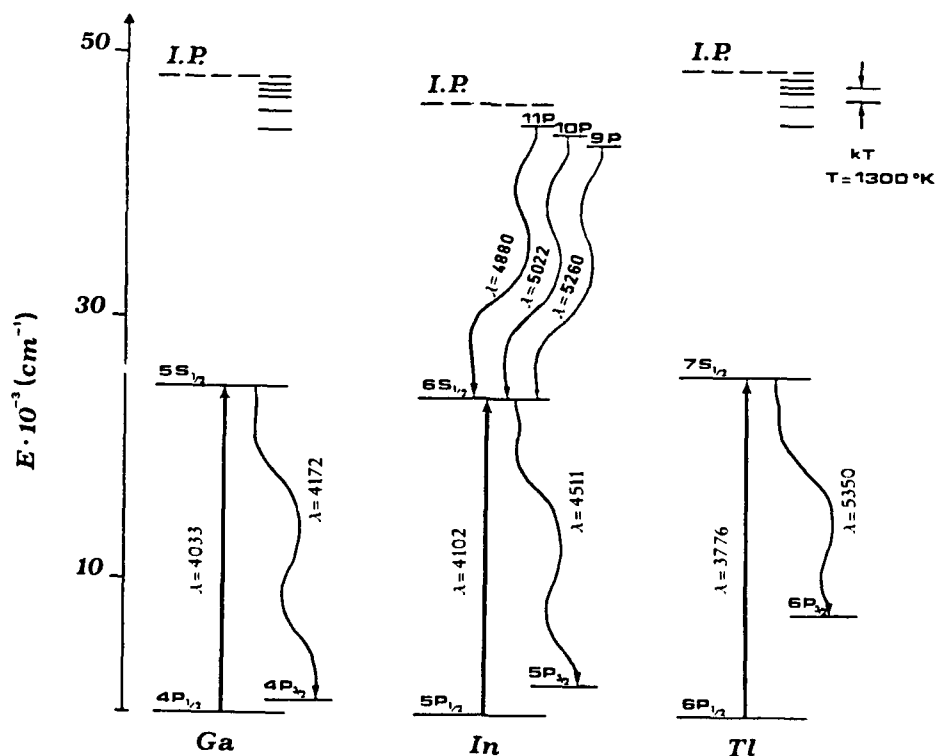
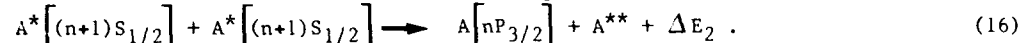
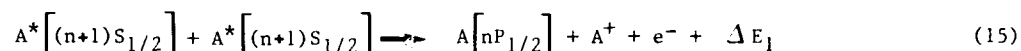


Figure 2. Simplified diagrams of the energy of the atomic levels of Ga, In and Tl. The value of the energy kT is also indicated in scale.

These elements present other motives of interest. Their ground state is a P level with a fine structure energy depending on the particular atom. Therefore we expect that the collisions of two excited atoms have two possible exit channels schematically represented in fig.1 and described by the reactions



Reaction (16) indicates the excitation of Rydberg levels (fig.1b). This reaction, as results from table 1 is not possible for Ga as ΔE_2 is always positive. In fig.2 a simplified diagram of the energy levels for the three atoms is shown.

We report in the following the very first preliminary results.

Experimental apparatus and preliminary results

In order to see this effect we started to work in a cell where high atomic densities are easily reached and it is also possible to add some buffer gas which plays the role of the third body in the collision process.

Ga, In and Tl have very low vapour pressure⁽²⁰⁾, so to achieve the same densities typical of analogous experiments in alkalis ($10^{12} \div 10^{14} \text{ cm}^{-3}$) it is necessary to work at very high temperatures as results from fig.3 where the densities of the three elements are plotted versus temperature.

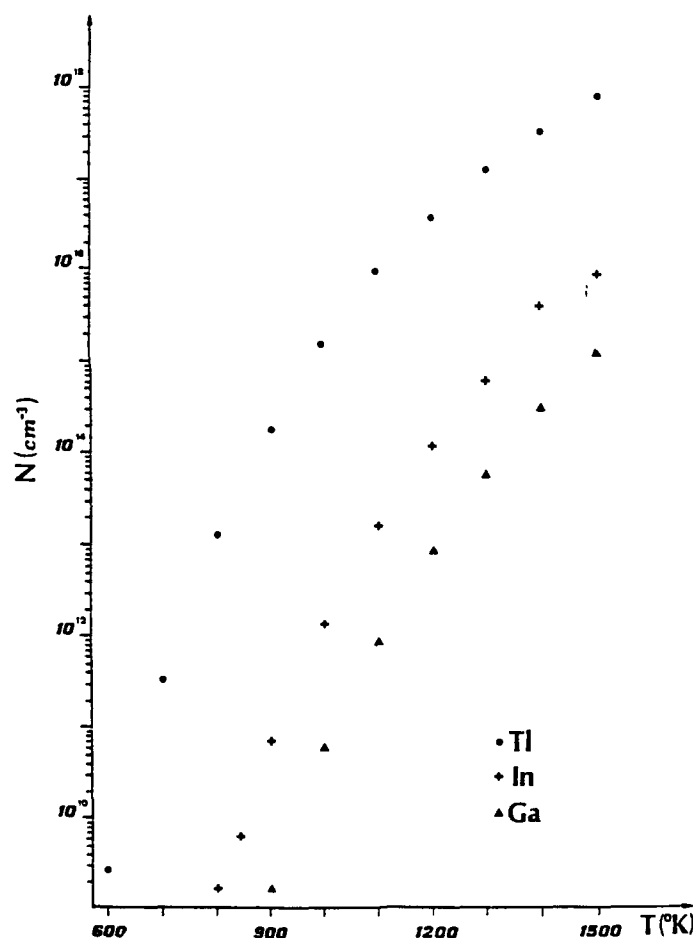


Figure 3. Densities of Ga, In and Tl plotted versus temperature. Data from reference (20).

Tl seems to be the easiest to handle with when temperature is concerned, but it is more difficult to get the laser wavelength resonant with the fundamental transition. For this reason we decided to start with In whose fundamental resonance ($\lambda = 4102 \text{ \AA}$) is achievable with the dye DPS. The useful temperature range goes from 800 to 1000 °C. At these temperatures In gets extremely reactive which creates difficulties in finding a suitable cell. As the HPO (heat pipe oven), more complicated in building, does not solve the problem at least for $T \geq 900 \text{ °C}$ ⁽²¹⁾, to observe the effect and to get the preliminary results we used a quartz cell. For $T < 800 \text{ °C}$

the cell contamination proceeds very slowly. For $T > 900^{\circ}\text{C}$ the contamination is so fast that the cell has to be changed after one day as an opaque layer covers its internal walls.

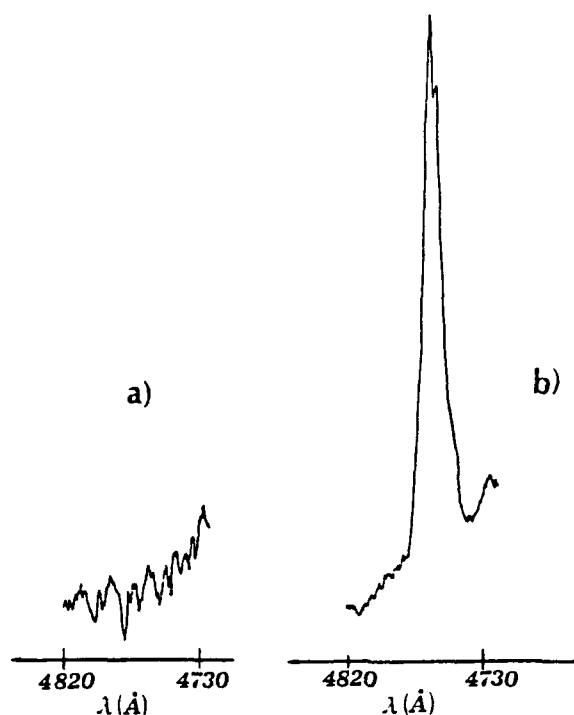


Figure 4. Portions of the spectrum detected at $T = 900^{\circ}\text{C}$, $\lambda_{\text{laser}} = 4102 \text{ Å}$ in a cell with In and 15 torr of Ne as buffer gas. a) Cell with clean walls; b) Cell with walls contaminated by In after about one day of work. The amplification in b) is decreased a factor of 5 with respect to a).

This layer not only reduces the transparency of the cell but, worse than that, gives rise to strong lines in the detected spectrum as shown in fig.4.

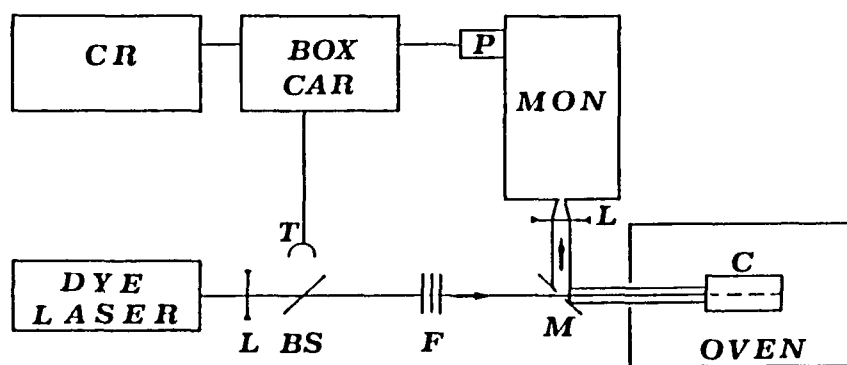


Figure 5. Experimental set-up.

C = Quartz cell; M = Mirror; MON = Monochromator; P = Photomultiplier; CR = Chart recorder;
T = Reference trigger; L = Converging lens; F = Neutral density filters.

Fig.5 shows a block diagram of the experimental set-up. A pulsed grazing incident dye laser (pumped by a commercial N_2 laser) - pulse duration 5 ns FWHM, maximum peak power $\approx 15 \text{ KW}$, repetition rate 10 Hz - is focused inside the cell kept in an oven whose temperature is controlled and may be raised up to 1200°C .

The fluorescence reflected by mirror M, dispersed by a 0.32 m focal length monochromator, is collected by a photomultiplier. The signal is analyzed by a box-car integrator and recorded by a chart recorder. The box-car is triggered by the laser pulse itself.

Both processes (15) and (16) can be detected by monitoring the fluorescence of the vapour irradiated by resonant light, even if they cannot be distinguished in these conditions. At low temperature only the lines corresponding to the $5P_{1/2} \rightarrow 6S_{1/2}$ (4102 Å) and $5P_{3/2} \rightarrow 6S_{1/2}$ (4511 Å) transitions show up and no other line appears. This excludes the presence of a high rate multiphoton ionization. When the temperature is increased and the atomic density gets high enough other lines appear in the spectrum.

Due to the short lifetime of the cell we analyzed only the short portion of the spectrum where some lines of the P series should appear. In this region we observed the lines corresponding to the transitions $6S \rightarrow 11P$ (4880 Å), $6S \rightarrow 10P$ (5022 Å) and $6S \rightarrow 9P$ (5260 Å) drawn in fig.2, while the transition $6S \rightarrow 12P$ (4790 Å), for example, is absent.

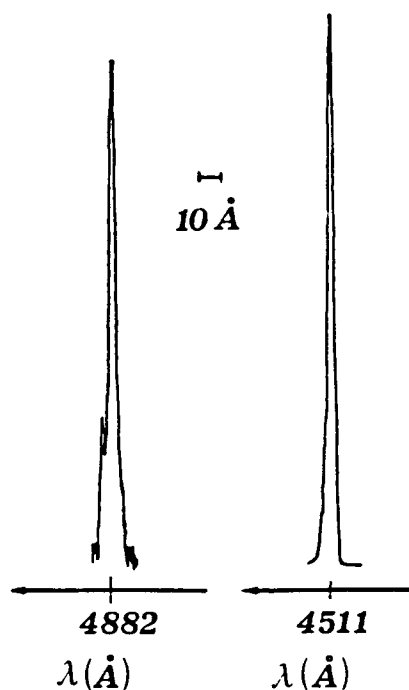


Figure 6. Signals corresponding to the transitions $6S \rightarrow 11P$ and $6S \rightarrow 5P_{3/2}$ respectively monitored in a cell with In and 15 torr of Ne as buffer gas at $T = 950^\circ\text{C}$, $\lambda_{\text{laser}} = 4102 \text{ Å}$. The $6S \rightarrow 11P$ line is amplified 400 times and only 3% of the $6S \rightarrow 5P_{3/2}$ light is collected.

In fig.6 the lines corresponding to the transitions $6S \rightarrow 11P$ and $6S \rightarrow 5P_{3/2}$ are reported in order to compare the relative intensities. Their ratio results to be 7.15×10^{-5} which is a reasonable value for collisional processes⁽¹²⁾. Even at high temperature the P series resonances disappear if the laser is slightly detuned from resonance. Up to now it was not possible to make accurate measurements of the dependence of the signal intensity on the laser intensity and the atomic density. These measurements are essential to give an undoubtable interpretation of the experiment. For the moment we can say that these signals are not due to multiphoton processes but to collisional ones and we presume that the latter are the ones we described before. On the other hand even with the mentioned measurements, there remain some puzzling aspects in the experiment such as, for example, the absence of the $6S \rightarrow 12P$ line as the 12P level is very close to the 11P level. Other collisional processes, unknown at the moment, cannot be excluded. For instance nothing is known about the molecules of these elements and they could play a role in the collision. It is also evident that a final interpretation cannot leave out the analysis of the entire spectrum.

In conclusion we have shown that the reported preliminary results come from collisional processes which we presume are the ones described in the text. To give a definite interpretation of the experiment we are trying to solve the problem of the short lifetime of the cell which is now too short to allow the analysis of the entire spectrum under the same experimental conditions.

References

1. L. I. Gudzenko and S. I. Yakovlenko, Sov. Phys. JETP 35, 877 (1972)
2. L. Moi, Acta Phys. Polonica, A69, 641 (1986)
3. Photons and continuum states of atoms and molecules, N. K. Rahman, C. Guidotti and M. Allegrini, Eds. (Springer-Verlag, Heidelberg, 1987)

4. V. S. Lisitsa and S. I. Yakovlenko, *Sov. Phys. JETP* 39, 759 (1974)
5. Ph. Cahuzac and P.E. Toschek, *Phys. Rev. Lett.* 40, 1087 (1978)
6. A. Kopystynska and L. Moi, *Phys. Rep.* 92, 135 (1982)
7. T.B. Lucatorto and T.J. McIlrath, *Appl. Optics* 19, 3948 (1980)
8. M. Allegrini, P. Bicchi and L. Moi, *Phys. Rev.* 28A, 1338 (1983)
9. J. Huennekens and A. Gallagher, *Phys. Rev.* 27A, 771 (1983)
10. M. Allegrini, C. Gabbanini, L. Moi and R. Colle, *Phys. Rev.* 32A, 2068 (1985)
11. S. Gozzini, S. A. Abdullah, M. Allegrini, A. Cremoncini and L. Moi, *Optics Comm.* 63, 97 (1987)
12. M. Allegrini, G. Alzetta, A. Kopystynska, L. Moi and G. Orriols, *Optics Comm.* 19, 96 (1976)
13. M. Allegrini, S. Gozzini, I. Longo, P. Savino and P. Bicchi, *Il Nuovo Cimento* 1D, 49 (1982)
14. T. Yabusaki, A. C. Tam, M. Hou, W. Happer and S. M. Curry, *Optics Comm.* 24, 305 (1978)
15. L. Barbier and M. Cheret, *J. Phys. B: At. Mol. Phys.* 16, 3213 (1983)
16. M. Allegrini, P. Bicchi, S. Gozzini and P. Savino, *Optics Comm.* 36, 449 (1981)
17. S. A. Abdullah, M. Allegrini, C. Gabbanini, S. Gozzini and L. Moi, in this book
18. P. Bicchi, K. R. Mah and F.W. Dalby, in this book
19. A. A. Radzig and B. M. Smirnov, *Reference data on atoms, molecules and ions* (Springer-Verlag, Heidelberg, 1985)
20. A. N. Nesmeyanov, *Vapour pressure of the chemical elements* (Elsevier, Amsterdam, 1963)
21. K. Niemax and H. K. Weber, *Appl. Phys.* B36, 177 (1985)

LIGHT MECHANICAL ACTIONS ON VAPORS

L. Moi and J. H. Xu*

Istituto di Fisica Atomica e Molecolare del C.N.R.
Via dei Giardini, 7 - 56100 Pisa, ITALY

*ICTP Fellow, Permanent address: Institute of Mechanics,
Chinese Academy of Sciences, Beijing, CHINA

Abstract

The light mechanical forces acting on vapors are discussed and the most recent experimental results are presented. Two effects are considered: the resonance radiation pressure (RRP) and the light induced drift (LID). In both cases important sodium vapor density variations have been observed. The influence of broad band laser excitation (lamp-laser) and of the atomic interaction with the cell walls have been analyzed.

Introduction

Light exerts forces on atoms which are able to modify their motion. These forces can be successfully exploited by using lasers that, due to the high achievable intensities, can deflect or cool down an atomic beam, as well as compress a vapor inside a cell. The experiments on the mechanical action of light (MAL) have been until now performed mostly on atomic beams, while very few of them have been done on vapors.

There are essentially two kinds of mechanical actions that light can usefully exert on vapors: the first is the resonance radiation pressure (RRP); the second is the light induced drift (LID) effect. Both of them can modify the equilibrium vapor density and eventually confine and compress the vapor in a part of the cell.

RRP is a well known effect due to the transfer of the photon momentum $h\nu/c$ to the atom during the absorption-emission process, where h =Planck's constant, c =velocity of light and ν laser frequency. If τ is the lifetime of the excited level the force acting on the atom is $F = h\nu/c\tau$ at the saturation. RRP pushes the atoms along the direction of the light propagation as it is schematically shown in fig. 1a for a single mode laser excitation. The arrow indicates the laser beam direction and the dots represent the atoms. RRP is maximum when the laser is perfectly on resonance inside the Doppler linewidth $\Delta\nu_D$.

RRP was demonstrated for the first time in 1933 by O. Frish⁽¹⁾, who was able to deflect a sodium atomic beam by using a resonance lamp. The advent of lasers made this kind of experiments easier by getting possible the deceleration and the cooling of atomic beams⁽²⁾. RRP on vapors instead was not demonstrated until the very recent experiment performed by J.H. Xu and L. Moi⁽³⁾.

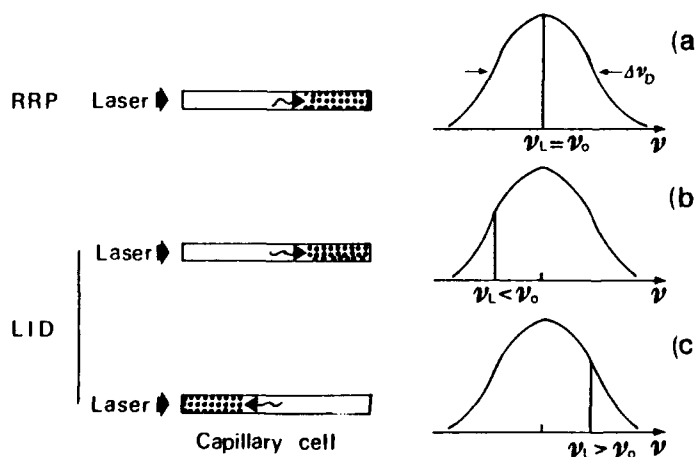


Fig. 1 - Schematic representation of the RRP and LID effects on vapors

LID is an effect proposed only few years ago by Gel'mukhanov and Shalaev⁽⁴⁾ and observed for the first time by Antsygin et al.⁽⁵⁾. It is due to the combined actions of resonant laser excitation and collision with a buffer gas. Both the difference between the diffusion coefficients of the ground and excited state atoms and the velocity selective laser excitation produce an asymmetry in the Maxwellian distribution of the atomic velocities and then a macroscopic flux of atoms inside the cell. As a consequence LID, differently from RRP, can both pull and push the atoms depending on the laser detuning (see fig. 1b and 1c) and it is maximum when the laser is slightly out of resonance.

RRP and LID are selective, through the resonant laser excitation, with respect to the atomic species, it is therefore evident their importance to study isotopic separation as well as

chemical reaction dynamics.

Experiments and results

In this paper the experiments performed on RRP and LID effects are described with special attention to the phenomena produced by multimode dye lasers having particular geometry and characteristics (lamp-laser) (6).

At least two important points must be considered when a MAL experiment is runned on a vapor: the first is represented by the collisions with the cell walls; the second by Doppler broadening of the absorption line.

When an atom hits the wall it remains for a given time T_a at the surface, where T_a depends on the adsorption energy E_a as

$$T_a = T_0 \exp(-E_a/KT) \quad (1)$$

with $T_0 = 10^{-13}$ s. This fact has two main consequences: the first is that for large T_a values an atomic layer is formed at the internal surface of the cell and this layer has to be removed to have any vapor density variation; the second one is that, in any case, the diffusion of the vapor is slowed down as a result of the many collisions with the cell walls undergone by the atoms in the diffusion process. The last effect is enhanced by the small transversal dimensions of the cell that have to match the laser beam diameter. Typical E_a values are in the 1 - 1.5 eV range for alkalis confined in a glass cell and the relative T_a is 10^{-3} s. By adopting a special coating, obtained from a heterodymetil polysilossane solution, T_a becomes 10^{-11} s (7). The coating reduces the formation of the surface atomic layer and it gets negligible the contribution of the wall friction to the diffusion time.

The Doppler broadening lowers the effective coupling of a single mode laser with the vapor (see insert in fig. 2) and this has non negligible consequences. For example the force acting on the vapor in the RRP effect

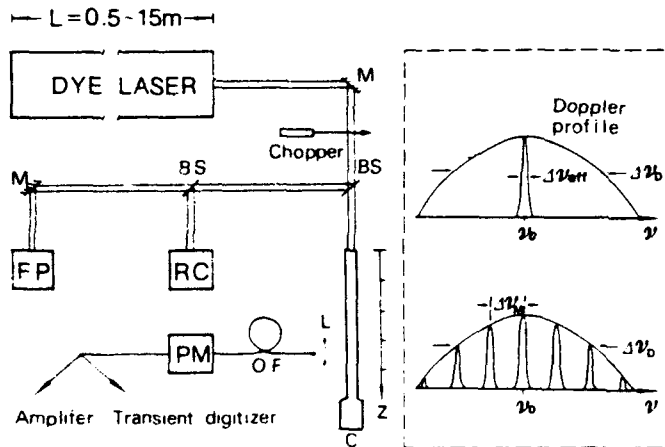


Fig. 2 - Sketch of the experimental apparatus;
 FP= Fabry Perot Interferometer;
 RC= reference cell; PM= photomultiplier;
 OF= optical fiber; C= capillary cell; L= lens;
 M= mirror; BS= beam splitter. The insert
 shows the coupling between the laser and vapor

depends on the number of atoms instantaneously interacting with the laser, and in LID the mentioned asymmetry in the Maxwellian velocity distribution is a function of the velocity groups involved in the excitation process. Therefore it is very important to control the fraction of excited atoms. To that purpose we have adopted a multimode laser having a long cavity in order to close up the frequency separation $\Delta\nu_M$ between the longitudinal modes and eventually to reduce it to a value that is smaller than the homogeneous linewidth of the absorbing line (8).

In fig. 2 the general scheme of the experimental apparatus used in both experiences is reported. Two different dye lasers have been used in order to check the highest efficiency of the broad band excitation: an actively stabilized single mode dye laser and a multimode dye laser whose cavity length L can be varied between .5 and 15 m, to a $\Delta\nu_M = 300$ MHz and a $\Delta\nu_M = 10$ MHz correspond respectively. The sodium vapor is confined in a capillary cell ($\phi = .2 \text{ cm}$) which has a length of about 15 cm in the LID experiments and 50 cm in the RRP experiments. In the first

case the cell is filled with few torr of Neon, while in the second one it is permanently connected to an ion pump in order to have a very low background gas pressure. The cell is made by following a particular procedure described elsewhere (9). The fluorescence is collected at right angle by means of an optical fiber which can be moved along z . At our experimental conditions, the fluorescence intensity I_f is proportional to the vapor density n and $\Delta n/n = \Delta I/I$.

1) Resonance Radiation Pressure: When a vapor is illuminated by a resonant laser it is submitted to a force F which, in stationary conditions, modifies the vapor density profile along the capillary as

$$n(z) = n_0 \exp(Fz/KT) \quad (2)$$

where n_0 is the equilibrium density and z is the position inside the cell. For a two level atom F is given by (3)

$$F = (h/\lambda\tau) \cdot (I_L/I_S) / (1 + I_L/I_S) \cdot \Delta\nu_{\text{eff}} / (\sqrt{\pi} \Delta\nu_D) \quad (3)$$

for a single mode excitation and by

$$F = \frac{\sum}{n} (h/\lambda \tau) \frac{I_n / I_S}{(1 + I_n / I_S)} - \frac{\Delta \nu_{\text{eff}} e^{-\left(\frac{n \Delta \nu_M}{\Delta \nu_D}\right)^2}}{\sqrt{\pi} \Delta \nu_D} \quad (4)$$

for a multimode laser excitation, where, λ = laser wavelength, I_S = saturation power density, I_n = intensity of each laser mode, $\Delta \nu_{\text{eff}} = \Delta \nu (1 + I_L / I_S)^{1/2}$ = effective linewidth of the absorption line, $\Delta \nu_n$ = natural atomic linewidth. The given F is calculated for laser absorption negligible over all the cell length. F is in general lower due to the Doppler shift of the excited atoms which are pushed out of resonance by the laser, unless a lamp laser is used⁽⁸⁾.

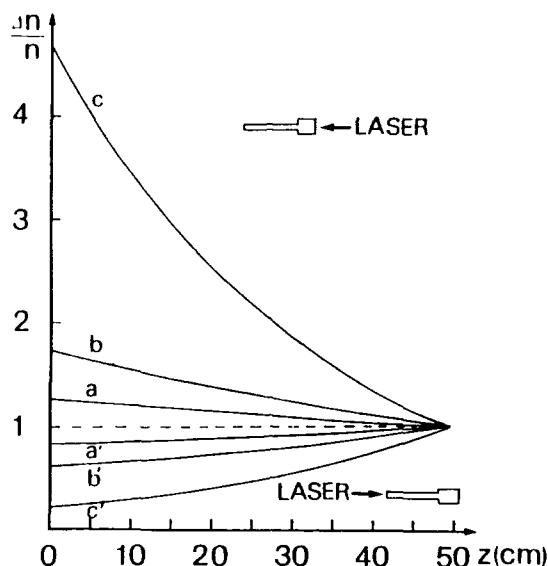


Fig. 3 - Relative vapor density variation calculated as function of z for single mode excitation (curves a and a'); multimode excitation from a standard dye laser ($L = .5m$) (curves b and b'); multimode excitation from a lamp laser ($L = 10 m$) (curves c and c')

In fig. 3 the $\Delta n/n$ versus z has been calculated for three different laser configurations and for both possible laser direction, as it is shown in the inserts. The calculations are made for $I_L = 2.5 W/cm^2$. At $z = 50$ cm it is located the sodium reservoir, therefore no density variations are there possible and the capillary is filled or emptied depending on the laser direction. In fig. 4 examples of fluorescence signals, obtained for the two possible directions of the laser (see inserts in the figure), are shown. At time $t = 0$

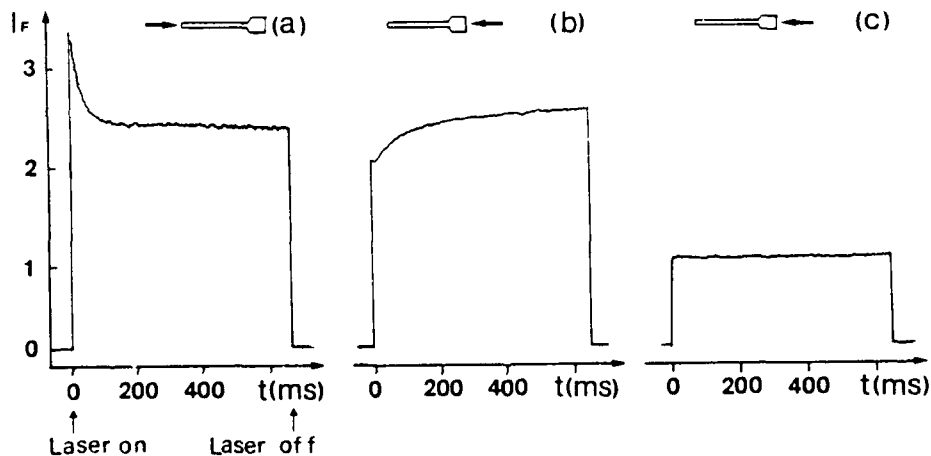


Fig. 4 - Fluorescence signals as function of time in presence of RRP; a) $W_L = 30$ mW, $z_0 = 15$ cm, $T = 190^\circ C$; b) $W_L = 40$ mW, $z_0 = 25$ cm, $T = 160^\circ C$; c) laser out of resonance

the laser is switched on and the fluorescence reaches its value determined by the local vapor density, then it starts decreasing (fig. 4a) or increasing (fig. 4b) under the radiation pressure. In fig. 4c the out of resonance signal is reported to allow a quantitative evaluation of the absolute density variation n . The maximum $\Delta n / n$ value measured in the preliminary experiment has been of the order of 70%. A plot of $\Delta n / n$ versus z is shown in fig. 5. It is evident the modification of the density profile produced by the RRP effect.

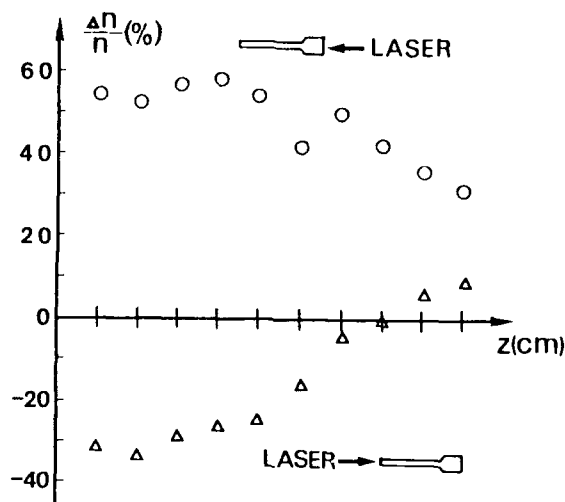


Fig. 5 - Plot of $\Delta n / n$ as function of z : Δ). $T = 190$ °C, $w_L = 30$ mW, $L = 10$ m; \circ). $T = 160$ °C, $w_L = 40$ mW, $L = 5$ m

ii) Light Induced Drift: This effect has been widely studied both theoretically⁽¹⁰⁾ and experimentally⁽¹¹⁾. We have put particular attention to the LID dependence on the atom-wall interaction and we have shown

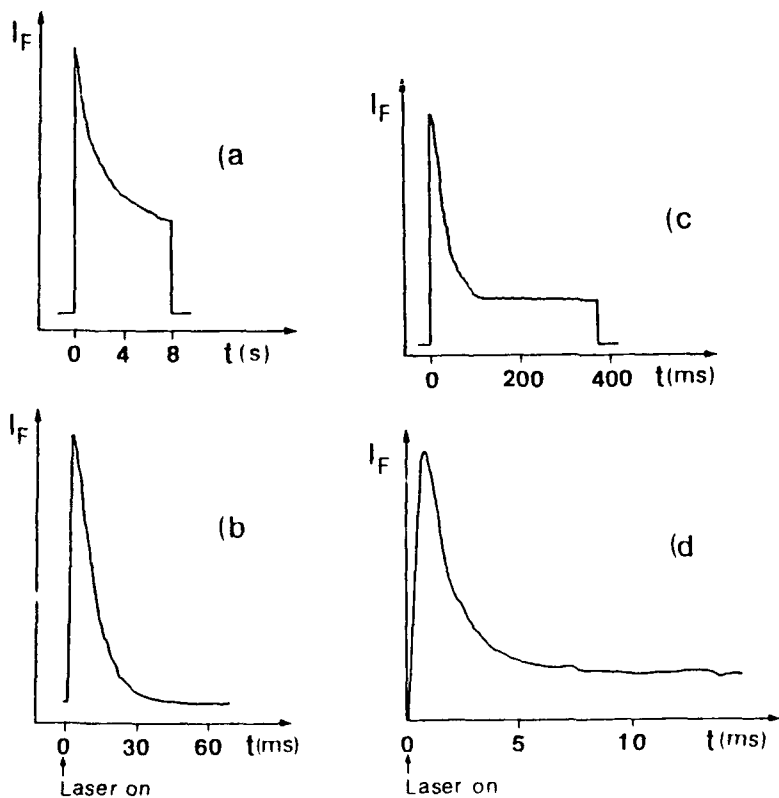


Fig. 6 - Fluorescence signals as function of time in presence of LID: a) uncoated cell, single mode excitation; b) uncoated cell, broad band excitation; c) coated cell, single mode excitation; d) coated cell, broad band excitation

that the used silane coating speeds up the effect⁽⁷⁾ by allowing the study of the LID stationary states for given laser intensity and frequency⁽¹²⁾.

Preliminary results have been obtained on the analysis of the laser bandwidth on the drift velocity v_{dr} . These results show that, by using the broad band dye laser described above, it is possible to increase v_{dr} . This can be understood by adopting an heuristic description for v_{dr} that is given by

$$v_{dr} = \frac{D_g - D_e}{D_g} v_L \eta \quad (5)$$

where D_e and D_g are the diffusion coefficient for the excited and ground state atoms respectively, η is the fraction of excited atoms and v_L is the mean laser selected atom velocity. η depends on the laser bandwidth as discussed above for RRP effect. While in RRP the laser bandwidth $\Delta\nu_L$ can be larger than the Doppler linewidth, in LID, owing to its dispersive behaviour, $\Delta\nu_L$ can not be as large as the Doppler profile because the net effect would be zero. Therefore by increasing $\Delta\nu_L$, v_{dr} reaches a maximum and then decreases again. This has been demonstrated for very high laser fields by Gel'mukhanov et al. (13). In this case it is the power broadening that increases the fraction of atoms interacting with the laser by inducing a v_{dr} increasing until the selective excitation is lost and v_{dr} decreases again.

In fig. 6 the signals produced by single mode and broad band laser excitations are reported both for uncoated and coated cells. These signals show the fluorescence variations obtained when the laser, suitable detuned, is switched on. The fluorescence increases up to the value determined by the equilibrium vapor density, then it decreases as the LID pushes the atoms away from the observation region. The transient time is proportional to the drift velocity, for given vapor density, laser intensity and detuning. The larger bandwidth speeds up the effect both in the coated and uncoated cells and in the second case the effect is even more spectacular. Further measurements are in progress to give a quantitative evaluation of v_{dr} in all these cases.

Conclusions

We have presented recent results on vapor MAL experiments which show a deep modification of the equilibrium density. The RRP is less effective than the LID as photon momenta are exchanged instead of atomic momenta, but it gives the possibility of performing a different kind of experiments like, for example, the laser cooling of a vapor. LID can be very effective in the isotopic separation and in the analysis of chemical equilibrium in vapor phase.

References

1. O.R.Frisch, Z. Phys. 86, 42 (1930)
2. For a review of these experiments see for example:
W.D.Phillips, J.V.Prodan and H.J.Metcalf, J.O.S.A. B 2, 1751 (1985)
3. J.H.Xu and L.Moi, submitted to Optics Commun.
4. F.Kh.Gel'mukhanov and A.M.Shalagin, JEPT Lett. 29, 711 (1979)
5. V.D.Antsygin, S.N.Atutov, F.Kh.Gel'mukhanov, G.G.Telegin and A.M.Shalagin, Sov.Phys. JEPT Lett. 30, 243 (1979)
6. J.Liang, L.Moi, C.Fabre, Optics Commun. 52, 131 (1984)
7. J.H.Xu, M.Allegri, S.Gozzini, E.Mariotti and L.Moi, Optics Commun. 63, 43 (1987)
8. L.Moi, Optics Commun. 50, 349 (1984)
9. M.Allegri, P.Bicchi and L.Moi, Phys. Rev. A 28, 1338 (1983)
10. See for example: G.Nienhuis, Phys. Rep. 138, 151 (1986) and references therein
11. See for example: H.G.C. Werij, J.E.M.Haverkort and J.P.Woerdman, Phys. Rev. A 33, 3270 (1986) and references therein
12. E.Mariotti, J.H.Xu, M.Allegri, G.Alzetta, S.Gozzini and L.Moi, Phys. Rev. A to be published
13. F.Kh.Gel'mukhanov, J.E.M.Haverkort, S.W.M.Borst and J.P.Woerdman, Phys. Rev. A 36, 164 (1987)

DYES FOR DYE LASERS: A MANUFACTURER'S VIEWPOINT

S. Edward Neister

President

Phase-R Corporation

Old Bay Road, New Durham, New Hampshire 03855

Abstract:

A review of dye lasers and the conditions that exist for good performance is made. The aspects of different dye laser types is discussed. The methods for determining dye lifetime are compared. The necessity for developing and using some standards for reporting new dyes and the methods of testing is requested for all persons involved in their development.

1.0 Early Observations

1.1 In The Beginning

Dr. Peter Sorokin began the use of organic dye material in liquid form as a laser source in 1967. While I was at General Laser Corporation, we developed the sealed coaxial flashlamp and as a result, the first commercially available dye laser. Figure 1 is a copy of the first dye laser advertisement placed in Laser Focus the winter of 1969. Figure 2 puts all together the basic concepts of what a dye laser is, how it is made, and what it does. The energy level diagram on the left with the broad S1 emission band is superimposed on top of the fluorescence band underneath the pictorial layout of a dye laser.

As the grating is rotated, the lasing output spectrum will change because the gain will shift to that wavelength which diffracts back through the dye cuvette to the output reflector. This will only occur over that part of the fluorescence spectrum in which the gain exceeds the dyes reabsorption.

The right graph shows the difference in spectral output when a flat reflector replaces the grating. Instead of the output linewidth being 7Å with the grating (or other dispersive device), it becomes broadened to about 40Å (3.8nm) because of the relative broad gain vs wavelength existing in the excited signlet state.

An interesting thing about dye lasers is that any dye will not lase at the same wavelength if it is excited or pumped by two different methods.

The following gives an expression how the losses in the cavity are related to the reflectivity and transmission of the reflectors. The emitted wavelength is also a function of not only the losses that exist, but also on the dye cell length and concentration.

L = Cavity Losses

l = Dye Cell Length

η = Dye Concentration

R = Mirror Reflectivities

T = Window Transmissions

$L = 1/2 L_{\eta} (R_1, R_2 T, T_2)$

Changes in wavelength estimated by

A good reference book on dye lasers is "Topics in Applied Physics Dye Lasers", Volume 1, Edited by F.P. Schafer. From that book Figure 3 shows the effect on lasing wavelength as the concentration is changed.

As the concentration is increased, the output shifts to the red. Figure 4 shows the effect by changing the length of the cell. So if you do a report that says that I have a half centimeter cell, expect a different wavelength if somebody else reports using a one centimeter cell.

1.2 Pump Methods

Lets look at the different methods of pumping in order to get everyone on the same ground. Figure 5 says ruby laser but you can substitute nitrogen laser, or Nd:Yag laser as the source for transverse laser pumping of the little dye cell. This is one method of making a dye laser, that is a laser pumped dye laser. Figure 5 also gives you a dramatic picture of what a CW dye laser looks like using an Argon or Kryton ion laser as the pump source.

This is from some of the early work that Ben Shavely at Kodak published. To some extent, this shows you why the flashlamp pumped dye laser is being used for high power work. Much more volume of dye can be excited with a flashlamp system, so therefore more output is obtained.

Figure 6 presents lasing output spectra from dye lasers pumped by the different methods. Pick any dye and notice how different they behave in lasing wavelength and relative output in each of the different systems.

One of the interesting things about the coaxial flashlamp is that it can pump dyes into the near UV.

I hope it is obvious that when data is presented, the method of pumping, the length of the cell or model of laser used must also be given.

2.0 Flashlamp Importance

Figure 7 shows the coaxial flashlamp. It differs from the linear flashlamp by the fact that the dye flows down the center of the coax. The linear flashlamp requires a reflector to get the light out of the linear flashlamp into the dye cell. The coax can be designed to get the maximum pumping efficiency into the dye cell. It has a different loss mechanism and different gain mechanism than any other excitation source. So if you are using a coax, you are going to get different performance numbers than if you use a linear, which is different from the Nd:Yag. Most important is that flashlamps can pump large volumes of dye, producing large energy pulses.

Figure 8 shows what a coax can do. This is one of the systems we developed for the Air Force quite a few years ago. This lamp produced 1.66% efficiency with Rhodamine 590 dye, at 1/3 μ s pulsewidth and less than 100ns risetime. The lamp was run at a kilowatt average power. The lamp proved to be very durable. It is an all metal to quartz seal coaxial flashlamp. The impressive thing about it is that we are getting 1.6% efficiency out of it.

The signature of the pulse out of the coax is a little bit different than some of the other systems (Figure 9). The coax typically has a very, very sharp rise. 50% of the risetime can be less than 20ns, so it really has pumped the dye hard. This pulse is a 3 Joule output pulse. It is about 1/2 microsecond pulsewidth, full width at half maximum. Its efficiency is probably in the order of about 1.1 to 1.2%. When Aaron Fletcher tested new dyes, he found some interesting correlations between dyes and this picture of the pulse. Differences from this norm may indicate what is happening with a particular dye.

Aaron Fletcher at the Naval Weapons Center, China Lake has probably been the fellow that has published more information on dye testing. He has done more testing than I think anyone else in the world. He has done an excellent job. Figure 10 presents a couple of things that Aaron has tried to get across to people. The degradation of the dyes can occur in several different ways. The left curve is what actually happens with a coax. I do not know what will happen with a linear. Aaron did a lot of his work with a coax but what is interesting, is the harder you pump the dye, the longer is its half life.

Aaron found that in order to measure the half life accurately it must be tested on an input energy level much above what is required for lasing threshold. Some data by others will not agree with Fletcher's. In most cases, they were not pumping sufficiently high enough above lasing threshold.

Figure 11 and 12 show the effect of dye efficiency and lasing threshold on repetition rate. This says that you must be real careful about how you make the measurement. Lasing thresholds will change, the rate of degradation will change depending upon how hard you are pumping them and how fast. Consistency is very necessary.

What was needed was an absorber with a lower cut off wavelength in order to maintain good life but not suffer efficiency (1)* suggested trying caffeine. He used caffeine in Biology as a tremendous UV absorbent. Figure 13 shows how the variation of its concentration effects its absorption. When you get into the order of about 1 gram per liter of caffeine, the optical density was measured to be about 9 and 10 below 3000A.

Caffeine was mixed into the cooling water of the triax (Figure 14). With it, efficiency was maintained as well as lifetime improvement. Caffeine prevented the break down of the alcohol solvents.

Figure 15 shows the results which were dramatic. The results indicate that flashlamp radiation below 3000A is breaking down the alcohols which greatly limits dye lifetime. Either a change in solvents, or a dye molecule not sensitive to these breakdown products is necessary to eliminate the need for this UV filter.

3.0 Testing Methods and Problems

The problem with measuring dye lifetime is horrendous. Aaron determined what he called the theoretical limit. He looked at it mathematically and generated some equations and said if you plot the data like figure 16 and from that calculate various constants, you can come up with numbers for the theoretical limit like 2 megajoules/liter or 4 megajoules/liter. This procedure is not trivial and is very time consuming if done correctly. There are so many variables that are changing; e.g., for different solvents, temperatures of the dyes, lasing efficiency, reflector alignment, that you really have to be a laser person to do this.

Figure 17 gives you an idea what some of Aaron's data looked like. All the numbers point to the FOM column of table 4 or what he calls the dyes figure of merit. FOM is obtained by measuring the dyes slope efficiency and multiplying it by some corrected lifetime. The problem is how can we compare this information with someone else's? It is very difficult unless the other person followed the exact same procedures.

In table 4 of figure 17 notice that when he used argon cover gas, typically he got much longer lifetime. He makes a statement that most Coumarin dyes have longer lifetime under argon. But there is a couple of Coumarin dyes where this is not true. For c8F and Coumarin 153, he gets longer lifetime with air. He explains this by saying the relative energy differences between the singlet and triplet states are different for those two dyes. So many different dyes have been tested that it seems that you can find some dyes tested on some laser which will help draw just about any conclusion you want.

(1)* The Use of Caffeine as a Liquid Filter in Coaxial Flashlamp Pumped Dye Lasers; John Calkins, Ed Colley, John Hazle, Optics Communications, Volume 42, no. 4, July 1982

Figure 18 is some of Aaron's latest data before he retired. The numbers are really starting to look impressive. The data was taken using a coaxial flashlamp. You should note that the Argon cover gas in Ethanol is the winner. But look at all the data he had to take.

We have to determine an easy method for testing and standardizing the lifetime recording of new dyes. Table 1 of figure 18 on the right is data from Schimitschek & Hammond. They took the relative number of laser shots to the 50% decline. That is all they did. They did not determine K numbers and C numbers, figure of merits but said, let's just pump it and see what happens. They had close agreement on relative lifetimes with Aaron for a common test, C1H and C2H. Aaron would not agree that this would produce the correct lifetime number.

But we have to start somewhere. Once you establish specific operating conditions, then comparisons can be made relative to one used as a base. To do absolute numbers, you are going to have to take data similar to what Aaron did.

One of the interesting things that we did was to watch how the dyes degrade. From figure 19, the laser produces a certain energy called E_0 at some charging voltage. If the lamp is flashed at that constant level, then there will be some number of shots when the output drops to $E_0/2$ which is called the half life. But if we instead start at $E_0/2$, and maintain that output, then four times as many shots can be put on the dye. This is accomplished by increasing the input energy until the voltage level reaches a value that is close to the operational limit.

Ben Shafer reported way back in the early 1970's that the spectral output can be shifted by changing its P.H. Figure 20 shows a dye which is the most dramatic shift I have seen to date. It was developed by Joel Kauffman. There are various things you can do to dyes and if the P.H. is not the same, you can possibly get different results.

Figure 21 is from Aaron's latest publication (2)**. This data shows what happens to the lasing efficiency if the temperature difference between the cooling water and the dye in the triax system is not correct. What is interesting is the significant change which can be made for only several tenths of a degree difference. The effect is very solvent dependent. Thus if you are going to do a lifetime measurement using the triax system, please make sure the temperatures are held constant. A temperature change can easily make any degradation data complete nonsense.

It is interesting to note that the dye was stopped in his "figure 6".

He kept the water flowing, but he stopped the dye. You notice that as the temperature of that inner tube approaches the optimum, the output reaches a maximum. This has nothing to do with the dye flush factor or index gradients or anything like that. So like I said earlier, you can make one rule of thumb with dyes, and I can show you something that will not follow.

When using a coaxial flashlamp, you can have a problem. The problem is that you tend to get a shock wave off the side of the tube during the pulse and some localized heating. Figure 22 shows how the index changes during the pulse. Figure 23 shows the effect of the shock wave as it propagates through the dye cell. So, if you test with too long a pulse, you can start getting other effects that are going to effect your efficiency.

4.0 Flashlamp Spectrum

Most papers talk about flashlamps in terms of its equivalent black body temperature. It is one method of trying to compare sources that are used to pump lasing materials.

Figure 24 is an uncalibrated optical multichannel analyser (OMA) spectrum of the flashlamp output. The OMA was checked by its sensitivity vs wavelength changes which makes a true calibration somewhat complicated.

By changing the center wavelength of the OMA, the output vs wavelength from different sources can be compared. The effective calibration overlapped on this spectrum would have the intensity at 4000Å increased by 2X and that at 3500Å increased by 4X.

What can be said is that the UV output is not increasing for shorter wavelengths as has been reported for linear flashlamps. We can only speculate the reasons, and say that the coax we use at about 10KA/cm² discharge current does not look like a black body, but is strictly a xenon discharge.

Reasons why we do not see the large UV can be possible because the inner tube has evidence of reaching very high (2000 degrees C) temperatures over a very thin layer during the discharge. Hot fused silica absorbs longer than normal wavelengths.

A possible other factor is that vapor fused silica (3)† produces emission spectra in the near UV that may have been misread as xenon emission. These lines can be very intense and may have lead to the conclusion about high black body temperatures.

Another interesting observation is that coaxial lamps can pump UV dyes directly to 3300Å. Even though efficiency is poor, enough UV is emitted which will successfully pump the dye. I am not aware of any linear flashlamp being able to pump UV dyes. If all the UV emission

(2)** Improving the Output and Lifetime of Flashlamp=Pumped Dye Lasers; Aaron N. Fletcher, Dan E. Bliss, Michael E. Pietrak, Naval Weapons Center

(3)† Persistent Enhanced UV Radiation from Double-Pulsed Flashlamps; H.W. Gandy, A.C. Kolb, W.H. Lupton and J.F. Weller; Applied Physics Letters, Vol. 4, Number 1, Jan. 1, 1964

does exist, I cannot see why some lasing should not be possible, even if the pulse risetime is a factor of 2 slower.

This leads to a different conclusion about the importance of separating the absorption and emission curves as much as possible. The dye absorption maxima near the peak emission of its source is best for pumping efficiency. Reducing self absorption at the lasing wavelength is best for lasing as well as overall efficiency.

5.0 Standardization of Testing

I have discussed most of the variables that occur with dyes and the dye laser in general. But figure 25 emphasizes something that I may not have stressed earlier. This is work that was done by Aaron Fletcher. When you do some measurements of the dye and you are using it in a laser, take a picture of the output. Use a photodiode and beam splitter so that you can see what is happening. Most of these pictures have linear type backs to the pulse. This seems to indicate triplet quenching. Different dyes react differently to the same excitation pulse. But it is very important to use all the information you can obtain to help understand the chemistry.

The manufacturer should tell the customer what an approximate lifetime is going to be for each dye. But any dye lases with enough efficiency to do the experiment at a specified wavelength. This efficiency is what we call D#. It is related to what the laser will produce using Rhodamine 590 which has a D# of 1. From figure 26, if the customer wants to use Rhodamine 640 in any laser, he can expect about 40% more intensity. For any given wavelength, a dye can be chosen that has the greatest efficiency. Because it is referenced to R590, the customer can approximate the laser's output at that point.

When you make your measurements and try to understand a new dye, you have got to come up with certain basic numbers. If we do not have those numbers, then comparisons cannot be made. You have to have the excitation wavelength. Initially, if you are going to excite the dye with a flashlamp or Nd:Yag or whatever, it is best not to have any tuning element in the cavity. Then the natural output wavelength is what we call Lambda Zero. This is where the dye will lase naturally with flat-flat reflectors when pumped in a specific manner. If the output reflector is about 95%, then some relative new but poor dyes may reach lasing threshold.

We want to know the efficiency. I always say relative to R590 - why? Because anyone that has a laser knows what that laser does with R590. R590 is the basic dye. It is a little more efficient than 6G and in any case people know what their laser does with that dye. You must also specify the solvent. We like to specify the solvent that gives the greatest efficiency. Some customers do not give a hoot about lifetime. They may just make 5 shots a week but they want the most photons they can get. So when we give them a D#, we like to specify the solvent that gives the best output. You may find that one dye lases very well in Methanol and in Ethanol it is 20% less efficient.

The lifetime rating for a new dye is the most difficult. Initially, an acceptable method would be to note the number of shots at a specified energy level that it took to reduce the output intensity to 50% when using one liter of dye.

When many dyes must be tested, we typically measure the amount of degradation that has occurred after 200 shots at 50 joules input energy per shot for 200ml of solution. This number helps sort out the week materials quickly.

As a summary, let me suggest the necessary information for a dye report.

- o excitation - flashlamp or whatever means used
- o Lambda Zero - wavelength of output with flat-flat reflectors
- o D# - relative efficiency to Rhodamine 590 - this means you must test R590 in the laser periodically
- o Solvent and Concentration - which gives the best D#
- o Lifetime - expressed as kilojoules per liter when pumped at some level above lasing threshold (suggest 4X)
 - the solvent for best lifetime
 - any cover gas
 - if UV filtered or not
 - the tuning range at 4X above threshold

For naming new dyes, there must be a basic methodology. I suggest:

1. New Identifier: related to some basic structure of the dye (Rhodamine etc.)
2. Wavelength: generally Lambda Zero when flashlamp excited
3. Modifications: using the alphabet for different modifications

Some examples: Coumarin 487

Oligo 381B

For a sample dye report, try the following:

	<u>Dye Report</u>
Name	Rhodamine 590
Excitation	FL. Coax - 10mm bore 6mm triax quartz
D#	1.1
Concentration	$8 \times 10^{-5} \text{M}$, Methanol
Tunable	595nm (flat-flat)
Lifetime	570 - 625nm @ 4X 100KJ/liter @ 4X Ethanol, caffeine argon, D# @ 0.9

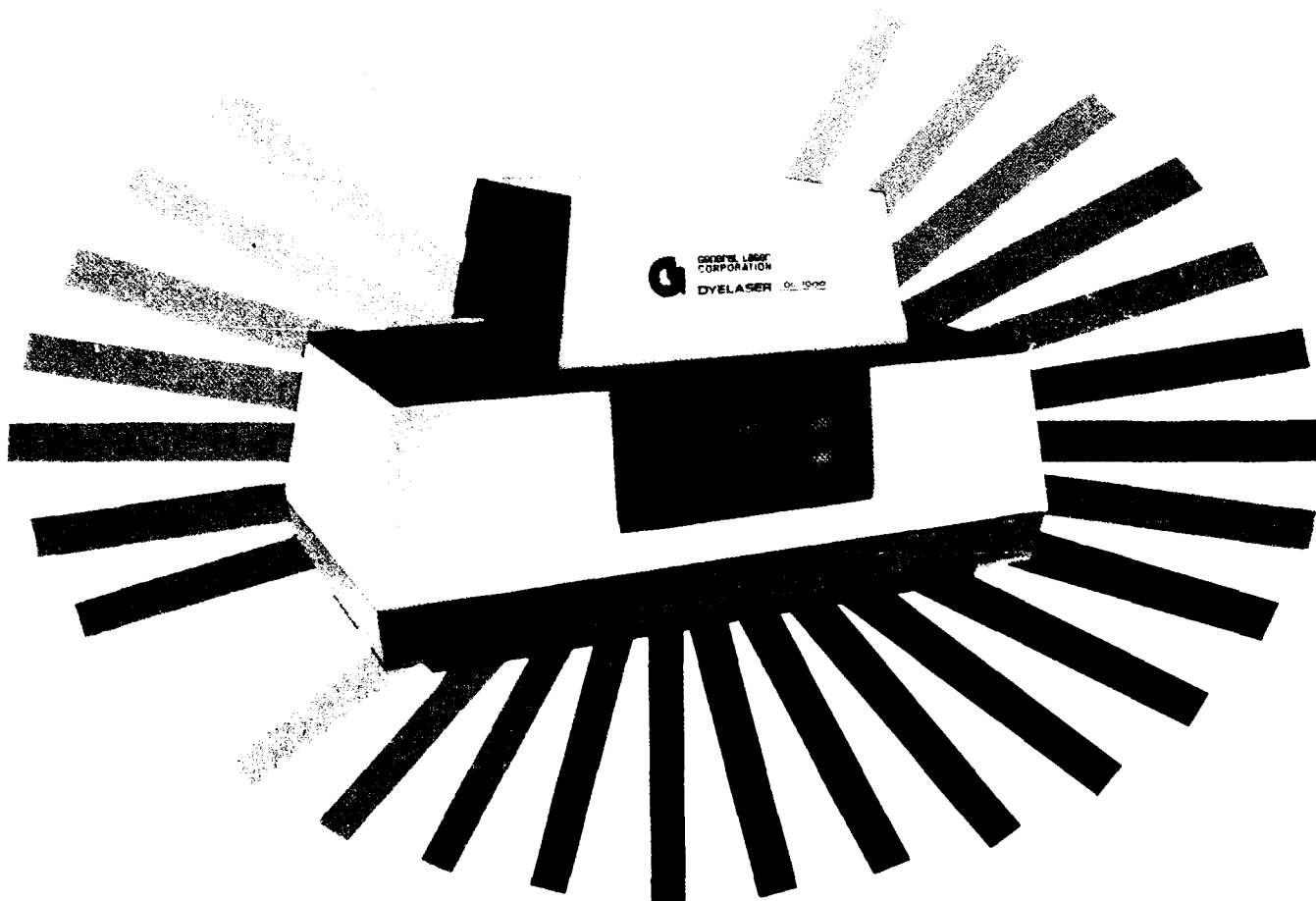
A general test procedure is shown in figure 27.

The dyes are first screened by measuring lasing threshold (V_{th}) and their lasing wavelength (λ_0).

Then, their performance is compared to existing dyes. A low threshold indicates a good dye. The threshold is changed by changing the reflectivity of the output (R_0). Then the output energy E_0 is compared to Rhodamine 590 to determine its relative efficiency (D#).

The test is complete when tunability ($\Delta\lambda$) and approximate half life ($\tau_{1/2}$) are measured.

The half life with caffeine as a UV filter $\tau_{1/2}^{cf}$ is important if the dye may be placed on the general market.



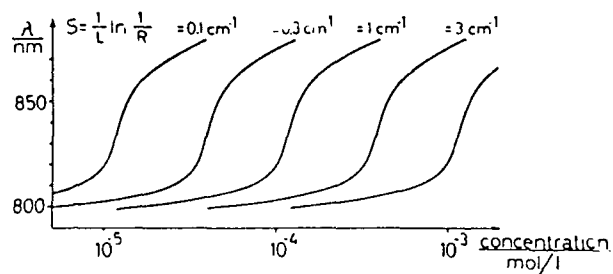
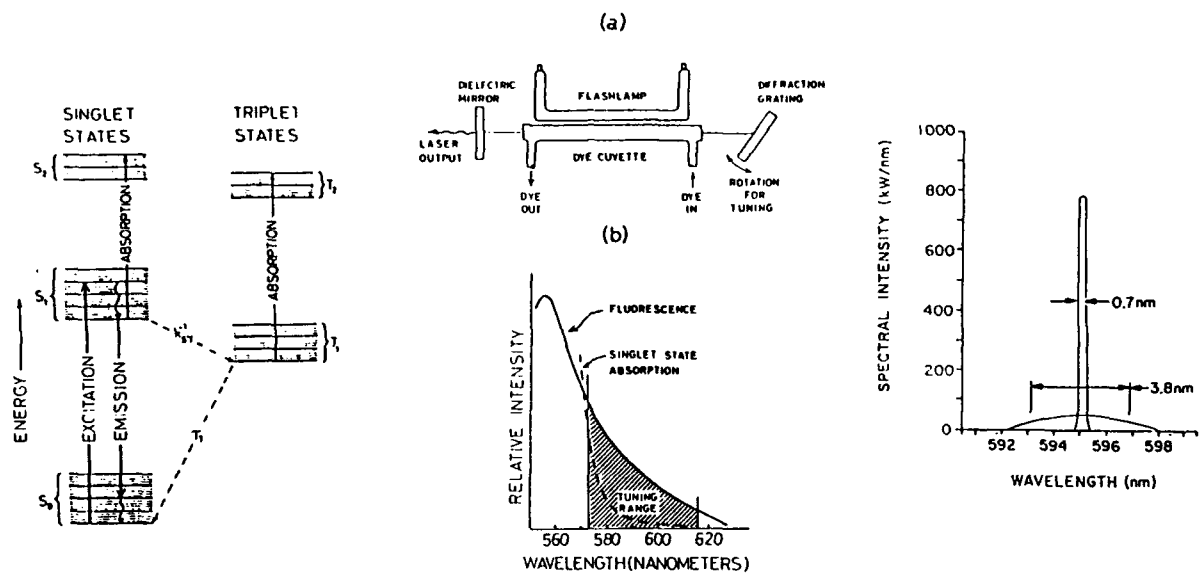


Fig. 3 Plot of calculated laser wavelength vs. concentration of the laser dye 3,3'-diethylthiatricobyanine bromide, with S as a parameter. (From SCHÄFER, 1968)

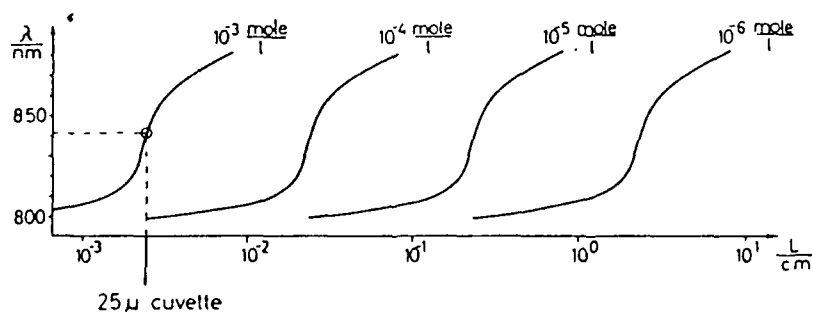


Fig. 4 Plot of calculated laser wavelength vs. active length of the laser cuvette, with the concentration of the solution of the dye 3,3'-diethylthiatricobyanine bromide as a parameter. (From SCHÄFER, 1968)

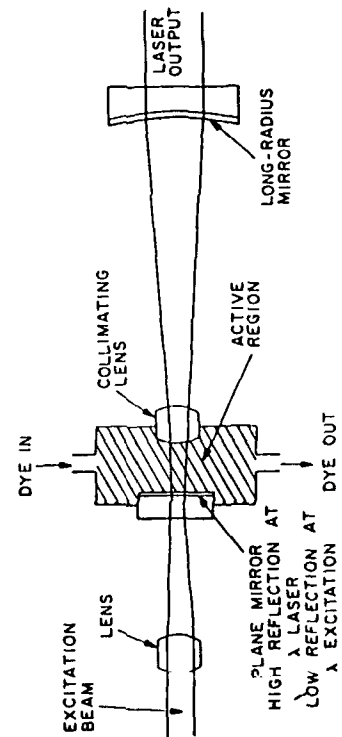
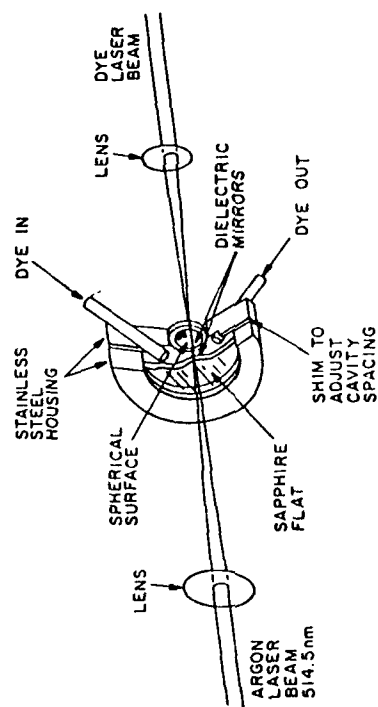
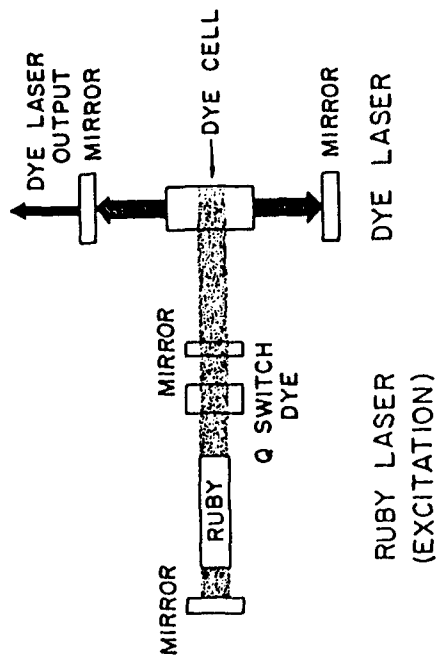
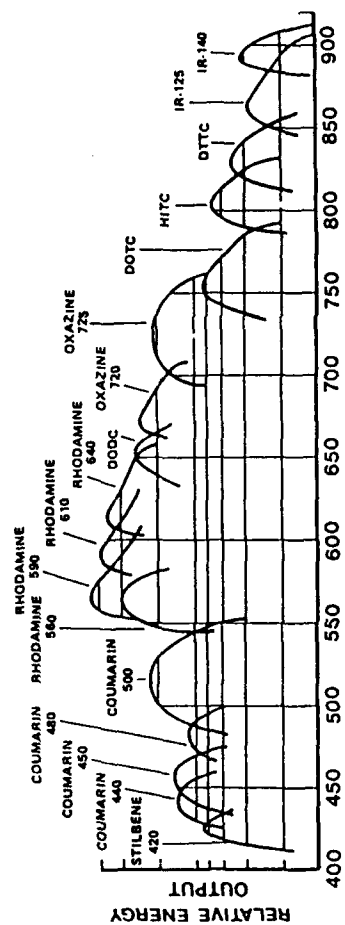
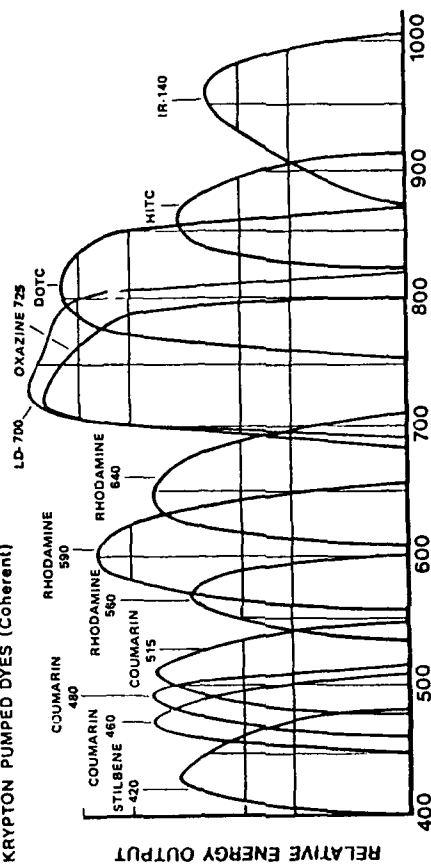


Figure 5

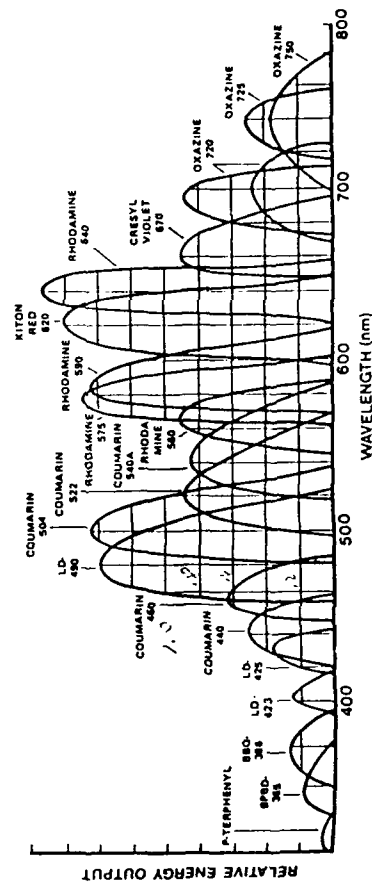
Nd:YAG PUMPED LASER DYES (Quintel International)



KRYPTON PUMPED DYES (Coherent)



COAXIAL FLASHLAMP PUMPED DYES (Phase-R)



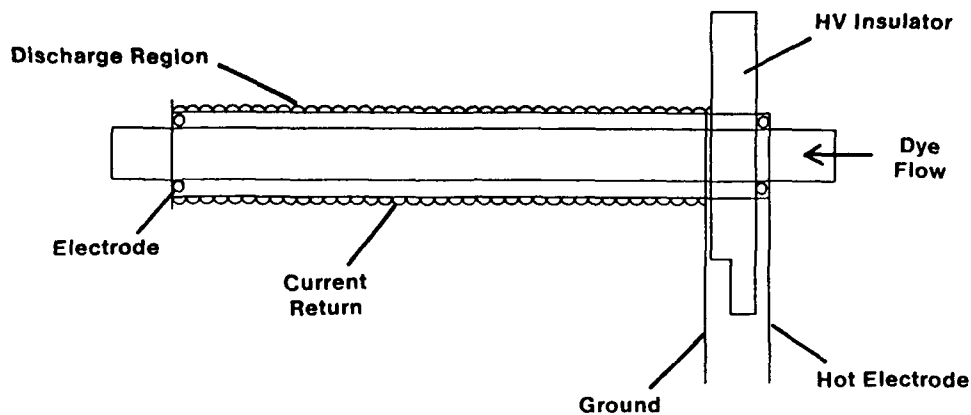
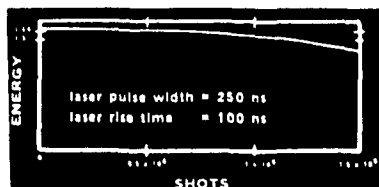


Figure 7

DL-13Sp COAXIAL FLASHLAMP

Improved for Longer Lifetime
Greater than 1.6% Efficiency



- Energy is single shot output of DL-2100D using Rhodamine 6G (methanol) with 100 joule input
- Shots accumulated at 100 joule per pulse at 10 Hz P.R.R.

Figure 8

DYE LASER PULSE OUTPUT

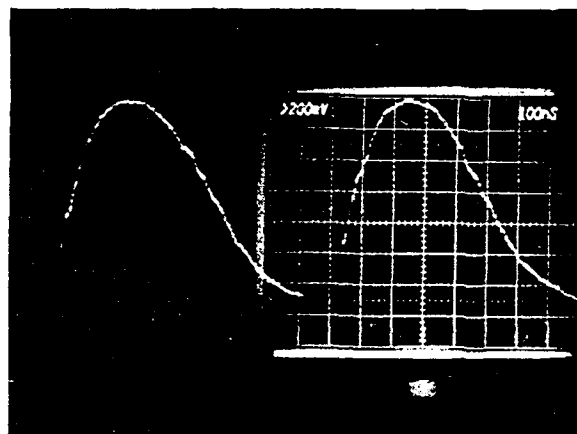
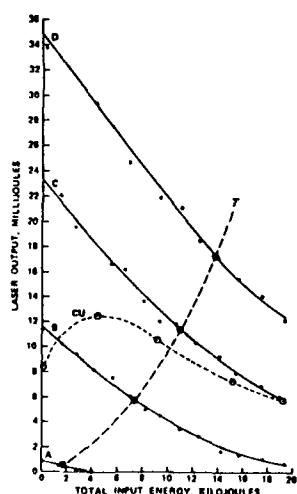
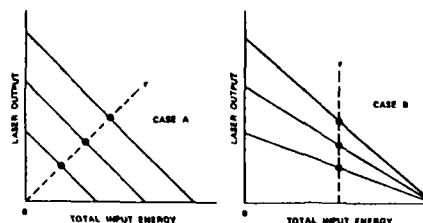


Figure 9

Laser Dye Stability: Part 2



Experimental variation of dye laser output during dye degradation. Curves A, B, C, and D are 10, 15, 20, and 25 J/flash, respectively. Curve CU is for the unfiltered solution at 20 J/flash. The line r traces the half-life points of the filtered solutions. The dye is 7-dimethylamino-4-methylcoumarin (coumarin 1) in ethanol.



Example of two types of half-life variation for different inputs per flash. Case A shows increasing half-lives while Case B shows constant half-lives. The line r traces the half-lives.

Figure 10

The graph shows the relationship between total input energy and calculated threshold for three different conditions (A, B, and C). The x-axis represents total input energy in kilojoules (0 to 140), and the y-axis represents the calculated threshold in joules (-2 to 16). Curve A starts at approximately 9.5 J at 0 kJ and increases to about 11.5 J at 130 kJ. Curve B starts at approximately 4.5 J at 0 kJ and increases to about 11.5 J at 130 kJ. Curve C starts at approximately -1 J at 0 kJ and increases to about 14.5 J at 130 kJ.

Total Input Energy (Kilojoules)	Calculated Threshold (Joule) - Curve A	Calculated Threshold (Joule) - Curve B	Calculated Threshold (Joule) - Curve C
0	9.5	4.5	-1.0
20	9.6	5.2	1.5
40	9.8	6.2	3.5
60	10.0	7.5	6.0
80	10.2	8.8	9.0
100	10.5	10.2	12.0
120	10.8	11.2	14.0
130	11.5	11.5	14.5

Figure 1 is a line graph showing the transmission spectra of polyacetylene films. The x-axis is labeled 'WAVELENGTH (in nm)' and ranges from 250 to 400 with major ticks every 50 units. The y-axis is labeled 'TRANSMISSION (relative to 400 nm)' and ranges from 0.0 to 1.0 with major ticks every 0.1 units. There are three curves plotted, corresponding to different concentrations of polyacetylene in benzene: 0.01 gm/L, 0.1 gm/L, and 1.0 gm/L. The 0.01 gm/L curve shows a broad absorption peak centered around 280 nm, with transmission dropping to approximately 0.3. The 0.1 gm/L and 1.0 gm/L curves show a sharp absorption edge around 300 nm, where transmission drops from 1.0 to near 0.0. Above 300 nm, the transmission for all three curves increases and levels off near 1.0, with the 1.0 gm/L curve being the highest and the 0.01 gm/L curve being the lowest in this region.

Diagram illustrating a dyeing apparatus. The apparatus consists of a central chamber with a Teflon top and Quartz walls. The chamber is divided into sections labeled FLASH, WATER, DYE, WATER, and FLASH. Arrows indicate the flow of dye from the central DYE section into the surrounding WATER sections. The chamber is sealed with an AR WINDOW on the left and right. At the bottom, there are two vertical tubes labeled DYE and WATER, with arrows indicating flow into the chamber. The bottom right corner is labeled IN.

Figure 1 is a semi-logarithmic plot showing the effect of caffeine on the fluorescence decay of coumarin 523. The y-axis is labeled "POWER in mW" and ranges from 10 to 500 on a logarithmic scale. The x-axis is labeled "TIME in minutes" and ranges from 0 to 120 on a linear scale. Two data series are plotted: "COUMARIN 523" (represented by open circles) and "caffeine" (represented by filled circles). The coumarin curve starts at approximately 200 mW at 0 minutes and decays rapidly, reaching 10 mW at 100 minutes. The caffeine curve starts at approximately 100 mW at 0 minutes and decays much more slowly, reaching 10 mW at 120 minutes. A label "14,000 shots" points to the end of the coumarin curve at 100 minutes.

A semi-logarithmic plot showing the power of a laser beam over time. The y-axis is labeled 'POWER in mW' and has a logarithmic scale with major ticks at 10, 50, 100, and 500. The x-axis is labeled 'TIME in minutes' and has a linear scale from 0 to 100 with major ticks every 20 minutes. Two data series are plotted: 'RHODAMINE 590' (represented by solid circles) and 'no caffeine' (represented by open circles). The 'RHODAMINE 590' series starts at approximately 250 mW at time 0 and decreases slowly to about 150 mW at 100 minutes. The 'no caffeine' series starts at approximately 250 mW at time 0 and decreases rapidly, reaching about 10 mW at 40 minutes. An arrow points to the x-axis at 100 minutes, labeled '14,000 shots'.

Time (minutes)	Power (mW) - RHODAMINE 590	Power (mW) - no caffeine
0	250	250
10	220	150
20	210	80
30	200	40
40	190	10
60	180	-
80	170	-
100	160	-

979

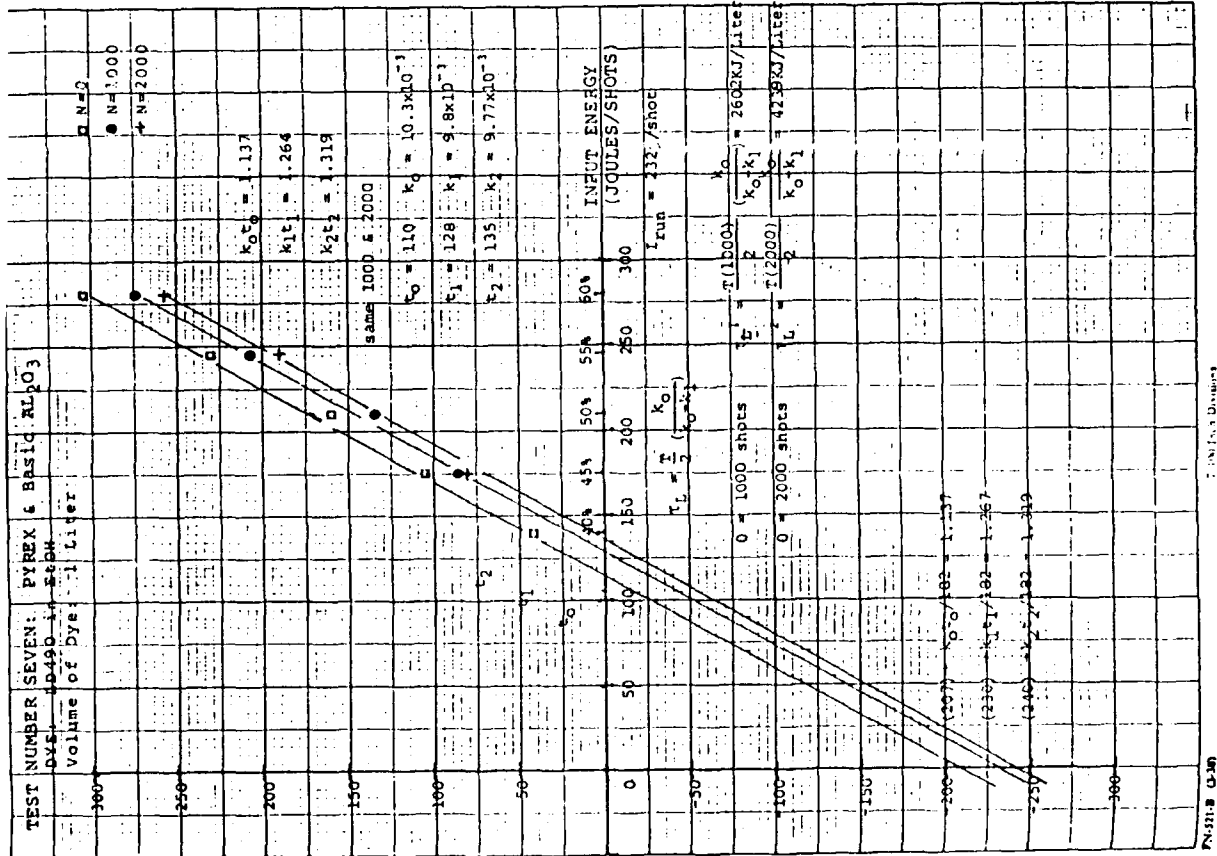


Figure 16

Laser Dye Stability Part 3.

Table 1. Comparison of stability data for ethanol solutions

Dye	Original designation	Dye No. in Fig. 1	This report	Large laser [°]	Flowing solution [2, 5]	Stable solution [3, 4]	Ratio values	
							static	"effective" or flowing t this report
ACJF	21	490	95° 180	6400	16100	2.39	14.0	
ACJF	22	490						1.6
CF	14	64		70°	250			1.2
CF	13	64			250			2.34
CF	32	140		6400	15000	2.39		34.0
CF	35	120		4700	11300	0.7		1.4
CF	17	140		50°	250			2.50
CF	8	74			7500*			7.1
CF	31	140		3000*	1000			8.2
CF	30	75	20° 75	3000*	1500			14.0
CF	38	118			4100			19.0
CF	33	350		6500	16000	2.50		56.0
CF	30	280		15700	37000	2.39		2.46
CF				3560	8800			2.29
CF				5330	12000			2.33
CF				3920	9100			2.91
CF				2190	6300			2.25
CF				2100	4500			2.43
CF								±0.018

* Pump light not filtered.

* In diode rather than ethanol.

* "Effective" values are static measurements divided by 2.43. The numerator only includes values having pump light filtered below 220 nm.

* t = 7 to 14 x 10⁻³ s using nitrogen laser pump [10].

* t = 1.6 to 7 x 10⁻³ s using nitrogen laser pump [10].

Table 4. Dye laser characterization constants for different cover gases for a series of 2.0 x 10⁻⁴ M dyes in ethanol

Trivial name of dye	Dye no.	Cover gas	I ₀ × 10 ³	I ₀ [J]	Lamp optical factor	Corrected I ₀ [Mden ⁻²]	FOM [Mden ⁻²]
Coum 102	17	Oxygen	1.10	39.8	0.70	0.24	0.26
		Air	1.23	23.9	0.65	0.66	1.0
		Argon	1.38	22.3	0.66	5.16	8.1
LD-490	18	Oxygen	1.58	29.1	0.63	1.66	2.6
		Air	1.79	22.7	0.63	4.28	7.6
		Argon	2.07	22.0	0.63	19.4	40.0
ACJF	22	Oxygen	1.43	22.5	0.47	18.5	26.0
		Air	1.45	28.0	0.42	40.7	59.0
		Argon	1.40	27.3	0.49	229.0	320.0
CF	30	Oxygen	1.10	31.4	0.62	16.4	18.0
		Air	1.19	27.3	0.62	84.5	100.0
		Argon	1.57	22.6	0.62	34.3	54.0
Coum 153	33	Oxygen	1.00	36.1	0.63	8.5	8.5
		Air	1.09	30.4	0.63	26.2	29.0
		Argon	1.40	24.8	0.63	10.6	15.0
Rhod 6G	-	Oxygen	3.14	16.0	0.54	43.2	140.0
Tetrafluoroborate ^a	-	Air	3.03	16.1	0.64	16.0	51.00
		Argon	3.35	15.9	0.58	345.0	1200.0

^a Found in [34]

^b 1.0 × 10⁻⁴ M

Figure 17

Lasing characteristics of p-ridyl substituted o-azobenzene dyes and comparison dyes at 2×10^{-4} molar.

Dye designation	Solvent	Cover gas	Lasing			
			Slope efficiency, $k_0 \times 10^3$	Threshold, t_0, J	Lifetime constant $1/\tau, M/dm^{-2}$	Wavelength, nm
4PyPO-HClO ₄	ethanol ^{a)}	air, argon	did not lase			
4PyPO-HClO ₄	water ^{a)}	air	0.38	43.0	n.d. b)	494-511
4PyPO-HClO ₄	water ^{a)}	argon	0.57	40.7	320.0	494-512
4PyPO-MePTS	ethanol	air	0.47	41.0	n.d. b)	492-507
4PyPO-MePTS	ethanol	argon	0.56	31.4	35.0	493-508
4PyPO-MePTS	water	air	0.51	35.8	107.0	494-512
4PyPO-MePTS	water	argon	0.67	34.2	157.0	494-512
4PyPO-MePTS	ethanol:water	air	0.59	35.5	112.0	496-507
4PyPO-MePTS	ethanol:water	argon	0.74	34.8	690.0	495-511
4PyMPO-MePTS	ethanol	air	n.d. b)	~50.0	n.d. b)	n.d. b)
4PyMPO-MePTS	ethanol ^{c)}	argon	1.6	21.0	2000.0	560-583
4PyMPO-MePTS	ethanol	argon	1.5	22.0	>10000.0	567-587
4PyMPO-MePTS	2-propanol ^{c)}	air	n.d. b)	~45.0	n.d. b)	n.d. b)
4PyMPO-MePTS	2-propanol ^{c)}	argon	1.4	16.9	16.0	559-582
4PyMPO-MePTS	methanol	argon	1.0	25.6	>10000.0	571-588
4PyMPO-MePTS	water	argon	0.45	41.0	n.d. b)	571-591
Coum 314	ethanol	air	1.9	19.8	2.8	492-504
Coum 314	ethanol	argon	2.1	17.3	1.6	492-507
Coum 314	methanol	air	1.9	19.3	4.0	496-508
Coum 487	ethanol	air	2.5	25.3	3.3	474-498
Coum 487	ethanol	argon	2.0	23.8	6.3	474-498
Coum 487	ethanol:water	air	2.4	24.8	6.3	487-507
Coum 487	ethanol:water	argon	2.2	24.1	10.0	487-507
Coum 487	methanol	air	4.1	21.1	2.4	481-503
Coum 487	methanol	argon	3.8	20.4	7.1	481-503
AC3F	ethanol	air	1.5	28.0	41.0	480-497
AC3F	ethanol	argon	1.4	27.3	239.0	480-497
AC3F	ethanol:water	air	1.7	27.1	313.0	490-514
AC3F	ethanol:water	argon	2.0	22.7	0.6	490-514
AC3F	methanol	air	1.2	30.1	80.0	482-509
AC3F	methanol	argon	1.2	28.3	113.0	484-512

Volume 16, number 3

Table I

Laser dye performance at 5 J energy input into flashlamp. This table can be directly compared with results previously reported [3]. Some differences in peak output power (e.g., C1 and C102) can be explained by the change in output mirror reflectivity.

Dye	Wavelength untuned (nm)	Initial peak output power (kW)	Relative number of laser shots to 50% decline of initial output
C111	466	8.0	480
C211	465	7.5	365
C311	450	1.0	10
C411	477	5.0	30
C611	490	7.0	255
C811	475	7.0	255
AC1F (a)	-	-	-
AC2F	490	9.0	650
Q1F	463	4.0	20
Q3F	477	5.0	160
Q4F	477	4.0	30
Q6F	473	10.0	180
AQ1F	452	6.0	100
C1 (b)	460	7.5	10
C2 (b)	458	6.5	10
C102 (b)	480	7.5	10
C120 (b)	440	8.0	10
C6 (b)	536	4.5	600
C30 (b)	503	6.0	450

(a) No lasing up to 5 J input.

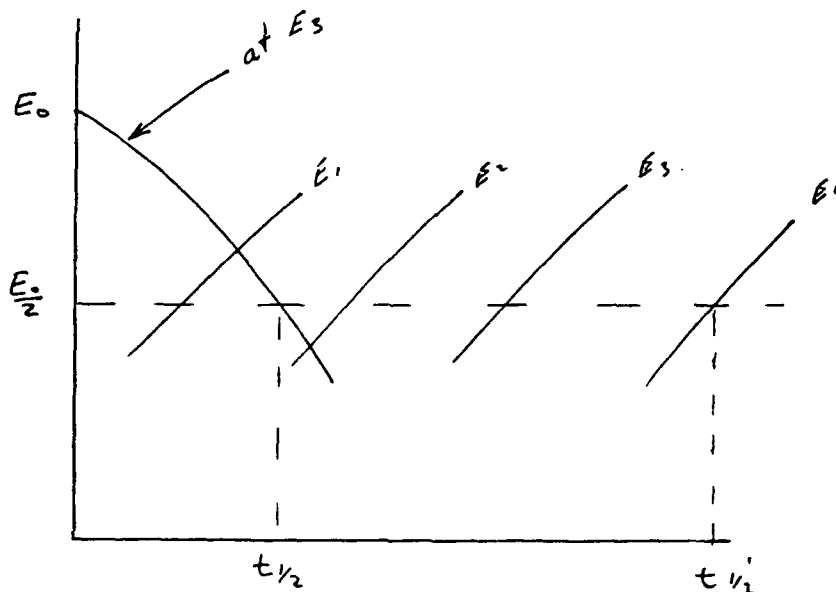
(b) Eastman Kodak dyes; structures given, for example, in ref. [4] and ref. [6].

^{a)} 10^{-2} molar in HClO₄. ^{b)} Not determined. ^{c)} Dye at 1×10^{-4} molar.

AC4F ethanol:water air 3.0

402 501 nm peak

Figure 18



Lifetime vs. Pump Level

Input $E_1 > E_2 > E_3 > E_4$

$t_{1/2}' > t_{1/2}$

Figure 19

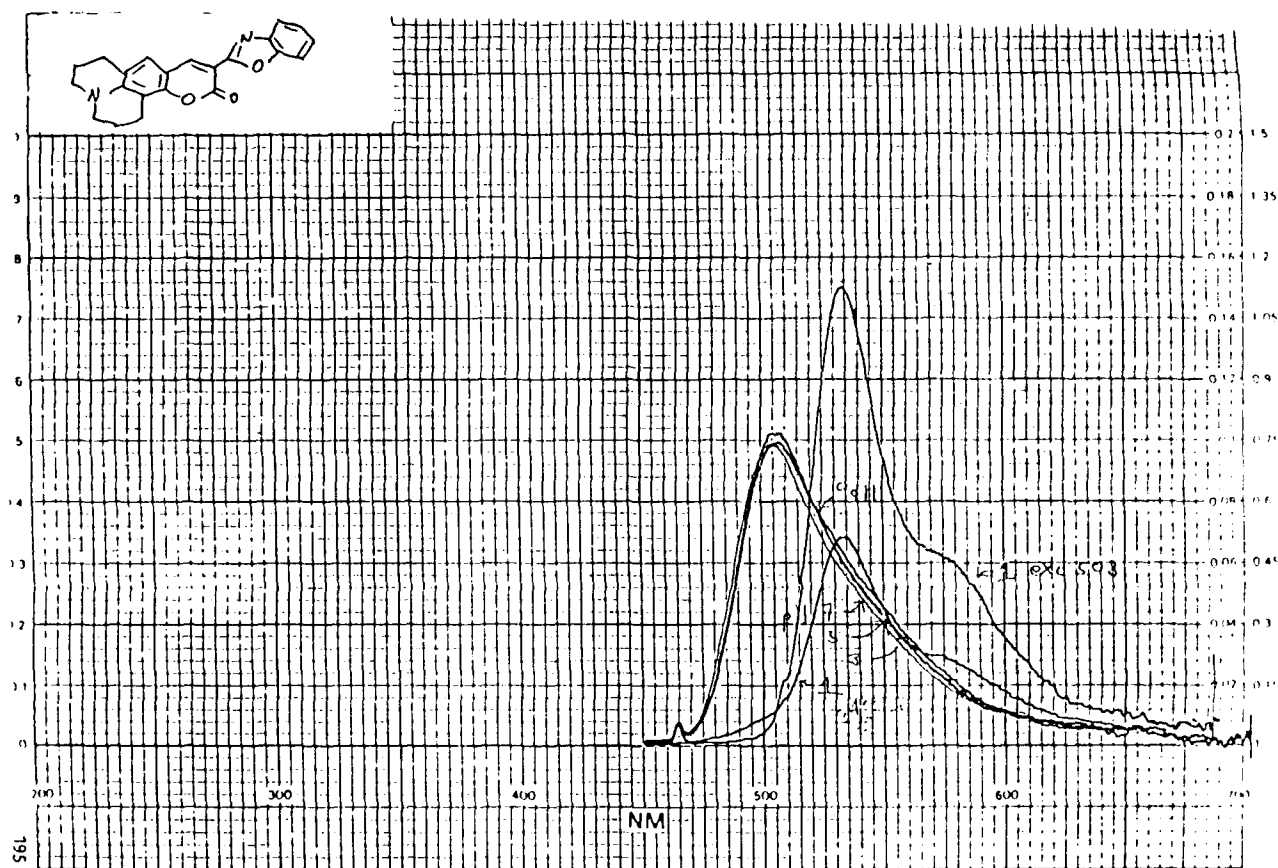


Figure 20

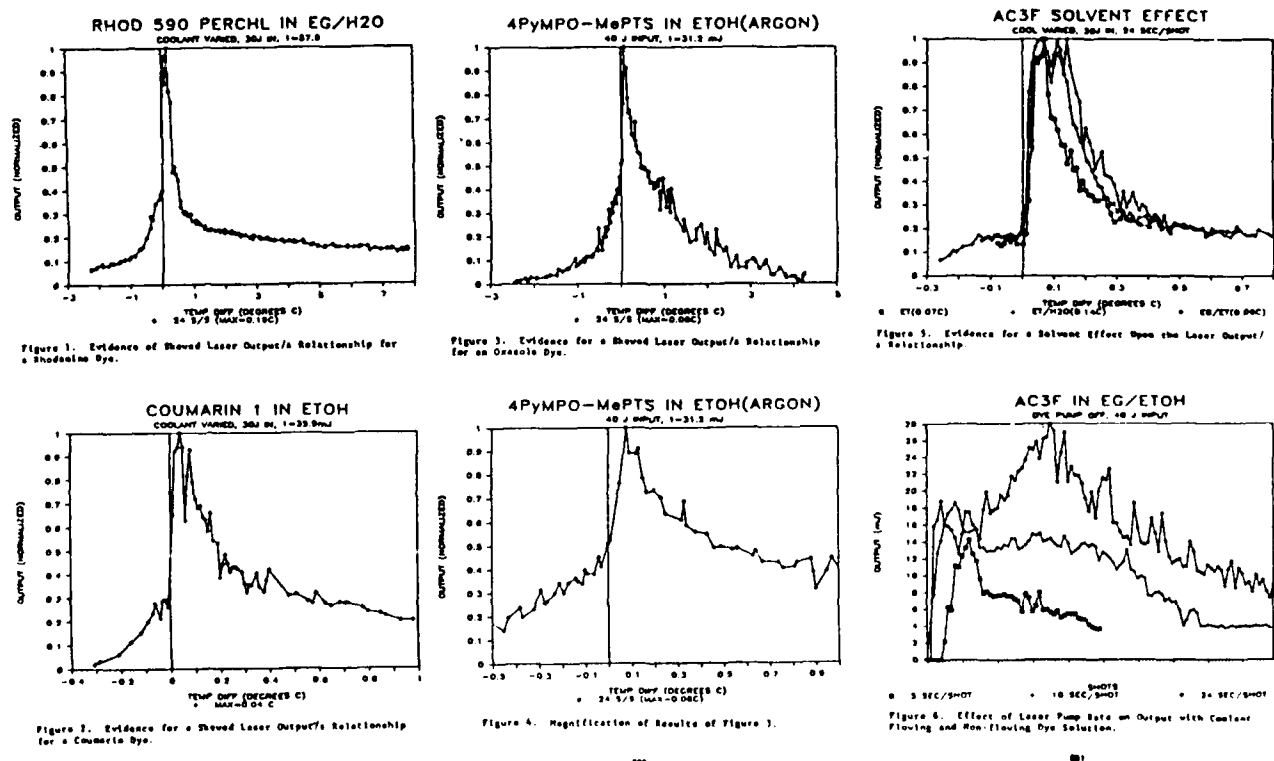


Figure 21

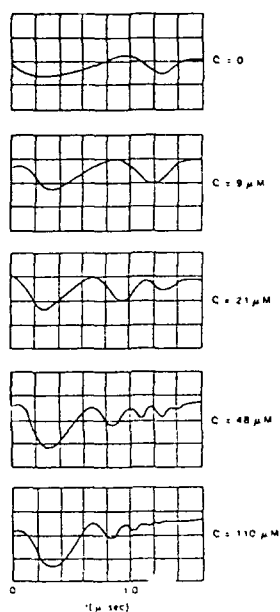


Fig. 22 Interferometer throughput for various dye concentrations in ethyl alcohol. Flashlamp energy is 60 J.

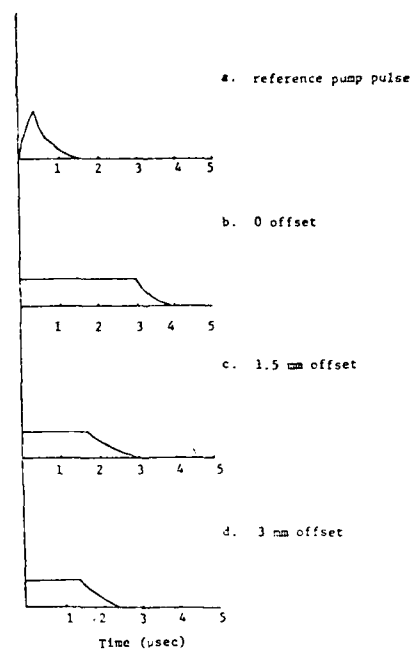


Figure 23 Transmission of a HeNe Beam Through a Dye Cell Filled with Ethanol

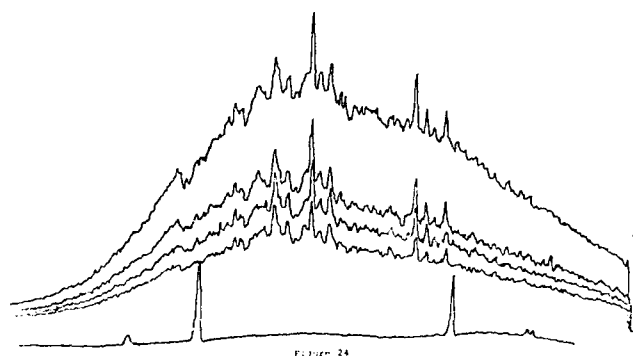


Figure 24

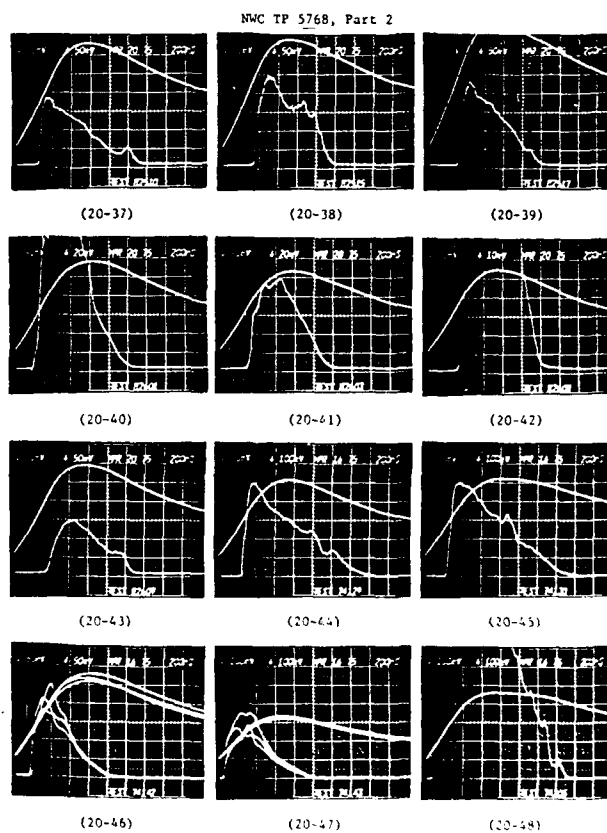


Figure 25



LASER DYES **COAXIAL FLASHLAMP PUMPED**

Wavelength (nm)	Excitation (nm)	Emission (nm)	Quantum Yield (%)	Stokes Shift (nm)	Notes
410-420	350-360	440-450	15	90	Excimer 100
420-430	360-370	450-460	15	90	Excimer 100
430-440	370-380	460-470	15	90	Excimer 100
440-450	380-390	470-480	15	90	Excimer 100
450-460	390-400	480-490	15	90	Excimer 100
460-470	400-410	490-500	15	90	Excimer 100
470-480	410-420	500-510	15	90	Excimer 100
480-490	420-430	510-520	15	90	Excimer 100
490-500	430-440	520-530	15	90	Excimer 100
500-510	440-450	530-540	15	90	Excimer 100
510-520	450-460	540-550	15	90	Excimer 100
520-530	460-470	550-560	15	90	Excimer 100
530-540	470-480	560-570	15	90	Excimer 100
540-550	480-490	570-580	15	90	Excimer 100
550-560	490-500	580-590	15	90	Excimer 100
560-570	500-510	590-600	15	90	Excimer 100
570-580	510-520	600-610	15	90	Excimer 100
580-590	520-530	610-620	15	90	Excimer 100
590-600	530-540	620-630	15	90	Excimer 100
600-610	540-550	630-640	15	90	Excimer 100
610-620	550-560	640-650	15	90	Excimer 100
620-630	560-570	650-660	15	90	Excimer 100
630-640	570-580	660-670	15	90	Excimer 100
640-650	580-590	670-680	15	90	Excimer 100
650-660	590-600	680-690	15	90	Excimer 100
660-670	600-610	690-700	15	90	Excimer 100
670-680	610-620	700-710	15	90	Excimer 100
680-690	620-630	710-720	15	90	Excimer 100
690-700	630-640	720-730	15	90	Excimer 100
700-710	640-650	730-740	15	90	Excimer 100
710-720	650-660	740-750	15	90	Excimer 100
720-730	660-670	750-760	15	90	Excimer 100
730-740	670-680	760-770	15	90	Excimer 100
740-750	680-690	770-780	15	90	Excimer 100
750-760	690-700	780-790	15	90	Excimer 100
760-770	700-710	790-800	15	90	Excimer 100
770-780	710-720	800-810	15	90	Excimer 100
780-790	720-730	810-820	15	90	Excimer 100
790-800	730-740	820-830	15	90	Excimer 100
800-810	740-750	830-840	15	90	Excimer 100
810-820	750-760	840-850	15	90	Excimer 100
820-830	760-770	850-860	15	90	Excimer 100
830-840	770-780	860-870	15	90	Excimer 100
840-850	780-790	870-880	15	90	Excimer 100
850-860	790-800	880-890	15	90	Excimer 100
860-870	800-810	890-900	15	90	Excimer 100
870-880	810-820	900-910	15	90	Excimer 100
880-890	820-830	910-920	15	90	Excimer 100
890-900	830-840	920-930	15	90	Excimer 100
900-910	840-850	930-940	15	90	Excimer 100
910-920	850-860	940-950	15	90	Excimer 100
920-930	860-870	950-960	15	90	Excimer 100
930-940	870-880	960-970	15	90	Excimer 100
940-950	880-890	970-980	15	90	Excimer 100
950-960	890-900	980-990	15	90	Excimer 100
960-970	900-910	990-1000	15	90	Excimer 100

All dyes test using DL-10 with DL-1100 Laser

* Tested using DL-5 with DL-1100 Laser

MOST EFFICIENT DYES

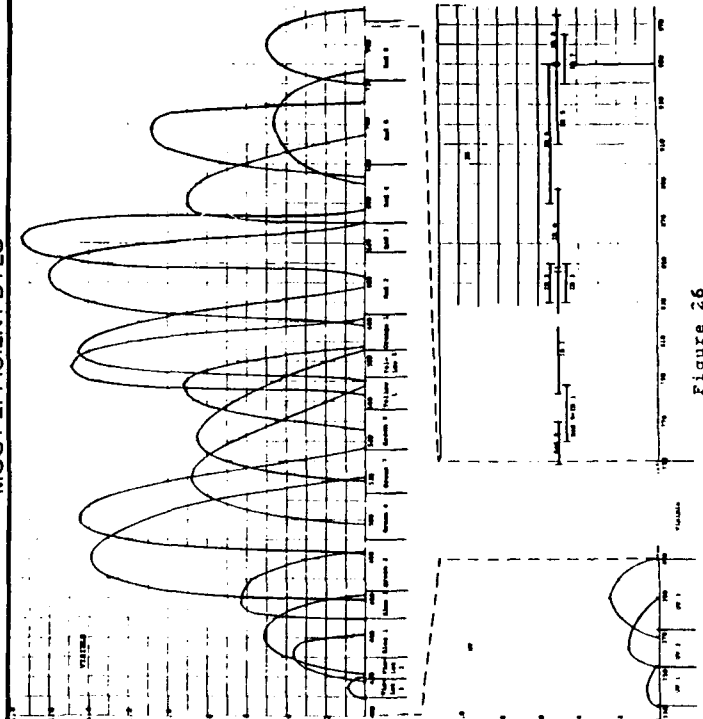


Figure 26

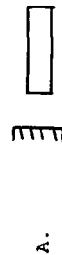
A. Dye Screen Test



Beam Splitter
(glass)

$V_{th} =$
 $\lambda_0 =$

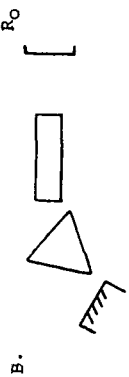
B. Performance Test



$R_0 = 30\%$

$V_{th} = 8-14KV =$ dye good
 $V_{th} > 14KV + R_0$ increase for
diagnostics
 $30\% < R_0 < 85\%$
 $E_0 @ V_{th} + 4KV$

Performance Test



$E_0 + 4/6 KV$
 $\lambda_{min} < \Delta < \lambda_{max}$

C. U.V. filter with caffeine

$\rho_{1/2}^{cf} =$

Data: $V_{th} =$
 $E_0 =$ D#
 $\lambda_b =$
 $\rho_{1/2} =$ No UV filter

Figure 27

NEW EFFICIENT UV LASER DYES THROUGH MOLECULAR ENGINEERING

Hans Güsten and Monika Rinke

Kernforschungszentrum Karlsruhe, Institut für Radiochemie,
7500 Karlsruhe, Postfach 3640, Federal Republic of Germany

Abstract

New UV laser dyes with improved lasing properties (conversion efficiency, tuning range, photochemical stability) superior to those previously available are obtained through molecular engineering. Sterically hindered and ring-bridged *p*-quaterphenyls exhibit laser dye emission in the 345 - 393 nm range with conversion efficiencies (slope efficiency) up to 20 % and with a low lasing threshold when pumped with an excimer laser operating on XeCl or KrF. Ring-bridging of *p*-quaterphenyl on adjacent rings by methylene, oxygen, and ethylene bridges causes a considerable decrease of the conversion efficiency in the order given, while the photochemical stability in dioxane increases with the same order of ring-bridging. From the photophysical parameters (fluorescence quantum yield and fluorescence decay time) of a potential laser dye the conversion efficiency can be predicted using the calculated cross-section of stimulated emission. The effect of the oxazolyl group on *p*-oligophenylenes reveals that terminally flanked oxazolyl groups reduce the laser performance of the *p*-oligophenylenes. When, however, the two oxazolyl groups are directly annellated to an aromatic ring, as in case of the benzo-bisoxazoles, a new class of efficient and photostable UV laser dyes is obtained.

Introduction

The concept of an ideal laser dye with all deactivation processes and attack mechanisms on the laser dye during its operation taken into account has been published recently¹. This hypothetical laser dye consists of a lasing dye moiety in the center encircled by one or two donor dyes covalently bound to it in order to increase the pump light absorption. In addition, a triplet quencher, a singlet oxygen quencher and a radical scavenger for the radicals produced photochemically from the solvents are chemically linked to the laser dye. Though several approaches towards an ideal laser dye have been made^{2, 3} its realization through skilled molecular engineering by organic chemists might remain a dream. Severe limitations on its realization are problems of solubility of the large molecule and, of course, costs of the synthesis.

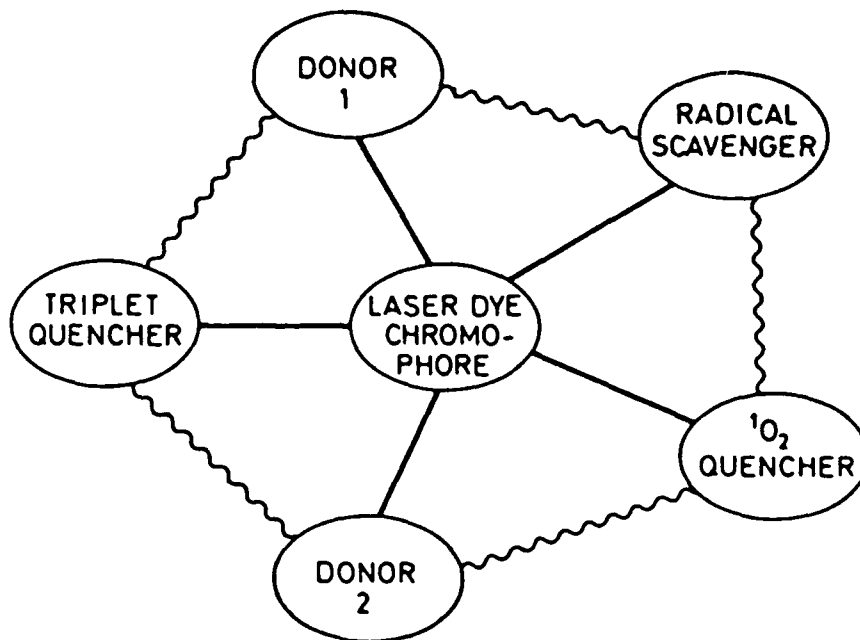


Figure 1 Scheme of an ideal laser dye¹.

More realistic improvements in the development of new and better laser dyes can be achieved through molecular engineering at a lower level. On the basis of spectroscopic and photophysical properties of a potential laser dye whose parent compound is known to show stimulated emission, improved laser dyes can be predicted. Consequently, the improvements of known laser dyes with spectroscopic and photophysical properties taken into account goes far beyond the principle of laser dye selection by trial and error.

In this paper we summarize our results on the laser performance of new tunable UV laser dyes of the class of substituted and ring-bridged *p*-quaterphenyls which have been preselected on account of their spectroscopic and photophysical properties^{4 - 6}.

Results and Discussion

To reach the threshold for stimulated emission of a laser dye in solution the wavelength dependent gain coefficient α for the light amplification must be optimized,

$$\alpha(\lambda) = N_1 \sigma_e(\lambda) - N_0 \sigma_a^0(\lambda) - N_1 \sigma_a^1(\lambda) - N_3 \sigma_a^3(\lambda) \quad (1)$$

stimulated emission
reabsorption
 $S_1 - S_n$ absorption
 $T_1 - T_n$ absorption

or, in other words, the loss processes such as reabsorption, $S_1 - S_n$ absorption and $T_1 - T_n$ absorption, must be minimized^{7, 8}. Once stimulated emission has started, a new loss term comprising all quenching reactions through photochemical degradation products has to be taken into account in Eq. 1. All cross-sections of the loss processes as well as the cross-section of stimulated emission are determined by spectroscopic and photophysical properties of the laser dye. Thus, the cross-section of stimulated emission, σ_e , is essentially determined by

$$\sigma_e = \text{const } Q_f / \tau_f, \quad (2)$$

the quotient of the fluorescence quantum yield, Q_f , and the fluorescence decay time, τ_f , of the laser dye in question. Thus, the organic molecule in question should have a high fluorescence quantum yield and a short fluorescence decay time in order to show stimulated emission. The pump threshold, in turn, is controlled by the reciprocal fluorescence quantum yield.

All these gain and loss processes are controlled and determined by the chemical structure and the geometry of the laser dye.

Sterically hindered and ring-bridged p-quaterphenyls

Among the p-oligophenylenes, the spectroscopic and photophysical properties of the p-quaterphenyls meet best the requirements for a good UV laser dye such as

- matching of the absorption spectrum with the emission of the most common excimer lasers operating on XeCl (308 nm) or KrF (248 nm),
- high molar absorption coefficients at the wavelength of the excimer pump laser⁴⁻⁶,
- broad spectral region of fluorescence and high fluorescence quantum yield^{4, 5},
- short fluorescence decay time^{4, 5},
- large Stokes' shift,
- little overlap of the fluorescence and triplet absorption spectral regions^{4, 5},
- photochemical stability,
- necessary solubility better than 10^{-3} M,
- ease of synthetic procedure.

In addition to excimer laser pumping, ring-bridged p-quaterphenyls have been suggested for flash-lamp pumping⁹. The p-quaterphenyl parent compound shows stimulated emission in the near UV range under flash-lamp excitation¹⁰ and in an XeCl pumped dye laser^{11, 12}. The low solubility, however, precludes its general use as a laser dye. The more soluble derivative 4, 4''-bis-(2-butyloctyloxy)-p-quaterphenyl, generally known as BiBuQ, has the disadvantage of a tenfold lower photochemical stability¹¹.

Tuning range and conversion efficiency

Higher pump light absorption of the common excimer laser emissions by a p-quaterphenyl can be achieved by molecular engineering. Figure 2 shows the influence of substitution by methyl groups and of ring-bridging on the absorption spectra of p-quaterphenyls.

A detailed study on the effect of substitution and ring-bridging in p-quaterphenyls on the spectroscopic and photophysical properties can be found in the work of Berlman¹³. In general, ring-bridging of p-quaterphenyls shifts the pump light absorption towards the wavelength of the XeCl excimer laser emission, methyl groups causing steric hindrance towards that of the KrF excimer laser emission. The same effect of substitution and ring-bridging can be observed in the tuning ranges of the p-quaterphenyls (see Figs. 3 and 4).

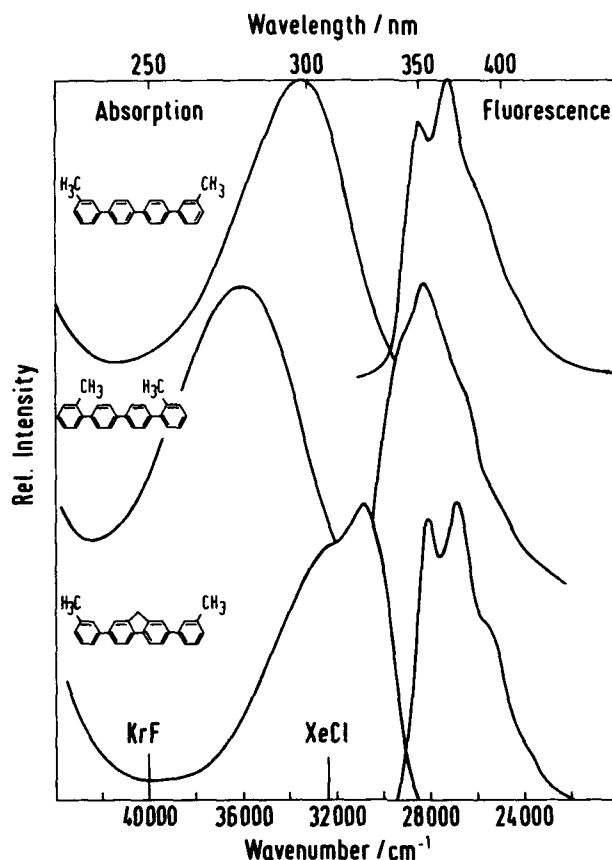


Figure 2 Absorption and fluorescence spectra of 3,3''-dimethyl-p-quaterphenyl, 2,2''-dimethyl-p-quaterphenyl and 2,7-di-m-tolylfluorene in dioxane at room temperature.

Generally, steric hindrance through methyl substitution in p-quaterphenyl produces shorter UV laser dye emission and lower conversion efficiencies. Contrary to methyl substituents, methoxy substituents do not show this hypsochromic effect of the tuning range (see Fig. 3). Ring-bridging of p-quaterphenyl generally gives rise to longer wavelength tuning ranges in comparison to sterically hindered p-quaterphenyls. The conversion efficiency of the ring-bridged p-quaterphenyls decreases in the order of $\text{CH}_2 > \text{O} > \text{CH}_2\text{-CH}_2$ bridging⁵.

Some remark should be added on the conversion efficiency and the tuning range of a laser dye. Both parameters depend on the dye laser system as well as on the mode of dye laser operation. Generally, dye laser performance measured in the narrow-band emission mode of the dye laser^{14, 15} gives rise to smaller tuning ranges and lower conversion efficiencies of a laser dye compared to a dye laser operating in the broad-band mode^{16, 17}. Figure 5 shows this effect for the conversion efficiency of [2,2']bifluorenyl in dioxane. The conversion efficiency is given as a quantum efficiency derived from the slope of a plot of the dye laser output energy vs. the pump energy (slope efficiency)¹⁸. The conversion efficiency measured in the broad-band mode is always higher compared to the narrow-band mode¹⁹. It is understandable that laser dye suppliers tend to report the conversion efficiency measured in the broad-band mode. However, for use in spectroscopy or analytical research the data measured in narrow-band mode are more meaningful.

A comparison of the laser performance of the ring-bridged and the sterically hindered p-quaterphenyls reveals that ring-bridged compounds tend to show smaller tuning ranges. Ring-bridging of p-quaterphenyl gives rise to smaller tuning ranges due to smaller Stokes' shifts of the more planar molecules as compared to sterically hindered p-quaterphenyls. Due to the smaller Stokes' shift, at the concentration used in a dye laser ($\sim 10^{-3} \text{ M}$), the tuning range is curtailed on the high energy side of the fluorescence spectrum⁵.

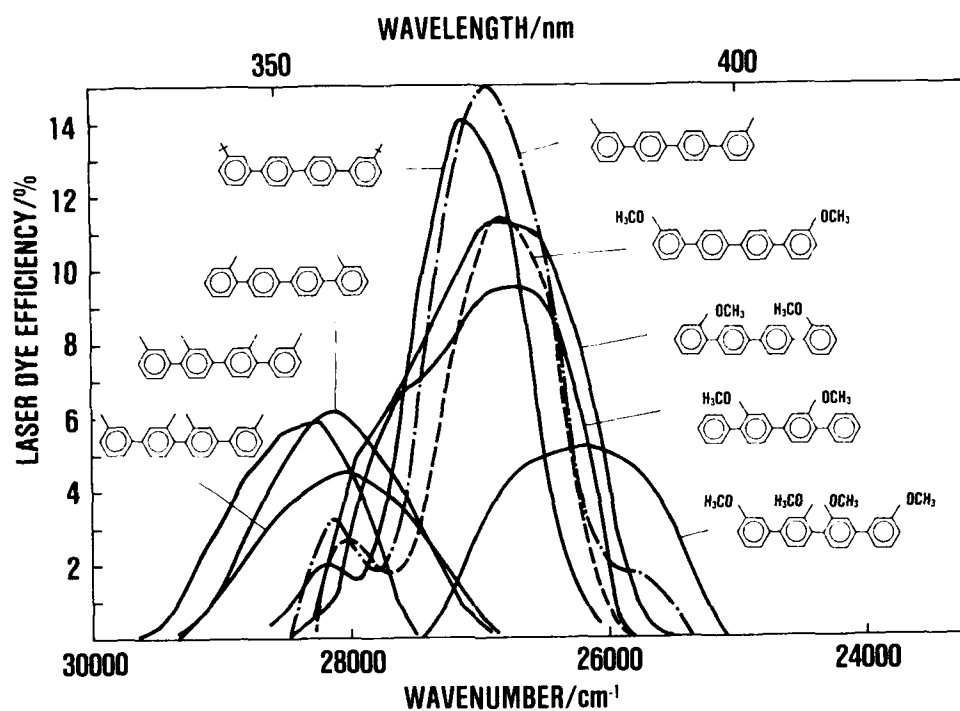


Figure 3 Tuning ranges vs. conversion efficiencies of sterically hindered p-quaterphenyls in dioxane and ethanol (XeCl excimer laser pumping)⁴.

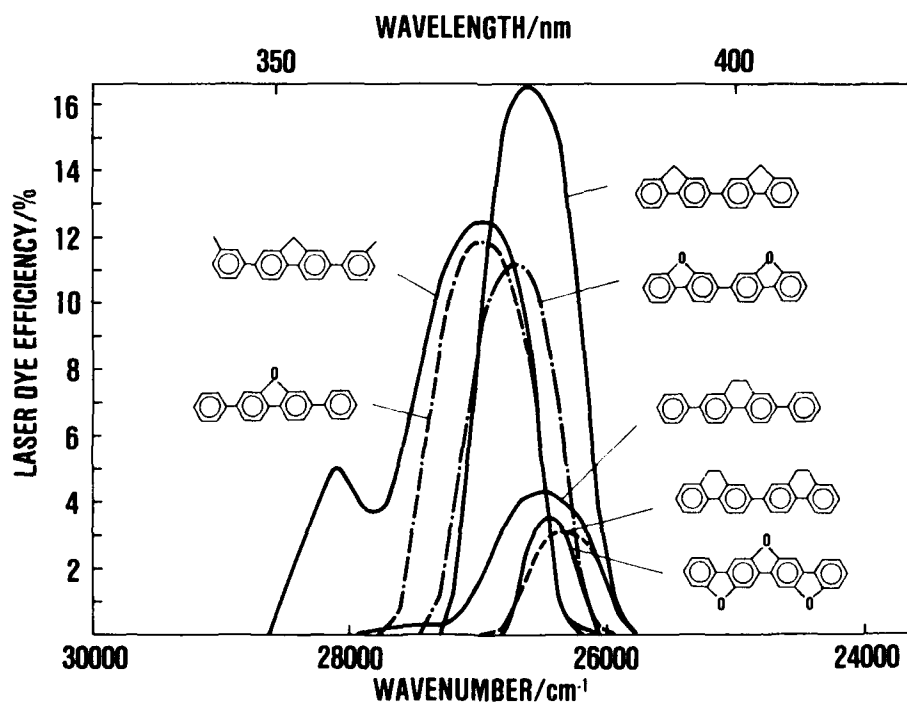


Figure 4 Tuning ranges vs. conversion efficiencies of ring-bridged p-quaterphenyls in dioxane. (XeCl excimer laser pumping)⁵.

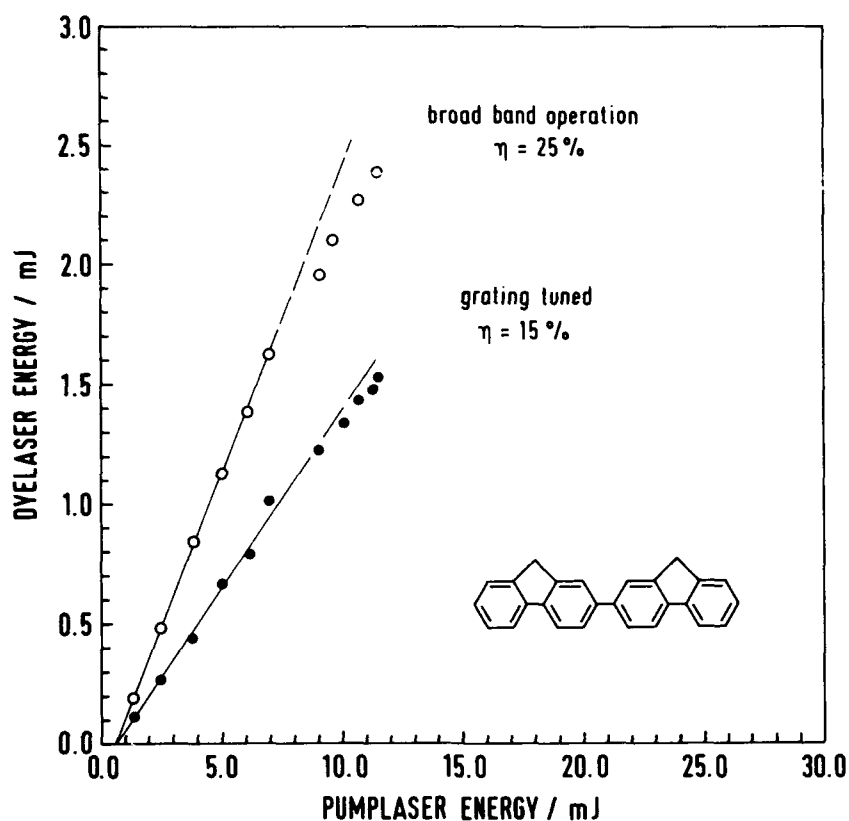
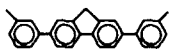
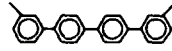
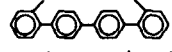
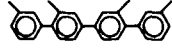
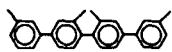
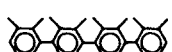


Figure 5 Slope efficiency of [2,2']-bifluorenyl in dioxane (XeCl excimer laser pumping) for different operation modes of the dye laser.

Table 1 summarizes the effect of methyl substitution and ring-bridging on the fluorescence properties and laser performance of the p-quaterphenyls.

Table 1

Fluorescence parameter and laser conversion efficiency of ring-bridged and sterically hindered p-quaterphenyls in dioxane

	Fluorescence λ_{max} [nm]	Fluorescence quantum yield Φ_f [%]	Conversion efficiency η [%]
	369	78	13
	367	77	15
	354	71	6
	354	71	6
	353	76	4.5
	299	6	-

With decreasing planarity of the p-quaterphenyl derivative the fluorescence is blue shifted and the fluorescence quantum yield decreases. Parallel to the decrease of the fluorescence quantum yield also the conversion efficiency of the laser dye decreases.

As was indicated in Eq. 2, the cross-section of stimulated emission of a potential laser dye is determined by the photophysical properties of the laser dye. In Fig. 6 the slope efficiencies of three double ring-bridged p-quaterphenyls are shown together with the photophysical properties of these compounds.

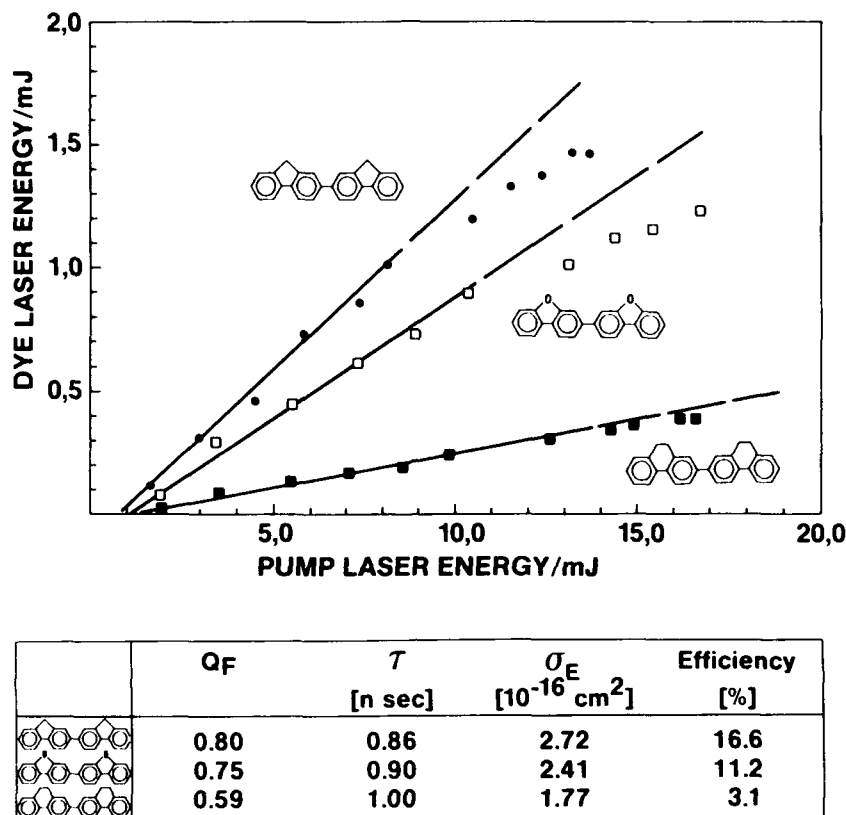


Figure 6 Slope efficiency of [2,2']-bifluorenyl, [3,3']-bidibenzofuranyl and 9,10,9',10'-tetrahydro[2,2']-biphenanthryl in dioxane and their photophysical properties.

The photophysical data given in Fig. 6 show that the conversion efficiency, derived from the slope efficiency, is proportional to the cross-section of stimulated emission σ_E of the laser dye. As, in turn, σ_E is connected via Eq. 2 with the fluorescence quantum yield, Q_f , and the fluorescence decay time, τ , the conversion efficiency of a potential laser dye can be estimated from these photophysical properties. It has been shown that this relation holds for a sizeable number of substituted and ring-bridged p-quaterphenyls⁵.

Photochemical stability

For high-power operation of dye lasers the photochemical stability of the laser dye is as important as the conversion efficiency and the tuning range are. In particular for long-term irradiation experiments with high photon fluxes of the pump laser, the stability of the laser dye can be the determining factor in the choice of a laser dye. The photochemical stability of a laser dye depends on the solvent¹¹ as well as on the photon energy of the pump laser²⁰. It was observed for the sterically hindered and ring-bridged p-quaterphenyls that the photochemical stability is approximately by a factor 10 to 20 better in dioxane than in ethanol^{2, 6}. As Figure 7 indicates, an exponential decay of the dye laser energy is observed with the increase in absorbed energy of the pump laser.

The photochemical stability was measured under comparative conditions, e. g. the concentration of the laser dye was such that at least 99 % of the pump laser light was absorbed in the transversely pumped dye laser cuvette. From the exponential decay curves in Fig. 7 a half-life energy $E_{1/2}$ can be calculated which is the total amount of the absorbed pump laser energy per liter of laser dye solution when the output energy of the dye laser has dropped to 50 % of its initial value. With the known concentration of the laser dye and the photon energy of the excimer laser used, the $E_{1/2}$ value can be expressed in a physically more meaningful lifetime as the number of photons absorbed per laser dye molecule when the output energy

of the dye laser has dropped to half of its initial energy output. A comprehensive investigation of visible and UV laser dye stabilities under excimer laser pumping has been published by Antonov and Hohla²¹.

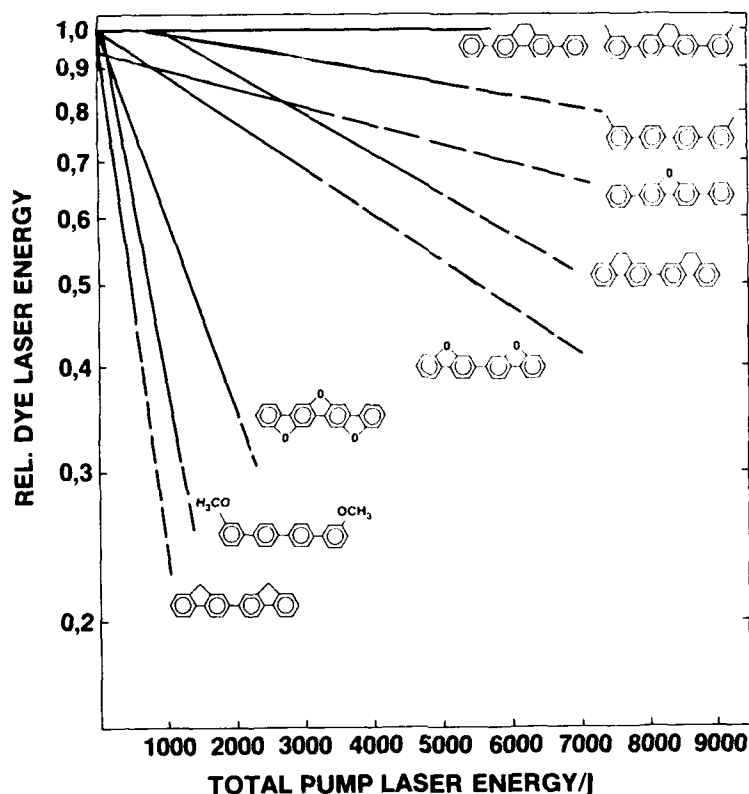
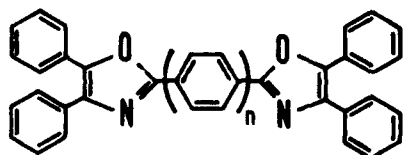


Figure 7 Photochemical degradation of substituted and ring-bridged p-quaterphenyls in dioxane as a function of the total absorbed XeCl pump laser energy.

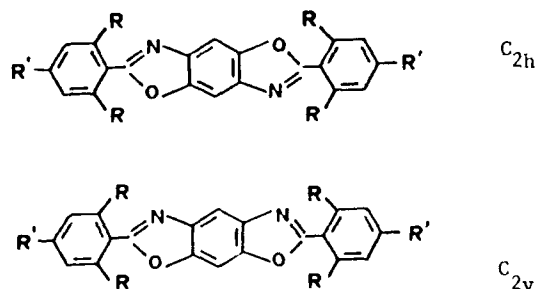
Figure 7 reveals that the photochemical stability of the ring-bridged p-quaterphenyls increases in the order of the bridge $\text{CH}_2 < \text{O} < \text{CH}_2\text{-CH}_2$. Mono ring-bridged p-quaterphenyls are more photostable than double bridged compounds which are, in turn, more stable than triple bridged p-quaterphenyls. It is interesting to note that the most photostable laser dyes of the ring-bridged p-quaterphenyls exhibit the lowest conversion efficiency⁵ (see also Fig. 6). In other words, the higher the conversion efficiency is the lower is the photochemical stability of the ring-bridged p-quaterphenyl. The mono ethylene-bridged p-quaterphenyls such as 2,7-diphenyl-9,10-dihydrophenanthrene are among the most stable photochemical laser dyes. Up to a total pump energy absorbed of 50 000 Joule per liter no photochemical degradation was noticeable. Methyl substitution of p-quaterphenyl results in much more stable laser dyes than methoxy substitution in the same position⁴.

Laser performance of oxazolyl substituted p-oligophenylenes

New aspects of laser dyes in molecular engineering can be derived by attaching oxazolyl groups to a known laser dye. It is well known that the oxazolyl group has a considerable chromophoric effect on the fluorescence of aromatic molecules because it enhances the fluorescence quantum yield without affecting the rate of non-radiative deactivation of the excited singlet state²². This fluorophoric effect of the oxazolyl group had been used in industrial fluorescers such as optical brighteners and organic scintillators long before laser dyes were discovered. We have synthesized p-oligophenylenes with two terminal oxazolyl groups as chromophores and a class of molecules, the benzo-bisoxazoles, in which two oxazolyl fluorophores are directly annellated to one aromatic ring. The benzo-bisoxazoles represent two classes of isomeric molecules of C_{2h} and C_{2v} symmetries.



$n = 0 - 3$



The photophysical properties such as fluorescence quantum yield and fluorescence decay time indicated that these compounds should lase^{23, 24}. Both classes of oxazoles, the w,w'-bis-oxazolyl-(2)-p-oligophenylenes and the 2,6-diphenylbenzo-bisoxazoles, show fluorescence quantum yields between 0.70 and 0.80 with fluorescence decay times well under one nanosecond^{23, 24}. Fig. 8 shows the chromophoric effect of the terminal oxazolyl groups in 4,4'-bis-[4,5-diphenyloxazolyl-(2)]-biphenyl ($n = 2$) which shifts the absorption and the fluorescence spectrum towards longer wavelengths. Compared to the p-oligophenylenes^{4, 5, 25} the triplet absorption is also strongly shifted to longer wavelengths. A strong energy separation between the singlet and triplet absorption bands is desirable in order to promote stimulated emission in a potential laser dye. This effect in regard to lasing has been extensively discussed by Pavlopoulos^{26, 27}.

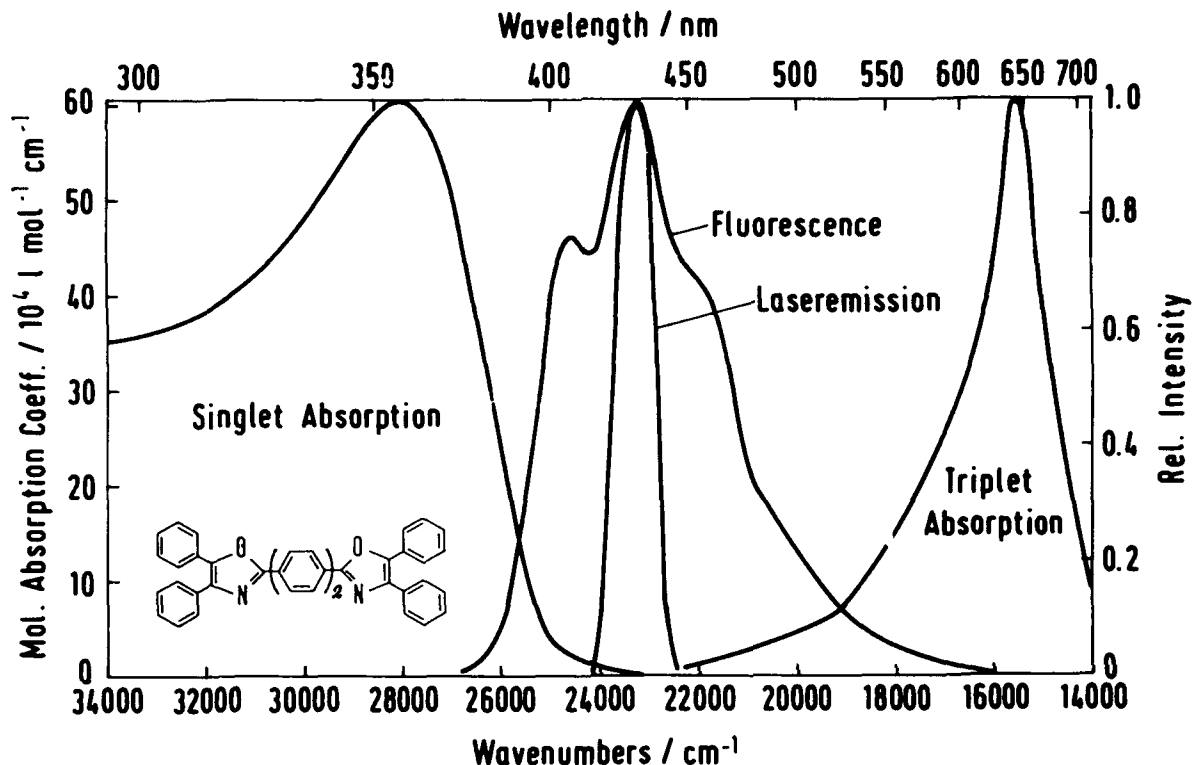


Figure 8 Singlet absorption, fluorescence, laser emission and triplet absorption spectra of 4,4'-bis[4,5-diphenyl-oxazolyl-(2)]biphenyl ($n = 2$) in dioxane at room temperature.

In Table 2 the laser performance data have been summarized of the substituted benzo-bisoxazoles and the w,w'-bis-oxazolyl-(2)-p-oligophenylenes.

Table 2

Laser performance of substituted 2,6-diphenyl-benzo-bisoxazoles (C_{2h} and C_{2v}) and w,w'-bis-oxazolyl-(2)-p-oligophenylenes ($n = 0 - 3$) in dioxane under XeCl excimer excitation

R'	R	Tuning range [nm]	Slope efficiency [%]	Photostability	
				Half-lifeenergy [10 ⁴ J/l]	Mean lifetime [photons / molecule]
C _{2h}					
C(CH ₃) ₃	H	381 - 393	14.1	303	7880
CH ₃	CH ₃	367 - 397	12.3	96	3800
C _{2v}					
C(CH ₃) ₃	H	371 - 384	5.1	57	1522
CH ₃	CH ₃	359 - 383	7.8	7	228
n = 0		409 - 421	3.0	2.3	53
n = 1		423 - 435	4.6	0.4	12
n = 2		421 - 438	8.6	0.4	16
n = 3		419 - 435	7.3	0.65	29

The conversion efficiency increases with the number of phenyl rings between the terminal oxazolyl groups. In the class of the isomeric benzo-bisoxazoles the symmetrical benzo-bisoxazoles are much better laser dyes than the unsymmetrical ones. Furthermore, the photochemical stability of the symmetrical benzo-bisoxazoles is much larger than that of the unsymmetrical benzo-bisoxazoles²⁴. This has been attributed to a much smaller overlap of the triplet absorption with the fluorescence spectrum in case of the symmetrical benzo-bisoxazoles²⁴.

Molecular engineering consisting in the introduction of steric hindrance in the parent benzo-bisoxazoles leads to a broader tuning range (see Fig. 9) due to a larger Stokes' shift. Introducing bulky methyl groups in the ortho, ortho' positions of the 2,6 positioned phenyl rings results in an unstructured absorption and less structured fluorescence spectrum and, hence, a broader tuning range.

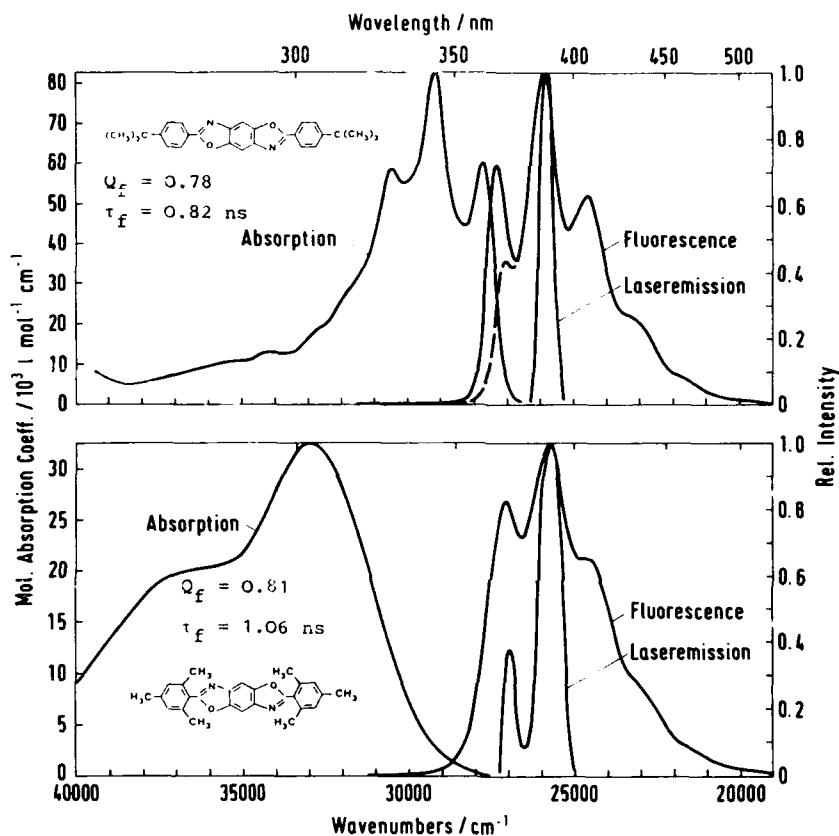


Figure 9 Singlet absorption, fluorescence spectra and tuning ranges of 2,6-di(4-tert.butylphenyl)-benzo[1,2d:4,5d'] bisoxazole and 2,6-dimesityl-benzo-[1,2d; 4,5d'] bisoxazole in dioxane (XeCl excimer laser pumping)²⁴

Furthermore, through molecular engineering the absorption maximum of the lower benzo-bisoxazole in Figure 9 can be shifted towards the 308 nm emission wavelength of the XeCl pumping laser and the solubility of this laser dye is increased due to the six methyl groups. The fluorescence quantum yield and the fluorescence decay time have been entered in Fig. 9. Due to a longer fluorescence decay time of the sterically hindered 2,6-dimesityl-benzo-bisoxazole this dye has a slightly lower conversion efficiency and a lower photochemical stability²⁴. While the photochemical stability of the w,w'-bis-oxazolyl-(2)-p-oligophenylenes is poor²³, the benzo-bisoxazoles with photochemical lifetimes on the order of thousands of absorbed photons per molecule are very photostable UV laser dyes²⁴. While the photophysical properties of the isomeric benzo-bis-oxazoles are almost identical differences can be noticed in their laser performance data²⁴. This demonstrates that besides the geometry the symmetry of a molecule can also have a large effect on the lasing properties of a potential laser dye.

References

1. F. P. Schäfer, *Laser Chem.* **3**, 265 (1983)
2. F. P. Schäfer, Z. Bor, W. Lüttke and B. Liphardt, *Chem. Phys. Lett.* **56**, 455 (1978)
3. B. Liphardt, B. Liphardt and W. Lüttke, *Optics Commun.* **38**, 207 (1981)
4. M. Rinke, H. Güsten and H. J. Ache, *J. Phys. Chem.* **90**, 2661 (1986)
5. M. Rinke, H. Güsten and H. J. Ache, *J. Phys. Chem.* **90**, 2666 (1986)
6. H. Güsten, M. Rinke and H. O. Wirth, *Appl. Phys. B*, in press

7. O. G. Peterson, J. P. Webb, W. C. McColgin and J. H. Eberly, *J. Appl. Phys.* **42**, 1917 (1971)
8. C. V. Shank, *Rev. Mod. Phys.* **47**, 649 (1975)
9. J. M. Kauffman, C. J. Kelly, A. Ghiorghis, E. Neister, L. Armstrong and P. R. Prause, *Laser Chem.* **7**, 343 (1987)
10. H. W. Furumoto and H. L. Ceecon, *IEEE J. Quant. Electron.* **QE6**, 262 (1970)
11. P. Cassard, P. B. Corkum and A. J. Alcock, *Appl. Phys.* **25**, 17 (1981)
12. R. S. Taylor and S. Minailov, *Appl. Phys. B* **38**, 131 (1985)
13. I. B. Berlman, *Handbook of Fluorescence Spectra of Aromatic Molecules* (Academic Press, New York, 1971)
14. L. D. Ziegler and B. S. Hudson, *Optics Commun.* **32**, 119 (1980)
15. D. M. Guthals and J. W. Nibler, *Optics Commun.* **29**, 322 (1979)
16. W. Zapka and U. Brackmann, *Appl. Phys.* **20**, 283 (1979)
17. O. Uchino, T. Mizunami, M. Maeda and Y. Miyazone, *Appl. Phys.* **19**, 35 (1979)
18. G. Marowski, *Optica Acta* **23**, 855 (1976)
19. M. Rinke and H. Güsten, *Ber. Bunsenges. Phys. Chem.* **90**, 439 (1986)
20. E. A. Stappaerts, *Appl. Opt.* **16**, 3079 (1977)
21. V. S. Antonov and K. L. Hohla, *Appl. Phys. B* **32**, 9 (1983)
22. A. Reiser, J. L. Leyshon, D. Saunders, M. V. Mijovic, A. Bright and J. Bogie, *J. Am. Chem. Soc.* **94**, 2414 (1972)
23. M. Rinke, H. Güsten and J. Heinze, *J. Photochem. Photobiol. A* **41**, 157 (1988)
24. H. Güsten, M. Rinke, C. Kao, Y. Zhou, M. Wang and J. Pan, *Optics Commun.* **59**, 379 (1986)
25. T. G. Pavlopoulos and P. R. Hammond, *J. Am. Chem. Soc.* **96**, 6568 (1974)
26. T. G. Pavlopoulos, *IEEE J. Quantum Electron.* **QE9**, 510 (1973)
27. T. G. Pavlopoulos, *Spectrochim. Acta* **42 A**, 47 (1986).

SYNTHESIS OF NEW COUMARIN LASER DYES BASED ON 1,1,7,7-
TETRAMETHYL-8-HYDROXYJULOLIDINE

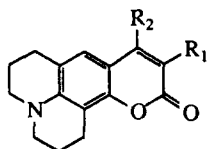
Chin H. Chen* and John L. Fox

Corporate Research Laboratories
Eastman Kodak Company
Rochester, New York 14650, U.S.A.

Abstract

Synthesis of 1,1,7,7-tetramethyl-8-hydroxyjulolidine and new coumarin dyes derived therefrom is described. The new synthesis offers advantages in ease of workup, purification and large scale preparation. These new dyes have similar spectral properties as those of the old coumarins. Tested by excimer laser, Coumarin 102T exhibits slightly better lasing efficiency than C-102.

Coumarins are the most widely used organic laser dyes for the blue-green region of the visible spectrum. Eastman Kodak Company manufactures and markets a large number of coumarin derivatives. Among which, the most interesting from the standpoint of quantum fluorescence efficiency and bathochromic spectral shifts are the 7-julolidylcoumarins as shown in the general structure 1.



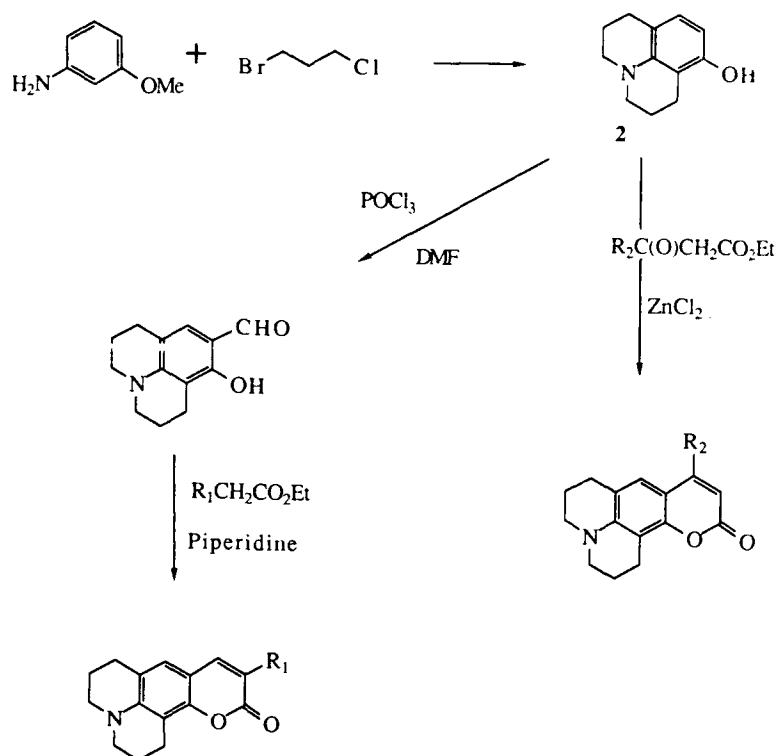
1

The synthesis of these julolidylcoumarins is depicted in Scheme 1. The most critical step in the entire synthesis is the preparation of 8-hydroxyjulolidine which was formed in about 30% yield by refluxing m-anisidine with excess 1-bromo-3-chloropropane.¹ In large scale preparation, the results were not always reproducible, thus, making the subsequent purification difficult. The major byproduct from this reaction has been identified to be the 8-methoxyjulolidine which apparently was not readily demethylated under the reaction condition. Examination of the mechanism under which the desired product is formed suggests that the bisalkylation and subsequent cyclization are probably favored by basic or near neutral condition, while the demethylation to eliminate CH₃X is favored under strong acidic condition. Therefore, it is difficult to optimize the reaction condition to favor the formation of 8-hydroxyjulolidine exclusively since the reaction turns gradually more acidic as more HBr and HCl evolve as reaction progresses.

Attempts to react m-aminophenol with 1-bromo-3-chloropropane directly failed to give any desired product, presumably, due to complications from competitive O-alkylation.

In search of a suitable substitute of 8-hydroxyjulolidine (2) so that the laser dyes derived from it would have similar and hopefully, better lasing characteristics as those of the original julolidylcoumarins, we have designed the 1,1,7,7-tetramethyl-8-hydroxyjulolidine depicted in 5 based on the following considerations: (1), To reduce the cost of large-scale preparation, it is desirable to start with m-aminophenol which is about five times cheaper than m-anisidine; (2), To facilitate the cyclization process during the synthesis of the julolidine ring, a better electrophile is required. Based on our previous work involving the ring closure of tetramethyl-5H,9H-quino[3,2,1-de]acridine² in acidic mediums, tetramethyl derivative would provide a more stable carbonium ion which is expected to enhance the electrophilic cyclization under acidic conditions; (3), To substitute the 1,1,7,7-benzylic hydrogens with methyl groups may enhance the photo stability of the julolidylcoumarin dyes as benzylic positions are often susceptible to oxidation; (4), Molecular orbital calculations of Coumarin 102 vs Coumarin 102T using a MOPAC AM1 program³ show only a slight increase of the LUMO level from -0.424 eV (C-102) to -0.404 eV (C-102T) while the HOMO level remains the same at about -8.165 eV. Most HOMO and LUMO coefficients as well as

Scheme 1. Synthesis of Julolidylcoumarins



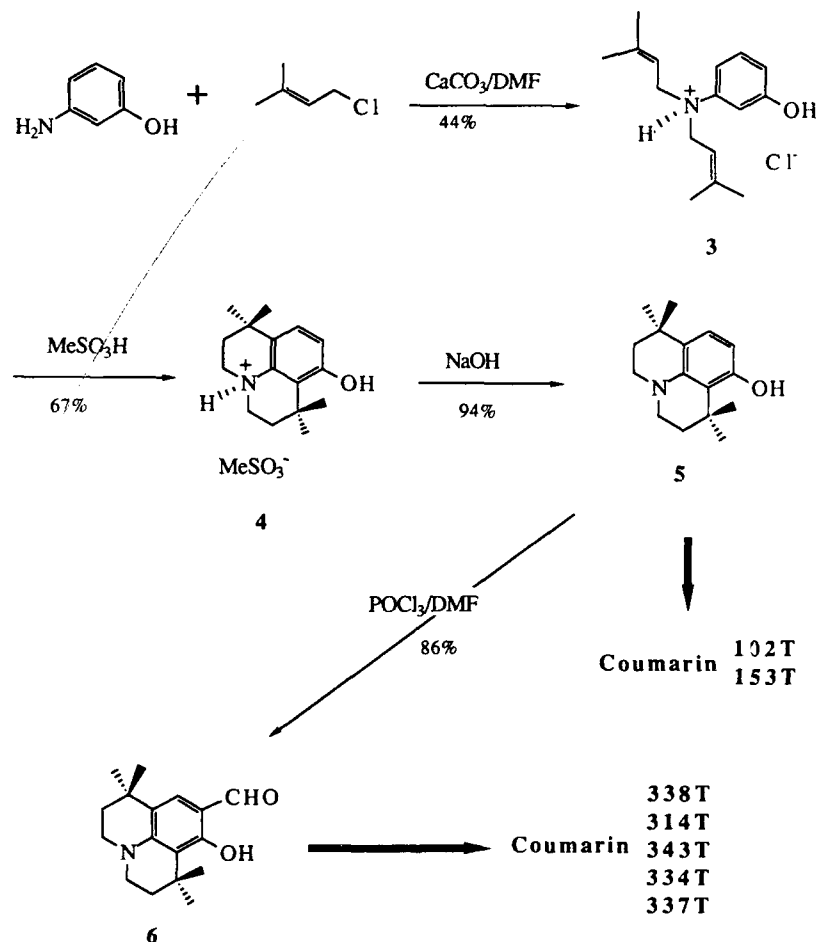
certain key bond angles and bond lengths in the ground states of both Coumarin 102 and 102T are similar. The major perturbation in the geometry of the new molecule lies in the bond angle of the *gem*-dimethyl substituted carbon near C-5 which is reduced to 83.4° in Coumarin 102T, while the other tertiary substituted carbon is tetrahedral which is around 110.7°. This distortion which apparently is due to the steric compression between the *gem*-dimethyl's and the *peri*-hydrogen at C-5 may contribute to further rigidize the julolidine ring system.

The synthesis of 1,1,7,7-tetramethyl-8-hydroxyjulolidine is outlined in Scheme 2.

The preparation of N,N-bis(allyl)-*m*-hydroxyaniline (**3**) as the HCl salt proceed in 44% yield. While the yield is relatively low, the material is readily isolated in pure form by precipitation from DMF with water and an isopropyl ether wash. The subsequent cyclization in methane sulfonic acid proceeds smoothly in 67% yield and is isolated in pure form by precipitation from the acid with water.

In order to facilitate the synthesis of the salicylaldehyde derivative which is needed for the subsequent coumarin dye synthesis, the aminium salt **4** needs to be deprotonated in a separate step which is effected in a two-phase, ethyl acetate/aqueous sodium hydroxide system in 94% yield. The final Vilsmeier reaction to introduce the formyl group proceeds in 86% yield. Considering the ease of isolation and purification involved in each of the intermediates, this synthesis is highly conducive to large-scale preparation. Overall yield of 8-hydroxy-tetramethyljulolidine from *m*-aminophenol is 28%.

Scheme 2. Synthesis of 8-Hydroxy-tetramethyljulolidine



The corresponding tetramethyljulolidylcoumarin derivatives are prepared similarly as depicted in Scheme 1. Their code names, absorption maxima, extinction coefficients, excitation and fluorescence maxima (all measured in EtOH) as well as the corresponding fluorescence quantum efficiencies are compared in Table 1. For comparison purposes, the same code names are used for both julolidylcoumarins with identical substituents R_1 and R_2 , except that the tetramethyl derivatives will bear a suffix T. As in the unsubstituted case, Coumarin 343T was prepared from Meldrum's acid.

In general, the tetramethyljulolidylcoumarins have similar (in certain cases, they are slightly better) fluorescence quantum efficiency as the old julolidylcoumarins. The dyes derived from 8-hydroxytetramethyljulolidine are slightly more soluble in both polar and non-polar solvents. This solubility difference may find applications where high solubility is desirable, such as EtOH in which most lasing performance data are measured.

Table I. Comparison of Spectral Properties Between Tetramethyljulolidyl and (Julolidyl)coumarins

Code	R ₁	R ₂	Abs λ max (nm)	ε ^a × 10 ⁴	Excit λ max (nm)	Fl λ max (nm)	η ^{**}
C-102T (102)	H	Me	388 388	2.14 2.19	452 452	464 464	0.60 0.58
C-338T (338)	CO ₂ Bu-t	H	432 432	4.24 4.28	432 432	476 476	0.79 0.78
C-314T (314)	CO ₂ ET	H	434 434	4.54 4.50	430 430	476 486	0.79 0.78
C-343T (343)	CO ₂ H	H	442 445	3.30 3.77	426 426	476 476	0.52 0.50
C-334T (334)	COMe	H	450 450	4.60 4.51	452 452	494 494	0.84 0.85
C-337T (337)	CN	H	442 442	4.18 4.33	444 444	486 486	0.80 0.83
C-153T (153)	H	CF ₃	420 422	1.96 1.97	430 430	532 532	0.50 0.48

^aε = Extinction coefficient

^{**}η = Fluorescence Quantum Yield

The lasing characteristics of these new tetramethyljulolidylcoumarins under excimer laser (XeCl) excitation at 308 nm⁴ and certain improved lifetime results under flashlamp pumped lasing conditions⁵ will be published elsewhere⁶. In these lasing measurements, a significant effort was devoted to ensure that dye lasing characteristics were assessed under identical experimental conditions.⁶ Narrow-linewidth performance of C-102T was assessed using the multiple-prism Littrow oscillators developed by Duarte and Piper.^{7,9} Here, 5% conversion efficiency was obtained at a linewidth ca. 1 GHz at FWHM.

References

1. Z. Valenta, P. Deslongchamps, R. A. Ellison, and K. Wiesner, J. Amer. Chem. Soc., **86**, 2533 (1964).
2. J. L. Fox, C. H. Chen, and J. F. Stenberg, Org. Proc. Prep. Internal., 169 (1985).
3. M. S. J. Dewar, E. G. Zoebisch, E. F. Healy, J. J. P. Stewart, J. Amer. Chem. Soc., **107**, 3902 (1985).
4. F. J. Duarte, C. H. Chen, and J. L. Fox, presented at the International Conference on Lasers '87, Lake Tahoe (1987), paper HO.7.
5. J. J. Ehrlich, S. D. Russell, S. Patterson, presented at the International Conference on Lasers '87, Lake Tahoe (1987), paper TH.7.
6. C. H. Chen, J. L. Fox, F. J. Duarte and J. J. Ehrlich, Applied Optics, **27**, February issue (1988).
7. F. J. Duarte and J. A. Piper, Opt. Commun. **35**, 100 (1980).
8. F. J. Duarte and J. A. Piper, Appl. Opt. **23**, 1391 (1984).

DYE CHROMOPHORES: TO LASE OR NOT TO LASE

James H. Bentley
U.S. Army Missile Command
Directed Energy Directorate
Redstone Arsenal, AL 35898-5245

Abstract

Lasing dyes form a gain medium possessing nanosecond fluorescence lifetimes, a large homogeneous nature, and extreme tunability. Low electrical efficiency, exacerbated by facile intersystem crossing, places strong constraints on the organic structures used for dye lasers.

Introduction

When dyes were first observed to lase, one of the first things done was to thumb through the chemical catalogs for dyes to see which could be made to lase. There were lots of dyes available. Euphoria soon turned to disillusionment, followed rapidly by panic and punishment of the innocent who were brash enough to predict great, huge, and wonderful varieties of lasing dyes for laser scientists. We are now in the formative stages of a definition of the problem, with which we are having quite a struggle.

During the disillusionment phase we discovered that the great majority of clothes dyes don't lase; and many more that did lase didn't do it very well. Somewhere in the disillusionment or panic phases we discovered that the triplet state is absolutely ubiquitous. That is if we kept the laser pulse going long enough, the triplet state population would grow to the point that triplet absorption losses were terrible no matter the dye. Now this is not to say that laser pulses cannot be stretched to many microseconds. They can, with the use of low k_{st} dyes and triplet state "quenchers", but at greatly reduced lasing levels generally.

Background

A typical molecular energy state diagram, Fig. 1, shows the time scale of the photophysical interaction of organic molecules with electromagnetic radiation. The times of excitation and deexcitation are generally typical, although certain times, such as the singlet/triplet or triplet/singlet intersystem crossing lifetimes, may vary considerably. These lifetimes correlate to their respective rate constants k_{st} and k_{ts} .

The fastest time is a photonic absorption, which corresponds to the time it takes a photon traveling at the speed of light in the medium to traverse the spacial extent of a typical dye molecule. If one assumes that a photon of a well defined wavelength is perhaps a couple of wavelengths long, then it takes a photon traveling at a velocity of say 2×10^{18} Angstroms per second about 10^{-15} seconds to traverse a point. If a molecule is located at that point and possesses a possible resonance for the photon wavelength, then absorption can occur. Looking at it another way, if a Bohr orbital electron is assumed to move at about 10^{16} Angstroms/second, then it can traverse a distance of 10 Angstroms in that same 10^{-15} second. ¹ One to

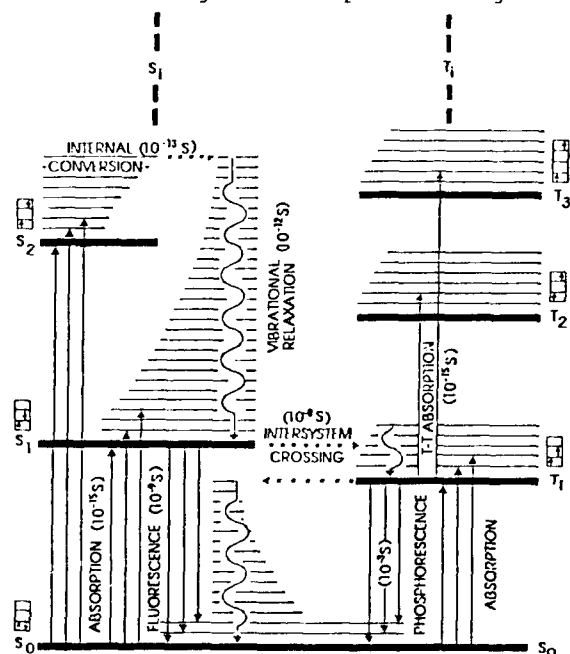


Fig. 1. Jablonski Diagram: Principal Photo-physical Processes in Laser Dyes

- 1.) HIGH EPSILON
- 2.) SMALL k_{st}
- 3.) LARGE SERVICE LIFETIME
- 4.) LONGER SINGLET (S_1) LIFETIME
- 5.) SHORTER TRIPLET (T_1) LIFETIME
- 6.) MINIMIZED S_x AND T_x MANIFOLD
ABSORPTION FOR LASER LINE

Fig. 2. Some Desirable Dye Characteristics

ten Angstroms is the order of the dipole size for a typical laser dye molecule.

The slowest times are the intersystem crossing times, in which case an electron must perform a spin flip, a zeroth order forbidden transition. These times vary enormously from 10^{-8} seconds to perhaps 30 seconds of natural lifetime. The single interaction, which for the most part, determines these lifetimes is a magnetic vector field couple, occurring in such a fashion so that a torque may be applied to the electron through its magnetic spin vector. This event requires a magnetic field varying spatially (or temporally) in the order of the size of the electron's own spin magnetic field.

Whether deexcitation occurs via fluorescence (10^{-9} sec) or phosphorescence (10^{-3} sec) there exists plenty of time for nuclear molecular motion to occur. This means that excited state dye molecules may change their physical shapes greatly, considering that nuclear motion single events are in the order of 10^{-13} to 10^{-12} seconds. This also allows time for solvent molecule re-orientation corresponding to dye molecule shape changes, implying that solvent indeed may be important to laser dye performance. This phenomenon is, of course, already well known.

Analysis

To truly define the problem of laser dyes, one needs to establish a successful model of a dye structure based, of necessity, on the proper meshing of quantum mechanics (QM) and observed data. Observed data alone is useful but inadequate. QM alone is impossible. Even a poor predictive model can point directions for the synthetic organic chemist. This can be of great aid considering the time and effort synthesis often takes. Any model should consider the desired characteristics listed in Fig. 2.

A partial list of specific structural contributors to the above requirements are found in Figures 3 and 4. These restrictions are obviously not separately independent, the asterisked items being exemplary.

One can choose to build a rigid, extended chromophore and expect considerable self-absorption for a laser frequency toward the intense part of the fluorescence spectrum. Or one can choose to incorporate rotation within part of the chromophore, and accept the reduced extinction coefficient that results. This is seen in Figure 5.

This method will generally yield a nice large Stokes shift and one will often observe a "natural" laser line (broad band resonator) somewhere close to the fluorescence maximum, as indicated in Fig. 6.

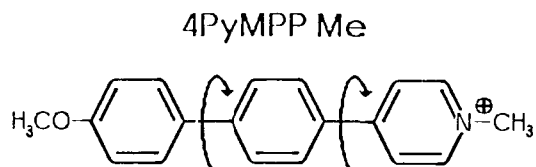
The largest pulse energy dyes are of the former, rigid chromophore type, in which advantage is taken of the homogeneous nature of laser dyes to "drain energy", so to speak, from the fluorescence band as a whole into a

- KETONIC CARBONYL - *TRIPLET FORMATION*
- BENZYLIC PROTONS - *EASILY OXIDIZED*
- POOR π ORBITAL OVERLAP - *LOW ϵ*
- * ● FREE ROTATION - *LOW ϵ*
- $N \rightarrow \pi^*$ EXCITATION - *TRIPLET FORMATION*
- * ● RESTRICTED ROTATION - *LOW STOKES SHIFT*
- $-\text{NO}_2$ GROUPS - *TRIPLET FORMATION*
- $-\text{C}=\text{C}-$ (NON-AROMATIC) - *DIMERIZATION*
- HIGH ATOMIC # ELEMENTS - *TRIPLET FORMATION*
- EXTENDED CONJUGATED STRUCTURES WITH LARGE RING CURRENTS - *TRIPLET FORMATION*
- $-\text{N}=\text{N}-$ GROUPS - *TRIPLET FORMATION*

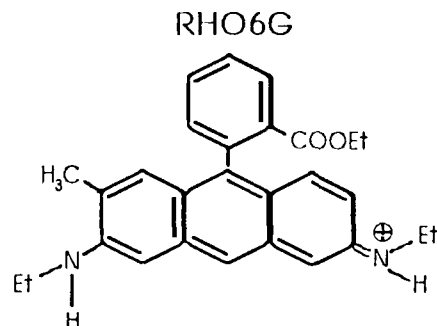
Fig. 3. Negative Dye Molecule Features

- HIGH ϵ 'S - *GOOD PUMPLIGHT ABSORPTION*
- CHARGE SEPARATION (PUSH - PULL) - *INCREASED ϵ AND STOKES SHIFT*
- * ● FREE ROTATION - *LARGE STOKES SHIFT*
- STRUCTURES THAT EXCITE $\pi \rightarrow \pi^*$ - *LOW K_{ST}*
- * ● RESTRICTED ROTATION - *HIGH ϵ*
- WIDE FLUORESCENCE BAND - *GOOD HOMOGENEOUS EXTRACTION OPPORTUNITY*
- LINEAR ORIENTED STRUCTURES - *LOW K_{ST}*

Fig. 4. Positive Dye Molecule Features



"FREE" ROTATION



"RESTRICTED" ROTATION

Fig. 5. Dye Molecular Structure Characteristics

laser line located typically far out on the long wavelength skirt of the fluorescence curve. One would like to predict that advantage could be taken of both extremes of structure so that a small amount of rotational freedom within a chromophore could increase the Stokes shift, while the large part of the chromophore was rigid with the corresponding large extinction coefficient. Such an ideal structure, coupled with the right auxochromes could yield an efficient, high energy dye.

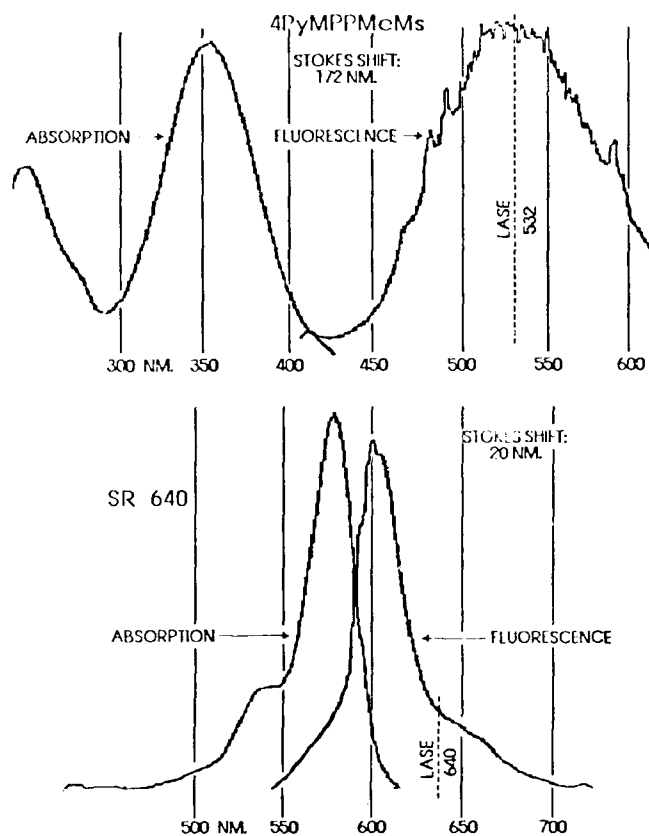


Fig. 6. Dye Stokes Shifts vs Wavelengths Absorption and Fluorescence Spectra (in nm)

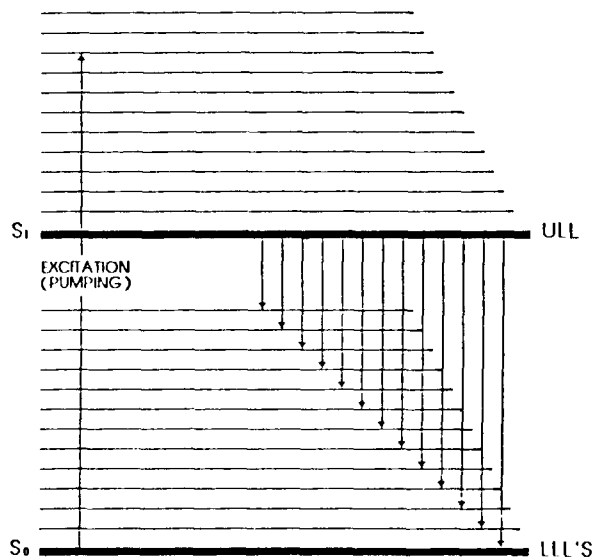


Fig. 7. Idealized Homogeneous Fluorescence Lasing

Now some mention of the concept of homogeneous lasers must be made since the concept is extremely important relative to how much laser line energy one can expect to extract from a given laser system. As illustrated in Fig. 7, if a laser system is truly perfectly homogeneous, then it has only one possible upper laser level (ULL) and the probabilities for spontaneous radiative deexcitation to any of a myriad of possible lower laser levels (LLL) are equivalent. This means that all the metastable pump energy "stored" in the lasing moiety is located in one quantum state (ULL) and that, if the system will lase at all, this total amount of energy can be lased out of the gain medium in one "line" that has a radiative decay to a single LLL. Reality is never as clean as the ideal, of course.

One can think of several ways to tune a laser, such as intracavity Fabry-Perot etalons, wavelength selective mirrors, prism assemblies, reflective refraction gratings, or combinations of each of these. One can specifically choose a laser line (and thus a LLL) or allow a spectrally unbiased optical system to choose its own line at which to establish maximum positive gain for stimulated emission. The latter case will result, in the case of dye lasers, in a laser line of say, 25-35

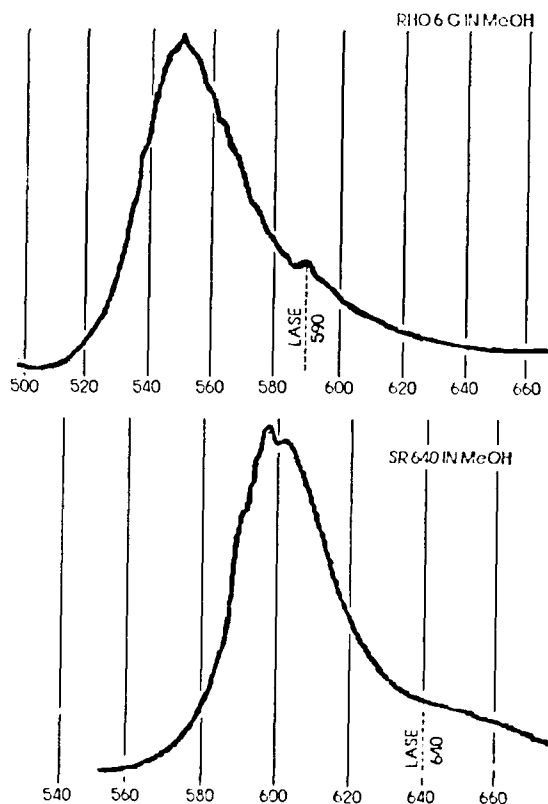


Fig. 8. Homogeneous Nature of Rhodamine Dyes Fluorescence Spectra (in nm)

Angstroms FWHM, demonstrating that while the dye laser is not a naturally perfect homogeneous laser, it nevertheless is a good approximation.

Another way of viewing this phenomenon is that for a perfectly homogeneous laser, all the possible ULL energy can be lased out of the system at any wavelength, under the fluorescence curve, that also has a system optical gain greater than one.

This is demonstrated nicely by Rhodamine 6G and Sulforhodamine 640 in Fig. 8. The fact that superior dye laser action is obtained from these dyes from the long wavelength skirt of the fluorescence curve is an indication of a well developed homogeneous nature to dye lasers. This is perhaps very fortunate for dye laser users since the self-absorption of singlet state manifolds for greatly rigidized structures is evidently quite large under most of the fluorescence curve.

It is one thing for a synthetic organic chemist (our molecular architect) to consider ways to provide molecules with high extinction coefficients and large fluorescent efficiencies; it is another matter to selectively shape a fluorescence curve to order.

Things may not be hopeless however, in that certain work by George Bird (Rutgers University) indicates the possibility of enhancing the long wavelength skirt of the long wavelength peak of the fluorescence curve, while sacrificing the peak's maximum fluorescence intensity.⁶ If this "red enhancement" can be done without shifting singlet absorption along also, lasing might be improved considerably for chromophores with rigid structures and the corresponding high extinction coefficients.

Conclusions

Triplet state absorption is extremely important to laser dye performance; so much so, that a dye with an extinction coefficient of only about 6000 can be made to lase, when triplet absorption is apparently not a problem.⁷ While it is evident that certain structural moieties and certain functional groups are quite efficient in generating triplet states in dye molecules, it is not evident that all auxochromes do not generate triplets at some rate or other. Neither is it apparent that any laser dye molecule can be made "triplet proof", so to speak, so that efficient lasing is terminated solely by means of thermal considerations. The difficulty does lie in the lack of adequate modeling. Inadequate modeling in turn lies not only in the predictive problems for any particular series of dye structures such as simple paraphenylenes, but in the fact that lasing moieties such as bimanenes⁷ exist at all. Who would have predicted a laser from a bimane type structure? And how many different molecular organic structures are there that might lase, which structures might be as different from the bimanenes as the bimanenes are different from oxazoles?

Any theory which hopes to treat new and better dyes must be able to deal with greatly disparate molecular structures; and any model which hopes to predict new individual structures must be able to deal effectively with the manner in which dye structures delocalize and stabilize electron density.⁸ To use an analogy, it appears that a good laser dye should be able to resonate with electromagnetic energy in the same manner as a bell or tuning fork resonates with mechanical energy. Can we learn something from the bell analogy and are our molecular architects up to the task of assembling such structures? This investigator feels that the greatest gain for future laser dyes will come with considerably rigid, (but not totally rigid) chromophores, with highly charge-dispersed push-pull mechanisms,⁸ in a lasing system that enhances the natural homogeneous nature of the dye fluorophore.

Such requirements may be applied to conventional or new and unusual structures, utilizing perhaps new and unusual atomic elements. The illuminating factor, ultimately, will always be how the electrons arrange over the changing molecular shape.

Bibliography

1. Turro, N.J., "Modern Molecular Photochemistry", Benjamin/Cummings, 1978.
2. McGlynn, Azumi, Kimoshita, "Molecular Spectroscopy of the Triplet State", Prentice-Hall, 1969.
3. Berlman, I.B., "Handbook of Fluorescence Spectra of Aromatic Molecules", AP, 1971.
4. Maeda, M., "Laser Dyes", AP, 1984.
5. Rhys-Williams, A.T., "An Introduction to Fluorescence Spectroscopy", Perkin-Elmer Publication.
6. Bird, George, Rutgers University; Unpublished Discussions.
7. Pavlopoulos, T.G.; Boyer, J.H.; Politzer, I.R.; Lau, Chun. "Laser Action from Syn-Methyl, Methyl Bimane", Journal of Applied Physics, Vol 60, p. 4028, 1986.
8. Kauffman, J.; Bentley, J.H., "Effect of Various Anions and Zwitterions on the Lasing Properties of a Photostable Cationic Laser Dye." Laser Chemistry, in press.

TWO-PHOTON LASER PHOTOCHEMISTRY OF A COUMARIN LASER DYE

Robert J. von Trebra, Robert P. Mahoney, and Tad H. Koch

Department of Chemistry and Biochemistry
University of Colorado, Boulder, CO 80309-0215

Abstract: Irradiation of 7-dimethylamino-4-methylcoumarin in aerobic ethanol solution with the partially focused output of a xenon chloride excimer laser at 308 nm resulted in the formation of yellow oligomeric material derived from the ethanol solvent. The efficiency of formation of the yellow material was dependent on the intensity of the excimer laser excitation. The oligomers are proposed to interfere with dye stimulated emission, and their formation is proposed to be initiated by sequential two-photon dye absorption followed by energy transfer to solvent. DABCO, 1,4-diazabicyclo[2.2.2]octane, suppressed the formation of oligomers and, consequently, is useful for prolonging the lifetime of coumarin and other dyes in excimer, nitrogen, and Nd:YAG laser pumped dye lasers.

Aminocoumarin dyes such as 7-dimethylamino-4-methylcoumarin (1, Coumarin 311) and 7-diethylamino-4-methylcoumarin (2, Coumarin 460) have been used extensively in dye lasers to produce tuneable light in the blue green region. A shortcoming of this class of dyes has been photoreactivity leading to the production of material absorbing at the fluorescence wavelength of the dye and consequently, interfering with stimulated emission. A photoproduct absorbing in the region of 460 nm which was identified earlier by Winters and co-workers from irradiation of Coumarin 460 is 7-diethylamino-4-carboxycoumarin (3).¹ Our investigations and those of others have revealed several photochemical processes of the aminocoumarins which destroy the dyes.²⁻⁵ These are formation of dye radicals in bimolecular processes and reaction of the dye radicals, dye triplet sensitization of singlet oxygen formation and subsequent dye oxidation by singlet oxygen, and reaction of dye excited states with triplet oxygen. Possibly the formation of 3 results from the latter process. None of these processes accounts for the rapid formation of photoproducts absorbing the region of 460 nm from XeCl excimer laser pumping of aerobic solutions of aminocoumarin dye in dye lasers.

We have recently observed that the efficiency of formation of products which interfere with stimulated emission from XeCl excimer laser excitation is a function of the degree of focusing of the XeCl excitation beam.⁶ Higher optical density was achieved with more focusing. Chromatographic separation of the higher molecular weight products from irradiation of an aerobic, 5×10^{-3} M, ethanol solution of Coumarin 311 afforded recovered coumarin in high yield, a small quantity of solvent adduct (7-N-(2-hydroxypropyl)-N-methylamino-4-methylcoumarin), and a yellow oil. Gaseous products, predominantly hydrogen and butane, were also formed as well as acetaldehyde. Spectroscopic and combustion analyses of the yellow oil indicated that it resulted from oxidative oligomerization of the solvent. Analogous results were obtained when Coumarin 311 was similarly irradiated in aerobic methanol. With benzene as the solvent, a black insoluble benzene polymer was rapidly formed.

The yellow oil from partially focused XeCl excimer laser excitation of the aminocoumarin laser dyes in ethanol or methanol solvent absorbs in the region of 460 nm. Since this is the predominant material formed absorbing in this region, we have proposed that the mixture of oxidized solvent oligomers is the material which interferes with stimulated emission in excimer laser pumped coumarin dye lasers.

The dye sensitized solvent oligomerization bears some resemblance to the photochemistry observed from vacuum UV excitation of the respective solvents.⁷⁻¹⁰ Consequently, we have proposed that the photochemistry in the dye laser results from upper dye excited state sensitization of the solvent followed by solvent C-H and C-O bond homolyses.⁶ Oligomers result from radical combination reactions and subsequent radical oxidations. The upper dye state is probably a triplet state resulting from absorption of a second photon by the first triplet state or energy transfer from a first excited dye singlet state to a first excited dye triplet state. The difference in the solvent photochemistry from that upon vacuum UV excitation possibly stems from the proposed difference in solvent excited state multiplicity, the concentration of radicals produced, and the presence of oxygen. Energy transfer from an upper triplet state of triphenylene to solvent has been implicated in the formation of a triphenylene solvent adduct.¹¹

Earlier we noted that DABCO, 1,4-diazabicyclo[2.2.2]octane, could be used to extend the useful lifetime of a variety of laser dyes in several types of dye lasers, especially excimer, nitrogen and Nd:YAG pumped dye lasers.¹² Its presence in aerobic solutions of the dyes inhibited formation of products absorbing at the fluorescence wavelengths of the dyes. We have now observed that DABCO inhibits the formation of the yellow solvent oligomers possibly by serving as an electron transfer triplet quencher and as a free radical scavenger.

Acknowledgment: The authors acknowledge the U. S. Army Research Office (contracts numbers DAAG-29-85-K-0014 and DAAL-87-K-0053) for financial support.

References

1. B. H. Winters, H. I. Mandelberg and W. B. Mohr, Appl. Phys. Lett. 25, 723 (1974).
2. R. von Trebra and T. H. Koch, Appl. Phys. Lett. 42, 129 (1983).
3. R. von Trebra and T. H. Koch, J. Photochem. 35, 33 (1986).
4. G. Jones, II, R. W. Bergmark and W. R. Jackson, Opt. Commun. 50, 320 (1984).
5. G. Jones, II, and W. R. Bergmark, J. Photochem. 27, 179 (1984).
6. R. von Trebra and T. H. Koch, J. Photochem. 41, 111 (1987).
7. R. J. Buenker, G. Olbrich, H. -P. Schuchmann, B. L. Schurmann and C. von Sonntag, J. Am. Chem. Soc. 106, 4362 (1984).
8. N. C. Yang, D. P. C. Tang, D. -M. Thap and J. S. Sallo, J. Am. Chem. Soc. 88, 2951 (1966).
9. C. von Sonntag, Z. Phys. Chem. N.F. 69, 292 (1970).
10. H. R. Ward and J. S. Wishnok, J. Am. Chem. Soc. 90, 5353 (1968).
11. M. Lamotte, J. Phys. Chem. 85, 2632 (1981); M. Lamotte, J. Pereyre, J. Jousset-Dubien and R. Lapouyade, J. Photochem. 38, 177 (1987).
12. R. J. von Trebra and T. H. Koch, Chem. Phys. Lett. 93, 315 (1982); T. H. Koch and R. J. von trebra, Stabilizer of Organic Dye Lasers, U.S. Patent No. 4,428,859, Jan. 31, 1984.

Effects of Detergents, Viscosity Modifiers, and Temperature Differential on the Output of Certain Laser Dyes

R. F. Kubin, A. N. Fletcher, M. C. Pietrak, and D. E. Bliss
Chemistry Division, Research Department
Naval Weapons Center, China Lake, California 93555-6001

Abstract

The effects of environment can significantly affect the performance of laser dyes. The addition of viscosity modifiers and detergents and control of the coolant-dye solution temperature differential (Δ) of flashlamp pumped dyes all have individual effects which are not totally independent of one another. Several viscosity modifiers were investigated with the goals of increasing the temperature differential range (FWHM) and reducing the optical distortion effects of thermal transients on a dye solution when lased in a static condition. At an established viscosity range, all viscosity modifiers reduced the lasing output. This effect was investigated by measurement of the fluorescence quantum yield of rhodamine 6G in various concentrations of the viscosity modifier Klucel H in a water-alcohol solvent. The quantum yield appeared to go through a maximum and fall sharply as the concentration of Klucel H was increased. Sodium dodecylsulfate added to water solutions of certain pyridinium oxazole salts was found to increase the lasing output by factors of two to greater than ten. Operating at the optimum temperature differential between coolant and dye solution can improve the output by factors of two to five. We note a synergistic effect on rhodamine 6G using both a detergent and viscosity modifier to increase the temperature differential range to 1.1°C.

Introduction

For a number of years this laboratory has been engaged in the study of factors that affect the output and lifetime of flashlamp pumped dye lasers.¹⁻¹⁸ This work continues our efforts to develop long lifetime, high output dye laser systems that can be field qualified. The effects of three parameters on several pyridinium oxazole salts and rhodamine 6G have been investigated with two goals in mind: (1) to find the optimum system among some very good dyes we have recently evaluated;¹⁹ and (2) to find conditions that would broaden the temperature differential range of a dye, where the temperature differential is defined as the coolant temperature minus the dye solution temperature in a flowing dye laser system. We have looked at the effects of poly(ethylene oxide), poly(vinylpyrrolidone), and several cellulosic viscosity modifiers. In general, increased viscosity reduced the lasing output. We chose three detergents, all well-known, that have been reported to increase the lasing output of certain organic dyes.²⁰ These three, ammonyx LO, triton X-100, and sodium dodecyl sulfate (SDS), are quite different chemically and one might reasonably predict the outcome when they are added to organic dyes that are themselves salts. Only SDS gave significant increases in output but not in all cases. We also wish to emphasize, in flowing dye systems, that the coolant dye temperature differential is an important experimental parameter and needs to be determined for each dye system. We have now observed a temperature differential range in excess of +1.0°C. With the dye systems studied, we have observed no negative Δ s. The coolant is always warmer for maximum output.

Experimental

Our dye laser system is a Phase R DL10Y laser head in a triaxial configuration. The cavity has a 100% reflector wide band rear mirror and for these tests used a 50% output coupler. Temperatures of coolant and dye solution can be controlled to 0.01°C as previously described.¹⁷ Quantum yield measurements were made using a Spex F 222 fluorometer. For the latter measurement, the dye solution absorbance was ≤ 0.014 resulting in dye concentrations in the 10^{-7} M range. Concentrations of dyes in the dye laser were 2×10^{-4} M. Viscosities were measured using a Brookfield digital readout viscometer.

Viscosity Effects

We chose a viscosity range of 1 to 5 poise to minimize the effects of thermal flux on the dye solution. For the viscosity studies, the laser was fired under two conditions, dye static and both dye and coolant static. In order

to avoid absorption effects as much as possible, we set a limit of $\leq 1\%$ by weight viscosity modifier. We also required that the viscosity modifier be shear stable and pseudo plastic. Of the eleven viscosity modifiers evaluated, five were chosen for study. These were Klucel H [a (hydroxypropyl cellulose)], hydroxyethyl cellulose methocel A (a hydroxymethyl-co-hydroxypropyl cellulose), polyox [poly(ethylene oxide)], and poly(vinylpyrrolidone). All but polyox met our criteria. Polyox, a shear sensitive polymer, was chosen to study the effect of shear stability. The first three listed form essentially a homologous series. In the viscosity range chosen, all modifiers reduced the lasing output compared to the same dye-solvent system without modifier. As the concentration of viscosity modifier is increased, the temperature differential range does increase but the increase at best can only be described as modest. Figures 1 and 2 show the effect of Klucel H on rhodamine 6G.

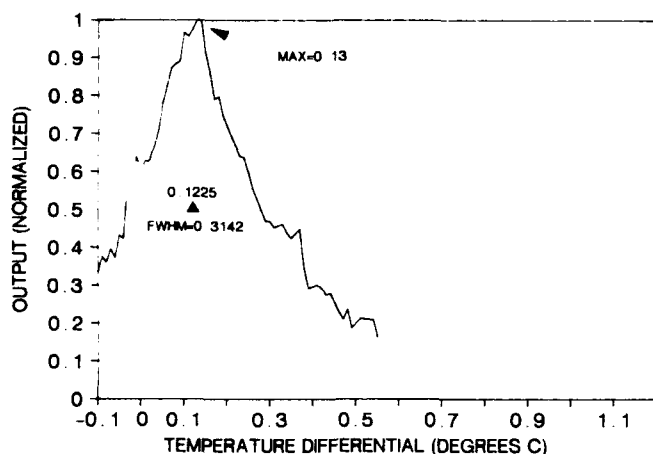


FIGURE 1. RH590 C1 + 0.5% Klucel H in EtOH/H₂O, Coolant Varied, 35 J Input, Max Output = 32.45 mJ.

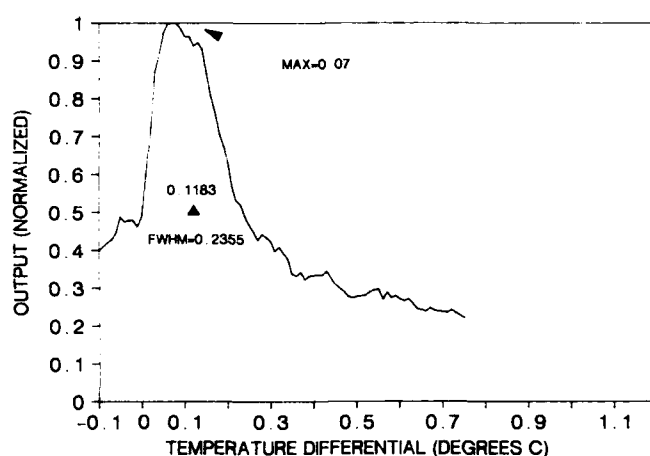


FIGURE 2. RH590 C1 + 0.3% Klucel H in EtOH/H₂O, Coolant Varied, 35 J Input, Max Output = 40.93 mJ.

In order to more fully investigate the reduced lasing output, we determined the fluorescence quantum yield of rhodamine 6G in various concentrations of Klucel H. Klucel H was chosen because it had the least effect of the modifiers studied on the lasing output. Table 1 gives the results of these measurements. The last two entries in the table are our measured quantum yields for the pure solvents. It would appear that there is a broad maximum peaking at about 0.3% Klucel H; however, it should be recognized that all the reported quantum yields in the range 0 to 0.4% Klucel H are within the experimental error of one another. At concentrations greater than 0.4% Klucel H, there is a definite fall off in the quantum yield. Unfortunately, it took 0.5% Klucel H to achieve a viscosity in our desired range. Again, comparison of Figures 1 and 2 show that upon lowering the Klucel H concentration to 0.3% the output increased by 25%. Because these experiments are quite time consuming we have not as yet tried a still lower concentration of Klucel H to see if the output falls.

TABLE 1. Fluorescence Quantum Yields Of Rhodamine 6G Perchlorate In EtOH/H₂O + Klucel H.

% Klucel H	Q	%Klucel H	Q
0.0	0.86	0.5	0.81
0.1	0.87	0.7	0.76
0.2	0.89	1.0	0.58
0.3	0.90	EtOH	0.95
0.4	0.89	H ₂ O	0.82

Detergent Effects

It has been known for some time that in highly polar solvents (essentially water) that certain detergents can increase the lasing output of particular dye classes. The detergent effect is ascribed to the breakup of dye dimers, trimers, etc., that form in highly polar solvents due to micelle formation of the detergent where a dye molecule

becomes associated with a micelle. Depending upon the hydrophobic, hydrophilic, and/or ionic properties of both dye and detergent micelle, the dye molecule can be inside or outside of the micelle. Each micelle, as a rule of thumb, may have 25 to 50 molecules of detergent. However, Chang and Kaler²¹ determined the molecular weight of the SDS micelle in water and deuterium oxide. From their results the number of SDS molecules per micelle in water is about 100. We investigated the effect of SDS on rhodamine 6G from mole ratios of less than 10:1 to 600:1. Initially, as SDS is added to rhodamine 6G, the solution turns purple and lasing is quenched. A plot of output versus SDS mole ratio shows an initial sharp drop in output followed by significant increases in output up to a mole ratio of about 100:1. With increase in the mole ratio, the curve reaches a maximum in output then gradually decreases by less than 10% at mole ratios exceeding 600:1. The value, 1.2% SDS, was chosen as being well into the plateau and corresponds to a mole ratio of about 400:1.

Figure 3 shows the structure of the five dyes tested. The nomenclature follows our recent paper.¹⁹ Ox 12 had the highest output (and short lifetime) of any pyridinium oxazole dye we have tested to date. Ox 15 has a reduced output but a lifetime rivaling that of Ox 2. Ox 26 was not reported previously.¹⁹ This dye was made and tested because of some evidence that alkyl substitution in the 4 position on the oxazole ring while reducing lifetime would increase output. Under our present test conditions, Ox 26 was poorer in both lifetime and output than Ox 2 (unsubstituted in the 4 position on the oxazole ring), which is the longest lived moderate output dye we have tested. Table 2 gives the lasing parameters of three of the pyridinium oxazole dyes tested plus some baseline data for comparison. For those not familiar with these constants, Table 3 gives some actual output energies for several energy input values. It can be seen that SDS increases the output of these dye systems by factors of 2 to >10. Ox 4 and Ox 15 are not included in these tables because, somewhat surprisingly, SDS had no effect on these two dyes. Again the effect of SDS on the value of the FWHM of the temperature differential range can only be described as modest, increasing somewhat as SDS is added.

TABLE 2. Lasing Data With SDS In Water.

DYE	1000 K*	t, J	1/C, MJ/l	FOM, kJ/l
Ox 2 - air	2.02	24.9	1,203.0	2,430.0
Ox 2 - argon	2.72	23.8	2,008.0	5,461.0
Ox 12 - air	2.39	20.8	19.68	47.0
Ox 12 - argon	2.82	17.1	44.40	125.2
Ox 26 - air	1.40	24.2	172.9	242.0
Ox 26 - argon	2.27	23.5	685.3	1,555.0
Ox 2 - argon - no SDS	1.64	33.9
Ox 12 - argon - no SDS	1.2	43.2	143.0	172.0
Ox 26 - argon - no SDS	0.472	48.9
RHO 6G - air - no SDS	1.05	28.2

*K is the slope efficiency, t is the lasing threshold, 1/C is the lifetime, FOM is the figure of merit.

TABLE 3. Comparison Of Lasing Outputs, mJ.

SYSTEM	Input, J				
	40	45	50	55	60
Ox 2/H ₂ O/air	2.7	6.0	10.6	15.4	20.1
Ox 2/H ₂ O/SDS/air	29.2	37.9	48.1
Ox 2/H ₂ O/Ar	10.1	18.2	25.7	36.9	44.6
Ox 2/H ₂ O/SDS/Ar	40.4	54.6
Ox 12/H ₂ O/Ar	...	2.7	8.4	13.6	19.2
Ox 12/H ₂ O/SDS/Ar	40.3 (35 J)
Ox 26/H ₂ O/air	0.5	2.8	5.1
Ox 26/H ₂ O/SDS/air	19.8	25.5	32.8	39.6	45.4
Ox 26/H ₂ O/Ar	...	3.5	8.1	12.5	16.8
Ox 26/H ₂ O/SDS/Ar	35.6	49.9

The other two detergents are non-ionic or strongly basic and one might predict they should have no effect on the pyridinium oxazole salts tested. This was essentially true for triton X-100. In the case of ammonyx LO (lauryl dimethylamine oxide) quenching or reduced output was observed which may be a pH effect because the pH of ammonyx LO is high (~11).

Temperature Differential Effect

We first reported our results on this parameter in a paper presented at Lasers '85.¹⁷ At that time we observed values of $\Delta = +0.2^\circ\text{C}$. We have now observed values of $\Delta > 1.0^\circ\text{C}$. Drake and Morse²² first reported an analysis of a coaxial flashlamp pumped dye laser cavity and predicted a value of $\Delta = 0.0$. Since that analysis, some papers have set the limits of $\Delta = \pm 0.05^\circ\text{C}$.^{23,24} We find that Δ is an experimental parameter of the particular dye, solvent-coolant system and must be determined for each case. If one operates within the FWHM range, the output can be from two to five times higher than values outside this range. Also, we note that on the dye systems that we have thus far tested the value of Δ has always been positive, i.e., the "coolant" is always warmer than the dye - which makes sense theoretically.²² In Figure 4 we present an interesting result. We had tested rhodamine 6G in the poly(hydroxyethyl cellulose) and found that its output was greatly reduced. At this point we added SDS to see if the output could be improved. The output was restored to that of rhodamine 6G with just SDS. The viscosity was reduced by a factor of about five. However, there was a synergistic effect in that range of Δ (FWHM value) increased from about a third of a degree to 1.1°C , the largest value so far observed. Also, Δ itself increased to over 1°C . At present we have no explanation for this effect of both viscosity modifier and detergent. Increasing the value of Δ reduces the criticality of the coolant - dye solution temperature control.

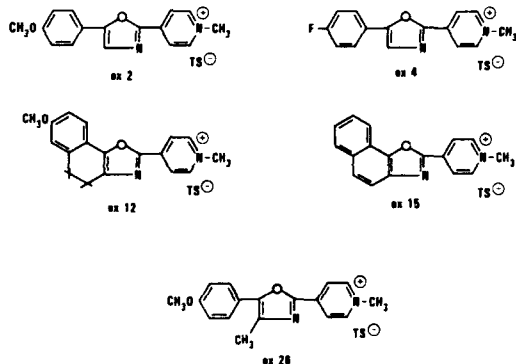


FIGURE 3. Dye Structures Investigated.

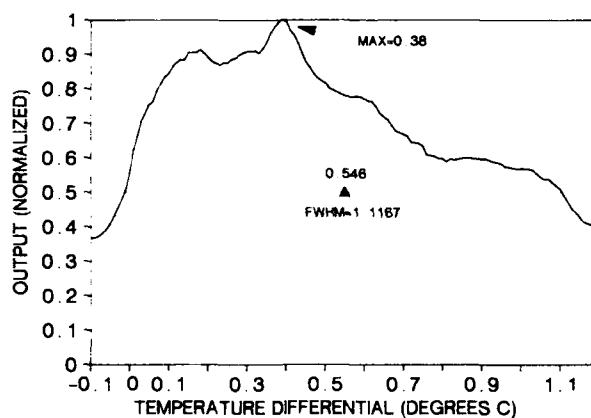


FIGURE 4. RH590 C1 + 0.5% QP-100 mH + 1.2% SDS in H₂O, Coolant Varied, 35J Input, Max Output = 32.87 mJ.

Acknowledgment

We wish to thank the following companies who supplied us samples of various viscosity modifiers: Dow Chemical Company (methocel), GAF Corporation (poly(vinylpyrrolidone)), Hercules (Klucel H), and Union Carbide (polyox, hydroxyethyl cellulose).

References

1. A. N. Fletcher, D. A. Fine, and D. E. Bliss, Appl. Phys 12, 29 (1977)
2. A. N. Fletcher, Appl. Phys. 12, 327 (1977)
3. A. N. Fletcher, Appl. Phys. 14, 295 (1977)
4. A. N. Fletcher, Appl. Phys. 16, 93 (1978)
5. A. N. Fletcher, and D. E. Bliss, Appl. Phys. 16, 289 (1978)
6. A. N. Fletcher, Appl. Phys. 22, 227 (1980)
7. A. N. Fletcher, R. H. Knipe, and M. E. Pietrak, Appl. Phys. 27, 93 (1982)
8. A. N. Fletcher, and R. H. Knipe, Appl. Phys. B29, 139 (1982)
9. R. F. Kubin and A. N. Fletcher, J. of Lumin 27, 455 (1982)
10. R. H. Knipe, Opt. and Quant. Electron. 15, 19 (1983)
11. A. N. Fletcher, Appl. Phys. B31, 19 (1983)
12. R. H. Knipe and A. N. Fletcher, Chem. Phys. Lett. 99, 49 (1983)
13. A. N. Fletcher, D. E. Bliss, and J. M. Kauffman, Opt. Comm. 47, 57 (1983)
14. A. N. Fletcher, R. A. Henry, R. F. Kubin, and R. A. Hollins, Opt. Comm. 48, 352 (1984)
15. R. H. Knipe and A. N. Fletcher, Opt. and Quant. Electron. 17, 47 (1985)
16. A. N. Fletcher, and M. E. Pietrak, Appl. Phys. B37, 151 (1985)
17. A. N. Fletcher, D. E. Bliss, M. E. Pietrak, and G. E. McManis III, presented at the International Conference on Lasers '85, Las Vegas (1985), Proceedings pg. 797.
18. A. N. Fletcher, M. E. Pietrak, and D. E. Bliss, Appl. Phys. B42, (1987)
19. A. N. Fletcher, R. A. Henry, M. E. Pietrak, D. E. Bliss, and J. H. Hall, Appl. Phys. B43, 155 (1987)
- 20a. O. G. Peterson, S. A. Fuccio, and B. B. Snively, Appl. Phys. Lett. 17, 245 (1970)
b. Z. Konefal, E. Lisicki, and T. Marszalek, Acta Phys. Pol. A (Poland) A52, 149 (1977)
21. N. J. Chang, and E. W. Kaler, J. Phys. Chem. 89, 2996 (1985)
22. J. M. Drake, and R. I. Morse, Opt. Comm. 12, 132 (1974)
23. R. M. Schotland, Appl. Opt. 20, 912 (1981)
24. L. G. Nair, Prog. Quant. Elect. 7, 153 (1982)

THE FREE ELECTRON LASER MEDICAL PROGRAM
B. L. Aronoff, M.D.
Director of Surgical Oncology and Laser Surgery
Baylor University Medical Center
3600 Gaston, Suite 558
Dallas, Texas 75246

ABSTRACT

For over three years, sporadic meetings about medical applications of the Free Electron laser have occurred. These culminated at a meeting at Los Alamos on February 1, 1984. At that time, more formal discussions were started as to possible medical applications. These have produced many theories and lines of research. At Baylor, we plan to work with the school of engineering of Southern Methodist University. They will do the material science and assist us in medical application. It seems that a wide variety of lasers will be available. We plan to explore the various "windows" in the electro magnetic spectrum to endeavor to destroy cancer in tissue at a depth beneath the skin. Newer fibers will assist in delivery of laser energy into remote parts of the body. These lasers should be more powerful and allow new interactions with tissue and probably better and deeper penetration when sensitizing dyes have been used. New combinations of lasers seems feasible for parenchymal tumors. New vistas will be explored in our endeavor to cure cancer.

I would like to discuss with you for the next few minutes what is going on with Free Electron laser in medicine and what we project for the future. As you all know, none of us have available in our institutions, a Free Electron laser. The one that most of the people that I'll talk about today have been using is the one at Stanford under John Madey, which has been operational for many months. It has been used primarily in the range of about 2.9 microns, which is one of the ideal wavelenghts for its use in medical practice. Now, actually, the whole program involves more than just medicine. It involves biophysics, DNA cellular molecular research, materials science and, of course, medicine.

A short history of how this program came about would seem important. Back in 1982, when the second meeting of American Society of Lasers in Medicine and Surgery was to be held at Hilton Head, Leon Goldman called several people and invited us to meet with John Madey and Kent Sokoloff. Now, you know that you can't go to Hilton Head and not play golf, just as you can't come out here and not ski. So, I went out early in the morning with my wife and we played golf and I returned in time to see John Madey. I did have a nice talk with Kent Sokoloff and in the next two years, there have been many visits between Dr. Madey and our group. These were very productive. In February, 1984, we received a phone call asking us to go to Los Alamos with a group to talk about the medical applications of the Free Electron laser. It was an interesting meeting because at first, they invited us to come early in the week and then told us that we could only come for one day because we did not have security clearance. After a brief discussion with the powers that be the evening before our performance, we let them know that we had secrets also that we did not want to jeopardize in our institution and things became smooth after that. The meeting, actually was very productive. In April, 1984, the same year, we got another phone call inviting us to go with the group to Washington, D.C. to see what we could do as far as legislation for the medical applications of the Free Electron laser. The first meeting was with the Administrative Assistant of the Senate Armed Services Committee, where we each presented our little dog and pony show. It was well received. In fact, this fellow said that he would write a check if he were able to do it. At any rate, he was very helpful. He had arranged meetings with several other people that he thought were important and over the next few months, many trips were made to Washington with many visits to various congressmen or their assistants, and, finally, we were fortunate to get into the Pentagon, where a personal friend was the Secretary of the Combined Chiefs of Staff. He arranged some very important meetings. By November, we knew that there would be a line item in the Department of Defense bill for ten million dollars a year for a period of five years. Originally, this was supposed to be a consortium of people to carry on related research in the program. Somehow or other, this got waylaid. At any rate, there was a final appropriation and we were fortunate enough to be in the group. The whole idea that we were trying to stimulate was that there would be centers, geographically distributed, so that when these programs were set up, there would be a free access by accredited people to do the research. For example, if a program was set up at Baylor in Dallas, this would serve the southwest. At any rate, things were going along and, finally, the various universities and hospitals were into the program, and, again, we were part of it.

There are several different types of Free Electron lasers. There is the linac at Stanford, number one, which is the one that Dr. Madey has. There is another super conducting radio frequency linac at Stanford. There is the Van DeGraff generator of 6 MEV at University of California at Santa Barbara. There is a Racetrack Microtron at the National Bureau of Standards, and, of course, Vanderbilt hopes to soon have a clone of Dr. Madey's laser. The original group included Baylor University Medical Center in Dallas, the Massachusetts General Hospital in Boston, Northwestern University in Chicago, the University of Utah at Salt Lake City, Stanford and the Lederman General Hospital in California. These institutions are still in the program and it is interesting that there are several programs of interest going on at each one. For example, Massachusetts General Hospital is working on the fragmentation of gallstones and kidney stones, femtosecond optical ranging, photodynamic therapy using two photon processes, tissue ablation mechanisms on the cornea and the lens and skin grafts and burn therapy, spectroscopic diagnosis techniques and laser angioplasty. All of these are being treated with modalities that we hope to obtain when the Free Electron laser is available. Now at Baylor University Medical Center in Dallas, we are working in two great areas. One is in the basic research, which includes the cellular level, the tissue level and the molecular level. In addition, we are working on infectious diseases, parasites, fungi, bacteria and, hopefully, on AIDS. We have been working with a lot of organic dyes, and at the moment, are working with about ten of these. We have models for micro thermal damage and DNA integrity. Now this has allowed us to get

together a group of scientists in the basic level that are working on the various components of cells. At the tissue level, there is also thermal modeling, particularly in the mid IR. This would include the 2.9, which is now available at Stanford, but also on the Hydrogen Fluoride laser. It has been used primarily in skin, muscle and liver and allows us to understand both micro thermal damage and damage to the various tissues. We have also been working on ablation mechanisms, using histology to find out about destruction of cells and, recently, we have working with dye uptake and specificity. We have had a very important work that we have been doing on animals that will have importance for bone marrow transfusions and we find that we can destroy the tumor cells in the bone marrow after the bone marrow has been harvested. Up to ninety-nine percent of tumor is destroyed and less than fifteen percent of the stimulating cells of the bone marrow. This has been tried in leukemia, lymphoma and some of the other diseases in which bone marrow is stored. The patient gets intensive chemotherapy or irradiation and then the bone marrow is returned to the patient. Now, our clinical work has been going on for fourteen years, starting with the CO² laser and, finally, into some of the other lasers. We have been doing liver resections with the CO² laser, putting on the T. Y. Lins clamp when we are doing right hepatic lobectomies or trisegmentectomies. We are able to take out large areas of liver with a minimal loss of blood. This has led us into other projects, which I will describe a little bit later on where we combine lasers to see if we could do any better by combining. We first combined the CO² and the Argon and it worked pretty good, but we didn't feel that it was good enough to use clinically and used it only in animals. The Free Electron laser promises us that in the future, we will have the availability of more than one wavelength simultaneous and, certainly, the CO² with the YAG or with the Argon or with other wavelengths that will certainly come up in the future, are very promising.

Another field that we have worked in extensively is in the Photodynamic Therapy and I would just like to mention two cases. One of the big problems we have with Photodynamic Therapy is the amount of penetration. We were presented with a lady that previously had had her lesion of her alveolus excised and within just a few months, showed up as a consult with two lesions in her palate. When the lesion was fluoresced, it showed at least five distinct lesions so we treated her rather vigorously, giving her 100 joules of energy per centimeter squared and the lesion faded out. I wish that this was the whole story. She has developed other lesions and has had to have further treatment. Another patient came along that had previously had a cancer of the larynx and came in with a new cancer fourteen years later on the posterior third of the tongue. Being he was in poor health, being eighty-four years of age and a cardiac, we elected to try irradiation. The irradiation was like giving him Vigoro because the tumor grew rather rapidly. We then gave him hematoporphyrin and, again, I used 100 joules per centimeter squared to the lesion. To our amazement, this lesion which was five centimeters thick and over five centimeters in diameter, began to necrose by the next day. The following week it showed extensive change, and the whole area of tumor, which was treated the second time, necrosed. Unfortunately, after he went home, about a week later, he had a heart attack and died.

Another project we are dealing with is the use of the Trimedyn laser in vascular occlusive disease. This is a new application of material that we saw at the meeting of the International Laser Society in Dallas in 1977. David Auth presented the combination of an Argon laser with a plastic blade to get hemostasis while he in surgery. Certainly, this is a very exciting field. At the moment, it is only being used in extremities clinically, but our projects are going on to try to use it in the coronary vessels.

Now, I would like to go over some of the other areas that have been doing work. The group at Salt Lake City has been going out to Stanford and has been able to fracture pigmented and cholesterol gallstones, and feel that there is definitely a tie in with the fracturing or removal of plaques, as well as these stones. They have also been working on two photon therapy and photodynamic therapy. Recently, I know that Dr. Strait and others have been out doing bone cutting with the laser with success. Now all of these clinical programs that are being done with the Free Electron laser at Stanford, are being done under a certain handicap because the beam, at the moment, is at one spot and the subject has to be moved. Secondly, the flexible delivery system to carry the beam has not been installed as yet.

Now, one of the areas of research that is going on in many institutions, not only those which are affiliated with the Free Electron laser, but around the world, has been the hunt for new dyes for Photodynamic Therapy. Some of the ones that have been interesting to us are Merocyanine and Carbocyanine. But there are many others that have been used, including the rhodamins, particularly Rhodamin 1,2,3, which will be reported on later in this meeting and then the work that has been done with Pheophorbidea, which has been used both with the Nd:YAG laser for excitation and for hyperthermia. There is a lot of other work being done on new dyes that are felt to be confidential and I could not secure the names of all these dyes.

There are obviously some characteristics of the Free Electron laser which makes it attractive for research. The broad wavelength selection seems to be available from the Free Electron laser. It is tunable through the spectrum and has high peak power with short duration pulses and high average power. These combine to get rid of some problems that we have with some of our conventional lasers. Now, at the moment, there are two frequently used lasers. The first one is the one at Stanford. It is in the near infra-red at around

2.9 - 3.1 microns. Also at U.C. Santa Barbara, they are using a laser at 100 microns. Both of them hope that in the near future, they will have much broader work in the infrared and the potential in the entire spectrum all the way down to the ultraviolet is predicted. Exactly the extent on either end is certainly not known. There is some very interesting work going on in China on tumor therapy by the stimulation of the immune system with ultraviolet lasers. This is to be discussed at our meeting in Dallas in April and it seems to me to have some very exciting possibilities.

While the challenge seems to be that if we can get much higher powers with our laser, that more therapeutic measures could be achieved and with other wavelengths, we can certainly find out certain characteristics that we don't know about at the moment. One of the projects that we are very interested in is the wave bands where the normal tissues, such as the skin, muscle and bone, will be traversed by the laser beam and it will hone in on an area that has been given a chromophore. Now this is not too far out when one considers that we are able to use the Argon laser going through normal tissue and also, the fact that we can get a little depth, not a whole lot, with hematoporphyrin with the destruction of tumor cells. So, to simply summarize what the project has been, we're working in the medical part, but all of our programs have chemistry, biology, physics and material sciences.

So far, there have been aggressive attacks into peripheral vessels with minimal attacks on coronary vessels percutaneous. Now we all know that Choy, Isner, Abella and others have done a lot of work on coronaries, but the percutaneous application of lasers into the coronary vessels is still in the near future. One of the areas that we told about when we first became involved in the Free Electron laser was PET imaging and certainly, this is a field of great interest to the people in various fields of medicine and surgery. We are looking to see that developed with rapidity once the laser is available. Now, just to review for a moment, some of the lasers. The original linear accelerator out at Stanford was 300 meters long and would take a pretty good size room to house this apparatus. The second, at Santa Barbara, the entire accelerator was fifty feet high. We were privileged to see the workings at Los Alamos and these fill a large building. Lastly, there are the prototypes that were developed at Stanford. Certainly, there have been considerable changes. They are using a 43 MEV linear accelerator and we all hope that in the near future, these will be in our institutions. I want to thank you for the privilege of the floor.

Summary

1. One laser with extensive wavelength possibilities.
2. Higher power wavelength - question more efficient.
3. Ability to secure multiple simultaneous wavelengths.
4. Advantage of high peak short impulses to avert thermal damage.
5. PET imaging.

To date, the main effect has been to stimulate research in universities and private institutions, more cooperation between M.D.'s and Ph.D.'s and taking a problem and finding a solution rather than trying to find some use for a new technique. Hopefully, a cure for the three dread diseases, cancer, heart disease and strokes, plus benefit gains in AIDS and Alzheimer's Disease.

EFFECTS OF THE Nd:YAG LASER ON NORMAL HUMAN FIBROBLAST CULTURES SENSITIZED WITH Q-SWITCH II DYE: STUDY OF A NEW FLUOROCHROME

Dan J. Castro, M.D; Romaine E. Saxton, Ph.D;
Harold R. Fetterman, Ph.D; Donna J. Castro, C.S.T; Paul H. Ward, M.D.

From the Division of Head and Neck Surgery (Otolaryngology) (DJC and PHW) and High Frequency High Speed Electronics Center (HRF), UCLA School of Medicine, Los Angeles, CA, 90024, Division of Surgical Oncology (RES), Veterans Administration Medical Center, Sepulveda, CA, and California Paramedical and Technical College (DJC), Long Beach, CA.

Recipient of the Lasers '87 Award

This study was supported by VA Medical Research Services, the Division of Head and Neck Surgery and the Jonsson Cancer Center, UCLA School of Medicine.

Abstract

For years, the development of effective methods for control of scar tissue has been the dream of many scientists around the world. Excessive deposition of collagen is a characteristic feature of cutaneous diseases with dermal fibrosis, such as keloids and hypertrophic scars, and no effective treatment is available for these conditions. Previous observations^{1,2} have suggested that the Nd:YAG laser may offer a novel mode of treatment for these diseases. In recent years, photodynamic therapy with lasers has regained popularity, specifically since the introduction of hematoporphyrin derivatives and Rhodamine-123 as chemosensitizing agents for the treatment of superficial malignancies. The search for a fluorochrome-specific for the Nd:YAG laser (near infrared, 1060 nm), has led us to investigate the potentials of Kodak Q-switch II Nd:YAG dye (absorption maxima at 1051 nm) as a new chemosensitizing agent on normal human fibroblast cultures. The results suggest that cells sensitized to Q-switch II dye are more sensitive to the effects of the Nd:YAG laser as compared to the effects of the laser alone. Significant suppression of DNA synthesis was observed at physiological temperatures as low as 28-34 °C, with cell death at 36 °C. This new technique of cell targetting with Q-switch II dye and specific Nd:YAG laser treatment may offer real advantages for the treatment of keloids of hypertrophic scars.

Materials and Methods

Nd:YAG Q-Switch II Dye

Eastman Q-switch II (Fig. 1) 8-(5-[2,4-Bis(4-pentyloxyphenyl)-6,7-dihydro-5H-1-benzopyran-8-yl]-2,4-pentadienylidene)-2,4-bis(4-pentyloxyphenyl)-5,6,7,8-tetrahydro-1-benzopyrilium Perchlorate is a pyrilium salt shown effective as an automatic Q-spoiler for Nd-glass lasers. It is a black crystalline solid with a molecular weight of 1079.75. The solvent of choice has been 1,2-dichloroethane, in which the dye is photochemically stable and has an excited state lifetime of 9.1×10^{-12} seconds. This dye has an absorption maxima at 1051 nm (Fig. 2) and it is rapidly bleached by UV and blue radiation.

Experimental Design of the Laser and Method of Dosimetry

The laser used in our experiments was a commercially available LS 880 Nd:YAG-CO₂ surgical laser system from Cooper LaserSonic Incorporation (Marlboro, Massachusetts). The Nd:YAG laser (Neodymium: Yttrium Aluminum Garnet) is a multimode, CW (continuous wave) laser, with a wavelength of 1060 nm (invisible, near infrared) and a maximum power output of 100 watts. The Nd:YAG laser beam is delivered either through an articulating arm or an optical fiber. The beam scan technique¹ was used to measure the spatial profile of the laser beam; this profile is complex¹ and does not assume the Gaussian distribution. The laser output passes through an aperture (slit) in a direction perpendicular to the direction of the beam propagation, and the light transmitted through the aperture is sensed by a detector. The measured beam profile, as registered by the chart recorder, is used to determine the peak intensity (watts/cm²), as well as the spot diameter at full width half maximum (FWHM), $1/e$ and $1/e^2$, respectively at 50%, 37% and 14% of the calculated intensity (Table 1). Numerical integration is used to analyze the measured beam profile to obtain the peak intensity using the formula:

$$P_0 = I_0 \int_0^{\infty} 2\pi r F_c(r) dr.$$

where P_0 is the power in watts, $F_c(r)$, the spatial distribution taken from the chart recorder and normalized to unity, and I_0 , the peak intensity axis of the beam in watts per square centimeter. A Simpson rule integration formula is used to evaluate this equation to obtain the peak intensity I_0 in each experiment. The Nd:YAG laser is outfitted with a time shutter to control the duration of exposure accurately. A thermopile power meter (model 210, Coherent, Palo Alto, California) is used to measure the average power transmitted through the fiber optic of the laser. The distance from the output to the target at 10.5 cm. as well as then angle of incidence (90 degrees) were measured and kept constant. Ten beam spatial profiles were recorded using the beam scanner. Analysis of these beams revealed a calculated spot diameter of 0.380 ± 0.008 cm. at FWHM, 0.457 ± 0.0 cm. at $1/e$ and 0.6324 ± 0.007 cm. at $1/e^2$. The calculated spot surface at $1/e^2$ ($S = \int_0^{\infty} \pi r F_c(r) dr$) was 0.154 ± 0.005 cm². The peak intensity in watts per square centimeter was 64.94 ± 4.1 w/cm² and kept constant. The time of exposure is varied to obtain different energy levels (Table 1). The largest spot diameter at $1/e^2$ was calibrated to 7% smaller than the diameter of the fibroblast culture wells, thus avoiding the interference of energy density between the vertical walls of the culture wells.

Using Beer's law ($I = I_0 e^{-\gamma L}$), we calculated the energy density absorbed by the Hank's medium, the culture plate and the fibroblasts (Table 1). By extrapolation, it appeared that 48% of the energy density incident was absorbed by the fibroblasts, while 52% was absorbed by the Hank's solution and culture plate.

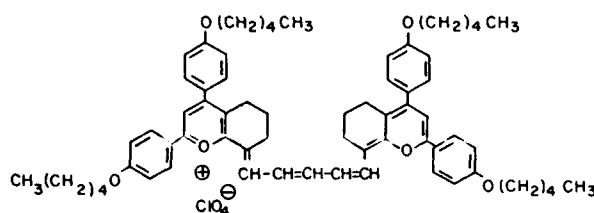


Fig. 1. Eastman Q-Switch II for Neodymium lasers.

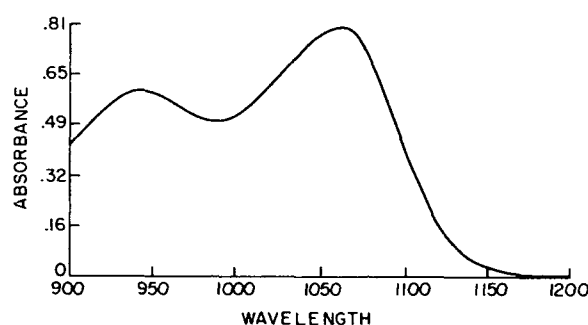


Fig. 2. Spectrum of absorption of Q-Switch II dye.

Normal Human Fibroblast cultures

Two normal human fibroblast cell lines, designated Micro II and B, were established in culture, respectively from a foreskin specimen (fetal fibroblast, rapidly dividing cells) and from a normal skin biopsy taken from an adult male at the time of surgical excision of a melanoma (primary adult fibroblast, slowly dividing cells).

Cells were cultivated at 37 °C in Roswell Park Memorial Institute tissue culture medium (RPMI) (model 1640, Irvine Scientific, Santa Ana, California), supplemented with 10% fetal calf serum (Irvine Scientific), 2 mM L-glutamine solution (GIBCO, Chagrin Falls, Ohio), 20 mM N-2-Hydroxyethylpiperazine-N-2-Ethanesulfonic acid (Hepes) buffer, pH-7.4 and 50 ug per milliliter of Gentamycin (Whitaker M.A. Bioproducts). The cells were plated in 75 cm² tissue culture flasks (Falcon 3024, Becton Dickinson Labware, Oxnard, California) and the medium was changed at three day intervals. Prior to laser treatment, the cells were removed by trypsinization and counted with a standard hemocytometer. Normal fibroblast cells (5x10⁴ cells/0.1 ml) were plated in one out of every fourth well of a 96-well culture plate (Model 3595, Costar Company, Cambridge, Massachusetts). This technique of cell plating was necessary to avoid interference of laser energy between the adjacent wells. The diameter of each well was 6.5 mm; for this reason we calibrated the laser beam diameter and surface at 1/e² to be 7% smaller than the culture wells utilized. The cells were allowed to attach and incubate for 24 hours prior to laser treatment.

Q-Switch II Dye Uptake

Q-switch II solid salt was obtained from Eastman Kodak Organic Chemicals (Rochester, New York). The solvent of choice has been 1,2-dichloroethane, however, because of its known hepato and cytotoxic effects, we used DMSO (Dimethyl Sulfoxide, 100%) as our solvent to obtain a stock solution with a concentration of 1 mg/ml. This dye solution appears to be stable in DMSO, as well as in distilled water and standard culture medium, without changes in its absorption curve as measured with a standard Carrie 20 spectrophotometer (Fig. 2). Further dye dilutions to 0.1 ug/ml were made in our standard culture medium mentioned above.

Prior to laser treatment, the culture medium in each plated well of the test group was replaced with 0.1 ml of this Q-switch II solution and incubated for one hour. Exposure to this dye was terminated by aspiration of the supernatant and washing of the cells twice with 0.1 ml of standard culture medium to remove excess Q-switch II not incorporated by the normal human fibroblast cells. After washing the cells, 0.1 ml of new culture medium was added to each well and incubated at 37 °C. This fresh medium was transparent, containing Hank's balanced salt solution (Microbiological Associates, Bethesda, Maryland) supplemented with 20 mM Hepes buffer solution (pH-7.4), 50 ug/ml of Streptomycin sulfate (GIBCO), and 2.5 ug/ml of Amphotericin B (GIBCO) without phenol red pH indicator. The culture medium in each plated well of the control groups (untreated, and treated with the Nd:YAG laser alone) was also replaced with this new medium prior to treatment. The step was necessary because previous experiments² indicated that most of the laser energy is absorbed by the phenol red of the standard culture medium. Confluency of the fibroblast cells was checked prior to laser treatment with a standard phase microscope and plates were used when cells covered 80-90% of each well. After laser treatment, the fibroblast cells were restored in the standard RPMI medium and incubated at 37 °C.

Determination of the Cell Viability

The cell viability was determined by the Trypan Blue exclusion test at six and 24 hours post-laser treatment. Incorporation of Trypan Blue in the cells indicated cell death. Percentage of viability was determined in control and laser treated fibroblast cells.

Determination of DNA Synthesis by [³H]-Thymidine Incorporation

Untreated controls as well as laser treated fibroblasts (test group sensitized to Q-switch II dye, control group treated with the laser alone) were incubated at 37 °C for six and 24 hours post-treatment and then tested for Thymidine uptake. At each time point, 5 µCi of tritiated Thymidine (specific activity 2.0 Ci/mmol; New England Nuclear, Boston, Massachusetts) was added to each well and the plates were incubated for an additional 24 hours. Incorporation of Thymidine was terminated by aspiration of the supernatant from each well followed by trypsinization of the cells from each well and transfer to 15 ml centrifuge tubes (Beral Scientific, Arlita, California). Pelleted cells were resuspended in 1 ml of Phosphate Buffered Saline (PBS) solution, x1 concentration, without calcium or magnesium (GIBCO Laboratories, Grand Island, New York) and heated at 90 °C in a water bath (Precision Company) for 30 minutes. The volume of each tube was increased to 8 ml with PBS and the tubes were centrifuged for 15 minutes at 2400 RPM (900 xg) in a centrifuge (Model TJ6; Beckman Instruments, Irvine, California). The supernatant were aspirated, the pellets washed with 3 ml of PBS (Grand Island) and then recentrifuged for 10 minutes. The supernatant were aspirated, 30 µg of 1% human serum albumin (Cutter Biological, Berkeley, California) and 5 ml of 10% iced TrichloroAcetic acid (Fisher Scientific Company, Fair Lawn, New Jersey) were added to each tube, and then cooled to below 4 °C for one hour. The TCA precipitate were collected by centrifugation for 10 minutes and the pellets washed again with 3 ml of 5% iced TrichloroAcetic acid. The tubes were recentrifuged for an additional 10 minutes and TCA precipitates from the pellets were dissolved overnight in 0.3 ml of 0.075N KOH. The hydrolysates were then transferred to standard scintillation vials (Beckman Instruments) containing 5 ml of Optifluor (United Technologies, Packard, Illinois) and after one hour, radioactivity in each vial was measured in a scintillation counter (LS 230; Beckman Instruments, Irvine, California). The results are expressed in CPM/well (Table 2).

Measurement of the Thermal Effects of the Laser Beam

The temperature in each well was measured prior to laser treatment (T_0) and immediately after laser exposure (T_{max}) by immersion of a microprobe, MT 23/8, connected to a thermometer, BAT-12 (with fast reading, super-accuracy, 0.1% of reading, +1 digit; Sontek Instruments, Clifton, New Jersey). The microprobe was immersed in the center of the Hank's medium of each well prior to and immediately after laser exposure. The thermal profile was recorded until the temperature in the treated well returned to the 20 °C ambient temperature (Tables I and II).

Statistical Method

The data were stored and analyzed with the computer software, SYSTAT, available at the Biostatistics Microcomputer Laboratory of the UCLA Health Science Computer Facility. Descriptive statistics, Scheffe's test for multiple comparisons and correlation test were performed by an independent evaluator from this department.

Results

In this study, we have examined the changes occurring in cell viability and DNA synthesis of two normal human fibroblast cell lines sensitized with Q-switch II dye as a result of Nd:YAG laser treatment at various energy densities and thermal levels. Using an accurate and reproducible method of dosimetry of laser energy and measurement of thermal changes in the medium prior and immediately post-laser treatment (T_0 , T_{max}), our data demonstrates that there is a significant linear correlation ($p < 0.001$) between those two parameters as we previously demonstrated.^{3,4,5} Therefore in the future, computers can be used to facilitate calculations so that one can quickly correlate total tissue dosage or thermal changes with immediate biological responses.

The viability of the test group fibroblasts sensitized with Q-switch II dye, as estimated by the Trypan Blue exclusion test at six and 24 hours post-laser treatment, was not affected at energy density and temperatures equal or lower than 950 J/cm² or 34 °C as compared with untreated cells. Above 1100 J/cm² or 36 °C, the cells were stained with Trypan Blue, indicating nonviability. However, the viability of the control group cells treated with the laser alone, was affected at higher energy density and temperature levels of 2000 J/cm² or 42 °C. Below this energy level, the viability was not affected as compared with untreated cells at six and 24 hours post-treatment. It indicates that fibroblast are more "sensitive" to the Nd:YAG laser treatment when first exposed to a nontoxic dose of Q-switch II dye. Cell killing was observed at temperatures equal or higher than 36 °C as compared to 42 °C when treated with the laser alone ($p < 0.001$) (Table 2, Figs. 3,4).

To evaluate the possible changes in cell duplication, fibroblast cultures sensitized with Q-switch II dye (test group) and control fibroblasts were incubated with [³H]-Thymidine after exposure to the Nd:YAG laser, and the uptake of Thymidine was measured at six and 24 hours post-treatment (Table 2, Figs. 3,4). For the test group (cells+Q-switch+laser) at energy levels between 314-950 J/cm² and corresponding temperatures between 28-34 °C, a significant inhibition of Thymidine uptake ($p < 0.001$) was noted both at six and 24 hours post-treatment (Table 2, Figs. 3,4). As mentioned above, cell viability as shown by the Trypan Blue exclusion test, was not affected at those energy densities and temperature ranges. At energy levels and temperatures equal to or higher than 1100 J/cm² (36 °C or above), Thymidine uptake for the test group was markedly suppressed both at six and 24 hours post-treatment ($p < 0.001$). This effect was accompanied by nonviability of the fibroblast cells, as demonstrated by the Trypan Blue exclusion test (Table 2, Figs. 3,4).

For the control group (cells+laser), significant inhibition of DNA synthesis was noted at higher energy densities and temperatures of 1700 J/cm² or 40 °C, both at six and 24 hours post-treatment as compared with untreated cells (Table 2, Figs. 3,4). As mentioned above, cell viability was not affected at those energy densities and temperature ranges. At energy levels and temperatures equal to or higher than 2000 J/cm² (42 °C or above), Thymidine uptake for the control group (cells + laser) was markedly suppressed and was accompanied by nonviability of the fibroblasts, both at six and 24 hours post-treatment (Table 2, Figs. 3,4).

Discussion

In this study, we have demonstrated that Q-switch II dye at nontoxic doses (0.1 µg/ml for one hour) to normal fibroblast cultures

enhances significantly the cytotoxic and cytostatic effects of the Nd:YAG laser at physiological temperatures as low as 28-36 °C.

Both stimulatory and inhibitory effects of different laser wavelengths on cell duplication have previously been reported.⁶⁻¹² However, many of the previous studies are difficult to interpret since information concerning the laser dosimetry is lacking. A primary emphasis of this study was to develop an accurate and reproducible method of delivery of energy densities and precise control of thermal changes in the fibroblast cultures. This technique¹ utilized is simple and reliable, based on laser beam geometry, dosimetry and temperatures as previously described.

Kodak Q-switch II is a new chemical with an absorption maxima at 1051 nm designed to be used as a Nd:YAG dye laser. The search for a fluorochrome-specific for the Nd:YAG laser has led our laboratory to test the effects of this dye on fibroblast cultures. In a previous study,¹³ two normal fibroblast cell lines were tested for sensitivity to various levels of this dye in-vitro. These cells were exposed to Q-switch II dye at concentrations of 0.01, 0.1, 1, 10, 50 and 100 µg/ml for one and 24 hours. Cell viability was assessed by the Trypan Blue exclusion test. Cell duplication and DNA synthesis were measured by the incorporation of ³H-Thymidine at six and 24 hours post-exposure to Q-switch II dye. At concentrations up to 10 µg/ml, both cell lines test lines tested showed no changes in cell viability. However, at concentrations equal to or higher than 50 µg/ml, more than 40% of the fibroblasts incorporated Trypan Blue after 24 hours of exposure to this dye, indicating significant cell killing. At concentrations between 0.01 to 10 µg/ml, an immediate and delayed significant stimulation of DNA synthesis was noted even after one hour of exposure to Q-switch II dye for both cell lines tested. However, at concentrations equal to or higher than 50 µg/ml, DNA synthesis was not statistically different than untreated control cells, but cell viability was affected for more than 40% of the treated cells after 24 hours of exposure to this dye. The results indicate that Q-switch II dye is nontoxic to normal human fibroblast cultures and showed a significant biostimulative effect on cell duplication at concentrations equal to or lower than 10 µg/ml. Therefore, in this present study, the concentration of 0.1 µg/ml was chosen as the "chemosensitizing" dose for the fibroblast cultures.

The effects of the Nd:YAG laser were more significant when fibroblast cultures were first "sensitized" to Q-switch II dye than when treated with the laser alone. Significant suppression of DNA synthesis was accompanied by non-viability of the fibroblast cultures at physiological temperatures as low as 36 °C and a corresponding energy density equal to or higher than 1100 J/cm² (Figs. 3,4). However, when fibroblast cultures were exposed to the Nd:YAG laser alone, similar cytotoxic effects were observed at temperatures of 42 °C or higher and corresponding energy densities equal to or higher than 2000 J/cm² (Figs. 3,4). It clearly indicates that Q-switch II sensitization enhances the cytotoxic effects of the Nd:YAG laser at non-thermal levels of energies on normal human fibroblast cultures.

In addition, a markedly delayed markedly reduced Thymidine incorporation which reflects lower DNA synthesis was observed at physiological temperatures as low as 28-34 °C (314-950 J/cm²) in fibroblast cultures sensitized to Q-switch II dye and exposed to the Nd:YAG laser (Figs. 3,4). The cells remained viable at these energy levels and temperature ranges as demonstrated by the Trypan Blue exclusion test. Similar effects of the Nd:YAG laser on fibroblast cultures NOT sensitized with Q-switch II dye were observed at higher temperature ranges of 40 °C (1700 J/cm²) as previously demonstrated.² The non-thermal range of effects of the Nd:YAG laser manifests itself at significantly reduced temperature ranges when cells are first sensitized with Q-switch II dye. This phenomenon demonstrates the advantages of photodynamic therapy with lasers which consists of the administration of a non-toxic chemosensitizing agent to cells (Q-switch II dye with a specific absorption maxima at 1051 nm), which is then activated using a carefully calibrated, monochromatic Nd:YAG laser at 1060 nm. Molecular mechanisms related to the specificity of binding or to the cellular site of action Q-switch II dye are still unknown. However, the cytotoxic effects observed at concentrations equal to or higher than 50 µg/ml suggest a direct uptake by cells of this dye and appears to be dose related. Furthermore, the unexpected biostimulative effects of cell duplication observed at concentrations equal to or lower than 10 µg/ml may suggest an intracellular target site of action.

Mitochondria and/or nuclei are potential targets for Q-switch II dye. It may stimulate cell duplication either by enhancing the energy-supplying metabolic processes of mitochondria and/or by alteration of the cell cycle time, or both. The cytotoxic and cytostatic effects of the Nd:YAG laser on fibroblast cultures sensitized to Q-switch II dyes at these physiological temperatures (28-36 °C) reinforce the concept of an intracellular site of action. "Activation" of the Q-switch II dye with the Nd:YAG laser may destroy or inhibit chains of metabolic processes in mitochondria which might result in the loss of capacity of division of the cells.

Eastman Q-switch II salt was shown to be effective as an automatic Q-spoiler for Nd:YAG dye laser. Its effects as a potential chemotoxic versus chemosensitizing agent on living cells have never been tested. However, the results of this study show surprising and promising future applications for this dye in-vitro¹³ as well as in-vivo.

1,2-dichloroethane has been the solvent of choice for the Q-switch II crystal, however, its hepatotoxic as well as cytotoxic effects in-vivo are well known. Therefore, we successfully attempted to dissolve this black crystalline solid in DMSO, which is used as a non-toxic in-vivo solvent for various compounds. Furthermore, this dye solution remains stable in distilled water and in regular culture medium, with a measured absorption maxima at 1051 nm (Fig. 2). Further research is currently in progress, trying to determine the intracellular target of this dye and its mechanism of action.

Photodynamic therapy has regained popularity in recent years, specifically since the introduction of lasers and fluorochromes as HPD and more recently Rhodamine-123^{3,4,5} for the treatment of superficial malignancies. Q-switch II dye may become an extremely efficacious photochemosensitizing agent for the treatment of keloids or hypertrophic scars, or connective tissue diseases, with the low-energy Nd:YAG laser.

Conclusion

Kodak Q-switch II dye has recently proven to be an effective biostimulative agent on normal human fibroblast cultures. The potential for this dye as a new chemosensitizing agent for the treatment of connective tissue diseases and wound healing with the Nd:YAG laser was examined. Two normal fibroblast cell lines were first sensitized to a non-toxic dose of Q-switch II dye (0.1 µg/ml for one hour), then subjected to treatment with a Neodymium:YAG laser at 1060 nm with varying levels of energy and temperatures determined by a reproducible method of dosimetry. The results indicate that Q-switch II dye at non-toxic doses of 0.1 µg/ml enhances the cytotoxic effects of the Nd:YAG laser at reduced temperatures as low as 36 °C. Furthermore, at physiological temperature ranges as low as 28-34 °C, significant inhibition of DNA synthesis or cell duplication was demonstrated while cell viability was not affected. Similar results were not observed when fibroblast cultures were treated with the laser alone. These observations suggest that Q-switch II dye is an effective chemosensitizing agent for the Nd:YAG laser and could potentially be used to reduce collagen deposition in conditions such as keloids and hypertrophic scars.

Acknowledgements

We wish to thank Judy Smith for her technical assistance and continued support of this work.

References

1. Castro DJ, Stuart A, Benvenuti D, et al: A new method of dosimetry: A study of comparative laser induced tissue damage. *Ann Plast Surg* 9:221-226, 1982.
2. Castro DJ, Abergel P, Meeker C, et al: Effects of the Nd:YAG laser on DNA synthesis and collagen production in human skin fibroblast cultures. *Ann Plast Surg* 11:214-222, 1983.
3. Castro DJ, Saxton RE, Fetterman HG, Castro DJ and Ward PH: Rhodamine-123 as a new photochemosensitizing agent with the Argon laser: "Non-thermal" and thermal effects on human squamous cells in-vitro. *Laryngoscope* 97(5):554-561, 1987.
4. Castro DJ, Saxton RE, Fetterman HG, Castro DJ and Ward PH: Rhodamine-123 as a chemosensitizing agent for Argon laser therapy: A new technique for treatment of superficial malignancies. *Arch Otolaryngol* 113:1176-1182, 1987.
5. Castro DJ, Saxton RE, Fetterman HG, Castro DJ and Ward PH: The effects of Argon laser on human melanoma cells sensitized with Rhodamine-123 in-vitro: Study of a new photochemosensitizing agent. *Amer J Otolaryngol* (Accepted for publication).
6. Gamaleya NF: In Wolbarsht ML (ed), *Laser Applications in Medicine and Biology*. Vol. 3, New York, Plenum Press, 1977, pp 1-13.
7. Haina D, Brunner R, Landthaler M, et al: Stimulierung der wundheilung mit laser licht. Klinische und tierexperimentelle untersuchungen. *Verhandl Der DDG*, 32, Tag. Munchen, Bermannverlag, 1981, pp 429-432.
8. Hell E, Lawrence JC: The initiation of epidermal wound healing in cuts and burns. *Br J Exp Path* 60:171, 1979.
9. Kana JS, Hutschenreiter G, Haina D, et al: The effect of low power density laser radiation on the healing of open skin wounds in rats. *Arch Surg* 116:293, 1981.
10. Mester E, Gyenes C, Tota JG: Experimentelle untersuchungen uber die wirkung von laserstrahlen auf die wundheilung. *Z Exp Chirurg* 2:94, 1969.
11. Mester E, Nagylueskay S, Waidelich W, et al: Uber den wirkungsmechanismus der direkten laserbestrahlung auf die menschlichen lymphocyten. *Arch Dermatol Res* 263:241, 1978.
12. Seipp W, Haina D, Justen V, et al: Laserstrahlen in der dermatologie. *Dtsch Dermatol* 26:557, 1978.
13. Castro DJ, Saxton RE, Fetterman HG, Castro DJ and Ward PH: Biostimulative effects of Nd:YAG Q-switch dye on normal human fibroblast cultures: Study of a new chemosensitizing agent for the Nd:YAG laser. *Laryngoscope* 97(12):1454-1459, 1987.

Measured Parameters	Power (P)	Spot Diameter $d1/d2$ (1)	Surface of Spot (S) $S = \pi r^2$ (cm ²)	Intensity (I) (2)	Time of Exposure (t) (3)	Total Energy Density Absorbed by Saline (Ea) (4)	Energy Density Delivered to Fibroblast (ED) (5)	Post Temperature T _{max} (7)
Energy Levels	Watts	(cm)	(cm ²)	(Watts/cm ²)	(sec)	(J/cm ²)	(J/cm ²)	(°C)
1	10±1	0.632±0.007	0.154±0.05	64.94±4.1	3.0±0.0	194.7	100.6	24±1
2	10±1	0.632±0.007	0.154±0.05	64.94±4.1	10.0±0.0	649.4	335.7	28±1
3	10±1	0.632±0.007	0.154±0.05	64.94±4.1	30.0±0.0	1948.2	1000.7	34±1
4	10±1	0.632±0.007	0.154±0.05	64.94±4.1	34.0±0.0	2207.9	1141.5	36±1
5	10±1	0.632±0.007	0.154±0.05	64.94±4.1	55.0±0.0	3571.7	1846.6	40±1
6	10±1	0.632±0.007	0.154±0.05	64.94±4.1	65.0±0.0	4221.1	2102.3	42±1

TABLE 1: Measured parameters with the Nd:YAG laser

Energy Density Absorbed by Cells (Joules/cm ²)	Control (1)	Control (2)	Q-Switch # (4) (0.1 µg/ml)	Q-Switch # (4) (0.1 µg/ml)	Nd:YAG Laser (5)	Nd:YAG Laser (5)	Nd:YAG Laser (5) - Q-Switch # (0.1 µg/ml)	Nd:YAG Laser (5) - Q-Switch # (0.1 µg/ml)
Post-Temperature T _{max} (°C)	ThyM (7) (CPM/Watt)	ThyM (7) (CPM/Watt)	ThyM (7) (CPM/Watt)	ThyM (7) (CPM/Watt)	ThyM (7) (CPM/Watt)	ThyM (7) (CPM/Watt)	ThyM (7) (CPM/Watt)	ThyM (7) (CPM/Watt)
Control	16852 81100 8 n=20	23010 711334 6 n=20	63082 812563 2 n=20	66136 813056 4 n=20				
84.1 (24±1 °C)	—	—	—	—	17090 81937 5 n=10	32632 811563 5 n=10	16627 311256 7 n=10	29520 811906 4 n=10
91.2 7 (28±1 °C)	—	—	—	—	17534 811079 5 n=10	32296 311631 5 n=10	4236 81077 5 n=10	5465 41077 2 n=10
94.8 6 (34±1 °C)	—	—	—	—	16125 811716 2 n=10	32065 311428 7 n=10	2927 81428 5 n=10	1665 81290 9 n=10
100.4 (36±1 °C)	—	—	—	—	16545 81011 1 n=10	30934 311562 5 n=10	182 8157 03 n=10	88 811310 n=10
1725 1 (48±1 °C)	—	—	—	—	6545 81716 5 n=10	5019 41530 7 n=10	70 7112 0 n=10	42 1110 2 n=10
2020 9 (52±1 °C)	—	—	—	—	157 4126 0 n=10	132 7126 0 n=10	40 8112 0 n=10	37 8110 0 n=10

TABLE 2: Thymidine counts versus energy levels and thermal profiles

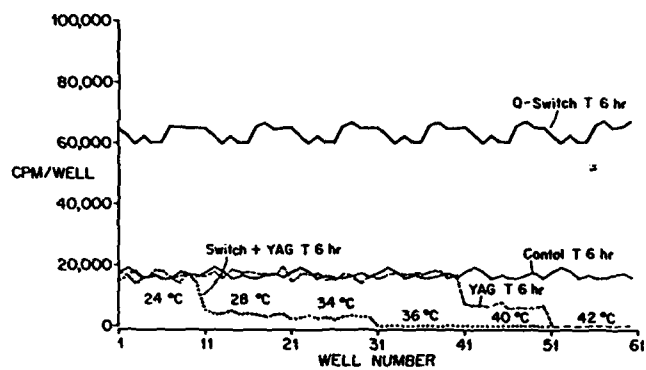


FIGURE 3: Thymidine counts at six hours

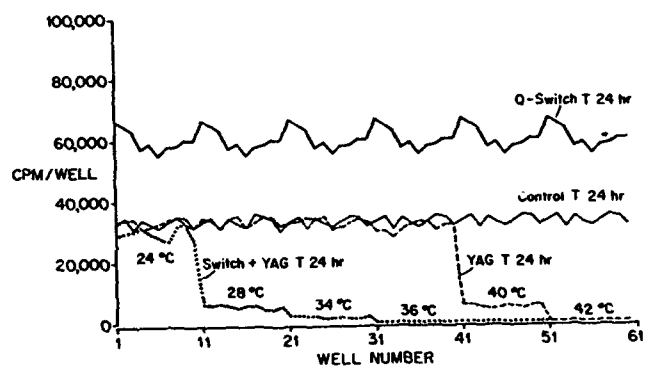


FIGURE 4: Thymidine counts at 24 hours

THE CO₂ LASER AS A TOOL FOR CORNEAL SURGERY

Joan M. Macdonald, Ph.D.*
Orman A. Simpson, Ph.D.**
Bernard E. McCarey, Ph.D.*
George O. Waring III, M.D.*

* Emory University, Department of Ophthalmology,
1327 Clifton Road NE, Atlanta, Georgia 30322

** Environmental Laser Systems, Inc.
3333 Chamblee Dunwoody Road, Atlanta, Georgia 30341

Abstract

The purpose of this study was to determine if the pulsed CO₂ laser could be used on the cornea with minimal thermal damage to the surrounding tissue. Human eye bank corneas were ablated and examined utilizing scanning and transmission electron microscopic techniques. The authors report no indication of coagulated protein or thermal damage to the bottom or side walls of ablations receiving three pulses to the same site. The linear ablations created sharp cleavage planes through the tissue, though the incisions were relatively jagged when compared to diamond knife incisions. Our preliminary work is promising, further investigation is needed to determine if the pulsed CO₂ laser can be used for precise surgical techniques on the cornea.

Introduction

The use of lasers for ophthalmic surgery has been successful in treating a variety of disorders. The suitability of a laser for a particular site of action depends upon properties of both the tissue and the laser, i.e. it is necessary for the laser wavelength to be absorbed at an absorption peak contained within the tissue. The principles of laser action dictate its feasibility for particular surgical techniques on the cornea. The properties of corneal surface surgery restrict the laser to wavelengths based on one of two principles: chemical or thermal interaction.

Absorption of ultraviolet energy results in chemical interaction that physically destroys intramolecular bonds^{1,2}. Preliminary results utilizing the excimer laser for corneal surgery have been promising^{1,2}, however, numerous disadvantages have been encountered. If the laser is to be commercially available, issues of high cost, low lifetime and possibility of mutagenesis must be addressed.

Thermal interaction relies upon water content to determine the effect produced by the CO₂ laser. The intracellular and extracellular water undergoes an abrupt phase change, creating steam and vaporizing the tissue. The dispersed energy can be absorbed by the tissue adjacent to the ablation, resulting in coagulation and carbonization of the remaining tissue. However, reducing the exposure time can minimize the thermal effect.

The features of the pulsed CO₂ laser that make it particularly suitable for corneal surgery are: 1) CO₂ laser energy is strongly absorbed by water molecules; and 2) the thermal relaxation time for water at the 10.6 μ m wavelength is 200 μ sec³. Since the cornea is composed of 78% water⁴, the corneal endothelium as well as other portions of the eye are protected from thermal damage from transmitted energy delivered with short exposure times. The thermal relaxation time of biological tissue is different from that of water, however, with a pulse width shorter than 200 μ sec, it should be possible to vaporize tissue without creating thermal damage to adjacent areas⁵. A large amount of power will need to be delivered during the short pulse duration, creating high power densities⁵. The poor hemostatic ability of the laser utilized in this fashion may be of concern in other tissues, but in an avascular tissue like the cornea, this is not relevant.

The purpose of the study was to evaluate the effect of the pulsed CO₂ laser in corneal tissue. We wished to determine if the laser could be used on corneal tissue with minimal damage to the adjacent stromal tissue. Ultimately, we question whether the laser will overcome complications encountered with the use of hand-held diamond knives during corneal surgery.

Methods and Materials

The CO₂ laser in this study was a high order mode system in which a small pinhole iris was used to deliver a single mode of the beam (Figure 1). Although the laser had a maximum output of 3 joules, it typically delivered 25 mjoules of power. The pulse delivered had a 150 nsec duration; the pulse clipper switched off at peak power and removed the nitrogen tail of the CO₂ pulse. The condenser divided the beam in half and the beam splitter removed another 50%. A helium-neon laser was used in conjunction with the CO₂ laser to ensure precise focusing of both lasers. A zinc selenide lens (0.5 inch focal length) focused the laser on the cornea placed onto a motor-mike driven translation stage (Oriental, 2.5 μ m stepping accuracy).

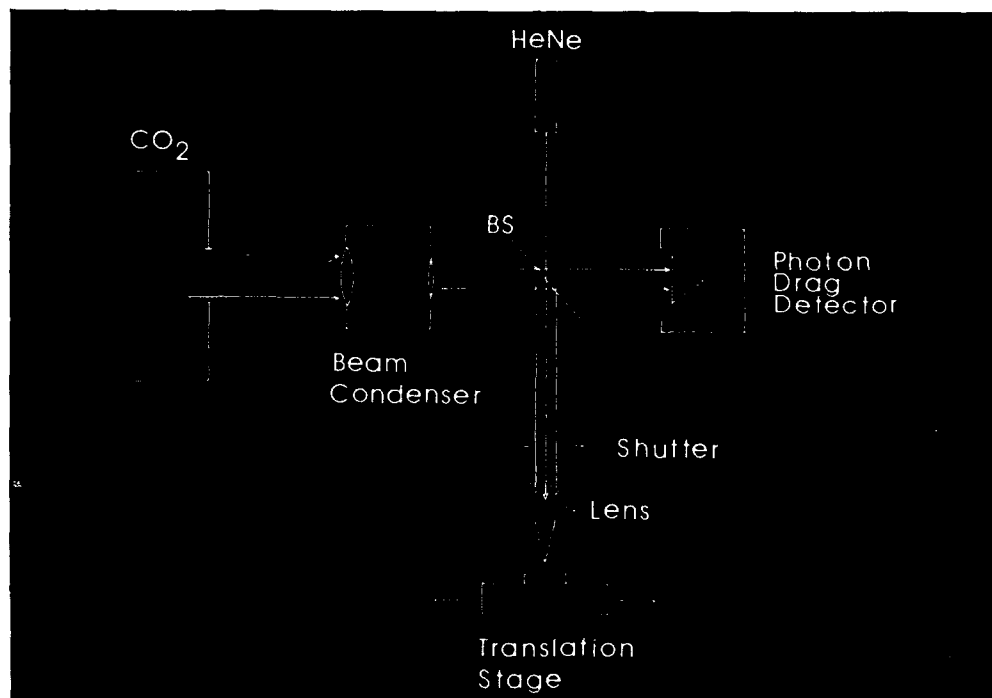


Figure 1. The schematic represents the CO₂ delivery system used in the study. The action of the condenser and beam splitter (BS) resulted in a 50% reduction of the beam at each location. The helium-neon (HeNe) laser was used to focus the beam through the 0.5 inch focal length zinc selenide lens.

Seven human eye bank corneas stored at 4 - 8 °C in K-Sol for 2 to 10 days (\bar{x} = 5.4 days) were used in the study. Two corneal buttons (5 mm diameter) were removed per cornea and were ablated with the CO₂ laser or incised with a diamond knife. To determine if the motion of the stage created any additional tissue disturbance, two types of laser ablations were made: incisional and single site. Following ablation, the button was bisected and both halves were placed into 2.5% glutaraldehyde in 0.2 M sodium cacodylate buffer. The specimens designated for transmission electron microscopy were subsequently sectioned for proper orientation during processing, post-fixed in 1% OsO₄ in 0.2 M sodium cacodylate, dehydrated in a series of increasing strengths of alcohol, infiltrated with a propylene oxide:Spurr mixture and embedded in Spurr resin. The ultra-thin sections were stained with lead citrate and uranyl acetate before viewing with a Jeol JEM-100 CXII microscope. The scanning electron microscopic specimens were removed from glutaraldehyde, dehydrated in a series of increasing strengths of alcohol, and critical point dried under a constant flow rate system. A gold-palladium element was used to sputter coat the specimens, they were mounted on aluminum stubs and were viewed with an International Scientific Instruments DS 130 microscope operated at 5 kV.

Results

The incisions and ablations in the tissue demonstrated several important findings. When comparing laser ablations of the cornea (Figure 2) to diamond knife incisions (Figure 3), scanning electron microscopy indicated a sharp cleavage plane through the tissue in both cases. The laser ablations resulted in a relatively jagged incision, which led us to perform single site ablations which removed the influence of the translation stage and allowed assessment of the uneven appearance of the incision, discriminating between movement of the stage or configuration of the beam. The smooth appearance of the walls of single site ablations (Figure 4) indicated the significant role the translation stage played in producing an uneven appearance.



Figure 2. Compared to the diamond knife incision, the linear ablation created by the pulsed CO₂ laser created a relatively jagged incision (X 600).



Figure 3. This micrograph of an incision made by a diamond knife demonstrates a sharply defined linear cut through the tissue. Note: the abnormal disrupted appearance of the epithelium is characteristic of changes that occur to corneal tissue during long-term storage in eye banking media (X 600).

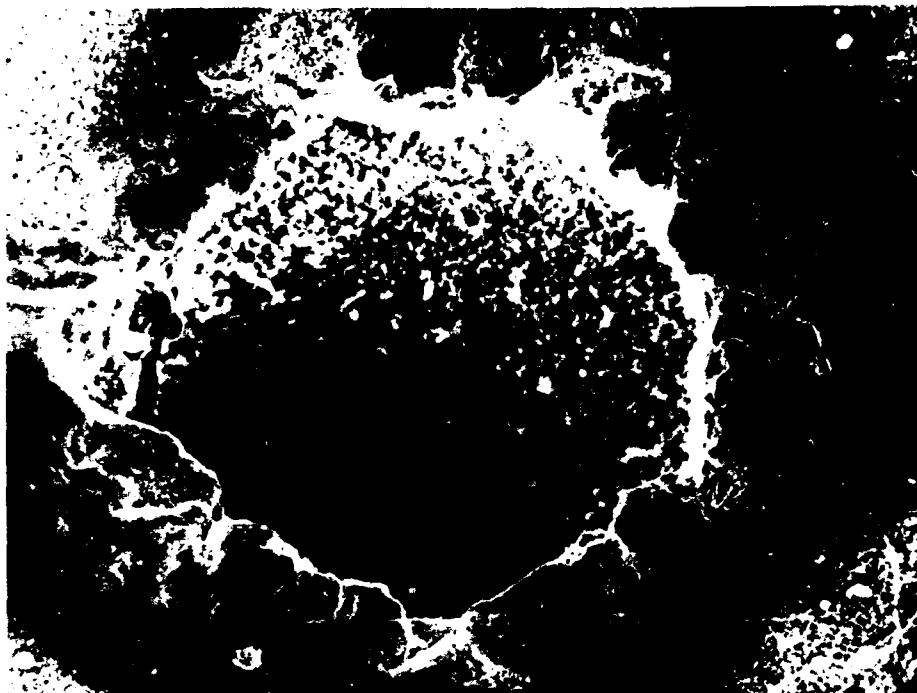


Figure 4. Scanning electron microscopy demonstrated a single site ablation in a human eye bank cornea that received three pulses with the pulsed CO₂ laser. Note the smooth sides of the ablation (X 1000).



Figure 5. A diamond knife incision created an irregular uneven lamellar pattern in the stroma of this human eye bank cornea as represented in this transmission electron micrograph (X 5500).

The incision made by a diamond knife had an irregular appearance (Figure 5). Presumably, the different angles and tensions of each lamellar layer of stroma resulted in an uneven surface along the wall of the incision. The side walls of the laser ablation appeared much smoother than the diamond knife incision (Figure 6). There was no indication of thermal damage to the bottom or side walls of an ablation that received three pulses to the same site.



Figure 6. This transmission electron micrograph clearly demonstrates a lack of thermal damage to the bottom or to the side wall of the human eye bank cornea that received three pulses to the site. Note: the presence of intrastromal edema is not unusual for a cornea during long-term storage in eye banking media (X 19200).

Discussion

We have demonstrated our goal to minimize thermal damage to areas adjacent to an ablation created by a CO₂ laser utilizing scanning and transmission electron microscopic techniques. This objective was predicted on the ability to deliver a CO₂ laser pulse of correct duration such that tissue could be vaporized without allowing excess energy to dissipate into surrounding tissue. Our observations have demonstrated several points. The translation stage played an important role in producing an uneven appearance to the incision and when this factor was eliminated, the walls of the ablation appeared smooth. The need for a stable translation stage has been illustrated. Additionally, the uneven appearance of the wall of the diamond knife incision was possibly created by the knife encountering the lamellar layers at different tensions and angles. However, the laser did not create an irregular appearance to the bottom or the sides of the ablation, but had created a smooth surface instead.

Laser corneal surgery involved in similar investigations has utilized the excimer laser. Although this work has demonstrated clean, precise ablations [1-2], there are numerous disadvantages associated with the excimer. The excimer laser utilizes similar technology to the CO₂ laser, but the corrosive halogens used in the excimer cause reliability problems not encountered with the CO₂ laser. The corrosive gases used in the excimer require special

mixing stations not needed by the CO₂ laser and these corrosive gases greatly diminish the shelf life of the eximer as well as cause degradation of the electrodes and optics of the laser system. The gases used in the CO₂ laser, CO₂, He and N₂, do not inhibit shelf life of the laser nor do they present the same safety hazards that halogens do in the eximer system.

Absorption of the ultraviolet energy of the eximer laser creates a chemical interaction that physically breaks intramolecular bonds. Because most organic molecules strongly absorb in the ultraviolet range, the hazards of biological complications by DNA damage from ultraviolet lasers remain a significant question. The clinical acceptance of the eximer laser will require an evaluation of the importance of ultraviolet-induced carcinogenesis and mutagenesis. The CO₂ laser emits a wavelength of 10.6 μ m which results in thermal interaction only.

In conclusion, the CO₂ laser, initially developed for military application, offers a safe, highly reliable, field-proven and cost-effective alternative to the eximer laser. Our preliminary work is promising, however, more work will be needed in the areas of wound healing and repair, stability of incisions and control of the delivery system. However, the effort will be well-spent if these obstacles are overcome.

Acknowledgments

This investigation was supported in part by the Division of Research Resources to Yerkes Regional Primate Research Center.

References

1. D.S. Aron-Rosa, C.F. Boerner, P. Bath, et al, Am J Ophthalmol 103/3II,454 (1987).
2. M.G. Kerr-Muir, S.L. Trokel, J. Marshall, et al, Am J Ophthalmol 103/3II,448 (1987).
3. A.J. Welch, IEEE (Inst Elec Electron Eng) J Quantum Electron QE 20,1471 (1984).
4. C.H. Dohlman in The Cornea, G. Smolin and R.A. Thoft, Eds. (Little, Brown and Company, Boston, Mass., 1987) pp. 3-16.
5. J.L. Boulnois, Lasers Med Sci 1,47 (1986).
6. D.S. Stark, P.H. Cross, H. Foster, IEEE (Inst Elec Electron Eng) J Quantum Electron QE 11,774 (1975).

LASER OPTIC FIBER SYSTEM REMOVAL OF PRIMARY INVASIVE SKIN CANCERS

Helen Ward

LRCP, MRCS (Lond.); BSC; MSc Physics (NSW); PhD Elec. Eng (NSW)
WARD MASRI, Medical Health and Research Center,
154 Avoca St., Randwick. NSW 2031 Australia.

and

Dept. of Optical Communications, School of Electrical Engineering,
University of New South Wales,
PO Box 1, Kensington, NSW 2033 Australia.

Abstract

Hitherto, traditional methods of skin cancer treatment such as liquid nitrogen, skin graft and cobalt therapy have resulted in regrowth of skin cancers or disfigurement. A laser optic fiber system and method of treatment was developed for application on an out-patient basis, to skin cancers. Skin cancers, such as Basal Cell Cancers (B.C.C.'s) and Squamous Cell Cancers (S.C.C.'s), ranging from early stages to widely invasive (6x10cm) lesions, and early primary melanomas, were treated. Results of the long-term, 9 year study showed that even very large lesions did not require skin grafts. Epithelial elements grew beneath a firm crust and formed new pink skin when the crusts fell off, leaving little residual mark (small scars were left if lesions were deeply invasive). Although some malignant lesions (approx. 10%) required 2 treatments close together, there was no recurrence after 9 years for several thousand cases of skin cancers. It is concluded that this optic fiber system is an important tool for eradicating a disfiguring and potentially fatal disease.

Introduction

Australia, especially Queensland, is the skin cancer capital of the world. It is closely followed by parts of California and Texas.

Australia has a population of 15.5 million people. Around 1500 deaths occur every year from skin cancer, and over one hundred and fifty thousand people are treated very year for skin cancer¹. Skin cancer is responsible for over 7,500 deaths in the USA per year².

Hitherto, traditional methods of treatment of advanced skin cancers such as liquid nitrogen, skin graft and cobalt therapy have resulted in either regrowth or disfigurement as is shown in fig. 1. This patient developed a Basal Cell Cancer of

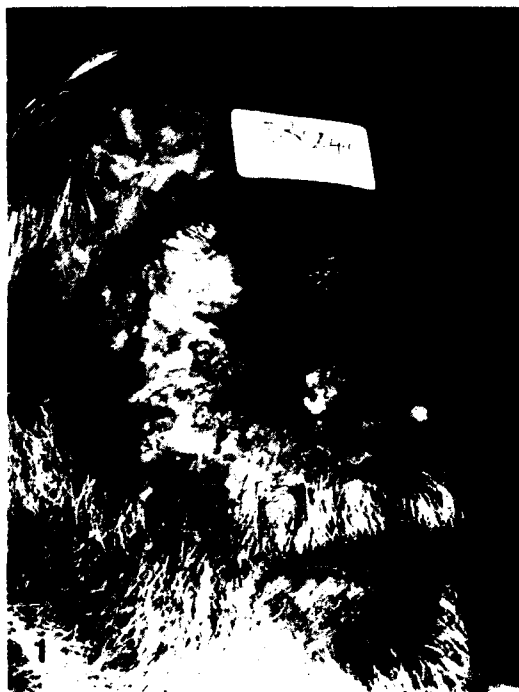


fig. 1: Disfigurement of patient following skin flap excision for B.C.C. of lower eyelid. Despite further subsequent excision; liquid nitrogen and CO₂ laser treatment, there is regrowth of B.C.C.'s along suture line.

his lower right eyelid 20 years ago, for which he was treated by excision and a skin flap. This resulted in loss of a tear duct and a permanent weeping ectropion of his lower eyelid. The B.C.C.'s recurred along the suture line and he was treated with a skin graft; liquid nitrogen; then with a pulsed CO₂ laser. But the B.C.C.'s returned.

Even treatments of early skin cancers such as liquid nitrogen, diathermy, excision, leave residual marks and have a high incidence of regrowth.

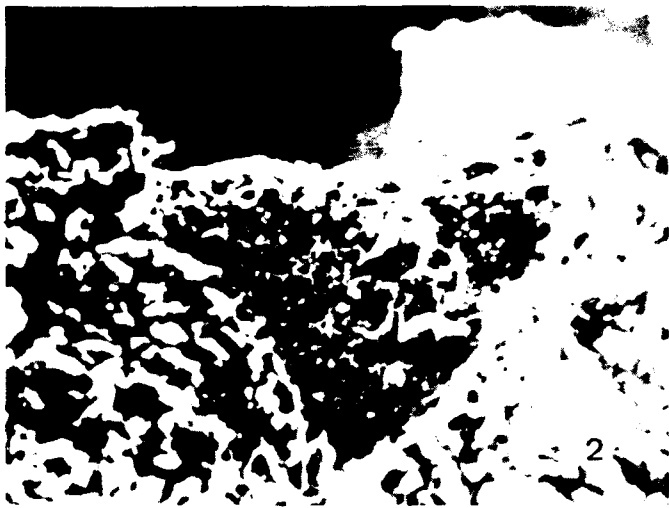


Fig 2: This electron micrograph shows the sharp borders of the crater caused by the pulsed Neodymium laser with little thermal damage to the surrounding tissue (in this case cardiac muscle). Fig 3: The electron micrograph of the CW argon laser crater shows a large area of thermal damage on the surface. Fig 4: Depicts a deep shaft with smaller zones of thermal damage with lasing by the CO₂ laser compared to Fig 5. Fig 5: Shows a shallow crater and relatively thick zones of thermal damage with the argon laser. Fig 6: In all three CW lasers, four zones of thermal damage are seen (1) explosive evaporation (2) vaporisation (charring) (3) conduction (4) "shock" or acoustic waves. Fig 7: The crests of the acoustic waves may be seen in this slide of CO₂ lasing of heart muscle taken by cinematography.

The following presentation is the result of a 9 year clinical study of laser removal of over seven thousand skin cancers.

Method

In 1976, with the view of developing a laser optic fiber system which I could apply to both my cardiac research and to a variety of skin lesions, I compared three main types of laser: CO₂, Nd-Yag, and argon³.

The absorption coefficient α of the three different lasers CO₂, Nd and Argon, has been found to be 200, 20, and 45 per cm respectively^{4,5,6}.

Using this coefficient in energy density calculations, and by experiments, I was able to come to the following conclusions:

With respect to continuous wave lasers, (i) for the CO₂ laser, most of the laser energy is used in vaporisation of tissue; (ii) for the Nd laser, a lot of the energy is used in scattering in tissue; (iii) for the Argon laser, most of the energy is absorbed by tissue pigments such as hemoglobin and melanin.

Hence, (a) much more laser energy is required to produce the same volume of vaporization (ie hole in tissue) with the argon laser than with the CO₂ or Nd lasers; (b) greater destruction to the tissue surrounding the crater walls occurred with the Argon laser than with the Nd or CO₂ lasers.

With respect to pulsed lasers: (1) a normal pulsed Nd laser produced much less damage to the walls of the tissue crater than any of the CW lasers: argon, Nd, CO₂, with the same energy density. (2) There was also much less surface damage with the pulsed Nd laser than with the CW lasers utilising the same energy density. This is shown in figs. 2 to 7.

However, the argon laser produces an additional acoustic wave owing to its absorption by melanin. Melanosomes act as heat sinks and also give out shock waves.

Figure 8 shows the optical density curve for melanin⁷, the main source of heat absorption in the skin.

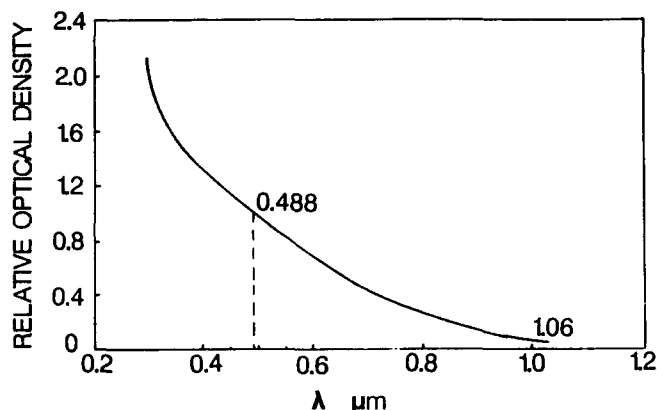


fig. 8: Optical Density curve for melanin⁷ shows marked absorption in U.V. and blue argon (488nm) wavelengths, with much less absorption in yellow, red and infra red wavelengths.

Absorption spectrum of (squid) melanin in a KBr pellet.

(Adapted from M. L. Wolbarsht et al., July 1981)

It shows that there is marked absorption by melanin in the UV to blue range of wavelengths, reducing markedly in the yellow, red and infra red wavelengths.

Hence the CW argon laser with its blue wavelengths results in maximum laser absorption by the tissue (compared for example with lasers with red or infra red wavelengths).

Treatment and Results

After experimenting with human volunteers since 1974, I developed (in 1978) an argon laser optic fiber system for the treatment of a variety of skin lesions.

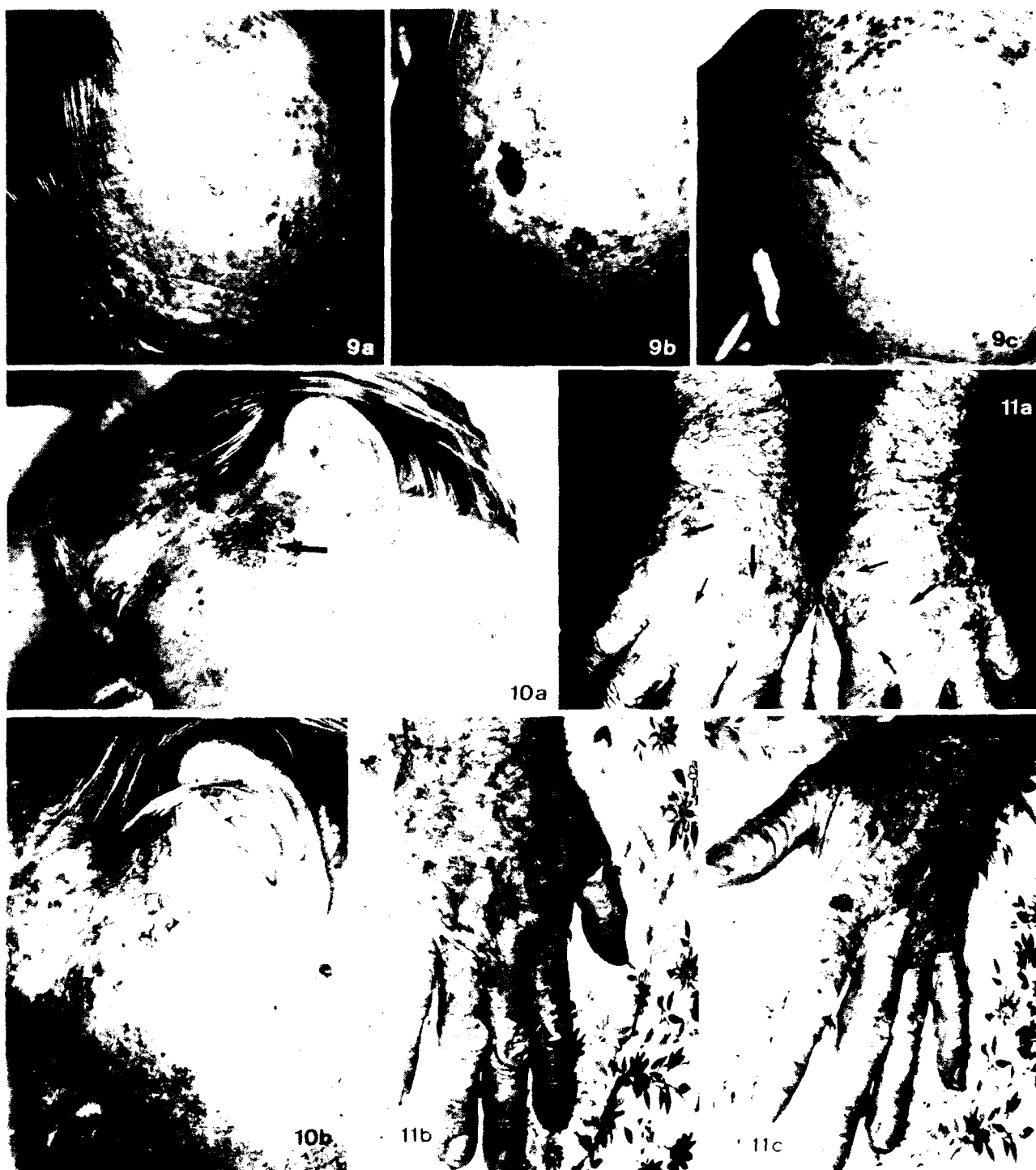
My breakthrough with skin cancers came when a patient with xeroderma pigmentosum presented, and I was able to study the results of my numerous treatments on him over a nine year period.

Xeroderma pigmentosum is a genetic condition characterised by development of multiple skin cancers of all histological types, throughout life from adolescence onwards.

Laser treatment of xeroderma pigmentosum is shown in figs 9 to 11.

Laser treatment of various basal cell cancers and squamous cell cancers are shown in figs 12 to 15.

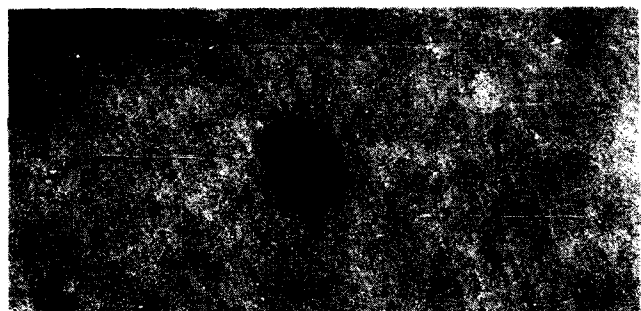
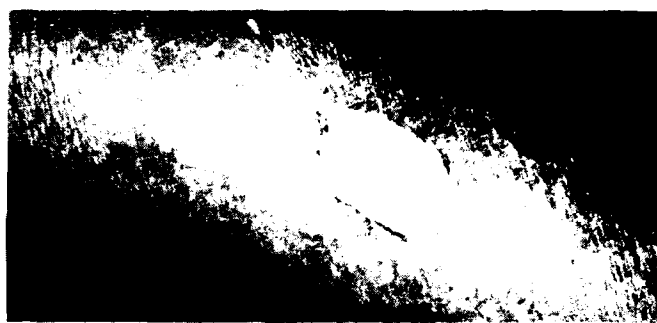
Different energies and energy densities were applied to different lesions depending upon lesion history, size, type and extent of invasion. Laser excision biopsies were performed.



Laser treatment of Xeroderma Pigmentosum. Fig 9a: Shows keratinised bleeding squamous cell cancers on the head of this patient with xeroderma pigmentosum. b: One of the lesions has just been lasered. c: Three years after laser treatment, there is no residual mark. Fig 10a: Shows a rapidly growing proliferative/bleeding squamous cell cancer which had grown in a month. b: No mark was left 3 months after lasing (there has been no recurrence in 5 years). Fig 11a: Shows the patient's hands with hyperkeratosis and squamous cell cancers. b,c: The hands seven years after laser treatment - no residual mark remains but a new squamous cell cancer has grown on one hand in a different position.



Laser treatment of various Basal cell and Squamous cell cancers. Fig 12a: Depicts a patient who has let an ulcerating SCC penetrate the skin of his neck. b: 1 week after lasing. Note a wide boundary of 5 to 8 mm was excised outside the visible margins of the lesion. c: Three weeks after lasing the lesion has healed leaving a small indented scar which occurred due to cancer penetration of the full thickness of the skin of the neck. Fig 13a: A B.C.C. is present in the outer edge of the eye (note the presence of other early B.C.C.'s). b: The same patient during lasing. c: 4 weeks later, virtually no visible mark remains. Fig 14a: An S.C.C. before lasing. b: During lasing. c: 3 weeks after lasing. Fig 15a: Depicts an invasive S.C.C. of the middle finger before lasing. Induration is present but the lesion was mobile. b: During lasing. c: 4 weeks after lasing. A dull pink mark remains. It has now faded to leave a barely perceptible scar.



Laser treatment of pigmented skin lesions. Fig 16a: Depicts a Hutchinson's freckle which has recently grown and become darker in some areas. b: The same lesion immediately after treatment. Fig 17a: This thirteen year old girl had a nodular melanoma on her stomach which had recently become elevated, darker and larger. b: 2 weeks after laser treatment, the lesion is healing well.

Laser treatment of difficult cases. Fig 18a: This figure reveals a recurrent multifocal diffuse B.C.C. on the patient's arm during laser treatment. There are other skin cancers present. They had all been treated previously by other means such as excision by scalpel. b: Shows a very large skin cancer being treated on the same patient's back. Fig 19a: This patient many years ago had half his right ear removed due to a skin cancer. I lased a large squamous cell skin cancer off the left half of his bottom lip. b: 6 months later after one treatment only, there was little perceptible residual mark on his lip.

Laser treatment of pigmented skin lesions is shown in figs 16 and 17.

Difficult Cases

Fig 18a and b shows another patient with xeroderma pigmentosum who only recently presented to me.

Unfortunately this gentleman has had over 5000 treatments since he was 14 years old including a craniotomy for a histiocytoma. He is a barrister in his forties and is disfigured facially. This is quite a difficult problem to treat by any method, at this late stage, and will require a lot of lasing. It is preferable to advise all cases of xeroderma pigmentosum at an early age to move to a shady climate such as England if they are to enjoy a reasonable quality of life.

Conversely, several cases of squamous cell cancers on lips (figs 19a, b) and eyelids have been treated and responded by healing very well.

Results of the long-term, 9 year study showed that although some malignant lesions (approx. 10%) required 2 treatments close together, there was no recurrence after 9 years for several thousand cases of skin cancers.

Conclusions

In conclusion, with respect to tumor treatment: this laser optic fiber system and method of treatment appears to selectively destroy rapidly growing abnormal cells and to spare normal epithelial elements.

In this way, a large lased area which would appear to be a third degree burn does not leave a residual ulcer and does not require a skin graft.

Patients were found to present earlier for treatment of skin cancers (especially melanomas) if they knew the treatment was relatively inexpensive, simple, quick and on an outpatient basis under local anaesthetic. It is concluded that this laser optic fiber system is an important tool for eradicating a disfiguring and potentially fatal disease.

References

1. A.J.J. Emmett and M.G.E. O'Rourke, Malignant Skin Tumours (Churchill Livingstone, New York, 1982), pp.4-9.
2. Cancer - A Cancer Journal for Clinicians, American Cancer Society 36(1), pp.9-17 (Jan/Feb 1986)
3. H. Ward, Laser Interaction with Matter at Moderate Intensities, MSc Physics (University of New South Wales, Sydney, 1980), pp.61-122
4. R. Verschueran, The CO₂ Laser in Tumor Surgery (Van Gorcum, Netherlands, 1976), p.42.
5. J.B. Hardy, H.T. Hammel and D. Murgatroyd, J. Appl. Physiol. 5, 257 (1956)
6. L.A. Priebe, in Laser Surgery, Pt II, I. Kaplan, Ed. p.242 (1978)
7. M.L. Wolbarsht, A.W. Walsh and G. George, Appl. Optics, 30, 13, 2184-2186 (1981)

INCISION HEALING AFTER MILLIWATT CO₂ LASER WELDING:
A COMPARISON OF RESULTS ACHIEVED WITH INSTRUMENTS OF VARYING DESIGN

Charlotte H. Greene, Ph.D.
Associate Professor of Physiology and Pharmacology
Philadelphia College of Osteopathic Medicine
4150 City Avenue
Philadelphia, Pennsylvania 19131
Domenic A. DeBias, Ph.D.
Professor and Chairman, Department of Physiology and Pharmacology
Philadelphia College of Osteopathic Medicine
4150 City Avenue
Philadelphia, Pennsylvania 19131
Wanda L. Young, B.A.
Senior Research Assistant
Philadelphia College of Osteopathic Medicine
4150 City Avenue
Philadelphia, Pennsylvania 19131
Maryanne J. Henderson, B.S.
Second Year Medical Student
Philadelphia College of Osteopathic Medicine
4150 City Avenue
Philadelphia, Pennsylvania 19131
Kiyoko I. Lehmann
Senior Research Associate
Philadelphia College of Osteopathic Medicine
4150 City Avenue
Philadelphia, Pennsylvania 19131
Scott A. Cosmi, B.S.
Supervisor of Electron Microscopy
Philadelphia College of Osteopathic Medicine
4150 City Avenue
Philadelphia, Pennsylvania 19131

Abstract

In this study the histology of CO₂ laser weld closures produced by two instruments of differing design were compared. Laser welding was also compared to conventional suture closure. Twelve New Zealand white rabbits were randomly assigned to one of two groups. Two full thickness incisions were made through the anterior aspect of the tongue in each animal. One incision was closed with focal welds using a different laser instrument for each group. The other incision was closed with interrupted sutures. Three animals in each group were sacrificed immediately and three were allowed to heal for eight days. Macroscopic and microscopic examination of the incision sites revealed no difference between the results obtained with either laser. In contrast, suture closure resulted in a longer healing time, a greater foreign body reaction in the involved tissue; it also necessitated a longer period of time to complete the repair.

Introduction

In this study the use of a Sharplan 1040 CO₂ surgical laser system was compared to a Bioquantum 7600 CO₂ microsurgical laser for tongue incision closure by laser welding. A comparison was also made between laser closure and conventional suture closure.

Increased clinical use of lasers has created a need for surgical training in the mechanics of handling the instruments and in the appropriate modification of existing procedures to incorporate the use of lasers. Since both of the lasers in this study are used for physician training in our institution, it is important to determine whether inherent design features of the particular laser or inexperience of the operator account for specific problems whenever they arise.

Therefore, we designed a surgical protocol that could be used with each of the lasers independently to determine whether similar results could be achieved with each in the hands of a single experienced operator. Although demonstration of equivalent results for this procedure may not extend to more complex applications where one laser may be more suitable than the other, the study does provide for an experience with each instrument which improves our ability to evaluate both laser and operator performances. Future studies are planned to examine other clinical procedures by applying a standard protocol while varying the type of laser instrument used.

Materials and Methods

Lasers

Both lasers operate at 1060 nm infrared in a gaussian mode. The Sharplan laser is continuously adjustable between 2 and 40 watts and 100 and 2,500 milliwatts. The beam is delivered through a spring balanced articulated arm which was coupled to an operating microscope and a manually controlled micromanipulator. The Bioquantum laser is continuously adjustable between 50 and 4,000 milliwatts. The beam is delivered through an adjustable optic coupled to an operating microscope and a manually controlled micromanipulator which has a variable gain setting that permits a range of sensitivities in the control of the joy stick.

The impact size of the focused beam at 250 milliwatts was determined by a modification of the method of Kiang and Lang¹. To find the correct focus isolated lines of single laser burn spots were made at different focus adjustments near the damage threshold of thermally sensitive paper. Impact size was evaluated microscopically because the visual focus does not necessarily coincide with the focus of the laser beam. Both systems were used with a 400 mm focal length lens.

The impact diameter of the focused Sharplan laser was measured at 0.42 mm with a cross-sectional area of 0.075 cm² using 250 milliwatt power measured at the target plane with a Diamond Ophier power meter. The irradiance was 340W/cm² and the energy fluence 170 joules/cm² with an exposure time of 0.5 seconds for each weld. The impact diameter of the focused Bioquantum laser was measured at 0.3 mm with a cross-sectional area of 0.71 cm² using 250 milliwatt power measured at the target plane. The irradiance was 354 W/cm² and the energy fluence 177 joules/cm² with an exposure time of 0.5 seconds for each weld.

Animals

Twelve New Zealand white rabbits weighing between 3 and 3.5 kg were randomly assigned to one of two groups. Group I was treated with the Sharplan laser and Group II with the Bioquantum laser; all other aspects of the protocol were identical for both groups. Operative procedures were performed under sodium pentobarbital anesthesia (30 mg/kg i.v.). Post operative analgesia and antibiotic therapy were administered to prevent pain and infection.

Surgical Procedure

The tongue was fully extended, immobilized and supported along the full length of the inferior surface. Two two-centimeter full-thickness incisions were made on each tongue anterior to the v-shaped solcus and to the right and left of the medial line. The edges of the left incisions were approximated and the incision closed with interrupted 6-0 absorbable sutures. Laser welds were performed on the right incisions by approximating the edges and then delivering focal welds at three sites; the most proximal and the most distal extensions of the incision and a site midway in-between. All welds were delivered at 250 mW for 0.5 seconds. Three animals in each group were sacrificed immediately following the surgical procedure; the remaining three animals in each group were sacrificed on the eighth day post surgery by intracardiac injection of a saturated MgCl₂ solution. The wound area was excised and prepared for histological examination using conventional techniques.

Results

Figure 1 shows the sites of the fresh welds produced by each laser. The initial effect with either laser was a flattening of the partially keratinized epithelium and a sealing of the side walls of the incision that occurred concurrently with hemostasis of the area. There was also some sloughing of cells and a loss of cellular detail in the uppermost layers. Penetration for both lasers appears to average approximately five-cell layers deep. Macroscopically, there was a faint zone of white discoloration following application of the laser; no charring was observed.

Figure 2 shows the sites of the healed welds on the eighth day post operative. There was minimal inflammatory response. The incision edges were directly opposed, and the collagen bridging made it difficult to measure any gap between the incision walls in either group. A small circumscribed area of epithelial cell thinning was noted in both groups in the impact area of the tissue.

Figure 3 shows the acute trauma due to suture placement. The average distance across the cleft between the walls of the incision is 0.9 mm, and the walls were not as closely aligned as with the laser welds. Higher magnification reveals the grossly hypoxic appearance of the tissue circumscribed by the suture.

Figure 4 shows the suture sites on the eighth day post operative. The suture trauma is only partially resolved. The channel is still open and contains remnants of suture material; it is also surrounded by fibroblasts and the adjacent tissue contains numerous polymorphonuclear granulocytes; other changes consistent with an active inflammatory

reaction were evident.

Discussion

The tissue changes produced by both lasers were equivalent. Each produced accelerated healing, minimal trauma, and reactive changes as opposed to conventional suturing. There were some differences in the ease of handling the laser beam because of different designs in the manually controlled micromanipulators. Differences were also found in the impact size which may become significant at higher energies, in procedures requiring finer control of the beam, and for procedures requiring uniform lasing of large areas. Nevertheless, the results obtained in the range of energy studied and with the type of tissue and procedure used, were satisfactory and similar.

Suture closure was found to be less satisfactory because of the increased trauma to the tissue, greater inflammatory response, delayed healing, and decreased precision in alignment of the incision walls.

References

1. Y.C. Kiang and R.W. Lang, Applied Optics 22(9), 1296 (1983).

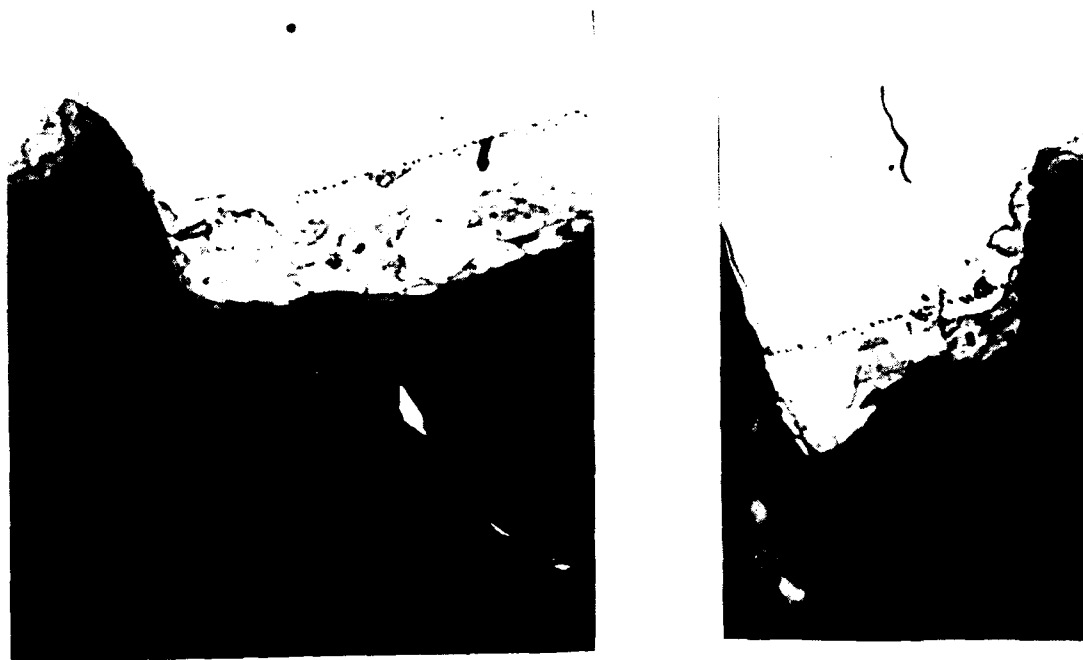


FIGURE 1. Site of fresh welds: Sharplan laser (left), Bioquantum laser (right). Epithelial cell flattening with sloughing of cells was evident. (Original magnification 125X).



FIGURE 2. Site of healed welds: Sharplan laser (left, above), Bioquantum laser (right, above). Epithelial cell thinning (arrows) was noted in the impact area (original magnification 125X).



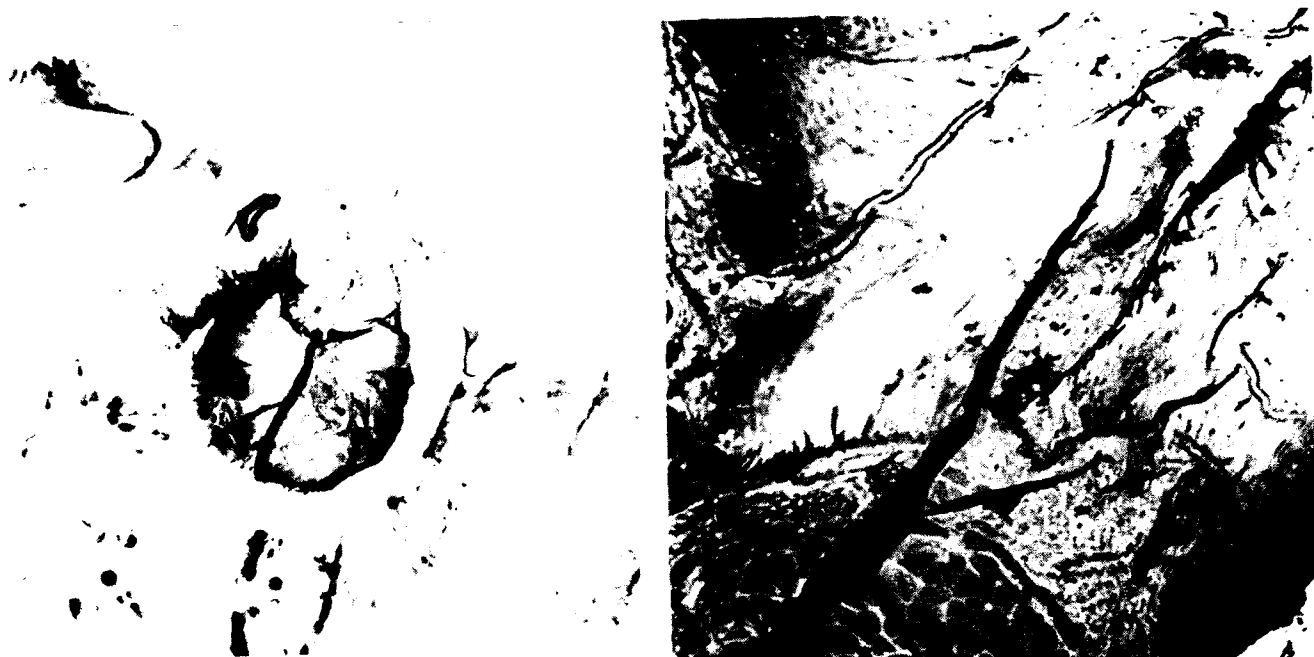
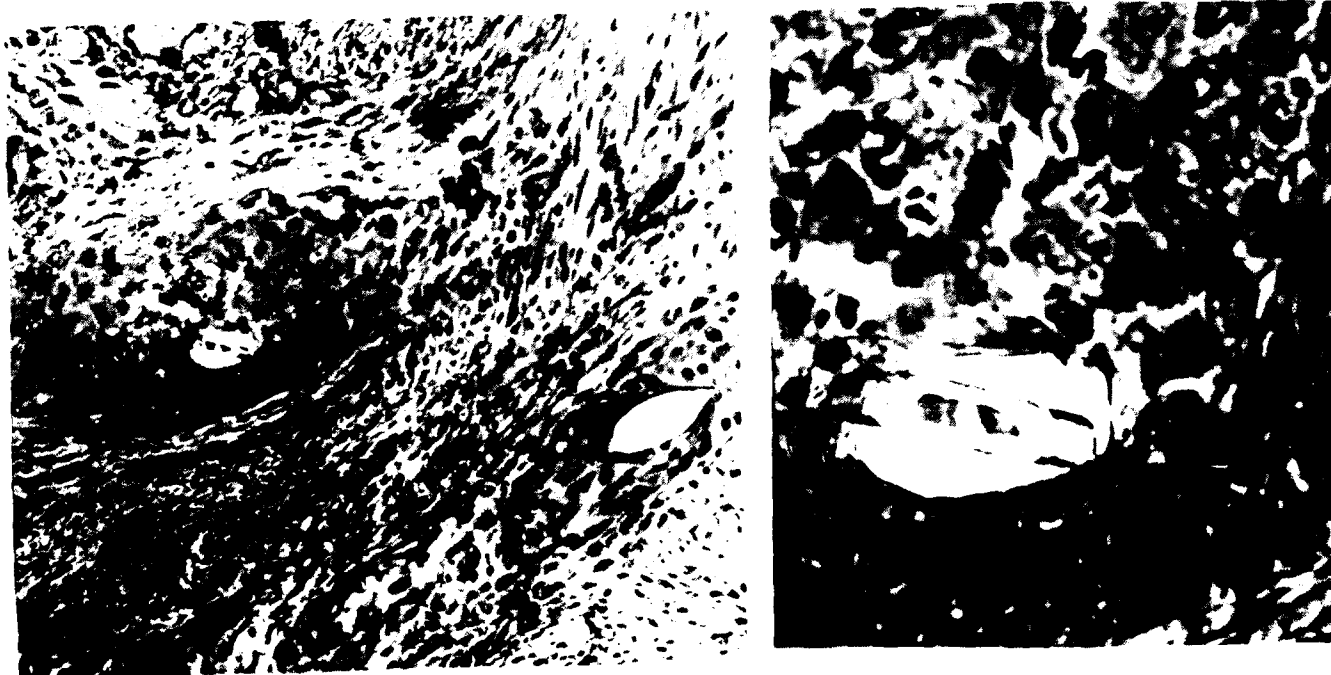


FIGURE 3. Site of acute trauma due to suture placement (above left) original magnification 31.25X; above right original magnification 125X).

FIGURE 4. Suture trauma is only partially resolved by the eighth day post-operative (below left, original magnification 31.25X; below right original magnification 500X).



LABORATORY MODELS FOR UTILIZING LASER TECHNIQUES IN EDUCATION AND RESEARCH

Domenic A. DeBias, Ph.D.

Professor and Chairman, Department of Physiology and Pharmacology

Philadelphia College of Osteopathic Medicine

4150 City Avenue

Philadelphia, PA 19131

Charlotte H. Greene, Ph.D.

Associate Professor, Department of Physiology and Pharmacology

Philadelphia College of Osteopathic Medicine

4150 City Avenue

Philadelphia, PA 19131

Ronald A. Kirschner, D.O.

Clinical Associate Professor, Department of Ear, Nose and Throat

Philadelphia College of Osteopathic Medicine

4150 City Avenue

Philadelphia, PA 19131

Leonard H. Finkelstein, D.O.

Professor of Surgery and Chairman, Division of Urology

Philadelphia College of Osteopathic Medicine

4150 City Avenue

Philadelphia, PA 19131

Abstract

Courses of instruction and research on the medical uses of lasers require adequate models. Undoubtedly, a wide variety of models are conceivable. In this report, several models that are satisfactorily used in the "hands-on" laser course offered by the Institute of Applied Laser Surgery and Philadelphia College of Osteopathic Medicine are described. Each has been demonstrated to be adequate for the respective specialties instruction in course. Others are in the process of development.

Introduction

Adequate training is a prerequisite to the efficacious use of lasers in medicine. With this in mind, laser courses offered jointly by the Institute of Applied Laser Surgery and the Philadelphia College of Osteopathic Medicine have provided intense "hands-on" experiences using animal models. Most of the models successfully used in the courses will be described in this report.

Procedures

All of the models are prepared on animals (dogs, rabbits, pigs) while in the surgical plane of anesthesia. The anesthetic most widely used is intravenous pentobarbital, 30 mg/kg; the ear veins of the rabbit and pig are readily accessible for infusion; the antecubital vein is used in the dog. In the case of the pigs, a preanesthetic cocktail consisting of Ketamine (22 mg/kg) and Promazine (1.1 mg/kg) is injected intramuscularly (gluteal muscle). Maintenance of anesthetic level is accomplished via anesthetic administration through indwelling catheters PRN. Upon completion of the "hands-on" laboratory, cardiac arrest is induced in the animals by administration of a large bolus of $MgCl_2$ intravenously. The carcasses are subsequently cremated. In cases where the animal models are used for research, the anesthetic procedures are the same as above. All surgical procedures are performed aseptically, and the animals are allowed to recover for further study, if necessary.

All housing and surgical procedures are in strict compliance with the NIH "Guidelines for the Care and Use of Laboratory Animals": (revised, 1985).

Bladder Neoplasm Simulation.

This model (30 kg male dog) is provided for the urology trainees¹. The model is prepared in two stages and is graphically illustrated in figures 1 and 2. In the first stage, the bladder is exposed via a midline abdominal incision. A $\frac{1}{2}$ inch incision is made through the trigone muscle. A strip of rectus muscle is separated and an end of the muscle is entered through the trigone incision and sutured to the bladder floor. At this time, a segment of ilium is "tacked" onto the serosal site of the bladder and will provide an opportunity for the trainee to observe any damage to the underlying structures when higher power densities are used.

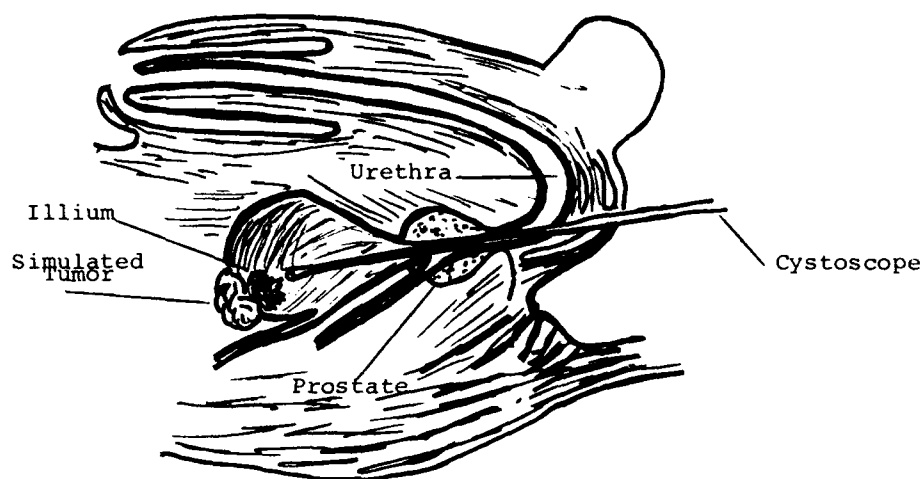


FIGURE 1. BLADDER MODEL WITH CYSTOSCOPE IN PLACE

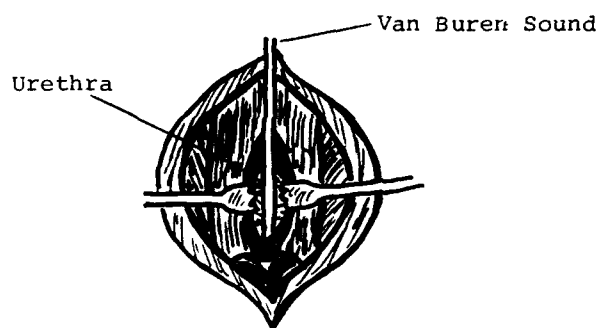


FIGURE 2. PERINEAL URETHROTOMY

In the second stage, the animal is prepared for cystoscopy. The dog's urethra has an acute curvature which prevents urethral cystoscopy. To circumvent this limitation, a perineal urethrotomy is performed. It is helpful to locate and expose the urethra if a 10 F catheter is passed through the urethra into the bladder. The exposed urethra is entered via a vertical incision and the edges are sutured to adjacent structures. A Van Buren sound is used to dilate the urethra before inserting the cystoscope and accompanying laser probe. With the cystoscope in place, the simulated neoplasm can be visualized and the lasing techniques can be initiated. The male dog also presents the prostate as an additional lasing site.

Tracheal Obstruction.

This model is provided for the bronchopulmonary trainees². The model is diagrammed in figure 3. The trachea is exposed via a midline incision. An inferiorly based pedicle from a split strap muscle is entered into the lumen of the trachea through a tracheostomy incision between two rings.

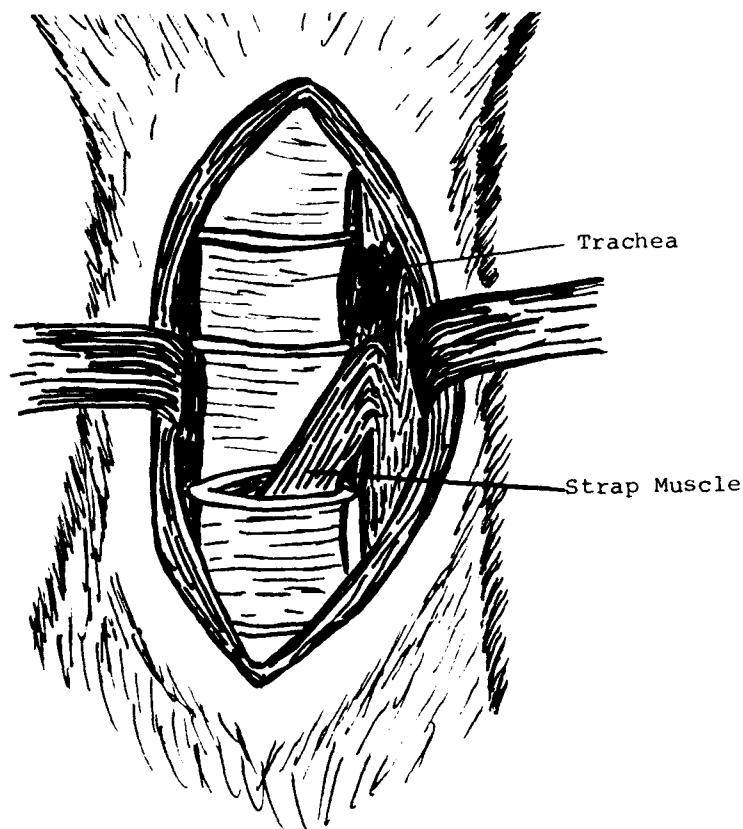


FIGURE 3. TRACHEAL OBSTRUCTION

End to End Anastomoses.

The feasibility of end to end anastomosing (i.e. blood vessels, tendons, veins, bowel, fallopian tubes, vas deferens, ureters, etc.) can be readily demonstrated in a mal models³. The structures to be anastomosed may be approximated with two stay sutures placed opposite to each other; a 7-0 suture stent may also be passed through the lumen. Following welding, patency of the lumen can be demonstrated by infusing a radio opaque dye through the lumen of the structure and visualization under fluoroscopy as seen in figure 4.

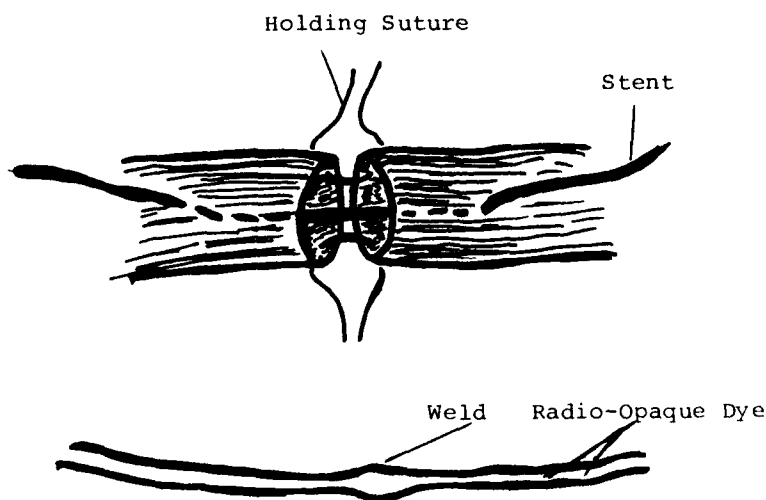


FIGURE 4. END TO END ANASTOMOSIS

Tattoo, Nevi, Hemangiomas.

In this model (figure 5), a tattooing instrument is used to introduce india ink inter-dermally to simulate tattoos, port wine nevi, and hemangiomas. Rabbit abdomen and backs present satisfactory surfaces for preparing the model and for ablation by lasers.

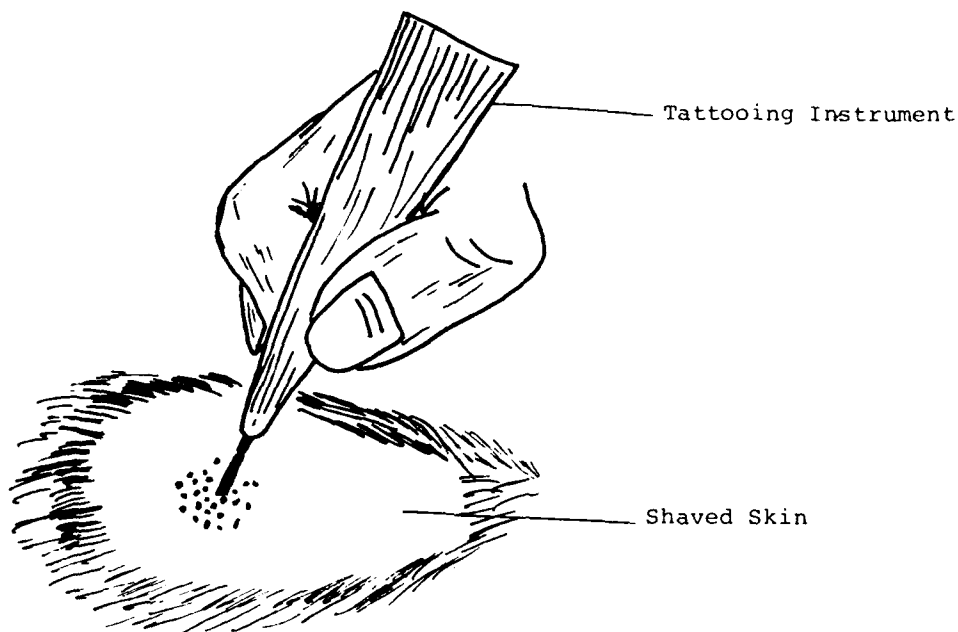


FIGURE 5. TATTOO

Also, the ear veins in the rabbit can serve as models for superficial varicoses and spider angiomas.

Other Possible Models.

Nephrectomy, partial hepatectomy, cervical conization and other models can be designed for instruction and/or research into the use of lasers in medicine.

References

1. Finkelstein, L.H., D.A. DeBias and C.H. Greene, Lasers in Medicine and Surgery. 6: 538 (1987).
2. Kirschner, R.A., M. Unger, D.A. DeBias, B.C. McDonnell and C.H. Greene, (Submitted for publication).
3. Weiner, P., L.H. Finkelstein, C.H. Greene and D.A. DeBias, Lasers in Medicine and Surgery. 6: 534 (1987).

ARTERIAL-VENOUS SIDE TO SIDE ANASTOMOSIS USING A COMPUTERIZED 1.32um Nd:YAG LASER
R. Nelson, D. Dew, T. Hsu, S. Martin, M. Cohen,
Orlando Regional Medical Center
Department of Surgery
1414 South Kuhl Avenue
Orlando, Fl 32806

Abstract

In this report, we show that arteriovenous side-to-side anastomosis of 3mm-5mm pig femoral vessels can readily be accomplished with a computer controlled 1.319 um, Nd:YAG laser system and standardized operative technique. At Orlando Regional Medical Center Laser Research and Demonstration Center we have greatly simplified laser tissue fusion and have successfully overcome many of the problems which have plagued laser tissue fusion in the past. Parameters which heretofore were left to the control of the surgeon are now automatically controlled by the computer, leaving the surgeon free to concentrate on principles of good operative technique. The technique is safe, fast and reproducible. Also, since the parameters are so well controlled, tissue bonding is maximized and tissue destruction is left to a minimum. We have had no incidence of pseudoaneurysm formation or anastomotic leaks. We feel that this system and operative technique is feasible for controlled clinical trials creating radiocephalic AV fistulas for purposes of renal dialysis. Once proven in human AV fistula trials, we foresee further clinical applications such as closure of femoral, carotid, and deep abdominal arteriotomies as well as anastomoses of various vascular autogenous grafts.

Introduction

In the past, the field of laser tissue fusion has been fraught with confusing results. Successful laser tissue fusion is dependent upon fine control of several variables including laser type, specific laser parameters, and operative technique. Several different types of lasers (argon, carbon dioxide, Nd:YAG) and operative techniques have been used for laser tissue fusion. Since the operative technique and laser parameters have not been standardized, it has been difficult to obtain reproducible results, either by the same experimenter, or from one experimenter to the next. Therefore, some type of standardization in the field of laser tissue fusion in order to insure more reliable results.

Laser tissue fusion is hypothesized to be made possible by the controlled heating and denaturation of tissue protein, resulting in a tissue bond formed by the protein coagulum. As tissue is heated, it goes through four sequential changes: heating; coagulation; evaporation; carbonization. Heating past 100 degrees centigrade results in evaporation of cellular water with subsequent charring and destruction of tissue. Therefore, for successful laser tissue fusion, it is essential to halt these tissue changes at the coagulation stage. In order to do this, several parameters have to be simultaneously controlled; laser type (argon, carbon dioxide, Nd:YAG), wave length, beam geometry, (which differs with laser type), exposure time, spot size, power level. At the Orlando Regional Medical Center Laser Research and Demonstration Laboratory we have successfully standardized these parameters through the development of a software driven 1.319 Nd:YAG laser system. By combining a computer controlled laser system with a standardized operative technique, we have greatly simplified laser tissue fusion and have overcome many of the problems which have plagued laser tissue fusion. As previously reported, we have standardized our methods through extensive animal studies in the rat. In this report, we show that arteriovenous side-to-side anastomosis of 3.0 to 5.0 mm. pig femoral vessels can readily be accomplished with our system and that our methods are feasible for human studies with potential applicability to the creation of arteriovenous fistulas for renal dialysis.

Materials

Our system consists of a specially modified Nd:YAG Laser operating at a wave length of 1.319 um. This totally programmable laser system is interfaced with an AT 80286 microprocessor. Critical data (e.g., exposure time, spot size, power level) is encoded on a floppy disk with hard disk backup that is accessed by the laser microprocessor system. The surgeon selects the appropriate tissue type (e.g. 3mm artery), and the microprocessor then automatically adjusts the laser parameters for ideal tissue fusion. The laser beam is delivered to the operative field through 400 um. fiber optic fiber which is connected to a specially designed hand piece which can be manipulated in much the same fashion and ease as an electrocautery. This maximizes operative flexibility and limits technical interference

with surgical procedures. The hand piece is fitted with an adjustable distance guide designed to keep the tip of the fiber-optic fiber a given distance from the tissue to be welded. Since the laser beam is cone-shaped, as the length of the distance guide is increased, the spot size at the tissue level is also increased and the energy transfer for a given volume of tissue is decreased.

We have chosen the Nd:YAG laser because it seems to be the ideal system for laser tissue fusion. CO₂ lasers are severely limited by water and argon lasers are severely limited by blood due to their absorption spectra. YAG laser beams are not absorbed well by either blood or by water and therefore are more practical for clinical laser tissue fusion since they are effective in wet, bloody or dry operative fields. The 1.319 Nd:YAG is much more effective in bloody fields than the 1.06 Nd:YAG and is therefore the wave length of choice. The relative penetration in blood for the argon, 1.06 Nd:YAG, and 1.319 Nd:YAG is shown below (Fig. 1).

Relative Penetration In Blood

Argon	1.0
1.06 Nd:YAG	4.2
1.32 Nd:YAG	11.3

Fig. 1. Relative penetration in blood for argon, 1.06 Nd:YAG, 1.32 Nd:YAG Lasers.

Methods

After adequate ketamine and nembutal anesthesia is obtained, the pig is placed in the supine position on the operating table and the femoral artery and vein exposed. Bulldog clamps are then placed on the artery and vein for proximal and distal control of the vessels. Heparinization is not necessary due to the very short clamp time needed. Small longitudinal openings are then made with a #11 scalpel blade in the artery and vein for a side-to-side anastomosis. It is essential that the arteriotomy and venotomy be clean-cut in that ragged edges are extremely difficult to approximate and may result in an anastomotic leak. Once the arteriotomy and venotomy have been completed, three #8-0 cardiovascular prolene stay sutures are placed in the posterior wall in order to approximate the vessel edges for laser tissue fusion. One stitch is placed at each end of the anastomosis and one in the center of the back wall. Once the walls are carefully approximated, the laser is used to sequentially spot weld the posterior wall of the anastomosis. It is essential that the distance guide keeps the tip of the laser fiber a constant distance from the tissue to be fused in order to assure consistent energy transfer at the tissue level and adequate tissue fusion without charring of the tissue. Once the posterior wall has been fused, a stay suture is then used to approximate the anterior wall. The anterior portion of the anastomosis is then completed with the laser, in the same fashion as the posterior wall. With the arteriovenous fistula completed, the distal vessel clamps are released and allowed to back bleed and the anastomosis inspected for leaks. The proximal clamps are then released and a thrill in the fistula is noted.

Results

At the time of this report, we have attempted seven arteriovenous anastomoses of pig femoral vessels. The vessels ranged from 3-5mm. in diameter and the pigs weighed from 150-180 pounds. Of the seven attempts, six procedures were successful with the immediate patency verified by a palpable thrill. There were no anastomotic leaks noted. All six of the successful AV fistulas were patent at the time the animals were sacrificed and there has been no evidence of pseudo-aneurism formation. Histologic studies show full thickness bonding at the anastomotic site with minimal tissue reaction as distinguished from the foreign body reaction seen with standard suture technique. Our first attempt at AV anastomosis with this technique and system was unsuccessful and this failure is attributed to difficulty in obtaining adequate anesthesia resulting in poor tissue approximation during the procedure. The anesthetic problems were readily resolved and as a result all subsequent procedures were technically simplified and were successful. The results of our studies are summarized in Table 1.

Table 1

Summary of Results of A-V Anastomosis in Pig
3-5 mm Femoral Vessels Using 1.319 Nd:YAG Lasers

<u>Attempts</u>	<u>Post Op Time</u>	<u>Patency</u>
1	0 Days	No
1	0 Days	Yes
1	4 Days	Yes
1	3 Weeks	Yes
1	3 Months	Yes
1	1 Year	Yes

Summary

We have shown that laser tissue fusion side-to-side arteriovenous anastomosis can readily be accomplished in 3-5mm pig femoral vessels with our computer controlled 1.319 Nd:YAG laser system. This system offers many advantages over those previously reported for use in laser tissue fusion. The parameters which heretofore were left to the control of the surgeon are now automatically controlled by the system, leaving the surgeon free to concentrate on principles of good surgical technique. The technique is fast, safe and reproducible. Also, since the parameters are well controlled, tissue bonding is maximized while tissue damage is left to a minimum. In contrast to CO₂ and argon systems, the 1.32 um. Nd:YAG permits tissue welding in relatively wet or bloody fields. Based upon these findings and previously reported animal studies performed at the Orlando Regional Laser Research and Demonstration Center we feel that the system and technique is feasible for use in controlled clinical trials creating radiocephalic AV fistulas for purposes of renal dialysis. Once proven in human AV fistula trials, we foresee further clinical applications such as closure of femoral, carotid, and deep abdominal arteriotomies as well as anastomoses of various vascular autogenous grafts.

ARGON LASER VASCULAR WELDING: THERMAL AND THROMBOGENIC ASPECTS

George E. Kopchok, Rodney A. White, M.D., Roy Fujitani, M.D., Geoffrey H. White, M.D., Jerry Vlasak, M.D., Leon Daykhovsky, M.D.*, Warren S. Grundfest, M.D.*

Division of Vascular Surgery, Harbor-UCLA Medical Center, 1000 West Carson Street, Torrance, CA 90509, (213) 533 2704 and the Department of Surgery and Division of Cardiology, Cedars-Sinai Medical Center, Los Angeles, CA.

ABSTRACT

The thermal properties and thrombogenicity of Argon laser assisted vascular repair (LAVR) and sutured vascular repair (SVR) was studied in canine arteries. Two sequential 1 cm length incisions were made in each artery, separated by a 4cm length of intact vessel. One was repaired by SVR using continuous 6-0 prolene and the other by LAVR from the adventitial surface. An AGA 782 digital thermographic camera and computer with spatial and thermal resolution of $\pm 0.2\text{mm}$ and $\pm 0.2^\circ\text{C}$ was used to continually record and analyze the LAVR. LAVR was performed using an HGM argon laser with a 300 micron optic fiber, 0.5 watt power, 0.066 cm^2 spot size, 150 seconds exposure, $1100\text{J}/\text{cm}^2$ energy fluence. Continuous irrigation (1 drop/second) of room temperature saline was used to cool the laser tissue. Autologous Indium-111 oxine labelled platelets were injected intravenously immediately after completion of all vascular repairs. The segments of LAVR and SVR and an equivalent segment of reference vessel were harvested 48 hours after injection and radioactivity was determined with a gamma counter. Anastomotic platelet adherence index (APAI) was calculated as the ratio of LAVR or SVR: reference vessel emissions.

Thermal measurements revealed a temperature increase to its maximum, then an instantaneous return to a baseline of 36° with each drop of saline. The maximum temperature recorded was 48.8°C , the mean maximum was $45.1 \pm 2.7^\circ\text{C}$ ($n=20$). There was a significant difference ($p<0.01$) in the APAI for the SVA (161 ± 76) compared to the LAVA (93 ± 41). The results suggest that the temperature increase did not have a detrimental effect on hemodynamic integrity or thrombogenicity. The lower platelet uptake on the LAVR compared to SVR may have a favorable effect on early vascular patency.

INTRODUCTION

The use of lasers to weld vascular tissue and form sutureless anastomosis has great potential. Numerous advantages have been described for welded anastomosis including lack of the foreign body reaction normally associated with sutures.¹⁻² This study was undertaken to test the hypothesis that the laser-induced increase in vessel wall temperature does not increase platelet adhesion to vascular repair. We measured the thermal properties of argon laser assisted vascular welding in conjunction with the early adhesion of platelets to the regions of vascular repair during the first 48 hours. Since platelets play a fundamental role in thrombus formation it is believed that decreased platelet adhesion will have a beneficial effect on early vascular patency.³

MATERIALS AND METHODS

Canine femoral ($n=16$) and carotid ($n=16$) arteries were isolated by standard surgical technique. Anticoagulation was induced with intravenous heparin (100 units/kg) and the proximal and distal portions of the artery were clamped. Two 1cm longitudinal incisions in the vessel wall were made separated by 4 cm. One incision (SVR) was closed using a continuous 6-0 prolene suture. The second incision (LAVR) was prepared for welding by placing a 6-0 prolene suture at each apex and at the midpoint, dividing the incision into two 5mm segments. Argon laser welding was accomplished with a 300 micron fiber held 1cm from the vessel edges, producing a spot size area of 0.066 cm^2 . An HGM* Argon laser was used at 0.50 watts power, 75 seconds exposure (15 pulses of 5 seconds separated by 0.2 seconds) and $570\text{ J}/\text{cm}^2$ energy fluence for each 5mm segment. The laser energy was moved back and forth along the anastomotic edge at a rate of approximately 1cm/sec. Cooling of the fusion site was accomplished by a low volume stream of saline at room temperature (1drop/sec, $\sim 3\text{ml}/\text{min}$). Position of the welded and sutured anastomosis was randomized.

Thermal images were recorded continuously with an AGA*** thermal camera which was positioned and focused 15cm from the vessel surface. Temperature calibration was achieved through the instruments built-in clamping and temperature compensating system which utilizes a liquid nitrogen cooled indium antimonide photon detector and has a spectral response of 3.5 to 5.6 microns. A focal distance of 15cm, in conjunction with 1.8mm aperture and 7° lens, resulted in a thermal and spatial resolution of $\pm 0.2^\circ\text{C}$ and $\pm 0.2\text{mm}$ respectively. Baseline temperatures were recorded before and after the welding process. The recorded thermal images were analyzed with the AGA thermovision computer and results detailed in a color coded temperature profile.

Platelet labelling studies were accomplished according to the method described by Hawker et.al. Indium 111 oxine*** was used to label the autologous canine platelets. This technique results in fast uptake, high labelling efficiency and a short (67 hour) half life.⁴ One hour prior to each operation, 25cc of venous blood was drawn into a syringe containing 3.0cc of sterile acid citrate. After meticulous separation and

* HGM Medical Laser Systems, Salt Lake City, Utah

** Agema Infrared Systems, Secaucus, New Jersey

*** Amersham Corp, Arlington Heights, IL

washing, the platelets were labelled with approximately 700uCi of Indium-111 oxine and incubated at 38°C for one minute. The labelled platelets were re-infused intravenously at the completion of each surgical procedure. In 48 hours the dogs were reanesthetised and the vessels excised. Three 1cm length samples were taken from each artery; the sutured repair, the welded repair and a 1cm control segment taken from normal vessel between the two. The radioactivity emitted from each specimen was determined with a gamma well counter (Searle Analytic, Inc.) using a wide field of view with a medium energy collimator and two 20% symmetric windows around the 173 and 247 KeV O-photopeaks of Indium-111. All counts were corrected for background activity and isotope decay. An anastomotic platelet adherence index (APAI) was calculated for each specimen by determining the ratio of platelet adherence to the sutured or laser-treated vessel compared to the platelet adherence to the control segment.

All animals used in the study received humane care in compliance with the "Principles of Laboratory Animal Care" formulated by the National Society of Medical Research and the "Guide for the Care of Laboratory Animals" prepared by the National Academy of Sciences and published by the National Institute of Health (NIH publication #80-23, revised 1978).

Results

All vessels were patent, hemostatic with no signs of postoperative complications. The temperatures incurred while argon laser welding were similar to previous experiments.⁵ The temperature increased rapidly but returned to baseline (~36°C) with each drop of saline. Saline controlled the maximum temperature and the duration of thermal exposure. The maximum temperature attained in this study was 48.8°C, the mean maximum was $45.1 \pm 2.7^\circ\text{C}$ (n=20).

The mean APAI at 48 hours for SVA was 161 ± 76 . This was significantly different from the mean of 93 ± 41 for LAVA ($p < 0.01$).

Discussion

Laser assisted vascular welding may be a useful adjunct to vascular surgery. Argon, CO₂ and Nd:YAG lasers have all been used to create hemostatic welds in medium size vessels. One of the major advantages of a laser welded anastomosis compared to suture repair appears to be the lack of suture acting as a foreign body. In a previous study, we observed an intimal hyperplastic response in sutured repairs which was not present after laser repair of identical canine arterial-venous fistulas at 8 weeks.² The laser repairs had minimal inflammatory reaction and more normal appearing collagen and elastin fiber orientation. It appears that argon laser sealing delays or inhibits the intimal hyperplastic response. Ashworth et al found similar results using the CO₂ laser to weld end-to-end canine carotid arteries.⁶ They found foreign-body giant cells invested the sutured repairs at 2, 4 and 6 weeks. The welded repairs showed no sign of intimal hyperplasia except at the stay suture site. As their technical skills improved the time required for laser repair was one third that needed for sutured repair.

Platelet adhesion appears to play a major role in early thrombosis and thrombogenic complications in vascular repair.³ When an injured vessel is exposed to blood, platelets adhere rapidly and undergo morphologic and biochemical changes which result in the release of platelet aggregation factors. The intensity of this reaction depends upon the reactivity of the injured vascular surface with platelets, the amount of blood exposed to the injury and platelet suppression and accumulation factors. In the present study, we found that despite the rise in temperature caused by argon laser induced fusion there was less platelet aggregation in comparison to sutured repair. The decrease in platelet adherence may be closely associated with the lack of a foreign body response to suture, although the laser energy itself or the welding mechanism may have some inhibitory factors not yet identified. Abergel et al described an ability to selectively suppress or stimulate collagen production by fibroblasts using the Nd:YAG Laser.⁷ At high powers they found the laser to have an inhibitory effect on collagen production while at low powers a stimulatory effect was observed.

The mechanism of argon laser fusion appears to be collagen to collagen bonding. The argon laser causes the collagen to denature or unwind, and cooling the fusion site before it coagulates causes the collagen to renature (recoil) and form a physiochemical bond of crosslinkages.⁸ The thermal findings in this study support this hypothesis since welding temperatures were in the range at which collagen denatures ($T_m = 40-60^\circ\text{C}$) and the maximum temperature of 48.8°C is well below the temperature at which protein coagulation occurs (~70°C).⁹⁻¹¹

In summary, in this study the increased temperature induced by Argon laser fusion did not have a detrimental effect on early platelet adhesion compared to control repairs, and indeed there was significantly less platelet adhesion to the laser repair site. This decrease in adhesion appears to be due to the lack of a foreign body in the blood stream although it is unclear what role the welding mechanism and laser exposure may play in the process.

Conclusion

We conclude that argon laser-assisted welding of canine vessels occurs at temperatures below 50°C and may exhibit numerous advantages over conventional suture repair. The temperature increase induced by laser fusion has no detrimental effect on early platelet adherence. In fact, the lack of a foreign body stimulus afforded with laser welds appears to significantly lower platelet accumulation when compared to suture repairs. Further studies are needed to delineate the thermal, photochemical and foreign body factors involved.

ACKNOWLEDGEMENT

Supported by Grant HL-32622 from USPHS, National Institutes of Health and by Imperial Grand Sweepstakes of Cedars-Sinai Medical Center.

REFERENCES

1. K.K. Jain, Lasers Surg. Med. 3, 311-2 (1984).
2. R.A. White, G.E. Kopchok, C. Donayre, G.H. White, R. Lyons, R. Fujitani, S.R. Klein, J. Uitto, J. Vascular Surg. 6, 447-453 (1987).
3. L.A. Harker, J.L. Richie, Circulation 62 (Suppl 5), 13-18 (1980).
4. R.J. Hawker, A.R. Wilkinson, L.M. Hawker, Clin. Sci. 58, 243-248 (1980).
5. G.E. Kopchok, W.S. Grundfest, R.A. White, C. Donayre, R. Fujitani, F. Litvack, G.H. White, S.R. Klein, L. Morgenstein, Soc. Optical Eng. 712, 260-263 (1986).
6. E.M. Ashworth, M.C. Dalsing, J.F. Olson, W.P. Hoagland, S.B. Baughman, J.L. Glover, Arch. Surg. 122, 673-677 (1987).
7. R.P. Abergel, C.A. Meeker, T.S. Lam, R.M. Dwyer, M.A. Lesavoy, J. Uitto, J. Am. Acad. Derm. 11, 1142-50 (1984).
8. R. Schober, F. Ulrich, T. Sander, Science 232, 1421-1422 (1986).
9. C.C. Danielson, Coll. Relat. Res. 2, 143 (1982).
10. D.K. Furuto, E.J. Miller, Biochem. 20, 1635-40 (1981).
11. D.K. Dew, Int. Soc. Optical Eng. 712, 255-257.

LASERS IN DENTISTRY

Donald E. Antonson and Marcus D. Benedetto

Donald E. Antonson, D.D.S., M.Ed.
Department of Operative Dentistry
College of Dentistry
University of Florida
Gainesville, Florida

Marcus D. Benedetto, M.S., Ph.D.
Ophthalmic Research Center
Orlando, Florida

The practice of Dentistry is changing at a most rapid pace. Since the advent of bonding (the process of fusing composite resin to enamel via acid etching) the day-in day-out dental treatment in most practices is quite different than that of just ten years ago. Additionally, the decay rate in young individuals is fifty percent less than it was twenty years ago. Furthermore, more sophisticated instrumentation is being developed for diagnosis and, even now, lasers are becoming available.

Twenty years ago, numerous investigators tried unsuccessfully to utilize lasers in performing dental procedures. This was because either the power densities were too high in magnitude or the units themselves were too large to be practical.

Today, however, the picture is quite different. Ever since Einstein discovered the concept of stimulated emission in 1917 researchers have continued to explore functional applications for this energy. Currently, technology and computer knowledge bring lasers into a position which shows them to be cost effective for the dental profession. The main types of lasers currently used in dentistry are CO₂, Argon, and YAG. The CO₂ has been demonstrated effective in caries detection and in soft tissue treatment such as gingivectomies and frenectomies. The Argon has demonstrated utility in soft tissue work targeting blood vessels. The YAG laser has functioned well for endodontic therapy for sterilizing canal walls.

In order for the practicing dentist to feel justified in purchasing new equipment he/she must be able to offset the cost of overhead by the generation of fees. This paper reviews the various applications of lasers in dentistry that make them practical instruments for the future.

One of the main benefits of the CO₂ laser in dentistry is its effect upon soft tissue. This ranges from a photophysical effect which is immediate, evidenced by either vaporization (ex. excision) or thermal (ex. dehydrated tissue), to a host response which is delayed and evidenced by necrosis or edema.

These soft tissue effects have been clinically applied by the dental profession in treating vascular tumors such as hemangiomas of the tongue and lips. Usually these types of tumors involve serious bleeding and sequela which have been shown to be diminished greatly by the coagulation effects of the laser. Without the benefit of coagulation, such surgeries would be difficult to manage and could cause life-threatening situations.

The current position of lasers in dentistry is predicated upon its history. The following review of past dental laser applications is summarized.

In 1972, Stern (1) showed that a laser may be beneficial for inhibiting dental caries formation. He used a superpulsed CO₂ laser on human enamel and found that it caused the enamel to be more resistant to caries. It appeared that the laser energy modified the enamel by increasing the concentration of the inorganic component of the outer enamel surface by vaporizing off some of the organic component. This resulted in recrystallization which could be seen under magnification.

In 1985, Sundstrom (2) from Sweden, used the laser to diagnose the dental caries by observing a luminescent reflection off of the enamel surface. Rebrov and Zelenov (3) in 1983, from Russia, showed successfully how lasers could be used to weld metal structures of clasps on removable partial dentures.

In 1984, a Japanese study (4) informed us that the laser induced chemical changes in the bonding state of hydroxyapatite which theoretically would help to decrease decay potential. Also, during this same year Melcer (5), in France, reported on treating decay with a CO₂ laser, and Leiberman (6) in Israel was fusing composite resin to lasered enamel. Leiberman found that composites fused in this manner were as tightly bound to the tooth as composites which were acid-etched bonded. This suggested that using the laser would decrease bonding time from three minutes to no more than fifteen seconds.

A year later, Antonson and Benedetto (7) reported at the Annual International Association of Dental Research Meeting that lasers can be used to diagnose enamel fissural caries. The technique uses a CO₂ laser which, when used at about 2 watts of power, targets higher organic areas in the outer layer of the enamel. These zones are areas where acidogenic bacteria have demineralized a portion of the enamel leaving a more organic zone. The laser photovaporizes the moisture present and carbonizes the areas with

higher organic concentrations. On the tooth surface these areas appear black. This allows the dentist to easily detect carious from healthy areas. Without the laser, the dentist has to rely upon an explorer (small dental instrument) to probe "soft" areas. Where it "sticks" the diagnosis is made. This technique has several problems; one of which is that the diagnosis is dependent upon the diameter of the explorer fine. This dulls and becomes thicker with usage, thus changing the criteria of the diagnosis. Also, the outer surface of the tooth has many grooves and fissures whose parallel walls allow for the explorer to frictionally lock thus giving a false diagnosis. Another problem with explorer diagnosis is that it can potentially cause small chipping in the pits or fissures that was not present initially. The laser makes the process more objective, and at the same time, allows the dental profession a true diagnosis of demineralized tooth structure.

Also in 1985, Stewart (8) successfully attached hydroxyapatite to a tooth to act as a pit and fissure sealant, and Myers (9) showed a laser could debride incipient caries. Currently, more and more reports are surfacing describing other dental applications for lasers.

Until recently lasers were about the size of a small compact car, with exotic current and external coolant requirements. Today lasers are available which are about the size of a small typewriter, portable, self-cooled and use normal 115 volt current. For example, Pfizer Laser Systems, Irvine, California, has a contraangle delivery system and allows dentists an easy transition from holding a traditional dental handpiece. It permits a CO₂ beam to be easily targeted to almost any area in the mouth. No longer is laser delivery an obstacle for dentistry, on the contrary, it is becoming a convenient modality. At a time when there is a high concern for preventing disease transmission in the dental environment (AIDS, Hepatitis, herpes, etc.) the laser is beneficial since no instrument contact occurs.

Initially, our first experiences using a laser involved using extracted teeth for determining dental caries. Next, thawed pig jaws provided early soft tissue surgery practice for performing gingivectomies, frenectomies and gingival sulcus deepening. The pig jaw is a very accurate laboratory model since its gingival tissues are abundant and quite similar to human gingiva. Additionally, they are easy to procure and inexpensive.

After much practice in the laboratory learning all of the laser's safety features, interlocks, and adjustments, the next step was to initiate treatment for patients. At first the authors were more skeptical than the patients. The patients were very receptive and sought out the laser technology. It is interesting to note that the "new" and the "sophisticated" lends itself to marketing parameters. After a short patient introduction to the laser, and after securing an informed consent, small fibromatous lesions were vaporized under local anesthesia. These were removed efficiently without any negative sequelae. Patients were very impressed with its result. Upon recall questioning, patients noted no post-operative discomfort. Healing was excellent. On the contrary, scalpel blade removal of these small lesions normally would be accompanied by continued bleeding and some discomfort. The laser experience was quite positive.

As we look to the future, some of the possible dental laser applications may include:

- 1) Sterilization of instruments
- 2) Periodontal surgery, frenectomy
- 3) Sulcus deepening
- 4) Fusion of porcelain to enamel in vivo
- 5) Polymerization of composites
- 6) Transillumination
- 7) Melting of marginal enamel adjacent to margin defects
- 8) Modification of surface enamel to close enamel defects
- 9) Splitting teeth by melting/fusing
- 10) Cavity preparation, caries removal and tooth structure sterilization
- 11) Dentin desensitization
- 12) Endodontics
- 13) Removing the smear layer
- 14) Diagnoses
- 15) Osteotomy
- 16) Removal of root tips
- 17) Heating of gutta percha
- 18) Apicoectomies
- 19) Hemostasis
- 20) Welding of non-precious alloys

As more dental laser applications are made known to the dental profession, one area of concern needs to be addressed. This involves laser safety standards for dental applications. A protocol needs to be developed and internationally distributed alerting dental personnel of laser safety. So far the dental profession has not addressed this issue. In the advent of other new portable CO₂ lasers of moderate cost, the forward thinking practitioner will be considering this new technology.

References

1. Stern, R.H. and Sognnaes, E.F., Laser inhibition of dental caries suggested by first tests in vivo. JADA Vol. 85, Nov. 1972.
2. Sundstrom, F., et al, Laser induced fluorescence from sound and carious tooth substance. Spectroscopic Studies. Swed. Dent. J. 1985; 9[2]: pp. 71-80.
3. Rebrov, V.I. and Zelenov, N.F., Reconstruction and restoration of clasp dentures using laser welding. Stomatologiya [Mosk] [USSR], May-Jun 1983; 62[3]: pp. 68-69.
4. Yamamoto, H. and Oaya, K., Potential of yttrium aluminum garnet laser in caries prevention. J. Oral Pathol. 3:7, 1974.
5. Melcer, J., et al. Treatment of dental decay by CO2 laser beam: preliminary results. Laser Surg. Med. 1984, 4:4, pp. 311-321.
6. Leiberman, R., Segal, T.H., Nordenberg, D. and Serebro, L.I., Adhesion of composite materials to enamel: comparison between the use of acid and lasing as pretreatment. Laser Surg. Med. 1984; 4:4, pp. 323-327.
7. Antonson, D.E. and Benedetto, M.D. Use of CO2 laser for visible detection of enamel fissure caries. Journal of Dental Research, Abstract Book, March 1986.
8. Stewart, L., Powell, G.L. and Wright, S. Hydroxyapatite attached by laser: a potential sealant for pits and fissures. Operative Dentistry, 1985, 10.
9. Meyers, T.D., Myers, W.L. In vivo caries removal utilizing the YAG laser. J. Michigan Dental Association, Vol. 67, Feb. 1985.

Reprint Requests To:

Dr. Marcus D. Benedetto, Director
Ophthalmic Research Center
4524-297 Curry Ford Road
Orlando, Florida 32812
(305) 896-5550

OBJECTIVE LASER DETERMINATION OF CARIES

Marcus D. Benedetto and Donald E. Antonson

Marcus D. Benedetto, M.S., Ph.D.
Ophthalmic Research Center
Orlando, Florida

Donald E. Antonson, D.D.S., M.Ed.
Department of Operative Dentistry
College of Dentistry
University of Florida
Gainesville, Florida

Abstract

The current method of detection of tooth decay (caries) is highly subjective and can yield as much as a 40% error in caries detection. Laser diagnostics reveal an objective method for the determination of caries.

Introduction

Normal saliva contains numerous types of bacteria of which some of the most predominant are cocci and filamentous. Bacteria such as streptococcus or lactobacillus combine with food substrate in the presence of food nutrients in the saliva to form caries (tooth decay). The primary areas where caries first develops are in the pits and fissures on the occlusal surfaces of teeth. Dentists routinely diagnose caries by looking intraorally with a mirror and an explorer at the visible surfaces of teeth. This is a small working area in which good visualization is needed.

The current method of caries detection is performed by employing an explorer. The limiting characteristics of caries determination by explorer are: A) Explorers come in different sizes. Caries determinations are therefore limited by the thickness of the tine and by the shape of the walls of the groove being investigated. There may be caries at the bottom of a groove, but if the tine is physically prevented from reaching this point due to the narrowness of the walls of the groove, then the caries will go undetected. B) Explorers are initially sharp and become dull with use and age. This can make them as much as 50% less accurate. C) Caries detection by explorer is subjective. Recent studies (1) have shown that there can be as much as a 40% error in caries determination by explorer. One of the charges of the International Symposium on Criteria for Placement and Replacement of Restorations which recently occurred was to find more accurate and reliable methodologies for caries detection. D) A tactile judgement is required. Occlusal fissure caries, as defined in Sturdevant's text (2), is best detected when an explorer tine placed into a pit or fissure provides "tug-back" or resistance to removal. According to criteria defined by the U.S. Public Health Service (3), signs of decay are: a) a softening at the base of the pit or fissure; b) an opacity surrounding the pit or fissure indicating undermining or demineralization of the enamel, and c) softened enamel that may be flaked away by the explorer. According to Gilmore (4), the diagnosis for occlusal caries is evident if, when the explorer is placed into grooves and pits, soft areas are found and are accompanied by chalky enamel or staining, or if the tooth structure cannot support the weight of the explorer. Deep pits, parallel grooves, "Y" junctures can cause a mechanical lock which yields the same sensation as caries. E) A final point for consternation is that an eight dollar instrument is used for the diagnosis of treatment which has hundred(s) dollar implications.

Materials and Methods

Apparatus.

A brand new AM Flex #23 (American Dental) explorer was used for the determination of caries by explorer. A Pfizer Laser Systems* portable CO₂ laser with contraangle delivery was used for the determination of caries by laser.

Procedures.

This study included seventy recently extracted teeth which were kept in a solution of water and thymol crystals to maintain hydration and to prevent further bacterialization. 6X mappings were made of the occlusal surface of each tooth. The teeth were then subjected to caries detection by explorer. The extent and locations of caries of each tooth were marked on the appropriate 6X map. These teeth were then subjected to the CO₂ laser at 4 watts of power and 18 pulses per second. The extent and locations of caries by laser determination were also noted on the appropriate 6X map. The agreement and discrepancies between laser and explorer were then compared.

Results

A tooth subjected to low power CO₂ laser energy would retain its natural coloration except at points of demineralization. These points were determined to be caries by virtue of the carbonized residue which remained when exposed to photovaporization by the CO₂ laser. These black carbonized areas, which were objectively verifiable, suggested the location of caries. There was a 70% agreement in the data. This means that, 70% of the time, where the explorer said there was caries, the laser determination agreed and where the explorer said there was no caries, the laser determination agreed that there was no caries. Conversely, 30% of the time there was disagreement. Moreover, 8% of the time, the laser found caries that was missed by the explorer. More importantly, 22% of the time, the laser found areas to be non-carious which were determined to be carious by explorer.

Discussion

The determination of caries by CO₂ laser appears to have several advantages. First and foremost, it is objective, verifiable, and replicable. This will permit the operator to physically demonstrate to his/her patient the desired treatment plan. This will serve to improve patient satisfaction and confidence. Additionally, the third party payers would greatly appreciate objective evidence that a particular restoration was needed. A photograph of the carious lesion can be placed in the patient's file for future reference and a copy can be sent to the third party payer. Second, the laser method is more rapid than the mechanical method (explorer). This will save the operator's valuable time. Third, it suggests a more conservative treatment plan. The laser, finding caries less often than the mechanical method, will result in more natural tooth structure remaining and less restorations being performed by 14% (the difference between 8% and 22%).

Summary

The current method of dental examination and detection of tooth decay (caries) consists of "feeling" the tooth with a metal dental instrument (called an "explorer") with a thin, curved, sharply pointed tine. This method is highly subjective and operator dependent. Recent studies have shown that there is as much as a 40% error in the detection of caries. A multitude of factors are involved: clinical experience, search strategy, quality of sensitive touch of the practitioner's hand, financial need, the philosophy of the institution where the practitioner was trained, diameter and condition of the explorer tine, and the topography of the tooth. Non-carious deep pits, parallel grooves, or Y-shaped junctures can all give the subjective sensation of being carious.

A CO₂ laser was used to evaluate seventy human teeth for the presence of occlusal fissure caries to determine if laser technology might be more objective than conventional explorer diagnosis. After explorer diagnosis, 6X mappings of each tooth were made with carious zones indicated. Next, the teeth were lasered, and where black zones were found indicating caries, these were compared to the carious zones found earlier by the explorer. There was only a 70% agreement between methodologies. The laser seemed to be more conservative in diagnosis than the explorer.

The use of a new method of objective caries determination by laser yields a consistent, more operator independent system of caries detection. In this double-blind study each of seventy teeth were examined by explorer and by laser and independently examined for caries. The results show a high degree of inconsistency between laser and explorer determined sites of caries. This correlates with the aforementioned 40% error.

References

1. Antonson, D.E., Soderholm, K.J., and Fischlschweiger, W., Observation of amalgam margin defects and recurrent decay frequency. J.Dent.Res. 1983;62: (Abstract #1138).
2. Sturdevant, C.M., et al, The Art and Science of Operative Dentistry. St. Louis, C.V. Mosby Co., 1985, p. 67.
3. Sturdevant, C.M., et al, The Art and Science of Operative Dentistry. St. Louis C.V. Mosby Co., 1985, p. 52.
4. Gilmore, H.W., Textbook of Operative Dentistry, Edition 1. St. Louis, C.V. Mosby Co., 1967, p. 38.

Reprint Request To:

Dr. Marcus D. Benedetto, Director
Ophthalmic Research Center
4524-297 Curry Ford Road
Orlando, Florida 32812
(305) 896-5550

* Pfizer Laser Systems
Pfizer, Inc.
66700 Red Hill Ave.
Irvine, CA 92714

ORAL BIOPSY BY PULSED CO2 LASER

Charles Liebow, D.M.D., Ph.D.,¹ Robert E. Braun, D.D.S.,¹

Laurie Hartman, D.D.S.,² and Joseph E. Margarone, D.D.S.¹

State University of New York at Buffalo, School of Dental Medicine, Buffalo, N.Y. 14214

¹ Department of Oral and Maxillofacial Surgery, SUNYAB School of Dental Medicine

² Department of Stomatology and Interdisciplinary Sciences,
Section on Oral Pathology, SUNYAB School of Dental Medicine

A b s t r a c t

Carbon Dioxide (CO₂) lasers have been used in soft tissue surgery in several sites of the body with significant success. This technique has certain advantages over conventional surgical approaches vis a' vis hemostasis, enhanced microsurgical capability, and a reduction in postoperative pain and inflammation. One problem in laser surgery is that tissue is routinely vaporized leaving no biopsy specimen, or if incisional techniques are employed, the heat generated by the laser can produce unacceptable artifacts or tissue destruction. Using a CO₂ laser with a high power density achieved by laser pulse, we are able to obtain excellent specimens with minimal tissue damage or specimen artifact while still preserving the benefits of laser surgery.

Introduction

Lasers have become increasingly valuable tools in surgery (1). Several types of lasers are in use, matching the specific characteristics of each laser type to the particular surgical need. Currently available lasers include: ruby, argon, neodymium-YAG, tuned dye, and, of course, the CO₂. Various lasers have various advantages, including ability to penetrate tissue, compatibility with fiberoptics, and selectivity of destruction. Though the CO₂ laser has none of these capabilities, it has certain characteristics suited to soft tissue surgery. It is capable of being focused into a small spot with maximal energy absorption producing tissue vaporization with minimal effect on adjacent tissue. This allows for precise removal of soft tissue with minimal inflammation. Also, the laser beam can produce hemostasis under certain conditions.

Laser surgery has been extensively used in various organs. Ophthalmology has made extensive use of lasers, utilizing the ability to penetrate tissue and perform internal alterations with minimal damage. Gynecology and otolaryngology have made extensive use of the laser. Gastroenterology, using fiberoptic devices, has begun to utilize the laser more extensively, along with many other fields of medicine. Laser surgery in the oral cavity offers the advantage of ease of approach and accessibility (2).

The principle of CO₂ laser surgery is that a maximum power density for a minimum duration minimizes the spread of heat to adjacent tissue (3). Though heat spread is sometimes useful, as in control of bleeding, minimizing the spread of heat will minimize damage to adjacent tissue. The less damage there is to adjacent tissue, the less inflammation, postoperative pain and delay of healing. When a biopsy is taken, peripheral damage occurs symmetrically to the tissue next to the excision and to the excised site. The quality of the biopsy, therefore, generally reflects the peripheral damage. Lasers are expected to create heat artifact damage and fulguration similar to electro-surgery, but more limited because of their superior control. Using a CO₂ laser at a high power density and small spot size along with spiked pulse mode and very short pulses should minimize the amount of tissue biopsy artifact and the amount of postoperative difficulty.

Methods

Fifteen patients have had surgery for various conditions involving soft tissue lesions of the oral cavity. The lesions have included: hemangiomas of the lips and buccal mucosa; leukoplakic lesions of the buccal mucosa and tongue; epuli; papillary hyperplasia; and periodontal pyogenic granuloma. These have been performed on an out-patient basis under local anesthesia on non-medically compromised patients. The lesions were excised with a CO₂ laser, Cooper Model 870. The power was varied between 5 and 20 watts using either a repeat spiked pulse beam at 2 KHz and 0.1 msec. or a continuous beam. Surgeries were either performed using a handpiece with a focusing guide tip, or through a Zeiss OMI-1 operating microscope.

Two general approaches were employed for tissue removal: ablation of the entire lesion, or excision of the lesion with the laser with retraction of the specimen. Ablation of the whole lesion generally was performed unless one of the following conditions existed: histological examination of the tissue was required; there was an operative reason not to cut the lesion itself (e.g., bleeding from the hemangiomas); or the bulk of the lesion would have necessitated excessive laser application and could be performed with less trauma and operating time by the latter method (e.g., transverse incision across the stalk of a pedunculated epulis). All tissues excised were fixed and evaluated for pathology and tissue damage produced by the laser.

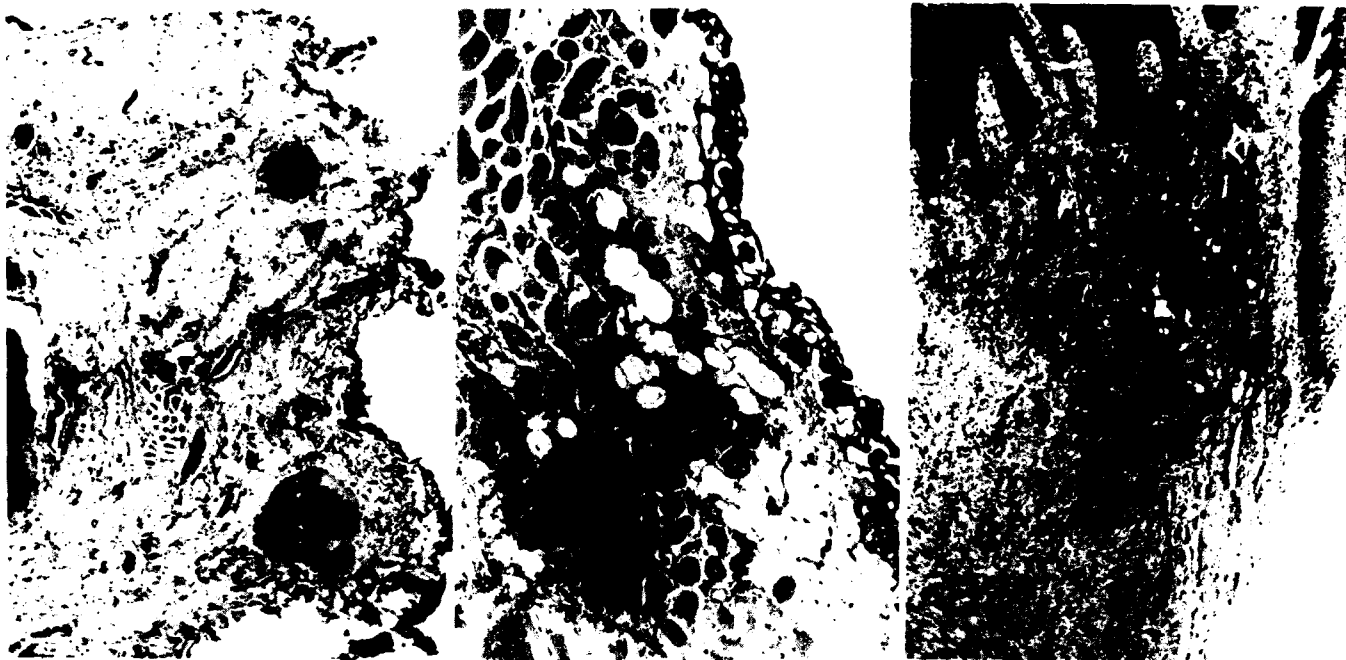
Results

All the surgeries have been performed to the satisfaction of both patient and doctor. No operative complications have occurred. The patients have all tolerated the procedure well and found it minimally stressful. Bleeding has been almost entirely prevented with either the continuous or pulsed modes. The technique for excision of the hemangiomas has been to excise the lesion by attempting to cut under the lesion through normal tissue and expose the feeder vessels. Once these are exposed, they are clamped, coagulated by slowly heating the vessels themselves with unfocused laser energy (not the clamp), and then released without recourse to vessel ligation. The clamp was used to prevent dissipation of heat by the flowing blood. In two cases the excision site was left open to granulate in, and in the other case the excision was sutured closed. In one instance, the hemangioma itself was perforated by the laser beam, and this produced some bleeding in the operating field. This bleeding was slowed by pressure application and cauterized with a diffuse laser beam. No other significant bleeding was noted in any of the surgeries, in spite of the fact that some of these areas are extremely vascular and prone to bleeding. As an example of the potential bleeding problems in these fields, we had difficulty containing the bleeding around the site of injection of the local anesthesia in one case, but no bleeding from the surgery.

There have been no significant post-operative complications from the laser surgeries, nor significant post-operative pain. Most of the patients refused post-operative analgesia. Two patients received a single dose of 750 mg aspirin. One patient had no post-operative discomfort for two days after surgery, and then developed an infection because of self-inflicted post-operative trauma (the patient bit the buccal mucosa while still under local anesthesia) and had to use analgesia. There was no post-operative bleeding even though almost all the sites were left open and no vessels were ligated. In the case of the periodontal surgery, no protective packing was employed (usually needed to reduce post-operative sensitivity).

The histological findings showed little damage to excised specimens. All specimens were adequate for pathological diagnosis, except for a few notable limited border areas produced by certain beam protocols where about 0.1 mm of fulguration artifact interfered with pathological assessment. The quality of the specimens can be seen in the five figures. Note the well preserved cellular structures including glands (Figures 3 & 4), muscles (Figure 2), blood vessels (Figures 1, 2, 4 & 5), etc. Figure 1 and 2 are 25 and 40 power views respectively of a cavernous hemangioma excised with a 7 watt pulsed beam. Note the thin darkened border in Figure 1 which represents tissue coagulation from fulguration. This border represents less than 0.1 mm of tissue damage. This tissue is loose and low in collagen content. In Figure 2, a higher power view of this same tissue, note that the fulguration is only one or two cells thick, and note that the muscles within about 0.1 mm of the incision are well preserved and their histology can be reliably determined. Figure 3 is a 100 power view of a periodontal abscess excised with a 15 watt pulsed beam. The incision is perfectly clear and sharp with no sign at all of fulguration or tissue coagulation. The inflammatory cells can be seen clearly in the center of the field and the epidermis is well defined. These figures show incisions with very little damage and maintenance of clear cellular morphology. These sections are adequate for pathological evaluation.

Figures 4 and 5 are 25 and 100 power views from an epulis excised by a 7 watt continuous beam. Two major differences exist between this sample and the two previously shown. One is that the former was cut with a continuous beam with a constant energy output as opposed to an intermittent beam with the "superpulsed" or spiked energy output. Also, this tissue has a higher collagen content than the hemangioma or even the periodontal abscess. The section in Figure 4 shows a cut downward from the keratinized epithelium, through a very fibrotic area, into and across a looser section of tissue including a minor salivary gland and many blood vessels. Note the very heavy area of fulguration at the site of incision through the epidermis, and the significant fulguration even through the less dense basilar portion of the incision. Note that the minor salivary gland right near the site of the incision is preserved, but that the cellular definition around the incision through the keratinized epithelium is vague and distorted. Figure 5 shows this area at higher power. The fulguration artifact is about 1mm thick here, and if this area included the margin of a malignancy, this would not be adequate as a biopsy sample.



Discussion



Figure 4



Figure 5

Figure 4. An epulis excised by a 7 watt continuous beam, 25 power. Two major differences exist between this sample and the two previously shown: this was cut with a continuous beam with a constant energy output as opposed to an intermittent beam with the "superpulsed" or spiked energy output; and, this tissue has a much higher collagen content than the hemangioma or even the periodontal abscess. This shows a cut downward from the keratinized epithelium, through a very fibrotic area, into and across a looser section of tissue including a minor salivary gland and many blood vessels. Note the very heavy area of fulguration at the site of incision through the epidermis, and the significant fulguration even through the less dense basilar portion of the incision. Note that the minor salivary gland right near the site of the incision has its remains well preserved, but that the cellular definition around the incision through the keratinized epithelium is vague and distorted.

Figure 5. A 100 power view of the same lesion. The fulguration artifact is about 1mm thick here, and if this area included the margin of a malignancy, this would not be adequate as a biopsy sample.

The patient response to laser surgery has been excellent. Patients tolerate the procedure well with little stress, possibly because they have no perception of the surgery because of the lack of pressure sensation. These procedures have been done under local anesthesia. The patients have reported no sensation whatsoever during the procedure. There is almost no postoperative pain from this procedure or other more extensive procedures. The most postoperative analgesic used by patients to date is one dose of 750 mg aspirin. It has been suggested that the laser may somehow desensitize surrounding nerve endings, but no definitive evidence has as yet been shown for this. The pain free postoperative course may be due instead to the lack of chemical signals for inflammation which would normally sensitize the nerves and make them hyper-reactive. The amount of post-operative discomfort is consistent with the minimal histological damage done to the incision site (assessed by the opposing face of the biopsy sample), so possibly no additional rationale is required to explain the excellent post-operative course.

This report shows that carbon dioxide lasers currently can fulfill a clinical role in soft tissue out-patient oral surgery and yield satisfactory biopsy samples when required. The extent of the role, a controlled comparison with other techniques, the use in hard tissue, and the use of other lasers with specific properties, all require a great deal of study, but the laser can routinely be employed today for certain oral surgical procedures.

Bibliography

1. Jako GJ. Lasers cut a swath in surgical and medical applications. IEEE Spectrum. 1985; 85:82-87.
2. Ossoff RH. Complications of CO2 laser surgery of the oral cavity and nasal cavity. In: Fried MP, Kelly JH, Strome M, eds. Complications of Laser Surgery of the Head and Neck. Chicago, Year Book Medical Publishers, Inc. 1986; pp. 94-98.
3. Mihashi S, Jako GJ, Incze J, Strong MS, Vaughan CW. Laser surgery in otolaryngology: Interaction of CO2 laser and soft tissue. Ann N Y Acad Sci. 1976; 267:263-294.

ULTRASHORT AR ION LASER PULSE SHAPES BY DOUBLE MODE-LOCKING IN THE CPM REGIME

E. Bourkoff

Department of Electrical & Computer Engineering, The Johns Hopkins University
Barton Hall, 34th & Charles Streets, Baltimore, Maryland 21218

Abstract

We have studied passive mode-locking of the Ar^+ laser using the saturable absorber R6G in four different regimes, as follows: when the Ar^+ laser operates in the colliding pulse mode-locking (CPM) configuration (i) with and (ii) without double mode-locking (DML) incorporated and also when the Ar^+ laser operates in the "conventional" configuration (iii) with and (iv) without double mode-locking incorporated. A detailed investigation of the Ar^+ and dye laser pulses from the double mode-locked Ar^+ -dye laser system has been made using correlation measurements. A direct display of a 67 psec Ar^+ pulse shape is measured. In addition, we review a technique of generating highly synchronous simultaneous pulse trains at three wavelengths, two of which are continuously tunable over a moderate range, which we call triple mode-locking.

Introduction

Passive mode-locking of Ar^+ laser has been recently reported [1-7]. In those systems, R6G (a dye normally used as a gain medium in the Ar^+ -pumped dye laser system) is inserted into the Ar^+ laser cavity as a saturable absorber to lock the Ar^+ modes *passively*. The mode-locked Ar^+ pulses in turn *intra-cavity* pump the R6G laser synchronously to generate short dye laser pulses [1,2,5-7]. However, either incompletely mode-locked dye laser pulses were reported [2,5], or no detailed characteristics of the dye laser pulses were given [1,6,7]. Some researchers [3,4,6,7] elaborated more extensively on the characteristics of the Ar^+ laser pulses, including arranging the Ar^+ laser to operate in the CPM regime [4,6]. Their results showed relatively broad pulsewidths [3,4,7], as compared to those from an actively mode-locked Ar^+ system. In [6], a combination of double and colliding pulse mode-locking (DCPM) of the Ar^+ and dye lasers was proposed, but only oscillographs having nsec resolution were reported.

In this talk, we present a system with an improved resonator design, while still using R6G as a saturable absorber, which allows for the flexibility to work in four different regimes. (A) The Ar^+ laser is in the "conventional" configuration and the saturable absorber is *lasing* (DML) [1,2,5,7]; (B) The Ar^+ laser is in the "conventional" configuration without DML [3,4]; (C) The Ar^+ laser is in the CPM configuration without DML [4]; (D) The Ar^+ laser is in the CPM configuration with DML [6]. The Ar^+ and dye laser pulses in each case are fully characterized, using a combination of correlation measurements and a fast photodiode. The measurements show both stable transform-limited Ar^+ pulse trains and completely mode-locked dye laser pulse trains with psec duration. In the

case when the Ar^+ laser is operating in the CPM regime, we are able to generate extremely short Ar^+ pulses (< 67 psec) [8], and to show the detailed Ar^+ pulse *shape*. In this talk, we also show the pulsewidth dependence on cavity length mismatch, wavelength, and intracavity bandwidth for each of the four cases outlined above [9].

Experimental Set-up

The schematic of our system is shown in Figure 1. Both ends of a Spectra-Physics model 171 Ar^+ laser cavity were extended, new mirrors M1, M2, M3, and M4 were positioned in such a way so as to include the dye jet stream inside the Ar^+ cavity. M1 was mounted on a linear translation stage for fine adjustment of the cavity length, and was either positioned as shown so that the dye jet was in the *center* of the cavity (cases C and D), or positioned close to mirror M2, in which case the system was *not* operating in the CPM regime (cases A and B). The Brewster prism shown in this figure maintains operation of the Ar^+ laser at 5145 Å, and also directs the dye laser beam to travel in its own cavity. M5 was a 7% Ar^+ output coupler with $R=\infty$. M1-M4 were coated for 4500-7500 Å in order to accommodate both the Ar^+ and dye wavelengths, and M6 was a flat high reflector used to redirect the dye laser beam. Various single-plate quartz birefringent filters of different thickness were positioned at Brewster angle, permitting dye laser operation with different bandwidths. Wavelength tuning was achieved by rotation of the intracavity crystal. The flat dye laser output coupler had a transmission of 2-4%, and was also mounted on a linear translation stage, such that the dye laser cavity length could be adjusted. The high-reflector focusing mirrors M2 and M3 had $R=5$ cm. The saturable absorber was a jet of R6G in ethylene glycol, and the jet nozzle was a modified Coherent Radiation model with its thickness reduced to about 100 μm .

The dye laser pulse durations were monitored by a rapid-scan autocorrelator, and were precisely measured by slow-scan autocorrelation using KDP. The Ar^+ pulses were monitored by an electronic detection system, consisting of a high speed photodiode, a sampling scope, and various accessories. The impulse response of the electronic detection system was 75 psec FWHM, characterized using the impulse-like psec dye laser pulses. The Ar^+ pulse durations were also measured by an alternative technique based on frequency up-conversion [10]. The Ar^+ and dye laser beams were collinear and mixed in a 3mm thick KDP crystal. By angle-tuning the crystal, the up-converted signal could be detected when both pulses overlapped and interacted in the crystal. The uv signal is proportional to the product of the instantaneous power of the Ar^+ and dye laser pulses. Therefore, the Ar^+ pulse shape

is depicted by recording the up-converted signal as a function of the delay between the Ar⁺ and impulse-like dye laser pulses.

Experimental Results

To examine cases A and B, we chose a system very similar to that shown in Figure 1, but with mirror M1 positioned very close to M2. We used R6G as the saturable absorber because of its high cross section at the 5145 Å Ar⁺ line. With only ethylene glycol in the jet stream, the (extended cavity) Ar⁺ output was cw, as expected. As we added and increased the R6G concentration, the Ar⁺ laser output became modulated, as monitored by our electronic detection system, and the threshold level of the Ar⁺ laser excitation current increased. When the R6G concentration increased further, the dye laser also reached threshold, and the Ar⁺ laser pulses were well mode-locked. Similar to conventional synchronous pumping, the cavity lengths of both Ar⁺ and dye lasers had to be matched to generate the shortest pulses. The effects of cavity length detuning were determined experimentally, as shown for case A in Figure 2. $\Delta L (\equiv L_{\text{dye}} - L_{\text{Ar}^+}) = 0$ indicates the position where we obtained the optimum Ar⁺ pulses. With minor deviation from $\Delta L = 0$, both the Ar⁺ and dye laser pulses could adjust themselves either forward or backward slightly in time, to conserve their pulse shapes at each cavity round-trip. When ΔL was increased ($\Delta L > 0$), the stimulated emission of R6G occurred too late to help shorten the Ar⁺ pulses effectively. As ΔL decreased ($\Delta L < 0$), the dye laser pulses were forced to arrive at the dye jet too early. The stimulated emission of R6G at the leading edge of the Ar⁺ pulses, in this case, perturbed the double mode-locking mechanism, causing instability of the Ar⁺ laser. This helps explain the asymmetry of the curve in Figure 2, which shows more tolerance for $\Delta L > 0$, in the sense that a larger cavity length mismatch is permitted before pulse instability sets in, compared to $\Delta L < 0$.

We found that it was not uncommon to have incompletely mode-locked dye laser pulses in this non-CPM regime, as reported elsewhere [2,5]. The dye laser was tunable from 5660 Å to 5920 Å, when $\Delta L \approx 0$, with a spectral bandwidth in the vicinity of 1 Å, determined by both the Brewster prism and the thickness of the birefringent filter plate. When the dye laser beam was obstructed (case B), the Ar⁺ laser operated in a purely "conventional" passive mode-locking regime, where the R6G relaxation time (≈ 6 nsec) was not short enough to induce good mode-locking, and an Ar⁺ laser pulse train of only nsec duration was obtained. Another disadvantage of the above configuration was that the short distance between the dye jet and the end mirror M1 did not allow R6G enough time to recover its absorbing ability prior to encountering the reflecting Ar⁺ pulse from M1. Summarizing thus far, in cases A and B, the Ar⁺ laser operated in the "conventional" passive mode-locking regime. With or without DML, this system was inferior to those systems using the traditional synchronous mode-locking arrangement.

We improved the system by moving the end mirror M1 further away from M2, and positioning it such that

the dye jet was in the center of the Ar⁺ laser cavity, i.e. the Ar⁺ laser operated in the CPM regime [11] (cases C and D). The advantages are threefold. Firstly, the two counterpropagating Ar⁺ pulses saturate the absorber more effectively, and the standing wave field of the overlapping pulses further reduce the loss in the strongly saturated regions of the absorber, allowing for higher output coupling of the Ar⁺ laser. Secondly, only one Ar⁺ pulse saturates the Ar⁺ plasma tube gain at any given time and gain competition is minimal since the pulse inter-arrival time in the Ar⁺ gain medium is equal. This helps to maximize and equalize the pulse amplitudes, increasing stability. Thirdly, reduction of the Ar⁺ pulse duration is expected over comparable single-pulse lasers [12].

We started again with only ethylene glycol in the jet stream, and added the R6G gradually until the dye laser reached threshold. The repetition rate of the Ar⁺ pulse train was monitored to ascertain that the Ar⁺ laser was, indeed, operating in the CPM regime, since two pulses per round-trip were then expected. The behavior of the colliding pulse mode-locked Ar⁺ laser without double mode-locking was first examined (case C), by blocking the dye laser beam. Figure 3 shows the Ar⁺ pulsewidth dependence on ΔL_{CPM} , the length difference between the two arms L_1 (M1 to jet) and L_2 (jet to M5). $\Delta L_{\text{CPM}} = 0$ corresponds to the position where the dye jet was located exactly in the center of the Ar⁺ laser cavity and where the optimum Ar⁺ pulses were obtained. The 130 psec FWHM Ar⁺ pulsewidth actually corresponds to 105 psec after deconvolution, due to the finite response time (75 psec) of the detection system. This is the minimum pulsewidth we found for case C. These properties were quite comparable to those previously reported in [4], where their Ar⁺ pulsewidth was determined only by correlation measurements. As shown in the inset oscillographs, the side lobe after the main Ar⁺ pulse and the long secondary tail (due to the slow recovery of the R6G saturable absorber) were clearly detected by our electronic detection system, whereas correlation measurements had difficulty resolving these features [4].

We then unblocked the dye laser beam, obtaining double mode-locking (case D). With precise matching of the lengths of the Ar⁺ and dye laser cavities, the side lobe and the secondary tail of the Ar⁺ pulse were eliminated. DML also helped to further shorten the Ar⁺ pulsewidth, in addition to providing a tunable dye laser pulse train with psec duration. The lasing bandwidth of the dye laser was varied by inserting single-plate quartz birefringent filters of different thicknesses. The tuning range of the dye laser was about 200 Å in the vicinity of 5800 Å (the emission peak of R6G in ethylene glycol at this relatively low concentration). The dye laser had an average output power of 20-30 mW and a peak power of ≈ 75 W, depending on the operating wavelength. When we replaced the 5.46 mm thick single-plate quartz birefringent filter by an 1.36mm thick one, the dye laser pulses had amplitude substructure due to the excess bandwidth, which indicates the phases of all the modes within this broadened lasing bandwidth were not locked together. The Ar⁺ pulses were characterized by cross-correlating them with the 5 psec dye laser pulses, a tech-

nique described in section II. Figure 4 shows not only the Ar^+ pulsewidth but also the detailed pulse shape with psec resolution. These Ar^+ pulsewidths are among the shortest reported from any mode-locked Ar^+ laser system, active or passive. The Ar^+ pulse shape was slightly asymmetric, with a sharper leading edge (≈ 30.6 psec) and a longer trailing edge (≈ 36.4 psec), each separately fitting a Gaussian pulse shape.

The spectral bandwidth of the Ar^+ laser was 6-7 GHz [13], corresponding to a time-bandwidth product < 0.5 , which shows the Ar^+ pulses were also transform-limited. The Ar^+ laser had an average output power of 90-120 mW and a peak power of ≈ 20 W, depending upon the Ar^+ excitation current. Additional Ar^+ excitation current was available, so it was possible to use higher Ar^+ laser output couplers, yielding larger output powers. The system performance as a function of either ΔL ($\equiv L_{\text{dye}} - L_{\text{Ar}^+}$) or ΔL_{CPM} ($\equiv L_1$ (M1 to jet) - L_2 (jet to M5)) was determined experimentally. The dependence of the Ar^+ and dye laser pulsewidths on ΔL , when $\Delta L_{\text{CPM}} = 0$, is shown in Figure 5, where we plot the Ar^+ and dye laser pulsewidths, Δt_{Ar^+} and Δt_{dye} , respectively, as a function of ΔL . $\Delta L = 0$ corresponds to the position where both the Ar^+ and dye laser pulses were optimized simultaneously. As shown in Figure 5, the Ar^+ and dye laser pulsewidths remain relatively constant over a mismatch range of about 2000 μm . Figure 6 shows the dependence of these pulsewidths on ΔL_{CPM} , when $\Delta L = 0$. Note that, by incorporating both CPM and double mode-locking, our system was very insensitive to cavity length mismatch, as evidenced by the greatly extended "stable region" shown in Figures 5 and 6, as compared to Figures 2 and 3.

Discussion

To generate mode-locked Ar^+ and dye laser pulses, negative gain is necessary before and after the propagation pulse, in order to establish a stable region of net gain within the pulse duration. In Figure 7, we consider the pulse shortening mechanism qualitatively [14]. We consider here the situation with $\Delta L = 0$. The saturated gain (G^{Ar^+}) experienced by the Ar^+ laser pulse (solid curve) remains essentially constant as the pulse (dashed curve) travels back and forth in the standing-wave cavity. This is due to the relatively long Ar^+ relaxation time, when compared to the cavity round-trip time. The Ar^+ pulse shaping is, thus, primarily due to the nonlinear saturation of the R6G absorber, $L^{\text{Ar}^+}(\tau)$, represented by the dash-dot curve. As shown at the bottom of Figure 7, this establishes a region of net gain for the Ar^+ pulse. Hence, the *net* pre-pulse gain for the Ar^+ pulse maintains negative values due to the presence of R6G, which introduces high nonlinear loss at low laser intensities. The net gain after the Ar^+ pulse is also negative due to the stimulated depletion of the S_1 state of R6G at the beginning of the trailing edge of the Ar^+ pulse, which not only causes a rapid restoration of the loss ($L^{\text{Ar}^+}(\tau)$) for the Ar^+ pulse (leading to compression of the trailing edge), but also provides synchronous R6G laser pulses. For the dye laser pulses, the R6G jet (the gain medium for the dye laser) is intracavity pumped by the short Ar^+ pulses. As shown at the

top of Figure 7, a net gain region for the dye laser pulses (occurring twice per cavity round-trip in our standing-wave configuration) results when the saturated gain, $G^{\text{dye}}(\tau)$ (dash-dot curve), exceeds its linear loss, L^{dye} (solid curve).

Generation of picosecond pulse trains at two tunable dye wavelengths by synchronous pumping has been reported previously [15,16]. In [15], a mode-locked Ar^+ laser was used to synchronously pump two separate dye lasers, and generated synchronized picosecond pulse trains at two independently tunable wavelengths. Another technique utilizes internal synchronous pumping, where a cw Ar^+ laser is used to pump a double mode-locked cw dye laser system [16], and dual-wavelength pulse trains of picosecond duration are obtained from the same cavity. The latter configuration was shown to have better synchronism between the two pulse trains [17]. In our present system, by adding a lasing dye as the saturable absorber for the R6G laser, the Ar^+ pulses would be synchronously pumping a double mode-locked dye laser internally, thus generating three synchronized pulse trains from our system, two of which arise from the dye laser cavity and are tunable over a moderate range. It should provide even better results than that previously reported [18], where the Ar^+ laser was *not* operating in the CPM regime.

Conclusions

Studies of passive mode-locking of the Ar^+ laser by the saturable absorber R6G in four different regimes has been presented. Our system outperformed *similar* passively mode-locked systems [1-7], especially in the case where the Ar^+ laser was in the CPM regime with double mode-locking incorporated. It provides somewhat broader dye laser pulses, compared to those from traditional synchronous mode-locking systems. However, it eliminates the use of sophisticated and expensive equipment needed to generate the Ar^+ pumping pulses actively. Detailed investigation of both the Ar^+ and dye laser pulses was undertaken, using correlation/photodiode measurement techniques. An actual determination of the Ar^+ pulse shape with psec resolution was made. High repetition rate (≈ 65 MHz) synchronous Ar^+ and dye laser pulse trains were reported. It is the first system to generate bandwidth-limited Ar^+ and dye laser pulses *simultaneously*. Parametric studies have shed light on some of the fundamental mechanisms involved in the generation of Ar^+ and dye laser pulses. They also indicate the system was relatively *insensitive* to cavity length mismatch.

Acknowledgments

Much of this work is a review of research described in the Ph.D. dissertation of Dr. Yu-lin Wang of Johns Hopkins University, in collaboration with the author. The research support of the National Science Foundation is most gratefully acknowledged.

References

- [1] W. Dietel, E. Dopel, and D. Kühlke, *Opt. Commun.* **35**, 445 (1980).
- [2] Z. A. Yasa and N. M. Amer, *Opt. Lett.* **6**, 67 (1981).
- [3] D. Y. Lin and A. Dienes, *Appl. Opt.* **20**, 3825 (1981).
- [4] D. Kühlke and W. Rudolph, *Opt. Commun.* **47**, 70 (1983).
- [5] C. H. Brito Cruz, H. L. Fragnito, R. Francalacci, M. A. F. Scarparo, and R. Srivastava, *Opt. and Quant. Electron.* **15**, 487 (1983).
- [6] C. Wang, Q. Xing, and X. Zhao, *Opt. Commun.* **55**, 135 (1985).
- [7] R. Selfridge and A. Dienes, *Appl. Opt.* **24**, 1724 (1985).
- [8] Y. Wang and E. Bourkoff, *Opt. Commun.* **65**, 264 (1988).
- [9] Y. Wang and E. Bourkoff, "Passive mode-locking of the Ar^+ laser," to be published in *Appl. Opt.* **27**, (1988).
- [10] H. Mahr and M. Hirsch, *Opt. Commun.* **13**, 96 (1975).
- [11] R. L. Fork, B. I. Greene, and C. V. Shank, *Appl. Phys. Lett.* **38**, 671 (1981).
- [12] M. S. Stix and E. P. Ippen, *IEEE J. Quantum Electron.* **QE-19**, 5209 (1983).
- [13] This is from the Spectra-Physics specification for ≈ 150 ps Ar^+ pulses generated by active mode-locking of model 171 Ar^+ laser.
- [14] Z. A. Yasa, *J. Appl. Phys.* **46**, 4895 (1975).
- [15] R. K. Jain and J. P. Heritage, *Appl. Phys. Lett.* **32**, 41 (1978).
- [16] Z. A. Yasa, A. Dienes, and J. R. Whinnery, *Appl. Phys. Lett.* **30**, 24 (1977).
- [17] E. Bourkoff and A. Dienes, *IEEE J. Quantum Electron.* **QE-16**, 425 (1980).
- [18] E. Bourkoff and Y. Wang, *Opt. Commun.* **61**, 397 (1987).

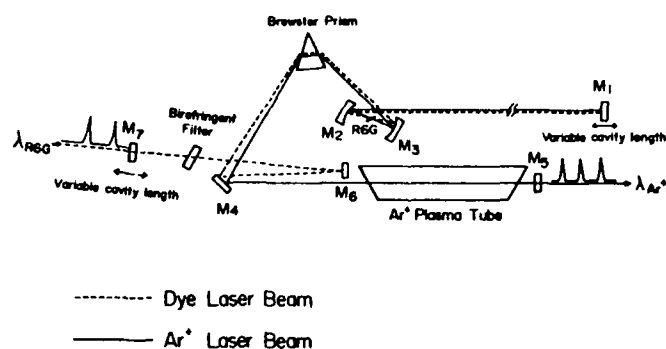


FIGURE 1

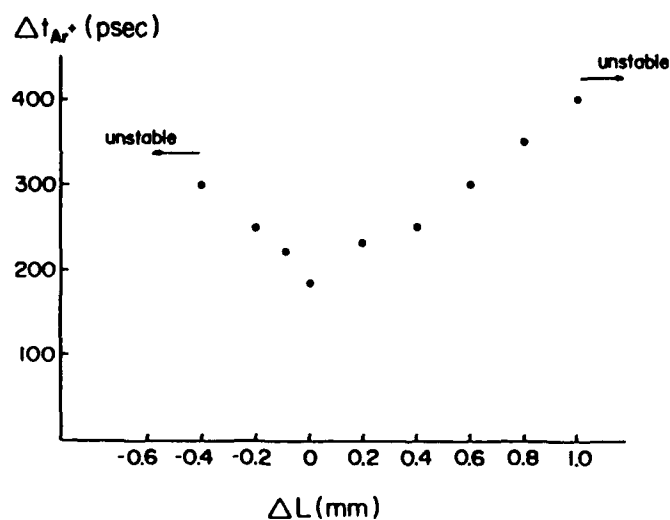


FIGURE 2

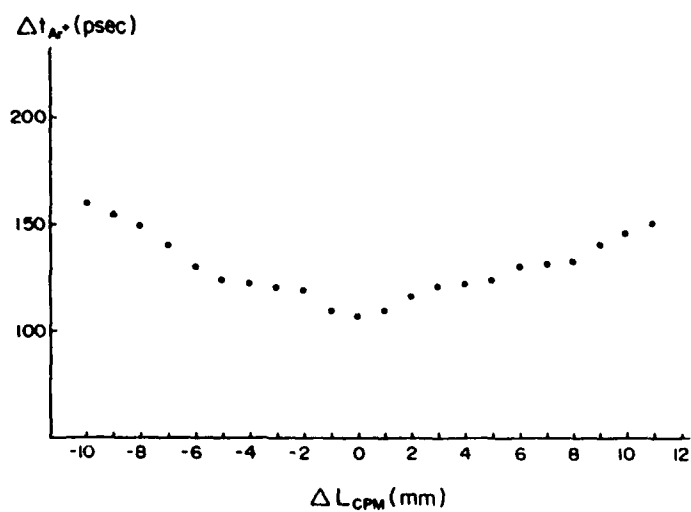


FIGURE 3

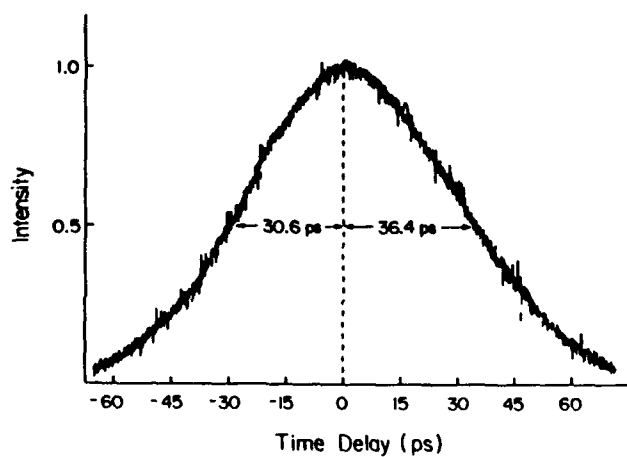


FIGURE 4

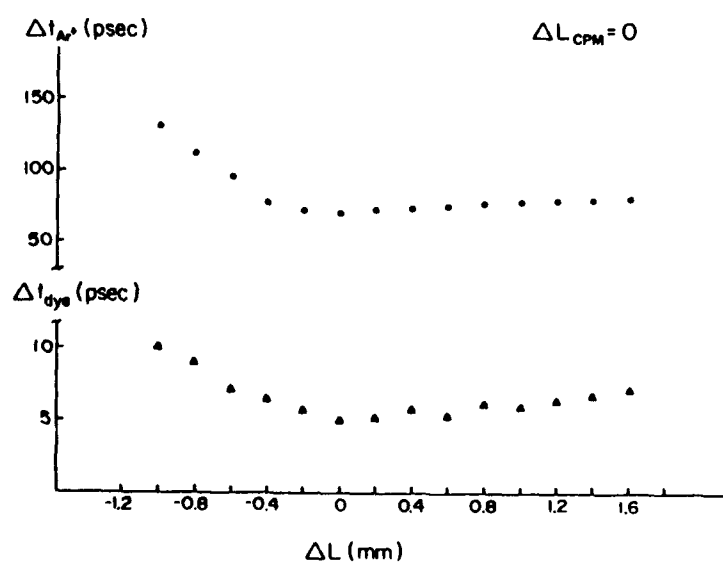


FIGURE 5

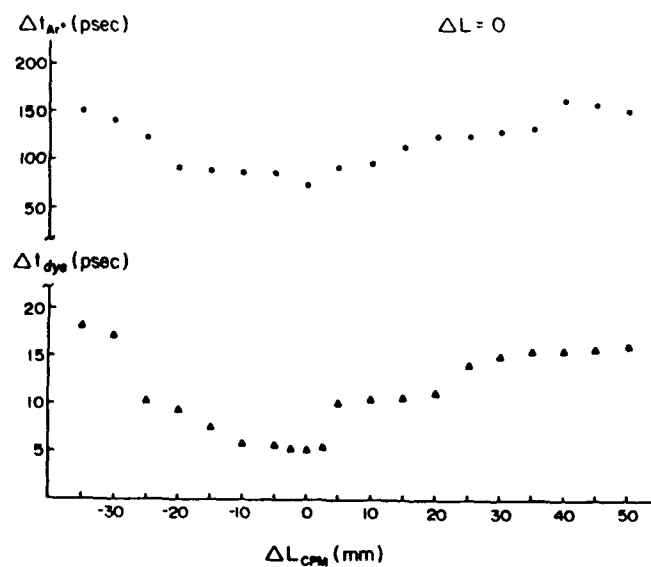


FIGURE 6

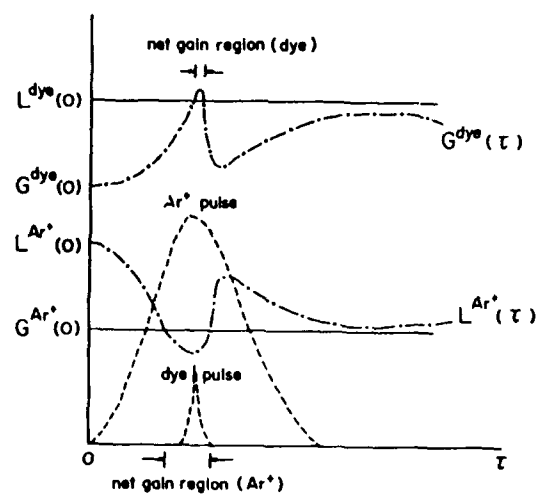


FIGURE 7

VARIABLE CAVITY MODE LOCKED Nd:glass LASER

by

N.H. Schiller
Hamamatsu Corporation
360 Foothill Road
Bridgewater, NJ 08807

and

X.C. Liang, Cheryl X.M. Zhao, L.M. Wang and R.R. Alfano
Institute for Ultrafast Spectroscopy and Lasers
Photonics Application Laboratory
Department of Electrical Engineering
The City College of New York
New York, NY 10031

Abstract

The design, performance, and characteristics of a mode-locked laser with effective cavity length for 5 to 21 meters is described. The pulse to pulse spacing of the pulse train is adjustable from about 35 to 140ns. The pulse duration was measured to be approximately 10ps for the early pulses in the train.

Introduction

Solid state mode-locked lasers have been used for many years for investigating nonlinear optical phenomena.⁽¹⁾ In a conventional mode-locked laser the cavity length ranges from 1 to 2 meters due to available limited space and mechanical stability.^(2,3) The pulse separation in such a conventional mode-locked laser is between 5 to 10 nanoseconds. For certain situations it would be desirable to have an ultra-long pulse spacing for applications such as ranging and remote sensing to mention a few. To produce such a pulse train requires either an ultra-long cavity or folding of a cavity.

This paper reports on a mode-locked laser design with an effective cavity length from 5 to 21 meters with overall length of 1.7 meters. The performance and characteristics of the laser such as parameters of energy, number of pulses, length of train and stability of the cavity is presented.

Experimental Arrangement

A schematic diagram of the compact design is shown in fig. 1. A Korad K-1 laser head equipped with (7 1/2" x 3/8") Brewster angle cut neodymium doped silicate rod and saturable absorber cell is located between several mirrors making up the cavity. The overall geometrical length of the laser is under 1.7 meters. The cavity contains a rear mirror (M_4) with a radius of curvature of 1.5 meters, three spherical⁽⁴⁾ optical path extender mirrors (M_1 to M_3) each with a radius of curvature of one meter, and an output mirror (M_0). The rear mirror and optical path extender mirrors were all coated for 100% reflectivity at 1.06 μ m. The output mirror (M_0) was coated for 65% reflectivity. The mode-locked dye cell was filled with Kodak #9860 dye dissolved in 1,2-Dichloroethane with transmission set at 70%.

The pulse train length and spacing was measured using an ultrafast Hamamatsu (C1083) pin diode coupled to a Tektronix 519 oscilloscope. The pulse duration was measured with a Hamamatsu C979X streak camera coupled to a video analyzer. The pulse train energy for each cavity length was measured using a Laser Precision Energy meter (RK-3230). Shot to shot stability of the laser appeared to be excellent for all cavity spacings.

The three optical path extender mirrors, (M_1 to M_3) were placed between the back mirror (M_4) and the dye cell. This provided a means of varying the optical path length of the cavity without changing its geometrical length. The distance between the mirrors was as follows; M_0 to M_1 was set at 1.7 meters, M_1 to M_2 and M_2 to M_3 was set at 1 meter each and M_3 to M_4 was set at 1.65 meters.

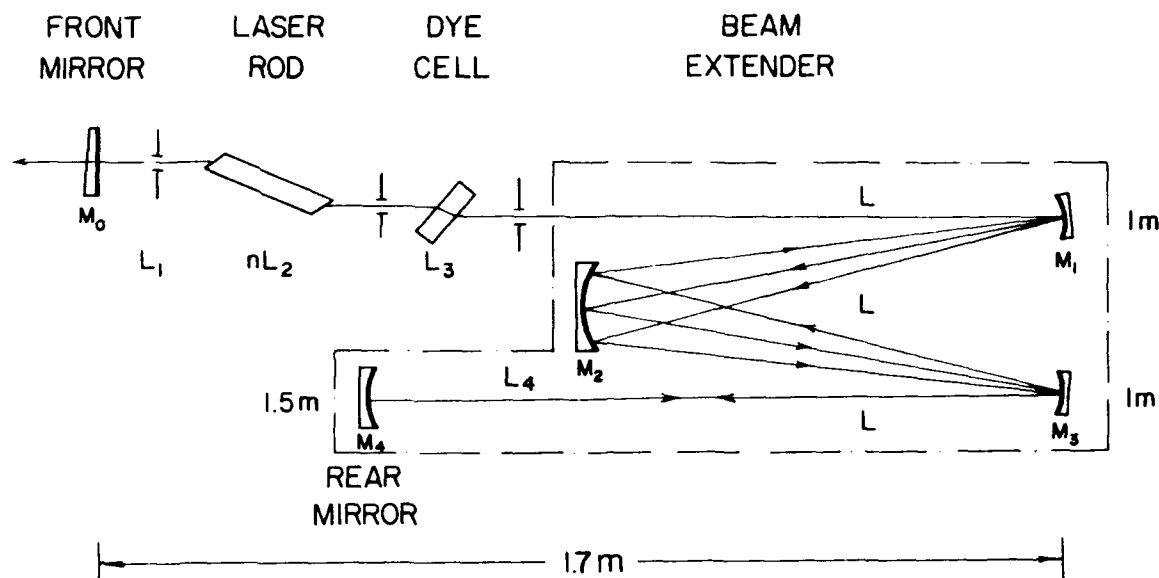


Figure 1. Schematic diagram of the variable cavity length Nd:glass mode-locked laser.

By adjusting mirror M_3 , the cavity length can be changed in 4 meter steps corresponding to approximately 13ns per step. The travel time for a pulse through the beam path extender section for N reflections off the central mirror M_2 is:

$$T = (2N+2) L/c \quad (1)$$

where L is the distance between mirrors M_1-M_2 and M_2-M_3 . The path length was measured from the pulse trains shown in Fig. 2 to be approximately 5.25, 9.25, 13.25, 17.25, and 21.25 meters. Figure 2 shows the oscilloscope traces of the pulse train for various number of reflections (N) in the path extender section for 1, 3, 5, and 7 dots. Each dot represents 4, 8, 12 and 16 path-lengths.

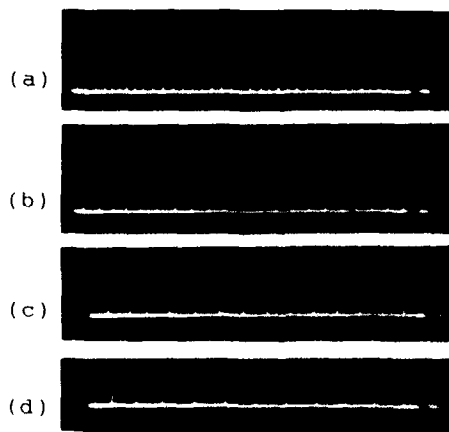


Figure 2. Oscilloscope traces of retouched photographs of mode-locked pulses emitted from the variable cavity length laser for each selectable spacing of (a) 5.25 meters, (b) 9.25 meters, (c) 13.25 meters, and (d) 17.25 meters.

Pulse to pulse spacings can easily be selected in steps of 13.2ns with the realignment of only one mirror (M_3), no other mirror is required to be realigned. For longer pulse separations this design can be scaled. With this cavity design we achieved a long optical path length in a short geometrical length (1.7m) thereby minimizing environment and mechanical effects providing a very stable configuration.

Laser thresholds, pulse to pulse time spacing, and pulse energies with respect to the number of passes through the path extender mirrors and the effective optical path length are summarized in table 1. The duration of a pulse early in the train is 10.5ps.

TABLE 1: LASER CHARACTERISTICS FOR MULTIPLE PASSES

PASSES IN PATH	Effective Cavity length	Threshold	Pulse Separation Distance	Energy
(N=)	(meter)	(kV)	(ns)	(mJ)
One	5.25	3.2	35	571
Three	9.25	3.8	61	562
Five	13.25	4.1	88	550
Seven	17.25	4.4	114	541
Nine	21.25	4.7	140	375

For various passes through the path extender section of the cavity the threshold energy increased slightly from 3.2kV to 4.7kV while the output energy remained fairly constant at about 550mJ with the exception of nine passes (N=9). For N=9 passes one of the reflections ran off the edge of the central mirror (M_2) resulting in a decrease in energy at the output.

The pulse train length was found to be extremely stable and long on the order of 5 μ s. This was attributed to the high stability of the cavity and the long pulse separation which we believe allows the lasing medium ample time to recover between successive passes of the optical pulse. In this case, the oscillator appears as an amplifier to the optical pulse which in turn is overcoming additional losses in the cavity due to multiple reflections off of each mirror. This may be viewed in essence as a "steady state" amplifier.

In summary, the overall size of the new laser design is 1.7 meters long by 0.3 meters wide. The pulse to pulse spacing is variable from approximately 35ns to 140ns. Train length was on the order of 5 μ s with about 100 pulses. The pulse duration of early pulses was measured to be 10.5ps. The stability diagram for the cavity was calculated using the matrix method. The physical size, stability and the elimination of devices external to the cavity are clear advantages over the standard two mirror cavity designs. Applications may include dynamical remote sensing and ranging of objects through the modulation of the pulse train.

This work is supported by Hamamatsu Photonics K.K.

References

1. R.R. Alfano and S.L. Shapiro, "Ultrafast phenomena in liquids and solids", Scientific American, 228, 42-57, (1973).
2. Ultrashort light pulses, Vol. 18, S.L. Shapiro, Ed. New York: Springer-Verlag, (1977).
3. R.R. Alfano, N.H. Schiller, and G.A. Reynolds, "Production of Picosecond Pulses by Mode Locking an Nd:Glass Laser with Dye #5", IEEE J. of Quan. Elec., QE-17, 290-291, (1981).
4. J. White, "Long Optical Paths of Large Aperature", J. Optical Society of America, 32, 285-288, (1942).

DESIGN OF A DIFFERENTIAL MODE HETERODYNE INTERFEROMETER*

Stephen Huber
Associate Professor of Physics
Beaver College
Glenside, PA 19038

Abstract

A design for a differential mode acousto-optic heterodyne laser interferometer is presented. The principle theoretical advantage of this interferometer is that it automatically cancels unwanted modulation interference noise generally present separately in each the reference beam and frequency shifted beam of the acousto-optic modulator. Disadvantages include 1) a more complex interferometer design including the need for two photodetectors and 2) the output signal has a more complex form. An application of this design would be real time monitoring and analysis of surface displacements with potential sensitivity on the Angstrom scale.

Introduction

The heterodyne mode of signal detection refers to a technique whereby the signal field to be measured is combined with a local oscillator reference field of slightly different frequency. The combined field is then detected with an appropriate photodetector. A review of this technique is readily available.

The attractive feature of heterodyne detection is that one can in principle achieve a signal to noise ratio approaching the quantum limit. This is accomplished by increasing the local oscillator reference field strength until the shot noise due to the local oscillator current dominates over any other noise contributions. However, there are instances where one prefers the signal strength and local oscillator field strength to be approximately equal. A case in point is the microinterferometer applications of Scott, Huber, and Sands.² These microinterferometers are driven by a frequency stabilized HeNe laser with and acousto-optic (A-O) modulator to produce two beams, one shifted by a frequency f_{AO} equal to the RF driving frequency of the A-O modulator. A typical value for f_{AO} is 40 MHz.

Minimum detectable signal levels are hampered in these interferometers by the reality that the two beams produced by the A-O modulator are not pure single sine waves but, rather, the reference beam and frequency shifted beam each have a small amount of 40 MHz beat signal interference "pollution" perhaps due to scattering of a fraction of the shifted signal back into the reference beam (and vice versa) within the A-O crystal. The presence of this beat signal in each of the two beams seriously hampers the ability to achieve theoretical minimum detectable signal levels.

Therefore, this paper proposes a differential mode microinterferometer design that overcomes this and other noise generation problems associated with interferometers employing techniques with approximately equal signal and reference field levels.

Interferometer Design

Figure 1 shows the design of an interferometer where all noise common to both beams is in principle greatly reduced. The frequency stabilize, polarized laser beam is split into two beams shifted in frequency by the A-O modulator frequency f_{AO} . Each of these beams is then split into two beams of equal intensity using beam splitting cubes. We now have four beams (labeled 1,2,3, and 4) at our disposal, two of which are shifted by the A-O modulator. Unmodulated reference beam (#2) is combined with modulated beam (#1) that is frequency shifted by f_{AO} and intercepted by photodetector #1. This superimposed beam is our new reference but carries the unwanted beat frequency "pollution" present in beams 1 and 2. The other unmodulated beam (#4) is reflected from a sample surface and recombined with the other modulated beam (#3). This superimposed beam now carries phase variation information from displacements in the sample surface as well as the unwanted beat frequency "pollution". By reversing the polarity on one of the photodetector outputs and adding to the other photodetector output the phase variation due to sample displacements can be extracted. Note that with zero input phase shift due to null displacement at the sample detection location there is (in principle) zero output signal. Hence, we have a differential mode of signal detection.

* Patent Pending

Schematic Diagram of Acousto-Optic Heterodyne Laser Interferometer

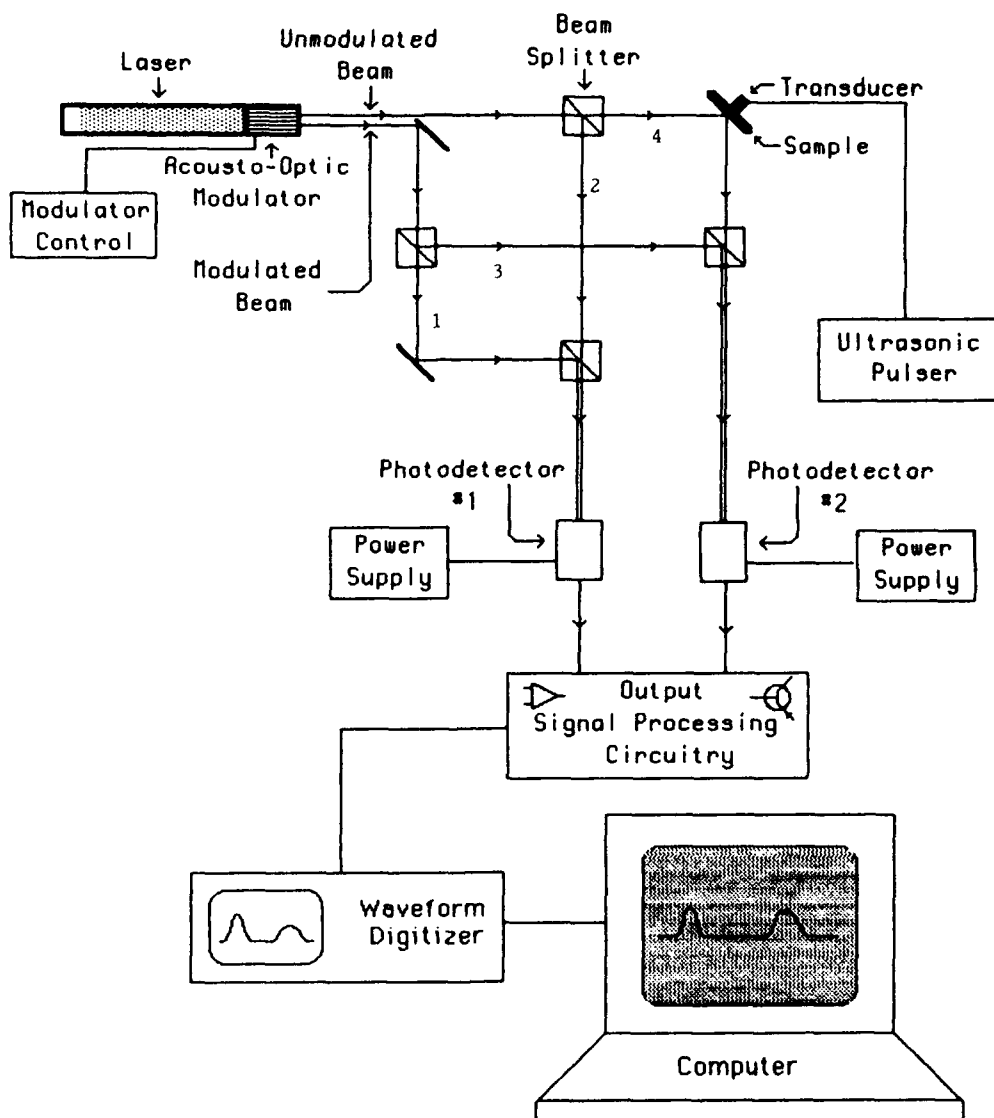


Figure 1

Analysis of Interferometer Output

Assume that the photodetectors are AC coupled so that only the time varying portion of the fields are detected. Photodetector #1 will then have an output voltage given by

$$y_1 = A_1 \sin(\omega t) + B \sin(\omega t + \delta_1) + C \sin(\omega t + \delta_2) \quad (1)$$

where the first term on the right represents the (intentional) beat frequency due to the recombination of beams 1 and 3. The second term on the right represents the unwanted f_{AO} beat noise due to beam 1 and likewise the third term represents the f_{AO} beat noise due to beam 2.

Likewise, photodetector #2 will have an output voltage given by

$$y_2 = A_2 \sin(\omega t + \Phi) + B \sin(\omega t + \delta_3) + C \sin(\omega t + \delta_4 + \Phi) \quad (2)$$

where the first term on the right represents the desired beat frequency and includes the time dependent phase shift

$$\Phi = \Phi(t) \quad (3)$$

due to surface displacements at the sample site. The second term on the right represents the unwanted f_{AO} beat noise due to beam 3 and likewise the third term represents the f_{AO} beat noise due to beam 4. The phase shifts

$$\delta_1, \delta_2, \delta_3, \delta_4 \quad (4)$$

take into account optical path length differences for the respective beat noises upon arrival at the respective photodetector.

When these voltage signals are combined after reversing polarity on the photodetector output #1 one obtains

$$\begin{aligned} y &= y_2 - y_1 \\ &= A_2 \sin(\omega t + \Phi) + B \sin(\omega t + \delta_3) + C \sin(\omega t + \delta_4 + \Phi) - A_1 \sin(\omega t) - B \sin(\omega t + \delta_1) - C \sin(\omega t + \delta_2) \end{aligned} \quad (5)$$

The amplitudes A_1 and A_2 can be controlled prior to reception by the photodetectors such that

$$A_1 = A_2 = A \quad (6)$$

Solving for the phase signal yields

$$\Phi(t) = \sin^{-1} \left(\frac{y - B \sin(\omega t + \delta_3) + A \sin(\omega t) + B \sin(\omega t + \delta_1) + C \sin(\omega t + \delta_2)}{A + C} \right) - \omega t \quad (7)$$

If the modulation frequency f_{AO} is on the order of 40 MHz, then the corresponding beat wavelength is on the order of 7.5 meters. Then phase differences for the beat noises present will be nearly equal. Using this approximation we may set

$$\delta_1 = \delta_2 = \delta_3 = \delta_4 = 0 \quad (8)$$

Then the information we desire is given by

$$\Phi(t) = \sin^{-1} \left(\frac{y}{A + C} + \sin(\omega t) \right) - \omega t \quad (9)$$

This result, although a bit cumbersome can be readily handled with an FM demodulator, waveform digitizer and computer.

Summary

The interferometer discussed in this report is appropriate for real time monitoring or analysis of surface displacements. Interrogation of mechanical properties of complex materials such as ceramic composites with surface resolution on the order of 1 micron is an application of particular interest. However, applications of the basic design can be quite diverse. This interferometer design is presently being investigated by the author. Preliminary results suggest that further development is appropriate.

References

1. A. Yariv, Optical Electronics (Holt, Rinehart and Winston, New York, 1985), pp. 352-355.
2. S. Huber, W.R. Scott, and R. Sands, in Review of Progress in Quantitative Non destructive Evaluation, vol 6A, D.O. Thompson and D.E. Chimenti, Ed. (Plenum, New York, 1987), pp. 1065-1073.
3. S. Huber, unpublished data.

A NEW OPTICAL METHOD FOR MEASURING SMALL ANGLE ROTATIONS.

Pan SHI ^{*} and Erik STIJNS

Vrije Universiteit Brussel, ALNA-TW
Pleinlaan 2, B-1050 Brussel, Belgium

Abstract

The measurement of rotations is an old mechanical problem ; different methods have been worked out. Often optical methods are used, as e.g. in shaft encoders, or Moiré techniques. More recently laser- and fibre gyroscopes were developed.

In this paper we describe an alternative approach. We build a Michelson interferometer, in which one of the mirrors (or both of them) are replaced by cornercubes which are fixed to the rotating table ; the optical pathlength depends on the angular position of the table. Rotating that table changes the pathlength, so the interference fringes shift ; this is measured by a counter. With this set-up it is possible to measure angular positions with an accuracy of 10^{-4} degree. By incorporating an up-down counter the apparatus is insensitive to vibrations. Moreover it worked well even if the distance between rotating table and the instrument is up to 4 meter.

1. Introduction

Although the measurement of rotations is a mechanical problem, optical methods are often used, as e.g. in optical shaft encoders or Moiré pattern techniques. We present here a method which uses only off-the-shelf lasers and optics, and which gives nevertheless satisfactory results as concerns sensitivity, easy of use, and insensitivity to parasitic vibrations.

2. Basic set-up

The basic idea consists in using a Michelson interferometer, in which one of the two mirrors is replaced by a black box. This black box has the two following properties :

- a) it reflects the light beam back on itself.
- b) the box can rotate around a vertical axis : when rotating, the optical pathlength in the box is a linear function of the angle of rotation.

Because of property (a) an interference pattern is formed at the screen : property (b) implies that the interference pattern shifts during the rotation of the black box. By measuring that shift one can, after calibration, calculate the rotation.

3. The right-angle prism as a retroreflector

The black box is realised by using a right-angle prism, as shown in figure 1. The laser ray is sent, via a beamsplitter, to that prism : the reflected beam is parallel to the incoming ray : it is then reflected on a fixed perpendicular mirror M2. Consequently, that ray follows exactly the same way back to the interferometer. This is also true when the prism

^{*} Permanent address : Department of Physics
Dalian Institute of Technology
Dalian, P.R. China

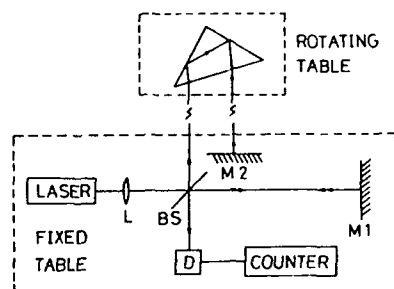


Figure 1 : Experimental set-up with a single prism.

is rotated, but then the optical pathlength changes, and the interference pattern shifts. In order to calculate that shift, consider figure 2. The light beam enters the prism in point D_0 ; the (vertical) axis of rotation is situated in point O . By geometrical arguments one can show that, after rotating over an angle θ , the change of the optical path is given by

$$\Delta P = \sqrt{2} a n (\cos \alpha - 1) + (\sqrt{2} a - 2\delta + 2y \tan \frac{\theta}{2}) \sin \theta \quad (1)$$

with $n \sin \alpha = \sin \theta$.

For small rotations this reduced to

$$\Delta P \approx (\sqrt{2} a - 2\delta) \theta + (y - \frac{a}{\sqrt{2} n}) \theta^2 \quad (2)$$

This formula shows that it is possible to improve the linearity by choosing

$$y = \frac{a}{\sqrt{2} n} \quad (3)$$

Only third-order deviations from linearity remain, and they are negligible for small rotations.

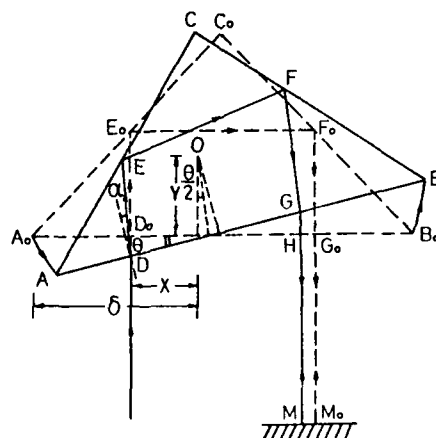


Figure 2 : Path of the light ray before and after rotation of the prism : the axis of rotation is displaced in the x- and y-directions.

4. The balanced set-up.

An improvement of the previous set-up was suggested by G.D. Chapman¹, and is shown in figure 3. The light beam of the second arm is also sent to the rotating table, where it is reflected by a second right-angle prism. Because of the symmetry, both the linearity and the sensitivity are greatly increased. If we take two equal prisms, with sides a and distance between them equal to l , the change of the optical pathlength can be shown to be

$$\Delta P = 2(\sqrt{2} a + l) \sin \theta \quad (4)$$

It turns out that the actual position of the axis of rotation has no importance : one always finds the same formula. Because formula (4) depends only on the sine of the angle and not, as formula (1) does, on other trigonometrical functions, the linearity of (4) for small angles is better than the linearity of (1). Moreover this symmetrical set-up can increase the sensitivity by more than an order of magnitude : it suffices therefore to take l large enough.

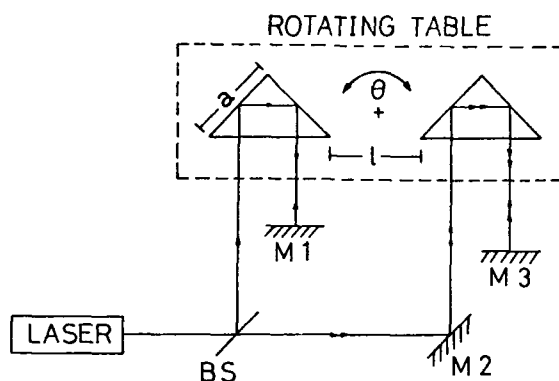


Figure 3 : Basic set-up with two prisms.

5. Experimental verification.

The set-up of figure 3 was realised and formula (4) was checked (figure 4). Two identical right-angle prisms, with sides $a = 30$ mm, were fixed on a perspex base : the distance between them was adjusted at $l = 48.2$ mm, in order to obtain 10^4 pulses per degree of rotation. A He-Ne laser was used as light source, and a lens diverges the beam a little bit. The shift of the interference pattern was measured with a photodiode. Each time the pattern

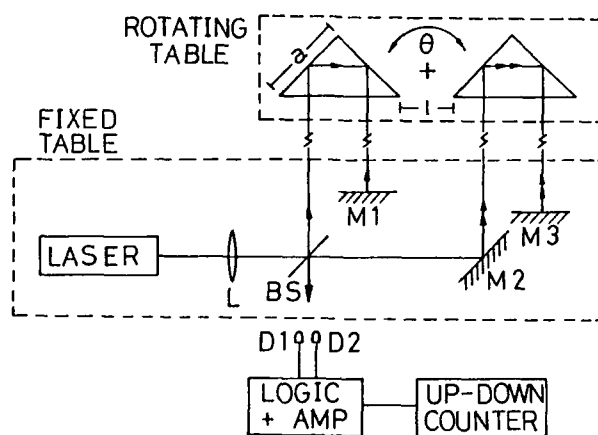


Figure 4 : Actual set-up of the experiment.

shifts over one fringe, the diode sees a pulse, which is amplified and send to an electronic counter. The number of pulses N is related to the change in optical path ΔP by

$$N = 2\Delta P/\lambda \quad (5)$$

In the actual set-up two photodiodes were used, positioned very close to each other (figure 5). Both signals were send, after amplification, to a logical controller. Both photodiodes see the same number of pulses, but because they are a little bit separated, there is a small phaseshift between the two signals. The sign of that phaseshift depends on the direction of movement of the fringe pattern, and consequently on the direction of rotation. The logical controller now gives each of the pulses a plus or minus sign, depending on the direction of movement. Those pulses, together with their signs, are send to an up-down counter, which counts the algebraic sum of the numbers. This set-up reduced the spurious pulses generated by vibrations. Indeed, vibrations around equilibrium give as much plus pulses as minus pulses, and consequently no net result is measured at the counter. So only real rotations are measured and vibrations are neglected. The experimental results are shown in figure 6. Each experimental point is the average of 20 measurements : the relative standard deviation σ/N ranges between 0.05 % and 0.2 %.

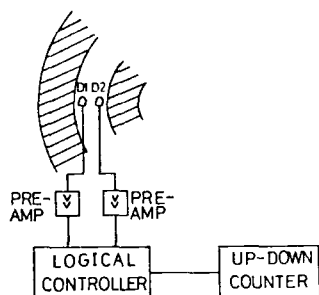


Figure 5 : Actual set-up of the measuring head.

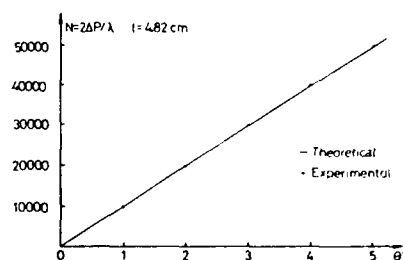


Figure 6 : Experimental points as compared to the theoretical curve.

6. Conclusions.

Measuring small angle rotations with a set-up with two right-angle prisms is a simple and accurate method. It has a good linearity : the sensitivity goes down to 10^{-4} degree $\approx 2 \times 10^{-3}$ mrad per fringe, and it is insensitive to vibrations. It is less sensitive, but easier to align and easier to use than the set-up of reference 2, and cheaper than the instrument of reference 3.

7. Acknowledgements.

We would like to acknowledge S. Cools who worked out a first experimental set-up, but especially G.D. Chapman whose remarks turned the original idea into a practical device. A preliminary version of this work was presented at the SPIE's Québec Conference⁴.

References.

1. G.D. Chapman : private communications.
2. G.D. Chapman, Appl. Opt. 13, 1646 (1974).
3. Hewlett-Packard Laser Measurement System 5526 A.
4. E. Stijns, presented at the SPIE Conference on Optical Testing and Metrology, Québec City, Canada (1986), paper 661-40.

LASER-EXCITED OPTICAL FILTERS:
COMPARISON OF RED- AND BLUE-SHIFTING FILTER CONCEPTS

T. M. Shay
Los Alamos National Laboratory
Chemical and Laser Sciences Division
P. O. Box 1663, MS E543
Los Alamos, N.M. 87545
(505)-667-8391

ABSTRACT

Laser-excited optical filter concepts in which blue shift or red shift photons are presented. We explore theoretically the potential performance of both laser-excited optical filter concepts.

Quantum-limited, wide field-of-view, narrow-bandwidth, atomic resonance optical filters with fast temporal responses are needed as receivers for blue-green underwater optical communications, remote sensing, and laser radar. The atomic Rb vapor laser-excited optical filters (LEOFs) are, in principle, electrically tunable, with narrow bandwidth (0.001 nm), a wide field-of-view (2π steradians), and high quantum efficiency. LEOFs offer simultaneously the resolution of a Fabry-Perot interferometer and an ideal field of view. Thus, these devices are ideally suited for extracting weak narrow bandwidth signals buried in strong nonresonant background radiation.

Narrow bandwidth operation of an atomic vapor LEOF was first demonstrated by Gelbwachs *et al.*,¹ Marling *et al.*,² and more recently by Chung *et al.*,^{3,4} Shay and Chung⁵ have presented a theoretical model for the blue-shifting LEOF. LEOFs are atomic resonance optical filters that use photon absorption from the first excited state of an atom to a higher lying level as the signal transition. To achieve efficient and selective excitation of the Rb(5p) atoms, a narrow bandwidth laser is used as the pump source. Fortunately, LEOFs do not require a high-power pump laser; on the contrary, reliable, efficient, low-power semiconductor lasers have been used to pump LEOFs.^{4,5} The ability of LEOFs to be pumped by diode lasers demonstrates the practicality of these optical filters.

The filtering process consists of the following four steps. First, limit the background noise spectrum with an optical bandpass filter. The most important function of this bandpass filter is to prevent any violet (for the blue-shifting LEOF) or red (for the red-shifting LEOF) noise photons from entering the LEOF cell. The second step consists of frequency upshifting the narrow bandwidth signal photons outside the residual background noise spectrum into a very low noise region of the spectrum (the violet or infrared region of the spectrum) by using a Rb LEOF cell. Third, the translated photons are isolated from the residual background noise by an optical filter that blocks the unshifted radiation and transmits only the shifted radiation. In the final step, the shifted signal photons are detected by the photodetector, while the background white noise is effectively rejected by the long wavelength stop filter. The net result of "sandwiching" the Rb LEOF cell between the optical prefilter and the optical low-pass filter is that the only incident light that is detected by the PMT is the light that has been shifted through the quantum absorption process in the Rb LEOF.

The physics of the narrow bandwidth frequency shifting process in the Rb LEOF is illustrated in Figs. 1 and 2 for the blue-shifting and red-shifting LEOFs, respectively. In both filters, the ground state Rb atoms are excited to the Rb(5p) state by the absorption of diode laser photons. The frequency shifting occurs when the signal photons are absorbed on the Rb($5p^2P_{1/2}$ to $10s^2S_{1/2}$) at 532.4 nm. When the Rb(10s) atoms are produced, they will, in the absence of significant collisional deactivation, radiatively decay to the np levels (where $6 \leq n \leq 9$) by emitting infrared photons. At this point, the operation of the two filter concepts differ. For the red-shifting LEOF, the infrared photons emitted on the Rb(10s \rightarrow np) transitions are the shifted photons. For the blue-shifting LEOF, the infrared photons emitted on those transitions are ignored and the subsequent emission of frequency translated (violet) photons on the Rb(np to 5s) transitions. These frequency shifted infrared or violet photons are proportional to the number of signal photons absorbed and are typically wavelength shifted to the red (blue) by more than 800 nm (100 nm). Because of this large spectral shift, simple color glass filters can effectively discriminate between shifted signal photons and unshifted noise photons. Rb LEOFs are based upon an atomic absorption process that is intrinsically isotropic and narrow bandwidth, and hence, LEOFs are inherently wide field-of-view ($\pm 90^\circ$) and, in the absence of collisional broadening, have Doppler-broadened linewidths (\sim GHz). The response time of this 532.4-nm filter is determined predominantly by the radiative lifetime of the Rb(10s) level, which has been calculated⁶ to be 471 ns.

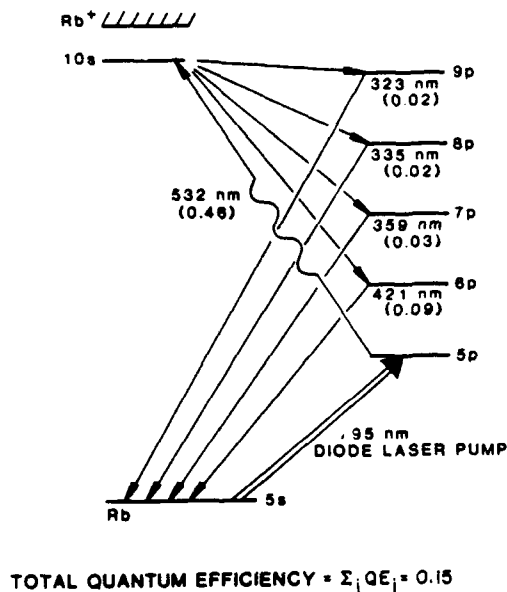


Fig. 1. A partial energy diagram of Rb indicating the two dominant processes for the blue shifting LEOF when 532-nm photons are absorbed in an actively pumped Rb. The numbers in the parenthesis correspond to the quantum efficiency of emission of that photon per signal photon absorbed.

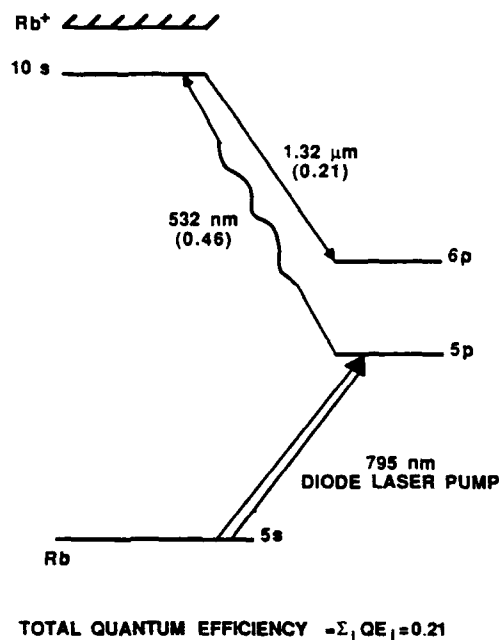


Fig. 2. A partial energy diagram of Rb indicating the important transitions for the red-shifting LEOF when 532.4-nm photons are absorbed.

The intrinsic quantum efficiency is defined as the number of infrared (violet) photons emitted per blue-green photon absorbed. In the absence of collisional deactivation of the Rb levels of interest, the intrinsic quantum efficiency for the red-shifting LEOF is simply the branching ratio for the Rb(10s to 6p) transition. For the blue-shifting LEOF, there is more than one violet transition of interest; in addition, the quantum efficiency is the product of a two-step process. Therefore, the intrinsic quantum efficiency for each of the violet np to 5s transitions can be calculated simply from the products of the branching ratios of the Rb(10s to np) and the respective Rb(np to 5s) transitions for ($6 \leq n \leq 9$).⁶ The total blue-shifting LEOF quantum efficiency (16%) is obtained by adding the quantum efficiency of these transitions.

For both filters, the ideal cell quantum efficiency (IQE) can only be achieved when (1) every signal photon incident upon the Rb cell is absorbed, (2) every violet photon emitted by a Rb atom escapes from the cell, and (3) collisional deactivation of the excited Rb atoms is negligible compared to radiative decay. In a practical system, these assumptions may not be strictly valid. In general, improved filter sensitivity and/or reduced filter pump power requires designs approaching those limits. Both the red- and blue-shifting LEOFs will have finite signal photon absorption and will violate some of the assumptions used in the quantum efficiency calculations as the ground state density, n_{5s} , is increased.

For the red-shifting LEOF, collisional deactivation of the Rb(10s) level causes a reduction in quantum efficiency. Assuming that the collisional deactivation of Rb(10s) occurs predominantly via collisions with Rb(5s) atoms, we can estimate the reduction in the quantum efficiency due to collisional quenching of the Rb(10s) atoms. The collisional quenching rates for the Rb(10s) atoms have not yet been measured. Therefore, I have calculated a quenching cross section for Rb(10s) atoms colliding with Rb(5s) atoms of $4.9 \cdot 10^{-13} \text{ cm}^2$, using the formula presented by Hugon *et al.*,⁷ which agrees with experimental measurements for high-lying Rb levels. Using this collision cross section, the quantum efficiency will be decreased by 10% (−0.46 db) and by 50% (−3 db) for n_{5s} equal to $1.11 \cdot 10^{12} \text{ cm}^{-3}$ and $9.61 \cdot 10^{13} \text{ cm}^{-3}$, respectively. Those vapor densities occur at the modest cell temperatures of 113 and 152°C respectively.

For blue-shifting LEOFs, there are two mechanisms that can lead to reduced quantum efficiency, the quenching that occurs for the red-shifting LEOF and for large diameter cells self-absorption of the frequency shifted photons. This latter mechanism is unique to the blue-shifted filter because for this filter the frequency shifted photons are emitted on four resonance transitions, as the Rb ground state atom density times cell radius product is increased the fraction of the frequency shifted photons that escape from the cell decreases. There are four violet resonance transitions and the cell transmission for each transition has been calculated on a computer. From these calculations, the escape probability of violet photons from the cell is decreased by 10% (-46 db) and 50% (-3 db), when n_{5s} equals $4.06 \cdot 10^{12} \text{ cm}^{-2}$ and $3.77 \cdot 10^{13} \text{ cm}^{-2}$, respectively.⁵ For small diameter cells ($r \sim 1 \text{ cm}$), the operating Rb(5s) densities exceed the densities for the -0.46 db and -3 db points for collisional quenching given in the previous paragraph, therefore collisional quenching is dominant for small diameter cells. However, for large diameter cells the quantum efficiency will be limited by the escape probability of violet photons. For example, a cylindrical blue-shifting Rb LEOF cell of 314 cm^2 aperture has -0.46 db and 3 db points when n_{5s} equals $4.06 \cdot 10^{11} \text{ cm}^{-3}$ and $3.77 \cdot 10^{12} \text{ cm}^{-3}$, respectively. Those vapor densities correspond to operating temperatures of 65 and 96°C, respectively.

Assuming that the signal photon bandwidth is much less than the absorption linewidth, then Beers law Eq. (1), can be utilized to calculate an accurate transmission probability, $P(\lambda_o)$, for the signal photons, as in

$$P(\lambda_o) = \exp [-n_{5p} \sigma(\lambda_o) d] \quad , \quad (1)$$

where, n_{5p} is the density of Rb(5p) atoms, $\sigma(\lambda_o)$ is the absorption cross section for the signal photons, and d is the average distance traveled by the signal photons in the Rb cell. However, the shortest distance that a signal photon can travel and escape from the cell is twice the cell length, namely $2L$, because all the Rb cell walls, except for the entrance window, are highly reflecting at the signal wavelength.⁵ Hence, replacing d by $2L$ guarantees that the probability of absorption of signal photons will always be greater than or equal to $P(\lambda_o)$. Because the Rb(5p) level is populated by the absorption of pump laser radiation, the required laser pump power is set by defining the specific value of the transmission probability $P(\lambda_o)$ for signal photons through the Rb cell. Thus, $P(\lambda_o)$ is a design parameter for the Rb LEOF.

Next, we need to evaluate the laser pump power required for our Rb LEOF. In our simplified model for a Rb LEOF, we make the following assumptions: (1) radiative loss processes are the dominant decay processes for Rb(5p) atoms; (2) the Rb cell walls have a fixed reflectivity R_p at the pump laser wavelength λ_p ; and (3) the Rb(5p) population is uniformly excited in the cell. Under those conditions, all of which are valid for the millitorr gas pressures of a Rb LEOF, we only need to replace the Rb pump photons that escape from the cell volume. Then, the laser pump power required for a LEOF is given in Eq. (2), as in

$$P_L = (1-R_p) n_{5p} L \pi r^2 h\nu_p A_{\text{eff}} \quad , \quad (2)$$

where, $L \pi r^2$ is the cell volume, $h\nu_p$ is the energy of the pump laser photons, and A_{eff} is the Einstein's coefficient for the resonance-trapped pumped photons in the Rb cell. For a Doppler-broadened atomic transition and a long cylindrical cell, Holstein and Bieberman⁸⁻¹⁰ obtained Eq. (3), for A_{eff} , as in

$$A_{\text{eff}} = \frac{1.6 \times A_{\text{rad}}}{\sigma(\lambda_p) n_{5s} r \left[\pi \ln \left\{ \sigma(\lambda_p) n_{5s} r \right\} \right]^{1/2}} \quad , \quad (3)$$

where A_{rad} is the Einstein A coefficient for λ_p photons. Note, that Eq. (2) shows that the A_{eff} is inversely proportional to $n_{5s} r$, so increasing $n_{5s} r$ decreases A_{eff} . The equation for the laser pump power required per unit area can be calculated by using Eqs. (1), (2), and (3) yielding

$$\frac{P_L}{\pi r^2} = \frac{(1-R_p) h\nu_p A_{\text{rad}} \times 1.6 \left[-\ln \left\{ P(\lambda_o) \right\} \right]}{2 \left[\sigma(\lambda_p) n_{5s} r \left[\pi \ln \left\{ \sigma(\lambda_p) n_{5s} r \right\} \right]^{1/2} \right] \sigma(\lambda_o)} \quad . \quad (4)$$

On the right-hand side of Eq. (4), there are only three variables that we can change. $P(\lambda_o)$ which is a design point for the filter, R_p the reflectivity of the cell walls at the pump wavelength (which you want as high as possible), and $n_{5s} r$, the product of the Rb(5s) density and cell radius. In practice, $P(\lambda_o)$ and R_p are fixed and only $n_{5s} r$ can be varied to reduce the required pump power. Therefore, the higher $n_{5s} r$ the lower the pump power required.

The pump power required can be calculated from Eq. (4), given A_{rad} , n_{5s} , R_p , and the pump and signal transition absorption cross sections. For our example calculations, we will assume that $R_p = 0.96$ and $P(\lambda_0) = 0.1$. For small diameter cells ($r = 1$ cm) both the red and blue shifting filter are limited by quenching of the Rb(10s) atoms therefore the ground-state atom density is limited to $1.12 \cdot 10^{12} \text{ cm}^{-3}$ (-0.46 db point) or $9.51 \cdot 10^{13} \text{ cm}^{-3}$ (-3 db point). These vapor densities correspond to 113 and 152°C , respectively. From Eq. (4), the required pump powers per square centimeter of cell aperture are 622 mW/cm^2 and 4.3 mW/cm^2 , respectively, for a cell with 1 cm radius. For a 10 -cm radius cell, the red-shifted filter is still limited by quenching of the Rb(10s) atoms from Eq. (4). We have calculated required pump powers of 3.4 mW/cm^2 and 0.36 mW/cm^2 for the -0.46 db and -3 db operating points. For a 10 -cm radius blue-shifting filter, the optical density of the self-absorption of the resonance transitions limits n_{5s} ; then from Eq. (4), we calculate 125 mW/cm^2 and 10.8 mW/cm^2 for the 3 db points of this filter. These ground-state atom densities correspond to temperatures of 66 and 96°C , respectively.

The response time of both filter concepts are predominantly determined by the radiative lifetime of the Rb(10s) level. The quantum efficiency is determined by the Doppler width of the signal transition and hence is almost identical for both filter concepts (~ 1 GHz). The quantum efficiency of the red-shifted filter is slightly higher (21%) than the quantum efficiency of the blue-shifted filter (16%). The laser pump power required for filter concepts is the same for small cell diameters (~ 1 cm or less). While for large diameter cells (20 cm), the required pump power decreases with cell aperture for the red-shifting filter and stays constant for the blue shifting filter. The operating temperature for large diameter cells is considerably lower for the blue-shifting concept. The main advantage of the blue-shifting filter is that sensitive low noise photomultiplier tubes can be used to detect the shifted photons whereas, the red-shifting filter must use photodiodes that do not have the internal gain of a photomultiplier.

In summary, the red- and blue-shifting LEOF concepts have been compared. We find that the largest difference between the two concepts is due to the different scaling of pump power per square centimeter of aperture with cell radius for large diameter cells. The processes limiting the quantum efficiency of both of these filters have been discussed. The blue shifting LEOF reaches a constant pump power per square centimeter of aperture large diameter cells, while the red-shifting LEOF sees a reduction in required pump power per unit area as the cell radius is increased. In applications where the ultimate in system sensitivity is required, the blue-shifting concept will be superior. In applications that have strong background noise and also require large apertures, the red-shifted filter requires lower pump power.

Acknowledgments

The authors wish to thank Dr. G. C. Mooradian and R. Anderson of NOSC for many fruitful discussions. We also thank Cmdr. R. Chatham for his support in the early stages of this work. This research was supported by SPAWAR, the Naval Ocean Systems Center, and the Department of Energy.

References

1. J. A. Gelbwachs, C. F. Klein, and J. E. Wessel, IEEE J. Quantum Electron., QE-14, 77 (1978).
2. J. B. Marling, J. Nilsen, L. C. West, and L. L. Wood, J. Appl. Phys. 50, 610 (1979).
3. Y. C. Chung, J. D. Dobbins, T. M. Shay, Technical Digest, Conference on Lasers and Electro-Optics, 64, April 1987, San Francisco, CA.
4. Y. C. Chung and T. M. Shay, to be published IEEE J. of Quantum Electron., May, (1988).
5. T. M. Shay and Y. C. Chung, to be published Optics Lett., (1988).
6. A. Lingard and S. E. Nielsen, Atomic Data and Nuclear Data Tables, 19, 533 (1977).
7. M. Hugon, F. Gounand, and P. R. Fournier, J. Phys. B: Atom. Molec. Phys. 13, L109, (1980).
8. T. Holstein, Phys. Rev. 72, 1212 (1947).
9. T. Holstein, Phys. Rev. 83, 1159 (1951).
10. L. M. Bieberman, J. Exptl. Theoret. Phys. (USSR), 17, 416 (1947).

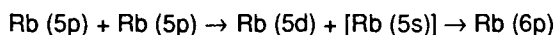
FUNDAMENTAL NOISE PROCESSES IN A LASER EXCITED OPTICAL FILTER

E. C. Apel
T. R. Gosnell
T. M. Shay
R. Samadani

Chemical and Laser Sciences Division
Los Alamos National Laboratory
Los Alamos, NM 87545

Abstract

A Rubidium narrow bandwidth optical filter is being investigated as a device for detecting weak narrow bandwidth radiation. In our configuration, the optical filter is actively pumped (or laser excited, i.e., LEOF). This configuration has a major inherent advantage over a passive optical filter, namely, wavelength versatility. One possible limitation to the Rb LEOF is due to an intrinsic noise source caused by the energy pooling of Rb 5p atoms which are produced by the pump laser. This process, i.e.,



produces Rb atoms in the 6p state which subsequently emit radiation within the bandwidth of the detection channel (420–323 nm). Hence, this constitutes a noise process since photons are produced at the detector in the absence of narrow bandwidth "signal" radiation. Herein, we present preliminary results on kinetic studies of the energy pooling process with the ultimate goal of quantifying the process (rate constant determination) and thus assessing its implications.

Introduction

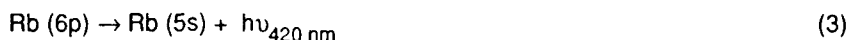
Narrow bandwidth optical filters are being investigated as devices for detecting weak, narrow bandwidth radiation. These filters can effectively reject both strong continuum radiation and strong narrow bandwidth radiation such as laser light. Potential applications of these filters can be found in laser communications, laser radar, and remote sensing. We have chosen to investigate the characteristics of an actively pumped (laser-excited) optical filter (LEOF) using Rb as the atomic medium.

The filtering process is a consequence of several steps. First, the incident signal radiation (what you want to detect) along with the background radiation is transmitted through a bandpass filter limiting the transmitted frequency range to $I(\nu) \pm \Delta\nu$ where $I(\nu)$ is the frequency of the signal laser and $\pm \Delta\nu$ are the cutoff points of the bandpass filter. The main purpose of the bandpass filter is to eliminate any violet background photons from entering the Rb cell. $I(\nu \pm \Delta\nu)$ is then allowed to traverse a heated cell containing Rb vapor in which the $5s \rightarrow 5p$ transition has been pumped by a diode laser (see Fig. 1). The signal laser is set to frequency match one of the $5p \rightarrow ns$ transitions. The prepared ns level subsequently decays to the np levels which, in turn, fluoresce to the ground state. The photons emitted from the np state are in the 420- to 323-nm wavelength range. This fluorescence is then passed through a long wavelength stop filter and allowed to impinge upon a photodetector. Thus, the only light hitting the photodetector is resultant from the initial signal laser frequency. The bandwidth is limited by the Doppler width of the atomic Rb absorption lines.

We are particularly concerned with the fundamental noise processes in the Rb LEOF. Noise in a LEOF arises from any process that produces photons at the detector when there is no signal present. Intrinsic noise produced in the Rb filter could limit the sensitivity of these devices. Therefore, it is important to identify and measure these processes. In the Rb LEOF, the intrinsic noise processes are collision-induced noise and blackbody noise. It has been shown that blackbody noise may be taken as negligible.¹

The following reactions are of interest





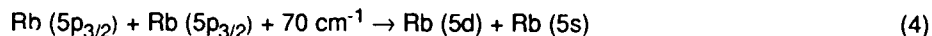
In the energy pooling process (1) Rb (5d) atoms are produced which subsequently decay to the Rb (6p) or Rb (5p) levels. The fraction of the decay which occurs to the Rb (6p) level contributes to the intrinsic noise of the LEOF filter since about half of the filter's quantum efficiency is produced by photons at 420 nm. We are interested, therefore, in measuring the rate constant for Reaction (1). Although there is one measurement of the rate constant which has been reported in the literature,² we feel that this result is potentially high in error as the result is dependent upon a theoretical ionization cross section. It should be noted that these experiments are very difficult and the results obtained by the authors in Reference 2 represent a very significant contribution to the understanding of the energy pooling processes in Rb.

Experimental

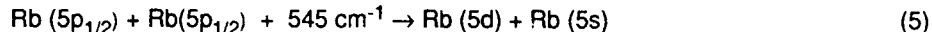
The experiment consists of pumping a heated Pyrex cell (80 - 250°C, 10 cm in length) containing Rb metal in a counter-propagating fashion using a diode laser (Hitachi 7802E) and an Ar⁺ pumped cw ring dye laser (Coherent 699). The frequency stabilized diode laser³ produces photons at $780.244 \pm 0.005 \text{ nm}$, which pump one of the hyperfine components of the $5s \rightarrow 5p$ transition. The $5p_{3/2}$ level is then pumped by the ring dye laser to a higher excited state (e.g., the 5d level). Fluorescence from excited states is then collected at a right angle relative to the laser beams either through a monochromator or through an interference filter, detected by a photomultiplier tube, and electronically processed.

Results and Discussion

Our initial objective was to obtain information on the energy pooling process. The energy pooling process for which the energy defect is the smallest is



We have chosen to quantify this process initially as a worst case scenario. In actual practice, one would choose to pump the $5p_{3/2}$ state (795 nm) as the energy defect for the reaction



is much greater than for Reaction (4). The laser diode, operating at 10 MW, is used to excite the $5p_{3/2}$ state. Evidence for the energy pooling process is observed at operational temperatures of $T \geq 390 \text{ K}$. This evidence is in the form of fluorescence that originates from higher (than 5p) excited state levels. The following transitions have been observed



In agreement with a previous study,² we found no evidence for fluorescence from any levels lying at higher energy than the 5d level. The energy defects for these levels are apparently too great ($>670 \text{ cm}^{-1}$). Observations of fluorescence from levels originating below the 5d level (e.g., 6p) is assumed to arise from a radiation cascading process (from 5d) and not an energy pooling process as the energy defect is probably too great.⁴

According to Reaction (1), the density of the 5d level varies as $\text{Rb [5p}_{3/2}]$.² Below (Fig. 2), we have plotted the pressure (number density) as a function of square root of the observed signal intensity (fluorescence from the 6p level to the 5s level, i.e., 421nm) for the case in which only the diode laser is used (to excite the $5p_{3/2}$ level). We have also plotted (Fig. 3) the square root of the signal intensity vs the 780 nm laser intensity at a given temperature (pressure). In each case a straight

line is observed, as expected from the kinetics of the system. Thus, we have further evidence of the observation of the energy pooling process.

Our next objective is to determine the rate coefficient for Reaction (1) to a high degree of accuracy. This will be accomplished using a ring dye laser (described in the experimental section) operating at 776.0 nm to pump the $5p_{3/2}$ level. The fluorescence resulting from the 5d level (or 6p) will be monitored as a function of the dye laser being on/off. This measurement, along with a number density measurement of the $5p_{3/2}$ level and assorted laser parameters will yield the rate constant for Reaction (1).

Summary

We have commenced our study of the intrinsic noise processes in Rb vapor. The main contributor to this noise process is the collisional energy pooling reaction described by Equation (1). We have observed evidence for the energy pooling process. The pooling mechanism is shown to follow the expected kinetics. We are in the process of determining, to a high degree of accuracy, the collisional cross section (rate constant) for this process. This work was supported by the Naval Oceans System Center.

References

- 1) T. M. Shay, paper #MJ.5, Lasers '87 conference.
- 2) L. Barbier and M. Cheret, J. Phys. B: At. Mol. Phys., 16, 3213 (1983)
- 3) Y. C. Chung and T. M. Shay, Elect. Lett, 23, 1044 (1987)
- 4) M. Allegrini, G. Alzetta, A. Kapystynka, L. Moi, and G. Orriols, Opt. Comm., 19, 96 (1976).

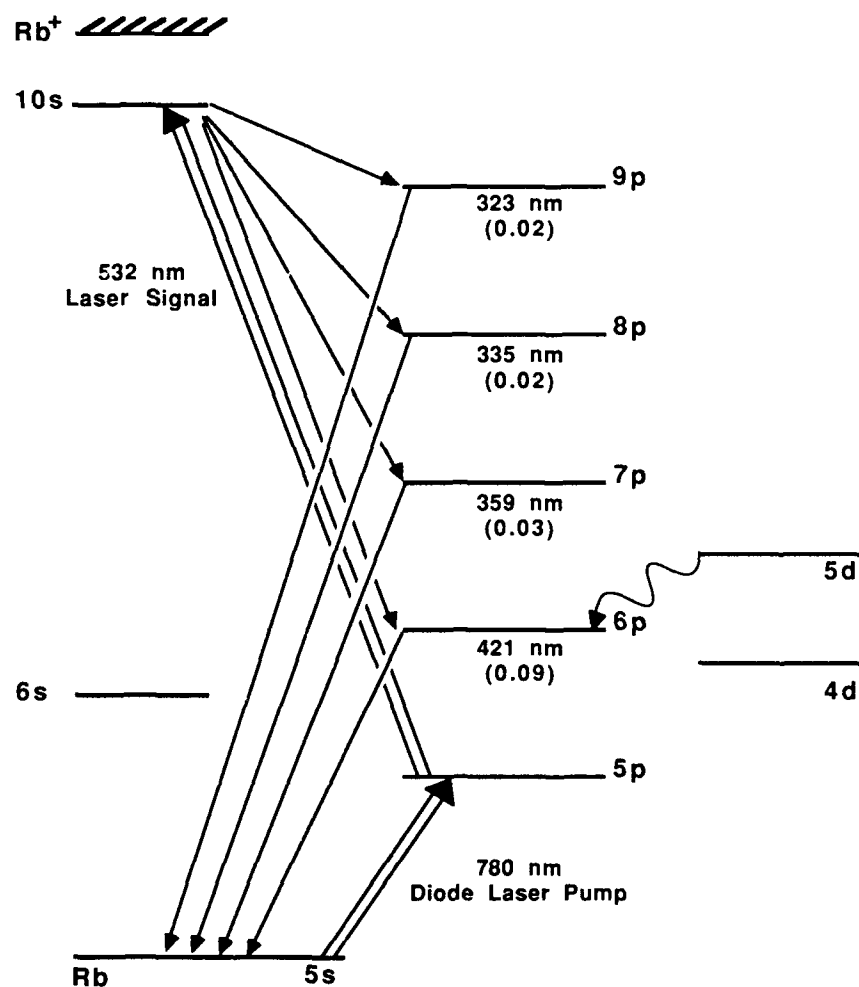


Fig. 1. Relevant energy levels diagram for Rb LEOF. The calculated intrinsic quantum efficiencies for the various P-levels are shown in brackets. The 5d level is populated by the energy pooling process.

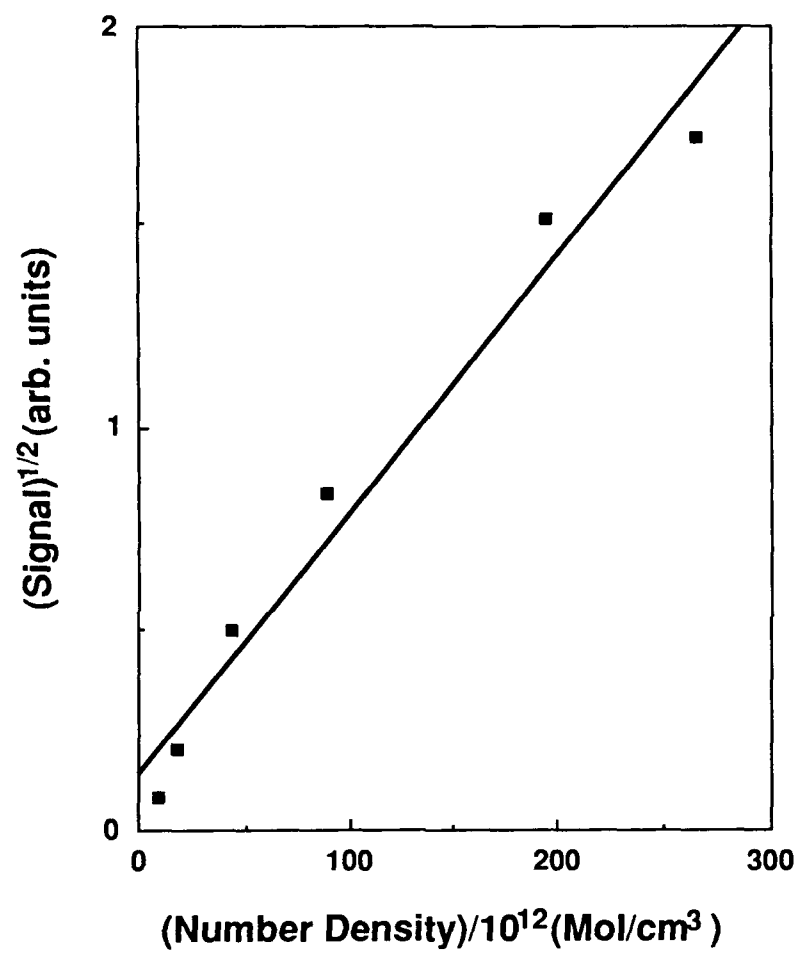


Fig. 2. Plot of the square root of the signal (6p-5s, 420nm) vs number density.

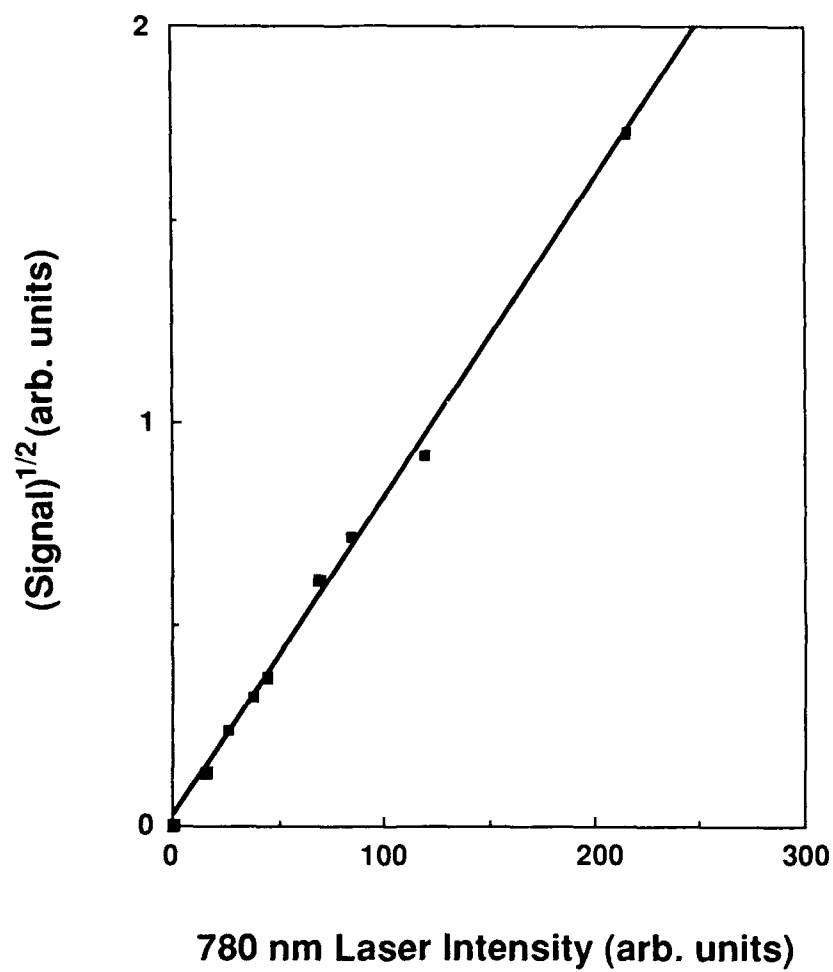


Fig. 3. Plot of the square root of the signal (6p-5s, 420 nm) vs 780 nm laser intensity at $T = 160^\circ\text{C}$.

MODE-LOCKED AND SYNCHRONOUSLY PUMPED CW LASERS
AND TIME-CORRELATED SINGLE PHOTON COUNTING:
A TIME RESOLUTION STUDY.

A. van Hoek and A.J.W.G. Visser

Departments of Molecular Physics and Biochemistry, Agricultural University,
De Dreijen 11, 6703 BC Wageningen, The Netherlands.

Abstract

In time-correlated single photon counting using deconvolution techniques the time resolution is determined by short-term instrumental response, temporal shifts and reproducibility. Pitfalls were traced and detection limits examined using ultrashort luminescence decays (5-10 ps).

Introduction

In picosecond luminescence experiments using synchronously pumped cw lasers and time correlated photon counting the temporal resolution is limited by the detection system. The excitation pulse width can be less than some picoseconds, but due to transit time jitter in the detection photomultiplier the width of the instrumental response is at least 47 ps¹. We used the technique to study biological materials² and applied deconvolution techniques to recover the decay time constants accurately³. When measuring rapidly decaying fluorescence (5-10 ps) it appears that not only the short term time resolution is important, but also reproducibility and long term temporal shifts influence the results. Transit time instabilities of components in the set-up (versus temperature, operating voltage, etc.) turned out to be important parameters.

Materials and methods

Three different pseudoazulenes, derivatives of 1,2-5,6 dibenzoxalene (DBO, systematic name benzo/b/indeno/1,2-e/piran) were purified as described previously⁴. N-hexane (Merck, fluorescence grade) was used to prepare solutions with a concentration corresponding to 0.2 OD at 300 nm. Pseudoazulenes do not exhibit any detectable emission arising from the S₁-S₀ transition, but from the S₂-S₀ transition the fluorescence quantum yield is in the order of 10⁻³ to 10⁻⁴. From the high polarisation of emission in low viscosity solutions⁵ an estimate can be made for the fluorescence decay time (less than 0.1 ns). We used the pseudoazulenes CH₃-DBO (1), Phe-DBO (2) and CHNOH-DBO (3)⁶, see figure 1. The quantum counter p-bis[2-(5-phenyloxazolyl)]benzene (POPOP), see (4) of figure 1, was purchased

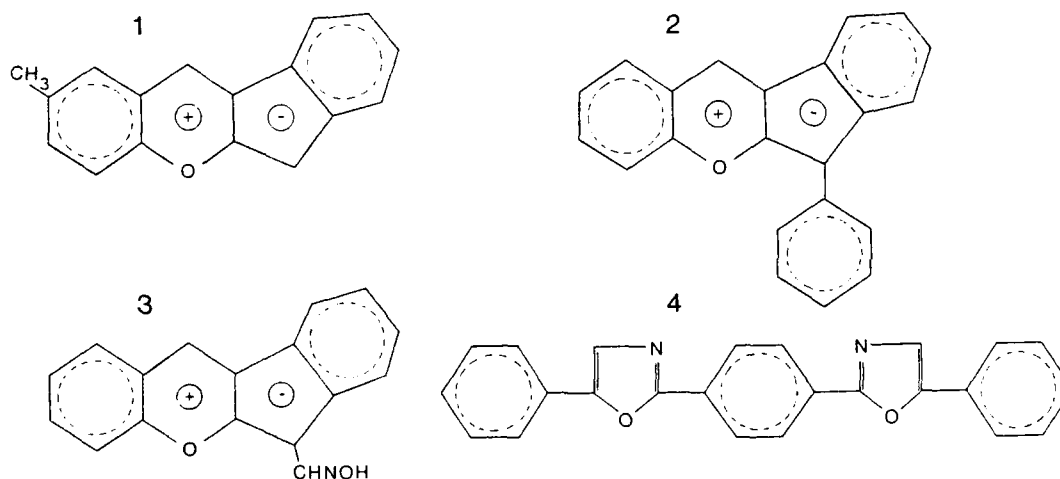


Fig.1 Chemical structures of CH₃-DBO (1), Phe-DBO (2), CHNOH-DBO (3) and POPOP (4).

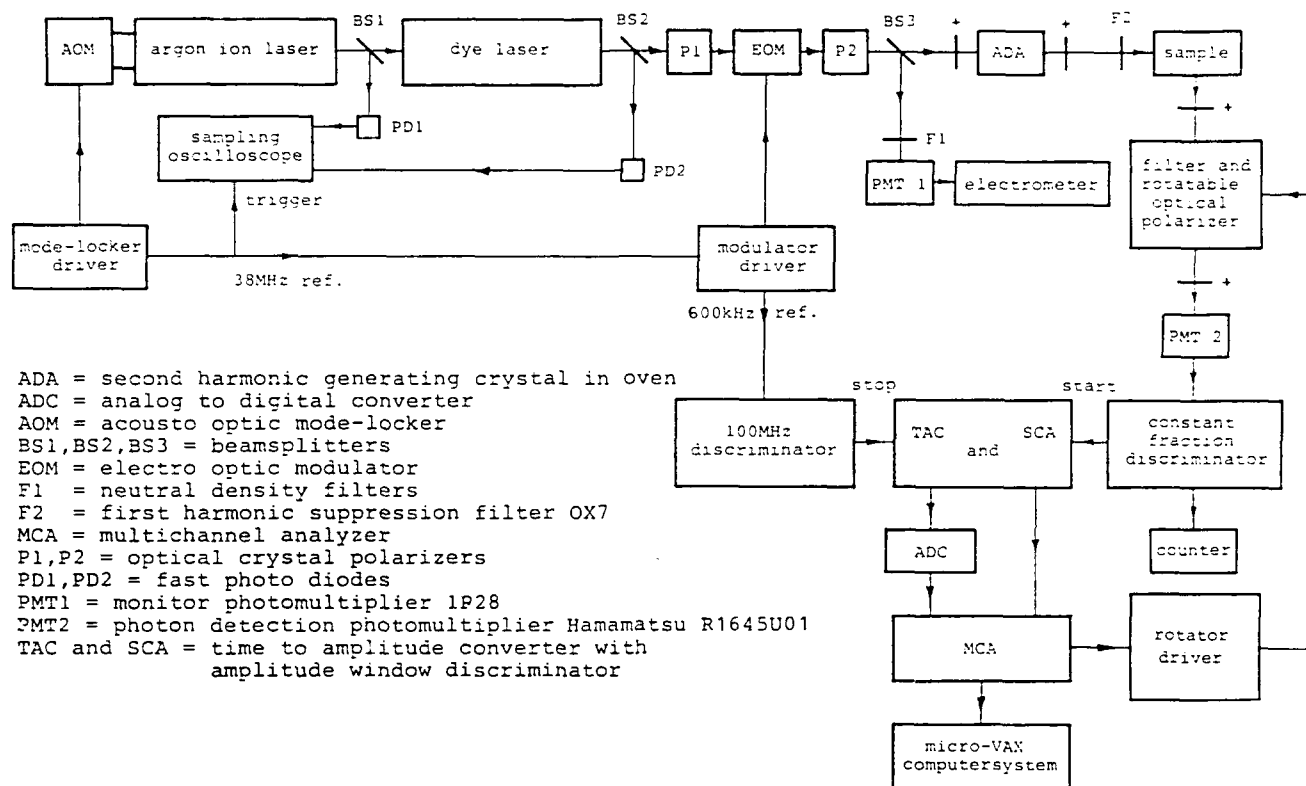


Fig.2 Block-diagram of the experimental set-up.

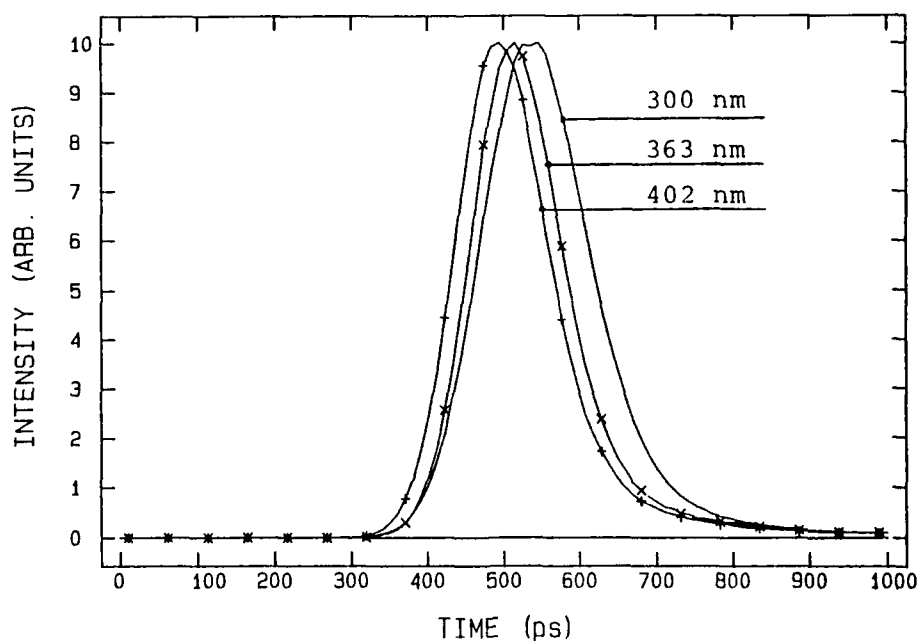


Fig.3 Graphs of the instrumental response at different wavelengths.

from Eastman Kodak (scintillation grade) and dissolved in ethanol (Merck, fluorescence grade), concentration corresponding to an OD of about 0.1 at 300 nm. Cis-parinaric acid was purchased from Molecular Probes and used as a 2 μ M solution in water.

In figure 2 a block diagram of the experimental set-up is shown. The time scale was calibrated using an Ortec 462 time calibrator, resulting in an overall accuracy of 0.1 %. The excitation is provided by the frequency doubled output of a synchronously pumped cw dye laser, resulting in pulses of some picoseconds duration at 300 nm wavelength. An electrooptic modulator set-up is used to reduce the rate of excitation pulses to 598 kHz⁷.

Fluorescence is detected at 90° with respect to the excitation direction and interference filters are used for scatter rejection. A sheet type polarizer in the fluorescence light path can be rotated in parallel or perpendicular position or, depending on experimental requirements, set under magic angle with respect to the direction of excitation polarisation. With neutral density filters the exciting beam is attenuated to have a maximum photon rate of 30 kHz³.

Reproducibility and temporal shifts

The width of the instrumental response (about 140 ps full width at half maximum, FWHM) is much wider than the decay times of the pseudoazulenes to be investigated. Therefore a deconvolution procedure is used. In figure 3 graphs are presented of the instrumental response at different wavelengths. It can be observed that in addition to a shift in time there is a variance in shape. These are mainly effects from the photomultiplier. The use of a proximity focussed type microchannel plate photomultiplier would minimize but not eliminate the wavelength dependency of properties¹. Therefore for deconvolution we use the reference or mimic method³. In that case the instrumental response is deconvoluted from a known (single) exponential fluorescence decay, recorded at the same wavelength as the unknown sample.

With the controls of the set-up fixed, the reproducibility of the time scale is much better than the mentioned accuracy. By determining (sub)nanosecond decay times of quantum counters the measurement has an accuracy sufficient to predict the sample temperature far within 1 °C. In particular when measuring picosecond decay times, the reproducibility may dramatically decrease when static or dynamic temporal shifts occur.

Static temporal shifts

With a time to amplitude converter (TAC) and analogue to digital converter (ADC) the time span between exciting light pulse and fluorescence photon is repeatedly measured, the data being gathered in the multichannel analyzer. When placing an optical filter in the exciting laser beam or the fluorescence light path, the time of arrival of a fluorescence photon will be delayed due to the difference in speed of light in air and in the filter. The delay will be about 1 ps per mm substrate, if an index of refraction of the filter material of about 1.4 is assumed.

When such shifts occur between measuring cycle of known and unknown fluorescence decay, an artificial short component will be found by the deconvolution procedure. This is another reason to measure unknown and reference sample at the same detection wavelength. The adjustment of the energy of excitation pulses is performed with a variable neutral density filter with metallic coating or by exchanging neutral density filters with metallic coating and equal thickness. In case of scanning a detection monochromator, not only a temporal broadening⁸ but also a shift may be introduced when the axis of rotation is not in the plane of the grating. In principle all these static shifts can be corrected for when their exact values are known.

Dynamic temporal shifts

More complications arise when there is a steady temporal drift because of ambient temperature changes. This drift is mainly originated by transit time variations versus temperature in discriminators, coaxial cables etc. Coaxial cables (50 Ω) are used as delay lines (~20 cm/ns) for positioning start and stop signals in the TAC time window. The temperature dependence of the transit time of a 100 ns delay line (RG 58 C/U) was measured to be -20 ps/°C.

The transit time instability of discriminators is determined by a complex of mechanisms, showing positive and negative coefficients. Therefore the temperature gradients induced by temperature variations have relatively much influence. One source of transit time drift is the threshold instability versus temperature, essentially not compensated by

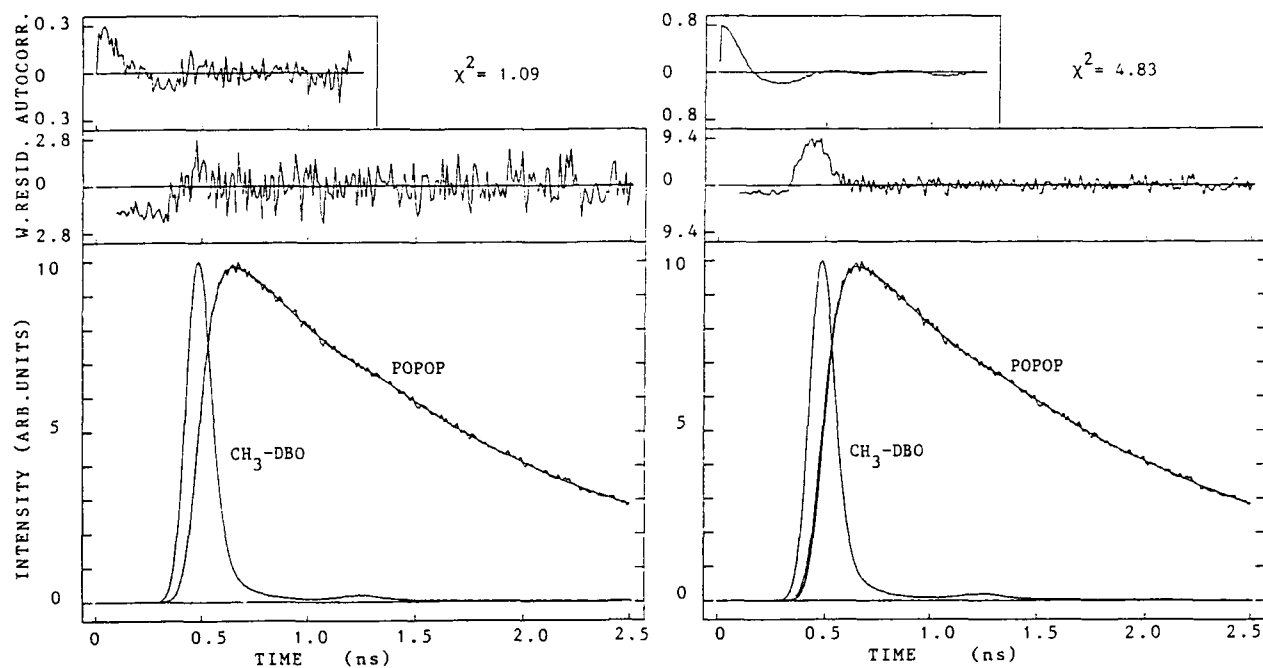


Fig. 4 Examples of the analysis of POPOP and CH₃-DBO fluorescence decays. The decay time of CH₃-DBO was fixed at 10 ps (left) and 50 ps (right).

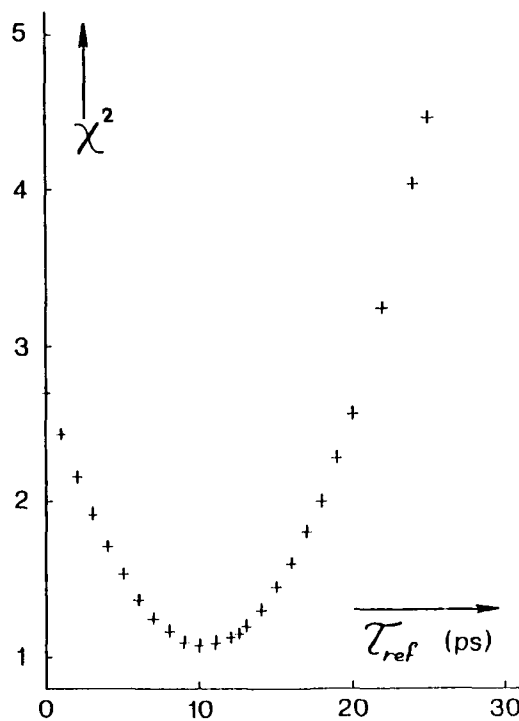


Fig. 5 Plot of χ^2 as function of the decay time of CH₃-DBO. All parameters were fixed in this case.

the constant fraction mechanism. In modern discriminators (Ortec 934, Tennelec TC454) this instability is less than 100 $\mu\text{V}/^\circ\text{C}$ and then a slope of the leading edge of 500 mV/ns results in a timing instability of 200 fs/ $^\circ\text{C}$.

From older discriminators (Ortec 436 and 463) the threshold instability is less than 500 $\mu\text{V}/^\circ\text{C}$, leading to a contribution to transit time instability of 1 ps/ $^\circ\text{C}$. It becomes worse when discriminating with the Ortec 436, 100 MHz discriminator, the shelf slope of the 38 MHz sinusoidal reference signal from the mode-locker driver (0.5 V_{pp}, slope 70 mV/ns at the zero crossing, resulting transit time instability 7 ps/ $^\circ\text{C}$) to have a timing signal for the modulator driver. In that case the signal must be amplified first⁸.

The propagation delay instability for modern discriminators is specified by the manufacturer (Ortec 934; <15 ps/ $^\circ\text{C}$ and Tennelec TC454; <10 ps/ $^\circ\text{C}$), indicating that threshold instability effects are relatively negligible. The overall transit time instability versus temperature of some discriminators was measured, using a negative fast pulse at the input, slope 500 mV/ns, amplitude 800 mV (Ortec 436; +8 ps/ $^\circ\text{C}$ and Canberra 1428A; +10 ps/ $^\circ\text{C}$). The temperature instability of the TAC (Ortec 457) is specified to be <±10 ps/ $^\circ\text{C}$ and measured to be -2 ps/ $^\circ\text{C}$ at the 50 ns range. The dependency of the photomultiplier transit time to the high voltage was measured to be -0.4 ps/V for the Hamamatsu R 1645 U/01. With a high voltage instability of 0.2 V/ $^\circ\text{C}$ at 3400 V (Bertan 205A-10N), a transit time instability of 80 fs/ $^\circ\text{C}$ can be awaited.

These results show that for picosecond accuracy the ambient temperature should be far within 1 $^\circ\text{C}$. Timing instability can be minimized by choosing components in such a way that the signs of temperature dependence coefficients of the transit time are the same in start and stop arm of the set-up.

Data analysis

Data were fitted to (single or multi-) exponential decay laws in an iteration process³, minimizing the weighted sum of squared residuals (reduced χ^2). Analysis could be performed with α 's and τ 's of reference and unknown compound fixed or as iteration variables. The relatively long decay time of the quantum counter POPOP is exactly known.

Results

In figure 3 not the pure instrumental responses at different wavelengths are presented, but only at the excitation wavelength 300 nm. The graphs corresponding to 363 and 402 nm are fluorescence "decays" of CH₃-DBO. From that fact some important conclusions can be drawn. The first conclusion is that the fluorescence decay time must be very short, possibly some picoseconds, because at 300 nm the FWHM of the response is broader than at 363 and 402 nm. A 100 ps fluorescence decay time (detected at 363 or 402 nm) would already give a substantial broadening of the 140 ps FWHM pulse profile. In this case the broadening is less than the wavelength effects at the cathode region of the photo-multiplier¹, giving broadening at shorter wavelengths.

The second conclusion is that the shift of the fluorescence peak to later points of time is also smaller than shift due to wavelength effects in the PMT. These effects make the peak shift to earlier points of time at longer wavelengths in this case. The effects were fully reproducible and care was taken that the experimental conditions were identical. For instance with changing filters (300, 363 and 402 nm) a negligible shift (less than 500 fs) was introduced and the photon rate was 30 kHz in all cases⁹.

Then data sets were analyzed using a data set of POPOP and one of the pseudoazulenes, all measured at the same wavelength, 402 nm. With fluorescence lifetimes of both compounds as free iteration variables χ^2 was optimized. The relatively long decay time of POPOP was recovered with high precision: 1294 ± 2 ps at 20 $^\circ\text{C}$. However, the lifetime of the pseudoazulene was found to yield a negative value, for CH₃-DBO: -7 ps ± 2 ps. That artificial value was found because the analysis program was forced to use single exponential decay laws for both compounds.

The negative value of the lifetime indicates that the rapid decay of the pseudoazulene competes with another rapid process from POPOP, most likely the internal conversion from excited vibronic states to the emitting S₁ state. The rate constant of such radiationless transitions is estimated to be in the THz range, yielding a time constant of a few picoseconds. Then a biexponential decay law was used for the POPOP fluorescence. When all parameters were free iteration variables, the deconvolution program could not find a unique solution in this case. From the expression for the convoluted fluorescence decay with the reference method³ it is clear that when reference and unknown decay time have to close values, no solution will be found by the program. So calculations were carried out with

decay time constants fixed. In figure 4 examples of analysis are given for two values of CH₃-DBO (for POPOP: $\alpha_1=-1$, $\alpha_2=1$, $\tau_1=1294$ ps and $\tau_2=5$ ps). When the lifetime of CH₃-DBO is varied systematically, a clear minimum can be found in the characteristic of reduced χ^2 as a function of the time constant of the pseudoazulene fluorescence (see figure 5). The τ -value of the fast component of the POPOP fluorescence decay did influence the point of minimum χ^2 but deviations were within reproducibility error.

By repeating the measurements and analyzing many datasets it becomes clear that the reproducibility is poor. And only when reference and unknown sample are recorded in a period of some minutes there is a chance for reasonable reproducibility. So now one measurement always consists of recording reference, unknown and again reference data as close in time as possible. Most times the two blocks of reference data are averaged (added) before analysis³. Despite of all these provisions it was not possible to give an accurate value for the fluorescence lifetimes of the pseudoazulenes. Only a range of values can be given and the reason is temporal drift during the measurements. For CH₃-DBO the fluorescence lifetime was found to be between 1 and 10 ps, for Phe-DBO between 1 and 6 ps, for CHNOH-DBO between 1 and 11 ps.

As can be deduced from figure 2 there are many components in the stop arm compared to the start arm of the set-up. It should be better to have a more direct stop signal, for instance from a photodiode excited by the laser pulses. But mainly because of the about 1 % conversion efficiency of the ADA crystal it was chosen to use all laser power for sample excitation purposes. We have planned to use in future a 300 nm transparent crystal polarizer behind the doubling crystal to separate the perpendicular polarized UV light

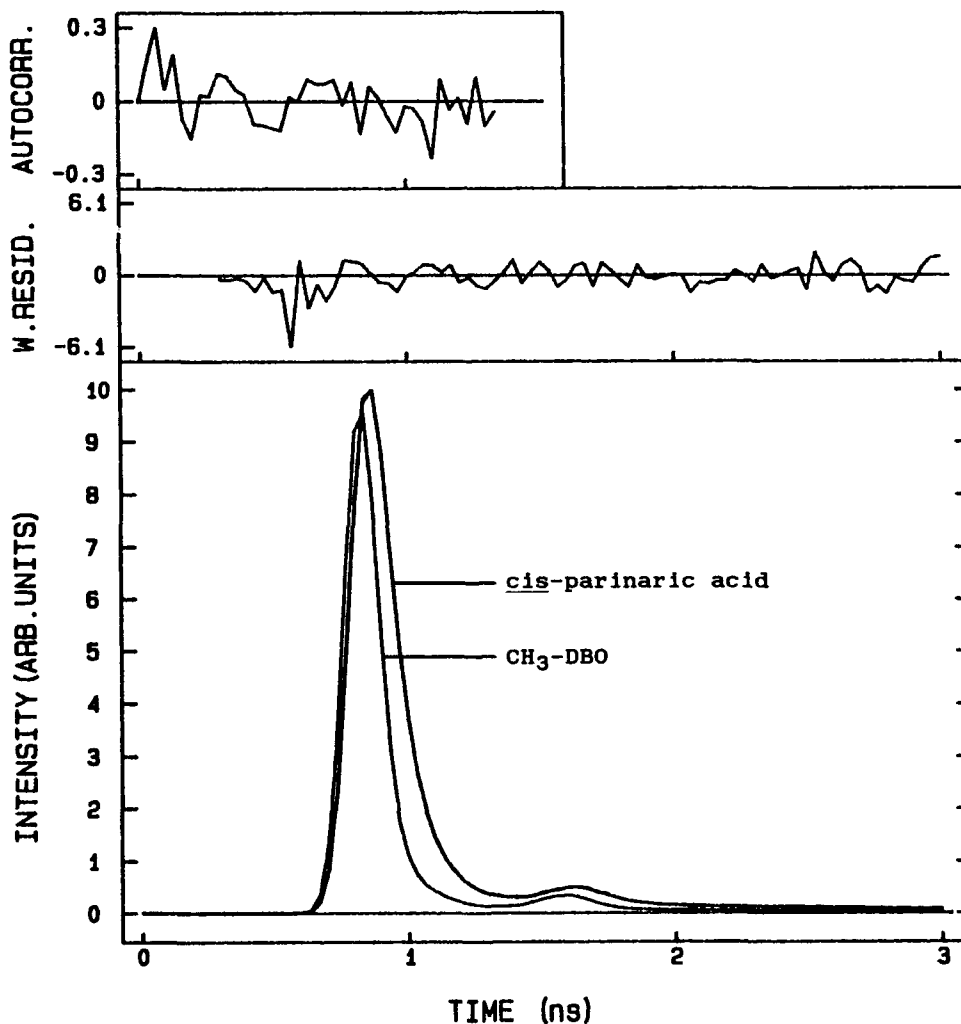


Fig.6 Analysis of 2 μ M cis-parinaric acid in water.

from the parallel polarized orange light. In that case the orange light can be used to trigger the (then much shorter) stop arm.

In order to illustrate the use of pseudoazulenes as reference compounds in experimental data of a biological sample, the fluorescence decay analysis of the natural fatty acid cis-parinaric acid is presented. The fatty acid in water probably forms micellar structures leading to extremely rapid fluorescence decay owing to a self-quenching mechanism. Using CH₃-DBO as reference compound for fluorescence at 422 nm it was possible to precisely determine the main fluorescence lifetime component ($\alpha = 0.993$, $\tau = 83 \pm 3$ ps) of cis-parinaric acid in water (see figure 6).

Conclusion

With the set-up as described fluorescence lifetimes can be measured on a picosecond timescale with single photon sensitivity. Transit time instability of components in start and stop arm as a function of temperature is the limiting factor for reproducibility and accuracy. The use of the pseudoazulenes as reference (or mimic) compound gives the possibility for analysis of picosecond decay processes with an accuracy that has not been shown before.

Acknowledgement

Dr. A.Olszowski (Technical University, Wroclaw, Poland) is kindly acknowledged for a gift of the pseudoazulenes.

References

1. D.Bebelaar, Rev.Sci.Instrum., 57, 1116 (1986)
2. A.van Hoek, K.Vos and A.J.W.G.Visser, IEEE J.Quant.Electron., QE-23, 1812 (1987)
3. K.Vos, A.van Hoek and A.J.W.G.Visser, Eur.J.Biochem., 165, 55 (1987)
4. A.Olszowski, J.Lipinski and H.J.Timpe, J.Mol.Struct., 53, 251 (1979)
5. F.Perrin, Ann.Phys., 12, 169 (1929)
6. A.J.W.G.Visser, T.Kulinski and A.van Hoek, J.Mol.Struct., (submitted)
7. A.van Hoek and A.J.W.G.Visser, Rev.Sci.Instrum., 52, 1199 (1981)
8. D.Bebelaar, Rev.Sci.Instrum., 57, 1686 (1986)
9. R.W.Wijnandts van Resandt, R.H.Vogel and S.W.Provencher, Rev.Sci.Instrum., 53, 1392 (1982)

MATERIALS SURFACE PROCESSING WITH EXCIMER LASERS

DAVID J. ELLIOTT
Vice President Marketing and Sales
and

BERNHARD P. PIWCZYK
President
LEITZ-IMAGE MICRO SYSTEMS CO.
900 Middlesex Turnpike, Bldg #8,
Billerica, Massachusetts 01821

Abstract

The evolution of the excimer laser from a research tool in the 1970's to the industrial models of the 1980's has opened up numerous applications in semiconductor manufacturing, materials processing, and biological and medical research. Present production-capable, computer-controlled excimer systems with handling equipment enabling efficient automation can now operate for up to 50 million shots before undergoing scheduled maintenance, with fluences remaining within $\pm 10\%$ in most cases. Thus, although many uses for the excimer laser are still research-oriented, production applications are rapidly emerging.

Introduction

Excimer lasers offer several key advantages as energy sources:

- First, they can provide deep-ultraviolet radiation at relatively high average power. Early UV lasers, such as double or triple harmonic Nd:YAG and ion lasers, had output power of less than one watt. Excimers, at similar wavelengths, deliver up to 50 watts: energy levels consistent with the production throughput rates needed for many processes (1) (2).
- Excimers have been shown to be essentially speckle-free, unlike earlier lasers operating in the ultraviolet spectrum. Speckle, an interference effect caused by high spatial coherence, causes localized excursions in the beam intensity profile which can result, for example, in non-uniform images in the photoresist used during semiconductor lithography. Excimers have relatively low spatial coherence, and are therefore essentially free of speckle.
- Excimers, as sources of deep ultraviolet radiation, are much more efficient than alternative light sources. The mercury arc lamp, with strong G-line, H-line and I-line peaks, falls off dramatically in the far ultraviolet region, just where the excimer begins. While mercury vapor and mercury halide lamps may have high conversion efficiencies ($\sim 50\%$), their high infrared content requires considerable output filtering. The excimer lasers on the other hand, produce essentially monochromatic radiation without the requirement of filtering.

The application of excimer lasers for microelectronic fabrication processes is particularly promising. The continued reduction of VLSI circuit geometries, together with increasingly higher levels of circuit integration create a demand for new circuit fabrication technologies. One of limitations of current IC fabrication technology is the use of high temperature processing. High temperatures distort silicon wafers, causing a loss of alignment control and resulting in a significant reduction in device yield. Excimer laser technology at very short ultra-violet wavelengths offers the possibility of low temperature processing, including the following major applications: Photoresist exposure, photoresist ablation over alignment marks, annealing, doping, and etching. In addition, applications in IC packaging, circuit personalization and fiber optics appear as very promising new applications for excimer laser technology in the electronics industry.

The most significant advantage of the excimer laser as a light source in VLSI processing is the range of short wavelengths available, below those used today for advanced optical microlithography (3) (4). This translates directly into better resolution. Argon Fluoride, for example, offers a 193nm wavelength at power levels exceeding those of the mercury lamp at G, H and I lines. Resist normally exposed in 200 mill seconds with mercury vapor sources can be exposed in 10-20 nanoseconds using an excimer laser with an output power of 200 mJ/pulse, operating at any of the principal excimer wavelengths; depending on the design of the optical imaging system, however, several pulses may be required, bringing the exposure time into the range of 50-100 milliseconds at a repetition rate of 200 Hz.

Ablation

Several years after the invention of the excimer laser, a light absorption phenomenon termed "ablative photodecomposition" or "photoablation" was discovered (5). This phenomenon occurs when pulsed ultraviolet radiation is absorbed on the surface of an organic solid; the high energy of UV photons is intensely absorbed by the polymer molecules, resulting in excitation within the molecules.

This energetic absorption results in bond breaking when the incoming UV energy exceeds the molecular bonding energy. The point at which such bond breaking occurs is termed the "ablation threshold". The ablation thresholds for a number of materials are given in the following table (6):

ABLATION THRESHOLDS FOR 193NM EXCIMER LASER
PULSE ENERGY (MJ/CM²)

PHOTOLYTIC:

Nitrocellulose	Less than 20
Novolak-Based Photoresist	30
Polycarbonate	40
Polyimide	45

PYROLYTIC:

Polysilicon	100
Silicon Nitride	195
Spin on-Glass	200
Silicon Dioxide	350
Silicon	Greater than 1000

The principal advantage of photoablation is the low thermal component of this process at low fluence levels. This property avoids undesirable melting or carbonization of organic molecules, a problem that often exists when visible or infrared laser radiation is used.

Organic polymer molecules consist of chains of smaller molecular units called monomers. A typical polymer chain will contain in the range of 1000-100,000 atoms of carbon, hydrogen, oxygen and nitrogen. These molecules absorb 95% of the incident energy at 193nm, and undergo a radiative lifetime (excited state) of about 0.1 nanosecond duration. The bond breaking lifetime is estimated to be in the 1-10 picosecond range (7). The depth of the absorption is less than 3000 angstroms, typically about 2000 angstroms, depending upon the particular polymer type, the fluence, and the area being exposed.

In photoablation reactions, the polymer molecules undergo bond scission, with excess energy remaining in the fragments in the form of thermal and kinetic energy. The rapid expansion created by this excitation and bond cleavage gives rise to the ejection of ablation products, gases and often small particles; the material transport time is estimated at about 10 microseconds. The accompanying fluorescence of ejected material often causes a plume of luminescence that can be readily observed. A scavenging nozzle designed to capture the by-products of ablative photodecomposition may be used to remove debris which can be a result of photoablation (8). Figure 1 shows the amount of material removed as a function of fluence for 3 excimer wavelengths. The target was polyimide.

Photolithography

The patterning of light-sensitive polymers for integrated circuit manufacturing requires extremely high imaging resolution (better than 0.5 μ m) and short exposure time. This resolution is essential in improving device packing density. In the short space of 10 years, the memory chip is evolving toward a 16 megabit device. Chip density is driven mainly by resolution capability. Short exposure times are required since imaging equipment is very capital intensive and only one wafer at a time can be processed.

In photolithography, radiation sensitive resists are patterned by sending light through a chrome-on-glass mask containing the IC pattern. The aerial image is transferred as a latent image in the photoresist, and the wafer is then developed, etched and selectively doped with ions. The excimer laser potentially offers both high resolution and extremely short exposure time for this crucial application.

Initial exposures made at 193nm show image resolution down to 0.4 microns in a one micron thick layer of positive photoresist. Figure 2 shows a high resolution test pattern imaged with a single pulse at 193nm.

Alignment Mark Ablation

Polymer ablation is also applicable in IC manufacturing for removing photoresist over the alignment marks on wafers prior to the patterning step, in order to avoid partial obscuration of the marks by the resist. Avoiding such obscuration of the alignment marks improves the overlay registration accuracy of the exposure system, in turn increasing the yield during device production. More importantly, it also permits the development of even higher resolution chip designs. Since IC devices now require up to 20 individual masking steps, overlay registration, the precise alignment of the current layer with those that lie under it, has become as important as resolution.

Initial tests have shown that overlay can be improved from 0.3 μ m (3 sigma) using die-by-die alignment with resist left above the marks to as little as 0.05 μ m, by first removing the resist with pulses of excimer laser light at 193nm. The typical beam fluence used to ablate the alignment marks is 500 mJ, an average of 15 pulses being sufficient to remove most layers of resist without damage to the underlying mark. (8)

Fiber Optic Communications

Optical fiber communications is another rapidly growing field in which the excimer laser is beginning to play an important role. Excimer laser micromachining of optical fibers can be used to create "tap" locations at which light signals can be extracted through the side of the fiber. The feasibility of welding optical fibers by means of a small number of excimer laser pulses has also been demonstrated.

These micromachining and fusing experiments were performed using a Leitz-IMS XLR-100 system at 193 nanometers within a fluence range of 5-12 J/cm², at various pulse repetition rates and with a computer controlled aperture shaping the beam in areas ranging from 10 to 140 microns on a side. The system is shown in Figures 3A and 3B, while the results of one such experiment are depicted in Figure 4.

Circuit Personalization and Repair

Patterning of gold for electronic conductors and interconnects is a key manufacturing process usually requiring multiple process steps. Gold on a hybrid circuit device can be structured in a single, "dry" step using the energetic photons from an excimer laser exposure system. The SEM photo shown in Figure 5 illustrates the resolution and edge acuity possible with photo-thermal ablation at 248 nanometers

(Krypton Fluoride). Photo-thermal reactions use thermal effects of photons rather than ablative photodecomposition for material removal.

Figure 5 shows a square hole made in a gold film by shaping the excimer laser beam with a computer controlled, multi-bladed aperture. A fluence of approximately 12J/cm² was used at a repetition rate of up to 200 Hz. Typical applications for this capability are integrated circuit personalization (link cutting) and removal of short circuits to repair interconnect patterns.

Integrated Circuit Packaging

VLSI devices with more than one or two hundred connections create a demand for new IC packages. In order to interconnect today's advanced integrated circuits, a new strategy involving the use of alternating layers of a di-electric material and a metallic conductor is emerging.

Frequently, the combination of choice is a thick (3-15um) dielectric layer of polyimide, together with a copper conductive layer. The excimer laser is used to create a series of openings or vias in the dielectric material, permitting electrical access to the conductor. Copper conductors can also be cleanly cut with the excimer. Figure 6 illustrates the sharp side walls in a copper conductor and the surrounding polyimide obtained by utilizing an excimer laser at a wavelength of 193 nm and a fluence of approximately 12 Joules/cm².

Biomedical Research

Because of the relatively minor thermal contribution in the action of the excimer laser as compared with the larger effect of ablative photodecomposition, such a system is an ideal tool for incising delicate specimens without significant thermal or structural damage. This property is of great advantage in genetic and biological research, permitting fine sectioning of living tissue with a minimum of collateral damage to the surrounding tissues.

Figure 7A is a SEM photograph of a human red blood cell, showing a cut performed by means of a finely focused excimer laser exposure at a wavelength of 193nm. A sharp, clean, high resolution cut is observed. Similarly, Figure 7B shows 0.3 micron punctures made in the cell membrane using a submicron beam size.

Summary and Conclusions

This paper has touched upon some promising new applications for excimer lasers in the fields of electronics manufacturing, fiber optic communications, and biomedical research. In most cases, results demonstrating the applicability of excimers to these fields have been presented.

Excimer laser light pulses at wavelengths of 193nm and 248nm have been used experimentally to improve alignment accuracy for wafer exposure systems; to micromachine fiber components for fiber optic networks; to incise cells for biological research; and to form submicron-resolution images for advanced integrated circuit fabrication.

Future generations of excimer laser systems will address as yet unforeseen production applications which are the outgrowth of current research. In the semiconductor manufacturing field alone, laser-assisted etching, deposition, doping and direct lithography are all techniques that show potential for significantly improving production efficiency and allowing products of vastly greater sophistication to be created. Today's excimer laser systems have reached a level of maturity which permits the groundwork to be laid for such future progress.

REFERENCES

1. H. Egger, H. Pummer, and C.K. Rhodes, EXCIMER LASERS FOR THE GENERATION OF EXTREME ULTRAVIOLET RADIATION, Laser Focus, June, 1982.
2. H. Pummer, THE STATUS OF COMMERCIAL EXCIMER LASER DEVELOPMENT, Lambda Physik, 2
89 Great Road, Acton, MA July, 1985.
3. K. Jain, C.G. Willson, B.J. Lin, ULTRAFast HIGH-RESOLUTION CONTACT LITHOGRAPHY, WITH EXCIMER LASERS, IBM, J. Res. Develop. Vol. 26, No. 2 March 1982.
4. K. Jain, SHORT-WAVELENGTH LASERS ARE HELPING FABRICATE EVER-SMALLER DEVICES, Laser Applications in Semiconductor Microlithography, Lasers and Applications, Sept. 1983.
5. B. Garrison, R. Srinivasan, LASER ABLATION OF ORGANIC POLYMERS: MICROSCOPIC MODELS FOR PHOTOCHEMICAL AND THERMAL PROCESSES, J. Appl. Phys. 57 (8), 15 April, 1
985.
6. R. Srinivasan and Bodil Braren, ABLATIVE PHOTODECOMPOSITION OF POLYMER FILMS BY PULSED FAR-ULTRAVIOLET (193NM) LASER RADIATION: DEPENDENCE OF ETCH DEPTH ON EXPERIMENTAL CONDITIONS, Journal of Polymer Science: Polymer Chemistry Edition, E
ol. 22, 2601-2609 (1984), John Wiley & Sons, Inc. V
7. D.J. Ehrlich, EARLY APPLICATIONS OF LASER DIRECT PATTERNING: DIRECT WRITING AND EXCIMER PROJECTION, Solid State Technology, December, 1985.
8. K.J. Polasko, D.J. Elliott, B.P. Piwczyk, VLSI PATTERN REGISTRATION IMPROVEMENT BY PHOTOABLATION OF RESIST-COVERED ALIGNMENT TARGETS, IEEE Triple Beams Meeting, Woodland Hill, CA, 1987.

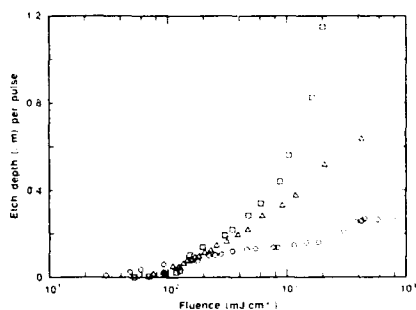
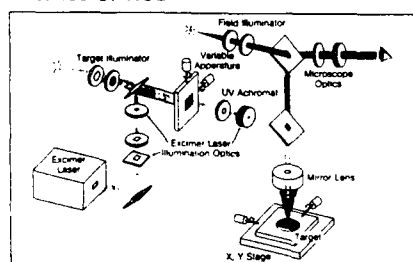


FIGURE 1: MATERIAL (POLYIMIDE) REMOVED PER PULSE AS A FUNCTION OF FLUENCE (SOURCE: R. SRINIVASAN, IBM)

XLR-100 OPTICS



XLR-100

FIGURE 3A: OPTICAL PATHS OF THE XLR-100

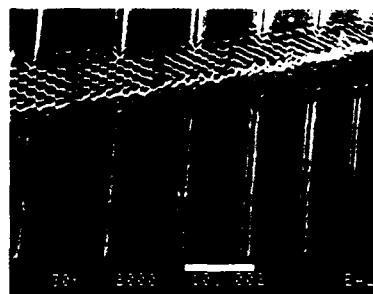


FIGURE 2: RESOLUTION PATTERN IMAGED WITH SINGLE PULSE AT 193NM



FIGURE 3B: XLR-100 EXCIMER LASER IMAGING SYSTEM

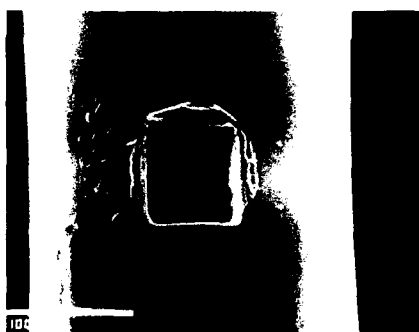


FIGURE 4: OPTICAL FIBER ABLATED AT 193NM (SOURCE LEITZ-IMS CO.)

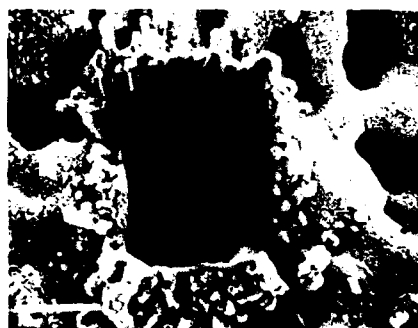


FIGURE 5: HYBRID CIRCUIT GOLD ABLATED AT 248NM WITH THE XLR-100 (SOURCE: LEITZ-IMS CO.)

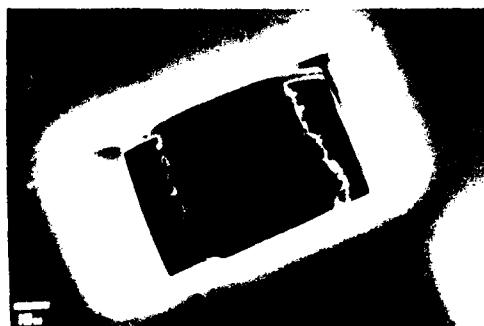


FIGURE 6: POLYIMIDE LAYER (50um THICK) ABLATED OVER COPPER



FIGURE 7A: HUMAN BLOOD CELL CUT AT 193NM (SOURCE: LEITZ-IMS CO.)



FIGURE 7B: HUMAN BLOOD CELL PUNCTURED AT 193NM (SOURCE: LEITZ-IMS CO.)

EXCIMER LASER ABLATION OF METALLIC THIN FILMS: APPLICATION TO ADHESION MEASUREMENT

P. H. Wojciechowski
Vacuum Coating Research Laboratory
Manufacturing Research and Engineering Organization
Eastman Kodak Company, Rochester, NY 14650

F. J. Duarte
Photographic Research Laboratories - Photographic Products Group
Eastman Kodak Company, Rochester, NY 14650

A. L. Hrycin
Optical Products Engineering Department - Kodak Apparatus Division
Eastman Kodak Company, Rochester, NY 14650

Abstract

Excimer laser ablation is used to investigate the adhesion of thin metal films vacuum deposited onto various substrates of both organic and inorganic materials. Correlation is established between the threshold energy required for laser-initiated film failure and conventional adhesion test results.

Introduction

Thin films ($< 1 \mu\text{m}$) of metals, dielectrics, and insulators are deposited on a broad range of organic and inorganic substrate materials and are used throughout the world in virtually all technology areas. The characteristics of these films (e.g., their physical and chemical properties, structure and morphology, and ultimate performance) all depend inter alia on film-to-substrate adhesion. Indeed, "adhesion" is central to thin-film technology and yet is one of its most elusive parameters.

Traditional techniques used to quantify film-to-substrate adhesion (such as peel, pull and scratch tests) are actually engineering tests of thin-film durability in a particular fracture mode and, although they yield reasonably reproducible, quantitative results in a relatively short time, there is considerable question about their accuracy and interpretation as tests of "adhesion". Clearly, advancing the state-of-the-art of adhesion research requires (i) continued development of a deeper, more fundamental understanding of adhesion phenomena and current measurement methods, and (ii) discovery and demonstration of new techniques that focus on adhesion at the film/substrate interface rather than on durability of the bulk film.

Reported here is a method that uses laser-initiated ablation of thin films to determine a threshold value of film attachment to the substrate. Before we describe the technique and its results, we present a brief background of adhesion and its associated key factors.

Adhesion Background

Can one really measure adhesion? If so, how? If not, why not, and what is measured instead? The answers to these questions rely, obviously, on a definition of adhesion. Mittal¹ defines two types of adhesion: basic and practical. We define basic adhesion as

that which is theoretically determinable from first principles. One of the fundamental building blocks of basic adhesion is the work by van der Waals² in 1873 to explain intermolecular attraction. By 1930, it was realized that three different effects contributed to the overall van der Waals' attractive potential energy U : for apolar atoms, the quantum mechanical or London³ effect (1930), given by

$$U_L \sim -[h\nu_1\nu_2/(\nu_1 + \nu_2)]\alpha_1\alpha_2/r^6 \quad (1)$$

(where h is Planck's constant, ν_i are the characteristic atomic frequencies, α_i are the polarizabilities, and r is the atomic separation); for interaction of permanent dipole moments, the molecular orientation or Keesom⁴ effect (1920), given by

$$U_K \sim -[(\mu_1\mu_2)^2/r^6](1/kT) \quad (2)$$

(where μ_i are the molecular dipole moments and k is the Boltzmann constant); and for the polarizing action induced by one molecule on another, the Debye⁵ effect (1920), given by

$$U_D \sim -(\alpha_1\mu_2^2 + \alpha_2\mu_1^2)/r^6. \quad (3)$$

All three contributions of the van der Waals' attraction potential fall off inversely as the sixth power of the atomic separation and are therefore effective over very short range. However, when integrated over the material volume, the force per unit area between adhering plates behaves as

$$F \sim A/R^3 \quad (4)$$

where A is referred to as the Hamaker⁶ constant, and R is the interaction distance of molecular arrays that make up the plates. Another approach to basic adhesion is the thermodynamic point-of-view in which the concepts of surface energy, contact angle, and wettability are considered.⁷

On the other hand, we define practical adhesion⁸ (also referred to as experimental adhesion or bond strength) as "the force required to remove the coating from the substrate". Practical adhesion is a function of (i) basic adhesion, and (ii) all other factors where "all other factors" may include such items as the internal and external stresses acting on the system, the nature of the adhesion testing method, the chemical environment, aging and corrosion phenomena, etc. Furthermore, it is argued⁹ that when two substances (A & B) are in adhesive contact with each other, the actual locus of failure may be in any of five different regions: (i) the bulk phase of substance A , (ii) the region of substance A influenced by the presence of substance B , (iii) the interface, which may be either sharp or diffuse on a molecular scale, (iv) the region of substance B influenced by the presence of substance A , and (v) the bulk phase of substance B . Obviously, chemical analysis by electron spectroscopy (ESCA) is of significant importance in determining the locus of failure and should be used in most situations when testing adhesion.

Indeed, practical factors such as these may exert much stronger influences over film adhesion than those of a more basic nature. Consequently, it is reasonable to advise the researcher new to the study of adhesion not to be "too pure", at least initially, about this broadly interdisciplinary art, but rather to be ever mindful of the specific end use of the system under study.

Several criteria are important to us in the development of adhesion testing and measurement methods. The test should (i) be quick, (ii) be reproducible, (iii) yield a quantitative result, (iv) address the problem, (v) have a reasonable chance of being modelled mechanistically, and (vi) be nonintrusive. Intrusive tests are those in which additional loading is imposed on the system being tested. For example, certain tests may require the use of epoxy cured at elevated temperatures. The application of epoxy can "load" the system (i) chemically (trace chemicals can migrate to the interface), (ii) thermally (cure conditions can physically alter the system constituents and their bond strength), and (iii) mechanically (addition of another layer, at the very least, increases the system stiffness). Such intrusions can severely influence adhesion test results.

Nonintrusive methods¹⁰ include both (i) static tests such as strain-induced failure and blister tests, and (ii) dynamic tests such as ultracentrifuge, ultrasonic, and forced vibrational¹¹ techniques. Another type of nonintrusive adhesion test involves the use of directed energy. In the work reported here we refer specifically to laser energy.

Laser Ablation of Thin Metal Films: Qualitative Description

The use of directed laser energy to investigate adhesion at the film/substrate interface was inspired by the work of Vossen.¹² In his tests a small, isolated dot of thin film material was detached from the substrate by impinging the laser beam (the size of which was significantly larger than the dot size) onto the back side of the substrate. Threshold values of laser energy density required to accomplish this detachment were correlated with thin film adhesion. In our experiments we measure the threshold laser energy density at which visible mechanical failure of the thin metal film occurs when the beam is directed at the front side of the film. The basic physical assumption is that the minimum laser energy density required to induce damage on a particular metal film depends on the physical characteristics of the film and on its bonding to the substrate.

A brief description of the events associated with failure can be utilized to describe the effect. First we consider the use of high laser energy density. Here, the incident energy density is sufficiently high to create a bright plasma emitting in the blue. That is, the incident laser energy is sufficient to vaporize the film and excite the resulting atomic population so that spontaneous photon emission occurs. In this case metal is totally ejected from the surface of the substrate.

By contrast, at threshold damage, the pattern of failure is associated with the deformed and fractured metal film physically removed from the substrate but still bonded, at the boundary, to the non-irradiated metal. In this instance, photon emission was not readily observed. Using high speed photography it was determined that the events described above take place at a time scale $< 200 \mu\text{s}$.

For films used here (for example, silver) reflection properties are very poor ($\sim 7\%$) at the wavelength of the XeCl laser ($B^2\Sigma_2^+ - X^2\Sigma_2^+$ transition, at $\lambda = 308 \text{ nm}$). Using a simple analysis it can be shown that most of the non-reflected energy is absorbed in the first 100 nm of the film thickness (typically $\sim 700 \text{ nm}$).

The mechanism we propose is that following the laser energy absorption at the upper layers of the film, a recoil compressive shock wave propagates through the remaining metal toward the film-substrate interface. There, part of the shock wave energy is

reflected back through the metal, and part is transmitted into the substrate. A closely following rarefaction wave is also reflected at the interface. This creates a region of strong tensile stress at the interface that acts to pull the metal from the surface. If this stress is greater than the sum of the stresses acting to bond the film to the substrate, film failure occurs. Thermal stresses may also contribute to failure. However, the speed of the thermal wave is considered to be much less than that of the mechanical shock wave and its associated expansion wave.

Using a simple energy approach, the conditions for threshold failure can be stated as

$$E_{B-X} \geq f \sum_{i=1}^N E_{A,i} + \sum_{i=1}^n E_{A-M,i} + \Delta E \quad (5)$$

where E_{B-X} is the energy provided by the XeCl laser, $E_{A,i}$ is the individual atomic binding energy, $E_{A-M,i}$ is the energy binding the atoms of the film to the molecules of the substrate at the interface, and ΔE is an energy defect resulting from losses during the energy-matter interaction at the upper layers of the film (this may include metal vaporization and photon excitation). N is the total number of atoms and f is the fraction of atoms that actually separate from each other. Also, n is the number of atoms that play a significant role in bonding at the interface ($n \ll N$).

Following the wave description given above, the threshold energy can be written in terms of

$$E_{B-X} - \Delta E \approx \chi \int [\Psi_0(x,y,z,t)]^2 dt + E_T \quad (6)$$

for the event involving the initial recoil compressive wave, where E_T is the fraction of the energy related to the thermal process. Here, $\Psi_0(x,y,z,t)$ represents a three-dimensional wave assumed to obey the usual wave equation behavior, and χ is a constant involving physical parameters necessary to convert intensity to power. Subsequently, the wave interaction can be described as

$$[\Psi_0(x,t,z,t)]^2 - \Delta I \approx \left[\sum_{m=1}^r \Psi_m(x,y,z,t) \right]^2 \quad (7)$$

where $\Psi_m(x,y,z,t)$ represents an m th three-dimensional wave participating in the process involving reflection and rarefaction waves responsible for separating the metal film from the substrate, and ΔI is an intensity loss due to propagation. Notice that this equation implies an interference of the various waves involved in the metal film failure mechanism.

An obvious consequence of this rudimentary description is that increasing N (the total number of atoms) should increase the energetic requirements for damage. Thus, testing between different films should be done for similar thicknesses. Also, removal of impurities affecting the binding energies via radiation and/or chemical processes should be encouraged.

At this stage it is too early to quantify this description. However, it is clear that this type of laser measurement may provide a direct connection with fundamental parameters used in the physical descriptions of adhesion described previously in this paper.

Experimental Details

Several different film/substrate combinations were used in our experiments. Thin films of Ag, Au, Ni, Cr, Co-Cr, Ni-Fe, as well as several metal oxides were deposited. Substrate materials included both organic [e.g., polyimide and poly(ethylene terephthalate) (PET)] and inorganic (e.g., ULE glass) types. Film thicknesses ranged from 50 to 700 nm. Polymeric substrate thicknesses ranged from 12.7 μm (0.0005 inches) to 178 μm (0.007 inches). Substrate pretreatment included conventional wash techniques, glow-discharge pre-etch, ion-beam pre-etch, or no treatment at all. The films were deposited by evaporation and sputtering. In the systems using organic web, a glow-discharge post treatment was sometimes used.

A XeCl excimer laser was used to irradiate the coatings under test. The 20-ns, 308-nm wavelength pulse from the laser has a measured output energy of approximately 50 mJ. The laser beam is focused by a 30-cm focal-length lens. The energy density impinging on the test sample is varied by moving the sample along the optical axis, between the lens and the focal plane. Threshold values for film failure are recorded as distance from the lens and then converted into energy density values.

Laser threshold failure results were compared with the results of other, more conventional, tests. For example, in the case of Ag deposited on PET by e-beam evaporation, the system must survive an extremely caustic bleach step in the post-deposition production process. Survivability of the Ag film is known to be a function of its adhesion to the PET as measured qualitatively by a tape test. Thus, both the bleach and the tape tests are compared against the results of the laser ablation test.

Two other tests were used whenever appropriate: the direct pull test and the dynamically loaded scratch test. For the pull test, we used the Sebastian II Adherence Tester manufactured by the Quad Group. It uses studs epoxy-bonded directly to the film. The tensile force required to pull the stud (and hence the film) from the substrate in the direction normal to the interface is measured and recorded. Both rigid and flexible substrates can be tested. Epoxy-coated backer plates are supplied for the flexible substrates. For the scratch test an LSRH (Laboratoire Suisse de Recherches Horlogeres) Revetest Automatic scratch tester was used. It continuously increases the stylus load on the thin film over a 10-mm scratch length. An acoustic emission (AE) sensor is attached for detecting the onset of coating delamination. This tester works best for brittle films on rigid substrates.

Results

A summary of the laser ablation adhesion tests is given in Table I, where we present the results for a representative sampling of three different systems. For the Ag/PET system, the pre- and post-treatments were done by an Ar/O_2 glow discharge. Approximately 700 nm of Ag was deposited by e-beam evaporation onto a moving Kodak Estar base web of 178- μm (0.007 inch) thickness. The "(S)" corresponds to an organic "subbing" layer that is applied to the PET surface to improve wettability. For the Cr and Ag on ULE glass systems, ion pre-etch and ion-assisted depositions were accomplished using a 3-cm Kaufman-type ion source, and the 100-nm thick films were deposited from filament sources. The glass substrates were 3.86-cm (1.52-inch) diameter x 0.63-cm ($\frac{1}{4}$ -inch) thick ULE roundels.

Table I

Results Summary

Sample No.	Deposited Mat'l	Substrate	Ion Bombardment		Method	Adhesion Test		Result	Laser Threshold Energy Density (mJ/cm ²)
			pre	simul. post		Result	Method		
1	Ag	PET (U)	x	x	KCl bl	(No Ag Removed)	Tape Test	No Failure	424
2	Ag	PET (S)	x	x	"	(80% Ag Removed)	"	Failure	303
3	Ag	PET (S)	x	x	"	"	"	"	303
4	Ag	PET (S)		x	"	(10% Ag Removed)	"	No Failure	333
5	Cr	ULE Glass			Seb II	10.4*kpsi	(Scratch Test w/ 200- μ m Diamond Stylus)	(Edge Left at 2N)	192
6	Cr	"	x		"	10.5		(Glass Substrate Fractured First)	237
7	Cr	"	x	x	"	10.4			251
8	Ag	ULE Glass			Seb II	0.0 [†]	(Scratch Test w/ 800- μ m Stainless Steel Stylus)	(a)	84
9	Ag	"	x		"	0.3		(b)	158
10	Ag	"	x	x	"	0.0		(c)	132

* Epoxy failure occurs ~ 10.5 kpsi (72.4 MPa) pull stress

† Adhesion was so poor that bonded stud fell off before pull test

(a) Total removal of wide track at 2.4 N

(b) Total removal of narrow track at 6.8 N

(c) Some thinning of wide track at 8-10 N

Correlation Discussion

Ag on Poly(ethylene terephthalate) (PET)

Excellent correlation is observed with the Ag/PET system laser tests. Sample #1 survived the bleach adhesion test very well. Virtually no silver was removed by a vigorous rub test in the bleach bath. The laser energy density for threshold failure of this sample was 424 mJ/cm². This corresponds to a position approximately 9 cm from the focal plane. For samples #2 and #3, the bleach bath resulted in catastrophic peeling of over 80% of the Ag film from the PET, and the corresponding energy density for threshold damage was 303 mJ/cm² (about 12 cm from the focal plane). In between, at 333 mJ/cm² laser energy density, the film survived the bleach test without the rub, but when rubbing was applied during submersion, the film underwent partial failure.

Cr on ULE Glass

For the Cr/ULE glass samples, all pull tests exhibited strengths that exceeded 71.7 MPa (10.4 Kpsi), which is the upper limit of this test (epoxy failure occurs at about 70 to 73 MPa). Thus, we had to rely on the scratch test for comparative information. The first Cr sample (#5) did not delaminate directly in the stylus track, but some lifting of

the film occurred along the track edge starting at a load of 2 N using a 200- μm diameter diamond stylus. The AE signature for this sample showed a drastic increase in acoustic activity as the load increased from 3 to 5 N. This could be attributed to the formation of tensile cracks in the coating which are seen at loads very much lower than those expected for substrate cracking. Tensile cracks are formed behind the stylus along zones of maximum tensile stress. The laser energy density for this test was 192 mJ/cm^2 .

Scratch test results for the next two Cr samples (#6 and #7) showed no film damage (with the 200- μm diamond stylus) for either sample prior to substrate failure. Increased adhesion due to the pre-etch removal of hydrocarbons is the probable reason for this. Adhesive forces are greater than the stylus-induced forces. The AE signatures for each of the samples are almost identical and show a smooth, gradual rise from 2 to 9 N, achieving a maximum of about only one-third of the maximum for sample #5. These AE signatures correspond to the failure of the glass substrate, and not the film. The laser threshold energy densities for these samples were 237 and 251 mJ/cm^2 , respectively. Thus, we again observe excellent correlation of the laser ablation test with conventional tests. In addition, for the laser ablation test, we see (i) an increased range above the pull-test limit, and (ii) an apparently finer distinction between two cases where the scratch test was unable to cause film failure.

Ag on ULE Glass

For the Ag/ULE glass samples, all pull tests again failed to provide adhesion information, but for reasons opposite those of the Cr/ULE glass system. For Ag samples #8 and #10, the epoxy-bonded stud/silver literally fell off of the substrate before it could be loaded into the pull tester. Sample #9 held together long enough to obtain a reading of 2067 kPa (300 psi). The wide difference in results between Cr and Ag ought to be expected. The adherence of metal films on oxide substrates is related to the free energy of oxide formation (ΔF_f). As free energy values become more negative, adhesion due to chemical bonding increases. The ΔF_f values for Ag and Cr are -0.112 and -10.9 eV/atom, respectively.

Thus, again we had to rely on the scratch tester for quantitative comparative information. With the 200- μm stylus, material removal occurred for all silver samples at an initial load of 1 N, which is the minimum load that can be applied. Using an 800- μm stainless steel stylus, a marked difference in the adhesion between the Ag samples could be observed. Post-scratch examination of the three Ag samples using both optical and scanning electron microscopy showed the following:

The silver film on the untreated sample (#8) was completely and cleanly removed across a substantial width of the stylus track. The corresponding threshold laser energy for this sample was 83.9 mJ/cm^2 . At the same loading condition (approximately 8.8 N), the Ag film on the pre-etched glass sample (#9) was again cleanly removed, but the track of removal was less than half that of sample #8. Threshold laser energy for this sample (the only sample with a nonzero pull test result) was 158 mJ/cm^2 . In contrast with the other two Ag samples, scratch results for the combined pre-etch and IAD Ag sample (#10) showed a very ductile, or thinning out, behavior of the metal over a track width somewhat wider than the untreated Ag sample (#8). Material removal was comparable with that of sample #9 but was smeared out over a significantly larger area. The corresponding threshold energy density is 132 mJ/cm^2 . Again, the laser test appears to give useful relative results where other tests cannot because of insufficient sensitivity.

Conclusions

Excimer laser energy is used to provide rapid, highly reproducible, quantitative information on the adherence of vacuum-deposited thin metal films grown on inorganic and organic substrates. Film-failure threshold energy delivered by the laser beam is observed to correlate with the degree of adhesion (as determined by alternate conventional techniques). The higher the degree of adhesion, the larger is the value of laser energy density required to initiate threshold failure of the thin film. The test is nonintrusive in that (i) extra thermal, chemical, or adhesive preparations are not required prior to performing the test, and (ii) no mechanical contact, loading, or pre-stressing of the film/substrate system occurs. Any or all of these effects may alter or obscure the test results. In addition, adhesion measurement by laser ablation provides differential information in cases where conventional tests fail. This is due to an increase in both the sensitivity and the range of adhesion measurements of a given system.

References

1. K. L. Mittal, in Adhesion Measurement of Thin Films, Thick Films, and Bulk Coatings, ASTM STP 640, K. L. Mittal, Ed., (American Society for Testing and Materials, Philadelphia, 1978) pp. 5-17.
2. J. D. van der Waals', Thesis, Leiden, 1873.
3. F. London, Z. Physik 63, 245 (1930); Trans. Faraday Soc. 33, 8 (1937).
4. W. H. Keesom, Proc. K. Ned. Akad. Wetenschap. 18, 636 (1915); 23, 939 (1920); Phys. Zeit. 22, 129 (1921); 22, 643 (1921).
5. P. Debye, Phys. Zeit. 21, 178 (1920); 22, 302 (1921).
6. H. C. Hamaker, Physica 4, 1058, (1937).
7. See for example: Contact Angle, Wettability, and Adhesion, R. F. Gould, Ed., ACS Advances in Chemistry Series #43, (American Chemical Society, Washington, D. C., 1964); R. G. Dillingham, D. J. Ondrus, F. J. Boerio, J. Adhesion 21, 95 (1987).
8. Ref. 1, p. 8.
9. R. J. Good, in Adhesion Measurement of Thin Films, Thick Films, and Bulk Coatings, ASTM STP 640, K. L. Mittal, Ed., (American Society for Testing and Materials, Philadelphia, 1978) pp 18-29.
10. See for example: Ref. 1; D. S. Campbell, in Handbook of Thin Film Technology, L. I. Maissel and R. Glang, Eds., (McGraw-Hill, New York, Chap. 12; J. Valli, J. Vac. Sci. Technol. A 4, 3007 (1986).
11. F. A. List and R. A. McKee, Thin Solid Films 151, 17 (1987).
12. J. L. Vossen, in Adhesion Measurement of Thin Films, Thick Films, and Bulk Coatings, ASTM STP 640, K. L. Mittal, Ed., (American Society for Testing and Materials, Philadelphia, 1978) pp. 122-133.

LASER CUTTING MACHINE FOR TEXTILE INDUSTRY (3)

Fernando D. Carvalho (1), M. Ribau Teixeira (1),
F. Carvalho Rodrigues (1), Cassiano Pais (1)
Jaime Alonso (1), Dietmar Appelt (2)

(1) LNETI - Optica, 1699 LISBOA CODEX, PORTUGAL
Telf: (01) 7589181

(2) EFACEC, PORTUGAL

(3) Research supported by grant for the Ministry of Industry and EFACEC.

ABSTRACT

A cutting machine using a 50 watts Carbon Dioxide laser is presented. The machine was developed for the textile industry under the Portuguese Research Program "ROBLAS", involving Industries, Textile Universities and a Government Research Center.

The laser, translation mechanisms and interface were developed and build for the machine, totally controlled through a Personal Computer.

INTRODUCTION

The machine presented on this paper is one of the results of a portuguese reasearch and development program named "ROBLAS".

The program was financed by the ministry of industry and has been executed by a group of researchers from:

LNETH - National Laboratory for Industrial Technology and Engineering

UBI - University of Covilhã

EID - A private research and development company on electronics.

EFACEC - A private company devoted to the production of laser technology and equipment for textile industry

The project of the "Laser Cutting Machine for Textile Industry" has involved four diferent areas:

Optics and Lasers

Electronics and Robotics

Mechanics

Software

The machine itself may be described as a table plotter without pen and with a laser.

There are four subsystems in the machine:

The laser

The translation table and structure

The interface

The software for the personal computer

THE LASER

The CO₂ laser used in the machine is a continuous wave, slow axial flow laser, emitting an output power level of 50 w.

The distance between the electrodes of the discharge tube is of 1.10 m and its internal bore is of 14 mm. The discharge tube is made of two glass walls, two electrodes, an entrance and exit gas aperture. Water is used for cooling the discharge which is circulating between the walls.

At both terminals, metallic supports are cemented at the external wall to receive through o-rings the metallic supports of the totally reflector mirror.

The cooling circuit has a radiator cooled by circulating air, a water pump and tubing.

The laser mixture used is: 10% CO₂, 10% N₂, 80% He. the elements of the gas circuitry are the vacuum rotary pump, the bottle of gaseous mixture, the pressure regulator and the needle valve.

The power supply, 3 Kw, 30 Kv is used for discharge breakdown (the discharge current is limited by two times 500 K Ω resistors).

The laser beam is emitted with a diameter of 7.5 mm with a divergence of 17,5 mrad.

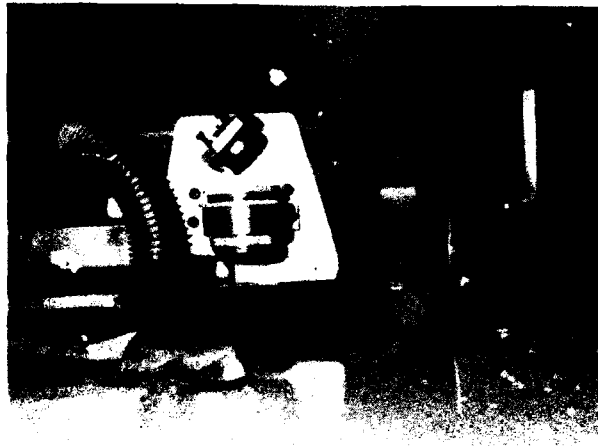
THE TRANSLATION TABLE AND STRUCTURE

The laser beam is translated to the cutting point through a XY mechanism which allows a total working area of 1,6 x 1 meter. to cover this area a double fixed rail is mounted on each of the shorter sides of the machine. A longer rail connects the two carriages and is moved along the shorter side of the table (y movement). Carriage of the rail contains the objective lens and aspiration shoe (x movement).

Movements are produced on step motors, 7,5 degree step, 0,1 nm of binary, and transmitted to the carriages through a timing belt. To prevent a twist effect on the y axis, its movement is transmitted by two belts, one on each rail, both with the same spindle.

Reduction of the transmission is made in such a way that a resolution of 0,4 mm is obtained.

In order to optimize space the laser system and power supply are totally installed under the top of the table. Laser tube is at an easy to reach position in order to facilitate the alignment procedures. The laser beam is deviated through four mirrors before reaching the lens with a focal of 50 mm creating a focus of tenth of a millimeter, under a depth of focus of 1 mm.



Carriage and optical system

THE INTERFACE

The machine is controlled from a personal computer through the parallel interface.

The interface, stepper drives, laser drive and logic power supply are housed in a rack with all the interconnections between units. The motherboard incorporates a connector for direct connection from the P.C.

The interface is designed to match the standard centronics port to the 4 - phase uni, dir stepping motor drives, SAA1027.

The centronics protocol has no formal specification but the timing diagrams are critical.

The eight lines of data control are used in the following way: two sets of three lines are used to control the two stepper motors another line identifies the laser on / laser off status.

THE SOFTWARE

The mxy system written in turbo Pascal, was developed as a set of separate programs using common utility routines and library files. They were then compiled as a set of modules directed by a menu - driven command interpreter. Memory requirements were minimized by placing each module (included file) in a separate overlay, with the interpreter and monitor in the main program.

The modules available in the program are listed in the top - level menu. Each module is accessed by typing the high lighted letter and generally responds with requests for necessary parameters or even file names.

Editor menu allows the development of data files which contains an analog model of the desired design and stores the pictures as geometric data attributes, and relationships. On the other hand, it's possible to add alphanumeric text.

Each picture corresponds to a data structure that contains most of the information. Most common structures are possible to be used in order to create the forms to be drawn. Text characters may be introduced at any time and are represented as a series of line segments. Special attributes such as speed laser on / laser off may be defined at this point.

Utilities are special database access - routines particularly designed for applications. They are associated with the positioning, scaling, rotating, skewing and copying of pictures. Utilities include a set of several filters that have been developed to adapt files from different CAD systems to data files possible to be used at this machine.

Once a data file has been finished it is possible to run that file in the machine, using the processing facilities. These, include a positioning capability through a manual mode by pressing cursor keys. Run mode, is used to cut a form accordingly with the data file in use.

Special attributes may be changed at any time to improve efficiency of the machine.

APPLICATIONS

The machine is now being used for testing its cutting capabilities at the industry.

Good results are being obtained since the usual cards are easily cut by machine at a convenient speed.

However this machine doesn't fulfill all the needs of the industry since a plotter is always necessary.

That is why a table plotter, based on the work made with this machine, was developed.

TECHNICAL CHARACTERISTICS

The machine presents a maximum working speed of 70 millimeters per second for a nominal speed of 50 mm/s. Any value smaller than that may be selected in a continuous way.

The total working area is 1.6 meter for 1 meter. Overall area repeatability is better than 1 millimeter. The resolution associated with a single step of the motor is 0.5 mm.

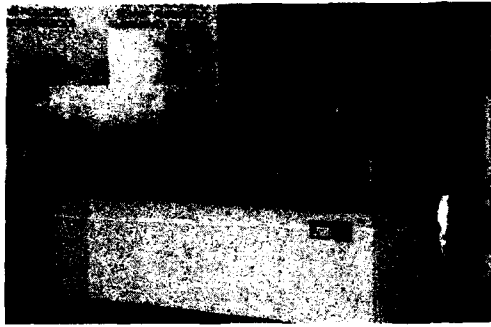
The machine has overall dimensions of 2 m for 1,4 m and 1 meter height.

Power consumption is 10 amps over 220 volts, single phase.

The weight of the machine is 300 kg.

Included as built-in equipment are:

- The CO2 laser ----- 50 watts
- High voltage supply ----- 30 Kv / 3Kw
- Vacuum system
- Closed water cooled system
- Smoke exhaust system
- Beam delivery accessories



The prototype of the Laser Cutting machine

FUTURE WORK

The prototype presented here is finished and being industrialized by EFAGEC.

A similar product, a table plotter, is now being commercialized.

The next objective of "ROBLAS" is to develop a machine with a double function: Plotter and laser cutter.

It is estimated that such a machine will be much more adapted to industrial needs instead of using two machines one plotter and one laser cutter.

HIGH THICKNESS LASER CUTTING

G. MANASSERO

Fiat Research Center

Strada Torino 50 - 10043 ORBASSANO (TO) - Italy

- ABSTRACT -

To verify laser technology benefits for dismantling nuclear power plants, experimental tests have been performed using CO₂ high power lasers for cutting metals and concrete.

A preliminary study was carried out to verify the possibility of propagating and controlling high power beams at long distance from commercial sources.

1 - INTRODUCTION

A high number of nuclear power plants already installed in the industrialized countries will involve, in the next future, the need for their dismantling. During operation some structures of the plants and some components of considerable dimensions will become partially radioactive or contaminated.

The feasible studies on dismantling are, as a consequence, based on the cutting of different types of materials, from stainless steel to reinforced concrete, into blocks of small dimensions. This in order to be better transportable in decontamination and final storage zones. During this dismantling phase it is often necessary to work at a safety distance both for radioactivity or presence of products resulted from the cutting process (particulate, smoke and vapours).

For the solution of the problem several techniques may be used among which, for instance, the mechanical or arch saw, the thermal lance, the oxyacetylenic flame, the explosive materials and finally the high power focalized laser beam.

The capacity of the last operative instrument to work at long distance from the source and to generate a limited quantity of drosses has activated the hope for its real utilization and, as a consequence, it was carried out this feasibility study.

Since 1981, at the FIAT Research Center (*) in the frame of a research program promoted from the European Community on the decommissioning of nuclear installations, are conducted experimental cutting and drilling tests on different materials with high thicknesses /1/.

Below are presented some of the significant results of this research.

2 - EXPERIMENTAL SET-UP

Experimental tests were carried on with two different high power CO₂ laser systems. One of these utilizes a 15² kW AVCO HPL source with an annular beam configuration and a Cassegrain focalizing optical system f/7. The cutting station has two linear and one rotating axes controlled by a CNC. This also keeps under control the laser beam power.

Fig. 1 shows the mechanical apparatus utilized in the cutting and welding station for the handling of samples to be cutted. The processing zone is limited by a metallic container, with a transparent window in order to prevent the cutting products to diffuse in the surrounding area.

With appropriate measurement instruments, the particulate emission was analyzed for granulometry and chemical composition.

The second system consisted of a 5 kW Spectra Physics laser source and a work station with only a linear and a rotating table. The cutting station which utilizes water cooled copper mirrors for beam propagation and directing and a focalizing ZnSe lens system with protection and assistance nozzles.

(*) Research supported by FIAT Components and Plants for Energy and Industry.

One of the objective of the research was to verify the utilization of the laser beam at long distance from the source and, mainly, to have a uniform process result in a large working area. This requires a laser beam as more as possible collimated in the selected range of distances between 5 and 30m from the source.

By knowing the laser beam parameters as the multimode coefficient, the diameter and position of the waist, obtained by a theoretical and experimental procedure in the case of welding and cutting cavity /2/, it was possible, with a mathematical model, to calculate the characteristics of the corrective mirrors and of the laser beam along the optical path /3/.

The optical system used is shown in Fig. 2. The laser beam, after a first reflection on mirror M1 goes on mirrors M2 and M3 which establish the collimator system (the curvature values are, respectively, -3600 mm and 5500 mm). When the mirror M4 intercept the beam the focal plane position obtained is at 5 m far from the output window of the source and, therefore, we are working at the lower limit of the selected operating area. On the other way the laser beam is directed by the plane mirrors M5, M6, M7, M8 and M9 and, after a path of 30 m, reaches the working plane.

In Fig. 3 the experimental realization is shown. The radiation is confined in metallic tubes both for protection and controlling of the gas flow uniformity in the inside in order to prevent for thermal effects along the beam path.

Having a flexible focalizing mechanical system it was possible to utilize the appropriate focal lenght for each thickness to be cutted .

In our specific problem it was found that it is better to use a 10 inches focal lenght for thicknesses between 5 and 15 mm and 20 inches for the range between 15 and 40 mm /3/.

The focalizing optical element could also be a water cooled metallic parabolic mirror with or without high reflecting surface coatings. The selection between reflective or transmissive optical element depends of the particular operating

situation. The lens permits to work axially with the beam direction and have a better uniformity and depth of focus but is more delicate and expensive than parabolic copper or other highly reflecting metallic mirrors for the infrared radiation.

In both situations it is necessary to work with appropriate protection of the final optic from particulate produced by the cutting process.

During the process optimization it was also evaluated the effect of varying the assistance nozzle type and the flow rate for different gases. Tubular metallic nozzles single and twin (with internal diameter between 0.5 and 1.5 mm) and coaxial nozzle (with variable aperture) were tested.

The tests have shown that better results, concerning the cutting depth, are obtained using the tubular nozzles. The presence of coaxial flow and a laminar flow between the focalizing optics and the sample give an additional protection against spatters and smoke.

The oxygen gas permits to obtain better results concerning the maximum obtainable cutting depth, for mild steel, but the advantages in comparison with others gases decrease with stainless steel and there are almost no differences for concrete.

3 - RESULTS OF CUTTING TESTS

The results of experimental tests have been obtained after an optimization fase of the different parameters concerning the cutting and drilling processes. In particular, in addition to the focal lenght and gas type variation, the following factors were considered :

- . nozzles position as regard to laser beam and sample;
- . focal position as regards the upper surface of the sample;
- . flow rate of assistance gas.

The dimensions of the utilized samples for cutting were 200 x 200x 200 mm and 150 x 150 x 150 mm for concrete blocks and circular or rectangular plates 15, 30, 40 and 45 mm thick of steel Fe42C and AISI 304.

3.1 - Concrete cutting

In Tab. 1 are reported some results on concrete cutting, obtained with the AVCO laser, utilizing a tubular nozzle with an internal diameter of 1.5 mm. This was positioned with an angle of 15° and at 5 mm from the upper surface of the sample to be cut. The best position for the focal plane resulted at 5 mm inside the material. The oxygen was utilized with 700 KPa pressure and 5000 l/h flow rate.

The data show that it is possible to cut concrete at a mean depth of 160 mm using a beam power of 10 kW at the speed of 0.01 m/min. The repeatability of depth cut value is about 10%. The maximum depth increases when the concrete is steel reinforced due to the exothermal reaction between oxygen and iron at high temperatures.

Fig. 4 shows a typical laser cut on concrete. As the depth increases the cutting kerf become large due to the focal plane position very close the upper surface. This set-up cannot be modified because it is necessary to have at the surface, especially for concrete, high power density in order to begin the melting and vaporization phenomena typical of the cutting processes.

Laser cutting is more easy when can be completed at once in order to facilitate fume and particulate expulsion below. The risk of damaging focalizing optical elements is also lower.

3.2 - Metals cutting

Laser cutting tests on metals have been carried out, mainly, on two materials largely used in the nuclear power plants: the mild steel Fe42C and the stainless steel AISI 304.

The nozzles used are the same as those for the concrete but the oxygen pressure was higher (800 KPa) and the focal plane was placed inside the material at a distance equal to 1/3 of the sample thickness.

In Tab. 2 are summarized the most significative cutting results using either the AVCO or the Spectra Physics source.

The mean depth from repeated cuts at various powers and speeds are reported. As shown the laser S.P. is more efficient than the AVCO one. This difference can be explained with different characteristics of the beam energy distribution which are very important for cutting processes. In fact, with the new fast axial flow laser sources having an oscillation cavity mode nearly TEM₀₀, it is possible to increase the cutting speeds without changing the others parameters. Anyway, with our laser sources, it was possible to cut more than 100 mm thickness of steel. The cutting quality was not taken into account because has no importance for dismantling processes.

In the case of Fe42C steel isothermal reactions help the cutting process but has a different behavior, compared with the stainless steel AISI 304, on the particulate emitted. The cutting products quantity produced and the particulate analysis aren't treated in this paper but, probably, it will be the result in this field of studies to establish if the laser cutting is competitive compared with more traditional thermal cutting processes.

In Tab. 3 are summarized the results for the AISI 304 steel cutting; the operation conditions are the same as those for Fe42C. From the data analysis appears that the cutting efficiency is lower, as compared to the mild steel, of about 20% on the cut depth; the difference between the two utilized sources remain.

In the Fig. 5 are shown some samples 15 mm thick after cutting with a laser power of 4.1 kW (S.P. source) and 0.3-0.5 m/min of speed.

4 - CONCLUSIONS

Several high thickness laser cutting tests have been carried out on metallic and concrete materials. The results demonstrate the feasibility of the process and that it is possible to cut thicknesses higher than 100 mm of carbon steel at a power of 10 kW. These values are valid if associated with the specific laser sources utilized in this research and might be improved with beams having an energy distribution more close to the fundamental mode.

With a beam propagation mathematical model which needed few characteristics of the used beam, some radiation properties were evaluated, in a working range between 5 and 30 m from the source. Computed parameter were beam diameter, collimation and focalizing degree of the beam.

The evaluation of the cutting particulate, especially for lower granulometry, will establish if laser could be competitive as regard to the traditional thermal cutting processes.

Among problems still to be solved we could mention the optics behaviour in presence of smoke and radioactive particulate, the remote control of the focalizing head and the visualization of the process in real time.

5 - BIBLIOGRAPHY

- /1/ B. MIGLIORATI, P. GAY "Advanced cutting techniques : laser and fissuration cutting"
Proceedings of the European Conference held in Luxembourg 22-24 May 1984 Edited by K.H. Schaller and B. Huber
- /2/ P. PERLO "Propagation at a multiki-lowatt laser beam : experimental characterization"
SPIE Vol. 650 (1986)
- /3/ G. MANASSERO "Investigation of specific application of laser cutting in the dismantling of nuclear power plants"
Contract FI - 100017 I (TT) of the European Community - Second progress report (April 87)

SINGLE NOZZLE INTERNAL DIAMETER : 1.5 mm		
OXYGEN PRESSURE : 700 KPa		
POSITION OF FOCAL PLANE : -5 mm FROM THE UPPER SURFACE		
DIMENSION OF THE SAMPLES : 200x200x200 AND 150x150x150 mm		
P (kW)	v (m/min)	h (mm)
5	0.02	78 ± 5
10	0.01	160 ± 23
10	0.02	94 ± 14
10	0.03	84 ± 6
10	0.04	81 ± 8
10	0.05	64 ± 5
10	0.06	60 ± 9

TAB. 1 - LASER CUTTING ON CONCRETE WITH AVCO HPL SOURCE

• SINGLE NOZZLE INTERNAL DIAMETER : 1.5 mm • OXYGEN PRESSURE : 800 KPa • POSITION FOCAL PLANE : -1/3 OF SAMPLE THICKNESS FROM THE UPPER SURFACE				
P (kW)	v (m/min)	h (mm)	Sample thickness (mm)	Laser source
5	0.2	23 ± 5	45	AVCO
5	0.27	19 ± 4	45	"
5	0.52	12 ± 1	45	"
7.5	0.2	31 ± 7	45	"
7.5	0.27	21 ± 4	45	"
7.5	0.41	16 ± 2	45	"
7.5	0.52	15 ± 1	45	"
10	0.2	35 ± 5	45	"
10	0.41	24 ± 1	45	"
4.1	0.45	15	15	S.P. 975
4.1	0.2	30	30	S.P. 975

TAB. 3 - LASER CUTTING ON AISI 304 STEEL WITH AVCO HPL AND SPECTRA PHYSICS 975 SOURCES

• SINGLE NOZZLE INTERNAL DIAMETER : 1.5 mm • OXYGEN PRESSURE : 800 KPa • POSITION FOCAL PLANE : -1/3 OF SAMPLE THICKNESS FROM THE UPPER SURFACE				
P (kW)	v (m/min)	h (mm)	Sample thickness (mm)	Laser source
5	0.2	31 ± 4	40	AVCO
7.5	0.2	35 ± 4	40	"
10	0.2	40	40	"
5	0.4	21 ± 7	40	"
7.5	0.4	19 ± 4	40	"
10	0.41	24 ± 6	40	"
5	0.6	15 ± 1	40	"
7.5	0.6	16 ± 1	40	"
4.1	0.5	15	15	S.P. 975
4.1	0.25	30	30	S.P. 975

TAB. 2 - LASER CUTTING ON MILD STEEL Fe42C AVCO HPL AND SPECTRA PHYSICS 975 SOURCES



FIG. 1 - ROTATING APPARATUS FOR SAMPLES HANDLING AND CUTTING PRODUCTS COLLECTOR

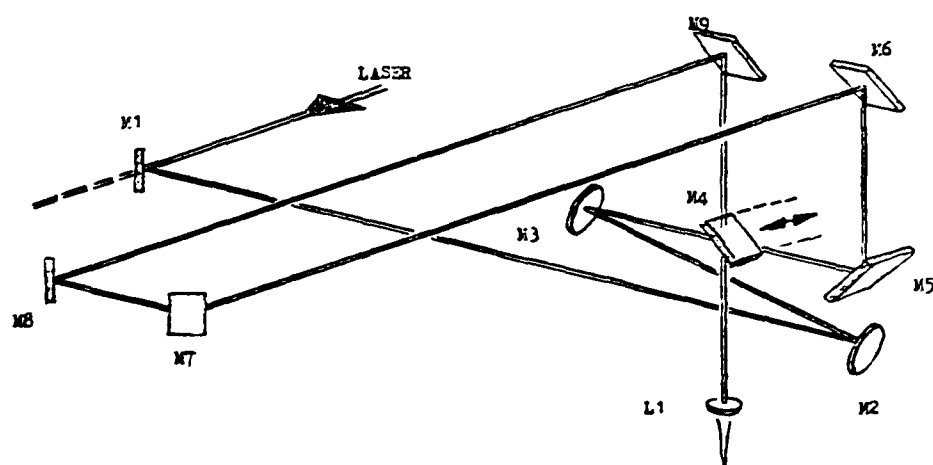


FIG. 2 - OPTICAL SYSTEM USED FOR STUDYING LASER BEAM PROPAGATION

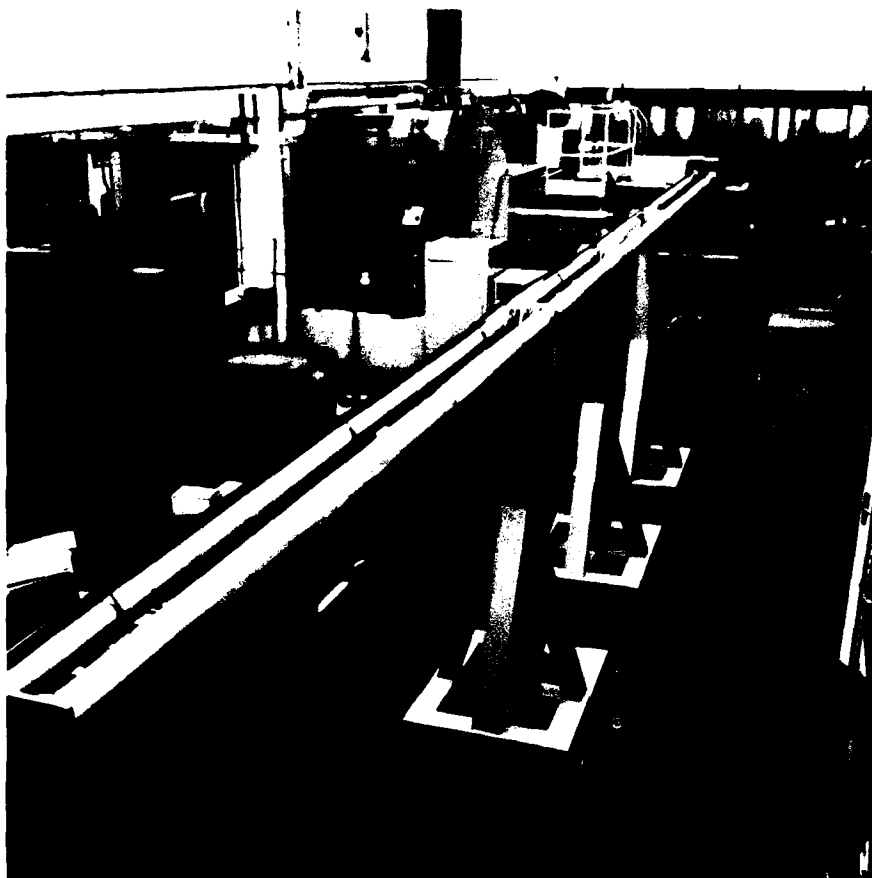


FIG. 3 - EXPERIMENTAL SET-UP OF THE OPTICAL SYSTEM
SHOWED IN FIG. 2

FIG. 4 - EXAMPLE OF LASER CUTTING ON
A CONCRETE BLOCK (200x200x200mm)
AT 10 kW AND 0.02 m/min.
(AVCO HPL SOURCE)



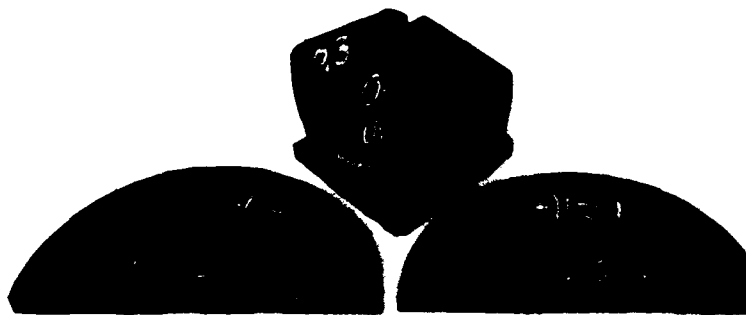


FIG. 5 - Fe42C MILD STEEL AND AISI 304 STEEL CUTS ON PLATES
15 mm THICK WITH 4.1 kW BEAM POWER AND 0.3-0.5 m/min
CUTTING SPEED (LASER SPECTRA PHYSICS MOD. 975)

UTILIZING LASERS IN TELEVISION

Louis Libin
NBC-TV

30 Rockefeller Plaza
New York, NY 10112
Room 1500W

ABSTRACT

This paper will introduce the laser to broadcasters and provide some applications to the television production and broadcast field. The applications will include laser cable marking, talent alignment, lighting effects, optical recording and high speed video recording using a pulsed laser for synchronized illumination.

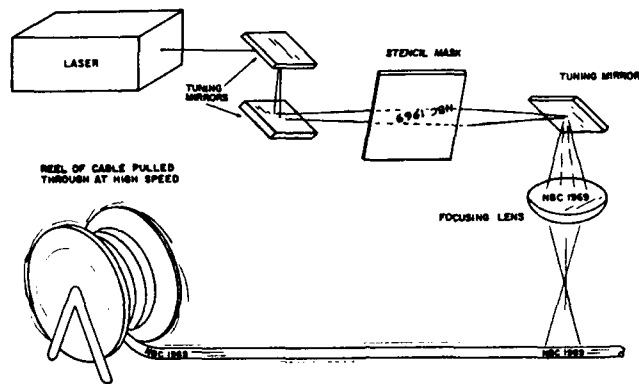
Since the laser was first developed by Theodore Maiman at Bell Laboratories in 1960 by flashing a lamp in the vicinity of a rod of synthetic ruby, the application of lasers to television broadcasting has been less than coherent and barely perceptible. However, when considering the laser's high intensity, purity of color, excellent focusing properties, and temporal coherence coupled with the short pulse duration, lasers are destined to have a dramatic impact on television. Lasers have the potential to improve imaging, lighting, and effects including 3-D reception. Lasers will be used as unique solutions to problems that are fundamental in nature to the broadcast industry.

Lasers are becoming more commonplace in television broadcast facilities today. Historically, television broadcasters use the latest technology, and lasers, being the latest technology can provide both elegant and trivial solutions to many commonplace problems.

In a large television network as in any large communications plant, there are many thousands of cables. Cables are normally numbered with a 2 digit alphanumeric prefix followed by an arbitrary 5-digit number. This information is printed on both ends of any size cable, whether 4 feet or 300 feet long. In an emergency, a considerable amount of time can be wasted by not knowing the cables purpose, destination and circuit. Bar code technology, using laser scanning can deliver on-the-spot alphanumeric information. Direct contact with the code is not required. An inexpensive He-Ne or semiconductor injection laser is usually used and has the advantage of small size and far-field beam pattern in the single transverse plane mode.

A new development, Laser Marking is now being considered for easy identification. Bar coding the cables provides a wealth of information, but laser marking the cables will allow for the easy identification, by either laser barcoding or alpha-numeric markings.

As the cable is fed through a high-speed mechanism, the laser beam, expanded, bounces off tuning mirrors through the X and Y- axis galvanometric deflecting mirrors, through focusing lens onto the mark field or the cable to be marked.



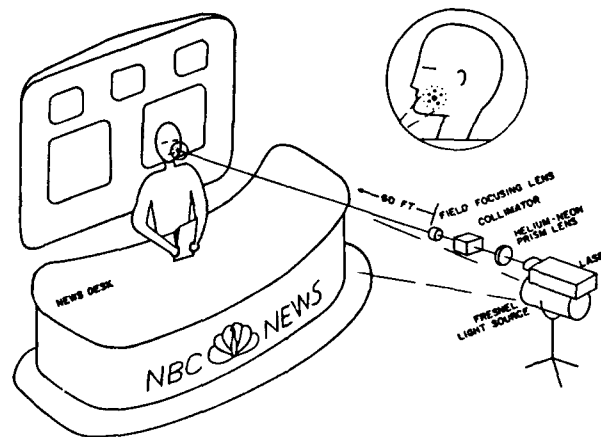
THE BEAM PATH OF AN IMAGE MASK PULSE-LASER CABLE MARKER

The characters, alphanumeric or bar code are formed by successive overlapping spots. The process is a clean process, leaving no hazardous debris. There are no inks or similar expense items required, therefore this is not a labor intensive process. This process is now being tested for cable marking and appears promising.

The design of complex lighting sets in large studios is made easier by utilizing two or three He-Ne lasers and observing the illuminated fields.

The beam is modulated through a series of prismatic and focusing lenses, designed to spread the beam in a gaussian manner, with the highest intensity in the center. The laser is mounted on the main fresnels and is used for precise aiming.

The studio to be calibrated is darkened, only one person is needed on the set; thus a substantial cost savings is introduced. We have tested this procedure for the set-up of news and entertainment shows using Red and Green lasers, and have shown that the cost of studio set-up can be significantly reduced. Using the inverse square rule, it can be shown that prismatic lenses can be used, along with a Keplerian collimator (an assembly of 2 convex mirrors) and focusing lense from a distance of more than 50 feet without significant divergence or fading.

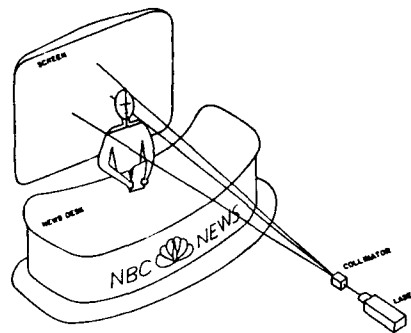


THE DESIGN OF COMPLEX LIGHTING SETS IS MADE EASIER BY USING HE-NE LASERS AND OBSERVING THE ILLUMINATED GAUSSIAN INTENSITY FIELDS ON THE SUBJECT.

The math of each of the lenses can be equated by performing a beam expansion ratio and beam expansion index using summation calculus.

As the cost of fiber-optics light guides decrease, it may become feasible to permanently mount on the fresnel light source a fiber-optic cable with a focusing lens assembly to be able to quickly set up studio lighting using one switching laser.

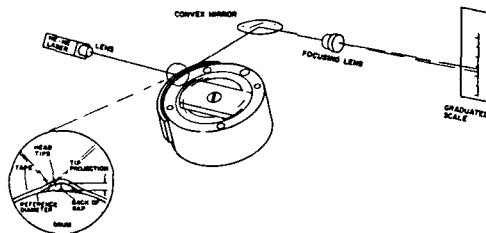
The same beam, projected through a collimator, can be used to align the talent to the exact, preprogrammed automatic camera locations. A line is projected, crossing with another onto the anchor person. The beam collimation is performed upstream of the cylindrical lens and beamsplitter (for crosshair generation).



FOR REPETITIVE NEWS SHOWS, LASER GENERATED
CROSSED-LINE PATTERNS CAN BE USED
TO ALIGN THE TALENT.

He-Ne lasers are used for the mechanical calibration of precise electro-mechanical tape transport mechanisms. A He-Ne laser, coupled to a convex mirror, whose surface reflects the tape head mechanism to be aligned, will deliver a magnified scale on a wall or screen with a much greater precision than can be measured mechanically. We use a field lens for a much tighter focus.

THE MECHANICAL CALIBRATION OF THE BROADCAST VIDEO TAPE HEAD USING A
HE-NE LASER FOR SCALE MAGNIFICATION.



TAPE/HEAD SEPARATION < 1 MICRON HEAD/GUIDE DIFFERENCE OF $> 1.33 \mu\text{m}$
WILL GIVE TIME BASE DIFFERENCES.

FOR EXAMPLE: AN ASPERITY OF $10 \mu\text{m}$ CAN RESULT IN A SIGNAL LOSS OF
5.5 db DUE TO TAPE/HEAD SEPARATION
FROM: SPACING LOSS (db) = $54.6 d/\lambda$.

In one of my experiments, we used a Helium-Neon laser to calibrate the video heads on a 3/4 inch tape machine. High-Speed videography techniques were used to capture the moving video head mechanism for later study.

LASER-BASED FIBER-OPTIC SYSTEMS

A fiber-optic network running at speeds over 500 Mb/s is currently being tested. In addition, methods of video bandwidth compression are being developed for multiple video channels per fiber transmission.

Broadcast quality video, audio and data are routinely carried through laser-based fiber optic systems more than 120 Km (75 miles) without repeaters. These Fii systems are modular and are used as short and long wavelength (840nm, 1300nm) for short distances and as long wavelength (1300nm, 1550 nm) single mode, lasers for long distances ([75 miles), without repeaters.

The systems in use today exceed the most stringent broadcast quality EIA transmission standard, the RS-250B for short haul. With the imminent introduction of advanced

Television transmission and display systems fiber optics is being considered as one of the most viable methods of home delivery of higher definition television systems.

Six channels of video may be transmitted through fiber optic systems using one single-mode cable. Three pairs of two high quality video signals would be multiplexed and inserted in a wavelength division multiplexer, operating in the 800-nm, 1300-nm and 1500-nm band. Excess loss ratios are less than 0.5 dB. The passband width in the multiplexer is wider than the oscillating wavelength deviation in the laser source, and the rejection-band attenuation is large enough to reduce signal degradation due to optical interchannel crosstalk. Laboratory experiments in closely spaced wavelength multiplexing have already achieved over 10 separate high speed signals from single frequency lasers spaced 1.3-nm apart. Current technology holds laser operation to ten gigabits/second, while detectors are generally limited to a higher order of magnitude. The unlimited bandwidth capabilities of single-mode fibers will rapidly develop when optical switches and device integration progresses. When this occurs, Terabit/second optical communication may become a reality. Experiments with signals requiring broadcast type bandwidths continue and may prove to be a very profitable venture for communication companies.

THROUGH THE AIR LASER MODULATION

In newsgathering environments television crews occasionally need studio to Transmitter Links and wireless access away from the newsgathering trucks. Microwave channels are usually used, however in busy urban areas it is becoming increasingly difficult to secure and temporarily license a microwave channel. As a result, employing a modulated laser through the air is becoming increasingly common.

Even in an optically congested area, there are large amounts of transmission space. For example, under optimal circumstances a system using only 1% of the center frequency of 3000-A light, could transmit 5×10^{12} Hz or 50,000 digital television channels of 100 MHz each. FCC authorization for optical video transmission is not required, however, the laser cannot be rated higher than Class II.

Semiconductor lasers are being used with success. If a digital system is used, then response time on the order of ten nanoseconds is needed to carry digital modulation.

OPTICAL PROCESSING AND RECORDING

Optical computers process information encoded in light beams. Digital optical computers utilize non-linear or bi-stable optical materials in a manner similar to the use of the transistor in an electronic computer. Another type of optical computer, the analog optical computer, applies the ability of a lens to perform a fourier transform and convolution to perform advanced mathematics such as matrix-matrix multiplication in linear algebra.

Commercially available, eraseable optical disk drives, are being developed now. One key concern is that optical disk standards are still in a state of flux. Data formats, track pitch and other parameters are nowhere near resolution. A 3-Mbyte/second multiple head optical disk drive has been developed and tested.

Progress is being made in using a single laser beam to perform a verifying "read" action while writing data. The data is scanned as a verifying action during the last tens of nanoseconds of each laser pulse width. The pulse duration is typically 50 ns. By detecting any shift in the reflected DC level of a disk that is tracking data, the reflection of the reading beam, can be used to flag the presence of already written data. In this way, by sensing previously written regions on the fly, the data-transfer rate will be sped up. Obviously the ultimate goal for broadcasters is the ability to record, edit and manipulate video information optically. This is one area where many experiments are being done.

LACRO BIT-PAU

Stable laser cavities, such as the He-Ne or Ruby lasers, produce a beam with a gaussian beam distribution and expansion. The spot size of the beam will expand by 2 when it has propagated a distance D_0 from $D=0$. In the far field the beam expands as if it were a spherical wave of limited angular extent and originating at $D=0$. Angle θ is the angular divergence of the beam given by:

$$\theta = \frac{2\lambda}{\pi a_0}$$

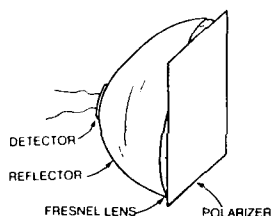
θ = ANGULAR DIVERGENCE

The Macro bit-pad is a large "interactive" grid with viewer control via hand-held He-Ne or Ruby low powered laser. (See Figure 1). The video is "chroma keyed onto the grid, which is a detector array covered by a polarizing sheet. The laser beam aims and when a trigger is pressed, a modulated signal is sent to only one segment of the detector array. Because the video is chroma keyed onto the detector array, high resolution graphics may appear as the final output.

The chroma key is a method of inserting one video signal into a background video. For example, when the weatherman is pointing to his video weather map, the screen that he's pointing to is actually a blank, flat, blue screen. A saturated flat blue is normally used, since blue is complementary or opposite in phase to human flesh tones. Thus, the chromance, or chroma key will create a hole in the final picture wherever blue occurs in the studio-camera signal.

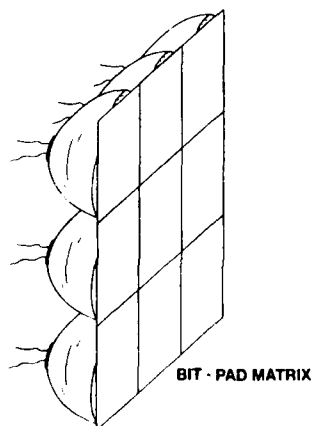
Since the key is formed strictly from the studio camera, the background scene, or in our case the many different screens we might want to interact with, may contain any color.

This resulting equation tells us that from a distance of 30 feet, a He-Ne with a beam diameter of 0.48 and a beam divergence of 1.7 mRAD will provide enough collimated light power to focus on a detector array with an area of 9 square inches. Thus, a laser with reasonably small cavity length can be used with normal angular divergence and its output on the detector matrix will be decodeable.



MACRO BIT-PAD SINGLE ELEMENT

Each Fresnel lens is covered by a one-way polarizing sheet to inhibit reflective scanning and focus incoming laser light on detector. The effects of hand stability will be attenuated by the somewhat large matrix element size. In the future if stability can be resolved the He-Ne or ruby laser can directly "Write" onto a large array with pixel resolution. Looking ahead, high powered visible beams may be used for added effect. There are many uses to the Macro-bit Pad. At present weather maps and election coverage appear to be the macro-bit pad's most promising primary users.



BIT-PAD MATRIX

HOLOGRAPHY

Holography seems to be a technology designed for television. A hologram is the recording and displaying of optical information. A photograph produces an image by reflection, whereas a hologram utilizes the principal of diffraction. Photographs record and display only intensity and color, but holograms record and display the complex amplitude of an optical wavefront that includes the entirety of information, intensity, color, and phase. The storage of all of the optical information gives rise to a large number of new possibilities that include the production of three-dimensional imaging - the most striking feature of holograms. The importance of the three-dimensional imaging is overshadowed by the extremely efficient recording capability. This extremely efficient, high density recording process stores tens of megabytes with a reference wave. Accessing this data for non-visual use (computers, random data storage) is being studied.

In 1972, RCA developed a holography based video tape machine, but the project was dropped in favor of a magnetic recording system. The system, called Holotape was a method of recording color programs on a special tape for later playback. The luminance and chrominance signals were converted to a pair of images that were recorded on photoresist-coated plastic tape in holographic form. The two major disadvantages of this system were coherent light readout and very expensive recording costs. The difficulties of forming good images with coherent light were severe, therefore hologram redundancy was used and producing the embossing master was a very complex process.

In one of the scenarios presently being studied, the transmitted signal consists of a time domain multiplexed (TDM) NTSC video signal and two control signals, one displaying phase and the other encompassing the additional optical and visual information. The two control signals are translated into laser modulated optical beams and is integrated with the NTSC display.

HIGH SPEED VIDEO RECORDING USING LASER LIGHT FOR ILLUMINATION

One of the inherent "problems" with the human eye is the lag or persistence of an image for approximately 1/10 second. The lag, coupled with the image integration performed by the brain, masks a large amount of the visual information available. The human eye cannot resolve motion that occurs in less than 1/4 second. This is where high-speed videography works well. An important advantage of slow-motion in video is the ability to manipulate time. We make time appear normal by recording the images at the same rate at which we intend to play them back. If we wish to slow time down, we merely record at a rate faster than it will be played back.

Pulsed high repetition laser light sources, such as the Argon or copper vapor laser (CU) are used as a strobe light source for high-speed video systems. The lasers have repetition rates of 4.6kHz and produce pulses of visible laser light with energy levels of 3-8 mJ.

Because of the coherent nature of laser light, source-to-subject distances of tens of meters are possible with negligible loss of illumination. The coherence factor also allows simple manipulation of field size inexpensive lenses. The copper vapor laser has performed well with the Eastman Kodak, Spin-Physics, SP-2000, capable of up to 12,000 pictures per second (P/S) on a split-screen basis. The system is monochrome, medium resolution and can record 2,000 P/S full field. Obviously events involving humans cannot be illuminated by lasers.

Extremely high-speed events however, can be shown in great detail. Projectiles such as bullets or balls can be played back detailing spin and spin rate and can be useful in demonstrating sporting events, science programs and promos and as a special effects device. Using available optical recording techniques, one could only imagine the quality of high-speed video attainable.

One reverse application, applying a video graphics system to analyze lasers is presently in use. Using two-dimensional CCD arrays, laser beam profiles can now be analyzed. Before this, laser beam profiles were analyzed aiming the laser at photo-sensitive paper and looking at the burn patterns. The video graphics system creates a pseudo-color representation of the intensity distribution for the full beam.

REFERENCES

- D.B. Carlin
"Multichannel Diode Laser Arrays For High-Data
Rate Optical Recording",
RCA Engineer, May 1986
- L.A. Cross
"Pulsed Semiconductor Lasers Find Use In
High-Speed Photography"
Laser Focus/Electro-Optics, August 1985
- M. Ettenberg
"Laser Diode Systems and Devices"
RCA Engineer, May 1986
- R.L. Fante
Proceeding IEEE Vol. 63 (1975) pg. 1658-9
- Goove, Abrahams and Mallon
"The Copper Vapor Laser - A Novel Light Source
for High-Speed Photography"
SMPTE Vol. 491, October 1984
- Ishida, Hayashi, Taneda, Motoki and Sugiura
"A 70-mm Film Laser Telecine for
High-Definition Television",
SMPTE Vol. 491, October 1984
- Lockwood, H.F. Mittke, J. P. Ettenberg, M.
"LED For High Data-Rate Optical Communications"
Opt. Comm. Vol. 16, 1976, pg. 192-4
- R.C. Plaisted, V.J. Stakun
"Holographic Document Viewers for the
Automated Support System, Man-Machine
Interface"
RCA Engineer, June 1976
- Sugiura, Nojiri and Okada
"HDTV Laser-Beam Recording on 35mm Color Film
and its Application for Electro-Cinematography"
SMPTE Journal, July 1984

CARBON ISOTOPES PRODUCTION BY THE COMBINED METHOD OF IR MULTIPHOTON DISSOCIATION
OF DIFLUOROCHLOROMETHANE MOLECULES AND LOW-TEMPERATURE RECTIFICATION OF CARBON MONOXIDE

V. Ju. Baranov, A. B. Bakhtadze, V. M. Vetsko, A. G. Kudziev, G. A. Tevzadze
I. V. Kurchatov Institute of Atomic Energy, Moscow, U.S.S.R.

Abstract

The production of carbon isotopes by IR multiphoton dissociation and low temperature rectification of CO is discussed.

Introduction

Production of carbon isotopes is nowadays performed by the countercurrent reversible process of low-temperature carbon monoxide rectification. Production yield scale of individual plants is of the order of several kilograms of carbon-13, enriched up to ~90%, per year.¹ Energy expenditure ϵ to perform this process is basically connected with gas-liquid phase transition at the sites of phase reversal and is proportional to the gas flow L_p circulating in the plant,²

$$\epsilon \sim L_p \sim \frac{P(x_p - x_F)}{x_F(1 - x_F)(a_p - 1)} \quad (1)$$

where a_p - is the elementary separation factor during rectification. As follows from Eq. (1), when the values of the product flow P and the desired isotope concentration x_p in it are fixed, the energy expenditure decreases with the increase of the desired isotope concentration in the feed flow x_F (Fig. 1). Due to this, the major part of energy expenditure is in the zone of the initial enrichment from the level of the natural (1%) up to the medium (20-30%) concentration of the desired isotope. If energy expenditure $\epsilon \sim 30$ keV/atom ^{13}C for (1-90%) concentration range, then for (30-90%) concentration range this value will be about 30 times less, ~ 1 keV/atom ^{13}C . Due to this to optimize the process of carbon isotopes production, it is recommended to use a more effective method than that of the low-temperature carbon monoxide rectification at the initial step of carbon-13 isotope enrichment.

Selective Multiphoton Dissociation

As an example of such method this paper discusses the method of isotope selective multiphoton dissociation of molecules.³ The experimental data study showed,⁴⁻⁶ that during the MPD of carbon containing molecules selectivities of the elemental separation step a_n are attainable, which substantially exceed the separation degree necessary to receive the desired isotope concentration of about $x_p \sim 20-30\%$, then for the initial enrichment step, it is advantageous to analyze the possibility of MPD of molecules in separating laser reactor (SLR) with multiplication of the degree of the desired isotope depletion Q .⁷ This scheme of SLR with the closed-loop gas circulation, containing the zone of laser beam irradiation, is the most simple for technical realization (Fig. 2).

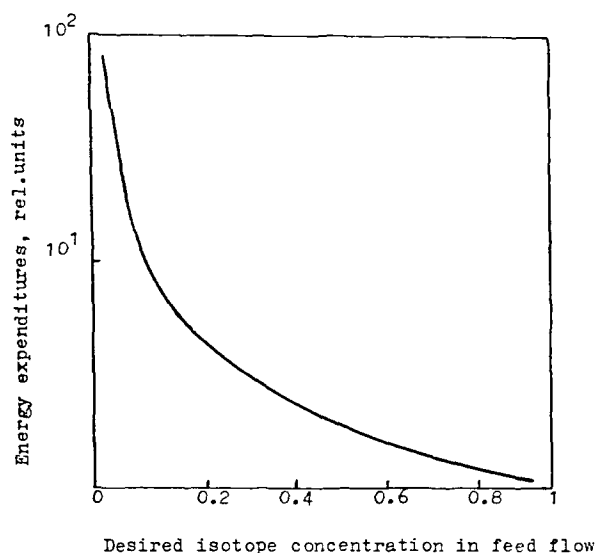
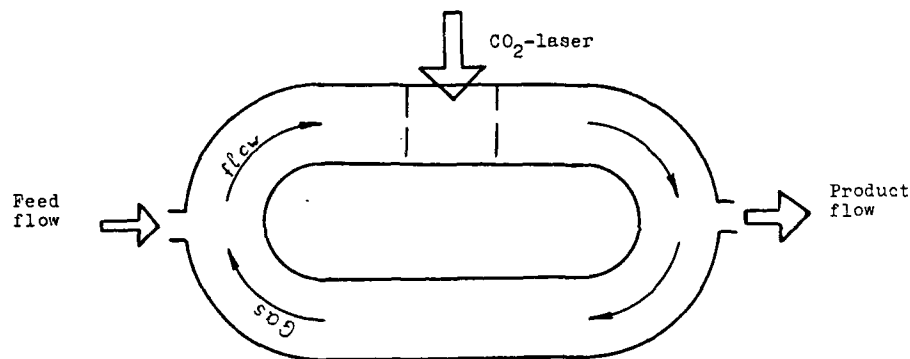


Fig.1



Separating laser reactor diagram

Fig.2

Let us perform a comparative analysis of the parameters of the separating laser reactor and rectifying plant (RP). Gas flows, circulating in SLR and RP may be determined from

$$L_{\Lambda} \sim \bar{P}_{\Lambda} / \beta_Y (1 - Q) x_F \quad (2)$$

$$L_p \sim \bar{P}_p / (a_p - 1) x_F$$

where β_Y - dissociation yield of the MPD process, \bar{P}_{Λ} , \bar{P}_p - product flows in SLR and RP respectively, calculated in terms of the pure desired isotope. It is obvious, that if $\beta_Y > (a_p - 1) / (1 - Q)$, then $L_{\Lambda} < L_p$. For low-temperature carbon monoxide rectification $a_p \sim 1.007$, therefore when $Q \sim 0.5$ (a relatively high degree of the desired isotope depletion), then even with low desired isotope dissociation yield, $\beta_Y \geq 10^{-2}$, the gas flow in SLR must be lower than that in RP for identical \bar{P} values. Expressions for the product flows of the desired isotope in SLR and RP may be presented as

$$\begin{aligned}\dot{P}_\Lambda &\sim \frac{P_\Lambda}{kT_\Lambda} f \ell S_\Lambda \beta_Y (1 - Q) x_P \\ \dot{P}_P &\sim \frac{P_P}{kT_P} \nu_P S_P (a_P - 1) x_F\end{aligned}\quad (3)$$

where P_Λ , P_P , T_Λ , T_P - pressures and temperatures of the working media in SLR and RP, ν_P , S_P - linear gas velocity and cross-section area of the separating columns in RP, f - laser pulse frequency, ℓ and S_Λ - linear dimension along the L_Λ flow and cross-section area of the laser irradiated zone, K - Boltzmann constant (Fig. 3). Let us study now expression (3). The $(a_P - 1)$ parameter determines the desired isotope portion, which may be removed from L_P gas flow in RP as a product flow $\dot{P}_P \cdot \beta_Y (1 - Q)$ parameter, exceeding $(a_P - 1)$ when $\beta_Y \geq 10^{-2}$ ($Q \sim 0.5$), as it was mentioned above, may be used as an analog for the above parameter. Linear gas flow velocity in RP is about 1 m/s. Linear velocity of the gas circulation through the laser irradiated zone into the SLR zone, $\nu_\Lambda = f \cdot \ell$ (Fig. 3), and when $\ell \sim 5$ cm and $f \sim 10^2 - 10^3$ cps [Ref. 3] it may exceed the ν_P value for more than one order of magnitude.

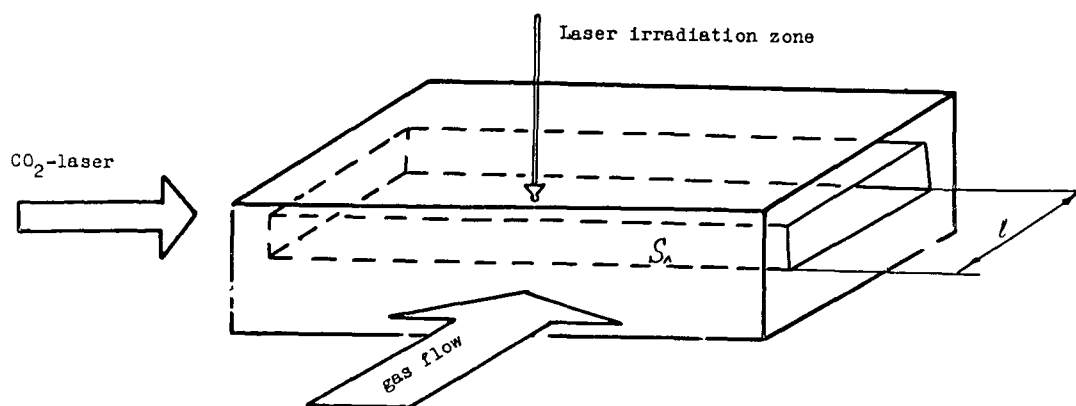


Diagram of the separating laser unit, included in the closed loop gas circulation line

Fig.3

Keeping in mind the above estimation let us compare the values of the specific product flows \dot{P}/S to determine the basic MPD parameters, such as dissociation yield β_Y of the desired isotope and resonance gas pressure P_Λ , which make the laser method more effective than that of the low-temperature carbon monoxide rectification. $\dot{P}_\Lambda/S_\Lambda$ and \dot{P}_P/S_P parameters characterize the desired isotope product flows, which may be obtained per unit cross-section in SLR and RP. When $P_P \sim 500$ Torr, $T_P \sim 80$ K, $a_P \sim 1.007$, $\nu_P \sim 0.5$ m/s we have for RP $\dot{P}_P/S_P \sim 4.4 \cdot 10^{-6}$ g¹³C/cm²s. Figure 4 shows dependencies of $\beta_Y(P_\Lambda)$, from which it follows that to provide $\dot{P}_\Lambda/S_\Lambda$ greater than \dot{P}_P/S_P the resonance gas pressure must be about $P_\Lambda \sim 100$ Torr. When, for example, $\beta_Y \sim 5 \cdot 10^{-2}$, then the specific production value in SLR will be of about one order of magnitude higher than that in RP. It should be mentioned that values of about $\beta_Y \leq 0.1$ are realistic values for the desired isotope dissociation yield.

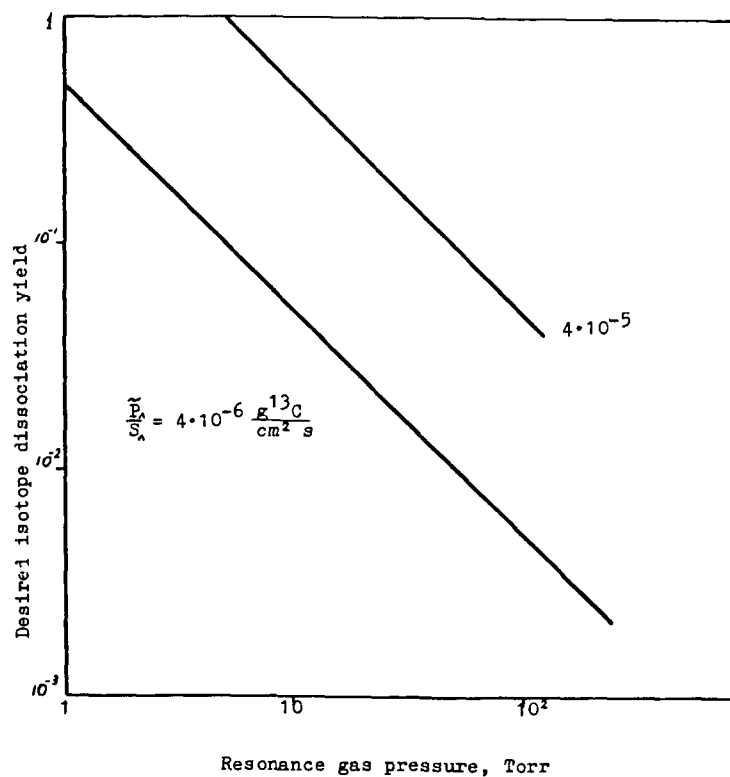


Fig.4

To provide the necessary regime in MPD the molecule of difluorochloromethane was chosen, which belongs to the group of smaller molecules characterized by the relatively high quasicontinuum boundary level and thus by the extended discrete network of vibrational levels. The molecules of this group are probably the most perspective for highly selective MPD of molecules.

The initial series of the experiments was performed using a CO_2 -laser with the following pulse specifications. The duration of the front pulse peak at its half-height was ~ 80 ns, and at its base ~ 250 ns; the pulse contained $\sim 50\%$ of energy; pulse tailing duration was ~ 1 μs . On the basis of the experimental data analysis we may note that dissociation yield and dissociation selectivity are weakly dependent on the buffer gas pressure (Fig. 5), but much more dependent on the proper resonance gas pressure (Fig. 6). Dissociation selectivity is high enough, $a \sim 10^3$, for the resonance gas pressure of interest, $P_A \sim 100$ Torr; however, dissociation yield is low, $\beta_y \sim 10^{-3}$. Threshold fluence for MPD is independent of the laser radiation frequency but is determined by the P_A resonance gas pressure (Fig. 7). Threshold fluence value increased with the resonance gas pressure rise.

Experimental data made it possible to presume that vibration-vibrational exchange has predominating influence on the multiphoton excitation and dissociation of the difluorochloromethane molecule. The qualitative model of the process was simulated, based on the fact that the main features of the process are connected with radiation excitation and vibration-vibrational exchange concurrence. In these conditions the resulting excitation rate may be expressed as

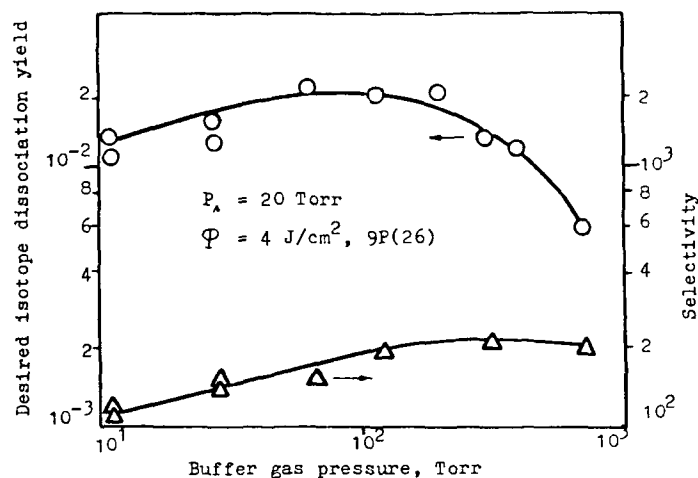


Fig. 5

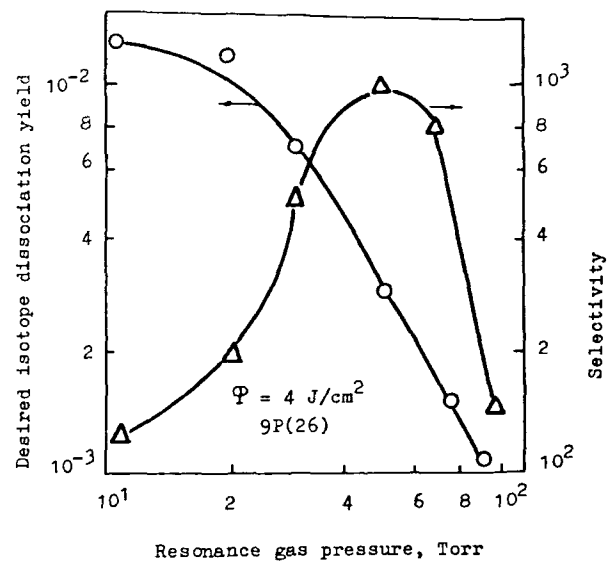


Fig. 6

$$W = GI - K_{v-v} - \nu P_A$$

(4)

where I - laser field intensity; G - effective excitation cross-section; K_{v-v} - vibrational exchange rate constant. To describe the distribution of molecules among the vibrational states in quasicontinuum we can use the relation⁸

$$N_n \sim q(\nu) \frac{(w\tau)^n}{n!} \exp(-w\tau)$$

(5)

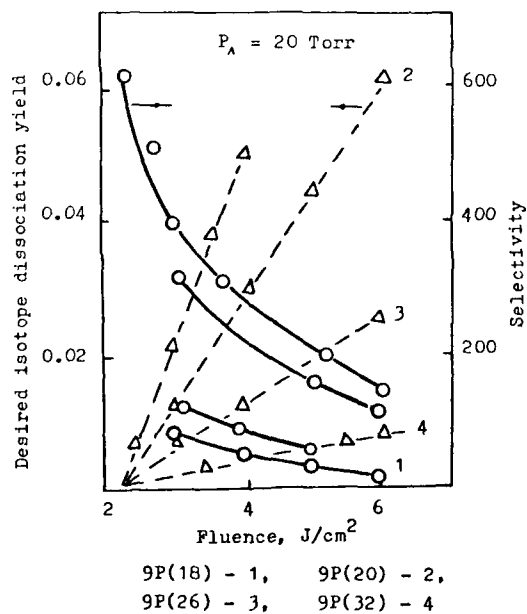


Fig. 7

where $q(\nu)$ - frequency factor, considering spectral dependence of the portion of molecules, excited into quasicontinuum; n - level number; τ - laser pulse duration. Finding that dissociation threshold is reached at such $\omega\tau$ mean vibrational excitation level, at which the velocity of the dissociation level population rise is the highest with $\omega\tau$ rise, we can obtain a simple threshold fluence estimate, above which an effective MPD molecule evolves at given P and τ values.

$$Q_n = \frac{1}{G} [K_{v-v} - v^P \tau + n_D - \sqrt{n_D}] \quad (6)$$

where n_D - dissociation level (for difluorochloromethane molecule, $n_D = 18$). Using experimental values of the threshold fluence we may receive the following constants: $G \sim 7.5 \times 10^{-19} \text{ cm}^2$, $K_{v-v} \sim 6.5 \times 10^6 \text{ Torr}^{-1} \text{ s}^{-1}$. The analysis of (6), allowing for G and K_{v-v} data shows that when the above values of laser irradiation duration, $\tau \sim 250 \text{ ns}$, and laser irradiation fluence, $\Phi \sim 4 \text{ J} \cdot \text{cm}^{-2}$ are used, dissociation yield of the desired isotope must be negligible, when $P_A \sim 100 \text{ Torr}$. In the meantime it follows from (6), that if laser pulse duration is shortened, dissociation threshold may remain at the same or lower level with the rise of the resonance gas pressure. Threshold fluence measurement for $P_A \sim 100 \text{ Torr}$ gives the admissible value $\Phi_n = 1 \text{ J} \cdot \text{cm}^{-2}$, if pulse duration is shortened down to $\tau \sim 20 \text{ ns}$.

Experiments performed with CO_2 -laser radiation with 20 ns pulse duration confirmed the above qualitative considerations. Optimal results were obtained for resonance gas pressure $P_A \sim 60 \text{ Torr}$, when the desired isotope dissociation yield was $\beta_y \sim 4 \times 10^{-2}$ and isotope concentration in the product $x_p \sim 30\%$, and specific energy expenditures $\epsilon \sim 4 \text{ keV/atom}^{13}\text{C}$. Here specific product yield for SLR was 5-times higher than that for RP.

Thus the combined method of carbon isotope production, consisting of high resonance gas pressure MPD method at the initial step of enrichment and low-temperature rectification method at the final step, provided substantial decrease of total energy expenditures and simultaneous increase of the desired isotope specific product yield. It follows from the above study that specific product yield increased 5-fold for the combined separation method compared to the low-temperature rectification method: from $4 \times 10^{-6} \text{ g}^{13}\text{C/cm}^2 \text{ s}$ up to $2 \times 10^{-5} \text{ g}^{13}\text{C/cm}^2 \text{ s}$, and total energy expenditures decreased from 30 down to 5 $\text{keV/atom}^{13}\text{C}$.

References

1. A. B. Bakhtadze, Stable Isotopes in the Life Sciences. International Atomic Energy Agency (IAEA), Vienna, 1977.
2. K. Koen, Theory of Isotope Separation (McGraw-Hill, New York, 1951).
3. E. P. Velikhov, V. Ju. Baranov, V. S. Letokhov, E. A. Ryabov, A. N. Starostin, Impul'snye CO_2 -lazery i ikh primeneniye dlya razdeleniya izotopov.-M., Nayka, 1983.
4. O. N. Avatkov, A. B. Bakhtadze, I. G. Gverdtsiteli, et al., CLEO-85, OSA/IEEE, Digest of technical papers, p. 36.
5. M. Gathier, C. G. Cureton, P. A. Hackett, et al., Applied Physics, B28, 43 (1982).
6. Yang Li-Shu, Wang Zheng-min, Liu Zong-cai et al., Chinese Physics Lasers, 13, 606 (1986).
7. V. M. Vetsko, O. A. Devdariani, S. A. Kalitin, Kvantovaya Elektronika, 12, 1254 (1985).
8. V. S. Letokhov, Nelineinye selektivnye fotoprotsessy v atomakh i molekulakh. M., Nayka, 1983, p. 228.

THERMOCHEMICAL EFFECT OF THE CONTINUOUS WAVE AND HIGH-REPETITION RATE LASERS ON METALS

V. Yu. Baranov, N. A. Zheleznov, F. K. Kosyrev, D. D. Malyuta, V. S. Mezhevov,
A. V. Rodin, and A. Yu. Sebrant
I. V. Kurchatov Institute of Atomic Energy, Moscow, USSR

Abstract

Thermochemical effects in CW and high pulse repetition frequency lasers are discussed.

Introduction

There is at present a growing interest in the problem of hardening the surface layers of steels and alloys by changing their chemical composition in order to improve the properties of these materials.¹

The most promising method for hardening the working surfaces of industrial products is thermochemical treatment of materials since it provides essential increase in hardness thus enhancing resistance of the material to mechanical wear.²

It is known that in the material treatment practice the most used is carburization of the surface layers of the low-carbon steels. The carburizing operation is carried out in practice at $T = 750-1100^{\circ}\text{C}$.³ Carburization of the surface layers of workpieces to a desired depth takes a long time (several hours). Attempts to speed up this operation increasing the temperature or the concentration of the carbon-containing gas in the furnace atmosphere do not give the desired result since increase in the temperature results in intense production of soot which prevents carbon from penetrating deep into the bulk of a material. Use of the gas glow discharge in the medium of ethanol, acetone or propane-butane mixture vapors is also unsuccessful since significant soot formation prevents maintaining a stable glow discharge.^{4,5}

However it is noted in Ref. 6 that the time of carburizing 12 KNZA steel in the glow discharge is reduced at $T = 1100-1300^{\circ}\text{C}$.

Of primary interest are investigations of the characteristics and features of the process of saturating the near-surface layers of low-carbon steels with carbon or nitrogen due to low-threshold laser-induced plasma, the so-called laser plasma treatment, described in Refs. 7 and 8. In these works carburization of the surface layers of low-carbon steels is accomplished on account of products of carbon-containing medium decomposition and carbon diffusion into the surface layers under the action of laser radiation upon the target. In Ref. 7 the plasma was formed by a high-repetition-rate CO_2 laser with pulse duration of $0.5-5.0 \mu\text{s}$ and the samples were irradiated in a chamber with the carbon-containing gas pressure not exceeding the atmospheric one. Using this method the surface layers of low-carbon steels can be carburized to 5% C concentration to a depth of some ten microns. In Ref. 8 the pulse duration was several milliseconds and carburization of the surface layers of the materials was reached due to a single pulse from the gaseous medium with a pressure of several dozens of atmospheres.

Lately at the I. V. Kurchatov Institute of Atomic Energy continuous wave lasers with an average power of some kilowatts and high-repetition-rate CO₂ lasers with pulse repetition frequencies up to 10³ Hz and peak powers exceeding 10⁶ W have been developed. This enabled investigations of thermochemical treatment of the metal and alloy surfaces by laser radiation to be performed within a wide range of laser parameters.

High-Repetition-Rate Mode

The experiments were carried out on a high-repetition-rate laser Svertchok (Fig. 1) with the following parameters:

Pulse energy 1-2 J (multimode)
Radiation pulse duration 0.5-100 μ s.
Pulse frequency up to 1 kHz
Average power up to 1 kW.



Fig. 1 View of a high-repetition-rate CO₂ laser "Svertchok".

The optical scheme of the experiment is shown in Fig. 2. The laser radiation was directed to the interaction chamber through a focusing lens. A part of the radiation was split to calorimeter K and photodetector. A sample to be treated was fixed on two-coordinate electrically-driven translator 7. The chamber was evacuated to about 1 Pa and then filled with the gas up to the desired pressure. Diagnostics of the plasma plume was accomplished by a quartz spectrograph ISP which recorded the time integrated spectrum of the plasma with a spatial resolution of about 0.1 mm along the incident laser beam axis. To obtain spectrograms with time resolution a spectral adapter SR (of SP-78 type) was used together with a streak-camera SK (of FER-7 type). High-speed cameras SK FER-7 and VFU-1 were also used for taking streak pictures of the plasma plume development and high-speed photography at a frequency of 5×10^5 frames/s. In some experiments the plasma plume transparency for the laser radiation was measured using the second photodetector and sample average heating was studied by means of thermocouples caulked into the sample microscope M installed on the chamber made it possible to control visually the process with respect to the quality of the surface obtained without removing the sample out of the chamber.

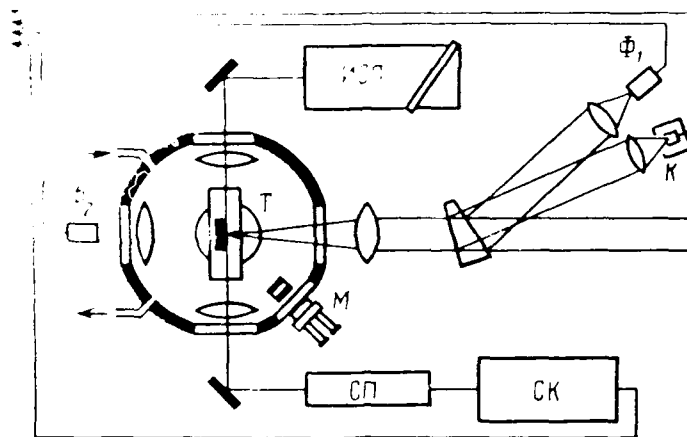


Fig. 2 Optical scheme of the experiment.

In the experiments metals Fe, W, Nb, Cr, Ta, Mo, and others were used. In all cases, layers with increased concentrations of carbon, nitrogen were obtained. The most detailed experiments have been carried out for the iron-carbon system which was the most convenient one for metal testing investigations.

Since the duration of the CO₂ laser pulse does not exceed 100 μ s the concentration of the dopant from the plasma formed on the melt during a single pulse is small, therefore tens and even hundreds of pulses are needed to obtain high concentrations. This results in that the zones with noticeable concentration of the alloying element have very uniform distribution of this element across the zone. However, a slight increase of the concentration is observed near the surface.

Irradiation of samples by means of the high-repetition-rate laser is performed in the scanning mode, selection of the pulse frequency and the scanning rate provides the desired number of pulses to a single point.

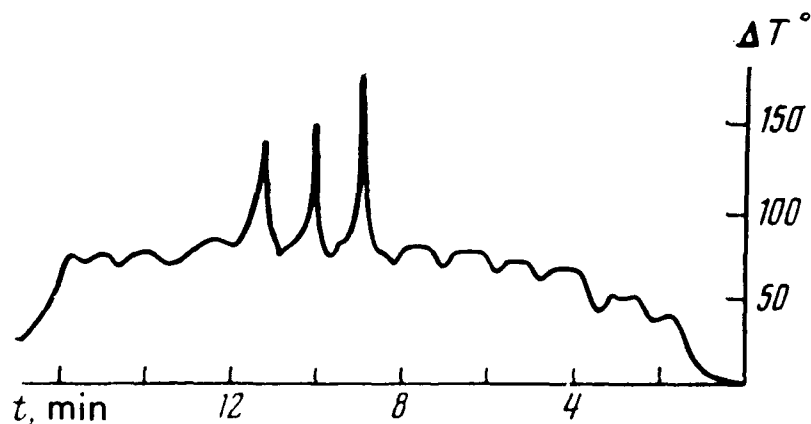


Fig. 3 Signal from the thermocouple caulked into the sample. The sample motion velocity is 0.9 mm/s, the average beam power is 200 W.

The high-repetition-rate mode of treatment leads to a peculiar thermal regime of the layer treated. Figure 3 presents the signal from the thermocouple caulked into the sample treated at a depth of 0.7 mm below the surface irradiated. There are no sharp peaks on the plot, showing melting occurring in the thin surface layer. The average heating increases with increase in the average power and in the deep-melt mode may amount to hundreds of degrees, which leads to change in the phase composition of the alloying layer compared with the layer which was only subject to rapid quenching after a single pulse. Investigations of the dependence of the laser-induced plasma parameters on the gas pressure and composition showed that, first, the temperature behind the laser-supported detonation wave front remains high enough (corresponding to an ionization degree of about 1) for several (3-4) μs , i.e., the melt can contact the alloying element ions (ion concentration is $>10^{17} \text{ cm}^{-3}$), not only during the pulse peak but also after bleaching the plasma (Fig. 4). The alloying element ion concentration, therefore, can be controlled by addition of a buffer gas. The presence of buffer gas prevents the undesirable increase of the threshold of plasma formation and plasma transparency with the gas pressure reduction.

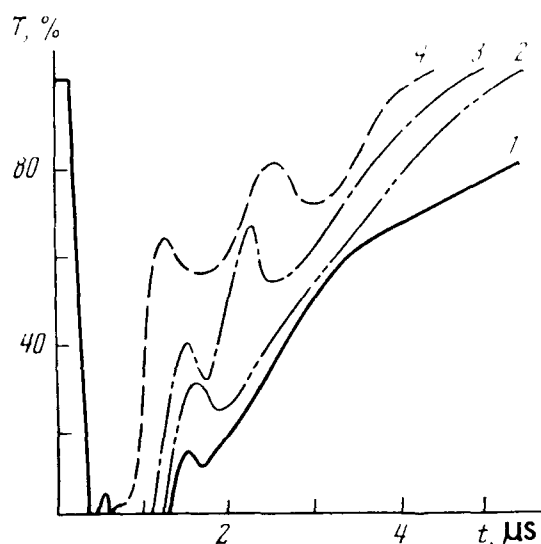


Fig. 4 Time dependence of the surface breakdown plasma transparency for different nitrogen pressures. Pulse energy is 1.5J, diameter of spot on the sample is 0.7 mm, and the material-tantalum pressures (kPa): 1-97; 2-48; 3-34; 4-17.

Therefore, alloying of the metal from the gas using the high-repetition-rate CO_2 lasers is a very flexible process.

Note that in some cases a gaseous medium surrounding the sample can be created by evaporation of the substance set into the beam reflected from the sample. In this case vacuum is maintained in the interaction chamber, which provides transportation of the jet of evaporated substance vapors to the melt on the sample. In the experiment with graphite pellets set into the reflected beam from the iron being melted in vacuum by the high-repetition-rate laser radiation, high-carbon steels have been obtained, close to those produced in propane.

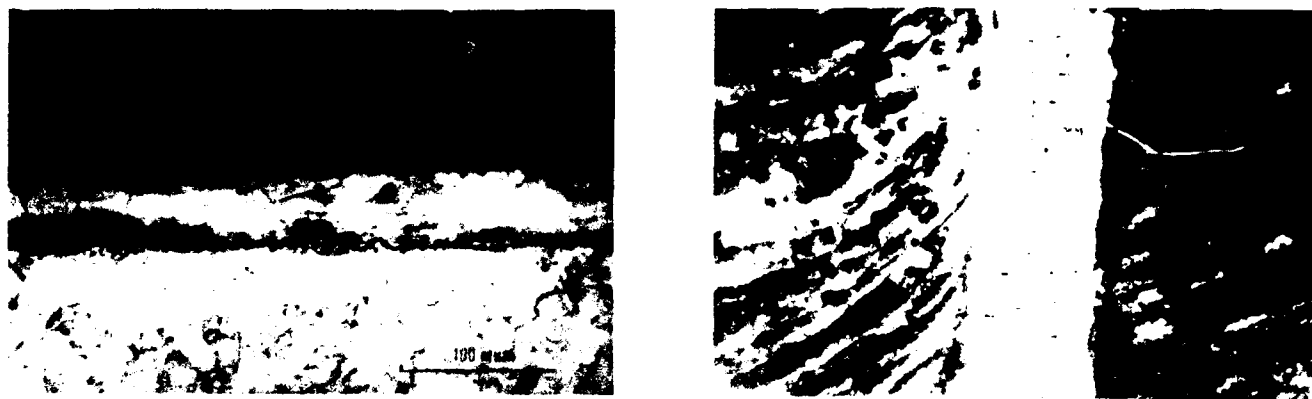


Fig. 5 Photographs of steel microsections after treatment in propane.

Figure 5 shows the photographs of microsections of the steel treated in propane at 25-50 MPa, the radiation energy density in the sample plane was 90 to 130 J/cm², taking into account that a part of the incident energy was absorbed in the gas. The number of pulses to the point was 50. The X-ray analysis showed that the lower boundary of the average carbon concentration in the layer irradiated was about 2%.

Continuous Wave Mode

In our opinion, the method under consideration opens significant prospects when using the continuous wave laser radiation. First, because the iron in liquid state dissolves easily the carbon in any of its modifications such as soot, graphite, cementite, etc., and, second, in the continuous wave laser-irradiation of the surface the time when the metal is in the melted state can be easily varied changing the diameter of the laser-heated spot and the velocity of the beam motion over the material surface (as well as the laser beam power). At the same time, the above considerations permit one to hope for obtaining high efficiency of this method when a high carbon concentration at a significant depth of the layer to be carburized (more than 1 mm) is reached.

In the present, we have investigated the features of the process of carburizing the surface layer of low-carbon steels in the carbon-containing gas medium in continuous wave irradiation with a 1 kW CO₂ laser of LT-1 type. The experimental setup is shown in Fig. 6.

The LT1 is the first Soviet industrial laser unit with a power of 5 kW. The laser head is smaller in comparison with any foreign units and the controlled multisection electrode system has no equal in the world practice. New designs have been copyrighted and patented in Great Britain, USA, France, FRG, Japan, DDR, etc.¹⁰⁻¹²

The options of the LT1 units (LT1-2, LT1-3, LT1-3 m, LT1-5, 2LT1-3 m, etc.) differ in their systems of working gas mixture blowing, power supply, cooling, control and regulation of working parameters, arrangement of components; they work within a wide range of the working gas mixture parameters (composition, velocity, pressure), current and voltage in the continuous wave and high-repetition-rate modes.

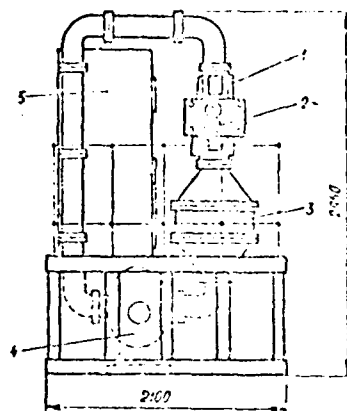


Fig. 6 Schematic view of LT-1
1 - discharge chamber; 2 - optical resonator; 3 - heat exchanger; 4 - blower;
5 - power supply.

In the experiments, 4 mm thick ARMCO-iron plates, previously rolled and cleaned from scale, were used as low-carbon steel samples. The samples were irradiated on a 5 kW LT-1 continuous wave unit in the jet of carbon-containing gas supplied to the zone of the CO₂ laser radiation interaction with the target. Propane was chosen as the carbon-containing gas, as well as its mixtures with such inert gases as Ar, He, N₂, etc. The samples were moved at a velocity of 1-100 mm/s and the laser output power reached 3.5 kW. The laser radiation was focused with a KCl lens with a focal distance of $F_0 = 200-400$ mm.

The structures of the paths treated were analyzed using the X-ray diffraction methods by means of a DRON-3x-ray diffractometer and URS-160 unit with a RKD camera, and optical metallography methods. The structures of the microsections were observed after their chemical etching in the 4% solution of strong nitric acid in ethanol. The microhardness of the samples obtained were measured by a PMT-3 microhardness meter at a load of 100 g. The measurement results were treated statistically.

Figure 7 shows a macrosection of the irradiated sample. The given path has been obtained in the following treatment mode: laser radiation power $P = 1.5$ kW, beam velocity $V = 10$ mm/s. The maximum depth of treatment reaches 0.3 mm. Changing the working regime it is possible to obtain paths with a width up to 10 mm and depth up to a few millimeters.



Fig. 7 Photograph of a macrosection of the path irradiated by a high-repetition-rate of CO₂ laser.

Carbon concentration and microhardness of the treated zone can be varied by choosing the parameters of laser interaction with the surface of a low-carbon steel.

Figure 8 shows the microsection structure obtained in the pure propane atmosphere with a pressure of 1.1 atm. at the limiting treatment parameters: velocity of the beam motion over the substrate $V = 1 \text{ mm/s}$, laser power $P = 3 \text{ kW}$.

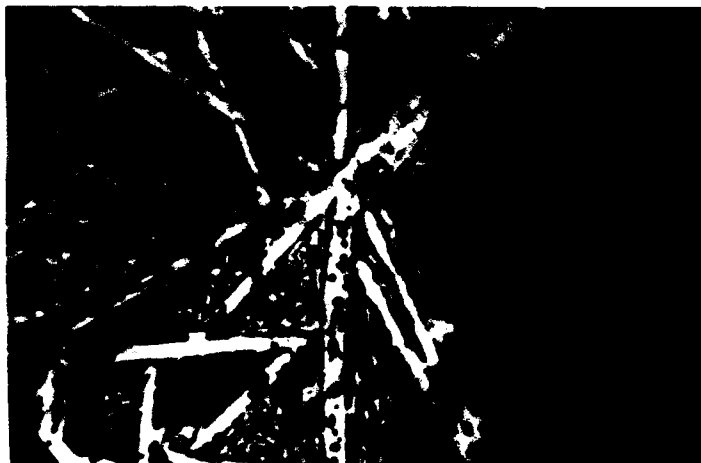


Fig. 8 Photograph of the treatment zone microstructure, 5%C.

The treatment zone is hypereutectic pig iron with a carbon concentration of about 5% C. In Fig. 8 plates of primary cementite in the ledeburite matrix, whose dimensions up to 100-150 μm are clearly seen. With reduction of the time of the radiation-target interaction (e.g., with increase in the velocity of beam motion over the substrate), the dimension of the primary cementite plates decrease noticeably.

When the beam motion velocity is increased, or the carbon-containing medium is diluted with inert gas, the carbon concentration in the zone of the radiation-target interaction is subsequently 7% C, 1.5% C, 0.5% C, and lower. Figure 9 is the photograph of a section with a carbon concentration of about 1.5% C. In this case, the carburization depth reached is 1 mm at a treatment rate of about 2 cm^2/s . The maximum carburization depth in the alloyed layers obtained with our equipment is as high as 4 mm.



Fig. 9 Photograph of the treatment zone microstructure, 1.5%C.

In all the carburization conditions microhardness in the treatment zone is higher than 6500 MPa and sometimes reaches 10000 MPa and higher values. High microhardness values appear to be due to hardening processes occurring in carbon saturation of melted metal as well as due to a high-concentration of the fine-dispersed carburization component in the treatment zone structure.

In all the microsections examined a white nonetchable zone between the treatment zone and the bulk metal was observed, which had a well-marked boundary both with the treatment zone and the base metal of the substrate. The microhardness in this white zone correspond to that of the layer carburized. Onset of this zone is likely to be connected with carbon diffusion from the melts to the solid.

The X-ray diffraction analysis revealed presence of ferrite and cementite having lattices with the practically constant parameters in the interaction zone for most treatment conditions. In the regimes with the average velocities of beam motion and in dilution of the carbon-containing medium with helium significant amounts of residual austenite were found in the structure components. When the carbon concentration was higher than 1% splitting of martensite duplex was not observed.

It must be noted that in the melted pool intense convective stirring of the liquid metal occurs, that results in a relative equalization of the carbon concentration to a depth of a few millimeters, which permits the above process to be developed with a high capability. At the same time under some treatment conditions, unstable behavior of carbon concentrations was observed along the line of the beam-substrate interaction, the microhardness in the zone treated remaining practically the same. Also, it should be pointed out that, in treatment of the surface some deterioration in its condition takes place, similar to that occurring in welding (weld reinforcement). In optimal choice of the carburization parameters a minimum reinforcement of the treatment zone (less than 0.1 mm), can be obtained. In some cases, pores were observed on the path surfaces.

Thermochemical and heat treatment of materials using the high-repetition-rate CO₂ lasers permits alloying layers as thin as about 100 μ m with controlled amount of alloying element to be obtained.

Use of the continuous wave radiation permits saturation of low carbon steel surface layers to a depth of several millimeters in the carbon-containing gaseous medium to be performed.

By varying the parameters of the above mentioned process (radiation power, laser spot diameter, velocity of beam motion over the substrate, gas medium composition), the carbon concentration in the layers treated can be easily changed, with the microhardness of irradiated zones reaching high values in all the cases.

References

1. Yu. M. Lakhtin and B. N. Ardamasov, Thermochemical Treatment of Metals. M., Metallurgiya 1985, p. 256.
2. I. V. Kragel'skii and V. V. Alisin. Friction, Wear and Lubrication, Handbook, v. 2. M., Mashinostroenie, 1979, p. 358.
3. E. Gudremon, Special Steels, v. 1, M., Metallurgizdat, 1958.
4. A. A. Babad-Zakhryapin and G. D. Kuznetsov, Thermochemical treatment in glow discharge, M., Atomizdat, 1975, p. 175.

5. V. S. Vanin, High-Temperature Ion Carburization. Metallovedenie I Termicheskaya Obrabotka Metallov, 1961, N 8, p. 22.
6. V. S. Vanin and V. G. Permyakov, Acceleration of High-Temperature Steel Carburization, Izv. AN SSSR, Otd. Lekhn, n. Ser. Metallurgiya I Toplivo, 1962, N 5.
7. V. N. Anisomov, Y. Yu. Baranov, L. A. Bolshov, L. I. Il'in, I. V., Kopetskii, V. S. Kraposhin, D. D. Malyuta, L. A. Matveeva, V. D. Pisimenny, and A. Yu. Sebrant, Carburization of Iron in Breakdown of Atmospheric Pressure Gas by the High-Repetition-Rate CO₂ Laser Radiation. Surface, Physics, Chemistry, Mechanics, M., 1984, N 9, 1984, p. 119-126.
8. A. A. Uglov and M. B. Ignat'ev, Abstracts of papers presented to All-Union meeting on laser application in machine-building technology, M., Nauka, 1982, p. 104.
9. F. K. Kosyrev, N. P. Kosyreva, A. P. Leonov, and V. A. Timofeev, LTl-2-5 kW commercial process laser unit. Avtomaticheskaya Svarka, 1978, N 10, p. 51-52.
10. U. S. Patent, 4,196,938 Apr. 8, 1980.
11. Great Britain Patent, 1,562,579, March 12, 1980.
12. Japan Patent 1,052,018, June 30, 1987.

OVERVIEW OF THE SDI PROGRAM IN SHORT WAVELENGTH CHEMICAL LASERS

C. R. Jones
Los Alamos National Laboratory
Los Alamos, New Mexico 87545

Abstract

Advanced chemical lasers promise to be effective space-based weapons against responsive threats. In this program, we are developing both CW and pulsed concepts for achieving this goal. Certain approaches may also be appropriate as ground-based weapons and fusion drivers.

I. Introduction

Space-based lasers (SBL) continue to be viable candidates for follow-on SDI architectures. Within this category, only spaced-based chemical lasers (SBCL) and space-based free-electron lasers (SBFEL) are being seriously considered at this time. Engineering maturity of SBCL, resulting from very active development programs over the past 15 years, has thrust this candidate into a leading directed energy weapon (DEW) role in a Milestone II architecture. Other DEW candidates, including ground-based FEL, neutral particle beams, ground-based excimers, and SBFEL, rely upon less mature technology and may be available in future architectures. Additionally, there is a lingering, ever-growing concern that sufficiently intense beams from GBLs cannot be propagated through the atmosphere to perform ballistic missile defense missions.

Current planning for SBCL includes capability growth of these lasers to address responsiveness of the threat. This performance enhancement primarily translates to laser brightness increase, although advances in device weight and expendable weight are obviously important goals as well.

The baseline SBCL concept incorporates the current Alpha hydrogen fluoride (HF) chemical laser operating at wavelengths near 2.7 μm . Growth in brightness can accrue from larger beam output apertures, from phasing separate apertures, and from lasing wavelength reductions. In this latter category, the nearest-term possibility is the operation on first-overtone transitions within the HF molecule at wavelengths near 1.3 μm . Another possibility, also in this wavelength range, is use of a chemical oxygen-iodine laser (COIL), a device requiring further development for effective space-based use.

There appear to be substantial gains to be made in reducing the wavelength even further. The SDI program charged with accomplishing this goal is the short-wavelength chemical laser (SWCL) program. In this basic research effort, we are attempting to develop viable chemical lasers operating in the visible and near-visible wavelength range. This paper overviews the SDIO SWCL program.

II. Status of Chemical Laser Technology

Most existing chemical lasers are based upon hydrogen-halide (HX) molecules operating on low-lying, single-quantum vibrational transitions within the electronic ground state of the HX product molecule. The most powerful and useful laser within this category is the HF laser, whose primary reaction step is the "cold" reaction,



This fast reaction effectively partitions its exoergicity of 35 kcal/mole into $\text{HF}(\nu = 1, 2, \text{ and } 3)$. The F-atoms for the above reaction are efficiently produced in a precombustor upstream of the supersonic mixing region for Reaction (1) by reacting D_2 with (excess) F_2 . Three important attributes of the HF laser are the low-mass reactants, reactant availability, and relative simplicity of the kinetics. Favorable fundamentals have driven this laser weapon candidate to a significant engineering maturity. A companion paper¹ describes this status.

COIL, discovered in 1978, is the only chemical laser operating on an electronic transition. In this laser, an energy-storage molecule is generated chemically and then collisionally transfers its energy to the lasing species. The robust energy-storage molecule is created in a solution reaction between gas-phase Cl_2 and liquid H_2O_2 . After being formed with near-unity efficiency, the O_2^* (singlet delta at $\sim 1 \text{ eV}$) diffuses through the liquid and flows in the gas phase to a

mixing region where I_2 is injected into the O_2 and diluent. The molecular iodine is first dissociated in collisions with O_2 after which collisional energy transfer occurs in the fast, near-resonant



The excited atomic iodine is the upper level of the well-characterized and favorable 1.3- μ m laser transition.

In addition to its operating wavelength being half that of the HF laser, a very positive feature of COIL is the achievable single-line output spectrum. This property will allow more efficient and simpler multiple-aperture systems. A major drawback to COIL, especially for space deployments, is the cumbersome 2-phase O_2^* generator.

III. Early SWCL Approaches

Serious efforts directed toward the development of visible-wavelength chemical lasers began in the early 1970s. The emphasis at this time was on identifying chemical reactions of sufficient energy release that electronically excited states in the product species would be energetically allowed. Metal-oxidizer gas-phase reactions dominated the picture.³ By today's standards, our view was quite primitive, due in large part to the paucity of literature at that time on the participation of electronic states in chemical reactions. At any rate, the generic reaction types were



and



Many of the flames resulting from these very energetic reactions were observed to be very bright, and in several cases, large yields of visible photons were measured. Unfortunately, these photons generally originated from a large number of states. Only modest specificity into electronically excited states was suggested in any of these early studies.

These results are not surprising in that a statistical distribution over product states should be expected in the absence of selection rules. The conservation of electronic spin is thought to be a "good" rule. Reactions (3) and (4) in most cases had no selection rules operating in their favor because the several energetically allowed states, including the ground states, were of the same symmetry. The precondition for the selective production of a specific excited state is that this state must differ in symmetry from the other energetically allowed states. This state will, therefore, be metastable. If it is strongly metastable, i.e., different spin from the ground state, then it is probably characterized by a radiative lifetime too long for a good upper laser level. This excited species, therefore, would be useful as a storage species, similar to O_2^* in COIL. For these reasons, it is now widely accepted that the direct chemical production of a good lasing species is unlikely, except in special circumstances.

IV. Later SWCL Approaches

Beginning in the late 1970s, there were several small efforts in SWCL research. Most of these had turned away from the earlier metal-oxidizer approaches to basically non-metal reactions for which spin-selection rules predicted favorable state specificity. There have been measurements on a few gas-phase chemical reactions showing quite specific production of an excited state. These reactions are shown in Table I.

Table I

Reaction	Excited State		Ref.
	Energy	Yield	
$H + NF_2 \rightarrow NF(a) + HF$	1.4 eV	0.90	4
$N + N_3 \rightarrow N_2(A) + N_2$	6.1	≥ 0.20	5
$O + CN \rightarrow N(^2D) + CO$	2.4	0.85	6

These reactions, along with the one producing O_2^* in COIL, provide positive support for the challenge of SWCL development. However, we must accept the fact that our attempts to increase the excitation energy of the excited species beyond the current 1 eV in the only existing chemically pumped electronic-transition laser lead to greater challenges. It can be argued that COIL is a somewhat special case, primarily having to do with the especially robust character of O_2^* , which, in turn, is due in large part to the low excitation energy of this species.

V. Current SWCL Program

A. General Approach

The SDIO SWCL program, which began in 1985, attempts to build upon the status prevailing at that time in order to develop a viable laser concept in a timely manner. We are seeking approaches offering high mass efficiency, near-uv or visible wavelength, simple reaction schemes, minimal electrical power requirements, and suitable reactants. The key guidelines are listed in Table II. The ambitious fuel efficiency goal of 1 MJ/kg is for an undiluted stoichiometric flow of the reacting species required in the laser concept.

Table II. Guidelines for Key SWCL Parameters

<u>Parameter</u>	<u>Requirement</u>	<u>Motivation</u>
• Laser Wavelength	$\lambda = \text{uv} - \text{visible}$	Brightness
• Transition Energy	$E = 2 - 4 \text{ eV}$	Direct
• Radiative Lifetime	$\tau_R \sim 10 \mu\text{s}$	Mixing
• Power in Flow	$\delta \geq 100 \text{ W/cm}^2$	Volume
• Fuel Efficiency	$\sigma \geq 1 \text{ MJ/kg}$	Weight
• Reactant Mass	$m_r \leq 300 \text{ amu}$	Weight

We envision a supersonic continuous-wave (CW) laser configuration similar to that for the HF laser. A simplified version is shown in Fig. 1, in which the flow is supersonic in the region of the laser axis by virtue of the nozzle expansion. The large excitation energies carried by the electronically excited states offer very high power density possibilities in the flow, which enables relatively compact systems. Using conservative assumptions, Table III shows the expected powers in flows of various excited-state densities through a 10 x 100-cm nozzle exit plane. If moderate densities of a few torr of excited states can be realized, significant SWCL payoffs in system volume and weight can be expected.

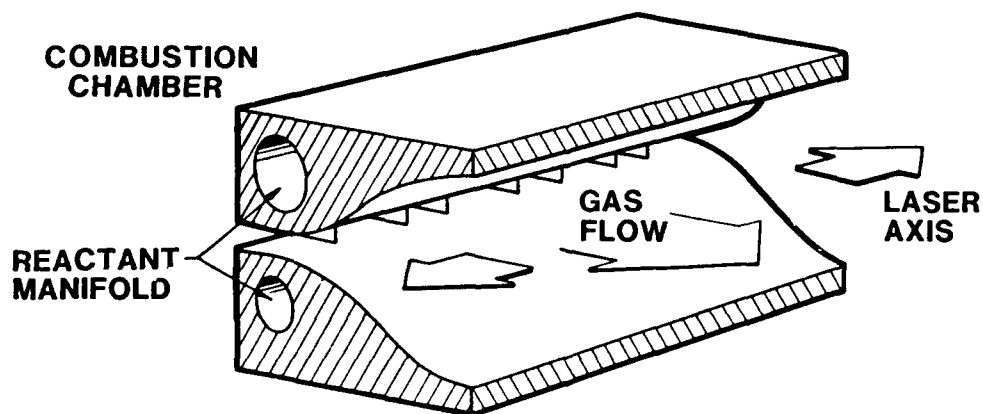


Fig. 1. Schematic of Simplified Supersonic Flow Nozzle for Chemical Lasers

Table III. Power Contained in Excited Flow Through Supersonic Nozzle Exit Plane

$V = 300 \text{ m/sec}$ $H = 10 \text{ cm}$ $L = 100 \text{ cm}$ $h\nu = 2 \text{ eV}$	
<u>Density</u>	<u>Power</u>
10^{17} cm^{-3}	1000 kW
10^{16}	100
10^{15}	10

The critical technical issues associated with the development of scalable SWCLs are shown in Table IV. Basically, these issues are related to the chemical production of a specific electronically excited state and maintaining it at usable densities over a period of time sufficient to use it. For example, it is undesirable for the excited state to radiate spontaneously at a much faster rate than the reagents can be mixed in the flow.

Table IV. Identified Critical Issues in SWCL Development

- Specific state production
- Species proliferation in flow
- Maintenance of high state densities
- Availability of reactants
- Reactant flow densities
- Radiative lifetime/mixing time
- Higher excited states have more loss channels
- Metastable transfer branching
- Existence of suitable acceptor/laser species

There are four basic approaches to SWCL development being pursued at this time:

1. direct chemical production of laser species,
2. indirect or storage species/transfer,
3. energy pooling of lower-energy species, and
4. pulsed, premixed schemes.

The first approach, as stated earlier, is expected to be effective only in special circumstances. The second case is preferred because very specific production of excited states can be realized. These states are sufficiently metastable that their energy must be collisionally transferred to be useful. A subset of this approach is the use of energy pooling, which is attractive because lower-energy species are apparently easier to generate and maintain at high densities. For example, pooling of $\text{NF}(a)$ and I^* is sufficiently energetic to produce $\text{NF}(b)$, which in transition to $\text{NF}(X)$ emits green photons. Finally, premixed schemes, by definition, obviate reagent mixing, one of the major SWCL issues. We imagine in this case that a chain reaction will be initiated in an energetic mixture, producing a pulse of excited states and pulsed lasing. Table V shows generic reactions for these four approaches. Lasing species are underlined.

Table V. Generic SWCL Reactions

- Direct

$$A + BC \rightarrow \underline{AB^*} + C$$
- Indirect

$$A + BC \rightarrow AB + C^M$$

$$C^M + XY \rightarrow C + \underline{XY^*}$$
- Energy Pooling

$$A^* + B^* \rightarrow C^*$$
- Pulsed

$$h\nu_p + ABC \rightarrow \text{Chain Reaction}$$

$$\rightarrow AB^*$$

B. Specific Concepts

Throughout the SDI SWCL program, approximately 15 concepts have been examined. Since space does not permit discussion of each of these, a few specific reaction systems will be overviewed. Further detail can be found in the open literature.

1. Direct chemical productions of laser species. The $O + N_3$ reaction represents one of several concepts based upon azide chemistry. Many azide reactions appear to be favorable SWCL candidates, based upon the energetic nature of the N_3 radical and the angular momentum constraints that may operate in specific reactions. As discussed earlier, a high degree of specificity is not expected in reactions creating states that are optically connected to the ground state. However, if the energetics of the reaction and the product are such that only a very few product states are energetically possible, then a statistical distribution over the product states may be sufficient for efficient laser operation. The $O + N_3$ reaction falls in this category because only the X, A, and B doublet states of NO are allowed on energetic grounds. One might expect a substantial fraction of the products to appear in NO(A) and NO(B). A significant yield of NO(A) has been measured.⁷ Other factors that make the NO γ -band laser candidate attractive are its successful lasing in direct optical pumping,⁸ low-mass reactants, and availability of the basic reagents. The rate coefficient for $O + N_3 \rightarrow NO + N_2$ has been measured to be $1 \times 10^{-11} \text{ cm}^3\text{sec}^{-1}$, and measurements are underway to quantify the yield.⁷ Experiments directed toward pulsed production of the reactants in a laser cell are in progress and are expected to lead to a demonstration of a pulsed, chemically driven NO(A \rightarrow X) laser.⁷

2. Storage species/collisional transfer. Chemical production of metastable species has been shown to occur with high specificity in a few instances. The generation of metastable nitrogen molecules by means of the azide reactions $N + N_3$ or $N_3 + N_3$ is believed to be moderately specific. One specific use of this energy is through the reaction sequence



In the case of CW operation the azide radical would be produced by



Again, the reagents are lightweight and appear to be readily obtainable. Pulsed demonstration of these kinetic steps is currently being pursued.

3. Energy pooling of lower-energy species. This approach is a subset of the one above but is important enough to be highlighted. High densities of species having excitation energies greater than ~2 eV are difficult because of the greater number of collisional loss channels for higher states. This limitation on the generation of 3-4 eV species can be circumvented by pooling the energy of two long-lived, low-energy excited states.

We are examining the efficient production of NF(b) by means of:



It is possible that this reaction scheme, suggested and researched earlier by Herbelin and Cohen⁹ can be effective in existing HF chemical laser devices, such as Alpha.

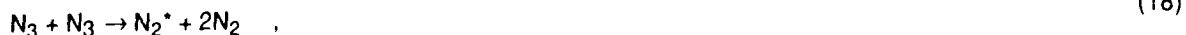
4. Pulsed, premixed reaction schemes. In order to circumvent the problem of slow fluid mixing, we are addressing the approach of initiating a chain reaction in an energetic mixture of reagents. The initiation energy, either optical or electrical, should be small compared with the chemical energy release in order that the laser system and fuel weight be acceptably low.

A hybrid chemical/excimer laser concept¹⁰ is being examined and has the following azide-based kinetic scheme occurring in premixed XeF₂/HN₃/diluent:



The chain reaction sequence is initiated by photolysis of XeF₂. This exciting concept will possibly combine the best features of chemical and excimer lasers. We expect that other reaction schemes within this hybrid category are also possible.

One other example of a pulsed SWCL candidate is one in which the lasing specie is the lead atom.¹¹ The reaction scheme is initiated by detonating solid lead azide, after which lasing would occur in the gas-phase expansion zone:



Again, the pump energy is generated by internal chemistry, but in this case, the required pump power density is reduced by virtue of the lasing specie being atomic.

A number of research groups from universities, industry, and a national laboratory have contributed to this program. Since all projects could not be specifically mentioned, the past and current participants are listed below:

Ben-Gurion University
Hercules, Inc.
Los Alamos National Laboratory
McDonnell Douglas Research Laboratory
Physical Sciences, Inc.
Rice University
Rocketdyne Division of Rockwell
Rockwell Science Center
Spectra Technologies, Inc.
SRI International
University of Denver
University of South Florida
University of Southern California

VI. Conclusions

A short-wavelength chemical laser is the Holy Grail¹² of high-performance, high-power lasers. We expect to take a large step in this quest within the next year through our current demonstration projects. A better understanding of SWCL operation and scaling relations should be the immediate outcome from this part of the SWCL program. Meanwhile, the basic research efforts will continue to germinate and nurture new concepts.

The primary impetus for pursuing this challenge is currently the large payoff expected for the high-brightness, space-laser weapon application. Other SDI missions may also be appropriate. Among these is a space-based illuminator or ground-based weapon. In this latter application, the higher efficiency that may be possible using internal chemistry in pulsed uv or visible laser concepts would be a large step in an SDI ground-based excimer laser improvement program. Finally, and also because of greater possible electrical efficiencies and the consequent reduced cost, pulsed SWCL concepts may one day be appropriate for advanced inertial confinement fusion drivers.

I would like to give a great deal of credit to the many fine researchers who have participated in this SDI research program. This program is sponsored by SDIO/T/IS and SDIO/T/DE and is managed by the Los Alamos National Laboratory.

References

1. Miller, J., these proceedings.
2. McDermott, W. E., N. R. Pchelkin, D. J. Bernard, and R. R. Bousek, Appl. Phys. Lett. 32, 469 (1978).
3. Cool, T. A., "Chemically Pumped Lasers," in Methods of Experimental Physics, Vol. 15B, C. L. Toug, ed., Ac. Press, New York (1979).
4. Malins, R. J., and D. W. Setser, J. Phys. Chem 57, 28 (1981).
5. David, S. J., and R. D. Coombe, J. Phys. Chem. 89, 5206 (1985).
6. Schmatjko, K. J., and J. Wolfrum, Ber. Bunsenges Phys. Chem. 82, 419 (1978).
7. Coombe, R. D., private communication.
8. Burrows, M. D., S. L. Baughcum, and R. C. Oldenborg, Appl. Phys. Lett. 46, 22 (1985).
9. Herbelin, J. M., and N. Cohen, Chem. Phys. Lett. 20, 603 (1973).
10. Mead, R. D., et al, Proceedings of SPIE Meeting, Conference on Short-Wavelength Lasers, 1988.
11. Bar, I., et al., ibid.
12. Marquet, L. C., not-so-private communication.

Advances in Laser Technology for Strategic Defense

J. H. Hammond, Neil Griff, R. L. Gullickson, B. J. Pierce, E. W. Pogue
Strategic Defense Initiative Organization, Washington, D. C.

Summary

Advances in laser and optics technology have enhanced the prospects for directed energy applications in strategic defense. We will describe progress in developing high brightness chemical, excimer, and free electron lasers and their associated beam control elements.

Chemical lasers represent our most mature high brightness laser technology. The ability of such systems to operate continuously at high power in the mid infrared (3.8 microns) with good beam quality has been demonstrated by the "MIRACL" chemical laser located at the White Sands Missile Range. MIRACL has now been successfully integrated with a 1.5 meter beam director and local loop adaptive optical system for improved beam quality. The Alpha HF chemical laser system is now being assembled. It will demonstrate the ability of a chemical laser system designed for space operation to operate at high power with good beam quality at 2.7 microns. The ability to improve beam quality through phase conjugation using stimulated Brillouin scattering has been demonstrated for pulsed chemical lasers, with substantial recent experimental evidence that continuous operation is possible.

Excimer lasers represent our most mature short wavelength laser candidate. We have demonstrated single pulse technology with pulse energies greater than a kilojoule and excellent beam quality using a Raman amplifier technique. The ability to operate the pulsed power technology for high power excimers was recently demonstrated at 100 Hz. These elements — high average power, excellent beam quality using Raman amplifiers — will be demonstrated by the EMRLD device operating with XeF at a (Raman shifted) wavelength of 411 nm.

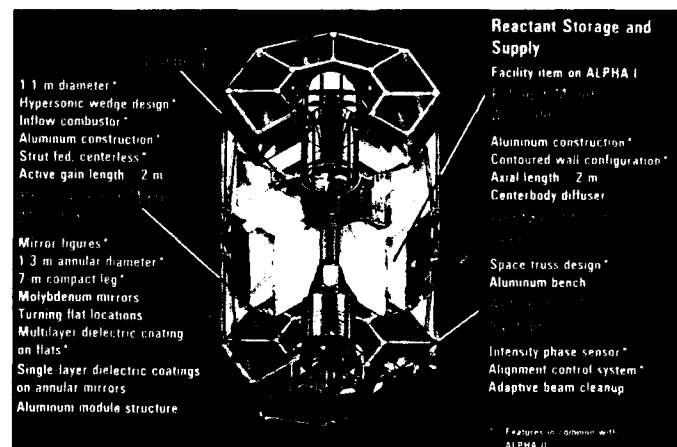
Free electron lasers represent a promising technology for ground and space applications. High current devices driven by induction linear accelerators have demonstrated extremely high efficiencies operating as amplifiers at microwave wavelengths. Recently, operation of these devices has been extended to 10.6 microns using the 50 MeV Advanced Test Accelerator. Two radiofrequency linear accelerator driven FELs have recently lased at 0.5 microns using respectively the superconducting accelerator (in a double pass recirculation mode) at Stanford and the new 120 MeV device at Boeing.

Chemical Laser Technology [1]

Figure 1: Several characteristics of the HF chemical laser make it ideally suited to operation in space. The device converts chemical energy directly to laser energy, so no external source of power is required. The large vacuum pumps required on the ground to exhaust the reactants while maintaining a low pressure in the reaction and lasing zone are replaced by the vacuum of space. The simple gain generator permitted by these attributes improves reliability.

The upper lasing level is an excited vibrational state of the HF molecule. Atomic fluorine is produced by the combustion of NF₃ with deuterium, seeded with atomic fluorine to initiate the process. The atomic fluorine produced by the combustion process reacts with hydrogen in a supersonic flow field. The combination of excited state lifetime and flow velocity provides an annular gain region several cm thick.

Key technologies for space-based HF chemical lasers will be validated with the Alpha I laser, a multi-megawatt device now being integrated and tested by TRW. The gain generator and optics are cylindrical, not linear, a geometry which is more convenient for launch and operation in space, and which simplifies scaling to higher powers.

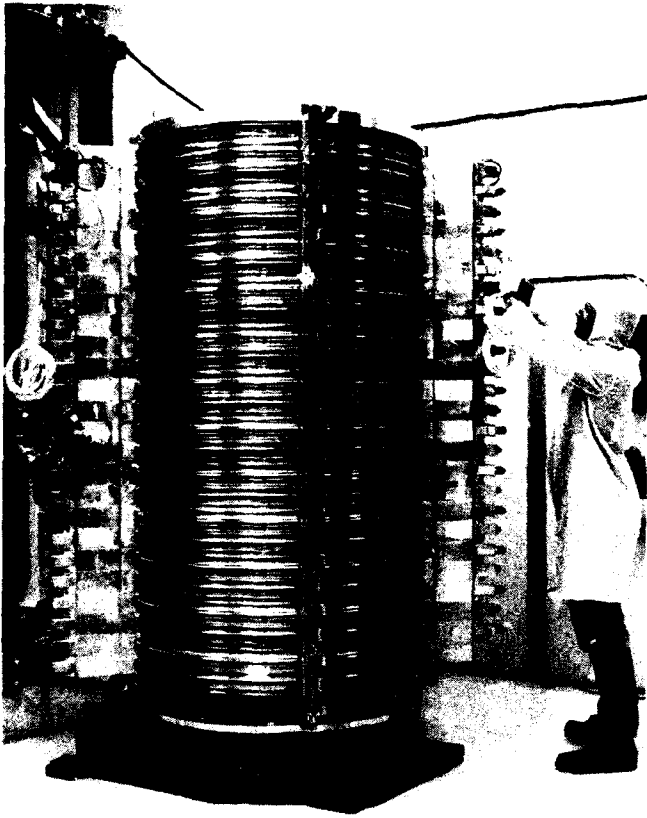


The Alpha HF Chemical Laser Device
Figure 1

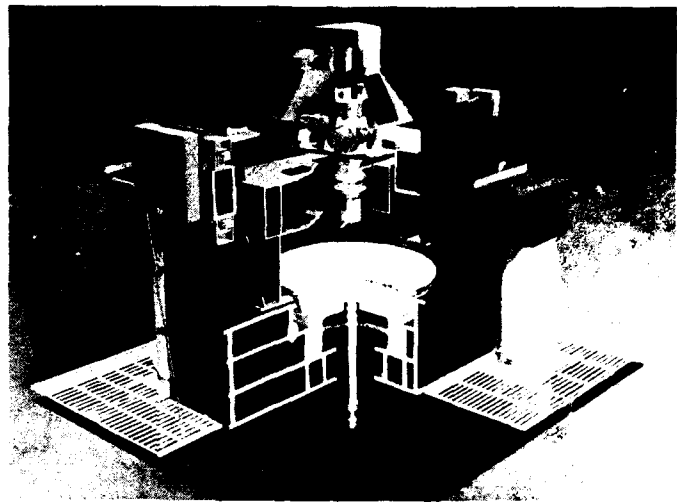
Figure 2: The two meter long cylindrical gain generator is shown here. It uses large (in comparison to the fine scale mixing nozzle used in the Mid Infrared Chemical Laser (MIRACL)) hypersonic wedge nozzle technology. [1] The use of these large nozzles is made possible by the low pressure exhaust conditions natural for space laser operation. The gain generator consists of 27 rings 1.1 m in diameter and 7.5 cm long. The nozzle rings are formed of extruded aluminum for affordability and ease of construction.

Figure 3: The optics for the cylindrical resonator design were produced at the Lawrence Livermore National Laboratory on a machine designed specifically for that purpose — the Large Optics Diamond Turning Machine (LODTM). LODTM can machine metal optics with cylindrical symmetry with diameters up to 1.5 m with a surface figure precision of $\lambda/100$. The high extraction decentered annular ring resonator produces uniform loading on optical surfaces and reduces sensitivity to aberrations.

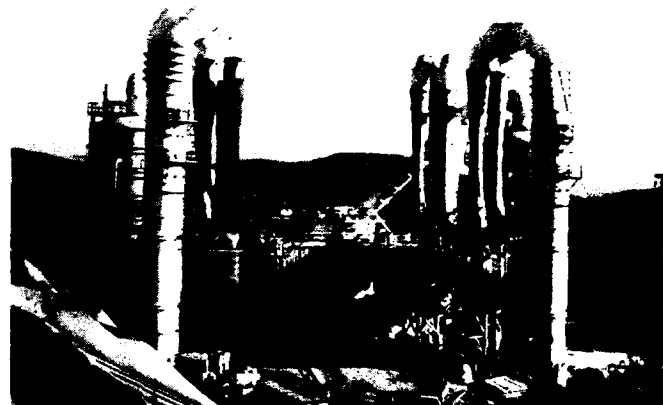
Figure 4: The large test facility required to reproduce the vacuum pumping capabilities of space is shown here. The steam ejectors must maintain a few Torr of vacuum for many seconds of device operation.



Alpha Gain Generator
Figure 2



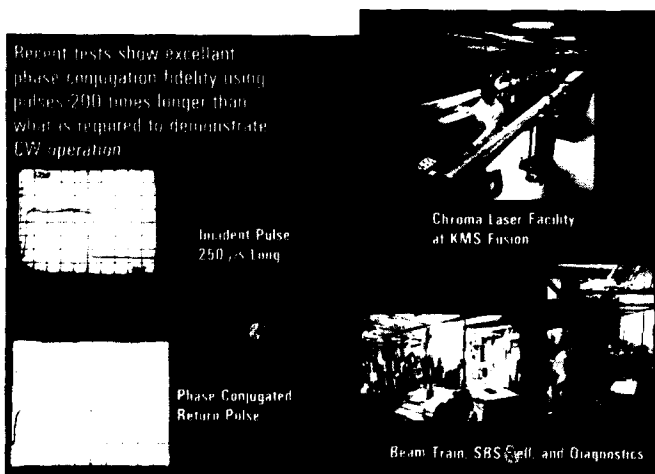
Large Optics Diamond Turning Machine
Figure 3



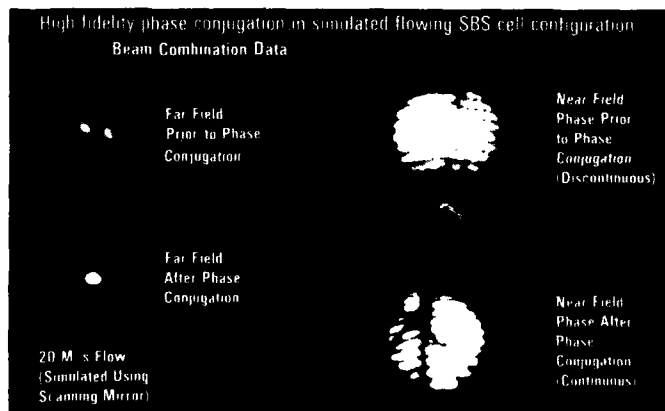
Alpha Facility
Figure 4

Figure 5: In order to study some of the issues regarding extension of the pulsed data to the CW regime, experiments were also carried out using the Chroma laser at KMS Fusion. Pulses were stretched to durations well beyond the decay time of the phonon scattering grating in the conjugating medium, high-pressure xenon (Chroma produced 170j, 150 usec pulses at 1.06 microns). This figure shows that excellent conjugation fidelity was maintained throughout the pulse.

Figure 6: The use of a flowing conjugation medium is essential to use of SBS with very high power CW beams, so the effects of relative motion between the wavefront and the conjugating medium were studied by sweeping the Chroma beam across a stationary SBS cell. The results confirm the concept for relative velocities of 10s of meters per second.



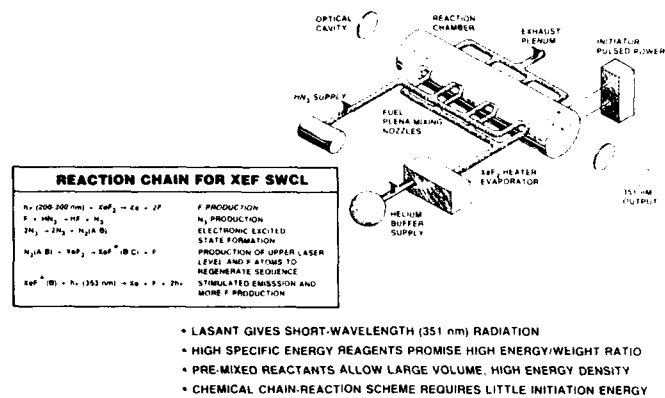
The Apache Long Pulse Experiments
Figure 5



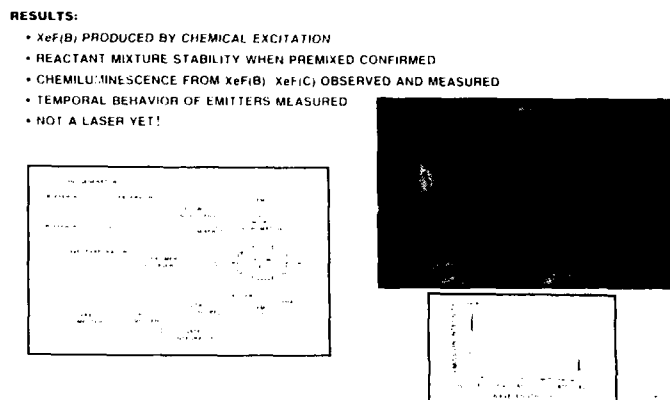
Results of the Long Pulse Experiments
Figure 6

Figure 7: SDIO is also investigating chemical lasers operating at shorter wavelengths. Figure 7 shows one example of such a concept. A light pulse triggers a chemical reaction in XeF₂ which produces atomic fluorine. In a five step reaction, an electronically excited nitrogen molecule transfers energy through collisions with XeF, a well studied excimer laser molecule. This approach provides short wavelength, high energy density, high fuel efficiency, with little initiation energy.

Figure 8: Spectra Technology has demonstrated the production of excited XeF by the optically initiated chemical reaction. They have confirmed the reactant stability of the premixed gases, and measured the chemiluminescence from several excited states of XeF as a function of time. However, this system has not yet operated with a resonator.



Chemical-Excimer Laser Concept
Figure 7



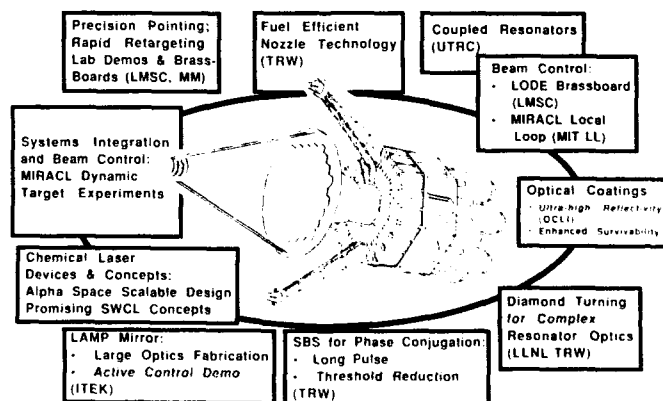
Chemical-Excimer Laser Status
Figure 8

Figure 9: Large optics is a critical technology for high energy lasers. The LAMP mirror, built by ITEK, is 4 m in diameter with active control. The mirror consists of seven segments of 17 mm thick ultra low expansion glass mounted on a graphite epoxy substate. Each segment can be independently positioned to control vibration. Fine figure actuators on each segment compensate for thermal distortion. All seven segments are now in position on the LAMP mirror. Closed loop control of the figure of the mirror segments has now been demonstrated using a low power helium neon laser in an interferometric configuration. The next step is to demonstrate segment phasing.



Large Active Mirror Program
Figure 9

Figure 10 summarizes the advances in space based chemical laser technology.



Summary of SBL Progress
Figure 10

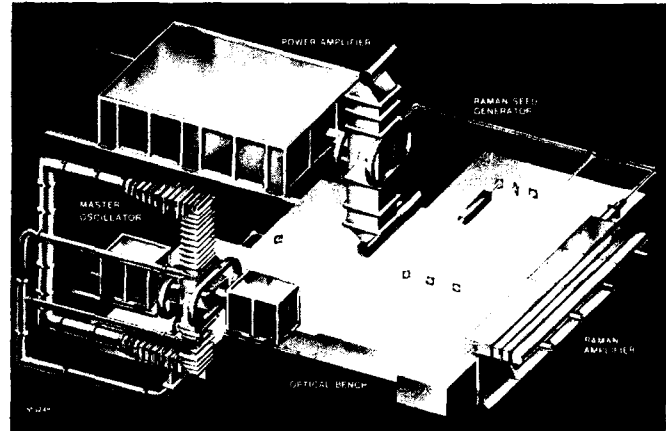
The Excimer Laser

The discharge excimer laser is a candidate for SDI applications as a reference source (beacon) for atmospheric compensation, UV ladars, illuminators for imaging space objects, designators for homing kinetic kill vehicles, optical guiding of electron beams, oscillators for FELs, and as a coherent source for Raman scattering experiments.

In the discharge excimer laser, x-rays preionize a gas consisting of rare gas halide molecules, producing a plasma. A high voltage discharge is sustained in the plasma, resulting in the excitation of the laser medium by electron collisions. The current state-of-the-art in discharge excimers is represented by the Highlight laser at Northrup. It has produced 100 j/pulse at 100 Hz. A four pulse burst has operated at up to 2 kHz rates. The beam quality is better than 2XDL.

Phase conjugation through nonlinear optics is already being used routinely in a discharge excimer laser. H. Komine at Northrup uses a static SF₆ cell at 10 atmospheres to compensate for thermal distortions in the gain medium [2]. The amplifier produces 1 J per pulse and operates at 2 Hz. With phase conjugation, the amplified beam quality improves from 2.4 to 1.4 with approximately three times more energy in the far field spot.

Figure 11: The electron beam pumped excimer laser represents SDIO's most mature short wavelength high power laser candidate. The state-of-the-art of our excimer technology is typified by the EMRLD excimer laser now being constructed by AVCO at the White Sands Missile Range. EMRLD consists of a closed flow loop master oscillator, open loop power amplifier, and Raman amplifier. EMRLD produces 100 pulses per second and operates with XeF at the Raman shifted wavelength of 411 nm.



EMRLD
Figure 11

The Raman amplifier configuration offers the advantage of combining the high beam quality of the master oscillator with the high power of the low beam quality amplifier. The high Fresnel number of the excimer laser configuration also facilitates adaptive optics for atmospheric compensation. The adaptive optical components can be installed after the master oscillator where the power levels are still low. The imposed phase on the wavefront is then amplified with a minimum of distortion.

Figure 12: The ability to perform phase conjugation using adaptive optics in a Raman look-through configuration has been recently demonstrated by AVCO and MIT Lincoln Lab. Using the Scale-Up excimer laser operating with XeF and producing 170 j per pulse, the 69 channel deformable mirror built by MIT Lincoln Lab was used to improve the beam brightness by a factor of 30. [3]

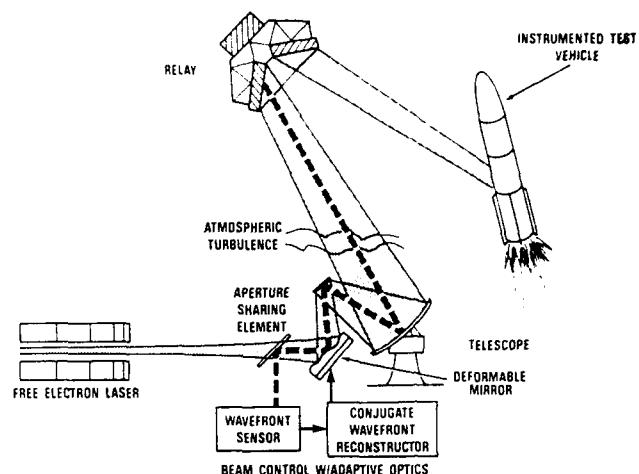


The EMRLD master oscillator is now being assembled. First light is expected in January, 1988. A megavolt gas blown spark gas switch was demonstrated at 100 Hz as a part of the EMRLD program. The ability of the MO to operate with high beam quality has also been confirmed. The Raman Beam Quality design verification test showed the ability of the Raman amplification process to combine the favorable beam quality of the master oscillator with the high power of the amplifier. The transient refractive index test unit examined the modification of the refractive index of the laser unit as a function of gain. The kinetics data base experiment examined the effect of different gas mixtures upon the laser gain and beam quality.

Raman Look-Through Demonstrated
Figure 12

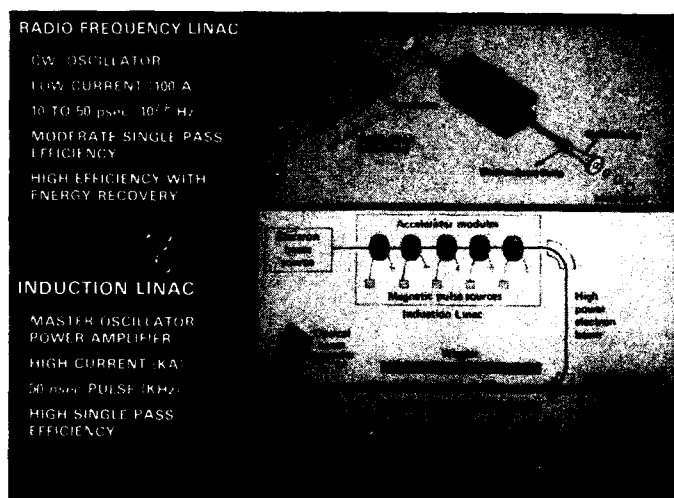
Free Electron Laser Technology [4, 5]

The Ground Based Free Electron Laser Experiment, shown in figure 13, will demonstrate the major land based elements of a ground based laser system. These elements include the laser device, beam control system, and atmospheric propagation capability. After demonstrating high power operation with high beam quality in the early 90's, this system will be used with a space relay mirror for a high power relay demonstration. Near term experiments will demonstrate relay mirror technology for low power lasers in the Relay Mirror Experiment (RME), to be deployed into a 400+ km orbit in 1988. RME will demonstrate the tracking of two ground based argon ion laser beams and the relay to a ground target of a pulsed Nd:YAG laser.

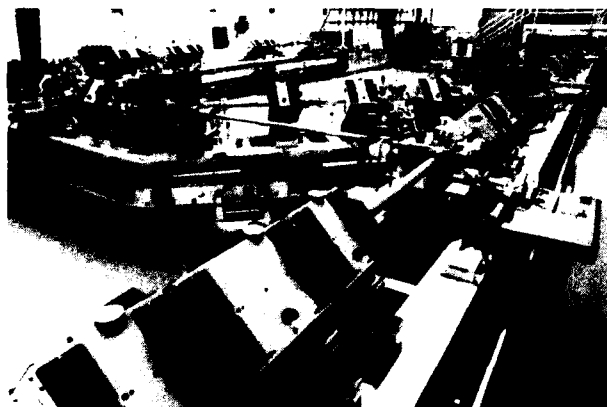


Ground Based Free Electron Laser Experiment
Figure 13

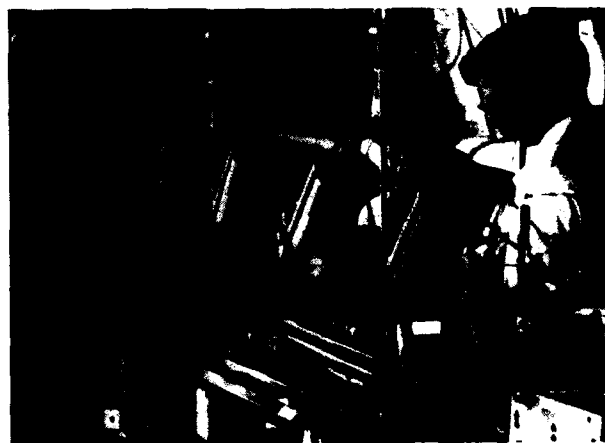
Figure 14 shows the parallel approaches for the ground based free electron laser program. The radio frequency linac approach offers a pulse format of closely spaced micropulses. This pulse format may offer atmospheric propagation advantages with lower losses to stimulated Raman scattering from rotational levels in nitrogen molecules. High efficiency is possible using energy recovery. Both oscillator and master oscillator power amplifier configurations should be possible. In two separate experiments at Stanford, with TRW [figure 15a]; and at Boeing [figure 15b], RF FELs have lased at 0.5 microns. The light weight accelerator cavities of the RF FEL also make this device promising as a space based laser. The use of superconducting cavities offers the promise of very compact accelerators with high current capability for space.



Parallel FEL Approaches
Figure 14

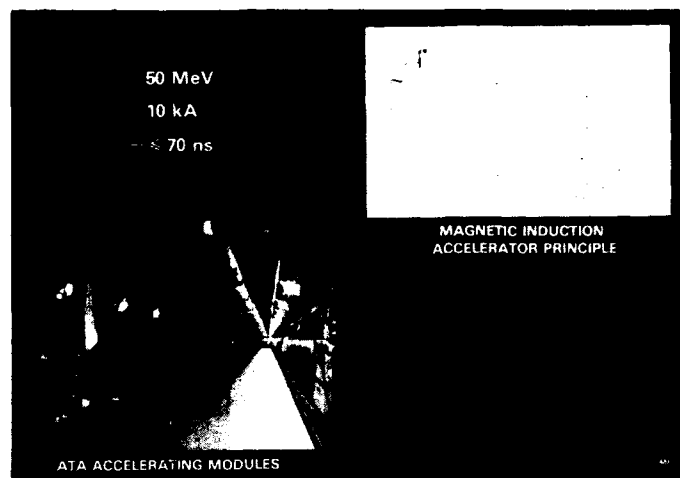


Radiofrequency Linac FEL at Boeing
Figure 15a



TRW/Stanford Superconducting FEL Achieves Visible Lasing
Figure 15b

The other approach is the high current induction linac. This produces longer pulses with a lower repetition rate. The high current (several kiloamps) possible with this approach lends itself to master oscillator power amplifier (MOPA) configurations. Induction linacs have produced extremely high efficiencies at cm wavelengths and have demonstrated high gain at wavelengths ranging from 9 mm to 10.6 microns. Figure 15c shows the 50 MeV Advanced Test Accelerator at LLNL used with currents of up to 2 kA for FEL experiments.

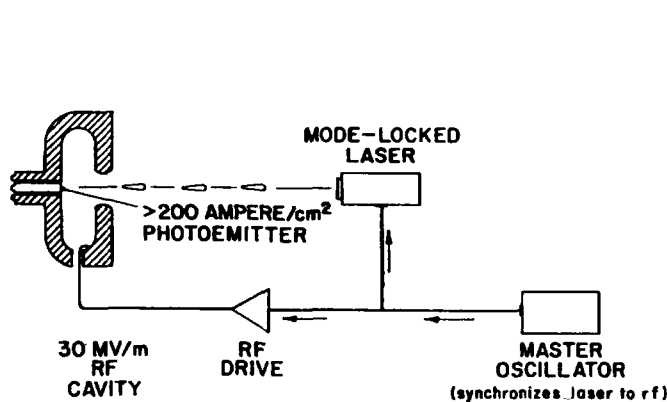


Advanced Test Accelerator Induction Linac
Figure 15c

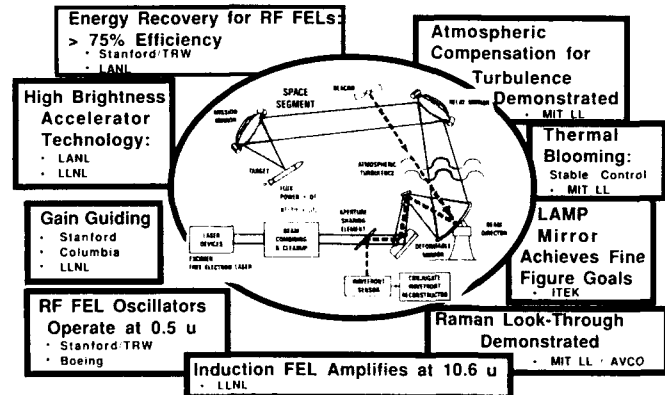
The goals of the current induction linac "Paladin" experiment, using ATA with wiggler lengths of up to 25 m, are to extend the high efficiency operation to the 10.6 micron wavelength and to demonstrate that refractive and gain guiding effects in intense electron beams can guide the amplified electromagnetic wave to reduce diffractive spreading in long wigglers. Preliminary results at LLNL suggest that gain guiding does occur in induction linac FELs as demonstrated earlier at Stanford (with a low current rf device) and at Columbia (using a low voltage diode machine.) [6]

Technology advanced have brought induction and RF linac operating characteristics closer together. The development of magnetic modulator technology to replace gas blown spark gas switches has allowed operation at higher repetition rate. Figure 16 shows a technology developed at LANL for FEL injectors which allows RF linacs to operate with higher current [5]. A doubled Nd:YAG laser causes photoemission of a high current electron pulse from a cathode. This bunch is accelerated to MV potential in a single step, reducing emittance growth. With this approach, not every micropulse is filled with electrons. This results in higher peak currents allowing high gain and operation in a MOPA configuration.

Figure 17 summarizes progress in ground based laser development.



Photoinjector for RF FEL
Figure 16



Summary of GBL Progress
Figure 17

Conclusions

Substantial progress has occurred in high power laser development. For chemical lasers, the ability to perform phase conjugation using nonlinear optics techniques may have a profound effect on the ability to phase together laser devices and may permit significant relaxation of optical tolerances.

Nonlinear optics has also been important for excimer lasers. The demonstration of phase preservation using the Raman look-through technique for an adaptive optical system has confirmed one of the main advantages of the excimer as a ground based laser candidate — the ability to perform atmospheric compensation on the low power oscillator.

All of our major FEL candidates have taken important steps toward demonstrating feasibility. Two different types of RF FELs have lased near 0.5 microns. The induction linac approach has demonstrated gain at 10.6 microns with a 15 m wiggler and verified code predictions. Several experiments have demonstrated gain guiding.

By the next International Conference on Lasers in 1988 several major SDIO high power laser facilities — Alpha and EMRLD — should have produced first light and provided substantial operating experience.

References

1. Joseph Miller, "High Power Hydrogen Fluoride Chemical Lasers: Power Scaling and Beam Quality," proceedings of this conference. Neil Griff and Douglas Kline, "Space Based Lasers for Ballistic Missile Defense," proceedings of this conference.
2. H. Komine, "Phase Conjugated XeCl Discharge Laser Amplification," Proc. of the Workshop on Nonlinear Optical Techniques for SDI Applications, October 28-31, 1986, published by W. J. Schafer Associates, Albuquerque, NM.
3. B. W. Nicholson, J. A. Russell, D. W. Trainor, T. Roberts, C. Higgs, "Phase Preservation in High Gain Raman Amplification," proceedings of this conference.
4. Proc. of the 1987 Particle Accelerator Conference, IEEE Conference Record. See invited papers by S. Penner on RF linac FELs and by R. Briggs on induction linac FELs.
5. Proc. of the 1987 Conference on Free Electron Lasers, Williamsburg, VA, (held September, 1987).
6. E. T. Scharlemann, "Free-Electron Laser Amplifiers," Draft LLNL UCRL Report, 26 October 1987.

"PANEL DISCUSSION"

MATURITY OF LASER TECHNOLOGY FOR STRATEGIC DEFENSE
DECEMBER 9, 1987, HARVEY'S RESORT HOTEL, LAKE TAHOE, NEVADA

Prof. Sproull:

We are blessed with a group of distinguished speakers this afternoon to discuss "The Maturity of Laser Technology for Strategic Defense". Now maturity is a value-laden word. It is pejorative at both ends. Mature implies closed-ended, not going anywhere. Immature implies brash, incompetent, and not able to perform as required. I guess the only positive way to come out would be something like rapidly maturing, still open-ended, but not overstating achievement.

Well, we shall see whether we come out at one end or the other or in the middle. Strategic defense is probably the most challenging mission of our generation. It demands the utmost from the development of a host of technologies. Laser technology is obviously prominent among them. Indeed it was the spectacular development of lasers that was primarily responsible for bringing strategic defense forward from the back burner position it occupied in the 1960's. The most eloquent reasons for revisiting strategic defense after 20 years were the achievements in laser technology. Now, whenever science and engineering have invaded extreme regions, fascinating new science has been learned and discoveries have been made. Ultra high temperatures, ultra low temperatures, ultra high power densities, ultra high electric or magnetic fields, ultra short times - any of these extreme regions has developed a host of new sciences and new discoveries. A little different kind of extreme is the extreme limit of accuracies, of gyros and accelerometers permitting an accuracy of inertial navigation that was unimaginable a generation ago. Another somewhat different kind of extreme is the extreme complexity of battle management and command control and communication when millions of objects are involved. So we can expect technologies to be challenged to the limit and we can expect discoveries and the development of new science and technology.

The laser technology related to strategic defense partakes of this stimulation by extremes. The most obvious and publicized rule is the boost and post boost intercept involving ultra powerful beams focused and agilely steered over distances like ten thousand kilometers. But lasers probably enter in vital roles in the discrimination and communication roles as well. These may be even more important in the near terms and are also highly stressing challenges to the technology.

Now to turn to our first speaker. I ask for your indulgence in a slight change in order to group the second, third and fourth talks together. I'd like to turn first then to Dr. Leon Goldman. Since the program was written he has changed affiliations. He is now with the Naval Hospital in San Diego, an expert in the use of lasers and various applications especially cancer phototherapy. Dr. Goldman.

Dr. Goldman:

My excuse, as a refractory gerontologist, and the least mature and the least informed on this Maturity of Laser Technology for Strategic Defense discussion, is that in laser medicine and laser surgery we view, what you all now call the mysterious photon, as a diagnostic and treatment modality. This very long sentence does not show our increasing impatience to go beyond our current faithful laser systems and to advance to other systems in order to deliver better health care. Nowhere in the present or in the immediate future at home or abroad is there an extensive, detailed, hopefully basic laser research as in SDI. For some time, before my departure to the Navy, I had condemned academia for their neglect of basic laser research in their public desire for uninformed and definitely unstudied politically biased polemics. Further, as laser experts, we should study in detail anything related to the defense of our country. We should read in detail and critically, not just quote from, the tough job of the APS report of Kumar Patel and Nicholas Floemergen and their associates. If it is possible we should plan to do bench work, not just library work, in the laboratory of SDI. For me, there is no SDI funding obligation, quite the contrary. With our experience from the Laser Laboratory for the Columbia C astronaut flight of January 12-18, 1986, a proposal was submitted to SDI for laser safety in space. In common with many of our laser proposals since 1961, this one on laser safety, was promptly rejected. Thus, I am here without any prejudice at all of any sort. (Laughter)

Our concerns for laser systems relate to the deployment of the new laser systems of SDI, to the laser medical research laboratory - and with due regard to our present economic environment - to the ambulatory surgical center, and the hospital operating rooms. If you

are not aware, laser surgery, when indicated, emphasizes medical cost savings through more out-patient facilities. To us, then, the spin-offs of laser SDI are:

1. New Laser Systems - excimer, chemical, FEL, and x-ray; systems, whether ground or space based, all have definite biomedical applications especially from the so-called small laser systems group of SDI
2. Super Computers
3. SDI communications and information handling technologies
4. Optics research, especially in adaptive lenses and fiber optics systems
5. The philosophy of cross fertilization which SDI endorses; this means physicists and engineers working actively with biologists and physicians

Also, in laser biomedicine, we definitely do not believe in the Chatham-Gulch Law that "New Lasers Never Work".

Now, what about the specific laser systems of SDI? In spite of SDI's interest in high output systems and not in 193 nm excimers, basic SDI research for excimers will help in the development of higher outputs, fiber optics, optical phase conjugation applications and perhaps even more about the concerns of mutagenesis and carcinogenesis which are very important, especially to the Food and Drug Administration in the U.S.A. Apparently, these concerns are not important to eye patients in Paris and also not to the military and to industry. With the new progress in excimer lasers shattering kidney and gall bladder stones, called the lithotripsy, basic research will help considerably in this area. TEA, superpulsed and Q-switched CO₂ lasers and also Er:YAG, even with its very fragile zirconium fluoride fibers, are now considered as "safer" rivals to excimer lasers in medicine.

It is time for laser medicine and surgery to become interested in the highly efficient chemical lasers of SDI. Not so much the powerful Alpha Project, but for safer instruments where a portable eye irrigator will not have to be placed next to the laser. So, the iodine is considered as again, a "safer rival" to the HF laser; it is portable and self contained; there not rapidly weakening chemicals as with many dyes, and good controls are to be considered. Also, shorter wavelength research and even harmonic generation are to be considered. Since there has been so much effective progress in the physics of chemical lasers in the past 18 months, consequently, and hopefully, there will be help also for the biomedical phase.

The recent increase in the biomedical R & D of FEL is very encouraging to our FEL committee of the American Society of Laser Medicine and Surgery of many years ago. We did dream of tuning all the way from microwaves to x-ray. The biomedical research with Straight, under the directions of Maday at Stanford, the detailed biomedical plans at Dallas, especially for PDT (photodynamic therapy) and the program at Vanderbilt all point to great dreams in the future for FEL, again primarily from the developments in SDI. Noted medical centers in the U.S.A., now there are at least five, will have operating units to determine whether a high output single precise tunable laser installation will answer all the needs from diagnostic phases, like PDT, to treatment facilities all from our dream of a single biomedical laser instrument. SDI already has demonstrated microwaves from FEL. Now we await new additional wavelengths from FEL besides IR. With the help and repeated annoyances to Dennis Matthews of Lawrence Livermore Laboratory, we have seen possible biomedical applications of their famed laboratory x-ray, other than x-ray holography.

Certainly, at present we can not speculate, in contrast to others, quite foolishly, that the laser x-ray is not ready to do away with the hospital x-ray division. With tissue cultures, with fresh slices of human tissues and our cooperative veterinary patients, we would suggest laboratory x-ray laser spin-off research in:

1. Cancer
2. Mutagenesis
3. Immunology
4. Photosynthesis
5. Isotope development in vivo
6. Micro x-ray diffraction studies in vivo

The problem is, "Can the cost of the x-ray laser individual impacts justify such cancer research at the cellular level at present?"

Super computers will have a definite role in the very rapid information gathering material, not only in the medical center, but also for the distant provision of medical care. Also, with precisions and rapidity, this will include computer programming for laser diagnostic and laser surgical procedures. Now, what does this laser movement in SDI, from

physics in the laboratory to the engineering world mean? It has been said that "the engineer can do for \$1 which any damn fool can do for \$2."

The greatest diagnostic medical instrument we have today is MRI (Magnetic Resonance Imagery). There are no x-ray concerns here, only powerful magnetic fields. We would like to have lasers make the imagery of MRI holographic. We would like laser spectroscopy determine the function of organs in MRI, the diagnostic of cancer according to Alfano, and the spread of cancer. We would like to have MRI show movement and with precision, which parts of the heart have adequate blood flow and which do not. We would like optical phase conjugation to be used in cancer diagnosis for early detection, even at microscopic level. Optical phase conjugation can be used for precise eye surgery as Stewart has suggested.

Now the unborn child can have examinations done with safety, under MRI. If instruments, called fetoscopes can be used inside the carrying mother for diagnosis and treatment, then laser fiberoptics can also be so used with much more precision and more efficient uses. Can we use lasers at chromosome level, as Berns has shown us to do biomedical engineering surgery for abnormal defects at chromosome level? That is possible.

Now, the laser engineers can, with SDI, help with the development of instruments going into cavities called endoscopes. These are for the lung, gastro-intestinal tract, the bladder, the gall bladder, the heart and blood vessels. With the new developments, including optical phase conjugation, there can be improvements even for the famed endoscope of MIT with its 19 optical fiber computer programmed heart for blood vessel diagnosis and treatment. This is the immediate great challenge for the need of man and the development for the medical laser market for the immediate future.

We need special laser diagnostic centers for the new area of laser non-surgical diagnosis and even medical treatment. This so-called "pure" laser medicine includes basic laser photobiography, Doppler circulation studies, immunology, exogenous chromophores for diagnosis and treatment beyond the ordinary endogenous chromophores that the body has. Endogenous chromophores are pigments which the body has, such as hemin of the red cells and melanin of skin color. It is the endogenous chromophores which make for specific local reactions with lasers 400-700 nm.

New instruments with new photons, again for diagnosis and treatment, make for the deliverance of better medical care. We can do this now in the real world, especially with the help of SDI. We in medicine can do this for the entire real world so that the have-not non-participants of SDI R & D in Europe and Asia do not feel that the U.S.A. and its allies have the only exclusive use of the evident spin-offs from SDI, for the good of man. We feel also that this interest in the biomedical applications from SDI is not premature or foolishly over enthusiastic. Again and again for the deliverance of better medical are we need more and more of those fabulous photons. (Applause).

Prof. Sproull:

Thank you very much. As I mentioned before, we will defer questions and comments until all the speakers have made their presentations. The next three speakers are, to a certain extent, a set, and we'll start with Jack Hammond whom you heard this morning. He is a physicist directing the Directed Energy Program at SDIO.

Dr. Hammond:

Thank you. Well, since we are a set, I'll try to keep my mark somewhat to a minimum here, the subject being "The Maturity of Laser Technology for Strategic Defense". First, I would like very much to say, and it is one of my major points, that this is a complicated issue - it's clearly one which we're constantly confronted with in the conduct of the SDI program. It is also one which I think is deserving of a very vigorous and informed public debate and one which I think deserves a bit of work on the debaters because it is a complicated issue. It's complicated because you have to understand several things. First, you have to understand which technologies we have in our set of tools to work with for SDI applications. You have to understand what their status is, both in terms of the physics reality, as well as how far they've been engineered. You have to understand clearly what you're trying to do and it's not just necessarily one mission that you're trying.

You're trying to do a range of missions. And finally, you have to understand what remains to be done in terms of new physics, and for the more mature system, what is required to be done in terms of engineering - how long that engineering will take or how long is it projected to take. Considering these elements, let's at least look at the first two and say, "What do we have as candidates?" and "What is their status?"

I think this type of meeting is a very excellent example of the increasing ability to get that sort of information for forming opinions. The extent to which we're able to talk

about the status of the technology in the open, without running into classification has been helped a lot by the fact that we have tried to formulate very precise classification guides to encourage publication as long as it does not violate national security interests. We've tried to cooperate within SDI with organizations, such as the APS, who have done a very excellent job in identifying what issues do exist. We may take issue with them on maturity and some of the specifics with the numbers but at least there is a very good compendium for looking at what exists and what some of the issues are.

Let me now turn to the second issue; I'll come back to the technologies we have in hand and what I think the status is. And certainly the status will be addressed by the next two speakers following me. But let me turn for a minute to the issue of what are we trying to do with lasers and what, in fact, SDI is trying to do, and to summarize very quickly what has been debated quite a bit in the press and elsewhere. Over the last six months or so, the DOD has been involved in a defense acquisition board review of the SDI program. The upshot of all of that is we have looked very carefully at several aspects of what SDI can do and what tools we need to do it. We've identified a phase I system architecture with candidate sub-elements and we've looked at follow-on systems that could be used as the threat grows. And when I say threat I mean that in a very detailed sense.

We have really looked at what is the current threat, the slower boosters which tend to give kinetic energy weapons longer times to do their job with their finite fly out times. We have also looked at how soon that threat may give way to faster busing and faster burn boosters - what the implications of mobile types of boosters might be - and we have tried to look at how that threat evolves and how the technologies which we can apply to addressing that responsive threat need to evolve. And there is understanding among the threat community and DOD in general, as to the need for looking both at near term technologies such as kinetic energy and far term technologies such as lasers. And looking at not only that but how lasers and some of the advanced technologies at say lower power levels play in the early phases, in the Phase I type of architecture. We have not made any decision to deploy any system. We have made a decision to accelerate certain of the sub-elements into a demonstration validation phase.

Well, at any rate, that's merely to say that we have looked at where lasers may play and we've looked at that with a considerable amount of detail. Let me just speak about what we have in the laser world and how might it play against those missions. As time progresses, there is a role in the fairly near term for illumination lasers, laser radars for discrimination - those types of technologies that I mentioned briefly this morning. And many of the technologies that you heard discussed in specific papers here play in those early phases. And there's not much engineering required for many of those systems. But, it is basically an engineering issue and those systems come along first. In terms of the follow-on systems, that is, the speed of light weapons systems, such as my office works on, we again have a range of technologies available ranging from chemical lasers, which in many ways are more mature. I think those will be addressed by Dr. Miller. I'll throw up a couple of slides since we're on video tape here and at least get the machine set up with these slides.

The lamp mirror is now complete. I unfortunately don't have the slide with me on my person at this time with all of the segments in place. But it is typical of the types of technologies being worked on for space based chemical lasers, that is a technology which has been under the development since the early to mid 70's and can furnish through the use of mirror technology - adaptive mirror technology such as this - which we pretty much have in hand and are able to scale up to brightness levels for initial application - that is to augment say for example, kinetic energy weapons systems. We're able to scale this optics technology - technology like that under development with the Alpha Laser program - annular resonator configurations for chemical lasers as quickly as any of the other technologies that we have in hand for high power applications.

I hesitate to say at the other end of the scale - lest they think that it's putting Dr. Briggs in a precarious position - and I even used an RF accelerator to typify the FEL. He claims that's at the other end of the scale. He works on another type of accelerator called induction Linacs. But here you can see sort of the state of the art in free electron lasers. This gives you more power on the ground and you don't have problems with space expendable fuels for the lasers. The mirrors are in space - the lasers aren't. This sort of laser looks more like a laboratory device. It is not a high average power device. It's looking at physics issues. So that's at the other end of the development scale. So to very quickly end up my points, I want say that maturity is a complicated issue - it's one in which we encourage an informed public debate and it is not one that one can very quickly summarize. Thank you.

Prof. Sproull:

Thank you very much. We are very pleased and fortunate to have Joseph Miller from TRW

here.

Dr. Miller:

Hi. Without arguing exactly what maturity means, in my opinion, the high energy laser technology is far more mature at this point and time than is generally perceived by the general public or even the technical community at large. In my opinion, we're building on a base of experience that's over twenty years old at this point and time. The first very high power lasers really came on line in the 1960's, those were the carbon dioxide gas dynamic lasers and electrical lasers. And although we're not working with that kind of laser now, we have used a great deal of the experience based on what was developed at that point and time.

Those lasers taught us how to build combusters and diffusers, fluid systems. The first cool high-power mirrors were developed on those lasers and are essentially the same as those in use today. The optical resonator configurations which would give us good saturations, good extraction efficiency, good mode control and high beam quality were developed on those lasers and are essentially very similar to what we are using today. Also, the alignment systems, the isolation of gas from optical systems, the development of computer models of wave optics phenomenology that are required in the high-power lasers and the diagnostics associated with high-power lasers were developed in the 1960's.

So, quite a legacy was established in the late 60's and early 70's that was borrowed directly as we entered the development of chemical lasers. The chemical lasers have gone essentially from 100KW scale lasers to megawatt scale lasers during the 1970's. The first large chemical laser came on line in 1973 and by 1980 we were operating with megawatt scale lasers, and these high power lasers have extensive test experience.

We have studied the propagation of the beams, the retention of beam quality, the acquisition of tracking and alignment of the beams on targets, the effects on those targets, and, of course, the technologies of the lasers have advanced. Higher power densities, higher efficiencies, more practical reactants, more practical hardwares systems have been developed. By the 80's, we are now operating reliably and consistently, at MW power levels, we are addressing light weight high efficiency space laser configurations, adaptive optics and techniques to provide very fine beam quality. And high powers, are coming on line and being applied to high power lasers themselves. The lamp mirror that Jack showed you is a very large optic whose figure is controlled to a very small fraction of the wavelength of the light that we have to operate within an adaptive optic sense. The wavefront sensing and actuation of those surfaces of the Alpha laser which will be coming on line in a few months is a embodiment of a very high power, high efficiency space laser configuration.

The work that we're doing in the 1980's, is literally a third generation of these devices and, in my opinion, our high power excimer lasers and the high power free electron lasers that will be coming next, will build on, and are building on that experience base as well as their own experience in high voltage, high power systems and in very large accelerators. In addition, there are some advanced technologies coming on which have been the subject of a good part of this meeting involving non-linear optical processes, stimulated Raman scattering, stimulated Brillouin scattering and the phase conjugation properties associated with them. The background in hardware and the expertise in high power lasers are not only issues of physics, they are issues of engineering. We have for these high power lasers engineering design criteria fabrication techniques.... Jack showed early today the diamond turning machines and some of the optical components and I discussed some of that yesterday... the assembly procedures. We moved out of the physics world and into the engineering world.

The extrapolations of what is required for near term strategic defense initiative applications are: The laser power has to go up by another factor something less than a factor of ten, the projecting optics have to get larger, a few times larger, ... the point is that the work, that we have done to this point in time and with these experiments that are coming in line, literally established the engineering design criteria for those systems. It is misleading, my opinion, to characterize what's required as a very large leap, factors of tens in laser powers and factors of tens in optics, and lets square that because the brightness goes up with the square, and so we're only a hundredth or thousandth of the way there. That really is a very misleading way to characterize the state of technology at this time. We really are able to design the near terms systems in many respects right now. In addition, as we look at this growth to the robust systems of the future, we really have to look at some of the advanced technologies. In particular, these non linear optics and phase conjugation technologies are very important because the physics within the last year or two have been established to really show that you can use these technologies to go to very much higher powers, very much larger projecting optic systems by synthesizing modules and by doing it in a way that's inexpensive and reliable.

The phase conjugation technologies let you build this high power hardware at much more comfortable engineering tolerances. It lets you build things faster and make them a lot less expensive. They eliminate a lot of high precision equipment involving stabilization systems, wavefront sensing, deformable mirrors, and they lead to very practical systems. So, in my opinion, people who paint the high energy laser technology as very risky, very immature and extremely difficult, who are not really able to extend to the SDI mission and who have good technical backgrounds, are actually performing a serious disservice to the community at large. Thank you.

Prof. Sproull:

Thank you very much. Next is Dr. Briggs from Lawrence Livermore National Laboratory.

Dr. Briggs:

I think one of the first things that came over me was that somehow I had a feeling of unease about this word maturity and the chairman of this session in fact even spoke a little bit about that at the outset. And so I grab my dictionary and start looking at what maturity means and, of course, one of the first definitions that you have is the attainment of a final and desired state. I think that's what most of us sort of sense we have in mind as far as the title of this session is concerned. How close are we to that final state? But of course, not surprisingly, there are other definitions in the dictionary. And one of them is reaching a set limit of time.

You all have savings bonds and you know that maturity sometimes is ten years and you've done it. And those who have children know that by the time they get to eighteen years old they're called mature. Sometimes they are and sometimes they aren't. So really, we have to be a little careful and I guess, after reading the dictionary, that sort of left me understanding why I had a little unease. Hanging around long enough is not the real criteria for maturity. The real question that we're addressing, of course is, "What are the chances that a given technology can meet the requirements?" and "How long will it take to develop, how much money of course will it take to develop?". That's the real question. That one isn't simple either. The real requirements in general terms: I think the APS study came out with a reasonable guideline there as far as laser devices and laser systems are concerned. How long is always a question of how hard you work.

So I always have a great deal of difficulty with that because I think there are too many examples in this country that are often quoted, that once we make up our mind we want to do something and in general have more than a vague notion of how to go about it, we can do it in an amazingly short period of time. So it is often a question of the national priority, whether the objective is viewed as sound enough. And I think that the debate over SDI in large part revolves around that in my opinion, which is the political question. Do we want to do this badly enough? I think time scales can often be heavily influenced by how hard you work at it. So those are a few sort of broader comments. I'm now going to get narrow just to be specific as far as the technical audience here is concerned and talk a little bit about the FEL amplifier which is about the only laser I know a whole lot about. I'm actually a refugee from plasma physics and accelerator physics. I don't get to too many laser conferences.

The basic point that I would like to make in talking about this example is that you have to understand the development of the technology that you're trying to develop well enough, and what that development plan is before you know how close you are to developing it. It may sound like an obvious statement, but let me take this particular example and talk a little bit about it. It has been talked about here at the conference in enough depth so you can hopefully get some piece of the message as to where we are in the development plan. We need laser requirements - I'm thinking here of ground base lasers considerably in excess of ten megawatts, fairly short wave lengths and fairly good beam quality of course. In the opinion of those of us who have been working on this technology, we feel we have a very good chance of meeting these requirements.

The FEL correctly has been viewed as a potential breakthrough in technology on very fundamental grounds - its not a question of sort of the latest idea that's slightly better because of some details here and there. It's a totally different kind of way to go at it. It involves radiation from electrons in vacuum. You don't have a laser media except the electron beam itself of course. So an awful lot of the problems that limit power density, the problems that basically limit power density in real lasers, are absent here.

You can have very high gains as in klystrons, which have 70-80 db gain in the microwave regime, and people often say that FEL is an extension of sort of microwave kind of technology into the visible spectrum, which I think is a pretty accurate description. And you can get very high conversion efficiencies, of course that's for SDI. I guess that

probably would be number one on the list as to why you care. Here's a generic picture of an FEL amplifier driven by an RF induction accelerator. For those who know the details of the competition that we're engaging in here, I hope you realize that I'm giving you an ecumenical speech here that is really aimed at talking about the FEL in a broad sense.

The only differences here for the present context are minor differences in pulse format as far as power amplifier configuration is concerned and the master oscillator choices. Wavelengths for FEL scale as one over electron beam energy squared. One little pulse of electrons runs through this amplifier with one little pulse of light and it amplifies. The conversion in that little pulse would give you a peak power but which is proportional to the electron beam power which involves the current and the voltage of course.

That's about as much technical definitions as I want to make for the purposes of these remarks. For the short wavelengths, you want a lot of MeV - the accelerator size in a linear accelerator gets longer the more MeV you ask for. If I have very high voltage particles and I want to extract a fair amount of their energy, it turns out I need longer and longer wigglers if I go to higher and higher voltage. So as I scale down in wavelength as I schematically indicate here, the bad news is that shorter wavelength devices tend to be bigger systems - it's kind of intriguing inverse scaling law here of some type. But the good news is that if I build an accelerator technology, which is the power source here, that operates at the right duty factor at the outset, then for short wavelengths, the powers achieved are really quite high in amplifiers or oscillators.

The development plan with FEL's involves a whole lot of identical modules. And so of course, you develop one module when you start out - that's part of the development plan - and you can build little sections of this and learn a whole lot about it. The physics of amplification is independent of the overall pulse length and the RFP rate and so on. And we can study that physics in fairly low RFP rate devices so the present development phase is sort of carrying two things in parallel with each other - this is where we are. We're doing amplifier physics - trying to understand this basic conversion efficiency - and believing that wavelength scalability in the physics is fairly minor, which I believe we do. Many of these experiments are done at even longer wavelengths than the final desired wavelength. In parallel with that, the program is developing the right kind of very high average power electron beam accelerators which do not exist at present. That is a considerable extension of the state of the art, by the way - high brightness, high average power electron accelerators in their two basic types - RF and induction.

At the present time at our stage of maturity, there have been some very fine early experiments - Los Alamos and Math Sciences Northwest collaborating with Boeing and TRW - checking some of the physics showing that you can extract energy in a tapered wiggler, about 4-5 percent of the energy out of the electron beam. Millimeter wave experiments have shown high extraction efficiencies and high gain simultaneously. That sort of checks the physics in a very different wavelength regime. Present experiments are really trying to focus very strongly on the proof of principle that you can make this kind of efficiency and as I've said in parallel with that high power electron beams, are being developed.

The plan here is that pieces of this technology are being developed. At this time, you ask us how much power we have out in a half micron or one micron from an FEL. We are very embarrassed to give the answer because basically the development plan is such that we have to develop these pieces then, when we integrate them, they will get integrated on a fairly large scale. And that, in my opinion, can be done very credibly, at acceptable risk, in something like the early 90's, at a scale which is already beginning to be significant for SDI. Thanks.

Prof. Sproull:

Thank you very much. We turn now to Arthur Kantrowitz. I guess it's true that he is occasionally at Earthouth but in my mind he is identified as a prominent contributor over the years, at AVCO, to the gas dynamic laser and the chemical laser.

Dr. Kantrowitz:

Thank you lot. Transportation costs to low earth orbit play a dominant role in the ability of any SDI architecture to meet the Nitzze criteria. This is especially true when transportation technologies and costs are not necessarily the same for the offense and the defense.

I want to point out to you that there is one kind of transportation technology where the defense has an inherent advantage over the offense in launching stuff into orbit. And that comes from the fundamental fact that the defense can be put into place over a period of years, whereas the offense, for maximum effectiveness, requires a sudden launching of many missiles at once. Laser propulsion to earth orbit exhibits that fundamental difference.

What I'd like to explain to you is laser propulsion, how it is supposed to work, and some of the very earliest results of a program (that is being conducted under Jack, my next door neighbor here) which has just started to examine the feasibility of laser propulsion. Then I will give you some estimates. Of course, estimates come a dime a dozen. I will give you some estimates of why I think there's a chance that it really can compete with other ways of launching stuff into orbit.

I can exhibit to you an example of laser propulsion very easily and the first view graph shows something being propelled by a laser. It's a dust particle and you hit it with a strong pulsed laser and you notice two things, both of which are important. One, the particle is propelled away from the laser, but not only that, the propulsion occurs at various angles. It is not along the laser beam but it angles to the laser beam. Now, this is most of the fundamental physics, so the rest is down hill. Of course, the mechanism of this propulsion is very simple. You evaporate stuff from a dust particle. This produces a jet and that propels. Of course, the velocities that you can achieve in this way are much larger than can be achieved with chemical rocketry. As you know, the kinds of pressures that are produced are not just enough to bust this dust particle. The kinds of pressures that can be produced in this way are the largest pressures that we know how to produce, hundreds of billions of atmospheres. In laser fusion experiments they get up to those kinds of pressures. So you can produce the forces, etc. There is no question about the Newtonian kinds of physics in this business.

The next viewgraph shows the energy to orbit, and the orbital velocities - G times the radius of the earth square root of that, and so that comes out to 4 kilowatt hours per pound. As you'll see, this process has no prayer of approaching a hundred percent efficiency. As a matter of fact, what we're shooting for in this feasibility program will amount to about 2 percent efficiency. So that, instead of a four kilowatt hours, it's two hundred kilowatt hours per pound. That still isn't a lot in cost. Now, let me next show you how. When you do something like this, there's a tendency to add bells and whistles. I want to say I favor an extreme attempt, which Freeman Dyson has referred to as dogmatic, to keep it simple. And that's this four P principle, we don't have aboard except the payload propellant which will evaporate and photons, nothing else. Now, I don't believe we will maintain that orthodoxy all the way to getting stuff in orbit, but we'll try. The next slide shows how you go about getting propulsion from a laser pulse.

A is a metering pulse which evaporates propellant P for half a microsecond or so. You then allow the gas to expand until it reaches the density that you want. Then, you follow that with a strong pulse, sufficient to ignite a laser supportive detonation wave, which will heat the gas typically to temperatures on the order of ten thousand Kelvin. Notice that these are above chemical temperatures, so you can get specific impulses which are much higher than you can get out of chemical rockets. Then, the plasma absorbs the beam by a process, an ancient process known as inverse Bremsstrahlung, and creates a laser supported detonation wave which is the main heating element. That is followed by the gas expanding over a period of microseconds, three to ten microseconds typically. Then, the exhaust dissipates and we repeat this about a hundred times a second. Now, may I have the next one Charlie? This shows a vehicle which so far does not violate the four P principle.

It starts out consistent of propellant and payload and the propellant is - you can think of ice. Ice is a pretty good propellant. We will want to add two kinds of things to it. You need more structural strength than ice has unless it's very cold and you need easily ionizable materials, so that you can produce laser supported detonation waves at low temperatures. Or you need this beautiful invention that Dennis Reilly made, where you imbed in the propellant, tiny antennas, which will ignite the laser supported detonation wave. That is a beautiful thing which apparently works very well. Notice that you can get thrust at an angle to the direction which you need to get angular momentum about the laser. And That was exhibited in the dust particle experiment. In this design, you need sixty degrees, which is a large angle. But then you can get the following trajectory, which is shown in the next slide. You don't need this sixty degrees, which I don't quite like, if you use a sphere and you make the trajectory a little trickier. That is shown in the next Viewgraph.

What we do here, is, we use a sphere. The size of the sphere is proportional to the mass left and it goes up to nine hundred kilometers and out into orbit. Unfortunately, I don't have the time to do more than just one thing. To say, if you analyze this process, presuming that we will be successful in getting about 40 percent of the laser energy into thrust, then this process can become very competitive with rockets, as long as you use the system more than about three percent of the time. Its costs will go down below that of rockets. And its launching capabilities are very large, enough that a ten Megawatt laser is capable of doing about 35 shuttle launches every year, in mass, into orbit. I think that would have an impact on SDI architecture and that impact is still fully to be assessed. Thank you.

Prof. Sproull:

We turn next to Kumar Patel, who, as all of you know, is a distinguished contributor to laser physics and technology. I think one of the reasons he is here today is, also, he was the Co-Chairman of the APS study on directed energy weapons.

Dr. Patel:

Thank you. I would like to very briefly discuss some of the aspects of the APS report as they deal with only the laser technology. One of the things that I think I should point out and I think it has been lost in translation many times is that the report has already been published in "Reviews of Modern Physics" and anybody who cares to read it, will find out that the report in no place says something will not work, that in no place it says that SDI should not be followed. What it really says is that if directed energy weapons are going to be useful in strategic defense, there are certain requirements and those requirements are laid out and then those are compared with where various technologies stand. We should also remember that SDI means different things to different people - shooting down an enemy satellite is in fact a part of SDI but it is a very small part of it. The requirement of power or technical expertise is considerably less than going after a boost phase defense. What the APS report does, is it plots out a scenario where directed energy weapons are, in fact, significant contributors to an overall defense of the type that was initially envisioned as the SDI to be, not a partial defense, but a total defense.

If you back off from that requirement, you can come up with a host of low requirements and, hence, a low amount of improvements, which may be necessary. But that is getting lost in the noise, where often the requirements are changed and arguments are made that what the report is saying is wrong. What I intend to do is very briefly review. Most of you, probably, have seen or heard about this report many times, so I am not going to bore you with the gory details. But what this report does, is describe the physics, science, and engineering of various laser and other directed energy weapons technologies which include particle beams. For the purposes of the present discussion, I will talk only about lasers, beam control, and delivery. Also, I will talk something about the beam materials interaction because that tells us how much energy is needed for destroying an object and, perhaps, I will say something about acquisition tracking, only because it is a very integral part of SDI. Lasers and other directed energy weapons have a very important role to play in the acquisition tracking and discrimination.

This rather busy slide tells us where various technologies are important - I talk about boost phase and mid course in terms of the flight of a missile and the re-entry vehicles. The various issues are detection, acquisition, tracking, discrimination and destruction. One of the things you'll find out is that laser technology plays an important role in almost all phases of SDI. The only place where it does not play any significant role is in detection of a launch, probably because the amount of energy that is given out by a chemical rocket is so large, that, it can be detected without any help from anything else. But the key point is that lasers have an important role to play in almost all phases of strategic defense. Now, let's look at the question of what lasers do that deliver lethal energies at thousands of kilometers at about the velocity of light.

For kill applications, the high value targets are the boosters and the post booster vehicles, because, for the destruction of one of these, it gives you roughly ten to one advantage in terms of the targets you have killed. Of course, for the re-entry vehicles and in the mid-course, the kill application is very important. In the mid-course, the interactive discrimination and the interactive radar play a very important role. Here lasers of various types can have a significant role. Now, what is needed - the top part that you don't see. What it says is that for the boost phase application, you need sufficient power or energy to kill the ballistic missiles or kill the post-boost vehicle. You need sufficient beam quality pointing accuracy and agility to deliver lethal power over long distances in the engagement time.

The present engagement time is in the order of ten minutes, which can be shortened and will be shortened, as one faces the responsive threat, but I will not get into that. For lasers, you need optical systems for transmitting beams from a source to the target, the various kinds of telescopes or what have you. Of course, you need accurate detection and location of the booster and plume. I'll say a word or two about that because some sort of interactive radar, whether it is laser or microwave, will play an important role. In the mid course you need power to kill and you need sufficient retargeting and the ability to be able to address various targets. Also, you need a mechanism for discriminating between the reentry vehicles and the decoys. Now, the various types of lasers are chemical lasers, excimer lasers, free-electron lasers and x-ray lasers - I'm not going to say anything about the details of these lasers - you heard something about that in the earlier talks - what I'm only going to point out here is that the American Physical Society did in fact look at various lasers - looked at their physics, science, and engineering and came to some conclusions about where the various technologies stand.

Before I go to that, let me just point out that a laser destroys a target by either melting, using CW lasers or impulse loading with pulse lasers of the type that Dr. Kantrowitz just mentioned, which create tremendous pressures by surface ablation. That is one way of destroying a target. The amount of energy you need for destroying a target: for a soft target you need about 1KJ/CM², typical booster ten 10KJ, hardened targets under 100's KJ in approximate numbers for just looking at what we are going to be doing. Starting from that, you can, assuming that you have a diffraction limited beam for a given mirror size and a given distance in terms of range, figure out how much power will have to be delivered to the target for killing the target. This is for 2.8 microns assuming no losses anywhere. One of the things that you see, is making the mirror larger does, in fact, reduce the amount of energy that is needed.

One can make mirrors arbitrarily or unreasonably large to reduce the requirements on the laser. If you're a ground based laser, such as the excimer laser or the free electron laser, you still need optics in space. As was mentioned earlier, you need two sets of optics: one is a relay mirror and the second is a mission mirror as shown there. You have the uplink and the downlink. The uplink has not necessarily a problem but a complication that arises from wave front destruction as the light propagates through the atmosphere. On the downlink, you can have a potential problem of SRS if you try to reach targets too far in the atmosphere. Some of these issues are listed here for chemical lasers. The issues are space based, and large optics because of long wavelengths. Free electron lasers and excimer lasers are ground based, but you need space optics multiple ground sites and so on.

These are some of the issues that are to be addressed. Just talking about the power of the laser is not enough. Many other things have to be addressed and they are not necessarily sequential issues, but issues that have to be addressed. Nobody ever multiplies difficulties in each of these issues and says everything becomes ten times difficult. The point is that each one of the technologies has its own problems. On this slide, I list, in a rough order of magnitude, how much improvement is necessary for various lasers to be able to do the kind of job that is required in SDI and the order of magnitude improvement goes from one to many, depending upon which specific technique you talk about. There are supporting technologies, phase correction, multiple aperture telescopes, aberration corrections, and so on.

One of the things you'll notice, is that mirror coatings have reached a point where we have the kind of mirrors that you need for handling the very large powers that will be required. Getting away from lasers and talking something about supporting technologies, one of things you need regardless of what you use for destroying a target - you've got to find the target - you've got to track the missile - you've got to have precision tracking and in the mid-course you need some sort of interactive discrimination. As far as detecting the launch, it's fairly easy. The plume emission is very large, I mentioned, very bright, and to miss is impossible. The problem is not so much that you can identify a launch, the question is how you find the target in a plume. The plume tends to be enormously large compared to the target that you are trying to find and, what you need there, is some sort of interactive discrimination, using lasers or some other technique. I will just give you a couple of insights from a recent DSB Task Force report.

These conclusions are also found in the APS report. It says precision tracking is uncertain at the present time, implying that a substantial amount of work has to be done. The same is true about discrimination. There are serious questions about discrimination between the RV and anything other than the most simplest kinds of decoys.

Finally, we talk about survivability. The DSB task force talked about the space based kinetic energy vehicles and the APS report talks about other space based systems. One of the key points is that these are, in fact, very vulnerable to attack from ground based lasers during the peacetime and I think that is something that one has to worry about. What I've given you here is a very brief outline of what the report says - again, I repeat, it doesn't say something will or will not work - it does not say why SDI should or should not be pursued - what it says, in as an objective way, as possible, is that there are a number of issues which need to be addressed and whether we address them or not, is going to be determined by our desire to get to a defense that we need. Thank you very much.

Prof. Sproull:

Thank you Dr. Patel. Dr. Seka works at the University of Rochester on laser fusion on the interactions between intense pulses of laser light and plasmas.

Dr. Seka:

Thank you very much. I suppose I'm somewhat of an outsider, being from laser fusion, and not being involved in any direct SDI projects at all. As such I represent, perhaps,

more the university point of view than anybody else. I would like to talk a little bit about some aspects of the SDI program, as I see it. Then on some of the more technical problems that I see, and, finally, address some of the problems that are outside purely technical ones. Most of the technical problems have already been addressed both here and during the last several days. The essential part, of course, is that lasers in various synchronizations are going to play an important role in any kind of SDI program, beginning in a boost phase, post-boost phase and mid course phase. There are lidars, laser radars, directed energy weapons and some other things that I feel are important.

To start, although I'm not a particular fan or enthusiast of SDI, I certainly am not an opponent to doing relevant research. But having listened the last two and a half days to SDI talks, I was struck by the incredible optimism of the progress that was relayed to this audience. Yesterday gave me the impression that there wasn't much left beyond development of deployment decisions. This morning, fortunately, some of this was mitigated a little bit. Coming from the laser fusion, as I do, whenever you hear the drums of success roll real loudly, you have a good measure of skepticism. You ask yourself an immediate question. What is happening in Washington? Is it perhaps budget time or something like it? So I would like to ignore some of this euphoria about the success and start from an outsider's viewpoint of the way I see SDI and the great problems involved in it. First and foremost, how are you going to track targets of meter dimensions over thousands of kilometers distance, which relates to a better than .01 microradian tracking accuracy - typically 30 nanoradians?

Now, that is a very tall order for anybody who works in a laboratory with a rather advanced laser, where ten times that kind of precision is somewhat difficult to come by. Of course, one has to discriminate between decoys and targets. In reading the APS report rather carefully, I noticed that there wasn't an awful lot said about it. So I proceeded to just look at what you do with a laser to detect the kind of motions that you could impart on a decoy with another somewhat more powerful laser. In the APS report that is given as a typical number of ten centimeters per second change in velocity. Now, if you were to just use a simple interferometer for heterodyne detection, you could certainly do that with a laser, but you would have to have a band width well below a megahertz band over millisecond periods of time. Those are certainly, again, very tall orders because you still need kilowatt powers and, as Kumar just told me, you also would need thousands of platforms in order to do this job. So, that is pretty much ruled out.

So you wonder. How do you do it? Since it is obviously not in the open literature, the various problems associated with atmospheric propagation of the laser beam have been discussed a number of times already, and it sounds like turbulence is reasonably in hand. I don't think thermal blooming is nearly as clear. I'd like to point out somewhat later that there may be some problems when you have real beams, high power beams, that are actually aberration corrected in the far field. I was extremely impressed with the report of mirror phasing using phase conjugation actually inside the laser, on the ground. Now that looks like a very good way of doing it and I think that will work very well for the ground based mirrors. I'm wondering whether anything like that can actually be applied to the mirrors up in space the first relay mirror being typically in a geo-stationary orbit at 40,000 kilometers, which is less than a half a second time of flight for photons. I don't know whether any phase conjugation technique is going to work for that.

Now, I'd like to go from the sublime of the expectations of SDI lasers and SDI optics to the ridiculous. Namely, what you have in a large laser facility as we have at our university, i.e., a multi-kilojoule multi-terawatt facility in the infrared, as well, as the ultraviolet. If you show the first viewgraph you can see what this looks like. It is not a very small facility. It is used for laser fusion experiments and this is it. You're looking at the output during an actual shot where we convert the infrared in the nonlinear crystals to the ultraviolet with high efficiency and then illuminate our targets, evaporate them and use the rocket motion, that we talked earlier, to actually compress them. Now, what are some of the problems that we encounter? This laser is not a stand-alone laser. It requires careful attention at all times. It is not a hands off laser. It has a lot of maintenance time and maintenance cost involved in keeping this laser going, but it does operate several times a week, as often as we can, with the limited manpower we have.

The performance characteristics of this laser are not really bad and in the next picture you can see what a typical beam actually looks like. What you do see here actually is a phase front diagnostic of it where we have done interferometry on the laser beam. We have imposed high frequency background field fringes, we have gotten into the Fourier transform plane and cut off the side lobes of the Fourier transform plane - this is shown in the lower left - while the two side lobes contain all the information about the phase. If you separate one of those side lobes, and transform it back, you obtain a phase front - a detailed phase front with an accuracy of about λ over fifty and that can still be improved. What you see is that we have a laser beam with a fairly good phase front of maximum distortion of one wave in infrared but corresponding to a roughly two to three times

the diffraction limited spot. Now you go into the ultraviolet as we do and that immediately transforms into 6 to 9 times the diffraction limit. Then you're in great trouble.

As you can see in the next image on the left side there's actually a calculated image using the phase information that you just saw in an actual near field distribution which is extremely uniform and you see a fairly benign looking far field in the infrared. In the ultraviolet it is totally broken up. Now that is not actually a far field, it is an intermediate field, this is where we typically use the laser on target. But this is a realistic thing that may actually be obtained in the lower atmosphere when you make phase front corrections for turbulence. In the near field, the lower atmosphere you will have very high intensity perturbations and you may find yourself with intensities that may go beyond Raman limits or may be very difficult to deal with thermal blooming. Now putting these together, I am quite convinced given the progress that has been reported as such that the basic requirements for SDI laser and optics will probably be met before too long. I have no doubt about that.

But when you look at this in the context of the actual numbers required, namely, many tens of laser stations, three times as many ground telescopes and all of them working for extended periods of time in a coalescent mode and then all of the sudden being readied for working in full operation. It is extremely difficult for me to see how that can work. Now, from the viewpoint of somebody who does not work in the SDI office or with any SDI projects it seems like the reports in the press indicate a rather strong stress on near-term goals for SDI, which certainly has a lot of prestige in the public, and for political purposes. As a cynic, I would say that maximizes the political and corporate profits but perhaps has some problems. One of the problems that I see is that it maximizes the effort in the industrial sector and somewhat minimizes the effort in the university sector which, after all, is tasked with producing the necessary future generations of scientists, and that is a real concern. We do have to have enough people who do get their degrees and will be able to produce effectively early next century.

Finally, another concern which, again, is somewhat off is that if we did succeed in the near term through some kind of crash program in putting a moderately effective shield into the sky will it be there to protect the viable economy and a worthwhile standard of living? That is a real concern. Thank you.

Prof. Sproull:

Thank you very much. The next speaker obviously needs no introduction but I might point out that I think it was William Sears or Arthur Kantrowitz who many years ago said that you didn't have to speculate on whether the martians had landed on earth or not - of course they had landed and the proof was that an outrageously competent group of people all emanated from Hungary at about the same time - von Karman, Von Neumann, Wigner and Edward Teller among others. My pleasure to introduce Dr. Teller...

Dr. Teller:

Thank you for your kind words. Actually when von Karman leaked the secret information about Mars, he added that the most important member of the group was Zsa Zsa Gabor. (Laughter).

I am very happy to be here. Right now I did not come all the way from mars, but from another very strange place, Washington, D.C. Yesterday, the treaty on Intermediate-Range Nuclear Force (INF) was signed. Verification raises a difficult question concerning any treaty, between an open society and a closed society. Therefore, such treaties are of necessity unequal. But the treaty that was just signed would eliminate 400 missiles carrying 1,200 separate atomic explosives. There is a reasonably good chance that most of them will be eliminated. Such a treaty, even if it is not perfect, can still be very useful.

The situation with the Strategic Defense Initiative (SDI) is similar. It is wrong to postulate that SDI won't work unless it works completely. It is wrong to postulate that arms reduction won't work unless it work completely. Arms reduction together with SDI has an incomparably better chance because the danger due to incomplete verification is decreased. Similarly, SDI together with arms reduction will be easier because the expected attack will be on a smaller scale.

A second introductory point I would like to make is about secrecy. We know that the Soviets have not only gone ahead with SDI, as Gorbachev has now stated; but we also know that they have vastly outspent us on lasers. We know that they are deploying laser installations. Unfortunately, we do not publish what we know. We, in turn, have made a great deal of progress in X-ray lasers. We also have remarkable results in laser fusion (not connected with SDI). Unfortunately, these results are secret and I cannot report on

them to you.

We should all work together in demanding openness in long-term scientific research. Secrecy in science does not work. Withholding information does more damage to us than to our competitors. Even in technical matters applied to defense, secrecy is of limited value; in many cases, it merely forces our opponents to spend a little more effort on espionage. We should try to bring about a more realistic and a more liberal policy on secrecy.

In discussing the use of lasers in defense and cooperation within the scientific community, I must mention the thorough study of the American Physical Society. One can be pessimistic about the use of lasers in SDI, but I am much more optimistic than the APS study appears to be. This is no reason for me to object to the study. It would have been, however, highly welcome if the study had contained more positive suggestions. Doubts in success would be far more welcome if they should be accompanied by novel ideas from the intelligent participants.

I want to start my objective discussion with the statement that lasers can do anything; therefore, they can also be used for SDI.

We now have a fresh competitor: High Temperature Superconductors. These also can do anything; therefore, I claim that lasers and high temperature superconductivity can accomplish everything, (Laughter)... hopefully including applications to SDI. I would now like to describe to you a simple experiment using a novel superconductor which also involves lasers.

One of my friends, Dick More, and I have written a paper which is available for your inspection. Its title is "On the Chemistry of Superconductivity." We assume the main arguments of the Bardeen-Cooper-Schrieffer (BCS) theory to be correct. But the distances over which the relevant interactions extend are shorter and the energies greater than in the BCS theory. We first consider the ceramic material studied in Zurich --lanthanum-copper-oxide. A Perovskite (CuO_2) layer is sandwiched between two neighboring monoxide LaO layers. A relatively small number of electrons are responsible for the superconductivity. These electrons have orbits which are superpositions of Bloch wavefunctions with a high probability amplitude in the two monoxide layers and a small probability amplitude in the intervening Perovskite layer. The quasi-momentum values, or k -values, in one superposition must be the same. Only low k -values will be occupied. The appropriate wave functions for these electrons have relatively low probability amplitudes in the Perovskite planes, but high probability amplitudes in the two monoxide planes. (At a later stage, all electron wave functions in these triple sandwiches have to be superposed.)

In the Perovskite planes, the electrons are near the top of the energy band and behave like positrons, but in the monoxide planes, they are near the bottom of the energy band and behave like holes or electrons. Hybridization of the wavefunctions in the neighboring layers is found to reduce the group velocity of the carriers, and this increases the strength of the interaction between the electrons and the slow-moving oxygen ions. This interaction leads to electron pairing at practically all temperatures and to ordering of the pairs below the transition temperature (T_c).

In Texas, a ceramic with a much higher transition temperature was found: yttrium-barium-copper-oxygen. In this compound, electrons in a single monoxide layer (CuO) interact with two Perovskite layers (CuO_2). In this case, the interacting layers are second neighbors, with barium oxide layers intervening. Otherwise, the situation is similar. The probability amplitudes are high in the monoxide layer and low in the Perovskite layers. And the motion is similar to that of electrons in the monoxide layer but similar to positrons in the Perovskite layers. The velocities are high in the Perovskite layers and low in the monoxide layer. The cancellation of velocities between the two types of layers may well be more complete in this more complex compound giving rise to an even higher value of the transition temperature (T_c).

I imagine that there may be a special kind of interaction in this complex yttrium compound that could give rise to peculiar optical phenomena. A vibration of oxygen ions of the barium oxide layer perpendicular to the x - y planes should change the coupling between the Perovskite and monoxide layers and thereby may have a sensitive influence on the group velocities. The maximum effect would be obtained if oxygens from the barium oxide layer approach the copper monoxide layer in a symmetric fashion and if they also recede from it symmetrically. This will change the mix in the hybridized superposition for the monoxide and Perovskite layers. For a given k -value, the group velocity of the electrons will change. If we consider a current carrying state in the x - y layer, the momentum values in the x - y layer will not change but the current will change as the oxygen ions vibrate. Thus, the current will be modulated and will radiate. At the same time, the current will have an effect on the position of the oxygen ions.

The Hamiltonian has a term proportional to the square of the current I^2 divided by the effective mass of the electrons. If a change of the oxygen positions influences the mix of the wavefunctions in the neighboring layers, the group velocity and the effective mass will change as well. The result is a change in the equilibrium position of the oxygen ions depending on I^2 . Indeed it is even possible to obtain a current in the lowest energy state as postulated by Bloch many decades ago, though this current-carrying state will have equal energy values for opposite directions of the current.

One proposed experiment would be to excite the oxygen vibration with the help of two laser beams with a frequency difference equal to the frequency of the oxygen vibration. The coupling is the same as in the Raman effect. The result will be that the two original laser beams will give rise to an infrared radiation whose frequency is the difference of the laser frequencies. The polarization will be parallel to the current and the intensity proportional to the square of the current. A similar experiment would use the yttrium compound in a magnetic field. Due to the Meissner effect, there will be electric currents on the surface of the superconducting particles. Excitation of the copper vibrations will cause the emission of radiation. In order to enhance the effect, small particles or thin superconducting layers should be used.

The experiments proposed here are, of course, based on a string of hypotheses. A positive result would provide a remarkable insight into the mechanism of high temperature superconductivity. The results may be important in optics and may even have interesting practical consequences including applications to SDI.

Prof. Sproull:

Thank you. Before opening up the session to all of us in the room to questions or comments, I'd like to give priority to the members of the table first. Could I call for that please? Anyone wish to take advantage of the opportunity?

Dr. Hammond:

I might quickly go through the points to indicate some of the work that is ongoing, to address the issues raised by Dr. Seka. First of all, the issue of tracking to one meter over a thousand kilometers is indeed the class of job which we have to do. I showed in my presentation this morning, a system - I think Dr. Seka mentioned it - it's very hard to get down to a few microradians in the laboratory, and having tried that, I understand. I showed a device, called the rapid retargeting precision pointing system, which is, in fact, a laboratory device mounted on one of the largest seismic masses in the U.S., which seeks to get at the accuracies necessary. I also pointed out this morning to a space experiment, the star lab experiment.

We have gone to space to get very long distances to show precision pointing. I can't discuss the exact ranges which we achieved, but I do point out that the skylight beam director and the ALL beam director were generically few microradian class types of devices - maybe somewhat greater again, I can't discuss exact numbers - but we are addressing those sorts of precisions. With the discrimination of targets, it was pointed out that realizing velocity changes of ten centimeters per second was difficult. I certainly agree with that and it does impose very severe band width constraints on radars. I personally favor larger delta V's if you want to do discrimination in that manner. Unfortunately, I tend to be somewhat of an advocate of my old office of kinetic energy for those types of applications. There are ways of looking at ten centimeters per second, there are also ways of perhaps producing higher delta V's. With the turbulence issue - I'm glad you conceded that turbulence correction, linear corrections, are easy - we still have a ways to go there.

The thermal blooming issue and the interaction with turbulence is, in fact, one of the key issues that we're looking at right now. We are looking at it computationally and we are looking very hard, for ways to quickly resolve the issue of thermal blooming instabilities. I will point out that we see some instabilities that tend very quickly to go to the same scale size as the mesh that you happen to be working on, so we have to sort out a few things in that area, and I understand that is an issue. With regard to mirrors in space - the issue of how one phases or controls the figure on mirrors in space - we are looking at techniques such as grazing incidence interferometry for phasing such mirrors as well as lasers in the general vicinity, for using some of the non linear techniques that we talked about. I think that the last issue was basically the question of how does one produce lasers with very good beam qualities. I think several papers here have dealt with issues such as Raman beam clean up methods and other non linear techniques for cleaning up beam quality, which are being addressed.

Finally, I would point out, with respect to his comment regarding industry versus university and near versus far term, that those are the tough trades that one has to make in the SDI business. However, I do point out that a number of the presentations in this

conference of very innovative techniques funded by SDIO, did come from the university environment.

Prof. Sproull:

Thank you. Any other comments from the table?

Lets then open it up for the floor. I'd like to ask you two things. One is, if you have a question, try to state it as loud as you can but try to address one member at the table and then, I'll ask that member at the table to rephrase the question because you do not have microphones out there and the tape recording may not be able to hear you. If you can't identify a particular member of the table, just ask your question anyway, and I will try to do my best. I will warn you in advance that it's a low pass filter and it might not come through very well. If you have a comment, all I can suggest, is that you just speak up because we won't be able to translate that. So, with those introductory suggestions, we're open for discussion from the floor.

QUESTION:

Note: This question was related to laser propulsion and why solar energy appears to be ignored in the SDI program.

Dr. Kantrowitz:

I find the question a little confusing because, while laser propulsion was first suggested at about the time of the energy embargo, that is simply a coincidence and they had nothing to do with each other.

Prof. Sproull:

But could you address the second part of the question, which was solar energy?

Dr. Kantrowitz:

I could give you an example of where it might be useful. If you make a very light decoy, such as is frequently proposed, it is worth noticing that even the pressure exerted by sunlight, which is very small, is enough to produce a measurable change in the ephemeris of a very light decoy. That is a conceivable method of discrimination, but it is, perhaps, superseded by other more positive ways.

Dr. Teller:

For missiles or for satellites?

Dr. Kantrowitz:

Even for decoys that just come along with an RV, solar pressure makes a difference of meters in the trajectory of a very light decoy, so that is a conceivable discrimination. This type of issue is not alone in a number of adventurous directions, which we now ignore at very great peril.

Dr. Lax:

A very important part of the SDI effort is in laser radars, and yet the APS report did not address that question. Would you comment?

Dr. Patel:

We do talk about laser radars in our report, in terms of what they are capable of doing, where they are needed, and the requirements of lasers to be used for radars in terms of the improvement that is required in the known or presently practiced laser technology. We don't go into the same sort of great detail as we go through regarding physics of other lasers, but we do, in fact, discuss this. In the talks, we don't talk about it because there are, primarily, other kinds of things to talk about. I missed my turn earlier to comment on other participants talks. I wish to apologize for not having spoken up at that time, but I do want to respond to one comment Dr. Teller made regarding APS, as well as academics not providing constructive suggestions.

I think that is just plain nonsense. The APS report is neither positive, neither optimistic nor pessimistic. It is about as objective a report as can be made. In fact, if one briefs through the report, we do point out possible directions in which potentials for progress lie. In academia, I am not a university person, so I really do not have a speaker

voice, but I will say that our skeptics, in fact, have made and will continue to make, very important contributions to SDI and SDI related efforts. I think that's a charge, which is not justified, that people in academia would not contribute to the SDI effort.

Dr. Teller:

I hope that whenever I write a report, and I hope not to write many, that it will be most optimistic and pessimistic. Objective reports do not exist. I am asking, and I continue to ask, for more contributions, and I am trying to compare the present process with something I have seen in the second World War, which at that time was very different. We had our critics and we had our optimist, who believed that it was done when it was not done, and we made our mistakes. I do not want particularly to criticize, but I do believe that most of the suggestions on SDI came from relatively narrow sources in the last four years, and I think that if I could be disproved in a very formal manner, particularly in the next year, it would be a great advantage.

QUESTION:

Who are those narrow sources?

Dr. Teller:

The narrow sources have been some industrial laboratories and some government laboratories. There has been, for instance, from the two weapons laboratories - Los Alamos and Livermore - a really great effort. It was based on the Stanford effort, originally on the FEL, and that is obviously a great contribution, which I am happy to acknowledge. Let me add, that in accelerator physics, there are now contributions from which a lot will probably come out. I hope that will be a very thorough way to make my objections irrelevant.

COMMENT:

I would like to agree with Dr. Teller in a negative way. That these people, these narrow sources, were trained by skeptics at the universities.

Dr. Teller:

I am not against the university.

COMMENT:

I found the APS report to be the only reasonably credible thing on SDI. I think Dr. Patel did a heroic effort, and to continue to hear these criticisms bothers me. I think it was an outstanding effort and I applaud him for it. (Applause)

Dr. Patel:

Thank you for the small number of supporters we have.

QUESTION:

Well, I have a question which might get a bit nasty for Dr. Patel. (Laughter). Dr. Patel stated here, and I think he also stated it to Physics Today, that the APS report nowhere says that SDI won't work. Am I wrong with that?

Dr. Patel:

...That is correct.

QUESTION:

...Right, and yet a couple of weeks after the report was published, there were a number of politicians on TV and all, except one, stated that the APS report concluded that SDI won't work. What do you think about those misrepresentations?

Dr. Patel:

...This is a free society and people are free to interpret things that they hear the way they want. The things that make news are not facts..(Laughter)..things that make news are, how facts are twisted to fit one persons or another persons political heart or some other view. The alternative is not acceptable, namely not to make facts available. So, I neither feel good nor bad about somebody using or misusing the report.

I think, in a free society we have to exercise our own judgement in deciding whether somebody has twisted something, twisted a given piece of information or not. I think that in all our little ways, we try to correct the misinformation that spreads around. I have been interpreted many times by newspapers, and I very clearly state that if you want to find out more of what is in the report, read the report. Do not look at excerpts of what's in there, because people will twist it the way they want it.

Dr. Miller:

I think it was a heroic effort. I think the details of the report are, in fact, a very good source of information on how various technologies work, and what the issues with them are. I think the APS has earned a little bit of criticism itself within the APS, as an institution, for two reasons: There are conclusions within the report, which I find, are not supported by the data in the report. The second reason is, when you start talking about the time required to develop various technologies, there really isn't much meat in the report that substantiates the time scale that is projected, and, that is subjective and judgmental. The report says some things that are not supported in detail. I think, also, that some of the press releases from the APS, which accompanied the report, do have a negative bent to them, and are different to the details in the report itself. Finally, I think that some confusion revolves around these points.

Dr. Patel:

Let me comment on the second aspect, which has to do with press releases. The study group was not, and is not, responsible for press releases. The specific press release that is being discussed has to do with the Council Resolution. The Council Resolution is the only one that went beyond the contents of the report. I invite you to read the council resolution in detail. I am getting very upset about people throwing the Council Resolution in my face. If anybody has read the Council Resolution, and not too many people have - I submit that less than one percent of the people have read what the Council Resolution said - it repeated some of the conclusions of the report, and then, explicitly says, "The council goes beyond what is said in the report and this is what it is." Now, that clearly defines a demarcation line. I think that the study group is not responsible for what goes on there.

So, I think that the criticism is really not valid. I think that people are free to use that as their needs or what have you. The question about time scale, is probably, the one aspect that a lot of judgement went in. The study group did have 16 or 17 members. The decade or so of the time scale that is required there, doesn't apply to any specific technology, but time required to assess the use of directed energy weapons in a full fledged SDI applications. It is an evaluation which was supported unanimously, by 17 people from both inside, as well as, outside of the SDI. It suddenly is not two years and it is not 50 years, which I think most people, if not all people, will agree. It argues that there is still substantial body of work to be done and that better be done, before one jumps into it with both feet.

Dr. Kantrowitz:

Do you associate yourself with the position with the second part, that went beyond the report? Or do you, as I believe Nicholas Bloembergen has done, disassociate yourself from them?

Dr. Patel:

I believe there is a letter in "Physics Today", on record, with my name attached to it, which says, "That the study group," - I think that there are 15 signatures; we could not reach two people who are in Europe - "which consists of 15 people, do in fact disassociate themselves from the second half of the Council Resolution." The study group made no effort to study those areas and we cannot make any more intelligent conclusions about that, than anybody else.

Dr. Lax:

I just want to make one comment, since some of this touches the political aspects. The decision to do SDI is a political one, and in a democracy, once a decision is made clear, it's important for a good scientist to participate, to keep it honest; otherwise, it is not going to work. As Dr. Teller said, many of us have worked in the military aspect of science and kept it vibrant and dynamic, and I think, effective, by working in the system, as well, as criticizing within the system, and by contributing.

Prof. Sproull:

Everyone hear that? It's a comment, I guess, rather than a question.

Dr. Teller:

Another comment..(Laughter). I have tried, and then again tried, to be moderate in my criticism of the APS report, and, also, moderate in whatever praise I have for the APS report. There is no question that a number of people, a prime number of people, have worked, and that's good. That they have agreed, I don't think that is terribly important. To have various views would have been as useful, if they are new, if they're original and if they are illuminating. I do not want to try to push for making it look better or making it look worse... You worked diligently. You looked. You were given classified information, which is very important, particularly because relatively few people have it. The main reason I talk now, again, is to reiterate one of my requests and to direct it at the APS and, very particularly, at the panel members.

One of our grave misfortunes is secrecy. I know that you have not been given all the facts, but most probably what you have not been given, is not essential. I don't want to have the illusion that in this complex system all secrets have been released .

They should have been, and I don't think that they have been, and that is certainly, most certainly, not your fault. But, I believe, having seen more than, much more than the physics community has seen, you could now do a very great service to speak to the effort to get everything that you have seen, out into the open. I think it is important for understanding, important for further progress. I don't think that we're differing on that and it is something that you could do.

Dr. Patel:

Just a small comment, not an exception, but a comment. I hope in Dr. Teller's remark, there is none of the strident view that is often held, that is... "If you knew what I know now, you wouldn't say what you're saying"... Dr. Teller, I think your suggestion about the lack of usefulness of secrecy is well taken and I think that we should all work towards reducing it as much as we can.

Dr. Teller:

My comment was that we have, and I think it is terrible, we have black projects which even you have not been taught to. The point is, that I have been in some of these projects and I find that one of the troubles is that so few people know about it -that true judgement on it is impossible. And I think that we should all do something to get things out on the table and on that, at least, we should fully agree.

Prof. Sproull:

I think that everyone in the room will agree on that. A lot of people working on black projects don't even know what the black programs are all about. (Laughter)

QUESTIONS:

I notice quite a lack of mention of cost in the panel discussion, except for Dr. Kantrowitz's discussion about a proposal that I didn't think was currently being considered. I happened to be talking to someone during the break, who suggested that as long as it doesn't defy any physical principles any of these ideas or concepts should be possible, if you just put enough time or manpower toward them. I would address to Dr. Teller and to Dr. Hammond, the question of what is the current status of the cost effectiveness for the cost consideration opposed to the technological aspects?

Dr. Hammond:

I think your question was, "What is the current status of examining the cost associated with the various systems for SDI." I mentioned a process within the Pentagon reviewing a Phase I and follow-on architecture for SDI. As you might expect, we have a bit more capability of estimating cost for things like rocketry and things we have more experience in producing. That was looked at in quite a bit of detail for the Phase I systems, but we also worked very hard to estimate, even knowing there was quite a bit of uncertainty in what the cost might be with the laser candidates that I talked about here earlier.

It is a very complex issue, not one that can be discussed here, but we are not out of the ball park in terms of cost associated with laser systems, vis-a-vis, other SDI alternatives. Those costs are reasonable in terms of cost exchange ratio and the usual measures of cost effectiveness, and we are already looking at that problem for lasers."

NOTE: Some 20-30 minutes of questions and comments have been deleted due to space constraints.

Prof. Sproull:

These last few comments have smoked me out. I wasn't going to give a speech but...(Laughter)..if you'll pardon the chairman from getting into the fray... First of all, let me say that this was a remarkably patient audience and a remarkably varied program. I don't know how much progress we have made here in assessing the maturity of laser technology in SDI, but the people at the table have demonstrated to you the remarkable richness and openness of the program. Talks like Dr. Goldman's, Dr. Kantrowitz's and Dr. Teller's show that we may be just beginning the infancy of some possible programs in SDI. What I really want to say is that I am terribly disturbed about the future of SDI (in its present format).

I suspect it will not last another 12 to 18 months. It is a political problem and an economical problem. It is uncertain whether it will survive the next election in a substantial way. Now that may not be so bad. In fact, if you change its name and it becomes a research program, a 6.1 or 6.2 type of thing, that may be the best thing that may come out. But, there are some big casualties that might happen with that. One, would be the type of expensive experiment. For example, looking at a plume against the earth's background, which is a difficult and expensive experiment, and was not really done, or done at all well, under the earlier setup, where you did not have central management under SDIO. You had the Army and DARPA as semi-independent players. Another casualty would be that the program would go back to just developing ingredients of a ballistic missile defense and a strategic defense, more generally, the way DARPA and the army were doing it, until the President's speech in March of 1983.

That would be unfortunate, because it would not allow work on the systems aspect, which is terribly important. Another aspect, namely, the battle management and command control and communications, those elements are desperately important in our strategic defense and were not being attacked when there was not central management. So, it would be a touch and go business, if under a different name, the program could be kept going. And I hope it can, as a more research oriented, long term program, with no hurry at all, unless the Soviet developments in defense, which are very considerable and formidable, become even more considerable and more formidable. I am not objecting to what the SDIO has done in the last few months. I think they needed to show that one should set up a conceptual system and show how it could evolve and get the support of the joint chiefs and so on. I think that exercise has been a very useful one, and it has been misinterpreted as being early deployment.

The combination of such a program and drastic reduction on warheads, down to the level of 300 to 500 for each of the major players, would make it a world that would be far safer and satisfactory than the world now. It would be especially more satisfactory to nations, such as France, England, Germany, Australia, even Canada, who are our friends, but we pay very little attention to them. A defense uppermost world, I think, could be attained in the 21st century in this way, and it would be a safer and more satisfactory world.

There is even a community now developing on how to make that transition in a stable way, a community that hadn't raised its head above the grass until quite recently. (It has people from organizations like Oakridge, Rand, and AT&T Labs). They are beginning to look at the interesting questions, on how you make the transition from a stable offense dominated to a stable defense dominated world, without going through a unstable intermediate position. The thing that has worried me the most, is that the natural friends, it seems to me, are the arms control community and the SDI community. Somehow or other they have been polarized to be enemies, especially on campuses, and on most campuses, the whole argument has been carried out at the bumper sticker level, which I find a disgrace. For my favorite institution, namely, the university, the role of the university should be to raise the level of discourse and not to lower the level of discourse. And the natural friends should be the arms control community and SDI. Instead, they have become a confrontation of confrontation politics.

So, I see a very promising future for the combination of drastic reduction of warheads, coupled with an SDI program. A totally nuclear disarmed world would be, according to most writers, a terrible dangerous world, partly because of the cheating threshold. But mostly because, although you can destroy nuclear weapons, you cannot destroy the capacity to make nuclear weapons and lots of countries could make weapons faster in their closed society than we could develop them, if nuclear weapons had been abolished completely, for say, a couple of decades. There's a lot more to the argument than that. This is a poor and one-dimensional representation of the argument that says that a total nuclear world would be

a dangerous world; nevertheless, I believe it.

So, I see a most promising future, in which laser technology will play a central and vital part. I think that all of us, who are interested in the laser, should take pride in that. I am sorry for the speech. I never intended to make it in the first place. (Applause)

Now, additional questions and comments or is it your pleasure that we should adjourn?... Seems to be a certain amount of enthusiasm for adjournment... Thank you very much....(Applause).

AUTHOR INDEX

- A - Abella, I. D. - 398
 Abdullah, S. A. - 947
 Adamovich, B. A. - 182
 Adams, Jr., J. E. - 774
 Aldag, H. R. - 330, 356
 Aleksandrov, K. S. - 378
 Aleksandrovsky, Y. S. - 378
 Alfano, R. R. - 423, 559, 580
 Allegrini, M. - 936, 947
 Alonso, J. - 1105
 Altpeter, L. L. - 707
 Amano, S. - 223
 Antonson, D. E. - 1048, 1051
 Apel, E. C. - 1077
 Apollonov, V. V. - 155, 498, 525
 Appelt, D. - 1105
 Apruzese, J. P. - 37, 44
 Arimondo, E. - 936
 Aronoff, B. L. - 1010
- B - Badreddine, B. - 612
 Baglin, F. G. - 931
 Bailey, R. T. - 502
 Baitsur, G. G. - 498
 Baker, G. L. - 565
 Bakhtadze, A. B. - 1124
 Ball, G. - 412
 Banet, M. - 867
 Baranov, V. Y. - 176, 182, 1124, 1130
 Barbini, R. - 493
 Barrow, V. - 59
 Basile, S. - 939
 Basov, N. G. - 230
 Bassett, D. - 59
 Beach, R. - 262
 Beedle, M. A. - 657
 Behn, R. - 531
 Benedetto, M. D. - 1048, 1051,
 Bennett, G. A. - 555
 Bentley, J. H. - 999
 Berik, E. - 381
 Bevan, J. W. - 882
 Bicchi, P. - 955, 959
 Bickers, L. - 851
 Bigio, I. - 268
 Blair, L. S. - 164
 Bliss, D. E. - 1005
 Boffa, V. - 95
 Bollanti, S. - 95
 Borisov, V. M. - 176
 Bourkoff, E. - 1057
 Bowden, M. D. - 550
 Braun, R. E. - 1053
 Briggs, R. G. - 1153
 Bron, W. E. - 570
 Burde, D. H. - 111, 126
 Burkhalter, G. - 37
 Burkhardt, C. E. - 936
 Burlamacchi, P. - 73
 Burton, D. J. - 898
 Butakov, A. L. - 729
- C - Carvalho, F. D. - 1105
 Casson, W. H. - 555
 Castro, Dan J. - 1014
 Castro, Donna J. - 1014
 Caulfield, H. J. - 18
 Chapman, R. - 249
- Chen, C. H. - 995
 Chen, J. - 653
 Christiansen, W. H. - 478
 Chung, K. P. - 599, 837
 Ciocca, M. - 936
 Cirkel, H. J. - 86
 Clark, R. W. - 44
 Coe, S. - 59
 Cohen, M. - 1042
 Colao, F. - 493
 Comeford, J. - 703
 Connolly, J. - 485
 Conrad, R. W. - 320, 665, 680
 Cooper, A. J. - 846
 Cooperstein, G. - 37
 Copeland, D. A. - 111
 Copic, M. - 437
 Cosmi, S. A. - 1033
 Cox, J. D. - 234
 Cox, J. W. - 696
 Cruickshank, F. R. - 502
- D - Dalby, F. W. - 955
 Davidenko, V. - 381
 Davis, J. - 37, 44
 Daykhovsky, L. - 1045
 Dearth, J. J. - 320
 De Silvestri, S. - 416, 740, 744
 DeBias, D. A. - 1033, 1038
 Deryugin, A. A. - 182
 Derzhavin, S. I. - 155
 Dew, D. K. - 1042
 Di Lazzaro, P. - 95
 Dosser, L. R. - 770
 Drutman, C. - 917
 Duarte, F. J. - 308, 364, 1097
 Dupertuis, M. A. - 531
- E - Edwards, J. - 59
 Ehrlich, J. - 320, 665
 Ehrlich, J. J. - 304, 308, 680
 Eichler, H. J. - 653
 Elliott, D. J. - 1090
 Endoh, M. - 223
 Endoh, A. - 349
 Eng, R. S. - 889
 Erickson, G. F. - 338, 342
 Essien, M. - 908
 Esterowitz, L. - 398
 Etemad, S. - 565
 Evans, W. - 707
 Everett, P. N. - 291, 297
 Evtushenko, G. S. - 729
- F - Falcone, R. W. - 66
 Falconer, I. S. - 550
 Fantini, M. - 73
 Farhoomand, J. - 539
 Fazliev, A. Z. - 387, 721
 Feilchenfeld, H. - 802
 Feldman, R. J. - 733
 Ferrante, G. - 939
 Fetterman, H. R. - 1014
 Ffitch, P. K. - 851
 Figueira, J. F. - 268
 Finkelstein, L. H. - 1038
 Firsov, K. N. - 498
 Fletcher, A. N. - 1005

- Fletcher, L. K. - 555, 703
 Fluckiger, D. U. - 685
 Flusberg, A. - 750
 Fong, C. K. - 674
 Forysiak, W. - 11
 Fox, J. L. - 995
 Freed, C. - 468
 Frey, L. - 160
 Friedrich, H. B. - 898
 Fujii, H. - 223
 Fujii, K. - 285
 Fujioka, T. - 223, 413
 Fujitani, R. - 1045
 Fulghum, S. F. - 680
- G - Gabbanini, C. - 947
 Garver, W. P. - 936
 Gayen, S. K. - 423
 Giordano, G. - 95
 Girmann, T. C. - 770
 Godlevskii, A. P. - 721
 Goldman, L. - 1153
 Golub, I. - 648
 Gordov, E. P. - 20, 721
 Gosnell, T. R. - 1077
 Cotoff, S. - 694, 703
 Gozzini, S. - 936, 947
 Grande, M. - 59
 Grant, I. - 783
 Green, R. B. - 902
 Greene, C. H. - 1033, 1038
 Greene, D. P. - 268
 Griff, N. - 205, 1146
 Gross, R. J. - 241
 Grundfest, W. S. - 1045
 Gullickson, R. L. - 1146
 Gusten, H. - 985
 Guyer, D. R. - 139
- H - Hachijin, M. - 518
 Hacura, A. - 931
 Hagan, D. J. - 584
 Hammond, J. H. - 1146, 1153
 Hanzel, D. - 437
 Harris, D. G. - 111, 126
 Harrison, R. G. - 11, 456
 Hartman, L. - 1053
 Hasama, T. - 150
 Hashimoto, T. - 518
 Henderson, M. J. - 1033
 Herbelin, J. M. - 218
 Herlach, F. - 544
 Hermesen, T. - 95
 Hertel, P. - 643
 Herziger, G. - 510
 Higgs, C. - 272
 Hill, G. A. - 839
 Hillman, L. W. - 4
 Ho, P. P. - 580
 Holland, P. L. - 694, 703
 Holmes, R. - 750
 Hommeau, F. - 103
 Hrycin, A. L. - 1097
 Hsing, T. R. - 837
 Hsu, T. - 1042
 Huber, S. - 1065
 Huff, P. - 851
 Hunter, H. T. - 555
 Hutchinson, D. P. - 555
- I - Itzkan, I. - 330
- J - James, R. W. - 550
 Janes, G. S. - 356
 Jansen, M. - 441
 Janssen, P. - 544
 Jedju, T. M. - 565
 Johnson, R. P. - 432
 Jones, C. R. - 1139
 Jones, J. - 703, 714
- K - Kannari, F. - 139
 Kantrowitz, A. R. - 1153
 Kapteyn, H. C. - 66
 Karpov, S. V. - 378
 Kashyap, R. - 859
 Kelley, J. D. - 936
 Kepple, P. C. - 44
 Key, M. H. - 59
 Keyes, R. J. - 685
 Khoo, I. C. - 636
 Khristoforov, O. B. - 176
 Kiehn, G. - 59
 Kimura, W. D. - 139
 Kintz, G. - 398
 Kirilov, A. E. - 729
 Kirschner, R. A. - 1038
 Kiryukhin, Y. B. - 176
 Kjelberg, I. - 531
 Klimek, D. E. - 680
 Kline, D. C. - 205
 Koch, T. H. - 1003
 Kochetov, I. V. - 182
 Kononov, I. G. - 498
 Konopleva, N. P. - 20
 Kopchok, G. E. - 1045
 Kosyrev, F. K. - 1130
 Kratzig, E. - 643
 Krishnan, M. - 51
 Krug, P. A. - 531, 550
 Krupke, W. F. - 262
 Kryukov, P. G. - 230
 Kubin, R. F. - 1005
 Kubodera, S. - 160
 Kudziev, A. G. - 1124
 Kurchatov, I. V. - 182, 1124
- L - Laporta, P. - 416, 740, 744
 Lax, B. - 889
 Lee, J. - 555
 Lee, L. - 441
 Lehmann, K. I. - 1033
 Leonell, J. - 707
 LePell, P. D. - 51
 Letardi, T. - 73, 95
 Letzring, S. - 412
 Leventhal, J. J. - 936
 Lewis, C. - 59
 Libin, L. - 1110
 Liebow, C. - 1053
 Lin, J. T. - 404, 604
 Lin, S-H. - 758
 Loosen, P. - 510
 Lowum, T. F. - 133
 Lukac, M. - 437
 Lukinykh, V. F. - 378
 Lysiak, R. J. - 657
- M - Ma, C. H. - 555
 MacDonald, J. M. - 1020
 MacFarlane, J. C. - 550
 Magni, V. - 416, 740, 744
 Mah, K. R. - 955
 Mahoney, R. P. - 1003

- Mal'tsev, A. N. - 729
 Malins, R. J. - 126
 Malyuta, D. D. - 182, 1130
 Manassero, G. - 1109
 Mansour, K. - 584
 Margarone, J. E. - 1053
 Marino, R. M. - 889
 Martin, S. - 1042
 Mathieu, P. - 463
 McCarey, B. E. - 1020
 McCown, A. W. - 268
 McDuff, O. P. - 612, 620, 628
 McGowan, R. B. - 320
 McMillan, K. - 882
 Mehlman, G. - 37
 Meier, B. - 370
 Menchi, E. - 936
 Menendez, R. C. - 837
 Merry, G. A. - 111
 Meucci, M. - 959
 Mezhevov, V. S. - 1130
 Miley, G. H. - 249
 Millar, P. S. - 160
 Miller, J. - 190, 1153
 Mirza, S. Y. - 729
 Miyazaki, K. - 150
 Miyoshi, T. - 518
 Moi, L. - 947, 959, 066
 Moloney, J. V. - 11
 Moncur, N. K. - 432
 Moore, C. L. - 696
 More, R. - 26
 Moriya, K. - 423
 Mosher, D. - 37
 Mulgaonkar, R. - 826
 Myslivets, S. A. - 378
- N - Nadler, J. - 249
 Nakano, S. - 518
 Napartovich, A. P. - 182
 Nash, T. - 51
 Neister, S. E. - 316, 971
 Nelson, R. - 1042
 Nicholson, B. W. - 272
 Novikov, V. P. - 176
- O - O'Brien, J. - 485
 O'Neill, D. - 59
 Ottinger, P. F. - 37
 Ou, S. - 441
- P - Pace, P. - 463
 Pacheco, D. P. - 330, 356
 Pais, C. - 1105
 Palucci, A. - 493
 Pape, H. - 643
 Parazzoli, C. G. - 917
 Patel, C. - 1153
 Patterson, S. P. - 304, 680
 Paziuk, V. S. - 230
 Penzkofer, A. - 370
 Perito, U. - 73
 Pert, G. - 59
 Peterson, T. - 160
 Petri, A. - 493
 Petricevic, V. - 423
 Phelps, K. - 694, 703
 Pickett, H. M. - 539
 Pierce, B. J. - 1146
 Pietrak, M. E. - 1005
 Pileri, D. - 791
 Piwczyk, B. P. - 1090
- Pogue, E. W. - 1146
 Polunin, Y. P. - 729
 Popov, A. K. - 378
 Prokhorov, A. M. - 155, 498, 525
 Pugh, D. - 502
 Pugh, L. A. - 111
- R - Radziemski, L. J. - 908
 Ramsden, S. - 59
 Reed, J. W. - 770
 Regan, C. - 59
 Ribezzo, S. - 493
 Richards, R. K. - 555
 Richter, K. - 653
 Rieger, H. - 257
 Rinke, M. - 985
 Roberts, T. - 272
 Rodin, A. V. - 1130
 Rodrigues, F. C. - 1105
 Rogers, S. K. - 733
 Rogerson, J. E. - 37
 Rose, S. - 59
 Rosocha, L. A. - 164
 Rostler, P. S. - 330
 Rothberg, L. - 565
 Russell, J. A. - 272
 Russell, S. D. - 680
- S - Sabia, E. - 95
 Saito, H. - 413
 Salib, S. K. - 810
 Salimbeni, R. - 73
 Salito, S. A. - 531
 Samadani, R. - 1077
 Sato, T. - 150
 Sauerbrey, R. - 160, 268
 Sawano, T. - 223
 Saxton, R. E. - 1014
 Schaefer, R. B. - 485
 Scherrer, V. E. - 37
 Schiller, N. H. - 1062
 Schlier, R. E. - 356
 Schneider, R. T. - 234
 Scully, M. O. - 1
 Seamans, J. F. - 139
 Sebrant, A. Y. - 1130
 Seka, W. - 412, 1153
 Seltzer, M. D. - 902
 Sergeant, M. - 441
 Shakir, Y. A. - 525
 Sharin, P. P. - 721
 Shaw, R. - 764
 Shay, T. M. - 268, 1073, 1077
 Shi, P. - 1069
 Shinn, M. - 262
 Shuker, R. - 648
 Siebert, L. D. - 432
 Siegrist, M. R. - 531
 Siiman, O. - 802
 Simon, J. D. - 867
 Simpson, O. A. - 1020
 Singh, J. P. - 146, 925
 Sirota, J. M. - 478
 Sirotkin, A. A. - 155
 Slabko, V. V. - 378
 Smakovski, Y. B. - 182
 Smirnov, V. S. - 387
 Smith, G. H. - 783
 Smith, P. - 268
 Smith, R. - 59
 Sneddon, J. - 908, 913
 Soileau, M. J. - 584

- Solarz, R. W. - 262
 Sorochenko, V. R. - 525
 Spangler, W. - 370
 Sperber, P. - 370
 Spiers, G. D. - 456
 Sproull, R. - 1153
 Stark, M. A. - 770
 Stepanov, Y. Y. - 176
 Stephanakis, S. J. - 37
 Stimson, P. A. - 550
 Stover, J. C. - 832
 Strel'tsov, A. P. - 182
 Su, S. G. - 867
 Sugimoto, K. - 518
 Sukhanov, V. B. - 729
 Svelto, O. - 740, 744
 Swecker, J. L. - 133
 Sylvan, A. - 456
 Sze, R. C. - 103, 268
- T - Takada, Y. - 413
 Takemori, S. - 518
 Tan, C. S. - 449
 Tardy, D. C. - 898
 Teixeira, M. R. - 1105
 Teller, E. - 26, 1153
 Tevzadze, G. A. - 1124
 Thomas, M. P. - 758
 Thornhill, J. W. - 37
 Tillotson, J. H. - 111, 126
 Tittel, F. K. - 268
 Torczynski, J. R. - 241
 Trainor, D. W. - 272
 Troitskii, V. O. - 729
 Trombetta, F. - 939
 Tsien, K. T. - 575
 Turner, Jr., C. E. - 111
- U - Uppal, J. S. - 11
- V - Vagin, N. P. - 230
 van Bockstal, L. - 544
 van der Burgt, M. - 544
 van der Laan, J. E. - 694, 703, 707, 714
 van Hoek, A. - 1083
 Van Stryland, E. W. - 584
 Vander Sluis, K. L. - 555
 Vannini, M. - 103, 268
 Vass, A. - 456
 Vaughn, V. V. - 320, 665
 Vetsko, V. M. - 1124
 Vidal, C. R. - 394
 Vinokhodov, A. Y. - 176
 Visser, A. J. W. G. - 1083
 Vlasak, J. - 1045
 von Trebra, R. J. - 1003
 Voronov, V. I. - 729
- W - Wang, L. Z. - 1
 Ward, H. - 1026
 Ward, P. H. - 1014
 Wark, J. - 59
 Waring, G. O. - 1020
 Warren, R. - 714
 Warwar, G. - 160
 Watanabe, M. - 349
 Watanabe, S. - 349
 Webb, C. E. - 276
 Welch, B. L. - 37
 Whitbourn, L. B. - 550
 White, G. H. - 1045
 White, R. A. - 1045
- Wilcox, J. Z. - 441
 Willi, O. - 59
 Williams, W. - 249
 Wisoff, P. J. - 160
 Witters, J. - 544
 Wojciechowski, P. H. - 1097
 Wong, S. - 463
 Wort, D. J. H. - 875
 Wu, Y. Y. - 584
- X - Hu, J. H. - 966
- Y - Yamada, K. - 150
 Yamagishi, K. - 423
 Yamschikov, V. A. - 498
 Yang, J. J. - 441
 Yang, T. T. - 111
 Yoder, M. J. - 485
 York, S. J. - 426
 Yoshida, S. - 223
 Young, F. C. - 37
 Young, W. L. - 1033
 Yu, C. - 449, 674
 Yueh, F. Y. - 925
 Yuryshev, N. N. - 230
- Z - Zheleznov, N. A. - 1130
 Zheng, C. E. - 95
 Zhiliba, A. I. - 20, 721
 Zollars, B. - 291, 297
 Zuev, V. E. - 721, 729
 Zuev, V. V. - 729